CARMEN: Center for Automated Vehicle Research with Multimodal Assured Navigation

A USDOT Tier-1 University Transportation Center

THE OHIO STATE UNIVERSITY
COLLEGE OF ENGINEERING

UCI University of California, Irvine

TEXAS
The University of Texas at Austin

University of CINCINNATI

PNT with Signals of Opportunity and Real-World Jammed and Spoofed Environments

Zak Kassas (https://orcid.org/0000-0002-4388-6142)

FINAL RESEARCH REPORT - November 30, **2023**

Contract # 69A3552047138

The contents of this report reflect the views of the authors, who are responsible for the facts and the accuracy of the information presented herein. This document is disseminated in the interest of information exchange. This report is funded, partially or entirely, by a grant from the U.S. Department of Transportation's University Transportation Centers Program. The U.S. Government assumes no liability for the contents or use thereof.

Project 6: PNT with Signals of Opportunity and Real-World Jammed and Spoofed Environments

In GNSS-degraded environments, whether the degradation is naturally occurring (e.g., in deep urban canyons) or intentional (e.g., in the presence of a jammer or a spoofer), ambient radio frequency (RF) signals can be exploited as an alternative positioning, navigation, and timing (PNT) source. These signals are commonly referred to as signals of opportunity (SOPs). SOPs can be terrestrial (e.g., cellular, digital television, and AM/FM transmitters) or space-based (e.g., low Earth orbit (LEO) satellites).

This project studied various aspects of exploiting cellular terrestrial and LEO-based SOPs as an alternative to GNSS for multi-modal highly automated transportation systems (HATS). The studies spanned theoretical analyses and modeling, extensive simulations, and real-world experimental demonstrations on ground vehicles, low-altitude unmanned aerial vehicles (UAVs), and high-altitude aircraft. Some studies were also conducted in a real-world GPS-jammed environment at Edwards Air Force Base, Mojave Desert, CA.

A total of 55 studies; each published as a journal, conference, or magazine paper; were conducted. In what follows, the main findings from each study, grouped by topical area, are summarized. The publications resulting from these studies are appended next.

I. Enhanced Integrity Monitoring with GNSS Fused with Terrestrial SOPs

1. Aerial vehicle protection level reduction by fusing GNSS and terrestrial signals of opportunity
   M. Maaref, J. Khalife, and Z. Kassas
   IEEE Transactions on Intelligent Transportation Systems, 2021, Vol. 22, Issue 9, pp. 5976–5993 (special issue)
   Summary: A method for reducing the protection levels (PLs) of aerial vehicles by fusing global navigation satellite sys- tems (GNSS) signals with terrestrial signals of opportu- nity (SOPs) is developed. PL is a navigation integrity parameter that guarantees the probability of position error exceeding a cer- tain value to be bounded by a target integrity risk. For unmanned aerial vehicles (UAVs), it is desirable to achieve as tight PLs as possible. This paper characterizes terrestrial cellular SOPs' mea- surement errors from extensive UAV flight campaigns, collected over the past few years in different environments and from dif- ferent providers, transmitting at different frequencies and band- widths. Next, the reduction in PLs due to fusing terrestrial SOPs with a traditional GNSS-based navigation system is analyzed. It is demonstrated that incorporating terrestrial SOP measurements is more effective in reducing the PLs over adding GNSS measure- ments. Experimental results are presented for a UAV traversing a trajectory of 823 m, during which the VPL of the GPS-based and GNSS-based navigation systems were reduced by 56.9% and 58.8%, respectively, upon incorporating SOPs; while the HPL of the GPS-based and GNSS-based navigation systems were reduced by 82.4% and 74.6%, respectively, upon incorporating SOPs.

2. Opportunistic autonomous integrity monitoring for enhanced UAV safety
   J. Khalife, M. Maaref, and Z. Kassas
   IEEE Aerospace and Electronic Systems Magazine, 2023, Vol. 38, no. 5, pp. 34-44 (special issue)
   Summary: An opportunistic advanced receiver autonomous integrity monitoring (OARAIM) algorithm for unmanned aerial vehicle (UAV) navigation is developed. This algorithm fuses ambient terrestrial signals of opportunity (SOPs) with global navigation satellite system (GNSS) signals to improve the ca- pability of detecting GNSS and SOP measurement faults and provide tight protection level (PL) bounds. A receiver is assumed to make pseudorange measurements on multiple GNSS satellites and terrestrial SOPs. Experimental tests are presented injecting simulated faults into the OARAIM algorithm which successfully detects the faults in GPS satellites and SOPs. Moreover, the OARAIM algorithm and the inclusion of the SOPs reduces the vertical and horizontal PLs by more than 55% and 70%, respectively, compared to only using GNSS measurements.
3. Performance analysis of opportunistic ARAIM for navigation with GNSS signals fused with terrestrial signals of opportunity
   M. Jia, J. Khalife, and Z. Kassas
   IEEE Transactions on Intelligent Transportation Systems, 2023, Vol. 24, no. 10, pp. 10587-10602
   Summary: Integrity monitoring of a vehicular navigation system that utilizes multi-constellation global navigation satellite systems (GNSS) signals fused with terrestrial signals of opportunity (SOPs) is considered. An opportunistic advanced receiver autonomous integrity monitoring (OARAIM) framework is developed to detect faults and calculate protection levels (PLs). The influence of fusing SOPs on the integrity performance is analyzed. It is shown that fusing a single SOP with GNSS signals essentially increases both the horizontal PL (HPL) and vertical PL (VPL), while fusing two or more SOPs could reduce the PLs and improves fault detection. Performance sensitivity analysis for the probability of SOP fault and user range error is conducted to characterize the fault-free HPL under different regimes. Experimental results on an unmanned aerial vehicle (UAV) navigating with GPS signals fused with cellular SOPs are presented to validate the effectiveness of the OARAIM framework and demonstrate the analysis of the integrity performance in the horizontal direction.
4. Urban road safety prediction: a satellite navigation perspective
   H. Lee, J. Seo, and Z. Kassas
   IEEE Intelligent Transportation Systems Magazine, 2022, Vol. 14, no. 6, pp. 94-106
   Summary: Predicting the safety of urban roads for navigation via global navigation satellite systems (GNSS) signals is considered. To ensure the safe driving of automated vehicles, a vehicle must plan its trajectory to avoid navigating on unsafe roads (e.g., icy conditions, construction zones, narrow streets, and so on). Such information can be derived from roads' physical properties, the vehicle's capabilities, and weather conditions. From a GNSS-based navigation perspective, the reliability of GNSS signals in different locales, which is heavily dependent on the road layout within the surrounding environment, is crucial to ensure safe automated driving. An urban road environment surrounded by tall objects can significantly degrade the accuracy and availability of GNSS

signals. This article proposes an approach to predict the reliability of GNSS-based navigation to ensure safe urban navigation. Satellite navigation reliability at a given location and time on a road is determined based on the probabilistic position error bound of the vehicle-mounted GNSS receiver. A metric for GNSS reliability for ground vehicles is suggested, and a method to predict the conservative probabilistic error bound of the GNSS navigation solution is proposed. A satellite navigation reliability map is generated for various navigation applications. As a case study, the reliability map is used in a proposed optimization problem formulation for automated ground vehicle safety-constrained path planning.

5. Evaluation of ground vehicle protection level reduction due to fusing GPS with faulty terrestrial signals of opportunity
   M. Jia, J. Khalife, and Z. Kassas
   ION International Technical Meeting, Jan. 25-28, 2021, San Diego, CA, pp. 354–365
   Summary: The protection level (PL) performance of an autonomous ground vehicle (AGV) due to fusing GPS signals with faulty terrestrial signals of opportunity (SOPs) is evaluated. The AGV is assumed to be equipped with receivers, which can produce a navigation solution from GPS and SOP pseudorange measurements. First, the effect of the number of SOPs on the PL reduction is analyzed. Then, the PL reduction under different assumptions of SOP fault probabilities is explored. The results show that while adding one SOP could increase the PL, adding two or more SOPs would significantly reduce the PLs. The results also demonstrate that even for highly unreliable SOPs (namely, those with fault probabilities as high as 10%), adding two or more SOPs would still reduce the PLs.
6. Ground vehicle navigation integrity monitoring for multi-constellation GNSS fused with cellular signals of opportunity
   M. Jia, H. Lee, J. Khalife, Z. Kassas, and J. Seo
   IEEE International Conference on Intelligent Transportation Systems, Sep. 19-22, 2021, Indianapolis, IN, pp. 3978–3983
   Summary: Integrity monitoring of a ground vehicle navigation system, utilizing multi-constellation global navigation satellite systems (GNSS) signals fused with ambient cellular signals of opportunity (SOPs) is considered. An advanced receiver autonomous integrity monitoring (ARAIM) framework is developed to detect and exclude multipath and non-line-ofsight errors. A method to conservatively predict the horizontal protection level (HPL) is proposed, utilizing ray-tracing and channel impulse response prediction in a three-dimensional (3D) building map of the environment. Simulation results are presented demonstrating the conservatively predicted HPL with different signals (GPS-only, GPS+GLONASS, GPS+SOP, and GPS+GLONASS+SOP). Experimental results are presented for a ground vehicle navigating a trajectory of 1380 m in an urban environment, showing the availability rates for GPS-only, GPS+GLONASS, GPS+SOP, and GPS+GLONASS+SOP being 52.53%, 75.66%, 76.87%, and 80.72%, respectively.
7. Kalman filter-based integrity monitoring for GNSS and 5G signals of opportunity integrated navigation
   M. Jia and Z. Kassas
   IFAC Symposium on Advances in Automotive Control, Aug. 29-31, 2022, Columbus, OH, pp. 273-278 (special session)

Summary: A Kalman filter-based receiver autonomous integrity monitoring algorithm (RAIM) is proposed to exploit sequential measurements from global navigation satellite systems (GNSS) and cellular 5G signals of opportunity (SOPs), to ensure safe vehicular navigation in urban environments. To deal with frequent threats caused by multipath and non-line-of-sight conditions, an innovation-based outlier rejection method is introduced. Next, a fault detection technique based on solution separation test is developed, and the quantification of protection levels is derived. Experimental results of a ground vehicle traveling in an urban environment, while making pseudorange measurements to GPS satellites and cellular 5G towers, are presented to demonstrate the efficacy of the proposed method. Incorporating 5G signals from only 2 towers is shown to reduce the horizontal protection level (HPL) by 0.22 m compared to using only GPS. Moreover, the proposed method is shown to reduce the HPL and vertical protection level (VPL) by 84.42% and 69.63%, respectively, over the snapshot advanced RAIM (ARAIM).

8. Fault detection and exclusion for INS/GPS/5G tightly-coupled navigation
   M. Jia and Z. Kassas
   IEEE/ION Position, Location, and Navigation Symposium, Apr. 25-27, 2023, Monterey, pp. 597-602
   Summary: A solution separation-based fault detection and exclusion (FDE) framework is developed for GPS and 5G signal of opportunity (SOP) aided inertial navigation system (INS). The proposed framework fuses an inertial measurement unit (IMU) with GPS and 5G pseudorange measurements in a tightly-coupled fashion via an extended Kalman filter to estimate the ground vehicles' attitude, position, velocity, and clock errors. Solution separation tests are exploited to detect and exclude faults from GPS and 5G signals due to transmitter failures and local threats in urban environments (e.g., multipath). Experimental results are presented to evaluate the efficacy of the proposed framework under different sensor fusion scenarios. It is shown that fusing 5G signals enhances the FDE performance of the multi-sensor system in a suburban scenario: while INS/GPS fails to detect faulty GPS measurements, the INS/GPS/SOP is able to detect the fault. Moreover, over a trajectory of 1.91 km traversed in 200 s, using signals from two 5G gNBs, the INS/GPS/5G system achieved a position root-mean squared error (RMSE) of 0.81 m and maximum position error of 2.17 m. The undetected GPS fault in the INS/GPS system increased the RMSE and maximum position error to 1.83 m and 4.25 m, respectively.

II. Cognitive Sensing and Navigation with Terrestrial 5G SOPs

1. Cognitive opportunistic navigation in private networks with 5G signals and beyond
   M. Neinavaie, J. Khalife, and Z. Kassas
   IEEE Journal of Selected Topics in Signal Processing, 2022, Vol. 16, no. 1, pp. 129-143
   Summary: A receiver architecture is proposed to cognitively extract navigation observables from fifth generation (5G) new radio (NR) signals of opportunity. Unlike conventional opportunistic receivers which require knowledge of the signal structure, particularly the reference signals (RSs), the proposed cognitive opportunistic navigation (CON) receiver requires knowledge of only the frame duration and carrier frequency of

the signal. In 5G NR, some of these RSs are only transmitted on demand, which limits the existing opportunistic navigation frameworks to signals which are on always-on; hence, limiting the exploitable RS bandwidth. To exploit the full available bandwidth and improve ranging accuracy, the proposed CON receiver is designed to estimate all the RSs contained in the transmitted signals corresponding to multiple 5G base stations, (i.e., gNBs). Navigation observables (pseudorange and carrier phase) are subsequently derived from the estimated RSs. The proposed receiver operates in two stages: (i) acquisition and (ii) tracking. The acquisition stage of the CON receiver is modeled as a sequential detection problem where the number of gNBs and their corresponding RSs and Doppler frequencies are unknown. The generalized likelihood ratio (GLR) test for sequentially detecting active gNBs is derived and used to estimate the number of gNBs and their RSs. In order for the receiver to refine and maintain the Doppler and RS estimates provided by the acquisition stage, tracking loops are designed. A sufficient condition on the Doppler estimation error to ensure that the proposed GLR asymptotically achieves a constant false alarm rate (CFAR) is derived. The output of the tracking loops, namely carrier phase and code phase, are then used to estimate the receiver's position. Extensive experimental results are presented demonstrating the capabilities of the proposed CON receiver with real 5G signals on ground and aerial platforms, with an experiment showing the first navigation results with real 5G signals on an unmanned aerial vehicle (UAV) navigating using the CON receiver over a 416 m trajectory with a position root mean-squared error (RMSE) of 4.35 m.

2. Exploiting on-demand 5G downlink signals for opportunistic navigation
   A. Abdallah, J. Khalife, and Z. Kassas
   IEEE Signal Processing Letters, 2023, Vol. 30, pp. 389-393
   Summary: This letter presents the first user equipment (UE)- based 5G navigation framework that exploits the "on-demand" 5G downlink signals. In this framework, the entire system bandwidth of incoming 5G signals is utilized in an opportunistic fashion. The proposed framework involves a cognitive approach to acquire the so-called ultimate reference signal (URS), which includes the "on-demand" as well as "always-on" reference signals (RSs). Experimental results are presented showing that the acquired URS: (i) spans the entire 5G downlink bandwidth, (ii) increases the carrier-to-noise ratio by 10 dB compared to state-of-the-art 5G user equipment (UE)-based opportunistic navigation receiver, and (iii) reduces significantly the carrier and code phase errors. A ranging error standard deviation of 2.75 m was achieved with proposed framework with a stationary receiver placed 290 m away from a 5G gNB in a clear line-of-sight environment, which is lower than the 5.05 m achieved when using the "always-on" 5G downlink signals.
3. Assessing real 5G signals for opportunistic navigation
   A. Abdallah, K. Shamaei, and Z. Kassas
   ION Global Navigation Satellite Systems Conference, Sep. 21-25, 2020, St. Louis, MO, pp. 2548–2559
   Summary: Cellular fifth-generation (5G) signals are assessed for opportunistic navigation. A carrier-aided code-based softwaredefined receiver (SDR) is presented, which produces navigation observables from received downlink 5G signals. These observables are analyzed to assess the performance of 5G signals for opportunistic navigation.

Experimental results are presented of a ground vehicle navigating with the 5G SDR while receiving signals from two 5G base stations (known as gNBs). It is shown that over a trajectory of 1.02 km traversed in 100 seconds, the position root mean-squared error (RMSE) was 14.9 m.

4. A machine learning multipath mitigation approach for opportunistic navigation with 5G signals
   M. Orabi, A. Abdallah, J. Khalife, and Z. Kassas
   ION Global Navigation Satellite Systems Conference, Sep. 20-24, 2021, St. Louis, MO, pp. 2895-2909
   Summary: The ability of different neural networks to mitigate multipath signals for opportunistic navigation with downlink 5G signals is assessed. Two neural networks, namely feed-forward neural networks (FFNNs) and time-delay neural networks (TDNNs), are designed to learn multipath-induced errors on a 5G receiver's code phase estimate. The neural networks use inputs from the autocorrelation function (ACF) to learn the errors in the code phase estimate of a conventional delay-locked loop (DLL). A ray tracing algorithm is used to produce high fidelity training data that could model the dynamics between the line of sight (LOS) component and the non-line of sight (NLOS) components. Cross-validation methods are used on FFNNs to examine the sensitivity of the out-of-sample error on the number of hidden layers, number of neurons per layer, and regularization constant that limits the complexity of the hypothesis space. Moreover, TDNNs with varying access to the time history of the ACF taps are assessed. Experimental results in a multipath-rich environment are presented demonstrating that the proposed TDNN achieved ranging root-mean squared error (RMSE) reduction of 27.1% compared to a conventional DLL.
5. Carpe signum: seize the signal – opportunistic navigation with 5G
   Z. Kassas, A. Abdallah, and M. Orabi
   Inside GNSS Magazine, Vol. 16, Issue 1, Feb. 2021, pp. 52–57
   Summary: Innovative features of cellular fifth-generation (5G) signals enable the wireless system to play a major role in autonomous technologies. Test results of a ground vehicle navigating with signals from five 5G base stations (gNBs) over a trajectory of 773 m traversed in 110 seconds show a position root mean-squared error of 4.1 m.
6. Universal receiver architecture for blind navigation with partially known terrestrial and extraterrestrial signals of opportunity
   J. Khalife, M. Neinavaie, and Z. Kassas
   ION Global Navigation Satellite Systems Conference, Sep. 20-24, 2021, St. Louis, MO, pp. 2201–2211
   Summary: A universal receiver architecture that is capable of exploiting partially known signals of opportunity (SOPs) for navigation is presented. A partially known signal refers to a signal to which only the center frequency and bandwidth are known to the receiver. Assuming that the SOP follows a standard modulation scheme, e.g., phase shift keying (PSK) or quadrature amplitude modulation (QAM), and a standard multiplexing scheme, e.g., code-division multiple access (CDMA) or orthogonal frequency-division multiplexing (OFDM), the proposed receiver architecture can blindly acquire and track the SOP to provide a navigation solution. Experimental results are presented showing the proposed

receiver successfully producing meter-level-accurate navigation solutions from different types of terrestrial and space signals: GPS, cellular 4G long-term evolution (LTE) and 5G, and Starlink LEO satellites, under the aforementioned partially known assumption.

7. Opportunistic navigation using sub-6 GHz 5G downlink signals: a case study on a ground vehicle

   A. Abdallah and Z. Kassas

   European Conference on Antennas and Propagation, Mar. 27 - Apr. 1, 2022, Madrid, Spain, pp. 1-5 (special session)

   Summary: A user equipment (UE)-based navigation framework that opportunistically exploits 5G signals is developed. The proposed framework exploits the "always on" 5G downlink signals in a time-domain-based receiver. To this end, a so-called ultimate synchronization signal (USS) is proposed to utilize the time-domain orthogonality of the orthogonal frequency division multiplexing (OFDM)-based 5G signals. This approach simplifies the receiver's complexity and enhances the performance of the 5G opportunistic navigation framework. Experimental results are presented to evaluate the efficacy of the proposed framework on a ground vehicle navigating in a suburban environment, while utilizing sub6 GHz 5G signals from two gNBs. It is shown that while a state-of-the-art frequency-domain-based 5G opportunistic navigation receiver can only reliably track the gNBs' signals over a trajectory of 1.02 km traversed in 100 seconds, producing a position root mean-squared error (RMSE) of 14.93 m; the proposed time-domain-based receiver was able to track over a trajectory of 2.17 km traversed in 230 seconds, achieving a position RMSE of 9.71 m.

8. Experimental characterization of received 5G signals carrier-to-noise ratio in indoor and urban environments

   A. Abdallah, J. Khalife, and Z. Kassas

   IEEE Vehicular Technology Conference, Apr. 25-28, 2021, Helsinki, Finland, pp. 1-5

   Summary: An extensive experimental study to characterize frequency range 1 (FR1) (i.e., sub-6 GHz) 5th generation (5G) signals from existing infrastructure for navigation is presented. The study uses a state-of-the-art 5G navigation software-defined radio (SDR) to track 5G signals in different environments and under different conditions to analyze the behavior of the received carrier-to-noise-ratio (C/N0), which directly affects the precision of the navigation performance. Three different experimental scenarios were conducted for this purpose with real 5G signals and 4th generation (4G) long-term evolution (LTE) signals for comparison purposes: (i) a stationary indoor scenario to study the effect of wall and floor partitions, (ii) a stationary outdoor scenario to study the effect of sampling rate, antenna grade, and clock quality, and (iii) a mobile outdoor experiment to study the C/N0 as a function of the range. All three scenarios confirmed the potential of downlink 4G and 5G signals for navigation

9. Multipath mitigation of 5G signals via reinforcement learning for navigation in urban environments

   A. Abdallah, M. Orabi, and Z. Kassas

   IEEE Vehicular Technology Conference, Jun. 19-22, 2022, Helsinki, Finland, pp. 1-5

   Summary: The ability of reinforcement learning (RL)-based convolutional neural network (CNN) to mitigate multipath signals for opportunistic navigation with downlink 5G signals

is assessed. The CNN uses inputs from the autocorrelation function (ACF) to learn the errors in the code phase estimates. A ray tracing algorithm is used to produce high fidelity training data that could model the dynamics between the line of sight (LOS) component and the non-line of sight (NLOS) components. Experimental results on a ground vehicle navigating with 5G signals for 902 m in a multipath-rich environment are presented, demonstrating that the proposed RL-CNN achieved a position root-mean squared error (RMSE) of 14.7 m compared to 20.6 m with a conventional delay-locked loop (DLL).

10. Joint detection and tracking of unknown beacons for navigation with 5G signals and beyond

    M. Neinavaie and Z. Kassas

    ION Global Navigation Satellite Systems Conference, Sep. 19-23, 2022, Denver, CO, pp. 921-932

    Summary: A receiver architecture is proposed to jointly detect and track unknown beacons to extract navigation observables from fifth generation (5G) new radio (NR) signals of opportunity and beyond. Unlike conventional opportunistic receivers which require knowledge of the signal structure, particularly the reference signals (RSs), the proposed receiver requires knowledge of only the RS period and carrier frequency of the signal. The transmitted RSs for private networks are unknown for an opportunistic receiver. Moreover, to use the spectrum more efficiently, some of these RSs are only transmitted on demand in 5G NR, which limits the existing opportunistic navigation frameworks to signals which are on always-on; hence, limiting the exploitable RS bandwidth. To exploit the full available bandwidth and improve ranging accuracy, the proposed receiver is designed to estimate all the RSs contained in the transmitted signals corresponding to multiple unknown sources. Navigation observables (pseudorange and carrier phase) are subsequently derived from the estimated RSs. The proposed receiver operates in two stages: (i) detection of unknown signals and (ii) tracking. The detection of unknown signals is modeled as a sequential detection problem where the number of sources and their corresponding RSs and Doppler frequencies are unknown. The generalized likelihood ratio (GLR) test for sequentially detecting active gNBs is used to estimate the number of sources and their RSs. In order for the receiver to refine and maintain the Doppler and RS estimates provided by the acquisition stage, tracking loops are used. The output of the tracking loops, namely carrier phase and code phase, are then used to estimate the receiver's position. Experimental results are presented demonstrating the capabilities of the proposed receiver with real 5G signals on ground and aerial platforms, with an experiment showing the navigation results with real 5G signals on an unmanned aerial vehicle (UAV) navigating using the proposed receiver over a 416 m trajectory with a position root mean-squared error (RMSE) of 4.35 m.

III. Navigation in GNSS-Denied Environments

1. I am not afraid of the GPS jammer: resilient navigation via signals of opportunity in GPS-denied environments

Z. Kassas, J. Khalife, A. Abdallah, and C. Lee
IEEE Aerospace and Electronic Systems Magazine, 2022, Vol. 37, no. 7, pp. 4-19
Summary: I am not afraid of the GPS jammer, as long as there are ambient signals of opportunity (SOPs) to exploit in the envi- ronment. In environments where GPS signals are challenged (e.g., indoors and deep urban canyons) or denied (e.g., under jamming and spoofing attacks), SOPs could serve as an alternative posi- tioning, navigation, and timing (PNT) source to GPS, and more generally, to global navigation satellite systems (GNSS). This paper presents a radio simultaneous localization and mapping (radio SLAM) approach that enables the exploitation of SOPs for resilient and accurate PNT. Radio SLAM estimates the states of the navigator-mounted receiver simultaneously with the SOPs' states. Radio SLAM could produce an SOP-derived navigation solution in a standalone fashion or by fusing SOPs with sensors (e.g., inertial measurement unit (IMU), lidar, etc.), digital maps, and/or other signals (e.g., GNSS). This paper presents the first published experimental results evaluating the efficacy of radio SLAM in a real GPS-denied environment. These experiments took place at Edwards Air Force Base, California, USA, during which GPS was intentionally jammed with jamming-to-signal (J/S) ratio as high as 90 dB. The paper evaluates the timing of two cellular long-term evolution (LTE) SOPs located in the jammed environment, showing timing stability over 95 minutes of GPS jamming. Moreover, the paper presents navigation results showcasing a ground vehicle traversing a trajectory of about 5 km in 180 seconds in the GPS-jammed environment. The vehicle's GPS-IMU system drifted from the vehicle's ground truth trajectory, resulting in a position root mean-squared error (RMSE) of 238 m. In contrast, the radio SLAM approach with a *single* cellular LTE SOP whose position was poorly known (an initial uncertainty on the order of several kilometers) achieved a position RMSE of 32 m.

2. No GPS no problem: exploiting cellular OFDM-based signals for accurate navigation
   Z. Kassas and A. Abdallah
   IEEE Transactions on Aerospace and Electronic Systems, 2023, accepted
   Summary: This paper presents a receiver that could exploit downlink orthogonal frequency-division multiplexing (OFDM)- based cellular signals to navigate opportunistically to meter-level accuracy in a real-world GPS-denied environment. The proposed receiver exploits signals from multiple logical antenna ports simultaneously, which dramatically improves the receiver's sensitivity. The efficacy of the proposed receiver is demonstrated experimentally in an environment under intentional GPS jamming, in which the ground vehicle-mounted receiver navigated for 5 km in 180 seconds. The receiver was able to acquire and track signals from 7 longterm evolution (LTE) eNodeBs, one of which was more than 25 km away, achieving a two-dimensional position root mean-squared error (RMSE) of 2.6 m.
3. I am not afraid of the jammer: navigating with signals of opportunity in GPS-denied environments
   Z. Kassas, J. Khalife, A. Abdallah, and C. Lee
   ION Global Navigation Satellite Systems Conference, Sep. 21-25, 2020, St. Louis, MO, pp. 1566–1585
   Summary: I am not afraid of the GPS jammer, as long as there are ambient signals of opportunity (SOPs) to exploit in the environment. In environments where GPS signals are

challenged (e.g., indoors and deep urban canyons) and denied (e.g., under jamming and spoofing attacks), SOPs could serve as an alternative navigation source to GPS, and more generally, to global navigation satellite systems (GNSS). This paper presents a radio simultaneous localization and mapping (radio SLAM) approach that enables the exploitation of SOPs for resilient and accurate navigation. Radio SLAM estimates the states of the navigator-mounted receiver simultaneously with the SOPs' states. Radio SLAM could produce an SOP-derived navigation solution in a standalone fashion or by fusing SOPs with sensors (e.g., inertial measurement unit (IMU), lidar, etc.), digital maps, and/or other signals (e.g., GNSS). The paper also overviews a core component of radio SLAM: a cognitive software-defined radio (SDR) called MATRIX: Multichannel Adaptive TRansceiver Information eXtractor, which produces navigation observables from terrestrial and space-based SOPs. Next, the paper showcases the most accurate navigation results to-date with terrestrial and space-based SOPs from low Earth orbit (LEO) satellites in different environments and on different platforms: indoor pedestrian, ground vehicles in urban and deep urban canyons, and aerial vehicles. Finally, the paper presents the first ever published experimental results for navigation with SOPs in a GPS-denied environment. These experiments took place at Edwards Air Force Base, California, USA, during which GPS was intentionally jammed with jamming-to-signal (J/S) ratio as high as 90 dB. The results showcase a ground vehicle traversing a trajectory of about 5 km in 180 seconds in the GPS-jammed environment, during which a GPS-IMU system drifted from the vehicle's ground truth trajectory, resulting in a position root mean-squared error (RMSE) of 238 m. In contrast, the radio SLAM approach with a single cellular long-term evolution (LTE) SOP whose position was poorly known (an initial uncertainty on the order of several kilometers) achieved a position RMSE of 32 m.

4. Demo: I am not afraid of the GPS jammer: exploiting cellular signals for accurate ground vehicle navigation in a GPS-denied environment
   A. Abdallah, Z. Kassas, and C. Lee
   ACM Workshop on Automotive and Autonomous Vehicle Security, Apr. 24, 2022, San Diego, CA, pp. 1-1
   Summary: This demo presents unprecedented attack-defense results of a ground vehicle navigating to a meter-level accuracy in a real-world GPS-denied environment, by exploiting ambient cellular signals exclusively and no other sensors.

IV. Low-Altitude UAV and High-Altitude Aircraft Navigation with Terrestrial SOPs

1. On the achievability of submeter-accurate UAV navigation with cellular signals exploiting loose network synchronization
   J. Khalife and Z. Kassas
   IEEE Transactions on Aerospace and Electronic Systems, 2022, Vol. 58, no. 5, pp. 4261-4278
   Summary: A framework that could achieve submeter-level unmanned aerial vehicle (UAV) horizontal navigation in multipath-free environments with cellular carrier phase measurements is developed. This framework exploits the "loose" synchronization between cellular base transceiver station (BTS) clocks. It is shown through extensive

experimental data that the beat frequency stability of cellular BTSs approaches that of atomic standards and that the clock deviations can be realized as a stable autoregressive moving average model. This BTS clock model is referred to as loose network synchronization. A rule-of-thumb is established for clustering the clock deviations to minimize the position estimation error, while significantly reducing the computational complexity. The presented models allow the UAV to achieve sustained carrier phase-based meter- to submeter-accurate navigation. To demonstrate the efficacy of the developed framework, this article presents three UAV flight experiments in Southern California, USA, utilizing signals from different cellular providers transmitting at different frequencies. The three experiments took place in open, semiurban environments with nearly multipath-free, line-ofsight (LOS) conditions, in which the UAV traveled 1.72, 3.07, and 0.61 km, achieving a horizontal position root mean squared error of 36.61, 88.58, and 89.33 cm, respectively, with respect to the UAV's on-board navigation system.

2. Assessment of cellular signals of opportunity for high altitude aircraft navigation
   Z. Kassas, J. Khalife, A. Abdallah, C. Lee, J. Jurado, S. Wachtel, J. Duede, Z. Hoeffner, T. Hulsey, R. Quirarte, and R. Tay
   IEEE Aerospace and Electronic Systems Magazine, 2022, Vol. 37, no. 10, pp. 4-19
   Summary: Opportunistic navigation with cellular signals is studied and demonstrated on a high altitude aircraft. An ex- tensive campaign was conducted by the Autonomous Systems Perception, Intelligence, and Navigation (ASPIN) Laboratory in collaboration with the US Air Force (USAF) to sample ambient cellular signals of opportunity (SOPs) at different altitudes in different regions in Southern California, USA. The carrier- to-noise ratio is characterized as a function of altitude and horizontal distance. It was found that signals from cellular transmitters can be reliably acquired and tracked for navigation purposes by receivers mounted on high dynamics aircraft flying at altitudes as high as 23,000 ft above ground-level (AGL) and horizontal distances as far as 100 km. The multipath channel is also characterized as a function of altitude, showing clean channels with a dominant line-of-sight component for altitudes up to 23,000 ft. To further assess the potential of cellular SOPs for aircraft navigation, a 51-km trajectory traversed over a period of 9 minutes was estimated exclusively using cellular SOPs (i.e., with no GPS or other sensors, except for barometric altimeter measurements), resulting in a three-dimensional (3–D) position 10.5 m position root mean-squared error (RMSE).
3. Differential framework for submeter-accurate vehicular navigation with cellular signals
   J. Khalife and Z. Kassas
   IEEE Transactions on Intelligent Vehicles, 2023, Vol. 8, no. 1, pp. 732-744
   Summary: A framework that could achieve submeter-levelaccurate horizontal navigation with carrier phase differential measurements from cellular signals is developed. This framework, termed CD-cellular, is composed of a base and a rover in a cellular environment, both making carrier phase measurements to the same cellular base transceiver stations (BTSs). The base shares its carrier phase measurements with the mobile rover, which in turn employs an extended Kalman filter to obtain a coarse estimate of its states, followed by a batch weighted nonlinear least squares (B-WNLS) estimator to solve for the integer ambiguities, and finally a point-solution WNLS to estimate its own

states. The framework is designed to guarantee that after some time, the rover's position error remains below a pre-defined threshold with a desired probability. This is achieved by leveraging models of the BTS positions from stochastic geometry. Experimental results on an unmanned aerial vehicle (UAV) in an open semi-urban environment with multipath-free, line-of-sight (LOS) conditions are presented, showing that the developed framework achieves a 70.48 cm position root mean-squared error (RMSE) over a trajectory of 2.24 km, measured with respect to the UAV's navigation solution from its onboard GPS-inertial navigation system (INS).

4. Flight demonstration of high altitude aircraft navigation with cellular signals
   Z. Kassas, J. Khalife, A. Abdallah, C. Lee, J. Jurado, S. Wachtel, J. Duede, Z. Hoeffner, T. Hulsey, R. Quirarte, and R. Tay
   IEEE Intelligent Transportation Systems Magazine, 2023, Vol. 15, no. 4, pp. 150–165
   Summary: This article presents the first demonstration of navigation with cellular signals of opportunity (SOPs) on a high-altitude aircraft. An extensive flight campaign was conducted by the Autonomous Systems Perception, Intelligence, and Navigation Laboratory in collaboration with the U.S. Air Force to sample ambient downlink cellular SOPs in different regions in Southern California, USA. Carrier phase measurements were produced from these signals, which were subsequently fused in an extended Kalman filter along with altimeter measurements to estimate the aircraft's state (position, velocity, and time). Three flights are performed in three different regions: 1) rural, 2) semiurban, and 3) urban. A multitude of flight trajectories and altitudes above ground level (AGL) was exercised in the three flights: 1) a 51-km trajectory of grid maneuvers with banking and straight segments at about 5,000 ft AGL, 2) a 57-km trajectory of a teardrop descent from 7,000 ft AGL down to touchdown at the runway, and 3) a 55-km trajectory of a holding pattern at about 15,000 ft AGL. The estimated aircraft trajectory is computed for each flight and compared with the trajectory from the aircraft's onboard navigation system, which utilized a GPS receiver coupled with an inertial navigation system and an altimeter. The cellular SOPs produced remarkable sustained navigation accuracy over the entire flight trajectories in all three flights, achieving a 3D position root mean-squared error of 10.53 m, 4.96 m, and 15.44 m, respectively.
5. UAV navigation with 5G carrier phase measurements
   A. Abdallah and Z. Kassas
   ION Global Navigation Satellite Systems Conference, Sep. 20-24, 2021, St. Louis, MO, pp. 3294-3306
   Summary: A framework for unmanned aerial vehicle (UAV) navigation using downlink cellular fifth-generation (5G) signals is presented. In the proposed framework, a software-defined receiver (SDR) is developed to extract carrier phase measurements from received 5G signals. The SDR utilizes the time-domain orthogonality of the orthogonal frequency division multiplexing (OFDM)-based 5G signals. A so-called ultimate synchronization signal (USS) to combine all available resources is proposed. The proposed 5G SDR includes two stages: (i) acquisition stage, in which only unique USS resources are utilized to detect the hearable gNBs and (ii) tracking stage, in which the entire USS is utilized to produce 5G carrier phase measurements. These measurements are processed in an extended Kalman filter (EKF) to assess the navigation performance of the proposed 5G opportunistic SDR.

Experimental results are presented of an UAV navigating with the proposed 5G SDR, while receiving signals from four 5G base stations (known as gNBs). It is shown that over a trajectory of 500 m traversed in 145 seconds, the position root mean-squared error (RMSE) was 3.35 m.

6. Received power characterization of terrestrial cellular signals on high altitude aircraft

   Z. Kassas, A. Abdallah, J. Khalife, C. Lee, J. Jurado, S. Wachtel, J. Duede, Z. Hoeffner, T. Hulsey, R. Quirarte, and R. Tay

   IEEE Aerospace Conference, Mar. 5-12, 2022, Big Sky, MT, pp. 1-8

   Summary: The received power of terrestrial cellular 3G code division multiple access (CDMA) and 4G long-term evolution (LTE) signals on a high altitude aircraft is experimentally characterized. The conducted experiments were performed on a Beechcraft C-12 Huron, a fixed-wing U.S. Air Force aircraft. Two types of flight patterns were performed: (i) teardrop-like patterns to characterize the carrier-to-noise ratio (C/N0) versus altitude and (ii) grid-like patterns to characterize C/N0 versus the horizontal distance between the aircraft and cellular towers. Flight campaigns in two regions were conducted: (i) a rural region in Edwards, California, USA, and (ii) an urban region in Riverside, California, USA. It was observed that cellular signals are surprisingly powerful at both (i) high altitudes, exhibiting C/N0 of 25–55 dB-Hz at altitudes of 2,000–23,000 ft above ground level (AGL) and (ii) faraway horizontal distances, exhibiting C/N0 of about 30 dB-Hz for towers as far as 50 km, while flying at about 16,000 ft AGL. In addition, two propagation models were evaluated to describe the behavior of the measured C/N0: (i) free-space path loss model and (ii) two-ray model. It was observed that the two-ray model fits the measured C/N0 sufficiently well, for towers more than 10 km away, while flying at an altitude of 16,000 ft AGL. For towers closer than 10 km, the antenna radiation pattern should be incorporated into the two-ray model to improve model fitting.

7. Protecting the skies: GNSS-less aircraft navigation with terrestrial cellular signals of opportunity

   Z. Kassas, A. Abdallah, C. Lee, J. Jurado, S. Wachtel, J. Duede, Z. Hoeffner, T. Hulsey, R. Quirarte, and R. Tay

   ION Global Navigation Satellite Systems Conference, Sep. 19-23, 2022, Denver, CO, pp. 1014-1025

   Summary: This paper shows how to protect our skies from harmful radio frequency interference (RFI) to global navigation satellite system (GNSS) signals, by offering terrestrial cellular signals of opportunity (SOPs) as a viable aircraft navigation system backup. An extensive flight campaign was conducted by the Autonomous Systems Perception, Intelligence, and Navigation (ASPIN) Laboratory in collaboration with the United States Air Force (USAF) to study the potential of cellular SOPs for high-altitude aircraft navigation. A multitude of flight trajectories and altitudes were exercised in the flight campaign in two different regions in Southern California, USA: (i) rural and (ii) semi-urban. Samples of the ambient downlink cellular SOPs were recorded, which were fed to ASPIN Laboratory's MATRIX (Multichannel Adaptive TRansceiver Information eXtractor) software-defined receiver (SDR), which produced carrier phase measurements from these samples. These measurements were fused with altimeter data via an extended Kalman

filter (EKF) to estimate the aircraft's trajectory. This paper shows for the first time that at altitudes as high as about 11,000 ft above ground level (AGL), more than 100 cellular long-term evolution (LTE) eNodeBs can be reliable tracked, many of which were more than 100 km away, with carrier-to-noise ratio (C/N0) exceeding 40 dB-Hz. The paper shows pseudorange and Doppler tracking results from cellular eNodeBs along with the C/N0 and number of tracked eNodeBs over the two regions, while performing ascending, descending, and grid maneuvers. In addition, the paper shows navigation results in the semi-urban and rural regions, showing a position root mean-squared error of 9.86 m and 10.37, respectively, over trajectories of 42.23 km and 56.56 km, respectively, while exploiting an average of about 19 and 10 eNodeBs, respectively.

8. Robust receiver design for high altitude aircraft navigation with terrestrial cellular signals

   Z. Kassas, S. Shahcheraghi, A. Kaiss, C. Lee, J. Jurado, S. Wachtel, J. Duede, Z. Hoeffner, T. Hulsey, R. Quirarte, and R. Tay

   IEEE/ION Position, Location, and Navigation Symposium, Apr. 25-27, 2023, Monterey, pp. 75-80

   Summary: A robust receiver design to exploit long-term evolution (LTE) terrestrial cellular signals of opportunity (SOPs) for high altitude aircraft navigation is presented. Conventional receivers employ phase-locked loops (PLLs) to track the carrier phase of received signals. In this paper, a Kalman filter (KF) is developed to replace the receiver's PLLs. To evaluate the performance of the proposed receiver, a flight campaign was conducted over two regions in California, USA: (i) Region A: Edwards Air Force Base (rural) and (ii) Region B: Palmdale (semi-urban). It is shown that the proposed receiver provides robust tracking of received LTE signals compared to a conventional PLL-based receiver, in which the latter could only track intermittently, especially during sharp turns. The produced carrier phase observables to 5 LTE eNodeBs in each region were fused with altimeter data via an extended Kalman filter (EKF) to estimate the aircraft's trajectory. Over trajectories of 51 km and 57 km in regions A and B, traversed in 9 min and 11 min, at flying altitudes of 5,000 and 7,000 ft above ground level, respectively, the proposed KF-based receiver reduced the position root-mean squared error (RMSE) by 74.8% and 30.7%, respectively, over the PLL-based receiver.

V. Exploiting LEO SOPs for PNT

1. The first carrier phase tracking and positioning results with Starlink LEO satellite signals

   J. Khalife, M. Neinavaie, and Z. Kassas

   IEEE Transactions on Aerospace and Electronic Systems, 2022, Vol. 58, no. 2, pp. 1487-1491

   Summary: This letter shows the first carrier phase tracking and positioning results with Starlink's low earth orbit (LEO) satellite signals. An adaptive Kalman filter based algorithm for tracking the beat carrier phase from the unknown Starlink signals is proposed.

Experimental results show carrier phase tracking of six Starlink satellites and a horizontal positioning error of 7.7 m with known receiver altitude.

2. Acquisition, Doppler tracking, and positioning with Starlink LEO satellites: first results
   M. Neinavaie, J. Khalife, and Z. Kassas
   IEEE Transactions on Aerospace and Electronic Systems, 2022, Vol. 58, no. 3, pp. 2606-2610
   Summary: This letter shows the first acquisition, Doppler tracking, and positioning results with Starlink's low Earth orbit satellite signals. A generalized-likelihood-ratio-based test is proposed to acquire Starlink's downlink signals. A Kalman-filter-based algorithm for tracking the Doppler frequency from the unknown Starlink signals is developed. Experimental results show Doppler tracking of six Starlink satellites, achieving a horizontal positioning error of 10 m.
3. Observability analysis of receiver localization via pseudorange measurements from a single LEO satellite
   R. Sabbagh and Z. Kassas
   IEEE Control Systems Letters, 2023, Vol. 7, pp. 571-576
   Summary: This letter presents an observability analysis for terrestrial receiver localization via pseudorange measurements extracted from a single low Earth orbit (LEO) satellite. It is shown that a stationary receiver with an unknown state (position and time) can theoretically localize itself with a LEO satellite with a known state (position, velocity, and time). In addition, bounds on the determinant of the l-step observability matrix are derived and geometric interpretations are presented indicating directions of poor observability. The implications of the analysis on observability-aided LEO satellite selection are discussed. Experimental results are presented showcasing the conclusions of the observability analysis for a receiver localizing itself with a single Starlink satellite or a single Orbcomm satellite.
4. Performance-driven design of carrier phase differential navigation frameworks with megaconstellation LEO satellites
   J. Khalife and Z. Kassas
   IEEE Transactions on Aerospace and Electronic Systems, 2023, Vol. 59, no. 3, pp. 2947–2966
   Summary: A navigation framework with carrier phase differential measurements from megaconstellation low Earth orbit (LEO) satellite signals is developed. The measurement errors due to ephemeris errors and ionospheric and tropospheric delays are derived and the statistics of the dilution of precision is characterized. Moreover, the joint probability density function of the megaconstellation LEO satellites' azimuth and elevation angles is derived to 1) enable performance characterization of navigation frameworks with LEO satellites in a computationally efficient way and 2) facilitate parameter design, namely, the differential baseline, to meet desired performance requirements. The Starlink constellation is used as a specific LEO megaconstellation example to demonstrate the developed carrier phase differential LEO (CD-LEO) navigation framework. Simulation results are presented demonstrating the efficacy of the proposed CD-LEO framework for an unmanned aerial vehicle (UAV) navigating for 15.1 km in 300 s, while using signals from

44 Starlink satellites, achieving a 3-D position root mean squared error (RMSE) of 2.2 m and a 2-D RMSE of 32.4 cm. Experimental results are presented showing UAV navigating for 2.28 km in 2 min over Aliso Viejo, CA, USA, using exclusively signals from only two Orbcomm LEO satellites, achieving an unprecedented position RMSE of 14.8 m.

5. Unveiling Starlink LEO satellite OFDM-like signal structure enabling precise positioning

   M. Neinavaie and Z. Kassas

   IEEE Transactions on Aerospace and Electronic Systems, 2023, accepted

   Summary: This letter unveils the unknown structure of Starlink low Earth orbit (LEO) satellites' orthogonal frequency division multiplexing (OFDM)-like reference signals (RSs). The spectrum of Starlink's dowlink signals is presented, and the frame length is estimated. A blind receiver is proposed, which acquires via a sequential generalized likelihood ratio test multiple satellites, estimates their RSs and respective Doppler, and tracks their carrier and code phases. Experimental results are presented showing six tracked Starlink LEO satellites, three of which transmitted pure tones, while the other transmitted OFDM-like signals. The achieved horizontal positioning error with the six satellites was 6.5 m.

6. Ephemeris tracking and error propagation analysis of LEO satellites with application to opportunistic navigation

   N. Khairallah and Z. Kassas

   IEEE Transactions on Aerospace and Electronic Systems, 2023, accepted

   Summary: A comprehensive study is performed for low Earth orbit (LEO) space vehicles (SVs) tracking by a receiver opportunistically extracting navigation observables from their downlink radio frequency signals. First, a framework to characterize the LEO SVs' orbital motion process noise covariance is developed. Second, the tracking performance via an extended Kalman filter (EKF) is analyzed via comprehensive Monte Carlo simulations for three different sets of observables: (i) pseudorange, (ii) Doppler, and (iii) fused pseudorange and Doppler measurements. Third, experimental results are presented demonstrating the efficacy of the opportunistic tracking framework in refining the ephemeris of a LEO SV from two-line element (TLE) files. The initial position and velocity errors of over 7.1 km and 7.3 m/s, respectively, of an Orbcomm LEO SV were reduced to 698.7 m and 1.8 m/s, respectively, in just over 6 minutes of tracking with carrier phase navigation observables, extracted opportunistically. Fourth, the error propagation from the LEO SV's state space to the measurement space and from the measurement space to the receiver's state space is analyzed in the context of stationary receiver localization. Bounds on the magnitude of pseudorange and Doppler residuals are first derived, and the magnitude of the receiver's estimation error is then characterized as a function of errors in the LEO SV's state space. Fifth, experimental results are presented of a stationary receiver tracking an Orbcomm LEO SV by fusing carrier phase observables via an EKF. The tracked LEO ephemeris is then used to localize another stationary receiver, showing a reduction in the receiver's initial horizontal error from 13,476 m to 343 m after just over 6 minutes. In contrast, it is shown that if the SGP4-propagated ephemeris was used in the EKF to localize the receiver, the error is reduced to 6,852 m, but the filter becomes inconsistent.

7. Opportunistic navigation with Doppler measurements from Iridium Next and Orbcomm LEO satellites
   M. Orabi, J. Khalife, and Z. Kassas
   IEEE Aerospace Conference, Mar. 6-13, 2021, Big Sky, MT, pp. 1-9
   Summary: A framework for opportunistic navigation with multiconstellation low Earth orbit (LEO) satellite signals is proposed. A receiver architecture suitable for processing both time division (TDMA) and frequency division multiple access (FMDA) signals from Orbcomm and Iridium NEXT satellites is presented to produce Doppler frequency measurements from multi-constellation LEO satellites. An extended Kalman filter (EKF)-based estimator is formulated to solve for a stationary receiver's position using the resulting Doppler measurements. Experimental results are presented showing receiver positioning with one Orbcomm satellite and four Iridium NEXT satellite with an unprecedented final position error 22.7 m.
8. Comparison of neural network architectures for simultaneous tracking and navigation with LEO satellites
   S. Kozhaya, J. Haidar-Ahmad, A. Abdallah, Z. Kassas, and S. Saab
   ION Global Navigation Satellite Systems Conference, Sep. 20-24, 2021, St. Louis, MO, pp. 2507–2520
   Summary: Machine learning (ML) frameworks are investigated for use in simultaneous tracking and navigation (STAN) with low Earth orbit (LEO) satellites. STAN is a navigation paradigm that utilizes specialized LEO receivers to extract navigation observables (e.g., pseudorange and Doppler) from LEO satellite signals. Two neural network architectures are compared: Feed Forward Neural Network (FFNN) and Recurrent Neural Network (RNN). Additionally, two ML-based orbit determination frameworks are compared: ephemeris propagation and residual error propagation. The objective of the comparison is to select an approach with the lowest open-loop propagation error as well as computational cost. Based on simulation results, a nonlinear autoregressive neural network with exogenous inputs (NARX) embedded within the residual error modeling framework is selected as the best ML approach among the compared candidates. Experimental results are presented demonstrating a ground vehicle navigating for a total of 258 seconds, while receiving signals from two Orbcomm LEO satellites. Global navigation satellite system (GNSS) signals were artificially cut off for the last 30 seconds, during which the vehicle traversed a trajectory of 871 m. Two navigation frameworks are compared to estimate the vehicle's trajectory: (i) LEO signal-aided inertial navigation system (INS) STAN framework using Simplified General Perturbation (SGP4) as its propagator and (ii) the proposed LEO signalaided INS STAN framework using ML as its propagator. The STAN with SGP4 achieved a three-dimensional (3-D) position root-mean squared error (RMSE) of 30 m. In contrast, the proposed STAN with SGP4+NARX framework achieved a 3-D position RMSE of 3.6 m.
9. Exploiting Starlink signals for navigation: first results
   M. Neinavaie, J. Khalife, and Z. Kassas
   ION Global Navigation Satellite Systems Conference, Sep. 20-24, 2021, St. Louis, MO, pp. 2766-2773

Summary: This paper demonstrates the first Doppler positioning-based results with Starlink low Earth orbit (LEO) satellites. A cognitive opportunistic framework is used to detect Starlink's LEO satellite signals and track the Doppler frequencies of each Starlink LEO satellite. To this end, a generalized likelihood ratio (GLR)-based test is developed to detect the LEO satellite signals and estimate their corresponding beacons. A chirp parameter estimator is also proposed to track the Doppler frequencies from the unknown Starlink signals. Experimental results are presented showing a horizontal positioning error of 10 m by tracking the Doppler of six Starlink LEO satellites.

10. An interacting multiple model estimator of LEO satellite clocks for improved positioning

    N. Khairallah and Z. Kassas

    IEEE Vehicular Technology Conference, Jun. 19-22, 2022, Helsinki, Finland, pp. 1-5

    Summary: An interacting multiple-model (IMM) estimator is developed to adaptively estimate the process noise covariance of low Earth orbit (LEO) satellite clocks for improved positioning. Experimental results are presented showing a stationary ground receiver localizing itself with carrier phase measurements from a single Orbcomm LEO satellite. The developed IMM is shown to reduce the localization error and improve filter consistency over two fixed mismatched extended Kalman filters (EKFs). Starting with an initial receiver position error of 1.45 km, the IMM yielded a final error of 111.26 m, while the errors of a conservative and optimistic EKFs converged to 254.71 m and 429.35 m, respectively.

11. A hybrid analytical-machine learning approach for LEO satellite orbit prediction

    J. Haidar-Ahmad, N. Khairallah, and Z. Kassas

    International Conference on Information Fusion, Jul. 4-7, 2022, Linköping, Sweden, pp. 1-7 (special session)

    Summary: A hybrid analytical-machine learning (ML) framework for improved low Earth orbit (LEO) satellite orbit prediction is developed. The framework assumes the following three stages. (i) LEO satellite first pass: A terrestrial receiver with knowledge of its position produces carrier phase measurements from received LEO satellite signals, enabling it to estimate the time of arrival. The LEO satellite's states are initialized with simplified general perturbations 4 (SGP4)-propagated two-line element (TLE) data, and are subsequently estimated via an extended Kalman filter (EKF) during the period of satellite visibility. (ii) LEO satellite not in view: a nonlinear autoregressive with exogenous inputs (NARX) neural network is trained on the estimated ephemeris and is used to propagate the LEO satellite orbit for the period where the satellite is not in view. (iii) LEO satellite second pass: a terrestrial receiver with no knowledge of its position uses the ML-predicted LEO ephemeris along with its carrier phase measurements from received LEO signals to estimate its own position via an EKF. Experimental results with with signals from an Orbcomm satellite are presented to demonstrate the efficacy of the proposed framework. It is shown that during the satellite's second pass, the ML-predicted ephemeris error is reduced by nearly 90% from that of an SGP4 propagation. In addition, it is shown that if the receiver was to use the SGP4-predicted satellite ephemeris to localize itself, the EKF's initial position error of 2.2 km increases to 6.7 km, while the proposed framework reduces

the position error to 448 m. Keywords—LEO satellites, machine learning, orbit determination, satellite tracking, signals of opportunity.

12. Blind receiver for LEO beacon estimation with application to UAV carrier phase differential navigation
    S. Kozhaya and Z. Kassas
    ION Global Navigation Satellite Systems Conference, Sep. 19-23, 2022, Denver, CO, pp. 2385-2397
    Summary: A receiver for blind beacon estimation of low Earth orbit (LEO) satellite signals with application to UAV navigation is presented. The receiver operates in three stages: (i) blind Doppler tracking that uses correlation in the frequency-domain as a frequency discriminator and tracks the Doppler using a frequency-locked loop (FLL), (ii) beacon estimation from the coherent accumulation of the received signal after wiping off the Doppler tracked by the FLL, and (iii) tracking LEO signals using the estimated beacon in the previous step to produce navigation observables. Experimental results are presented showing: (i) successful blind estimation of the navigation beacon of the Orbcomm LEO constellation and (ii) a UAV navigating using the estimated beacons of two Orbcomm LEO satellites via a carrier phase differential navigation framework, achieving a three-dimensional position root mean-squared error (RMSE) of 13.9 m with only Orbcomm signals fused with an altimeter, over a trajectory of 2.28 km traversed in 2 minutes.
13. Observability analysis of opportunistic receiver localization with LEO satellite pseudorange measurements
    R. Sabbagh and Z. Kassas
    ION Global Navigation Satellite Systems Conference, Sep. 19-23, 2022, Denver, CO, pp. 1890-1901
    Summary: An observability analysis of terrestrial receiver localization via pseudorange measurements extracted from a single low Earth orbit (LEO) satellite is presented. It is concluded that a stationary receiver with an unknown state (position and time) can localize itself with measurements from a LEO satellite with a known state (position, velocity, and time). In addition, bounds on the determinant of the observability matrix are derived. The relationship between the satellite's relative orbital inclination angle and geometric diversity of the line-of-sight vectors from the receiver to the satellite is analyzed, leading to geometric interpretations indicating directions of poor observability. Experimental results are presented showcasing the conclusions of the observability analysis for a receiver localizing itself with a single Starlink LEO satellite or a single Orbcomm LEO satellite. Finally, an observability-aided LEO satellite selection strategy is discussed.
14. Navigation with multi-constellation LEO satellite signals of opportunity: Starlink, OneWeb, Orbcomm, and Iridium
    Z. Kassas, S. Kozhaya, H. Kanj, J. Saroufim, S. Hayek, M. Neinavaie, N. Khairallah, and J. Khalife
    IEEE/ION Position, Location, and Navigation Symposium, Apr. 25-27, 2023, Monterey, pp. 338-343
    Summary: This paper summarizes current state-of-the-art navigation results with multi-constellation low Earth orbit (LEO) satellite signals of opportunity. Experimental results

with four LEO satellite constellations are presented: Starlink, OneWeb, Orbcomm, and Iridium. Two receiver designs are presented: (R1) a cognitive opportunistic navigation approach, which utilizes minimal, publicly available prior knowledge about the LEO satellite signal structure and (R2) a blind approach, which assumes no prior knowledge of the signals. Stationary positioning and mobile ground vehicle navigation results are presented. For the ground vehicle, results with two frameworks are presented: (N1) a LEOaided inertial navigation system (INS) simultaneous tracking and navigation (STAN) and (N2) a LEO-aided differential STAN. The results reveal the tremendous promise of exploiting multiconstellation LEO satellite signals of opportunity for navigation. For positioning: (i) with R1, starting with an initial estimate about 179 km away, by exploiting signals from 6 Starlink, 1 Orbcomm, and 4 Iridium, a final two-dimensional (2–D) position error of 6.5 m was achieved and (ii) with R2, starting with an initial estimate about 3,600 km away, by exploiting signals from 4 Starlink, 2 OneWeb, 1 Orbcomm, and 1 Iridium, a final 2–D position error of 5.1 m was achieved. For navigation, a ground vehicle was equipped with an industrial-grade inertial measurement unit (IMU) and an altimeter. (i) With R1 and N1, the vehicle traversed 4.15 km in 150 seconds (GNSS signals were only available for the first 2.33 km). By exploiting signals from 3 Starlink, 2 Orbcomm, and 1 Iridium, the 3–D position root mean squared error (RMSE) and final 3-D error were 18.4 m and 27.1 m, respectively. The GNSS-aided INS position RMSE and final 3-D error were 118.5 m and 472.7 m, respectively. (ii) With R2 and N2, the vehicle traversed 1.03 km in 110 seconds (GNSS signals were only available for the first 0.11 km). By exploiting signals from 4 Starlink, 1 OneWeb, 2 Orbcomm, and 1 Iridium, the 3–D position RMSE and final 3-D error were 9.5 m and 4.4 m, respectively. The GNSS-aided INS position RMSE and final 3-D error were 205 m and 525 m, respectively.

15. Signal mode transition detection in Starlink LEO satellite downlink signals
    M. Neinavaie and Z. Kassas
    IEEE/ION Position, Location, and Navigation Symposium, Apr. 25-27, 2023, Monterey, pp. 360-364
    Summary: A receiver architecture for detection and tracking of Starlink orthogonal frequency division multiplexing (OFDM)- based signals is proposed. The proposed receiver enables exploiting all the transmitted periodic beacons of Starlink low Earth orbit (LEO) signals to draw carrier phase, code phase, and Doppler observables. The reference signals (RSs) of modern OFDM-based systems contain both always-on and on-demand components. These components can be unknown and subject to dynamic transmission modes. Thanks to a matched subspacebased detection algorithm, the proposed receiver is shown to be capable of cognitive detection of both always-on and ondemand components in the Starlink OFDM-based RSs. It is shown that despite the dynamic nature of Starlink RSs, the proposed matched subspace detector senses the transition between the transmission modes of Starlink RSs, and detects all the accessible RSs with a predetermined probability of false alarm. Experimental results are provided to validate the performance of the proposed receiver in transmission mode detection in Starlink downlink signals.
16. Multi-constellation blind beacon estimation, Doppler tracking, and opportunistic positioning with OneWeb, Starlink, Iridium NEXT, and Orbcomm LEO satellites

S. Kozhaya, H. Kanj, and Z. Kassas
IEEE/ION Position, Location, and Navigation Symposium, Apr. 25-27, 2023, Monterey, pp. 1184-1195

Summary: A novel blind spectral approach is proposed for blind beacon estimation, Doppler tracking, and opportunistic positioning with unknown low Earth orbit (LEO) satellite signals. The framework is agnostic to the modulation and multiple access scheme adopted by LEO satellites. First, an analytical derivation of the received signal frequency spectrum is presented, which accounts for the highly dynamic channel between the LEO satellite and a terrestrial receiver. Second, a frequency domain-based blind Doppler discriminator is proposed. Third, a Kalman filter (KF)-based Doppler tracking algorithm is developed. Fourth, a blind beacon estimation framework for LEO satellites is proposed and its convergence properties are studied. Simulation results are presented showing successful beacon estimation and Doppler tracking of Starlink LEO satellites transmitting 5G orthogonal division multiple access (OFDM) signals. Experimental results are presented demonstrating the efficacy of the proposed framework on multi-constellation LEO satellites, namely OneWeb, Starlink, Orbcomm, and Iridium NEXT. Despite adopting different modulation and multiple access transmission schemes, the proposed framework is capable of successfully estimating the beacon and tracking the Doppler, in a blind fashion, of 8 LEO satellites (2 OneWeb, 4 Starlink, 1 Iridium NEXT, and 1 Orbcomm) over a period of about 560 seconds with Hz-level accuracy. The produced Doppler measurements were fused through a nonlinear least-squares estimator to localize a stationary receiver to an unprecedented level of accuracy. Starting with an initial estimate about 3,600 km away, a final three-dimensional (3–D) position error of 5.8 m and 2–D position error of 5.1 m was achieved. Aside from achieving this unprecedented accuracy, these results represent the first successful opportunistic tracking of unknown OneWeb LEO signals and their exploitation for positioning.

17. Positioning with Starlink LEO satellites: A blind Doppler spectral approach
S. Kozhaya and Z. Kassas
IEEE Vehicular Technology Conference, Jun. 20-23, 2023, Florence, Italy, pp. 1-5

Summary: A blind Doppler spectral approach is proposed for exploiting unknown Starlink low Earth orbit (LEO) satellite signals for positioning. First, an analytical derivation of the received signal frequency spectrum is presented, which accounts for the highly dynamic channel between the LEO satellite and a ground-based receiver. Second, a frequency domain-based blind Doppler discriminator is proposed. Third, a Kalman filter (KF)- based Doppler tracking algorithm is developed. Finally, experimental results are presented of a stationary receiver tracking the Doppler, in a blind fashion, of six Starlink LEO satellites over a period of about 800 seconds with Hz-level accuracy. The Doppler measurements were fused through a nonlinear leastsquares estimator to localize the receiver to an unprecedented level of accuracy. Starting with an initial estimate 200 km away, the proposed approach achieved a final horizontal twodimensional (2D) position error of 4.3 m.

18. Joint Doppler and azimuth DOA tracking for positioning with Iridium LEO satellites
S. Shahcheraghi, F. Gourabi, M. Neinavaie, and Z. Kassas

ION Global Navigation Satellite Systems Conference, Sep. 11-15, 2023, Denver, CO, pp. 2373-2383

Summary: A receiver capable of estimating the Doppler and azimuth direction-of-arrival (DOA) of Iridium NEXT low Earth orbit (LEO) signals of opportunity (SOPs) is presented. The proposed receiver operates in three stages: (i) Fast Fourier Transform (FFT)- based Doppler acquisition, (ii) Kalman filter (KF)-based Doppler tracking, and (iii) Doppler-compensated MUltiple SIgnal Classification (MUSIC)-based algorithm for DOA tracking. Experimental results are presented demonstrating successful tracking of the Doppler frequency and azimuth DOA of an Iridium NEXT LEO satellite, achieving a Doppler root mean square error (RMSE) of 8.1 Hz over 120 seconds and an azimuth DOA RMSE of 1.04 degrees over 60 seconds. The Doppler and azimuth DOA measurements are fused via an extended Kalman filter (EKF) to localize a stationary receiver. Starting with an initial estimate 7 km away from the true receiver's position, the Doppler-only measurements yielded a final positioning error of 656.m, while the Doppler and azimuth DOA measurements reduced the error to 289.5 m.

19. Acquisition and tracking of Starlink LEO satellite signals in low SNR regime
    H. Kanj, S. Kozhaya, and Z. Kassas
    ION Global Navigation Satellite Systems Conference, Sep. 11-15, 2023, Denver, CO, pp. 3420-3431

    Summary: Acquisition and tracking of Starlink low Earth orbit (LEO) satellite signals in low signal-to-noise ratio (SNR) regime is considered. Starlink's highly dynamic downlink LEO signal model is derived, leading to coherence conditions for which the signals can be blindly tracked in low SNR regime. Next, the full-bandwidth Starlink beacon is estimated, and a time-bandwidth analysis of this beacon is presented. Finally, joint code and carrier phase Kalman filter-based loop is proposed for tracking Stralink LEO downlink signals in low SNR regime. Experimental results are presented showing successful Doppler tracking of 10 Starlink LEO satellites with a stationary receiver in low SNR regime. The Doppler observables were fused in a batch nonlinear least-squares estimator to yield a two-dimensional (2D) positioning error of 21.2 m, starting from an initial estimate 100 km away from the receiver's true position.

20. Evaluation of orbit errors and measurement corrections in differential navigation with LEO satellites
    J. Saroufim, S. Hayek, and Z. Kassas
    ION Global Navigation Satellite Systems Conference, Sep. 11-15, 2023, Denver, CO, pp. 2823-2834

    Summary: Ephemeris errors and measurement corrections in differential navigation with low Earth orbit (LEO) space vehicles (SVs) are analyzed. First, orbit errors are characterized for the non-differential case, showing the dependency of the range measurement errors on the receiver-to-SV geometry. The study is then extended to the differential case, where the maximum differential range error is found to occur when the baseline is normal to the projected measurement vector from one receiver onto the local navigation frame. A simulation study is presented to assess the differential navigation performance with 14 Starlink and 11 OneWeb LEO satellites. The framework fused differenced pseudorange measurements from a base and rover to LEO SVs with inertial measurement unit (IMU)

measurements via an extended Kalman filter (EKF) in a tightly-coupled fashion to estimate the rover's states. The simulation considered an aerial vehicle equipped with a tactical-grade IMU, an altimeter, a GNSS receiver, and a LEO receiver making pseudorange measurements to the LEO SVs. During 300 seconds of flight time, the vehicle traveled a distance of 28 km, the last 23 km of which were without GNSS, achieving a three-dimensional (3-D) position root mean squared error (RMSE) of 52 cm, compared to 12.5 m using the non-differential framework. Experimental results are presented, showing the potential of differential navigation in reducing ephemeris, clocks, and atmospheric errors. A ground vehicle traversed a distance of 540 m in 60 seconds, the last 492 m of which without GNSS signals, while making Doppler measurements to 2 Orbcomm and 1 Iridium LEO SVs, whose ephemerides were obtained from two-line element (TLE) files, propagated with simplified general perturbation 4 (SGP4) orbit propagator. The differential framework yielded a position RMSE of 7.13 m, compared to 41.29 m using non-differential measurements, and 87.74 m with GNSS-aided IMU.

21. Blind Doppler tracking and positioning with NOAA LEO satellite signals
S. Kozhaya, H. Kanj, and Z. Kassas
ION Global Navigation Satellite Systems Conference, Sep. 11-15, 2023, Denver, CO, pp. 363-372
Summary: A spectral approach for blind acquisition and Doppler tracking of low Earth orbit (LEO) satellite signals is applied to National Oceanic and Atmospheric Administration (NOAA) satellites. The approach accounts for the high LEO satellites' dynamic channel, by deriving an appropriate model for the received signal frequency spectrum. A frequency-domain-based Doppler discriminator is utilized along with a Kalman filter-based Doppler tracking algorithm. Experimental results are presented showing successful acquisition and Doppler tracking of NOAA LEO satellite signals. Next, the approach is demonstrated in multi-constellation LEO acquisition and tracking, showing Hz-level Doppler tracking of 4 Starlink, 2 OneWeb, 1 Iridium NEXT, 1 Orbcomm, and 1 NOAA LEO satellites. Carrier phase observables were constructed from the tracked Doppler and fused through a nonlinear least-squares estimator to localize a stationary receiver. Starting with an initial estimate 3,600 km away from the receiver's true position, the proposed approach is shown to achieve a two-dimensional (2D) error of 5.1 m.

22. Enter LEO on the GNSS stage: navigation with Starlink satellites
Z. Kassas, M. Neinavaie, J. Khalife, N. Khairallah, S. Kozhaya, J. Haidar-Ahmad, and Z. Shadram
Inside GNSS Magazine, Vol. 16, Issue 6, Dec. 2021, pp. 42-51 (cover article)
Summary: We are witnessing a space renaissance. Tens of thousands of broadband low Earth orbit (LEO) satellites are expected to be launched by the end of this decade. These planned megaconstellations of LEO satellites along with existing constellations will shower the Earth with a plethora of signals of opportunity, diverse in frequency and direction. These signals could be exploited for navigation in the inevitable event that GNSS signals become unavailable (e.g., in deep urban canyons, under dense foliage, during unintentional interference, and intentional jamming) or untrustworthy (e.g., under malicious spoofi ng attacks). This article shows the first multi-constellation navigation results with Starlink, Orbcomm, and Iridium LEO satellites.

23. A look at the stars: navigation with multi-constellation LEO satellite signals of opportunity
    Z. Kassas, S. Kozhaya, J. Saroufim, H. Kanj, and S. Hayek
    Inside GNSS Magazine, Vol. 18, Issue 4, Aug. 2023, pp. 38–47 (cover article)
    Summary: Experimental and simulation results from Starlink, OneWeb, Orbcomm and Iridium LEO satellite constellations are presented, demonstrating the effi cacy and tremendous promise the proposed LEO-agnostic blind opportunistic navigation frameworks.

VI. GNSS and SOP SDR

1. GNSS software defined radio: History, current developments, and standardization efforts
   D. Akos, J. Arribas, M. Bhuiyan, P. Closas, F. Dovis, I. Fernandez-Hernandez, C. Fernández–Prades, S. Gunawardena, T. Humphreys, Z. Kassas, J. López Salcedo, M. Nicola, T. Pany, M. Psiaki, A. Rügamer, Y. Song, and J. Won
   NAVIGATION, Journal of the Institute of Navigation, 2023, accepted
   Summary: Taking the work conducted by the global navigation satellite system (GNSS) software-defined radio (SDR) working group during the last decade as a seed, this contribution summarizes for the first time the history of GNSS SDR development. It highlights selected SDR implementations and achievements that are available to the public or that influenced the general SDR development. The relation to the standardization process of intermediate frequency (IF) sample data and metadata is discussed, and an update of the Institute of Navigation (ION) SDR Standard is proposed. The work focuses on GNSS SDR implementations on general purpose processors and leaves aside developments conducted on field programmable gate array (FPGA) and application-specific integrated circuits (ASICs) platforms. Data collection systems (i.e., front-ends) have always been of paramount importance for GNSS SDRs, and are thus partly covered in this work. The work represents the knowledge of the authors but is not meant as a complete description of SDR history.
2. GNSS software defined radio: History, current developments, and standardization efforts
   D. Akos, J. Arribas, M. Bhuiyan, P. Closas, F. Dovis, I. Fernandez-Hernandez, C. Fernández–Prades, S. Gunawardena, T. Humphreys, Z. Kassas, J. López Salcedo, M. Nicola, T. Pany, M. Psiaki, A. Rügamer, Y. Song, and J. Won
   ION Global Navigation Satellite Systems Conference, Sep. 19-23, 2022, Denver, CO, pp. 3180-3209
   Summary: Taking the work conducted by the Global Navigation Satellite System (GNSS) Software Defined Radio (SDR) working group during the last decade as a seed, this contribution summarizes for the first time the history of GNSS SDR development. It highlights selected SDR implementations and achievements that are available to the public or influenced the general SDR development. The relation to the standardization process of Intermediate Frequency (IF) sample data and metadata is discussed, and a

recent update of the Institute of Navigation (ION) SDR standard is recapitulated. The work focuses on GNSS SDR implementations on general purpose processors and leaves aside developments conducted on Field Programmable Gate Array (FPGA) and Application-Specific Integrated Circuits (ASICs) platforms. Data collection systems (i.e., front-ends) have always been of paramount importance for GNSS SDRs and are thus partly covered in this work. The work represents the knowledge of the authors but is not meant as a complete description of SDR history. Part of the authors plan to coordinate a more extensive work on this topic in the near future.

Acquisition and Tracking of Starlink LEO Satellite Signals in Low SNR Regime

Haitham Kanj, Sharbel Kozhaya, and Zaher M. Kassas
The Ohio State University

BIOGRAPHY

Haitham Kanj is a Ph.D student in the Department of Electrical and Computer Engineering at The Ohio State University and a member of the Autonomous Systems Perception, Intelligence, and Navigation (ASPIN) Laboratory. He received a B.E. in Electrical Engineering from the Lebanese American University. His current research interests include opportunistic navigation, low Earth orbit (LEO) satellites, and cognitive software-defined radio. He is the recipient of the 2023 IEEE/ION Position, Location, and Navigation Symposium (PLANS) best student paper award.

Sharbel Kozhaya is a Ph.D student in the Department of Electrical and Computer Engineering at The Ohio State University and a member of the Autonomous Systems Perception, Intelligence, and Navigation (ASPIN) Laboratory. He received a B.E. in Electrical Engineering from the Lebanese American University. His current research interests include opportunistic navigation, low Earth orbit (LEO) satellites, cognitive software-defined radio, and 5G. He is the recipient of the 2023 IEEE/ION Position, Location, and Navigation Symposium (PLANS) best student paper award.

Zaher (Zak) M. Kassas is a professor at The Ohio State University and TRC Endowed Chair in Intelligent Transportation Systems. He is the Director of the Autonomous Systems Perception, Intelligence, and Navigation (ASPIN) Laboratory. He is also director of the U.S. Department of Transportation Center: CARMEN (Center for Automated Vehicle Research with Multimodal AssurEd Navigation), focusing on navigation resiliency and security of highly automated transportation systems. He received a B.E. in Electrical Engineering from the Lebanese American University, an M.S. in Electrical and Computer Engineering from The Ohio State University, and an M.S.E. in Aerospace Engineering and a Ph.D. in Electrical and Computer Engineering from The University of Texas at Austin. He is a recipient of the National Science Foundation (NSF) CAREER award, Office of Naval Research (ONR) Young Investigator Program (YIP) award, Air Force Office of Scientific Research (AFOSR) YIP award, IEEE Walter Fried Award, Institute of Navigation (ION) Samuel Burka Award, and ION Col. Thomas Thurlow Award. He is an Associate Editor of the IEEE Transactions on Aerospace and Electronic Systems and the IEEE Transactions on Intelligent Transportation Systems. He is a Fellow of the ION and a Distinguished Lecturer of the IEEE Aerospace and Electronic Systems Society. His research interests include cyber-physical systems, navigation systems, and intelligent transportation systems.

ABSTRACT

Acquisition and tracking of Starlink low Earth orbit (LEO) satellite signals in low signal-to-noise ratio (SNR) regime is considered. Starlink's highly dynamic downlink LEO signal model is derived, leading to coherence conditions for which the signals can be blindly tracked in low SNR regime. Next, the full-bandwidth Starlink beacon is estimated, and a time-bandwidth analysis of this beacon is presented. Finally, joint code and carrier phase Kalman filter-based loop is proposed for tracking Stralink LEO downlink signals in low SNR regime. Experimental results are presented showing successful Doppler tracking of 10 Starlink LEO satellites with a stationary receiver in low SNR regime. The Doppler observables were fused in a batch nonlinear least-squares estimator to yield a two-dimensional (2D) positioning error of 21.2 m, starting from an initial estimate 100 km away from the receiver's true position.

I. INTRODUCTION

Due to the known limitations of global navigation satellite systems (GNSS), there is an ever increasing interest in alternative positioning, navigation, and timing (PNT) systems. Literature over the past decade explored the use of ambient terrestrial radio frequency signals of opportunity (SOPs) for PNT (Raquet *et al.*, 2021; Souli et al., 2022; Fokin and Volgushev, 2022). Examples of terrestrial SOPs exploited for PNT include: (i) AM/FM radio (Chen et al. (2020)), (ii) cellular (e.g., 3G (Khalife et al. (2016)), 4G (Tian et al. (2023)), and 5G (del Peral-Rosado et al. (2022)), and (iii) digital television (Jiao et al., 2023).

The birth of low Earth orbit (LEO) satellite megaconstellations has resulted in tremendous interest in exploring the use of their signals for PNT (Kassas et al., 2019; Jardak and Jault, 2022; Prol et al., 2022; Janssen et al., 2023; Menzione and Paonni, 2023; Prol et al., 2023). Numerous studies have been published over the past few years addressing various challenges in opportunistic PNT with LEO, from addressing space vehicle (SV) orbit, clock, and propagation errors (Mortlock and Kassas, 2021; Morton et al., 2022; Cassel et al., 2022; Wang et al., 2023; Zhao et al., 2023; Wu et al., 2023; Jiang et al., 2023; Ye et al., 2023; Saroufim

et al., 2023); receiver and signal design (Tan et al., 2019; Wei et al., 2020; Bilardi, 2021; Kassas et al., 2021; Egea-Roca et al., 2022; Huang et al., 2022; Pinell et al., 2023; Yang et al., 2023); and analyzing the estimation performance (Farhangian et al., 2021; Hartnett, 2022; Singh et al., 2022; Jiang et al., 2022; More et al., 2022; Shi et al., 2023; Guo et al., 2023; Kanamori et al., 2023; Sabbagh and Kassas, 2023).

Whenever the LEO downlink signal structure is sufficiently known, designing a receiver that could acquire and track such signals becomes a "classic" receiver design problem. Examples of LEO constellations with sufficient knowledge about their downlink signal include Orbcomm and Iridium. Nevertheless, new LEO megaconstellations, such as Starlink and OneWeb, do not disclose public information about their signals. This challenge can be addressed with blind signal processing techniques. Previous research was capable of estimating downlink sequences in direct sequence spread spectrum communication systems (Tsatsanis and Giannakis, 1997; Burel and Bouder, 2000; Choi and Moon, 2020; Li et al., 2023), for GPS/GNSS signals under non-cooperative conditions (Merwe et al., 2020; Rui et al., 2022), and for orthogonal frequency-division multiplexing (OFDM) signals (Bolcskei, 2001; Tanda, 2004; Liu et al., 2010). In the context of LEO, (Neinavaie et al., 2021; Kozhaya and Kassas, 2022) developed blind Doppler tracking approaches for Obrcomm LEO SVs; while (Khalife et al., 2022) was the first to successfully apply blind signal processing techniques on Starlink LEO signals, yielding carrier phase observables, from which a stationary receiver was localized with a two-dimensional (2D) error of 25.9 m with signals from six Starlink LEO SVs. Another blind approach, based on matched subspace detection, was developed in (Neinavaie et al., 2022; Neinavaie and Kassas, 2023b), yielding Doppler observables, from which a stationary receiver was localized with a 2D error of 10 m (with pure tones) and 6.5 m (with OFDM signals in addition to pure tones) from the same six Starlink LEO SVs. A blind spectral-based approach was developed in (Kozhaya and Kassas, 2023), yielding Doppler observables, from which a stationary receiver was localized with a 2D error of 4.3 m with the same six Starlink LEO SVs. In (Kozhaya et al., 2023; Kassas et al., 2023), it was demonstrated that this approach is rather general, referred to as LEO-agnostic, and is capable of acquiring and tracking LEO signals regardless of their modulation and multiple access schemes. In addition to Starlink LEO, the approach was successfully applied to OneWeb, Orbcomm, and Iridium LEO SVs, yielding Hz-level-accurate Doppler tracking, from which a stationary receiver was localized with a 2D error of 5.1 m with 2 OneWeb, 4 Starlink, 1 Iridium, and 1 Orbcomm LEO SVs. Starlink's OFDM signal structure was later disclosed in (Humphreys et al., 2023), while (Yang and Soloviev, 2023; Jardak and Adam, 2023) studied tracking of Starlink's pure tones with a low-noise block (LNB) and (Stock et al., 2023) analyzed the Starlink user uplink signals for PNT.

In general, the fact that LEO SVs are closer to Earth implies a higher received signal-to-noise ratio (SNR). However, new LEO constellations, such as Starlink, employ phased antenna arrays (Chi et al., 2023) to beamform their signals toward their *subscribing* users (Neinavaie and Kassas, 2022, 2023a). As such, the SNR is only high whenever an *opportunistic* receiver is in the vicinity of an active user terminal. This phenomenon was witnessed whenever the previously designed blind algorithms (Neinavaie and Kassas, 2023b; Kozhaya and Kassas, 2023), which successfully tracked Starlink LEO signals in Southern California, USA, in which active Starlink user terminals were nearby; failed to track Starlink signals in Columbus, Ohio, USA, which, at the time of performing the experiments, was not within Starlink's coverage. This paper addresses the challenge of tracking LEO SVs in low SNR regime, from which navigation observables can be generated. To the author's knowledge, this challenge has not been addressed yet in the literature.

This paper focuses makes the following contributions: (i) derives the conditions under which Starlink's downlink LEO signals can be blindly tracked in low SNR regime, (ii) presents a time-bandwidth analysis of the estimated downlink beacon, (iii) designs a joint code and carrier phase Kalman filter (KF)-based tracking loop capable of tracking LEO SVs in low SNR regime, and (iv) presents experimental results of 10 Starlink LEO SVs tracked in low SNR regime, from which a stationary receiver was localized with a 2D error of 21.2 m, starting from an initial estimate 100 km away from the receiver's true position.

The paper is organized as follows. Section II derives the signal model. Section III presents the Starlink blind beacon estimation framework. Section IV presents the proposed signal acquisition and tracking approach. Section V shows the experimental tracking and positioning results in low SNR regime. Section VI gives concluding remarks.

II. SIGNAL MODEL

This section derives the received signal model under assumptions associated with a highly dynamic channel between a LEO SV and a ground based opportunistic receiver. This paper assumes the existence of repetitive sequences in the downlink LEO SV signal. Almost all communication channels require a periodic sequence referred to as the beacon. Examples of such periodic sequences are: (i) pseudorandom noise codes used in spread spectrum code division multiple access (CDMA) systems like cellular 3G (3GPP2 (2011)), GPS (Navstar GPS (2015)), and Globalstar LEO Hendrickson (1997), and (ii) the primary synchronization block utilized in OFDM modulation in cellular 4G (3GPP (2010)) and cellular 5G (3GPP (2018)). Let $s(t)$ and $m(t)$ denote the beacon with period T_{sub} and the user data sent by a LEO SV, respectively. This paper assumes that these two signal components are uncorrelated. Define, $x(t) \triangleq s(t) + m(t)$ as the transmitted LEO signal which becomes $x_c(t) \triangleq x(t)\exp(j2\pi f_c t)$ after carrier modulation, where f_c is the carrier frequency. Define the variables $\delta_{LOS}(t)$ as the line-of-sight time-of-flight between the LEO SV and the opportunistic receiver, $\delta_{atm}(t)$ as the atmospheric delay the transmitted

signal experiences as a result of propagating through the ionosphere and troposphere, and $\delta_{clk}(t)$ as the clock mismatch between the LEO SV and the opportunistic receiver. Now, define $\tau(t) \triangleq \delta_{LOS}(t) + \delta_{atm}(t) + \delta_{clk}(t)$ as the apparent delay observed at the receiver. Therefore, the received signal before carrier wipe-off can be expressed as

$$\begin{aligned} r_c(t) &\triangleq x_c\left(t-\tau(t)\right) + n_c(t) \\ &= x(t-\tau(t)) \exp\left[\, j2\pi f_c \left[t-\tau\left(t\right)\right]\right] + n_c(t). \end{aligned} \tag{1}$$

$x(t)$ captures the channel noise, which is modeled as a complex Gaussian white random process with power spectral density of $\frac{N_0}{2}$. After carrier wipe-off and filtering, the received base-band signal is expressed as

$$\begin{aligned} r_b(t) &\triangleq r_c(t) \exp\left[\, -j2\pi(f_c - f_e)t\right] \\ &= x(t-\tau(t)) \exp\{j\left[\, \theta(t) + 2\pi f_e t\right]\} + n_b(t), \end{aligned}$$

where f_e is the frequency error of the LNB down-converter, $\theta(t) \triangleq -2\pi f_c \tau(t)$ and $n_b(t)$ is the base-band low-pass filtered version of $n_c(t)$. Note that because a commercial LNB utilizes a temperature-compensated crystal oscillator (TCXO) with expected error in the $\left[0, 30\right]$ kHz range and the clock is not disciplined to GNSS, f_e cannot be ignored. Define the support function $w_{T_{sub}}(t)$ as

$$w_{T_{sub}}(t) \triangleq \begin{cases} 1, & t \in [0, T_{sub}) \\ 0, & \text{otherwise.} \end{cases}$$

In this paper, $\theta_k(t) \triangleq \theta(t) w_{T_{sub}}(t - t_k)$ is approximated by its second order Taylor series expansion (TSE) at time instant $t_k = t_0 + kT_{sub}$, where t_0 is some initial time, and k is the sub-accumulation index, according to

$$\begin{aligned} \theta_k(t) &\approx \theta_0(t_k) + \dot{\theta}(t_k)(t-t_k) + \frac{1}{2}\ddot{\theta}(t_k)(t-t_k)^2 \\ &= \theta_0(t_k) + f_D(t_k)(t-t_k) + \frac{1}{2}\dot{f}_D(t_k)(t-t_k)^2, \end{aligned} \tag{2}$$

where $f_D(t)$ is the apparent Doppler shift, $\dot{f}_D(t)$ is the apparent Doppler rate, and $t \in [0, T_{sub})$. Equivalently, $\tau(t)$ can be expressed as

$$\tau_k(t) \approx \tau_0(t_k) + \dot{\tau}(t_k)(t-t_k) + \frac{1}{2}\ddot{\tau}(t_k)(t-t_k)^2. \tag{3}$$

Furthermore, the received signal $r_k^*(t)$ before carrier phase wipe-off using the carrier phase estimate denoted $\hat{\theta}_k(t)$ generated by the tracking loop discussed in Section IV at the k-th sub-accumulation can be expressed as

$$\begin{aligned} r_k^*(t) &\triangleq r_b(t) w_{T_{sub}}(t - t_k) \\ &= s_k(t) \exp\left\{j\left[\theta_k(t) + 2\pi f_e t\right]\right\} + n_k^*(t), \end{aligned} \tag{4}$$

where $s_k(t) \triangleq s(t - \tau_k(t)) w_{T_{sub}}(t)$ and the term $n_k^*(t) \triangleq \left[n_b(t-\tau_k(t)) + m(t-\tau_k(t))\right] w_{T_{sub}}(t)$ represents the lumped user data and channel noise. The received signal $r_k(t)$ after carrier wipe-off using the carrier phase estimate, denoted $\hat{\theta}_k(t)$, generated by the tracking loop discussed in Section IV, can be expressed as

$$\begin{aligned} r_k(t) &= r_k^*(t) \exp\{-j\left[\hat{\theta}_k(t) + 2\pi \hat{f}_e t\right]\} \\ &= s_k(t) \exp\left[\, j\tilde{\theta}_k(t)\right] + n_k(t), \end{aligned} \tag{5}$$

where $\tilde{\theta}_k(t) = \theta_k(t) - \hat{\theta}_k(t) + 2\pi(f_e - \hat{f}_e)t$ is the residual carrier phase and $\hat{f}_e$ is the Doppler ambiguity estimate of the LNB clock error generated in Section IV.

III. STARLINK DOWNLINK BEACON ESTIMATION

This section presents the beacon estimation framework used to estimate Starlink LEO SV's downlink beacon. Next it analyzes the time-frequency characteristics of this beacon.

1. Signal Capture Setup

This subsection presents the blind beacon estimation framework to estimate the repetitive sequence in Starlink's LEO downlink signals. For this purpose, a high-gain signal capture setup was used (see Figure 1). An LNB with 2.5 dB noise figure is mounted on a 30 dBi Ku-Band parabolic antenna to collect high SNR Starlink signals. The RF signal is then fed into a stationary National Instrument (NI) universal software radio peripheral (USRP) X-410 whose sampling frequency was set to 500 MHz. This allows for estimation of the full bandwidth beacon of Starlink which spans 240 MHz. The total experiment duration was 60 seconds.

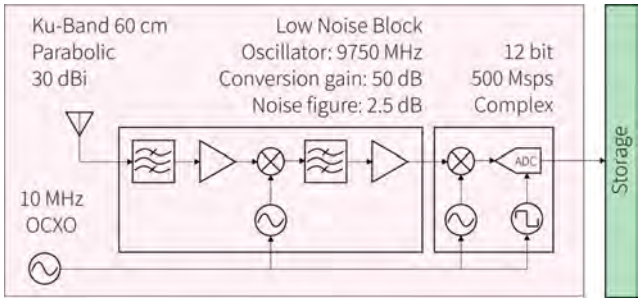

Figure 1: Block diagram of high-gain Starlink signal capture setup.

2. Blind Beacon Estimation

The continuous-time signal in (4) was sampled at a constant sampling interval $T_s = 1/F_s$. The discrete-time received signal before carrier wipe-off at the k-th sub-accumulation can be written as

$$r_k^*[n] = s[n - d_k[n]] \exp\left(j\Theta_k[n]\right) + n_k^*[n], \tag{6}$$

where $n \in [0, L-1]$; $s[n]$ is the discrete-time equivalent of $s(t)$ with period $L = T_{sub}/T_s$; $\Theta_k[n]$ and d_k are the discrete-time carrier phase and code phase, respectively, of the received signal at the k-th sub-accumulation; and $n_k^*[n]$ is the discrete-time equivalent of $n_k^*(t)$. Note that $\Theta_k[n]$ is made to include the effects of the frequency clock error f_e for ease of further analysis. Let M denote the number of sub-accumulations used per accumulation. In order to maintain carrier phase coherence in any correlation-based receiver over the accumulation interval, the following condition must be satisfied

$$2\tilde{f}_D M T_{sub} + \tilde{\dot{f}}_D (M T_{sub})^2 \ll \frac{1}{2}, \tag{7}$$

where $\tilde{f}_D$ and $\tilde{\dot{f}}_D$ are the errors associated with the estimates of the Doppler f_D and Doppler rate $\dot{f}_D$. Also, to maintain code phase coherence over the accumulation interval, the following condition must be satisfied

$$\tilde{\dot{\tau}} M T_{sub} + \tilde{\ddot{\tau}} (M T_{sub})^2 \ll \frac{1}{F_s}, \tag{8}$$

where $\tilde{\dot{\tau}}$ and $\tilde{\ddot{\tau}}$ are the errors associated with the estimates of the code phase rate $\dot{\tau}$ and code phase acceleration $\ddot{\tau}$. Knowing that the maximum realized Doppler rate for Starlink is $\dot{f}_D \approx 3$ kHz and that $\ddot{\tau} = \frac{-\dot{f}_D}{F_c}$, it can be seen that the maximum error $\tilde{\ddot{\tau}} \approx 0.27\,\mu\text{s/s}^2$. Therefore, for a reasonable choice of number of sub-accumulations M, $\ddot{\tau}$ can be ignored and (8) simplifies to $\tilde{\dot{\tau}} M T_{sub} F_s \ll 1$.

The first step in beacon estimation is verifying the existence of a repetitive sequence. Figure 2 shows the normalized auto-correlation profile of a 100 ms window of the collected signal. The repetitive peaks with spacing T_{sub} = 4/3 ms validates the existence of the repetitive sequence. Furthermore, in the beacon estimation stage, choosing M = 1 is sufficient given the high signal to noise ratio (SNR) of the collected signal. Let T denote the total number of accumulations used for beacon estimation, which was chosen to be 70 herein. Given these choice of T and M under the conditions (7) and (8), the blind beacon estimator should be able to resolve for the relative carrier phase shift, Doppler shift, and code phase shift between the different accumulations.

Let $\boldsymbol{r}_k$ denote the complex vector form of (6) such that

$$\boldsymbol{r}_k \triangleq \left[r_k^*[0], \ldots, r_k^*[L-1]\right], \quad \boldsymbol{y} \triangleq \left[\boldsymbol{r}_1^\mathsf{T}, \ldots, \boldsymbol{r}_T^\mathsf{T}\right],$$

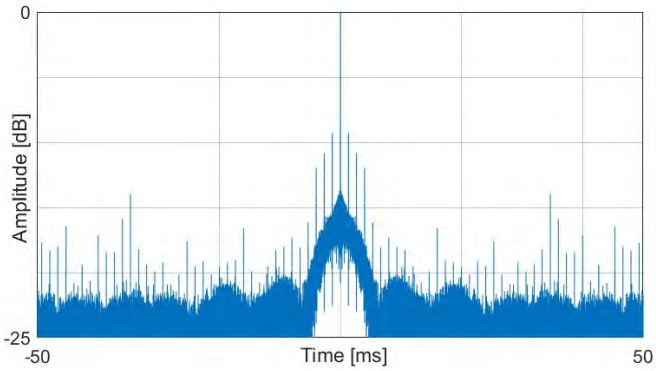

Figure 2: Normalized auto-correlation of a 100 ms window of Starlink's received signal.

Algorithm 1 Beacon Estimation Algorithm

Input $\mathbf{y},\ T_s,\ \gamma$
Output $\hat{\mathbf{s}}$

$\hat{\mathbf{s}} \leftarrow \mathbf{y}[0],\ w \leftarrow 0$
for $k = \{1, \ldots, T-1\}$ **do**
  $[\Delta\hat{d}_k, \Delta\hat{f}_D] = \text{argmax}_{d,\Delta f_D} \left| \left(\hat{\mathbf{s}} \star \boldsymbol{r}_k^{\mathsf{T}} \exp[j2\pi\Delta f_D n T_s]\right)[d] \right|^2$
  $R = \left(\hat{\mathbf{s}} \star \boldsymbol{r}_k^{\mathsf{T}} \exp[j2\pi\Delta\hat{f}_D n T_s]\right)[\Delta\hat{d}_k]$
  if $|R| > \gamma$ **then**
    $w \leftarrow w + 1$
    $\hat{\mathbf{s}} \leftarrow \frac{w}{w+1}\hat{\mathbf{s}} + \frac{1}{w+1}\text{circshift}\left(\boldsymbol{r}_k^{\mathsf{T}}, \Delta\hat{d}_k\right) \exp[j(2\pi\Delta f_D n T_s + \angle R)]$
  else
    continue
  end if
end for

where $\boldsymbol{y}$ is a matrix containing all T sub-accumulations of the received signal described in (6) that will be used for beacon estimation. Next, the beacon estimation algorithm is performed according to Algorithm 1. First, the initial accumulation is taken as a reference signal. Second, the reference signal is correlated with the next available accumulation in search for the best estimates of the relative code phase shift $\Delta\hat{d}_k$ and relative Doppler shift $\Delta\hat{f}_D$, which maximize the correlation between the beacon estimate $\hat{\boldsymbol{s}}$ and the current available accumulation. Note that this method works only under the assumption of high SNR data, i.e. the correlation between two consecutive accumulations is capable of producing a prominent peak. Let,

$$(\mathbf{s} \star \mathbf{r})[d] = \sum_{n=1}^{L} \mathbf{s}^*[n]\mathbf{r}\left[\text{mod}(n+d, L)\right],$$

denote the discrete-time circular cross-correlation of $\boldsymbol{s}$ and $\boldsymbol{r}$ where $\text{mod}(\cdot,\cdot)$ denotes the modulo operator. Next, if the magnitude of the correlation passes the predetermined threshold γ, the beacon estimate is updated using the estimates $\Delta\hat{d}_k$, $\Delta\hat{f}_D$, and the current accumulation. This process is repeated until the all the M accumulations are used, and then the beacon estimation process is complete. Note that because the algorithm relies on initializing the reference signal as an arbitrary accumulation, the resulting beacon contains a Doppler ambiguity. However, this carrier phase ambiguity can be resolved by tracking an arbitrary Starlink SV Doppler using the tracking loops in Section IV. After that, for beacon estimation purposes only, the position of the receiver is used to generate the expected Doppler measurements from the TLE + SGP4, and then the Doppler ambiguity would be the Doppler shift that would minimize the total error between the measured Doppler and estimated Doppler from TLE + SGP4.

3. Beacon Analysis

This section analyzes the Starlink LEO beacon in the downlink channel. Figure 3 shows the amplitude of 40 ms of the high SNR Starlink LEO downlink signal. It is observed that the downlink signal is non-stationary with varying power levels, even between two consecutive sub-accumulation intervals. This highlights the importance of (i) increasing the number of sub-accumulations

used, M, for any correlation-based receiver to increase the probability of getting higher power frames per accumulation, and (ii) the threshold γ defined in the beacon estimation stage which prevents low power sub-accumulations from skewing the beacon estimate. The auto-correlation profile of the beacon versus signal bandwidth is shown in Figure 4. As expected, the auto-correlation profile peak width decreases as the bandwidth of the beacon increases to reach the full bandwidth at 240 MHz. However, under condition (8), it is most favorable to choose the lowest F_s sufficient for acquisition and tracking purposes. Furthemore, let $R_x[d] = (x \star x)[d]$ denote the discrete circular auto-correlation function. It is also observed that for an F_s of 2.5 MHz, $\angle R_x[1] \approx \angle R_x[0] + \pi$ and $|R_x[1]| \approx 0.33\,|R_x[0]|$. This implies that a large choice of M results in worse correlations in the absence of code phase rate compensation. This amplifies the importance of satisfying condition (8) for code phase coherence.

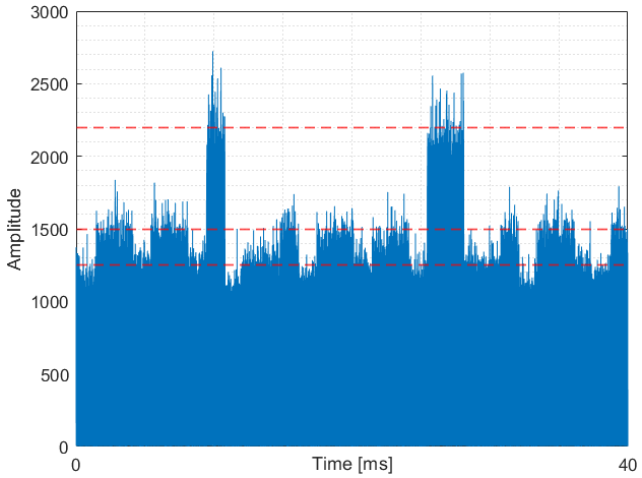

Figure 3: Amplitude of 40 ms of received signal.

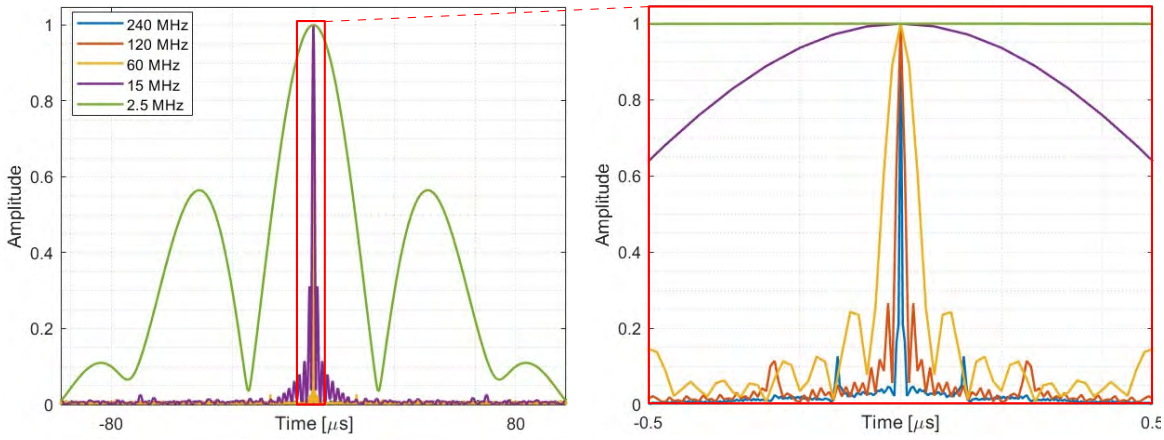

Figure 4: Auto-correlation profile of estimated beacon versus bandwidth.

IV. STARLINK SIGNAL ACQUISITION AND TRACKING

This section explains the acquisition stage and tracking loops used to track Starlink LEO SVs' Doppler without a high gain signal capture setup. All what follows assumes that M = 5 and F_s = 2.5 MHz to satisfy conditions (7) and (8). Let, K denote the accumulation index and $n \in \left[0, \frac{MT_{sub}}{Ts} - 1\right]$.

1. Acquisition

The acquisition stage follows the typical maximum likelihood estimator of the code phase $\hat{d}_K$ and $\hat{f}_{D,K}$, expressed as

$$[\hat{d}_K, \hat{f}_{D,K}] = \text{argmax}_{d,f_D} \left| \left(\hat{\mathbf{s}} \star \boldsymbol{r}_K^{\mathsf{T}} \exp[j2\pi f_D n T_s]\right)[d] \right|^2$$

It is noted that the granularity of the Doppler search space, call it Δf_D, should satisfy condition (7) such that maximum Doppler error is $\tilde{f}_D = \frac{\Delta f_D}{2}$ and the maximum Doppler rate error is $\tilde{\dot{f}}_D = 3$ kHz/s^2.

2. Kalman Filter Tracking

A KF approach is proposed to track both the code and carrier phase. Note that even though the estimated beacon is unambiguous, the resulting Doppler measurements will still contain an ambiguous Doppler shift term. This is because the LNB is expected to have nonzero frequency error at the time of data collection. This is the reason why the following tracking model will assume disjoint dynamics between the code phase and carrier phase. However, the ambiguity term can still be resolved by minimizing the error between the rate of the tracked code phase and the tracked Doppler after tracking is complete. Let $\boldsymbol{x}(t) \triangleq \left[\theta(t),\ \dot{\theta}(t),\ \ddot{\theta}(t),\ \tau(t),\ \dot{\tau}(t)\right]^{\mathsf{T}}$ be the state vector whose dynamics is modeled as $\dot{\boldsymbol{x}}(t) = \mathbf{A}\boldsymbol{x}(t) + \boldsymbol{w}(t)$,

$$\mathbf{A} \triangleq \begin{bmatrix} 0 & 1 & 0 & 0 & 0 \\ 0 & 0 & 1 & 0 & 0 \\ 0 & 0 & 0 & 0 & 0 \\ 0 & 0 & 0 & 0 & 1 \\ 0 & 0 & 0 & 0 & 0 \end{bmatrix},$$

where $\boldsymbol{w}(t)$ is a zero-mean white noise process with covariance matrix $\mathbf{Q} = \text{diag}\left[0, 0, (2\pi 0.2)^2, 0, 1\right]$. The discrete equivalent of the above model is $\boldsymbol{x}_{K+1} = \mathbf{F}\boldsymbol{x}_K + \boldsymbol{w}_K$, discretized at uniform intervals of MT_{sub} with $\boldsymbol{x}_K \triangleq \left[\theta_K,\ \dot{\theta}_K,\ \ddot{\theta}_K,\ d_K,\ \dot{d}_K\right]^{\mathsf{T}}$, where

$$\mathbf{F} = e^{\mathbf{A}MT_{sub}}, \quad \mathbf{Q}_d = \int_0^{MT_{sub}} e^{\mathbf{A}t}\mathbf{Q}\left(e^{\mathbf{A}t}\right)^{\mathsf{T}} dt,$$

such that $\mathbf{Q}_d$ is the covariance matrix of $\boldsymbol{w}_K$, which is the discrete-time equivalent of $\boldsymbol{w}(t)$. The observation model is $\boldsymbol{z}_K = \mathbf{C}\boldsymbol{x}_K + \boldsymbol{v}_K$ where,

$$\mathbf{C} \triangleq \begin{bmatrix} 0 & 1 & 0 & 0 & 0 \\ 0 & 0 & 0 & 1 & 0 \end{bmatrix}, \quad \boldsymbol{v}_k \sim \mathcal{N}\left(\begin{bmatrix} 0 \\ 0 \end{bmatrix}, \begin{bmatrix} \sigma_{\dot{\theta}}^2 & 0 \\ 0 & \sigma_{\tau}^2 \end{bmatrix}\right),$$

where the measurement noise variances $\sigma_{\dot{\theta}}^2$ and σ_{τ}^2 are set to $(2\pi 0.2)^2$ Hz^2 and 3.9 μs^2 respectively. Define the prompt, early, and late correlations in both time and frequency as

$$\begin{aligned} S^p(K) &= \left|\langle r_K[n], s[n]\rangle\right|^2 \\ S_t^e(K) &= \left|\langle r_K[n], s[n - B_t F_s]\rangle\right|^2 \\ S_t^l(K) &= \left|\langle r_K[n], s[n + B_t F_s]\rangle\right|^2 \\ S_f^e(K) &= \left|\langle r_K[n], s[n]\exp[-j2\pi B_f n T_s]\rangle\right|^2 \\ S_f^l(K) &= \left|\langle r_K[n], s[n]\exp[+j2\pi B_f n T_s]\rangle\right|^2, \end{aligned}$$

where term B_t is chosen to be 0.2 μs in accordance with the auto-correlation profile in Figure 4, and B_f is chosen to be 500 Hz to approximate the 3 dB bandwidth of the beacon correlation in the frequency-domain. Finally, the measurement pre-fit residual is defined as $\tilde{\boldsymbol{y}}_K = \left[\tilde{\dot{\theta}}_K,\ \tilde{d}_K\right]^{\mathsf{T}}$ where

$$\tilde{\dot{\theta}}_K = \frac{S_f^e(K) - S_f^l(k)}{S_f^e(K) + S_f^l(K)}, \quad \tilde{d}_K = \frac{S_t^e(K) - S_t^l(K)}{S_t^e(K) + S_t^l(K)}.$$

Note that without a high gain signal capture setup, the KF relies on non-zero user activity to remain in a locked state. However, as can be seen from Figure 3, the received signal power is non-stationary. Therefore, in intervals were no user activity is present, the KF must at least have a rough estimate of the Doppler rate and code phase rate. This is to allow the filter to propagate the dynamic model and remain in a locked state when frame activity returns. Define $\hat{\dot{\theta}}_K$ and $\hat{\dot{d}}_K$ as the estimates of the Doppler rate and code rate, respectively. Linear regression is used to estimate these variables from the last N KF estimates of d_K and

$\dot{\theta}_K$ that satisfy the condition $S^p(K) > \lambda$, where N and λ are both tunable parameters. These estimates allow continuous KF tracking with non-stationary user activity.

V. EXPERIMENTAL RESULTS

This section presents experimental tracking and positioning results that can be achieved with the presented framework. To this end a stationary NI-USRP X-410 was set to record the Starlink downlink channel from 4 different LNBs with the carrier frequency f_c set to 11.325 GHz, the sampling frequency F_s was set to 2.5 MHz, and the total recording duration was set to 1500 seconds. The LNBs were placed in a rhombus formation so that Starlink SV signals can be captured from all directions. Figure 5(a) shows the tracked Doppler versus TLE + SGP4 generated Doppler measurements.

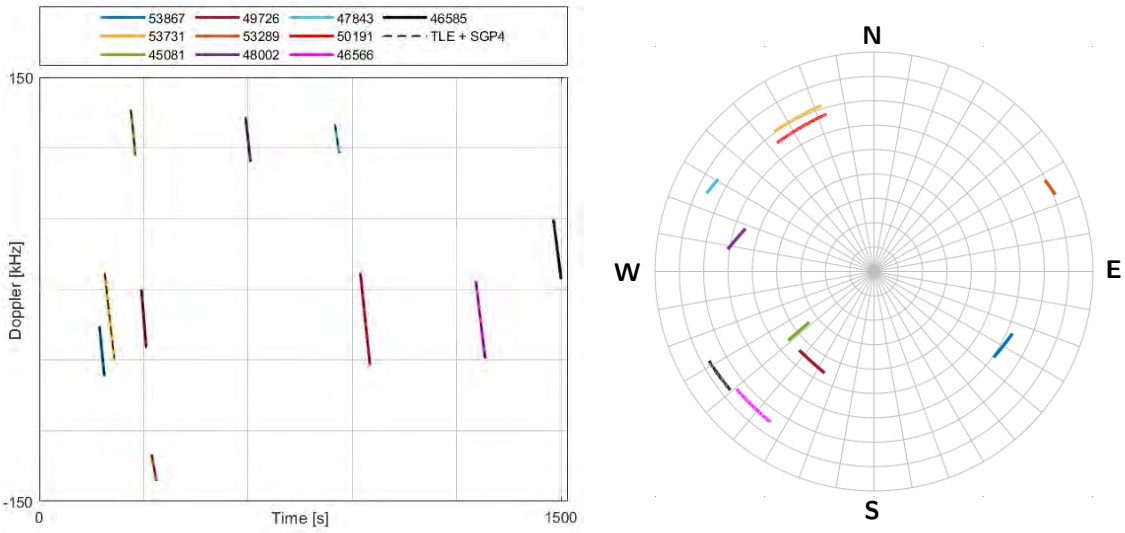

Figure 5: (a) Reciever tracked Doppler vs. TLE + SGP4 estimated Doppler.(b) Skyplot of tracked Starlink LEO SVs.

1. Measurement Model

The tracked Doppler measurements were integrated to generate carrier phase observables, calculated as

$$\Phi_s(K) \triangleq \frac{cMT_{sub}}{2\pi f_c} \sum_{i=0}^{K-1} \hat{\dot{\theta}}_i, \tag{9}$$

where $s \in [1, S]$ denotes the SV index, c is the speed-of-light, and S is the total number of tracked SVs. The carrier phase model is expressed as

$$\Phi_s(K) = \|\boldsymbol{r}_r - \boldsymbol{r}_s(K)\|_2 + \delta t_s(K) + N_s + v_s(K), \tag{10}$$

where $\boldsymbol{r}_r \triangleq [x_r, y_r, z_r]^\intercal$ is the receiver's 3D position; $\boldsymbol{r}_s \triangleq [x_s, y_s, z_s]^\intercal$ is the 3D position of the *s-th* SV; $\delta t_s(K)$ is a term modeling the lumped effects of clock errors and atmospheric delays; N_s is the carrier phase ambiguity of the *s-th* SV; v_s is the discrete-time measurement noise modeled as zero-mean white whose variance is derived from the estimation covariance of the KF. Note that in order to simplify the formulation of the nonlinear least-squares (NLS) filter, this model assumes that the signal time-of-flight has negligible effect on the SVs' positions and clock biases. Furthermore, $\delta_s(K)$ and N_s are lumped and approximated by their first-order TSE to rewrite (10) as

$$\Phi_s(K) \approx \|\boldsymbol{r}_r - \boldsymbol{r}_s(k)\|_2 + a_s + b_s K(MT_{sub}) + v_s(K),$$

where a_s and b_s are the zeroth- and first-order TSE coefficients.

2. Positioning Filter

Define a state vector $\boldsymbol{x} \triangleq \left[\boldsymbol{r}_r{}^{\mathsf{T}}, a_1, b_1, \ldots, a_S, b_S\right]^{\mathsf{T}}$ where the total number of tracked SVs is $S = 10$. Let, $\boldsymbol{\Phi}(K)$ denote the carrier phase measurements available from all S SVs at time instant K stacked into a column. Let, $\boldsymbol{z}$ denote the column vector containing $\boldsymbol{\Phi}(K)$ for every available K. Then, one can readily write the measurement model $\boldsymbol{z} = h(\boldsymbol{x}) + \boldsymbol{v}$ where $h(\boldsymbol{x})$ is a nonlinear vector function mapping the state space to the measurement space, and $\boldsymbol{v}$ is the measurement noise vector. At this point, the SV positions are propagated using TLE + SGP4. It is important to note that the TLE epoch time was adjusted such that it minimizes the range residuals for each SV to account for ephemeris timing errors. Finally, an NLS is used to estimate the stationary receivers true position. The solution results are shown in Figure 6. The initial position estimate was set 100 km away from the receiver's true position, and the final 2D error converged to within 21.2 m.

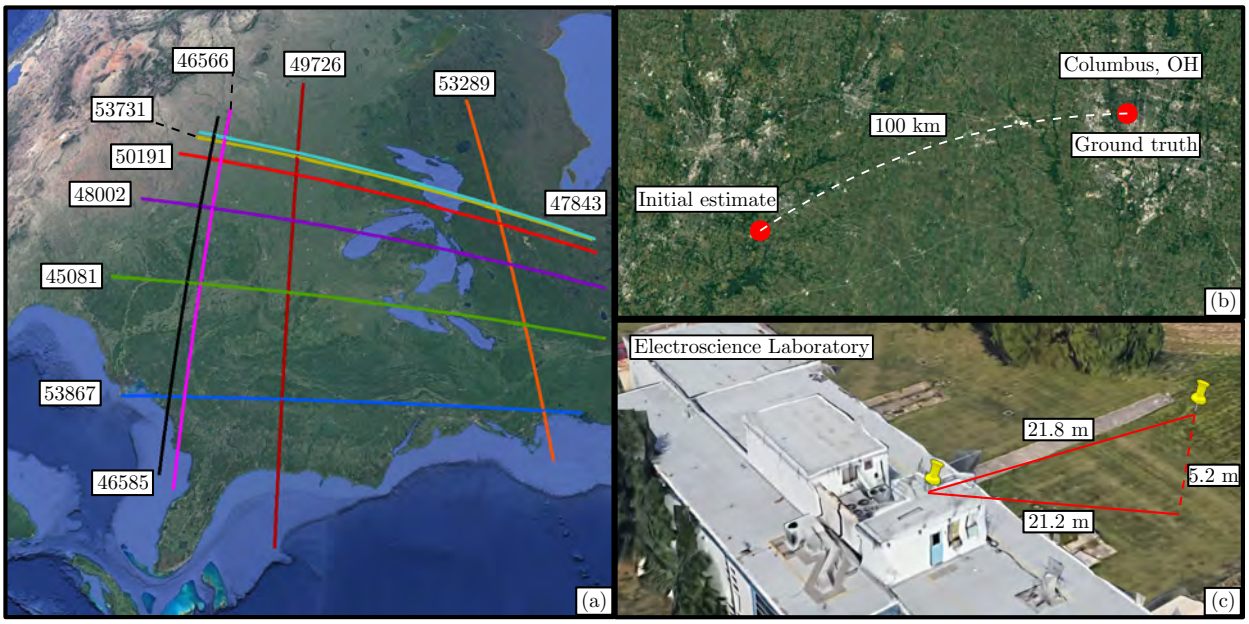

Figure 6: (a) Starlink LEO SVs' trajectories, (b) initial estimate distance from ground truth, and (c) final positioning solution and errors.

VI. CONCLUSION

This paper considered acquisition and tracking of Starlink LEO signals in low SNR regime, enabling exploitation of such signals for opportunistic PNT. Coherence conditions for which Starlink's signals can be blindly tracked in low SNR regime were derived. The full-bandwidth Starlink beacon was estimated, and a time-bandwidth analysis of this beacon was presented. A KF-based tracking loop was proposed for joint code and carrier phase tracking. Experimental results were presented showing successful Doppler tracking of 10 Starlink LEO SVs with a stationary receiver in low SNR regime. The Doppler observables were fused in a batch NLS estimator to yield a 2D positioning error of 21.2 m, starting from an initial estimate 100 km away from the receiver's true position.

ACKNOWLEDGMENTS

This work was supported in part by the Office of Naval Research (ONR) under Grants N00014-19-1-2511 and N00014-22-1-2242, in part by the Air Force Office of Scientific Research (AFOSR) under Grant FA9550-22-1-0476, and in part by the U.S. Department of Transportation (USDOT) under Grant 69A3552047138.

REFERENCES

3GPP (2010). Evolved universal terrestrial radio access (E-UTRA); multiplexing and channel coding. TS 36.212, 3rd Generation Partnership Project (3GPP).

3GPP (2018). Physical channels and modulation. TS 38.211, 5G; NR; 3rd Generation Partnership Project (3GPP).

3GPP2 (2011). Physical layer standard for cdma2000 spread spectrum systems (C.S0002-E). TS C.S0002-E, 3rd Generation Partnership Project 2 (3GPP2).

Bilardi, S. (2021). A GNSS signal simulator and processor for evaluating acquisition and tracking of GPS-like signals from satellites in LEO. Master's thesis, University of Colorado at Boulder, CO, USA.

Bolcskei, H. (2001). Blind estimation of symbol timing and carrier frequency offset in wireless OFDM systems. *IEEE Transactions on Communications*, 49(6):988–999.

Burel, G. and Bouder, C. (2000). Blind estimation of the pseudo-random sequence of a direct sequence spread spectrum signal. In *Proceedings of IEEE Military Communications Conference*, volume 2, pages 967–970.

Cassel, R., Scherer, D., Wilburne, D., Hirschauer, J., and Burke, J. (2022). Impact of improved oscillator stability on LEO-based satellite navigation. In *Proceedings of ION International Technical Meeting*, pages 893–905.

Chen, X., Wei, Q., Wang, F., Jun, Z., Wu, S., and Men, A. (2020). Super-resolution time of arrival estimation for a symbiotic FM radio data system. *IEEE Transactions on Broadcasting*, 66(4):847–856.

Chi, Y., Park, J., and Park, S. (2023). Hybrid multibeamforming receiver with high-precision beam steering for low Earth orbit satellite communication. *IEEE Transactions on Antennas and Propagation*, 71(7):5695–5707.

Choi, H. and Moon, H. (2020). Blind estimation of spreading sequence and data bits in direct-sequence spread spectrum communication systems. *IEEE Access*, 8:148066–148074.

del Peral-Rosado, J., Nolle, P., Rothmaier, F., Razavi, S., Lindmark, G., Jiang, X., Shrestha, D., Gunnarsson, F., Parsawar, S., Mundlamuri, R., Kaltenberger, F., Sirola, N., Sarkka, O., Noman, U., Rostrom, J., Vaarala, K., Miettinen, P., Garlaschi, S., Canzian, L., Babaroglu, H., Rastorgueva-Foi, E., Turunen, M., Talvitie, J., and Flachs, D. (2022). Proof-of-concept of dedicated aerial 5G and GNSS testbed for enhanced hybrid positioning. In *Proceedings of ION GNSS Conference*, pages 2362–2376.

Egea-Roca, D., Lopez-Salcedo, J., Seco-Granados, G., and Falletti, E. (2022). Performance analysis of a multi-slope chirp spread spectrum signal for PNT in a LEO constellation. In *Proceedings of Workshop on Satellite Navigation Technology*, pages 1–9.

Farhangian, F., Benzerrouk, H., and Landry, R. (2021). Opportunistic in-flight INS alignment using LEO satellites and a rotatory IMU platform. *Aerospace*, 8(10):280–281.

Fokin, G. and Volgushev, D. (2022). Software-defined radio network positioning technology design. problem statement. In *Proceedings of Systems of Signals Generating and Processing in the Field of on Board Communications*, pages 1–6.

Guo, F., Yang, Y., Ma, F., Liu, Y. Z. H., and Zhang, X. (2023). Instantaneous velocity determination and positioning using doppler shift from a LEO constellation. *Satellite Navigation*, 4:9–21.

Hartnett, M. (2022). Performance assessment of navigation using carrier Doppler measurements from multiple LEO constellations. Master's thesis, Air Force Institute of Technology, Ohio, USA.

Hendrickson, R. (1997). Globalstar for the military. In *Proceedings of IEEE Military Communications Conference*, volume 3, pages 1173–1178.

Huang, C., Qin, H., Zhao, C., and Liang, H. (2022). Phase - time method: Accurate Doppler measurement for Iridium NEXT signals. *IEEE Transactions on Aerospace and Electronic Systems*, 58(6):5954–5962.

Humphreys, T., Iannucci, P., Komodromos, Z., and Graff, A. (2023). Signal structure of the Starlink Ku-band downlink. *IEEE Transactions on Aerospace and Electronics Systems*. accepted.

Janssen, T., Koppert, A., Berkvens, R., and Weyn, M. (2023). A survey on IoT positioning leveraging LPWAN, GNSS and LEO-PNT. *IEEE Internet of Things Journal*, 10(13):11135–11159.

Jardak, N. and Adam, R. (2023). Practical use of Starlink downlink tones for positioning. *Sensors*, 23(6):3234–3253.

Jardak, N. and Jault, Q. (2022). The potential of LEO satellite-based opportunistic navigation for high dynamic applications. *Sensors*, 22(7):2541–2565.

Jiang, M., Qin, H., Su, Y., Li, F., and Mao, J. (2023). A design of differential-low Earth orbit opportunistically enhanced GNSS (D-LoeGNSS) navigation framework. *Remote Sensing*, 15(8):2136–2158.

Jiang, M., Qin, H., Zhao, C., and Sun, G. (2022). LEO Doppler-aided GNSS position estimation. *GPS Solutions*, 26(1):1–18.

Jiao, Z., Chen, L., Lu, X., Liu, Z., Zhou, X., Zhuang, Y., and Guo, G. (2023). Carrier phase ranging with DTMB signals for urban pedestrian localization and GNSS aiding. *Remote Sensing*, 15(2):423–446.

Kanamori, H., Kobayashi, K., and Kubo, N. (2023). A map-matching based positioning method using Doppler tracking and estimation by a software-defined receiver for multi-constellation LEO satellites. In *Proceedings of ION International Technical Meeting*, pages 649–663.

Kassas, Z., Kozhaya, S., Saroufim, J., Kanj, H., and Hayek, S. (2023). A look at the stars: Navigation with multi-constellation LEO satellite signals of opportunity. *Inside GNSS Magazine*, 18(4):38–47.

Kassas, Z., Morales, J., and Khalife, J. (2019). New-age satellite-based navigation – STAN: simultaneous tracking and navigation with LEO satellite signals. *Inside GNSS Magazine*, 14(4):56–65.

Kassas, Z., Neinavaie, M., Khalife, J., Khairallah, N., Haidar-Ahmad, J., Kozhaya, S., and Shadram, Z. (2021). Enter LEO on the GNSS stage: Navigation with Starlink satellites. *Inside GNSS Magazine*, 16(6):42–51.

Khalife, J., Neinavaie, M., and Kassas, Z. (2022). The first carrier phase tracking and positioning results with Starlink LEO satellite signals. *IEEE Transactions on Aerospace and Electronic Systems*, 56(2):1487–1491.

Khalife, J., Shamaei, K., and Kassas, Z. (2016). A software-defined receiver architecture for cellular CDMA-based navigation. In *Proceedings of IEEE/ION Position, Location, and Navigation Symposium*, pages 816–826.

Kozhaya, S., Kanj, H., and Kassas, Z. (2023). Multi-constellation blind beacon estimation, Doppler tracking, and opportunistic positioning with OneWeb, Starlink, Iridium NEXT, and Orbcomm LEO satellites. In *Proceedings of IEEE/ION Position, Location, and Navigation Symposium*, pages 1184–1195.

Kozhaya, S. and Kassas, Z. (2022). Blind receiver for LEO beacon estimation with application to UAV carrier phase differential navigation. In *Proceedings of ION GNSS Conference*, pages 2385–2397.

Kozhaya, S. and Kassas, Z. (2023). Positioning with Starlink LEO satellites: A blind Doppler spectral approach. In *Proceedings of IEEE Vehicular Technology Conference*, pages 1–5.

Li, L., Zhang, H., Du, S., Liang, T., and Gao, L. (2023). Blind despreading and deconvolution of asynchronous multiuser direct sequence spread spectrum signals under multipath channels. *IET Signal Processing*, 17(5):1–14.

Liu, W., Wang, J., and Li, S. (2010). Blind detection and estimation of OFDM signals in cognitive radio contexts. In *Proceedings of International Conference on Signal Processing Systems*, volume 2, pages 347–351.

Menzione, F. and Paonni, M. (2023). LEO-PNT mega-constellations: a new design driver for the next generation MEO GNSS space service volume and spaceborne receivers. In *Proceedings of IEEE/ION Position, Location, and Navigation Symposium*, pages 1196–1207.

Merwe, J., Bartl, S., O'Driscoll, C., Rügamer, A., Förster, F., Berglez, P., Popugaev, A., and Felber, W. (2020). GNSS sequence extraction and reuse for navigation. In *Proceedings of ION GNSS+ Conference*, pages 2731–2747.

More, H., Cianca, E., and Sanctis, M. (2022). Positioning performance of LEO mega constellations in deep urban canyon environments. In *Proceedings of International Symposium on Wireless Personal Multimedia Communications*, pages 256–260.

Mortlock, T. and Kassas, Z. (2021). Assessing machine learning for LEO satellite orbit determination in simultaneous tracking and navigation. In *Proceedings of IEEE Aerospace Conference*, pages 1–8.

Morton, Y., Xu, D., and Jiao, Y. (2022). Ionospheric scintillation effects on signals transmitted from LEO satellites. In *Proceedings of ION GNSS Conference*, pages 2980–2988.

Navstar GPS (2015). Space segment/navigation user interfaces interface specification IS-GPS-200. `http://www.gps.gov/technical/icwg/`.

Neinavaie, M. and Kassas, Z. (2022). Unveiling beamforming strategies of Starlink LEO satellites. In *Proceedings of ION GNSS Conference*, pages 2525–2531.

Neinavaie, M. and Kassas, Z. (2023a). Signal mode transition detection in Starlink leo satellite downlink signals. In *Proceedings of IEEE/ION Position, Location, and Navigation Symposium*, pages 360–364.

Neinavaie, M. and Kassas, Z. (2023b). Unveiling Starlink LEO satellite OFDM-like signal structure enabling precise positioning. *IEEE Transactions on Aerospace and Electronic Systems*. accepted.

Neinavaie, M., Khalife, J., and Kassas, Z. (2021). Blind Doppler tracking and beacon detection for opportunistic navigation with LEO satellite signals. In *Proceedings of IEEE Aerospace Conference*, pages 1–8.

Neinavaie, M., Khalife, J., and Kassas, Z. (2022). Acquisition, Doppler tracking, and positioning with Starlink LEO satellites: First results. *IEEE Transactions on Aerospace and Electronic Systems*, 58(3):2606–2610.

Pinell, C., Prol, F., Bhuiyan, M., and Praks, J. (2023). Receiver architectures for positioning with low earth orbit satellite signals: a survey. *EURASIP Journal on Advances in Signal Processing*, 2023:60–80.

Prol, F., Ferre, R., Saleem, Z., Välisuo, P., Pinell, C., Lohan, E., Elsanhoury, M., Elmusrati, M., Islam, S., Celikbilek, K., Selvan, K., Yliaho, J., Rutledge, K., Ojala, A., Ferranti, L., Praks, J., Bhuiyan, M., Kaasalainen, S., and Kuusniemi, H. (2022). Position, navigation, and timing (PNT) through low earth orbit (LEO) satellites: A survey on current status, challenges, and opportunities. *IEEE Access*, 10:83971–84002.

Prol, F., Kaasalainen, S., Lohan, E., Bhuiyan, M., Praks, J., and Kuusniemi, H. (2023). Simulations using LEO-PNT systems: A brief survey. In *Proceedings of IEEE/ION Position, Location, and Navigation Symposium*, pages 1381–387.

Raquet *et al.*, J. (2021). Position, navigation, and timing technologies in the 21st century. volume 2, Part D: Position, Navigation, and Timing Using Radio Signals-of-Opportunity, chapter 35–43, pages 1115–1412. Wiley-IEEE.

Rui, Z., Ouyang, X., Zeng, F., and Xu, X. (2022). Blind estimation of GPS M-Code signals under noncooperative conditions. *Wireless Communications and Mobile Computing*, 2022.

Sabbagh, R. and Kassas, Z. (2023). Observability analysis of receiver localization via pseudorange measurements from a single LEO satellite. *IEEE Control Systems Letters*, 7(3):571–576.

Saroufim, J., Hayek, S., and Kassas, Z. (2023). Simultaneous LEO satellite tracking and differential LEO-aided IMU navigation. In *Proceedings of IEEE/ION Position Location and Navigation Symposium*, pages 179–188.

Shi, C., Zhang, Y., and Li, Z. (2023). Revisiting Doppler positioning performance with LEO satellites. *GPS Solutions*, 27(3):126–137.

Singh, U., Shankar, M., and Ottersten, B. (2022). Opportunistic localization using LEO signals. In *Proceedings of Asilomar Conference on Signals, Systems, and Computers*, pages 894–899.

Souli, N., Kolios, P., and Ellinas, G. (2022). Online relative positioning of autonomous vehicles using signals of opportunity. *IEEE Transactions on Intelligent Vehicles*, 7(4):873–885.

Stock, W., Hofmann, C., and Knopp, A. (2023). LEO-PNT with Starlink: Development of a burst detection algorithm based on signal measurements. In *Proceedings of International ITG Workshop on Smart Antennas and Conference on Systems, Communications, and Coding*, pages 1–6.

Tan, Z., Qin, H., Cong, L., and Zhao, C. (2019). Positioning using IRIDIUM satellite signals of opportunity in weak signal environment. *Electronics*, 9(1):37.

Tanda, M. (2004). Blind symbol-timing and frequency-offset estimation in OFDM systems with real data symbols. *IEEE Transactions on Communications*, 52(10):1609–1612.

Tian, J., Fangchi, L., Yafei, T., and Dongmei, L. (2023). Utilization of non-coherent accumulation for LTE TOA estimation in weak LOS signal environments. *EURASIP Journal on Wireless Communications and Networking*, 2023(1):1–31.

Tsatsanis, M. and Giannakis, G. (1997). Blind estimation of direct sequence spread spectrum signals in multipath. *IEEE Transactions on Signal Processing*, 45(5):1241–1252.

Wang, D., Qin, H., and Huang, Z. (2023). Doppler positioning of LEO satellites based on orbit error compensation and weighting. *IEEE Transactions on Instrumentation and Measurement*, 72:1–11.

Wei, Q., Chen, X., and Zhan, Y. (2020). Exploring implicit pilots for precise estimation of LEO satellite downlink Doppler frequency. *IEEE Communications Letters*, 24(10):2270–2274.

Wu, N., Qin, H., and Zhao, C. (2023). Long-baseline differential doppler positioning using space-based SOP based on BPVGMM. *IEEE Transactions on Instrumentation and Measurement*, 72:1–10.

Yang, C. and Soloviev, A. (2023). Starlink Doppler and Doppler rate estimation via coherent combining of multiple tones for opportunistic positioning. In *Proceedings of IEEE/ION Position, Location, and Navigation Symposium*, pages 1143–1153.

Yang, C., Zang, B., Gu, B., Zhang, L., Dai, C., Long, L., Zhang, Z., Ding, L., and Ji, H. (2023). Doppler positioning of dynamic targets with unknown LEO satellite signals. *Electronics*, 12(11):2392–2404.

Ye, L., Gao, N., Yang, Y., Deng, L., and Li, H. (2023). Three satellites dynamic switching range integrated navigation and positioning algorithm with clock bias cancellation and altimeter assistance. *Aerospace*, 10(5):411–438.

Zhao, C., Qin, H., Wu, N., and Wang, D. (2023). Analysis of baseline impact on differential doppler positioning and performance improvement method for LEO opportunistic navigation. *IEEE Transactions on Instrumentation and Measurement*, 72:1–10.

Acquisition, Doppler Tracking, and Positioning With Starlink LEO Satellites: First Results

Letter

This letter shows the first acquisition, Doppler tracking, and positioning results with Starlink's low Earth orbit satellite signals. A generalized-likelihood-ratio-based test is proposed to acquire Starlink's downlink signals. A Kalman-filter-based algorithm for tracking the Doppler frequency from the unknown Starlink signals is developed. Experimental results show Doppler tracking of six Starlink satellites, achieving a horizontal positioning error of 10 m.

I. INTRODUCTION

Theoretical and experimental studies have demonstrated the potential of low Earth orbit (LEO) broadband communication satellites as promising reliable sources for navigation [1]–[4]. Companies like Amazon, Telesat, and SpaceX are deploying so-called *megaconstellations* to provide global broadband internet [5]. In particular, launching thousands of space vehicles (SVs) into LEO by SpaceX can be considered as a turning point in the future of LEO-based navigation technologies. Although they suffer from higher Doppler effect, signals received from LEO SVs can be about 30 dB stronger than signals received from medium Earth orbit (MEO) SVs, where global navigation satellite systems (GNSSs) SVs reside [4].

Research has shown that one could exploit LEO SV broadband communication signals opportunistically for navigation purposes [3]. Three of the main challenges of navigation with Starlink SV signals are as follows:

1) Limited information about the signal structure.
2) Very-high dynamics of Starlink LEO SVs.
3) Poorly known ephemerides.

Assuming that Starlink LEO SV downlink signals contains a periodic reference signal, this letter tackles the first

Manuscript received July 16, 2021; released for publication October 12, 2021. Date of publication November 11, 2021; date of current version June 9, 2022.

DOI. No. 10.1109/TAES.2021.3127488

Refereeing of this contribution was handled by M. Baum.

This work was supported in part by the Office of Naval Research (ONR) under Grant N00014-19-1-2511; in part by the U.S. Department of Transportation (USDOT) under Grant 69A3552047138 for the CARMEN University Transportation Center (UTC); and in part by the Air Force Office of Scientific Research (AFOSR) under the Young Investigator Program (YIP) award.

Authors' addresses: Joe Khalife and Mohammad Neinavaie are with the Department of Mechanical and Aerospace Engineering, University of California, Irvine, CA 92697 USA, E-mail: (khalifej@uci.edu; mneinava@uci.edu); Zaher M. Kassas is with Department of Mechanical and Aerospace Engineering, University of California, Irvine, CA 92697 USA, and also with The Ohio State University, Columbus, OH 43210 USA, E-mail: (zkassas@ieee.org). *(Corresponding author: Zaher M. Kassas.)*

0018-9251 © 2021 IEEE

Authorized licensed use limited to: The Ohio State University. Downloaded on October 12,2022 at 17:16:27 UTC from IEEE Xplore. Restrictions apply.

challenge by formulating a *matched subspace detection* problem to detect the unknown RS of Starlink SVs and estimate the unknown period and Doppler frequency. The second challenge is addressed by adopting a second-order model to capture the dynamics of the Doppler frequency, and designing a Kalman filter (KF)-based algorithm that is capable of tracking the unknown parameters of the Doppler model. A blind approach was presented in [6] and [7] to exploit partially known signals for navigation purposes. However, these approaches were designed for M-ary phase-shift keying signaling and are incapable of deciphering sophisticated signals, such as Starlink's orthogonal frequency-division multiple access (OFDMA) signals.

This letter makes the following contributions. First, a model for the Starlink LEO SV's downlink signals is presented. Second, an algorithm is proposed to acquire the Starlink LEO SV signals and track the Doppler frequency of each detected SV. Third, next to [8], the first experimental positioning results with Starlink downlink signals are presented in this letter. In [8], an adaptive KF is used to track the carrier phase of Starlink LEO SVs. However, the method presented in [8] relies on tracking the phase of a single carrier. When a more complicated signal structure is used in the downlink signal, e.g., OFDMA, a more sophisticated method should be developed to exploit the entire signal bandwidth for navigation purposes. Indeed, the method in [8] is not capable of exploiting the entire signal bandwidth, and it only relies on tracking a single frequency component. In this letter, by considering a general model for the Starlink downlink signals, the unknown parameters of the signal are estimated for the first time for Starlink LEO SVs, and are subsequently used to detect the Starlink LEO SVs and track their corresponding Doppler frequencies. The proposed method enables one to estimate the synchronization signals of the Starlink LEO SVs.

II. RECEIVED SIGNAL MODEL

A. Starlink Downlink Signals

Except for the carrier frequencies and the bandwidths, more detailed signal specifications of Starlink downlink signals are unavailable to the public. SpaceX uses the Ku-band spectrum for the satellite-to-user links (both uplink and downlink) and the satellite-to-ground contacts are carried out in Ka-band [9]. Software-defined radios (SDRs) allow one to sample bands of the radio frequency spectrum. However, Ku/Ka-bands are beyond the carrier frequency of most commercial SDRs. Hence, in the experiments carried out in this letter, a 10-GHz mixer is employed between the antenna and the SDR to downconvert Starlink LEO SV signals from 11.325 GHz to 1.325 GHz.

In order to formulate a detection problem to detect the activity of Starlink downlink signals, a signal model is proposed that solely relies on the periodicity of the transmitted signals. The logic behind the proposed signal model is that in most commercial communication systems, a periodic RS is transmitted for synchronization purposes, e.g., primary synchronization signals (PSSs) in long-term evolution (LTE) and the fifth generation (5G) signals. The following subsection presents a model for the Starlink LEO SV's downlink signals.

B. Baseband Signal Model

As mentioned previously, in most commercial communication systems, a periodic RS is transmitted, e.g., PSS in OFDMA-based and spreading codes in code division multiple access-based signals. In this letter, the Starlink LEO SV downlink signal is modeled as an unknown periodic signal in the presence of interference and noise. If an RS, such as PSS in OFDMA-based signals, is being periodically transmitted, it will be detected and estimated by the proposed method. The received baseband signal is modeled as

$$r[n] = \alpha c[\tau_n - t_s[n]] \exp\left(j\theta[\tau_n]\right) + d[\tau_n - t_s[n]] \exp\left(j\theta[\tau_n]\right) + w[n] \quad (1)$$

where $r[n]$ is the received signal at the nth time instant; α is the complex channel gain between the receiver and the Starlink LEO SV; τ_n is the sample time expressed in the receiver time; $c[\tau_n]$ represents the samples of the complex periodic RS with a period of L samples; $t_s[n]$ is the code-delay between the receiver and the Starlink LEO SV at the nth time instant; $\theta[\tau_n] = 2\pi f_D[n] T_s n$ is the carrier phase in radians, where $f_D[n]$ is the instantaneous Doppler frequency at the nth time instant and T_s is the sampling time; $d_i[\tau_n]$ represents the complex samples of some data transmitted from the Starlink LEO SV; and $w[n]$ is measurement noise, which is modeled as a complex, zero-mean, independent, and identically distributed random sequence with variance σ_w^2.

Starlink LEO SV's signals suffer from very high Doppler shifts. Higher lengths of processing intervals require higher order Doppler models. In order for a Doppler estimation algorithm to provide an accurate estimate of the Doppler frequency, the processing interval should be large enough to accumulate enough power. According to the considered processing interval length in the experiments, it was observed that during the kth processing interval, the instantaneous Doppler frequency is nearly a linear function of time, i.e., $f_D[n] = f_{D_k} + \beta_k n$, where f_{D_k} is referred to as constant Doppler, and β_k is the Doppler rate at the kth processing interval. The coherent processing interval (CPI) is defined as the time interval in which the constant Doppler, f_{D_k}, and the Doppler rate, β_k, are constant.

The received signal at the nth time instant when the Doppler rate is wiped-off is denoted by $r'[n] \triangleq \exp(-j2\pi\beta_k n^2) r[n]$. One can define *the desired RS* which is going to be detected in the acquisition stage as

$$s[n] \triangleq \alpha c[\tau_n - t_s[n]] \exp\left(j2\pi f_{D_k} T_s n\right) \quad (2)$$

and the equivalent noise as

$$w_{\text{eq}}[n] = d[\tau_n - t_s[n]] \exp\left(j2\pi f_{D_k} T_s n\right)$$

Authorized licensed use limited to: The Ohio State University. Downloaded on October 12,2022 at 17:16:27 UTC from IEEE Xplore. Restrictions apply.

$$+\exp\left(-j2\pi\beta n^2\right) w[n]. \tag{3}$$

Hence, $r'[n] = s[n] + w_{\text{eq}}[n]$. Due to the periodicity of the RS, $s[n]$ has the following property:

$$s[n+mL] = s[n]\exp\left(j\omega_k mL\right) \quad 0 \le n \le L-1 \tag{4}$$

where $\omega_k \triangleq 2\pi f_{D_k} T_s$ is the normalized Doppler at the kth CPI, and $-\pi \le \omega_k \le \pi$. A vector of L observation samples corresponding to the mth period of the signal is formed as

$$\mathbf{z}_m \triangleq [r'[mL], r'[mL+1], \ldots, r'[(m+1)L-1]]^{\mathsf{T}}. \tag{5}$$

The kth CPI vector is constructed by concatenating M vectors of length L to form the $ML \times 1$ vector

$$\mathbf{y}_k = [\mathbf{z}_{kM}^{\mathsf{T}}, \mathbf{z}_{kM+1}^{\mathsf{T}}, \ldots, \mathbf{z}_{(k+1)M-1}^{\mathsf{T}}]^{\mathsf{T}}. \tag{6}$$

Therefore,

$$\mathbf{y}_k = \mathbf{H}_k\mathbf{s} + \mathbf{w}_{\text{eq}_k} \tag{7}$$

where $\mathbf{s} = [s[1], s[2], \ldots, s[L]]^{\mathsf{T}}$, and the $ML \times L$ Doppler matrix is defined as

$$\mathbf{H}_k \triangleq [\mathbf{I}_L, \exp\left(j\omega_k L\right)\mathbf{I}_L, \ldots, \exp\left(j\omega_k(M-1)L\right)\mathbf{I}_L]^{\mathsf{T}} \tag{8}$$

where $\mathbf{I}_L$ is an $L \times L$ identity matrix and $\mathbf{w}_{\text{eq}_k}$ is the equivalent noise vector.

III. PROPOSED FRAMEWORK

This section presents the structure of the proposed framework. The proposed receiver consists of two main stages: (i) acquisition and (ii) tracking. In the acquisition stage, an estimate of the period of the RS in the Downlink signal of Starlink SV, and an initial estimate for the Doppler parameters are provided at $k = 0$, which is discussed in the following subsection. In order for the receiver to refine and maintain the Doppler estimate, a tracking stage is also presented.

A. Acquisition

In this section, a detection scheme is proposed to detect the existence of Starlink LEO SVs in the carrier frequency of 11.325 GHz within a bandwidth of 2.5 MHz, at $k = 0$. The following binary hypothesis test is used to detect the Starlink LEO SV signal

$$\begin{cases} \mathcal{H}_0: & \mathbf{y}_0 = \mathbf{w}_{\text{eq}_0} \\ \mathcal{H}_1: & \mathbf{y}_0 = \mathbf{H}_0\mathbf{s} + \mathbf{w}_{\text{eq}_0}. \end{cases} \tag{9}$$

For a given set of unknown variables $\mathcal{W}_0 = \{L, \omega_0, \beta_0\}$, the generalized likelihood ratio (GLR) detector for the testing hypothesis (9) is known as matched subspace detector [10], [11], and is derived as (see [12, Th. 9.1])

$$\mathcal{L}(\mathbf{y}_0|\mathcal{W}_0) = \frac{\mathbf{y}_0^{\mathsf{H}}\mathbf{P}_{\mathbf{H}_0}\mathbf{y}_0}{\mathbf{y}_0^{\mathsf{H}}\mathbf{P}_{\mathbf{H}_0}^{\perp}\mathbf{y}_0} \underset{\mathcal{H}_0}{\overset{\mathcal{H}_1}{\gtrless}} \eta \tag{10}$$

where $\mathbf{y}_0^{\mathsf{H}}$ is the Hermitian transpose of $\mathbf{y}_0$, $\mathbf{P}_{\mathbf{H}_0} \triangleq \mathbf{H}_0(\mathbf{H}_0^{\mathsf{H}}\mathbf{H}_0)^{-1}\mathbf{H}_0^{\mathsf{H}}$ denotes the projection matrix to the column space of $\mathbf{H}_0$, $\mathbf{P}_{\mathbf{H}_0}^{\perp} \triangleq \mathbf{I} - \mathbf{P}_{\mathbf{H}_0}$ denotes the projection matrix onto the space orthogonal to the column space of $\mathbf{H}_0$, and η is the threshold, which is predetermined according to the probability of false alarm. Since, $\mathbf{H}_k^{\mathsf{H}}\mathbf{H}_k = M\mathbf{I}_L$ for all k, the likelihood $\mathcal{L}(\mathbf{y}_0|\mathcal{W}_0)$ can be rewritten as $\mathcal{L}(\mathbf{y}_0|\mathcal{W}_0) = \frac{1}{\frac{\|\mathbf{y}_0\|^2}{\frac{1}{M^2}\|\mathbf{H}_0^{\mathsf{H}}\mathbf{y}_0\|^2} - 1}$, which is a monotonically increasing function of $\frac{\|\mathbf{H}_0^{\mathsf{H}}\mathbf{y}_0\|^2}{\|\mathbf{y}_0\|^2}$. Hence, the GLR detector (10) is equivalent to

$$\frac{\|\mathbf{H}_0^{\mathsf{H}}\mathbf{y}_0\|^2}{\|\mathbf{y}_0\|^2} \underset{\mathcal{H}_0}{\overset{\mathcal{H}_1}{\gtrless}} \eta' \tag{11}$$

where η' is determined according to a desired probability of false alarm. The maximum likelihood estimate of $\mathcal{W}_0$ is

$$\hat{\mathcal{W}}_0 = \text{argmax}_{L,\omega_0,\beta_0}\|\mathbf{H}_0^{\mathsf{H}}\mathbf{y}_0\|^2. \tag{12}$$

It should be pointed out that the estimated Doppler using (12) results in a constant ambiguity denoted by $\omega_a = 2\pi f_a$. This constant ambiguity is accounted for the navigation filter.

Fig. 1 demonstrates the likelihood in terms of Doppler frequency and the period for real Starlink downlink signals. The CPI was set to be 200 times the period. As it can be seen in Fig. 1, a Starlink LEO SV downlink signal is detected with a period of 32 μs and at a Doppler frequency of -2745 Hz.

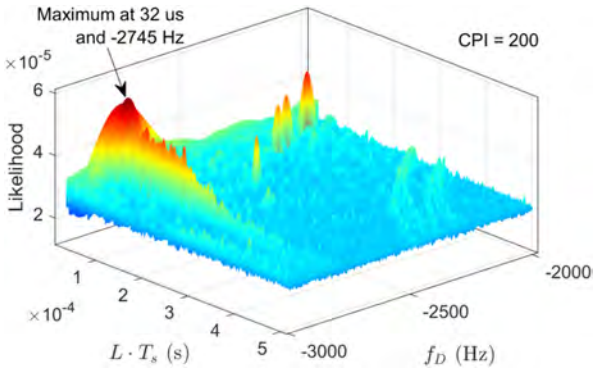

Fig. 1. Acquisition: The likelihood function versus Doppler frequency and the period at Starlink downlink carrier frequency of 11.325 GHz.

B. Doppler Tracking Algorithm

It is important to note that the receiver does not have knowledge of the Doppler ambiguity f_a. The Doppler frequency that will be tracked by the receiver contains this constant ambiguity. In order to track the Doppler, a KF-based tracking loop is developed. The KF formulation allows for arbitrary Doppler model order selection, which is crucial due to the LEO SVs' high dynamics. The KF-based Doppler tracking algorithm is described as follows.

1) *Doppler Dynamics Model:* The time-varying component of the continuous-time true Doppler, denoted by $f(t)$, is a function of (i) the true range rate between the LEO SV and the receiver, denoted by $\dot{d}(t)$, and the (ii) time-varying difference between the receiver's and LEO SV's clock bias rate, denoted by $\dot{b}(t)$, expressed in meters

Authorized licensed use limited to: The Ohio State University. Downloaded on October 12,2022 at 17:16:27 UTC from IEEE Xplore. Restrictions apply.

per second. Hence, $\omega(t) = 2\pi[-\frac{\dot{d}(t)}{\lambda} + \frac{\dot{b}(t)}{\lambda} + f_a]$, where, $\omega(t) = 2\pi f(t)$, and λ is the carrier wavelength. The clock bias is assumed to have a constant drift, i.e., $b(t) = a \cdot (t - t_0) + b_0$, where a is the clock drift, b is the constant bias, and t_0 is the initial time. Moreover, simulations with Starlink LEO SVs show that the kinematic model $\ddot{d}(t) = \tilde{w}(t)$, where $\tilde{w}$ is a zero-mean white noise process with power spectral density $q_{\tilde{w}}$ holds for short periods of time. Let k denote the time index corresponding to $t_k = kT + t_0$, where $T = MLT_s$ is the sampling interval also known as subaccumulation period, and ML is the number of subaccumulated samples. The vector $\boldsymbol{\omega}_k \triangleq [\omega_k, \dot{\omega}_k]^{\mathsf{T}}$ is considered as the Doppler state vector for the proposed tracking algorithm. The initial state is given by $\boldsymbol{\omega}_0 = [2\pi f_a + \frac{2\pi}{\lambda}(a - \dot{d}(t_0)), -\frac{2\pi}{\lambda}\ddot{d}(t_0)]^{\mathsf{T}}$.

2) *KF-Based Doppler Tracking:* Let $\hat{\boldsymbol{\omega}}_{k|l}$ and $\mathbf{P}_{k|l}$ denote the KF estimate of $\boldsymbol{\omega}_k$ and corresponding estimation error covariance, respectively, given all measurements up to time-step $l \leq k$. The initial estimate $\hat{\boldsymbol{\omega}}_{0|0}$ with a corresponding $\mathbf{P}_{0|0}$ are provided from the acquisition stage. The KF-based tracking algorithm follows a regular KF for the time update. The measurement update is discussed next. The KF measurement update equations are carried out based on the maximum likelihood estimate of the Doppler. The Doppler wipe-off is performed as $\tilde{r}_k[i] = r[i + kML] \exp[-j\hat{\theta}_{k+i|k}]$, where $\hat{\theta}_{k+i|k}$ is obtained according to $\hat{\theta}_{k+i|k} = \hat{\omega}_{k|k} i T_s + \hat{\dot{\omega}}_{k|k} \frac{i^2}{2} T_s^2$, for $i = 0, \ldots, ML - 1$. The vector $\tilde{\mathbf{y}}_{k+1}$ is constructed as $\tilde{\mathbf{y}}_{k+1} = [\tilde{r}_k[0], \ldots, \tilde{r}_k[ML - 1]]^{\mathsf{T}}$. One can show that [cf. (7)]

$$\tilde{\mathbf{y}}_{k+1} = \tilde{\mathbf{H}}_{k+1}\mathbf{s} + \tilde{\mathbf{w}}_{\mathrm{eq}_{k+1}} \tag{13}$$

where the residual Doppler matrix is

$$\tilde{\mathbf{H}}_{k+1} \triangleq [\mathbf{I}_L, \exp\left(j\Delta\omega_k L\right)\mathbf{I}_L, \ldots, \exp\left(j\Delta\omega_{k+1}(M-1)L\right)\mathbf{I}_L]^{\mathsf{T}} \tag{14}$$

and $\Delta\omega_{k+1} = \omega_{k+1} - \hat{\omega}_{k+1|k}$. The proposed KF innovation is given by

$$\nu_{k+1} = \mathrm{argmax}_{\Delta\omega_{k+1}} \frac{1}{M} \|\tilde{\mathbf{H}}_{k+1}^{\mathsf{H}} \tilde{\mathbf{y}}_{k+1}\|^2 \tag{15}$$

which is a direct measure of the Doppler error. The measurement noise is chosen proportional to the Doppler search step size. The initial estimates of the Doppler $\hat{\omega}_{0|0}$ and the Doppler rate $\hat{\dot{\omega}}_{0|0}$ are obtained from the acquisition stage.

IV. EXPERIMENTAL RESULTS

This section provides the first results for blind Doppler tracking and positioning with Starlink signals of opportunity. A stationary National Instrument (NI) universal software radio peripheral (USRP) 2945R was equipped with a consumer-grade Ku antenna and low-noise block (LNB) downconverter to receive Starlink signals in the Ku-band. The sampling rate was set to 2.5 MHz and the carrier frequency was set to 11.325 GHz, which is one of the Starlink downlink frequencies. The samples of the Ku signal were stored for offline processing. The tracking results are presented next.

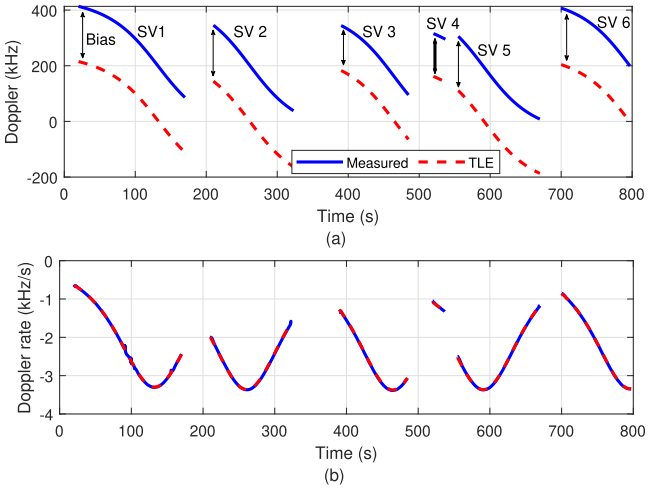

Fig. 2. Experimental results showing measured and predicted. (a) Doppler frequencies and (b) Doppler frequency rates from six Starlink LEO SVs.

A. Blind Doppler Tracking Results

The USRP was set to record Ku signals over a period of 800 s. During this period, a total of six Starlink SVs transmitting at 11.325 GHz passed over the receiver, one at a time. The framework discussed in Section III was used to acquire the downlink signals and track the Doppler frequencies and rates from these LEO SVs, which are shown in Fig. 2 along with the ones predicted from two-line element (TLE) files [3]. It can be seen that the proposed algorithm is tracking the Doppler and the Doppler rate of six Starlink LEO SVs. It can also be seen that the estimated Doppler frequencies have a constant bias compared to the predicted ones from the TLEs.

B. Position Estimation

Next, pseudorange rate observables are formed from the tracked Doppler frequencies by downsampling by a factor D to avoid large time correlations in the pseudorange observables and multiplying by the wavelength to express the Doppler frequencies in meters per second. Let $i \in \{1, 2, 3, 4, 5, 6\}$ denote the SV index. The pseudorange rate observable to the ith SV at time step $\kappa = k \cdot D$, expressed in meters, is modeled as

$$z_i(\kappa) = \frac{\dot{\boldsymbol{r}}_{\mathrm{SV}_i}^{\mathsf{T}}(\kappa)\left[\boldsymbol{r}_r - \boldsymbol{r}_{\mathrm{SV}_i}(\kappa)\right]}{\left\|\boldsymbol{r}_r - \boldsymbol{r}_{\mathrm{SV}_i}(\kappa)\right\|_2} + a_i + v_{z_i}(\kappa) \tag{16}$$

where $\boldsymbol{r}_r$ and $\boldsymbol{r}_{\mathrm{SV}_i}(\kappa)$ are the receiver's and ith Starlink SV 3-D position vectors, $\dot{\boldsymbol{r}}_{\mathrm{SV}_i}(\kappa)$ is the ith Starlink SV 2-D velocity vector, a_i is the constant bias due to the unknown Doppler frequency ambiguity f_a, and $v_{z_i}(\kappa)$ is the measurement noise, which is modeled as a zero-mean, white Gaussian random variable with variance $\sigma_i^2(\kappa)$. The value of $\sigma_i^2(\kappa)$ is the first diagonal element of $\mathbf{P}_{\kappa|\kappa}$, expressed in $\mathrm{m}^2/\mathrm{s}^2$. Next, define the parameter vector $\boldsymbol{x} \triangleq [\boldsymbol{r}_r{}^{\mathsf{T}}, a_1, \ldots, a_6]^{\mathsf{T}}$. Let $\boldsymbol{z}$

Authorized licensed use limited to: The Ohio State University. Downloaded on October 12,2022 at 17:16:27 UTC from IEEE Xplore. Restrictions apply.

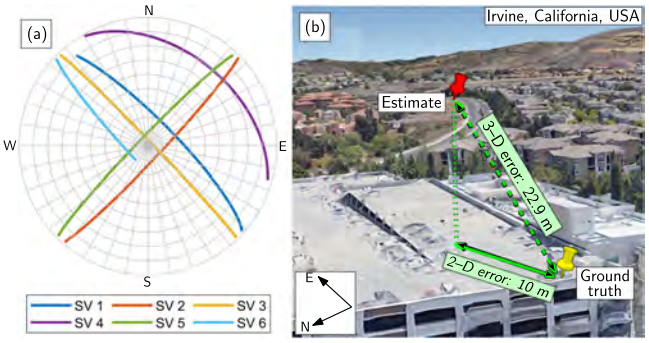

Fig. 3. (a) Skyplot showing the Starlink SVs' trajectories during the experiment. (b) Environment layout and positioning results.

denote the vector of all the pseudorange observables stacked together, and let $\boldsymbol{v}_z$ denote the vector of all measurement noises stacked together, which is a zero-mean Gaussian random vector with a diagonal covariance $\mathbf{R}$ whose diagonal elements are given by $\sigma_i^2(\kappa)$. Then, one can readily write the measurement equation given by $\boldsymbol{z} = \boldsymbol{g}(\boldsymbol{x}) + \boldsymbol{v}_z$, where $\boldsymbol{g}(\boldsymbol{x})$ is a vector-valued function that maps the parameter $\boldsymbol{x}$ to the pseudorange rate observables according to (16). Next, a weighted nonlinear least-squares (WNLS) estimator with weight matrix $\mathbf{R}^{-1}$ is solved to obtain an estimate of $\boldsymbol{x}$ given by $\hat{\boldsymbol{x}} = [\hat{\boldsymbol{r}}_r^{\mathsf{T}}, \hat{a}_1, \ldots, \hat{a}_6]^{\mathsf{T}}$. The SV positions were obtained from TLE files and SGP4 software. It is important to note that the TLE epoch time was adjusted for each SV to account for ephemeris errors. This was achieved by minimizing the pseudorange rate residuals for each SV.

Subsequently, the receiver position was estimated using the aforementioned WNLS. The 3-D position error was found to be 22.9 m, while the 2-D position error was 10 m. A skyplot of the Starlink SVs and the environment layout summarizing the positioning results are shown in Fig. 3.

V. CONCLUSION

This letter showed the first Doppler tracking and positioning results with real Starlink LEO SV signals. A model of a Starlink SV's received signal and a detection problem to detect Starlink downlink SV signals were formulated. A KF-based Doppler tracking algorithm was developed to track the Doppler of Starlink downlink signals. Experimental results showed carrier phase tracking of six Starlink LEO SVs over a period of approximately 800 s. The experiments also show a 10-m 2-D and 22.9-m 3-D position errors.

MOHAMMAD NEINAVAIE, Graduate Student Member, IEEE
JOE KHALIFE, Member, IEEE
ZAHER M. KASSAS, Senior Member, IEEE
University of California, Irvine Irvine, CA USA
The Ohio State University, Columbus, OH USA

REFERENCES

[1] N. Levanon
Quick position determination using 1 or 2 LEO satellites
IEEE Trans. Aerosp. Electron. Syst., vol. 34, no. 3, pp. 736–754, Jul. 1998.

[2] T. Reid *et al.*
"Navigation from low Earth orbit—Part 1: Concept, current capability, and future promise
in *Position, Navigation, and Timing Technologies in the 21st Century: Integrated Satellite Navigation, Sensor Systems, and Civil Applications*, vol. 2, J. Morton, F. van Diggelen, J. Spilker, Jr., and B. Parkinson, Eds. Hoboken, NJ, USA: Wiley, 2021, ch. 43, pp. 1359–1379.

[3] Z. Kassas
Navigation from low Earth orbit—part 2: Models, implementation, and performance
In *Position, Navigation, and Timing Technologies in the 21st Century: Integrated Satellite Navigation, Sensor Systems, and Civil Applications*, vol. 2, J. Morton, F. van Diggelen, J. Spilker, Jr., and B. Parkinson, Eds. Hoboken, NJ, USA: Wiley, 2021, ch. 43, pp. 1381–1412.

[4] A. Nardin, F. Dovis, and J. Fraire
Empowering the tracking performance of LEO-based positioning by means of meta-signals
IEEE J. Radio Freq. Identif., vol. 5, no. 3, pp. 244–253, Sep. 2021.

[5] T. Reid *et al.*
Satellite navigation for the age of autonomy
in *Proc. IEEE/ION Position, Location Navigat. Symp.*, 2020, pp. 342–352.

[6] M. Neinavaie, J. Khalife, and Z. Kassas
Blind opportunistic navigation: Cognitive deciphering of partially known signals of opportunity
In *Proc. 33rd Int. Tech. Meeting Satell. Division Inst. Navigat.*, Sep. 2020, pp. 2748–2757.

[7] M. Neinavaie, J. Khalife, and Z. Kassas
Blind doppler tracking and beacon detection for opportunistic navigation with LEO satellite signals
In *Proc. IEEE Aerosp. Conf.*, Mar. 2021, pp. 1–8.

[8] J. Khalife, M. Neinavaie, and Z. Kassas
The first carrier phase tracking and positioning results with starlink LEO satellite signals
IEEE Trans. Aerosp. Electron. Syst., to be published, doi: 10.1109/TAES.2021.3113880.

[9] I. Del Portillo, B. Cameron, and E. Crawley
A technical comparison of three low earth orbit satellite constellation systems to provide global broadband
Acta Astronautica, vol. 159, pp. 123–135, 2019.

[10] L. Scharf and B. Friedlander
Matched subspace detectors
IEEE Trans. Signal Process., vol. 42, no. 8, pp. 2146–2157, Aug. 1994.

[11] F. Gini and A. Farina
Vector subspace detection in compound-Gaussian clutter. Part I: Survey and new results
IEEE Trans. Aerosp. Electron. Syst., vol. 38, no. 4, pp. 1295–1311, Oct. 2002.

[12] S. Kay
Fundamentals of Statistical Signal Processing: Detection Theory, vol. II. Upper Saddle River, NJ, USA: Prentice-Hall, 1993.

Authorized licensed use limited to: The Ohio State University. Downloaded on October 12,2022 at 17:16:27 UTC from IEEE Xplore. Restrictions apply.

Aerial Vehicle Protection Level Reduction by Fusing GNSS and Terrestrial Signals of Opportunity

Mahdi Maaref, Joe Khalife, *Member, IEEE*, and Zaher M. Kassas, *Senior Member, IEEE*

***Abstract*— A method for reducing the protection levels (PLs) of aerial vehicles by fusing global navigation satellite systems (GNSS) signals with terrestrial signals of opportunity (SOPs) is developed. PL is a navigation integrity parameter that guarantees the probability of position error exceeding a certain value to be bounded by a target integrity risk. For unmanned aerial vehicles (UAVs), it is desirable to achieve as tight PLs as possible. This paper characterizes terrestrial cellular SOPs' measurement errors from extensive UAV flight campaigns, collected over the past few years in different environments and from different providers, transmitting at different frequencies and bandwidths. Next, the reduction in PLs due to fusing terrestrial SOPs with a traditional GNSS-based navigation system is analyzed. It is demonstrated that incorporating terrestrial SOP measurements is more effective in reducing the PLs over adding GNSS measurements. Experimental results are presented for a UAV traversing a trajectory of 823 m, during which the VPL of the GPS-based and GNSS-based navigation systems were reduced by 56.9% and 58.8%, respectively, upon incorporating SOPs; while the HPL of the GPS-based and GNSS-based navigation systems were reduced by 82.4% and 74.6%, respectively, upon incorporating SOPs.**

***Index Terms*— Integrity, protection level, signals of opportunity, GNSS, navigation, UAV.**

I. Introduction

AVIATION is undergoing a monumental transformation with the introduction of unmanned aerial vehicles (UAVs) into the national airspace. UAVs promise to create a significant number of technical jobs and transform numerous industries, such as construction, surveying, transportation, delivery, agriculture, entertainment, among others [1]. Moreover, UAVs can be tasked with hazardous and humanly prohibitive tasks, such as infrastructure inspection, hurricane relief, and firefighting. As UAVs perform increasingly complex tasks in a semi-autonomous or a fully-autonomous fashion, the requirements on the accuracy and safety of their navigation system become ever more stringent [2].

UAVs are equipped with a suite of sensors with different modalities, including passive signal-based (e.g., global navigation satellite system (GNSS)) and dead-reckoning (DR) (e.g., inertial navigation system (INS)). These sensing modalities can be classified into two major categories: (i) local sensing modalities, which provide the location of the UAV relative to its own coordinate system and (ii) global sensing modalities, which provide the absolute location of the UAV within a global frame. Navigation systems onboard today's UAVs mainly rely on GNSS, which has monopolized global sensing technologies in outdoor applications for the past few decades. However, GNSS signals are challenged in urban environments [3]–[5] and could be easily compromised via interference, jamming, or spoofing [6], [7]. Integrity monitoring is one criterion to evaluate GNSS performance, which refers to the ability of the navigation system to provide timely warnings when the information given by its on-board sensors is not trustworthy [8]–[11]. Integrity monitoring frameworks are divided into two categories: internal and external [12]. External methods (e.g., ground-based augmentation system (GBAS), satellite-based augmentation system (SBAS), etc.) leverage a network of ground monitoring stations to monitor the transmitted signals, while internal methods (e.g., receiver autonomous integrity monitoring (RAIM)) typically use the redundant information within the transmitted navigation signals.

RAIM checks the consistency in the redundant measurements to perform fault detection and exclusion. RAIM also assesses the availability performance by calculating the vertical and horizontal protection levels (VPL and HPL). By definition, the protection level (PL) is defined as a confidence bound on the size of the position domain error given a specified target integrity risk [13]. Constructing tight PLs (i.e., VPL and HPL) has been the subject of several studies, and many different RAIM schemes incorporating other sensing modalities have been proposed, such as multi-constellation RAIM (e.g., Galileo-GPS [14] and GLONASS-GPS [15]), INS-GPS RAIM [16], and lidar-GPS RAIM [17]. This paper considers exploiting terrestrial signals of opportunity (SOPs) as an additional "constellation" and develops RAIM for SOP-GNSS to reduce the PLs even further. SOPs are ambient radio signals that are not intended for navigation or timing purposes, such as AM/FM radio [18], [19], cellular [20]–[24], digital

Manuscript received March 16, 2020; revised October 4, 2020 and June 8, 2021; accepted June 15, 2021. Date of publication July 16, 2021; date of current version September 1, 2021. This work was supported in part by the Office of Naval Research (ONR) under Grant N00014-19-1-2613, in part by the U.S. Department of Transportation (USDOT) for the CARMEN University Transportation Center (UTC) under Grant 69A3552047138, and in part by the National Science Foundation (NSF) under Grant 1929965. The Associate Editor for this article was E. Atkins. *(Corresponding author: Zaher M. Kassas.)*

The authors are with the Department of Mechanical and Aerospace Engineering, University of California, Irvine, CA 92521 USA (e-mail: mmaaref@uci.edu; khalifej@uci.edu; zkassas@ieee.org).

This article has supplementary downloadable material available at https://doi.org/10.1109/TITS.2021.3095184, provided by the authors.

Digital Object Identifier 10.1109/TITS.2021.3095184

1558-0016 © 2021 IEEE. Personal use is permitted, but republication/redistribution requires IEEE permission.
See https://www.ieee.org/publications/rights/index.html for more information.

Authorized licensed use limited to: The Ohio State University. Downloaded on October 13,2023 at 15:52:26 UTC from IEEE Xplore. Restrictions apply.

television [25], [26], low Earth orbit (LEO) satellite signals [27]–[30], and Wi-Fi [31], [32]. In contrast to DR-type sensors, *absolute* position information may be extracted from SOPs. Moreover, SOPs are practically unaffected by dense smoke, fog, rain, snow, and other poor weather conditions. SOPs enjoy several inherently desirable attributes: (i) abundance in most locales of interest, (ii) transmission at a wide range of frequencies and directions, (iii) reception at carrier-to-noise ratio that is commonly tens of dBs higher than that of GNSS signals, and (iv) they are free to use, since their infrastructure is already operational [33], [34]. The literature demonstrated the benefit of fusing SOP and GNSS signals to reduce the vertical dilution of precision (VDOP) [35].

This paper proposes a GNSS-SOP RAIM approach, which exploits the favorable transmitter-to-receiver geometry to significantly reduce a UAV's PL. Since all GNSS satellites are typically above the UAV-mounted receiver, GNSS measurements lack elevation angle diversity, which in turn degrades the VPL. In contrast, terrestrial SOP transmitters are inherently at low elevation angles. As a consequence, a combined GNSS-SOP system will benefit from a *doubled* elevation angle range. In addition, certain SOPs possess favorable geometric configurations by construction, e.g., cellular towers are placed at the center of hexagonal cells. This yields well-spaced azimuth angles, which is desirable for HPL reduction.

An initial work that considered fusing GPS and SOP signals for UAV integrity monitoring was conducted in [36]. This paper extends the previous work through the following contributions. First, cellular SOP measurement errors are characterized from hours of UAV flight campaigns over the past few years, which collected extensive SOP data in different environments. The presented SOP measurements represent the most extensive characterization to-date of cellular SOPs in various environments and from different cellular providers, transmitting at different frequencies and bandwidths. Probability density function (pdf) and cumulative distribution function (cdf)-based overbounding are established and compared. Moreover, the SOP measurements' fault rate is calculated. Second, in contrast to the previous work where only GPS signals were considered, the combined GNSS-SOP performance is evaluated in this paper. Third, different sources for SOP measurement error are evaluated, including multipath, clock bias error, and poor geometric conditions. Fourth, a real-world experiment with cellular long-term evolution (LTE) SOPs are presented demonstrating the proposed GNSS-SOP system to reduce the UAV's PLs. The experimental results using eleven cellular LTE SOPs show that the proposed framework reduces the VPL over GPS-based and GNSS-based navigation systems by 56.9% and 58.8%, respectively; while the framework resulted in HPL reduction over GPS-based and GNSS-based navigation systems by 82.4% and 74.6%, respectively.

The structure of this paper is organized as follows. Section II details the motivation and background of this work. Section III formulates the GPS-SOP navigation solution. Section IV studies empirically the salient attributes of the SOP measurements. This methodology can be applied to other terrestrial SOP classes. Section V discusses the enhancement in the RAIM PL by incorporating the SOP measurement. Sections VI and VII present simulation and experimental results with cellular LTE signals, evaluating the efficacy and accuracy of the proposed framework. Concluding remarks are given in Section VIII.

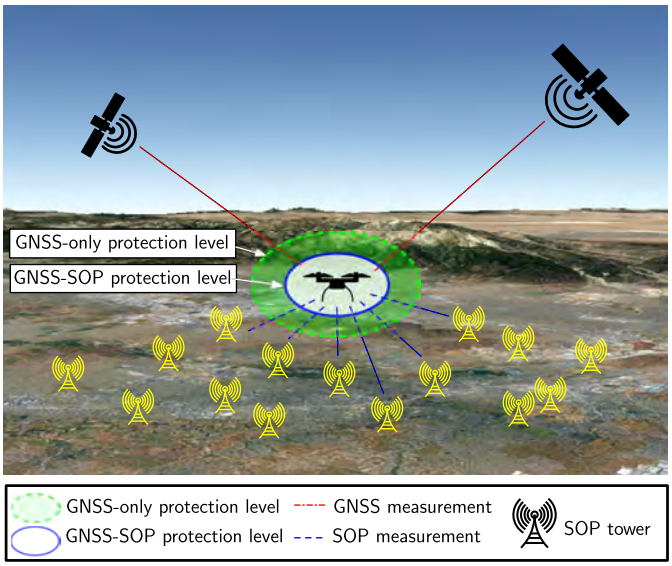

Fig. 1. The proposed method which combines pseudoranges obtained from GNSS satellites and terrestrial SOP transmitters to reduce the PL. Note the abundance of cellular LTE SOPs in this environment: Riverside, California, USA. Many other types of SOPs are also present in the environment but are not plotted here.

II. Background and Motivation

This paper proposes a GNSS-SOP framework for UAV navigation, which significantly reduces the UAV's PL compared to traditional GNSS-based frameworks. The UAV employs a RAIM-based algorithm to calculate the PL. This paper aims at investigating the enhancement in the transmitter-to-receiver geometry, considering the fact that terrestrial SOP measurements are received from negative elevation angles, as the UAV can fly above the terrestrial SOPs. Fig. 1 demonstrates the proposed GNSS-SOP framework. In contrast to GBAS-based frameworks, the expected reduction in PL can be obtained without installing dedicated, costly ground-based stations.

The integrity of GNSS measurements can be established via the navigation message, which specifies anomalies related to satellite operation, such as transmitters' clock errors and satellite service failure. However, the integrity information provided by the navigation message is not desirable for real-time applications as the ground control segment (GCS) requires a few hours to broadcast a failure [37]. Hence, integrity monitoring is usually obtained by means of additional frameworks. These frameworks include external sensor fusion-based techniques as well as internal techniques. Sensor fusion techniques leverage onboard navigation sensors to monitor the navigation solution, while internal techniques typically use the redundant information within the transmitted navigation signals for this purpose. In [17], a method was proposed to leverage lidar measurements to improve both the integrity of the navigation solution and the fault detection capabilities. The proposed method employed an unscented Kalman

Authorized licensed use limited to: The Ohio State University. Downloaded on October 13,2023 at 15:52:26 UTC from IEEE Xplore. Restrictions apply.

filter (UKF) to fuse Lidar and GPS data. Then, an algorithm was described to extract the lidar odometry covariance to construct the RAIM test statistic. Considering the fact that the urban structures and tall buildings, which block GNSS signals, are rich with features detectable by lidar, this method was shown to be very effective for urban environment integrity monitoring. In [38], a method to incorporate an INS for fault detection was proposed. This method, employed an extended Kalman filter (EKF) to fuse INS and GPS measurements. Then, a sliding window estimator was formulated that solves the full-nonlinear maximum *a posteriori* estimate in real-time. Finally, the resulting window of residuals was used to implement an improved fault detection strategy, which is robust against EKF linearization errors. In [39], a method to combine GNSS, lidar, and inertial measurement unit (IMU) was proposed that calculates the integrity measures by analyzing the lidar return light intensity.

Finally, [8] proposed a method that incorporate data from camera and map-matching for both positioning and calculating the integrity of the navigation solution. In contrast to external integrity monitoring methods, RAIM alleviates the need for costly, bulky, and computationally intensive infrastructures.

Over the past few decades, a multitude of algorithms for RAIM have been introduced, including RAIM for GPS-only and multi-constellation GNSS frameworks. With the expected increase in the number of pseudorange sources, new RAIM methods have been studied to exploit the pseudoranges made on different GNSS satellites. Two of the existing algorithms include least-squares (LS) RAIM and multiple hypothesis solution separation (MHSS).

- **LS RAIM algorithm:** LS RAIM considers two scenarios for each satellite: fault-free and faulty operation. In the faulty case, a bias is added in one of the measurements. Since the position error is not directly observable, LS RAIM employs a residual-based test statistic to evaluate the consistency of pseudorange measurements. Fault detection is achieved by comparing the test statistic against a threshold [12]. Initially, the LS RAIM algorithm relied on the assumption that only one failure occurs at a time [11]. Later on, more sophisticated LS RAIM-based algorithms were developed to account for simultaneous faults [40], [41]. In [14], the performance of LS RAIM for combined Galileo-GPS was evaluated. Another variation of the LS RAIM is known as forward-backward (FB) RAIM. FB RAIM is similar to the LS RAIM in its core and consists of two phases: forward and backward. The forward phase includes four tests: (i) geometry preliminary check, (ii) global test to check the measurements' consistency, (iii) local test to identify the outlier, and (iv) separability test to check the measurements' correlation. The backward phase includes a global test to re-introduce the erroneously-rejected measurements. FB RAIM was shown to be a robust algorithm for multi-constellation frameworks. In [42], GPS-Galileo FB RAIM was investigated in a signal-degraded environments. An initial study on the differential SOP system (where a baseline between the base and rover is present) was conducted in [43], where the reduction in the PL was analyzed. This paper differs from [43] trough the following. First, in this paper, the terrestrial pseudoranges are directly injected into the estimator alongside GNSS pseudoranges. With the differential SOP system, the base and rover were making pseudorange measurements to the same SOP transmitters, while the rover had no access to GNSS signals. Second, [43] assumed the presence of a stationary agent in the navigator's environment, referred to as the base, which has knowledge of its own state at all time. The base's purpose was to estimate the dynamic stochastic clock errors of SOP transmitters and to share these estimates with the navigator. It was assumed that the base had direct line-of-sight (LOS) to all SOP towers. This assumption may not be practical in the real-world. Therefore, developing a self-contained solution is desirable. To this end, this paper develops a self-contained UAV navigation framework that fuses GNSS and SOP pseudoranges, to simultaneously localize the UAV-mounted receiver and estimate the receiver's and transmitters' clock errors.
- **MHSS algorithm:** The MHSS algorithm, was first introduced in [44] and [45]. MHSS constructs a fault tree, which refers to a set of assumptions about the environment in which a RAIM algorithm is applied. The measurements are supposed to be in one out of a set of different branches of the fault tree, to each of which an *a priori* probability of occurrence is assigned. MHSS evaluates the different fault modes given the specified probabilities of fault and determines the optimal probability of missed detection for each mode. MHSS considers the potential usage of multi-constellation GNSS observations and is designed to account for multiple faults [46], [47]. In [14] and [15], MHSS was employed to study the integrity of GPS-Galileo and GPS-GLONASS multi-constellation frameworks, respectively.

As mentioned above, all RAIM algorithms employ a preliminary check to verify the geometry conditions. Favorable geometric conditions significantly enhances the capabilities of integrity monitoring processes. The notion of incorporating more measurements from GNSS augmentation systems (GBAS and SBAS) has been investigated in the literature [48]–[52]. More recently, it was demonstrated in [53] that GNSS-based VPL and HPL were reduced by 57% and 65%, respectively, when GBAS corrections were used. Instead of using dedicated GBAS and SBAS infrastructure, this paper proposes a combined GNSS-SOP RAIM and aims to investigate the improvement in the transmitters' geometry by incorporating terrestrial SOPs. SOP towers are more abundant than dedicated infrastructure and are freely available. Also, SOPs are not limited to airport vicinities; hence, UAVs navigating in urban environments could benefit from SOPs' transmitted signals. Moreover, in contrast to satellites, terrestrial SOPs inherently transmit at low elevation angles. What is more, UAVs typically fly above terrestrial SOPs, enabling reception from negative elevation angles. As a result, a significant improvement in the geometry is expected by adding terrestrial SOP measurements. This paper, first, studies the SOP pseudorange characterization. This allows different assumptions to be

Authorized licensed use limited to: The Ohio State University. Downloaded on October 13,2023 at 15:52:26 UTC from IEEE Xplore. Restrictions apply.

placed on GNSS-SOP RAIM. Next, this paper evaluates the performance of the proposed GNSS-SOP RAIM from a PL standpoint.

III. Navigation Framework

This section formulates a weighted nonlinear least-squares (WNLS)-based framework for standalone UAV navigation with GNSS-SOP measurements. The navigation environment comprises a UAV, N SOP towers, and M GNSS satellites. The SOP towers are assumed to be stationary with known 3-dimensional (3-D) positions. This assumption implicitly places stringent requirements on a database integrity. In practice, one could map the SOP transmitter via several approaches, such as radio mapping or satellite images and store them in a local and/or cloud-hosted database, which is continuously maintained. This has been the subject of prior research [54], [55]. It was shown that the location of the SOPs can be mapped *a priori* using one method or a combination of several methods from the list below:

- Extracting from satellite imagery, such as Google database [56].
- Extracting from publicly available database [57].
- Estimating according to the frameworks presented in [55], [58].

The UAV is equipped with a GNSS receiver that makes pseudorange measurements to GNSS satellites at discrete-time instants $k = 0, 1, \ldots$, according to

$$z'_{\mathrm{GNSS}_m}(k) = \left\| \boldsymbol{r}_r(k) - \boldsymbol{r}_{\mathrm{GNSS}_m}(k) \right\|_2 + c \cdot \left[\delta t_r(k) - \delta t_{\mathrm{GNSS}_m}(k) \right] + \upsilon_{\mathrm{GNSS}_m}(k),$$

where $z'_{\mathrm{GNSS}_m} \triangleq z_{\mathrm{GNSS}_m} - c \cdot \delta t_{\mathrm{iono}} - c \cdot \delta t_{\mathrm{tropo}}$; δt_{iono} and $\delta t_{\mathrm{tropo}}$ are the known ionospheric and tropospheric delays, respectively; c is the speed of light; $\boldsymbol{r}_{\mathrm{GNSS}_m}$ and $\delta t_{\mathrm{GNSS}_m}$ are the position and clock bias of the m-th GNSS satellite, respectively; and $\boldsymbol{r}_r \triangleq [x_r, y_r, z_r]^{\mathsf{T}}$ and δt_r are the receiver's position and clock bias, respectively. The term $\upsilon_{\mathrm{GNSS}_m}$ is the m-th GNSS satellite measurement noise, which is modeled as a zero-mean white Gaussian random sequence with variance $\sigma^2_{\mathrm{GNSS}_m}$.

The UAV is also equipped with an SOP receiver that makes pseudorange measurements to terrestrial SOPs. A model of the pseudorange measurement, after mild approximations discussed in [59], is given by

$$z_{\mathrm{SOP}_n}(k) = \left\| \boldsymbol{r}_r(k) - \boldsymbol{r}_{\mathrm{SOP}_n} \right\|_2 + c \cdot \left[\delta t_r(k) - \delta t_{\mathrm{SOP}_n}(k) \right] + \upsilon_{\mathrm{SOP}_n}(k),$$

where $\boldsymbol{r}_{\mathrm{SOP}_n}$ and $\delta t_{\mathrm{SOP}_n}$ are the position and clock bias of the n-th SOP transmitter, respectively, and $\upsilon_{\mathrm{SOP}_n}$ is the n-th SOP measurement noise, which is modeled as a zero-mean white Gaussian random sequence with variance $\sigma^2_{\mathrm{SOP}_n}$.

The UAV estimates its state vector $\boldsymbol{x}_r \triangleq \left[\boldsymbol{r}_r{}^{\mathsf{T}}, c\delta t_r\right]^{\mathsf{T}}$ by fusing these measurements using a WNLS estimator. The clock biases $\{\delta t_{\mathrm{SOP}_n}\}_{n=1}^{N}$ are modeled as first-order polynomials, i.e., $\delta t_{\mathrm{SOP}_n}(k) \approx \dot{\delta} t_{\mathrm{SOP}_n} kT + \delta t_{\mathrm{SOP}_n,0}$, where $\dot{\delta} t_{\mathrm{SOP}_n}$ is the constant clock drift of the n-th transmitter, $\delta t_{\mathrm{SOP}_n,0}$ is the corresponding initial bias, T is the sampling time, and k is the time-step. The parameters of the first-order polynomials, i.e., $\delta t_{\mathrm{SOP}_n,0}$ and $\dot{\delta} t_{\mathrm{SOP}_n}$, can be transmitted to the user from a ground-based station, or can be calculated by the UAV itself from GNSS data and the measured pseudoranges using a LS estimator according to the method described in [60]. Note that $\delta t_{\mathrm{SOP}_n,0}$ and $\dot{\delta} t_{\mathrm{SOP}_n}$ can be assumed as constant parameters; therefore, the UAV does not need to employ a Kalman filter (KF) to continuously estimate them over time. More details about the first-order polynomial model of the SOP clock bias is discussed in [43], [61]. The impact of model mismatch due to using the first-order polynomial model on the measurement accuracy is discussed in Subsection VI-E.

Subsequently, the vector of all measurements given by

$$\boldsymbol{z} \triangleq \left[z'_{\mathrm{GNSS}_1}, \ldots, z'_{\mathrm{GNSS}_M}, z_{\mathrm{SOP}_1}, \ldots, z_{\mathrm{SOP}_N}\right]^{\mathsf{T}},$$

The UAV-mounted receiver's state vector is estimated using WNLS. The model is linearized according to

$$\Delta \boldsymbol{z} = \mathbf{H}\, \Delta \boldsymbol{x}_r + \boldsymbol{v},$$

where $\Delta \boldsymbol{z} \triangleq \boldsymbol{z} - \hat{\boldsymbol{z}}$ is the difference between the measurement vector $\boldsymbol{z}$ and its estimate $\hat{\boldsymbol{z}}$, $\Delta \boldsymbol{x}_r \triangleq \boldsymbol{x}_r - \hat{\boldsymbol{x}}_r$ is the difference between the receivers's state vector $\boldsymbol{x}_r$ and its estimate $\hat{\boldsymbol{x}}_r$, and $\boldsymbol{v} \triangleq \left[\upsilon_{\mathrm{GNSS}_1}, \ldots, \upsilon_{\mathrm{GNSS}_M}, \upsilon_{\mathrm{SOP}_1}, \ldots, \upsilon_{\mathrm{SOP}_N}\right]^{\mathsf{T}}$. The measurement Jacobian used in the WNLS estimator is $\mathbf{H} = \left[\mathbf{H}^{\mathsf{T}}_{\mathrm{GNSS}}, \mathbf{H}^{\mathsf{T}}_{\mathrm{SOP}}\right]^{\mathsf{T}}$, where $\mathbf{H}_{\mathrm{GNSS}}$ and $\mathbf{H}_{\mathrm{SOP}}$, shown at the bottom of the page, where $\mathtt{C}(\cdot)$ and $\mathtt{S}(\cdot)$ denote the cosine and sine functions, respectively; el_{GNSS_m} and az_{GNSS_m} are the elevation and azimuth angles of the m-th GNSS satellites, respectively; and el_{SOP_n} and az_{SOP_n} are the elevation and azimuth angles of the n-th SOP transmitter, respectively. All elevation and azimuth angles are expressed in the East, North, Up (ENU) local coordinate frame, centered at the receiver's position. The weighting matrix in the WNLS is chosen as the inverse of the measurement noise covariance

$$\mathbf{R} = \mathrm{diag}\left[\sigma^2_{\mathrm{GNSS}_1}, \ldots, \sigma^2_{\mathrm{GNSS}_M}, \sigma^2_{\mathrm{SOP}_1}, \ldots, \sigma^2_{\mathrm{SOP}_N}\right],$$

where diag$(\cdot)$ denotes a diagonal matrix.

$$\mathbf{H}_{\mathrm{GNSS}} \triangleq \begin{bmatrix} -\mathtt{C}(el_{\mathrm{GNSS}_1})\mathtt{S}(az_{\mathrm{GNSS}_1}) & -\mathtt{C}(el_{\mathrm{GNSS}_1})\mathtt{C}(az_{\mathrm{GNSS}_1}) & -\mathtt{S}(el_{\mathrm{GNSS}_1}) & 1 \\ \vdots & \vdots & \vdots & \vdots \\ -\mathtt{C}(el_{\mathrm{GPS}_M})\mathtt{S}(az_{\mathrm{GPS}_M}) & -\mathtt{C}(el_{\mathrm{GPS}_M})\mathtt{C}(az_{\mathrm{GPS}_M}) & -\mathtt{S}(el_{\mathrm{GPS}_M}) & 1 \end{bmatrix}$$

$$\mathbf{H}_{\mathrm{SOP}} \triangleq \begin{bmatrix} -\mathtt{C}(el_{\mathrm{SOP}_1})\mathtt{S}(az_{\mathrm{SOP}_1}) & -\mathtt{C}(el_{\mathrm{SOP}_1})\mathtt{C}(az_{\mathrm{SOP}_1}) & -\mathtt{S}(el_{\mathrm{SOP}_1}) & 1 \\ \vdots & \vdots & \vdots & \vdots \\ -\mathtt{C}(el_{\mathrm{SOP}_N})\mathtt{S}(az_{\mathrm{SOP}_N}) & -\mathtt{C}(el_{\mathrm{SOP}_N})\mathtt{C}(az_{\mathrm{SOP}_N}) & -\mathtt{S}(el_{\mathrm{SOP}_N}) & 1 \end{bmatrix},$$

Authorized licensed use limited to: The Ohio State University. Downloaded on October 13,2023 at 15:52:26 UTC from IEEE Xplore. Restrictions apply.

TABLE I
CHARACTERISTICS OF RECORDED CELLULAR SOPS

Environment	Platform	Number of towers	Signal type	Freq. [MHz]	Bandwidth [MHz]	Length [s]	Date [DD/MM/YYYY]
Open sky	Stationary	2	LTE	2125 and 1955	20	–	13/5/2019
Semi-urban and urban	GV	2	LTE	2145 and 1955	20	1500	15/11/2016
	GV	3	LTE	2145 and 1955	20	2000	20/1/2017
	GV	4	LTE	2145 and 739	20 and 10	1600	22/6/2018
	GV	5	LTE	1955 and 739	20 and 10	580	27/6/2016
	GV	3	LTE	739	10	825	5/11/2017
	GV	5	LTE	1955 and 739	20 and 10	1800	22/8/2018
Deep Urban	GV	2	LTE	2145 and 1955	20	345	12/10/2018
	GV	2	LTE	2145 and 1955	20	500	24/8/2018
Open sky and Semi-urban	UAV	2	CDMA	882.75	1.23	3300	13/5/2017
	UAV	7	CDMA	882.75	1.23	2900	22/2/2017
	UAV	8	CDMA	882.75	1.23	2200	1/10/2017
	UAV	8	CDMA	882.75	1.23	2600	1/10/2017
	UAV	2	CDMA	882.75	1.23	3500	15/11/2017
Urban	UAV	11	LTE	739, 1955, 2125, and 2145	10	605	16/6/2019

IV. SOP PSEUDORANGE ERROR CHARACTERIZATION

In order to incorporate SOP measurements into a RAIM-type framework and determine the integrity of the combined SOP-GNSS system, one must statistically characterize SOP pseudorange measurements, namely determine their accuracy and failure rates. While recent research have studied fault and error sources in SOP-based navigation [43], this paper is focuses on the statistical properties of these resulting errors. In this paper, the data collected by the Autonomous Systems Perception, Intelligence, and Navigation (ASPIN) Laboratory over several years of experimental campaigns was used to characterize the statistics of cellular SOP pseudorange measurements. Cellular SOP pseudoranges were recorded with UAVs for an aggregate of several hours of flights. These pseudoranges were obtained using the Multichannel Adaptive TRansceiver Information eXtractor (MATRIX) [62] software-defined receiver (SDR) in (i) different environments; (ii) at different carrier frequencies; and (iii) for different signal types, including long-term evolution (LTE) and code-division multiple access (CDMA) signals. In order to perform these experiments in different environmental conditions, the data collection was carried out in California, USA: Riverside (open sky), San Bernardino (semi-urban), Aliso Viejo (urban), and Riverside (deep urban). While this paper tries to characterize the impact of the most well-known SOP error sources, such as multipath, clock model mismatch, poor geometric configuration, etc., accounting for all possible sources of errors (e.g., software bugs, communication drops, hardware failure, etc.) requires continuous data collection for thousands of hours, which is considered for future work. The characteristics of the recorded data are tabulated in Table I. As expected, the quality of these measurements is highly dependent on the environment. Note that the data collected by ground vehicles (GVs) was used to characterize cellular SOP measurements, mimicking UAVs flying at low altitudes (e.g., during takeoff and landing phases and performing missions such as goods delivery).

Note that the method that was used in this paper to characterize the SOP pseudorange error was DeCleene's single cdf-overbounding approach. Generally, an overbounding approach considers the worst-case scenario, given the stored data available in the database. Because of this, it is acceptable to apply DeCleene algorithm on the recorded data in post-processing and then, update the overbounding cdf's parameteres in the database, from which the navigator can pull these parameters. This can be achieved in post-process or in real-time. Next, the pseudorange measurements' errors were characterized using the method discussed in [36] via the following three steps.

- **Step 1:** The true ranges between the receiver and SOP transmitter (i.e., $\left\| \boldsymbol{r}_r(k) - \boldsymbol{r}_{\mathrm{SOP}_n}(k) \right\|_2$) are removed from the recorded pseudoranges $z_{\mathrm{SOP}_n}(k)$. The true ranges are known *a priori* from the knowledge of the transmitters' location and receiver's ground truth position. The resulting measurement after removing the true range is given by:

$$\begin{aligned} z'_{\mathrm{SOP}_n}(k) &\triangleq z_{\mathrm{SOP}_n}(k) - \left\| \boldsymbol{r}_r(k) - \boldsymbol{r}_{\mathrm{SOP}_n}(k) \right\|_2 \\ &= c \cdot \left[\delta t_r(k) - \delta t_{\mathrm{SOP}_n}(k) \right] + v_{\mathrm{SOP}_n}(k). \end{aligned}$$

- **Step 2:** The error term due to the difference between the receiver's and the transmitter's clock biases (i.e., $c \cdot \left[\delta t_r(k) - \delta t_{\mathrm{SOP}_n}(k) \right]$) is removed from the measurement $z'_{\mathrm{SOP}_n}(k)$. To this end, a first-order polynomial approximation with a constant initial clock bias $c\delta t_{\mathrm{r,SOP}_{n,0}}$ and drift $c\dot{\delta} t_{\mathrm{r,SOP}_{n,0}}$ is used to model the difference

Authorized licensed use limited to: The Ohio State University. Downloaded on October 13,2023 at 15:52:26 UTC from IEEE Xplore. Restrictions apply.

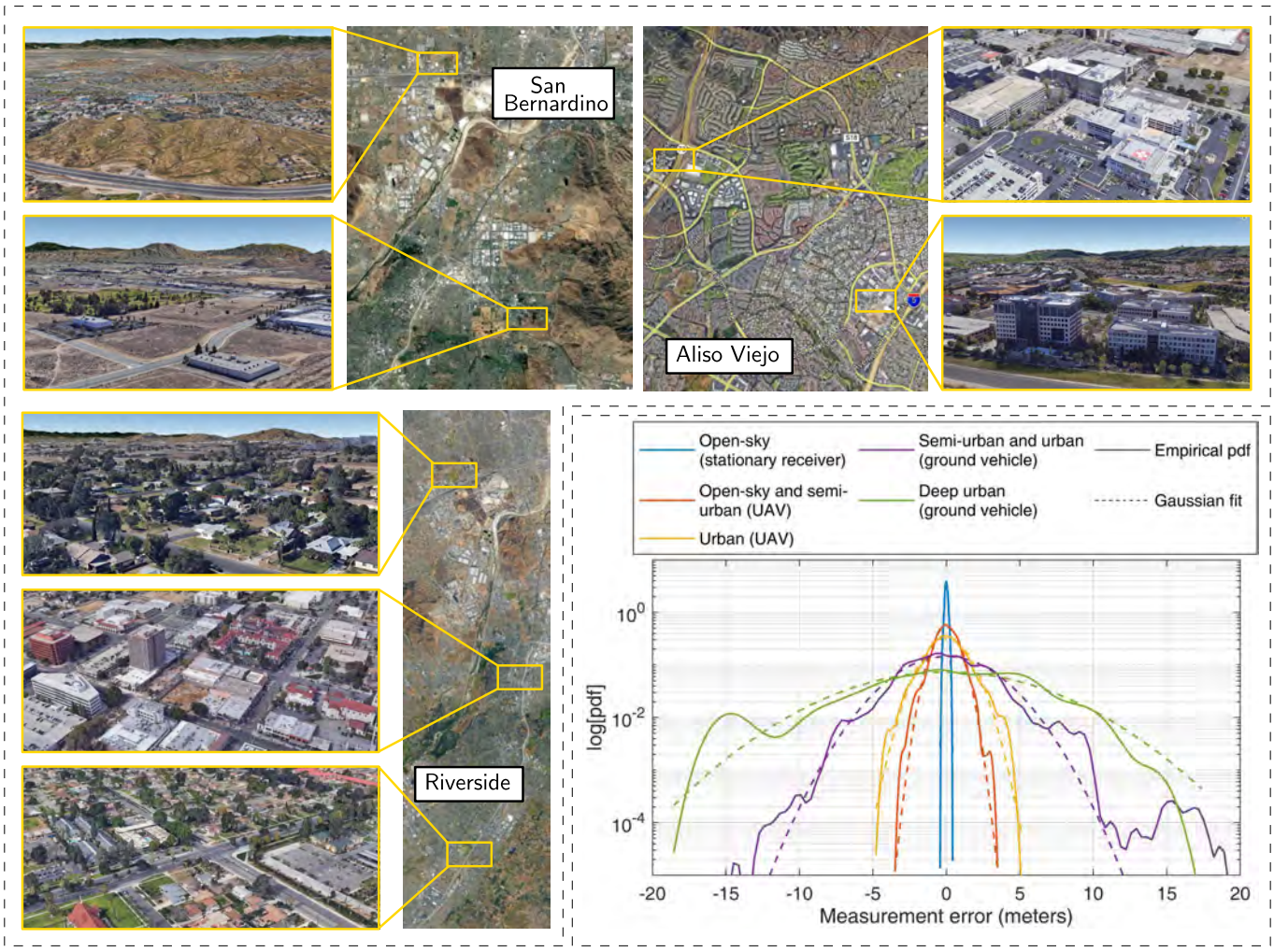

Fig. 2. Characterization of cellular SOP pseudoranges: SOPs environments in different locales in California, USA and corresponding pdfs.

between the receiver's and transmitter's clock biases, i.e.,

$$c \cdot \left[\delta t_r(k) - \delta t_{\mathrm{SOP}_n}(k)\right] = c\dot{\delta t}_{\mathrm{r,SOP}_{n,0}}\, kT + c\delta t_{\mathrm{r,SOP}_{n,0}}.$$

The constants $c\dot{\delta t}_{\mathrm{r,SOP}_{n,0}}$ and $c\delta t_{\mathrm{r,SOP}_{n,0}}$ are estimated by post-processing the recorded data from time-step 0 to time-step K via an LS estimator, which minimizes the cost function $\mathbf{G}$ given by

$$\mathbf{G} \triangleq \left\| \boldsymbol{y} - \mathbf{S}\begin{bmatrix} c\dot{\delta t}_{\mathrm{r,SOP}_{n,0}} \\ c\delta t_{\mathrm{r,SOP}_{n,0}} \end{bmatrix} \right\|_2^2,$$

$$\mathbf{S} \triangleq \begin{bmatrix} 0 & T & \dots & KT \\ 1 & 1 & \dots & 1 \end{bmatrix}^{\mathsf{T}},$$

where the LS observation vector $\boldsymbol{y}$ is given by

$$\boldsymbol{y} \triangleq \left[z'_{\mathrm{SOP}_n}(0), \dots, z'_{\mathrm{SOP}_n}(K)\right]^{\mathsf{T}}.$$

The resulting measurement after removing the error due to clock bias difference is given by:

$$z''_{\mathrm{SOP}_n}(k) \triangleq z'_{\mathrm{SOP}_n}(k) - c\dot{\delta t}_{\mathrm{r,SOP}_{n,0}}\, kT - c\delta t_{\mathrm{r,SOP}_{n,0}} \simeq v_{\mathrm{SOP}_n}(k).$$

Although using the first-order polynomial approximation for modeling the SOP clock has been thoroughly studied in the literature [60], [61], this approximation may introduce faults that are not monitored. In Subsection VI-E, the effect of model mismatch in the aforementioned clock model on the measurement error is analyzed.

- **Step 3:** The sample mean and sample variance of the measurement error's pdf are calculated from

$$\hat{\mu}_{\mathrm{SOP}_n} = \frac{1}{K+1}\sum_{k=0}^{K} z''_{\mathrm{SOP}_n}(k),$$

$$\hat{\sigma}^2_{\mathrm{SOP}_n} = \frac{1}{K}\sum_{k=0}^{K}\left[z''_{\mathrm{SOP}_n}(k) - \hat{\mu}_{\mathrm{SOP}_n}\right]^2.$$

Fig. 2 illustrates the empirical pdfs found from the collected measurements. Overlayed on these pdfs are the Gaussian pdf fits with the calculated sample mean $\hat{\mu}_{\mathrm{pdf,sample}}$ and sample variance $\hat{\sigma}_{\mathrm{pdf,sample}}$ over all SOPs. Table II summarizes $\hat{\mu}_{\mathrm{pdf,sample}}$ and $\hat{\sigma}_{\mathrm{pdf,sample}}$ in different environments. Note that the calculated sample means are almost zero due to **Step 2** described above.

With respect to integrity, an overbounding function is conservative if it predicts the occurrence of large navigation errors to be at least as frequent as their actual occurrence [13]. Since both the empirical and overbound plots in Fig. 2 are pdfs and

Authorized licensed use limited to: The Ohio State University. Downloaded on October 13,2023 at 15:52:26 UTC from IEEE Xplore. Restrictions apply.

TABLE II

SAMPLE MEAN ($\hat{\mu}_{\text{pdf,sample}}$) AND SAMPLE VARIANCE ($\hat{\sigma}_{\text{pdf,sample}}$) OF GAUSSIAN PDFS OF PSEUDORANGE MEASUREMENT ERROR IN DIFFERENT ENVIRONMENTS

Altitude	Environment	$\hat{\mu}_{\text{pdf,sample}}$	$\hat{\sigma}_{\text{pdf,sample}}$
–	Open sky	1.41×10^{-15} m	0.11 m
Low altitude	Urban and semi-urban	-1.24×10^{-16} m	2.74 m
	Deep urban	-1.05×10^{-15} m	5.42 m
High altitude	Semi-urban	-3.66×10^{-18} m	0.75 m
	Urban	7.10×10^{-18} m	1.32 m

TABLE III

SINGLE-CDF APPROACH-BASED ($\hat{\mu}_{\text{cdf,overbound}}$) AND SAMPLE VARIANCE ($\hat{\sigma}_{\text{cdf,overbound}}$) OF GAUSSIAN CDFS OF PSEUDORANGE MEASUREMENT ERROR IN DIFFERENT ENVIRONMENTS

Altitude	Environment	$\hat{\mu}_{\text{cdf,overbound}}$	$\hat{\sigma}_{\text{cdf,overbound}}$
–	Open sky	0 m	0.22 m
Low altitude	Urban and semi-urban	0 m	3.02 m
	Deep urban	0 m	5.97 m
High altitude	Semi-urban	0 m	0.97 m
	Urban	0 m	2.64 m

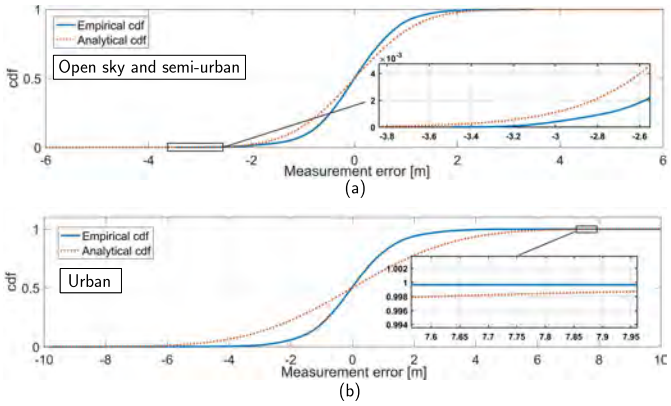

Fig. 3. Characterization of cellular SOP pseudorange measurement accuracy in different environments in which the pseudoranges were collected. Empirical cdf of pseudorange errors and analytical Gaussian cdfs obtained from a single-cdf approach are illustrated for each environment: (a) Open sky and semi-urban and (b) urban.

integrate to one, it is not possible for the pdf overbound to hold for all values of the empirical pdf. In fact, there exists small residuals around the tails, which are not necessarily characterized by a Gaussian distribution. Since the integrity requirements impose constraints at 10^{-7} level, this aspect needs to be analyzed further, validating that the integrity risk is ensured, especially around the tails. Over the past few years, different bounding strategies have been investigated in the literature to construct conservative bounds, which represent the empirical measurement error. The first overbounding approach that successfully provided conservative bounds for the empirical measurement error was DeCleene's single cdf-overbounding approach [63]. In [63], it was proven that the assumption for a zero-mean Gaussian error distribution can be replaced by a requirement that the error distribution is symmetric, unimodal, and whose cdf is bounded by a Gaussian error distribution overbounded for errors less than the mean and underbounded for errors greater than the mean, i.e.,

$$G_o > G_a, \quad G_a \leq 0.5$$
$$G_o \leq G_a, \quad G_a > 0.5,$$

where G_o and G_a are the overbound cdf and the empirical cdf, respectively. To ensure the integrity risk around the tails, the single-cdf overbounding method [63] was implemented. Fig. 3 illustrates the empirical cdfs found from the collected measurements. Overlayed on these cdfs are the cdf overbounds obtained from DeCleene's single cdf-overbounding approach. Table III summarizes $\hat{\mu}_{\text{cdf,overbound}}$ and $\hat{\sigma}_{\text{cdf,overbound}}$ in different environments. As it can be seen from Fig. 3, the integrity is ensured over all empirical measurement errors. Therefore, DeCleene's single cdf-overbounding method was used in this paper during simulations and real-world experiments.

Calculating the SOP measurements' fault rate is a more challenging problem as no official SOP measurement integrity standard has been issued yet. According to the Air Force GPS Standard Positioning Service Performance Standard (SPS PS) [64], the GPS measurement fault is defined by an error greater than 4.42 times the broadcast User Range Accuracy (URA). However, this cannot directly apply to SOP measurements. On one hand, URA cannot be assessed from the measurements and the user needs to receive this parameter from external entities, which ensure the integrity level. On the other hand, the SOP navigation message does not include URA information. The lack of SOP integrity information is analogous to the lack of GLONASS integrity information over the first years of operation, where no URA data was available in the GLONASS's Receiver Independent Exchange Format (RINEX) file. Using the methods that evaluate the GLONASS fault rate without having access to the broadcast URA [15], [65], the SOP fault rate can be approximated. It is first important to establish the type of operating environment. In this paper low-altitude UAV navigation in urban/deep urban environments is considered. One can see from Fig. 2 that the pseudorange error in these environments does not exceed 19.12 m (solid purple curve). Therefore, it is reasonable to consider an induced bias larger than 20 m as a fault. Table III shows that $\hat{\sigma}_{\text{cdf,overbound}} = 5.97$ m for a low-altitude UAV in an urban/deep urban environment. Consequently, the 20 m fault threshold corresponds to 3.35 times the standard deviation of the overbound cdf, which in turn implies that the probability of a cellular SOP transmitter being in a faulty state is 8.08×10^{-4}. The approximated fault bias and the corresponding probability are demonstrated in Fig. 4. It is important to note that the reliability of cellular SOPs has not yet been fully characterized. This is a tedious process that requires thousands of hours of data collection. The SOP integrity parameters obtained in this paper are still preliminary and used as a proof of concept. As the database of collected SOP data grows, these parameters can be further refined. The

Authorized licensed use limited to: The Ohio State University. Downloaded on October 13,2023 at 15:52:26 UTC from IEEE Xplore. Restrictions apply.

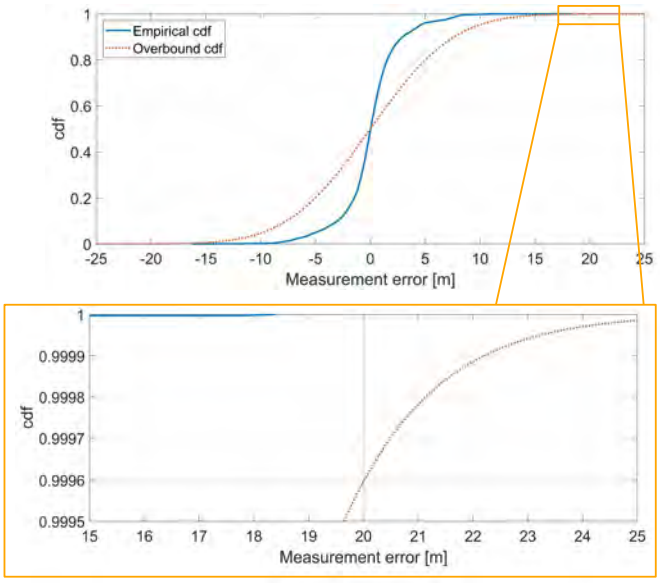

Fig. 4. The approximated fault bias and its corresponding probability. A fault bias of 20 m in magnitude corresponds to an 8.08×10^{-4} fault probability.

aim of this paper is to present a methodology to calculate these parameters and how to use them for UAV integrity monitoring. As such, an 8.08×10^{-4} fault probability could be either conservative or optimistic. However, in the case of the latter, it has been shown in [66] that incorporating SOPs would still yield improvement over GPS-only for high and unlikely SOP fault probabilities of 10^{-2}.

V. PL Reduction via Adding SOPs

RAIM algorithms provide the user with an estimate of the confidence in the position information via PL. Several methods to calculate PL have been proposed in the literature. This paper considers the MHSS-based PL presented in [67], [68] to study the effect of adding SOPs into the transmitter-to-receiver geometry. Formulating other types of RAIM for other SOP-GNSS navigation frameworks is similar and could be investigated in future work. The associated VPL and HPL under fault-free hypothesis are obtained from

$$\begin{aligned}
\mathrm{VPL} &= K_v\, d_{\mathrm{UP}}, \quad d_{\mathrm{UP}} = \sqrt{\sum_{i=1}^{M+N} \mathbf{S}^2{}_{3,i}\, \mathbf{R}_{i,i}}, \\
\mathrm{HPL} &= K_h d_{\mathrm{H}}, \quad d_{\mathrm{H}}^2 = \frac{{d_{\mathrm{E}}}^2 + {d_{\mathrm{N}}}^2}{2} \\
&\quad + \sqrt{\left(\frac{{d_{\mathrm{E}}}^2 - {d_{\mathrm{N}}}^2}{2}\right)^2 + {d_{\mathrm{EN}}}^2}, \\
d_{\mathrm{E}} &= \sqrt{\sum_{i=1}^{M+N} \mathbf{S}^2{}_{1,i}\, \mathbf{R}_{i,i}}, \quad d_{\mathrm{N}} = \sqrt{\sum_{i=1}^{M+N} \mathbf{S}^2{}_{2,i}\, \mathbf{R}_{i,i}}, \\
d_{\mathrm{EN}} &= \sqrt{\sum_{i=1}^{M+N} \mathbf{S}_{1,i}\mathbf{S}_{2,i}\, \mathbf{R}_{i,i}}, \qquad (1)
\end{aligned}$$

where $\mathbf{S} \triangleq \left(\mathbf{H}^{\mathsf{T}}\mathbf{R}^{-1}\mathbf{H}\right)^{-1}\mathbf{H}^{\mathsf{T}}\mathbf{R}^{-1}$ and $\mathbf{X}_{ij}$ denotes the element of i-th row and j-th column of a matrix $\mathbf{X}$. The coefficients K_v and K_h are defined according to

$$K_v \triangleq \Phi^{-1}(1 - \beta_v/2), \quad K_h \triangleq \Phi^{-1}(1 - \beta_h/2),$$

where Φ denotes the cdf of the standard Gaussian distribution and β_v and β_h are the integrity budget for the vertical and horizontal components, whose values are set to 9.8×10^{-8} and 2×10^{-9}, respectively. The risk under potential failure conditions can be evaluated by a faulted hypothesis. The PL for the faulted hypothesis is formulated in [68].

In contrast to the GNSS-only approaches, where the elevation range is limited between some elevation mask and 90 degrees, the proposed GNSS-SOP framework can double the elevation angle range to -90 to 90 degrees. This is due to the fact that UAVs can fly even above the terrestrial SOPs. It is important to note that the improvement in transmitter-to-receiver geometry is highly dependent on the initial configuration of the satellites to which the SOPs are added. For example, if no GNSS satellite at zenith is considered, the reduction obtained by adding a SOP will be much larger. In order to perform a fair comparison and to account for as many as possible satellite configurations, Monte Carlo simulations are adopted with 10^4 realizations, which is large enough to cover a variety of initial satellite configuration.

Next, the PL reduction by incorporating additional GNSS measurements versus additional SOP measurements is investigated as follows. In each Monte Carlo realization, M GNSS satellite azimuth and elevation angles were generated according to

$$\begin{aligned}
az_{\mathrm{GNSS}_m} &\sim \mathcal{U}(-180, 180), \quad m = 1, \ldots, M \\
el_{\mathrm{GNSS}_m} &\sim \mathcal{U}(el_{\mathrm{mask}}, 90), \quad m = 1, \ldots, M,
\end{aligned}$$

where $\mathcal{U}(a, b)$ is the uniform distribution over the interval $[a, b]$ and el_{mask} is a pre-defined elevation mask. Then, an additional measurement at el_{new} and az_{new} was generated according to

$$\begin{aligned}
az_{\mathrm{new}} &\sim \mathcal{U}(-180, 180), \\
el_{\mathrm{new}} &\in \{-90, -80, \ldots, 80, 90\}.
\end{aligned}$$

This model is equivalent to adding a new transmitter into a pre-deployed random set of transmitters, while the elevation angle of the new transmitter can be swept between -90 and 90 degrees. Next, The reduction in the PLs due to adding this new transmitter was recorded at each elevation angle between -90 and 90 degrees. The average and standard deviation of the corresponding PLs' reduction for introducing this additional transmitter at a sweeping elevation angle $-90 \leq el_{\mathrm{new}} \leq 90$ degrees is plotted in Fig. 5 for different values of the pre-deployed transmitters M and different elevation mask el_{mask}. The PLs are calculated using (1).

Fig. 5 clearly shows that while adding more measurements from other satellites decreases the PLs, measurements from transmitters at low elevation angles are more effective in minimizing the PL than transmitters at elevation angles between 0 and 90 degrees. Moreover, by comparing the solid lines and dashed lines from the same colors, it is evident that in the environment with high elevation mask (e.g., deep urban), the amount of reduction in the PL due to adding SOPs

Authorized licensed use limited to: The Ohio State University. Downloaded on October 13,2023 at 15:52:26 UTC from IEEE Xplore. Restrictions apply.

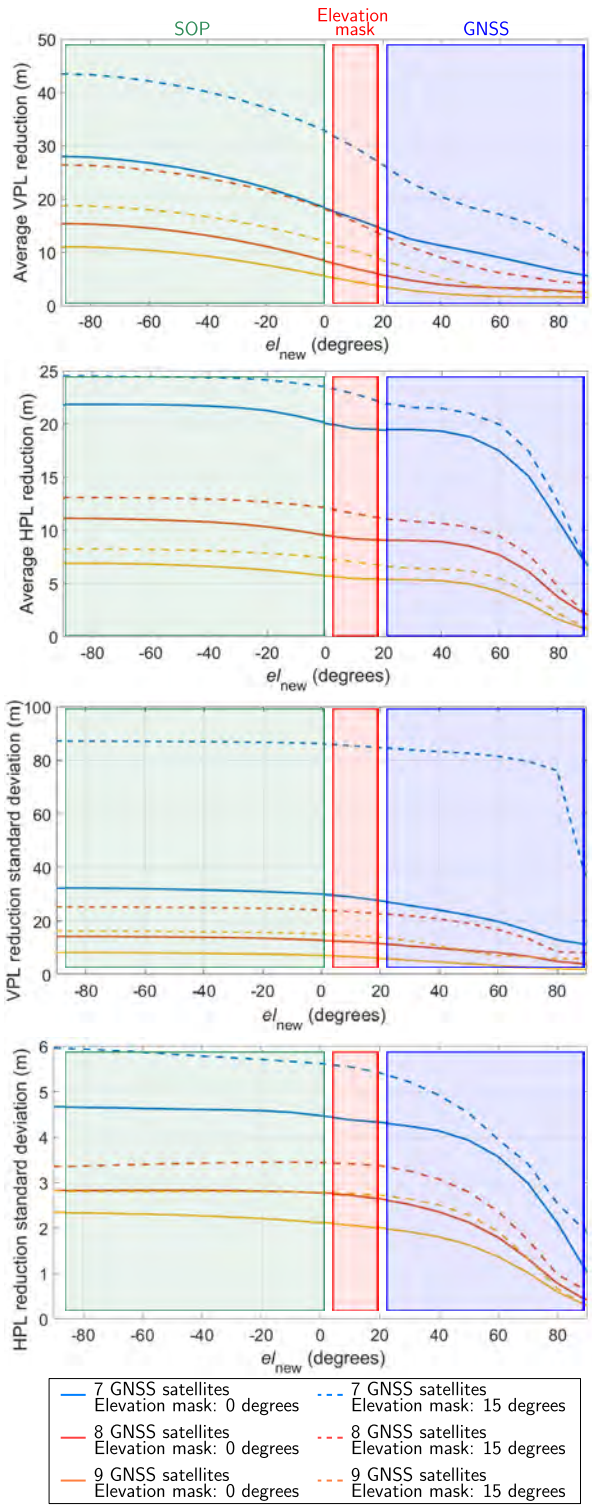

Fig. 5. The average and standard deviation of the reduction in VPL and HPL after adding an additional measurement at an elevation angle $-90 \leq el_{\text{new}} \leq 90$ degrees for $M = 7, \ldots, 9$ and elevation masks: 0 and 15 degrees. The initial values of the VPLs for $M = 7, \ldots, 9$ and elevation masks 0 degrees were 31.67 m, 18.79 m, and 14.31 m; and the initial values of the VPLs for $M = 7, \ldots, 9$ and elevation masks 15 degrees were 47.07, m 29.72 m, and 22.00 m, respectively. This shows the proposed method was able to reduce the VPLs by more than 50%.

is significantly larger than the reduction in the PL due to adding satellites (specifically for VPL). Finally, the Monte Carlo-based analysis under same simulation conditions and

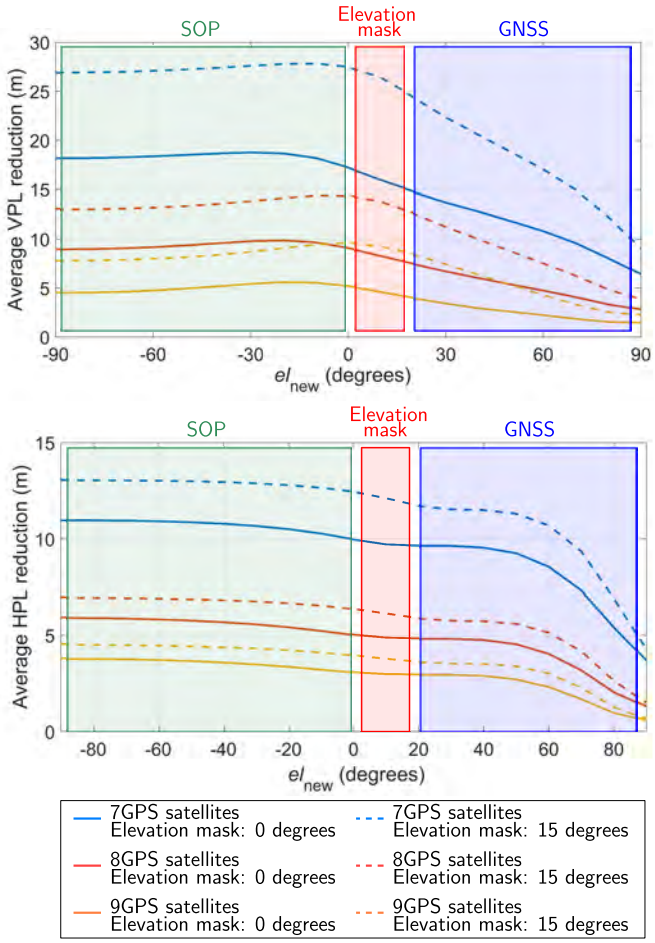

Fig. 6. The reduction in LS RAIM-based VPL and HPL after adding an additional measurement at an elevation angle $-90 \leq el_{\text{new}} \leq 90$ degrees for $M = 7, \ldots, 9$ and elevation masks: 0 and 15 degrees.

data set was repeated for a VPL and a HPL constructed from LS RAIM. The results are shown in Fig. 6. As it can be seen, the results of the LS RAIM was similar to the MHSS-RAIM, which was demonstrated in Fig. 5.

VI. Simulation Results

A simulation test was set up to evaluate the potential of exploiting SOPs for RAIM. To compare the PL of a GPS-only solution with that of a GPS-SOP solution, a stationary receiver at the Madrid Deep Space Communications Complex (MDSCC) was considered. The elevation and azimuth angles of the GPS satellite constellation above the receiver over a 24-hour period was computed using GPS ephemeris files collected at the MDSCC. To illustrate the PL reduction by incorporating SOP observations, 5 additional SOP transmitters were simulated at the test environment, and the resulting PL was evaluated. Throughout different simulations provided in this section, the number of SOP transmitters is fixed (5 SOPs) and their positions are listed in IV. However, in Subsection VI-D, the impact of the number of SOPs on the achieved PL is evaluated by varying the number of SOPs from 0 to 10. The simulation settings are given in Table IV. In Table IV, the UAV's and towers' positions are expressed in Geographic coordinate system.

Authorized licensed use limited to: The Ohio State University. Downloaded on October 13,2023 at 15:52:26 UTC from IEEE Xplore. Restrictions apply.

TABLE IV
SIMULATION SETTINGS

Parameter	Definition	Value
$\{z_{\mathrm{GPS}_m}\}_{m=1}^{M}$	GPS pseudorange measurements	Extracted from the navigation RINEX file (20 July 2006 to 21 July 2006)
β_v	Integrity budget for the vertical component	9.8×10^{-8}
$\boldsymbol{r}_r$	UAV's position	$[40.429200, -4.249700, 900]$
N	Number of SOP transmitters	0-10
M	Number of GPS satellites	5 to 9
T	Sampling time	0.1 s
	SOP clock type	High-quality OCXO
	Receiver clock type	Typical OCXO
$\{\sigma_{\mathrm{GPS}_m}\}_{m=1}^{M}$	GPS measurement noise standard deviation	3 m
$\{\sigma_{\mathrm{SOP}_n}\}_{n=1}^{N}$	SOP measurement noise standard deviation	2 m
$\{\boldsymbol{r}_{\mathrm{SOP}_n}\}_{n=1}^{5}$	Towers' position	$[40.432549, -4.265973, 871]$
		$[40.443643, -4.255776, 1089]$
		$[40.438886, -4.243743, 806]$
		$[40.430516, -4.228286, 778]$
		$[40.421916, -4.248156, 766]$

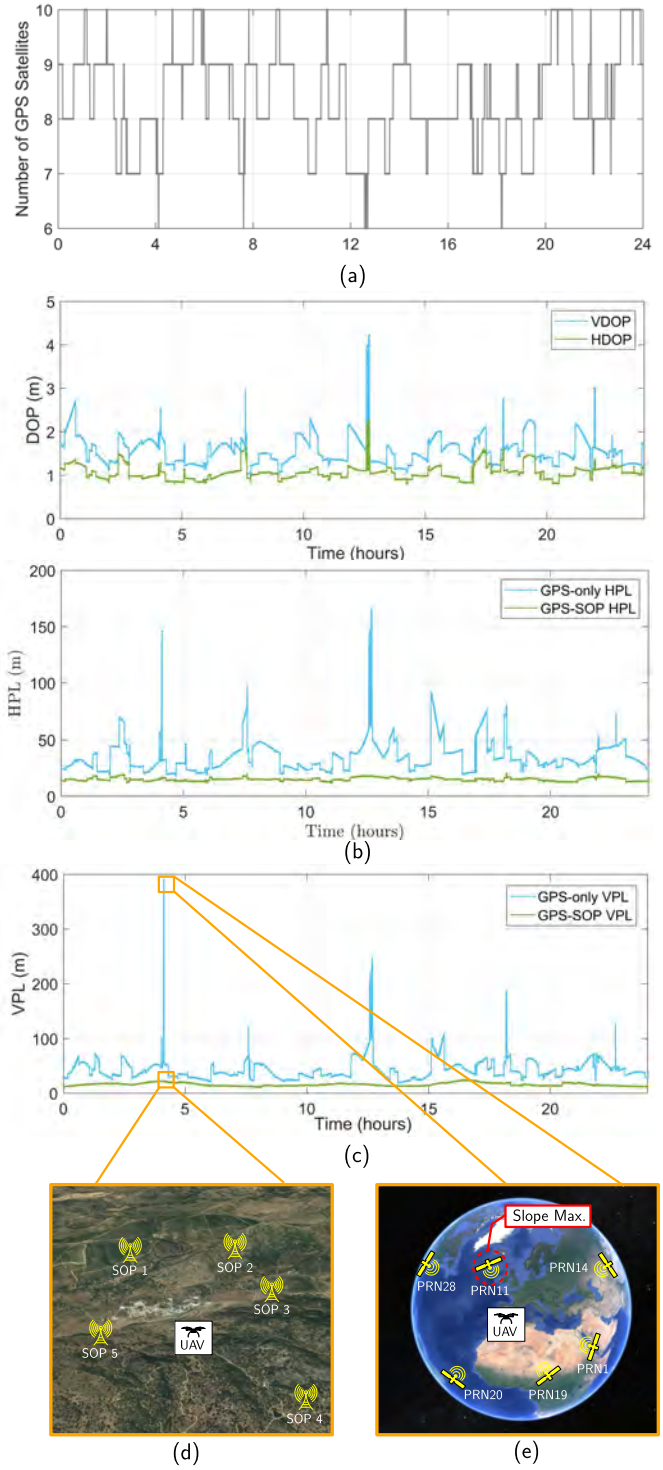

Fig. 7. Simulation environment and the simulation results: (a) The number of available GPS satellites for a 24-hour period. (b) The VDOP and HDOP of available GPS satellites for a 24-hour period, (c) Comparison between GPS-only and GPS-SOP PLs over 24 hours. (d) The simulation environment layout at Madrid Deep Space Communications Complex (MDSCC), the location of the receiver, and position of the SOP towers. (e) An instance where GPS-only VPL was 350 m due to poor satellite-to-receiver geometry.

A. PL Reduction via Adding SOPs

Fig. 7 (a) and (b) illustrates the associated number of available GPS satellites for a 24-hour period and the corresponding DOP metrics. Fig. 7 (c) illustrates the VPL and HPL obtained by the GPS-only solution (blue line) and the proposed GPS-SOP solution (green line). The average GPS-only VPL over 24 hours was 43.36 m, whereas the average GPS-SOP VPL was 16 m. Fig. 7 (c) also shows a few instances where the GPS-only VPL exceeds 200 m. By comparing Fig. 7 (a),(b) and Fig. 7 (c), it is evident that these instances correspond to poor satellite-to-receiver geometry, where the receiver had LOS to only 6 GPS satellites and VDOP is larger than 2.5. Fig. 7 (d) illustrates the simulation environment along with the location of the SOP towers. Fig. 7 (e) illustrates the GPS satellites configuration at a particular instance where the GPS-only VPL and HPL were around 350 m and 150 m, respectively. It can be seen that the PLs are significantly reduced in this instance by incorporating SOP transmitters.

B. Evaluating Different Elevation Masks

Next, the performance of the proposed framework for different elevation mask angles is evaluated. To this end, a simulation was conducted for elevation masks 0 to 23 degrees. The other simulation settings are the same as what has been tabulated in Table IV. In each run, GPS-only PLs and the proposed GPS-SOP PLs were calculated. The results are shown in Fig. 8. As can be seen, the GPS-only PLs were significantly increased by increasing the elevation mask, while the GPS-SOP PLs remained nearly constant. Hence, in the environment with large GPS elevation mask (e.g., deep urban

Authorized licensed use limited to: The Ohio State University. Downloaded on October 13,2023 at 15:52:26 UTC from IEEE Xplore. Restrictions apply.

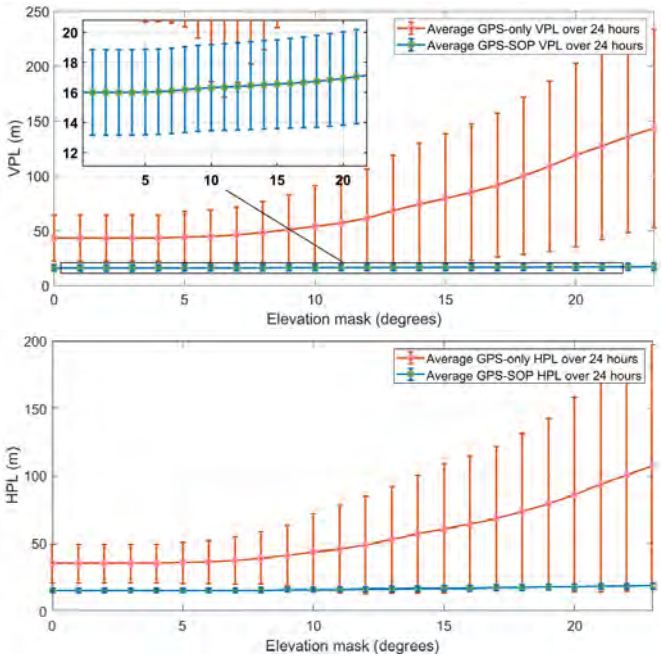

Fig. 8. Comparison between GPS-only PLs and the proposed GPS-SOP PLs for different elevation masks. As can be seen, the GPS-only PLs were significantly increased for large elevation masks, while the GPS-only PLs remained nearly constant. The vertical lines in top plot represent the error bar.

canyon), incorporating SOP measurements can effectively reduce the PLs.

C. Evaluating the Impact of SOP Configuration

This subsection, extends the analysis presented in Subsection VI-A to consider the geometries, which are poor from SOP configuration point of view. The statistics of cellular SOPs' configuration have been studied in the literature. In [69], it was shown that for cellular LTE SOPs, the distribution of the N transmitters' location can be modeled by a binomial point process (BPP) in an annular region $\mathbb{B}_o\,(d_{\min}, d_{\max})$ where o is the origin, $d_{\min}$ is the far-field distance, and $d_{\max}$ is the maximum distance for which the receiver can reliably hear the SOPs (see Fig. 9(a)). Subsequently, the azimuth angles of the SOPs are uniformly distributed between 0 and 2π (see Fig. 9(b)). In [70], [71], it was demonstrated that terrestrial cellular SOPs as far as 3 km can be reliably acquired and tracked by UAVs. As such $d_{\max}$ is set to 3 km. It was also noted experimentally that $d_{\min}$ and can be approximated by 5 m.

The BPP model is used to evaluate the impact of the number of SOPs N on the performance of the proposed framework. To this end, the simulation with a setup presented in Subsection VI-A was conducted for $N = 0$ (GPS-only case) and $N = 1, 2, \ldots, 10$ (GPS-SOP case).

Throughout this test, the location of these 10 SOPs were fixed. Each of these 10 locations was generated using the BPP model. Then, for each of these cases, the simulation configuration tabulated in Table IV was applied and results were re-generated over 24 hours period. Finally, the average

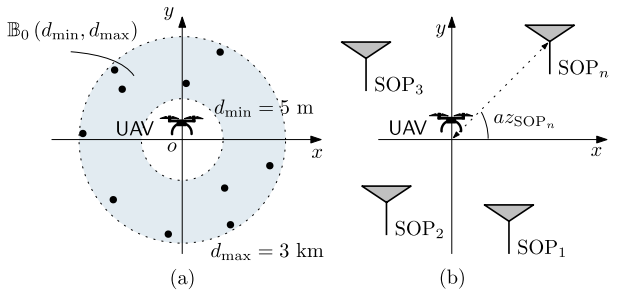

Fig. 9. (a) BPP realization with $N = 10$. (b) The azimuth angles in a BPP are uniformly distributed between 0 and 2π.

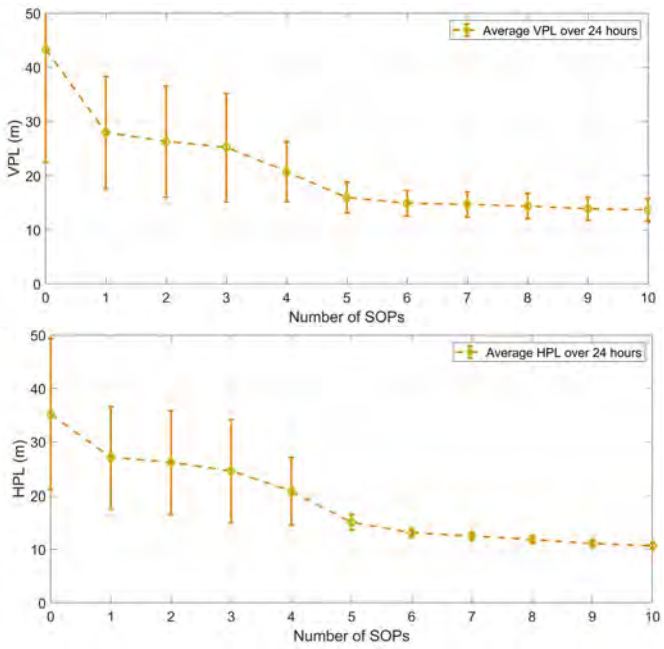

Fig. 10. Impact of the number of SOPs on the achieved PLs over a 24-hour period. The vertical lines in each plot represent the error bar.

of the observed PLs were calculated. The results are shown in Fig. 10. The following can be concluded from this simulation. First, with $N = 1$, the proposed approach achieved an average VPL of 28 m compared to an average VPL of 43.36 m with the GPS-only case ($N = 0$). This shows that even adding one SOP transmitter can significantly reduce the VPL (same conclusion holds for HPL). Second, the results demonstrate the expected behavior that exploiting more SOPs yields higher PL reduction. However, the PL reduction is nearly constant after adding 6 or more SOPs. Third, as can be seen from Fig. 10, SOPs will not contribute negatively, even when the geometry configuration is poor.

D. Considering Other GNSS Constellations

The results presented in Subsection VI-A only considered GPS. In order to study the reduction in PL via adding SOP measurements, while considering other GNSS constellations the simulation setup presented in Subsection VI-A was extended to account for both GPS and GLONASS. To this end, the GLONASS satellites' Keplerian elements

Authorized licensed use limited to: The Ohio State University. Downloaded on October 13,2023 at 15:52:26 UTC from IEEE Xplore. Restrictions apply.

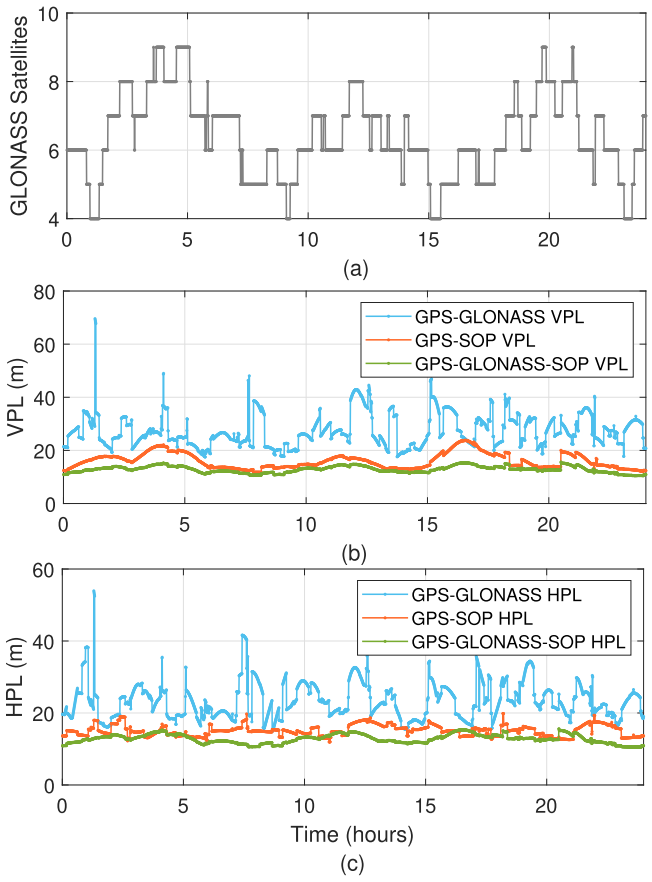

Fig. 11. Simulation results for a GNSS-based navigation system: (a) The number of available GLONASS satellites for a 24-hour period. (b) Comparison between GPS-GLONASS and GPS-GLONASS-SOP PLs over 24 hours. (c) Comparison between GPS-GLONASS and GPS-GLONASS-SOP HPLs over 24 hours.

parameterizing the orbits were extracted from the North American Aerospace Defense Command (NORAD) publicly available database [72]. The orbit's parameters are updated daily in the two-line element (TLE) files. Using TLEs and orbit determination algorithms, the positions and velocities of the GLONASS satellites were calculated for the time and location described in Subsection VI-A. Fig. 11 (a) illustrates the associated number of available GLONASS satellites for a 24-hour period. Fig. 11 (b)-(c) illustrate the VPL and HPL obtained by the GPS-GLONASS solution (blue line), GPS-SOP solution (orange line), and the proposed GPS-GLONASS-SOP solution (green line). Over 24-hours, the average GPS-GLONASS VPL was 27.28 m, the average GPS-SOP VPL was 15.59 m, and the average GPS-GLONASS-SOP VPL was 12.82 m. By comparing Fig. 7 and Fig. 11, it is evident that even in GNSS-based navigation systems, introducing SOP measurements can reduce the VPL by more than 50%. It is important to note that while the number of SOPs were fixed to 5, the number of GLONASS satellites was greater than or equal to 5 in about 99% of the time over 24-hours. Therefore, another important conclusion that can be drawn from this plot is that while the number of GLONASS satellites is more than the SOP transmitters, adding SOP transmitters is more effective in reducing the PLs (compare orange and blue lines). This shows the effectiveness of the proposed method, validating that while adding more measurements from other satellite constellations decreases the PL, measurements from transmitters at (i) low elevation angles are more effective in minimizing the VPL than transmitters at elevation angles between 0 and 90 degrees and (ii) uniformly distributed azimuth angles (which is inherent in certain SOPs by construction, e.g., cellular SOPs), are more effective in minimizing the HPL.

E. Evaluating SOP Clock Model Mismatch

In Section IV, the mismatch between the time evolution of the true clock bias and its first-order polynomial approximation was analyzed. This subsection analyzes the impact of this mismatch component on the measurement error. Define

$$\delta t_{\mathrm{SOP}_n}(k) \triangleq \dot{\delta} t_{\mathrm{SOP}_n} kT + \delta t_{\mathrm{SOP}_{n,0}} + \eta_{r,s_n},$$

where η_{r,s_n} is the mismatch between the true time evolution of $\delta t_{\mathrm{SOP}_n}(k)$ and its first-order approximation. In [43], it was shown that η_{r,s_n} is a zero-mean white random sequence with variance σ^2_{η,r,s_n} and is obtained from the k-th element of the vector

$$\boldsymbol{\eta}_{r,s_n} = \mathbf{GF_1 w_1} + \mathbf{GF_2 w_2}, \tag{2}$$

where

$$\mathbf{w_1} \triangleq \left[w_{\delta t_{r,s_n}}(0), \ldots, w_{\delta t_{r,s_n}}(K-2)\right]^{\mathsf{T}},$$

$$\mathbf{w_2} \triangleq \left[w_{\dot{\delta} t_{r,s_n}}(0), \ldots, w_{\dot{\delta} t_{r,s_n}}(K-3)\right]^{\mathsf{T}},$$

$$\mathbf{F_1} \triangleq \begin{bmatrix} 0 & 0 & \ldots & 0 \\ 1 & 0 & \ldots & 0 \\ \vdots & \vdots & \ddots & \vdots \\ 1 & 1 & \ldots & 1 \end{bmatrix}_{(K)\times(K-1)},$$

$$\mathbf{F_2} \triangleq \begin{bmatrix} 0 & 0 & \ldots & 0 \\ 0 & 0 & \ldots & 0 \\ T & 0 & \ldots & 0 \\ 2T & T & \ldots & 0 \\ \vdots & \vdots & \ddots & \vdots \\ (K-2)T & (K-3)T & \ldots & T \end{bmatrix}_{(K)\times(K-2)},$$

$$\mathbf{G} = \left[\mathbf{I} - \mathbf{S}(\mathbf{S}^{\mathsf{T}}\mathbf{S})^{-1}\mathbf{S}^{\mathsf{T}}\right], \quad \mathbf{S} \triangleq \begin{bmatrix} 0 & T & \ldots & (K-1)T \\ 1 & 1 & \ldots & 1 \end{bmatrix}^{\mathsf{T}},$$

where K is the total number of processed samples; $\mathbf{I}$ is the Identity matrix; and $w_{\delta t_{r,s_n}}$ and $w_{\dot{\delta} t_{r,s_n}}$ are the noise corresponding to the time evolution of the clock bias and clock drift, respectively. Equation (2) implies that the impact of the mismatch error component on the measurement accuracy depends on the quality of the oscillators used in the receiver and in the SOPs' transmitters. Fig. 12 shows σ_{η,r,s_n} for a transmitter equipped with a high-quality oven-controlled crystal oscillator (OCXO), which is a reasonable assumption [54], [73], and four different receivers: (i) a receiver equipped with a high-quality OCXO, (ii) a receiver equipped with a typical OCXO, a receiver equipped with a typical temperature-compensated crystal oscillator (TCXO), and (iv) a receiver equipped with a low-quality TCXO. From Fig. 12, one can see the conservativeness of the mismatch $\eta_{r,s_n}(k)$ due

Authorized licensed use limited to: The Ohio State University. Downloaded on October 13,2023 at 15:52:26 UTC from IEEE Xplore. Restrictions apply.

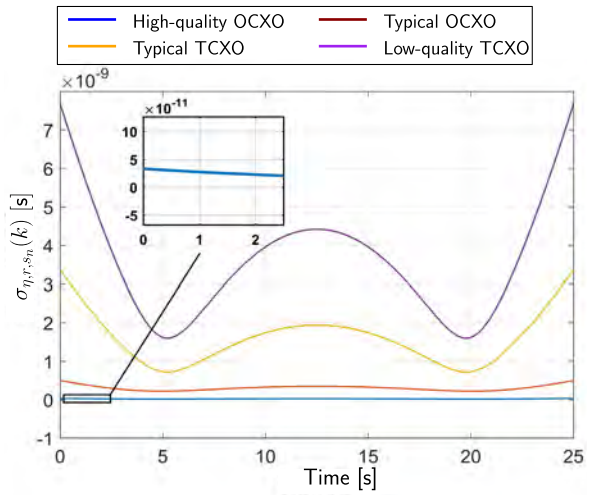

Fig. 12. The standard deviation $\{\sigma_{\eta,r,s_n}(k)\}_{k=0}^{K-1}$ of the vector $\boldsymbol{\eta}_{r,s_n}$ for four receivers, equipped with different oscillators: (i) high-quality OCXO, (ii) typical OCXO, (iii) typical TCXO, and (iv) low-quality TCXO. Here, $K = 2,500$ samples and $T = 0.01$ s.

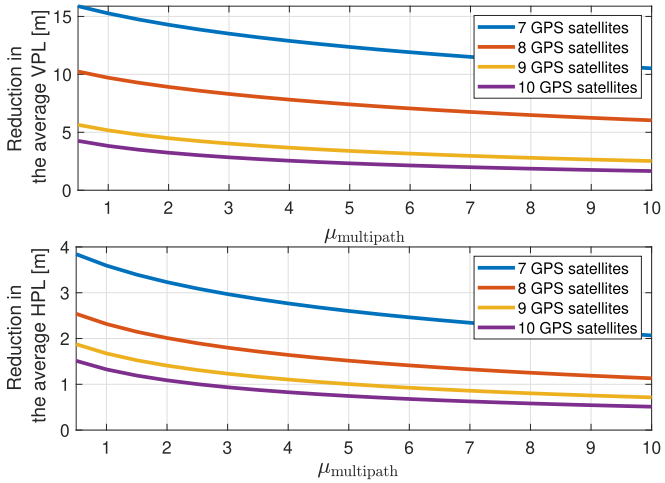

Fig. 13. The expected reduction in VPL and HPL by adding one SOP measurement into the navigation system in a multipath environment. These tests were performed at 10 degrees elevation mask.

to different clock types. The clock bias process noise power spectral densities of the receivers equipped with high-quality OCXO, typical OCXO, typical TCXO, and low-quality TCXO were set to be 1.3×10^{-22} s, 4×10^{-20} s, 4.7×10^{-20} s, and 1×10^{-19} s respectively. As it can be seen from Fig. 12, the mismatch error standard deviation component in the receiver equipped with a high-quality OCXO is about 1 centimeter and in the receiver equipped with a typical OCXO is nearly 10 centimeters. Comparing this with the cdf-overbound variances calculated in Section IV validates that using a first-order polynomial for a fairly stable oscillator is conservative.

F. Evaluating the Effect of Multipath on SOPs

Although cellular SOPs undergo severe multipath effects due to the low elevation angle of the received signal, the literature have shown that the high transmission bandwidth of these signals make them more robust to multipath compared to GNSS signals [74]. Cellular SOP multipath analysis for navigation in urban environment has been investigated in [23], [75], [76], where the statistics of the measurement error in a multipath and multipath-free environment was analyzed. It was shown that the multipath error can be reduced from 15 m to 50 cm by increasing bandwidth from 1.4 MHz to 20 MHz. The impact of the SOP multipath on the integrity of the navigation solution was discussed in [43]. In this subsection, the impact of SOP short multipath delay on VPL reduction is evaluated. For this analysis, LTE SOP is considered. This methodology can be applied to other terrestrial SOP types. In the case of short multipath delays, biases will be induced in the pseudorange measured by the receiver. In [77], a method was proposed to characterize this bias using the channel impulse response (CIR). It was shown that the induced bias can be formulated according to

$$b_n = c\frac{\chi_n}{\kappa}, \quad \kappa \triangleq -\frac{4\pi A^2 \cos\left(\frac{\pi}{2M}\right)}{M\left[\sin\left(\frac{\pi}{2M}\right)\right]^3}, \tag{3}$$

where $M \triangleq \left\lfloor \frac{N_r}{6} \right\rfloor$, N_r denotes the number of subcarriers in the received LTE signal, A denotes signal amplitude, and $\lfloor . \rfloor$ denotes the integer floor function. The term χ_n in (3) denotes the effect of multipath interference on the receiver's delay-locked loop (DLL) and is function of the subcarrier interval, the DLL correlator spacing, the number of subcarrier symbols in the LTE pilot signal, the signal power due to antenna gain and implementation loss, and the normalized symbol timing error. As one can expect, in the presense of significant multipath, this error component gets larger values, therefore, its contribution to the measurement noise gets larger. This effect can be characterized by increasing the ratio between the SOP measurement noise (which has been corrupted by multipath) and GPS measurement noise. In fact, inflating the measurement noise variance to account for multipath is a well-known technique in the multipath mitigation approaches that has been proposed in the literature [78], [79]. Accordingly, it is proposed that the induced bias can be characterized by adding an inflation term to the SOP measurement error. This inflation factor can be formulated as $\mu_{\text{multipath}} \triangleq \sigma^2_{\text{SOP}}/\sigma^2_{\text{GPS}}$. To evaluate the effect of incorporating SOPs in multipath environment, the analysis presented in Section V was performed by swiping the inflation factor $\mu_{\text{multipath}}$ from 0.5 to 10. The results are shown in Fig. 13, where the expected reduction by incorporating one SOP is plotted, considering different values for $\mu_{\text{multipath}}$ and different number of pre-existing GPS satellites. From this figure, it can be seen that the VPL and HPL reduction does not change significantly by increasing $\mu_{\text{multipath}}$, especially for the cases where 8 or more satellites are available in the environment. It is important to mention that this analysis does not aim at formulating SOP multipath, which has been already formulated in (3). In contrast, this analysis aim at evaluating the impact of SOP multipath on the expected reduction in the VPL via the proposed method. Therefore, from Fig. 13, it can be concluded that even in the multipath environments, introducing the SOP transmitter will reduce the PLs. It is evident from this figure that when

Authorized licensed use limited to: The Ohio State University. Downloaded on October 13,2023 at 15:52:26 UTC from IEEE Xplore. Restrictions apply.

Fig. 14. Experimental hardware setup and the traversed trajectory along with the position of cellular LTE SOP towers.

multipath is high, this reduction is less. However, even in multipath environments, incorporating SOP transmitters will not negatively contribute in VPL calculations.

VII. Experimental Results

This section describes the experimental hardware setup and presents the results demonstrating the proposed GNSS-SOP framework for UAV PL reduction.

A. Hardware Setup

A DJI Matrice 600 drone was equipped with a National Instrument (NI) universal software radio peripheral (USRP)-2955 to sample LTE signals at four different carrier frequencies. For this experiment, LTE carrier frequencies 1955, 2145, 2125, and 739 MHz were used, which are allocated to USA operators AT&T, T-Mobile, and Verizon. The sampling rate was set to 10 MSps and the sampled LTE signals were recorded on a laptop. The UAV was also equipped with a Septentrio AsteRx-i V integrated GNSS-IMU sensor [80]. Over the course of the experiment, the ground-truth trajectory of the UAV was obtained from this integrated GNSS-IMU navigation system, while the raw GPS measurements were used to estimate the receiver's position via the framework presented in Section III and to calculate the PL via the approach presented in Section V. Septentrio's post-processing software development kit (PP-SDK) was used to process carrier phase observables collected by the AsteRx-i V and by a nearby differential GPS base station to obtain a carrier phase-based navigation solution. This integrated GNSS-IMU real-time kinematic (RTK) system was used to produce the ground-truth results with which the proposed navigation framework was compared. Fig. 14 shows the experimental hardware setup, the environmental layout of the experiment, the location of the SOP towers, and the ground truth.

Over the course of the experiment, the receiver traversed a trajectory of 823 m over 240 s, while listening to 11 cellular LTE SOP towers. The locations of the towers in the environment were mapped before the experiment. The towers' cell IDs and their corresponding carrier frequencies are presented in Table V.

TABLE V
SOP Towers' Characteristics

Cell ID	Carrier frequency (MHz)
78	2145
104, 352	1955
308, 358, 224, 58, 354	2125
492, 5, 27	739

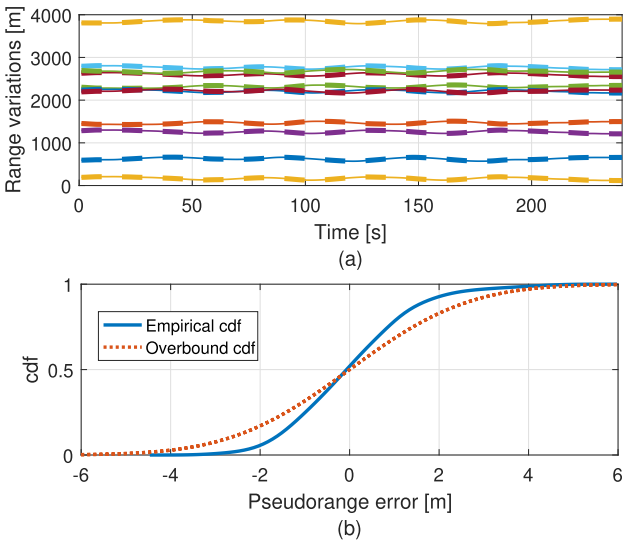

Fig. 15. (a) LTE pseudorange (solid lines) and true range (dashed lines) variations for towers 1 through 11 (different colors correspond to different towers). (b) Empirical cdf and the overbound cdf of the LTE pseudoranges for towers 1 through 11.

The sampled LTE signals were processed offline using the proposed LTE SDR in [23], which was developed in MATLAB. The resulting measurements were used to estimate the receiver's location using the proposed navigation framework.

B. Experimental Results

1) Measurements: Fig. 15 (a) shows LTE pseudorange (solid lines) and true range (dashed lines) variations and Fig. 15 (b) shows the empirical cdf of the LTE pseudorange measurement errors. The overbound cdf obtained from the DeCleene' method [63] are overlayed on this plot. The pseudorange measurement errors were obtained by subtracting the pseudorange measurement from the true range measurement, i.e., $z_{\mathrm{SOP}_n}(k) - \left\| \boldsymbol{r}_r(k) - \boldsymbol{r}_{\mathrm{SOP}_n}(k) \right\|_2$, for $n = 1, \ldots, 11$. The true ranges are known from the knowledge of the transmitters' location and receiver's ground truth position, which was obtained from the integrated GNSS-IMU RTK system. The standard deviations of the pseudoranges for towers 1 through 11 were calculated to be 0.95, 1.54, 0.8, 1.72, 1.03, 1.74, 1.30, 1.78, 1.43, 0.86, and 1.28 m, respectively. It is worth noting that one cannot fairly compare the results of these

Authorized licensed use limited to: The Ohio State University. Downloaded on October 13,2023 at 15:52:26 UTC from IEEE Xplore. Restrictions apply.

TABLE VI
COMPARISON BETWEEN NAVIGATION SOLUTION PERFORMANCE

Scenario	2-D RMSE [m]	3-D RMSE [m]	Average HPE [m]	Average HPL [m]	Average VPE [m]	Average VPL [m]
GPS-only solution	2.34	4.37	2.34	26.32	3.70	27.83
GPS-SOP solution	1.13	3.63	1.13	4.64	3.44	11.99
Reduction	51.46%	16.98%	51.7%	82.37%	7.02%	56.91%

measurements with each other since the received signals from these towers have experienced different carrier-to-noise ratio and multipath conditions.

2) Adding SOPs in the GPS-Based Navigation System: The UAV flew for 240 s, while collecting LTE signals from 11 LTE towers in the environment. The stored LTE signals were then processed by the LTE module of the MATRIX SDR to produce LTE SOP pseudoranges, which were then fused with raw GPS pseudorange measurements obtained from the Septentrio receiver to produce the navigation solution along with the corresponding VPL and HPL. Two sets of results were produced to evaluate the impact of SOP measurements on navigation and on PL: (i) a navigation solution and MHSS RAIM-based PL measures using GPS measurements only and (ii) a navigation solution and MHSS RAIM-based PL using GPS and cellular SOP measurements. The 2-D and 3-D position root-mean squared errors (RMSEs) and the vertical position error (VPE) are tabulated in Table VI for both navigation solutions: GPS-only and GPS-SOP. As it can been from Table VI, incorporating the proposed method reduced the VPL and HPL by 56.91% and 82.37%, respectively. However, comparing the VPLs of GPS-only and GPS-SOP systems alone could be an incomplete comparison as these systems operate on different measurement sets. To address this concern, the gaps between VPL and VPE (i.e., VPL-VPE) is also considered. According to Table VI, the gap between VPL and VPE in GPS-only system is 24.13 m, while the gap between VPL and VPE in GPS-SOP system is 8.55 m. This indicates that the proposed approach was able to provide the navigation system with a tighter vertical bound. As can be seen from Table VI, incorporating SOPs resulted more reduction in the HPL, compared to the VPL. This happened based on the geometric distribution of the satellites in this experiment. The change in the satellites' geometric configuration will result in different reduction rates in HPL and VPL.

Fig. 16 (a) illustrates the GPS satellites' sky plot over Aliso Viejo, California, USA at time 4:40 pm, coordinated universal time (UTC), on June 16, 2019. The elevation and azimuth angles of GPS satellites were computed using GPS ephemeris files extracted from the recorded RINEX file. Fig. 16 (b) illustrates the sky plot for both GPS and SOP transmitters. The red region in Fig. 16 (a)–(b) corresponds to negative elevation angles, at which the SOPs' measurements were received. For

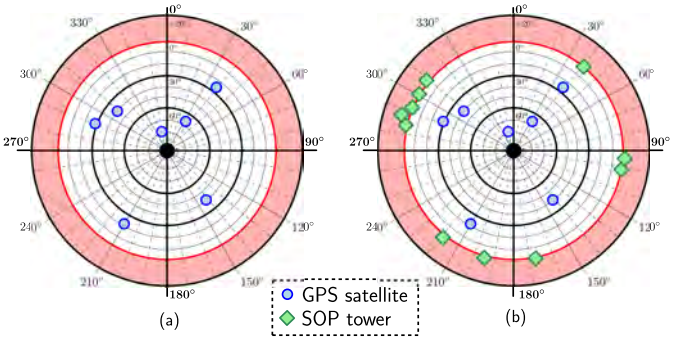

Fig. 16. Sky plot of GPS satellites and SOP towers over Aliso Viejo, California, USA at 4:40 pm, coordinated universal time (UTC), June 16, 2019. The sky plot shows elevation and azimuth angles of transmitters. The red region corresponds to the negative elevation angles, at which the SOPs' measurements were received. (a) GPS satellites. (b) GPS satellites and SOP towers.

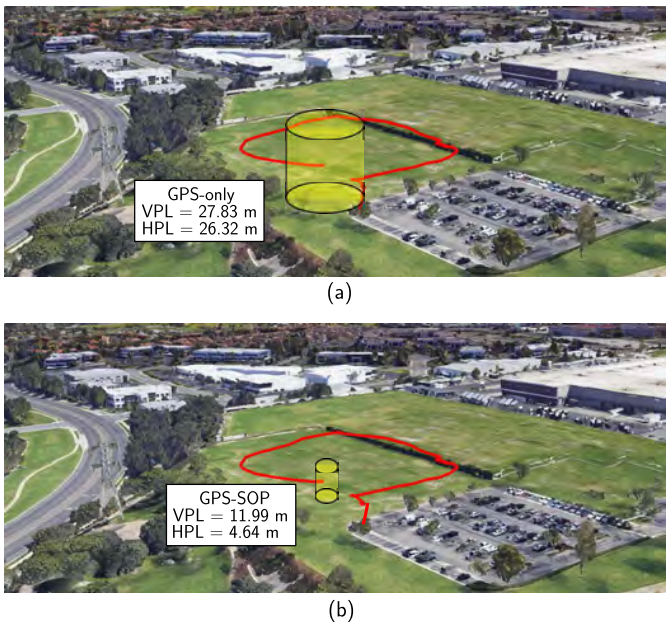

Fig. 17. Comparison between GPS-only and GPS-SOP frameworks. It is evident that incorporating the SOP signals significantly reduces the PLs.

a comparative analysis, the results achieved by the proposed framework is compared to the results achieved by the GBAS framework presented in [53], where it was shown that the VPL and HPL are reduced by 57% and 65%, respectively, when GBAS corrections were used. While the VPL reduction obtained from GBAS is comparable with that obtained from SOPs, the HPL reduction obtained with SOPs is larger than GBAS. Moreover, SOP towers are more abundant than GBAS infrastructure, and SOPs are not limited to airport vicinities; hence, and UAVs navigating in urban environments could benefit from SOPs' transmitted signals.

Fig. 17 (a)–(b) shows the calculated PLs without and with incorporating the SOP signals, respectively.

3) Adding SOPs in the GNSS-Based Navigation System: Next, the impact of adding SOPs in the GNSS-based navigation framework was evaluated. To this end, the experimental results were extended to account for both GPS and GLONASS

Authorized licensed use limited to: The Ohio State University. Downloaded on October 13,2023 at 15:52:26 UTC from IEEE Xplore. Restrictions apply.

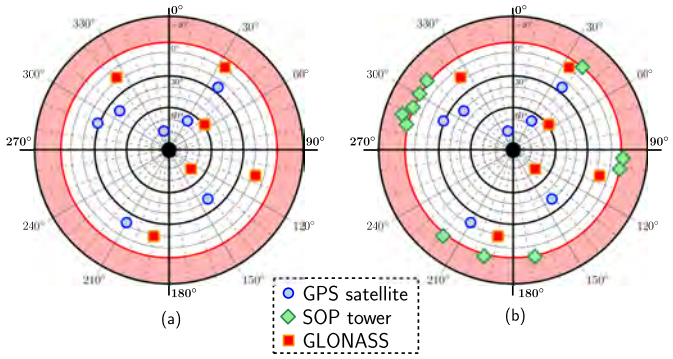

Fig. 18. Sky plot of GNSS satellites and SOP towers over Aliso Viejo, California, USA. (a) GNSS satellites. (b) GNSS satellites and SOP towers.

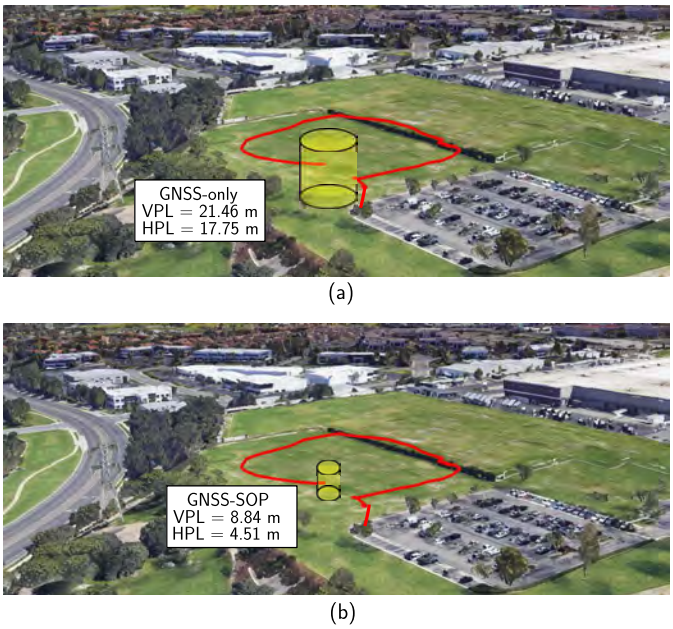

Fig. 19. Comparison between the PLs of (a) GNSS-only and (b) GNSS-SOP frameworks.

satellites. The GLONASS satellites' Keplerian elements parameterizing the orbits were extracted from the navigation RINEX file produced by the Septentrio receiver. Similarly, the GLONASS pseudorange measurements were extracted from the observation RINEX file. Fig. 18 (a) illustrates the GPS and GLONASS satellites' sky plot, while Fig. 18 (b) illustrates the sky plot for the GPS, GLONASS, and SOP transmitters. Fig. 19 (a) and Fig. 19 (b) shows the calculated VPL and HPL using GNSS measurements and using GNSS plus SOP measurements, respectively.

The VPL of the GNSS-only navigation solution was 21.46 m, while the VPL of the proposed GNSS-SOP was 8.84 m. The HPL of the GNSS-only navigation solution was 17.75 m, while the HPL of the proposed GNSS-SOP was 4.51 m. Hence, incorporating the developed framework in this paper reduced the VPL and HPL by 58.8% and 74.6%, respectively. Note that the GNSS-SOP HPL is larger than the GPS-SOP HPL. This could be due to the increased dimensionality of the RAIM algorithm by adding more measurements. More importantly, adding SOPs to GPS only and GNSS improves their respective performances.

VIII. Conclusion

This paper developed a method for reducing the VPL and HPL for a UAV by incorporating SOP measurements into both GPS-based and GNSS-based navigation systems. First, the statistics of cellular SOP measurement errors were characterized from extensive data collected over the past few years in different environments and from different providers, transmitting at different frequencies and bandwidths. Then, It was demonstrated that the VPL of the GNSS-only solution can be reduced by exploiting the inherently small elevation angles of terrestrial SOPs and the HPL can be reduced by exploiting the SOPs' well-spaced azimuth angles. The impact of common SOP measurement errors were evaluated, including clock bias and multipath errors. Finally, a real-world experimental test over a total traversed trajectory of 823 m was performed to validate the efficacy of the proposed framework. Results showed that introducing the SOP measurements into GPS and GNSS navigation systems reduced VPL by 56.9% and 58.8%, respectively, while the HPL was reduced by 82.4% and 74.6%, respectively. It is important to note that the GNSS satellite configuration benefits from more favorable geometry, compared to GPS-only satellite configuration. As a result, it is harder to improve the GNSS-geometry further by incorporating SOPs, compared to improving the GPS-only geometry. Nevertheless, as shown in the paper, incorporating SOPs reduces the HPL and VPL for both GPS-only and GNSS-only. Although it was shown that incorporating SOPs can improve both navigation accuracy and reduce the PL, the lack of commitment from SOP providers can be considered as a drawback of the proposed approach, which could be the subject of future work.

Acknowledgment

The authors would like to thank Kimia Shamaei for her help with data collection and processing.

References

[1] T. Murfin, "UAV report: Growth trends & opportunities for 2019," *GPS World Mag.*, vol. 29, no. 10, pp. S2–S9, Oct. 2018.
[2] Z. M. Kassas, P. Closas, and J. Gross, "Navigation systems panel report navigation systems for autonomous and semi-autonomous vehicles: Current trends and future challenges," *IEEE Aerosp. Electron. Syst. Mag.*, vol. 34, no. 5, pp. 82–84, May 2019.
[3] S. M. Saab and Z. M. Kassas, "Power matching approach for GPS coverage extension," *IEEE Trans. Intell. Transp. Syst.*, vol. 7, no. 2, pp. 156–166, Jun. 2006.
[4] J.-I. Meguro, T. Murata, J.-I. Takiguchi, Y. Amano, and T. Hashizume, "GPS multipath mitigation for urban area using omnidirectional infrared camera," *IEEE Trans. Intell. Transp. Syst.*, vol. 10, no. 1, pp. 22–30, Mar. 2009.
[5] C. Rose, J. Britt, J. Allen, and D. Bevly, "An integrated vehicle navigation system utilizing lane-detection and lateral position estimation systems in difficult environments for GPS," *IEEE Trans. Intell. Transp. Syst.*, vol. 15, no. 6, pp. 2615–2629, Dec. 2014.
[6] R. T. Ioannides, T. Pany, and G. Gibbons, "Known vulnerabilities of global navigation satellite systems, status, and potential mitigation techniques," *Proc. IEEE*, vol. 104, no. 6, pp. 1174–1194, Jun. 2016.
[7] D. Borio, F. Dovis, H. Kuusniemi, and L. L. Presti, "Impact and detection of GNSS jammers on consumer grade satellite navigation receivers," *Proc. IEEE*, vol. 104, no. 6, pp. 1233–1245, Jun. 2016.

Authorized licensed use limited to: The Ohio State University. Downloaded on October 13,2023 at 15:52:26 UTC from IEEE Xplore. Restrictions apply.

[8] R. Toledo-Moreo, D. Betaille, and F. Peyret, "Lane-level integrity provision for navigation and map matching with GNSS, dead reckoning, and enhanced maps," *IEEE Trans. Intell. Transp. Syst.*, vol. 11, no. 1, pp. 100–112, Mar. 2010.

[9] D. Salos, "Integrity monitoring applied to the reception of GNSS signals in urban environments," Ph.D. dissertation, Dept. Mathématiques Informatique Télécommun., Nat. Polytech. Inst. Toulouse, Univ. Toulouse, Toulouse, France, 2012.

[10] K. Ansari, Y. Feng, and M. Tang, "A runtime integrity monitoring framework for real-time relative positioning systems based on GPS and DSRC," *IEEE Trans. Intell. Transp. Syst.*, vol. 16, no. 2, pp. 980–992, Apr. 2015.

[11] N. Zhu, J. Marais, D. Betaille, and M. Berbineau, "GNSS position integrity in urban environments: A review of literature," *IEEE Trans. Intell. Transp. Syst.*, vol. 19, no. 9, pp. 2762–2778, Sep. 2018.

[12] Q. Sun and J. Zhang, "RAIM method for improvement on GNSS reliability and integrity," in *Proc. IEEE/AIAA 28th Digit. Avionics Syst. Conf.*, Oct. 2009, pp. 3–11.

[13] J. Rife, S. Pullen, P. Enge, and B. Pervan, "Paired overbounding for nonideal LAAS and WAAS error distributions," *IEEE Trans. Aerosp. Electron. Syst.*, vol. 42, no. 4, pp. 1386–1395, Oct. 2006.

[14] A. Ene, J. Blanch, and T. Walter, "Galileo-GPS RAIM for vertical guidance," in *Proc. Nat. Tech. Meeting Inst. Navigat.*, Jan. 2006, pp. 18–20.

[15] T. Walter, J. Blanch, M. J. Choi, T. Reid, and P. Enge, "Incorporating GLONASS into aviation RAIM receivers," in *Proc. Int. Tech. Meeting Inst. Navigat.*, Jan. 2013, pp. 239–249.

[16] P. Roysdon and J. Farrell, "GPS-INS outlier detection and elimination using a sliding window filter," in *Proc. Amer. Control Conf.*, May 2017, pp. 1244–1249.

[17] A. V. Kanhere and G. X. Gao, "Integrity for GPS/LiDAR fusion utilizing a RAIM framework," in *Proc. 31st Int. Tech. Meeting Satell. Division Inst. Navigat. (ION GNSS+)*, Oct. 2018, pp. 3145–3155.

[18] J. McEllroy, "Navigation using signals of opportunity in the AM transmission band," M.S. thesis, Dept. Air Force, Air Force Inst. Technol., Air Univ., Wright-Patterson Air Force Base, OH, USA, 2006.

[19] A. Popleteev, "Indoor positioning using FM radio signals," Ph.D. dissertation, Univ. Trento, Trento, Italy, 2011.

[20] C. Yang and T. Nguyen, "Tracking and relative positioning with mixed signals of opportunity," *Navigation*, vol. 62, no. 4, pp. 291–311, Dec. 2015.

[21] J. Khalife and Z. M. Kassas, "Navigation with cellular CDMA signals—Part II: Performance analysis and experimental results," *IEEE Trans. Signal Process.*, vol. 66, no. 8, pp. 2204–2218, Apr. 2018.

[22] J. del Peral-Rosado, J. López-Salcedo, F. Zanier, and G. Seco-Granados, "Position accuracy of joint time-delay and channel estimators in LTE networks," *IEEE Access*, vol. 6, pp. 25185–25199, 2018.

[23] K. Shamaei and Z. M. Kassas, "LTE receiver design and multipath analysis for navigation in urban environments," *Navigation*, vol. 65, no. 4, pp. 655–675, Dec. 2018.

[24] Z. Kassas, A. Abdallah, and M. Orabi, "Carpe signum: Seize the signal—Opportunistic navigation with 5G," *Inside GNSS Mag.*, vol. 16, no. 1, pp. 52–57, 2021.

[25] L. Chen, O. Julien, P. Thevenon, D. Serant, A. G. Pena, and H. Kuusniemi, "TOA estimation for positioning with DVB-T signals in outdoor static tests," *IEEE Trans. Broadcast.*, vol. 61, no. 4, pp. 625–638, Dec. 2015.

[26] C. Yang, T. Nguyen, and E. Blasch, "Mobile positioning via fusion of mixed signals of opportunity," *IEEE Aerosp. Electron. Syst. Mag.*, vol. 29, no. 4, pp. 34–46, Apr. 2014.

[27] D. Lawrence *et al.*, "Navigation from LEO: Current capability and future promise," *GPS World Mag.*, vol. 28, no. 7, pp. 42–48, Jul. 2017.

[28] T. G. R. Reid, A. M. Neish, T. Walter, and P. K. Enge, "Broadband LEO constellations for navigation," *Navigation*, vol. 65, no. 2, pp. 205–220, Jun. 2018.

[29] Z. Kassas, J. Morales, and J. Khalife, "New-age satellite-based navigation—STAN: Simultaneous tracking and navigation with LEO satellite signals," *Inside GNSS Mag.*, vol. 14, no. 4, pp. 56–65, 2019.

[30] Z. Kassas, J. Khalife, M. Neinavaie, and T. Mortlock, "Opportunity comes knocking: Overcoming GPS vulnerabilities with other satellites' signals," *Inside Unmanned Syst. Mag.*, pp. 30–35, Jun./Jul. 2020.

[31] R. M. Faragher and R. K. Harle, "Towards an efficient, intelligent, opportunistic smartphone indoor positioning system," *Navigation*, vol. 62, no. 1, pp. 55–72, Mar. 2015.

[32] Y. Zhuang, Z. Syed, Y. Li, and N. El-Sheimy, "Evaluation of two WiFi positioning systems based on autonomous crowdsourcing of handheld devices for indoor navigation," *IEEE Trans. Mobile Comput.*, vol. 15, no. 8, pp. 1982–1995, Aug. 2016.

[33] R. Faragher, "Effects of multipath interference on radio positioning systems," Ph.D. dissertation, Dept. Phys., Univ. Cambridge, Cambridge, U.K., 2007.

[34] L. A. Merry, R. M. Faragher, and S. Schedin, "Comparison of opportunistic signals for localisation," in *Proc. IFAC Symp. Intell. Auton. Veh.*, Sep. 2010, pp. 109–114.

[35] J. Morales, J. Khalife, and Z. Kassas, "Opportunity for accuracy," *GPS World Mag.*, vol. 27, no. 3, pp. 22–29, Mar. 2016.

[36] M. Maaref and Z. M. Kassas, "UAV integrity monitoring measure improvement using terrestrial signals of opportunity," in *Proc. 32nd Int. Tech. Meeting Satell. Division Inst. Navigat. (ION GNSS+)*, Oct. 2019, pp. 3045–3056.

[37] E. Kaplan and C. Hegarty, *Understanding GPS: Principles and Applications*, 2nd ed. Norwood, MA, USA: Artech House, 2005.

[38] T. G. Needham and M. S. Braasch, "Gravity model error considerations for high-integrity GNSS-aided INS operations," in *Proc. IEEE/ION Position, Location Navigat. Symp. (PLANS)*, Apr. 2018, pp. 822–832.

[39] A. Hassani, N. Morris, M. Spenko, and M. Joerger, "Experimental integrity evaluation of tightly-integrated IMU/LiDAR including return-light intensity data," in *Proc. 32nd Int. Tech. Meeting Satell. Division Inst. Navigat. (ION GNSS+)*, Oct. 2019, pp. 2637–2658.

[40] J. E. Angus, "RAIM with multiple faults," *Navigation*, vol. 53, no. 4, pp. 249–257, Dec. 2006.

[41] M. Joerger, F. Chan, and B. Pervan, "Solution separation versus residual-based RAIM," *J. Navigat.*, vol. 61, no. 61, pp. 237–330, Jun. 2014.

[42] D. Borio and C. Gioia, "Galileo: The added value for integrity in harsh environments," *Sensors*, vol. 16, no. 1, p. 111, Jan. 2016.

[43] M. Maaref and Z. M. Kassas, "Measurement characterization and autonomous outlier detection and exclusion for ground vehicle navigation with cellular signals," *IEEE Trans. Intell. Vehicles*, vol. 5, no. 4, pp. 670–683, Dec. 2020.

[44] R. Brown and P. McBurney, "Self-contained GPS integrity checks using maximum solution separation as the test statistic," in *Proc. Int. Tech. Meeting Satell. Division The Inst. Navigat.*, Sep. 1987, pp. 263–268.

[45] B. S. Pervan, S. P. Pullen, and J. R. Christie, "A multiple hypothesis approach to satellite navigation integrity," *Navigation*, vol. 45, no. 1, pp. 61–71, Mar. 1998.

[46] J. Blanch *et al.*, "A proposal for multi-constellation advanced RAIM for vertical guidance," in *Proc. Int. Tech. Meeting Satell. Division The Inst. Navigat.*, Sep. 2011, pp. 2665–2680.

[47] J. Blanch *et al.*, "Advanced RAIM user algorithm description: Integrity support message processing, fault detection, exclusion, and protection level calculation," in *Proc. ION GNSS Conf.*, Sep. 2012, pp. 2828–2849.

[48] B. Belabbas, P. Remi, and M. Meurer, "Performance assessment of GBAS CAT III using GPS and Galileo," in *Proc. ION GNSS Conf.*, Sep. 2008, pp. 2945–2952.

[49] T. Dautermann, C. Mayer, F. Antreich, A. Konovaltsev, B. Belabbas, and U. Kälberer, "Non-Gaussian error modeling for GBAS integrity assessment," *IEEE Trans. Aerosp. Electron. Syst.*, vol. 48, no. 1, pp. 693–706, Jan. 2012.

[50] Z. Wang, C. Macabiau, J. Zhang, and A. Escher, "Prediction and analysis of GBAS integrity monitoring availability at LinZhi airport," *GPS Solutions*, vol. 18, pp. 27–40, 2014.

[51] R. Sabatini, T. Moore, and C. Hill, "Avionics-based GNSS integrity augmentation synergies with SBAS and GBAS for safety-critical aviation applications," in *Proc. IEEE/AIAA Digit. Avionics Syst. Conf.*, Sep. 2016, pp. 1–10.

[52] M. Caamano, M. Felux, M. Circiu-Simona, and D. Gerbeth, "Multi-constellation GBAS: How to benefit from a second constellation," in *Proc. IEEE/ION Position, Location Navigat. Symp.*, Apr. 2016, pp. 833–841.

[53] Y. Zhu, Y. Liu, Z. Wang, and Q. Li, "Evaluation of GBAS flight trials based on BDS and GPS," *IET Radar, Sonar, Navigat.*, vol. 14, no. 2, pp. 233–241, Feb. 2020.

[54] Z. Kassas, V. Ghadiok, and T. Humphreys, "Adaptive estimation of signals of opportunity," in *Proc. ION GNSS Conf.*, Sep. 2014, pp. 1679–1689.

[55] J. J. Morales and Z. M. Kassas, "Optimal collaborative mapping of terrestrial transmitters: Receiver placement and performance characterization," *IEEE Trans. Aerosp. Electron. Syst.*, vol. 54, no. 2, pp. 992–1007, Apr. 2018.

Authorized licensed use limited to: The Ohio State University. Downloaded on October 13,2023 at 15:52:26 UTC from IEEE Xplore. Restrictions apply.

[56] A. Rodriguez, C. Tiberius, R. Bree, and Z. Geradts, "Google timeline accuracy assessment and error prediction," *Forensic Sci. Res.*, vol. 3, no. 3, pp. 240–255, 2018.
[57] General Data Resources, Inc. (2020). *Antenna Database*. [Online]. Available: http://antennasearch.com
[58] J. Morales and Z. Kassas, "Tightly-coupled inertial navigation system with signals of opportunity aiding," *IEEE Trans. Aerosp. Electron. Syst.*, vol. 57, no. 3, pp. 1930–1948, Jun. 2021.
[59] Z. M. Kassas and T. E. Humphreys, "Observability analysis of collaborative opportunistic navigation with pseudorange measurements," *IEEE Trans. Intell. Transp. Syst.*, vol. 15, no. 1, pp. 260–273, Feb. 2014.
[60] K. Shamaei, J. Khalife, and Z. Kassas, "Performance characterization of positioning in LTE systems," in *Proc. ION GNSS Conf.*, Sep. 2016, pp. 2262–2270.
[61] F. Knutti, M. Sabathy, M. Driusso, H. Mathis, and C. Marshall, "Positioning using LTE signals," in *Proc. Navigat. Conf. Eur.*, Apr. 2015, pp. 1–8.
[62] Z. Kassas, J. Khalife, A. Abdallah, and C. Lee, "I am not afraid of the jammer: Navigating with signals of opportunity in GPS-denied environments," in *Proc. ION GNSS Conf.*, Sep. 2020, pp. 1566–1585.
[63] B. DeCleene, "Defining pseudorange integrity-overbounding," in *Proc. Int. Tech. Meeting Satell. Division Inst. Navigat.*, Sep. 2000, pp. 1916–1924.
[64] GPS Directorate. (Sep. 2008). *Global Positioning System Standard Positioning Service Performance Standard (GPS SPS PS)*. [Online]. Available: http://www.gps.gov/technical/ps/
[65] L. Heng, "Safe satellite navigation with multiple constellations: Global monitoring of GPS and GLONASS signal-in-space anomalies," Ph.D. dissertation, Dept. Elect. Eng., Stanford Univ., Stanford, CA, USA, 2012.
[66] M. Jia, J. Khalife, and Z. Kassas, "Evaluation of ground vehicle protection level reduction due to fusing GPS with faulty terrestrial signals of opportunity," in *Proc. ION Int. Tech. Meeting*, Jan. 2021, pp. 354–365.
[67] *Minimum Operational Performance Standards for Global Positioning System/Wide Area Augmentation System Airborne Equipment*, RTCA, Washington, DC, USA, Dec. 2001.
[68] V. Kropp and G. Berz, "Optimized MHSS ARAIM user algorithms: Assumptions, protection level calculation and availability analysis,"' in *Proc. IEEE/ION Position, Location Navigat. Symp. (PLANS)*, May 2014, pp. 308–323.
[69] M. Haenggi, J. G. Andrews, F. Baccelli, O. Dousse, and M. Franceschetti, "Stochastic geometry and random graphs for the analysis and design of wireless networks," *IEEE J. Sel. Areas Commun.*, vol. 27, no. 7, pp. 1029–1046, Sep. 2009.
[70] K. Shamaei and Z. Kassas, "Sub-meter accurate UAV navigation and cycle slip detection with LTE carrier phase," in *Proc. ION GNSS Conf.*, Sep. 2019, pp. 2469–2479.
[71] J. Khalife and Z. Kassas, "Opportunistic UAV navigation with carrier phase measurements from asynchronous cellular signals," *IEEE Trans. Aerosp. Electron. Syst.*, vol. 56, no. 4, pp. 3285–3301, Aug. 2020.
[72] North American Aerospace Defense Command (NORAD). *Two-Line Element Sets*. Accessed: Feb. 23, 2020. [Online]. Available: http://celestrak.com/NORAD/elements/
[73] K. Wesson, K. Pesyna, J. Bhatti, and T. Humphreys, "Opportunistic frequency stability transfer for extending the coherence time of GNSS receiver clocks," in *Proc. ION GNSS Conf.*, Sep. 2010, pp. 2959–2968.
[74] S. Aditya, A. F. Molisch, and H. M. Behairy, "A survey on the impact of multipath on wideband time-of-arrival based localization," *Proc. IEEE*, vol. 106, no. 7, pp. 1183–1203, Jul. 2018.
[75] C. Gentner, T. Jost, W. Wang, S. Zhang, A. Dammann, and U.-C. Fiebig, "Multipath assisted positioning with simultaneous localization and mapping," *IEEE Trans. Wireless Commun.*, vol. 15, no. 9, pp. 6104–6117, Sep. 2016.
[76] C. Yang and A. Soloviev, "Positioning with mixed signals of opportunity subject to multipath and clock errors in urban mobile fading environments," in *Proc. 31st Int. Tech. Meeting Satell. Division Inst. Navigat. (ION GNSS+)*, Oct. 2018, pp. 223–243.
[77] B. Yang, K. B. Letaief, R. S. Cheng, and Z. Cao, "Timing recovery for OFDM transmission," *IEEE J. Sel. Areas Commun.*, vol. 18, no. 11, pp. 2278–2291, Nov. 2000.
[78] F. Nievinski, "Forward and inverse modeling of GPS multipath for snow monitoring," Ph.D. dissertation, Univ. Colorado, Boulder, CO, USA, 2013.
[79] S. Tay and J. Marais, "Weighting models for GPS pseudorange observations for land transportation in urban canyons," in *Proc. Eur. Workshop GNSS Signals Signal Process.*, Dec. 2013, pp. 1–4.
[80] (2018). *Septentrio AsteRx-i V*. [Online]. Available: https://www.septentrio.com/products

Mahdi Maaref received the B.S. and M.S. degrees from the University of Tehran in 2008 and 2011, respectively, and the Ph.D. degree in electrical engineering from Shahid Beheshti University in 2016. In 2016, he was a Visiting Research Collaborator with the University of Alberta, Edmonton, Canada. He is currently a Post-Doctoral Research Fellow with the University of California, Irvine. He is a member of the Autonomous Systems Perception, Intelligent, and Navigation (ASPIN) Laboratory. His research interests include autonomous ground vehicles, opportunistic perception, and autonomous integrity monitoring.

Joe Khalife (Member, IEEE) received the B.E. degree in electrical engineering and the M.S. degree in computer engineering from Lebanese American University (LAU), and the Ph.D. degree in electrical engineering and computer science from the University of California, Irvine. From 2012 to 2015, he was a Research Assistant at LAU. Since 2015, he has been a member of the ASPIN Laboratory. He is currently a Post-Doctoral Fellow with the University of California, Irvine. He is a member of the Autonomous Systems Perception, Intelligence, and Navigation (ASPIN) Laboratory. His research interests include opportunistic navigation, autonomous vehicles, and software-defined radio. He was a recipient of the 2016 IEEE/ION Position, Location, and Navigation Symposium (PLANS) Best Student Paper Award and the 2018 IEEE Walter Fried Award.

Zaher (Zak) M. Kassas (Senior Member, IEEE) received the B.E. degree in electrical engineering from Lebanese American University, the M.S. degree in electrical and computer engineering from The Ohio State University, and the M.S.E. degree in aerospace engineering and the Ph.D. degree in electrical and computer engineering from The University of Texas at Austin. He is currently an Associate Professor with the University of California, Irvine, and the Director of the Autonomous Systems Perception, Intelligence, and Navigation (ASPIN) Laboratory. He is also the Director of the U.S. Department of Transportation, Center for Automated Vehicles Research with Multimodal AssurEd Navigation (CARMEN), focusing on navigation resiliency and security of highly automated transportation systems. His research interests include cyber-physical systems, estimation theory, navigation systems, autonomous vehicles, and intelligent transportation systems. He was a recipient of the 2018 National Science Foundation (NSF) Faculty Early Career Development Program (CAREER) Award, the 2019 Office of Naval Research (ONR) Young Investigator Program (YIP) Award, the 2018 IEEE Walter Fried Award, the 2018 Institute of Navigation (ION) Samuel Burka Award, and the 2019 ION Col. Thomas Thurlow Award. He is an Associate Editor for the IEEE TRANSACTIONS ON AEROSPACE AND ELECTRONIC SYSTEMS and the IEEE TRANSACTIONS ON INTELLIGENT TRANSPORTATION SYSTEMS.

Authorized licensed use limited to: The Ohio State University. Downloaded on October 13,2023 at 15:52:26 UTC from IEEE Xplore. Restrictions apply.

An Interacting Multiple Model Estimator of LEO Satellite Clocks for Improved Positioning

Nadim Khairallah and Zaher M. Kassas
Department of Mechanical and Aerospace Engineering, University of California, Irvine, USA
Emails: khairaln@uci.edu and zkassas@ieee.org

***Abstract*—An interacting multiple-model (IMM) estimator is developed to adaptively estimate the process noise covariance of low Earth orbit (LEO) satellite clocks for improved positioning. Experimental results are presented showing a stationary ground receiver localizing itself with carrier phase measurements from a single Orbcomm LEO satellite. The developed IMM is shown to reduce the localization error and improve filter consistency over two fixed mismatched extended Kalman filters (EKFs). Starting with an initial receiver position error of 1.45 km, the IMM yielded a final error of 111.26 m, while the errors of a conservative and optimistic EKFs converged to 254.71 m and 429.35 m, respectively.**

***Index Terms*—IMM, navigation, signals of opportunity, low Earth orbit satellites, adaptive estimation.**

I. Introduction

Opportunistic navigation has gained significant attention in recent years to overcome the limitations of global navigation satellite systems (GNSS). This paradigm aims to exploit ambient signals of opportunity (SOPs) in the environment [1], [2]. Various generations of terrestrial cellular signals (3G code-division multiple-access (CDMA), 4G long-term evolution (LTE), and 5G [3]–[6]), have shown the potential of meter-level level accuracy on ground and aerial vehicles [7]–[9]. As for space-based SOPs, low Earth orbit (LEO) space vehicles (SVs) have received significant attention recently, as they could revolutionize satellite-based navigation [10]–[17].

LEO SVs' inherent characteristics make them desirable for navigation. First, LEO SVs are abundant, with around 3,800 active SVs in orbit. The number of LEO SVs is projected to increase dramatically over this decade due to the launch of so-called megaconstellations (e.g., Starlink, Kuiper, etc.) [18]. Second, LEO SVs' configuration relative to a receiver anywhere on Earth yields a low geometric dilution of precision (GDOP), which improves navigation accuracy [19]. Third, LEO SVs transmit in a wide range of frequency bands (e.g., Orbcomm SVs transmit in the very-high frequency band, while Starlink SVs transmit in the Ku-band), which reduces vulnerability to interference. Fourth, LEO SVs are around twenty times closer to Earth than GNSS SVs, which reside in medium Earth orbit (MEO), making the power of received LEO signals up to 2,400 times more powerful than GNSS [20].

However, there are two main challenges to opportunistic navigation using LEO SVs. First, the proprietary signals transmitted by LEO SVs are partially known. This issue can be tackled with the design of specialized receivers that leverage the periodic signals with favorable correlation properties transmitted by the LEO SVs [21], [22]. Even when LEO signals are unknown, cognitive signal processing approaches have been shown to yield useful navigation observables [23], [24]. Second, unlike GNSS SVs, LEO SVs generally do not openly transmit information about their ephemeris and clock error states in their downlink signals. On one hand, among the most accurate publicly available information on ephemerides are two-line element (TLE) file, published and updated periodically by the North American Aerospace Defense Command (NORAD) [25]. These TLE files consist of a set of mean Keplerian elements at a specified epoch that an analytical Simplified General Perturbation (SGP4) model [26] can propagate to any inquiry time. TLEs, however, suffer from errors of a few kilometers at epoch and this error grows throughout propagation. On the other hand, the quality of oscillators onboard LEO SVs is generally unknown and no information is available on the degree of synchronicity of clocks across the constellation network.

As such, LEO SVs' states are uncertain at best (ephemeris) or completely unknown (clock errors). One approach to deal with this is via the simultaneous tracking and navigation (STAN) framework, which estimates the SVs' states simultaneously with the receiver's states [11], [27]. Another approach was proposed in [28], in which LEO SVs' position and velocity process noise was estimated by a receiver, which tracked the LEO SVs by utilizing pseudorange and/or Doppler measurements from LEO SVs' signals.

This paper focuses on the challenge of estimating the process noise covariance of unknown LEO SVs' clocks. Prior work in the context of mapping unknown cellular towers with a mobile ground-based receiver has demonstrated that adaptive estimation of terrestrial SOP clocks improves the estimation performance [29]. This paper considers a "dual" problem in which a stationary receiver localizes itself from signals transmitted by a single LEO SV, while adaptively estimating the unknown clock of the SV. To this end, an interacting multiple-model (IMM) estimator, which uses a bank of extended Kalman filters (EKFs), is developed. IMMs have shown tremendous potential in a variety of applications [30], [31] and have been "adapted" to estimating process and measurement noise statistics [32].

The rest of the paper is organized as follows. Section II presents the clock dynamics and measurement models. Section III details the estimation framework to adaptively localize a stationary receiver using LEO SVs. Section IV presents

experimental results. Section V gives concluding remarks.

II. Model Description

A. Clock Dynamics Model

The receiver and LEO SV clock error states are modeled according to the standard double integrator model with bias δt and drift $\dot{\delta t}$, which evolve according to

$$\dot{\boldsymbol{x}}_{\text{clk}}(t) = \mathbf{A}_{\text{clk}}\,\boldsymbol{x}_{\text{clk}}(t) + \tilde{\boldsymbol{w}}_{\text{clk}}(t), \tag{1}$$

$$\boldsymbol{x}_{\text{clk}} = \begin{bmatrix} \delta t \\ \dot{\delta t} \end{bmatrix}, \quad \tilde{\boldsymbol{w}}_{\text{clk}} = \begin{bmatrix} \tilde{w}_{\delta t} \\ \tilde{w}_{\dot{\delta t}} \end{bmatrix}, \quad \mathbf{A}_{\text{clk}} = \begin{bmatrix} 0 & 1 \\ 0 & 0 \end{bmatrix},$$

where $\tilde{w}_{\delta t}$ and $\tilde{w}_{\dot{\delta t}}$ are zero-mean, mutually independent white noise processes with power spectral density $S_{\tilde{w}_{\delta t}}$ and $S_{\tilde{w}_{\dot{\delta t}}}$, respectively. These power spectra $S_{\tilde{w}_{\delta t}}$ and $S_{\tilde{w}_{\dot{\delta t}}}$ can be related to the power-law coefficients $\{h_\alpha\}_{\alpha=-2}^{2}$, which have been shown through laboratory experiments to be adequate to characterize the power spectral density of the fractional frequency deviation $y(t)$ of an oscillator from nominal frequency, which takes the form $S_y(f) = \sum_{\alpha=-2}^{2} h_\alpha f^\alpha$ [33]. It is common to approximate the clock error dynamics by considering only the frequency random walk coefficient h_{-2} and the white frequency coefficient h_0, which lead to $S_{\tilde{w}_{\delta t}} \approx \frac{h_0}{2}$ and $S_{\tilde{w}_{\dot{\delta t}}} \approx 2\pi^2 h_{-2}$ [34].

Discretizing (1) at a constant sampling period T yields

$$\boldsymbol{x}_{\text{clk}}(k+1) = \mathbf{F}_{\text{clk}}\,\boldsymbol{x}_{\text{clk}}(k) + \boldsymbol{w}_{\text{clk}}(k), \quad k = 0, 1, 2, \ldots \tag{2}$$

where $\boldsymbol{w}_{\text{clk}}$ is a zero-mean white noise sequence with covariance $\mathbf{Q}_{\text{clk}}$

$$\mathbf{Q}_{\text{clk}} = \begin{bmatrix} S_{\tilde{w}_{\delta t}} T + S_{\tilde{w}_{\dot{\delta t}}} \frac{T^3}{3} & S_{\tilde{w}_{\dot{\delta t}}} \frac{T^2}{2} \\ S_{\tilde{w}_{\dot{\delta t}}} \frac{T^2}{2} & S_{\tilde{w}_{\dot{\delta t}}} T \end{bmatrix}, \; \mathbf{F}_{\text{clk}} = \begin{bmatrix} 1 & T \\ 0 & 1 \end{bmatrix}. \tag{3}$$

B. Carrier Phase Measurement Model

The receiver opportunistically extracts carrier phase navigation observables from the LEO SV signals. These carrier phase measurements between the receiver and the m^{th} LEO SV at time-step k corresponding to time $t_k = t_0 + kT$ for some initial time t_0 are modeled according to

$$\begin{aligned} z_m(k) = {} & \|\boldsymbol{r}_r(k) - \boldsymbol{r}_{\text{sv}_m}(k')\|_2 + c\left[\delta t_r(k) - \delta t_{\text{sv}_m}(k')\right] \\ & + \lambda_m N_m + c\delta t_{\text{tropo}_m}(k) + c\delta t_{\text{iono}_m}(k) + v_m(k), \end{aligned} \tag{4}$$

where k' is the time-step corresponding to $t_{k'} = t_k - \delta_{\text{TOF}}$ with δ_{TOF} being the true time-of-flight of the signal from the m^{th} LEO SV to the receiver; $\boldsymbol{r}_r \triangleq [x_r, y_r, z_r]^\mathsf{T}$ and $\boldsymbol{r}_{\text{sv}_m} \triangleq [x_{\text{sv}_m}, y_{\text{sv}_m}, z_{\text{sv}_m}]^\mathsf{T}$ are the receiver's and m^{th} LEO SV's 3-D position, respectively, expressed in the Earth-centered, Earth-fixed (ECEF) reference frame; c is the speed of light; δt_r and δt_{sv_m} are the receiver's and the m^{th} LEO SV's clock bias, respectively; λ_m is the m^{th} LEO SV's carrier wavelength; N_m is the m^{th} LEO SV's carrier phase ambiguity; $\delta t_{\text{tropo}_m}$ and δt_{iono_m} are the tropospheric and ionospheric delays associated with the m^{th} LEO SV's signals, respectively; and $v_m(k)$ is the measurement noise, which is modeled as a zero-mean white Gaussian sequence with variance $\sigma_m^2(k)$.

Assuming no cycle slip occurs when the receiver tracks the carrier phase (i.e., the carrier phase ambiguity remains constant), the difference between the receiver and the m^{th} LEO SV range-equivalent clock biases and the range-equivalent carrier phase ambiguity are lumped into a single term $c\Delta\delta t_m(k)$, simplifying the carrier phase measurement model to

$$\begin{aligned} z_m(k) = {} & \|\boldsymbol{r}_r(k) - \boldsymbol{r}_{\text{sv}_m}(k')\|_2 + c\Delta\delta t_m(k) \\ & + c\delta t_{\text{tropo}_m}(k) + c\delta t_{\text{iono}_m}(k) + v_m(k), \end{aligned} \tag{5}$$

$$c\Delta\delta t_m(k) \triangleq c\left[\delta t_r(k) - \delta t_{\text{sv}_m}(k')\right] + \lambda_m N_m. \tag{6}$$

III. Adaptive Estimation Framework

In multiple-model (MM) estimation, a bank of filters, traditionally Kalman filters (KFs), run in parallel, with each filter in the bank matched to a mode. The output of the MM estimator is obtained by weighing each filter's estimate by their respective innovation likelihood [34]. For systems modeled with Markovian switching probabilities between modes, the computational cost of the exhaustive MM estimator, which keeps track of all mode combinations, grows exponentially with time. Several sub-optimal filters such as the generalized pseudo-Bayesian (GPB) algorithms have been developed to remedy this issue by considering the one-step time history for GPB1 (r hypotheses) and two-step time history for GPB2 (r^2 hypotheses), where r is the number of modes [34]. The interacting multiple-model (IMM) was developed to allow for a two-step history processing using only r filters running in parallel via a mixing stage that computes the initial condition fed to each filter. As a result, the IMM, which has the computational cost of GPB1 but with comparable performance to GPB2, offers a tradeoff between complexity and adaptation capability [35], and is selected as the adaptive filter used in this study.

A single cycle of the IMM for r modes is depicted in Fig. 1, with the following notational definitions:

r	Number of filters
i	$\{1, \ldots, r\} \in \mathbb{N}$
$\hat{\boldsymbol{x}}^i(k-1\|k-1)$	State estimate of filter i
$\mathbf{P}^i(k-1\|k-1)$	Estimation error covariance of filter i
$\mathbf{M}(k-1\|k-1)$	Mixing probability matrix
$\hat{\boldsymbol{x}}^{0i}(k-1\|k-1)$	Mixed initial condition matched to filter i
$\mathbf{P}^{0i}(k-1\|k-1)$	Estimation error covariance associated with $\hat{\boldsymbol{x}}^{0i}(k-1\|k-1)$
$\boldsymbol{z}(k)$	Measurement
$\Lambda_i(k)$	Innovation likelihood of filter i
$\hat{\boldsymbol{x}}^i(k\|k)$	Updated state estimate of filter i
$\mathbf{P}^i(k\|k)$	Updated estimation error covariance of filter i
$\boldsymbol{\pi}$	Mode transition probability matrix
$\boldsymbol{\mu}(k)$	Mode probability vector
$\hat{\boldsymbol{x}}(k\|k)$	Combined state estimate
$\mathbf{P}(k\|k)$	Combined estimation error covariance

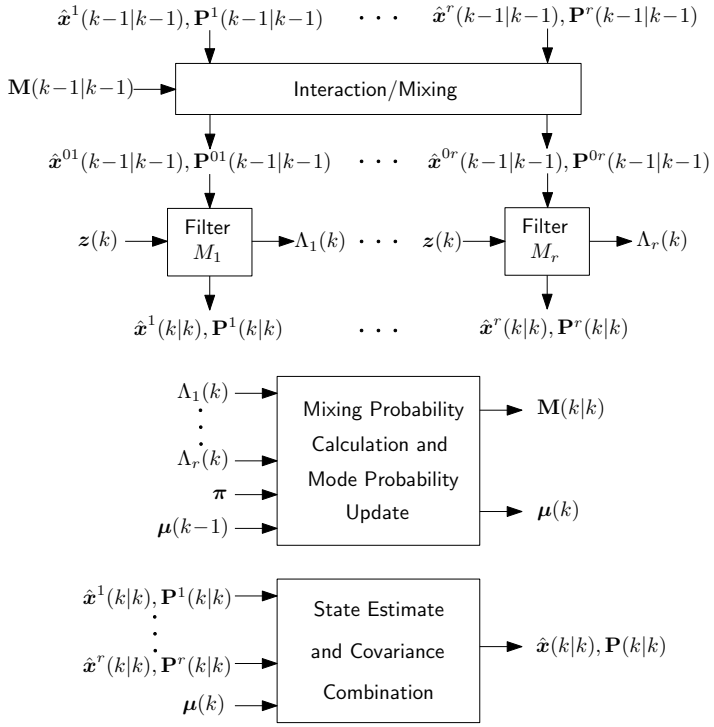

Fig. 1. A single cycle of the IMM filter with r modes.

The IMM algorithm consists of the four following stages, shown in Fig. 1, repeated recursively:

Interaction/mixing: This stage calculates the initial conditions $\hat{\boldsymbol{x}}^{0i}(k{-}1|k{-}1)$ and $\mathbf{P}^{0i}(k{-}1|k{-}1)$ fed to each filter in the bank by combining $\hat{\boldsymbol{x}}^{i}(k{-}1|k{-}1)$ and $\mathbf{P}^{i}(k{-}1|k{-}1)$ using the mixing probability matrix $\mathbf{M}(k{-}1|k{-}1)$.

Mode-matched filtering: This stages performs a regular KF update (prediction and correction), for each KF in the bank, where each filter is matched to a particular mode. It also calculates the innovation likelihood of each filter.

Mixing probability and mode probability update: This stage computes the mixing probability matrix and updates the mode probability vector, based on the innovation likelihood of each filter in the bank.

State estimate and covariance combination: This stage combines the state estimates and estimation error covariances from the individual filters by weighting $\hat{\boldsymbol{x}}^{i}(k|k)$ and $\mathbf{P}^{i}(k|k)$ by their respective mode probabilities from $\boldsymbol{\mu}(k)$.

In this study, an IMM adaptive filter is implemented to estimate the clock error states' process noise covariance online to improve the positioning of an unknown receiver.

The process noise covariance of the clock error states depends on the corresponding oscillator stability. The quality of oscillators vary widely between temperature-compensated crystal oscillator (TCXO), oven-controlled crystal oscillator (OCXO), and chip-scale atomic clock (CSAC). The discrete-time process noise covariance for clock error states is readily calculated from (3), where the power spectral densities $S_{\tilde{w}_{\delta t}}$ and $S_{\tilde{w}_{\delta_t}}$ depend on the power-law coefficients associated with the oscillator stability. Table I summarizes the power-law coefficients of various clock qualities.

The process noise covariance $\mathbf{Q}$ associated with the range-equivalent lumped term (6) only depends on the receiver's and LEO SV's stochastic clock error states as the range-equivalent carrier phase ambiguity is deterministic, and is given by

$$\mathbf{Q} = c^2 \left[\mathbf{Q}_{\mathrm{clk}_r} + \mathbf{Q}_{\mathrm{clk}_{\mathrm{sv}}}\right], \tag{7}$$

where $\mathbf{Q}_{\mathrm{clk}_r}$ and $\mathbf{Q}_{\mathrm{clk}_{\mathrm{sv}}}$ are computed from (3) by using the receiver's and LEO SV's oscillator power spectra, respectively.

TABLE I
CLOCK QUALITY POWER-LAW COEFFICIENT VALUES.

Quality	Coefficients $\{h_0, h_{-2}\}$
Worst TCXO	$\{2.0 \times 10^{-19}, 2.0 \times 10^{-20}\}$
Typical TCXO	$\{9.4 \times 10^{-20}, 3.8 \times 10^{-21}\}$
Typical OCXO	$\{8.0 \times 10^{-20}, 4.0 \times 10^{-23}\}$
Best OCXO	$\{2.6 \times 10^{-22}, 4.0 \times 10^{-26}\}$
CSAC	$\{7.2 \times 10^{-21}, 2.7 \times 10^{-27}\}$

IV. Experimental Results

To demonstrate the improvements in receiver positioning accuracy and filter consistency, achieved via the adaptation in the IMM over mismatched EKFs, Orbcomm SV signals were collected by a stationary receiver. Orbcomm was chosen for this experiment since its SVs openly transmit ephemeris information in their downlink signals [36]. The ephemeris data was decoded by the receiver and used in the estimators as the SV's ground truth trajectory.

A. Experimental Setup and Filter Parameters

A VHF quadrifilar helix antenna was connected to an Ettus E312 Universal Software Radio Peripheral (USRP) disciplined by a NI CDA-2990 OctoClock to sample Orbcomm LEO SV signals at 137-138 MHz at a sampling rate of 2.4 MSps.

An IMM estimator and two fixed mismatched EKFs were implemented to estimate the receiver's position and the lumped term (6) and its rate of change. It is assumed that the receiver has knowledge of its height (e.g., through altimeter measurements) so that the filters effectively estimate the receiver's planar two-dimensional position in a local North-East-Down (NED) frame.

It is hypothesized that the receiver's clock quality lies between a worst TCXO and a best OCXO and that the LEO SV's clock quality lies between a typical TCXO and a CSAC. As a result, the IMM filter runs $r = 4$ different modes, one for each possible combination of receiver-LEO SV clock quality. The IMM filter is initialized with $\mu_i(0) = 1/r,\ i = 1, \ldots, r$ as no prior is available on the oscillators' stability and the Markovian mode transition matrix is given by $\boldsymbol{\pi}_{ij} = \begin{cases} 1-p, & \text{if } i = j = 1, \ldots, r \\ p/(r-1), & \text{if } i \neq j \end{cases}$ where p is the probability of transition to another mode, which is set to 10^{-4}.

The IMM's performance is also compared to that of two mismatched EKFs: a conservative filter which overbounds $\mathbf{Q}$ by assuming a receiver-LEO SV joint clock quality equivalent to a worst TCXO-typical TCXO pair and an optimistic filter which underestimates $\mathbf{Q}$ by assuming a receiver-LEO SV joint clock quality equivalent to a typical OCXO-best OCXO pair.

B. Experimental Results

The USRP sampled downlink signals from Orbcomm FM116 SV for around 4.5 minutes. Carrier phase navigation observables were opportunistically extracted by the receiver and were corrected for tropospheric and ionospheric delays using standard models [37]. The measurement noise variance was time-varying and was calculated based on the LEO SV's elevation angle. All filters were initialized with the same initial receiver position estimate, drawn from a Gaussian distribution with the mean being the true receiver's location and a variance of 10^6 m^2 in the North and East directions as seen in Fig. 2. The initial receiver position error was 1.45 km.

Fig. 2 and Table II summarize the receiver localization performance of the IMM and the two fixed EKFs. The following observations can be drawn from these results. First, the IMM yielded better localization performance than the two mismatched EKFs by decreasing the initial positioning error from 1.45 km to 111.26 m versus 254.71 m and 429.35 m for the conservative and optimistic EKFs, respectively. Second, the IMM's covariance captures well the uncertainty in the positioning error whereas the uncertainty for the EKF overbounding $\mathbf{Q}$ is too conservative and the uncertainty for the EKF underestimating $\mathbf{Q}$ is too optimistic. The above observations can be explained by the fact that mismatched process noise covariances lead to less accurate estimates and filter inconsistency or even divergence as in the case of the optimistic EKF [29]. The adaptation capability of the IMM filter addresses the unknown process noise covariance by estimating it online along the receiver position states. Third, the uncertainty ellipses of all three filters are elongated in the same direction as can be seen in Fig. 2(a). This is explained by the motion of the LEO SV relative to the receiver: more information is available in the direction parallel to the LEO SV's motion, resulting in more uncertainty (i.e., elongated covariance ellipses) in the direction orthogonal to the LEO SV's trajectory depicted in the skyplot of Fig. 2(b).

Fig. 3 shows the time evolution of the IMM mode probabilities and suggests that the combined receiver-LEO SV clocks have comparable stability to a typical TCXO-best OCXO oscillator pair.

If a cycle slip occurs in the carrier phase observables, a sharp step equal to the number of cycles slipped multiplied by the carrier wavelength is suddenly introduced in the time evolution of the lumped term (6). This step will act as a disturbance to any filter estimating (6). It is expected that after the transient period following the cycle slip disturbance, the IMM mode probabilities converge back to the values that correctly characterize the clock error states' process noise covariance.

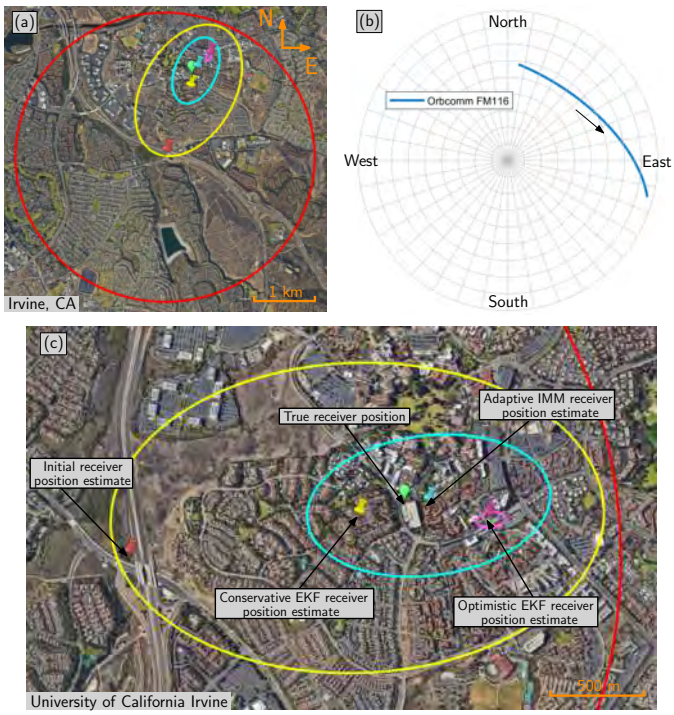

Fig. 2. (a) Experimental results showing true receiver position (green) along with estimates and corresponding 95^{th}-percentile uncertainty ellipses: (i) red: initial estimate, (ii) yellow: conservative EKF, (iii) purple: optimistic EKF, and (iv) blue: IMM. (b) Skyplot of Orbcomm FM116 SV's trajectory relative to the receiver. (c) Zoomed view on the localization performance of different filters. Map data: Google Earth.

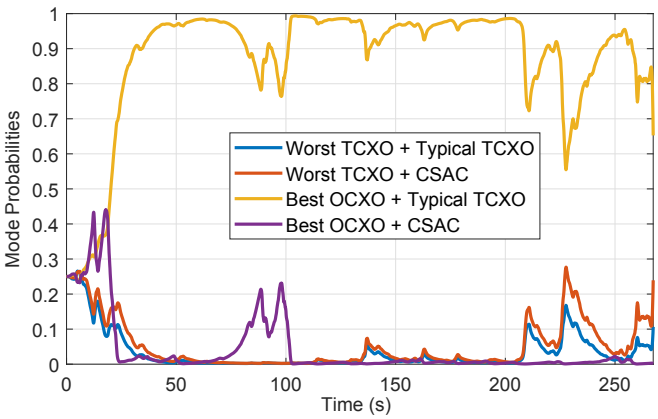

Fig. 3. IMM mode probabilites.

TABLE II
COMPARISON OF IMM VERSUS MISMATCHED FIXED EKFS.

	Adaptive IMM	Conservative EKF	Optimistic EKF
Final error (m)	111.26	254.71	429.35

V. CONCLUSION

This paper developed an IMM estimator to localize a receiver using carrier phase measurements extracted from a single LEO SV's signals. The IMM adaptively estimated the process noise covariance of the combined receiver-LEO SV clock error states. The accuracy and consistency advantages of

the IMM adaptation were showcased experimentally against two fixed mismatched EKFs. The IMM reduced the initial receiver position error from 1.45 km to 111.26 m, while a conservative EKF yielded a final error of 254.71 m and an optimistic EKF diverged to an error of 429.35 m.

ACKNOWLEDGMENTS

This work was supported in part by the Office of Naval Research (ONR) under Grant N00014-19-1-2511 and Grant N00014-19-1-2613, in part by the National Science Foundation (NSF) under Grant 1929965, and in part by the U.S. Department of Transportation (USDOT) under Grant 69A3552047138 for the CARMEN University Transportation Center (UTC). The authors would like to thank Sharbel Kozhaya for his help with data collection and processing.

REFERENCES

[1] J. Raquet *et al.*, "Position, navigation, and timing technologies in the 21st century," J. Morton, F. van Diggelen, J. Spilker, Jr., and B. Parkinson, Eds. Wiley-IEEE, 2021, vol. 2, Part D: Position, Navigation, and Timing Using Radio Signals-of-Opportunity, ch. 35–43, pp. 1115–1412.

[2] N. Souli, P. Kolios, and G. Ellinas, "Online relative positioning of autonomous vehicles using signals of opportunity," *IEEE Transactions on Intelligent Vehicles*, pp. 1–1, 2021.

[3] J. Khalife and Z. Kassas, "Navigation with cellular CDMA signals – part II: Performance analysis and experimental results," *IEEE Transactions on Signal Processing*, vol. 66, no. 8, pp. 2204–2218, April 2018.

[4] P. Wang and Y. Morton, "Multipath estimating delay lock loop for LTE signal TOA estimation in indoor and urban environments," *IEEE Transactions on Wireless Communications*, vol. 19, no. 8, pp. 5518–5530, 2020.

[5] J. Gante, L. Sousa, and G. Falcao, "Dethroning GPS: Low-power accurate 5G positioning systems using machine learning," *IEEE Journal on Emerging and Selected Topics in Circuits and Systems*, vol. 10, no. 2, pp. 240–252, June 2020.

[6] H. Dun, C. Tiberius, and G. Janssen, "Positioning in a multipath channel using OFDM signals with carrier phase tracking," *IEEE Access*, vol. 8, pp. 13 011–13 028, 2020.

[7] C. Yang, T. Nguyen, and E. Blasch, "Mobile positioning via fusion of mixed signals of opportunity," *IEEE Aerospace and Electronic Systems Magazine*, vol. 29, no. 4, pp. 34–46, April 2014.

[8] J. del Peral-Rosado, O. Renaudin, C. Gentner, R. Raulefs, E. Dominguez-Tijero, A. Fernandez-Cabezas, F. Blazquez-Luengo, G. Cueto-Felgueroso, A. Chassaigne, D. Bartlett, F. Grec, L. Ries, R. Prieto-Cerdeira, J. Lopez-Salcedo, and G. Seco-Granados, "Physical-layer abstraction for hybrid GNSS and 5G positioning evaluations," in *Proceedings of IEEE Vehicular Technology Conference*, September 2019, pp. 1–6.

[9] A. Abdallah and Z. Kassas, "UAV navigation with 5G carrier phase measurements," in *Proceedings of ION GNSS Conference*, September 2021, pp. 3294–3306.

[10] R. Landry, A. Nguyen, H. Rasaee, A. Amrhar, X. Fang, and H. Benzerrouk, "Iridium Next LEO satellites as an alternative PNT in GNSS denied environments–part 1," *Inside GNSS Magazine*, vol. 14, no. 3, pp. 56–64., May 2019.

[11] Z. Kassas, J. Morales, and J. Khalife, "New-age satellite-based navigation – STAN: simultaneous tracking and navigation with LEO satellite signals," *Inside GNSS Magazine*, vol. 14, no. 4, pp. 56–65, 2019.

[12] T. Reid, B. Chan, A. Goel, K. Gunning, B. Manning, J. Martin, A. Neish, A. Perkins, and P. Tarantino, "Satellite navigation for the age of autonomy," in *Proceedings of IEEE/ION Position, Location and Navigation Symposium*, 2020, pp. 342–352.

[13] Q. Wei, X. Chen, and Y. Zhan, "Exploring implicit pilots for precise estimation of LEO satellite downlink Doppler frequency," *IEEE Communications Letters*, vol. 24, no. 10, pp. 2270–2274, 2020.

[14] S. Thompson, S. Martin, and D. Bevly, "Single differenced Doppler positioning with low Earth orbit signals of opportunity and angle of arrival estimation," in *Proceedings of ION International Technical Meeting*, 2020, pp. 497–509.

[15] A. Nardin, F. Dovis, and J. Fraire, "Empowering the tracking performance of LEO'-based positioning by means of meta-signals," *IEEE Journal of Radio Frequency Identification*, pp. 1–1, 2021.

[16] R. Cassel, D. Scherer, D. Wilburne, J. Hirschauer, and J. Burke, "Impact of improved oscillator stability on LEO-based satellite navigation," in *Proceedings of ION International Technical Meeting*, January 2022, pp. 893–905.

[17] J. Khalife, M. Neinavaie, and Z. Kassas, "The first carrier phase tracking and positioning results with Starlink LEO satellite signals," *IEEE Transactions on Aerospace and Electronic Systems*, vol. 56, no. 2, pp. 1487–1491, April 2022.

[18] S. Liu, Z. Gao, Y. Wu, D. Kwan Ng, X. Gao, K. Wong, S. Chatzinotas, and B. Ottersten, "LEO satellite constellations for 5G and beyond: How will they reshape vertical domains?" *IEEE Communications Magazine*, vol. 59, no. 7, pp. 30–36, July 2021.

[19] Z. Kassas, M. Neinavaie, J. Khalife, N. Khairallah, J. Haidar-Ahmad, S. Kozhaya, and Z. Shadram, "Enter LEO on the GNSS stage: Navigation with Starlink satellites," *Inside GNSS Magazine*, vol. 16, no. 6, pp. 42–51, 2021.

[20] D. Lawrence, H. Cobb, G. Gutt, M. OConnor, T. Reid, T. Walter, and D. Whelan, "Navigation from LEO: Current capability and future promise," *GPS World Magazine*, vol. 28, no. 7, pp. 42–48, July 2017.

[21] F. Farhangian and R. Landry, "Multi-constellation software-defined receiver for Doppler positioning with LEO satellites," *Sensors*, vol. 20, no. 20, pp. 5866–5883, October 2020.

[22] C. Pinell, "Receiver architectures for positioning with low Earth orbit satellite signals," Master's thesis, Lulea University of Technology, School of Electrical Engineering, Sweden, 2021.

[23] M. Neinavaie, J. Khalife, and Z. Kassas, "Blind Doppler tracking and beacon detection for opportunistic navigation with LEO satellite signals," in *Proceedings of IEEE Aerospace Conference*, March 2021, pp. 1–8.

[24] M. Neinavaie, J. Khalife, and Z. Kassas, "Acquisition, Doppler tracking, and positioning with Starlink LEO satellites: First results," *IEEE Transactions on Aerospace and Electronic Systems*, 2021, accepted.

[25] North American Aerospace Defense Command (NORAD), "Two-line element sets," http://celestrak.com/NORAD/elements/.

[26] D. Vallado and P. Crawford, "SGP4 orbit determination," in *Proceedings of AIAA/AAS Astrodynamics Specialist Conference and Exhibit*, August 2008, pp. 6770–6799.

[27] S. Kozhaya, J. Haidar-Ahmad, A. Abdallah, Z. Kassas, and S. Saab, "Comparison of neural network architectures for simultaneous tracking and navigation with LEO satellites," in *Proceedings of ION GNSS Conference*, September 2021, pp. 2507–2520.

[28] N. Khairallah and Z. Kassas, "Ephemeris closed-loop tracking of LEO satellites with pseudorange and Doppler measurements," in *Proceedings of ION GNSS Conference*, September 2021, pp. 2544–2555.

[29] Z. Kassas, V. Ghadiok, and T. Humphreys, "Adaptive estimation of signals of opportunity," in *Proceedings of ION GNSS Conference*, September 2014, pp. 1679–1689.

[30] S. Kim, J. Choi, and Y. Kim, "Fault detection and diagnosis of aircraft actuators using fuzzy-tuning IMM filter," *IEEE Transactions on Aerospace and Electronic Systems*, vol. 44, no. 3, pp. 940–952, July 2008.

[31] M. Gomaa, O. De Silva, G. Mann, and G. Gosine, "Observability-constrained VINS for MAVs using interacting multiple model algorithm," *IEEE Transactions on Aerospace and Electronic Systems*, vol. 57, no. 3, pp. 1423–1442, June 2021.

[32] R. Li, X., and Y. Bar-Shalom, "A recursive multiple model approach to noise identification," *IEEE Transactions on Aerospace and Electronic Systems*, vol. 30, no. 3, pp. 671–684, July 1994.

[33] A. Thompson, J. Moran, and G. Swenson, *Interferometry and Synthesis in Radio Astronomy*, 2nd ed. John Wiley & Sons, 2001.

[34] Y. Bar-Shalom, X. Li, and T. Kirubarajan, *Estimation with Applications to Tracking and Navigation*. New York, NY: John Wiley & Sons, 2002.

[35] H. Blom and Y. Bar-Shalom, "The interacting multiple model algorithm for systems with Markovian switching coefficients," *IEEE Transactions on Automatic Control*, vol. 33, no. 8, pp. 780–783, August 1988.

[36] M. Kenny, "Ever wondered what is on the Orbcomm satellite downlink?" http://mdkenny.customer.netspace.net.au/Orbcomm.pdf, 2002.

[37] P. Misra and P. Enge, *Global Positioning System: Signals, Measurements, and Performance*, 2nd ed. Ganga-Jamuna Press, 2010.

Assessing Real 5G Signals for Opportunistic Navigation

Ali A. Abdallah, Kimia Shamaei, and Zaher M. Kassas
University of California, Irvine, USA

BIOGRAPHIES

Ali A. Abdallah is a Ph.D student in the Department of Electrical Engineering and Computer Science at the University of California, Irvine and a member of the Autonomous Systems Perception, Intelligence, and Navigation (ASPIN) Laboratory. He received a B.E. in Electrical Engineering from the Lebanese American University (LAU). His current research interests include opportunistic navigation, software-defined radio, long-term evolution (LTE), 5G, and indoor localization.

Kimia Shamaei received a Ph.D. in Electrical Engineering from the University of California, Irvine and a B.S. and M.S. in Electrical Engineering from the University of Tehran. She was a member of the ASPIN Laboratory. She is a recipient of the 2018 Institute of Navigation (ION) Samuel Burka Award and 2020 ION Bradford Parkinson Award.

Zaher (Zak) M. Kassas is an associate professor at the University of California, Irvine and director of the ASPIN Laboratory. He received a B.E. in Electrical Engineering from the Lebanese American University, an M.S. in Electrical and Computer Engineering from The Ohio State University, and an M.S.E. in Aerospace Engineering and a Ph.D. in Electrical and Computer Engineering from The University of Texas at Austin. In 2018, he received the National Science Foundation (NSF) Faculty Early Career Development Program (CAREER) award, and in 2019, he received the Office of Naval Research (ONR) Young Investigator Program (YIP) award. He is a recipient of 2018 IEEE Walter Fried Award, 2018 ION Samuel Burka Award, and 2019 ION Col. Thomas Thurlow Award. He is an Associate Editor for the IEEE Transactions on Aerospace and Electronic Systems and the IEEE Transactions on Intelligent Transportation Systems. His research interests include cyber-physical systems, estimation theory, navigation systems, autonomous vehicles, and intelligent transportation systems.

ABSTRACT

Cellular fifth-generation (5G) signals are assessed for opportunistic navigation. A carrier-aided code-based software-defined receiver (SDR) is presented, which produces navigation observables from received downlink 5G signals. These observables are analyzed to assess the performance of 5G signals for opportunistic navigation. Experimental results are presented of a ground vehicle navigating with the 5G SDR while receiving signals from two 5G base stations (known as gNBs). It is shown that over a trajectory of 1.02 km traversed in 100 seconds, the position root mean-squared error (RMSE) was 14.9 m.

I. INTRODUCTION

Over the past few years, the third-generation partnership project (3GPP) has been developing the fifth-generation (5G) (also known as new radio (NR)) as the next wireless communication system [1, 2]. 5G provides faster data transfer speeds, lower latency, higher capacity, lower transmission power, and network slicing over the previous fourth-generation cellular system, also known as long-term evolution (LTE). These features allow 5G to play a major role in autonomous technologies. For example, autonomous vehicles involve enormous quantity of data collection, processing, and communication. This data includes navigation trajectory, traffic information, and surrounding vehicles and obstacles. 5G could revolutionize autonomous vehicle's capabilities, from data sharing to navigation and situational awareness. This paper focuses on assessing the potential of 5G signals for opportunistic navigation.

Recent research has considered the use of signals of opportunity (SOPs) as complementary and alternative navigation sources in global navigation satellite systems (GNSS)-challenged environments. SOPs are signals not intended for navigation purposes; however; can be exploited for navigation, such as AM/FM [3–5], Wi-Fi [6–8], digital television [9–11] , low earth orbit (LEO) [12–14], and cellular [15–17]. Cellular signals, namely code-division multiple access

Copyright © 2020 by A. A. Abdallah, K. Shamaei, and Z. M. Kassas

Preprint of the 2020 ION GNSS+ Conference St. Louis, Missouri, September 21–25, 2020

(CDMA) and LTE, have shown high ranging and localization accuracy using specialized software-defined receivers (SDRs) [18–22]. The performance of these SDRs have been evaluated with different navigation frameworks, both indoors [23–25] and outdoors [26–28], where experimental results demonstrated meter-level accuracy positioning accuracy on ground-mounted receivers with LTE and CDMA signals [29–31] and sub-meter-level positioning accuracy on aerial vehicle-mounted receivers with real LTE and CDMA signals [32, 33].

The cellular 5G system will be the first system to coexist with the previous system, LTE. The 5G system deploys a structure that is similar to the one deployed for LTE, where both systems use orthogonal frequency division multiplexing (OFDM) for downlink transmission. The 5G system is very attractive by design for navigation purposes due to its following qualities:

- High carrier frequencies: 5G is designed to transmit at two main frequency ranges (FRs): (i) FR1, which spans frequencies from 450 MHz to 6 GHz and (ii) FR2, which spans frequencies from 24.25 to 52.6 GHz [34]. High carrier frequencies yield precise carrier phase navigation observables and reduce multipath effect due to high path signal loss, especially for FR2.
- Abundance: the 5G design tackles the problem of high signal path loss of millimeter waves (mmWaves) by using beamforming techniques and small cells, which makes the 5G base stations (also known as gNodeBs (gNB)) ubiquitous.
- Geometric diversity: cellular towers have favorable geometry by construction of the cells to provide better coverage.
- Large bandwidth: While a single LTE signal has a bandwidth up to 20 MHz, a single 5G signal has a bandwidth up to 100 MHz and 400 MHz bandwidth for FR1 and FR2, respectively. This makes it less susceptible to multipath errors, i.e., it can differentiate multipath components with shorter delays from the line-of-sight (LOS) signal.
- High received power: the received carrier-to-noise-ratio C/N_0 of cellular signals from nearby cellular towers is more than 20 dB-Hz higher than global position system (GPS) signals.

The positioning capabilities of 5G has been studied over the past few years. Different approaches have been proposed, in which direction-of-arrival (DOA), direction-of-departure (DOD), time-of-arrival (TOA), or a combination thereof were used to achieve accurate positioning from 5G signals. In [35], the authors investigated the positioning performance of six different 5G impulse radio waveforms, where 5G had no generally accepted waveform at the time. The performance analysis showed the capability of mmWaves in achieving sub-meter level accuracy, where the best performance was achieved when using Guassian raised-cosine, Guassian pulse, and Sinc-RCP impulse radio waveforms. The capability of massive multiple-input-multiple-output (mMIMO) systems in providing very accurate localization when relying on DOA was studied in [36]. The paper addressed the limitation of DOA in mMIMO systems in the presence of multipath by proposing a compressed sensing navigation framework and relied on the channel properties to distinguish LOS from multipath components. The proposed algorithm showed sub-meter accuracy in simulation. Another approach to reduce 5G small cell interference and multipath effect in angular localization methods by combining near-field and far-field effects was proposed in [37]. Simulation results showed that the proposed approach improved the angular resolution by orders of magnitude. In [38], a GNSS/5G integrated positioning framework based on a particle filter was proposed, in which device-to-device (D2D) range and angle measurements were utilized between mobile terminals (MTs). An experiment was performed assuming real GNSS data and emulated 5G D2D data, where the integrated system reduced the GNSS position root mean-squared error (RMSE) from around 5 m to 2-3 m, assuming 10 MTs. In [39], a network-based positioning framework using joint TOA and DOA was proposed using cascaded extended Kalman filters (EKFs). The proposed framework considered the clock biases between the user equipment (UE) and the gNBs, and among the gNBs themselves. The framework was evaluated by simulating a real 5G scenario using three-dimensional (3-D) ray tracing, where sub-meter-level positioning accuracy was demonstrated.

All the aforementioned were limited to theoretical analyses, simulations, or laboratory-emulated 5G signals. This is due to:

- The structure of 5G signals has been recently finalized.
- 5G has been implemented only in a few major cities.
- The hardware limitation for both reception and transmission 5G systems, where mmWaves systems are still in development.
- The proposed navigation approaches require a network-based approach, in which the user's privacy is revealed

for the network. This also limits the UE to a single serving cellular provider, which limits the number of gNBs in sight.

This paper tackles the aforementioned challenges by

- Studying opportunistic navigation of 5G signals and presenting potential signals to be exploited for navigation purposes.
- Presenting an SDR to extract navigation observables from 5G signals
- Implementing a navigation framework using an EKF to estimate the receiver's position, along with the clock biases of the receiver and gNBs from extracted 5G navigation observables.
- Performing the first experimental demonstration of navigation with real cellular 5G signals.

The remainder of the paper is organized as follows. Section II discusses the 5G received signal structure and the potential reference signals for opportunistic navigation. Section III presents the carrier-aided code-based 5G receiver-design. Section IV proposes a 5G navigation framework. Section V validates the performance of the proposed navigation framework in a suburban environment over a 1.02 km trajectory traversed in 100 seconds. The achieved two-dimensional (2-D) RMSE is shown to be 14.93 m, while listening to two gNBs. Concluding remarks are given in Section VI.

II. 5G SIGNAL STRUCTURE

OFDM with cyclic prefix (CP) is used as a modulation technique for 5G downlink signals, which is the same waveform LTE has adopted for its downlink signal. This paper discusses an opportunistic UE-based navigation approach; thus, only 5G downlink signal structure is discussed. In OFDM, a multi-carrier transmission scheme is used, where transmitted data symbols are mapped into multiple narrowband subcarriers in the frequency-domain, which reduces frequency selective fading effect caused by multipath. The serial data symbols $\{S_1, \cdots, S_{N_r}\}$ are parallelized in group symbols, each of length N_r, where N_r is the number of subcarriers carrying the data. Then, a guard band in the frequency-domain is applied by zero-padding both sides of the signal and extending the N_r subcarriers into N_c subcarriers. At this step, an inverse fast Fourier transform (IFFT) is taken, and the last L_{CP} elements are repeated in the beginning, which serves as a guard band in the time-domain to protect the OFDM signals from inter-symbol interference (ISI).

At the receiver, the transmitted symbols are demodulated by executing the aforementioned steps in reverse order. The obtained OFDM signals are arranged in a 2-D frame. The structure of this frame depends on the transmission type of the 5G signal, which can be either time division duplexing (TDD) or frequency division duplexing (FDD). This paper will use 5G signals from FR1, where most cellular providers are using FDD due to its superior performance in providing better coverage and less latency.

Compared to LTE numerology (i.e., subcarrier spacing (SCS) and symbol length), which supports only one type of subcarrier spacing, $\Delta f = 15$ kHz, 5G supports different types of subcarrier spacing. Fig. 1 shows the different types, where μ denotes the numerology.

The duration of the FDD 5G frame is

$$T_f = \frac{\Delta f_{\max} N_f}{100} \cdot T_c = 10\,\text{ms},$$

where, $\Delta f_{\max} = 480\,\text{kHz}$, $N_f = 4096$, and $T_c = \frac{1}{\Delta f_{\max} N_f} = 0.509$ ns is the basic time unit for 5G. Each 5G frame consists of ten subframes, with duration 1 ms each. The number of OFDM symbols per subframe is $N_{\text{symb}}^{\text{subframe},\mu} = N_{\text{symb}}^{\text{slot}} N_{\text{slot}}^{\text{subframe},\mu}$. The frame is divided into two equally-sized half-frames consisting of five subframes each and denoted by: (i) half-frame 0 consisting of subframes 0-4 and (ii) half-frame 1 consisting of subframes 5-9.

For a predefined μ, the number of slots is denoted by $n_s^\mu \in \{0, 1, \cdots, N_{\text{slot}}^{\text{subframe},\mu}\}$ or $n_s^\mu \in \{0, 1, \cdots, N_{\text{slot}}^{\text{frame},\mu}\}$ in an increasing order within a subframe or a frame, respectively. The number of symbols per slot $N_{\text{symb}}^{\text{slot}}$ depends on the type of cyclic prefix and the specified numerology. Table I shows for different numerologies: the number of OFDM symbols per slot, number of slots per frame, number of slots per subframe, and CP duration.

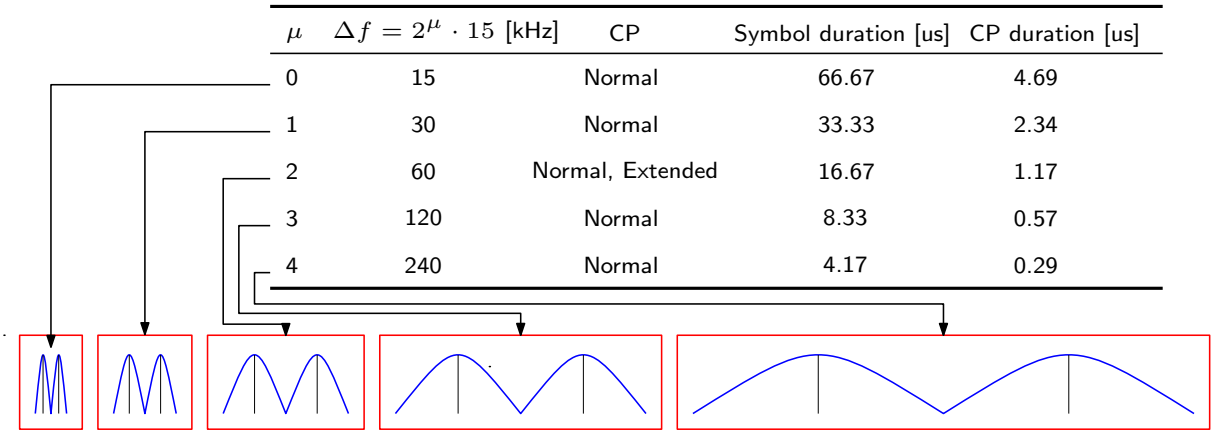

Fig. 1. Different numerologies of 5G and the corresponding: subcarrier spacing, CP type, OFDM symbol duration, CP duration, and two-subcarriers representation.

TABLE I

NUMBER OF OFDM SYMBOLS PER SLOT, SLOTS PER FRAME, AND SLOTS PER SUBFRAME

μ	**Cyclic prefix**	$N^{\text{slot}}_{\text{symb}}$	$N^{\text{frame},\mu}_{\text{slot}}$	$N^{\text{subframe},\mu}_{\text{slot}}$
0	Normal	14	10	1
1	Normal	14	20	2
2	Normal	14	40	4
2	Extended	12	40	4
3	Normal	14	80	8
4	Normal	14	160	16

A resource block (RB) is defined as $N^{\text{RB}}_{\text{sc}} = 12$ subcarriers in the frequency-domain and has the time length of a resource grid $N^{\text{subframe},\mu}_{\text{symb}}$. A resource block consists of resource elements. The minimum and maximum number of resource blocks along with the corresponding bandwidth for different numerologies are summarized in Table II. Each element in the 5G frame is uniquely identified for a specific antenna port p and subcarrier configuration μ by $(k, l)_{p,\mu}$, where k is the index in frequency domain l is the symbol position in the time domain relative to some reference point. In the 5G protocol, "Point A" serves as a common reference point and can be obtained as reported in [40].

TABLE II

THE MINIMUM AND MAXIMUM NUMBER OF RESOURCE BLOCKS AND THE CORRESPONDING BANDWIDTHS FOR DIFFERENT NUMEROLOGIES.

μ	$N^{\text{min}}_{\text{RB}}$	$N^{\text{max}}_{\text{RB}}$	**Minimum bandwidth [Mhz]**	**Maximum bandwidth [Mhz]**
0	24	275	4.32	49.5
1	24	275	8.64	99
2	24	275	17.28	198
3	24	275	34.56	396
4	24	138	69.12	397.44

At the receiver side, the received 5G signal must be converted to frame structure before extracting signals of interest. To do so, the frame start time should be known. For the purpose of providing the frame start time, the gNB broadcasts synchronization signals (SS) with a pre-specified symbol mapping in the 5G frame. The SS includes two reference signals: primary synchronization signal (PSS) and secondary synchronization signal (SSS), which provide symbol and frame timing, respectively. Once the frame start time is known, the CPs can be removed and a fast Fourier transform (FFT) is taken to construct the OFDM symbols in the frame. The SS, the physical broadcast channel (PBCH), and its associated demodulation reference signal (DM-RS) are transmitted in the same 4 symbols block called the SS/PBCH block. The SS/PBCH block consists of 240 contiguous subcarrier (20 RBs) and four consecutive OFDM symbols. Within the SS/PBCH, the subcarriers are numbered in an ascending order from 0 to

239. Fig. 2 shows the SS/PBCH block structure and the corresponding OFDM symbols and subcarriers mapping of the different signals within the block. Note that the position of PBCH-DM-RS varies with v, and the value v changes depending on the physical cell ID N_{ID}^{Cell}. The SS/PBCH block is transmitted every two frames and is transmitted numerous times, where each set of these transmitted block is called an SS/PBCH burst. The SS/PBCH burst has to be confined within a half-frame window (5 ms). Each block in the SS/PBCH burst is beamformed in a different direction. The frequency location of the SS/PBCH within the 5G frame depends on the 5G high-level signaling. The time location of the SS/PBCH block and the size of the SS/PBCH burst in the frame depends on the transmission frequency f_c and the numerology μ as shown in Table III, where index 0 corresponds to the first OFDM symbol of the first slot in a half-frame.

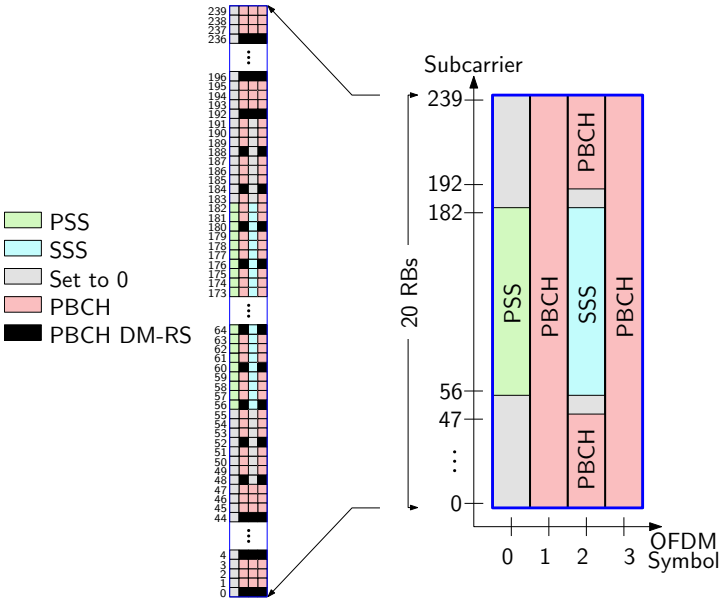

Signal	Symbol number	Subcarrier number
PSS	0	56, 57, $\cdots$, 182
SSS	0	56, 57, $\cdots$, 182
Set to zero	0	0, 1, $\cdots$, 55 183, 184, $\cdots$, 239
	2	48, 49, $\cdots$, 55 183, 184, $\cdots$, 239
PBCH	1, 3	0, 1, $\cdots$, 239
	2	0, 1, $\cdots$, 47 192, 193, $\cdots$, 239
DM-RS	1, 3	$0+v$, $4+v$, $236+v$
	2	$0+v$, $4+v$, $44+v$ $192+v$, $196+v$, $236+v$

$v = N_{ID}^{Cell} \bmod 4$

Fig. 2. SS/PBCH block structure and the corresponding OFDM symbols and subcarriers mapping of the different signals within the block.

TABLE III
SYMBOL NUMBERS CONTAINING SS/PBCH BLOCK FOR DIFFERENT NUMEROLOGIES AND FREQUENCY BANDS

subcarrier spacing (kHz)	**Carrier frequency**	**Symbol number**	**Slot number n**
Case A: 15	$f_c \leq 3$ GHz $3 < f_c \leq 6$ GHz	$\{2, 8\} + 14n$	$\{0, 1\}$ $\{0, \cdots, 3\}$
Case B: 30	$f_c \leq 3$ GHz $3 < f_c \leq 6$ GHz	$\{4, 8, 16, 20\} + 28n$	$\{0\}$ $\{0, 1\}$
Case C: 30	$f_c \leq 3$ GHz $3 < f_c \leq 6$ GHz	$\{2, 8\} + 14n$	$\{0, 1\}$ $\{0, \cdots, 3\}$
Case D: 120	$f_c > 6$ GHz	$\{4, 8, 16, 20\} + 28n$	$\{0, \cdots, 3,$ $5, \cdots, 8,$ $10, \cdots, 13,$ $15, \cdots, 18\}$
Case E: 240	$f_c > 6$ GHz	$\{8, 12, 16, 20, 32,$ $36, 40, 44\} + 56n$	$\{0, \cdots, 8\}$

The PSS and SS are two orthogonal maximum-length sequences (m-sequences) of length 127 and are transmitted on contiguous subcarriers. The PSS has three possible sequences $N_{ID}^{(2)} \in \{0, 1, 2\}$, each of which maps to an integer representing the sector ID of the gNB. The SSS has 336 possible sequences $N_{ID}^{(1)} \in \{0, \cdots, 335\}$, each of which maps

to an integer representing the group identifier of the gNB. See Section 7.4.2 of [40]. Both $N_{ID}^{(1)}$ and $N_{ID}^{(2)}$ define the physical cell identity of the gNB according to

$$N_{ID}^{Cell} = 3N_{ID}^{(1)} + N_{ID}^{(2)}.$$

PBCH is a physical channel that is used to transmit the system information required to establish the connection between the gNB and the UE. The decoding of the PBCH parameters is explained in details in [41]. The DM-RS signal associated with the PBCH is used for decoding purposes and estimate the channel frequency response. The PBCH DM-RS sequence is generated as explained in Section 7.4.1.4 of [40].

III. 5G RECEIVER STRUCTURE

This section presents a carrier-aided code SDR to opportunistically extract TOA measurements from 5G signals. The receiver is a modified version from the receiver developed in [41], and it has three main stages: (i) 5G carrier frequency extraction, (ii) acquisition, and (iii) tracking. The rest of this section overviews each of the these stages.

A. 5G Carrier Frequency Extraction

This stage is required if the carrier frequency of the transmitted 5G signal is unknown to the UE. Otherwise, if this information is known, this stage can be skipped, and the UE can start at the acquisition stage. At this stage, a blind search is performed over all candidate 5G frequency bands in order to find the carrier frequency of the transmitted 5G signals. To do so, the UE searches for available SS/PBCH block, which is carried by the synchronization raster. The synchronization raster indicates the frequency positions of the synchronization block that can be used by the UE for system acquisition when explicit signaling of the synchronization block position is not present. The center frequency of the synchronization raster is the center subcarrier of the SS/PBCH block, i.e., the 121-th subcarrier denoted by SS_{REF}. The frequency position of SS_{REF} is defined with corresponding to global synchronization channel number (GSCN) [34]. The parameters defining the SS_{REF} and GSCN for all frequency ranges are presented in Table IV. More details can be found in Section 5.4.3 in [34].

TABLE IV
GSCN PARAMETERS FOR THE GLOBAL FREQUENCY RASTER

Frequency range [MHz]	SS_{REF} **frequency position**	**GSCN**	**Range of GSCN**
0 – 3,000	$N \cdot 1,200$ kHz $+M \cdot 50$ kHz $N = 1:1:2,499,\ M \in \{1,3,5\}^*$	$3N + (M-3)/2$	2 – 7,498
3,000 – 24,250	$3,000$ MHz $+N \cdot 1.44$ MHz $N = 1:1:14,756$	$7,499 + N$	7,499 – 22,255
24,250 – 100,000	$24,250.08$ MHz $+N \cdot 17.28$ MHz $N = 1:1:4,383$	$22,256 + N$	22,256 – 26,639

* The default value for operating bands with SCS spaced channel raster is $M = 3$.

B. Acquisition

Knowing the frequency position of SS_{REF}, the UE starts sampling the 5G signals with at least a sufficient sampling rate to capture the entire SS/PBCH bandwidth. Then, the received signal is converted to the baseband domain by wiping out the carrier frequency. At this level, a coarse estimate of the frame start time and $N_{ID}^{(2)}$ are obtained by acquiring the PSS signal. The frame start time is used to control the FFT window timing. The CP elements are removed and an FFT is taken to convert the signal into the 5G frame structure. Then, the SS/PBCH block is extracted, and the received SSS signal is correlated with the possible locally generated sequences to determine $N_{ID}^{(1)}$, and calculate N_{ID}^{Cell} of the gNB. Note that the frequency reuse of 5G is 1, i.e., the received signal may have a 5G signal from multiple gNBs with different N_{ID}^{Cell}, In this case, multiple PSS and SSS peaks can be observed corresponding to more than one gNB. Once the UE determines the N_{ID}^{Cell} of the acquired signal, it maps the DM-RS

subcarriers and extract it from the SS/PBCH block. The extracted DM-RS is correlated with all possible sequences, and the one with the highest peak is used to estimate the channel frequency response (CFR). Knowing the CFR, the estimated channel distortion is reversed using a channel equalizer. Then, the PBCH message is decoded and the second and fourth symbols of the SS/PBCH block are used to refine the frame start time estimate using estimation of signal parameters via rotational invariance techniques (ESPRIT) algorithm, where in this paper, the frame start time represents the TOA of the received 5G signal. A coarse estimate of Doppler frequency $\hat{f}_D$ is obtained by looking at the phase difference between the CFR estimated from two distinct symbols in the SS/PBCH block.

C. Tracking

In this stage, a phase-locked loop (PLL)-aided delay-locked loop (DLL) is used to track the TOA of the received signal. At each tracking loop iteration, the phase effect is wiped off from the received signal, which is assumed constant over a duration of two frames and calculated by integrating $\hat{f}_D$ over time. Then, the TOA is normalized by the sampling time T_s, where the integer part of samples $\text{Int}\{.\}$ is used to control the FFT window timing and the fractional part of samples $0 \leq \text{Frac}\{\cdot\} < 1$ is removed from the signal using a phase rotation in the frequency-domain. The remaining code and carrier phase errors are estimated using a DLL and PLL, respectively.

The carrier phase discriminator can be defined as the phase of the integrated CFRs over the entire subcarrier as shown in [42]. Then, a second-order loop filter at the output of the discriminator can be used to estimate the rate of change of the carrier phase error $2\pi\hat{f}_D$, expressed in rad/s. For code tracking, an early-power-minus-late-power discriminator is used to derive the normalized timing error $\tilde{e}_\tau$ [43]. Assuming that the symbol timing error has linear variations, a second-order loop is used to achieve zero steady-state error. Finally, the TOA estimate $\hat{e}_\tau$ is updated according to

$$\hat{e}_\tau \longleftarrow \hat{e}_\tau + \frac{T_f}{T_s}\left(v_{DLL} - v_{PLL}\right),$$

where $T_f = 20$ ms and v_{DLL} and v_{PLL} are the outputs of the DLL and PLL filters, respectively.

IV. 5G NAVIGATION FRAMEWORK

An EKF is used to estimate the state vector from the 5G pseudorange measurements $\boldsymbol{z} \triangleq c\hat{\boldsymbol{e}}_\tau \triangleq c\left[\hat{e}_\tau^{(1)}, \cdots, \hat{e}_\tau^{(U)}\right] = \left[\rho^{(1)}, \cdots, \rho^{(U)}\right]$, where c and U are the speed of light and the number of gNBs, respectively. The pseudorange between the receiver and the u-th gNB at the i-th time-step can be expressed as

$$\rho^{(u)}(i) = \left\|\boldsymbol{r}_r(i) - \boldsymbol{r}_{s,u}\right\|_2 + c \cdot \left[\delta t_r(i) - \delta t_{s,u}(i)\right] + \nu_u(i), \quad i = 1, 2, \cdots$$

where $\boldsymbol{r}_r = [x_r, y_r, z_r]^\mathsf{T}$ is the receiver's 3-D position vector, $\boldsymbol{r}_{s,u} = [x_{s,u}, y_{s,u}, z_{s,u}]^\mathsf{T}$ is the gNB's 3-D position vector, c is the speed of light, δt_r is the receiver's clock bias, $\delta t_{s,u}$ is the gNB's clock bias, and ν_u is the measurement noise, which is modeled as a zero-mean, white Gaussian random sequence with variance σ_2^u. The gNBs positions $\{\boldsymbol{r}_{s,u}\}_{u=1}^U$ are assumed to be known, e.g., from radio mapping or cloud-hosted databases. The EKF estimates the state vector defined as

$$\boldsymbol{x} \triangleq \left[\boldsymbol{x}_r^\mathsf{T}, \boldsymbol{x}_{\text{clk}}^\mathsf{T}\right]^\mathsf{T},$$

where $\boldsymbol{x}_r = \left[\boldsymbol{r}_r^\mathsf{T}, \dot{\boldsymbol{r}}_r^\mathsf{T}\right]$ and $\boldsymbol{x}_{\text{clk}}$ is the clock state vector $\boldsymbol{x}_{\text{clk}}$ defined as $\boldsymbol{x}_{\text{clk}} \triangleq \left[c\Delta\delta t_1, c\Delta\dot{\delta} t_1, \cdots, c\Delta\delta t_U, c\Delta\dot{\delta} t_U\right]^\mathsf{T}$, where $\{\Delta\delta t_u \triangleq \delta t_r - \delta t_{s,u}\}_{u=1}^U$ and $\{\Delta\dot{\delta} t_u \triangleq \dot{\delta} t_r - \dot{\delta} t_{s,u}\}_{u=1}^U$ are the relative clock bias and drift between the receiver and the u-th gNB. The clock error dynamics are assumed to evolve according to the following discrete-time dynamics

$$\boldsymbol{x}_{\text{clk}_j}(i+1) = \mathbf{F}_{\text{clk}}\boldsymbol{x}_{\text{clk}_j}(i) + \boldsymbol{w}_{\text{clk}_j}(i),$$

where

$$\boldsymbol{x}_{\text{clk}_j} \triangleq \begin{bmatrix} c\delta t_i \\ c\dot{\delta} t_i \end{bmatrix}, \quad \mathbf{F}_{\text{clk}} = \begin{bmatrix} 1 & T \\ 0 & 1 \end{bmatrix}, \quad \boldsymbol{w}_{\text{clk}_j} = \begin{bmatrix} w_{\delta t_i} \\ w_{\dot{\delta} t_i} \end{bmatrix}, \quad \text{for } j \in \{r, s_u\},$$

where $T \equiv T_f$ is the measurement's sampling time and $\boldsymbol{w}_{\text{clk}_j}$ is the process noise, which is modeled as a discrete-time zero-mean white sequence with covariance $\mathbf{Q}_{\text{clk}_j}$ with

$$\mathbf{Q}_{\text{clk}_j} \triangleq c^2 \cdot \begin{bmatrix} S_{\tilde{w}_{\delta t_j}} T + S_{\tilde{w}_{\dot{\delta} t_j}} \frac{T^3}{3} & S_{\tilde{w}_{\delta t_j}} \frac{T^2}{2} \\ S_{\tilde{w}_{\dot{\delta} t_j}} \frac{T^2}{2} & S_{\tilde{w}_{\dot{\delta} t_j}} T \end{bmatrix},$$

where $S_{\tilde{w}_{\delta t,i}}$ and $S_{\tilde{w}_{\dot{\delta} t,i}}$ are the clock bias and drift process noise power spectra, respectively. The values of $S_{\tilde{w}_{\delta t,i}}$ and $S_{\tilde{w}_{\dot{\delta} t,i}}$ depend on the clock's quality [44].

The receiver is assumed to move in a 2-D plane with a constant known height $z_r \equiv z_0$. The receiver's motion is assumed to evolve according to a nearly constant velocity dynamics, i.e.,

$$\ddot{\boldsymbol{r}}(t) = \tilde{\boldsymbol{w}},$$

where $\tilde{\boldsymbol{w}}$ is a process noise vector, which is modeled as zero-mean white random process with power spectral density $\tilde{\mathbf{Q}}_{\text{ped}} = \text{diag}[\tilde{q}_x, \tilde{q}_y]$, where $\tilde{q}_x$ and $\tilde{q}_y$ are the power spectral densities of the acceleration in the $x-$ and $y-$ directions, respectively [45]. The receiver's discrete-time dynamics are hence given by

$$\boldsymbol{x}_r(i+1) = \mathbf{F}_r \boldsymbol{x}_r(i) + \boldsymbol{w}_r(i),$$

where

$$\boldsymbol{x} \triangleq \begin{bmatrix} x_r \\ y_r \\ \dot{x}_r \\ \dot{y}_r \end{bmatrix}, \quad \mathbf{F}_r = \begin{bmatrix} 1 & 0 & T & 0 \\ 0 & 1 & 0 & T \\ 0 & 0 & 1 & 0 \\ 0 & 0 & 0 & 1 \end{bmatrix},$$

and $\boldsymbol{w}_r$, the process noise, which is modeled as a discrete-time zero-mean white sequence with covariance $\mathbf{Q}_r$, where

$$\mathbf{Q}_r = \begin{bmatrix} \tilde{q}_x \frac{T^3}{3} & 0 & \tilde{q}_x \frac{T^2}{2} & 0 \\ 0 & \tilde{q}_y \frac{T^3}{3} & 0 & \tilde{q}_y \frac{T^2}{2} \\ \tilde{q}_x \frac{T^2}{2} & 0 & \tilde{q}_x T & 0 \\ 0 & \tilde{q}_y \frac{T^2}{2} & 0 & \tilde{q}_y T \end{bmatrix}.$$

V. EXPERIMENTAL RESULTS

This section validates the proposed 5G opportunistic navigation framework experimentally in a suburban environment using ambient 5G signals. To the best of the author's knowledge, this is the first navigation solution produced using 5G signals from serving gNBs.

A. Experimental Setup and Environmental Layout

The experiment was performed on the Fairview road in Costa Mesa, California, USA. In this experiment, a quad-channel National Instrument (NI) universal software radio peripheral (USRP)-2955 was mounted on a vehicle, where only two channels were used to sample 5G signals with a sampling ratio of 10 MSps. The receiver was equipped with two consumer-grade cellular omnidirectional Laird antennas. The USRP was tuned to listen to two carrier frequencies corresponding to two U.S. cellular providers whose characteristics are summarized in Table V. The USRP was driven by a GPS-disciplined oscillator (GPSDO) and the sampled data were stored for post-processing. The vehicle was equipped with a Septentrio AsteRx-i V integrated GNSS-IMU whose x-axis pointed toward the front of the vehicle, y-axis pointed to the right side of the vehicle, and z-axis pointed upward. AsteRx-i V is equipped with a dual-antenna multi-frequency GNSS receiver and a VectorNav VN-100 micro-electromechanical system (MEMS) IMU. The loosely-coupled GNSS-IMU with satellite-based augmentation system (SBAS) navigation solution produced by AsteRx-i V was used as ground truth in this experiment. Fig. 3 shows the experimental hardware and software setup.

TABLE V
gNBs's Characteristics

gNB	Carrier frequency [MHz]	N_{ID}^{Cell}	Cellular provider
1	632.55	398	T-Mobile
2	872	608	AT&T

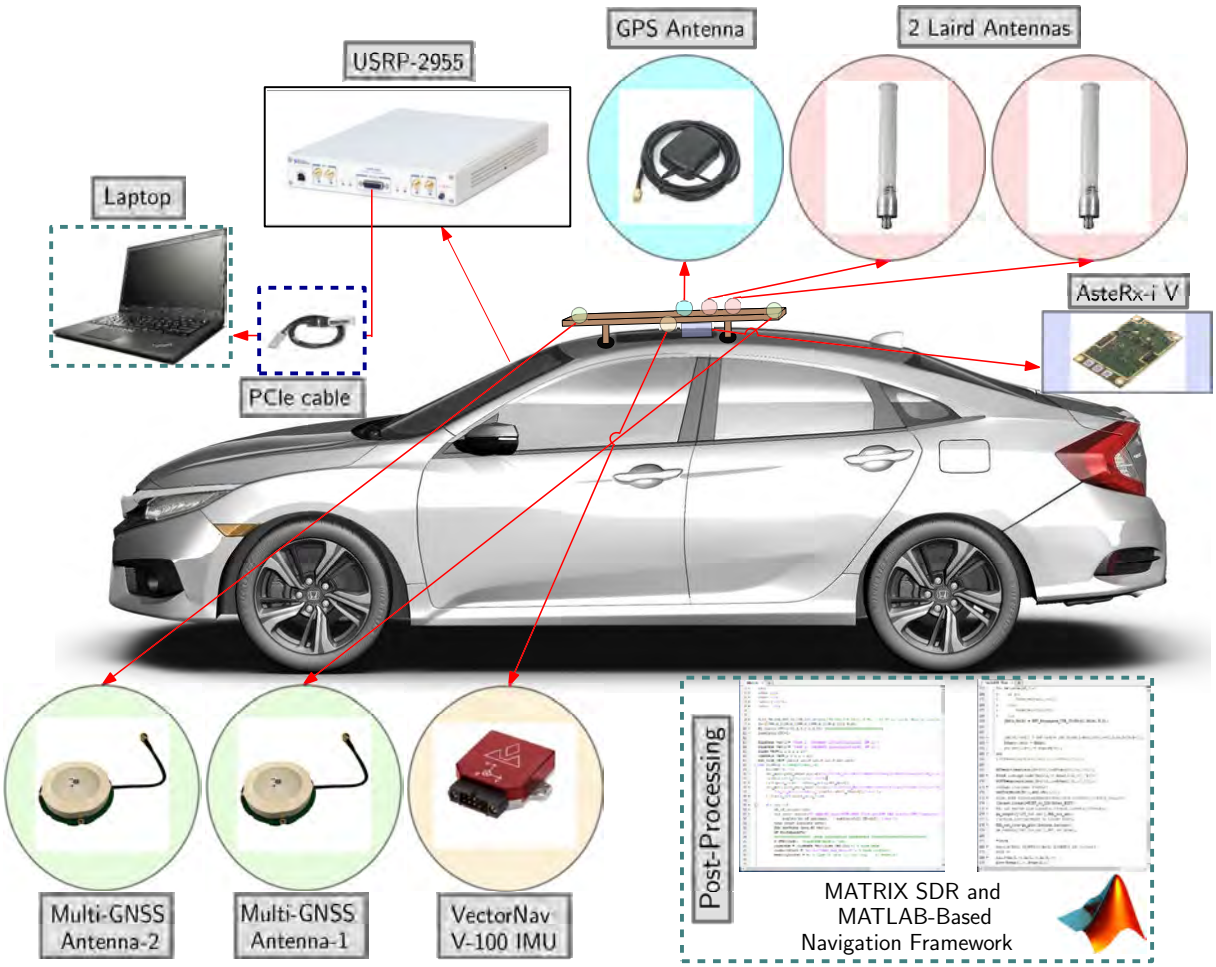

Fig. 3. Experimental hardware and software setup.

B. Navigation Solution

The vehicle traversed a distance of 1.02 km in 100 seconds. The tracking results of the PSS and the SSS of the received 5G signals produced by Multichannel Adaptive TRansceiver Information eXtractor (MATRIX) SDR from both gNBs are shown in Figs. 4. The SDR's DLL bandwidth was tuned to 0.05 Hz, while the PLL bandwidth was tuned to 4 Hz. The true range and Doppler measurements were obtained using the ground truth positions throughout the experiment and the surveyed location of the gNBs. The receiver's position and velocity state vectors and their corresponding covariances were initialized using the output of the GNSS-IMU system. The initial relative clock biases were eliminated, i.e., the EKF's relative clock biases were initialized to zero. The first two 5G measurements were dropped, where the first two position from the GNSS-IMU system were used to initialize the relative clock drifts. The receiver's and gNBs' clocks were modeled as oven-controlled crystal (OCXO) with $S_{\tilde{w}_{\delta t_j}} = 1.3 \times 10^{-22}$ and $S_{\tilde{w}_{\dot{\delta} t_j}} = 7.9 \times 10^{-25}$ [44]. The process noise power spectral densities $\tilde{q}_x$ and $\tilde{q}_y$ were set to 0.1 ($\mathrm{m}^2/\mathrm{s}^3$). The measurement noise standard deviations were set to 3 m and 6 m for gNBs 1 and 2, respectively, which were obtained empirically.

Fig. 5 shows the environmental layout, the location of the gNBs, the navigation solution of the proposed 5G framework, and the receiver's ground truth. The performance of the opportunistic navigation framework with two gNBs is summarized in Table VI.

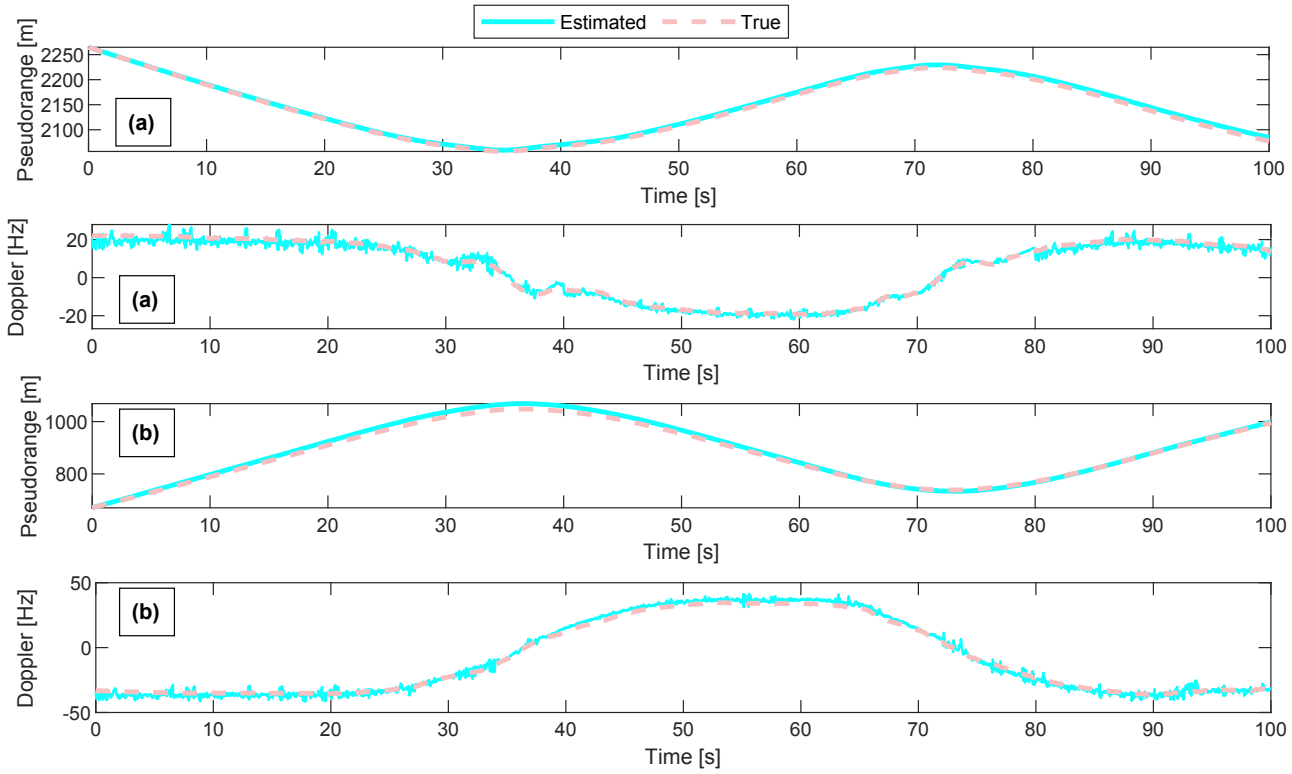

Fig. 4. The estimated pseudorange and Doppler versus true range and Doppler measurements for (a) the T-Mobile gNB with $N_{ID}^{Cell} = 398$ (b) the AT&T gNB with $N_{ID}^{Cell} = 608$.

TABLE VI
EXPERIMENTAL RESULTS

Metric	Value
Trajectory length	1.02 km
Trip time	100 seconds
Position RMSE	14.93 m
Standard deviation	8.28 m
Maximum error	25.87 m

VI. CONCLUSION

This paper presented a navigation framework in which 5G signals are exploited for navigation purposes in an opportunistic fashion. The framework includes: (i) a carrier-aided code-based SDR that produces navigation observables from 5G signals and (ii) a navigation filter in which the observables are processed to estimate the UE's position and velocity. An experiment was conducted on a mobile ground vehicle to assess the navigation performance of 5G signals. In the experiment, the vehicle-mounted receiver navigated using 5G signals from two gNBs for 1.02 km in 100 seconds. The proposed 5G navigation framework demonstrated a position RMSE of 14.93 m, while listening to signals from two gNBs only.

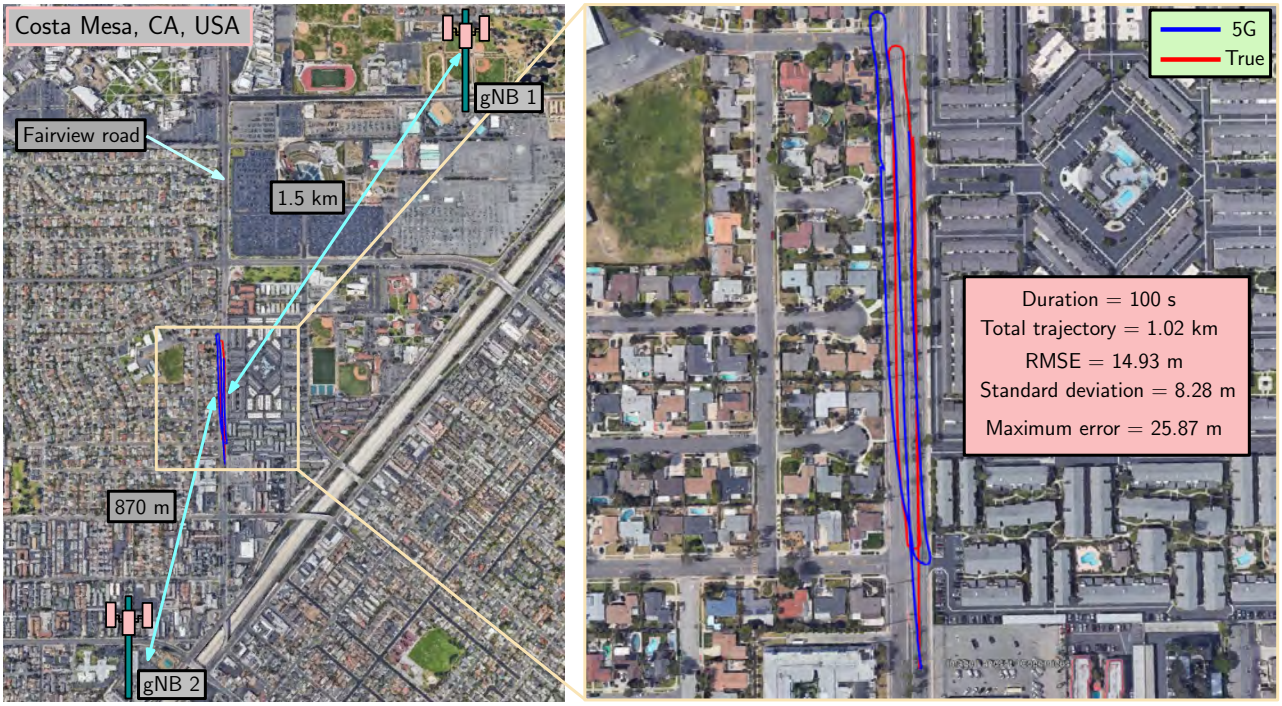

Fig. 5. Environmental layout, gNBs' locations, and the traversed trajectory. The 5G navigation solution exhibited a postion RMSE of 14.93 m versus to the GNSS-IMU with SBAS navigation solution produced by AsterX-i V. Image: Google Earth.

ACKNOWLEDGMENT

The authors would like to thank Joe Khalife for his help in data collection. This work was supported in part by the Office of Naval Research (ONR) under Grant N00014-19-1-2511; in part under the financial assistance award 70NANB17H192 from U.S. Department of Commerce, National Institute of Standards and Technology (NIST); and in part by the U.S. Department of Transportation (USDOT) under University Transportation Center (UTC) Program Grant 69A3552047138.

References

[1] F. Boccardi, R. Heath, A. Lozano, T. Marzetta, and P. Popovski, "Five disruptive technology directions for 5G," *IEEE Communications Magazine*, vol. 52, no. 2, pp. 74–80, February 2014.

[2] M. Agiwal, A. Roy, and N. Saxena, "Next generation 5G wireless networks: A comprehensive survey," *IEEE Communications Surveys Tutorials*, vol. 18, no. 3, pp. 1617–1655, February 2016.

[3] A. Popleteev, "Indoor positioning using FM radio signals," Ph.D. dissertation, University of Trento, Italy, 2011.

[4] V. Moghtadaiee and A. Dempster, "Indoor location fingerprinting using FM radio signals," *IEEE Transactions on Broadcasting*, vol. 60, no. 2, pp. 336–346, June 2014.

[5] M. Psiaki and B. Slosman, "Tracking of digital FM OFDM signals for the determination of navigation observables," in *Proceedings of ION GNSS Conference*, September 2019, pp. 2325–2348.

[6] Y. Bai, S. Wu, G. Retscher, A. Kealy, L. Holden, M. Tomko, A. Borriak, B. Hu, H. Wu, and K. Zhang, "A new method for improving Wi-Fi-based indoor positioning accuracy," *Journal of Location Based Services*, vol. 8, no. 3, pp. 135–147, July 2014.

[7] R. Faragher and R. Harle, "Towards an efficient, intelligent, opportunistic smartphone indoor positioning system," *NAVIGATION, Journal of the Institute of Navigation*, vol. 62, no. 1, pp. 55–72, 2015.

[8] H. Zou, M. Jin, H. Jiang, L. Xie, and C. Spanos, "WinIPS: WiFi-based non-intrusive indoor positioning system with online radio map construction and adaptation," *IEEE Transactions on Wireless Communications*, vol. 16, no. 12, pp. 8118–8130, 2017.

[9] P. Thevenon, S. Damien, O. Julien, C. Macabiau, M. Bousquet, L. Ries, and S. Corazza, "Positioning using mobile TV based on the DVB-SH standard," *NAVIGATION, Journal of the Institute of Navigation*, vol. 58, no. 2, pp. 71–90, 2011.

[10] J. Yang, X. Wang, M. Rahman, S. Park, H. Kim, and Y. Wu, "A new positioning system using DVB-T2 transmitter signature waveforms in single frequency networks," *IEEE Transactions on Broadcasting*, vol. 58, no. 3, pp. 347–359, September 2012.

[11] L. Chen, O. Julien, P. Thevenon, D. Serant, A. Pena, and H. Kuusniemi, "TOA estimation for positioning with DVB-T signals in outdoor static tests," *IEEE Transactions on Broadcasting*, vol. 61, no. 4, pp. 625–638, 2015.

[12] R. Landry, A. Nguyen, H. Rasaee, A. Amrhar, X. Fang, and H. Benzerrouk, "Iridium Next LEO satellites as an alternative PNT in GNSS denied environments–part 1," *Inside GNSS Magazine*, pp. 56–64., May 2019.

[13] Z. Kassas, J. Morales, and J. Khalife, "New-age satellite-based navigation – STAN: simultaneous tracking and navigation with LEO satellite signals," *Inside GNSS Magazine*, vol. 14, no. 4, pp. 56–65, 2019.

[14] Z. Kassas, J. Khalife, M. Neinavaie, and T. Mortlock, "Opportunity comes knocking: overcoming GPS vulnerabilities with other satellites' signals," *Inside Unmanned Systems Magazine*, pp. 30–35, June/July 2020.

[15] M. Ulmschneider and C. Gentner, "Multipath assisted positioning for pedestrians using LTE signals," in *Proceedings of IEEE/ION Position, Location, and Navigation Symposium*, April 2016, pp. 386–392.

[16] Z. Kassas, J. Khalife, K. Shamaei, and J. Morales, "I hear, therefore I know where I am: Compensating for GNSS limitations with cellular signals," *IEEE Signal Processing Magazine*, pp. 111–124, September 2017.

[17] J. del Peral-Rosado, R. Raulefs, J. López-Salcedo, and G. Seco-Granados, "Survey of cellular mobile radio localization methods: From 1G to 5G," *IEEE Communications Surveys Tutorials*, vol. 20, no. 2, pp. 1124–1148, 2018.

[18] J. del Peral-Rosado, J. Lopez-Salcedo, G. Seco-Granados, F. Zanier, P. Crosta, R. Ioannides, and M. Crisci, "Software-defined radio LTE positioning receiver towards future hybrid localization systems," in *Proceedings of International Communication Satellite Systems Conference*, October 2013, pp. 14–17.

[19] C. Yang, T. Nguyen, and E. Blasch, "Mobile positioning via fusion of mixed signals of opportunity," *IEEE Aerospace and Electronic Systems Magazine*, vol. 29, no. 4, pp. 34–46, April 2014.

[20] M. Driusso, C. Marshall, M. Sabathy, F. Knutti, H. Mathis, and F. Babich, "Indoor positioning using LTE signals," in *Proceedings of International Conference on Indoor Positioning and Indoor Navigation*, October 2016, pp. 1–8.

[21] J. Khalife, K. Shamaei, and Z. Kassas, "Navigation with cellular CDMA signals – part I: Signal modeling and software-defined receiver design," *IEEE Transactions on Signal Processing*, vol. 66, no. 8, pp. 2191–2203, April 2018.

[22] K. Shamaei, J. Khalife, and Z. Kassas, "Exploiting LTE signals for navigation: Theory to implementation," *IEEE Transactions on Wireless Communications*, vol. 17, no. 4, pp. 2173–2189, April 2018.

[23] C. Gentner, E. Munoz, M. Khider, E. Staudinger, S. Sand, and A. Dammann, "Particle filter based positioning with 3GPP-LTE in indoor environments," in *Proceedings of IEEE/ION Position, Location and Navigation Symposium*, April 2012, pp. 301–308.

[24] C. Gentner, B. Ma, M. Ulmschneider, T. Jost, and A. Dammann, "Simultaneous localization and mapping in multipath environments," in *Proceedings of IEEE/ION Position Location and Navigation Symposium*, April 2016, pp. 807–815.

[25] A. Abdallah, K. Shamaei, and Z. Kassas, "Performance characterization of an indoor localization system with LTE code and carrier phase measurements and an IMU," in *Proceedings of International Conference on Indoor Positioning and Indoor Navigation*, September 2019, pp. 1–8.

[26] M. Driusso, C. Marshall, M. Sabathy, F. Knutti, H. Mathis, and F. Babich, "Vehicular position tracking using LTE signals," *IEEE Transactions on Vehicular Technology*, vol. 66, no. 4, pp. 3376–3391, April 2017.

[27] Z. Kassas, M. Maaref, J. Morales, J. Khalife, and K. Shamaei, "Robust vehicular localization and map matching in urban environments through IMU, GNSS, and cellular signals," *IEEE Intelligent Transportation Systems Magazine*, vol. 12, no. 3, pp. 36–52, June 2020.

[28] A. Abdallah and Z. Kassas, "Deep learning-aided spatial discrimination for multipath mitigation," in *Proceedings of IEEE/ION Position, Location, and Navigation Symposium*, April 2020, pp. 1324–1335.

[29] C. Yang and T. Nguyen, "Tracking and relative positioning with mixed signals of opportunity," *NAVIGATION, Journal of the Institute of Navigation*, vol. 62, no. 4, pp. 291–311, December 2015.

[30] J. Khalife and Z. Kassas, "Navigation with cellular CDMA signals – part II: Performance analysis and experimental results," *IEEE Transactions on Signal Processing*, vol. 66, no. 8, pp. 2204–2218, April 2018.

[31] K. Shamaei, J. Morales, and Z. Kassas, "A framework for navigation with LTE time-correlated pseudorange errors in multipath environments," in *Proceedings of IEEE Vehicular Technology Conference*, April 2019, pp. 1–6.

[32] J. Khalife, K. Shamaei, S. Bhattacharya, and Z. Kassas, "Centimeter-accurate UAV navigation with cellular signals," in *Proceedings of ION GNSS Conference*, September 2018, pp. 2321–2331.

[33] K. Shamaei and Z. Kassas, "Sub-meter accurate UAV navigation and cycle slip detection with LTE carrier phase," in *Proceedings of ION GNSS Conference*, September 2019, pp. 2469–2479.

[34] 3GPP, "Base station (BS) radio transmission and reception," 3rd Generation Partnership Project (3GPP), TS 38.104, July 2018. [Online]. Available: https://www.etsi.org/deliver/etsi-ts/138100-138199/138104/15.02.00-60/ts-138104v150200p.pdf

[35] X. Cui, T. Gulliver, J. Li, and H. Zhang, "Vehicle positioning using 5G millimeter-wave systems," *IEEE Access*, vol. 4, pp. 6964–6973, 2016.

[36] N. Garcia, H. Wymeersch, E. Larsson, A. Haimovich, and M. Coulon, "Direct localization for massive MIMO," *IEEE Transactions on Signal Processing*, vol. 65, no. 10, pp. 2475–2487, May 2017.

[37] K. Han, Y. Liu, Z. Deng, L. Yin, and L. Shi, "Direct positioning method of mixed far-field and near-field based on 5G massive MIMO system," *IEEE Access*, vol. 7, pp. 72 170–72 181, 2019.

[38] L. Yin, Q. Ni, and Z. Deng, "A GNSS/5G integrated positioning methodology in D2D communication networks," *IEEE Transactions on Signal Processing*, vol. 36, no. 2, pp. 351–362, February 2018.

[39] M. Koivisto, M. Costa, J. Werner, K. Heiska, J. Talvitie, K. Leppanen, V. Koivunen, and M. Valkama, "Joint device positioning and clock synchronization in 5G ultra-dense networks," *IEEE Transactions on Wireless Communications*, vol. 16, no. 5, pp. 2866–2881, May 2017.

[40] 3GPP, "Physical channels and modulation," https://www.etsi.org/deliver/etsi-ts/138200-138299/138211/15.02.00-60/ts-138211v150200p.pdf, 5G; NR; 3rd Generation Partnership Project (3GPP), TS 38.211, July 2018.

[41] K. Shamaei and Z. Kassas, "Opportunistic navigation with 5G signals," *IEEE Transactions on Wireless Communications*, 2020, submitted.

[42] K. Shamaei and Z. Kassas, "LTE receiver design and multipath analysis for navigation in urban environments," *NAVIGATION, Journal of the Institute of Navigation*, vol. 65, no. 4, pp. 655–675, December 2018.

[43] B. Yang, K. Letaief, R. Cheng, and Z. Cao, "Timing recovery for OFDM transmission," *IEEE Journal on Selected Areas in Communications*, vol. 18, no. 11, pp. 2278–2291, November 2000.

[44] Z. Kassas, V. Ghadiok, and T. Humphreys, "Adaptive estimation of signals of opportunity," in *Proceedings of ION GNSS Conference*, September 2014, pp. 1679–1689.

[45] Z. Kassas and T. Humphreys, "Observability analysis of collaborative opportunistic navigation with pseudorange measurements," *IEEE Transactions on Intelligent Transportation Systems*, vol. 15, no. 1, pp. 260–273, February 2014.

IEEE
Aerospace and Electronic
SYSTEMS
magazine

October 2022
ISSN 0885-8985
Volume 37, Number 10

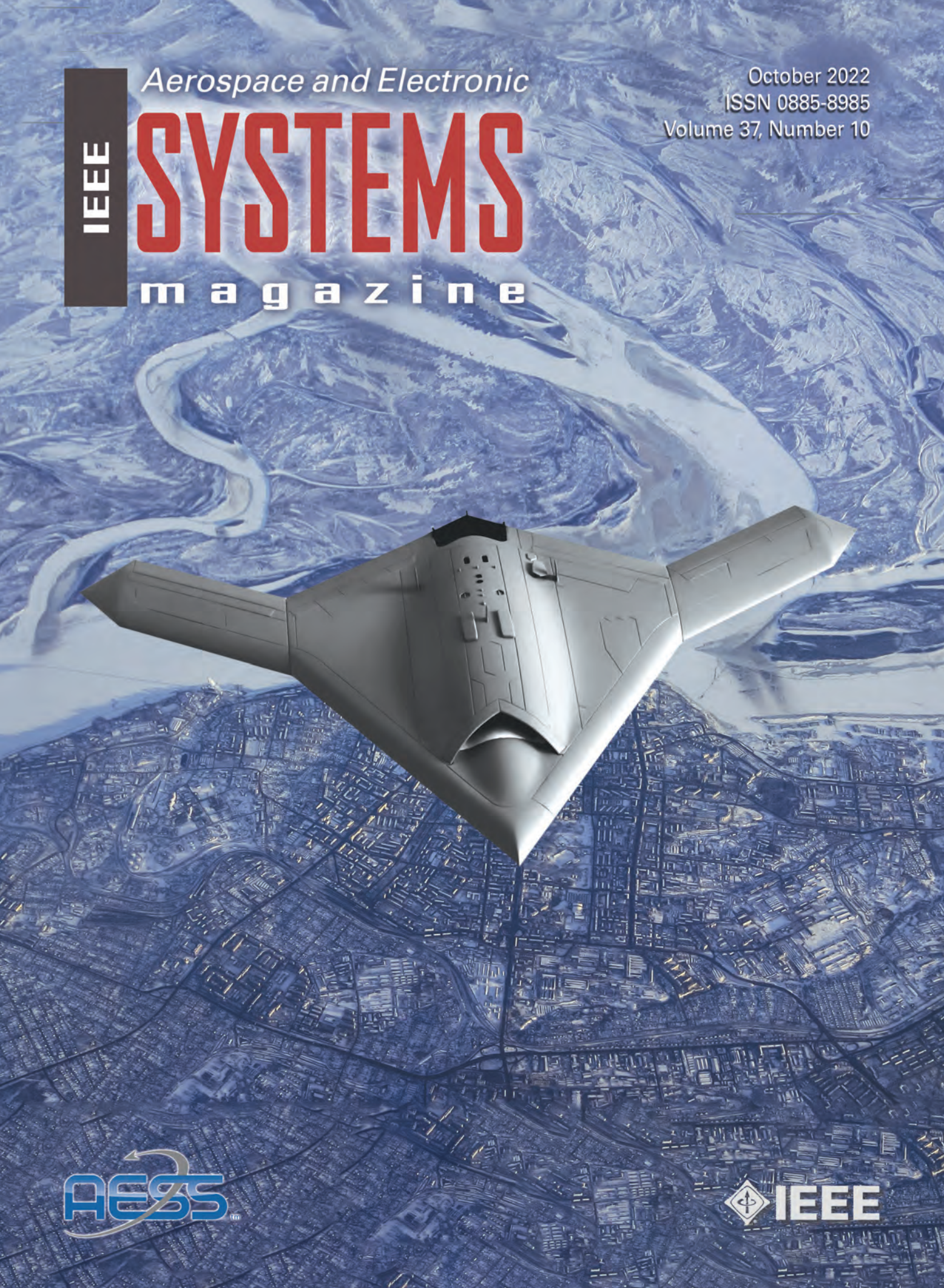

AESS

IEEE

Feature Article:

DOI. No. 10.1109/MAES.2022.3187142

Assessment of Cellular Signals of Opportunity for High-Altitude Aircraft Navigation

Zaher (Zak) M. Kassas, **The Ohio State University, Columbus, OH 43210 USA**
Joe Khalife and Ali Abdallah, **University of California, Irvine, Irvine, CA 92697 USA**
Chiawei Lee, Juan Jurado, Steven Wachtel, Jacob Duede, Zachary Hoeffner, Thomas Hulsey and Rachel Quirarte, **U.S. Air Force, Edwards, CA 93524 USA**
RunXuan Tay, **Republic of Singapore Air Force, Singapore**

INTRODUCTION

Modern aircraft navigation systems are highly dependent on global navigation satellite system (GNSS) signals and their augmentation systems (e.g., ground-based augmentation system and space-based augmentation system). GNSS provides the aircraft with an accurate and reliable position, speed, and time estimate at any point and without interruption. GNSS is also relied on in aviation communications, navigation, and surveillance systems as well as air traffic management [1].

Over the past few years, GNSS radio frequency interference (RFI) incidents skyrocketed, jeopardizing safe and efficient aviation operations. RFI sources include repeaters and pseudolites, GNSS jammers, and systems transmitting outside the GNSS frequency bands [2]. According to EUROCONTROL, a pan-European, civil-military organization dedicated to supporting European aviation, there were 4364 GNSS outages reported by pilots in 2018, which represents more than a 2000% increase over the previous year [3]. What is alarming is that while the majority of RFI hotspots appear related to conflict zones, they affect civil aviation at distances of up to 300 km from these zones. What is also alarming is that the majority of RFI (about 81%) affects en-route flights, even though this is where RFI should be at its lowest, as the aircraft is as far away from a ground-based interferer as possible. In 2019, the International Civil Aviation Organization issued a Working Paper titled "An Urgent Need to Address Harmful Interferences to GNSS," where it concluded that harmful RFI to GNSS would prevent the full continuation of safety and efficiency benefits of GNSS-based services. Moreover, there was a call for supporting the multidisciplinary development of alternative positioning, navigation, and timing (PNT) strategy and solutions to complement the use of GNSS in aviation [4].

In 2021, the U.S. Department of Transportation released the "Complementary Positioning, Navigation, and Timing (PNT) and GPS Backup Technologies Demonstration Report" to the U.S. Congress. The report concluded that while there are suitable, mature, and commercially available technologies to back up or to complement GPS, none of these systems alone can universally back up the PNT capabilities provided by GPS and its augmentations, necessitating a diverse universe of PNT technologies [5]. Moreover, in 2021, the National Institute of Standards and Technology issued a report on "Foundational PNT Profile: Applying the Cybersecurity Framework for the Responsible Use of PNT Services," where it identified signals of opportunity (SOPs) and terrestrial RF sources (e.g., cellular) as a mitigation category that apply to the PNT profile [6]. Indeed, SOPs [7], particularly from cellular infrastructure [8]–[13], have shown tremendous promise over the past decade as an alternative PNT source [14]. This is due to their inherently desirable attributes for navigation purposes as follows:

i) they are ubiquitous;

ii) they are transmitted in a wide range of frequencies and in many directions, which makes them spectrally and geometrically diverse;

Authors' current addresses: Zaher (Zak) M. Kassas, The Ohio State University, Columbus, OH 43210 USA (e-mail: zkassas@ieee.org); Joe Khalife and Ali Abdallah, University of California, Irvine, Irvine, CA 92697 USA; Chiawei Lee, Juan Jurado, Steven Wachtel, Jacob Duede, Zachary Hoeffner, Thomas Hulsey, and Rachel Quirarte U.S. Air Force, Edwards, CA 93524 USA; RunXuan Tay, Republic of Singapore Air Force, Singapore. (*Corresponding author: Zaher M. Kassas*).
Manuscript received 28 June 2021, revised 13 January 2022; accepted 1 June 2022, and ready for publication 29 June 2022.
Review handled by Erik Blasch.
0885-8985/22/$26.00 © 2022 IEEE

Authorized licensed use limited to: The Ohio State University. Downloaded on October 13,2022 at 17:51:17 UTC from IEEE Xplore. Restrictions apply.

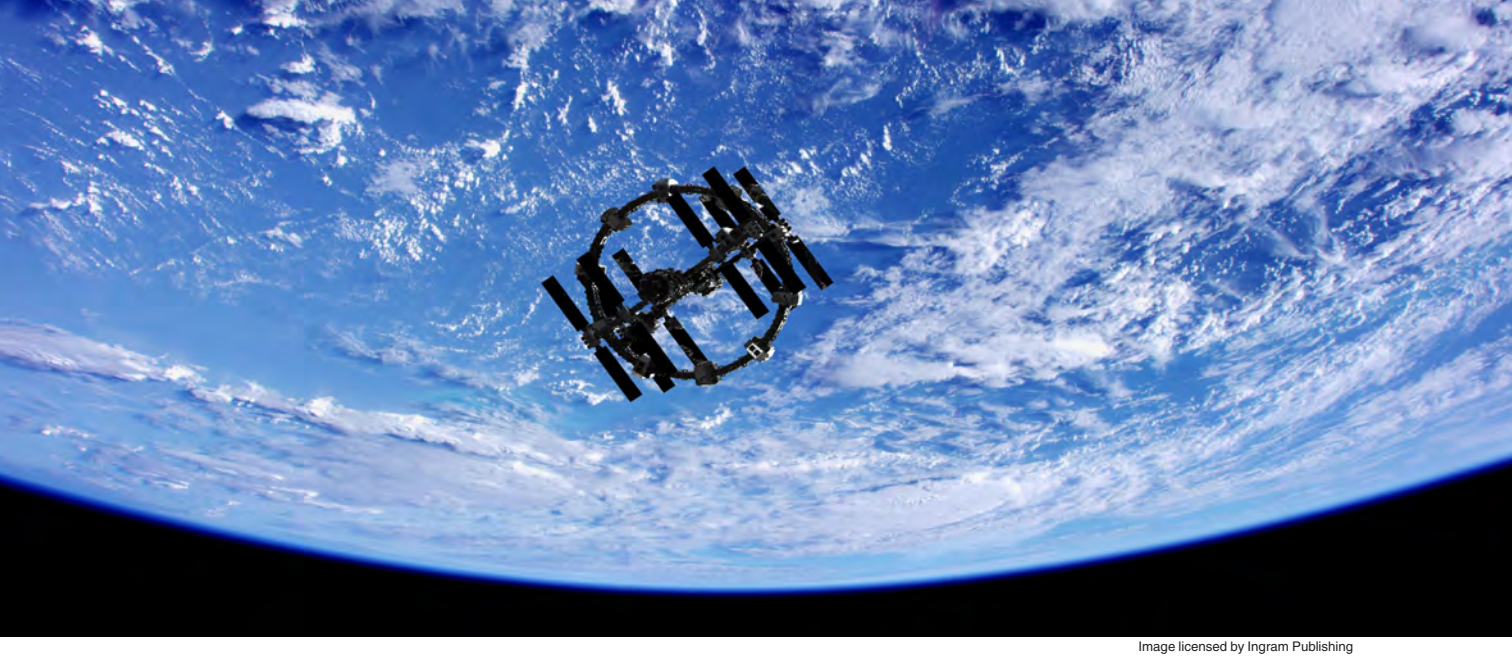

Image licensed by Ingram Publishing

iii) they possess a high received carrier-to-noise (CNR) ratio (tens of dBs higher than GPS); and

iv) they are readily available for free as their infrastructure is well established and the signals are broadcasted to billions of users worldwide.

Recent results have shown the ability of cellular SOPs to yield meter-level-accurate navigation on ground vehicles [15]–[18] in urban environments and submeter-level-accurate navigation on UAVs [19], [20]. Moreover, the robustness and availability of cellular SOPs have been demonstrated in a GPS-jammed environment [21].

Assessing cellular signals for aerial vehicles has been the subject of several studies recently [22], [23]. These studies span radio channel modeling [24]–[26]; evaluation of signal quality in terms of received signal power [27], [28], interference from cellular transmitters [29]–[31], and coverage and connectivity [32], [33]; and standards recommendations [34], [35]. According to existing studies, commercial cellular networks are capable of providing connectivity to aerial vehicles at low altitudes. However, the majority of published studies focused on evaluating cellular signals for communication purposes with little attention to evaluating them for navigation purposes [36]. Moreover, these studies only considered i) UAVs flying at low altitudes (up to 500 ft) and ii) slow speeds (up to 50 km/h). As such, existing studies are insufficient to reveal the potential and challenges associated with aviation operations. On the one hand, there is a lack of understanding of cellular signal attenuation and interference issues when received by aircraft flying at higher altitudes. On the other hand, there is a lack of assessment of the Doppler effect on tracking cellular synchronization signals for aircraft traveling at high speeds. Consider, for example, a Piper PA-18, a Boeing 747, and an F22 Raptor, which could reach speeds of 200, 1000, and 2400 km/h, respectively, yielding Doppler frequency shifts at cellular frequencies of few hundred to several thousand Hz [37]. This study aims to perform the first assessment of cellular SOPs for high-altitude aircraft navigation by addressing the following questions:

1) Can cellular SOPs be received and exploited properly at aircraft altitudes and speeds to produce a robust navigation solution?

2) Does the downward tilt of cellular base station antennas prohibit reliable reception at high altitudes?

3) Is there a sufficient number of hearable cellular base stations to produce a navigation solution over long trajectories for high-altitude aircraft?

To answer these questions, an unprecedented aerial campaign was conducted in March 2020 by the Autonomous Systems Perception, Intelligence, and Navigation (ASPIN) Laboratory in collaboration with the United States Air Force (USAF) at the Edwards Air Force Base (AFB), California, USA. The cellular software-defined radios (SDRs) of the ASPIN Laboratory were flown on a USAF Beechcraft C-12 Huron, a fixed-wing aircraft, to collect ambient cellular 3G code-division multiple access (CDMA) and 4G long-term evolution (LTE) signals over Southern California. This unique dataset consists of combinations of flight run over three different environments (rural, semiurban, and urban) with altitudes ranging up to 23,000 ft and a multitude of trajectories and maneuvers including straight segments, banking turns, holding patterns, and ascending and descending teardrops, performed by members of the USAF Test Pilot School. This article assesses the collected signals for navigation purposes, with the aim to show that should GNSS signals become unavailable or unreliable midflight, cellular SOPs could be used to produce a sustainable and accurate navigation solution. In particular, this article characterizes the CNR as a function of altitude and horizontal distance.

Authorized licensed use limited to: The Ohio State University. Downloaded on October 13,2022 at 17:51:17 UTC from IEEE Xplore. Restrictions apply.

Figure 1.
USAF Pilots and ASPIN researchers with the C-12 aircraft.

The CNR influences the precision of the navigation observables produced by a navigation receiver. It is found that up to a dozen base stations can be acquired and tracked at 23,000 ft above ground level (AGL). Furthermore, the multipath channel is analyzed at different altitudes in different regions. Multipath can cause significant biases in navigation observables, compromising the accuracy of the navigation solution. Ground reflections could be a concern for strong multipath. However, the data shows clean channels between the aircraft and the cellular base stations with a dominantly strong line-of-sight (LOS) component at all altitudes, which in turn means that the navigation observables from cellular SOPs will have high accuracy. To demonstrate the feasibility of aircraft navigation with cellular SOPs, a sample trajectory of the C-12 aircraft was estimated using cellular SOPs only, yielding a three-dimensional (3D) 10.5 m position root-mean-squared error (RMSE) over a 51-km trajectory traversed over a period of 9 minutes at approximately 5000 ft AGL.

The rest of this article is organized as follows. The "Experimental Setup and Flight Regions" section describes the hardware and software setup with which the aircraft was equipped and overviews the environments in which the flight campaigns took place. The "Ground-to-Air Channel Characterization" section studies the i) downlink cellular channel (ground-to-air) in terms of received CNR at different aircraft altitudes, aircraft-to-transmitter range, and in different regions and ii) multipath effects in terms of the channel impulse response (CIR). The "Aircraft Navigation With Cellular Signals" section presents experimental aircraft navigation results exclusively with cellular signals. The "Conclusion" section summarizes the main findings of this article.

EXPERIMENTAL SETUP AND FLIGHT REGIONS

This section overviews the hardware and software setup used for data collection and processing. It also describes the flight regions and aircraft maneuvers.

HARDWARE AND SOFTWARE SETUP

For this study, the C-12 aircraft, called Ms. Mabel, was equipped with the following.

- A quad-channel universal software radio peripheral (USRP)-2955.
- Three consumer-grade 800/1900-MHz Laird cellular antennas.
- A peripheral component interconnect express cable.
- A desktop computer equipped with a solid-state drive for data storage.
- A laptop computer running the ASPIN Laboratory's SDR, called MATRIX: Multichannel Adaptive TRansceiver Information eXtractor, for real-time monitoring of the signals, which was operated during the flight by a flight engineer to determine when, where, and what cellular signals were available to tune the USRP accordingly.
- A GPS antenna to i) feed GPS measurements for the aircraft navigation system and ii) discipline the USRP's onboard GPS-disciplined oscillator.

Figure 1 shows the C-12 aircraft and the USAF pilots and ASPIN researchers (this article's co-authors). The equipment was assembled at the ASPIN Laboratory on a special rack provided by the USAF and was shipped to be mounted on the C-12 aircraft. The three Laird antennas were connected to the USRP to capture impinging 3G and 4G signals, and the USRP was tuned to listen to three carrier frequencies corresponding to two 4G United States cellular providers and one 3G United States cellular provider, as shown in Figure 2. Terabytes of in-phase and quadrature samples were collected throughout the experiment with a sampling rate of 10 MSps per channel. The 3G and 4G cellular modules of the MATRIX SDR [38], [39] were then used to postprocess the stored samples to produce navigation observables: Doppler frequency, carrier phase, and pseudorange, along with

Authorized licensed use limited to: The Ohio State University. Downloaded on October 13,2022 at 17:51:17 UTC from IEEE Xplore. Restrictions apply.

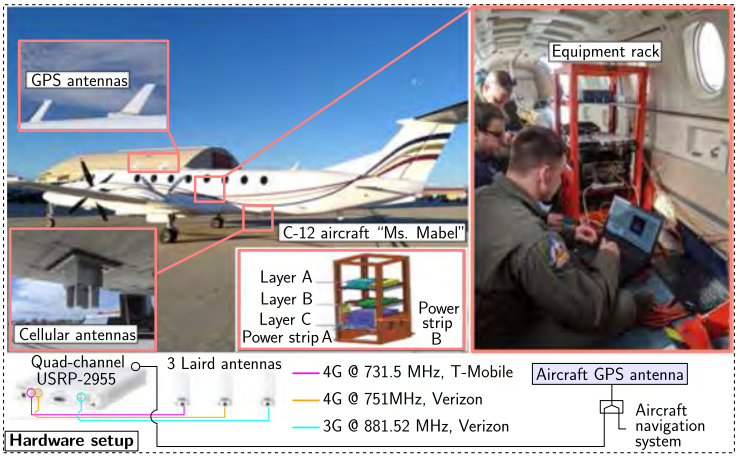

Figure 2.
Hardware setup with which the C-12 aircraft was equipped.

corresponding CNRs. The hardware and software setup are shown in Figures 2 and 3, respectively.

FLIGHT REGIONS AND AIRCRAFT MANEUVERS

The campaign took place in three regions as follows.

i) *Region A:* A rural region in Edwards AFB, California.

ii) *Region B:* A semiurban region in Palmdale, California.

iii) *Region C*: An urban region in Riverside, California.

Different maneuvers were planned over the three regions to test several aspects of aircraft navigation with cellular SOPs. Figure 4 shows the regions in which the experiments were performed. More than 70 3G base transceiver stations (BTSs) and 4G eNodeBs were mapped throughout the experiment via the method described in [40]. The mapped towers were cross-checked via Google Earth and online databases and are shown in Figure 4. This article investigates the potential of cellular SOPs for navigation; therefore, mapping the SOPs will not be discussed. The different maneuvers performed by the aircraft are described next.

Two main types of maneuvers were performed in each region. The first was a teardrop-like pattern while climbing/descending. The patterns have a focal point that is aligned with geographic points of interest (see Figure 4). The measurements used to characterize the CNR and multipath were taken exactly above the geographic point of interest to maintain the horizontal distance between the aircraft and the cellular base stations. The second was a grid-like pattern with many turns and straight segments. Such patterns were used as stress-test for the navigation receivers to assess their ability to track cellular synchronization signals in a robust and accurate fashion as well as navigation solution evaluation. The two types of maneuvers are shown in Figure 5.

GROUND-TO-AIR CHANNEL CHARACTERIZATION

This section characterizes the ground-to-air radio channel by analyzing the CNR and multipath at different altitudes and horizontal distances in Regions A, B, and C.

CNR RATIO CHARACTERIZATION

The CNR influences the precision of the pseudorange navigation observable. The pseudorange is obtained by correlating the received cellular signal with known replicas of

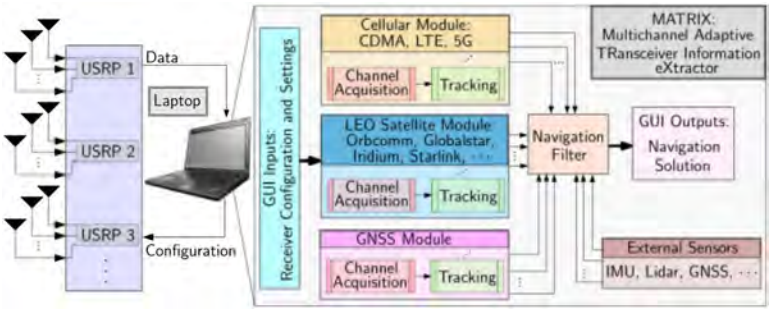

Figure 3.
Software setup used for cellular SOP signal collection.

Authorized licensed use limited to: The Ohio State University. Downloaded on October 13,2022 at 17:51:17 UTC from IEEE Xplore. Restrictions apply.

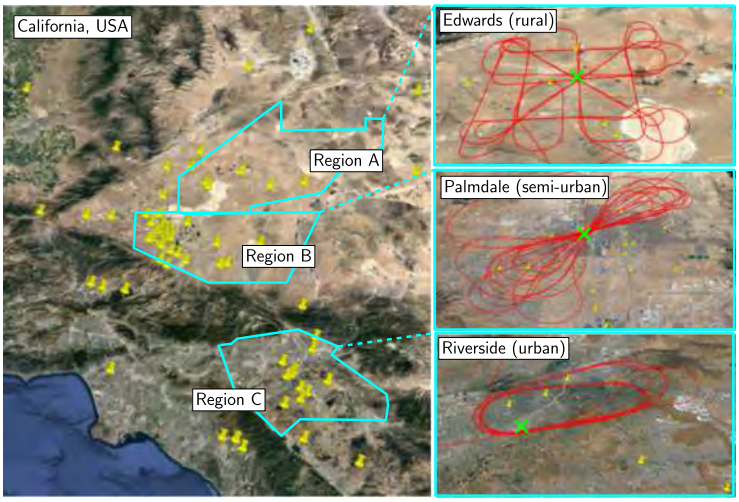

Figure 4.
Regions A, B, and C in which the flight campaigns took place. The yellow pins represent 3G and 4G cellular towers that were mapped and analyzed in this study. The right figures show the aircraft trajectory in all regions (shown in red). Geographic points of interest in each region, shown in green crosses, were chosen according to the designed trajectories.

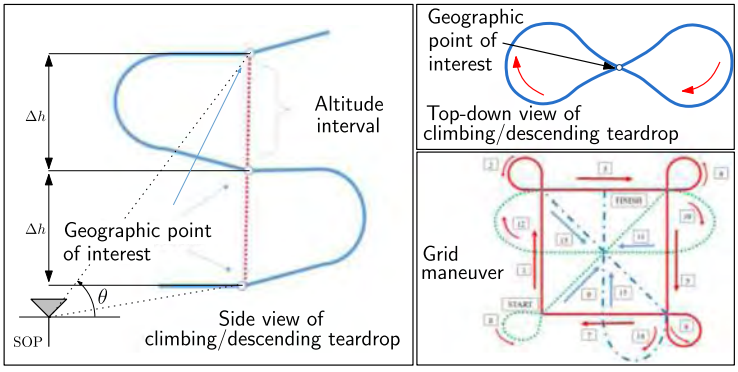

Figure 5.
Maneuvers performed by the C-12 aircraft. The altitude step is denoted by Δh and θ denotes the elevation angle.

the synchronization sequences contained therein, such as the pseudorandom noise (PN) sequence in 3G CDMA and the primary synchronization signal and secondary synchronization signal in 4G LTE. The pseudorange observable is the delay of the autocorrelation peak, expressed in meters. The pseudorange is typically acquired through an exhaustive search over code phase shifts and Doppler frequencies then tracked with delay-locked loops (DLLs). Generally, the variance of the pseudorange error in a DLL is inversely proportional to the CNR. Roughly, the CNR must be above 20 dB-Hz for robust acquisition and tracking. High sensitivity receivers can acquire and track lower CNR signals, which is the subject of active research. The CNR can be calculated according to [41]

$$\mathrm{CNR} = \frac{C}{N_0} = \frac{C}{\sigma^2_{\mathrm{noise}} T} \tag{1}$$

where C is the carrier power in Watts (W), N_0 is the noise power spectral density in W/Hz, which can be expressed as $N_0 = \sigma^2_{\mathrm{noise}} T$, where $\sigma^2_{\mathrm{noise}}$ is the discretized noise variance and T is the accumulation period, or the period over which correlation in the DLL is performed. A cellular SOP receiver estimates $\sigma^2_{\mathrm{noise}}$ by calculating the average power of the autocorrelation function of the received signal with a "fictitious" sequence that has similar properties as the transmitted sequences (e.g., a PN sequence that is not transmitted by any transmitter). The carrier power C is estimated by subtracting the noise variance from the peak power. The mapping between the CNR and the pseudorange error variance expressed in m^2 for a 3G cellular SOP receiver using a first-order DLL with a coherent discriminator is given by [38]

$$\sigma^2_{3\mathrm{G}} = c^2 \frac{B_{n,\mathrm{DLL}} q(t_{\mathrm{eml}})}{2\left(1 - 2B_{n,\mathrm{DLL}} T\right)\mathrm{CNR}} \tag{2}$$

Authorized licensed use limited to: The Ohio State University. Downloaded on October 13,2022 at 17:51:17 UTC from IEEE Xplore. Restrictions apply.

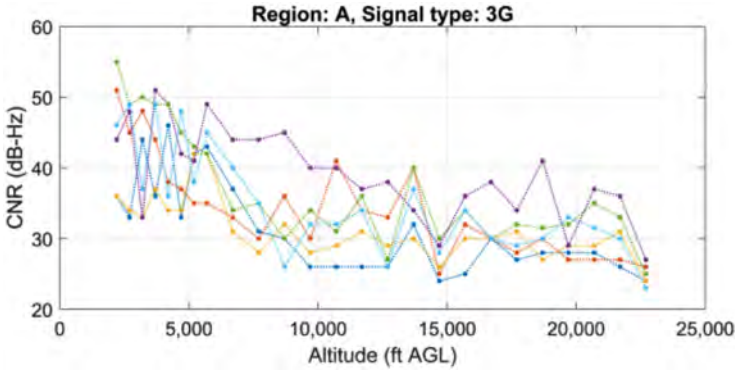

Figure 6.
CNR of 6 3G BTSs as a function of altitude in Region A for 3G signals. Different lines corresponds to different cellular towers.

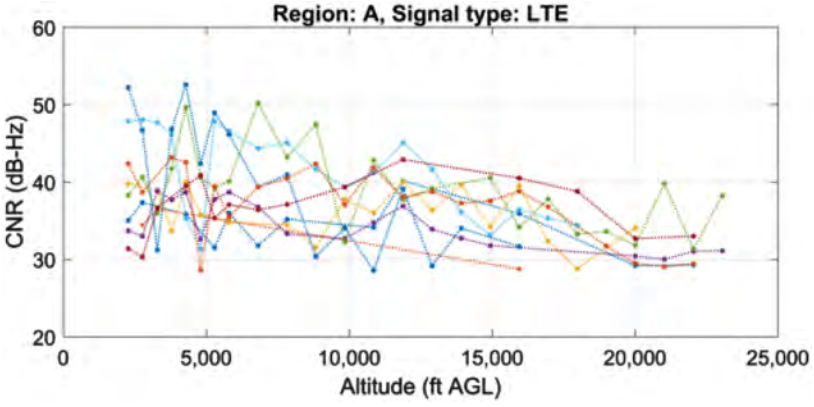

Figure 7.
CNR of 9 LTE eNodeBs as a function of altitude in Region A for LTE signals. Different lines corresponds to different cellular towers.

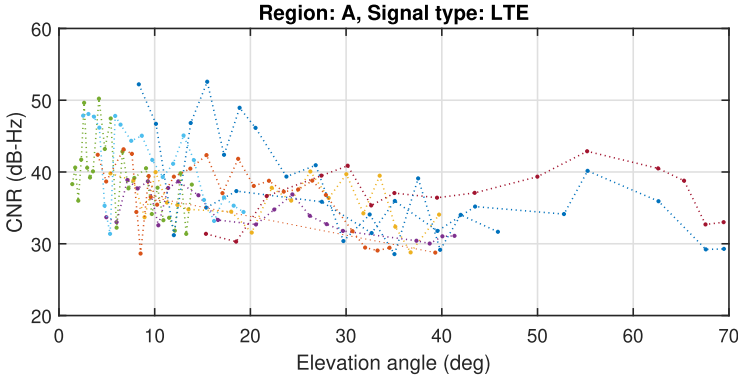

Figure 8.
CNR of 9 LTE eNodeBs as a function of elevation in Region A for LTE signals. Different lines corresponds to different cellular towers

where c is the speed of light, $B_{n,\mathrm{DLL}}$ is the DLL's noise equivalent bandwidth, and $q(t_{\mathrm{eml}})$ is a sensitivity parameter that is a function of the autocorrelation function of the 3G cellular signal and the early minus-late time. For 4G LTE signals, this relationship becomes [39]

$$\sigma^2_{4\mathrm{G}} = c^2 \frac{\pi^2 T_s^2}{128 \lfloor \frac{N_r}{6} \rfloor \mathrm{CNR}} \tag{3}$$

where T_s is the sample duration and N_r is the number of orthogonal frequency-division multiplexing subcarriers used in the synchronization sequence, and $\lfloor \cdot \rfloor$ is the floor

Authorized licensed use limited to: The Ohio State University. Downloaded on October 13,2022 at 17:51:17 UTC from IEEE Xplore. Restrictions apply.

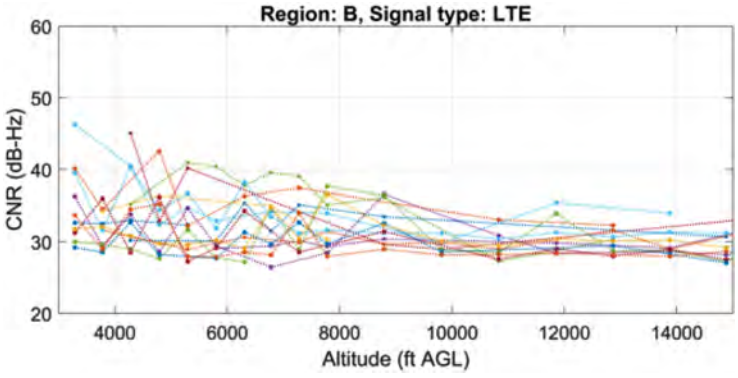

Figure 9.
CNR of 16 LTE eNodeBs as a function of altitude in Region B for LTE signals. Different lines corresponds to different cellular towers

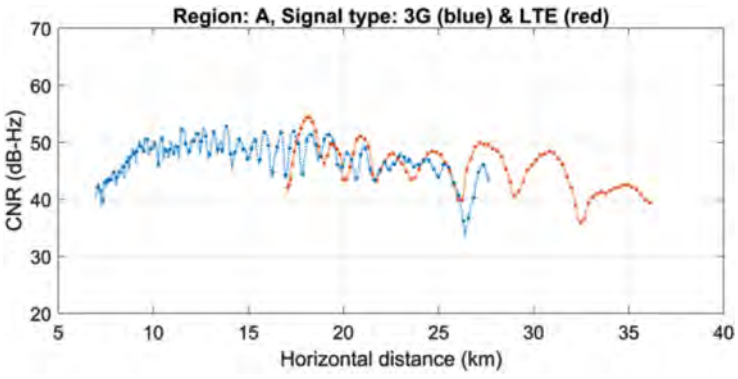

Figure 10.
CNR as a function of the horizontal distance for one 3G BTS (blue) and one LTE eNodeB (red). The aircraft was flying at about 5000 ft AGL.

function. It can be seen from (2) and (3) that the CNR is a crucial parameter in the precision of pseudorange measurements and must be characterized for aviation. In this experimental campaign, the CNRs were measured for i) a fixed horizontal distance and different altitudes and ii) a fixed altitude and different horizontal distances. The CNR as a function of altitude for Region A and both 3G and 4G signals are shown in Figures 6 and 7, respectively. Figure 8 shows the CNR as a function of elevation for 4G LTE signals in Region A. Figure 9 shows the CNR as a function of altitude for 4G LTE signals in Region B.

Figures 6–9 reveal that a significant number of cellular SOPs (namely, 73.33%) can be reliably acquired and tracked at altitudes up to 23,000 ft AGL. The reliable acquisition is qualified by the ability of detecting the presence of the signal along with producing a coarse estimate of the corresponding delays and Doppler shifts. Reliable tracking is qualified by maintaining bounded code and carrier phase errors. These bounded errors guarantee the reliability of the tracked signals to produce navigation observable(s) (pseudorange and carrier phase) which are used to produce a navigation solution. Typical path loss models would predict a linear decrease of the CNR as the distance increases. One reason for seeing a sharp decrease over low altitudes is the directivity of cellular antennas in the elevation direction. It was observed that an elevation angle of about 20° seems to be a cutoff angle for the main lobe, above which the CNR decreases almost linearly with distance. However, the cellular SOP receivers were able to successfully track the signals all the way to 23,000 ft AGL, which corresponded to a maximum elevation angle of approximately 70°. This indicates that there is enough signal power in the side lobes to exploit for navigation purposes. The sharp decrease in CNR at low elevation angles also indicates that the cellular SOP navigation receiver would significantly benefit from a few degrees of an upward adjustment of cellular base station antennas. Although cellular providers require the downward tilt to minimize interference between different cells, the results shown in this article indicate that an upward adjustment is worth considering.

The CNRs for two base stations in Region A are plotted as a function of the horizontal distance in Figure 10. The curves in Figure 10 were expected to decrease as the horizontal distance increased. While this trend is visible, the CNRs also exhibit periodic behavior. This behavior could be due to the two-ray model, where ground

Authorized licensed use limited to: The Ohio State University. Downloaded on October 13,2022 at 17:51:17 UTC from IEEE Xplore. Restrictions apply.

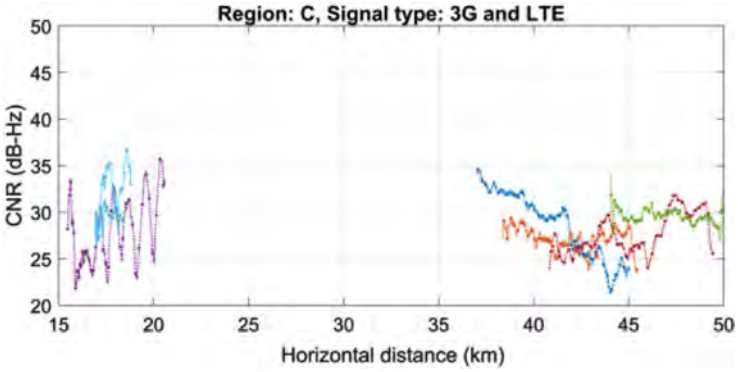

Figure 11.
CNR as a function of the horizontal distance for four 3G BTSs (blue, red, yellow, and purple) and two LTE eNodeBs (green and light blue). The aircraft was flying at an altitude of more than 16,000 ft AGL.

reflections cause constructive and destructive interference. This behavior was observed in reported results in the literature by other experimental campaigns [26].

The CNRs for six base stations in Region C are plotted as a function of the horizontal distance in Figure 11. It is worth noting that the aircraft was flying at an altitude of a little above 16,000 ft AGL, more than 11,000 ft higher than in Figure 11. At such altitudes, the elevation angles are very high. Since cellular base station antennas are tilted downward and are directional in the elevation direction, the loss due to the directive radiation pattern of cellular base station antennas dominates the path loss. This could explain why some of the CNRs in Figure 11 have an increasing trend, especially at shorter horizontal distances where the change in elevation angle is more significant. It is worth mentioning that the big hole in Figure 11 is purely due to this flight scenario, where the cellular base stations happened to be located either too close or too far with respect to the trajectory traversed by the aircraft.

MULTIPATH CHARACTERIZATION

The abovementioned study characterized the precision of pseudorange measurements via the CNR. Next, the accuracy of such measurements is characterized via the multipath channel. Severe- and short-delay multipath can introduce significant biases in the pseudorange measurement, which in turn degrades the navigation solution. One approach to characterize the multipath channel is by estimating the CIR. The cell-specific reference signal (CRS) in 4G LTE is transmitted for channel estimation purposes. The CIR is calculated at different altitudes in Regions A and B. Representative results for each region are shown in Figure 12. The bandwidth of the LTE signal used to estimate the CIRs was 10 MHz.

Figure 12 shows that the LOS signal dominates the CIR over altitudes up to 23,000 ft AGL. Figure 12 suggests that, as expected, multipath is most prominent at low altitudes. This is due to the fact that less reflective surfaces are standing between the transmitter and the receiver. This can be seen as the CIRs are predominantly multipath-free or are experiencing low multipath. This implies high accuracy in the pseudorange measurements. Note that the CIRs seem to slightly degrade at altitudes of around 15,000 ft (AGL) and higher. That is due mostly to channel noise rather than multipath, as indicated in the CNR plots in Figures 6 and 7.

AIRCRAFT NAVIGATION WITH CELLULAR SIGNALS

The previous section established that cellular 3G and 4G SOPs are acquirable and trackable at altitudes as high as 23,000 ft AGL and that the channel possesses a dominant LOS component at the same range of altitudes. This section evaluates the navigation solution obtained exclusively with cellular SOP pseudoranges (without fusing any other sensors or signals, except for barometric altimeter measurements).

EXPERIMENT LAYOUT

The test trajectory consisted of a 1-2-3 leg from the grid pattern in Figure 4. Specifically, Leg 1 is a 24-km straight segment, followed by Leg 2, which is a 270° banking turn of length 18 km, and Leg 3 is a 9-km straight segment. The total distance traveled by the aircraft was over 51 km completed in 9 minutes. The aircraft's trajectory is shown in Figure 13. The aircraft maintained an altitude of approximately 5000 ft AGL over the trajectory. Three radio frequency channels were sampled as follows:

i) 881.52 MHz, which is a 3G channel allocated for cellular provider Verizon Wireless;

ii) 731.5 MHz, a 4G LTE channel allocated for AT&T; and

Authorized licensed use limited to: The Ohio State University. Downloaded on October 13,2022 at 17:51:17 UTC from IEEE Xplore. Restrictions apply.

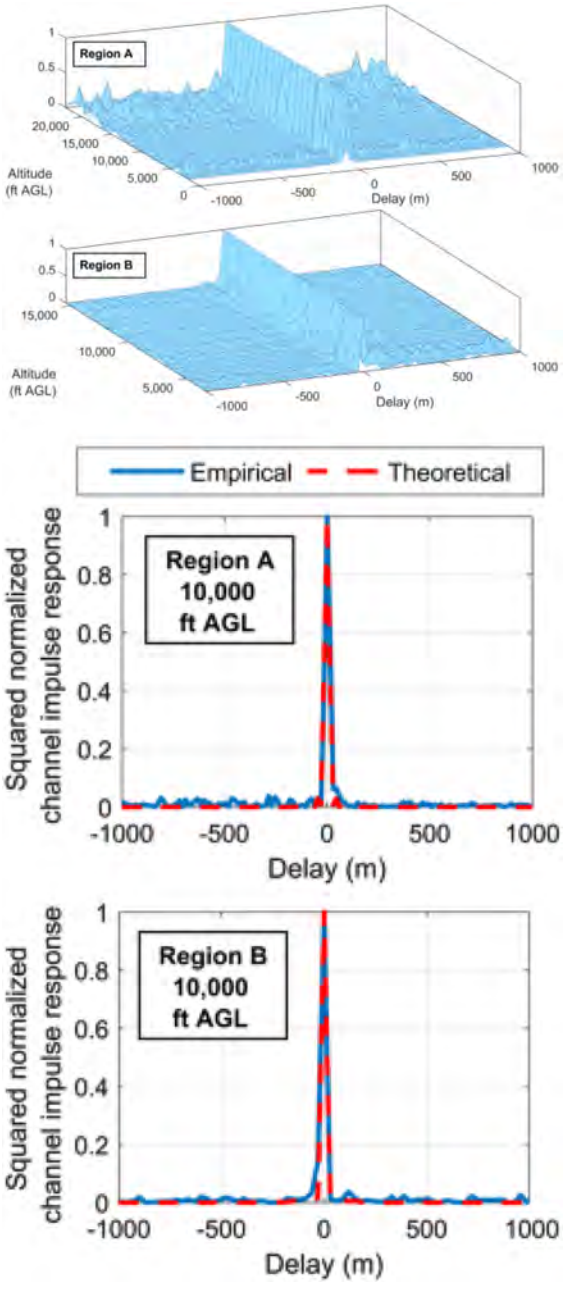

Figure 12.
Top: Surface plots of the CIR as a function of altitude for representative eNodeBs in Regions A and B. Bottom: Snapshots of empirical CIR in Regions A and B at 10,000 ft AGL along with the theoretical CIR.

iii) 751 MHz, also a 4 G LTE channel allocated for T-Mobile.

A total of 11 cellular SOPs were heard over the three channels during the experiment as follows:

a) six 3G BTSs; and

b) five 4G eNodeBs.

TRACKING RESULTS

The 11 cellular SOPs were acquired at different times and tracked for different durations based on signal quality. The pseudorange to the nth base station can be modeled as [14]

$$z_n(k) = \|\boldsymbol{r}_r(k) - \boldsymbol{r}_{s_n}\|_2 + c\delta t_n(k) + v_n(k) \tag{4}$$

where $\boldsymbol{r}_{s_n}$ is the nth base station's 3tD position, c is the speed of light, $\{\delta t_n(k)\}_{n=1}^{N}$ is the difference between the aircraft-mounted receiver's and the nth cellular SOP's clock biases, with N being the total number of cellular SOPs, and $v_n(k)$ is the measurement noise, which is modeled as a zero-mean white sequence with variance $\sigma_n^2(k)$ obtained from the instantaneous CNR using the expression in (2) for 3G signals and the expression in (3) for 4G signals. Figures 14–16 show the time history of i) measured CNRs, ii) pseudorange measurements, and iii) pseudorange error (pseudorange minus the true range), for all 11 cellular SOPs, respectively. The true range is obtained from the known cellular SOPs' position and the aircraft's position throughout the entire flight, the latter of which was obtained from the aircraft's onboard navigation system.

The solid lines in Figure 15 depict the true range between the aircraft and the cellular SOPs, while the dashed lines show the receiver's pseudorange after removing the initial clock bias, i.e.

$$z_n'(k) = z_n(k) - c\hat{\delta}t_n(0)$$

where $\hat{\delta}t_n(0)$ is the initial clock bias estimate, obtained by differencing the true range between the aircraft and the cellular SOP position with the initial pseudorange measurement $z_n(0)$ produced by the receiver.

One can see from Figure 15 that pseudorange tracking is lost for some of the cellular SOPs at or around 300 s, which is when the aircraft starts banking to perform the 270° turn. It is suspected that the aircraft's wings and body block or severely attenuate some of the signals during banking, causing loss of tracking.

It is important to note that the average distance between the aircraft and the BTSs or eNodeBs was around 30 km over the entire trajectory, with eNodeB 4 being tracked at a 100-km distance in the first part of the trajectory. It is worth pointing that this study is a proof of concept to show the potential of exploiting cellular SOPs for aircraft navigation. The developed receiver is not a fully autonomous receiver and does not perform reacquisition of the same SOP after losing track. However, these signals were reacquirable (e.g., after banking).

NAVIGATION SOLUTION

Several estimators could be employed to estimate the aircraft's states (position, velocity, heading, and time) from

Authorized licensed use limited to: The Ohio State University. Downloaded on October 13,2022 at 17:51:17 UTC from IEEE Xplore. Restrictions apply.

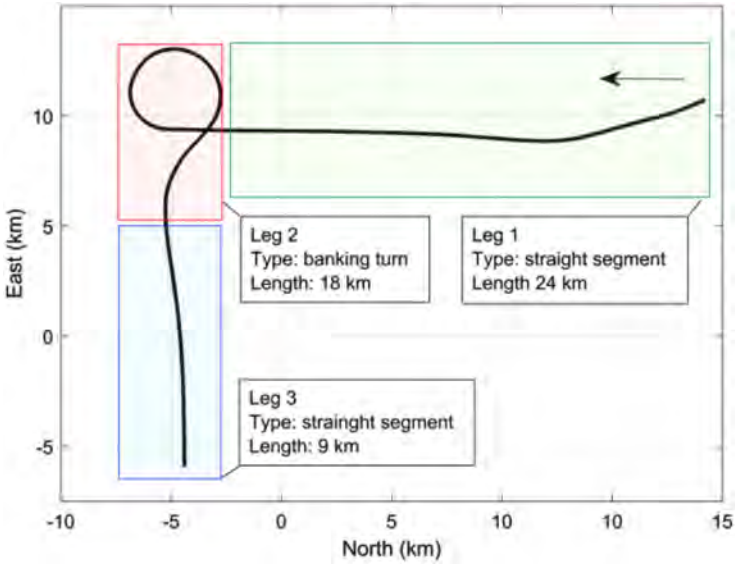

Figure 13.
Aircraft trajectory for the aerial navigation experiment over Region A. The aircraft was flying at about 5000 ft AGL.

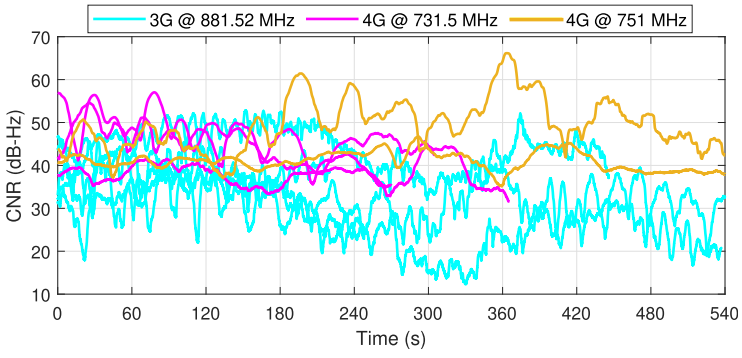

Figure 14.
Time history of the CNRs for all the base stations used to compute the navigation solution.

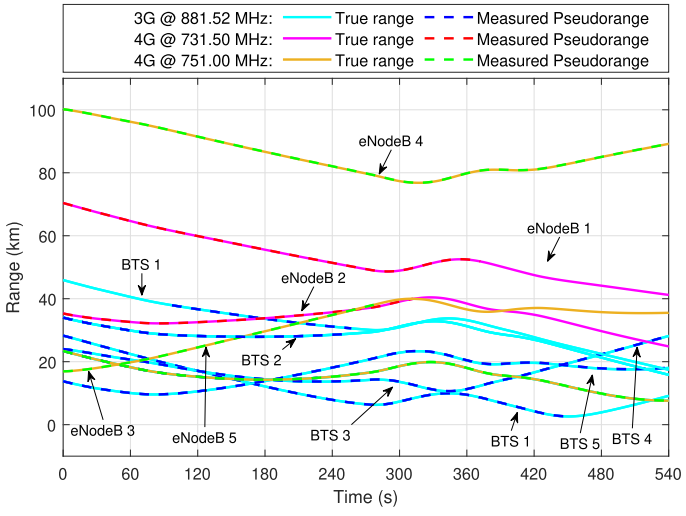

Figure 15.
Time history of the pseudoranges estimated by the cellular SOP receivers and the corresponding true range. The initial values of the pseudoranges and ranges were subtracted out for ease of comparison.

Authorized licensed use limited to: The Ohio State University. Downloaded on October 13,2022 at 17:51:17 UTC from IEEE Xplore. Restrictions apply.

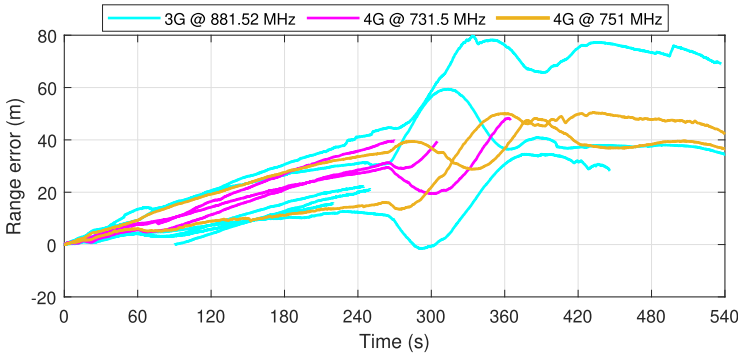

Figure 16.
Time history of the pseudorange error (pseudorange minus the true range) for all cellular SOPs. The error is driven by a common term, which is the receiver's clock bias. The errors increase significantly at around 275 s, which is when the turn starts. The high dynamics of a banking turn inject stress on the tracking loops. The initial values of the pseudorange errors were subtracted out for ease of comparison.

pseudorange measurements. Moreover, data from other sensors [e.g., inertial measurement unit (IMU), radar, lidar, vision, etc.] and/or dynamical constraints could be fused with the pseudorange measurements to improve the navigation solution accuracy. However, the objective of this study is to test the potential of cellular SOPs to produce a navigation solution. Any additional sensors or dynamical constraints will only improve the performance of what is presented next. Since cellular SOPs suffer from low diversity in the vertical direction, only altitude measurements from the aircraft's navigation system were fused with the pseudorange measurements. The position of the cellular SOPs was assumed to be known, although it can be estimated on-the-fly as well [42]. However, the clock biases are dynamic and stochastic and must be estimated along with the aircraft's states. This results in an underdetermined system (i.e., one where the dimension of the state vector is larger than the dimension of the measurement vector), which makes using a point estimator (e.g., nonlinear least squares) infeasible [43]. To circumvent this, an extended Kalman filter (EKF) is used to produce the navigation solution with cellular pseudorange measurements and altimeter data derived from the aircraft's onboard navigation system. The aircraft's 3D position and velocity, denoted by $\boldsymbol{r}_{\mathrm{r}}$ and $\dot{\boldsymbol{r}}_{\mathrm{r}}$, respectively, were estimated in an North–East–Down frame centered at the geographical point of interest of Region A. A simple, yet effective nearly constant velocity dynamical model was used to describe the dynamics of the aircraft, with power spectra given by q_N, q_E, and q_D for the acceleration process noise in the N, E, and D directions, respectively. A double integrator driven by process noise was used to model the receiver and base stations' clock biases [14]. The clock state of the receiver or any base station therefore consists of a time-varying, stochastic bias δt and drift $\dot{\delta} t$, with process noise power spectra $S_{\tilde{w}_{\delta t}}$ and $S_{\tilde{w}_{\dot{\delta} t}}$, respectively. The EKF was implemented using the framework described in [44]. To this end, define the state vector

$$\begin{aligned}\boldsymbol{x}(k) \triangleq \big[&\boldsymbol{r}_{\mathrm{r}}(k), \dot{\boldsymbol{r}}_{\mathrm{r}}(k), c\delta t_1(k), c\dot{\delta} t_1(k),\\ &\ldots, c\delta t_N(k), c\dot{\delta} t_N(k)\big]^{\mathsf{T}} \in \mathbb{R}^{6+2\,N}.\end{aligned} \tag{5}$$

The discrete-time dynamics of $\boldsymbol{x}$ is given by

$$\boldsymbol{x}(k+1) = \mathbf{F}\boldsymbol{x}(k) + \boldsymbol{w}(k) \tag{6}$$

where $\mathbf{F} \triangleq \mathrm{diag}[\mathbf{F}_{\mathrm{pv}}, \mathbf{F}_{\mathrm{clk}}, \ldots, \mathbf{F}_{\mathrm{clk}}]$

$$\mathbf{F}_{\mathrm{pv}} \triangleq \begin{bmatrix} \mathbf{I}_{3\times 3} & T\mathbf{I}_{3\times 3} \\ \mathbf{0}_{3\times 3} & \mathbf{I}_{3\times 3} \end{bmatrix}, \quad \mathbf{F}_{\mathrm{clk}} \triangleq \begin{bmatrix} 1 & T \\ 0 & 1 \end{bmatrix}$$

and T is the measurement update period, which is chosen to be the accumulation period in the receiver, and $\boldsymbol{w}(k)$ is the discrete-time process noise vector, which is modeled as a zero-mean white sequence with covariance $\mathbf{Q} \triangleq \mathrm{diag}[\mathbf{Q}_{\mathrm{pv}}, c^2\mathbf{Q}_{\mathrm{clk}}]$

$$\mathbf{Q}_{\mathrm{pv}} \triangleq \begin{bmatrix} \mathbf{S}_{\mathrm{pv}}\frac{T^3}{3} & \mathbf{S}_{\mathrm{pv}}\frac{T^2}{2} \\ \mathbf{S}_{\mathrm{pv}}\frac{T^2}{2} & \mathbf{S}_{\mathrm{pv}}T \end{bmatrix}, \quad \mathbf{S}_{\mathrm{pv}} \triangleq \mathrm{diag}[q_N, q_E, q_D]$$

$$\mathbf{Q}_{\mathrm{clk}} = \boldsymbol{\Gamma}\mathbf{Q}_{\mathrm{clk,r}}\boldsymbol{\Gamma}^{\mathsf{T}} + \mathbf{Q}_{\mathrm{clk,sop}}, \quad \boldsymbol{\Gamma} \triangleq [\mathbf{I}_{2\times 2}\ \ldots, \mathbf{I}_{2\times 2}]^{\mathsf{T}}$$

$$\mathbf{Q}_{\mathrm{clk,sop}} \triangleq \mathrm{diag}\left[\mathbf{Q}_{\mathrm{clk,sop}_1}, \ldots, \mathbf{Q}_{\mathrm{clk,sop}_N}\right]$$

$$\mathbf{Q}_{\mathrm{clk},i} = \begin{bmatrix} S_{\tilde{w}_{\delta t_i}}T + S_{\tilde{w}_{\dot{\delta} t_i}}\frac{T^3}{3} & S_{\tilde{w}_{\dot{\delta} t_i}}\frac{T^2}{2} \\ S_{\tilde{w}_{\dot{\delta} t_i}}\frac{T^2}{2} & S_{\tilde{w}_{\dot{\delta} t_i}}T \end{bmatrix}$$

where $i \in \{\mathrm{r}, \mathrm{sop}_1, \ldots, \mathrm{sop}_N\}$ and $S_{\tilde{w}_{\delta t_i}}$ and $S_{\tilde{w}_{\dot{\delta} t_i}}$ are the receiver or SOP-specific clock bias and drift noise power spectra.

The measurement (4) can be expressed in vector form as

$$\begin{aligned}&\boldsymbol{z}(k) = \boldsymbol{h}[\boldsymbol{x}(k)] + \boldsymbol{v}(k) \\ &\boldsymbol{z}(k) \triangleq [z_1(k), \ldots, z_N(k), z_{\mathrm{alt}}(k)]^{\mathsf{T}} \in \mathbb{R}^{N+1} \\ &\boldsymbol{v}(k) \triangleq [v_1(k), \ldots, v_N(k), v_{\mathrm{alt}}(k)]^{\mathsf{T}}\end{aligned} \tag{7}$$

where $\boldsymbol{h}[\boldsymbol{x}(k)]$ is a vector-valued function readily obtained from (4) and z_{alt} is the aircraft's altitude measurement. Let $\mathbf{R}(k)$ denote the covariance of the measurement noise vector $\boldsymbol{v}(k)$, which has the form $\mathbf{R}(k) =$

Authorized licensed use limited to: The Ohio State University. Downloaded on October 13,2022 at 17:51:17 UTC from IEEE Xplore. Restrictions apply.

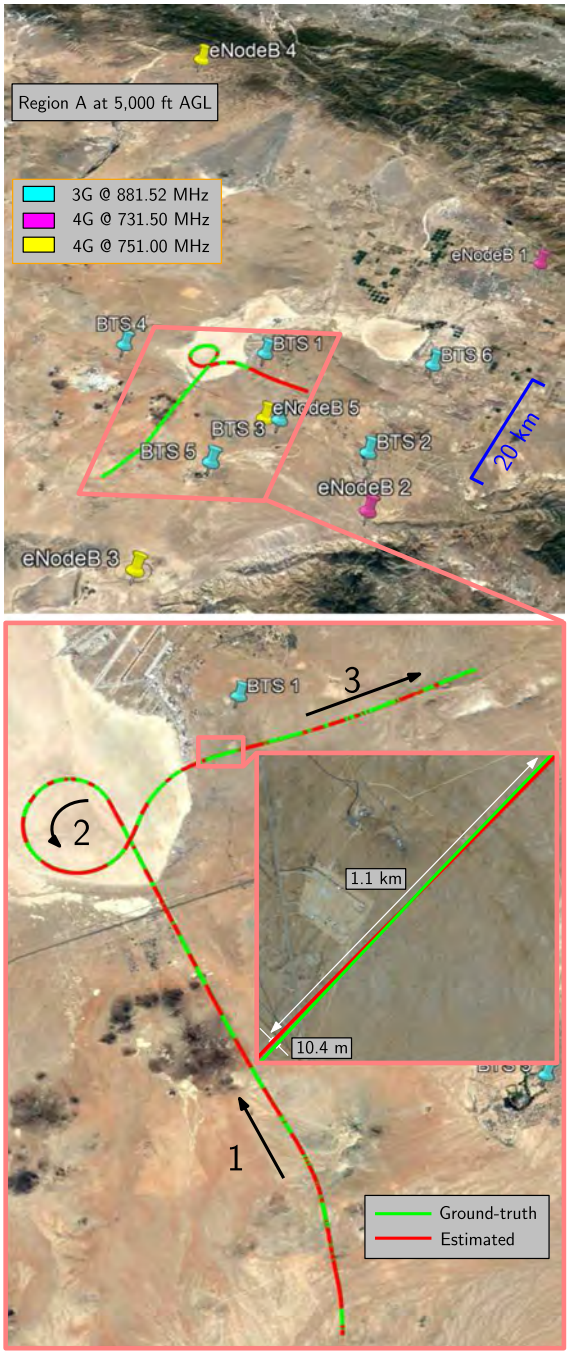

Figure 17.
Experimental layout and results showing: i) BTS and eNodeB positions, ii) true aircraft trajectory, and iii) aircraft trajectory estimated exclusively using cellular SOPs. The aircraft traversed a total distance of 51-km traversed in 9 minutes during the experiment. The 3D position RMSE over the entire trajectory was found to be 10.5 m.

$\text{diag}[\sigma_1^2, \ldots, \sigma_N^2, \sigma_{\text{alt}}^2]$. The noise variances $\sigma_n^2(k)$ were obtained from the instantaneous CNR using the expression in (2) for 3G signals and the expression in (3) for 4G signals, while σ_{alt}^2 was set to 3 m^2.

An EKF is then implemented based on the dynamics and measurement models in (6) and (7), respectively, to yield and estimate $\hat{\boldsymbol{x}}(k|k)$ of $\boldsymbol{x}(k)$ using all measurements up to time-step k, with an associated estimation error covariance denoted by $\mathbf{P}(k|k)$. The initial estimate and covariance are obtained from two consecutive measurements and corresponding position estimates taken from the aircraft's navigation system [44]. The receiver and base station clock process noise covariance matrices were chosen to be

$$\mathbf{Q}_{\text{clk},r} = \begin{bmatrix} 9.57 \times 10^{-5} & 2.52 \times 10^{-8} \\ 2.52 \times 10^{-8} & 1.89 \times 10^{-6} \end{bmatrix} \tag{8}$$

$$\mathbf{Q}_{\text{clk},s_n} = \begin{bmatrix} 3.11 \times 10^{-7} & 2.52 \times 10^{-11} \\ 2.52 \times 10^{-11} & 1.89 \times 10^{-9} \end{bmatrix}. \tag{9}$$

The abovementioned clock process noise covariance matrices assumed the receiver to be equipped with a typical-quality oven-controlled crystal oscillator (OCXO), while the cellular base stations are equipped with high-quality OCXOs [14]. The measurement rate was $T = 0.08/3$ s. The power spectral densities of the acceleration in north and east directions were set to high values to account for not having an accurate dynamical model of the C-12 aircraft [45], specifically $q_N = q_E = 5\ \text{m}^2/\text{s}^3$. However, the power spectral density of the acceleration in the down direction was set to be small, since there was little change in altitude throughout the flight, specifically $q_D = 0.5\,\text{m}^2/\text{s}^3$.

Figure 17 shows the environment layout and the true and estimated trajectories. The total position 3D RMSE was calculated to be 10.5 m over the 51-km trajectory, traversed in 9 minutes. It is important to note that the position error in the EKF is the largest during the turn. This is due to i) the measurement errors due to the high dynamics of the banking turn, which severely stressed the tracking loops, and ii) the mismatch in the dynamics model assumed in the EKF since a 270° banking turn has significantly different dynamics than the assumed nearly constant velocity. However, as mentioned earlier, the purpose of this study is to highlight the minimum performance that can be achieved with SOPs. Any additional sensors, dynamical constraints, or adaptive estimators would improve the performance [46], [47]. Figure 18 shows the EKF estimation error plots and corresponding sigma-bounds for the aircraft's position and velocity states. The 3D navigation performance over the 51-km trajectory is summarized in Table 1.

DISCUSSION

This study showed the potential of cellular 3G and 4G SOPs as reliable sources for high-altitude aircraft navigation. The results presented herein, although promising, can be further improved upon in several ways. The following are key takeaways and design considerations for reliable aircraft navigation with cellular SOPs.

Authorized licensed use limited to: The Ohio State University. Downloaded on October 13,2022 at 17:51:17 UTC from IEEE Xplore. Restrictions apply.

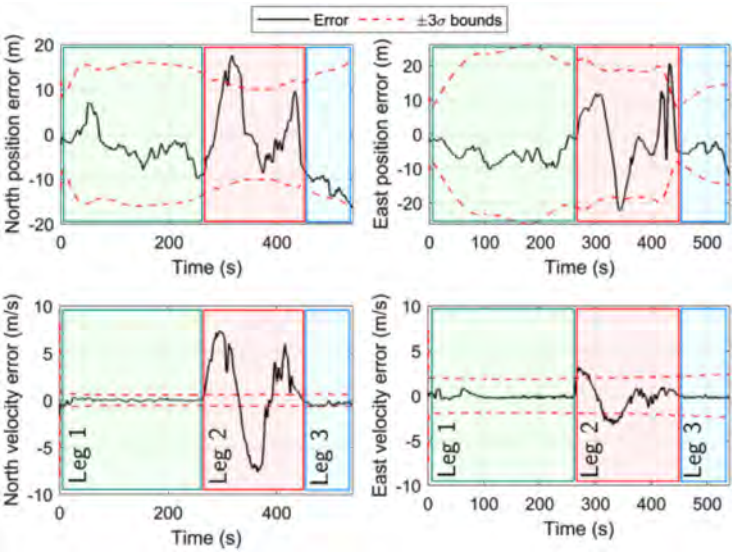

Figure 18.
EKF plots showing the time history of the position and velocity errors as well as the $\pm 3\sigma$ bounds. As expected, the EKF performs poorly in the second leg, where the mismatch between the true aircraft dynamics and the assumed EKF model is highest.

- *Long integration periods:* The period over which correlations were performed in the receiver could be extended to achieve higher CNRs where necessary, especially at altitudes above 23,000 ft. However, one would need a stable oscillator in the receiver clock to achieve coherent integration. As such, highly stable OCXOs or chip-scale atomic clocks could be used to drive the receiver's clock.
- *Mitigate self-blockage:* As discussed previously, the aircraft's body and wings caused signal blockage or severe attenuation during banking. One way to mitigate this is by mounting multiple antennas onto the aircraft in such a way that at least one antenna remains within LOS to the cellular base station of interest (e.g., at the tip of both wings). This guarantees continuous availability of pseudorange measurements. Another mitigation approach is to use synthetic aperture navigation (e.g., [48])
- *Accounting for the high dynamics:* Aircraft, such as the C-12, can perform highly dynamic maneuvers. As such, it is crucial to design tracking loops in the receivers that can cope with such dynamics. Moreover, the dynamics model employed in the EKF in this study led to mismatches and larger estimation errors during the 270° turn. This mismatch can be mitigated by using appropriate dynamical models for fixed-wing aircraft or more elaborate dynamical models (e.g., Wiener process acceleration, Singer acceleration, mean-adaptive acceleration, semi-Markov jump process, circular motion, curvilinear motion, coordinated turn, among others [45]) adaptive estimation techniques [46], [47], and/or a kinematic model with IMU measurements, as is the case with most INS aiding techniques [16], [42].
- *Vertical dilution of precision:* At high altitudes, there is very little vertical diversity with respect to terrestrial cellular towers. As such, the aircraft's cellular-based navigation solution vertical dilution of precision will be large. Nevertheless, the aircraft's vertical position can still be estimated from the pseudoranges extracted from cellular towers, albeit with less accuracy compared to the results presented in this article, which fused altimeter-based measurements. For example, if the altimeter-based altitude measurements are not used in the demonstrated flight, a 2D and 3D RMSE of 30.41 and 117.55 m are achieved, respectively, compared to 10.53 and 10.55 m, respectively, when using altitude measurements.
- *Intrachannel interference:* The proposed receiver exploits the synchronization sequences or reference signals broadcast by cellular towers. These signals are designed to have low cross-correlation properties between different towers. For

Table 1.

Navigation Performance With Cellular Signals			
Metric	**Leg 1**	**Leg 2**	**Leg 3**
Position RMSE [m]	7.57	12.85	12.87
Velocity RMSE [m/s]	0.62	4.87	0.46
Maximum position error [m]	10.46	22.67	20.46
Maximum velocity error [m/s]	4.15	7.64	0.74

Authorized licensed use limited to: The Ohio State University. Downloaded on October 13,2022 at 17:51:17 UTC from IEEE Xplore. Restrictions apply.

example, in 3G systems, a 32768-long QPSK pseudonoise (PN) sequence and Walsh codes are used to spread the transmitted data. The PN sequence is shifted by an integer multiple of 64 chips by each cellular tower sector, which allows a maximum of 512 possible shifts. In this case, the cross-correlation between the PN sequence and its shifted version is negligible. As such, for two towers to significantly interfere at the receiver, their relative range must be at least 15 km (corresponding to 64-chip offset). However, in practice, adjacent towers are offset by at least 4×64 chips, requiring a minimum of 60-km relative range for strong interference to occur. In addition, the 60-km relative range implies a 95 dB difference in the path loss (assuming the free space propagation model), which means that one signal will be completely buried in the noise floor of the other. Even for a relative range of 15 km, the difference in the path loss is 83 dB. In conclusion, it is very unlikely for intrachannel interference to be an impediment for exploiting 3G signals for aerial navigation. This could explain why interference from fear and far cells have not been detected in the case of 3G signals. The same discussion holds for 4G signals, except that the synchronization signals were not used in the 4G module in order to avoid interference, since some of these sequences are common between different eNodeBs. Instead, only the CRS was used, which is unique for each eNodeB and has very low cross-correlation properties.

CONCLUSION

This study demonstrated that reliable acquisition and tracking of cellular 3G CDMA and 4G LTE signals can be performed by high dynamics aircraft flying at altitudes up to 23,000 ft AGL and horizontal distances up to 100 km, making them a reliable source for aircraft navigation. This finding is further validated by experimental results showing a USAF C-12 aircraft navigating for 51 km at around 5000 ft AGL over a 9-minute period exclusively with cellular SOPs, achieving a 3D position RMSE of 10.5 m.

ACKNOWLEDGMENTS

The authors would like to thank Edwards AFB and Holloman AFB for inviting the ASPIN Laboratory to conduct experiments on Air Force aircraft in the "SNIFFER: Signals of opportunity for Navigation In Frequency-Forbidden EnviRonments" flight campaign. They would also like to thank Joshua Morales, Kimia Shamaei, Mahdi Maaref, Kyle Semelka, MyLinh Nguyen, and Trier Mortlock for their help with preparing for data collection. DISTRIBUTION STATEMENT A. Approved for public release; Distribution is unlimited 412TW-PA-20146. This work was supported in part by the Office of Naval Research (ONR) under Grant N00014-19-1-2511 and Grant N00014-19-1-2613, in part by the Sandia National Laboratories under Grant 1655264, in part by the National Science Foundation (NSF) under Grant 1929965, and in part by the U.S. Department of Transportation (USDOT) under Grant 69A3552047138 for the CARMEN University Transportation Center (UTC).

REFERENCES

[1] R. Sabatini *et al.*, "Avionics systems panel research and innovation perspectives," *IEEE Aerosp. Electron. Syst. Mag.*, vol. 37, no. 12, pp. 58–72, Dec. 2020.

[2] E. Blasch *et al.*, "Cyber awareness trends in avionics," in *Proc. IEEE/AIAA Digit. Avionics Syst. Conf.*, 2019, pp. 1–8.

[3] EUROCONTROL, Aviation Intelligence Unit, "Does radio frequency interference to satellite navigation pose an increasing threat to network efficiency, cost-effectiveness and ultimately safety?," Brussels, Belgium, Tech. Rep., Mar. 2021. [Online]. Available: https://www.eurocontrol.int/sites/default/files/2021-03/eurocontrol-think-paper-9-radio-frequency-intereference-satellite-navigation.pdf

[4] International Civil Aviation Organization (ICAO), "An urgent need to address harmful interferences to GNSS," Montreal, QC, Canada, Tech. Rep., May 2019. [Online]. Available: https://www.iata.org/contentassets/d7e421981aa64169af1a8d6b37438d4d/tib-gnss-interference-final.pdf

[5] A. Hansen *et al.*, "Complementary PNT and GPS backup technologies demonstration report: Sections 1 through 10," Cambridge, MA, USA, John A. Volpe Nat. Transp. Syst. Center Tech. Rep. DOT-VNTSC-20-07, 2021.

[6] M. Bartock *et al.*, "Foundational PNT profile: Applying the cybersecurity framework for the responsible use of positioning, navigation, and timing (PNT) services," Gaithersburg, MD, USA, Nat. Inst. Standards and Technol. (NIST), Tech. Rep. NISTIR 8323, Feb. 2021.

[7] J. Raquet *et al.*, "Part D: Position, navigation, and timing using radio signals-of-opportunity," in *Position, Navigation, and Timing Technologies in the 21st Century: Integrated Satellite Navigation, Sensor Systems, and Civil Applications*, J. Morton, F. van Diggelen, J. Spilker, Jr., and B. Parkinson, Eds. Hoboken, NJ, USA: Wiley-IEEE, 2021, vol. 2, ch. 35–43, pp. 1115–1412.

[8] J. del Peral-Rosado, R. Raulefs, J. López-Salcedo, and G. Seco-Granados, "Survey of cellular mobile radio localization methods: From 1G to 5G," *IEEE Commun. Surv. Tut.*, vol. 20, no. 2, pp. 1124–1148, Apr.–Jun. 2018.

Authorized licensed use limited to: The Ohio State University. Downloaded on October 13,2022 at 17:51:17 UTC from IEEE Xplore. Restrictions apply.

[9] T. Kang, H. Lee, and J. Seo, "TOA-based ranging method using CRS in LTE signals," *J. Adv. Navigation Technol.*, vol. 23, no. 5, pp. 437–443, Oct. 2019.

[10] P. Wang and Y. Morton, "Multipath estimating delay lock loop for LTE signal TOA estimation in indoor and urban environments," *IEEE Trans. Wireless Commun.*, vol. 19, no. 8, pp. 5518–5530, Aug. 2020.

[11] J. Gante, L. Sousa, and G. Falcao, "Dethroning GPS: Low-power accurate 5G positioning systems using machine learning," *IEEE Trans. Emerg. Sel. Topics Circuits Syst.*, vol. 10, no. 2, pp. 240–252, Jun. 2020.

[12] H. Dun, C. Tiberius, and G. Janssen, "Positioning in a multipath channel using OFDM signals with carrier phase tracking," *IEEE Access*, vol. 8, pp. 13011–13028, 2020.

[13] A. Abdallah and Z. Kassas, "UAV navigation with 5G carrier phase measurements," in *Proc. ION GNSS Conf.*, 2021, pp. 3294–3306.

[14] Z. Kassas, "Navigation with cellular signals of opportunity," in *Position, Navigation, and Timing Technologies in the 21st Century: Integrated Satellite Navigation, Sensor Systems, and Civil Applications*, J. Morton, F. van Diggelen, J. Spilker, Jr., and B. Parkinson, Eds. Hoboken, NJ, USA: Wiley-IEEE, vol. 2, ch. 38, 2021, pp. 1171–1223.

[15] C. Yang, T. Nguyen, and E. Blasch, "Mobile positioning via fusion of mixed signals of opportunity," *IEEE Aerosp. Electron. Syst. Mag.*, vol. 29, no. 4, pp. 34–46, Apr. 2014.

[16] Z. Kassas, M. Maaref, J. Morales, J. Khalife, and K. Shamaei, "Robust vehicular localization and map matching in urban environments through IMU, GNSS, and cellular signals," *IEEE Intell. Transp. Syst. Mag.*, vol. 12, no. 3, pp. 36–52, Jun. 2020.

[17] J. del Peral-Rosado *et al.*, "Physical-layer abstraction for hybrid GNSS and 5G positioning evaluations," in *Proc. IEEE Veh. Technol. Conf.*, 2019, pp. 1–6.

[18] M. Maaref and Z. Kassas, "Autonomous integrity monitoring for vehicular navigation with cellular signals of opportunity and an IMU," *IEEE Trans. Intell. Transp. Syst.*, vol. 23, no. 6, pp. 5586–5601, Jun. 2022.

[19] K. Shamaei and Z. Kassas, "Sub-meter accurate UAV navigation and cycle slip detection with LTE carrier phase," in *Proc. 32nd Int. Tech. Meeting Satell. Division Inst. Navigation Conf.*, 2019, pp. 2469–2479.

[20] J. Khalife and Z. Kassas, "On the achievability of sub-meter-accurate UAV navigation with cellular signals exploiting loose network synchronization," *IEEE Trans. Aerosp. Electron. Syst.*, early access, Mar. 31, 2022, doi: 10.1109/TAES.2022.3162770.

[21] Z. Kassas, J. Khalife, A. Abdallah, and C. Lee, "I am not afraid of the GPS jammer: Resilient navigation via signals of opportunity in GPS-denied environments," *IEEE Aerosp. Electron. Syst. Mag.*, vol. 37, no. 7, pp. 4–19, Jul. 2022.

[22] Qualcomm Technologies Inc., "LTE unmanned aircraft systems," San Diego, CA, USA, Tech. Rep. 1.0.1, May 2017. [Online]. Available: https://www.qualcomm.com/documents/lte-unmanned-aircraft-systems-trial-report/

[23] Y. Zeng, Q. Wu, and R. Zhang, "Accessing from the sky: A tutorial on UAV communications for 5G and beyond," *Proc. IEEE*, vol. 107, no. 12, pp. 2327–2375, Dec. 2019.

[24] R. Amorim, H. Nguyen, P. Mogensen, I. Kovacs, J. Wigard, and T. Sorensen, "Radio channel modeling for UAV communication over cellular networks," *IEEE Wireless Commun. Lett.*, vol. 6, no. 4, pp. 514–517, Aug. 2017.

[25] X. Cai *et al.*, "An empirical air-to-ground channel model based on passive measurements in LTE," *IEEE Trans. Veh. Technol.*, vol. 68, no. 2, pp. 1140–1154, Feb. 2019.

[26] W. Khawaja, I. Guvenc, D. Matolak, U. Fiebig, and N. Schneckenburger, "A survey of air-to-ground propagation channel modeling for unmanned aerial vehicles," *IEEE Commun. Surv. Tut.*, vol. 21, no. 3, pp. 2361–2391, Jul.–Sep. 2019.

[27] K. Matheou *et al.*, "Analysis of at-altitude LTE power spectra for small unmanned aircraft system C2 communications," in *Proc. Integr. Commun., Navigation, Surveill. Conf.*, 2019, pp. 1–12.

[28] X. Cai *et al.*, "Low altitude air-to-ground channel characterization in LTE network," in *Proc. Eur. Conf. Antennas Propag.*, 2019, pp. 1–5.

[29] B. Van DerA. BerghChiumento, and S. Pollin, "LTE in the sky: Trading off propagation benefits with interference costs for aerial nodes," *IEEE Commun. Mag.*, vol. 54, no. 5, pp. 44–50, May 2016.

[30] I. Kovacs, R. Amorim, H. Nguyen, J. Wigard, and P. Mogensen, "Interference analysis for UAV connectivity over LTE using aerial radio measurements," in *Proc. IEEE Veh. Technol. Conf.*, 2017, pp. 1–6.

[31] R. J. Amorim, I. Wigard Kovacs, and T. Sorensen, "UAV Communications for 5G and Beyond," *Performance Enhancements for LTE-Connected UAVs: Experiments and Simulations*, Y. Zeng, I. R. Guvenc Zhang, G. Geraci, and D. Matolak, Eds. Hoboken, NJ, USA: Wiley-IEEE, 2021, ch. 5, pp. 139–161.

[32] E. Teng, J. Diogo Falcao, and B. Iannucci, "Holes-in-the-sky: A field study on cellular-connected UAS," in *Proc. Int. Conf. Unmanned Aircr. Syst.*, 2017, pp. 1165–1174.

[33] G. Athanasiadou, M. Batistatos, D. Zarbouti, and G. Tsoulos, "LTE ground-to-air field measurements in the context of flying relays," *IEEE Wireless Commun.*, vol. 26, no. 1, pp. 12–17, Feb. 2019.

[34] A. Abdalla and V. Marojevic, "Communications standards for unmanned aircraft systems: The 3GPP perspective and research drivers," *IEEE Commun. Standards Mag.*, vol. 5, no. 1, pp. 70–77, Mar. 2021.

[35] H. Maattanen, "UAV communications for 5G and beyond," *3GPP Standardization for Cellular-Supported UAVs*, Y. Zeng, I. Guvenc, R. Zhang, G. Geraci, and D. Matolak, Eds. Hoboken, NJ, USA: Wiley-IEEE,2021, ch. 6, pp. 163–180.

Authorized licensed use limited to: The Ohio State University. Downloaded on October 13,2022 at 17:51:17 UTC from IEEE Xplore. Restrictions apply.

[36] E. Kim and Y. Shin, "Feasibility analysis of LTE-based UAS navigation in deep urban areas and DSRC augmentation," *Sensors*, vol. 19, no. 9, pp. 4192–4207, Apr. 2019.

[37] B. Stevens and M. Younis, "Detection algorithm for cellular synchronization signals in airborne applications," *IEEE Access*, vol. 9, pp. 55555–55566, Apr. 2021.

[38] J. Khalife, K. Shamaei, and Z. Kassas, "Navigation with cellular CDMA signals—Part I: Signal modeling and software-defined receiver design," *IEEE Trans. Signal Process.*, vol. 66, no. 8, pp. 2191–2203, Apr. 2018.

[39] K. Shamaei and Z. Kassas, "LTE receiver design and multipath analysis for navigation in urban environments," *Navigation, J. Inst. Navigation*, vol. 65, no. 4, pp. 655–675, Dec. 2018.

[40] J. Morales and Z. Kassas, "Optimal collaborative mapping of terrestrial transmitters: Receiver placement and performance characterization," *IEEE Trans. Aerosp. Electron. Syst.*, vol. 54, no. 2, pp. 992–1007, Apr. 2018.

[41] P. Misra and P. Enge, *Global Positioning System: Signals, Measurements, and Performance*, 2nd ed. Lincoln, MA, USA: Ganga-Jamuna Press, 2010.

[42] J. Morales and Z. Kassas, "Tightly-coupled inertial navigation system with signals of opportunity aiding," *IEEE Trans. Aerosp. Electron. Syst.*, vol. 57, no. 3, pp. 1930–1948, Jun. 2021.

[43] Z. Kassas and T. Humphreys, "Receding horizon trajectory optimization in opportunistic navigation environments," *IEEE Trans. Aerosp. Electron. Syst.*, vol. 51, no. 2, pp. 866–877, Apr. 2015.

[44] J. Khalife and Z. Kassas, "Opportunistic UAV navigation with carrier phase measurements from asynchronous cellular signals," *IEEE Trans. Aerosp. Electron. Syst.*, vol. 56, no. 4, pp. 3285–3301, Aug. 2020.

[45] X. Li and V. Jilkov, "Survey of maneuvering target tracking. Part I: Dynamic models," *IEEE Trans. Aerosp. Electron. Syst.*, vol. 39, no. 4, pp. 1333–1364, Oct. 2003.

[46] M. Yeddanapudi, Y. Bar-Shalom, and K. Pattipati, "IMM estimation for multitarget-multisensor air traffic surveillance," *Proc. IEEE*, vol. 85, no. 1, pp. 80–96, Jan. 1997.

[47] J. Dunik, O. Kost, O. Straka, and E. Blasch, "Navigation and estimation improvement by environmental-driven noise mode detection," in *Proc. IEEE/ION Position, Location, Navigation Symp.*, 2020, pp. 925–932.

[48] A. Abdallah and Z. Kassas, "Deep learning-aided spatial discrimination for multipath mitigation," in *Proc. IEEE/ION Position, Location, Navigation Symp.*, 2020, pp. 1324–1335.

Authorized licensed use limited to: The Ohio State University. Downloaded on October 13,2022 at 17:51:17 UTC from IEEE Xplore. Restrictions apply.

A Hybrid Analytical-Machine Learning Approach for LEO Satellite Orbit Prediction

Jamil Haidar-Ahmad[1], Nadim Khairallah[2], and Zaher M. Kassas[1,2]
[1]Department of Electrical Engineering and Computer Science, University of California, Irvine, USA
[2]Department of Mechanical and Aerospace Engineering, University of California, Irvine, USA
Emails: jhaidara@uci.edu, khairaln@uci.edu, and zkassas@ieee.org

***Abstract*—A hybrid analytical-machine learning (ML) framework for improved low Earth orbit (LEO) satellite orbit prediction is developed. The framework assumes the following three stages. (i) LEO satellite first pass: A terrestrial receiver with knowledge of its position produces carrier phase measurements from received LEO satellite signals, enabling it to estimate the time of arrival. The LEO satellite's states are initialized with simplified general perturbations 4 (SGP4)-propagated two-line element (TLE) data, and are subsequently estimated via an extended Kalman filter (EKF) during the period of satellite visibility. (ii) LEO satellite not in view: a nonlinear autoregressive with exogenous inputs (NARX) neural network is trained on the estimated ephemeris and is used to propagate the LEO satellite orbit for the period where the satellite is not in view. (iii) LEO satellite second pass: a terrestrial receiver with *no* knowledge of its position uses the ML-predicted LEO ephemeris along with its carrier phase measurements from received LEO signals to estimate its own position via an EKF. Experimental results with with signals from an Orbcomm satellite are presented to demonstrate the efficacy of the proposed framework. It is shown that during the satellite's second pass, the ML-predicted ephemeris error is reduced by nearly 90% from that of an SGP4 propagation. In addition, it is shown that if the receiver was to use the SGP4-predicted satellite ephemeris to localize itself, the EKF's initial position error of 2.2 km increases to 6.7 km, while the proposed framework reduces the position error to 448 m.**

***Keywords*—LEO satellites, machine learning, orbit determination, satellite tracking, signals of opportunity.**

I. Introduction

Future low Earth orbit (LEO) satellite constellations will weave a virtual blanket cover around the globe, bringing forth signals diverse in frequency and direction, which are also received at much higher power than global navigation satellite system (GNSS) signals [1], [2]. As such, LEO satellites are considered highly attractive from a positioning, navigation, and timing (PNT) perspective. LEO satellites' signals of opportunity could complement and safeguard GNSS to provide high levels of performance and operational resilience [3]–[5].

To exploit LEO satellites signals opportunistically, one must overcome three main challenges: (i) develop specialized receivers to extract navigation observables from these signals; (ii) estimate the satellites' clocks, which, unlike GNSS, are neither transmitted publicly nor are as stable and as tightly synchronized; and (iii) estimate the satellite's ephemeris with minimal error. The first two challenges have been the subject of extensive research recently [5]–[15]. This paper focuses on addressing the third challenge.

Several analytical and numerical satellite orbit determination algorithms have been developed to propagate satellites' states as well as associated uncertainty [16]. These propagators take into consideration, to various extents, multiple sources of perturbing forces, e.g., Earth's non-uniform gravitational field, atmospheric drag, solar radiation pressure, and third-body attraction (eg., Sun and Moon) [17]. The simplified general perturbations 4 (SGP4) [18] analytical propagator is used to generate ephemerides from a set of mean orbital elements given at a reference epoch in two-line elements (TLE) files, which are published and updated periodically by the North American Aerospace Defense Command (NORAD) [19]. However, analytical orbit determination methods are based on limited dynamical models and mean elements which may not meet PNT accuracy requirements [20], [21]. Space agencies usually employ high-precision orbit propagators (HPOP), which are numerical propagators used in conjunction with precise force models. However, numerical propagators require large amounts of data and significant computation time, which renders them undesirable for real-time PNT purposes.

Machine learning (ML) has shown tremendous potential in radar and communications [22], and its powerful modeling capabilities have been recently studied to provide a less parameter-reliant orbit propagation solution [23], [24]. In [25], [26], distribution regression was used for orbit determination of objects in LEO. Propagating LEO satellite orbits was studied in [27], [28] via artificial neural networks (ANNs), support vector machines (SVMs), and Gaussian processes (GPs). A simulation study developed in [28], [29] showed that ANNs possess high regression capabilities compared to SVMs and GPs. Several neural network (NN) architectures, such as the Time Delayed Neural Network (TDNN) and Long Short-Term Memory (LSTM) NNs were studied in [30]. However, utilizing ML in full orbit determination, allowing for completely replacing standard propagators, is yet to be achieved. Promising preliminary result were presented in [31], in which a TDNN was trained using the data from two Orbcomm LEO satellites, which broadcast their three-dimensional (3-D) position in the Earth-centered, Earth-fixed (ECEF) coordinate frame from onboard GNSS receivers. Finally, [32] utilized HPOP along with decoded Orbcomm satellite ephemeris messages to train a NN that was capable of estimating the position of the satellite to meter-level accuracy in a short time period.

Authorized licensed use limited to: The Ohio State University. Downloaded on October 21,2022 at 17:06:26 UTC from IEEE Xplore. Restrictions apply.

This paper proposes a hybrid analytical-ML approach for LEO satellite orbit prediction where the receiver has no prior knowledge on the satellite's position except for publicly available TLE files. The paper makes the following contributions:

- A hybrid analytical-ML propagator is developed in a three-step framework: (i) refine LEO satellite's ephemeris via opportunistic tracking, initialized from an SGP4-propagated TLE, using an extended Kalman filter (EKF), (ii) train the ML propagator on the refined ephemeris *without* relying on the true ephemeris as was the case in [31], [32], and (iii) localize a receiver opportunistically with the ML-propagated ephemeris.
- The ephemeris propagation performance of the hybrid analytical-ML framework is compared with that of standalone propagators using true decoded Orbcomm ephemeris data.
- Experimental results are presented to demonstrate the efficacy of the proposed framework with a first pass of an Orbcomm satellite during which the tracking to refine the ephemeris is performed and a second pass of the same satellite during which the opportunistic localization performance using ML-propagated ephemeris and SGP4-propagated ephemeris are compared.

The paper is organized as follows. Section II describes the measurement model. Section III details the proposed analytical-ML orbit prediction framework. Section IV presents experimental results. Section V gives concluding remarks.

II. Carrier Phase Measurement Model

This section describes the carrier phase measurement model, which is used to both track the LEO satellite during its first pass and to localize the receiver from LEO satellite signals during the second pass. A LEO receiver extracts continuous-time carrier phase measurements from LEO satellites' signals by integrating the Doppler measurement over time [33]. The carrier phase measurement (expressed in meters) made by the receiver on the LEO satellite at time-step k, which represents discrete-time instant $t_k = kT + t_0$ for an initial time t_0, can be modeled in discrete-time as [2]

$$\begin{aligned}\phi(k) = \left\|\boldsymbol{r}_{\mathrm{r}}(k) - \boldsymbol{r}_{\mathrm{leo}}(k')\right\|_2 + c\left[\delta t_r(k) - \delta t_{\mathrm{leo}}(k'_l)\right] + \lambda N \\ + c\delta t_{\mathrm{iono}}(k) + c\delta t_{\mathrm{tropo}}(k) + v(k), \quad k = 1, 2, \ldots \quad (1)\end{aligned}$$

where k' represents discrete-time at $t_{k'} = kT + t_0 - \delta t_{\mathrm{TOF}}$, with δt_{TOF} being the true time-of-flight of the signal from the LEO satellite to the receiver; c is the speed-of-light; $\boldsymbol{r}_r$ and $\boldsymbol{r}_{\mathrm{leo}}$ are the receiver's and LEO satellite's 3-D position vectors expressed in the same reference frame; δt_r and δt_{leo} are the receiver's and LEO satellite's clock biases, respectively; λ is the wavelength of the carrier signal transmitted by the LEO satellite; N is the carrier phase ambiguity of the LEO satellite carrier phase measurement; δt_{iono} and $\delta t_{\mathrm{tropo}}$ are the ionospheric and tropospheric delays, respectively; and v is the measurement noise, which is modeled as a zero-mean white Gaussian random sequence with variance σ^2_ϕ.

Assuming no cycle slip occurs when the receiver tracks the carrier phase (i.e., the carrier phase ambiguity remains constant), the difference between the receiver and LEO satellite clock biases and the carrier phase ambiguity are lumped into a single term $c\Delta\delta t(k)$, simplifying (1) as

$$\begin{aligned}z(k) \triangleq \phi(k) = \left\|\boldsymbol{r}_r(k) - \boldsymbol{r}_{\mathrm{leo}}(k')\right\|_2 + c\Delta\delta t(k) \\ + c\delta t_{\mathrm{tropo}}(k) + c\delta t_{\mathrm{iono}}(k) + v(k), \quad (2)\end{aligned}$$

$$c\Delta\delta t(k) \triangleq c\left[\delta t_r(k) - \delta t_{\mathrm{sv}}(k')\right] + \lambda N. \quad (3)$$

III. Orbit Prediction Framework

PNT with measurements from overhead satellites require knowledge of the satellites' ephemeris. The best estimate available publicly for a LEO satellite's ephemeris would be from an initial ephemeris at a given time provided by TLE files published by NORAD, which would then be propagated through a propagator (e.g., SGP4). However, this initial ephemeris could be off by a few kilometers, and with SGP4 propagating the satellite's ephemeris through time, the error would continue to increase, only to be corrected when a new TLE file is published the next day. This limits the use of LEO signals for PNT, since such large ephemerides errors translate to unacceptably large positioning errors. The proposed framework mitigates the issue of relying on an ephemeris that is off by several kilometers. A base station with known position opportunistically tracks and refines the satellite's ephemeris when it is overhead. Next, an NN trains on this refined ephemeris and predicts the satellite's future position and velocity. Finally, a receiver with unknown position is given this predicted ephemeris to use it to localize itself when the same satellite passes overhead. Fig. 1 summarizes the proposed framework. The following subsections describe each stage of the proposed framework.

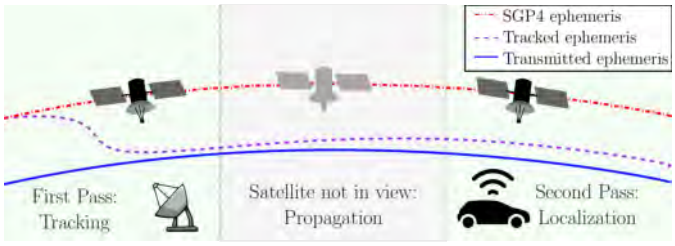

Fig. 1. Proposed framework. (i) LEO satellite first pass: A terrestrial receiver with knowledge of its position tracks the LEO satellite. The LEO satellite's states are initialized with SGP4-propagated TLE data, and are subsequently estimated via an EKF during the period of satellite visibility, utilizing the carrier phase measurements. (ii) LEO satellite not in view: an NN is trained on the estimated ephemeris and is used to propagate the LEO satellite orbit for the period where the satellite is not in view. (iii) LEO satellite second pass: a terrestrial receiver with *no* knowledge of its position uses the ML-predicted LEO ephemeris along with its carrier phase measurements from received LEO signals to estimate its own position via an EKF.

A. Opportunistic Tracking

This subsection formulates the EKF utilized as the tracking filter used to estimate the LEO satellite's ephemeris during the first LEO satellite pass in the proposed framework. The filter assumes a base station with known position making carrier

Authorized licensed use limited to: The Ohio State University. Downloaded on October 21,2022 at 17:06:26 UTC from IEEE Xplore. Restrictions apply.

phase measurements modeled in (1). The EKF state vector is given by

$$\boldsymbol{x}_{\text{leo}} \;=\; \left[\boldsymbol{r}_{\text{leo}}^{\mathsf{T}},\, \dot{\boldsymbol{r}}_{\text{leo}}^{\mathsf{T}},\, c\Delta\delta t,\, c\Delta\dot{\delta} t\right]^{\mathsf{T}}.$$

For the satellite's time update between measurements, a two-body model including the most significant non-zero mean perturbing acceleration, which corresponds to J_2 effects, is adopted as the LEO satellite orbit dynamics model in the Earth-centered inertial (ECI) reference frame. This model offers a trade-off between accurate open-loop state prediction, while maintaining a simple analytical Jacobian for estimation error covariance propagation [34], and is given as

$$\ddot{\boldsymbol{r}}_{\text{leo}} = \boldsymbol{a}_{\text{grav},J_2} + \tilde{\boldsymbol{w}}_{\text{leo}}, \qquad \boldsymbol{a}_{\text{grav},J_2} = \frac{dU_{J_2}}{d\boldsymbol{r}_{\text{leo}}}, \tag{4}$$

where $\boldsymbol{r}_{\text{leo}} \triangleq [x_{\text{leo}},\, y_{\text{leo}},\, z_{\text{leo}}]^{\mathsf{T}}$ is the 3-D position vector of the LEO satellite in the ECI frame, $\boldsymbol{a}_{\text{grav},J_2}$ is the acceleration due to Earth's non-uniform gravity including J_2 effects, U_{J_2} is the non-uniform gravity potential of Earth including J_2 effects at the satellite, and $\tilde{\boldsymbol{w}}_{\text{leo}}$ is a process noise vector with power spectral density $\tilde{\mathbf{Q}}_{\text{leo}}$, which attempts to capture the overall acceleration perturbations including the unmodeled non-uniformity of Earth's gravitational field, atmospheric drag, solar radiation pressure, third-body gravitational forces (e.g., gravity of the Sun and Moon), and general relativity [17].

The components of $\boldsymbol{a}_{\text{grav},J_2} = [\ddot{x}_{\text{grav}},\, \ddot{y}_{\text{grav}},\, \ddot{z}_{\text{grav}}]^{\mathsf{T}}$ are

$$\begin{aligned}
\ddot{x}_{\text{grav}} &= -\frac{\mu x_{\text{leo}}}{\|\boldsymbol{r}_{\text{leo}}\|^3}\left[1 + J_2\frac{3}{2}\left(\frac{R_E}{\|\boldsymbol{r}_{\text{leo}}\|}\right)^2\left(1 - 5\frac{z_{\text{leo}}^2}{\|\boldsymbol{r}_{\text{leo}}\|^2}\right)\right],\\
\ddot{y}_{\text{grav}} &= -\frac{\mu y_{\text{leo}}}{\|\boldsymbol{r}_{\text{leo}}\|^3}\left[1 + J_2\frac{3}{2}\left(\frac{R_E}{\|\boldsymbol{r}_{\text{leo}}\|}\right)^2\left(1 - 5\frac{z_{\text{leo}}^2}{\|\boldsymbol{r}_{\text{leo}}\|^2}\right)\right],\\
\ddot{z}_{\text{grav}} &= -\frac{\mu z_{\text{leo}}}{\|\boldsymbol{r}_{\text{leo}}\|^3}\left[1 + J_2\frac{3}{2}\left(\frac{R_E}{\|\boldsymbol{r}_{\text{leo}}\|}\right)^2\left(3 - 5\frac{z_{\text{leo}}^2}{\|\boldsymbol{r}_{\text{leo}}\|^2}\right)\right],
\end{aligned} \tag{5}$$

where μ is Earth's standard gravitational parameter and R_E is the mean radius of the Earth. The clock error dynamics are assumed to evolve according to the standard double integrator model, driven by process noise [2].

B. ML-Based Orbit Prediction

After refining the satellite's ephemeris, the proposed ML model discussed in the following subsections trains on this ephemeris and then propagates it in time for usage in PNT.

1) Data Preparation: After tracking a satellite's ephemeris, this ephemeris is pre-processed for use in training the ML model. First, the accuracy of the two-body with J_2 propagation model on a short period of time is utilized for smoothing the tracked ephemeris. The tracked ephemeris is propagated over the entire tracking period allowing for a smoother training dataset and more training data points. The features selected as input candidates for the NN are satellite's 3-D position $\{x, y, z\}$ and velocity $\{\dot{x}, \dot{y}, \dot{z}\}$. The coordinate reference frame chosen is the ECI frame since this eliminates the time-varying effect of Earth's rotation in the ECEF frame.

2) Architecture: Two NNs, depicted in Figs. 2 and 3, are studied. The TDNN is based on a feed-forward NN (FFNN), which simply propagates from input to output in one direction. The time delay aspect is the NN's outputs being fed back as delayed inputs. Predicting a satellite's ephemeris can be seen as a time series prediction problem. The NARX architecture has been shown to be highly capable of learning long-term dependencies [35] and predicting time series [36]–[38]. The NARX takes SGP4 propagated position states as inputs. It also has a feedback loop where its output, the estimated ephemeris state values, are fed back as additional input.

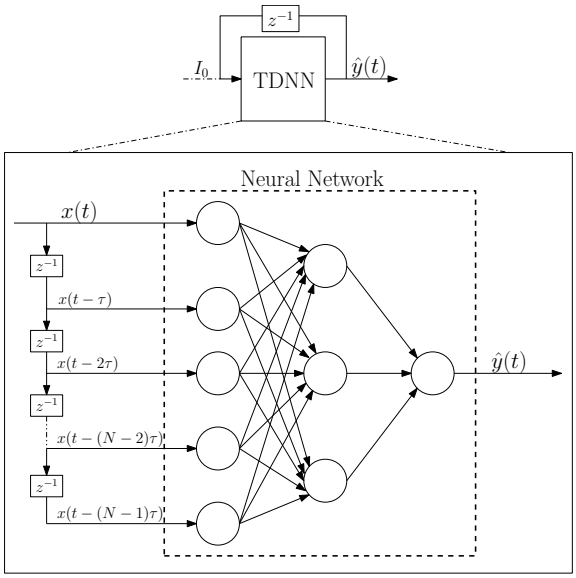

Fig. 2. TDNN Architecture.

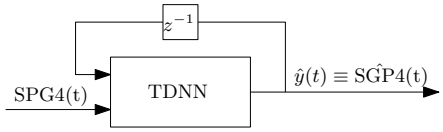

Fig. 3. NARX Architecture.

3) Optimization and Hyper-parameter Tuning: Next, hyper-parameters were chosen to best fit the learned model. Choosing the dimensions of the NN, such as how wide or how deep it is, will greatly affect its performance and ability to generalize, not memorize. Furthermore, since the dynamics of the error between SGP4 propagated ephemeris (initialized from a TLE file) and true satellite ephemeris are unknown and appear to be nonlinear, multiple activation functions must be investigated, including oscillatory functions (e.g., snake function). These hyper-parameters were carefully tuned, using a Bayesian optimization method, as well as compared with hyper-parameters selected by a HyperBand optimizer. Additionally, the number of time-delayed inputs was varied along with which states were fed into the NN. Finally, optimization was performed for incrementally decreasing the learning rate as training loss decreases, and early stopping was implemented to avoid over-fitting. Table I summarizes the search space the NNs were tuned on.

Authorized licensed use limited to: The Ohio State University. Downloaded on October 21,2022 at 17:06:26 UTC from IEEE Xplore. Restrictions apply.

TABLE I
HYPER-PARAMETER SEARCH SPACE

Parameter	Value
Activation Function	Linear, ReLU, Tanh, Sigmoid, Snake [39]
Hidden Layers	[0,5]
Nodes per Layer	[2,128]
Optimizer	Adam [40], Adagrad [41], SGD, Yogi [42]

4) Results: After tuning the NN and comparing different possible combinations of hyper-parameters, it was concluded that a wide NN is capable of modeling SGP4-TLE ephemeris error, and any added layers in depth for introducing higher levels of abstraction are unnecessary. Moreover, increasing the number of delayed inputs degrades the performance as the dimensionality of the input increases without adding much information to the model. An important observation to note is that increasing the number of estimated states results in worse estimated ephemeris. This could be attributed to the limited size of data trained and validated on as well as the incrementally increasing levels of accuracy and abstraction required from the NN as more states are added. Finally, three NNs were trained, each estimating a position state and its time derivative. The NARX architecture given SGP4-ephemeris as exogenous inputs offered the best orbit propagation accuracy and therefore is chosen for the propagation step.

C. Localization

This subsection formulates the EKF used to estimate the receiver's position during the second LEO satellite pass in the proposed framework. The filter assumes a stationary receiver with unknown position and clocks. The receiver opportunistically extracts carrier phase measurements as modeled in (1). The EKF state vector is given by

$$\boldsymbol{x}_{\mathrm{r}} \;=\; \left[\boldsymbol{r}_{\mathrm{r}}^{\mathsf{T}},\, c\Delta\delta t_{\mathrm{r}},\, c\Delta\dot{\delta} t_{\mathrm{r}}\right]^{\mathsf{T}}.$$

IV. EXPERIMENTAL RESULTS

This section demonstrates the proposed framework experimentally by (i) comparing the LEO tracking performance with a filter using the refined ML-propagated ephemeris versus using SGP4-propagated ephemeris initialized from TLE and (ii) localizing a stationary receiver with both ephemerides. An Orbcomm satellite was chosen, since it transmits the satellite's ephemeris. Signals from Orbcomm FM107 were collected, from which carrier phase measurements were opportunistically extracted. The satellite's downlink signals, which include the satellite's true ephemeris generated by on-board GPS receivers, were decoded for use as ground truth. Finally, ionospheric and tropospheric delays were corrected in the carrier phase measurements [43].

A. Experimental Setup

A very high frequency (VHF) quadrifilar helix antenna was connected to an Ettus E312 Universal Software Radio Peripheral (USRP) to sample Orbcomm LEO satellites' signals at 137-138 MHz at a sampling rate of 2.4 MSps. The USRP's oscillator was disciplined by an external, freely-running NI CDA-2990 OctoClock. The recording was repeated twice to record two consecutive passes of Orbcomm FM107 over Irvine, California, USA. The measurements extracted from the LEO satellite's signals during the first pass were used to track Orbcomm FM107 and refine its ephemeris. Then, this refined ephemeris was used as an input to the supervised training of the hybrid analytical-ML propagator. This propagator was subsequently employed to propagate the ephemeris of Orbcomm FM107 for around 100 minutes, which corresponds to its orbital period, until the satellite is visible again overhead. During the second pass, the measurements extracted from Orbcomm FM107 signals were used to opportunistically localize the receiver, while using the hybrid analytical-ML propagated ephemeris. The localization performance was compared to that obtained using the SGP4-propagated TLE ephemeris. The skyplot showing the trajectory of the satellite for both consecutive passes is shown in Fig. 4.

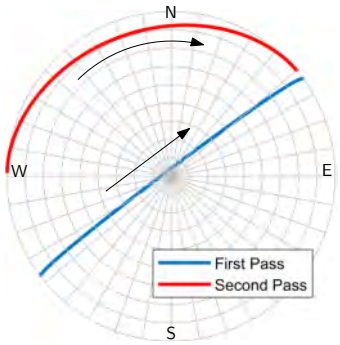

Fig. 4. Skyplot of satellite Orbcomm FM107 during the tracking (first pass) and localization (second pass).

B. Tracking

A receiver with known position tracks the LEO satellite according to the framework described in Section III-A. The state estimates are initialized according to

$$\hat{\boldsymbol{x}}_{\mathrm{leo}}(0|0) = [\boldsymbol{r}_{\mathrm{leo}}^{\mathsf{T}}(0), \dot{\boldsymbol{r}}_{\mathrm{leo}}^{\mathsf{T}}(0), \boldsymbol{z}(0) - \|\boldsymbol{r}_r - \boldsymbol{r}_{\mathrm{leo}}(0)\|_2, 0]^{\mathsf{T}},$$

where $[\boldsymbol{r}_{\mathrm{leo}}^{\mathsf{T}}(0), \dot{\boldsymbol{r}}_{\mathrm{leo}}^{\mathsf{T}}(0)]^{\mathsf{T}}$ is the satellite's initial state given from the SGP4-propagated ephemeris initialized from TLE. The initial estimation error covariance was set to

$$\begin{aligned}
&\mathbf{P}_{\boldsymbol{x}_{\mathrm{leo}}}(0|0) \triangleq \mathrm{diag}[\mathbf{P}_i(0|0), \mathbf{P}_{\mathrm{clk}}(0|0)]\\
&\mathbf{P}_i(0|0) \equiv {}^{i}_{b}\bar{\mathbf{R}}(0)\mathbf{P}_b(0|0)\,{}^{i}_{b}\bar{\mathbf{R}}^{\mathsf{T}}(0)\\
&{}^{i}_{b}\bar{\mathbf{R}}(0) = \mathrm{diag}[{}^{i}_{b}\mathbf{R}(0), {}^{i}_{b}\mathbf{R}(0)]\\
&\mathbf{P}_b(0|0) \equiv \mathrm{diag}[5\times10^5, 3\times10^3, 10^5, 0.05, 0.01, 0.2]\\
&\mathbf{P}_{\mathrm{clk}}(0|0) \equiv \mathrm{diag}[100, 10]
\end{aligned}$$

where $\mathbf{P}_i$ and $\mathbf{P}_b$ are the initial error covariance in the ECI frame and the satellite's body frame respectively, and ${}^{i}_{b}\mathbf{R}$ is the rotation matrix from the body frame to the ECI frame. This method initializes the estimate error covariance in the body frame which is more intuitive than initializing in the ECI frame, as most of the error is usually in the along-track. This

Authorized licensed use limited to: The Ohio State University. Downloaded on October 21,2022 at 17:06:26 UTC from IEEE Xplore. Restrictions apply.

allows to capture the elliptical nature of the error covariance and initializes cross terms in the ECI frame which would allow for faster and better convergence. The measurement noise covariance was set to 0.5 m^2. The satellite was tracked for 517 seconds, during which, the satellite's position error magnitude decreased from 980 m to 56 m. Figs. 5 and 6 show the EKF error plots of the satellite's ephemeris in the body frame. The cross track direction is the least observable, which is consistent with [44]. Fig. 7 shows the position error magnitude of the tracked ephemeris compared to SGP4 propagated from TLE.

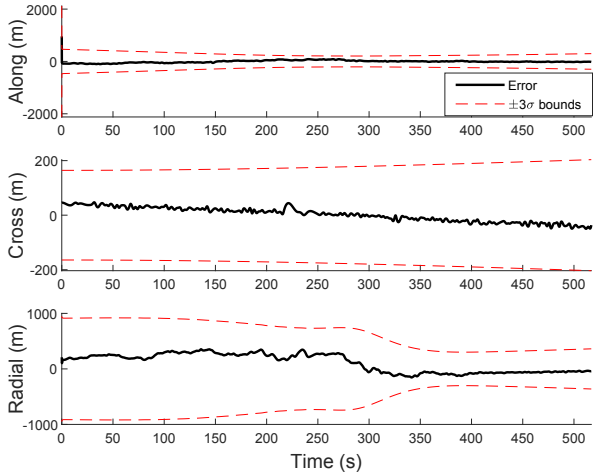

Fig. 5. EKF position plots in the satellite's body frame.

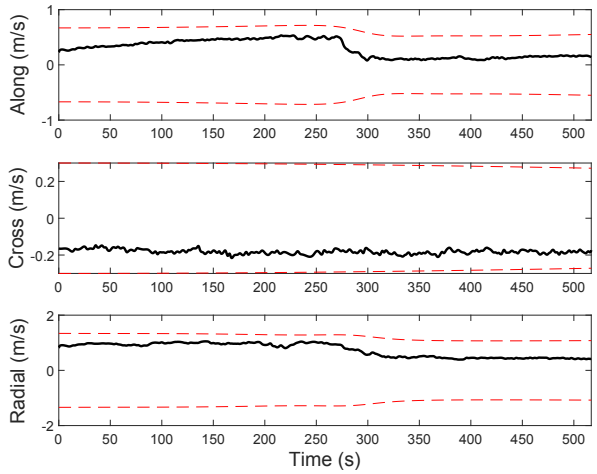

Fig. 6. EKF velocity plots in the satellite's body frame.

C. Propagation

Upon completion of satellite tracking, the estimated ephemeris at the final time of tracking is considered to be the best estimate for the satellite's ephemeris. This ephemeris is then back-propagated using the J_2 orbit propagation model to smooth over the tracking period. This smoothed ephemeris is now ready to be trained on. The ML model is given the SGP4 ephemeris propagated from TLE as exogenous input and the tracked and smoothed ephemeris as ground truth. The ML model then trains on this data and learns a mapping from the SGP4-TLE ephemeris to the tracked ephemeris. Finally, the ML model starts propagating and extrapolating satellite

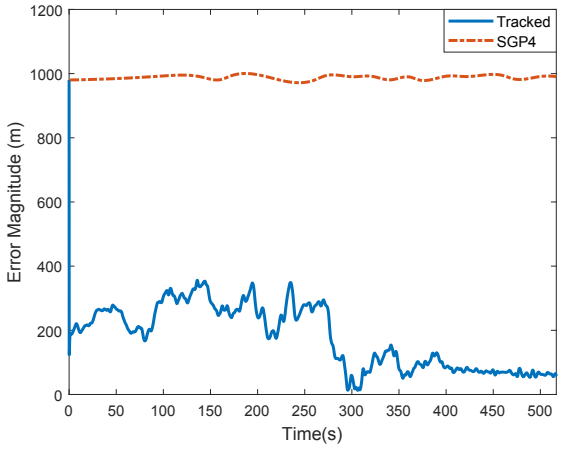

Fig. 7. Position error magnitude of SGP4 ephemeris initialized from TLE versus tracked ephemeris.

ephemeris, taking as its input the SGP4-TLE ephemeris at each time-step and its own outputs at previous time steps, and outputting a corrected ephemeris at that time-step. The ML model is propagated for 5,870 seconds until the satellite comes back to view. The ephemeris is then further propagated for a period of 363 seconds for this ephemeris to be used in localization. Fig. 8 shows the position error magnitude of the ML-propagated ephemeris and the SGP4-propagated ephemeris during the satellite's second pass.

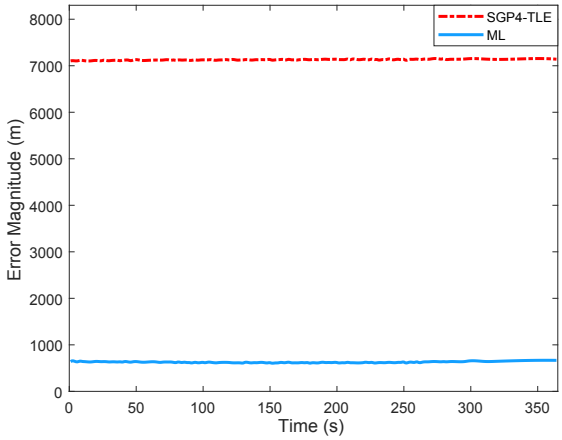

Fig. 8. Position error magnitude of SGP4 ephemeris initialized from TLE versus propagated ephemeris through the proposed ML framework.

D. Localization Results

The framework in Section III-C was adopted to localize a ground stationary receiver with the initial state estimates

$$\hat{\boldsymbol{x}}_r(0|0) = [\hat{\boldsymbol{r}}_r^{\mathsf{T}}(0|0), z(0) - \left\|\hat{\boldsymbol{r}}_r(0|0) - \boldsymbol{r}_{\text{leo}}^{j}(0)\right\|_2, 0]^{\mathsf{T}}$$

where $\hat{\boldsymbol{r}}_r(0|0)$ is the receiver's initial position estimate, which was drawn as $\hat{\boldsymbol{r}}_{\text{r}}(0|0) \sim \mathcal{N}[\boldsymbol{r}_r, \mathbf{P}_e(0|0)]$, in the ECEF frame. The estimate $c\Delta\delta t$ was initialized as the difference between the initial measurement and the estimated initial range, where

Authorized licensed use limited to: The Ohio State University. Downloaded on October 21,2022 at 17:06:26 UTC from IEEE Xplore. Restrictions apply.

Fig. 9. Experimental results showing the initial and final 2-D stationary receiver localization errors and associated 95% uncertainty ellipses using (i) SGP4-propagated ephemeris and (ii) ML-propagated ephemeris. Map data: Google Earth.

$j \in \{\mathrm{ML}, \mathrm{SGP4}\}$ is the index of the satellite ephemeris used. The initial error covariance matrices were set as

$$\mathbf{P}_{\boldsymbol{x}_r}(0|0) \triangleq \mathrm{diag}[\mathbf{P}_e(0|0), \mathbf{P}_{\mathrm{clk}}(0|0)]$$
$$\mathbf{P}_e(0|0) \equiv {}^e_l\bar{\mathbf{R}}\mathbf{P}_l(0|0)\,{}^e_l\bar{\mathbf{R}}^{\mathsf{T}}$$
$$\mathbf{P}_l(0|0) \equiv \mathrm{diag}[10^6, 10^6, 0.1]$$
$$\mathbf{P}_{\mathrm{clk}}(0|0) \equiv \mathrm{diag}[10^8, 10^4]$$

where $\mathbf{P}_e(0|0)$ and $\mathbf{P}_l(0|0)$ are the initial receiver position error covariance in the ECEF frame and the local East-North-Up (ENU) frame, respectively, and ${}^e_l\mathbf{R}$ is the rotation matrix from the local ENU frame to the ECEF frame. This allows for comparing with the two-dimensional (2-D) North-East error only since the Up direction is poorly estimable from satellite measurements only. The measurement noise covariance was set to 0.5 m^2. The receiver was localized for 363 seconds, using the ML-propagated ephemeris as the satellite's ephemeris in the EKF filter. The 2-D magnitude of error decreased from an initial error of 2,219 m to 448 m. However, when the SGP4-propagated ephemeris was utilized with the same measurement noise covariance, the error increased to 6,718 m. Fig. 9 shows the the initial and final 2-D localization estimates and associated 95% uncertainty ellipses using (i) SGP4-propagated ephemeris and (ii) ML-propagated ephemeris. Fig. 10 shows the EKF error trajectories in the ENU frame.

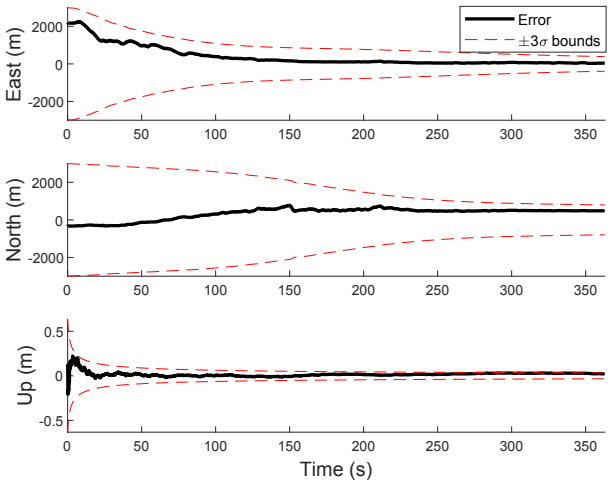

Fig. 10. EKF position plots for stationary localization using ML generated ephemeris.

V. Conclusion

This paper proposed a hybrid analytical-ML approach for LEO satellite orbit prediction, where the receiver has no prior knowledge on the satellite's position except for publicly available TLE files. During the LEO satellite's first pass, a stationary receiver tracks using carrier phase measurements the LEO satellite via an EKF initialized with SGP4-propagated TLE. A NARX NN is trained on the estimated ephemeris, which is then used to propagate the LEO ephemeris when the satellite is not in view. During the LEO satellite's second pass, a receiver with unknown position uses the ML-predicted LEO ephemeris to localize itself via an EKF. Experimental results with an Orbcomm LEO satellite are presented showing the efficacy of the proposed framework in reducing the initial receiver error from 2.22 km to 448 m, while the SGP4-ephemeris localization yielded a final error of 6.7 km.

Acknowledgments

This work was supported in part by the Office of Naval Research (ONR) under Grants N00014-19-1-2511 and N00014-19-1-2613, in part by the U.S. Department of Transportation (USDOT) under Grant 69A3552047138 for the CARMEN University Transportation Center (UTC), and in part by the Air Force Office of Scientific Research (AFOSR) under the Young Investigator Program award. The authors would like to thank Sharbel Kozhaya for his help with data collection and processing.

Authorized licensed use limited to: The Ohio State University. Downloaded on October 21,2022 at 17:06:26 UTC from IEEE Xplore. Restrictions apply.

REFERENCES

[1] T. Reid, T. Walter, P. Enge, D. Lawrence, H. Cobb, G. Gutt, M. O'Conner, and D. Whelan, "Position, navigation, and timing technologies in the 21st century," J. Morton, F. van Diggelen, J. Spilker, Jr., and B. Parkinson, Eds. Wiley-IEEE, 2021, vol. 2, ch. 43: Navigation from low Earth orbit – Part 1: Concept, Current Capability, and Future Promise, pp. 1359–1379.

[2] Z. Kassas, "Position, navigation, and timing technologies in the 21st century," J. Morton, F. van Diggelen, J. Spilker, Jr., and B. Parkinson, Eds. Wiley-IEEE, 2021, vol. 2, ch. 43: Navigation from low Earth orbit – Part 2: models, implementation, and performance, pp. 1381–1412.

[3] T. Reid, B. Chan, A. Goel, K. Gunning, B. Manning, J. Martin, A. Neish, A. Perkins, and P. Tarantino, "Satellite navigation for the age of autonomy," in *Proceedings of IEEE/ION Position, Location and Navigation Symposium*, 2020, pp. 342–352.

[4] A. Nardin, F. Dovis, and J. Fraire, "Empowering the tracking performance of LEO'-based positioning by means of meta-signals," *IEEE Journal of Radio Frequency Identification*, pp. 1–1, 2021.

[5] Z. Kassas, M. Neinavaie, J. Khalife, N. Khairallah, J. Haidar-Ahmad, S. Kozhaya, and Z. Shadram, "Enter LEO on the GNSS stage: Navigation with Starlink satellites," *Inside GNSS Magazine*, vol. 16, no. 6, pp. 42–51, 2021.

[6] R. Landry, A. Nguyen, H. Rasaee, A. Amrhar, X. Fang, and H. Benzerrouk, "Iridium Next LEO satellites as an alternative PNT in GNSS denied environments–part 1," *Inside GNSS Magazine*, vol. 14, no. 3, pp. 56–64, May 2019.

[7] F. Farhangian and R. Landry, "Multi-constellation software-defined receiver for Doppler positioning with LEO satellites," *Sensors*, vol. 20, no. 20, pp. 5866–5883, October 2020.

[8] Z. Kassas, J. Morales, and J. Khalife, "New-age satellite-based navigation – STAN: simultaneous tracking and navigation with LEO satellite signals," *Inside GNSS Magazine*, vol. 14, no. 4, pp. 56–65, 2019.

[9] Q. Wei, X. Chen, and Y. Zhan, "Exploring implicit pilots for precise estimation of LEO satellite downlink Doppler frequency," *IEEE Communications Letters*, vol. 24, no. 10, pp. 2270–2274, 2020.

[10] T. Mortlock and Z. Kassas, "Performance analysis of simultaneous tracking and navigation with LEO satellites," in *Proceedings of ION GNSS Conference*, September 2020, pp. 2416–2429.

[11] F. Farhangian, H. Benzerrouk, and R. Landry, "Opportunistic in-flight INS alignment using LEO satellites and a rotatory IMU platform," *Aerospace*, vol. 8, no. 10, pp. 280–281, 2021.

[12] M. Neinavaie, J. Khalife, and Z. Kassas, "Acquisition, Doppler tracking, and positioning with Starlink LEO satellites: First results," *IEEE Transactions on Aerospace and Electronic Systems*, 2021, accepted.

[13] R. Cassel, D. Scherer, D. Wilburne, J. Hirschauer, and J. Burke, "Impact of improved oscillator stability on LEO-based satellite navigation," in *Proceedings of ION International Technical Meeting*, January 2022, pp. 893–905.

[14] C. Pinell, "Receiver architectures for positioning with low Earth orbit satellite signals," Master's thesis, Lulea University of Technology, School of Electrical Engineering, Sweden, 2021.

[15] N. Khairallah and Z. Kassas, "An interacting multiple model estimator of LEO satellite clocks for improved positioning," in *Proceedings of IEEE Vehicular Technology Conference*, 2022, accepted.

[16] B. Schutz, B. Tapley, and G. Born, *Statistical orbit determination*. Elsevier, 2004.

[17] J. Vetter, "Fifty years of orbit determination: Development of modern astrodynamics methods," *Johns Hopkins APL Technical Digest*, vol. 27, no. 3, pp. 239–252, November 2007.

[18] D. Vallado and P. Crawford, "SGP4 orbit determination," in *Proceedings of AIAA/AAS Astrodynamics Specialist Conference and Exhibit*, August 2008, pp. 6770–6799.

[19] North American Aerospace Defense Command (NORAD), "Two-line element sets," http://celestrak.com/NORAD/elements/.

[20] K. DeMars, R. Bishop, and M. Jah, "Entropy-based approach for uncertainty propagation of nonlinear dynamical systems," *Journal of Guidance, Control, and Dynamics*, vol. 36, no. 4, pp. 1047–1057, July-August 2013.

[21] X. Tian, G. Chen, E. Blasch, K. Pham, and Y. Bar-Shalom, "Comparison of three approximate kinematic models for space object tracking," in *Proceedings of International Conference on Information Fusion*, 2013, pp. 1005–1012.

[22] U. Majumder, E. Blasch, and D. Garren, *Deep Learning for Radar and Communications Automatic Target Recognition*. Norwood, MA: Artech House, 2020.

[23] Y. Wang, X. Bai, H. Peng, G. Chen, D. Shen, E. Blasch, and C. Sheaff, "Gaussian-binary classification for resident space object maneuver detection," *Acta Astronautica*, vol. 187, pp. 438–446, October 2021.

[24] S. Shen, C. Sheaff, M. Guo, E. Blasch, K. Pham, and G. Chen, "Three-dimensional convolutional neural network (3D-CNN) for satellite behavior discovery," in *Proceedings of SPIE Sensors and Systems for Space Applications*, vol. 11755, 2021, pp. 1–18.

[25] S. Sharma and J. Cutler, "Robust orbit determination and classification: A learning theoretic approach," *IPN Progress Report*, pp. 42–203, 2015.

[26] F. Feng, Y. Zhang, H. Li, Y. Fang, Q. Huang, and X. Tao, "A novel space-based orbit determination method based on distribution regression and its sparse solution," *IEEE Access*, vol. 7, pp. 133 203–133 217, 2019.

[27] H. Peng and X. Bai, "Limits of machine learning approach on improving orbit prediction accuracy using support vector machine," in *Proceedings of Advanced Maui Optical and Space Surveillance Technologies Conference*, 2017, pp. 1–22.

[28] H. Peng and X. Bai, "Artificial neural network–based machine learning approach to improve orbit prediction accuracy," *Journal of Spacecraft and Rockets*, vol. 55, no. 5, pp. 1248–1260, 2018.

[29] H. Peng and X. Bai, "Comparative evaluation of three machine learning algorithms on improving orbit prediction accuracy," *Astrodynamics*, vol. 3, no. 4, pp. 325–343, 2019.

[30] N. Salleh, S. Yuhaniz, N. Azmi, and S. Sabri, "Enhancing simplified general perturbations-4 model for orbit propagation using deep learning: a review," in *Proceedings of International Conference on Software and Computer Applications*, 2019, pp. 5937–5941.

[31] T. Mortlock and Z. Kassas, "Assessing machine learning for LEO satellite orbit determination in simultaneous tracking and navigation," in *Proceedings of IEEE Aerospace Conference*, March 2021, pp. 1–8.

[32] S. Kozhaya, J. Haidar-Ahmad, A. Abdallah, Z. Kassas, and S. Saab, "Comparison of neural network architectures for simultaneous tracking and navigation with LEO satellites," in *Proceedings of ION GNSS Conference*, September 2021, pp. 2507–2520.

[33] P. Misra and P. Enge, *Global Positioning System: Signals, Measurements, and Performance*, 2nd ed. Ganga-Jamuna Press, 2010.

[34] J. Morales, J. Khalife, U. Santa Cruz, and Z. Kassas, "Orbit modeling for simultaneous tracking and navigation using LEO satellite signals," in *Proceedings of ION GNSS Conference*, September 2019, pp. 2090–2099.

[35] T. Lin, B. Horne, P. Tino, and C. Giles, "Learning long-term dependencies in NARX recurrent neural networks," *IEEE Transactions on Neural Networks*, vol. 7, no. 6, pp. 1329–1338, 1996.

[36] H. Siegelmann, B. Horne, and C. Giles, "Computational capabilities of recurrent NARX neural networks," *IEEE Transactions on Systems, Man, and Cybernetics, Part B (Cybernetics)*, vol. 27, no. 2, pp. 208–215, 1997.

[37] H. Xie, H. Tang, and Y. Liao, "Time series prediction based on NARX neural networks: An advanced approach," in *Proceedings of IEEE International Conference on Machine Learning and Cybernetics*, vol. 3, 2009, pp. 1275–1279.

[38] J. Menezes, P. Maria, and G. Barreto, "Long-term time series prediction with the NARX network: An empirical evaluation," *Neurocomputing*, vol. 71, no. 16-18, pp. 3335–3343, 2008.

[39] L. Ziyin, T. Hartwig, and M. Ueda, "Neural networks fail to learn periodic functions and how to fix it," *Advances in Neural Information Processing Systems*, vol. 33, pp. 1583–1594, 2020.

[40] D. Kingma and J. Ba, "Adam: A method for stochastic optimization," *arXiv preprint arXiv:1412.6980*, 2014.

[41] J. Duchi, E. Hazan, and Y. Singer, "Adaptive subgradient methods for online learning and stochastic optimization," *Journal of Machine Learning Research*, vol. 12, no. 7, pp. 2121–2159, 2011.

[42] M. Zaheer, S. Reddi, D. Sachan, S. Kale, and S. Kumar, "Adaptive methods for nonconvex optimization," in *Proceedings of International Conference on Neural Information Processing Systems*, vol. 31, 2018, pp. 9815–9825.

[43] J. Khalife, M. Neinavaie, and Z. Kassas, "Navigation with differential carrier phase measurements from megaconstellation LEO satellites," in *Proceedings of IEEE/ION Position, Location, and Navigation Symposium*, April 2020, pp. 1393–1404.

[44] N. Khairallah and Z. Kassas, "Ephemeris closed-loop tracking of LEO satellites with pseudorange and Doppler measurements," in *Proceedings of ION GNSS Conference*, September 2021, pp. 2544–2555.

Authorized licensed use limited to: The Ohio State University. Downloaded on October 21,2022 at 17:06:26 UTC from IEEE Xplore. Restrictions apply.

The Ohio State University

2023 Publications

Title

A Look at the Stars: Navigation with Multi-Constellation LEO Satellite Signals of Opportunity

Journal

Inside GNSS Magazine, (18)4

Authors

Kassas, Z.
Kozhaya, S.
Saroufim, J.
Kanj, H.
Hayek, S.

Publication Date

2023-08

July/August 2023 | Engineering Solutions from the Global Navigation Satellite System Community | www.insidegnss.com

InsideGNSS+

Published by Autonomous Media

GPS | GALILEO | GLONASS | BEIDOU

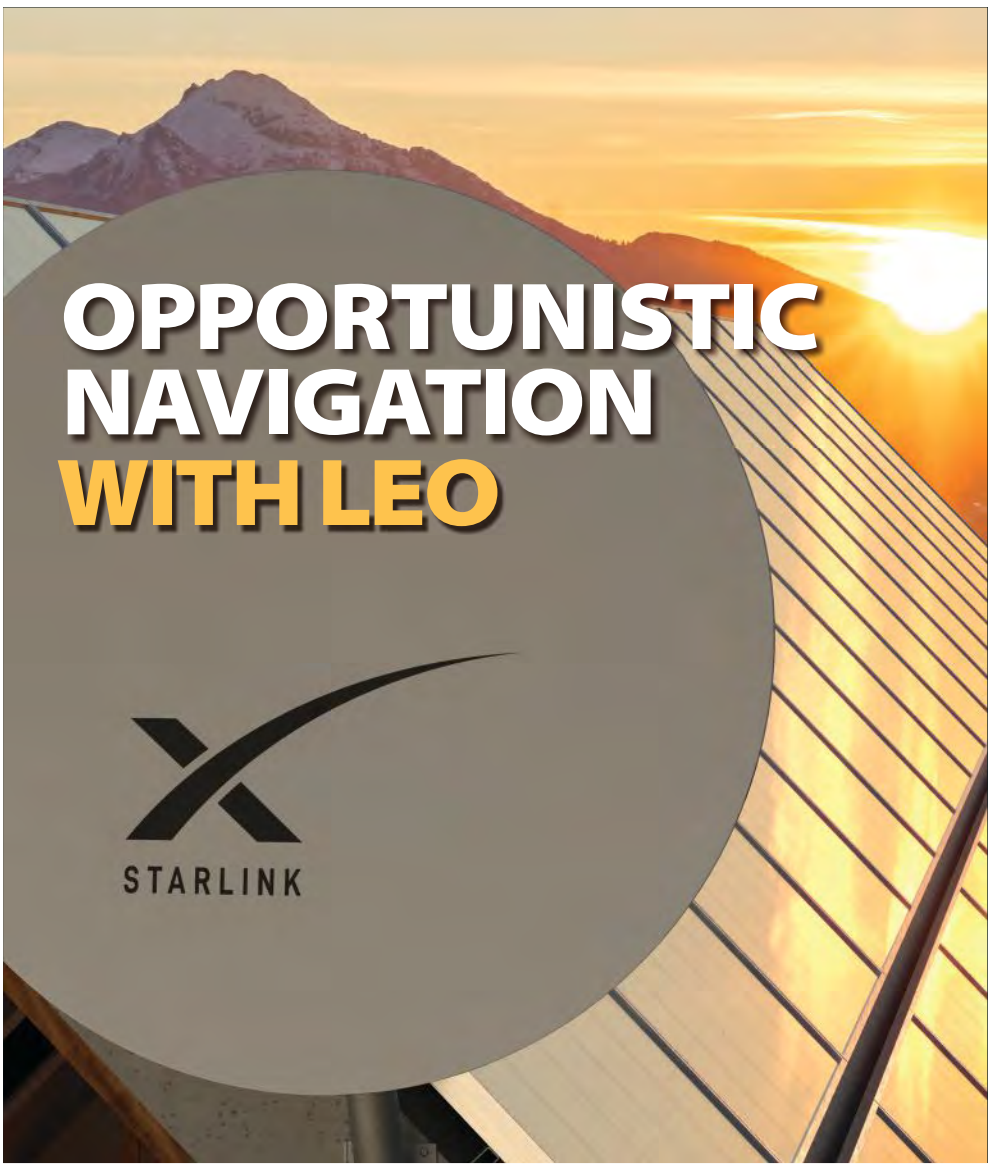

OPPORTUNISTIC NAVIGATION WITH LEO

FIGURE 1 LEO satellite constellations Starlink, OneWeb, Orbcomm and Iridium.

A Look at the Stars:
Navigation with Multi-Constellation LEO Satellite Signals of Opportunity

Experimental and simulation results from Starlink, OneWeb, Orbcomm and Iridium LEO satellite constellations are presented, demonstrating the efficacy and tremendous promise the proposed LEO-agnostic blind opportunistic navigation frameworks.

ZAHER (ZAK) M. KASSAS, SHARBEL KOZHAYA, JOE SAROUFIM, HAITHAM KANJ, SAMER HAYEK
AUTONOMOUS SYSTEMS PERCEPTION, INTELLIGENCE, & NAVIGATION (ASPIN) LABORATORY, THE OHIO STATE UNIVERSITY, COLUMBUS, OHIO

We are witnessing a renewed space race. From technology giants, to startups, to governments, everyone is claiming a stake in launching their own low Earth orbit (LEO) satellite constellation. These constellations promise to transform our daily lives, offering broadband connectivity anywhere on Earth, and will benefit scientific inquiry in fields such as remote sensing. However, not all such constellations are created equal. So-called mega-constellations comprising tens of thousands of satellites are on their way to becoming a reality. SpaceX's Starlink is the clear frontrunner, with the ambitious plan to deploy nearly 12,000 LEO satellites. These constellations will be welcomed by current constellations inhabiting LEO, and collectively they could usher in a new era for positioning, navigation and timing (PNT).

This article presents current state-of-the-art PNT results with multi-constellation LEO satellite signals of opportunity (SOPs) from four LEO satellite constellations (Starlink, OneWeb, Orbcomm and Iridium) and provides an overview of a LEO-agnostic opportunistic navigation receiver, which assumes no prior knowledge of the LEO downlink signals. The receiver is capable of acquiring and tracking unknown LEO satellite signals in a blind fashion, producing Doppler navigation observables with Hz-level accuracy. A differential simultaneous tracking and navigation (DSTAN) framework is developed to deal with the poorly known nature of LEO satellite ephemerides and unknown clock errors.

Experimental navigation results on a stationary receiver and a ground vehicle also are presented. For the stationary receiver, starting with an initial estimate about 3,600 km away, by exploiting signals from 4 Starlink, 2 OneWeb, 1 Orbcomm, and 1 Iridium, a final 2D position error of 5.1 m was achieved. The ground vehicle, equipped with an industrial-grade inertial measurement unit (IMU) and an altimeter, traversed 1.03 km in 110 seconds (GNSS signals were only available for the first 0.11 km). By exploiting signals from 4 Starlink, 1 OneWeb, 2 Orbcomm, and 1 Iridium, the 3D position root-mean squared error (RMSE) and final 3D error of DSTAN were 9.5 m and 4.4 m, respectively. These results represent the first exploitation of unknown OneWeb LEO satellite signals for PNT purposes and the first multi-constellation LEO PNT with Starlink, OneWeb, Orbcomm and Iridium satellites.

The article concludes by presenting simulation results serving as a peak to the future when Starlink and OneWeb constellations are deployed. DSTAN could achieve decimeter-level and meter-level accuracy with pseudorange and Doppler measurements, respectively, over a 23-km trajectory without GNSS.

LEO Satellites: The Benefits and Challenges

Mega-constellations of LEO satellites are being born (e.g., Starlink, OneWeb and Kuiper), joining existing LEO constellations (e.g., Orbcomm, Globalstar, Iridium, among others) [1]. These satellites will shower the Earth with a plethora of signals, diverse in frequency and direction, which could be used for PNT in a dedicated fashion or opportunistically. **Figure 1** depicts the four LEO satellite constellations considered in this article.

To compensate for the limitations of GNSS, researchers have studied the exploitation of terrestrial SOPs for PNT over the last decade [2]. Exploiting SOPs did not stay Earthly, as LEO satellites have received considerable attention recently as potential SOPs. Several theoretical and experimental studies have been conducted on LEO-based PNT [3-5].

LEO satellites possess desirable attributes for PNT: (i) they are around 20 times closer to Earth compared to GNSS satellites that reside in medium Earth orbit (MEO) and could yield significantly higher carrier-to-noise ratio (CNR); (ii) they are becoming abundant as tens of thousands of broadband internet satellites are expected to be deployed into LEO; and (iii) they transmit in different frequency bands and are placed in varying orbits, making LEO satellite signals diverse in frequency and direction. However, exploiting LEO satellite signals for PNT purposes in an opportunistic fashion comes with challenges, as they are owned by private

AUTONOMOUS MEDIA

Get Inside our Autonomous Future

IG Inside GNSS

INSIDE**GNSS**.COM

Free Subscription Offer

inside unmanned systems

INSIDE ENGINEERING, POLICY AND PRACTICE

INSIDE**UNMANNED**SYSTEMS.COM

Free Subscription Offer

INSIDE AUTONOMOUS VEHICLES

INSIDE**AUTONOMOUS**VEHICLES.COM

Free Subscription Offer

PUBLISHED BY **AUTONOMOUS MEDIA, LLC**

operators that typically do not disclose crucial information about the satellites' ephemerides, clock synchronization and stability, and signal specifications.

LEO Satellite Signal Model

To exploit the unknown signals transmitted by LEO satellites, this article relies on the existence of repetitive sequences (also known as beacon) in their transmitted signals. The continuous-time baseband signal model at the receiver's front-end after propagating in an additive white Gaussian channel (AWGN) is expressed as

$$r_k(t) = s\big(t-\tau_k(t)\big)\exp\big(j\theta_k(t)\big) + n_k(t), \quad (1)$$

where $r_k(t)$ is the received signal at $t_k=t_0+kT_0$, where t_0 is an initial time, $k\in\mathbb{N}$ is a discrete index (referred to as sub-accumulation index), T_0 is the beacon length, $s(t)$ is the beacon, and $\tau_k(t)$ is the apparent delay between the transmitted signal and the received signal at the receiver's antenna (also known as the code phase). The apparent delay is the composition of multiple effects: (i) the time-of-flight along the line-of-sight between the transmitter and receiver, (ii) combined effect of the transmitter's and receiver's clock biases, (iii) ionospheric and tropospheric delays, and (iv) other unmodeled errors. Moreover, $\theta_k(t)$ is the carrier phase, which is related to the code phase by $\theta_k(t)=-2\pi f_c\,\tau_k(t)$, where f_c is the carrier frequency of the transmitted signal. Finally, $n_k(t)$ is the sequence of the lumped channel noise and random user data. It is important to note the channel between the LEO satellite and the opportunistic receiver is highly dynamic, thus, high Doppler shift and rate will be observed by the receiver.

Blind Doppler Tracking and Navigation Beacon Estimation

To deal with the unknown time-varying parameters modulating the received navigation beacon $s(t)$, a blind estimation framework was proposed in [6] to track the Doppler as well as estimate the change in the code and carrier phase. The main idea behind this blind Doppler tracker is that the repetitive beacon present in the transmitted signal exhibits a prominent feature in the received signal's spectrum. This blind estimator uses the initial received spectrum as a template and cross-correlates it with the upcoming sub-accumulations to keep track of the change in Doppler as well as to refine the estimated beacon spectrum. Working initially in a non-coherent fashion in the frequency-domain alleviates the need to deal with the complexity invoked by working in a code-carrier coherent fashion. In other words, the Doppler manifests as compression and dilation in the time-domain, as well as high drift in the code phase between consecutive sub-accumulation. These effects cannot be neglected when increasing the coherent processing interval and estimating the navigation beacon.

Figure 2 shows the block diagram of the blind Doppler estimator, where $\bar{r}_k[n]$ denotes the received signal after baseband mixing and filtering; NCO denotes a numerically-controlled oscillator; and $R_k[f]$ and $\hat{S}_k[f]$ are the fast Fourier transform (FFT) of $r_k[n]$ and $s[n]$, respectively.

After successful Doppler and code phase tracking and wiping off the effect of the time-varying quantities in (1) using the proposed blind tracker, the received signal can be readily expressed as a linear model $\boldsymbol{y=Hx+w}$. Based on this observation model, the beacon can be estimated (e.g., using least-squares). Additional details can be found in [6].

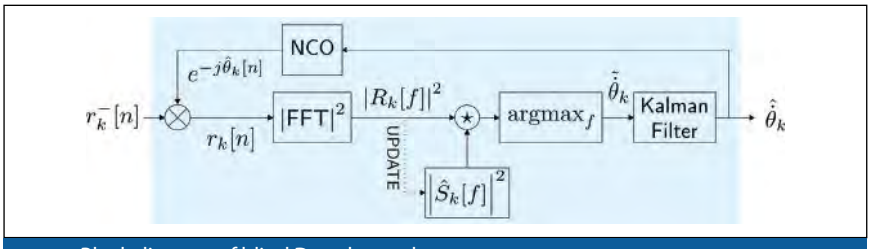

FIGURE 2 Block diagram of blind Doppler tracker.

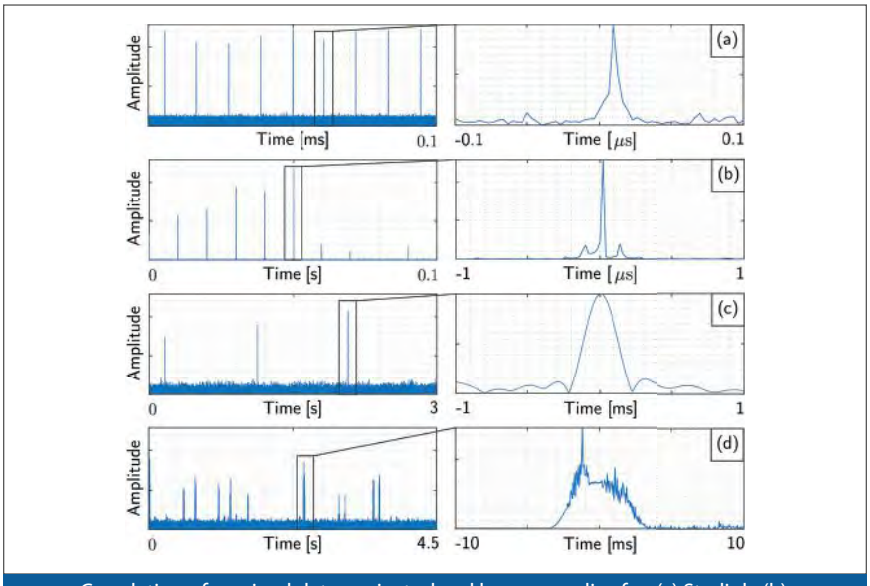

FIGURE 3 Correlation of received data against a local beacon replica for: (a) Starlink, (b) OneWeb, (c) Orbcomm and (d) Iridium.

Navigation Beacon of Starlink, OneWeb Orbcomm and Iridium LEO Constellations

This section presents experimental results demonstrating successful beacon estimation and blind Doppler tracking for four LEO constellations, namely Starlink, OneWeb, Orbcomm and Iridium, which transmit their downlink signals according to the specifications summarized in **Table 1.**

Starlink LEO Constellation

The signal capture setup for Starlink used the NI-USRP x410 to collect raw IQ measurements. The sampling rate was set to 500 MHz and the carrier frequency was set to 11.325 GHz, which is

Parameter	Starlink	OneWeb	Orbcomm	Iridium
Bandwidth	240 MHz	230 MHz	4.8 kHz	31.5 kHz
Beacon length	4/3 ms	10 ms	1 s	90 ms
Active satellites	3,660	542	36	66
Modulation	OFDM	OFDM	SD-QPSK	DE-QPSK
Frequency band	Ku, Ka	Ku, Ka	VHF	L
Number of channels	8	8	2	240
Number of beams	≈ 48	16	N/A	48
Altitude [km]	550	1,200	750	780

TABLE 1 Comparison of LEO constellation's signal parameters.

roughly at the center of one of Starlink's downlink channels in the Ku band. According to the Federal Communications Commission (FCC), the Starlink user downlink signal spectrum spans the 10.7 to 12.7 GHz frequency band. This spectrum is dissected into eight equidistant channels, each with an effective bandwidth of 240 MHz. The period of the repetitive sequence was determined by inspecting the auto-correlation function of a data snapshot that entails many frames. The repetitive sequence present in the frames of the data snapshot induces an impulse train in the auto-correlation function with spacing that was recorded to be equal to 4/3 ms. The NI-USRP x410 was set to record for a duration of 900 seconds. The proposed framework was used to acquire and track the signals present in the collected data.

OneWeb LEO Constellation

The signal capture setup for OneWeb downlink signals was the same as Starlink, with the sampling rate set to 50 MHz and the carrier frequency set to 11.075 GHz. According to the FCC, OneWeb's user downlink signal spectrum spans the 10.7 to 12.7 GHz frequency band. This spectrum is dissected into eight equidistant channels, each with absolute bandwidth of 250 MHz. The repetitive sequence period was estimated to be 10 ms from the data snapshot auto-correlation function. The proposed blind beacon estimation framework was capable of estimating a repetitive sequence that can be used to generate Doppler and code phase observables.

Orbcomm LEO Constellation

The proposed blind beacon estimation method was applied to downlink Orbcomm LEO satellite signals. To this end, a stationary NI-USRP E312 was equipped with a commercial Orbcomm antenna to receive signals in the VHF band. The sampling rate was set to 2.4 MHz and the carrier frequency was set to 137 MHz. The duration of the recorded data was 900 seconds. Orbcomm satellites transmit at a predefined set of frequency pairs in the user downlink spectrum with an effective channel bandwidth of 4.8 kHz. After collection, the Orbcomm signal was fed to the proposed blind beacon estimator and Doppler tracker.

Iridium LEO Constellation

An NI-USRP E312 was used to capture raw signal measurements received by a commercial Iridium antenna. The

NavtechGPS brings you ...

Tallysman AJ977XF AntiJam Triple Band GNSS Antenna

- Low Elevation Angle Nulling Antenna (LEANA)
- Tallysman eXtended Filter
- Ideal for Hostile Environments
- Functions with SBAS in Available Regions
- RoHS and REACH Compliant
- IP67 Weather-Proof Housing

Contact Us for Details!

NavtechGPS

+1-703-256-8900 • 800-628-0885
https://www.navtechgps.com/products

Essential GNSS Courses for 2023


Hegarty


Pue


Vaujin

Live Remote Courses with Real-Time Engagement Taught by World-Class GNSS Experts

9:00 AM-4:30 PM EST

- 346: GPS/GNSS Operation for Engineers and Technical Professionals. *Instructor: Dr. Chris Hegarty.* For those needing a well-coordinated, intensive introduction to GNSS concepts, design and operation; and for those wanting a greater understanding of colleagues' work to become a more productive member of the team. (4 Days, December 5-8)
- 122: GPS/GNSS Fundamentals and Enhancements. *Instructor: Dr. Chris Hegarty.* Take the first two days of 346 for an overview of how the GPS/GNSS system works (2 Days, December 5-6)
- 557: Inertial Systems, Kalman Filtering, and GPS/INS Integration. *Instructors: Dr. Alan Pue and Mr. Michael Vaujin.* Immerse yourself in the fundamentals and practical implementations that fuse GPS receiver measurements with strapdown inertial navigation. (5 Days, December 11-15)

Questions? Contact Trevor at tboynton@navtechgps.com

NavtechGPS

+1-703-256-8900 • 800-628-0885
https://www.navtechgps.com/gps-gnss-training/courses/

sampling rate was set to 2.4 MHz, the carrier frequency was set to 1626.2708 MHz in the L band, which coincides with the ring alert (RA) channel of Iridium satellites, and the total capture duration was 600 seconds. Iridium satellites employ both time division multiple access (TDMA) and frequency division multiple access (FDMA). The Iridium spectrum consists of multiple channels, namely, the RA, paging channel, voice channel, and duplex user channels. The RA channel bandwidth is 41.667 kHz, and the beacon period is 90 ms.

The captured samples from the four LEO constellations were processed via a software-defined radio implementation (SDR) of the proposed blind Doppler tracking framework discussed in [6].

Despite each LEO constellation adopting different modulation and multiple-access strategies, the success of the proposed LEO-agnostic navigation beacon estimation framework is evident in **Figure 3,** which shows consistent repetitive cross-correlation peaks between the received signal and locally-generated beacon for Starlink, OneWeb, Orbcomm and Iridium.

Positioning with Multi-Constellation LEO Satellites

This section presents a multi-constellation positioning solution using signals from Starlink, OneWeb, Orbcomm and Iridium LEO constellations. The carrier phase navigation observables produced by the proposed blind beacon estimation and Doppler tracking framework are used to localize a stationary receiver.

Carrier Phase Measurement Model

Let $i \in [1,L]$ denote the satellite's index, where L is the total number of satellites. The carrier phase observable $\Phi_k(k)$ obtained by integrating the Doppler measurement to the i-th satellite at time-step k, expressed in meters, is modeled as

$$\Phi_k(k) = \|\boldsymbol{r}_r - \boldsymbol{r}_{SV,i}(k')\|_2 + c.[\delta t_r(k) - \delta t_{SV,i}(k')] + c.[\delta_{trop,i}(k) + \delta_{iono,i}(k)] + \lambda_i N_i + \nu_i(k), \quad (2)$$

where $\boldsymbol{r}_r$ is the stationary receiver's 3D position vector in the East-North-Up (ENU) frame; $\boldsymbol{r}_{SV,i}$ is the i-th satellite's 3D position vector in the ENU frame; δt_r and $\delta t_{SV,i}$ are the receiver's and i-th satellite's clock biases, respectively; $\delta_{trop,i}$ and $\delta_{iono,i}$ are the ionospheric and tropospheric delays between the receiver and i-th satellite, respectively; c is the speed-of-light; λ_i is the wavelength of the i-th satellite's signal; N_i is the carrier phase ambiguity between the receiver and i-th satellite; and ν_i is the measurement noise, which is modeled as a discrete-time zero-mean white sequence with variance $\sigma^2_{\Phi,i}$.

In **Equation 2,** the time index k' represents discrete time-step $t_k = t_0 + kT_0 - \delta t_{TOF,i}$, where $\delta t_{TOF,i}$ is the time-of-flight of the signal from the i-th satellite to the receiver. This article assumes k'≈k to simplify the formulation of nonlinear least-squares positioning. This approximation introduces an error in the LEO satellite position and clock bias. The error introduced by this approximation in the LEO satellite position is negligible compared to the position error in two-line element (TLE) files, which can be as high as a few kilometers. The receiver and LEO satellite clock error states (bias and drift) are modeled according to the standard double integrator model [4]. These terms will be lumped together and approximated as a first-order Taylor series expansion (TSE). Under these assumptions, **Equation 2** can be approximated as

$$\Phi_i(k) \approx \|\boldsymbol{r}_r - \boldsymbol{r}_{SV,i}(k)\|_2 + a_i + b_i k T_0 + \nu_i(k), \quad (3)$$

where $a_i \triangleq c.(\delta t_r - \delta t_{SV,i} + \delta_{trop,i} + \delta_{\text{iono,i}})$, and $b_i \triangleq c.(\delta t_r - \delta t_{SV,i} + \delta_{trop,i} + \delta_{\text{iono,i}})$ are the zero- and first-order TSE terms, respectively, of the lumped clock errors and atmospheric delays.

Tracking Results

Signals from 4 Starlink, 2 OneWeb, 1 Orbcomm, and 1 Iridium LEO satellites were collected. **Figure 4(a)** shows the skyplot of the LEO satellites, while **Figure 4(b)** shows the hardware used for

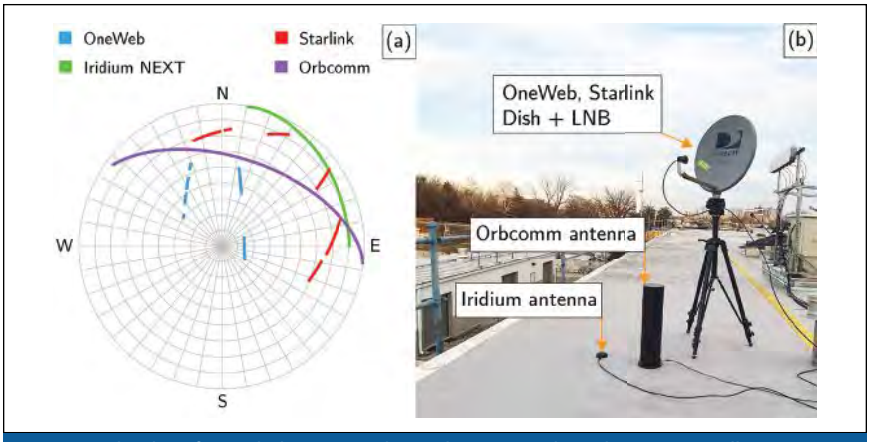

FIGURE 4 (a) Skyplot of 4 Starlink, 2 OneWeb, 1 Orbcomm and 1 Iridium LEO satellites.

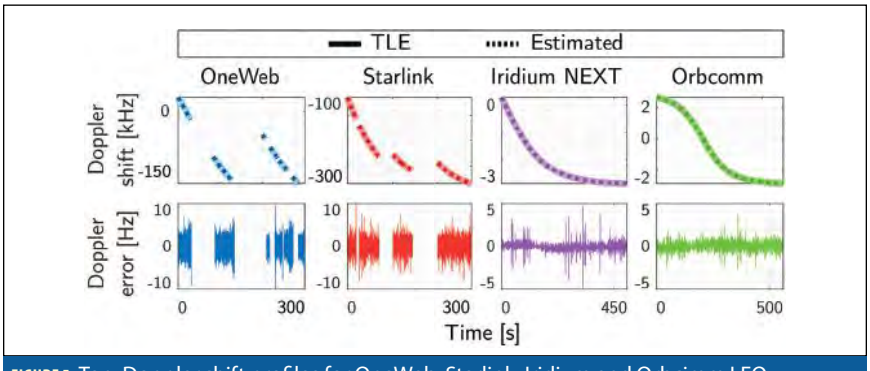

FIGURE 5 Top: Doppler shift profiles for OneWeb, Starlink, Iridium and Orbcimm LEO satellitess. Solid curves denote the estimated Doppler from the proposed framework, while dotted curves denote the predicted Doppler from TLE+SGP4. Bottom: Doppler error during the tracking period of each satellite.

data collection. The hardware included: (i) a low-noise block (LNB) with conversion gain of 50 dB and noise figure of 2.5 dB connected to a Ku-band 60 cm parabolic offset dish with a gain of 30 dBi to receive Starlink and OneWeb satellite signals, (ii) a commercial Orbcomm antenna and (iii) a commercial Iridium antenna.

Tracking results of eight different satellites are shown in **Figure 5.** The top row in the figure shows the estimated (dashed) versus the TLE+SGP4-predicted (solid) Doppler shift profile for each tracked satellite. The bottom row shows the Doppler error during the tracking period. It is worth noting that even though the studied LEO constellations suffer from high Doppler (up to ~250 kHz), the blind Doppler tracking framework was able to track the Doppler with an error less than 10 Hz.

Positioning Solution

Next, a batch nonlinear least-squares estimator was employed using measurements from all LEO satellites to estimate the stationary receiver. The satellite positions were obtained from TLE files and an SGP4 orbit determination software. The TLE epoch time was adjusted for each satellite to account for ephemeris errors. This was achieved by minimizing the carrier phase residuals for each satellite [7]. The estimator's formulation is described in [6]. The receiver's initial position estimate was set on the roof of the Engineering parking structure at the University of California, Irvine, approximately 3,600 km away from the true position, which was on the roof of The Ohio State University's ElectroScience Laboratory (ESL) in Columbus, Ohio. **Figure 6** summarizes the positioning results. Specifically, **Figure 6(a)** shows the trajectories of the eight satellites from the four LEO constellations, **Figure 6(b)** shows the initial position estimate versus true receiver's position, and **Figure 6(c)** shows the true and estimated receiver's position. The final 3D position error was found to be 5.8 m, while the 2D position error was 5.1 m (i.e., upon considering only the east and north coordinates in the ENU frame).

Simultaneous Tracking and Navigation with Differential Measurements

Today's vehicular navigation systems rely on a GNSS-aided inertial navigation system (INS). This GNSS/INS integration, which can be loose, tight, or deep, provides a navigation solution that benefits both the short-term accuracy of the INS and the long-term stability of GNSS [8]. In the STAN framework [9], LEO satellite signals are opportunistically exploited to produce navigation observables as an INS-aiding source, thus serving as a complement or even an alternative to GNSS signals. GNSS satellites are equipped with highly stable atomic clocks, are synchronized across the constellation network, and transmit their ephemeris data and clock errors to the user in their navigation message. In contrast, LEO satellites do not possess the aforementioned attributes because they are not designed for PNT purposes. Their on-board clocks are not necessarily of atomic standard nor as tightly synchronized. Moreover, they do not publicly transmit their ephemeris and clock error data in their proprietary signals.

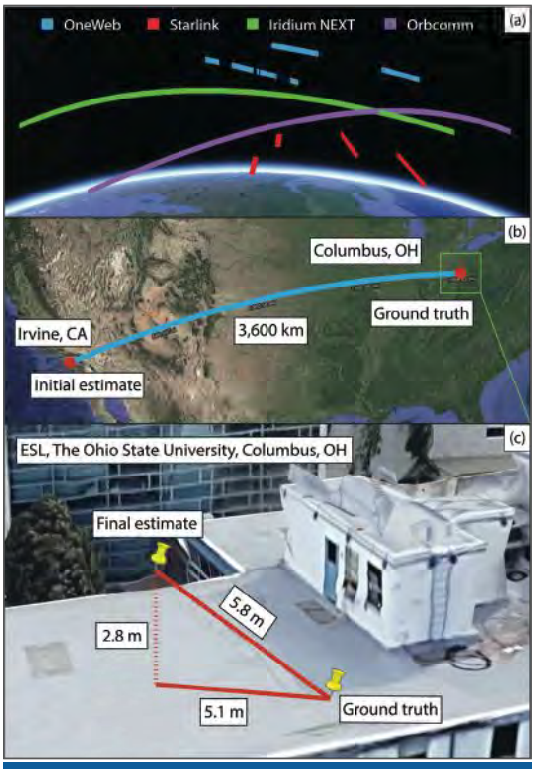

FIGURE 6 Positioning results with Starlink, OneWeb, Orbcomm and Iridium LEO constellations: (a) LEO satellite trajectories. (b) Initial and final estimated positions. (c) Final errors relative to receiver's true position.

To overcome these challenges, the STAN framework was proposed, in which the navigating vehicle's states are simultaneously estimated with the states of the LEO satellites [9-12]. STAN employs a filter, e.g., an extended Kalman filter (EKF), to aid the vehicle's INS with navigation observables extracted from LEO satellites' signals in a tightly coupled fashion.

Differential positioning is a multiple-receiver PNT technique that entails computing corrections at a known base station to improve the positioning solution at an unknown rover [13-14]. To compensate for common mode errors, namely LEO space vehicle (SV) ephemerides, LEO SV clocks, and ionospheric and tropospheric delays, DSTAN was proposed to incorporate additional measurements extracted from the same LEO satellites from known base station(s), which are communicated to the navigating vehicle as shown in **Figure 7** [15].

Measurement Models

This subsection describes the LEO satellite receiver pseudorange and Doppler measurement models. The differential pseudorange measurement model across the rover and the base at time-step k, which represents discrete-time at $t_k = t_0 + kT_0$ for an initial time t_0 and sampling time T_0, is defined as

$$z_l^{(R,B)} = \rho_l^{(R)}(k) - \rho_l^{(B)}(k) = \left\| \boldsymbol{r}_{r,R}(k) - \boldsymbol{r}_{leo,l}(k) \right\|_2 - \left\| \boldsymbol{r}_{r,B}(k) - \boldsymbol{r}_{leo,l}(k) \right\|_2 + c\delta t_r^{(R,B)}(k) + c\delta t_{trop,l}^{(R,B)}(k) + c\delta t_{iono,l}^{(R,B)}(k) + \nu_{\rho,l}^{(R,B)}(k), \quad (4)$$

where $\rho_l^{(R)}$ and $\rho_l^{(B)}$ are the pseudorange measurements at the rover and base station, respectively, to the l-th LEO satellite; $\boldsymbol{r}_{r,R}$, $\boldsymbol{r}_{r,B}$, and $\boldsymbol{r}_{leo,l}$ are the rover, base, and LEO satellite position vectors, respectively; c is the speed of light; $\delta t_r^{(R,B)}$ is the clock bias difference between the

rover and the base; $\delta t_{trop,l}^{(R,B)}$ and $\delta t_{iono,l}^{(R,B)}$ are tropospheric and ionospheric delay differences between the rover and the base from the l-th LEO satellite, respectively; and $v_{\rho,l}^{(R,B)}$ is the pseudorange measurement noise difference between the rover and the base. The Doppler measurement f_D extracted by the LEO receiver is related to the pseudorange rate measurement $\dot{\rho} = -\frac{c}{f_c} f_D$ where f_C is the LEO SV carrier frequency. The differential pseudorange rate measurement model across the rover and the base is defined as

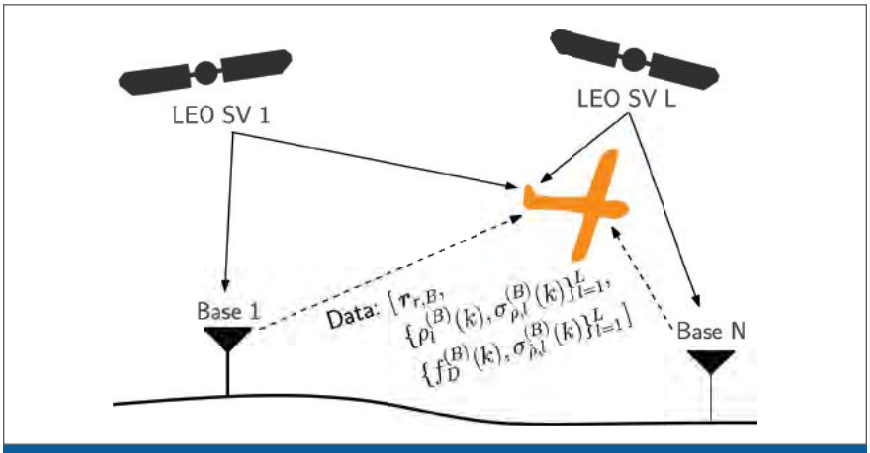

FIGURE 7 DSTAN framework: *N* base stations with known positions and a rover (UAV) with unknown states make pseudorange or Doppler measurements to the same *L* LEO SVs. The base stations transmit a data packet containing the base's position $\boldsymbol{r}_{r,B}$ and its pseudorange $\rho_l^{(B)}(k)$ or Doppler $f_D^{(B)}(k)$ measurements to all LEO SVs along with the measurements' standard deviation $\sigma_{(\rho,l)}^{(B)}(k)$ and $\sigma_{(\dot{\rho},l)}^{(B)}(k)$, respectively. The rover aids its onboard inertial measurement unit (IMU) with differential measurements and navigates while estimating its own states simultaneously with the LEO SVs' states.

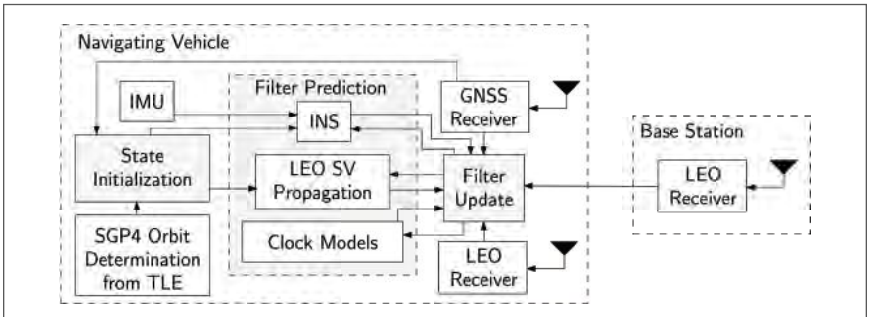

FIGURE 8 LEO-aided INS DSTAN framework.

FIGURE 9 Navigating rover's hardware setup.

$$
\begin{aligned}
z_l^{(R,B)} &= \dot{\rho}_l^{(R)}(k) - \dot{\rho}_l^{(B)}(k) \\
&= \left[\dot{\boldsymbol{r}}_{r,R}(k) - \dot{\boldsymbol{r}}_{leo,l}(k)\right]^T \frac{\boldsymbol{r}_{r,R}(k) - \boldsymbol{r}_{leo,l}(k)}{\left\|\boldsymbol{r}_{r,R}(k) - \boldsymbol{r}_{leo,l}(k)\right\|_2} \\
&\quad - \left[\dot{\boldsymbol{r}}_{r,B}(k) - \dot{\boldsymbol{r}}_{leo,l}(k)\right]^T \frac{\boldsymbol{r}_{r,B}(k) - \boldsymbol{r}_{leo,l}(k)}{\left\|\boldsymbol{r}_{r,B}(k) - \boldsymbol{r}_{leo,l}(k)\right\|_2} \\
&\quad + c\dot{\delta}t_r^{(R,B)}(k) + c\dot{\delta}t_{trop,l}^{(R,B)}(k) + c\dot{\delta}t_{iono,l}^{(R,B)}(k) + v_{\dot{\rho},l}^{(R,B)}(k)
\end{aligned} \tag{5}
$$

Where $\dot{\rho}_l^{(R)}$ and $\dot{\rho}_l^{(B)}$ are the pseudorange rate measurements at the rover and base station, respectively, to the l-th LEO satellite; $\dot{\boldsymbol{r}}_{r,R}$, $\dot{\boldsymbol{r}}_{r,B}$, and $\dot{\boldsymbol{r}}_{leo,l}$ are the rover, base, and LEO satellite velocity vectors, respectively; $\dot{\delta}t_r^{(R,B)}$ is the clock drift difference between the rover and the base; $\dot{\delta}t_{trop,l}^{(R,B)}$ and $\dot{\delta}t_{iono,l}^{(R,B)}$ are tropospheric and ionospheric delay rate differences between the rover and the base from the l-th LEO satellite, respectively; and $v_{\dot{\rho},l}^{(R,B)}$ is the pseudorange rate measurement noise difference between the rover and base.

Filter Formulation

Figure 8 shows the block diagram of the DSTAN framework. The vehicle's state vector $\boldsymbol{x}_r$ consists of the vehicle's body frame orientation with respect to the Earth-centered Earth-fixed (ECEF) reference frame ${}_e^b\boldsymbol{q}$, the vehicle's 3D position $\boldsymbol{r}_r$ and velocity $\dot{\boldsymbol{r}}_r$ in ECEF, and the gyroscope $\boldsymbol{b}_{gyr}$ and accelerometer $\boldsymbol{b}_{acc}$ biases, namely,

$$
\boldsymbol{x}_r = \left[{}_e^b\boldsymbol{q}^T, \boldsymbol{r}_r^T, \dot{\boldsymbol{r}}_r^T, \boldsymbol{b}_{gyr}^T, \boldsymbol{b}_{acc}^T\right]^T. \tag{6}
$$

The clock state vector consists of the relative clock bias and drift difference between the rover and all bases, i.e.,

$$
\boldsymbol{x}_{clk} = c \cdot \left[\delta t^{(R,B_1)}, \dot{\delta t}^{(R,B_1)}, \ldots, \delta t^{(R,B_n)}, \dot{\delta t}^{(R,B_n)}\right]^T. \tag{7}
$$

The l-th LEO satellite's state vector $\boldsymbol{x}_{leo,l}$ consists of its 3D position and velocity, expressed in the ECEF reference frame

$$
\boldsymbol{x}_{leo,l} = \left[\boldsymbol{r}_{leo,l}^T, \dot{\boldsymbol{r}}_{leo,l}^T\right]^T. \tag{8}
$$

The state vector estimated in the DSTAN EKF is formed by augmenting the vehicles' states, clock states and each LEO satellite's states, namely,

$$
\boldsymbol{x} = \left[\boldsymbol{x}_r, \boldsymbol{x}_{clk}, \boldsymbol{x}_{leo,1}, \ldots, \boldsymbol{x}_{leo,L}\right]^T. \tag{9}
$$

Ground Vehicle Navigation with LEO-aided DSTAN

This section presents experimental results demonstrating the performance of ground vehicle navigation with 4 Starlink, 1 OneWeb, 2 Orbcomm and 1 Iridium LEO satellites via the DSTAN framework. The vehicle traversed a 1.03

km trajectory in 110 seconds, while a differential base station with known position was set up at the ElectroScience Lab at The Ohio State University, about 1.5 km away from the vehicle. The vehicle was equipped with a Septentrio AsteRx SBi3 Pro+ integrated GNSS-INS system with an industrial-grade IMU and an altimeter, which provided the ground truth. The vehicle was also equipped with antennas and radio frequency front ends to receive LEO signals. **Figure 9** shows the vehicle's hardware setup. The base station's setup is the same as the one shown in **Figure 4.**

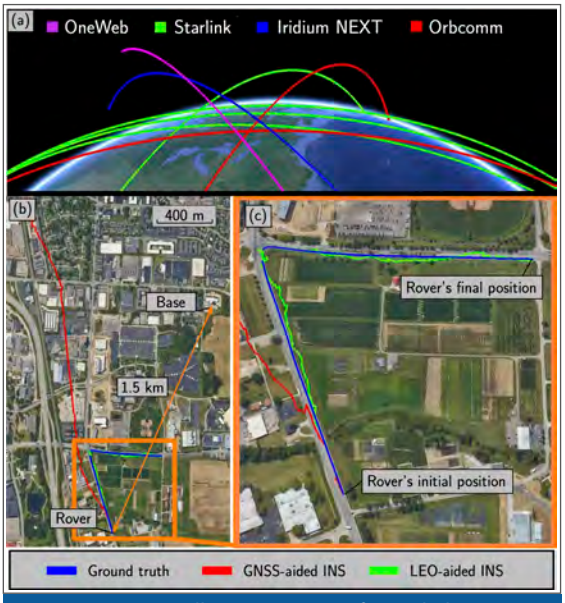

FIGURE 10 (a) LEO satellite trajectories of 4 Starlink, 1 OneWeb, 2 Orbcomm, and 1 Iridium LEO satellites whose signals were exploited for ground vehicle navigation, (b) relative distance between the base and rover (ground vehicle), (c) navigation results: ground truth trajectory (blue), GNSS-aided INS (red), and DSTAN LEO-aided INS (green).

LEO satellite signals from the four constellations were collected at the base station and the rover (ground vehicle) and were used to generate Doppler navigation observables from the receiver presented in [6]. GNSS signals were available for the first 7 seconds of the experiment but were virtually cut off for the last 103 seconds, during which the vehicle traversed a 0.92 km distance. **Figure 10** shows the LEO satellites' trajectories, relative distance between the base and rover, and the ground truth trajectory traversed by the rover versus the GNSS-INS and DSTAN navigation solutions.

Simulation Results: A Sneak Peak to the Future

This section presents simulation results via a high fidelity simulator demonstrating the potential of DSTAN with 14 Starlink, 11 OneWeb, 3 Iridium, and 1 Orbcomm LEO satellites.

Simulation Overview

The simulation considered a fixed-wing aerial vehicle that traveled a 28 km trajectory for 300 seconds over Columbus, Ohio. The vehicle was equipped with a tactical-grade IMU, an altimeter, a GNSS receiver and a LEO receiver that produced pseudorange and Doppler measurements. The simulated environment also included three base stations equipped with LEO receivers that produced pseudorange and Doppler observables that were communicated to the aerial vehicle along with the base positions and measurement noise variances.

The mean baseline distances between the aerial vehicle along its simulated trajectory and the three base stations was 5.37, 6.01 and 4.84 km. GNSS signals were made available to the aerial vehicle for the first 60 seconds of flight time, during which GNSS measurements were fused with the INS in a loosely coupled fashion. The LEO observables were used to refine the estimates of the LEO SVs ephemerides and the rover-base(s) clock differences. During the last 240 seconds, GNSS signals were made unavailable to the vehicle, which operated in STAN mode. The altimeter measurements and LEO observables aided the on-board INS, while simultaneously estimating the LEO SVs' ephemerides and clock differences. The LEO satellite trajectories were generated via Analytical Graphics Inc. (AGI) Systems Tool Kit (STK) using a High-Precision Orbit Propagator (HPOP). The LEO SVs, consisting of 14 Starlink, 11 OneWeb, 3 Iridium, and 1 Orbcomm satellites, were found to be visible from Columbus on January 9, 2023, at 17:00 UTC. The orbits of these SVs are shown in **Figure 11.**

	Total	No GNSS
Distance [km]	1.03	0.92
Time [s]	130	123
	GNSS-INS	**LEO-INS DSTAN**
Position RMSE [m]	788	9.5
Final Error [m]	1,877	4.4

TABLE 2 Summary of experimental results.

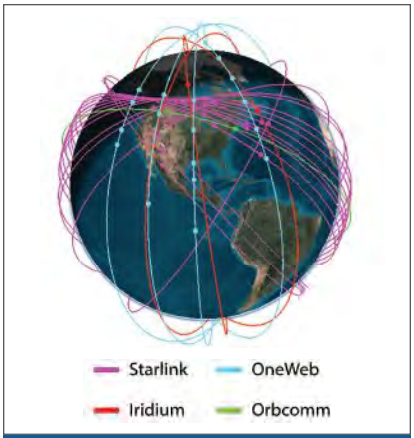

FIGURE 11 Simulated satellite trajectories.

Pseudorange and Doppler measurements were generated from the aerial vehicle and the three base stations to all visible LEO satellites. The measurement noise variances were calculated based on the predicted CNR ratio according to the log distance path loss model described in [13].

To demonstrate the benefit of the DSTAN framework, two cases were considered:

1. Standalone STAN: The aerial vehicle relied solely on the LEO observables that were extracted from its LEO receiver.
2. Differential STAN: The aerial vehicle differenced its LEO measurements from those communicated from one, two or three base stations.

Both configurations were simulated using pseudorange or Doppler observables from the LEO receivers. **Table 3** summarizes the achieved results.

Results and Discussion

The simulation environment is depicted in **Figure 12,** showing the base station locations and the aerial vehicle's ground truth and estimated trajectories via the

	GNSS-INS	STAN	DSTAN		
			1 Base	2 Bases	3 Bases
Pseudorange					
RMSE [m]	528	7.90	0.40	0.34	0.31
Final Error [m]	1,795	5.70	0.32	0.08	0.29
Doppler					
RMSE [m]	528	14.80	5.13	3.10	1.37
Final Error [m]	1,796	8.20	3.24	3.89	0.96

TABLE 3 Summary of Simulation Results.

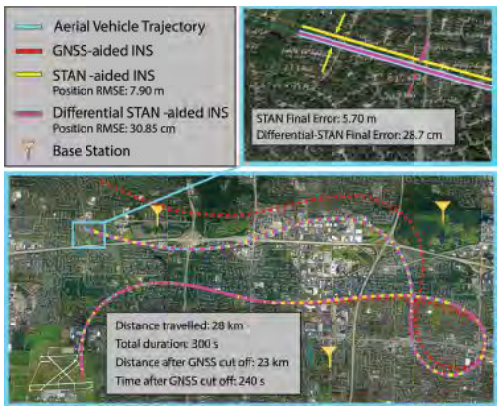

FIGURE 12 Simulation environment and navigation results.

GNSS-aided INS, STAN-aided INS, and 3-base DSTAN-aided INS frameworks.

Figure 13 and **Figure 14** compare the EKF errors and associated ±3σ bounds of the aerial vehicle's position and velocity states in the East and North directions of GNSS-INS, STAN, and one base DSTAN with (i) LEO pseudorange-aided INS and (ii) LEO Doppler-aided INS, respectively. As expected, it can be seen that the GNSS-INS errors quickly diverge after GNSS cutoff. In contrast, the STAN errors diverge at a slower rate, while DSTAN significantly reduces the divergence rate. The errors of pseudorange-aiding were smaller than Doppler-aiding. Note that altimeter measurements provided non-diverging errors in the up direction in all configurations.

Figure 15 and **Figure 16** show the effect of incorporating additional base stations on the navigation solution with pseudorange and Doppler measurements, respectively. The addition of the first base leads to significantly tighter position error uncertainty bounds, while this improvement gradually decreases with the incorporation of the second and third base stations.

This significant improvement in the navigation solution presented by the differential framework can be attributed to (i) elimination of the LEO satellite clock states from the EKF vector, (ii) additional information provided by the measurements of base stations whose positions are known, and (iii) compensation of LEO SVs' ephemerides errors. IG

Acknowledgments

This work was supported in part by the Office of Naval Research (ONR) under Grants N00014-19-1-2511 and N00014-22-1-2242, in part by the Air Force Office of Scientific Research (AFOSR) under Grant FA9550-22-1-0476, in part by the National Science Foundation (NSF) under Grant 2240512, and in part by the U.S. Department of Transportation (USDOT) under Grant 69A3552047138 for the CARMEN University Transportation Center (UTC).

References

(1) N. Jardak and Q. Jault, "The potential of LEO satellite-based opportunistic navigation for high dynamic applications," Sensors, vol. 22, no. 7, pp. 2541–2565, 2022

(2) Z. Kassas, J. Khalife, A. Abdallah, and C. Lee, "I am not afraid of the GPS jammer: resilient navigation via signals of opportunity in GPS-denied environments," IEEE Aerospace and Electronic Systems Magazine, vol. 37, no. 7, pp. 4–19, July 2022.

(3) T. Reid, T. Walter, P. Enge, D. Lawrence, H. Cobb, G. Gutt, M. O'Conner, and D. Whelan, "Position, navigation, and timing technologies in the 21st century," J. Morton, F. van Diggelen, J. Spilker, Jr., and B. Parkinson, Eds. Wiley-IEEE, 2021, vol. 2, ch. 43: Navigation from low Earth orbit–Part 1: concept, current capability, and future promise, pp. 1359–1379.

(4) Z. Kassas, "Position, navigation, and timing technologies in the 21st century," J. Morton, F. van Diggelen, J. Spilker, Jr., and B. Parkinson, Eds. Wiley-IEEE, 2021, vol. 2, ch. 43: Navigation from low Earth orbit–Part 2: models, implementation, and performance, pp. 1381–1412.

(5) M. Hartnett, "Performance assessment of navigation using carrier Doppler measurements from multiple LEO constellations," Master's thesis, Air Force Institute of Technology, Ohio, USA, 2022.

(6) S. Kozhaya, H. Kanj, and Z. M. Kassas, "Multi-constellation blind beacon estimation, Doppler tracking, and opportunistic positioning with OneWeb, Starlink, Iridium NEXT, and Orbcomm LEO satellites," in Proceedings of IEEE/

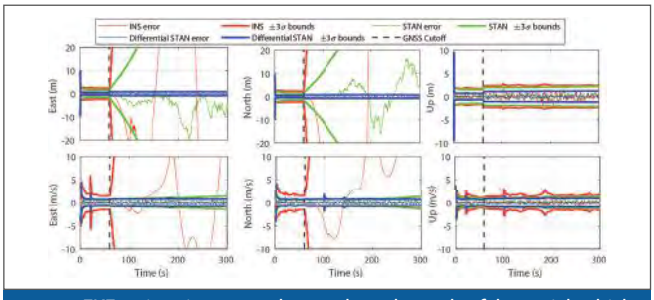

FIGURE 13 EKF estimation error plots and ±3σ bounds of the aerial vehicle states for GNSS-INS, STAN, and one base DSTAN LEO pseudorange-aided INS. The first and second rows correspond to the position and velocity states, respectively, of the vehicle in the ENU frame.

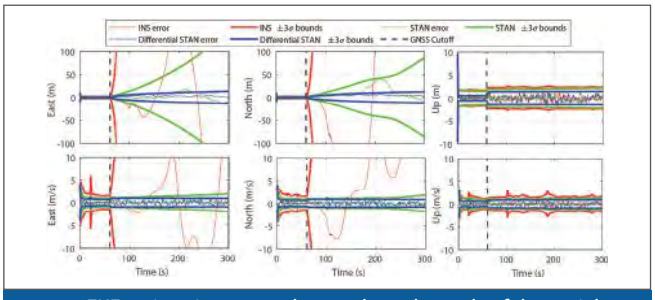

FIGURE 14 EKF estimation error plots and ±3σ bounds of the aerial vehicle states GNSS-INS, STAN and one base DSTAN LEO Doppler-aided INS. The first and second rows correspond to the position and velocity states, respectively, of the vehicle in the ENU frame.

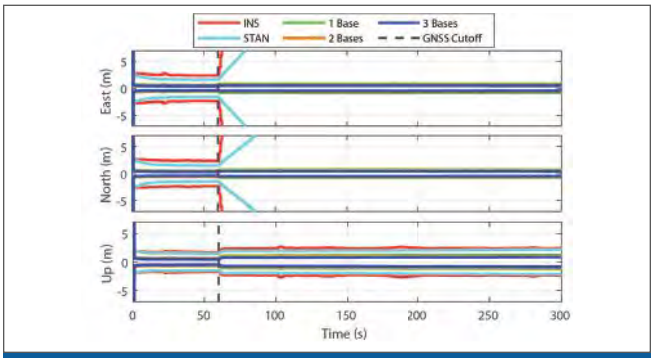

FIGURE 15 EKF ±3σ estimation error bounds of the aerial vehicle states in the ENU frame with pseudorange-aided INS for varying number of base stations.

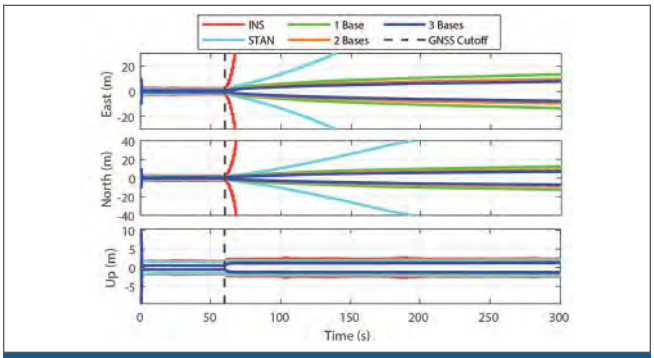

FIGURE 16 EKF ±3σ estimation error bounds of the aerial vehicle states in the ENU frame with Doppler-aided INS for varying number of base stations.

ION Position, Location and Navigation Symposium, 2023, pp. 1184–1195.

(7) J. Khalife, M. Neinavaie, and Z. Kassas, "The first carrier phase tracking and positioning results with Starlink LEO satellite signals," IEEE Transactions on Aerospace and Electronic Systems, vol. 56, pp. 1487–1491, 2022.

(8) D. Gebre-Egziabher, "What is the difference between 'loose', 'tight', 'ultra-tight' and 'deep' integration strategies for INS and GNSS," *Inside GNSS* Magazine, pp. 28–33, 2007.

(9) Z. Kassas, N. Khairallah, and S. Kozhaya, "Ad astra: Simultaneous tracking and navigation with megaconstellation LEO satellites," *IEEE Aerospace and Electronic Systems* Magazine, 2023, accepted.

(10) Z. Kassas, J. Morales, and J. Khalife, "New-age satellite-based navigation–STAN: simultaneous tracking and navigation with LEO satellite signals," *Inside GNSS* Magazine, pp. 56–65, 2019.

(11) T. Mortlock and Z. Kassas, "Performance analysis of simultaneous tracking and navigation with LEO satellites," in Proceedings of ION GNSS Conference, pp. 2416–2429, 2020.

(12) Z. Kassas, M. Neinavaie, J. Khalife, N. Khairallah, J. Haidar-Ahmad, S. Kozhaya, and Z. Shadram, "Enter LEO on the GNSS stage: Navigation with Starlink satellites," Inside GNSS Magazine, pp. 42–51, 2021.

(13) B. Parkinson and P. Enge, "Differential GPS," Global Positioning System: Theory and applications., vol. 2, pp. 3–50, 1996.

(14) J. Khalife and Z. Kassas, "Performance-driven design of carrier phase differential navigation frameworks with megaconstellation LEO satellites," IEEE Transactions on Aerospace and Electronic Systems, pp. 1–20, 2023, accepted.

(15) J. Saroufim, S. W. Hayek, and Z. M. Kassas, "Simultaneous LEO satellite tracking and differential LEO-aided IMU navigation," in Proceedings of IEEE/ION Position, Location and Navigation Symposium, 2023, pp. 179–188.

Authors

Zaher (Zak) M. Kassas is a Professor of Electrical & Computer Engineering (ECE) at The Ohio State University and TRC Endowed Chair of Intelligent Transportation Systems (ITS). He is also Director of the Autonomous Systems Perception, Intelligence, & Navigation (ASPIN) Laboratory and Director of the U.S. Department of Transportation Center: CARMEN (Center for Automated Vehicle Research with Multimodal AssurEd Navigation), focusing on navigation resiliency and security of highly automated transportation systems. He received a B.E. in Electrical Engineering from the Lebanese American University (LAU), M.S. in ECE from The Ohio State University, and M.S.E. in Aerospace Engineering and Ph.D. in ECE from The University of Texas at Austin. He is a recipient of the National Science Foundation (NSF) CAREER award, Office of Naval Research (ONR) Young Investigator Program (YIP) award, Air Force Office of Scientific Research (AFOSR) YIP award, IEEE Walter Fried Award, Institute of Navigation (ION) Samuel Burka Award, and ION Col. Thomas Thurlow Award. He is a Fellow of the ION and a Distinguished Lecturer of the IEEE Aerospace and Electronic Systems Society. His research interests include cyber-physical systems, navigation systems and ITS.

Sharbel Kozhaya is a Ph.D. student in the Department of Electrical Engineering and Computer Science at The Ohio State University and a member of the ASPIN Laboratory. He received a B.E. in Electrical Engineering from LAU. His current research interests include cognitive sensing, opportunistic navigation, software-defined radio and low Earth orbit satellites.

Joe Saroufim is a Ph.D. student in the Department of Electrical Engineering and Computer Science at The Ohio State University and a member of the ASPIN Laboratory. He received a B.E. in Mechanical Engineering from LAU. His current research interests include situational awareness, autonomous vehicles and sensor fusion.

Haitham Kanj is a Ph.D. student in the Department of Electrical Engineering and Computer Science at The Ohio State University and a member of the ASPIN Laboratory. He received a B.E. in Electrical Engineering from LAU. His current research interests include cognitive sensing, 5G and satellite-based navigation.

Samer Watchi Hayek is a Ph.D. student in the Department of Electrical Engineering and Computer Science at The Ohio State University and a member of the ASPIN Laboratory. He received a B.E. in Mechanical Engineering from LAU. His current research interests include autonomous vehicles, sensor fusion, simultaneous localization and mapping.

A Machine Learning Multipath Mitigation Approach for Opportunistic Navigation with 5G Signals

Mohamad Orabi, Ali A. Abdallah, Joe Khalife, and Zaher M. Kassas
University of California, Irvine

BIOGRAPHIES

Mohamad Orabi is a Ph.D. student in the Department of Electrical Engineering and Computer Science at the University of California, Irvine and a member of the Autonomous Systems Perception, Intelligence, and Navigation (ASPIN) Laboratory. He received a B.E. in Electrical Engineering from the Lebanese American University (LAU). His current research interest include machine learning; opportunistic navigation; multipath mitigation; and software-defined radio for 5G, LTE, and low Earth orbit (LEO) signals.

Ali A. Abdallah is a Ph.D student in the Department of Electrical Engineering and Computer Science at the University of California, Irvine and a member of the ASPIN Laboratory. He received a B.E. in Electrical Engineering from LAU. His current research interests include opportunistic navigation, software-defined radio, long-term evolution (LTE), 5G, and indoor localization.

Joe Khalife is a postdoctoral fellow at the University of California, Irvine and member of the ASPIN Laboratory. He received a B.E. in Electrical Engineering and an M.S. in Computer Engineering from LAU, and a Ph.D. in Electrical Engineering and Computer Science from the University of California, Irvine. From 2012 to 2015, he was a research assistant at LAU. He has been a member of the ASPIN Laboratory since 2015. He is a recipient of the 2016 IEEE/ION Position, Location, and Navigation Symposium (PLANS) Best Student Paper Award and the 2018 IEEE Walter Fried Award. His research interests include opportunistic navigation, autonomous vehicles, and software-defined radio.

Zaher (Zak) M. Kassas is an associate professor at the University of California, Irvine and director of the Autonomous Systems Perception, Intelligence, and Navigation (ASPIN) Laboratory. He is also director of the U.S. Department of Transportation Center: CARMEN (Center for Automated Vehicle Research with Multimodal AssurEd Navigation), focusing on navigation resiliency and security of highly automated transportation systems. He received a B.E. in Electrical Engineering from the Lebanese American University, an M.S. in Electrical and Computer Engineering from The Ohio State University, and an M.S.E. in Aerospace Engineering and a Ph.D. in Electrical and Computer Engineering from The University of Texas at Austin. He is a recipient of the 2018 National Science Foundation (NSF) Faculty Early Career Development Program (CAREER) award, 2019 Office of Naval Research (ONR) Young Investigator Program (YIP) award, 2018 IEEE Walter Fried Award, 2018 Institute of Navigation (ION) Samuel Burka Award, and 2019 ION Col. Thomas Thurlow Award. His research interests include cyber-physical systems, estimation theory, navigation systems, autonomous vehicles, and intelligent transportation systems.

Abstract

The ability of different neural networks to mitigate multipath signals for opportunistic navigation with downlink 5G signals is assessed. Two neural networks, namely feed-forward neural networks (FFNNs) and time-delay neural networks (TDNNs), are designed to learn multipath-induced errors on a 5G receiver's code phase estimate. The neural networks use inputs from the autocorrelation function (ACF) to learn the errors in the code phase estimate of a conventional delay-locked loop (DLL). A ray tracing algorithm is used to produce high fidelity training data that could model the dynamics between the line of sight (LOS) component and the non-line of sight (NLOS) components. Cross-validation methods are used on FFNNs to examine the sensitivity of the out-of-sample error on the number of hidden layers, number of neurons per layer, and regularization constant that limits the complexity of the hypothesis space. Moreover, TDNNs with varying access to the time history of the ACF taps are assessed. Experimental results in a multipath-rich environment are presented demonstrating that the proposed TDNN achieved ranging root-mean squared error (RMSE) reduction of 27.1% compared to a conventional DLL.

Copyright © 2021 by M. Orabi, A. Abdallah, and J. Khalife, Z. Kassas

Preprint of the 2021 ION GNSS+ Conference St. Louis, Missouri, September 20–24, 2021

I. Introduction

Accurate and reliable positioning, navigation, and timing (PNT) is a crucial enabler of autonomy. For decades, global navigation satellite systems (GNSS) have been the leading providers of PNT. However, as more semi-autonomous and fully-autonomous systems started depending on GNSS for PNT, the vulnerabilities of GNSS signals have become more apparent. Their severe attenuation indoors and in deep urban canyons and susceptibility to unintentional interference, intentional jamming, and malicious spoofing [1–4] prove to be critical limitations standing in the way of autonomy. Recently, considerable attention has been devoted to exploiting ambient radio frequency signals of opportunity (SOPs) [5], such as cellular, AM/FM radio, satellite communication, digital television, and Wi-Fi, as a standalone alternative to GNSS or to complement GNSS-based navigation [6–15]. Among the different SOPs, cellular 5G signals are particularly attractive due to their ubiquity, geometric diversity, high received signal power, and large bandwidth [16–24].

The positioning capabilities of 5G systems have been studied over the past few years. Different approaches have been proposed, in which direction-of-arrival (DOA), direction-of-departure (DOD), time-of-arrival (TOA), or combination thereof is used to achieve accurate positioning from 5G signals. The study in [25] derived the Cramer-Rao bound on position and orientation estimation uncertainty, as well as presented an algorithm that achieves the bound for average to high signal-to-noise ratio. In [26], the capability of massive multiple-input multiple-output (mMIMO) systems in providing very accurate localization when relying on DOA was studied. The work in [27] presented an algorithm to mitigate the near-field errors in angular positioning with 5G system. A compressed sensing approach was proposed to address the limitations of DOA in mMIMO systems in the presence of multipath, showing the potential of achieving submeter accuracy in a simulated environment. In contrast to the aforementioned approaches, [21, 28] were the first to present experimental navigation results on a ground vehicle, achieving meter level accuracy.

Given the low elevation angles from which cellular signals are received, these signals suffer from non-LOS and multipath conditions [29]. While these are not too problematic for communication purposes, they can induce very large errors when used for positioning purposes. Multipath signals distort the autocorrelation function used in the receiver's DLLs and phase-locked loops (PLLs), introducing biases in the code and carrier phase estimates, which in turn introduce errors in the navigation solution [30]. Several techniques have been developed to mitigate the effect of mulitpath in GNSS systems, most of which could be grouped into two main categories: (i) antenna techniques [31] and (ii) signal processing techniques, such as the narrow correlator [32], strobe edge correlator [33], and high resolution correlator (HRC) [34]. While the aforementioned approaches have been shown to outperform the standard early-minus-late (E-L) DLL, they are still susceptible to severe multipath. Moreover, while signal processing techniques could be extended to receivers that exploit cellular signals opportunistically for navigation, antenna techniques that mitigate multipath by filtering out signals with lower elevation angles are not useful, since most received signals from terrestrial 5G bas stations (referred to as gNBs) have low elevation angles.

Machine learning (ML) algorithms and neural networks (NNs) have managed to find their way into several fields with applications ranging from speech recognition and object detection to medical diagnosis and many others. In recent years, emerging NNs have gained significantly more attention as they surpassed model-based algorithms in their capabilities in achieving their intended goals such as DeepFake [35] and WaveNet [36], the first being an NN with the ability of generating very convincing fake footage, and the latter being a text to speech system that outperforms the existing state of the art model based systems. NNs have also outperformed human rivals. An example of such NN is OpenAI Five's large scale deep reinforcement learning system [37], which became the first AI system to defeat the world champions at an esports game that presents novel challenges for AI systems such as long time horizons, imperfect information, and complex continuous state-action spaces. These noteworthy achievements could be attributed to the ability of NNs to learn complex multi-dimensional relationships by observing training data, and leveraging that to take decisions on new data that it has never seen before. Machine learning algorithms have also found their way into the navigation field. In [38], a deep NN was developed to spatially discriminate multipath signals in a synthetic aperture fashion and beamform towards the LOS component. This NN was then coupled with a zero velocity update (ZUPT)-aided inertial measurement unit (IMU) to achieve an accuracy of about one-meter indoors over a trajectory of 600 m [39]. In [40], a wavelet NN approach that predicts the satellite's clock bias using its values at previous epochs was introduced. An NN-based DLL (NNDLL) was proposed in [41] for multipath mitigation in GPS receivers. The type of multipath environment and receiver motion was identified via a NN in [42] in order to adjust the receiver's tracking strategy.

This paper assesses the ability of different NNs to learn multipath errors that corrupt the TOA estimate in a 5G opportunistic navigation receiver. First, feed-forward NNs (FFNNs) are examined and a cross-validation approach is used to study the performance of NNs belonging to hypothesis spaces of different complexities. Second, time-delay NNs (TDNNs) are assessed for the same problem by extending the inputs of the FFNN to include a delayed version of the inputs. A TDNN could leverage the time history of the inputs to learn the dynamics of the errors introduced by multipath signals. Several TDNNs with different amounts of access to the time history are trained and their multipath mitigation performance is assessed. Finally, experimental results are presented to test the proposed TDNN approach on real 5G signals.

This paper is organized as follows. Section II introduces the structure of 5G signals and models the synchronization signals being exploited for navigation. Section III offers a mathematical model for NNs and the concept of generalization. Section IV formally defines the learning problem as well as the target function for the goal of multipath mitigation. Section V, discusses the simulator that was used to generate the training and testing data needed for the learning machine, as well as the input pre-processing. Section VII demonstrates the ability of the proposed TDNN trained via the simulation data to show robustness against multipath via experimental results.

II. 5G Signal Structure

This section discusses the 5G signal structure and provides a model for 5G reference signals that can be exploited for opportunistic navigation.

A. 5G Frame Structure

5G systems implement orthogonal frequency-division multiplexing (OFDM) with an adaptive subcarrier spacing $\Delta f = 2^{\mu} \times 15$ kHz, where $\mu \in \{0, 1, 2, 3, 4\}$ is defined as the numerology. 5G is designed to support transmission at different frequency ranges (from 450 MHz to 52.6 GHz). In the time domain, 5G signals are transmitted in frames of duration $T_f = 10$ ms, which are divided into 10 subframes with a duration of 1 ms each. Subframes are then further divided into 2^{μ} time slots which contain 14 OFDM symbols each of duration $T_{\text{symb}} = \frac{1}{\Delta f}$. In the frequency domain, subframes are divided into a number of resource grids consisting of resource blocks with 12 subcarriers each. The number of resource grids in a frame is determined by higher level parameters. Moreover, a resource element defines the smallest unit of the resource grid spanning a duration of one OFDM symbol and a bandwidth of one subcarrier. The 5G frame structure is further illustrated in Fig. 1(a).

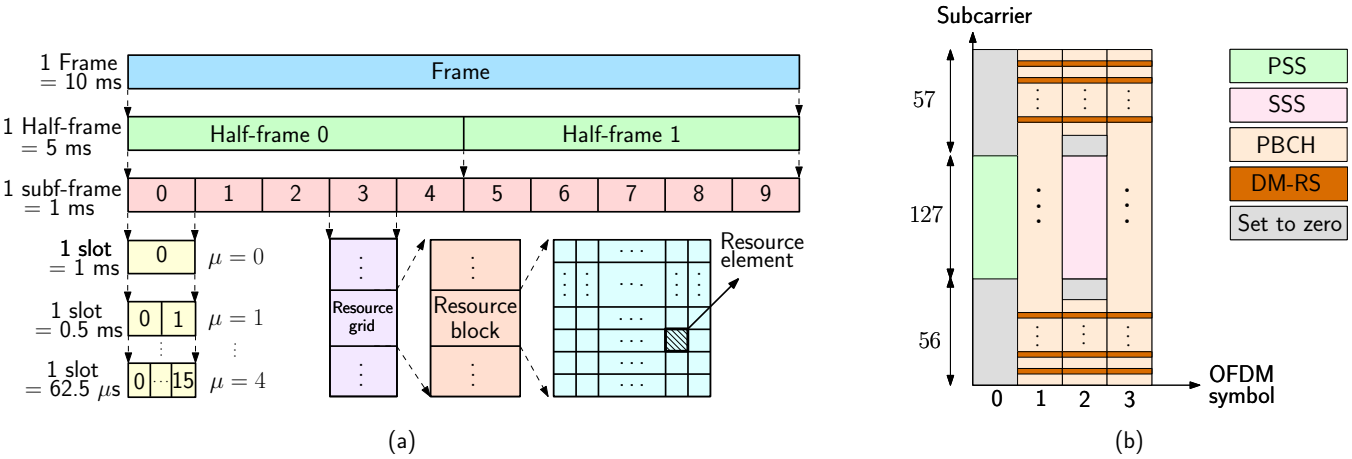

Fig. 1. (a) 5G frame structure. (b) SS/PBCH block structure.

5G systems utilize two maximal-length synchronization signals (SS) of length $N_{\text{SS}} = 127$, known as the primary synchronization signal (PSS) and secondary synchronization signal (SSS) to enable cell search and synchronization at the user equipment (UE). There is a total of three possible PSS sequences, each mapped to an integer representing the sector ID of the gNB denoted by $N_{\text{ID}}^{(2)}$. On the other hand, the SSS is one of 336 possible sequences, each mapped

TABLE I

SYMBOL NUMBERS CONTAINING SS/PBCH BLOCK FOR DIFFERENT NUMEROLOGIES AND FREQUENCY BANDS

subcarrier spacing (kHz)	**Carrier frequency**	**Symbol number**	**Slot number n**
Case A: 15	$f_c \leq 3$ GHz $3 < f_c \leq 6$ GHz	$\{2, 8\} + 14n$	$\{0, 1\}$ $\{0, \cdots, 3\}$
Case B: 30	$f_c \leq 3$ GHz $3 < f_c \leq 6$ GHz	$\{4, 8, 16, 20\} + 28n$	$\{0\}$ $\{0, 1\}$
Case C: 30	$f_c \leq 3$ GHz $3 < f_c \leq 6$ GHz	$\{2, 8\} + 14n$	$\{0, 1\}$ $\{0, \cdots, 3\}$
Case D: 120	$f_c > 6$ GHz	$\{4, 8, 16, 20\} + 28n$	$\{0, \cdots, 3,$ $5, \cdots, 8,$ $10, \cdots, 13,$ $15, \cdots, 18\}$
Case E: 240	$f_c > 6$ GHz	$\{8, 12, 16, 20, 32,$ $36, 40, 44\} + 56n$	$\{0, \cdots, 8\}$

to an integer representing the gNB's group identifier denoted by $N_{\text{ID}}^{(1)}$. This results in a total of 1008 cell identifiers denoted by $N_{\text{ID}}^{\text{cell}} = 3N_{\text{ID}}^{(1)} + N_{\text{ID}}^{(2)}$.

The SS are transmitted along with the physical broadcast channel (PBCH) signal and its associated demodulation reference signal (DM-RS) on a block known as the SS/PBCH block, which spans 20 resource blocks (i.e., 240 subcarriers) and four consecutive OFDM symbols. Fig. 1(b) shows an SS/PBCH block along with the position of each signal within that block. The resource allocation of the SS/PBCH block is determined as summarized in Table I [43], where index 0 corresponds to the first OFDM symbol of the first slot in a half-frame. In fact, the SS/PBCH is transmitted numerous times, where each set of these transmitted block is called an SS/PBCH burst. However, each SS/PBCH block in the burst is beamformed in a different direction with a periodicity that can be 5 ms, 10 ms, 20 ms, 40 ms, 80 ms or 160 ms.

B. Signal Model

For the purpose of opportunistic navigation with 5G, the signals of interest for a given $N_{\text{ID}}^{\text{cell}}$ could be modeled as

$$s_{\text{SS}}(t) = \begin{cases} \text{IFT}\{S_{\text{PSS}}(f)\}, & \text{for } t \in (0, T_{\text{symb}}) \\ \text{IFT}\{S_{\text{SSS}}(f)\}, & \text{for } t \in (2T_{\text{symb}}, 3T_{\text{symb}}) \\ 0, & \text{otherwise,} \end{cases}$$

where $S_{\text{PSS}}(f)$ and $S_{\text{SSS}}(f)$ are the frequency-domain representations of the PSS and SSS, respectively, corresponding to the transmitting gNB's cell ID $N_{\text{ID}}^{\text{cell}}$. Fig. 2 presents an SS in the time and frequency domains for $N_{\text{ID}}^{\text{cell}} = 420$. A navigation receiver correlates the replicated SS signal with the received signal forming the autocorrelation function (ACF), denoted by $R(\tau)$ according to

$$\begin{aligned} R(\tau) &\stackrel{\triangle}{=} y(t) \circledast s_{\text{SS}}(t) \\ &= \text{IFFT}\{Y(f) S_{\text{SS}}^*(f)\} \qquad (1) \\ &= \text{sinc}\,(B\tau) \qquad (2) \end{aligned}$$

where the symbols $\circledast$ and * denote the circular correlation and the complex conjugate operators, respectively, IFFT denotes the inverse fast Fourier transform, and $y(t)$ and $Y(f)$ are the time and frequency domain representations of the received signal with a bandwidth of $B = N_{\text{subcarriers}} \cdot \Delta f$, where $N_{\text{subcarriers}}$ is the number of subcarriers allocated for the synchronization signal. Since each symbol of the SS is mapped onto one subcarrier, then $N_{\text{subcarriers}} = N_{\text{SS}} = 127$. It is important to note that while the ACF takes a triangular shape for GPS signals, the ACF produced by the correlator of an opportunistic receiver exploiting 5G signals takes the shape of the sinc function. This follows from the OFDM modulation of the two maximal-length sequences (m-sequences) PSS and SSS. Equation (2) follows from (1) since $S_{\text{SS}}(f)$ is an m-sequence that takes the values $\{-1, +1\}$, and $S_{\text{SS}}(f) S_{\text{SS}}^*(f) = |S_{\text{SS}}(f)|^2 = \text{rect}(\frac{f}{B})$, where rect denotes the standard rectangular function with a bandwidth of B.

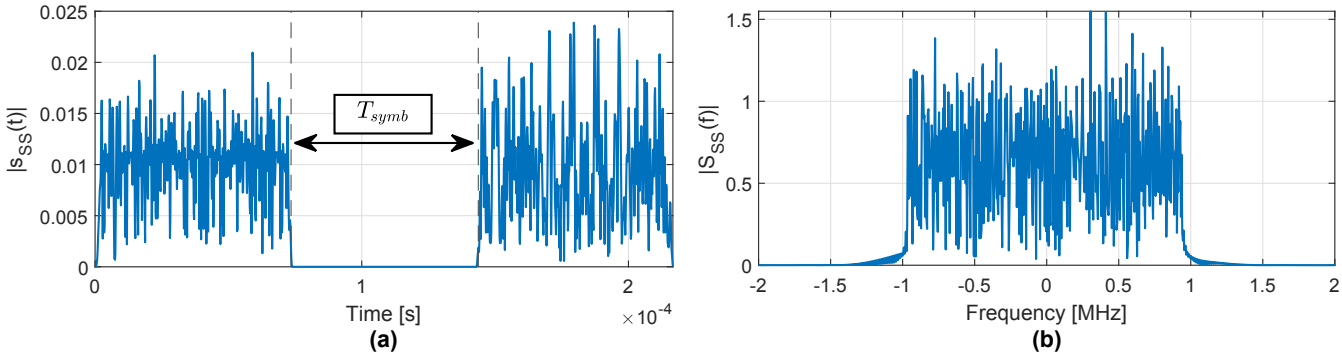

Fig. 2. Time (a) and Frequency (b) Domain SS for $N_{\mathrm{ID}}^{\mathrm{cell}} = 420$.

III. Overview of NNs

This section presents the mathematical model for NNs and introduces the concepts of in-sample and out-of-sample errors as well as generalization. Learning machines, or NNs, are in essence function approximators [44]. Consider some input $x \in \mathcal{X}$ that is mapped to $y \in \mathcal{Y}$ by an unknown target function $f : \mathcal{X} \mapsto \mathcal{Y}$. Given some examples $\{(x_1, y_1), (x_2, y_2), \ldots, (x_N, y_N)\}$, one can begin to learn more about the target function and formulate hypothesis as to what the true function could be. NNs are a family of parametric functions $\hat{y} = h(x, w) : \mathcal{X} \mapsto \mathcal{Y}$, where $h(x, w)$ belongs to some hypothesis space $\mathcal{H}$ and is parameterized by its weights and biases that are lumped into the term w. The goal of the learning machine is to find the optimal hypothesis space $\mathcal{H}^*$ (e.g. quadratic, cubic, etc.) and optimal weights w^* such that $h^*(x, w^*) \in \mathcal{H}^*$ is a good approximation of $f(x)$ which minimizes some cost function $C(y, h^*(x, w^*))$ that penalizes the difference between the true and approximated mappings (e.g. L_2-norm $||y - \hat{y}||^2$). The performance of a learning machine h is assessed based on its generalization capabilities, which is measured by the concept of risk, or out-of-sample error defined as [45]

$$\begin{aligned} E_{\mathrm{out}}(h) &= \mathbb{E}[C(y, h(x, w))] \\ &= \int_{\mathcal{X},\mathcal{Y}} C\left(f\left(x\right), h\left(x, w\right)\right) p(x, y) dx dy \end{aligned} \tag{3}$$

Note that the assumption of a probability distribution $p(x, y)$ in Equation (3) allows the modeling of uncertainty in the input data, such as in the presence of noise. However, E_{out} cannot be computed in learning problems since only a noisy subset of the input and output spaces $x_i \in \mathcal{X}$ and $y_i \in \mathcal{Y}$ is available. Thus, a learning algorithm will seek to mizimize the emperical risk, or in-sample error given by

$$E_{\mathrm{in}}(h) = \frac{1}{N} \sum_{i=1}^{N} C(y_i, h(x_i, w)) \tag{4}$$

Finding the optimal weights w^* corresponding to some hypothesis h is done via a learning algorithm that minimizes the in-sample risk according to

$$w^* \triangleq \arg\min_{w} E_{\mathrm{in}}(h(x, w))$$

The challenge in training NNs is that the true function being minimized is the in-sample error, while the function to be minimized is the out-of-sample error. To this end, K-fold cross-validation [46] was used to estimate the out-of-sample risk to ensure that $E_{\mathrm{out}}(h) \approx E_{\mathrm{in}}(h)$ and prevent the over-fitting of data by networks with a high complexity hypothesis space where the in-sample error becomes much smaller than the out-of-sample error (i.e. $E_{\mathrm{in}}(h) \ll E_{\mathrm{out}}(h)$).

IV. Problem Formulation

This section presents the problem formulation of ML-based multipath mitigation and discusses the input and output spaces of its target function. In model-based approaches, different types of DLLs are utilized to track the code phase of the received signal, where the choice of the discriminator function proved to be an important design parameter. Discriminator functions could be coherent, non-coherent, and even quasi-coherent, with varying number of taps. More sophisticated DLL architectures like the multipath estimating delay-locked loop (MEDLL) try to estimate the parameters of the nuisance NLOS components to mitigate the effects of multipath [47]. These discriminator functions and even the more sophisticated algorithms could be thought of as functions $f : \mathcal{X} \mapsto \mathcal{Y}$ that map the input space $\mathcal{X}$, being taps from the autocorrelation function, to the output space $\mathcal{Y}$, which is the code phase estimate of the LOS component $\hat{\tau}$.

At each time-step k, the discriminator function $f(x_k)$ of a conventional DLL uses N_x taps from the correlator output $x_k \in \mathcal{X}$ to produce an estimate of the code phase error $\tilde{\tau}_k \triangleq \tau_k - \hat{\tau}_k$, which is then used to update the code phase estimate at the next time-step $\hat{\tau}_{k+1}$. The presence of multipath corrupts the ACF taps x_k resulting in errors in the estimate of $\tilde{\tau}_k$. This process is illustrated in the following equations where the errors due to multipath are denoted by $e(x_k)$.

$$\begin{aligned} f(x_k) &\approx \tilde{\tau}_k \\ &= \tilde{\tau}_k + e(x_k) \\ \hat{\tau}_{k+1} &= \hat{\tau}_k + \tilde{\tau}_k + e(x_k) \end{aligned} \tag{5}$$

The aim of this paper is to mitigate the effects of the NLOS components on the tracking performance of the conventional DLL by training machine learning algorithms to approximate the function $e : \mathcal{X} \mapsto \mathcal{Y}$. In general, the impact of multipath depends on the amplitude, delay, phase, and phase rate of the NLOS components relative to the LOS component. Consider a NLOS component assosiated with a "virtual" transmitter location corrupting the ACF by interfering constructively with the LOS component. As the receiver moves within the environment the interference could change or even oscillate between constructive and destructive, causing the code phase estimate produced by the DLL to display some oscillation behavior. It is speculated that the ML algorithm would learn to leverage such dynamics in the input data x_k to estimate the errors introduced by multipath $\hat{y}_k = e(x_k)$. Fig. 3 depicts the block diagram of the proposed approach.

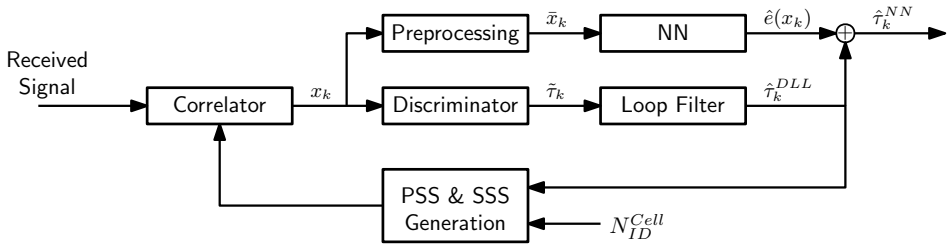

Fig. 3. Block diagram of the proposed NN approach.

V. Training and Data Generation

To simulate a realistic environment, map and terrain data were obtained through OpenStreetMap [48] and Global Multiresolution Terrain Elevation Data (GMTED) [49] for the area around Aldrich Park at the University of California Irvine. An opportunistic 5G receiver was then simulated to be moving around the park at a walking speed of 2 m/s. The simulated environment and trajectory are presented in Fig. 4(a). Moreover, the location of the simulated gNB reflects the real gNB position on top of the Engineering Tower. The power, delay, and phase of each path were then computed for the entire trajectory using the ray tracing methods available through MATLAB's RadioFrequency (RF) toolbox [50]. The channel impulse response (CIR) was generated in this manner to ensure that the simulator would capture the dynamics between the LOS and NLOS components. Fig. 4(b) shows the simulation environment in MATLAB with the rays traced from the gNB to four sample points within the trajectory along with the received power for each path. It is worth noting that the material used for buildings was concrete with a relative permittivity of 5.31 and a conductivity of 0.0548 Simens per meter. These values were chosen according to the international

telecommunication union (ITU) recommendations, which provide methods, equations, and values used to calculate real relative permittivity, conductivity, and complex relative permittivity for common materials [51].

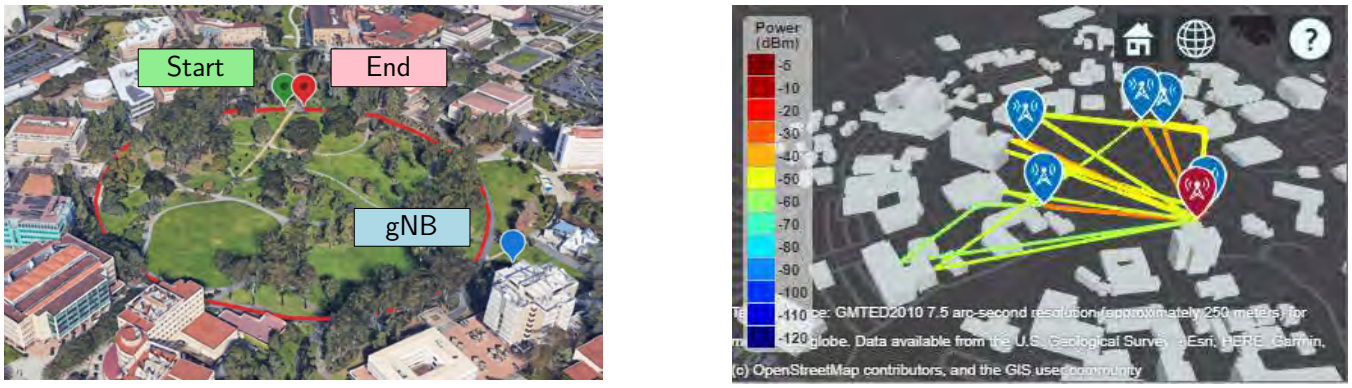

(a) (b)

Fig. 4. (a) Receiver Trajectory around Aldirch Park. (b) Rays traced from transmitter (red) to sample points of trajectory (blue).

Next, the obtained CIR is used to simulate the tracking results for an opportunistic 5G receiver traversing the aforementioned trajectory shown in Fig. (a) 4. The tracking loops of the receiver uses inputs from the output of the correlator $R(\tau)$, which is simulated from the CIR according to

$$R_k(\tau) = \sum_{i=1}^{N_k^{\text{paths}}} \alpha_k^i R(\tau - \tau_k^i)$$

where k is the time index with a duration equivalent to that of the SS (set to 20 ms based on an observation of a real 5G transmission scenario), $R_k(\tau)$ is the correlator output of the opportunistic receiver accounting for the different traversed paths at the k-th time-step, $R(.)$ is the ACF of the synchronization signal defined in (2), N_k^{paths} is the total number of paths traversed by the signal, $\alpha_k^i \in \mathcal{C}$ is a complex number representing the power and phase of the signal component corresponding to the i-th path, and τ_k^i represents its delay (time of flight).

Finally, the simulated data contained samples (x_k, y_k) with an equivalent duration of 438.51 seconds. The input $x_k \in \mathcal{C}^{2N_x+1}$ is formed of $2N_x + 1$ samples of the correlator output at the k-th time-step centered around the DLL's code phase estimate, such that $x_k = [x_k^{-N_x}, \ldots, x_k^{N_x}]^T$, where $x_k^d = R_k(\tau + \hat{\tau}_k^{\text{DLL}} + d/f_s)$ and f_s is the frequency at which the ACF was sampled. For the remainder of this paper, the sampling frequency is set to $f_s \triangleq 4B = 7.62$, and the number of ACF taps used as inputs is $2N_x + 1 = 11$. The sample target points $y_k \in \mathcal{R}$ are the errors incurred by the DLL estimate $e(x_k) = \tau_k^{\text{LOS}} - \hat{\tau}_k^{\text{DLL}}$, where the true LOS delays at the k-th time-step τ_k^{LOS} are obtained from the simulated CIR. It is important to note the dependence of the training data generation on the output of the DLL. A different choice of tracking algorithm would change the dynamics of the inputs extracted from the ACF. Moreover, the NN learns the errors that are specific to the type of algorithm being used. This implies that the final implementation will include both a DLL and an NN, as shown in Fig. 3, with the output of the former being fed back into the correlator, while the output of the latter would be fed to the navigation filter in order to produce more accurate position estimates. This implementation assures that the input space that the NN operates on contains the same dynamics as the input space presented to the NN during training.

Each input vector x_k is then normalized by the tap with maximum magnitude, and the complex values in the resulting vector and separated into their real and imaginary components forming $\bar{x}_k \in \mathcal{R}^{2(2N_x+1)}$, where the first $2N_x + 1$ inputs are the real components of x_k, and the last $2N_x + 1$ inputs are the imaginary components. Fig. 5 shows the input vectors before and after pre-processing denoted by x_k and $\bar{x}_k$, respectively. This type of pre-processing standardizes the data making it more invariant to changes that should not affect the output such as the carrier power. Note that this transformation preserves all the information about the relative amplitude, delay, and phase of the peaks corresponding to different paths.

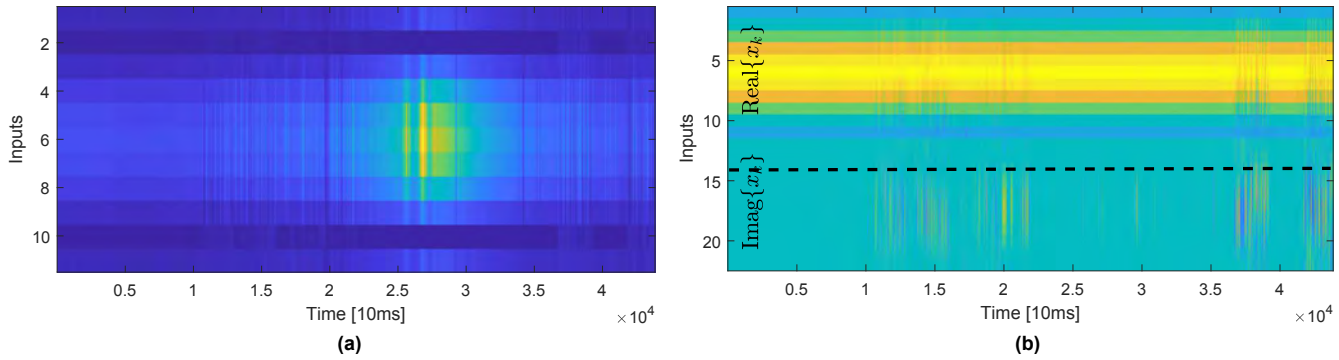

Fig. 5. (a) Raw Input Data x_k. (b) Processed Input Data $\bar{x}_k$.

VI. Simulation Results

This section assesses the multipath mitigation performance of different FFNN and TDNN architectures via simulations.

A. Feed-Forward Neural Networks (FFNN)

To select the optimal hypothesis $\mathcal{H}^*$ space for generalization with FFNNs, the out-of-sample error $E_{\text{out}}(h)$ is estimated while varying the complexity of the hypothesis space by varying the number of layers and number of neurons per layer. The out-of-sample error was estimated via 5-fold cross-validation, in which the data samples $\{(x_k, y_k); k = 1, \ldots, N\}$ are split into five disjoint subsets $\mathcal{X}_1, \ldots, \mathcal{X}_5$. An estimate of the total risk that would promote generalization is then produced according to

$$E_i(h) = \frac{5}{N} \sum_{\mathcal{X}_i} C(y, \hat{y})$$

$$\hat{E}_{\text{out}}(h) = \frac{1}{5} \sum_{i=1}^{5} E_i(h),$$

where each subset $\mathcal{X}_i$ is used to estimate the risk $E_i(h)$ for the model $h(x, w)$ trained on the remaining four subsets. The values obtained by iterating over each subset are then averaged to obtain an estimate of the out-of-sample risk $\hat{E}_{\text{out}}(h)$ associated with the network h that is closer to the true out-of-sample error $E_{\text{out}}(h)$.

Fig. 6 shows the 5-fold cross-validation risk estimates achieved by $h \in \mathcal{H}(N_{\text{layers}}, N_{\text{neurons}})$, a FFNN parameterized by the number of hidden layers $N_{\text{layers}} \in \{1, 2, 3, 4\}$ and number of neurons per layer $N_{\text{neurons}} \in \{10, 25, 50\}$. This is done to study the effect of varying the complexity of the hypothesis space, in an effort to find a model that promotes generalization. Fig. 6 shows that that for the problem at hand, a wide NN is preferred over a deep NN. The model with the best risk estimate ($N_{\text{layers}} = 3$, $N_{\text{neurons}} = 50$) is then re-trained on the first 350.81 seconds of the original data sample, leaving the remaining 87.7 seconds for testing. The performance of the aforementioned model is presented in Fig. 7. The FFNN achieved a ranging root mean-squared error (RMSE) reduction of 40% and 30% over the conventional DLL in the training and test sets, respectively.

After selecting the parameters $N_{\text{layers}} = 3$ and $N_{\text{neurons}} = 50$ a regularization term λ is added to the cost function such that $C(y, \hat{y}) = ||y - \hat{y}||^2 + \lambda||w||^2$. Regularization is a technique used to prevent over-fitting and promote generalization. 5-Fold cross-validation was performed again on the previously selected model to produce risk estimates for $\lambda = \{n \cdot 5 \times 10^{-7}; n = 0, \ldots 40\}$. The results, presented in Fig. 8, imply that the model trained with $\lambda = 4 \times 10^{-6}$ yields the best generalization behavior. Hence, an NN with $N_{\text{layers}} = 3$, $N_{\text{neurons}} = 50$, and $\lambda = 4 \times 10^{-6}$ is trained on the first 350.81 seconds of the simulated data samples and tested on the remaining 87.7 seconds. The tracking results for the aforementioned NN are presented in Fig. 9, where the FFNN achieved a ranging RMSE reduction of 38.58% and 29.08% over the conventional DLL was achieved in the training and test sets, respectively. Table II summarizes the DLL versus FFNN ranging RMSE performance.

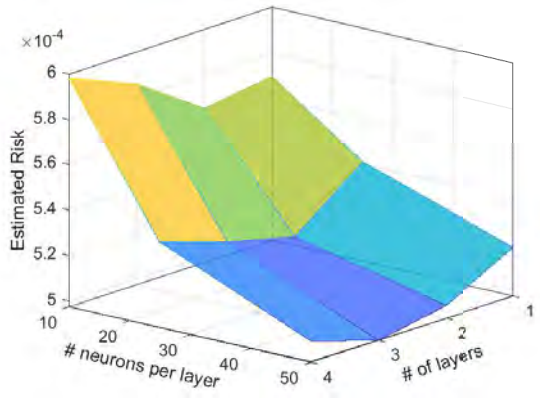

Fig. 6. 5-Fold cross validation for FFNN model order complexity selection.

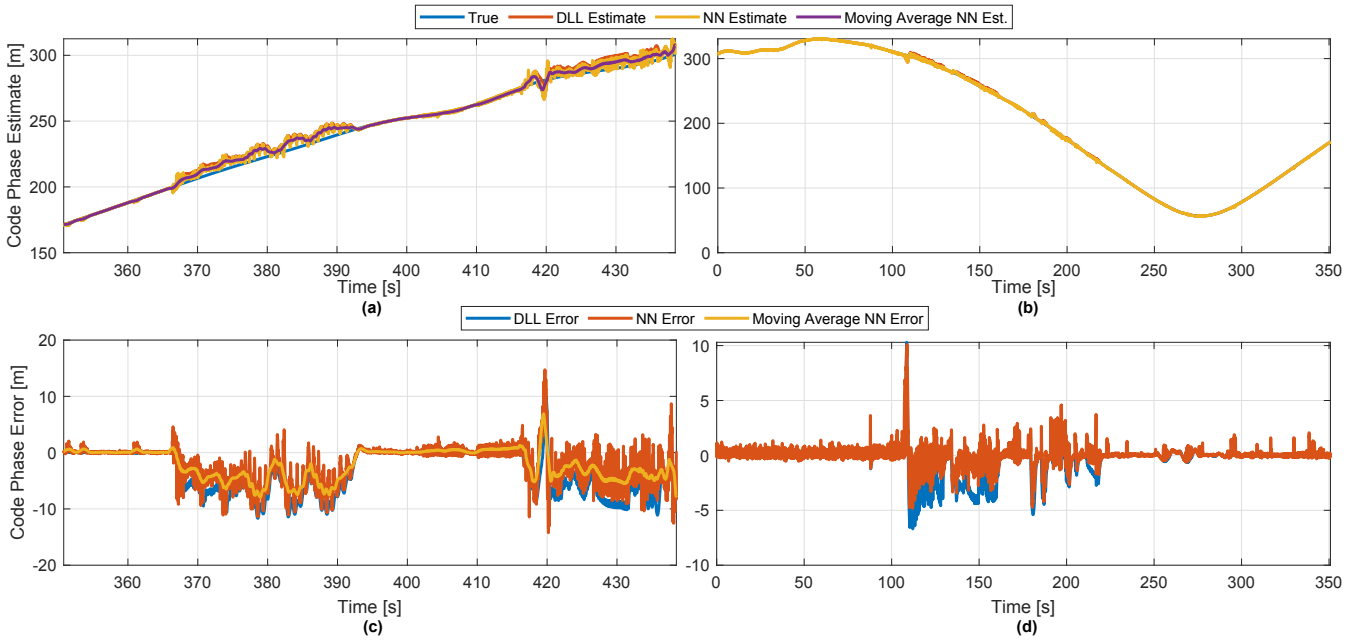

Fig. 7. Tracking results for FFNN selected via 5 fold cross-validation ($N_{\text{layers}} = 3$, $N_{\text{neurons}} = 50$): (a) Code phase estimates for test set. (b) Code phase estimates for training set. (c) Code phase errors for test set. (d) Code phase errors for training set.

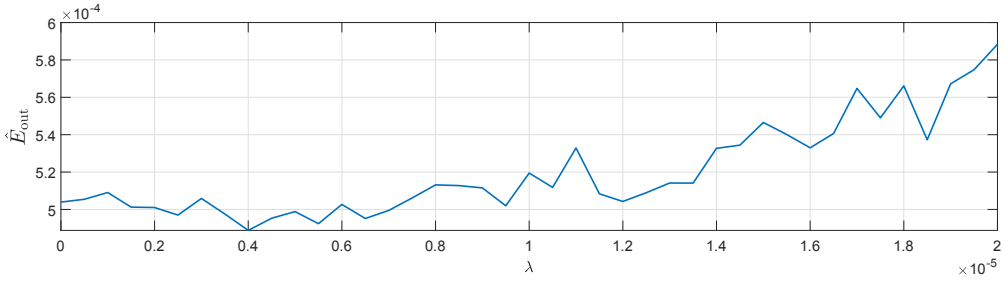

Fig. 8. 5-Fold Cross Validation for FFNN regularization parameter λ.

B. Time-Delay Neural Networks (TDNN)

A TDNN could be thought of as an extension of the FFNN architecture with the delays on the input layer. This means that the input layer for a TDNN could be viewed as the input layer for an FFNN expanded to include the time history of its inputs. This change in the input space is illustrated in Fig. 10, representing the input layers for an FFNN and TDNN respectively. To motivate the TDNN approach for the problem of code phase estimation in

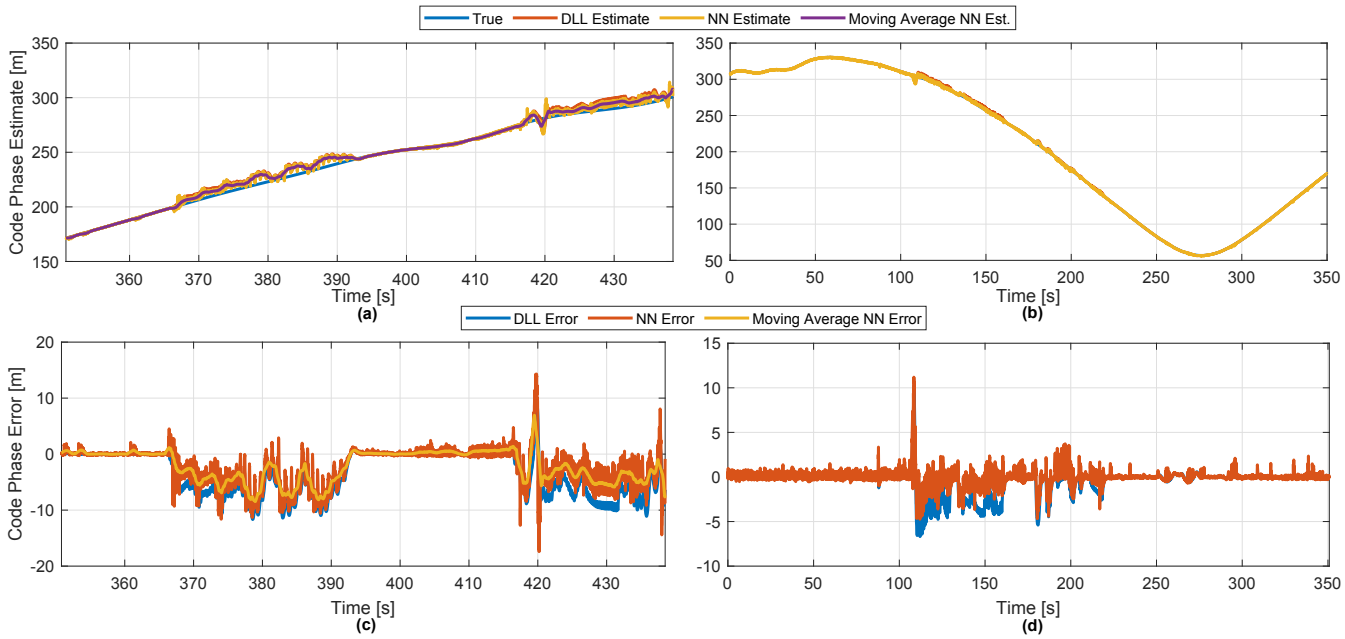

Fig. 9. Tracking results for FFNN selected via 5 fold cross-validation ($\lambda = 4 \times 10^{-6}$): (a) Code phase estimates for test set. (b) Code phase estimates for training set. (c) Code phase errors for test set. (d) Code phase errors for training set.

TABLE II
FFNN Ranging RMSE for Training and Testing Sets.

	Ranging RMSE [m]	
	Training Set	Validation Set
DLL	0.6556	3.7196
FFNN	0.3929	2.5872
Regularized FFNN	0.4027	2.6379

multipath scenarios, Fig. 10 presents the ACF in a region corrupted by multipath for a single time-step k as well as its variation over time. It is hard to extract meaningful information about the LOS delay from the single time-step view. However, with access to the time history of the ACF taps, it becomes easier to visualize the dynamics between the peak due to the LOS component and the peaks due to the NLOS components. Thus, the inputs to the TDNN are now given by

$$x_k^{\text{TDNN}} = [x_k, \ldots, x_{k-n_{\text{delay}}^i}, \ldots, x_{k-n_{\text{delay}}^{N_{\text{delays}}}}],$$

where N_{delays} is the total number of delay taps. A TDNN approach gives rise to the question of how varying the width of the time window of the inputs available $n_{\text{delay}}^{N_{\text{delays}}}$ affects the multipath mitigation performance of the NN. To this end, five TDNNs were examined with two hidden layers, where the first layer contains 20 neurons while the second layer contained 5 neurons. The number of delay taps was kept constant at $N_{\text{delays}} = 10$, while $n_{\text{delay}}^{N_{\text{delays}}}$ was varied such that $n_{\text{delay}}^{N_{\text{delays}}} \in \{10, 20, 30, 40, 50\}$. The total number of tap delays was kept constant as increasing it would lead to an increase in the effective number of inputs, adding to the complexity of the NN. The added complexity of TDNN relative to FFNN makes out-of-sample error estimation via cross-validation unfeasible due to the increase in computational requirements. Instead, the networks were trained using a Bayesian regularization learning algorithm, which could reduce or eliminate the need for lengthy cross-validation [52]. Training was stopped when the validation loss corresponding to the last 87.7 seconds of the generated data did not fall below its minimal value for 10 epochs; then, the TDNN with the lowest validation loss was selected. The results of this analysis are presented in Fig. 11, which suggests that increasing the width of the delay time window improves the multipath mitigation performance on both the training and validation sets. Moreover, the tracking performance of the TDNN with the lowest validation loss ($n_{\text{delay}}^{N_{\text{delays}}} = 50$) is presented in Fig. 12, showing a ranging RMSE reduction of 55.8% and 59.6% over the conventional DLL in the training and test sets, respectively. These results validate the intuition

that giving the NN access to the time history could help the learning algorithm exploit the dynamics caused by the mutlipath on the target function $e(x_k)$. Moreover, the trained network displayed a marginally higher performance improvement in that validation set than it did on the training set. This is considered a good sign for the generalization capabilities of the network as it shows that the discrepancy between the in-sample error and out-of-sample error is small. Table III summarizes the DLL and TDNN ranging RMSE performance.

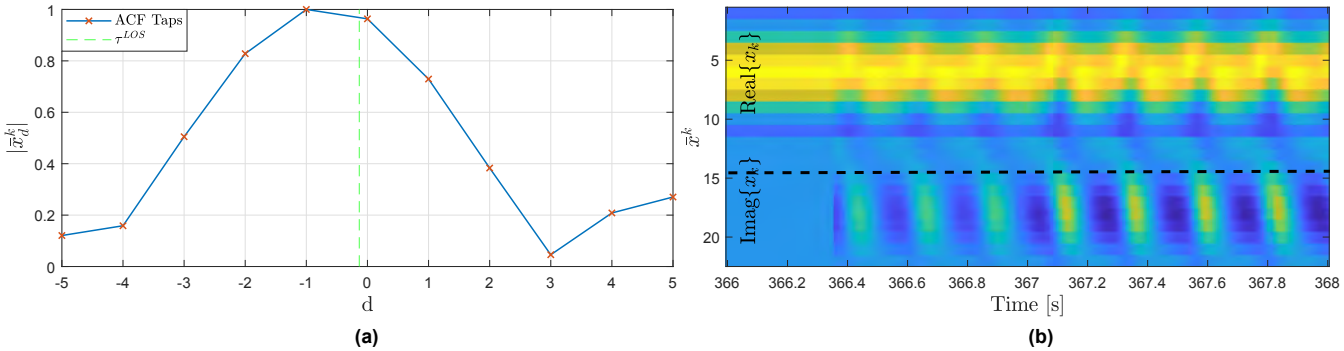

Fig. 10. (a) Multipath corrupted ACF taps for $t = 369$ s. (b) Multipath corrupted pre-processed inputs for $t \in [366, 368]$ s.

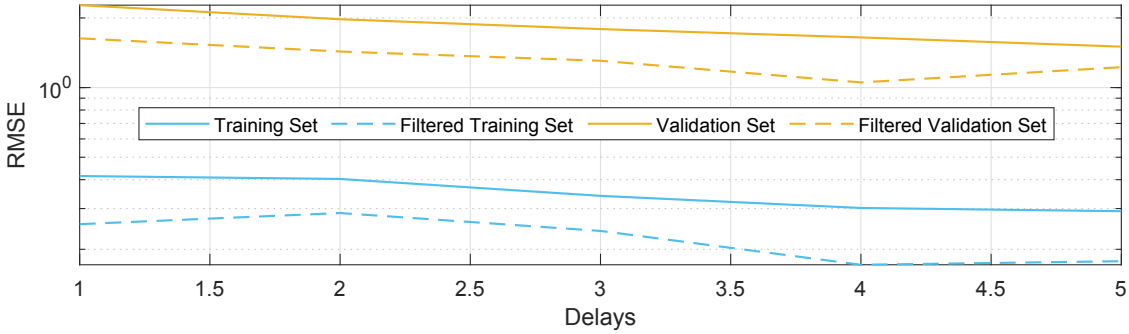

Fig. 11. Validation and test RMSE of TDNN vs delay window.

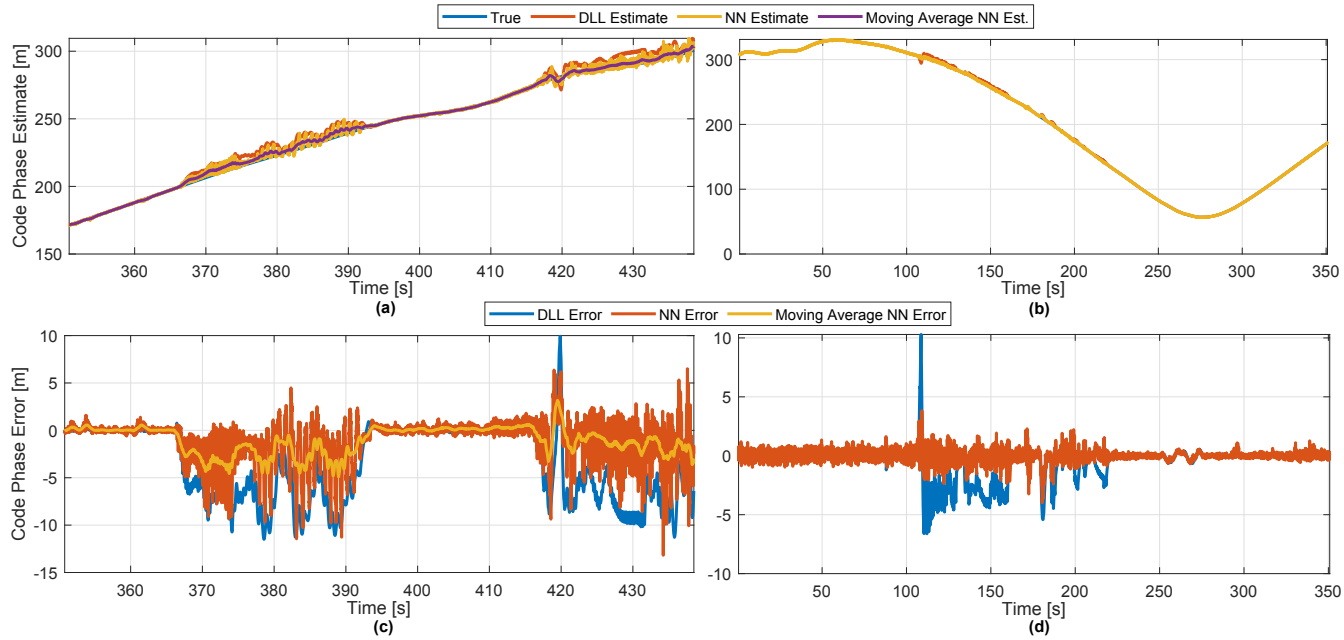

Fig. 12. Tracking results for TDNN ($n_{\text{delay}}^{N_{\text{delays}}} = 50$): (a) Code phase estimates for test set. (b) Code phase estimates for training set. (c) Code phase errors for test set. (d) Code phase errors for training set.

TABLE III
TDNN Ranging RMSE for Training and Testing Sets.

	Ranging RMSE [m]	
	Training Set	Validation Set
DLL	0.6556	3.7196
TDNN	0.2923	1.5033

VII. Experimental Validation

This section presents experimental results to verify the validity of the proposed ML approach for multipath mitigation.

A. Experimental Setup and Environmental Layout

The experiment was conducted in Aldrich Park, University of California, Irvine. Data was collected with a quad channel National Instrument (NI) universal software radio peripheral (USRP)-2955, where only one channel was used to sample 5G signals with a sampling frequency of 5 MSps. The receiver was equipped with a consumer-grade cellular omnidirectional Laird antenna and listened to cellular signals from a gNB implementing a subcarrier spacing $\Delta f = 15$ kHz, with $N_{\text{ID}}^{\text{cell}} = 420$, and a carrier frequency of 632.55 MHz. The USRP was driven by a GPS-disciplined oscillator (GPSDO) and the sampled signals were stored for post-processing. A MATLAB-based opportunistic software defined radio (SDR) designed to exploit 5G signals was then used to acquire and track the collected signals, as well as extract the NN input data x_k. The architecture of the aforementioned SDR was based on the work in [22].

B. Experimental Results

The ACF taps x_k extracted from the correlator of the SDR were processed by the NN that displayed the best generalization capabilities, i.e., TDNN with $n_{\text{delay}}^{N_{\text{delays}}} = 50$. The collected data was corrupted by multipath in the time interval $t \in [21, 26]$ seconds. The multipath corrupted region is highlighted in Fig. 13, which shows the experimental tracking results, and the delay estimates produced by both the DLL and TDNN. Fig. 14 shows the opportunistic receiver's correlator output $R_k(\tau)$ as well as the pre-processed input data $\bar{x}_k$ for $t = 22.82$ s and $t \in [21, 27]$ s respectively, corresponding to the multipath corrupted region. The effect of multipath on the tracking performance and inputs observed in Figs. 13 and 14 are similar to the effects present in the simulated training data in Figs. 10 and 12. This shows that the generated training data reflected the input data that would be processed in real scenarios.

Unlike GNSS satellites, cellular towers do not transmit any clock correction parameters and have less stable clocks than GNSS's atomic clocks, which introduce clock biases and drifts to the code phase estimates. In order to provide a fair evaluation of the DLL and NN estimates, the clock drift terms are estimated as the slope of the linear curve that best fits the code phase errors. It is also worth noting that the first 10 seconds of the data is skipped to allow for any transient periods to pass. The effect of the clock drift is apparent in Fig. 15, which shows the errors corresponding to both the DLL and NN estimates increasing linearly with time, along with their best linear fit. Fig. 15 also presents the true and estimated code phase values both before and after accounting for the clock drift, showing an overall RMSE reduction of 27% with a reduction of 38% in the highlighted multipath region.

The code phase estimates produced by the TDNN which compensates for the multipath errors $e(x_k)$ presented in Fig. 13 display a higher resilience to the bias introduced in the multipath corrupted region. While the DLL's estimate displays a sudden jump in the multipath corrupted region, the TDNN's estimate becomes more noisy while staying closer to the true code phase. This increase in variance within the multipath corrupted regions displayed in both simulation and experimental results could prove beneficial, since code phase measurements are weighted according to their variance in the navigation filter which ultimately produces the navigation solution. This noisy behavior could be thought of as an indicator of bad measurement which could improve the positioning solution by giving more weights to other measurements that aren't corrupted by multipath.

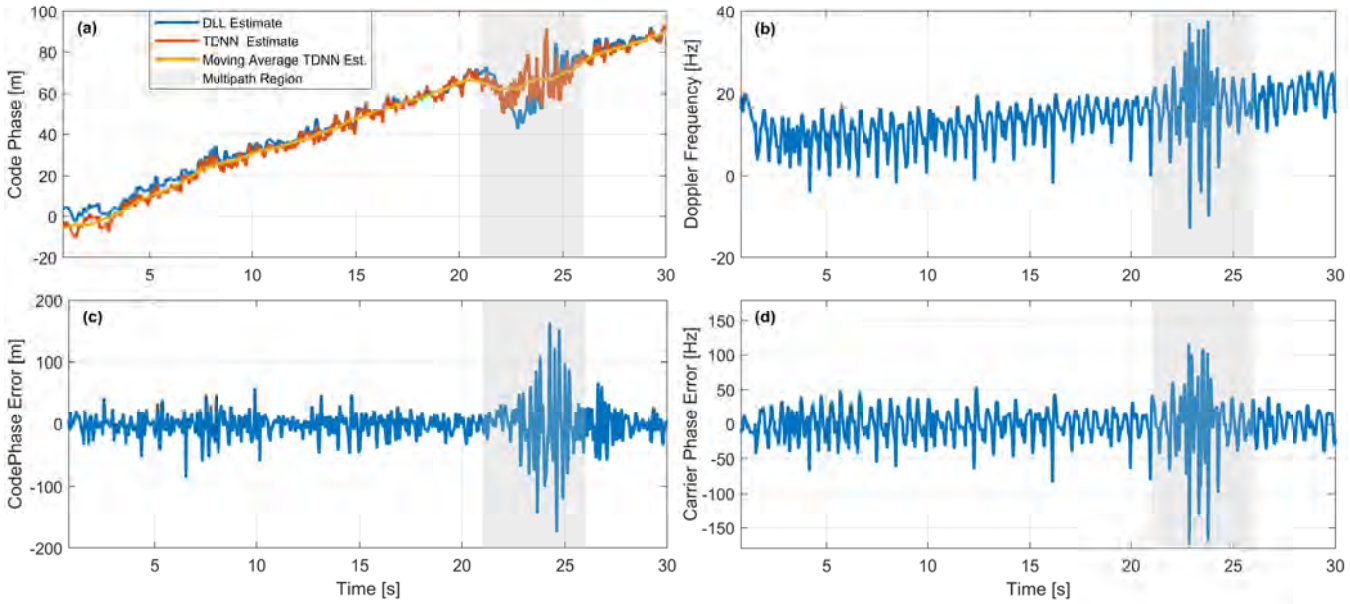

Fig. 13. Experimental tracking results: (a) Code phase estimate. (b) Doppler frequency estimate. (c) Code phase error estimate. (d) Carrier phase error estimate.

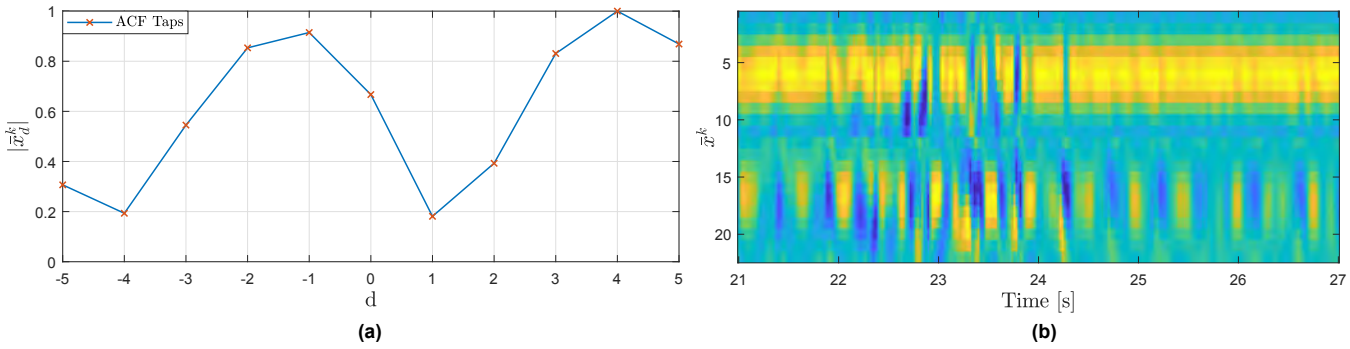

Fig. 14. (a) Multipath corrupted ACF taps for $t = 22.82$ s. (b) Multipath corrupted pre-processed inputs for $t \in [21, 27]$ s.

TABLE IV
RANGING RMSE FOR EXPERIMENTAL DATA.

	Ranging RMSE [m]	
	Overall	Multipath Region
DLL	6.7360	12.6551
TDNN	4.9074	7.8348

VIII. Conclusion

This paper assessed FFNNs and TDNNs for multipath mitigation in an opportunistic receiver that exploits 5G signals for navigation. A ray tracing based simulator was used to generate the training data, which was used to assess the performance and generalization capabilities of networks for model order selection. Simulation results showed that both TDNNs and FFNNs offered an RMSE reduction of 29.1% and 59.6%, respectively, over a conventional DLL over the test set. TDNNs were able to outperform FFNNs due to their additional access to the time history of the inputs, which present an opportunity to extract information from the dynamics of the LOS and NLOS signals. Finally, an experiment was conducted to test the generalization capability of the designed TDNN to real environments, where it was successfully able to mitigate the bias caused by multipath. The TDNN showed an overall RMSE reduction of 27.1% with a reduction of 38% in the most severe multipath region.

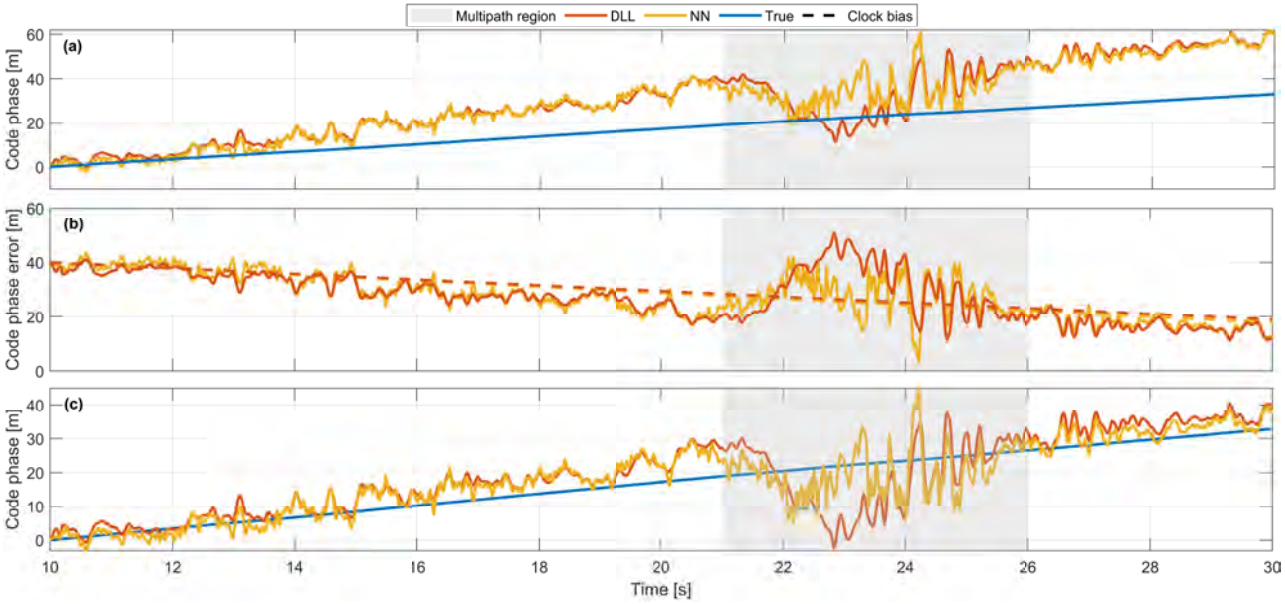

Fig. 15. (a) Code phase estimates. (b) True code phase errors. (c) Code phase estimates after accounting for clock drift.

Acknowledgments

This work was supported in part by the Office of Naval Research (ONR) under Grant N00014-19-1-2511 and Grant N00014-19-1-2613, in part by the U.S. Department of Transportation (USDOT) under Grant 69A3552047138 for the CARMEN University Transportation Center (UTC), and in part under the financial assistance award 70NANB17H192 from U.S. Department of Commerce, National Institute of Standards and Technology (NIST). Map data copyrighted OpenStreetMap contributors and available from https://www.openstreetmap.org.

References

[1] E. Costa, "Simulation of the effects of different urban environments on GPS performance using digital elevation models and building databases," *IEEE Transactions on Intelligent Transportation Systems*, vol. 12, no. 3, pp. 819–829, September 2011.

[2] D. Borio, F. Dovis, H. Kuusniemi, and L. Presti, "Impact and detection of GNSS jammers on consumer grade satellite navigation receivers," *Proceedings of the IEEE*, vol. 104, no. 6, pp. 1233–1245, February 2016.

[3] D. Miralles, A. Bornot, P. Rouquette, N. Levigne, D. Akos, Y.-H.Chen, S. Lo, and T. Walter, "An assessment of GPS spoofing detection via radio power and signal quality monitoring for aviation safety operations," *IEEE Intelligent Transportation Systems Magazine*, vol. 12, no. 3, pp. 136–146, June 2020.

[4] C. Hegarty, D. Bobyn, J. Grabowski, and A. Van Dierendonck, "An overview of the effects of out-of-band interference on GNSS receivers," *NAVIGATION, Journal of the Institute of Navigation*, vol. 67, no. 1, pp. 143–161, March 2020.

[5] "Position, navigation, and timing technologies in the 21st century," J. Morton, F. van Diggelen, J. Spilker, Jr., and B. Parkinson, Eds. Wiley-IEEE, 2021, vol. 2, Part D: Position, Navigation, and Timing Using Radio Signals-of-Opportunity, ch. 35–43, pp. 1115–1412.

[6] C. Yang, T. Nguyen, and E. Blasch, "Mobile positioning via fusion of mixed signals of opportunity," *IEEE Aerospace and Electronic Systems Magazine*, vol. 29, no. 4, pp. 34–46, April 2014.

[7] R. Faragher and R. Harle, "Towards an efficient, intelligent, opportunistic smartphone indoor positioning system," *NAVIGATION, Journal of the Institute of Navigation*, vol. 62, no. 1, pp. 55–72, 2015.

[8] L. Chen, O. Julien, P. Thevenon, D. Serant, A. Pena, and H. Kuusniemi, "TOA estimation for positioning with DVB-T signals in outdoor static tests," *IEEE Transactions on Broadcasting*, vol. 61, no. 4, pp. 625–638, 2015.

[9] M. Ulmschneider and C. Gentner, "Multipath assisted positioning for pedestrians using LTE signals," in *Proceedings of IEEE/ION Position, Location, and Navigation Symposium*, April 2016, pp. 386–392.

[10] J. del Peral-Rosado, R. Raulefs, J. López-Salcedo, and G. Seco-Granados, "Survey of cellular mobile radio localization methods: From 1G to 5G," *IEEE Communications Surveys Tutorials*, vol. 20, no. 2, pp. 1124–1148, 2018.

[11] A. Abdallah and Z. Kassas, "Multipath mitigation via synthetic aperture beamforming for indoor and deep urban navigation," *IEEE Transactions on Vehicular Technology*, vol. 70, no. 9, pp. 8838–8853, September 2021.

[12] M. Psiaki and B. Slosman, "Tracking of digital FM OFDM signals for the determination of navigation observables," in *Proceedings of ION GNSS Conference*, September 2019, pp. 2325–2348.

[13] T. Kang, H. Lee, and J. Seo, "TOA-based ranging method using CRS in LTE signals," *Journal of Advanced Navigation Technology*, vol. 23, no. 5, pp. 437–443, October 2019.

[14] Z. Kassas, J. Khalife, A. Abdallah, and C. Lee, "I am not afraid of the jammer: navigating with signals of opportunity in GPS-denied environments," in *Proceedings of ION GNSS Conference*, 2020, pp. 1566–1585.

[15] M. Orabi, J. Khalife, and Z. Kassas, "Opportunistic navigation with Doppler measurements from Iridium Next and Orbcomm LEO satellites," in *Proceedings of IEEE Aerospace Conference*, March 2021, pp. 1–9.

[16] X. Cui, T. Gulliver, J. Li, and H. Zhang, "Vehicle positioning using 5G millimeter-wave systems," *IEEE Access*, vol. 4, pp. 6964–6973, 2016.

[17] J. Peral-Rosado, J. Lopez-Salcedo, S. Kim, and G. Seco-Granados, "Feasibility study of 5G-based localization for assisted driving," in *Proceedings of International Conference on Localization and GNSS*, June 2016, pp. 1–6.

[18] Z. Abu-Shaban, X. Zhou, T. Abhayapala, G. Seco-Granados, and H. Wymeersch, "Performance of location and orientation estimation in 5G mmwave systems: Uplink vs downlink," in *Proceedings of IEEE Wireless Communications and Networking Conference*, April 2018, pp. 1–6.

[19] E. Menta, N. Malm, R. Jäntti, K. Ruttik, M. Costa, and K. Leppänen, "On the performance of AoA-based localization in 5G ultra-dense networks," *IEEE Access*, vol. 7, pp. 33 870–33 880, 2019.

[20] A. Tobie, A. Garcia-Pena, P. Thevenon, J. Vezinet, and M. Aubault, "Hybrid navigation filters performances between GPS, Galileo and 5G TOA measurements in multipath environment," in *Proceedings of ION GNSS Conference*, 2020, pp. 2107–2140.

[21] A. Abdallah, K. Shamaei, and Z. Kassas, "Assessing real 5G signals for opportunistic navigation," in *Proceedings of ION GNSS Conference*, 2020, pp. 2548–2559.

[22] K. Shamaei and Z. Kassas, "Receiver design and time of arrival estimation for opportunistic localization with 5G signals," *IEEE Transactions on Wireless Communications*, vol. 20, no. 7, pp. 4716–4731, 2021.

[23] A. Abdallah, J. Khalife, and Z. Kassas, "Experimental characterization of received 5G signals carrier-to-noise ratio in indoor and urban environments," in *Proceedings of IEEE Vehicular Technology Conference*, April 2021, pp. 1–5.

[24] A. Abdallah and Z. Kassas, "UAV navigation with 5G carrier phase measurements," in *Proceedings of ION GNSS Conference*, September 2021, accepted.

[25] A. Shahmansoori, G. Garcia, G. Destino, G. Seco-Granados, and H. Wymeersch, "Position and orientation estimation through millimeter-wave MIMO in 5G systems," *IEEE Transactions on Wireless Communications*, vol. 17, no. 3, March 2018.

[26] N. Garcia, H. Wymeersch, E. Larsson, A. Haimovich, and M. Coulon, "Direct localization for massive MIMO," *IEEE Transactions on Signal Processing*, vol. 65, no. 10, pp. 2475–2487, May 2017.

[27] K. Han, Y. Liu, Z. Deng, L. Yin, and L. Shi, "Direct positioning method of mixed far-field and near-field based on 5G massive MIMO system," *IEEE Access*, vol. 7, pp. 72 170–72 181, 2019.

[28] Z. Kassas, A. Abdallah, and M. Orabi, "Carpe signum: seize the signal – opportunistic navigation with 5G," *Inside GNSS Magazine*, vol. 16, no. 1, pp. 52–57, 2021.

[29] K. Shamaei and Z. Kassas, "LTE receiver design and multipath analysis for navigation in urban environments," *NAVIGATION, Journal of the Institute of Navigation*, vol. 65, no. 4, pp. 655–675, December 2018.

[30] P. Wang and Y. Morton, "Multipath estimating delay lock loop for LTE signal TOA estimation in indoor and urban environments," *IEEE Transactions on Wireless Communications*, vol. 19, no. 8, pp. 5518–5530, 2020.

[31] D. Aloi and M. Sharawi, "High fidelity antenna model validation results of a GNSS multipath limiting antenna," *IEEE Transactions on Aerospace and Electronic Systems*, vol. 47, no. 1, pp. 3–14, January 2011.

[32] A. van Dierendonck, P. Fenton, and T. Ford, "Theory and performance of narrow correlator spacing in a GPS receiver," *NAVIGATION, Journal of the Institute of Navigation*, vol. 39, no. 3, pp. 265–283, September 1992.

[33] L. Garin, F. van Diggelen, and J. Rousseau, "Strobe and edge correlator multipath mitigation for code," in *Proceedings of ION International Technical Meeting*, January 1996, pp. 657–664.

[34] G. McGraw and M. Braasch, "GNSS multipath mitigation using gated and high resolution correlator concepts," in *Proceedings of ION National Technical Meeting*, January 1999, pp. 333–342.

[35] Y. Li, X. Yang, P. Sun, H. Qi, and S. Lyu, "Celeb-df: A large-scale challenging dataset for deepfake forensics," in *Proceedings of the IEEE/CVF Conference on Computer Vision and Pattern Recognition*, 2020, pp. 3207–3216.

[36] A. Oord, S. Dieleman, H. Zen, K. Simonyan, O. Vinyals, A. Graves, N. Kalchbrenner, A. Senior, and K. Kavukcuoglu, "Wavenet: A generative model for raw audio," *arXiv preprint arXiv:1609.03499*, 2016.

[37] C. Berner, G. Brockman, B. Chan, V. Cheung, P. Dębiak, C. Dennison, D. Farhi, Q. Fischer, S. Hashme, C. Hesse *et al.*, "Dota 2 with large scale deep reinforcement learning," *arXiv preprint arXiv:1912.06680*, 2019.

[38] A. Abdallah and Z. Kassas, "Deep learning-aided spatial discrimination for multipath mitigation," in *Proceedings of IEEE/ION Position, Location, and Navigation Symposium*, April 2020, pp. 1324–1335.

[39] A. Abdallah, C. Jao, Z. Kassas, and A. Shkel, "A pedestrian indoor navigation system using deep-learning-aided cellular signals and ZUPT-aided foot-mounted IMUs," *IEEE Sensors Journal*, 2021, accepted.

[40] Y. Wang, Z. Lu, Y. Qu, L. Li, and N. Wang, "Improving prediction performance of GPS satellite clock bias based on wavelet neural network," *GPS solutions*, vol. 21, no. 2, pp. 523–534, April 2017.

[41] M. Orabi, J. Khalife, A. Abdallah, Z. Kassas, and S. Saab, "A machine learning approach for GPS code phase estimation in multipath environments," in *Proceedings of IEEE/ION Position, Location, and Navigation Symposium*, April 2020, pp. 1224–1229.

[42] N. Sokhandan, N. Ziedan, A. Broumandan, and G. Lachapelle, "Context-aware adaptive multipath compensation based on channel pattern recognition for gnss receivers," *NAVIGATION, Journal of the Institute of Navigation*, vol. 70, no. 5, pp. 944–962, September 2017.

[43] 3GPP, "Physical layer procedures for control," 3rd Generation Partnership Project (3GPP), TS 38.213, July 2018. [Online]. Available: https://www.etsi.org/deliver/etsi_ts/138200_138299/138213/15.02.00_60/ts_138213v150200p.pdf

[44] K. Hornik, M. Stinchcombe, and H. White, "Multilayer feedforward networks are universal approximators," *Neural networks*, vol. 2, no. 5, pp. 359–366, 1989.

[45] Y. Abu-Mostafa, I. Magdon-Ismail, and H. Lin, *Learning from data*. AMLBook New York, NY, USA:, 2012, vol. 4.

[46] T. Fushiki, "Estimation of prediction error by using K-fold cross-validation," *Statistics and Computing*, vol. 21, no. 2, pp. 137–146, 2011.

[47] M. Sanchez-Fernandez, M. Aguilera-Forero, and A. Garcia-Armada, "Performance analysis and parameter optimization of DLL and MEDLL in fading multipath environments for next generation navigation receivers," *IEEE Transactions on Consumer Electronics*, vol. 53, no. 4, pp. 1302–1308, November 2007.

[48] OpenStreetMap contributors, "Planet dump retrieved from https://planet.osm.org," https://www.openstreetmap.org, 2017.

[49] J. Danielson and D. Gesch, *Global multi-resolution terrain elevation data 2010 (GMTED2010)*. US Department of the Interior, US Geological Survey, 2011.

[50] "Matlab RF toolbox," https://www.mathworks.com/help/rf/index.html, 2021.

[51] P. Series, "Effects of building materials and structures on radiowave propagation above about 100 MHz," *Recommendation ITU-R*, pp. 2040–1, 2015.

[52] F. Burden and D. Winkler, "Bayesian regularization of neural networks," *Artificial neural networks*, pp. 23–42, 2008.

Blind Doppler Tracking and Positioning with NOAA LEO Satellite Signals

Sharbel Kozhaya, Haitham Kanj, and Zaher M. Kassas
The Ohio State University

BIOGRAPHY

Sharbel Kozhaya is a Ph.D student in the Department of Electrical and Computer Engineering at The Ohio State University and a member of the Autonomous Systems Perception, Intelligence, and Navigation (ASPIN) Laboratory. He received a B.E. in Electrical Engineering from the Lebanese American University. His current research interests include opportunistic navigation, low Earth orbit (LEO) satellites, cognitive software-defined radio, and 5G. He is the recipient of the 2023 IEEE/ION Position, Location, and Navigation Symposium (PLANS) best student paper award.

Haitham Kanj is a Ph.D student in the Department of Electrical and Computer Engineering at The Ohio State University and a member of the Autonomous Systems Perception, Intelligence, and Navigation (ASPIN) Laboratory. He received a B.E. in Electrical Engineering from the Lebanese American University. His current research interests include opportunistic navigation, low Earth orbit (LEO) satellites, and cognitive software-defined radio. He is the recipient of the 2023 IEEE/ION Position, Location, and Navigation Symposium (PLANS) best student paper award.

Zaher (Zak) M. Kassas is a professor at The Ohio State University and TRC Endowed Chair in Intelligent Transportation Systems. He is the Director of the Autonomous Systems Perception, Intelligence, and Navigation (ASPIN) Laboratory. He is also director of the U.S. Department of Transportation Center: CARMEN (Center for Automated Vehicle Research with Multimodal AssurEd Navigation), focusing on navigation resiliency and security of highly automated transportation systems. He received a B.E. in Electrical Engineering from the Lebanese American University, an M.S. in Electrical and Computer Engineering from The Ohio State University, and an M.S.E. in Aerospace Engineering and a Ph.D. in Electrical and Computer Engineering from The University of Texas at Austin. He is a recipient of the National Science Foundation (NSF) CAREER award, Office of Naval Research (ONR) Young Investigator Program (YIP) award, Air Force Office of Scientific Research (AFOSR) YIP award, IEEE Walter Fried Award, Institute of Navigation (ION) Samuel Burka Award, and ION Col. Thomas Thurlow Award. He is an Associate Editor of the IEEE Transactions on Aerospace and Electronic Systems and the IEEE Transactions on Intelligent Transportation Systems. He is a Fellow of the ION and a Distinguished Lecturer of the IEEE Aerospace and Electronic Systems Society. His research interests include cyber-physical systems, navigation systems, and intelligent transportation systems.

ABSTRACT

A spectral approach for blind acquisition and Doppler tracking of low Earth orbit (LEO) satellite signals is applied to National Oceanic and Atmospheric Administration (NOAA) satellites. The approach accounts for the high LEO satellites' dynamic channel, by deriving an appropriate model for the received signal frequency spectrum. A frequency-domain-based Doppler discriminator is utilized along with a Kalman filter-based Doppler tracking algorithm. Experimental results are presented showing successful acquisition and Doppler tracking of NOAA LEO satellite signals. Next, the approach is demonstrated in multi-constellation LEO acquisition and tracking, showing Hz-level Doppler tracking of 4 Starlink, 2 OneWeb, 1 Iridium NEXT, 1 Orbcomm, and 1 NOAA LEO satellites. Carrier phase observables were constructed from the tracked Doppler and fused through a nonlinear least-squares estimator to localize a stationary receiver. Starting with an initial estimate 3,600 km away from the receiver's true position, the proposed approach is shown to achieve a two-dimensional (2D) error of 5.1 m.

I. INTRODUCTION

Navigation from low Earth orbit (LEO) satellites promises to revolutionize satellite-based navigation (Kassas et al., 2019; Jardak and Jault, 2022; Prol et al., 2022; Janssen et al., 2023; Menzione and Paonni, 2023; Prol et al., 2023). As such, it is not surprising to witness the tremendous interest from governments and private technology giants, launching their own LEO constellations, some of which dubbed "megaconstellations" as they will comprise thousands of LEO satellites (Curzi et al., 2020; Liu et al., 2021).

Using LEO satellite signals for navigation offers several desirable attributes (Reid et al., 2021; Kassas, 2021): (i) higher received signal power compared to GNSS satellites that reside in medium Earth orbit (MEO), (ii) high availability and favorable geometry, and (iii) spectral diversity in the radio frequency spectrum. However, exploiting broadband LEO satellite signals of opportunity

Copyright © 2023 by Sharbel E. Kozhaya and Z. M. Kassas

Preprint of the 2023 ION GNSS+ Conference
Denver, Colorado, September 11–15, 2023

for navigation purposes comes with challenges, as they are owned by private operators that typically do not disclose crucial information about the satellites': (i) ephemerides, (ii) clock synchronization and stability, and (iii) signal specifications.

Several studies have been published over the past few years addressing the aforementioned challenges, from addressing satellite orbit, clock, and propagation errors (Mortlock and Kassas, 2021; Khairallah and Kassas, 2021; Morton et al., 2022; Cassel et al., 2022; Wang et al., 2023; Zhao et al., 2023; Wu et al., 2023; Jiang et al., 2023; Ye et al., 2023; Khalife and Kassas, 2023; Saroufim et al., 2023; Kassas et al., 2023a); to receiver and signal design (Tan et al., 2019; Wei et al., 2020; Bilardi, 2021; Orabi et al., 2021; Kassas et al., 2021; Neinavaie et al., 2022b; Egea-Roca et al., 2022; Huang et al., 2022; Pinell et al., 2023; Yang et al., 2023; Humphreys et al., 2023; Yang and Soloviev, 2023); to analyzing the estimation performance (Farhangian et al., 2021; Psiaki, 2021; Hartnett, 2022; Singh et al., 2022; Jiang et al., 2022; More et al., 2022; Shi et al., 2023; Guo et al., 2023; Kanamori et al., 2023; Sabbagh and Kassas, 2023; Farhangian and Landry, 2023; Ries et al., 2023).

This paper focuses on addressing the challenge of extracting navigation observables from unknown LEO satellite signals. Whenever the LEO downlink signal structure is sufficiently known, designing a receiver that could acquire and track such signals becomes a "classic" receiver design problem. Examples of LEO constellations with sufficient knowledge about their downlink signal include Orbcomm and Iridium NEXT. Nevertheless, new LEO megaconstellations, such as Starlink and OneWeb, do not disclose public information about their signals. This challenge can be addressed with blind signal processing techniques. Previous research was capable of estimating downlink sequences in direct sequence spread spectrum communication systems (Tsatsanis and Giannakis, 1997; Burel and Bouder, 2000; Choi and Moon, 2020; Li et al., 2023), for GPS/GNSS signals under non-cooperative conditions (Merwe et al., 2020; Rui et al., 2022), and for orthogonal frequency-division multiplexing (OFDM) signals (Bolcskei, 2001; Tanda, 2004; Liu et al., 2010). However, LEO downlink channels pose a challenge making the aforementioned approaches not straightforwardly applicable, namely the high dynamics of the channel between the LEO satellite and the ground-based receiver. To address this challenge in the context of LEO, (Neinavaie et al., 2021; Kozhaya and Kassas, 2022) developed blind Doppler tracking approaches that were used to navigate an unmanned aerial vehicle (UAV) with Obrcomm LEO satellites; while (Khalife et al., 2022) was the first to successfully apply blind signal processing techniques on Starlink LEO signals, yielding carrier phase observables, from which a stationary receiver was localized with a two-dimensional (2D) error of 25.9 m with signals from six Starlink LEO satellites. Another blind approach, based on matched subspace detection, was developed in (Neinavaie et al., 2022a; Neinavaie and Kassas, 2023), yielding Doppler observables, from which a stationary receiver was localized with a 2D error of 10 m (with pure tones) and 6.5 m (with OFDM signals in addition to pure tones) from the same six Starlink LEO satellites. A blind spectral-based approach was developed in (Kozhaya and Kassas, 2023), yielding Doppler observables, from which a stationary receiver was localized with a 2D error of 4.3 m with the same six Starlink LEO satellites. In (Kozhaya et al., 2023; Kassas et al., 2023b), it was demonstrated that this approach is rather general, referred to as LEO-agnostic, and is capable of acquiring and tracking LEO signals regardless of their modulation and multiple access schemes. In addition to Starlink LEO, the approach was successfully applied to OneWeb, Orbcomm, and Iridium NEXT LEO satellites, yielding Hz-level-accurate Doppler tracking, from which a stationary receiver was localized with a 2D error of 5.1 m with 2 OneWeb, 4 Starlink, 1 Iridium NEXT, and 1 Orbcomm LEO satellites. This paper shows that this LEO-agnostic approach is capable of exploiting the signals of a fifth LEO constellation: National Oceanic and Atmospheric Administration (NOAA) satellites.

This paper offers the following contributions: (i) derive an analytical approximation of the received signal frequency spectrum for highly dynamic channels and (ii) develop a blind Doppler spectral estimator via frequency-domain cross-correlation and a Kalman filter (KF)-based tracking loop. The proposed approach relies on the presence of a repetitive sequence in the LEO satellite's downlink, to which the blind spectral Doppler tracker locks and cross-correlation is used to track the Doppler shift. Experimental results are presented showing successful acquisition and Doppler tracking of NOAA LEO satellite signals with the proposed approach. In addition, experimental results are presented showing Hz-level Doppler tracking of 4 Starlink, 2 OneWeb, 1 Iridium NEXT, 1 Orbcomm, and 1 NOAA LEO satellites. Carrier phase observables are constructed from the tracked Doppler and fused through a nonlinear least-squares (NLS) estimator to localize a stationary receiver. Starting with an initial estimate 3,600 km away from the receiver's true position, the proposed approach is shown to achieve a two-dimensional (2D) error of 5.1 m.

This paper is organized as follows. Section II derives the signal model. Section III discusses the blind Doppler discriminator and tracking approach. Section IV presents NOAA LEO tracking results. Section V presents multi-constellation LEO tracking and positioning with Starlink, OneWeb, Iridium NEXT, Orbcomm, and NOAA LEO satellites. Section VI gives concluding remarks.

II. SIGNAL MODEL

This section presents a model of the received signal, which takes into account the high dynamics channel between the LEO satellite and ground-based receiver. Then, it derives an analytical expression of the signal's frequency spectrum.

1. Received Baseband Signal Model

Let $x(t)$ be the unknown LEO satellite signal, expressed at baseband. The proposed framework does not assume any particular modulation or multiplexing scheme. The only assumption is that $x(t)$ can be written as $x(t) = s(t) + n_d(t)$, where $s(t)$ is a deterministic repetitive signal and $n_d(t)$ is a random signal driven by the user data. Examples of repetitive sequences are the pseudorandom noise (PRN) used in GPS (Flores (2022)), Globalstar LEO satellites (Hendrickson (1997)), and CDMA2000 (3GPP2 (2011)) and the primary and secondary synchronization sequences (PSS and SSS) used in 4G long-term evolution (LTE) (3GPP (2010)) and 5G (3GPP (2018)). The proposed framework assumes the following properties of $s(t)$:

1. It is periodic with period T_0.
2. It is uncorrelated with the data $n_d(t)$.
3. It is zero-mean, has a stationary power spectral density (PSD) with $\left|\mathcal{F}\left\{s(t)w_{T_0}(t)\right\}\right|^2 = S_s(f)$, where $w_{T_0}(t)$ is a windowing function that is unity within the interval $[0, T_0]$ and zero elsewhere.

Consider $x(t)$ being transmitted at a carrier frequency f_c. Let $\tau_d(t)$ denote the apparent delay between the transmitted signal $x_c(t) \triangleq x(t)\exp(j2\pi f_c t)$ and the received signal at the receiver's antenna. The apparent delay $\tau_d(t)$ is composed of (i) the time-of-flight along the line-of-sight (LOS) between the transmitter and receiver (i.e., $d_{LOS}(t)/c$, where $d_{LOS}(t)$ is the LOS distance between the LEO satellite's transmitter and the receiver and c is the speed of light); (ii) combined effect of the transmitter's and receiver's clock biases, denoted $\delta t_{clk}(t)$; (iii) ionospheric and tropospheric delays $\delta t_{iono}(t)$ and $\delta t_{tropo}(t)$, respectively; and (iv) other unmodeled errors. After propagating in an additive white Gaussian channel, the resulting received signal before baseband mixing can be expressed as

$$\bar{r}(t) = x_c\left(t - \tau_d(t)\right) + \bar{n}(t) = x(t - \tau_d(t))\exp\left(j2\pi f_c\left[t - \tau_d\left(t\right)\right]\right) + \bar{n}(t),$$

where $\bar{n}(t)$ is a complex white Gaussian noise with PSD $N_0/2$.

Let $r(t) \triangleq \bar{r}(t)\exp\left(-j2\pi f_c t\right)$ denote the received signal after baseband mixing and filtering. Then, $r(t)$ can be expressed as $r(t) = x(t - \tau_d(t))\exp\left(j\theta(t)\right) + n(t)$, where $n(t)$ is the low-pass filter output of $\bar{n}(t)$, and $\theta(t) = -2\pi f_c \tau_d(t)$ is the carrier phase of the received signal. Using a Taylor series expansion, at time instant $t_k = t_0 + kT_0$, where k is the sub-accumulation index and t_0 is some initial time, the carrier phase of the signal can be expressed as

$$\theta(t) = \theta(t_k) + \dot{\theta}(t_k)t + \frac{1}{2}\ddot{\theta}(t_k)t^2 + H.O.T. \tag{1}$$

Denote $\theta_k(t)$ as $\theta(t)$ in (1), after dropping the higher-order terms ($H.O.T.$). By definition, $f_D(t) \triangleq \frac{\dot{\theta}(t)}{2\pi}$ is the apparent Doppler shift and $\dot{f}_D(t)$ is the apparent Doppler rate.

It is important to note that the channel between the LEO satellite and the ground-based receiver is highly dynamic, thus, high Doppler shift and rate will be observed by the receiver. On the other hand, at the k-th sub-accumulation, $\tau_d(t)$ is approximated by its zero-order term $d_k = \tau_d(t_k)$, while the higher order terms are dropped to simplify the following signal analysis. Due to the first property, one can arbitrarily choose $\tau_d(t)$ to denote the code start time. It is important to note that the higher order terms in $\tau_d(t)$ stretch or contract the code in the time-domain, but this paper ignores this effect, which seems to be of little impact on Starlink LEO satellite codes.

Finally, the expression of the received signal at the k-th sub-accumulation can be written as $r_k^-(t) = r(t)w_{T_0}(t - t_k) = s_k(t)\exp\left(j\theta_k(t)\right) + n_k^-(t)$, where $s_k(t) = s(t - d_k)w_{T_0}(t)$ and $n_k^-(t) = n(t - d_k)w_{T_0}(t)$. The received signal $r_k(t)$ after carrier wipe-off using the carrier phase estimate, denoted $\hat{\theta}_k(t)$, generated by the tracking loop discussed in Section III.2, can be expressed as

$$r_k(t) = r_k^-(t)\exp(-j\hat{\theta}_k(t)) = s_k(t)\exp(j\tilde{\theta}_k(t)) + n_k(t), \tag{2}$$

where $\tilde{\theta}_k(t) = \theta_k(t) - \hat{\theta}_k(t)$ is the residual carrier phase.

2. Frequency Spectrum of the Received Signal

The received signal's frequency spectrum at the k-th sub-accumulation is $S_{r_k}(f) = |\mathcal{F}\{r_k(t)\}|^2$. Using the third property of $s(t)$, the Wigner distribution function (WDF) of $s_k(t)$ for $t \in [0, T_0]$ can be written as

$$W_s(t,f) \triangleq \int_{-\infty}^{\infty} s_k\left(t+\frac{\tau}{2}\right) s_k^*\left(t-\frac{\tau}{2}\right) \exp(-2\pi f\tau)\, d\tau = \frac{S_s(f)}{T_0}.$$

It can be shown that the WDF of the residual carrier phase at the k-th sub-accumulation $C_k(t) = \exp(j\tilde{\theta}_k(t))$, for $t \in [0, T_0]$, is $W_{C_k}(t,f) = \delta\left(f - \frac{\dot{\tilde{\theta}}_k}{2\pi} - \frac{\ddot{\tilde{\theta}}_k}{2\pi}t\right)$, where $\delta(\cdot)$ denotes the Dirac delta function. Using the second property of $s(t)$, the WDF of $r_k(t)$ in (2), for $t \in [0, T_0]$, can be written as

$$W_{r_k}(t,f) = \frac{S_s(f)}{T_0} \circledast \delta\left(f - \frac{\dot{\tilde{\theta}}_k}{2\pi} - \frac{\ddot{\tilde{\theta}}_k}{2\pi}t\right) + W_{n_k}(t,f),$$

where $(f \circledast g)(t) = \int_{-\infty}^{\infty} f(\tau)g(t-\tau)d\tau$ is the convolution, $W_{n_k}(t,f)$ is the WDF of the noise and data at the k-th sub-accumulation. Using the projection property of WDF, the following follows

$$\begin{aligned} S_{r_k}(f) &\triangleq \int_0^{T_0} W_{r_k}(t,f)\, dt = \frac{S_s(f)}{T_0} \circledast \int_0^{T_0} \delta\left(f - \frac{\dot{\tilde{\theta}}_k}{2\pi} - \frac{\ddot{\tilde{\theta}}_k}{2\pi}t\right) dt + S_{n_k}(f) \\ &= S_s(f) \circledast \frac{2\pi}{\left|\ddot{\tilde{\theta}}_k\right| T_0} \int_0^{T_0} \delta\left(t - \frac{2\pi f - \dot{\tilde{\theta}}_k}{\ddot{\tilde{\theta}}_k}\right) dt + S_{n_k}(f) = S_s(f) \circledast \Pi\left(f; \dot{\tilde{\theta}}_k, \ddot{\tilde{\theta}}_k\right) + S_{n_k}(f), \end{aligned} \tag{3}$$

where $S_{n_k}(f) = \int_0^{T_0} W_{n_k}(t,f)\, dt$ and

$$\Pi\left(f; \dot{\theta}, \ddot{\theta}\right) = \frac{2\pi}{\left|\ddot{\theta}\right| T_0} \begin{cases} 1, & \left| f - \dfrac{\dot{\theta} + \dfrac{|\ddot{\theta}|}{2} T_0}{2\pi} \right| < \dfrac{|\ddot{\theta}|}{4\pi} T_0, \\ 0, & \text{elsewhere.} \end{cases}$$

Equation (3) states that the received signal's frequency spectrum consists of a shifted and dilated version of the repetitive sequence's frequency spectrum alongside a noise floor. The shifting in the received spectrum is mainly due to residual Doppler $\dot{\tilde{\theta}}_k$ and the dilation is due to residual Doppler rate $\ddot{\tilde{\theta}}_k$.

III. BLIND DOPPLER TRACKING

This section derives the Doppler discriminator and formulates the KF-based Doppler tracking loop.

1. Frequency-Domain Based Doppler Discriminator

The nonlinear NLS estimator of the residual Doppler $\dot{\tilde{\theta}}_k$ at the k-th sub-accumulation is given by

$$\begin{aligned} \dot{\tilde{\theta}}_k &= \underset{\dot{\theta}}{\operatorname{argmin}} \left\| S_{r_k}(f) - S_s(f) \circledast \Pi\left(f; \dot{\theta}, \ddot{\theta}\right) \right\|^2 \\ &= \underset{\dot{\theta}}{\operatorname{argmin}} \left\| S_{r_k}(f) \right\|^2 + \left\| S_s(f) \circledast \Pi\left(f; \dot{\theta}, \ddot{\theta}\right) \right\|^2 - 2\left(S_{r_k} \star S_s\right)(f) \circledast \Pi\left(f; \dot{\theta}, \ddot{\theta}\right) \qquad (4) \\ &= \underset{\dot{\theta}}{\operatorname{argmax}} \left(S_{r_k} \star S_s\right)(f) \circledast \Pi\left(f; \dot{\theta}, \ddot{\theta}\right) \cong \underset{\dot{\theta}}{\operatorname{argmax}} \left(S_{r_k} \star S_s\right)(f) \circledast \delta\left(f - \frac{\dot{\theta}}{2\pi}\right), \quad \text{for} \quad \ddot{\tilde{\theta}}_k \approx 0 \\ &= 2\pi \underset{f}{\operatorname{argmax}} \left(S_{r_k} \star S_s\right)(f), \qquad (5) \end{aligned}$$

where $(f \star g)(\tau) = \int_{-\infty}^{\infty} f^*(t)g(t+\tau)dt$ is the cross-correlation. The first two terms in the minimization problem (4) are a constant function of the search parameter $\dot{\theta}$; therefore, they are ignored. As the blind receiver does not have prior knowledge of $S_s(f)$, it starts with an initial estimate $\hat{S}_s(f) \triangleq S_{r_0}(f)$ and refines the repetitive sequence's spectrum with every sub-accumulation. It is worth pointing that the regime of small residual Doppler rate values assumed in (5) is a reasonable assumption, since the Doppler rate between two consecutive sub-accumulations is nearly constant.

2. Kalman Filter-Based Tracking Loop

The continuous-time signal in (2) is sampled at a sampling interval $T_s = 1/F_s$, the discrete-time received signal before carrier wipe-off at the k-th sub-accumulation can be written as

$$r_k^-[n] = s[n - d_k] \exp\left(j\tilde{\Theta}_k[n]\right) + n_k^-[n],$$

where $n \in [0, L-1]$, $s[n]$ is the discrete-time sequence of $s(t)$ with period $L = T_0/T_s$ and $\tilde{\Theta}_k[n]$ and d_k are the discrete-time carrier phase and code start time, respectively, of the received signal at the k-th sub-accumulation.

The carrier phase state vector is defined as $\boldsymbol{\theta}(t) \triangleq \left[\theta(t),\ \dot{\theta}(t),\ \ddot{\theta}(t)\right]^{\mathsf{T}}$, whose dynamics is modeled as

$$\dot{\boldsymbol{\theta}}(t) = \mathbf{A}\boldsymbol{\theta}(t) + \mathbf{B}\boldsymbol{w}(t), \tag{6}$$

$$\mathbf{A} \triangleq \begin{bmatrix} 0 & 1 & 0 \\ 0 & 0 & 1 \\ 0 & 0 & 0 \end{bmatrix}, \quad \mathbf{B} \triangleq \begin{bmatrix} 0 \\ 0 \\ 1 \end{bmatrix},$$

where $\boldsymbol{w}(t)$ is a zero-mean white noise process with power spectral density q_w. The continuous-time dynamics in (6) is discretized at a sampling time $T_0 = LT_s$, leading to $\boldsymbol{\Theta}_{k+1} = \mathbf{F}\boldsymbol{\Theta}_k + \mathbf{w}_k$, where $\boldsymbol{\Theta}_k \triangleq \left[\theta_k,\ \dot{\theta}_k,\ \ddot{\theta}_k\right]^{\mathsf{T}}$, $\mathbf{F} \triangleq e^{\mathbf{A}T_0}$ is the state transition matrix, $\mathbf{w}_k$ is a discrete-time process noise vector, which is a zero-mean white sequence with covariance $\mathbf{Q} = q_{\tilde{w}} \int_0^{T_0} e^{\mathbf{A}t}\mathbf{B}\left(e^{\mathbf{A}t}\mathbf{B}\right)^{\mathsf{T}} dt$. The reconstructed sequence of the carrier phase used to perform carrier wipe-off can be written as a second order piece-wise polynomial given by $\hat{\Theta}_k[n] = \hat{\theta}_{k-1} + \hat{\dot{\theta}}_k nT_s + \frac{1}{2}\hat{\ddot{\theta}}_k (nT_s)^2$, $n \in [0, L-1]$. After carrier wipe-off, the received signal's sequence can be expressed as

$$r_k[n] = s[n - d_k] \exp\left(j\tilde{\Theta}_k[n]\right) + n_k[n]. \tag{7}$$

Equation (7) will be used to determine the residual Doppler $\tilde{\dot{\theta}}_k$ at the k-th sub-accumulation, which is fed as innovation to a KF loop that uses the observation model $z_k = \mathbf{H}\boldsymbol{\Theta}_k + v_k$, where $\mathbf{H} \triangleq [0\ 1\ 0]$ and v_k is a discrete-time zero-mean white noise sequence with variance $\sigma_{\dot{\theta}}^2$. The KF innovation ν_k is the fast Fourier transform (FFT)-based discrete-time version of (5).

$$\nu_k = \tilde{\dot{\theta}}_k = \underset{\dot{\theta}}{\operatorname{argmax}} \left|R_k[\dot{\theta}]\right|^2 \star \left|\hat{S}_k[\dot{\theta}]\right|^2.$$

It is worth noting that the Doppler tracked using the proposed approach has a real-valued ambiguity part $\dot{\theta}_N$ that needs to be resolved to retrieve back the actual Doppler shift.

IV. EXPERIMENTAL RESULTS: NOAA LEO ACQUISITION AND TRACKING

This section demonstrates the proposed blind Doppler estimator and tracking loop with NOAA LEO satellite signals. To this end, a stationary National Instrument (NI) universal software radio peripheral (USRP) E312 was equipped with a consumer-grade very high frequency (VHF) Quadrifilar Helical antenna to receive NOAA LEO satellite signals. The sampling bandwidth was set to 2.4 MHz and the carrier frequency f_c was set to 137.0 MHz. Samples of the VHF signal were stored for off-line processing via a software-defined radio (SDR).

The USRP was set to record for a period of 800 seconds. During this period, one NOAA satellite passed over the receiver. The framework discussed in Section III was used to acquire and track the signal from the satellite with $q_w = (0.1)^2$ rad^2/s^6 and $\sigma_{\dot{\theta}} = \frac{\pi}{6}$ rad/s. The estimated beacon spectrum and tracked Doppler from the satellite is shown in Figure 1.

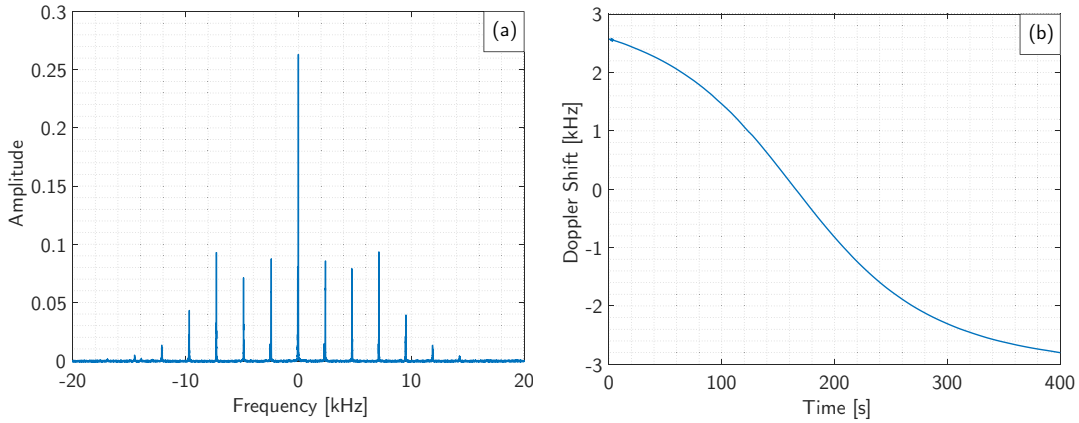

Figure 1: (a) NOAA LEO satellite estimated beacon spectrum. (b) Blindly tracked Doppler from a NOAA satellite using the spectral-based approach.

V. EXPERIMENTAL RESULTS: STARLINK, ONEWEB, ORBCOMM, IRIDIUM NEXT, AND NOAA LEO TRACKING AND POSITIONING

This section presents multi-constellation tracking and positioning results, exploiting signals from Starlink, OneWeb, Orbcomm, Iridium NEXT, and NOAA LEO constellations. The hardware used for data collection (see Figure 2) included: (i) an LNB with conversion gain of 50 dB and noise figure of 2.5 dB connected to a Ku-band 60 cm parabolic offset dish with gain of 30 dBi to receive Starlink and OneWeb satellite signals, (ii) a commercial Orbcomm antenna to receive Orbcomm and NOAA signals, and (iii) a commercial Iridium NEXT antenna.

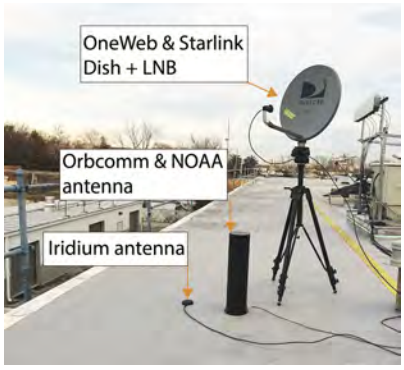

Figure 2: Hardware setup.

Figure 3 shows the tracked Doppler and Doppler error from multi-constellation LEO satellites (4 Starlink, 2 OneWeb, 1 Orbcomm, 1 Iridium NEXT, and 1 NOAA) as well as their respective trajectories during their passing overhead.

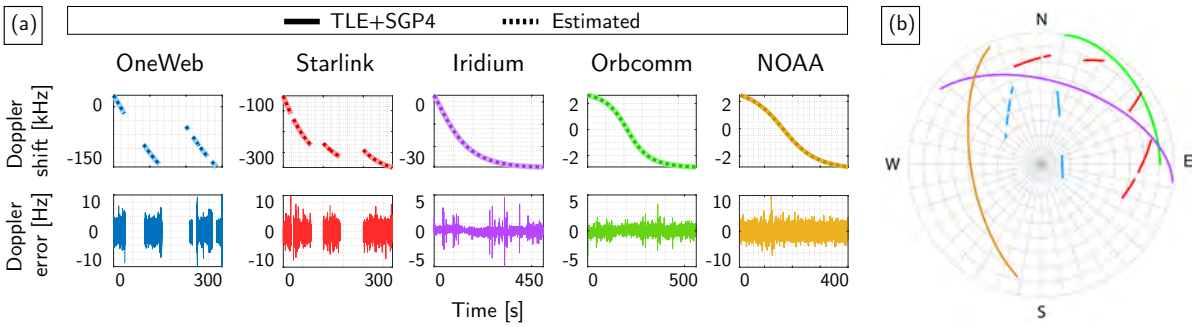

Figure 3: (a) Top: Doppler curves generated by the proposed framework (dashed) and calculated from propagated satellite orbit using TLE+SGP4 (solid). Bottom: the innovation of the KF tracking loops. (b) Skyplot showing the trajectories of the tracked LEO satellites.

After tracking, carrier phase measurements were reconstructed by integrating the tracked Doppler and fed to a batch NLS estimator to estimate the position of the stationary receiver. The measurement model and positioning filter formulation were adopted from (Kozhaya et al., 2023). The receiver's initial position estimate was set on the roof of the Engineering parking structure at the University of California, Irvine, USA, approximately 3,600 km away from the true position, which was on the roof of the ElectroScience Laboratory at the The Ohio State University, Columbus, OH, USA. Figure 4(a) shows the trajectories of the 9 satellites from the 5 LEO constellations. Figure 4(b) shows the initial and final position estimates. Figure 4(c) shows the true and estimated receiver's position. The final 3D position error was found to be 5.8 m, while the 2D position error was 5.1 m (i.e., upon considering only the east and north coordinates in the ENU frame). It is worth noting that the addition of the NOAA satellite Doppler measurements did not reduce the positioning error by much (reduction on the order of centimeters), compared to using 4 Starlink, 2 OneWeb, 1 Orbcomm, 1 Iridium NEXT LEO satellites (as presented in (Kozhaya et al., 2023)). This is due to the already favorable geometry of the four constellations.

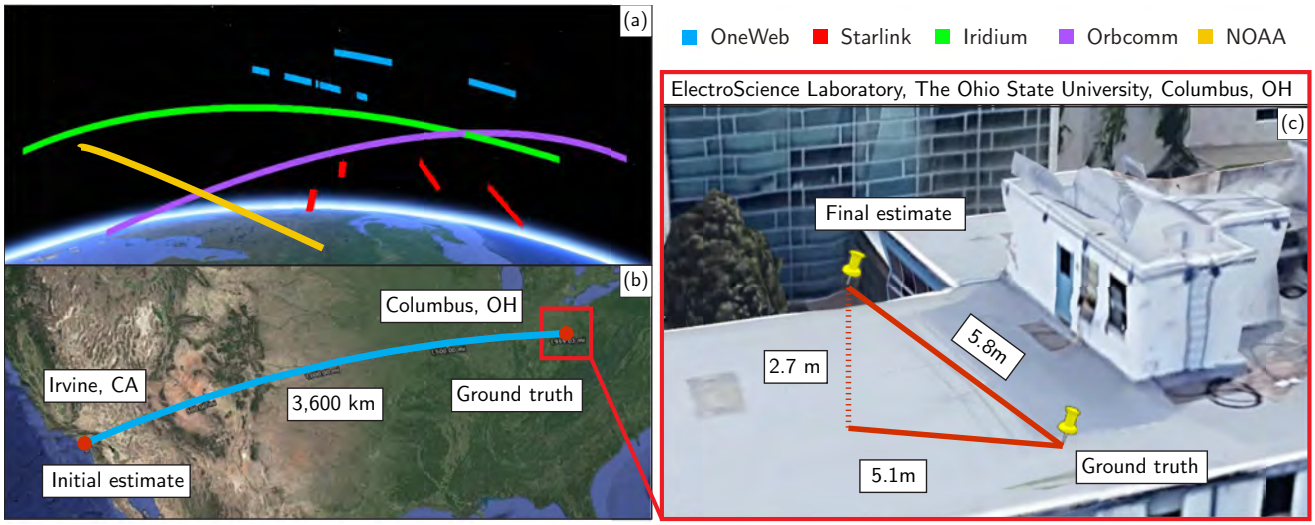

Figure 4: Positioning results with 4 Starlink, 2 OneWeb, 1 Orbcomm, 1 Iridium NEXT, and 1 NOAA LEO satellites: (a) LEO satellite trajectories. (b) Initial and final estimated positions. (c) Final errors relative to the receiver's true position.

VI. CONCLUSION

This paper showcased that the previously developed LEO-agnostic spectral-based approach is capable of acquiring and tracking a new LEO constellation: NOAA LEO satellites. Experimental results were also presented showing Hz-level Doppler tracking of 5 different LEO satellite constellations: Starlink, OneWeb, Orbcomm, Iridium NEXT, and NOAA. Carrier phase observables were constructed from the tracked Doppler and fused through an NLS estimator to localize a stationary receiver. Starting with an initial estimate 3,600 km away from the receiver's true position, the proposed approach achieved a 2D error of 5.1 m.

ACKNOWLEDGMENTS

This work was supported in part by the Office of Naval Research (ONR) under Grants N00014-19-1-2511 and N00014-22-1-2242, in part by the Air Force Office of Scientific Research (AFOSR) under Grant FA9550-22-1-0476, and in part by the U.S. Department of Transportation (USDOT) under Grant 69A3552047138 for the CARMEN University Transportation Center (UTC).

REFERENCES

3GPP (2010). Evolved universal terrestrial radio access (E-UTRA); multiplexing and channel coding. TS 36.212, 3rd Generation Partnership Project (3GPP).

3GPP (2018). Physical channels and modulation. TS 38.211, 5G; NR; 3rd Generation Partnership Project (3GPP).

3GPP2 (2011). Physical layer standard for cdma2000 spread spectrum systems (C.S0002-E). TS C.S0002-E, 3rd Generation Partnership Project 2 (3GPP2).

Bilardi, S. (2021). A GNSS signal simulator and processor for evaluating acquisition and tracking of GPS-like signals from

satellites in LEO. Master's thesis, University of Colorado at Boulder, CO, USA.

Bolcskei, H. (2001). Blind estimation of symbol timing and carrier frequency offset in wireless OFDM systems. *IEEE Transactions on Communications*, 49(6):988–999.

Burel, G. and Bouder, C. (2000). Blind estimation of the pseudo-random sequence of a direct sequence spread spectrum signal. In *Proceedings of IEEE Military Communications Conference*, volume 2, pages 967–970.

Cassel, R., Scherer, D., Wilburne, D., Hirschauer, J., and Burke, J. (2022). Impact of improved oscillator stability on LEO-based satellite navigation. In *Proceedings of ION International Technical Meeting*, pages 893–905.

Choi, H. and Moon, H. (2020). Blind estimation of spreading sequence and data bits in direct-sequence spread spectrum communication systems. *IEEE Access*, 8:148066–148074.

Curzi, G., Modenini, D., and Tortora, P. (2020). Large constellations of small satellites: A survey of near future challenges and missions. *Aerospace*, 7(9):1–18.

Egea-Roca, D., Lopez-Salcedo, J., Seco-Granados, G., and Falletti, E. (2022). Performance analysis of a multi-slope chirp spread spectrum signal for PNT in a LEO constellation. In *Proceedings of Workshop on Satellite Navigation Technology*, pages 1–9.

Farhangian, F., Benzerrouk, H., and Landry, R. (2021). Opportunistic in-flight INS alignment using LEO satellites and a rotatory IMU platform. *Aerospace*, 8(10):280–281.

Farhangian, F. and Landry, R. (2023). High-order pseudorange rate measurement model for multi-constellation LEO/INS integration: Case of Iridium-NEXT, Orbcomm, and Globalstar. *Proceedings of the Institution of Mechanical Engineers, Part G: Journal of Aerospace Engineering*, 237(4):925–939.

Flores, A. (2022). NAVSTAR GPS space segment/navigation user interfaces. `https://www.gps.gov/technical/icwg/IS-GPS-200N.pdf`.

Guo, F., Yang, Y., Ma, F., Liu, Y. Z. H., and Zhang, X. (2023). Instantaneous velocity determination and positioning using doppler shift from a LEO constellation. *Satellite Navigation*, 4:9–21.

Hartnett, M. (2022). Performance assessment of navigation using carrier Doppler measurements from multiple LEO constellations. Master's thesis, Air Force Institute of Technology, Ohio, USA.

Hendrickson, R. (1997). Globalstar for the military. In *Proceedings of IEEE Military Communications Conference*, volume 3, pages 1173–1178.

Huang, C., Qin, H., Zhao, C., and Liang, H. (2022). Phase - time method: Accurate Doppler measurement for Iridium NEXT signals. *IEEE Transactions on Aerospace and Electronic Systems*, 58(6):5954–5962.

Humphreys, T., Iannucci, P., Komodromos, Z., and Graff, A. (2023). Signal structure of the Starlink Ku-band downlink. *IEEE Transactions on Aerospace and Electronics Systems*. accepted.

Janssen, T., Koppert, A., Berkvens, R., and Weyn, M. (2023). A survey on IoT positioning leveraging LPWAN, GNSS and LEO-PNT. *IEEE Internet of Things Journal*, 10(13):11135–11159.

Jardak, N. and Jault, Q. (2022). The potential of LEO satellite-based opportunistic navigation for high dynamic applications. *Sensors*, 22(7):2541–2565.

Jiang, M., Qin, H., Su, Y., Li, F., and Mao, J. (2023). A design of differential-low Earth orbit opportunistically enhanced GNSS (D-LoeGNSS) navigation framework. *Remote Sensing*, 15(8):2136–2158.

Jiang, M., Qin, H., Zhao, C., and Sun, G. (2022). LEO Doppler-aided GNSS position estimation. *GPS Solutions*, 26(1):1–18.

Kanamori, H., Kobayashi, K., and Kubo, N. (2023). A map-matching based positioning method using Doppler tracking and estimation by a software-defined receiver for multi-constellation LEO satellites. In *Proceedings of ION International Technical Meeting*, pages 649–663.

Kassas, Z. (2021). Position, navigation, and timing technologies in the 21st century. volume 2, chapter 43: Navigation from low Earth orbit – Part 2: models, implementation, and performance, pages 1381–1412. Wiley-IEEE.

Kassas, Z., Khairallah, N., and Kozhaya, S. (2023a). Ad astra: Simultaneous tracking and navigation with megaconstellation LEO satellites. *IEEE Aerospace and Electronic Systems Magazine*. accepted.

Kassas, Z., Kozhaya, S., Saroufim, J., Kanj, H., and Hayek, S. (2023b). A look at the stars: Navigation with multi-constellation LEO satellite signals of opportunity. *Inside GNSS Magazine*, 18(4):38–47.

Kassas, Z., Morales, J., and Khalife, J. (2019). New-age satellite-based navigation – STAN: simultaneous tracking and navigation with LEO satellite signals. *Inside GNSS Magazine*, 14(4):56–65.

Kassas, Z., Neinavaie, M., Khalife, J., Khairallah, N., Haidar-Ahmad, J., Kozhaya, S., and Shadram, Z. (2021). Enter LEO on the GNSS stage: Navigation with Starlink satellites. *Inside GNSS Magazine*, 16(6):42–51.

Khairallah, N. and Kassas, Z. (2021). Ephemeris closed-loop tracking of LEO satellites with pseudorange and Doppler measurements. In *Proceedings of ION GNSS Conference*, pages 2544–2555.

Khalife, J. and Kassas, Z. (2023). Performance-driven design of carrier phase differential navigation frameworks with mega-constellation LEO satellites. *IEEE Transactions on Aerospace and Electronic Systems*, 59(3):2947–2966.

Khalife, J., Neinavaie, M., and Kassas, Z. (2022). The first carrier phase tracking and positioning results with Starlink LEO satellite signals. *IEEE Transactions on Aerospace and Electronic Systems*, 56(2):1487–1491.

Kozhaya, S., Kanj, H., and Kassas, Z. (2023). Multi-constellation blind beacon estimation, Doppler tracking, and opportunistic positioning with OneWeb, Starlink, Iridium NEXT, and Orbcomm LEO satellites. In *Proceedings of IEEE/ION Position, Location, and Navigation Symposium*, pages 1184–1195.

Kozhaya, S. and Kassas, Z. (2022). Blind receiver for LEO beacon estimation with application to UAV carrier phase differential navigation. In *Proceedings of ION GNSS Conference*, pages 2385–2397.

Kozhaya, S. and Kassas, Z. (2023). Positioning with Starlink LEO satellites: A blind Doppler spectral approach. In *Proceedings of IEEE Vehicular Technology Conference*, pages 1–5.

Li, L., Zhang, H., Du, S., Liang, T., and Gao, L. (2023). Blind despreading and deconvolution of asynchronous multiuser direct sequence spread spectrum signals under multipath channels. *IET Signal Processing*, 17(5):1–14.

Liu, S., Gao, Z., Wu, Y., Kwan Ng, D., Gao, X., Wong, K., Chatzinotas, S., and Ottersten, B. (2021). LEO satellite constellations for 5G and beyond: How will they reshape vertical domains? *IEEE Communications Magazine*, 59(7):30–36.

Liu, W., Wang, J., and Li, S. (2010). Blind detection and estimation of OFDM signals in cognitive radio contexts. In *Proceedings of International Conference on Signal Processing Systems*, volume 2, pages 347–351.

Menzione, F. and Paonni, M. (2023). LEO-PNT mega-constellations: a new design driver for the next generation MEO GNSS space service volume and spaceborne receivers. In *Proceedings of IEEE/ION Position, Location, and Navigation Symposium*, pages 1196–1207.

Merwe, J., Bartl, S., O'Driscoll, C., Rügamer, A., Förster, F., Berglez, P., Popugaev, A., and Felber, W. (2020). GNSS sequence extraction and reuse for navigation. In *Proceedings of ION GNSS+ Conference*, pages 2731–2747.

More, H., Cianca, E., and Sanctis, M. (2022). Positioning performance of LEO mega constellations in deep urban canyon environments. In *Proceedings of International Symposium on Wireless Personal Multimedia Communications*, pages 256–260.

Mortlock, T. and Kassas, Z. (2021). Assessing machine learning for LEO satellite orbit determination in simultaneous tracking and navigation. In *Proceedings of IEEE Aerospace Conference*, pages 1–8.

Morton, Y., Xu, D., and Jiao, Y. (2022). Ionospheric scintillation effects on signals transmitted from LEO satellites. In *Proceedings of ION GNSS Conference*, pages 2980–2988.

Neinavaie, M. and Kassas, Z. (2023). Unveiling Starlink LEO satellite OFDM-like signal structure enabling precise positioning. *IEEE Transactions on Aerospace and Electronic Systems*. accepted.

Neinavaie, M., Khalife, J., and Kassas, Z. (2021). Blind Doppler tracking and beacon detection for opportunistic navigation with LEO satellite signals. In *Proceedings of IEEE Aerospace Conference*, pages 1–8.

Neinavaie, M., Khalife, J., and Kassas, Z. (2022a). Acquisition, Doppler tracking, and positioning with Starlink LEO satellites: First results. *IEEE Transactions on Aerospace and Electronic Systems*, 58(3):2606–2610.

Neinavaie, M., Shadram, Z., Kozhaya, S., and Kassas, Z. M. (2022b). First results of differential Doppler positioning with unknown Starlink satellite signals. In *Proceedings of IEEE Aerospace Conference*, pages 1–14.

Orabi, M., Khalife, J., and Kassas, Z. (2021). Opportunistic navigation with Doppler measurements from Iridium Next and Orbcomm LEO satellites. In *Proceedings of IEEE Aerospace Conference*, pages 1–9.

Pinell, C., Prol, F., Bhuiyan, M., and Praks, J. (2023). Receiver architectures for positioning with low earth orbit satellite signals: a survey. *EURASIP Journal on Advances in Signal Processing*, 2023:60–80.

Prol, F., Ferre, R., Saleem, Z., Välisuo, P., Pinell, C., Lohan, E., Elsanhoury, M., Elmusrati, M., Islam, S., Celikbilek, K., Selvan, K., Yliaho, J., Rutledge, K., Ojala, A., Ferranti, L., Praks, J., Bhuiyan, M., Kaasalainen, S., and Kuusniemi, H. (2022). Position, navigation, and timing (PNT) through low earth orbit (LEO) satellites: A survey on current status, challenges, and opportunities. *IEEE Access*, 10:83971–84002.

Prol, F., Kaasalainen, S., Lohan, E., Bhuiyan, M., Praks, J., and Kuusniemi, H. (2023). Simulations using LEO-PNT systems: A brief survey. In *Proceedings of IEEE/ION Position, Location, and Navigation Symposium*, pages 1381–387.

Psiaki, M. (2021). Navigation using carrier Doppler shift from a LEO constellation: TRANSIT on steroids. *NAVIGATION, Journal of the Institute of Navigation*, 68(3):621–641.

Reid, T., Walter, T., Enge, P., Lawrence, D., Cobb, H., Gutt, G., O'Conner, M., and Whelan, D. (2021). Position, navigation, and timing technologies in the 21st century. volume 2, chapter 43: Navigation from low Earth orbit – Part 1: concept, current capability, and future promise, pages 1359–1379. Wiley-IEEE.

Ries, L., Limon, M., Grec, F., Anghileri, M., Prieto-Cerdeira, R., Abel, F., Miguez, J., Perello-Gisbert, J., d'Addio, S., R. Ioannidis and, A. O., Rapisarda, M., Sarnadas, R., and Testani, P. (2023). LEO-PNT for augmenting Europe's space-based PNT capabilities. In *Proceedings of IEEE/ION Position, Location, and Navigation Symposium*, pages 329–337.

Rui, Z., Ouyang, X., Zeng, F., and Xu, X. (2022). Blind estimation of GPS M-Code signals under noncooperative conditions. *Wireless Communications and Mobile Computing*, 2022.

Sabbagh, R. and Kassas, Z. (2023). Observability analysis of receiver localization via pseudorange measurements from a single LEO satellite. *IEEE Control Systems Letters*, 7(3):571–576.

Saroufim, J., Hayek, S., and Kassas, Z. (2023). Simultaneous LEO satellite tracking and differential LEO-aided IMU navigation. In *Proceedings of IEEE/ION Position Location and Navigation Symposium*, pages 179–188.

Shi, C., Zhang, Y., and Li, Z. (2023). Revisiting Doppler positioning performance with LEO satellites. *GPS Solutions*, 27(3):126–137.

Singh, U., Shankar, M., and Ottersten, B. (2022). Opportunistic localization using LEO signals. In *Proceedings of Asilomar Conference on Signals, Systems, and Computers*, pages 894–899.

Tan, Z., Qin, H., Cong, L., and Zhao, C. (2019). Positioning using IRIDIUM satellite signals of opportunity in weak signal environment. *Electronics*, 9(1):37.

Tanda, M. (2004). Blind symbol-timing and frequency-offset estimation in OFDM systems with real data symbols. *IEEE Transactions on Communications*, 52(10):1609–1612.

Tsatsanis, M. and Giannakis, G. (1997). Blind estimation of direct sequence spread spectrum signals in multipath. *IEEE Transactions on Signal Processing*, 45(5):1241–1252.

Wang, D., Qin, H., and Huang, Z. (2023). Doppler positioning of LEO satellites based on orbit error compensation and weighting. *IEEE Transactions on Instrumentation and Measurement*, 72:1–11.

Wei, Q., Chen, X., and Zhan, Y. (2020). Exploring implicit pilots for precise estimation of LEO satellite downlink Doppler frequency. *IEEE Communications Letters*, 24(10):2270–2274.

Wu, N., Qin, H., and Zhao, C. (2023). Long-baseline differential doppler positioning using space-based SOP based on BPVGMM. *IEEE Transactions on Instrumentation and Measurement*, 72:1–10.

Yang, C. and Soloviev, A. (2023). Starlink Doppler and Doppler rate estimation via coherent combining of multiple tones for opportunistic positioning. In *Proceedings of IEEE/ION Position, Location, and Navigation Symposium*, pages 1143–1153.

Yang, C., Zang, B., Gu, B., Zhang, L., Dai, C., Long, L., Zhang, Z., Ding, L., and Ji, H. (2023). Doppler positioning of dynamic targets with unknown LEO satellite signals. *Electronics*, 12(11):2392–2404.

Ye, L., Gao, N., Yang, Y., Deng, L., and Li, H. (2023). Three satellites dynamic switching range integrated navigation and positioning algorithm with clock bias cancellation and altimeter assistance. *Aerospace*, 10(5):411–438.

Zhao, C., Qin, H., Wu, N., and Wang, D. (2023). Analysis of baseline impact on differential doppler positioning and performance improvement method for LEO opportunistic navigation. *IEEE Transactions on Instrumentation and Measurement*, 72:1–10.

Blind Receiver for LEO Beacon Estimation with Application to UAV Carrier Phase Differential Navigation

Sharbel E. Kozhaya and Zaher M. Kassas
The Ohio State University

BIOGRAPHIES

Sharbel E. Kozhaya is a Ph.D student in the Department of Electrical and Computer Engineering at The Ohio State University and a member of the Autonomous Systems Perception, Intelligence, and Navigation (ASPIN) Laboratory. He received a B.E. in Electrical Engineering from the Lebanese American University. His current research interests include opportunistic navigation, Low Earth Orbit (LEO) satellites, software-defined radio, signal fusion, and 5G.

Zaher (Zak) M. Kassas Zaher (Zak) M. Kassasis a Professor at The Ohio State University and director of the Autonomous Systems Perception, Intelligence, and Navigation (ASPIN) Laboratory. He is also director of the U.S. Department of Transportation Center: CARMEN (Center for Automated Vehicle Research with Multimodal AssurEd Navigation), focusing on navigation resiliency and security of highly automated transportation systems. He received a B.E. in Electrical Engineering from the Lebanese American University, an M.S. in Electrical and Computer Engineering from The Ohio State University, and an M.S.E. in Aerospace Engineering and a Ph.D. in Electrical and Computer Engineering from The University of Texas at Austin. He is a recipient of the 2018 National Science Foundation (NSF) CAREER award, 2019 Office of Naval Research (ONR) Young Investigator Program (YIP) award, 2022 Air Force Office of Scientific Research (AFOSR) YIP award, 2018 IEEE Walter Fried Award, 2018 Institute of Navigation (ION) Samuel Burka Award, and 2019 ION Col. Thomas Thurlow Award. He is a Senior Editor of the IEEE Transactions on Intelligent Vehicles and an Associate Editor of the IEEE Transactions on Aerospace and Electronic Systems and the IEEE Transactions on Intelligent Transportation Systems. His research interests include cyber-physical systems, navigation systems, autonomous vehicles, and intelligent transportation systems.

ABSTRACT

A receiver for blind beacon estimation of low Earth orbit (LEO) satellite signals with application to UAV navigation is presented. The receiver operates in three stages: (i) blind Doppler tracking that uses correlation in the frequency-domain as a frequency discriminator and tracks the Doppler using a frequency-locked loop (FLL), (ii) beacon estimation from the coherent accumulation of the received signal after wiping off the Doppler tracked by the FLL, and (iii) tracking LEO signals using the estimated beacon in the previous step to produce navigation observables. Experimental results are presented showing: (i) successful blind estimation of the navigation beacon of the Orbcomm LEO constellation and (ii) a UAV navigating using the estimated beacons of two Orbcomm LEO satellites via a carrier phase differential navigation framework, achieving a three-dimensional position root mean-squared error (RMSE) of 13.9 m with only Orbcomm signals fused with an altimeter, over a trajectory of 2.28 km traversed in 2 minutes.

I. INTRODUCTION

The potential of signals of opportunity (SOPs) as a reliable navigation source has been undoubtedly uncovered in the past decade (Raquet *et al.*, 2021). Terrestrial SOPs include cellular (Gadka et al., 2019; Shamaei and Kassas, 2021a; Souli et al., 2021b; Kazaz et al., 2022; Xhafa et al., 2021; Wang and Morton, 2022), FM radio (Chen et al., 2020; Psiaki and Slosman, 2022; Aziz and Allen, 2018), and digital television (Yang and Soloviev, 2020; Hong et al., 2021; Souli et al., 2021a), among which, cellular provided the most accuracy. Previous literature showed meter-level accurate ground vehicle navigation (Yang et al., 2020; Soderini et al., 2020; Hong et al., 2021; Maaref and Kassas, 2022; Lapin et al., 2022) and sub-meter-level accurate unmanned aerial vehicle (UAV) navigation with cellular SOPs (Khalife and Kassas, 2022).

Exploiting SOPs did not stay earthly, as space vehicles have received considerable attention recently as potential SOPs (Reid et al., 2021; Kassas, 2021; Gao et al., 2021; Prol et al., 2022; Jardak and Jault, 2022). Many theoretical and experimental studies have been conducted on the use of low Earth orbit (LEO) satellite signals as an alternative to global navigation satellite system (GNSS) (Leng et al., 2016; Tan et al., 2019a; Wei et al., 2020; Farhangian and Landry, 2020; Farhangian et al., 2021; Psiaki, 2021; Nardin et al., 2021; Wang and El-Mowafy, 2022; Hartnett, 2022; Cassel et al., 2022; Huang et al., 2022; Jiang et al.,

Copyright © 2022 by S. Kozhaya and Z. Kassas

Preprint of the 2022 ION GNSS+ Conference
Denver, Colorado, September 19–23, 2022

2022; Iannucci and Humphreys, 2022; Li et al., 2022; Khalife et al., 2022; Zhao et al., 2022). LEO satellites possess desirable attributes for positioning in GNSS-challenged environments: (i) they are around twenty times closer to the Earth compared to GNSS satellites, which reside in medium Earth orbit (MEO), making their received signal power between 24 to 34 dB higher than GNSS signals; (ii) they are becoming abundant as thousands of broadband Internet satellites are expected to be deployed into LEO; and (iii) they transmit in different frequency bands, making LEO satellite signals diverse in frequency and direction. Figure 1 depicts some of the existing and future broadband LEO constellations.

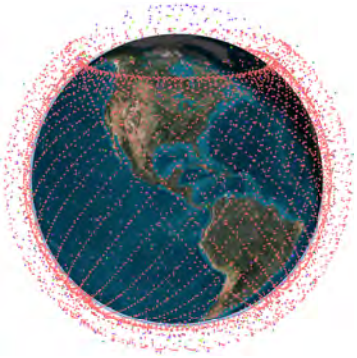

Constellation	Number of Satellites	Frequency Band
Orbcomm	36	VHF
Globalstar	48	S and C
Iridium NEXT	66	L and Ka
OneWeb	648	Ku and Ka
Starlink	42,404	Ku, Ka, and V
Boeing	147	V and Ka
Kuiper	3,276	Ku and Ka

Figure 1: Visualization of some of the existing and future broadband LEO satellites.

While such results bring hope to solving the problem of reliable navigation in GNSS-challenged environments, one must emphasize that navigating with LEO satellites comes with several challenges. The main challenges are (i) the poorly known nature of LEO satellites' ephemeris due to many LEO operators not making such information publicly available, (ii) the unknown and potentially loose nature of LEO satellites' timing and synchronization protocols, and (iii) the unknown nature of LEO satellites' signals due to being proprietary.

To address the first challenge, several approaches have been recently proposed, including differential navigation utilizing a known base receiver (Khalife et al., 2020), simultaneous tracking and navigation (STAN) (Kassas et al., 2021)), and analytical/machine-learning satellite orbit tracking (Shen et al., 2019; Khairallah and Kassas, 2021; Kozhaya et al., 2021; Haidar-Ahmad et al., 2022)). To address the second challenge, an approach to adaptively estimate LEO satellites' clock stability has been recently developed (Khairallah and Kassas, 2022), while (Wang and El-Mowafy, 2022) proposed a model that considered the systematic effects related to the environment and relativistic effects to improve LEO clock prediction. To address the third challenge, the recently established paradigm of cognitive opportunistic navigation (Neinavaie et al., 2022), which estimates the minimally known LEO satellite signals in a blind fashion has been showing tremendous promise (Neinavaie et al., 2020, 2021). Most recently, this paradigm allowed for the exploitation of the unknown Starlink LEO satellites, from which navigation observables were produced, allowing for localizing a stationary receiver to within 10 m, with 6 Starlink LEO satellites.

At the core of the blind receiver is the ability to detect periodically transmitted signals, estimate and track them, and finally generate navigation observables. One can be reasonably confident that beacons are present in every communication system. For example, a primary and secondary synchronization sequence (PSS) and (SSS), respectively, are transmitted in 4G LTE and 5G NR systems for symbol timing recovery. Such sequences were exploited for opportunistic navigation purposes (Shamaei and Kassas, 2021b; Yang et al., 2022). However, these repeated sequences are published and maintained by the 3rd Generation Partnership Project (3GPP), and it is assumed that the receiver perfectly knows the synchronization sequences and can correlate local replicas of these sequences with the received signals. In the case where these sequences are unknown, as is the case of future broadband LEO satellite systems, acquiring and tracking these satellite signals becomes impossible for a regular opportunistic receiver, as such, designing receivers that can blindly and adaptively estimate these sequences is a crucial need for the future of opportunistic navigation.

The problem of detecting and estimating periodically transmitted signals is not new in the literature. Blind orthogonal frequency division multiplexing (OFDM) symbol timing recovery methods have been successfully employed in the wireless communications and cognitive radio literature (Tanda, 2004; Al-Dweik, 2006; Liu et al., 2010). Other methods have considered blind estimation of spreading sequence and data bits in direct-sequence spread spectrum (DSSS) communication systems both in the absence and presence of multipath (Tsatsanis and Giannakis, 1997; Choi and Moon, 2020). Other methods considered eigenvalue decomposition (Burel and Bouder, 2000; Bouder et al., 2004) and neural betwork (NN) unsupervised learning (Bouder and Burel, 2000; Zhang et al., 2012). However, the proposed approaches make assumptions that do not hold for the case of LEO satellite transmitters, mainly the low magnitude of the frequency offset and stationarity of the channel. Unfortunately, as a result of the high dynamics of LEO satellites transmitting in the K-band, large shift and rate changes will be observed in both the carrier and code phase of the received signal. In this case, it is nearly impossible to coherently integrate the signal to

accumulate enough power for reliable detection of synchronization signals.

While carrier phase (Khalife et al., 2020) and Doppler (Tan et al., 2019b; Farhangian and Landry, 2020; Orabi et al., 2021) measurements have been successfully extracted from Orbcomm and Iridium NEXT LEO satellites, these approaches so far relied on the knowledge of the structure of the transmitted signals. For example, Orbcomm and Iridium satellites uses Symmetric Differential Phase Shift Keying (SD-PSK) modulation (Orbcomm, 2002; Iridium Constellation LLC, 2013), which fail to generalize to OFDM-based constellations.

There is still little information about the signal structure of future constellations that will bring thousands of satellites into LEO. This paper aims to develop a blind LEO receiver unrestrained from the challenges discussed above, i.e., agnostic to the modulation scheme used (M-ary PSK, ODFM, or other) and the dynamics of the satellite. The paper's main contributions are as follows. First, a receiver design for blind opportunistic navigation using broadband LEO satellites is presented. The proposed receiver produces Doppler, carrier, and code phase observables. Second, the performance of the proposed receiver is assessed experimentally for UAV navigation with real signals from two Orbcomm LEO satellites. It is shown that the proposed receiver successfully extracted the aforementioned observables. A base with known states was set up in the UAV's vicinity, which produced navigation observables to the same Orbcomm satellites. The differential carrier phase observables were fed to an extended Kalman filter (EKF) to estimate the UAV's trajectory. Over the UAV's 2.28 km trajectory, a position root mean-squared error of 13.9 m was achieved exclusively with the Orbcomm satellite signals.

The rest of the paper is organized as follows. Section II overviews the blind receiver structure and details the received signal models, tracking loops, and navigation beacon estimation. Section III presents the experimental results. Section IV gives concluding remarks.

II. BLIND RECEIVER STRUCTURE

1. Blind Receiver Overview

The receiver operates in three stages : (i) blind Doppler tracking that uses correlation in the frequency-domain as a frequency discriminator and tracks the Doppler using a frequency-locked loop (FLL), (ii) beacon estimation from the coherent accumulation of the received signal after wiping off the Doppler tracked by the FLL, and (iii) tracking LEO signals using the estimated beacon in the previous step to produce navigation observables. Figure 2 summarizes the block diagram of the proposed receiver.

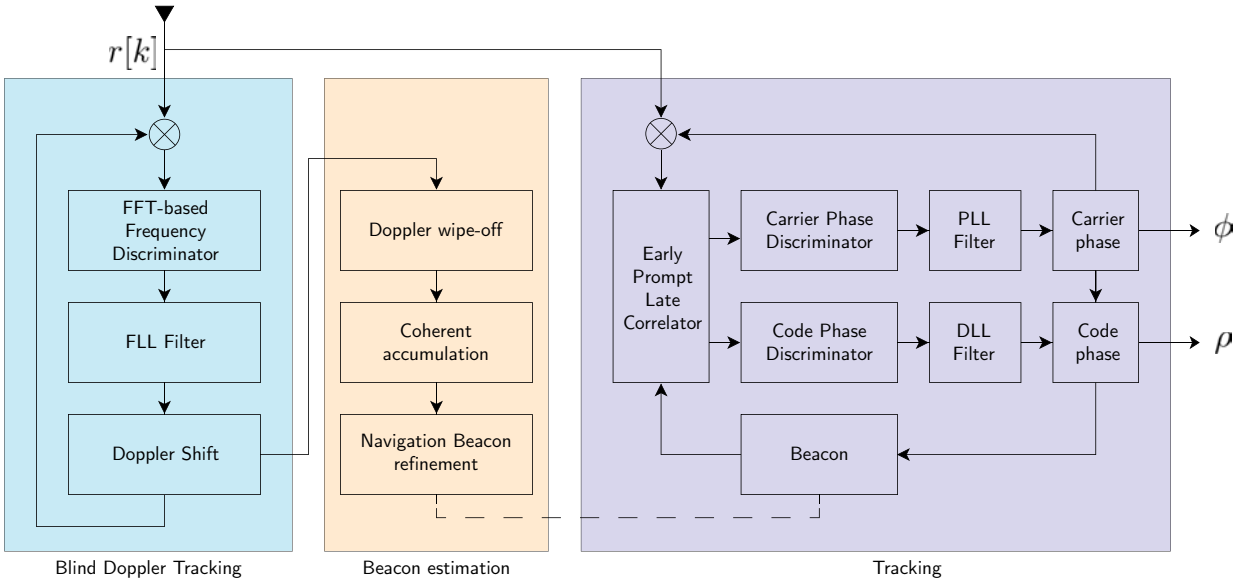

Figure 2: Structure of the proposed blind receiver

2. Continuous-Time Transmitted Baseband Signal Model

Let $x(t)$ be the unknown signal transmitted by a navigation source. The proposed framework does not assume any particular modulation or multiplexing scheme. The only assumption is that the transmitted signal $x(t)$ comprises M periodic synchronization signals $\{s_m(t)\}_{m=1}^{M}$, with the m-th signal having a period T_m. The total number of periodic signals M may be unknown.

Furthermore, these periodic signals may be multiplexed in time, frequency, and/or code. As such, $x(t)$ is modeled as

$$x(t) = \sum_{n=-\infty}^{\infty} \sum_{m=1}^{M} s_m(t - nT_m) + m(t), \tag{1}$$

where $m(t)$ denotes the remaining, non-periodic signals in the original transmitted signal $x(t)$. Let T_0 denote the least common multiplier of $\{T_m\}_{m=1}^{M}$. Subsequently, one can define a periodic signal $s^*(t)$ that encompasses all periodic signals contained in $x(t)$ with period T_0 as

$$s^*(t) = \sum_{m=1}^{M} s_m(t),$$

where,

$$s(t) = \sum_{n=-\infty}^{\infty} s^*(t - nT_0).$$

The signal can now be expressed as $x(t) = s(t) + m(t)$. The signal $x(t)$ is then transmitted at a carrier frequency f_c as

$$x_c(t) = x(t) \exp\left(j2\pi f_c t\right). \tag{2}$$

3. Continuous-Time and Discrete-Time Received Baseband Signal Model

Let $\tau_d(t)$ denote the time it takes until the transmitted signal reaches the receiver's antenna. This duration entails the (i) length of the line of sight (LOS) between the transmitter and the receiver $d(t)/c$, (ii) aggregated transmitter and receiver's clock bias $\delta t_{clk}(t)$, (iii) ionospheric and tropospheric delays $\delta t_{iono}(t)$ and $\delta t_{tropo}(t)$, and (iv) other unmodeled delays. After propagating in an additive white Gaussian channel, the resulting time-domain received signal before baseband mixing can be expressed as

$$\begin{aligned} \bar{r}(t) &= x_c\left(t - \tau_d(t)\right) + \bar{n}(t) \\ &= x(t - \tau_d(t)) \exp\left(j2\pi f_c \left[t - \tau_d\left(t\right)\right]\right) + \bar{n}(t), \end{aligned} \tag{3}$$

where $\bar{n}(t)$ is the complex, zero-mean, white Gaussian noise with power spectral density N_0. Let $r(t)$ denote the received signal after baseband mixing and filtering. Then, $r(t)$ can be expressed as

$$\begin{aligned} r(t) &= \bar{r}(t) \exp\left(-j2\pi f_c t\right) \\ &= x'(t - \tau_d(t)) \exp\left(j\theta(t)\right) + n(t), \end{aligned} \tag{4}$$

where $x'(t)$ and $n(t)$ are the low-pass filter output of $x(t)$ and $\bar{n}(t)$, respectively, and $\theta(t)$ is the carrier phase of the received signal expressed as $\theta(t) = -2\pi f_c \tau_d(t)$.

After sampling at a sampling interval T_s, the discrete-time received signal at the k-th sub-accumulation can be approximated as

$$r_k^{'}[n] = s[n - d_k] \exp\left(j\Theta_k[n]\right) + n_k'[n], \tag{5}$$

where $n \in [0, L-1]$; $s[n]$ is the discrete-time version of $s(t)$ with period $L = T_0/T_s$; $\Theta_k[n]$ and d_k are the discrete carrier phase and code phase in samples, respectively, of the received signal at the k-th sub-accumulation; and $n_k'[n]$ is the sequence representing the data and noise at the k-th sub-accumulation.

4. Received Signal Dynamical Model

By using a Taylor series expansion, the carrier phase of the signal can be written as

$$\theta(t) = \theta_0 + \dot{\theta}(t)t + \frac{1}{2}\ddot{\theta}(t)t^2 + ... \tag{6}$$

Let $f_D(t) \triangleq \frac{\dot{\theta}(t)}{2\pi}$ denote the apparent Doppler shift. It is important to note that the transmitter or receiver may be experiencing very high dynamics, such in the case of LEO satellite communication or a receiver mounted on a highly dynamic aircraft. As

such, a high Doppler shift may be induced in the transmitted signal. In this paper, the carrier phase will be approximated up to its second order, and the signal state vector is defined as $\boldsymbol{x}(t) \triangleq \left[\theta(t),\ \dot{\theta}(t),\ \ddot{\theta}(t),\ \tau_d(t)\right]^{\mathsf{T}}$. The dynamics of the signal is modeled as

$$\dot{\boldsymbol{x}}(t) = \mathbf{A}\boldsymbol{x}(t) + \mathbf{B}\tilde{w}(t), \tag{7}$$

$$\mathbf{A} \triangleq \begin{bmatrix} 0 & 1 & 0 & 0 \\ 0 & 0 & 1 & 0 \\ 0 & 0 & 0 & 0 \\ 0 & \frac{-1}{2\pi f_c} & 0 & 0 \end{bmatrix}, \quad \mathbf{B} \triangleq \begin{bmatrix} 0 \\ 0 \\ 1 \\ 0 \end{bmatrix},$$

where $\tilde{w}(t)$ is a zero-mean white noise process with power spectral density $q_{\tilde{w}}$. The continuous-time model (7) is discretized at a sampling time $T_0 = LT_s$ yielding

$$\mathbf{x}_{k+1} = \mathbf{F}\mathbf{x}_k + \mathbf{w}_k, \tag{8}$$

where $\mathbf{F} \triangleq e^{\mathbf{A}T_0}$, $\mathbf{w}_k$ is a discrete-time process noise vector, which is a zero-mean white sequence with covariance $\mathbf{Q} = q_{\tilde{w}} \int_0^{T_0} e^{\mathbf{A}t}\mathbf{B} \left(e^{\mathbf{A}t}\mathbf{B}\right)^{\mathsf{T}} dt$.

5. Kalman Filter-Based Tracking Loop

A joint frequency, carrier, and code phase Kalman filter (KF)-based tracking loop is presented in this section. Let $\hat{\boldsymbol{\Theta}}_k \triangleq \left[\hat{\theta}_k,\ \hat{\dot{\theta}}_k,\ \hat{\ddot{\theta}}_k\right]^{\mathsf{T}}$ denote the carrier phase state estimate at the k-th sub-accumulation. The reconstructed sequence of the carrier phase can be written as a second order piece-wise polynomial given by

$$\hat{\Theta}_k[n] = \hat{\theta}_{k-1} + \hat{\dot{\theta}}_k n T_s + \frac{1}{2}\hat{\ddot{\theta}}_k \left(nT_s\right)^2, \quad n \in [0, L] \tag{9}$$

$$\hat{\theta}_k \triangleq \begin{cases} \hat{\Theta}_k[L] & \text{if} \quad k > 0 \\ 0 & \text{if} \quad k \leq 0 \end{cases} \tag{10}$$

The code phase estimates $\hat{\tau}_k$, expressed in seconds, and $\hat{d}_k$ expressed in samples, are defined as

$$\hat{\tau}_k \triangleq -\frac{\hat{\theta}_k}{2\pi f_c}, \quad \hat{d}_k \triangleq \left\lfloor \frac{\hat{\tau}_k}{T_s} \right\rceil. \tag{11}$$

Note that practically $\hat{\theta}_0$ and $\hat{\tau}_0$ are non-zero constants given by $\theta(0)$ and $\frac{\theta(0)}{2\pi c}$, respectively. But for simplicity, they are defined initially as zero and this will only shift the reference of the tracking and estimation framework.

The expression of the received signal after performing carrier wipe-off using the best estimate of the carrier can be written as

$$\begin{aligned} r_k[n] &\triangleq r_k^{'}[n] \exp\left(-j\hat{\Theta}_{k|k-1}[n]\right) \\ &= s[n - d_k] \exp\left(j\tilde{\Theta}_k[n]\right) + n_k[n], \end{aligned} \tag{12}$$

where $\tilde{\Theta}_k[n] = \Theta_k[n] - \hat{\Theta}_k[n]$, and $\tilde{\boldsymbol{\Theta}}_k \triangleq \left[\tilde{\theta}_k,\ \tilde{\dot{\theta}}_k,\ \tilde{\ddot{\theta}}_k\right]^{\mathsf{T}}$ is the estimation error of the carrier phase state. The sequence $r_k[n]$ will be used to determine the: (i) carrier phase error $\tilde{\theta}_k$, (ii) Doppler error $\tilde{\dot{\theta}}_k$, and (iii) code phase error $\tilde{\tau}_k$ at the k-th sub-accumulation by using respective discriminators discussed in the following section.

After calculating the carrier and Doppler errors, their values are fed as innovations to a KF loop that uses the observation model

$$\mathbf{z}_k = \mathbf{H}\mathbf{x}_k + \mathbf{v}_k, \tag{13}$$

$$\mathbf{H} \triangleq \begin{bmatrix} 1 & 0 & 0 & 0 \\ 0 & 1 & 0 & 0 \\ 0 & 0 & 0 & 1 \end{bmatrix}, \quad \mathbf{R} \triangleq \begin{bmatrix} \sigma_\theta^2 & 0 & 0 \\ 0 & \sigma_{\dot{\theta}}^2 & 0 \\ 0 & 0 & \sigma_\tau^2 \end{bmatrix},$$

where $\mathbf{v}_k$ is a discrete-time zero-mean white noise process with covariance $\mathbf{R}$. After calculating the innovation and performing a measurement update, the posterior carrier phase state estimate is $\hat{\mathbf{\Theta}}_{k|k}$, which will be used in the refinement of the navigation beacon. In the beginning phase of blind tracking, the framework is not coherent and relies heavily on frequency errors to bring the Doppler and Doppler rate errors close to zero. The frequency error is calculated using the cross-correlation in the frequency-domain as shown in the following section. After frequency lock, the receiver reaches the nominal operating region, in which the carrier and code phase errors produced by the nonlinear discriminators are acceptable.

6. Navigation Beacon Estimation

Since the receiver does not have any prior information about the repetitive sequence transmitted by the SOP, the receiver will take the first sub-accumulation ($k = 0$) as initial prior for the beacon estimate $\hat{s}_0[n]$ and attempt to sequentially refine it given the new incoming stream ($k > 0$) as

$$\hat{s}_0[n] = r_0[n] = s[n] \exp\left(j\tilde{\Theta}_0[n]\right) + w_0[n], \tag{14}$$

$$\hat{s}_k[n] = \alpha s_{k-1}[n] + (1-\alpha) r_k^*[n + \hat{d}_k] \exp\left(-j\hat{\Theta}_{k|k}[n]\right), \tag{15}$$

where $\alpha \in (0, 1)$ is a fading memory average parameter. The goal is to drive $\hat{s}_k[n]$ to converge to $\hat{s}[n]$ which might be a shifted version of the true sequence in time by $\tilde{d}_0$ and rotated by a phase of $\tilde{\theta}_0$.

7. Blind Doppler Tracking using Frequency-Domain Cross-Correlation

Under the assumption that the Doppler rate is nearly constant between two sub-accumulation, and by using (5), the nonlinear least squares (NLS) estimator for the Doppler shift $\dot{\theta}_k$ at the k-th sub-accumulation can be written as

$$\begin{aligned}
\hat{\dot{\theta}}_k &= \underset{\dot{\theta}}{\operatorname{argmin}} \left\| r_k^{'}[n] - \hat{s}_k[n - d_k] \exp\left(-j\Theta[n]\right) \right\|^2 \\
&= \underset{\dot{\theta}}{\operatorname{argmax}} \Re \left\{ \exp(-j\theta_k) \sum_0^{L-1} r_k^{'}[n] s_k^*[n - d_k] \exp(-j\dot{\theta}_k n T_s) \right\} \\
&= 2\pi \cdot \underset{f}{\operatorname{argmax}} \left| R_k^{'}(f) \circledast \hat{S}_k^*(-f) \exp(j2\pi d_k f) \right| \\
&= 2\pi \cdot \underset{f}{\operatorname{argmax}} \left| R_k^{'}(f) \star \hat{S}_k(f) \right|,
\end{aligned} \tag{16}$$

where $\dot{\theta} = 2\pi f$, $(f \star g)(\tau) = \int_{-\infty}^{\infty} f^*(t) g(t+\tau) dt$ is the cross-correlation operator, and $(f \circledast g)(t) = \int_{-\infty}^{\infty} f(\tau) g(t-\tau) d\tau$ is the convolution. Using (16), the Doppler error can be tracked blindly and fed to the KF discussed before to refine the Doppler shift and rate estimates.

III. EXPERIMENTAL RESULTS

This section presents experimental results validating the proposed receiver on Orbcomm LEO satellite signals.

1. Estimated Navigation Beacon from Orbcomm LEO Satellites

Orbcomm LEO signals were recorded using an Ettus E312 USRP with carrier frequency set to 137 MHz and sampling bandwidth of 2.4 MHz. The duration of the recorded data was 100 seconds. The recorded Orbcomm signals were fed to the proposed blind receiver. Apart from the proposed blind receiver, Orbcomm's transmitted data were decoded using the scheme described in (Orbcomm, 2002). After decoding, the data was cross-correlated with itself and showed repetitive behavior every T_0 equals to 1 second. The decoded data was averaged in a T_0 window over the 100 seconds. The averaging process increases the effective energy of the pseudo-random (PRN) sequence. Finally, the blindly estimated navigation beacon was compared against the true PRN sequence obtained by the averaging process. Figure 3(a) shows the true vs estimated PRN in-quadrature waveform. Figure 3(b) shows the in-phase/quadrature (IQ) plot of the estimated PRN sequence. Figure 3(c) shows the cross-correlation function

between the true and estimated PRN sequence. The prominent peak indicates successful estimation of the PRN sequence.

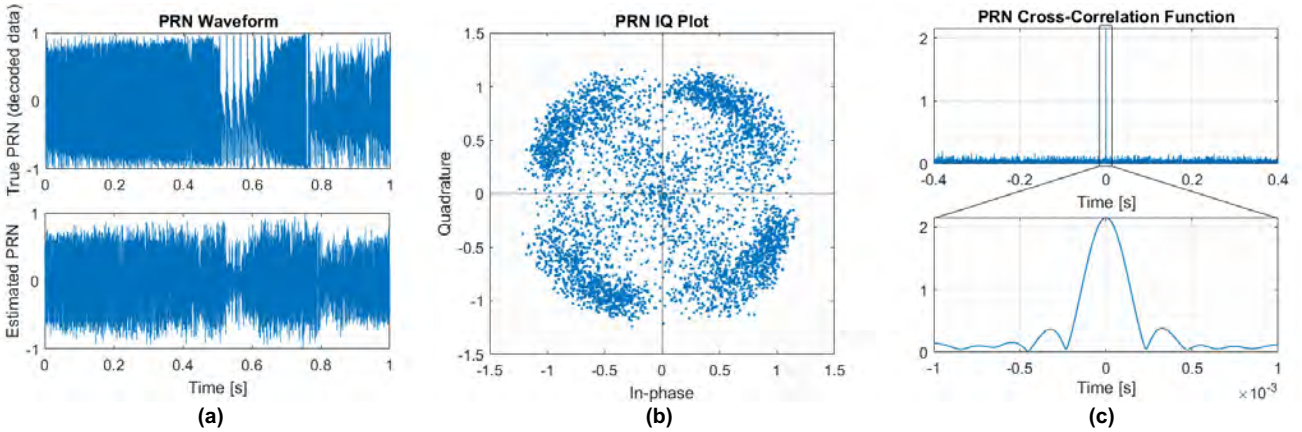

Figure 3: (a) True vs estimated PRN In-quadrature waveform. (b) Estimated PRN IQ plot. (c) Cross-correlation function between the true and estimated PRN.

2. UAV Differential Carrier Phase Navigation using Orbcomm LEO Satellites

To assess the performance of a receiver using the blindly estimated navigation beacon discussed in the previous section, a carrier phase differential (CD-LEO) experiment was conducted using the framework discussed in (Khalife et al., 2020). The rover was a DJI Matrice 600 UAV equipped with an Ettus E312 USRP, a high-end VHF antenna, and a small consumer-grade GPS antenna to discipline the onboard oscillator. The base was a stationary receiver equipped with an Ettus E312 USRP, a custom-made VHF antenna, and a small consumer-grade GPS antenna to discipline the onboard oscillator. The receivers were tuned to a 137 MHz carrier frequency with 2.4 MHz sampling bandwidth, which covers the 137–138 MHz band allocated to Orbcomm satellites. Samples of the received signals were stored for off-line post-processing. The LEO carrier phase measurements were produced at a rate of 24 Hz and were downsampled to 10 Hz. The UAV trajectory was taken from its on-board navigation system, which uses GNSS (GPS and GLONASS), an inertial measurement unit (IMU), and other sensors. The experimental setup is shown in Figure 4. The UAV traversed a total trajectory of 2.28 km in 120 seconds. Over the course of the experiment, the receivers on-board the base and the UAV were listening to 2 Orbcomm satellites, namely FM 108 and FM 116.

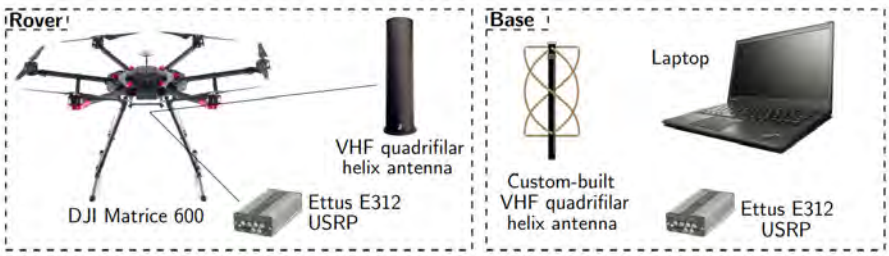

Figure 4: The architecture of the proposed blind receiver

a) Acquisition and Tracking of Orbcomm Satellites

The receivers at the base and rover used the estimated navigation beacon to acquire the visible Orbcomm satellites during the experiment. A joint Doppler and Code phase search was performed and successfully detected the Orbcomm satellites. Figure 5 shows the acquisition plots for the base's receiver. After acquisition, the KF-based tracking loop was initialized using the initial Doppler shift and code phase, and generated carrier phase observables from Orbcomm satellites. Figure 6(a) visualizes the skyplot of the tracked Orbcomm satellites. Figure 6(b) summarizes the tracking results of the two satellites seen by the UAV. It should be noted that the carrier phase error exhibit sudden $\pm\frac{\pi}{2}$ phase jumps because of the presence of user data alongside with the SD-PSK modulation employed in the transmitted signal. The SD-PSK modulation used in Orbcomm and Iridium NEXT renders the PRN-based carrier phase tracking loop sensitive to user data and more prone to exhibit cycle slips. But in general, one can assume that the transmitted SD-PSK modulated signals employ effective source and channel coding schemes that equalize the probability of every symbol in the alphabet. Consequently, the average of the phase jumps due to user data is expected to be zero.

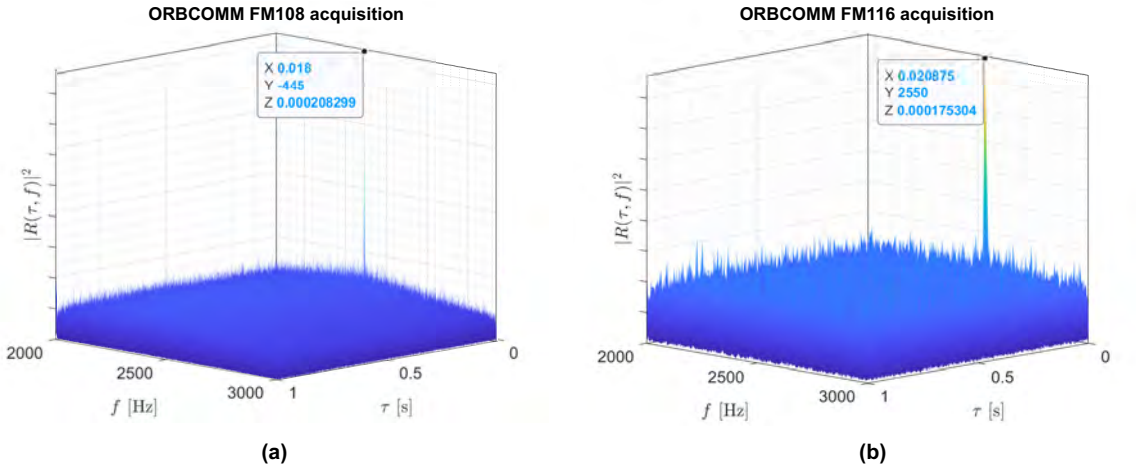

(a) (b)

Figure 5: 2-D Doppler and Code phase acquisition plots for Orbcomm FM108 (a) and FM116 (b) at the Base receiver.

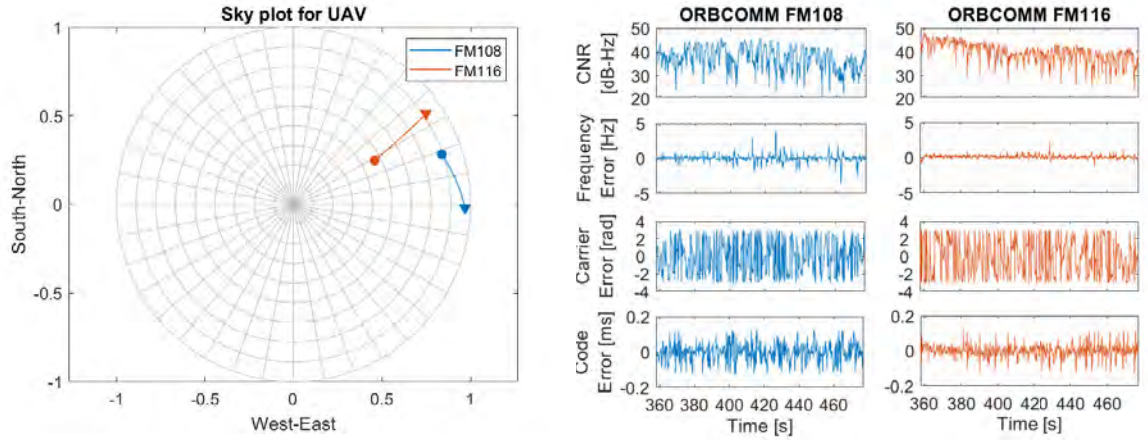

(a) (b)

Figure 6: (a) Sky plot of the geometry of the 2 Orbcomm satellites for the UAV during the experiment. (b) Tracking results of the two satellites seen by the UAV.

b) Carrier Differential Navigation with Orbcomm Satellites

The employed carrier phase model is discussed in detail in (Khalife et al., 2020) and given by

$$\Phi_i^j(k) = \left\|\mathbf{r}_{r_i}(k) - \mathbf{r}_{SV_j}(k')\right\|_2 + c\delta t_{r_i}(k) + c\delta t_{SV_j}(k') + c\delta t_{trop_{ij}}(k) + c\delta t_{iono_{ij}}(k) + \lambda_j N_{ij} + \nu_{ij}(k), \tag{17}$$

where $i \in \{1,2\}$ is the index of the stationary base and mobile rover, respectively; $j \in \{1,2\}$ is the index of the LEO satellite; $k' = k - \delta t_{TOF_{ij}}$ where $\delta t_{TOF_{ij}}$ is the time of flight of signal from the j-th satellite to the i-th receiver; $\mathbf{r}_{r_i} \triangleq [x_{r_i}, y_{r_i}, z_{r_i}]^\intercal$ is the i-th receiver's position vector in East-North-Up (ENU) frame; $\mathbf{r}_{SV_i} \triangleq [x_{SV_i}, y_{SV_i}, z_{SV_i}]^\intercal$ is the j-th satellite's position vector in ENU; δt_{r_i} and δt_{SV_j} are the i-th receiver's and j-th satellite's clock biases, respectively; $\delta t_{trop_{ij}}$ and $\delta t_{iono_{ij}}$ are the ionospheric and tropospheric delays between the i-th receiver and j-th satellite, respectively; λ_j is the wavelength of the j-th satellite's signal; N_{ij} is the carrier phase ambiguity between the i-th receiver and j-th satellite; and ν_{ij} is the measurement noise, which is modeled as a discrete-time zero-mean white Gaussian sequence with variance σ_{ij}^2. The difference between the carrier phase measurement at the base and rover to the j-th satellite can be expressed as

$$\Delta\Phi^j(k) = \Phi_2^j(k) - \Phi_1^j(k) = \left\|\mathbf{r}_{r_2}(k) - \mathbf{r}_{SV_j}(k')\right\|_2 - \left\|\mathbf{r}_{r_1} - \mathbf{r}_{SV_j}(k')\right\|_2 + c\Delta\delta t_r(k) + \lambda_j \Delta N_j + \nu_j(k), \tag{18}$$

where it is assumed that $\delta t_{trop_{1j}} \approx \delta t_{trop_{2j}}$ and $\delta t_{iono_{1j}} \approx \delta t_{iono_{2j}}$, and $\Delta\delta t_r = \delta t_{r_2} - \delta t_{r_1}$ is the lumped clock bias term of the base and rover. Let $\Delta\hat{\Phi}_{TLE}^j(k)$ denote the estimated differential carrier phase calculated using from two-line element

(TLE) files and an SGP4 propagator, which can be expressed as

$$\Delta\hat{\Phi}^j_{TLE}(k) = \hat{\Phi}^j_{2,TLE}(k) - \hat{\Phi}^j_{1,TLE}(k) = \left\|\mathbf{r}_{r_2}(k) - \mathbf{r}_{SV_j}(k')\right\|_2 - \left\|\mathbf{r}_{r_1} - \mathbf{r}_{SV_j}(k')\right\|_2 . \tag{19}$$

Figure 7(a) shows the differential carrier phase $\Delta\Phi^j(k)$ for both satellites without the initial carrier phase ambiguity ΔN_j using: (i) observables calculated from TLE+SGP4 (equation 19) and (ii) the real tracked signals (equation 18). The difference between the measured differential carrier phase and the one calculated from TLE+SGP4 is

$$\Delta\Phi^j(k) - \Delta\hat{\Phi}^j_{TLE}(k) = c\Delta\delta t_r(k) + \lambda_j\Delta N_j + \nu_j(k), \tag{20}$$

which is plotted in Figure 7(b). Note that ideally, the two curves in Figure 7(b) should superimpose because they are plotting the same $\Delta\delta t_r$, however, due to measurement noise and unresolved carrier phase cycle slips, the two curves do not perfectly superimpose, nevertheless, they show the same trend.

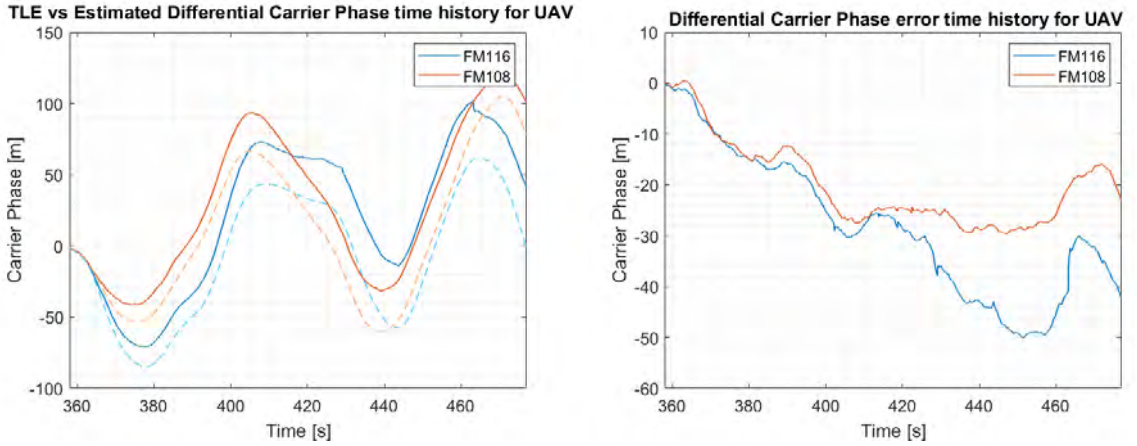

Figure 7: (a) Differential carrier phase seen by the UAV for Orbcomm FM116 and FM108 from: observables calculated from TLE (plotted in dashed), and the real tracked signals (plotted in solid). (b) Error between the TLE-calculated and real differential carrier phase.

The single-difference carrier phase measurement fed to the EKF is given by

$$z^j(k) \triangleq \Delta\Phi^j(k) + \left\|\mathbf{r}_{r_1}(k) - \mathbf{r}_{SV_j}(k')\right\|_2 \tag{21}$$

The UAV's position and velocity were assumed to evolve according to a nearly constant velocity model, and the common clock state was assumed to evolve according to the standard model of double integrator driven by noise as discussed in (Khalife et al., 2020). A prior for the UAV's position and velocity was obtained from the UAV's on-board navigation system. The prior was used to initialize the EKF. After initialization, the EKF used altimeter measurements and single-difference Orbcomm LEO satellites measurements to estimate the states of the UAV. The position of FM 108 and FM 116 was obtained by propagating the TLE files using SGP4. The UAV navigated for 2.28 km exclusively from only two Orbcomm LEO satellites with a position RMSE of 13.9 m over a period of 2 minutes. Figure 8(a) illustrates the true versus estimated trajectory of the UAV. Figure 8(b) shows the EKF position estimation error and $\pm 3\sigma$ bounds for the carrier phase differential navigation solution.

IV. CONCLUSION

This paper presented a receiver for blind beacon estimation of LEO satellite signals. The receiver operates in three stages: (i) blind Doppler tracking, (ii) beacon estimation from the coherent accumulation of the received signal after wiping off the Doppler tracked by the FLL, and (iii) tracking LEO signals using the estimated beacon to produce navigation observables. Experimental results were presented showing successful blind estimation of the navigation beacon of the Orbcomm LEO constellation. In addition, experimental results were presented of a UAV navigating using the estimated beacons of two Orbcomm LEO satellites via a carrier phase differential navigation framework, achieving a three-dimensional position RMSE of 13.9 m, over a trajectory of 2.28 km traversed in 2 minutes.

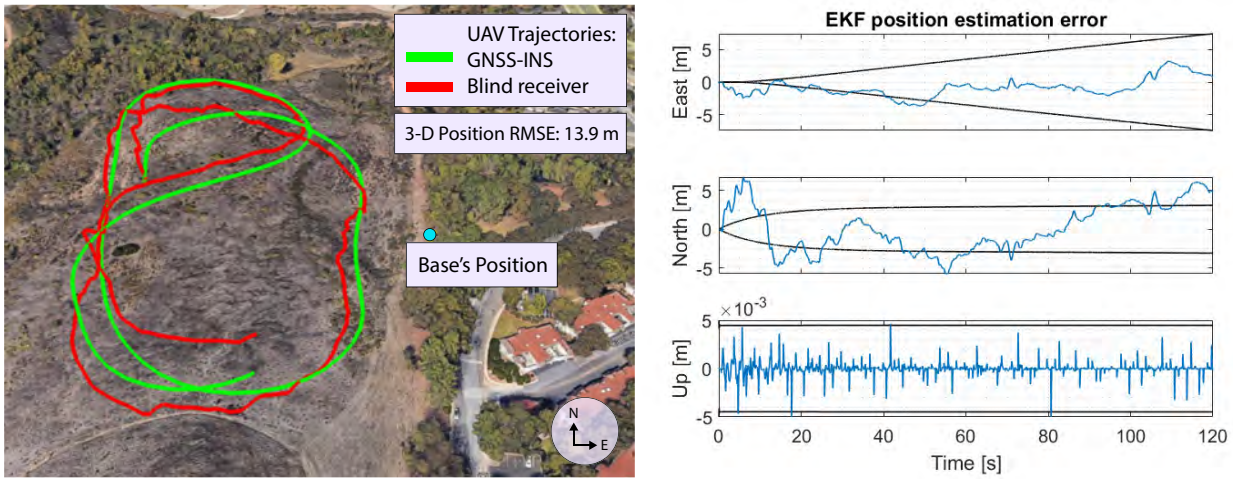

Figure 8: (a) True (from GNSS-INS) and estimated (from blind Orbcomm LEO receiver with carrier phase differential measurments) trajectories of the UAV. (b) EKF position estimation error of the UAV and $\pm 3\sigma$ bounds for the carrier phase differential navigation solution.

ACKNOWLEDGEMENTS

This work was supported in part by the Office of Naval Research (ONR) under N00014-19-1-2511 and Grant N00014-22-1-2242, in part by the Air Force Office of Scientific Research (AFOSR) under Grant FA9550-22-1-0476, and in part by the U.S. Department of Transportation (USDOT) under Grant 69A3552047138 for the CARMEN University Transportation Center (UTC).

REFERENCES

Al-Dweik, A. (2006). A novel non-data-aided symbol timing recovery technique for OFDM systems. *IEEE Transactions on Communications*, 54(1):37–40.

Aziz, M. and Allen, C. (2018). Experimental results of a differential angle-of-arrival based 2D localization method using signals of opportunity. *International Journal of Navigation and Observation*, 2018(5470895):1–6.

Bouder, C., Azou, S., and Burel, G. (2004). Performance analysis of a spreading sequence estimator for spread spectrum transmissions. *Journal of the Franklin Institute*, 341(7):595–614.

Bouder, C. and Burel, G. (2000). Spread spectrum codes identification by neural networks. *Systems and Control: Theory and Applications*, pages 257–262.

Burel, G. and Bouder, C. (2000). Blind estimation of the pseudo-random sequence of a direct sequence spread spectrum signal. In *Proceedings of IEEE Military Communications Conference*, volume 2, pages 967–970.

Cassel, R., Scherer, D., Wilburne, D., Hirschauer, J., and Burke, J. (2022). Impact of improved oscillator stability on LEO-based satellite navigation. In *Proceedings of ION International Technical Meeting*, pages 893–905.

Chen, X., Wei, Q., Wang, F., Jun, Z., Wu, S., and Men, A. (2020). Super-resolution time of arrival estimation for a symbiotic FM radio data system. *IEEE Transactions on Broadcasting*, 66(4):847–856.

Choi, H. and Moon, H. (2020). Blind estimation of spreading sequence and data bits in direct-sequence spread spectrum communication systems. *IEEE Access*, 8:148066–148074.

Farhangian, F., Benzerrouk, H., and Landry, R. (2021). Opportunistic in-flight INS alignment using LEO satellites and a rotatory IMU platform. *Aerospace*, 8(10):280–281.

Farhangian, F. and Landry, R. (2020). Multi-constellation software-defined receiver for Doppler positioning with LEO satellites. *Sensors*, 20(20):5866–5883.

Gadka, P., Sadowski, J., and Stefanski, J. (2019). Detection of the first component of the received LTE signal in the OTDoA method. *Wireless Communications and Mobile Computing*, pages 1–12.

Gao, Y., Zhao, X., Wang, S., Xiang, Y., Huang, C., and Hua, Y. (2021). Positioning via GEO communication satellites' signals of opportunity. *IET Radar, Sonar Navigation*, 15(11):1472–1482.

Haidar-Ahmad, J., Khairallah, N., and Kassas, Z. (2022). A hybrid analytical-machine learning approach for LEO satellite orbit prediction. In *Proceedings of International Conference on Information Fusion*, pages 1–7.

Hartnett, M. (2022). Performance assessment of navigation using carrier Doppler measurements from multiple LEO constellations. Master's thesis, Air Force Institute of Technology, Wright-Patterson Air Force Base, Ohio, USA.

Hong, T., Sun, J., Jin, T., Yi, Y., and Qu, J. (2021). Hybrid positioning with DTMB and LTE signals. In *Proceedings of International Wireless Communications and Mobile Computing*, pages 303–307.

Huang, C., Qin, H., Zhao, C., and Liang, H. (2022). Phase - time method: Accurate Doppler measurement for Iridium NEXT signals. *IEEE Transactions on Aerospace and Electronic Systems*, pages 1–9.

Iannucci, P. and Humphreys, T. (2022). Fused low-Earth-orbit GNSS. *IEEE Transactions on Aerospace and Electronics Systems*. accepted.

Iridium Constellation LLC (2013). Iridium NEXT engineering statement. `http://licensing.fcc.gov/myibfs/download.do?attachment_key=1031348`.

Jardak, N. and Jault, Q. (2022). The potential of LEO satellite-based opportunistic navigation for high dynamic applications. *Sensors*, 22(7):2541–2565.

Jiang, M., Qin, H., Zhao, C., and Sun, G. (2022). LEO Doppler-aided GNSS position estimation. *GPS Solutions*, 26(1):1–18.

Kassas, Z. (2021). Position, navigation, and timing technologies in the 21st century. volume 2, chapter 43: Navigation from low Earth orbit – Part 2: models, implementation, and performance, pages 1381–1412. Wiley-IEEE.

Kassas, Z., Neinavaie, M., Khalife, J., Khairallah, N., Haidar-Ahmad, J., Kozhaya, S., and Shadram, Z. (2021). Enter LEO on the GNSS stage: Navigation with Starlink satellites. *Inside GNSS Magazine*, 16(6):42–51.

Kazaz, T., Janssen, G., Romme, J., and Van der Veen, A. (2022). Delay estimation for ranging and localization using multiband channel state information. *IEEE Transactions on Wireless Communications*, 21(4):2591–2607.

Khairallah, N. and Kassas, Z. (2021). Ephemeris closed-loop tracking of LEO satellites with pseudorange and Doppler measurements. In *Proceedings of ION GNSS Conference*, pages 2544–2555.

Khairallah, N. and Kassas, Z. (2022). An interacting multiple model estimator of LEO satellite clocks for improved positioning. In *Proceedings of IEEE Vehicular Technology Conference*, pages 1–5.

Khalife, J. and Kassas, Z. (2022). Differential framework for submeter-accurate vehicular navigation with cellular signals. *IEEE Transactions on Intelligent Vehicles*. accepted.

Khalife, J., Neinavaie, M., and Kassas, Z. (2020). Navigation with differential carrier phase measurements from megaconstellation LEO satellites. In *Proceedings of IEEE/ION Position, Location, and Navigation Symposium*, pages 1393–1404.

Khalife, J., Neinavaie, M., and Kassas, Z. (2022). The first carrier phase tracking and positioning results with Starlink LEO satellite signals. *IEEE Transactions on Aerospace and Electronic Systems*, 56(2):1487–1491.

Kozhaya, S., Haidar-Ahmad, J., Abdallah, A., Kassas, Z., and Saab, S. (2021). Comparison of neural network architectures for simultaneous tracking and navigation with LEO satellites. In *Proceedings of ION GNSS Conference*, pages 2507–2520.

Lapin, I., Granados, G., Samson, J., Renaudin, O., Zanier, F., and Ries, L. (2022). STARE: Real-time software receiver for LTE and 5G NR positioning and signal monitoring. In *Proceedings of Workshop on Satellite Navigation Technology*, pages 1–11.

Leng, M., Quitin, F., Tay, W., Cheng, C., Razul, S., and See, C. (2016). Anchor-aided joint localization and synchronization using SOOP: Theory and experiments. *IEEE Transactions on Wireless Communications*, 15(11):7670–7685.

Li, M., Xu, T., Guan, M., Gao, F., and Jiang, N. (2022). LEO-constellation-augmented multi-GNSS real-time PPP for rapid re-convergence in harsh environments. *GPS Solutions*, 26(1):1–12.

Liu, W., Wang, J., and Li, S. (2010). Blind detection and estimation of OFDM signals in cognitive radio contexts. In *Proceedings of International Conference on Signal Processing Systems*, volume 2, pages 347–351.

Maaref, M. and Kassas, Z. (2022). Autonomous integrity monitoring for vehicular navigation with cellular signals of opportunity and an IMU. *IEEE Transactions on Intelligent Transportation Systems*, 23(6):5586–5601.

Nardin, A., Dovis, F., and Fraire, J. (2021). Empowering the tracking performance of LEO-based positioning by means of meta-signals. *IEEE Journal of Radio Frequency Identification*, 5(3):244–253.

Neinavaie, M., Khalife, J., and Kassas, Z. (2020). Blind opportunistic navigation: Cognitive deciphering of partially known signals of opportunity. In *Proceedings of ION GNSS Conference*, pages 2748–2757.

Neinavaie, M., Khalife, J., and Kassas, Z. (2021). Blind Doppler tracking and beacon detection for opportunistic navigation with LEO satellite signals. In *Proceedings of IEEE Aerospace Conference*, pages 1–8.

Neinavaie, M., Khalife, J., and Kassas, Z. (2022). Cognitive opportunistic navigation in private networks with 5G signals and beyond. *IEEE Journal of Selected Topics in Signal Processing*, 16(1):129–143.

Orabi, M., Khalife, J., and Kassas, Z. (2021). Opportunistic navigation with Doppler measurements from Iridium Next and Orbcomm LEO satellites. In *Proceedings of IEEE Aerospace Conference*, pages 1–9.

Orbcomm (2002). Ever wondered what is on the Orbcomm satellite downlink? `http://mdkenny.customer.netspace.net.au/Orbcomm.pdf`.

Prol, F., Ferre, R., Välisuo, Z. S. P., Pinell, C., Lohan, E., Elsanhoury, M., Elmusrati, M., Islam, S., Celikbilek, K., Selvan, K., Yliaho, J., Rutledge, K., Ojala, A., Ferranti, L., andM. Bhuiyan, J. P., Kaasalainen, S., and Kuusniemi, H. (2022). Position, navigation, and timing (PNT) through low earth orbit (LEO) satellites: A survey on current status, challenges, and opportunities. *IEEE Access*, 10:83971–84002.

Psiaki, M. (2021). Navigation using carrier Doppler shift from a LEO constellation: TRANSIT on steroids. *NAVIGATION, Journal of the Institute of Navigation*, 68(3):621–641.

Psiaki, M. and Slosman, B. (2022). Tracking digital FM OFDM signals for the determination of navigation observables. *NAVIGATION, Journal of the Institute of Navigation*, 69(2).

Raquet *et al.*, J. (2021). Position, navigation, and timing technologies in the 21st century. volume 2, Part D: Position, Navigation, and Timing Using Radio Signals-of-Opportunity, chapter 35–43, pages 1115–1412. Wiley-IEEE.

Reid, T., Walter, T., Enge, P., Lawrence, D., Cobb, H., Gutt, G., O'Conner, M., and Whelan, D. (2021). Position, navigation, and timing technologies in the 21st century. volume 2, chapter 43: Navigation from low Earth orbit – Part 1: Concept, Current Capability, and Future Promise, pages 1359–1379. Wiley-IEEE.

Shamaei, K. and Kassas, Z. (2021a). A joint TOA and DOA acquisition and tracking approach for positioning with LTE signals. *IEEE Transactions on Signal Processing*, pages 2689–2705.

Shamaei, K. and Kassas, Z. (2021b). Receiver design and time of arrival estimation for opportunistic localization with 5G signals. *IEEE Transactions on Wireless Communications*, 20(7):4716–4731.

Shen, D., Lu, J., Chen, G., Blasch, E., Sheaff, C., Pugh, M., and Pham, K. (2019). Methods of machine learning for space object pattern classification. In *Proceedings of IEEE National Aerospace and Electronics Conference*, pages 565–572.

Soderini, A., Thevenon, P., Macabiau, C., Borgagni, L., and Fischer, J. (2020). Pseudorange measurements with LTE physical channels. In *Proceedings of ION International Technical Meeting*, pages 817–829.

Souli, N., Kolios, P., and Ellinas, G. (2021a). Online relative positioning of autonomous vehicles using signals of opportunity. *IEEE Transactions on Intelligent Vehicles*, pages 1–1.

Souli, N., Makrigiorgis, R., Kolios, P., and Ellinas, G. (2021b). Real-time relative positioning system implementation employing signals of opportunity, inertial, and optical flow modalities. In *Proceedings of International Conference on Unmanned Aircraft Systems*, pages 229–236.

Tan, Z., Qin, H., Cong, L., and Zhao, C. (2019a). New method for positioning using IRIDIUM satellite signals of opportunity. *IEEE Access*, 7:83412–83423.

Tan, Z., Qin, H., Cong, L., and Zhao, C. (2019b). Positioning using IRIDIUM satellite signals of opportunity in weak signal environment. *Electronics*, 9(1):37.

Tanda, M. (2004). Blind symbol-timing and frequency-offset estimation in OFDM systems with real data symbols. *IEEE Transactions on Communications*, 52(10):1609–1612.

Tsatsanis, M. and Giannakis, G. (1997). Blind estimation of direct sequence spread spectrum signals in multipath. *IEEE Transactions on Signal Processing*, 45(5):1241–1252.

Wang, K. and El-Mowafy, A. (2022). LEO satellite clock analysis and prediction for positioning applications. *Geo-spatial Information Science*, 25(1):14–33.

Wang, P. and Morton, Y. (2022). Impact analysis of inter-cell interference in cellular networks for navigation applications. *IEEE Transactions on Aerospace and Electronic Systems*. accepted.

Wei, Q., Chen, X., and Zhan, Y. (2020). Exploring implicit pilots for precise estimation of LEO satellite downlink Doppler frequency. *IEEE Communications Letters*, 24(10):2270–2274.

Xhafa, A., del Peral-Rosado, J., López-Salcedo, J., and Seco-Granados, G. (2021). Evaluation of 5G positioning performance based on UTDoA, AoA and base-station selective exclusion. *Sensors*, 22(1):101–118.

Yang, C., Arizabaleta-Diez, M., Weitkemper, P., and Pany, T. (2022). An experimental analysis of cyclic and reference signals of 4g LTE for TOA estimation and positioning in mobile fading environments. *IEEE Aerospace and Electronic Systems Magazine*, 37(9):16–41.

Yang, C., Pany, T., and Weitkemper, P. (2020). Effect of antenna ports on TOA estimation with 4G LTE signals in urban mobile environments. In *Proceedings of ION International Technical Meeting*, pages 2166–2181.

Yang, C. and Soloviev, A. (2020). Mobile positioning with signals of opportunity in urban and urban canyon environments. In *Proceedings of IEEE/ION Position, Location, and Navigation Symposium*, pages 1043–1059.

Zhang, T., Dai, S., Zhang, W., Ma, G., and Gao, X. (2012). Blind estimation of the PN sequence in lower SNR DS-SS signals with residual carrier. *Digital Signal Processing*, 22(1):106–113.

Zhao, C., Qin, H., and Li, Z. (2022). Doppler measurements from multiconstellations in opportunistic navigation. *IEEE Transactions on Instrumentation and Measurement*, 71:1–9.

UC Irvine
UC Irvine Previously Published Works

Title
Carpe signum: seize the signal – opportunistic navigation with 5G

Permalink
https://escholarship.org/uc/item/7392n44c

Authors
Kassas, Zak
Abdallah, Ali
Orabi, Mohamad

Publication Date
2021-01-25

Peer reviewed

eScholarship.org Powered by the California Digital Library
University of California

January/February 2021 | Engineering Solutions from the Global Navigation Satellite System Community | www.insidegnss.com

InsideGNSS

Published by **Autonomous Media**

GPS | GALILEO | GLONASS | BEIDOU

SUPERCORRELATION

Inertially-aided Extended Coherent Integration Combats Multipath

Carpe Signum: Seize the Signal
Opportunistic Navigation with 5G

Innovative features of cellular fifth-generation (5G) signals enable the wireless system to play a major role in autonomous technologies. Test results of a ground vehicle navigating with signals from five 5G base stations (gNBs) over a trajectory of 773 m traversed in 110 seconds show a position root mean-squared error of 4.1 m.

ZAHER (ZAK) M. KASSAS,
ALI A. ABDALLAH AND MOHAMAD ORABI,
UNIVERSITY OF CALIFORNIA, IRVINE

Also known as new radio (NR), the next wireless communication system 5G provides faster data transfer speeds, lower latency, higher capacity, lower transmission power, and network slicing over fourth-generation (4G) long-term evolution (LTE). Autonomous vehicles involve enormous quantity of data collection, processing, and communication for navigation trajectory, traffic information, and surrounding vehicles and obstacles. 5G could revolutionize autonomous vehicles' capabilities, from data sharing to navigation and situational awareness. This article assesses the potential of 5G signals for opportunistic navigation.

A carrier-aided code-based software-defined receiver (SDR) in this research produces navigation observables from received downlink 5G signals. These observables are analyzed to assess the performance of 5G signals for opportunistic navigation.

A wealth of recent research has considered the use of signals of opportunity (SOPs) as complementary and alternative navigation sources in GNSS-challenged environments [1]. SOPs are signals not intended for navigation purposes; however, they can be exploited for navigation, such as Wi-Fi [2], AM/FM [3], digital television [4], low-Earth orbit [5], and cellular [6[. Cellular signals, code-division multiple access (CDMA) and LTE, have shown high ranging and localization accuracy using specialized software-defined receivers (SDRs). See Reference [7]. To date, all 5G navigation results published in the literature have been limited to theoretical analyses, simulations, or laboratory-emulated 5G signals, due to:

- The structure of 5G signals has been recently finalized.
- 5G has been implemented only in a few major cities.
- The hardware for both reception and transmission in 5G systems, in which millimeter waves (mmWaves) are used, is still in development.
- The proposed navigation approaches require a network-based approach, in which the user's privacy is revealed for the network. This also limits the user equipment (UE) to a single serving cellular provider, which limits the number of gNBs in sight. See **sidebar 5G Characteristics**.

This article describes the first experimental demonstration of navigation with real cellular 5G signals, tackling the aforementioned challenges by:

- Studying opportunistic navigation of 5G signals and presenting potential signals to be exploited for navigation purposes.
- Presenting an SDR to extract navigation observables from 5G signals.
- Implementing a navigation framework using an extended Kalman filter (EKF) to estimate the receiver's position, along with

the clock biases of the receiver and gNBs from extracted 5G navigation observables.

5G Signal Structure

Orthogonal frequency multiplexing (OFDM) with cyclic prefix (CP) is used as a modulation technique for 5G downlink signals, which is the same waveform LTE has adopted for its downlink signal. Here, we implement an opportunistic UE-based navigation approach; thus, only 5G downlink signal structure is discussed. OFDM uses a multi-carrier transmission scheme: transmitted data symbols are mapped into multiple narrowband subcarriers in the frequency-domain, which reduces frequency selective fading effect caused by multipath. The serial data symbol $\{S_1,\ldots,S_N\}$ are parallelized in group symbols, each of length N_R, where N_R is the number of subcarriers carrying the data. Then, a guard band in the frequency-domain is applied by zero-padding both sides of the signal and extending the N_R subcarriers into N_c subcarriers. At this step, an inverse fast Fourier transform (IFFT) is taken, and the last L_{CP} elements are repeated in the beginning, which serves as a guard band in the time-domain to protect the OFDM signals from inter-symbol interference (ISI).

At the receiver, the transmitted symbols are demodulated by executing these steps in reverse order. The obtained OFDM signals are arranged in a 2-D frame. The structure of this frame depends on the transmission type of the 5G signal, which can be either time division duplexing (TDD) or frequency division duplexing (FDD). Here, we use 5G signals from frequency range 1 (FR1), where most cellular providers are using FDD due to its providing better coverage and less latency.

Compared to LTE numerology (i.e., subcarrier spacing (SCS) and symbol length), which supports only one type of subcarrier spacing, Δf=15kHz, 5G supports different types of subcarrier spacing. **Figure 1** shows the different types, where μ denotes the numerology.

The duration of the FDD 5G frame is

$$T_f = \frac{\Delta f_{\max} N_f}{100} T_c = 10 \text{ ms} \quad (1)$$

where $\Delta f_{\max}$=480 kHz, N_f=4096, and $T_c=\frac{1}{\Delta f_{max} N_f}$=0.509 ns is the basic time unit for 5G. Each 5G frame consists of ten subframes, with duration 1 ms each. The number of OFDM symbols per subframe is $N_{\text{symb}}^{\text{subframe},\mu}=N_{\text{symb}}^{\text{slot}} N_{\text{slot}}^{\text{subframe},\mu}$. The frame is divided into two equally-sized half-frames consisting of five subframes each and denoted by: (i) half-frame 0 consisting of subframes 0-4 and (ii) half-frame 1 consisting of subframes 5-9.

For a predefined μ, the number of slots is denoted by $n_s^\mu \in \{0, 1, \ldots, N_{\text{slot}}^{\text{subframe},\mu}\}$ or $n_s^\mu \in \{0, 1, \ldots, N_{\text{slot}}^{\text{frame},\mu}\}$ in an increasing order within a subframe or a frame, respectively. The number of symbols per slot $N_{\text{symb}}^{\text{slot}}$ depends on the type of cyclic prefix and the specified numerology.

The table in Figure 1 shows for different numerologies: the number of OFDM symbols per slot, number of slots per frame, number of slots per subframe, and CP type.

A resource block (RB) is defined as N_{sc}^{RB}=12 subcarriers in the frequency-domain and has the time length of a resource grid $N_{\text{symb}}^{\text{subframe},\mu}$. A resource block consists of resource elements. The minimum and maximum number of resource blocks along with the corresponding bandwidth for different numerologies are summarized in **Table 1.** Each element in the 5G frame is uniquely identified for a specific antenna port p and subcarrier configuration μ by (k,l)p,μ, where k is the index in frequency domain and l is the symbol position in the time domain relative to some reference point. In the 5G protocol, "Point A" serves as a common reference point.

μ	Δ f [kHz]	CP	$N_{\text{symb}}^{\text{slot}}$	$N_{\text{slot}}^{\text{frame},\mu}$	Symbol duration [μs]	CP duration [μs]
0	15	N	14	10	66.67	4.69
1	30	N	14	20	33.33	2.34
2	60	N/E	14/12	40	16.67	1.17
3	120	N	14	80	8.33	0.57
4	240	N	14	160	4.17	0.29

N: normal; E: extended; CP: cyclic prefix

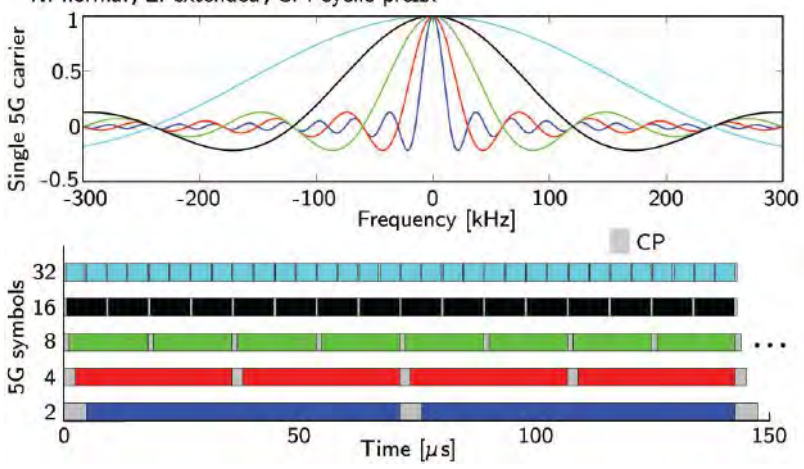

FIGURE 1 Different numerologies of 5G and the corresponding: single OFDM carrier and timing of two consecutive OFDM symbols guarded by CPs.

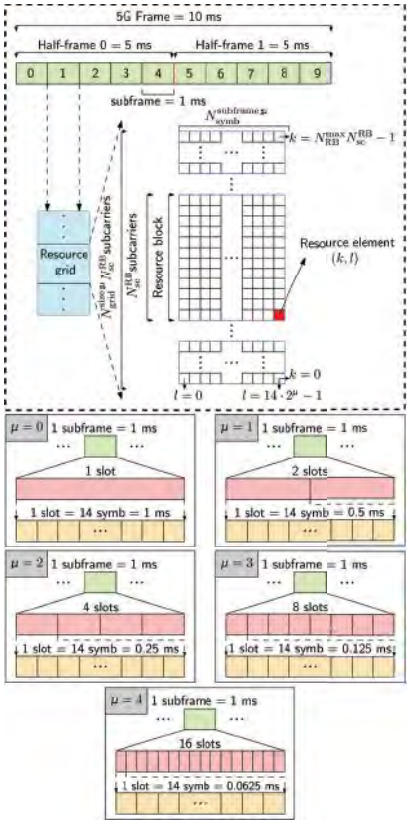

FIGURE 2 5G frame structure.

Signal	Symbol number	Subcarrier number
PSS	0	56, 57, ⋯, 182
SSS	0	56, 57, ⋯, 182
Set to zero	0	0, 1, ⋯, 55 183, 184, ⋯, 239
	2	48, 49, ⋯, 55 183, 184, ⋯, 239
PBCH	1, 3	0, 1, ⋯, 239
	2	0, 1, ⋯, 47 192, 193, ⋯, 239
DM-RS	1, 3	$0+v, 4+v, 236+v$
	2	$0+v, 4+v, 44+v$ $192+v, 196+v, 236+v$

$v = N_{ID}^{Cell} \bmod 4$

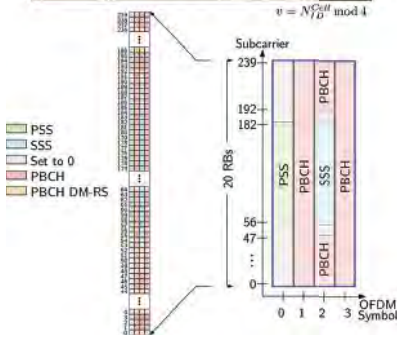

FIGURE 3 SS/PBCH block structure and the corresponding OFDM symbols and subcarriers mapping of the different signals within the block.

Figure 2 summarizes the 5G frame structure.

At the receiver side, the received 5G signal must be converted to frame structure before extracting signals of interest. To do so, the frame start time should be known. For the purpose of providing the frame start time, the gNB broadcasts synchronization signals (SS) with a pre-specified symbol mapping in the 5G frame. The SS includes two reference signals: primary synchronization signal (PSS) and secondary synchronization signal (SSS), which provide symbol and frame timing, respectively. Once the frame start time is known, the CPs can be removed and a fast Fourier transform (FFT) is taken to construct the OFDM symbols in the frame. The SS, the physical broadcast channel (PBCH), and its associated demodulation reference signal (DM-RS) are transmitted in the same 4 symbols block called the SS/PBCH block. The SS/PBCH block consists of 240 contiguous subcarrier (20 RBs) and four consecutive OFDM symbols. Within the SS/PBCH, the subcarriers are numbered in an ascending order from 0 to 239. **Figure 3** shows the SS/PBCH block structure and the corresponding OFDM symbols and subcarriers mapping of the different signals within the block. Note that the position of PBCH-DM-RS varies with v, and the value v changes depending on the physical cell ID. The SS/PBCH block is transmitted every two frames and is transmitted numerous times, where each set of these transmitted block is called an SS/PBCH burst. The SS/PBCH burst has to be confined within a half-frame window (5 ms). Each block in the SS/PBCH burst is beamformed in a different direction. The frequency location of the SS/PBCH within the 5G frame depends on the 5G high-level signaling. The time location of the SS/PBCH block and the size of the SS/PBCH burst in the frame depends on the transmission frequency fc and the numerology μ.

The PSS and SSS are two orthogonal maximum-length sequences (m-sequences) of length 127 and are transmitted on contiguous subcarriers. The PSS has three possible sequences $N_{ID}^{(2)} \in \{0,1,2\}$, each of which maps to an integer representing the sector ID of the gNB. The SSS has 336 possible sequences $N_{ID}^{(1)} \in \{0,1,\ldots,335\}$, each of which maps to an integer representing the group identifier of the gNB. Both $N_{ID}^{(1)}$ and $N_{ID}^{(2)}$ define the physical cell identity of the gNB according to

$$N_{ID}^{\text{Cell}} = 3N_{ID}^{(1)} + N_{ID}^{(2)} \quad (2)$$

PBCH is a physical channel that is used to transmit the system information required to establish the connection between the gNB and the UE. The DM-RS signal associated with the PBCH is used for decoding purposes and estimate the channel frequency response.

5G Receiver and Navigation Framework

A carrier-aided SDR is used to opportunistically extract TOA measurements from 5G signals. The receiver has three main stages: 5G carrier frequency extraction, acquisition, and tracking.

Assuming the knowledge of the gNBs' locations, the estimated TOA measurements are fed to an EKF to estimate the state vector defined as $\boldsymbol{x} \triangleq [\boldsymbol{x}_r^{\mathrm{T}}, \boldsymbol{x}_{\text{clk}}^{\mathrm{T}}]^{\mathrm{T}}$; where $\boldsymbol{x}_r$ is the 3-D position and velocity of the receiver and $\boldsymbol{x}_{\text{clk}}$ is the relative clock bias and drift between the receiver and each of the gNBs. The receiver dynamics are assumed to evolve accord-

μ	$N_{\min}^{RB}$	$N_{\max}^{RB}$	Minimum bandwidth [MHz]	Maximum bandwidth [MHz]
0	24	275	4.32	49.5
1	24	275	8.64	99
2	24	275	17.28	198
3	24	275	34.56	396
4	24	138	69.12	397.44

TABLE 1 The minimum and maximum number of resource blocks and the corresponding bandwidths for different numerologies.

5G Characteristics

5G will coexist with the previous 4G LTE. 5G deploys a similar structure to LTE, both using orthogonal frequency division multiplexing (OFDM) for downlink transmission. The 5G system is very attractive by design for navigation purposes due to its:

- **HIGH CARRIER FREQUENCIES:** 5G is designed to transmit at two main frequency ranges (FRs): FR1, which spans 450 MHz to 6 GHz; and FR2, which spans 24.25 to 52.6 GHz. High carrier frequencies yield precise carrier-phase navigation observables and reduce multipath effect due to high signal path loss, especially for FR2.
- **ABUNDANCE:** the 5G design tackles the problem of high signal path loss of millimeter waves (mmWaves) by using beamforming techniques and small cells, which makes the gNBs ubiquitous.
- **GEOMETRIC DIVERSITY:** cellular towers have favorable geometry by construction of the cells to provide better coverage.
- **LARGE BANDWIDTH:** While a single LTE signal has a bandwidth up to 20 MHz, a single 5G signal has a bandwidth up to 100 MHz and 400 MHz bandwidth for FR1 and FR2, respectively. This makes it less susceptible to multipath errors; it can differentiate multipath components with shorter delays from the line-of-sight (LOS) signal.
- **HIGH RECEIVED POWER:** the received carrier-to-noise-ratio C/N0 of cellular signals from nearby cellular towers is more than 20 dB-Hz higher than GPS signals.

ing to nearly constant velocity dynamics, while the clock error dynamics are assumed to evolve according to the standard double integrator model driven by noise.

Experimental Demonstration

To the best of the authors' knowledge, this demonstration of 5G opportunistic navigation for a ground vehicle navigating in a challenging urban environment is the first navigation solution produced using ambient 5G signals from serving gNBs.

Experimental Setup and Layout. The experiment was performed on Main Street, Santa Ana, California. A quad-channel National Instrument (NI) universal software radio peripheral (USRP)-2955 was mounted on a vehicle; only two channels were used to sample 5G signals with a sampling ratio of 10 MSps. The receiver was equipped with two consumer-grade cellular omnidirectional Laird antennas. The USRP was tuned to two carrier frequencies corresponding to two U.S. cellular providers summarized in **Table 2.** The USRP was driven by a GPS-disciplined oscillator (GPSDO) and the sampled data were stored for post-processing. The vehicle was equipped with a Septentrio AsteRx-i V integrated GNSS-IMU whose x-axis pointed toward the front of the vehicle, y-axis pointed to the right side of the vehicle, and z-axis pointed upward. AsteRx-i V is equipped with a dual-

NavtechGPS brings you ...

NEW! xNAV650 INS

Ideal for SWaP constrained drones, mobile mapping, and UAV based applications where long flight times are needed

OXTS Inertial+GNSS

- Compact: 77 x 63 x 24 mm; Light weight: 130g
- Dual antenna, quad constellation, 2 cm position accuracy
- PTP time stamp for LiDAR synchronization
- Riegl, Velodyne, Z+F, and other sensors supported
- Robust post-processing software included
- High accuracy: 0.05 pitch and roll
- Tactical grade, *No magnetometer, No ITAR restrictions*

Contact us about integrating the xNAV650 into your applications.

NavtechGPS

+1-703-256-8900 • 800-628-0885

www.navtechgps.com/xnav650-mems-imu-receiver/

Your ONE source for GNSS products and solutions

April and May GNSS Training


Hegarty


Pue


Vaujin

Live Remote Courses with Real-Time Engagement Taught by World-Class GPS/GNSS/INS Experts

- 557: Inertial Systems, Kalman Filtering, and GPS/INS Integration. *Instructors: Dr. Alan Pue and Mr. Michael Vaujin.* Immerse yourself in the fundamentals and practical implementations that fuse GPS receiver measurements with strapdown inertial navigation. (Five days, May 17-21)
- 346: GPS/GNSS Operation for Engineers and Technical Professionals. *Instructor: Dr. Chris Hegarty.* For those needing a well-coordinated, intensive introduction to GNSS concepts, design and operation; and for those wanting a greater understanding of colleagues' work to become a more productive member of the team. (Four days, April 27-30)
- 122: GPS/GNSS Fundamentals and Enhancements. *Instructor: Dr. Chris Hegarty.* Take the first two days of 346 for an overview of how the GPS/GNSS system works (Two days, April 27-28)

Questions? Contact Carolyn at cmcdonald@navtechgps.com

NavtechGPS

+1-703-256-8900 • 800-628-0885

www.navtechgps.com/gps-gnss-training/courses/

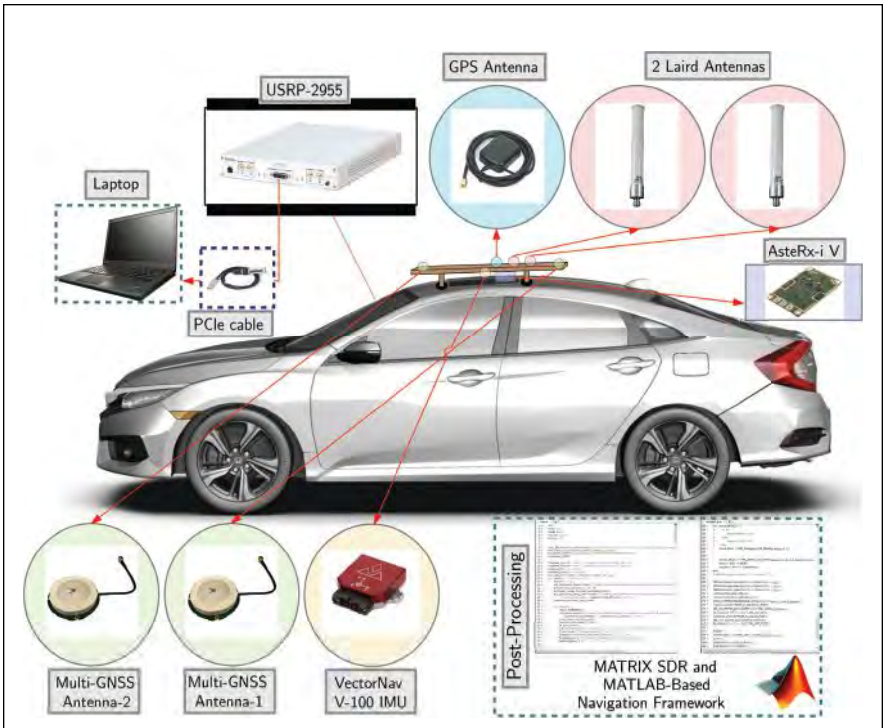

FIGURE 4 Experimental hardware and software setup.

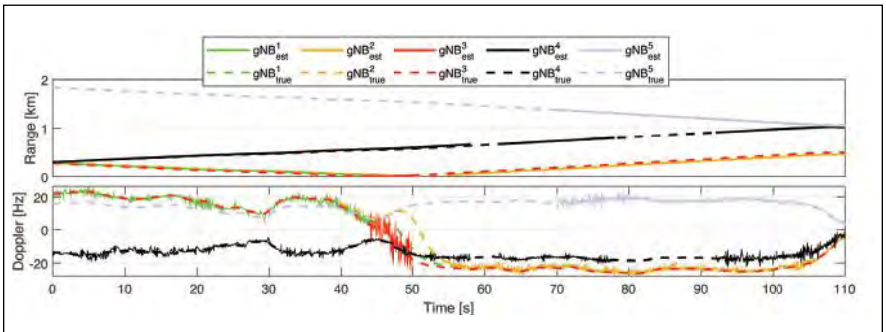

FIGURE 5 Estimated pseudorange and Doppler versus true range and Doppler measurements for the five exploited gNBs.

gNB	Carrier frequency [MHz]	N_{ID}^{Cell}	Cellular provider
1	872	239	AT&T
2	872	918	AT&T
3	872	81	AT&T
4	632.55	103	T-Mobile
5	632.55	354	T-Mobile

TABLE 2 gNBs characteristics.

antenna multi-frequency GNSS receiver and a VectorNav VN-100 MEMS IMU. The GNSS-IMU with SBAS navigation solution produced by AsteRx-i V was used as the ground truth in this experiment. **Figure 4** shows the experimental hardware and software setup.

Navigation Solution. The vehicle traversed a distance of 773 m in 110 seconds. **Figure 5** shows the true pseudorange and Doppler to all 5G gNBs versus the estimated pseudorange and Doppler as produced by ASPIN Laboratory's Multichannel Adaptive TRansceiver Information eXtractor (MATRIX) SDR. The true range and Doppler measurements were obtained using the vehicle's ground truth trajectory and the surveyed locations of the gNBs.

The EKF's position and velocity state vectors and their corresponding covariances were initialized using the output of the GNSS-IMU system. The initial relative clock biases were eliminated, i.e., the EKF's relative clock biases were initialized to zero. The first two 5G measurements were dropped, as the first two position estimates from the GNSS-IMU system were used to initialize the relative clock drifts. **Figure 6** shows the environmental layout, the location of the gNBs, the opportunistic 5G navigation solution, and the vehicle's ground truth trajectory.

Acknowledgments

The authors thank Joe Khalife for help in data collection. This work was supported in part by the Office of Naval Research under Grant N00014-19-1-2511; in part under the financial assistance award 70NANB17H192 from U.S. Department of Commerce, National Institute of Standards and Technology; and in part by the U.S. Department of Transportation under University Transportation Center Program Grant 69A3552047138.

This article is drawn from a paper at ION GNSS+ 2020, (see *www.ion.org/publications/browse.cfm)* though it presents new results.

References

(1) Z. Kassas, J. Khalife, A. Abdallah, and C. Lee, "I am not afraid of the jammer: navigating with signals of opportunity in GPS-denied environments," in Proc. of ION GNSS+ Conference, 2020, pp. 1566-1585.

(2) R. Faragher and R. Harle, "Towards an efficient, intelligent, opportunistic smartphone indoor positioning system," NAVIGATION, (62)1, pp. 55–72, 2015.

(3) V. Moghtadaiee and A. Dempster, "Indoor location fingerprinting using FM radio signals," IEEE Trans. on Broadcasting, (40)2, pp. 336–346, 2014.

(4) C. Yang, T. Nguyen, and E. Blasch, "Mobile positioning via fusion of mixed signals of opportunity," IEEE Aerospace and Electronic Systems, (29)4, pp. 34–46, 2014.

(5) Z.Kassas, J. Khalife, M. Neinavaie, T. Mortlock, "Opportunity Comes Knocking," Inside Unmanned Systems, pp. 30–35, June 2020.

(6) K. Shamaei and Z. Kassas, "LTE receiver design and multipath analysis for navigation in urban environments," NAVIGATION, (65)4, pp. 655–675, 2018.

(7) A. Abdallah, K. Shamaei, and Z. Kassas, "Assessing real 5G signals for opportunistic navigation," in Proc. of ION GNSS+ Conference, 2020, pp. 2548-2559.

Authors

Zaher (Zak) M. Kassas is an associate professor at the University of California, Irvine and Director of the Autonomous Systems Perception, Intelligence, and Navigation (ASPIN) Laboratory. He is also Director of the US DOT Center for Automated Vehicles Research with Multimodal AssurEd Navigation (CARMEN). He received a Ph.D. in electrical and computer engineering from the University of Texas at Austin. He is a recepient of the 2018 National Science Foundation (NSF) CAREER award, 2019 Office of Naval Research (ONR) Young Investigator Program award, 2018 IEEE Walter Fried award, 2018 ION Burka award, and 2019 ION Col. Thomas Thurlow award.

Ali A. Abdallah is a Ph.D. student in the Department of Electrical Engineering and Computer Science at the University of California, Irvine and a member of the ASPIN Laboratory.

Mohamad Orabi is a Ph.D. student in the Department of Electrical Engineering and Computer Science at University of California, Irvine and a member of the ASPIN Laboratory.

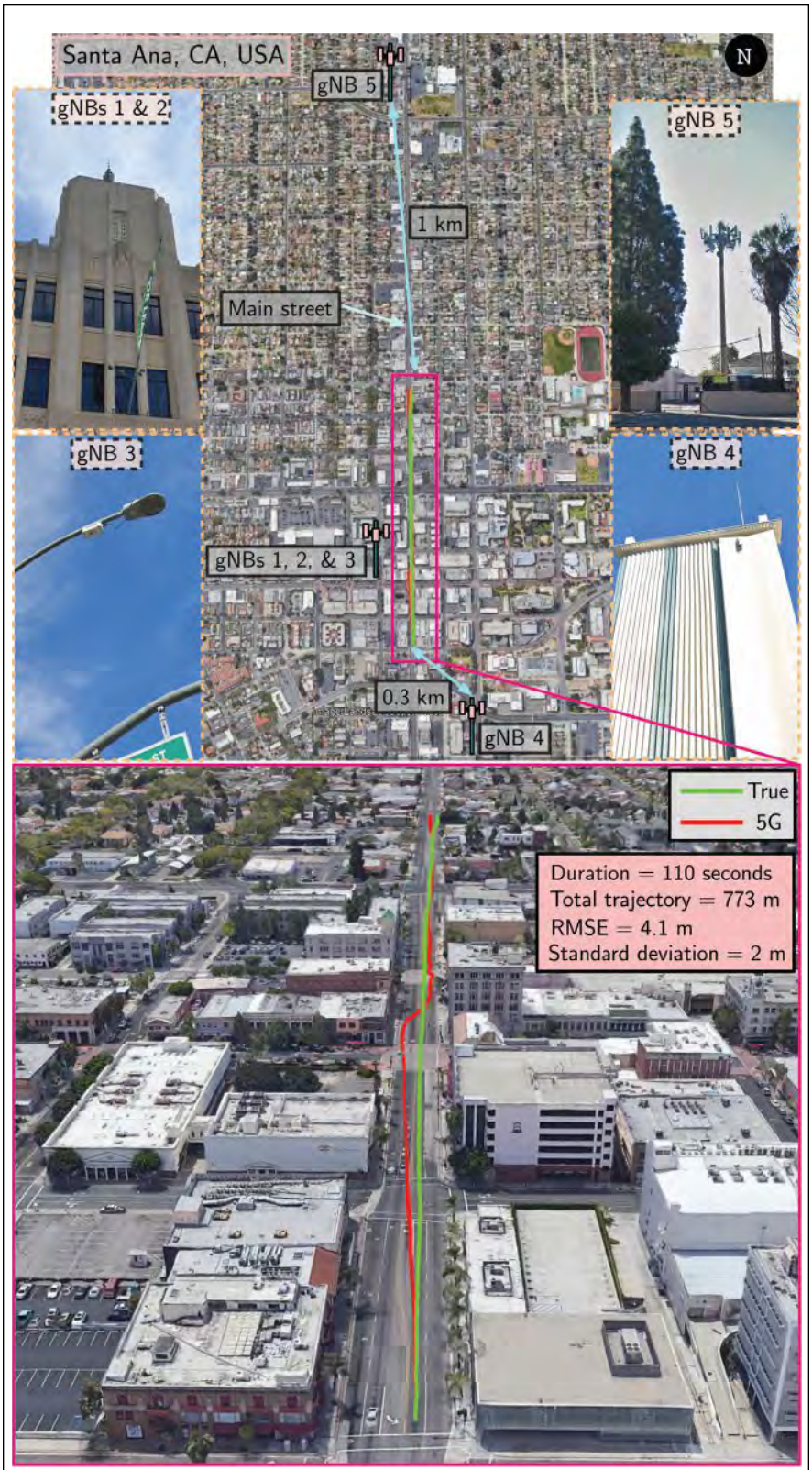

FIGURE 6 Environmental layout, gNBs' locations, and the traversed trajectory. The 5G navigation solution exhibited a postion RMSE of 4.1 m versus to the GNSS-IMU with SBAS navigation solution produced by AsterX-i V. *Image: Google Earth.*

Cognitive Opportunistic Navigation in Private Networks With 5G Signals and Beyond

Mohammad Neinavaie, *Graduate Student Member, IEEE*, Joe Khalife, and Zaher M. Kassas, *Senior Member, IEEE*

***Abstract*—A receiver architecture is proposed to cognitively extract navigation observables from fifth generation (5G) new radio (NR) signals of opportunity. Unlike conventional opportunistic receivers which require knowledge of the signal structure, particularly the reference signals (RSs), the proposed cognitive opportunistic navigation (CON) receiver requires knowledge of only the frame duration and carrier frequency of the signal. In 5G NR, some of these RSs are only transmitted on demand, which limits the existing opportunistic navigation frameworks to signals which are on *always-on*; hence, limiting the exploitable RS bandwidth. To exploit the full available bandwidth and improve ranging accuracy, the proposed CON receiver is designed to estimate all the RSs contained in the transmitted signals corresponding to multiple 5G base stations, (i.e., gNBs). Navigation observables (pseudorange and carrier phase) are subsequently derived from the estimated RSs. The proposed receiver operates in two stages: (i) acquisition and (ii) tracking. The acquisition stage of the CON receiver is modeled as a sequential detection problem where the number of gNBs and their corresponding RSs and Doppler frequencies are unknown. The generalized likelihood ratio (GLR) test for sequentially detecting active gNBs is derived and used to estimate the number of gNBs and their RSs. In order for the receiver to refine and maintain the Doppler and RS estimates provided by the acquisition stage, tracking loops are designed. A sufficient condition on the Doppler estimation error to ensure that the proposed GLR asymptotically achieves a constant false alarm rate (CFAR) is derived. The output of the tracking loops, namely carrier phase and code phase, are then used to estimate the receiver's position. Extensive experimental results are presented demonstrating the capabilities of the proposed CON receiver with real 5G signals on ground and aerial platforms, with an experiment showing the first navigation results with real 5G signals on an unmanned aerial vehicle (UAV) navigating using the CON receiver over a 416 m trajectory with a position root mean-squared error (RMSE) of 4.35 m.**

***Index Terms*—5G, new radio, cognitive radio, signals of opportunity, navigation, positioning.**

Manuscript received May 29, 2021; revised August 29, 2021; accepted September 23, 2021. Date of publication October 14, 2021; date of current version February 2, 2022. This work was supported in part by the Office of Naval Research (ONR) under Grant N00014-19-1-2511 and in part by the U.S. Department of Transportation (USDOT) under Grant 69A3552047138 for the CARMEN University Transportation Center (UTC). The guest editor coordinating the review of this manuscript and approving it for publication was Dr. Octavia Dobre. *(Corresponding Author: Zaher M. Kassas.)*

The authors are with the Department of Mechanical and Aerospace Engineering, University of California Irvine (UCI), Irvine, CA 92617 USA (e-mail: mneinava@uci.edu; khalifej@uci.edu; zkassas@ieee.org).

This article has supplementary downloadable material available at https://doi.org/10.1109/JSTSP.2021.3119929, provided by the authors.

Digital Object Identifier 10.1109/JSTSP.2021.3119929

I. Introduction

CURRENT capabilities offered by fourth generation (4G) mobile communications will not meet the demands of emerging applications such as Internet of Things (IOT) and autonomous vehicles [1], [2]. To address such demands, fifith generation (5G) has been developed, with a focus on features such as enhanced mobile broadband, ultra-reliable low-latency communications, and massive machine type communications [3]. Based on the performance requirements set by the international telecommunication union (ITU), the third generation partnership project (3GPP) began 5G standardization in 2015 and released its first specifications on a 5G system in June 2018, which included both the new air interface, known as new radio (NR), and 5G core network (5GC) [4]. One main characteristic of 5G signals is high data rate, which necessitates a higher transmission bandwidth and more sophisticated multiplexing techniques. The scarcity of unlicensed spectrum in lower frequencies called for using millimeter waves (mmWaves) for NR signal transmission [5]. The high path loss of propagated mmWave signals can be compensated for by beamforming techniques and massive multiple-input multiple-output (mMIMO) antenna structures [6]. Beamforming in 5G requires the knowledge of the user's location, which means that 5G-based positioning is not only an auxiliary service, but is essential for resource allocation and beamforming for high data rate transmission [7]. Different types of positioning techniques have been evaluated by the 3GPP in Release 15 and 16 [8].

Cellular positioning techniques in the literature can be classified into *network-based* and *opportunistic* approaches [9], [10]. Network-based approaches require two-way communication with the network and the transmission of a pre-specified positioning reference signal (PRS) and some system parameters such as the number of transmission antennas and the beamforming matrix. Network-based positioning capabilities in wireless communication systems have been defined since 4G systems [11]. In a contrast to network-based approaches, in opportunistic approaches, the user equipment (UE) estimates its position from downlink signals, without communicating back with the network. As such, opportunistic approaches are more attractive than network-based approaches since: they (i) do not require additional overhead or bandwidth, (ii) preserve the UE's privacy, (iii) do not require paying subscription to the network, and (iv) enable the UE to exploit signals from multiple

1932-4553 © 2021 IEEE. Personal use is permitted, but republication/redistribution requires IEEE permission.
See https://www.ieee.org/publications/rights/index.html for more information.

Authorized licensed use limited to: The Ohio State University. Downloaded on October 12,2022 at 17:21:12 UTC from IEEE Xplore. Restrictions apply.

cellular providers simultaneously, which improves the positioning accuracy.

Opportunistic navigation frameworks usually rely on the broadcast reference signals (RSs), which are used to derive direction-of-arrival (DOA) and time-of-arrival (TOA) [12]. These signals are known at the UE and are universal across network operators. Hence, they can be exploited for positioning without the need for the UE to be a network subscriber. In cellular long-term evolution (LTE) networks, several RSs, such as the cell-specific reference signal (CRS), are broadcast at regular and known time intervals, regardless of the number of UEs in the environments. This *always-on* type of transmitted RSs reduces the network's energy efficiency and increases operational expenses and interference. One of the main features of 5G signals is *ultra-lean* transmission, which minimizes the transmission of always-on signals. For instance, CRS which used to be an always-on RS in LTE, is not necessarily being continuously transmitted in 5G signals. Up until now, 5G opportunistic navigation methods relied on the always-on signals, e.g., the primary and secondary synchronization signals (PSS and SSS, respectively) and the physical broadcast channel (SB/PBCH) block, none of which use the entire signal bandwidth [13]–[15].

This paper presents a cognitive opportunistic navigation framework (CON) by developing a 5G receiver architecture to simultaneously detect the active gNBs in the environment, estimate the number of gNBs and their unknown RSs which are not necessarily *always-on*, and exploit them to derive navigation observables in a cognitive fashion. There are four main RSs in 5G signals: demodulation RSs, phase tracking RSs, sounding RSs, and channel state information (CSI) RSs. These RSs are only transmitted on demand, which limits the efficacy of conventional opportunistic navigation frameworks which rely on always-on RSs. For instance, while the receiver proposed in [14] was the first 5G-based opportunistic navigation receiver, it relies on the always-on SB/PBCH block. The downside of relying only on the SB/PBCH block is the limited bandwidth. Higher signal bandwidth translates to more accurate TOA estimates. In order to exploit the full ranging accuracy achievable with 5G signals, the proposed CON receiver is designed to cognitively estimate the RSs present in the entire bandwidth and exploit them to obtain navigation observables (pseudoranges and carrier phase). Not only the proposed receiver is capable of exploiting RSs which are not always-on, but the cognitive nature of the proposed receiver enables opportunistic navigation with future communication standards with unknown or partially known signal specifications. The proposed receiver architecture relies solely on the periodicity of the RSs and requires very limited information about the 5G signal, namely it only assumes knowledge of the frame duration and the carrier frequency. It should be pointed out that an energy detector can be used to provide an estimate of the carrier frequency and using the current literature, e.g., the period estimator in [16], the frame duration can also be estimated in a pre-processing stage. One main challenge faced by the CON receiver is the problem of distinguishing signals from multiple 5G base stations, i.e., gNBs, multiplexed over the same channel. This task is relatively simple when the RSs are known, as RSs are usually designed to have desirable autocorrelation and cross-correlation properties. Since this paper does not assume knowledge of the RSs, it is desirable for the CON receiver to be able to detect multiple gNBs and distinguish their signals. To this end, a subspace-based detection scheme leveraging the Doppler frequency subspace is proposed to estimate the number of available gNBs and estimate their RSs.

Specifically, the contributions of this work are as follows:

- A CON receiver design is presented, which could estimate the unknown RSs of a gNB. The cognitive nature of the proposed receiver enables estimating both always-on and on demand RSs which are not necessarily always-on. Using extensive experiments, it is shown that the estimated RSs posses higher bandwidth compared to conventional 5G opportunistic navigation receivers, which allows for producing more precise navigation observables.
- A sequential generalized likelihood ratio (GLR) detector is derived to detect the presence of multiple gNBs on the same channel and provide an estimate of the number of active gNBs. The detector relies on matched subspace detection, where the signal subspace is defined by the Doppler frequencies of the gNBs. The sequential GLR detector estimates the number of gNBs, and their Doppler frequencies, and it provides an initial estimate of their unknown RSs, which are then used and refined in the tracking loops.
- A sufficient condition on the Doppler estimation error to ensure that the proposed GLR asymptotically achieves a constant false alarm rate (CFAR) is derived.
- Extensive experimental results are presented demonstrating the capabilities of the proposed CON receiver with real 5G signals on ground and aerial platforms. On a ground vehicle, it is demonstrated that the CON receiver yields a reduction of 10% and 37.7% in the estimated delay and Doppler root mean squared error (RMSE), respectively, over that achieved with a conventional opportunistic navigation 5G receiver that has complete knowledge of the transmitted RSs but only relies on always-on RSs. On an unmanned aerial vehicle (UAV), it is demonstrated that the proposed CON receiver enables the UAV to navigate over a 416m trajectory with two 5G NR gNBs achieving a position RMSE of 4.35 m. To evaluate the performance of the CON receiver in a scenario where the RSs are always-on, another experiment is conducted in which a UAV navigates with long-term evolution (LTE) eNodeBs, achieving a position RMSE of 2.07 m, which is identical to the performance achieved with a conventional opportunistic navigation 4G receiver that has complete knowledge of the transmitted RSs.

The rest of the paper is organized as follows. Section II surveys related research on navigation with 4G and 5G signals. Section III describes the received baseband signal model. Section IV presents the proposed CON receiver architecture. Section V presents the experimental results. Section VI gives concluding remarks.

Authorized licensed use limited to: The Ohio State University. Downloaded on October 12,2022 at 17:21:12 UTC from IEEE Xplore. Restrictions apply.

II. Related Work

1) Opportunistic Navigation: Over the past decade, opportunistic navigation has been demonstrated in the literature with different types of signals, also known as signals of opportunity (SOPs). SOP examples include cellular [9], [10], digital television [17], [18], AM/FM [19], [20], Wi-Fi [21], [22], and low-earth orbit (LEO) satellite signals [23], [24]. Among SOPs, cellular signals have attracted considerable attentions due to their desirable attributes, including: (i) large transmission bandwidth, (ii) high carrier-to-noise ratio, and (iii) desirable geometric diversity [25]. While meter-level and decimeter-level SOP-based navigation solutions were demonstrated on ground vehicles and UAVs, respectively, the aforementioned approaches relied on the knowledge of a subset of the RSs transmitted by the SOP. These methods would fail if (i) the receiver enters an unknown SOP environment where the number of active SOPs and their corresponding RSs are unknown, or (ii) some signal parameters change due to the dynamic nature of wireless protocols. This paper addresses these issues by estimating all available RSs within the SOP with minimal prior knowledge.

2) Positioning With 5G Signals: The characteristics of mmWave signals were evaluated for positioning in [26]. Cramér-Rao lower bounds (CRLBs) of the direction-of-departure (DOD), DOA, and TOA for both uplink and downlink mmWave signals were derived in [27], [28], showing sub-meter positioning error, and sub-degree orientation error. To exploit the sparsity of mmWave channels, tools relying on compressed sensing were proposed in [29], [30] to estimate DOD, DOA, and TOA of the UE, showing sub-meter level position error via simulation results. The DOD and UE's position were estimated in a two-stage Kalman filter using the signal strength from multiple base stations in [31], which yielded sub-meter-level three-dimensional (3-D) position accuracy. The joint estimation of the position and orientation of the UE, as well as the location of reflectors or scatterers in the absence of the line-of-sight (LOS) path, were considered in [32], showing less than 15m position RMSE and less than 7° orientation RMSE. A two-way distributed localization protocol was proposed in [33] to remove the effect of the clock bias in TOA estimates. In [7], a positioning method for multiple-output single-input systems was proposed, where the DOD and TOA of the received signal were used to localize a UE. In [34], estimation of signal parameters via rotational invariant techniques (ESPRIT) was used to estimate the DOA and DOD of the signal. Experimental results in [14] and [13] showed meter-level navigation using TOA estimates from 5G signals. The results presented therein rely only on the PSS and SSS for TOA estimation. It is shown that the proposed receiver yields a narrower RS autocorrelation function, which translates to more accurate TOA estimates. Moreover, the proposed receiver architecture can be readily adapted to any type of signal containing periodic RSs.

Detection of Unknown Signals in the Presence of Noise and Interference: The acquisition stage of the CON receiver is modeled as a sequential matched subspace detection problem, which comprises estimating the number of gNBs, an initial estimate of normalized Doppler, and an initial estimate of the RSs. The detection problem of an unknown source in the presence of other interfering signals falls into the paradigm of *matched subspace detectors* which has been widely studied in the classic detection literature [35]–[37]. Matched subspace detectors are used frequently in radar signal processing, e.g., in source localization in multiple-input multiple-output (MIMO) radars [38] and passive bistatic radar [39]. In [40], the design of subspace matched filters in the presence of mismatch in the steering vector was addressed. The performance of low-rank adaptive normalized matched subspace detectors was studied in [41]. In [42], the idea of subspace matching was used to present a solution to the problem of detecting the number of signals in both white and colored noise. In [43], the structure of the noise covariance matrix was exploited to enhance the matched subspace detection performance. In [44], adaptive vector subspace detection in partially homogeneous Gaussian disturbance was addressed. Recently, machine learning approaches have been proposed for unknown transmitter detection, identification, and classification [45], [46]. In the navigation literature, detection of unknown signals has been studied to design frameworks which are capable of navigating with unknown or partially known signals. The problem of detecting Galileo and Compass satellites signals was studied in [47], which revealed the spread spectrum codes for these satellites. Preliminary experiments on navigation with partially known signals from low and medium Earth orbit satellites were conducted in [48]–[51]. In particular, a chirp parameter estimator was used in [49] to blindly estimate the GPS pseudorandom noise (PRN) codes. In [50], a blind channel estimator was proposed to exploit Orbcomm satellite signals for navigation purposes. In [51], OFDM signals were emulated from Orbcomm LEO satellites and an FFT-based Doppler estimator was proposed to exploit these signals for navigation purposes. While these approaches yielded useful insights, they either exploited signals that have a simpler structure compared to 5G or proposed different receiver structures than the one developed in this paper. In particular, this paper uses the concept of matched subspace detection to design a full receiver architecture, whose performance is analyzed analytically and is subsequently tested experimentally with real 5G signals. It is shown that the proposed receiver is capable of detecting the number of active gNBs, along with their corresponding RSs and Doppler frequencies with only the prior knowledge of the frame duration and the carrier frequency.

III. Received Baseband Signal Model

This section provides a brief review of the NR RSs, and presents the signal model.

A. Brief Review of NR RSs

NR adopts orthogonal frequency division multiplexing (OFDM) scheme, as was the case in 4G. In OFDM-based transmission, the symbols are mapped onto multiple carrier frequencies, referred to as subcarriers, with a particular spacing known as subcarrier spacing. Unlike the 4G signal standard, which considers a fixed subcarrier spacing of 15 kHz, subcarrier spacing values of $15 \times 2^{\mu}$, with $\mu \in \{0, 1, 2, 3\}$ are supported

Authorized licensed use limited to: The Ohio State University. Downloaded on October 12,2022 at 17:21:12 UTC from IEEE Xplore. Restrictions apply.

by NR. The system selects subcarrier spacing values based on carrier frequency, and/or other requirements and scenarios. Once the subcarrier spacing is configured, the frame structure is identified. An NR frame has a duration of 10ms and consists of 10 subframes with durations of 1 ms [4]. In the proposed receiver, only the frame duration and carrier frequency are assumed to be known. In the frequency-domain, each subframe is divided into numerous resource grids, each of which has multiple resource blocks with 12 subcarriers. The number of resource grids in the frame is provided to the UE from higher level signallings. A resource element is the smallest element of a resource grid that is defined by its symbol and subcarrier number [4].

To provide frame timing to the UE, a gNB broadcasts synchronization signals (SS) on pre-specified symbol numbers. An SS includes PSS and SSS, which provide symbol and frame timing, respectively. The PSS and SSS are transmitted along with the PBCH signal and its associated demodulation reference signal (DM-RS) on a block called SS/PBCH block. The SS/PBCH block consists of four consecutive OFDM symbols and 240 consecutive subcarriers. The SS/PBCH block has a periodicity of 20 ms and is transmitted numerous times on one of the half frames, also known as SS/PBCH burst.

B. Signal Model

As it was mentioned previously, the SS/PBCH block is not transmitted on the whole signal's bandwidth. Therefore, methods which only rely on SS/PBCH block, cannot exploit the full ranging accuracy that can be achieved by 5G signals. Other periodic RSs are not necessarily *always-on* and the cognitive receiver should be able to exploit them to be able to achieve the available ranging accuracy. In this paper, with a focus on exploiting navigation observables using the RSs in the entire 5G bandwidth, the 5G NR signal is modeled as an unknown periodic signal in the presence of interference and noise. If an RS is being periodically transmitted, it will be detected by the receiver, estimated, and used to derive navigation observables. The estimated RS will involve an estimation of always-on signals such as the SSs and any other active reference signal that is being periodically transmitted. It will be shown experimentally in section V that the exploited bandwidth by the proposed cognitive method is larger than that of the method which only relies on always-on signals. The received baseband signal model can be expressed as

$$r[n] = \sum_{i=1}^{N} \left(\alpha_i c_i[\tau_n - t_{s_i}[n]] \exp\left(j\theta_i[\tau_n]\right)\right. \\ \left. + d_i[\tau_n - t_{s_i}[n]] \exp\left(j\theta_i[\tau_n]\right)\right) + w[n], \quad (1)$$

where $r[n]$ is the received signal at the nth time instant; α_i is the complex channel gain between the UE and the ith gNB; τ_n is the sample time expressed in the receiver time; N is the number of gNBs; $c_i[n]$ is the periodic RS with a period of L samples; $t_{s_i}[n]$ is the code-delay corresponding to the UE and the ith gNB at the nth time instant; $\theta_i[\tau_n] = 2\pi f_{D_i}[n] T_s n$ is the carrier phase in radians, where $f_{D_i}[n]$ is the Doppler frequency at the nth time instant and T_s is the sampling time; $d_i[\tau_n]$ represents the samples of some data transmitted from the ith gNB; and $w[n]$ is a zero-mean independent and identically distributed noise with $\mathbb{E}\{w[m]w^*[n]\} = \sigma_w^2 \delta[m-n]$, where $\delta[n]$ is the the Kronecker delta function, and X^* denotes the complex conjugate of random variable X.

According to (1), the channel between the ith gNB and the UE is considered to have a single tap with the complex channel gain α_i. The desired RS from the ith gNB is defined as

$$s_i[n] \triangleq \alpha_i c_i[\tau_n - t_{s_i}[n]] \exp\left(j\theta_i[\tau_n]\right), \quad (2)$$

and the equivalent noise is

$$w_{\mathrm{eq}_i}[n] = d_i[\tau_n - t_{s_i}[n]] \exp\left(j\theta_i[\tau_n]\right) + w[n]. \quad (3)$$

Hence, the signal model can be rewritten as

$$r[n] = \sum_{i=1}^{N} \left(s_i[n] + w_{\mathrm{eq}_i}[n]\right). \quad (4)$$

It should be noted that due to the periodicity of the RS, assuming a constant Doppler in the processing time, i.e., $f_{D_i}[n] = f_{D_i}$, the desired RS has the following property

$$s_i[n + mL] = s[n] \exp\left(j\omega_i mL\right) \quad 0 \le n \le L-1, \quad (5)$$

where $\omega_i = 2\pi f_{D_i} T_s$ is the normalized Doppler, and $-\pi \le \omega_i \le \pi$. The acquisition stage will estimate $s_i[n]$ and the estimation of $s_i[n]$ will be used at the receiver to obtain the navigation observables.

Definition: The coherent processing interval (CPI) is defined as the time interval during which the Doppler, delay, and channel gains are considered to be constant.

One can form a vector of L observation samples corresponding to the kth period of the signal as

$$\mathbf{y}_k \triangleq [r[(k-1)L+1], r[(k-1)L+2], \ldots, r[kL]]^{\mathsf{T}}. \quad (6)$$

Considering a CPI of length $K \times L$ samples, the observation vector is constructed as $\mathbf{y} = [\mathbf{y}_1^{\mathsf{T}}, \mathbf{y}_2^{\mathsf{T}}, \ldots, \mathbf{y}_K^{\mathsf{T}}]^{\mathsf{T}}$. Therefore,

$$\mathbf{y} = \sum_{i=1}^{N} \mathbf{H}_i \mathbf{s}_i + \mathbf{w}_{\mathrm{eq}_i}, \quad (7)$$

where $\mathbf{s}_i = [s_i[1], s_i[2], \ldots, s_i[L]]^{\mathsf{T}}$, $\mathbf{w}_{\mathrm{eq}_i}$ is the equivalent noise vector corresponding to the ith source, and the $KL \times L$ Doppler matrix corresponding to the ith source is defined as

$$\mathbf{H}_i \triangleq [\mathbf{I}_L, \exp\left(j\omega_i L\right)\mathbf{I}_L, \ldots, \exp\left(j\omega_i (K-1)L\right)\mathbf{I}_L]^{\mathsf{T}}, \quad (8)$$

where $\mathbf{I}_L$ is an $L \times L$ identity matrix.

IV. CON Receiver Structure

This section presents the structure of the proposed receiver. The proposed receiver consists of two main stages: (i) acquisition and (ii) tracking. Each of these stages are discussed in details next.

A. Acquisition

In this paper, the acquisition stage is modeled as a sequential matched subspace detection problem. The acquisition stage comprises estimating the number of gNBs, an initial estimate

Authorized licensed use limited to: The Ohio State University. Downloaded on October 12,2022 at 17:21:12 UTC from IEEE Xplore. Restrictions apply.

of normalized Doppler, and the RSs, i.e., N, ω_i, and $\mathbf{s}_i$, respectively. At each step of the acquisition, a test is performed to detect the most powerful gNB when the subspace of the previously detected gNBs are nulled. In the following subsection, matched subspace detection is overviewed and the hypothesis test for detection of multiple gNBs is formulated.

1) Matched Subspace Detector: As it was mentioned previously, in the first step of the proposed sequential algorithm, the presence of a single gNB is tested and if the null hypothesis is accepted, then $\hat{N} \equiv 0$, which means that no gNB is detected to be present in the environment under the test. If the test rejects the null hypothesis, the algorithm verifies the presence of at least one source and performs the test to detect the presence of other gNBs in the presence of the previously detected gNBs. The unknown Doppler and the RS of each gNBs are estimated at each step.

In general, if the null hypothesis at the ith level of the sequential algorithm is accepted, the algorithm is terminated and the estimated number of gNBs will be $\hat{N} = i - 1$.

In order to test the presence of $\mathbf{s}_i$, at the ith stage of the acquisition algorithm, the observation vector can be written as

$$\mathbf{y} = \mathbf{H}_i \mathbf{s}_i + \mathbf{B}_{i-1}\boldsymbol{\theta}_{i-1} + \mathbf{w}_{\mathrm{eq}_i}, \tag{9}$$

$$\mathbf{B}_{i-1} \triangleq [\mathbf{H}_1, \mathbf{H}_2, \ldots, \mathbf{H}_{i-1}],\ \boldsymbol{\theta}_{i-1} \triangleq [\mathbf{s}_1^{\mathsf{T}}, \mathbf{s}_2^{\mathsf{T}}, \ldots, \mathbf{s}_{i-1}^{\mathsf{T}}]^{\mathsf{T}}. \tag{10}$$

The following binary hypothesis test is used to detect the ith gNB:

$$\begin{cases} \mathcal{H}_0^i :\ \mathbf{y} = \mathbf{B}_{i-1}\boldsymbol{\theta}_{i-1} + \mathbf{w}_{\mathrm{eq}_i} \\ \mathcal{H}_1^i :\ \mathbf{y} = \mathbf{H}_i \mathbf{s}_i + \mathbf{B}_{i-1}\boldsymbol{\theta}_{i-1} + \mathbf{w}_{\mathrm{eq}_i}. \end{cases} \tag{11}$$

For a given set of Doppler frequencies, $\mathcal{W}_i = \{\omega_1, \omega_2, \ldots, \omega_i\}$, the GLR at the ith stage is derived as (see Appendix A)

$$\mathcal{L}_i(\mathbf{y}|\mathcal{W}_i) = \frac{\mathbf{y}^{\mathsf{H}}\mathbf{P}_{\mathbf{S}_i}\mathbf{y}}{\mathbf{y}^{\mathsf{H}}\mathbf{P}^{\perp}_{\mathbf{B}_{i-1}}\mathbf{P}^{\perp}_{\mathbf{S}_i}\mathbf{P}^{\perp}_{\mathbf{B}_{i-1}}\mathbf{y}}, \tag{12}$$

where $\mathbf{y}^{\mathsf{H}}$ is the Hermitian transpose of $\mathbf{y}$, $\mathbf{P}_{\mathbf{X}} \triangleq \mathbf{X}(\mathbf{X}^{\mathsf{H}}\mathbf{X})^{-1}\mathbf{X}^{\mathsf{H}}$, denotes the projection matrix to the column space of $\mathbf{X}$, and

$$\mathbf{P}^{\perp}_{\mathbf{X}} \triangleq \mathbf{I} - \mathbf{X}\left(\mathbf{X}^{\mathsf{H}}\mathbf{X}\right)^{-1}\mathbf{X}^{\mathsf{H}}, \tag{13}$$

denotes the projection matrix onto the space orthogonal to the column space of $\mathbf{X}$, and $\mathbf{S}_i = \mathbf{P}^{\perp}_{\mathbf{B}_{i-1}}\mathbf{H}_i$. Intuitively, in (12) the subspace of previously detected gNBs, i.e., $\mathbf{B}_{i-1}$, is nulled to detect the ith gNB.

Remark 1 (Vector space interpretation of (12)): If the subspace spanned by the columns of $\mathbf{S}_i = \mathbf{P}^{\perp}_{\mathbf{B}_{i-1}}\mathbf{H}_i$, is viewed as the *ith gNB's signal subspace*, and the orthogonal subspace as the *noise subspace*, then the likelihood (12) can be interpreted as an estimated signal to noise ratio (SNR). The reader is referred to [35] for further interpretations of matched subspace detectors.

Remark 2: At the ith stage of the proposed sequential algorithm, the GLR requires an estimate of the set $\mathcal{W}_i$. The sequential nature of the algorithm enables a single variable estimation of the Doppler frequency at each step. For instance, at the first step of the algorithm, a single dimensional search is required to obtain the maximum likelihood (ML) estimate of ω_1, denoted by $\hat{\omega}_1$. In the second stage of the algorithm, $\hat{\omega}_1$ is used to construct the projection matrix to null the subspace of the first gNB. Consequently, at the ith step of the algorithm, invoking the previously estimated Dopplers, a single dimensional search is required to estimate ω_i, and construct the estimated projection matrix and the estimated Doppler matrix for the corresponding stage, denoted by $\hat{\mathbf{P}}_{\mathbf{S}_i}$ and $\hat{\mathbf{H}}_i$, respectively.

The following lemma simplifies the likelihood function (12).

Lemma 1: In the likelihood function (12), the following equality holds

$$\mathbf{H}_i^{\mathsf{H}}\mathbf{P}^{\perp}_{\mathbf{B}_{i-1}}\mathbf{H}_i = \lambda_i \mathbf{I}, \tag{14}$$

where the scalar λ_i is the Schur complement of block $\mathbf{C}_{i-1}$, i.e., the upper $(i-1)\times(i-1)$ block of the matrix $\mathbf{C}_i$,* where

$$\mathbf{C}_i = \begin{bmatrix} c_{11} & c_{12} & \ldots & c_{1i} \\ c_{21} & c_{22} & \ldots & c_{2i} \\ \vdots & \ddots & \ddots & \vdots \\ c_{i1} & c_{i2} & \ldots & c_{ii} \end{bmatrix}, \tag{15}$$

and $c_{ij} \triangleq \sum_{k=0}^{K-1} \exp(j(\omega_j - \omega_i)Lk)$.

Proof: See Appendix B.

According to Lemma 1, the likelihood (12) at the ith stage can be simplified as

$$\mathcal{L}_i(\mathbf{y}) = \frac{\|\hat{\lambda}_i^{-1}\hat{\mathbf{H}}_i^{\mathsf{H}}\hat{\mathbf{P}}^{\perp}_{\mathbf{B}_{i-1}}\mathbf{y}\|^2}{\|\hat{\mathbf{P}}^{\perp}_{\mathbf{B}_{i-1}}\mathbf{y}\|^2 - \|\hat{\lambda}_i^{-1}\hat{\mathbf{H}}_i^{\mathsf{H}}\hat{\mathbf{P}}^{\perp}_{\hat{\mathbf{B}}_{i-1}}\mathbf{y}\|^2} \underset{\mathcal{H}_0^i}{\overset{\mathcal{H}_1^i}{\gtrless}} \eta_i. \tag{16}$$

where η_i is a predetermined threshold at the ith stage. The ML estimate of $\hat{\omega}_i$, is obtained by maximizing the likelihood function under $\mathcal{H}_1^i$ which yields

$$\hat{\omega}_i = \arg\max_{\omega_i} \|\mathbf{H}_i^{\mathsf{H}}\mathbf{P}^{\perp}_{\mathbf{B}_{i-1}}\mathbf{y}\|^2, \tag{17}$$

and is used to construct $\hat{\mathbf{P}}_{\mathbf{B}_{i-1}}$, $\hat{\mathbf{H}}_i$, and $\hat{\lambda}_i$.

For a known ω_i, the least squares (LS) estimate of the ith source, i.e., $\mathbf{s}_i$, is given by

$$\hat{\mathbf{s}}_i = \frac{1}{\lambda_i}\mathbf{H}_i^{\mathsf{H}}\mathbf{P}^{\perp}_{\mathbf{B}_{i-1}}\mathbf{y}, \tag{18}$$

It should be noted that the estimated RS, i.e., $\hat{\mathbf{s}}_i$, contains the effect of the channel between the gNB and the UE. Small values of $|\alpha_i|$ degrades the estimation quality of the desired RS and, consequently, affects the acquisition and tracking performance. It should also be pointed out that $\frac{1}{\lambda_i}\mathbf{H}_i^{\mathsf{H}}\mathbf{P}^{\perp}_{\mathbf{B}_{i-1}}\mathbf{y} = \mathbf{s}_i + \mathbf{w}_{\mathrm{acq}_i}$, where $\mathbf{w}_{\mathrm{acq}_i} = \frac{1}{\lambda_i}\mathbf{H}_i^{\mathsf{H}}\mathbf{P}^{\perp}_{\mathbf{B}_{i-1}}\mathbf{w}_{\mathrm{eq}_i}$. In other words, for a known Doppler frequency, the LS estimator of the ith source is an unbiased estimator, i.e., $\mathbb{E}\{\hat{\mathbf{s}}_i\} = \mathbf{s}_i$. However, since the true Doppler is not known to the CON receiver, the ML estimate of the Doppler is used to compute the LS estimate of the ith RS instead. Moreover, it can be shown that

$$\frac{1}{\hat{\lambda}_i}\hat{\mathbf{H}}_i^{\mathsf{H}}\hat{\mathbf{P}}_{\mathbf{B}_{i-1}}\mathbf{H}_i = \beta_{\mathrm{acq}_i}\mathbf{I}, \tag{19}$$

*Consider $p \times p$ matrix $\mathbf{A}$, $p \times 1$ vectors $\mathbf{b}$ and $\mathbf{c}$ and scalar d. For the matrix $\begin{bmatrix} \mathbf{A} & \mathbf{b} \\ \mathbf{c}^{\mathsf{T}} & d \end{bmatrix}$, the Schur complement of block $\mathbf{A}$ is defined as $d - \mathbf{c}^{\mathsf{T}}\mathbf{A}^{-1}\mathbf{b}$.

Authorized licensed use limited to: The Ohio State University. Downloaded on October 12,2022 at 17:21:12 UTC from IEEE Xplore. Restrictions apply.

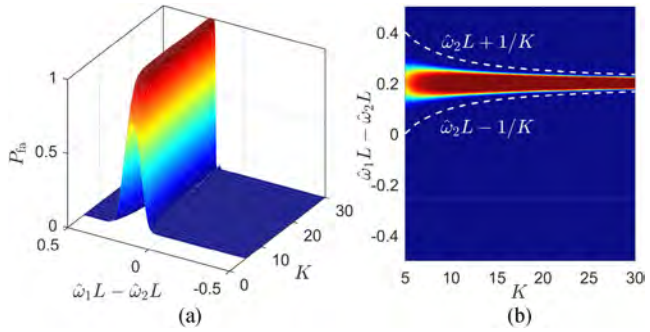

Fig. 1. Simulation results demonstrating Theorem 1. (a) A surface plot of P_{fa} for varying values of K and $\hat{\omega}_1 L - \hat{\omega}_2 L$. (b) A heat map of P_{fa} along with the CFAR convergence boundaries in dashed white lines, as determined by Theorem 1.

where β_{acq_i} is some complex scalar. As such, the LS estimate of the RS using the ML estimate of the Doppler becomes

$$\hat{\mathbf{s}}_i = \frac{1}{\hat{\lambda}_i} \hat{\mathbf{H}}_i^{\mathsf{H}} \hat{\mathbf{P}}^{\perp}_{\mathbf{B}_{i-1}} \mathbf{y} = \beta_{\text{acq}_i} \mathbf{s}_i + \hat{\mathbf{w}}_{\text{acq}_i}, \tag{20}$$

where $\hat{\mathbf{w}}_{\text{acq}_i} \triangleq \frac{1}{\hat{\lambda}_i} \hat{\mathbf{H}}_i^{\mathsf{H}} \hat{\mathbf{P}}^{\perp}_{\mathbf{B}_{i-1}} \mathbf{w}_{\text{eq}_i}$. Furthermore, the asymptotically efficient property of the ML estimator results in $|\beta_{\text{acq}_i}| \to 1$ as $K \to \infty$ [52].

2) Asymptotic CFAR Property: The Doppler estimation error affects the probability of detection and the probability of false alarm. For known subspaces and the corresponding projection matrices, using Theorem 7.1 in [53], one can show that the probability of false alarm for the ith stage of the likelihood in (12) asymptotically tends to

$$P_{\text{fa}_i} = \exp\left(-L\eta_i\right) \sum_{n=0}^{L-1} \frac{(L\eta_i)^n}{n!}, \tag{21}$$

for a large number of observation samples. In other words, the detector is not a function of unknown parameters for known Doppler frequencies, which means that it ensures CFAR property. Next, the effect of Doppler estimation error on the probability of false alarm is assessed. The following theorem gives a sufficient condition to ensure the CFAR property for a scenario with two gNBs for a large enough CPI.

Theorem 1: Consider two gNBs with Doppler frequencies ω_1 and ω_2 and corresponding estimates $\hat{\omega}_1$ and $\hat{\omega}_2$, respectively. Define the Doppler estimation error of ω_1 as $\Delta\omega_1 \triangleq \omega_1 - \hat{\omega}_1$. As $K \to \infty$, sufficient conditions for the matched subspace detector in (12) to be a CFAR detector in the second stage are (i) $|\Delta\omega_1 L| \ll \frac{1}{K}$ and (ii) $|\hat{\omega}_2 L - \hat{\omega}_1 L| > \frac{1}{K}$.

Proof: See Appendix C.

Numerical simulations were conducted in order to visualize the results of Theorem 1. To this end, 5G-like signals were simulated for two different sources at: (i) $\omega_1 L = 0$ and (ii) $\omega_2 L = 0.2$. Then, the CPI length was varied from $K = 5$ to $K = 30$ and $(\hat{\omega}_1 L - \hat{\omega}_2 L)$ was varied from -0.5 to 0.5. For each $(K, \hat{\omega}_1 L - \hat{\omega}_2 L)$ pair, 10^5 realizations of the noise $\mathbf{w}_{\text{eq}_i}$ were used to numerically calculate P_{fa}. The detection threshold was selected such that $P_{\text{fa}} = 0.001$ in the absence of the second source. The results are shown in Fig. 1 indicating that P_{fa} for $|\hat{\omega}_i L - \hat{\omega}_j L| > \frac{1}{K}$ is almost constant at 0.001, and approaches 1 otherwise, which demonstrates Theorem 1.

It should be pointed out that in the experiments, (21) is used to select the threshold for a given probability of false alarm. According to Theorem 7.1 in [53], (21) holds for a large number of observation samples and for known subspaces. Due to the asymptotic efficiency property of the ML estimator, it is assumed that the subpsapce estimation error tends to zero for a large number of observation samples. In the experiments, the number of samples in a CPI is selected to be large and (21) holds asymptotically. The acquisition algorithm is summarized in Algorithm 1.

Algorithm 1: Sequential Matched Subspace Detector.

Input: $\mathbf{y}$, P_{fa}
Output: $\hat{N}$, $\hat{\omega}_i$, and $\hat{\mathbf{s}}_i$ for $i = 1, \ldots, \hat{N}$
1: Initialization: $i = 1$, $\mathbf{P}^{\perp}_{\mathbf{B}_0} = \mathbf{I}$
2: Calculate $\mathcal{L}_i(\mathbf{y})$ according to (16) and the threshold using (21).
3: **if** $\mathcal{L}_i(\mathbf{y}) < \eta_i$ **then**
4: $\quad \hat{N} = i - 1$.
5: $\quad$ Break
6: **end if**
7: Estimate ω_i according to (17), and construct $\hat{\mathbf{H}}_i$, $\hat{\mathbf{P}}^{\perp}_{\mathbf{B}_{i-1}}$, and $\hat{\lambda}_i$
8: $\hat{\mathbf{s}}_i = \frac{1}{\hat{\lambda}_i} \hat{\mathbf{H}}_i^{\mathsf{H}} \hat{\mathbf{P}}^{\perp}_{\mathbf{B}_{i-1}} \mathbf{y}$
9: $i \leftarrow i + 1$, update $\hat{\mathbf{P}}^{\perp}_{\mathbf{B}_{i-1}}$ using $\hat{\omega}_i$, and go to step 2.

B. Tracking

After obtaining coarse estimates of the Doppler frequencies and estimates of the RSs in the acquisition step, the receiver refines and maintains these estimates. Specifically, phase-locked loops (PLLs) are employed to track the carrier phases of the detected RSs and carrier-aided delay-locked loops (DLLs) are used to track the RSs' code phases. Each detected source has its own dedicated tracking loop. Therefore, for compactness of notation, the source index i is dropped in the subsequent analysis. The tracking loops are discussed next.

1) RS Estimate Update: The acquisition step provides a coarse initial estimate of the RS, denoted by $\hat{\mathbf{s}}_{\text{acq}}[n]$. From (20), the nth symbol of the estimated RS can be expressed as $\hat{s}_{\text{acq}}[n] = \beta_{\text{acq}} s[n] + \hat{w}_{\text{acq}}[n]$, where β_{acq} is obtained according to (19) and $x[n]$ is the nth element of vector $\mathbf{x}$. Recall that β_{acq} depends on the Doppler estimation error in the acquisition stage. Let $\hat{t}_{s_k}$ and $\hat{f}_{D_k}$ be the code phase and the Doppler estimates at time-step k in the tracking loop, respectively. In this step of the tracking loop, the RS estimate is updated by coherently integrating the observations after delay compensation and Doppler wipe-off. As such, the RS estimate at the kth iteration of the tracking loops is given by

$$\hat{s}_k[n] = \frac{k}{k+1} \hat{s}_{k-1}[n] + \frac{1}{k+1} y_k[n + \hat{n}_{d_k}] \exp\left(-j2\pi \hat{f}_{D_k} n\right)$$

Authorized licensed use limited to: The Ohio State University. Downloaded on October 12,2022 at 17:21:12 UTC from IEEE Xplore. Restrictions apply.

$$= \frac{1}{k+1}\left[\hat{s}_{\text{acq}}[n] + \sum_{m=1}^{k} y_m[n+\hat{n}_{d_m}] \times \exp\left(-j2\pi \hat{f}_{D_m} n\right)\right], \quad (22)$$

where $\hat{n}_{d_m} \triangleq \lfloor \frac{\hat{t}_{s_m}}{T_s} \rceil$ and $\lfloor \cdot \rceil$ denotes rounding to the closest integer.

2) PLL: The PLL consists of a phase discriminator, a loop filter, and a numerically-controlled oscillator (NCO). It was found that the receiver could easily track the carrier phase with a second-order PLL with a loop filter transfer function

$$F_{\text{PLL}}(s) = \frac{2\kappa\omega_n s + \omega_n^2}{s}, \quad (23)$$

where $\kappa \equiv \frac{1}{\sqrt{2}}$ is the damping ratio and ω_n is the undamped natural frequency, which can be related to the PLL noise-equivalent bandwidth $B_{n,\text{PLL}}$ by $B_{n,\text{PLL}} = \frac{\omega_n}{8\zeta}(4\zeta^2+1)$ [54]. The loop filter transfer function in (23) is discretized at a sampling period $T_{\text{sub}} \triangleq LT_s$, which is the time interval at which the loop filters are updated and is typically known as the subaccumulation interval. The discretized transfer function is realized in state-space. The output of the loop filter at time-step k, denoted by $v_{\text{PLL},k}$, is the rate of change of the carrier phase error, expressed in rad/s. The Doppler frequency estimate at time-step k is deduced by dividing $v_{\text{PLL},k}$ by 2π. The loop filter transfer function in (23) is discretized and realized in state-space. The noise-equivalent bandwidth is chosen to range between 4 and 8 Hz. The carrier phase estimate at time-step k is updated according to

$$\hat{\theta}_k = \hat{\theta}_{k-1} + v_{\text{PLL}} \cdot T_{\text{sub}}, \quad (24)$$

where $\hat{\theta}_0 \equiv 0$. A measure of the change in distance between the transmitter and receiver can be formed from the carrier phase as $z(k) = -\frac{c}{2\pi f_c}\hat{\theta}_k$, where c is the speed-of-light and f_c is the carrier frequency. The term z is typically referred to as the carrier phase expressed in meters. The model relating z to the receiver's position is discussed in Subsection V-B.

3) DLL: The carrier-aided DLL employs an early-minus-late discriminator. The early and late correlations at time-step k used in the discriminator are denoted by Z_{e_k} and Z_{l_k}, respectively, which are calculated by correlating the received signal with an early and a delayed version of the estimated RS, respectively. The time shift between Z_{e_k} and Z_{l_k} is defined as the early-minus-late time, denoted by ξ. The DLL loop filter is a simple gain K_{DLL}, with a noise-equivalent bandwidth $B_{n,\text{DLL}} = \frac{K_{\text{DLL}}}{4} \equiv$ 0.5 Hz. The output of the DLL loop filter v_{DLL} is the rate of change of the code phase, expressed in s/s. Assuming low-side mixing at the radio frequency front-end, the code phase estimate is updated according to

$$\hat{t}_{s_{k+1}} = \hat{t}_{s_k} - \left(v_{\text{DLL},k} + \frac{v_{\text{PLL},k}}{2\pi f_c}\right) \cdot T_{\text{sub}}. \quad (25)$$

The code phase estimate can be used to readily deduce the pseudorange observables.

V. Experimental Results

This section validates the proposed CON receiver experimentally. To this end, three experiments are conducted: (i) an experiment on a ground vehicle with real 5G NR signals, (ii) an experiment on UAV with real 5G NR signals, and (iii) an experiment on UAV with real 4G LTE signals. The objective of these experiments are to: (i) validate the signal model, (ii) evaluate the acquisition and tracking performance of the CON receiver, (iii) demonstrate the capability of detecting multiple sources, i.e., gNBs in 5G and eNodeBs in LTE, transmitting on the same carrier frequency, (iv) showcase the navigation solution obtained via the CON receiver, (iv) and evaluate the navigation performance of the CON receiver in a scenario where the RSs are always-on and compare it to the navigation solution obtained with a conventional opportunistic navigation receiver which has complete knowledge of the RSs. The parameters considered in the experiments are listed in Table I.

A. CON With Real 5G Signals: Comparison With a Conventional 5G Receiver on a Ground Vehicle

The first experiment aims to compare the acquisition and tracking performance of the CON receiver with the conventional 5G receiver [14] which only relies on the always-on RSs. The experimental setup and results for the experiment with real 5G NR signals are discussed next.

1) Experimental Setup and Environmental Layout: In this experiment, a ground vehicle was equipped with a quad-channel National Instrument (NI) universal software radio peripheral (USRP)-2955 and four consumer grade 800/1900 MHz cellular antennas to sample 5G signals near Fairview Road in Costa Mesa, California, USA. Only one channel from the USRP was used and was tuned to a 872 MHz carrier frequency, which is a 5G NR frequency allocated to the U.S. cellular provider AT&T. The sampling rate was set to 10 Mega-samples per second (MSps) and the sampled 5G signals were stored on a laptop for post-processing. In order to obtain ground-truth, the vehicle was equipped with a Septentrio AsteRx-i V GNSS-aided inertial navigation system (INS), which is a dual antenna, multi-frequency GNSS receiver with real-time kinematics (RTK) capabilities. The GNSS receiver is coupled with a Vectornav VN-100 micro electromechanical systems (MEMS) inertial measurement unit (IMU) to estimate the position and orientation of the ground vehicle at a rated horizontal accuracy of 0.6 cm in clear sky conditions (RTK performance). The vehicle traversed a trajectory of 4.1 km in 315 seconds. Fig. 2 shows the environment layout and the vehicle trajectory. The acquisition results are presented next.

2) Signal Model Validation: The signal model (1) considers a channel with a single tap, which corresponds to the LOS path with an arbitrary complex channel gain α_i. In other words, the channel is modeled as $h_i[n] = \alpha_i \delta[n - \lfloor t_{s_i}[n] \rceil]$, where α_i is the complex channel gain between the ith gNB and the UE, $t_{s_i}[n]$ is the code-delay corresponding to the UE and the ith gNB, and $\lfloor \cdot \rceil$ is the rounding operation to the closest integer. Note that this channel models flat fading, where multiple received "close" signal paths are combined into a single α_i. To justify the signal

Authorized licensed use limited to: The Ohio State University. Downloaded on October 12,2022 at 17:21:12 UTC from IEEE Xplore. Restrictions apply.

TABLE I
RECEIVER PARAMETERS

Parameter	LTE	5G
Carrier frequency	1955, 2145, 2125, and 739 MHz [12]	632.55, and 872 MHz [13]
Sampling rate	10 MHz	10 MHz
η	1.012 for $P_{fa} = 10^{-4}$ (21)	1.007 for $P_{fa} = 10^{-4}$ (21)
$B_{n,\mathrm{PLL}}$	4-8 Hz (empirically)	4-8 Hz (empirically)
$B_{n,\mathrm{DLL}}$	0.5 Hz (empirically)	0.5 Hz (empirically)
T_{sub}	10 ms [12]	20 ms [13]
K	40 (empirically)	40 (empirically)

Fig. 2. Experimental setup and vehicle trajectory for the 5G NR experiment with ground vehicle.

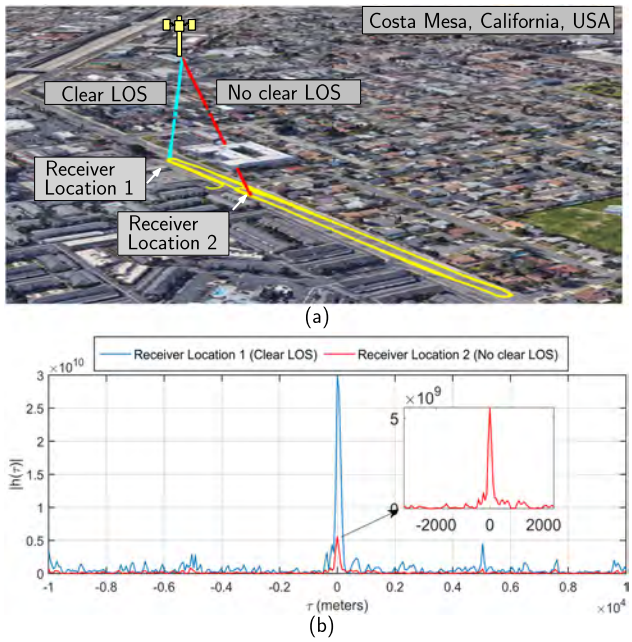

Fig. 3. (a) Receiver locations for two cases: with and without clear LOS. (b) Channel impulse response at the two receiver locations.

model in the tested scenario, two test points are considered for the ground vehicle (see Fig. 3(a)). In this figure, the term *clear LOS* refers to a scenario where the signal is not blocked by an obstacle, e.g., a building. The two test points, i.e., receiver location 1 and receiver location 2, are considered based on the existence of the clear LOS with respect to the 5G gNB. Receiver location 1 has a clear LOS and is also closer to the gNB. On the other hand, receiver location 2 is blocked by a building and does not have a clear LOS. The magnitude of the channel impulse response for both locations are plotted in Fig. 3(b). The magnitudes of the channel impulse responses are estimated by reconstructing the frame as described in [13]. As it can be seen in this figure, the channel impulse response for receiver location 2 is weaker than that of receiver location 1 which is due to blockage of the signal by an obstacle. The complex channel gain in (1) captures this effect by attenuating the LOS signal. If the acquisition of a gNB is performed when the receiver does not have a clear LOS, e.g., receiver location 2, the detection performance will be degraded, which in turn affects the tracking performance. Fig. 4 demonstrates the likelihood at the first stage of acquisition for receiver location 1 and 2. As can be seen in Fig. 4, the likelihood is degraded at receiver location 2 due to signal blockage. Note that in both receiver locations, $|h(\tau)|$ does not exhibit multiple taps (i.e., $h_i[n] = \sum_{j=1}^{M} \alpha_{i,j}\delta[n - \lfloor t_{s_{i,j}}[n] \rceil]$, where M is the number of paths), which corresponds to the impulse response of a frequency selective channel. While the considered signal model is simple, yet valid for the conducted experiments, more sophisticated channel models, e.g., frequency selective channels, can be considered in future work [55].

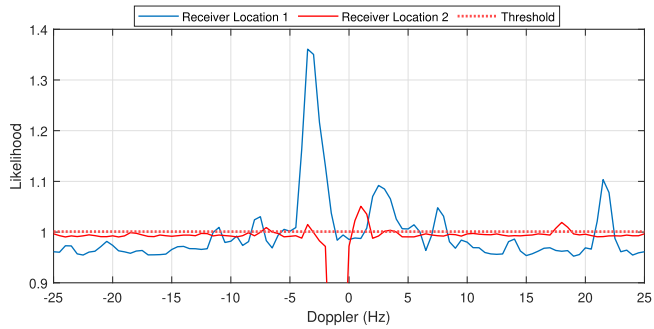

Fig. 4. The likelihood (12) calculated at receiver location 1 and 2 for $i = 1$ demonstrates that no clear line of sight dramatically degrades the likelihood function.

3) Acquisition Results: The recorded 5G signals were processed in two ways for comparison: (i) using the proposed CON receiver and (ii) using the conventional 5G receiver proposed in [14]. The conventional 5G receiver detected 1 gNB with an initial Doppler frequency of -7.2 Hz. Note that the limited

Authorized licensed use limited to: The Ohio State University. Downloaded on October 12,2022 at 17:21:12 UTC from IEEE Xplore. Restrictions apply.

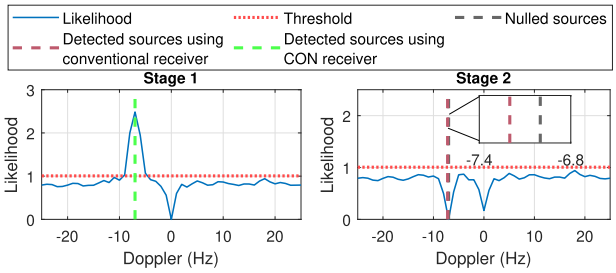

Fig. 5. Acquisition stages in the CON receiver for 5G NR signals on a ground vehicle showing the likelihood function at each stage and the detected and nulled sources. The DC component, i.e., at zero Doppler frequency, was nulled as it was saturating the detector.

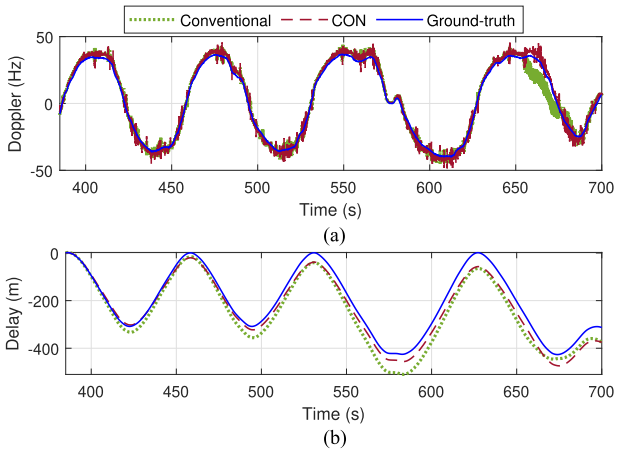

Fig. 6. (a) Doppler tracking and (b) delay tracking results for the 5G NR ground vehicle experiment. The ground-truth is calculated according to the true position of the vehicle and the gNBs.

number of gNBs was expected as 5G gNBs are sparsely deployed at the present time. The location of the gNB was mapped prior to the experiment. Next, the signal acquisition stage was applied to detect the ambient 5G gNB. The detection threshold was set such that $P_{\text{fa}} = 10^{-4}$, which yielded $\eta = 1.008$, K was set to 40, and T_{sub} was set to 20 ms. Doppler estimation was performed by searching for the maximizer of the likelihood function according to (17) with a step size of 1 Hz. The acquisition stages in the CON receiver is shown in Fig. 5. As it can be seen in this figure, in the first stage of the acquisition, one gNB is detected at frequency -7 Hz. In the second stage, the Doppler subspace of this gNB is nulled and the resulting likelihood is less than the threshold for all Doppler frequencies. This implies that, no other gNBs are detected in the second stage of the acquisition or equivalently $\hat{N} = 1$.

4) Tracking Results: After acquiring the Doppler and RSs, the tracking loops are initialized and the signal is tracked. Fig. 6 show the resulting Doppler frequency and delay, expressed in meters, obtained using the CON and conventional receivers. As it can be seen in Fig. 6(b) the estimated delays for the CON and the conventional receivers are slightly drifting away from the ground-truth which is due to the clock drifts. The effect of clock drift is considered in the carrier phase model (see equation (26)). Note that the initial value of the delays were subtracted out

TABLE II
DELAY AND DOPPLER RMSE FOR THE CON AND CONVENTIONAL RECEIVERS

	Delay RMSE (m)	Doppler RMSE (Hz)
Conventional	24.33	3.66
CON	21.88	2.28

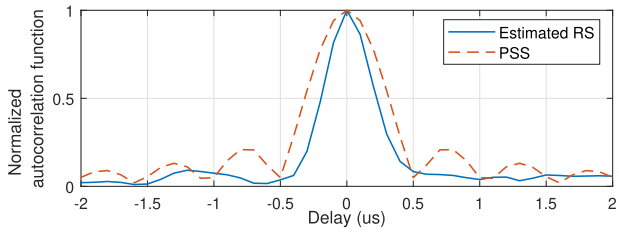

Fig. 7. Normalized autocorrelation function of the RS estimated with the CON receiver compared to that of a 5G PSS.

to facilitate comparison. The Doppler and delay RMSE values were calculated from ground-truth for both receivers and are summarized in Table II, which shows that the CON receiver outperforms the conventional one.

A main reason behind the CON receiver performing better than a conventional 5G receiver is that the former exploits the RSs in the entire bandwidth, making the bandwidth of estimated RS higher than the RSs used in the conventional receiver (mainly, PSS and SSS). Fig. 7 shows this: the normalized autocorrelation function of the RS estimated with the CON receiver is narrower than that of a 5G PSS.

Remark 3: The conventional and the proposed cognitive methods use tracking loops which involve the same computational complexity. The main difference between the computational complexity of the proposed cognitive receiver and a conventional receiver stems from the acquisition stage. The number of complex operations is considered as a metric for computational complexity. In the likelihood function (12), the size of the projection matrices increases with the detection stage, i.e., i. However, in [56] (Appendix 8B), a recursive formula is provided to calculate the projection matrix at the ith stage based on the already calculated projection matrix at $(i-1)$th stage. Using the recursive formula presented in this appendix, the complexity of the projection matrix is $\mathcal{O}(K^2)$ where $\mathcal{O}(\cdot)$ denotes the rate of growth of a function, i.e., its order. Consequently, the number of complex operations to calculate the matched subspace detector is $\mathcal{O}((5(KL)^2 + KL)N)$.

B. CON With Real 5G Signals: The First Navigation Results on a UAV

The second experiment aims to find a navigation solution on a UAV using the CON receiver. To the best of author's knowledge this is the first navigation results with real 5G signals on a UAV.

1) Experimental Setup and Environment Layout: In this experiment, the navigator was an Autel Robotics X-Star Premium UAV equipped with a single-channel Ettus 312 USRP connected to a consumer-grade 800/1900 MHz cellular antenna and a small consumer-grade GPS antenna to discipline the on-board oscillator. The cellular receivers were tuned to the cellular

Authorized licensed use limited to: The Ohio State University. Downloaded on October 12,2022 at 17:21:12 UTC from IEEE Xplore. Restrictions apply.

Fig. 8. Environment layout and UAV trajectory for the 5G NR UAV experiment.

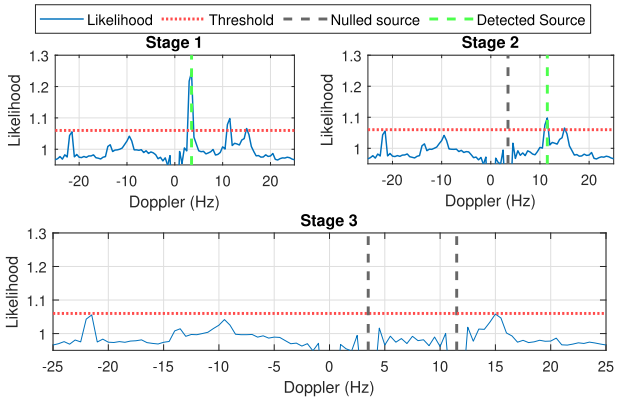

Fig. 9. Acquisition stages in the CON receiver for 5G NR signals on a UAV showing the likelihood function at each stage and the detected and nulled sources. The DC component, i.e., at zero Doppler frequency, was nulled as it was saturating the detector.

carrier frequency 632.55 MHz, which is a 5G NR frequency allocated to the U.S. cellular provider T-Mobile. Samples of the received signals were stored for off-line post-processing. The ground-truth reference trajectory was taken from the on-board Ettus 312 USRP GPS solution. The UAV traversed a trajectory of 416 m. Fig. 8 shows the environment layout and the vehicle trajectory. The acquisition results are presented next.

2) Acquisition Results: Next, the signal acquisition stage was applied to detect the ambient 5G gNBs. The CON 5G receiver detected 2 gNBs with initial Doppler frequencies of 3.5 Hz and 11.5 Hz. The location of the gNBs was mapped prior to the experiment.

The acquisition stages in the CON receiver are shown in Fig. 9.

3) Tracking Results: After acquiring the Doppler and the RSs, the tracking loops are initialized and the signal is tracked. Fig. 10 shows the resulting Doppler frequencies and delays, expressed in meters, obtained using the CON receiver.

4) Navigation Solution: In the following, it is assumed that (i) the UAV's altitude is known at all time and (ii) the UAV has an estimate of its position at time-step k_0, prior to navigating with 5G signals. The carrier phase to the i-th gNB $z_i(k)$ at time-step

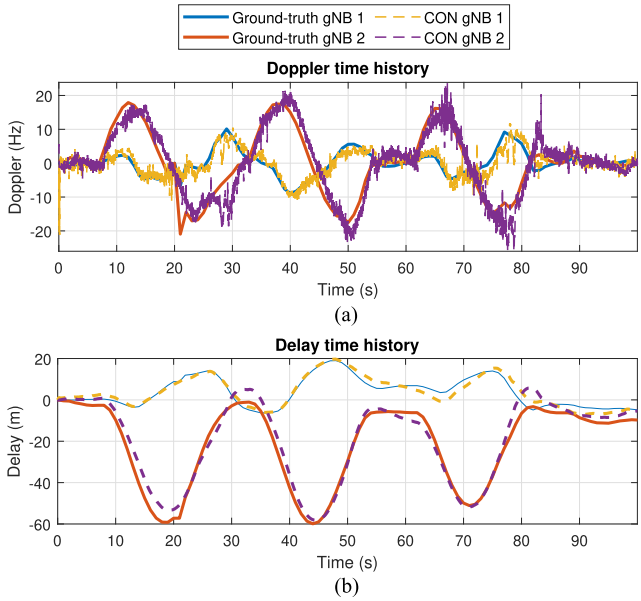

Fig. 10. (a) Doppler tracking and (b) delay tracking results for the UAV 5G experiment. The ground-truth is calculated according to the true position of the vehicle and the gNBs.

k expressed in meters can be modeled as

$$z_i(k) = \|\boldsymbol{r}_r(k) - \boldsymbol{r}_{s_i}\|_2 + c\delta t_r(k) - c\delta t_{s_i} + v_i(k), \quad (26)$$

where $\boldsymbol{r}_r$ and $\boldsymbol{r}_{s_i}$ are the three-dimensional (3–D) position vectors of the UAV-mounted receiver and the i-th gNB, respectively; c is the speed of light; δt_r is the UAV-mounted receiver's clock bias; δt_{s_i} models the i-th gNB's clock bias and carrier phase ambiguity; and $v_i(k)$ is the measurement noise, which is modeled as a zero-mean Gaussian random variable with variance σ_i^2 [57]. Note that since the UAV's altitude is known, e.g., using an altimeter, only its two-dimensional (2–D) position is estimated. The time reference for the transmitter and receiver clocks is chosen such that $\delta t_r(k_0) = 0$.

Using the position estimate at k_0 and the fact that $\delta t_r(k_0) = 0$, the gNBs clock biases can be estimated from $z_i(k_0)$ resulting in the estimate $\hat{\delta} t_{s_i}$. Next, define the corrected carrier phase measurement $\bar{z}_i(k) \triangleq z_i(k) + \hat{\delta} t_{s_i}$ which can be approximated as

$$\bar{z}_i(k) \approx \|\boldsymbol{r}_r(k) - \boldsymbol{r}_{s_i}\|_2 + c\delta t_r(k) + v_i(k), \quad \forall k > k_0. \quad (27)$$

Subsequently, the corrected carrier phase measurements were fed to an extended Kalman filter (EKF) to solve the state vector $\boldsymbol{x}(k) \triangleq [\boldsymbol{r}_r(k), \dot{\boldsymbol{r}}_r(k), c\delta t_r(k), c\dot{\delta} t_r(k)]^{\mathsf{T}}$, where $\dot{\boldsymbol{r}}_r(k)$ is the UAV's 2–D velocity vector and $\dot{\delta} t_r(k)$ is the receiver's clock drift. A nearly constant velocity model was used for the UAV's position and velocity dynamics, and a standard double integrator driven by process noise was used to model the clock bias and drift dynamics [58]. As such, the discrete-time dynamics model of $\boldsymbol{x}$ are given by

$$\boldsymbol{x}(k+1) = \mathbf{F}\boldsymbol{x}(k) + \boldsymbol{w}(k), \quad (28)$$

where $\mathbf{F}$ is the state transition matrix obtained according to [58] and $\boldsymbol{w}(k)$ is the process noise vector, which is modeled as a

Authorized licensed use limited to: The Ohio State University. Downloaded on October 12,2022 at 17:21:12 UTC from IEEE Xplore. Restrictions apply.

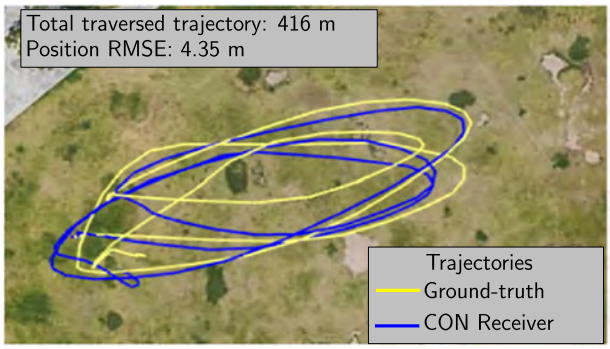

Fig. 11. Ground-truth and estimated trajectories using CON receiver for 5G NR signals on a UAV. The CON receiver yielded a UAV position RMSE of 4.35m. Map data: Google Earth.

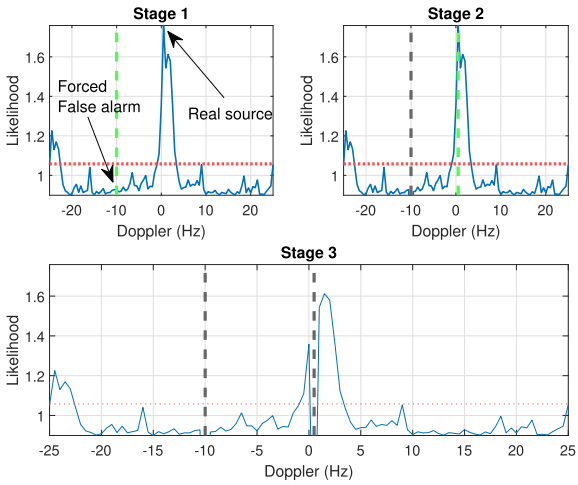

Fig. 12. Likelihood function for the UAV 5G experiment: In stage 1, a non-existent source at a corresponding Doppler of -10 Hz was fictitiously induced to pass the threshold (i.e., forced false alarm). In stage 2, this fictitious source is nulled and a valid source of 0 Hz is detected.

zero-mean Gaussian random vector with covariance matrix $\mathbf{Q}$ obtained according to [58]. The UAV's x, y acceleration process noise spectra in the nearly constant velocity model were set to $\tilde{q}_x = \tilde{q}_y = 10\ \mathrm{m}^2/\mathrm{s}^3$, and the receiver's clock process noise was chosen to be that of a typical temperature-compensated crystal oscillator (TCXO) [58]. Note that $\boldsymbol{r}_r(k)$ is expressed in an East-North-Up (ENU) frame centered at the UAV's true initial position. The EKF state estimate was initialized at $\hat{\boldsymbol{x}} = \mathbf{0}_{6\times 1}$ with an initial covariance of $\boldsymbol{\Sigma} = 4 \cdot \mathbf{I}_{6\times 6}$. The measurement noise covariance was set to $\mathbf{R} = 2 \cdot \mathbf{I}_{2\times 2}$.

The position RMSE of the UAV was calculated to be 4.35 m with the aforementioned parameters. The true and estimated UAV trajectories are shown in Fig. 11.

5) Effect of False Alarm: The effect of a false alarm on the performance of the tracking loops is assessed next. It will be demonstrated that if at the acquisition stage a false alarm happens and a gNB is mistakenly detected, the carrier phase error will not converge in the tracking loops. In this case, the proposed method should neglect the detected source. To demonstrate this experimentally, Fig. 12 plots the likelihood function. In this experiment, the acquisition stage is forced to detect a false alarm,

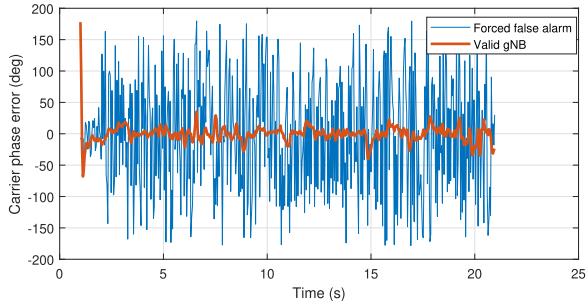

Fig. 13. Carrier phase error for a valid gNB (at 0 Hz) and a forced false alarm gNB (at -10 Hz) shown in Fig 12.

i.e., the acquisition stage is confirming the existence of a source which does not exist. Fig. 13 demonstrates the carrier phase error for the valid gNB and the false alarm gNB. As it can be seen in Fig. 13, the carrier phase error for the valid gNB converges whereas the carrier phase error for the false alarm is not. It should also be noted that P_{fa} can be selected based on the operating environments.

C. CON With LTE Signals: Comparing With a Conventional Receiver When the RSs are Always-On

This experiment was conducted with real LTE signals on a UAV to (i) compare the navigation performance with a receiver which exploits all the available RSs in a scenario where the RSs are always-on, and (ii) to evaluate the performance of the CON receiver in an environment with multiple LTE eNodeBs operating in the same carrier frequency. The experimental setup and results are discussed next.

1) Experimental Setup: In this experiment, a DJI Matrice 600 UAV was equipped with the NI USRP-2955 and four consumer grade 800/1900 MHz cellular antennas to sample LTE signals near Aliso Viejo, California, USA. The channels of the USRP were tuned to 1955, 2145, 2125, and 739 MHz carrier frequencies, respectively, which are 4G LTE frequencies allocated to the U.S. cellular providers AT&T, T-Mobile, and Verizon. The sampling rate for each channel was set to 10 MSps and the sampled LTE signals were stored on a laptop for post-processing. The UAV was equipped with the same Septentrio GNSS-aided INS described in Subsection V-A for ground-truth.

2) Acquisition Results: The recorded LTE signals were processed in two ways for comparison: (i) using the proposed CON receiver and (ii) using the conventional LTE receiver developed in [59]. The conventional LTE receiver detected 11 eNodeBs over the 4 channels. The locations of the eNodeBs were mapped prior to the experiment and are shown in Fig. 14. Next, the signal acquisition stage was applied to detect the ambient LTE eNodeBs. The detection threshold was set such that $P_{\mathrm{fa}_i} = 10^{-4}$, which yielded $\eta_i = 1.012$, K was set to 40, and T_{sub} was set to 10 ms for all i. Doppler estimation was performed in a similar as the previous experiment. The acquisition stages for the 1955 MHz carrier frequency are shown in Fig. 15. In particular, Fig. 15 shows how the likelihood function changes as sources are detected and nulled by the CON receiver. The conventional

Authorized licensed use limited to: The Ohio State University. Downloaded on October 12,2022 at 17:21:12 UTC from IEEE Xplore. Restrictions apply.

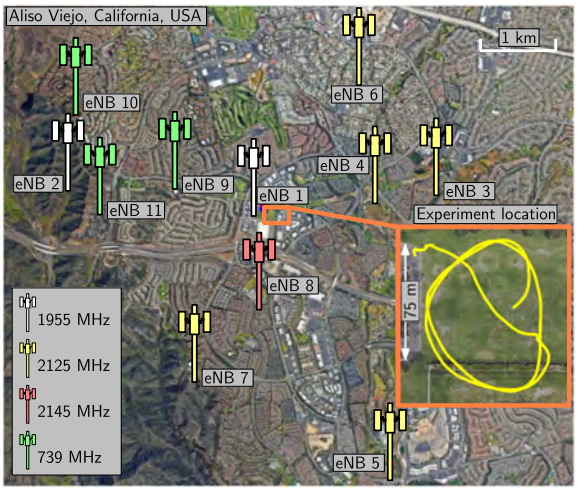

Fig. 14. Layout of eNodeBs and UAV trajectory for the 4G LTE experiment.

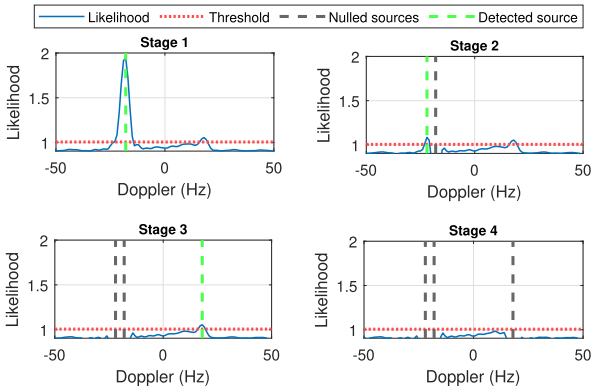

Fig. 15. Acquisition stages for the 1955 MHz carrier frequency showing the likelihood function at each stage and the detected and nulled sources.

LTE receiver detected two eNodeBs at the 1955 MHz carrier frequency, denoted by eNodeB 1 and eNodeB 2 in Fig. 14, with eNodeB 1 having a Doppler frequency of -18.5 Hz and eNodeB 2 having a Doppler frequency of -17.5 Hz. The CON receiver detected 3 eNodeBs at the 1955 MHz carrier frequency with Doppler frequencies -22 Hz, -18, and 18 Hz. The eNodeBs detected by the CON receiver were manually associated with the ones detected by the conventional receiver by matching the Doppler and delay profiles. Sophisticated data association techniques could be employed to perform this step; however, it is out of the scope of the current paper. After performing data association, it was found that only one of the Doppler frequencies detected by the CON receiver pertains to the ones detected by the conventional LTE receiver. Specifically, the CON receiver detected eNodeB 1 at a -18 Hz Doppler frequency, which is 0.5 Hz off from the one estimated by the conventional receiver. This error is due to the 1 Hz step size used in the Doppler search. For $K = 40$, the condition from Theorem 1 for the CON receiver to be able to distinguish between eNodeB 1 and eNodeB 2 at the specified $P_{\text{fa}_i} = 10^{-4}$ is that the difference between their Doppler frequencies must be greater than 1.25 Hz. However, the Doppler frequency difference between eNodeB 1 and 2 measured by the conventional receiver is 1 Hz which violates the

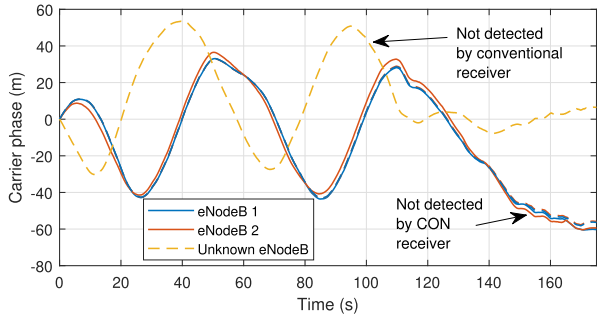

Fig. 16. Tracking results showing the carrier phase, expressed in meters, obtained from the CON and conventional receivers for the 1955 MHz carrier frequency. Solid lines represent the carrier phases tracked by the conventional receiver while the dashed lines represent the ones tracked by the CON receiver.

TABLE III
CARRIER PHASE RMSE BETWEEN THE CON AND CONVENTIONAL LTE RECEIVERS AND GROUND-TRUTH

eNodeB	1	4	5	7	8	10
CON RMSE (m)	3.34	3.00	2.80	2.37	2.85	5.13
Conventional RMSE (m)	3.39	2.52	2.70	2.92	2.84	3.40

aforementioned condition. This direct consequence of Theorem 1 explains why the CON receiver could not detect eNodeB 2. Similar acquisition results are obtained with the remaining carrier frequencies. A total of 11 eNodeBs were acquired by the CON receiver. After manual data association, it is found that only 6 of them pertain to the ones detected by the conventional receiver (eNodeBs 1, 4, 5, 7, 8, and 10) and the rest pertain to unknown eNodeBs that were not detected by the conventional receiver.

3) Tracking Results: After acquiring the Doppler frequencies and the RSs, the tracking loops are initialized and the signals are tracked. Fig. 16 shows the resulting carrier phases, expressed in meters, obtained using the CON and conventional receivers for the eNodeBs acquired on the 1955 MHz carrier frequency. The carrier phase expressed in meters is a smoother estimate of the true range than the RS delays. The subsequent analyses focus on carrier phase measurements since they will be used to compute the navigation solution. The carrier phase RMSE values are summarized in Table III. Note that eNodeBs 2, 3, 6, 9, and 11 are not included in Table III since they were not detected by the CON receiver; however, as mentioned previously, the CON receiver acquired and tracked 5 unknown eNodeBs that were not detected by the conventional LTE receiver. One example is shown in Fig. 16. For fair comparison, only the common eNodeBs will be used to compute a navigation solution.

4) Navigation Solution: The navigation framework discussed in SubSection V-A is employed to compute the UAV's 2–D position from the navigation observables produced by the CON and conventional receivers. Two position estimates were calculated using six carrier phase measurements from the eNodeBs in Table III: (i) for the conventional receiver and (ii) for the CON receiver. The position RMSE of the conventional and CON receivers were both calculated to be 2.07 m. The true and estimated UAV trajectories are shown in Fig. 17.

Authorized licensed use limited to: The Ohio State University. Downloaded on October 12,2022 at 17:21:12 UTC from IEEE Xplore. Restrictions apply.

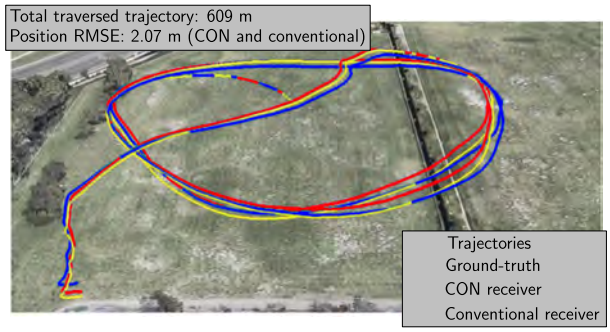

Fig. 17. Ground-truth and estimated trajectories using CON and a conventional LTE receivers. Both approaches yielded a UAV position RMSE of 2.07m. Map data: Google Earth.

VI. Conclusion

A CON receiver architecture was proposed to extract navigation observables from 5G signals, without requiring knowledge of the 5G RSs. To exploit the full ranging accuracy that can be achieved with 5G signals, the proposed CON receiver was designed to estimate the RSs from multiple 5G gNBs and exploit them for navigation purposes. The acquisition stage of the CON receiver was modeled as a sequential detection problem. The GLR test was derived to sequentially estimate the number of active gNBs, their RSs, and Doppler frequencies. Tracking loops were also designed in order to refine and maintain the estimates provided by the acquisition stage. Real 5G signals were used to assess the capabilities of the proposed CON receiver. Extensive experimental results were presented demonstrating the capabilities of the proposed CON receiver with real 5G and 4G signals on ground and aerial platforms. On a ground vehicle, it was demonstrated that the CON receiver yields a reduction of 10% and 37.7% in the estimated delay and Doppler RMSE, respectively, over that achieved with a conventional opportunistic navigation 5G receiver. On a UAV, it was demonstrated that the CON receiver enables the UAV to navigate over 416 m trajectory with 5G NR gNBs, achieving a position RMSE of 4.35 m.

Appendix A
Derivation of Likelihood Function (12)

For a known $\mathcal{W}_i$, the singular value decomposition (SVD) of the matrix $\mathbf{B}_{i-1}$ can be written as

$$\mathbf{B}_{i-1} = [\mathbf{W}_{i-1}\ \mathbf{U}_{i-1}] \begin{bmatrix} \mathbf{\Sigma}_{i-1} & \mathbf{0} \\ \mathbf{0} & \mathbf{0} \end{bmatrix} \begin{bmatrix} \mathbf{W}_{i-1}^{\mathsf{H}} \\ \mathbf{U}_{i-1}^{\mathsf{H}} \end{bmatrix} \tag{29}$$

where $\mathbf{W}_{i-1}$ and $\mathbf{U}_{i-1}$ are $KL \times (i-1)L$ and $KL \times (KL - (i-1)L)$ orthogonal matrices that span the column space of $\mathbf{B}_{i-1}$ and orthogonal column space of $\mathbf{B}_{i-1}$, respectively. In other words, $\mathbf{U}_{i-1}^{\mathsf{H}}\mathbf{B}_{i-1} = \mathbf{0}$. Therefore,

$$\mathbf{U}_{i-1}^{\mathsf{H}}\mathbf{y} = \mathbf{U}_{i-1}^{\mathsf{H}}\mathbf{H}_i\mathbf{s}_i + \mathbf{U}_{i-1}^{\mathsf{H}}\mathbf{w}_{\mathrm{eq_i}}. \tag{30}$$

As it was mentioned previously, the complex envelope of the OFDM signals can be considered to be asymptotically white and Gaussian [60]. Here, the GLR test is derived assuming that $\mathbf{w}_{\mathrm{eq}_i} \sim \mathcal{N}(\mathbf{0}, \sigma_w^2\mathbf{I})$. It should be noted that since $\mathbf{U}_{i-1}^{\mathsf{H}}\mathbf{U}_{i-1} = \mathbf{I}$, the statistical characteristics of noise is preserved, i.e., $\mathbf{U}_{i-1}^{\mathsf{H}}\mathbf{w}_{\mathrm{eq_i}} \sim \mathcal{N}(\mathbf{0}, \sigma_w^2\mathbf{I})$. By multiplying the observation vector by $\mathbf{U}_{i-1}^{\mathsf{H}}$, (11) can be written as

$$\begin{cases} \mathcal{H}_0^i:\ \mathbf{U}_{i-1}^{\mathsf{H}}\mathbf{y} = \mathbf{U}_{i-1}^{\mathsf{H}}\mathbf{w}_{\mathrm{eq_i}}, \\ \mathcal{H}_1^i:\ \mathbf{U}_{i-1}^{\mathsf{H}}\mathbf{y} = \mathbf{U}_{i-1}^{\mathsf{H}}\mathbf{H}_i\mathbf{s}_i + \mathbf{U}_{i-1}^{\mathsf{H}}\mathbf{w}_{\mathrm{eq_i}}. \end{cases} \tag{31}$$

For the linear detection problem (31), the GLR can is derived as [53, Section 9.4.3]

$$\mathcal{L}_i(\mathbf{y}|\mathcal{W}_i) = \frac{\mathbf{y}^{\mathsf{H}}\mathbf{P}_{\mathbf{S_i}}\mathbf{y}}{\mathbf{y}^{\mathsf{H}}\mathbf{P}^{\perp}_{\mathbf{B_{i-1}}}\mathbf{P}^{\perp}_{\mathbf{S_i}}\mathbf{P}^{\perp}_{\mathbf{B_{i-1}}}\mathbf{y}}, \tag{32}$$

where $\mathbf{P}_{\mathbf{S_i}} \triangleq \mathbf{P}^{\perp}_{\mathbf{B}_{i-1}}\mathbf{H}_i$ and

$$\mathbf{P}^{\perp}_{\mathbf{B}_{i-1}} \triangleq \mathbf{U}_{i-1}\mathbf{U}_{i-1}^{\mathsf{H}} = \mathbf{I} - \mathbf{B}_{i-1}\left(\mathbf{B}_{i-1}^{\mathsf{H}}\mathbf{B}_{i-1}\right)^{-1}\mathbf{B}_{i-1}^{\mathsf{H}}. \tag{33}$$

Appendix B
Proof of Lemma 1

The matrices $\mathbf{H}_i$ and $\mathbf{P}^{\perp}_{\mathbf{B}_{i-1}}$ can be written as

$$\mathbf{H}_i = \mathbf{h}_i \otimes \mathbf{I}_L, \quad \mathbf{P}^{\perp}_{\mathbf{B}_{i-1}} = \bar{\mathbf{P}}^{\perp}_{i-1} \otimes \mathbf{I}_L, \tag{34}$$

where, $\mathbf{h}_i \triangleq [1, \exp(j\omega_i L), \ldots, \exp(j\omega_i(K-1)L)]^{\mathsf{T}}$, $\bar{\mathbf{P}}^{\perp}_{i-1} \triangleq (\mathbf{I} - \mathbf{b}_{i-1}(\mathbf{b}_{i-1}^{\mathsf{H}}\mathbf{b}_{i-1})\mathbf{b}_{i-1}^{\mathsf{H}})$, $\mathbf{b}_{i-1} \triangleq [\mathbf{h}_1, \ldots, \mathbf{h}_{i-1}]$, and $\otimes$ denotes the Kronecker product. Hence, one can write

$$\mathbf{H}_i^{\mathsf{H}}\mathbf{P}^{\perp}_{\mathbf{B}_{i-1}}\mathbf{H}_i = \left(\mathbf{h}_i^{\mathsf{H}}\bar{\mathbf{P}}^{\perp}_{i-1}\mathbf{h}_i\right) \otimes \mathbf{I}_L. \tag{35}$$

The scalar $\mathbf{h}_i^{\mathsf{H}}\bar{\mathbf{P}}^{\perp}_{i-1}\mathbf{h}_i$ can be written as

$$\mathbf{h}_i^{\mathsf{H}}\bar{\mathbf{P}}^{\perp}_{i-1}\mathbf{h}_i = c_{ii} - \begin{bmatrix} c_{i1}, \ldots, c_{i(i-1)} \end{bmatrix} \cdot \begin{bmatrix} c_{11} & c_{12} & \ldots & c_{1(i-1)} \\ c_{21} & c_{22} & \ldots & c_{2i} \\ \vdots & \ddots & \ddots & \vdots \\ c_{i1} & c_{i2} & \ldots & c_{(i-1)(i-1)} \end{bmatrix}^{-1} \begin{bmatrix} c_{1i} \\ c_{2i} \\ \vdots \\ c_{(i-1)i} \end{bmatrix}, \tag{36}$$

which is the Schur complement of $\mathbf{C}_{i-1}$ of matrix $\mathbf{C}_i$ in (15), with $c_{ij} \triangleq \sum_{k=0}^{K-1} \exp(j(\omega_j - \omega_i)Lk)$.

Appendix C
Proof of Theorem 1

Proof: To prove that the likelihood ensures the CFAR property, the asymptotic distributions of the numerator and the denominator of the likelihood in (12) are determined under the null hypothesis. It is then shown that as $K \to \infty$, the asymptotic distribution of the likelihood is not a function of unknown parameters if the Doppler frequencies and their estimates satisfy the conditions described in Theorem 1.

According to (9), under the null hypothesis of the second stage, i.e., $\mathcal{H}_0^2$, the received signal vector can be written as $\mathbf{y} = \mathbf{B}_1\boldsymbol{\theta}_1 + \mathbf{w}_{\mathrm{eq}_2}$, where in a scenario with two sources with Doppler frequencies ω_1 and ω_2 one has $\mathbf{B}_1 = \mathbf{H}_1$ and $\boldsymbol{\theta}_1 = \mathbf{s}_1$. Hence, replacing $\mathbf{y} = \mathbf{B}_1\boldsymbol{\theta}_1 + \mathbf{w}_{\mathrm{eq}_2}$ in the numerator of the likelihood (12) results in

$$N(\mathbf{y}) = \mathbf{s}_1^{\mathsf{H}}\mathbf{H}_1^{\mathsf{H}}\hat{\mathbf{P}}_{\mathbf{S}_2}\mathbf{H}_1\mathbf{s}_1 + \mathbf{w}_{\mathrm{eq}_2}^{\mathsf{H}}\hat{\mathbf{P}}_{\mathbf{S}_2}\mathbf{w}_{\mathrm{eq}_2} + 2\Re\left\{\mathbf{s}_1^{\mathsf{H}}\mathbf{H}_1^{\mathsf{H}}\hat{\mathbf{P}}_{\mathbf{S}_2}\mathbf{w}_{\mathrm{eq}_2}\right\}, \tag{37}$$

Authorized licensed use limited to: The Ohio State University. Downloaded on October 12,2022 at 17:21:12 UTC from IEEE Xplore. Restrictions apply.

where $\hat{\mathbf{P}}_{\mathbf{S}_2} \triangleq \hat{\mathbf{P}}^{\perp}_{\mathbf{H}_1}\hat{\mathbf{H}}_2(\hat{\mathbf{H}}_2^{\mathsf{H}}\hat{\mathbf{P}}^{\perp}_{\mathbf{H}_1}\hat{\mathbf{H}}_2)^{-1}\hat{\mathbf{H}}_2^{\mathsf{H}}\hat{\mathbf{P}}^{\perp}_{\mathbf{H}_1}$, and $\Re\{\cdot\}$ denotes the real part. Since, for all values of $i \neq j$, one has $\mathbf{H}_i^{\mathsf{H}}\mathbf{H}_i = K\mathbf{I}_L$, and $\mathbf{H}_i^{\mathsf{H}}\mathbf{H}_j = \exp(j(\omega_j-\omega_i)(K-1)L/2)\frac{\sin(\frac{(\omega_j-\omega_i)KL}{2})}{\sin(\frac{(\omega_j-\omega_i)L}{2})}\mathbf{I}_L$, it can be shown that

$$\mathbf{s}_1^{\mathsf{H}}\mathbf{H}_1^{\mathsf{H}}\hat{\mathbf{P}}_{\mathbf{S}_2}\mathbf{H}_1\mathbf{s}_1 = \left|\mathcal{S}(\omega_1,\hat{\omega}_2) - \frac{\mathcal{S}(\omega_1,\hat{\omega}_1)\mathcal{S}(\hat{\omega}_1,\hat{\omega}_2)}{K}\right|^2 \times \frac{K}{K^2-|\mathcal{S}(\hat{\omega}_1,\hat{\omega}_2)|^2}\mathbf{s}_1^{\mathsf{H}}\mathbf{s}_1, \tag{38}$$

where $\mathcal{S}(\omega_1,\omega_2) \triangleq \frac{\sin(\frac{(\omega_1-\omega_2)KL}{2})}{\sin(\frac{(\omega_1-\omega_2)L}{2})}$. If the Doppler estimation error of ω_1, defined as $\Delta\omega_1 \triangleq \omega_1 - \hat{\omega}_1$, satisfies $|\Delta\omega_1 L| \ll \frac{1}{K}$, and the difference between the estimate of the Doppler frequencies of the 2nd gNB and the 1st gNB satisfies $|\hat{\omega}_2 L - \hat{\omega}_1 L| > \frac{1}{K}$; then, the following limit holds

$$\lim_{K\to\infty}\left|\mathcal{S}(\omega_1,\hat{\omega}_2) - \frac{\mathcal{S}(\omega_1,\hat{\omega}_1)\mathcal{S}(\hat{\omega}_1,\hat{\omega}_2)}{K}\right|^2 \times \frac{K}{K^2-|\mathcal{S}(\hat{\omega}_1,\hat{\omega}_2)|^2}\mathbf{s}_1^{\mathsf{H}}\mathbf{s}_1 = 0. \tag{39}$$

The last term on the right hand side of (37) is a random variable with mean $\mathbb{E}\{\mathbf{s}_1^{\mathsf{H}}\mathbf{H}_1^{\mathsf{H}}\hat{\mathbf{P}}_{\mathbf{S}_2}\mathbf{w}_{\mathrm{eq}_2}\} = 0$ and variance $\sigma^2\mathbf{s}_1^{\mathsf{H}}\mathbf{H}_1^{\mathsf{H}}\hat{\mathbf{P}}_{\mathbf{S}_2}\mathbf{H}_1\mathbf{s}_1$, which according to (39), asymptotically tends to zero as $K \to \infty$. Therefore,

$$\lim_{K\to\infty} N(\mathbf{y}) = \mathbf{w}_{\mathrm{eq}_2}^{\mathsf{H}}\hat{\mathbf{P}}_{\mathbf{S}_2}\mathbf{w}_{\mathrm{eq}_2}, \tag{40}$$

with probability one. Using similar steps for the denominator of (12), denoted by $D(\mathbf{y})$, it can be shown that

$$\lim_{K\to\infty} D(\mathbf{y}) = \mathbf{w}_{\mathrm{eq}_2}^{\mathsf{H}}\left(\hat{\mathbf{P}}^{\perp}_{\mathbf{H}_1} - \hat{\mathbf{P}}_{\mathbf{S}_2}\right)\mathbf{w}_{\mathrm{eq}_2}, \tag{41}$$

with probability one. According to equation (2.29) in [53], since $\hat{\mathbf{P}}_{\mathbf{S}_2}$ and $\hat{\mathbf{P}}_{\mathbf{H}_1}$ are idempotent matrices, $\frac{N(\mathbf{y})}{\sigma_w^2} \sim \boldsymbol{\chi}^2_{2L}$, and $\frac{D(\mathbf{y})}{\sigma_w^2} \sim \chi^2_{2(KL-L)}$ as $K \to \infty$. Hence, the asymptotic distribution of the likelihood (12) is not a function of the noise variance and the unknown Doppler frequencies which proves the CFAR property.

REFERENCES

[1] F. Boccardi, R. Heath, A. Lozano, T. Marzetta, and P. Popovski, "Five disruptive technology directions for 5G," *IEEE Commun. Mag.*, vol. 52, no. 2, pp. 74–80, Feb. 2014.

[2] M. Agiwal, A. Roy, and N. Saxena, "Next generation 5G wireless networks: A comprehensive survey," *IEEE Commun. Surv. Tut.*, vol. 18, no. 3, pp. 1617–1655, Jul.–Sep. 2016.

[3] S. Parkvall *et al.*, "5G NR release 16: Start of the 5G evolution," *IEEE Commun. Standards Mag.*, vol. 4, no. 4, pp. 56–63, Dec. 2020.

[4] K. Takeda, H. Xu, T. Kim, K. Schober, and X. Lin, "Understanding the heart of the 5G air interface: An overview of physical downlink control channel for 5G new radio," *IEEE Commun. Standards Mag.*, vol. 4, no. 3, pp. 22–29, Sep. 2020.

[5] J. Baenke *et al.*, "Millimeter-wave downlink coverage extension strategies," *IEEE Commun. Mag.*, vol. 58, no. 9, pp. 74–78, Sep. 2020.

[6] M. Giordani, M. Polese, A. Roy, D. Castor, and M. Zorzi, "A tutorial on beam management for 3GPP NR at mmWave frequencies," *IEEE Commun. Surv. Tut.*, vol. 21, no. 1, pp. 173–196, Jan.–Mar. 2019.

[7] A. Fascista, A. Coluccia, H. Wymeersch, and G. Seco-Granados, "Millimeter-wave downlink positioning with a single-antenna receiver," *IEEE Trans. Wireless Commun.*, vol. 18, no. 9, pp. 4479–4490, Sep. 2019.

[8] 3GPP, "Study on NR positioning support," 3rd Generation Partnership Project (3GPP), Tech. Rep. TR 38.855, Mar. 2019. [Online]. Available: https://www.3gpp.org/ftp/Specs/archive/38_series/38.855/

[9] J. del Peral-Rosado, R. Raulefs, J. López-Salcedo, and G. Seco-Granados, "Survey of cellular mobile radio localization methods: From 1G to 5G," *IEEE Commun. Surv. Tut.*, vol. 20, no. 2, pp. 1124–1148, Apr.–Jun. 2018.

[10] Z. Kassas, "Navigation from low earth orbit—part 2: models, implementation, and performance," in *Position, Navigation, and Timing Technologies in the 21st Century*, J. Morton, F. van Diggelen, J. Spilker, Jr., and B. Parkinson, Eds., Hoboken, NJ, USA: Wiley, 2021, vol. 2, ch. 43, pp. 1381–1412.

[11] J. del Peral-Rosado, J. López-Salcedo, F. Zanier, and G. Seco-Granados, "Position accuracy of joint time-delay and channel estimators in LTE networks," *IEEE Access*, vol. 6, no. 25185–25199, 2018, doi: 10.1109/ACCESS.2018.2827921.

[12] K. Shamaei and Z. Kassas, "A joint TOA and DOA acquisition and tracking approach for positioning with LTE signals," *IEEE Trans. Signal Process.*, vol. 69, pp. 2689–2705, 2021, doi: 10.1109/TSP.2021.3068920.

[13] A. Abdallah, K. Shamaei, and Z. Kassas, "Assessing real 5G signals for opportunistic navigation," in *Proc. Int. Tech. Meeting Satell. Division Inst. Navigation Conf.*, 2020, pp. 2548–2559.

[14] K. Shamaei and Z. Kassas, "Receiver design and time of arrival estimation for opportunistic localization with 5G signals," *IEEE Trans. Wireless Commun.*, vol. 20, no. 7, pp. 4716–4731, Jul. 2021.

[15] Z. Kassas, A. Abdallah, and M. Orabi, "Carpe signum: Seize the signal - opportunistic navigation with 5G," *Inside GNSS Mag.*, vol. 16, no. 1, pp. 52–57, 2021.

[16] E. Conte, A. Filippi, and S. Tomasin, "ML period estimation with application to vital sign monitoring," *IEEE Signal Process. Lett.*, vol. 17, no. 11, pp. 905–908, Nov. 2010.

[17] J. Yang, X. Wang, M. Rahman, S. Park, H. Kim, and Y. Wu, "A new positioning system using DVB-T2 transmitter signature waveforms in single frequency networks," *IEEE Trans. Broadcast.*, vol. 58, no. 3, pp. 347–359, Sep. 2012.

[18] L. Chen, O. Julien, P. Thevenon, D. Serant, A. Pena, and H. Kuusniemi, "TOA estimation for positioning with DVB-T signals in outdoor static tests," *IEEE Trans. Broadcast.*, vol. 61, no. 4, pp. 625–638, Dec. 2015.

[19] J. McEllroy, "Navigation using signals of opportunity in the AM transmission band," Master's thesis, Air Force Inst. Technol., Wright-Patterson Air Force Base, Ohio, USA, 2006.

[20] A. Popleteev, "Indoor positioning using FM radio signals," Ph.D. dissertation, Univ. Trento, Italy, 2011.

[21] R. Faragher and R. Harle, "Towards an efficient, intelligent, opportunistic smartphone indoor positioning system," *NAVIGATION, J. Inst. Navigation*, vol. 62, no. 1, pp. 55–72, 2015.

[22] H. Zou, M. Jin, H. Jiang, L. Xie, and C. Spanos, "WinIPS: WiFi-based non-intrusive indoor positioning system with online radio map construction and adaptation," *IEEE Trans. Wireless Commun.*, vol. 16, no. 12, pp. 8118–8130, Dec. 2017.

[23] M. Orabi, J. Khalife, and Z. Kassas, "Opportunistic navigation with Doppler measurements from Iridium Next and Orbcomm LEO satellites," in *Proc. IEEE Aerosp. Conf.*, 2021, pp. 1–9.

[24] J. Khalife, M. Neinavaie, and Z. Kassas, "The first carrier phase tracking and positioning results with Starlink LEO satellite signals," *IEEE Trans. Aerosp. Electron. Syst.*, early access, 2021, doi: 10.1109/TAES.2021.3113880.

[25] Z. Kassas, J. Khalife, A. Abdallah, and C. Lee, "I am not afraid of the jammer: Navigating with signals of opportunity in GPS-denied environments," in *Proc. 33rd Int. Tech. Meeting Satell. Division Inst. Navigation Conf.*, 2020, pp. 1566–1585.

[26] H. Wymeersch, G. Seco-Granados, G. Destino, D. Dardari, and F. Tufvesson, "5G mmWave positioning for vehicular networks," *IEEE Wireless Commun.*, vol. 24, no. 6, pp. 80–86, Dec. 2017.

[27] Z. Abu-Shaban, X. Zhou, T. Abhayapala, G. Seco-Granados, and H. Wymeersch, "Error bounds for uplink and downlink 3D localization in 5G millimeter wave systems," *IEEE Trans. Wireless Commun.*, vol. 17, no. 8, pp. 4939–4954, Aug. 2018.

[28] Z. Abu-Shaban, X. Zhou, T. Abhayapala, G. Seco-Granados, and H. Wymeersch, "Performance of location and orientation estimation in 5G mmwave systems: Uplink vs downlink," in *Proc. IEEE Wireless Commun. Netw. Conf.*, 2018, pp. 1–6.

[29] J. Lee, G. Gil, and Y. Lee, "Exploiting spatial sparsity for estimating channels of hybrid MIMO systems in millimeter wave communications," in *Proc. IEEE Glob. Commun. Conf.*, 2014, pp. 3326–3331.

Authorized licensed use limited to: The Ohio State University. Downloaded on October 12,2022 at 17:21:12 UTC from IEEE Xplore. Restrictions apply.

[30] D. Yacong, "Channel estimation for massive MIMO systems based on sparse representation and sparse signal recovery," Ph.D. dissertation, Univ. California, San Diego, CA, USA, 2018.
[31] E. Rastorgueva-Foi, M. Costa, M. Koivisto, K. Leppanen, and M. Valkama, "User positioning in mmW 5G networks using beam-RSRP measurements and Kalman filtering," in *Proc. Int. Conf. Inf. Fusion*, 2018, pp. 1–7.
[32] R. Mendrzik, H. Wymeersch, and G. Bauch, "Joint localization and mapping through millimeter wave MIMO in 5G systems," in *Proc. IEEE Glob. Commun. Conf.*, 2018, pp. 1–6.
[33] Z. Abu-Shaban, H. Wymeersch, T. Abhayapala, and G. Seco-Granados, "Distributed two-way localization bounds for 5G mmwave systems," in *Proc. IEEE Globecom Workshops*, 2018, pp. 1–6.
[34] W. Ma, C. Qi, and G. Li, "High-resolution channel estimation for frequency-selective mmWave massive MIMO systems," *IEEE Trans. Wireless Commun.*, vol. 19, no. 5, pp. 3517–3529, May 2020.
[35] L. Scharf and B. Friedlander, "Matched subspace detectors," *IEEE Trans. Signal Process.*, vol. 42, no. 8, pp. 2146–2157, Aug. 1994.
[36] S. Kraut, L. Scharf, and L. McWhorter, "Adaptive subspace detectors," *IEEE Trans. Signal Process.*, vol. 49, no. 1, pp. 1–16, Jan. 2001.
[37] F. Gini and A. Farina, "Vector subspace detection in compound-Gaussian clutter. Part I: Survey and new results," *IEEE Trans. Aerosp. Electron. Syst.*, vol. 38, no. 4, pp. 1295–1311, Oct. 2002.
[38] M. Korso, R. Boyer, A. Renaux, and S. Marcos, "Statistical resolution limit for source localization with clutter interference in a MIMO radar context," *IEEE Trans. Signal Process.*, vol. 60, no. 2, pp. 987–992, Feb. 2012.
[39] A. Zaimbashi, M. Derakhtian, and A. Sheikhi, "GLRT-based CFAR detection in passive bistatic radar," *IEEE Trans. Aerosp. Electron. Syst.*, vol. 49, no. 1, pp. 134–159, Jan. 2013.
[40] I. Atitallah, A. Kammoun, M. Alouini, and T. Al-Naffouri, "Optimal design of large dimensional adaptive subspace detectors," *IEEE Trans. Signal Process.*, vol. 64, no. 19, pp. 4922–4935, Oct. 2016.
[41] A. Combernoux, F. Pascal, and G. Ginolhac, "Performance of the low-rank adaptive normalized matched filter test under a large dimension regime," *IEEE Trans. Aerosp. Electron. Syst.*, vol. 55, no. 1, pp. 459–468, Feb. 2019.
[42] M. Wax and A. Adler, "Detection of the number of signals by signal subspace matching," *IEEE Trans. Signal Process.*, vol. 69, pp. 973–985, 2021, doi: 10.1109/TSP.2021.3053495.
[43] Z. Wang, G. Li, and H. Chen, "Adaptive persymmetric subspace detectors in the partially homogeneous environment," *IEEE Trans. Signal Process.*, vol. 68, pp. 5178–5187, 2020, doi: 10.1109/TSP.2020.3020156.
[44] D. Ciuonzo, A. De Maio, and D. Orlando, "On the statistical invariance for adaptive radar detection in partially homogeneous disturbance plus structured interference," *IEEE Trans. Signal Process.*, vol. 65, no. 5, pp. 1222–1234, Mar. 2017.
[45] D. Roy, T. Mukherjee, M. Chatterjee, E. Blasch, and E. Pasiliao, "RFAL: Adversarial learning for RF transmitter identification and classification," *IEEE Trans. Cogn. Commun. Netw.*, vol. 6, no. 2, pp. 783–801, Jun. 2019.
[46] M. Baek, S. Kwak, J. Jung, H. Kim, and D. Choi, "Implementation methodologies of deep learning-based signal detection for conventional MIMO transmitters," *IEEE Trans. Broadcast.*, vol. 65, no. 3, pp. 636–642, Sep. 2019.
[47] G. Gao, "Towards navigation based on 120 satellites: Analyzing the new signals," Ph.D. dissertation, Stanford Univ., Stanford, CA, USA, 2008.
[48] J. Merwe *et al.*, "GNSS sequence extraction and reuse for navigation," in *Proc. Int. Tech. Meeting Satell. Division Inst. Navigation Conf.*, 2020, pp. 2731–2747.
[49] M. Neinavaie, J. Khalife, and Z. Kassas, "Blind opportunistic navigation: Cognitive deciphering of partially known signals of opportunity," in *Proc. Int. Tech. Meeting Satell. Division Inst. Navigation Conf.*, 2020, pp. 2748–2757.
[50] M. Neinavaie, J. Khalife, and Z. Kassas, "Blind doppler tracking and beacon detection for opportunistic navigation with LEO satellite signals," in *Proc. IEEE Aerosp. Conf.*, 2021, pp. 1–8.
[51] J. Khalife, M. Neinavaie, and Z. Kassas, "Blind doppler tracking from OFDM signals transmitted by broadband LEO satellites," in *Proc. IEEE Veh. Technol. Conf.*, 2021, pp. 1–6.
[52] T. Zhao and T. Huang, "Cramer-Rao lower bounds for the joint delay-Doppler estimation of an extended target," *IEEE Trans. Signal Process.*, vol. 64, no. 6, pp. 1562–1573, Mar. 2016.
[53] S. Kay, *Fundamentals of Statistical Signal Processing: Detection Theory*, vol. II. Upper Saddle River, NJ, USA: Prentice-Hall, 1993.
[54] P. Misra and P. Enge, *Global Positioning System: Signals, Measurements, and Performance*, 2nd ed. Kathmandu, Nepal: Ganga-Jamuna Press, 2010.
[55] D. Tse and P. Viswanath, *Fundamentals of Wireless Communication*. Cambridge, U.K.: Cambridge Univ. Press, 2005.
[56] S. Kay, *Fundamentals of Statistical Signal Processing: Estimation Theory*, vol. I. Upper Saddle River, NJ, USA: Prentice-Hall, 1993.
[57] K. Shamaei and Z. Kassas, "Sub-meter accurate UAV navigation and cycle slip detection with LTE carrier phase," in *Proc. Int. Tech. Meeting Satell. Division Inst. Navigation Conf.*, 2019, pp. 2469–2479.
[58] Z. Kassas and T. Humphreys, "Observability analysis of collaborative opportunistic navigation with pseudorange measurements," *IEEE Trans. Intell. Transp. Syst.*, vol. 15, no. 1, pp. 260–273, Feb. 2014.
[59] K. Shamaei and Z. Kassas, "LTE receiver design and multipath analysis for navigation in urban environments," *NAVIGATION, J. Inst. Navigation*, vol. 65, no. 4, pp. 655–675, Dec. 2018.
[60] H. Ochiai and H. Imai, "On the distribution of the peak-to-average power ratio in OFDM signals," *IEEE Trans. Commun.*, vol. 49, no. 2, pp. 282–289, Feb. 2001.

Mohammad Neinavaie (Graduate Student Member, IEEE) received the M.S. degree in digital communication systems from Shiraz University, Shiraz, Iran. He is a Ph.D. Student with the University of California, Irvine, CA, USA, and a Member of the Autonomous Systems Perception, Intelligence, and Navigation (ASPIN) Laboratory. His research interests include opportunistic navigation, cognitive radio, wireless communication systems, and software-defined radio.

Joe Khalife received the B.E. degree in electrical engineering, the M.S. degree in computer engineering from the Lebanese American University (LAU), Beirut, Lebanon, and the Ph.D. degree in electrical engineering and computer science from the University of California, Irvine, CA, USA. He is a Postdoctoral Fellow with the University of California, Irvine and a Member of the Autonomous Systems Perception, Intelligence, and Navigation (ASPIN) Laboratory. From 2012 to 2015, he was a Research Assistant with LAU, and has been a Member of the ASPIN Laboratory since 2015. His research interests include opportunistic navigation, autonomous vehicles, and software-defined radio. He was the recipient of the 2016 IEEE/ION Position, Location, and Navigation Symposium (PLANS) Best Student Paper Award and the 2018 IEEE Walter Fried Award.

Zaher (Zak) M. Kassas (Senior Member, IEEE) received the B.E. degree in electrical engineering from the Lebanese American University, Beirut, Lebanon, the M.S. degree in electrical and computer engineering from The Ohio State University, Columbus, OH, USA, the M.S.E. degree in aerospace engineering, and the Ph.D. degree in electrical and computer engineering from The University of Texas at Austin, Austin, TX, USA. He is an Associate Professor with the University of California, Irvine, CA, USA, and the Director of the Autonomous Systems Perception, Intelligence, and Navigation (ASPIN) Laboratory. He is also the Director of the U.S. Department of Transportation Center: CARMEN (Center for Automated Vehicle Research with Multimodal AssurEd Navigation), focusing on navigation resiliency and security of highly automated transportation systems. He was the recipient of the 2018 National Science Foundation (NSF) Faculty Early Career Development Program (CAREER) Award, and 2019 Office of Naval Research (ONR) Young Investigator Program (YIP) Award, the 2018 IEEE Walter Fried Award, 2018 Institute of Navigation (ION) Samuel Burka Award, and 2019 ION Col. Thomas Thurlow Award. He is the Senior Editor of the IEEE TRANSACTIONS ON INTELLIGENT VEHICLES and an Associate Editor for the IEEE TRANSACTIONS ON AEROSPACE AND ELECTRONIC SYSTEMS, and the IEEE TRANSACTIONS ON INTELLIGENT TRANSPORTATION SYSTEMS. His research interests include cyber-physical systems, estimation theory, navigation systems, autonomous vehicles, and intelligent transportation systems.

Authorized licensed use limited to: The Ohio State University. Downloaded on October 12,2022 at 17:21:12 UTC from IEEE Xplore. Restrictions apply.

Comparison of Neural Network Architectures for Simultaneous Tracking and Navigation with LEO Satellites

Sharbel E. Kozhaya [†], Jamil A. Haidar-Ahmad[†], Ali A. Abdallah[†], Zaher M. Kassas[†], and Samer S. Saab[‡]
[†] *University of California, Irvine, USA*
[‡] *Lebanese American University, Byblos, Lebanon*

BIOGRAPHIES

Sharbel E. Kozhaya is a Ph.D student in the Department of Electrical Engineering and Computer Science at the University of California, Irvine and a member of the ASPIN Laboratory. He received a B.E. in Electrical Engineering from LAU. His current research interests include opportunistic navigation, software-defined radio, and low earth orbit satellites.

Jamil A. Haidar-Ahmad is a Ph.D student in the Department of Electrical Engineering and Computer Science at the University of California, Irvine and a member of the Autonomous Systems Perception, Intelligence, and Navigation (ASPIN) Laboratory. He received a B.E. in Mechatronics Engineering with honors and Minor in Computer Science from the Lebanese American University (LAU). His current research interests include opportunistic navigation, software-defined radio, signal fusion, 5G, and indoor localization.

Ali A. Abdallah is a Ph.D student in the Department of Electrical Engineering and Computer Science at the University of California, Irvine and a member of the ASPIN Laboratory. He received a B.E. in Electrical Engineering from LAU. His current research interests include opportunistic navigation, software-defined radio, long-term evolution (LTE), 5G, and indoor localization.

Zaher (Zak) M. Kassas is an associate professor at the University of California, Irvine and director of the Autonomous Systems Perception, Intelligence, and Navigation (ASPIN) Laboratory. He is also director of the U.S. Department of Transportation Center: CARMEN (Center for Automated Vehicle Research with Multimodal AssurEd Navigation), focusing on navigation resiliency and security of highly automated transportation systems. He received a B.E. in Electrical Engineering from the Lebanese American University, an M.S. in Electrical and Computer Engineering from The Ohio State University, and an M.S.E. in Aerospace Engineering and a Ph.D. in Electrical and Computer Engineering from The University of Texas at Austin. He is a recipient of the 2018 National Science Foundation (NSF) Faculty Early Career Development Program (CAREER) award, 2019 Office of Naval Research (ONR) Young Investigator Program (YIP) award, 2018 IEEE Walter Fried Award, 2018 Institute of Navigation (ION) Samuel Burka Award, and 2019 ION Col. Thomas Thurlow Award. His research interests include cyber-physical systems, estimation theory, navigation systems, autonomous vehicles, and intelligent transportation systems.

Samer S. Saab received the B.S., M.S., and Ph.D. degrees in electrical engineering in 1988, 1989, and 1992, respectively, and the M.A. degree in applied mathematics in 1990, from the University of Pittsburgh, PA, USA. He is currently the Dean of Graduate Studies and Research at the Lebanese American University. He served on the Editorial Board of the IEEE Transactions on Control Systems Technology from 2005 to 2011 and on the Editorial Board of the IEEE Control Systems Society-Conference from 2005 to 2009. Since September 2015, he has been serving on the Editorial Board of the IEEE Transactions on Automatic Control. His research interests include iterative learning control, Kalman filtering, navigational positioning systems, and wireless communications.

ABSTRACT

Machine learning (ML) frameworks are investigated for use in simultaneous tracking and navigation (STAN) with low Earth orbit (LEO) satellites. STAN is a navigation paradigm that utilizes specialized LEO receivers to extract navigation observables (e.g., pseudorange and Doppler) from LEO satellite signals. Two neural network architectures are compared: Feed Forward Neural Network (FFNN) and Recurrent Neural Network (RNN). Additionally, two ML-based orbit determination frameworks are compared: ephemeris propagation and residual error propagation. The

Copyright © 2021 by S. Kozhaya, J. Haidar-Ahmad, A. Abdallah, Z. Kassas, and S. Saab

Preprint of the 2021 ION GNSS+ Conference St. Louis, Missouri, September 20–24, 2021

objective of the comparison is to select an approach with the lowest open-loop propagation error as well as computational cost. Based on simulation results, a nonlinear autoregressive neural network with exogenous inputs (NARX) embedded within the residual error modeling framework is selected as the best ML approach among the compared candidates. Experimental results are presented demonstrating a ground vehicle navigating for a total of 258 seconds, while receiving signals from two Orbcomm LEO satellites. Global navigation satellite system (GNSS) signals were artificially cut off for the last 30 seconds, during which the vehicle traversed a trajectory of 871 m. Two navigation frameworks are compared to estimate the vehicle's trajectory: (i) LEO signal-aided inertial navigation system (INS) STAN framework using Simplified General Perturbation (SGP4) as its propagator and (ii) the proposed LEO signal-aided INS STAN framework using ML as its propagator. The STAN with SGP4 achieved a three-dimensional (3-D) position root-mean squared error (RMSE) of 30 m. In contrast, the proposed STAN with SGP4+NARX framework achieved a 3-D position RMSE of 3.6 m.

I. INTRODUCTION

Over the past decades, the ambitious and glorified image of an Earth connected through a web weaved from low earth orbit (LEO) satellites had taken the world by storm, promising high-resolution images; remote sensing; space-based optical mesh networks; global, high-availability, high-bandwidth, and low-latency internet [1–3]. Many companies such as Globalstar, Iridium, ICO, and Teledesic made haste in securing their position in space as more constellations and satellite systems were born [4]. This dream was short-lived; however, as these companies suffered financial problems, and the reliability and viability of LEO constellations were scrutinized and suffered from skepticism. In the past decade, with the ground-breaking recent developments in satellite technologies and launch reduction costs, the world has set its sights on LEO satellites once again. The demand for LEO satellites has never been higher, as LEO satellites have the potential to serve as the foundation for supporting new technologies and advancements in satellite imaging, remote sensing, and revolutionizing communication technologies such as 5G which demands higher data rates [5–7]. Furthermore, the commercialization of LEO mega-constellations, LEO satellites' popularity has soared, with major technology giants such as SpaceX, Amazon, and Boeing rushing to enter this field by launching and scheduling the launch of tens of thousands of satellites for internet connectivity and communication purposes [8, 9].

Signals transmitted by the tens of thousands of LEO satellites that are about to orbit the earth could be utilized as signals of opportunity (SOPs) for navigation purposes. SOPs come in different forms and multiple sources ranging from terrestrial signals such as digital television, cellular, and AM/FM to extraterrestrial signals such as signals coming from LEO or Medium Earth Orbit (MEO) satellites [10]. When it comes to navigation, these SOPs are a very attractive source in environments where global navigation satellite systems (GNSS) are unavailable (e.g., under interference or jamming attacks), unusable (e.g., indoors), too weak (e.g., deep urban canyons or under dense canopy), or untrustworthy (e.g., under spoofing attacks). Utilizing different SOPs for navigation in GNSS-challenged environments has been studied for: (i) terrestrial signals [11–19] and (ii) LEO signals [20–27]. As megaconstellations of LEO satellites get launched, LEO satellites will provide virtually a blanket cover around the globe, bringing forth abundant signals diverse in frequency (allowing for spoofing detection) and in direction (yielding a low geometric dilution of precision). They will also provide significantly more powerful signals compared to GNSS satellites which reside in MEO.

Since most LEO constellations are not intended for navigation purposes, three challenges must be tackled to exploit their signals for navigation: (i) develop specialized receivers to extract navigation observables from their downlink signals [28–33], (ii) compensate for lack of tight synchronization of satellites' clocks [34, 35], and (iii) estimate the satellites' ephemerides [36, 37]. This paper focuses on the latter challenge.

Several orbital determination methods have been developed in the literature [38–41]. These methods differ in complexity and accuracy. Numerous dynamics models which estimate the state of LEO satellites (position and velocity), as well as these estimates' uncertainty, have been developed over the years [42, 43]. The state of a satellite can be parametrized by its Keplerian elements, also known as classical orbital elements (COE). These orbital elements, along with some other information about a satellite' states, can be found in two-line element sets (TLEs) which are publicly published on a daily basis by the North American Aerospace Defense Command (NORAD) [44].

One way to mathematically propagate a satellite's states given its position vector in an inertial reference frame is to solve a second order differential equation relating the satellite's position and acceleration. This is also known

as a Kepler orbit, which is an unperturbed orbit where for any values of the initial state vector, the Kepler orbit corresponding to the solution can be found. However, utilizing these elements in determining an orbit through unperturbed Keplerian orbital models numerically or analytically leads to highly inaccurate results as there are several sources of perturbing forces that cannot be ignored, e.g., atmospheric drag, the Earth's oblateness causing a non-uniform gravitational field, solar radiation pressure, and other sources of gravitational forces (e.g., the Sun and the Moon). Therefore, perturbed models (e.g., two-body J2 propagator which takes into consideration the previously mentioned perturbations) are typically utilized, where an extra term is added as process noise in an attempt to capture the overall perturbation in acceleration, including multiple sources of forces which could offset the satellite's ephemeris from following an unperturbed path.

Numerical methods, such as the two body, two body with J2 model, and the High-Precision Orbit Propagator (HPOP) are capable of producing highly accurate orbits; however, they require heavy computational loads to forecast the satellite orbit, rendering them unsuitable in real-time navigation systems. Meanwhile, their analytical counterparts, such as the Simplified General Perturbation (SGP4) [45], are computationally more efficient, allowing for real-time propagation at the cost of introducing larger satellite position errors. The currently available parameters from NORAD, such as values from TLE files, do not provide enough data for achieving a desirable state accuracy, where utilizing these elements for orbital determination with a standard SGP4 propagator could lead to errors in the order of several kilometers, which accumulate and drift over time. These errors are in reality greater due to the fact that the initial estimation of the satellite's position purely from the TLE file parameters could be off by as much as 2.5 km [46, 47]. Recent studies had shown that more accurate results can be achieved in LEO-based navigation by simultaneously tracking the satellite's states in a navigation filter, or what is referred to as simultaneous tracking and navigation (STAN) framework [21]. STAN simultaneously estimates the LEO satellites' states together with the navigator's states. The SGP4 propagator would be a candidate model for usage within the STAN framework. However, the SGP4 propagator not only inherits TLE errors, but it cannot be initialized using any *a priori* knowledge of the position and velocity of the satellite– this means it depends exclusively on TLE files, which are periodically updated every 24 hours.

In the past decade, there has been increased interest in utilizing the powerful capabilities of machine learning (ML) for providing an orbital propagation solution. In [48] and [49], distribution regression was used for orbital determination of objects in LEO and GEO space. Propagating LEO space debris orbits was studied through the use of support vector machines (SVMs) [50, 51], and LEO satellite orbital states were modeled using artificial neural networks (ANNs), SVMs, and gaussian processes (GPs).

A simulation study showed that ANNs possess high regression capabilities compared to SVMs and GPs [51, 52]. However, these results compared the performance of different ML methods against each other, not taking into consideration the high accuracy of standard numerical and analytical propagators. Time delayed neural networks (TDNNs) and long short-term memory (LSTM) neural networks have been studied in [53]. However, utilizing ML in full orbital determination, allowing to completely replace standard propagators, is yet to be achieved.

A promising preliminary study was conducted in [37], in which a TDNN was trained using the data from two Orbcomm LEO satellites, which broadcast their 3-D position, which are obtained from onboard GNSS receivers. The TDNN's output was used in the STAN framework.

This paper builds on the results of [37] and makes the following contributions:

- It conducts a comprehensive performance analysis between different ANN architectures for short and long-term satellite orbit prediction, namely TDNNs and LSTMs.
- It studies the performance of the numerical and analytical propagators powered by a ML approach to account for residual error correction.
- It assesses the validation and generalization of the proposed ML-based orbital propagator for different orbits.
- It demonstrates experimentally the performance of the proposed ML-based STAN framework in estimating a ground vehicle's position.

The remainder of the paper is organized as follows. Section II briefly explains ML-based orbital determination and provides background on what has been achieved in literature. Section III describes the proposed architectures and the improvements compared to previous approaches. Section IV presents a series of numerical experiments where the ML models are investigated and discussed. Finally, concluding remarks are given in Section V.

II. OVERVIEW OF THE PROPOSED SYSTEM

This section presents a high-level block diagram of the proposed system. The proposed system builds on the traditional STAN framework introduced in [21]. The performance of the EKF-STAN framework has been previously demonstrated in realistic simulation environments and experimentally on a ground vehicle and on an unmanned aerial vehicle (UAV), showing the potential of achieving meter-level-accurate navigation [21, 37].

The EKF-STAN framework utilizes specialized LEO receivers to extract navigation observables, such as ephemeris messages, if available; pseudorange; and Doppler measurements from the LEO satellite signals. Furthermore, a model-based LEO propagator, such as SGP4, is employed in estimating the LEO satellite's states (position and velocity). The EKF-ML-STAN framework instead replaces the model-based propagator with a ML-based propagator to achieve potentially more accurate propagated LEO states. The framework includes GNSS receivers, which produce a navigation solution from GNSS signals, when such signals are available and useable. Finally, an IMU which reports the vehicle's specific force, angular rate, and orientation, is embedded within an INS. The INS provides the vehicle's position state, which along with the LEO signals, propagated LEO states, GNSS signals, and clock models which compensate for timing bias and phase shifts, are fed into an Extended Kalman Filter (EKF). The employed EKF then simultaneously estimates the vehicle's states, tracks the LEO satellite's states, and estimates timing biases as well as the confidence of the estimated values. When GNSS signals are available, the framework uses these signals for navigating the vehicle and tracking the LEO satellites. Once the GNSS signals cut off, the ML model propagates the LEO satellite states within the STAN framework. Fig. 1 depicts the proposed EKF-ML-STAN framework.

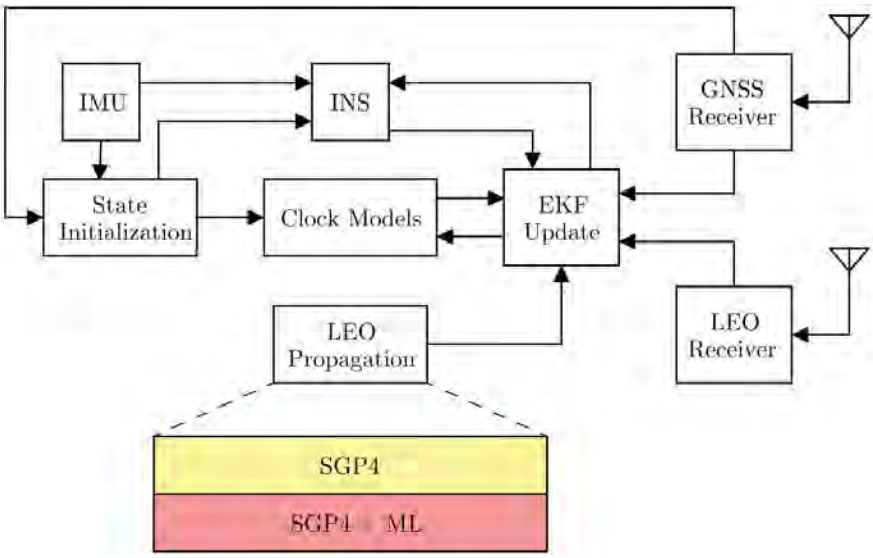

Fig. 1. Proposed improvements on the STAN system.

The proposed ML propagator approach could take one of two forms. The first form replaces the LEO propagation block with a specialized ML propagation block capable of directly estimating LEO satellite ephemeris. The second form adds an error correction block to the STAN framework right after the LEO propagation block. The error correction block learns the mapping between a standard propagator, such as SGP4, and a highly accurate propagator, such as HPOP.

III. ML-BASED ORBITAL DETERMINATION

ML attempts to build a model based on training data, which is subsequently utilized in several applications, such as making predictions or inferences, classifying data, or making decisions. ML has been utilized in solving highly dynamic, nonlinear, and highly uncertain problems. ML can be categorized into: (i) supervised learning, where the model is given both the input and expected output; (ii) unsupervised learning, where the model is only given the inputs; (iii) reinforced learning, where the model is given rewards or penalties according to the decisions it makes.

For orbital determination, a ML model would be given the task of taking previous LEO satellite positions as inputs and using this information to predict the satellite's future ephemeris. A complex ML model would be capable of embedding the highly dimensional dynamical orbital propagation models. The desired ML model should also propagate any initial *a priori* knowledge of a satellite's state. To this end, the model is expected to learn the behavior of highly accurate propagators, which would otherwise not be usable in real-time applications, such as HPOP. The model will serve as a substitute to highly accurate propagators with lower computational complexity, as inference times are usually low. The SGP4 propagator will be treated as the baseline for comparison with the proposed ML models. SGP4 is used to calculate orbital state vectors of satellites within an Earth-centered inertial (ECI) coordinate system. It is an analytical orbital propagator that uses TLE files, produced by NORAD and the National Aeronautics and Space Administration (NASA) daily. It is widely used in real-time orbital determination as it takes into consideration the perturbations a multitude of external forces. In order to compare the performance of the ML models with SGP4, a more accurate, yet computationally heavy propagator, HPOP, is considered as ground truth [54].

ANNs are systems capable of approximating any continuous function and are therefore known as "Universal Approximators" [55]. Consider some input $x \in \mathcal{X}$ that is mapped to $y \in \mathcal{Y}$ by an unknown function $f : \mathcal{X} \mapsto \mathcal{Y}$. Given enough compact subsets of data points mapping the input space and output space $\{(x_1, y_1), \ldots, (x_n, y_n)\}$, the neural network (NN) forms probability-weighted associations, effectively approximating the function that maps the two spaces. NNs are capable of achieving this by funneling the inputs through a multitude of "neuron" blocks, where every neuron computes $\sigma(x, w, b) = \sigma(w \cdot x + b)$, where w is the weight associated with every input, b is the bias associated with every input, and σ is the activation function of the neuron which could either be linear or could add nonlinearity to the system.

Once the estimated output $\hat{y}$, is computed, the error between the observed output y and $\hat{y}$ is calculated through a cost function $C(y, \hat{y})$, which the NN aims to minimize. There is an abundance of cost functions used in ML, each allowing for an intuitive understanding of the difference between the observed and estimated output. The mean-squared error (MSE) will be used as a cost function to assess the performance in the proposed approach, which can be expressed as

$$C(y, \hat{y})_{\text{MSE}} = \frac{1}{n} \sum_{i=1}^{n} (y_i - \hat{y}_i)^2 \tag{1}$$

where n is the number of data points, y_i is the observed values, and $\hat{y}_i$ is the estimated values. Once the cost function is computed, each layer's weights and biases are updated according to how much those weights and biases contributed to the each layer's error output.

To achieve a computationally feasible ML solution for orbital determination and propagation, this paper presents two frameworks: (i) ephemeris prediction and (ii) error prediction. First, the ephemeris propagation framework presents an architecture that is capable of propagating a satellite's orbit from historical state data, where each state is given by $S = [r, \dot{r}]^\intercal$, where r and $\dot{r}$ are the LEO satellite's 3-D position and velocity in the ECEF frame. There has been previous work in training a TDNN to model a satellite's path for a short time window (approximately 30 seconds) in [37]. However, this model used the LEO satellite's state which are transmitted by onboard GPS receiver and transmitted in the downlink signal. While this approach produced promising results with Orbcomm LEO satellites, this cannot be generalized to other LEO satellite constellations, since they do not necessarily transmit their states openly. As such, a more realistic approach would be to train the NN to model a computationally heavy yet highly accurate propagator, such as HPOP. This model would look at historical HPOP data during training, and then take d previous consecutive states to output the next state: $\hat{S}_t = \Lambda(\hat{S}_{t-1}, \hat{S}_{t-2}, \ldots, \hat{S}_{t-d})$, where Λ is the function that maps previous states to the next state. A key constraint to the complexity of this model in allowing higher dimensionality is the time needed for inference, as the model should stay within real-time timing constraints.

Second, the error propagation framework models the error between a fast and less accurate propagator, such as SPG4, with a more accurate propagator, such as HPOP. This method is attractive since both propagators already handle the computation of highly dynamic parameters, leaving the NN to simply "close the gap" between already two close propagators. The model is trained to find the mapping from SPG4 propagated state vectors to HPOP propagated state vectors $\hat{S}_{\text{HPOP}} = \Gamma(S_{\text{SGP4}})$, where Γ is the mapping between the two states.

A. FRAMEWORK 1: Ephemeris Propagation

This section presents a ML model specialized for predicting LEO satellite orbits for short time windows.

A.1 TRAINING

The proposed ANN models are investigated to study their ability and accuracy in predicting a LEO satellite's state vector (3-D position and velocity). Ground truth data in the ECEF reference frame was acquired using the Analytical Graphics Inc. System Tool Kit (AGI-STK) software, which is capable of generating highly accurate orbits through the usage of the HPOP, a numerical propagator with high dimensionality and high fidelity [56]. The AGI-STK allows for exporting such orbits for usage in a ML environment. The satellite chosen for the simulation study is the Orbcomm F107 satellite (NORAD ID: 40087). AGI-STK provides its own database of satellite models, where this satellite's model parameters, such as its inertial mass distribution, are available. The toolkit provides a HPOP propagator with updated force models from its database. The force models include gravitational effects of the sun, moon, and options to include Jupiter, Venus, Saturn, and other planetary gravitational forces. The gravitational effects include Earth's gravitational model (2008) with high order and degree. Other forces include drag models, taking into account area/mass ratio, atmospheric density models, low altitude density models, and solar flux/geomagnetic models. Additionally, solar radiation pressure is utilized by the propagator while taking into account central body radiation pressure and eclipsing central bodies of the Earth and Moon. This makes the AGI-STK tool suitable for exporting propagated LEO satellite ephemeris to be used for training, validation, and testing.

A.2 DESIGN

To achieve a ML model which could take initial historical data and start propagating the satellite's orbit, using its previous output as new input, this model should be capable of time series prediction, as the satellite's state elements could be seen as its own time series. Feed forward neural networks (FFNN) [57,58], which simply propagate from input to output in one direction. However, other NNs like recurrent NNs (RNNs), close the loop and provide a feedback to the NN. For this reason, the RNNs are expected to perform well in modeling highly nonlinear and harmonic data [59–62].

TDNNs are simple FFNNs, except that in TDNNs the input is fed as a time series, which allows the NN to learn the dynamics of the system. For orbital determination, the output $\hat{y}(t)$ is the state vector $S_{\text{LEO}}(t)$ at time t, and the input is $I(0,1,\ldots,N-1) = \{x(t), x(t-\tau), \ldots, x(t-(N-1)\tau)\}$ for N previous state vector data points. The TDNN's output is connected to the input I through a delay block, closing the loop, and effectively creating a nonlinear auto-regressive (NAR) prediction model. The TDNN model is given an initial input I_0, and it predicts the next state of the satellite which is fed back as the new input. Fig. 2 depicts the structure of TDNN.

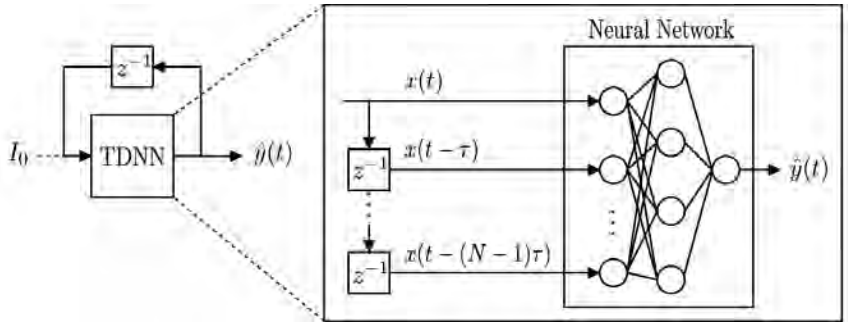

Fig. 2. TDNN architecture.

LSTMs are mainly composed of a cell which remembers values over time intervals (memory cell), an input gate, output gate, and a forget gate which regulates the flow of information into and out of the cell [63]. Fig. 3 presents the structure of LSTM NN.

The next subsection compares the performance of TDNN and LSTM for short orbital prediction.

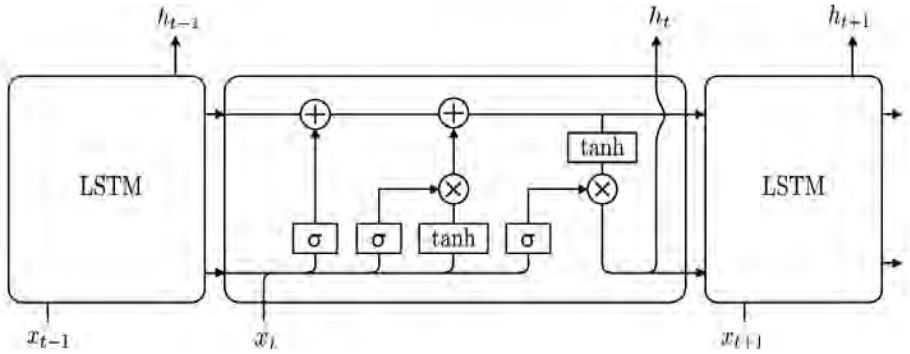

Fig. 3. Generic LSTM Architecture.

A.3 RESULTS

A simulation study was conducted using the data generated from the AGI-STK software corresponding to the an Orbcomm LEO satellite. Table I summarizes the simulation settings. Fig. 4 plots the training and validation MSEs as a function of training epochs. The validation errors for the TDNN design are low, showcasing its ability to function within an acceptable margin of error with new data. The LSTM is shown to be capable of following the profile of the LEO satellite's orbit, however, its accuracy was much lower.

TABLE I
SIMULATION SETTINGS.

Parameter	Value
Satellite name	Orbcomm F107
Duration [hours]	10
Sampling time [seconds]	1
Training Period [hours]	5
Testing Period [hours]	5

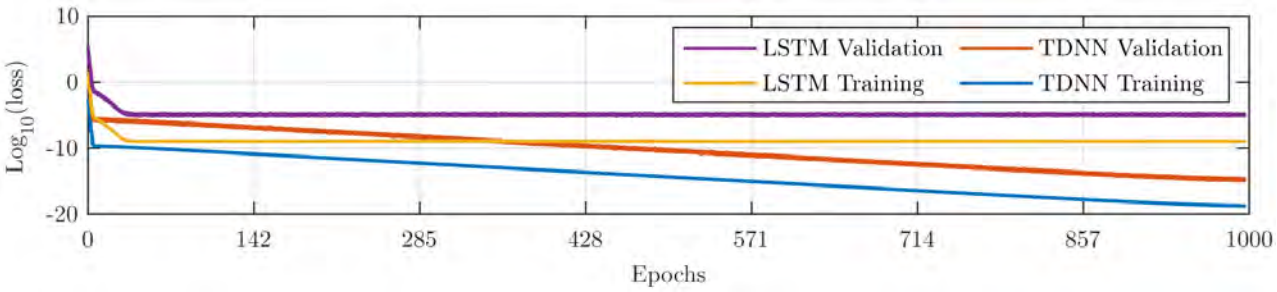

Fig. 4. Validation loss (MSE) versus number of training epochs of proposed models.

The training and validation errors show that the TDNN architecture outperforms the LSTM. The TDNN model is assessed by predicting the satellite's ephemeris in a closed-loop fashion. A TDNN model was trained for every output pair of parameters in the orbital state $S = \{x, y, z, vx, vy, vz\}$. The input and output were chosen as pairs of the position and velocity in each dimension at a time. Simulation results showed promising propagation accuracy for long-term windows, while using the proposed TDNN-based approach compared to the conventional SGP4 model. Fig. 5 depicts the error comparison of SPG4 and the TDNN corresponding to the $\{x, \dot{x}\}$ pair.

The results suggests that the TDNN model is capable of following the HPOP propagator for a short time window. The TDNN showed an acceptable performance for about one orbit, after which, the performance starts degrading.

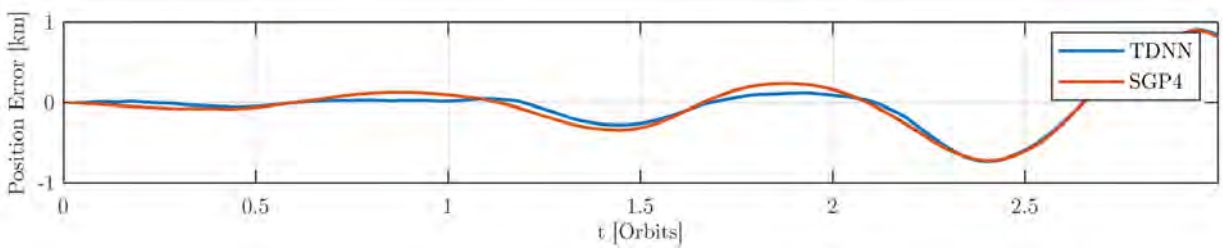

Fig. 5. LEO satellite's position error comparison between SGP4 and TDNN.

B. FRAMEWORK 2: Residual Error Propagation

The errors of the proposed ANNs with respect to HPOP were close to those of SGP4. This could be attributed to the complexity of the LEO satellite's orbit, as well as the highly dimensional properties of HPOP. SGP4 itself is accurate as well, though not as accurate as HPOP, in propagating the ephemeris. Therefore, a nonlinear autoregressive with exogenous inputs (NARX) model was devised to map the output of an SGP4 propagator to those of a well-initialized HPOP propagator.

B.1 TRAINING

To compare both proposed frameworks, the same training, validation, and testing data extracted from AGI-STK's HPOP propagated ephemeris are utilized.

B.2 DESIGN

The NARX model essentially functions similar to a NAR model, with the only difference being that exogenous inputs, which are propagated SPG4 ephemeris, are utilized in predicting the output, as seen in Fig. 6. The NARX architecture has been shown to be highly capable of learning long-term dependencies [64] and predicting time series [65–67]; even chaotic time series [68].

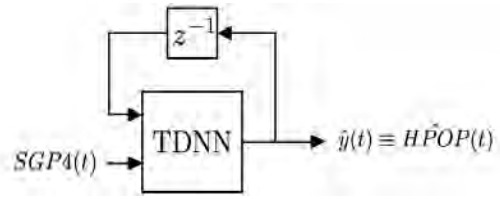

Fig. 6. Proposed NARX model.

The NARX architecture takes SGP4 propagated position states as inputs. It also has a feedback loop where its output, the estimated HPOP state values, are fed back as additional input. This way, the model takes SGP4 as input as well as previous estimated $\hat{\text{HPOP}}(t-1,\ldots,t-d)$ values, and it outputs new estimated $\hat{\text{HPOP}}(t)$ values.

B.3 RESULTS

The simulation settings shown in Table I for the Orbcomm LEO satellite were used. Fig. 7 and Table II shows the position error magnitude of the SGP4 versus the propagated SGP4+NARX approach. Because the SGP4 propagator is initialized with TLE files, which are a compact mean to achieve modestly fast and accurate calculation, its initial position error can reach up to 1 km [69]. Fig. 7 (a) shows the SGP4 position error magnitude while keeping the initial error. Fig. 7 (b) shows the SGP4 position error magnitude while removing the initial error of the TLE file for comparison. The results shows that SGP4+NARX is accumulating error at a much slower rate compared to SGP4.

From these results, one concludes that SGP4+NARX offers promising orbit propagation.

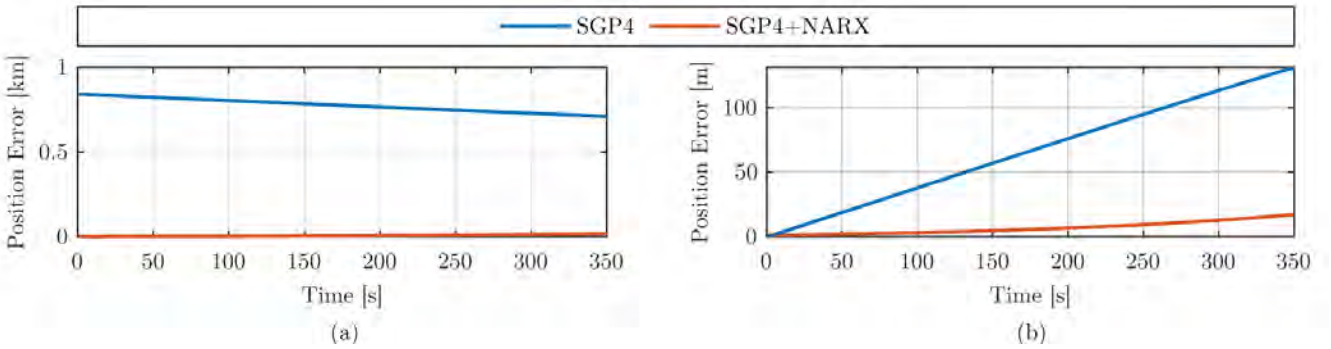

Fig. 7. 3-D Position error magnitude for Orbcomm FM107's trajectory (a) without removing the initial error of SGP4 and (b) with removing the initial error of SGP4.

TABLE II
LEO PROPAGATION PERFORMANCE IN SIMULATION FOR 350 SECONDS.

RMSE [m]	**Orbcomm-FM107**
SGP4 (with TLE initial error)	773
SGP4 (without TLE initial error)	54
SGP4+NARX	8

IV. EXPERIMENTAL RESULTS

In this section, the performance of the proposed STAN navigation framework is assessed experimentally. Here, the performance utilizing propagation via SGP4 ill be compared to the one achieved with the proposed SGP4+NARX. In the experiment, Orbcomm LEO satellites signals were collected, where a ground-truth reference of the satellite ephemeris was obtained by decoding the satellites' positions transmitted from their on-board GPS receivers [28]. The error estimation NARX architecture was chosen, as it has demonstrated the highest accuracy amongst the studied ML frameworks.

A. ENVIRONMENTAL LAYOUT AND EXPERIMENTAL SETUP

A ground vehicle was equipped with the following hardware and software setup:

- A quadrifilar helix antenna to receive the Orbcomm SV downlink signals, which are transmitted at frequencies between 137 and 138 MHz
- A USRP E312 to sample Orbcomm symmetric differential phase shift keying (SDPSK) signals.
- These samples were then processed by the Multi-channel Adaptive TRansceiver Information eXtractor (MATRIX) software-defined radio developed by the Autonomous Systems Perception, Intelligence, and Navigation (ASPIN) Laboratory to perform carrier synchronization, extract pseudorange rate observables, and decode Orbcomm ephemeris messages [28].
- A Septentrio AsteRx-i V integrated GNSS-IMU, which is equipped with a dual-antenna, multi-frequency GNSS receiver and a Vectornav VN-100 micro-electromechanical system (MEMS) IMU. Septentrio's post-processing software development kit (PP-SDK) was used to process GPS carrier phase observables collected by the AsteRxi V and by a nearby differential GPS base station to obtain a carrier phase-based navigation solution. This integrated GNSS-IMU real-time kinematic (RTK) system [70] was used to produce the ground truth results with which the proposed navigation framework was compared.

The experimental setup is shown in Fig. 8. The ground vehicle was driven along U.S. Interstate 5 near Irvine, California, USA, for 7,495 m over 258 seconds, during which 2 Orbcomm LEO satellites were available. The standard deviation of the Orbcomm Doppler measurements was set to be 4.7 Hz, which was obtained empirically. Two navigation frameworks were implemented to estimate the vehicle's trajectory: (i) the LEO signal-aided INS STAN framework using SGP4 as its propagator and (ii) the LEO signal-aided INS STAN framework using the NARX as its

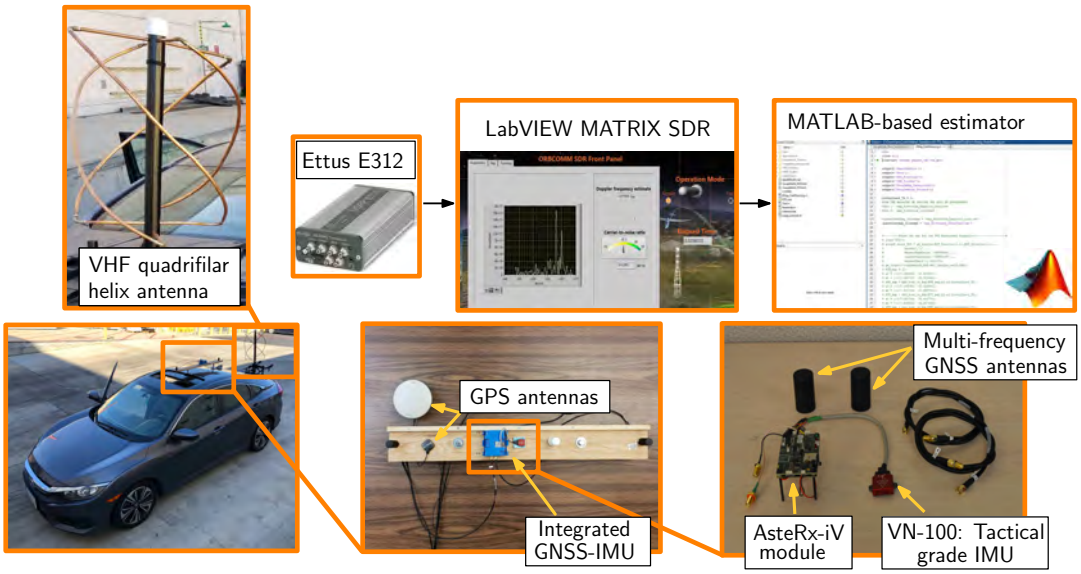

Fig. 8. Experimental Setup.

propagator. The SGP4 propagated ephemeris was initialized from the corresponding TLE file published by NORAD. The HPOP ephemeris utilized for training was properly initialized through STK, using the Orbcomm LEO satellite's positions decoded from the first measurement epoch. To perform a fair comparison between the propagation of SGP4+NARX that uses the first decoded ephemeris point for initialization and the performance of SGP4 that uses a relatively old TLE file, we generated a new TLE file the transmitted ephemeris, propagated it with SGP4, and used it for the comparison. Fig. 9 sketches the data generation and testing method.

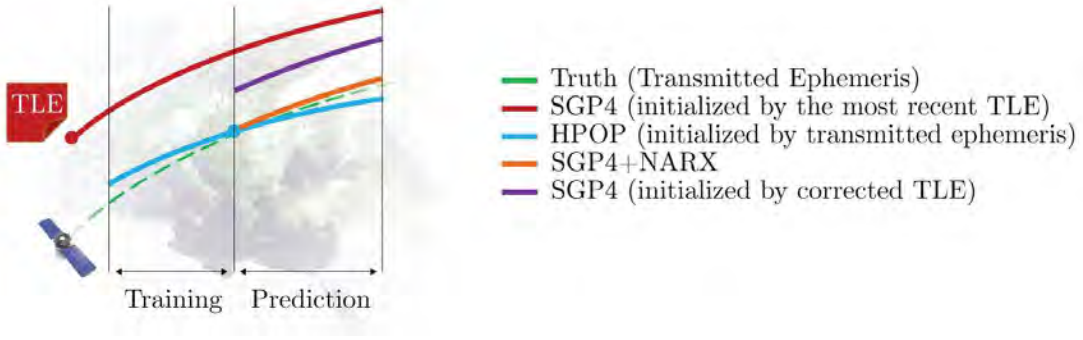

Fig. 9. Sketch illustrating the training phase of the NARX model (using TLE-SGP4 and HPOP) as its prediction phase.

B. RESULTS

First, the performance of the SGP4+NARX model as a propagator is compared with SGP4. The ephemeris position error $E_{\text{LEO}} = \{E_x, E_y, E_z\}$ of both tracked satellites and the total positional error characterized by $E_r = \sqrt{E_x^2 + E_y^2 + E_z^2}$ are shown in Fig. 10 and summarized in Table III.

The improved results in LEO satellite position estimation translate directly to a better navigation performance for a ground vehicle. Fig. 11 shows the vehicle's true trajectory compared to estimates from the original STAN framework and the proposed STAN with SGP4+NARX. The results are summarized in Table IV. The results show how the NARX model's ability in better estimating the LEO satellites' ephemeris leads to a more accurate navigation solution.

TABLE III
LEO Propagation Performance in an experimental scenario.

RMSE [m]	Orbcomm FM112	Orbcomm FM117
SGP4	558	1,226
SGP4+NARX	74	38

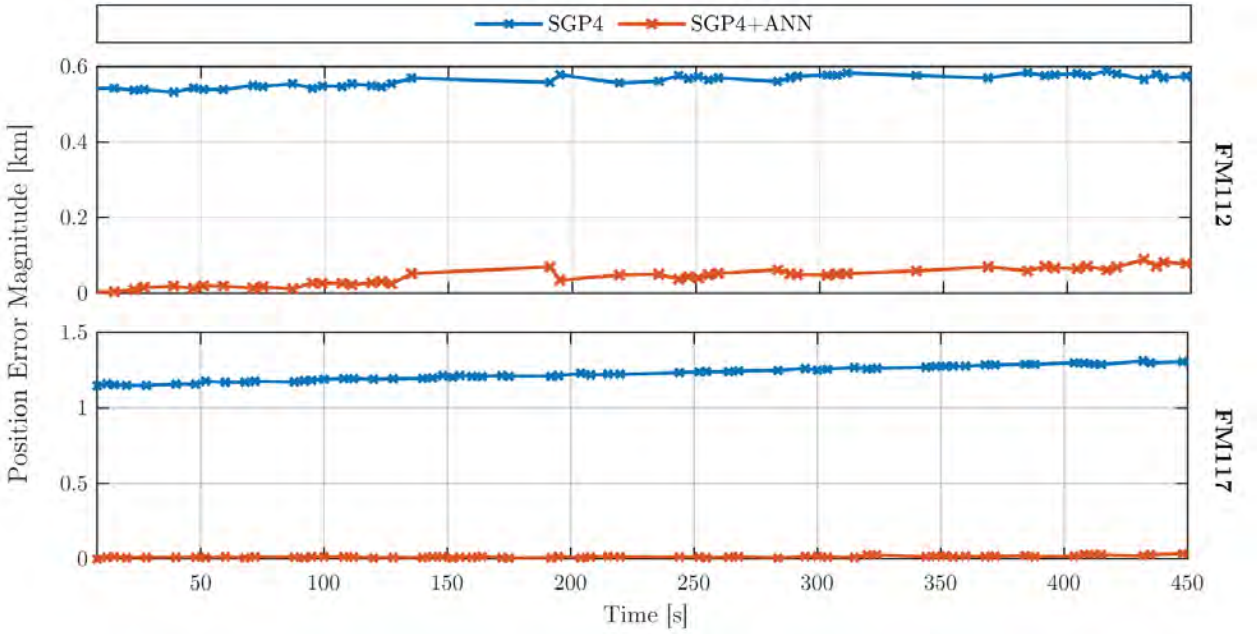

Fig. 10. Comparison between SGP4 and SGP4+NARX propagation

V. CONCLUSION

This paper investigated the performance of multiple ML models (TDNN, LSTM, NAR, and NARX) in propagating LEO satellite ephemeris and in correcting SGP4 ephemeris to map to a more accurate HPOP ephemeris. Both the ephemeris propagation framework and the error modeling framework were studied under the same simulation environment. The error modeling framework performed better and was thus chosen as the LEO propagator in the STAN framework. Experiments were conducted with a ground vehicle navigating while extracting Doppler measurements from two Orbcomm LEO satellites. The training data for the ML model was historical HPOP ephemeris data of the satellite's orbit. The performance of the SGP4+NARX model in tracking the LEO satellites' ephemeris was compared with the results of a traditional LEO propagation model using SPG4. The EKF with SGP4+NARX framework noticeably outperformed the traditional EKF with SGP4 framework's accuracy. The STAN with SGP4 achieved a ground vehicle 3-D position RMSE of 30 m. In contrast, the proposed STAN with SGP4+NARX framework achieved a 3-D position RMSE of 3.6 m.

ACKNOWLEDGMENT

This work was supported in part by the Office of Naval Research (ONR) under Grant N00014-19-1-2511 and Grant N00014-19-1-2613, and in part by the U.S. Department of Transportation (USDOT) under Grant 69A3552047138 for the CARMEN University Transportation Center (UTC). The authors would like to thank Analytical Graphics, Inc. (AGI) for making Systems Tool Kit (STK) available for research purposes.

TABLE IV
GROUND VEHICLE NAVIGATION PERFORMANCE.

Performance Measure	STAN with SGP4	STAN with SGP4+NARX
RMSE [m]	30	3.6
Final Error [m]	30	8.3

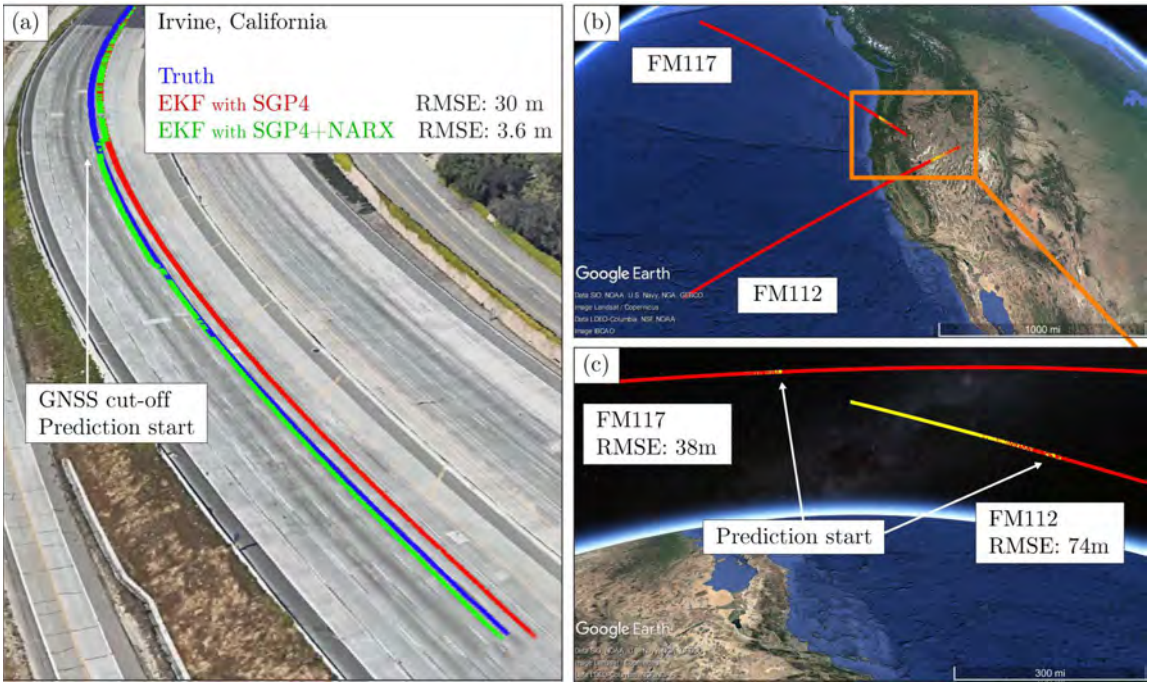

Fig. 11. Experimental results showing (a) the trajectory of a ground vehicle navigating with the proposed approach. The truth (white) is compared to the STAN with SGP4 estimate (red) and the STAN with SGP4+NARX estimate (green). (b, c) the trajectory of the 2 Orbcomm LEO satellites generated by SGP4+NARX predictions (yellow) versus the truth trajectories (red) obtained from onboard GPS receivers. Map data: Google Earth.

References

[1] S. Hackel, O. Montenbruck, P. Steigenberger, U. Balss, C. Gisinger, and M. Eineder, "Model improvements and validation of TerraSAR-X precise orbit determination," *Journal of Geodesy*, vol. 91, no. 5, pp. 547–562, 2017.

[2] D. King, A. Farrel, and Z. Chen, "An evolution of optical network control: From earth to space," in *Proceedings of the IEEE International Conference on Transparent Optical Networks*, 2020, pp. 1–4.

[3] D. Cho, W. Choi, M. Kim, J. Kim, E. Sim, and H. Kim, "High-resolution image and video CubeSat (HiREV): development of space technology test platform using a low-cost CubeSat platform," *International Journal of Aerospace Engineering*, 2019.

[4] D. Crosbie, "The new space race: Satellite mobile communications," *IEE review*, vol. 39, no. 3, pp. 111–114, 1993.

[5] O. Kodheli, A. Guidotti, and A. Vanelli-Coralli, "Integration of satellites in 5G through LEO constellations," in *Proceedings of the IEEE Global Communications Conference*, 2018, pp. 1–6.

[6] G. Giambene, S. Kota, and P. Pillai, "Satellite-5G integration: A network perspective," *IEEE Network*, vol. 32, no. 5, pp. 25–31, 2018.

[7] B. Di, L. Song, Y. Li, and V. Poor, "Ultra-dense LEO: Integration of satellite access networks into 5G and beyond," *IEEE Wireless Communications*, vol. 26, no. 2, pp. 62–69, 2019.

[8] D. Bhattacherjee, W. Aqeel, I. Bozkurt, A. Aguirre, B. Chandrasekaran, P. Godfrey, G. Laughlin, B. Maggs, and A. Singla, "Gearing up for the 21st century space race," in *Proceedings of the ACM Workshop on Hot Topics in Networks*, 2018, pp. 113–119.

[9] M. Harris, "Tech giants race to build orbital internet [news]," *IEEE Spectrum*, vol. 55, no. 6, pp. 10–11, 2018.

[10] "Position, navigation, and timing technologies in the 21st century," J. Morton, F. van Diggelen, J. Spilker, Jr., and B. Parkinson, Eds. Wiley-IEEE, 2021, vol. 2, Part D: Position, Navigation, and Timing Using Radio Signals-of-Opportunity, ch. 35–43, pp. 1115–1412.

[11] A. Popleteev, "Indoor positioning using FM radio signals," Ph.D. dissertation, University of Trento, Italy, 2011.

[12] C. Gentner, "Channel-SLAM: Multipath assisted positioning," Ph.D. dissertation, Ulm University, 2018.

[13] A. Shahmansoori, G. Garcia, G. Destino, G. Seco-Granados, and H. Wymeersch, "Position and orientation estimation through millimeter-wave MIMO in 5G systems," *IEEE Transactions on Wireless Communications*, vol. 17, no. 3, March 2018.

[14] J. Khalife and Z. Kassas, "Opportunistic UAV navigation with carrier phase measurements from asynchronous cellular signals," *IEEE Transactions on Aerospace and Electronic Systems*, vol. 56, no. 4, pp. 3285–3301, August 2020.

[15] C. Yang and A. Soloviev, "Mobile positioning with signals of opportunity in urban and urban canyon environments," in *IEEE/ION Position, Location, and Navigation Symposium*, April 2020, pp. 1043–1059.

[16] Z. Kassas, J. Khalife, A. Abdallah, and C. Lee, "I am not afraid of the jammer: navigating with signals of opportunity in GPS-denied environments," in *Proceedings of ION GNSS Conference*, 2020, pp. 1566–1585.

[17] Z. Kassas, A. Abdallah, and M. Orabi, "Carpe signum: seize the signal – opportunistic navigation with 5G," *Inside GNSS Magazine*, vol. 16, no. 1, pp. 52–57, 2021.

[18] T. Kazaz, G. Janssen, J. Romme, and A. Van der Veen, "Delay estimation for ranging and localization using multiband channel state information," *IEEE Transactions on Wireless Communications*, pp. 1–16, September 2021.

[19] A. Abdallah and Z. Kassas, "UAV navigation with 5G carrier phase measurements," in *Proceedings of ION GNSS Conference*, September 2021, accepted.

[20] D. Lawrence, H. Cobb, G. Gutt, M. OConnor, T. Reid, T. Walter, and D. Whelan, "Navigation from LEO: Current capability and future promise," *GPS World Magazine*, vol. 28, no. 7, pp. 42–48, July 2017.

[21] Z. Kassas, J. Morales, and J. Khalife, "New-age satellite-based navigation – STAN: simultaneous tracking and navigation with LEO satellite signals," *Inside GNSS Magazine*, vol. 14, no. 4, pp. 56–65, 2019.

[22] T. Reid, K. Gunning, A. Perkins, S. Lo, and T. Walter, "Going back for the future: Large/mega LEO constellations for navigation," in *Proceedings of ION GNSS Conference*, September 2019, pp. 2452–2468.

[23] Z. Kassas, J. Khalife, M. Neinavaie, and T. Mortlock, "Opportunity comes knocking: overcoming GPS vulnerabilities with other satellites' signals," *Inside Unmanned Systems Magazine*, pp. 30–35, June/July 2020.

[24] F. Farhangian, H. Benzerrouk, and R. Landry, "Opportunistic in-flight INS alignment using LEO satellites and a rotatory IMU platform," *Aerospace*, vol. 8, no. 10, pp. 280–281, 2021.

[25] S. Thompson, S. Martin, and D. Bevly, "Single differenced doppler positioning with low Earth orbit signals of opportunity and angle of arrival estimation," in *Proceedings of ION International Technical Meeting*, 2020, pp. 497–509.

[26] M. Psiaki, "Navigation using carrier doppler shift from a LEO constellation: TRANSIT on steroids," *NAVIGATION, Journal of the Institute of Navigation*, vol. 68, no. 3, pp. 621–641, September 2021.

[27] M. Neinavaie, J. Khalife, and Z. Kassas, "Exploiting Starlink signals for navigation: first results," in *Proceedings of ION GNSS Conference*, September 2021, accepted.

[28] J. Khalife and Z. Kassas, "Receiver design for Doppler positioning with LEO satellites," in *Proceedings of IEEE International Conference on Acoustics, Speech and Signal Processing*, May 2019, pp. 5506–5510.

[29] R. Landry, A. Nguyen, H. Rasaee, A. Amrhar, X. Fang, and H. Benzerrouk, "Iridium Next LEO satellites as an alternative PNT in GNSS denied environments–part 1," *Inside GNSS Magazine*, vol. 14, no. 3, pp. 56–64., May 2019.

[30] Z. Tan, H. Qin, L. Cong, and C. Zhao, "New method for positioning using IRIDIUM satellite signals of opportunity," *IEEE Access*, vol. 7, pp. 83 412–83 423, 2019.

[31] M. Neinavaie, J. Khalife, and Z. Kassas, "Blind Doppler tracking and beacon detection for opportunistic navigation with LEO satellite signals," in *Proceedings of IEEE Aerospace Conference*, March 2021, pp. 1–8.

[32] J. Khalife, M. Neinavaie, and Z. Kassas, "Blind Doppler tracking from OFDM signals transmitted by broadband LEO satellites," in *Proceedings of IEEE Vehicular Technology Conference*, April 2021, pp. 1–6.

[33] J. Khalife, M. Neinavaie, and Z. Kassas, "The first carrier phase tracking and positioning results with Starlink LEO satellite signals," *IEEE Transactions on Aerospace and Electronic Systems*, 2021, accepted.

[34] J. Khalife, M. Neinavaie, and Z. Kassas, "Navigation with differential carrier phase measurements from megaconstellation LEO satellites," in *Proceedings of IEEE/ION Position, Location, and Navigation Symposium*, April 2020, pp. 1393–1404.

[35] T. Mortlock and Z. Kassas, "Performance analysis of simultaneous tracking and navigation with LEO satellites," in *Proceedings of ION GNSS Conference*, September 2020, pp. 2416–2429.

[36] J. Morales, J. Khalife, U. Santa Cruz, and Z. Kassas, "Orbit modeling for simultaneous tracking and navigation using LEO satellite signals," in *Proceedings of ION GNSS Conference*, September 2019, pp. 2090–2099.

[37] T. Mortlock and Z. Kassas, "Assessing machine learning for LEO satellite orbit determination in simultaneous tracking and navigation," in *Proceedings of IEEE Aerospace Conference*, March 2021, pp. 1–8.

[38] X. Bai and J. Junkins, "Modified chebyshev-picard iteration methods for orbit propagation," *The Journal of the Astronautical Sciences*, vol. 58, no. 4, pp. 583–613, 2011.

[39] J. Aristoff and A. Poore, "Implicit runge-kutta methods for orbit propagation," in *AIAA/AAS Astrodynamics Specialist Conference*, 2012, p. 4880.

[40] J. Sullivan, S. Grimberg, and S. DAmico, "Comprehensive survey and assessment of spacecraft relative motion dynamics models," *Journal of Guidance, Control, and Dynamics*, vol. 40, no. 8, pp. 1837–1859, 2017.

[41] S. Shuster, *A survey and performance analysis of orbit propagators for LEO, GEO, and highly elliptical orbits*. Utah State University, 2017.

[42] X. Tian, G. Chen, E. Blasch, K. Pham, and Y. Bar-Shalom, "Comparison of three approximate kinematic models for space object tracking," in *Proceedings of International Conference on Information Fusion*, 2013, pp. 1005–1012.

[43] Y. Luo and Z. Yang, "A review of uncertainty propagation in orbital mechanics," *Progress in Aerospace Sciences*, vol. 89, pp. 23–39, February 2017.

[44] North American Aerospace Defense Command (NORAD), "Two-line element sets," http://celestrak.com/NORAD/elements/.

[45] D. Vallado, P. Crawford, R. Hujsak, and T. Kelso, "Revisiting spacetrack report# 3," in *Proceedings of the Astrodynamics Specialist Conference and Exhibit*, 2006, p. 6753.

[46] M. Zaheer, "Kinematic orbit determination of low earth orbiting satellites, using satellite-to-satellite tracking data and comparison of results with different propagators," 2014.

[47] D. Racelis and M. Joerger, "High-integrity TLE error models for MEO and GEO satellites," in *Proceedings of AIAA SPACE and Astronautics Forum and Exposition*, September 2018, pp. 1–13.

[48] S. Sharma and J. Cutler, "Robust orbit determination and classification: A learning theoretic approach," *IPN Progress Report*, pp. 42–203, 2015.

[49] F. Feng, Y. Zhang, H. Li, Y. Fang, Q. Huang, and X. Tao, "A novel space-based orbit determination method based on distribution regression and its sparse solution," *IEEE Access*, vol. 7, pp. 133 203–133 217, 2019.

[50] H. Peng and X. Bai, "Limits of machine learning approach on improving orbit prediction accuracy using support vector machine," in *Proceedings of the Advanced Maui Optical and Space Surveillance*, 2017, pp. 1–22.

[51] H. Peng and X. Bai, "Artificial neural network–based machine learning approach to improve orbit prediction accuracy," *Journal of Spacecraft and Rockets*, vol. 55, no. 5, pp. 1248–1260, 2018.

[52] H. Peng and X. Bai, "Comparative evaluation of three machine learning algorithms on improving orbit prediction accuracy," *Astrodynamics*, vol. 3, no. 4, pp. 325–343, 2019.

[53] N. Salleh, S. Yuhaniz, N. Azmi, and S. Sabri, "Enhancing simplified general perturbations-4 model for orbit propagation using deep learning: a review," in *Proceedings of the International Conference on Software and Computer Applications*, 2019, 5937–5941.

[54] C. Chao, J. Cook, J. Cox, T. Starchville, R. Thompson, and L. Wagner, "Independent verification and validation for analytical graphics, inc. of three astrodynamic functions of the satellite tool kit: version 4.1. 0," *Journal of The Aerospace Corporation ATR*, 2000.

[55] K. Hornik, M. Stinchcombe, and H. White, "Multilayer feedforward networks are universal approximators," *Neural networks*, vol. 2, no. 5, pp. 359–366, 1989.

[56] Analytical graphics, inc., systems tool kit (STK).

[57] M. Refan and A. Dameshghi, "GDOP classification and approximation by implementation of time delay neural network method for low-cost GPS receivers," *Iranian Journal of Electrical and Electronic Engineering*, vol. 16, no. 2, pp. 192–200, 2020.

[58] V. Peddinti, D. Povey, and S. Khudanpur, "A time delay neural network architecture for efficient modeling of long temporal contexts," in *Proceedings of the International Speech Communication Association Conference*, 2015.

[59] X. Yang, H. Sun, X. Sun, M. Yan, Z. Guo, and K. Fu, "Position detection and direction prediction for arbitrary-oriented ships via multitask rotation region convolutional neural network," *IEEE Access*, vol. 6, pp. 50 839–50 849, 2018.

[60] H. Kim and T. Bae, "Deep learning-based GNSS network-based real-time kinematic improvement for autonomous ground vehicle navigation," *Journal of Sensors*, 2019.

[61] M. Jiménez-Guarneros, P. Gómez-Gil, R. Fonseca-Delgado, M. Ramírez-Cortés, and V. Alarcón-Aquino, "Long-term prediction of a sine function using a LSTM neural network," *Journal of Nature-Inspired Design of Hybrid Intelligent Systems*, pp. 159–173, 2017.

[62] A. Hatata and M. Eladawy, "Prediction of the true harmonic current contribution of nonlinear loads using NARX neural network," *Alexandria Engineering Journal*, vol. 57, no. 3, pp. 2018–1518, 2007.

[63] F. Gers, J. Schmidhuber, and F. Cummins, "Learning to forget: Continual prediction with LSTM," *Neural computation*, vol. 12, no. 10, pp. 2451–2471, 2000.

[64] T. Lin, B. Horne, P. Tino, and C. Giles, "Learning long-term dependencies in NARX recurrent neural networks," *IEEE Transactions on Neural Networks*, vol. 7, no. 6, pp. 1329–1338, 1996.

[65] H. Siegelmann, B. Horne, and C. Giles, "Computational capabilities of recurrent NARX neural networks," *IEEE Transactions on Systems, Man, and Cybernetics, Part B (Cybernetics)*, vol. 27, no. 2, pp. 208–215, 1997.

[66] H. Xie, H. Tang, and Y. Liao, "Time series prediction based on NARX neural networks: An advanced approach," in *Proceedings of IEEE International conference on machine learning and cybernetics*, vol. 3, 2009, pp. 1275–1279.

[67] J. Menezes, P. Maria, and G. Barreto, "Long-term time series prediction with the NARX network: An empirical evaluation," *Neurocomputing*, vol. 71, no. 16-18, pp. 3335–3343, 2008.

[68] E. Diaconescu, "The use of NARX neural networks to predict chaotic time series," *Wseas Transactions on computer research*, vol. 3, no. 3, pp. 182–191, 2008.

[69] B. Li, J. Sang, and J. Ning, "TLE generation from sparse tracking data and its performance," *Advances in the Astronautical Sciences*, vol. 158, pp. 4003–4014, 2016.

[70] "Septentrio AsteRx-i V," https://www.septentrio.com/products, 2018.

Demo: I Am Not Afraid of the GPS Jammer: Exploiting Cellular Signals for Accurate Ground Vehicle Navigation in a GPS-Denied Environment

Ali A. Abdallah†, Zaher M. Kassas†, and Chiawei Lee‡
† University of California, Irvine, USA
‡ US Air Force Test Pilot School, Edwards Air Force Base, California, USA
abdalla2@uci.edu, zkassas@ieee.org, and chiawei.lee@us.af.mil
Video Demonstration: https://www.youtube.com/watch?v=kwpCRXz-5gM

THIS demo presents unprecedented attack-defense results of a ground vehicle navigating to a meter-level accuracy in a real-world GPS-denied environment, by exploiting ambient cellular signals exclusively and no other sensors.

Today's vehicular navigation systems fuse information from a global navigation satellite system (GNSS) receiver (e.g., GPS) and an inertial measurement unit (IMU). Relying on GNSS alone to aid an IMU poses an alarming vulnerability: GNSS signals could become unavailable or unreliable in environments under a malicious attack (jamming or spoofing). Without GNSS, the IMU errors will accumulate and eventually diverge, compromising the vehicle's safe and efficient operation.

Current trends to supplement a navigation system when GNSS signals become unreliable are traditionally sensor-based (e.g., vision, lidar, sonar, and odometers). These sensors extract *relative* motion information to reduce the IMU's error divergence rate. However, these are dead-reckoning-type sensors; therefore, during prolonged periods of GNSS outage, the error will eventually diverge. Moreover, these sensors only provide *local* position estimates, may not properly function in all environments (e.g., fog, snow, rain, dust, nighttime, etc.), and are still susceptible to malicious attacks.

The authors developed a defense mechanism that exploits ambient cellular signals to produce an accurate, sustained navigation solution without GNSS. In contrast to the aforementioned sensors, *absolute* position information could be extracted from cellular signals to provide bounded IMU errors. Moreover, cellular signals are more difficult to jam and spoof than GNSS and are practically unaffected by poor weather conditions. To demonstrate the efficacy of this mechanism in a real-world GPS-denied environment, the authors were invited to participate in live GPS jamming experiments, called NAVFEST, at Edwards Air Force Base (AFB), California, USA. GPS signals were jammed with high-powered jammers, spread over an area of around 50 miles, which transmitted a variety of waveforms at jamming-to-signal ratio (J/S) exceeding 100 dB (see Fig. 1).

The vehicle was driven into the jammed environment, where it traversed 5 km in 180 seconds, of which, GPS signals were unavailable for the last 3.9 km. During the jamming attack, the vehicle-mounted navigation system, which utilized a commercial high-end GPS receiver (Septentrio AsteRx-i V) with a tactical-grade IMU (Vectornav VN-100) accumulated a position root mean-squared error (RMSE) of 238 m. In contrast, the developed defense mechanism exploited signals from eight cellular long-term evolution (LTE) towers, whose positions were mapped prior to the experiment, from the U.S. cellular providers T-Mobile and Verizon, one of which was more than 52 km away from the ground vehicle. These signals were processed by the author's software-defined radio (SDR) to produce pseudorange measurements, which were fused through an extended Kalman filter to estimate the vehicle's trajectory. The defense mechanism achieved a position RMSE of 2.6 m exclusively with cellular LTE signals and no other sensors. The results are summarized in Fig. 2. Note that to obtain the vehicle's ground truth trajectory, a vehicle-mounted GNSS-IMU system was used, which utilized signals from the non-jammed GNSS constellations (Galileo and GLONASS). It is worth noting that the unprecedented 2.6 position RMSE achieved in this demo are an order of magnitude smaller than previously published results in the same environment, which achieved a position RMSE of 29.4 m. Further details can be found in the video.

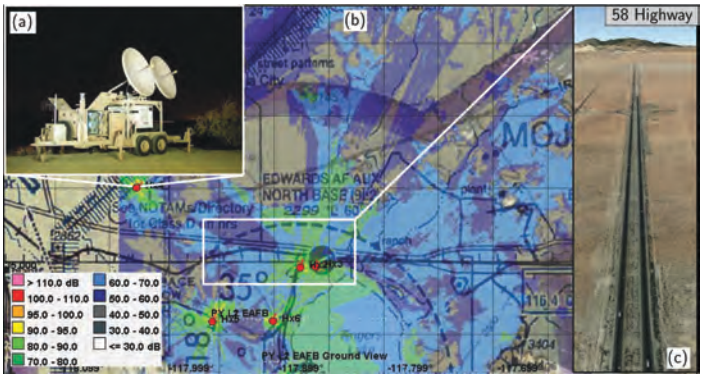

Fig. 1. NAVFEST GPS jamming laydown: (a) one of the jammers used in the experiment, (b) J/S heat map and the jammers' locations, (c) the 58 Highway, where the ground vehicle was driven. Map data: Edwards AFB.

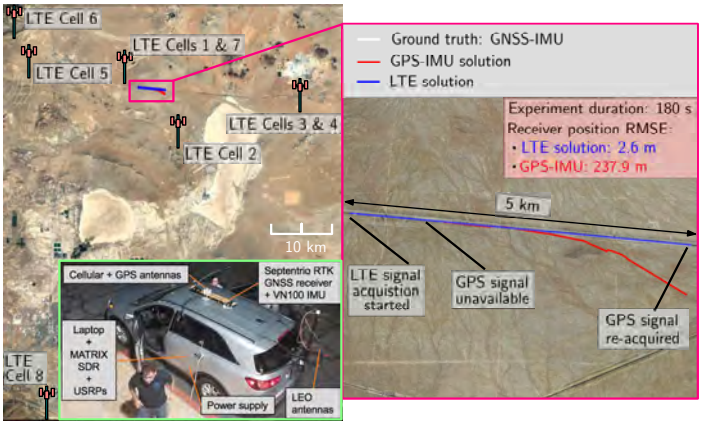

Fig. 2. Navigation solutions for (i) GPS-IMU, (ii) cellular LTE, and (iii) GNSS-IMU ground truth. Map data: Google Earth.

This work was supported by ONR grant N00014-19-1-2511, NSF grant 1929965, and DOT grant 69A3552047138. DISTRIBUTION STATEMENT A. Approved for public release; Distribution is unlimited 412TW-PA-20399.
Workshop on Automotive and Autonomous Vehicle Security (AutoSec) 2022
24 April 2022, San Diego, CA, USA
ISBN 1-891562-68-1
https://dx.doi.org/10.14722/autosec.2022.23049
www.ndss-symposium.org

Differential Framework for Submeter-Accurate Vehicular Navigation With Cellular Signals

Joe Khalife, *Member, IEEE*, and Zaher M. Kassas, *Senior Member, IEEE*

***Abstract*—A framework that could achieve submeter-level-accurate horizontal navigation with carrier phase differential measurements from cellular signals is developed. This framework, termed CD-cellular, is composed of a base and a rover in a cellular environment, both making carrier phase measurements to the same cellular base transceiver stations (BTSs). The base shares its carrier phase measurements with the mobile rover, which in turn employs an extended Kalman filter to obtain a coarse estimate of its states, followed by a batch weighted nonlinear least squares (B-WNLS) estimator to solve for the integer ambiguities, and finally a point-solution WNLS to estimate its own states. The framework is designed to guarantee that after some time, the rover's position error remains below a pre-defined threshold with a desired probability. This is achieved by leveraging models of the BTS positions from stochastic geometry. Experimental results on an unmanned aerial vehicle (UAV) in an open semi-urban environment with multipath-free, line-of-sight (LOS) conditions are presented, showing that the developed framework achieves a 70.48 cm position root mean-squared error (RMSE) over a trajectory of 2.24 km, measured with respect to the UAV's navigation solution from its onboard GPS-inertial navigation system (INS).**

***Index Terms*—Carrier phase, fifth-generation (5G), integer ambiguity resolution, LTE, navigation, RTK, signals of opportunity, UAV.**

NOMENCLATURE

i	$\in \{\text{UAV(U)}, \text{Base(B)}\}$, receiver index.
n	$\in \{1, \ldots, N\}$, BTS index.
N	Total number of BTSs.
k	Discrete-time index.
c	Speed of light.
λ	Signal wavelength.
$z_n^{(i)}(k)$	Carrier phase measurement from i-th receiver to n-th BTS at time-step k.
$\boldsymbol{r}_{r_i}$	$\triangleq [x_{r_i}, y_{r_i}]^\mathsf{T}$, i-th receiver's two-dimensional (2-D) position vector.
$\boldsymbol{r}_{s_n}$	$\triangleq [x_{s_n}, y_{s_n}]^\mathsf{T}$, n-th BTS's 2-D position vector.
$\Delta z_{r_i,s_n}$	Altitude difference between i-th receiver and n-th BTS.
$N_n^{(i)}$	Carrier phase ambiguity between i-th receiver and n-th BTS.
δt_{r_i}	i-th receiver's clock bias.
δt_{s_n}	n-th BTS's clock bias.
$v_n^{(i)}$	Measurement noise between i-th receiver and n-th BTS.
$(\sigma_n^{(i)})^2$	Variance of $v_n^{(i)}$.
$C/N_{0,n}^{(i)}$	Carrier-to-noise ratio of n-th BTS measured by i-th receiver.
$B_{i,\text{PLL}}$	i-th receiver's PLL noise equivalent bandwidth.
$z_{n,1}^{(\text{U,B})}$	Double-difference carrier phase measurment for n-th BTS.
$h_{n,1}^{\text{U}}$	Single-difference range for n-th BTS.
$N_{n,1}^{(\text{U,B})}$	Double-difference integer ambiguity for n-th BTS.
$v_{n,1}^{(\text{U,B})}$	Double-difference measurement noise for n-th BTS.
$\boldsymbol{z}_{\text{U,B}}$	Vector of all double-difference measurements.
$\boldsymbol{h}[\boldsymbol{r}_{r_\text{U}}]$	Vector of all single-difference ranges.
$\boldsymbol{N}$	Vector of all double-difference integer ambiguities.
$\boldsymbol{v}_{\text{U,B}}$	Vector of all double-difference measurement noise.
$\mathbf{R}_{\text{U,B}}$	Covariance matrix of $\boldsymbol{v}_{\text{U,B}}$.
α	Confidence level.
ζ	Desired position error threshold.
k_ζ	Cutoff time beyond which position error bound holds.
$\mathbf{z}_{\text{U,B}}^{k_\zeta}$	Collection of all double-difference measurement vectors up to time-step k_ζ.
$\mathbf{r}_{\boldsymbol{r}_\text{U}}^{k_\zeta}$	Time history of receiver U's position up to time-step k_ζ in vector form.
$\mathbf{h}[\mathbf{r}_{\boldsymbol{r}_\text{U}}^{k_\zeta}]$	Collection of all single-difference range vectors up to time-step k_ζ.
$\mathbf{v}_{\text{U,B}}^{k_\zeta}$	Collection of all double-difference measurement noise vectors up to time-step k_ζ.
$\mathbf{R}_{\text{U,B}}^{k_\zeta}$	Covariance matrix of $\mathbf{v}_{\text{U,B}}^{k_\zeta}$.
$\hat{\mathbf{r}}_{\boldsymbol{r}_\text{U}}^{k_\zeta}$	B-WNLS float estimate of $\hat{\mathbf{r}}_{\boldsymbol{r}_\text{U}}^{k_\zeta}$.
$\hat{\boldsymbol{N}}^{k_\zeta}$	B-WNLS float estimate of $\boldsymbol{N}$.
$\check{\boldsymbol{N}}^{k_\zeta}$	B-WNLS integer estimate of $\boldsymbol{N}$.
$\tilde{\boldsymbol{N}}^{k_\zeta}$	Integer ambiguity errors.
$\check{\mathbf{r}}_{\boldsymbol{r}_\text{U}}^{k_\zeta}$	B-WNLS estimate of $\hat{\mathbf{r}}_{\boldsymbol{r}_\text{U}}^{k_\zeta}$ after integer fix.
$\tilde{\mathbf{G}}$	Double-difference geometry matrix.

Manuscript received 6 June 2022; accepted 18 June 2022. Date of publication 1 August 2022; date of current version 23 January 2023. This work was supported in part by the Office of Naval Research under Grant N00014-19-1-2511, in part by the National Science Foundation under Grant 1929965, and in part by the U.S. Department of Transportation under Grant 69A3552047138 for the CARMEN University Transportation Center. (*Corresponding author: Zaher M. Kassas.*)

Joe Khalife is with the Department of Mechanical and Aerospace Engineering, University of California, Irvine, CA 92697 USA (e-mail: khalifej@uci.edu).

Zaher M. Kassas is with the Department of Electrical and Computer Engineering, the Ohio State University, Columbus, OH 43210 USA (e-mail: zkassas@ieee.org).

Color versions of one or more figures in this article are available at https://doi.org/10.1109/TIV.2022.3187957.

Digital Object Identifier 10.1109/TIV.2022.3187957

2379-8858 © 2022 IEEE. Personal use is permitted, but republication/redistribution requires IEEE permission.
See https://www.ieee.org/publications/rights/index.html for more information.

Authorized licensed use limited to: The Ohio State University. Downloaded on April 13,2023 at 05:03:54 UTC from IEEE Xplore. Restrictions apply.

$\lambda_{\max}(\mathbf{A})$ Maximum eigenvalue of some matrix $\mathbf{A}$.
$\lambda_{\min}(\mathbf{A})$ Minimum eigenvalue of some matrix $\mathbf{A}$.
$f^{-1}_{\chi^2,M}(\cdot)$ Inverse chi-square cdf with M degrees of freedom.

I. Introduction

As AUTONOMOUS vehicles (AVs) get endowed with higher levels of autonomy, the accuracy and resiliency requirements of their navigation systems become evermore stringent. For example, for an automated driving system to be classified as SAE J3016^{TM} Level 4 (high automation), the driving system must be able to precisely and safely execute driving maneuvers, such as lane changes or turns at intersections. In order to execute such driving maneuvers, localization accuracies of 0.1 m with a confidence of 95% must be realized [1]. On the other hand, while similar clear-cut requirements for unmanned aerial vehicles (UAVs) have not been established yet [2], [3], it is not far-fetched to imagine submeter-level navigation requirements for certain flight operations, e.g., beyond visual line-of-sight (BVLOS) in urban environments and in large-scale swarms.

Today's AVs rely on an inertial navigation system (INS) aided by global navigation satellite system (GNSS) signals. While such systems can meet the submeter-level accuracy requirement in certain clear line-of-sight conditions, they are at the mercy of GNSS signal vulnerabilities. These signals are jammable, spoofable, and may become unusable in certain environments (e.g., deep urban canyons) [4]–[7]. Moreover, a GNSS receiver may simply fail altogether. When GNSS signals are compromised or unusable, the error in the INS-derived navigation solution will quickly drift unboundedly, violating the navigation accuracy requirement and jeopardizing the safe operation of the AV. On one hand, aiding sensors such as lidars or cameras can be used to limit the drift of the INS [8], [9]. However, such sensors can only provide position information in a *local* map and they too could drift over time [10], [11]. One way to circumvent this issue is to create high-fidelity global maps of lidar point clouds or camera images and localize the AV in such global maps using map matching [12]. However, building these high-fidelity maps for different environment is tedious and performing map matching requires high computational power and resources to run in real-time [13], [14]. On the other hand, signals of opportunity (SOPs) (e.g., low Earth orbit (LEO) satellite [15]–[17], digital television [18], [19], and cellular [20]–[26]) possess desirable attributes to serve as an alternative aiding source to GNSS signals. Navigation with SOPs has been demonstrated on ground vehicles and unmanned aerial vehicles (UAVs), achieving a localization accuracy ranging from meters to tens of meters, with the latter accuracy corresponding to ground vehicles in deep urban canyons with severe multipath conditions [27]–[33]. Cellular SOPs, particularly 3G code-division multiple access (CDMA), 4G long-term evolution (LTE), and 5G new radio (NR), are among the most attractive SOP candidates for navigation. These signals are abundant, received at a much higher power than GNSS signals, offer a favorable horizontal geometry, are free to use, and can provide position information in a *global* map. While cellular signals are jammable and spoofable [34]–[36], they are typically received at high powers (more than 30 dB than GNSS signals [37]) and are transmitted in multiple frequency bands. The cellular 3G, 4G, and 5G spectrum spans the 700 MHz to nearly 6 GHz bands. The 5G millimeter wave (mmWave) spectrum is envisioned to span several GHz of spectrum, with some bands reaching up to 400 MHz of bandwidth. This makes staging a successful, clandestine attack on cellular SOPs generally challenging, as the attacker would need to target the entire cellular spectrum with very high power.

A challenge that arises in cellular-based navigation is the unknown states of cellular base transceiver stations (BTSs), namely their position and clock errors (bias and drift). This is in sharp contrast to GNSS-based navigation, where the states of the satellites are transmitted to the receiver in the navigation message. Since cellular BTSs are spatially stationary, their positions may be mapped prior to navigation (e.g., by a dedicated mapping campaign or from satellite imagery and cellular databases). While mapping BTS positions is also tedious, the number of BTSs in an environment is orders of magnitude lower than the number of points in a lidar point cloud or pixels in image maps. While BTS positions can be mapped once and stored for later use, BTS clock errors must be continuously estimated since these errors are stochastic and dynamic. To deal with this challenge, a base/rover framework was proposed in [20], [38], in which the base and rover make pseudorange measurements to the same BTSs in the environment. The base was assumed to have complete knowledge of its states (e.g., by having access to GNSS signals), while estimating the states of BTSs in its environment, and sharing these estimates with a rover that had no knowledge of its states. Another framework was developed in which the rover estimated its states simultaneously with the states of the BTSs in the environment, i.e., performed radio simultaneous localization and mapping (radio SLAM) [39], [40].

It is well-known that carrier phase measurements are much more precise than code phase (pseudorange) measurements. While meter-level accuracy is achievable with pseudorange measurements, submeter-level (centimeter to decimeter) is achievable in carrier phase differential GNSS (CD-GNSS), also known as real-time kinematic (RTK) [41], [42]. However, the literature on differential cellular-based navigation frameworks is sparse. A preliminary study of cellular carrier phase-based navigation were conducted in [43], [44], in which the received carrier phase of cellular signals was exploited to produce submeter-level accurate navigation solutions on a UAV flying in an open semi-urban environment. The framework was based on carrier phase differential (CD)-cellular measurements, requiring an additional base receiver. The CD-cellular navigation framework was analyzed through Monte Carlo simulations. One advantage of the CD-cellular framework is that it requires very few base receivers to cover large areas [44] (1 base in about 6 km radius). One challenge with using differential carrier phase measurements is having to resolve the integer ambiguities [41], [45], [46]. Several solutions have been proposed for this problem, most notably the Local Minima Search (LMS) method [47] and the Least-squares Ambiguity Decorrelation Adjustment (LAMBDA) method [48]–[50] and its variants [51]. These methods rely on either (i) multiple-frequency measurements, both code and carrier phase measurements, (ii) the GNSS satellite geometry to change significantly

Authorized licensed use limited to: The Ohio State University. Downloaded on April 13,2023 at 05:03:54 UTC from IEEE Xplore. Restrictions apply.

with time as the receiver remains stationary, or (iii) dedicated ground-based GPS integrity beacons [52]. However, code phase measurements are not necessarily available from cellular BTSs, nor do BTSs necessarily transmit synchronized signals on different frequencies; and BTSs are stationary. To overcome this issue, a CD-cellular framework that leverages UAV motion to resolve the integer ambiguities and achieve a submeter-accurate navigation solution was proposed in [44]. However, the work in [44] suffers from two major limitations: (i) the navigation solution prior to resolving the ambiguities lacks rigorous reliability guarantees and (ii) the size of the batch filter that resolves the ambiguities is pre-set, which does not guarantee any navigation performance requirements.

This paper presents the first complete study for submeter-accurate horizontal navigation using CD-cellular measurements. The framework requires a base receiver making carrier phase measurements to the same BTSs as the navigating rover and assumes a communication channel between the base and rover. While this framework could be employed for ground or aerial vehicles (as long as multipath and signal blockage conditions are properly mitigated or accounted for), this study focuses on UAV applications, due to the favorable multipath-free, line-of-sight (LOS) channels between the BTS and the UAV. It is important to note that the algorithms presented in the paper are agnostic to the signal type. The CD-cellular framework only assumes carrier phase measurements available from nearby cellular towers, which can be produced from 3G, 4G, 5G, and future generations. In particular, this paper extends [43] and [44] by making the following four contributions:

1) First, a three-stage framework for navigating with CD-cellular measurements is developed. The first stage employs an extended Kalman filter (EKF) to obtain a coarse estimate of the UAV's position. An EKF initialization scheme is provided. In the second stage, a batch solution is obtained to fix the integer ambiguities. In the third stage, the UAV navigates with the CD-cellular measurements and fixed ambiguities.
2) A probabilistic upper bound on the position error after resolving the integer ambiguities is established. The probabilistic upper bound captures mainly the effect of the integer ambiguity error on the UAV position error. Models of the BTS positions from stochastic geometry are leveraged to determine the upper bound that holds with a desired probability, for a given number of BTSs.
3) The derived probabilistic upper bound is used to formulate a test that determines when to solve the batch estimator and fix the integer ambiguities in order to guarantee that the UAV position error remains under a pre-defined threshold, with a certain probability.
4) Experimental results are presented demonstrating the proposed CD-cellular framework. The experiments show a UAV navigating at submeter-level accuracy in an open semi-urban environment and multipath-free, LOS conditions, while remaining in the same BTS sectors. The UAV achieves a horizontal position root mean-squared error (RMSE) of 70.48 cm over a trajectory of 2.24 km, measured with respect to the UAV's navigation solution from its onboard GPS-INS.

The remainder of the paper is organized as follows. Section II describes the cellular carrier phase observable model. Section III formulats the base/rover CD-cellular framework. Section IV provides experimental results demonstrating the proposed framework, showing submeter-level UAV navigation accuracy. Concluding remarks are given in Section V.

II. Cellular Carrier Phase Observable Model

In the rest of this paper, availability of code phase, Doppler frequency, and carrier phase measurements of cellular CDMA and LTE signals is assumed (e.g., from specialized navigation receivers [18], [20], [53]–[56]). The continuous-time carrier phase observable can be obtained by integrating the Doppler measurement over time [41]. The carrier phase (expressed in cycles) made by the i-th receiver on the n-th SOP is given by

$$\phi_n^{(i)}(t) = \phi_n^{(i)}(t_0) + \int_{t_0}^{t} f_{D_n}^{(i)}(\tau)d\tau, \quad n = 1, \ldots, N, \tag{1}$$

where $f_{D_n}^{(i)}$ is the Doppler measurement made by the i-th receiver on the n-th cellular SOP, $\phi_n^{(i)}(t_0)$ is the initial carrier phase, and N is the total number of SOPs. In (1), i denotes either the base (B) or the rover UAV (U). Assuming a constant Doppler during a subaccumulation period T, (1) can be discretized to yield

$$\phi_n^{(i)}(t_k) = \phi_n^{(i)}(t_0) + \sum_{l=0}^{k-1} f_{D_n}^{(i)}(t_l)T, \tag{2}$$

where $t_k \triangleq t_0 + kT$. In what follows, the time argument t_k will be replaced by k for simplicity of notation. Note that the receiver will make noisy carrier phase measurements. Adding measurement noise to (2) and expressing the carrier phase observable in meters yields

$$z_n^{(i)}(k) = \lambda\phi_n^{(i)} + \lambda T \sum_{l=0}^{k-1} f_{D_n}^{(i)}(l) + v_n^{(i)}(k), \tag{3}$$

where λ is the wavelength of the carrier signal and $v_n^{(i)}(k)$ is the measurement noise, which is modeled as a discrete-time zero-mean white Gaussian sequence with variance $[\sigma_n^{(i)}(k)]^2$. The carrier phase in (3) can be parameterized in terms of the receiver and cellular SOP states as

$$\begin{aligned} z_n^{(i)}(k) = & \sqrt{\|\boldsymbol{r}_{r_i}(k) - \boldsymbol{r}_{s_n}\|_2^2 + \Delta z_{r_i,s_n}^2(k)} \\ & + c\left[\delta t_{r_i}(k) - \delta t_{s_n}(k)\right] + \lambda N_n^{(i)} + v_n^{(i)}(k), \end{aligned} \tag{4}$$

where $\boldsymbol{r}_{r_i} \triangleq [x_{r_i}, y_{r_i}]^{\mathsf{T}}$ is the receiver's two-dimensional (2–D) position vector; $\boldsymbol{r}_{s_n} \triangleq [x_{s_n}, y_{s_n}]^{\mathsf{T}}$ is the cellular BTS's known 2–D position vector; $\Delta z_{r_i,s_n} \triangleq z_{r_i}(k) - z_{s_n}$ is the difference between the receiver' and BTS's altitude; c is the speed of light; δt_{r_i} and δt_{s_n} are the receiver's and cellular BTS's clock biases, respectively; and $N_n^{(i)}$ is the carrier phase ambiguity. Note that a coherent PLL may be employed in CDMA and LTE navigation receivers since the cellular synchronization and reference signals do not carry any data. As such, the measurement noise variance can be expressed as [41]

$$\left[\sigma_n^{(i)}(k)\right]^2 = \lambda^2 \frac{B_{i,\text{PLL}}}{C/N_{0,n}(k)}, \tag{5}$$

Authorized licensed use limited to: The Ohio State University. Downloaded on April 13,2023 at 05:03:54 UTC from IEEE Xplore. Restrictions apply.

where $B_{i,\text{PLL}}$ is the receiver's PLL noise equivalent bandwidth and $C/N_{0,n}(k)$ is the cellular SOP's measured carrier-to-noise ratio at time-step k. The remainder of this paper assumes zero-mean Gaussian measurement noise. The actual measurement noise statistics may differ from the what is assumed in (5). Therefore, instead of using (5), Gaussian overbounds of the true measurement noise distribution could be used, if known. Methods described in [57]–[59] could be used to compute overbounds of the measurement noise statistics in different environments. Note that small UAVs and hearable cellular BTSs are typically at comparable altitudes, which makes the vertical diversity very poor. Therefore, one can only estimate the UAV's horizontal position using cellular SOPs without introducing significant errors. As such, the proposed framework assumes that the UAV and BTS altitudes, $z_r(k)$ and z_{s_n}, respectively, are known and only the UAV's 2–D position is estimated.

It is important to note that the channels between the UAVs and the cellular BTSs do not suffer from severe multipath, as a strong LOS component is usually observed in the received signal [60], [61]. In the case of severe multipath or non-LOS (NLOS) conditions, it is assumed that either (i) signal processing techniques at the SOP receiver level [24], [28], [56], [62]–[67] or (ii) measurement outlier rejection techniques [57] are used to mitigate mulitpath or exclude measurements with large errors due to multipath. Concepts of receiver autonomous integrity monitoring (RAIM) may also be used to exclude measurements with large errors, which can be considered as faulty measurements [68]–[71]. Alternatively, multipath error models may be used to predict and mitigate large measurement errors, either through multipath prediction maps [58], [72] or statistical models [73]. To this end, it is assumed in the rest of the paper that the effect of multipath has either (i) been mitigated or (ii) included in the measurement model (4).

III. Navigation with Carrier Phase Differential Cellular Measurements

This section develops the CD-cellular navigation framework and establishes guarantees on its achievable performance. The framework consists of two receivers in an environment comprising N cellular BTSs. The receivers are assumed to be listening to the same BTSs, with the BTS locations being known. The first receiver, referred to as the base (B), is assumed to have knowledge of its own position state (e.g., a stationary receiver deployed at a surveyed location or a high-flying aerial vehicle with access to GNSS). The second receiver, referred to as the rover UAV (U), does not know its position and aims to navigate using the CD-cellular framework. The base communicates its own position and carrier phase observables with the rover. Fig. 1 illustrates the base/rover framework.

A. CD-Cellular Measurement Model

In what follows, the objective is to estimate the rover's position, which will be achieved by double-differencing the measurements (4). It is subsequently assumed that the UAV and the base are within the same sector of a particular BTS. As such, there will be clock bias discrepancies due to sector mismatch

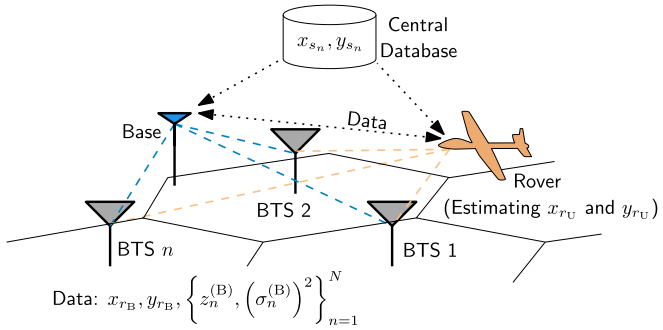

Fig. 1. CD-cellular base/rover framework.

[20]. Without loss of generality, let the measurements to the first SOP be taken as references to form the single difference

$$z_{n,1}^{(i)}(k) \triangleq z_n^{(i)}(k) - z_1^{(i)}(k), \tag{6}$$

for $n = 2, \ldots, N$. Subsequently, define the double difference between U and B as

$$\begin{aligned} z_{n,1}^{(\text{U,B})}(k) &\triangleq z_{n,1}^{(\text{U})}(k) - z_{n,1}^{(\text{B})}(k) \\ &\quad + \sqrt{\|\boldsymbol{r}_{r_\text{B}}(k) - \boldsymbol{r}_{s_n}\|_2^2 + \Delta z_{r_\text{B},s_n}^2(k)} \\ &\quad - \sqrt{\|\boldsymbol{r}_{r_\text{B}}(k) - \boldsymbol{r}_{s_1}\|_2^2 + \Delta z_{r_\text{B},s_1}^2(k)} \\ &\triangleq h_{n,1}^{(\text{U})}(k) + \lambda N_{n,1}^{(\text{U,B})} + v_{n,1}^{(\text{U,B})}(k), \end{aligned} \tag{7}$$

where $h_{n,1}{}^{(\text{U})}(k) \triangleq \sqrt{\|\boldsymbol{r}_{r_\text{U}}(k) - \boldsymbol{r}_{s_n}\|_2^2 + \Delta z_{r_\text{U},s_n}^2(k)} - \sqrt{\|\boldsymbol{r}_{r_\text{U}}(k) - \boldsymbol{r}_{s_1}\|_2^2 + \Delta z_{r_\text{U},s_1}^2(k)}$, $N_{n,1}^{(\text{U,B})} \triangleq N_n^{(\text{U})} - N_n^{(\text{B})} - N_1^{(\text{U})} + N_1^{(\text{B})}$, $v_{n,1}^{(\text{U,B})}(k) \triangleq v_n^{(\text{U})}(k) - v_n^{(\text{B})}(k) - v_1^{(\text{U})}(k) + v_1^{(\text{B})}(k)$, and $n = 2, \ldots, N$. Note that (7) holds only when the UAV and base carrier phase measurements are synchronized. Synchronization is done using the cellular system time. The detected reference signals are used to synchronize the measurements from both receivers. Synchronization errors between the base and UAV receivers translate to differencing carrier phase measurements shifted in time. As such, the residual error in this case will be a function of the synchronization error Δt, the UAV speed v, and the receiver drifts $\dot{\delta}t$. It can be shown that the residual CD-cellular measurement error Δz due to synchronization errors between the base and rover is bounded according to

$$|\Delta z| \leq 2(v_\text{max} + \dot{\delta}t_\text{max})\Delta t, \tag{8}$$

where v_max is the maximum UAV speed and $\dot{\delta}t_\text{max}$ is the maximum clock drift. It is shown in [44] that in typical open semi-urban cells, the synchronization error is less than 60 μs. As such, for $v_\text{max} = 14$ m/s, which is considered high for small UAVs, and a 150 Hz drift at a carrier frequency of 882.75 MHz for the receiver clocks, which was observed from experimental data, the residual errors in the CD-cellular measurement will be less than 8 mm according to (8). Therefore, full synchronization is assumed. In vector form, the measurement model (7) becomes

$$\boldsymbol{z}_{\text{U,B}}(k) \triangleq \boldsymbol{h}\left[\boldsymbol{r}_{r_\text{U}}(k)\right] + \lambda \boldsymbol{N} + \boldsymbol{v}_{\text{U,B}}(k), \tag{9}$$

Authorized licensed use limited to: The Ohio State University. Downloaded on April 13,2023 at 05:03:54 UTC from IEEE Xplore. Restrictions apply.

where

$$\boldsymbol{z}_{\mathrm{U,B}}(k) \triangleq \left[z_{2,1}^{(\mathrm{U,B})}(k), \ldots, z_{N,1}^{(\mathrm{U,B})}(k)\right]^{\mathsf{T}}$$

$$\boldsymbol{h}\left[\boldsymbol{r}_{r_{\mathrm{U}}}(k)\right] \triangleq \left[h_{2,1}^{(\mathrm{U})}(k), \ldots, h_{N,1}^{(\mathrm{U})}(k)\right]^{\mathsf{T}}$$

$$\boldsymbol{N} \triangleq \left[N_{2,1}^{(\mathrm{U,B})}, \ldots, N_{N,1}^{(\mathrm{U,B})}\right]^{\mathsf{T}}$$

$$\boldsymbol{v}_{\mathrm{U,B}}(k) \triangleq \left[v_{2,1}^{(\mathrm{U,B})}(k), \ldots, v_{N,1}^{(\mathrm{U,B})}(k)\right]^{\mathsf{T}},$$

where $\boldsymbol{v}_{\mathrm{U,B}}(k)$ has a covariance $\mathbf{R}_{\mathrm{U,B}}(k)$, which can be readily shown to be

$$\mathbf{R}_{\mathrm{U,B}}(k) = \mathbf{R}^{(1)}(k) + \left[\sigma_1^{(\mathrm{U,B})}(k)\right]^2 \mathbf{1}_{N-1}\mathbf{1}_{N-1}^{\mathsf{T}}, \tag{10}$$

where $[\sigma_1^{(\mathrm{U,B})}(k)]^2 \triangleq [[\sigma_1^{(\mathrm{B})}(k)]^2 + [\sigma_1^{(\mathrm{U})}(k)]^2]$,

$$\mathbf{R}^{(1)}(k) \triangleq \mathrm{diag}\left[\left[\sigma_2^{(\mathrm{B})}(k)\right]^2 + \left[\sigma_2^{(\mathrm{U})}(k)\right]^2, \ldots, \left[\sigma_N^{(\mathrm{B})}(k)\right]^2 + \left[\sigma_N^{(\mathrm{U})}(k)\right]^2\right],$$

and $\mathbf{1}_{N-1}$ is an $(N-1)\times 1$ vector of ones. Note that the vector $\boldsymbol{N}$ is now a vector of $N-1$ integers and has to be solved for along with the rover UAV's position $\boldsymbol{r}_{r_{\mathrm{U}}}$. The next subsections present a framework to obtain a navigation solution with CD-cellular measurements.

B. Navigation Strategy

It is important to first establish the navigation strategy employed by the UAV. To this end, assume CD-cellular measurements are given at $k = 0, 1, 2, \ldots$. It is desired that, with probability greater than $1-\alpha$, the 2-norm of the position error be less than a desired threshold ζ for all $k \geq k_\zeta$. Let $\delta\boldsymbol{r}_{r_{\mathrm{U}}}(k)$ denote the position error at time-step k. Then, it is desired that

$$\Pr\left[\|\delta\boldsymbol{r}_{r_{\mathrm{U}}}(k)\|_2^2 \leq \zeta^2\right] \geq 1-\alpha, \quad \forall\, k \geq k_\zeta. \tag{11}$$

For $k < k_\zeta$, the UAV will use an EKF to produce a "rough" estimate of its position and the integer ambiguities. Measurements at $k=0$ and $k=1$ are used to initialize the EKF. Then, at $k = k_\zeta$, a batch weighted nonlinear least-squares (B-WNLS) estimator for all measurements from $k=0$ to k_ζ is used to obtain an estimate of the integer ambiguities that guarantees (11) for $k \geq k_\zeta$. The EKF solution is used to initialize the B-WNLS. For $k > k_\zeta$, the UAV will solve for its position using $\boldsymbol{z}_{\mathrm{U,B}}(k)$ and the estimated ambiguities through a point solution weighted nonlinear least-squares (PS-WNLS). The time-step k_ζ is determined on-the-fly by the UAV via the test developed in the remaining of this section. Fig. 2 summarizes the aforementioned navigation strategy.

The blocks in Fig. 2 are subsequently described.

C. EKF Model and Initialization

Define the vector $\boldsymbol{x}_{\mathrm{EKF}} \triangleq [\boldsymbol{r}_{r_{\mathrm{U}}}^{\mathsf{T}}, \dot{\boldsymbol{r}}_{r_{\mathrm{U}}}^{\mathsf{T}}, \boldsymbol{N}^{\mathsf{T}}]^{\mathsf{T}}$ as the state vector to be estimated by the EKF, where $\dot{\boldsymbol{r}}_{r_{\mathrm{U}}}^{\mathsf{T}}$ is the 2–D velocity vector of the UAV. The UAV's position and velocity states are assumed

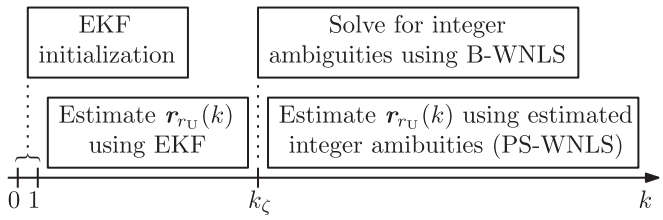

Fig. 2. Diagram of the proposed CD-cellular navigation strategy.

to evolve according to a velocity random walk model [31]. Note that only the float solution of $\boldsymbol{N}$ is estimated in the EKF, i.e., the integer constraint is relaxed. The EKF will produce an estimate $\hat{\boldsymbol{x}}_{\mathrm{EKF}}(k|j)$, i.e., an estimate of $\boldsymbol{x}_{\mathrm{EKF}}(k)$ using all measurements $\boldsymbol{z}_{\mathrm{U,B}}(k)$ up to time-step $j \leq k$, along with an estimation error covariance $\mathbf{P}_{\mathrm{EKF}}(k|j) \triangleq \mathbb{E}[\tilde{\boldsymbol{x}}_{\mathrm{EKF}}(k|j)\tilde{\boldsymbol{x}}_{\mathrm{EKF}}^{\mathsf{T}}(k|j)]$ where $\tilde{\boldsymbol{x}}_{\mathrm{EKF}}(k|j) \triangleq \boldsymbol{x}_{\mathrm{EKF}}(k) - \hat{\boldsymbol{x}}_{\mathrm{EKF}}(k|j)$ is the estimation error. The UAV's random walk dynamics and the measurement model in (9) are used to derive the EKF time-update and measurement-update equations. The EKF initialization is discussed next. Note that the measurement $\boldsymbol{z}_{\mathrm{U,B_{ini}}} \triangleq [\boldsymbol{z}_{\mathrm{U,B}}^{\mathsf{T}}(0), \boldsymbol{z}_{\mathrm{U,B}}^{\mathsf{T}}(1)]^{\mathsf{T}}$ may be parameterized as

$$\boldsymbol{z}_{\mathrm{U,B_{ini}}} = \begin{bmatrix}\boldsymbol{z}_{\mathrm{U,B}}(0)\\ \boldsymbol{z}_{\mathrm{U,B}}(1)\end{bmatrix} = \boldsymbol{h}_{\mathrm{ini}}\left[\boldsymbol{x}_{\mathrm{EKF}}(1)\right] + \boldsymbol{v}_{\mathrm{U,B_{ini}}}, \tag{12}$$

$$\boldsymbol{h}_{\mathrm{ini}}\left[\boldsymbol{x}_{\mathrm{EKF}}(1)\right] \triangleq \begin{bmatrix}\boldsymbol{h}\left[\boldsymbol{r}_{r_{\mathrm{U}}}(1) - T\dot{\boldsymbol{r}}_{r_{\mathrm{U}}}(1)\right] + \lambda\boldsymbol{N}\\ \boldsymbol{h}\left[\boldsymbol{r}_{r_{\mathrm{U}}}(1)\right] + \lambda\boldsymbol{N}\end{bmatrix},$$

where T is the sampling time and $\boldsymbol{v}_{\mathrm{U,B_{ini}}} \triangleq [\boldsymbol{v}_{\mathrm{U,B}}^{\mathsf{T}}(0), \boldsymbol{v}_{\mathrm{U,B}}^{\mathsf{T}}(1)]^{\mathsf{T}}$ is the overall initial measurement noise, which is modeled as a zero-mean Gaussian random vector with covariance $\mathbf{R}_{\mathrm{ini}} \triangleq \mathrm{diag}[\mathbf{R}_{\mathrm{U,B}}(0), \mathbf{R}_{\mathrm{U,B}}(1)]$. The measurement equation in (12) can be solved in a weighted nonlinear least-squares (WNLS) estimator (e.g., using the Gauss-Newton algorithm) with a weighting matrix $\mathbf{R}_{\mathrm{ini}}^{-1}$ [74]. Solving the WNLS yields an estimate of $\boldsymbol{x}_{\mathrm{EKF}}(1)$, denoted $\hat{\boldsymbol{x}}_{\mathrm{EKF,ini}}$, and an associated estimation error covariance, denoted $\mathbf{P}_{\mathrm{EKF,ini}}$. Finally, the EKF initial estimate and estimation error covariance are initialized according to

$$\hat{\boldsymbol{x}}_{\mathrm{EKF}}(1|1) \equiv \hat{\boldsymbol{x}}_{\mathrm{EKF,ini}}, \quad \mathbf{P}_{\mathrm{EKF}}(1|1) \equiv \mathbf{P}_{\mathrm{EKF,ini}}. \tag{13}$$

Note that the size of $\boldsymbol{z}_{\mathrm{U,B_{ini}}}$ must be greater than or equal to the size of $\boldsymbol{x}_{\mathrm{EKF}}$ to perform the steps described above, i.e., N must satisfy $K_B(N-1) \geq ((N-1)+4)$, where K_B is the batch size. In the case where $K_B = 2$, as in (12), then N must be 5 or more. If $N < 5$, then the batch size must be increased. However, N must satisfy $N \geq 2$, otherwise the CD-cellular measurements cannot be formed.

D. B-WNLS Solution

When $k = k_\zeta$, the B-WNLS estimate of the UAV's position and the integer ambiguities is computed. Define the collection of carrier phase measurements from time-step 0 to k_ζ as

$$\mathbf{z}_{\mathrm{U,B}}^{k_\zeta} \triangleq \left[\boldsymbol{z}_{\mathrm{U,B}}^{\mathsf{T}}(0), \ldots, \boldsymbol{z}_{\mathrm{U,B}}^{\mathsf{T}}(k_\zeta)\right]^{\mathsf{T}}, \tag{14}$$

Authorized licensed use limited to: The Ohio State University. Downloaded on April 13,2023 at 05:03:54 UTC from IEEE Xplore. Restrictions apply.

which can be expressed as

$$\mathbf{z}_{\mathrm{U,B}}^{k_\zeta} = \mathbf{h}\left[\mathbf{r}_{r_\mathrm{U}}^{k_\zeta}\right] + \lambda \bar{\mathbf{I}}^{k_\zeta} \boldsymbol{N} + \mathbf{v}_{\mathrm{U,B}}^{k_\zeta}, \tag{15}$$

$$\mathbf{r}_{r_\mathrm{U}}^{k_\zeta} \triangleq \begin{bmatrix} \boldsymbol{r}_{r_\mathrm{U}}(0) \\ \vdots \\ \boldsymbol{r}_{r_\mathrm{U}}(k_\zeta) \end{bmatrix}, \ \mathbf{v}_{\mathrm{U,B}}^{k_\zeta} \triangleq \begin{bmatrix} \boldsymbol{v}_{\mathrm{U,B}}(0) \\ \vdots \\ \boldsymbol{v}_{\mathrm{U,B}}(k_\zeta) \end{bmatrix},$$

$$\mathbf{h}\left[\mathbf{r}_{r_\mathrm{U}}^{k_\zeta}\right] \triangleq \begin{bmatrix} \boldsymbol{h}\left[\boldsymbol{r}_{r_\mathrm{U}}(0)\right] \\ \vdots \\ \boldsymbol{h}\left[\boldsymbol{r}_{r_\mathrm{U}}(k_\zeta)\right] \end{bmatrix}, \ \bar{\mathbf{I}}^{k_\zeta} \triangleq \begin{bmatrix} \mathbf{I}_{(N-1)\times(N-1)} \\ \vdots \\ \mathbf{I}_{(N-1)\times(N-1)} \end{bmatrix},$$

where $\mathbf{v}_{\mathrm{U,B}}^{k_\zeta}$ is the overall carrier phase measurement noise with covariance $\mathbf{R}_{\mathrm{U,B}}^{k_\zeta} \triangleq \mathrm{diag}[\mathbf{R}_{\mathrm{U,B}}(0), \ldots, \mathbf{R}_{\mathrm{U,B}}(k_\zeta)]$.

Let $\boldsymbol{x}_{\mathrm{B-WNLS}}^{k_\zeta} \triangleq [(\mathbf{r}_{r_\mathrm{U}}^{k_\zeta})^\mathsf{T}, \boldsymbol{N}^\mathsf{T}]^\mathsf{T}$ denote the parameters to be estimated. A B-WNLS estimator with weight matrix $(\mathbf{R}_{\mathrm{U,B}}^{k_\zeta})^{-1}$ is used to obtain an estimate $\hat{\boldsymbol{x}}_{\mathrm{B-WNLS}}^{k_\zeta} \triangleq [(\hat{\mathbf{r}}_{r_\mathrm{U}}^{k_\zeta})^\mathsf{T}, (\hat{\boldsymbol{N}}^{k_\zeta})^\mathsf{T}]^\mathsf{T}$ of $\boldsymbol{x}_{\mathrm{B-WNLS}}^{k}$ and an associated estimation error covariance $\mathbf{P}_{\mathrm{B-WNLS}}^{k_\zeta}$, given by

$$\mathbf{P}_{\mathrm{B-WNLS}}^{k_\zeta} = \begin{bmatrix} \mathbf{P}_{\mathbf{r}_\mathrm{U}}^{k_\zeta} & \mathbf{P}_{\mathbf{r}_\mathrm{U},\boldsymbol{N}}^{k_\zeta} \\ \left(\mathbf{P}_{\mathbf{r}_\mathrm{U},\boldsymbol{N}}^{k_\zeta}\right)^\mathsf{T} & \mathbf{P}_{\boldsymbol{N}}^{k_\zeta} \end{bmatrix}. \tag{16}$$

Note the dependency of $\hat{\boldsymbol{N}}^{k_\zeta}$ on k_ζ.

The vector $\boldsymbol{N}$ consists of integers; however, its estimate, the vector $\hat{\boldsymbol{N}}^{k_\zeta}$, is not necessarily a vector of integers. As such, the vector $\hat{\boldsymbol{N}}^{k_\zeta}$ must be "fixed" to the correct integers. This is achieved using the LAMBDA method [49], which produces the vector of fixed integers denoted by $\check{\boldsymbol{N}}^{k_\zeta}$ obtained from the float solution $\hat{\boldsymbol{N}}^{k_\zeta}$ and $\mathbf{P}_{\boldsymbol{N}}^{k_\zeta}$. Specifically, the vector $\check{\boldsymbol{N}}^{k_\zeta}$ is defined as

$$\check{\boldsymbol{N}}^{k_\zeta} \triangleq \underset{\boldsymbol{N}\in\mathbb{Z}^{N-1}}{\mathrm{argmin}} \left[\left(\hat{\boldsymbol{N}}^{k_\zeta} - \boldsymbol{N}\right)^\mathsf{T} \left(\mathbf{P}_{\boldsymbol{N}}^{k_\zeta}\right)^{-1} \left(\hat{\boldsymbol{N}}^{k_\zeta} - \boldsymbol{N}\right)\right], \tag{17}$$

where $\mathbb{Z}$ is the set of integers. After fixing the integer ambiguities, the UAV's fixed position estimates $\check{\mathbf{r}}_{r_\mathrm{U}}^{k}$ are obtained according to

$$\check{\mathbf{r}}_{r_\mathrm{U}}^{k_\zeta} = \hat{\mathbf{r}}_{r_\mathrm{U}}^{k_\zeta} - \mathbf{P}_{\mathbf{r}_\mathrm{U},\boldsymbol{N}}^{k_\zeta} \mathbf{P}^{k_\zeta\,-1}_{\boldsymbol{N}} \left(\hat{\boldsymbol{N}}^{k_\zeta} - \check{\boldsymbol{N}}^{k_\zeta}\right). \tag{18}$$

Note that the B-WNLS solution is initialized with the EKF estimates of the UAV positions and ambiguities.

E. PS-WNLS

Once the integer ambiguities are determined, the carrier phase measurements at time-step $k \geq k_\zeta$ are used to determine the point solution $\hat{\boldsymbol{r}}_{r_\mathrm{U}}(k)$ and an associated estimation error covariance $\mathbf{P}_{\boldsymbol{r}_\mathrm{U}}(k)$ using a WNLS, i.e., the estimate of $\boldsymbol{r}_{r_\mathrm{U}}(k)$ using $\boldsymbol{z}_{\mathrm{U,B}}(k)$ and $\tilde{\boldsymbol{N}}^{k_\zeta}$ through a WNLS. To this end, define the integer ambiguity estimation error as $\tilde{\boldsymbol{N}}^{k_\zeta} \triangleq \boldsymbol{N} - \check{\boldsymbol{N}}^{k_\zeta}$. Hence, the carrier phase measurement vector for $k \geq k_\zeta$ can be parameterized by

$$\boldsymbol{z}_{\mathrm{U,B}}(k) \triangleq \boldsymbol{h}\left[\boldsymbol{r}_{r_\mathrm{U}}(k)\right] + \lambda \check{\boldsymbol{N}}^{k_\zeta} + \lambda \tilde{\boldsymbol{N}}^{k_\zeta} + \boldsymbol{v}_{\mathrm{U,B}}(k). \tag{19}$$

The difference between (9) and (19) is that now an estimate of $\boldsymbol{N}$ is known to the UAV, and it can therefore estimate its position vector instantaneously using $\boldsymbol{z}_{\mathrm{U,B}}(k)$. However, $\lambda\tilde{\boldsymbol{N}}^{k_\zeta}$ is now introduced as an additional measurement error, where $\tilde{\boldsymbol{N}}^{k_\zeta}$ can be modeled as a zero-mean random vector with covariance $\mathbf{P}_{\boldsymbol{N}}^{k_\zeta}$. The weight matrix in the PS-WNLS is chosen to be

$$\boldsymbol{\Sigma}^{-1}(k) \triangleq \left[\lambda^2 \mathbf{P}_{\boldsymbol{N}}^{k_\zeta} + \mathbf{R}_{\mathrm{U,B}}(k)\right]^{-1}. \tag{20}$$

In the following sections, k_ζ is determined to satisfy (11) $\forall\, k \geq k_\zeta$. To this end, the position error is first probabilistically upper bounded and a test on k is derived to determine when (11) will hold.

F. Probabilistic Position Error Upper Bound

The carrier phase measurement noise standard deviation calculated from (5) is on the order of a 1.5 cm for a carrier-to-noise ratio of 35 dB-Hz and a wavelength of 34 cm (800 MHz cellular band). Moreover, typical carrier-to-noise ratios for cellular signals are observed to be much higher than 35 dB-Hz for low-altitude receivers, reaching 60 dB-Hz or more in the case of LTE and 5G signal [37]. As such, it is assumed that the contribution of $\boldsymbol{v}_{\mathrm{U,B}}(k)$ to the estimation error is insignificant compared to $\tilde{\boldsymbol{N}}^{k_\zeta}$. The position error due to $\tilde{\boldsymbol{N}}^{k_\zeta}$ can be approximated by

$$\delta\boldsymbol{r}_{r_\mathrm{U}}(k) = \lambda \left[\tilde{\mathbf{G}}^\mathsf{T}(k)\boldsymbol{\Sigma}^{-1}(k)\tilde{\mathbf{G}}(k)\right]^{-1} \tilde{\mathbf{G}}^\mathsf{T}(k)\boldsymbol{\Sigma}^{-1}(k)\tilde{\boldsymbol{N}}^{k_\zeta}, \tag{21}$$

$$\tilde{\mathbf{G}}(k) = \begin{bmatrix} \frac{\hat{\boldsymbol{r}}_{r_\mathrm{U}}^\mathsf{T}(k) - \boldsymbol{r}_{s_2}^\mathsf{T}}{\sqrt{\left\|\hat{\boldsymbol{r}}_{r_\mathrm{U}}(k) - \boldsymbol{r}_{s_2}\right\|_2^2 + \Delta z_{r_\mathrm{U},s_2}^2(k)}} - \frac{\hat{\boldsymbol{r}}_{r_\mathrm{U}}^\mathsf{T}(k) - \boldsymbol{r}_{s_1}^\mathsf{T}}{\sqrt{\left\|\hat{\boldsymbol{r}}_{r_\mathrm{U}}(k) - \boldsymbol{r}_{s_1}\right\|_2^2 + \Delta z_{r_\mathrm{U},s_1}^2(k)}} \\ \vdots \\ \frac{\hat{\boldsymbol{r}}_{r_\mathrm{U}}^\mathsf{T}(k) - \boldsymbol{r}_{s_N}^\mathsf{T}}{\sqrt{\left\|\hat{\boldsymbol{r}}_{r_\mathrm{U}}(k) - \boldsymbol{r}_{s_N}\right\|_2^2 + \Delta z_{r_\mathrm{U},s_N}^2(k)}} - \frac{\hat{\boldsymbol{r}}_{r_\mathrm{U}}^\mathsf{T}(k) - \boldsymbol{r}_{s_1}^\mathsf{T}}{\sqrt{\left\|\hat{\boldsymbol{r}}_{r_\mathrm{U}}(k) - \boldsymbol{r}_{s_1}\right\|_2^2 + \Delta z_{r_\mathrm{U},s_1}^2(k)}} \end{bmatrix}. \tag{22}$$

The estimation error covariance associated with the position estimate is expressed as

$$\mathbf{P}_{\boldsymbol{r}_\mathrm{U}}(k) = \left[\tilde{\mathbf{G}}^\mathsf{T}(k)\boldsymbol{\Sigma}^{-1}(k)\tilde{\mathbf{G}}(k)\right]^{-1}. \tag{23}$$

In what follows, the time argument will be omitted for compactness of notation. Let $\boldsymbol{\Sigma}^{\frac{1}{2}}$ denote a square root of $\boldsymbol{\Sigma}$. Using the submultiplicative property of the 2-norm, it can be shown from (21) that

$$\|\delta\boldsymbol{r}_{r_\mathrm{U}}\|_2^2 \leq \lambda^2 \left\|\left[\tilde{\mathbf{G}}^\mathsf{T}\boldsymbol{\Sigma}^{-1}\tilde{\mathbf{G}}\right]^{-1} \tilde{\mathbf{G}}^\mathsf{T}\boldsymbol{\Sigma}^{-\frac{1}{2}}\right\|_2^2 \left\|\boldsymbol{\Sigma}^{-\frac{1}{2}}\tilde{\boldsymbol{N}}^{k_\zeta}\right\|_2^2. \tag{24}$$

Using the fact that the square of the 2-norm of some real matrix $\mathbf{A}$ is the maximum eigenvalue of $\mathbf{A}\mathbf{A}^\mathsf{T}$ [75, p. 266 & 341], denoted by $\lambda_{\max}(\mathbf{A}\mathbf{A}^\mathsf{T})$, the term $\|[\tilde{\mathbf{G}}^\mathsf{T}\boldsymbol{\Sigma}^{-1}\tilde{\mathbf{G}}]^{-1}\tilde{\mathbf{G}}^\mathsf{T}\boldsymbol{\Sigma}^{-\frac{1}{2}}\|_2^2$ is calculated to be

$$\begin{aligned} \left\|\left[\tilde{\mathbf{G}}^\mathsf{T}\boldsymbol{\Sigma}^{-1}\tilde{\mathbf{G}}\right]^{-1} \tilde{\mathbf{G}}^\mathsf{T}\boldsymbol{\Sigma}^{-\frac{1}{2}}\right\|_2^2 &= \lambda_{\max}\left(\left[\tilde{\mathbf{G}}^\mathsf{T}\boldsymbol{\Sigma}^{-1}\tilde{\mathbf{G}}\right]^{-1}\right) \\ &= \lambda_{\max}\left(\mathbf{P}_{\boldsymbol{r}_\mathrm{U}}\right), \end{aligned} \tag{25}$$

Authorized licensed use limited to: The Ohio State University. Downloaded on April 13,2023 at 05:03:54 UTC from IEEE Xplore. Restrictions apply.

where the last equality follows from (23). Subsequently, $\|\delta \boldsymbol{r}_{r_{\mathrm{U}}}\|_2^2$ can be further bounded according to

$$\|\delta \boldsymbol{r}_{r_{\mathrm{U}}}\|_2^2 \leq \lambda^2 \lambda_{\max}\left(\mathbf{P}_{\boldsymbol{r}_{\mathrm{U}}}\right) \left\|\boldsymbol{\Sigma}^{-\frac{1}{2}} \tilde{\boldsymbol{N}}^{k_\zeta}\right\|_2^2. \tag{26}$$

Note that

$$\begin{aligned}\mathbf{P}_{\boldsymbol{r}_{\mathrm{U}}} &\preceq \lambda_{\max}\left(\boldsymbol{\Sigma}\right)\left(\tilde{\mathbf{G}}^{\mathsf{T}}\tilde{\mathbf{G}}\right)^{-1} \\ &\preceq \lambda_{\max}\left(\boldsymbol{\Sigma}\right) \underbrace{\operatorname{trace}\left[\left(\tilde{\mathbf{G}}^{\mathsf{T}}\tilde{\mathbf{G}}\right)^{-1}\right]}_{\triangleq \mathrm{HDOP}^2} \mathbf{I}_{2\times 2},\end{aligned} \tag{27}$$

where the horizontal dilution of precision (HDOP) depends on the current geometry between the UAV and the cellular BTSs. With probability β, the HDOP is probabilistically upper bounded according to

$$\Pr\left[\mathrm{HDOP} \leq \mathrm{HDOP}_{\max}\right] = \beta, \tag{28}$$

where $\mathrm{HDOP}_{\max}$ can be calculated in advance from the known cellular BTS using stochastic geometry models, as discussed in the next subsection. Subsequently, $\lambda_{\max}(\mathbf{P}_{\boldsymbol{r}_{\mathrm{U}}})$ can be bounded according to

$$\lambda_{\max}\left(\mathbf{P}_{\boldsymbol{r}_{\mathrm{U}}}\right) \leq \lambda_{\max}\left(\boldsymbol{\Sigma}\right) \mathrm{HDOP}_{\max}^2, \tag{29}$$

which in turn implies that with a probability greater than β, the following holds

$$\|\delta \boldsymbol{r}_{r_{\mathrm{U}}}\|_2^2 \leq \lambda^2 \lambda_{\max}\left(\boldsymbol{\Sigma}\right) \mathrm{HDOP}_{\max}^2 \left\|\boldsymbol{\Sigma}^{-\frac{1}{2}} \tilde{\boldsymbol{N}}^{k_\zeta}\right\|_2^2. \tag{30}$$

G. Determination of $HDOP_{max}$

In order to determine the distribution of HDOP and hence $\mathrm{HDOP}_{\max}$, stochastic geometry is used to model the relative geometry between the UAV and BTSs. Specifically, the BTS positions are modeled as a binomial point process (BPP) and the total number of hearable BTSs is assumed to be known [76], [77]. The BTS position distribution is parameterized by the minimum and maximum hearable distance to a BTS, denoted by $d_{\min}$ and $d_{\max}$, respectively. However, the HDOP can be parameterized by the bearing angles only; hence, the dependency on $d_{\min}$ and $d_{\max}$ is eliminated. Then, several realizations of the BTS bearing angles are realized for a given value of N and the empirical cumulative density function (cdf) of the HDOP is characterized. Finally, the value $\mathrm{HDOP}_{\max}$ is identified from the emprical cdf for a desired β. Fig. 3(a) illustrates a realization of the BPP for $N = 15$ ($d_{\min} = 50$ m and $d_{\max} = 5000$ m) and Fig. 3(b) shows $\mathrm{HDOP}_{\max}$ for various N and β obtained from 10^5 BPP realizations.

H. Probabilistic Integer Ambiguity Error Upper Bound

With a probability greater than $1-p$, $\tilde{\boldsymbol{N}}^{k_\zeta}$ will be within the confidence region defined as

$$\left(\tilde{\boldsymbol{N}}^{k_\zeta}\right)^{\mathsf{T}} \left(\mathbf{P}_{\boldsymbol{N}}^{k_\zeta}\right)^{-1} \tilde{\boldsymbol{N}}^{k_\zeta} \leq \gamma(p), \tag{31}$$

where $\gamma(p) \triangleq f^{-1}_{\chi^2,N-1}(1-p)$ and $f^{-1}_{\chi^2,M}(\cdot)$ is the inverse cdf of a chi-square distributed random variable with M degrees of freedom. Note that the left-hand side of (31) would not be chi-square distributed in the presence of unmodeled errors such as multipath biases due to deep fading or cycle slips. In such cases, the measurement noise variance must be inflated to overbound these unmodeled errors. This can be investigated further in future work. By defining

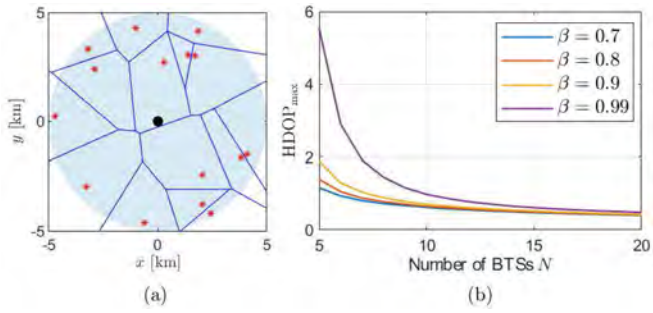

Fig. 3. (a) Voronoi diagram for a realization of the BPP for $N = 15$. The red asterisks indicate the BTS locations and the black disc at the origin inidcates the UAV location. The shaded blue area is the ring defined between $d_{\min}$ and $d_{\max}$. (b) $\mathrm{HDOP}_{\max}$ that satisfies $\Pr[\mathrm{HDOP} \leq \mathrm{HDOP}_{\max}] = \beta$ for various N and β values. The empirical cdf of the HDOP was calculated from 10^5 BPP realizations.

$$\bar{\mathbf{P}}_{\boldsymbol{N}}^{k_\zeta} \triangleq \boldsymbol{\Sigma}^{-\frac{1}{2}} \mathbf{P}_{\boldsymbol{N}}^{k_\zeta} \boldsymbol{\Sigma}^{-\frac{1}{2}}, \tag{32}$$

the inequality in (31) may be re-written as

$$\left(\boldsymbol{\Sigma}^{-\frac{1}{2}} \tilde{\boldsymbol{N}}^{k_\zeta}\right)^{\mathsf{T}} \left(\bar{\mathbf{P}}_{\boldsymbol{N}}^{k_\zeta}\right)^{-1} \boldsymbol{\Sigma}^{-\frac{1}{2}} \tilde{\boldsymbol{N}}^{k_\zeta} \leq \gamma(p). \tag{33}$$

Note that (33) implies the inequality

$$\Pr\left[\left\|\boldsymbol{\Sigma}^{-\frac{1}{2}} \tilde{\boldsymbol{N}}^{k_\zeta}\right\|_2^2 \leq \lambda_{\max}\left(\bar{\mathbf{P}}_{\boldsymbol{N}}^{k_\zeta}\right) \gamma(p)\right] \geq 1-p. \tag{34}$$

I. Eigenvalue Test for Batch Size Determination

Assuming that the HDOP and $\tilde{\boldsymbol{N}}$ are independent, the following inequality holds

$$\begin{aligned}&\Pr\left[\|\delta \boldsymbol{r}_{r_{\mathrm{U}}}\|_2^2 \leq \lambda^2 \lambda_{\max}(\boldsymbol{\Sigma})\, \mathrm{HDOP}_{\max}^2 \lambda_{\max}\left(\bar{\mathbf{P}}_{\boldsymbol{N}}^{k_\zeta}\right) \gamma(p)\right] \\ &\quad \geq \beta(1-p).\end{aligned} \tag{35}$$

Recall that (11) is desired; therefore, satisfying

$$\begin{aligned}&\lambda^2 \lambda_{\max}\left(\boldsymbol{\Sigma}\right) \mathrm{HDOP}_{\max}^2 \lambda_{\max}\left(\bar{\mathbf{P}}_{\boldsymbol{N}}^{k_\zeta}\right) \gamma(p) \leq \zeta^2 \\ &\qquad \Rightarrow \quad \lambda_{\min}\left(\left(\bar{\mathbf{P}}_{\boldsymbol{N}}^{k_\zeta}\right)^{-1}\right) \geq g\left(\zeta, p\right),\end{aligned} \tag{36}$$

achieves (11), where $\lambda_{\min}(\mathbf{A})$ denotes the smallest eigenvalue of matrix $\mathbf{A}$, $g(\zeta,p) \triangleq (\frac{1}{\zeta^2})[\lambda^2 \lambda_{\max}(\boldsymbol{\Sigma}) \mathrm{HDOP}_{\max}^2 \gamma(p)]$, and $p = 1-(1-\alpha)/\beta$. Note that the inequality in (36) is in the form of a test that can be performed after each measurement is added to the batch filter.

Remark: It is easier to compute $(\bar{\mathbf{P}}_{\boldsymbol{N}}^{k_\zeta})^{-1}$ rather than $\bar{\mathbf{P}}_{\boldsymbol{N}}^{k_\zeta}$ without having to solve the batch WNLS; hence, the test is on $\lambda_{\min}((\bar{\mathbf{P}}_{\boldsymbol{N}}^{k_\zeta})^{-1})$. Appendix A shows that the inversion of 2×2 matrices only is needed to compute $(\bar{\mathbf{P}}_{\boldsymbol{N}}^{k_\zeta})^{-1}$.

Authorized licensed use limited to: The Ohio State University. Downloaded on April 13,2023 at 05:03:54 UTC from IEEE Xplore. Restrictions apply.

IV. Experimental Results

This section presents experimental results demonstrating submeter-level UAV navigation results via the framework developed in this paper. As mentioned in Section III, only the 2–D position of the UAV is estimated as its altitude may be obtained using other sensors (e.g., altimeter). The UAV's position is estimated in the horizontal plane of an East-North-Up (ENU) frame centered at the average of the BTS positions. In the following experiments, the altitude of the UAV was obtained from its on-board navigation system. Alternatively, the UAV's altitude may be obtained from a barometric altimeter. Moreover, the noise equivalent bandwidths of the receivers' PLLs were set to $B_{\mathrm{U,PLL}} = B_{\mathrm{B,PLL}} = B_{\mathrm{PLL}} = 3$ Hz in all experiments and the measurement noise covariances were calculated according to (5).

A. Experimental Layout and Setup

In order to demonstrate the CD-cellular framework discussed in Section III, two Autel Robotics X-Star Premium UAVs were equipped each with an Ettus E312 universal software radio peripheral (USRP), a consumer-grade 800/1900 MHz cellular antenna, and a small consumer-grade GPS antenna to discipline the on-board oscillator for ground-truth collection. Note that one UAV acted as a base and the other as a navigating UAV. The base was mounted on a UAV since access to building roofs was restricted in the experiment area. The receivers were tuned to a 882.75 MHz carrier frequency (i.e., $\lambda = 33.96$ cm), which is a cellular CDMA channel allocated for the U.S. cellular provider Verizon Wireless. Samples of the received signals were stored for off-line post-processing. The cellular carrier phase measurements were given at a rate of 12.5 Hz, i.e., $T = 0.08$ s. The ground-truth reference for each UAV trajectory was taken from its on-board integrated navigation system, which uses GPS, an inertial measurement unit (IMU), and other sensors. The hovering horizontal precision of the Autel Robotics X-Star Premium UAVs are reported to be 2 m.

The navigating UAV's total traversed trajectory was 2.24 km, which was completed in 4 minutes with a total trajectory radius of 270 m. The trajectory radius is defined as the distance between the centre of the trajectory and the furthest point on the trajectory. Over the course of the experiment which took place in an open semi-urban environment and mulitpath-free, LOS conditions near Riverside, California, USA, the receivers were listening to 9 BTSs, whose 3–D positions were mapped prior to the experiment according to the framework in [78]. Some errors may arise due to uncertainties in the BTS positions, which were verified from Google Earth imagery. While the accuracy of Google Earth is not officially known, studies show that it is below 20 cm in the areas of interest [79]. A panorama of the environment from the UAV's vantage point is shown in Fig. 4, and the channel impulse response measured using the autocorrelation function of the CDMA shortcode for all 9 BTSs over 300 seconds is shown in Fig. 5. The curves in Fig. 5 demonstrate a dominant LOS component and nearly multipath-free conditions. Throughout the experiments, the UAV remained in the same BTS sectors as the base receiver. The CD-cellular measurements were used to estimate the navigating UAV's trajectory via the base/UAV framework developed in Section III. The experimental setup, the cellular BTS layout, and the true trajectory (from the UAV's on-board integrated navigation system) and estimated trajectory (from the proposed CD-cellular framework) of the navigating UAV are shown in Fig. 7. A plot of the carrier-to-noise ratios of all the BTSs measured by the rover and the time history of the delta ranges (deviation from the initial range) are given in Fig. 6(a) and Fig. 6(b), respectively. The base measured similar carrier-to-noise values.

Fig. 4. Panorama of the environment from the UAV's vantage point for the environment near Riverside, California, USA.

TABLE I
Experimental Results ($k_\zeta T = 120$ s)

	$k < k_\zeta$	$k \geq k_\zeta$	$\forall k$
Duration	120 s	120 s	240 s
Distance traveled	0.96 km	1.28 km	2.24 km
Trajectory radius	330 m	168 m	270 m
EKF RMSE	24.15 m	3.95 m	14.53 m
B–WNLS RMSE	65.79 cm	–	–
PS–WNLS RMSE	65.79 cm	74.83 cm	70.48 cm
No Test RMSE	–	–	12.26 m

B. Navigation Results

The probabilities β and α were set to 0.99 and 0.4, respectively, and the desired position error threshold was set to (i) $\zeta \equiv \zeta_1 = \sqrt{2}$ m and (ii) $\zeta \equiv \zeta_2 = 3$ m. For these parameters, $k_{\zeta_1}T$ was found to be 120 s and $k_{\zeta_2}T$ was found to be 99 s. The position RMSE for $k < k_{\zeta_1}$ was found to be 24.15 m (from the EKF), and 74.89 cm for $k \geq k_{\zeta_1}$ (from the PS-WNLS, after resolving the integer ambiguities through the B-WNLS). The estimated trajectories are also shown in Fig. 7 and the position error and associated $\pm 3\sigma$ bounds are shown in Fig. 8. Similarly, the position RMSE for $k < k_{\zeta_2}$ was found to be 24.15 m (from the EKF), and 2.65 m for $k \geq k_{\zeta_2}$. The time history of $\lambda_{\min}((\bar{\mathbf{P}}_{\boldsymbol{N}}^{k_\zeta})^{-1})$ is shown in Fig. 9(a) along with $g(\zeta_1, p)$ and $g(\zeta_2, p)$, and the empirical cdfs of the position RMSE for $k \geq 0$ and for $k \geq k_\zeta$ (after resolving the ambiguities through the B-WNLS) are shown in Fig. 9(b) and (c) for ζ_1 and ζ_2, respectively. The position RMSEs for each part of the trajectory are shown in Tables I and II for ζ_1 and ζ_2, respectively. It can be seen from Fig. 9(b) that $\Pr[\|\delta \boldsymbol{r}_{r_{\mathrm{U}}}\|_2^2 \leq \zeta_1^2] = 0.62 \geq 1 - \alpha$ and

Authorized licensed use limited to: The Ohio State University. Downloaded on April 13,2023 at 05:03:54 UTC from IEEE Xplore. Restrictions apply.

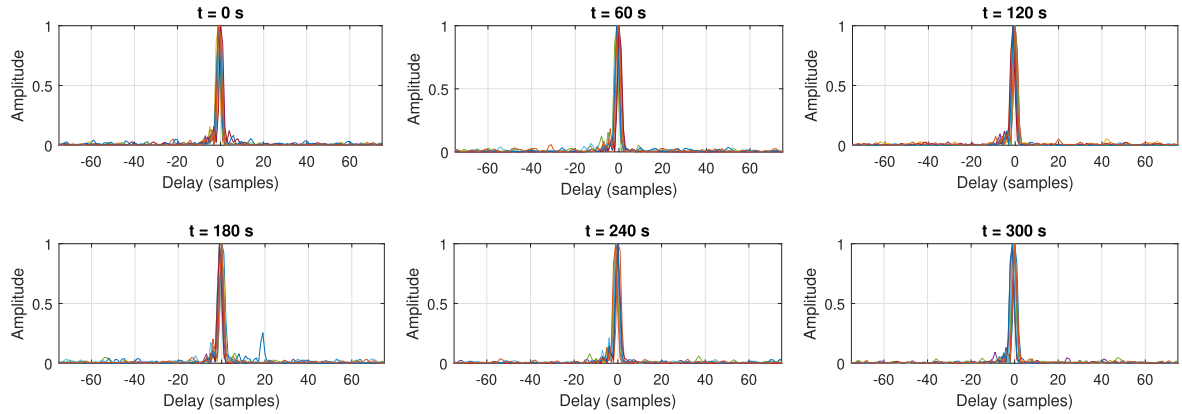

Fig. 5. Channel impulse response measured using the autocorrelation function of the CDMA shortcode for all 9 BTSs over 300 seconds in the environment near Riverside, California, USA.

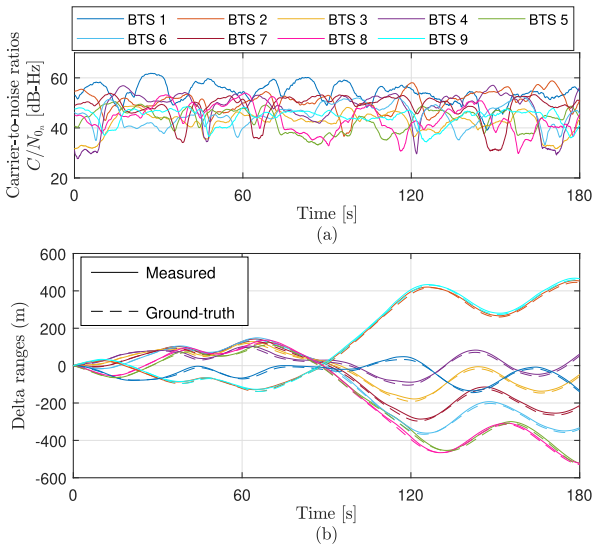

Fig. 6. (a) Carrier-to-noise ratios $\{C/N_{0_n}\}_{n=1}^{9}$ of all the cellular BTSs measured by the rover in the experiment. The carrier-to-noise ratios measured by the base were of similar values. (b) Measured and calculated delta ranges to all the cellular BTSs from the rover in the experiment. Similarly, the base's measured delta ranges closely matched the calculated delta ranges.

TABLE II
EXPERIMENTAL RESULTS ($k_\zeta T = 99$ S)

	$k < k_\zeta$	$k \geq k_\zeta$	$\forall k$
Duration	99 s	141 s	240 s
Distance traveled	0.68 km	1.56 km	2.24 km
Trajectory radius	175 m	282 m	270 m
EKF RMSE	22.11 m	4.05 m	14.53 m
B–WNLS RMSE	2.5 m	–	–
PS–WNLS RMSE	2.5 m	2.65 m	2.59 m
No Test RMSE	–	–	12.26 m

from Fig. 9(c) that $\Pr[\|\delta \boldsymbol{r}_{r_U}\|_2^2 \leq \zeta_2^2] = 0.88 \geq 1 - \alpha$, where α was chosen to be 0.4 for both experiments. This demonstrates that the proposed navigation strategy achieves the bounded-error requirement. For comparison, a navigation solution referred to as "No Test" trajectory was computed at the second time-step instead of determining k_ζ from the proposed test. The RMSE of

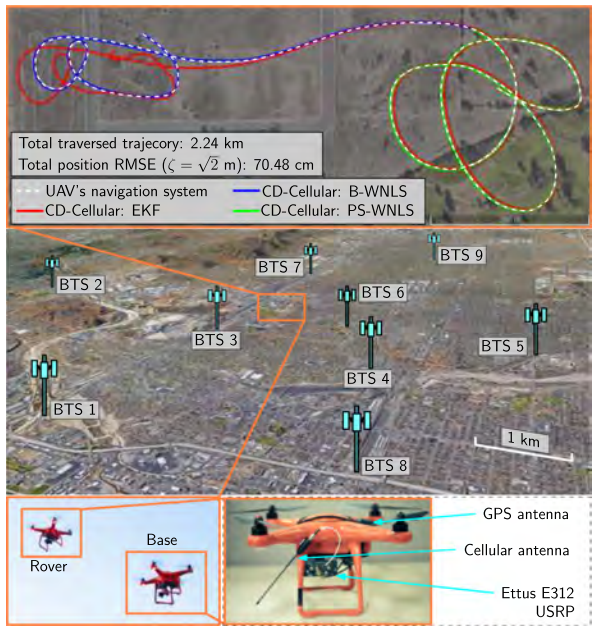

Fig. 7. Experimental setup, the cellular BTS layout, and the true trajectory (from the UAV's on-board integrated navigation system) and estimated trajectory (from the proposed CD-cellular framework for $\zeta = \sqrt{2}$ m) of the navigating UAV. The ground-truth trajectory is shown in white, the EKF trajectory estimate in red, the B-WNLS solution in blue, and the P-WNLS solution in green. The white curve coincides almost completely with the blue and green curves. Map data: Google Earth.

the No Test trajectory was found to be 12.26 m, which is also summarized in Table I and Table II.

It is important to note that the proposed CD-cellular framework is designed to guarantee a positioning performance under integer ambiguity errors only. However, when measurement noise dominates and in the presence of unmodeled errors (e.g., multipath), the effect the integer ambiguity errors may have on the positioning error becomes less significant. As a result, there is a fundamental lower bound on the position error that is a function of the unknown environment. This also implies that the proposed framework performs well in a practical regime of the design parameters α, β, ζ, and N. Nevertheless, the proposed method

Authorized licensed use limited to: The Ohio State University. Downloaded on April 13,2023 at 05:03:54 UTC from IEEE Xplore. Restrictions apply.

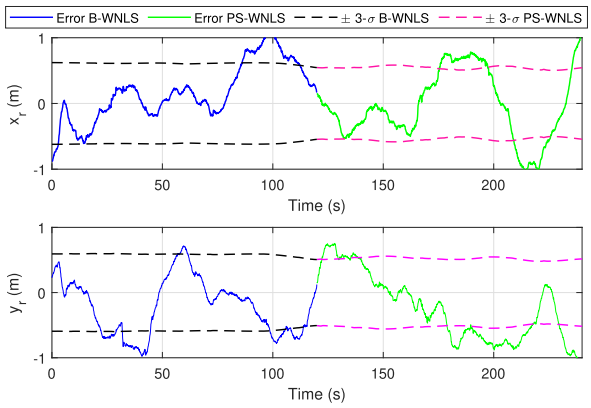

Fig. 8. Position error and associated ± 3-σ bounds for $\zeta = \sqrt{2}$ m.

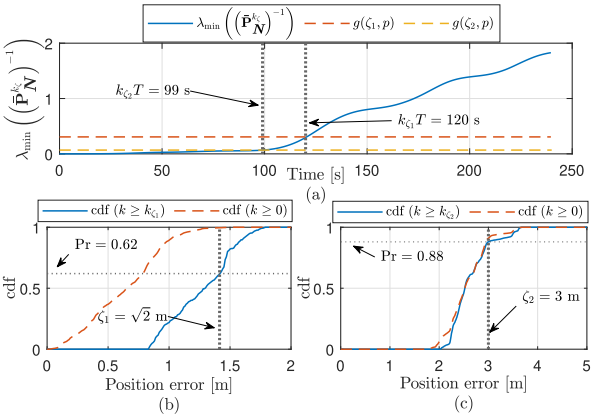

Fig. 9. (a) Time history of $\lambda_{\min}((\bar{\mathbf{P}}_{\boldsymbol{N}}^{k_\zeta})^{-1})$ and the thresholds $g(\zeta_1, p)$ and $g(\zeta_2, p)$. It can be seen that the tests are satisfied for $k_{\zeta_1}T = 120$ s and $k_{\zeta_2}T = 99$ s, respectively. (b) Cdf of the position error for $k \geq k_{\zeta_1}$ and $k \geq 0$, using the B-WNLS estimate for $k < k_{\zeta_1}$. It can be empirically seen that $\Pr\left[\|\delta \boldsymbol{r}_{r_U}\|_2^2 \leq \zeta_1^2\right] = 0.62 \geq 1 - \alpha$, where $\alpha = 0.4$. (c) Cdf of the position error for $k \geq k_{\zeta_2}$ and $k \geq 0$, using the B-WNLS estimate for $k < k_{\zeta_2}$. It can be empirically seen that $\Pr\left[\|\delta \boldsymbol{r}_{r_U}\|_2^2 \leq \zeta_2^2\right] = 0.88 \geq 1 - \alpha$, where $\alpha = 0.4$.

guarantees with a desired confidence level that the position error due to integer ambiguity errors remains below a desired threshold.

C. Discussion

The following are key takeaways and remarks from the experimental results presented above. First, it is important to note that the RMSEs were calculated with respect to the trajectory returned by the UAVs' on-board navigation system. Although these systems use multiple sensors for navigation, they are not equipped with high precision GPS receivers, e.g., RTK systems. Therefore, some errors are expected in what is considered to be "true" trajectories taken from the on-board sensors. The hovering horizontal precision of the UAVs are reported to be 2 m. It is worth noting that ideally, one would set the base to be stationary at an accurately surveyed position. However, considering the nature and limitations of the conducted experiment, the base was a hovering UAV. In such case, if the base's reported position from its GPS-INS system exhibited a bias, such bias would get consumed into the integer ambiguity term (cf. (7)), which is subsequently estimated. Note that the framework still achieved the desired performance on the rover UAV, despite the use of a non-stationary base UAV.

Second, the experiments showed that reliable navigation with cellular signals is possible when the proper models are used in an open semi-urban environment. The experiments lasted 4 minutes, indicating that the UAV could rely *exclusively* on cellular carrier phase measurements for sustained submeter-level accurate navigation. Note that the proposed framework does not account for unmodeled errors, such as multipath or signal blockage. Such errors could be partially mitigated (i) at the receiver level [24], [66], (ii) via outlier rejection techniques [57], [80], or (iii) included in the measurement model [59], [73], after which the proposed framework must be adapted. It is expected for the performance to degrade in the presence of such errors. Extending the proposed framework to account for such errors could be the subject of future work.

Third, not only the UAV can navigate at submeter-level accuracy in the absence of GPS signals, but it can do so with bounded errors. This is inherent to the formulation of the CD-cellular framework. Fig. 9(b) is clearly satisfying (11) for $\beta = 0.99$, $\alpha = 0.4$, and $\zeta = \sqrt{2}$ m.

Fourth, throughout the experiments, the UAV and base remained within the same BTS or eNB sectors. BTSs and eNBs typically transmit in three different sectors, each of which covering 120 degrees. When crossing between sectors, the receiver would need to perform a "handover," which involves acquiring and tracking the signal from the new sector [20]. The CD-cellular framework is robust against the BTS sectors not being completely synchronized when the UAV and the base are listening the same BTS sectors. However, errors in the measurements may be introduced when the UAV and base are in different sectors of a particular BTSs. One way to reduce the effect of the errors introduced by crossing BTS sectors is to use the approach proposed in [38].

Fifth, the distance between the base and rover varied from 272 m to 580 m throughout the experiment. The CD-cellular measurement model in (7) does not require a minimum or maximum separation between the base and navigating UAV. However, the maximum separation is dependent on the signal quality. It was shown in [44] that a cellular SOP receiver can acquire and track a BTS signal reliably up to a distance of 6 km. As such, the base and the UAV must each be within 6 km of a BTS to form differential measurement to that particular BTS. Several bases could be deployed to cover a larger area.

Sixth, in the CD-cellular framework formulation, the UAV-mounted receiver's clock bias is canceled by differencing measurements. As such, the magnitude of the receiver's clock bias should not affect the position estimate. This implies that the quality of the receiver's clock should not affect the navigation performance, as long as the receiver can maintain track of the signals.

Authorized licensed use limited to: The Ohio State University. Downloaded on April 13,2023 at 05:03:54 UTC from IEEE Xplore. Restrictions apply.

Seventh, in order to assess the effect of altimeter errors on the 2–D navigation solution, a zero-mean, Gaussian measurement noise error was simulated in $\Delta z_{r,s_n}$ with a 100 m^2 variance. The 2–D position RMSE for all k for the experiment was 78.8 cm (increase of 8.32 cm) for $\zeta = \sqrt{2}$ m. The degradation in the 2–D navigation solution is up to two orders of magnitudes less than the altimeter errors.

Eighth, some of the position errors are due to vehicle dynamics, mainly during turns. The dynamic stress on the receiver's tracking loops will induce carrier phase measurements error, which in turn translate to position errors. The effects of dynamics can be seen by comparing Fig. 6 and Fig. 8. One can see that the error trend in Fig. 8 follows the variations due to turns in the delta range shown in Fig. 6. Higher order loops or vector tracking loops could be used in the cellular receiver to minimize the effects of dynamics on the measurements.

Ninth, while the experimental results presented herein are not extensive, they present solid evidence of the potential of the proposed approach. Beside the submeter-level RMSE achieved, it is evident from the $\pm 3-\sigma$ bounds shown in Fig. 8, which remain below 1 m in magnitude, that the position error is not expected to grow over time if the navigating UAV traveled a longer distance.

Tenth, it can be seen from Table I and Table II that not performing the proposed test results in a jump in the position RMSE. This indicates that a probabilistic bound can be guaranteed only when the proposed test is satisfied.

V. Conclusion

This paper presented a framework for submeter-accurate UAV horizontal navigation with cellular carrier phase measurements. The proposed framework, called CD-cellular framework, relies on a base receiver and a navigating receiver on-board a navigating UAV, also known as rover. Both receivers make carrier phase measurements to the same sectors of the same cellular SOPs to produce the cellular carrier phase double difference measurements, referred to as CD-cellular measurements. The main strategy behind the CD-cellular framework is to navigate in three stages. In the first stage, an EKF is employed to produce a coarse estimate of the UAV's position. In the second stage, which is determined by a proposed test on the estimation error covariance, the UAV fixes the integer ambiguities in a batch solver. The proposed test guarantees that the position error of the UAV will remain less than a pre-defined threshold with a desired probability after the batch solution is calculated. In the third stage, the UAV navigates with high precision with the CD-cellular measurements and fixed integer ambiguities. The proposed method is designed for environments with strong LOS signal. Further analysis should be conducted to extend the proposed approach to multipath environments. Experimental results demonstrated not only that the proposed framework guarantees a desired navigation performance, but it also showed a UAV navigating in an open semi-urban environment and multipath-free, LOS conditions with a 70.48 cm horizontal position RMSE over a trajectory of 2.24 km with reference to the UAV's navigation solution from its onboard GPS-INS system.

Appendix A
Proof That Only 2×2 Matrices Are Needed to be Inverted to Compute $(\bar{\mathbf{P}}_{\boldsymbol{N}}^{k_\zeta})^{-1}$

From (20) and (32), one can readily see that

$$\begin{aligned}\left(\bar{\mathbf{P}}_{\boldsymbol{N}}^{k_\zeta}\right)^{-1} &= \left[\lambda^2\mathbf{P}_{\boldsymbol{N}}^{k_\zeta} + \mathbf{R}_{\mathrm{U,B}}\right]^{\frac{1}{2}}\left(\mathbf{P}_{\boldsymbol{N}}^{k_\zeta}\right)^{-1}\left[\lambda^2\mathbf{P}_{\boldsymbol{N}}^{k_\zeta} + \mathbf{R}_{\mathrm{U,B}}\right]^{\frac{1}{2}} \\ &= \left[\lambda^2\mathbf{I} + \left(\mathbf{P}_{\boldsymbol{N}}^{k_\zeta}\right)^{-1}\mathbf{R}_{\mathrm{U,B}}\right]^{\frac{1}{2}}\left[\lambda^2\mathbf{I} + \mathbf{R}_{\mathrm{U,B}}\left(\mathbf{P}_{\boldsymbol{N}}^{k_\zeta}\right)^{-1}\right]^{\frac{1}{2}},\end{aligned}$$

which shows that the calculation of $(\bar{\mathbf{P}}_{\boldsymbol{N}}^{k_\zeta})^{-1}$ entails knowing $(\mathbf{P}_{\boldsymbol{N}}^{k_\zeta})^{-1}$. The estimation error covariance of the B-WNLS $\mathbf{P}_{\mathrm{B-WNLS}}^{k_\zeta}$ is given by

$$\mathbf{P}_{\mathrm{B-WNLS}}^{k_\zeta} = \left[\left(\tilde{\mathbf{H}}^{k_\zeta}\right)^{\mathsf{T}}\left(\mathbf{R}_{\mathrm{U,B}}^{k_\zeta}\right)^{-1}\tilde{\mathbf{H}}^{k_\zeta}\right]^{-1}, \tag{37}$$

where $\tilde{\mathbf{H}}^{k_\zeta} = [\tilde{\mathbf{G}}^{k_\zeta}\; \bar{\mathbf{I}}^{k_\zeta}]$, $\tilde{\mathbf{G}}^{k_\zeta} \triangleq \mathrm{diag}[\tilde{\mathbf{G}}(0), \ldots, \tilde{\mathbf{G}}(k_\zeta)]$. Note that $\tilde{\mathbf{G}}(k)$ is evaluated at the EKF position estimate at k. Expanding (37) and using matrix block inversion, $(\mathbf{P}_{\boldsymbol{N}}^{k_\zeta})^{-1}$ may be expressed as

$$\begin{aligned}\left(\mathbf{P}_{\boldsymbol{N}}^{k_\zeta}\right)^{-1} = \lambda^2\sum_{\kappa=0}^{k_\zeta}\Big[&\mathbf{R}_{\mathrm{U,B}}^{-1}(\kappa) - \mathbf{R}_{\mathrm{U,B}}^{-1}(\kappa)\tilde{\mathbf{G}}(\kappa) \\ &\cdot\left[\tilde{\mathbf{G}}^{\mathsf{T}}(\kappa)\mathbf{R}_{\mathrm{U,B}}^{-1}(\kappa)\tilde{\mathbf{G}}(\kappa)\right]^{-1}\tilde{\mathbf{G}}^{\mathsf{T}}(\kappa)\mathbf{R}_{\mathrm{U,B}}^{-1}(\kappa)\Big].\end{aligned} \tag{38}$$

The calculation of $\mathbf{R}_{\mathrm{U,B}}^{-1}(\kappa)$ is straightforward from the structure of $\mathbf{R}_{\mathrm{U,B}}(\kappa)$ in (10) and the Sherman-Morrison formula, which is given by

$$\begin{aligned}\mathbf{R}_{\mathrm{U,B}}^{-1}(\kappa) = &\left[\mathbf{R}^{(1)}(\kappa)\right]^{-1} \\ &- \frac{\left[\mathbf{R}^{(1)}(\kappa)\right]^{-1}\mathbf{1}_{N-1}\mathbf{1}_{N-1}^{\mathsf{T}}\left[\mathbf{R}^{(1)}(\kappa)\right]^{-1}}{\frac{1}{\left[\sigma_1^{(\mathrm{U,B})}(\kappa)\right]^2} + \mathbf{1}_{N-1}^{\mathsf{T}}\left[\mathbf{R}^{(1)}(\kappa)\right]^{-1}\mathbf{1}_{N-1}}.\end{aligned} \tag{39}$$

Recall that $\mathbf{R}^{(1)}(\kappa)$ is a diagonal matrix and its inverse can be trivially obtained. Consequently, calculating $(\mathbf{P}_{\boldsymbol{N}}^{k_\zeta})^{-1}$ and subsequently $(\bar{\mathbf{P}}_{\boldsymbol{N}}^{k_\zeta})^{-1}$ requires inverting only the matrices $\{\tilde{\mathbf{G}}^{\mathsf{T}}(\kappa)\mathbf{R}_{\mathrm{U,B}}^{-1}(\kappa)\tilde{\mathbf{G}}(\kappa)\}_{\kappa=0}^{k_\zeta}$, each of which is a 2×2 matrix.

Acknowledgment

The authors would like to thank Joshua Morales, Kimia Shamaei, and Mahdi Maaref for their help in data collection.

References

[1] T. Reid et al., "Localization requirements for autonomous vehicles," *SAE Int. J. Connected Automated Veh.*, vol. 2, no. 3, pp. 173–190, Sep. 2019.
[2] Federal Aviation Administration, "NextGen annual report: A report on the history, current status, and future of national airspace system modernization," pp. 1–154, 2020.

Authorized licensed use limited to: The Ohio State University. Downloaded on April 13,2023 at 05:03:54 UTC from IEEE Xplore. Restrictions apply.

[3] R. Sabatini et al., "Avionics systems panel research and innovation perspectives," *IEEE Aerosp. Electron. Syst. Mag.*, vol. 35, no. 12, pp. 58–72, Dec. 2020.

[4] D. Borio, F. Dovis, H. Kuusniemi, and L. Presti, "Impact and detection of GNSS jammers on consumer grade satellite navigation receivers," *Proc. IEEE*, vol. 104, no. 6, pp. 1233–1245, Jun. 2016.

[5] R. Ioannides, T. Pany, and G. Gibbons, "Known vulnerabilities of global navigation satellite systems, status, and potential mitigation techniques," *Proc. IEEE*, vol. 104, no. 6, pp. 1174–1194, Jun. 2016.

[6] N. Kbayer and M. Sahmoudi, "Performances analysis of GNSS NLOS bias correction in urban environment using a threedimensional city model and GNSS simulator," *IEEE Trans. Aerosp. Electron. Syst.*, vol. 54, no. 4, pp. 1799–1814, Aug. 2018.

[7] D. Miralles et al. "An assessment of GPS spoofing detection via radio power and signal quality monitoring for aviation safety operations," *IEEE Intell. Transp. Syst. Mag.*, vol. 12, no. 3, pp. 136–146, Fall. 2020.

[8] D. Venable and J. Raquet, "Large scale image aided navigation," *IEEE Trans. Aerosp. Electron. Syst.*, vol. 52, no. 6, pp. 2849–2860, Dec. 2016.

[9] K. Takeyama, T. Machida, Y. Kojima, and N. Kubo, "Improvement of dead reckoning in urban areas through integration of low-cost multisensors," *IEEE Trans. Intell. Veh.*, vol. 2, no. 4, pp. 278–287, Dec. 2017.

[10] J. Zhang and S. Singh, "Visual-lidar odometry and mapping: Low-drift, robust, and fast," in *Proc. IEEE Int. Conf. Robot. Automat.*, 2015, pp. 2174–2181.

[11] J. Khalife, S. Ragothaman, and Z. Kassas, "Pose estimation with lidar odometry and cellular pseudoranges," in *Proc. IEEE Intell. Veh. Symp.*, 2017, pp. 1722–1727.

[12] L. Li, M. Yang, L. Guo, C. Wang, and B. Wang, "Hierarchical neighborhood based precise localization for intelligent vehicles in urban environments," *IEEE Trans. Intell. Veh.*, vol. 1, no. 3, pp. 220–229, Sep. 2016.

[13] Z. Wang, J. Fang, X. Dai, H. Zhang, and L. Vlacic, "Intelligent vehicle self-localization based on double-layer features and multilayer LIDAR," *IEEE Trans. Intell. Veh.*, vol. 5, no. 4, pp. 616–625, Dec. 2020.

[14] Y. Ren, B. Liu, R. Cheng, and C. Agia, "Lightweight semantic-aided localization with spinning LiDAR sensor," *IEEE Trans. Intell. Veh.*, to be published, doi: 10.1109/TIV.2021.3099022.

[15] T. Reid, A. Neish, T. Walter, and P. Enge, "Broadband LEO constellations for navigation," *Navigation: J. Inst. Navigation*, vol. 65, no. 2, pp. 205–220, 2018.

[16] Z. Kassas et al. "Enter LEO on the GNSS stage: Navigation with Starlink satellites," *Inside GNSS Mag.*, vol. 16, no. 6, pp. 42–51, 2021.

[17] C. Zhao, H. Qin, and Z. Li, "Doppler measurements from multiconstellations in opportunistic navigation," *IEEE Trans. Instrum. Meas.*, vol. 71, 2022, Art. no. 8500709.

[18] C. Yang, T. Nguyen, and E. Blasch, "Mobile positioning via fusion of mixed signals of opportunity," *IEEE Aerosp. Electron. Syst. Mag.*, vol. 29, no. 4, pp. 34–46, Apr. 2014.

[19] L. Chen, P. Thevenon, G. Seco-Granados, O. Julien, and H. Kuusniemi, "Analysis on the TOA tracking with DVB-T signals for positioning," *IEEE Trans. Broadcast.*, vol. 62, no. 4, pp. 957–961, Dec. 2016.

[20] J. Khalife, K. Shamaei, and Z. Kassas, "Navigation with cellular CDMA signals—Part I: Signal modeling and software-defined receiver design," *IEEE Trans. Signal Process.*, vol. 66, no. 8, pp. 2191–2203, Apr. 2018.

[21] C. Gentner, "Channel-SLAM: Multipath assisted positioning," Ph.D. dissertation, Ulm University, Ulm, Germany, 2018.

[22] J. del Peral-Rosado, R. Raulefs, J. López-Salcedo, and G. Seco-Granados, "Survey of cellular mobile radio localization methods: From 1G to 5G," *IEEE Commun. Surv. Tuts.*, vol. 20, no. 2, pp. 1124–1148, Apr.–Jul. 2018.

[23] T. Kang, H. Lee, and J. Seo, "TOA-based ranging method using CRS in LTE signals," *J. Adv. Navigation Technol.*, vol. 23, no. 5, pp. 437–443, Oct. 2019.

[24] P. Wang and Y. Morton, "Multipath estimating delay lock loop for LTE signal TOA estimation in indoor and urban environments," *IEEE Trans. Wireless Commun.*, vol. 19, no. 8, pp. 5518–5530, Aug. 2020.

[25] J. Gante, L. Sousa, and G. Falcao, "Dethroning GPS: Low-power accurate 5G positioning systems using machine learning," *IEEE Trans. Emerg. Sel. Topics Circuits Syst.*, vol. 10, no. 2, pp. 240–252, Jun. 2020.

[26] A. Abdallah and Z. Kassas, "UAV navigation with 5G carrier phase measurements," in *Proc. ION GNSS Conf.*, 2021, pp. 3294–3306.

[27] C. Gentner, T. Jost, W. Wang, S. Zhang, A. Dammann, and U. Fiebig, "Multipath assisted positioning with simultaneous localization and mapping," *IEEE Trans. Wireless Commun.*, vol. 15, no. 9, pp. 6104–6117, Sep. 2016.

[28] J. del Peral-Rosado, J. López-Salcedo, F. Zanier, and G. Seco-Granados, "Position accuracy of joint time-delay and channel estimators in LTE networks," *IEEE Access*, vol. 6, pp. 25185–25199, 2018.

[29] Z. Kassas, M. Maaref, J. Morales, J. Khalife, and K. Shamaei, "Robust vehicular localization and map matching in urban environments through IMU, GNSS, and cellular signals," *IEEE Intell. Transp. Syst. Mag.*, vol. 12, no. 3, pp. 36–52, Fall 2020.

[30] R. Landry, A. Nguyen, H. Rasaee, A. Amrhar, X. Fang, and H. Benzerrouk, "Iridium Next LEO satellites as an alternative PNT in GNSS denied environments–part 1," *Inside GNSS Mag.*, vol. 14, no. 3, pp. 56–64, May 2019.

[31] J. Khalife and Z. Kassas, "Opportunistic UAV navigation with carrier phase measurements from asynchronous cellular signals," *IEEE Trans. Aerosp. Electron. Syst.*, vol. 56, no. 4, pp. 3285–3301, Aug. 2020.

[32] C. Yang and A. Soloviev, "Mobile positioning with signals of opportunity in urban and urban canyon environments," in *Proc. IEEE/ION Position, Location, Navigation Symp.*, 2020, pp. 1043–1059.

[33] N. Souli, P. Kolios, and G. Ellinas, "Online relative positioning of autonomous vehicles using signals of opportunity," *IEEE Trans. Intell. Veh.*, to be published, doi: 10.1109/TIV.2021.3124727.

[34] M. Lichtman, R. Rao, V. Marojevic, J. Reed, and R. Jover, "5G NR jamming, spoofing, and sniffing: Threat assessment and mitigation," in *Proc. IEEE Int. Conf. Commun. Workshops*, 2018, pp. 1–6.

[35] A. Gupta, R. Jha, P. Gandotra, and S. Jain, "Bandwidth spoofing and intrusion detection system for multistage 5G wireless communication network," *IEEE Trans. Veh. Technol.*, vol. 67, no. 1, pp. 618–632, Jan. 2018.

[36] W. Xu, C. Yuan, S. Xu, H. Ngo, and W. Xiang, "On pilot spoofing attack in massive MIMO systems: Detection and countermeasure," *IEEE Trans. Inf. Forensics Secur.*, vol. 16, pp. 1396–1409, 2021.

[37] A. Abdallah, J. Khalife, and Z. Kassas, "Experimental characterization of received 5G signals carrier-to-noise ratio in indoor and urban environments," in *Proc. IEEE Veh. Technol. Conf.*, 2021, pp. 1–5.

[38] J. Khalife and Z. Kassas, "Navigation with cellular CDMA signals—Part II: Performance analysis and experimental results," *IEEE Trans. Signal Process.*, vol. 66, no. 8, pp. 2204–2218, Apr. 2018.

[39] C. Yang and A. Soloviev, "Simultaneous localization and mapping of emitting radio sources-SLAMERS," in *Proc. ION GNSS Conf.*, 2015, pp. 2343–2354.

[40] J. Morales and Z. Kassas, "Tightly-coupled inertial navigation system with signals of opportunity aiding," *IEEE Trans. Aerosp. Electron. Syst.*, vol. 57, no. 3, pp. 1930–1948, Jun. 2021.

[41] P. Misra and P. Enge, *Global Positioning System: Signals, Measurements, and Performance*, 2nd ed., Lincoln, MA, USA: Ganga-Jamuna Press, 2010.

[42] D. Yoon, C. Kee, J. Seo, and B. Park, "Position accuracy improvement by implementing the DGNSS-CP algorithm in smartphones," *Sensors*, vol. 16, no. 6, pp. 910–925, 2016.

[43] J. Khalife and Z. Kassas, "Precise UAV navigation with cellular carrier phase measurements," in *Proc. IEEE/ION Position, Location, Navigation Symp.*, 2018, pp. 978–989.

[44] J. Khalife, K. Shamaei, S. Bhattacharya, and Z. Kassas, "Centimeter-accurate UAV navigation with cellular signals," in *Proc. ION GNSS Conf.*, 2018, pp. 2321–2331.

[45] P. Teunissen and S. Verhagen, "GNSS carrier phase ambiguity resolution: Challenges and open problems," in *Observing our Changing Earth*. Berlin/Heidelberg, Germany: Springer, 2009, pp. 785–792.

[46] K. Berntorp, A. Weiss, and S. Cairano, "Integer ambiguity resolution by mixture Kalman filter for improved GNSS precision," *IEEE Trans. Aerosp. Electron. Syst.*, vol. 56, no. 4, pp. 3170–3181, Aug. 2020.

[47] M. Pratt, B. Burke, and P. Misra, "Single-epoch integer ambiguity resolution with GPS-GLONASS L1 data," in *Proc. Annu. Meeting The Inst. Navigation*, 1997, pp. 691–699.

[48] P. Teunissen, "Least-squares estimation of the integer GPS ambiguities," in *Proc. Invited Lecture, Sect. IV Theory And Methodol., IAG Gen. Meeting*, 1993, pp. 1–16.

[49] P. Teunissen, "The least-squares ambiguity decorrelation adjustment: A method for fast GPS integer ambiguity estimation," *J. Geodesy*, vol. 70, no. 1, pp. 65–82, Nov. 1995.

[50] P. Teunissen, "Carrier phase integer ambiguity resolution," in *Springer Handbook of Global Navigation Satellite Systems*, New York, NY, USA: Springer, 2017, pp. 661–685.

[51] X. Chang, X. Yang, and T. Zhou, "MLAMBDA: A modified LAMBDA method for integer least-squares estimation," *J. Geodesy*, vol. 79, no. 9, pp. 552–565, 2005.

Authorized licensed use limited to: The Ohio State University. Downloaded on April 13,2023 at 05:03:54 UTC from IEEE Xplore. Restrictions apply.

[52] B. Pervan and B. Parkinson, "Cycle ambiguity estimation for aircraft precision landing using the Global Positioning System," *J. Guidance, Control, Dyn.*, vol. 20, no. 4, pp. 681–689, Jul./Aug. 1997.
[53] J. del Peral-Rosado et al., "Software-defined radio LTE positioning receiver towards future hybrid localization systems," in *Proc. AIAA Int. Commun. Satell. Syst. Conf.*, 2013, pp. 1–11.
[54] M. Ulmschneider and C. Gentner, "Multipath assisted positioning for pedestrians using LTE signals," in *Proc. IEEE/ION Position, Location, Navigation Symp.*, 2016, pp. 386–392.
[55] M. Driusso, C. Marshall, M. Sabathy, F. Knutti, H. Mathis, and F. Babich, "Vehicular position tracking using LTE signals," *IEEE Trans. Veh. Technol.*, vol. 66, no. 4, pp. 3376–3391, Apr. 2017.
[56] A. Abdallah and Z. Kassas, "Multipath mitigation via synthetic aperture beamforming for indoor and deep urban navigation," *IEEE Trans. Veh. Technol.*, vol. 70, no. 9, pp. 8838–8853, Sep. 2021.
[57] M. Maaref and Z. Kassas, "Measurement characterization and autonomous outlier detection and exclusion for ground vehicle navigation with cellular signals," *IEEE Trans. Intell. Veh.*, vol. 5, no. 4, pp. 670–683, Dec. 2020.
[58] S. Ragothaman, M. Maaref, and Z. Kassas, "Autonomous ground vehicle path planning in urban environments using GNSS and cellular signals reliability maps: Models and algorithms," *IEEE Trans. Aerosp. Electron. Syst.*, vol. 57, no. 2, pp. 1562–1580, Jun. 2021.
[59] M. Maaref, J. Khalife, and Z. Kassas, "Aerial vehicle protection level reduction by fusing GNSS and terrestrial signals of opportunity," *IEEE Trans. Intell. Transp. Syst.*, vol. 22, no. 9, pp. 5976–5993, Sep. 2021.
[60] Qualcomm Technologies, Inc., "LTE unmanned aircraft systems," Tech. Rep. 1.0.1, May 2017. [Online]. Available: https://www.qualcomm.com/documents/lte-unmanned-aircraft-systems-trial-report/
[61] Z. Kassas et al., "Assessment of cellular signals of opportunity for high altitude aircraft navigation," *IEEE Aerospace and Electronic Systems Magazine*, to be published, doi: 10.1109/MAES.2022.3187142.
[62] X. Chen, F. Dovis, and M. Pini, "An innovative multipath mitigation method using coupled amplitude delay lock loops in GNSS receivers," in *Proc. IEEE/ION Position, Location Navigation Symp.*, 2010, pp. 1118–1126.
[63] K. Shamaei and Z. Kassas, "LTE receiver design and multipath analysis for navigation in urban environments," *Navigation: J. Inst. Navigation*, vol. 65, no. 4, pp. 655–675, Dec. 2018.
[64] Y. Quan, L. Lau, G. Roberts, X. Meng, and C. Zhang, "Convolutional neural network based multipath detection method for static and kinematic GPS high precision positioning," *Remote Sens.*, vol. 10, no. 12, pp. 2052–2069, Dec. 2018.
[65] P. Gadka, J. Sadowski, and J. Stefanski, "Detection of the first component of the received LTE signal in the OTDoA method," *Wireless Commun. Mobile Comput.*, 2019, pp. 1–12, Apr. 2019.
[66] H. Dun, C. Tiberius, and G. Janssen, "Positioning in a multipath channel using OFDM signals with carrier phase tracking," *IEEE Access*, vol. 8, pp. 13011–13028, 2020.
[67] P. Wang, Y. Wang, and J. Morton, "Signal tracking algorithm with adaptive multipath mitigation and experimental results for LTE positioning receivers in urban environments," *IEEE Trans. Aerosp. Electron. Syst.*, vol. 58, no. 4, pp. 2779–2795, Aug. 2022.
[68] M. Joerger and B. Pervan, "Fault detection and exclusion using solution separation and chi-squared ARAIM," *IEEE Trans. Aerosp. Electron. Syst.*, vol. 52, no. 2, pp. 726–742, Apr. 2016.
[69] N. Zhu, J. Marais, D. Betaille, and M. Berbineau, "GNSS position integrity in urban environments: A. review of literature," *IEEE Trans. Intell. Transp. Syst.*, vol. 19, no. 9, pp. 2762–2778, Sep. 2018.
[70] N. Zhu, D. Betaille, J. Marais, and M. Berbineau, "GNSS integrity monitoring schemes for terrestrial applications in harsh signal environments," *IEEE Intell. Transp. Syst. Mag.*, vol. 12, no. 3, pp. 81–91, Fall 2020.
[71] M. Jia, H. Lee, J. Khalife, Z. Kassas, and J. Seo, "Ground vehicle navigation integrity monitoring for multi-constellation GNSS fused with cellular signals of opportunity," in *Proc. IEEE Int. Conf. Intell. Transp. Syst.*, 2021, pp. 3978–3983.
[72] N. Ziedan, "Multipath channel estimation and pattern recognition for environment-based adaptive tracking," in *Proc. 25th Int. Tech. Meeting Satell. Division Inst. Navigation*, 2012, pp. 394–407.
[73] Y. Wang, X. Chen, and P. Liu, "Statistical multipath model based on experimental GNSS data in static urban canyon environment," *Sensors*, vol. 18, no. 4, pp. 1149–1165, Apr. 2018.
[74] Y. Bar-Shalom, X. Li, and T. Kirubarajan, *Estimation with Applications to Tracking and Navigation*. New York, NY: Wiley, 2002.
[75] B. Noble and J. Daniel, *Applied Linear Algebra*. Upper Saddle River, NJ, USA: Prentice Hall, 1998.
[76] M. Haenggi, J. Andrews, F. Baccelli, O. Dousse, and M. Franceschetti, "Stochastic geometry and random graphs for the analysis and design of wireless networks," *IEEE J. Sel. Areas Commun.*, vol. 27, no. 7, pp. 1029–1046, Sep. 2009.
[77] J. Schloemann, H. Dhillon, and R. Buehrer, "A tractable metric for evaluating base station geometries in cellular network localization," *IEEE Wireless Commun. Lett.*, vol. 5, no. 2, pp. 140–143, Apr. 2016.
[78] J. Morales and Z. Kassas, "Optimal collaborative mapping of terrestrial transmitters: Receiver placement and performance characterization," *IEEE Trans. Aerosp. Electron. Syst.*, vol. 54, no. 2, pp. 992–1007, Apr. 2018.
[79] J. Wirth, E. Bonugli, and M. Freund, "Assessment of the accuracy of google earth imagery for use as a tool in accident reconstruction," in *Proc. SAE World Congr. & Exhib.*, 2015, pp. 1–17.
[80] M. Maaref and Z. Kassas, "Autonomous integrity monitoring for vehicular navigation with cellular signals of opportunity and an IMU," *IEEE Trans. Intell. Transp. Syst.*, vol. 23, no. 6, pp. 5586–5601, Jun. 2022.

Joe Khalife (Senior Member, IEEE) received the B.E. degree in electrical engineering and the M.S. degree in computer engineering from Lebanese American University (LAU), Beirut, Lebanon, and the Ph.D. degree in electrical engineering and computer science from the University of California Irvine, Irvine, CA, USA. He is currently a Postdoctoral Fellow with the University of California Irvine, and a Member of the Autonomous Systems Perception, Intelligence, and Navigation (ASPIN) Laboratory. From 2012 to 2015, he was a Research Assistant at LAU and has been a Member of the ASPIN Laboratory since 2015. His research interests include opportunistic navigation, autonomous vehicles, and software-defined radio. He was the recipient of the 2016 IEEE/ION Position, Location, and Navigation Symposium (PLANS) Best Student Paper Award and the 2018 IEEE Walter Fried Award.

Zaher (Zak) M. Kassas (Senior Member, IEEE) received the B.E. degree in electrical engineering from the Lebanese American University, Beirut, Lebanon, the M.S. degree in electrical and computer engineering from The Ohio State University, Columbus, OH, USA, the M.S.E. degree in aerospace engineering and the Ph.D. in electrical and computer engineering from The University of Texas at Austin, Austin, TX, USA. He is currently a Professor of electrical and computer engineering at The Ohio State University and Director of the Autonomous Systems Perception, Intelligence, and Navigation (ASPIN) Laboratory. He is also the Director of the U.S. Department of Transportation Center: CARMEN (Center for Automated Vehicle Research with Multimodal AssurEd Navigation), focusing on navigation resiliency and security of highly automated transportation systems. His research interests include cyber-physical systems, estimation theory, navigation systems, autonomous vehicles, and intelligent transportation systems. He was the recipient of the 2018 National Science Foundation (NSF) Faculty Early Career Development Program (CAREER) Award, 2019 Office of Naval Research (ONR) Young Investigator Program (YIP) Award, 2022 Air Force Office of Scientific Research (AFOSR) YIP Award, 2018 IEEE Walter Fried Award, 2018 Institute of Navigation (ION) Samuel Burka Award, and 2019 ION Col. Thomas Thurlow Award. He is a Senior Editor of the IEEE TRANSACTIONS ON INTELLIGENT VEHICLES and an Associate Editor for the IEEE TRANSACTIONS ON AEROSPACE AND ELECTRONIC SYSTEMS and IEEE TRANSACTIONS ON INTELLIGENT TRANSPORTATION SYSTEMS.

Authorized licensed use limited to: The Ohio State University. Downloaded on April 13,2023 at 05:03:54 UTC from IEEE Xplore. Restrictions apply.

UC Irvine
UC Irvine Previously Published Works

Title
Enter LEO on the GNSS Stage: Navigation with Starlink Satellites

Permalink
https://escholarship.org/uc/item/9td3n8wd

Authors
Kassas, Zak
Neinavaie, Mohammad
Khalife, Joe
et al.

Publication Date
2021-11-01

Peer reviewed

eScholarship.org Powered by the California Digital Library
University of California

November/December 2021 | Engineering Solutions from the Global Navigation Satellite System Community | www.insidegnss.com

InsideGNSS

Published by **Autonomous Media**

GPS | GALILEO | GLONASS | BEIDOU

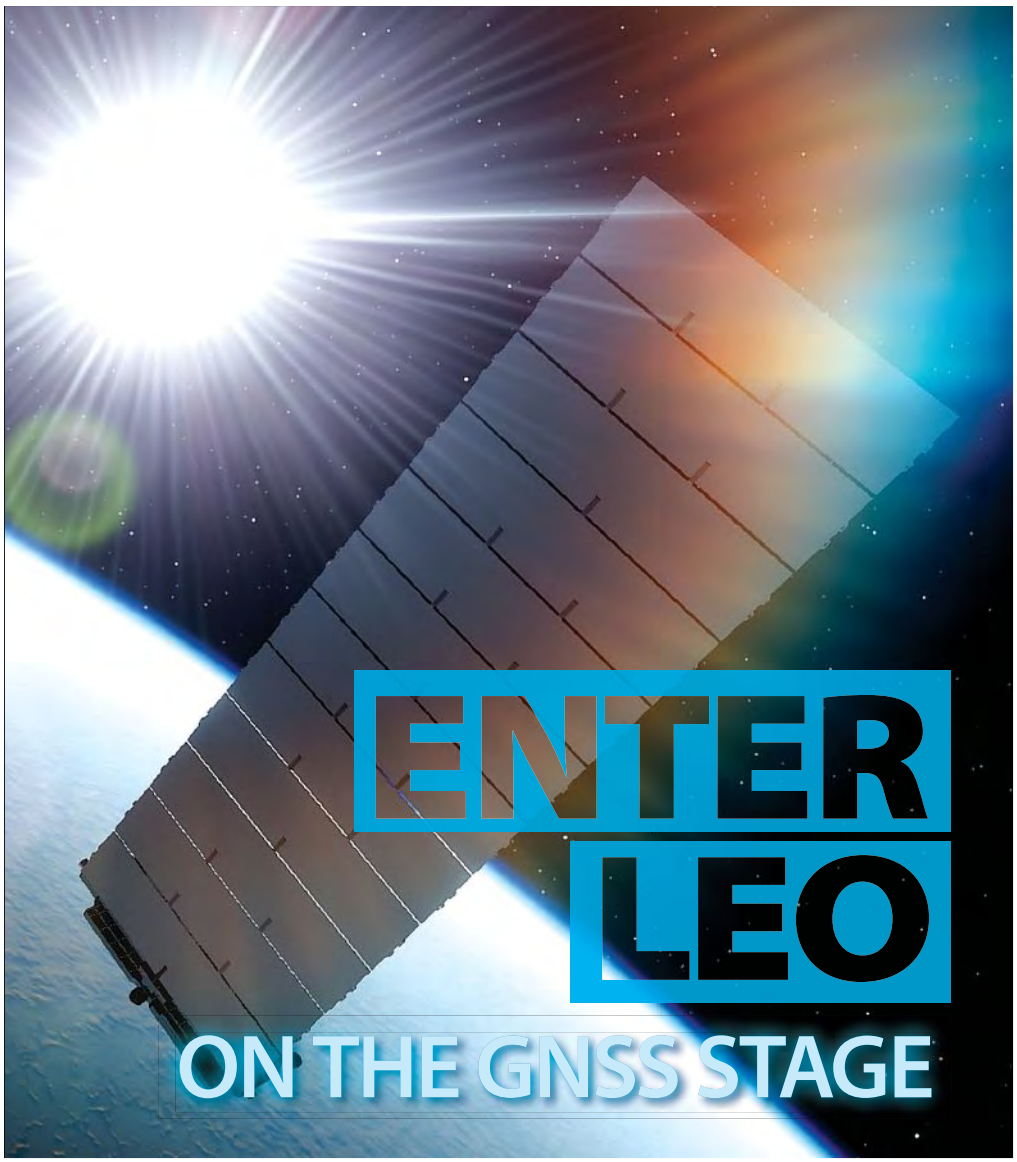

Photo courtesy of AleksandrMorrisovich/Shutterstock.com.

ENTER LEO on the GNSS Stage

Navigation with Starlink Satellites

We are witnessing a space renaissance. Tens of thousands of broadband low Earth orbit (LEO) satellites are expected to be launched by the end of this decade. These planned megaconstellations of LEO satellites along with existing constellations will shower the Earth with a plethora of signals of opportunity, diverse in frequency and direction. These signals could be exploited for navigation in the inevitable event that GNSS signals become unavailable (e.g., in deep urban canyons, under dense foliage, during unintentional interference, and intentional jamming) or untrustworthy (e.g., under malicious spoofing attacks).

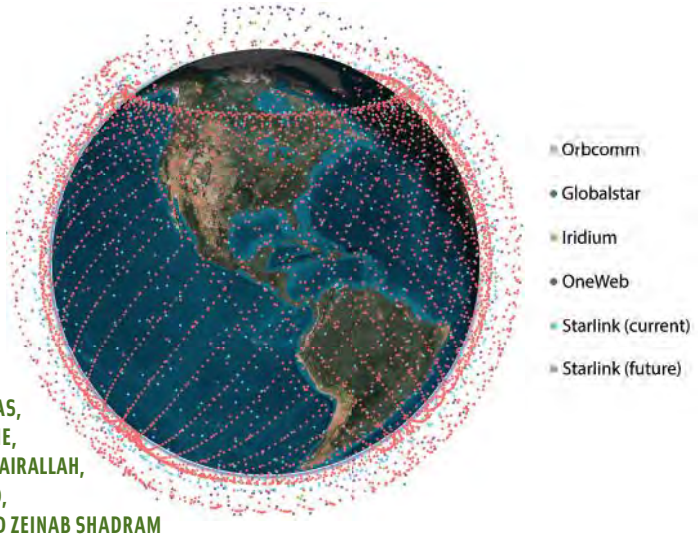

FIGURE 1 Some existing and future LEO satellite constellations.

ZAHER (ZAK) M. KASSAS, MOHAMMAD NEINAVAIE, JOE KHALIFE, NADIM KHAIRALLAH, JAMIL HAIDAR-AHMAD, SHARBEL KOZHAYA AND ZEINAB SHADRAM
AUTONOMOUS SYSTEMS PERCEPTION, INTELLIGENCE AND NAVIGATION (ASPIN) LABORATORY

The ambitious and glorified image of an Earth connected through a web woven from low-Earth orbit (LEO) satellites is taking the world by storm, promising high-resolution images; remote sensing; and global, high-availability, high-bandwidth and low-latency Internet. Many corporations, such as Orbcomm, Globalstar, and Iridium, made haste in securing their position in space as LEO constellations were born. With the recent developments in satellite technology, reduction in launch costs and commercialization of LEO megaconstellations, LEO satellites' popularity is soaring. Major technology giants such as SpaceX, Amazon and OneWeb rush to enter this field by launching and scheduling the launch of thousands of satellites for Internet connectivity and communication purposes.

The promise of utilizing LEO satellites for navigation has been the subject of recent studies [1]–[4]. *(The online version of this article contains an extensive reference list, omitted here for space reasons.)*

While some studies call for tailoring the transmission protocol to support navigation capabilities [5], other studies propose to exploit the transmitted signals

for navigation in an opportunistic fashion [6]. The former studies allow for simpler receiver architectures and navigation algorithms. However, they require significant investment in satellite infrastructure and spectrum allocation, the cost of which private companies; such as OneWeb, SpaceX, Amazon, among others; which are planning to aggregately launch tens of thousands of satellites into LEO (see **Figure 1** and **Table 1**) may not be willing to pay.

Moreover, if the aforementioned companies agree to that additional cost, there will be no guarantees that they would not charge for "extra navigation services." As such, exploiting LEO satellite signals opportunistically for navigation becomes the more viable approach. This article studies opportunistic navigation with the Starlink megaconstellation of LEO satellites.

To address the limitations and vulnerabilities of GNSS, opportunistic navigation has received significant attention over the past decade or so. Opportunistic navigation is a paradigm that relies on exploiting ambient radio signal of opportunity (SOPs) for positioning and timing [7]. Besides LEO satellite signals, other SOPs include AM/FM radio, digital television, WiFi, and cellular, with the latter showing the promise of a submeter-accurate navigation on unmanned aerial vehicles (UAVs) [8] and meter-level navigation on ground vehicles [9],[10].

LEO satellites possess desirable attributes for navigation. First, LEO satellites are around twenty times closer to Earth compared to GNSS satellites that reside in medium-Earth orbit (MEO), making LEO satellites' received signals significantly more powerful than GNSS (more than 30 dB). Second, LEO satellites orbit the Earth at much faster rates compared to GNSS satellites, making LEO satellites' Doppler measurements attractive to exploit.

Third, LEO megaconstellations will shower Earth with signals diverse in frequency, improving robustness to interference and cyberattacks. Fourth, LEO satellites will provide virtually a blanket cover around the globe, yielding low geometric dilution of precision (GDOP), which in turn gives more precise position estimates. These are not ungrounded promises. As of mid-2021, SpaceX has launched over 1,600 Starlink satellites into LEO, with the total being projected to be up to 42,000 satellites, 12,000 of which are already approved by the Federal Communications Commission (FCC).

Figure 2 and **Figure 3** show a heat map of the number of currently visible versus future Starlink LEO satellites, respectively,

Constellation	Number of Satellites	Frequency Band
Orbcomm	36	VHF
Globalstar	48	S and C
Iridium	66	L and Ka
OneWeb	882	Ku and Ka
Boeing	147	V and Ka
Starlink (SpaceX)	11,943	Ku, Ka and V
Kuiper (Amazon)	3,236	Ku and Ka

TABLE 1 Existing and future LEO constellations: number of satellite and transmission bands.

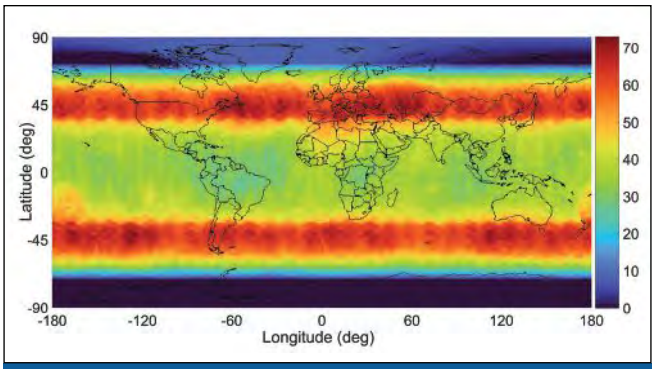

FIGURE 2 Heat map showing the number of currently visible Starlink LEO satellites above a 5-degree elevation mask.

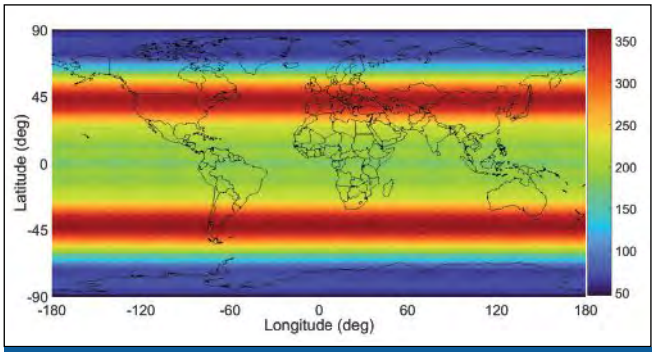

FIGURE 3 Heat map showing the number of future visible Starlink LEO satellites above a 5-degree elevation mask.

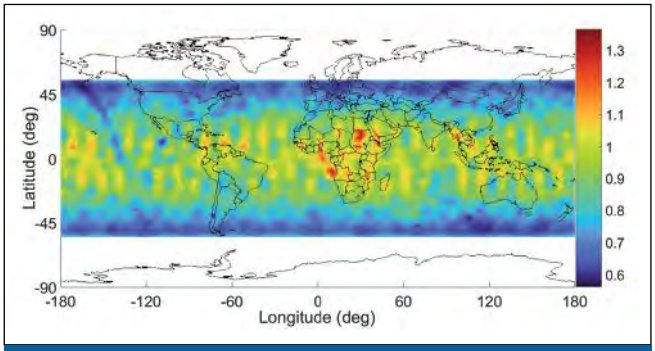

FIGURE 4 Heat map showing PDOP for the current Starlink LEO constellation above a 5-degree elevation mask.

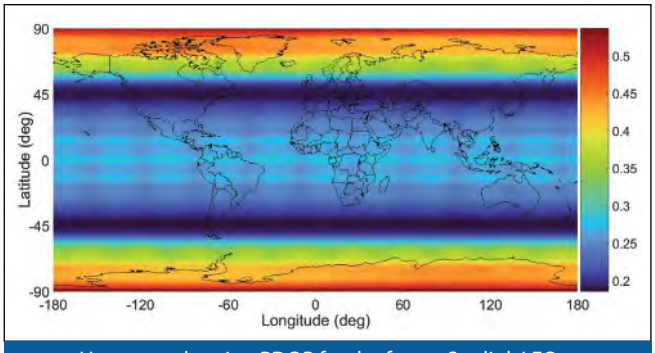

FIGURE 5 Heat map showing PDOP for the future Starlink LEO constellation above a 5-degree elevation mask.

above an elevation mask of 5 degrees. Figure 4 and Figure 5 present heat maps of the position dilution of precision (PDOP) for the current versus future Starlink constellation, respectively.

However, there is no such thing as a free lunch. A multitude of challenges must be addressed to be able to exploit LEO satellite signals in an opportunistic fashion.

First, since LEO satellites are not designed for navigation purposes, they do not necessarily transmit their satellites' ephemerides, and in occasions that they do, we might not have access to such data as non-subscribers. The position and velocity of a satellite can be parametrized by its Keplerian elements. These elements, along with some other information about a satellite's states, can be found in two-line element (TLE) files, which are tracked and publicly published on a daily basis by the North American Aerospace Defense Command (NORAD) [11]. However, utilizing these elements in determining the satellites' orbits introduces errors on the order of kilometers, as these elements are dynamic and deviate due to several sources of perturbing forces, which include atmospheric drag, the Earth's oblateness causing a non-uniform gravitational field, solar radiation pressure, and other sources of gravitational forces (e.g., the Sun and the Moon) [12]. Furthermore, with Starlink satellites orbiting at very low altitudes, the effect of these forces is amplified.

Second, unlike GNSS satellites, LEO satellites are not necessarily equipped with atomic clocks, nor they are as tightly synchronized. The stability of LEO satellites' clocks and their synchronicity are unknown. In contrast to GNSS, where the satelites' clock errors are periodically transmitted to the receiver in the navigation message, such information is unavailable to the receiver.

Finally, LEO satellites are owned and operated by private entities, which adopt proprietary transmission protocols; making their signals "mysterious" for non-subscribers. As such, to exploit these signals, we need to build specialized receivers that are capable of extracting navigation observables.

Navigation with Starlink Satellites

Here, we present two approaches to exploit unknown Starlink signals for navigation. The first approach relies on the single or multiple carrier signals transmitted by Starlink satellites. An adaptive Kalman filter (KF)-based phase-locked loop (PLL) algorithm is used in the first approach to extract carrier phase observables from received satellite signals. In the second approach, Starlink signals are acquired and tracked without assuming any prior knowledge on the signal. This approach considers a more generic model for the transmitted synchronization signals to provide Dopplernavigation observables.

Extracting Carrier-Phase Observables. (Approach 1) A look at the magnitude of the fast Fourier transform (FFT) of the Starlink downlink signal at 11.325 GHz carrier frequency and sampling rate of 2.5 MHz shows nine peaks (Figure 6a). Figure 6b demonstrates the Waterfall plot of the FFT over an 80-second interval.

The peaks are uniformly separated by approximately 44 kHz and vary in amplitude over time. One approach to extract navigation observables from Starlink signals is to consider the peaks as carriers and develop a software-defined radio (SDR) to acquire and track them to generate beat carrier phase measurements. Since the receiver does not know the position of the tracked peak relative to the center frequency of the signal, a Doppler ambiguity is present, and it is accounted for in the navigation filter used to generate the position solution. The continuous-time model of the beat carrier phase is a function of

- the true range between the LEO satellite and the receiver,
- the time-varying difference between the receiver's and LEO satellite's clock bias, and
- the beat carrier frequency.

The clock bias is assumed to have an initial value and a constant drift. An adaptive KF-based algorithm tracks the beat carrier phase. The KF-based tracking operates similarly to Costas loops, except that the loop filter is replaced with a KF, where the measurement noise variance is varied adaptively. More details are discussed in [13].

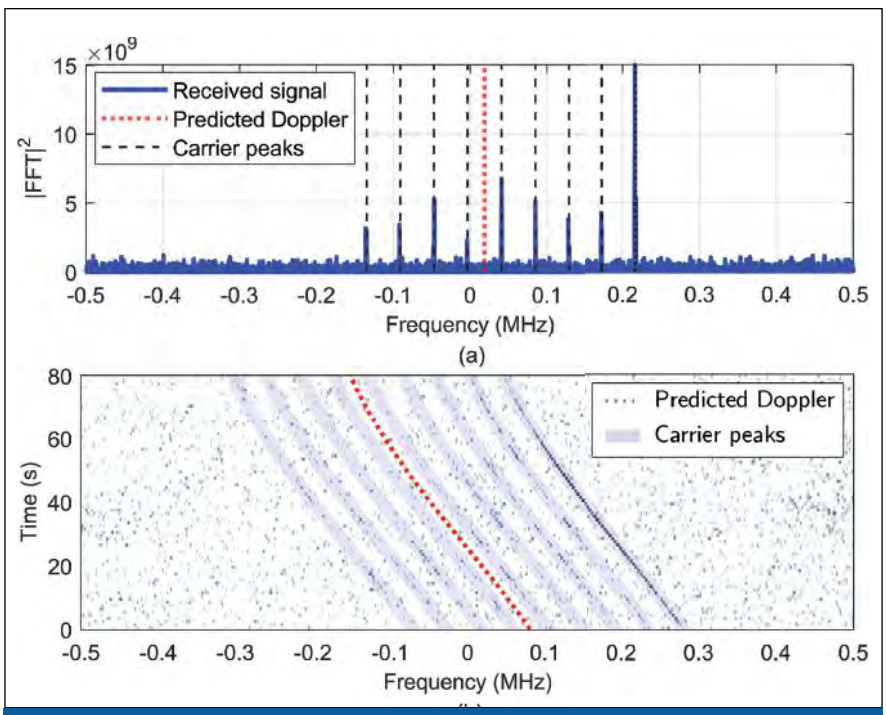

FIGURE 6 (a) the square of the magnitude of the signal's FFT and (b) the Waterfall plot of the FFT over an 80-second interval.

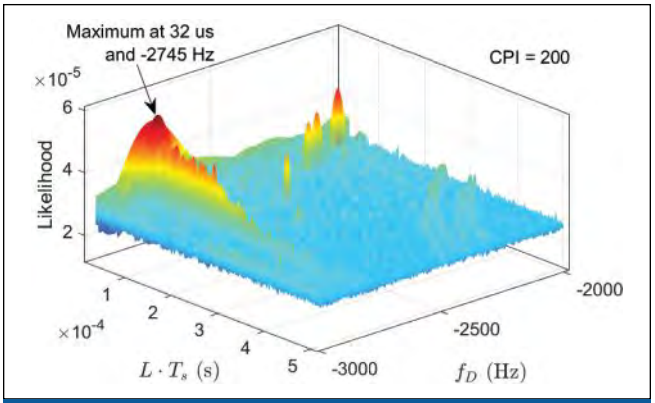

FIGURE 7 The likelihood function versus Doppler frequency and the period at Starlink downlink carrier frequency of 11.325 GHz.

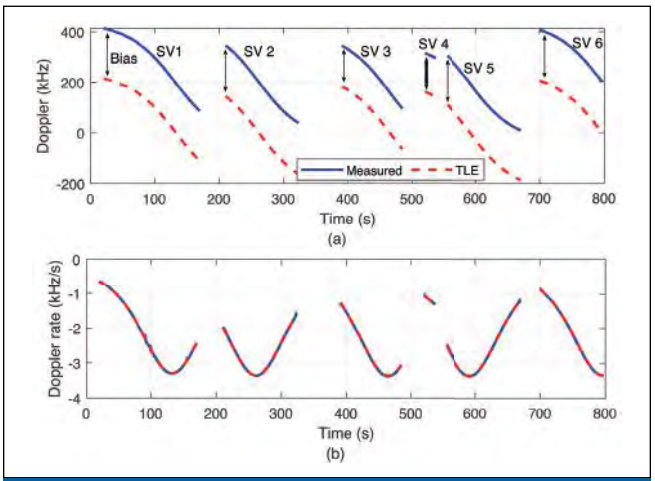

FIGURE 8 Estimated Doppler frequencies and Doppler rates of six Starlink space vehicles (SVs).

Estimating the Synchronization Signal. (Approach 2) In most communication systems, a periodic signal is transmitted for synchronization purposes, e.g., spreading codes in 3G code division multiple access (CDMA) and primary synchronization signal (PSS) in 4G LTE and 5G. Unlike data, the synchronization signals are periodic. One can model the Starlink downlink signal as an unknown periodic signal. The detection of unknown periodic signals in the presence of noise and interference falls into the paradigm of matched subspace detectors, which has been studied in the detection literature.

The second approach consists of two main stages: acquisition and tracking. In the acquisition stage, an estimate of the parameters of the synchronization signal and its period, denoted by L, along with an initial estimate of the Doppler frequency f_D is produced. The acquisition stage is modeled as a binary hypothesis testing problem as:

$$\begin{cases} H_0: \text{No Starlink signal is present} \\ H_1: \text{Starlink signal is present.} \end{cases}$$

Solving the detection problem produces a likelihood function which involves a two-dimensional search over the

NavtechGPS brings you ...

NovAtel OEM7™ Series GNSS Receivers

- Built-in interference detection and mitigation!
- L-Band and SPAN® GNSS+INS functionality
- 555 available channels
- Multi-constellation, multi-frequency
- TerraStar™ ready for centimeter-level positioning
- Field upgradable to all OEM7 software options

Contact us for model details and options

NavtechGPS
+1-703-256-8900 • 800-628-0885
https://www.navtechgps.com/novatel_oem7_gnss_receivers/

Live Stream GNSS Courses

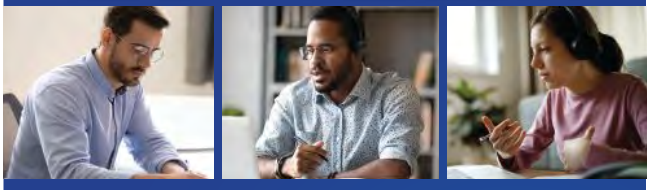

Your Team, Your Training, Your Timetable!

Private group training with real-time engagement

- 557: Inertial Systems, Kalman Filtering, and GPS/INS Integration. Instructors: Dr. Alan Pue and Mr. Michael Vaujin *(advanced aided inertial systems and GPS, 5 days)*
- 551: Using Advanced GPS/GNSS Signals and Systems. Instructor: Dr. John Betz *(deep drill into systems, signals, and receiver design, 5 days)*
- 346: GPS/GNSS Operation for Engineers and Technical Professionals. Instructor: Dr. Chris Hegarty *(GPS overview, DGPS intro, 4 days)*
- 335: Military GPS Receiver Performance in Jamming, with Mitigations *(for U.S. military and U.S. contractors).* Instructor: Dr. John Betz (2.5 days)
- 122: GPS/GNSS Fundamentals and Enhancements. Instructor: Dr. Chris Hegarty *(just the basics, 2 days)*

Questions? Contact Trevor Boynton at tboynton@navtechgps.com

NavtechGPS
+1-703-256-8900 • 800-628-0885
https://www.navtechgps.com/gps-gnss-training/gnss-group-training/

Doppler frequency and period. **Figure 7** demonstrates the likelihood in terms of Doppler frequency and the period for Starlink downlink signals in the acquisition stage.

After producing these initial estimates in the acquisition stage, the estimated Doppler frequency is tracked using a Doppler tracking algorithm. To capture the high dynamics of Starlink LEO satellites, a linear chirp model is considered. More precisely, it is assumed that during the coherent processing interval (CPI), the Doppler is a linear function of time. An FFT-based chirp parameter tracking is used to track the chirp parameters which are the Doppler frequency and Doppler rate. **Figure 8** demonstrates the tracked Doppler frequencies and Doppler rates of six Starlink satellites transmitting at 11.325 GHz versus those predicted from TLE files. The estimated Doppler frequencies have a constant bias compared to those predicted from TLE. This bias is present because the exact carrier frequency of the transmitted signals is unknown. This constant bias is estimated in the navigation filter. More details are discussed in [14].

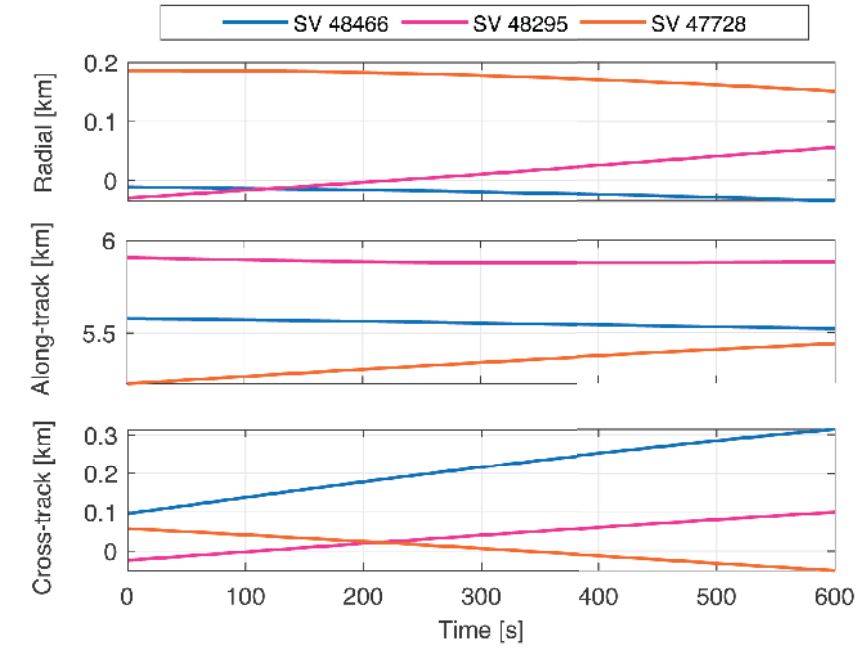

FIGURE 9 Breakdown of the position error of three Starlink satellites in the Radial, In-track, and Cross-track frame.

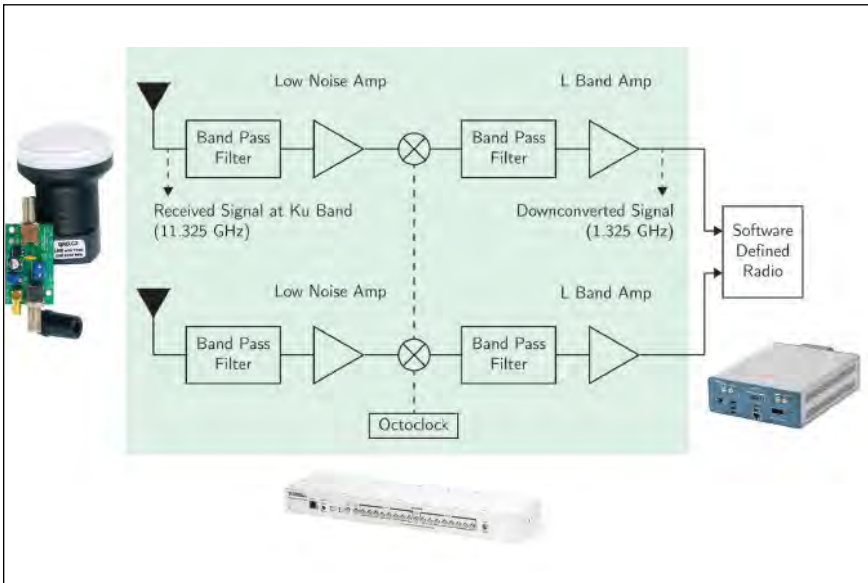

FIGURE 10 Hardware set-up.

Starlink LEO Ephemerides Error

One source of error to consider when navigating with LEO satellite signals arises from imperfect knowledge of the LEO satellites' ephemerides. This is due to time-varying Keplerian elements caused by several perturbing accelerations acting on the satellite. Mean Keplerian elements and perturbing acceleration parameters are contained in publicly available TLE files. The information in these files may be used to initialize simplified general perturbations (SGP) models, which propagate LEO satellite's orbit. SGP propagators (e.g., SGP4 [15]) are optimized for speed by replacing complicated perturbing acceleration models that require numerical integrations with analytical expressions to propagate a satellite posi-tion from an epoch time to a specified future time.

The tradeoff is in satellite position accuracy: the SGP4 propagator has around 3 km in position error at epoch and the propagated orbit will continue to deviate from the true one until the TLE files are updated the following day. **Figure 9** shows the breakdown of the position error of three Starlink satellites in the radial, along-track and cross-track frame. The errors are generated by propagating Starlink satellites using SGP4 and comparing to a "ground truth," generated by the High Precision Orbit Propagator (HPOP), which was initialized using the state vector published by Starlink. **Figure 9** shows that most of the error reside along the track. More details are discussed in [16],[17].

Positioning with Starlink Carrier Phase and Doppler Measurements

This section presents the first stationary positioning results with Starlink signals. A National Instruments (NI) universal software radio peripheral (USRP) 2945R was equipped with two consumer-grade antennas and low-noise block (LNB) downconverters to receive Starlink signals in the Ku-band from two different angles. An octo-clock was used to synchronize the USRP clocks and the downconverters. The sampling rate was set to 2.5 MHz and the carrier frequency was set to 11.325 GHz, which is one of the Starlink downlink frequencies. **Figure 10** shows the hardware setup.

A weighted nonlinear least-squares (WNLS) estimator was used to estimate the receiver's position using the six detected Starlink satellites. To account for ephemeris errors, the TLE epoch time for each Starlink satellite was shifted in time to minimize the error residuals.

The receiver's position was initialized as the centroid of all Starlink satellite positions, projected onto the surface of the Earth, yielding an initial position error of 179 km. The clock biases and drifts were initialized to zero.

The environment layout and the posi-tioning results are shown in **Figure 11** and **Table 2,** respectively. The 3–D position error was found to be 33.5 m and 22.9 m for Approach 1 and 2, respective-ly. Upon equipping the receiver with an altimeter (to know its attitude) the 2–D position error was reduced to 7.7 m and 10 m for Approach 1 and Approach 2, respectively. More details are discussed in [13],[14].

Differential Doppler Positioning

A common approach to compensate for ephemeris errors, ionospheric and tropospheric delays, clock errors, and other common mode errors is to employ a differential framework, composed of a base and a rover. In differential Doppler positioning, the rover estimates its states by subtracting its Doppler measurements to Starlink satellites from Doppler measurements to the same satellites made by a base receiver with known position. This leads to fewer unknown terms that need to be estimated and to reducing the effect of common mode errors. More details are dis-cussed in [18].

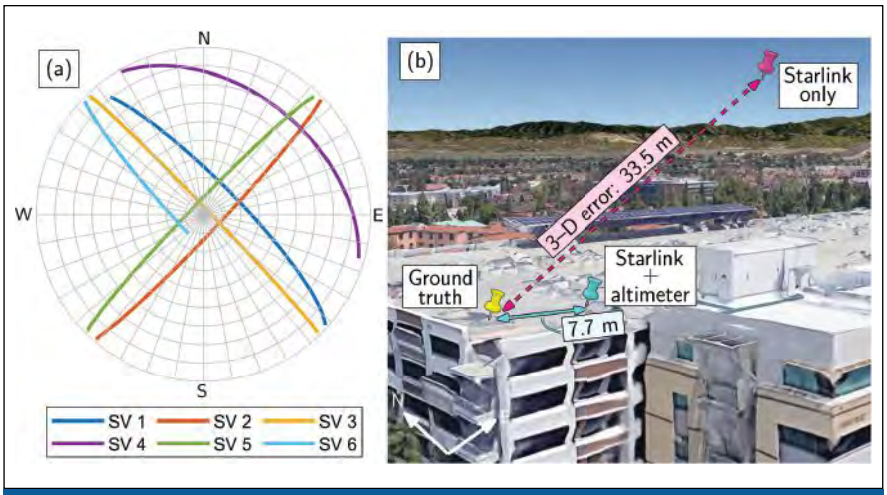

FIGURE 11 (a) Skyplot showing the trajectory of the six Starlink satellites over a 600 s period. (b) Environment layout and positioning results for approach 1.

	Approach 1	Approach 2
3-D position error	33.5 m	22.9 m
2-D position error	7.7 m	10 m

TABLE 2 Experimental results with 6 Starlink LEO satellites for a stationary receiver.

Experimental Results with Starlink Differential Doppler Measurements

This section presents experimental results of positioning with differential Doppler measurements from Starlink LEO satellites.

A stationary scenario is considered in which the base was equipped with an Ettus E312 USRP with a consumer-grade antenna and LNB downconverter to receive Starlink signals in the Ku-band, and the rover was equipped with USRP 2974 with the same downconverter. The Octoclocks were used to synchronize between the USRPs' clocks and the downconverters at the base and at the rover. The sampling rate was set to 2.5 MHz, and the carrier frequency was set to 11.325 GHz. Over the course of the experiment, the receivers on-board the base and the rover were listening to 3 Starlink satellites: 44740, 48295, and 47728. The satellites were visible for 320 seconds. **Figure 12** shows the likelihood as a function of the Doppler frequency and period of Starlink downlink signals. The CPI was set to be 200 times the period. It can be seen that three Starlink LEO satellites were detected in the acquisition stage. **Figure 13** shows the measured differential Doppler for the three satellites. The spike in the estimated differential Doppler is due to channel outage and burst error, which is common in satellite communications. The distance between the base and the rover was 1.004 km. The rover's initial estimate was approximately 200 km away from its true position. Upon employing the differential Doppler positioning framework, the 3–D position error was found to be 33.4 m, while the 2–D position error was 5.6 m. **Figure 14** shows the positions of the base and the rover as well as the rover's initial estimate and its final 3–D and 2–D estimates.

Simultaneous LEO Satellite Tracking and Ground Vehicle Navigation

Whether navigating on water, over land, or in air, most vehicles traditionally rely on a GNSS-aided inertial navigation system (INS). This GNSS/INS integration—which can be loose, tight, or deep—provides a navigation solution that benefits from both the short-term accuracy of the INS and the long-term stability of GNSS [19]. LEO satellites' signals could be opportunistically exploited as an INS-aiding source, thus serving as a complement or even an alternative to GNSS signals.

GNSS satellites are equipped with highly stable atomic clocks, are synchronized across the network, and they transmit their ephemeris data and clock errors to the user in their navigation message. In contrast, LEO satellites are not designed for navigation purposes. As such, their on-board clocks are not necessarily of atomic standards nor as tightly synchronized. Moreover, LEO satellites typically do not openly transmit their ephemeris and clock error data in their proprietary signals.

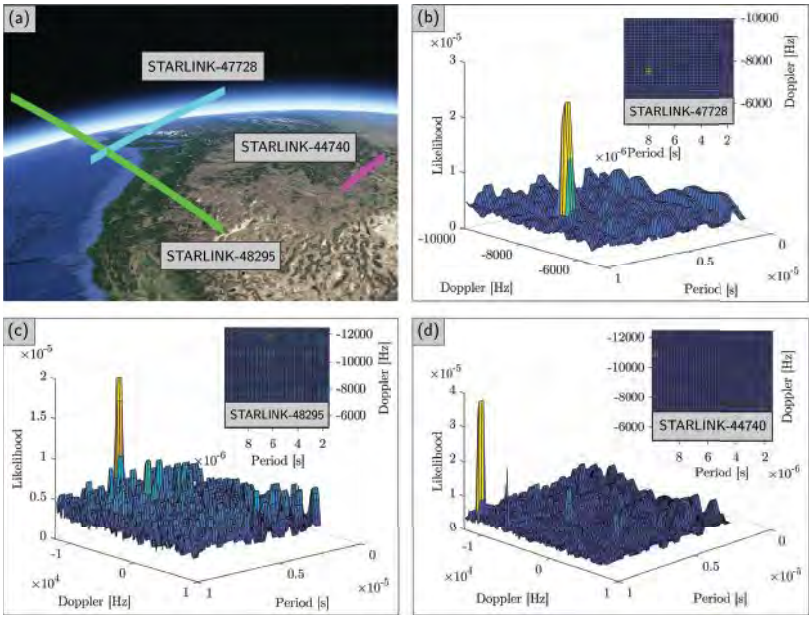

FIGURE 12 (a) Trajectories of the three Starlink satellites used in the differential Doppler positioning experiment. (b)-(d) Acquisition of the three Starlink satellites' signals.

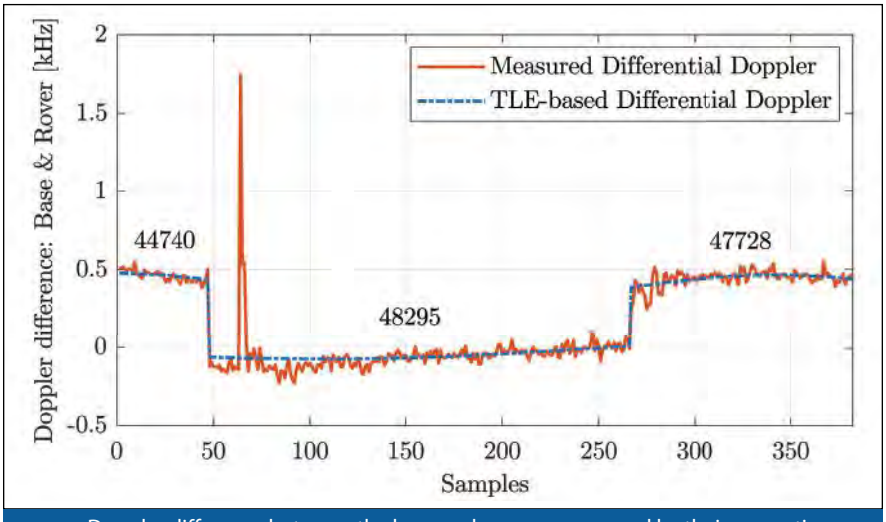

FIGURE 13 Doppler difference between the base and rover as measured by their respective receivers versus TLE-based calculations.

To remedy these challenges, the simultaneous tracking and navigation (STAN) framework was proposed, in which the navigating vehicle's states are simultaneously estimated with the states of the LEO satellites [2],[20]. STAN employs a filter, e.g., an extended Kalman filter (EKF), to aid the vehicle's INS with navigation observables (e.g., carrier phase and Doppler), extracted from LEO satellites' signals in a tightly coupled fashion.

Figure 15 shows a block diagram of the STAN framework. The vehicle's state vector xv, estimated in the STAN framework, is the vehicle's body frame orientation with respect to the Earth-centered Earth-fixed (ECEF) reference frame, the vehicle's 3-D position and velocity in ECEF, and the gyroscope and accelerometer biases, namely

$$x_v = [{}^b_e\bar{q}^T, r_v^T, \dot{r}_v^T, b_g^T, b_a^T]^T \quad (5)$$

The m-th LEO satellite's state vector x_{LEOm} consists of its 3-D position and velocity, expressed in the Earth-centered inertial (ECI) reference frame and the relative clock bias and clock drift between the receiver and the LEO satellite, i.e.,

$$x_{LEO_m} = [r_{LEO_m}^T, \dot{r}_{LEO_m}^T, c\delta t_m, c\dot{\delta} t_m]^T \quad (6)$$

The state vector estimated in the STAN EKF is formed by augmenting the vehicles' states with each LEO satellite's states, i.e.,

$$x_{STAN} = [x_v^T, x_{LEO_1}^T, \ldots, x_{LEO_m}^T]^T \quad (7)$$

Experimental Results: Ground Vehicle Navigation with Starlink and Orbcomm LEO Satellites

This section presents simulation results

FIGURE 14 (a) Rover position initial estimate, (b) Base and rover true locations, and (c) True and estimated positions of the rover.

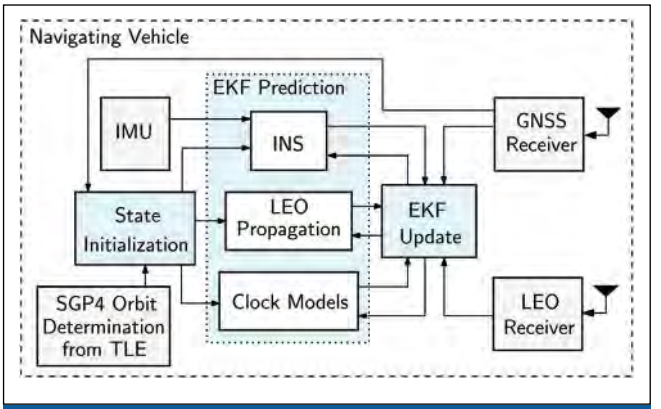

FIGURE 15 STAN framework block diagram.

demonstrating the performance of ground vehicle navigation with 3 Starlink and 2 Orbcomm LEO satellites via the STAN framework. The vehicle was driven along the CA-55 freeway in California, USA, for 4.15 km in 150 seconds. The vehicle was equipped with a Septentrio AsteRx-I V integrated GNSS-INS system, a VectorNav VN-100 microelectro-mechanical systems (MEMS) tactical-grade inertial measurement unit (IMU), two LNBs connected to a USRP-2974 to sample Starlink satellites signals at 11.325 GHz, and a VHF antenna connected to an Ettus E312 USRP to sample Orbcomm signals at 137-138 MHz, as shown in **Figure 16**.

During the first 80 seconds, GNSS signals available, but they were fictitiously cut off for the last 70 seconds of the experiment, during which the vehicle traveled for 1.82 km. The GNSS-INS navigation solution drifted to a 3-D position root mean squared error (RMSE) of 118.5 m from the actual trajectory, while the STAN LEO- aided INS yielded a 3-D position RMSE of 21.6 m.

Figure 17 illustrates the true and estimated trajectories and **Table 3** summarizes the navigation results.

Simulation Results: A Glimpse to the Future

This section presents simulation results demonstrating the achievable opportunistic navigation performance with the future Starlink megasconstellation upon launching its 12,000 LEO satellites that are approved by the FCC. A fixed-wing UAV was equipped with a tactical-grade IMU, an oven-controlled crystal oscillator (OCXO), and GNSS and Starlink LEO receivers. The Starlink receiver produced Doppler measurements to visible Starlink satellites. The Starlink satellites were equipped with chip-scale atomic clocks (CSACs). The Doppler measurement noise variances ranged between 500–1,500 Hz^2, which were varied based on predicted carrier-to-noise ratio, as calculated based on satellites' elevation angle. The simulated UAV compares in performance to a small private plane with a cruise speed of roughly 50 m/s. The UAV flew over Irvine, California, USA for a 300-second trajectory covering 15.43 km.

The trajectory consisted of a straight climbing segment, followed by a figure-eight pattern, and then a final descent into a straight segment. The UAV, initially at 1 km altitude, climbed to an altitude of 1.5 km, where it began executing rolling and yawing maneuvers before descending back down to 1 km in the straight segment. The Starlink satellite states were initialized using TLE files and the trajectories of the 74 Starlink LEO satellites used to navigate the UAV are shown in **Figure 18** (the trajectories are colored in red when the satellites are outside the 20° elevation mask and in green when they are visible to the UAV). GNSS was available for the first 60 s of the flight and STAN with Starlink satellites was performed without GNSS for the last 240 s of the trajectory. **Figure 18** illustrates the simulation results and **Table 4** summarizes the navigation results.

FIGURE 16 Hardware setup for the ground vehicle experiment.

FIGURE 17 Experimental results of a ground vehicle traveling 4.15 km in 150 seconds where the last 70 seconds are in an emulated GNSS-denied environment.

	GNSS-INS	STAN: LEO-INS
RMSE [m]	118.5	21.6
Final Error [m]	472.7	53.6

TABLE 3 Experimental results: ground vehicle navigating with 3 Starlink and 2 Orbcomm LEO satellites over a 1.82 km trajectory without GNSS, traversed in 70 s.

	GNSS-INS	STAN: LEO-INS
RMSE [m]	2,713	13.75
Final Error [m]	5,554	28.49

TABLE 4 Simulation results: UAV navigating with 74 Starlink satellites over a 12.28 km trajectory without GNSS, traversed in 240 s.

References

[1] T. Reid, A. Neish, T. Walter, and P. Enge, "Broadband LEO constellations for navigation," *NAVIGATION, Journal of the Institute of Navigation*, vol. 65, no. 2, pp. 205–220, 2018.

[2] Z. Kassas, J. Morales, and J. Khalife, "New-age satellite-based navigation – STAN: simultaneous tracking and navigation with LEO satellite signals," *Inside GNSS Magazine*, vol. 14, no. 4, pp. 56–65, 2019.

[3] F. Farhangian and R. Landry, "Multi-constellation software-defined receiver for Doppler positioning with LEO satellites," *Sensors*, vol. 20, no. 20, pp. 5866–5883, 2020.

[4] M. Psiaki, "Navigation using carrier doppler shift from a LEO constellation: TRANSIT on steroids," *NAVIGATION, Journal of the Institute of Navigation*, vol. 68, no. 3, pp. 621–641, 2021.

[5] P. Iannucci and T. Humphreys, "Economical fused LEO GNSS," *Proceedings of IEEE/ION Position, Location and Navigation Symposium*, 2020, pp. 426– 443.

[6] M. Orabi, J. Khalife, and Z. Kassas, "Opportunistic navigation with Doppler measurements from Iridium Next and Orbcomm LEO satellites," *Proceedings of IEEE Aerospace Conference*, 2021, pp. 1–9.

[7] "Position, navigation, and timing technologies in the 21st century," J. Morton, F. van Diggelen, J. Spilker, Jr., and B. Parkinson, Eds. Wiley-IEEE, 2021, vol. 2, *Part D: Position, Navigation, and Timing Using Radio Signals-of-Opportunity*, ch. 35– 43, pp. 1115–1412.

[8] J. Khalife and Z. Kassas, "Precise UAV navigation with cellular carrier phase measurements," *Proceedings of IEEE/ ION Position, Location, and Navigation Symposium*, 2018, pp. 978–989.

[9] M. Maaref and Z. Kassas, "Autonomous integrity monitoring for vehicular navigation with cellular signals of opportunity and an IMU," *IEEE Transactions on Intelligent Transportation Systems*, 2021, accepted.

[10] C. Yang and A. Soloviev, "Mobile positioning with signals of opportunity in urban and urban canyon environments," *Proceedings of IEEE/ION Position, Location, and Navigation Symposium*, 2020, pp. 1043–1059.
[11] North American Aerospace Defense Command, "Two-line element sets," http://celestrak.com/NORAD/elements/
[12] B. Tapley, B. Schutz, and G. Born, Statistical Orbit Determination. Burlington, MA: Elsevier Academic Press, 2004.
[13] J. Khalife, M. Neinavaie, and Z. Kassas, "The first carrier phase tracking and positioning results with Starlink LEO satellite signals," *IEEE Transactions on Aerospace and Electronic Systems*, 2021, accepted.
[14] M. Neinavaie, J. Khalife, and Z. Kassas, "Acquisition, Doppler tracking, and positioning with Starlink LEO satellites: first results," *IEEE Transactions on Aerospace and Electronic Systems*, 2021, accepted.
[15] D. Vallado and P. Crawford, "SGP4 orbit determination," *Proceedings of AIAA/AAS Astrodynamics Specialist Conference and Exhibit*, 2008, pp. 1–29.
[16] N. Khairallah and Z. Kassas, "Ephemeris closed-loop tracking of LEO satellites with pseudorange and Doppler measurements," *Proceedings of ION GNSS+ Conference*, 2021, pp. 2544-2555.
[17] S. Kozhaya, J. Haidar-Ahmad, A. Abdallah, S. Saab, and Z. Kassas, "Comparison of neural network architectures for simultaneous tracking and navigation with LEO satellite," *Proceedings of ION GNSS+ Conference*, 2021, pp. 2507–2520.
[18] J. Khalife and Z. Kassas, "Navigation with differential carrier phase measurements from megaconstellation LEO satellites," *Proceedings of IEEE/ION Position, Location and Navigation* Symposium, 2020, pp. 1393– 1404.
[19] D. Gebre-Egziabher, "What is the difference between 'loose', 'tight', 'ultra-tight' and 'deep' integration strategies for INS and GNSS," *Inside GNSS Magazine*, pp. 28–33, 2007.
[20] T. Mortlock and Z. Kassas, "Performance analysis of simultaneous tracking and navigation with LEO satellites," *Proceedings of ION GNSS+ Conference*, 2020, pp. 2416–2429.

Acknowledgment

This work was supported in part by the Office of Naval Research (ONR) under Grant N00014-16-1-2305, in part by the National Science Foundation (NSF) under Grant 1929965, in part by the U.S. Department of Transportation (USDOT) under Grant 69A3552047138 for the CARMEN University Transportation Center (UTC), and in part by the Air Force Office of Scientific Research (AFOSR) under the Young Investigator Program (YIP) Grant. IG

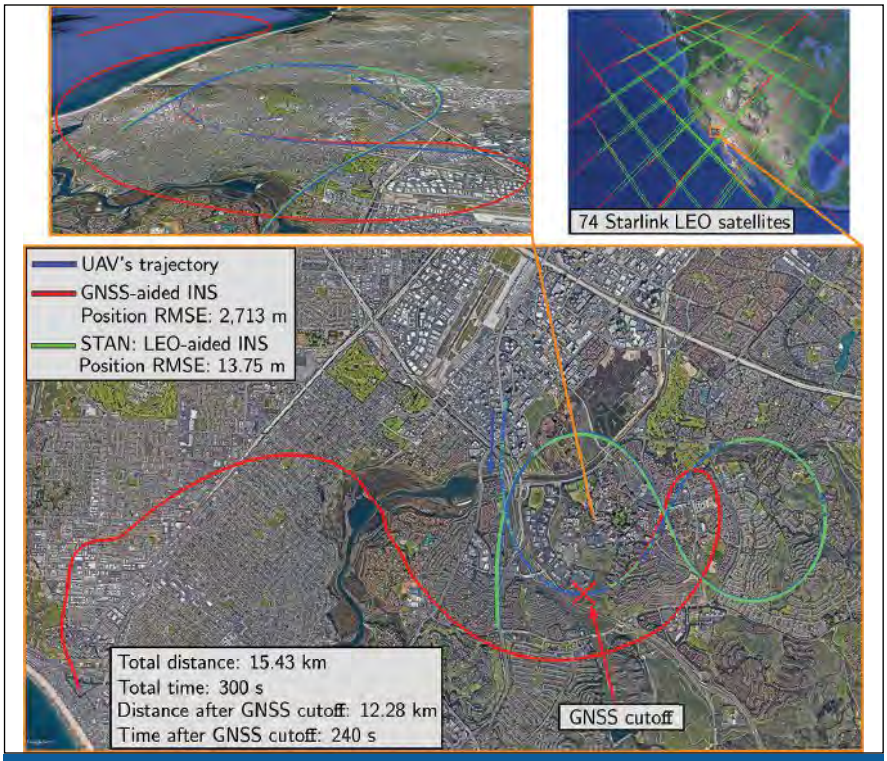

FIGURE 18 Simulation results of a UAV traveling 15.43 km in 300 seconds, where the last 240 seconds are without GNSS signals.

Authors

Zaher (Zak) Kassas is an associate professor at the University of California, Irvine (UCI) and The Ohio State University. He is director of the ASPIN Lab and also director of the U.S. Department of Transportation Center for Automated Vehicle Research with Multimodal AssurEd Navigation (CARMEN). His research interests include cyber-physical systems, navigation systems, and intelligent transportation systems.

Mohammad Neinavaie is a Ph.D. student at UCI and a member of the ASPIN Lab. His research interests include cognitive radio.

Joe Khalife is postdoctoral scholar at the ASPIN Lab. His research interests include modeling and analysis of signals of opportunity.

Nadim Khairallah is a Ph.D. student at UCI and a member of the ASPIN Lab. His research interests include opportunistic navigation.

Sharbel Kozhaya is a Ph.D. student at UCI and a member of the ASPIN Lab. His research interests include cognitive soft-ware defined radio.

Jamil Haidar-Ahmad is a Ph.D. student at UCI and a member of the ASPIN Lab. His research interests include satellite-based navigation

Zeinab Shadram is a postdoctoral scholar at the ASPIN Lab. Her research interests include modeling and analysis of signals of opportunity.

Ephemeris Tracking and Error Propagation Analysis of LEO Satellites with Application to Opportunistic Navigation

Nadim Khairallah and Zaher M. Kassas, *Senior Member, IEEE*

***Abstract*—A comprehensive study is performed for low Earth orbit (LEO) space vehicles (SVs) tracking by a receiver opportunistically extracting navigation observables from their downlink radio frequency signals. First, a framework to characterize the LEO SVs' orbital motion process noise covariance is developed. Second, the tracking performance via an extended Kalman filter (EKF) is analyzed via comprehensive Monte Carlo simulations for three different sets of observables: (i) pseudorange, (ii) Doppler, and (iii) fused pseudorange and Doppler measurements. Third, experimental results are presented demonstrating the efficacy of the opportunistic tracking framework in refining the ephemeris of a LEO SV from two-line element (TLE) files. The initial position and velocity errors of over 7.1 km and 7.3 m/s, respectively, of an Orbcomm LEO SV were reduced to 698.7 m and 1.8 m/s, respectively, in just over 6 minutes of tracking with carrier phase navigation observables, extracted opportunistically. Fourth, the error propagation from the LEO SV's state space to the measurement space and from the measurement space to the receiver's state space is analyzed in the context of stationary receiver localization. Bounds on the magnitude of pseudorange and Doppler residuals are first derived, and the magnitude of the receiver's estimation error is then characterized as a function of errors in the LEO SV's state space. Fifth, experimental results are presented of a stationary receiver tracking an Orbcomm LEO SV by fusing carrier phase observables via an EKF. The tracked LEO ephemeris is then used to localize another stationary receiver, showing a reduction in the receiver's initial horizontal error from 13,476 m to 343 m after just over 6 minutes. In contrast, it is shown that if the SGP4-propagated ephemeris was used in the EKF to localize the receiver, the error is reduced to 6,852 m, but the filter becomes inconsistent.**

***Index Terms*—LEO satellites, ephemeris tracking, pseudorange, Doppler, error propagation, opportunistic navigation.**

I. Introduction

As of January 2022, over 4,000 space vehicles (SVs) were orbiting Earth at altitudes between 160 and 1,000 km [1]. This orbital altitude range is referred to as low Earth orbit (LEO) [2] and is the zone where the next space race is currently booming [3], fueled by broadband Internet megaconstellations (e.g., Starlink, Project Kuiper, among others). Currently, SpaceX leads this race with over 2,500 Starlink SVs already launched, of which more than 2,200 are operational [4]. Furthermore, SpaceX is already approved by the Federal Communications Commission (FCC) to launch over 12,000 SVs and has filed to increase the number of SVs of their Starlink megaconstellation to over 42,000 [5].

This space race, however, can have dire consequences on the sustainability and integrity of space as a shared environment for humanity [6]. With many SVs and space debris already in orbit, a domino effect of space junk generation is likely to happen. This scenario is known as the Kessler Syndrome [7] and is named after the NASA astrophysicist who hypothesized it in 1978. The Kessler Syndrome states that any collision between space objects would generate numerous pieces of space debris that in turn can cause further collisions, thus creating a cascading effect of increasing space debris orbiting Earth. This exponential self-sustaining growth in space junk would pollute space enough that it would render this environment unsustainable for humanity. Space collisions have already happened, the most notable of which being the Iridium 33 – Cosmos 2251 collision that occured in 2009 [8]. The overpopulation of space, particularly in the LEO zone, increases the likelihood of such collisions that would fuel and intensify the effect of the Kessler Syndrome [9].

To prevent such a catastrophe, the field of space situational awareness (SSA) was born [10], [11]. SSA aims at keeping track of all SVs and space debris orbiting the Earth with the goal of preventing collisions. The current state-of-the-art orbit determination technologies for SSA rely on an array of large telescopes, electro-optical surveillance systems, and radars scattered around the globe as part of the Space Surveillance Network (SSN). Operated by the Combined Space Operations Center (CSpOC), the SSN keeps track of more than 23,000 objects in orbit for SSA purposes [12] using range, angle, and optical measurements from radars, telescopes, and electro-optical surveillance systems.

The LEO SVs' ephemeris tracked by the SSN is, however, not released to the public. The most accurate publicly available source to calculate the ephemeris of LEO SVs are two-line element (TLE) sets published online and updated periodically by the North American Aerospace Defense Command (NORAD) using SSN observations. TLE sets consist of a list of mean orbital elements (inclination angle, right ascension of ascending node, eccentricity, argument of perigee, mean anomaly, and mean motion) and corrective terms given at a specified time epoch [13] that a simplified general perturbation model SGP4, can propagate to a desired inquiry time [14]. Although SGP4 takes into account the variation of the orbital

This work was supported in part by the Air Force Office of Scientific Research (AFOSR) under Grant FA9550-22-1-0476, the Office of Naval Research (ONR) under Grant N00014-19-1-2511, and in part by the U.S. Department of Transportation (USDOT) under Grant 69A3552047138 for the CARMEN University Transportation Center (UTC).

N. Khairallah was with the Department of Mechanical and Aerospace Engineering at the University of California, Irvine, USA. Z. Kassas is with the Department of Electrical and Computer Engineering at The Ohio State University. (email: khairaln@uci.edu and zkassas@ieee.org). *Corresponding author: Z. Kassas.*

elements due to Earth's oblateness, atmospheric drag, and various short and long-term perturbations, the TLE-propagated satellite ephemerides suffer from error of a few km in position and a few meters per second in velocity compared to the actual satellite ephemerides.

Despite being launched for communication and broadband Internet [15], LEO SVs present a remarkable potential for both SSA and navigation [16]–[30]. On one hand, their signals can be exploited to track LEO satellites, reducing the ephemeris error by orders of magnitude from open-loop propagators (e.g., SGP4) alleviating the need to install expensive radars, telescopes, and electro-optical surveillance systems [31]–[33]. On the other hand, LEO SVs offer both geometric and spectral diversities, which are desirable attributes for accurate and resilient navigation, respectively. Moreover, LEO SVs are around twenty times closer to Earth than GNSS SVs, which reside in medium Earth orbit (MEO), making LEO signals received with more than 30 dB higher power than their GNSS counterparts [34].

However, there are two main challenges facing opportunistic navigation using LEO SVs. First, their proprietary signals are partially known or completely unknown. For the former case, specialized receivers have been developed, which leverage public knowledge about LEO SVs' periodic signals [35]–[39]. Even when LEO signals are unknown, cognitive signal processing approaches [40] have been shown to yield useful navigation observables [41], [42]. Second, unlike GNSS SVs, LEO SVs generally do not openly transmit information about their clock error states and ephemeris in their downlink signals. To tackle this challenge, the simultaneous tracking and navigation (STAN) framework was proposed, in which the receiver estimates its own states simultaneously with the states of the LEO SVs (position, velocity, and clock error) [43]. To deal with the challenge of now knowing the stability of LEO SVs' clocks, an interacting multiple-model estimator was developed in [44] to estimate online the clock error states process noise covariance.

Concerning the uncertain LEO SVs' ephemerides challenge, SGP4 is the de facto propagator for the publicly available TLE files [45]. However, the magnitude of the LEO SV position error as calculated from the SGP4-propagated TLE ephemeris can range from a few hundred meters to a few km, with most of the error concentrated in the along-track axis of the LEO SV's motion (i.e., along the SV's velocity vector). Beyond SGP4, which is a low-fidelity analytical propagator that improves computational efficiency at the cost of orbit determination accuracy, semi-analytical and high-fidelity numerical propagators [46] that perform costly numerical integration with complex force models can achieve higher propagation accuracies [47]–[52]. However, all numerical and semi-analytical propagators require sufficient prior knowledge of various force model parameters (e.g., atmospheric drag, solar radiation pressure, etc.) as well as an accurate initial estimate [53], [54], which are not readily available. Additionally, erroneous model parameters or initial estimates will cause these propagators to diverge due to model mismatches. Recently, machine learning was explored to tackle the orbit determination problem [31], [33], [55]–[60]. Although showing great promise, these machine learning approaches lack formal guarantees of performance.

This paper aims to study the tracking of LEO SVs by a receiver opportunistically extracting navigation observables (pseudorange, carrier phase, and/or Doppler) from its radio frequency downlink signals to tackle the uncertain ephemeris challenge. The goal of this study is twofold: (i) offer a framework to track LEO SVs via their navigation observables and (ii) enable LEO-based navigation by opportunistically refining publicly available ephemeris information from TLE files, without requiring accurate ephemeris not publicly available. Moreover, the effect of errors in the LEO SVs' states on the localization performance of a stationary receiver is analyzed. The contributions of this paper are:

- A methodology to characterize the LEO SV's orbital motion process noise covariance is first presented. Then, a realistic and comprehensive Monte Carlo (MC) simulation study is performed to assess opportunistic LEO SV tracking performance against the open-loop SGP4-propagation of TLEs for three different sets of observables: (i) pseudorange, (ii) Doppler, and (iii) fused pseudorange and Doppler measurements. These simulations extend [32] by performing MC simulations over various SVs with different elevation profiles with respect to the tracking receiver and with the SGP4 propagator performance evaluated for all realizations.
- Bounds on the pseudorange and Doppler residuals are derived as a function of LEO SV's ephemeris errors and clocks error states magnitude. Additionally, the magnitude of receiver state estimation error is characterized as a function of the errors in the LEO SV's states. Subsequently, the error propagation from the LEO SV's state space to the measurement space and then to the receiver's state space is analyzed.
- Experimental results are presented demonstrating the efficacy of the LEO SV tracking framework with a refinement of the Orbcomm FM107 SV's TLE-derived ephemeris from initial position and velocity errors of over 7.1 km and 7.3 m/s down to final errors of 698.7 m and 1.8 m/s, respectively, in just over 6 minutes of tracking. Furthermore, the derived bounds on measurement residuals and magnitude of receiver state estimation errors are verified experimentally. The tracked LEO ephemeris is then used to localize another stationary receiver, showing a reduction in the receiver's initial horizontal error from 13,476 m to 343 m. In contrast, it is shown that if the SGP4-propagated ephemeris was used in the EKF to localize the receiver, the error is reduced to 6,852 m, but the filter becomes inconsistent.

The remainder of the paper is organized as follows. Section II describes the LEO satellites' orbital dynamics and measurement models. Section III discusses the LEO satellite tracking framework and showcases the MC simulation setup and results. Section IV presents derivations of error propagation from the LEO satellites' ephemeris to the measurements and from the measurements to the estimated states. Section V provides experimental results demonstrating the opportunistic tracking of an Orbcomm satellite. Section VI gives concluding remarks.

II. Model Description

This section describes the LEO satellite orbital dynamics and measurement models used in the opportunistic tracking framework.

A. LEO Satellite Dynamics

A two-body model including the most significant non-zero mean perturbing acceleration is adopted as the LEO satellite orbital dynamics model in the Earth-centered inertial (ECI) reference frame. This model offers a trade-off between accurate open-loop state prediction while maintaining a simple analytical Jacobian for estimation error covariance propagation. The most significant perturbing accelerations for a LEO satellite are due to Earth's non-uniform gravity $\boldsymbol{a}_{\text{grav}}$. The two-body model can be written generally as

$$\ddot{\boldsymbol{r}}_{\text{leo}}(t) = \boldsymbol{a}_{\text{grav}}(t) + \tilde{\boldsymbol{w}}_{\text{leo}}(t), \qquad \boldsymbol{a}_{\text{grav}}(t) = \frac{\partial U(t)}{\partial \boldsymbol{r}_{\text{leo}}(t)}, \quad (1)$$

where $\boldsymbol{r}_{\text{leo}} \triangleq [x_{\text{leo}}, y_{\text{leo}}, z_{\text{leo}}]^{\mathsf{T}}$ is the position vector of the LEO satellite in the ECI frame, U is the non-uniform gravitational potential of Earth at the satellite, and $\tilde{\boldsymbol{w}}_{\text{leo}}$ is a process noise vector in the ECI frame with power spectral density (PSD) $\tilde{\mathbf{Q}}_{\text{leo}}$, which attempts to capture the overall acceleration perturbations including the unmodeled non-uniformity of Earth's gravitational field, atmospheric drag, solar radiation pressure, third-body gravitational forces (e.g., gravity of the Moon and Sun), and general relativity [61].

Several models have been developed for Earth's gravitational potential U. For a satellite requiring accuracies of a few meters, the JGM-3 model developed by Goddard Space Flight Center is usually sufficient [62]. Here, the tesseral and sectoral terms of the JGM-3 model are neglected, since they are several orders of magnitude smaller than the zonal terms (denoted $\{J_n\}_{n=2}^{\infty}$). This yields [63]

$$U = \frac{\mu}{\|\boldsymbol{r}_{\text{leo}}\|}\left[1 - \sum_{n=2}^{N} J_n \frac{R_e^n}{\|\boldsymbol{r}_{\text{leo}}\|^n} P_n\left[\sin(\varphi)\right]\right], \quad (2)$$

where μ is Earth's standard gravitational parameter, P_n is a Legendre polynomial with harmonic n, J_n is the n-th zonal coefficient, R_e is the mean radius of the Earth, $\sin(\varphi) = z_{\text{leo}}/\|\boldsymbol{r}_{\text{leo}}\|$ (i.e., φ being the LEO SV's latitude), and $N = \infty$. Since the acceleration due to the J_2 coefficient is approximately three orders of magnitude greater than the acceleration due to the other zonal coefficients modeling Earth's oblateness, the perturbation due to non-uniform gravity will be approximated by using only the term corresponding to J_2. Taking the partial derivative of (2) with respect to the components of $\boldsymbol{r}_{\text{leo}}$ with $N \equiv 2$ gives the components of $\boldsymbol{a}_{\text{grav}} \triangleq [\ddot{x}_{\text{grav}}, \ddot{y}_{\text{grav}}, \ddot{z}_{\text{grav}}]^{\mathsf{T}}$ in the ECI frame as

$$\begin{aligned}
\ddot{x}_{\text{grav}} &= -\frac{\mu x_{\text{leo}}}{\|\boldsymbol{r}_{\text{leo}}\|^3}\left[1 + J_2\frac{3}{2}\left(\frac{R_e}{\|\boldsymbol{r}_{\text{leo}}\|}\right)^2\left(1 - 5\frac{z_{\text{leo}}^2}{\|\boldsymbol{r}_{\text{leo}}\|^2}\right)\right],\\
\ddot{y}_{\text{grav}} &= -\frac{\mu y_{\text{leo}}}{\|\boldsymbol{r}_{\text{leo}}\|^3}\left[1 + J_2\frac{3}{2}\left(\frac{R_e}{\|\boldsymbol{r}_{\text{leo}}\|}\right)^2\left(1 - 5\frac{z_{\text{leo}}^2}{\|\boldsymbol{r}_{\text{leo}}\|^2}\right)\right],\\
\ddot{z}_{\text{grav}} &= -\frac{\mu z_{\text{leo}}}{\|\boldsymbol{r}_{\text{leo}}\|^3}\left[1 + J_2\frac{3}{2}\left(\frac{R_e}{\|\boldsymbol{r}_{\text{leo}}\|}\right)^2\left(3 - 5\frac{z_{\text{leo}}^2}{\|\boldsymbol{r}_{\text{leo}}\|^2}\right)\right].
\end{aligned} \quad (3)$$

B. Clock Dynamics Model

The receiver's and LEO SVs' clock error state dynamics are assumed to evolve in discrete-time according to [64]

$$\boldsymbol{x}_{\text{clk},i}(k+1) = \mathbf{F}_{\text{clk}}\,\boldsymbol{x}_{\text{clk},i}(k) + \boldsymbol{w}_{\text{clk},i}(k), \quad (4)$$

$$\boldsymbol{x}_{\text{clk},i} \triangleq \left[c\delta t_i,\, c\dot{\delta} t_i\right]^{\mathsf{T}}, \quad \mathbf{F}_{\text{clk}} = \begin{bmatrix} 1 & T \\ 0 & 1 \end{bmatrix},$$

where $i = \{r, \text{leo}\}$, δt_i is the clock bias, $\dot{\delta} t_i$ is the clock drift, c is the speed of light, T is the constant sampling interval, and $\boldsymbol{w}_{\text{clk},i}$ is the process noise, which is modeled as a discrete-time white noise sequence with covariance

$$\mathbf{Q}_{\text{clk},i} = c^2 \cdot \begin{bmatrix} S_{\tilde{w}_{\delta t_i}} T + S_{\tilde{w}_{\dot{\delta} t_i}} T^3/3 & S_{\tilde{w}_{\dot{\delta} t_i}} T^2/2 \\ S_{\tilde{w}_{\dot{\delta} t_i}} T^2/2 & S_{\tilde{w}_{\dot{\delta} t_i}} T \end{bmatrix}, \quad (5)$$

The terms $S_{\tilde{w}_{\delta t_i}}$ and $S_{\tilde{w}_{\dot{\delta} t_i}}$ are the clock bias and drift process noise PSDs, respectively, which can be related to the power-law coefficients, $\{h_{\alpha_i}\}_{\alpha_i=-2}^{2}$, which have been shown through laboratory experiments to characterize the power spectral density of the fractional frequency deviation of an oscillator from nominal frequency according to $S_{\tilde{w}_{\delta t_i}} \approx \frac{h_{0,i}}{2}$ and $S_{\tilde{w}_{\dot{\delta} t_i}} \approx 2\pi^2 h_{-2,i}$ [65]. The receiver's and LEO SVs' process noise covariances $\mathbf{Q}_{\text{clk},r}$ and $\mathbf{Q}_{\text{clk,leo}}$ are calculated from (5) using the PSDs associated with the receiver's and LEO SVs' oscillator quality, respectively.

C. Pseudorange Measurement Model

A LEO receiver extracts pseudorange measurements ρ from LEO SVs by estimating the time-of-arrival. The pseudorange ρ from the LEO SV to the receiver at time-step k, which represents discrete-time instant $t_k = kT + t_0$ for an initial time t_0, is modeled as

$$\begin{aligned}
\rho(k) = \|\boldsymbol{r}_r(k) - \boldsymbol{r}_{\text{leo}}(k')\|_2 + c\cdot[\delta t_r(k) - \delta t_{\text{leo}}(k')]\\
+ c\delta t_{\text{iono}}(k) + c\delta t_{\text{tropo}}(k) + v_\rho(k),
\end{aligned} \quad (6)$$

where k' represents discrete-time at $t_{k'} = kT + t_0 - \delta t_{\text{TOF}}$, with δt_{TOF} being the true time-of-flight of the signal from the LEO SV to the receiver; $\boldsymbol{r}_r$ and $\boldsymbol{r}_{\text{leo}}$ are the receiver's and LEO SV's three-dimensional (3-D) position vectors expressed in the same reference frame, respectively; c is the speed of light; δt_r and δt_{leo} are the receiver's and LEO SV transmitter's clock biases, respectively; δt_{iono} and δt_{tropo} are the ionospheric and tropospheric delays affecting the LEO SV's signal, respectively; and $v_\rho(k)$ is the pseudorange measurement noise, which is modeled as a zero-mean white Gaussian random sequence with variance $\sigma_\rho^2(k)$.

D. Doppler Measurement Model

A LEO receiver extracts Doppler frequency measurements f_D from LEO satellites by subtracting the nominal carrier frequency from the received signal frequency. A pseudorange rate measurement $\dot{\rho}$ can be obtained from

$$\dot{\rho}(t) = -\frac{c}{f_c} f_D(t), \quad (7)$$

where f_c is the carrier frequency.

The pseudorange rate measurement $\dot{\rho}$ from the LEO SV to the receiver at time-step k can be modeled as

$$\dot{\rho}(k) = \left[\dot{\boldsymbol{r}}_r(k) - \dot{\boldsymbol{r}}_{\text{leo}}(k')\right]^{\mathsf{T}} \frac{\left[\boldsymbol{r}_r(k) - \boldsymbol{r}_{\text{leo}_l}(k')\right]}{\left\|\boldsymbol{r}_r(k) - \boldsymbol{r}_{\text{leo}}(k')\right\|_2} + c \cdot \left[\dot{\delta t}_r(k) - \dot{\delta t}_{\text{leo}}(k')\right] + c\dot{\delta t}_{\text{iono}}(k) + c\dot{\delta t}_{\text{tropo}}(k) + v_{\dot{\rho}}(k), \tag{8}$$

where $\dot{\boldsymbol{r}}_r$ and $\dot{\boldsymbol{r}}_{\text{leo}}$ are the receiver's and LEO SV's 3-D velocity vectors expressed in the same reference frame, respectively; $\dot{\delta t}_r$ and $\dot{\delta t}_{\text{leo}}$ are the receiver's and LEO SV's transmitter clock drifts, respectively; $\dot{\delta t}_{\text{iono}}$ and $\dot{\delta t}_{\text{tropo}}$ are the ionospheric and tropospheric delay rates affecting the LEO SV's signal, respectively; and $v_{\dot{\rho}}(k)$ is the pseudorange rate measurement noise, which is modeled as a zero-mean white Gaussian random sequence with variance $\sigma^2_{\dot{\rho}}(k)$.

E. Carrier Phase Measurement Model

The continuous-time carrier phase observable can be obtained by integrating the Doppler measurement over time [66]. The carrier phase measurement ϕ (expressed in meters) made by the receiver on the LEO SV at time-step k can be modeled in discrete-time as

$$\phi(k) = \left\|\boldsymbol{r}_r(k) - \boldsymbol{r}_{\text{leo}}(k')\right\|_2 + c \cdot \left[\delta t_r(k) - \delta t_{\text{leo}}(k')\right] + \lambda N + c\delta t_{\text{iono}}(k) + c\delta t_{\text{tropo}}(k) + v_{\phi}(k), \tag{9}$$

where λ is the wavelength of the carrier signal transmitted by the LEO SV, N is the carrier phase ambiguity of the LEO SV carrier phase measurement, and $v_{\phi}(k)$ is the measurement noise, which is modeled as a zero-mean white Gaussian random sequence with variance $\sigma^2_{\phi}(k)$.

III. Opportunistic LEO Satellite Tracking

This section formulates the LEO SV tracking framework and presents simulation results comparing the tracking performance with pseudorange, Doppler, and fused pseudorange and Doppler versus SGP4's open-loop propagation.

A. Tracking Filter Formulation

An extended Kalman filter (EKF) is implemented to perform the tracking of LEO SVs by a receiver opportunistically extracting navigation observables from the satellite's downlink signals. The state vector estimated by the EKF is defined as

$$\boldsymbol{x} \triangleq \left[\boldsymbol{x}_{\text{leo}}^{\mathsf{T}}, \boldsymbol{x}_{\text{clk}}^{\mathsf{T}}\right]^{\mathsf{T}}, \quad \boldsymbol{x}_{\text{leo}} \triangleq \left[\boldsymbol{r}_{\text{leo}}^{\mathsf{T}}, \dot{\boldsymbol{r}}_{\text{leo}}^{\mathsf{T}}\right],$$

$$\boldsymbol{x}_{\text{clk}} \triangleq \left[c \cdot (\delta t_r - \delta t_{\text{leo}}) \ , \ c \cdot \left(\dot{\delta t}_r - \dot{\delta t}_{\text{leo}}\right)\right]^{\mathsf{T}},$$

where $\boldsymbol{r}_{\text{leo}}$ and $\dot{\boldsymbol{r}}_{\text{leo}}$ are the LEO SV's 3-D position and velocity vectors, expressed in the ECI reference frame, respectively.

The propagation of the LEO SV's position $\boldsymbol{r}_{\text{leo}}$ and velocity $\dot{\boldsymbol{r}}_{\text{leo}}$ is performed by numerical integration of the orbital dynamics equations of motion in (3) during the prediction step of the EKF.

B. LEO Orbital Motion Process Noise Characterization

Since the process noise covariance matrix $\mathbf{Q}_{\boldsymbol{r}\dot{\boldsymbol{r}}_{\text{leo}}}$ of the LEO SV's orbital motion (position and velocity states) not only affects the uncertainty propagation, but also the states' estimates in the tracking filter, it is critical to accurately characterize $\mathbf{Q}_{\boldsymbol{r}\dot{\boldsymbol{r}}_{\text{leo}}}$. To this end, the following general MC-based methodology is adopted.

1) A NORAD-generated publicly available TLE reference file is selected for a LEO SV. The reference TLE epoch as well as the six mean Keplerian elements and corrective terms given at this TLE epoch fully define the orbit of the Orbcomm SV. This reference TLE is propagated for a duration of K seconds spanning just over one orbital period (e.g., $K = 6,000$ for Orbcomm), with a time-step of one second using the SGP4 propagator. The predicted SV position and velocity are saved in $\boldsymbol{x}_{\boldsymbol{r}\dot{\boldsymbol{r}},\text{ref}}(k)$, $k = 1, 2, \ldots, K+1$.
2) N MC realizations are generated by drawing samples from a Gaussian distribution centered at the reference TLE mean Keplerian elements. For each of these N realizations, a TLE file is generated with the same epoch and corrective terms as the reference TLE but with the randomized mean Keplerian elements.
3) Each of the N randomized TLE realizations of the reference TLE are propagated for K seconds with a time-step of one second using the SGP4 propagator and the predicted SV position and velocity $\boldsymbol{x}_{\boldsymbol{r}\dot{\boldsymbol{r}},j}(k)$ are stored at each time-step k for each realization j, where $k = 1, 2, \ldots, K+1$ and $j = 1, 2, \ldots, N$.
4) For each realization j, the value of the process noise $\boldsymbol{w}_{\boldsymbol{r}\dot{\boldsymbol{r}},j}$ is calculated at each time-step $k = 1, \ldots, K$ according to $\boldsymbol{w}_{\boldsymbol{r}\dot{\boldsymbol{r}},j}(k) = \boldsymbol{x}_{\boldsymbol{r}\dot{\boldsymbol{r}},j}(k+1) - \boldsymbol{f}_{\boldsymbol{r}\dot{\boldsymbol{r}}}\left[\boldsymbol{x}_{\boldsymbol{r}\dot{\boldsymbol{r}},j}(k)\right]$, where $\boldsymbol{f}_{\boldsymbol{r}\dot{\boldsymbol{r}}}$ is the nonlinear dynamics model used in the filter's prediction step to propagate the SV's position and velocity states. In this article, $\boldsymbol{f}_{\boldsymbol{r}\dot{\boldsymbol{r}}}$ is specifically taken to be such that $\boldsymbol{f}_{\boldsymbol{r}\dot{\boldsymbol{r}}}(\boldsymbol{r}) = \dot{\boldsymbol{r}}$ and $\boldsymbol{f}_{\boldsymbol{r}\dot{\boldsymbol{r}}}(\dot{\boldsymbol{r}}) = \ddot{\boldsymbol{r}}$, where $\ddot{\boldsymbol{r}}$ are described by the two-body with J2 perturbations equations of motion in (3).
5) The empirical covariance $\mathbf{Q}_{\boldsymbol{r}\dot{\boldsymbol{r}},\text{emp}}$ of the process noise is computed at each time-step k by averaging $\boldsymbol{w}_{\boldsymbol{r}\dot{\boldsymbol{r}},j}(k)\boldsymbol{w}^{\mathsf{T}}_{\boldsymbol{r}\dot{\boldsymbol{r}},j}(k)$ across MC realizations according to $\mathbf{Q}_{\boldsymbol{r}\dot{\boldsymbol{r}},\text{emp}}(k) = \frac{1}{N}\sum_{j=1}^{N} \boldsymbol{w}_{\boldsymbol{r}\dot{\boldsymbol{r}},j}(k)\boldsymbol{w}^{\mathsf{T}}_{\boldsymbol{r}\dot{\boldsymbol{r}},j}(k)$, $k = 1, \ldots, K$.

Since both the SGP4 propagation $\boldsymbol{x}_{\boldsymbol{r}\dot{\boldsymbol{r}},j}(k+1)$ and the filter's prediction $\boldsymbol{f}_{\boldsymbol{r}\dot{\boldsymbol{r}}}\left[\boldsymbol{x}_{\boldsymbol{r}\dot{\boldsymbol{r}},j}(k)\right]$ are performed in the ECI reference frame, the process noise vectors $\boldsymbol{w}_{\boldsymbol{r}\dot{\boldsymbol{r}},j}(k)$ are also expressed in the ECI frame. As a result, $\mathbf{Q}_{\boldsymbol{r}\dot{\boldsymbol{r}},\text{emp}}(k)$ will be the empirical process noise covariance at each time-step expressed in the ECI frame.

To provide an intuitive interpretation of the effect of the process noise on the LEO SV's motion, the rotation matrix $\mathbf{R}_i^o$ from the ECI frame, denoted $\{i\}$, to the SV's Radial-Transverve-Normal (RTN) frame, denoted $\{o\}$ for orbital frame, where the transverse and normal axes correspond to along-track and cross-track directions, respectively, is computed at each time-step k. The empirical process noise covariance determined by the MC analysis described above

${}^{i}\mathbf{Q}_{\boldsymbol{r}\dot{\boldsymbol{r}},\text{emp}}(k)$ is then rotated to form ${}^{o}\mathbf{Q}_{\boldsymbol{r}\dot{\boldsymbol{r}},\text{emp}}(k)$, $k = 1, 2, \ldots, K$.

In addition, ${}^{o}\mathbf{Q}_{\boldsymbol{r}\dot{\boldsymbol{r}},\text{emp}}$ is more invariant than ${}^{i}\mathbf{Q}_{\boldsymbol{r}\dot{\boldsymbol{r}},\text{emp}}$ since in the SV's RTN frame, the SV's motion is constrained to be in the along-track – radial plane (orbital plane) with the velocity in the along-track direction and with no motion in the cross-track direction; whereas in the ECI frame, the LEO SV's motion has generally components in all directions which are time-varying as the SV orbits Earth. Moreover, the invariance brought by the expression of the process noise covariance matrix in the SV's RTN frame allows for a generalization of ${}^{o}\mathbf{Q}_{\boldsymbol{r}\dot{\boldsymbol{r}},\text{emp}}$ to all LEO SVs, which have similar motion characteristics in the RTN frame, while ${}^{i}\mathbf{Q}_{\boldsymbol{r}\dot{\boldsymbol{r}},\text{emp}}$ would only be applicable for the reference SV chosen in the MC framework at a specific time determined by the SV's position in the ECI frame. To further enhance the generalization of the process noise covariance matrix, the invariance of ${}^{o}\mathbf{Q}_{\boldsymbol{r}\dot{\boldsymbol{r}},\text{emp}}$ is leveraged to define ${}^{o}\bar{\mathbf{Q}}_{\boldsymbol{r}\dot{\boldsymbol{r}},\text{emp}} \triangleq \frac{1}{K}\sum_{k=1}^{K} {}^{o}\mathbf{Q}_{\boldsymbol{r}\dot{\boldsymbol{r}},\text{emp}}(k)$, which will be used in the LEO SV tracking filter. The 95^{th}-percentile error ellipsoid associated with the LEO SV's position states (i.e, top-left 3×3 block of ${}^{o}\bar{\mathbf{Q}}_{\boldsymbol{r}\dot{\boldsymbol{r}},\text{emp}}$) can be visualized in Fig. 1.

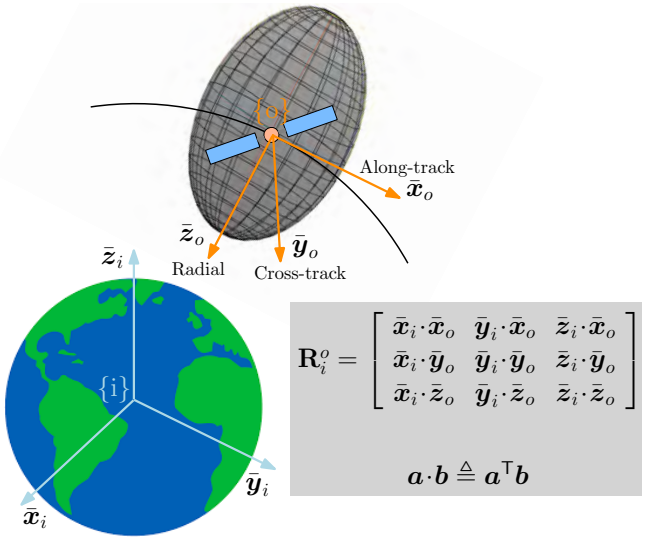

Fig. 1. Visualization of the 95^{th}-percentile error ellipsoid of the averaged process noise covariance characterized for one orbital period for the LEO SV's position states. The rotation matrix $\mathbf{R}_i^o$ rotates the coordinates of a vector expressed in the ECI frame $\{i\}$ into the LEO SV's RTN frame $\{o\}$. The principal directions of $\{i\}$ and $\{o\}$ are represented by the unit vectors $\bar{\boldsymbol{x}}_i$, $\bar{\boldsymbol{y}}_i$, $\bar{\boldsymbol{z}}_i$ and $\bar{\boldsymbol{x}}_o$, $\bar{\boldsymbol{y}}_o$, $\bar{\boldsymbol{z}}_o$, respectively. The notation $a \cdot b$ denotes the inner product of vectors a and b.

To validate this methodology, the empirical position and velocity covariance matrix ${}^{i}\mathbf{P}_{\boldsymbol{r}\dot{\boldsymbol{r}},\text{emp}}(k) = \frac{1}{N}\sum_{j=1}^{N} \tilde{\boldsymbol{x}}_{\boldsymbol{r}\dot{\boldsymbol{r}},j}(k)\tilde{\boldsymbol{x}}_{\boldsymbol{r}\dot{\boldsymbol{r}},j}^{\mathsf{T}}(k)$, where $\tilde{\boldsymbol{x}}_{\boldsymbol{r}\dot{\boldsymbol{r}},j}(k) \triangleq \boldsymbol{x}_{\boldsymbol{r}\dot{\boldsymbol{r}},\text{ref}}(k) - \boldsymbol{x}_{\boldsymbol{r}\dot{\boldsymbol{r}},j}(k)$, is computed from $N = 100$ MC runs of SGP4 propagation of different TLE realizations. In parallel, the filter's open-loop formal covariance is computed by propagating the *initial* empirical position and velocity covariance matrix ${}^{i}\mathbf{P}_{\boldsymbol{r}\dot{\boldsymbol{r}},\text{emp}}(1)$ via the nonlinear dynamics $\boldsymbol{f}_{\boldsymbol{r}\dot{\boldsymbol{r}}}$ coupled to the ${}^{o}\bar{\mathbf{Q}}_{\boldsymbol{r}\dot{\boldsymbol{r}},\text{emp}}$ term to account for the process noise of the SV's position and velocity states and is denoted by ${}^{i}\mathbf{P}_{\boldsymbol{r}\dot{\boldsymbol{r}},\text{prop}}(k)$. At each time-step k, ${}^{o}\bar{\mathbf{Q}}_{\boldsymbol{r}\dot{\boldsymbol{r}},\text{emp}}$ was rotated using the current rotation matrix $\mathbf{R}_o^i(k)$ to form ${}^{i}\bar{\mathbf{Q}}_{\boldsymbol{r}\dot{\boldsymbol{r}},\text{emp}}(k)$ and perform the propagation of ${}^{i}\mathbf{P}_{\boldsymbol{r}\dot{\boldsymbol{r}},\text{prop}}$ in the ECI frame. Finally, the absolute difference between the empirical and propagated position standard deviations is plotted in Fig. 2 in the LEO SV's RTN frame for $k = 1, \ldots, K+1$.

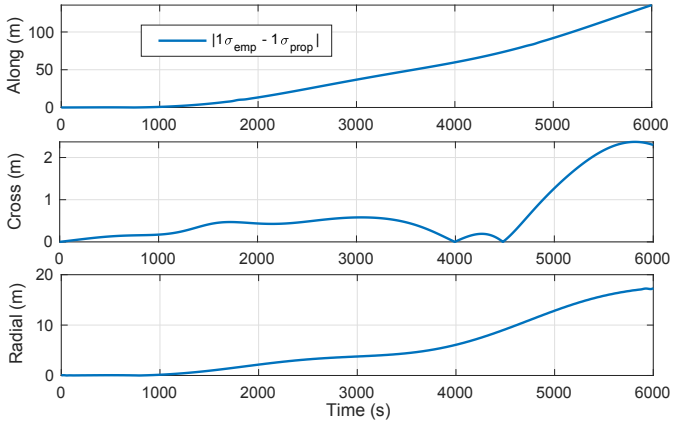

Fig. 2. Absolute difference between the empirical and propagated formal position standard deviations in the RTN frame for one orbital period.

The following comments and observations can be made. First, although the difference between the SGP4-propagated ephemerides and the orbital dynamics model $\boldsymbol{f}_{\boldsymbol{r}\dot{\boldsymbol{r}}}$ used is deterministic, the randomness in this approach stems from the initial dispersion of TLEs around the reference TLE in step 2 of the above methodology. Second, SGP4 was chosen as the source of truth orbit model since using a higher-fidelity analytical propagator would result in a less representative ephemeris without accurate knowledge of the ballistic coefficient [53], [54], which is not readily available. Third, the deviation of the SGP4 predictions from the actual truth ephemeris is small for 1-second propagation intervals and justifies the use of SGP4 as the source of orbit truth in this analysis. Fourth, the error ellipsoid of the LEO SV's position states process noise covariance matrix is mostly elongated in the radial direction (see Fig. 1). This can be explained by the fact that most of the acceleration perturbations are in this direction and are mainly caused by the unmodeled non-uniformity of Earth's gravitational potential beyond the J_2 term. Fifth, the absolute difference between the empirical and propagated LEO SV position states standard deviations is the largest for the along-track axis, revealing that the LEO SV position process noise covariance was matched the least in this direction. Nevertheless, the absolute difference for the position in the along-track axis is less than 150 m after more than one orbit of open-loop propagation around Earth as shown in Fig. 2. For time spans less than 10 minutes, during which a LEO SV is typically visible to a receiver, this absolute difference is very small. Finally, the close agreement between the empirical and formal covariances in Fig. 2 demonstrates that the orbital motion process noise covariance characterized by the averaging approach in the above methodology is reliable to be used in the tracking filter.

C. Simulation Setup

A comprehensive MC simulation is performed to study the efficacy of opportunistic LEO SV tracking using 3 different sets of observables: (i) pseudorange measurements, (ii) Doppler measurements, and (iii) fused pseudorange and Doppler measurements. In this simulation, 103 SVs with diverse elevation profiles and geometries relative to the receiver, as depicted in the skyplot in Fig. 3, are tracked with each set of measurements at a rate of 1 Hz for a duration of 5 minutes. For each of the 103 SVs, 100 MC runs are simulated resulting in a total of 10,300 tracking runs for each set of observables. In each MC run, the initial SV's position and velocity is obtained from a randomized TLE, which is generated with realistic errors consistent with uncertainties observed in NORAD-published TLEs. Moreover, the time evolution of the receiver's and LEO SVs' clock error states as well as the measurement noise are randomized for each MC run. The simulation setup and randomization settings are presented next.

1) Receiver and LEO Satellites' Trajectories: The tracking receiver was simulated to be stationary with a known location on the University of California, Irvine, USA campus. The receiver was placed on the top of a parking structure to garantee an open sky environment with no obstructed views in all directions. Consequently, multipath effects affecting the incoming SV downlink signals are assumed to be negligible for the tracking receiver. Also, since the LEO SV tracking is performed in the ECI frame, the receiver's position and velocity is also found in the ECI frame by converting the stationary Earth-centered, Earth-fixed (ECEF) position while accounting for Earth's rotation, nutation and precession effects, and polar motion.

The FCC-approved 12,000-satellite Starlink LEO constellation was simulated using orbital parameters found in the FCC filings. The LEO SV' trajectories were obtained through SGP4 propagations of simulated TLEs for the Starlink satellite megaconstellation. The elevation angle mask was set to 10°.

2) Clock Errors: The receiver was assumed to be equipped with a typical-quality oven-controlled crystal oscillator (OCXO) and the LEO SVs were assumed to have high-quality OCXOs. The power-law coefficients of these oscillators are given in Table I and can be used to compute the discrete-time process noise covariance for the clock error states $\mathbf{Q}_{\text{clk},r}$ and $\mathbf{Q}_{\text{clk,leo}}$. The clock bias and drift of the LEO receiver and LEO SV transmitters were simulated according to the standard two-state clock error model [64]. The values of the receiver's clock error states $\boldsymbol{x}_{\text{clk},r}(0) \triangleq \left[c\delta t_r(0), c\dot{\delta} t_r(0)\right]$ were initialized as $\boldsymbol{x}_{\text{clk},r}(0) \sim \mathcal{N}\left[\mathbf{0}_{2\times 1}, \mathbf{P}_{\text{clk},r}\right]$, where $\mathbf{P}_{\text{clk},r} = \text{diag}\left[9\times 10^4, 9\times 10^{-2}\right]$ with units of [m^2, (m/s)^2] corresponding to a 1σ of 1 μs and 1 ns/s for the clock bias and drift, respectively. The values of the LEO SVs' clock error states $\boldsymbol{x}_{\text{clk,leo}}(0) \triangleq \left[c\delta t_{\text{leo}}(0), c\dot{\delta} t_{\text{leo}}(0)\right]$ were initialized as $\boldsymbol{x}_{\text{clk,leo}}(0) \sim \mathcal{N}\left[\mathbf{0}_{2\times 1}, \mathbf{P}_{\text{clk,leo}}\right]$, where $\mathbf{P}_{\text{clk,leo}} = \text{diag}\left[9\times 10^2, 9\times 10^{-4}\right]$ with units of [m^2, (m/s)^2] corresponding to a 1σ of 0.1 μs and 0.1 ns/s for the clock bias and drift, respectively.

3) Measurements: Pseudorange navigation observables to all visible LEO SVs were generated according to (6). The time-varying pseudorange measurement noise variances were calculated from the predicted carrier-to-noise (C/N_0), which was found from the log-distance path loss model

$$(C/N_0)_l(k) = P_0 - 10\log_{10}\left(d_l(k)/D_0\right), \tag{10}$$

where $P_0 = 56$ dB-Hz is the nominal C/N_0 at a distance $D_0 = 1{,}000$ km and $d_l(k) \triangleq \|\boldsymbol{r}_r(k) - \boldsymbol{r}_{\text{leo}_l}(k)\|_2$ is the distance between the receiver and the l-th LEO SV. The pseudorange measurement noise variances are proportional to the square root of the inverse of C/N_0, expressed in linear units, and ranged between 0.43 and 3.73 m^2.

Pseudorange rate measurements to all visible LEO SVs were generated according to (8). Pseudorange rate measurements are directly proportional to Doppler frequency observables as demonstrated in (7) but are independent of the carrier frequency. Hence, pseudorange rate measurements were preferred over Doppler to obtain comparable measurements from different constellations which transmit downlink signals at frequencies that are orders of magnitude apart. From (10), based on the distance between the receiver and SVs, the pseudorange rate measurement noise variances, expressed in linear units, ranged between 0.13 and 1.17 (m/s)^2.

The simulated measurements were assumed to have been corrected for tropospheric and ionospheric effects using available models in the literature [66]. The remaining modeling errors are lumped in the white measurement noise, with temporal correlations being neglected for simplicity. Future studies could readily generalize these simulations by incorporating such correlations.

TABLE I
RECEIVER'S AND LEO SVS' OSCILLATOR PARAMETERS

Quality	**Coefficients** $\{\boldsymbol{h_0}, \boldsymbol{h_{-2}}\}$
Receiver's typical-quality OCXO	$\{8.0\times 10^{-20}, 4.0\times 10^{-23}\}$
LEO SVs' high-quality OCXO	$\{2.6\times 10^{-22}, 4.0\times 10^{-26}\}$

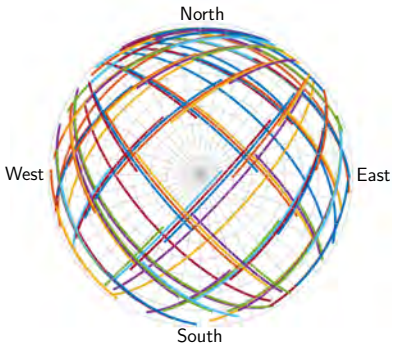

Fig. 3. Skyplot of simulated trajectories of 103 SVs.

D. Filter Initialization

The l-th LEO SV position and velocity state estimates $\hat{\boldsymbol{x}}_{\boldsymbol{r}\dot{\boldsymbol{r}}_{\text{leo},l}}(0|0) \triangleq \left[\hat{\boldsymbol{r}}^{\mathsf{T}}_{\text{leo},l}(0|0), \hat{\dot{\boldsymbol{r}}}^{\mathsf{T}}_{\text{leo},l}(0|0)\right]^{\mathsf{T}}$ were initialized in the ECI frame, denoted by $\{i\}$, as follows

$$\hat{\boldsymbol{x}}_{\boldsymbol{r}\dot{\boldsymbol{r}}_{\text{leo},l}}(0|0) \sim \mathcal{N}\left[\boldsymbol{x}_{\boldsymbol{r}\dot{\boldsymbol{r}}_{\text{leo},l}}(0), \mathbf{P}_{\boldsymbol{x}_{\boldsymbol{r}\dot{\boldsymbol{r}}_{\text{leo},l}}}(0|0)\right]$$

$$\mathbf{P}_{\boldsymbol{x}_{\boldsymbol{r}\dot{\boldsymbol{r}}_{\mathrm{leo},l}}}(0|0) \triangleq \mathrm{diag}\left[\mathbf{P}_{\boldsymbol{x}_{\boldsymbol{r}_{\mathrm{leo},l}}}(0|0), \mathbf{P}_{\boldsymbol{x}_{\dot{\boldsymbol{r}}_{\mathrm{leo},l}}}(0|0)\right]$$

$$\mathbf{P}_{\boldsymbol{x}_{\boldsymbol{r}_{\mathrm{leo},l}}}(0|0) = \mathbf{R}^{i}_{o_{\mathrm{leo},l}}(0)\,{}^{o_{\mathrm{leo}}}\mathbf{P}_{\boldsymbol{x}_{\boldsymbol{r}_{\mathrm{leo}}}}(0|0)\left[\mathbf{R}^{i}_{o_{\mathrm{leo},l}}(0)\right]^{\mathsf{T}}$$

$$\mathbf{P}_{\boldsymbol{x}_{\dot{\boldsymbol{r}}_{\mathrm{leo},l}}}(0|0) = \mathbf{R}^{i}_{o_{\mathrm{leo},l}}(0)\,{}^{o_{\mathrm{leo}}}\mathbf{P}_{\boldsymbol{x}_{\dot{\boldsymbol{r}}_{\mathrm{leo}}}}(0|0)\left[\mathbf{R}^{i}_{o_{\mathrm{leo},l}}(0)\right]^{\mathsf{T}},$$

where $\boldsymbol{x}_{\boldsymbol{r}\dot{\boldsymbol{r}}_{\mathrm{leo},l}}(0)$ is the l-th LEO SV's true position and velocity states in ECI and $\mathbf{P}_{\boldsymbol{x}_{\boldsymbol{r}\dot{\boldsymbol{r}}_{\mathrm{leo},l}}}(0|0)$ is the associated initial covariance; ${}^{o_{\mathrm{leo}}}\mathbf{P}_{\boldsymbol{x}_{\boldsymbol{r}_{\mathrm{leo}}}}(0|0) \triangleq \mathrm{diag}\left[4\times10^{6}, 10^{2}, 10^{4}\right]$ m^2 and ${}^{o_{\mathrm{leo}}}\mathbf{P}_{\boldsymbol{x}_{\dot{\boldsymbol{r}}_{\mathrm{leo}}}}(0|0) \triangleq \mathrm{diag}\left[4\times10^{-2}, 10^{-4}, 4\right]$ $(\mathrm{m/s})^2$ are the initial LEO SV's position and velocity covariances in the SV's orbital RTN frame $\{o_{\mathrm{leo}}\}$, respectively; and $\mathbf{R}^{i}_{o_{\mathrm{leo},l}}(0)$ is the initial rotation matrix from the l-th LEO SV's orbital RTN frame $\{o_{\mathrm{leo}_l}\}$ to the ECI frame $\{i\}$. The first entry of the LEO SV's position and velocity covariances in the SV's RTN frame corresponds to the SVs' along-track axis, the second entry is associated with the cross-track direction, and the last entry is for the radial axis. These values were carefully selected to closely match the uncertainties inherent to TLE files with the most uncertainty being in the along-track position and radial velocity, while the cross-track direction TLE errors are the least substantial as the SVs' motion is constrained in the orbital (along-track – radial) plane.

The LEO SVs' position and velocity states process noise covariance ${}^{o}\bar{\mathbf{Q}}_{\boldsymbol{r}\dot{\boldsymbol{r}},\mathrm{emp}}$ found from the methodology in Subsection III-B was used in the EKF to account for the effect of unmodeled uncertainties in the LEO SVs' orbital motion. This process noise covariance matrix expressed in the SV's RTN frame was rotated to the ECI frame at each EKF time update step for every LEO SV. Note that the time-step of 1 second, chosen in Subsection III-B, is consistent with the propagation time-step in the EKF, as the measurement updates are performed at a rate of 1 Hz.

The filter's clock error states $\boldsymbol{x}_{\mathrm{clk}}(0|0)$ were initialized as $\boldsymbol{x}_{\mathrm{clk}}(0|0) \sim \mathcal{N}\left[\mathbf{0}_{2\times1}, \mathbf{P}_{\mathrm{clk}}(0|0)\right]$, where $\mathbf{P}_{\mathrm{clk}}(0|0) = \mathbf{P}_{\mathrm{clk},r} + \mathbf{P}_{\mathrm{clk,leo}}$. The process noise covariance for the filter's clock error states is set to $\mathbf{Q}_{\mathrm{clk}} = \mathbf{Q}_{\mathrm{clk},r} + \mathbf{Q}_{\mathrm{clk,leo}}$, with $\mathbf{Q}_{\mathrm{clk},r}$ and $\mathbf{Q}_{\mathrm{clk,leo}}$ computed from (5) using the oscillator parameters found in Table I.

E. Tracking Results

This subsection presents MC tracking simulation results for the 3 observable sets: (i) pseudorange measurements, (ii) Doppler measurements, and (iii) fused pseudorange and Doppler measurements.

The EKF-tracked position and velocity root mean-squared errors (RMSEs) were computed for each SV by averaging over the ensemble of 100 MC realizations performed for each SV. These position and velocity RMSEs were then averaged over all 103 SVs tracked in the simulation. Furthermore, open-loop SGP4 propagations of the randomized TLE, which served to initialize the EKF's initial position and velocity estimates, were performed for each MC realization. The average performance of SGP4 is computed in a similar fashion to EKF tracking: an ensemble average over the MC realizations for each SV is then averaged over all SVs. Figs. 4 and 5, respectively, show the position and velocity RMSEs expressed in the RTN frame of the open-loop SGP4-propagated ephemerides as well as the ephemerides tracked using the 3 different set of observables: (i) pseudorange measurements, (ii) Doppler measurements, and (iii) fused pseudorange and Doppler measurements. Fig. 6 shows the magnitude of the LEO SV position error for the open-loop SGP4 propagation and the tracking using the 3 measurement sets. The EKF-tracked clock states RMSEs were also computed with respect to the simulated clock error states in Subsection III-C2 by first averaging over the 100 MC realizations for each SV, then by averaging over all 103 simulated SVs. Fig. 7 shows the clock error states RMSEs for opportunistic LEO SV tracking with the 3 different set of measurements.

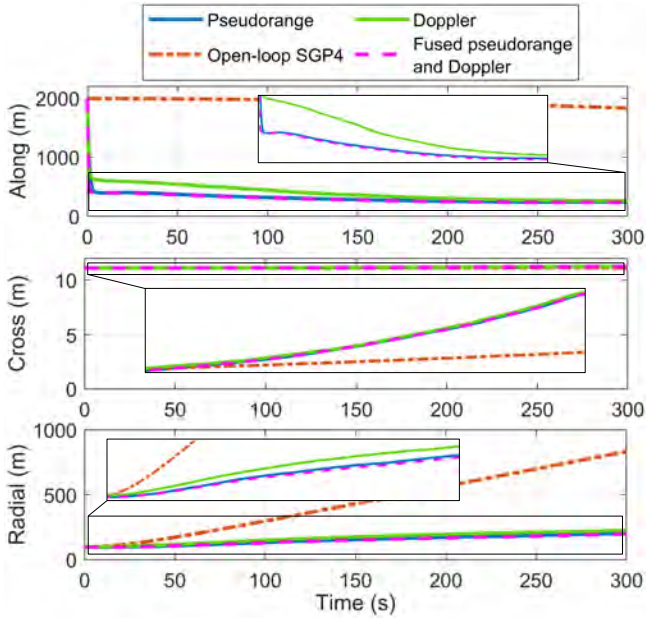

Fig. 4. Position RMSEs for tracking using pseudorange, Doppler, and fused pseudorange and Doppler versus SGP4's open-loop position RMSE.

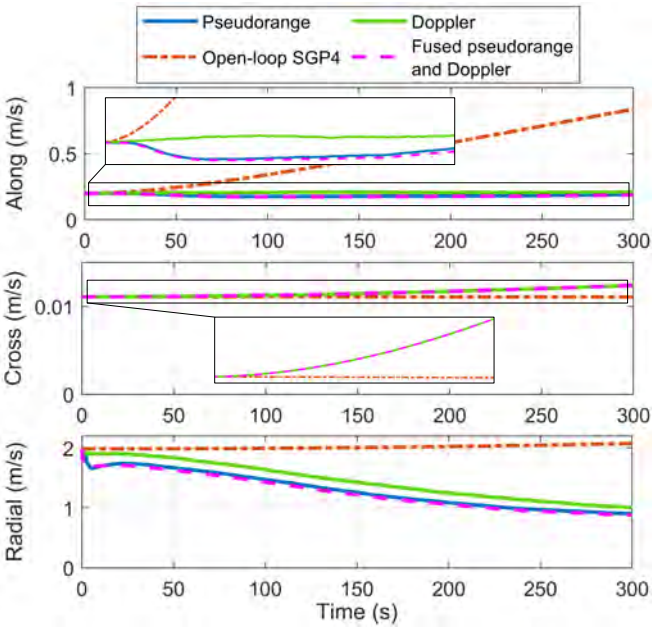

Fig. 5. Velocity RMSEs for tracking using pseudorange, Doppler, and fused pseudorange and Doppler versus SGP4's open-loop position RMSE.

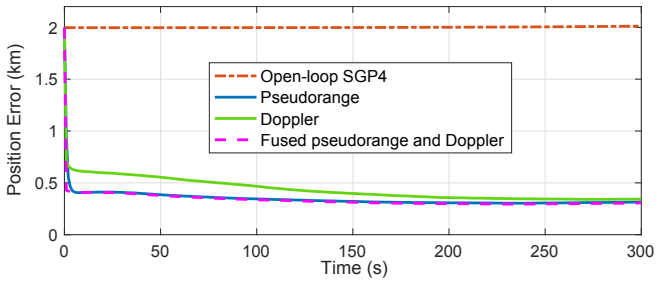

Fig. 6. Magnitude of position error for tracking using pseudorange, Doppler, and fused pseudorange and Doppler versus SGP4's open-loop position error.

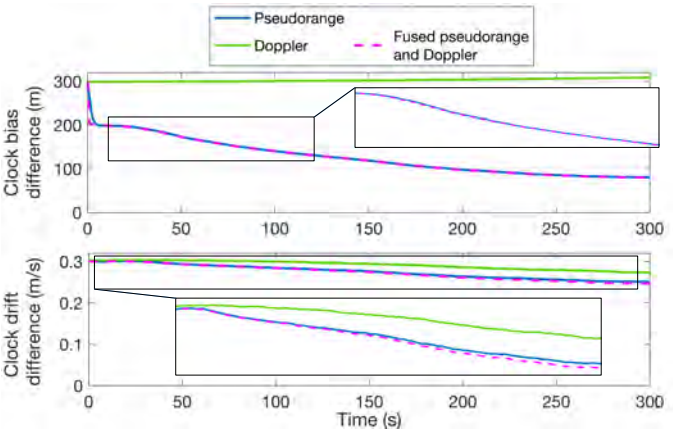

Fig. 7. Clock bias and drift difference RMSEs for tracking using pseudorange, Doppler, and fused pseudorange and Doppler.

This comprehensive MC study reveals the average performance of the opportunistic LEO tracking framework presented in this paper. The following conclusions can be made from these simulations. First, it can be seen that the cross-track direction is the least observable for both position and velocity states. This can be explained by the fact that the SV's motion is restricted in the along-track–radial plane. As a result, the cross-track direction is not excited during the SV's motion, which leads to poor estimability of the corresponding states. Second, it can be seen from Figs. 4-6 that using pseudorange measurements yield better LEO SV tracking performance than Doppler measurements. Third, fusing both pseudorange and Doppler measurements yields negligible improvements over pseudorange-only tracking. This is suggested by the fact that both types of measurements are highly dependent (cf. (7), thus leading to a negligible information increase when augmenting the pseudorange measurement vector to include both navigation observables. Fourth, it is worth noting that the clock bias term $c\left[\delta t_r - \delta t_{\text{leo}}\right]$ is unobservable with Doppler measurements only and is consequently not actively estimated during LEO SV tracking with this set of observables. This can be seen in the top plot in Fig. 7, where the clock bias RMSE diverges for LEO SV tracking with Doppler measurements. Fifth, the relative clock error states tracking performance is comparable to the relative position and velocity tracking performance with the different sets of measurements: pseudorange observables yield smaller RMSEs than Doppler observables and combining both type of measurements result in a negligible improvement in the tracking performance over pseudorange-only tracking.

IV. Effect of LEO Satellite State Errors on Navigation Performance

This section studies the measurement errors resulting from SVs' state errors and analyzes the effect of these measurement errors on the localization error of a stationary unknown receiver.

A. Measurement Errors Due to LEO Satellite State Errors

Let $\hat{\boldsymbol{r}}_{\text{leo}_l}(k)$ and $\hat{\dot{\boldsymbol{r}}}_{\text{leo}_l}(k)$ be the l-th LEO SV erroneous position and velocity obtained using TLEs at time-step k, respectively. Define $\tilde{\boldsymbol{r}}_{\text{leo}_l}(k)$ and $\tilde{\dot{\boldsymbol{r}}}_{\text{leo}_l}(k)$ to be the errors at time-step k of propagated LEO ephemerides (e.g., from SGP4) of the l-th LEO SV position and velocity, respectively, as

$$\tilde{\boldsymbol{r}}_{\text{leo}_l}(k) \triangleq \boldsymbol{r}_{\text{leo}_l}(k) - \hat{\boldsymbol{r}}_{\text{leo}_l}(k)$$
$$\tilde{\dot{\boldsymbol{r}}}_{\text{leo}_l}(k) \triangleq \dot{\boldsymbol{r}}_{\text{leo}_l}(k) - \hat{\dot{\boldsymbol{r}}}_{\text{leo}_l}(k),$$

where $\boldsymbol{r}_{\text{leo}_l}(k)$ and $\dot{\boldsymbol{r}}_{\text{leo}_l}(k)$ are the l-th LEO SV true position and velocity at time-step k, respectively.

Define $c\tilde{\delta t}$ and $c\tilde{\dot{\delta}}t$ to be the errors in the clock error states estimates as

$$c\tilde{\delta t}_l(k) \triangleq c\left[\delta t_r(k) - \delta t_{\text{leo}_l}(k'_l)\right] - c\left[\hat{\delta t}_r(k) - \hat{\delta t}_{\text{leo}_l}(k'_l)\right]$$
$$c\tilde{\dot{\delta}}t_l(k) \triangleq c\left[\dot{\delta t}_r(k) - \dot{\delta t}_{\text{leo}_l}(k'_l)\right] - c\left[\hat{\dot{\delta}}t_r(k) - \hat{\dot{\delta}}t_{\text{leo}_l}(k'_l)\right]$$

Next, bounds on pseudorange and pseudorange rate measurement errors are derived as a function of SVs' state errors.

1) Bound on Pseudorange Measurements: A receiver only having access to TLEs would produce an estimated pseudorange measurement $\hat{\rho}_l(k)$ to the l-th LEO SV as

$$\hat{\rho}_l(k) = \left\|\boldsymbol{r}_r(k) - \hat{\boldsymbol{r}}_{\text{leo}_l}(k'_l)\right\|_2 + c\left[\hat{\delta t}_r(k) - \hat{\delta t}_{\text{leo}_l}(k'_l)\right] \quad (11)$$

where $c\left[\hat{\delta t}_r(k) - \hat{\delta t}_{\text{leo}_l}(k'_l)\right]$ is the clock error bias estimate that the receiver's filter maintains. If no prior is available for this clock error bias, different initialization schemes could be implemented, such as initializing this term to zero or setting this term to be the difference between the true measurement and the estimated range, thus effectively setting the value of the clock bias error to make the predicted measurement match the true measurement.

Performing a first-order Taylor series expansion of the erroneous pseudorange measurement estimate $\hat{\rho}_l(k)$ in (11) about the l-th LEO SV true position $\boldsymbol{r}_{\text{leo}_l}(k)$ and true clock bias difference $c\left[\delta t_r(k) - \delta t_{\text{leo}_l}(k'_l)\right]$ yields

$$\hat{\rho}_l(k) \approx \rho_l(k) + \boldsymbol{h}_l^{\mathsf{T}}(k)\tilde{\boldsymbol{r}}_{\text{leo}_l}(k) - c\tilde{\delta t}_l(k), \quad (12)$$

where $\boldsymbol{h}_l(k) \triangleq \frac{\boldsymbol{r}_r(k) - \boldsymbol{r}_{\text{leo}_l}(k'_l)}{\left\|\boldsymbol{r}_r(k) - \boldsymbol{r}_{\text{leo}_l}(k'_l)\right\|_2}$ is the unit line-of-sight (LOS) vector pointing from the l-th LEO SV to the receiver at time-step k.

Defining the pseudorange residual $\Delta\rho_l(k)$ of the l-th LEO SV as

$$\Delta\rho_l(k) \triangleq \rho_l(k) - \hat{\rho}_l(k)$$

and substituting (12) for $\hat{\rho}_l(k)$ yields

$$\Delta\rho_l(k) \approx -\boldsymbol{h}_l^{\mathsf{T}}(k)\tilde{\boldsymbol{r}}_{\mathrm{leo}_l}(k) + c\tilde{\delta}t_l(k) \tag{13}$$

The magnitude of the range residual $\Delta\rho_l(k)$ can be bounded by invoking the triangular inequality as follows

$$|\Delta\rho_l(k)| \leq \sum_{j=1}^{3} \left| {}^{\{o_l\}}h_l^j(k)\, {}^{\{o_l\}}\tilde{r}_{\max}^j \right| + c\tilde{\delta}t_{\max}, \tag{14}$$

where ${}^{\{o_l\}}\boldsymbol{h_l}(k)$ is $\boldsymbol{h_l}(k)$ expressed in the l-th SV RTN frame denoted $\{o_l\}$, ${}^{\{o_l\}}\tilde{\boldsymbol{r}}_{\max}$ is a vector bounding the SVs' position errors in the RTN frame (i.e., ${}^{\{o_l\}}\tilde{\boldsymbol{r}}_{\max} \succeq {}^{\{o_l\}}\tilde{\boldsymbol{r}}_{\mathrm{leo}_l}(k)$ for all k, where $\succeq$ denotes the element-wise operation), superscript j indexes the component of vectors ${}^{\{o_l\}}\boldsymbol{h_l}(k)$ and ${}^{\{o_l\}}\tilde{\boldsymbol{r}}_{\max}$, and $c\tilde{\delta}t_{\max} \geq \left|c\tilde{\delta}t_l(k)\right|$ for all k.

2) Bound on Pseudorange Rate Measurements: A receiver only having access to TLEs would produce an estimated pseudorange rate measurement $\hat{\dot{\rho}}_l(k)$ to the l-th LEO SV as

$$\hat{\dot{\rho}}_l(k) = \left[\dot{\boldsymbol{r}}_r(k) - \hat{\dot{\boldsymbol{r}}}_{\mathrm{leo}_l}(k_l')\right]^{\mathsf{T}} \frac{\left[\boldsymbol{r}_r(k) - \hat{\boldsymbol{r}}_{\mathrm{leo}_l}(k_l')\right]}{\left\|\boldsymbol{r}_r(k) - \hat{\boldsymbol{r}}_{\mathrm{leo}_l}(k_l')\right\|_2} + c\left[\hat{\dot{\delta}}t_r(k) - \hat{\dot{\delta}}t_{\mathrm{leo}_l}(k_l')\right] \tag{15}$$

where $c\left[\hat{\dot{\delta}}t_r(k) - \hat{\dot{\delta}}t_{\mathrm{leo}_l}(k_l')\right]$ is the clock error drift estimate that the receiver's filter maintains. If no prior is available for this clock error drift, this term can be initialized to zero.

Performing a first-order Taylor series expansion of the erroneous pseudorange rate measurement estimate $\hat{\dot{\rho}}_l(k)$ in (15) about the l-th LEO SV true position $\boldsymbol{r}_{\mathrm{leo}_l}(k)$ and velocity $\dot{\boldsymbol{r}}_{\mathrm{leo}_l}(k)$ and true clock drift difference $c\left[\dot{\delta}t_r(k) - \dot{\delta}t_{\mathrm{leo}_l}(k_l')\right]$ yields

$$\hat{\dot{\rho}}_l(k) \approx \dot{\rho}_l(k) + \boldsymbol{g}_l^{\mathsf{T}}(k)\tilde{\boldsymbol{r}}_{\mathrm{leo}_l}(k) + \boldsymbol{h}_l^{\mathsf{T}}(k)\tilde{\dot{\boldsymbol{r}}}_{\mathrm{leo}_l}(k) - c\tilde{\dot{\delta}}t_l(k), \tag{16}$$

where $\boldsymbol{g}_l^{\mathsf{T}}(k) \triangleq \frac{\left[\dot{\boldsymbol{r}}_r(k) - \dot{\boldsymbol{r}}_{\mathrm{leo}_l}(k_l')\right]^{\mathsf{T}}}{\left\|\boldsymbol{r}_r(k) - \boldsymbol{r}_{\mathrm{leo}_l}(k_l')\right\|_2}\left[\mathbf{I}_{3\times 3} - \boldsymbol{h}_l(k)\boldsymbol{h}_l^{\mathsf{T}}(k)\right]$.

Defining the pseudorange rate residual $\Delta\dot{\rho}_l(k)$ of the l-th LEO SV as

$$\Delta\dot{\rho}_l(k) \triangleq \dot{\rho}_l(k) - \hat{\dot{\rho}}_l(k)$$

and substituting (16) for $\hat{\dot{\rho}}_l(k)$ yields

$$\Delta\dot{\rho}_l(k) \approx -\boldsymbol{g}_l^{\mathsf{T}}(k)\tilde{\boldsymbol{r}}_{\mathrm{leo}_l}(k) - \boldsymbol{h}_l^{\mathsf{T}}(k)\tilde{\dot{\boldsymbol{r}}}_{\mathrm{leo}_l}(k) + c\tilde{\dot{\delta}}t_l(k) \tag{17}$$

The magnitude of the pseudorange rate residual $\Delta\dot{\rho}_l(k)$ can be bounded by invoking the triangular inequality as follows

$$|\Delta\dot{\rho}_l(k)| \leq \left| {}^{\{o_l\}}\boldsymbol{h}_l^{\mathsf{T}}(k)\, {}^{\{o_l\}}\tilde{\dot{\boldsymbol{r}}}_{\max} \right| + \left| \frac{{}^{\{o_l\}}\left[\dot{\boldsymbol{r}}_r(k) - \dot{\boldsymbol{r}}_{\mathrm{leo}_l}(k_l')\right]^{\mathsf{T}}}{\left\|\boldsymbol{r}_r(k) - \boldsymbol{r}_{\mathrm{leo}_l}(k_l')\right\|_2} \left[{}^{\{o_l\}}\boldsymbol{h}_l(k)\, {}^{\{o_l\}}\boldsymbol{h}_l^{\mathsf{T}}(k) - \mathbf{I}_{3\times 3}\right] {}^{\{o_l\}}\tilde{\boldsymbol{r}}_{\max} \right| + c\tilde{\dot{\delta}}t_{\max}, \tag{18}$$

where ${}^{\{o_l\}}\tilde{\dot{\boldsymbol{r}}}_{\max}$ is a vector bounding the SVs' velocity errors in the RTN frame (i.e., ${}^{\{o_l\}}\tilde{\dot{\boldsymbol{r}}}_{\max} \succeq {}^{\{o_l\}}\tilde{\dot{\boldsymbol{r}}}_{\mathrm{leo}_l}(k)$ for all k) and $c\tilde{\dot{\delta}}t_{\max} \geq \left|c\tilde{\dot{\delta}}t_l(k)\right|$ for all k.

It is important to note that the bounds derived above on pseudorange and pseudorange rate residuals can easily be reduced to bounds on range and range rate measurement residuals by setting the bounds on the clock errors $c\tilde{\delta}t_{\max}$ and $c\tilde{\dot{\delta}}t_{\max}$ to zero in (14) and (18), respectively.

To validate the derived bounds, 20 circular orbits of LEO SVs having an orbital height of 700 km were simulated with various geometries with respect to a receiver stationary on a spherical rotating Earth as can be seen from the skyplot in Fig. 8. SV1 is on the top left quadrant of the skyplot going from West to North and the trajectories of the SVs progressively move until SV10 which goes from South to East in the bottom right quadrant. Similarly, SV11 goes from South to West in the bottom left quadrant of the skyplot and SV20 goes from East to North in the top right quadrant. Each of these 20 orbits were randomized in 100 MC runs with position errors drawn from a uniform distribution with maximum magnitude ${}^{\{b\}}\tilde{\boldsymbol{r}}_{\max} \triangleq \left[4\times 10^3, 20, 200\right]^{\mathsf{T}}$ m in the LEO SV's RTN frame to emulate TLE errors. The velocities were then modified accordingly to maintain the circularity of the orbit and ${}^{\{b\}}\tilde{\dot{\boldsymbol{r}}}_{\max}$ was taken to be the maximum velocity errors in the LEO SV's RTN frame's axes. Furthermore, clock bias and drift errors were introduced for the receiver's and LEO SV's oscillators. It is first assumed, without loss of generality, that the oscillator of the receiver and the LEO SV are nominally synchronized (i.e., the true pseudorange and pseudorange rate measurements are in fact range and range rate measurements, respectively). Then, the maximum deviation from the nominally synchronized clock states is set to 100 and 10 ns for the receiver's and LEO SV's clock biases, respectively, and to 1 and 0.1 ns/s for the receiver's and LEO SV's clock drifts, respectively, when generating the simulated pseudorange and pseudorange rate measurements according to (6) and (8), respectively. Consequently, $c\tilde{\delta}t_{\max}$ and $c\tilde{\dot{\delta}}t_{\max}$ are taken to be equal to $c\left[(100+10)\times(1+0.1)\, t_{\mathrm{vis}}\right]\times 10^{-9}$ m and $c\,(1+0.1)\times 10^{-9}$ m/s, respectively, where t_{vis} is the duration (in seconds) of the LEO SV visibility from the receiver.

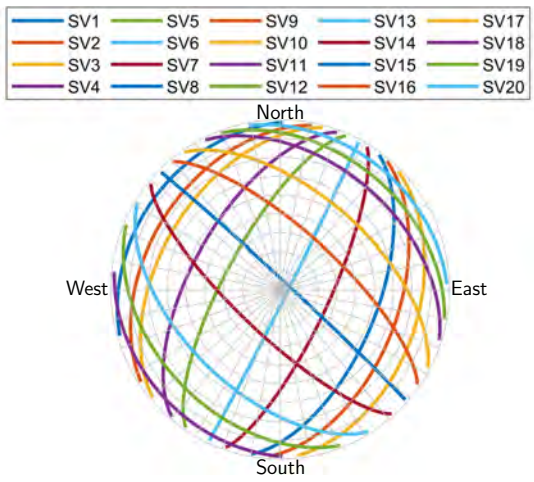

Fig. 8. Skyplot of 20 SVs simulated to validate the bounds.

The magnitude of pseudorange and pseudorange rate residuals for the 100 MC realizations as well as the derived bounds in (14) and (18) for 2 SVs are shown in Figs. 9 and 10, respectively. It can be seen that the derived bounds are valid

for the entire duration of LEO SV visibility and for all MC realizations. Moreover, similar behavior was observed for all the 20 simulated SVs.

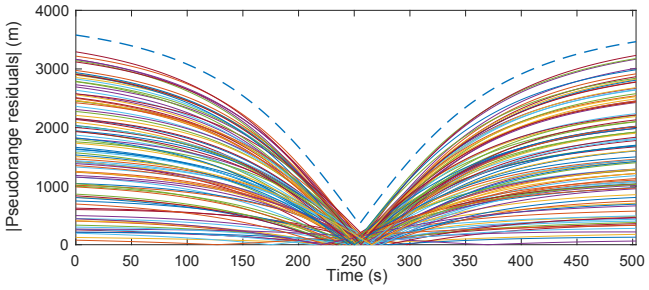

Fig. 9. Magnitude of pseudorange residuals for 100 MC realizations of randomized LEO states (solid) with bound (dashed) for SV 12.

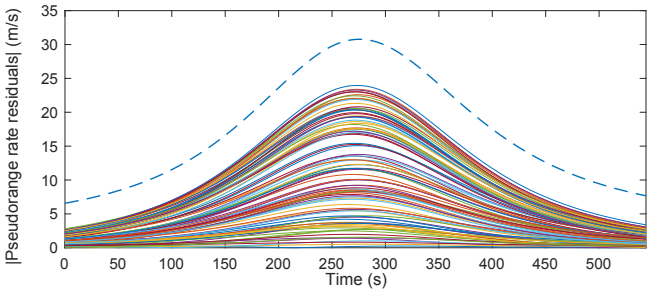

Fig. 10. Magnitude of pseudorange rate residuals for 100 MC realizations of randomized LEO states (solid) with bound (dashed) for SV 2.

Finally, it is worth noting that pseudorange measurement residuals change signs at around the time the SV passes zenith in its trajectory with respect to the receiver while pseudorange rate measurement residuals don't change signs (i.e., either remain positive or negative for the entire duration of the SV pass). This can be explained by the fact that most of the TLE position errors are in the along-track direction of the SV's motion as has been observed experimentally (this will be discussed in Section V, cf. Fig. 19), which leads to the TLE-derived SV position to either lag or lead the true SV position along the orbit as depicted in Fig. 11 (a) and (b), respectively. In the case where the TLE-derived SV position lags the true SV position, the TLE-derived range between the receiver and the SV is initially greater than the true range between the receiver and the SV, then both ranges become equal at around the SV's zenith, and finally the true range becomes greater than the TLE-derived range, thus resulting in residuals continuously going from negative to positive values along the pass. The opposite happens when the TLE-derived position leads the true SV position: range residuals are initially positive, then cross zero at around the zenith, before becoming negative. TLE errors in the cross-track and radial directions, and more importantly clock bias errors, result in the pseudorange residuals not crossing zero at exactly the SV's zenith. For range rate measurements, both the true range and the TLE-derived range decrease (negative range rate) before reaching the closest point to the receiver (zero range rate) then increase afterwards (positive range rate) but the lag/lead of the TLE-derived SV position results in a shifted range rate curve with respect to the true range rate curve. These two curves do not overlap, meaning there will be no sign shift in the range rate residuals, and the separation between them is the greatest at around the SV's zenith which explains the higher magnitudes of pseudorange rate residuals around the SV's zenith in Fig. 10. Furthermore, the time evolution of the true and TLE-derived ranges and range rates are depicted in Fig. 11 for both the case when the TLE-derived SV position lags (a) and leads (b) the true SV position to facilitate the visualization of these claims on range and range rate residuals sign change.

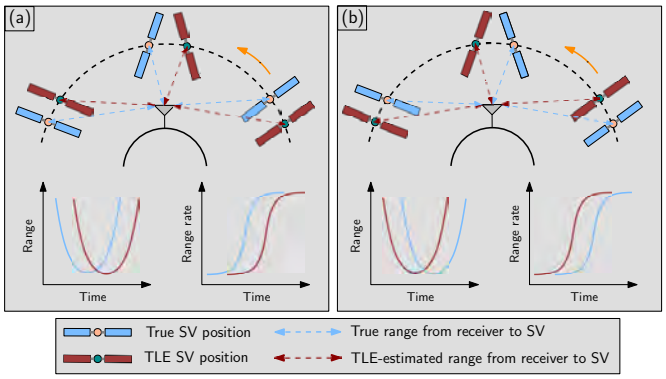

Fig. 11. Schematic to visualize TLE errors' effects on range and range rate residuals. In (a), the TLE-derived SV position lags the true SV position along the orbit while the TLE-derived SV position leads the true SV position along the orbit in (b).

B. State Estimation Errors Due to Measurement Errors

To study the propagation of errors from the measurements to the estimated receiver's states $\boldsymbol{x}$ (consisting of the stationary 3–D ECEF position $\boldsymbol{r}_r$ and clock error states $\boldsymbol{x}_{\text{clk}}$), assume first that the receiver's states are perfectly known (e.g., through optimal filtering of measurements with knowledge of the ground truth LEO SV ephemeris). Then, errors in the LEO SV's ephemeris and clock error states are suddenly introduced in the receiver's knowledge. This will consequently lead to discrepancies between the extracted measurements, which are consistent with the true SV's ephemeris and nominal clock error states, and the predicted measurements by the receiver using the erroneous ephemeris and clock error states information. These discrepancies will cause the receiver to update the estimates of its states to fit the measurements extracted from the LEO SV's signals to its erroneous model. This perturbation analysis can be captured in one iteration of the nonlinear least-squares (NLS) below

$$\boldsymbol{\Delta x} = \left(\mathbf{H}^{\mathsf{T}}\mathbf{H}\right)^{-1}\mathbf{H}^{\mathsf{T}}\boldsymbol{\Delta z}, \tag{19}$$

where $\boldsymbol{\Delta x}$ is the state estimate error vector, $\mathbf{H}$ is the measurement Jacobian matrix, and $\boldsymbol{\Delta z} = [\Delta z(1), \ldots, \Delta z(K)]^{\mathsf{T}}$ is the measurement innovations vector for the entire duration of satellite visibility, with K being the last time-step index. The stationary receiver's clock error states consist of the differenced clock error bias and drift between the receiver's and the SV's oscillator when using pseudorange measurements but only the differenced drift error states when using pseudorange rate measurements.

Although several iterations are usually required for the NLS estimator to converge, one iteration captures the majority of the errors introduced in the receiver state estimates, since the perturbation in the LEO SV's states is relatively small (i.e., TLE ephemeris errors are negligible compared to the distance between the receiver and LEO SV and do not considerably affect the unit LOS vector between the receiver and LEO SV).

One way to bound the receiver state estimation error $\boldsymbol{\Delta x}$ is by invoking the Cauchy-Schwarz inequality on (19) as follows

$$\|\boldsymbol{\Delta x}\|_2 \leq \left\| \left(\mathbf{H}^\mathsf{T}\mathbf{H}\right)^{-1}\mathbf{H}^\mathsf{T} \right\|_2 \|\boldsymbol{\Delta z}\|_2 , \tag{20}$$

where $\|\mathbf{A}\|_2 = \sigma_{\max}(\mathbf{A})$, i.e., the maximum singular value of the matrix $\mathbf{A}$.

In Subsection IV-A, a bound on $|\Delta z(k)|$ was found for all k as a function of the receiver-SV geometry; maximum LEO SV ephemeris errors ${}^{\{b\}}\tilde{\boldsymbol{r}}_{\max}$ and ${}^{\{b\}}\tilde{\dot{\boldsymbol{r}}}_{\max}$, expressed in the SV's RTN frame; and maximum clock bias $c\tilde{\delta}t_{\max}$ and drift $c\tilde{\dot{\delta}}t_{\max}$ errors, for $z \in \{\rho, \dot{\rho}\}$.

Since the pseudorange rate residuals do not change sign (i.e., either remain positive or negative) during the LEO SV visibility period as explained in Subsection IV-A and as can be seen from Fig. 10, $\|\boldsymbol{\Delta\dot{\rho}}\|_2$ can easily be bounded by $\|\boldsymbol{\Delta\dot{\rho}'}\|_2$ where each component of $\boldsymbol{\Delta\dot{\rho}'}$ is computed from (18). Using (20), this yields the following upper bound on receiver state estimation errors

$$\|\boldsymbol{\Delta x}_{\dot{\boldsymbol{\rho}}}\|_2 \leq \left\| \left(\mathbf{H}_{\dot{\rho}}^\mathsf{T}\mathbf{H}_{\dot{\rho}}\right)^{-1}\mathbf{H}_{\dot{\rho}}^\mathsf{T} \right\|_2 \|\boldsymbol{\Delta\dot{\rho}'}\|_2 \tag{21}$$

which is represented by the solid line in Fig. 13.

Pseudorange residuals, however, switch sign around the LEO SV's zenith (i.e., maximum elevation angle) with respect to the receiver as demonstrated in Subsection IV-A and as can be seen in Fig. 9. As a result of this sign change in $\boldsymbol{\Delta\rho}$, (14) has to be modified resulting in $\Delta\rho'(k) \triangleq^{\{b\}} \boldsymbol{h}^\mathsf{T}(k){}^{\{b\}}\tilde{\boldsymbol{r}}_{\max} + c\tilde{\delta}t_{\max}$. Unfortunately, although $\|\boldsymbol{\Delta\rho'}\|_2$ is greater than $\|\boldsymbol{\Delta\rho}\|_2$ for the majority of realizations, this is not guaranteed. As a result, the strict bound in (21) is not transposable to pseudorange measurements. In practice, however, using the equivalent of (21) with pseudorange measurements yields a very loose upper bound on the magnitude of the state estimation errors, which is 3 orders of magnitude greater than the actual errors and is thus too loose to be useful, as seen in Fig. 12. This can be explained by the fact that only a small component of the vectors $\boldsymbol{\Delta\rho'}$ and $\boldsymbol{\Delta\dot{\rho}'}$ are scaled by the maximum singular value of the linear map $\left(\mathbf{H}^\mathsf{T}\mathbf{H}\right)^{-1}\mathbf{H}^\mathsf{T}$, where $\mathbf{H}$ is the corresponding measurement Jacobian for each observable type. Effectively, $\boldsymbol{\Delta\rho'}$ and $\boldsymbol{\Delta\dot{\rho}'}$ are almost orthogonal to the right singular vector associated with the maximum singular value of $\left(\mathbf{H}^\mathsf{T}\mathbf{H}\right)^{-1}\mathbf{H}^\mathsf{T}$ with respective angles of 90.04° and 90.06° on average for all SVs of Fig. 8. Additionally, the looseness of the bound for pseudorange compared to pseudorange rate stems from the fact that $\|\boldsymbol{\Delta\rho'}\|_2 \gg \|\boldsymbol{\Delta\dot{\rho}'}\|_2$.

Another way to approximate the magnitude of receiver state estimate errors resulting from error in measurements is by plugging in $\boldsymbol{\Delta z'}$ in (19) resulting in

$$\|\boldsymbol{\Delta x}_{\boldsymbol{z}}\|_2 \approx \|\boldsymbol{\Delta x}'_{\boldsymbol{z}}\|_2 = \left\| \left(\mathbf{H}_{\boldsymbol{z}}^\mathsf{T}\mathbf{H}_{\boldsymbol{z}}\right)^{-1}\mathbf{H}_{\boldsymbol{z}}^\mathsf{T}\boldsymbol{\Delta z'} \right\|_2 , \ \boldsymbol{z} \in \{\boldsymbol{\rho}, \boldsymbol{\dot{\rho}}\} \tag{22}$$

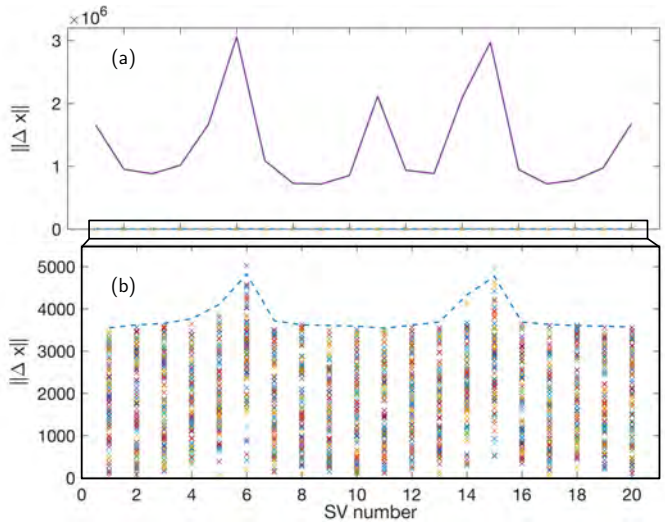

Fig. 12. Magnitude of receiver state estimation error for 100 MC realizations of randomized ephemerides (cross) with bound (solid) and tight bound approximation (dashed) computed using pseudorange measurements for each of the 20 SVs shown in Fig. 8.

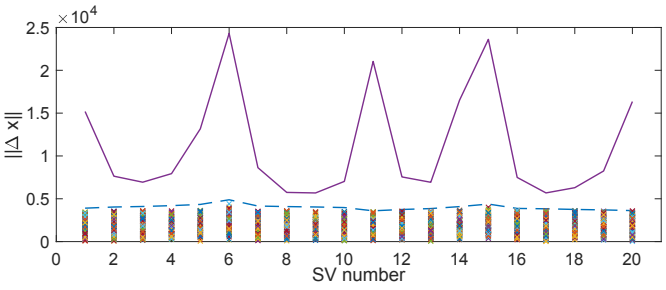

Fig. 13. Magnitude of receiver state estimation error for 100 MC realizations of randomized ephemerides (cross) with bound (solid) and tight bound approximation (dashed) computed using pseudorange rate measurements for each of the 20 SVs shown in Fig. 8.

The above expression is not a strict bound per se as it is slightly violated for only 3 realizations (out of 2,000 for pseudorange measurements with less than 4.2% error), but rather a good approximation of the maximum magnitude of receiver state estimate errors as depicted in Figs. 12(b) and 13. Note that the realizations for which the approximation in (22) does not overbound the magnitude of the state estimation errrors occur mainly for SVs with high maximum elevation angles with respect to the receiver (i.e., SV6 and SV15 as can be seen from the skyplot in Fig. 8). It is also interesting to observe that these SVs with high maximum elevation angles approach the singular unobservable case in which the receiver is in the orbital plane (i.e., maximum elevation angle of 90° with non-rotating Earth) [67] and that this reduction in estimability is reflected in the higher value of both the magnitude of state estimation errors (crosses) and the tight approximation of the upper bound (dashed) in Fig. 12(b) for these SVs. The intuition for this approximation results from the fact that (19) is the vector which premultiplied by $\mathbf{H}$ gives the orthogonal projection of $\boldsymbol{\Delta z}$ onto the range space of $\mathbf{H}$, thus resulting in the least squares solution. Similarly, $\mathbf{H}\boldsymbol{\Delta x'}$

gives the orthogonal projection of $\boldsymbol{\Delta z'}$ onto the range space of $\mathbf{H}$ in (22). Assuming $|\boldsymbol{\Delta z'}| \succeq |\boldsymbol{\Delta z}|$ (which is always true for $\boldsymbol{z} = \dot{\boldsymbol{\rho}}$ but not guaranteed for $\boldsymbol{z} = \boldsymbol{\rho}$), a sufficient condition to ensure that $\|\boldsymbol{\Delta x'}\|_2 \geq \|\boldsymbol{\Delta x}\|_2$ is to have $\boldsymbol{v_i} \succeq \mathbf{0}$ or $\boldsymbol{v_i} \preceq \mathbf{0}$, where $\boldsymbol{v_i}$ are the vectors forming the orthonormal basis of the range space of $\mathbf{H}$ with $i = 1, \ldots, n$ where n is the number of estimated states. This condition ensures that the coordinates of the projection of $\boldsymbol{\Delta z'}$ onto the range space of $\mathbf{H}$ expressed in the orthornormal basis are element-wise greater in absolute value than their counterparts for the projection of $\boldsymbol{\Delta z}$, which in turn implies $\|\boldsymbol{\Delta x'}\|_2 \geq \|\boldsymbol{\Delta x}\|_2$. It is interesting to note that the vectors forming the orthonormal basis of the range space of $\mathbf{H}$ for pseudorange measurements of SV6 and SV15 have entries that often fluctuate signs. This behavior is suspected to cause the upper bound approximation in (22) to underestimate the magnitude of state estimation errors for some realizations for these high maximum elevation angle SVs.

Finally, as in the opportunistic LEO SV tracking with Doppler measurements in Section III, note that the difference between the receiver's and LEO SV's clock bias is not estimated in localization since this quantity is not observable with pseudorange rate measurements. As a result, the receiver state estimation error vector $\boldsymbol{\Delta x}_{\dot{\boldsymbol{\rho}}}$ is composed of only 4 elements whereas $\boldsymbol{\Delta x}_{\boldsymbol{\rho}}$ has 5 entries. It is also interesting to note that the estimation errors in the clock error states are negligible with respect to the error in the receiver's estimated 3–D position. Consequently, the magnitude of position error and both tight upper bound approximation and strict loose upper bound on position errors are indistinguishably below the magnitude of all state errors represented respectively by the crosses, dashed line, and solid line in Figs. 12 and 13.

V. Experimental Results

This section presents the results of an experiment performed with a stationary receiver on the University of California, Irvine, USA campus opportunistically extracting carrier phase navigation observables from an Orbcomm LEO SV's downlink signals. The Orbcomm LEO constellation was chosen for this experiment as Orbcomm SVs openly transmit ephemeris information obtained from their on-board GPS receivers in their downlink signals [68]. As a result, the receiver can decode this accurate ephemeris information which will serve as a ground truth to assess the performance of the LEO SV tracking framework developed in this paper in comparison to the open-loop SPG4-propagated TLE ephemeris. Additionally, the ground truth ephemeris will also serve to verify the bounds derived in Section IV.

A. Experimental Setup and Filter Settings

A very-high frequency (VHF) antenna was connected to an Ettus E312 Universal Software Radio Peripheral (USRP) to receive Orbcomm downlink signals at 137-138 MHz and sample them at 2.4 MSps. The USRP's oscillator was driven by an external, freely-running CDA-2990 OctoClock. The receiver was placed on the top of a parking structure in an open sky environemnent to prevent multipath effects. Carrier phase navigation observables were opportunistically extracted by the receiver and were corrected for ionospheric and tropospheric effects using standard models from [66]. These measurements were then filtered at a rate of 1 Hz in the EKF developed in Subsection III-A to perform the tracking of the Orbcomm FM107 SV for around 6 minutes.

The LEO SV's position and velocity estimates were initialized from the SGP4-propagated ephemeris of the most recent TLE available for the Orbcomm FM107 SV tracked in this experiment. The associated initial position and velocity covariances were set to ${}^{o}\mathbf{P}_{\boldsymbol{x_r}}(0|0) \triangleq \text{diag}\left[10^7, 10^3, 10^4\right]$ m^2 and ${}^{o}\mathbf{P}_{\boldsymbol{x_{\dot{r}}}}(0|0) \triangleq \text{diag}\left[10^{-2}, 10^{-1}, 10^2\right]$ $(\text{m/s})^2$ in the SV's RTN frame, respectively. The Orbcomm FM107 SV's initial position and velocity covariance was set to be consistent with the observed SGP4-propagated TLE ephemeris errors (computed with respect to the truth ephemeris that is obtained by decoding it from the Orbcomm SV's downlink signals). It is worth noting that such magnitude of errors (with more than 7 km along-track error as shown in Fig. 19) is not common for TLEs and may have been caused by the Orbcomm SV performing a maneuver that altered the ballistic trajectory that was fit in the TLE published by NORAD. The covariance about the SV's orbital states in the simulations of Subsection III-D was selected to be more representative of the actual errors expected from a TLE. It is stated in [69] that the position error of TLEs is usually around 1 km at epoch and grows with the propagation time. The daily cadence of TLE updates for SVs in LEO results in the ephemeris errors being usually on the order of a 1–3 km at any point in time. In practical situations where initial covariance sizing cannot be performed to be consistent with the TLE errors since the SV's truth ephemeris is not known, a bank of filters with different initial covariance sizes can be implemented in a multiple-model estimation framework. The better matched filter with the most appropriate covariance size will have the most consistent innovation residuals than the other more mismatched filters. Consequently, the best matched filter's state estimate and associated covariance will dominate the other filters' in the combination step of the multiple-model estimator and the unknown initial covariance sizing problem is circumvented.

Since carrier phase measurements are used in this experiment, the clock bias difference term of $\boldsymbol{x}_{\text{clk}}$ is modified by adding the carrier phase ambiguity term from (9) and becomes $c\left[\delta t_r - \delta t_{\text{leo}}\right] + \lambda N$. This term is initialized by subtracting the initial estimated range from the first carrier phase measurement. The clock drift term was initialized to 0 and the clock error states' covariance was initialized to $\mathbf{P}_{\boldsymbol{x}_{\text{clk}}} \triangleq \text{diag}\left[10^7, 10^2\right]$ with units of [m^2, $(\text{m/s})^2$] corresponding to a 1σ of around 11 μs and 33 ns/s for the clock bias and drift, respectively.

The process noise covariance of the Orbcomm SV's orbital motion was set to ${}^{o}\bar{\mathbf{Q}}_{\boldsymbol{r\dot{r}},\text{emp}}$ found in Subsection III-B, where ${}^{o}\bar{\mathbf{Q}}_{\boldsymbol{r\dot{r}},\text{emp}}$ was rotated to the ECI frame at each time-step to propagate the estimation error covariance of the LEO SV's position and velocity states. The process noise covariance of the clock error states was set to be equivalent to a combination of a typical-quality temperature-compensated crystal oscillator (TCXO)–high-quality OCXO pair. The power-law coefficients of these oscillators are given in Table II. This choice was

motivated by findings in [44] that characterized the combined oscillators' quality for the clock on-board Orbcomm SVs and the CDA-2990 OctoClock used to discipline the receiver's clock in this experiment. The time-varying measurement noise variance was set to be proportional to the inverse of the predicted C/N_0 from (10), expressed in linear units, and it ranged between 3.49 and 4.84 m^2.

TABLE II
EXPERIMENTAL OSCILLATOR PARAMETERS

Quality	**Coefficients** $\{h_0, h_{-2}\}$
Typical-quality TCXO	$\{9.4 \times 10^{-20}, 3.8 \times 10^{-21}\}$
High-quality OCXO	$\{2.6 \times 10^{-22}, 4.0 \times 10^{-26}\}$

B. Experimental Tracking Results

Figs. 14 and 15 respectively show the position and velocity EKF error plots and associated $\pm 3\sigma$ bounds as well as the open-loop SGP4-propagated ephemeris errors in the SV's RTN frame. Figs. 16 and 17 respectively show the 3–D position and velocity errors magnitude for the EKF-tracked and the open-loop SGP4-propagated ephemeris. The initial position and velocity errors of over 7.1 km and 7.3 m/s obtained from the SGP4 propagation of the most recent TLE of the Orbcomm FM107 SV were reduced to final errors of 698.7 m and 1.8 m/s, respectively, in just over 6 minutes of tracking.

The following are key takeaways from these experimental tracking results. First, note that the LEO SV tracking performance with carrier phase observables is similar to that using pseudorange measurements as both measurement models only differ by the carrier phase ambiguity (6)-(9) and the effect of the ionosphere on the measurements: δt_{iono} acts as delay for pseudoranges and as an advance for carrier phases. After correcting for the atmospheric effects, accounting for the carrier phase ambiguity term is done by lumping it with the clock bias difference term estimated in the filter. Second, as can be seen from Figs. 14 and 15, the open-loop SGP4-propagated ephemeris errors stay relatively constant over the entire experiment. Moreover, opportunistic tracking mostly reduces the along-track position and radial velocity errors, which are usually where most of the errors in ephemerides obtained from TLEs lie. The radial position and along-track velocity errors, however, increase slightly during tracking as compared to their open-loop SGP4 counterparts. Third, as demonstrated in simulations in Subsection III-E, the cross-track direction is verified experimentally to be the least observable for both position and velocity. Fourth, note that the oscillations observed in the Orbcomm SV's velocity EKF plots in Fig. 15 between 0 and 30 seconds are due to the noisy decoding of the ground truth ephemeris information transmitted by the SV in its downlink signals. This happens at the beginning of the tracking period as the Orbcomm SV's elevation is still low (below 16° before 30 seconds), thus leading to errors in the ephemeris packet decoding as a result of low C/N_0.

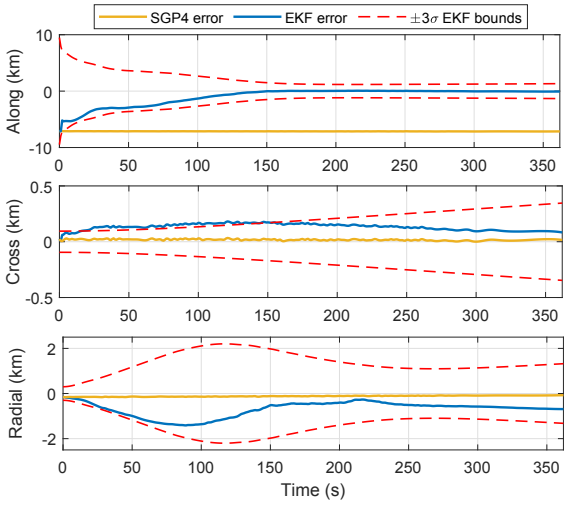

Fig. 14. EKF-tracked position errors with associated $\pm 3\sigma$ bounds versus open-loop SGP4 errors for Orbcomm FM107 SV.

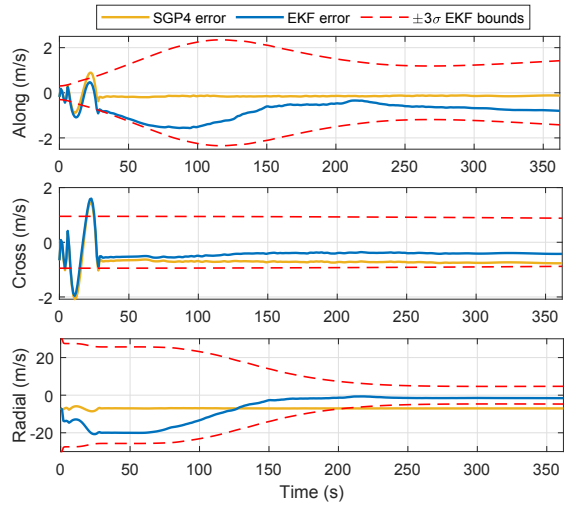

Fig. 15. EKF-tracked velocity errors with associated $\pm 3\sigma$ bounds versus open-loop SGP4 errors for Orbcomm FM107 SV.

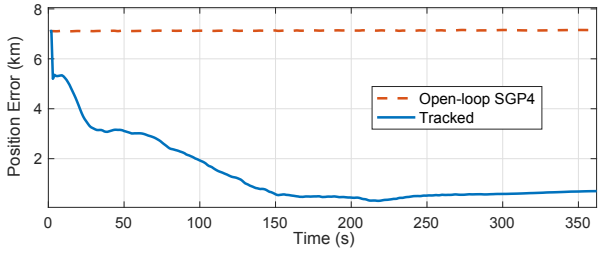

Fig. 16. EKF-tracked 3–D position error magnitude versus open-loop SGP4 errors for Orbcomm FM107 SV.

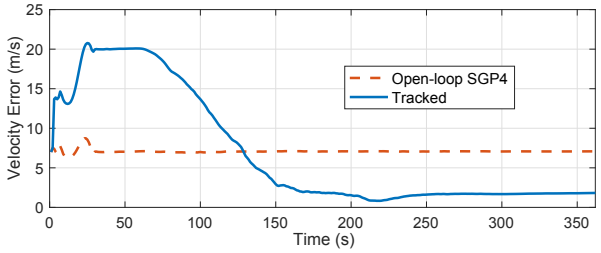

Fig. 17. EKF-tracked 3–D velocity error magnitude versus open-loop SGP4 errors for Orbcomm FM107 SV.

C. Experimental Receiver Localization Results

To demonstrate the practical advantages of LEO SV ephemeris refinement via the opportunistic tracking framework presented in this paper, an EKF is implemented to localize another stationary receiver extracting measurements opportunistically from Orbcomm FM107 SV's downlink signals using the open-loop SGP4-propagated ephemeris on one hand and the refined ephemeris resulting from the tracking performed in Subsection V-B by the tracking receiver on the other hand. It is assumed that the receiver to be localized has knowledge of its height (e.g., through altimeter measurements). Since the localization of the unknown receiver serves the purpose of demonstrating the efficacy of the tracking receiver in refining the satellite's ephemeris over the publicly available knowledge in TLE files, the unknown receiver was placed in an open sky environment. As such, multipath effects are also ignored in this case for simplicity of this proof of concept.

The state vector estimated by the EKF is $\boldsymbol{x} \triangleq \left[\boldsymbol{r}_r^{\mathsf{T}}, \boldsymbol{x}_{\mathrm{clk}}^{\mathsf{T}}\right]$, where $\boldsymbol{r}_r$ is the receiver' 3-D position in the ECEF reference frame and $\boldsymbol{x}_{\mathrm{clk}}$ is the same as in Subsection V-B with the carrier phase ambiguity term added to the clock bias difference. Since the fixed ECEF position of the receiver is estimated, the Orbcomm SV's ephemeris is also computed in the ECEF frame, denoted $\{e\}$. The TLE-generated ephemeris ${}^{e}\boldsymbol{x}_{\mathrm{leo,SGP4}}$ is computed by performing the SGP4 propagations of the most recent TLE for the Orbcomm FM107 SV in the ECEF frame. The refined ephemeris is obtained by propagating backward in time the last tracked position and velocity estimate in the ECI frame by numerical integration of the two-body with J_2 equations of motion (3). This is done since the last state estimate produced by the tracking receiver is the most refined state vector describing the SV's ephemeris. Consequently, the backwards propagation from this most refined state vector results in the most refined orbit for the SV's ECI ephemeris, which is then rotated to ECEF to yield the refined ephemeris ${}^{e}\boldsymbol{x}_{\mathrm{leo,tracked}}$ that is used by the stationary receiver localizing itself. It is worth mentioning that this tracked ephemeris back propagation is performed in post-processing in these experimental results, i.e., the last SV position and velocity states estimated by the tracking receiver at the end of the SV's pass are used in the refined ephemeris computation. However, this is not required as one can have such a system operating in real-time: the most up-to-date estimated state vector by the tracking receiver can be propagated via the SV's dynamics to generate the refined ephemeris that is fed to the receiver localizing itself. This process can run sequentially as the tracking receiver continues on refining the ephemeris of the LEO SV over the duration of its pass, while the unknown receiver keeps on improving its localization performance with the incrementally improved ephemeris it gets from the tracking receiver.

The EKF using the SGP4 open-loop ephemeris ${}^{e}\boldsymbol{x}_{\mathrm{leo,SGP4}}$ and the EKF using the refined ephemeris ${}^{e}\boldsymbol{x}_{\mathrm{leo,tracked}}$ were both initialized with the same initial receiver position estimate, drawn from a Gaussian distribution with the mean being the true receiver's location and a variance of 10^8 m^2 in the East and North directions as seen in Fig. 18. The initial receiver position error was 13.48 km. The clock error states' covariance was initialized to $\mathbf{P}_{\boldsymbol{x}_{\mathrm{clk}}} \triangleq \mathrm{diag}\left[10^8, 10^2\right]$ with units of [m^2, (m/s)^2] corresponding to a 1σ of around 33 μs and 33 ns/s for the clock bias and drift, respectively. The clock error states process noise covariance and time-varying measurement noise were identical to those in Subsection V-B.

The experimental localization results are shown in Fig. 18 and Table III and are summarized next. The 2-D positioning error of the receiver localized using the refined tracked ephemeris ${}^{e}\boldsymbol{x}_{\mathrm{leo,tracked}}$ was decreased from its initial value of around 13.48 km to 343 m while the localization performed using the SGP4-propagated ephemeris ${}^{e}\boldsymbol{x}_{\mathrm{leo,SGP4}}$ diverged to over 6.85 km in error. The localization estimate using the ${}^{e}\boldsymbol{x}_{\mathrm{leo,SGP4}}$ is inconsistent as its associated uncertainty ellipse does not include the true receiver position (green pin is outside yellow ellipse in Fig. 18). This is due to a model mismatch, as the SGP4-propagated ephemeris fed to the EKF is over 7.13 km away from the true SV's ephemeris, on average, and is causing filter divergence [70]. Additionally, note that the shape, size, and orientation of the uncertainty ellipses of both EKFs in Fig. 18 are similar. This is explained by both EKFs having the same initial estimation error covariance, process noise covariance, time-varying measurement noise and the fact that the measurement Jacobians of both EKFs are nearly identical: the time history of the unit LOS vectors pointing from the SV to the estimated receiver location are very close for both ${}^{e}\boldsymbol{x}_{\mathrm{leo,tracked}}$ and ${}^{e}\boldsymbol{x}_{\mathrm{leo,SGP4}}$.

TABLE III
HORIZONTAL 2–D POSITIONING ERRORS FOR EKF USING OPEN-LOOP SGP4-PROPAGATED EPHEMERIS AND EKF USING REFINED TRACKED EPHEMERIS.

	Initial	Final (SGP4)	Final (refined)
Horizontal error (m)	13,476	6,852	343

D. Experimental Bound Validation

In this subsection, the derived results of Section IV are verified with the data from the Orbcomm FM107 SV experiment. Figs. 19 and 20 show the magnitudes of the carrier phase and Doppler residuals along with the corresponding bounds from (14) and (18) scaled by f_c/c, respectively. The residuals were calculated by subtracting the predicted measurements computed from (9) and (7)-(8) using the TLE-generated ephemeris from the true measurements extracted by the receiver. The differenced clock bias and drift states used in the predicted measurement calculations were set to the difference between the first carrier phase measurement and the initial true range, and zero, respectively, to focus on the effects of the TLE errors on the measurement residuals. The maximum LEO SV's state errors ${}^{\{b\}}\tilde{\boldsymbol{r}}_{\max}$, ${}^{\{b\}}\dot{\tilde{\boldsymbol{r}}}_{\max}$, $c\tilde{\delta t}_{\max}$, and $c\dot{\tilde{\delta t}}_{\max}$ were computed using the TLE-propagated ephemeris, the ground truth decoded ephemeris, and the true measurements. Fig. 19 also shows the 3–D position error of the Orbcomm FM107 SV's TLE-derived ephemeris along with its component in the SV's RTN frame, demonstrating that most of the TLE-propagated ephemeris position error is the along-track direction. It is interesting to note that the experimental

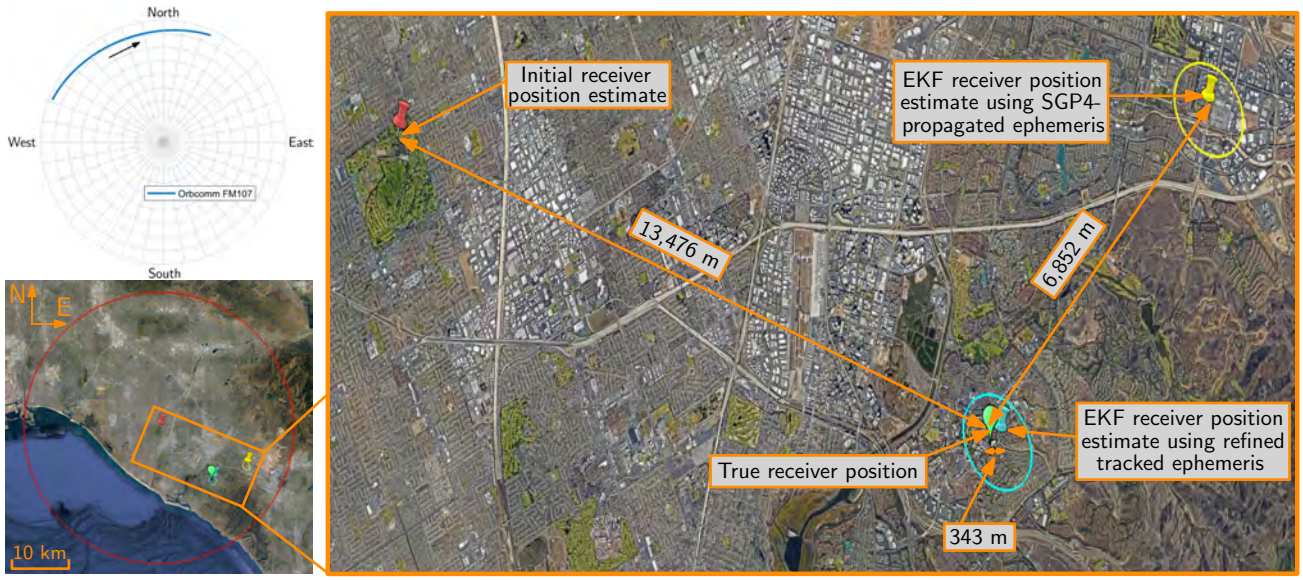

Fig. 18. Experimental results: skyplot of Orbcomm LEO SV trajectory and true receiver position (green) along with estimates and corresponding 95^{th}-percentile horizontal uncertainty ellipses: (i) red: initial estimate, (ii) yellow: EKF using ${}^{e}\boldsymbol{x}_{\mathrm{leo,SGP4}}$ ephemeris, and (iii) blue: EKF using ${}^{e}\boldsymbol{x}_{\mathrm{leo,tracked}}$ ephemeris. Map data: Google Earth.

carrier phase residual switches signs around 50 seconds earlier than the minimum of the bound curve that corresponds to an approximation of the SV's zenith in Fig. 19. This 50-second difference is caused by the discrepancy in the clock bias term between the true and predicted measurements, which results in the true and predicted carrier phase curves having the same value when the SV is not yet at zenith, i.e., residual curve crossing zero before zenith. Table IV shows the magnitude of the receiver's states estimation errors from one iteration of the NLS (19) using carrier phase and Doppler measurements. The approximation of a tight upper bound and the strict loose upper bound on this magnitude are also computed. Note that the results in Table IV are consistent with those observed in simulations in Figs. 12 and 13.

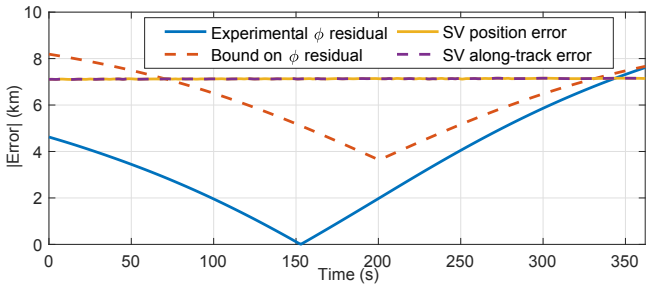

Fig. 19. Experimental carrier phase residuals magnitudes along with bound and 3–D position error with its along-track component for Orbcomm FM107 SV.

TABLE IV
MAGNITUDE OF RECEIVER'S STATE ESTIMATION ERRORS CALCULATED USING CARRIER PHASE AND DOPPLER FOR THE TLE-DERIVED EPHEMERIS, THE APPROXIMATION OF THE TIGHT UPPER BOUND, AND THE LOOSE STRICT UPPER BOUND. VALUES ARE IN METERS.

	TLE ephemeris	Bound approximation	Loose bound
$\left\|\boldsymbol{\Delta x}_{\boldsymbol{\phi}}\right\|_2$ $(\times 10^3)$	6.8	7.1	1.0×10^4
$\left\|\boldsymbol{\Delta x}_{\boldsymbol{f_D}}\right\|_2$ $(\times 10^3)$	3.7	6.8	2.8×10^3

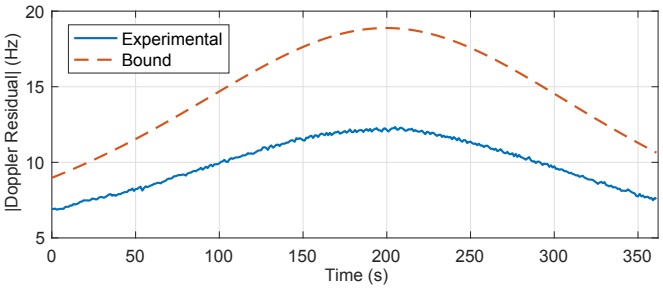

Fig. 20. Experimental Doppler residuals magnitudes along with bound for Orbcomm FM107 SV.

VI. CONCLUSION

This paper presented a complete framework to perform LEO SVs tracking by a receiver opportunistically extracting navigation observables from their downlink signals. The performance of the tracking filter was studied via MC simulations for 103 SVs with diverse geometries with respect to the receiver and for three different set of observables: (i) pseudorange, (ii) Doppler, and (iii) fused pseudorange and Doppler measurements. Additionally, the performance of the tracking filter was compared to the average performance of the open-loop SGP4 propagation of randomized TLE realizations. This comparison revealed ephemeris refinement capability of the tracking filter, particularly in the along-track position and radial velocity, where most of the TLE-propagated ephemeris errors lie. Additionally, bounds on pseudorange and Doppler residuals were derived and the magnitude of stationary receiver state estimation errors were characterized as a function of LEO SV's state errors. In other words, the error propagation from the LEO SV's state space to the measurement space to the receiver's state space was analyzed. Finally, experimental results were presented demonstrating the performance of the

opportunistic tracking framework and error propagation analysis. The initial position error of the Orbcomm FM107 SV calculated from TLE-derived ephemeris was reduced by an order of magnitude. Receiver localization via an EKF with the tracked ephemeris from the Orbcomm FM107 LEO SV showed the initial horizontal error reducing from 13,476 m to 343 m. In contrast, it was shown that if the EKF employed SGP-4 propagated ephemeris, the error reduced to 6,852, but dangerously, the filter's estimate was inconsistent. Finally, the observed experimental errors are contained within the derived bounds.

ACKNOWLEDGMENT

The authors would like to thank Jamil Haidar-Ahmad and Sharbel Kozhaya for their help with data collection and processing.

REFERENCES

[1] Union of Concerned Scientists, "UCS satellite database," https://www.ucsusa.org/resources/satellite-database, January 2022.

[2] L. Boldt-Christmas, "Low Earth orbit," http://www.esa.int/ESA_Multimedia/Images/2020/03/Low_Earth_orbit, March 2020.

[3] D. Bhattacherjee, W. Aqeel, I. Bozkurt, A. Aguirre, B. Chandrasekaran, P. Godfrey, G. Laughlin, B. Maggs, and A. Singla, "Gearing up for the 21st century space race," in *Proceedings of the ACM Workshop on Hot Topics in Networks*, 2018, pp. 113–119.

[4] S. Clark, "SpaceX passes 2,500 satellites launched for Starlink internet network," https://spaceflightnow.com/2022/05/13/spacex-passes-2500-satellites-launched-for-companys-starlink-network/, May 2022.

[5] J. Brodkin, "SpaceX says 12,000 satellites isn't enough, so it might launch another 30,000," https://arstechnica.com/information-technology/2019/10/spacex-might-launch-another-30000-broadband-satellites-for-42000-total, October 2019.

[6] A. Boley and M. Byers, "Satellite mega-constellations create risks in Low Earth Orbit, the atmosphere and on Earth," *Scientific Reports*, vol. 11, no. 1, pp. 1–8, 2021.

[7] D. Kessler, N. Johnson, J.-C. Liou, and M. Matney, "The Kessler Syndrome: implications to future space operations," *Advances in the Astronautical Sciences*, vol. 137, no. 8, 2010.

[8] J. Nicholas, "The collision of Iridium 33 and Cosmos 2251: the shape of things to come," in *Proceedings of International Astronautical Congress*, 2009.

[9] J.-C. Liou and N. Johnson, "Instability of the present LEO satellite populations," *Advances in Space Research*, vol. 41, no. 7, pp. 1046–1053, 2008.

[10] J. Kennewell and B. Vo, "An overview of space situational awareness," in *Proceedings of International Conference on Information Fusion*, 2013, pp. 1029–1036.

[11] E. Blasch, M. Pugh, C. Sheaff, J. Raquepas, and P. Rocci, "Big data for space situation awareness," in *Proceedings of SPIE*, vol. 10196, 2017, pp. 1–13.

[12] USSTRATCOM, "U.S. Strategic Command Fact Sheet Combined Space Operations Center / 614th Air Operations Center," https://www.stratcom.mil/Portals/8/Documents/CSpOC_Factsheet_2018.pdf, July 2018.

[13] North American Aerospace Defense Command (NORAD), "Two-line element sets," http://celestrak.com/NORAD/elements/.

[14] D. Vallado and P. Crawford, "SGP4 orbit determination," in *Proceedings of AIAA/AAS Astrodynamics Specialist Conference and Exhibit*, August 2008, pp. 6770–6799.

[15] S. Liu, Z. Gao, Y. Wu, D. Kwan Ng, X. Gao, K. Wong, S. Chatzinotas, and B. Ottersten, "LEO satellite constellations for 5G and beyond: How will they reshape vertical domains?" *IEEE Communications Magazine*, vol. 59, no. 7, pp. 30–36, July 2021.

[16] T. Reid, K. Gunning, A. Perkins, S. Lo, and T. Walter, "Going back for the future: Large/mega LEO constellations for navigation," in *Proceedings of ION GNSS Conference*, September 2019, pp. 2452–2468.

[17] B. Li, H. Ge, M. Ge, L. Nie, Y. Shen, and H. Schuh, "LEO enhanced global navigation satellite system (LeGNSS) for real-time precise positioning services," *Advances in Space Research*, vol. 63, no. 1, pp. 73–93, 2019.

[18] R. Landry, A. Nguyen, H. Rasaee, A. Amrhar, X. Fang, and H. Benzerrouk, "Iridium Next LEO satellites as an alternative PNT in GNSS denied environments–part 1," *Inside GNSS Magazine*, vol. 14, no. 3, pp. 56–64, May 2019.

[19] S. Thompson, S. Martin, and D. Bevly, "Single differenced Doppler positioning with low Earth orbit signals of opportunity and angle of arrival estimation," in *Proceedings of ION International Technical Meeting*, 2020, pp. 497–509.

[20] T. Reid, B. Chan, A. Goel, K. Gunning, B. Manning, J. Martin, A. Neish, A. Perkins, and P. Tarantino, "Satellite navigation for the age of autonomy," in *Proceedings of IEEE/ION Position, Location and Navigation Symposium*, 2020, pp. 342–352.

[21] J. Khalife, M. Neinavaie, and Z. Kassas, "Navigation with differential carrier phase measurements from megaconstellation LEO satellites," in *Proceedings of IEEE/ION Position, Location, and Navigation Symposium*, April 2020, pp. 1393–1404.

[22] Q. Wei, X. Chen, and Y. Zhan, "Exploring implicit pilots for precise estimation of LEO satellite downlink Doppler frequency," *IEEE Communications Letters*, vol. 24, no. 10, pp. 2270–2274, 2020.

[23] F. Farhangian, H. Benzerrouk, and R. Landry, "Opportunistic in-flight INS alignment using LEO satellites and a rotatory IMU platform," *Aerospace*, vol. 8, no. 10, pp. 280–281, 2021.

[24] A. Nardin, F. Dovis, and J. Fraire, "Empowering the tracking performance of LEO-based positioning by means of meta-signals," *IEEE Journal of Radio Frequency Identification*, vol. 5, no. 3, pp. 244–253, 2021.

[25] L. Ye, Y. Yang, X. Jing, L. Deng, and H. Li, "Single-satellite integrated navigation algorithm based on broadband LEO constellation communication links," *Remote Sensing*, vol. 13, no. 4, pp. 703–729, February 2021.

[26] P. Iannucci and T. Humphreys, "Fused low-Earth-orbit GNSS," *IEEE Transactions on Aerospace and Electronics Systems*, 2022, accepted.

[27] M. Psiaki, "Navigation using carrier Doppler shift from a LEO constellation: TRANSIT on steroids," *NAVIGATION, Journal of the Institute of Navigation*, vol. 68, no. 3, pp. 621–641, September 2021.

[28] Z. Kassas, M. Neinavaie, J. Khalife, N. Khairallah, J. Haidar-Ahmad, S. Kozhaya, and Z. Shadram, "Enter LEO on the GNSS stage: Navigation with Starlink satellites," *Inside GNSS Magazine*, vol. 16, no. 6, pp. 42–51, 2021.

[29] R. Cassel, D. Scherer, D. Wilburne, J. Hirschauer, and J. Burke, "Impact of improved oscillator stability on LEO-based satellite navigation," in *Proceedings of ION International Technical Meeting*, January 2022, pp. 893–905.

[30] J. Khalife, M. Neinavaie, and Z. Kassas, "The first carrier phase tracking and positioning results with Starlink LEO satellite signals," *IEEE Transactions on Aerospace and Electronic Systems*, vol. 56, no. 2, pp. 1487–1491, April 2022.

[31] S. Kozhaya, J. Haidar-Ahmad, A. Abdallah, Z. Kassas, and S. Saab, "Comparison of neural network architectures for simultaneous tracking and navigation with LEO satellites," in *Proceedings of ION GNSS Conference*, September 2021, pp. 2507–2520.

[32] N. Khairallah and Z. Kassas, "Ephemeris closed-loop tracking of LEO satellites with pseudorange and Doppler measurements," in *Proceedings of ION GNSS Conference*, September 2021, pp. 2544–2555.

[33] J. Haidar-Ahmad, N. Khairallah, and Z. Kassas, "A hybrid analytical-machine learning approach for LEO satellite orbit prediction," in *Proceedings of International Conference on Information Fusion*, 2022, pp. 1–7.

[34] D. Lawrence, H. Cobb, G. Gutt, M. OConnor, T. Reid, T. Walter, and D. Whelan, "Navigation from LEO: Current capability and future promise," *GPS World Magazine*, vol. 28, no. 7, pp. 42–48, July 2017.

[35] J. Khalife and Z. Kassas, "Receiver design for Doppler positioning with LEO satellites," in *Proceedings of IEEE International Conference on Acoustics, Speech and Signal Processing*, May 2019, pp. 5506–5510.

[36] F. Farhangian and R. Landry, "Multi-constellation software-defined receiver for Doppler positioning with LEO satellites," *Sensors*, vol. 20, no. 20, pp. 5866–5883, October 2020.

[37] M. Orabi, J. Khalife, and Z. Kassas, "Opportunistic navigation with Doppler measurements from Iridium Next and Orbcomm LEO satellites," in *Proceedings of IEEE Aerospace Conference*, March 2021, pp. 1–9.

[38] C. Pinell, "Receiver architectures for positioning with low Earth orbit satellite signals," Master's thesis, Lulea University of Technology, School of Electrical Engineering, Sweden, 2021.

[39] C. Zhao, H. Qin, and Z. Li, "Doppler measurements from multiconstellations in opportunistic navigation," *IEEE Transactions on Instrumentation and Measurement*, vol. 71, pp. 1–9, 2022.

[40] M. Neinavaie, J. Khalife, and Z. Kassas, "Cognitive opportunistic navigation in private networks with 5G signals and beyond," *IEEE Journal of Selected Topics in Signal Processing*, vol. 16, no. 1, pp. 129–143, 2022.
[41] M. Neinavaie, J. Khalife, and Z. Kassas, "Blind Doppler tracking and beacon detection for opportunistic navigation with LEO satellite signals," in *Proceedings of IEEE Aerospace Conference*, March 2021, pp. 1–8.
[42] M. Neinavaie, J. Khalife, and Z. Kassas, "Acquisition, Doppler tracking, and positioning with Starlink LEO satellites: First results," *IEEE Transactions on Aerospace and Electronic Systems*, vol. 58, no. 3, pp. 2606–2610, June 2022.
[43] Z. Kassas, J. Morales, and J. Khalife, "New-age satellite-based navigation – STAN: simultaneous tracking and navigation with LEO satellite signals," *Inside GNSS Magazine*, vol. 14, no. 4, pp. 56–65, 2019.
[44] N. Khairallah and Z. Kassas, "An interacting multiple model estimator of LEO satellite clocks for improved positioning," in *Proceedings of IEEE Vehicular Technology Conference*, 2022, pp. 1–5.
[45] F. Hoots and R. Roehrich, "Spacetrack Report NO. 3," http://celestrak.com/NORAD/documentation/spacetrk.pdf, December 1988, compiled by TS Kelso.
[46] Systems Tool Kit (STK), "High-Precision Orbit Propagator (HPOP)," https://help.agi.com/stk/11.0.1/Content/hpop/hpop.htm, September 2016.
[47] D. Vallado, "An analysis of state vector propagation using differing flight dynamics programs," in *Proceedings of the AAS Space Flight Mechanics Conference*, vol. 120, January 2005, pp. 1563–1592.
[48] X. Tian, G. Chen, E. Blasch, K. Pham, and Y. Bar-Shalom, "Comparison of three approximate kinematic models for space object tracking," in *Proceedings of International Conference on Information Fusion*, 2013, pp. 1005–1012.
[49] M. Hough, "Closed-form nonlinear covariance prediction for two-body orbits," *Journal of Guidance, Control, and Dynamics*, vol. 37, no. 1, pp. 26–35, 2014.
[50] K. Vishwajeet, P. Singla, and M. Jah, "Nonlinear uncertainty propagation for perturbed two-body orbits," *Journal of Guidance, Control, and Dynamics*, vol. 37, no. 5, pp. 1415–1425, May 2014.
[51] Z. Yang, Y. Luo, V. Lappas, and A. Tsourdos, "Nonlinear analytical uncertainty propagation for relative motion near $j2$-perturbed elliptic orbits," *Journal of Guidance, Control, and Dynamics*, vol. 43, no. 4, pp. 888–903, April 2018.
[52] B. Jones and R. Weisman, "Multi-fidelity orbit uncertainty propagation," *Acta Astronautica*, vol. 155, pp. 406–417, 2019.
[53] O. Montenbruck and E. Gill, *Satellite orbits: models, methods, and applications*. Springer, 2000.
[54] B. Schutz, B. Tapley, and G. Born, *Statistical orbit determination*. Elsevier, 2004.
[55] S. Sharma and J. Cutler, "Robust orbit determination and classification: A learning theoretic approach," *IPN Progress Report*, pp. 42–203, 2015.
[56] B. Lee, W. Kim, J. Lee, and Y. Hwang, "Machine learning approach to initial orbit determination of unknown LEO satellites," in *Proceedings of AIAA SpaceOps Conference*, 2018, pp. 1–11.
[57] H. Peng and X. Bai, "Comparative evaluation of three machine learning algorithms on improving orbit prediction accuracy," *Astrodynamics*, vol. 3, no. 4, pp. 325–343, 2019.
[58] H. Peng and X. Bai, "Machine learning approach to improve satellite orbit prediction accuracy using publicly available data," *The Journal of the Astronautical Sciences*, vol. 67, no. 2, pp. 762–793, 2020.
[59] B. Li, J. Huang, Y. Feng, F. Wang, and J. Sang, "A machine learning-based approach for improved orbit predictions of LEO space debris with sparse tracking data from a single station," *IEEE Transactions on Aerospace and Electronic Systems*, vol. 56, no. 6, pp. 4253–4268, 2020.
[60] T. Mortlock and Z. Kassas, "Assessing machine learning for LEO satellite orbit determination in simultaneous tracking and navigation," in *Proceedings of IEEE Aerospace Conference*, March 2021, pp. 1–8.
[61] J. Vetter, "Fifty years of orbit determination: Development of modern astrodynamics methods," *Johns Hopkins APL Technical Digest*, vol. 27, no. 3, pp. 239–252, November 2007.
[62] B. Tapley, M. Watkins, C. Ries, W. Davis, R. Eanes, S. Poole, H. Rim, B. Schutz, C. Shum, R. Nerem, F. Lerch, J. Marshall, S. Klosko, N. Pavlis, and R. Williamson, "The Joint Gravity Model 3," *Journal of Geophysical Research*, vol. 101, no. B12, pp. 28 029–28 049, December 1996.
[63] J. Vinti, *Orbital and Celestial Mechanics*. American Institute of Aeronautics and Astronautics, 1998.
[64] R. Brown and P. Hwang, *Introduction to Random Signals and Applied Kalman Filtering*, 3rd ed. John Wiley & Sons, 2002.
[65] A. Thompson, J. Moran, and G. Swenson, *Interferometry and Synthesis in Radio Astronomy*, 2nd ed. John Wiley & Sons, 2001.
[66] P. Misra and P. Enge, *Global Positioning System: Signals, Measurements, and Performance*, 2nd ed. Ganga-Jamuna Press, 2010.
[67] R. Sabbagh and Z. Kassas, "Observability analysis of receiver localization via pseudorange measurements from a single LEO satellite," *IEEE Control Systems Letters*, vol. 7, no. 3, pp. 571–576, 2023.
[68] M. Kenny, "Ever wondered what is on the Orbcomm satellite downlink?" http://mdkenny.customer.netspace.net.au/Orbcomm.pdf, 2002.
[69] D. Vallado, P. Crawford, R. Hujsak, and T. Kelso, "Revisiting spacetrack report# 3," in *Proceedings of the Astrodynamics Specialist Conference and Exhibit*, 2006, p. 6753.
[70] J. Morales, J. Khalife, U. Santa Cruz, and Z. Kassas, "Orbit modeling for simultaneous tracking and navigation using LEO satellite signals," in *Proceedings of ION GNSS Conference*, September 2019, pp. 2090–2099.

Nadim Khairallah received his M.S. in Mechanical and Aerospace Engineering from the University of California, Irvine and B.E. in Mechanical Engineering with High Distinction from the American University of Beirut. He was a member of the Autonomous Systems Perception, Intelligence, and Navigation (ASPIN) Laboratory. He is a recipient of the 2021 US Department of Transportation Graduate Student of the Year award and the 2022 IEEE Vehicular Technology Conference best student paper award. His research interests include satellite-based opportunistic navigation, sensor fusion, and estimation theory.

Zaher (Zak) M. Kassas (S'98-M'08-SM'11) is a professor at The Ohio State University and TRC Endowed Chair in Intelligent Transportation Systems. He is the Director of the Autonomous Systems Perception, Intelligence, and Navigation (ASPIN) Laboratory. He is also director of the U.S. Department of Transportation Center: CARMEN (Center for Automated Vehicle Research with Multimodal AssurEd Navigation), focusing on navigation resiliency and security of highly automated transportation systems. He received a B.E. in Electrical Engineering from the Lebanese American University, an M.S. in Electrical and Computer Engineering from The Ohio State University, and an M.S.E. in Aerospace Engineering and a Ph.D. in Electrical and Computer Engineering from The University of Texas at Austin. He is a recipient of the National Science Foundation (NSF) CAREER award, Office of Naval Research (ONR) Young Investigator Program (YIP) award, Air Force Office of Scientific Research (AFOSR) YIP award, IEEE Walter Fried Award, Institute of Navigation (ION) Samuel Burka Award, and ION Col. Thomas Thurlow Award. He is an Associate Editor of the IEEE Transactions on Aerospace and Electronic Systems and the IEEE Transactions on Intelligent Transportation Systems. He is a Fellow of the ION and a Distinguished Lecturer of the IEEE Aerospace and Electronic Systems Society. His research interests include cyber-physical systems, navigation systems, and intelligent transportation systems.

Evaluation of Ground Vehicle Protection Level Reduction due to Fusing GPS with Faulty Terrestrial Signals of Opportunity

Mu Jia, Joe Khalife, and Zaher M. Kassas
University of California, Irvine, USA

BIOGRAPHY

Mu Jia is a Ph.D. student at the University of California, Irvine and a member of the Autonomous Systems Perception, Intelligence, and Navigation (ASPIN) Laboratory. He received a B.E. in Vehicle Engineering from Shandong University, an M.E. in Mechanical Engineering from University of Defense Technology, and an M.S. in Mechanical Engineering from Duke University. His current research interests include autonomous ground vehicles, autonomous integrity monitoring, and opportunistic navigation.

Joe Khalife is a postdoctoral fellow at the University of California, Irvine and member of the Autonomous Systems Perception, Intelligence, and Navigation (ASPIN) Laboratory. He received a B.E. in Electrical Engineering, an M.S. in Computer Engineering from the Lebanese American University (LAU) and a Ph.D. in Electrical Engineering and Computer Science from the University of California, Irvine. From 2012 to 2015, he was a research assistant at LAU, and has been a member of the ASPIN Laboratory since 2015. He is a recipient of the 2016 IEEE/ION Position, Location, and Navigation Symposium (PLANS) Best Student Paper Award and the 2018 IEEE Walter Fried Award. His research interests include opportunistic navigation, autonomous vehicles, and software-defined radio.

Zaher (Zak) M. Kassas is an associate professor at the University of California, Irvine and director of the Autonomous Systems Perception, Intelligence, and Navigation (ASPIN) Laboratory. He received a B.E. in Electrical Engineering from the Lebanese American University, an M.S. in Electrical and Computer Engineering from The Ohio State University, and an M.S.E. in Aerospace Engineering and a Ph.D. in Electrical and Computer Engineering from The University of Texas at Austin. In 2018, he received the National Science Foundation (NSF) Faculty Early Career Development Program (CAREER) award, and in 2019, he received the Office of Naval Research (ONR) Young Investigator Program (YIP) award. He is a recipient of 2018 IEEE Walter Fried Award, 2018 Institute of Navigation (ION) Samuel Burka Award, and 2019 ION Col. Thomas Thurlow Award. His research interests include cyber-physical systems, estimation theory, navigation systems, autonomous vehicles, and intelligent transportation systems.

ABSTRACT

The protection level (PL) performance of an autonomous ground vehicle (AGV) due to fusing GPS signals with faulty terrestrial signals of opportunity (SOPs) is evaluated. The AGV is assumed to be equipped with receivers, which can produce a navigation solution from GPS and SOP pseudorange measurements. First, the effect of the number of SOPs on the PL reduction is analyzed. Then, the PL reduction under different assumptions of SOP fault probabilities is explored. The results show that while adding one SOP could increase the PL, adding two or more SOPs would significantly reduce the PLs. The results also demonstrate that even for highly unreliable SOPs (namely, those with fault probabilities as high as 10%), adding two or more SOPs would still reduce the PLs.

I. INTRODUCTION

The past few years have witnessed intense interest in pushing ground vehicles towards higher levels of automation, with the ultimate objective of achieving full autonomy, also known as Level 5 [1]. The potential impacts of deploying autonomous ground vehicles (AGVs) into our streets are promising, including reducing congestion and travel time and increased safety. However, there remains critical gaps between the capabilities of current technology and the stringent requirements of fully autonomous driving. Accurate, reliable, and resilient navigation is a key enabler of autonomous driving. Higher levels of automation not only rely on lane-level navigation accuracy, but also on tight protection levels (PLs) and integrity measures, especially on crowded urban roads, in which the AGV is surrounded by other vehicles, pedestrians, and bicyclists. Accurate navigation coupled with integrity monitoring (IM) are essential to guarantee the safety of the AGV itself, and most importantly the safety of humans in it and surrounding it. Virtually all current ground vehicles rely on global navigation satellite systems (GNSS) to estimate their position in a global frame. However, GNSS signals are jammable, spoofable, and may not be available

in deep urban canyons [2–4]. Recently, using signals of opportunity (SOPs) as a complement or an alternative to GNSS signals in GNSS-challenged environments has proven to improve the accuracy and integrity of the navigation solution [5]. However, SOPs are not designed for the safety-critical function of navigation; hence, their reliability as a navigation source is still under study. This paper addresses the following question: Could the navigation system integrity be improved by exploiting signals with unknown reliability? This paper answers this question by studying the effect of the number of SOPs and fault probabilities on IM performance.

Current ground vehicles are equipped with a suite of navigation sensors: GNSS receivers, vision-based sensors (red-green-blue (RGB) and infrared (IR) cameras), inertial navigation system (INS), and active range-finding sensors (lidar and radar). These sensors produce two categories of navigation functionality: (i) local navigation, which provides the position of the vehicle in a local coordinate system and (ii) global navigation, which provides the position of the vehicle in a global coordinate system. Over the past few decades, GNSS has monopolized global navigation. Future AGVs will require reliable lane-level-accurate navigation to travel safely, especially on urban roads. However, current GNSS technologies cannot sufficiently support the transition of ground vehicles from partial to full automation in terms of accuracy, integrity, and availability. For example, single point positioning (SPP), currently relied upon by ground and aerial vehicles, can only achieve meter-level accuracy [6]. Certain approaches, such as augmentation systems and real-time kinematic (RTK), could improve navigation accuracy and achieve sub-meter-level accuracy under certain conditions. However, these approaches cannot overcome the vulnerabilities of GNSS signals in deep urban canyons, where AGVs are expected to be ubiquitous.

Recent work have demonstrated how SOPs could improve navigation system accuracy in GNSS-challenged environments. SOPs (e.g. cellular signals [7–12], digital television signals [13–15], AM/FM radio signals [16–18], and low Earth orbit satellite (LEO) signals [19–24] have been exploited to produce navigation solutions in a standalone fashion or as an aiding source for an INS in the absence of GNSS signals [25]. For vehicular navigation, cellular signals are particularly attractive with their favorable characteristics, such as abundance in urban canyons, geometric and spectral diversity, high received power, and large bandwidth [26]. Cellular SOPs have been demonstrated to achieve meter-level accuracy for ground vehicles in a standalone fashion [27, 28] and when fused with an INS [29] and lane-level accuracy when fused with lidar [30].

Aside from accuracy, the trustworthiness of the navigation solution is another major concern in safety-critical applications, such as autonomous driving. The trustworthiness in the correctness of information by a positioning, navigation, and timing (PNT) system is measured as integrity. To improve the integrity of a navigation system, IM is usually used to detect anomalies or faults and to quantify the confidence of system integrity. There are two categories of IM frameworks, namely internal methods and external methods. External methods monitor the system's integrity by using external data sources such as ground-based augmentation system (GBAS) [31, 32] and satellite-based augmentation system (SBAS) [33]. In contrast, internal methods (e.g., receiver autonomous integrity monitoring (RAIM) and advanced RAIM (ARAIM)) leverage redundant measurements from existing signals [34, 35]. RAIM is a cost-effective technique for IM, since it does not require building additional infrastructure. Multi-constellation measurements [36] (e.g. Galileo, GLONASS, and Beidou) and aiding sensors (e.g., INS-GPS [37], lidar-GPS [6] and vision-GPS [38]) have been recently considered to improve the IM performance. In addition, several SOP-based IM studies have been conducted recently. In [39], cellular SOPs have been characterized and outlier detection and exclusion methods have been developed to deal with environment-induced faults, such as severe multipath conditions. In [40], a RAIM framework for ground vehicle navigation using cellular SOPs and an inertial measurement unit (IMU) was developed. GPS-SOP RAIM was proposed in [41] to support safe autonomous driving. GPS-SOP RAIM was also considered in [42] to improve the IM of unmanned aerial vehicles (UAVs).

While previous research have demonstrated that fusing cellular SOPs could improve the navigation accuracy and integrity, an open question remains unanswered: when does fusing SOPs benefit IM? While SOPs have favorable characteristics for enhancing the system integrity, the reliability of SOP transmitters has not been completely characterized and is very likely to be lower than that of GPS satellites, since the stakes of SOP transmitter faults are much lower than that of GPS satellite faults. This unknown reliability of SOPs compared to GPS satellites raises a question about the boundary condition under which incorporating SOPs in the navigation system can still improve the integrity of the system, particularly in terms of the number of available SOPs and their fault probability. This paper analyzes the PL reduction in different scenarios to answer the above question. This paper considers an AGV equipped with an SOP receiver that can produce pseudorange measurements from multiple terrestrial SOPs and a GPS receiver that can produce pseudorange measurements from multiple GPS satellites. The AGV produces a navigation solution from the SOP and GPS measurements. Moreover, the AGV performs IM using ARAIM aided by SOPs, which is referred to as ARAIM+SOP framework in this paper. This paper analyzes the performance of the ARAIM+SOP framework under different operation regimes through Monte Carlo numerical simulations. First, a simulator is constructed to characterize the influence of the number of SOPs on the horizontal PL (HPL) and vertical PL (VPL). Second, the PL reduction under different assumptions of SOP fault probabilities is analyzed.

The remainder of the paper is organized as follows. Section II. describes the measurement and SOP models employed in the paper. Section III. summarizes the ARAIM+SOP framework. Section IV. characterizes the PL reduction through Monte Carlo simulations. Concluding remarks are given in Section V.

II. MODEL DESCRIPTION

This paper considers an AGV navigating in an environment that comprises N_{GPS} GPS satellites and N_{SOP} cellular transmitters. The cellular transmitters are stationary with known positions. The AGV is equipped with (i) a GPS receiver capable of producing pseudorange measurements from the N_{GPS} GPS satellites (e.g., [43–45]) and (ii) a receiver capable of producing pseudorange measurements from the N_{SOP} SOP transmitters (e.g., [8,9,27,46]). The AGV uses a weighted nonlinear least-squares (WNLS)-based estimator to compute the navigation solutions from the GPS and SOP pseudorange measurements and simultaneously performs IM and fault detection and exclusion (FDE). The IM algorithm, discussed in Section III, is based on the baseline ARAIM framework [34]. Although ARAIM handles multiple GNSS constellations, this paper considers only the GPS constellation. The proposed framework can be readily generalized to multiple GNSS constellations. The rest of this section presents the GPS and SOP pseudorange measurement models and the WNLS-based estimator used in the ARAIM+SOP framework, as well as the models of the GPS satellites and SOP transmitters' azimuth and elevation angles used to evaluate the ARAIM+SOP framework.

1. GPS and SOP Pseudorange Measurement Models

a) GPS Pseudorange Measurement Model

The m-th GPS pseudorange measurement after compensating for ionospheric delays, tropospheric delays, and the satellite's clock bias is modeled as:

$$z_{GPS_m}(k) = \|\boldsymbol{r}_r(k) - \boldsymbol{r}_{GPS_m}(k)\|_2 + c \cdot \delta t_{r,ck}(k) + v_{GPS_m}(k), \qquad k = 0, 1, \ldots, \quad m = 1, \ldots, N_{GPS}, \tag{1}$$

where $z_{GPS_m}(k) = z'_{GPS_m}(k) - c \cdot \hat{\delta} t_{iono}(k) - c \cdot \hat{\delta} t_{tropo}(k) - c \cdot \hat{\delta} t_{GPS_m}(k)$; with $z'_{GPS_m}(k)$ being the uncompensated pseudorange; $\hat{\delta} t_{GPS_m}(k)$ is the estimated clock bias of the m-th GPS satellite; $\hat{\delta} t_{iono}(k)$ and $\hat{\delta} t_{tropo}(k)$ are the estimated ionospheric and tropospheric delays, respectively; c is the speed of light; $\boldsymbol{r}_r(k)$ and $\boldsymbol{r}_{GPS_m}(k)$ are the receiver and m-th satellite's three-dimensional (3-D) position vectors, respectively; $\delta t_{r,ck}(k)$ is the receiver's clock bias; and $v_{GPS_m}(k)$ denotes the measurement noise, which is modeled as a zero-mean Gaussian random sequence with a variance $\sigma^2_{GPS_m}$.

b) SOP Pseudorange Measurement Model

The n-th SOP pseudorange measurement can be modeled as [47]

$$\bar{z}_{SOP_n}(k) = \|\boldsymbol{r}_r(k) - \boldsymbol{r}_{SOP_n}(k)\|_2 + c \cdot [\delta t_{r,ck}(k) - \delta t_{SOP_n}(k)] + \bar{v}_{SOP_n}(k), \qquad k = 0, 1, \ldots, \quad n = 1, \ldots, N_{SOP}, \tag{2}$$

where $\boldsymbol{r}_{SOP_n}(k)$ and $\delta t_{SOP_n}(k)$ are the position and clock bias of the n-th SOP transmitter, respectively; and $\bar{v}_{SOP_n}$ is the SOP measurement noise, which is modeled as a zero-mean Gaussian random sequence with a variance σ^2_{user,SOP_n}. The model for σ^2_{user,SOP_n} is given in Subsection III.1. It was noted in [48] that the difference $c \cdot [\delta t_{r,ck}(k) - \delta t_{SOP_n}(k)]$ can be modeled as

$$c \cdot [\delta t_{r,ck}(k) - \delta t_{SOP_n}(k)] = c\delta t_{r,SOP}(k) + c\delta t_{SOP_n,0} + \epsilon_n(k), \qquad k = 0, 1, \ldots, \quad n = 1, \ldots, N_{SOP}, \tag{3}$$

where $c\delta t_{r,SOP}(k)$ is a common term driving the difference between the receiver and SOP clock biases, $c\delta t_{SOP_n,0}$ is an initial bias, and $\epsilon_n(k)$ is an error term modeled as a zero-mean Gaussian random variable with variance $\sigma^2_{\epsilon_n}$. The value of $\sigma^2_{\epsilon_n}$ is discussed in Subsection III.1. It is assumed that the initial biases $\{c\delta t_{SOP_n,0}\}_{n=1}^{N_{SOP}}$ were calibrated prior to IM. Finally, after initial bias calibration, the n-th SOP pseudorange measurement z_{SOP_n} can be expressed as

$$z_{SOP_n} = \|\boldsymbol{r}_r(k) - \boldsymbol{r}_{SOP_n}(k)\|_2 + c\delta t_{r,SOP}(k) + v_{SOP_n}(k), \qquad k = 0, 1, \ldots, \quad n = 1, \ldots, N_{SOP}, \tag{4}$$

where $v_{SOP_n}(k) \triangleq \epsilon_n(k) + \bar{v}_{SOP_n}(k)$.

2. Navigation Solution

The AGV aims to estimate its position vector using GPS and SOP pseudorange measurements using a WNLS. To this end, the GPS and SOP receivers' clock biases must be estimated alongside the AGV's position to avoid biasing the navigation solution. The vector to be estimated is given by

$$\boldsymbol{x}(k) \triangleq \left[\boldsymbol{r}_r{}^{\mathsf{T}}(k), c\delta t_{r,ck}(k), c\delta t_{r,SOP}(k)\right]^{\mathsf{T}}.$$

The time argument is omitted in the following for compactness of notation. The all-in-view combined GPS-SOP measurement vector can be formed according to

$$\boldsymbol{z} \triangleq \left[z_{GPS_1}, \ldots, z_{GPS_{N_{GPS}}}, z_{SOP_1}, \ldots, z_{SOP_{N_{SOP}}}\right]^{\mathsf{T}}.$$

A WNLS is then iterated to obtain an estimate of $\boldsymbol{x}$, denoted by $\hat{\boldsymbol{x}}$, using $\boldsymbol{z}$. Let l denote the iteration number, $\hat{\boldsymbol{x}}_l$ the estimate at iteration l, and $\hat{\boldsymbol{z}}_l$ the measurement prediction calculated using $\hat{\boldsymbol{x}}_l$. The all-in-view navigation solution update is obtained from the normal equations according to

$$\Delta\boldsymbol{x}_l = \left(\mathbf{H}_l{}^{\mathsf{T}}\mathbf{W}\mathbf{H}_l\right)^{-1}\mathbf{H}_l{}^{\mathsf{T}}\mathbf{W}\left(\boldsymbol{z} - \hat{\boldsymbol{z}}_l\right), \tag{5}$$

where $\mathbf{H}_l$ is the measurement Jacobian evaluated at $\hat{\boldsymbol{x}}_l$ and $\mathbf{W}$ is the weight matrix given by $\mathbf{W} = \mathbf{C}_{int}^{-1}$, where $\mathbf{C}_{int}$ is a diagonal matrix whose diagonal elements $\{\mathbf{C}_{int}(j,j)\}_{j=1}^{N_{GPS}+N_{SOP}}$ are the measurement noise variances used for integrity. The values of the diagonal elements of $\mathbf{C}_{int}$ are discussed in Subsection III.3. The WNLS estimate at the $(l+1)$-th iteration is updated according to

$$\hat{\boldsymbol{x}}_{l+1} = \hat{\boldsymbol{x}}_l + \Delta\boldsymbol{x}_l,$$

and the iteration number is subsequently increased according to $l \leftarrow l+1$. After convergence, the all-in-view navigation solution is denoted $\hat{\boldsymbol{x}}^{(0)}$, the measurement prediction after convergence is denoted $\hat{\boldsymbol{z}}^{(0)}$, and the residual at convergence is denoted $\boldsymbol{y}$, which is given by

$$\boldsymbol{y} \triangleq \boldsymbol{z} - \hat{\boldsymbol{z}}^{(0)}.$$

Let $\mathbf{H}$ denote the measurement Jacobian after convergence, which can be parameterized by the GPS satellites' and SOP transmitters' azimuth and elevation angles according to

$$\mathbf{H} = \begin{bmatrix} \mathbf{H}_{GPS} \\ \mathbf{H}_{SOP} \end{bmatrix}, \tag{6}$$

where

$$\mathbf{H}_{GPS} \triangleq \begin{bmatrix} -\cos(el_{GPS_1})\sin(az_{GPS_1}) & -\cos(el_{GPS_1})\cos(az_{GPS_1}) & -\sin(el_{GPS_1}) & 1 & 0 \\ \vdots & \vdots & \vdots & \vdots & \vdots \\ -\cos(el_{GPS_{N_{GPS}}})\sin(az_{GPS_{N_{GPS}}}) & -\cos(el_{GPS_{N_{GPS}}})\cos(az_{GPS_{N_{GPS}}}) & -\sin(el_{GPS_{N_{GPS}}}) & 1 & 0 \end{bmatrix},$$

$$\mathbf{H}_{SOP} \triangleq \begin{bmatrix} -\cos(el_{SOP_1})\sin(az_{SOP_1}) & -\cos(el_{SOP_1})\cos(az_{SOP_1}) & -\sin(el_{SOP_1}) & 0 & 1 \\ \vdots & \vdots & \vdots & \vdots & \vdots \\ -\cos(el_{SOP_{N_{SOP}}})\sin(az_{SOP_{N_{SOP}}}) & -\cos(el_{SOP_{N_{SOP}}})\cos(az_{SOP_{N_{SOP}}}) & -\sin(el_{SOP_{N_{SOP}}}) & 0 & 1 \end{bmatrix},$$

where az_{GPS_m} and el_{GPS_m} are the m-th GPS satellite's azimuth and elevation angles, respectively, and az_{SOP_n} and el_{SOP_n} are the n-th SOP's azimuth and elevation angles, respectively.

3. GPS Satellite Azimuth and Elevation Angle Characterization

As it can be seen from the expression of $\mathbf{H}$ in (6), the GPS satellites' and SOP transmitters' azimuth and elevation angles are enough to characterize the geometry between the AGV and the navigation sources. This paper assumes a stationary receiver located in Orange County, California, USA. The receiver position is fixed at $\boldsymbol{r}_r \equiv 10^6 \times [-2.482345,\ -4.700049,\ 3.513616]^{\mathsf{T}}$ expressed in the Earth-Centered-Earth-Fixed (ECEF) frame. The azimuth and elevation angles of all visible satellites at that location and at any point in time can be readily calculated. Since the nominal orbital period of a GPS satellites is 11 hours 58 minutes, which is almost exactly half of a sidereal day, the same exact GPS satellite configuration will repeat itself above the specified location after one full day on Earth [49]. As such, to obtain a realization of GPS azimuth and elevation angles, a random time is chosen from a 24-hour interval at which the satellite positions are determined. Subsequently, the azimuth and elevation angles are calculated and only GPS satellites above an elevation angle mask $el_{mask} = 5^\circ$ are retained.

4. SOP Azimuth and Elevation Angle Models

The cellular SOP network is modeled as a binomial point process (BPP), where the horizontal positions of N SOPs are independently and uniformly distributed over an annular region centered at the receiver, i.e., $\mathbb{B}_r(d_{SOP_{\min}}, d_{SOP_{\max}}) = \pi(d^2_{SOP_{\max}} - d^2_{SOP_{\min}})$ [50], where $d_{SOP_{\min}}$ is the minimum horizontal distance required for the far-field assumption to

hold and $d_{SOP_{\max}}$ is the maximum horizontal distance for which ranging signals can be detected by the receiver (see Figure 1(a) for $N = 15$). The altitudes of the SOPs relative to the receiver are assumed to be uniformly distributed between $h_{SOP_{\min}}$ and $h_{SOP_{\max}}$. As shown in Figure 1(b), the location of the n-th SOP is represented by $(d_{SOP_n}, h_{SOP_n}, az_{SOP_n})$, where d_{SOP_n} and h_{SOP_n} are the horizontal and vertical distances between the n-th SOP and the receiver, respectively. As a result, the elevation angle of the n-th SOP and the range to the n-th SOP r_{SOP_n} can be calculated as

$$el_{SOP_n} = \tan^{-1}\left(\frac{h_{SOP_n}}{d_{SOP_n}}\right), \qquad r_{SOP_n} = \sqrt{d_{SOP_n}^2 + h_{SOP_n}^2}.$$

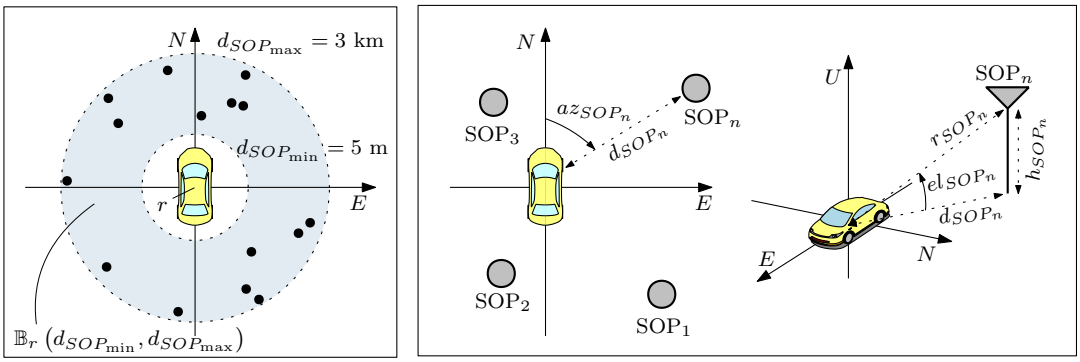

Figure 1: (a) BPP realization with $N = 15$, SOP transmitters uniformly lie in the annular region. (b) Parametrization of the n-th SOP position by its range r_{SOP_n}, azimuth angle az_{SOP_n} and elevation angle el_{SOP_n}.

III. ARAIM+SOP FRAMEWORK

This section introduces the ARAIM+SOP framework adopted by this paper to perform IM. ARAIM+SOP is developed based on the baseline multiple hypothesis solution separation (MHSS) ARAIM introduced in [34]. The MHSS ARAIM framework is capable of incorporating different navigation signals with different signal properties, e.g., different error variance, maximum nominal biases, and probability of single or constellation faults. The ARAIM+SOP framework utilizes this flexibility of multiple-source ARAIM to incorporate SOPs as a navigation constellation. While multiple GNSS constellations can be handled by the ARAIM+SOP framework, this paper considers GPS-SOP ARAIM as an initial study. The ARAIM+SOP framework is readily extendable to multiple GNSS constellations. Table 1 summarizes the inputs for the ARAIM+SOP algorithm.

The ARAIM+SOP algorithm first determines the fault modes to be monitored based on the Integrity Support Message (ISM) and SOP signal error characterization obtained from experimental campaigns. The prior probabilities of the fault modes are also computed in this step. During IM, the ARAIM+SOP conducts solution separation tests to detect and exclude potential faults in the system. The ARAIM+SOP framework also includes a chi-squared test which serves as a sanity check for potential faults outside the fault modes obtained by the algorithm. A brief description of the ARAIM+SOP is provided by the following sections. Detailed descriptions can be found in [34].

1. SOP Integrity Parameters

In order to perform IM with SOP pseudoranges, their integrity parameters must be known, mainly $\{\sigma_{URA,SOP_n}\}_{n=1}^{N_{SOP}}$, $\{\sigma_{URE,SOP_n}\}_{n=1}^{N_{SOP}}$, $\{b_{nom,SOP_n}\}_{n=1}^{N_{SOP}}$, $\{P_{SOP_n}\}_{n=1}^{N_{SOP}}$, and $P_{const,SOP}$. The performance of the ARAIM+SOP framework is characterized for various values of N_{SOP} and $\{P_{SOP_n}\}_{n=1}^{N_{SOP}}$. Moreover, this paper will not consider GPS or SOP constellation faults, as the probability of either to happen is assumed to be extremely low. Therefore, $P_{const,GPS}$ and $P_{const,SOP}$ are set to be 0. The rest of the SOP integrity parameters are discussed below.

a) SOP User Range Accuracy (URA) Standard Deviation

Figure 2(a) shows experimentally recorded data corresponding to a realization of $c\cdot[\delta t_{r,GPS}(k) - \delta t_{SOP_n}(k)]$ for three SOPs, after initial bias calibration, over a period of 24 hours. It can be clearly seen from Figure 2(a) that $\{c \cdot [\delta t_{r,GPS}(k) - \delta t_{SOP_n}(k)]\}_{n=1}^{3}$ are driven by a common term, justifying the right hand side of (3). Figure 2(b) shows the resulting $\epsilon_n(k)$, representing the deviation of $c \cdot [\delta t_{r,GPS}(k) - \delta t_{SOP_n}(k)]$ from the common term, for the realization in Figure 2(a). Figure 2(b) shows that $\{\epsilon_n\}_{n=1}^{3}$ can be considered as noise terms. Assuming ergodicity, the values of $\{\sigma_{\epsilon_n}\}_{n=1}^{3}$ range from 0.6 to 0.73 m. Therefore, σ_{URA,SOP_n} is chosen to be 1 m for all n, to guarantee that $\sigma_{\epsilon_n} \leq \sigma_{URA,SOP_n}$.

Table 1: Inputs to the ARAIM+SOP Algorithm

Input	Description	Obtained from
$\{z_{GPS_m}\}_{m=1}^{N_{GPS}}$	Pseudorange for m-th GPS satellite after dual frequency correction, tropospheric correction, and smoothing are performed	Receiver
$\{z_{SOP_n}\}_{n=1}^{N_{SOP}}$	Pseudorange for n-th SOP	Receiver
$\{\sigma_{URA,GPS_m}\}_{m=1}^{N_{GPS}}$	Standard deviation of the clock and ephemeris error of m-th satellite used for integrity	ISM
$\{\sigma_{URE,GPS_m}\}_{m=1}^{N_{GPS}}$	Standard deviation of the clock and ephemeris error of m-th satellite used for accuracy and continuity	ISM
$\{\sigma_{URA,SOP_n}\}_{n=1}^{N_{SOP}}$	Standard deviation of the clock error of n-th SOP used for integrity	Discussed in Subsection III.1
$\{\sigma_{URE,SOP_n}\}_{n=1}^{N_{SOP}}$	Standard deviation of the clock error of n-th SOP used for accuracy and continuity	Discussed in Subsection III.1
$\{b_{nom,GPS_m}\}_{m=1}^{N_{GPS}}$	Maximum nominal bias for GPS used for integrity	ISM
$\{b_{nom,SOP_n}\}_{n=1}^{N_{SOP}}$	Maximum nominal bias for SOP used for integrity	Discussed in Subsection III.1
$\{P_{GPS_m}\}_{m=1}^{N_{GPS}}$	Probability of a single GPS fault	ISM
$\{P_{SOP_n}\}_{n=1}^{N_{SOP}}$	Probability of a single SOP fault	Varied
$P_{const,GPS}$	Probability of GPS constellation fault	0
$P_{const,SOP}$	Probability of SOP constellation fault	0

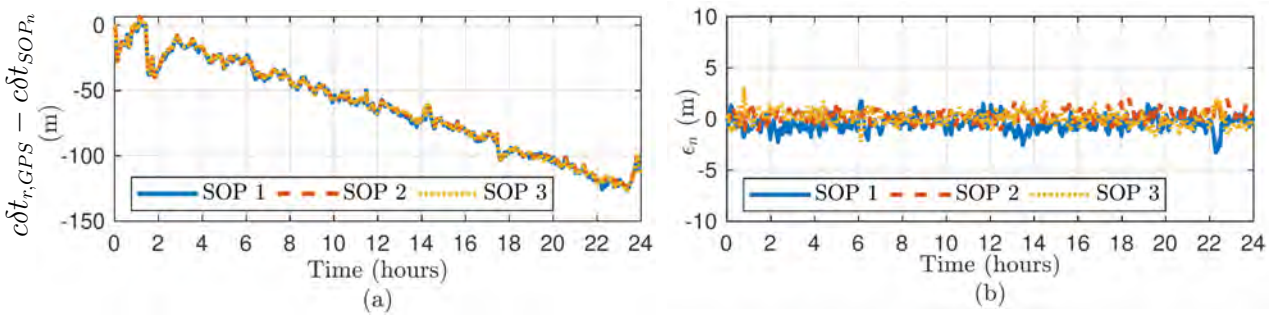

Figure 2: (a) Experimentally recorded data corresponding to a realization of $c \cdot [\delta t_r(k) - \delta t_{SOP_n}(k)]$ for three SOPs, after initial bias calibration, over a period of 24 hours. (b) Resulting $\epsilon_n(k)$ for the three SOPs in (a).

b) SOP User Range Error (URE) Standard Deviation

In GPS, it is usually assumed

$$\sigma_{URE,GPS} = \frac{2}{3}\sigma_{URA,GPS}.$$

This relationship is also used for $\sigma_{URE,SOP}$ and $\sigma_{URA,SOP}$.

c) SOP Maximum Nominal Bias

The maximum nominal bias typically used in GPS ARAIM applications is around 1 m. Due to the difference in the propagation channels, the SOP maximum nominal bias is taken to be threefold that of GPS; hence, b_{nom,SOP_n} is chosen to be 3 m for all n.

2. Determination of Fault Modes to be Monitored

The first step of the ARAIM+SOP framework is to determine the fault modes to be monitored and calculate their prior probabilities. The objective of this step is to choose the smallest subset of all the possible fault modes and make sure that the sum of the probabilities of the modes that are not monitored do not exceed a predefined threshold P_{THRES}. The algorithm moves the fault modes from the list of not monitored to the monitored list until the total probability of the remaining modes' occurrence is under P_{THRES}. The fault modes are selected from the fault modes with smaller number of faulty satellites (which is defined as the degree of the fault modes) to fault modes with larger degrees. Note that the maximum number of simultaneous faults is determined by the probability of single transmitter fault, constellation fault probability, and P_{THRES}.

After the $N_{faultmodes}$ fault modes are determined, the prior probability of each fault mode $P_{fault}^{(i)}$ is calculated based on the probability of single transmitter fault and constellation fault of GPS and SOP.

3. Covariance Matrix For Integrity

The ARAIM+SOP framework computes the pseudorange error diagonal covariance matrices $\mathbf{C}_{int,GPS}$ (used for integrity) and $\mathbf{C}_{acc,GPS}$ (used for accuracy and continuity) using the equation given by [34]:

$$\mathbf{C}_{int,GPS}(m,m) = \sigma_{URA,GPS_m}^2 + \sigma_{user,GPS_m}^2$$

$$\mathbf{C}_{acc,GPS}(m,m) = \sigma_{URE,GPS_m}^2 + \sigma_{user,GPS_m}^2,$$

where σ_{user,GPS_m} is the standard deviation of the GPS code noise and multipath error, which is calculated as

$$\sigma_{user,GPS_m} = \sqrt{\frac{f_{L1}^4 + f_{L5}^4}{(f_{L1}^2 - f_{L5}^2)^2}} \sqrt{\sigma_{MP}^2 + \sigma_{Noise}^2},$$

where f_{L1} and f_{L5} are the L1 an L5 frequency of GPS signal, $\sigma_{MP} = 0.13 + 0.53 \cdot \exp(-el_{GPS_m}/6.9)$ and $\sigma_{MP} = 0.15 + 0.43 \cdot \exp(-el_{GPS_m}/6.9)$.

Similarly, the SOP pseudorange error diagonal covariance matrices are given by

$$\mathbf{C}_{int,SOP}(n,n) = \sigma_{URA,SOP_n}^2 + \sigma_{user,SOP_n}^2$$

$$\mathbf{C}_{acc,SOP}(n,n) = \sigma_{URE,SOP_n}^2 + \sigma_{user,SOP_n}^2,$$

where σ_{user,SOP_m} is the standard deviation of the SOP multipath error which can be calculated as a function of the distance between the receiver and the SOP transmitter. The equation for σ_{user,SOP_m} is given in [50] (cf. (10)).

The pseudorange error diagonal covariance matrices for the overall system are given by

$$\mathbf{C}_{int} = \text{blkdiag}\left[\mathbf{C}_{int,GPS}, \mathbf{C}_{int,SOP}\right]$$

$$\mathbf{C}_{acc} = \text{blkdiag}\left[\mathbf{C}_{acc,GPS}, \mathbf{C}_{acc,SOP}\right],$$

where blkdiag donates block diagonal matrix.

4. Solution Separation Test

The ARAIM+SOP conducts multiple hypothesis testing to detect and locate the faults. Each fault mode determined by the previous step corresponds to one hypothesis. For each alternative hypothesis, a fault-tolerant solution is defined as the navigation solution obtained from measurements excluding the hypothesized faulty measurements in the corresponding fault mode. The difference between the fault-tolerant solutions and the all-in-view solution serves as the test statistics for each alternative hypothesis. The difference vector for the i-th fault mode is computed as

$$\Delta\hat{\boldsymbol{x}}^{(i)} = \hat{\boldsymbol{x}}^{(i)} - \hat{\boldsymbol{x}}^{(0)} = (\mathbf{S}^{(i)} - \mathbf{S}^{(0)})\boldsymbol{y}, \tag{7}$$

where $\hat{\boldsymbol{x}}^{(i)}$ and $\hat{\boldsymbol{x}}^{(0)}$ are the i-th fault-tolerant solution and the all-in-view solution, respectively; $\boldsymbol{y}$ is the residual vector from the all-in-view solution; and

$$\mathbf{S}^{(i)} \triangleq (\mathbf{H}^{\mathsf{T}}\mathbf{W}^{(i)}\mathbf{H})^{-1}\mathbf{H}^{\mathsf{T}}\mathbf{W}^{(i)}, \tag{8}$$

where $\mathbf{W}^{(i)}$ is the diagonal weighing matrix, which is defined as

$$\mathbf{W}^{(i)}(j,j) = \begin{cases} \mathbf{C}_{int}^{-1}(j,j) & \text{if measurement } j \text{ is hypothesized faulty,} \\ 0 & \text{otherwise.} \end{cases}$$

The test threshold for the q-th coordinate ($q = 1, 2,$ or 3) of fault mode i is denoted by $T_{i,q}$. The thresholds can be computed from the variance of $\Delta\hat{\boldsymbol{x}}^{(i)}$ and the continuity budget. For each i and q, the solution separation test is

$$|\hat{x}_q^{(i)} - \hat{x}_q^{(0)}| \overset{?}{\leq} T_{i,q}. \tag{9}$$

If the test fails for any i and q, the algorithm will try to perform fault exclusion.

5. Chi-squared Test

Other than the solution separation tests, the ARAIM-SOP framework conducts a chi-squared test as a sanity check for faults outside of the fault modes monitored in the framework. The chi-squared statistic is an upper bound of all solution separation test, i.e., the detectable faults will manifest themselves in this test statistic [34].

6. Protection Level Calculation

After all the fault detection and exclusion is performed, the HPL can be calculated. The algorithm first computes HPL_q for the two horizontal directions, i.e., $q \equiv 1, 2$, from the well-established equation [34]

$$2Q\left(\frac{HPL_q - b_q^{(0)}}{\sigma_q^{(0)}}\right) + \sum_{i=1}^{N_{fault,modes}} P_{fault}^{(i)} Q\left(\frac{HPL_q - T_{k,i} - b_q^{(i)}}{\sigma_q^{(i)}}\right) = \frac{1}{2} PHMI_{HOR}\left(1 - \frac{P_{fault,notmonitored}}{PHMI_{VERT} + PHMI_{HOR}}\right), \tag{10}$$

where Q is the tail distribution function of the standard Gaussian distribution; $b_q^{(i)}$ is the worst case impact of the nominal bias in the q direction; $\sigma_q^{(i)}$ is the variance of the fault-tolerant position estimate; $P_{fault}^{(i)}$ is the probability of fault mode i; $P_{fault,notmonitored}$ is the probability of the faults that are not included in the fault modes; and $PHMI_{VERT}$ and $PHMI_{HOR}$ are the integrity budget for the vertical and horizontal components, respectively. The HPL is further given by

$$HPL = \sqrt{HPL_1^2 + HPL_2^2}. \tag{11}$$

The VPL can be calculated from an equation similar to equation (10), except that $q \equiv 3$.

IV. PROTECTION LEVEL REDUCTION CHARACTERIZATION

Monte Carlo simulations are conducted to characterize the PL in different scenarios. In each simulation, it is assumed that there are 6 GPS satellites available above the elevation mask $el_{mask} = 5^\circ$. The GPS satellite positions are randomly drawn as discussed in Subsection II.3. Cellular base stations are placed randomly based on the BPP model mentioned in Subsection II.4. The vertical distances between the user receiver and the SOP transmission antenna are assumed to be uniformly distributed between 5 m to 25 m, i.e., $h_{SOP_n} \sim \mathcal{U}(5, 25)$ for $n = 1, \ldots, N_{SOP}$. The SOP elevation angles $el_{SOP,n}$ and pseudorange noise standard deviations σ_{user,SOP_n} are calculated according to h_{SOP_n}, d_{SOP_n}, and az_{SOP_n}. The simulation settings are tabulated in Table 2.

Table 2: SIMULATION SETTINGS

Parameter	Definition	Value
N_{GPS}	Number of available GPS satellites included in the navigation solution	6
N_{SOP}	Number of SOP transmitters included in the navigation solution	0 to 7
$PHMI_{HOR}$	Integrity budget for the horizontal component	10^{-7}
$PHMI_{VERT}$	Integrity budget for the vertical component	10^{-9}
PFA_{HOR}	Continuity budget allocated to the horizontal component	10^{-7}
PFA_{VERT}	Continuity budget allocated to the vertical component	10^{-9}
$\{\sigma_{URA,GPS_m}\}_{m=1}^{N_{GPS}}$	Standard deviation of the clock and ephemeris error of satellite m used for integrity	1 m
$\{\sigma_{URA,SOP_n}\}_{n=1}^{N_{SOP}}$	Standard deviation of the clock error of SOP n used for integrity	1 m

1. Evaluating Number of SOPs

The first study is to characterize the effect of the number of SOPs on the PL reduction. The VPL and HPL are first computed with the GPS measurements only. Then, the number of SOP transmitters was varied as $N_{SOP} \in \{1, \ldots, 7\}$. For each N_{SOP}, 10^5 realizations are drawn to compute the average PL reductions from GPS-only solutions to GPS-SOP solutions. The SOP fault probability was set to 10^{-4}. The results are shown in Figure 3.

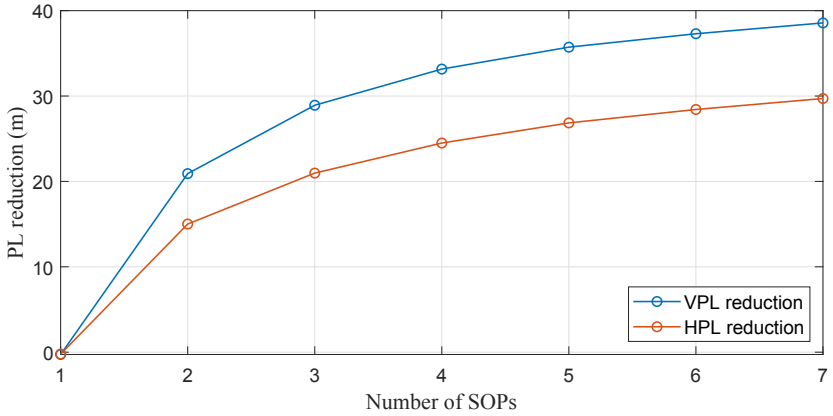

Figure 3: The average reduction in VPL and HPL after adding different number of SOP measurements. Each data point is obtained by averaging over 10^5 Monte Carlo realizations.

The following may be concluded from Figure 3. The number of SOP measurements plays an important role in PL reduction. Surprisingly, incorporating one SOP measurement in the framework *degrades* the IM performance. This is likely because the probability of single SOP transmitter fault is higher than that of GPS. The increased redundancy is not enough to compensate for the effects of increased probability of fault and larger number of fault modes. Furthermore, adding two or more SOPs will improve the IM performance significantly under the assumption of SOP fault probability being 10^{-4}. The PL reduction does not vary by much as N_{SOP} exceeds 5.

2. Evaluating Probability of Faults

As the probability of SOP fault has not been thoroughly characterized, it is essential to evaluate the performance of the ARAIM+SOP framework under different probability of fault assumptions. In these simulations, the probability of single SOP fault P_{SOP_n} is swept from 10^{-5} to 10^{-1}. The SOP measurement is considered to be faulty when multipath or non-line-of-sight (NLOS) conditions cause unmodeled biases or the SOP transmitter encounters anomalies which induce errors in the estimated position. The lower bound of P_{SOP_n} is chosen based on the assumption that the SOP measurements are less reliable than GPS measurements. It is also worth noting that P_{SOP_n} is not likely to be as high as 10^{-1}. However, 10^{-1} is chosen as an extreme case to study the performance in extreme regimes. For each N_{SOP} and P_{SOP_n} pair, 10^5 realizations are drawn to compute the average PL reduction. The results are shown in Figure 4.

The following conclusions may be drawn from Figure 4. Generally, the PL reduction will decrease with the probability of SOP transmitter fault increasing. However, in reasonable fault probability ranges (10^{-5} to 10^{-3}), the IM performance is more sensitive to the number of SOPs than the probability of fault. With enough SOP transmitters available, the less reliable SOP measurements (with P_{SOP_n} up to 10^{-3}) can still reduce the PLs significantly. Although less significant, PL reductions can still be achieved with high probability of SOP fault. It is worth re-iterating that these scenarios are not likely to happen in real life.

V. CONCLUSION

The performance of ARAIM+SOP was characterized by Monte Carlo numerical simulations. The paper analyzed the effect of the number of SOPs and the SOPs' fault probabilities on PL reduction. The following conclusions can be drawn from these analyses. First, the number of SOPs affects the PLs of the ARAIM+SOP framework significantly. Adding only one SOP could degrade the IM perofrmance. However, adding two or more SOPs will significantly improve the performance, and this improvement significantly grows up until about 5 SOPs. Beyond 5 SOPs, the improvement does not vary by much. Second, while incorporating a single faulty SOP does not benefit PL reduction, incorporating multiple highly unreliable SOPs will reduce the PL.

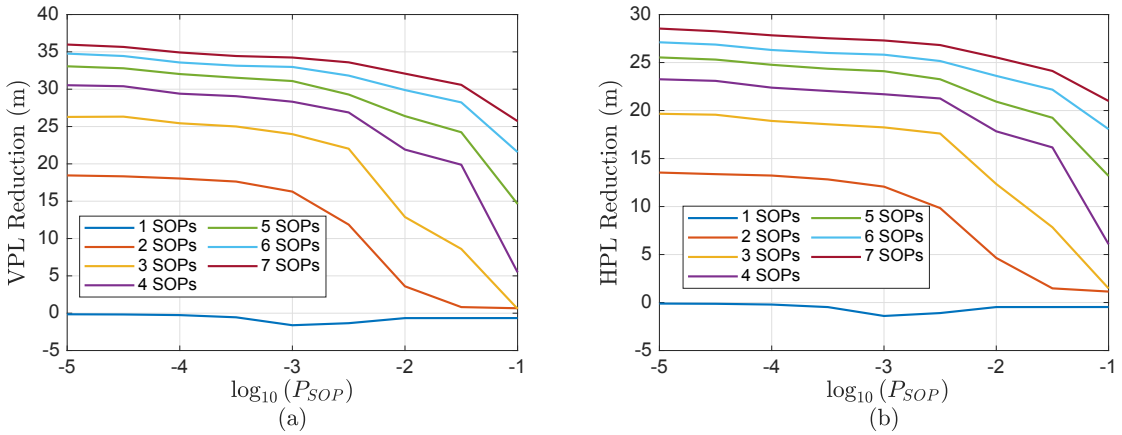

Figure 4: The reduction in VPL and HPL for adding different number of SOPs with different probability of SOP fault. (a) VPL reduction. (b) HPL reduction.

ACKNOWLEDGEMENTS

This work was supported in part by the U.S. Department of Transportation (USDOT) under Grant 69A3552047138 for the CARMEN University Transportation Center (UTC) and in part by the National Science Foundation (NSF) under Grant 1929965.

REFERENCES

[1] SAE International, "Taxonomy and definitions for terms related to driving automation systems for on-road motor vehicles," Tech. Rep., June 2018.

[2] R. Ioannides, T. Pany, and G. Gibbons, "Known vulnerabilities of global navigation satellite systems, status, and potential mitigation techniques," *Proceedings of the IEEE*, vol. 104, no. 6, pp. 1174–1194, February 2016.

[3] D. Borio, F. Dovis, H. Kuusniemi, and L. Presti, "Impact and detection of GNSS jammers on consumer grade satellite navigation receivers," *Proceedings of the IEEE*, vol. 104, no. 6, pp. 1233–1245, February 2016.

[4] N. Zhu, J. Marais, D. Betaille, and M. Berbineau, "GNSS position integrity in urban environments: A review of literature," *IEEE Transactions on Intelligent Transportation Systems*, vol. 19, no. 9, pp. 2762–2778, September 2018.

[5] Z. Kassas, J. Khalife, A. Abdallah, and C. Lee, "I am not afraid of the jammer: navigating with signals of opportunity in GPS-denied environments," in *Proceedings of ION GNSS Conference*, 2020, pp. 1566–1585.

[6] D. Imparato, A. El-Mowafy, and C. Rizos, "Integrity monitoring: From airborne to land applications," in *Multifunctional Operation and Application of GPS*. IntechOpen, 2018, pp. 23–43.

[7] C. Gentner, T. Jost, W. Wang, S. Zhang, A. Dammann, and U. Fiebig, "Multipath assisted positioning with simultaneous localization and mapping," *IEEE Transactions on Wireless Communications*, vol. 15, no. 9, pp. 6104–6117, September 2016.

[8] M. Driusso, C. Marshall, M. Sabathy, F. Knutti, H. Mathis, and F. Babich, "Vehicular position tracking using LTE signals," *IEEE Transactions on Vehicular Technology*, vol. 66, no. 4, pp. 3376–3391, April 2017.

[9] K. Shamaei, J. Khalife, and Z. Kassas, "Exploiting LTE signals for navigation: Theory to implementation," *IEEE Transactions on Wireless Communications*, vol. 17, no. 4, pp. 2173–2189, April 2018.

[10] J. Khalife and Z. Kassas, "Navigation with cellular CDMA signals – part II: Performance analysis and experimental results," *IEEE Transactions on Signal Processing*, vol. 66, no. 8, pp. 2204–2218, April 2018.

[11] J. del Peral-Rosado, J. López-Salcedo, F. Zanier, and G. Seco-Granados, "Position accuracy of joint time-delay and channel estimators in LTE networks," *IEEE Access*, vol. 6, no. 25185–25199, p. April, 2018.

[12] Z. Kassas, A. Abdallah, and M. Orabi, "Carpe signum: seize the signal – opportunistic navigation with 5G," *Inside GNSS Magazine*, vol. 16, no. 1, pp. 52–57, 2021.

[13] P. Thevenon, S. Damien, O. Julien, C. Macabiau, M. Bousquet, L. Ries, and S. Corazza, "Positioning using mobile TV based on the DVB-SH standard," *NAVIGATION, Journal of the Institute of Navigation*, vol. 58, no. 2, pp. 71–90, 2011.

[14] C. Yang, T. Nguyen, and E. Blasch, "Mobile positioning via fusion of mixed signals of opportunity," *IEEE Aerospace and Electronic Systems Magazine*, vol. 29, no. 4, pp. 34–46, April 2014.

[15] L. Chen, O. Julien, P. Thevenon, D. Serant, A. Pena, and H. Kuusniemi, "TOA estimation for positioning with DVB-T signals in outdoor static tests," *IEEE Transactions on Broadcasting*, vol. 61, no. 4, pp. 625–638, 2015.

[16] S. Fang, J. Chen, H. Huang, and T. Lin, "Is FM a RF-based positioning solution in a metropolitan-scale environment? A probabilistic approach with radio measurements analysis," *IEEE Transactions on Broadcasting*, vol. 55, no. 3, pp. 577–588, September 2009.

[17] A. Popleteev, "Indoor positioning using FM radio signals," Ph.D. dissertation, University of Trento, Italy, 2011.

[18] V. Moghtadaiee and A. Dempster, "Indoor location fingerprinting using FM radio signals," *IEEE Transactions on Broadcasting*, vol. 60, no. 2, pp. 336–346, June 2014.

[19] R. Landry, A. Nguyen, H. Rasaee, A. Amrhar, X. Fang, and H. Benzerrouk, "Iridium Next LEO satellites as an alternative PNT in GNSS denied environments–part 1," *Inside GNSS Magazine*, pp. 56–64., May 2019.

[20] Z. Tan, H. Qin, L. Cong, and C. Zhao, "New method for positioning using IRIDIUM satellite signals of opportunity," *IEEE Access*, vol. 7, pp. 83 412–83 423, 2019.

[21] Z. Kassas, J. Morales, and J. Khalife, "New-age satellite-based navigation – STAN: simultaneous tracking and navigation with LEO satellite signals," *Inside GNSS Magazine*, vol. 14, no. 4, pp. 56–65, 2019.

[22] Z. Kassas, J. Khalife, M. Neinavaie, and T. Mortlock, "Opportunity comes knocking: overcoming GPS vulnerabilities with other satellites' signals," *Inside Unmanned Systems Magazine*, pp. 30–35, June/July 2020.

[23] F. Farhangian and R. Landry, "Multi-constellation software-defined receiver for Doppler positioning with LEO satellites," *Sensors*, vol. 20, no. 20, pp. 5866–5883, October 2020.

[24] M. Orabi, J. Khalife, and Z. Kassas, "Opportunistic navigation with Doppler measurements from Iridium Next and Orbcomm LEO satellites," in *Proceedings of IEEE Aerospace Conference*, March 2021, accepted.

[25] J. Morales and Z. Kassas, "Tightly-coupled inertial navigation system with signals of opportunity aiding," *IEEE Transactions on Aerospace and Electronic Systems*, 2021, accepted.

[26] Z. Kassas, J. Khalife, K. Shamaei, and J. Morales, "I hear, therefore I know where I am: Compensating for GNSS limitations with cellular signals," *IEEE Signal Processing Magazine*, pp. 111–124, September 2017.

[27] K. Shamaei and Z. Kassas, "LTE receiver design and multipath analysis for navigation in urban environments," *NAVIGATION, Journal of the Institute of Navigation*, vol. 65, no. 4, pp. 655–675, December 2018.

[28] A. Abdallah and Z. Kassas, "Deep learning-aided spatial discrimination for multipath mitigation," in *Proceedings of IEEE/ION Position, Location, and Navigation Symposium*, April 2020, pp. 1324–1335.

[29] Z. Kassas, M. Maaref, J. Morales, J. Khalife, and K. Shamaei, "Robust vehicular localization and map matching in urban environments through IMU, GNSS, and cellular signals," *IEEE Intelligent Transportation Systems Magazine*, vol. 12, no. 3, pp. 36–52, June 2020.

[30] M. Maaref, J. Khalife, and Z. Kassas, "Lane-level localization and mapping in GNSS-challenged environments by fusing lidar data and cellular pseudoranges," *IEEE Transactions on Intelligent Vehicles*, vol. 4, no. 1, pp. 73–89, March 2019.

[31] M. Caamano, M. Felux, D. Gerbeth, J. Juan, G. Gonzalez-Casado, and J. Sanz, "Network-based ionospheric gradient monitoring to support GBAS," in *Proceedings of ION GNSS Conference*, 2019, pp. 2888–2902.

[32] M. Yoon, J. Lee, and S. Pullen, "Integrity risk evaluation of impact of ionospheric anomalies on GAST D GBAS," *NAVIGATION, Journal of the Institute of Navigation*, vol. 67, no. 2, pp. 223–234, 2020.

[33] E. Kaplan and C. Hegarty, *Understanding GPS: Principles and Applications*, 2nd ed. Artech House, 2005.

[34] J. Blanch, T. Walter, P. Enge, Y. Lee, B. Pervan, M. Rippl, and A. Spletter, "Advanced RAIM user algorithm description: Integrity support message processing, fault detection, exclusion, and protection level calculation," in *Proceedings of ION GNSS Conference*, September 2012, pp. 2828–2849.

[35] V. Kropp, "Advanced receiver autonomous integrity monitoring for aircraft guidance using GNSS," Ph.D. dissertation, University of Munich, Germany, 2018.

[36] J. Blanch, T. Walter, P. Enge, S. Wallner, F. Amarillo Fernandez, R. Dellago, R. Ioannides, I. F. Hernandez, B. Belabbas, A. Spletter *et al.*, "Critical elements for a multi-constellation advanced RAIM," *NAVIGATION, Journal of the Institute of Navigation*, vol. 60, no. 1, pp. 53–69, 2013.

[37] P. Roysdon and J. Farrell, "GPS-INS outlier detection and elimination using a sliding window filter," in *Proceedings of American Control Conference*, May 2017, pp. 1244–1249.

[38] S. Bhamidipati and G. Gao, "SLAM-based integrity monitoring using GPS and fish-eye camera," in *Proceedings of ION GNSS Conference*, September 2019, pp. 4116–4129.

[39] M. Maaref and Z. Kassas, "Measurement characterization and autonomous outlier detection and exclusion for ground vehicle navigation with cellular signals," *IEEE Transactions on Intelligent Vehicles*, vol. 5, no. 4, pp. 670–683, December 2020.

[40] M. Maaref and Z. Kassas, "Autonomous integrity monitoring for vehicular navigation with cellular signals of opportunity and an IMU," *IEEE Transactions on Intelligent Transportation Systems*, 2021, accepted.

[41] M. Maaref, J. Khalife, and Z. Kassas, "Enhanced safety of autonomous driving by incorporating terrestrial signals of opportunity," in *Proceedings of IEEE International Conference on Acoustics, Speech and Signal Processing*, May 2020, pp. 9185–9189.

[42] M. Maaref and Z. Kassas, "UAV integrity monitoring measure improvement using terrestrial signals of opportunity," in *Proceedings of ION GNSS Conference*, September 2019, pp. 3045–3056.

[43] K. Borre, D. Akos, N. Bertelsen, P. Rinder, and S. Jensen, *A Software-defined GPS and Galileo Receiver: A Single-frequency Approach*. Birkhäuser, 2007.

[44] T. Pany, *Navigation Signal Processing for GNSS Software Receivers*. Artech House, 2010.

[45] M. Braasch and A. Dempster, "Tutorial: GPS receiver architectures, front-end and baseband signal processing," *IEEE Aerospace and Electronic Systems Magazine*, vol. 34, no. 2, pp. 20–37, February 2019.

[46] J. del Peral-Rosado, J. Lopez-Salcedo, G. Seco-Granados, F. Zanier, P. Crosta, R. Ioannides, and M. Crisci, "Software-defined radio LTE positioning receiver towards future hybrid localization systems," in *Proceedings of International Communication Satellite Systems Conference*, October 2013, pp. 14–17.

[47] Z. Kassas and T. Humphreys, "Observability analysis of collaborative opportunistic navigation with pseudorange measurements," *IEEE Transactions on Intelligent Transportation Systems*, vol. 15, no. 1, pp. 260–273, February 2014.

[48] J. Khalife and Z. Kassas, "Precise UAV navigation with cellular carrier phase measurements," in *Proceedings of IEEE/ION Position, Location, and Navigation Symposium*, April 2018, pp. 978–989.

[49] S. Saab and Z. Kassas, "Power matching approach for GPS coverage extension," *IEEE Transactions on Intelligent Transportation Systems*, vol. 7, no. 2, pp. 156–166, June 2006.

[50] S. Aditya, H. Dhillon, A. Molisch, R. Buehrer, and H. Behairy, "Characterizing the impact of SNR heterogeneity on time-of-arrival-based localization outage probability," *IEEE Transactions on Wireless Communications*, vol. 18, no. 1, pp. 637–649, January 2019.

Evaluation of Orbit Errors and Measurement Corrections in Differential Navigation With LEO Satellites

Joe Saroufim, Samer Hayek, and Zaher M. Kassas
The Ohio State University

BIOGRAPHY

Joe Saroufim is a Ph.D student in the Department of Electrical and Computer Engineering at The Ohio State University and a member of the Autonomous Systems Perception, Intelligence, and Navigation (ASPIN) Laboratory. He received a B.E. in Mechanical Engineering from the Lebanese American University. His current research interests include low Earth orbit satellites, situational awareness, autonomous vehicles, and sensor fusion.

Samer Hayek is a Ph.D student in the Department of Electrical and Computer Engineering at The Ohio State University and a member of the ASPIN Laboratory. He received a B.E. in Mehchanical Engineering from the Lebanese American University. His current research interests include low Earth orbit satellites, autonomous vehicles, sensor fusion, and simultaneous localization and mapping.

Zaher (Zak) M. Kassas is a professor at The Ohio State University and TRC Endowed Chair in Intelligent Transportation Systems. He is the Director of the Autonomous Systems Perception, Intelligence, and Navigation (ASPIN) Laboratory. He is also director of the U.S. Department of Transportation Center: CARMEN (Center for Automated Vehicle Research with Multimodal AssurEd Navigation), focusing on navigation resiliency and security of highly automated transportation systems. He received a B.E. in Electrical Engineering from the Lebanese American University, an M.S. in Electrical and Computer Engineering from The Ohio State University, and an M.S.E. in Aerospace Engineering and a Ph.D. in Electrical and Computer Engineering from The University of Texas at Austin. He is a recipient of the National Science Foundation (NSF) CAREER award, Office of Naval Research (ONR) Young Investigator Program (YIP) award, Air Force Office of Scientific Research (AFOSR) YIP award, IEEE Walter Fried Award, Institute of Navigation (ION) Samuel Burka Award, and ION Col. Thomas Thurlow Award. He is an Associate Editor of the IEEE Transactions on Aerospace and Electronic Systems and the IEEE Transactions on Intelligent Transportation Systems. He is a Fellow of the ION and a Distinguished Lecturer of the IEEE Aerospace and Electronic Systems Society. His research interests include cyber-physical systems, navigation systems, and intelligent transportation systems.

ABSTRACT

Ephemeris errors and measurement corrections in differential navigation with low Earth orbit (LEO) space vehicles (SVs) are analyzed. First, orbit errors are characterized for the non-differential case, showing the dependency of the range measurement errors on the receiver-to-SV geometry. The study is then extended to the differential case, where the maximum differential range error is found to occur when the baseline is normal to the projected measurement vector from one receiver onto the local navigation frame. A simulation study is presented to assess the differential navigation performance with 14 Starlink and 11 OneWeb LEO satellites. The framework fused differenced pseudorange measurements from a base and rover to LEO SVs with inertial measurement unit (IMU) measurements via an extended Kalman filter (EKF) in a tightly-coupled fashion to estimate the rover's states. The simulation considered an aerial vehicle equipped with a tactical-grade IMU, an altimeter, a GNSS receiver, and a LEO receiver making pseudorange measurements to the LEO SVs. During 300 seconds of flight time, the vehicle traveled a distance of 28 km, the last 23 km of which were without GNSS, achieving a three-dimensional (3-D) position root mean squared error (RMSE) of 52 cm, compared to 12.5 m using the non-differential framework. Experimental results are presented, showing the potential of differential navigation in reducing ephemeris, clocks, and atmospheric errors. A ground vehicle traversed a distance of 540 m in 60 seconds, the last 492 m of which without GNSS signals, while making Doppler measurements to 2 Orbcomm and 1 Iridium LEO SVs, whose ephemerides were obtained from two-line element (TLE) files, propagated with simplified general perturbation 4 (SGP4) orbit propagator. The differential framework yielded a position RMSE of 7.13 m, compared to 41.29 m using non-differential measurements, and 87.74 m with GNSS-aided IMU.

I. INTRODUCTION

Existing low Earth orbit (LEO) satellite constellations, each of which totaling less than a hundred satellites (e.g., Orbcomm, Globalstar, Iridium NEXT), are being joined by megaconstellations of LEO satellites, each of which comprising up to thousands

of LEO satellites (e.g., OneWeb, Starlink, Project Kuiper). SpaceX is currently dominating these megaconstellations with about 4,000 functioning Starlink space vehicles (SVs) in LEO, with a possible extension to 42,000. Uninterrupted signals from these satellites will soon cover the Earth, heralding a new age for opportunistic position, navigation, and timing (PNT) (Kassas et al., 2019; Jardak and Jault, 2022; Janssen et al., 2023; Menzione and Paonni, 2023; Prol et al., 2023).

Conventional navigation methods that rely on fusing global navigation satellite system (GNSS) receivers with inertial measurement units (IMUs) raise alarming concerns when GNSS signals become unavailable or unreliable due to (i) intentional jamming (Miralles et al., 2020) or spoofing (Bhatti and Humphreys, 2017), (ii) signal obstruction and multipath in deep urban canyons (McGraw and Braasch, 1999), and (iii) unintentional interference (Hegarty et al., 2020), leading to unbounded accumulation of IMU errors.

To address the shortcomings of GNSS, opportunistic navigation using terrestrial signals of opportunity (SOPs) has been studied extensively, achieving lane-level positioning on ground vehicles (Peral-Rosado et al., 2016; Maaref et al., 2019; Whiton et al., 2022), and sub-meter-level accuracy on unmanned aerial vehicles (UAVs) (Khalife and Kassas, 2022). The boom in LEO satellites has attracted researchers' attention in recent years towards exploiting LEO signals for PNT in either a standalone fashion (Khalife et al., 2022; Huang et al., 2022; Zhao et al., 2022) or an IMU aiding fashion (Kassas et al., 2019; Farhangian et al., 2021).

Besides their large abundance around the Earth, several desirable characteristics qualify LEO SVs as promising PNT sources (Prol et al., 2022): (i) being twenty times closer to Earth than GNSS SVs that reside in medium Earth orbit (MEO) satellites results in higher received carrier-to-noise ratio, (ii) residing at different altitudes ranging from 160 to 1,000 km with different orbit orientations offers favorable geometric dilution of precision for accurate position and velocity estimation (Kennewell and Vo, 2013), and (iii) orbiting at high speed compared to MEO SVs yields more informative Doppler measurements.

However, exploiting broadband LEO satellite SOPs for navigation purposes comes with challenges, as they are owned by private operators that typically do not disclose crucial information about the satellites': (i) ephemerides, (ii) clock synchronization and stability, and (iii) signal specifications. Several studies have been published over the past few years to address satellite orbit, clock, and propagation errors (Kozhaya et al., 2021; Khairallah and Kassas, 2021; Morton et al., 2022; Cassel et al., 2022; Wang et al., 2023; Zhao et al., 2023; Wu et al., 2023; Jiang et al., 2023a; Ye et al., 2023; Khalife and Kassas, 2023; Saroufim et al., 2023; Kassas et al., 2023a); receiver and signal design (Tan et al., 2019; Wei et al., 2020; Bilardi, 2021; Orabi et al., 2021; Kassas et al., 2021; Neinavaie et al., 2022; Egea-Roca et al., 2022; Huang et al., 2022; Pinell et al., 2023; Yang et al., 2023; Humphreys et al., 2023; Yang and Soloviev, 2023); and navigation framework design (Farhangian et al., 2021; Psiaki, 2021; Hartnett, 2022; Singh et al., 2022; Jiang et al., 2022; More et al., 2022; Shi et al., 2023; Guo et al., 2023; Kanamori et al., 2023; Sabbagh and Kassas, 2023; Farhangian and Landry, 2023; Ries et al., 2023).

Although LEO SVs typically do not transmit their position in their downlink signals, they may be calculated from the publicly available two-line element (TLE) sets published and updated daily by the North American Aerospace Defense Command (NORAD). The first line in the TLE contains designation and temporal data, whereas the second line consists of a list of the standard orbital elements (inclination angle, right ascension of ascending node, eccentricity, argument of perigee, mean anomaly, and mean motion) defined at a certain time epoch. Using this information, orbit determination algorithms, such as simplified general perturbation 4 (SGP4), can be used to estimate any LEO SV's ephemeris (Vallado and Crawford, 2008). Nonetheless, although SGP4 takes into account atmospheric drag and satellites perturbations, its corresponding propagated TLE ephemeris results in state error ranging from hundreds of meters to a few kilometers, mostly concentrated in the tangential or along-track axis of the LEO satellite's body frame (Khairallah and Kassas, 2021). Even sophisticated high-fidelity numerical propagators incorporating complex force models, which showed improved propagation accuracy, require prior knowledge of force parameters that are not publicly available (Vallado, 2005; Hough, 2014; Jones and Weisman, 2019).

Modeling orbit errors has been studied recently for improved opportunistic PNT with LEO satellites. Precise orbit determination and LEO navigation augmentation were proposed to achieve GNSS-like positioning (Michalak et al., 2021; Meng et al., 2021); however, access to a GNSS receiver onboard the LEO SVs would be needed, posing additional challenges. An orbit error compensation method was introduced in (Wang et al., 2023) to improve Doppler positioning accuracy.

Differential navigation offers an alternative technique to correct for satellite orbit, atmospheric, and clock errors (Yan and Zhang, 2022; Jiang et al., 2023b). This technique consists of a base station with a known position, listening to the same satellites as a navigating rover with an unknown state. The base station transmits measurement corrections to the rover (Parkinson and Enge, 1996; Hwang et al., 1999). At a sufficiently small baseline distance, differenced measurements from the two receivers significantly reduce the aforementioned common mode errors mentioned. LEO-based differential navigation was studied using carrier phase measurements from Orbcomm (Khalife and Kassas, 2019; Khalife et al., 2020), and Doppler observables from Starlink (Neinavaie et al., 2022; Saroufim et al., 2023) and Iridium (Zhao et al., 2023). A recent study involving a multi-constellation differential simultaneous tracking and navigation (D-STAN) framework using differenced Doppler measurements from Starlink, OneWeb, Orbcomm, and Iridium SVs showed promisingly accurate navigation performance, achieving meter-level accuracy over a trajectory of about a kilometer (Kassas et al., 2023b).

This paper analyzes the dominating along-track error in the LEO SVs orbit and maps this error to the ranging error as seen by a ground-based receiver. It also analyzes the substantial benefit of the differential framework to reduce this error. This paper makes the following contributions. First, the pseudorange measurement model is presented for the non-differential and differential frameworks, and the propagation of ephemeris error onto the measurement model is derived. The analysis is conducted first in the SV's orbital plane for the non-differential framework, showing the effect of receiver-to-SV orientation on the measurement error and receiver localization. The analysis is then extended to the differential scenario, where the receiver-to-SV orientation is shown to hold a major impact on the differential error. Next, a numerical simulation study is presented, demonstrating the efficacy of differential navigation in reducing the effect of LEO ephemeris error on the navigation solution. The simulation considered an aerial vehicle equipped with a tactical-grade IMU, an altimeter, and a LEO satellites receiver listening to 14 Starlink and 11 OneWeb satellites, while a base station communicates its pseudorange measurements from the same LEO SVs to help with the measurement error corrections and improve the rover navigation performance. The rover traveled a distance of 28 km in 300 seconds, where GNSS signals were available for the first 60 seconds. The proposed framework achieved a position three-dimensional (3-D) root mean-squared error (RMSE) of 52 cm. Finally, experimental results are presented for a ground vehicle navigating for 540 m in 60 s with differential Doppler measurement from 2 Orbcomm and 1 Iridium NEXT LEO satellites, achieving a 3-D position RMSE of 7.13 m, despite using erroneous LEO SV ephemerides obtained from TLE+SGP4.

The rest of the paper is organized as follows: Section II presents the non-differential and differential measurement models. Section III shows the effect of ephemeris error on the range measurements. Section IV discusses the simulation results of a LEO-aided differential navigation. Section V shows experimental results validating the benefit of differential navigation. Section VI gives concluding remarks.

II. MODEL DESCRIPTION

This section presents the LEO satellites' pseudorange measurement model in both differential and non-differential frameworks.

1. Non-Differential Measurement Model

Pseudorange measurements ρ from a LEO satellite l extracted by a LEO receiver at time-step k, representing discrete-time instant $t_k = kT + t_0$, is modeled as

$$\rho_l(k) \;=\; \|\boldsymbol{r}_r(k) - \boldsymbol{r}_{leo,l}(k')\|_2 + c\cdot[\delta t_r(k) - \delta t_{leo,l}(k')] + c\delta t_{trop,l}(k) + c\delta t_{iono,l}(k) + \epsilon_{\rho,l}(k),$$

where k' represents discrete-time at $t_{k'} = kT + t_0 - \delta t_{TOF}$, with δt_{TOF} being the true time-of-flight of the signal from the LEO satellite to the receiver; $\boldsymbol{r}_r$ and $\boldsymbol{r}_{leo,l}$ are the 3-D position vectors of the receiver and the l-th LEO SV in the Earth-centered-Earth-fixed (ECEF) reference frame; c is the speed of light; δt_r and $\delta t_{leo,l}$ are the clock biases of the receiver and the l-th LEO SV, respectively; $\delta t_{iono,l}(k)$ and $\delta t_{trop,l}(k)$ are the ionospheric and tropospheric delays from the l-th LEO SV to the receiver at time-step k, respectively; and $\epsilon_{\rho,l}$ is the pseudorange measurement noise, which is modeled as a discrete-time zero-mean white Gaussian sequence with variance $\sigma^2_{\rho,l}(k)$.

2. Differential Measurement Model

The differential pseudorange measurement model across the rover R and the base B is defined as

$$\begin{aligned} z_l^{(R,B)}(k) \;&=\; \rho_l^{(R)}(k) - \rho_l^{(B)}(k) \\ &= \|\boldsymbol{r}_{r,R}(k) - \boldsymbol{r}_{leo,l}(k')\|_2 - \|\boldsymbol{r}_{r,B}(k) - \boldsymbol{r}_{leo,l}(k')\|_2 + c\delta t_r^{(R,B)}(k) + c\delta t_{trop,l}^{(R,B)}(k) + c\delta t_{iono,l}^{(R,B)}(k) + \epsilon_{\rho,l}^{(R,B)}(k), \end{aligned}$$

where

$$\begin{aligned} \delta t_r^{(R,B)}(k) \;&\triangleq\; \delta t_r^{(R)}(k) - \delta t_r^{(B)}(k) \\ \epsilon_{\rho,l}^{(R,B)}(k) \;&\triangleq\; \epsilon_{\rho,l}^{(R)}(k) - \epsilon_{\rho,l}^{(B)}(k). \end{aligned}$$

III. EFFECT OF EPHEMERIS ERROR ON LEO SATELLITES MEASUREMENTS

Each satellite is characterized by its orbital plane, where its motion along the orbit is defined by the rate of change in its true anomaly. Therefore, a satellite state error that is concentrated in the along-track axis in a low eccentricity orbit can be represented as a true anomaly angle error. To assess the error at this level, a theoretical analysis is conducted in the satellite's orbital plane, where exact relations can be derived and generalized for all LEO SVs' orbits. This section addresses the LEO SV state errors reflected in the range measurement for the non-differential and differential configurations.

1. Non-Differential Framework

Define $\hat{\boldsymbol{r}}_{leo,l}$, $\hat{\dot{\boldsymbol{r}}}_{leo,l}$ as the estimated "erroneous" position and velocity of the l^{th} LEO satellite extracted from the TLEs; $\hat{\rho}_l$ is the corresponding pseudorange measurement; $\boldsymbol{r}_l$ and $\hat{\boldsymbol{r}}_l$ are the range vectors from the receiver to the l^{th} true and estimated LEO SV, respectively. To study the impact of the LEO satellite state error on the pseudorange, for simplicity, perfect clocks are assumed. Hence, the range error ν can be written as

$$\begin{aligned} \nu &= \rho_l - \hat{\rho}_l \\ &= \|\boldsymbol{r}_l\| - \|\hat{\boldsymbol{r}}_l\| \\ &= \|\boldsymbol{r}_r - \boldsymbol{r}_{leo,l}\| - \|\boldsymbol{r}_r - \hat{\boldsymbol{r}}_{leo,l}\|. \end{aligned}$$

Given that most of the state error resides in the satellite's in-track direction, it is beneficial to study this effect in each satellite's orbital plane, where all SVs would behave similarly regardless of their orbital elements. Figure 1 illustrates the orbital plane of satellite l with the projection of the receiver position vector onto this plane. Define $\boldsymbol{e}$ to be the error vector of a LEO satellite in its orbital plane, namely

$$\begin{aligned} \boldsymbol{e} &= \hat{\boldsymbol{r}}_{leo,l} - \boldsymbol{r}_{leo,l} \\ &= \hat{\boldsymbol{r}}_l - \boldsymbol{r}_l. \end{aligned}$$

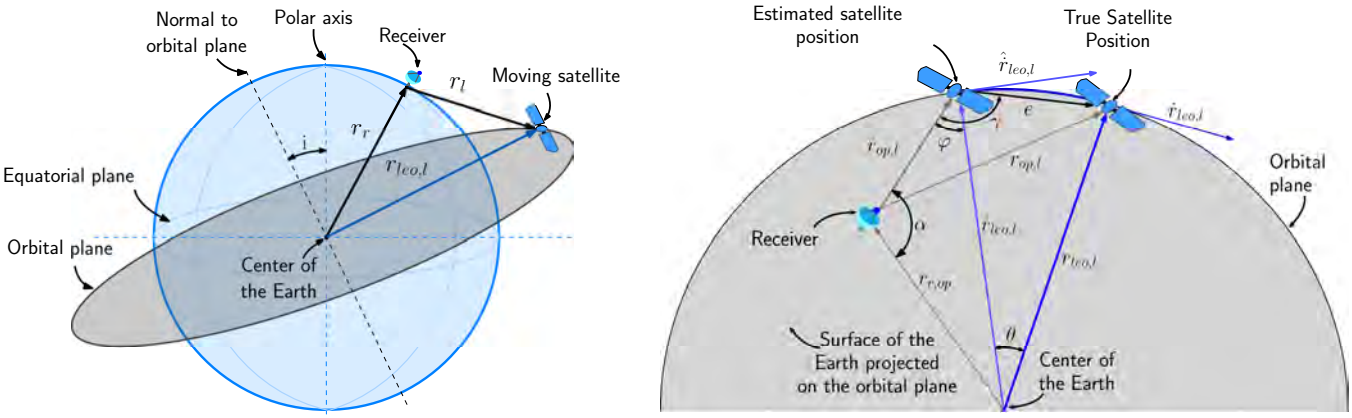

Figure 1: Earth and satellite's orbit (left). Orbital plane for a non-differential scenario: estimated and actual LEO satellite positions with corresponding range measurements to a stationary receiver projected onto the satellite's orbital plane (right).

Denote a variable 'a' as the L2 norm of its corresponding vector form, i.e., $a = \|\boldsymbol{a}\|$. Also, let $\boldsymbol{r}_{op,l}$, $\hat{\boldsymbol{r}}_{op,l}$, and $\boldsymbol{r}_{r,op}$ represent the projections of $\boldsymbol{r}_l$, $\hat{\boldsymbol{r}}_l$, and $\boldsymbol{r}_r$, respectively, on the l^{th} LEO satellite's orbital plane. Hence, the true orbital plane range can be written as

$$r_{op} = \sqrt{\hat{r}_{op}^2 + e^2 - 2\hat{r}_{op}.\cos\gamma}.$$

Assuming a circular orbit for a small in-track error e, leads to $\hat{r}_{leo} \approx r_{leo}$. From Figure 1, it can be seen that γ can be written as

$$\gamma = \varphi + \frac{\pi - \theta}{2}.$$

Knowing that the along-track error e is at the order of few kilometers, and the magnitude of the LEO satellite's position vector in the ECEF coordinate system, $\hat{r}_{leo}$ is in the range $6550 - 7500$ km, resulting in a true anomaly error $\theta \approx 0.01°$, making the assumption $\cos\gamma \approx \sin\varphi$ valid. Taking the satellite position error to be along the direction of motion, the range error can be written as $\nu = |r_{op} - \hat{r}_{op}|$, where the only variable is φ, leading to

$$\nu = \hat{r}_{op}\left(\sqrt{1 \pm \frac{2.e.\sin\varphi}{\hat{r}_{op}}} - 1\right). \tag{1}$$

Without prior knowledge of the ephemeris, it is difficult to estimate the magnitude of the SV state error. To circumvent this, a differential framework is adapted to reduce the effect of SV ephemeris error on the navigation solution.

2. Differential Framework

This subsection analyzes the effect of a satellite ephemeris error at a single time epoch on the differential range measurements from two stationary receivers. A fixed baseline is assumed to study the impact of the orientation of two receivers with respect to the satellite on the differential range measurements subjected to orbital errors.

Let r_{r_i} and b denote the projection of the i^{th} receiver position and baseline onto the LEO satellite orbital plane, respectively, as illustrated in Figure 2. Following (1), the true range and range residual ν in the orbital plane can be calculated as

$$r_i = \hat{r}_i \left(\sqrt{1 + \frac{2.e.\sin\varphi_{r_i}}{\hat{r}_i}} \right)$$

$$\nu = \hat{r}_1 \left(\sqrt{1 + \frac{2.e.\sin\varphi_{r_1}}{\hat{r}_1}} - 1 \right) - \hat{r}_2 \left(\sqrt{1 + \frac{2.e}{\hat{r}_2}.\sin\left(\varphi_{r_1} - \varphi_{r_1,r_2}\right)} - 1 \right), \tag{2}$$

where the first and second terms in (2) represent the range errors at the first and second receivers, respectively, and

$$\varphi_{r_{r_1,r_2}} = \arccos\left(\frac{\hat{r}_1^2 + \hat{r}_2^2 - b^2}{2\hat{r}_1\hat{r}_2} \right).$$

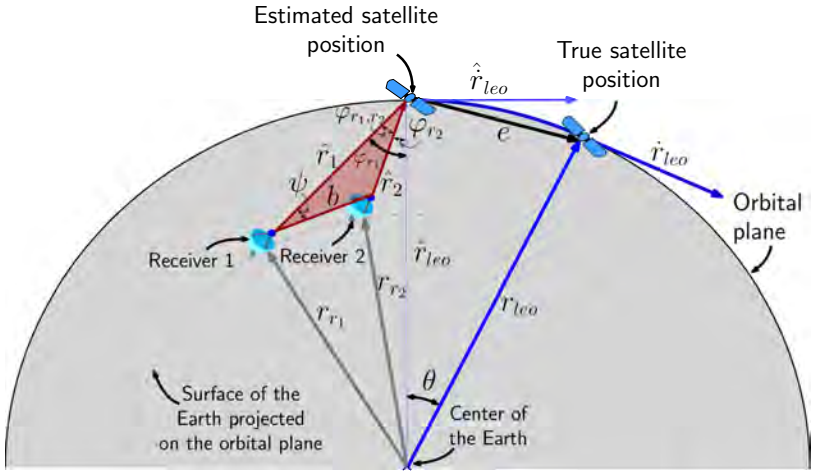

Figure 2: Differential scenario in the orbital plane: estimated and actual LEO satellite positions with corresponding range measurements to two stationary receivers projected onto the satellite's orbital plane.

Fixing receiver 1 and the orbital plane baseline b, receiver 2 may take any position along the circle centered at receiver 1 with radius b. Hence, the only variable affecting the differential residual becomes $\varphi_{r_{r_1,r_2}}$, revealing the relationship between the orientation of the second receiver and measurement error at a specific time step. It can be shown from (2) that the error at the second receiver eliminates its counterpart on the first receiver when $\varphi_{r_{r_1,r_2}}$ is zero, while the largest residual error occurs when $\varphi_{r_{r_1,r_2}}$ is maximum, i.e., when $|\psi| = \frac{\pi}{2}$, which is the angle between the estimated range at the fixed receiver and the baseline.

A simulation was conducted to demonstrate these relationships. A receiver was placed at The Ohio State University, Columbus, Ohio, USA, and was assumed to listen to a Starlink LEO satellite, producing an estimated range measurement. The second receiver was moved along 100 different locations centered at the first receiver, with a radius of 5 km, shown in Figure 3(a). The true satellite position was simulated with a 4 km in-track error along the direction of motion, where the true reference range measurement was obtained. The two receivers listened to the same SV at each epoch, and the measurements were differenced at the estimated and true satellite positions for every baseline orientation. The differential residuals at each location of the second receiver are shown in Figure 3(b) studied in the satellite's orbital plane, where the maximum differential error was recorded when the baseline is normal to the projected estimated range vector on the orbital plane. The maximum differential residual for

a 4 km in-track error and 5 km baseline with the Starlink LEO satellite used was found to be 23 m, while almost zero differential residual is achieved when the baseline is co-linear with the projected estimated range vector at the fixed receiver.

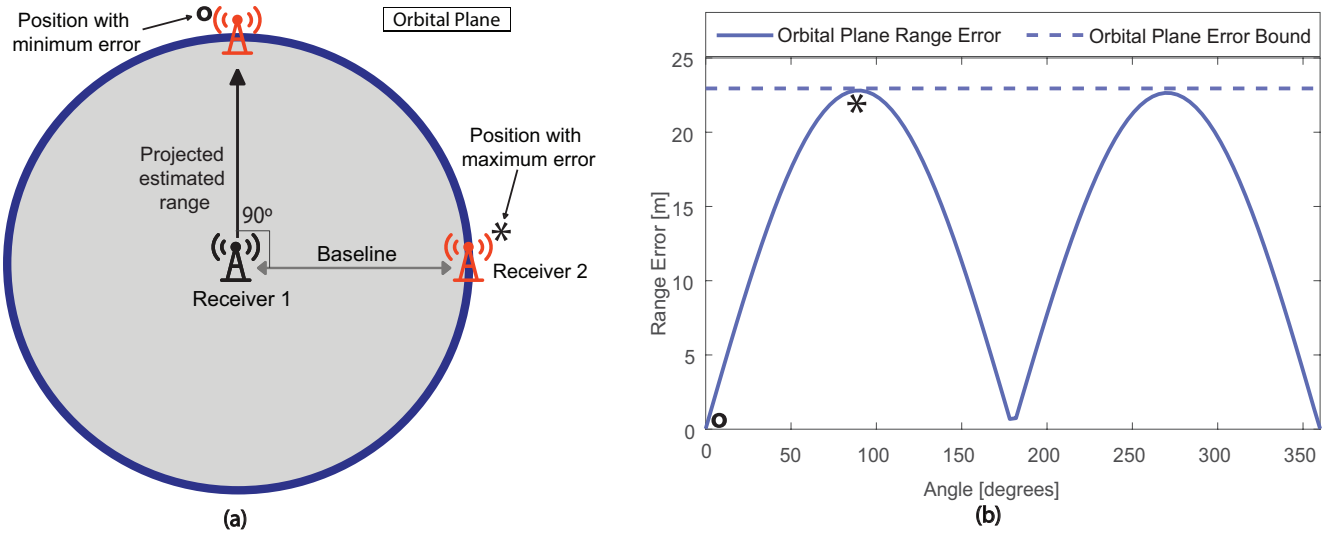

Figure 3: (a) Baseline orientation showing the locations of maximum and minimum differential range errors. (b) Differential range error and maximum range error with varying receivers-SV orientation in the orbital plane.

IV. SIMULATION OF DIFFERENTIAL NAVIGATION WITH LEO SATELLITES

This section presents simulation results of a differential framework comprising a moving rover with unknown states and a stationary basestation with a known position. The rover and base make pseudorange measurements to L LEO satellites, where the base communicates its position, pseudorange measurements, and measurement noise variance $\sigma^{2}_{\rho,l}{}^{(B)}$ to the rover. Figure 4 depicts a block diagram of the differential framework adapted by the rover, where IMU measurements are tightly coupled with GNSS and LEO pseudoranges via an extended Kalman filter (EKF). The following subsections formulate the EKF and present the EKF error plots.

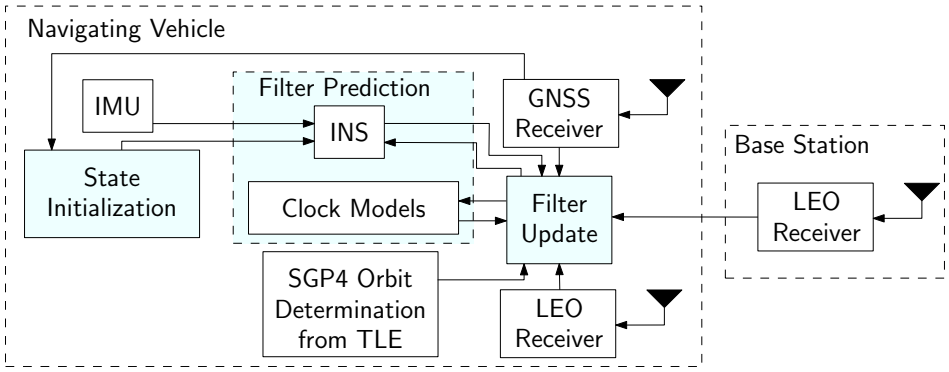

Figure 4: LEO-aided INS differential framework

1. EKF Formulation

The EKF for the differential framework shown in Figure 4 is implemented to estimate the moving rover's states and clock state difference between the base and rover. The state vector is defined as

$$\begin{aligned} \boldsymbol{x} &= [\boldsymbol{x}_r{}^{\mathsf{T}},\, \boldsymbol{x}_{clk}{}^{\mathsf{T}}]^{\mathsf{T}} \\ \boldsymbol{x}_r &= [{}^{b}_{g}\bar{\boldsymbol{q}}^{\mathsf{T}},\, \boldsymbol{r}_r^{\mathsf{T}},\, \dot{\boldsymbol{r}}_r^{\mathsf{T}},\, \boldsymbol{b}_{gyr}^{\mathsf{T}},\, \boldsymbol{b}_{acc}^{\mathsf{T}}]^{\mathsf{T}} \\ \boldsymbol{x}_{clk} &= [c\delta t_r^{(R,B)}, c\dot{\delta} t_r^{(R,B)}] \end{aligned}$$

where $\boldsymbol{x}_r$ is the vehicle's state vector, composed of ${}^{b}_{g}\bar{\boldsymbol{q}}$, which is a four-dimensional unit quaternion representing the orientation of the body frame $\{b\}$ fixed at the inertial navigation system (INS) with respect to the global frame $\{g\}$; $\boldsymbol{r}_r$ and $\dot{\boldsymbol{r}}_r$ are the 3-D position and velocity of the vehicle expressed in $\{g\}$; and $\boldsymbol{b}_{gyr}$ and $\boldsymbol{b}_{acc}$ are the 3-D biases of the IMU's gyroscope and accelerometer, respectively, expressed in $\{\mathrm{b}\}$. The vector $\boldsymbol{x}_{clk}$ is the clock state, composed of the difference between the rover and the base clock bias and drift. The IMU and clock dynamics models are detailed in (Saroufim et al., 2023), whereas the strap-down INS kinematic equations used to estimate the orientation, position, and velocity of the rover can be found in (Kassas et al., 2023a).

2. Simulation

The simulation environment comprised a stationary receiver located at the Electroscience Laboratory, at The Ohio State University, Columbus, Ohio, USA. The base was equipped with a LEO receiver producing pseudorange measurements to 14 Starlink and 11 OneWeb LEO SVs. A fixed-wing aerial vehicle was simulated to fly for 300 seconds over Columbus, traveling a total distance of 28 km. The vehicle was equipped with a tactical-grade IMU, an altimeter, a GNSS receiver, and an opportunistic LEO receiver making pseudorange measurements to the same 25 LEO satellites. For the first 60 seconds, GNSS and altimeter measurements were fused in a loosly coupled fashion to aid the onboard INS, before cutting off GNSS signals for the remaining 240 seconds. After GNSS cutoff, the aerial vehicle fused altimeter, Starlink, and OneWeb LEO pseudorange measurements, along with the communicated pseudoranges from the base-station to navigate the rover. The gyroscope and accelerometer readings were simulated from the vehicle's kinematics as explained in (Saroufim et al., 2023). The two receivers were equipped with a high-quality oven-controlled crystal oscillator (OCXO) clocks. Finally, the LEO satellites' ephemerides were generated via the Analytical Graphics Inc. (AGI) System Tool Kit (STK) and propagated using High Precision Orbit Propagator (HPOP) with an elevation mask of 15 degrees.

Table 1: Simulation Environment.

Metric	Total	No GNSS
Distance [km]	28	23
Time [s]	300	240

Figure 5 illustrates the LEO SVs' trajectories and the aerial vehicle trajectories: ground truth, GNSS-aided INS, non-differential LEO-aided INS, and differential LEO-aided INS, while Figure 6 shows the EKF error plots. Note that the GNSS-INS error bounds diverge rapidly after GNSS-cutoff, and hence are not shown in the EKF plots. Tables 1 and 2 summarize the results.

The geometric and orbital diversity of Starlink and OneWeb shown in Fig. 5 reduce the position dilution of precision (PDOP) in the east and north directions, causing the vehicle's states to remain observable in these directions. The error convergence in the up direction is mainly due to the presence of altimeter corrections throughout the simulation period. These results present the potential of a sub-meter accuracy with a differential LEO-aided INS navigation, and the significant reduction of common mode errors including ephemeris and clock effects.

Table 2: Simulation results.

Framework	2-D position RMSE [m]	Final error [m]
GNSS-INS	528	1,795
Non-differential LEO-aided INS	12.5	7.1
Differential LEO-aided INS	0.52	0.10

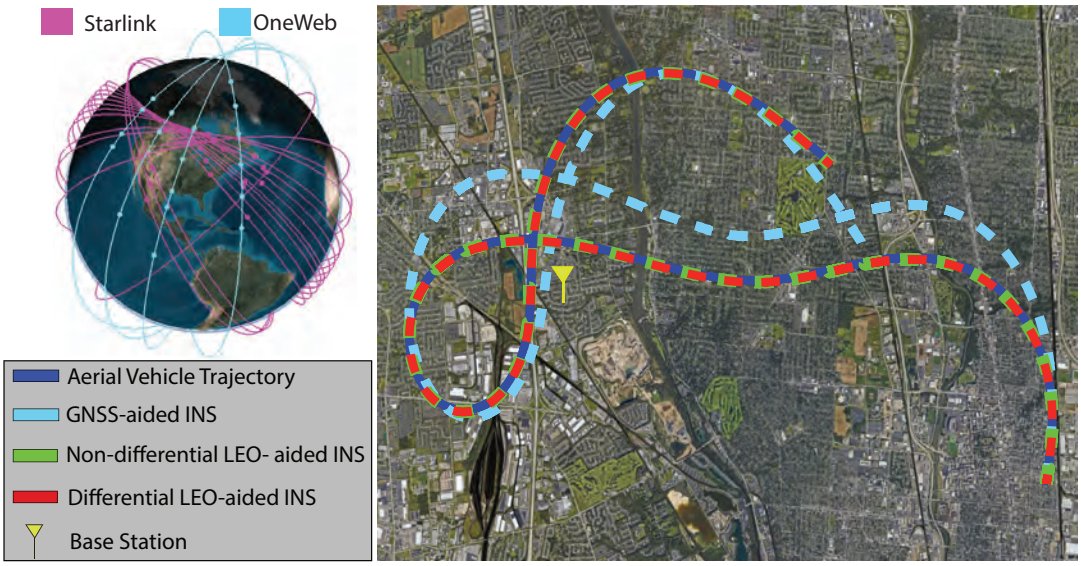

Figure 5: Simulation results showing the aerial vehicle trajectory, estimated trajectory with GNSS-aided INS, non-differential LEO-aided INS, and differential LEO-aided INS, as well as the SVs' trajectories used in the study.

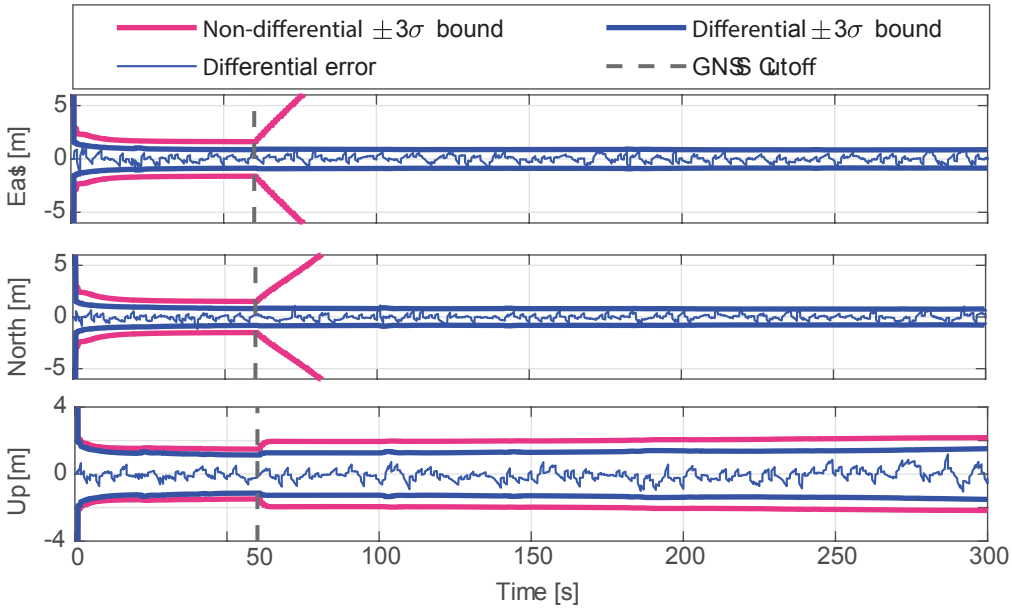

Figure 6: EKF estimation error plots and $\pm 3\sigma$ bounds of the aerial vehicle position for differential and non-differential LEO-aided INS in the ENU frame.

V. EXPERIMENTAL RESULTS

This section demonstrates the significance of differential navigation with LEO satellites experimentally. A ground vehicle navigated with Doppler measurements from 2 Orbcomm and 1 Iridium NEXT LEO SVs. Note since pseudorange measurements were not available from these LEO SVs, Doppler measurements were used instead. The vehicle's ground truth was obtained from a Septentrio AsteRx SBi3 Pro+ integrated GNSS-INS system with real-time kinematic (RTK), and using an industrial-grade IMU. The vehicle traveled a total distance of 540 m in 60 seconds in Columbus, Ohio, USA, while a differential base-station with known position was installed on top of the ElectroScience Laboratory, at The Ohio State University, with a mean baseline distance of 1.1 km from the ground vehicle (see Fig. 7). During the experiment, the LEO receivers on the base and ground vehicle were listening to the same 3 SVs. GNSS signals were available for the first 20 seconds, then made virtually unavailable for the remaining 40 seconds, during which the vehicle traversed 492 m.

Table 3: Trajectory settings

Metric	Total	No GNSS
Distance [km]	0.54	0.492
Time [s]	60	40

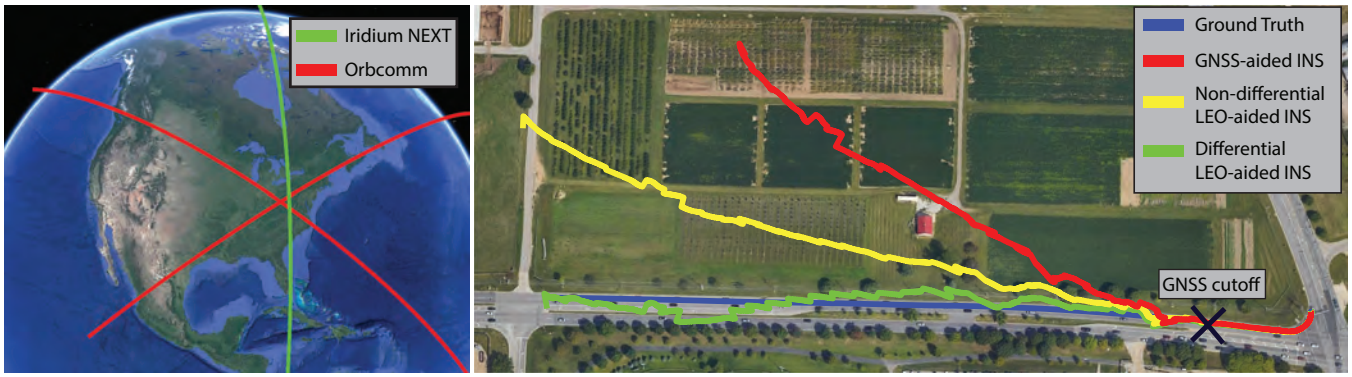

Figure 7: Experimental results showing Orbcomm and Iridium LEO SVs' trajectories (left), and the navigating vehicle's trajectory, GNSS-aided INS trajectory, non-differential LEO-aided INS, and differential LEO-aided INS (right).

To demonstrate the benefit of differential navigation with LEO satellites, the ground vehicle's attitude, 3-D position and velocity were estimated and compared to: (i) non-differential LEO-aided INS and (ii) GNSS-aided INS where the vehicle relies solely on the IMU measurements after GNSS signals were cut off. Fig. 7 shows the vehicle's true trajectory, GNSS-aided INS, non-differential LEO-aided INS, and differential LEO-aided INS. Tables 3 and 4 summarize the results.

Table 4: Experimental results

Framework	2-D position RMSE [m]	Final error [m]
GNSS-INS	87.74	212.53
Non-differential LEO-aided INS	41.29	112.56
Differential LEO-aided INS	7.13	5.38

VI. CONCLUSION

This paper analyzed the effect of the dominating along-track ephemeris error on the orbital plane range measurement error for a fixed base-station. The study was then extended to the differential framework, showing that the differential range error due to ephemeris bias is closely related to the receiver-to-SV orientation. A simulation study was conducted to evaluate the performance of the differential framework using pseudorange measurements from 14 Starlink and 11 OneWeb LEO SVs. The results showed a 3-D position RMSE of 52 cm along a 28 km trajectory, compared to 12.5 m using the non-differential framework. Finally, experimental results of a moving ground vehicle using Doppler measurements from 2 Orbcomm and 1 Iridium SVs reduced the position RMSE from 87.74 m using GNSS-aided INS, and 41.29 m using non-differential LEO-aided INS, to 7.13 m with the proposed differential LEO-aided INS framework.

ACKNOWLEDGEMENTS

This work was supported in part by the Office of Naval Research (ONR) under Grant N00014-19-1-2511, in part by the Air Force Office of Scientific Research (AFOSR) under Grant FA9550-22-1-0476, in part by the U.S. Department of Transportation (USDOT) under Grant 69A3552047138, and in part by The Aerospace Corporation under Award 4400000428. The authors would like to thank Sharbel Kozhaya and Haitham Kanj for their help in experimental data collection and processing.

REFERENCES

Bhatti, J. and Humphreys, T. (2017). Hostile control of ships via false GPS signals: Demonstration and detection. *NAVIGATION, Journal of the Institute of Navigation*, 64(1):51–66.

Bilardi, S. (2021). A GNSS signal simulator and processor for evaluating acquisition and tracking of GPS-like signals from satellites in LEO. Master's thesis, University of Colorado at Boulder, CO, USA.

Cassel, R., Scherer, D., Wilburne, D., Hirschauer, J., and Burke, J. (2022). Impact of improved oscillator stability on LEO-based satellite navigation. In *Proceedings of ION International Technical Meeting*, pages 893–905.

Egea-Roca, D., Lopez-Salcedo, J., Seco-Granados, G., and Falletti, E. (2022). Performance analysis of a multi-slope chirp spread spectrum signal for PNT in a LEO constellation. In *Proceedings of Workshop on Satellite Navigation Technology*, pages 1–9.

Farhangian, F., Benzerrouk, H., and Landry, R. (2021). Opportunistic in-flight INS alignment using LEO satellites and a rotatory IMU platform. *Aerospace*, 8(10):280–281.

Farhangian, F. and Landry, R. (2023). High-order pseudorange rate measurement model for multi-constellation LEO/INS integration: Case of Iridium-NEXT, Orbcomm, and Globalstar. *Proceedings of the Institution of Mechanical Engineers, Part G: Journal of Aerospace Engineering*, 237(4):925–939.

Guo, F., Yang, Y., Ma, F., Liu, Y. Z. H., and Zhang, X. (2023). Instantaneous velocity determination and positioning using doppler shift from a LEO constellation. *Satellite Navigation*, 4:9–21.

Hartnett, M. (2022). Performance assessment of navigation using carrier Doppler measurements from multiple LEO constellations. Master's thesis, Air Force Institute of Technology, Ohio, USA.

Hegarty, C., Bobyn, D., Grabowski, J., and Van Dierendonck, A. (2020). An overview of the effects of out-of-band interference on GNSS receivers. *NAVIGATION, Journal of the Institute of Navigation*, 67(1):143–161.

Hough, M. (2014). Closed-form nonlinear covariance prediction for two-body orbits. *Journal of Guidance, Control, and Dynamics*, 37(1):26–35.

Huang, C., Qin, H., Zhao, C., and Liang, H. (2022). Phase - time method: Accurate Doppler measurement for Iridium NEXT signals. *IEEE Transactions on Aerospace and Electronic Systems*, 58(6):5954–5962.

Humphreys, T., Iannucci, P., Komodromos, Z., and Graff, A. (2023). Signal structure of the Starlink Ku-band downlink. *IEEE Transactions on Aerospace and Electronics Systems*. accepted.

Hwang, P., McGraw, G., and Bader, J. (1999). Enhanced differential GPS carrier-smoothed code processing using dual-frequency measurements. *NAVIGATION, Journal of the Institute of Navigation*, 46(2):127–138.

Janssen, T., Koppert, A., Berkvens, R., and Weyn, M. (2023). A survey on IoT positioning leveraging LPWAN, GNSS and LEO-PNT. *IEEE Internet of Things Journal*, 10(13):11135–11159.

Jardak, N. and Jault, Q. (2022). The potential of LEO satellite-based opportunistic navigation for high dynamic applications. *Sensors*, 22(7):2541–2565.

Jiang, M., Qin, H., Su, Y., Li, F., and Mao, J. (2023a). A design of differential-low Earth orbit opportunistically enhanced GNSS (D-LoeGNSS) navigation framework. *Remote Sensing*, 15(8):2136–2158.

Jiang, M., Qin, H., Su, Y., Li, F., and Mao, J. (2023b). A design of differential-low Earth orbit opportunistically enhanced GNSS (D-LoeGNSS) navigation framework. *Remote Sensing*, 15(8):1–23.

Jiang, M., Qin, H., Zhao, C., and Sun, G. (2022). LEO Doppler-aided GNSS position estimation. *GPS Solutions*, 26(1):1–18.

Jones, B. and Weisman, R. (2019). Multi-fidelity orbit uncertainty propagation. *Acta Astronautica*, 155:406–417.

Kanamori, H., Kobayashi, K., and Kubo, N. (2023). A map-matching based positioning method using Doppler tracking and estimation by a software-defined receiver for multi-constellation LEO satellites. In *Proceedings of ION International Technical Meeting*, pages 649–663.

Kassas, Z., Khairallah, N., and Kozhaya, S. (2023a). Ad astra: Simultaneous tracking and navigation with megaconstellation LEO satellites. *IEEE Aerospace and Electronic Systems Magazine*. accepted.

Kassas, Z., Kozhaya, S., Kanj, H., Saroufim, J., Hayek, S., Neinavaie, M., Khairallah, N., and Khalife, J. (2023b). Navigation with multi-constellation LEO satellite signals of opportunity: Starlink, Oneweb, Orbcomm, and Iridium. In *Proceedings of IEEE/ION Position, Location, and Navigation Symposium*, pages 338–343.

Kassas, Z., Morales, J., and Khalife, J. (2019). New-age satellite-based navigation – STAN: simultaneous tracking and navigation with LEO satellite signals. *Inside GNSS Magazine*, 14(4):56–65.

Kassas, Z., Neinavaie, M., Khalife, J., Khairallah, N., Haidar-Ahmad, J., Kozhaya, S., and Shadram, Z. (2021). Enter LEO on the GNSS stage: Navigation with Starlink satellites. *Inside GNSS Magazine*, 16(6):42–51.

Kennewell, J. and Vo, B. (2013). An overview of space situational awareness. In *Proceedings of International Conference on Information Fusion*, pages 1029–1036.

Khairallah, N. and Kassas, Z. (2021). Ephemeris closed-loop tracking of LEO satellites with pseudorange and Doppler measurements. In *Proceedings of ION GNSS Conference*, pages 2544–2555.

Khalife, J. and Kassas, Z. (2019). Assessment of differential carrier phase measurements from Orbcomm LEO satellite signals for opportunistic navigation. In *Proceedings of ION GNSS Conference*, pages 4053–4063.

Khalife, J. and Kassas, Z. (2022). On the achievability of submeter-accurate UAV navigation with cellular signals exploiting loose network synchronization. *IEEE Transactions on Aerospace and Electronic Systems*, 58(5):4261–4278.

Khalife, J. and Kassas, Z. (2023). Performance-driven design of carrier phase differential navigation frameworks with mega-constellation LEO satellites. *IEEE Transactions on Aerospace and Electronic Systems*, 59(3):2947–2966.

Khalife, J., Neinavaie, M., and Kassas, Z. (2020). Navigation with differential carrier phase measurements from megaconstellation LEO satellites. In *Proceedings of IEEE/ION Position, Location, and Navigation Symposium*, pages 1393–1404.

Khalife, J., Neinavaie, M., and Kassas, Z. (2022). The first carrier phase tracking and positioning results with Starlink LEO satellite signals. *IEEE Transactions on Aerospace and Electronic Systems*, 56(2):1487–1491.

Kozhaya, S., Haidar-Ahmad, J., Abdallah, A., Kassas, Z., and Saab, S. (2021). Comparison of neural network architectures for simultaneous tracking and navigation with LEO satellites. In *Proceedings of ION GNSS Conference*, pages 2507–2520.

Maaref, M., Khalife, J., and Kassas, Z. (2019). Lane-level localization and mapping in GNSS-challenged environments by fusing lidar data and cellular pseudoranges. *IEEE Transactions on Intelligent Vehicles*, 4(1):73–89.

McGraw, G. and Braasch, M. (1999). GNSS multipath mitigation using gated and high resolution correlator concepts. In *Proceedings of ION National Technical Meeting*, pages 333–342.

Meng, L., Chen, J., Wang, J., and Zhang, Y. (2021). Broadcast ephemerides for LEO augmentation satellites based on nonsingular elements. *GPS Solutions*, 25(4):129–139.

Menzione, F. and Paonni, M. (2023). LEO-PNT mega-constellations: a new design driver for the next generation MEO GNSS space service volume and spaceborne receivers. In *Proceedings of IEEE/ION Position, Location, and Navigation Symposium*, pages 1196–1207.

Michalak, G., Glaser, S., Neumayer, K., and König, R. (2021). Precise orbit and earth parameter determination supported by LEO satellites, inter-satellite links and synchronized clocks of a future gnss. *Advances in Space Research*, 68(12):4753–4782.

Miralles, D., Bornot, A., Rouquette, P., Levigne, N., Akos, D., Y.-H.Chen, Lo, S., and Walter, T. (2020). An assessment of GPS spoofing detection via radio power and signal quality monitoring for aviation safety operations. *IEEE Intelligent Transportation Systems Magazine*, 12(3):136–146.

More, H., Cianca, E., and Sanctis, M. (2022). Positioning performance of LEO mega constellations in deep urban canyon environments. In *Proceedings of International Symposium on Wireless Personal Multimedia Communications*, pages 256–260.

Morton, Y., Xu, D., and Jiao, Y. (2022). Ionospheric scintillation effects on signals transmitted from LEO satellites. In *Proceedings of ION GNSS Conference*, pages 2980–2988.

Neinavaie, M., Shadram, Z., Kozhaya, S., and Kassas, Z. M. (2022). First results of differential Doppler positioning with unknown Starlink satellite signals. In *Proceedings of IEEE Aerospace Conference*, pages 1–14.

Orabi, M., Khalife, J., and Kassas, Z. (2021). Opportunistic navigation with Doppler measurements from Iridium Next and Orbcomm LEO satellites. In *Proceedings of IEEE Aerospace Conference*, pages 1–9.

Parkinson, B. and Enge, P. (1996). Differential GPS. *Global Positioning System: Theory and applications.*, 2:3–50.

Peral-Rosado, J., Lopez-Salcedo, J., Kim, S., and Seco-Granados, G. (2016). Feasibility study of 5G-based localization for assisted driving. In *Proceedings of International Conference on Localization and GNSS*, pages 1–6.

Pinell, C., Prol, F., Bhuiyan, M., and Praks, J. (2023). Receiver architectures for positioning with low earth orbit satellite signals: a survey. *EURASIP Journal on Advances in Signal Processing*, 2023:60–80.

Prol, F., Ferre, R., Saleem, Z., Välisuo, P., Pinell, C., Lohan, E., Elsanhoury, M., Elmusrati, M., Islam, S., Celikbilek, K., Selvan, K., Yliaho, J., Rutledge, K., Ojala, A., Ferranti, L., Praks, J., Bhuiyan, M., Kaasalainen, S., and Kuusniemi, H. (2022). Position, navigation, and timing (PNT) through low earth orbit (LEO) satellites: A survey on current status, challenges, and opportunities. *IEEE Access*, 10:83971–84002.

Prol, F., Kaasalainen, S., Lohan, E., Bhuiyan, M., Praks, J., and Kuusniemi, H. (2023). Simulations using LEO-PNT systems: A brief survey. In *Proceedings of IEEE/ION Position, Location, and Navigation Symposium*, pages 1381–387.

Psiaki, M. (2021). Navigation using carrier Doppler shift from a LEO constellation: TRANSIT on steroids. *NAVIGATION, Journal of the Institute of Navigation*, 68(3):621–641.

Ries, L., Limon, M., Grec, F., Anghileri, M., Prieto-Cerdeira, R., Abel, F., Miguez, J., Perello-Gisbert, J., d'Addio, S., R. Ioannidis and, A. O., Rapisarda, M., Sarnadas, R., and Testani, P. (2023). LEO-PNT for augmenting Europe's space-based PNT capabilities. In *Proceedings of IEEE/ION Position, Location, and Navigation Symposium*, pages 329–337.

Sabbagh, R. and Kassas, Z. (2023). Observability analysis of receiver localization via pseudorange measurements from a single LEO satellite. *IEEE Control Systems Letters*, 7(3):571–576.

Saroufim, J., Hayek, S., and Kassas, Z. (2023). Simultaneous LEO satellite tracking and differential LEO-aided IMU navigation. In *Proceedings of IEEE/ION Position Location and Navigation Symposium*, pages 179–188.

Shi, C., Zhang, Y., and Li, Z. (2023). Revisiting Doppler positioning performance with LEO satellites. *GPS Solutions*, 27(3):126–137.

Singh, U., Shankar, M., and Ottersten, B. (2022). Opportunistic localization using LEO signals. In *Proceedings of Asilomar Conference on Signals, Systems, and Computers*, pages 894–899.

Tan, Z., Qin, H., Cong, L., and Zhao, C. (2019). Positioning using IRIDIUM satellite signals of opportunity in weak signal environment. *Electronics*, 9(1):37.

Vallado, D. (2005). An analysis of state vector propagation using differing flight dynamics programs. In *Proceedings of the AAS Space Flight Mechanics Conference*, volume 120, pages 1563–1592.

Vallado, D. and Crawford, P. (2008). SGP4 orbit determination. In *Proceedings of AIAA/AAS Astrodynamics Specialist Conference and Exhibit*, pages 6770–6799.

Wang, D., Qin, H., and Huang, Z. (2023). Doppler positioning of LEO satellites based on orbit error compensation and weighting. *IEEE Transactions on Instrumentation and Measurement*, 72:1–11.

Wei, Q., Chen, X., and Zhan, Y. (2020). Exploring implicit pilots for precise estimation of LEO satellite downlink Doppler frequency. *IEEE Communications Letters*, 24(10):2270–2274.

Whiton, R., Chen, J., Johansson, T., and Tufvesson, F. (2022). Urban navigation with LTE using a large antenna array and machine learning. In *Proceedings of IEEE Vehicular Technology Conference*, pages 1–5.

Wu, N., Qin, H., and Zhao, C. (2023). Long-baseline differential doppler positioning using space-based SOP based on BPVGMM. *IEEE Transactions on Instrumentation and Measurement*, 72:1–10.

Yan, Z. and Zhang, X. (2022). Assessment of the performance of GPS/Galileo PPP-RTK convergence using ionospheric corrections from networks with different scales. *Earth, Planets and Space*, 74(1):1–19.

Yang, C. and Soloviev, A. (2023). Starlink Doppler and Doppler rate estimation via coherent combining of multiple tones for opportunistic positioning. In *Proceedings of IEEE/ION Position, Location, and Navigation Symposium*, pages 1143–1153.

Yang, C., Zang, B., Gu, B., Zhang, L., Dai, C., Long, L., Zhang, Z., Ding, L., and Ji, H. (2023). Doppler positioning of dynamic targets with unknown LEO satellite signals. *Electronics*, 12(11):2392–2404.

Ye, L., Gao, N., Yang, Y., Deng, L., and Li, H. (2023). Three satellites dynamic switching range integrated navigation and positioning algorithm with clock bias cancellation and altimeter assistance. *Aerospace*, 10(5):411–438.

Zhao, C., Qin, H., and Li, Z. (2022). Doppler measurements from multiconstellations in opportunistic navigation. *IEEE Transactions on Instrumentation and Measurement*, 71:1–9.

Zhao, C., Qin, H., Wu, N., and Wang, D. (2023). Analysis of baseline impact on differential doppler positioning and performance improvement method for LEO opportunistic navigation. *IEEE Transactions on Instrumentation and Measurement*, 72:1–10.

Experimental Characterization of Received 5G Signals Carrier-to-Noise Ratio in Indoor and Urban Environments

Ali A. Abdallah[1], Joe Khalife[2], and Zaher M. Kassas[1,2]
[1]Department of Electrical Engineering and Computer Science, University of California, Irvine, USA
[2]Department of Mechanical and Aerospace Engineering, University of California, Irvine, USA
Emails: abdalla2@uci.edu, khalifej@uci.edu, zkassas@ieee.org

***Abstract*—An extensive experimental study to characterize frequency range 1 (FR1) (i.e., sub-6 GHz) 5th generation (5G) signals from existing infrastructure for navigation is presented. The study uses a state-of-the-art 5G navigation software-defined radio (SDR) to track 5G signals in different environments and under different conditions to analyze the behavior of the received carrier-to-noise-ratio (C/N_0), which directly affects the precision of the navigation performance. Three different experimental scenarios were conducted for this purpose with real 5G signals and 4th generation (4G) long-term evolution (LTE) signals for comparison purposes: (i) a stationary indoor scenario to study the effect of wall and floor partitions, (ii) a stationary outdoor scenario to study the effect of sampling rate, antenna grade, and clock quality, and (iii) a mobile outdoor experiment to study the C/N_0 as a function of the range. All three scenarios confirmed the potential of downlink 4G and 5G signals for navigation.**

***Index Terms*— 5G, 4G, LTE, carrier-to-noise ratio, navigation.**

I. Introduction

The 5th generation (5G) cellular system (also known as new radio (NR)) has been showing a great potential in many applications beyond wireless communication, such as enabling new capabilities in future smart device connectivity, handling large data exchange for autonomous vehicles, and providing alternative positioning, navigation, and timing (PNT) solutions. This paper focuses on the latter application by characterizing the received power of sub-6GHz 5G signals.

The 5G system employs a similar structure to the 4th generation (4G) long-term evolution (LTE) system, as both systems use orthogonal frequency division multiplexing (OFDM) for downlink transmission. By design, the 5G system is very attractive for navigation purposes due to its following attributes: (1) high carrier frequencies (two main frequency ranges (FRs): (i) FR1, which spans frequencies from 450 MHz to 6 GHz and (ii) FR2, which spans frequencies from 24.25 to 52.6 GHz [1]), (2) abundance, (3) geometric diversity, (4) large bandwidth (up to 100 MHz and 400 MHz bandwidth for FR1 and FR2, respectively), and (5) high received power. This paper studies experimentally the received power of 5G signals. More specifically, the carrier to noise ratio (C/N_0) is characterized through extensive experiments. The C/N_0 is an important metric in determining the navigation performance with 5G signal: the higher the C/N_0, the better the navigation precision.

The positioning capabilities of 5G have been studied in the recent years. Different approaches have been proposed, in which the direction-of-arrival (DOA), direction-of-departure (DOD), time-of-arrival (TOA), or a combination thereof is used to achieve accurate positioning with 5G signals. In [2], the authors investigated the positioning performance of six different 5G impulse radio waveforms, at the time when there were no generally accepted 5G waveforms yet. The analysis showed the capability of millimeter waves (mmWaves) in achieving sub-meter level accuracy, and the best performance was achieved with Gaussian raised-cosine, Gaussian pulse, and Sinc-RCP impulse radio waveforms. The capability of massive multiple-input-multiple-output (mMIMO) systems in providing accurate localization through DOA measurements was studied in [3]. The paper addressed the limitation of DOA estimation in mMIMO systems in the presence of multipath by proposing a compressed sensing navigation framework, which relies on the channel properties to distinguish line-of-sight (LOS) from multipath components. The proposed algorithm showed sub-meter positioning accuracy in simulation. Another approach to reduce 5G small cell interference and multipath effect in angular localization methods by combining near-field and far-field effects was proposed in [4]. Simulation results showed that the proposed approach improves the angular resolution by orders of magnitude. In [5], an integrated global navigation satellite system (GNSS)/5G framework was developed with a particle filter, in which device-to-device (D2D) range and angle measurements were assumed between mobile terminals (MTs). An experiment was performed with simulated GNSS data and emulated 5G D2D data, where the integrated system reduced the GNSS position root mean-squared error (RMSE) from around 5 m to about 3 m assuming 10 MTs. In [6], a network-based positioning framework using joint TOA and DOA measurements was proposed using cascaded extended Kalman filters (EKFs). The proposed framework considered the clock biases between the user equipment (UE) and the 5G base stations (also knows as gNodeBs or gNBs), and among the gNBs themselves. The framework was evaluated by simulating a real 5G scenario using three-dimensional (3-D) ray tracing, where a sub-meter-level positioning accuracy was demonstrated.

All the aforementioned studies are limited to unrealistic

assumptions, simulations only, and/or laboratory emulated 5G signals without any experimental demonstrations. The lack of experiments in the 5G literature is due to: (i) 5G gNBs being rolled over only recently in a few major cities, (ii) hardware limitations in transmitting and receiving mmWave signals, or (iii) the proposed navigation approaches are network-based approaches and require the user to subscribe to the network. In the latter situation, the positioning performance will be limited as only gNBs from a single serving cellular provider are used. Alternatively, 5G signals could be exploited opportunistically [7]–[9], increasing the number of available gNBs without compromising the user's privacy by requiring network subscription. This paper characterizes a critical metric for measuring opportunistic navigation performance with 5G signals, namely the received C/N_0. The paper studies experimentally (i) the effect of different indoor structures and floors on the 5G received C/N_0, (ii) the effect of receiver antenna grade, receiver's clock quality, and sampling rate on the C/N_0, and (iii) the effect of distance between the receiver and the gNB.

The remainder of the paper is organized as follows. Section II discusses the methodology for calculating the C/N_0 of received 5G signals. Section III presents experimental results for both 5G and 4G signals in three different scenarios: (i) a stationary indoor scenario to study the effect of wall and floor partitions, (ii) a stationary outdoor scenario to study the effect of sampling rate, antenna grade, and clock quality, and (iii) a mobile outdoor experiment to study the effect of range. Concluding remarks are given in Section IV.

II. Methodology

This paper characterizes 5G signals from FR1, where most cellular providers use frequency division duplexing (FDD) due to its superior performance in providing better coverage and lower latency. The C/N_0 is obtained by tracking the primary synchronization signal (PSS) and the secondary synchronization signal (SSS) using the software-defined radio (SDR) proposed in [10]–[12]. The C/N_0 is calculated as

$$
\begin{aligned}
C/N_0 &= 10\log_{10}\left[\frac{\Delta f(C-\sigma_n^2)}{\sigma_n^2}\right], \\
C &= \max_t \{|\boldsymbol{h}(t)|\}, \\
\sigma_n^2 &= \frac{1}{\lceil \frac{3}{4}M\rceil - \lceil \frac{1}{4}M\rceil} \sum_{t_i=\lceil \frac{1}{4}M\rceil}^{\lceil \frac{3}{4}M\rceil} |\boldsymbol{h}(t_i)|^2,
\end{aligned}
$$

where Δf is the subcarrier frequency, C is the carrier power, σ_n^2 is the noise power, $\boldsymbol{h}(t)$ is the impulse response estimated in the tracking loop of the navigation SDR, M is the length of $\boldsymbol{h}(t)$, and $\lceil\cdot\rceil$ denotes integer rounding towards $+\infty$.

III. Experimental Results

This section characterizes the signal power of existing sub-6Ghz 5G signals currently in service and assesses their use for opportunistic navigation in different environments and setups. Three scenarios are presented comparing the C/N_0 of 5G and 4G signals: (1) a stationary, indoor scenario to study the effect of wall and floor partitions, (2) a stationary, outdoor scenario to study the effect of the sampling rate, antenna grade, and receiver clock quality, and (3) a mobile, outdoor experiment to study the C/N_0 as a function of range.

A. Scenario 1: Stationary Indoors

This scenario studies the C/N_0 of 4G and 5G signals in indoor environments.

1) Experimental Setup: In the first scenario, the C/N_0 of FR1-5G and 4G signals are characterized indoors, where the effect of wall and floor partitions are studied. To this end, 5G and 4G signals were collected over durations of five minutes at 14 different locations in the Engineering Gateway building at the University of California, Irvine (UCI), USA. Out of the 14 locations, 12 are labeled with a number and a letter according to "ij", where $i \in \{1,2,3,4\}$ corresponds to the floor number and $j \in \{a,b,c,d,e,f\}$ corresponds to a building area. The remaining two locations are labeled "bridge" (an indoor bridge with glass walls on the 3-rd floor connecting the two buildings) and "elevator" (an elevator in the middle of the building which was going up and down between floors 1 and 4 during data collection). At each location, signals from two U.S. cellular providers were received: T-Mobile and AT&T, transmitting at four different frequencies in total, as summarized in Table I. Both gNB1 and eNodeB1 were located on top of the Engineering Tower building on the UCI campus. In addition to being from the same operator, gNB2 and eNodeB2 have the same cell ID. As a result, they are most likely co-located; however, their exact locations is not known. The receiver was equipped with four omnidirectional, low-grade, magnetic mount antennas connected to a quad-channel National Instruments (NI) universal software radio peripheral (USRP)-2955R to simultaneously down-mix and synchronously sample signals at the four carrier frequencies with a sampling rate of 10 mega sampled per second (Msps). The signals were processed in a post-processing fashion using the 4G and 5G modules of the Multichannel Adaptive TRansceiver Information eXtractor (MATRIX) SDR implemented in MATLAB [10], [13]. Fig. 1 shows the environment layout in which the experiment was performed, the eNodeBs' and gNBs' positions from which signals were collected, and the experimental hardware and software setup.

TABLE I
eNodeB's and gNB's Characteristics

Base station	Carrier frequency [MHz]	N_{ID}^{Cell}	Cellular provider
gNB 1	872	872	AT&T
gNB 2	632.55	394	T-Mobile
eNodeB 1	739	93	AT&T
eNodeB 2	731.5	394	T-Mobile
eNodeB 3	751/2125	221	T-Mobile

2) Experimental Results: The C/N_0 values of the eNodeBs and gNBs in Table I at each location are shown in Fig. 2. The following can be concluded from these plots:

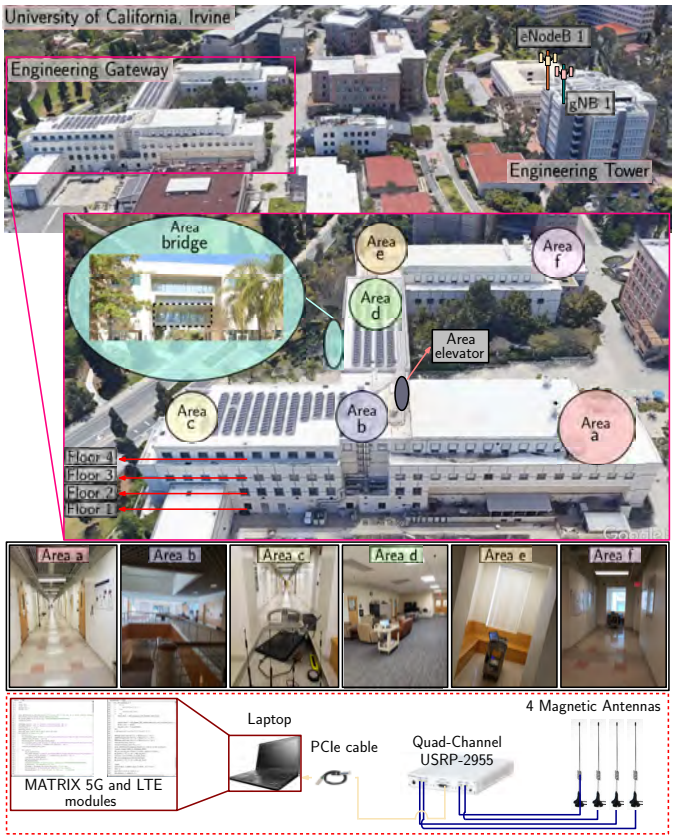

Fig. 1. Environment layout and hardware and software setup of scenario 1. Map data: Google Earth.

- Both 4G and 5G signals from both providers have consistently similar C/N_0 values at the different locations. As a result, similar navigation accuracy is expected with FR1-5G signals as with 4G signals.
- There does not seem to be a clear pattern in the C/N_0 behavior on different floors or areas in the building. This conclusion is surprising and implies that a consistent navigation performance is expected throughout the entire building.
- Although the elevator walls are metal, the signals inside the elevator are surprisingly powerful. This can be particularly useful as pedestrian-mounted receivers going up or down the floors can maintain track of 4G and 5G signals and do not need to re-acquire.

B. Scenario 2: Stationary Outdoors

In this scenario, the effect of sampling rate, antenna grade, and receiver clock quality on the C/N_0 is studied.

1) Experimental Setup: The receiver was placed on the roof of the Anteater parking structure on UCI campus, 300 m away from gNB1 and eNodeB1 with direct LOS. The hardware setup is similar to that of the stationary indoors setup in scenario 1, except that two of the omnidirectional low-grade antennas were replaced by two high-grade 10 Watts, omnidirectional Laird antennas with a gain of 1.5 dBi. The antennas were connected to the same USRP mentioned in the previous setup to simultaneously down-mix and synchronously sample signals at the four carrier frequencies, which are then post-processed by the MATRIX SDR. The USRP's oscillator was operated in two modes: (i) as a GPS-disciplined oscillator (GPSDO) (precise frequency standard) and (ii) free running internal oscillator (typical oven-controlled oscillator (OCXO)). Moreover, the signals were sampled at (i) 10 Msps and (ii) 20 Msps to study the effect of the sampling rate on the C/N_0. Fig. 3 shows the experimental hardware and software setup.

2) Experimental Results: The C/N_0 values of the 4G and 5G signals for different antenna grades, clock qualities, and sampling rates are shown in Fig. 4. The following can be concluded from these plots:

- As expected, the C/N_0 values with the high-grade (HG) antenna are consistently 3–6 dB higher than that with the low-grade (LG) antenna. While these results imply that investing in a high-grade antenna (around $40 USD price difference) yields a 3–6dB gain in the C/N_0, which goes a long way in low signal-to-noise ratio (SNR) applications, it is also important to notice that the C/N_0 values with the low-grade antenna are mainly above 50 dB-Hz. Such C/N_0 is high enough to produce a reliable navigation solution. Similar values were obtained indoors with the low-grade antenna, as indicated in Fig. 2.
- When operating with the GPSDO, the receiver produces stable values of C/N_0. When operating with the USRP's internal OCXO, the C/N_0 values are less stable initially, but appear to stabilize around high enough C/N_0 values as time progresses. This implies that such signals are useful in GNSS-challenged environments (e.g., scenario 1 and in deep urban canyons) or in environments under spoofing or jamming attacks.
- There does not seem to be any noticeable gain in increasing the sampling rate from 10 Msps to 20 Msps, as the bandwidth of the 4G and 5G signals under study was 10 MHz.

C. Scenario 3: Mobile Outdoors

This scenario characterizes the C/N_0 as a function of the range r between the receiver and the gNB.

1) Experimental Setup: In this third scenario, the experiment was conducted on Fairview Road in Costa Mesa, California, USA. One of the high-grade Laird antennas was connected to the USRP, which was in turn mounted on a vehicle and tuned to listen to FR1-5G signals at a 872 MHz carrier frequency, which corresponds to the U.S. cellular provider AT&T. The gNB cell ID was 608 and its location was surveyed prior to the experiment. The USRP's GPSDO was used throughout this experiment. The vehicle was equipped with a Septentrio AsteRx-i V integrated GNSS-inertial measurement unit (IMU) whose x-axis pointed toward the front of the vehicle, y-axis pointed to the right side of the vehicle, and z-axis pointed upward. AsteRx-i V is equipped with a dual-antenna multi-frequency GNSS receiver and a VectorNav VN-100 micro-electromechanical system (MEMS) IMU. The loosely-coupled GNSS-IMU with satellite-based augmentation system (SBAS)

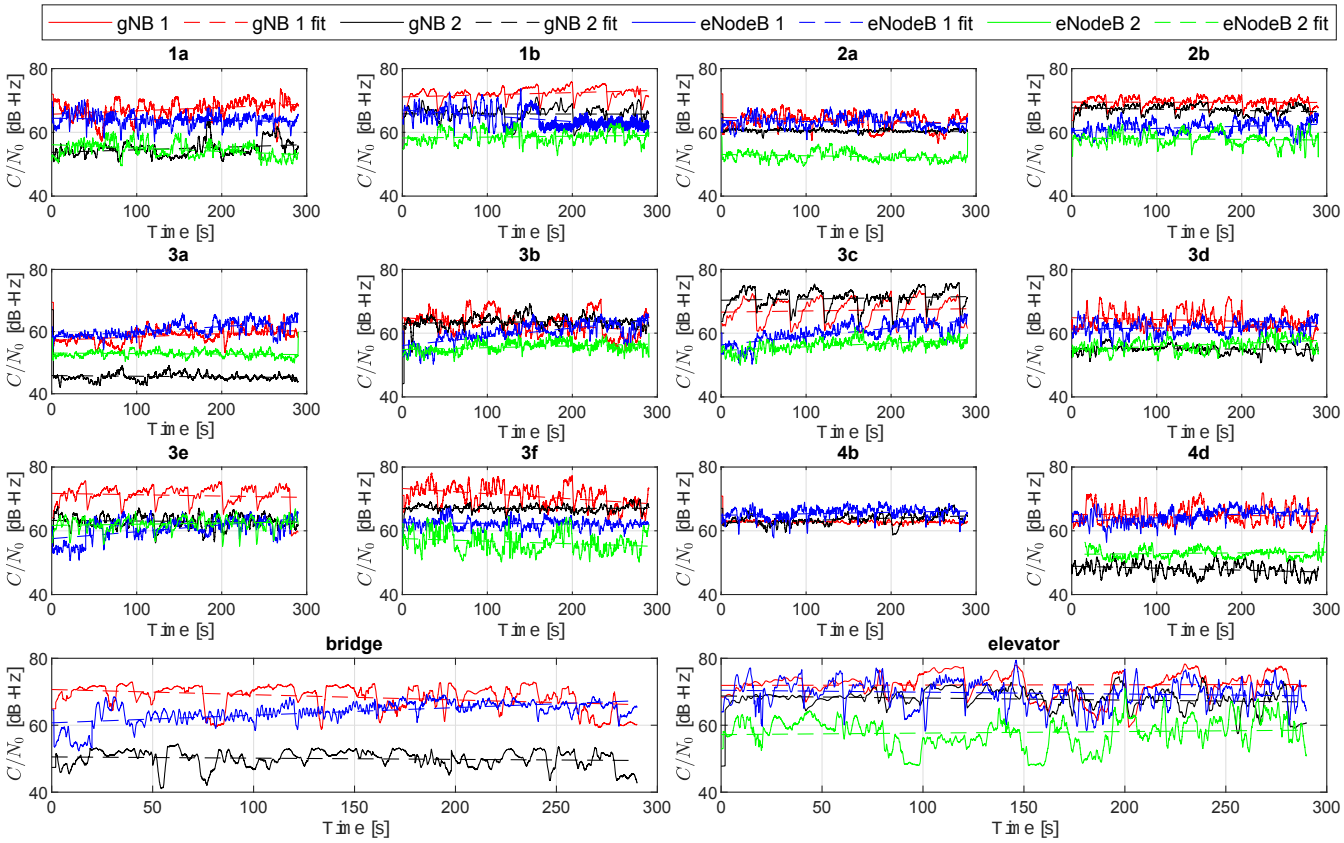

Fig. 2. Experimental results of scenario 1 showing the C/N_0 values of the 2 gNBs and eNodeBs 1 & 2 from Table I in different locations in the Engineering Gateway building on UCI campus. The solid and dash lines represents the estimated C/N_0 time history and the corresponding linear fit, respectively.

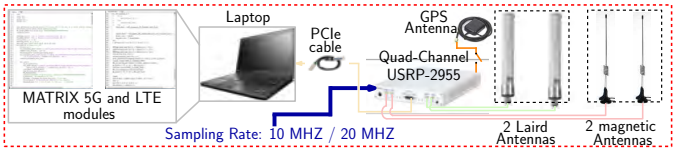

Fig. 3. Hardware and software setup of scenario 2. Map data: Google Earth.

navigation solution produced by AsteRx-i V was used as ground truth in this experiment. Fig. 5 shows the environment layout and the experimental hardware and software setup.

2) Experimental Results: The C/N_0 was computed along the trajectory and plotted as a function of the range between the gNB and the receiver and is shown in Fig. 6 along with a linear fit. The following can be concluded from this plot. While simple, the linear model seems to fit well the behavior of the C/N_0 in this semi-urban environment. Such models can be particularly useful for navigation framework design and analyses. Moreover, the received 5G signals are surprising powerful at more than 55 dB-Hz beyond 2 km, which is a typical cell size in semi-urban environments. This results implies that the receiver could reliably track signals from numerous 5G gNBs, which directly improves the navigation performance.

IV. Conclusion

The received power of 5G signals is assessed experimentally for opportunistic navigation using real 5G signals from existing infrastructure and a state-of-the-art 5G navigation SDR. The C/N_0 ratio of 5G signals was studied in three different scenarios: (i) a stationary indoor experiment, (ii) a stationary outdoor experiment, and (iii) a mobile outdoor experiment on a ground vehicle. The stationary indoor experiment assessed the C/N_0 of 4G and 5G signals for different floors and room structures, showing consistent behavior across locations. As a result, similar navigation accuracy is expected with FR1 5G signals as with 4G signals. The stationary outdoor experiment studied the effect of sampling rate, antenna grade, and clock quality on the received C/N_0, showing that acceptable performance could be obtained with low-grade antennas and free-running OCXOs. The mobile experiment demonstrated that the C/N_0 could be modeled as a linear function of the range, and shows that the C/N_0 remains powerful beyond 2 km, which in turn implies that numerous gNBs can be used for navigation.

Acknowledgment

This work was supported in part by the Office of Naval Research (ONR) under Grant N00014-19-1-2511; in part under the financial assistance award 70NANB17H192 from U.S. Department of Commerce, National Institute of Standards

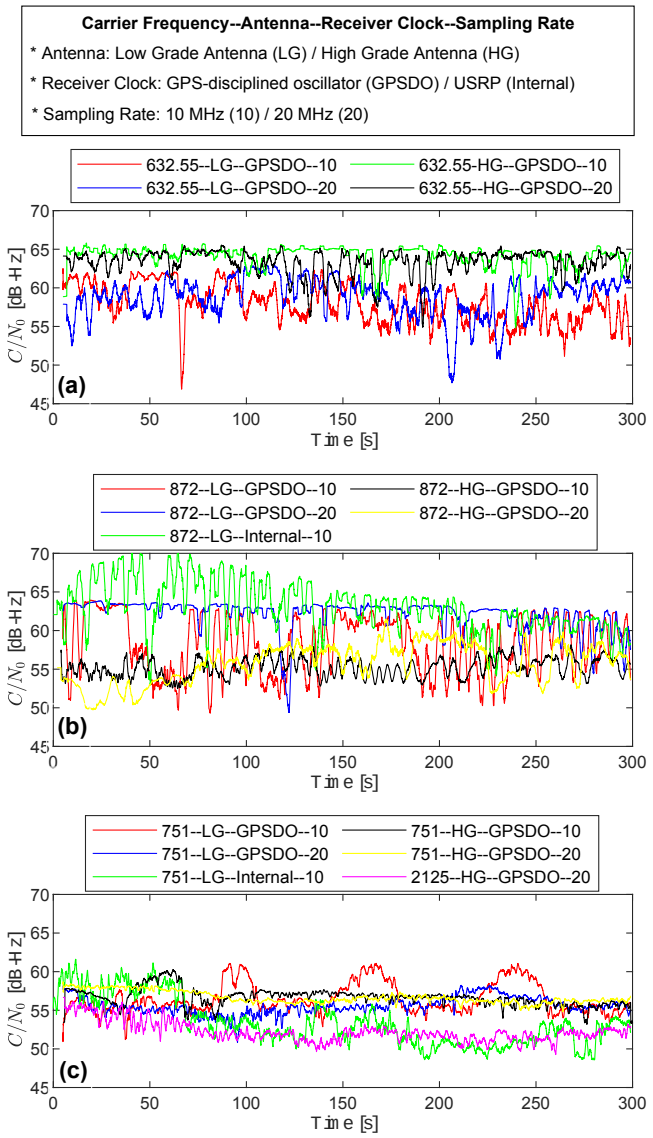

Fig. 4. Experimental results of scenario 2 showing the C/N_0 values of gNBs 1 & 2 and eNodeB3 from Table I for a stationary outdoor receiver and for different antenna grade, receiver clock quality, and sampling rate.

and Technology (NIST); and in part by the U.S. Department of Transportation (USDOT) under University Transportation Center (UTC) Program Grant 69A3552047138. The authors would like to thank Mohamad Orabi for his help with data collection.

REFERENCES

[1] 3GPP, "Base station (BS) radio transmission and reception," 3rd Generation Partnership Project (3GPP), TS 38.104, July 2018. [Online]. Available: https://www.etsi.org/deliver/etsi-ts/138100-138199/138104/15.02.00-60/ts-138104v150200p.pdf

[2] X. Cui, T. Gulliver, J. Li, and H. Zhang, "Vehicle positioning using 5G millimeter-wave systems," *IEEE Access*, vol. 4, pp. 6964–6973, 2016.

[3] N. Garcia, H. Wymeersch, E. Larsson, A. Haimovich, and M. Coulon, "Direct localization for massive MIMO," *IEEE Transactions on Signal Processing*, vol. 65, no. 10, pp. 2475–2487, May 2017.

[4] K. Han, Y. Liu, Z. Deng, L. Yin, and L. Shi, "Direct positioning method of mixed far-field and near-field based on 5G massive MIMO system," *IEEE Access*, vol. 7, pp. 72 170–72 181, 2019.

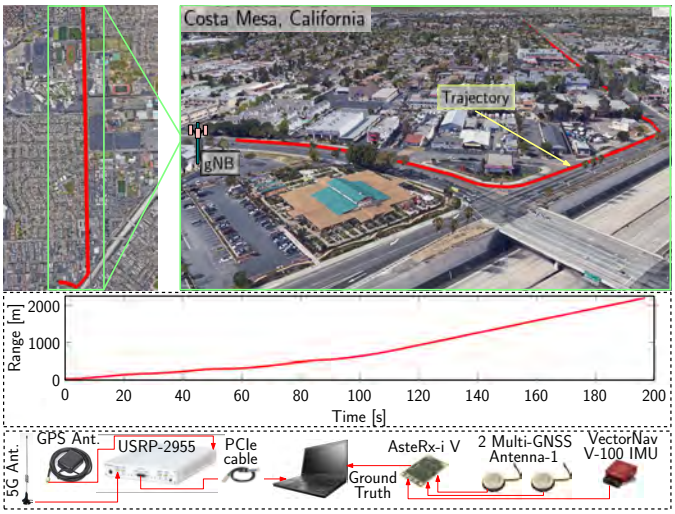

Fig. 5. Scenario 3: environment layout, hardware and software setup, and the range between the ground vehicle-mounted receiver and the gNB over the entire experiment. Map data: Google Earth.

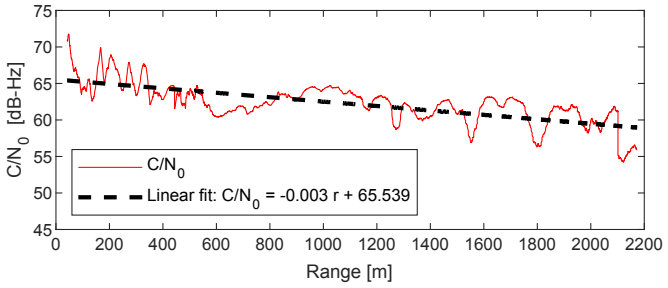

Fig. 6. Experimental results of scenario 3 showing the C/N_0 values of a gNB in a semi-urban environment as a function of the range between the gNB and an outdoor mobile receiver mounted on a vehicle.

[5] L. Yin, Q. Ni, and Z. Deng, "A GNSS/5G integrated positioning methodology in D2D communication networks," *IEEE Transactions on Signal Processing*, vol. 36, no. 2, pp. 351–362, February 2018.

[6] M. Koivisto, M. Costa, J. Werner, K. Heiska, J. Talvitie, K. Leppanen, V. Koivunen, and M. Valkama, "Joint device positioning and clock synchronization in 5G ultra-dense networks," *IEEE Transactions on Wireless Communications*, vol. 16, no. 5, pp. 2866–2881, May 2017.

[7] C. Yang, T. Nguyen, and E. Blasch, "Mobile positioning via fusion of mixed signals of opportunity," *IEEE Aerospace and Electronic Systems Magazine*, vol. 29, no. 4, pp. 34–46, April 2014.

[8] M. Driusso, C. Marshall, M. Sabathy, F. Knutti, H. Mathis, and F. Babich, "Vehicular position tracking using LTE signals," *IEEE Transactions on Vehicular Technology*, vol. 66, no. 4, pp. 3376–3391, April 2017.

[9] Z. Kassas, J. Khalife, K. Shamaei, and J. Morales, "I hear, therefore I know where I am: Compensating for GNSS limitations with cellular signals," *IEEE Signal Processing Magazine*, pp. 111–124, September 2017.

[10] K. Shamaei and Z. Kassas, "Receiver design and time of arrival estimation for opportunistic localization with 5G signals," *IEEE Transactions on Wireless Communications*, 2021, accepted.

[11] A. Abdallah, K. Shamaei, and Z. Kassas, "Assessing real 5G signals for opportunistic navigation," in *Proceedings of ION GNSS Conference*, 2020, pp. 2548–2559.

[12] Z. Kassas, A. Abdallah, and M. Orabi, "Carpe signum: seize the signal – opportunistic navigation with 5G," *Inside GNSS Magazine*, vol. 16, no. 1, pp. 52–57, 2021.

[13] K. Shamaei, J. Khalife, and Z. Kassas, "Exploiting LTE signals for navigation: Theory to implementation," *IEEE Transactions on Wireless Communications*, vol. 17, no. 4, pp. 2173–2189, April 2018.

Exploiting On-Demand 5G Downlink Signals for Opportunistic Navigation

Ali Abdallah, *Student Member, IEEE*, Joe Khalife, *Member, IEEE*, and Zaher M. Kassas, *Senior Member, IEEE*

***Abstract*—This letter presents the first user equipment (UE)-based 5G navigation framework that exploits the "on-demand" 5G downlink signals. In this framework, the entire system bandwidth of incoming 5G signals is utilized in an opportunistic fashion. The proposed framework involves a cognitive approach to acquire the so-called ultimate reference signal (URS), which includes the "on-demand" as well as "always-on" reference signals (RSs). Experimental results are presented showing that the acquired URS: (i) spans the entire 5G downlink bandwidth, (ii) increases the carrier-to-noise ratio by 10 dB compared to state-of-the-art 5G user equipment (UE)-based opportunistic navigation receiver, and (iii) reduces significantly the carrier and code phase errors. A ranging error standard deviation of 2.75 m was achieved with proposed framework with a stationary receiver placed 290 m away from a 5G gNB in a clear line-of-sight environment, which is lower than the 5.05 m achieved when using the "always-on" 5G downlink signals.**

***Index Terms*—5G, positioning, navigation.**

I. Introduction

FIFTH-GENERATION (5G) cellular signals are envisioned to play a major role in various positioning and navigation applications, e.g., automated driving systems (ADSs), Internet of things (IoT), etc. Network-based positioning approaches have promised sub-meter-level accuracy with 5G signals [1], [2], [3], [4]. These approaches require the user to be a subscriber in the network in order to utilize the downlink/uplink channels between the 5G base station (also known as gNodeB (gNB)) and the user equipment (UE). This compromises the user's privacy by revealing their accurate location and limits the user to only gNBs from the network to which they are subscribed. To compensate for this, UE-based approaches have been studied recently and showed meter-level positioning accuracy on ground and aerial vehicles utilizing sub-6 GHz infrastructure [5], [6], [7], [8]. However, unlike previous cellular systems, 5G applies an ultra-lean transmission policy, which minimizes the transmission of "always-on" signals; hence, limiting UE-based opportunistic navigation to only synchronization signals. To demonstrate the impact of this limitation, consider the possible 5G downlink bandwidth $B_{\rm p}$, which ranges between 4.32 to 397.44 MHz, with synchronization signals spanning a bandwidth $B_{\rm s}$ that ranges between 3.6 to 57.6 MHz. As such, for $B_{\rm p} = 397.44$ and $B_{\rm s} = 57.6$, only 14.5% of the bandwidth is being exploited opportunistically with synchronization signals alone. Higher bandwidth signals yield more precise time-of-arrival estimates and facilitate differentiating the line-of-sight (LOS) signal from multipath components.

This letter makes the following contributions. First, the 5G downlink signals are discussed and a model for exploiting the *entire* bandwidth is presented. Second, an opportunistic navigation framework that exploits on-demand 5G downlink signals is proposed. Third, experimental results of the first signal acquisition and tracking of the so-called ultimate reference signal (URS) is presented, showing that the acquired URS: (i) spans the entire 5G downlink bandwidth, (ii) increases the carrier-to-noise (CNR) ratio by 10 dB compared to state-of-the-art 5G user equipment (UE)-based opportunistic navigation receiver, and (iii) reduces significantly the carrier and code phase errors. The proposed framework is shown to exhibit a ranging error standard deviation of 2.75 m, which is lower than the 5.05 m achieved with "always-on" 5G downlink signals.

II. 5G Known "always-On" Downlink Signals

This letter proposes a UE-based framework; thus, it only considers the 5G downlink signal, which employs orthogonal frequency division multiplexing (OFDM) with cyclic prefix (CP) for modulation. A 5G frame has a duration of 10 ms, which consists of 10 subframes, each with a duration of 1 ms. Each subframe breaks down into numerous slots, each of which contains 14 OFDM symbols for a normal CP length. The subcarrier spacing in 5G is flexible and is defined as $\Delta f = 2^{\mu} \times 15$ [kHz], where $\mu \in \{0, \ldots, 4\}$ is a pre-defined numerology. Each subframe is divided into numerous resource grids, each of which has multiple resource blocks with 12 subcarriers. A resource element is the smallest element of a resource grid, defined by its symbol and subcarrier number.

The 5G frame contains two synchronization signals that can be exploited for navigation: primary synchronization signal (PSS) and secondary synchronization signal (SSS), which are two orthogonal maximal length sequences of length 127. PSS has 3 possible sequences and specifies the sector ID of the gNB, and SSS has 336 possible sequences, which specifies the group identifier of the gNB. Together, they provide the frame start time and gNB physical cell ID $N_{ID}^{\rm Cell}$. The physical broadcast channel (PBCH) demodulation reference signal (DM-RS) is also transmitted in the same symbols as the synchronization signals. Altogether, they form what is called as SS/PBCH block. The length of the block is 240 subcarriers.

Manuscript received 30 July 2022; revised 17 November 2022; accepted 1 December 2022. Date of publication 6 January 2023; date of current version 19 April 2023. This work was supported in part by the Office of Naval Research (ONR) under Grant N00014-19-1-2511, and in part by the U.S. Department of Transportation (USDOT) under Grant 69A3552047138 for the CARMEN University Transportation Center (UTC). The associate editor coordinating the review of this manuscript and approving it for publication was Dr. Koby Todros. *(Corresponding author: Zaher M. Kassas.)*

Ali Abdallah and Joe Khalife were with the Department of Electrical Engineering & Computer Science, University of California, Irvine, CA 92697 USA (e-mail: abdalla2@uci.edu; khalifej@uci.edu).

Zaher M. Kassas is with the Department of Electrical & Computer Engineering, The Ohio State University, Columbus, OH 43210 USA (e-mail: zkassas@ieee.org).

Digital Object Identifier 10.1109/LSP.2023.3234496

1070-9908 © 2023 IEEE. Personal use is permitted, but republication/redistribution requires IEEE permission.
See https://www.ieee.org/publications/rights/index.html for more information.

Authorized licensed use limited to: The Ohio State University. Downloaded on October 13,2023 at 15:56:35 UTC from IEEE Xplore. Restrictions apply.

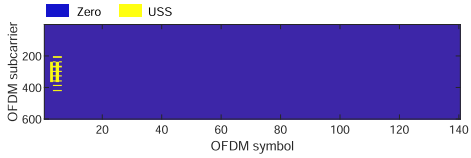

Fig. 1. The 5G OFDM locally-generated frame.

III. State-of-The-Art 5G Opportunistic Receivers

A. "always-On" Approach

A carrier-aided code phase 5G receiver was developed in [5], [9] to extract navigation observables from known "always-on" 5G downlink synchronization signals (SSs). A so-called ultimate SS (USS) was proposed, utilizing the time-domain orthogonality of downlink signals. The USS is essentially the 5G frame with a normalized SS/PBCH and zeros elsewhere. This approach is limited by the ratio of USS bandwidth versus the entire downlink bandwidth $r_{\mathrm{B,USS}}$ and the duty factor $r_{\mathrm{T,USS}}$, which limit the accuracy of the delay and carrier phase estimates, respectively [10]. For different configurations, $r_{\mathrm{B,USS}}$ and $r_{\mathrm{T,USS}}$ range between 14.5%–36% and 0.0104%–5.33%, respectively. Fig. 1 shows the USS locally-generated 5G frame in the frequency-domain, where only the yellow resource elements are known to the UE and the rest is set to zero. The depicted frame represents a 5G downlink signal with $\mu = 0$, 10 MHz bandwidth, $r_{\mathrm{B,USS}} = 36\%$, and $r_{\mathrm{T,USS}} = 1.33\%$.

B. Cognitive Approach

The "always-on" approach requires knowing the signal structure, specifically the reference signals (RSs). To alleviate this, a cognitive opportunistic navigation (CON) framework was proposed in [11] to exploit all available RSs, including ones unknown to the UE. The CON framework successfully estimated a periodic 5G RS, which was subsequently tracked, and exploited for navigation. However, the following question arises: How much of the available resources does the cognitively-acquired RS capture compared to the "always-on" (i.e., USS)? Given that the OFDM frame start time is unknown in the CON framework, the only way to assess the acquired signal is to look at the narrowness of the normalized autocorrelation function (ACF) of both RSs, which gives an estimate of the bandwidth that is being exploited (i.e., r_{B}). The results in [11] showed $r_{\mathrm{B,CON}} = 25\%$ versus $r_{\mathrm{B,USS}} = 36\%$.

The CON framework suffers from the following limitations

- The acquisition in the CON framework is challenged by the propagation channel fading and stationarity, which limits the coherent processing interval (CPI), i.e., the time interval in which the Doppler, delay, and channel gains are considered constant. Short CPI means less resources to be captured in the cognitively-acquired signal.
- The CON framework requires the UE to be in motion to exploit multiple gNBs transmitting on the same channel. Yet, to do so, the CON framework uses Doppler subspace to differentiate between gNBs; thus, the framework acquires only the most powerful gNB among different gNBs with similar Doppler profile. This results in acquiring less gNBs than the "always-on" approach.
- The 5G frame start time remains unknown in the CON framework; hence, it is not possible to construct the frame structure of the acquired signal. As such, pre-filtering and power allocation of different RSs cannot be performed, which affects the fidelity of the acquired signal.

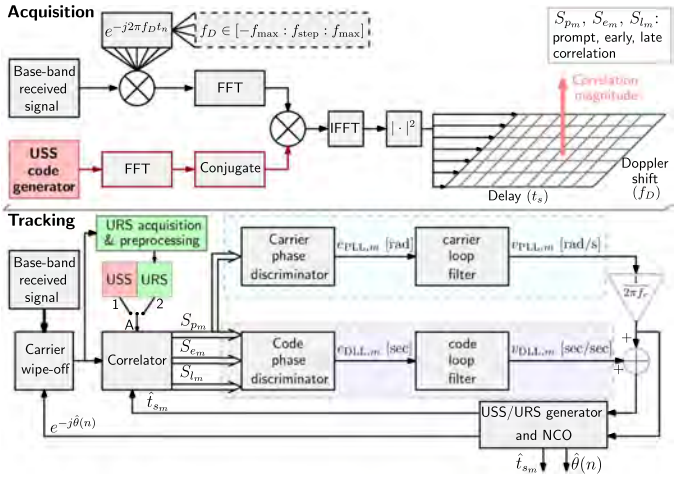

Fig. 2. Block diagram of proposed framework.

IV. Proposed Framework

This section presents the proposed framework in which the on-demand 5G signals are exploited. The framework aims to maximize r_{B} and r_{T} by exploiting other periodic RSs in the 5G downlink signals that are unknown to the UE, such as: channel state information RS (CSI-RS); other DM-RSs for the physical downlink control channel (PDCCH) and physical data shared channel (PDSCH); and phase tracking RS (PTRS).

A. Signal Model

The received baseband signal model can be expressed as

$$r[n] = \sum_{i=1}^{N} \left(\alpha_i c_i[\tau_n - t_{s_i}[n]] \exp\left(j\theta_i[\tau_n]\right) + d_i[\tau_n - t_{s_i}[n]] \exp\left(j\theta_i[\tau_n]\right)\right) + w[n], \quad (1)$$

where $r[n]$ is the received signal at the nth time instant; α_i is the complex channel gain between the UE and the i-th gNB; τ_n is the sample time expressed in the receiver time; N is the number of gNBs; $c_i[n]$ is the periodic RS with a period of L samples; $t_{s_i}[n]$ is the code-delay corresponding to the UE and the i-th gNB at the nth time instant; $\theta_i[\tau_n] = 2\pi f_{D_i}[n] T_s n$ is the carrier phase in radians, with $f_{D_i}[n]$ being the Doppler frequency at the nth time instant and T_s is the sampling time; $d_i[\tau_n]$ represents the samples of some data transmitted from the i-th gNB; and $w[n]$ is a zero-mean independent and identically distributed noise with $\mathbb{E}\{w[m]w^*[n]\} = \sigma_w^2 \delta[m-n]$, where $\delta[n]$ is the Kronecker delta function, and X^* denotes the complex conjugate of random variable X.

B. Proposed Approach

The structure of the proposed framework is shown in Fig. 2. This framework utilizes a so-called URS for 5G opportunistic navigation, which takes advantage of both "always-on" and "on-demand' 5G downlink RSs. Since the USS is always transmitted in the 5G downlink signal, it is used as a prior to acquire OFDM resources, which (i) extends the CPI, (ii) uses the USS subspace to exploit all available gNBs (even gNBs with similar Doppler

Authorized licensed use limited to: The Ohio State University. Downloaded on October 13,2023 at 15:56:35 UTC from IEEE Xplore. Restrictions apply.

profile), and (iii) allows preprocessing of the acquired replica to suppress noise and interference and maintain equally-distributed power among different RSs.

1) USS-Based Acquisition and Tracking: In the acquisition stage, the USS is used to determine which gNBs are in the UE's proximity and obtain a coarse estimate of their corresponding code start times $\{\hat{t}_{s_{i,0}}\}_{i=1}^{I}$ and Doppler frequencies $\{\hat{f}_{D_{i,0}}\}_{i=1}^{I}$, where I is the total number of gNBs.

In the tracking stage, the receiver refines these coarse estimates via a phase-locked loop (PLL) and a carrier-aided delay-locked loop (DLL). At first, node A in Fig. 2 is connected to 1 and the tracking loops use the USS as the local replica.

2) URS Acquisition: After the tracking loop achieves lock, acquisition of the URS is performed as

$$\mathbf{URS}_i \triangleq \frac{1}{K}\sum_{k=1}^{K}\hat{\boldsymbol{y}}_{i,k}, \tag{2}$$

where K is the total number of 5G frames used to capture the URS and $\hat{\boldsymbol{y}}_{i,k}$ is the received k-th 5G frame, defined as

$$\hat{\boldsymbol{y}}_{i,k} \triangleq \exp(-j2\pi\hat{f}_{D_{i,k}}[\boldsymbol{\tau}_k]) \odot \boldsymbol{r}_k[(n - \lfloor \hat{t}_{s_{i,k}} \cdot f_s \rceil)_L], \tag{3}$$

where $\boldsymbol{a} \odot \boldsymbol{b}$ is the element-wise product, $\lfloor \cdot \rceil$ rounds the argument to the nearest integer, $(\cdot)_L$ denotes modulo-L operation, f_s is the sampling frequency, and $\boldsymbol{r}_k$ and $\boldsymbol{\tau}_k$ are defined as

$$\boldsymbol{r}_k \triangleq [r[(k-1)L+1], r[(k-1)L+2], \ldots, r[kL]]^{\mathsf{T}},$$

$$\boldsymbol{\tau}_k \triangleq \left[\tau_{(k-1)L+1}, \tau_{(k-1)L+2}, \ldots, \tau_{kL}\right]^{\mathsf{T}}.$$

3) URS Preprocessing: A main advantage of the proposed framework is its ability to estimate the 5G OFDM frame start time. This allows converting the captured time-domain URS into 5G frame structure (i.e., frequency-domain) where the transmitted symbols are generated, which gives access to each received 5G resource element separately. This capability can be utilized to pre-filter the acquired URS and minimize interference. The preprocessing is summarized in Algorithm 1, where γ is a predefined threshold chosen empirically between 0 and 1, which depends on the fading channel between the gNB and UE. The preprocessing stage outputs a modified version of the URS signal denoted by $\mathbf{URS}'_i$.

4) URS Tracking: After acquiring and preprocessing the URS, node A switches to 2 and uses the URS as the local replica in standard tracking loops (e.g., as in [12]).

Algorithm 1: URS Preprocessing.

Input: $\mathbf{URS}_i$
Output: $\mathbf{URS}'_i$

Convert $\mathbf{URS}_i$ to frame structure $\mathbf{URS}_i^f$ (i.e., time-domain serial array to matrix)
Normalize by maximum magnitude of resource elements

$$\mathbf{URS}_i^f = \mathbf{URS}_i^f / \mathrm{URS_m}, \quad \mathrm{URS_m} \triangleq \max\left\{\left|\mathbf{URS}_i^f\right|\right\}$$

for $x = 0, x{+}{+}$, while $x <$ Number of symbols **do**
  for $y = 0, y{+}{+}$, while $y <$ Number of subcarriers **do**
    if $|\mathbf{URS}_i^f(x,y)| < \gamma$ **then**
      $\mathbf{URS}_i^f(x,y) \leftarrow 0$
    end if
  end for
end for
Normalize element-wise: $\mathbf{URS}_i^f = \mathbf{URS}_i^f ./ |\mathbf{URS}_i^f|$
Convert $\mathbf{URS}_i^f$ into time-domain $\mathbf{URS}'_i$

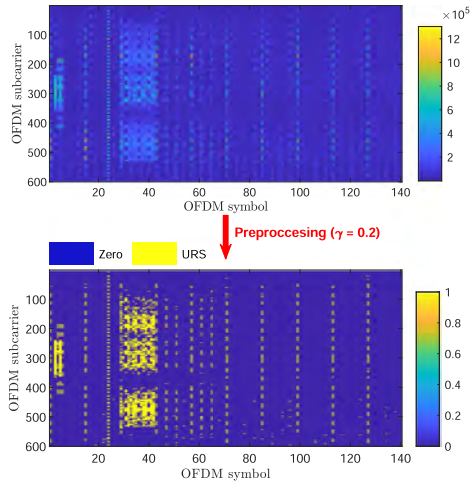

Fig. 3. Fame structure of the URS before and after preprocessing.

V. Experimental Results

This section presents the first UE-based carrier and code phase tracking, exploiting the entire sampled 5G downlink bandwidth. To this end, a stationary National Instrument (NI) universal software radio peripheral (USRP)-2955 was equipped with a consumer-grade omnidirectional Laird antenna to receive 5G downlink signals. The bandwidth was set to 10 MHz and the carrier frequency was set to 632.55 MHz, which corresponds to the U.S. cellular provider T-Mobile. The collected data was stored on a laptop for off-line processing. URS acquisition, preprocessing, and tracking results are presented next.

A. URS Acquisition and Preprocessing

The USRP recorded 5G signals for 300 seconds. The USS was used to detect a nearby gNB as in [5]. The gNB was mapped prior to the experiment and its location was known to the receiver. The receiver determined the gNB cell ID, Doppler, and code start time through a correlation approach detailed in [5], [9]. The cell ID was obtained from the detected synchronization sequences as summarized in Section II. A gNB with $N_{ID}^{\mathrm{Cell}} = 394$ was detected. The processing needed to track the Doppler and code start time followed the steps outlined in Section IV-B, with $\gamma = 0.2$. Due to the limited space in letters, the reader is directed to [5], [9] for the implementation details of Doppler and code start time tracking of gNB signals.

After the tracking loops achieved lock, the proposed framework acquired the URS signal for 4 seconds. Then, the acquired signal was preprocessed as discussed in Algorithm 1. Fig. 3 shows the frame structure of acquired URS before and after preprocessing.

To study URS's spectral efficiency $r_{\mathrm{B,URS}}$ and duty factor $r_{\mathrm{T,URS}}$, the number of active subcarriers and symbols was obtained from the preprocessed URS as shown in Fig. 4. Assuming that a URS symbol is active if 10 or more subcarriers are active within that symbol results in having 32 active symbols; hence, $r_{\mathrm{T,URS}} = 22.86\%$ compared to $r_{\mathrm{T,USS}} = 2.86\%$. For the bandwidth ratio, Fig. 4 shows that $r_{\mathrm{B,URS}} = 100\%$ compared

Authorized licensed use limited to: The Ohio State University. Downloaded on October 13,2023 at 15:56:35 UTC from IEEE Xplore. Restrictions apply.

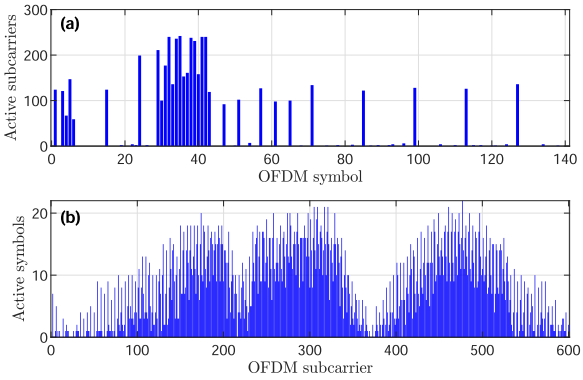

Fig. 4. (a) Number of active subcarriers for each URS symbol and (b) number of active symbols for each URS subcarrier.

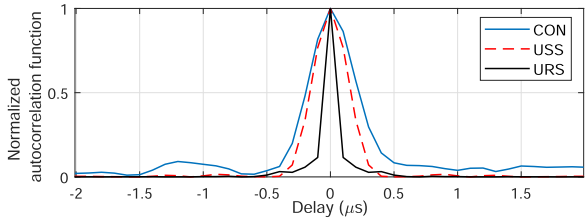

Fig. 5. Normalized autocorrelation function of the RS estimated with the CON receiver compared to the USS.

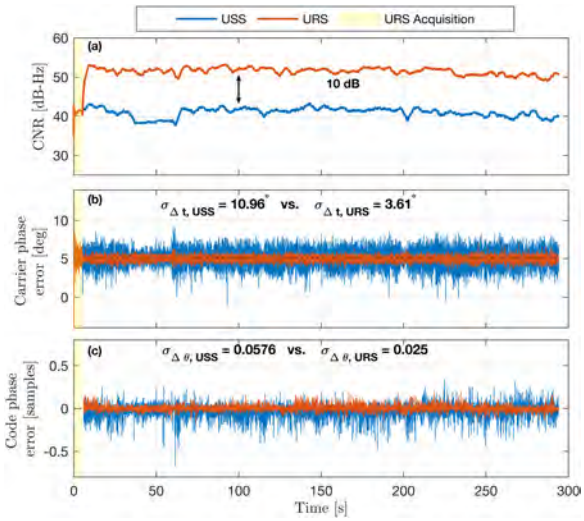

Fig. 6. Cellular 5G tracking results of the proposed URS versus USS: (a) CNR, (b) carrier phase error, and (c) code phase error.

to $r_{\mathrm{B,USS}} = 36\%$ and $r_{\mathrm{B,CON}} = 25\%$. The advantage of this increase in bandwidth ratio can be seen in the narrowness of the URS-ACF as shown in Fig. 5, which gives higher resolution in the time-domain to discriminate the LOS from multipath components.

B. URS Tracking Results

Next, the receiver switched to using the URS for tracking the signal parameters. Fig. 6 shows the tracking results of the proposed framework utilizing the entire sampled 5G bandwidth compared to the USS-based approach. It can be seen how the

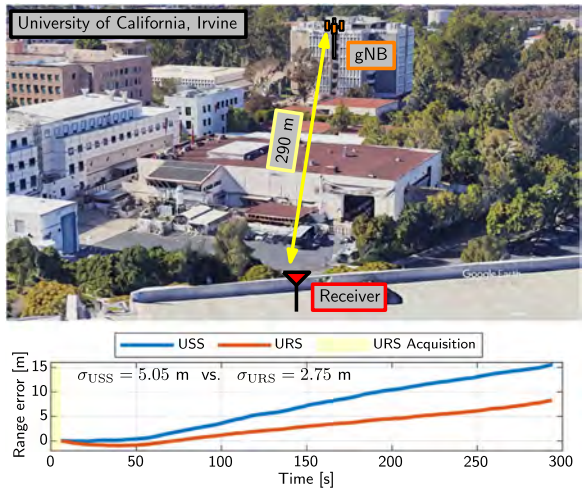

Fig. 7. Environment layout and ranging error of USS and URS frameworks.

CNR significantly increased by approximately 10 dB when using the acquired URS. This is due to the fact that in typical time-of-arrival based ranging, the variance of the ranging error is a decreasing function of (i) the signal bandwidth and (ii) the signal-to-noise ratio. In the proposed approach, the bandwidth of the synchronization signal was increased by learning more synchronization sequences in higher subcarriers. Moreover, synchronization sequences were learnt in different symbols of the frame. This resulted in a 10 dB increase in CNR as shown in Fig. 6. Consequently, the standard deviation of the URS-based method is significantly decreased compared to that of the USS-based method. Also, smaller carrier and code phase errors were obtained by the proposed approach, which translates to better ranging performance. It is worth noting that the CNR increase comes with an additional complexity complexity on the order of $O(K \cdot n)$, from (2) and (3). Also, the URS cannot be used until after K time-steps. However, this delay is reasonably short, e.g., 4 seconds in the results herein.

C. Ranging Results

This subsection assesses the ranging performance of the proposed framework. In this stationary scenario, the true range is fixed (290 m); hence, removing the initial range error results in the time history of the range error as seen in Fig. 7. Note that the range error of the proposed URS-based framework drifts slower than that of the USS-based framework. The range error's standard deviation of the USS and URS frameworks were 5.05 m and 2.75 m, respectively.

VI. Conclusion

This letter proposed a framework to exploit the on-demand 5G downlink bandwidth for navigation. The limitations of existing state-of-the-art "always-on" and cognitive user-based frameworks were discussed. A model of the 5G received signal was formulated, and an acquisition approach to capture the on-demand RSs denoted by URS was presented. Experimental results showed that proposed approach: (i) acquired a URS that spans the entire 5G downlink bandwidth, (ii) achieved 10 dB increase in the C/N_0, and (iii) resulted in significantly more precise code and carrier phase measurements.

Authorized licensed use limited to: The Ohio State University. Downloaded on October 13,2023 at 15:56:35 UTC from IEEE Xplore. Restrictions apply.

REFERENCES

[1] N. Garcia, H. Wymeersch, E. Larsson, A. Haimovich, and M. Coulon, "Direct localization for massive MIMO," *IEEE Trans. Signal Process.*, vol. 65, no. 10, pp. 2475–2487, May 2017.

[2] M. Koivisto et al., "Joint device positioning and clock synchronization in 5G ultra-dense networks," *IEEE Trans. Wireless Commun.*, vol. 16, no. 5, pp. 2866–2881, May 2017.

[3] Qualcomm, "Demonstrating advanced 5G innovations [video]," Jun. 2021. [Online]. Available: https://www.qualcomm.com/news/onq/2021/06/27/demonstrating-advanced-5g-innovations

[4] M. Pan et al., "Efficient joint DOA and TOA estimation for indoor positioning with 5G picocell base stations," *IEEE Trans. Instrum. Meas.*, vol. 71, pp. 1–19, 2022, Art. no. 8005219.

[5] A. Abdallah and Z. Kassas, "UAV navigation with 5G carrier phase measurements," in *Proc. ION GNSS Conf.*, 2021, pp. 3294–3306.

[6] I. Lapin, G. Seco-Granados, O. Renaudin, F. Zanier, and L. Ries, "Joint delay and phase discriminator based on ESPRIT for 5G NR positioning," *IEEE Access*, vol. 9, pp. 126550–126563, 2021.

[7] L. Chen, X. Zhou, F. Chen, L. Yang, and R. Chen, "Carrier phase ranging for indoor positioning with 5G NR signals," *IEEE Internet Things J.*, vol. 9, no. 13, pp. 10908–10919, Jul. 2022.

[8] J. Del Peral-Rosado et al., "Design considerations of dedicated and aerial 5G networks for enhanced positioning services," in *Proc. Workshop Satell. Navigation Technol.*, 2022, pp. 1–12.

[9] A. Abdallah and Z. Kassas, "Opportunistic navigation using sub-6 GHz 5G downlink signals: A case study on a ground vehicle," in *Proc. Eur. Conf. Antennas Propag.*, 2022, pp. 1–5.

[10] A. Graff, W. Blount, P. Iannucci, J. Andrews, and T. Humphreys, "Analysis of OFDM signals for ranging and communications," in *Proc. ION GNSS Conf.*, 2021, pp. 2910–2924.

[11] M. Neinavaie, J. Khalife, and Z. Kassas, "Cognitive opportunistic navigation in private networks with 5G signals and beyond," *IEEE J. Sel. Topics Signal Process.*, vol. 16, no. 1, pp. 129–143, Jan. 2022.

[12] M. Braasch and A. Dempster, "Tutorial: GPS receiver architectures, front-end and baseband signal processing," *IEEE Aerosp. Electron. Syst. Mag.*, vol. 34, no. 2, pp. 20–37, Feb. 2019.

Authorized licensed use limited to: The Ohio State University. Downloaded on October 13,2023 at 15:56:35 UTC from IEEE Xplore. Restrictions apply.

Exploiting Starlink Signals for Navigation: First Results

Mohammad Neinavaie, Joe Khalife, and Zaher M. Kassas
University of California, Irvine

BIOGRAPHIES

Mohammad Neinavaie is a Ph.D. student at the University of California, Irvine and member of the Autonomous Systems Perception, Intelligence, and Navigation (ASPIN) Laboratory. He received a B.E. in electrical engineering and an M.S. in digital communication systems from Shiraz University. His research interests include opportunistic navigation, blind opportunistic navigation, cognitive radio, wireless communication systems and software-defined radio.

Joe J. Khalife is a postdoctoral fellow at the University of California, Irvine and member of the Autonomous Systems Perception, Intelligence, and Navigation (ASPIN) Laboratory. He received a B.E. in electrical engineering, an M.S. in computer engineering from the Lebanese American University (LAU) and a Ph.D. in electrical engineering from the University of California, Irvine. From 2012 to 2015, he was a research assistant at LAU. His research interests include opportunistic navigation, autonomous vehicles, and software-defined radio.

Zaher (Zak) M. Kassas is an associate professor at the University of California, Irvine and director of the Autonomous Systems Perception, Intelligence, and Navigation (ASPIN) Laboratory. He is also director of the U.S. Department of Transportation Center: CARMEN (Center for Automated Vehicle Research with Multimodal AssurEd Navigation), focusing on navigation resiliency and security of highly automated transportation systems. He received a B.E. in Electrical Engineering from the Lebanese American University, an M.S. in Electrical and Computer Engineering from The Ohio State University, and an M.S.E. in Aerospace Engineering and a Ph.D. in Electrical and Computer Engineering from The University of Texas at Austin. He is a recipient of the 2018 National Science Foundation (NSF) Faculty Early Career Development Program (CAREER) award, 2019 Office of Naval Research (ONR) Young Investigator Program (YIP) award, 2018 IEEE Walter Fried Award, 2018 Institute of Navigation (ION) Samuel Burka Award, and 2019 ION Col. Thomas Thurlow Award. His research interests include cyber-physical systems, estimation theory, navigation systems, autonomous vehicles, and intelligent transportation systems.

ABSTRACT

This paper demonstrates the first Doppler positioning-based results with Starlink low Earth orbit (LEO) satellites. A cognitive opportunistic framework is used to detect Starlink's LEO satellite signals and track the Doppler frequencies of each Starlink LEO satellite. To this end, a generalized likelihood ratio (GLR)-based test is developed to detect the LEO satellite signals and estimate their corresponding beacons. A chirp parameter estimator is also proposed to track the Doppler frequencies from the unknown Starlink signals. Experimental results are presented showing a horizontal positioning error of 10 m by tracking the Doppler of six Starlink LEO satellites.

I. INTRODUCTION

Theoretical and experimental studies demonstrated the potential of low Earth orbit (LEO) broadband communication satellites as promising reliable sources for navigation [1–14]. Companies like Amazon, Telesat, OneWeb, and SpaceX are deploying so-called *megaconstellations* to provide global broadband internet [15, 16]. In particular, launching thousands of space vehicles (SVs) into LEO by SpaceX, can be considered as a turning-point in the future of LEO-based navigation technologies. Signals received by LEO SVs can be about 30 dB stronger than signals received from medium Earth orbit (MEO) where global navigation satellite systems (GNSS) SVs are placed [17].

Research has shown that one could exploit LEO SV broadband communication signals opportunistically for navigation purposes [18, 19]. Opportunistic navigation exempts the broadband provider from radical system changes, and does not require additional costly services and infrastructures. However, in order to draw navigation observables, an opportunistic framework needs knowledge of the LEO SV signal structure which may not be publicly available. Three of the main challenges of navigation with Starlink SV signals are (i) limited information about the signal structure, (ii) very-high

Copyright © 2021 by Z. M. Kassas

Preprint of the 2021 ION GNSS+ Conference
St. Louis, Missouri, September 20–24, 2021

dynamics of Starlink LEO SVs, and (iii) unknown ephemerides. This paper mainly concentrates on the first and second challenges.

The detection problem of an unknown source in the presence of other interfering signals falls into the paradigm of *matched subspace detectors* which has been widely studied in the classic detection literature [20–22]. Matched subspace detectors are used frequently in radar signal processing, e.g., in source localization in multiple-input multiple-output (MIMO) radars [23] and passive bistatic radar [24]. In [25], the design of subspace matched filters in the presence of mismatch in the steering vector was addressed. The performance of low-rank adaptive normalized matched subspace detectors was studied in [26]. In [27], the idea of subspace matching was used to present a solution to the problem of detecting the number of signals in both white and colored noise. In [28], the structure of the noise covariance matrix was exploited to enhance the matched subspace detection performance. In [29], adaptive vector subspace detection in partially homogeneous Gaussian disturbance was addressed. In the navigation literature, detection of unknown signals has been studied to design frameworks which are capable of navigating with unknown or partially known signals. The problem of detecting Galileo and Compass SV signals was studied in [30], which revealed the spread spectrum codes for these SVs. Preliminary experiments on navigation with partially known signals from low and medium Earth orbit satellites were conducted in [31–33]. In [34], a cognitive opportunistic navigation framework was proposed to exploit 5G signals for navigation purposes. This paper builds on the concept of cognitive opportunistic navigation by presenting a receiver architecture, which is capable of exploiting Starlink signals for navigation. Assuming that Starlink LEO SV downlink signals contains a periodic reference signal (RS), this paper formulates a *matched subspace detection* problem to detect the unknown RSs of Starlink SVs and estimating the unknown period and Doppler frequency.

This paper makes the following contributions. First, a model for the Starlink LEO SV's downlink signals is presented. Second, an algorithm is proposed to (i) acquire the Starlink LEO SV signals and (ii) track the Doppler frequency of each detected SV. Third, next to [19], the first experimental results with Starlink downlink signals is presented in this paper. In [19], a phase-locked loop was used to track the carrier phase of Starlink LEO SVs. However, the method presented in [19] relies on tracking the phase of a single carrier at a time, but does not generalize to more complicated sturctures, e.g., orthogonal frequency-division multiple access (OFDMA). In this paper, by considering a general model for the Starlink downlink signals, the unknown parameters of the signal are estimated and used to detect Starlink LEO SVs. Indeed, the proposed method enables one to estimate the synchronization signals of the Starlink LEO SVs. A demonstration of the first Starlink LEO SVs detection, Doppler tracking, and positioning results with real Starlink signals is presented, showing a horizontal position error of 10 m with six Starlink SVs.

The rest of the paper is organized as follows. Section II presents the hardware setup. Section III describes the received baseband signal model. Section IV and V present the proposed acquisition and Doppler tracking methods, respectively. Section VI presents the experimental results. Section VII gives concluding remarks.

II. DOWNCONVERTING STARLINK LEO SV SIGNALS

Detailed signal specifications of Starlink downlink signals are not available to the public. The only known information about these signals are the carrier frequencies and the bandwidths. The Ku-band is used by SpaceX for the satellite-to-user links (both uplink and downlink) [35]. In order to sample bands of the radio frequency, software-defined radios (SDRs) can be used. However, Ku/Ka bands are beyond the carrier frequency of most commercial SDRs.

In this paper, a hardware setup is proposed based on downconverting the Starlink LEO SV signals to the L band. A 10 GHz mixer is employed between the antenna and the SDR to downconvert Starlink LEO SV signals from the Ku band (10.7–12.75 GHz) to the L band (950–2150 MHz). In particular, the hardware downconverts the Starlink LEO SV Ku band signals, namely 11.325 GHz, to 1.325 GHz. The hardware block diagram can be seen in Fig. 1.

In order to formulate a detection problem to detect the activity of Starlink downlink signals, a signal model is proposed which solely relies on the periodicity of the transmitted signals. The logic behind the proposed signal model is that in most commercial communication systems, a periodic RS is transmitted for synchronization purposes, e.g., primary synchronization signals (PSS) in long term evolution (LTE) and the fifth generation (5G) signals [36]. The following subsection, presents a model for the Starlink LEO SV's downlink signals. Moreover, in order to capture the high dynamics of the Starlink LEO SVs, the proposed signal model considers a *second-order polynomial* model for the variations of the Doppler frequency in the processing interval.

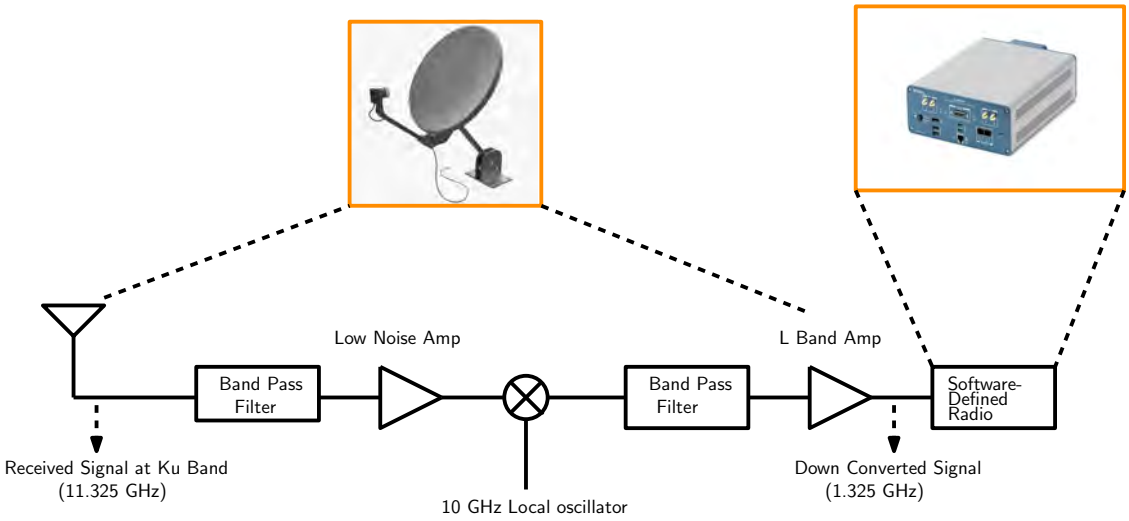

Fig. 1. Two stages down-convertor.

III. PROPOSED SIGNAL MODEL FOR STARLINK LEO SV DOWNLINK SIGNALS

As it was mentioned previously, in most commercial communication systems, a periodic RS is transmitted, e.g., PSS in OFDMA-based and spreading codes in code division multiple access (CDMA)-based signals [37]. In this paper, the Starlink LEO SV downlink signal is modeled as an unknown periodic signal in the presence of interference and noise. If an RS such as PSS in OFDMA-based signals is being periodically transmitted, it will be detected and estimated by the proposed method. The proposed signal model is

$$\begin{aligned} r[n] &= \alpha c[\tau_n - t_s[n]] \exp\left(j\theta[\tau_n]\right) \\ &\quad + d[\tau_n - t_s[n]] \exp\left(j\theta[\tau_n]\right) + w[n], \end{aligned} \tag{1}$$

where $r[n]$ is the received signal at the nth time instant; α is the complex channel gain between the receiver and the Starlink LEO SV; τ_n is the sample time expressed in the receiver time; $c[\tau_n]$ represents the samples of the complex periodic RS with a period of L samples; $t_s[n]$ is the code-delay corresponding to the receiver and the Starlink LEO SV at the nth time instant; $\theta[\tau_n] = 2\pi f_D[n] T_s n$ is the carrier phase in radians, where $f_D[n]$ is the instantaneous Doppler frequency at the nth time instant and T_s is the sampling time; $d_i[\tau_n]$ represents the complex samples of some data transmitted from the Starlink LEO SV; and $w[n]$ is the complex zero-mean independent and identically distributed noise with variance σ_w^2.

Starlink LEO SV's signals suffer from very high Doppler shifts. Higher lengths of processing intervals require higher order Doppler models. In order for a Doppler estimation algorithm to provide an accurate estimation of the Doppler frequency, the processing interval should be large enough to accumulate enough energy. According to the considered processing interval length in the experiments, it is observed that during the kth processing interval the instantaneous Doppler frequency is almost a linear function of time, i.e., $f_D[n] = f_{D_k} + \beta_k n$, where f_{D_k} is referred to as constant Doppler, and β_k is the Doppler rate at the kth processing interval. The coherent processing interval (CPI) is defined as the time interval in which the constant Doppler, f_{D_k}, and the Doppler rate, β_k, are constant.

The received signal at the nth time instant when the Doppler rate is wiped-off is denoted by $r'[n] \triangleq \exp(-j2\pi\beta_k n^2) r[n]$. One can define *the desired RS* which is going to be detected in the acquisition stage as

$$s[n] \triangleq \alpha c[\tau_n - t_s[n]] \exp\left(j2\pi f_{D_k} T_s n\right), \tag{2}$$

and the equivalent noise as

$$\begin{aligned} w_{\text{eq}}[n] &= d[\tau_n - t_s[n]] \exp\left(j2\pi f_{D_k} T_s n\right) \\ &\quad + \exp\left(-j2\pi\beta n^2\right) w[n]. \end{aligned} \tag{3}$$

Hence, $r'[n] = s[n] + w_{\text{eq}}[n]$. Due to the periodicity of the RS, $s[n]$ has the following property

$$s[n + mL] = s[n] \exp\left(j\omega_k mL\right) \quad 0 \le n \le L-1, \tag{4}$$

where $\omega_k = 2\pi f_{D_k} T_s$ is the normalized Doppler at the kth CPI, and $-\frac{1}{2} \leq \omega_k \leq \frac{1}{2}$. A vector of L observation samples corresponding to the mth period of the signal is formed as

$$\mathbf{z}_m \triangleq [r'[mL], r'[mL+1], \ldots, r'[(m+1)L-1]]^{\mathsf{T}}. \tag{5}$$

The kth CPI vector is constructed by concatenating M vectors of length L to form the $ML \times 1$ vector

$$\mathbf{y}_k = [\mathbf{z}_{kM}^{\mathsf{T}}, \mathbf{z}_{kM+1}^{\mathsf{T}}, \ldots, \mathbf{z}_{(k+1)M-1}^{\mathsf{T}}]^{\mathsf{T}}. \tag{6}$$

Therefore,

$$\mathbf{y}_k = \mathbf{H}_k \mathbf{s} + \mathbf{w}_{\mathrm{eq}_k}, \tag{7}$$

where $\mathbf{s} = [s[1], s[2], \ldots, s[L]]^{\mathsf{T}}$, and the $ML \times L$ Doppler matrix is defined as

$$\mathbf{H}_k \triangleq [\mathbf{I}_L, \exp(j\omega_k L)\,\mathbf{I}_L, \ldots, \exp(j\omega_k (M-1)L)\,\mathbf{I}_L]^{\mathsf{T}}, \tag{8}$$

where $\mathbf{I}_L$ is an $L \times L$ identity matrix, and $\mathbf{w}_{\mathrm{eq}_\mathbf{k}}$ is the equivalent noise vector.

IV. ACQUISITION

In this section, a detection scheme is proposed to detect the existence of Starlink LEO SVs in the carrier frequency of 11.325 GHz within a bandwidth of 2.5 MHz, at $k = 0$. The following binary hypothesis test is used to detect the Starlink LEO SV

$$\begin{cases} \mathcal{H}_0: & \mathbf{y}_0 = \mathbf{w}_{\mathrm{eq}_0} \\ \mathcal{H}_1: & \mathbf{y}_0 = \mathbf{H}_0 \mathbf{s} + \mathbf{w}_{\mathrm{eq}_0}. \end{cases} \tag{9}$$

For a given set of unknown variables $\mathcal{W}_0 = \{L, \omega_0, \beta_0\}$, the GLR detector for the testing hypothesis (9) is known as matched subspace detector [20, 22], and is derived as (see Theorem 9.1 in [38])

$$\mathcal{L}(\mathbf{y}_0|\mathcal{W}_0) = \frac{\mathbf{y}_0^H \mathbf{P}_{\mathbf{H_0}} \mathbf{y}_0}{\mathbf{y}_0^H \mathbf{P}_{\mathbf{H_0}}^{\perp} \mathbf{y_0}} \underset{\mathcal{H}_0}{\overset{\mathcal{H}_1}{\gtrless}} \eta, \tag{10}$$

where $\mathbf{y}_0^{\mathsf{H}}$ is the Hermitian transpose of $\mathbf{y}_0$, $\mathbf{P}_{\mathbf{H_0}} \triangleq \mathbf{H_0}(\mathbf{H_0^H H_0})^{-1}\mathbf{H_0^H}$ denotes the projection matrix to the column space of $\mathbf{H}_0$, $\mathbf{P}_{\mathbf{H_0}}^{\perp} \triangleq \mathbf{I} - \mathbf{P}_{\mathbf{H_0}}$ denotes the projection matrix onto the space orthogonal to the column space of $\mathbf{H}_0$, and η is the threshold which is predetermined according to the probability of false alarm. Since, $\mathbf{H}_k^{\mathsf{H}}\mathbf{H}_k = M\mathbf{I_L}$ for all k, the likelihood can be rewritten as $\mathcal{L}(\mathbf{y}_0|\mathcal{W}_0) = \frac{1}{\frac{\|\mathbf{y}_0\|^2}{\frac{1}{M^2}\|\mathbf{H}_0^{\mathsf{H}}\mathbf{y}_0\|^2} - 1}$, which is a monotonically increasing function of $\frac{\|\mathbf{H}_0^{\mathsf{H}}\mathbf{y}_0\|^2}{\|\mathbf{y}_0\|^2}$. Hence, the GLR detector (10) is equivalent to

$$\frac{\|\mathbf{H}_0^{\mathsf{H}}\mathbf{y}_0\|^2}{\|\mathbf{y}_0\|^2} \underset{\mathcal{H}_0}{\overset{\mathcal{H}_1}{\gtrless}} \eta', \tag{11}$$

where η' is determined according to the desired probability of false alarm. The maximum likelihood of the set $\mathcal{W}_0$ is

$$\hat{\mathcal{W}}_0 = \mathrm{argmax}_{L,\omega_0,\beta_0} \|\mathbf{H}_0^{\mathsf{H}}\mathbf{y}_0\|^2, \tag{12}$$

It should be pointed out that the estimated Doppler using (12) results in a constant ambiguity denoted by $\omega_0 = 2\pi f_0$. This constant ambiguity is accounted for in the navigation filter.

Fig. 2 demonstrates the likelihood in terms of Doppler frequency and the period for real Starlink downlink signals. The CPI is considered to be 200 times the period. The Doppler-beacon length subspace for two time instances t_0 and t_1 where $t_1 - t_0 = 1s$. As it can be seen in this figure, the likelihood's location is changed from t_0 to t_1 in the subspace which demonstrates a Doppler rate of 1609 Hz/s for this Starlink LEO SV.

V. Doppler Tracking

The low effective SNR per *degree of freedom* in many scenarios, e.g., OFDMA-based signals, may impose a large CPI. The Doppler estimator in the proposed receiver processes one CPI at a time to estimate the Doppler parameters corresponding to the CPI. To accumulate enough energy, the number of samples in one CPI, i.e., M, has to be large enough to include

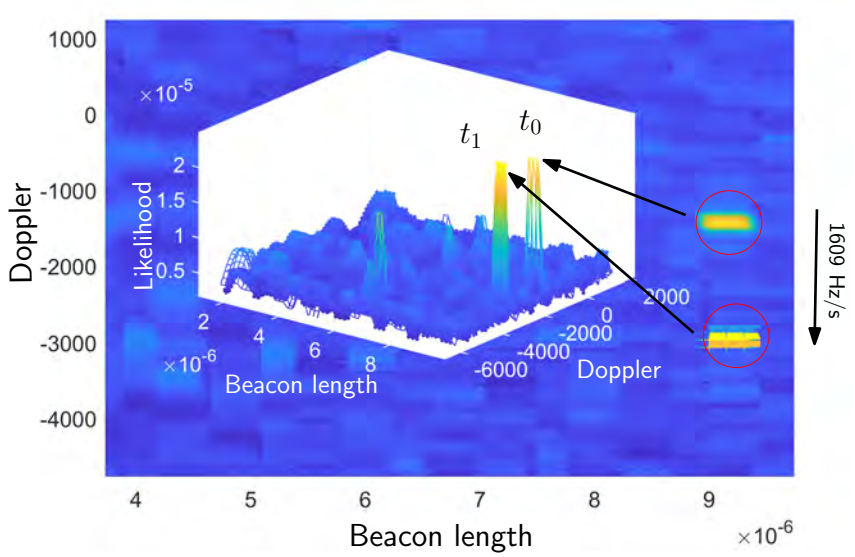

Fig. 2. Matched subspace detection for real Starlink signals: The Doppler-beacon length subspace for two time instances t_0 and t_1 where $t_1 - t_0 = 1s$. In this experiment, the likelihood's location is changed from t_0 to t_1 in the subspace which demonstrates a Doppler rate of 1609 Hz/s for this Starlink LEO SV.

a sufficient number of complete cycles of the beacon signal. As it was mentioned previously, the Doppler frequency $f_D[n]$ cannot be assumed to be constant during the CPI. The signal part of the observation includes a periodic beacon $s[n]$ of length L and its Fourier transform can be written as a pulse train with period $f_0 = \frac{1}{L}$. More precisely,

$$\mathcal{F}\left\{\sum_{i=-\infty}^{\infty} \alpha \exp\left(j2\pi f_D[n]n\right) s[n - iL - n_d]\right\} = \sum_{i=-\infty}^{\infty} \alpha S\left(if_0\right) \Pi\left(f - f_{D_k} - if_0\right), \tag{13}$$

where $S(f) = \mathcal{F}\{s[n]\}$ is the discrete Fourier transform of $s[n]$ and $\Pi(f)$ is the pulse resulting from the time-varying Doppler. As such, a proper sliding band-pass filter, is capable of tracking the Doppler frequency changes in different CPIs from $S(f)$. Tracking the pulse trains from (13) results in an ambiguity of an integer multiple of f_0 in the Doppler estimate. Assuming the Doppler frequency can be modeled as a time polynomial of order p, it can be shown that the peak-tracking estimator will yield an estimation error that is a time polynomial of order $p-1$. Therefore, the magnitude of the estimation error may grow unacceptably large in a peak-tracking estimator. In many practical scenarios, the instantaneous Doppler frequency can be modeled as a time polynomial during one CPI; therefore, a more sophisticated estimator must be employed. Signals whose frequencies increase or decrease as a time polynomial are referred to as *chirp signals*. A linear chirp can be written as [39]

$$c(t) = \exp\left(j2\pi(\beta t + \gamma)t\right), \tag{14}$$

where β and γ are the parameters of the linear chirp signal. In order for the proposed receiver to have a reliable track of the instantaneous Doppler frequency, the chirp parameters have to be taken into account.

A. Wigner Distribution and Chirp Parameter Estimation

One classic way of estimating the parameters of a chirp is through the Wigner distribution [39], which for a single chirp signal $c(t)$ is given by

$$W(t, f) = \int_{-\infty}^{\infty} c\left(t + \frac{\tau}{2}\right) c^*\left(t - \frac{\tau}{2}\right) \exp\left(-j2\pi f\tau\right) d\tau. \tag{15}$$

For a linear chirp, i.e., $c(t) = \exp\left(j2\pi(\beta t^2 + \gamma t)\right)$,

$$W(t, f) = \delta\left(f - (2\beta t + \gamma)\right), \tag{16}$$

where $\delta(\cdot)$ is the Dirac delta function. The Wigner distribution concentrates the energy on the time history of the instantaneous frequency and can be used to estimate the parameters of a chirp. Direct implementation of (15) is computationally

inefficient, as the complexity grows with $(ML)^3 \log ML$ [40]. Alternatively, one can search over certain values of Doppler rate, i.e., β_k, wipe-off the effect of β_k in the received signal, and take the FFT of the wiped-off signal to estimate f_{D_k}. This reduces the overall computational complexity of chirp parameter estimation dramatically.

VI. EXPERIMENTAL RESULTS

This section provides the first results for blind Doppler tracking and positioning with Starlink signals of opportunity. A stationary National Instrument (NI) universal software radio peripheral (USRP) 2945R was equipped with a consumer-grade Ku antenna and low-noise block (LNB) downconverter to receive Starlink signals in the Ku band. The sampling rate was set to 2.5 MHz and the carrier frequency was set to 11.325 GHz, which is one of the Starlink downlink frequencies. The samples of the Ku signal were stored for off-line processing.

Next, pseudorange rate observables were formed from the tracked Doppler frequencies by (i) downsampling by a factor D to avoid large time-correlations in the pseudorange observables and (ii) multiplying by the wavelength to express the Doppler frequencies in meters per second.

Let $i \in \{1, 2, 3, 4, 5, 6\}$ denote the SV index. The pseudorange rate observable to the ith SV at time-step $\kappa = k \cdot D$, expressed in meters, is modeled as

$$z_i(\kappa) = \frac{\dot{\boldsymbol{r}}_{\mathrm{SV_i}}^{\mathsf{T}}(\kappa)\left[\boldsymbol{r}_r - \boldsymbol{r}_{\mathrm{SV_i}}(\kappa)\right]}{\left\|\boldsymbol{r}_r - \boldsymbol{r}_{\mathrm{SV_i}}(\kappa)\right\|_2} + a_i + v_{z_i}(\kappa), \tag{17}$$

where $\boldsymbol{r}_r$ and $\boldsymbol{r}_{\mathrm{SV_i}}(\kappa)$ are the receiver's and ith Starlink SV three-dimensional (3–D) position vectors, $\dot{\boldsymbol{r}}_{\mathrm{SV_i}}(\kappa)$ is the ith Starlink SV 2–D velocity vector, a_i is the constant bias due to the unknown Doppler frequency ambiguity f_0, and $v_{z_i}(\kappa)$ is the measurement noise, which is modeled as a zero-mean, white Gaussian random variable with variance $\sigma_i^2(\kappa)$. The value of $\sigma_i^2(\kappa)$ is the first diagonal element of $\mathbf{P}_{\kappa|\kappa}$, expressed in $\mathrm{m}^2/\mathrm{s}^2$. Next, define the parameter vector $\boldsymbol{x} \triangleq \left[\boldsymbol{r}_r{}^{\mathsf{T}}, a_1, \ldots, a_6\right]^{\mathsf{T}}$. Let $\boldsymbol{z}$ denote the vector of all the pseudorange observables stacked together, and let $\boldsymbol{v}_z$ denote the vector of all measurement noises stacked together, which is a zero-mean Gaussian random vector with a diagonal covariance $\mathbf{R}$ whose diagonal elements are given by $\sigma_i^2(\kappa)$. Then, one can readily write the measurement equation given by $\boldsymbol{z} = \boldsymbol{g}(\boldsymbol{x}) + \boldsymbol{v}_z$, where $\boldsymbol{g}(\boldsymbol{x})$ is a vector-valued function that maps the parameter $\boldsymbol{x}$ to the pseudorange rate observables according to (17). Next, a weighted nonlinear least-squares (WNLS) estimator with weight matrix $\mathbf{R}^{-1}$ is solved to obtain an estimate of $\boldsymbol{x}$ given by $\hat{\boldsymbol{x}} = \left[\hat{\boldsymbol{r}}_r^{\mathsf{T}}, \hat{a}_1, \ldots, \hat{a}_6\right]^{\mathsf{T}}$. The SV positions were obtained from TLE files and SGP4 software. It is important to note that the TLE epoch time was adjusted for each SV to account for ephemeris errors. This was achieved by minimizing the pseudorange rate residuals for each SV.

Subsequently, the receiver position was estimated using the aforementioned WNLS. The 3–D position error was found to be 22.9 m, while the 2–D position error was 10 m.

A skyplot of the Starlink SVs as well as the environment layout along with the positioning results are shown in Fig. 3.

VII. CONCLUSION

The first Doppler positioning-based results with Starlink LEO SVs was demonstrated. In order to detect Starlink's LEO SV signals and track the Doppler frequencies of each Starlink LEO SV, a cognitive opportunistic framework was used. To this end, a GLR-based test was developed to detect the LEO SV signals and estimate their corresponding beacons. A chirp parameter estimator was also proposed to track the Doppler frequencies from the unknown Starlink signals. Experimental results showed a horizontal positioning error of 10 m by tracking the Doppler of six Starlink LEO SVs.

ACKNOWLEDGMENTS

This work was supported in part by the Office of Naval Research (ONR) under Grant N00014-19-1-2511, in part by the U.S. Department of Transportation (USDOT) under Grant 69A3552047138 for the CARMEN University Transportation Center (UTC), and in part by the National Science Foundation (NSF) under Grant 1929965.

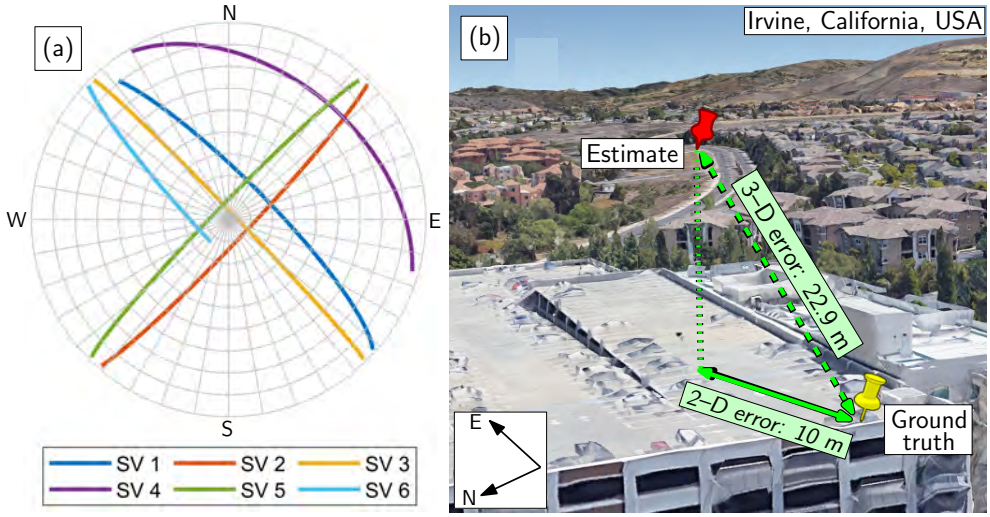

Fig. 3. (a) Skyplot showing the Starlink SVs' trajectories during the experiment. (b) Environment layout and positioning results.

References

[1] M. Rabinowitz, B. Parkinson, C. Cohen, M. O'Connor, and D. Lawrence, "A system using LEO telecommunication satellites for rapid acquisition of integer cycle ambiguities," in *Proceedings of IEEE/ION Position Location and Navigation Symposium*, April 1998, pp. 137–145.

[2] N. Levanon, "Quick position determination using 1 or 2 LEO satellites," *IEEE Transactions on Aerospace and Electronic Systems*, vol. 34, no. 3, pp. 736–754, July 1998.

[3] M. Joerger, L. Gratton, B. Pervan, and C. Cohen, "Analysis of Iridium-augmented GPS for floating carrier phase positioning," *NAVIGATION, Journal of the Institute of Navigation*, vol. 57, no. 2, pp. 137–160, 2010.

[4] T. Reid, A. Neish, T. Walter, and P. Enge, "Broadband LEO constellations for navigation," *NAVIGATION, Journal of the Institute of Navigation*, vol. 65, no. 2, pp. 205–220, 2018.

[5] D. Racelis, B. Pervan, and M. Joerger, "Fault-free integrity analysis of mega-constellation-augmented GNSS," in *Proceedings of ION GNSS Conference*, January 2019, pp. 465–484.

[6] P. Iannucci and T. Humphreys, "Economical fused LEO GNSS," in *Proceedings of IEEE/ION Position, Location and Navigation Symposium*, 2020, pp. 426–443.

[7] J. Khalife, M. Neinavaie, and Z. Kassas, "Navigation with differential carrier phase measurements from megaconstellation LEO satellites," in *Proceedings of IEEE/ION Position, Location, and Navigation Symposium*, April 2020, pp. 1393–1404.

[8] Z. Kassas, J. Khalife, M. Neinavaie, and T. Mortlock, "Opportunity comes knocking: overcoming GPS vulnerabilities with other satellites' signals," *Inside Unmanned Systems Magazine*, pp. 30–35, June/July 2020.

[9] R. Morales-Ferre, E. Lohan, G. Falco, and E. Falletti, "GDOP-based analysis of suitability of LEO constellations for future satellite-based positioning," in *Proceedings of IEEE International Conference on Wireless for Space and Extreme Environments*, 2020, pp. 147–152.

[10] Z. Kassas, "Position, navigation, and timing technologies in the 21st century," J. Morton, F. van Diggelen, J. Spilker, Jr., and B. Parkinson, Eds. Wiley-IEEE, 2021, vol. 2, ch. 43: Navigation from low Earth orbit – Part 2: models, implementation, and performance, pp. 1381–1412.

[11] T. Reid, T. Walter, P. Enge, D. Lawrence, H. Cobb, G. Gutt, M. O'Conner, and D. Whelan, "Position, navigation, and timing technologies in the 21st century," J. Morton, F. van Diggelen, J. Spilker, Jr., and B. Parkinson, Eds. Wiley-IEEE, 2021, vol. 2, ch. 43: Navigation from low Earth orbit – Part 1: Concept, Current Capability, and Future Promise, pp. 1359–1379.

[12] S. Thompson, S. Martin, and D. Bevly, "Single differenced doppler positioning with low Earth orbit signals of opportunity and angle of arrival estimation," in *Proceedings of ION International Technical Meeting*, 2020, pp. 497–509.

[13] N. Khairallah and Z. Kassas, "Ephemeris closed-loop tracking of LEO satellites with pseudorange and Doppler measurements," in *Proceedings of ION GNSS Conference*, September 2021, accepted.

[14] S. Kozhaya, J. Haidar-Ahmad, A. Abdallah, S. Saab, and Z. Kassas, "Comparison of neural network architectures for simultaneous tracking and navigation with LEO satellites," in *Proceedings of ION GNSS Conference*, September 2021, accepted.

[15] T. Reid, K. Gunning, A. Perkins, S. Lo, and T. Walter, "Going back for the future: Large/mega LEO constellations for navigation," in *Proceedings of ION GNSS Conference*, September 2019, pp. 2452–2468.

[16] T. Reid, B. Chan, A. Goel, K. Gunning, B. Manning, J. Martin, A. Neish, A. Perkins, and P. Tarantino, "Satellite navigation for the age of autonomy," in *Proceedings of IEEE/ION Position, Location and Navigation Symposium*, 2020, pp. 342–352.

[17] A. Nardin, F. Dovis, and J. Fraire, "Empowering the tracking performance of LEO-based positioning by means of meta-signals," *IEEE Journal of Radio Frequency Identification*, pp. 1–1, 2021.

[18] Z. Kassas, J. Morales, and J. Khalife, "New-age satellite-based navigation – STAN: simultaneous tracking and navigation with LEO satellite signals," *Inside GNSS Magazine*, vol. 14, no. 4, pp. 56–65, 2019.

[19] J. Khalife, M. Neinavaie, and Z. Kassas, "The first carrier phase tracking and positioning results with Starlink LEO satellite signals," *IEEE Transactions on Aerospace and Electronic Systems*, 2021, accepted.

[20] L. Scharf and B. Friedlander, "Matched subspace detectors," *IEEE Transactions on signal processing*, vol. 42, no. 8, pp. 2146–2157, 1994.

[21] S. Kraut, L. Scharf, and L. McWhorter, "Adaptive subspace detectors," *IEEE Transactions on Signal Processing*, vol. 49, no. 1, pp. 1–16, 2001.

[22] F. Gini and A. Farina, "Vector subspace detection in compound-Gaussian clutter. part I: survey and new results," *IEEE Transactions on Aerospace and Electronic Systems*, vol. 38, no. 4, pp. 1295–1311, 2002.

[23] M. Korso, R. Boyer, A. Renaux, and S. Marcos, "Statistical resolution limit for source localization with clutter interference in a MIMO radar context," *IEEE Transactions on Signal Processing*, vol. 60, no. 2, pp. 987–992, 2012.

[24] A. Zaimbashi, M. Derakhtian, and A. Sheikhi, "GLRT-based CFAR detection in passive bistatic radar," *IEEE Transactions on Aerospace and Electronic Systems*, vol. 49, no. 1, pp. 134–159, 2013.
[25] I. Atitallah, A. Kammoun, M. Alouini, and T. Al-Naffouri, "Optimal design of large dimensional adaptive subspace detectors," *IEEE Transactions on Signal Processing*, vol. 64, no. 19, pp. 4922–4935, 2016.
[26] A. Combernoux, F. Pascal, and G. Ginolhac, "Performance of the low-rank adaptive normalized matched filter test under a large dimension regime," *IEEE Transactions on Aerospace and Electronic Systems*, vol. 55, no. 1, pp. 459–468, 2019.
[27] M. Wax and A. Adler, "Detection of the number of signals by signal subspace matching," *IEEE Transactions on Signal Processing*, vol. 69, pp. 973–985, 2021.
[28] Z. Wang, G. Li, and H. Chen, "Adaptive persymmetric subspace detectors in the partially homogeneous environment," *IEEE Transactions on Signal Processing*, vol. 68, pp. 5178–5187, 2020.
[29] D. Ciuonzo, A. De Maio, and D. Orlando, "On the statistical invariance for adaptive radar detection in partially homogeneous disturbance plus structured interference," *IEEE Transactions on Signal Processing*, vol. 65, no. 5, pp. 1222–1234, 2017.
[30] G. Gao, "Towards navigation based on 120 satellites: Analyzing the new signals," Ph.D. dissertation, Stanford University, 2008.
[31] J. Merwe, S. Bartl, C. O'Driscoll, A. Rügamer, F. Förster, P. Berglez, A. Popugaev, and W. Felber, "GNSS sequence extraction and reuse for navigation," in *Proceedings of ION GNSS+ Conference*, 2020, pp. 2731–2747.
[32] M. Neinavaie, J. Khalife, and Z. Kassas, "Blind Doppler tracking and beacon detection for opportunistic navigation with LEO satellite signals," in *Proceedings of IEEE Aerospace Conference*, March 2021, pp. 1–8.
[33] J. Khalife, M. Neinavaie, and Z. Kassas, "Blind Doppler tracking from OFDM signals transmitted by broadband LEO satellites," in *Proceedings of IEEE Vehicular Technology Conference*, April 2021, pp. 1–6.
[34] M. Neinavaie, J. Khalife, and Z. Kassas, "Cognitive opportunistic navigation in private networks with 5G signals and beyond," *IEEE Journal of Selected Topics in Signal Processing*, 2021, accepted.
[35] I. Del Portillo, B. Cameron, and E. Crawley, "A technical comparison of three low earth orbit satellite constellation systems to provide global broadband," *Acta Astronautica*, vol. 159, pp. 123–135, 2019.
[36] K. Shamaei and Z. Kassas, "Receiver design and time of arrival estimation for opportunistic localization with 5G signals," *IEEE Transactions on Wireless Communications*, vol. 20, no. 7, pp. 4716–4731, 2021.
[37] D. Tse and P. Viswanath, *Fundamentals of wireless communication*. Cambridge university press, 2005.
[38] S. Kay, *Fundamentals of statistical signal processing: Detection Theory*. Prentice-Hall, Upper Saddle River, NJ, 1993, vol. II.
[39] P. Djuric and S. Kay, "Parameter estimation of chirp signals," *IEEE Transactions on Acoustics, Speech, and Signal Processing*, vol. 38, no. 12, pp. 2118–2126, 1990.
[40] M. Vishwanath, R. Owens, and M. Irwin, "The computational complexity of time-frequency distributions," in *Proceedings of IEEE Workshop on Statistical Signal and Array Processing*, 1992, pp. 444–447.

Fault Detection and Exclusion for INS/GPS/5G Tightly-Coupled Navigation

Mu Jia and Zaher M. Kassas
Department of Electrical and Computer Engineering
The Ohio State University, Columbus, OH, USA
jia.641@osu.edu, zkassas@ieee.org

***Abstract*—A solution separation-based fault detection and exclusion (FDE) framework is developed for GPS and 5G signal of opportunity (SOP) aided inertial navigation system (INS). The proposed framework fuses an inertial measurement unit (IMU) with GPS and 5G pseudorange measurements in a tightly-coupled fashion via an extended Kalman filter to estimate the ground vehicles' attitude, position, velocity, and clock errors. Solution separation tests are exploited to detect and exclude faults from GPS and 5G signals due to transmitter failures and local threats in urban environments (e.g., multipath). Experimental results are presented to evaluate the efficacy of the proposed framework under different sensor fusion scenarios. It is shown that fusing 5G signals enhances the FDE performance of the multi-sensor system in a suburban scenario: while INS/GPS fails to detect faulty GPS measurements, the INS/GPS/SOP is able to detect the fault. Moreover, over a trajectory of 1.91 km traversed in 200 s, using signals from two 5G gNBs, the INS/GPS/5G system achieved a position root-mean squared error (RMSE) of 0.81 m and maximum position error of 2.17 m. The undetected GPS fault in the INS/GPS system increased the RMSE and maximum position error to 1.83 m and 4.25 m, respectively.**

***Index Terms*—opportunistic navigation, RAIM, fault detection, solution separation, 5G.**

I. Introduction

The world is fast approaching an era of autonomous driving, which is powered by recent developments in artificial intelligence (AI), computing, communication as well high-precision navigation technologies. However, ensuring safety of the automated driving function is one of the most significant obstacles facing the development, commercialization, and adoption of fully-automated vehicles. Analysis of reported accidents that involved automated vehicles indicate that most of the wrong decisions from the self-driving system are triggered by failures in the positioning, navigation, and perception system [1].

Ground vehicle navigation systems utilize global navigation satellite system (GNSS) receivers and a suite of onboard sensors, e.g., lidar, camera, radar, inertial navigation system (INS), etc. GNSS receivers are relied upon to provide a navigation solution in a global frame and to correct for accumulating errors due to the bias and drift of sensor dead reckoning. While achieving higher levels of navigation accuracy has been a classic requirement, the trustworthiness in the navigation solution, commonly assessed by integrity measures, as well as the ability of fault detection and exclusion (FDE) is evermore vital in the safety-critical application of automated driving. To ensure safe navigation, automated vehicles need to instantaneously detect receiver and sensor failures and have the capability of excluding possible faults to maintain continuous high-integrity navigation.

Current GNSS technologies are insufficient to support the transition of ground vehicles to full automation in terms of accuracy, integrity, and availability [2]. While analysis indicates that driverless vehicles will need centimeter-level navigation accuracy on local and residential streets [3], single point positioning (SPP) can only achieve meter-level accuracy [4]. Integration of GNSS receivers with an INS improves the navigation solution by taking advantage of the short-term accuracy of the INS, coupled with the long-term stability of the GNSS solution. However, sub-meter-level accuracy is achievable with certain augmentation systems and real-time kinematic (RTK) only under certain favorable conditions [5]. In terms of integrity and availability, recent work demonstrated that in a sample downtown environment (Chicago urban corridor), availability of GPS-only positioning was less than 10% at most locations. While integration of multi-constellation GNSS, INS, wheel speed sensors, zero velocity updates, and vehicle kinematic constraint improved the availability significantly, it was still challenging to maintain availability after the vehicle traversed 4,500 m in an urban environment [6].

Recently, signals of opportunity (SOPs) [7]; e.g., cellular signals [8]–[11], digital television [12], and FM [13]; have been been demonstrated as an attractive alternative or supplement to GNSS signals. For vehicular navigation in urban environments [14]–[16], cellular SOPs are particularly attractive due to their inherent attributes: abundance, geometric and spectral diversity, high received power, and large bandwidth. With the fast deployment of fifth-generation (5G) cellular systems, their navigation capabilities have attracted extensive research efforts [17]–[22]. Recent literature exploited downlink 5G signals and showed favorable positioning accuracy [23], [24].

Integrity monitoring of multi-sensor integrated navigation has attracted research efforts during the last couple of decades [25]. Receiver autonomous integrity monitoring (RAIM), which was initially introduced in aviation, has been adapted to account for multi-constellation GNSS measurements [26]

This work was supported in part by the U.S. Department of Transportation (USDOT) under Grant 69A3552047138 for the CARMEN University Transportation Center (UTC) and in part by the National Science Foundation (NSF) under Grant 2240512.

(e.g., Galileo [27], GLONASS [28], and Beidou [29]), aiding sensors (e.g., INS-GPS [30], lidar-GNSS [31], vision-GPS [32], and multi-sensor collaborative [33]), and terrestrial SOPs [34]–[36]. As tightly-coupled GNSS/INS is widely adopted for vehicular navigation, different integrity monitoring frameworks have been proposed, e.g., extended RAIM [37], solution separation [38], residual-based method [39], and innovation-based method [40]. Initial studies to characterize the integrity monitoring improvement for automated driving, upon fusing GPS signals with terrestrial SOPs, was conducted in [41], [42]. However, the research on FDE for opportunistic navigation, especially for SOP-aided inertial navigation is rarely found in the literature. An extended Kalman filter (EKF)-based solution separation RAIM, which fuses sequential GNSS and SOP measurements was proposed in [43]. Nevertheless, a simple vehicle dynamics models was adopted and no fault exclusion results were presented. This paper extends the previous work by incorporating an INS and developing the FDE algorithm. To this end, a solution separation-based FDE framework is developed for INS/GPS/5G. Solution separation tests are exploited to detect and exclude faults from GPS and 5G signals due to transmitter failures and local threats in urban environments (e.g., multipath). Experimental results are presented to evaluate the efficacy of the proposed framework under different sensor fusion scenarios. It is shown that fusing 5G signals enhances the FDE performance of the multi-sensor system in a suburban scenario: while INS/GPS fails to detect faulty GPS measurements, the INS/GPS/SOP is able to detect the fault. Moreover, over a trajectory of 1.91 km traversed in 200 s, using signals from two 5G gNBs, the INS/GPS/5G system achieved a position root-mean squared error (RMSE) of 0.81 m and maximum position error of 2.17 m. The undetected GPS fault in the INS/GPS system increased the RMSE and maximum position error to 1.83 m and 4.25 m, respectively.

The rest of the paper is organized as follows. Section II introduces navigation models for GPS/SOP-aided INS. Section III describes the proposed integrity monitoring framework. Section IV presents the experiment results in a suburban environment and compares the FDE performance of different sensor fusion scenarios. Section V concludes the paper.

II. GPS/SOP-Aided Inertial Navigation

This section describes foundational models for the INS/GPS/SOP tightly coupled navigation framework, including the GPS and terrestrial SOP pseudorange measurement models, the aided INS states, the dynamics of the vehicle-mounted receiver and cellular SOP clocks, and the EKF-based navigation framework.

A. GPS Pseudorange Measurement Model

The ground vehicle is equipped with a receiver which makes pseudorange measurements to M GPS satellites. Let $\boldsymbol{z}^{\mathrm{G}}(k)$ denote the GPS measurement vector at time-step k defined as

$$\boldsymbol{z}^{\mathrm{G}}(k) = [z_1^{\mathrm{G}}(k), \ldots, z_m^{\mathrm{G}}(k), \ldots, z_M^{\mathrm{G}}(k)]^{\mathsf{T}},$$

where $z_m^{\mathrm{G}}(k)$ is the m-th GPS pseudorange measurement at time-step k, after compensating for ionospheric and tropospheric delays and satellite's clock bias, which is modeled as

$$z_m^{\mathrm{G}}(k) = \|\boldsymbol{r}_r(k) - \boldsymbol{r}_m^{\mathrm{G}}(k)\|_2 + c \cdot \delta t_r(k) + v_m^{\mathrm{G}}(k), \quad (1)$$

where $\boldsymbol{r}_r(k)$ and $\boldsymbol{r}_m^{\mathrm{G}}(k)$ are the receiver and m-th satellite's three-dimensional (3–D) position vectors, respectively; c is the speed of light; $\delta t_r(k)$ is the GPS receiver's clock bias; and v_m^{G} is the measurement noise, which is modeled as a zero-mean white Gaussian sequence with variance $(\sigma_m^{\mathrm{G}})^2(k)$.

B. Terrestrial SOP Pseudorange Measurement Model

The ground vehicle-mounted receiver also makes pseudorange measurements from N terrestrial SOPs, which are assumed to be stationary with known positions. Let $\boldsymbol{z}^{\mathrm{S}}(k)$ denote the SOP measurement vector at time-step k, defined as

$$\boldsymbol{z}^{\mathrm{S}}(k) = [z_1^{\mathrm{S}}(k), \ldots, z_n^{\mathrm{S}}(k), \ldots, z_N^{\mathrm{S}}(k)]^{\mathsf{T}},$$

where $z_n^{\mathrm{S}}(k)$ is the n-th SOP measurement at time-step k, which can be modeled as

$$z_n^{\mathrm{S}}(k) = \|\boldsymbol{r}_r(k) - \boldsymbol{r}_n^{\mathrm{S}}\|_2 + c \cdot [\delta t_r^{\mathrm{S}}(k) - \delta t_n^{\mathrm{S}}(k)] + v_n^{\mathrm{S}}(k), \quad (2)$$

where $\boldsymbol{r}_n^{\mathrm{S}}$ and $\delta t_n^{\mathrm{S}}(k)$ are the 3–D position and clock bias of the n-th SOP transmitter, respectively; $\delta t_r^{\mathrm{S}}(k)$ is the the receiver's clock bias (assumed to be different than the GPS receiver's clock bias $\delta t_r(k)$); and $v_n^{\mathrm{S}}(k)$ is the measurement noise, which is modeled as a zero-mean white Gaussian sequence with variance $(\sigma_n^{\mathrm{S}})^2(k)$.

C. Aided INS

The vehicle-mounted IMU produces 3–D angular velocity measurements $\boldsymbol{\omega}_{imu}(k)$ and specific force measurements $\boldsymbol{a}_{imu}$. An EKF is used to fuse IMU, GPS, and 5G SOP measurements [44]. The EKF state vector is defined as

$$\boldsymbol{x} \triangleq [{}_e^b\boldsymbol{q}^{\mathsf{T}}, \boldsymbol{r}_r^{\mathsf{T}}, \dot{\boldsymbol{r}}_r^{\mathsf{T}}, \boldsymbol{b}_{gyr}^{\mathsf{T}}, \boldsymbol{b}_{acc}^{\mathsf{T}}, \boldsymbol{x}_{\mathrm{clk},r}^{\mathsf{T}}, \boldsymbol{x}_{\mathrm{clk}}^{\mathrm{S}\ \mathsf{T}}]^{\mathsf{T}}, \quad (3)$$

where ${}_e^b\boldsymbol{q}$ is the 4–D unit quaternion, representing the vehicle's orientation, i.e., rotation from Earth-centered, Earth-fixed (ECEF) frame {e} to vehicle body frame {b}, $\dot{\boldsymbol{r}}_r$ is the vehicle's speed, $\boldsymbol{b}_{gyr}$ is the gyroscope's 3–D bias, $\boldsymbol{b}_{acc}$ is the accelerometer's 3–D bias, $\boldsymbol{x}_{\mathrm{clk},r} = [\delta t_r, \dot{\delta} t_r]^{\mathsf{T}}$ is the GPS receiver clock error state vector, with $\dot{\delta} t_r$ denoting the receiver clock drift; and $\boldsymbol{x}_{\mathrm{clk}}^{\mathrm{S}}$ captures the difference between the SOP receiver and each of the SOPs' transmitters clock errors.

The discrete-time dynamics of $\boldsymbol{x}_{\mathrm{clk},r}$ and $\boldsymbol{x}_{\mathrm{clk}}^{\mathrm{S}}$ is assumed to follow the standard double integrator model, driven by process noise [44].

The time-update of ${}_e^b\boldsymbol{q}$, $\boldsymbol{r}_r$, and $\dot{\boldsymbol{r}}_r$ are performed using ECEF strapdown mechanization equations with the gyroscope and accelerometer measurements [45]. The EKF measurement-update corrects the time-updated states $\hat{\boldsymbol{x}}(k+1|k)$ using available GPS and SOP pseudorange measurements. The EKF measurement-updated states $\hat{\boldsymbol{x}}(k+1|k+1)$ and associated estimation error covariance $\mathbf{P}(k+1|k+1)$ are computed using standard EKF update equations [44].

III. Solution Separation-Based RAIM with FDE

This section describes the solution separation-based RAIM for aided INS, which fuses measurements from IMU, GPS, and SOPs, to detect and exclude faults from GPS and SOP measurements. Note that the proposed frameworks assume no fault condition in IMU measurements.

A. Framework Overview

As shown in Fig. 1, the proposed aided INS RAIM framework extends the framework developed in [43] by incorporating INS and fault detection functionality. The integrity monitoring system utilizes a bank of filters, upon which solution separation tests are conducted to detect potential faults from the ranging measurement, while assuming the INS is faultless. When faults are detected, exclusions are tried to resume normal operation.

B. Solution Separation Test

The test statistics are chosen to be the difference between the position estimates from the main filter, $\hat{\boldsymbol{r}}^{(0)}(k|k)$, and the position estimates from the subfilters, $\hat{\boldsymbol{r}}^{(i)}(k|k)$ [43]. The test statistics vector can be expressed as

$$\boldsymbol{x}_{ss}^{(i)}(k) = \hat{\boldsymbol{r}}^{(0)}(k|k) - \hat{\boldsymbol{r}}^{(i)}(k|k), \qquad i = 1, \ldots, N_{ss}, \quad (4)$$

where N_{ss} is the number of subfilters, i.e., the number of faulted hypotheses to be monitored.

As shown in [46], the covariance of the i-th solution separation vector can be computed as

$$\boldsymbol{\Sigma}_{ss}^{(i)}(k) = \mathbf{P}^{(i)}(k|k) - \mathbf{P}^{(0)}(k|k). \quad (5)$$

This enables the framework to calculate $\boldsymbol{\Sigma}_{ss}^{(i)}$ without having the cross-correlation between the main filter and subfilters.

The test threshold for the i-th hypothesis in the q-th direction is set to meet a predefined probability of false alert P_{fa} under nominal conditions according to

$$T_{i,q} = Q^{-1}(\alpha_{i,q} P_{fa}) \sigma_{ss,q}^{(i)}, \quad (6)$$

where $Q^{-1}(\cdot)$ is the inverse Q-function, $\alpha_{i,q}$ is the allocation coefficients of the false alert budget to q direction of the i-th fault mode, and $\sigma_{ss,q}^{(i)}$ is the q-th diagonal element of $\boldsymbol{\Sigma}_{ss}^{(i)}$.

C. FDE and Filter Management

After each time-step, when the system receives new pseudorange measurements, the test statistics of all subsets on all three directions are compared with their corresponding test thresholds. The system will be determined as in normal operation if all the tests pass, i.e.,

$$x_{ss,q}^{(i)} < T_{i,q}, \qquad i = 1, \ldots, N_{ss}, q = 1, 2, 3. \quad (7)$$

Otherwise, if any of the above tests fails, the system is deemed as in faulty conditions and the fault exclusion algorithm tries to recover the system by excluding the measurements associated with the failed tests.

The fault exclusion algorithm consists of reconstructing the filters and recalculating the estimation solutions. For example, if any of the three tests for the i-th subset fails at time-step k_d, the subsets will be reconstructed based on the measurements excluding the ones associated with the i-th subset. The new subsets will be reinitialized based on the estimation solution from the main filter at time-step $k_d - k_{con}$, where k_{con} is a design parameter to allow the reconstructed subsets to converge. The reconstructed subsets will be propagated from time $k_d - k_{con}$ to the current time k_d. The purpos of the recalculation is twofold: (i) to rule out the possibility that the faulty measurements have contaminated the navigation solution before time-step k, and (ii) to recover the convergence of the reconstructed subfilter, so that the system can resume normal operation immediately, rather than waiting for future measurements until the filters converge. If the new subsets pass all the solution separation tests at time-step k_d, the system resume to normal operation with the remaining measurements after the exclusion. Otherwise, an alarm will be raised, as no possible exclusion is available. Algorithm 1 summarizes the FDE and filter management calcululations.

Algorithm 1 FDE and filter management

Input: N_{ss}, k, k_{con}, $\{\hat{\boldsymbol{x}}^{(0)}(j|j)\}_{j=1}^{k}$, $\{\mathbf{P}^{(0)}(j|j)\}_{j=1}^{k}$, $\{\hat{\boldsymbol{x}}^{(i)}(k|k)\}_{i=0}^{N_{ss}}$, $\{\mathbf{P}^{(i)}(k|k)\}_{i=0}^{N_{ss}}$, $\{\boldsymbol{z}(j)\}_{j=1}^{k}$, $\{\boldsymbol{\omega}_{imu}(j)\}_{j=1}^{k}$, $\{\boldsymbol{a}_{imu}(j)\}_{j=1}^{k}$

Output: $\{\hat{\boldsymbol{x}}^{(i)}(k|k)\}_{i=0}^{N_{ss}}$, $\{\mathbf{P}^{(i)}(k|k)\}_{i=0}^{N_{ss}}$

```
f ← 0
for i ∈ {1, ..., N_ss} do
    if any test (6) fails for x̂^(i)(k|k) then
        f ← i
        break
    end if
end for
if f ≠ 0 then
    {z_e(j)}_{j=1}^k ← {z(j)}_{j=1}^k excluding {z_f(j)}_{j=1}^k
    k_e ← k − k_con
    Reconstruct subsets at k_e
    Initialize {x̂_e^(i)(k_e|k_e)}_{i=0}^{N_ss−1}, {P_e^(i)(k_e|k_e)}_{i=0}^{N_ss−1} with corresponding element from x̂^(0)(k_e|k_e), P^(0)(k_e|k_e)
    Propagate filters to calculate {x̂_e^(i)(k|k)}_{i=0}^{N_ss−1}, {P_e^(i)(k|k)}_{i=0}^{N_ss−1}
    for i ∈ {1, ..., N_ss − 1} do
        if any test (6) fails for x̂_e^(i)(k|k) then
            Return Fault with no exclusion
        end if
    end for
    {x̂^(i)(k|k)}_{i=0}^{N_ss} ← {x̂_e^(i)(k|k)}_{i=0}^{N_ss−1}
    {P^(i)(k|k)}_{i=0}^{N_ss} ← {P_e^(i)(k|k)}_{i=0}^{N_ss−1}
    N_ss ← N_ss − 1
    return Fault with exclusion
else
    return No fault
end if
```

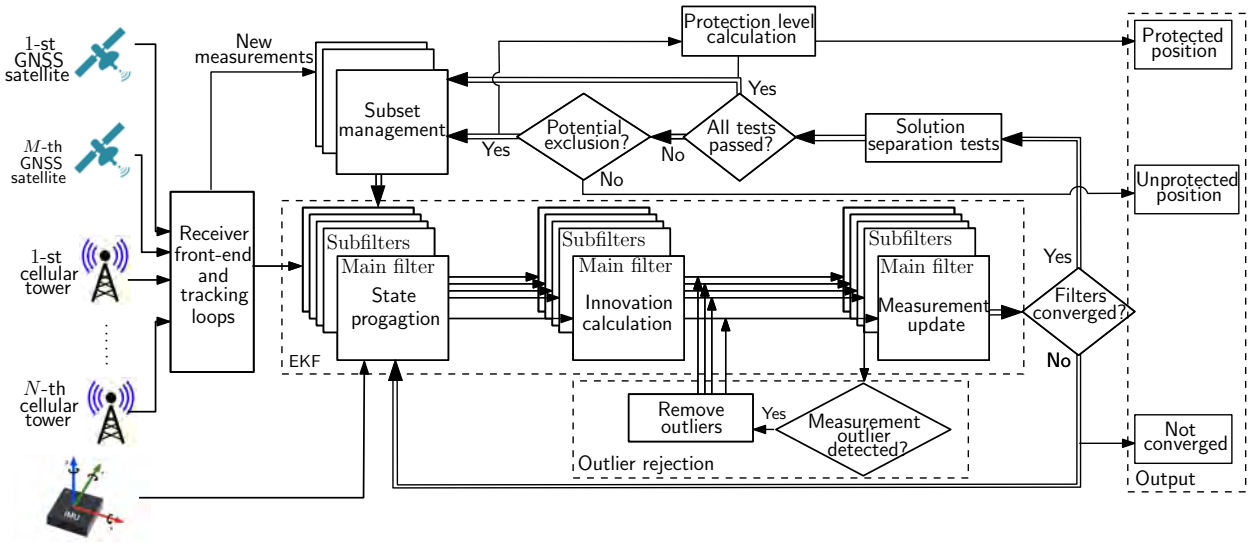

Fig. 1. Solution separation RAIM for INS/GPS/SOP tightly-coupled navigation.

IV. Experimental Results

To demonstrate the proposed FDE framework and evaluate its performance under different sensor fusion scenarios, i.e., INS/GPS and INS/GPS/SOP, an experiment was conducted with a ground vehicle navigating in a suburban environment while collecting measurements from the on-board IMU, GPS, and two 5G gNBs.

A. Experimental Setup and RAIM Parameters

The experiment was conducted in Costa Mesa, California, USA. Two consumer-grade cellular omnidirectional Laird antennas were connected to a quadchannel National Instrument (NI) universal software radio peripheral (USRP)-2955 which was mounted on a ground vehicle. Two channels of the USRP was set up to sample 5G signals, which were processed by a software-defined radio (SDR) receiver to produce SOP pseudorange measurements. The vehicle was also equipped with a Septentrio AsteRx-i V integrated GNSS-IMU system to produce an RTK-corrected navigation solution, which are used as ground truth in this experiment. The raw IMU measurements and GPS pseudoranges from the Septentrio GNSS-IMU system are fed into the proposed framework to produce an INS/GPS/5G navigation solution and support FDE.

During the experiment, the ground vehicle was able to track 9 GPS satellites and receive 5G signals from 2 ambient gNB towers. The experiment environment and 5G tower locations are shown in Fig. 2.

The integrity risk budget. i.e., probability of hazardous misleading information (PHMI), are set to be 10^{-4}/h. The probability of false alert is targeted at 10^{-3}/h. The probability of fault for both GPS and 5G towers is set to be 10^{-2}/h and the time of influence for each fault is set to be 120 s . Considering the measurement rate in this experiment is 5 Hz yields RAIM parameters in the notation of per point as shown in Table I.

TABLE I
RAIM Parameters

Parameter	Definition	Value
$\{\sigma^{\text{GPS}}_{\text{URA},m}\}_{m=1}^{M}$	User Range Error for GPS	5 m
$\{\sigma^{\text{S}}_{\text{URA,n}}\}_{n=1}^{N}$	User Range Error for SOP	5.48 m
$PHMI_{\text{HOR}}$	Integrity budget for the horizontal component	1.1×10^{-9}
$PHMI_{\text{VERT}}$	Integrity budget for the vertical component	1.1^{-11}
$P_{\text{fa,HOR}}$	Continuity budget allocated to the vertical component	5.6×10^{-8}
$P_{\text{fa,VERT}}$	Continuity budget allocated to the vertical component	5.6×10^{-10}
$\{P_{\text{GPS}_m}\}_{m=1}^{M}$	Probability of a single GPS satellite fault	5.6×10^{-7}
$\{P_{\text{SOP}_n}\}_{n=1}^{N}$	Probability of a single SOP fault	5.6×10^{-7}

B. Experimental Results

Since the experiment was conducted in a suburban environment, which was not as challenging for GPS and 5G signals, and the GPS and 5G pseudorange measurements were produced by advanced receivers, no faults appeared in the pseudoranges. To mimic GPS faults, it was hypothesized that the ionospheric and troposhperic errors for the GPS satellite with PRN 7 were not properly corrected, which caused ranging errors with an average magnitude of 4.57 m.

The ground vehicle traversed a trajectory of 1.91 km in 200 seconds. The proposed framework was first implemented by fusing INS and GPS measurements. As shown in Fig. 3, the test statistic of INS/GPS did not surpass the test threshold, which indicates that the system failed to detect the hypothesized fault in the GPS satellite. However, in the case where two 5G towers were fused, the test statistic increased and test threshold decreased to a level that the system could detect the GPS fault.

Fig. 2. Experiment layout, ground-truth trajectory (green), and navigation solutions with hypothesized fault GPS measurements: INS/GPS (blue) and INS/GPS/5G (red).

After the fault got excluded by the FDE algorithm described in Section III-C, the INS/GPS/5G achieved a position RMSE of 0.81 m and maximum position error of 2.17 m. The undetected GPS fault increased the RMSE and maximum position error to 1.83 m and 4.25 m, respectively, as summarized in Table II.

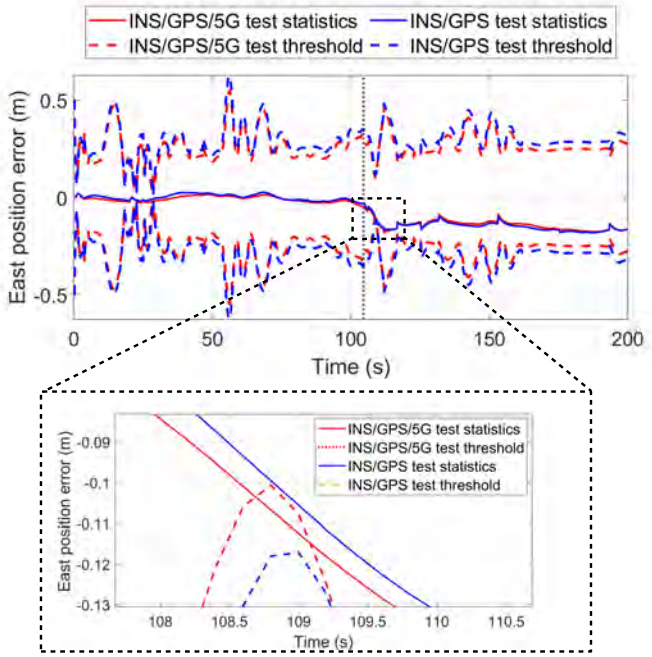

Fig. 3. Test statistics (solid) and test thresholds (dashed) for INS/GPS (blue) and INS/GPS/5G (red)

TABLE II
PERFORMANCE COMPARISON BETWEEN INS/GPS AND INS/GPS/5G

	INS/GPS	**INS/GPS/SOP**
RMSE (m)	1.8309	0.8116
Maximum error (m)	4.2505	2.1686

V. CONCLUSION

This paper developed a solution separation-based RAIM framework for INS/GPS/SOP tightly-coupled navigation systems. This framework conducts solution separation tests to instantaneously detect and exclude ranging measurement faults from GPS and SOP. The FDE performance of the proposed framework was validated experimentally, where 5G signals were exploited to improve FDE over fusing INS only with GPS signals. It was shown that fusing 5G enables the system to detect a fault from GPS satellites, which fusing only INS and GPS fails to detect. With the faulty measurements detected and excluded, INS/GPS/5G achieved a position RMSE of 0.81 m, while INS/GPS yielded a RMSE of 1.83 m. The FDE also reduced the maximum error from 4.25 m to 2.17 m.

ACKNOWLEDGMENT

The authors would like to thank Ali Abdallah for his help with data collection and processing.

REFERENCES

[1] H. Jing, Y. Gao, S. Shahbeigi, and M. Dianati, "Integrity monitoring of GNSS/INS based positioning systems for autonomous vehicles: State-of-the-art and open challenges," *IEEE Transactions on Intelligent Transportation Systems*, vol. 23, no. 9, pp. 14 166–14 187, 2022.

[2] N. Zhu, D. Betaille, J. Marais, and M. Berbineau, "GNSS integrity monitoring schemes for terrestrial applications in harsh signal environments," *IEEE Intelligent Transportation Systems Magazine*, vol. 12, no. 3, pp. 81–91, 2020.

[3] T. Reid, S. Houts, R. Cammarata, G. Mills, S. Agarwal, A. Vora, and G. Pandey, "Localization requirements for autonomous vehicles," *SAE International Journal of Connected and Automated Vehicles*, vol. 2, no. 3, pp. 173–190, September 2019.

[4] D. Imparato, A. El-Mowafy, and C. Rizos, "Integrity monitoring: From airborne to land applications," in *Multifunctional Operation and Application of GPS*. IntechOpen, 2018, pp. 23–43.

[5] T. Humphreys, M. Murrian, and L. Narula, "Deep-urban unaided precise global navigation satellite system vehicle positioning," *IEEE Intelligent Transportation Systems Magazine*, vol. 12, no. 3, pp. 109–122, 2020.

[6] K. Nagai, M. Spenko, R. Henderson, and B. Pervan, "Fault-free integrity and continuity for driverless urban vehicle navigation with multi-sensor integration: A case study in downtown Chicago," in *Proceedings of ION GNSS+ Conference*, September 2022, pp. 1350–1365.

[7] N. Souli, P. Kolios, and G. Ellinas, "Relative positioning of autonomous systems using signals of opportunity," in *Proceedings of IEEE Vehicular Technology Conference*, 2020, pp. 1–6.

[8] H. Dun, C. Tiberius, and G. Janssen, "Positioning in a multipath channel using OFDM signals with carrier phase tracking," *IEEE Access*, vol. 8, pp. 13 011–13 028, 2020.

[9] M. Pan, P. Liu, S. Liu, W. Qi, Y. Huang, X. You, X. Jia, and X. Li, "Efficient joint DOA and TOA estimation for indoor positioning with 5G picocell base stations," *IEEE Transactions on Instrumentation and Measurement*, vol. 71, pp. 1–19, 2022.

[10] Y. Wang, H. Zhu, T. Liang, and J. Qian, "Signals of opportunity navigation using LTE downlink signals," in *Proceedings of IEEE International Conference on Communication Technology*, September 2022, pp. 1070–1074.

[11] C. Jao, A. Abdallah, C. Chen, M. Seo, S. Kia, Z. Kassas, and A. Shkel, "PINDOC: Pedestrian indoor navigation system integrating deterministic, opportunistic, and cooperative functionalities," *IEEE Sensors Journal*, vol. 22, no. 14, pp. 14 424–14 435, July 2022.

[12] Z. Jiao, L. Chen, X. Lu, Z. Liu, X. Zhou, Y. Zhuang, and G. Guo, "Carrier phase ranging with DTMB signals for urban pedestrian localization and GNSS aiding," *Remote Sensing*, vol. 15, no. 2, pp. 423–446, 2023.

[13] X. Chen, Q. Wei, F. Wang, Z. Jun, S. Wu, and A. Men, "Super-resolution time of arrival estimation for a symbiotic FM radio data system," *IEEE Transactions on Broadcasting*, vol. 66, no. 4, pp. 847–856, December 2020.

[14] K. Strandjord, Y. Morton, and P. Wang, "Evaluating the urban signal environment for GNSS and LTE signals," in *Proceedings of ION GNSS+ Conference*, 2021, pp. 2166–2182.

[15] A. Abdallah and Z. Kassas, "Opportunistic navigation using sub-6 GHz 5G downlink signals: A case study on a ground vehicle," in *Proceedings of European Conference on Antennas and Propagation*, 2022, pp. 1–5.

[16] R. Whiton, J. Chen, T. Johansson, and F. Tufvesson, "Urban navigation with LTE using a large antenna array and machine learning," in *Proceedings of IEEE Vehicular Technology Conference*, 2022, pp. 1–5.

[17] C. Olone, H. Dhillon, and R. Buehrer, "Single-anchor localizability in 5G millimeter wave networks," *IEEE Wireless Communications Letters*, vol. 9, no. 1, pp. 65–69, 2020.

[18] A. Xhafa, J. del Peral-Rosado, J. López-Salcedo, and G. Seco-Granados, "Evaluation of 5G positioning performance based on UTDoA, AoA and base-station selective exclusion," *Sensors*, vol. 22, no. 1, pp. 101–118, 2021.

[19] A. Abdallah, J. Khalife, and Z. Kassas, "Experimental characterization of received 5G signals carrier-to-noise ratio in indoor and urban environments," in *Proceedings of IEEE Vehicular Technology Conference*, April 2021, pp. 1–5.

[20] I. Lapin, G. Granados, J. Samson, O. Renaudin, F. Zanier, and L. Ries, "STARE: Real-time software receiver for LTE and 5G NR positioning and signal monitoring," in *Proceedings of Workshop on Satellite Navigation Technology*, April 2022, pp. 1–11.

[21] J. del Peral-Rosado, P. Nolle, F. Rothmaier, S. Razavi, G. Lindmark, X. Jiang, D. Shrestha, F. Gunnarsson, S. Parsawar, R. Mundlamuri, F. Kaltenberger, N. Sirola, O. Sarkka, U. Noman, J. Rostrom, K. Vaarala, P. Miettinen, S. Garlaschi, L. Canzian, H. Babaroglu, E. Rastorgueva-Foi, M. Turunen, J. Talvitie, and D. Flachs, "Proof-of-concept of dedicated aerial 5G and GNSS testbed for enhanced hybrid positioning," in *Proceedings of ION GNSS Conference*, September 2022, pp. 2362–2376.

[22] C. Jin, W. Tay, K. Zhao, K. V. Ling, and K. Sin, "A 5G/GNSS integrated positioning method," in *Proceedings of ION GNSS Conference*, September 2022, pp. 2429–2443.

[23] A. Abdallah and Z. Kassas, "UAV navigation with 5G carrier phase measurements," in *Proceedings of ION GNSS Conference*, September 2021, pp. 3294–3306.

[24] Z. Liu, L. Chen, X. Zhou, Z. Jiao, G. Guo, and R. Chen, "Machine learning for time-of-arrival estimation with 5G signals in indoor positioning," *IEEE Internet of Things Journal*, 2023, accepted.

[25] N. Zhu, J. Marais, D. Betaille, and M. Berbineau, "GNSS position integrity in urban environments: A review of literature," *IEEE Transactions on Intelligent Transportation Systems*, vol. 19, no. 9, pp. 2762–2778, September 2018.

[26] J. Blanch, T. Walter, P. Enge, S. Wallner, F. Amarillo Fernandez, R. Dellago, R. Ioannides, I. Fernandez Hernandez, B. Belabbas, A. Spletter *et al.*, "Critical elements for a multi-constellation advanced RAIM," *NAVIGATION, Journal of the Institute of Navigation*, vol. 60, no. 1, pp. 53–69, 2013.

[27] A. Ene, J. Blanch, and T. Walter, "Galileo-GPS RAIM for vertical guidance," in *Proceedings of National Technical Meeting of The Institute of Navigation*, January 2006, pp. 18–20.

[28] T. Walter, J. Blanch, M. J. Choi, T. Reid, and P. Enge, "Incorporating GLONASS into aviation RAIM receivers," in *Proceedings of International Technical Meeting of the Institute of Navigation*, January 2013, pp. 239–249.

[29] Y. Liu, J. Zhang, R. Xue, and Z. Wang, "Performance analysis of advanced RAIM with the inclusion of BeiDou," in *Proceedings of ION International Technical Meeting*, 2014, pp. 3629–3636.

[30] P. Roysdon and J. Farrell, "GPS-INS outlier detection and elimination using a sliding window filter," in *Proceedings of American Control Conference*, May 2017, pp. 1244–1249.

[31] T. Li, L. Pei, Y. Xiang, Q. Wu, S. Xia, L. Tao, X. Guan, and W. Yu, "P3-LOAM: PPP/LiDAR loosely coupled SLAM with accurate covariance estimation and robust RAIM in urban canyon environment," *IEEE Sensors Journal*, vol. 21, no. 5, pp. 6660–6671, 2021.

[32] L. Fu, J. Zhang, R. Li, X. Cao, and J. Wang, "Vision-aided RAIM: A new method for GPS integrity monitoring in approach and landing phase," *Sensors*, vol. 15, no. 9, pp. 22 854–22 873, 2015.

[33] J. Xiong, J. Cheong, A. Dempster, and Z. Xiong, "An integrity monitoring method for multi-sensor collaborative navigation," in *Proceedings of IEEE/ION Position, Location, and Navigation Symposium*, April 2020, pp. 461–468.

[34] M. Maaref and Z. Kassas, "Measurement characterization and autonomous outlier detection and exclusion for ground vehicle navigation with cellular signals," *IEEE Transactions on Intelligent Vehicles*, vol. 5, no. 4, pp. 670–683, December 2020.

[35] M. Maaref and Z. Kassas, "Autonomous integrity monitoring for vehicular navigation with cellular signals of opportunity and an IMU," *IEEE Transactions on Intelligent Transportation Systems*, vol. 23, no. 6, pp. 5586–5601, June 2022.

[36] J. Khalife, M. Maaref, and Z. Kassas, "Opportunistic autonomous integrity monitoring for enhanced UAV safety," *IEEE Aerospace and Electronics Systems Magazine*, 2022, accepted.

[37] S. Hewitson and J. Wang, "Extended receiver autonomous integrity monitoring (eRAIM) for GNSS/INS integration," *Journal of Surveying Engineering*, vol. 136, no. 1, pp. 13–22, 2010.

[38] J. Blanch, T. Walter, L. Norman, K. Gunning, and L. de Groot, "Solution separation-based fd to mitigate the effects of local threats on ppp integrity," in *Proceedings of IEEE/ION Position, Location and Navigation Symposium*, April 2020, pp. 1085–1092.

[39] O. O. Crespillo, A. Grosch, J. Skaloud, and M. Meurer, "Innovation vs residual kf based GNSS/INS autonomous integrity monitoring in single fault scenario," in *Proceedings of ION GNSS+ Conference*, September 2017, pp. 2126–2136.

[40] C. Tanil, S. Khanafseh, M. Joerger, and B. Pervan, "Probabilistic data association techniques for target tracking with applications to sonar, radar and EO sensors," *IEEE Aerospace and Electronic Systems Magazine*, vol. 54, no. 1, pp. 131–143, 2018.

[41] M. Maaref, J. Khalife, and Z. Kassas, "Enhanced safety of autonomous driving by incorporating terrestrial signals of opportunity," in *Proceedings of IEEE International Conference on Acoustics, Speech and Signal Processing*, May 2020, pp. 9185–9189.

[42] M. Jia, J. Khalife, and Z. Kassas, "Evaluation of ground vehicle protection level reduction due to fusing GPS with faulty terrestrial signals of opportunity," in *Proceedings of ION International Technical Meeting*, January 2021, pp. 354–365.

[43] M. Jia and M. Kassas, "Kalman filter-based integrity monitoring for GNSS and 5G signals of opportunity integrated navigation," in *Proceedings of IFAC on Advances in Automotive Control*, vol. 55, August 2022, pp. 273–278.

[44] J. Morales and Z. Kassas, "Tightly-coupled inertial navigation system with signals of opportunity aiding," *IEEE Transactions on Aerospace and Electronic Systems*, vol. 57, no. 3, pp. 1930–1948, 2021.

[45] P. Groves, *Principles of GNSS, Inertial, and Multisensor Integrated Navigation Systems*, 2nd ed. Artech House, 2013.

[46] R. Young and G. McGraw, "Fault detection and exclusion using normalized solution separation and residual monitoring methods," *NAVIGATION, Journal of the Institute of Navigation*, vol. 50, no. 3, pp. 151–169, 2003.

Flight Demonstration of High Altitude Aircraft Navigation With Cellular Signals

IMAGE LICENSED BY INGRAM PUBLISHING

Zaher (Zak) M. Kassas*
Is with the Department of Electrical and Computer Engineering, The Ohio State University, Columbus, OH 43210 USA.
E-mail: zkassas@ieee.org

Joe Khalife and Ali A. Abdallah
Were with the Autonomous Systems Perception, Intelligence, and Navigation Laboratory, University of California, Irvine CA 92697 USA.
E-mail: khalifej@uci.edu; abdalla2@uci.edu

Digital Object Identifier 10.1109/MITS.2023.3236890
Date of current version: 9 May 2023

*Corresponding author

Authorized licensed use limited to: The Ohio State University. Downloaded on October 13,2023 at 15:30:15 UTC from IEEE Xplore. Restrictions apply.

1939-1390/23©2023IEEE

Chiawei Lee, Juan Jurado, Steven Wachtel, Jacob Duede, Zachary Hoeffner, Thomas Hulsey, and Rachel Quirarte

Are with the Test Pilot School, U.S. Air Force, Edwards Air Force Base, Edwards, CA 93524 USA. E-mail: chiawei.lee@us.af.m; jdjurado@icloud.com; steven.wachtel.1@us.af.mil; jacob.duede@us.af.mil; zachary.hoeffner.1@us.af.mil; thomas.hulsey.2@us.af.mil; rachel.quirarte@us.af.mil

RunXuan Tay

Is with the Air Warfare Center, Republic of Singapore Air Force, Singapore. E-mail: rxtay@outlook.com

Abstract—This article presents the first demonstration of navigation with cellular signals of opportunity (SOPs) on a high-altitude aircraft. An extensive flight campaign was conducted by the Autonomous Systems Perception, Intelligence, and Navigation Laboratory in collaboration with the U.S. Air Force to sample ambient downlink cellular SOPs in different regions in Southern California, USA. Carrier phase measurements were produced from these signals, which were subsequently fused in an extended Kalman filter along with altimeter measurements to estimate the aircraft's state (position, velocity, and time). Three flights are performed in three different regions: 1) rural, 2) semiurban, and 3) urban. A multitude of flight trajectories and altitudes above ground level (AGL) was exercised in the three flights: 1) a 51-km trajectory of grid maneuvers with banking and straight segments at about 5,000 ft AGL, 2) a 57-km trajectory of a teardrop descent from 7,000 ft AGL down to touchdown at the runway, and 3) a 55-km trajectory of a holding pattern at about 15,000 ft AGL. The estimated aircraft trajectory is computed for each flight and compared with the trajectory from the aircraft's onboard navigation system, which utilized a GPS receiver coupled with an inertial navigation system and an altimeter. The cellular SOPs produced remarkable sustained navigation accuracy over the entire flight trajectories in all three flights, achieving a 3D position root mean-squared error of 10.53 m, 4.96 m, and 15.44 m, respectively.

Introduction

A quick search of the phrase "Global Positioning System (GPS)" on the Aviation Safety Reporting System (ASRS) returns 579 navigation-related incidents since January 2000. The ASRS is a publicly available reporting system established by NASA to identify and address issues reported by frontline personnel in the aviation system [1]. A deeper look at the data reveals that, out of these 579 incidents, a malfunction or failure was detected in navigation sensors with the following occurrences: 508 in "GPS & Other Satellite Navigation," 34 in "Navigational Equipment and Processing," 14 in "Flight Dynamics Navigation and Safety," 12 in "Altimeter," and 6 in "Positional/Directional Sensing." Among these incidents, 100 are suspected to be due to GPS jamming and interference, leading to the loss of the main and auxiliary GPS units in some cases. What is alarming is the increasing trend of GPS interference—the majority of the aforementioned incidents took place since 2019. What is more, previously undisclosed U.S. Federal Aviation Administration data for a few months in 2017 and 2018 detail hundreds of aircraft losing GPS reception. On a single day in March 2018, 21 aircraft reported GPS problems to air traffic controllers near Los Angeles, CA, USA [2]. These and other incidents uncover the vulnerabilities of existing aircraft navigation systems, which are highly dependent on global navigation satellite system (GNSS) signals and their augmentation systems (e.g., ground-based augmentation systems and space-based augmentation systems) [3], [4]. There is an urgent need for complementary robust and accurate navigation systems to ensure aviation safety.

In 2019, the International Civil Aviation Organization issued a working paper titled "An Urgent Need to Address Harmful Interferences to GNSS," where it concluded that harmful radio-frequency (RF) interference to GNSS signals would prevent the full continuation of safety and efficiency benefits of GNSS-based services. Moreover, there was a call for supporting multidisciplinary development of alternative positioning, navigation, and timing strategy and solutions to complement the use of GNSS in aviation [5]. In 2021, the U.S. Department of Transportation released the "Complementary Positioning, Navigation, and Timing (PNT) and GPS Backup Technologies Demonstration Report" to Congress. The report concluded that, while there are suitable, mature, and commercially available technologies to back up or complement GPS, none of these systems alone can universally back up the PNT capabilities provided by GPS and its augmentations, necessitating a diverse universe of PNT technologies [6]. Moreover, in 2021, the National Institute of Standards and Technology issued a report on "Foundational PNT Profile: Applying the

Authorized licensed use limited to: The Ohio State University. Downloaded on October 13,2023 at 15:30:15 UTC from IEEE Xplore. Restrictions apply.

The cellular SOPs produced remarkable navigation accuracy in all three flights, achieving a position RMSE of 10.53 m, 4.96 m, and 15.44 m, respectively.

Cybersecurity Framework for the Responsible Use of PNT Services," where it identified signals of opportunity (SOPs) and terrestrial RF sources (e.g., cellular) as a mitigation category that applies to the PNT profile [7].

Among terrestrial RF SOPs, cellular signals have shown tremendous potential as an alternative PNT source [8] because of their inherently desirable attributes:

- *Abundance*: Cellular base stations are abundant in most locales, with the number of base stations slated to increase dramatically with future cellular generations.
- *Geometric diversity*: Cellular base stations are placed in favorable geometric configurations by construction of the cellular infrastructure.
- *Frequency diversity*: In contrast to GNSS signals, cellular signals are transmitted at a wide range of frequencies, which makes them more difficult to be simultaneously jammed or spoofed.
- *High received power*: The received cellular carrier-to-noise ratio (CNR) is commonly tens of decibels higher than that of GNSS signals, even in deep urban canyons and indoor environments [9].
- *High bandwidth*: Downlink cellular signals can be up to 20 MHz [in 4G long-term evolution (LTE)] and even higher in future generations, which yields precise time-of-arrival estimates.
- *Free to use*: The cellular infrastructure is already operational; thus, with specialized receivers, navigation observables (pseudorange, carrier phase, and Doppler) can be extracted from the "always-on" transmitted signals.

Recent results have shown the ability of cellular SOPs to yield meter-level-accurate navigation on ground vehicles [10], [11] in urban environments and submeter-level-accurate navigation on unmanned aerial vehicles (UAVs) [12], [13]. Moreover, the robustness and availability of cellular SOPs have been demonstrated in a GPS-jammed environment [14].

Assessing cellular signals for aerial vehicles has been the subject of several studies recently [15]. These studies span radio channel modeling [16], [17]; evaluation of signal quality in terms of received signal power [18], [19], interference from cellular transmitters [20], [21], [22], and coverage and connectivity [23], [24], [25]; and standards recommendations [26], [27]. However, the majority of these studies focused on evaluating cellular signals for communication purposes with little attention to evaluating them for navigation purposes [28]. Moreover, they considered UAVs flying at low altitudes (up to 500 ft) and slow speeds (up to 50 km/h). A recent study revealed that cellular signals can be acquired and tracked at altitudes as high as 23,000 ft above ground level (AGL) and at horizontal distances of more than 100 km from cellular transmitters [29]. However, the potential of cellular SOPs for high-altitude aircraft navigation has not been thoroughly assessed. This article aims to perform the first assessment of cellular SOPs for aircraft navigation by addressing the following question: Can cellular SOPs be received and exploited at aircraft altitudes to produce a robust navigation solution?

To answer this question, an *unprecedented* aerial flight campaign was conducted in March 2020 by the Autonomous Systems Perception, Intelligence, and Navigation (ASPIN) Laboratory in collaboration with the U.S. Air Force (USAF) at the Edwards Air Force Base (AFB), CA, USA. The cellular software-defined radios (SDRs) of the ASPIN Laboratory were flown over on a USAF Beechcraft C-12 Huron, a fixed-wing aircraft, to collect ambient cellular signals. This unique dataset consists of combinations of flight runs over three different environments (rural, semiurban, and urban) with altitudes ranging up to 23,000 feet and a multitude of trajectories and maneuvers, including straight segments, banking turns, holding patterns, and ascending and descending teardrops performed by members of the USAF Test Pilot School. During these large-scale experiments, terabytes of samples of 3G code-division multiple access (CDMA) and 4G LTE signals were recorded under various conditions.

This article provides the first extensive demonstrations of their kind of utilizing cellular SOPs for navigation purposes on high-altitude aircraft. The aim of these demonstrations is to show that, should GNSS signals become unavailable or unreliable mid-flight, cellular SOPs could be used to produce a sustained and accurate navigation solution over trajectories spanning tens of kilometers.

To demonstrate the feasibility of aircraft navigation with cellular SOPs, three flights are performed in three different regions: 1) rural, 2) semiurban, and 3) urban. A multitude of flight trajectories and altitudes AGL was exercised in the three flights: 1) a 51-km trajectory of grid maneuvers with banking and straight segments at about 5,000 ft AGL, 2) a 57-km trajectory of a teardrop descent from 7,000 ft AGL down to touchdown at the runway, and 3) a 55-km trajectory of a holding pattern at about 15,000 ft AGL.

The aircraft's trajectory is estimated for each flight exclusively from cellular SOPs using an extended Kalman filter (EKF). The estimated aircraft trajectory is compared with the aircraft's onboard navigation system, which used a GPS-aided inertial navigation system (INS) and an

Authorized licensed use limited to: The Ohio State University. Downloaded on October 13,2023 at 15:30:15 UTC from IEEE Xplore. Restrictions apply.

altimeter. The cellular SOPs produced remarkable navigation accuracy in all three flights, achieving a position root mean-squared error (RMSE) of 10.53 m, 4.96 m, and 15.44 m, respectively.

The rest of this article is organized as follows. The "Model Description" section describes the aircraft dynamics and cellular SOP measurement model. The "Navigation Framework" section formulates the EKF navigation framework. The "Experimental Setup and Flight Regions" section describes the experimental setup with which the aircraft was equipped and overviews the environments in which the flight campaigns took place. The "Aerial Navigation Results" section presents experimental aircraft navigation results exclusively with cellular signals. The "Conclusion" section gives concluding remarks.

ASPIN Laboratory's SDR, called the *Multichannel Adaptive Transceiver Information Extractor*, produces several types of navigation observables.

Model Description

This section describes the aircraft dynamics and cellular SOP measurement models used in the rest of the article.

Aircraft Dynamics Model

Depending on the aircraft's motion and sensor suite, different dynamic models can be used to describe its dynamics. The goal of this article is to assess the minimum performance of aircraft navigation with cellular SOPs exclusively. As such, a simple, yet effective continuous Wiener process acceleration model is employed, which upon discretization at a constant sampling interval T, is given by

$$\boldsymbol{x}_{\text{pva}}(k+1) = \mathbf{F}_{\text{pva}}\boldsymbol{x}_r(k) + \boldsymbol{w}_{\text{pva}}(k), \quad k = 0, 1, 2, \ldots$$
$$\mathbf{F}_{\text{pva}} = \begin{bmatrix} \mathbf{I}_{3\times3} & T\mathbf{I}_{3\times3} & \frac{T^2}{2}\mathbf{I}_{3\times3} \\ \mathbf{0}_{3\times3} & \mathbf{I}_{3\times3} & T\mathbf{I}_{3\times3} \\ \mathbf{0}_{3\times3} & \mathbf{0}_{3\times3} & \mathbf{I}_{3\times3} \end{bmatrix} \tag{1}$$

where $\boldsymbol{x}_{\text{pva}} \triangleq [\boldsymbol{r}_r^\intercal, \dot{\boldsymbol{r}}_r^\intercal, \ddot{\boldsymbol{r}}_r^\intercal]^\intercal$, $\boldsymbol{r}_r \triangleq [x_r, y_r, z_r]^\intercal$ is the 3D position of the aircraft expressed in a North-East-Down (NED) frame, and $\boldsymbol{w}_{\text{pva}}$ is a discrete-time zero-mean white noise sequence with covariance $\mathbf{Q}_{\text{pva}}$ given by

$$\mathbf{Q}_{\text{pva}} = \begin{bmatrix} \frac{T^5}{20} & \frac{T^4}{8} & \frac{T^3}{6} \\ \frac{T^4}{8} & \frac{T^3}{3} & \frac{T^2}{2} \\ \frac{T^3}{6} & \frac{T^2}{2} & T \end{bmatrix} \otimes \tilde{\mathbf{S}}_{\text{NED}}$$

where $\otimes$ denotes the Kronecker product, and $\tilde{\mathbf{S}}_{\text{NED}} \triangleq \text{diag}[\tilde{q}_N, \tilde{q}_E, \tilde{q}_D]$, where $\tilde{q}_N$, $\tilde{q}_E$, and $\tilde{q}_D$ are the NED jerk continuous-time noise power spectra, respectively. It should be noted that more complicated dynamic models can be used to describe the aircraft's dynamics, e.g., Singer acceleration, mean-adaptive acceleration, circular motion, curvilinear motion, and coordinated turn, among others [30]. Of course, if an INS is available, its measurements can be used to describe the aircraft's motion, while the INS is aided with cellular SOPs [31].

Clock Error Dynamics Model

Wireless standards require cellular base stations to be synchronized to within a few microseconds, which is order of magnitudes higher than the nanosecond requirements in GNSS. As such, the base station clock errors, which are dynamic and stochastic, must be accounted for in the navigation filter when navigating with cellular SOPs. A typical model for the dynamics of the clock error states is the so-called *two-state model*, composed of the clock bias δt and clock drift $\dot{\delta t}$, given by

$$\boldsymbol{x}_{\text{clk}}(k+1) = \mathbf{F}_{\text{clk}}\boldsymbol{x}_{\text{clk}}(k) + \boldsymbol{w}_{\text{clk}}(k) \tag{2}$$

where $\boldsymbol{w}_{\text{clk}}$ is a discrete-time zero-mean white noise sequence with covariance $\mathbf{Q}_{\text{clk}}$, and

$$\mathbf{F}_{\text{clk}} = \begin{bmatrix} 1 & T \\ 0 & 1 \end{bmatrix}, \quad \mathbf{Q}_{\text{clk}} = \begin{bmatrix} S_{\tilde{w}_{\delta t}} T + S_{\tilde{w}_{\dot{\delta t}}} \frac{T^3}{3} & S_{\tilde{w}_{\dot{\delta t}}} \frac{T^2}{2} \\ S_{\tilde{w}_{\dot{\delta t}}} \frac{T^2}{2} & S_{\tilde{w}_{\dot{\delta t}}} T \end{bmatrix}. \tag{3}$$

The power spectra $S_{\tilde{w}_{\delta t}}$ and $S_{\tilde{w}_{\dot{\delta t}}}$ are determined by the quality of the oscillator from which the clock signal is derived [32].

SOP Measurement Model

ASPIN Laboratory's SDR, called the *Multichannel Adaptive Transceiver Information Extractor* (*MATRIX*), produces several types of navigation observables. To get the highest possible precision, carrier phase observables are exploited for navigation, which after some manipulations can be modeled as [14]

$$z_n(k) = \| \boldsymbol{r}_r(k) - \boldsymbol{r}_{s_n} \|_2 + c\delta t_n(k) + v_n(k), \quad n = 1, 2, \ldots, N \tag{4}$$

where $\boldsymbol{r}_{s_n}$ is the nth cellular base station's 3D position vector; c is the speed of light; δt_n is the overall clock error in the nth carrier phase measurement, which combines the effect of receiver and base station clock biases and the initial carrier phase ambiguity; N is the total number of available base

Authorized licensed use limited to: The Ohio State University. Downloaded on October 13,2023 at 15:30:15 UTC from IEEE Xplore. Restrictions apply.

stations; and $v_n(k)$ is the measurement noise, which is modeled as a discrete-time zero-mean white Gaussian sequence with variance $\sigma_n^2(k)$. The measurement noise variance can be modeled as a function of the CNR [33], [34].

Altimeter Measurement Model

Since cellular base stations appear to have similar altitudes for a high-flying aircraft, their vertical dilution of precision (VDOP) will be very large. To circumvent this issue, the altimeter data z_{alt} derived from the aircraft's onboard navigation system is used in addition to the cellular carrier phase measurements in the measurement-update step in the EKF.

Navigation Framework

This section formulates the EKF navigation framework based on the models presented in the "Model Description" section.

EKF Model

Let $\boldsymbol{x} \triangleq [\boldsymbol{x}_{\text{pv}}^{\mathsf{T}}, \boldsymbol{x}_{\text{clk}_1}^{\mathsf{T}}, \ldots, \boldsymbol{x}_{\text{clk}_N}^{\mathsf{T}}]^{\mathsf{T}}$ denote the state to be estimated, where $\boldsymbol{x}_{\text{clk}_n} \triangleq [c\delta t_n, c\dot{\delta} t_n]^{\mathsf{T}}$. Using (1) and (2), one can write the dynamics of $\boldsymbol{x}$ as

$$\boldsymbol{x}(k+1) = \mathbf{F}\boldsymbol{x}(k) + \boldsymbol{w}(k) \tag{5}$$

where $\mathbf{F} \triangleq \text{diag}[\mathbf{F}_{\text{pva}}, \mathbf{F}_{\text{clk}}, \ldots, \mathbf{F}_{\text{clk}}]$ and $\boldsymbol{w}(k)$ is the overall process noise vector, which is a zero-mean white sequence with covariance $\mathbf{Q} \triangleq \text{diag}[\mathbf{Q}_{\text{pva}}, \bar{\mathbf{Q}}_{\text{clk}}]$, and

$$\bar{\mathbf{Q}}_{\text{clk}} \triangleq \begin{bmatrix} \mathbf{Q}_{\text{clk}_r} + \mathbf{Q}_{\text{clk}_{s1}} & \mathbf{Q}_{\text{clk}_r} & \cdots & \mathbf{Q}_{\text{clk}_r} \\ \mathbf{Q}_{\text{clk}_r} & \mathbf{Q}_{\text{clk}_r} + \mathbf{Q}_{\text{clk}_{s2}} & \cdots & \mathbf{Q}_{\text{clk}_r} \\ \vdots & \vdots & \ddots & \vdots \\ \mathbf{Q}_{\text{clk}_r} & \mathbf{Q}_{\text{clk}_r} & \cdots & \mathbf{Q}_{\text{clk}_r} + \mathbf{Q}_{\text{clk}_{s_N}} \end{bmatrix}$$

where $\mathbf{Q}_{\text{clk}_r}$ and $\{\mathbf{Q}_{\text{clk}_{sn}}\}_{n=1}^{N}$ have the same form as in (3), except that $S_{\tilde{w}_{\delta t}}$ and $S_{\tilde{w}_{\dot{\delta} t}}$ are replaced with the receiver and nth base station's clock process noise spectra, respectively. Note that the cross correlations in $\bar{\mathbf{Q}}_{\text{clk}}$ come from combining the effect of the receiver and cellular base station clocks in the same state. Since the receiver clock bias is common to all clock states, the cross correlations in $\bar{\mathbf{Q}}_{\text{clk}}$ will be the receiver clock's process noise covariance [35].

The measurement vector defined by $\boldsymbol{z}(k) \triangleq [z_{\text{alt}}(k), z_1(k), \ldots, z_N(k)]^{\mathsf{T}}$ is used to estimate $\boldsymbol{x}$ in the EKF. In vector form, the measurement equation is given by

$$\boldsymbol{z}(k) = \boldsymbol{h}[\boldsymbol{x}(k)] + \boldsymbol{v}(k) \tag{6}$$

where $\boldsymbol{h}[\boldsymbol{x}(k)]$ is a vector-valued function defined as $\boldsymbol{h}[\boldsymbol{x}(k)] \triangleq [h_{\text{alt}}[\boldsymbol{x}(k)], h_1[\boldsymbol{x}(k)], \ldots, h_N[\boldsymbol{x}(k)]]^{\mathsf{T}}$ with $h_{\text{alt}}[\boldsymbol{x}(k)] = z_r(k) + v_{\text{alt}}(k)$, $h_n[\boldsymbol{x}(k)] \triangleq \| \boldsymbol{r}_r(k) - \boldsymbol{r}_{s_n} \|_2 + c\delta t_n(k)$, and $\boldsymbol{v}(k) \triangleq [v_{\text{alt}}(k), v_1(k), \ldots, v_N(k)]^{\mathsf{T}}$ is the measurement noise vector, which is modeled as a zero-mean white Gaussian random vector with covariance $\mathbf{R}(k) \triangleq \text{diag}[\sigma_{\text{alt}}^2(k), \sigma_1^2(k), \ldots, \sigma_N^2(k)]$.

An EKF is implemented given the dynamics and measurement models in (5) and (6) to produce an estimate of $\boldsymbol{x}(k)$ using all measurements up to time step k, denoted by $\hat{\boldsymbol{x}}(k|k)$, and an associated estimation error covariance denoted by $\mathbf{P}(k|k)$. The EKF is initialized from two successive position priors according to the framework discussed in [35]. The EKF process and measurement noise covariances are described in the next section.

EKF Settings

The measurement rate was $T = 0.08/3$ s; the jerk process noise spectra were chosen to be $\tilde{q}_N = 18\ \text{m}^2/\text{s}^5$, $\tilde{q}_E = 18\ \text{m}^2/\text{s}^5$, and $\tilde{q}_D = 0.5\ \text{m}^2/\text{s}^5$; and the receiver and base station clock process noise covariance matrices were chosen to be

$$\mathbf{Q}_{\text{clk},r} = \begin{bmatrix} 9.57 \times 10^{-5} & 2.52 \times 10^{-8} \\ 2.52 \times 10^{-8} & 1.89 \times 10^{-6} \end{bmatrix} \tag{7}$$

$$\mathbf{Q}_{\text{clk},s_n} = \begin{bmatrix} 3.11 \times 10^{-7} & 2.52 \times 10^{-11} \\ 2.52 \times 10^{-11} & 1.89 \times 10^{-9} \end{bmatrix}. \tag{8}$$

These clock process noise covariance matrices assumed the receiver to be equipped with a typical temperature-compensated crystal oscillator (TCXO), while the cellular base stations are equipped with a typical oven-controlled crystal oscillator (OCXO) [8].

The altimeter measurement error variance $\sigma_{\text{alt}}^2(k)$ was assumed to be $5\ \text{m}^2$. The cellular measurement noise variances were calculated as a function of the CNR and receiver parameters, as discussed in [33] and [34]. The range of values taken by the measurement noise variances is explicitly stated for each region in the "Aerial Navigation Results" section.

Experimental Setup and Flight Regions

This section overviews the experimental setup used for data collection and processing. It also describes the flight regions.

Hardware and Software Setup

The C-12 aircraft was equipped with a universal software radio peripheral (USRP) with consumer-grade cellular antennas to sample three cellular bands and store the samples on a desktop computer for offline processing. The stored samples were postprocessed with the 3G and 4G cellular modules of MATRIX. The SDR produces navigation observables: Doppler frequency, carrier phase, and pseudorange, along with corresponding CNRs. The hardware setup is shown in Figure 1.

The aircraft's ground-truth trajectory was taken from the C-12's onboard Honeywell H764-ACE EGI INS/GPS, which provided time–space–position information at a 1-Hz data rate. The accuracy specifications are tabulated in Table 1.

Flight Regions

Three flights are reported in this article, each of which took place in one of three regions: 1) Region A: a rural region in

Authorized licensed use limited to: The Ohio State University. Downloaded on October 13,2023 at 15:30:15 UTC from IEEE Xplore. Restrictions apply.

Edwards AFB, CA; 2) Region B: a semiurban region in Palmdale, CA; and 3) Region C: an urban region in Riverside, CA. Different maneuvers were planned over the three regions to test several aspects of aircraft navigation with cellular SOPs.

Figure 2 shows the regions in which the experiments were performed as well as the aircraft trajectory for each flight. The 3G base transceiver stations (BTSs) and 4G eNodeBs were mapped via the method described in [36]. The mapped towers were cross-checked via Google Earth and online databases and are shown in Figure 2. This article investigates the potential of cellular SOPs for navigation; therefore, mapping the SOPs will not be discussed.

Aerial Navigation Results

This section presents experimental results demonstrating high-altitude aircraft navigation using the framework discussed in the "Model Description" section in the three regions shown in Figure 2.

Aerial Navigation in Region A

The test trajectory in Region A consisted of 1) a 24-km straight segment, followed by 2) a 270° banking turn of length 18 km, and 3) a final 9-km straight segment. The total distance traveled by the aircraft was more than 51 km, completed in 9 min. The aircraft maintained an altitude of approximately 5,000 ft AGL throughout the trajectory. During this flight, three RF channels were sampled at 1) 881.52 MHz, which is a 3G channel allocated for the U.S. cellular provider Verizon Wireless; 2) 731.5 MHz, a 4G LTE channel allocated for T-Mobile; and 3) 751 MHz, also a 4G LTE channel allocated for Verizon. A total of 11 cellular SOPs were heard during the experiment: six 3G BTSs and five 4G eNodeBs. The 11 cellular SOPs were acquired at different times and tracked for different durations based on signal quality. Figure 3(a)–(c) shows the time history of the 1) measured CNRs, 2) pseudorange measurements, and 3) pseudorange error (pseudorange minus the true range) for all 11 cellular SOPs, respectively. One can see from Figure 3(c) that

Table 1. Honeywell H764-ACE EGI accuracy.

Metric	Blended INS/GPS Accuracy
Position	5 m, spherical error probable
Velocity	0.01 m/s
Heading	0.015°
Pitch/Roll	0.01°

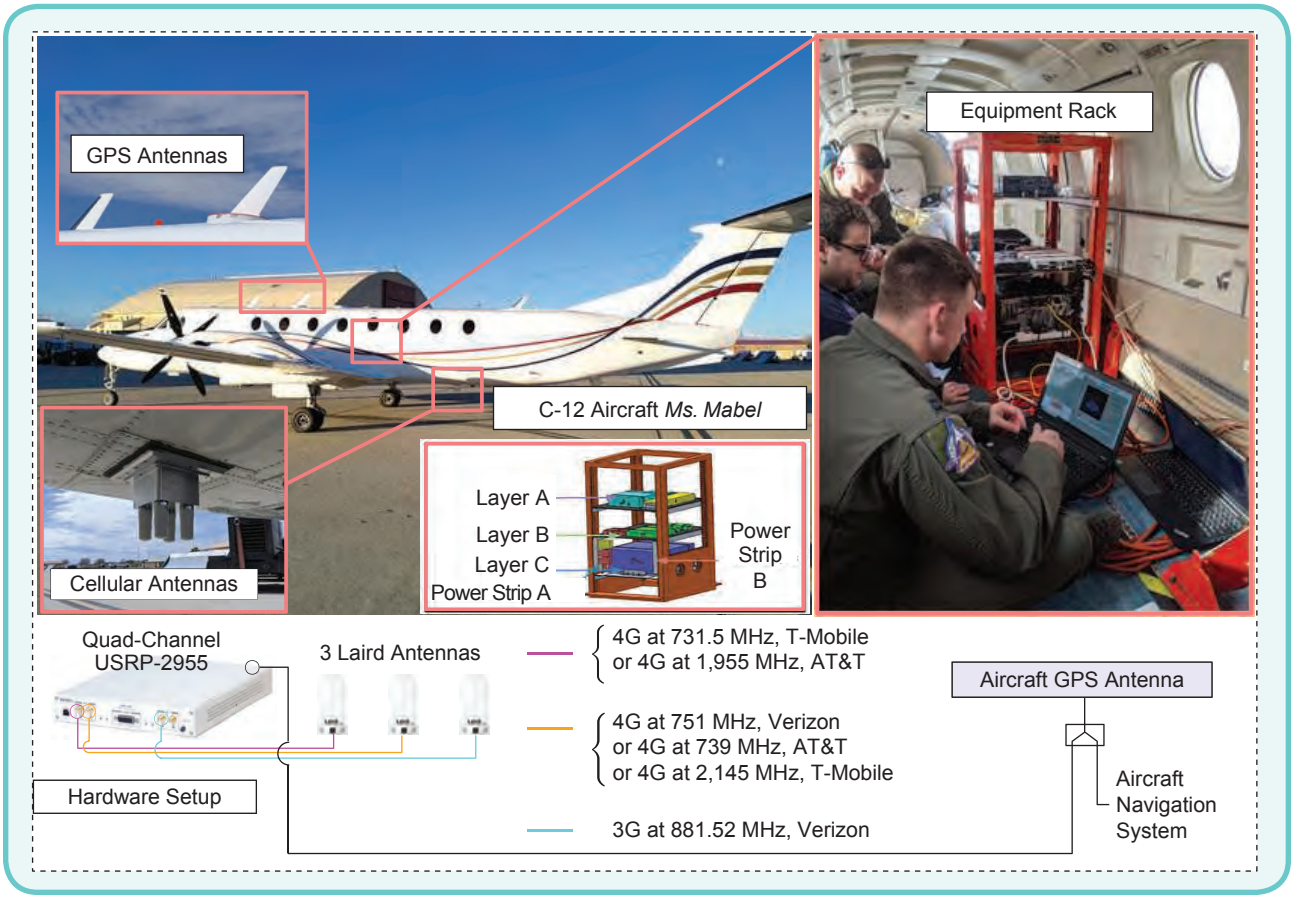

FIG 1 Hardware setup with which the C-12 aircraft was equipped.

Authorized licensed use limited to: The Ohio State University. Downloaded on October 13,2023 at 15:30:15 UTC from IEEE Xplore. Restrictions apply.

It is suspected that the aircraft's wings and body block or severely attenuate some of the signals during banking, causing loss of tracking.

pseudorange tracking is lost for some of the cellular SOPs at or around 300 s, which is when the aircraft starts banking to perform the 270° turn. In addition to the high dynamics of the banking turn, it is suspected that the aircraft's wings and body block or severely attenuate some of the signals during banking, causing loss of tracking. Using the expressions of the measurement noise variances as a function of the CNR and receiver parameters in [33] and [34], $\sigma_n(k)$ was found to vary between 1.44 and 9.47 m.

Next, the state vector $\boldsymbol{x}$ of the aircraft was estimated using the carrier phase measurements obtained from the cellular SOP receivers via the EKF discussed in the "EKF Model" section. The total position RMSE was calculated to be 10.5 m over the 51-km trajectory, traversed in 9 min. Figure 4 shows the aircraft's true and estimated trajectories. Figure 5 shows the EKF estimation error plots and corresponding sigma bounds for the aircraft's position and velocity states. It is important to note that the position error in the EKF is the largest during the turn. This is due to 1) the measurement errors due to the high dynamics of the banking turn, which severely stressed the tracking loops, and 2) the mismatch in the dynamics model assumed in the EKF since a 270° banking turn has significantly different dynamics than the assumed continuous Wiener process acceleration model. However, as mentioned earlier, the purpose of this study is to highlight the minimum performance that can be achieved with cellular SOPs. It is important to note that the average distance between the aircraft and the BTSs or eNodeBs was around 30 km over the entire trajectory, with eNodeB 4 being tracked at a 100-km distance in the first part of the trajectory.

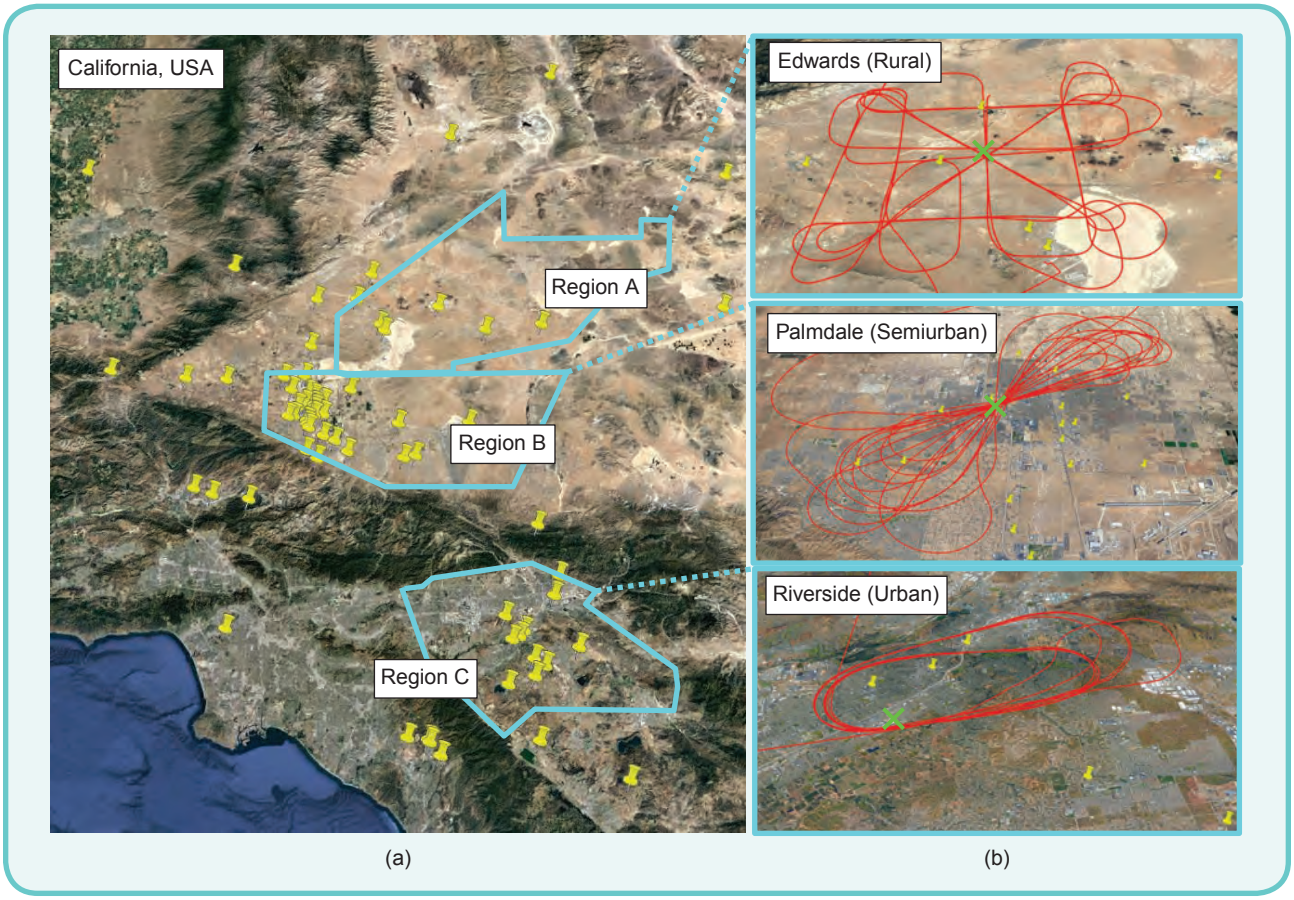

FIG 2 (a) Regions A, B, and C in which the flight campaigns took place. The yellow pins represent 3G and 4G cellular towers that were mapped and analyzed in this study. (b) The aircraft trajectories in all regions (shown in red). Geographic points of interest in each region, shown by green crosses, were chosen according to the designed trajectories.

Authorized licensed use limited to: The Ohio State University. Downloaded on October 13,2023 at 15:30:15 UTC from IEEE Xplore. Restrictions apply.

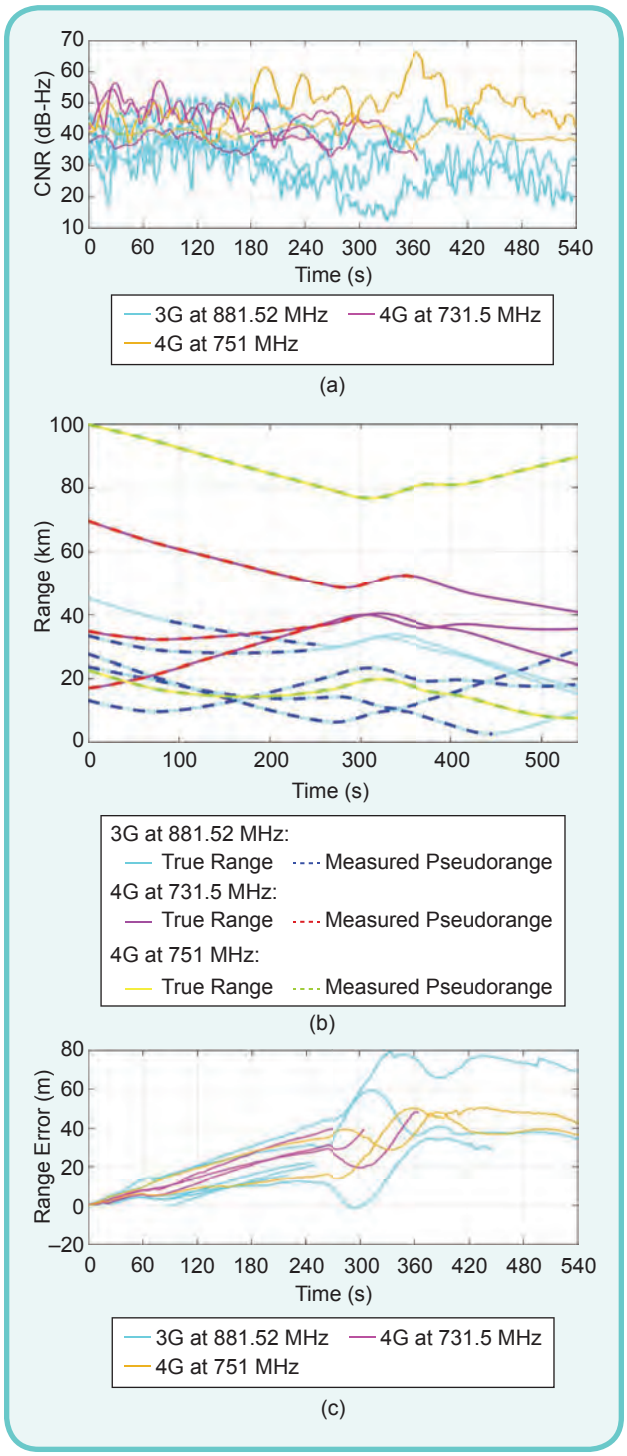

FIG 3 (a) Time history of the CNRs for all of the base stations used to compute the navigation solution in Region A. (b) Time history of the pseudoranges estimated by the cellular SOP receivers and the corresponding true range in Region A. The initial values of the pseudoranges and ranges were subtracted out for ease of comparison. (c) Time history of the pseudorange error (pseudorange minus the true range) for all cellular SOPs in Region A. The error is driven by a common term, which is the receiver's clock bias. The errors increase significantly at around 300 s, which is when the turn starts. The high dynamics of a banking turn inject stress on the tracking loops. The initial values of the pseudorange errors were subtracted out for ease of comparison.

Aerial Navigation in Region B

The test trajectory in Region B consisted of 1) an approach to General William J. Fox Airfield, followed by 2) a touch and go. The total distance traveled by the aircraft was more than 57 km completed in 11 min. The aircraft descended from an

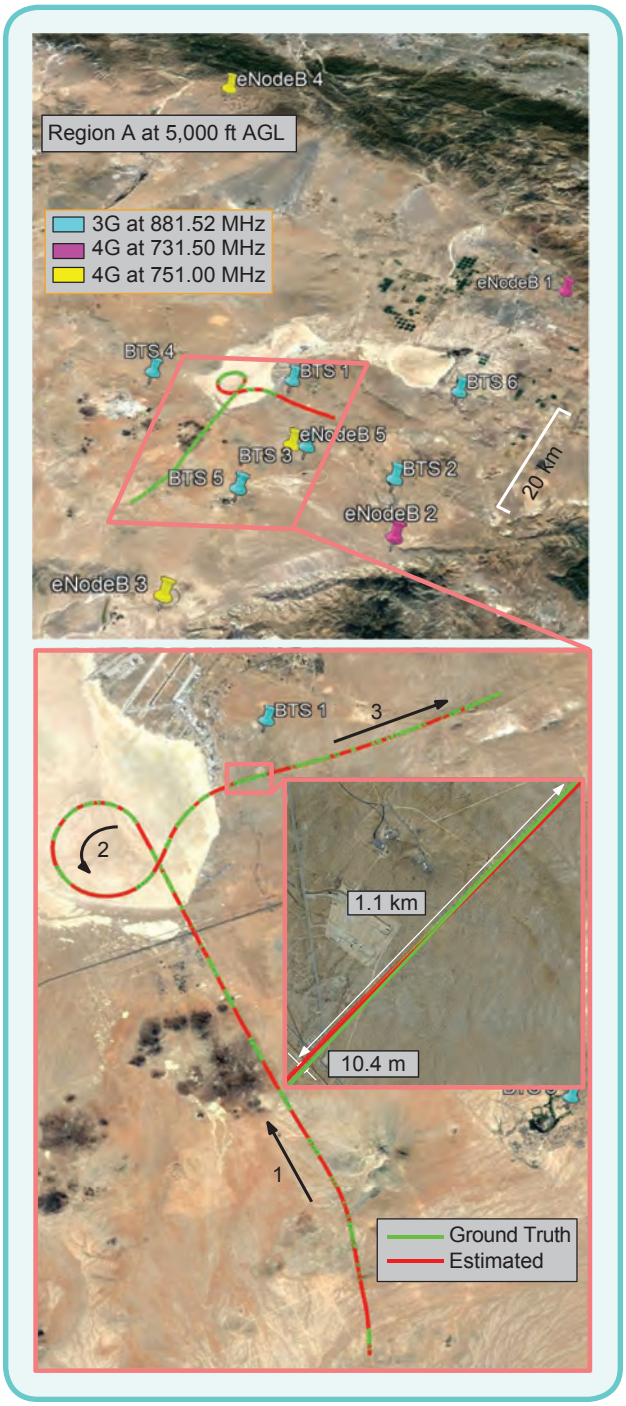

FIG 4 Experimental layout and results in Region A showing BTS and eNodeB positions, true aircraft trajectory, and aircraft trajectory estimated exclusively using cellular SOPs. The aircraft traversed a total distance of 51 km in 9 min during the experiment. The position RMSE over the entire trajectory was found to be 10.5 m.

Authorized licensed use limited to: The Ohio State University. Downloaded on October 13,2023 at 15:30:15 UTC from IEEE Xplore. Restrictions apply.

altitude of 7,000 ft AGL. During this flight, three RF channels were sampled at 1) 881.52 MHz, which is a 3G channel allocated for the U.S. cellular provider Verizon Wireless; 2) 731.5 MHz, a 4G LTE channel allocated for T-Mobile; and 3) 739 MHz, also a 4G LTE channel allocated for AT&T. A total of 14 cellular SOPs were heard during the experiment: nine 3G BTSs and five 4G eNodeBs. The 14 cellular SOPs were acquired at different times and tracked for different durations based on signal quality. Figure 6(a)–(c) shows the time history of 1) measured CNRs, 2) pseudorange measurements, and 3) pseudorange error (pseudorange minus the true range) for all 14 cellular SOPs, respectively. Using the expressions of the measurement noise variances as a function of the CNR and receiver parameters in [33] and [34], $\sigma_n(k)$ was found to vary between 1.3 to 4.43 m.

Next, the state vector $\boldsymbol{x}$ of the aircraft was estimated using the carrier phase measurements obtained from the cellular SOP receivers via the EKF discussed in the "EKF Model" section. The total position RMSE was calculated to be 4.95 m over the 57-km trajectory, traversed in 11 min. Figure 7 shows the aircraft's true and estimated trajectories. Figure 8 shows the EKF estimation error plots and corresponding sigma bounds for the aircraft's position and velocity states. It is important to note that the aircraft's position estimate on touchdown is less than 3 m away from the true position and is well within the runway. In addition, the geometric diversity becomes poor after the sixth minute as the aircraft is flying on one side of the SOPs. This explains the increasing sigma bounds in Figure 8.

Aerial Navigation in Region C

The test trajectory in Region C consisted of a holding pattern over Riverside Municipal Airport. The total distance traveled by the aircraft was more than 55 km, completed in 8.5 min. The aircraft maintained an altitude of approximately 15,000 ft AGL throughout the trajectory. During this flight, two RF channels were sampled at 1) 881.52 MHz, which is a 3G channel allocated for the U.S. cellular provider Verizon Wireless; 2) 1,955 MHz, a 4G LTE channel allocated for AT&T; and 3) 2,145 MHz, a 4G LTE channel allocated for T-Mobile. A total of 11 cellular SOPs were heard during the experiment: seven 3G BTSs and four 4G eNodeBs. The 11 cellular SOPs were acquired at different times and tracked for different durations based on signal quality. Figure 9(a)–(c) shows the time history of 1) measured CNRs, 2) pseudorange measurements, and 3) pseudorange error (pseudorange minus the true range), for all 9 cellular SOPs, respectively. Similar to the first flight, one can see from Figure 9(c) that pseudorange tracking is lost for some

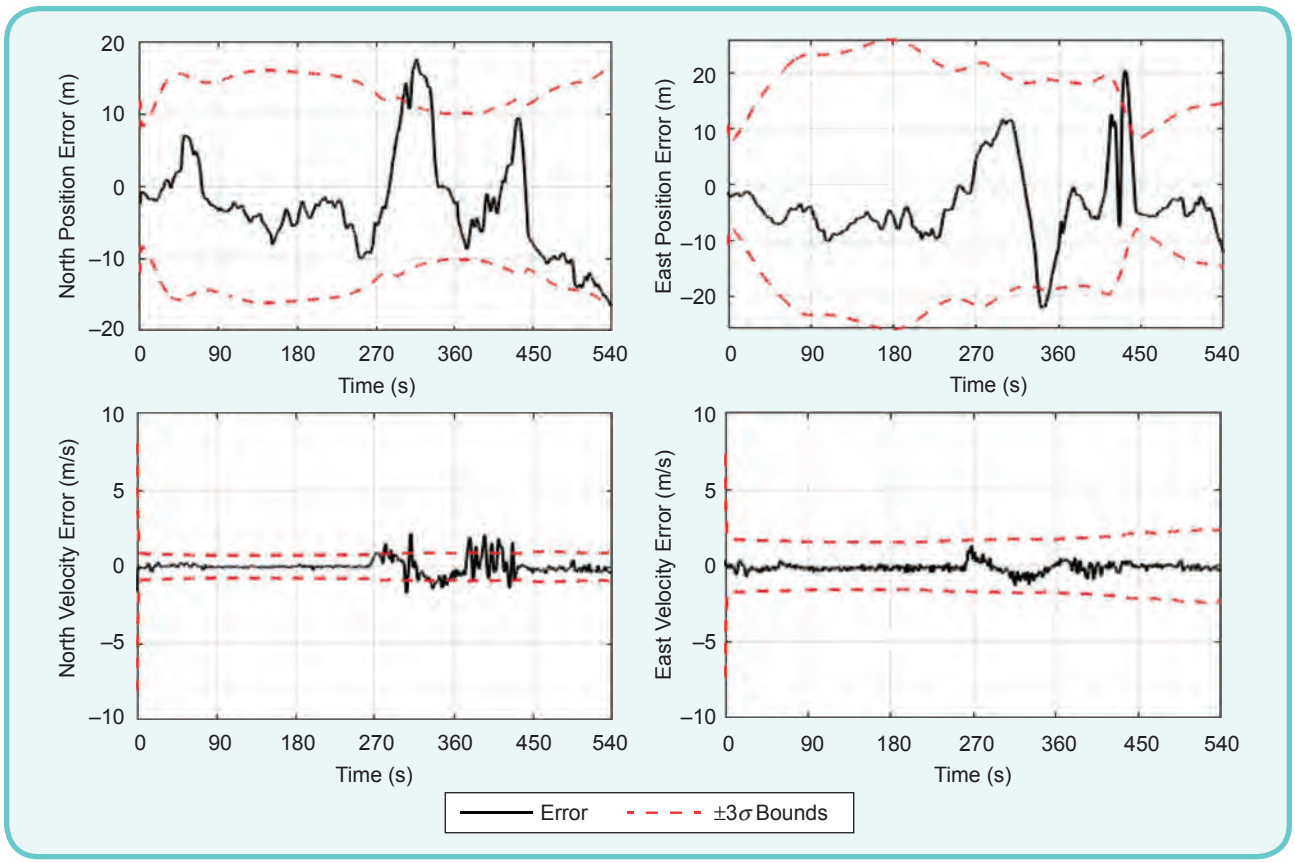

FIG 5 EKF plots showing the time history of the position and velocity errors in Region A as well as the $\pm 3\sigma$ bounds. As expected, the EKF performs poorly in the second leg, where the mismatch between the true aircraft dynamics and the assumed EKF model is highest.

Authorized licensed use limited to: The Ohio State University. Downloaded on October 13,2023 at 15:30:15 UTC from IEEE Xplore. Restrictions apply.

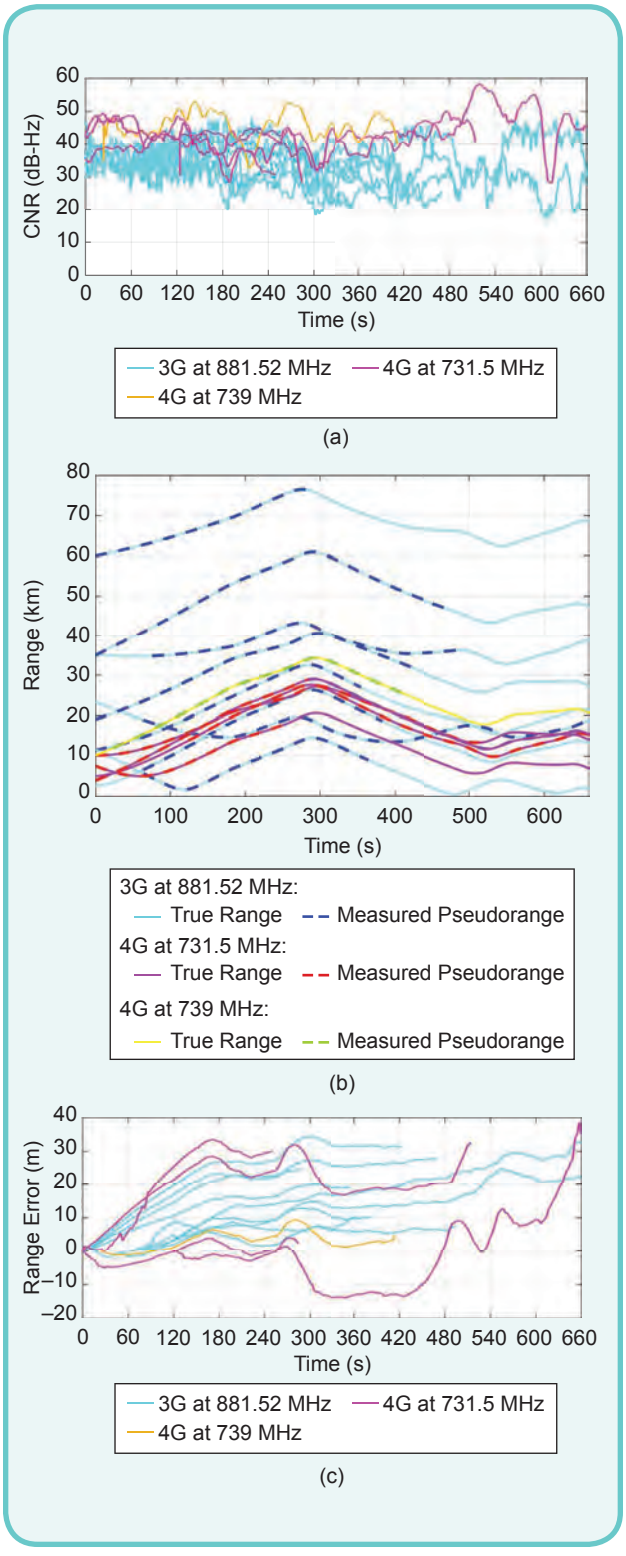

FIG 6 (a) Time history of the CNRs for all of the base stations used to compute the navigation solution in Region B. (b) Time history of the pseudoranges estimated by the cellular SOP receivers and the corresponding true range in Region B. The initial values of the pseudoranges and ranges were subtracted out for ease of comparison. (c) Time history of the pseudorange error (pseudorange minus the true range) for all cellular SOPs in Region B.

of the cellular SOPs when the aircraft starts banking to perform the turns in the holding pattern. Using the expressions of the measurement noise variances as a function of the CNR and receiver parameters in [33] and [34], $\sigma_n(k)$ was found to vary between 1.73 and 5.69 m.

Next, the state vector $\boldsymbol{x}$ of the aircraft was estimated using the carrier phase measurements obtained from the cellular SOP receivers via the EKF discussed in the "EKF Model" section. The total position RMSE was calculated to be 15.44 m over the 55-km trajectory, traversed in 8.5 min. Figure 10 shows the aircraft's true and estimated trajectories. Figure 11 shows the EKF estimation error plots and corresponding sigma

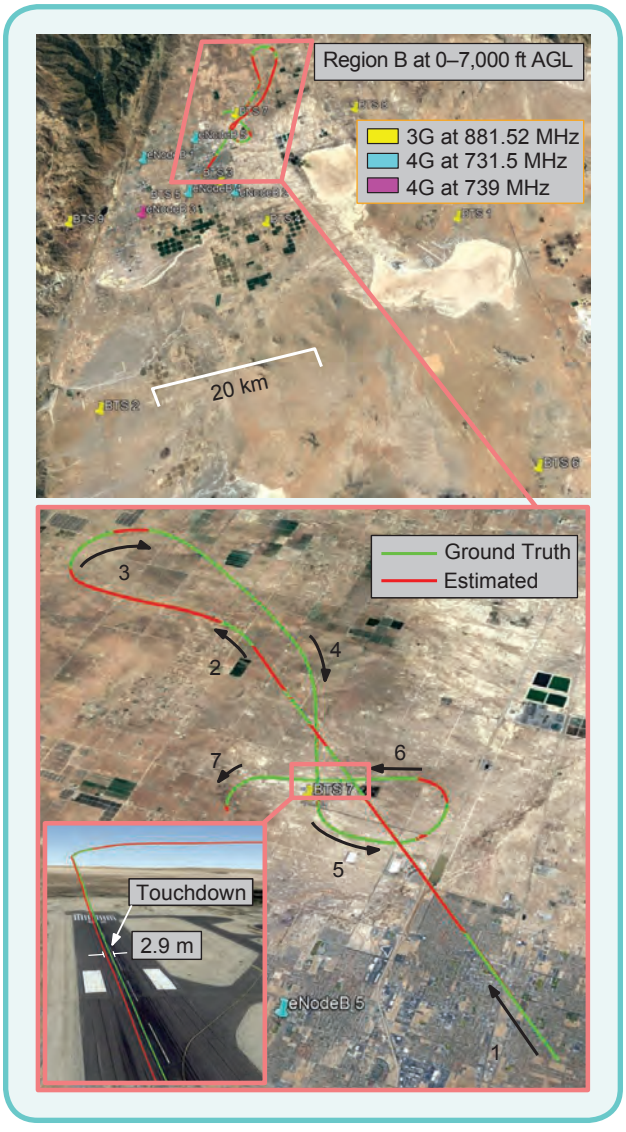

FIG 7 Experimental layout and results in Region B showing BTS and eNodeB positions, true aircraft trajectory, and aircraft trajectory estimated exclusively using cellular SOPs. The aircraft traversed a total distance of 57 km in 11 min during the experiment. The position RMSE over the entire trajectory was found to be 4.96 m. Note that the position estimate on touchdown is less than 3 m away from the true aircraft position and is well within the runway.

Authorized licensed use limited to: The Ohio State University. Downloaded on October 13,2023 at 15:30:15 UTC from IEEE Xplore. Restrictions apply.

The achieved results unveiled the remarkable potential of utilizing cellular SOPs for sustained accurate high-altitude aircraft navigation.

bounds for the aircraft's position and velocity states. As expected, the measurement errors and the mismatch in the dynamics model assumed in the EKF are more severe during the turns.

Discussion

The navigation performance in all three regions is summarized in Table 2.

The achieved results unveiled the remarkable potential of utilizing cellular SOPs for sustained accurate high-altitude aircraft navigation. The results presented herein, although promising, can be further improved upon in several ways. The following are key takeaways and design considerations for reliable aircraft navigation with cellular SOPs:

- *Accounting for the aircraft dynamical model mismatch*: Aircraft, such as the C-12, can perform a variety of highly dynamic maneuvers. The dynamics model employed in the EKF in this study did not perfectly capture the aircraft dynamics throughout its trajectory, leading to an increased estimation error due to the mismatch between the actual aircraft's dynamics and the dynamical model assumed by the EKF. This mismatch can be mitigated by using appropriate dynamical models for fixed-wing aircraft or more elaborate dynamical models (e.g., Wiener process acceleration, Singer acceleration, mean-adaptive acceleration, a semi-Markov jump process, circular motion, curvilinear motion, and coordinated turns, among others [30]) coupled with adaptive estimation techniques [37], [38], [39], [40], [41], [42]. Alternatively, if access to raw inertial measurement unit (IMU) data is available, a kinematic model with IMU measurements can be used as is the case with most INS-aiding techniques [10], [31].
- *Accounting for statistical model mismatch*: The aircraft's process noise covariance assumed by the EKF's dynamical model was found via offline tuning and by

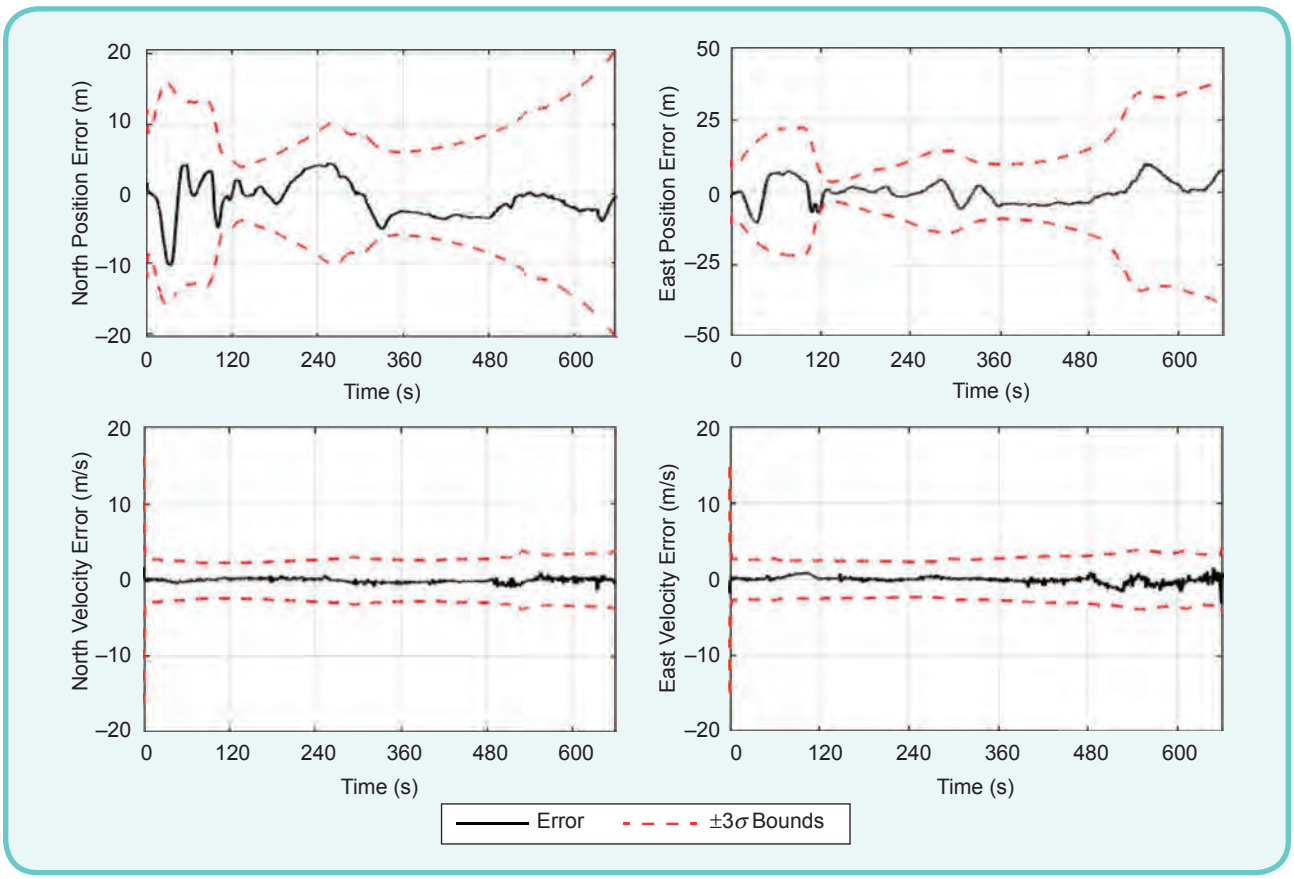

FIG 8 EKF plots showing the time history of the position and velocity errors in Region B as well as the $\pm 3\sigma$ bounds.

Authorized licensed use limited to: The Ohio State University. Downloaded on October 13,2023 at 15:30:15 UTC from IEEE Xplore. Restrictions apply.

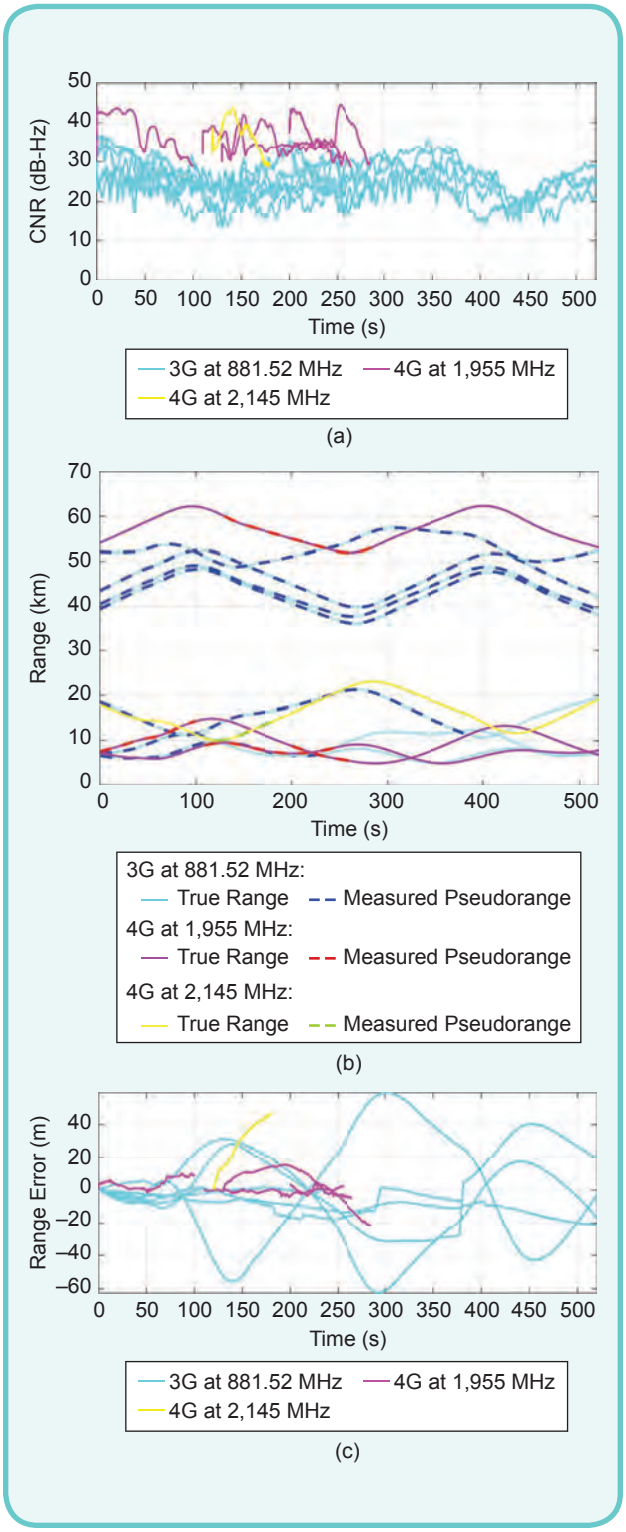

FIG 9 (a) Time history of the CNRs for all of the base stations used to compute the navigation solution in Region C. (b) Time history of the pseudoranges estimated by the cellular SOP receivers and the corresponding true range in Region C. The initial values of the pseudoranges and ranges were subtracted out for ease of comparison. (c) Time history of the pseudorange error (pseudorange minus the true range) for all cellular SOPs in Region C. The error is driven by a common term, which is the receiver's clock bias.

analyzing the aircraft's maneuvers from ground-truth data. In addition, the process noise covariances of the aircraft's receiver clock were set at typical TCXO values, and the cellular SOP transmitter clocks were set at typical OCXO values. While these values represent good approximations for the aircraft's receiver clock quality as well as the quality of typical cellular SOP transmitters, mismatches between the assumed values and the actual values can be mitigated via adaptive estimation techniques [43], [44], [45], which would improve

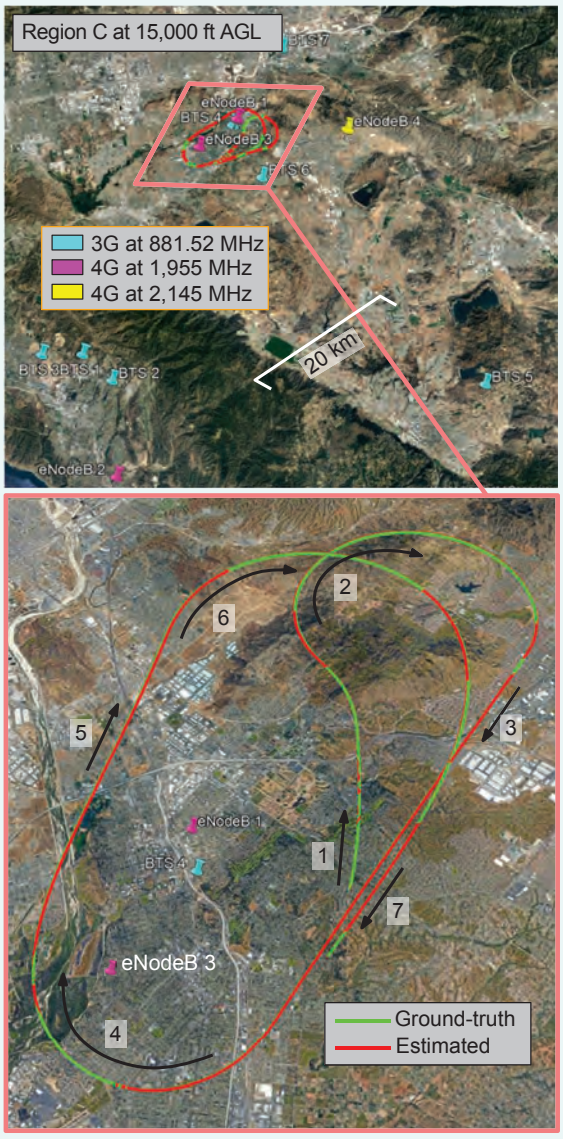

FIG 10 Experimental layout and results in Region C showing BTS and eNodeB positions, true aircraft trajectory, and aircraft trajectory estimated exclusively using cellular SOPs. The aircraft traversed a total distance of 55 km in 8.5 min during the experiment. The position RMSE over the entire trajectory was found to be 15.44 m.

Authorized licensed use limited to: The Ohio State University. Downloaded on October 13,2023 at 15:30:15 UTC from IEEE Xplore. Restrictions apply.

the estimation performance. Adaptive estimation techniques would also mitigate the errors arising from mismatches between the actual measurement noise variances and calculated measurement noise variances.

- *Vertical dilution of precision*: At high altitudes, there is very little vertical diversity with respect to terrestrial cellular towers. As such, the aircraft's cellular-based navigation solution VDOP will be large. Nevertheless, the aircraft's vertical position can still be estimated from the pseudoranges extracted from cellular towers, albeit with less accuracy compared to the results presented in this article, which fused altimeter-based measurements.
- *Mapping cellular SOPs*: This article assumed cellular SOPs to be mapped a priori. This was achieved via a mapping campaign according to the method described in [36]. Nevertheless, such an assumption can be relaxed via the radio simultaneous localization and mapping framework, which maps the unknown SOPs simultaneously with localizing the aircraft [14], [31].

Table 2. Navigation performance with cellular signals.

Metric	Region A	Region B	Region C
Cellular towers {3G,4G}	{6,5}	{9,5}	{7,4}
Cellular frequencies (MHz)	881.52	881.52	881.52
	731.5	731.5	1,955
	751	739	2,145
Flight duration (min)	9	11	8.5
Flight length (km)	51	57	55
Altitude AGL (ft)	5,000	0–7,000	15,000
Position RMSE (m)	10.53	4.96	11.67
Velocity RMSE (m/s)	0.58	0.5	0.71
Maximum position error (m)	22.67	15.04	25.89
Maximum velocity error (m/s)	2.29	3.19	3.94

Conclusion

This article demonstrated robust high-altitude aircraft navigation with 3G CDMA and 4G LTE cellular SOPs. An EKF was used to fuse cellular carrier phase measurements to estimate the aircraft's position, velocity, and time. The EKF utilized a simple, yet effective continuous Wiener process acceleration model to describe the aircraft dynamics. A multitude of flight trajectories and altitudes AGL was exercised in the three flights: 1) a 51-km trajectory of grid maneuvers with banking and straight segments at about

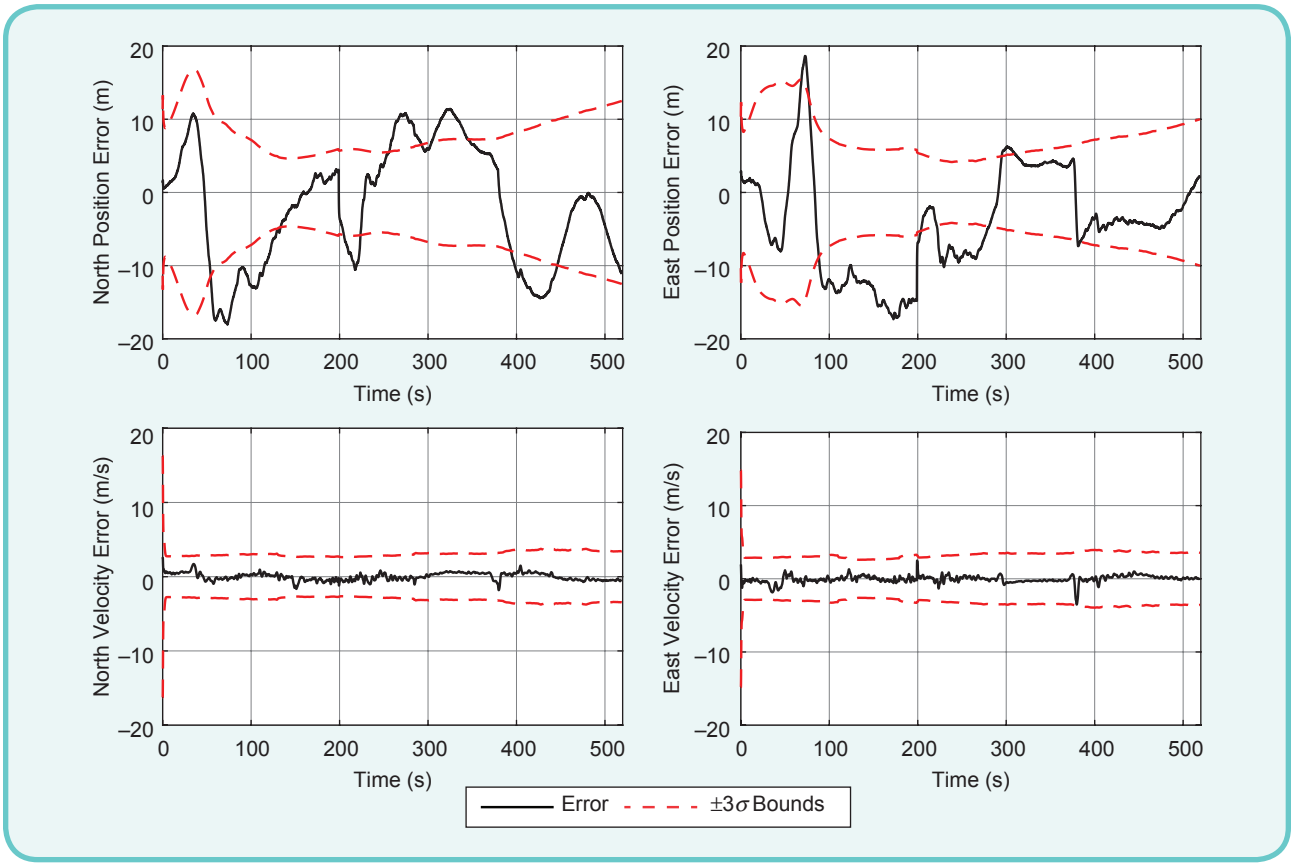

FIG 11 EKF plots showing the time history of the position and velocity errors in Region C as well as the $\pm 3\sigma$ bounds. As expected, the EKF performs poorly in the second leg, where the mismatch between the true aircraft dynamics and the assumed EKF model is highest.

Authorized licensed use limited to: The Ohio State University. Downloaded on October 13,2023 at 15:30:15 UTC from IEEE Xplore. Restrictions apply.

5,000 ft AGL, 2) a 57-km trajectory of a teardrop descent from 7,000 ft AGL down to touchdown at the runway, and 3) a 55-km trajectory of a holding pattern at about 15,000 ft AGL. Cellular SOPs produced remarkable navigation accuracy in all three flights, achieving a 3D position RMSE of 10.53 m, 4.96 m, and 15.44 m, respectively. These unprecedented results demonstrate the potential of cellular signals as a viable alternative to GNSS for high-altitude aircraft navigation. While the presented outcomes are encouraging, more accurate navigation results can be achieved by fusing cellular SOP observables with an INS.

> The EKF utilized a simple, yet effective continuous Wiener process acceleration model to describe the aircraft dynamics.

Acknowledgment

This work was supported in part by the Office of Naval Research under grant N00014-19-1-2511 and grant N00014-19-1-2613, in part by Sandia National Laboratories under award 1655264, in part by the National Science Foundation under grant 1929965, and in part by the U.S. Department of Transportation under grant 69A3552047138 for the Center for Automated Vehicles Research with Multimodal Assured Navigation University Transportation Center.

The authors would like to thank Edwards AFB and Holloman AFB for inviting the ASPIN Laboratory to conduct experiments on USAF aircraft in the "Signals of Opportunity for Navigation in Frequency-Forbidden Environments" flight campaign. The authors would like to thank Joshua Morales, Kimia Shamaei, Mahdi Maaref, Kyle Semelka, MyLinh Nguyen, and Trier Mortlock for their help in preparing for data collection. DISTRIBUTION STATEMENT A. Approved for public release; distribution is unlimited. 412TW-PA-20146.

About the Authors

Zaher (Zak) M. Kassas (zkassas@ieee.org) earned his B.E. degree in electrical engineering from the Lebanese American University, his M.S. degree in electrical and Computer Engineering from The Ohio State University, and his M.S.E. degree in aerospace engineering and Ph.D. degree in electrical and computer engineering from The University of Texas at Austin. He is a professor of Electrical and Computer Engineering at The Ohio State University, Columbus, OH 43210 USA, and director of the Autonomous Systems Perception, Intelligence, and Navigation Laboratory (ASPIN). He is also director of the U.S. Department of Transportation Center for Automated Vehicle Research with Multimodal Assured Navigation (CARMEN), focusing on navigation resiliency and security of highly automated transportation systems. His research interests include cyberphysical systems, estimation theory, navigation systems, autonomous vehicles, and intelligent transportation systems. He is a recipient of the 2018 National Science Foundation CAREER award, 2019 Office of Naval Research Young Investigator Program (YIP) award, 2022 Air Force Office of Scientific Research YIP award, 2018 IEEE Walter Fried Award, 2018 Institute of Navigation (ION) Samuel Burka Award, and 2019 ION Col. Thomas Thurlow Award. He is an associate editor of *IEEE Transactions on Aerospace and Electronic Systems* and *IEEE Transactions on Intelligent Transportation Systems*. He is a fellow of the ION and a Distinguished Lecturer of the IEEE Aerospace and Electronic Systems Society.

Joe Khalife (khalifej@uci.edu) earned his B.E. degree in electrical engineering and his M.S. degree in computer engineering from the Lebanese American University and his Ph.D. degree in electrical engineering and computer science from the University of California, Irvine. He was a postdoctoral fellow at the University of California, Irvine, and a member of the Autonomous Systems Perception, Intelligence, and Navigation (ASPIN) Laboratory, University of California, Irvine, CA 92697 USA. From 2012 to 2015, he was a research assistant at the Lebanese American University and has been a member of the ASPIN Laboratory since 2015. His research interests include opportunistic navigation, autonomous vehicles, and software-defined radio. He is a recipient of the 2016 IEEE/Institute of Navigation Position, Location, and Navigation Symposium Best Student Paper Award, 2018 IEEE Walter Fried Award, and 2021 IEEE AESS Robert T. Hill Best Dissertation Award. He is a Member of IEEE.

Ali A. Abdallah (abdalla2@uci.edu) earned his B.E. degree in electrical engineering from the Lebanese American University and M.S. degree in electrical engineering and computer science from the University of California, Irvine. He was a member of the Autonomous Systems Perception, Intelligence, and Navigation Laboratory, University of California, Irvine, CA 92697 USA. He is a recipient of the Best Student Paper Award at the 2020 IEEE/Institute of Navigation Position, Location, and Navigation Symposium. He is a Student Member of IEEE.

Authorized licensed use limited to: The Ohio State University. Downloaded on October 13,2023 at 15:30:15 UTC from IEEE Xplore. Restrictions apply.

Chiawei Lee (chiawei.lee@us.af.mil) earned his B.S. degree in aerospace engineering from the University of California, Los Angeles, and his M.S. degree in aero/astro engineering from Stanford University. He is an assistant professor and instructor flight test engineer at the U.S. Air Force Test Pilot School, Edwards Air Force Base, Edwards, CA 93524 USA. He serves as the test management program director, overseeing about a dozen student and staff-led flight test projects each year. In addition, he is the chief test safety officer responsible for the safe execution of curriculum and flight test project safety packages.

Juan Jurado (jdjurado@icloud.com) earned his B.S. degree from Texas A&M University, his M.S. degree from the U.S. Air Force Test Pilot School, and M.S. and Ph.D. degrees from the Air Force Institute of Technology. He is a U.S. Air Force lieutenant colonel and the director of education at the U.S. Air Force Test Pilot School, Edwards Air Force Base, Edwards, CA 93524 USA. Previously, he served as director of engineering for the 413th Flight Test Squadron and oversaw various C-130, V-22, and H-1 flight test programs. His research interests include aircraft performance modeling, online sensor calibration, image processing, visual–inertial navigation, and statistical sensor management for multisensor navigation problems.

Steven Wachtel (steven.wachtel.1@us.af.mil) earned his B.S. degree in mechanical engineering from The Ohio State University, an M.S. degree in flight test engineering from the U.S. Air Force Test Pilot School, and an M.S. degree in systems engineering from the Air Force Institute of Technology. He is a U.S. Air Force captain and a flight test engineer assigned to the 780th Test Squadron at the U.S. Air Force Test Pilot School, Edwards Air Force Base, Edwards, CA 93524 USA.

Jacob Duede (jacob.duede@us.af.mil) earned his M.S. degree in engineering from the University of Arkansas and his M.S. degree in flight test engineering from Air University. He is a major in the U.S. Air Force and is with the U.S. Air Force Test Pilot School at Edwards Air Force Base, Edwards, CA 93524 USA. He was trained as a communication/navigation/mission systems apprentice on C-17 Globmaster II aircraft and stationed at McChord Air Force Base, WA. He graduated from the U.S. Air Force Academy as a commissioned officer with a B.S. in mechanical engineering. He attended the undergraduate pilot training at Columbus Air Force Base, MS. In 2020, he graduated from the U.S. Air Force Test Pilot School at Edwards Air Force Base. He is a senior pilot with more than 2,000 h.

Zachary Hoeffner (zachary.hoeffner.1@us.af.mil) earned his B.S degree in nuclear engineering from the U.S. Air Force Academy, his M.S. degree in flight test engineering from the U.S. Air Force Test Pilot School, his M.S. degree in engineering physics and applied physics from the Air Force Institute of Technology, and his M.S. degree in nuclear engineering from the Air Force Institute of Technology. He is a flight test engineer for the U.S. Air Force with the U.S. Air Force Test Pilot School at Edwards Air Force Base, Edwards, CA 93524 USA.

Thomas Hulsey (thomas.hulsey.2@us.af.mil) earned his B.S. degree in aerospace engineering from the Missouri University of Science and Technology, his M.S. degree in aeronautical engineering from the Air Force Institute of Technology, and his M.S. degree in experimental flight test engineering from the U.S. Air Force Test Pilot School. He is a U.S. Air Force Flight Commander of Operations Engineering with the U.S. Air Force Test Pilot School at Edwards Air Force Base, Edwards, CA 93524 USA.

Rachel Quirarte (rachel.quirarte@us.af.mil) earned her B.S. degree in aeronautical engineering from the U.S. Air Force Academy, her M.S. degree in flight test engineering from the U.S. Air Force Test Pilot School, and her M.S. degree in mechanical engineering from Rice University. She is a KC-46 and KC-135 programmatic flight commander and test pilot in the 418th Flight Test Squadron in the U.S. Air Force and is with the U.S. Air Force Test Pilot School at Edwards Air Force Base, Edwards, CA 93524 USA.

RunXuan Tay (rxtay@outlook.com) earned his B.S. degree in electrical engineering from the University of California, San Diego, and his M.S. degree in flight test engineering from the U.S. Air Force Test Pilot School. He is currently a test pilot at the Air Warfare Center, Republic of Singapore Air Force, Singapore, where he works on fixed-wing test programs.

Authorized licensed use limited to: The Ohio State University. Downloaded on October 13,2023 at 15:30:15 UTC from IEEE Xplore. Restrictions apply.

References

[1] "ASRS database online," ASRS/NASA, Washington, DC, USA. [Online]. Available: https://asrs.arc.nasa.gov/search/database.html

[2] M. Harris, "FAA files reveal a surprising threat to airline safety," *IEEE Spectr.*, Jan. 2021. [Online]. Available: https://spectrum.ieee.org/faa-files-reveal-a-surprising-threat-to-airline-safety-the-us-militarys-gps-tests

[3] D. Miralles et al., "An assessment of GPS spoofing detection via radio power and signal quality monitoring for aviation safety operations," *IEEE Intell. Transp. Syst. Mag.*, vol. 12, no. 3, pp. 136–146, Jun. 2020, doi: 10.1109/MITS.2020.2994117.

[4] F. Dovis, L. Ruotsalainen, R. Toledo-Moreo, Z. Kassas, and V. Gikas, "Recent advancement on the use of global navigation satellite system-based positioning for intelligent transport systems," *IEEE Intell. Transp. Syst. Mag.*, vol. 12, no. 3, pp. 6–9, Jun. 2020, doi: 10.1109/MITS.2020.2994923.

[5] "An urgent need to address harmful interferences to GNSS," Int. Civil Aviation Org., Montreal, QC, Canada, Tech. Rep. A40-WP/188, May 2019. [Online]. Available: https://www.iata.org/contentassets/e45e5219cc8c4277a0e80562590793da/address-harmful-interferences-gnss.pdf

[6] A. Hansen et al., "Complementary PNT and GPS backup technologies demonstration report: Sections 1 through 10," John A. Volpe National Transportation Systems Center (US), U.S. Dept. Transp., Washington, DC, USA, no. DOT-VNTSC-20-07, Jan. 2021.

[7] M. Bartock et al., "Foundational PNT profile: Applying the cybersecurity framework for the responsible use of positioning, navigation, and timing (PNT) services," Nat. Inst. Standards Technol. (NIST), Gaithersburg, MD, USA, NISTIR 8323, Feb. 2021.

[8] Z. Kassas, "Position, navigation, and timing technologies in the 21st century," in *Navigation with Cellular Signals of Opportunity*, vol. 2, J. Morton, F. van Diggelen, J. Spilker Jr., and B. Parkinson, Eds. New York, NY, USA: Wiley, 2021, ch. 38, pp. 1171–1223.

[9] A. Abdallah, J. Khalife, and Z. Kassas, "Experimental characterization of received 5G signals carrier-to-noise ratio in indoor and urban environments," in *Proc. IEEE Veh. Technol. Conf.*, Apr. 2021, pp. 1–5, doi: 10.1109/VTC2021-Spring51267.2021.9448729.

[10] Z. Kassas, M. Maaref, J. Morales, J. Khalife, and K. Shamaei, "Robust vehicular localization and map matching in urban environments through IMU, GNSS, and cellular signals," *IEEE Intell. Transp. Syst. Mag.*, vol. 12, no. 3, pp. 36–52, Jun. 2020, doi: 10.1109/MITS.2020.2994110.

[11] M. Maaref and Z. Kassas, "Autonomous integrity monitoring for vehicular navigation with cellular signals of opportunity and an IMU," *IEEE Trans. Intell. Transp. Syst.*, vol. 23, no. 6, pp. 5586–5601, Jun. 2022, doi: 10.1109/TITS.2021.3055200.

[12] J. Khalife and Z. Kassas, "On the achievability of submeter-accurate UAV navigation with cellular signals exploiting loose network synchronization," *IEEE Trans. Aerosp. Electron. Syst.*, vol. 58, no. 5, pp. 4261–4278, Oct. 2022, doi: 10.1109/TAES.2022.3162770.

[13] J. Khalife and Z. Kassas, "Differential framework for submeter-accurate vehicular navigation with cellular signals," *IEEE Trans. Intell. Veh.*, early access, 2022, doi: 10.1109/TIV.2022.3187957.

[14] Z. Kassas, J. Khalife, A. Abdallah, and C. Lee, "I am not afraid of the GPS jammer: resilient navigation via signals of opportunity in GPS-denied environments," *IEEE Aerosp. Electron. Syst. Mag.*, vol. 37, no. 7, pp. 4–19, Jul. 2022, doi: 10.1109/MAES.2022.3154110.

[15] Y. Zeng, Q. Wu, and R. Zhang, "Accessing from the sky: A tutorial on UAV communications for 5G and beyond," *Proc. IEEE*, vol. 107, no. 12, pp. 2327–2375, Dec. 2019, doi: 10.1109/JPROC.2019.2952892.

[16] X. Cai et al., "An empirical air-to-ground channel model based on passive measurements in LTE," *IEEE Trans. Veh. Technol.*, vol. 68, no. 2, pp. 1140–1154, Feb. 2019, doi: 10.1109/TVT.2018.2886961.

[17] W. Khawaja, I. Guvenc, D. Matolak, U. Fiebig, and N. Schneckenburger, "A survey of air-to-ground propagation channel modeling for unmanned aerial vehicles," *IEEE Commun. Surveys Tuts.*, vol. 21, no. 3, pp. 2361–2391, Thirdquarter 2019, doi: 10.1109/COMST.2019.2915069.

[18] K. Matheou et al., "Analysis of at-altitude LTE power spectra for small unmanned aircraft system C2 communications," in *Proc. Integr. Commun., Navig. Surveillance Conf.*, Apr. 2019, pp. 1–12, doi: 10.1109/ICNSURV.2019.8735287.

[19] X. Cai et al., "Low altitude air-to-ground channel characterization in LTE network," in *Proc. Eur. Conf. Antennas Propag.*, Apr. 2019, pp. 1–5.

[20] B. Van Der Bergh, A. Chiumento, and S. Pollin, "LTE in the sky: trading off propagation benefits with interference costs for aerial nodes," *IEEE Commun. Mag.*, vol. 54, no. 5, pp. 44–50, May 2016, doi: 10.1109/MCOM.2016.7470934.

[21] I. Kovacs, R. Amorim, H. Nguyen, J. Wigard, and P. Mogensen, "Interference analysis for UAV connectivity over LTE using aerial radio measurements," in *Proc. IEEE Veh. Technol. Conf.*, Sep. 2017, pp. 1–6.

[22] R. Amorim, J. Wigard, I. Kovacs, and T. Sorensen, "UAV communications for 5G and beyond," in *Performance Enhancements for LTE-Connected UAVs: Experiments and Simulations*, Y. Zeng, I. Guvenc, R. Zhang, G. Geraci, and D. Matolak, Eds. New York, NY, USA: Wiley, 2021, ch. 5, pp. 139–161.

[23] E. Teng, J. Diogo Falcao, and B. Iannucci, "Holes-in-the-sky: A field study on cellular-connected UAS," in *Proc. Int. Conf. Unmanned Aircraft Syst.*, Jun. 2017, pp. 1165–1174, doi: 10.1109/ICUAS.2017.7991402.

[24] X. Lin et al., "The sky is not the limit: LTE for unmanned aerial vehicles," *IEEE Commun. Mag.*, vol. 56, no. 4, pp. 204–210, Apr. 2018, doi: 10.1109/MCOM.2018.1700643.

[25] G. Athanasiadou, M. Batistatos, D. Zarbouti, and G. Tsoulos, "LTE ground-to-air field measurements in the context of flying relays," *IEEE Wireless Commun.*, vol. 26, no. 1, pp. 12–17, Feb. 2019, doi: 10.1109/MWC.2018.1800225.

[26] A. Abdalla and V. Marojevic, "Communications standards for unmanned aircraft systems: The 3GPP perspective and research drivers," *IEEE Commun. Standards Mag.*, vol. 5, no. 1, pp. 70–77, Mar. 2021, doi: 10.1109/MCOMSTD.001.2000032.

[27] H. Maattanen, "3GPP standardization for cellular-supported UAVs," in *UAV Communications for 5G and Beyond*, Y. Zeng, I. Guvenc, R. Zhang, G. Geraci, and D. Matolak, Eds. New York, NY, USA: Wiley, 2021, ch. 6, pp. 163–180.

[28] E. Kim and Y. Shin, "Feasibility analysis of LTE-based UAS navigation in deep urban areas and DSRC augmentation," *Sensors*, vol. 19, no. 19, pp. 4192–4207, Apr. 2019, doi: 10.3390/s19194192.

[29] Z. Kassas et al., "Assessment of cellular signals of opportunity for high altitude aircraft navigation," *IEEE Aerosp. Electron. Syst. Mag.*, vol. 37, no. 10, pp. 4–19, Oct. 2022, doi: 10.1109/MAES.2022.3187142.

[30] X. Li and V. Jilkov, "Survey of maneuvering target tracking. Part I: Dynamic models," *IEEE Trans. Aerosp. Electron. Syst.*, vol. 39, no. 4, pp. 1333–1364, Oct. 2003, doi: 10.1109/TAES.2003.1261132.

[31] J. Morales and Z. Kassas, "Tightly-coupled inertial navigation system with signals of opportunity aiding," *IEEE Trans. Aerosp. Electron. Syst.*, vol. 57, no. 3, pp. 1930–1948, Jun. 2021, doi: 10.1109/TAES.2021.3054067.

[32] J. Barnes et al., "Characterization of frequency stability," *IEEE Trans. Instrum. Meas.*, vol. IM-20, no. 2, pp. 105–120, May 1971, doi: 10.1109/TIM.1971.5570702.

[33] J. Khalife, K. Shamaei, and Z. Kassas, "Navigation with cellular CDMA signals – Part I: Signal modeling and software-defined receiver design," *IEEE Trans. Signal Process.*, vol. 66, no. 8, pp. 2191–2203, Apr. 2018, doi: 10.1109/TSP.2018.2799167.

[34] K. Shamaei and Z. Kassas, "LTE receiver design and multipath analysis for navigation in urban environments," *Navig., J. Inst. Navig.*, vol. 65, no. 4, pp. 655–675, Dec. 2018, doi: 10.1002/navi.272.

[35] J. Khalife and Z. Kassas, "Opportunistic UAV navigation with carrier phase measurements from asynchronous cellular signals," *IEEE Trans. Aerosp. Electron. Syst.*, vol. 56, no. 4, pp. 3285–3301, Aug. 2020, doi: 10.1109/TAES.2019.2948452.

[36] J. Morales and Z. Kassas, "Optimal collaborative mapping of terrestrial transmitters: Receiver placement and performance characterization," *IEEE Trans. Aerosp. Electron. Syst.*, vol. 54, no. 2, pp. 992–1007, Apr. 2018, doi: 10.1109/TAES.2017.2773238.

[37] M. Yeddanapudi, Y. Bar-Shalom, and K. Pattipati, "IMM estimation for multitarget-multisensor air traffic surveillance," *Proc. IEEE*, vol. 85, no. 1, pp. 80–96, Jan. 1997, doi: 10.1109/5.554210.

[38] A. Mohamed and K. Schwarz, "Adaptive Kalman filtering for INS/GPS," *J. Geodesy*, vol. 73, no. 4, pp. 193–203, May 1999, doi: 10.1007/s001900050236.

[39] P. Hanlon and P. Maybeck, "Multiple-model adaptive estimation using a residual correlation Kalman filter bank," *IEEE Trans. Aerosp. Electron. Syst.*, vol. 36, no. 2, pp. 393–406, Apr. 2000, doi: 10.1109/7.845216.

[40] C. Hide, T. Moore, and M. Smith, "Adaptive Kalman filtering for low-cost INS/GPS," *J. Navig.*, vol. 56, no. 1, pp. 143–152, Jan. 2003, doi: 10.1017/S0373463302002151.

[41] W. Ding, J. Wang, C. Rizos, and D. Kinlyside, "Improving adaptive Kalman estimation in GPS/INS integration," *J. Navig.*, vol. 60, no. 3, pp. 517–529, Sep. 2007, doi: 10.1017/S0373463307004316.

[42] M. Yu, "INS/GPS integration system using adaptive filter for estimating measurement noise variance," *IEEE Trans. Aerosp. Electron. Syst.*, vol. 48, no. 2, pp. 1786–1792, Apr. 2012, doi: 10.1109/TAES.2012.6178100.

[43] Z. Kassas, V. Ghadiok, and T. Humphreys, "Adaptive estimation of signals of opportunity," in *Proc. ION GNSS Conf.*, Sep. 2014, pp. 1679–1689.

[44] J. Dunik, O. Straka, O. Kost, and J. Havlik, "Noise covariance matrices in state-space models: A survey and comparison of estimation methods—Part I," *Int. J. Adaptive Control Signal Process.*, vol. 31, no. 11, pp. 1505–1543, May 2017, doi: 10.1002/acs.2783.

[45] J. Dunik, O. Kost, O. Straka, and E. Blasch, "Navigation and estimation improvement by environmental-driven noise mode detection," in *Proc. IEEE/ION Position, Location, Navig. Symp.*, 2020, pp. 925–932.

ITS

Authorized licensed use limited to: The Ohio State University. Downloaded on October 13,2023 at 15:30:15 UTC from IEEE Xplore. Restrictions apply.

Received <day> March 2023 | Revised <day> <month> <year> | Accepted <day> <month> <year>

DOI: xxx/xxxx

ARTICLE TYPE

GNSS Software Defined Radio: History, Current Developments, and Standardization Efforts

Thomas Pany[1] | Dennis Akos[2] | Javier Arribas[3] | M. Zahidul H. Bhuiyan[4] | Pau Closas[5] | Fabio Dovis[6] | Ignacio Fernandez-Hernandez[7] | Carles Fernández–Prades[3] | Sanjeev Gunawardena[8] | Todd Humphreys[9] | Zaher M. Kassas[10] | José A. López Salcedo[11] | Mario Nicola[12] | Mark L. Psiaki[13] | Alexander Rügamer[14] | Young-Jin Song[15] | Jong-Hoon Won[15]

[1]University of the Bundeswehr Munich, Neubiberg, Germany
[2]University of Colorado, Boulder, USA
[3]Centre Tecnològic de Telecomunicacions de Catalunya, Barcelona, Spain
[4]Finnish Geospatial Research Institute, Kirkkonummi, Finland
[5]Northeastern University, Boston, USA
[6]Politecnico di Torino, Turin, Italy
[7]European Commission, Brussels, Belgium
[8]Air Force Institute of Technology, Wright-Patterson AFB, USA
[9]The University of Texas at Austin, Austin, USA
[10]The Ohio State University, Columbus, USA
[11]Universitat Autònoma de Barcelona, Cerdanyola del Vallès, Spain
[12]LINKS Foundation, Turin, Italy
[13]Virginia Tech, Blacksburg, USA
[14]Fraunhofer Institute for Integrated Circuits IIS, Erlangen, Germany
[15]Inha University, Incheon, South Korea

Summary

Taking the work conducted by the global navigation satellite system (GNSS) software-defined radio (SDR) working group during the last decade as a seed, this contribution summarizes for the first time the history of GNSS SDR development. It highlights selected SDR implementations and achievements that are available to the public or that influenced the general SDR development. The relation to the standardization process of intermediate frequency (IF) sample data and metadata is discussed, and an update of the Institute of Navigation (ION) SDR Standard is proposed. The work focuses on GNSS SDR implementations on general purpose processors and leaves aside developments conducted on field programmable gate array (FPGA) and application-specific integrated circuits (ASICs) platforms. Data collection systems (*i.e.*, front-ends) have always been of paramount importance for GNSS SDRs, and are thus partly covered in this work. The work represents the knowledge of the authors but is not meant as a complete description of SDR history.

KEYWORDS
GNSS, software-defined radio

1 | INTRODUCTION

Receiver development has always been an integral part of satellite navigation, ever since the early studies conducted for the U.S. Global Positioning System (GPS). The very first receivers were huge devices, realizing the correlation of the received satellite signal with internally generated code and carrier replicas by a mixture of digital and analog electronics (Eissfeller & Won, 2017). Advances in semiconductor technology soon enabled signal processing on dedicated chips. This technology was of course complex to handle and mostly located within the U.S. industry. Despite the success of GPS and its Russian counterpart Globalnaya Navigazionnaya Sputnikovaya Sistema (GLONASS), receiver internal technology was barely accessible to the broader research community for a long time, as it seemed to be impossible to realize GNSS signal processing on low-cost computers. Even in the year 1996 a key receiver design pioneer expressed skepticism that general purpose microprocessors were, or would ever be, a suitable platform for implementing a GNSS receiver (Kaplan, 1996).

The situation radically changed when the algorithms of a GPS receiver were first implemented as Matlab software on a desktop personal computer (PC) and estimates of digital signal processor (DSP) resources required to run the algorithms in real-time were encouraging (D. Akos & Braasch, 1996; D. M. Akos, 1997). Soon after, real-time processing was demonstrated even on conventional PCs and the widespread use of software radio technology took off with exponential growth. Interestingly, software radio technology did not replace existing hardware receivers usually realized as one or more ASICs, but complemented these, allowing researchers to easily implement and test new algorithms or to develop highly specialized receivers with reasonable effort. Today, this is a well-established approach for military, scientific, and even commercial applications as described by Curran et al. (2018).

As different research groups developed their own software radios, they used different data collection systems to sample the GNSS signals. Whereas the data format of the digital GNSS signal streams is comparably easy to describe, the widespread use of software radio technology made it necessary to introduce a certain level of standardization, which was finally achieved by a group of researchers as documented by Gunawardena et al. (2021). The result was the so-called ION SDR Standard (ION SDR Working Group, 2020).

As technology further evolved, new GNSS software radios emerged and some deficiencies of the ION SDR Standard became apparent (Clements et al., 2021). These conditions prompted the present paper, whose contributions are four-fold. First, it presents the first history of GNSS SDR development (Section 2). Second, it offers a detailed description of select GNSS SDRs (Section 3). Third, it overviews recent front-end developments (Section 4). Finally, it summarizes the history of the ION SDR Standard and proposes an update thereto (Section 5).

2 | GNSS SOFTWARE DEFINED RADIO HISTORY

The history of GNSS SDR requires more than a bit of recollection, which can be fraught with inaccuracies, none of which are intentional in the present work. Corrections would always be welcome.

GNSS SDR traces its roots to Ohio University's Avionics Engineering Center around 1994. Professor Michael Braasch, a newly-minted faculty member of the Electrical and Computer Engineering Department and already recognized as an expert in GNSS multipath, was interested in creating a high-fidelity simulation of the internal signal processing within GPS and GLONASS receivers. Dennis Akos, a Ph.D. student in the Department, was intrigued by the idea. Already harboring a keen interest in computer science and programming, Akos took on the simulation project at Braasch's request under the FAA/NASA Joint University Program. Meanwhile, publication of "The Software Radio Architecture" in the 1995 IEEE Communication Magazine (Mitola, 1995) fueled Akos's and Braasch's thinking that this "simulation" could instead be targeted toward an actual software radio implementation. The result was the first publication on GNSS SDR, which appeared in the proceedings of the 1996 ION Annual Meeting (D. Akos & Braasch, 1996).

Development of this initial simulation/implementation was significantly furthered through cooperation with Dr. James B. Y. Tsui of Wright Patterson Air Force Base. Well-recognized as an expert in digital receivers, Tsui had recently taken an interest in satellite navigation. In 1995, two summer interns, Dennis Akos from Ohio University and Michael Stockmaster from The Ohio State University, worked under Tsui's guidance to develop a Matlab implementation of the signal processing required for basic GPS receiver operation. A digital oscilloscope was used to capture the initial IF data that were critical to developing and debugging those early algorithms. Akos was responsible for the lower-level signal processing (acquisition as well as code/carrier tracking), while Stockmaster implemented the navigation solution. The cumulative result was the first ever GPS SDR implementation. Although fully operational, it was "slow as molasses": processing 30 seconds of IF data required hours of computation time. Tsui published the first textbook on GPS SDR in 2000 (Tsui, 2000). A parallel contribution of this initial effort was the direct radio frequency (RF) sampling front-end, which garnered significant interest and pushed advances in analog-to-digital converter development (D. Akos et al., 1999).

After receiving his Ph.D. in 1997, Akos started his academic career as an Assistant Professor in the Systemteknik Department of Luleå University of Technology in Sweden, where he taught a course on computer architecture. It was here that GPS SDR first achieved real time operation. For a class project, Akos provided a Matlab-based GPS SDR and challenged a group of students to "get it to run as fast as possible" subject to the requirement that the complex accumulation products for each channel were within 10% of those produced by the original Matlab-based GPS SDR. It was in 1999 that the first "real time" operation was possible, processing 60 seconds of IF data in 55 seconds. This was a notable achievement at the time given that renowned GPS expert Philip Ward, who was responsible for some of the first GPS receivers, had recently expressed skepticism about the prospect of a

fully software-defined real-time GPS SDR, writing “The integrate-and-dump accumulators provide filtering and resampling at the processor baseband input rate, which is around 200 Hz [... and] well within the interrupt servicing rate of modern high-speed microprocessors. But the 5- to 50-MHz rates [of intermediate frequency samples] would not be manageable” (Kaplan, 1996). This real time implementation effort was led by student Per-Ludvig Normark and led to the results published by D. M. Akos et al. (2001).

In the meantime, Kai Borre, a geodesy professor from Aalborg University, had also developed in the mid-late 1990s Matlab code for GPS receivers. Borre’s code focused on the navigation block and including functions for conversion of coordinates and time references, satellite position determination, and atmospheric corrections. The joint efforts of Akos, Borre, and others would later lead to the well-known book (Borre et al., 2007), a primary reference for GNSS SDR over the next years, and the related SoftGPS Matlab receiver.

Upon graduation, Normark continued his GNSS receiver development with the GPS Laboratory at Stanford University and then returned home to Sweden where he co-founded NordNav Technologies, which developed the first Galileo SDR, and helped establish the architecture, together with Cambridge Silicon Radio (CSR), to push GNSS to a price point acceptable to the mobile phone adoption. CSR, at the time a dominant supplier of Bluetooth hardware to the mobile phone market, acquired NordNav in 2006 and they jointly redesigned the CSR 2.4 GHz radio to multiplex to the 1575.42 MHz GPS L1 band, exploiting the fact that most Bluetooth applications have a relatively low duty cycle. This approach, coupled with the real-time software GPS implementation, provided a near-zero-added-cost GPS receiver.

There have been numerous contributions to GNSS SDR development since these early years, many of which are from the co-authors of this paper. Selected developments by the authors are outlined in Section 3 including a survey of achievements by other researchers in Section 3.11. The authors are aware that many other important contributions are missing, and make no claims of establishing a comprehensive description. In order to give the reader a better orientation about the chronological order of all developments, we present Tab. 1 , reiterating that the selection of references is partly subjective and often similar developments have been carried out by several research groups. The timeline demonstrates the flexibility of SDR technology, i.e., the same code base is used for GPS L1 C/A code signals and for signals of opportunity (SOP) from cellular terrestrial transmitters or from communication satellites in low Earth orbit (LEO).

3 | CURRENT STATUS OF GNSS SOFTWARE DEFINED RADIOS

In June 2023, a quick internet search did not reveal any comprehensive listing of all GNSS SDRs and Wikipedia (2023) lists seven entries, which is far below the number of receivers known by the authors, even if the following criterion is applied to limit the scope: a GNSS SDR (or software receiver) is defined as a piece of software running on a general purpose computer converting samples of a received GNSS signal into a position velocity and time (PVT) estimate. It is clearly understood that a front-end including analog-to-digital conversion (ADC) is required to sample the received signal, but other than that no further functionality is allowed to be realized via hardware. With this definition, three categories of software receivers can be introduced:

real-time receivers: monolithic or modular software packages written in an efficient low-level programming language (like C or C++) typically optimized for run-time efficiency and stability

teaching/research tools: software packages written in a high level programming language like Python or Matlab optimized for code readability and flexibility

snapshot receivers: receivers optimized for very short batches of signal samples

Furthermore, the software package shall allow some configuration flexibility and (at least theoretically) support the ION SDR Standard. The following subsections introduce a few selected developments, emphasizing the rationale behind design choices and current status. Each sub-section is represented by one entry in Tab. 2 to give the reader a quick overview of the main characteristics of each development. Section 3.1 describes the work of Psiaki, Ledvina, and Humphreys and their efforts in real-time processing on DSPs with the bit-wise-parallel approach proving to be highly successful even for space applications. Section 3.2 covers work of Pany/others in their efforts with multiconstellation/multifrequency GNSS. Section 3.3 and Section 3.4 cover the efforts of Borre and others in a readable open source Matlab GPS SDR started in (Borre et al., 2007), with the most recent GNSS update reported in Borre et al. (2022). Akos has also continued this academic development of a suite of open source GNSS SDRs (Bernabeu et al., 2021). The widely used open-source receiver GNSS-SDR is described in Section 3.5.

TABLE 1 Timeline of GNSS SDR developments

Year	Milestone with comment	Reference
1995	Emergence of software radio approach	(Mitola, 1995)
1996	First publication of a GPS SDR development	(D. Akos & Braasch, 1996)
1999	First real-time software receiver with GPS L1 C/A code	(D. M. Akos et al., 2001)
2000	First text book on GPS SDR published	(Tsui, 2000)
2002+	Use of bit-wise correlation and SIMD instructions	(Ledvina et al., 2003; Pany et al., 2003)
2002+	GNSS SDRs as commercial products	NordNav, IFEN, Trimble, Locus Lock, ...
2004	First multi-GNSS/multi-frequency GNSS SDRs	(Ledvina, Psiaki, Sheinfeld, et al., 2004; Pany, Eissfeller, et al., 2004)
2004	First real-time GNSS/INS integration with SDR	(Gunawardena et al., 2004)
2005	GNSS SDR consolidation at Politecnico di Torino and LINKS Foundation	Section 3.9
2005	Demonstration of vector tracking with a GNSS SDR	(Pany et al., 2005)
2006	First real-time all-in-view embeddable GNSS SDR	(T. Humphreys et al., 2006)
2006	First use of SDR technology for AM signals of opportunity	(McEllroy, 2006; McEllroy et al., 2006)
2007	Start of wide-spread adoption of SDR technology in GNSS research	(Borre et al., 2007)
2007	First development of a snapshot receiver	Section 3.8
2009	First multi-core GNSS SDR	(T. E. Humphreys et al., 2009)
2010	Adoption of a computer science best practice collaborative framework	Section 3.5
2010	First use of GPUs for correlation	(Hobiger et al., 2010)
2011+	Use of GNSS SDR for ionospheric research	(O'Hanlon et al., 2011; Peng & Morton, 2011)
2012+	SDR developments at the Finnish Geospatial Research Institute	(Borre et al., 2022; Söderholm et al., 2016)
2012	Use of a DVB-T ultra-low-cost front-end for GNSS SDR	Section. 3.5
2012+	Use of SDR technology for LTE signals of opportunity	(del Peral-Rosado et al., 2013; Driusso et al., 2017; Shamaei et al., 2018)
2014+	Use of GNSS SDRs in space	(Lightsey et al., 2014; Murrian et al., 2021)
2014	Use of SDRs for mixed cellular 3G GSM/CDMA and DTV SOP	(Yang et al., 2014)
2015+	Abundance of processing power for GNSS SDR available	(Dampf et al., 2015; Nichols et al., 2022)
2017+	Use of SDRs for 3G CDMA and 4G LTE SOP	(Kassas et al., 2017)
2018	First use of Python for dedicated teaching of GNSS SDR	Section 3.7
2018	First SDR enabling sub-meter-level carrier-phase-based UAV navigation with 3G CDMA and 4G LTE SOP	(Khalife & Kassas, 2018 2022)
2020	Formal adoption of ION SDR Standard	Section 5
2020	Use of SDR for stationary positioning with multi-constellation Orbcomm and Iridium LEO SOP	(Farhangian & Landry, 2020; Orabi et al., 2021)
2021	First SDR for 5G SOP	(Shamaei & Kassas, 2021b)
2021+	Use of GNSS SDR to support development of new navigation satellite systems	(Miller et al., 2023; Song et al., 2021)
2021	First SDR enabling vehicle navigation with multi-constellation LEO SOP	(Kassas et al., 2023 2021)
2022	First SDR enabling aircraft navigation with cellular SOP	(Kassas, Abdallah, et al., 2022; Kassas, Khalife, Abdallah, Lee, Jurado, et al., 2022)

TABLE 2 Overview of GNSS SDRs discussed in Section 3

Name	Main language	Open source	Main focus
GRID	C++	No	Real-time operation of advanced algorithms on embedded devices
MuSNAT	C++	No	Analysis of navigation signal processing and algorithm prototyping
SoftGPS	MATLAB	Yes	Suite of GNSS SDRs with widespread use and accompanying book
FGI-GSRx	MATLAB	Yes	Multi-GNSS SDR with accompanying book
GNSS-SDR	C++	Yes	Real-time SDR with modular structure and widespread use
AutoNav-SDR	MATLAB	No	Support for KPS-development, API, and GPU
PyChips	Python	No	Multi-GNSS and optimized for use in teaching classes
UAB Snapshot GNSS Receiver	MATLAB	No	Snapshot receiver that can be operated in the cloud
NGene	ANSI C	No	Efficient GNSS SDR used in numerous Galileo-related projects
MATRIX	MATLAB, C++	No	Combined processing of GNSS with cellular 3G/4G/5G and LEO (Starlink, OneWeb, Orbcomm, Iridium, and Globalstar) signals

The AUTONAV receiver used to support the development of Korean Positioning System (KPS) is discussed in Section 3.6 and PyChips (cf. Section 3.7) is the basis for tutorial classes of the ION. The UAB snapshot GNSS software receiver is described in Section 3.8, while Section 3.9 discusses a SDR used e.g. to the authentication schemes, reflectometry or to assess the influence of non-standard GNSS transmissions. Section 3.10 extends the scope of SDR to non-GNSS signals.

Whereas at the beginning of the GNSS SDR development the different receivers were linked to specific persons or research institutes, today often different receivers, tools or code bases are used at the same institute. On the other hand, code bases first developed by a single institute spread into different institutes. For example, the developments of Borre et al. (2007) forked into several branches [e.g. (Bernabeu et al., 2021; FGI, 2022; Zhang, 2022)], as discussed in Section 3.3 and Section 3.4.

3.1 | Bit-Wise Parallelism and the Emergence of GRID

The original real-time GNSS software radio work by D. M. Akos (1997) inspired an effort within the Cornell GPS group. Psiaki had been working with non-real-time software GNSS signal processing in Matlab for about two years when he started to wonder whether the slow Matlab operations could be translated to run in real-time on a general desktop workstation. The bottleneck in GNSS digital signal processing occurs when doing the operations that initially process the high-frequency RF front-end samples. RF front-ends typically sample at 4 MHz or faster. A 12 channel receiver would have to perform on the order of 400 million operations per second or more in order do all of the needed signal processing. Psiaki conceived the concept of bit-wise parallel processing as a means of addressing this challenge. He recruited then-Ph.D. candidate Brent Ledvina to make an attempt at implementing these ideas in the C programming language on a Real-Time Linux desktop workstation. Ledvina succeeded in developing a 12-channel real-time L1 C/A-code receiver after about 6 months' effort (Ledvina et al., 2003).

The main concept of bit-wise parallelism is to work efficiently with RF front-end data that have a low number of quantization bits. If an RF front-end produces a 1-bit digital output stream, then 32 successive sign-bit samples can be stored in a single 32-bit unsigned integer word on a general-purpose processor. Thirty-two successive output samples of a 2-bit RF front-end can be stored in two 32-bit words, one containing the successive sign bits and the other containing the successive magnitude bits. Each channel of the software receiver generates a 1-bit or a 2-bit representation of 32 successive samples of its IF carrier replica, both in-phase and quadrature, and the successive samples are stored in parallel in 32-bit unsigned integer words. Similarly, it generates a 1-bit representation of 32 successive samples of its prompt pseudo-random noise (PRN) code replica and stores them in parallel in a single 32-bit unsigned integer word. It also generates an early-minus-late PRN code replica that requires 1.5 bits per sample, which takes up two 32-bit unsigned integer words to store 32 samples. These replica signals can be generated very efficiently by using pre-tabulated 32-bit words. The software receiver then performs a series of bit-wise AND, OR, XOR, and similar operations that have the effect of performing PRN code mixing and IF-to-baseband carrier mixing. The outputs of the mixing operations are contained in a small number of 32-bit words, the number of which depends on the number of bits in each RF front-end output sample and the number of bits in the IF carrier replicas.

The final operation is accumulation of the results in the 32-bit words. This involves sets of bit-wise Boolean operations, as per Ledvina et al. (2003), followed by summation of the number of 1-bits in the resulting 32-bit unsigned integer words. The bit summation operations proved to be a challenge in terms of minimizing execution time. Ledvina solved this problem by using a pre-computed 1-dimensional data table whose input was the unsigned integer and whose output was the number of 1-bits. In order to keep the table size reasonable, it only counted the bits in a 16-bit unsigned integer word. The original receiver's 32-bit words were split in half, two table look-ups were performed, and the results summed in order to count all the 1-bits. The original algorithms are defined by Ledvina et al. (2003), Ledvina, Psiaki, Powell, & Kintner (2004), and Ledvina, Psiaki, Powell, & Kintner (2006).

When using very long PRN codes, such as the L2C CL code, the original method's whole-period PRN code tables of the proper 32-bit words at various code phases became impractically large. Therefore, a new method was developed for long PRN codes. It tabulates 32-bit words of short generic PRN code chip sequences, with all possible combinations of a short sequences of chips considered at various PRN code offsets relative to the start of the samples of the 32-bit word. Those methods are described by Psiaki (2006) and by Ledvina et al. (2007). This technique proved invaluable for dealing with long codes.

A processor that can operate on wider segments of data, up to 512 bits for current single instruction multiple data (SIMD) instructions, gains substantial additional signal processing speed increases (Nichols et al., 2022). Note, however, that the speed increase factors over brute-force integer calculations are typically not as high as the number of bits per word. That is, the techniques do not speed up the operations by a factor of 32 when processing 32 samples in parallel by using 32-bit words to represent 32 samples. For a 2-bit RF front-end and a 32-bit processor, the speed-up factor might be only 4 because the bit-wise parallel approach requires multiple operations due to, say, a simple multiplication of one time series by another. If one doubles the number of bits per word, however, then the speed tends to double. A particularly helpful feature of some recent processor designs is their inclusion of a hardwired command to count all the 1 bits in a word. This "popcount" intrinsic obviates the table look-ups that counted 1-bits in the original bitwise parallel design. If the number of bits increases in the RF front-end samples and/or the IF carrier replicas, however, then the bit-wise parallel method of signal processing slows down. Signals represented by 3 or 4 bits might cause the processing speed gains of bit-wise parallel algorithms to be limited or even non-existent.

After getting the basic algorithms working in real-time using 32-bit words, the Cornell group showcased the efficacy of real-time GNSS software radio by using the techniques to develop a dual-frequency L1 C/A and L2C receiver (Ledvina, Psiaki, Sheinfeld, et al., 2004) and a GPS/Galileo L1 civilian receiver (Ledvina, Psiaki, Humphreys, et al., 2006). These real-time software GNSS receivers each required only several person-days to develop them from the original L1 C/A code receiver. Of course, the L1/L2 receiver required a new dual-frequency RF front-end. The GPS/Galileo receiver required knowledge of the civilian Galileo E1 PRN codes, which had not been published at that time. This requirement led to a supporting effort which successfully deduced the Galileo GIOVE-A E1 PRN codes by recording their raw RF front-end samples and post-processing those samples using a suite of custom-designed SDR signal processing algorithms in order to pull the chips out of the noise (Psiaki et al., 2006).

The next development was to re-implement the bit-wise parallel code for embedded (low-power, low-cost) processing. Initially targeting a Texas Instruments DSP, this work was accomplished in 2006 by then-Ph.D. candidate Todd Humphreys (T. Humphreys et al., 2006). Later, as a professor at The University of Texas at Austin, Humphreys and his students—notably Jahshan Bhatti and Matthew Murrian—undertook a sequence of significant expansions and improvements to this receiver. Called GRID, the C++-based UT Austin receiver is by now a highly-optimized science-grade multicore GNSS SDR (T. E. Humphreys et al., 2009; Nichols et al., 2022) with its main features summarized in Tab. 3 . It was the first GNSS SDR to be adapted for spoofing (T. E. Humphreys et al., 2008), the first GNSS SDR to operate in space (Lightsey et al., 2014), the first receiver of any kind to show that centimeter-accurate GNSS positioning is possible with a smartphone antenna (K. M. Pesyna Jr. et al., 2014), the first receiver to be used to locate terrestrial sources of GNSS interference from low-Earth orbit (Murrian et al., 2021), and is the basis of the current state-of-the-art in urban precise (dm-level) positioning (T. E. Humphreys et al., 2020; Yoder & Humphreys, 2023). As detailed in (Nichols et al., 2022), GRID has also reaffirmed the commercial viability of GNSS SDR in widespread low-cost applications: it was recently licensed by a major aerospace company for use across all company operations, including in the thousands of satellites of the company's broadband Internet mega-constellation.

3.2 | Multi Sensor Navigation Analysis Tool

The Multi Sensor Navigation Analysis Tool (MuSNAT) is an object-oriented but monolithic C++ software receiver maintained by the University of the Bundeswehr Munich (UniBwM) and has been first mentioned in its present form by Pany et al. (2019).

TABLE 3 Main features of GRID

GRID		
Feature	Solution	Remark
Operating System	GNU/Linux, macOS, Windows	
Programming environment	C++	
IF sample file input source	A wide array of formats	Proposed ION SDR Standard will accommodate
Real-time sample input	Yes	See Nichols et al. (2022)
Additional sensors	IMU, Cameras, LiDAR	Requires PpEngine module
Supported GNSS	GPS, Galileo, BeiDou, SBAS, QZSS, CDMA	Nearly all open spreading codes and navigation message streams supported
Acquisition	Multi-threaded and FFT-optimized	
Tracking	Vectorized, multicore, Intel SIMD (SSE2 through AVX-512) and ARM NEON (64-bit and 128-bit) accelerations	Correlation no longer the primary bottleneck under some configurations; see Nichols et al. (2022)
Measurement output	All standard GNSS observables	Proprietary GBX format plus RINEX, NMEA, RTCM, Matlab MAT-file, KML
Navigation	Extended Kalman filter based on pseudorange and Doppler measurements	Carrier-phase-based positioning available with PpEngine module
Further features	Vector tracking, multi-antenna, IMU integration, space-ready, interference mitigation & detection	
Availability	Source code available via commercial license from UT Austin	Turnkey solutions available via Locus Lock

It started as an operational real-time receiver development, but currently it mostly serves to develop and demonstrate innovative signal processing and navigation algorithms. Furthermore, it is used for teaching. It is freely available as executable for academic purposes from (UniBwM, 2023). Its main characteristics can be found in Tab. 4 . In contrast to the bit-wise approach of Section 3.1 (that allows to design very power-efficient implementations), the design idea of MuSNAT and its predecessors was to realize a high-end receiver running on powerful PCs or workstations. The bit-wise approach was replaced by using SIMD instructions of Intel/AMD central processing units (CPUs). This allows to represent samples as 8-bit or 16-bit values and SIMD instructions like AVX-512 currently allow processing of registers of up to 512 bit (i.e. 32 16-bit samples) in parallel.

The GNSS software receiver developments started at UniBwM in 2002 after it became clear that the software radio approach discovered by D. Akos would provide useful insights into GNSS receiver technology and thus will be indirectly very helpful to design and build the Galileo navigation satellite system. The first software receiver at UniBwM was GPS L1 C/A only and was realized as a Matlab/Simulink project working in post-processing. To sample the GNSS signals, a commercial ADC with a peripheral component interconnect express (PCIe) connector from NI was used (PXI 5112) that was connected either to a low-bandwidth GPS L1 C/A code front-end based on the Plessey GP 2010 RF chip set and later on to one GPS L1/L2 high-bandwidth front-end, which was specifically developed by Fraunhofer IIS (Pany, Förster, & Eissfeller, 2004). Soon after, the software to communicate with the ADC (written in C++ making use of the Microsoft Foundation classes) was upgraded to a full GPS L1 C/A plus L2CS (L2 medium length code was supported only, not the long code) receiver. A detailed analysis published by Pany et al. (2003) revealed that not only the SIMD instruction set was important for the real-time capability but also the size and structure of the CPU caches. Memory bandwidth is one of the key issues when representing samples by multiple bits. One of the first achievements with this receiver was the demonstration of vector tracking (Pany et al., 2005).

Based on those results, funding to support a group of five researches over three years was secured. This allowed starting a new software receiver project, this time making full use of C++ features for object-oriented development, and development of a graphical user interface (GUI) connected to the processing core via a clearly defined interface also allowing to run the core without GUI. The overarching development goal at that time was to realize a high-quality multi-GNSS multi-frequency receiver on a desktop PC or powerful laptop that could potentially be operated on a continuous basis to replace the (at that time) rather inflexible and expensive commercial GNSS receivers at continuously operating reference stations (CORSs). A concise overview of the development during those years was written by Stöber et al. (2010) and shows the improvements compared to the start of the project layed down by Pany, Eissfeller, et al. (2004).

A loose cooperation with IFEN GmbH was initiated that eventually resulted in the SX3 receiver (IFEN GmbH, 2022). IFEN used the processing core as initial basis, improved the core, replaced the GUI, and developed new dedicated front-ends. The C++ code was further optimized to support more channels at higher bandwidth and almost instantaneous high-sensitivity acquisition with the graphics processing unit (GPU) (GPS World staff, 2012). Also, semi-codeless tracking of GPS L2P(Y) (i.e. P-code aided cross-correlation) was implemented. The cooperation of UniBwM with IFEN lasted until 2013 when the development directions started to diverge. IFEN used the software mostly as base receiver platform with an application programming interface (API) to support different applications, whereas UniBwM continued to modify the core, which was not always beneficial for software stability if seen from a commercial point of view.

The focus at UniBwM switched in 2017 as the old GUI could not be maintained anymore. Furthermore, real-time operation became less important as most scientific results were obtained in post-processing. The result was that a new GUI was developed and attached to the proven processing core. Any run-time optimizations within the processing core degrading navigation performance (i.e. mostly causing additional noise in the code tracking loop) were removed. The core's logging output was directed to a SQL database to store all different kind of intermediate results in a single file (additionally to the legacy ASCII logging into multiple files). A dedicated visualization tool for this database was developed.

The use of Windows and Visual Studio for developing a software radio is a little unusual, but is explained as follows. At UniBwM, most researchers use Windows PCs to allow easy document exchange with each other and most importantly within the European space industry. For this reason, all software receiver developments were done for Windows only. In terms of numerical performance and code optimization, Intel provided and still provides with the Intel C++ compiler and the Intel Performance Primitives the same quality on Windows as for Linux. Over the years it became, however, also clear that the potential use of the processing core on embedded devices and long-term stability might have been easier to achieve on the Linux operating system. IFEN ported part of the core to Linux, but not the full software receiver, and showed that conventional desktop CPUs and embedded CPUs provided an impressive processing capability already in the year 2015 (Dampf et al., 2015).

As already mentioned, code optimization to achieve fast (and real-time) signal tracking was a main research focus in the first years. Different studies on CPU assembler instructions, CPU architecture and bottlenecks resulted in dedicated assembler implementations. Extensive lookup-tables were used and one very efficient correlator implementation with the Intel x86 pmaddubsw-instruction was based on a signal sample representation as unsigned integers (including the necessary rewriting of the correlation formulae due to the switch from the standard representation of samples as signed integers to unsigned integers). FFT based acquisition was already very efficient on the CPU and even more efficient on the GPU. The use of FFT libraries provided by NVIDIA made the acquisition code porting from CPU to GPU comparably easy. The situation is different for signal tracking. The tracking code has been transferred to the GPU, and some optimization have been applied to minimize the amount of data transfer between CPU and GPU. However, since the correlation parameters are slightly different for each signal tracked, the correlation code is called multiple times and the latency to start one thread on the GPU generated significant overhead. GPU-based tracking is thus currently only beneficial if a very large number (several hundreds) of correlators is configured per tracking channel, as pointed out by Pany et al. (2019). As modern desktop and laptop CPUs continue to improve and make use of a many-core structure, the need to port signal tracking to the GPU becomes less important. Furthermore, the use of dedicated assembler code required over the years continuous adaptation to new CPU instruction sets (e.g. from SSE to AVX instructions). The performance gained by using hand-coded assembler routines compared to the use of the libraries provided by Intel (IPP) is not always worth the effort and was not further actively pursued. Instead, dot-product routines (2 x 16-bit signed input to 64-bit output) from the IPP are employed for signal tracking.

The C++ universe is huge, and it is easy to integrate external source code. For example, the famous RTKLIB and the ION SDR sample reader code have been integrated. The current research work with MuSNAT focuses on GNSS/INS/LiDAR integration, support of massive antenna arrays (Dötterböck et al., 2023), vector tracking and deep GNSS/INS coupling, support for LTE/5G-signals and GNSS signal simulation. It has to be admitted that the maintenance of the huge C++ code-base of MuSNAT at a

TABLE 4 Main Features of MuSNAT

MuSNAT		
Feature	Solution	Remark
Operating System	Windows 10/11	Compiles as GUI or as command line version (port of command line version to Linux under preparation)
Programming environment	Microsoft Visual Studio 2019 C++	CUDA, Intel OneAPI, vcpkg and .net for GUI
IF sample file input source	ION SDR Standard and proprietary file readers	proprietary readers faster than ION SDR reader
Real-time sample input	yes, via TCP/IP	server available via LabView for selected NI USRPs
Additional sensors	LiDAR, IMU	LiDAR uses PCL format, IMU proprietary ASCII format, video formats supported but not yet used
Supported GNSS	GPS, Galileo, BeiDou, GLONASS, SBAS, OFDM (LTE, 5G, ...)	nearly all open spreading codes available and at least for each system one navigation message decoder
Acquisition	optimized fast Fourier transform (FFT) method	CPU and GPU supported
Tracking	dot-product from Intel Performance Primitives (CUDA version for massive multi-correlator applications)	computational performance mostly limited by memory bus width
Further features	multi-antenna, signal-generator, primary-secondary tracking, SQL database for logging, vector tracking, GNSS/INS integration, RTKLIB	via Matlab-interface support of Galileo OSNMA/HAS and synthetic aperture processing
Availability	Executable plus data visualizer downloadable via UniBwM (2023)	Source code available for research projects with UniBwM

University institute with a high fluctuation of researchers is partly demanding. The learning curve for good C++ development in this context is steep and for the purposes of obtaining a PhD degree often an inefficient way. Therefore, interfaces from the C++ code to Matlab were established and for example Open Service Navigation Message Authentication (OSNMA) decoding, PPP-computation for High Accuracy Service (HAS) or LiDAR odometry are implemented in Matlab. Another development is to use MuSNAT to generate multi-correlator values that are then used within a full Matlab based receiver to emulate signal correlation via interpolation (Bochkati et al., 2022). Bochkati et al. (2023) use this for ease of development of synthetic aperture algorithms.

UniBwM has initially used front-ends from Fraunhofer IIS and the software receiver included low-level universal serial bus (USB) drivers for real-time data transfer. The same approach was used to connect the front-ends from IFEN GmbH to the processing core. The effort to write stable high data-rate low-level drivers is significant and introduces a dependency on libraries and support from the USB chip manufacturers. To reduce these kinds of development efforts, the decision to connect front-ends via TCP/IP was felt. This approach is powerful in terms of bandwidth and also generic and a first version of it is described in (Arizabaleta et al., 2021). Furthermore, with e.g. LabVIEW from NI it is comparably easy to develop a simple TCP/IP signal source for universal software radio peripheral (USRP) frontends. At the time of writing this paper, a more efficient firmware for USRPs with direct FPGA programming is being developed and shall allow to synchronously capture data from an inertial measurement unit (IMU) together with the GNSS signal samples.

3.3 | SoftGPS, SoftGNSSv3.0, and Derivatives

As abovementioned, (Borre et al., 2007) and the associated Matlab receiver was a cornerstone for GNSS SDR development. This receiver, initially called SoftGPS, then SoftGNSS (usually referred to as SoftGNSSv3.0), included the basic processing functions for GPS L1 C/A in a readable format, was very useful for educational purposes. These included signal FFT-based acquisition, frequency, carrier phase and code phase tracking, data synchronization and demodulation, pseudorange generation, and eventually PVT. The Matlab code, together with some samples, was provided in a CD with the book, and was also available at Aalborg University's Danish GPS lab website. Apart from K. Borre and D. Akos, SoftGNSS included relevant contributions by D. Plausinaitis and others. Unfortunately, Kai Borre passed away in 2017 and the Danish GPS Lab was discontinued. However, SoftGNSS and its derivatives remain quite alive. Here are some examples:

- A new SDR GNSS book, (Borre et al., 2022), extending SoftGPS functionality to several frequencies, GNSS and architectures, can be considered as the successor of (Borre et al., 2007). A main building block of this book is FGI-GSRx, described in the following section, but the book also includes other Matlab receivers. In particular, DF-GSRx (Dual-Frequency GNSS Software Receiver), developed by Borre's PhD student P. Bolla, is a dual-frequency GPS L1/L5 receiver that includes dual-frequency acquisition techniques, measurements combination (iono-free in particular) and positioning. The book also includes a GPS L1 C/A snapshot receiver developed by Borre's former PhD student I. Fernandez-Hernandez, more modest than that described later in Section 3.8, but simple and quick to execute and therefore possibly useful for educational purposes.
- The Easy Suite libraries (Borre, 2003 2009), still publicly available and used, provide an excellent educational tool to dive into basic functions of GNSS receivers, such as calculating satellite positions from the ephemerides, datum conversions, or computing the receiver position and its accuracy in multiple ways (least squares, Kalman filter, carrier phase ambiguity resolution, etc.)
- (Bernabeu et al., 2021), as above mentioned, provides a collection of open source SDRs developed at University of Colorado Boulder and based on SoftGNSS.
- (Zhang, 2022) provides a repository with adaptations of SoftGNSS for different front-ends.

3.4 | Finnish Geospatial Research Institute's Multi-GNSS Software Receiver

The software receiver developed by Finnish Geospatial Research Institute (FGI) is famously known as the FGI-GSRx (FGI's GNSS Software Receiver). The development of the FGI-GNSS Software Receiver (GSRx) software receiver started in 2012 from the open source GNSS software receiver released in 2007 by Prof. Borre and his colleagues Borre et al. (2007). The software receiver was able to track two IOV (In-Orbit Validation) satellites called GIOVE A and GIOVE B from the European GNSS system Galileo. Since then, the researchers at FGI have been continuously developing new capabilities to the software receiver with the inclusion of Galileo in 2013 (Söderholm et al., 2016), the Chinese satellite navigation system BeiDou in early 2014 (M. Bhuiyan et al., 2015; M. Z. Bhuiyan et al., 2014), the Indian regional satellite navigation System NavIC in late 2014 (Thombre et al., 2015) , and the Russian satellite navigation system GLONASS in 2015 (Honkala, 2016).

The FGI-GSRx software receiver has been extensively used as a research platform for the last one decade in different national and international research and development projects to develop, test and validate novel receiver processing algorithms for robust, resilient and precise position navigation and timing (PNT). At present, the FGI-GSRx can process GNSS signals from multiple constellations, including GPS, Galileo, BeiDou, GLONASS, and NavIC. The software receiver is intended to process raw IF signals in post-processing. The processing chain of the software receiver consists of GNSS signal acquisition, code and carrier tracking, decoding the navigation message, pseudorange estimation, and PVT estimation. The software architecture is built in such a way that any new algorithm can be developed and tested at any stage in the receiver processing chain without requiring significant changes to the original codes. FGI-GSRx provides a unique and easy-to-use platform not only for research and development, but also for whoever is interested in learning about GNSS receivers. Some of the main features of FGI-GSRx are listed in Tab. 5 .

The software receiver was released as open source in February 2022 (FGI, 2022). FGI-GSRx receiver was also accompanied by the book 'GNSS Software Receivers', a next edition of one of the fundamental GNSS textbooks, published in 2022 by Cambridge University Press (Borre et al., 2022). The book systematically introduced the software receiver processing functionalities

TABLE 5 Main features of FGI-GSRx

FGI-GSRx		
Feature	Solution	Remark
Operating System	Windows 10	Compiles in Windows 10 environment. The software receiver should run in other OS which can host MATLAB or OCTAVE.
Programming environment	MATLAB	Executes in MATLAB 2019 or any other later version. The software receiver can be also executed in OCTAVE.
IF sample file input source	ION SDR Standard	Read input data files following ION SDR Standard.
Processing mode	Only operate as post-processing GNSS receiver	It can read raw IF data for a complete receiver processing, or it can load previously saved acquisition and/or tracking data in order to skip acquisition and/or tracking operation to be able to process navigation solution depending on parameters set in the user configuration file.
Supported GNSS	GPS L1, Galileo E1, BeiDou B1, GLONASS L1, NavIC L5	Open source FGI-GSRx only supports single frequency multi-GNSS processing.
Acquisition	FFT-based signal acquisition	Sophisticated research specific implementation for high sensitive acquisition is not published as open source.
Tracking	Table-based three-stage tracking	Based on the tracking status of each individual satellite, the software receiver switches among three stages: i) PULL IN, ii) COARSE TRACKING and iii) FINE TRACKING.
Navigation	Traditional Least Square (LS)	Users can select SNR or elevation cut-off mask in order to decide on the satellites that contribute to the position computation.

with experimental results for GPS L1 C/A signal in Section 2 (“GPS L1 C/A Receiver Processing”, 2022), GLONASS L1OF signal in Section 3 (“GLONASS L1OF Receiver Processing”, 2022), Galileo E1 OS signal in Section 4 (“Galileo E1 Receiver Processing”, 2022), BeiDou B1I signal in Section 5 (“BeiDou B1I Receiver Processing”, 2022), NavIC L5 signal in Section 6, (“NavIC L5 Receiver Processing”, 2022) and a single frequency multi-constellation solution with three GNSS signals in Section 7 (“A Multi-GNSS Software Receiver”, 2022). The readers can easily follow the fundamental receiver processing chain for each individual GNSS signal with the distinctive changes among those signals discussed and highlighted with figures. One of the noteworthy contributions of the book was the integration method of several GNSS signals to form a single-frequency multi-GNSS PVT solution presented in Section 7.

The FGI-GSRx software receiver can be utilized in universities and other research institutes as a tool for training graduate level students and early-stage researchers for getting hands-on experience on GNSS receiver development. It can also be utilized in the vast GNSS industry as a benchmark software defined receiver implementation. The software receiver is already being used in the ‘GNSS Technologies’ course offered widely in Finland - at the University of Vaasa, Tampere University, Aalto University and the Finnish Institute of Technology.

3.5 | GNSS-SDR, an Open-Source Software-Defined GNSS Receiver

The software receiver developed by the Centre Tecnològic de Telecomunicacions de Catalunya (CTTC), uncreatively named GNSS-SDR (but not related to the ION SDR Standard), is another example of a multi-band, multi-system receiver. It has been

TABLE 6 Main features of GNSS-SDR

GNSS-SDR		
Feature	Solution	Remark
Operating System	GNU/Linux, macOS, Windows OS through WSL.	Included as a software package in Debian and Ubuntu, and in Macports for macOS. Tested on ArchLinux, CentOS 7, Fedora, OpenSUSE, Rocky Linux.
Programming environment	C++	Software linters are automatically run at each code change to ensure meeting high-quality coding standards.
Processing mode	Real-Time and Post-Processing.	It can work in real-time using a wide assortment of commercial RF front-ends, and in post-processing mode with a number of file formats (including input files produced by the ION SDR Standard conversion tools).
Supported GNSS	GPS L1, L2C, L5; Galileo E1, E5a, E5b, E6; Glonass L1 CA, L2 CA; Beidou B1, B3.	The modular design allows for easy inclusion of new signals.
Acquisition	FFT-based signal acquisition.	A-GNSS capabilities to accelerate the Time To First Fix.
Tracking	Multicorrelator-based Data and Pilot signal tracking.	Customizable DLL, PLL, FLL. High-dynamics capabilities. SIMD-accelerated both in i686 and ARM CPUs (see Fernández–Prades et al. (2016a)).
Navigation	Traditional Least Square (LS), code and carrier-based positioning modes.	Positioning engine based on RTKLIB implementation (Takasu & Yasuda, 2009). All possible supported GNSS signals combinations are allowed.

constantly evolving since 2010, keeping pace with the newest GNSS algorithms and signals over more than a decade. It originated as a by-product of a CTTC research staff initiative, with the aim of providing a collaborative framework with other researchers seeking to accelerate research and development of software-defined GNSS receiver technology. The receiver particularly focuses on baseband signal processing, although it has the ability to run a navigation engine (refer to Tab. 6). The early stages of development baked slowly under a personal side-project scheme, with no funding, but with the purely exploratory objective of designing an optimal architecture specifically suitable for GNSS signal processing, where concepts such as testability, extensibility, reusability, scalability, maintainability, portability, adaptability to new non-standard requirements, and adoption of Computer Science best practices considered from scratch.

Its first popularity peak came on August 2012, with the reporting of the usage for GNSS of extremely cheap (about $25) DVB-T receivers based on the Taiwan's Realtek RTL2832U chipset, sold in form of USB dongles that allow users to watch over-the-air DVB-T European broadcast television on their personal computers. Normally, those devices send partially-decoded MPEG transport frames over the USB, but exploiting an undocumented mode of operation of the demodulator chip, the user was able to obtain raw I&Q samples, stream them through USB to a personal computer and then apply the GNSS-SDR software processing, turning the DVB-T receiver into a GNSS receiver and delivering position in real-time (see Fernández–Prades et al. (2013)). On a parallel development, in November 2013, the European Space Agency acknowledged GNSS-SDR as one of the first 50 users worldwide to achieve a successful Galileo position fix.

The project gained momentum and maturity over the years, and today it enjoys a solid and valuable user base continuously providing feedback, enhancements, and new features. Current versions are included in major GNU/Linux distributions, such as Debian and Ubuntu, and in Macports for Apple's macOS. The software package has been used in several public and private-funded research projects (including EUSPA, European Space Agency (ESA), NSF and NASA activities, as well as in educational programs such as Google Summer of Code), and it has been reportedly used for research purposes worldwide. The authors opened

a discussion of quality metrics and key performance indicators for any generic software-defined receiver (Fernández–Prades et al. (2016b), extended online version available at `https://gnss-sdr.org/design-forces/`) and proposed the concept of *continuous reproducibility* in GNSS signal processing (Fernández–Prades et al. (2018)).

The full project and source code documentation can be found online at `https://gnss-sdr.org`, a website with over 5000 unique visitors per month, which contributes to raising awareness on GNSS technology. The website content is also on a GitHub repository at `https://github.com/gnss-sdr/geniuss-place`, hence undergoing public scrutiny. The project is also well-connected to its software ecosystem and existing SDR platforms. It builds on a wide range of GNU/Linux distributions and versions (from most recent releases to those released in 2014), and it provides a Yocto / Openembedded layer, which allows its portability to a wide range of embedded platforms (see Fernández–Prades (2022)).

The software produces standard outputs for observables and navigation data (RINEX files and RTCM-104 v3.2 messages as defined by the Networked Transport of RTCM via Internet Protocol, NTRIP), as well as position fixes in application-specific messages (*e.g.*, NMEA 0183), a variety of GIS-oriented file formats (KML, GeoJSON, GPX), and custom binary outputs that allow the observability of internal signal processing sub-products.

3.6 | AutoNav SDR

The AutoNav SDR is a MATLAB-based multi-GNSS and multi-frequency software receiver that was developed by the Autonomous Navigation Laboratory of Inha University, South Korea (Song et al., 2021). Its main features are arranged in Tab. 7 . The critical point considered in the design phase of this SDR is the maximization of reconfigurability. Since South Korea is developing its own satellite navigation system, KPS which is targeted to operate from 2035 as reported by Ministry of Science and ICT of Korea (2021), a flexible receiver that can process not yet existent signals is highly required. The AutoNav SDR is profoundly designed to provide full reconfigurability in terms of target signal combinations and signal characteristics, especially for easy addition of the new signal proposals. To do so, a basic framework of software receiver was designed with a well-designed processing functional architecture and data structure in consideration of the expandability of the signals and then applied to realize an SDR for GPS L1 C/A code signal as a first realization example by reconfiguring a configuration file via a GUI. Then, different signals of the other constellations (GLONASS, Galileo, BeiDou navigation satellite system (BDS), Quasi-Zenith Satellite System (QZSS), NavIC) and frequencies (L1, L2, L5) were added quickly by utilizing this expandability. In this way, KPS signal candidates can be easily added to the SDR to evaluate and compare the performance of each candidate in the signal design phase. Similarly, a reconfigurable GNSS simulator was developed at the same time with the same idea. This is a MATLAB-based IF level GNSS/KPS simulator which can be ideally suited to test the navigation performance of any GNSS signals as well as new KPS signals by reconfiguring signal design parameters via a GUI.

Although the AutoNav SDR is targeted for post-processing only, the original correlation operation in MATLAB with variables of double precision was too slow at the beginning of its design phase. So, two simple accelerations were applied to the SDR: a GPU-based acquisition module and a MEX correlator for tracking. The GPU-based signal acquisition module was implemented in a very simple way using the Parallel Computing Toolbox of MATLAB. If the GPU is usable, local variables for the correlation (i.e., code and carrier replicas) are generated in the GPU memory using the gpuArray function. Then, FFT and inverse fast Fourier transform (IFFT), and correlations are performed in the GPU automatically. Finally, the correlation results are extracted using a gather function. With this simple approach, it has approximately 2.12 times faster execution time compared to the general CPU-based acquisition, without the relatively complex development using CUDA.

Since the most time-consuming process of the receiver is the correlator in the signal tracking, a MEX function is employed to reduce the computational burden. The MEX function connects the MATLAB environment to the external function written in C/C++ language with an appropriate wrapper function, so the user can call it within MATLAB. The MEX correlator was written in the standard C language and uses integer-based variables. The SDR pre-generates the code and carrier replica tables at the initialization process with resolutions of 18 bits and 8 bits, respectively. The code and carrier NCOs have a resolution of 32 bits, so the indices of the tables for current code and carrier replica generation are calculated using bit shift operations of 14 bits and 24 bits, respectively. With these implementations, the overall execution time became much faster (approximately 5 times) than the original double precision-based code, but it still cannot operate in real-time. Currently, Inha University is developing the FPGA-based real-time GNSS receiver that only the correlator would be substituted by the FPGA board at the original AutoNav SDR.

To further enhance the flexibility, the AutoNav SDR also provides APIs at each part of the signal processing chain (such as ring buffer, acquisition, tracking, navigation message extraction, position calculation, etc.). The API design was influenced by

TABLE 7 Main features of AutoNav SDR

AutoNav SDR		
Feature	Solution	Remark
Operating system	Windows	
Programming environment	MATLAB and C	
Processing mode	Post-processing	
Supported GNSS	GPS (L1 C/A, L2C, L5), GLONASS L1, Galileo (E1, E5a, E5b), BDS (B1I, B1C, B2a), QZSS (L1 C/A, L1C, L2C, L5), NavIC L5	Free selection of signal combination
Acquisition	GPU-based acquisition	Simple implementation using Parallel Computing Toolbox of MATLAB
Tracking	MEX correlator	18/8 bits code/carrier replica tables, 32 bits code/-carrier numerically controlled oscillators (NCOs), bit shift operations
Further features	API, easy addition of new signals, RINEX observation logging, Radio Frequency Interference (RFI) mitigation based on pulse blanking, direct state tracking Kalman filter	

the ipexSR of Stöber et al. (2010) and was implemented similarly using the dynamic link library (DLL). Since MATLAB can load a library from DLL and call a function within the library, the API concept of the C/C++-based software can also be used analogously in the MATLAB environment. If the SDR is converted to an executable file (.exe) and provided to a user, the user can freely modify functions or develop algorithms by generating the DLL, without the need for the whole source codes.

3.7 | PyChips

Pychips is a relatively new object-oriented satnav SDR that has been developed from scratch since 2018. It is based on the experience gained from two previous implementations, namely the MATLAB SDR that was distributed with Wideband TRIGR (see Section 5) and the ChameleonChips GNSS SDR Toolbox for MATLAB (Gunawardena, 2014).

One of the key promises of SDRs is their flexibility, and hence its utility as an education and research tool. In the satnav context, various publicly available SDRs can be used to teach basic courses on satnav systems, signal processing, and receiver design. However, there is an implicit assumption that students have the relevant programming language skills for that particular SDR. Students are expected to understand the inner workings of the SDR in detail, and, more importantly, to make modifications to the code to add advanced capabilities and/or revisions as part of their graduate research projects. While somewhat valid, this programming language proficiency assumption may not always hold true. Further, given the situation, it may be far more efficient and beneficial to have grad students make deeper progress on their research rather than spending time becoming programming language experts. PyChips was developed from the ground up to support this notion. A more detailed introduction to PyChips can be found in Gunawardena (2021). Its main features are summarized in Tab. 8 . It is implemented in Python with C++ bindings where performance is absolutely essential for reasonably fast execution.

The current version of PyChips supports the creation and definition of entire constellations of satellites with advanced next-generation signal structures, along with interference sources and channel effects. This simulation portion of PyChips (comprising of numerous source objects) synthesizes these signals at the sample level on to one or more sample streams that are grouped into objects called stream containers. A stream container is an abstraction of a satnav receiver's antenna(s) and RF front-end subsystem. This could be multi-frequency, multi-element, with different sample rates and bandwidths, IF or baseband sampling architecture, and any and all combinations thereof. If live-sky signal processing is the use case, then one or more sampled SDR

TABLE 8 Main features of PyChips

PyChips		
Feature	Solution	Remark
Operating System	Windows x64	Due to pre-compiled C/C++ bindings that currently use the Windows API for file reading and threading. Linux support under development.
Programming environment	Signal and ARchitecture Description Language (SARDL), Python, C/C++	SDR entirely specified using JSON-based SARDL. Assembles pre-built configurable Python and C/C++ objects at runtime according to user SARDL specification.
IF sample file input source	ION SDR Standard	Parses ION metadata hierarchy to select the appropriate decoder kernel written in C++. Sample decoding is split across multiple threads using a data parallel architecture
Real-time sample input	Not currently supported	
Additional sensors	None	
Supported GNSS	Supports all civilian satnav signals (GPS, GLONASS, Galileo, BeiDou, QZSS, NavIC, SBAS)	Spreading codes defined as memory codes. Code replicas specified as an assembly of sequence objects (static, subcarrier, overlay, mux, ..., see Gunawardena (2021))
Acquisition	FFT-based generic acquisition engine with configurable coherent and non-coherent integration settings	Auto detects and implements circular vs. non-circular frequency-domain correlation based on code length
Tracking	Generic tracking module assembled from configurable functional blocks (e.g. carrier-wipeoff, code replica, correlator, gearbox, accumulator, ...) and a generic controller object – all defined in SARDL	Employs split-sum correlation Gunawardena & van Graas (2006). Always operates on 1-millisecond block of samples and retires current block before operating on next block (no sample shifting to align with SV time-of-transmission). Direct initialization of tracking objects configured for other signals from same SV (e.g. GPS L1 C/A to L1C, L2C, and L5)
Measurement output	Yes	CSV format
Availability	Versions distributed at ION conference tutorials	Versions used at ION tutorials

data files can be specified to instantiate a stream container object that is functionally identical and imperceptible from a simulated one. PyChips uses the ION SDR Standard to determine the appropriate C/C++ decoder/unpacker/re-quantizer kernel to use for reading and parsing these SDR files.

The sample streams contained in a PyChips stream container are processed using numerous sink objects. Currently, implemented examples include virtual oscilloscopes and spectrum analyzers, as well as acquisition engines and signal tracking modules.

The unique feature of PyChips is that, all of the functionality described above is defined/specified using a draft SDR language called Signal and ARchitecture Description Language (SARDL). SARDL is implemented as a grouping of JavaScript Object Notation (JSON) files. Current and next-generation advanced satnav signal structures and the receiver architectures to process them are constructed by assembling together pre-built low-level functional blocks. For example, as described in Gunawardena (2021), the user can build receiver tracking modules to process GPS L1C TMBOC(6, 1, 4/33) and Galileo E1OS CBOC(6, 1, 1/11) MBOC signals as simple BOC(1, 1) signals to model a low-cost low-power mass market receiver, or a high-end survey-grade receiver taking full advantage of these ‘dual personality’ signals.

TABLE 9 Main features of UAB Snapshot GNSS Receiver

UAB Snapshot GNSS Receiver		
Feature	Solution	Remark
Operating system	Any supported by MATLAB	
Programming environment	MATLAB	MATLAB version 6.0 (R12, 2000) or higher.
Processing mode	Post-processing	
Supported GNSS	GPS (L1 C/A, L5), Galileo (E1C, E5a)	
Acquisition	FFT-based signal acquisition	Implementing the double-FFT algorithm for both code correlation and bit synchronization. Long correlations can be implemented by non-coherently combining a set of coherent correlations. Assisted-GNSS (A-GNSS) is used to narrow the acquisition search space. Compatible with 3GPP RRLP-compliant XML data.
Tracking	None	No tracking is implemented because the receiver architecture is based on snapshot mode (i.e. acquisition-only).
Navigation	Weighted Least Squares (WLS)	Coarse-time navigation is implemented.
Further features	Implements near-far detection and interference detection.	

Indeed, at this stage, the goal of the PyChips project is to hone SARDL with a vast number of diverse signal specifications, use cases, and applications – in order explore the concept of a 'satnav signals and systems specification language.' Today, the reference SDR that implements SARDL is written in Python and is therefore called PyChips. However, the ultimate goal of this effort is to contribute towards satnav SDR implementations that have the performance, power efficiency, and scalability of ASICs with the flexibility, reconfigurability, adaptability, and ease-of-use of software.

3.8 | UAB Snapshot GNSS Software Receiver

The UAB snapshot GNSS software receiver (cf. Tab. 9) was originally developed as part of the research activities on indoor GNSS positioning that were carried out by the Signal Processing for Communications and Navigation (SPCOMNAV) group at Universitat Autònoma de Barcelona (UAB), back in 2007. At that time, the group was involved in one of the two parallel contracts that ESA awarded to assess the feasibility of indoor GNSS positioning, under the project named DINGPOS. The proposed strategy was to rely on a combination of technologies such as WiFi, ultra wideband (UWB), 2G/3G cellular networks and GNSS as discussed by López-Salcedo et al. (2008). As far as GNSS was concerned, UAB was in charge of developing the software implementation of a so-called high-sensitivity GNSS (HS-GNSS) receiver, which could be able to operate under the extremely-weak signal conditions experienced indoors. This involves working under 10 to 40 dB attenuation losses, which drive the effective carrier power to noise power spectral density, i.e. C/N_0, down to values where conventional GNSS receivers are not able to operate anymore.

The proposed HS-GNSS receiver implementation was based on a snapshot architecture where a batch of input samples were processed at a time to provide the user's position. This approach is often referred to in the literature as 'push-to-fix' or 'acquisition-only', since no tracking stage is actually implemented at the receiver. This means that the receiver operates in open-loop mode by providing at its output the observables obtained straightaway from the acquisition stage. The implementation of the HS-GNSS software receiver was strongly influenced by the work already initiated by Gonzalo Seco-Granados before joining UAB, during his period from 2002 to 2005 as technical staff at the European Space Research and Technology Center (ESTEC) of ESA in The Netherlands, where he was leading the activities concerning indoor GNSS and snapshot GNSS

receivers. Actually, the core of the UAB snapshot GNSS receiver was inspired on the same concept of double-FFT acquisition already introduced by Jiménez-Baños et al. (2006). This algorithm uses two consecutive FFT operations for implementing the correlation of the received signal with the local code replica, and then the simultaneous estimation of the fine Doppler and bit synchronization. Interested readers on the double-FFT algorithm and on a detailed description of the UAB snapshot GNSS receiver implementation will find a comprehensive description written by Seco-Granados et al. (2012).

From a general perspective, the UAB snapshot GNSS software receiver implements a set of specific signal processing techniques that are tailored to the particular working conditions indoors. Nevertheless, the implementation is flexible and it does not prevent the receiver to be operated efficiently in other scenarios, such as outdoors. Regarding the indoor environment, the most important impairment to be counteracted is certainly the severe attenuation due to the propagation through building materials and other obstacles. Attenuation up to 40 dB can easily be experienced, thus requiring a specific action to recover as much of the lost power in order to still be able to detect GNSS satellites. Since it is the received energy what matters from a signal detection and estimation point of view, and energy is nothing but power times the observation time, the only way to compensate for an extremely weak received power is by increasing the observation time. This means processing a longer piece of received signal, which means implementing very long correlation integration times at the GNSS receiver, on the order of hundreds of milliseconds or even a few seconds. Unfortunately, increasing the correlation time is hindered by the presence of the navigation message data symbols, residual Doppler errors and clock instabilities. So the approach adopted in practice by most snapshot GNSS receivers, particularly those intended for high-sensitivity applications, is to split a long correlation into pieces of shorter, but long-enough coherent correlations, whose outputs are then noncoherently accumulated. This combination of coherent and noncoherent correlation has proven to be successful in increasing the receiver sensitivity and thus still be able to detect a few GNSS satellites indoors. Actually, an interesting discussion on how important having long-enough coherent integrations was discussed by Pany et al. (2009).

The correlation between the received signal and the local replica is therefore the most important operation of a snapshot GNSS receiver. The reason is that with such correlation, the most accurate code delay and Doppler observables need to be estimated. This is because no tracking stage is implemented, and thus there will be no chance to further refine these observables in subsequent stages of the receiver. It is for this reason that the correlation must be implemented in the most optimal way, taking into account subtle details that might be ignored in conventional GNSS receiver implementations. Such optimality is actually brought by the double-FFT algorithm implemented in the UAB snapshot GNSS receiver, which implements the optimal joint estimation of the code-delay and fine Doppler over a long period of time, where potentially sign transitions may occur due to the presence of data modulating symbols. Additional considerations such as how to handle a non-integer number of samples when performing the FFT, the interpolation between consecutive correlation peaks, the code-Doppler effect over a long correlation period, etc. can be found in Seco-Granados et al. (2012).

The code delay and Doppler estimates provided by the acquisition stage are then directly used by the navigation module to compute the user's position. Such code-delay estimates are ambiguous at one code period because no absolute time reference is available, and therefore no other time-delay information can be provided but that contained with a PRN code period. This is because just a batch of received samples is processed, and thus no access to the transmission time encoded onto the navigation message is available in general. As a result, the user's position needs to be computed without such time reference, which becomes a very specific feature of snapshot GNSS receivers. This problem can be solved thanks to what is known as coarse-time navigation, where the conventional navigation equations are augmented to include an additional unknown that represents the missing absolute time reference. The interested readers will find in (Van Diggelen, 2009, Ch.4) an excellent description of this method.

Since its development in 2008, the UAB snapshot GNSS receiver has been a key tool for many research activities at the SPCOMNAV group. This software has been used for instance, to characterize the multipath propagation indoors (López-Salcedo et al., 2009), to assess the feasibility of using GNSS receivers in missions to the Moon, where the weak-signal problem is very similar to the indoor one (Manzano-Jurado et al., 2014), to test near-far mitigation techniques that may appear in indoor/Space applications (Locubiche-Serra et al., 2016), to assess the impact of phase noise (Gómez-Casco et al., 2016), and to provide GNSS positioning to internet of things (IOT) sensors in smart cities (Minetto et al., 2020) by means of a cloud-based implementation of the UAB snapshot GNSS receiver that was developed from 2016 to 2018.

The migration of the UAB snapshot receiver into a cloud-based implementation was certainly a major milestone that attracted the interest of the community and opened the door for totally new applications and use cases. The interest in cloud GNSS positioning was motivated by the fact that GNSS software receivers were running at that time in local computers next to the user who collected the samples to be processed. However, with the advent and widespread deployment of cloud computing platforms such as Amazon Web Services (AWS), Microsoft Azure and Google Cloud, such local computers could actually be

placed anywhere, and remote access could be granted to upload and process GNSS samples in a remote server in a scalable manner. Furthermore, this approach fitted pretty well with a snapshot GNSS receiver implementation, where a batch of samples could be sent to a remote server where the user's position would then be computed using the same tools as in any other snapshot GNSS receiver. That is, using A-GNSS for reducing the acquisition search space, making extensive use of FFT operations and computing the user's position by means of coarse-time navigation techniques.

This was the idea behind the so-called 'cloudGNSSrx', the cloud-based implementation of the UAB snapshot GNSS receiver as described in SPCOMNAV (2019). The architecture was based on a dockerized compilation of the Matlab source code implementing the UAB snapshot GNSS receiver. Then a system of job queues, schedulers and load balancers were built on AWS to automate and scale the remote execution of the receiver, and an API was developed for machine-to-machine communication, facilitating the provision of GNSS positioning to small IOT sensors (Lucas-Sabola et al. (2016)). In this way, IOT sensors requiring GNSS positioning were able to offload most of the computational load to a remote server, thus significantly reducing the power consumption and thus extending their battery lifetime.

Low-power GNSS positioning is actually one of the main applications of cloud GNSS software receivers, since for snapshots shorter than a few tens on milliseconds, the energy spent in sending the GNSS samples to the cloud pays off for the significant energy that is saved at the user's terminal for not processing such samples, and doing it at the cloud instead (Lucas-Sabola et al., 2017). This feature was actually acknowledged by the former GSA, now the European Union Agency for the Space Programme (EUSPA), who identified the UAB cloud GNSS receiver as one of the promising technologies for the future adoption of GNSS in the IOT domain (European Union Agency for the Space Programme, 2018). The cloud GNSS software receiver developed by UAB was then licensed in 2019 to the startup company Loctio, who improved very significantly the initial prototype and made it a commercial product.

It is important to remark that apart from the low-power consumption use case, cloud GNSS software receivers can also be used to provide access to sophisticated signal processing techniques that cannot be implemented in conventional receivers. For instance, advanced signal monitoring techniques, spoofing detection or authenticated/certified positioning, the latter being reported by Rügamer et al. (2016). There is therefore a brilliant future ahead for cloud GNSS software receivers with many exciting new applications still to come.

3.9 | The NGene Family of Receivers at Politecnico di Torino and LINKS

The development of NGene, a GNSS software receiver, originated at Politecnico di Torino and LINKS Foundation in the early 2000s. At that time, the Navigation Signal Analysis and Simulation Group (NavSAS) was already engaged in software implementation of various sections of GNSS baseband processing. This endeavor capitalized on the group's extensive expertise in digital signal processing and specifically in simulating complex communication systems.

The initial focus was optimizing the acquisition and tracking stages, both as post-processing tools and as core processing units on programmable hardware. In 2005, under regional funding, the research team, partially affiliated with the Istituto Superiore Mario Boella (now part of the LINKS Foundation), commenced the development of a fully software-based, real-time GNSS receiver for GPS and forthcoming Galileo signals.

The outcome of the work was NGene, the software receiver, as documented by Molino et al. (2009). NGene demonstrated real-time processing capabilities for GPS, Galileo, and EGNOS signal components transmitted on the L1/E1 band. Prior to processing, the signals were subjected to IF downconversion and digitalization by an external analog front-end device. Communication between the front-end device and the software receiver occurred via a USB connection. The hardware part of the receiving chain consisted solely of the antenna, and its low noise amplifier (LNA), the A/D converter with front-end filtering, with all other components being software-based. This fundamental architecture has laid the groundwork for subsequent enhancements and has been the essential building block of the NGene receiver family.

NGene, thanks to the reconfigurable and modular structure, has long served as the primary tool for in-lab analysis, development, and prototyping of signal processing algorithms and architectures. Thanks to its flexible implementation, NGene was adapted to process the Galileo In-Orbit Validation signals (GIOVE-A) and subsequently to process the first Galileo signals immediately upon their availability, as detailed in Margaria et al. (2012). As a result, the research team was among the first worldwide to achieve a position fix using the initial four Galileo satellites. Over time, the software receiver continued to evolve and was tailored to address diverse applications, leveraging the advantages of software radio implementation (see Tab. 10).

Today, the NGene family offers configurable support for various RF-to-IF front-ends, which connect to the software processor via USB, meeting the requirements of numerous activities and projects. A simplified, low-complexity version was developed to

TABLE 10 Main features of NGene receiver family

NGene receiver family		
Feature	Solution	Remark
Operating System	GNU/Linux-based	Since based on standard libraries, it can run on Windows too
Programming environment	ANSI C and assembly (Intel x86 and ARM SIMD instructions)	Eclipse IDE and GNU Compiler Collection (GCC) compiler
IF sample file input source	Binary file	
Processing mode	Real Time and Post-processing	It can work in real-time from USB-based RF front-ends and in post-processing mode with binary file formats.
Additional sensors	No	
Supported GNSS	GPS L1 C/A, Galileo E1	
Acquisition	FFT-based algorithm	
Tracking	Multi-Correlator based Data tracking loop	
Measurement output	Yes	Acquisition, tracking and PVT results available as binary/text log files
Availability	Restricted	Licensing of a public release currently under discussion
Further features	Scintillation monitoring, Interference detection, Galileo OSNMA authentication	Specific modified versions for research purposes

enable GNSS positioning capabilities on ARM-based embedded processors (Troglia Gamba, Nicola, & Falletti, 2015). Additional branches of the software were adapted for GNSS-R receiver deployment in reflectometry tests (Troglia Gamba, Marucco, et al., 2015), evaluation of anti-jamming algorithms, detection of non-standard code transmission and its effects on Galileo positioning (Dovis et al., 2017), as well as being the tool for the study of the 2019 Galileo outage event (Dovis et al., 2019). One of the latest branches of the NGene family encompasses algorithms for authenticating Galileo messages using the OSNMA, as described in Nicola et al. (2022); Troglia Gamba et al. (2020a). Furthermore, a set of functions is being developed to support future GPS Chimera authentication service processing (Troglia Gamba et al., 2020b).

3.10 | The MATRIX SDR for Navigation with Signals of Opportunity

MATRIX (Multichannel Adaptive TRansceiver Information eXtractor) is a state-of-the-art cognitive SDR, developed at Kassas' Autonomous Systems Perception, Intelligence, and Navigation (ASPIN) Laboratory, for navigation with terrestrial and space-based SOPs (Kassas et al., 2020). MATRIX continuously searches for opportune signals from which it draws navigation and timing information, employing signal characterization on-the-fly as necessary. MATRIX could produce a navigation solution in a standalone fashion (Shamaei & Kassas, 2021a) or by fusing SOPs with sensors (e.g., IMU (Morales & Kassas, 2021), LiDAR (Maaref et al., 2019), etc.), digital maps (Maaref & Kassas, 2020), and/or other signals (e.g., GNSS) (Kassas et al., 2017). Figure 1 shows MATRIX's architecture and Tab. 11 lists the main features.

On one hand, MATRIX has achieved the most accurate navigation results to-date in the published literature with cellular SOPs (3G CDMA, 4G LTE, and 5G NR), achieving meter-level navigation indoors (Abdallah & Kassas, 2021) and on ground vehicles (Maaref & Kassas, 2022) and submeter-level navigation on unmanned aerial vehicles (Khalife & Kassas, 2022). In addition, MATRIX's efficacy has been demonstrated in a real-world GPS-denied environment (Kassas, Khalife, Abdallah, & Lee, 2022), achieving a position root-mean squared error of 2.6 m with 7 cellular LTE eNodeBs over a trajectory of 5 km (one of which was more than 25 km away), during which GPS was intentionally jammed (Abdallah et al., 2022). MATRIX has also achieved remarkable results on high-altitude aircraft, where it was able to acquire and track cellular 3G CDMA and 4G LTE signals at

TABLE 11 Main features of MATRIX

MATRIX		
Feature	Solution	Remark
Operating System	Linux, Windows	
Programming environment	C++, MATLAB, LabVIEW	
IF sample file input source	Binary file	
Real-time sample input	Yes	Some SOP modules supports real-time processing
Additional sensors	IMU, GNSS	
Supported GNSS	GPS L1 C/A	
Acquisition	FFT-based signal acquisition	
Tracking	DLL, PLL, FLL, Kalman filter	Different tracking loops per SOP module
Measurement output	Yes	Acquisition, tracking, and PVT results available as text/CSV files and via GUI
Navigation	Weighted least squares; Kalman filter; Doppler, code- and carrier-based positioning modes	
Availability	Restricted	Licensing options available via The Ohio State University

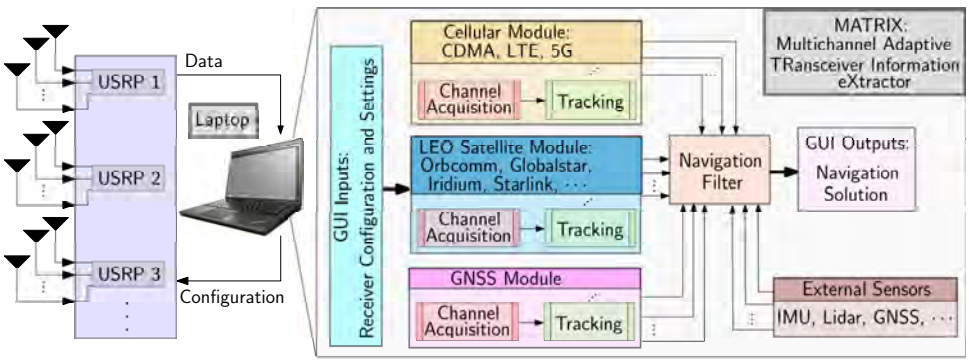

FIGURE 1 MATRIX cognitive SDR architecture. The SDR consists of: (i) USRPs to collect different radio signals, (ii) various modules to produce navigation observables from different types of signals (e.g., cellular, LEO satellites, etc.), (iii) external sensors (e.g., IMU, LiDAR, GNSS receivers, etc.), whose measurements can be fused with the navigation observables produced by the signal modules, and (iv) navigation filter that fuses all measurements to produce a navigation solution.

altitudes as high as 23,000 ft above ground level and from cellular towers more than 100 km away (Kassas, Khalife, Abdallah, Lee, Jurado, et al., 2022). What is more, meter-level high-altitude aircraft navigation was demonstrated over aircraft trajectories exceeding 50 km, by fusing MATRIX's cellular navigation observables with an altimeter (Kassas, Abdallah, et al., 2022).

On the other hand, MATRIX has achieved the first published results in the literature for exploiting unknown SpaceX's Starlink LEO satellite signals for positioning, achieving a horizontal positioning error of 10 m with Doppler observables (Neinavaie et al., 2021) and 7.7 m with carrier phase observables (Khalife et al., 2022). In addition, the first ground vehicle navigation results with multi-constellation LEO (Orbcomm, Iridium NEXT, and Starlink satellites) were achieved with MATRIX (Kassas et al., 2021), upon coupling its LEO navigation observables with an inertial navigation system (INS) in a tightly-coupled fashion through the simultaneous tracking and navigation (STAN) framework (Kassas et al., 2019).

3.11 | Other Achievements with GNSS SDRs

Apart from the success stories of the previous subsections a number of other achievements have been accomplished with GNSS SDRs. They are listed in this subsection.

The first real-time GNSS/INS integration with an SDR was achieved by Gunawardena et al. (2004) and one of the first GNSS SDR implementation on a GPU was reported in Hobiger et al. (2010).

GNSS SDRs are known to achieve the highest possible sensitivity as different integration schemes or data wipe-off procedures can be performed in post-processing. This enables very long coherent integration times, which is beneficial for sensitivity or multipath mitigation as reported in Section 3.8. Characterization of the GPS transmit antenna pattern with a 30-second long coherent integration resulting in 0 dBHz sensitivity is discussed by Donaldson et al. (2020). The same sensitivity was achieved by 300 noncoherent integrations, each 1 second long for the purpose of indoor timing by iPosi Inc. (2015).

Graphical programming languages, such as LabVIEW and Simulink, are attractive choices for implementing SDRs, due to their flexibility, modularity, and upgradability. Moreover, since SDRs are conceptualized as block diagrams, graphical programming languages enable a one-to-one correspondence between the architectural conceptualization and software implementation (Hamza et al., 2009; Kassas et al., 2013).

The scope of SDRs was first extended to non-GNSS signals by McEllroy et al. (2006). SDRs became the implementation of choice in numerous studies aimed at exploiting SOPs for navigation purposes (Diouf et al., 2021 2019; Kassas et al., 2017), such as (i) cellular 3G code division multiple access (CDMA) (Khalife et al., 2018; K. Pesyna et al., 2011; Yang & Soloviev, 2018), 4G long term evolution (LTE) (del Peral-Rosado et al., 2017; Ikhtiari, 2019; Kang et al., 2019; Shamaei & Kassas, 2018; Shamaei et al., 2018; Wang et al., 2022; Yang et al., 2022), and 5G new radio (NR) (Abdallah & Kassas, 2022; del Peral-Rosado et al., 2022; Fokin & Volgushev, 2022; Lapin et al., 2022; Santana et al., 2021; Shamaei & Kassas, 2021b; Tang & Peng, 2022); (ii) AM/FM radio (Chen et al., 2020; McEllroy, 2006; Psiaki & Slosman, 2022; Souli et al., 2021); (iii) digital television (Souli et al., 2020 2022; Yang & Soloviev, 2020); and (iv) LEO satellites (Farhangian et al., 2021; Farhangian & Landry, 2020; Nardin et al., 2021; Orabi et al., 2021; Pinell, 2021; Zhao et al., 2022) .

Due to the enhanced analysis possibilities of GNSS SDR they proved to be very useful to understand ionospheric scintillation and the first dedicated SDRs are described by O'Hanlon et al. (2011); Peng & Morton (2011). The authors used a general purpose front-end being reconfigurable for multi-GNSS multi-band signals, and a custom dual-frequency front-end, respectively. The first system further evolved into an intelligent, scintillation event-driven data collection, as reported by Morton et al. (2015).

Commercialization of academic SDR developments was partly discussed in the previous sections. Also, a major receiver manufacturer provides GNSS SDRs, first starting with a timing receiver (Trimble Inc., 2005) and then moving to a flexible narrow-band receiver (Trimble Inc., 2017). Wide-band signals were later added, with some signal processing now done on an FPGA as reported in PR Newswire (2021). The most recent commercial activity can be found in LocusLock (2022) and builds upon the software described in the Section 3.1.

4 | SDR FRONT-ENDS

As outlined before, a front-end is required to obtain digital samples for the SDR processing. The front-end's tasks are to receive, filter, amplify, down-convert, and further digitize and quantize the analog RF signal entering the GNSS antenna. Many different types of front-ends were used for GNSS SDRs. Roughly, five different categories can be identified:

discrete components: using RF-connectable components like LNAs, filters or ADCs it is comparable easy to realize the function of a front-end and log IF or baseband samples. Those setups are easy to realize, but often bulky and sometimes prone to interference.

commercial signal recorders: several companies offer GNSS signal recorders to allow to record (and often to replay) one or more GNSS frequency band. Usually they do not implement a real-time connection to an SDR.

generic non-GNSS front-ends: SDR technology is used in many different fields of electrical engineering and front-ends covering a wide frequency are available. Their price ranges from a few Dollars (Fernández–Prades et al., 2013) to highly sophisticated multi-channel front-ends costing several ten-thousands of Dollars. The oscillator quality, bit-width or RF-filter characteristics is not always optimal for GNSS signal processing.

dedicated GNSS real-time front-ends: built for the purpose to realize a real-time GNSS SDR. A good example is described in Section 4.1. They are compact and build with discrete components.

ASICs: some RF-ASICs seem to target GNSS SDR use and evaluation kits allow streaming of IF samples, e.g. NTLAB, UAB (2022); RF Micro Devices, Inc., Greensboro (2006).

GNSS signals need a comparable high sampling rate of the front-end and when connected to a PC via a USB cable the transfer was not always reliable in the early years. Various optimizations and workarounds have been implemented like watermarking the IF sample stream and skipping lost sample packets as invented by Foerster & Pany (2013). With the advent of USB 3.0 or PCIe those solutions became obsolete.

In the following section, we describe Fraunhofer USB front-ends as an example of user needs, main features and general architectures of GNSS SDR front-ends. For a broader perspective of GNSS-compatible front-ends in the market, the interested reader can refer to (Borre et al., 2022, Ch.12).

4.1 | Fraunhofer USB Front-ends

The scientific community, along with some industrial partners, required a multi-band solution for the upcoming civil multi-band signals in GPS and Galileo planning. In 2006, Fraunhofer IIS developed a front-end called the L125 Triband USB (see Fig. 2 a), which allowed recording of fixed frequencies of L1/E1, L2, and L5/E5a. This front-end had one antenna input and could record via two USB 2.0 connectors data streams with up to 40 MSPS sampling rate and a 2 or 4 bit ADC resolution, and one antenna input. However, increasing customer demands for portable and flexible solutions led to a complete redesign of the USB front-end concept. One major request was reconfigurability on the SDR front-end side. To meet these different requirements in one SDR front-end hardware, a new version of the USB front-end was developed that realizes the signal conditioning to an onboard FPGA enabling desired reconfigurability on the fly. This was necessary to allow for a single-band receiver with a low sampling rate for specific real-time SDR projects, as well as a wideband and multi-frequency front-end for other projects.

In 2012 Fraunhofer IIS (Rügamer et al., 2012) introduced the Flexiband multi-system, multi-band USB front-end depicted in Fig. 2 b. Within the last ten years, this front-end has been used and validated in numerous scientific and industrial projects. Furthermore, it has been commercialized and is distributed as the 'MGSE REC' product of TeleOrbit GmbH (2022).

A regular Flexiband unit consists of up to three analog reception boards, a carrier board with ADCs and FPGA, and a USB 3.0 interface board. A common antenna input port is supported, and separate front-end input signals for up to three antenna inputs. Three dual-channel ADCs sample the incoming signal with 81 MSPS and 8 bits I/Q. The raw data stream is received by an FPGA in which different digital operations like filtering, mixing, data rate, and bit-width reduction, as well as a digital automatic gain control (AGC) are applied. Finally, a single multiplexed data stream is formed together with a checksum. This multiplexed stream is sent via an USB 3.0 interface to the PC. Data rates of up to 1296 MBit/s or 162 MByte/s raw data stream are supported. The Flexiband GUI software receives the raw multiplexed stream, checks its integrity, and demultiplexes it. The data streamed can be either written to hard disk or sent to a customer application (e.g., a software receiver). The raw samples can be stored as a multiplexed data stream, in an 8 bit/sample format, or directly as a .mat file for MATLAB. In parallel, the ION Metadata *.sdrx is provided.

Due to its bandwidth, sampling rates, quantization, and multiplexing schema flexibility, the ION SDR Standard was a perfect fit to clearly and unambiguously define the configuration for the user. Therefore, right after the first conclusion of the ION SDR Standard, each binary raw-data output file of the Flexiband front-end was equipped with an 'sdrx' metadata file specifying the raw data format.

Finally, a replay variant of this Flexiband exists that reads in the raw IF samples on hard disk using the ION SDR Standard specification and replays the digital data as an analog RF output stream supporting multiple GNSS bands at the same time.

5 | ION SDR STANDARD

The previous sections already made clear that data exchange between the various SDRs requires a certain level of standardization. The events that led up to the suggestion to develop what became the ION SDR Standard (also known as ION GNSS Metadata Standard, ION SDR Metadata Standard, GNSS SDR Sampled Data Metadata Standard or GNSS SDR Metadata Standard), can be traced back to circa 1999. Building upon the successful contributions made by Akos, the Ohio University Avionics

(a) TriBand USB2.0 Front-end from 2006

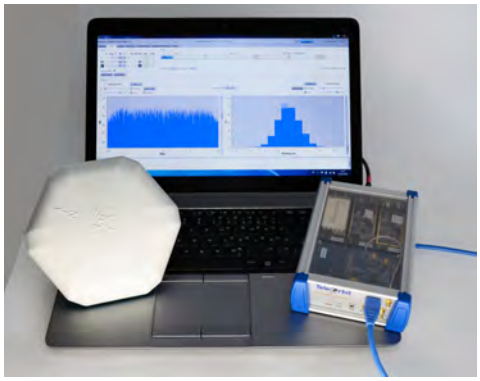

(b) Flexiband USB3.0 Front-end from 2012 onwards

FIGURE 2 Two examplary USB Front-end from Fraunhofer IIS

Engineering Center undertook several research projects leveraging GPS SDRs. One such project was called the GPS Anomalous Event Monitor (GAEM) (Snyder et al., 1999). This was sponsored by the FAA Technical Center and led by Prof. Frank van Graas. Commercial GPS receivers within prototype LAAS ground facilities were experiencing brief unexplained outages. GAEM kept a continuous 10-second history of IF samples in a circular memory buffer. When an outage occurred, GAEM was triggered to dump this buffer to disk and collect for a further 10 seconds. These sample files were then post-processed in MATLAB to determine the cause of the anomaly. Early versions of GAEM used commercial data collection cards and had numerous issues related to their proprietary drivers. Around 2001, Gunawardena developed a refined version of GAEM that was based on one of the earliest PCI-based dual-ADC-plus-FPGA development cards commercially available. It collected two GPS L1 data streams at 5 MSPS and 2 MHz bandwidth. This version of GAEM was fielded at three airports and operated continuously for over 3 years and helped to characterize numerous anomalous events (Gunawardena et al., 2009). This GAEM also supported a continuous collection mode, and was used for several research projects including the characterization of GPS multipath over water (Zhu & Van Graas, 2009) and GPS/IMU deep integration demonstrations in flight (Soloviev et al., 2004). For the latter, the 2 kHz raw data from a MEMS IMU were interleaved with the SDR samples thanks to the FPGA-based architecture that allowed for such custom capabilities.

Circa 2002, as these research projects progressed, the 2 MHz bandwidth limitation of GAEM became apparent. There was a pressing need to support emerging research opportunities related to GPS L5, as well as high fidelity GPS signal quality monitoring. A multi-band and higher-bandwidth (24 MHz) front-end and SDR data collection system was needed. There were only a handful of vendors selling such systems at the time, and it wasn't clear if these would serve the purpose for satnav SDR application (sampling coherency concerns, etc.). However, by far, the >$350k price tag of these systems precluded any hope of purchasing them for university research. It was decided to develop this capability in-house. In 2003, a 2-channel L1/L5 front-end with 24 MHz bandwidth and 56.32 MSPS was developed (Gunawardena et al., Winter 2007-2008). It was based on connectorized RF components. The sampling and collection subsystems were carried over from GAEM.

The capabilities of the dual-frequency high-bandwidth system attracted interest from several universities, government research groups, as well as a defense contractor. To support these opportunities, the development of a new system known as Wideband Transform-domain Instrumentation GNSS Receiver (TRIGR) was completed in 2008 (Gunawardena & Van Graas, 2011). The front-end was miniaturized to a single-frequency custom PCB module. Up to 8 such modules (with the required frequency options) were combined with an 8-channel 12-bit ADC to create modular systems for various sponsors. The raw samples from the ADC are transferred to a PCIe FPGA card where the 8 streams are packed in various formats according to the user's selection in a GUI. Supported formats range from any one stream at 1-bit sample depth, any 2 streams at 12 bits (sign extended to 16), to all 8 streams at 4 bits. The sustained data transfer rate from the PCIe FPGA card to the RAID storage array was limited to 240 MB/sec. As such, the appropriate format had to be selected to balance between the required capability and transfer rate. The generated file names embed a UTC timestamp as well as the packed stream order and sample depth.

The event-based data collection feature of GAEM needed to be incorporated into Wideband TRIGR. However, the >10× data rate meant that a 10-second circular buffer could not be easily implemented in RAM using 32-bit systems of the day. This issue was addressed by writing data as a sequence of smaller files, where a new file was spawned before the current file was closed – with some sample overlap for data integrity – a technique known as temporal splitting. A separate process was used to delete

older files from the RAID array to make room for new ones – unless an event was received – in which case the files surrounding the event were moved to a folder for post-processing.

With the myriad of sample packing formats available with Wideband TRIGR, along with the temporal splitting-based file generation scheme, it became clear that a machine-readable metadata file needed to be included with every collection. An XML schema was designed for this purpose.

Up until this time, apart from the FPGA-based real-time GPS receiver that was developed and used for certain projects, all SDR files generated by GAEM and Wideband TRIGR were post processed in MATLAB. As others have mentioned, this was excruciatingly slow – especially for Wideband TRIGR data. To address this issue, as well as to support the rapid emergence of multi-band and multi-constellation satnav signals, Gunawardena wrote and distributed a MATLAB SDR toolbox where correlation was performed in optimized C code and also leveraged multi-threading in a data parallel architecture. This toolbox, known as ChameleonChips, also read the XML metadata files produced by Wideband TRIGR to determine the appropriate sample unpacking kernel to use. This work was presented at ION GNSS+ 2013 in Nashville, TN (Gunawardena, 2013). During this presentation, it was suggested that the satnav SDR community should adopt a metadata standard – similar to the one developed for Wideband TRIGR – in order to alleviate the numerous headaches associated with sharing such files. This was met with widespread support and enthusiasm. Longstanding ION members Phillip Ward, Jade Morton, and Michael Braasch helped to pitch this idea to the ION Executive Committee.

During the January 2014 Council Meeting in San Diego, ION approved the process for establishing a formal standard (Gunawardena et al., 2021). The ION GNSS SDR Metadata Working Group (WG) was formed in April 2014 with Thomas Pany and Gunawardena as co-chairs (James Curran was added later as a third co-chair). Membership represented academia, industry (including satnav SDR product vendors as well as traditional satnav equipment manufacturers), non-profit research entities, and government agencies spanning countries in Europe, America, Asia, and Australia. The working group developed the standard as well as associated normative software over a course of six years. With regard to the normative software, while many individuals contributed, initial development of the C++ object model was performed by Michael Mathews of Loctronix while James Curran wrote much of the functionality to decode packed samples based on the metadata specification. The draft standard was adopted as the formal ION SDR Standard in January 2020.

5.1 | Use of the ION SDR Standard

Today the ION SDR Standard serves as a reference to describe IF formats and is for example useful for public tenders or if for some means an established format is needed. A number of SDRs do include the C++ libraries to read meta-data and IF samples.

The level of exchange of IF samples between research groups is to some extent limited and much less executed compared to e.g. exchange of RINEX files. This is of course related to the huge size of IF sample files and to the fact that for the majority of GNSS use cases, RINEX observation data or PVT exchange is sufficient. Furthermore, GNSS SDRs still tend to use mostly the same front-end and once the respective data format is known, there is obviously no need to describe it via the XML format. A disadvantage of the C++ routines is their generic design, which renders sample reading quite slow, as each sample is isolated via a number of for-loops from the input files. Clements et al. (2021) did propose an algorithm to automatically generate optimized code for sample reading for a given IF format, but this proposal did not yet manifest into a usable implementation.

5.2 | ION SDR Standard Extension

Already during the standardization process a number of features for the standard were identified, that appear to be useful, but lack of resources did not allow including them in the formal standardization procedure. Those features are described in the App. II of (ION SDR Working Group, 2020). Within the ION-GNSS+ 2022 meeting in September, the following points have been discussed and will be included in App. II of the next - draft-version V1.1 of the ION SDR Standard:

5.2.1 | Flexible bit layout

The ION SDR Standard defines a 'Lump' as the ordered containment of all samples occurring within an interval. The ordered containment is understood in a regular way holding the samples of the individual streams together. Clements et al. (2021) see this as a limitation, as highly efficient SDRs may use efficient bit-packing schemes to optimize data transfer over communication lines that need buffering. They identify a need to distribute the samples of different Streams in interleaved ways over the Lump. This interleaving cannot be described by the V1.0 of the ION SDR Standard. To overcome this limitation, the authors propose a

new but optional attribute for the Lump object, called 'Layout'. In case Layout is present, further information on the bit packing scheme needs to be provided, describing in an explicit way the type of each bit of a Lump. The authors make a detailed proposal for this new Lump layout following the structure of the existing standard. The proposal even includes more advanced bit use cases, like puncturing (e.g. explicit omitting of bits) and overwriting of bits by time markers.

5.2.2 | Refined sample rate/epoch definitions

Clements et al. (2021) note that the V1.0 of the ION SDR Standard makes implicit assumptions about the timing of the sampling process and staggered sampling cannot be described by it. Staggered sampling occurs if the sampling instants of different GNSS signals are delayed with respect to each other, and might be of use to increase observability of GNSS interference in a multi-antenna system. To overcome this limitation, the authors propose to add two new attributes for 'Stream' objects to shift the sampling epochs of different GNSS stream with respect to each other.

5.2.3 | JSON format for metadata files

Comment ID 22 of the initial Request for Comments (RFC1) makes a suggestion that the WG considers markup languages other than XML for metadata files, specifically JSON, YAML and TOML (Anonymous, 2017). In 2017, this comment was addressed by asserting that the XML format will be maintained for the time being, since normative software that parses XML had already been developed. However, the WG responded with the assurance that "other markup languages will be considered in the future based on community need and interest."

As of the time of this writing, and with the experience gained from developing PyChips (which is a satnav SDR that is completely described using a draft signal/system specification language based on JSON, as described in Section 3.7), it is this author's opinion that JSON may have some distinct advantages over XML for future applications and use cases. For example, JSON streaming is a methodology for transferring object-oriented data over communications protocols (Wikipedia, 2022) and is widely used in well-known applications such as Plotly (2022). Hence, streaming JSON could be one way to parse SDR sample streams whose formats are changing dynamically.

Figure 3 shows a notional listing for a JSON formatted metadata description for the Flexiband front-end XML metadata listing found in Gunawardena et al. (2021).

To maintain compatibility with the existing and formally adopted XML-based metadata specification, it is understood that any adoption of another markup language such as JSON must include open source normative software and tools to convert between these formats. Adoption of JSON based metadata is currently being considered for future versions of PyChips. If and when a successful implementation has been achieved, consideration for adopting JSON as another valid option for representing ION SDR Standard-compliant metadata in a future version of the standard will be requested.

SUMMARY AND CONCLUSION

Since GPS SDR developments started in the mid 90's, together with the operational declaration of GPS, its feasibility has been widely proven by several platforms and their derivatives. We define GNSS SDR platforms as those implementing the receiver functions in general purpose software and processors, and divide them in real-time receivers, teaching/research tools, and snapshot receivers. We then describe some of them, with focus on those related to the authors but also including other developments. In particular, and based on the pioneering work by D. Akos, we describe the bit-wise parallelism platform by the Cornell GPS group, which led to GRID by UT Austin; the MuSNAT receiver by UniBwM, which also led to IFEN GmbH's SX3 commercial receiver; The SoftGPS Matlab receiver and associated book, widely used for GNSS teaching and also influencing other platforms, such as FGI-GSRx; the popular C++ open source GNSS-SDR by CTTC; AutoNav SDR by Inha University; PyChips by S. Gunawardena and based on Python; the snapshot GNSS receiver by UAB, leading to cloudGNSSrx; the real-time N-GENE receiver by LINKS, used for early testing of Galileo first signals and OSNMA and the MATRIX receiver by ASPIN for navigation with terrestrial and space-based SOP among others. We provide an overview of the tasks and components of SDR front-ends, and for this purpose we describe Fraunhofer developments from the last years as a reference. Finally, we discuss the ION SDR Standard, officially approved by ION in 2020, and its current extensions.

In view of the impact in the GNSS community and the progress in the last decades, we conclude that GNSS SDR has a promising future and will continue coexisting with FPGA and ASIC receivers for the decades to come.

```
{"system": {
    "id": "Flexiband", "comment": "Front-end variant:II-4e PRS (E6abc/E1abc/uBlox)",
    "freqbase": {"format": "MHz", "value": 8.10e+01 },
    "equipment": "Flexiband Multi-band receiver", "types": "Flexiband Multi-band receiver",
    "sessions": {
      "0": {
        "comment": "flexiband", "toa": "2022-09-30T00:00:00.00Z",
        "contact": "J. Doe", "campaign": "Example Campaign", "scenario": "Example Scenario",
        "position": {"lat": "0.0", "lon": "0.0", "height": "0.0"},
        "files": {
          "0": {
            "url": "flexiband.usb", "timestamp": "2022-09-30T00:00:00.00Z", "owner": "Example Owner",
            "lanes": {
              "0": {
                "id": "Data",
                "block": {
                  "cycles": 506, "sizeheader": 6, "sizefooter": 6,
                  "chunk": {
                    "sizeword": 1, "countwords": 2, "endian": "undefined", "padding": "none", "wordshift": "left",
                    "lump": {
                      "streams": {
                        "E6abc_B3": {
                          "other_specs": {"Amp": "162", "Antenna power": "false", "AGC": "false"},
                          "ratefactor": 1, "quantization": 4, "packedbits": 4, "alignment": "undefined",
                          "shift": "undefined", "format": "IQ", "encoding": "INT",
                          "bands": {
                            "E6abc_B3": {
                              "centerfreq": {"format": "MHz", "value": 1.27e+03},
                              "translatedfreq": { "format": "kHz", "value": 8.75e+03},
                              "delaybias": { "format": "sec", "value": 0.0e+00},
                              "bandwidth": { "format": "Hz", "value": 0.0e+00}
                            }
                          }
                        },
                        "L1_E1abc_B1_G1": {
                          "other_specs": { "Amp": "120", "Antenna power": "false", "AGC": "false"},
                          "ratefactor": 1, "quantization": 4, "packedbits": 4, "alignment": "undefined",
                          "shift": "undefined", "format": "IQ", "encoding": "INT",
                          "bands": {
                            "L1_E1abc_B1_G1": {
                              "centerfreq": {"format": "MHz", "value": 1.58e+03},
                              "translatedfreq": {"format": "kHz", "value": -4.58e+03},
                              "delaybias": {"format": "sec", "value": 0.0e+00},
                              "bandwidth": {"format": "Hz", "value": 0.0e+00}
                            }}}}}}}}}}}}}}}
```

FIGURE 3 Notional JSON Representation of Flexiband Front-End Metadata from Gunawardena et al. (2021)

ACKNOWLEDGEMENTS AND REMARKS

The authors are mainly listed in alphabetical order to reflect the variety and importance of all contributions. The contributions have been partly edited by Thomas Pany, who also takes the responsibility for the structure of the work, the abstract and the introduction and is thus listed as first author. The article is based on a contribution by the same authors to the ION-GNSS+ conference 2022 in Denver, CO.

The GNSS SDR developments at the University of the Bundeswehr Munich of Section 3.2 were supported by via numerous research projects administered by the German DLR and were financed by the German Federal Ministry for Economic Affairs and Climate Action (BMWK). The authors acknowledge the financial support by the University of the Bundeswehr München for this publication.

At Northeastern University, support has been partially provided by the National Science Foundation (NSF) under Awards ECCS-1845833 and CCF-2326559.

The UAB snapshot GNSS software receiver was supported in part by numerous ESA-funded research projects and by the Spanish State Research Agency (AEI) project PID2020-118984GB-I00.

The MATRIX SDR development at the ASPIN Laboratory was supported by the Office of Naval Research (ONR) under Grants N00014-16-1-2305, N00014-19-1-2613, and N00014-19-1-2511; the Air Force Office of Scientific Research (AFOSR) under Grant FA9550-22-1-0476; the U.S. Department of Transportation (USDOT) under Grant 69A3552047138 for the CARMEN University Transportation Center (UTC); and the National Institute of Standards and Technology (NIST) under Grant 70NANB17H192.

The authors would like to acknowledge the work of Prof. Kai Borre, who passed away in 2017, for his influential contributions to the GNSS SDR field over the last decades.

The views expressed in this article are those of the individual authors and do not reflect the official policy or position of any state or government entity.

References

Abdallah, A., & Kassas, Z. (2021, September). Multipath mitigation via synthetic aperture beamforming for indoor and deep urban navigation. *IEEE Transactions on Vehicular Technology*, *70*(9), 8838–8853. https://doi.org/10.1109/TVT.2021.3094807

Abdallah, A., & Kassas, Z. (2022). Opportunistic navigation using sub-6 GHz 5G downlink signals: A case study on a ground vehicle. In *Proceedings of European Conference on Antennas and Propagation* (pp. 1–5). IEEE. https://doi.org/10.23919/EuCAP53622.2022.9769276

Abdallah, A., Kassas, Z., & Lee, C. (2022). Demo: I am not afraid of the GPS jammer: exploiting cellular signals for accurate ground vehicle navigation in a GPS-denied environment. In *Proceedings of Workshop on Automotive and Autonomous Vehicle Security* (pp. 1–1). https://dx.doi.org/10.14722/autosec.2022.23049

Akos, D., & Braasch, M. (1996, June). A software radio approach to global navigation satellite system receiver design. In *Proc. of the Annual Meeting of The Institute of Navigation* (pp. 455–463). Institute of Navigation.

Akos, D., S, Stockmaster, M., J.B.Y., T., & Caschera, J. (1999). Direct bandpass sampling of multiple distinct RF signals. *IEEE Transactions on Communications*, *47*(7), 983–988. https://doi.org/10.1109/26.774848

Akos, D. M. (1997). *A software radio approach to global navigation satellite system receiver design* (Doctoral dissertation, Fritz J. and Dolores H. Russ College of Engineering and Technology Ohio University). `https://web.stanford.edu/group/scpnt/gpslab/pubs/theses/DennisAkosThesis97.pdf`

Akos, D. M., Normark, P.-L., Enge, P., Hansson, A., & Rosenlind, A. (2001). Real-time GPS software radio receiver. In *Proc. of the ION National Technical Meeting* (pp. 809–816). Institute of Navigation.

Anonymous. (2017). *RFC1 comments and responses.* `https://sdr.ion.org/RFC1_Comments_Responses.html`. [Accessed on 09/30/2022]

Arizabaleta, M., Ernest, H., Dampf, J., Kraus, T., Sanchez-Morales, D., Dötterböck, D., … Pany, T. (2021). Recent enhancements of the multi-sensor navigation analysis tool (MuSNAT). In *Proc. of the ION GNSS+ Meeting* (pp. 2733–2753). https://doi.org/10.33012/2021.17960

BeiDou B1I receiver processing. (2022). In *GNSS software receivers* (pp. 153–163). Cambridge University Press. https://doi.org/10.1017/9781108934176.007

Bernabeu, J., Palafox, F., Li, Y., & Akos, D. (2021, Jan.). A collection of SDRs for global navigation satellite systems (GNSS). In *Proc. of the ION International Technical Meeting* (pp. 906–919). Institute of Navigation. https://doi.org/10.33012/2022.18230

Bhuiyan, M., Söderholm, S., Thombre, S., Ruotsalainen, L., & Kuusniemi, H. (2015, May). Performance analysis of a dual-frequency software-defined BeiDou receiver with B1 and B2 signals. In *Proc. of the China Satellite Navigation Conference*

(CSNC) (pp. 827–839). Springer. http://dx.doi.org/10.1007/978-3-662-46638-4_72

Bhuiyan, M. Z., Söderholm, S., Thombre, S., Ruotsalainen, L., & Kuusniemi, H. (2014). Overcoming the challenges of BeiDou receiver implementation. *Sensors*, *14*(11), 22082–22098. https://doi.org/10.3390/s141122082

Bochkati, M., Dampf, J., & Pany, T. (2022). On the use of multi-correlator values as sufficient statistics as basis for flexible ultra-tight GNSS/INS integration developments. In *2022 25th International Conference on Information Fusion (FUSION)* (pp. 1–8). IEEE. https://doi.org/10.23919/FUSION49751.2022.9841253

Bochkati, M., Dampf, J., & Pany, T. (2023). Receiver clock estimation for RTK-grade multi-GNSS multi-frequency synthetic aperture processing. In *Proc. of the IEEE/ION PLANS meeting* (pp. 968–976). https://doi.org/10.1109/PLANS53410.2023.10140032

Borre, K. (2003). The GPS easy suite–Matlab code for the GPS newcomer. *GPS Solutions*, *7*(1), 47–51. https://doi.org/10.1007/s10291-003-0049-3

Borre, K. (2009). GPS easy suite II. *InsideGNSS*, *2*, 48–51.

Borre, K., Akos, D., Bertelsen, N., Rinder, P., & Jensen, S. H. (2007). *A software-defined GPS and galileo receiver, single frequency approach*. Birkhäuser, Boston. ISBN:9780817643904

Borre, K., Fernandez-Hernandez, I., Lopez-Salcedo, J. A., & Bhuiyan, M. Z. H. (2022). *GNSS software receivers*. Cambridge University Press, Cambridge. https://doi.org/10.1017/9781108934176

Chen, X., Wei, Q., Wang, F., Jun, Z., Wu, S., & Men, A. (2020, December). Super-resolution time of arrival estimation for a symbiotic FM radio data system. *IEEE Transactions on Broadcasting*, *66*(4), 847–856. https://doi.org/10.1109/TBC.2019.2957666

Clements, Z., Iannucci, P. A., Humphreys, T. E., & Pany, T. (2021, Oct.). Optimized bit-packing for bit-wise software-defined GNSS radio. In *Proc. of the ION GNSS+ Meeting*. Institute of Navigation. https://doi.org/10.33012/2021.18015

Curran, J. T., Fernández–Prades, C., Morrison, A., & Bavaro, M. (2018, Jan.). Innovation: The continued evolution of the GNSS software-defined radio. *GPS World*, *29*(1), 43–49.

Dampf, J., Pany, T., Bär, W., Winkel, J., Stöber, C., Fürlinger, K., … Garcia-Molina, J. A. (2015). More than we ever dreamed possible: Processor technology for GNSS software receivers in the year 2015. *Inside GNSS*, *10*(4), 62–72.

del Peral-Rosado, J., Estatuet-Castillo, R., Lopez-Salcedo, J., Seco-Granados, G., Chaloupka, Z., Ries, L., & Garcoa-Molina, J. (2017, January). Evaluation of hybrid positioning scenarios for autonomous vehicle applications. In *Proc. of the ION International Technical Meeting* (pp. 2541–2553). https://doi.org/10.33012/2017.15220

del Peral-Rosado, J., Nolle, P., Razavi, S., Lindmark, G., Shrestha, D., Gunnarsson, F., … Flachs, D. (2022, April). Design considerations of dedicated and aerial 5G networks for enhanced positioning services. In *Proceedings of Workshop on Satellite Navigation Technology (NAVITEC)* (pp. 1–12). IEEE. https://doi.org/10.1109/NAVITEC53682.2022.9847557

del Peral-Rosado, J., Lopez-Salcedo, J., Seco-Granados, G., Zanier, F., Crosta, P., Ioannides, R., & Crisci, M. (2013, October). Software-defined radio LTE positioning receiver towards future hybrid localization systems. In *Proceedings of AIAA International Communication Satellite Systems Conference* (pp. 1–11). https://doi.org/10.2514/6.2013-5610

Diouf, C., Janssen, G., Dun, H., Kazaz, T., & Tiberius, C. (2021). A USRP-based testbed for wideband ranging and positioning signal acquisition. *IEEE Transactions on Instrumentation and Measurement*, *70*, 1–15. https://doi.org/10.1109/TIM.2021.3065449

Diouf, C., Janssen, G., Kazaz, T., Dun, H., Chamanzadeh, F., & Tiberius, C. (2019). A 400 Msps SDR platform for prototyping accurate wideband ranging techniques. In *Proceedings of Workshop on Positioning, Navigation and Communications* (pp. 1–6). IEEE. https://doi.org/10.1109/WPNC47567.2019.8970251

Donaldson, J. E., Parker, J. J., Moreau, M. C., Highsmith, D. E., & Martzen, P. D. (2020). Characterization of on-orbit GPS transmit antenna patterns for space users. *Navigation, Journal of the Institute of Navigation*, *67*(2), 411–438. https://doi.org/10.1002/navi.361

Dovis, F., Linty, N., Berardo, M., Cristodaro, C., Minetto, A., Nguyen Hong, L., … Troglia Gamba, M. (2017, Jun.). Anomalous GPS signals reported from svn49. *GPS World*. `https://www.gpsworld.com/anomalous-{GPS}-signals-reported-from-svn49`.

Dovis, F., Minetto, A., Nardin, A., Falletti, E., Margaria, D., Nicola, M., & Vannucchi, M. (2019, Jul.). What happened when Galileo experienced a week-long service outage. *GPS World*. `https://www.gpsworld.com/why-galileo-experienced-a-week-long-service-outage`.

Driusso, M., Marshall, C., Sabathy, M., Knutti, F., Mathis, H., & Babich, F. (2017, April). Vehicular position tracking using LTE signals. *IEEE Transactions on Vehicular Technology*, *66*(4), 3376–3391. https://doi.org/10.1109/TVT.2016.2589463

Dötterböck, D., Pany, T., Lesjak, R., Prechtl, T., & Tabatabaei, A. (2023). PRN sequence estimation with a self-calibrating 40-element antenna array. *Navigation, Journal of the Institute of Navigation*, *70*(4), 1–1. https://doi.org/10.33012/navi.600

Eissfeller, B., & Won, J.-H. (2017). Receiver architecture. In P. J. Teunissen & O. Montenbruck (Eds.), *Springer handbook of global navigation satellite systems* (pp. 365–400). Springer. https://doi.org/10.1007/978-3-319-42928-1

European Union Agency for the Space Programme. (2018). *GNSS User Technology Report.* `https://www.gsa.europa.eu/system/files/reports/gnss_user_tech_report_2018.pdf`. [Accessed on 23-Sep-2022]

Farhangian, F., Benzerrouk, H., & Landry, R. (2021). Opportunistic in-flight INS alignment using LEO satellites and a rotatory IMU platform. *Aerospace*, *8*(10), 280–281. https://doi.org/10.3390/aerospace8100280

Farhangian, F., & Landry, R. (2020, October). Multi-constellation software-defined receiver for Doppler positioning with LEO satellites. *Sensors*, *20*(20), 5866–5883. https://doi.org/10.3390/s20205866

Fernández–Prades, C. (2022). *Yocto geniux.* Online: `https://github.com/carlesfernandez/yocto-geniux`. [Accessed: 12-Sep-2022] https://doi.org/10.5281/zenodo.7848142

Fernández–Prades, C., Arribas, J., & Closas, P. (2016a, Sept.). Accelerating GNSS software receivers. In *Proc. of the ION GNSS+ Meeting* (pp. 44–61). . https://doi.org/10.33012/2016.14576

Fernández–Prades, C., Arribas, J., & Closas, P. (2016b, Dec.). Assessment of software-defined GNSS receivers. In *2016 8th ESA Workshop on Satellite Navigation Technologies and European Workshop on GNSS Signals and Signal Processing (NAVITEC).* IEEE. https://doi.org/10.1109/NAVITEC.2016.7931740

Fernández–Prades, C., Closas, P., & Arribas, J. (2013, Sept.). Turning a television into a GNSS receiver. In *Proc. of the ION GNSS+ Meeting* (pp. 1492–1507). Institute of Navigation.

Fernández–Prades, C., Vilà–Valls, J., Arribas, J., & Ramos, A. (2018, Apr.). Continuous reproducibility in GNSS signal processing. *IEEE Access*, *6*(1), 20451–20463. https://doi.org/10.1109/ACCESS.2018.2822835

FGI. (2022). *The fgi-gsrx software defined GNSS receiver goes open source.* `https://www.maanmittauslaitos.fi/en/topical_issues/fgi-gsrx-software-defined-gnss-receiver-goes-open-source`. [Accessed 11-Aug-2022]

Foerster, F., & Pany, T. (2013). *Device and method for producing a data stream on the basis of data packets provided with packet sequence marks, and satellite receivers for providing the data stream* (Nos. US patent no. 8451170, 2011-03-03; German patent no. 102008014981, 2009-10-15).

Fokin, G., & Volgushev, D. (2022, Mar.). Software-defined radio network positioning technology design. problem statement. In *Proceedings of Systems of Signals Generating and Processing in the Field of on Board Communications* (pp. 1–6). IEEE. https://doi.org/10.1109/IEEECONF53456.2022.9744391

Galileo E1 receiver processing. (2022). In *GNSS software receivers* (pp. 140–152). Cambridge University Press. https://doi.org/10.1017/9781108934176.006

GLONASS L1OF receiver processing. (2022). In *GNSS software receivers* (pp. 126–139). Cambridge University Press. https://doi.org/10.1017/9781108934176.005

Gómez-Casco, D., López-Salcedo, J. A., & Seco-Granados, G. (2016). Generalized integration techniques for high-sensitivity GNSS receivers affected by oscillator phase noise. In *2016 IEEE Statistical Signal Processing Workshop (SSP)* (pp. 1–5). IEEE. https://doi.org/10.1109/SSP.2016.7551809

GPS World staff. (2012, Sept.). *Innovation: Software GNSS receiver - GPS world : GPS world.* `https://www.gpsworld.com/software-{GNSS}-receiver-an-answer-for-precise-positioning-research/`. [Accessed on 07/04/2022]

GPS L1 C/A receiver processing. (2022). In *GNSS software receivers* (pp. 108–125). Cambridge University Press. https://doi.org/10.1017/9781108934176.004

Gunawardena, S. (2013). A universal GNSS software receiver matlab® toolbox for education and research. In *Proc. of the ION GNSS+ Meeting* (pp. 1560–1576). Institute of Navigation.

Gunawardena, S. (2014). A universal GNSS software receiver toolbox. *Inside GNSS*, 58–67.

Gunawardena, S. (2021). A high performance easily configurable satnav SDR for advanced algorithm development and rapid capability deployment. In *Proc. of the ION International Technical Meeting* (pp. 539–554). Institute of Navigation. https://doi.org/10.33012/2021.17808

Gunawardena, S., Pany, T., & Curran, J. (2021). ION GNSS software-defined radio metadata standard. *Navigation, Journal of the Institute of Navigation*, *68*(1), 11–20. `https://navi.ION.org/content/68/1/11` https://doi.org/10.1002/navi.407

Gunawardena, S., Soloviev, A., & van Graas, F. (2004). Real time implementation of deeply integrated software GPS receiver and low cost IMU for processing low-CNR GPS signals. In *Proc. of the Annual Meeting of The Institute of Navigation* (pp. 108–114). Institute of Navigation.

Gunawardena, S., Soloviev, A., & Van Graas, F. (Winter 2007-2008). Wideband transform-domain GPS instrumentation receiver for signal quality and anomalous event monitoring. *Navigation, Journal of the Institute of Navigation*, *54*(4), 317–331. https://www.ion.org/publications/abstract.cfm?articleID=102456

Gunawardena, S., & van Graas, F. (2006). Split-sum correlator simplifies range computations in GPS receiver. *Electronics Letters*, *42*, 1469-1471. https://doi.org/10.1049/el:20062921

Gunawardena, S., & Van Graas, F. (2011). Multi-channel wideband GPS anomalous event monitor. In *Proc. of the International Technical Meeting of the Satellite Division of the ION* (pp. 1957–1968). Institute of Navigation.

Gunawardena, S., Zhu, Z., Uijt de Haag, M., & Van Graas, F. (2009). Remote-controlled, continuously operating GPS anomalous event monitor. *Navigation, Journal of the Institute of Navigation*, *56*(2), 97–113. https://www.ION.org/publications/abstract.cfm?articleID=102491

Hamza, G., Zekry, A., & Motawie, I. (2009). Implementation of a complete GPS receiver using Simulink. *IEEE Circuits and Systems Magazine*, *9*(4), 43–51. https://doi.org/10.1109/MCAS.2009.934706

Hobiger, T., Gotoh, T., Amagai, J., Koyama, Y., & Kondo, T. (2010). A GPU based real-time GPS software receiver. *GPS solutions*, *14*(2), 207–216. http://dx.doi.org/10.1007/s10291-009-0135-2

Honkala, S. (2016). *GLONASS satellite navigation signal implementation in a software-defined multi-constellation satellite navigation receiver* (Unpublished master's thesis). Aalto University.

Humphreys, T., Psiaki, M., Kintner, P., & Ledvina, B. (2006). GNSS receiver implementation on a DSP: Status, challenges, and prospects. In *Proc. of the International Technical Meeting of the Satellite Division of the ION* (pp. 2370–2382). Institute of Navigation.

Humphreys, T. E., Bhatti, J., Pany, T., Ledvina, B., & O'Hanlon, B. (2009, Sept.). Exploiting multicore technology in software-defined GNSS receivers. In *Proc. of the ION GNSS meeting* (p. 326-338). Institute of Navigation.

Humphreys, T. E., Ledvina, B. M., Psiaki, M. L., O'Hanlon, B. W., & Kintner, P. M., Jr. (2008, Sept.). Assessing the spoofing threat: development of a portable GPS civilian spoofer. In *Proc. of the ION GNSS meeting* (pp. 2314–2325). Institute of Navigation.

Humphreys, T. E., Murrian, M. J., & Narula, L. (2020). Deep-urban unaided precise global navigation satellite system vehicle positioning. *IEEE Intelligent Transportation Systems Magazine*, *12*(3), 109–122. https://doi.org/10.1109/MITS.2020.2994121

IFEN GmbH. (2022). *SX3 GNSS Software Receiver — ifen.com.* https://www.ifen.com/products/sx3-{GNSS}-software-receiver/. [Accessed 01-Sep-2022]

Ikhtiari, N. (2019). *Navigation in GNSS denied environments using software defined radios and LTE signals of opportunities* (Unpublished master's thesis). University of Canterbury, Christchurch, New Zealand.

ION SDR Working Group. (2020). *Global navigation satellite systems software defined radio sampled data metadata standard, revision 1.0.* https://sdr.{ION}.org.

iPosi Inc. (2015). *iPosi GNSS signal processing and assistance; performance.* https://iposi.com/technology/Performance. [Accessed on 2022-09-26]

Jiménez-Baños, D., Blanco-Delgado, N., López-Risueño, G., Seco-Granados, G., & Garcia-Rodriguez, A. (2006). Innovative techniques for GPS indoor positioning using a snapshot receiver. In *Proc. of the International Technical Meeting of the Satellite Division of the ION* (pp. 2944–2955). Institute of Navigation.

Kang, T., Lee, H., & Seo, J. (2019, October). Analysis of the maximum correlation peak value and RSRQ in LTE signals according to frequency bands and sampling frequencies. In *International Conference on Control, Automation and Systems* (pp. 1182–1186). IEEE. https://doi.org/10.23919/ICCAS47443.2019.8971462

Kaplan, E. (1996). *Understanding GPS principles and applications*. Artech House Publishers. ISBN:0890067937

Kassas, Z., Abdallah, A., Lee, C., Jurado, J., Duede, J., Hoeffner, Z., … Tay, R. (2022, September). Protecting the skies: GNSS-less accurate aircraft navigation with terrestrial cellular signals of opportunity. In *Proc. of the ION GNSS+ Meeting* (pp. 1014–1025). Institute of Navigation. accepted https://doi.org/10.33012/2022.18579

Kassas, Z., Bhatti, J., & Humphreys, T. (2013, December). A graphical approach to GPS software-defined receiver implementation. In *Proceedings of IEEE Global Conference on Signal and Information Processing* (pp. 1226–1229). https://doi.org/10.1109/GlobalSIP.2013.6737129

Kassas, Z., Khalife, J., Abdallah, A., & Lee, C. (2020). I am not afraid of the jammer: navigating with signals of opportunity in GPS-denied environments. In *Proc. of the ION GNSS+ Meeting* (pp. 1566–1585). Institute of Navigation. https://doi.org/10.33012/2020.17737

Kassas, Z., Khalife, J., Abdallah, A., & Lee, C. (2022, July). I am not afraid of the GPS jammer: resilient navigation via signals of opportunity in GPS-denied environments. *IEEE Aerospace and Electronic Systems Magazine*, *37*(7), 4–19. https://doi.org/10.1109/MAES.2022.3154110

Kassas, Z., Khalife, J., Abdallah, A., Lee, C., Jurado, J., Wachtel, S., … Tay, R. (2022, Oct.). Assessment of cellular signals of opportunity for high altitude aircraft navigation. *IEEE Aerospace and Electronic Systems Magazine*, *37*(10). https://doi.org/10.1109/MAES.2022.3187142

Kassas, Z., Khalife, J., Shamaei, K., & Morales, J. (2017, September). I hear, therefore I know where I am: Compensating for GNSS limitations with cellular signals. *IEEE Signal Processing Magazine*, *34*(5), 111–124. https://doi.org/10.1109/MSP.2017.2715363

Kassas, Z., Kozhaya, S., Saroufim, J., Kanj, H., & Hayek, S. (2023). A look at the stars: Navigation with multi-constellation LEO satellite signals of opportunity. *Inside GNSS Magazine*, *18*(4), 38–47.

Kassas, Z., Morales, J., & Khalife, J. (2019). New-age satellite-based navigation – STAN: simultaneous tracking and navigation with LEO satellite signals. *Inside GNSS*, *14*(4), 56–65.

Kassas, Z., Neinavaie, M., Khalife, J., Khairallah, N., Haidar-Ahmad, J., Kozhaya, S., & Shadram, Z. (2021). Enter LEO on the GNSS stage: Navigation with Starlink satellites. *Inside GNSS*, *16*(6), 42–51.

Khalife, J., & Kassas, Z. (2018, April). Precise UAV navigation with cellular carrier phase measurements. In *Proc. of the IEEE/ION PLANS meeting* (pp. 978–989). IEEE. https://doi.org/10.1109/PLANS.2018.8373476

Khalife, J., & Kassas, Z. (2022, Oct.). On the achievability of submeter-accurate UAV navigation with cellular signals exploiting loose network synchronization. *IEEE Transactions on Aerospace and Electronic Systems*, *58*(5), 4261–4278. https://doi.org/10.1109/TAES.2022.3162770

Khalife, J., Neinavaie, M., & Kassas, Z. (2022, April). The first carrier phase tracking and positioning results with Starlink LEO satellite signals. *IEEE Aerospace and Electronic Systems Magazine*, *56*(2), 1487–1491. https://doi.org/10.1109/TAES.2021.3113880

Khalife, J., Shamaei, K., & Kassas, Z. (2018, April). Navigation with cellular CDMA signals – part I: Signal modeling and software-defined receiver design. *IEEE Transactions on Signal Processing*, *66*(8), 2191–2203. https://doi.org/10.1109/TSP.2018.2799167

Lapin, I., Granados, G., Samson, J., Renaudin, O., Zanier, F., & Ries, L. (2022, April). STARE: Real-time software receiver for LTE and 5G NR positioning and signal monitoring. In *Proceedings of Workshop on Satellite Navigation Technology (NAVITEC)* (pp. 1–11). IEEE. https://doi.org/10.1109/NAVITEC53682.2022.9847544

Ledvina, B., Powell, S., Kintner, P., & Psiaki, M. (2003). A 12-channel real-time GPS L1 software receiver1. In *Proc. of the ION National Technical Meeting* (pp. 767–782). Institute of Navigation.

Ledvina, B., Psiaki, M., Humphreys, T., Powell, S., & Kintner, P. (2006). A real-time software receiver for the GPS and Galileo L1 signals. In *Proc. of the International Technical Meeting of the Satellite Division of the ION* (pp. 2321–2333). Institute of Navigation.

Ledvina, B., Psiaki, M., Powell, S., & Kintner, P. (2004, Sept.). Bit-wise parallel algorithms for efficient software correlation applied to a GPS software receiver. *IEEE Transactions on Wireless Communications*, *3*(5), 1469–1473. https://doi.org/10.1109/TWC.2004.833467

Ledvina, B., Psiaki, M., Powell, S., & Kintner, P. (2006, Mar.). *Real-time software receiver; US patent no. 7010060, 2006-03-07* (No. US patent no. 7010060).

Ledvina, B., Psiaki, M., Powell, S., & Kintner, P. (2007, Dec.). *Real-Time Software Receiver; US patent no. 7305021; 2007-12-04* (No. US patent no. 7305021).

Ledvina, B., Psiaki, M., Sheinfeld, D., Cerruti, A., Powell, S., & Kintner, P. (2004). A real-time GPS civilian L1/L2 software receiver. In *Proc. of the International Technical Meeting of the Satellite Division of the ION* (pp. 986–1005). Institute of Navigation.

Lightsey, G., Humphreys, T., Bhatti, J., Joplin, A., O'Hanlon, B., & Powell, S. (2014). Demonstration of a space capable miniature dual frequency GNSS receiver. *Navigation, Journal of the Institute of Navigation*, *61*(1), 53–64. https://doi.org/10.1002/navi.52

Locubiche-Serra, S., López-Salcedo, J. A., & Seco-Granados, G. (2016). Statistical near-far detection techniques for GNSS snapshot receivers. In *Proc. of the IEEE International Conference on Acoustics, Speech, and Signal Processing* (pp. 6570–6574). IEEE. https://doi.org/10.1109/ICASSP.2016.7472943

LocusLock. (2022). *Reliable, accurate, and intelligent GPS lock.* `https://locuslock.com`. [Accessed on 2022-09-30]

López-Salcedo, J. A., Capelle, Y., Toledo, M., Seco, G., López-Vicario, J., Kubrak, D., … Jiménez, D. (2008). DINGPOS: a hybrid indoor navigation platform for GPS and Galileo. In *Proc. of the International Technical Meeting of the Satellite Division of the ION* (pp. 1780–1791). Institute of Navigation.

López-Salcedo, J. A., Parro-Jiménez, J. M., & Seco-Granados, G. (2009). Multipath detection metrics and attenuation analysis using a GPS snapshot receiver in harsh environments. In *2009 3rd European Conference on Antennas and Propagation (EuCAP)* (pp. 3692–3696). IEEE.

Lucas-Sabola, V., Seco-Granados, G., López-Salcedo, J. A., García-Molina, J., & Crisci, M. (2017). Efficiency analysis of cloud GNSS signal processing for IoT applications. In *Proc. of the ION GNSS+ Meeting* (pp. 3843–3852). Institute of Navigation. https://doi.org/10.33012/2017.15237

Lucas-Sabola, V., Seco-Granados, G., López-Salcedo, J. A., García-Molina, J. A., & Crisci, M. (2016). Cloud GNSS receivers: New advanced applications made possible. In *2016 International Conference on Localization and GNSS (ICL-GNSS)* (pp. 1–6). IEEE. https://doi.org/10.1109/ICL-GNSS.2016.7533852

Maaref, M., & Kassas, Z. (2020, July). Ground vehicle navigation in GNSS-challenged environments using signals of opportunity and a closed-loop map-matching approach. *IEEE Transactions on Intelligent Transportation Systems*, *21*(7), 2723–2723. https://doi.org/10.1109/TITS.2019.2907851

Maaref, M., & Kassas, Z. (2022, June). Autonomous integrity monitoring for vehicular navigation with cellular signals of opportunity and an IMU. *IEEE Transactions on Intelligent Transportation Systems*, *23*(6), 5586–5601. https://doi.org/10.1109/TITS.2021.3055200

Maaref, M., Khalife, J., & Kassas, Z. (2019, March). Lane-level localization and mapping in GNSS-challenged environments by fusing Lidar data and cellular pseudoranges. *IEEE Transactions on Intelligent Vehicles*, *4*(1), 73–89. https://doi.org/10.1109/TIV.2018.2886688

Manzano-Jurado, M., Alegre-Rubio, J., Pellacani, A., Seco-Granados, G., López-Salcedo, J. A., Guerrero, E., & García-Rodríguez, A. (2014). Use of weak GNSS signals in a mission to the moon. In *2014 7th ESA Workshop on Satellite Navigation Technologies and European Workshop on GNSS signals and Signal Processing (NAVITEC)* (pp. 1–8). IEEE. http://dx.doi.org/10.1109/NAVITEC.2014.7045151

Margaria, D., Linty, N., Favenza, A., Nicola, M., Musumeci, L., Falco, G., … Dovis, F. (2012, Jan.-Feb.). Contact! - first acquisition and tracking of IOV Galileo signals. *Inside GNSS*, *7*, 45–55.

McEllroy, J. (2006). *Navigation using signals of opportunity in the* AM *transmission band* (Unpublished master's thesis). Air Force Institute of Technology, Wright-Patterson Air Force Base, Ohio, USA.

McEllroy, J., Raquet, J., & Temple, M. (2006). Use of a software radio to evaluate signals of opportunity for navigation. In *Proc. of the ION GNSS meeting* (pp. 126–133). Institute of Navigation.

Miller, N. S., Koza, T. J., Morgan, S. C., Martin, S. M., Neish, A., Grayson, R., & Reid, T. (2023). SNAP: A Xona Space Systems and GPS software-defined receiver. In *Proc. of the IEEE/ION PLANS meeting* (pp. 897–904). https://doi.org/10.1109/PLANS53410.2023.10139956

Minetto, A., Dovis, F., Vesco, A., Garcia-Fernandez, M., López-Cruces, À., Trigo, J. L., … others (2020). A testbed for GNSS-based positioning and navigation technologies in smart cities: The HANSEL project. *Smart Cities*, *3*(4), 1219–1241. https://doi.org/10.3390/smartcities3040060

Ministry of Science and ICT of Korea. (2021). *Launch to become the world's seventh 'space powerhouse'!* `https://www.msit.go.kr/bbs/view.do?sCode=engŹmId=4ŹmPid=2ŹbbsSeqNo=42ŹnttSeqNo=568`. [Accessed on 14-Sep-2022]

Mitola, J. (1995). The software radio architecture. *IEEE Communications Magazine*, *33*(5), 26–38. https://doi.org/10.1109/35.393001

Molino, A., Nicola, M., Pini, M., & Fantino, M. (2009). N-GENE GNSS software receiver for acquisition and tracking algorithms validation. In *European signal processing conference* (pp. 2171–2175). IEEE. Print ISBN:978-161-7388-76-7

Morales, J., & Kassas, Z. (2021). Tightly-coupled inertial navigation system with signals of opportunity aiding. *IEEE Transactions on Aerospace and Electronic Systems*, *57*(3), 1930–1948. https://doi.org/10.1109/TAES.2021.3054067

Morton, Y., Jiao, Y., & Taylor, S. (2015). High-latitude and equatorial ionospheric scintillation based on an event-driven multi-GNSS data collection system. *Proc. Ionospheric Effect Sym.*.

A multi-GNSS software receiver. (2022). In *GNSS software receivers* (pp. 174–188). Cambridge University Press. https://doi.org/10.1017/9781108934176.009

Murrian, M. J., Narula, L., Iannucci, P. A., Budzien, S., O'Hanlon, B. W., Powell, S. P., & Humphreys, T. E. (2021). First results from three years of GNSS interference monitoring from low Earth orbit. *Navigation, Journal of the Institute of Navigation*,

68(4), 673–685. https://doi.org/10.1002/navi.449

Nardin, A., Dovis, F., & Fraire, J. (2021). Empowering the tracking performance of LEO-based positioning by means of meta-signals. *IEEE Journal of Radio Frequency Identification*, *5*(3), 244–253. https://doi.org/10.1109/JRFID.2021.3077082

NavIC L5 receiver processing. (2022). In *GNSS software receivers* (pp. 164–173). Cambridge University Press. https://doi.org/10.1017/9781108934176.008

Neinavaie, M., Khalife, J., & Kassas, Z. (2021, June). Acquisition, Doppler tracking, and positioning with Starlink LEO satellites: First results. *IEEE Transactions on Aerospace and Electronic Systems*, *58*(3), 2606–2610. https://doi.org/10.1109/TAES.2021.3127488

Nichols, H. A., Murrian, M. J., & Humphreys, T. E. (2022). Software-defined GNSS is ready for launch. In *Proc. of the ION GNSS+ Meeting* (pp. 996–1013). https://doi.org/10.33012/2022.18313

Nicola, M., Motella, B., Pini, M., & Falletti, E. (2022, March). Galileo OSNMA public observation phase: Signal testing and validation. *IEEE Access*, *10*, 27960–27969. https://doi.org/10.1109/ACCESS.2022.3157337

NTLAB, UAB. (2022). *Unique ICs for GNSS Receivers.* `https://ntlab.lt/`. [Accessed on 2022-09-26]

O'Hanlon, B. W., Psiaki, M. L., Powell, S., Bhatti, J. A., Humphreys, T. E., Crowley, G., & Bust, G. S. (2011). Cases: A smart, compact GPS software receiver for space weather monitoring. In *Proc. of the International Technical Meeting of the Satellite Division of the ION* (pp. 2745–2753). https://doi.org/10.15781/T2N010949

Orabi, M., Khalife, J., & Kassas, Z. (2021, March). Opportunistic navigation with Doppler measurements from Iridium Next and Orbcomm LEO satellites. In *Proc. of the IEEE aerospace conference* (pp. 1–9). IEEE. https://doi.org/10.1109/AERO50100.2021.9438454

Pany, T., Dötterböck, D., Gomez-Martinez, H., Hammed, M. S., Hörkner, F., Kraus, T., … Ebert, D. (2019). The multi-sensor navigation analysis tool (MuSNAT) – architecture, LiDAR, GPU/CPU GNSS signal processing. In *Proc. of the ION GNSS+ Meeting* (pp. 4087–4115). Institute of Navigation. https://doi.org/10.33012/2019.17128

Pany, T., Eissfeller, B., Hein, G., Moon, S., & Sanroma, D. (2004). IPEXSR: A PC based software GNSS receiver completely developed in europe. In *Proc. ENC-GNSS 2004.*

Pany, T., Förster, F., & Eissfeller, B. (2004). Real-time processing and multipath mitigation of high-bandwidth L1/L2 GPS signals with a PC-based software receiver. In *Proc. of the International Technical Meeting of the Satellite Division of the ION* (pp. 971–985). Institute of Navigation.

Pany, T., Kaniuth, R., & Eissfeller, B. (2005, Sept.). Deep integration of navigation solution and signal processing. In *Proc. of the ION GNSS meeting* (pp. 1095–1102). Institute of Navigation.

Pany, T., Moon, S. W., Irsigler, M., Eissfeller, B., & Fürlinger, K. (2003). Performance assessment of an under-sampling SWC receiver for simulated high-bandwidth GPS/Galileo signals and real signals. In *Proc. of the International Technical Meeting of the Satellite Division of the ION* (pp. 103–116). Institute of Navigation.

Pany, T., Riedl, B., Winkel, J., Wörz, T., Schweikert, R., Niedermeier, H., … Jiménez-Baños, D. (2009). Coherent integration time: The longer, the better. *Inside GNSS*, *4*(6), 52–61.

Peng, S., & Morton, Y. (2011). A USRP2-based multi-constellation and multi-frequency GNSS software receiver for ionosphere scintillation studies. In *Proc. of the ION International Technical Meeting* (pp. 1033–1042). Institute of Navigation.

Pesyna, K., Kassas, Z., Bhatti, J., & Humphreys, T. (2011, September). Tightly-coupled opportunistic navigation for deep urban and indoor positioning. In *Proc. of the ION GNSS meeting* (pp. 3605–3617). Institute of Navigation.

Pesyna, K. M., Jr., Heath, R. W., Jr., & Humphreys, T. E. (2014). Centimeter positioning with a smartphone-quality GNSS antenna. In *Proc. of the ION GNSS+ Meeting* (pp. 1568–1577). Institute of Navigation.

Pinell, C. (2021). *Receiver architectures for positioning with low Earth orbit satellite signals* (Unpublished master's thesis). Lulea University of Technology, School of Electrical Engineering, Sweden.

Plotly. (2022). *Plotly JSON chart schema.* `https://plotly.com/chart-studio-help/json-chart-schema/`. [Accessed on 09/30/2022]

PR Newswire. (2021). *New trimble DA2 receiver boosts performance of trimble catalyst GNSS positioning service.* `https://www.prnewswire.com/news-releases/new-trimble-da2-receiver-boosts-performance-of-trimble-catalyst-GNSS-positioning-service-301381160.html`. [Accessed on 2022-09-29]

Psiaki, M. (2006, March). Real-time generation of bit-wise parallel representations of over-sampled PRN codes. *IEEE Transactions on Wireless Communications*, *5*(3), 487–491. https://doi.org/10.1109/TWC.2006.1611075

Psiaki, M., Humphreys, T., Mohiuddin, S., Powell, S., Cerruti, A., & Kintner, P. (2006). Searching for Galileo. In *Proc. of the International Technical Meeting of the Satellite Division of the ION* (pp. 1567–1575). Institute of Navigation.

Psiaki, M., & Slosman, B. (2022). Tracking digital FM OFDM signals for the determination of navigation observables. *Navigation, Journal of the Institute of Navigation*, *69*(2). https://doi.org/10.33012/navi.521

RF Micro Devices, Inc., Greensboro. (2006). *RFMD announces availability of the RFMD(R) GPS RF8110 scalable GPS solution.* `https://ir.qorvo.com/node/12736/pdf`. [Accessed on 2022-09-29]

Rügamer, A., Förster, F., Stahl, M., & Rohmer, G. (2012). A flexible and portable multiband GNSS front-end system. In *Proc. of the International Technical Meeting of the Satellite Division of the ION* (pp. 2378–2389). Institute of Navigation.

Rügamer, A., Rubino, D., Lukcin, I., Taschke, S., Stahl, M., & Felber, W. (2016). Secure position and time information by server side PRS snapshot processing. In *Proc. of the ION GNSS+ Meeting* (pp. 3002–3017). Institute of Navigation. https://doi.org/10.33012/2016.14781

Santana, G., de Cristo, R., & Branco, K. (2021). Integrating cognitive radio with unmanned aerial vehicles: An overview. *Sensors*, *21*(3), 830–856. https://doi.org/10.3390/s21030830

Seco-Granados, G., López-Salcedo, J. A., Jiménez-Baños, D., & López-Risueño, G. (2012). Challenges in indoor global navigation satellite systems: Unveiling its core features in signal processing. *IEEE Signal Processing Magazine*, *29*(2), 108–131. https://doi.org/10.1109/MSP.2011.943410

Shamaei, K., & Kassas, Z. (2018, December). LTE receiver design and multipath analysis for navigation in urban environments. *Navigation, Journal of the Institute of Navigation*, *65*(4), 655–675. https://doi.org/10.1002/navi.272

Shamaei, K., & Kassas, Z. (2021a). A joint TOA and DOA acquisition and tracking approach for positioning with LTE signals. *IEEE Transactions on Signal Processing*, 2689–2705. https://doi.org/10.1109/TSP.2021.3068920

Shamaei, K., & Kassas, Z. (2021b). Receiver design and time of arrival estimation for opportunistic localization with 5G signals. *IEEE Transactions on Wireless Communications*, *20*(7), 4716–4731. https://doi.org/10.1109/TWC.2021.3061985

Shamaei, K., Khalife, J., & Kassas, Z. (2018, April). Exploiting LTE signals for navigation: Theory to implementation. *IEEE Transactions on Wireless Communications*, *17*(4), 2173–2189. https://doi.org/10.1109/TWC.2018.2789882

Snyder, C., Feng, G., & Van Graas, F. (1999). GPS Anomalous Event Monitor(GAEM). In *Proc. of the Annual Meeting of The Institute of Navigation* (pp. 185–189). Institute of Navigation.

Söderholm, S., Bhuiyan, M., Thombre, S., Ruotsalainen, L., & Kuusniemi, H. (2016). A multi-GNSS software-defined receiver: Design, implementation, and performance benefits. *Annals of Telecommunications*, *71*, 399–410. https://doi.org/10.1007/s12243-016-0518-7

Soloviev, A., Gunawardena, S., & Van Graas, F. (2004). Deeply integrated GPS/low-cost IMU for low CNR signal processing: Flight test results and real time implementation. In *Proc. of the International Technical Meeting of the Satellite Division of the ION* (pp. 1598–1608). Institute of Navigation.

Song, Y. J., Lee, H. B., & Won, J. H. (2021, Jun.). Design of multi-constellation and multi-frequency GNSS SDR with fully reconfigurable functionality. *Journal of Positioning, Navigation, and Timing*, *10*(2), 91–102. https://doi.org/10.11003/JPNT.2021.10.2.91

Souli, N., Kolios, P., & Ellinas, G. (2020). Relative positioning of autonomous systems using signals of opportunity. In *Proceedings of IEEE Vehicular Technology Conference* (pp. 1–6). IEEE. https://doi.org/10.1109/VTC2020-Spring48590.2020.9128912

Souli, N., Kolios, P., & Ellinas, G. (2021). Online relative positioning of autonomous vehicles using signals of opportunity. *IEEE Transactions on Intelligent Vehicles*, 873–885. https://doi.org/10.1109/TIV.2021.3124727

Souli, N., Kolios, P., & Ellinas, G. (2022). Adaptive frequency band selection for accurate and fast positioning utilizing SOPs. In *Proceedings of International Conference on Unmanned Aircraft Systems* (pp. 1309–1315). https://doi.org/10.48550/arXiv.2206.04312

SPCOMNAV. (2019). *Cloud GNSS Receiver.* `http://cloudGNSSrx.com`. [Accessed on 23-Sep-2022]

Stöber, C., Anghileri, M., Ayaz, A. S., Dötterböck, D., Krämer, I., Kropp, V., … Pany, T. (2010, Sept.). ipexSR: a real-time multi-frequency software GNSS receiver. In *Proceedings ELMAR-2010* (pp. 407–416). IEEE.

Takasu, T., & Yasuda, A. (2009). Development of the low-cost RTK-GPS receiver with an open source program package RTKLIB. In *International symposium on GPS/GNSS* (Vol. 1). International Convention Center Jeju Korea.

Tang, G., & Peng, A. (2022). 5G receiver design based on downlink intermittent signals tracking algorithm. In *Proceedings of china satellite navigation conference* (pp. 462–471). Springer. https://doi.org/10.1007/978-981-19-2576-4_41

TeleOrbit GmbH. (2022). *MGSE REC: GNSS Radio frequency front-end.* `https://teleorbit.eu/en/satnav/mgse-rec/`. [Accessed on 09/06/2022]

Thombre, S., Bhuiyan, M., Söderholm, S., Kirkko-Jaakkola, M., Ruotsalainen, L., & Kuusniemi, H. (2015). A software multi-GNSS receiver implementation for the Indian regional navigation satellite system. *IETE Journal of Research*, 246–256. https://doi.org/10.1080/03772063.2015.1093968

Trimble Inc. (2005). *Trimble introduces future-ready GNSS positioning technology.* `https://investor.trimble.com/news-releases/news-release-details/trimble-introduces-future-ready-GNSS-positioning-technology`. [Accessed on 2022-09-29]

Trimble Inc. (2017). *Trimble DA1 catalyst GNSS systems.* `https://geospatial.trimble.com/products-and-solutions/trimble-da1`. [Accessed on 2022-09-29]

Troglia Gamba, M., Marucco, G., Pini, M., Ugazio, S., Falletti, E., & Lo Presti, L. (2015, Nov). Prototyping a GNSS-based passive radar for UAVs: An instrument to classify the water content feature of lands. *Sensors*, *15*(11), 28287–28313. https://doi.org/10.3390/s151128287

Troglia Gamba, M., Nicola, M., & Falletti, E. (2015). eNGene: An ARM based embedded real-time software GNSS receiver. In *Proc. of the International Technical Meeting of the Satellite Division of the ION* (Vol. 4, pp. 3178–3187). Institute of Navigation.

Troglia Gamba, M., Nicola, M., & Motella, B. (2020a, Jun.). Galileo OSNMA: An implementation for ARM-based embedded platforms. In *2020 International Conference on Localization and GNSS, ICL-GNSS 2020 - Proceedings* (pp. 1–6). https://doi.org/10.1109/ICL-GNSS49876.2020.9115539

Troglia Gamba, M., Nicola, M., & Motella, B. (2020b, September). GPS chimera: A software profiling analysis. In *Proc. of the ION GNSS+ Meeting* (pp. 3781–3793). https://doi.org/10.33012/2020.17717

Tsui, J. B.-Y. (2000). *Fundamentals of global positioning system receivers: A software approach*. Wiley-Interscience. https://doi.org/10.1002/0471200549

UniBwM. (2023). *MuSNAT — LRT 9.* `https://www.unibw.de/lrt9/lrt-9.2/software-packages/MuSNAT`. [Accessed on 23/06/2023]

Van Diggelen, F. (2009). *A-GPS: Assisted GPS, GNSS, and SBAS*. Artech House. Electronic ISBN: 9781596933750

Wang, P., Wang, Y., & Morton, J. (2022, August). Signal tracking algorithm with adaptive multipath mitigation and experimental results for LTE positioning receivers in urban environments. *IEEE Transactions on Aerospace and Electronic Systems*, *58*(4), 2779–2795. https://doi.org/10.1109/TAES.2021.3139569

Wikipedia. (2022). *JSON streaming.* `https://en.wikipedia.org/wiki/JSON_streaming`. [Accessed on 09/30/2022]

Wikipedia. (2023). *GNSS software-defined receiver.* `https://en.wikipedia.org/wiki/GNSS_software-defined_receiver`. [Accessed 23-Jun-2023]

Yang, C., Arizabaleta-Diez, M., Weitkemper, P., & Pany, T. (2022). An experimental analysis of cyclic and reference signals of 4G LTE for TOA estimation and positioning in mobile fading environments. *IEEE Aerospace and Electronic Systems Magazine*, *37*(9), 16–41. https://doi.org/10.1109/MAES.2022.3186650

Yang, C., Nguyen, T., & Blasch, E. (2014, April). Mobile positioning via fusion of mixed signals of opportunity. *IEEE Aerospace and Electronic Systems Magazine*, *29*(4), 34–46. https://doi.org/10.1109/MAES.2013.130105

Yang, C., & Soloviev, A. (2018). Positioning with mixed signals of opportunity subject to multipath and clock errors in urban mobile fading environments. In *Proc. of the ION GNSS+ Meeting* (pp. 223–243). Institute of Navigation. https://doi.org/10.33012/2018.15833

Yang, C., & Soloviev, A. (2020, April). Mobile positioning with signals of opportunity in urban and urban canyon environments. In *Proc. of the IEEE/ION PLANS meeting* (pp. 1043–1059). IEEE. https://doi.org/10.1109/PLANS46316.2020.9109876

Yoder, J. E., & Humphreys, T. E. (2023). Low-cost inertial aiding for deep-urban tightly-coupled multi-antenna precise GNSS. *Navigation, Journal of the Institute of Navigation*, *70*(1). https://doi.org/10.33012/navi.561

Zhang, X. (2022, Sept. 9). *GitHub - TMBOC/SoftGNSS: current working ver. of SoftGNSS v3.0 for GN3sV2, GN3sV3, NT1065EVK, and NUT4NT samplers.* `https://github.com/TMBOC/SoftGNSS`.

Zhao, C., Qin, H., & Li, Z. (2022). Doppler measurements from multiconstellations in opportunistic navigation. *IEEE Transactions on Instrumentation and Measurement*, *71*, 1–9. https://doi.org/10.1109/TIM.2022.3147315

Zhu, Z., & Van Graas, F. (2009). Earth-surface multipath detection and error modeling for aircraft GPS receivers. *Navigation, Journal of the Institute of Navigation*, *56*(1), 45–56. `https://www.{ION}.org/publications/abstract.cfm?articleID=102487` https://doi.org/10.1002/j.2161-4296.2009.tb00443.x

How to cite this article: Thomas Pany Akos D., Arribas J. M. Zahidul H. Bhuiyan Pau Closas Fabio Dovis Ignacio Fernandez-Hernandez Carles Fernández–Prades Sanjeev Gunawardena Todd Humphreys Zaher M. Kassas José A. López Salcedo Mario Nicola Mark L. Psiaki Alexander Rügamer Young-Jin Song Jong-Hoon Won , GNSS SDR History and Status. *NAVIGATION*, xxxx;yyy:z–t.

GNSS Software Defined Radio: History, Current Developments, and Standardization Efforts

Dennis Akos, *University of Colorado, Boulder*
Javier Arribas, *Centre Tecnològic de Telecomunicacions de Catalunya*
M. Zahidul H. Bhuiyan, *Finnish Geospatial Research Institute*
Pau Closas, *Northeastern University*
Fabio Dovis, *Politecnico di Torino, Italy*
Ignacio Fernandez-Hernandez, *European Commission*
Carles Fernández–Prades, *Centre Tecnològic de Telecomunicacions de Catalunya*
Sanjeev Gunawardena, *Air Force Institute of Technology*
Todd Humphreys, *The University of Texas at Austin*
Zaher M. Kassas, *The Ohio State University*
José A. López Salcedo, *Universitat Autònoma de Barcelona*
Mario Nicola, *LINKS foundation, Italy*
Thomas Pany, *Universität der Bundeswehr München*
Mark L. Psiaki, *Virginia Tech*
Alexander Rügamer, *Fraunhofer Institute for Integrated Circuits IIS, Germany*
Young-Jin Song, *Inha University, Incheon, South Korea*
Jong-Hoon Won, *Inha University, Incheon, South Korea*

BIOGRAPHY

Dennis Akos completed the Ph.D. degree in Electrical Engineering at Ohio University within the Avionics Engineering Center and is currently a faculty member with the Aerospace Engineering Sciences Department at the University of Colorado, Boulder.

Javier Arribas is a Senior Researcher in the Navigation & Positioning Research Unit at Centre Tecnològic de Telecomunicacions de Catalunya (CTTC/CERCA), Spain.

M. Zahidul H. Bhuiyan is a Research Professor at Finnish Geospatial Research Institute. His main research interests include multi-GNSS receiver development, PNT robustness and resilience, seamless positioning, etc.

Pau Closas is Associate Professor in Electrical and Computer Engineering at Northeastern University, Boston MA. His research interest include robust estimation and filtering for resilient GNSS receivers.

Fabio Dovis is a Full professor and leader of the Navigation Signal Analysis and Simulation group at the Electronics and Telecommunications Department of Politecnico di Torino, Italy. His research interests include advanced signal processing techniques for GNSS

Ignacio Fernandez-Hernandez works at the European Commission, DG DEFIS, as responsible for Galileo high accuracy and authentication. He is also an adjunct professor at KU Leuven.

Carles Fernández-Prades is a Senior Researcher and serves as Head of the Navigation & Positioning Research Unit at Centre Tecnològic de Telecomunicacions de Catalunya (CTTC/CERCA), Spain.

Sanjeev Gunawardena is a Research Associate Professor of Electrical Engineering with the Autonomy & Navigation Technology (ANT) Center at the Air Force Institute of Technology (AFIT). His research interests include RF design, digital systems design, high performance computing, SDR, and all aspects of satnav and associated signal processing.

Todd Humphreys is Professor of Aerospace Engineering at The University of Texas at Austin, where he leads the Radionavigation Laboratory and the Wireless Networking and Communications Group.

Zaher (Zak) Kassas is Professor of Electrical and Computer Engineering at The Ohio State University and Director of the U.S. Department of Transportation Center CARMEN (Center for Automated Vehicle Research with Multimodal AssurEd Navigation).

José A. López Salcedo is professor at Universitat Autònoma de Barcelona. His research interests lie in the field of statistical signal processing with application to snapshot GNSS receivers and future GNSS/PNT evolutions.

Mario Nicola is a researcher in the Space and Navigation Technologies research area at LINKSFoundation, Italy. His main activity is the implementation of algorithms for software radio GPS/Galileo receivers.

Thomas Pany is professor for satellite navigation at the Universität der Bundeswehr München and highly interested in GNSS signal processing and software radio technology.

Mark L. Psiaki is Professor and Crofton Faculty Chair of Aerospace and Ocean Engineering at Virginia Tech. His research interests are navigation, attitude and orbit determination, remote sensing, and general estimation and filtering.

Alexander Rügamer works in GNSS receiver development at the Fraunhofer Institute for Integrated Circuits IIS. His research interests are GNSS multi-band reception, integrated circuits, and immunity to interference.

Young-Jin Song is a Ph. D. student in the Department of Electrical and Computer Engineering at Inha University, South Korea. His research interests are GNSS software receiver, FPGA-based simulator/receiver, and weak signal processing.

Jong-Hoon Won is a professor and leader of Autonomous Navigation Laboratory in the Department of Electrical Engineering at Inha University, Incheon, South Korea. His research interests include GNSS signal design, receivers, navigation, target tracking systems, and self-driving cars.

ABSTRACT

Taking the work conducted by the Global Navigation Satellite System (GNSS) Software Defined Radio (SDR) working group during the last decade as a seed, this contribution summarizes for the first time the history of GNSS SDR development. It highlights selected SDR implementations and achievements that are available to the public or influenced the general SDR development. The relation to the standardization process of Intermediate Frequency (IF) sample data and metadata is discussed, and a recent update of the Institute of Navigation (ION) SDR standard is recapitulated. The work focuses on GNSS SDR implementations on general purpose processors and leaves aside developments conducted on Field Programmable Gate Array (FPGA) and Application-Specific Integrated Circuits (ASICs) platforms. Data collection systems (*i.e.*, front-ends) have always been of paramount importance for GNSS SDRs and are thus partly covered in this work. The work represents the knowledge of the authors but is not meant as a complete description of SDR history. Part of the authors plan to coordinate a more extensive work on this topic in the near future.

I. INTRODUCTION

Receiver development has always been an integral part of satellite navigation, ever since the early studies conducted for the American Global Positioning System (GPS). The very first receivers were huge devices, realizing the correlation of the received satellite signal with internally generated code and carrier replicas by a mixture of digital and analog electronics (Teunissen and Montenbruck, 2017). The advance of semiconductor technology soon after enabled signal processing on dedicated chips. This technology was of course complex to handle and mostly located within the US industry. Despite the success of GPS and its Russian counterpart Globalnaya Navigazionnaya Sputnikovaya Sistema (GLONASS), receiver internal technology was barely accessible to the broader research community for a long time, as it seemed to be impossible to realize GNSS signal processing on low-cost computers. Even in the year 1996 a key receiver design pioneer expressed skepticism that general purpose microprocessors were, or would ever be, a suitable platform for implementing an GNSS receiver (Kaplan, 1996).

The situation radically changed when the algorithms of a GPS receiver were first implemented as Matlab software on a desktop Personal Computer (PC) and estimates of Digital Signal Processor (DSP) processing power to run the algorithms in real-time were encouraging (Akos and Braasch, 1996; Akos, 1997). Soon after, real-time processing was demonstrated even on conventional PCs and the widespread use of software radio technology took off with exponential growth. Interestingly, software radio technology did not replace existing hardware receivers usually realized as one or more ASICs, but complemented these, allowing researchers to easily implement and test new algorithms or to develop highly specialized receivers with reasonable effort. Today, this is a well-established approach for military, scientific, and even commercial applications as described by Curran et al. (2018).

As different research groups developed their own software radios, they used different data collection systems to sample the GNSS signals. Whereas the data format of the digital GNSS signal streams is comparably easy to describe, the widespread use of software radio technology made it necessary to introduce a certain level of standardization, which was finally achieved by a group of researchers as documented by Gunawardena et al. (2021).

Technology further evolved, and not only new GNSS software radios appeared, but also some deficiencies of the standard (Clements et al., 2021). This triggered this work to recap the roots of GNSS SDR development in sect. II with a more detailed

focus on some receivers in sect. III and on front-end developments in sect. IV. Section V summarizes the history and the proposed update of the GNSS SDR standard.

II. GNSS SOFTWARE DEFINED RADIO HISTORY

The history of the Global Positioning System (GPS), or now more broadly known as the Global Navigation Satellite System (GNSS) Software Defined Radio (SDR), requires more than a bit of recollection which always can be fraught with inaccuracies, none of which are intentional, and corrections would always be welcome.

GNSS SDR traces its roots to Ohio University's Avionics Engineering Center around 1994. Professor Michael Braasch, a newly-minted faculty member of the Electrical and Computer Engineering department and already recognized as an expert in GNSS multipath, was interested in creating in a high-fidelity simulation of the internal signal processing within GPS and GLONASS receivers. Dennis Akos, a Ph.D. student in the Ohio University Electrical and Computer Engineering department/Avionics Engineering Center, was intrigued by the idea. Already harboring a keen interest in computer science and programming, Akos took on the simulation project at Braasch's request under the FAA/NASA Joint University Program. Meanwhile, publication of "The Software Radio Architecture" within the 1995 IEEE Communication Magazine Mitola (1995) fueled Akos's and Braasch's thinking that this "simulation" could instead be targeted toward an actual software radio implementation. The result was the first publication on GNSS SDR, which appeared in the proceedings of the 1996 ION Annual Meeting Akos and Braasch (1996).

Development of this initial simulation/implementation was significantly furthered through cooperation with Dr. James B. Y. Tsui of Wright Patterson Air Force Base. Well recognized as an expert in digital receivers, Tsui had recently taken an interest in satellite navigation. In 1995, two summer interns, Dennis Akos from Ohio University and Michael Stockmaster from The Ohio State University, worked under Tsui's guidance to develop a Matlab implementation of the signal processing required for basic GPS receiver operation. A digital oscilloscope was used to capture the initial IF data that were critical to developing and debugging those early algorithms. Akos was responsible for the lower-level signal processing (acquisition as well as code/carrier tracking), while Stockmaster implemented the navigation solution. The cumulative result was the first ever GPS SDR implementation. Although fully operational, it was "slow as molasses": processing 30 seconds of IF data required hours of computation time. Tsui published the first textbook on GPS SDR in 2000 (Tsui, 2000). A parallel contribution of this initial effort was the direct Radio Frequency (RF) sampling front-end, which garnered significant interest as well as pushed advances in analog-to-digital converter development (Akos et al., 1999).

After receiving his Ph.D. in 1997, Akos started his academic career as an Assistant Professor in the Systemteknik Department of Luleå University of Technology in Sweden, where he taught a course on computer architecture. It was here that GPS SDR first achieved real time operation. For a class project, Akos provided a Matlab-based GPS SDR and challenged a group of students to "get it to run as fast as possible" subject to the requirement that the complex accumulation products for each channel were within 10% of those produced by the original Matlab-based GPS SDR. It was in 1999 that the first "real time" operation was possible, processing 60 seconds of IF data in 55 seconds. This was a notable achievement at the time as renowned GPS expert Philip Ward, who was responsible for some of the first GPS receivers, wrote: "the integrate and dump accumulators provide filtering and resampling at the processor baseband input rate, which is around 200 Hz (...). The 200 Hz is well within the interrupt servicing rate of modern high-speed microprocessors, but the 5- or 50 MHz rates would not be manageable" in (Kaplan, 1996). This real time implementation effort was led by student Per-Ludvig Normark and led to the results published by Akos et al. (2001).

In the meantime, Kai Borre, a geodesy professor from Aalborg University, had also developed in the mid-late 1990s Matlab code for GPS receivers. Borre's code focused on the navigation block and including functions for e.g. conversion of coordinates and time references, satellite position determination and atmospheric corrections. The joint efforts of Akos, Borre and others would later lead to the well-known book (Borre et al., 2007), a main reference for GNSS SDR over the next years, and the related SoftGPS Matlab receiver.

Upon graduation, Normark continued his GNSS receiver development with the GPS Laboratory at Stanford University and then returned home to Sweden where he co-founded NordNav Technologies, which developed the first Galileo SDR, and helped establish the architecture, with Cambridge Silicon Radio (CSR) out of Cambridge, UK, to push GNSS to a price point acceptable to the mobile phone adoption. CSR, at the time a dominant supplier of Bluetooth hardware to the mobile phone market, acquired NordNav in 2006, and redesigned the 2.4 GHz radio to multiplex to the 1575.42 MHz GPS L1 band, exploiting the fact that most Bluetooth applications have a relatively low duty cycle. This approach, coupled with the real time software GPS implementation, provided a near-zero-added-cost GPS receiver.

There has been numerous contributions to GNSS SDR development since these early years, many of which are from the co-authors of this paper. Some selected developments are outlined in the next section. The authors of this paper are aware that many other important contributions are missing herein and agreed at the ION GNSS+ 2022 conference to extend this endeavor to a larger format, like a special issue of NAVIGATION, thereby maximizing the inclusion of all relevant contributors.

III. CURRENT STATUS OF GNSS SOFTWARE DEFINED RADIOS

In June 2022, a quick internet search did not reveal a comprehensive listing of all GNSS SDRs and Wikipedia (2022) lists six entries, which is far below the number of receivers known by the authors, even if the following criterion is applied to limit the scope: *a GNSS SDR (or software receiver) is defined as a piece of software running on a general purpose computer converting samples of a received GNSS signal into a Position Velocity and Time (PVT) estimate.* It is clearly understood that a front-end including Analog-to-Digital Conversion (ADC) is required to sample the received signal, but other than that no further functionality is allowed to be realized via hardware. With this definition, three categories of software receivers can be introduced:

- **real-time receivers:** monolithic or modular software packages written in an efficient low-level programming language (like C or C++) typically optimized for run-time efficiency and stability
- **teaching/research tools:** software packages written in a high level programming language like Python or Matlab optimized for code readability and flexibility
- **snapshot receivers:** receivers optimized for very short batches of signal samples

Furthermore, the software package shall allow some configuration flexibility and (at least theoretically) support the ION SDR standard. The following subsections introduce a few selected developments, emphasizing the rationale behind design choices and current status. Section III.1 describes the work of Psiaki, Ledvina, and Humphreys and their efforts in real-time processing on DSPs with the bit-wise approach proving to be highly successful even for space applications. Sect. III.2 covers work of Pany/others in their efforts with multiconstellation/multifrequency GNSS. Sect. III.3 and Sect. III.4 cover the efforts of Borre and others in a readable open source Matlab GPS SDR started in (Borre et al., 2007), with the most recent GNSS update reported in Borre et al. (2022). Akos has also continued this academic development of a suite of open source GNSS SDRs (Bernabeu et al., 2021). The widely used open-source receiver GNSS-SDR is described in III.5. The AUTONAV receiver used to support the development of Korean Positioning System (KPS) is discussed in sect. III.6 and PyChips (cf. sect. III.7) is the basis for tutorial classes of the ION. The snapshot approach is outlined in sect. III.8 and sect. III.9 discusses a SDR used e.g. to the authentication schemes, reflectometry or to assess the influence of non-standard GNSS transmissions. Section III.10 extends the scope of SDR to non-GNSS signals.

Whereas at the beginning of the GNSS SDR development the different receivers were linked to specific persons or research institutes, today often different receivers, tools or code bases are used at the same institute. On the other hand, code bases first developed by a single institute spread into different institutes. For example, the developments of Borre et al. (2007) forked into several branches [e.g. (FGI, 2022; Bernabeu et al., 2021; Zhang, 2022)], as discussed in sect. III.3 and sect. III.4.

Many key contributions to GNSS in general have been achieved with SDRs. Other SDR key publications cover implementations or algorithms which were in principle already known, but have been implemented for the first time with SDR technology. Some of those contributions are listed in the following subsections. Apart from them it is worthwhile to mention that the first real-time GNSS/INS integration with an SDR was achieved by Gunawardena et al. (2004) and one of the first GNSS SDR implementation on a Graphics Processing Unit (GPU) was reported in Hobiger et al. (2010). Furthermore, GNSS SDRs are known to achieve the highest possible sensitivity as different integration schemes or data wipe-off procedures can be performed in post-processing. This enables very long coherent integration times which is beneficial for sensitivity or multipath mitigation as reported in sect. III.8. Characterization of the GPS transmit antenna pattern with a 30-second long coherent integration resulting in 0 dBHz sensitivity is discussed by Donaldson et al. (2020). The same sensitivity was achieved by 300 noncoherent integrations each 1 second long for the purpose of indoor timing by iPosi Inc. (2015). On the other hand, graphical programming languages, such as LabVIEW and Simulink, are attractive choices for implementing SDRs, due to their flexibility, modularity, and upgradability. Moreover, since SDRs are conceptualized as block diagrams, graphical programming languages enable a one-to-one correspondence between the architectural conceptualization and software implementation (Hamza et al., 2009; Kassas et al., 2013).

The scope of SDRs was first extended to non-GNSS signals by McEllroy et al. (2006). SDRs became the implementation of choice in numerous studies aimed at exploiting signals of opportunity (SOPs) for navigation purposes (Kassas et al., 2017; Diouf et al., 2019, 2021), such as (i) cellular 3G code-division multiple-access (CDMA) (Pesyna et al., 2011; Yang and Soloviev, 2018; Khalife et al., 2018), 4G long-term evolution (LTE) (del Peral-Rosado et al., 2017; Shamaei et al., 2018; Shamaei and Kassas, 2018; Ikhtiari, 2019; Kang et al., 2019; Wang et al., 2022; Yang et al., 2022), and 5G new radio (NR) (Shamaei and Kassas, 2021b; Santana et al., 2021; Fokin and Volgushev, 2022; Abdallah and Kassas, 2022; Lapin et al., 2022; Tang and Peng, 2022; Del Peral-Rosado et al., 2022); (ii) AM/FM radio (McEllroy, 2006; Chen et al., 2020; Souli et al., 2021; Psiaki and Slosman, 2022); (iii) digital television (Souli et al., 2020; Yang and Soloviev, 2020; Souli et al., 2022); and (iv) Low Earth Orbit (LEO) satellites (Farhangian and Landry, 2020; Orabi et al., 2021; Farhangian et al., 2021; Pinell, 2021; Nardin et al., 2021; Zhao et al., 2022) .

Due to the enhanced analysis possibilities of GNSS SDR they proved to be very useful to understand ionospheric scintillation and

the first dedicated SDRs are described by Peng and Morton (2011); O'Hanlon et al. (2011). The authors used a general purpose front-end being reconfigurable for multi-GNSS multi-band signals, and a custom dual-frequency front-end, respectively. The first system further evolved into an intelligent, scintillation event-driven data collection as reported by Morton et al. (2015).

Commercialization of academic SDR developments is partly discussed in the following sections. Also a major receiver manufacturer provides GNSS SDRs, first starting with a timing receiver (Trimble Inc., 2005) and then moving to a flexible narrow-band receiver (Trimble Inc., 2017). Wide-band signals were later added with some signal processing now done on an FPGA as reported in PR Newswire (2021). The most recent commercial activity can be found in LocusLock (2022) and builds upon the software described in the following section.

1. Bit-Wise Parallelism for the High-Bandwidth Digital Signal Processing Receiver Operations

The original real-time GNSS software radio work by Akos (1997) inspired an effort within the Cornell GPS group. Psiaki had been working with non-real-time software GNSS signal processing in MATLAB for about 2 years when he started to wonder whether the slow MATLAB operations could be translated to run in real-time on a general desktop workstation. The bottleneck in GNSS digital signal processing occurs when doing the operations that initially process the high-frequency RF front-end samples. RF front-ends typically sample at 4 MHz or faster. A 12 channel receiver would have to perform on the order of 400 million operations per second or more in order do all of the needed signal processing. Psiaki conceived the concept of bit-wise parallel processing as a means of addressing this challenge. He recruited then-Ph.D. candidate Brent Ledvina to make an attempt at implementing these ideas in the C programming language on a Real-Time Linux desktop workstation. Ledvina succeeded in developing a 12-channel real-time L1 C/A-code receiver after about 6 months effort. The first publication about this receiver was (Ledvina et al., 2003).

The main concept of bit-wise parallelism is to work efficiently with RF front-end data that have a low number of quantization bits. If an RF front-end produces a 1-bit digital output stream, then 32 successive sign-bit samples can be stored in a single 32-bit unsigned integer word on a general-purpose processor. Thirty-two successive output samples of a 2-bit RF front-end can be stored in two 32-bit words, one containing the successive sign bits and the other containing the successive magnitude bits. Each channel of the software receiver generates a 1-bit or a 2-bit representation of 32 successive samples of its IF carrier replica, both in-phase and quadrature, and the successive samples are stored in parallel in 32-bit unsigned integer words. Similarly, it generates a 1-bit representation of 32 successive samples of its prompt Pseudo-Random Noise (PRN) code replica and stores them in parallel in a single 32-bit unsigned integer word. It also generates an early-minus-late PRN code replica that requires 1.5 bits per sample, which takes up two 32-bit unsigned integer words to store 32 samples. These replica signals can be generated very efficiently by using pre-tabulated 32-bit words. The software receiver then performs a series of bit-wise AND, OR, XOR, and similar operations that have the effect of performing PRN code mixing and IF-to-baseband carrier mixing. The outputs of the mixing operations are contained in a small number of 32-bit words, the number of which depends on the number of bits in each RF front-end output sample and the number of bits in the IF carrier replicas.

The final operation is accumulation of the results in the 32-bit words. This involves sets of bit-wise Boolean operations, as per Ledvina et al. (2003), followed by summation of the number of 1-bits in the resulting 32-bit unsigned integer words. The bit summation operations proved to be a challenge in terms of minimizing execution time. Ledvina solved this problem by using a pre-computed 1-dimensional data table whose input was the unsigned integer and whose output was the number of 1-bits. In order to keep the table size reasonable, it only counted the bits in a 16-bit unsigned integer word. The original receiver's 32-bit words were split in half, 2 table look-ups were performed, and the results summed in order to count all the 1-bits. The original algorithms are defined by Ledvina et al. (2003), Ledvina et al. (2004a) and Ledvina et al. (2006b).

When using very long PRN codes, such as the L2C CL code, the original method's whole-period PRN code tables of the proper 32-bit words at various code phases became impractically large. Therefore, a new method was developed for long PRN codes. It tabulates 32-bit words of short generic PRN code chip sequences, with all possible combinations of a short sequences of chips considered at various PRN code offsets relative to the start of the samples of the 32-bit word. Those methods are described by Psiaki (2006) and by Ledvina et al. (2007). This technique proved invaluable for dealing with long codes.

After getting the basic algorithms working in real-time, the Cornell group show-cased the efficacy of real-time GNSS software radio by using the techniques to develop a dual-frequency L1 C/A and L2C receiver (Ledvina et al., 2004b) and a GPS/Galileo L1 civilian receiver (Ledvina et al., 2006a). These real-time software GNSS receivers each required only several person-days to develop them from the original L1 C/A code receiver. Of course, the L1/L2 receiver required a new dual-frequency RF front-end. The GPS/Galileo receiver required knowledge of the civilian Galileo E1 PRN codes, which had not been published at that time. That led to a supporting effort which successfully deduced the Galileo GIOVE-A E1 PRN codes by listening to them and doing a lot of signal processing in order to pull the chips out of the noise (Psiaki et al., 2006).

The next development was to re-implement the bit-wise parallel code for embedded (low-power, low-cost) processing. Initially targeting a Texas Instruments DSP, this work was accomplished in 2006 by then-Ph.D. candidate Todd Humphreys (Humphreys et al., 2006). Later, as a professor at The University of Texas at Austin, Humphreys and his students—notably Jahshan Bhatti

and Matthew Murrian—undertook a sequence of significant expansions and improvements to this receiver. Called GRID/PpRx, the C++-based UT Austin receiver is by now a highly-optimized science-grade multicore GNSS SDR (Humphreys et al., 2009; Nichols et al., 2022). It was the first GNSS SDR to be adapted for spoofing (Humphreys et al., 2008), the first GNSS SDR to operate in space (Lightsey et al., 2014), the first receiver of any kind to show that centimeter-accurate GNSS positioning is possible with a smartphone antenna (Pesyna et al., 2014), the first receiver to be used to locate terrestrial sources of GNSS interference from low-Earth orbit (Murrian et al., 2021), and is the basis of the current state-of-the-art in urban RTK positioning (Humphreys et al., 2020; Yoder and Humphreys, 2022). As detailed in (Nichols et al., 2022), GRID/PpRx has also reaffirmed the commercial viability of GNSS SDR in widespread low-cost applications: it was recently licensed by a major aerospace company for use across all company operations, including in the thousands of satellites of the company's broadband Internet mega-constellation.

A processor that can operate on wider segments of data, up to 512 bits for current single instruction, multiple data (Single Instruction Multiple Data (SIMD)) instructions, gains substantial additional signal processing speed increases (Nichols et al., 2022). Note, however, that the speed increase factors over brute-force integer calculations are typically not as high as the number of bits per word. That is, the techniques do not speed up the operations by a factor of 32 when processing 32 samples in parallel by using 32-bit words to represent 32 samples. For a 2-bit RF front-end and a 32-bit processor, the speed-up factor might be only 4 because the bit-wise parallel approach requires multiple operations due to, say, a simple multiplication of one time series by another. If one doubles the number of bits per word, however, then the speed tends to double. A particularly helpful feature of some recent processor designs is their inclusion of a hardwired command to count all the 1 bits in a word. This "popcount" intrinsic obviates the table look-ups that counted 1-bits in the original bitwise parallel design. If the number of bits increases in the RF front-end samples and/or the IF carrier replicas, however, then the bit-wise parallel method of signal processing slows down. Signals represented by 3 or 4 bits might cause the processing speed gains of bit-wise parallel algorithms to be limited or even non-existent.

2. Multi Sensor Navigation Analysis Tool

The Multi Sensor Navigation Analysis Tool (MuSNAT) is an object-oriented but monolithic C++ software receiver maintained by the Universität der Bundeswehr München (UniBwM) and has been first mentioned in its present form by Pany et al. (2019). It started as an operational real-time receiver development, but currently it mostly serves to develop and demonstrate innovative signal processing and navigation algorithms. Furthermore, it is used for teaching. It is freely available as executable for academic purposes from (UniBwM, 2022). Its main characteristics can be found in Tab. 1. In contrast to the bit-wise approach of sect. III.1 (that allows to design very power-efficient implementations), the design idea of MuSNAT and its predecessors was to realize a high-end receiver running on powerful PCs or workstations. The bit-wise approach was replaced by using SIMD instructions of Intel/AMD Central Processing Units (CPUs). This allows to represent samples as 8-bit or 16-bit values and SIMD instructions like AVX-512 currently allow processing of registers of up to 512 bit (i.e. 32 16-bit samples) in parallel.

The GNSS software receiver developments started at UniBwM in 2002 after it became clear that the software radio approach discovered by D. Akos would provide useful insights into GNSS receiver technology and thus will be indirectly very helpful to design and build the Galileo navigation satellite system. The first software receiver at UniBwM was GPS L1 C/A only and was realized as a Matlab/Simulink project working in post-processing. To sample the GNSS signals a commercial ADC with a Peripheral Component Interconnect Express (PCIe) connector from NI was used (PXI 5112) that was connected either to a low-bandwidth GPS L1 C/A code front-end based on the Plessey GP 2010 RF chip set and later on to one GPS L1/L2 high-bandwidth front-end, which was specifically developed by Fraunhofer IIS (Pany et al., 2004b). Soon after, the software to communicate with the ADC (written in C++ making use of the Microsoft Foundation classes) was upgraded to a full GPS L1 C/A plus L2CS (L2 medium length code was supported only, not the long code) receiver. A detailed analysis published by Pany et al. (2003) revealed that not only the SIMD instruction set was important for the real-time capability but also the size and structure of the CPU caches. Memory bandwidth is one of the key issues when representing samples by multiple bits. One of the first achievements with this receiver was the demonstration of vector tracking (Pany et al., 2005).

Based on those results, funding to support a group of five researches over three years was secured. This allowed starting a new software receiver project, this time making full use of C++ features for object oriented development, and development of a Graphical User Interface (GUI) connected to the processing core via a clearly defined interface also allowing to run the core without GUI. The overarching development goal at that time was to realize a high-quality multi-GNSS multi-frequency receiver on a desktop PC or powerful laptop that could potentially be operated on a continuous basis to replace the (at that time) rather inflexible and expensive commercial GNSS receivers at Continuously Operating Reference Stations (CORSs). A concise overview of the development during those years was written by Stöber et al. (2010) and shows the improvements compared to the start of the project layed down by Pany et al. (2004a).

A loose cooperation with IFEN GmbH was initiated that eventually resulted in the SX3 receiver (IFEN GmbH, 2022). IFEN used the processing core as initial basis, improved the core, replaced the GUI, and developed new dedicated front-ends. The C++ code was further optimized to support more channels at higher bandwidth and almost instantaneous high-sensitivity acquisition

Table 1: Summary of MuSNAT

MuSNAT		
Feature	Solution	Remark
Operating System	Windows 10/11	Compiles as GUI or as command line version
Programming environment	C++ and CUDA	Microsoft Visual Studio and vcpkg
IF sample file input source	ION SDR standard and proprietary file readers	proprietary readers faster than ION SDR reader
real-time sample input	yes, via TCP/IP	server available via LabView for selected NI USRPs
additional sensors	LiDAR, IMU	LiDAR uses PCL format, IMU proprietary ASCII format, video formats supported but not yet used
Supported GNSS	GPS, Galileo, BeiDou, GLONASS, SBAS, OFDM (LTE, 5G)	nearly all open spreading codes available and at least for each system one navigation message decoder
acquisition	optimized Fast Fourier Transform (FFT) method	CPU and GPU supported
tracking run-time optimization	dot-product from Intel Performance Primitives	computational performance mostly limited by memory bus width
further features	multi-antenna, signal-generator, primary-secondary tracking, SQL database for logging, vector tracking, GNSS/INS integration, Matlab-interface, RTKLIB	

with the GPU (GPS World staff, 2012). Also semi-codeless tracking of GPS L2P(Y) (i.e. P-code aided cross-correlation) was implemented. The cooperation of UniBwM with IFEN lasted until 2013 when the development directions started to diverge. IFEN used the software mostly as base receiver platform with an Application Programming Interface (API) to support different applications, whereas UniBwM continued to modify the core, which was not always beneficial for software stability if seen from a commercial point of view.

The focus at UniBwM switched in 2017 as the old GUI could not be maintained anymore. Furthermore, real-time operation became less important as most scientific results were obtained in post-processing. The result was that a new GUI was developed and attached to the proven processing core. Any run-time optimizations within the processing core degrading navigation performance (i.e. mostly causing additional noise in the code tracking loop) were removed. The core's logging output was directed to a SQL database to store all different kind of intermediate results in a single file (additionally to the legacy ASCII logging into multiple files). A dedicated visualization tool for this database was developed.

The use of Windows and Visual Studio for developing a software radio is a little unusual, but is explained as follows. At UniBwM most researchers use Windows PCs to allow easy document exchange with each other and most importantly within the European Space industry. For this reason, all software receiver developments were done for Windows only. In terms of numerical performance and code optimization, Intel provided and still provides with the Intel C++ compiler and the Intel Performance Primitives the same quality on Windows as for Linux. Over the years it became, however, also clear that the potential use of the processing core on embedded devices and long-term stability might have been easier to achieve on the Linux operating system. IFEN ported part of the core to Linux, but not the full software receiver and showed that conventional desktop CPUs and embedded CPUs provided an impressive processing capability already in the year 2015 (Dampf et al., 2015).

As already mentioned, code optimization to achieve fast (and real-time) signal tracking was a main research focus in the first years. Different studies on CPU assembler instructions, CPU architecture and bottlenecks resulted in dedicated assembler implementations. Extensive lookup-tables were used and one very efficient correlator implementation with the Intel x86 pmaddubsw-instruction was based on a signal sample representation as unsigned integers (including the necessary rewriting of the correlation formulae due to the switch from the standard representation of samples as signed integers to unsigned integers). Fast Fourier Transform (FFT) based acquisition was already very efficient on the CPU and even more efficient on the GPU. The use of FFT libraries provided by NVIDIA made the acquisition code porting from CPU to GPU comparably easy. The situation is different for signal tracking. The tracking code has been transferred to the GPU and some optimization have been applied to minimize the amount of data transfer between CPU and GPU. However, since the correlation parameters are slightly different for each signal tracked, the correlation code is called multiple times and the latency to start one thread on the GPU

generated significant overhead. GPU-based tracking is thus currently only beneficial if a very large number (several hundreds) of correlators is configured per tracking channel, as pointed out by Pany et al. (2019). As modern desktop and laptop CPUs continue to improve and make use of a many-core structure, the need to port signal tracking to the GPU becomes less important. Furthermore, the use of dedicated assembler code required over the years continuous adaptation to new CPU instruction sets (e.g. from SSE to AVX instructions). The performance gained by using hand-coded assembler routines compared to the use of the libraries provided by Intel (IPP) is not always worth the effort and was not further actively pursued. Instead, dot-product routines (2 x 16-bit signed input to 64-bit output) from the IPP are employed for signal tracking.

The C++ universe is huge, and it is easy to integrate external source code. For example, the famous RTKLIB and the ION SDR sample reader code have been integrated. The current research work with MuSNAT focuses on GNSS/INS/LiDAR integration, support of massive antenna arrays, vector tracking and deep GNSS/INS coupling, support for LTE/5G-signals and GNSS signal simulation. It has to be admitted that the maintenance of the huge C++ code-base of MuSNAT at a University institute with a high fluctuation of researchers is partly demanding. The learning curve for good C++ development in this context is steep and for the purposes of obtaining a PhD degree often an inefficient way. Therefore, interfaces from the C++ code to Matlab were established and for example Open Service Navigation Message Authentication (OSNMA) decoding, PPP-computation for HAS or LiDAR odometry are implemented in Matlab. Another development is to use MuSNAT to generate multi-correlator values that are then used within a full Matlab based receiver to emulate signal correlation via interpolation (Bochkati et al., 2022).

UniBwM has initially used front-ends from Fraunhofer IIS and the software receiver included low-level Universal Serial Bus (USB) drivers for real-time data transfer. The same approach was used to connect the front-ends from IFEN GmbH to the processing core. The effort to write stable high data-rate low-level drivers is significant and introduces a dependency on libraries and support from the USB chip manufacturers. To reduce these kinds of development efforts, the decision to connect front-ends via TCP/IP was felt. This approach is powerful in terms of bandwidth and also generic and a first version of it is described in (Arizabaleta et al., 2021). Furthermore, with e.g. LabVIEW from NI it is comparably easy to develop a simple TCP/IP signal source for Universal Software Radio Peripheral (USRP) frontends. At the time of writing this paper, a more efficient firmware for USRPs with direct FPGA programming is being developed and shall allow to synchronously capture data from an Inertial Measurement Unit (IMU) together with the GNSS signal samples.

3. SoftGPS, SoftGNSSv3.0 and Derivatives

As abovementioned, (Borre et al., 2007) and the associated Matlab receiver was a cornerstone for GNSS SDR development. This receiver, initially called SoftGPS, then SoftGNSS (usually referred to as SoftGNSSv3.0), included the basic processing functions for GPS L1 C/A in a readable format, very useful for educational purposes. These included signal FFT-based acquisition, frequency, carrier phase and code phase tracking, data synchronization and demodulation, pseudorange generation, and eventually PVT. The Matlab code, together with some samples, was provided in a CD with the book, and was also available at Aalborg University's Danish GPS lab website. Apart from K. Borre and D. Akos, SoftGNSS included relevant contributions by D. Plausinaitis and others. Unfortunately, Kai Borre passed away in 2017 and the Danish GPS Lab was discontinued. However, SoftGNSS and its derivatives remain quite alive. Here are some examples:

- A new SDR GNSS book, (Borre et al., 2022), extending SoftGPS functionality to several frequencies, GNSS and architectures, can be considered as the successor of (Borre et al., 2007). A main building block of this book is FGI-GSRx, described in the following section, but the book includes also other Matlab receivers. In particular, DF-GSRx (Dual-Frequency GNSS Software Receiver), developed by Borre's PhD student P. Bolla, is a dual-frequency GPS L1/L5 receiver that includes dual-frequency acquisition techniques, measurements combination (iono-free in particular) and positioning. The book also includes a GPS L1 C/A snapshot receiver developed by Borre's former PhD student I. Fernandez-Hernandez, more modest than that described later in III.8, but simple and quick to execute and therefore possibly useful for educational purposes.
- The Easy Suite libraries (Borre, 2003, 2009), still publicly available and used, provide an excellent educational tool to dive into basic functions of GNSS receivers, such as calculating satellite positions from the ephemerides, datum conversions, or computing the receiver position and its accuracy in multiple ways (least squares, Kalman filter, carrier phase ambiguity resolution, etc.)
- (Bernabeu et al., 2021), as above mentioned, provides a collection of open source SDRs developed at University of Colorado Boulder and based on SoftGNSS.
- (Zhang, 2022) provides a respository with adaptations of SoftGNSS for different front-ends.

4. Finnish Geospatial Research Institute's Multi-GNSS Software Receiver

The software receiver developed by Finnish Geospatial Research Institute (FGI) is famously known as the FGI-GSRx (FGI's GNSS Software Receiver). The development of the FGI-GNSS Software Receiver (GSRx) software receiver started in 2012

Table 2: Main features of FGI-GSRx

FGI-GSRx		
Feature	Solution	Remark
Operating System	Windows 10	Compiles in Windows 10 environment. The software receiver should run in other OS which can host MATLAB or OCTAVE.
Programming environment	MATLAB	Executes in MATLAB 2019 or any other later version. The software receiver can be also executed in OCTAVE.
IF sample file input source	ION SDR standard	Read input data files following ION SDR standard.
Processing mode	Only operate as post-processing GNSS receiver	It can read raw IF data for a complete receiver processing, or it can load previously saved acquisition and/or tracking data in order to skip acquisition and/or tracking operation to be able to process navigation solution depending on parameters set in the user configuration file.
Supported GNSS	GPS L1, Galileo E1, BeiDou B1, GLONASS L1, NavIC L5	Open source FGI-GSRx only supports single frequency multi-GNSS processing.
Acquisition	FFT-based signal acquisition	Sophisticated research specific implementation for high sensitive acquisition is not published as open source.
Tracking	Table-based three-stage tracking	Based on the tracking status of each individual satellite, the software receiver switches among three stages: i) PULL IN, ii) COARSE TRACKING and iii) FINE TRACKING.
Navigation	Traditional Least Square (LS)	Users can select SNR or elevation cut-off mask in order to decide on the satellites that contribute to the position computation.

from the open source GNSS software receiver released in 2007 by Prof. Borre and his colleagues Borre et al. (2007). The software receiver was able to track two IOV (In-Orbit Validation) satellites called GIOVE A and GIOVE B from the European GNSS system Galileo. Since then, the researchers at FGI have been continuously developing new capabilities to the software receiver with the inclusion of Galileo in 2013 (Söderholm et al., 2016), the Chinese satellite navigation system BeiDou in early 2014 (Bhuiyan et al., 2014, 2015), the Indian regional satellite navigation System NavIC in late 2014 (Thombre et al., 2015) , and the Russian satellite navigation system GLONASS in 2015 (Honkala, 2016).

The FGI-GSRx software receiver has been extensively used as a research platform for the last one decade in different national and international research and development projects to develop, test and validate novel receiver processing algorithms for robust, resilient and precise Position Navigation and Timing (PNT). At present, the FGI-GSRx can process GNSS signals from multiple constellations, including GPS, Galileo, BeiDou, GLONASS, and NavIC. The software receiver is intended to process raw IF signals in post-processing. The processing chain of the software receiver consists of GNSS signal acquisition, code and carrier tracking, decoding the navigation message, pseudorange estimation, and PVT estimation. The software architecture is built in such a way that any new algorithm can be developed and tested at any stage in the receiver processing chain without requiring significant changes to the original codes. FGI-GSRx provides a unique and easy-to-use platform not only for research and development, but also for whoever is interested in learning about GNSS receivers. The software receiver was released as open source in February 2022 (FGI, 2022). FGI-GSRx receiver is also tied with the book 'GNSS Software Receivers' by Cambridge University Press, a next edition of one of the fundamental GNSS textbooks, which is now in press to be published in the second half of 2022. Some of the main features of FGI-GSRx is listed in Tab. 2.

The FGI-GSRx software receiver can be utilized in universities and other research institutes as a tool for training graduate level students and early-stage researchers for getting hands-on experience on GNSS receiver development. It can also be utilized in the vast GNSS industry as a benchmark software defined receiver implementation. The software receiver is already being used in the 'GNSS Technologies' course offered widely in Finland - at the University of Vaasa, Tampere University, Aalto University and the Finnish Institute of Technology.

Table 3: Main features of GNSS-SDR

GNSS-SDR		
Feature	Solution	Remark
Operating System	GNU/Linux, macOS, Windows OS through WSL.	Included as a software package in Debian and Ubuntu, and in Macports for macOS. Tested on ArchLinux, CentOS 7, Fedora, OpenSUSE, Rocky Linux.
Programming environment	C++	Software linters are automatically run at each code change to ensure meeting high-quality coding standards.
Processing mode	Real-Time and Post-Processing.	It can work in real-time using a wide assortment of commercial RF front-ends, and in post-processing mode with a number of file formats (including input files produced by the ION standard conversion tools).
Supported GNSS	GPS L1, L2C, L5; Galileo E1, E5a, E5b, E6; Glonass L1 CA, L2 CA; Beidou B1, B3.	The modular design allows for easy inclusion of new signals.
Acquisition	FFT-based signal acquisition.	A-GNSS capabilities to accelerate the Time To First Fix.
Tracking	Multicorrelator-based Data and Pilot signal tracking.	Customizable DLL, PLL, FLL. High-dynamics capabilities. SIMD-accelerated both in i686 and ARM CPUs (see Fernández–Prades et al. (2016a)).
Navigation	Traditional Least Square (LS), code and carrier-based positioning modes.	Positioning engine based on RTKLIB implementation (Takasu and Yasuda, 2009). All possible supported GNSS signals combinations are allowed.

5. GNSS-SDR, an Open-Source Software-Defined GNSS Receiver

The software receiver developed by the Centre Tecnològic de Telecomunicacions de Catalunya (CTTC), uncreatively named GNSS-SDR (but not related to the ION SDR standard), is another example of a multi-band, multi-system receiver. It has been constantly evolving since 2010, keeping pace with the newest GNSS algorithms and signals over more than a decade. It originated as a by-product of a CTTC research staff initiative, with the aim of providing a collaborative framework with other researchers seeking to accelerate research and development of software-defined GNSS receiver technology. The receiver particularly focuses on baseband signal processing, although it has the ability to run a navigation engine (refer to Table 3). The early stages of development baked slowly under a personal side-project scheme, with no funding, but with the purely exploratory objective of designing an optimal architecture specifically suitable for GNSS signal processing, where concepts such as testability, extensibility, reusability, scalability, maintainability, portability, adaptability to new non-standard requirements, and adoption of Computer Science best practices considered from scratch.

Its first popularity peak came on August 2012, with the reporting of the usage for GNSS of extremely cheap (about $25) DVB-T receivers based on the Taiwan's Realtek RTL2832U chipset, sold in form of USB dongles that allow users to watch over-the-air DVB-T European broadcast television on their personal computers. Normally, those devices send partially-decoded MPEG transport frames over the USB, but exploiting an undocumented mode of operation of the demodulator chip, the user was able to obtain raw I&Q samples, stream them through USB to a personal computer and then apply the GNSS-SDR software processing, turning the DVB-T receiver into a GNSS receiver and delivering position in real-time (see Fernández–Prades et al. (2013)). On a parallel development, in November 2013, the European Space Agency acknowledged GNSS-SDR as one of the first 50 users worldwide to achieve a successful Galileo position fix.

The project gained momentum and maturity over the years, and today it enjoys a solid and valuable user base continuously providing feedback, enhancements, and new features. Current versions are included in major GNU/Linux distributions, such as Debian and Ubuntu, and in Macports for Apple's macOS. The software package has been used in several public and private-funded research projects (including EUSPA, European Space Agency (ESA), NSF and NASA activities, as well as in educational programs such as Google Summer of Code), and it has been reportedly used for research purposes worldwide. The authors opened a discussion of quality metrics and key performance indicators for any generic software-defined receiver (Fernández–Prades et al. (2016b), extended online version available at `https://gnss-sdr.org/design-forces/`) and proposed the concept of *continuous reproducibility* in GNSS signal processing (Fernández–Prades et al. (2018)).

Table 4: Main features of AutoNav SDR

AutoNav SDR		
Feature	Solution	Remark
Operating system	Windows	
Programming environment	MATLAB and C	
Processing mode	Post-processing	
Supported GNSS	GPS (L1 C/A, L2C, L5), GLONASS L1, Galileo (E1, E5a, E5b), BDS (B1I, B1C, B2a), QZSS (L1 C/A, L1C, L2C, L5), NavIC L5	Free selection of signal combination
Acquisition	GPU-based acquisition	Simple implementation using Parallel Computing Toolbox of MATLAB
Tracking	MEX correlator	18/8 bits code/carrier replica tables, 32 bits code/carrier Numerically Controlled Oscillators (NCOs), bit shift operations
Further features	API, easy addition of new signals, RINEX observation logging, Radio Frequency Interference (RFI) mitigation based on pulse blanking, direct state tracking Kalman filter	

The full project and source code documentation can be found online at `https://gnss-sdr.org`, a website with over 5000 unique visitors per month, which contributes to raising awareness on GNSS technology. The website content is also on a GitHub repository at `https://github.com/gnss-sdr/geniuss-place`, hence undergoing public scrutiny. The project is also well-connected to its software ecosystem and existing SDR platforms. It builds on a wide range of GNU/Linux distributions and versions (from most recent releases to those released in 2014), and it provides a Yocto / Openembedded layer, which allows its portability to a wide range of embedded platforms (see Fernández–Prades (2022)).

The software produces standard outputs for observables and navigation data (RINEX files and RTCM-104 v3.2 messages as defined by the Networked Transport of RTCM via Internet Protocol, NTRIP), as well as position fixes in application-specific messages (*e.g.*, NMEA 0183), a variety of GIS-oriented file formats (KML, GeoJSON, GPX), and custom binary outputs that allow the observability of internal signal processing sub-products.

6. AutoNav SDR

The AutoNav SDR is a MATLAB-based multi-GNSS and multi-frequency software receiver that was developed by the Autonomous Navigation Laboratory of Inha University, South Korea (Song et al., 2021). Its main features are arranged in Tab. 4. The critical point considered in the design phase of this SDR is the maximization of reconfigurability. Since South Korea is developing its own satellite navigation system, KPS which is targeted to operate from 2035 as reported by Ministry of Science and ICT of Korea (2021), a flexible receiver that can process not yet existent signals is highly required. The AutoNav SDR is profoundly designed to provide full reconfigurability in terms of target signal combinations and signal characteristics, especially for easy addition of the new signal proposals. To do so, a basic framework of software receiver was designed with a well-designed processing functional architecture and data structure in consideration of the expandability of the signals and then applied to realize an SDR for GPS L1 C/A code signal as a first realization example by reconfiguring a configuration file via GUI. Then, different signals of the other constellations (GLONASS, Galileo, BeiDou Navigation Satellite System (BDS), Quasi-Zenith Satellite System (QZSS), NavIC) and frequencies (L1, L2, L5) were added quickly by utilizing this expandability. In this way, KPS signal candidates can be easily added to the SDR to evaluate and compare the performance of each candidate in the signal design phase. Similarly, a reconfigurable GNSS simulator was developed at the same time with the same idea. This is a MATLAB-based IF level GNSS/KPS simulator which can be ideally suited to test the navigation performance of any GNSS signals as well as new KPS signals by reconfiguring signal design parameters via GUI.

Although the AutoNav SDR is targeted for post-processing only, the original correlation operation in MATLAB with variables of double precision was too slow at the beginning of its design phase. So, two simple accelerations were applied to the SDR: a GPU-based acquisition module and a MEX correlator for tracking. The GPU-based signal acquisition module was implemented in a very simple way using the Parallel Computing Toolbox of MATLAB. If the GPU is usable, local variables for the correlation

Table 5: Main features of PyChips

PyChips		
Feature	Solution	Remark
Operating System	Windows x64 (8, 10, 11)	Due to pre-compiled C/C++ bindings that currently use the Windows API for file reading and threading
Programming environment	Python 3.10	
IF sample file input source	ION SDR Metadata Standard	Parses ION metadata hierarchy to select the appropriate decoder kernel written in C++. Sample decoding is split across multiple threads using a data parallel architecture
Real-time sample input	Not currently supported	
Additional sensors	None	
Supported GNSS	Supports all civilian satnav signals (GPS, GLONASS, Galileo, BeiDou, QZSS, NavIC, SBAS)	Spreading codes defined as memory codes
Acquisition	FFT based generic acquisition engine with configurable coherent and non-coherent integration settings	Auto detects and implements circular vs. non-circular frequency-domain correlation based on code length
Tracking	User configurable generic tracking module object	Employs split-sum correlation Gunawardena and van Graas (2006). Always operates on 1 millisecond block of samples and retires current block before operating on next block (no sample shifting to align with SV time-of-transmission)
Measurement output	Yes	CSV format
Availability	Release to public GIT repository pending	Versions used at ION tutorials

(i.e., code and carrier replicas) are generated in the GPU memory using the gpuArray function. Then, FFT and Inverse Fast Fourier Transform (IFFT), and correlations are performed in the GPU automatically. Finally, the correlation results are extracted using a gather function. With this simple approach, it has approximately 2.12 times faster execution time compared to the general CPU-based acquisition, without the relatively complex development using CUDA.

Since the most time-consuming process of the receiver is the correlator in the signal tracking, a MEX function is employed to reduce the computational burden. The MEX function connects the MATLAB environment to the external function written in C/C++ language with an appropriate wrapper function, so the user can call it within MATLAB. The MEX correlator was written in the standard C language and uses integer-based variables. The SDR pre-generates the code and carrier replica tables at the initialization process with resolutions of 18 bits and 8 bits, respectively. The code and carrier Numerically Controlled Oscillators (NCOs) have a resolution of 32 bits, so the indices of the tables for current code and carrier replica generation are calculated using bit shift operations of 14 bits and 24 bits, respectively. With these implementations, the overall execution time became much faster (approximately 5 times) than the original double precision-based code, but it still cannot operate in real-time. Currently, Inha University is developing the FPGA-based real-time GNSS receiver that only the correlator would be substituted by the FPGA board at the original AutoNav SDR.

To further enhance the flexibility, the AutoNav SDR also provides APIs at each part of the signal processing chain (such as ring buffer, acquisition, tracking, navigation message extraction, position calculation, etc.). The API design was influenced by the ipexSR of Stöber et al. (2010) and was implemented similarly using the Dynamic Link Library (DLL). Since MATLAB can load a library from DLL and call a function within the library, the API concept of the C/C++-based software can also be used analogously in the MATLAB environment. If the SDR is converted to an executable file (.exe) and provided to a user, the user can freely modify functions or develop algorithms by generating the DLL, without the need for the whole source codes.

7. PyChips

Pychips is a relatively new object-oriented satnav SDR that has been developed from scratch since 2018. It is based on the experience gained from two previous implementations, namely the MATLAB SDR that was distributed with Wideband TRIGR (see section V) and the ChameleonChips GNSS SDR Toolbox for MATLAB (Gunawardena, 2014).

One of the key promises of SDRs is their flexibility and hence its utility as an education and research tool. In the satnav context, various publicly available SDRs can be used to teach basic courses on satnav systems, signal processing, and receiver design. However, there is an implicit assumption that students have the relevant programming language skills for that particular SDR. Students are expected to understand the inner workings of the SDR in detail, and, more importantly, to make modifications to the code to add advanced capabilities and/or revisions as part of their graduate research projects. While somewhat valid, this programming language proficiency assumption may not always hold true. Further, given the situation, it may be far more efficient and beneficial to have grad students make deeper progress on their research rather than spending time becoming programming language experts. PyChips was developed from the ground up to support this notion. A more detailed introduction to PyChips can be found in Gunawardena (2021). It is implemented in Python with C++ bindings where performance is absolutely essential for reasonably fast execution.

The current version of PyChips supports the creation and definition of entire constellations of satellites with advanced next-generation signal structures, along with interference sources and channel effects. This simulation portion of PyChips (comprising of numerous source objects) synthesizes these signals at the sample level on to one or more sample streams that are grouped into objects called stream containers. A stream container is an abstraction of a satnav receiver's antenna(s) and RF front-end subsystem. This could be multi-frequency, multi-element, with different sample rates and bandwidths, IF or baseband sampling architecture, and any and all combinations thereof. If live-sky signal processing is the use case, then one or more sampled SDR data files can be specified to instantiate a stream container object that is functionally identical and imperceptible from a simulated one. PyChips uses the ION SDR Metadata standard to determine the appropriate C/C++ decoder/unpacker/re-quantizer kernel to use for reading and parsing these SDR files.

The sample streams contained in a PyChips stream container are processed using numerous sink objects. Currently implemented examples include virtual oscilloscopes and spectrum analyzers, as well as acquisition engines and signal tracking modules.

The unique feature of PyChips is that, all of the functionality described above is defined/specified using a grouping of JavaScript Object Notation (JSON) files. Current and next-generation advanced satnav signal structures and the receiver architectures to process them are constructed by assembling together pre-built low-level functional blocks. For example, as described in Gunawardena (2021), the user can build receiver tracking modules to process GPS L1C TMBOC(6, 1, 4/33) and Galileo E1OS CBOC(6, 1, 1/11) MBOC signals as simple BOC(1, 1) signals to model a low-cost low-power mass market receiver, or a high-end survey-grade receiver taking full advantage of these 'dual personality' signals.

Indeed, at this stage, the goal of the PyChips project is to hone the JSON specification layer with a vast number of diverse signal specifications, use cases and applications, in order to have it become a 'satnav signals and systems specification language.' Today, the reference SDR that implements this language is written in Python and is therefore called PyChips. However, the ultimate goal of this effort is to contribute towards satnav SDR implementations that have the performance, power efficiency, and scalability of ASICs with the flexibility, reconfigurability, adaptability, and ease-of-use of software.

8. UAB Snapshot GNSS Software Receiver

The UAB snapshot GNSS software receiver (cf. Tab. 6) was originally developed as part of the research activities on indoor GNSS positioning that were carried out by the Signal Processing for Communications and Navigation (SPCOMNAV) group at Universitat Autònoma de Barcelona (UAB), back in 2007. At that time, the group was involved in one of the two parallel contracts that ESA awarded to assess the feasibility of indoor GNSS positioning, under the project named DINGPOS. The proposed strategy was to rely on a combination of technologies such as WiFi, Ultra Wideband (UWB), 2G/3G cellular networks and GNSS as discussed by López-Salcedo et al. (2008). As far as GNSS was concerned, UAB was in charge of developing the software implementation of a so-called high-sensitivity GNSS (HS-GNSS) receiver, which could be able to operate under the extremely-weak signal conditions experienced indoors. This involves working under 10 to 40 dB attenuation losses, which drive the effective C/N0 down to values where conventional GNSS receivers are not able to operate anymore.

The proposed HS-GNSS receiver implementation was based on a snapshot architecture where a batch of input samples were processed at a time to provide the user's position. This approach is often referred to in the literature as *push-to-fix* or *acquisition-only*, since no tracking stage is actually implemented at the receiver. This means that the receiver operates in open-loop mode by providing at its output the observables obtained straightaway from the acquisition stage. The implementation of the HS-GNSS software receiver was strongly influenced by the work already initiated by Gonzalo Seco-Granados before joining UAB, during his period from 2002 to 2005 as technical staff at the European Space Research and Technology Center (ESTEC) of ESA in The Netherlands, where he was leading the activities concerning indoor GNSS and snapshot GNSS receivers. Actually, the core of the UAB snapshot GNSS receiver was inspired on the same concept of double-FFT acquisition already introduced by Jiménez-Baños et al. (2006). This algorithm uses two consecutive FFT operations for implementing the correlation of the received signal with the local code replica, and then the simultaneous estimation of the fine Doppler and bit synchronization. Interested readers on the double-FFT algorithm and on a detailed description of the UAB snapshot GNSS receiver implementation will find a comprehensive description written by Seco-Granados et al. (2012).

From a general perspective, the UAB snapshot GNSS software receiver implements a set of specific signal processing techniques that are tailored to the particular working conditions indoors. Nevertheless, the implementation is flexible and it does not prevent the receiver to be operated efficiently in other scenarios, such as outdoors. Regarding the indoor environment, the most important impairment to be counteracted is certainly the severe attenuation due to the propagation through building materials and other obstacles. Attenuation up to 40 dB can easily be experienced, thus requiring a specific action to recover as much of the lost power in order to still be able to detect GNSS satellites. Since it is the received energy what matters from a signal detection and estimation point of view, and energy is nothing but power times the observation time, the only way to compensate for an extremely weak received power is by increasing the observation time. This means processing a longer piece of received signal, which means implementing very long correlation integration times at the GNSS receiver, on the order of hundreds of milliseconds or even a few seconds. Unfortunately, increasing the correlation time is hindered by the presence of the navigation message data symbols, residual Doppler errors and clock instabilities. So the approach adopted in practice by most snapshot GNSS receivers, particularly those intended for high-sensitivity applications, is to split a long correlation into pieces of shorter, but long-enough coherent correlations, whose outputs are then noncoherently accumulated. This combination of coherent and noncoherent correlation has proven to be successful in increasing the receiver sensitivity and thus still be able to detect a few GNSS satellites indoors. Actually, an interesting discussion on how important having long-enough coherent integrations was discussed by Pany et al. (2009).

The correlation between the received signal and the local replica is therefore the most important operation of a snapshot GNSS receiver. The reason is that with such correlation, the most accurate code delay and Doppler observables need to be estimated. This is because no tracking stage is implemented, and thus there will be no chance to further refine these observables in subsequent stages of the receiver. It is for this reason that the correlation must be implemented in the most optimal way, taking into account subtle details that might be ignored in conventional GNSS receiver implementations. This is one of the advantages of the double-FFT algorithm implemented in the UAB snapshot GNSS receiver, which implements the optimal joint estimation of the code-delay and fine Doppler over a long period of time, where potentially sign transitions may occur due to the presence of data modulating symbols. Additional considerations such as how to handle a non-integer number of samples when performing the FFT, the interpolation between consecutive correlation peaks, the code-Doppler effect over a long correlation period, etc. can be found in Seco-Granados et al. (2012).

The code delay and Doppler estimates provided by the acquisition stage are then directly used by the navigation module to compute the user's position. Such code-delay estimates are ambiguous at one code period because no absolute time reference is available, and therefore no other time-delay information can provided but that contained with a PRN code period. This is because just a batch of received samples is processed, and thus no access to the transmission time encoded onto the navigation message is available in general. As a result, the user's position needs to be computed without such time reference, which becomes a very specific feature of snapshot GNSS receivers. This problem can be solved thanks to what is known as coarse-time navigation, where the conventional navigation equations are augmented to include an additional unknown that represents the missing absolute time reference. The interested readers will find in (Van Diggelen, 2009, Ch.4) an excellent description of this method.

Since its development in 2008, the UAB snapshot GNSS receiver has been a key tool for many research activities at the SPCOMNAV group. This software has been used for instance, to characterize the multipath propagation indoors (López-Salcedo et al., 2009), to assess the feasibility of using GNSS receivers in missions to the Moon, where the weak-signal problem is very similar to the indoor one (Manzano-Jurado et al., 2014), to test near-far mitigation techniques that may appear in indoor/Space applications (Locubiche-Serra et al., 2016), to assess the impact of phase noise (Gómez-Casco et al., 2016), and to provide GNSS positioning to Internet of Things (IOT) sensors in smart cities (Minetto et al., 2020) by means of a cloud-based implementation of the UAB snapshot GNSS receiver that was developed from 2016 to 2018.

The migration of the UAB snapshot receiver into a cloud-based implementation was certainly a major milestone that attracted the interest of the community and opened the door for totally new applications and use cases. The interest in cloud GNSS positioning was motivated by the fact that GNSS software receivers were running at that time in local computers next to the user who collected the samples to be processed. However, with the advent and widespread deployment of cloud computing platforms such as Amazon Web Services (AWS), Microsoft Azure and Google Cloud, such local computers could actually be placed anywhere, and remote access could be granted to upload and process GNSS samples in a remote server in a scalable manner. Furthermore, this approach fitted pretty well with a snapshot GNSS receiver implementation, where a batch of samples could be sent to a remote server where the user's position would then be computed using the same tools as in any other snapshot GNSS receiver. That is, using A-GNSS for reducing the acquisition search space, making extensive use of FFT operations and computing the user's position by means of coarse-time navigation techniques.

This was the idea behind the so-called "cloudGNSSrx", the cloud-based implementation of the UAB snapshot GNSS receiver as described in SPCOMNAV (2019). The architecture was based on a dockerized compilation of the Matlab source code implementing the UAB snapshot GNSS receiver. Then a system of job queues, schedulers and load balancers were built on AWS to automate and scale the remote execution of the receiver, and an API was developed for machine-to-machine communication,

Table 6: Main features of UAB Snapshot GNSS Receiver

UAB Snapshot GNSS Receiver		
Feature	Solution	Remark
Operating system	Any supported by MATLAB	
Programming environment	MATLAB	MATLAB version 6.0 (R12, 2000) or higher.
Processing mode	Post-processing	
Supported GNSS	GPS (L1 C/A, L5), Galileo (E1C, E5a)	
Acquisition	FFT-based signal acquisition	Implementing the double-FFT algorithm for both code correlation and bit synchronization. Long correlations can be implemented by non-coherently combining a set of coherent correlations. Assisted-GNSS (A-GNSS) is used to narrow the acquisition search space. Compatible with 3GPP RRLP-compliant XML data.
Tracking	None	No tracking is implemented because the receiver architecture is based on snapshot mode (i.e. acquisition-only).
Navigation	Weighted Least Squares (WLS)	Coarse-time navigation is implemented.
Further features	Implements near-far detection and interference detection.	

facilitating the provision of GNSS positioning to small IOT sensors (Lucas-Sabola et al. (2016)). In this way, IOT sensors requiring GNSS positioning were be able to offload most of the computational load to a remote server, thus significantly reducing the power consumption and thus extending their battery lifetime.

Low-power GNSS positioning is actually one of the main applications of cloud GNSS software receivers, since for snapshots shorter than a few tens on milliseconds, the energy spent in sending the GNSS samples to the cloud pays off for the significant energy that is saved at the user's terminal for not processing such samples, and doing it at the cloud instead (Lucas-Sabola et al., 2017). This feature was actually acknowledged by the former GSA, now the European Union Agency for the Space Programme (EUSPA), who identified the UAB cloud GNSS receiver as one of the promising technologies for the future adoption of GNSS in the IOT domain (European Union Agency for the Space Programme, 2018). The cloud GNSS software receiver developed by UAB was then licensed in 2019 to the startup company Loctio, who enormously developed the initial prototype and made it a commercial product.

It is important to remark that apart from the low-power consumption use case, cloud GNSS software receivers can also be used to provide access to sophisticated signal processing techniques that cannot be implemented in conventional receivers. For instance, advanced signal monitoring techniques, spoofing detection or authenticated/certified positioning, the latter being reported by Rügamer et al. (2016). There is therefore a brilliant future ahead for cloud GNSS software receivers with many exciting new applications still to come.

9. The NGene Family of Receivers at Politecnico di Torino and LINKS

The development of the GNSS software receiver, noted as NGene, at Politecnico di Torino and LINKS foundation, roots back to the early years of 2000. At such time the Navigation Signal Analysis and Simulation Group (NavSAS) was already working on the software implementation of several sections of the GNSS baseband processing leveraging on the strong background of the group at Politecnico di Torino on digital signal processing and in particular in the digital simulation of complex communications system.

Such early work was addressing the optimized implementation of the acquisition and tracking stages, both as post processing tool, or as core processing units on programmable hardware. In 2005, under regional funding, the research team, at that time affiliated also partially to the Istituto Superiore Mario Boella (now part of the LINKS foundation) started to develop a fully software, real time GNSS receiver for GPS and for the upcoming Galileo signals.

The outcome of the work was the first release of the software receiver NGene as reported by Molino et al. (2009), which was able to process in real-time the GPS, Galileo and EGNOS signal components broadcast on the L1/E1 band, after Intermediate Frequency downconversion and digitalization of the signal ensemble reaching the antenna. IF downconversion and digitalization

were demanded to an external analog front-end device, which communicated via USB connection with the personal computer hosting the software receiver. The A/D converter with front-end filtering, along with the antenna and its Low-Noise Amplifier, were the only non-software elements of the receiving chain. Since then, many features were added on top of that fundamental architecture, which has remained since today the distinguishing feature of the NGene family of receivers. This reconfigurable software receiver has been since long time the principal development tool for in-lab analysis, development and prototyping of signal processing algorithms and architectures.

For example, thanks to the flexible implementation, NGene was adapted to process the Galileo In-Orbit validation signals (GIOVE-A) and later to excitingly process the first Galileo signals as soon as they were available as described in Margaria et al. (2012). Later it allowed the research team to be one of the first worldwide to obtain a position fix from the first four Galileo satellites.

The software receiver kept evolving and it has been adapted to address different applications, maximising the benefits of the software radio implementation. Today the NGene family is configurable to support many different RF-to-IF front-ends, USB connected with the software processor, responding to the needs of tens of activities and projects. A simplified, low-complexity version implements GNSS positioning capabilities in ARM-based embedded processors as described by Troglia Gamba et al. (2015b). Other branches of the software were adapted to fly a GNSS-R receiver for reflectometry tests (Troglia Gamba et al., 2015a) , to test antijamming algorithms, and in 2017 to support the detection of the transmission of a Non-standard code and the effects on Galileo positioning (Dovis et al., 2017) as well as during the Galileo outage event in 2019 (Dovis et al., 2019).

The implementation of the algorithms to authenticate the Galileo message via the OS Navigation Message Authentication mechanism (OSNMA) is one of the most recent branches of the NGene family (Nicola et al., 2022; Troglia Gamba et al., 2020a), together with the implementation of the set of functions to elaborate the future GPS Chimera authentication service (Troglia Gamba et al., 2020b).

10. The MATRIX SDR for Navigation with Signals of Opportunity

MATRIX (Multichannel Adaptive TRansceiver Information eXtractor) is a state-of-the-art cognitive SDR, developed at Kassas' Autonomous Systems Perception, Intelligence, and Navigation (ASPIN) Laboratory, for navigation with terrestrial and space-based SOPs (Kassas et al., 2020). MATRIX continuously searches for opportune signals from which it draws navigation and timing information, employing signal characterization on-the-fly as necessary. MATRIX could produce a navigation solution in a standalone fashion (Shamaei and Kassas, 2021a) or by fusing SOPs with sensors (e.g., IMU (Morales and Kassas, 2021), LiDAR (Maaref et al., 2019), etc.), digital maps (Maaref and Kassas, 2020), and/or other signals (e.g., GNSS) (Kassas et al., 2017). Fig. 1 shows MATRIX's architecture.

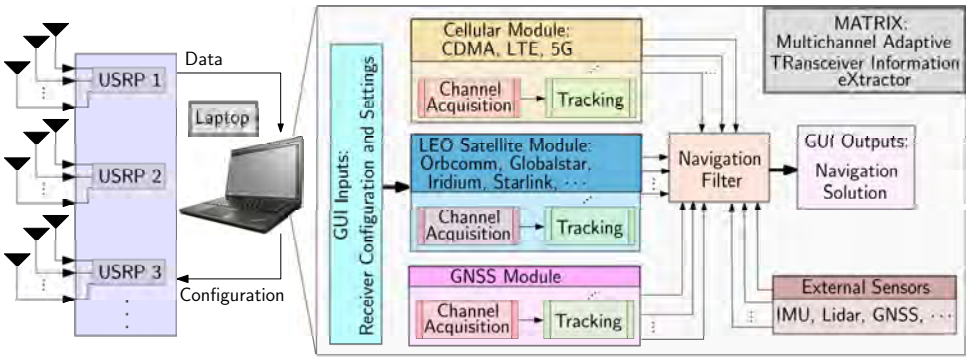

Figure 1: MATRIX cognitive SDR architecture. The SDR consists of: (i) USRPs to collect different radio signals, (ii) various modules to produce navigation observables from different types of signals (e.g., cellular, LEO satellites, etc.), (iii) external sensors (e.g., IMU, LiDAR, GNSS receivers, etc.), whose measurements can be fused with the navigation observables produced by the signal modules, and (iv) navigation filter that fuses all measurements to produce a navigation solution.

On one hand, MATRIX has achieved the most accurate navigation results to-date in the published literature with cellular SOPs (3G CDMA, 4G LTE, and 5G NR), achieving meter-level navigation indoors (Abdallah and Kassas, 2021) and on ground vehicles (Maaref and Kassas, 2022) and submeter-level navigation on unmanned aerial vehicles (Khalife and Kassas, 2022). In addition, MATRIX's efficacy has been demonstrated in a real-world GPS-denied environment (Kassas et al., 2022b), achieving a position root-mean squared error of 2.6 m with 7 cellular LTE eNodeBs over a trajectory of 5 km (one of which was more than 25 km away), during which GPS was intentionally jammed (Abdallah et al., 2022). MATRIX has also achieved remarkable results on high-altitude aircraft, where it was able to acquire and track cellular 3G CDMA and 4G LTE signals at altitudes as high as 23,000 ft above ground level and from cellular towers more than 100 km away (Kassas et al., 2022c). What is more,

meter-level high-altitude aircraft navigation was demonstrated over aircraft trajectories exceeding 50 km, by fusing MATRIX's cellular navigation observables with an altimeter (Kassas et al., 2022a).

On the other hand, MATRIX has achieved the first published results in the literature for exploiting unknown SpaceX's Starlink LEO satellite signals for positioning, achieving a horizontal positioning error of 10 m with Doppler observables (Neinavaie et al., 2021) and 7.7 m with carrier phase observables (Khalife et al., 2022). In addition, the first ground vehicle navigation results with multi-constellation LEO (Orbcomm, Iridium NEXT, and Starlink satellites) were achieved with MATRIX (Kassas et al., 2021), upon coupling its LEO navigation observables with an inertial navigation system (INS) in a tightly-coupled fashion through the simultaneous tracking and navigation (STAN) framework (Kassas et al., 2019).

IV. SDR FRONT-ENDS

A front-end is required to obtain digital samples for the SDR processing. The front-end's tasks are to receive, filter, amplify, down-convert, and further digitize and quantize the analog RF signal entering the GNSS antenna. Many different types of front-ends were used for GNSS SDRs. Roughly, five different categories can be identified:

- **discrete components:** Using RF-connectable components like Low Noise Amplifiers (LNAs), filters or ADCs it is comparable easy to realize the function of a front-end and log IF or baseband samples. Those setups are easy to realize but often bulky and sometimes prone to interference.
- **commercial signal recorders:** several companies offer GNSS signal recorders to allow to record (and often to replay) one or more GNSS frequency band. Usually they do not implement a real-time connection to an SDR.
- **generic non-GNSS front-ends:** SDR technology is used in many different fields of electrical engineering and front-ends covering a wide frequency are available. Their price ranges from a few Dollars (Fernández–Prades et al., 2013) to highly sophisticated multi-channel front-ends costing several ten-thousands of Dollars. The oscillator quality, bit-width or RF-filter characteristics is not always optimal for GNSS signal processing.
- **dedicated GNSS real-time front-ends**: Built for the purpose to realize a real-time GNSS SDR. A good example is described in sect. IV.1. They are compact and build with discrete components.
- **ASICs**: Some RF-ASICs seem to target GNSS SDR use and evaluation kits allow streaming of IF samples, e.g. RF Micro Devices, Inc., Greensboro (2006); NTLAB, UAB (2022).

GNSS signals need a comparable high sampling rate of the front-end and when connected to a PC via a USB cable the transfer was not always reliable in the early years. Various optimizations and workarounds have been implemented like watermarking the IF sample stream and skipping lost sample packets as invented by Foerster and Pany (2013). With the advent of USB 3.0 or PCIe those solutions became obsolete.

In the following section, we describe Fraunhofer USB front-ends as an example of user needs, main features and general architectures of GNSS SDR front-ends. For a broader perspective of GNSS-compatible front-ends in the market, the interested reader can refer to (Borre et al., 2022, Ch.12).

1. Fraunhofer USB Front-ends

With the upcoming civil multi-band signals in GPS, and Galileo planning progressing, there was a need for the scientific community but also with some industrial partners, to have a multi-band SDR front-end solution, to enable also multi-band SDR development.

In 2006, Fraunhofer IIS developed a front-end, called the L125 Triband USB (see Fig. 2a), which allows a fixed frequency recording of L1/E1, L2, and L5/E5a via two USB 2.0 data streams with up to 40 MSPS sampling rate, a 2 or 4 bit ADC resolution, and one antenna input.

However, increasing customer requests for portable and flexible solutions concerning frequency band selection, adjustable sampling rates, intermediate frequencies, and multi-antenna support led to completely redesigning this USB front-end concept. One major request was reconfigurability on the SDR front-end side. While for specific projects, a single band receiver with a low-sampling rate is desired (i.e. to realize a real-time SDR), in other projects, a wideband and multi-frequency front-end may be needed. To cope with these different requirements in one SDR front-end hardware, a new version of the USB front-end was developed that realizes the signal conditioning to an on-board FPGA enabling the desired reconfigurability on the fly.

In 2012 Fraunhofer IIS (Rügamer et al., 2012) introduced the Flexiband multi-system, multi-band USB front-end depicted in Fig. 2b. Within the last ten years, this front-end has been used and validated in numerous scientific and industrial projects. Furthermore, it has been commercialized and is distributed as the "MGSE REC" product of TeleOrbit GmbH (2022).

(a) TriBand USB2.0 Front-end from 2006

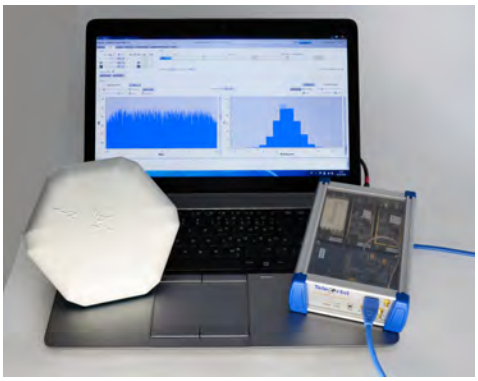

(b) Flexiband USB3.0 Front-end from 2012 onwards

Figure 2: Two examplery USB Front-end from Fraunhofer IIS

A regular Flexiband unit consists of up to three analog reception boards, a carrier board with ADCs and FPGA, and a USB 3.0 interface board. A common antenna input port is supported, and separate front-end input signals for up to three antenna inputs. Three dual-channel ADCs sample the incoming signal with 81 MSPS and 8 bits I/Q. The raw data stream is received by an FPGA in which different digital operations like filtering, mixing, data rate, and bit-width reduction, as well as a digital Automatic Gain Control (AGC) are applied. Finally, a single multiplexed data stream is formed together with a checksum. This multiplexed stream is sent via an USB 3.0 interface to the PC. Data rates of up to 1296 MBit/s or 162 MByte/s raw data stream are supported. The Flexiband GUI software receives the raw multiplexed stream, checks its integrity, and demultiplexes it. The data streamed can be either written to hard disk or sent to a customer application (e.g., a software receiver). The raw samples can be stored as a multiplexed data stream, in an 8 bit/sample format, or directly as a .mat file for MATLAB. In parallel, the ION Metadata *.sdrx is provided.

Due to its bandwidth, sampling rates, quantization, and multiplexing schema flexibility, the ION metadata standard was a perfect fit to clearly and unambiguously define the configuration for the user. Therefore, right after the first conclusion of the ION metadata standard, each binary raw-data output file of the Flexiband front-end was equipped with an "sdrx" metadata file specifying the raw data format.

Finally, a replay variant of this Flexiband exists that reads in the raw IF samples on hard disk using the ION metadata standard specification and replays the digital data as an analog RF output stream supporting multiple GNSS bands at the same time.

V. ION SDR METADATA STANDARD

The events that led up to the suggestion to develop what became the ION SDR Metadata Standard can be traced back to circa 1999. Building upon the successful contributions made by Akos, the Ohio University Avionics Engineering Center undertook several research projects leveraging GPS SDRs. One such project was called the GPS Anomalous Event Monitor (GAEM) (Snyder et al., 1999). This was sponsored by the FAA Technical Center and led by Prof. Frank van Graas. Commercial GPS receivers within prototype LAAS ground facilities were experiencing brief unexplained outages. GAEM kept a continuous 10-second history of IF samples in a circular memory buffer. When an outage occurred, GAEM was triggered to dump this buffer to disk and collect for a further 10 seconds. These sample files were then post-processed in MATLAB to determine the cause of the anomaly. Early versions of GAEM used commercial data collection cards and had numerous issues related to their proprietary drivers. Around 2001, Gunawardena developed a refined version of GAEM that was based on one of the earliest PCI-based dual-ADC-plus-FPGA development cards commercially available. It collected two GPS L1 data streams at 5 MSPS and 2 MHz bandwidth. This version of GAEM was fielded at three airports and operated continuously for over 3 years and helped to characterize numerous anomalous events (Gunawardena et al., 2009). This GAEM also supported a continuous collection mode, and was used for several research projects including the characterization of GPS multipath over water (Zhu and Van Graas, 2009) and GPS/IMU deep integration demonstrations in flight (Soloviev et al., 2004). For the latter, the 2 kHz raw data from a MEMS IMU were interleaved with the SDR samples thanks to the FPGA-based architecture that allowed for such custom capabilities.

Circa 2002, as these research projects progressed, the 2 MHz bandwidth limitation of GAEM became apparent. There was a pressing need to support emerging research opportunities related to GPS L5, as well as high fidelity GPS signal quality monitoring. A multi-band and higher-bandwidth (24 MHz) front-end and SDR data collection system was needed. There were only a handful of vendors selling such systems at the time, and it wasn't clear if these would serve the purpose for satnav SDR

application (sampling coherency concerns, etc.). However, by far, the >$350k price tag of these systems precluded any hope of purchasing them for university research. It was decided to develop this capability in-house. In 2003, a 2-channel L1/L5 front-end with 24 MHz bandwidth and 56.32 MSPS was developed (Gunawardena et al., 2008). It was based on connectorized RF components. The sampling and collection subsystems were carried over from GAEM.

The capabilities of the dual-frequency high-bandwidth system attracted interest from several universities, government research groups, as well as a defense contractor. To support these opportunities, the development of a new system known as Wideband Transform-domain Instrumentation GNSS Receiver (TRIGR) was completed in 2008 (Gunawardena and Van Graas, 2011). The front-end was miniaturized to a single-frequency custom PCB module. Up to 8 such modules (with the required frequency options) were combined with an 8-channel 12-bit ADC to create modular systems for various sponsors. The raw samples from the ADC are transferred to a PCIe FPGA card where the 8 streams are packed in various formats according to the user's selection in a GUI. Supported formats range from any one stream at 1-bit sample depth, any 2 streams at 12 bits (sign extended to 16), to all 8 streams at 4 bits. The sustained data transfer rate from the PCIe FPGA card to the RAID storage array was limited to 240 MB/sec. As such, the appropriate format had to be selected to balance between the required capability and transfer rate. The generated file names embed a UTC timestamp as well as the packed stream order and sample depth.

The event-based data collection feature of GAEM needed to be incorporated into Wideband TRIGR. However, the >10× data rate meant that a 10-second circular buffer could not be easily implemented in RAM using 32-bit systems of the day. This issue was addressed by writing data as a sequence of smaller files, where a new file was spawned before the current file was closed – with some sample overlap for data integrity – a technique known as temporal splitting. A separate process was used to delete older files from the RAID array to make room for new ones – unless an event was received – in which case the files surrounding the event were moved to a folder for post processing.

With the myriad of sample packing formats available with Wideband TRIGR, along with the temporal splitting-based file generation scheme, it became clear that a machine-readable metadata file needed to be included with every collection. An XML schema was designed for this purpose.

Up until this time, apart from the FPGA-based real-time GPS receiver that was developed and used for certain projects, all SDR files generated by GAEM and Wideband TRIGR were post processed in MATLAB. As others have mentioned, this was excruciatingly slow – especially for Wideband TRIGR data. To address this issue, as well as to support the rapid emergence of multi-band and multi-constellation satnav signals, Gunawardena wrote and distributed a MATLAB SDR toolbox where correlation was performed in optimized C code and also leveraged multi-threading in a data parallel architecture. This toolbox, known as ChameleonChips, also read the XML metadata files produced by Wideband TRIGR to determine the appropriate sample unpacking kernel to use. This work was presented at ION GNSS+ 2013 in Nashville, TN (Gunawardena, 2013). During this presentation, it was suggested that the satnav SDR community should adopt a metadata standard – similar to the one developed for Wideband TRIGR – in order to alleviate the numerous headaches associated with sharing such files. This was met with widespread support and enthusiasm. Longstanding ION members Phillip Ward, Jade Morton, and Michael Braasch helped to pitch this idea to the ION Executive Committee.

During the January 2014 Council Meeting in San Diego, ION approved the process for establishing a formal standard (Gunawardena et al., 2021). The ION GNSS SDR Metadata Working Group (WG) was formed in April 2014 with Thomas Pany and Gunawardena as co-chairs (James Curran was added later as a third co-chair). Membership represented academia, industry (including satnav SDR product vendors as well as traditional satnav equipment manufacturers), non-profit research entities, and government agencies spanning countries in Europe, America, Asia, and Australia. The working group developed the standard as well as associated normative software over a course of six years. With regards to the normative software, while many individuals contributed, initial development of the C++ object model was performed by Michael Mathews of Loctronix while James Curran wrote much of the functionality to decode packed samples based on the metadata specification. The draft standard was adopted as a formal ION standard in January 2020.

1. Use of GNSS SDR Standard

Today the GNSS SDR standard serves as a reference to describe IF formats and is for example useful for public tenders or if for some means an established format is needed. A number of SDRs do include the C++ libraries to read meta-data and IF samples.

The level of exchange of IF samples between research groups is to some extent limited and much less executed compared to e.g. exchange of RINEX files. This is of course related to the huge size of IF sample files and to the fact that for the majority of GNSS use cases, RINEX observation data or PVT exchange is sufficient. Furthermore, GNSS SDRs still tend to use mostly the same front-end and once the respective data format is known, there is obviously no need to describe it via the XML format. A disadvantage of the C++ routines is their generic design, which renders sample reading quite slow, as each sample is isolated via a number of for-loops from the input files. Clements et al. (2021) did propose an algorithm to automatically generate optimized code for sample reading for a given IF format, but this proposal did not yet manifest into a usable implementation.

2. Standard Extension

Already during the standardization process a number of features for the standard were identified, that appear to be useful but lack of resources did not allow including them in the formal standardization procedure. Those features are described in the App. II of (ION SDR Working Group, 2020). Within the ION-GNSS+ 2022 meeting in September, the following points have been discussed and will be included in App. II of the next - draft-version V1.1 of the standard:

a) Flexible bit layout

The SDR metadata standard defines a "Lump" as the ordered containment of all samples occurring within an interval. The ordered containment is understood in a regular way holding the samples of the individual streams together. The authors of (Clements et al., 2021) see this as a limitation, as highly efficient SDRs may use efficient bit-packing schemes to optimize data transfer over communication lines that need buffering. They identify a need to distribute the samples of different Streams in interleaved ways over the Lump. This interleaving cannot be described by the V1.0 of the SDR metadata standard. To overcome this limitation, the authors propose a new but optional attribute for the Lump object, called "Layout". In case Layout is present, further information on the bit packing scheme needs to be provided, describing in an explicit way the type of each bit of a Lump. The authors propose a detailed proposal following the structure of the existing standard can be found for this new Lump layout. The proposal even includes more advanced bit use cases, like puncturing (e.g. explicit omitting of bits) and overwriting of bits by time markers.

b) Refined sample rate/epoch definitions

In the work (Clements et al., 2021), the authors note that the V1.0 of the SDR metadata standard makes implicit assumptions about the timing of the sampling process and staggered sampling cannot be described by it. Staggered sampling occurs if the sampling instants of different GNSS signals are delayed with respect to each other, and might be of use to increase observability of GNSS interference in a multi-antenna system. To overcome this limitation, the authors propose to add two new attributes for stream objects to shift the sampling epochs of different GNSS stream with respect to each other.

c) JSON format for metadata files

Comment ID 22 of the initial Request for Comments (RFC1) makes a suggestion that the WG considers markup languages other than XML for metadata files, specifically JSON, YAML and TOML (Anon, 2017). In 2017, this comment was addressed by asserting that the XML format will be maintained for the time being since normative software that parses XML had already been developed. However, the WG responded with the assurance that "other markup languages will be considered in the future based on community need and interest."

As of the time of this writing, and with the experience gained from developing PyChips (which is a satnav SDR that is completely described using a draft signal/system specification language based on JSON, as described in III.7), it is this author's opinion that JSON may have some distinct advantages over XML for future applications and use cases. For example, JSON streaming is a methodology for transferring object-oriented data over communications protocols (Wikipedia, 2022) and is widely used in well-known applications such as Plotly (2022). Hence, streaming JSON could be one way to parse SDR sample streams whose formats are changing dynamically.

Figure 3 shows a notional listing for a JSON formatted metadata description for the Flexiband front-end XML metadata listing found in Gunawardena et al. (2021).

To maintain compatibility with the existing and formally adopted XML-based metadata specification, it is understood that any adoption of another markup language such as JSON must include open source normative software and tools to convert between these formats. Adoption of JSON based metadata is currently being considered for future versions of PyChips. If and when a successful implementation has been achieved, consideration for adopting JSON as another valid option for representing ION Standard-compliant metadata in a future version of the standard will be requested.

SUMMARY AND CONCLUSION

Since GPS SDR developments started in the mid 90's, together with the operational declaration of GPS, its feasibility has been widely proven by several platforms and their derivatives. We define GNSS SDR platforms as those implementing the receiver functions in general purpose software and processors, and divide them in real-time receivers, teaching/research tools, and snapshot receivers. We then describe some of them, with focus on those related to the authors but also including other developments. In particular, and based on the pioneering work by D. Akos, we describe the Bit-Wise Parallelism platform by the Cornell GPS group, which led to GRID/PpRx by UT Austin; the MuSNAT receiver by UniBwM, which also led to IFEN GmbH's SX3 commercial receiver; The SoftGPS Matlab receiver and associated book, widely used for GNSS teaching and also influencing other platforms, such as FGI-GSRx; the popular C++ open source GNSS-SDR by CTTC; AutoNav SDR by Inha University; PyChips by S. Gunawardena and based on Python; the snapshot GNSS receiver by UAB, leading to cloudGNSSrx;

```
{"system": {
    "id": "Flexiband", "comment": "Front-end variant:II-4e PRS (E6abc/E1abc/uBlox)",
    "freqbase": {"format": "MHz", "value": 8.10e+01 },
    "equipment": "Flexiband Multi-band receiver", "types": "Flexiband Multi-band receiver",
    "sessions": {
      "0": {
        "comment": "flexiband", "toa": "2022-09-30T00:00:00.00Z",
        "contact": "J. Doe", "campaign": "Example Campaign", "scenario": "Example Scenario",
        "position": {"lat": "0.0", "lon": "0.0", "height": "0.0"},
        "files": {
          "0": {
            "url": "flexiband.usb", "timestamp": "2022-09-30T00:00:00.00Z", "owner": "Example Owner",
            "lanes": {
              "0": {
                "id": "Data",
                "block": {
                  "cycles": 506, "sizeheader": 6, "sizefooter": 6,
                  "chunk": {
                    "sizeword": 1, "countwords": 2, "endian": "undefined", "padding": "none", "wordshift": "left",
                    "lump": {
                      "streams": {
                        "E6abc_B3": {
                          "other_specs": {"Amp": "162", "Antenna power": "false", "AGC": "false"},
                          "ratefactor": 1, "quantization": 4, "packedbits": 4, "alignment": "undefined",
                          "shift": "undefined", "format": "IQ", "encoding": "INT",
                          "bands": {
                            "E6abc_B3": {
                              "centerfreq": {"format": "MHz", "value": 1.27e+03},
                              "translatedfreq": { "format": "kHz", "value": 8.75e+03},
                              "delaybias": { "format": "sec", "value": 0.0e+00},
                              "bandwidth": { "format": "Hz", "value": 0.0e+00}
                            }
                          }
                        },
                        "L1_E1abc_B1_G1": {
                          "other_specs": { "Amp": "120", "Antenna power": "false", "AGC": "false"},
                          "ratefactor": 1, "quantization": 4, "packedbits": 4, "alignment": "undefined",
                          "shift": "undefined", "format": "IQ", "encoding": "INT",
                          "bands": {
                            "L1_E1abc_B1_G1": {
                              "centerfreq": {"format": "MHz", "value": 1.58e+03},
                              "translatedfreq": {"format": "kHz", "value": -4.58e+03},
                              "delaybias": {"format": "sec", "value": 0.0e+00},
                              "bandwidth": {"format": "Hz", "value": 0.0e+00}
                            }}}}}}}}}}}}}}}
```

Figure 3: Notional JSON Representation of Flexiband Front-End Metadata from Gunawardena et al. (2021)

the real-time N-GENE receiver by LINKS, used for early testing of Galileo first signals and OSNMA and the MATRIX receiver by ASPIN for navigation with terrestrial and space-based SOP among others. We provide an overview of the tasks and components of SDR front-ends, and for this purpose we describe Fraunhofer developments from the last years as a reference. Finally, we discuss the SDR Metadata Standard, officially approved by ION in 2020, and its current extensions.

In view of the impact in the GNSS community and the progress in the last decades, we conclude that GNSS SDR has a promising future and will continue coexisting with FPGA and ASIC receivers for the decades to come.

ACKNOWLEDGEMENTS AND REMARKS

The authors are listed in alphabetical order to reflect the variety and importance of all contributions. The contributions have been partly edited by Thomas Pany, who also takes the responsibility for the structure of the work, the abstract and the introduction.

The GNSS SDR developments at the Universität der Bundeswehr München of sect. III.2 were supported by via numerous research projects administered by the German DLR and were financed by the German Federal Ministry for Economic Affairs and Climate Action (BMWK).

The UAB snapshot GNSS software receiver was supported in part by numerous ESA-funded research projects and by the Spanish State Research Agency (AEI) project PID2020-118984GB-I00.

The MATRIX SDR development at the ASPIN Laboratory was supported by the Office of Naval Research (ONR) under Grants N00014-16-1-2305, N00014-19-1-2613, and N00014-19-1-2511; the Air Force Office of Scientific Research (AFOSR) under Grant FA9550-22-1-0476; the U.S. Department of Transportation (USDOT) under Grant 69A3552047138 for the CARMEN University Transportation Center (UTC); and the National Institute of Standards and Technology (NIST) under Grant 70NANB17H192.

The authors would like to acknowledge the work of Prof. Kai Borre, who passed away in 2017, for his influential contributions to the GNSS SDR field over the last decades.

REFERENCES

Abdallah, A. and Kassas, Z. (2021). Multipath mitigation via synthetic aperture beamforming for indoor and deep urban navigation. *IEEE Transactions on Vehicular Technology*, 70(9):8838–8853.

Abdallah, A. and Kassas, Z. (2022). Opportunistic navigation using sub-6 GHz 5G downlink signals: A case study on a ground vehicle. In *Proceedings of European Conference on Antennas and Propagation*, pages 1–5.

Abdallah, A., Kassas, Z., and Lee, C. (2022). Demo: I am not afraid of the GPS jammer: exploiting cellular signals for accurate ground vehicle navigation in a GPS-denied environment. In *Proceedings of Workshop on Automotive and Autonomous Vehicle Security*, pages 1–1.

Akos, D. and Braasch, M. (1996). A Software Radio Approach to Global Navigation Satellite System Receiver Design. In *Proceedings of the 52nd Annual Meeting of The Institute of Navigation*, pages 455–463.

Akos, D., S andockmaster, M., J.B.Y., T., and Caschera, J. (1999). Direct bandpass sampling of multiple distinct RF signals. *IEEE Transactions on Communications*, 47(7):983–988.

Akos, D. M. (1997). *A Software Radio Approach to Global Navigation Satellite System Receiver Design*. PhD thesis, Fritz J. and Dolores H. Russ College of Engineering and Technology Ohio University.

Akos, D. M., Normark, P.-L., Enge, P., Hansson, A., and Rosenlind, A. (2001). Real-time gps software radio receiver. In *Proceedings of the 2001 National Technical Meeting of the Institute of Navigation*, pages 809–816.

Anon (2017). RFC1 Comments and Responses. `https://sdr.ion.org/RFC1_Comments_Responses.html`. [Accessed on 09/30/2022].

Arizabaleta, M., Ernest, H., Dampf, J., Kraus, T., Sanchez-Morales, D., Dötterböck, D., Schütz, A., and Pany, T. (2021). Recent enhancements of the multi-sensor navigation analysis tool (musnat). In *Proceedings of the 34th International Technical Meeting of the Satellite Division of The Institute of Navigation (ION GNSS+ 2021)*, pages 2733–2753.

Bernabeu, J., Palafox, F., Li, Y., and Akos, D. (2021). A collection of sdrs for global navigation satellite systems (gnss). In *Proceedings of the 2022 International Technical Meeting of The Institute of Navigation*, pages 906–919.

Bhuiyan, M., Söderholm, S., Thombre, S., Ruotsalainen, L., and Kuusniemi, H. (2015). Performance Analysis of a Dual-

Frequency Software-Defined BeiDou Receiver with B1 and B2 Signals. In *Proc. of the China Satellite Navigation Conference (CSNC)*.

Bhuiyan, M. Z., Söderholm, S., Thombre, S., Ruotsalainen, L., and Kuusniemi, H. (2014). Overcoming the Challenges of BeiDou Receiver Implementation. *Sensors 2014*, 14(11):22082–22098.

Bochkati, M., Dampf, J., and Pany, T. (2022). On the use of multi-correlator values as sufficient statistics as basis for flexible ultra-tight gnss/ins integration developments. In *2022 25th International Conference on Information Fusion (FUSION)*, pages 1–8. IEEE.

Borre, K. (2003). The GPS Easy Suite–Matlab code for the GPS newcomer. *GPS Solutions*, 7(1):47–51.

Borre, K. (2009). GPS Easy suite II. *InsideGNSS*, 2:48–51.

Borre, K., Akos, D., Bertelsen, N., Rinder, P., and Jensen, S. H. (2007). *A Software-Defined GPS and Galileo Receiver, Single Frequency Approach*. Birkhäuser, Boston.

Borre, K., Fernandez-Hernandez, I., Lopez-Salcedo, J. A., and Bhuiyan, M. Z. H. (2022). *GNSS Software Receivers*. Cambridge University Press, Cambridge.

Chen, X., Wei, Q., Wang, F., Jun, Z., Wu, S., and Men, A. (2020). Super-resolution time of arrival estimation for a symbiotic FM radio data system. *IEEE Transactions on Broadcasting*, 66(4):847–856.

Clements, Z., Iannucci, P. A., Humphreys, T. E., and Pany, T. (2021). Optimized bit-packing for bit-wise software-defined GNSS radio. In *Proceedings of the 34th International Technical Meeting of the Satellite Division of The Institute of Navigation (ION-GNSS+ 2021)*. Institute of Navigation.

Curran, J. T., Fernández–Prades, C., Morrison, A., and Bavaro, M. (2018). Innovation: The continued evolution of the GNSS software-defined radio. *GPS World*, 29(1):43–49.

Dampf, J., Pany, T., Bär, W., Winkel, J., Stöber, C., Fürlinger, K., Closas, P., and Garcia-Molina, J. A. (2015). More than we ever dreamed possible: Processor technology for gnss software receivers in the year 2015. *Inside GNSS*, 10(4):62–72.

del Peral-Rosado, J., Estatuet-Castillo, R., Lopez-Salcedo, J., Seco-Granados, G., Chaloupka, Z., Ries, L., and Garcoa-Molina, J. (2017). Evaluation of hybrid positioning scenarios for autonomous vehicle applications. In *Proceedings of ION International Technical Meeting Conference*, pages 2541–2553.

Del Peral-Rosado, J., Nolle, P., Razavi, S., Lindmark, G., Shrestha, D., Gunnarsson, F., Kaltenberger, F., Sirola, N., Särkkä, O., Roström, J., Vaarala, K., Miettinen, P., Pojani, G., Canzian, L., Babaroglu, H., Rastorgueva-Foi, E., Talvitie, J., and Flachs, D. (2022). Design considerations of dedicated and aerial 5G networks for enhanced positioning services. In *Proceedings of Workshop on Satellite Navigation Technology (NAVITEC)*, pages 1–12.

Diouf, C., Janssen, G., Dun, H., Kazaz, T., and Tiberius, C. (2021). A USRP-based testbed for wideband ranging and positioning signal acquisition. *IEEE Transactions on Instrumentation and Measurement*, 70:1–15.

Diouf, C., Janssen, G., Kazaz, T., Dun, H., Chamanzadeh, F., and Tiberius, C. (2019). A 400 Msps SDR platform for prototyping accurate wideband ranging techniques. In *Proceedings of Workshop on Positioning, Navigation and Communications*, pages 1–6.

Donaldson, J. E., Parker, J. J., Moreau, M. C., Highsmith, D. E., and Martzen, P. D. (2020). Characterization of on-orbit gps transmit antenna patterns for space users. *NAVIGATION: Journal of the Institute of Navigation*, 67(2):411–438.

Dovis, F., Linty, N., Berardo, M., Cristodaro, C., Minetto, A., Nguyen Hong, L., Pini, M., Falco, G., Falletti, E., Margaria, D., Marucco, G., Motella, B., Nicola, M., and Troglia Gamba, M. (2017). Anomalous gps signals reported from svn49. *GPS World*.

Dovis, F., Minetto, A., Nardin, A., Falletti, E., Margaria, D., Nicola, M., and Vannucchi, M. (2019). What happened when Galileo experienced a week-long service outage. *GPS World*.

European Union Agency for the Space Programme (2018). GNSS User Technology Report. `https://www.gsa.europa.eu/system/files/reports/gnss_user_tech_report_2018.pdf`. [Accessed on 23-Sep-2022].

Farhangian, F., Benzerrouk, H., and Landry, R. (2021). Opportunistic in-flight INS alignment using LEO satellites and a rotatory IMU platform. *Aerospace*, 8(10):280–281.

Farhangian, F. and Landry, R. (2020). Multi-constellation software-defined receiver for Doppler positioning with LEO satellites. *Sensors*, 20(20):5866–5883.

Fernández–Prades, C. (2022). Yocto Geniux. Online: https://github.com/carlesfernandez/yocto-geniux. [Accessed: 12-Sep-2022]. doi: 10.5281/zenodo.4743667.

Fernández–Prades, C., Arribas, J., and Closas, P. (2016a). Accelerating GNSS software receivers. In *Proc. 29th Int. Tech. Meeting Sat. Div. Inst. Navig.*, pages 44–61, Portland, OR. doi: 10.33012/2016.14576.

Fernández–Prades, C., Arribas, J., and Closas, P. (2016b). Assessment of software-defined GNSS receivers. In *Proc. 8th ed. of NAVITEC Conf.*, ESA/ESTEC, Noordwijk, The Netherlands. doi: 10.1109/NAVITEC.2016.7931740.

Fernández–Prades, C., Closas, P., and Arribas, J. (2013). Turning a television into a GNSS receiver. In *Proc. 26th Int. Tech. Meeting Sat. Div. Inst. Navig.*, pages 1492–1507, Nashville, TN.

Fernández–Prades, C., Vilà–Valls, J., Arribas, J., and Ramos, A. (2018). Continuous reproducibility in GNSS signal processing. *IEEE Access*, 6(1):20451–20463. doi: 10.1109/ACCESS.2018.2822835.

FGI (2022). The FGI-GSRx Software Defined GNSS Receiver Goes Open Source. https://www.maanmittauslaitos.fi/en/topical_issues/fgi-gsrx-software-defined-gnss-receiver-goes-open-source. [Accessed 11-Aug-2022].

Foerster, F. and Pany, T. (2013). Device and method for producing a data stream on the basis of data packets provided with packet sequence marks, and satellite receivers for providing the data stream; us patent no. 8451170, 2011-03-03; german patent no. 102008014981, 2009-10-15. US Patent 8,451,170.

Fokin, G. and Volgushev, D. (2022). Software-defined radio network positioning technology design. problem statement. In *Proceedings of Systems of Signals Generating and Processing in the Field of on Board Communications*, pages 1–6.

Gómez-Casco, D., López-Salcedo, J. A., and Seco-Granados, G. (2016). Generalized integration techniques for high-sensitivity GNSS receivers affected by oscillator phase noise. In *2016 IEEE Statistical Signal Processing Workshop (SSP)*, pages 1–5. IEEE.

GPS World staff (2012). Innovation: Software gnss receiver - gps world : Gps world. https://www.gpsworld.com/software-gnss-receiver-an-answer-for-precise-positioning-research/. (Accessed on 07/04/2022).

Gunawardena, S. (2013). A Universal GNSS Software Receiver MATLAB® Toolbox for Education and Research. In *Proceedings of the 26th International Technical Meeting of the Satellite Division of The Institute of Navigation (ION GNSS+ 2013)*, pages 1560–1576. Institute of Navigation.

Gunawardena, S. (2014). A universal gnss software receiver toolbox. *Inside GNSS*, pages 58–67.

Gunawardena, S. (2021). A High Performance Easily Configurable Satnav SDR for Advanced Algorithm Development and Rapid Capability Deployment. In *Proceedings of the 2021 International Technical Meeting of The Institute of Navigation (ION ITM 2021)*, pages 539–554. Institute of Navigation.

Gunawardena, S., Pany, T., and Curran, J. (2021). ION GNSS software-defined radio metadata standard. *NAVIGATION: Journal of the Institute of Navigation*, 68(1):11–20.

Gunawardena, S., Soloviev, A., and van Graas, F. (2004). Real time implementation of deeply integrated software GPS receiver and low cost IMU for processing low-CNR GPS signals. In *Proceedings of the 60th Annual Meeting of The Institute of Navigation (2004)*, pages 108–114.

Gunawardena, S., Soloviev, A., and Van Graas, F. (2007-2008). Wideband Transform-Domain GPS Instrumentation Receiver for Signal Quality and Anomalous Event Monitoring. *NAVIGATION: Journal of the Institute of Navigation*, 54(4):317–331.

Gunawardena, S. and van Graas, F. (2006). Split-sum correlator simplifies range computations in gps receiver. *Electronics Letters*, 42:1469–1471.

Gunawardena, S. and Van Graas, F. (2011). Multi-Channel Wideband GPS Anomalous Event Monitor. In *Proceedings of the 24th International Technical Meeting of the Satellite Division of The Institute of Navigation (ION GNSS 2011)*, pages 1957–1968. Institute of Navigation.

Gunawardena, S., Zhu, Z., Uijt de Haag, M., and Van Graas, F. (2009). Remote-Controlled, Continuously Operating GPS Anomalous Event Monitor. *NAVIGATION: Journal of the Institute of Navigation*, 56(2):97–113.

Hamza, G., Zekry, A., and Motawie, I. (2009). Implementation of a complete GPS receiver using Simulink. *IEEE Circuits and Systems Magazine*, 9(4):43–51.

Hobiger, T., Gotoh, T., Amagai, J., Koyama, Y., and Kondo, T. (2010). A GPU based real-time GPS software receiver. *GPS solutions*, 14(2):207–216.

Honkala, S. (2016). GLONASS Satellite Navigation Signal Implementation in a Software-defined Multi-constellation Satellite Navigation Receiver. Master's thesis, Aalto University.

Humphreys, T., Psiaki, M., Kintner, P., and Ledvina, B. (2006). GNSS Receiver Implementation on a DSP: Status, Challenges, and Prospects. In *Proceedings of the 19th International Technical Meeting of the Satellite Division of The Institute of Navigation (ION GNSS 2006)*, pages 2370–2382. Institute of Navigation.

Humphreys, T. E., Bhatti, J., Pany, T., Ledvina, B., and O'Hanlon, B. (2009). Exploiting multicore technology in software-defined GNSS receivers. In *Proceedings of the ION GNSS Meeting*, pages 326–338, Savannah, GA. Institute of Navigation.

Humphreys, T. E., Ledvina, B. M., Psiaki, M. L., O'Hanlon, B. W., and Kintner, Jr., P. M. (2008). Assessing the spoofing threat: Development of a portable GPS civilian spoofer. In *Proceedings of the ION GNSS Meeting*, Savannah, GA. Institute of Navigation.

Humphreys, T. E., Murrian, M. J., and Narula, L. (2020). Deep-urban unaided precise global navigation satellite system vehicle positioning. *IEEE Intelligent Transportation Systems Magazine*, 12(3):109–122.

IFEN GmbH (2022). SX3 GNSS Software Receiver — ifen.com. `https://www.ifen.com/products/sx3-gnss-software-receiver/`. [Accessed 01-Sep-2022].

Ikhtiari, N. (2019). Navigation in GNSS denied environments using software defined radios and LTE signals of opportunities. Master's thesis, University of Canterbury, Christchurch, New Zealand.

ION SDR Working Group (2020). Global Navigation Satellite Systems Software Defined Radio Sampled Data Metadata Standard, Revision 1.0. `https://sdr.ion.org`.

iPosi Inc. (2015). iPosi GNSS Signal Processing and Assistance; Performance. `https://iposi.com/technology/Performance`. [Accessed on 2022-09-26].

Jiménez-Baños, D., Blanco-Delgado, N., López-Risueño, G., Seco-Granados, G., and Garcia-Rodriguez, A. (2006). Innovative techniques for GPS indoor positioning using a snapshot receiver. In *Proceedings of the 19th International Technical Meeting of the Satellite Division of The Institute of Navigation (ION GNSS 2006)*, pages 2944–2955.

Kang, T., Lee, H., and Seo, J. (2019). Analysis of the maximum correlation peak value and RSRQ in LTE signals according to frequency bands and sampling frequencies. In *International Conference on Control, Automation and Systems*, pages 1182–1186.

Kaplan, E. (1996). *Understanding GPS Principles and Applications*. Artech House Publishers.

Kassas, Z., Abdallah, A., Lee, C., Jurado, J., Duede, J., Hoeffner, Z., Hulsey, T., Quirarte, R., Wachtel, S., and Tay, R. (2022a). Protecting the skies: GNSS-less accurate aircraft navigation with terrestrial cellular signals of opportunity. In *Proceedings of ION GNSS Conference*. accepted.

Kassas, Z., Bhatti, J., and Humphreys, T. (2013). A graphical approach to GPS software-defined receiver implementation. In *Proceedings of IEEE Global Conference on Signal and Information Processing*, pages 1226–1229.

Kassas, Z., Khalife, J., Abdallah, A., and Lee, C. (2020). I am not afraid of the jammer: navigating with signals of opportunity in GPS-denied environments. In *Proceedings of ION GNSS Conference*, pages 1566–1585.

Kassas, Z., Khalife, J., Abdallah, A., and Lee, C. (2022b). I am not afraid of the GPS jammer: resilient navigation via signals of opportunity in GPS-denied environments. *IEEE Aerospace and Electronic Systems Magazine*, 37(7):4–19.

Kassas, Z., Khalife, J., Abdallah, A., Lee, C., Jurado, J., Wachtel, S., Duede, J., Hoeffner, Z., Hulsey, T., Quirarte, R., and Tay, R. (2022c). Assessment of cellular signals of opportunity for high altitude aircraft navigation. *IEEE Aerospace and Electronic Systems Magazine*. accepted.

Kassas, Z., Khalife, J., Shamaei, K., and Morales, J. (2017). I hear, therefore I know where I am: Compensating for GNSS limitations with cellular signals. *IEEE Signal Processing Magazine*, pages 111–124.

Kassas, Z., Morales, J., and Khalife, J. (2019). New-age satellite-based navigation – STAN: simultaneous tracking and navigation with LEO satellite signals. *Inside GNSS Magazine*, 14(4):56–65.

Kassas, Z., Neinavaie, M., Khalife, J., Khairallah, N., Haidar-Ahmad, J., Kozhaya, S., and Shadram, Z. (2021). Enter LEO on the GNSS stage: Navigation with Starlink satellites. *Inside GNSS Magazine*, 16(6):42–51.

Khalife, J. and Kassas, Z. (2022). On the achievability of submeter-accurate UAV navigation with cellular signals exploiting loose network synchronization. *IEEE Transactions on Aerospace and Electronic Systems*. accepted.

Khalife, J., Neinavaie, M., and Kassas, Z. (2022). The first carrier phase tracking and positioning results with Starlink LEO satellite signals. *IEEE Transactions on Aerospace and Electronic Systems*, 56(2):1487–1491.

Khalife, J., Shamaei, K., and Kassas, Z. (2018). Navigation with cellular CDMA signals – part I: Signal modeling and software-defined receiver design. *IEEE Transactions on Signal Processing*, 66(8):2191–2203.

Lapin, I., Granados, G., Samson, J., Renaudin, O., Zanier, F., and Ries, L. (2022). STARE: Real-time software receiver for LTE and 5G NR positioning and signal monitoring. In *Proceedings of Workshop on Satellite Navigation Technology*, pages 1–11.

Ledvina, B., Powell, S., Kintner, P., and Psiaki, M. (2003). A 12-Channel Real-Time GPS L1 Software Receiver. In *Proceedings of the 2003 National Technical Meeting of The Institute of Navigation*, pages 767–782. Institute of Navigation.

Ledvina, B., Psiaki, M., Humphreys, T., Powell, S., and Kintner, P. (2006a). A Real-Time Software Receiver for the GPS and Galileo L1 Signals. In *Proceedings of the 19th International Technical Meeting of the Satellite Division of The Institute of Navigation (ION GNSS 2006)*, pages 2321–2333. Institute of Navigation.

Ledvina, B., Psiaki, M., Powell, S., and Kintner, P. (2004a). Bit-Wise Parallel Algorithms for Efficient Software Correlation Applied to a GPS Software Receiver. *IEEE Transactions on Wireless Communications*, 3(5):1469–1473.

Ledvina, B., Psiaki, M., Powell, S., and Kintner, P. (2006b). Real-Time Software Receiver; US patent no. 7010060, 2006-03-07.

Ledvina, B., Psiaki, M., Powell, S., and Kintner, P. (2007). Real-Time Software Receiver; US patent no. 7305021; 2007-12-04.

Ledvina, B., Psiaki, M., Sheinfeld, D., Cerruti, A., Powell, S., and Kintner, P. (2004b). A Real-Time GPS Civilian L1/L2 Software Receiver. In *Proceedings of the 17th International Technical Meeting of the Satellite Division of The Institute of Navigation (ION GNSS 2004)*, pages 986–1005. Institute of Navigation.

Lightsey, G., Humphreys, T., Bhatti, J., Joplin, A., O'Hanlon, B., and Powell, S. (2014). Demonstration of a Space Capable Miniature Dual Frequency GNSS Receiver. *NAVIGATION, Journal of the Institute of Navigation*, 61(1):53–64.

Locubiche-Serra, S., López-Salcedo, J. A., and Seco-Granados, G. (2016). Statistical near-far detection techniques for GNSS snapshot receivers. In *2016 IEEE International Conference on Acoustics, Speech and Signal Processing (ICASSP)*, pages 6570–6574. IEEE.

LocusLock (2022). Reliable, accurate, and intelligent GPS LOCK. `https://locuslock.com`. [Accessed on 2022-09-30].

López-Salcedo, J., Capelle, Y., Toledo, M., Seco, G., Vicario, J. L., Kubrak, D., Monnerat, M., Mark, A., and Jiménez, D. (2008). DINGPOS: a hybrid indoor navigation platform for GPS and Galileo. In *Proceedings of the 21st International Technical Meeting of the Satellite Division of The Institute of Navigation (ION GNSS 2008)*, pages 1780–1791.

López-Salcedo, J. A., Parro-Jiménez, J. M., and Seco-Granados, G. (2009). Multipath detection metrics and attenuation analysis using a GPS snapshot receiver in harsh environments. In *2009 3rd European Conference on Antennas and Propagation (EuCAP)*, pages 3692–3696.

Lucas-Sabola, V., Seco-Granados, G., López-Salcedo, J. A., García-Molina, J., and Crisci, M. (2017). Efficiency analysis of cloud GNSS signal processing for IoT applications. In *Proceedings of the 30th International Technical Meeting of the Satellite Division of The Institute of Navigation (ION GNSS+ 2017)*, pages 3843–3852.

Lucas-Sabola, V., Seco-Granados, G., López-Salcedo, J. A., García-Molina, J. A., and Crisci, M. (2016). Cloud GNSS receivers: New advanced applications made possible. In *2016 International Conference on Localization and GNSS (ICL-GNSS)*, pages 1–6. IEEE.

Maaref, M. and Kassas, Z. (2020). Ground vehicle navigation in GNSS-challenged environments using signals of opportunity and a closed-loop map-matching approach. *IEEE Transactions on Intelligent Transportation Systems*, 21(7):2723–2723.

Maaref, M. and Kassas, Z. (2022). Autonomous integrity monitoring for vehicular navigation with cellular signals of opportunity and an IMU. *IEEE Transactions on Intelligent Transportation Systems*, 23(6):5586–5601.

Maaref, M., Khalife, J., and Kassas, Z. (2019). Lane-level localization and mapping in GNSS-challenged environments by fusing lidar data and cellular pseudoranges. *IEEE Transactions on Intelligent Vehicles*, 4(1):73–89.

Manzano-Jurado, M., Alegre-Rubio, J., Pellacani, A., Seco-Granados, G., López-Salcedo, J. A., Guerrero, E., and García-Rodríguez, A. (2014). Use of weak GNSS signals in a mission to the moon. In *2014 7th ESA Workshop on Satellite Navigation Technologies and European Workshop on GNSS Signals and Signal Processing (NAVITEC)*, pages 1–8. IEEE.

Margaria, D., Linty, N., Favenza, A., Nicola, M., Musumeci, L., Falco, G., Falletti, E., Pini, M., Fantino, M., and Dovis, F. (2012). Contact! - first acquisition and tracking of IOV galileo signals. *Inside GNSS*, 7:45–55.

McEllroy, J. (2006). Navigation using signals of opportunity in the AM transmission band. Master's thesis, Air Force Institute of Technology, Wright-Patterson Air Force Base, Ohio, USA.

McEllroy, J., Raquet, J., and Temple, M. (2006). Use of a software radio to evaluate signals of opportunity for navigation. In *Proceedings of the 19th International Technical Meeting of the Satellite Division of The Institute of Navigation (ION GNSS 2006)*, pages 126–133.

Minetto, A., Dovis, F., Vesco, A., Garcia-Fernandez, M., López-Cruces, À., Trigo, J. L., Molina, M., Pérez-Conesa, A., Gáñez-Fernández, J., Seco-Granados, G., et al. (2020). A testbed for GNSS-based positioning and navigation technologies in smart cities: The HANSEL project. *Smart Cities*, 3(4):1219–1241.

Ministry of Science and ICT of Korea (2021). Launch to Become the World's Seventh 'Space Powerhouse'! `https://www.msit.go.kr/bbs/view.do?sCode=eng&mId=4&mPid=2&bbsSeqNo=42&nttSeqNo=568`. [Accessed on 14-Sep-2022].

Mitola, J. (1995). The software radio architecture. *IEEE Communications Magazine*, 33(5):26–38.

Molino, A., Nicola, M., Pini, M., and Fantino, M. (2009). N-GENE GNSS software receiver for acquisition and tracking algorithms validation. In *European Signal Processing Conference*, pages 2171–2175.

Morales, J. and Kassas, Z. (2021). Tightly-coupled inertial navigation system with signals of opportunity aiding. *IEEE Transactions on Aerospace and Electronic Systems*, 57(3):1930–1948.

Morton, Y., Jiao, Y., and Taylor, S. (2015). High-latitude and equatorial ionospheric scintillation based on an event-driven multi-gnss data collection system. *Proc. Ionospheric Effect Sym., Alexandria, Va*.

Murrian, M. J., Narula, L., Iannucci, P. A., Budzien, S., O'Hanlon, B. W., Powell, S. P., and Humphreys, T. E. (2021). First results from three years of GNSS interference monitoring from low Earth orbit. *Navigation, Journal of the Institute of Navigation*, 68(4):673–685.

Nardin, A., Dovis, F., and Fraire, J. (2021). Empowering the tracking performance of LEO-based positioning by means of meta-signals. *IEEE Journal of Radio Frequency Identification*, 5(3):244–253.

Neinavaie, M., Khalife, J., and Kassas, Z. (2021). Acquisition, Doppler tracking, and positioning with Starlink LEO satellites: First results. *IEEE Transactions on Aerospace and Electronic Systems*, 58(3):2606–2610.

Nichols, H. A., Murrian, M. J., and Humphreys, T. E. (2022). Software-defined GNSS is ready for launch. In *Proceedings of the ION GNSS+ Meeting*.

Nicola, M., Motella, B., Pini, M., and Falletti, E. (2022). Galileo osnma public observation phase: Signal testing and validation. *IEEE Access*, 10:27960–27969.

NTLAB, UAB (2022). Unique ICs for GNSS Receivers. `https://ntlab.lt/`. [Accessed on 2022-09-26].

O'Hanlon, B. W., Psiaki, M. L., Powell, S., Bhatti, J. A., Humphreys, T. E., Crowley, G., and Bust, G. S. (2011). Cases: A smart, compact gps software receiver for space weather monitoring. In *Proceedings of the 24th International Technical Meeting of The Satellite Division of the Institute of Navigation (ION GNSS 2011)*, pages 2745–2753.

Orabi, M., Khalife, J., and Kassas, Z. (2021). Opportunistic navigation with Doppler measurements from Iridium Next and Orbcomm LEO satellites. In *Proceedings of IEEE Aerospace Conference*, pages 1–9.

Pany, T., Dötterböck, D., Gomez-Martinez, H., Hammed, M. S., Hörkner, F., Kraus, T., Maier, D., Sanchez-Morales, D., Schütz, A., Klima, P., and Ebert, D. (2019). The multi-sensor navigation analysis tool (MuSNAT) – architecture, LiDAR, GPU/CPU GNSS signal processing. In *Proceedings of the 32nd International Technical Meeting of the Satellite Division of The Institute of Navigation (ION GNSS+ 2019)*, pages 4087–4115. Institute of Navigation.

Pany, T., Eissfeller, B., Hein, G., Moon, S., and Sanroma, D. (2004a). IPEXSR: A PC based software GNSS receiver completely developed in Europe. In *Proc. ENC-GNSS 2004*.

Pany, T., Förster, F., and Eissfeller, B. (2004b). Real-time processing and multipath mitigation of high-bandwidth l1/l2 gps signals with a pc-based software receiver. In *Proceedings of the 17th International Technical Meeting of the Satellite Division of The Institute of Navigation (ION GNSS 2004)*, pages 971–985.

Pany, T., Kaniuth, R., and Eissfeller, B. (2005). Deep integration of navigation solution and signal processing. In *Proceedings of the 18th International Technical Meeting of the Satellite Division of The Institute of Navigation (ION GNSS 2005)*, pages 1095–1102.

Pany, T., Moon, S. W., Irsigler, M., Eissfeller, B., and Fürlinger, K. (2003). Performance assessment of an under-sampling swc receiver for simulated high-bandwidth gps/galileo signals and real signals. In *Proceedings of the 16th International Technical Meeting of the Satellite Division of The Institute of Navigation (ION GPS/GNSS 2003)*, pages 103–116.

Pany, T., Riedl, B., Winkel, J., Wörz, T., Schweikert, R., Niedermeier, H., Lagrasta, S., López-Risueño, G., and Jiménez-Baños, D. (2009). Coherent integration time: The longer, the better. *Inside GNSS*, 4(6):52–61.

Peng, S. and Morton, Y. (2011). A usrp2-based multi-constellation and multi-frequency gnss software receiver for ionosphere scintillation studies. In *Proceedings of the 2011 International Technical Meeting of The Institute of Navigation*, pages 1033–1042.

Pesyna, K., Kassas, Z., Bhatti, J., and Humphreys, T. (2011). Tightly-coupled opportunistic navigation for deep urban and indoor positioning. In *Proceedings of ION GNSS Conference*, pages 3605–3617.

Pesyna, Jr., K. M., Heath, Jr., R. W., and Humphreys, T. E. (2014). Centimeter positioning with a smartphone-quality GNSS antenna. In *Proceedings of the ION GNSS+ Meeting*.

Pinell, C. (2021). Receiver architectures for positioning with low Earth orbit satellite signals. Master's thesis, Lulea University of Technology, School of Electrical Engineering, Sweden.

Plotly (2022). Plotly JSON chart schema. `https://plotly.com/chart-studio-help/json-chart-schema/`. [Accessed on 09/30/2022].

PR Newswire (2021). New Trimble DA2 Receiver Boosts Performance of Trimble Catalyst GNSS Positioning Service. `https://www.prnewswire.com/news-releases/new-trimble-da2-receiver-boosts-performance-of-trimble-catalyst-gnss-positioning-service-301381160.html`. [Accessed on 2022-09-29].

Psiaki, M. (2006). Real-Time Generation of Bit-Wise Parallel Representations of Over-Sampled PRN Codes. *IEEE Transactions on Wireless Communications*, 5(3):487–491.

Psiaki, M., Humphreys, T., Mohiuddin, S., Powell, S., Cerruti, A., and Kintner, P. (2006). Searching for Galileo. In *Proceedings of the 19th International Technical Meeting of the Satellite Division of The Institute of Navigation (ION GNSS 2006)*, pages 1567–1575. Institute of Navigation.

Psiaki, M. and Slosman, B. (2022). Tracking digital FM OFDM signals for the determination of navigation observables. *NAVIGATION, Journal of the Institute of Navigation*, 69(2).

RF Micro Devices, Inc., Greensboro (2006). RFMD Announces Availability of the RFMD(R) GPS RF8110 Scalable GPS Solution. `https://ir.qorvo.com/node/12736/pdf`. [Accessed on 2022-09-29].

Rügamer, A., Förster, F., Stahl, M., and Rohmer, G. (2012). A Flexible and Portable Multiband GNSS front-end System. In *Proceedings of the 25th International Technical Meeting of the Satellite Division of The Institute of Navigation (ION GNSS 2012)*, pages 2378–2389. Institute of Navigation.

Rügamer, A., Rubino, D., Lukcin, I., Taschke, S., Stahl, M., and Felber, W. (2016). Secure position and time information by server side PRS snapshot processing. In *Proceedings of the 29th International Technical Meeting of the Satellite Division of the Institute of Navigation (ION GNSS+ 2016)*, pages 3002–3017.

Santana, G., de Cristo, R., and Branco, K. (2021). Integrating cognitive radio with unmanned aerial vehicles: An overview. *Sensors*, 21(3):830–856.

Seco-Granados, G., López-Salcedo, J. A., Jiménez-Baños, D., and López-Risueño, G. (2012). Challenges in indoor global navigation satellite systems: Unveiling its core features in signal processing. *IEEE Signal Processing Magazine*, 29(2):108–131.

Shamaei, K. and Kassas, Z. (2018). LTE receiver design and multipath analysis for navigation in urban environments. *NAVIGATION, Journal of the Institute of Navigation*, 65(4):655–675.

Shamaei, K. and Kassas, Z. (2021a). A joint TOA and DOA acquisition and tracking approach for positioning with LTE signals. *IEEE Transactions on Signal Processing*, pages 2689–2705.

Shamaei, K. and Kassas, Z. (2021b). Receiver design and time of arrival estimation for opportunistic localization with 5G signals. *IEEE Transactions on Wireless Communications*, 20(7):4716–4731.

Shamaei, K., Khalife, J., and Kassas, Z. (2018). Exploiting LTE signals for navigation: Theory to implementation. *IEEE Transactions on Wireless Communications*, 17(4):2173–2189.

Snyder, C., Feng, G., and Van Graas, F. (1999). GPS Anomalous Event Monitor (GAEM). In *Proceedings of the 55th Annual Meeting of The Institute of Navigation (ION AM 1999)*, pages 185–189. Institute of Navigation.

Söderholm, S., Bhuiyan, M., Thombre, S., Ruotsalainen, L., and Kuusniemi, H. (2016). A Multi-GNSS Software-defined Receiver: Design, Implementation, and Performance Benefits. *Annals of Telecommunications*, 71:399–410.

Soloviev, A., Gunawardena, S., and Van Graas, F. (2004). Deeply Integrated GPS/Low-Cost IMU for Low CNR Signal Processing: Flight Test Results and Real Time Implementation. In *Proceedings of the 17th International Technical Meeting of the Satellite Division of The Institute of Navigation (ION GNSS 2004)*, pages 1598–1608. Institute of Navigation.

Song, Y. J., Lee, H. B., and Won, J. H. (2021). Design of multi-constellation and multi-frequency gnss sdr with fully reconfigurable functionality. *Journal of Positioning, Navigation, and Timing*, 10(2):91–102.

Souli, N., Kolios, P., and Ellinas, G. (2020). Relative positioning of autonomous systems using signals of opportunity. In *Proceedings of IEEE Vehicular Technology Conference*, pages 1–6.

Souli, N., Kolios, P., and Ellinas, G. (2021). Online relative positioning of autonomous vehicles using signals of opportunity. *IEEE Transactions on Intelligent Vehicles*, pages 1–1.

Souli, N., Kolios, P., and Ellinas, G. (2022). Adaptive frequency band selection for accurate and fast positioning utilizing SOPs. In *Proceedings of International Conference on Unmanned Aircraft Systems*, pages 1309–1315.

SPCOMNAV (2019). Cloud GNSS Receiver. `http://cloudGNSSrx.com`. [Accessed on 23-Sep-2022].

Stöber, C., Anghileri, M., Ayaz, A. S., Dötterböck, D., Krämer, I., Kropp, V., Won, J.-H., Eissfeller, B., Güixens, D. S., and Pany, T. (2010). ipexsr: A real-time multi-frequency software gnss receiver. In *Proceedings ELMAR-2010*, pages 407–416. IEEE.

Takasu, T. and Yasuda, A. (2009). Development of the low-cost RTK-GPS receiver with an open source program package RTKLIB. In *International symposium on GPS/GNSS*, volume 1. International Convention Center Jeju Korea.

Tang, G. and Peng, A. (2022). 5G receiver design based on downlink intermittent signals tracking algorithm. In *Proceedings of China Satellite Navigation Conference*, pages 462–471.

TeleOrbit GmbH (2022). MGSE REC: GNSS Radio Frequency Front-End. `https://teleorbit.eu/en/satnav/mgse-rec/`. [Accessed on 09/06/2022].

Teunissen, P. J. and Montenbruck, O., editors (2017). *Receiver Architecture*, pages 365–400. Springer International Publishing, Cham.

Thombre, S., Bhuiyan, M., Söderholm, S., Kirkko-Jaakkola, M., Ruotsalainen, L., and Kuusniemi, H. (2015). A Software Multi-GNSS Receiver Implementation for the Indian Regional Navigation Satellite System. *IETE Journal of Research*, pages 246–256.

Trimble Inc. (2005). Trimble Introduces Future-Ready GNSS Positioning Technology. `https://investor.trimble.com/news-releases/news-release-details/trimble-introduces-future-ready-gnss-positioning-technology`. [Accessed on 2022-09-29].

Trimble Inc. (2017). Trimble DA1 Catalyst GNSS Systems . `https://geospatial.trimble.com/products-and-solutions/trimble-da1`. [Accessed on 2022-09-29].

Troglia Gamba, M., Marucco, G., Pini, M., Ugazio, S., Falletti, E., and Lo Presti, L. (2015a). Prototyping a gnss-based passive radar for uavs: An instrument to classify the water content feature of lands. *Sensors*, 15(11):28287–28313.

Troglia Gamba, M., Nicola, M., and Falletti, E. (2015b). eNGene: An ARM based embedded real-time software GNSS receiver. In *28th International Technical Meeting of the Satellite Division of the Institute of Navigation, ION GNSS 2015*, volume 4, pages 3178–3187.

Troglia Gamba, M., Nicola, M., and Motella, B. (2020a). Galileo osnma: An implementation for arm-based embedded platforms. In *2020 International Conference on Localization and GNSS, ICL-GNSS 2020 - Proceedings*, page 1–6.

Troglia Gamba, M., Nicola, M., and Motella, B. (2020b). Gps chimera: A software profiling analysis. In *Proceedings of the 33rd International Technical Meeting of the Satellite Division of the Institute of Navigation, ION GNSS+ 2020*, pages 3781–3793.

Tsui, J. B.-Y. (2000). *Fundamentals of Global Positioning System Receivers: A Software Approach*. Wiley-Interscience.

UniBwM (2022). MuSNAT — LRT 9. `https://www.unibw.de/lrt9/lrt-9.2/software-packages/musnat`. [Accessed on 07/04/2022].

Van Diggelen, F. (2009). *A-GPS: Assisted GPS, GNSS, and SBAS*. Artech House.

Wang, P., Wang, Y., and Morton, J. (2022). Signal tracking algorithm with adaptive multipath mitigation and experimental results for LTE positioning receivers in urban environments. *IEEE Transactions on Aerospace and Electronic Systems*, 58(4):2779–2795.

Wikipedia (2022). GNSS software-defined receiver. `https://en.wikipedia.org/wiki/GNSS_software-defined_receiver`. [Accessed 27-Jun-2022].

Wikipedia (2022). JSON streaming. `https://en.wikipedia.org/wiki/JSON_streaming`. [Accessed on 09/30/2022].

Yang, C., Arizabaleta-Diez, M., Weitkemper, P., and Pany, T. (2022). An experimental analysis of cyclic and reference signals of 4g LTE for TOA estimation and positioning in mobile fading environments. *IEEE Aerospace and Electronic Systems Magazine*, 37(9):16–41.

Yang, C. and Soloviev, A. (2018). Positioning with mixed signals of opportunity subject to multipath and clock errors in urban mobile fading environments. In *Proceedings of ION GNSS Conference*, pages 223–243.

Yang, C. and Soloviev, A. (2020). Mobile positioning with signals of opportunity in urban and urban canyon environments. In *Proceedings of IEEE/ION Position, Location, and Navigation Symposium*, pages 1043–1059.

Yoder, J. E. and Humphreys, T. E. (2022). Low-cost inertial aiding for deep-urban tightly-coupled multi-antenna precise GNSS. *Navigation, Journal of the Institute of Navigation*. To be published.

Zhang, X. (2022). GitHub - TMBOC/SoftGNSS: Current working ver. of SoftGNSS v3.0 for GN3sV2, GN3sV3, NT1065EVK, and NUT4NT samplers. `https://github.com/TMBOC/SoftGNSS`. [Accessed on 2022-09-09].

Zhao, C., Qin, H., and Li, Z. (2022). Doppler measurements from multiconstellations in opportunistic navigation. *IEEE Transactions on Instrumentation and Measurement*, 71:1–9.

Zhu, Z. and Van Graas, F. (2009). Earth-Surface Multipath Detection and Error Modeling for Aircraft GPS Receivers. *NAVIGATION: Journal of the Institute of Navigation*, 56(1):45–56.

Ground Vehicle Navigation Integrity Monitoring for Multi-Constellation GNSS Fused with Cellular Signals of Opportunity

Mu Jia[1], Halim Lee[2], Joe Khalife[1], Zaher M. Kassas[1], and Jiwon Seo[2]

Abstract— **Integrity monitoring of a ground vehicle navigation system, utilizing multi-constellation global navigation satellite systems (GNSS) signals fused with ambient cellular signals of opportunity (SOPs) is considered. An advanced receiver autonomous integrity monitoring (ARAIM) framework is developed to detect and exclude multipath and non-line-of-sight errors. A method to conservatively predict the horizontal protection level (HPL) is proposed, utilizing ray-tracing and channel impulse response prediction in a three-dimensional (3D) building map of the environment. Simulation results are presented demonstrating the conservatively predicted HPL with different signals (GPS-only, GPS+GLONASS, GPS+SOP, and GPS+GLONASS+SOP). Experimental results are presented for a ground vehicle navigating a trajectory of 1380 m in an urban environment, showing the availability rates for GPS-only, GPS+GLONASS, GPS+SOP, and GPS+GLONASS+SOP being 52.53%, 75.66%, 76.87%, and 80.72%, respectively.**

I. Introduction

Passenger safety in ground vehicles depend on the accuracy and reliability of the vehicle's navigation system. This is particularly the case for semi- and fully-automated vehicles. Ground vehicle navigation systems utilize global navigation satellite systems (GNSS) receivers and a suite of onboard sensors, e.g., lidar, camera, radar, inertial navigation system (INS), etc. GNSS are relied upon to provide a navigation solution in a global frame and to correct for accumulating errors due to sensor dead reckoning.

While achieving higher levels of navigation accuracy has been a classic requirement, the trustworthiness in the navigation solution, commonly assessed by integrity measures, is evermore vital in the safety critical application of automated driving. To ensure safe navigation, automated vehicles need to tightly bound the navigation errors and ensure that the probability of navigation errors being not properly bounded is below a certain limit. Current GNSS technologies are insufficient to support the transition of ground vehicles to full automation in terms of accuracy, integrity, and availability [1]. In terms of accuracy, sub-meter-level accuracy is achievable with certain augmentation systems and real-time kinematic (RTK) only under certain favorable conditions [2]; while single point positioning (SPP) can only achieve meter-level accuracy [3]. In terms of integrity and availability, recent work demonstrated that in a sample downtown environment (Chicago urban corridor), availability of GPS-only positioning was less than 10% at most locations. While using multi-constellation GNSS (GPS, GLONASS, Galileo, and Beidou) improved the availability significantly, it was still lower than 80% at certain points; concluding that multi-constellation GNSS cannot provide continuous vehicle positioning along the street [4].

Recently, signals of opportunity (SOPs), e.g., cellular signals [5] and digital television signals [6], have been been demonstrated as an attractive alternative or supplement to GNSS signals. SOPs could provide a navigation solution in a global frame in a standalone fashion [7], [8] or aid dead reckoning sensors (e.g., INS [9]). For vehicular navigation in urban environments, cellular SOPs are particularly attractive due to their inherent attributes: abundance, geometric and spectral diversity, high received power, and large bandwidth. When used alongside GNSS signals, SOPs could improve the accuracy, integrity, and availability of the navigation system.

GNSS-based integrity monitoring has been studied extensively [10]. Among the proposed frameworks, receiver autonomous integrity monitoring (RAIM) is exceptionally attractive, as it is cost-effective and does not require building additional infrastructure [11]. RAIM has been adapted to account for multi-constellation GNSS measurements [12] (e.g. Galileo [13], GLONASS [14], and Beidou [15]), aiding sensors (e.g., INS-GPS [16], lidar-GNSS [17], and vision-GPS [18]), and terrestrial SOPs [19], [20]. An initial study to characterize the integrity monitoring improvement for automated driving, upon fusing GPS signals with terrestrial SOPs, was conducted in [21]. However, this study assumed fault-free measurements, which is not realistic in urban environments, in which multipath effects and non-line-of-sight (NLOS) conditions are prevalent. In [22], the protection level reduction due to fusing GPS and terrestrial SOPs was studied; however, multipath and NLOS effects in GNSS and SOP measurements were not explicitly considered.

This paper makes three contributions. First, an advanced RAIM (ARAIM) framework is proposed to incorporate multi-constellation GNSS and cellular long-term evolution (LTE) SOPs. Second, a method to conservatively predict the horizontal protection level (HPL) is proposed, utilizing ray-tracing and channel impulse response prediction in a three-dimensional (3D) building map of the environment. Third, simulation and experimental results are presented demonstrating the efficacy of fusing multi-constellation GNSS with cellular terrestrial SOPs in terms of reducing the HPL.

The rest of this paper is organized as follows. Section II

This work was supported in part by the U.S. Department of Transportation (USDOT) under Grant 69A3552047138 for the CARMEN University Transportation Center (UTC) and in part by the National Science Foundation (NSF) under Grant 1929965.

[1]Department of Mechanical and Aerospace Engineering, University of California, Irvine, muj2@uci.edu, khalifej@uci.edu, zkassas@ieee.org

[2]School of Integrated Technology, Yonsei University, Korea, halim.lee@yonsei.ac.kr, jiwon.seo@yonsei.ac.kr

describes the GNSS and cellular SOP pseudorange measurement models and estimator used to fuse these measurements. Section III formulates the method to conservatively predict the HPL. Section IV presents simulation and experimental results. Section V gives concluding remarks.

II. Model Description

This section describes the GNSS and cellular pseudorange measurement models and the weighted nonlinear least square (WNLS) estimator used to estimate the vehicle's position. Furthermore, this section provides an overview of the ARAIM algorithm for integrity monitoring with multi-constellation GNSS and cellular SOPs.

A. GNSS Pseudorange Measurement Model

The ground vehicle-mounted receiver makes pseudorange measurements to M GNSS satellites from N_{const} GNSS constellations. Let $i \in \{1, \ldots, N_{\text{const}}\}$ denote the index of the constellation to which the m-th GNSS satellite belongs. The m-th GNSS pseudorange measurement at time-step k, after compensating for ionospheric delays, tropospheric delays, and the satellite's clock bias, is modeled as

$$\begin{aligned} z_{\text{GNSS}_m}(k) =& \|\boldsymbol{r}_r(k) - \boldsymbol{r}_{\text{GNSS}_m}(k)\|_2 + c \cdot \delta t_{r,i}(k) \\ &+ b_{\text{GNSS}_m}(k) + v_{\text{GNSS}_m}(k), \end{aligned} \tag{1}$$

where $z_{\text{GNSS}_m}(k) = z'_{\text{GNSS}_m}(k) + c\hat{\delta}t_{\text{GNSS}_m}(k) - c \cdot \hat{\delta}t_{\text{iono}}(k) - c \cdot \hat{\delta}t_{\text{tropo}}(k)$; $z'_{\text{GNSS}_m}(k)$ is the pseudorange from the m-th GNSS satellite before corrections; c is the speed of light; $\hat{\delta}t_{\text{GNSS}_m}(k)$ is the m-th GNSS satellite's clock bias estimate; $\hat{\delta}t_{\text{iono}}(k)$ and $\hat{\delta}t_{\text{tropo}}(k)$ are the estimated ionospheric and tropospheric delays, respectively; $\boldsymbol{r}_r(k)$ and $\boldsymbol{r}_{GNSS_m}(k)$ are the receiver and m-th satellite's 3D position vectors, respectively; $\delta t_{r,i}(k)$ is the receiver's clock bias with respect to the i-th GNSS constellation's reference time; $b_{\text{GNSS}_m}(k)$ is the bias caused by multipath interference and/or NLOS effects; and v_{GNSS_m} is the measurement noise, which is modeled as a zero-mean, white Gaussian sequence with variance $\sigma^2_{\text{GNSS}_m}$. The prediction of $b_{\text{GNSS}_m}(k)$ via ray-tracing simulations is addressed in Section III-A.

B. Cellular SOP Pseudorange Measurement Model

The ground vehicle-mounted receiver also makes pseudorange measurements from N cellular base stations, which are assumed to be stationary with known positions. The n-th SOP measurement at time-step k can be modeled as

$$\begin{aligned} \bar{z}_{\text{SOP}_n} =& \|\boldsymbol{r}_r(k) - \boldsymbol{r}_{\text{SOP}_n}\|_2 + c \cdot [\bar{\delta}t_{r,\text{SOP}}(k) \\ &- \delta t_{\text{SOP}_n}(k)] + b_{\text{SOP}_n}(k) + \bar{v}_{\text{SOP}_n}(k), \end{aligned} \tag{2}$$

where $\boldsymbol{r}_{\text{SOP}_n}$ and $\delta t_{\text{SOP}_n}(k)$ are the position and clock bias of the n-th SOP transmitter with respect to cellular system time, respectively; $\bar{\delta}t_{r,\text{SOP}}(k)$ is the the receiver's clock bias with respect to cellular system time; $b_{\text{SOP}_n}(k)$ is the bias caused by multipath interference and/or NLOS effects for the SOP; and $\bar{v}_{\text{SOP}_n}$ is the measurement noise, which is modeled as a zero-mean white Gaussian sequence with variance $\sigma^2_{\text{user,SOP}_n}$. Based on [23], the difference $c \cdot [\bar{\delta}t_{r,\text{SOP}}(k) - \delta t_{\text{SOP}_n}(k)]$ can be modeled as

$$\begin{aligned} c \cdot [\bar{\delta}t_{r,\text{SOP}}(k) - \delta t_{\text{SOP}_n}(k)] =& c\delta t_{r,\text{SOP}}(k) + c\delta t_{\text{SOP}_n,0} \\ &+ \epsilon_n(k), \end{aligned} \tag{3}$$

where $c\delta t_{r,\text{SOP}}(k)$ is a common term driving the difference between the receiver and SOP clock biases, $c\delta t_{\text{SOP}_n,0}$ is an initial bias, and $\epsilon_n(k)$ is an error term modeled as a zero-mean Gaussian random variable with variance $\sigma^2_{\epsilon_n}$. It is assumed that the initial biases $\left\{c\delta t_{\text{SOP}_n,0}\right\}_{n=1}^{N}$ were calibrated prior to integrity monitoring. Finally, after initial bias calibration, the n-th SOP pseudorange measurement z_{SOP_n} can be expressed as

$$\begin{aligned} z_{\text{SOP}_n} =& \|\boldsymbol{r}_r(k) - \boldsymbol{r}_{\text{SOP}_n}(k)\|_2 + c\delta t_{r,\text{SOP}}(k) \\ &+ b_{\text{SOP}_n}(k) + v_{\text{SOP}_n}(k), \end{aligned} \tag{4}$$

where $v_{\text{SOP}_n}(k) \triangleq \epsilon_n(k) + \bar{v}_{\text{SOP}_n}(k)$. The variances for the noise terms are characterized in [22]. The prediction of the bias term for SOPs is discussed in Section III-B.

C. Navigation Solution

The ground vehicle estimates its position vector using GNSS and SOP pseudorange measurements via a WNLS. The vector to be estimated is given by

$$\boldsymbol{x}(k) \triangleq \left[\boldsymbol{r}_r{}^{\mathsf{T}}(k), c\delta t_{r,1}(k), \ldots, c\delta t_{r,N_{\text{const}}}(k), c\delta t_{r,\text{SOP}}(k)\right]^{\mathsf{T}}.$$

The time argument is omitted in the following for compactness of notation. The all-in-view combined GNSS-SOP measurement vector can be formed according to

$$\boldsymbol{z} \triangleq \left[z_{\text{GNSS}_1}, \ldots, z_{\text{GNSS}_M}, z_{\text{SOP}_1}, \ldots, z_{\text{SOP}_N}\right]^{\mathsf{T}}.$$

A WNLS is then iterated to obtain an estimate of $\boldsymbol{x}$, denoted by $\hat{\boldsymbol{x}}$, using $\boldsymbol{z}$. Let h denote the iteration number, $\hat{\boldsymbol{x}}_h$ the estimate at iteration h, and $\hat{\boldsymbol{z}}_h$ the measurement prediction calculated using $\hat{\boldsymbol{x}}_h$. The all-in-view navigation solution update is obtained from the normal equations according to

$$\Delta\boldsymbol{x}_h = \left(\mathbf{H}_h{}^{\mathsf{T}}\mathbf{W}\mathbf{H}_h\right)^{-1}\mathbf{H}_h{}^{\mathsf{T}}\mathbf{W}\left(\boldsymbol{z} - \hat{\boldsymbol{z}}_h\right), \tag{5}$$

where $\mathbf{H}_h$ is the measurement Jacobian evaluated at $\hat{\boldsymbol{x}}_h$ and $\mathbf{W}$ is the weight matrix. The weight matrix is given by $\mathbf{W} = \mathbf{C}_{\text{int}}^{-1}$, where $\mathbf{C}_{\text{int}}$ is a diagonal matrix whose diagonal elements $\left\{\mathbf{C}_{\text{int}}(j,j)\right\}_{j=1}^{N+M}$ are the measurement noise variances used for integrity. The WNLS estimate at the $(h+1)$-th iteration is updated according to

$$\hat{\boldsymbol{x}}_{h+1} = \hat{\boldsymbol{x}}_h + \Delta\boldsymbol{x}_h,$$

and the iteration number is subsequently increased according to $h \leftarrow h + 1$. After convergence, the all-in-view navigation solution is denoted $\hat{\boldsymbol{x}}^{(\infty)}$, the measurement prediction after convergence is denoted $\hat{\boldsymbol{z}}^{(\infty)}$, and the residual at convergence is denoted $\boldsymbol{y}$, which is given by

$$\boldsymbol{y} \triangleq \boldsymbol{z} - \hat{\boldsymbol{z}}^{(\infty)}.$$

Let $\mathbf{H}$ denote the measurement Jacobian after convergence. $\mathbf{H}$ is an $(N+M) \times (3 + N_{\text{const}} + 1)$ matrix, which can be

parameterized by the GNSS satellites and SOP transmitters' azimuth and elevation angles as $\mathbf{H} \triangleq [\mathbf{G}, \mathbf{B}]$, where $\mathbf{G}$ is the geometry matrix, and $\mathbf{B}$ is the time matrix. The j-th row of $\mathbf{G}$ matrix can be defined as

$$\mathbf{G}_j \triangleq \left[-c(El_j)s(Az_j) \ -c(El_j)c(Az_j) \ -s(El_j)\right],$$

where $c(\cdot)$ and $s(\cdot)$ denote the $\cos(\cdot)$ and $\sin(\cdot)$ functions, respectively, and El_j and Az_j are elevation angle and azimuth angle, respectively, of j-th GNSS satellite or cellular base station. The clock bias Jacobian $\mathbf{B}$ can be expressed as

$$\mathbf{B} \triangleq \begin{bmatrix} \mathbf{B}' & \mathbf{0}_{M\times 1} \\ \mathbf{0}_{N\times N_{\text{const}}} & \mathbf{1}_{N\times 1} \end{bmatrix}, \tag{6}$$

where $\mathbf{B}'$ is an $M \times N_{\text{const}}$ matrix denoting the GNSS clock bias Jacobian, whose m, i-th entry, denoted by B'_{mi}, is

$$B'_{mi} = \begin{cases} 1 & \text{if } m\text{-th satellite belongs to } i\text{-th constellation,} \\ 0 & \text{otherwise.} \end{cases}$$

D. ARAIM with SOP Framework

This article extends the ARAIM with SOP framework proposed in [22] to incorporate multi-constellation GNSS and pseudorange measurements. ARAIM performs fault detection and exclusion (FDE) and HPL calculation based on the multiple hypothesis solution separation (MHSS) algorithm. The reasons for choosing ARAIM are twofold: (i) flexibility of the multiple-source ARAIM framework allows it to incorporate pseudorange measurements from different GNSS constellations and SOPs and (ii) due to the high probability of large biases caused by NLOS and multipath interference in urban environments, multiple faults should be considered.

III. Conservative HPL Prediction

This section describes the proposed method to analyze the performance of the ARAIM with SOP framework in an urban environment. The framework predicts conservative HPLs using ray-tracing simulations with 3D city models. The availability of high quality 3D models has enabled the performance evaluation of GNSS in urban canyons [24]. Ray-tracing has been utilized to predict signal propagation and visibility in mobile and wireless communication systems, and to estimate multipath and NLOS biases [25]. Conservative HPLs were also predicted for GPS only using ray-tracing simulations. Due to 3D map imperfections and other perturbations that arise in practice, e.g., signal blockage by foliage and surrounding vehicles, predicting the exact HPL of an AGV at a certain location and time is practically impossible. Therefore, this article predicts conservative HPLs by producing an upper bound for multipah and NLOS biases.

A flow chart for predicting the conservative HPLs is shown in Fig. 1. The proposed method first uses ray-tracing software, e.g., Wireless Insite, to simulate the channel impulse response (CIR) between each point on the map and the GNSS satellites or LTE base stations. The bias bounds are estimated from the CIRs using the methods described in the following subsections. Finally, FDE is conducted using the bias bounds and conservative HPLs are calculated accordingly.

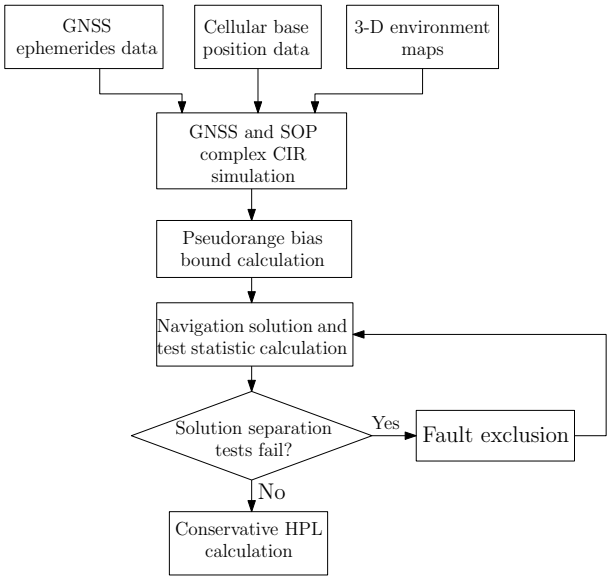

Fig. 1: Flowchart of proposed GNSS+SOP ARAIM.

A. GNSS Pseudorange Bias Prediction

Multipath/NLOS bias due to signal reflection and/or blockage by surrounding buildings is captured by $b_{\text{GNSS}_m}(k)$ in (1), which was predicted through ray-tracing simulations with a 3D building map. This term can be modeled as [26]

$$b_{\text{GNSS}_m}(k) = b_{\text{NLOS}_m}(k) + b_{\text{multipath}_m}(k), \tag{7}$$

where $b_{\text{NLOS}_m}(k)$ denotes the extra traveled distance between the reflected path and direct path when only NLOS signals are received and $b_{\text{multipath}_m}(k)$ denotes a bias caused by multipath. Note that in line-of-sight (LOS) conditions, $b_{\text{NLOS}_m}(k)$ becomes zero.

When the satellite positions, receiver position, and the 3D building map are given, the reflected paths can be simulated by finding the reflection point on the 3D building model using ray-tracing simulation. The position of the satellites at a specific time can be calculated from almanac data. The direct path can be determined by simply calculating the distance between satellites and the receiver. When there are multiple reflected paths, $b_{\text{NLOS}_m}(k)$ is calculated from the shortest reflected path.

If the ground vehicle receives multiple reflected signals, a multipath bias $b_{\text{multipath}_m}(k)$ can occur. The amount of multipath bias is determined by the correlator design of the code tracking loop in the receiver. In this paper, the *a posteriori* multipath estimation (APME) method [27] is assumed to be used for correlator design, and the multipath error is estimated using its noise envelope. The noise envelope is a function of the difference in traveled distance, received amplitude, and phase between the reflected and direct path. The multipath bias $b_{\text{NLOS}_m}(k)$ is modeled as

$$\begin{aligned} b_{\text{multipath}_m}(k) = \text{N}E(&R_{\text{reflected}_m}(k) - R_{\text{direct}_m}(k), \\ &A_{\text{reflected}_m}(k) - A_{direct_m}(k), \\ &\phi_{\text{reflected}_m}(k) - \phi_{\text{direct}_m}(k)), \end{aligned} \tag{8}$$

where $NE(\cdot)$ denotes the noise envelope function of the APME method (details are given on [27]); R denotes the simulated signal's traveled distance; A denotes the simulated received signal amplitude; ϕ denotes the simulated received signal phase; and subscript $_{\text{reflected}}$ and $_{\text{direct}}$ denote the reflected path and direct path, respectively. The time-of-arrival (TOA), received signal amplitude, and received signal phase were simulated by ray-tracing simulation and used to calculate the $b_{\text{multipath}_m}(k)$. Considering the possible blockage of GNSS signals by nearby vehicles, an elevation mask of 25° was conservatively set for the calculation.

B. SOP Pseudorange Bias Prediction

The bias term in (4) can be expressed as

$$b_{\text{SOP}_n}(k) = c \cdot \tau(k,0) - d_{\text{LOS}} + \chi_1(k) + \chi_2(k), \qquad (9)$$

where $c{\cdot}\tau(k,0)$ denotes the TOA of the first path; d_{LOS} is the LOS path length; and $\chi_1(k)$ and $\chi_2(k)$ are the biases due to multipath [28]. When the LOS signal is completely blocked or severely attenuated, the first path will be a reflected path. Therefore, $c \cdot \tau(k,0)$ will be larger than the true distance between the receiver and the LTE base station. As such, the pseudorange bias caused by NLOS effects becomes the difference between $c \cdot \tau(k,0)$ and d_{LOS}.

The complex CIR at the vehicle's position at time-step k can be modeled as [28]

$$r(k,\tau) = \sum_{l=0}^{L-1} \alpha(k,l)\delta(\tau - \tau(k,l)), \qquad (10)$$

where L is the number of multipath components; $\alpha(k,l)$ and $\tau(k,l)$ are the relative attenuation and delay components, respectively, of the l-th path with respect to the first path; and $\delta(\cdot)$ is the Dirac delta function. As Fig. 1 shows, the CIR can be simulated by ray-tracing with using a 3D building map, LTE base station locations and LTE signal properties.

The NLOS error and multipath interference can be predicted based on the simulated CIR. For the NLOS error, if the first simulated path is the LOS path, the NLOS error will be zero. Otherwise, the NLOS error is the difference between the delay for the first reflected path and LOS path.

Note that the effect of the delay of the reflected signal, $\tau(l)$, can be constructive or destructive. As the wavelength of LTE signals is only decimeters, small imperfections in the 3D models can induce large perturbations in the phase of $\alpha(l)$. Monte Carlo simulations are performed to calculate a pseudorange bias bound. For each Monte Carlo realization, the phase of $\alpha(l)$ is perturbed by $\Delta\phi \sim \mathcal{U}(-\pi,\pi)$. The relative amplitude $|\alpha(l)|$ is not varied in the Monte Carlo simulation, because it is assumed that the perturbation of amplitude due to map imperfections is relatively small. The bias bound is set to the maximum absolute bias out of all the Monte Carlo simulations.

IV. Simulation and Experimental Results

This section analyzes the performance of the proposed framework with SOP and multi-constellation GNSS signals.

A. Simulation Results

This subsection characterizes the integrity performance for the navigation system with GPS, GLONASS, and LTE pseudorange measurements. A simulation study was conducted on an area located in Riverside, CA, USA. The CIRs and conservative HPLs are simulated for a grid of locations with the resolution of 5 meters. The number of subcarrier symbols in the LTE pilot signal, was set to $B = 200$ with a bandwidth of 20 MHz and the time shift in the tracking loop was set to 0.5. The cell-specific reference signal (CRS) was used as the pilot signal [28]. The time epoch for the simulation is assumed to be 3:53 AM, on June 23rd 2018 UTC. As Fig. 2 (a) shows, there are 5 LTE base stations available in this area. Commercial 3D city maps (e.g., Fig. 2 (b)) from 3dbuildings [29] and ray-tracing software, Wireless Insite [30], are used to simulate the CIRs. Fig. 3 shows the CIR for the signal coming from transmitter 5 at the receiver position showing in Fig. 2. The upper bounds of the the pseudorange biases are further predicted using the method introduced in Section III. As an example, the pseudorange biases for transmitter 5 are plotted in Fig. 4. Finally, the conservative HPLs are further calculated by the ARAIM+SOP framework.

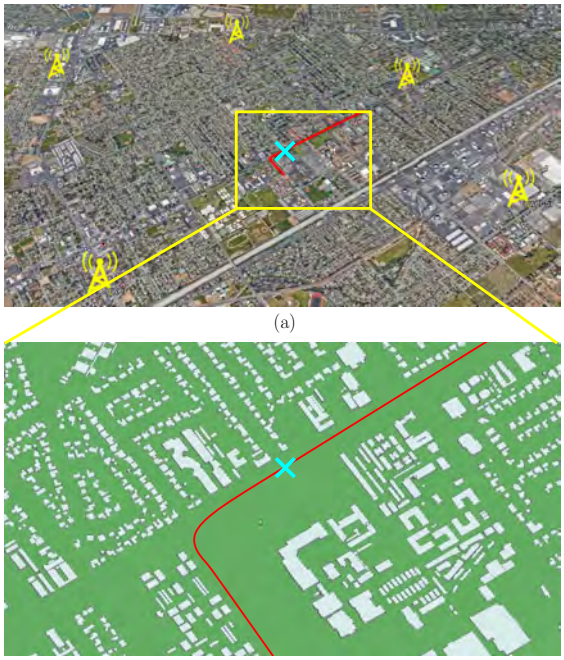

(a)

(b)

Fig. 2: (a) Simulation and experiment environment showing LTE tower locations and (b) 3D map of simulation environment. The receiver location is marked by an "X" for which the CIR is shown in Fig. 3. The vehicle trajectory is shown in red.

The parameters for the ARAIM+SOP framework are tabulated in Table I. Four scenarios of signal availability are considered in this paper: (i) GPS-only; (ii) GPS+GLONASS; (iii) GPS+SOP; and (iv) GPS+GLONASS+SOP. There are 11 GPS satellite and 7 GLONASS satellites available above the elevation mask during the simulation period. After FDE, the HPLs for the above four scenarios are plotted in Fig. 5.

Two conclusions can be drawn from Fig. 5. First, adding

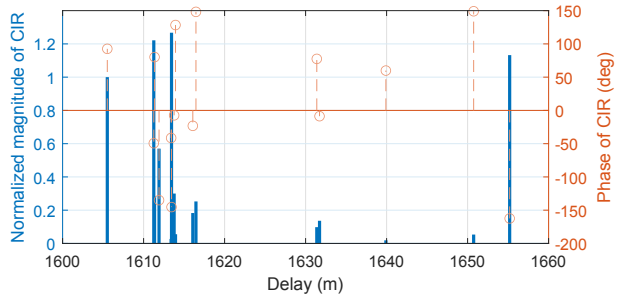

Fig. 3: CIR of the signal from transmitter 5 at the receiver position marked by an "X" in Fig. 2. The x-axis is the path delay expressed in meters.

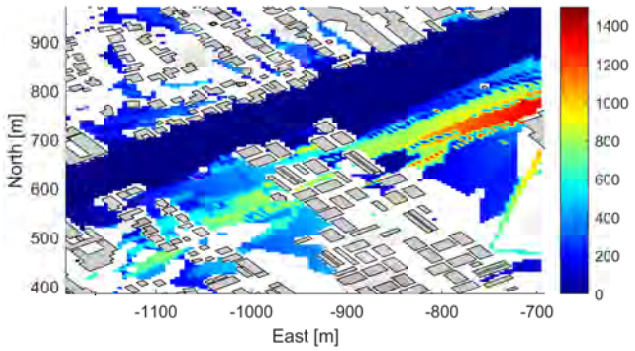

Fig. 4: Predicted range bias for transmitter 5.

the GLONASS and/or SOP will reduce the HPLs at some certain area. Second, adding GNSS or SOP constellations can reduce the availability. This is because that the ARAIM+SOP framework considers NLOS and large multipath biases as outliers to be detected. In urban environments, the NLOS and multipath errors could be common, which makes the probability of fault larger than the value used in the framework. As a result, there are scenarios where the number of simultaneous faults surpasses the maximum number of faults. For these scenarios, the measurement consistency will not satisfy the requirements after the FDE. The RAIM will consider the system as unavailable. There are two techniques to solve the problem of reduced availability. First, the integrity parameters can be characterized based on experiment campaigns in urban environments. Second, receivers can apply strategies to decide which constellation to use for navigation based on integrity maps.

B. Experimental Results

An experiment was conducted to demonstrate the proposed framework. In this experiment, a ground vehicle was equipped with two consumer-grade 800/1900 MHz cellular omnidirectional Laird antennas to receive the LTE signals. A National Instruments (NI) dual-channel universal software radio peripheral (USRP) 2954R, driven by a GPS disciplined oscillator (GPSDO) was used to down-mix and sample LTE signals. A Septentrio AsteRx-i V integrated GNSS-IMU sensor was used to provide the ground-truth trajectory. The ground vehicle traveled along a trajectory shown in Fig. 2.

TABLE I: RAIM Parameters

Parameter	Definition	Value
$\{\sigma_{URA,GNSS_m}\}_{m=1}^{M}$	User Range Error for GNSS	1 m
$\{\sigma_{URA,SOP_n}\}_{n=1}^{N}$	User Range Error for SOP	1 m
$PHMI_{HOR}$	Integrity budget for the horizontal component	10^{-7}
$PHMI_{VERT}$	Integrity budget for the vertical component	10^{-9}
PFA_{HOR}	Continuity budget allocated to the vertical component	10^{-7}
PFA_{VERT}	Continuity budget allocated to the vertical component	10^{-9}
$\{P_{GNSS_m}\}_{m=1}^{M}$	Probability of a single GNSS satellite fault	10^{-5}
$\{P_{SOP_n}\}_{n=1}^{N}$	Probability of a single SOP fault	10^{-4}

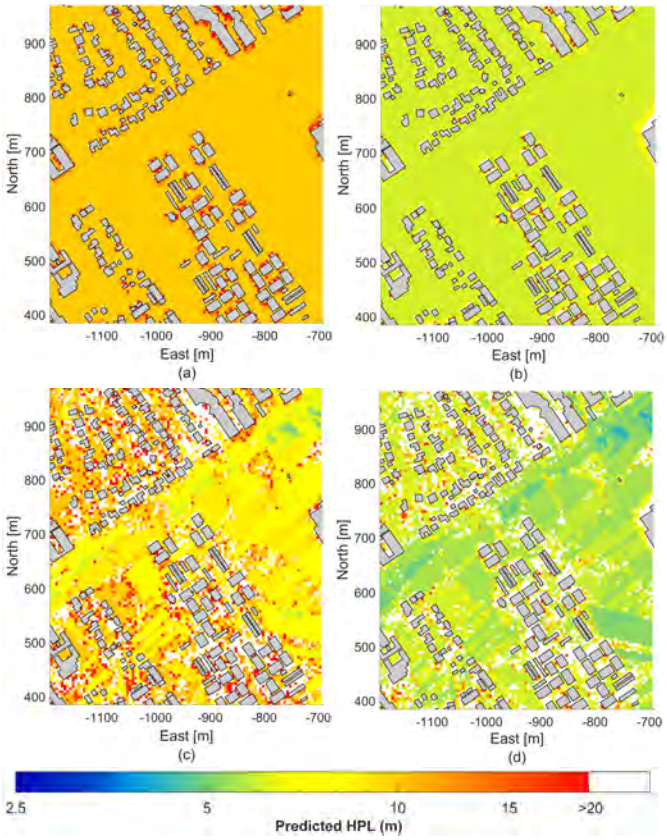

Fig. 5: Maps of conservatively predicted HPL for different navigation constellations: (a) GPS-only; (b) GPS+GLONASS; (c) GPS+SOP; (d) GPS+GLONASS+SOP.

The HPLs along the trajectory are plotted in Fig. 6. The horizontal alarm limit (HAL) is set to 20 m. It can be seen that (i) incorporating GLONASS and SOP pseudorange measurements reduces the HPLs and (ii) adding SOPs can be more effective than adding GLONASS in terms of reducing HPLs. For most of the trajectory, the HPL for GPS+SOP is smaller than GPS+GLONASS. It is worth highlighting that it is unfair to compare GLONASS with SOPs, as there were 7 GLONASS satellites available while only 5 SOPs were available during the experiment. Along the course of this experiment, the availability rates for GPS-only, GPS+GLONASS, GPS+SOP, and GPS+SOP+GLONASS were calculated to be 52.53%, 75.66%, 76.87%, and 80.72%, respectively.

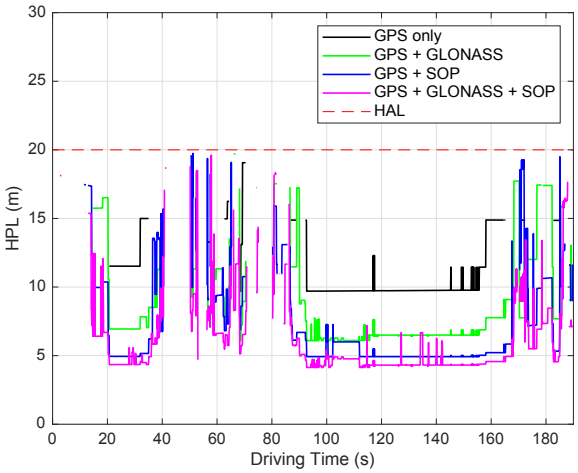

Fig. 6: HPLs over the course of the experiment trajectory. The HPL values above the HAL are truncated from the plot.

V. Conclusion

This paper proposed an ARAIM+SOP framework with multi-constellation GNSS and LTE pseudorange measurements for ground vehicle navigation. A method to predict conservative HPLs based on ray-tracing was introduced to produce the integrity map. Simulation and experiment results show that by incorporating multi-constellation GNSS and SOP pseudoranges, the HPLs are reduced. Experimental results for a ground vehicle navigating in an urban environment, showed the availability rates for GPS-only, GPS+GLONASS, GPS+SOP, and GPS+GLONASS+SOP to be 52.53%, 75.66%, 76.87%, and 80.72%, respectively.

References

[1] N. Zhu, D. Betaille, J. Marais, and M. Berbineau, "GNSS integrity monitoring schemes for terrestrial applications in harsh signal environments," *IEEE Intelligent Transportation Systems Magazine*, vol. 12, no. 3, pp. 81–91, 2020.

[2] T. Humphreys, M. Murrian, and L. Narula, "Deep-urban unaided precise global navigation satellite system vehicle positioning," *IEEE Intelligent Transportation Systems Magazine*, vol. 12, no. 3, pp. 109–122, 2020.

[3] D. Imparato, A. El-Mowafy, and C. Rizos, "Integrity monitoring: From airborne to land applications," in *Multifunctional Operation and Application of GPS*. IntechOpen, 2018, pp. 23–43.

[4] K. Nagai, T. Fasoro, M. Spenko, R. Henderson, and B. Pervan, "Evaluating GNSS navigation availability in 3-D mapped urban environments," in *Proceedings of IEEE/ION Position, Location and Navigation Symposium*, 2020, pp. 639–646.

[5] Z. Kassas, A. Abdallah, and M. Orabi, "Carpe signum: seize the signal – opportunistic navigation with 5G," *Inside GNSS Magazine*, vol. 16, no. 1, pp. 52–57, 2021.

[6] C. Yang, T. Nguyen, and E. Blasch, "Mobile positioning via fusion of mixed signals of opportunity," *IEEE Aerospace and Electronic Systems Magazine*, vol. 29, no. 4, pp. 34–46, April 2014.

[7] C. Yang and A. Soloviev, "Mobile positioning with signals of opportunity in urban and urban canyon environments," in *IEEE/ION Position, Location, and Navigation Symposium*, April 2020, pp. 1043–1059.

[8] Z. Kassas, J. Khalife, A. Abdallah, and C. Lee, "I am not afraid of the jammer: navigating with signals of opportunity in GPS-denied environments," in *Proceedings of ION GNSS Conference*, 2020, pp. 1566–1585.

[9] Z. Kassas, M. Maaref, J. Morales, J. Khalife, and K. Shamaei, "Robust vehicular localization and map matching in urban environments through IMU, GNSS, and cellular signals," *IEEE Intelligent Transportation Systems Magazine*, vol. 12, no. 3, pp. 36–52, June 2020.

[10] N. Zhu, J. Marais, D. Betaille, and M. Berbineau, "GNSS position integrity in urban environments: A review of literature," *IEEE Transactions on Intelligent Transportation Systems*, vol. 19, no. 9, pp. 2762–2778, September 2018.

[11] J. Blanch, T. Walter, P. Enge, Y. Lee, B. Pervan, M. Rippl, and A. Spletter, "Advanced RAIM user algorithm description: Integrity support message processing, fault detection, exclusion, and protection level calculation," in *Proceedings of ION GNSS Conference*, September 2012, pp. 2828–2849.

[12] J. Blanch, T. Walter, P. Enge, S. Wallner, F. Amarillo Fernandez, R. Dellago, R. Ioannides, I. F. Hernandez, B. Belabbas, A. Spletter *et al.*, "Critical elements for a multi-constellation advanced RAIM," *NAVIGATION, Journal of the Institute of Navigation*, vol. 60, no. 1, pp. 53–69, 2013.

[13] A. Ene, J. Blanch, and T. Walter, "Galileo-GPS RAIM for vertical guidance," in *Proceedings of National Technical Meeting of The Institute of Navigation*, January 2006, pp. 18–20.

[14] T. Walter, J. Blanch, M. J. Choi, T. Reid, and P. Enge, "Incorporating GLONASS into aviation RAIM receivers," in *Proceedings of International Technical Meeting of the Institute of Navigation*, January 2013, pp. 239–249.

[15] Y. Liu, J. Zhang, R. Xue, and Z. Wang, "Performance analysis of advanced RAIM with the inclusion of BeiDou," in *Proceedings of ION International Technical Meeting*, 2014, pp. 3629–3636.

[16] P. Roysdon and J. Farrell, "GPS-INS outlier detection and elimination using a sliding window filter," in *Proceedings of American Control Conference*, May 2017, pp. 1244–1249.

[17] T. Li, L. Pei, Y. Xiang, Q. Wu, S. Xia, L. Tao, X. Guan, and W. Yu, "P3-LOAM: PPP/LiDAR loosely coupled SLAM with accurate covariance estimation and robust RAIM in urban canyon environment," *IEEE Sensors Journal*, vol. 21, no. 5, pp. 6660–6671, 2021.

[18] L. Fu, J. Zhang, R. Li, X. Cao, and J. Wang, "Vision-aided RAIM: A new method for GPS integrity monitoring in approach and landing phase," *Sensors*, vol. 15, no. 9, pp. 22 854–22 873, 2015.

[19] M. Maaref and Z. Kassas, "Measurement characterization and autonomous outlier detection and exclusion for ground vehicle navigation with cellular signals," *IEEE Transactions on Intelligent Vehicles*, vol. 5, no. 4, pp. 670–683, December 2020.

[20] M. Maaref and Z. Kassas, "Autonomous integrity monitoring for vehicular navigation with cellular signals of opportunity and an IMU," *IEEE Transactions on Intelligent Transportation Systems*, 2021, accepted.

[21] M. Maaref, J. Khalife, and Z. Kassas, "Enhanced safety of autonomous driving by incorporating terrestrial signals of opportunity," in *Proceedings of IEEE International Conference on Acoustics, Speech and Signal Processing*, May 2020, pp. 9185–9189.

[22] M. Jia, J. Khalife, and Z. Kassas, "Evaluation of ground vehicle protection level reduction due to fusing GPS with faulty terrestrial signals of opportunity," in *Proceedings of ION International Technical Meeting*, January 2021, pp. 354–365.

[23] J. Khalife and Z. Kassas, "Precise UAV navigation with cellular carrier phase measurements," in *Proceedings of IEEE/ION Position, Location, and Navigation Symposium*, April 2018, pp. 978–989.

[24] L. Wang, P. Groves, and M. Ziebart, "Multi-constellation GNSS performance evaluation for urban canyons using large virtual reality city models," *Journal of Navigation*, vol. 65, pp. 459–476, 2012.

[25] N. Ziedan, "Urban positioning accuracy enhancement utilizing 3-D buildings model and accelerated ray tracing algorithm," in *Proceedings of ION GNSS Conference*, September 2017, pp. 3253–3268.

[26] G. Zhang and L. Hsu, "A new path planning algorithm using a GNSS localization error map for UAVs in an urban area," *Journal of Intelligent and Robotic Systems*, vol. 94, pp. 219–235, 2019.

[27] J. Sleewaegen and F. Boon, "Mitigating short delay multipath: a promising new technique," in *Proceedings of ION International Technical Meeting Conference*, September 2010, pp. 204–213.

[28] K. Shamaei and Z. Kassas, "LTE receiver design and multipath analysis for navigation in urban environments," *NAVIGATION, Journal of the Institute of Navigation*, vol. 65, no. 4, pp. 655–675, December 2018.

[29] "3dbuildings," https://3dbuildings.com.

[30] Remcom Inc., "Wireless insite," https://www.remcom.com/.

IEEE Aerospace and Electronic SYSTEMS magazine

July 2022
ISSN 0885-8985
Volume 37, Number 7

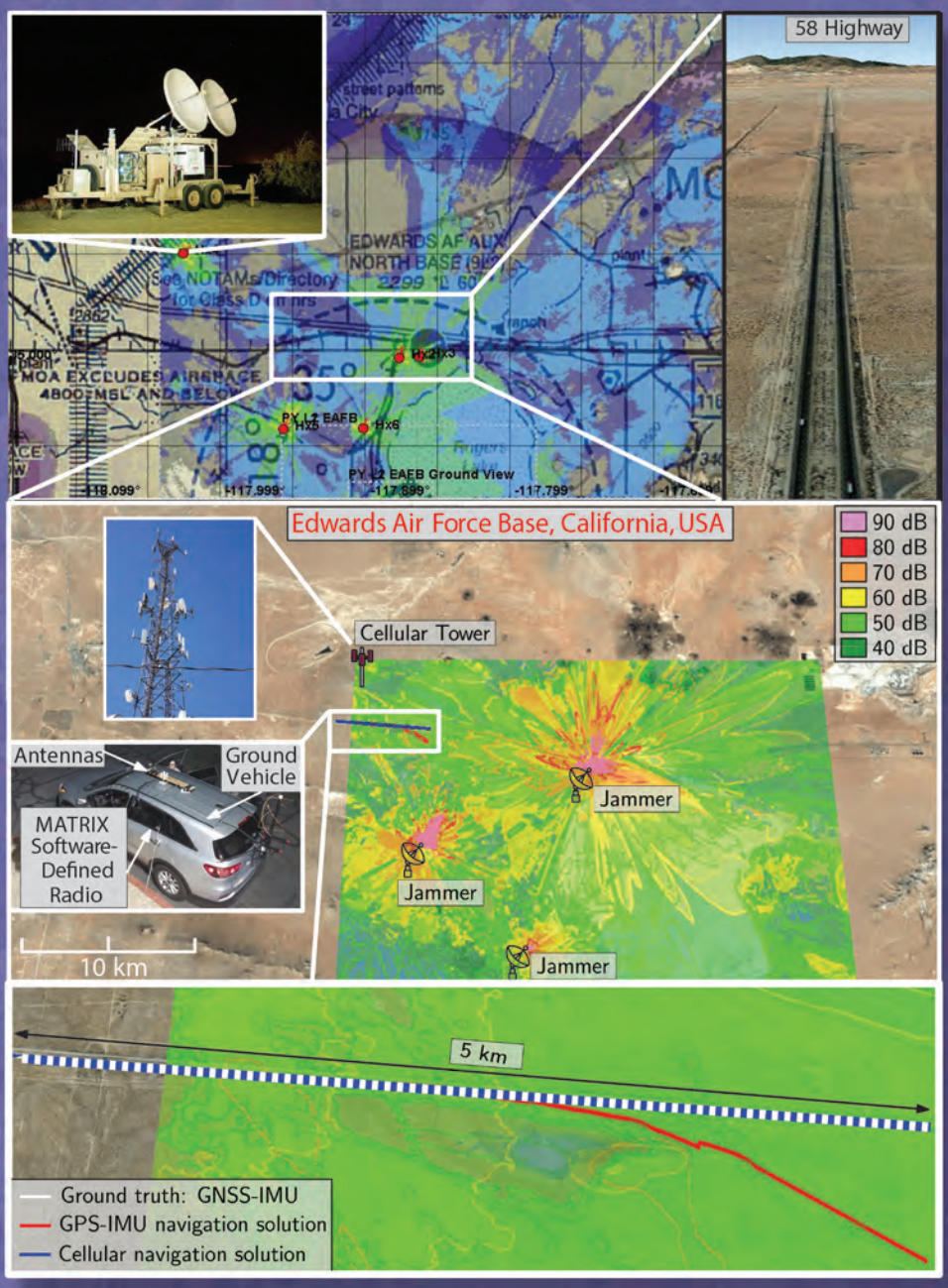

AESS

IEEE

Feature Article:

DOI. No. 10.1109/MAES.2022.3154110

I Am Not Afraid of the GPS Jammer: Resilient Navigation Via Signals of Opportunity in GPS-Denied Environments

Zaher M. Kassas, Joe Khalife, and Ali A. Abdallah, University of California, Irvine, CA 92697, USA
Chiawei Lee, U.S. Air Force Test Pilot School, Edwards, CA 93524, USA

INTRODUCTION

Global navigation satellite systems (GNSS) are at the heart of numerous technologies that fuel our modern day life. It is estimated that there are currently about 8 billion GNSS devices worldwide, reaching 9 billion by 2025. The economic benefits of GPS to the U.S. private sector between 1984 and 2017 is estimated to be nearly $1.8 trillion, and 15 of the 18 U.S. critical infrastructures rely on GPS. While losing accurate positioning, navigation, and timing (PNT) can be a nuisance in nonsafety critical applications, the impact can be catastrophic in safety-critical applications, such as transportation, aviation, military operations, among others. Over the last few years, GNSS jamming and spoofing incidents have been happening with increasing frequency, exposing the inherent vulnerabilities of GNSS, and rendering them a single point of failure [1]–[4]. GNSS jamming and spoofing have affected hundreds of vessels in South Korea; disrupted navigation over the South China Sea islands; caused chaos on smartphones and rideshares in Moscow; put tens of vessels into disarray in the Black Sea; caused dozens of unmanned aerial vehicles (UAVs) to plummet during a Hong Kong air show, resulting in hundreds of thousands of dollars in damages; are suspected to have been utilized to hijack UAVs and oil tankers in the Persian Gulf; disrupted airport operations around the world; and are becoming commonplace in military conflict [5]. What is particularly alarming is that jamming and spoofing are no longer confined to sophisticated rogue organizations, with jammers being sold online and marketed as personal privacy devices, and hackers publishing spoofing software-defined radio (SDR) code online. Today's navigation systems, particularly those onboard ground, aerial, and surface vehicles, fuse information from a GNSS receiver and an inertial measurement unit (IMU) [6]. The integration of these two systems, typically referred to as a GNSS-aided inertial navigation system (INS), takes advantage of the complementary attributes of each system: the long-term stability of a GNSS navigation solution aids the short-term accuracy of an INS. Sensors (e.g., cameras, lasers, sonar, and odometers) have been commonly adopted to supplement a navigation system for the inevitable event that GNSS signals become unreliable or unavailable. These sensors could be used to extract relative motion information to reduce the INS's error divergence rate. However, they are still dead-reckoning-type sensors; therefore, during prolonged periods of GNSS outage, the error would eventually diverge. Moreover, these sensors only provide local position estimates, may not properly function in all environments (e.g., fog, snow, rain, dust, nighttime, etc.), and are still susceptible to malicious spoofing attacks [7].

Signals of opportunity (SOPs) have been considered to enable navigation whenever GNSS signals become unavailable or unreliable [8]. SOPs are ambient radio signals that are not intended for navigation or timing purposes, such as AM/FM radio [9], [10], WiFi [11], [12], cellular [13]–[16], digital television [17], [18], and low-Earth orbit (LEO) satellite siganls [19]–[21]. In contrast to the aforementioned dead-reckoning-type sensors, absolute position information could be extracted from SOPs to provide bounded INS errors. Moreover, many SOPs are practically unaffected by dense smoke, fog, rain, snow, and other poor weather conditions.

Authors' current addresses: Zaher M. Kassas, Joe Khalife, and Ali Abdallah are with the Department of Mechaincal and Aerospace Engineering, University of California, Irvine, Irvine, CA 92697 USA (e-mails: zkassas@ieee.org; jjkhalife@gmail.com; abdalla2@uci.edu); Chiawei Lee is with the U.S. Air Force Test Pilot School, Edwards, CA 93524 USA (e-mail: chiawei.lee@us.af.mil). *(Corresponding author: Zaher M. Kassas)*.
Manuscript received 8 June 2021, revised 23 October 2021; accepted 2 February 2022, and ready for publication 22 February 2022.
Review handled by Jason Gross.
0885-8985/22/$26.00 © 2022 IEEE

Authorized licensed use limited to: The Ohio State University. Downloaded on September 16,2022 at 02:22:47 UTC from IEEE Xplore. Restrictions apply.

Image licensed by Ingram Publishing

SOPs enjoy several inherently desirable attributes for navigation purposes:

1) abundance in most locales of interest;
2) transmission at a wide range of frequencies and directions;
3) reception at a carrier-to-noise ratio (C/N_0) that is commonly tens of dBs higher than that of GNSS signals;
4) they are free to use, since their infrastructure is already operational.

While SOPs are jammable and spoofable [22]–[24], they are transmitted in multiple frequency bands and are typically received outdoors at high C/N_0. In the case of cellular SOPs, for example, they are received at more than 30 dBs higher C/N_0 than GNSS signals [25]. They also span the 700 MHz to nearly 6 GHz bands, excluding the 5G millimeter wave (mmWave) spectrum, which is envisioned to span several GHz of spectrum, with some bands reaching up to 400 MHz of bandwidth. This makes staging a successful, clandestine attack on cellular SOPs generally challenging, as the attacker would need to target the entire cellular spectrum with very high power. A typical challenge that arises in SOP-based navigation is that unlike GNSS, whose satellite states are transmitted in their navigation message, the states of SOPs, namely their position and clock states, are typically unknown *a priori* and must be estimated. To overcome this challenge, a radio simultaneous localization and mapping (radio SLAM) framework was proposed in which the states of the navigating vehicle are simultaneously estimated with the states of the SOPs [26], while aiding the INS in a tightly coupled fashion [27]. Recent works have demonstrated meter-level-accurate navigation with SOPs on ground vehicles and pedestrians indoors [28], [29] and submeter-level accurate navigation on aerial vehicles [30]. While published results in the literature have demonstrated experimentally the efficacy of SOPs as PNT sources in a standalone fashion (i.e., without fusing SOPs with other signals or sensors) and in an integrated fashion (i.e., fusing SOPs with INS and lidar), experiments were never conducted in actual GNSS-denied environments. These results were achieved by "fictitiously" cutting GNSS signals from the navigation filter. In September 2019, the authors' Autonomous Systems Perception, Intelligence, and Navigation (ASPIN) Laboratory was invited to participate in live GPS jamming experiments, called Developmental Test Navigation Festival (DT NAVFEST), at Edwards Air Force Base (AFB), California, USA. Experiments with stationary antennas and ground vehicles were conducted to study SOPs for PNT. This article reports findings from these experiments, which represent the first published results evaluating the efficacy of SOPs for PNT in a real GPS-denied environment. In particular, this article analyzes the clock errors of terrestrial cellular long-term evolution (LTE) SOPs located inside the jammed region, showing timing stability over 95 min of GPS jamming. Moreover, this article showcases the efficacy of the radio SLAM approach on a ground vehicle navigating in the jammed environment, while exploiting a terrestrial cellular LTE SOP. The results show the vehicle navigating during GPS jamming for 5 km in 180 s, during which the position root mean-squared error (RMSE) of a traditional GPS-aided INS grew to nearly 238 m. In contrast, the radio SLAM approach with a *single* cellular LTE SOP whose position was poorly known (an initial uncertainty on the order of several kilometers) achieved a position RMSE of 32 m. To the best of authors' knowledge, these are the first published results of navigation with SOPs in real GPS-denied environments, under jamming conditions. Preliminary results of this study were presented in Kassas *et al.*'s work [5]. However, considering the nonpeer reviewed nature of Kassas *et al.*'s work [5], the results therein only focused on showing the navigation solution. In contrast, this article

1) formulates the mathematical details of radio SLAM by describing the navigator's dynamics model via an INS kinematics formulation versus a dynamics

Authorized licensed use limited to: The Ohio State University. Downloaded on September 16,2022 at 02:22:47 UTC from IEEE Xplore. Restrictions apply.

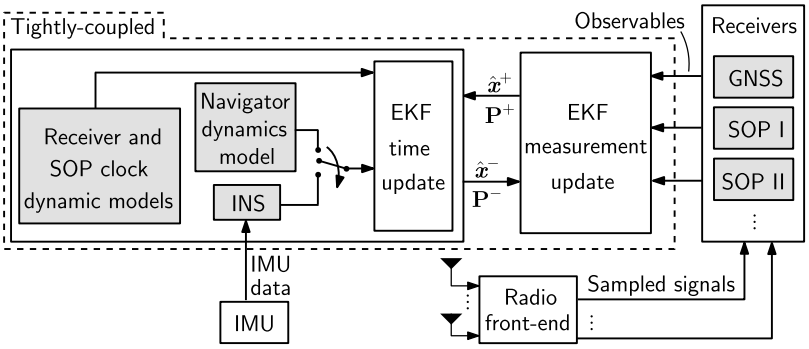

Figure 1.
Overview of a tightly coupled radio SLAM framework. The radio front-end collects signals, which are processed in the navigation receivers. The EKF time update is performed based on the toggling switch: (i) using a dynamical model that describes the navigator's dynamics or (ii) using an INS, when available. The EKF measurement update is performed using navigation observables from received SOP signals and GNSS signals, when available.

model formulation; clock error dynamics model; and SOP measurement model;

2) gives explicit description of the experiments including filter initialization and software and hardware setup;

3) provides further analyses and experimental results of the C/N_0 experienced during jamming as well as the filter's estimation error.

The rest of this article is organized as follows. The section "Radio Slam" provides and overview of the radio SLAM framework. The section "GPS-Jammed Environment and Experimental Setup" describes the GPS-jammed environment and hardware and software setup. "PNT Experimental Results in the GPS-Jammed Environment" presents PNT experimental results. Finally, the "Conclusion" is presented.

RADIO SLAM

This section overviews radio SLAM framework as well as the navigator's dynamics model, clock error dynamics, and SOP measurement models.

FRAMEWORK OVERVIEW

Radio SLAM estimates the states of the navigator-mounted receiver simultaneously with the SOPs' states. Radio SLAM produces an SOP-derived navigation solution in a standalone fashion [26], [31] or an integrated fashion by fusing SOPs with sensors (e.g., IMU, lidar, etc.) and digital maps [32].

Observability of radio SLAM was analyzed in the authors' work [26], [33], leading to establishing the minimal *a priori* knowledge needed about the navigator-mounted receiver's and/or SOP transmitters' states. The most significant conclusion from these observability analyzes is that if a mobile navigator with knowledge of its initial states (position, velocity, clock bias, and clock drift), denoted $\boldsymbol{x}_r$, makes pseudorange measurements to $M \geq 1$ terrestrial SOPs whose states (position, clock bias, and clock drift), denoted $\{\boldsymbol{x}_{s,i}\}_{i=1}^{M}$ are unknown, then the environment is fully observable, i.e., the navigator can estimate its states simultaneously with the states of the SOPs. The conclusions from these observability analyzes will be used in estimating the mobile ground vehicle's and SOP's states in the section "Experiment 2: Mobile Receiver."

A simple, yet effective estimator that could be employed in radio SLAM is the extended Kalman filter (EKF). Here, one could employ a similar architecture to a tightly coupled GNSS-INS. This architecture i) performs the EKF measurement update (yielding the corrected estimate $\hat{\boldsymbol{x}}^{+}$ and corrected error covariance $\mathbf{P}^{+}$) whenever GNSS observables (e.g., pseudorange and carrier phase) are available and ii) performs the EKF time update (yielding the predicted estimate $\hat{\boldsymbol{x}}^{-}$ and prediction error covariance $\mathbf{P}^{-}$) with raw IMU data between GNSS measurement epochs. The added complexity with SOPs is that the EKF state vector is composed of both the navigator's states and the SOPs' states, i.e., $\boldsymbol{x} \triangleq \left[\boldsymbol{x}_r^{\mathsf{T}}, \boldsymbol{x}_{s,1}^{\mathsf{T}}, \ldots, \boldsymbol{x}_{s,M}^{\mathsf{T}}\right]^{\mathsf{T}}$. If no INS is used, then a proper dynamical model for the navigator dynamics can be used for the EKF time update. Of course, this would introduce a mismatch between the true navigator's dynamics and the model used in the EKF; nevertheless, advanced methods such as adaptive filters (e.g., interacting multiple models [34] and noise covariance estimation [35] could alleviate this mismatch.

Figure 1 depicts a high-level block diagram of tightly coupled radio SLAM, which operates in the following two modes.

- **Mapping mode:** GNSS observables are available. Here, GNSS and SOP observables are fused in the EKF to aid the INS (if available), producing a more accurate estimate of $\boldsymbol{x}_r$ while mapping the SOP

Authorized licensed use limited to: The Ohio State University. Downloaded on September 16,2022 at 02:22:47 UTC from IEEE Xplore. Restrictions apply.

radio environment (i.e., estimating the unknown states of the SOPs $\{\boldsymbol{x}_{s,i}\}_{i=1}^{M}$.

- **Radio SLAM mode:** GNSS observables are unavailable. Here, SOP observables aid the INS (if available) to simultaneously estimate the navigator-mounted states $\boldsymbol{x}_r$ while continuing to refine estimates of the SOPs' states.

NAVIGATOR DYNAMICS MODEL

In a tightly coupled radio SLAM framework, either an INS kinematics model or a dynamics model for the navigator is utilized to perform the EKF time update. In what follows, a description of each is discussed.

INS KINEMATICS FORMULATION

Let $\{b\}$ denote a body frame fixed at the navigator, and let $\{g\}$ denote a global frame, e.g., the Earth-centered inertial frame [36]. Moreover, let $\boldsymbol{\theta}_b \in \mathbb{R}^3$ represent the three-dimensional (3-D) orientation vector of the body frame with respect to the global frame and ${}^g\boldsymbol{r}_b \in \mathbb{R}^3$ the 3-D position vector of the navigator expressed in $\{g\}$. Given the INS's true 3-D rotational rate vector ${}^b\boldsymbol{\omega} \in \mathbb{R}^3$ in the body frame and its 3-D acceleration ${}^g\boldsymbol{a}_b \in \mathbb{R}^3$ in the global frame, the standard strapdown kinematics equations can be expressed in continuous time as

$$\dot{\boldsymbol{\theta}}_b(t) = {}^b\boldsymbol{\omega}(t) \tag{1}$$

$${}^g\ddot{\boldsymbol{r}}_b(t) = {}^g\boldsymbol{a}_b(t). \tag{2}$$

The 3-D orientation vector of the body frame with respect to the global frame can be represented by the 4-D quaternion vector ${}^b_g\bar{\boldsymbol{q}} \in \mathbb{R}^4$.

The navigator's IMU is assumed to contain a triad-gyroscope and a triad-accelerometer, which produce measurements $\boldsymbol{z}_{\text{imu}} \triangleq \left[\boldsymbol{\omega}_{\text{imu}}^{\mathsf{T}}, \boldsymbol{a}_{\text{imu}}^{\mathsf{T}}\right]^{\mathsf{T}}$ of the angular rate and specific force, which are modeled as

$$\boldsymbol{\omega}_{\text{imu}}(k) = {}^b\boldsymbol{\omega}(k) + \boldsymbol{b}_{\text{gyr}}(k) + \boldsymbol{n}_{\text{gyr}}(k) \tag{3}$$

$$\boldsymbol{a}_{\text{imu}}(k) = \mathbf{R}\left[{}^b_g\bar{\boldsymbol{q}}(k)\right]({}^g\boldsymbol{a}_b(k) - {}^g\boldsymbol{g}(k)) + \boldsymbol{b}_{\text{acc}}(k) + \boldsymbol{n}_{\text{acc}}(k) \tag{4}$$

where $\mathbf{R}\left[{}^b_g\bar{\boldsymbol{q}}\right]$ is the equivalent rotation matrix of ${}^b_g\bar{\boldsymbol{q}}$; ${}^g\boldsymbol{g}$ is the acceleration due to gravity acting on the navigator in the global frame; $\boldsymbol{b}_{\text{gyr}} \in \mathbb{R}^3$ and $\boldsymbol{b}_{\text{acc}} \in \mathbb{R}^3$ are the gyroscope and accelerometer biases, respectively; and $\boldsymbol{n}_{\text{gyr}}$ and $\boldsymbol{n}_{\text{acc}}$ are measurement noise vectors, which are modeled as zero-mean white noise sequences with covariances $\mathbf{Q}_{\boldsymbol{n}_{\text{gyr}}}$ and $\mathbf{Q}_{\boldsymbol{n}_{\text{acc}}}$, respectively. Integrating IMU specific force data to perform a time update of the position and velocity in a rotating coordinate frame introduces a centrifugal and Coriolis term due to the rotation rate of the Earth [37]. However, a short integration interval is considered in this article, where the variation of the Coriolis force was considered negligible for simplicity. Further details about neglecting the Coriolis force over short integration intervals can be found in Morales and Kassas [27].

The gyroscope and accelerometer biases in (3) and (4) are dynamic and stochastic; hence, they must be estimated in the EKF as well. As such, the INS 16-state vector is given by

$$\boldsymbol{x}_{\text{ins}} = \left[\begin{array}{cccc} {}^b_g\bar{\boldsymbol{q}}^{\mathsf{T}}, & {}^g\boldsymbol{r}_b^{\mathsf{T}}, & {}^g\dot{\boldsymbol{r}}_b^{\mathsf{T}}, & \boldsymbol{b}_{\text{gyr}}^{\mathsf{T}}, \quad \boldsymbol{b}_{\text{acc}}^{\mathsf{T}} \end{array}\right]^{\mathsf{T}}$$

where $\dot{\boldsymbol{r}}_b \in \mathbb{R}^3$ is the 3-D velocity of the navigator.

The INS states evolve in time according to

$$\boldsymbol{x}_{\text{ins}}(k+1) = \boldsymbol{f}_{\text{ins}}\left[\boldsymbol{x}_{\text{ins}}(k), {}^b\boldsymbol{\omega}(k), {}^g\boldsymbol{a}_b(k)\right]$$

where $\boldsymbol{f}_{\text{ins}}$ is a vector-valued function of standard strapdown kinematic equation [38], which discretizes (1) and (2) by integrating ${}^b\boldsymbol{\omega}$ and ${}^g\boldsymbol{a}_b$ to produce ${}^b_g\bar{\boldsymbol{q}}(k+1)$, $\boldsymbol{r}_b(k+1)$, and $\dot{\boldsymbol{r}}_b(k+1)$, and uses a velocity random walk model for the biases, which is given by

$$\begin{aligned} \boldsymbol{b}_{\text{gyr}}(k+1) &= \boldsymbol{b}_{\text{gyr}}(k) + \boldsymbol{w}_{\text{gyr}}(k) \\ \boldsymbol{b}_{\text{acc}}(k+1) &= \boldsymbol{b}_{\text{acc}}(k) + \boldsymbol{w}_{\text{acc}}(k) \end{aligned}$$

where $\boldsymbol{w}_{\text{gyr}}$ and $\boldsymbol{w}_{\text{acc}}$ are process noise vectors that drive the in-run bias variation (or bias instability) and are modeled as white noise sequences with covariance $\mathbf{Q}_{\boldsymbol{w}_{\text{gyr}}}$ and $\mathbf{Q}_{\boldsymbol{w}_{\text{acc}}}$, respectively.

DYNAMICS MODEL FORMULATION

Generally, the navigator's dynamics can be described as

$$\dot{\boldsymbol{x}}(t) = \boldsymbol{f}[\boldsymbol{x}(t), \boldsymbol{u}(t), t] + \boldsymbol{w}(t)$$

where $\boldsymbol{x}$ is the navigator's state vector, $\boldsymbol{u}$ represents known exogenous inputs, and $\boldsymbol{w}$ is the process noise. Depending on the navigator's platform (pedestrian or ground, aerial, or maritime) and motion, different dynamic models can be used to describe the navigator's dynamics, such as polynomial (e.g., white noise acceleration and Wiener process acceleration), singer acceleration, mean-adaptive acceleration, semi-Markov jump process, circular motion, curvilinear motion, coordinated turn, among others [39].

A simple, yet effective dynamical model that has been successfully employed for navigators with "low dynamics," which sufficiently captures the dynamics between EKF measurement updates is the white noise acceleration, given by

$$\dot{\boldsymbol{x}}_{\text{pv}}(t) = \mathbf{A}_{\text{pv}}\,\boldsymbol{x}_{\text{pv}}(t) + \mathbf{D}_{\text{pv}}\tilde{\boldsymbol{w}}_{\text{pv}}(t) \tag{5}$$

$$\mathbf{A}_{\text{pv}} = \begin{bmatrix} \mathbf{0}_{3\times3} & \mathbf{I}_{3\times3} \\ \mathbf{0}_{3\times3} & \mathbf{0}_{3\times3} \end{bmatrix}, \quad \mathbf{D}_{\text{pv}} = \begin{bmatrix} \mathbf{0}_{3\times3} \\ \mathbf{I}_{3\times3} \end{bmatrix}$$

Authorized licensed use limited to: The Ohio State University. Downloaded on September 16,2022 at 02:22:47 UTC from IEEE Xplore. Restrictions apply.

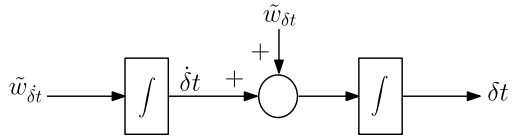

Figure 2.
Clock error states dynamics model.

where $\boldsymbol{x}_{\text{pv}} \triangleq \left[\boldsymbol{r}_r^{\mathsf{T}}, \dot{\boldsymbol{r}}_r^{\mathsf{T}}\right]^{\mathsf{T}}$, $\boldsymbol{r}_r \triangleq [x_r, y_r, z_r]^{\mathsf{T}}$ is the 3-D position of the navigator-mounted receiver, and $\tilde{\boldsymbol{w}}_{\text{pv}} = \left[\tilde{w}_x, \tilde{w}_y, \tilde{w}_z\right]^{\mathsf{T}}$ is the process noise vector, whose elements of are modeled as zero-mean, mutually independent white noise processes with power spectral densities $\tilde{q}_x$ $\tilde{q}_y$, and $\tilde{q}_z$, respectively. Note that here, the superscript g is dropped and the subscript r is used to denote the navigator-mounted receiver's position instead of b, since the navigator in this case is not relying on an INS and the orientation of its body is not estimated.

Discretizing the navigator's dynamics (5) at a constant sampling period T yields the discrete-time model

$$\boldsymbol{x}_{\text{pv}}(k+1) = \mathbf{F}_{\text{pv}}\, \boldsymbol{x}_r(k) + \boldsymbol{w}_{\text{pv}}(k), \quad k = 0, 1, 2, \ldots$$
$$\mathbf{F}_{\text{pv}} = \begin{bmatrix} \mathbf{I}_{3\times 3} & T\mathbf{I}_{3\times 3} \\ \mathbf{0}_{3\times 3} & \mathbf{I}_{3\times 3} \end{bmatrix}$$

where $\boldsymbol{w}_{\text{pv}}$ is a discrete-time zero-mean white noise sequence with covariance $\mathbf{Q}_{\text{pv}}$ given by

$$\mathbf{Q}_{\text{pv}} = \begin{bmatrix} x\frac{T^3}{3} & 0 & 0 & \tilde{q}_x\frac{T^2}{2} & 0 & 0 \\ 0 & \tilde{q}_y\frac{T^3}{3} & 0 & 0 & \tilde{q}_y\frac{T^2}{2} & 0 \\ 0 & 0 & \tilde{q}_z\frac{T^3}{3} & 0 & 0 & \tilde{q}_z\frac{T^2}{2} \\ \tilde{q}_x\frac{T^2}{2} & 0 & 0 & \tilde{q}_x T & 0 & 0 \\ 0 & \tilde{q}_y\frac{T^2}{2} & 0 & 0 & \tilde{q}_y T & 0 \\ 0 & 0 & \tilde{q}_z\frac{T^2}{2} & 0 & 0 & \tilde{q}_z T \end{bmatrix}.$$

CLOCK ERROR DYNAMICS MODEL

GNSS satellites are equipped with atomic clocks, are synchronized, and their clock errors are transmitted in the navigation message along with the satellites' positions. Therefore, in GNSS-based navigation, only the receiver's clock error is estimated. In contrast, SOPs are equipped with less stable oscillators than GNSS satellites, are typically roughly synchronized to GNSS, and their clock error states (bias and drift) are mostly unknown. As such, the SOP clock errors must be simultaneously estimated with the receiver's clock error. To facilitate this estimation in the radio SLAM framework, the clock error state dynamics must be specified. To this end, a typical model for the dynamics of the clock error states is the so-called two-state model, composed of the clock bias δt and clock drift $\dot{\delta t}$, as depicted in Figure 2.

Table 1.

Typical h_0 and h_{-2} Values for Different TCXO and OCXO Oscillators [41]

Oscillator	h_0	h_{-2}
TCXO	2.0×10^{-19}	2.0×10^{-20}
TCXO	1.0×10^{-21}	2.0×10^{-20}
TCXO	9.4×10^{-20}	3.8×10^{-21}
TCXO	3.9×10^{-22}	2.4×10^{-22}
TCXO	3.5×10^{-20}	8.5×10^{-22}
TCXO	1.9×10^{-21}	2.5×10^{-23}
OCXO	2.6×10^{-22}	4.0×10^{-26}
OCXO	8.0×10^{-20}	4.0×10^{-23}
OCXO	3.4×10^{-22}	1.3×10^{-24}

The clock error states evolve according to

$$\dot{\boldsymbol{x}}_{\text{clk}}(t) = \mathbf{A}_{\text{clk}}\, \boldsymbol{x}_{\text{clk}}(t) + \tilde{\boldsymbol{w}}_{\text{clk}}(t)$$

$$\boldsymbol{x}_{\text{clk}} = \begin{bmatrix} \delta t \\ \dot{\delta t} \end{bmatrix}, \quad \tilde{\boldsymbol{w}}_{\text{clk}} = \begin{bmatrix} \tilde{w}_{\delta t} \\ \tilde{w}_{\dot{\delta t}} \end{bmatrix}, \quad \mathbf{A}_{\text{clk}} = \begin{bmatrix} 0 & 1 \\ 0 & 0 \end{bmatrix} \tag{6}$$

where the elements of $\tilde{\boldsymbol{w}}_{\text{clk}}$ are modeled as zero-mean, mutually independent white noise processes, and the power spectral density of $\tilde{\boldsymbol{w}}_{\text{clk}}$ is given by $\tilde{\mathbf{Q}}_{\text{clk}} = \text{diag}\left[S_{\tilde{w}_{\delta t}}, S_{\tilde{w}_{\dot{\delta t}}}\right]$. The power spectra $S_{\tilde{w}_{\delta t}}$ and $S_{\tilde{w}_{\dot{\delta t}}}$ can be related to the power-law coefficients $\{h_\alpha\}_{\alpha=-2}^{2}$, which have been shown through laboratory experiments to be adequate to characterize the power spectral density of the fractional frequency deviation $y(t)$ of an oscillator from nominal frequency, which takes the form $S_y(f) = \sum_{\alpha=-2}^{2} h_\alpha f^\alpha$[40]. It is common to approximate the clock error dynamics by considering only the frequency random walk coefficient h_{-2} and the white frequency coefficient h_0, which lead to $S_{\tilde{w}_{\delta t}} \approx \frac{h_0}{2}$ and $S_{\tilde{w}_{\dot{\delta t}}} \approx 2\pi^2 h_{-2}$[34].

Many SOPs of interest, particularly cellular transmitters, are equipped with oven-controlled crystal oscillators (OCXOs). On the other hand, many receivers are equipped with less stable oscillators, e.g., temperature-compensated crystal oscillator (TCXO). Typical TCXO and OCXO values for h_0 and h_{-2} are given in Table 1.

Discretizing dynamics (6) at a sampling interval T yields the discrete-time-equivalent model

$$\boldsymbol{x}_{\text{clk}}(k+1) = \mathbf{F}_{\text{clk}}\, \boldsymbol{x}_{\text{clk}}(k) + \boldsymbol{w}_{\text{clk}}(k)$$

Authorized licensed use limited to: The Ohio State University. Downloaded on September 16,2022 at 02:22:47 UTC from IEEE Xplore. Restrictions apply.

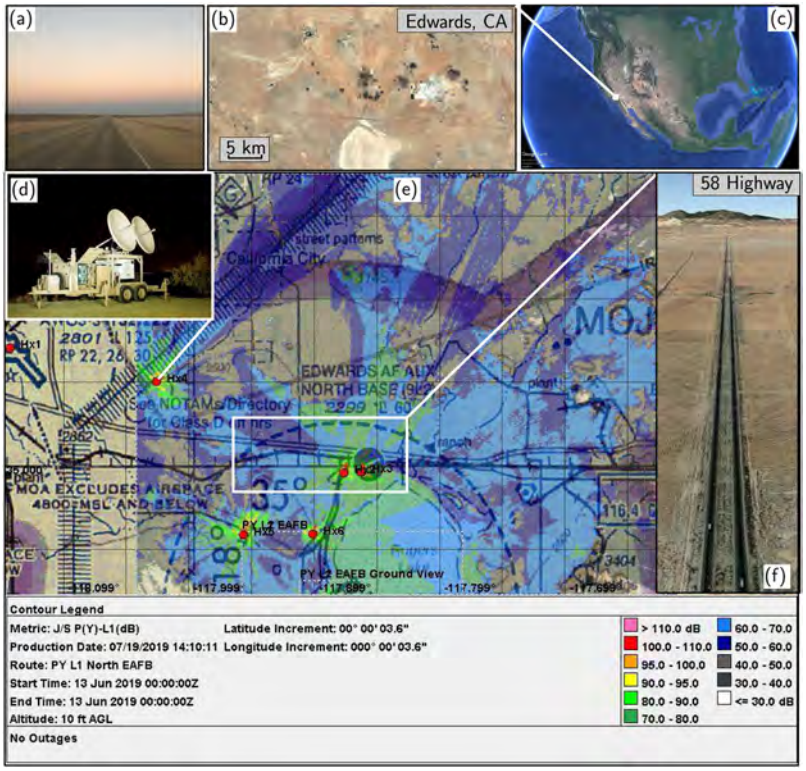

Figure 3.
DT NAVFEST GPS jamming laydown: (a) highway taken toward Edwards AFB, (b) photo of Edwards AFB, CA, (c) location of the experiment, (d) photo of one of the jammers used in the experiment, (e) heat map showing the jamming power and jammers' location, (f) photo of the 58 Highway, where the ground vehicle experiment was performed. Map data: Google Earth.

where $\boldsymbol{w}_{\text{clk}}$ is a discrete-time zero-mean white noise sequence with covariance $\mathbf{Q}_{\text{clk}}$, and

$$\mathbf{F}_{\text{clk}} = \begin{bmatrix} 1 & T \\ 0 & 1 \end{bmatrix}, \quad \mathbf{Q}_{\text{clk}} = \begin{bmatrix} S_{\tilde{w}_{\delta t}} T + S_{\tilde{w}_{\delta t}} \frac{T^3}{3} & S_{\tilde{w}_{\delta t}} \frac{T^2}{2} \\ S_{\tilde{w}_{\delta t}} \frac{T^2}{2} & S_{\tilde{w}_{\delta t}} T \end{bmatrix}. \tag{7}$$

SOP MEASUREMENT MODEL

A specialized receiver could produce a pseudorange measurement to an SOP, which after discretization and mild approximations discussed in the work of Kassas and Humphrey [26], can be modeled as

$$\rho(k) = \|\boldsymbol{r}_r(k) - \boldsymbol{r}_s\|_2 + c \cdot [\delta t_r(k) - \delta t_s(k)] + v_\rho(k) \tag{8}$$

where c is the speed of light and v_ρ is a DT zero-mean white Gaussian sequence with variance $\sigma_\rho^2(k)$.

Another, more precise navigation observable that can be produced is the carrier phase, which can be modeled as

$$\lambda\phi(k) = \|\boldsymbol{r}_r(k) - \boldsymbol{r}_s\|_2 + c[\delta t_r(k) - \delta t_s(k)] + \lambda N + v_\phi(k) \tag{9}$$

where λ is the wavelength of the carrier signal, N represents the carrier phase ambiguity (namely, the initial phase difference between the receiver and the SOP), and $v_\phi(k)$ is the measurement noise, which is modeled as a discrete-time zero-mean white Gaussian sequence with variance $\sigma_\phi^2(k)$.

Note that the term N in (9) is not necessarily an integer [42]. Single- or double-difference carrier phase measurements will have integer ambiguities. If the SOP carrier phase measurements are used in a differential framework, the Least-squares AMBiguity Decorrelation Adjustment (LAMBDA) method [43], or its variants, e.g., the modified LAMBDA method [44], could be used to resolve the integer ambiguities. If SOP carrier phase measurements are used in a nondifferential framework, the carrier phase ambiguity is treated as a real-valued constant offset that can be assimilated into the SOP's initial clock bias [45]. In both differential and nondifferential frameworks, cycle slips in carrier phase tracking may occur, which could introduce integer "jumps" in N. In such cases, cycle slip detection and mitigation methods may be used to reduce their effects on carrier phase measurements [46]. The rest of this article focuses on a pseudorange-based navigation solution.

RADIO SLAM EKF FORMULATION

The observables to all SOPs in the environment, whether pseudoranges and/or carrier phases are augmented into

Authorized licensed use limited to: The Ohio State University. Downloaded on September 16,2022 at 02:22:47 UTC from IEEE Xplore. Restrictions apply.

Table 2.

Jammer Laydown

Site	Latitude (N)	Longitude (W)	Terrain height (ft MSL)	Antenna height (ft AGL)	Antenna azimuth true (deg)	Antenna elevation (deg)	Antenna gain (dBi)		EIRP (dBm)		Waveform
							L1	L2	L1	L2	
Hx1	35° 04′ 12.4″	118° 08′ 41.82″	2769	10	57	15	24.2	24.5	83.8	84.1	CW, BBN
Hx2	34° 59′ 43.52″	117° 52′ 42.35″	2313	10	15	15	24.2	24.5	83.8	84.1	CW, BBN
Hx3	34° 59′ 45.57″	117° 51′ 52.65″	2289	10	13	15	24.2	24.5	83.8	84.1	CW, BBN
Hx4	35° 02′ 59.59″	118° 01′ 40.87″	2528	10	43	15	24.2	24.5	83.8	84.1	CW, BBN
Hx5	34° 57′ 29.35″	117° 57′ 31.78″	2429	10	24	15	24.2	24.5	83.8	84.1	CW, BBN
Hx6	34° 57′ 30.83″	117° 54′ 12.65″	2441	10	17	15	24.2	24.5	83.8	84.1	CW, BBN
Nx1	34° 54′ 42.45″	117° 54′ 5.5″	2309	29	49	-30	14.1	12.9	-12.4	-13.6	CW, BBN

MSL: Mean sea level; AGL: Above ground level; dBi: Decibel isotropic; dBm: Decibel referenced to 1 mW; EIRP: Equivalent, isotropically radiated power (EIRP) values accounted for estimated 1.5 dB line loss between amplifier and antenna; CW: Continuous wave; BBN: Broad-band noise

the measurement vector z, which is used to estimate $\boldsymbol{x} \triangleq \left[\boldsymbol{x}_r^{\mathsf{T}}, \boldsymbol{x}_{s,1}^{\mathsf{T}}, \ldots, \boldsymbol{x}_{s,M}^{\mathsf{T}}\right]^{\mathsf{T}}$, where $\boldsymbol{x}_{s,i} \triangleq \left[\boldsymbol{r}_{s_i}^{\mathsf{T}}, \boldsymbol{x}_{\mathrm{clk},s_i}^{\mathsf{T}}\right]^{\mathsf{T}} \in \mathbb{R}^5$ is the state of the ith SOP. If an INS is used as discussed in the section "INS Kinematics Formulation," $\boldsymbol{x}_r \triangleq \left[\boldsymbol{x}_{\mathrm{ins}}^{\mathsf{T}}, \boldsymbol{x}_{\mathrm{clk},r}^{\mathsf{T}}\right]^{\mathsf{T}} \in \mathbb{R}^{18}$. If the white noise acceleration model is used as discussed in the section "Dynamics Model Formulation," $\boldsymbol{x}_r \triangleq \left[\boldsymbol{x}_{\mathrm{pv}}^{\mathsf{T}}, \boldsymbol{x}_{\mathrm{clk},r}^{\mathsf{T}}\right]^{\mathsf{T}} \in \mathbb{R}^8$.

GPS-JAMMED ENVIRONMENT AND EXPERIMENTAL SETUP

This section overviews the GPS-jammed environment during DT NAVFEST live GPS jamming at Edwards AFB, as well as the hardware and software setup.

JAMMING LAYDOWN

From the information made available to the participants, six high-powered jammers (HPJ) and one portable box jammer (PBJ) were spread over an area of approximately 50 miles north of Edwards AFB, as shown in Figure 3. The term "Hx" denotes an HPJ, one of them seen in Figure 3, and "Nx" denotes a PBJ. The initial locations and characteristics of the jammers are summarized in Table 2. The experiments conducted by the ASPIN team took place just outside the perimeters of Edwards AFB, mainly on the 58 Highway pictured in Figure 3 and near the Mojave Airport.

SOP LTE ENODEB LAYOUT

An SOP radio mapping campaign with the cognitive SDR Multichannel Adaptive TRansceiver Information eXtractor (MATRIX), discussed in the section "MATRIX Cognitive SDR," was conducted a month before DT NAVFEST to survey available LTE eNodeBs in the area. Since Edwards AFB is largely unpopulated, only two LTE eNodeBs (SOP 1 and SOP 2) were hearable in the scheduled jamming area and were located at the same site, as shown in Figure 4. The eNodeBs were transmitting at high power to service large macrocells in the sparsely populated area. The eNodeBs corresponded to two U.S. cellular providers (Verizon Wireless and T-Mobile), and they were

Authorized licensed use limited to: The Ohio State University. Downloaded on September 16,2022 at 02:22:47 UTC from IEEE Xplore. Restrictions apply.

Figure 4.
SOP LTE eNodeB layout. Map data: Google Earth.

transmitting on dual frequencies. The characteristics of the two eNodeBs are summarized in Table 3.

HARDWARE SETUP

The ground vehicle was equipped with hardware setup shown in Figure 5, which was comprised of i) Septentrio GNSS-INS system and ii) LTE front-end. The hardware setup is described in the following.

SEPTENTRIO GNSS-INS SYSTEM

The Septentrio GNSS-INS system consists of the following: a multifrequency GNSS AsteRx-i V receiver, a tactical-grade Vectornav VN-100 microelectromechanical system IMU, and a dual-GNSS antenna system. AsteRx-i V processes the dual antenna multifrequency GNSS signals with IMU measurements to generate an accurate and reliable position and orientation solution. Multi-GNSS

Table 3.

eNodeBs' Characteristics			
eNodeB	Carrier frequency [MHz]	$N_{\mathrm{ID}}^{\mathrm{Cell}}$	Cellular provider
1	751 / 2125	377	Verizon
2	731.5 / 2145	491	T-Mobile

antennas 1 and 2 were mounted on a wooden board that was mounted on the roof of the vehicle and aligned with the vehicle's main axis. Antenna-1, i.e., the main antenna, was toward the back of the vehicle. Antenna-2, i.e., the auxiliary antenna, was toward the front of the vehicle. The VN-100 IMU was mounted on the wooden board as well, with its x-axis pointing toward the front of the vehicle, the y-axis pointing to the right of the vehicle (as seen from behind the vehicle), and the z-axis pointing downward. It is worth noting that only GPS was jammed, while signals from other GNSS constellations (Galileo and GLONASS) were available. The GNSS-INS system was used to obtain the vehicle's ground truth trajectory by using signals from the nonjammed GNSS constellations.

LTE FRONT-END

The LTE front-end comprised of the following:

1) a quad-channel universal software radio peripheral (USRP)-2955;

Figure 5.
Ground vehicle and hardware setup.

Authorized licensed use limited to: The Ohio State University. Downloaded on September 16,2022 at 02:22:47 UTC from IEEE Xplore. Restrictions apply.

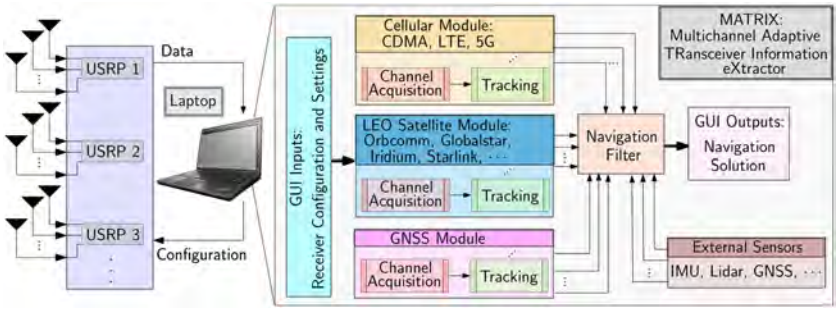

Figure 6.
MATRIX cognitive SDR architecture. The SDR consists of the following: (i) USRPs to collect different radio signals, (ii) various modules to produce navigation observables from different types of signals (e.g., cellular, LEO satellites, etc.), (iii) external sensors (e.g., IMU, lidar, GNSS receivers, etc.), whose measurements can be fused with the navigation observables produced by the signal modules, and (iv) navigation filter that fuses all measurements to produce a navigation solution.

2) two consumer-grade 800/1900 MHz Laird cellular antennas;
3) a PCIe cable;
4) a laptop;
5) a consumer-grade GPS antenna to discipline the USRP's onboard GPS-disciplined oscillator (GPSDO).

The two Laird antennas were connected to the USRP to capture impinging LTE signals, and the USRP was tuned to listen to two carrier frequencies corresponding to the eNodeBs in Table 3.

SOFTWARE SETUP

The software setup used in the performed experiment included the following: i) Septentrio's postprocessing software development kit and ii) MATRIX, which are described in the following.

SEPTENTRIO POSTPROCESSING SOFTWARE DEVELOPMENT KIT (PPSDK) TOOL

Septentrio's PP-SDK was used to process GNSS observables collected by the AsteRx-i V to obtain a GNSS-INS navigation solution. This integrated GNSS-INS system was used to produce the ground truth results with which the produced navigation solution was compared.

MATRIX COGNITIVE SDR

MATRIX is a state-of-the-art cognitive SDR, developed at the ASPIN Laboratory, for navigation with terrestrial and space-based SOPs [47]–[51]. MATRIX continuously searches for

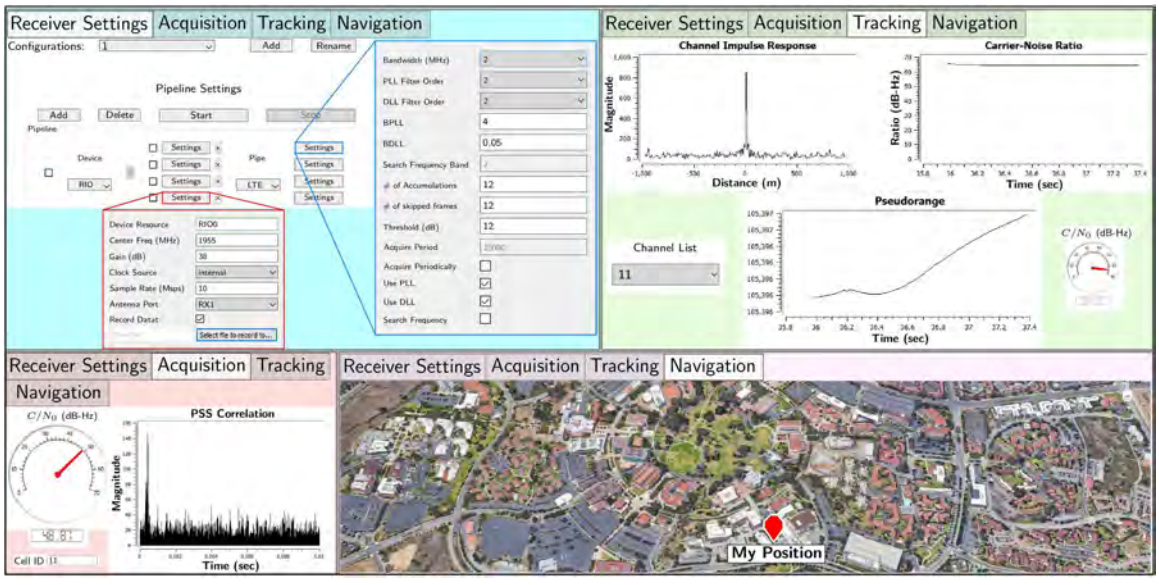

Figure 7.
GUI of the LTE module of the MATRIX SDR. The interface has four main windows: (i) Receiver Settings: to be set by the user; (ii) Acquisition and (iii) Tracking: show the resulting signals in real-time; and (iv) Navigation: plots the navigation solution.

Authorized licensed use limited to: The Ohio State University. Downloaded on September 16,2022 at 02:22:47 UTC from IEEE Xplore. Restrictions apply.

opportune signals from which it draws navigation and timing information, employing signal characterization on-the-fly as necessary. MATRIX could produce a navigation solution in a standalone fashion or by fusing SOPs with sensors (e.g., IMU, lidar, etc.), digital maps, and/or other signals (e.g., GNSS). Figure 6 shows MATRIX's architecture. The conducted experiment used MATRIX's carrier-aided code phase-based LTE module [48] to produce LTE navigation observables. Figure 7 shows the graphical user interface (GUI) front panel of the LTE module of MATRIX.

PNT EXPERIMENTAL RESULTS IN THE GPS-JAMMED ENVIRONMENT

Two experiments were conducted to study the behavior of SOPs in the presence of real GPS jamming and to assess their potential as PNT sources. The results from each experiment are presented as follows.

EXPERIMENT 1: STATIONARY RECEIVER

Cellular SOPs are typically equipped with GPSDOs to meet the synchronization requirements set by the 3rd Generation Partnership Project (3GPP). Some opportunistic navigation frameworks exploit the resulting stability of cellular SOPs' clock [30], making it important to evaluate the clock stability of cellular SOPs under GPS jamming to determine their suitability in radio SLAM.

SETUP

The setup described in the sections "Hardware Setup" and "Software Setup" was deployed outside the jamming area to listen to two LTE eNodeBs (SOP 1 and SOP 2) located in an area affected by jamming. The jamming-to-signal (J/S) at the eNodeBs was around 60 dBs. During this experiment, the jammers were periodically turned on for 10 min, then turned off for 2 min. The MATRIX SDR sampled LTE signals synchronously at 10 Msps for 95 min on carrier frequencies 751 MHz and 731.5 MHz, which are frequencies allocated to U.S. cellular providers Verizon Wireless and T-Mobile, respectively. Figure 8 shows the setup of the first experiment.

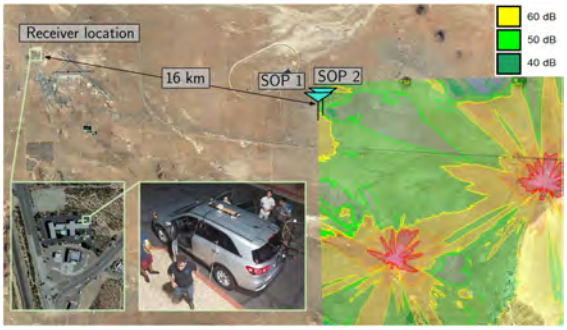

Figure 8.
Experiment 1 setup. The setup discussed in sections "Hardware Setup" and "Software Setup" was deployed outside the GPS-jammed area to listen to two SOPs located in an area where J/S was around 60 dB. Map data: Google Earth.

RESULTS

The LTE signal samples were processed by the LTE module of MATRIX to produce pseudorange observables to the two eNodeBs. The two LTE eNodeBs as well as the receiver were stationary and at known locations. The true range between the receiver and each eNodeB was subtracted from the corresponding pseudorange measurements [cf. (8)]. Figure 9(a) shows the time history of the remaining term (after subtracting the initial pseudorange values). Note that a 5-min dataloss occurred around the 35th minute due to a hardware malfunction. Recalling that the measurement noise is appropriately modeled as white, the trend in the variations, as shown in Figure 9(a) is mainly due to the relative clock biases between the eNodeBs and the receiver. After a short initial transient due to the receiver's GPSDO, the clock biases seem to stabilize. Moreover, both clock biases appear to be driven by a common term, which is likely to be the receiver's bias. To evaluate the relative

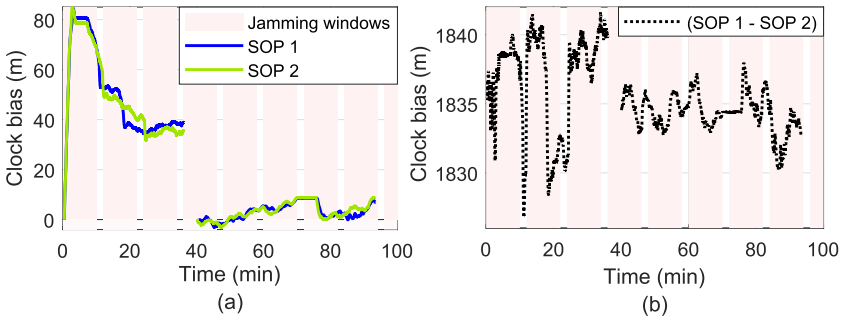

Figure 9.
Experiment 1 results. (a) Time history of clock biases corresponding to SOP 1 and SOP 2. The initial pseudorange values were subtracted. A hardware malfunction around the 35th min caused a 5-min dataloss. (b) Clock bias difference between SOP 1 and SOP 2, without subtracting the initial pseudoranges. The stable difference shows that the relative stability between LTE SOPs is maintained for a period of over 95 min during GPS jamming.

Authorized licensed use limited to: The Ohio State University. Downloaded on September 16,2022 at 02:22:47 UTC from IEEE Xplore. Restrictions apply.

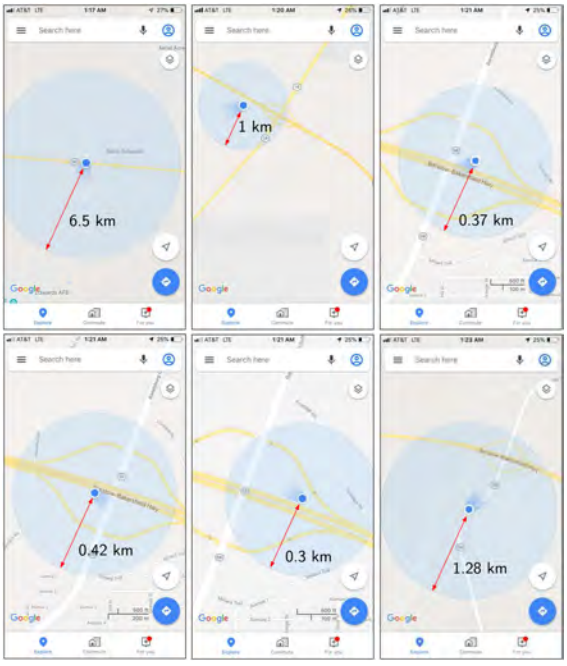

Figure 10.
Screenshots from Google Maps on an iPhone 8 during Experiment 2. The uncertainty grew to a radius over 6 km.

stability between the SOP biases, the difference of the biases (without subtracting their initial values) is plotted in Figure 9(b), which shows a stable difference hovering around 1835 m. Figure 9 does not show significant correlation between the stability of the clock biases and the jamming window, leading to the conclusion that the LTE SOPs' relative stability is maintained for a period of over 95 min during GPS jamming. This could be attributed to either: i) the oscillators equipped on the eNodeBs are disciplined by other GNSS constellations or ii) the free-running oscillators remained stable during the jamming period.

EXPERIMENT 2: MOBILE RECEIVER

Another experiment was conducted to demonstrate the radio SLAM framework with LTE SOPs under real GPS jamming. The experimental setup and results are discussed as follows.

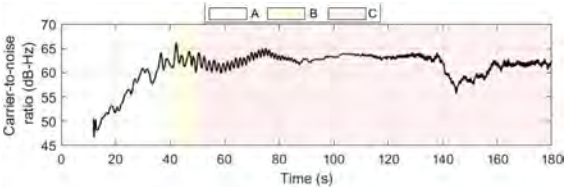

Figure 11.
C/N_0 to the LTE SOP as measured by the ground vehicle. The experiment consists of three time segments: (A) GPS signals available, (B) GPS signals intermittent, and (C) GPS signals were unavailable.

SETUP

In this experiment, a ground vehicle was driven in the east direction along the 58 Highway, as shown in Figure 3. Over the course of the experiment, only one LTE eNodeB (SOP 1) was hearable at 751 MHz. LTE samples were collected at 10 Msps for 8 min. The vehicle started west of the jamming area. The experiment was composed of the following three segments:

1) GPS signals were available (0–40 s);
2) GPS signals were intermittent (40–50 s);
3) GPS signals were not available (50–180 s).

During this experiment, the jammers were operating continuously. The SOP pseudorange measurements were fed to the tightly coupled radio SLAM framework depicted in Figure 1 to estimate the states for two scenarios:

Scenario 1: SOP position was assumed to be *fully known* (from the prior mapping campaign). Here, the estimated state vector in the EKF was $\boldsymbol{x}_r \triangleq \left[\boldsymbol{r}_r^{\mathsf{T}}, \dot{\boldsymbol{r}}_r^{\mathsf{T}}, c \cdot (\boldsymbol{x}_{\mathrm{clk},r}^{\mathsf{T}} - \boldsymbol{x}_{\mathrm{clk},s}^{\mathsf{T}})\right]^{\mathsf{T}}$.

Scenario 2: SOP position was assumed to be *unknown*, (a prior with a large uncertainty was used). Here, the estimated state vector in the EKF was $\boldsymbol{x}_r \triangleq \left[\boldsymbol{r}_r^{\mathsf{T}}, \dot{\boldsymbol{r}}_r^{\mathsf{T}}, \boldsymbol{r}_s^{\mathsf{T}}, c \cdot (\boldsymbol{x}_{\mathrm{clk},r}^{\mathsf{T}} - \boldsymbol{x}_{\mathrm{clk},s}^{\mathsf{T}})\right]^{\mathsf{T}}$.

Table 4.

Experiment 2 Results			
Framework	Position RMSE (m)	Final error (m)	SOP final error (m)
Scenario 1: Radio SLAM with known SOP position	29.4	69.4	–
Secnario 2: Radio SLAM with unknown SOP position	32.2	84.5	5.5
GPS-IMU	237.9	766.0	–

Authorized licensed use limited to: The Ohio State University. Downloaded on September 16,2022 at 02:22:47 UTC from IEEE Xplore. Restrictions apply.

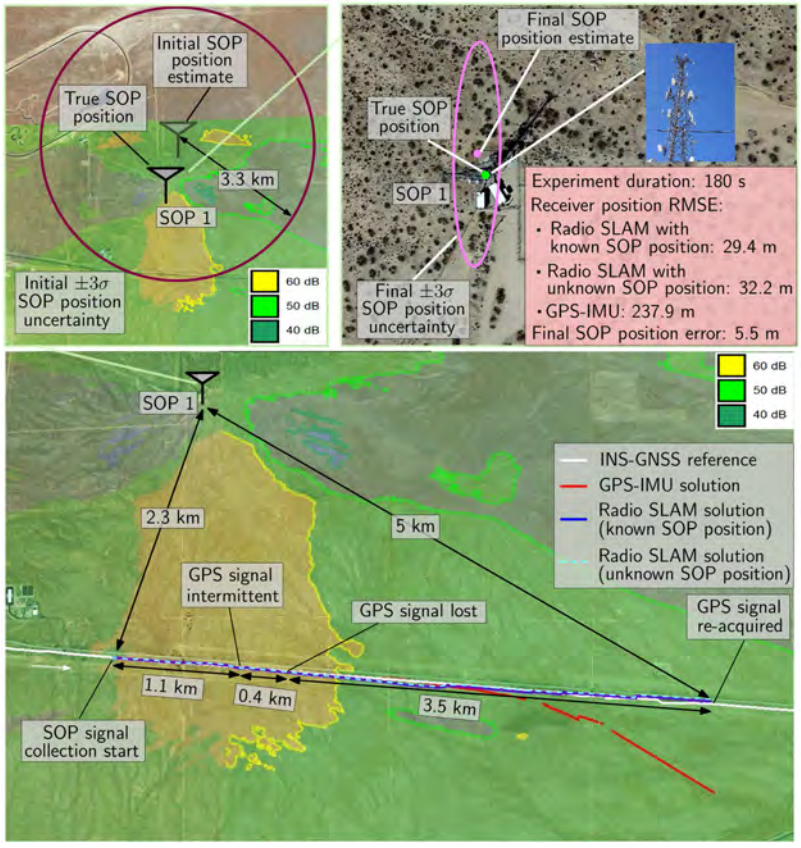

Figure 12.
Experiment 2 results for both scenarios. Map data: Google Earth.

Due to a hardware storage malfunction, the raw IMU data were not properly saved. As such, the radio SLAM with the white noise acceleration dynamical model discussed in the section "Dynamics Model Formulation" was used. The process noise spectral densities were set as $\tilde{q}_x = \tilde{q}_y = 0.01$ m^2/s^3, and $\tilde{q}_z = 0.001$ m^2/s^3 and the receiver's and SOP's oscillators were set to be high quality OCXOs with parameters $h_0 = 2.6 \times 10^{-22}$ and $h_{-2} = 4.0 \times 10^{-26}$. The results are presented as follows.

RESULTS

Results from a smartphone navigation application are provided first to showcase the impact of real GPS jamming on a GPS receiver. Figure 10 shows screenshots from Google Maps running on an iPhone 8 during the ground vehicle's trajectory. Essentially, the navigation solution stopped updating, would sporadically jump around by hundreds of meters, and the blue "halo" representing the estimated position uncertainty grew to a radius over 6 km. Note the time progression shown in the screenshots as the vehicle was driving along the 58 Highway in one direction; nevertheless, the estimated position reported by the iPhone kept jumping around.

In both scenarios, the receiver had access to GPS signals for the first 50 s only. The receiver's last produced GPS navigation solution before GPS signals were

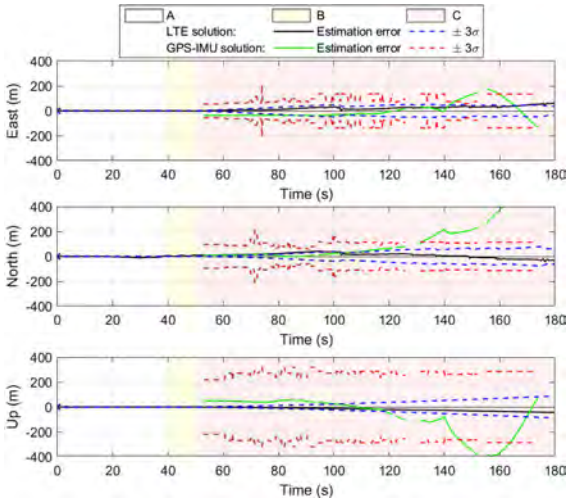

Figure 13.
Experiment 2 EKF results: receiver position error and associated $\pm 3\sigma$ bounds for Scenario 1: assuming *fully known* SOP position. (A) GPS signals available, (B) GPS signals intermittent, and (C) GPS signals unavailable.

Authorized licensed use limited to: The Ohio State University. Downloaded on September 16,2022 at 02:22:47 UTC from IEEE Xplore. Restrictions apply.

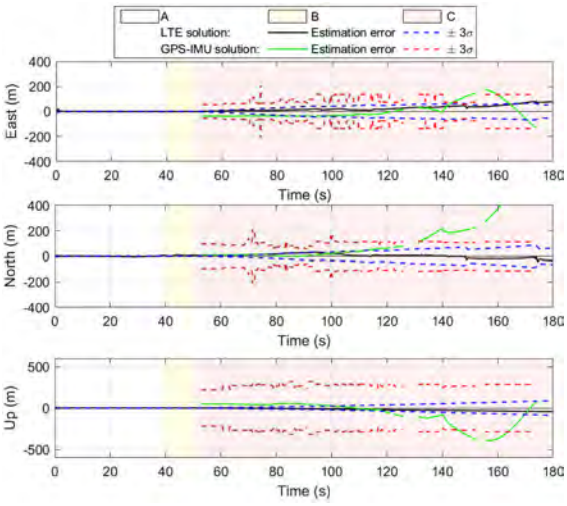

Figure 14.
Experiment 2 EKF results: receiver position error and associated $\pm 3\sigma$ bounds for Scenario 2: assuming *unknown* SOP position. (A) GPS signals available, (B) GPS signals intermittent, and (C) GPS signals unavailable.

lost was used to initialize the position states in both radio SLAM scenarios, and the receiver's and SOP's positions were expressed in an East–North–UP frame, centered at the receiver's initial position. The initial state estimate for Scenario 1 was $\hat{\boldsymbol{x}}^- = \mathbf{0}_{8\times 1}$, while the initial state estimate for Scenario 2 was $\hat{\boldsymbol{x}}^- = [\mathbf{0}_{1\times 6}, 976.9, 3221.3, 58.9, \mathbf{0}_{1\times 2}]^{\mathsf{T}}$. The initial estimation error covariance for Scenario 1 was $\mathbf{P}^- = \mathrm{diag}[1, 1, 1, 10, 10, 10, 1\times 10^9, 45]$, while the initial estimation error covariance for Scenario 2 was $\mathbf{P}^- = \mathrm{diag}[1, 1, 1, 10, 10, 10, 12\times 10^5, \ 12\times 10^5, 1, 1\times 10^9, 45]$. For Scenario 2, the SOP position was randomly initialized around the true SOP position with an initial 2-D $\pm 3\sigma$ radius of about 3.3 km. For the random realization used in the EKF, the initial SOP position error was 1.07 km. Figure 11 shows C/N_0 as measured by the vehicle-mounted receiver to the LTE SOP.

For Scenario 1, the receiver's 2-D position RMSE was found to be 29.4 m with a final 2-D position error of 69.4 m. For Scenario 2, the receiver's final 2-D position RMSE was found to be 32.2 m with a final 2-D position error of 84.5 m. The SOP's final 2-D position error was 5.5 m. For comparison, a GPS-IMU solution was produced using Septentrio's PPSDK tool for the same trajectory. The receiver's 2-D position RMSE was found to be 237.9 m from the GPS-IMU solution with a final 2-D position error of 766.0 m. Table 4 and Figure 12 summarize the results of Experiment 2.

The EKF position error and associated $\pm 3\sigma$ bounds for Scenario 1 are shown in Figure 13. The EKF position error and associated $\pm 3\sigma$ bounds for Scenario 2 are shown in Figure 14 for the receiver and in Figure 15 for the SOP. It can be seen from these figures that, as expected, the GPS-

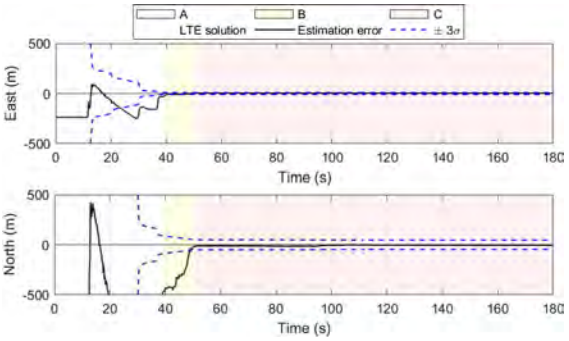

Figure 15.
Experiment 2 EKF results: SOP position error and $\pm 3\sigma$ bounds. (A) GPS signals available, (B) GPS signals intermittent, and (C) GPS signals unavailable.

IMU errors diverge unboundedly in the GPS-jammed region. What appears to be alarming is that these errors are inconsistent with the reported σ-bounds. In contrast, the errors for both Scenarios 1 and 2 in the east and north directions are consistent with the σ-bounds and are drifting at a much lower rate. This drift could be attributed to poor estimability—recall that a *single* SOP is being used and that the vehicle is quickly moving away from the SOP. Of course, using an IMU would reduce this drift as it would provide more precise time updates than the assumed white noise acceleration dynamical model. In fact, this slowly drifting behavior is consistent with the results presented in the work of Morales and Kassas [27] with a single SOP. Using signals from two or more SOPs was shown to alleviate this drift and yield bounded errors. The divergence in the Up direction is simply due to poor geometric diversity in the vertical direction, which could be readily accounted for with an external sensor (e.g., altimeter).

DISCUSSION

The following can be concluded from the aforementioned results. First, Experiment 1 shows that cellular SOP clocks remain relatively stable during the jamming period. This could be attributed to: i) the jamming was intermittent, as shown in Figure 9, which could have allowed the SOPs' on-board GPSDOs to relock to GPS and ii) by design, cellular transmitter clocks are required to maintain $\pm 3\,\mu$s synchronization with GPS time, even after 8 h of GPS signal loss [52]. Future studies could consider longer periods of GPS jamming (more than 8 h), to fully characterize the behavior of cellular SOP clocks in the presence of a persistent GPS jammer.

Second, as expected, the performance of radio SLAM with unknown SOP position is worse than that of radio SLAM with known SOP positions. This is due to the poorer estimability of the state space in Scenario 2, as more states are being estimated from the same pseudorange measurements. The final position errors in Scenarios

Authorized licensed use limited to: The Ohio State University. Downloaded on September 16,2022 at 02:22:47 UTC from IEEE Xplore. Restrictions apply.

1 and 2 highlight this degradation in the performance. However, the EKF error is a random process itself, and can theoretically take arbitrary realizations from an underlying distribution at any point in time. As such, the position RMSE is a more insightful measure of the filter performance. What is interesting is that the degradation of the RMSE performance between Scenarios 1 and 2 is about 3 m, which is on the same order of magnitude as the SOP position estimation error in Scenario 2.

Third, the nature of the experiment makes it difficult to be performed in an urban region. The environment in which the experiment took place was rural, where cellular SOPs tend not to be as abundant as urban regions. Within the same region, one could receive signals from faraway SOPs on an aerial platform compared to a ground platform. As such, future studies could consider conducting the experiments on an aerial platform, which would increase the number of hearable SOPs.

CONCLUSION

This article justified why I am not afraid of the GPS jammer, as long as there are ambient SOPs to exploit in the environment. A radio SLAM approach was presented, which enables the exploitation of SOPs for resilient navigation in environments where GPS signals are challenged or denied. Radio SLAM could produce an SOP-derived navigation solution in a standalone fashion or by fusing SOPs with sensors, digital maps, and/or other signals (e.g., GNSS). This article presented the first published experimental results for navigation with SOPs in a GPS-denied environment. These experiments took place at Edwards AFB, during DT NAVFEST, in which GPS was intentionally jammed with J/S as high as 90 dB. The results analyzed the clock stability of two cellular SOP LTE eNodeBs in the jammed area, showing that the relative stability between the LTE SOPs is maintained for a period of more than 95 min during GPS jamming. Moreover, the results showcased a ground vehicle traversing a trajectory of about 5 km in 180 s in the GPS-jammed environment, during which a GPS-IMU system drifted from the vehicle's ground truth trajectory, resulting in a position RMSE of 238 m. In contrast, the radio SLAM approach with a *single* cellular LTE SOP whose position was poorly known (an initial uncertainty on the order of several kilometers) achieved a position RMSE of 32 m.

ACKNOWLEDGMENTS

This work was supported in part by the Office of Naval Research (ONR) under Grant N00014-19-1-2511 and Grant N00014-19-1-2613, in part by the National Science Foundation (NSF) under Grant 1929965, and in part by part by the U.S. Department of Transportation (USDOT) under Grant 69A3552047138 for the CARMEN University Transportation Center (UTC). The authors would like to thank Edwards AFB for inviting the ASPIN Laboratory to conduct experiments during DT NAVFEST. The authors would also like to thank J. Morales, K. Shamaei, M. Maaref, K. Semelka, M. Nguyen, and T. Mortlock for their help with data collection.

Distribution Statement A. Approved for public release; Distribution is unlimited 412TW-PA-20399.

REFERENCES

[1] D. Borio, F. Dovis, H. Kuusniemi, and L. Presti, "Impact and detection of GNSS jammers on consumer grade satellite navigation receivers," *Proc. IEEE*, vol. 104, no. 6, pp. 1233–1245, Feb. 2016.

[2] M. Psiaki and T. Humphreys, "GNSS spoofing and detection," *Proc. IEEE*, vol. 104, no. 6, pp. 1258–1270, Jun. 2016.

[3] R. Ioannides, T. Pany, and G. Gibbons, "Known vulnerabilities of global navigation satellite systems, status, and potential mitigation techniques," *Proc. IEEE*, vol. 104, no. 6, pp. 1174–1194, Feb. 2016.

[4] C. Hegarty, D. Bobyn, J. Grabowski, and A. Van Dierendonck, "An overview of the effects of out-of-band interference on GNSS receivers," *NAVIGATION, J. Inst. Navigat.*, vol. 67, no. 1, pp. 143–161, Mar. 2020.

[5] Z. Kassas, J. Khalife, A. Abdallah, and C. Lee, "I am not afraid of the jammer: Navigating with signals of opportunity in GPS-denied environments," in *Proc. 33rd Int. Tech. Meeting Satell. Division Inst. Navigat.*, 2020, pp. 1566–1585.

[6] D. Gebre-Egziabher, "What is the difference between 'loose', 'tight', 'ultra-tight' and 'deep' integration strategies for INS and GNSS," *Inside GNSS*, 2007, pp. 28–33.

[7] J. Petit, B. Stottelaar, M. Feiri, and F. Kargl, "Remote attacks on automated vehicles sensors: Experiments on camera and lidar," *Black Hat Europe*, 2015.

[8] J. Morton, F. van Diggelen, J. Spilker Jr., and B. Parkinson, Eds., "Position, navigation, and timing technologies in the 21st century," in *Part D: Position, Navigation, and Timing Using Radio Signals-of-Opportunity*, vol. 2. Berlin, Germany: Wiley, 2021, ch. 35–43, pp. 1115–1412.

[9] J. McEllroy, "Navigation using signals of opportunity in the AM transmission band," Master's thesis, Air Force Institute of Technology, Wright-Patterson Air Force Base, OH, USA, 2006.

[10] X. Chen, Q. Wei, F. Wang, Z. Jun, S. Wu, and A. Men, "Super-resolution time of arrival estimation for a symbiotic FM radio data system," *IEEE Trans. Broadcast.*, vol. 66, no. 4, pp. 847–856, Dec. 2020.

[11] R. Faragher and R. Harle, "Towards an efficient, intelligent, opportunistic smartphone indoor positioning system," *NAVIGAT., J. Inst. Navigat.*, vol. 62, no. 1, pp. 55–72, 2015.

Authorized licensed use limited to: The Ohio State University. Downloaded on September 16,2022 at 02:22:47 UTC from IEEE Xplore. Restrictions apply.

[12] A. Makki, A. Siddig, M. Saad, and C. Bleakley, "Survey of WiFi positioning using time-based techniques," *Comput. Netw.*, vol. 88, pp. 218–233, 2015.

[13] C. Gentner, T. Jost, W. Wang, S. Zhang, A. Dammann, and U. Fiebig, "Multipath assisted positioning with simultaneous localization and mapping," *IEEE Trans. Wireless Commun.*, vol. 15, no. 9, pp. 6104–6117, Sep. 2016.

[14] J. del Peral-Rosado, R. Raulefs, J. López-Salcedo, and G. Seco-Granados, "Survey of cellular mobile radio localization methods: From 1 G to 5 G," *IEEE Commun. Surv. Tut.*, vol. 20, no. 2, pp. 1124–1148, Apr.–Jun. 2018.

[15] Z. Kassas, "Navigation With Cellular Signals of Opportunity," in *Position, Navigation, and Timing Technologies in the 21st Century*, vol. 2, J. Morton, F. van Diggelen, J. Spilker Jr., and B. Parkinson, Eds. Berlin, Germany: Wiley, ch. 37, pp. 1171–1223, 2021.

[16] A. Abdallah and Z. Kassas, "UAV navigation with 5 G carrier phase measurements," in *Proc. ION GNSS Conf.*, 2021, pp. 3294–3306.

[17] C. Yang, T. Nguyen, and E. Blasch, "Mobile positioning via fusion of mixed signals of opportunity," *IEEE Aerosp. Electron. Syst. Mag.*, vol. 29, no. 4, pp. 34–46, Apr. 2014.

[18] L. Chen, O. Julien, P. Thevenon, D. Serant, A. Pena, and H. Kuusniemi, "TOA estimation for positioning with DVB-T signals in outdoor static tests," *IEEE Trans. Broadcast.*, vol. 61, no. 4, pp. 625–638, Dec. 2015.

[19] T. Reid, A. Neish, T. Walter, and P. Enge, "Broadband LEO constellations for navigation," *NAVIGAT., J. Inst. Navigat.*, vol. 65, no. 2, pp. 205–220, 2018.

[20] R. Landry, A. Nguyen, H. Rasaee, A. Amrhar, X. Fang, and H. Benzerrouk, "Iridium next LEO satellites as an alternative PNT in GNSS denied environments—Part 1," *Inside GNSS Mag.*, vol. 14, no. 3, pp. 56–64, May 2019.

[21] Z. Kassas, J. Morales, and J. Khalife, "New-age satellite-based navigation—STAN: Simultaneous tracking and navigation with LEO satellite signals," *Inside GNSS Mag.*, vol. 14, no. 4, pp. 56–65, 2019.

[22] M. Lichtman, R. Jover, M. Labib, R. Rao, V. Marojevic, and J. Reed, "LTE/LTE-A jamming, spoofing, and sniffing: Threat assessment and mitigation," *IEEE Commun. Mag.*, vol. 54, no. 4, pp. 54–61, Apr. 2016.

[23] A. Gupta, R. Jha, P. Gandotra, and S. Jain, "Bandwidth spoofing and intrusion detection system for multistage 5 G wireless communication network," *IEEE Trans. Veh. Technol.*, vol. 67, no. 1, pp. 618–632, Jan. 2018.

[24] W. Xu, C. Yuan, S. Xu, H. Ngo, and W. Xiang, "On pilot spoofing attack in massive MIMO systems: Detection and countermeasure," *IEEE Trans. Inf. Forensics Security*, vol. 16, pp. 1396–1409, 2021, doi: 10.1109/TIFS.2020.3036805.

[25] A. Abdallah, J. Khalife, and Z. Kassas, "Experimental characterization of received 5 G signals carrier-to-noise ratio in indoor and urban environments," in *Proc. IEEE Veh. Technol. Conf.*, 2021, pp. 1–5.

[26] Z. Kassas and T. Humphreys, "Observability analysis of collaborative opportunistic navigation with pseudorange measurements," *IEEE Trans. Intell. Transp. Syst.*, vol. 15, no. 1, pp. 260–273, Feb. 2014.

[27] J. Morales and Z. Kassas, "Tightly-coupled inertial navigation system with signals of opportunity aiding," *IEEE Trans. Aerosp. Electron. Syst.*, vol. 57, no. 3, pp. 1930–1948, Jun. 2021.

[28] M. Driusso, C. Marshall, M. Sabathy, F. Knutti, H. Mathis, and F. Babich, "Vehicular position tracking using LTE signals," *IEEE Trans. Veh. Technol.*, vol. 66, no. 4, pp. 3376–3391, Apr. 2017.

[29] A. Abdallah and Z. Kassas, "Deep learning-aided spatial discrimination for multipath mitigation," in *Proc. IEEE/ION Position, Location, Navigat. Symp.*, 2020, pp. 1324–1335.

[30] J. Khalife and Z. Kassas, "Precise UAV navigation with cellular carrier phase measurements," in *Proc. IEEE/ION Position, Location, Navigat. Symp.*, 2018, pp. 978–989.

[31] C. Yang and A. Soloviev, "Simultaneous localization and mapping of emitting radio sources-SLAMERS," in *Proc. ION GNSS Conf.*, 2015, pp. 2343–2354.

[32] Z. Kassas, M. Maaref, J. Morales, J. Khalife, and K. Shamaei, "Robust vehicular localization and map matching in urban environments through IMU, GNSS, and cellular signals," *IEEE Intell. Transp. Syst. Mag.*, vol. 12, no. 3, pp. 36–52, Jun. 2020.

[33] J. Morales and Z. Kassas, "Stochastic observability and uncertainty characterization in simultaneous receiver and transmitter localization," *IEEE Trans. Aerosp. Electron. Syst.*, vol. 55, no. 2, pp. 1021–1031, Apr. 2019.

[34] Y. Bar-Shalom, X. Li, and T. Kirubarajan, *Estimation With Applications to Tracking and Navigation*. New York, NY, USA: Wiley, 2002.

[35] J. Dunik, O. Kost, O. Straka, and E. Blasch, "State and measurement noise in positioning and tracking: Covariance matrices estimation and gaussianity assessment," in *Proc. IEEE/ION Position, Location, Navigat. Symp.*, 2018, pp. 1326–1335.

[36] M. Shuster, "A survey of attitude representations," *J. Astronautical Sci.*, vol. 41, no. 4, pp. 439–517, Oct. 1993.

[37] P. Groves, *Principles of GNSS, Inertial, and Multisensor Integrated Navigation Systems*, 2nd ed. Norwood, MA, USA: Artech House, 2013.

[38] M. Braasch, "Inertial navigation systems," in *Aerospace Navigation Systems*. Hoboken, NJ, USA: Wiley, 2016.

[39] X. Li and V. Jilkov, "Survey of maneuvering target tracking. Part I: Dynamic models," *IEEE Trans. Aerosp. Electron. Syst.*, vol. 39, no. 4, pp. 1333–1364, Oct. 2003.

[40] A. Thompson, J. Moran, and G. Swenson, *Interferometry and Synthesis in Radio Astronomy*, 2nd ed. New York, NY, USA: Wiley, 2001.

[41] J. Curran, G. Lachapelle, and C. Murphy, "Digital GNSS PLL design conditioned on thermal and oscillator phase noise," *IEEE Trans. Aerosp. Electron. Syst.*, vol. 48, no. 1, pp. 180–196, Jan. 2012.

Authorized licensed use limited to: The Ohio State University. Downloaded on September 16,2022 at 02:22:47 UTC from IEEE Xplore. Restrictions apply.

[42] M. Psiaki and S. Mohiuddin, "Modeling, analysis, and simulation of GPS carrier phase for spacecraft relative navigation," *J. Guid., Control, Dyn.*, vol. 30, no. 6, pp. 1628–1639, Nov./Dec. 2007.

[43] P. Teunissen, "The least-squares ambiguity decorrelation adjustment: A method for fast GPS integer ambiguity estimation," *J. Geodesy*, vol. 70, no. 1, pp. 65–82, Nov. 1995.

[44] X. Chang, X. Yang, and T. Zhou, "MLAMBDA: A modified LAMBDA method for integer least-squares estimation," *J. Geodesy*, vol. 79, no. 9, pp. 552–565, 2005.

[45] J. Khalife and Z. Kassas, "Opportunistic UAV navigation with carrier phase measurements from asynchronous cellular signals," *IEEE Trans. Aerosp. Electron. Syst.*, vol. 56, no. 4, pp. 3285–3301, Aug. 2020.

[46] K. Shamaei and Z. Kassas, "Sub-meter accurate UAV navigation and cycle slip detection with LTE carrier phase," in *Proc. ION GNSS Conf.*, 2019, pp. 2469–2479.

[47] J. Khalife, K. Shamaei, and Z. Kassas, "Navigation with cellular CDMA signals—Part i: Signal modeling and software-defined receiver design," *IEEE Trans. Signal Process.*, vol. 66, no. 8, pp. 2191–2203, Apr. 2018.

[48] K. Shamaei and Z. Kassas, "LTE receiver design and multipath analysis for navigation in urban environments," *NAVIGAT., J. Inst. Navigat.*, vol. 65, no. 4, pp. 655–675, Dec. 2018.

[49] K. Shamaei and Z. Kassas, "Receiver design and time of arrival estimation for opportunistic localization with 5G signals," *IEEE Trans. Wireless Commun.*, vol. 20, no. 7, pp. 4716–4731, Jul. 2021.

[50] M. Orabi, J. Khalife, and Z. Kassas, "Opportunistic navigation with Doppler measurements from Iridium Next and Orbcomm LEO satellites," in *Proc. IEEE Aerosp. Conf.*, 2021, pp. 1–9.

[51] J. Khalife, M. Neinavaie, and Z. Kassas, "The first carrier phase tracking and positioning results with starlink LEO satellite signals," *IEEE Trans. Aerosp. Electron. Syst.*, vol. 58, no. 2, pp. 1487–1491, Apr. 2022, doi: 10.1109/TAES.2021.3113880.

[52] 3GPP2, "Recommended minimum performance standards for cdma2000 spread spectrum base stations," 3rd Generation Partnership Project 2 (3GPP2), TS C.S0010-E, Mar. 2014. [Online]. Available: http://www.arib.or.jp/english/html/overview/doc/STD-T64v7_00/Specification/ARIB_STD-T64-C.S0010-Ev2.0.pdf

Transform lives

Bring the promise of technology — and the knowledge and power to leverage it, to people around the globe. **Donate now to the IEEE Foundation and make a positive impact on humanity.**

- **Inspire technology education**
- **Enable innovative solutions for social impact**
- **Preserve the heritage of technology**
- **Recognize engineering excellence**

IEEE Foundation

Discover how you can do a world of good today.

Learn more about the IEEE Foundation at **ieeefoundation.org**.
To make a donation now, go to **ieeefoundation.org/donate.**

IEEE

Authorized licensed use limited to: The Ohio State University. Downloaded on September 16,2022 at 02:22:47 UTC from IEEE Xplore. Restrictions apply.

I am Not Afraid of the Jammer: Navigating with Signals of Opportunity in GPS-Denied Environments

Zak M. Kassas, Joe Khalife, and Ali Abdallah
University of California, Irvine, USA
Chiawei Lee
US Air Force Test Pilot School, USA

BIOGRAPHIES

Zaher (Zak) M. Kassas is an associate professor at the University of California, Irvine and director of the Autonomous Systems Perception, Intelligence, and Navigation (ASPIN) Laboratory. He received a B.E. in Electrical Engineering from the Lebanese American University, an M.S. in Electrical and Computer Engineering from The Ohio State University, and an M.S.E. in Aerospace Engineering and a Ph.D. in Electrical and Computer Engineering from The University of Texas at Austin. In 2018, he received the National Science Foundation (NSF) Faculty Early Career Development Program (CAREER) award, and in 2019, he received the Office of Naval Research (ONR) Young Investigator Program (YIP) award. He is a recipient of 2018 IEEE Walter Fried Award, 2018 Institute of Navigation (ION) Samuel Burka Award, and 2019 ION Col. Thomas Thurlow Award. He is an Associate Editor for the IEEE Transactions on Aerospace and Electronic Systems and the IEEE Transactions on Intelligent Transportation Systems. His research interests include cyber-physical systems, estimation theory, navigation systems, autonomous vehicles, and intelligent transportation systems.

Joe Khalife is a postdoctoral fellow at the University of California, Irvine and member of the Autonomous Systems Perception, Intelligence, and Navigation (ASPIN) Laboratory. He received a B.E. in Electrical Engineering, an M.S. in Computer Engineering from the Lebanese American University (LAU) and a Ph.D. in Electrical Engineering and Computer Science from the University of California, Irvine. From 2012 to 2015, he was a research assistant at LAU, and has been a member of the ASPIN Laboratory since 2015. He is a recipient of the 2016 IEEE/ION Position, Location, and Navigation Symposium (PLANS) Best Student Paper Award and the 2018 IEEE Walter Fried Award. His research interests include opportunistic navigation, autonomous vehicles, and software-defined radio.

Ali A. Abdallah is a Ph.D student in the Department of Electrical Engineering and Computer Science at the University of California, Irvine and a member of the Autonomous Systems Perception, Intelligence, and Navigation (ASPIN) Laboratory. He received a B.E. in Electrical Engineering from the Lebanese American University (LAU). His current research interests include opportunistic navigation, software-defined radio, long-term evolution (LTE), 5G, and indoor localization.

Chiawei (Wei) Lee is an Instructor Flight Test Engineer at the United States Air Force Test Pilot School. His primary role is as Director of the school's Test Management Program which executes about a dozen real-world flight test projects a year. He also serves as the Chief Test Safety Officer and Flight Test Foundations Branch Chief for USAF TPS. His previous flight test experience includes weapons and electronic warfare testing on the F-16, F-22, F-35, B-1, and B-2. He received a B.S. in Aerospace Engineering from the University of California at Los Angeles and an M.S. in Aeronautics and Astronautics from Stanford University.

ABSTRACT

I am not afraid of the GPS jammer, as long as there are ambient signals of opportunity (SOPs) to exploit in the environment. In environments where GPS signals are challenged (e.g., indoors and deep urban canyons) and denied (e.g., under jamming and spoofing attacks), SOPs could serve as an alternative navigation source to GPS, and more generally, to global navigation satellite systems (GNSS). This paper presents a radio simultaneous localization and mapping (radio SLAM) approach that enables the exploitation of SOPs for resilient and accurate navigation. Radio

Copyright © 2020 by Z. Kassas, J. Khalife, A. Abdallah, and C. Lee

Preprint of the 2020 ION GNSS+ Conference St. Louis, Missouri, September 21–25, 2020

SLAM estimates the states of the navigator-mounted receiver simultaneously with the SOPs' states. Radio SLAM could produce an SOP-derived navigation solution in a standalone fashion or by fusing SOPs with sensors (e.g., inertial measurement unit (IMU), lidar, etc.), digital maps, and/or other signals (e.g., GNSS). The paper also overviews a core component of radio SLAM: a cognitive software-defined radio (SDR) called MATRIX: Multichannel Adaptive TRansceiver Information eXtractor, which produces navigation observables from terrestrial and space-based SOPs. Next, the paper showcases the most accurate navigation results to-date with terrestrial and space-based SOPs from low Earth orbit (LEO) satellites in different environments and on different platforms: indoor pedestrian, ground vehicles in urban and deep urban canyons, and aerial vehicles. Finally, the paper presents the first ever published experimental results for navigation with SOPs in a GPS-denied environment. These experiments took place at Edwards Air Force Base, California, USA, during which GPS was intentionally jammed with jamming-to-signal (J/S) ratio as high as 90 dB. The results showcase a ground vehicle traversing a trajectory of about 5 km in 180 seconds in the GPS-jammed environment, during which a GPS-IMU system drifted from the vehicle's ground truth trajectory, resulting in a position root mean-squared error (RMSE) of 238 m. In contrast, the radio SLAM approach with a *single* cellular long-term evolution (LTE) SOP whose position was poorly known (an initial uncertainty on the order of several kilometers) achieved a position RMSE of 32 m.

I. INTRODUCTION

Global navigation satellite systems (GNSS) are at the heart of numerous technologies that fuel our modern day life. It is estimated that there are currently about 8 billion GNSS devices worldwide, reaching 9 billion by 2025 [1]. The economic benefits of GPS to the U.S. private sector between 1984 and 2017 is estimated to be nearly $1.8 trillion [2], and 15 of the 18 U.S. critical infrastructures rely on GPS [3]. While losing accurate positioning, navigation, and timing (PNT) can be a nuisance in non-safety critical applications, the impact can be catastrophic in safety-critical applications, such as transportation, aviation, military operations, among others. Over the last few years, GNSS jamming [4] and spoofing [5] incidents have been happening with increasing frequency, exposing the inherent vulnerabilities of GNSS, and rendering them a single point of failure. GNSS jamming and spoofing have disrupted airport operations in the United States [6]; affected hundreds of vessels and airplanes in South Korea [7]; disrupted navigation over South China sea islands [8]; caused chaos on smartphones and rideshares in Moscow [9]; put tens of vessels into disarray in the Black Sea [10]; caused dozens of UAVs to plummet during a Hong Kong air show, resulting in hundreds of thousands of dollars in damages [11]; are suspected to have been utilized to hijack unmanned aerial vehicles (UAVs) and oil tankers in the Persian Gulf [12]; and are becoming commonplace in military conflicts [13]. What is particularly alarming is that jamming and spoofing are no longer confined to sophisticated rogue organizations [14, 15], with jammers being sold online and marketed as personal privacy devices [16], and hackers publishing spoofing SDR code online [17]. It is no surprise that the White House issued in February 2020 an Executive Order on "Strengthening National Resilience through Responsible Use of Positioning, Navigation, and Timing Services" [18].

Today's navigation systems, particularly those onboard ground and aerial vehicles, fuse information from a GNSS receiver and an inertial measurement unit (IMU). The integration of these two systems, typically referred to as a GNSS-aided inertial navigation system (INS), takes advantage of the complementary properties of each system: the long-term stability of a GNSS navigation solution aids the short-term accuracy of an INS. Current trends to supplement a navigation system in the inevitable event that GNSS signals become unreliable are traditionally sensor-based (e.g., cameras, lasers, sonar, and odometers). These sensors could be used to extract relative motion information to reduce the INS's error divergence rate. However, they are still dead-reckoning-type sensors; therefore, during prolonged periods of GNSS outage, the error will eventually diverge. Moreover, these sensors only provide local position estimates, may not properly function in all environments (e.g., fog, snow, rain, dust, nighttime, etc.), and are still susceptible to malicious spoofing attacks [19].

Recently, signals of opportunity (SOPs) have been considered to enable navigation whenever GNSS signals become unavailable or unreliable [20–22]. SOPs are ambient radio signals that are not intended for navigation or timing purposes, such as AM/FM radio [23–25], cellular [26–33], digital television [34–37], low Earth orbit (LEO) satellite signals [38–44], and Wi-Fi [45–49]. In contrast to the aforementioned dead-reckoning-type sensors, absolute position information may be extracted from SOPs to provide bounded INS errors. Moreover, many SOPs are practically unaffected by dense smoke, fog, rain, snow, and other poor weather conditions.

SOPs enjoy several inherently desirable attributes for navigation purposes: (i) abundance in most locales of interest, (ii) transmission at a wide range of frequencies and directions, (iii) reception at a carrier-to-noise ratio that is commonly tens of dBs higher than that of GNSS signals, and (iv) they are free to use, since their infrastructure is already operational. However, unlike GNSS, whose satellite states are transmitted in their navigation message, the states of SOPs, namely their position and clock states, are typically unknown *a priori* and must be estimated. To overcome this challenge, a radio simultaneous localization and mapping (radio SLAM) framework was proposed in which the states of the navigating vehicle are simultaneously estimated with the states of the SOPs, while aiding the INS in a tightly-couple fashion [50–52]. Recent work have demonstrated meter-level-accurate navigation with SOPs on ground vehicles and pedestrians indoors [53–58] and centimeter-level accurate navigation on aerial vehicles [59–61]. With appropriately designed navigation receivers and estimation frameworks, SOPs have been exploited as aiding sources for INS [62, 63] and lidar [64, 65].

While recent work has demonstrated experimentally the efficacy of SOPs as PNT sources in a standalone fashion (i.e., without fusing SOPs with any other signals or sensors) and in an integrated fashion (i.e., with fusing SOPs with INS and lidar), experiments were never conducted in actual GNSS-denied environments. The navigation results in such work were achieved by "fictitiously" cutting GNSS signals from the navigation filter. In September 2019, the Autonomous Systems Perception, Intelligence, and Navigation (ASPIN) Laboratory was invited to participate in live GPS jamming experiments at Edwards Air Force Base (AFB), California, USA, called Developmental Test Navigation Festival (DT NAVFEST). Several experiments with stationary antennas and ground vehicles were conducted to study SOPs for PNT. This paper reports findings from these jamming experiments. In particular, the paper analyzes the clock errors of terrestrial SOPs within the jamming region. Moreover, the paper showcases the efficacy of the radio SLAM approach on a ground vehicle navigating in the GPS-denied environment, while exploiting terrestrial SOPs. The experimental results show the vehicle navigating in a jammed GPS region for 5 km in 180 seconds, during which the position root mean-squared error (RMSE) of a traditional GPS-aided INS grew to nearly 238 m, while the radio SLAM approach final position RMSE was around 32 m. To the authors' knowledge, these are the first published results in the literature of navigation with SOPs in real GPS-denied environments, under jamming conditions.

The rest of the paper is organized as follows. Section overviews the radio SLAM framework and the cognitive SDR used to exploit terrestrial and space-based SOPs for PNT. Section III presents experimental navigation results with terrestrial and space-based SOPs from LEO satellites in different environments and on different platforms: ground vehicles in urban and deep urban canyons, aerial vehicles, and indoor pedestrian. Section IV describes the GPS-jammed environment at Edwards AFB and the experimental setup. Section V presents PNT experimental results in the GPS-jammed environment. Section VI gives concluding remarks.

II. RADIO SLAM

This section overviews radio SLAM and the cognitive SDR used to exploit terrestrial and space-based SOPs for PNT.

A. Framework Overview

Radio SLAM estimates the states of the navigator-mounted receiver simultaneously with the SOPs' states. Observability of radio SLAM was analyzed in [66–69], leading to establishing the minimal *a priori* knowledge needed about the navigator-mounted receiver's and/or SOP transmitters' states. Radio SLAM could produce an SOP-derived navigation solution in a standalone fashion [27, 28, 32, 55, 59] or by fusing SOPs with sensors (e.g., inertial measurement unit (IMU) [51, 52, 62], lidar [64, 65], etc.), digital maps [63, 70], and/or signals (e.g., GNSS [27, 71, 72]). Fig. 1 illustrates a high-level block diagram of radio SLAM.

B. MATRIX Cognitive SDR

MATRIX (Multichannel Adaptive TRansceiver Information eXtractor) is a state-of-the-art, cognitive SDR, developed at the ASPIN Laboratory, for navigation with terrestrial and space-based SOPs. MATRIX continuously searches for opportune signals from which it draws navigation and timing information, employing signal characterization on-the-fly as necessary. Fig. 2 shows the architecture of MATRIX.

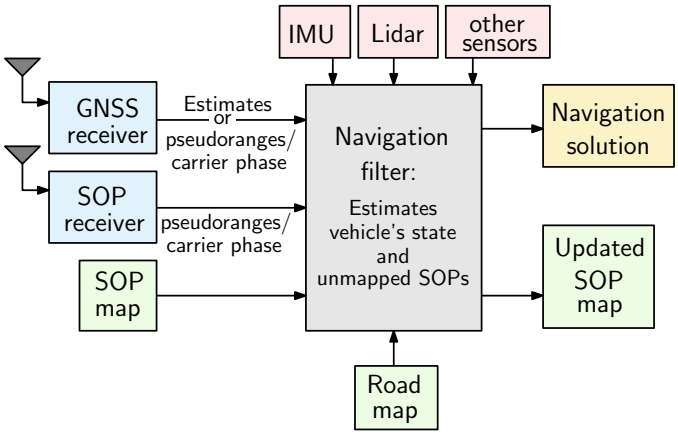

Fig. 1. Radio SLAM framework.

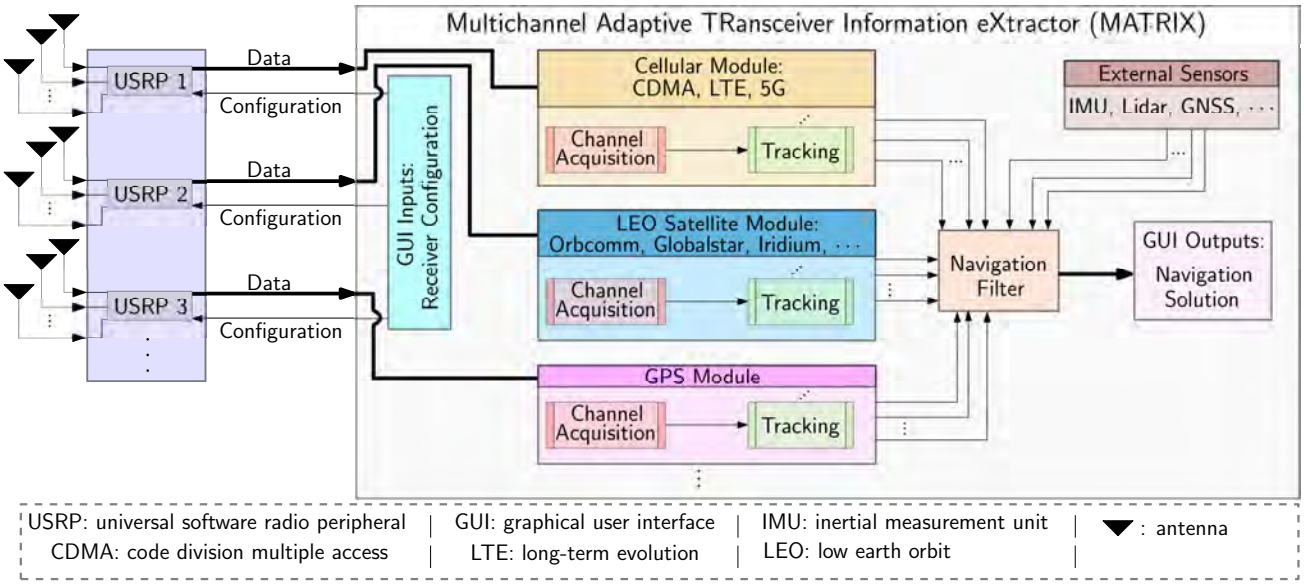

Fig. 2. MATRIX cognitive SDR architecture.

III. NAVIGATION WITH TERRESTRIAL AND LEO SATELLITE SOPS

The radio SLAM framework with MATRIX has been validated experimentally with terrestrial SOPs (cellular code division multiple access (CDMA), LTE, and 5G) and space-based SOPs from LEO satellites (Orbcomm and Iridium constellations) in different environments and on different platforms: ground vehicles in urban and deep urban canyons, aerial vehicles, and indoor pedestrian. This section illustrates these navigation results, which are considered the most accurate to-date for navigation with SOPs.

A. Ground Vehicle Navigation

A.1 Navigation with Standalone LTE SOPs

Fig. 3 shows the navigation performance with standalone LTE signals in an urban environment in Riverside, California, USA, on a ground vehicle [32]. Here, the positions of the LTE towers (also known as eNodeBs) were pre-surveyed and the radio SLAM framework did not estimate these positions, but it estimated the eNodeBs' clock errors along with the ground vehicle's position and velocity. The ground vehicle traversed a trajectory of 1.44 km, achieving a position RMSE of 3.17 m with four eNodeBs. The ground truth was obtained from the GPS navigation solution, produced from 10 GPS satellites.

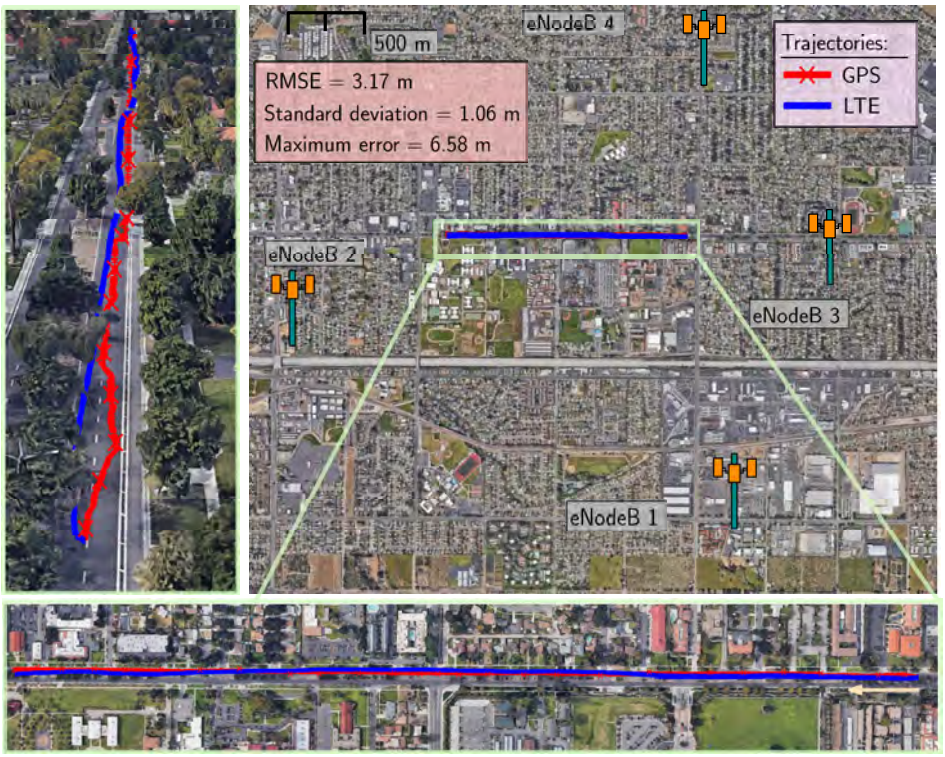

Fig. 3. Ground vehicle navigation with LTE SOPs in an urban environment in downtown Riverside, California, USA. This figure shows the environmental layout, the four LTE eNodeBs' locations, and the traversed trajectory. Over a trajectory of 1.44 km, the LTE navigation solution exhibited a position RMSE of 3.17 m, standard deviation of 1.06 m, and maximum error of 6.58 m from the GPS navigation solution obtained with 10 GPS satellites [32]. Map data: Google Earth.

A.2 Navigation with GPS, LTE, IMU, and Map Matching

Fig. 4 shows the navigation performance with an integrated navigation system, which used GPS and LTE SOPs along with an IMU and map matching in a deep urban environment in downtown Riverside, California, USA, on a ground vehicle [63]. The positions of the LTE eNodeBs were pre-surveyed and the radio SLAM framework did not estimate these positions, but it estimated the eNodeBs' clock errors along with the INS's states. The ground truth was obtained with a Septentrio AsteRx-i V integrated GPS–IMU system, which was equipped with a dual-antenna multi-frequency GNSS receiver and a Vectornav VN-100 microelectromechanical system IMU. The carrier phase observables recorded by the Septentrio system were fused with nearby differential GPS base stations' measurements to produce the carrier phase-based real-time kinematic (RTK) solution [73]. Due to non-line-of-sight, the vehicle encountered 15 seconds of a GPS unavailability period, causing the GPS-IMU solution to accumulate errors due to IMU drift, resulting in a position RMSE of 5.1 m. In contrast, exploiting two LTE eNodeBs in the environment and employing map matching, reduced the position RMSE by 33%, achieving 3.43 m.

A.3 Navigation with LEO Satellite SOPs and IMU

Fig. 5 shows the navigation performance with LEO-aided INS. Here, the radio SLAM framework is more complex due to the poorly known and dynamic, stochastic nature of LEO satellites. The navigation framework is termed STAN: simultaneous tracking and navigation, to emphasize the fact that LEO satellites are *tracked* in their orbit. The ground vehicle traversed a trajectory of 7,495 m in 258 seconds along Interstate 5 in Orange County, California, USA, achieving a position RMSE of 188.6 m when using LEO-aided INS with periodic LEO satellite position updates (transmitted by the LEO satellites) and 195.6 m without satellite position updates (LEO satellite states estimated from two-line element (TLE) files and orbit propagation algorithms), compared to a position RMSE of 1,419 m when using the INS only [74]. The ground truth was obtained using the Septentrio AsteRx-i V integrated GPS–IMU system discussed in Subsection III-A.2.

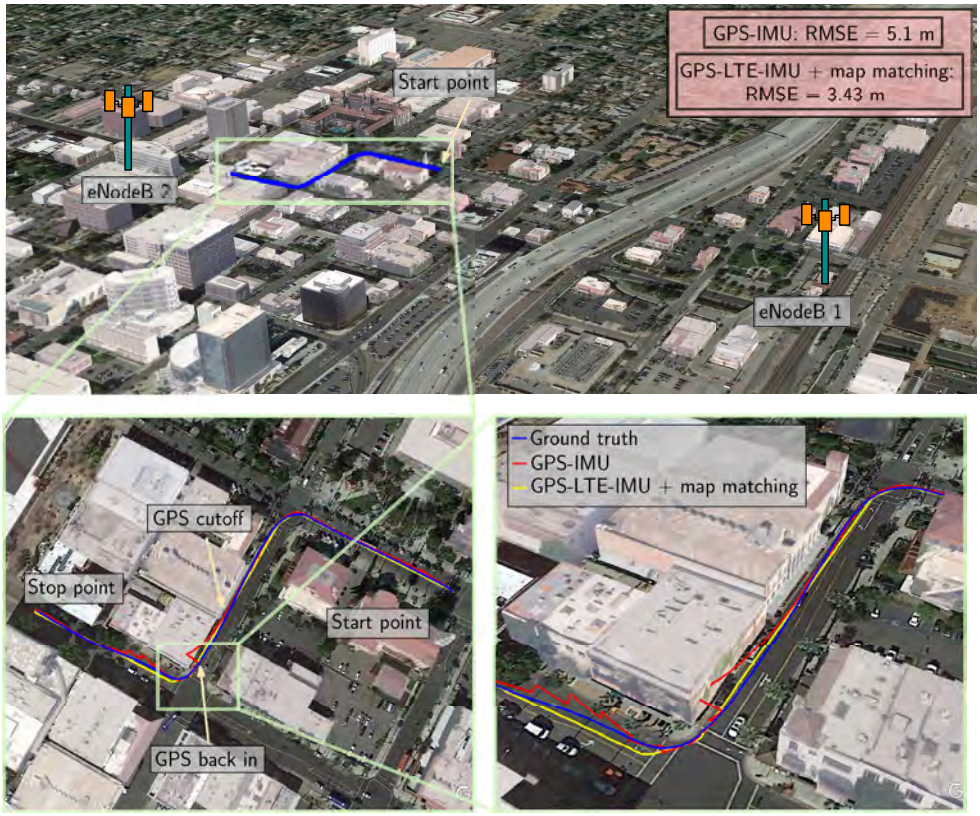

Fig. 4. Ground vehicle navigation with an integrated navigation system, which used GPS and LTE SOPs along with an IMU and map matching in a deep urban environment in downtown Riverside, California, USA. The figure shows the environmental layout, LTE eNodeBs' locations, traversed trajectory, and the different navigation solutions. Over a trajectory of 345 m, the GPS-LTE-IMU with map matching exhibited a position RMSE of 3.43 m compared to 5.1 m achieved using GPS-IMU only [63]. Map data: Google Earth.

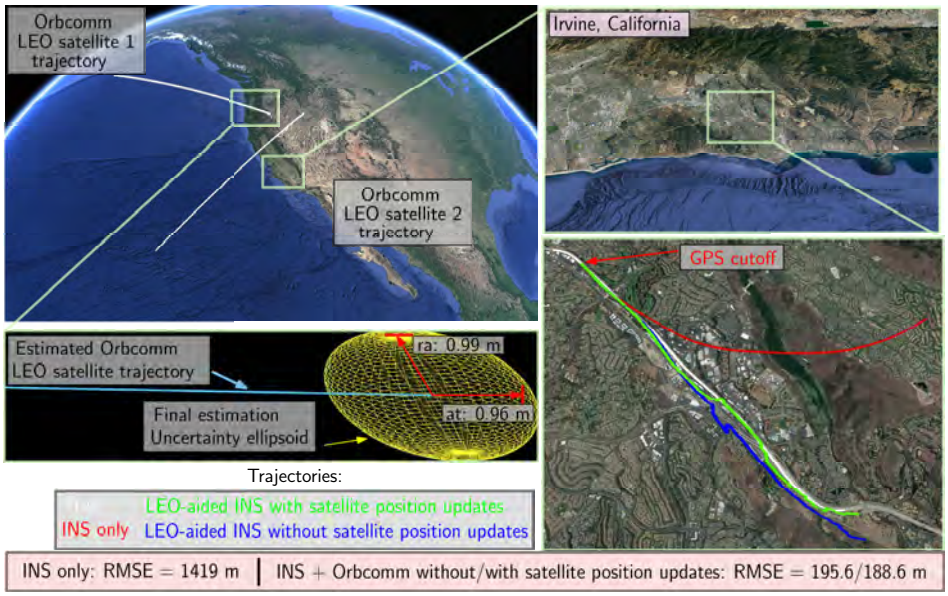

Fig. 5. Ground vehicle navigation with LEO satellite-aided INS in Orange County, California, USA. The figure shows the trajectory of the two Orbcomm LEO satellites, estimated trajectory of one of the satellites and corresponding final position uncertainty, and true and estimated trajectories of the ground vehicle. Over a trajectory of 7,495 m in 258 seconds, the LEO-aided INS exhibited a position RMSE of 188.6 m when using LEO-aided INS with periodic LEO satellite position updates (transmitted by LEO satellites) and 195.6 m without satellite position updates, compared to a position RMSE of 1,419 m with INS only [74]. Map data: Google Earth.

B. Aerial Vehicle Navigation

B.1 Navigation with Standalone CDMA and LTE SOPs

On aerial vehicles and exploiting carrier phase observables, sub-meter level-accurate navigation with standalone cellular CDMA and LTE SOPs can be achieved. Fig. 6 shows the navigation performance with cellular CDMA SOPs for a UAV flown in Colton, California, USA [60]. Here, the positions of the CDMA towers (also known as base transceiver stations (BTSs)) were pre-surveyed and the radio SLAM framework did not estimate these positions. These results were obtained via a carrier phase differential cellular (CD-cellular) CDMA navigation framework. The navigation solution exhibited a two-dimensional (2-D) position RMSE of 62.11 cm over a trajectory of 1.72 km flown in 3 minutes. The solution from the UAV's onboard integrated navigation system was used as ground truth.

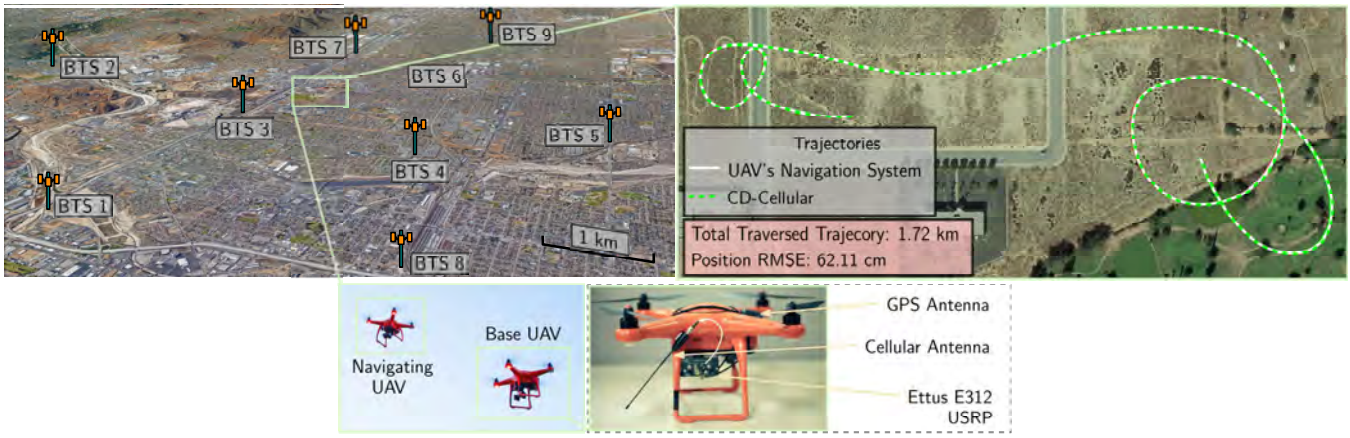

Fig. 6. UAV navigation results with CD-cellular CDMA SOPs in Colton, California, USA [60]. The figure shows the environmental layout, CDMA BTSs' locations, true trajectory (from the UAV's onboard integrated navigation system), and the carrier phase differential cellular (CD-cellular) CDMA navigation solution in the base/rover framework. The CD-cellular navigation solution exhibited a position RMSE of 62.11 cm over a trajectory of 1.72 km flown over a period of 3 minutes. Map data: Google Earth.

Fig. 7 shows the navigation performance with standalone cellular LTE SOPs for a UAV flown in Mission Viejo, California, USA [61]. The figure shows the environmental layout, LTE eNodeBs' locations, true trajectory (from a Septentrio AsteRx-i V GNSS-INS with RTK system), and the carrier phase LTE navigation solution. An altimeter was used in the navigation framework to estimate the UAV's altitude. In contrast to the results shown in Fig. 6, no base was used here. The navigation solution exhibited a 2-D and 3-D position RMSE of 81 cm and 86 cm, respectively, for a traversed trajectory of 605 m over 175 seconds.

B.2 Navigation with CDMA SOPs and IMU

Fig. 8 shows the navigation performance with standalone cellular CDMA SOPs for a UAV flown in Riverside, California, USA [52]. The figure shows the environmental layout, CDMA SOPs' locations, true trajectory (from UAV's onboard integrated navigation system), and the cellular CDMA SOP-aided INS navigation solution. In contrast to the results shown in Fig. 6 and 7, this experiment (1) did *not* assume knowledge of the SOPs' locations: the positions of these SOPs were simulataneously estimated in a radio SLAM fashion, (2) utilized an INS, and (3) used SOP pseudorange measurements.

B.3 Navigation with LEO Satellite SOPs and IMU

Fig. 9 shows experimental results of a UAV navigating via the LEO-aided INS in Irvine, California, USA. The UAV exhibited a final position error of 5.7 m (with LEO satellite position updates) and 29.9 m (without LEO satellite position updates– here, LEO satellite states were estimated from TLE files and orbit propagation algorithms), compared to 123.5 m with an INS only [42].

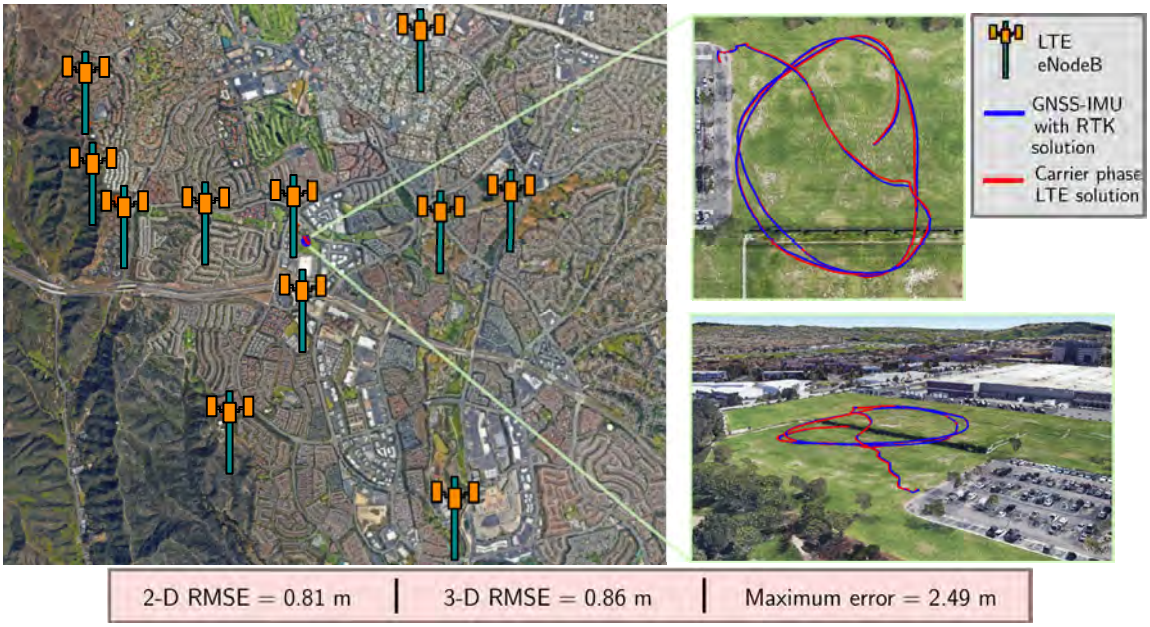

Fig. 7. UAV navigation results with LTE SOPs in Mission Viejo California, USA [61]. This figure shows the environmental layout, LTE eNodeBs' locations, experimental setup, UAV's true trajectory (obtained using a Septentrio AsteRx-i V GNSS-INS with RTK system), and the carrier phase LTE navigation solution. The UAV traversed a trajectory of 605 m over 175 seconds. The results show a 2-D position RMSE of 81 cm and a 3-D position RMSE of 86 cm. Map data: Google Earth.

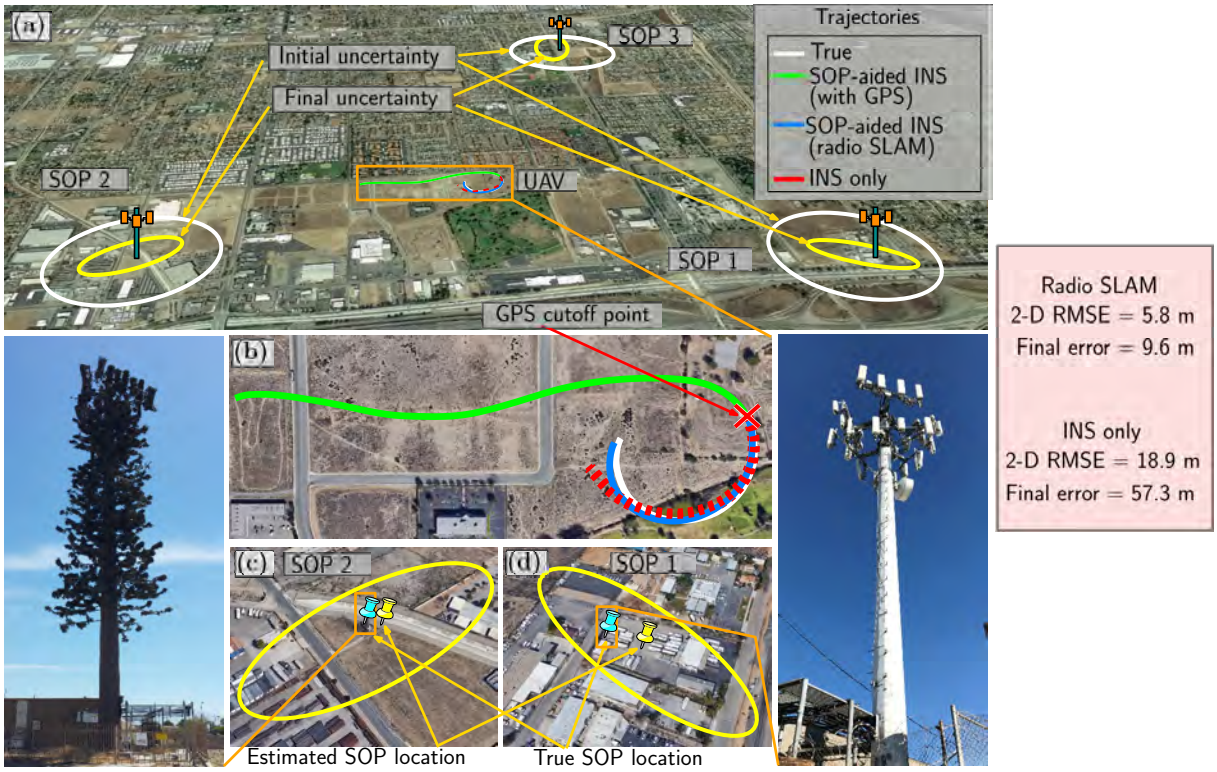

Fig. 8. UAV navigation results with cellular CDMA SOP-aided INS in Riverside California, USA for 80 seconds, the last 30 seconds of which were without GPS [52]. (a) Experimental environment showing the UAV's trajectory, cellular SOPs' locations, initial SOPs' position uncertainties, and final position uncertainties. (b) UAV's trajectory before and after GPS cutoff: (i) white: ground truth, (ii) green: SOP-aided INS before GPS cutoff, (iii) blue: SOP-aided INS after GPS cutoff, and (iv) red: GPS aided INS after GPS cutoff, i.e., INS only. (c) and (d) True and estimated SOP locations and corresponding final uncertainty ellipses. Map data: Google Earth.

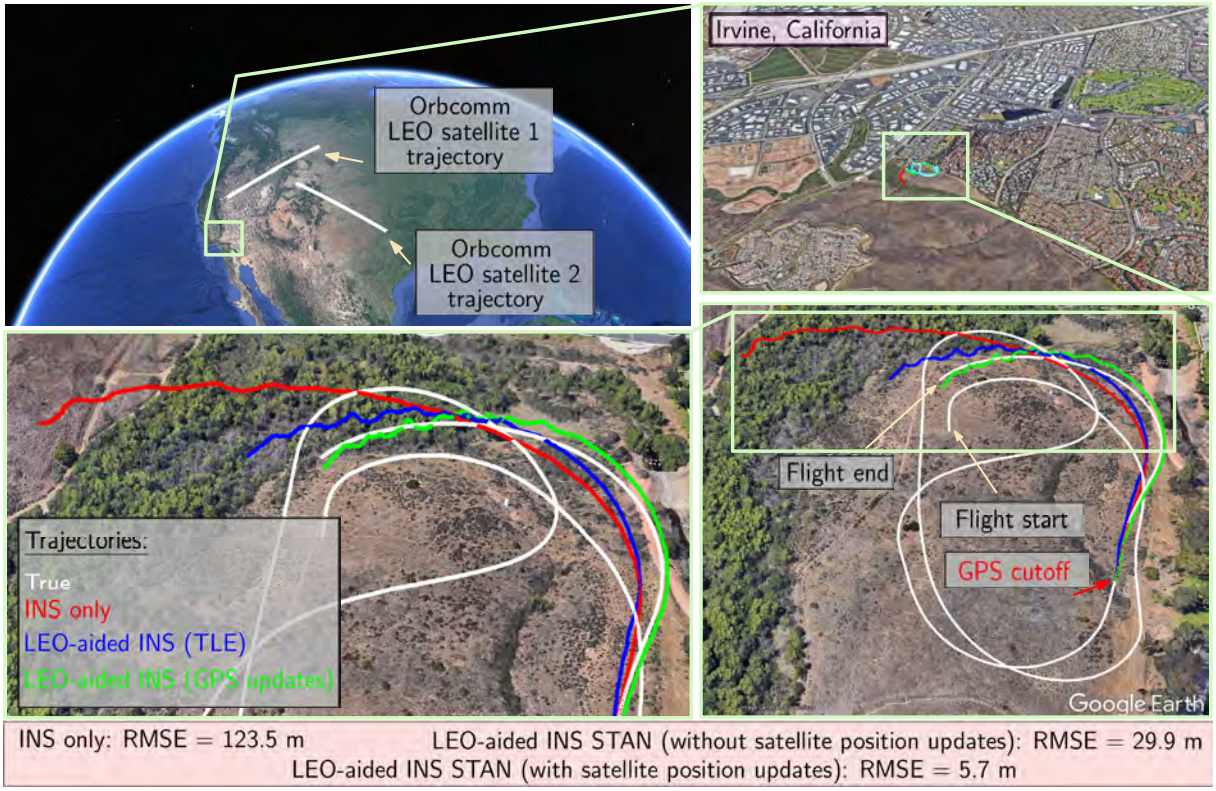

Fig. 9. UAV navigation with LEO satellite-aided INS in Irvine, California, USA, for 155 seconds, the last 30 seconds of which were without GPS [42]. This figure shows: the trajectory of the two Orbcomm LEO satellites, zoom on the UAV's final position and final position estimates, and true and estimated trajectories of the UAV. Map data: Google Earth.

B.4 Navigation with Standalone LEO Satellite SOPs

Fig. 10 shows experimental results of a UAV navigating with carrier phase differential LEO (CD-LEO) satellite signals in Mission Viejo, California, USA [75]. This framework employs a rover and a base receiver. In contrast to the results presented in Fig. 9, no INS was used here. Also, no LEO satellite position updates were used, instead, the LEO satellite states were estimated from TLE files and orbit propagation algorithms. The UAV traversed a trajectory of 2.2 km, achieving a 2-D position RMSE of 15.03 m.

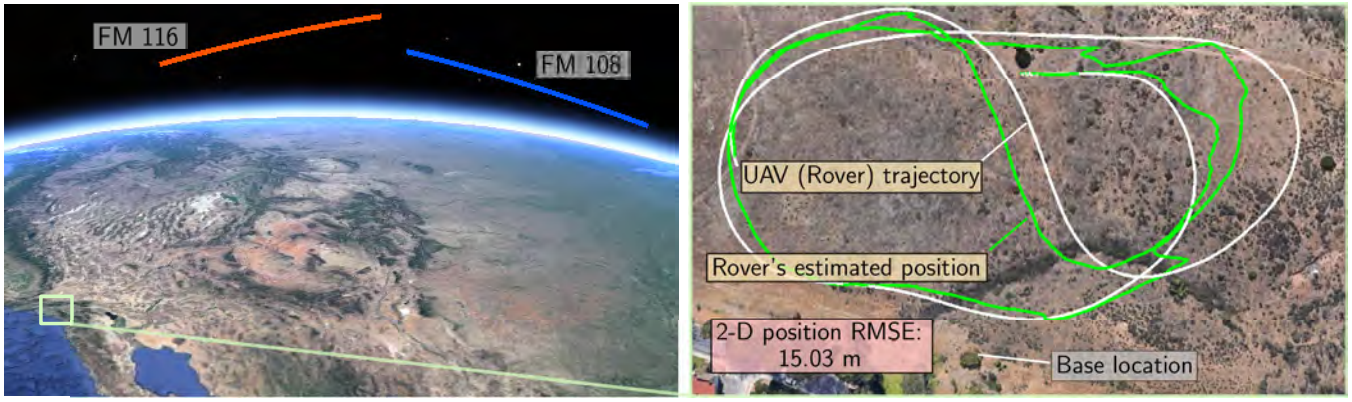

Fig. 10. UAV navigation results with CD-LEO satellite signals in Mission Viejo, California, USA [75]. Here, the UAV (acted as the rover) and a stationary receiver (acted as the base). This figure shows trajectory of the two Orbcomm LEO satellites, true trajectory of the UAV (rover), and the estimated trajectory of the rover using CD-LEO. The UAV traversed a trajectory of 2.2 km, achieving a 2-D position RMSE of 15.03 m. Google Earth.

C. Pedestrian Indoor Navigation

Indoor environments are particularly challenging for SOP-based navigation due to severe signal attenuation and multipath effects. Nevertheless, LTE SOPs have shown tremendous potential in indoor environments, with MATRIX being able to acquire and track LTE signals deep inside buildings, in rooms without windows, and on different floors [76].

Fig. 11(a) shows the navigation performance with LTE SOPs, coupled with a synthetic aperture navigation (SAN) framework to minimize multipath effects by utilizing beamforming. The LTE-SAN navigation solution demonstrated a 2-D position RMSE of 3.93 m compared to 7.19 m from standalone LTE (without SAN) over a traversed trajectory of 126.8 m in 100 seconds and while listening to six LTE eNodeBs [57]. Fig. 11(b) shows the navigation performance of an LTE-aided IMU. The LTE-IMU navigation solution exhibited a 2-D position RMSE of 2.92 m compared to 5.09 m and 9.48 m from standalone LTE and standalone IMU, respectively, for a traversed trajectory of 109 m over 50 seconds and while listening to five LTE eNodeBs [58]. In both experiments, the LTE eNodeBs locations were pre-surveyed.

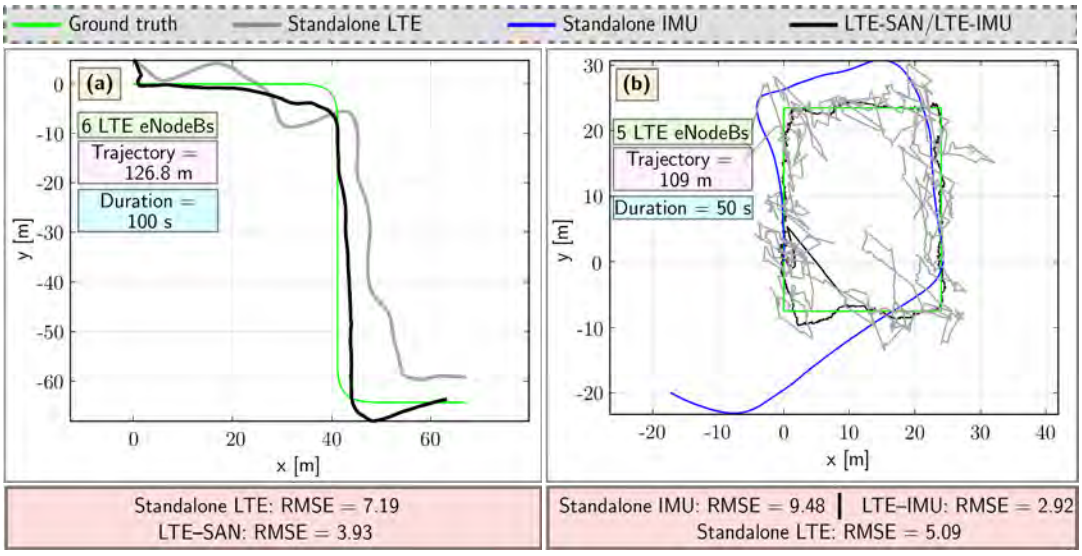

Fig. 11. (a) Pedestrian indoor navigation with LTE SOP signals, at the University of California, Irvine, USA [57]. The figure shows the pedestrian's ground truth trajectory versus the navigation solution from: (i) standalone LTE (without SAN) and (ii) LTE-SAN. (b) Pedestrian indoor navigation with LTE SOP signals and IMU, at the University of California, Riverside, USA [58]. The figure shows the pedestrian's ground truth trajectory versus the navigation solution from: (i) standalone LTE (without IMU) and (ii) LTE-IMU.

IV. GPS-JAMMED ENVIRONMENT AND EXPERIMENTAL SETUP

All SOP-based experimental results presented in Section III were conducted in environments in which GPS signals were *not* jammed. Essentially, GPS signals were "fictitiously" cut off from the navigation filter. In September 2019, the ASPIN Laboratory was invited to conduct experiments during DT NAVFEST live GPS jamming at Edwards AFB, California, USA. This section overviews the GPS-jammed environment and experimental setup.

A. Jamming Laydown

From the information made available to the participants, six high-powered jammers (HPJ) and one portable box jammer (PBJ) were spread over an area of approximately 50 miles north of Edwards AFB, as shown in Fig. 12. The term "Hx" denotes an HPJ, one of them seen in Fig. 12, and "Nx" denotes a PBJ. The initial locations and characteristics of the jammers are summarized in Table I. The experiments conducted by the ASPIN team took place just outside the perimeters of Edwards AFB, mainly on the 58 Highway pictured in Fig. 12 and near the Mojave airport.

TABLE I

JAMMER LAYDOWN

Site	Latitude (N)	Longitude (W)	Terrain height (ft MSL)	Antenna height (ft AGL)	Antenna azimuth true (deg)	Antenna elevation (deg)	Antenna gain (dBi)		EIRP (dBm)		Wave-form
							L1	L2	L1	L2	
Hx1	35° 04′ 12.4”	118° 08′ 41.82”	2769	10	57	15	24.2	24.5	83.8	84.1	CW, BBN
Hx2	34° 59′ 43.52”	117° 52′ 42.35”	2313	10	15	15	24.2	24.5	83.8	84.1	CW, BBN
Hx3	34° 59′ 45.57”	117° 51′ 52.65”	2289	10	13	15	24.2	24.5	83.8	84.1	CW, BBN
Hx4	35° 02′ 59.59”	118° 01′ 40.87”	2528	10	43	15	24.2	24.5	83.8	84.1	CW, BBN
Hx5	34° 57′ 29.35”	117° 57′ 31.78”	2429	10	24	15	24.2	24.5	83.8	84.1	CW, BBN
Hx6	34° 57′ 30.83”	117° 54′ 12.65”	2441	10	17	15	24.2	24.5	83.8	84.1	CW, BBN
Nx1	34° 54′ 42.45”	117° 54′ 5.5”	2309	29	49	-30	14.1	12.9	-12.4	-13.6	CW, BBN

MSL: Mean sea level
AGL: Above ground level
dBi: Decibel isotropic
dBm: Decibel referenced to 1 milliwatt
EIRP: Equivalent, isotropically radiated power. EIRP values accounted for estimated 1.5 dB line loss between amplifier and antenna
CW: Continuous wave
BBN: broad-band noise

B. SOP LTE eNodeB Layout

An SOP radio mapping campaign with MATRIX was conducted a month before DT NAVFEST to survey available LTE eNodeBs in the area [77]. Since Edwards AFB is largely unpopulated, only two LTE eNodeBs (SOP 1 and SOP 2) were hearable in the scheduled jamming area and were located at the same site, as shown in Fig. 13. The eNodeBs were transmitting at high power to service large macrocells in the sparsely populated area. The eNodeBs corresponded to two U.S. cellular providers, and they were transmitting on dual frequencies. The characteristics of the two eNodeBs are summarized in Table II.

TABLE II

ENODEBS' CHARACTERISTICS

eNodeB	Carrier frequency [MHz]	N_{ID}^{Cell}	Cellular provider
1	751/2125	377	Verizon
2	731.5/2145	491	T-Mobile

C. Hardware Setup

The hardware setup used in the performed experiment included: (i) Septentrio GNSS-INS system and (ii) LTE front-end, which are described next.

C.1 Septentrio GNSS-INS System

The Septentrio GNSS-INS system consists of: (i) a multi-frequency GNSS AsteRx-i V receiver, a tactical-grade Vectornav VN-100 micro-electromechanical system (MEMS) IMU, and a dual-GNSS antenna system. AsteRx-i V processes the dual antenna multi-frequency GNSS signals with IMU measurements to generate an accurate and reliable position and orientation solution. Multi-GNSS antennas 1 and 2 were mounted on a wooden board that was mounted on the roof of the vehicle and aligned with the vehicle's main axis. Antenna-1, i.e., the main antenna, was toward the back of the vehicle. Antenna-2, i.e., the auxiliary antenna, was toward the front of the vehicle. The VN-100 IMU was mounted on the wooden board as well, with its x-axis pointing toward the front of the vehicle, the

y-axis pointing to the right of the vehicle (as seen from behind the vehicle), and the z-axis pointing downward. It is worth noting that only GPS was jammed, while signals from other GNSS constellations (Galileo and GLONASS) were available. The GNSS-INS system was used to obtain the vehicle's ground truth trajectory by using signals from the non-jammed GNSS constellations.

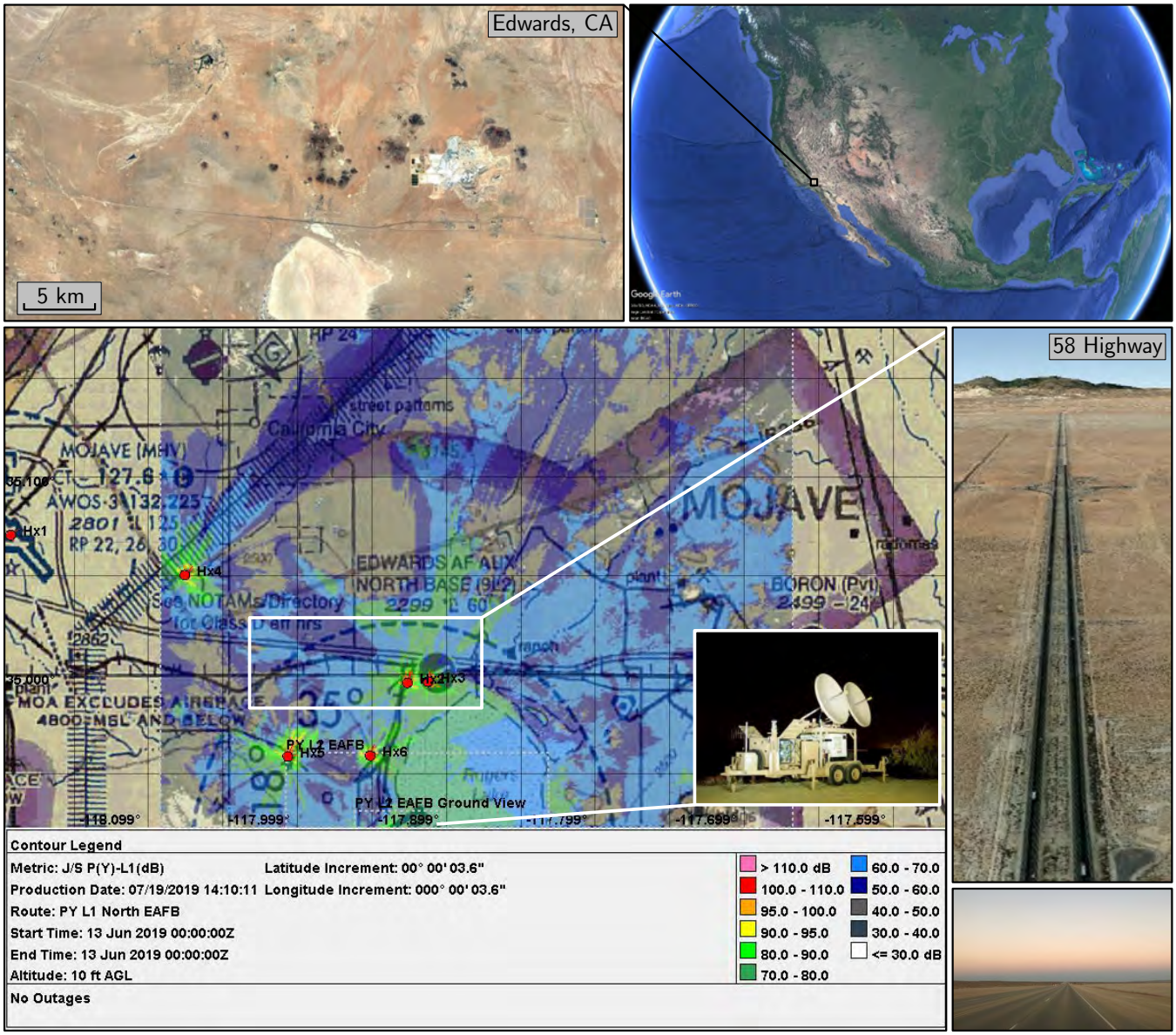

Fig. 12. DT NAVFEST GPS jamming layout. Map data: Google Earth.

C.2 LTE Front-End

The LTE front-end comprised: (i) a quad-channel universal software radio peripheral (USRP)-2955, (ii) two consumer-grade 800/1900 MHz Laird cellular antennas [78], (iii) a PCIe cable, (iv) a laptop, and (v) a consumer-grade GPS antenna to discipline the USRP's onboard GPS-disciplined oscillator (GPSDO). The two Laird antennas were connected to the USRP to capture impinging LTE signals, and the USRP was tuned to listen to two carrier frequencies corresponding to the eNodeBs in Table II.

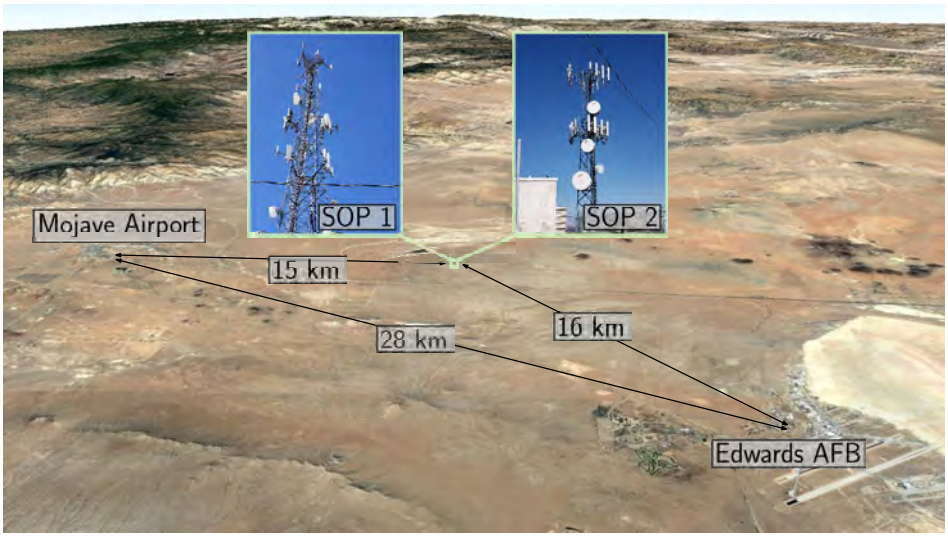

Fig. 13. SOP LTE eNodeB layout.

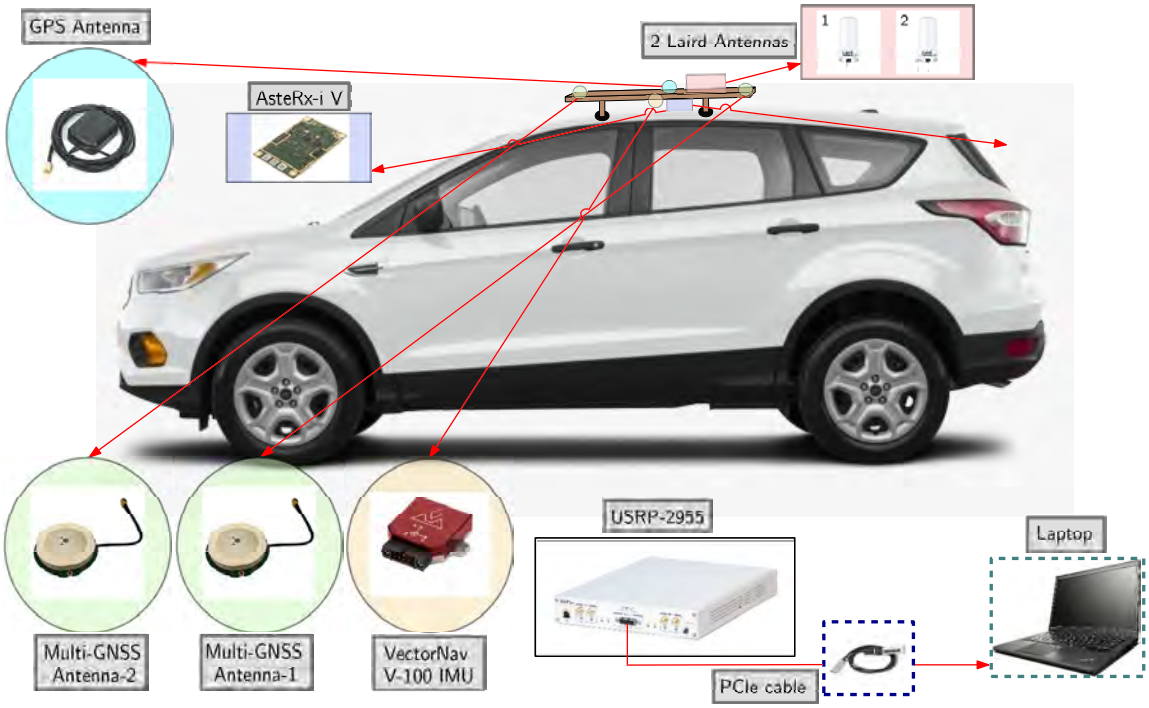

Fig. 14. Ground vehicle and hardware setup.

D. Software Setup

The software setup used in the performed experiment included: (i) Septentrio's post-processing software development kit and (ii) MATRIX, which are described next.

D.1 Septentrio PPSDK Tool

Septentrio's post-processing software development kit (PP-SDK) was used to process GNSS observables collected by the AsteRx-i V to obtain a GNSS-INS navigation solution. This integrated GNSS-INS system [73] was used to produce the ground truth results with which the produced navigation solution was compared.

D.2 MATRIX: LTE-Module

The conducted experiment used the MATRIX SDR's carrier-aided code phase-based LTE module to produce navigation observables from received LTE signals. Fig. 15 shows the GUI front panel of the LTE module of MATRIX.

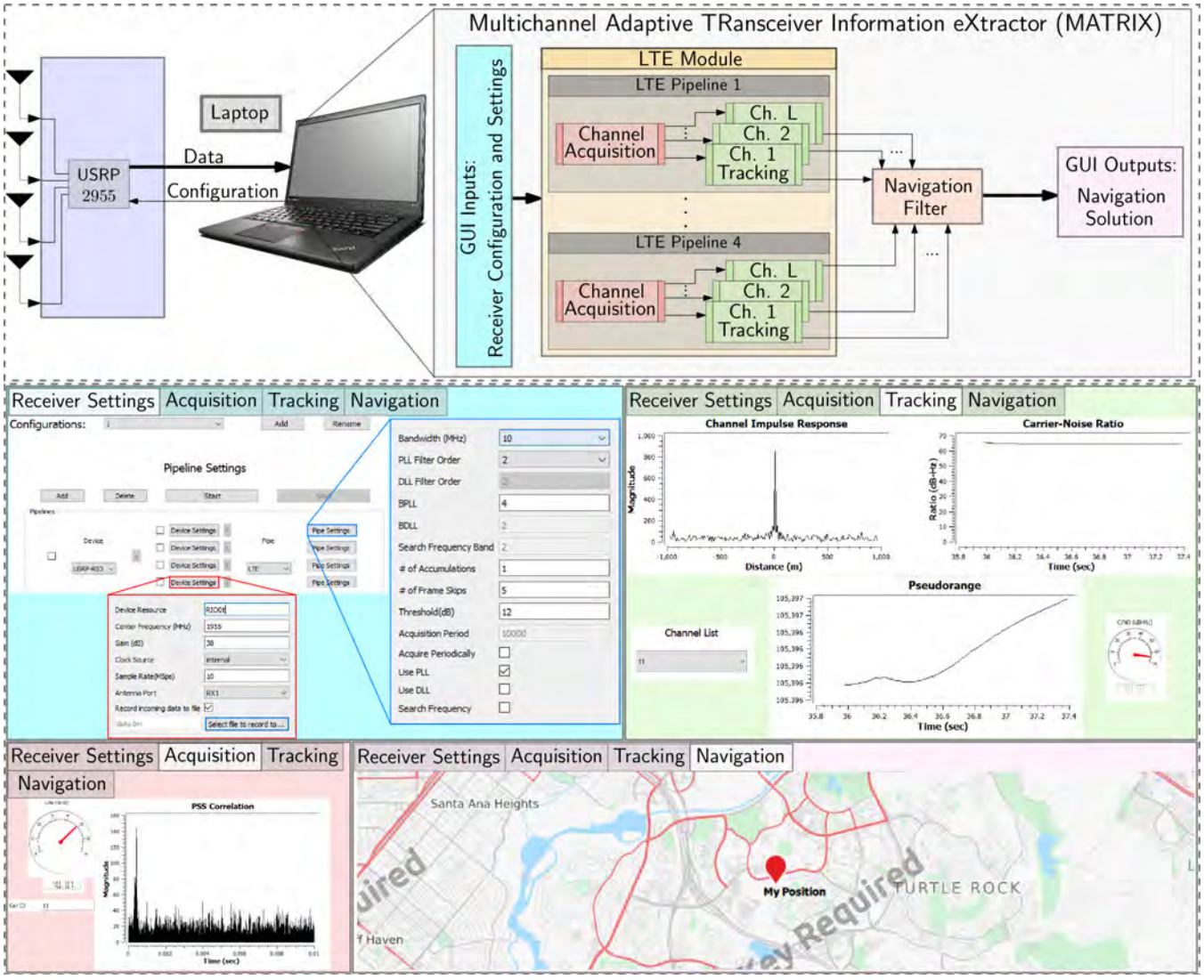

Fig. 15. GUI of the LTE module of the MATRIX SDR.

V. PNT EXPERIMENTAL RESULTS IN GPS-JAMMED ENVIRONMENT

Two experiments were conducted to study the behavior of SOPs in the presence of real GPS jamming and to assess their potential as PNT sources. The results from each experiment are presented next.

A. Experiment 1: Stationary Receiver

Cellular CDMA BTSs and LTE eNodeBs are typically equipped with GPSDOs to meet the synchronization requirements set by the 3GPP [79]. Some opportunistic navigation frameworks exploit the resulting stability of cellular SOPs' clocks [59,61,80]. It is therefore important to evaluate the clock stability of cellular SOPs under GPS jamming to determine their suitability in the opportunistic frameworks discussed in Section III.

A.1 Setup

The setup described in Subsections IV-C and IV-D was deployed outside of the jamming area to listen to the two LTE eNodeBs (SOP 1 and SOP 2) located in an area affected by jamming. The J/S at the eNodeBs was around 60 dBs. During this experiment, the jammers were periodically turned on for 10 minutes, then turned off for 2 minutes. The MATRIX SDR sampled LTE signals synchronously at 10 Msps for 95 minutes on carrier frequencies 751 MHz and 731.5 MHz, which are frequencies allocated to U.S. cellular providers Verizon Wireless and T-Mobile, respectively. Fig. 16 shows the setup of the first experiment.

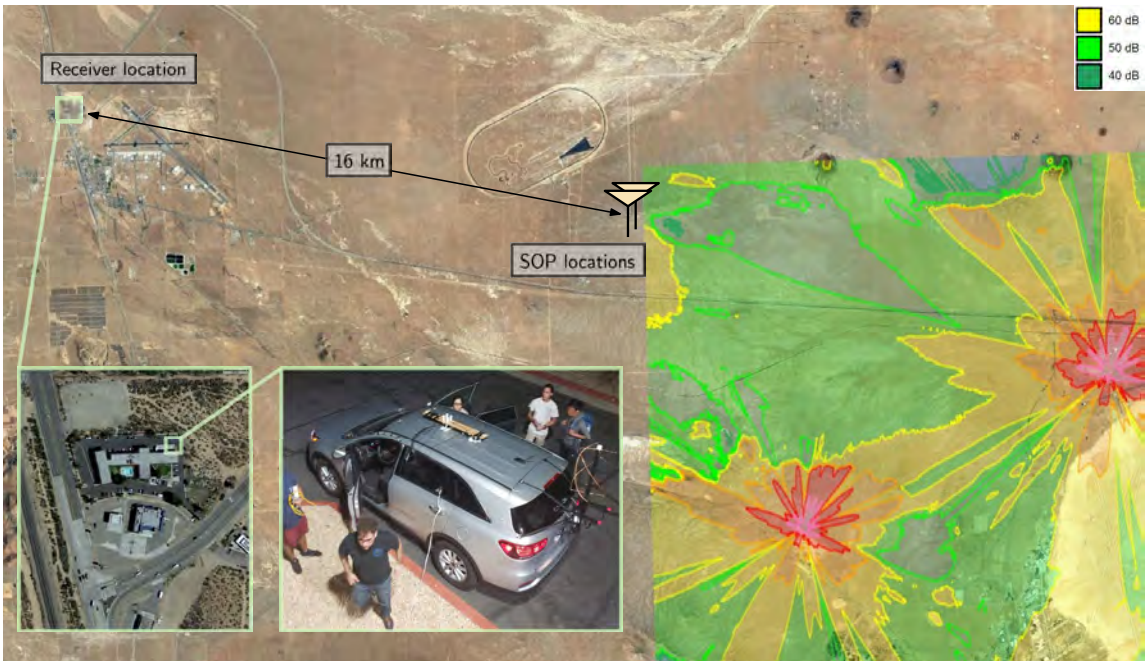

Fig. 16. Experiment 1 setup. The setup discussed in Subsections IV-C and IV-D was deployed outside of the GPS-jammed area to listen to the two SOPs located in an area where J/S was around 60 dB. Map data: Google Earth.

A.2 Results

The LTE signal samples were processed by the LTE module of MATRIX to produce pseudorange observables to the two eNodeBs. Since both the eNodeBs and the receiver were stationary, the variations in the resulting pseudoranges were mainly due to the relative clock biases between the eNodeBs and the receiver. Fig. 17(a) shows the time history of the SOPs' clock biases, which were obtained from their pseudoranges after subtracting the initial pseudorange values. Note that a 5-minute dataloss occurred around the 35^{th} minutes due to a hardware malfunction. After a short initial transient due to the receiver's GPSDO, the clock biases seem to stabilize. Moreover, both clock biases appear to be driven by a common term, which is likely to be the receiver's bias. To evaluate the relative stability between the SOP biases, the difference of the biases (without subtracting their initial values) is plotted in Fig. 17(b), which shows a stable difference around hovering around 1835 m. Fig. 17 does not show significant correlation between the stability of the clock biases and the jamming window, leading to the conclusion that the LTE SOPs' relative stability is maintained for a period of more than an hour during GPS jamming. This could be attributed to either: (i) the oscillators equipped on the towers are disciplined by other GNSS constellations or (ii) the free-running oscillators remained stable during the jamming period.

B. Experiment 2: Mobile Receiver

A second experiment was conducted to demonstrate the radio SLAM framework with real LTE signals under real GPS jamming. The experimental setup and results are discussed next.

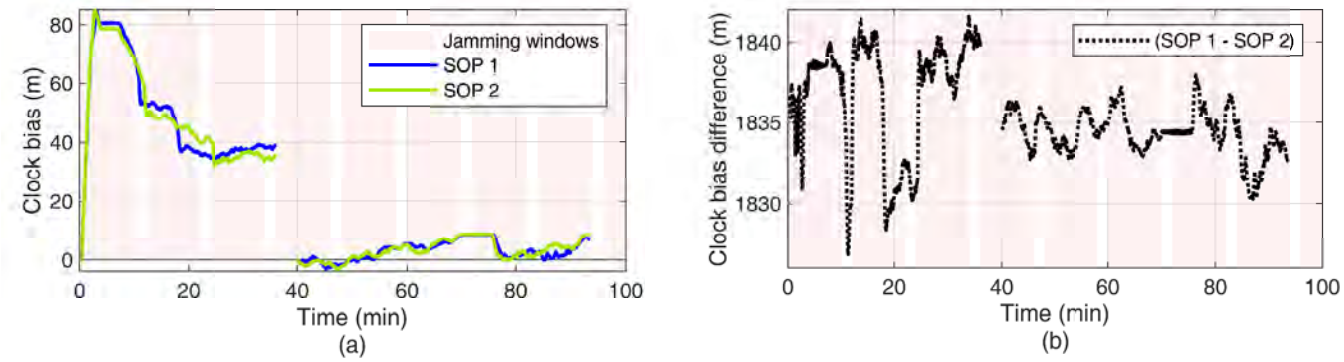

Fig. 17. Experiment 1 results. (a) Time history of clock biases corresponding to SOP 1 and SOP 2. The initial pseudorange values were subtracted. A hardware malfunction around the 35^{th} minute caused a 5-minute dataloss. (b) Clock bias difference between SOP 1 and SOP 2, without subtracting the initial pseudoranges. The stable difference shows that the relative stability between LTE SOPs is maintained for a period of more than an hour during GPS jamming.

B.1 Setup

In this experiment, a ground vehicle was driven in the East direction along the 58 Highway, shown in Fig. 12. Over the course of the experiment, only one LTE eNodeB (SOP 1) was hearable at 751 MHz. LTE samples were collected at 10 Msps for 8 minutes. The vehicle started west of the jamming area, and entered the jamming area around 30 seconds after LTE signal collection started. Then, 10 seconds later, GPS signals became intermittent, after which they were completely lost 10 seconds later. GPS became available again 130 seconds later. During this experiment, the jammers were operating continuously. Two radio SLAM scenarios were considered: (i) the SOP position was assumed to be fully known (from the prior mapping campaign) and (ii) the SOP position was assumed to be unknown, (a prior with a large uncertainty was used). In both scenarios, an EKF was used to produce an estimate of the receiver's and SOP's states from SOP pseudorange measurements. Statistical models were used to propagate the receiver's and SOP's state estimates between GPS or SOP updates. The results are presented next.

B.2 Results

Results from a smartphone navigation application are provided first for comparison. Screenshots from Google Maps running on an iPhone 8 during the ground vehicle's trajectory are shown in Fig. 18. Essentially, the navigation solution stopped updating, would sporadically jump around by hundreds of meters, and the blue "halo" representing the estimated position uncertainty grew to a radius over 6 km.

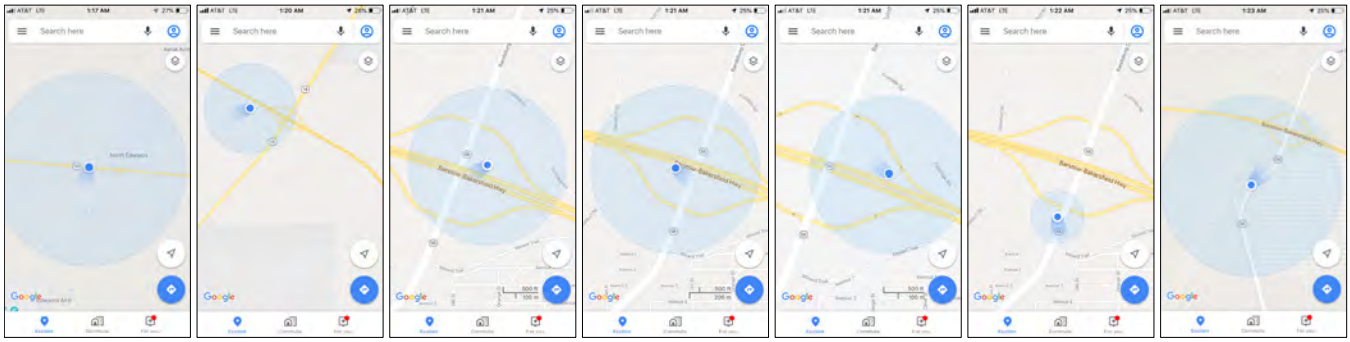

Fig. 18. Screenshots from Google Maps on an iPhone 8 during Experiment 2. The uncertainty grew to a radius over 6 km.

In both radio SLAM scenarios, the receiver had access to GPS signals for the first 50 seconds only. For the SLAM with known SOP position scenario, the SOP position was assumed to be fully known. The receiver's 2-D position RMSE was found to be 29.4 m with a final 2-D position error of 69.4 m. For the radio SLAM with unknown SOP position scenario, the SOP initial position was poorly known. In particular, the SOP position was randomly initialized around the true SOP position with an initial 2-D $\pm 3\sigma$ radius of 3.3 km. For the random realization used

in the EKF, the initial SOP position error was 1.07 km. The receiver's final 2-D position RMSE was found to be 32.2 m with a final 2-D position error of 84.5 m. Table III and Fig. 19 summarize the results of Experiment 2. For comparison, a GPS-IMU solution was produced using Septentrio's PPSDK tool for the same trajectory as the radio SLAM scenarios. The receiver's 2-D position RMSE was found to be 237.9 m from the GPS-IMU solution with a final 2-D position error of 766.0 m.

TABLE III
EXPERIMENT 2 RESULTS

Framework	**Receiver RMSE (m)**	**Receiver final error (m)**	**SOP final error (m)**
Radio SLAM with known SOP position	29.4	69.4	–
Radio SLAM with unknown SOP position	32.2	84.5	5.2
GPS-IMU	237.9	766.0	–

VI. CONCLUSION

This paper justified why I am not afraid of the GPS jammer, as long as there are ambient SOPs to exploit in the environment. This paper presented a radio SLAM approach that enables the exploitation of SOPs for resilient and accurate navigation in environments where GPS signals are challenged (e.g., indoors and deep urban canyons) or denied (e.g., under jamming and spoofing attacks). Radio SLAM could produce an SOP-derived navigation solution in a standalone fashion or by fusing SOPs with sensors (e.g., IMU, lidar, etc.), digital maps, and/or other signals (e.g., GNSS). The paper overviewed MATRIX, a cognitive SDR, which produces navigation observables from terrestrial and space-based SOPs. The paper showcased the most accurate navigation results to-date with terrestrial and space-based SOPs from LEO satellites in different environments and on different platforms: ground vehicles in urban and deep urban canyons, aerial vehicles, and indoor pedestrian. Moreover, the the paper presented the first ever published experimental results for navigation with SOPs in a GPS-denied environment. These experiments took place at Edwards AFB, California, USA, during DT NAVFEST, in which GPS was intentionally jammed with J/S as high as 90 dB. The results analyzed the clock stability of two cellular SOP LTE eNodeBs in the jammed area, showing that the relative stability between the LTE SOPs is maintained for a period of more than an hour during GPS jamming. Moreover, the results showcased a ground vehicle traversing a trajectory of about 5 km in 180 seconds in the GPS-jammed environment, during which a GPS-IMU system drifted from the vehicle's ground truth trajectory, resulting in a position RMSE of 238 m. In contrast, the radio SLAM approach with a *single* cellular LTE SOP whose position was poorly known (an initial uncertainty on the order of several kilometers) achieved a position RMSE of 32 m.

ACKNOWLEDGMENTS

The authors would like to thank Edwards AFB for inviting the ASPIN Laboratory to conduct experiments during DT NAVFEST. The authors would like to thank Joshua Morales, Kimia Shamaei, Mahdi Maaref, Kyle Semelka, MyLinh Nguyen, and Trier Mortlock for their help with data collection. This work was supported in part by the Office of Naval Research (ONR) under Grant N00014-19-1-2511 and Grant N00014-19-1-2613; in part by the National Science Foundation (NSF) under Grant 1929965; and in part by the U.S. Department of Transportation (USDOT) under University Transportation Center (UTC) Program Grant 69A3552047138. DISTRIBUTION STATEMENT A. Approved for public release; Distribution is unlimited 412TW-PA-20399.

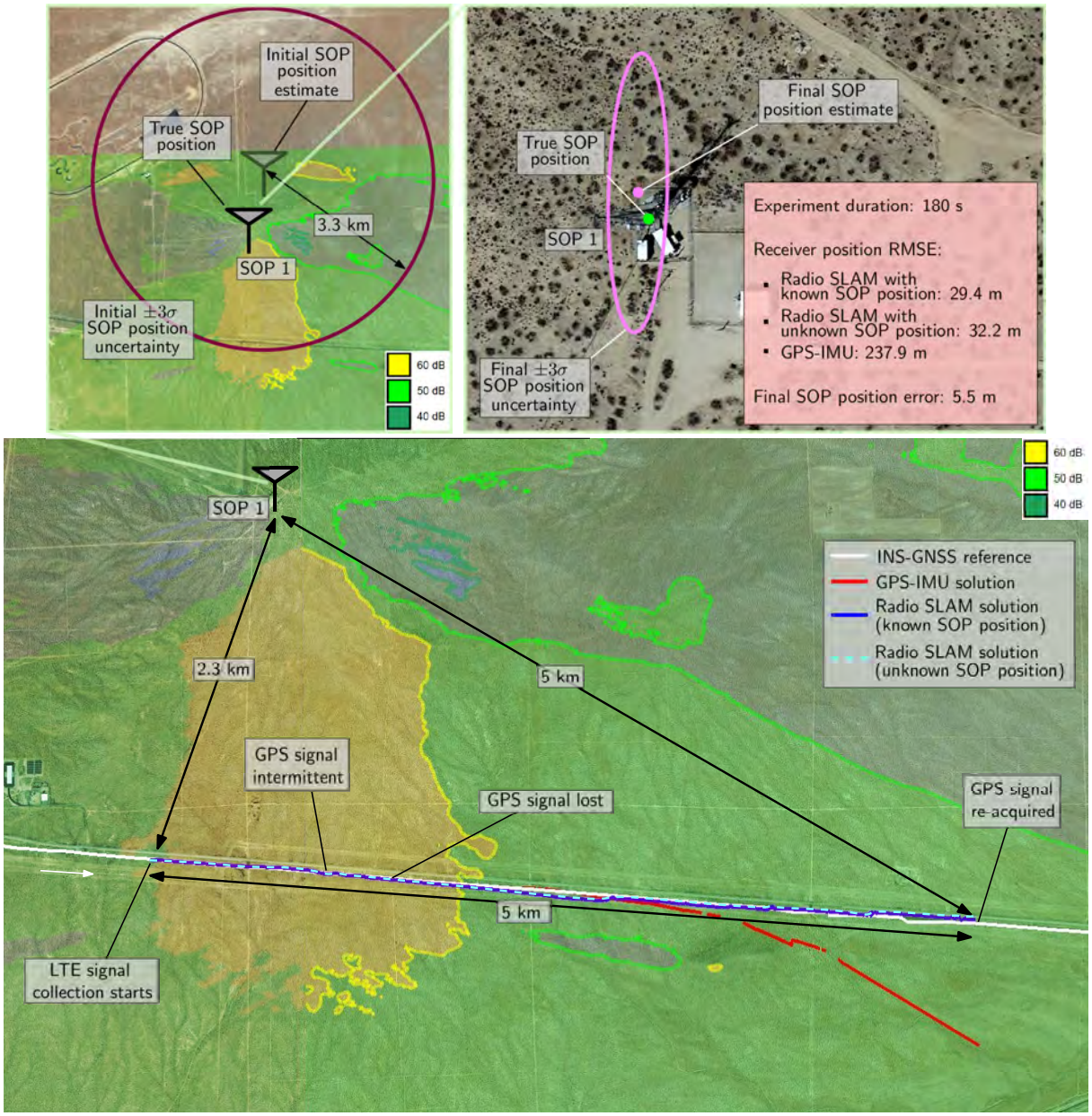

Fig. 19. Experiment 2 layout and results for both scenarios: (i) fully known SOP position and (ii) unknown SOP position.

References

[1] European GNSS Agency (GSA), "GNSS market report," https://www.gsa.europa.eu/system/files/reports/gnss_mr_2017.pdf, May 2017.

[2] RTI International, "Economic benefits of the Global Positioning System," https://www.rti.org/sites/default/files/gps_finalreport.pdf, June 2019.

[3] M. Graham, "GPS use in U.S. critical infrastructure and emergency communications," https://www.gps.gov/multimedia/presentations/2012/10/USTTI/graham.pdf, October 2012.

[4] D. Borio, F. Dovis, H. Kuusniemi, and L. L. Presti, "Impact and detection of GNSS jammers on consumer grade satellite navigation receivers," *Proceedings of the IEEE*, vol. 104, no. 6, pp. 1233–1245, February 2016.

[5] M. Psiaki and T. Humphreys, "GNSS spoofing and detection," *Proceedings of the IEEE*, vol. 104, no. 6, pp. 1258–1270, June 2016.

[6] S. Pullen and G. Gao, "GNSS jamming in the name of privacy: Potential threat to GPS aviation," *Inside GNSS*, pp. 34–43, March/April 2012.

[7] Inside GNSS News, "North Korea's GPS jamming prompts South Korea to endorse nationwide eLoran system," http://www.insidegnss.com/node/3532, April 2013.

[8] Sputnik News, "China jams US spy drones over disputed South China Sea islands," https://sputniknews.com/us/201505221022471108/, May 2015.

[9] C. Sebastian, "Getting lost near the Kremlin? Russia could be 'GPS spoofing'," http://money.cnn.com/2016/12/02/technology/kremlin-gps-signals/index.html, December 2016.

[10] Inside GNSS News, "Reports of mass GPS spoofing attack in the Black Sea strengthen calls for PNT backup," https://insidegnss.com/reports-of-mass-gps-spoofing-attack-in-the-black-sea-strengthen-calls-for-pnt-backup/, July 2017.

[11] D. Divis, "Dozens of drones crash after GPS jammed causing HK$1M in damages, criminal investigation launched," https://insideunmannedsystems.com/dozens-of-drones-crash-after-gps-jammed-causing-hk1m-in-damages-criminal-investigation-launched, October 2018.

[12] Inside GNSS, "Iran is reportedly jamming ship GPS navigation systems to get them to wander into Iranian waters," https://www.businessinsider.com/iran-is-jamming-ship-gpsnavigation-systems-to-seize-them-2019-8, August 2019.

[13] O. Pawlyk, "General: Electronic jamming a growing problem for aircraft in Syria," https://www.military.com/dodbuzz/2018/04/30/general-electronic-jamming-growing-problem-aircraft-syria.html, April 2018.

[14] J. Bhatti and T. Humphreys, "Hostile control of ships via false GPS signals: Demonstration and detection," *NAVIGATION, Journal of the Institute of Navigation*, vol. 64, no. 1, pp. 51–66, 2017.

[15] Inside GNSS, "Tesla Model S and Model 3 prove vulnerable to GPS spoofing attacks, research from Regulus cyber shows," https://insidegnss.com/tesla-model-s-and-model-3-prove-vulnerable-to-gps-spoofing-attacks-research-from-regulus-cyber-shows, June 2019.

[16] GPS World, "FCC to fine Chinese jammer retailer $34.9M for online U.S. sales," http://gpsworld.com/fcc-to-fine-chinese-jammer-retailer-34-9m-for-online-u-s-sales, June 2014.

[17] GPS World, "Inexpensive hack spoofs GPS in smartphones, drones," http://gpsworld.com/inexpensive-hack-spoofs-gps-in-smartphones-drones, August 2015.

[18] United States, Executive Office of the President, "Executive order on strengthening national resilience through responsible use of positioning, navigation, and timing services," Febraury 2020.

[19] J. Petit, B. Stottelaar, M. Feiri, and F. Kargl, "Remote attacks on automated vehicles sensors: Experiments on camera and lidar," *Black Hat Europe*, vol. 11, 2015.

[20] J. Raquet and R. Martin, "Non-GNSS radio frequency navigation," in *Proceedings of IEEE International Conference on Acoustics, Speech and Signal Processing*, March 2008, pp. 5308–5311.

[21] L. Merry, R. Faragher, and S. Schedin, "Comparison of opportunistic signals for localisation," in *Proceedings of IFAC Symposium on Intelligent Autonomous Vehicles*, September 2010, pp. 109–114.

[22] Z. Kassas, "Collaborative opportunistic navigation," *IEEE Aerospace and Electronic Systems Magazine*, vol. 28, no. 6, pp. 38–41, 2013.

[23] J. McEllroy, J. Raquet, and M. Temple, "Use of a software radio to evaluate signals of opportunity for navigation," in *Proceedings of ION GNSS Conference*, September 2006, pp. 126–133.

[24] A. Popleteev, "Indoor positioning using FM radio signals," Ph.D. dissertation, University of Trento, Italy, 2011.

[25] M. Psiaki and B. Slosman, "Tracking of digital FM OFDM signals for the determination of navigation observables," in *Proceedings of ION GNSS Conference*, September 2019, pp. 2325–2348.

[26] C. Yang and T. Nguyen, "Tracking and relative positioning with mixed signals of opportunity," *NAVIGATION, Journal of the Institute of Navigation*, vol. 62, no. 4, pp. 291–311, December 2015.

[27] Z. Kassas, J. Khalife, K. Shamaei, and J. Morales, "I hear, therefore I know where I am: Compensating for GNSS limitations with cellular signals," *IEEE Signal Processing Magazine*, pp. 111–124, September 2017.

[28] J. Khalife and Z. Kassas, "Navigation with cellular CDMA signals – part II: Performance analysis and experimental results," *IEEE Transactions on Signal Processing*, vol. 66, no. 8, pp. 2204–2218, April 2018.

[29] J. del Peral-Rosado, J. López-Salcedo, F. Zanier, and G. Seco-Granados, "Position accuracy of joint time-delay and channel estimators in LTE networks," *IEEE Access*, vol. 6, no. 25185–25199, p. April, 2018.

[30] J. del Peral-Rosado, R. Raulefs, J. López-Salcedo, and G. Seco-Granados, "Survey of cellular mobile radio localization methods: From 1G to 5G," *IEEE Communications Surveys Tutorials*, vol. 20, no. 2, pp. 1124–1148, 2018.

[31] C. Gentner, "Channel-SLAM: Multipath assisted positioning," Ph.D. dissertation, Ulm University, 2018.

[32] K. Shamaei and Z. Kassas, "LTE receiver design and multipath analysis for navigation in urban environments," *NAVIGATION, Journal of the Institute of Navigation*, vol. 65, no. 4, pp. 655–675, December 2018.

[33] A. Abdallah, K. Shamaei, and Z. Kassas, "Assessing real 5g signals for opportunistic navigation," in *Proceedings of ION GNSS Conference*, 2020, accepted.

[34] M. Rabinowitz and J. Spilker, Jr., "A new positioning system using television synchronization signals," *IEEE Transactions on Broadcasting*, vol. 51, no. 1, pp. 51–61, March 2005.

[35] P. Thevenon, S. Damien, O. Julien, C. Macabiau, M. Bousquet, L. Ries, and S. Corazza, "Positioning using mobile TV based on the DVB-SH standard," *NAVIGATION, Journal of the Institute of Navigation*, vol. 58, no. 2, pp. 71–90, 2011.

[36] J. Yang, X. Wang, M. Rahman, S. Park, H. Kim, and Y. Wu, "A new positioning system using DVB-T2 transmitter signature waveforms in single frequency networks," *IEEE Transactions on Broadcasting*, vol. 58, no. 3, pp. 347–359, September 2012.

[37] L. Chen, O. Julien, P. Thevenon, D. Serant, A. Pena, and H. Kuusniemi, "TOA estimation for positioning with DVB-T signals in outdoor static tests," *IEEE Transactions on Broadcasting*, vol. 61, no. 4, pp. 625–638, 2015.

[38] L. Gill, D. Grenier, and J. Chouinard, "Use of XM radio satellite signal as a source of opportunity for passive coherent location," *IET Radar, Sonar Navigation*, vol. 5, no. 5, pp. 536–544, June 2011.

[39] D. Lawrence, H. Cobb, G. Gutt, M. OConnor, T. Reid, T. Walter, and D. Whelan, "Navigation from LEO: Current capability and future promise," *GPS World Magazine*, vol. 28, no. 7, pp. 42–48, July 2017.

[40] T. Reid, A. Neish, T. Walter, and P. Enge, "Broadband LEO constellations for navigation," *NAVIGATION, Journal of the Institute of Navigation*, vol. 65, no. 2, pp. 205–220, 2018.

[41] R. Landry, A. Nguyen, H. Rasaee, A. Amrhar, X. Fang, and H. Benzerrouk, "Iridium Next LEO satellites as an alternative PNT in GNSS denied environments–part 1," *Inside GNSS Magazine*, pp. 56–64., May 2019.

[42] Z. Kassas, J. Morales, and J. Khalife, "New-age satellite-based navigation – STAN: simultaneous tracking and navigation with LEO satellite signals," *Inside GNSS Magazine*, vol. 14, no. 4, pp. 56–65, 2019.

[43] J. Khalife, M. Neinavaie, and Z. Kassas, "Navigation with differential carrier phase measurements from megaconstellation LEO satellites," in *Proceedings of IEEE/ION Position, Location, and Navigation Symposium*, April 2020, pp. 1393–1404.

[44] Z. Kassas, J. Khalife, M. Neinavaie, and T. Mortlock, "Opportunity comes knocking: overcoming GPS vulnerabilities with other satellites' signals," *Inside Unmanned Systems Magazine*, pp. 30–35, June/July 2020.

[45] J. Khalife, Z. Kassas, and S. Saab, "Indoor localization based on floor plans and power maps: Non-line of sight to virtual line of sight," in *Proceedings of ION GNSS Conference*, September 2015, pp. 2291–2300.

[46] R. Faragher and R. Harle, "Towards an efficient, intelligent, opportunistic smartphone indoor positioning system," *NAVIGATION, Journal of the Institute of Navigation*, vol. 62, no. 1, pp. 55–72, 2015.

[47] A. Makki, A. Siddig, M. Saad, and C. Bleakley, "Survey of WiFi positioning using time-based techniques," *Computer Networks*, vol. 88, pp. 218–233, 2015.

[48] Y. Zhuang, Z. Syed, Y. Li, and N. El-Sheimy, "Evaluation of two WiFi positioning systems based on autonomous crowdsourcing of handheld devices for indoor navigation," *IEEE Transactions on Mobile Computing*, vol. 15, no. 8, pp. 1982–1995, August 2016.

[49] Z. Zhang, S. He, Y. Shu, and Z. Shi, "A self-evolving WiFi-based indoor navigation system using smartphones," *IEEE Transactions on Mobile Computing*, vol. 19, no. 8, pp. 1760–1774, 2020.

[50] Z. Kassas, "Analysis and synthesis of collaborative opportunistic navigation systems," Ph.D. dissertation, The University of Texas at Austin, USA, 2014.

[51] J. Morales, P. Roysdon, and Z. Kassas, "Signals of opportunity aided inertial navigation," in *Proceedings of ION GNSS Conference*, September 2016, pp. 1492–1501.

[52] J. Morales and Z. Kassas, "Tightly-coupled inertial navigation system with signals of opportunity aiding," *IEEE Transactions on Aerospace and Electronic Systems*, 2019, submitted.

[53] C. Yang, T. Nguyen, and E. Blasch, "Mobile positioning via fusion of mixed signals of opportunity," *IEEE Aerospace and Electronic Systems Magazine*, vol. 29, no. 4, pp. 34–46, April 2014.

[54] M. Driusso, C. Marshall, M. Sabathy, F. Knutti, H. Mathis, and F. Babich, "Vehicular position tracking using LTE signals," *IEEE Transactions on Vehicular Technology*, vol. 66, no. 4, pp. 3376–3391, April 2017.

[55] K. Shamaei, J. Khalife, and Z. Kassas, "Exploiting LTE signals for navigation: Theory to implementation," *IEEE Transactions on Wireless Communications*, vol. 17, no. 4, pp. 2173–2189, April 2018.

[56] K. Shamaei, J. Morales, and Z. Kassas, "A framework for navigation with LTE time-correlated pseudorange errors in multipath environments," in *Proceedings of IEEE Vehicular Technology Conference*, April 2019, pp. 1–6.

[57] A. Abdallah, K. Shamaei, and Z. Kassas, "Indoor localization with LTE carrier phase measurements and synthetic aperture antenna array," in *Proceedings of ION GNSS Conference*, September 2019, pp. 2670–2679.

[58] A. Abdallah, K. Shamaei, and Z. Kassas, "Performance characterization of an indoor localization system with LTE code and carrier phase measurements and an IMU," in *Proceedings of International Conference on Indoor Positioning and Indoor Navigation*, September 2019, pp. 1–8.

[59] J. Khalife and Z. Kassas, "Precise UAV navigation with cellular carrier phase measurements," in *Proceedings of IEEE/ION Position, Location, and Navigation Symposium*, April 2018, pp. 978–989.

[60] J. Khalife, K. Shamaei, S. Bhattacharya, and Z. Kassas, "Centimeter-accurate UAV navigation with cellular signals," in *Proceedings of ION GNSS Conference*, September 2018, pp. 2321–2331.

[61] K. Shamaei and Z. Kassas, "Sub-meter accurate UAV navigation and cycle slip detection with LTE carrier phase," in *Proceedings of ION GNSS Conference*, September 2019, pp. 2469–2479.

[62] Z. Kassas, J. Morales, K. Shamaei, and J. Khalife, "LTE steers UAV," *GPS World Magazine*, vol. 28, no. 4, pp. 18–25, April 2017.

[63] Z. Kassas, M. Maaref, J. Morales, J. Khalife, and K. Shamaei, "Robust vehicular localization and map matching in urban environments through IMU, GNSS, and cellular signals," *IEEE Intelligent Transportation Systems Magazine*, vol. 12, no. 3, pp. 36–52, June 2020.

[64] J. Khalife, S. Ragothaman, and Z. Kassas, "Pose estimation with lidar odometry and cellular pseudoranges," in *Proceedings of IEEE Intelligent Vehicles Symposium*, June 2017, pp. 1722–1727.

[65] M. Maaref, J. Khalife, and Z. Kassas, "Lane-level localization and mapping in GNSS-challenged environments by fusing lidar data and cellular pseudoranges," *IEEE Transactions on Intelligent Vehicles*, vol. 4, no. 1, pp. 73–89, March 2019.

[66] Z. Kassas and T. Humphreys, "Observability analysis of collaborative opportunistic navigation with pseudorange measurements," *IEEE Transactions on Intelligent Transportation Systems*, vol. 15, no. 1, pp. 260–273, February 2014.

[67] Z. Kassas and T. Humphreys, "Receding horizon trajectory optimization in opportunistic navigation environments," *IEEE Transactions on Aerospace and Electronic Systems*, vol. 51, no. 2, pp. 866–877, April 2015.

[68] J. Morales and Z. Kassas, "Stochastic observability and uncertainty characterization in simultaneous receiver and transmitter localization," *IEEE Transactions on Aerospace and Electronic Systems*, vol. 55, no. 2, pp. 1021–1031, April 2019.

[69] J. Khalife and Z. Kassas, "Opportunistic UAV navigation with carrier phase measurements from asynchronous cellular signals," *IEEE Transactions on Aerospace and Electronic Systems*, vol. 56, no. 4, pp. 3285–3301, August 2020.

[70] M. Maaref and Z. Kassas, "Ground vehicle navigation in GNSS-challenged environments using signals of opportunity and a closed-loop map-matching approach," *IEEE Transactions on Intelligent Transportation Systems*, pp. 1–16, June 2019.

[71] M. Maaref and Z. Kassas, "UAV integrity monitoring measure improvement using terrestrial signals of opportunity," in *Proceedings of ION GNSS Conference*, September 2019, pp. 3045–3056.

[72] M. Maaref, J. Khalife, and Z. Kassas, "Enhanced safety of autonomous driving by incorporating terrestrial signals of opportunity," in *Proceedings of IEEE International Conference on Acoustics, Speech and Signal Processing*, May 2020, pp. 9185–9189.

[73] "Septentrio AsteRx-i V," https://www.septentrio.com/products, 2018.

[74] C. Ardito, J. Morales, J. Khalife, A. Abdallah, and Z. Kassas, "Performance evaluation of navigation using LEO satellite signals with periodically transmitted satellite positions," in *Proceedings of ION International Technical Meeting Conference*, 2019, pp. 306–318.

[75] J. Khalife and Z. Kassas, "Assessment of differential carrier phase measurements from orbcomm LEO satellite signals for opportunistic navigation," in *Proceedings of ION GNSS Conference*, September 2019, pp. 4053–4063.

[76] A. Abdallah, K. Shamaei, and Z. Kassas, "Indoor positioning based on LTE carrier phase measurements and an inertial measurement unit," in *Proceedings of ION GNSS Conference*, September 2018, pp. 3374–3384.

[77] J. Morales and Z. Kassas, "Optimal collaborative mapping of terrestrial transmitters: receiver placement and performance characterization," *IEEE Transactions on Aerospace and Electronic Systems*, vol. 54, no. 2, pp. 992–1007, April 2018.

[78] "Laird phantom 3G/4G multiband antenna NMO mount white TRA6927M3NB," https://www.lairdtech.com/products/phantom-series-antennas.

[79] 3GPP2, "Recommended minimum performance standards for cdma2000 spread spectrum base stations," 3rd Generation Partnership Project 2 (3GPP2), TS C.S0010-E, March 2014. [Online]. Available: http://www.arib.or.jp/english/html/overview/doc/STD-T64v7_00/Specification/ARIB_STD-T64-C.S0010-Ev2.0.pdf

[80] J. Khalife and Z. Kassas, "Evaluation of relative clock stability in cellular networks," in *Proceedings of ION GNSS Conference*, September 2017, pp. 2554–2559.

Joint Detection and Tracking of Unknown Beacons for Navigation with 5G Signals and Beyond

Mohammad Neinavaie and Zaher M. Kassas
The Ohio State University

BIOGRAPHIES

Mohammad Neinavaie is a Ph.D. student at The Ohio State University and member of the Autonomous Systems Perception, Intelligence, and Navigation (ASPIN) Laboratory. He received a B.E. in electrical engineering and an M.S. in digital communication systems from Shiraz University. His research interests include opportunistic navigation, blind opportunistic navigation, cognitive radio, wireless communication systems and software-defined radio.

Zaher (Zak) M. Kassas is a Professor at The Ohio State University and director of the Autonomous Systems Perception, Intelligence, and Navigation (ASPIN) Laboratory. He is also director of the U.S. Department of Transportation Center: CARMEN (Center for Automated Vehicle Research with Multimodal AssurEd Navigation), focusing on navigation resiliency and security of highly automated transportation systems. He received a B.E. in Electrical Engineering from the Lebanese American University, an M.S. in Electrical and Computer Engineering from The Ohio State University, and an M.S.E. in Aerospace Engineering and a Ph.D. in Electrical and Computer Engineering from The University of Texas at Austin. He is a recipient of the 2018 National Science Foundation (NSF) CAREER award, 2019 Office of Naval Research (ONR) Young Investigator Program (YIP) award, 2022 Air Force Office of Scientific Research (AFOSR) YIP award, 2018 IEEE Walter Fried Award, 2018 Institute of Navigation (ION) Samuel Burka Award, and 2019 ION Col. Thomas Thurlow Award. His research interests include cyber-physical systems, navigation systems, autonomous vehicles, and intelligent transportation systems.

ABSTRACT

A receiver architecture is proposed to jointly detect and track unknown beacons to extract navigation observables from fifth generation (5G) new radio (NR) signals of opportunity and beyond. Unlike conventional opportunistic receivers which require knowledge of the signal structure, particularly the reference signals (RSs), the proposed receiver requires knowledge of only the RS period and carrier frequency of the signal. The transmitted RSs for private networks are unknown for an opportunistic receiver. Moreover, to use the spectrum more efficiently, some of these RSs are only transmitted on demand in 5G NR, which limits the existing opportunistic navigation frameworks to signals which are on *always-on*; hence, limiting the exploitable RS bandwidth. To exploit the full available bandwidth and improve ranging accuracy, the proposed receiver is designed to estimate all the RSs contained in the transmitted signals corresponding to multiple unknown sources. Navigation observables (pseudorange and carrier phase) are subsequently derived from the estimated RSs. The proposed receiver operates in two stages: (i) detection of unknown signals and (ii) tracking. The detection of unknown signals is modeled as a sequential detection problem where the number of sources and their corresponding RSs and Doppler frequencies are unknown. The generalized likelihood ratio (GLR) test for sequentially detecting active gNBs is used to estimate the number of sources and their RSs. In order for the receiver to refine and maintain the Doppler and RS estimates provided by the acquisition stage, tracking loops are used. The output of the tracking loops, namely carrier phase and code phase, are then used to estimate the receiver's position. Experimental results are presented demonstrating the capabilities of the proposed receiver with real 5G signals on ground and aerial platforms, with an experiment showing the navigation results with real 5G signals on an unmanned aerial vehicle (UAV) navigating using the proposed receiver over a 416 m trajectory with a position root mean-squared error (RMSE) of 4.35 m.

I. INTRODUCTION

To address the demands of emerging applications such as internet of things (IOT) and autonomous vehicles, fifith generation (5G) has been developed, with a focus on features such as enhanced mobile broadband, ultra-reliable low-latency communications, and massive machine type communications (Parkvall et al., 2020). Based on the performance requirements set by the international telecommunication union (ITU), the third generation partnership project (3GPP) began 5G standardization in 2015 and released its first specifications on a 5G system in June 2018, which included both the new air interface, known as new radio (NR), and 5G core network (5GC) (Takeda et al., 2020). One main characteristic of 5G signals is high data rate, which necessitates a higher transmission bandwidth and more sophisticated multiplexing techniques. The scarcity of unlicensed spectrum in lower

frequencies called for using millimeter waves (mmWaves) for NR signal transmission (Baenke et al., 2020). The high path loss of propagated mmWave signals can be compensated for by beamforming techniques and massive multiple-input multiple-output (mMIMO) antenna structures (Giordani et al., 2019). Beamforming in 5G requires the knowledge of the user's location, which means that 5G-based positioning is not only an auxiliary service, but is essential for resource allocation and beamforming for high data rate transmission (Fascista et al., 2019). Different types of positioning techniques have been evaluated by the 3GPP in Release 15 and 16.

Cellular positioning techniques in the literature can be classified into *network-based* and *opportunistic* approaches (del Peral-Rosado et al., 2018b; Kassas, 2021). Network-based approaches require two-way communication with the network and the transmission of a pre-specified positioning reference signal (PRS) and some system parameters such as the number of transmission antennas and the beamforming matrix. Network-based positioning capabilities in wireless communication systems have been defined since 4G systems (del Peral-Rosado et al., 2018a). In a contrast to network-based approaches, in opportunistic approaches, the user equipment (UE) estimates its position from downlink signals, without communicating back with the network. As such, opportunistic approaches are more attractive than network-based approaches since: they (i) do not require additional overhead or bandwidth, (ii) preserve the UE's privacy, (iii) do not require paying subscription to the network, and (iv) enable the UE to exploit signals from multiple cellular providers simultaneously, which improves the positioning accuracy. Opportunistic navigation frameworks usually rely on the broadcast reference signals (RSs), which are used to derive direction-of-arrival (DOA) and time-of-arrival (TOA) (Shamaei and Kassas, 2021a). These signals are known at the UE and are universal across network operators. Hence, they can be exploited for positioning without the need for the UE to be a network subscriber. In cellular long-term evolution (LTE) networks, several RSs, such as the cell-specific reference signal (CRS), are broadcast at regular and known time intervals, regardless of the number of UEs in the environments. This *always-on* type of transmitted RSs reduces the network's energy efficiency and increases operational expenses and interference. One of the main features of 5G signals is *ultra-lean* transmission, which minimizes the transmission of always-on signals. For instance, CRS which used to be an always-on RS in LTE, is not necessarily being continuously transmitted in 5G signals. Up until now, 5G opportunistic navigation methods relied on the always-on signals, e.g., the primary and secondary synchronization signals (PSS and SSS, respectively) and the physical broadcast channel (SS/PBCH) block, none of which use the entire signal bandwidth (Shamaei and Kassas, 2021b).

This paper presents the cognitive opportunistic navigation (CON) framework originally presented in (Neinavaie et al., 2022b) as a joint detection and tracking algorithm which develops a receiver architecture to simultaneously detect the active unknown beacons in the environment, estimate the number of unknown beacons and their unknown RSs which are not necessarily *always-on*, and exploit them to derive navigation observables. There are four main RSs in 5G signals: demodulation RSs, phase tracking RSs, sounding RSs, and channel state information (CSI) RSs. These RSs are only transmitted on demand, which limits the efficacy of conventional opportunistic navigation frameworks which rely on always-on RSs. For instance, while the receiver proposed in (Shamaei and Kassas, 2021b) was the first 5G-based opportunistic navigation receiver, it relies on the always-on SB/PBCH block. The downside of relying only on the SB/PBCH block is the limited bandwidth. Higher signal bandwidth translates to more accurate TOA estimates. In order to exploit the full ranging accuracy achievable with 5G signals, the CON receiver is designed to cognitively estimate the RSs present in the entire bandwidth and exploit them to obtain navigation observables (pseudoranges and carrier phase). Not only the proposed receiver is capable of exploiting RSs which are not always-on, but the cognitive nature of the proposed receiver enables opportunistic navigation with future communication standards with unknown or partially known signal specifications. The proposed receiver architecture relies solely on the periodicity of the RSs and requires very limited information about the 5G signal, namely it only assumes knowledge of the frame duration and the carrier frequency. It should be pointed out that an energy detector can be used to provide an estimate of the carrier frequency and using the current literature, e.g., the period estimator in (Conte et al., 2010), the frame duration can also be estimated in a pre-processing stage.

The rest of the paper is organized as follows. Section II surveys related research. Section III describes the received baseband signal model. Section IV presents the proposed proposed receiver architecture. Section V presents the experimental results. Section VI gives concluding remarks.

II. RELATED WORK

1. Opportunistic Navigation

Over the past decade, opportunistic navigation has been demonstrated in the literature with different types of signals, also known as signals of opportunity (SOPs). SOP examples include cellular (Gadka et al., 2019; Hong et al., 2021; Kazaz et al., 2022; Lapin et al., 2022; Maaref and Kassas, 2022; Shamaei and Kassas, 2021a; Soderini et al., 2020; Souli et al., 2021b; Strandjord et al., 2021; Wang and Morton, 2022; Xhafa et al., 2021), digital television (Hong et al., 2021; Souli et al., 2021a; Yang and Soloviev, 2020), FM radio (Aziz and Allen, 2018; Chen et al., 2020; Psiaki and Slosman, 2022), and low-earth orbit (LEO) satellite signals (Farhangian and Landry, 2020; Hartnett, 2022; Huang et al., 2022; Iannucci and Humphreys, 2022; Khalife et al., 2022; Kozhaya and Kassas, 2022; Leng et al., 2016; Wei et al., 2020). Among terrestrial SOPs, cellular signals have attracted

considerable attention due to their desirable attributes, including: (i) large transmission bandwidth, (ii) high carrier-to-noise ratio, and (iii) desirable geometric diversity. Cellular SOPs have been demonstrated to yield meter-level accuracy in urban and indoor environments experiencing severe multipath (Abdallah and Kassas, 2021; Dun et al., 2020; Jao et al., 2022; Wang and Morton, 2020; Wang and Morton, 2020; Wang et al., 2022; Whiton et al., 2022) and sub-meter-level positioning accuracy on unmanned aerial (UAVs) (Khalife and Kassas, 2022a,b).

Nevertheless, the aforementioned approaches relied on the knowledge of a subset of the RSs transmitted by the SOP. These methods would fail if (i) the receiver enters an unknown SOP environment where the number of active SOPs and their corresponding RSs are unknown, or (ii) some signal parameters change due to the dynamic nature of wireless protocols. This paper addresses these issues by estimating all available RSs within the SOP with minimal prior knowledge.

2. Positioning with 5G Signals

The characteristics of mmWave signals were evaluated for positioning in (Wymeersch et al., 2017). Cramér-Rao lower bounds (CRLBs) of the direction-of-departure (DOD), DOA, and TOA for both uplink and downlink mmWave signals were derived in (Abu-Shaban et al., 2018; Abu-Shaban et al., 2018), showing sub-meter positioning error, and sub-degree orientation error. To exploit the sparsity of mmWave channels, tools relying on compressed sensing were proposed in (Lee et al., 2014),(Yacong, 2018) to estimate DOD, DOA, and TOA of the UE, showing sub-meter level position error via simulation results. The DOD and UE's position were estimated in a two stage Kalman filter using the signal strength from multiple base stations in (Rastorgueva-Foi et al., 2018), which yielded sub-meter-level three-dimensional (3-D) position accuracy. The joint estimation of the position and orientation of the UE, as well as the location of reflectors or scatterers in the absence of the line-of-sight (LOS) path were considered in (Mendrzik et al., 2018), showing less than 15 m position RMSE and less than 7 degree orientation RMSE. A two-way distributed localization protocol was proposed in (Abu-Shaban et al., 2018) to remove the effect of the clock bias in TOA estimates. In (Fascista et al., 2019), a positioning method for multiple-output single-input systems was proposed, where the DOD and TOA of the received signal were used to localize a UE. In (Ma et al., 2020), estimation of signal parameters via rotational invariant techniques (ESPRIT) was used to estimate the DOA and DOD of the signal. Experimental results in (Abdallah and Kassas, 2022) showed meter-level navigation using TOA estimates from 5G signals. The results presented therein rely only on the PSS and SSS for TOA estimation. It is shown that the proposed receiver yields a narrower RS autocorrelation function, which translates to more accurate TOA estimates. Moreover, the proposed receiver architecture can be readily adapted to any type of signal containing periodic RSs.

3. Detection of Unknown Signals in the Presence of Noise and Interference

The acquisition stage of the proposed receiver is modeled as a sequential matched subspace detection problem, which comprises estimating the number of gNBs, an initial estimate of normalized Doppler, and an initial estimate of the RSs. The detection problem of an unknown source in the presence of other interfering signals falls into the paradigm of *matched subspace detectors* which has been widely studied in the classic detection literature (Gini and Farina, 2002; Kraut et al., 2001; Scharf and Friedlander, 1994). Matched subspace detectors are used frequently in the signal processing literature, e.g., in source localization in multiple-input multiple-output (MIMO) radars (Korso et al., 2012) , passive bistatic radar (Zaimbashi et al., 2013), and navigation with unknown signals (Neinavaie et al., 2022a,b). In the navigation literature, detection of unknown signals has been studied to design frameworks which are capable of navigating with unknown or partially known signals. The problem of detecting Galileo and Compass satellites signals was studied in (Gao, 2008), which revealed the spread spectrum codes for these satellites. Preliminary experiments on navigation with partially known signals from low and medium Earth orbit satellites were conducted in (Khalife et al., 2021, 2022; Merwe et al., 2020; Neinavaie et al., 2021, 2022a). While these approaches yielded useful insights, they exploited signals that have a simpler structure compared to 5G. In (Neinavaie et al., 2022b), using the concept of matched subspace detection, a full receiver architecture is derived, analyzed and tested with real 5G signals. It was shown that the proposed receiver was capable of detecting the number of active gNBs, along with their corresponding RSs and Doppler frequencies with only the prior knowledge of the frame duration and the carrier frequency.

III. RECEIVED BASEBAND SIGNAL MODEL

As it was mentioned previously, the SS/PBCH block is not transmitted on the whole signal's bandwidth. Therefore, methods which only rely on SS/PBCH block, cannot exploit the full ranging accuracy that can be achieved by 5G signals. Other periodic RSs are not necessarily *always-on* and the cognitive receiver should be able to exploit them to be able to achieve the available ranging accuracy. In this paper, with a focus on exploiting navigation observables using the RSs in the entire 5G bandwidth, the 5G NR signal is modeled as an unknown periodic signal in the presence of interference and noise. If an RS is being periodically transmitted, it will be detected by the receiver, estimated, and used to derive navigation observables. The estimated RS will involve an estimation of always-on signals such as the SSs and any other active reference signal that is being periodically transmitted. It will be shown experimentally in section V that the exploited bandwidth by the proposed cognitive method is

larger than that of the method which only relies on always-on signals. The received base-band signal model can be expressed as

$$r[n] = \sum_{i=1}^{N} \alpha_i c_i[\tau_n - t_{s_i}[n]] \exp\left(j\theta_i[\tau_n]\right) + d_i[\tau_n - t_{s_i}[n]] \exp\left(j\theta_i[\tau_n]\right) + w_i[n], \tag{1}$$

where $r[n]$ is the received signal at the nth time instant; α_i is the complex channel gain between the UE and the ith gNB; τ_n is the sample time expressed in the receiver time; N is the number of gNBs; $c_i[n]$ is the periodic RS with a period of L samples; $t_{s_i}[n]$ is the code-delay corresponding to the UE and the ith gNB at the nth time instant; $\theta_i[\tau_n] = 2\pi f_{D_i}[n] T_s n$ is the carrier phase in radians, where $f_{D_i}[n]$ is the Doppler frequency at the nth time instant and T_s is the sampling time; $d_i[\tau_n]$ represents the samples of some data transmitted from the ith gNB; and $w_i[n]$ is zero-mean independent and identically distributed noise with $\mathbb{E}\left\{w_i[m] w_i[n]\right\} = \sigma_{w_i}^2 \delta[m-n]$, where $\delta[n]$ is the the Kronecker delta function. The desired RS from the ith gNB is defined as

$$s_i[n] \triangleq \alpha_i c_i[\tau_n - t_{s_i}[n]] \exp\left(\theta_i[\tau_n]\right), \tag{2}$$

and the equivalent noise is

$$w_{\mathrm{eq}_i}[n] = d_i[\tau_n - t_{s_i}[n]] \exp\left(\theta_i[\tau_n]\right) + w_i[n]. \tag{3}$$

Hence, the system model can be rewritten as

$$r[n] = \sum_{i=1}^{N} s_i[n] + w_{\mathrm{eq}_i}[n]. \tag{4}$$

It should be noted that due to the periodicity of the RS, assuming a constant Doppler in the processing time, i.e., $f_{D_i}[n] = f_{D_i}$, the desired RS has the following property

$$s_i[n + mL] = s[n] \exp\left(j\omega_i mL\right) \quad 0 \leq m \leq L-1, \tag{5}$$

where $\omega_i = 2\pi f_{D_i} T_s$ is the normalized Doppler, and $-\frac{1}{2} \leq \omega_i \leq \frac{1}{2}$. The acquisition stage will estimate $s_i[n]$ and the estimation of $s_i[n]$ will be used at the receiver to obtain the navigation observables.

Definition: The coherent processing interval (CPI) is defined as the time interval during which the Doppler, delay, and channel gains are considered to be constant.

One can form a vector of L observation samples corresponding to the kth period of the signal as

$$\mathbf{y}_k \triangleq [r[(k-1)L+1], r[(k-1)L+2], \ldots, r[kL]]^{\mathsf{T}}. \tag{6}$$

Considering a CPI of length $K \times L$ samples, the observation vector is constructed as $\mathbf{y} = [\mathbf{y}_1^{\mathsf{T}}, \mathbf{y}_2^{\mathsf{T}}, \ldots, \mathbf{y}_K^{\mathsf{T}}]^{\mathsf{T}}$. Therefore,

$$\mathbf{y} = \sum_{i=1}^{N} \mathbf{H}_i \mathbf{s}_i + \mathbf{w}_{\mathrm{eq}_i}, \tag{7}$$

where $\mathbf{s}_i = [s_i[1], s_i[2], \ldots, s_i[L]]$, $\mathbf{w}_{\mathrm{eq}_i}$ is the equivalent noise vector corresponding to the ith source, and the $KL \times L$ Doppler matrix corresponding to the ith source is defined as

$$\mathbf{H}_i \triangleq [\mathbf{I}_L, \exp\left(j\omega_i L\right) \mathbf{I}_L, \ldots, \exp\left(j\omega_i (K-1) L\right) \mathbf{I}_L]^{\mathsf{T}}, \tag{8}$$

where $\mathbf{I}_L$ is an $L \times L$ identity matrix.

IV. PROPOSED RECEIVER STRUCTURE

This section presents the structure of the proposed receiver. The proposed receiver consists of two main stages: (i) acquisition and (ii) tracking. Each of these stages are discussed in details next.

1. Acquisition

In this paper, the acquisition stage is modeled as a sequential matched subspace detection problem. The acquisition stage comprises estimating the number of gNBs, an initial estimate of normalized Doppler, and the RSs, i.e., N, ω_i, and $\mathbf{s}_i$, respectively. At each step of the acquisition, a test is performed to detect the most powerful gNB when the subspace of the previously detected gNBs are nulled. In the following subsection, matched subspace detection is overviewed and the hypothesis test for detection of multiple gNBs is formulated.

a) Matched Subspace Detector

As it was mentioned previously, in the first step of the proposed sequential algorithm, the presence of a single gNB is tested and if the null hypothesis is accepted, then $\hat{N} \equiv 0$, which means that no gNB is detected to be present in the environment under the test. If the test rejects the null hypothesis, the algorithm verifies the presence of at least one source and performs the test to detect the presence of other gNBs in the presence of the previously detected gNBs. The unknown Doppler and the RS of each gNBs are estimated at each step. In general, if the null hypothesis at the ith level of the sequential algorithm is accepted, the algorithm is terminated and the estimated number of gNBs will be $\hat{N} = i - 1$.

In order to test the presence of $\mathbf{s}_i$, at the ith stage of the acquisition algorithm, the observation vector can be written as

$$\mathbf{y} = \mathbf{H}_i \mathbf{s}_i + \mathbf{B}_{i-1}\boldsymbol{\theta}_{i-1} + \mathbf{w}_{\mathrm{eq}_i}, \tag{9}$$

$$\mathbf{B}_{i-1} \triangleq [\mathbf{H}_1, \mathbf{H}_2, \ldots, \mathbf{H}_{i-1}],\ \boldsymbol{\theta}_{i-1} \triangleq [\mathbf{s}_1^{\mathsf{T}}, \mathbf{s}_2^{\mathsf{T}}, \ldots, \mathbf{s}_{i-1}^{\mathsf{T}}]^{\mathsf{T}}. \tag{10}$$

The following binary hypothesis test is used to detect the ith gNB:

$$\begin{cases} \mathcal{H}_0^i: & \mathbf{y} = \mathbf{B}_{i-1}\boldsymbol{\theta}_{i-1} + \mathbf{w}_{\mathrm{eq}_i} \\ \mathcal{H}_1^i: & \mathbf{y} = \mathbf{H}_i \mathbf{s}_i + \mathbf{B}_{i-1}\boldsymbol{\theta}_{i-1} + \mathbf{w}_{\mathrm{eq}_i}. \end{cases} \tag{11}$$

For a given set of Doppler frequencies, $\mathcal{W}_i = \{\omega_1, \omega_2, \ldots, \omega_i\}$, the GLR at the ith stage is derived as (Neinavaie et al., 2022b)

$$\mathcal{L}_i(\mathbf{y}|\mathcal{W}_i) = \frac{\mathbf{y}^{\mathsf{H}}\mathbf{P}_{\mathbf{s}_i}\mathbf{y}}{\mathbf{y}^{\mathsf{H}}\mathbf{P}_{B_{i-1}}^{\perp}\mathbf{P}_{\mathbf{s}_i}^{\perp}\mathbf{P}_{B_{i-1}}^{\perp}\mathbf{y}}, \tag{12}$$

where $\mathbf{y}^{\mathsf{H}}$ is the Hermitian transpose of $\mathbf{y}$, $\mathbf{P}_{\mathbf{X}} \triangleq \mathbf{X}(\mathbf{X}^{\mathsf{H}}\mathbf{X})^{-1}\mathbf{X}^{\mathsf{H}}$, denotes the projection matrix to the column space of $\mathbf{X}$, and

$$\mathbf{P}_{\mathbf{X}}^{\perp} \triangleq \mathbf{I} - \mathbf{X}\left(\mathbf{X}^{\mathsf{H}}\mathbf{X}\right)\mathbf{X}^{\mathsf{H}}, \tag{13}$$

denotes the projection matrix onto the space orthogonal to the column space of $\mathbf{X}$, and $\mathbf{s}_i = \mathbf{P}_{\mathbf{B}_{i-1}}^{\perp}\mathbf{H}_i$.

The reader is referred to (Scharf and Friedlander, 1994) for further interpretations of matched subspace detectors.

The ML estimate of $\hat{\omega_i}$, is obtained by maximizing the likelihood function under $\mathcal{H}_1^i$ which yields

$$\hat{\omega_i} = \arg\max_{\omega_i} \|\mathbf{H}_i^{\mathsf{H}}\mathbf{P}_{\mathbf{B}_{i-1}}^{\perp}\mathbf{y}\|^2, \tag{14}$$

and is used to construct $\hat{\mathbf{P}}_{\mathbf{B}_{i-1}}$, $\hat{\mathbf{H}}_i$, and $\hat{\lambda}_i$. For a known ω_i, the least squares (LS) estimate of the ith source, i.e., $\mathbf{s}_i$, is given by

$$\hat{\mathbf{s}}_i = \frac{1}{\lambda_i}\mathbf{H}_i^{\mathsf{H}}\mathbf{P}_{\mathbf{B}_{i-1}}^{\perp}\mathbf{y}, \tag{15}$$

2. Tracking

After obtaining coarse estimates of the Doppler frequencies and estimates of the RSs in the acquisition step, the receiver refines and maintains these estimates. Specifically, phase-locked loops (PLLs) are employed to track the carrier phases of the detected RSs and carrier-aided delay-locked loops (DLLs) are used to track the RSs' code phases. The details of the tracking loops are presented in (Neinavaie et al., 2022b).

V. EXPERIMENTAL RESULTS

This section validates the proposed proposed receiver experimentally. To this end, three experiments are conducted: (i) an experiment on a ground vehicle with real 5G NR signals, (ii) and an experiment on UAV with real 5G NR signals. The objective of these experiments are to: (i) evaluate the acquisition and tracking performance of the proposed receiver, (ii) demonstrate the capability of detecting multiple sources transmitting on the same carrier frequency, (iii) and showcase the navigation solution obtained via the proposed receiver.

1. Real 5G Signals: Comparison with a Conventional 5G Receiver on a Ground Vehicle

The first experiment aims to compare the acquisition and tracking performance of the proposed receiver with the conventional 5G receiver (Shamaei and Kassas, 2021b) which only relies on the always-on RSs. The experimental setup and results for the experiment with real 5G NR signals are discussed next.

a) Experimental Setup and Environmental Layout

In this experiment, a ground vehicle was equipped with a quad-channel National Instrument (NI) universal software radio peripheral (USRP)-2955 and four consumer grade 800/1900 MHz cellular antennas to sample 5G signals near Fairview Road in Costa Mesa, California, USA. Only one channel from the USRP was used and was tuned to a 872 MHz carrier frequency, which is a 5G NR frequency allocated to the U.S. cellular provider AT&T. The sampling rate was set to 10 Mega-samples per second (MSps) and the sampled 5G signals were stored on a laptop for post-processing. In order to obtain ground-truth, the vehicle was equipped with a Septentrio AsteRx-i V GNSS-aided inertial navigation system (INS), which is a dual antenna, multi-frequency GNSS receiver with real-time kinematics (RTK) capabilities. The GNSS receiver is coupled with a Vectornav VN-100 micro electromechanical systems (MEMS) inertial measurement unit (IMU) to estimate the position and orientation of the ground vehicle at a rated horizontal accuracy of 0.6 cm in clear sky conditions (RTK performance). The vehicle traversed a trajectory of 4.1 km in 315 seconds. The acquisition results are presented next.

b) Acquisition Results

The recorded 5G signals were processed in two ways for comparison: (i) using the proposed proposed receiver and (ii) using the conventional 5G receiver proposed in (Shamaei and Kassas, 2021b). The conventional 5G receiver detected 1 gNB with an initial Doppler frequency of -7.2 Hz. Note that the limited number of gNBs was expected as 5G gNBs are sparsely deployed at the present time. The location of the gNB was mapped prior to the experiment. Next, the signal acquisition stage was applied to detect the ambient 5G gNB. The detection threshold was set such that $P_{\text{fa}} = 10^{-4}$, which yielded $\eta = 1.008$, K was set to 40, and T_{sub} was set to 20 ms. Doppler estimation was performed by searching for the maximizer of the likelihood function according to (14) with a step size of 1 Hz. The acquisition stages in the proposed receiver is shown in Fig. 1.

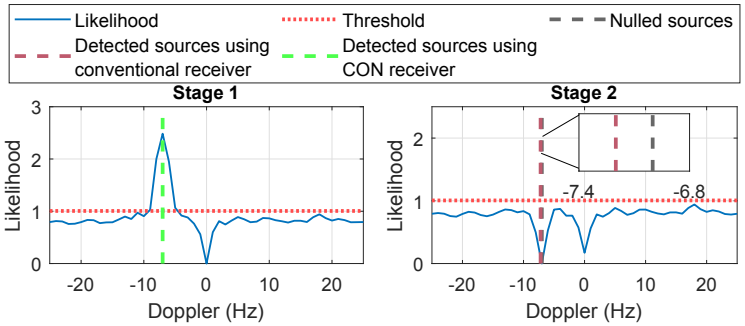

Figure 1: Acquisition stages in the proposed receiver for 5G NR signals on a ground vehicle showing the likelihood function at each stage and the detected and nulled sources. The DC component, i.e., at zero Doppler frequency, was nulled as it was saturating the detector.

c) Tracking Results

After acquiring the Doppler and the RSs, the tracking loops are initialized and the signal is tracked. Fig. 2 show the resulting Doppler frequency and delay, expressed in meters, obtained using the proposed and conventional receivers. As it can be seen in Fig. 2(b) the estimated delays for the proposed and the conventional receivers are slightly drifting away from the ground-truth which is due to the clock drifts. The effect of clock drift is considered in the carrier phase model (see equation (16)). Note that the initial value of the delays were subtracted out to facilitate comparison. The Doppler and delay RMSE values were calculated from ground-truth for both receivers and are summarized in Table 1, which shows that the proposed receiver outperforms the conventional one.

One main reason behind proposed performing better than a conventional 5G receiver is the fact that the latter exploits the RSs in

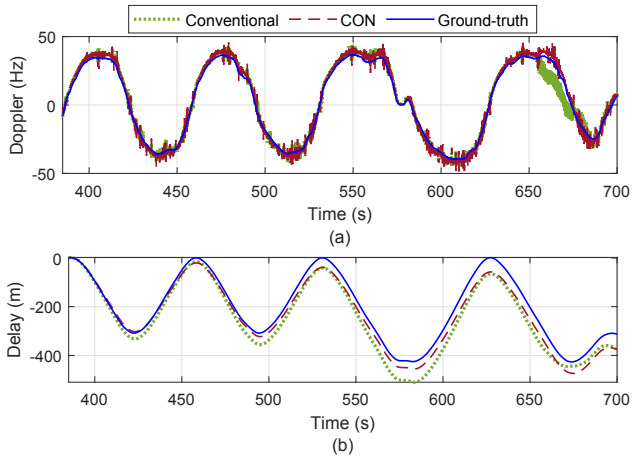

Figure 2: (a) Doppler tracking and (b) delay tracking results for the 5G NR ground vehicle experiment. The ground-truth is calculated according to the true position of the vehicle and the gNBs.

the entire bandwidth, making the bandwidth of the estimated RS higher than the RSs used in the conventional receiver, mainly the PSS and SSS. Fig. 3 illustrates this showing a narrower normalized autocorrelation function of the RS estimated with the proposed receiver compared to that of a 5G PSS.

Table 1: Delay and Doppler RMSE for the proposed and conventional receivers.

	Delay RMSE (m)	Doppler RMSE (Hz)
Conventional	24.3	3.66
proposed	21.88	2.28

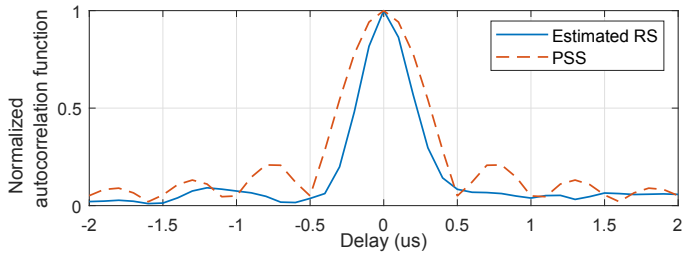

Figure 3: Normalized autocorrelation function of the RS estimated with the proposed receiver compared to that of a 5G PSS.

2. Real 5G signals: The First Navigation Results on a UAV

The second experiment aims to find a navigation solution on a UAV using the proposed receiver. To the best of author's knowledge this is the first navigation results with real 5G signals on a UAV.

a) Experimental Setup and Environment Layout

In this experiment, the navigator was an Autel Robotics X-Star Premium UAV equipped with a single-channel Ettus 312 USRP connected to a consumer-grade 800/1900 MHz cellular antenna and a small consumer-grade GPS antenna to discipline the on-board oscillator. The cellular receivers were tuned to the cellular carrier frequency 632.55 MHz, which is a 5G NR frequency allocated to the U.S. cellular provider T-Mobile. Samples of the received signals were stored for off-line post-processing. The ground-truth reference trajectory was taken from the on-board Ettus 312 USRP GPS solution. The UAV traversed a trajectory of 416 m. Fig. 4 shows the environment layout and the vehicle trajectory. The acquisition results are presented next.

b) Acquisition Results

Next, the signal acquisition stage was applied to detect the ambient 5G gNBs. The proposed receiver detected 2 gNBs with initial Doppler frequencies of 3.5 Hz and 11.5 Hz. The location of the gNBs was mapped prior to the experiment. The acquisition stages in the proposed receiver are shown in Fig. 5.

Figure 4: Environment layout and UAV trajectory for the 5G NR UAV experiment

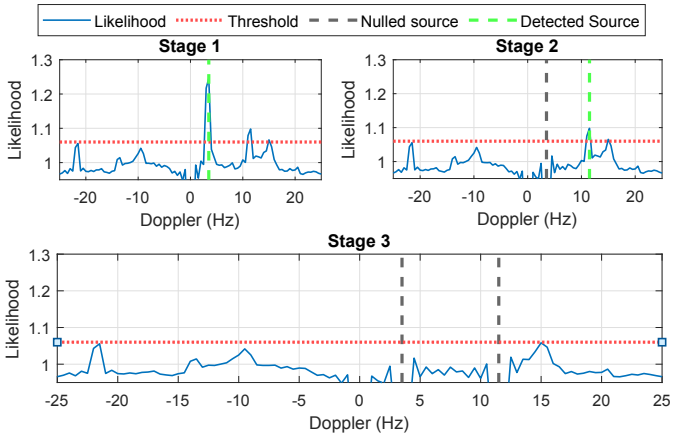

Figure 5: Acquisition stages in the proposed receiver for 5G NR signals on a UAV showing the likelihood function at each stage and the detected and nulled sources. The DC component, i.e., at zero Doppler frequency, was nulled as it was saturating the detector.

c) Tracking Results

After acquiring the Doppler and the RSs, the tracking loops are initialized and the signal is tracked. Fig. 6 shows the resulting Doppler frequencies and delays, expressed in meters, obtained using the proposed receiver.

d) Navigation Solution

In the following, it is assumed that (i) the UAV's altitude is known at all time and (ii) the UAV has an estimate of its position at time-step k_0, prior to navigating with 5G signals. The carrier phase to the i-th gNB $z_i(k)$ at time-step k expressed in meters can be modeled as

$$z_i(k) = \|\boldsymbol{r}_r(k) - \boldsymbol{r}_{s_i}\| + c\delta t_r(k) - c\delta t_{s_i} + v_i(k), \tag{16}$$

where $\boldsymbol{r}_r$ and $\boldsymbol{r}_{s_i}$ are the three-dimensional (3–D) position vectors of the UAV-mounted receiver and the i-th gNB, respectively; c is the speed of light; δt_r is the UAV-mounted receiver's clock bias; δt_{s_i} models the i-th gNB's clock bias and carrier phase ambiguity; and $v_i(k)$ is the measurement noise, which is modeled as a zero-mean Gaussian random variable with variance σ_i^2 (Shamaei and Kassas, 2019). Note that since the UAV's altitude is known, e.g., using an altimeter, only its two-dimensional (2–D) position is estimated. The time reference for the transmitter and receiver clocks is chosen such that $\delta t_r(k_0) = 0$. Using the position estimate at k_0 and the fact that $\delta t_r(k_0) = 0$, the gNBs clock biases can be estimated from $z_i(k_0)$ resulting in the estimate $\hat{\delta} t_{s_i}$. Next, define the corrected carrier phase measurement $\bar{z}_i(k) \triangleq z_i(k) + \hat{\delta} t_{s_i}$ which can be approximated as

$$\bar{z}_i(k) \approx \|\boldsymbol{r}_r(k) - \boldsymbol{r}_{s_i}\| + c\delta t_r(k) + v_i(k), \quad \forall\, k > k_0. \tag{17}$$

Subsequently, the corrected carrier phase measurements were fed to an extended Kalman filter (EKF) to solve the state vector $\boldsymbol{x}(k) \triangleq \left[\boldsymbol{r}_r^{\mathsf{T}}(k), \dot{\boldsymbol{r}}_r^{\mathsf{T}}(k), c\delta t_r(k), c\dot{\delta} t_r(k)\right]^{\mathsf{T}}$, where $\dot{\boldsymbol{r}}_r(k)$ is the UAV's 2–D velocity vector and $\dot{\delta} t_r(k)$ is the receiver's clock

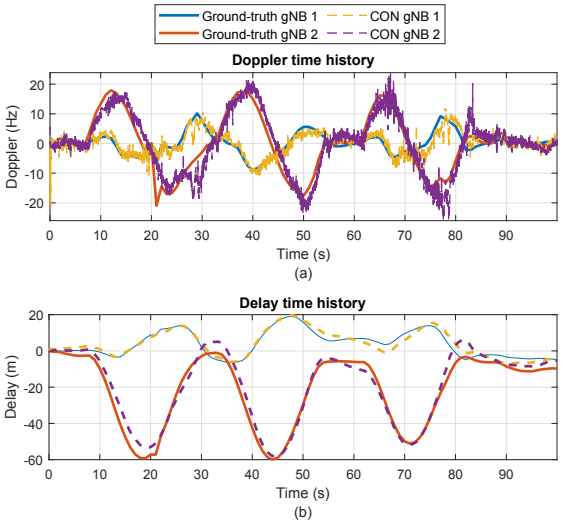

Figure 6: (a) Doppler tracking and (b) delay tracking results for the UAV 5G experiment. The ground-truth is calculated according to the true position of the vehicle and the gNBs.

drift. A nearly constant velocity model was used for the UAV's position and velocity dynamics, and a standard double integrator driven by process noise was used to model the clock bias and drift dynamics (Kassas, 2021). As such, the discrete-time dynamics model of $\boldsymbol{x}$ are given by $\boldsymbol{x}(k+1) = \mathbf{F}\boldsymbol{x}(k) + \boldsymbol{w}(k)$, where $\mathbf{F}$ is the state transition matrix obtained according to (Kassas, 2021) and $\boldsymbol{w}(k)$ is the process noise vector, which is modeled as a zero-mean Gaussian random vector with covariance matrix $\mathbf{Q}$ obtained according to (Kassas, 2021). The UAV's x, y acceleration process noise spectra in the nearly constant velocity model were set to $q_x = q_y = 10$ m^2/s^5, and the receiver's clock process noise was chosen to be that of a typical temperature-compensated crystal oscillator (TCXO) (Kassas, 2021). Note that $\boldsymbol{r}_r(k)$ is expressed in an East-North-Up (ENU) frame centered at the UAV's true initial position. The EKF state estimate was initialized at $\hat{\boldsymbol{x}} = \mathbf{0}_{6\times 1}$ with an initial covariance of $\boldsymbol{\Sigma} = 4 \cdot \mathbf{I}_{6\times 6}$. The measurement noise covariance was set to $\mathbf{R} = 2 \cdot \mathbf{I}_{2\times 2}$. The position RMSE of the UAV was calculated to be 4.35 m with the aforementioned parameters. The true and estimated UAV trajectories are shown in Fig. 7.

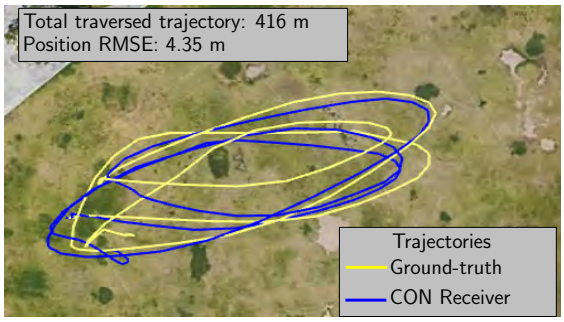

Figure 7: Ground-truth and estimated trajectories using proposed receiver for 5G NR signals on a UAV. The proposed receiver yielded a UAV position RMSE of 4.35 m. Map data: Google Earth.

VI. CONCLUSION

A joint detection and tracking method was proposed to extract navigation observables from 5G signals, without requiring knowledge of the 5G RSs. To exploit the full ranging accuracy that can be achieved with 5G signals, the proposed receiver was designed to estimate the RSs from multiple 5G gNBs and exploit them for navigation purposes. The acquisition stage of the receiver was modeled as a sequential detection problem. The GLR test was used to sequentially estimate the number of active gNBs, their RSs, and Doppler frequencies. Tracking loops were also designed in order to refine and maintain the estimates provided by the acquisition stage. Extensive experimental results were presented demonstrating the capabilities of the proposed receiver with real 5G signals on ground and aerial platforms. On a ground vehicle, it was demonstrated that the proposed receiver yields a reduction of 10% and 37.7% in the estimated delay and Doppler RMSE, respectively, over that achieved with a conventional opportunistic navigation 5G receiver. On a UAV, it was demonstrated that the proposed receiver enables the UAV to navigate over 416 m trajectory with 5G NR gNBs, achieving a position RMSE of 4.35 m.

ACKNOWLEDGEMENTS

This work was supported in part by the Office of Naval Research (ONR) under N00014-19-1-2511, in part by the Air Force Office of Scientific Research (AFOSR) under Grant FA9550-22-1-0476, and in part by the U.S. Department of Transportation (USDOT) under Grant 69A3552047138 for the CARMEN University Transportation Center (UTC).

REFERENCES

Abdallah, A. and Kassas, Z. (2021). Multipath mitigation via synthetic aperture beamforming for indoor and deep urban navigation. *IEEE Transactions on Vehicular Technology*, 70(9):8838–8853.

Abdallah, A. and Kassas, Z. (2022). Opportunistic navigation using sub-6 GHz 5G downlink signals: A case study on a ground vehicle. In *Proceedings of European Conference on Antennas and Propagation*, pages 1–5.

Abu-Shaban, Z., Wymeersch, H., Abhayapala, T., and Seco-Granados, G. (2018). Distributed two-way localization bounds for 5G mmwave systems. In *Proceedings of IEEE Globecom Workshops*, pages 1–6.

Abu-Shaban, Z., Zhou, X., Abhayapala, T., Seco-Granados, G., and Wymeersch, H. (2018). Error bounds for uplink and downlink 3D localization in 5G millimeter wave systems. *IEEE Transactions on Wireless Communications*, 17(8):4939–4954.

Abu-Shaban, Z., Zhou, X., Abhayapala, T., Seco-Granados, G., and Wymeersch, H. (2018). Performance of location and orientation estimation in 5G mmwave systems: Uplink vs downlink. In *Proceedings of IEEE Wireless Communications and Networking Conference*, pages 1–6.

Aziz, M. and Allen, C. (2018). Experimental results of a differential angle-of-arrival based 2D localization method using signals of opportunity. *International Journal of Navigation and Observation*, 2018(5470895):1–6.

Baenke, J., Chaudhuri, K., Deshpande, A., Halder, A., Irizarry, M., Saxena, N., Sharma, S., and Yang, R. (2020). Millimeter-Wave downlink coverage extension strategies. *IEEE Communications Magazine*, 58(9):74–78.

Chen, X., Wei, Q., Wang, F., Jun, Z., Wu, S., and Men, A. (2020). Super-resolution time of arrival estimation for a symbiotic FM radio data system. *IEEE Transactions on Broadcasting*, 66(4):847–856.

Conte, E., Filippi, A., and Tomasin, S. (2010). ML period estimation with application to vital sign monitoring. *IEEE Signal Processing Letters*, 17(11):905–908.

del Peral-Rosado, J., López-Salcedo, J., Zanier, F., and Seco-Granados, G. (2018a). Position accuracy of joint time-delay and channel estimators in LTE networks. *IEEE Access*, 6:25185–25199.

del Peral-Rosado, J., Raulefs, R., López-Salcedo, J., and Seco-Granados, G. (2018b). Survey of cellular mobile radio localization methods: From 1G to 5G. *IEEE Communications Surveys Tutorials*, 20(2):1124–1148.

Dun, H., Tiberius, C., and Janssen, G. (2020). Positioning in a multipath channel using OFDM signals with carrier phase tracking. *IEEE Access*, 8:13011–13028.

Farhangian, F. and Landry, R. (2020). Multi-constellation software-defined receiver for Doppler positioning with LEO satellites. *Sensors*, 20(20):5866–5883.

Fascista, A., Coluccia, A., Wymeersch, H., and Seco-Granados, G. (2019). Millimeter-wave downlink positioning with a single-antenna receiver. *IEEE Transactions on Wireless Communications*, 18(9):4479–4490.

Gadka, P., Sadowski, J., and Stefanski, J. (2019). Detection of the first component of the received LTE signal in the OTDoA method. *Wireless Communications and Mobile Computing*, pages 1–12.

Gao, G. (2008). *Towards navigation based on 120 satellites: Analyzing the new signals*. PhD thesis, Stanford University.

Gini, F. and Farina, A. (2002). Vector subspace detection in compound-Gaussian clutter. part I: survey and new results. *IEEE Transactions on Aerospace and Electronic Systems*, 38(4):1295–1311.

Giordani, M., Polese, M., Roy, A., Castor, D., and Zorzi, M. (2019). A tutorial on beam management for 3GPP NR at mmWave frequencies. *IEEE Communications Surveys Tutorials*, 21(1):173–196.

Hartnett, M. (2022). Performance assessment of navigation using carrier Doppler measurements from multiple LEO constellations. Master's thesis, Air Force Institute of Technology, Wright-Patterson Air Force Base, Ohio, USA.

Hong, T., Sun, J., Jin, T., Yi, Y., and Qu, J. (2021). Hybrid positioning with DTMB and LTE signals. In *Proceedings of International Wireless Communications and Mobile Computing*, pages 303–307.

Huang, C., Qin, H., Zhao, C., and Liang, H. (2022). Phase - time method: Accurate Doppler measurement for Iridium NEXT signals. *IEEE Transactions on Aerospace and Electronic Systems*, pages 1–9.

Iannucci, P. and Humphreys, T. (2022). Fused low-Earth-orbit GNSS. *IEEE Transactions on Aerospace and Electronics Systems*. accepted.

Jao, C., Abdallah, A., Chen, C., Seo, M., Kia, S., Kassas, Z., and Shkel, A. (2022). Sub-meter accurate pedestrian indoor navigation system with dual ZUPT-aided INS, machine learning-aided LTE, and UWB signals. In *Proceedings of ION GNSS+ Conference*. accepted.

Kassas, Z. (2021). Position, navigation, and timing technologies in the 21st century. volume 2, chapter 38: Navigation with Cellular Signals of Opportunity, pages 1171–1223. Wiley-IEEE.

Kazaz, T., Janssen, G., Romme, J., and Van der Veen, A. (2022). Delay estimation for ranging and localization using multiband channel state information. *IEEE Transactions on Wireless Communications*, 21(4):2591–2607.

Khalife, J. and Kassas, Z. (2022a). Differential framework for submeter-accurate vehicular navigation with cellular signals. *IEEE Transactions on Intelligent Vehicles*. accepted.

Khalife, J. and Kassas, Z. (2022b). On the achievability of submeter-accurate UAV navigation with cellular signals exploiting loose network synchronization. *IEEE Transactions on Aerospace and Electronic Systems*. accepted.

Khalife, J., Neinavaie, M., and Kassas, Z. (2021). Blind Doppler tracking from OFDM signals transmitted by broadband LEO satellites. In *Proceedings of IEEE Vehicular Technology Conference*, pages 1–6.

Khalife, J., Neinavaie, M., and Kassas, Z. (2022). The first carrier phase tracking and positioning results with Starlink LEO satellite signals. *IEEE Transactions on Aerospace and Electronic Systems*, 56(2):1487–1491.

Korso, M., Boyer, R., Renaux, A., and Marcos, S. (2012). Statistical resolution limit for source localization with clutter interference in a MIMO radar context. *IEEE Transactions on Signal Processing*, 60(2):987–992.

Kozhaya, S. and Kassas, Z. (2022). Blind receiver for LEO beacon estimation with application to UAV carrier phase differential navigation. In *Proceedings of ION GNSS Conference*. accepted.

Kraut, S., Scharf, L., and McWhorter, L. (2001). Adaptive subspace detectors. *IEEE Transactions on Signal Processing*, 49(1):1–16.

Lapin, I., Granados, G., Samson, J., Renaudin, O., Zanier, F., and Ries, L. (2022). STARE: Real-time software receiver for LTE and 5G NR positioning and signal monitoring. In *Proceedings of Workshop on Satellite Navigation Technology*, pages 1–11.

Lee, J., Gil, G., and Lee, Y. (2014). Exploiting spatial sparsity for estimating channels of hybrid MIMO systems in millimeter wave communications. In *Proceedings of IEEE GLOBECOM*, pages 3326–3331.

Leng, M., Quitin, F., Tay, W., Cheng, C., Razul, S., and See, C. (2016). Anchor-aided joint localization and synchronization using SOOP: Theory and experiments. *IEEE Transactions on Wireless Communications*, 15(11):7670–7685.

Ma, W., Qi, C., and Li, G. (2020). High-resolution channel estimation for frequency-selective mmwave massive MIMO systems. *IEEE Transactions on Wireless Communications*, 19(5):3517–3529.

Maaref, M. and Kassas, Z. (2022). Autonomous integrity monitoring for vehicular navigation with cellular signals of opportunity and an IMU. *IEEE Transactions on Intelligent Transportation Systems*, 23(6):5586–5601.

Mendrzik, R., Wymeersch, H., and Bauch, G. (2018). Joint localization and mapping through millimeter wave MIMO in 5G systems. In *Proceedings of IEEE Global Communications Conference*, pages 1–6.

Merwe, J., Bartl, S., O'Driscoll, C., Rügamer, A., Förster, F., Berglez, P., Popugaev, A., and Felber, W. (2020). GNSS sequence extraction and reuse for navigation. In *Proceedings of ION GNSS+ Conference*, pages 2731–2747.

Neinavaie, M., Khalife, J., and Kassas, Z. (2021). Blind Doppler tracking and beacon detection for opportunistic navigation with LEO satellite signals. In *Proceedings of IEEE Aerospace Conference*, pages 1–8.

Neinavaie, M., Khalife, J., and Kassas, Z. (2022a). Acquisition, Doppler tracking, and positioning with Starlink LEO satellites: First results. *IEEE Transactions on Aerospace and Electronic Systems*, 58(3):2606–2610.

Neinavaie, M., Khalife, J., and Kassas, Z. (2022b). Cognitive opportunistic navigation in private networks with 5G signals and beyond. *IEEE Journal of Selected Topics in Signal Processing*, 16(1):129–143.

Parkvall, S., Blankenship, Y., Blasco, R., Dahlman, E., Fodor, G., Grant, S., Stare, E., and Stattin, M. (2020). 5G NR release 16: Start of the 5G evolution. *IEEE Communications Standards Magazine*, 4(4):56–63.

Psiaki, M. and Slosman, B. (2022). Tracking digital FM OFDM signals for the determination of navigation observables. *NAVIGATION, Journal of the Institute of Navigation*, 69(2).

Rastorgueva-Foi, E., Costa, M., Koivisto, M., Leppanen, K., and Valkama, M. (2018). User positioning in mmw 5G networks using beam-RSRP measurements and Kalman filtering. In *Proceedings of International Conference on Information Fusion*, pages 1–7.

Scharf, L. and Friedlander, B. (1994). Matched subspace detectors. *IEEE Transactions on signal processing*, 42(8):2146–2157.

Shamaei, K. and Kassas, Z. (2019). Sub-meter accurate UAV navigation and cycle slip detection with LTE carrier phase. In *Proceedings of ION GNSS Conference*, pages 2469–2479.

Shamaei, K. and Kassas, Z. (2021a). A joint TOA and DOA acquisition and tracking approach for positioning with LTE signals. *IEEE Transactions on Signal Processing*, pages 2689–2705.

Shamaei, K. and Kassas, Z. (2021b). Receiver design and time of arrival estimation for opportunistic localization with 5G signals. *IEEE Transactions on Wireless Communications*, 20(7):4716–4731.

Soderini, A., Thevenon, P., Macabiau, C., Borgagni, L., and Fischer, J. (2020). Pseudorange measurements with LTE physical channels. In *Proceedings of ION International Technical Meeting*, pages 817–829.

Souli, N., Kolios, P., and Ellinas, G. (2021a). Online relative positioning of autonomous vehicles using signals of opportunity. *IEEE Transactions on Intelligent Vehicles*, pages 1–1.

Souli, N., Makrigiorgis, R., Kolios, P., and Ellinas, G. (2021b). Real-time relative positioning system implementation employing signals of opportunity, inertial, and optical flow modalities. In *Proceedings of International Conference on Unmanned Aircraft Systems*, pages 229–236.

Strandjord, K., Morton, Y., and Wang, P. (2021). Evaluating the urban signal environment for GNSS and LTE signals. In *Proceedings of ION GNSS+ Conference*, pages 2166–2182.

Takeda, K., Xu, H., Kim, T., Schober, K., and Lin, X. (2020). Understanding the heart of the 5G air interface: An overview of physical downlink control channel for 5G new radio. *IEEE Communications Standards Magazine*, 4(3):22–29.

Wang, P. and Morton, Y. (2020). Multipath estimating delay lock loop for LTE signal TOA estimation in indoor and urban environments. *IEEE Transactions on Wireless Communications*, 19(8):5518–5530.

Wang, P. and Morton, Y. (2020). Performance comparison of time-of-arrival estimation techniques for LTE signals in realistic multipath propagation channels. *NAVIGATION, Journal of the Institute of Navigation*, 67(4):691–712.

Wang, P. and Morton, Y. (2022). Impact analysis of inter-cell interference in cellular networks for navigation applications. *IEEE Transactions on Aerospace and Electronic Systems*. accepted.

Wang, P., Wang, Y., and Morton, J. (2022). Signal tracking algorithm with adaptive multipath mitigation and experimental results for LTE positioning receivers in urban environments. *IEEE Transactions on Aerospace and Electronic Systems*, 58(4):2779–2795.

Wei, Q., Chen, X., and Zhan, Y. (2020). Exploring implicit pilots for precise estimation of LEO satellite downlink Doppler frequency. *IEEE Communications Letters*, 24(10):2270–2274.

Whiton, R., Chen, J., Johansson, T., and Tufvesson, F. (2022). Urban navigation with LTE using a large antenna array and machine learning. In *Proceedings of IEEE Vehicular Technology Conference*, pages 1–5.

Wymeersch, H., Seco-Granados, G., Destino, G., Dardari, D., and Tufvesson, F. (2017). 5G mmWave positioning for vehicular networks. *IEEE Wireless Communications*, 24(6):80–86.

Xhafa, A., del Peral-Rosado, J., López-Salcedo, J., and Seco-Granados, G. (2021). Evaluation of 5G positioning performance based on UTDoA, AoA and base-station selective exclusion. *Sensors*, 22(1):101–118.

Yacong, D. (2018). *Channel Estimation for Massive MIMO Systems Based on Sparse Representation and Sparse Signal Recovery*. PhD thesis, University of California, San Diego.

Yang, C. and Soloviev, A. (2020). Mobile positioning with signals of opportunity in urban and urban canyon environments. In *Proceedings of IEEE/ION Position, Location, and Navigation Symposium*, pages 1043–1059.

Zaimbashi, A., Derakhtian, M., and Sheikhi, A. (2013). GLRT-based CFAR detection in passive bistatic radar. *IEEE Transactions on Aerospace and Electronic Systems*, 49(1):134–159.

Joint Doppler and Azimuth DOA Tracking for Positioning with Iridium LEO Satellites

Shaghayegh Shahcheraghi, Forough Nasihati Gourabi, Mohammad Neinavaie, and Zaher M. Kassas
The Ohio State University

BIOGRAPHY

Shaghayegh Shahcheraghi is a Ph.D. student at The Ohio State University and member of the Autonomous Systems Perception, Intelligence, and Navigation (ASPIN) Laboratory. She received a B.E. in Electrical Engineering and an M.S. in Telecommunication engineering from Shiraz University. She obtained her second M.S. degree in Telecommunication engineering with the focus on signal processing from Polytechnic University of Milan, Italy. Her research interests include opportunistic navigation, blind opportunistic navigation, cognitive radio, wireless communication systems, and software-defined radio.

Forough Nasihati Gourabi is a postdoctoral scholar at The Ohio State University and a member of the Autonomous Systems Perception, Intelligence, and Navigation (ASPIN) Laboratory. She received a Ph.D. in Aerospace Engineering from the Sharif University of Technology. Her research interests include optimal estimation, opportunistic navigation, and satellite orbit determination.

Mohammad Neinavaie is a Ph.D. student at The Ohio State University and member of the Autonomous Systems Perception, Intelligence, and Navigation (ASPIN) Laboratory. He received a B.E. in electrical engineering and an M.S. in digital communication systems from Shiraz University. His research interests include opportunistic navigation, blind opportunistic navigation, cognitive radio, wireless communication systems and software-defined radio.

Zaher (Zak) M. Kassas is a professor at The Ohio State University and TRC Endowed Chair in Intelligent Transportation Systems. He is the Director of the Autonomous Systems Perception, Intelligence, and Navigation (ASPIN) Laboratory. He is also director of the U.S. Department of Transportation Center: CARMEN (Center for Automated Vehicle Research with Multimodal AssurEd Navigation), focusing on navigation resiliency and security of highly automated transportation systems. He received a B.E. in Electrical Engineering from the Lebanese American University, an M.S. in Electrical and Computer Engineering from The Ohio State University, and an M.S.E. in Aerospace Engineering and a Ph.D. in Electrical and Computer Engineering from The University of Texas at Austin. He is a recipient of the National Science Foundation (NSF) CAREER award, Office of Naval Research (ONR) Young Investigator Program (YIP) award, Air Force Office of Scientific Research (AFOSR) YIP award, IEEE Walter Fried Award, Institute of Navigation (ION) Samuel Burka Award, and ION Col. Thomas Thurlow Award. He is an Associate Editor of the IEEE Transactions on Aerospace and Electronic Systems and the IEEE Transactions on Intelligent Transportation Systems. He is a Fellow of the ION and a Distinguished Lecturer of the IEEE Aerospace and Electronic Systems Society. His research interests include cyber-physical systems, navigation systems, and intelligent transportation systems.

ABSTRACT

A receiver capable of estimating the Doppler and azimuth direction-of-arrival (DOA) of Iridium NEXT low Earth orbit (LEO) signals of opportunity (SOPs) is presented. The proposed receiver operates in three stages: (i) Fast Fourier Transform (FFT)-based Doppler acquisition, (ii) Kalman filter (KF)-based Doppler tracking, and (iii) Doppler-compensated MUltiple SIgnal Classification (MUSIC)-based algorithm for DOA tracking. Experimental results are presented demonstrating successful tracking of the Doppler frequency and azimuth DOA of an Iridium NEXT LEO satellite, achieving a Doppler root mean square error (RMSE) of 8.1 Hz over 120 seconds and an azimuth DOA RMSE of 1.04 degrees over 60 seconds. The Doppler and azimuth DOA measurements are fused via an extended Kalman filter (EKF) to localize a stationary receiver. Starting with an initial estimate 7 km away from the true receiver's position, the Doppler-only measurements yielded a final positioning error of 656.m, while the Doppler and azimuth DOA measurements reduced the error to 289.5 m.

I. INTRODUCTION

Over the past decade, the tremendous potential of signals of opportunity (SOPs) for navigation has been unveiled (Raquet *et al.*, 2021; Souli et al., 2021; Fokin and Volgushev, 2022; Kassas et al., 2022). SOPs include cellular (Wang and Morton, 2023; Liu et al., 2023; Tian et al., 2023; Kassas and Abdallah, 2023), FM radio (Moghtadaiee and Dempster, 2014; Aziz and Allen, 2018; Chen et al., 2020; Psiaki and Slosman, 2019), digital television (Yang and Soloviev, 2020; Hong et al., 2021; Souli et al., 2022; Jiao et al., 2023), low Earth orbit (LEO) satellites (Jardak and Jault, 2022; Huang et al., 2022; Zhao et al., 2023; Kassas et al., 2023a), and geostationary Earth orbit (GEO) satellites (Gao et al., 2021).

Among terrestrial SOPs, the most accurate navigation results have been demonstrated with cellular signals, achieving meter-level accuracy on ground vehicles (Soderini et al., 2020; Yang et al., 2022; Maaref and Kassas, 2022; Lapin et al., 2022) and sub-meter-level accuracy on unmanned aerial vehicles (UAVs) (Khalife and Kassas, 2023). Different techniques have been studied for cellular-based navigation. In (Shamaei et al., 2018; Shamaei and Kassas, 2021a), a long-term evolution (LTE) receiver was proposed, where the direction-of-arrival (DOA) and time-of-arrival (TOA) were jointly estimated, showing sub-meter-level positioning accuracy with 5 LTE eNodeBs. TOA estimates from real fifth generation (5G) signals showed meter-level ranging accuracy (Shamaei and Kassas, 2021b). Cramer-Rao lower bounds (CRLBs) of the direction-of-departure (DOD), DOA, and TOA for both uplink and downlink millimeter wave (mmWave) signals were derived in (Abu-Shaban et al., 2018), showing sub-meter positioning error, and sub-degree orientation error. To exploit the sparsity of mmWave channels, compressed sensing-based framework were proposed in (Lee et al., 2014) to estimate DOD, DOA, and TOA of the user equipment (UE), showing sub-meter-level position error via numerical simulation. The joint estimation of the position and orientation of the UE, as well as the location of reflectors or scatterers in the absence of the line-of-sightg (LOS) path were considered in (Mendrzik et al., 2018), showing less than 15 m position root-mean squared (RMSE) and less than 7 degrees orientation RMSE. The DOD and UE's position were estimated in a two-stage Kalman filter (KF) using the signal strength from multiple base stations in (Rastorgueva-Foi et al., 2018), which yielded sub-meter-level three-dimensional (3-D) position accuracy. In (Fascista et al., 2019), a positioning method for multiple-output single-input systems was proposed, where the DOD and TOA of the received signal were used to localize a UE. In (Ma et al., 2020), estimation of signal parameters via rotational invariant techniques (ESPRIT) was used to estimate the DOA and DOD of the signal.

LEO satellite SOPs have attracted considerable attention in recent years (Prol et al., 2022; Hartnett, 2022; Shi et al., 2023), due to their desirable characteristics for navigation: (i) compared with global navigation satellite systems (GNSS) which reside in medium Earth orbit (MEO), LEO satellites are about twenty times closer to Earth, which could result in higher received signal power; (ii) there are thousands of satellites in LEO, and it is expected that tens of thousands more space vehicles (SVs) will be deployed into LEO in the upcoming decade, which could provide more coverage and availability compared with terrestrial SOPs; and (iii) LEO SVs are deployed in different orbits and transmit in a wide range of frequency bands, providing both spatial and spectral diversity.

The potential of LEO signals for navigation have been the subject of several recent studies (Leng et al., 2016; Wei et al., 2020; Psiaki, 2021). Orbcomm LEO satellite signals were exploited for stationary receiver positioning in (Khalife and Kassas, 2019) and UAV navigation in (Khalife et al., 2020; Kozhaya and Kassas, 2022). Iridium NEXT LEO satellites were exploited for stationary receiver positioning in (Tan et al., 2019a) and aerial vehicle navigation in (Benzerrouk et al., 2019). Orbcomm and Iridium NEXT LEO satellites were jointly exploited for stationary receiver positioning in (Farhangian and Landry, 2020; Orabi et al., 2021) and for ground and aerial vehicle navigation in (Farhangian et al., 2021). Starlink signals were first acquired, tracked, and exploited for stationary receiver positioning in (Khalife et al., 2022). Ground vehicle navigation with Starlink, Orbcomm, and Iridium NEXT was first demonstrated in (Kassas et al., 2021). OneWeb signals were first acquired and tracked in (Kozhaya et al., 2023) and were used alongside Starlink, Orcomm, and Iridium for stationary receiver positioning, while ground vehicle navigation with these four constellations was demonstrated in Kassas et al. (2023b).

Nevertheless, all the aforementioned work relied on either the Doppler frequency or the carrier phase for positioning and navigation. While DOA estimation for positioning with terrestrial SOPs has been the subject of many studies (Pan et al., 2022), DOA estimation from LEO SOPs has not received similar attention. In (Islam et al., 2021), Doppler and DOA estimation of satellites in the UHF and VHF bands were studied. Using an L-shaped antenna array, DOA was estimated using the interferometer and MUltiple SIgnal Classification (MUSIC) techniques. The developed DOA estimation method was implemented only for amplitude shift keying (ASK) modulated signals, and in the UHF and VHF bands. In (Thompson et al., 2021), by incorporating the DOA, a differenced Doppler positioning method was proposed to address the issue of lack of knowledge about the precise location of satellites. DOA was estimated at the stationary base and shared with the roving receiver to derive the geometry matrix to eliminate the need for information about SVs' states. The simulation results showed that the DOA measurements should be very accurate to enable acceptable position estimation in case only a single LEO satellite is used. This work did not study how to estimate DOA of LEO SVs. In this paper, a Doppler compensated-aided MUSIC framework is proposed to track the azimuth DOA of the signals coming from Iridium NEXT satellites. To the authors' knowledge, this is the first study to consider joint Doppler and azimuth DOA tracking of Iridium NEXT LEO satellite SOPs for positioning.

Iridium NEXT LEO signals consist of multiple channels, namely, the ring alart (RA), paging channel, voice channel, and duplex user channels, which are transmitted over the 1,616–1,626.5 MHz band to provide different communication services globally. A small part of this spectrum, namely 1,626–1,626.5 MHz is used for paging and acquisition (Iridium Constellation LLC, 2013). In this paper, by setting the receiver frequency to 1,626.2708 MHz in the L–band, signals are collected from the RA channel of Iridium NEXT satellites to estimate the Doppler frequency. The RA channel bandwidth is B = 41.667 kHz. The Iridium NEXT constellation consists of 75 active satellites that orbit the Earth in 6 different orbital planes, spaced 30° apart (Iridium Constellation LLC, 2013).

The IRIDIUM NEXT signal employs both time division multiple access (TDMA) and frequency division multiple access

(FDMA) and consists of three parts, namely tone (no modulation), unique word (Binary Phase Shift Keying (BPSK) modulation) and information (Quadrature Phase Shift Keying (QPSK) modulation). In this paper, pure tone, BPSK and QPSK signals are exploited simultaneously for Doppler tracking of Iridium NEXT signals, enabling more precise Doppler estimation (Tan et al., 2019b) compared with tracking only the pure tone part of the signal. In addition to estimating the Doppler frequency, the paper also presents an approach for azimuth DOA estimation with a Uniform Linear Array (ULA).

This paper's contributions are as follows. First, a receiver architecture that could produce Doppler frequency and azimuth DOA observables from Iridium NEXT LEO satellites is presented. Second, the Doppler and azimuth DOA observables are fused via an extended Kalman filter (EKF) to localize a stationary receiver with a single Iridium NEXT LEO satellite. Starting with an initial estimate 7 km away from the true receiver's position, the Doppler-only measurements yielded a final positioning error of 656.m, while Doppler and azimuth DOA measurements reduced the error to 289.5 m.

The rest of the paper is organized as follows. Section II describes the received baseband signal model. Section III presents the proposed receiver architecture. Section IV presents the experimental results for Doppler and Azimuth DOA tracking along with receiver positioning with these observables. Section V gives concluding remarks.

II. RECEIVED BASEBAND SIGNAL MODEL

At the receiver, a ULA with M antenna elements where all the antennas are separated by the same distance d is used to estimate the azimuth DOA of the Iridium downlink signal using the phase difference of the received signal at different antenna elements and different samples. A very small gap between the antenna elements reduces directivity, while large spacing introduces grating lobes resulting in ambiguity in DOA estimation. Therefore, the spacing between antenna elements is typically chosen to be equal to half the wavelength ($d = \frac{\lambda}{2}$), where $\lambda = \frac{c}{f_c}$ is the received signal wavelength, c is the speed-of-light, and f_c is the carrier frequency (Clerckx and Oestges, 2013). The baseband signal samples of Iridium NEXT SVs received by the mth antenna element can be written as

$$r_m[n] = \sum_{i=1}^{N} \gamma_{i,m}(\tau_n) a_i[n] e^{j2\pi f_{D_{i,m}}[n] T_s n} e^{j\frac{2\pi}{\lambda} d \cdot \sin(\phi_i[n])(m-1)} + w_m[n], \tag{1}$$

where $r_m[n]$ is the received signal by the mth antenna element at the nth time instant; N is the total number of Iridium NEXT satellites; $\gamma_{i,m}(\tau_n)$ is the complex channel gain between the mth antenna element and the ith Iridium NEXT space vehicle (SV); τ_n is the sample time expressed in the receiver time; $a_i[n]$ represents the transmitted symbol at the nth time instant drawn from an $M-$ary phase shift keying constellation, i.e., $a = e^{j\frac{2\pi q}{M}}$ for $q \in \{0, \cdots, M-1\}$; $\phi_i[n]$ is the angle between the beam arriving from ith Iridium NEXT satellite and the orthogonal line to the ULA at the nth time instant; $f_{D_{i,m}}[n]$ is the instantaneous Doppler frequency at the mth antenna element at the nth time instant, T_s is the sampling time; and $w_m[n]$ captures the effect of noise and transmitted data at the mth antenna element, which is modeled as a complex zero-mean independent and identically distributed noise with variance σ_w^2. Processing the received signal is performed in some processing intervals, named as coherent processing intervals (CPIs). Small CPIs cannot capture enough power to enable signal processing and precise estimation. On the other hand, due to the high dynamics of the channel between the SVs and the receiver, the instantaneous Doppler frequency varies during large CPI. It is observed that for Iridium NEXT LEO SVs, a CPI large enough to yield acceptable performance is one resulting in the instantaneous Doppler frequency $f_{D_i}[n]$ being modeled as a linear function of time. In particular, $f_{D_i}[n]$ at the kth CPI can be modeled as

$$f_{D_i}[n] = f_{D_{k,i}} + \beta_{k,i} n T_s, \qquad k = 0, \cdots, K-1, \tag{2}$$

where $f_{D_{k,i}}$ is referred to as constant Doppler, $\beta_{k,i}$ is the Doppler rate at the kth processing interval corresponding to the ith Iridium NEXT satellite, and K is the total number of CPIs. During the defined CPI, the channel gain $\gamma_{i,m}(\tau_n)$, Doppler $f_{D_{k,i}}$, and the Doppler rate $\beta_{k,i}$ are all constant. Since channel gain is considered to be constant during one CPI, the channel gain can be denoted as the function of CPI index, i.e., $\gamma_{i,m}(\tau_n) = \gamma_{k,i,m}$. The received signal at the mth antenna element at nth time instant when the Doppler rate is wiped-off can be written as $r'_m[n] = \exp\big(-j\pi\beta_{k,i,m} n^2 T_s^2\big) r_m[n]$

$$r'_m[n] \quad = \sum_{i=1}^{N} \gamma_{k,i,m} a_i[n] e^{j2\pi f_{D_{k,i,m}} T_s n} e^{j\frac{2\pi}{\lambda} d.\sin(\phi_{k,i}[n])(m-1)} + w_{\mathrm{eq_m}}[n].$$

The next section discusses the receiver architecture for Doppler acquisition and Doppler and DOA tracking. For simplicity of notations the subscripts (i and m), which denote the ith Iridium NEXT SV and mth antenna element respectively, will be dropped in the sequel, unless it is required. Note that the Doppler estimation method is similar for all antenna elements.

III. RECEIVER ARCHITECTURE

This section overviews the proposed receiver architecture. The proposed receiver performs Doppler and DOA estimation in two sequential steps. In the first step, the Doppler frequency of each antenna element is estimated, and in the second step, the DOA is estimated. The Doppler frequency of each antenna element is estimated in two stages: (i) acquisition and (ii) tracking. Each of these stages is discussed in detail next.

1. Doppler Frequency Acquisition

As discussed in Section II, based on the selected CPI length herein, the instantaneous Doppler frequency is appropriately modeled as a linear function of time.

Iridium NEXT signals consist of three components (i) an un-modulated tone, (ii) a unique word with binary phase shift keying (BPSK) modulation, and (iii) information data with quadrature phase shift keying (QPSK) modulation that are always transmitted from Iridium NEXT SVs to the receiver (Shahriar, 2008). In order to avoid a phase shift arising from the unique word (BPSK) and the information data (QPSK), the baseband samples in each CPI are raised to the 4th power to wipe off the BPSK and QPSK symbols, resulting in a pure tone. As such, in addition to the pure tone that was exploited in (Orabi et al., 2021), unique word signals and information signals are also exploited for Doppler frequency estimation (Tan et al., 2019b). Then, a fast Fourier transform (FFT) of the signal of first and second CPI is taken, and the Doppler rate is calculated based on the shift in Doppler frequency during one CPI. Note that in the frequency-domain, the impulse-like peak occurs at the frequency which is equal to four times of the true Doppler frequency due to the fact that the signal samples were raised to the 4th power. As a result, the obtained Doppler rate and Doppler frequency should be normalized by four to get the appropriate estimates. After wiping off the normalized Doppler rate, an FFT of the 4th power of the samples in the first CPI is taken. The initial Doppler frequency is acquired by normalizing the frequency at which the impulse-like peak of FFT occurs.

2. KF-Based Doppler Frequency Tracking

After obtaining coarse estimates of the Doppler rate and Doppler frequency in the acquisition step, the receiver refines and maintains these estimates via a KF. Due to the SVs'high dynamics and the CPI length, employing a KF allows for improved Doppler estimation, since its formulation allows for arbitrary Doppler model order selection. The KF-based Doppler tracking algorithm is described next.

a) Doppler Dynamics Model

The time-varying component of the continuous-time true Doppler is a function of the true range rate between the LEO SV and the receiver and the time-varying difference between the receiver's and LEO SV's clock bias rate (i.e., drift). It assumed that the clock drift is constant, so it has a constant contribution to the Doppler. The discrete-time dynamic model of the Doppler state vector $\boldsymbol{x}_k = [f_{D_k}, \beta_k]^{\mathsf{T}}$ is given by

$$\boldsymbol{x}_{k+1} = \mathbf{F}\boldsymbol{x}_k + \mathbf{w}_k, \tag{3}$$

$$\mathbf{F} = \begin{bmatrix} 1 & T \\ 0 & 1 \end{bmatrix}, \qquad \mathbf{Q} = q_{\tilde{w}} \begin{bmatrix} \frac{T^3}{3} & \frac{T^2}{2} \\ \frac{T^2}{2} & T \end{bmatrix}, \tag{4}$$

where $\mathbf{F}$ is the discrete-time state transition matrix, $\mathbf{w}_k$ is a discrete-time process noise with zero-mean and covariance matrix $\mathbf{Q}$, $q_{\tilde{w}}$ is the power spectral density of the continuous-time-equivalent of the process noise driving the Doppler rate acceleration, and T is the time interval between two measurements, which is set to the CPI length.

b) KF-Based Doppler Tracking

Let $\hat{\boldsymbol{x}}_{k|l}$ denotes the KF estimate of $\boldsymbol{x}_k$ given all the measurements up to time-step $l \leqslant k$, and $\mathbf{P}_{k|l}$ denotes the corresponding estimation error covariance. Using the estimated Doppler and Doppler rate in the acquisition stage, $\hat{\mathbf{x}}_{0|0}$ and its corresponding $\mathbf{P}_{0|0}$ are estimated. The KF-based tracking algorithm follows the standard time-update procedure in KF. The KF measurement update is implemented based on the FFT estimate of the Doppler, which is discussed next. First, the Doppler rate wipe-off is performed as $r'_k[n] = \exp\big(-j2\pi\beta_k n^2\big) r_k[n]$, where n corresponds to all the samples in each CPI. Next, the following steps are performed sequentially: (i) the samples of each CPI are raised to the power 4, (ii) FFT is taken, (iii) the frequency at which the peak occurs is detected, and (iv) after normalizing this frequency by 4, $f_{D_{k+1}}$, which is used in calculating the innovation, is estimated. The proposed KF innovation is obtained as

$$\nu_{k+1} = f_{D_{k+1}} - \hat{f}_{D_{k+1|k}}, \tag{5}$$

which is a direct measure of the Doppler estimation error. Using the innovation and performing a measurement-update, the posterior Doppler state vector $\hat{\mathbf{x}}_{k|k}$ is estimated.

3. Doppler-Compensated-based MUSIC for DOA Tracking

The estimated Doppler frequency is wiped-off from the baseband received samples of each antenna element according to $\tilde{r}_m[n] \triangleq \exp\Big(-j2\pi\hat{f}_{D_m}[n]T_s n\Big)r_m[n]$. Hence, the received signal at the mth antenna element at nth time instant when the Doppler frequency is wiped-off can be written as

$$\tilde{r}_m[n] = \gamma_m(\tau_n)a[n]e^{j\zeta_m[n]}e^{j\frac{2\pi}{\lambda}d\sin(\phi[n])(m-1)} + \tilde{w}[n], \tag{6}$$

where $\zeta_m[n] = 2\pi(f_{D_m}[n] - \hat{f}_{D_m}[n])T_s n$, which represents the effect of the residual Doppler.
Collecting the Doppler compensated samples for all the antennas, an $M \times L$ matrix $\mathbf{Y}$ is formed, whose mth row includes L Doppler-compensated samples received by the mth antenna element. In order to estimate the DOA, the MUSIC algorithm is applied. MUSIC is a subspace-based super-resolution algorithm that relies on the eigenvalue decomposition of the sample covariance matrix of the received signal (Paulraj et al., 1993). Let, $\mathbf{R}_y = \frac{1}{L}\sum_{l=1}^{L}\boldsymbol{y}_l\boldsymbol{y}_l^{\mathsf{H}}$ be the sample covariance matrix of the received signal, where $\boldsymbol{y}_l$ denotes the lth column of $\mathbf{Y}$. The intuition behind MUSIC comes from the fact that given a sufficient received signal power, $\mathbf{R}_y$ can be decomposed into two almost orthogonal subspaces: a noise subspace and a signal subspace. The eigenvalues corresponding to the signal subspace will be significantly larger than the ones associated with the noise subspace. The eigenvectors associated with the near-zero eigenvalues of $\mathbf{R}_y$ span the noise subspace and constitute the columns of the noise matrix, $\mathbf{U}_n$. Finally, the angular MUSIC spectrum can be computed as $\mathrm{P}_{MUSIC}(\phi) = \frac{1}{\boldsymbol{a}^{\mathsf{H}}(\phi)\mathbf{U}_n\mathbf{U}_n^{\mathsf{H}}\boldsymbol{a}(\phi)}$ for different values of ϕ, when $\boldsymbol{a}^{\mathsf{T}}(\phi) = \Big[1, e^{j\frac{2\pi}{\lambda}d\sin(\phi)}, ..., e^{j\frac{2\pi}{\lambda}d\sin(\phi)(M-1)}\Big]$ is the steering vector associated with the azimuth angle ϕ. Whenever the steering vector is related to the true angle of the received signal, the noise subspace and the steering vector becomes almost orthogonal to each other, resulting in sharp peaks in the angular MUSIC spectrum. These peaks represent the DOA estimates of the received signals.

IV. EXPERIMENTAL RESULTS

This section presents experimental results of Doppler and azimuth DOA tracking of signals from an unknown Iridium NEXT LEO SV via the proposed framework. Also, the positioning accuracy of a stationary receiver is compared for two scenarios, (i) only Doppler is exploited for positioning, (ii) both Doppler and azimuth angle are used for positioning. In what follows, the experimental setup is first discussed. Next, results from the Doppler acquisition, Doppler tracking, and azimuth DOA tracking of the Iridium NEXT are presented. Finally, Doppler-only and Doppler+azimuth DOA positioning results are presented.

1. Experimental Setup

To demonstrate the performance of the proposed receiver, an experiment was performed in Columbus, Ohio, USA. A stationary receiver was equipped with

- A National Instrument (NI) four-channel universal software radio peripherals (USRPs)-2955 to simultaneously down-mix and synchronously sample the Iridium NEXT signals received by four antennas at a sampling rate of 2.4 Msps and a carrier frequency of $1,626.2708$ MHz in the L–band.
- Four GPS antennas to record Iridium NEXT signals in the L–band. The antennas feature a multi-point feeding design in order to provide high phase center stability. Also, these wide-beamwidth antennas are designed to receive low elevation signals with high gain. The antennas were arranged in a 4×1 ULA array structure with $d = \lambda = 18.4$ cm. It should be pointed out that ideally the antenna elements should be spaced $d = \frac{\lambda}{2}$ apart to avoid angle ambiguity, however, due to the large diameter of GPS antennas used in this experiment, the antenna spacing was set to λ, which will be discussed in Section IV.2.c.
- A host laptop computer to store the samples of the received signals for off-line post-processing.
  The experimental setup is shown in Figure 1.

It should be noted that DOA estimation is very sensitive to the phase shift between different antenna elements. All antennas, amplifiers, and cables must be similar. Also, all the channels are required to be phase synchronized. To meet these requirements, similar antennas, amplifiers, and matched-length cables were used in this experiment. Moreover, a GPS antenna was used to discipline the USRP's oscillator to maintain the oscillator as stable as possible. However, other elements such as the filters, mixers, amplifiers, and phase locked loops of the USRP can cause a time-varying phase error on the signals received from different antenna elements. Time, temperature, and mechanical conditions are other factors that can introduce a phase error over time. Moreover, mutual coupling between antennas can affect the signals captured by each antenna element. As a result, performing calibration is a crucial step for each experiment to remove the phase and amplitude differences between all the channels with the reference channel.

Figure 1: Experimental hardware setup.

2. Experimental Results

The USRP sampled signals with the sampling bandwidth Fs of 2.4 MHz over a period of about 120 seconds at a carrier frequency of 1626.2708 MHz in the L–band, which coincides with the ring alert (RA) channel of Iridium NEXT SVs. The proposed framework was used to track the Doppler frequency and the azimuth angle of the Iridium NEXT LEO SV with NORAD Catalog Number 42811. It should be noted that since the aim of this paper is to track the azimuth angle and evaluate its effect on positioning accuracy, signals coming from only one Iridium NEXT signal is studied.

a) Acquisition result

As discussed in Section III, in the first step, initial Doppler rate and Doppler are acquired. Figure 2 shows the FFT of the 4th power of the baseband received signal for two successive CPIs, which led to initial Doppler rate estimation. Note that the CPI was set to 2 seconds. After wiping-off the Doppler rate, the FFT of the 4th power of the baseband received signal is taken. The initial Doppler is acquired by normalizing the frequency at which the peak occurs.

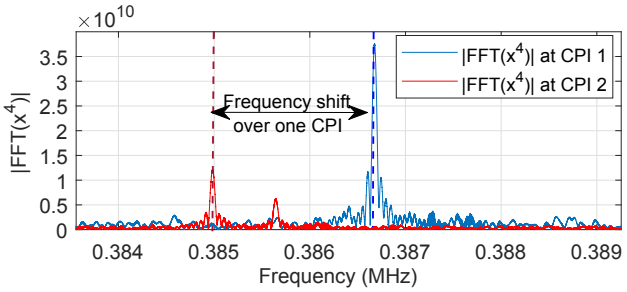

Figure 2: FFT of the 4th power of the received Iridium NEXT signal for two successive CPIs. The frequency shift during a 2-second CPI gives an estimate of $4\beta_0$. Normalizing this value by four gives the initial estimate of the Doppler rate in the acquisition stage.

b) Doppler Tracking Results

In the next step, the Doppler frequency of the signals captured by each antenna element is tracked. The results are compared with the predicted Doppler obtained from two-line element (TLE) files and an SGP4 orbit determination software. Figure 3 demonstrates the estimated (dashed) versus the TLE+SGP4-predicted (solid) Doppler frequency profile for each antenna element. It can be seen that the estimated Doppler frequency matches the predicted Doppler from TLE+SGP4.

c) DOA Tracking Result

In this step, the estimated Doppler frequency is wiped-off from signals received by each antenna element. Collecting the Doppler-compensated samples corresponding to all 4 antennas at each CPI, the sample covariance matrix is calculated to get the MUSIC angular spectrum, as described in Section III.3. Figure 4(a) illustrates the MUSIC angular spectrum over time, where the peaks occur at the estimated azimuth DOA of each CPI. The estimated azimuth angle $\hat{\phi}$ represents the estimated angle between the incoming signal and the orthogonal line to the ULA. Since the array is located along the South-North direction, and the predicted azimuth angle obtained from TLE file, ϕ_{TLE}, is measured from the North direction, the estimated angle and its corresponding azimuth angle from TLE are complementary angles, and they are related through, $\hat{\phi} = 90^\circ - \phi_{TLE} + \alpha_0$, where α_0 represents the initial ambiguity arising from the fact that the distance between the antenna elements equals to λ. This constant ambiguity is resolved in the navigation filter. The estimated angles are disambiguated by comparing them with the azimuth angles from TLE files.

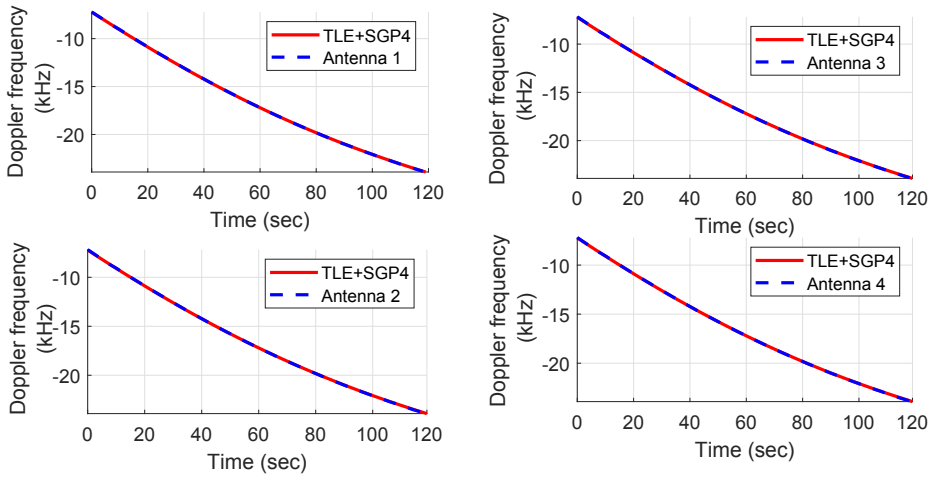

Figure 3: The estimated (dashed) versus the TLE+SGP4-predicted (solid) Doppler frequency profile during the tracking period for all 4 antenna elements.

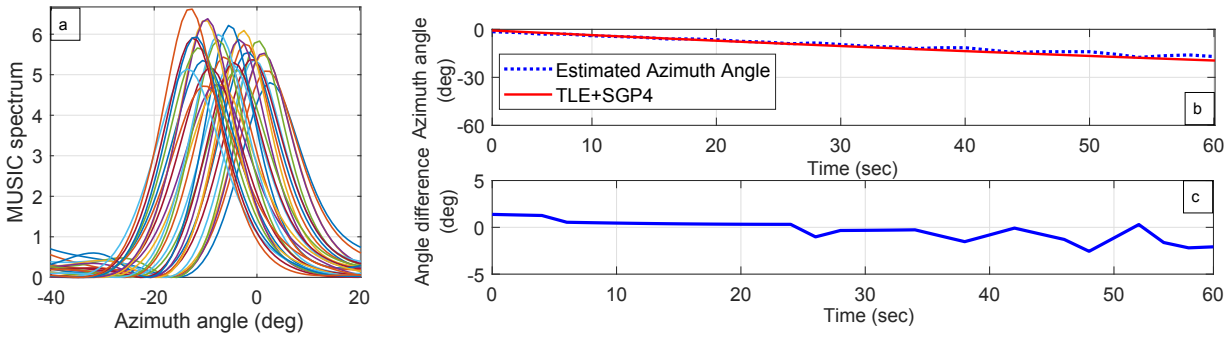

Figure 4: (a) MUSIC angular spectrum of detected Iridium NEXT over time. (b) The estimated (dotted) versus the TLE+SGP4-predicted (solid) azimuth angle profile. (c) Angle estimation error over 60 seconds of Iridium LEO SV visibility.

Figure 4(b) shows the profile of estimated (dotted) versus the TLE+SGP4-predicted (solid) azimuth angle variation. Figure 4(c) demonstrates the error of angle estimation during the tracking period. The experimental results show that the azimuth angles are tracked with an root mean squared-error (RMSE) of 1.04 degrees and with the maximum error of less than 3 degrees during 60 seconds. It can be seen that as the SV approaches the horizon, the angle estimation becomes more erroneous because the received signal power decreases. Antenna element displacements, misalignment of the array due to the slope of the ground, and low number of antenna elements can also contribute in DOA estimation error.

d) Navigation Solution

This section presents positioning results of a stationary receiver with Doppler-only versus Doppler and azimuth DOA measurements produced by the proposed receiver. Pseudorange rate observables $\dot{\rho}$ are formed from the tracked Doppler frequencies according to $\rho = -\frac{c}{f_c} f_D$, where c is the speed of light and $f_c = 1626.2708$ MHz is the carrier frequency. The measurements relating the receiver coordinates to the satellite's estimated pseudorange rate and azimuth DOA from the proposed receiver are modeled as

$$\dot{\rho}(k) = \frac{-\dot{\boldsymbol{r}}_{\mathrm{SV}}^{\top}(k)\left[\boldsymbol{r}_r - \boldsymbol{r}_{\mathrm{SV}}(k)\right]}{\|\boldsymbol{r}_r - \boldsymbol{r}_{\mathrm{SV}}(k)\|} + a_1 + v_{\dot{\rho}}(k) \tag{7}$$

$$\phi(k) = \mathrm{atan2}(y_{r,SV}^{NED}(k),\ x_{r,SV}^{NED}(k)) + a_2 + a_3\, k + v_{\phi}(k), \tag{8}$$

where $\dot{\rho}(k)$ and $\phi(k)$ represent the pseudorange rate and azimuth angle measurements, respectively, at time instant k. $\boldsymbol{r}_{\mathrm{SV}}$ and $\dot{\boldsymbol{r}}_{\mathrm{SV}}$ denote the satellite position and velocity vectors in the Earth-centered Earth-fixed (ECEF) coordinates, with $\boldsymbol{r}_r = [x_r\ y_r\ z_r]^{\top}$ being the receiver position vector; the constant a_1 is assumed to account for the difference between the receiver and the satellite's clocks, i.e., $a_1 = c[\dot{\delta}_r(k) - \dot{\delta}_{SV}(k)]$, where $\dot{\delta}_r$ and $\dot{\delta}_{SV}$ are the receiver's and LEO satellite's clock drifts, respectively; and

$x_{r,SV}^{NED}(k)$ and $y_{r,SV}^{NED}(k)$ are the first and second components of the vector $\boldsymbol{r}_{r,SV}^{NED}(k)$, i.e., the range vector from receiver to satellite in the local North-East-Down (NED) frame,

$$\boldsymbol{r}_{r,SV}^{NED}(k) = \begin{bmatrix} -\sin(\theta_1)\cos(\theta_2) & -\sin(\theta_1)\sin(\theta_2) & \cos(\theta_1) \\ -\sin(\theta_2) & \cos(\theta_2) & 0 \\ -\cos(\theta_1)\cos(\theta_2) & -\cos(\theta_1)\sin(\theta_2) & -\sin(\theta_1) \end{bmatrix} [\boldsymbol{r}_{\mathrm{SV}}(k) - \boldsymbol{r}_{\mathrm{r}}(k)], \tag{9}$$

Note that, a_2 and a_3 form a time-varying term compensating for unmodeled effects, such as clock errors and ionospheric and tropospheric delays. Moreover, $v_{\dot{\rho}}$ and v_{ϕ} are the measurement noise which are modeled as white Gaussian random variables with variances $\sigma_{\dot{\rho}}^2$ and σ_{ϕ}^2, respectively. Finally, θ_1 and θ_2 are the geodetic latitude and longitude of the unknown receiver defined by $\theta_1 = \arcsin(z_r/\|\boldsymbol{r}_r\|)$ and $\theta_2 = \arctan(y_r/x_r)$. The receiver positioning is achieved via an EKF in two cases of measurement types. First, Doppler measurements are employed to estimate the state vector, $\boldsymbol{x} = \left[\boldsymbol{r}_r^\top, a_1\right]^\top$ with an initial error covariance matrice in the ECEF frame as

$$\mathbf{P}0|0) = \mathrm{diag}[\mathbf{T}\,\mathbf{P}_{NED}(0|0)\,\mathbf{T}^\top, \mathbf{P}_a(0|0)]$$

where $\mathbf{T}$ is the rotation matrix from the NED frame to the ECEF frame, $\mathbf{P}_{NED}(0|0)$ is the initial error covariance matrix in the ECEF frame set to $\mathrm{diag}[6.7 \times 10^3, 6.7 \times 10^3, 0.1]$ and $\mathbf{P}_a(0|0)$ is the initial error covariance corresponding to a_1 and is set to 10^4. Afterward, the azimuth measurements are added to the Doppler to solve the positioning problem. In this case, the state vector is augmented to $\boldsymbol{x} = \left[\boldsymbol{r}_r^\top, a_1, a_2, a_3\right]^\top$, where $\mathbf{P}_{NED}(0|0)$ remains the same while $\mathbf{P}_a(0|0)$ is changed to $[10^4, 10^4, 10^4]$. The measurement noise variances for Doppler and azimuth where calculated empirically and ranged between $1 - 25$ Hz^2 and $0.25 - 2.25$ deg^2, respectively. Figure 5 summarizes the positioning results, which demonstrates the benefit of fusing azimuth DOA alongside Doppler measurements.

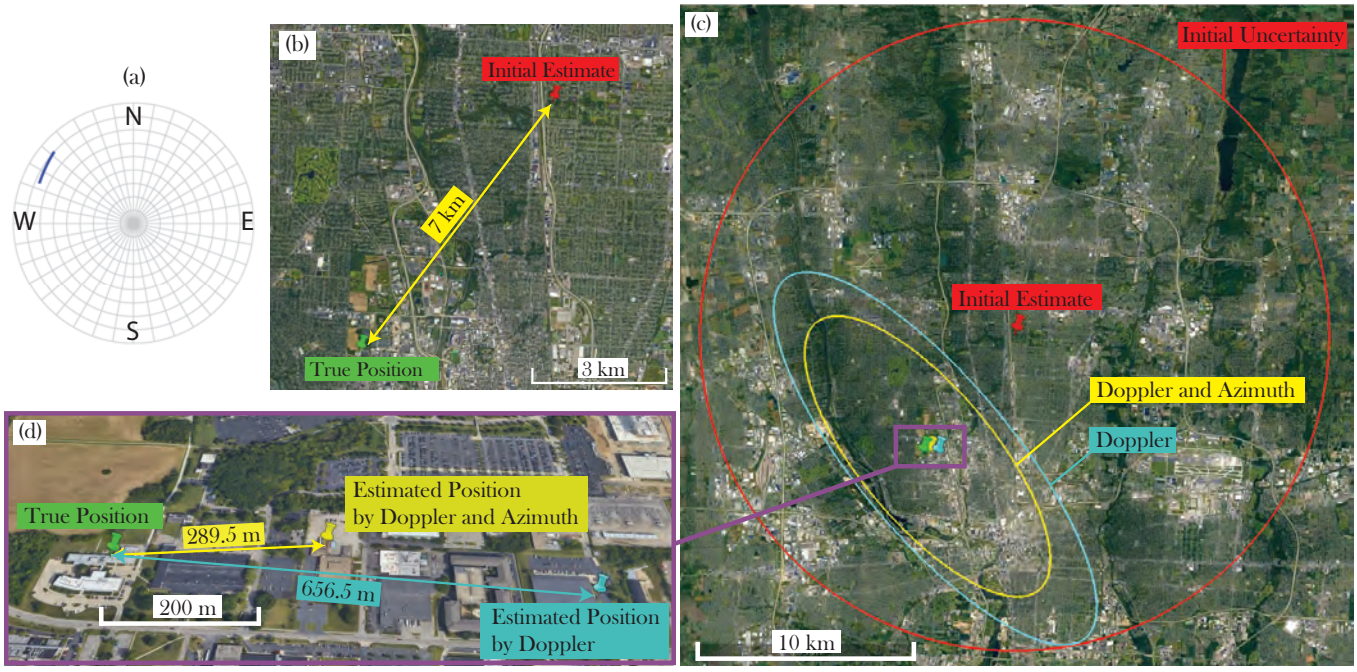

Figure 5: (a) Skyplot showing the trajectory of the Iridium LEO satellite. (b) Initial estimate versus true receiver position. (c) Initial estimate and its corresponding 95% uncertainty ellipses and estimated position with (i) Doppler-only measurements and (ii) Doppler and azimuth DOA along with corresponding 95% uncertainty ellipses. (d) Zoomed view on positioning errors. Map data: Google Earth.

V. CONCLUSION

This paper presented a receiver for Doppler and Azimuth DOA estimation of Iridium NEXT LEO satellite signals. Experimental results were presented demonstrating successful tracking of the Doppler frequency and azimuth DOA of an Iridium NEXT LEO satellite, achieving a Doppler RMSE of 8.1 Hz over 120 seconds and an azimuth DOA RMSE of 1.04 degrees over 60 seconds. The Doppler and azimuth DOA measurements are fused via an EKF to localize a stationary receiver. Starting with an initial estimate 7 km away from the true receiver's position, Doppler-only measurements yielded a final positioning error of 656.m, while the Doppler and azimuth DOA measurements reduced the error to 289.5 m.

ACKNOWLEDGEMENTS

This work was supported in part by the Office of Naval Research (ONR) under Grant N00014-19-1-2511 and in part by the Air Force Office of Scientific Research (AFOSR) under Grant FA9550-22-1-0476. The authors would like to thank Justin Kuric for helpful discussions.

REFERENCES

Abu-Shaban, Z., Zhou, X., Abhayapala, T., Seco-Granados, G., and Wymeersch, H. (2018). Error bounds for uplink and downlink 3D localization in 5G millimeter wave systems. *IEEE Transactions on Wireless Communications*, 17(8):4939–4954.

Aziz, M. and Allen, C. (2018). Experimental results of a differential angle-of-arrival based 2D localization method using signals of opportunity. *International Journal of Navigation and Observation*, 2018(5470895):1–6.

Benzerrouk, H., Nguyen, Q., Xiaoxing, F., Amrhar, A., Nebylov, A., and Landry, R. (2019). Alternative PNT based on Iridium Next LEO satellites Doppler/INS integrated navigation system. In *Proceedings of Saint Petersburg International Conference on Integrated Navigation Systems*, pages 1–10.

Chen, X., Wei, Q., Wang, F., Jun, Z., Wu, S., and Men, A. (2020). Super-resolution time of arrival estimation for a symbiotic FM radio data system. *IEEE Transactions on Broadcasting*, 66(4):847–856.

Clerckx, B. and Oestges, C. (2013). *MIMO Wireless Networks: Channels, Techniques and Standards for Multi-Antenna, Multi-User and Multi-Cell Systems*. Academic Press, Inc., Orlando, FL, USA, 2nd edition.

Farhangian, F., Benzerrouk, H., and Landry, R. (2021). Opportunistic in-flight INS alignment using LEO satellites and a rotatory IMU platform. *Aerospace*, 8(10):280–281.

Farhangian, F. and Landry, R. (2020). Multi-constellation software-defined receiver for Doppler positioning with LEO satellites. *Sensors*, 20(20):5866–5883.

Fascista, A., Coluccia, A., Wymeersch, H., and Seco-Granados, G. (2019). Millimeter-wave downlink positioning with a single-antenna receiver. *IEEE Transactions on Wireless Communications*, 18(9):4479–4490.

Fokin, G. and Volgushev, D. (2022). Software-defined radio network positioning technology design. problem statement. In *Proceedings of Systems of Signals Generating and Processing in the Field of on Board Communications*, pages 1–6.

Gao, Y., Zhao, X., Wang, S., Xiang, Y., Huang, C., and Hua, Y. (2021). Positioning via GEO communication satellites' signals of opportunity. *IET Radar, Sonar Navigation*, 15(11):1472–1482.

Hartnett, M. (2022). Performance assessment of navigation using carrier Doppler measurements from multiple LEO constellations. Master's thesis, Air Force Institute of Technology, Ohio, USA.

Hong, T., Sun, J., Jin, T., Yi, Y., and Qu, J. (2021). Hybrid positioning with DTMB and LTE signals. In *Proceedings of International Wireless Communications and Mobile Computing*, pages 303–307.

Huang, C., Qin, H., Zhao, C., and Liang, H. (2022). Phase - time method: Accurate Doppler measurement for Iridium NEXT signals. *IEEE Transactions on Aerospace and Electronic Systems*, 58(6):5954–5962.

Iridium Constellation LLC (2013). Iridium NEXT engineering statement. `http://licensing.fcc.gov/myibfs/download.do?attachment_key=1031348`.

Islam, M., Wang, T., Wade, S., Bessell, T., Spitzer, T., and Hallett, J. (2021). Doppler and angle of arrival estimation from digitally modulated satellite signals in passive RF space domain awareness. In *Proceedings of Advanced Maui Optical and Space Surveillance Technologies Conference*, pages 1–14.

Jardak, N. and Jault, Q. (2022). The potential of LEO satellite-based opportunistic navigation for high dynamic applications. *Sensors*, 22(7):2541–2565.

Jiao, Z., Chen, L., Lu, X., Liu, Z., Zhou, X., Zhuang, Y., and Guo, G. (2023). Carrier phase ranging with DTMB signals for urban pedestrian localization and GNSS aiding. *Remote Sensing*, 15(2):423–446.

Kassas, Z. and Abdallah, A. (2023). No GPS no problem: Exploiting cellular OFDM-based signals for accurate navigation. *IEEE Transactions on Aerospace and Electronic Systems*. accepted.

Kassas, Z., Khairallah, N., and Kozhaya, S. (2023a). Ad astra: Simultaneous tracking and navigation with megaconstellation LEO satellites. *IEEE Aerospace and Electronic Systems Magazine*. accepted.

Kassas, Z., Khalife, J., Abdallah, A., and Lee, C. (2022). I am not afraid of the GPS jammer: resilient navigation via signals of opportunity in GPS-denied environments. *IEEE Aerospace and Electronic Systems Magazine*, 37(7):4–19.

Kassas, Z., Kozhaya, S., Kanj, H., Saroufim, J., Hayek, S., Neinavaie, M., Khairallah, N., and Khalife, J. (2023b). Navigation with multi-constellation LEO satellite signals of opportunity: Starlink, Oneweb, Orbcomm, and Iridium. In *Proceedings of IEEE/ION Position, Location, and Navigation Symposium*, pages 338–343.

Kassas, Z., Neinavaie, M., Khalife, J., Khairallah, N., Haidar-Ahmad, J., Kozhaya, S., and Shadram, Z. (2021). Enter LEO on the GNSS stage: Navigation with Starlink satellites. *Inside GNSS Magazine*, 16(6):42–51.

Khalife, J. and Kassas, Z. (2019). Receiver design for Doppler positioning with LEO satellites. In *Proceedings of IEEE International Conference on Acoustics, Speech and Signal Processing*, pages 5506–5510.

Khalife, J. and Kassas, Z. (2023). Differential framework for submeter-accurate vehicular navigation with cellular signals. *IEEE Transactions on Intelligent Vehicles*, 8(1):732–744.

Khalife, J., Neinavaie, M., and Kassas, Z. (2020). Navigation with differential carrier phase measurements from megaconstellation LEO satellites. In *Proceedings of IEEE/ION Position, Location, and Navigation Symposium*, pages 1393–1404.

Khalife, J., Neinavaie, M., and Kassas, Z. (2022). The first carrier phase tracking and positioning results with Starlink LEO satellite signals. *IEEE Transactions on Aerospace and Electronic Systems*, 56(2):1487–1491.

Kozhaya, S., Kanj, H., and Kassas, Z. (2023). Multi-constellation blind beacon estimation, Doppler tracking, and opportunistic positioning with OneWeb, Starlink, Iridium NEXT, and Orbcomm LEO satellites. In *Proceedings of IEEE/ION Position, Location, and Navigation Symposium*, pages 1184–1195.

Kozhaya, S. and Kassas, Z. (2022). Blind receiver for LEO beacon estimation with application to UAV carrier phase differential navigation. In *Proceedings of ION GNSS Conference*, pages 2385–2397.

Lapin, I., Granados, G., Samson, J., Renaudin, O., Zanier, F., and Ries, L. (2022). STARE: Real-time software receiver for LTE and 5G NR positioning and signal monitoring. In *Proceedings of Workshop on Satellite Navigation Technology*, pages 1–11.

Lee, J., Gil, G., and Lee, Y. (2014). Exploiting spatial sparsity for estimating channels of hybrid MIMO systems in millimeter wave communications. In *Proceedings of IEEE GLOBECOM*, pages 3326–3331.

Leng, M., Quitin, F., Tay, W., Cheng, C., Razul, S., and See, C. (2016). Anchor-aided joint localization and synchronization using SOOP: Theory and experiments. *IEEE Transactions on Wireless Communications*, 15(11):7670–7685.

Liu, Z., Chen, L., Zhou, X., Jiao, Z., Guo, G., and Chen, R. (2023). Machine learning for time-of-arrival estimation with 5G signals in indoor positioning. *IEEE Internet of Things Journal*, 10(11):9782–9795.

Ma, W., Qi, C., and Li, G. (2020). High-resolution channel estimation for frequency-selective mmwave massive MIMO systems. *IEEE Transactions on Wireless Communications*, 19(5):3517–3529.

Maaref, M. and Kassas, Z. (2022). Autonomous integrity monitoring for vehicular navigation with cellular signals of opportunity and an IMU. *IEEE Transactions on Intelligent Transportation Systems*, 23(6):5586–5601.

Mendrzik, R., Wymeersch, H., and Bauch, G. (2018). Joint localization and mapping through millimeter wave MIMO in 5G systems. In *Proceedings of IEEE Global Communications Conference*, pages 1–6.

Moghtadaiee, V. and Dempster, A. (2014). Indoor location fingerprinting using FM radio signals. *IEEE Transactions on Broadcasting*, 60(2):336–346.

Orabi, M., Khalife, J., and Kassas, Z. (2021). Opportunistic navigation with Doppler measurements from Iridium Next and Orbcomm LEO satellites. In *Proceedings of IEEE Aerospace Conference*, pages 1–9.

Pan, M., Liu, P., Liu, S., Qi, W., Huang, Y., You, X., Jia, X., and Li, X. (2022). Efficient joint DOA and TOA estimation for indoor positioning with 5G picocell base stations. *IEEE Transactions on Instrumentation and Measurement*, 71:1–19.

Paulraj, A., Ottersten, B., Roy, R., Swindlehurst, A., Xu, G., and Kailath, T. (1993). 16 subspace methods for directions-of-arrival estimation. *Handbook of Statistics*, 10:693–739.

Prol, F., Ferre, R., Saleem, Z., Välisuo, P., Pinell, C., Lohan, E., Elsanhoury, M., Elmusrati, M., Islam, S., Celikbilek, K., Selvan, K., Yliaho, J., Rutledge, K., Ojala, A., Ferranti, L., Praks, J., Bhuiyan, M., Kaasalainen, S., and Kuusniemi, H. (2022). Position, navigation, and timing (PNT) through low earth orbit (LEO) satellites: A survey on current status, challenges, and opportunities. *IEEE Access*, 10:83971–84002.

Psiaki, M. (2021). Navigation using carrier Doppler shift from a LEO constellation: TRANSIT on steroids. *NAVIGATION, Journal of the Institute of Navigation*, 68(3):621–641.

Psiaki, M. and Slosman, B. (2019). Tracking of digital FM OFDM signals for the determination of navigation observables. In *Proceedings of ION GNSS Conference*, pages 2325–2348.

Raquet *et al.*, J. (2021). Position, navigation, and timing technologies in the 21st century. volume 2, Part D: Position, Navigation, and Timing Using Radio Signals-of-Opportunity, chapter 35–43, pages 1115–1412. Wiley-IEEE.

Rastorgueva-Foi, E., Costa, M., Koivisto, M., Leppanen, K., and Valkama, M. (2018). User positioning in mmw 5G networks using beam-RSRP measurements and Kalman filtering. In *Proceedings of International Conference on Information Fusion*, pages 1–7.

Shahriar, C. (2008). A scheme to mitigate interference from Iridium satellite's downlink signal captured by omnidirectional antenna array. In *Proceedings of IEEE Antennas and Propagation Society International Symposium*, pages 1–4.

Shamaei, K. and Kassas, Z. (2021a). A joint TOA and DOA acquisition and tracking approach for positioning with LTE signals. *IEEE Transactions on Signal Processing*, 69:2689–2705.

Shamaei, K. and Kassas, Z. (2021b). Receiver design and time of arrival estimation for opportunistic localization with 5G signals. *IEEE Transactions on Wireless Communications*, 20(7):4716–4731.

Shamaei, K., Khalife, J., and Kassas, Z. (2018). A joint TOA and DOA approach for positioning with LTE signals. In *Proceedings of IEEE/ION Position, Location, and Navigation Symposium*, pages 81–91.

Shi, C., Zhang, Y., and Li, Z. (2023). Revisiting Doppler positioning performance with LEO satellites. *GPS Solutions*, 27(3):126–137.

Soderini, A., Thevenon, P., Macabiau, C., Borgagni, L., and Fischer, J. (2020). Pseudorange measurements with LTE physical channels. In *Proceedings of ION International Technical Meeting*, pages 817–829.

Souli, N., Kolios, P., and Ellinas, G. (2022). Online relative positioning of autonomous vehicles using signals of opportunity. *IEEE Transactions on Intelligent Vehicles*, 7(4):873–885.

Souli, N., Makrigiorgis, R., Kolios, P., and Ellinas, G. (2021). Real-time relative positioning system implementation employing signals of opportunity, inertial, and optical flow modalities. In *Proceedings of International Conference on Unmanned Aircraft Systems*, pages 229–236.

Tan, Z., Qin, H., Cong, L., and Zhao, C. (2019a). New method for positioning using IRIDIUM satellite signals of opportunity. *IEEE Access*, 7:83412–83423.

Tan, Z., Qin, H., Cong, L., and Zhao, C. (2019b). Positioning using IRIDIUM satellite signals of opportunity in weak signal environment. *Electronics*, 9(1):37.

Thompson, S., Martin, S., and Bevly, D. (2021). Single differenced Doppler positioning with low Earth orbit signals of opportunity and angle of arrival estimation. In *Proceedings of ION International Technical Meeting Conference*, pages 497–509.

Tian, J., Fangchi, L., Yafei, T., and Dongmei, L. (2023). Utilization of non-coherent accumulation for LTE TOA estimation in weak LOS signal environments. *EURASIP Journal on Wireless Communications and Networking*, 2023(1):1–31.

Wang, P. and Morton, Y. (2023). Impact analysis of inter-cell interference in cellular networks for navigation applications. *IEEE Transactions on Aerospace and Electronic Systems*, 59(1):685–694.

Wei, Q., Chen, X., and Zhan, Y. (2020). Exploring implicit pilots for precise estimation of LEO satellite downlink Doppler frequency. *IEEE Communications Letters*, 24(10):2270–2274.

Yang, C., Arizabaleta-Diez, M., Weitkemper, P., and Pany, T. (2022). An experimental analysis of cyclic and reference signals of 4G LTE for TOA estimation and positioning in mobile fading environments. *IEEE Aerospace and Electronic Systems Magazine*, 37(9):16–41.

Yang, C. and Soloviev, A. (2020). Mobile positioning with signals of opportunity in urban and urban canyon environments. In *Proceedings of IEEE/ION Position, Location, and Navigation Symposium*, pages 1043–1059.

Zhao, C., Qin, H., Wu, N., and Wang, D. (2023). Analysis of baseline impact on differential doppler positioning and performance improvement method for LEO opportunistic navigation. *IEEE Transactions on Instrumentation and Measurement*, 72:1–10.

Kalman Filter-Based Integrity Monitoring for GNSS and 5G Signals of Opportunity Integrated Navigation

Mu Jia * **and Zaher M. Kassas** *

* *The Ohio State University, Columbus, OH 43210, USA*
(e-mail: jia.641@osu.edu; zkassas@ieee.org)

Abstract: A Kalman filter-based receiver autonomous integrity monitoring algorithm (RAIM) is proposed to exploit sequential measurements from global navigation satellite systems (GNSS) and cellular 5G signals of opportunity (SOPs), to ensure safe vehicular navigation in urban environments. To deal with frequent threats caused by multipath and non-line-of-sight conditions, an innovation-based outlier rejection method is introduced. Next, a fault detection technique based on solution separation test is developed, and the quantification of protection levels is derived. Experimental results of a ground vehicle traveling in an urban environment, while making pseudorange measurements to GPS satellites and cellular 5G towers, are presented to demonstrate the efficacy of the proposed method. Incorporating 5G signals from only 2 towers is shown to reduce the horizontal protection level (HPL) by 0.22 m compared to using only GPS. Moreover, the proposed method is shown to reduce the HPL and vertical protection level (VPL) by 84.42% and 69.63%, respectively, over the snapshot advanced RAIM (ARAIM).

Keywords: opportunistic navigation, Kalman filter, RAIM, solution separation, 5G.

1. INTRODUCTION

Passenger safety in automated vehicles depends on the accuracy and reliability of the vehicle's navigation system. With the continuous improvements of navigation system accuracy due to incorporation of multiple sensors (e.g., global navigation satellite systems (GNSS) receivers, lidar, camera, radar, and inertial measurement unit (IMU)), the notion of navigation integrity becomes evermore crucial as vehicles get endowed with autonomous capabilities. GNSS receivers are relied upon to calibrate sensors, correct for accumulating errors due sensor dead reckoning, and provide a navigation solution in a global frame. However, the GNSS-based navigation solution is unreliable in deep urban canyons, due to blockage, reflection, or diffraction of signals by buildings and nearby objects. Recently, cellular signals of opportunity (SOPs) have been demonstrated as a complement or alternative to GNSS signals in GNSS-challenged (Maaref and Kassas, 2020) and GNSS-denied (Kassas et al., 2022) environments. Fusing GNSS signals with cellular SOPs has shown significant improvement in the robustness, accuracy, and integrity of the navigation solution for ground (Kassas et al., 2020) and aerial (Maaref et al., 2021) vehicles.

To ensure safe navigation, automated vehicles need to tightly bound the navigation errors and ensure that the probability of navigation errors being not properly bounded is below a certain limit. Current GNSS technologies are insufficient to support the transition of ground vehicles to full automation in terms of accuracy, integrity, and availability (Zhu et al., 2020). In terms of accuracy, sub-meter-level accuracy is achievable with certain augmentation systems and real-time kinematic (RTK) only under certain favorable conditions (Humphreys et al., 2020); while single point positioning (SPP) can only achieve meter-level accuracy (Imparato et al., 2018). In terms of integrity and availability, recent work demonstrated that in a sample downtown environment (Chicago urban corridor), availability of GPS-only positioning was less than 10% at most locations. While using multi-constellation GNSS (GPS, GLONASS, Galileo, and Beidou) improved the availability significantly, it was still lower than 80% at certain locales; concluding that multi-constellation GNSS cannot provide continuous vehicle positioning (Nagai et al., 2020).

GNSS-based integrity monitoring has been extensively studied (Kropp, 2018). Among the proposed frameworks, receiver autonomous integrity monitoring algorithm (RAIM) is exceptionally attractive, as it is cost-effective and does not require installing additional infrastructure (Blanch et al., 2012). RAIM has been adapted to account for multi-constellation GNSS measurements (e.g., Galileo (Ene et al., 2006), GLONASS (Walter et al., 2013), Beidou (Liu et al., 2014), and low Earth orbit (LEO) mega-constellation-augmented GNSS (Racelis and Joerger, 2020)), aiding sensors (e.g., INS-GPS (Needham and Braasch, 2018), lidar-GNSS (Li et al., 2021), and vision-GPS (Fu et al., 2015)), and terrestrial SOPs (Maaref and Kassas, 2022). Initial studies to characterize the integrity monitoring improvement for automated driving, upon fusing GPS signals with terrestrial SOPs, were conducted in (Maaref et al., 2020; Jia et al., 2021a). However,

⋆ This work was supported in part by the U.S. Department of Transportation (USDOT) under Grant 69A3552047138 for the CARMEN University Transportation Center (UTC) and in part by the National Science Foundation (NSF) under Grant 1929965.

these studies assumed fault-free measurements, which is not realistic in urban environments, where multipath and non-line-of-sight (NLOS) conditions are prevalent. The influence of multipath and NLOS on integrity and availability in urban environments was considered in (Jia et al., 2021b). Nevertheless, the availability rates are still not fully characterized for assured navigation.

Up until recently, most of the integrity monitoring frameworks have relied on snapshot RAIM, i.e., RAIM based on static (e.g., weighted least square) estimators, due to their straightforward projection of measurement error distribution on the solution domain. However, frequent and severe multipath effects can easily cause snapshot RAIM to fail. This is because RAIM is built on the assumption that nearly the full set of the measurements from each time-step can form a consistent set. Otherwise, snapshot RAIM is likely to fail to locate the unfaulted subset of measurements. Furthermore, multipath and NLOS errors are environment dependent, so it is difficult to model the multipath and NLOS errors as a deterministic distribution, which is a necessary prior for the threats to be monitored by RAIM. To improve the measurement redundancy, this paper develops a novel Kalman filter-based RAIM framework to fuse sequential measurements from GNSS and terrestrial SOPs. Furthermore, it introduces an innovation-based outlier rejection method to pre-filter measurement outliers. Solution separation tests are conducted to monitor and exclude faults.

This paper makes three contributions. First, a Kalman filter-based RAIM for GNSS and 5G SOP integrated navigation is proposed. Second, the technique of incorporating outlier rejection into RAIM is studied. Third, experimental results of a ground vehicle traveling in an urban environment, while making pseudorange measurements to GPS satellites and cellular 5G towers, are presented to demonstrate the efficacy of the proposed method. Incorporating 5G signals from only 2 towers is shown to reduce the horizontal protection level (HPL) by 0.22 m compared to using only GPS. Moreover, the proposed method is shown to reduce the HPL and vertical protection level (VPL) by 84.42% and 69.63%, respectively, over the snapshot advanced RAIM (ARAIM).

The paper is organized as follows. Section 2 presents the navigation system. Section 3 describes the proposed integrity monitoring framework. Section 4 presents experimental results. Section 5 concludes the paper.

2. MODEL DESCRIPTION

This section describes the GNSS and cellular pseudorange measurement models, the dynamics of the vehicle mounted receiver and cellular SOP clocks, and the extended Kalman filter (EKF)-based navigation framework.

2.1 GNSS Pseudorange Measurement Model

The ground vehicle-mounted receiver makes pseudorange measurements to M GNSS satellites from N_{const} GNSS constellations. Let $i \in \{1, \ldots, N_{\text{const}}\}$ denote the index of the constellation to which the m-th GNSS satellite belongs. The m-th GNSS pseudorange measurement at time-step k, after compensating for ionospheric and tropospheric delays, and satellite's clock bias, is modeled as

$$z_{\text{GNSS}_m}(k) = \|\boldsymbol{r}_r(k) - \boldsymbol{r}_{\text{GNSS}_m}(k)\|_2 + c \cdot \delta t_r(k) + v_{\text{GNSS}_m}(k), \quad (1)$$

where $\boldsymbol{r}_r(k)$ and $\boldsymbol{r}_{\text{GNSS}_m}(k)$ are the receiver and m-th satellite's three-dimensional (3–D) position vectors, respectively; c is the speed of light; $\delta t_r(k)$ is the receiver's clock bias; and v_{GNSS_m} is the measurement noise, which is modeled as a zero-mean white Gaussian sequence with variance $\sigma^2_{\text{GNSS}_m}(k)$.

2.2 Terrestrial SOP Pseudorange Measurement Model

The ground vehicle-mounted receiver also makes pseudorange measurements from N terrestrial SOPs, which are assumed to be stationary with known positions. The n-th SOP measurement at time-step k can be modeled as

$$z_{\text{SOP}_n}(k) = \|\boldsymbol{r}_r(k) - \boldsymbol{r}_{\text{SOP}_n}\|_2 + c \cdot [\delta t_{r,\text{SOP}}(k) - \delta t_{\text{SOP}_n}(k)] + v_{\text{SOP}_n}(k), \quad (2)$$

where $\boldsymbol{r}_{\text{SOP}_n}$ and $\delta t_{\text{SOP}_n}(k)$ are the 3–D position and clock bias of the n-th SOP transmitter, respectively; $\delta t_{r,\text{SOP}}(k)$ is the the SOP receiver's clock bias; and $v_{\text{SOP}_n}(k)$ is the measurement noise, which is modeled as a zero-mean white Gaussian sequence with variance $\sigma^2_{\text{SOP}_n}(k)$.

2.3 Receiver and Terrestrial SOP Dynamics Model

The vehicle is assumed to follow a white noise acceleration dynamics (e.g., as in (Kassas et al., 2022)). The vehicle-mounted receiver state vector is defined as $\boldsymbol{x}_v \triangleq [\boldsymbol{r}_r^\mathsf{T}, \dot{\boldsymbol{r}}_r^\mathsf{T}, \boldsymbol{x}_{\text{clk},r}^\mathsf{T}, \boldsymbol{x}_{\text{clk,SOP}}^\mathsf{T}]^\mathsf{T}$, where $\boldsymbol{x}_{\text{clk},r} = [\delta t_r, \dot{\delta} t_r]^\mathsf{T}$ is the GNSS receiver clock error state vector, with $\dot{\delta} t_r$ denoting the receiver clock drift; and $\boldsymbol{x}_{\text{clk,SOP}}$ captures the difference between the SOP receiver and each of the SOPs' transmitters clock errors.

Since the SOP pseudorange measurement (2) is parameterized by the difference between the receiver's and the SOPs' clock biases, one needs to only estimate the difference in clock biases and clock drifts. Therefore, the clock state associated with the n-th SOP can be defined

$$\Delta \boldsymbol{x}_{\text{clk,SOP}_n} \triangleq \left[c\Delta\delta t_n, c\Delta\dot{\delta} t_n\right]^\mathsf{T},$$

where $\Delta\delta t_n = \delta t_{r,\text{SOP}} - \delta t_{\text{SOP}_n}$ is the difference between the receiver's clock bias δt_r and the n-th SOP's clock bias δt_n and $\Delta\dot{\delta} t_n = \dot{\delta} t_{r,\text{SOP}} - \dot{\delta} t_{\text{SOP}_n}$ is the difference between the receiver's clock drift $\dot{\delta} t_r$ and the n-th SOP's clock drift $\dot{\delta} t_n$. The augmented clock error state is defined as

$$\boldsymbol{x}_{\text{clk,SOP}} \triangleq \left[\Delta \boldsymbol{x}_{\text{clk,SOP}_1}^\mathsf{T}, \ldots, \Delta \boldsymbol{x}_{\text{clk,SOP}_n}^\mathsf{T}\right]^\mathsf{T} \quad (3)$$

The discrete-time dynamics of $\boldsymbol{x}_{\text{clk,SOP}}$ is assumed to follow the standard double integrator model, driven by process noise (see (Bar-Shalom et al., 2002)).

2.4 EKF time and measurement update

An EKF is used to fuse the measurements from GNSS and SOPs to estimate $\boldsymbol{x}_v$. The EKF measurement update corrects the time-updated states $\hat{\boldsymbol{x}}(k+1|k)$ using available GNSS and SOP measurements. The innovation vector is computed as

$$\tilde{\boldsymbol{z}}(k+1) = \boldsymbol{z}(k) - \boldsymbol{h}\left[\hat{\boldsymbol{x}}(k+1|k)\right],$$

where $\boldsymbol{z}(k)$ the measurement vector at time-step k, and $\boldsymbol{h}(\cdot)$ is the nonlinear measurement model. The EKF

measurement-updated states $\hat{\boldsymbol{x}}(k+1|k+1)$ and associated estimation error covariance $\mathbf{P}(k+1|k+1)$ are computed using standard EKF update equations.

When a signal is fully blocked at a time-step, or detected as an outlier by prefiltering techniques, e.g., the outlier rejection method introduced in Subsection 3.2, the signal is considered as intermittent and the time-updated state estimate and prediction error covariance are passed to the next time-step, skipping the measurement update step.

3. EKF-BASED RAIM WITH OUTLIER REJECTION

This section describes the EKF-based solution separation RAIM, which fuses sequential measurements from GNSS and SOPs, to detect and exclude faults.

3.1 Framework Overview

The flowchart of the proposed EKF RAIM framework is shown in Fig. 1. The integrity monitoring system utilizes a bank of filters, among which there is one that incorporates the all in-view signals, while each of the remaining filters excludes certain signals. These two types of filters are referred to as main filter and subfilters, respectively. Each subfilter excludes one of the signals, so that the subfilter is not influenced by potential faults from the excluded signal. In order to improve the stability and availability of the system, the RAIM algorithm first screens the outliers in the measurements using the innovation-based outlier rejection method. The RAIM algorithm conducts solution separation tests to detect potential faults in the signals, and exclude detected faulty signal to maintain navigation integrity. After all the detection and exclusions, the protection level is computed based on integrity requirements.

3.2 Outlier Rejection

The outlier rejection algorithm uses the innovation filtering technique to remove measurements contaminated by severe multipath and NLOS interference caused by buildings and nearby objects. Measurements suffering from temporary biases are considered as outliers instead of faulty signals to (i) reduce the burden of fault detection and exclusion and (ii) improve measurement redundancy, as only measurement outliers for a short period of time instead of the entire duration are removed from the system. The metrics for detecting outliers is chosen to be the normalized innovation (Groves, 2013).

3.3 Solution Separation Test

This paper develops the fault detection algorithm based on the solution separation test for Kalmen filter navigation developed in (Young and McGraw, 2003; Blanch et al., 2020). The test statistics are chosen to be the difference of the position estimates from the main filter, $\hat{\boldsymbol{r}}^{(0)}(k|k)$, and the position estimates from the subfilters, $\hat{\boldsymbol{r}}^{(i)}(k|k)$. The test statistics vector can be expressed as

$$\boldsymbol{x}_{ss}^{(i)}(k) = \hat{\boldsymbol{r}}^{(0)}(k|k) - \hat{\boldsymbol{r}}^{(i)}(k|k), \qquad i = 1, \ldots, N_{ss}, \quad (4)$$

where N_{ss} is the number of subfilters, i.e., the number of faulted hypotheses to be monitored.

Young and McGraw (2003) showed that the covariance of the i-th solution separation vector can be computed as

$$\boldsymbol{\Sigma}_{ss}^{(i)}(k) = \mathbf{P}^{(i)}(k|k) - \mathbf{P}^{(0)}(k|k).$$

This enables the framework to calculate $\boldsymbol{\Sigma}_{ss}^{(i)}$ without having the cross-correlation between the main filter and subfilters.

The test threshold for the i-th hypothesis in the q-th direction is set to meet a predefined probability of false alert P_{fa} under nominal conditions,

$$T_{i,q} = Q^{-1}(\alpha_{i,q} P_{fa}) \sigma_{ss,q}^{(i)},$$

where $Q^{-1}(\cdot)$ is the inverse Q-function, $\alpha_{i,q}$ is the allocation coefficients of the false alert budget to q direction of the i-th fault mode, and $\sigma_{ss,q}^{(i)}$ is the q-th diagonal element of $\boldsymbol{\Sigma}_{ss}^{(i)}$.

3.4 Protection level computation

The protection level is a statistical error bound computed to guarantee the probability of error exceeding the bound is smaller than the defined integrity risk (Zhu et al., 2018). The predefined integrity risk budget is referred to as probability of hazardous misleading information (PHMI). Suppose that the total integrity risk budget is equally allocated to all the fault mode, the protection level in the q-th direction can be calculated by

$$PL_q = \max_i \left(T_{i,q} + Q^{-1}\left(\frac{PHMI_q}{N_{ss} P(H_i)} \right) \sigma_{ss,q}^{(i)} \right),$$

where $PHMI_q$ is the integrity budget allocated to the q-th direction, and $P(H_i)$ is the probability of the i-th fault mode. The horizontal protection level (HPL) is calculated as the the square root of the protection levels on the horizontal plane, i.e., $q = 1, 2$. The vertical protection level $VPL = PL_3$.

4. EXPERIMENTAL RESULTS

This section presents experimental results of a ground vehicle navigating with GPS and cellular 5G SOPs in an urban environment. The protection levels of the integrated GPS-SOP are compared with those of GPS only to demonstrate the performance improvement of fusing terrestrial 5G SOP measurements. The performance of the proposed framework is also compared with the snapshot ARAIM.

4.1 Experiment setup

In the experiment, a ground vehicle, mounted with antennas to receive GNSS and cellular signals, traveled on Fairview Road in Costa Mesa, California, USA. Two high-grade omnidirectional Laird antennas were connected to a quad-channel National Instruments (NI) universal software radio peripheral (USRP)-2955R to simultaneously down-mix and synchronously sample signals. The USRP were tuned to to Frequency Range 1 (FR1) 5G signals at a carrier frequency of 872 MHz and 632.55 MHz, which corresponded to the U.S. cellular provider AT&T and T-Mobile, respectively. The gNB cell IDs were 608 and 398, respectively. The 5G tower's geodetic locations were [33.652043, -117.907206, 42] and [33.670968, -117.909894, 40], which were surveyed prior to the experiment. Fig. 2 shows the environment layout.

The signals were processed in a post-processing fashion using the Multichannel Adaptive TRansceiver Information

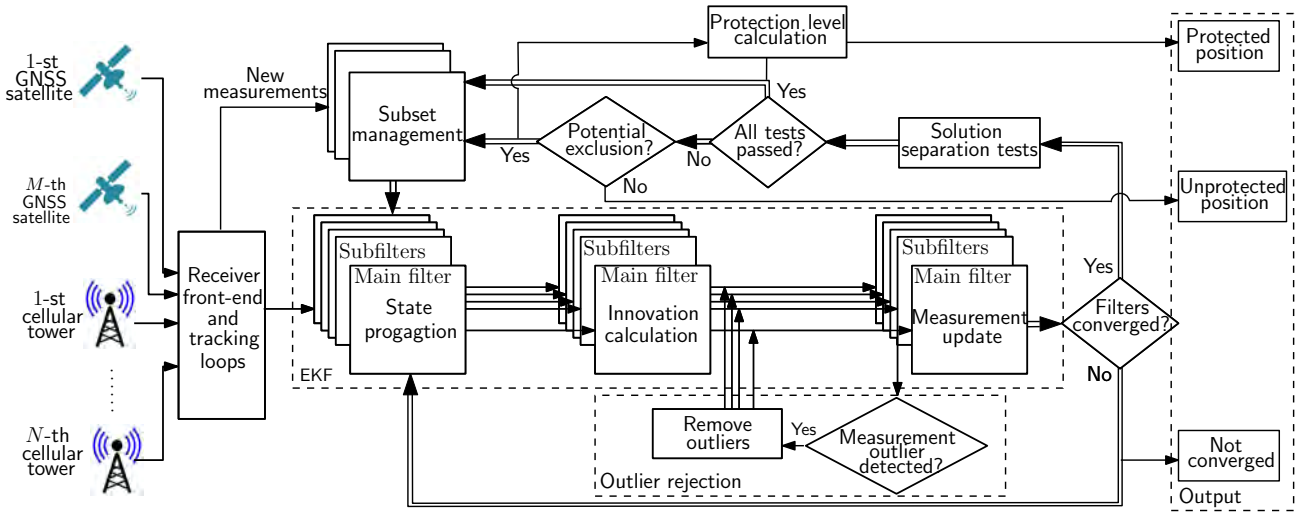

Fig. 1. Flowchart of the EKF-based RAIM with outlier rejection.

eXtractor (MATRIX) software-defined radio (SDR) (Abdallah and Kassas, 2022). The vehicle was equipped with a Septentrio AsteRx-i V integrated GNSS-IMU whose x-axis pointed toward the front of the vehicle, y-axis pointed to the right side of the vehicle, and z-axis pointed upward. AsteRx-i V is equipped with a dual-antenna multi-frequency GNSS receiver and a VectorNav VN-100 micro-electromechanical system (MEMS) IMU. The integrated GNSS receiver provides GPS pseudorange measurements, which were fed to the EKF estimator discussed in Subsection 2.4, to produce the GPS-SOP navigation solution. The tightly-coupled GNSS-IMU with satellite-based augmentation system (SBAS) navigation solution produced by AsteRx-i V was used as ground truth. The GNSS and SOP measurement rate was 5 Hz.

The budget for integrity risk were set to be 10^{-4}/h. The probability of false alert was targeted at 10^{-3}/h. The probability of fault for both GPS and 5G was set to 10^{-2}/h and the time of influence for each fault was set to 120 s. The RAIM parameters are summarized in Table 1.

Table 1. RAIM Parameters

Parameter	Definition	Value
$\{\sigma_{\text{URA,GPS}_m}\}_{m=1}^{M}$	User Range Error for GPS	5 m
$\{\sigma_{\text{URA,SOP}_n}\}_{n=1}^{N}$	User Range Error for SOP	5.48 m
$PHMI_{\text{HOR}}$	Integrity budget for the horizontal component	1.1×10^{-9}
$PHMI_{\text{VERT}}$	Integrity budget for the vertical component	1.1^{-11}
$P_{\text{fa,HOR}}$	Continuity budget allocated to the vertical component	5.6×10^{-8}
$P_{\text{fa,VERT}}$	Continuity budget allocated to the vertical component	5.6×10^{-10}
$\{P_{\text{GPS}_m}\}_{m=1}^{M}$	Probability of a single GPS satellite fault	5.6×10^{-7}
$\{P_{\text{SOP}_n}\}_{n=1}^{N}$	Probability of a single SOP fault	5.6×10^{-7}

4.2 Experimental results

During the experiment, the vehicle travelled for 125 seconds along the trajectory shown in Fig. 2. Pseudorange measurements from 9 GPS satellites and 2 5G towers were used to produce the navigation solutions. The position errors, EKF $\pm 3\sigma$ error bounds, and protection levels are plotted in Fig. 3, showing that the EKF estimator is consistent and the protection levels successfully bound the position errors.

To demonstrate the influence of fusing 5G signal on the integrity performance, the protection levels of using only GPS signals are computed and compared with the GPS+5G solution. The HPL and VPL along the trajectory for GPS+5G and GPS only are plotted in Fig. 4. The average HPL and VPL are shown in Table 2. The results show that fusing only 2 5G towers reduces the average HPL by 0.22 m at the cost of slightly increasing the VPL.

The performance of the proposed EKF-based RAIM is compared with the snapshot ARAIM using a nonlinear least-squares (NLS) estimator. Fig. 5 shows that the proposed framework significantly reduces both HPL and VPL. The average protection levels over the trajectory are given in Table 2, indicating that EKF-based RAIM reduces average HPL and VPL by 84.42% and 69.63%, respectively, over the snapshot ARAIM.

It is worth noting that using the EKF increased the root mean square error (RMSE) over NLS. This could be due to the over-simplified vehicle dynamics model adopted: white noise acceleration. The position accuracy can be improved by incorporating an IMU (Morales and Kassas, 2021; Souli et al., 2021) or using an elaborate vehicle dynamics model with well tuned parameters (Li and Jilkov, 2003).

Table 2. Performance comparison of different algorithms and signal usage

	RMSE	Avg. HPL	Avg. VPL
Snapshot RAIM with GPS only	1.1075 m	102.3792 m	53.5740 m
Snapshot RAIM with GPS+5G	1.1007 m	102.5703 m	53.7070 m
EKF RAIM with GPS only	1.1421 m	16.2013 m	16.2509 m
EKF RAIM with GPS+5G	1.1772 m	15.9801 m	16.3097 m

Fig. 2. Experiment layout and navigation solutions: ground-truth (green) and proposed framework (yellow).

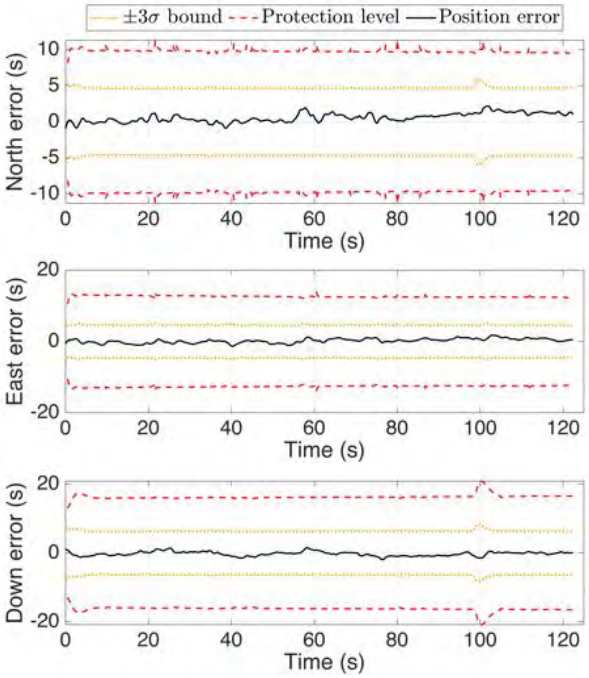

Fig. 3. EKF position errors, 3σ bounds, and protection levels with GPS and 5G signals.

5. CONCLUSION

This paper proposed a Kalman filter-based RAIM algorithm for GNSS and 5G SOP integrated navigation. To deal with frequent threats caused by multipath and NLOS conditions, an innovation-based outlier rejection method was introduced. Furthermore, a fault detection technique based on solution separation test was developed, and a quantification of protection levels was derived. The experimental results on a ground vehicle traveling in an urban environment demonstrated the efficacy of the proposed method. Incorporating cellular 5G SOPs from only 2 tower was shown to reduce the HPL by 0.22 m over using only GPS. The proposed method was also shown to reduce HPL and VPL by 84.42% and 69.63%, respectively, over the snapshot ARAIM.

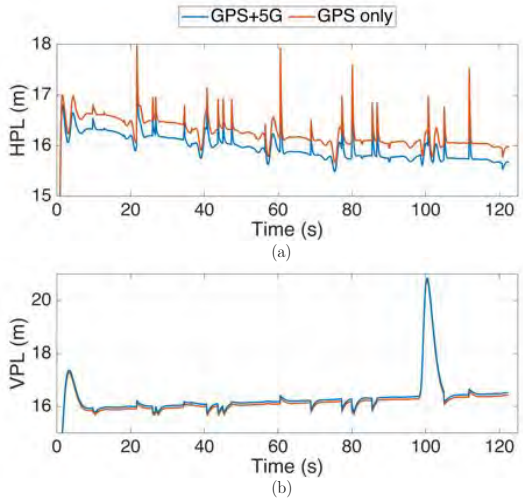

Fig. 4. Protection levels for GPS+5G and GPS only: (a) HPL and (b) VPL.

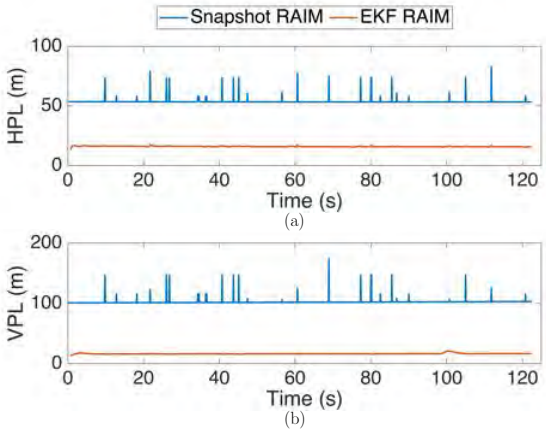

Fig. 5. Protection levels of snapshot ARAIM and EKF RAIM with GPS+5G: (a) HPL and (b) VPL.

REFERENCES

Abdallah, A. and Kassas, Z. (2022). Opportunistic navigation using sub-6 GHz 5G downlink signals: A case study on a ground vehicle. In *Proceedings of European Conference on Antennas and Propagation*, 1–5.

Bar-Shalom, Y., Li, X., and Kirubarajan, T. (2002). *Estimation with Applications to Tracking and Navigation*. John Wiley & Sons, New York, NY.

Blanch, J., Walter, T., Enge, P., Lee, Y., Pervan, B., Rippl, M., and Spletter, A. (2012). Advanced RAIM user algorithm description: Integrity support message processing, fault detection, exclusion, and protection level calculation. In *Proceedings of ION GNSS Conference*, 2828–2849.

Blanch, J., Walter, T., Norman, L., Gunning, K., and de Groot, L. (2020). Solution separation-based fd to mitigate the effects of local threats on ppp integrity. In *Proceedings of IEEE/ION Position, Location and Navigation Symposium*, 1085–1092.

Ene, A., Blanch, J., and Walter, T. (2006). Galileo-GPS RAIM for vertical guidance. In *Proceedings of National Technical Meeting of The Institute of Navigation*, 18–20.

Fu, L., Zhang, J., Li, R., Cao, X., and Wang, J. (2015). Vision-aided RAIM: A new method for GPS integrity monitoring in approach and landing phase. *Sensors*, 15(9), 22854–22873.

Groves, P. (2013). *Principles of* GNSS*, Inertial, and Multisensor Integrated Navigation Systems*. Artech House, second edition.

Humphreys, T., Murrian, M., and Narula, L. (2020). Deep-urban unaided precise global navigation satellite system vehicle positioning. *IEEE Intelligent Transportation Systems Magazine*, 12(3), 109–122.

Imparato, D., El-Mowafy, A., and Rizos, C. (2018). Integrity monitoring: From airborne to land applications. In *Multifunctional Operation and Application of GPS*, 23–43. IntechOpen.

Jia, M., Khalife, J., and Kassas, Z. (2021a). Evaluation of ground vehicle protection level reduction due to fusing GPS with faulty terrestrial signals of opportunity. In *Proceedings of ION International Technical Meeting*, 354–365.

Jia, M., Lee, H., Khalife, J., Kassas, Z., and Seo, J. (2021b). Ground vehicle navigation integrity monitoring for multi-constellation GNSS fused with cellular signals of opportunity. In *Proceedings of IEEE International Conference on Intelligent Transportation Systems*, 3978–3983.

Kassas, Z., Khalife, J., Abdallah, A., and Lee, C. (2022). I am not afraid of the GPS jammer: resilient navigation via signals of opportunity in GPS-denied environments. *IEEE Aerospace and Electronic Systems Magazine*, 37(7), 4–19.

Kassas, Z., Maaref, M., Morales, J., Khalife, J., and Shamaei, K. (2020). Robust vehicular localization and map matching in urban environments through IMU, GNSS, and cellular signals. *IEEE Intelligent Transportation Systems Magazine*, 12(3), 36–52.

Kropp, V. (2018). *Advanced receiver autonomous integrity monitoring for aircraft guidance using GNSS*. Ph.D. thesis, University of Munich, Germany.

Li, T., Pei, L., Xiang, Y., Wu, Q., Xia, S., Tao, L., Guan, X., and Yu, W. (2021). P3-LOAM: PPP/LiDAR loosely coupled SLAM with accurate covariance estimation and robust RAIM in urban canyon environment. *IEEE Sensors Journal*, 21(5), 6660–6671.

Li, X. and Jilkov, V. (2003). Survey of maneuvering target tracking. Part I: Dynamic models. *IEEE Transactions on Aerospace and Electronic Systems*, 39(4), 1333–1364.

Liu, Y., Zhang, J., Xue, R., and Wang, Z. (2014). Performance analysis of advanced RAIM with the inclusion of BeiDou. In *Proceedings of ION International Technical Meeting*, 3629–3636.

Maaref, M. and Kassas, Z. (2020). Measurement characterization and autonomous outlier detection and exclusion for ground vehicle navigation with cellular signals. *IEEE Transactions on Intelligent Vehicles*, 5(4), 670–683.

Maaref, M. and Kassas, Z. (2022). Autonomous integrity monitoring for vehicular navigation with cellular signals of opportunity and an IMU. *IEEE Transactions on Intelligent Transportation Systems*, 23(6), 5586–5601.

Maaref, M., Khalife, J., and Kassas, Z. (2020). Enhanced safety of autonomous driving by incorporating terrestrial signals of opportunity. In *Proceedings of IEEE International Conference on Acoustics, Speech and Signal Processing*, 9185–9189.

Maaref, M., Khalife, J., and Kassas, Z. (2021). Aerial vehicle protection level reduction by fusing GNSS and terrestrial signals of opportunity. *IEEE Transactions on Intelligent Transportation Systems*, 22(9), 5976–5993.

Morales, J. and Kassas, Z. (2021). Tightly-coupled inertial navigation system with signals of opportunity aiding. *IEEE Transactions on Aerospace and Electronic Systems*, 57(3), 1930–1948.

Nagai, K., Fasoro, T., Spenko, M., Henderson, R., and Pervan, B. (2020). Evaluating GNSS navigation availability in 3-D mapped urban environments. In *Proceedings of IEEE/ION Position, Location and Navigation Symposium*, 639–646.

Needham, T. and Braasch, M. (2018). Gravity model error considerations for high-integrity GNSS-aided INS operations. In *Proceedings of IEEE/ION Position, Location and Navigation Symposium*, 822–832.

Racelis, D. and Joerger, M. (2020). Impact of cascading faults on mega-constellation-augmented GNSS PPP integrity. In *Proceedings of ION GNSS Conference*, 3055–3070.

Souli, N., Makrigiorgis, R., Kolios, P., and Ellinas, G. (2021). Real-time relative positioning system implementation employing signals of opportunity, inertial, and optical flow modalities. In *Proceedings of International Conference on Unmanned Aircraft Systems*, 229–236.

Walter, T., Blanch, J., Choi, M.J., Reid, T., and Enge, P. (2013). Incorporating GLONASS into aviation RAIM receivers. In *Proceedings of International Technical Meeting of the Institute of Navigation*, 239–249.

Young, R. and McGraw, G. (2003). Fault detection and exclusion using normalized solution separation and residual monitoring methods. *NAVIGATION, Journal of the Institute of Navigation*, 50(3), 151–169.

Zhu, N., Betaille, D., Marais, J., and Berbineau, M. (2020). GNSS integrity monitoring schemes for terrestrial applications in harsh signal environments. *IEEE Intelligent Transportation Systems Magazine*, 12(3), 81–91.

Zhu, N., Marais, J., Betaille, D., and Berbineau, M. (2018). GNSS position integrity in urban environments: A review of literature. *IEEE Transactions on Intelligent Transportation Systems*, 19(9), 2762–2778.

Multipath Mitigation of 5G Signals via Reinforcement Learning for Navigation in Urban Environments

Ali A. Abdallah[1], Mohamad Orabi[1], and Zaher M. Kassas[1,2]
[1]Department of Electrical Engineering and Computer Science, University of California, Irvine, USA
[2]Department of Mechanical and Aerospace Engineering, University of California, Irvine, USA
Emails: abdalla2@uci.edu, orabim@uci.edu, zkassas@ieee.org

***Abstract*—The ability of reinforcement learning (RL)-based convolutional neural network (CNN) to mitigate multipath signals for opportunistic navigation with downlink 5G signals is assessed. The CNN uses inputs from the autocorrelation function (ACF) to learn the errors in the code phase estimates. A ray tracing algorithm is used to produce high fidelity training data that could model the dynamics between the line of sight (LOS) component and the non-line of sight (NLOS) components. Experimental results on a ground vehicle navigating with 5G signals for 902 m in a multipath-rich environment are presented, demonstrating that the proposed RL-CNN achieved a position root-mean squared error (RMSE) of 14.7 m compared to 20.6 m with a conventional delay-locked loop (DLL).**

***Index Terms*— 5G, reinforcement learning, multipath, navigation.**

I. Introduction

Multipath phenomenon is a major error source in signal-based navigation technologies including: (i) global navigation satellite systems (GNSS) [1] and (ii) alternative technologies, such as cellular, AM/FM radio, satellite communication, digital television, and Wi-Fi [2]–[11]. Among alternative signal-based technologies, cellular 5G signals are particularly attractive due to their ubiquity, geometric diversity, high received signal power, and large bandwidth [12]–[14].

The positioning capabilities of 5G systems have been studied over the past few years. Different approaches have been proposed, in which direction-of-arrival (DOA), direction-of-departure (DOD), time-of-arrival (TOA), or combination thereof is used to achieve accurate positioning from 5G signals. The study in [15] derived the Cramér-Rao lower bound on position and orientation estimation uncertainty and presented an algorithm that achieves the bound for average to high signal-to-noise ratio. In [16], the capability of massive multiple-input multiple-output (mMIMO) systems in providing very accurate localization when relying on DOA was studied. The work in [17] presented an algorithm to mitigate the near-field errors in angular positioning with 5G system. A compressed sensing approach was proposed to address the limitations of DOA in mMIMO systems in the presence of multipath, showing the potential of achieving submeter accuracy in a simulated environment. In contrast to the aforementioned approaches, [18]–[20] were the first to present experimental navigation results on ground and aerial vehicles, achieving meter-level accuracy.

Several techniques have been developed to mitigate the effect of multipath in GNSS systems, most of which could be grouped into three main categories: (i) antenna techniques [21], (ii) signal processing techniques, such as the narrow correlator [22], strobe edge correlator [23], and high resolution correlator (HRC) [24], and (iii) a combination thereof [25]. While the aforementioned approaches have been shown to outperform the standard early-minus-late (E-L) delay-locked loop (DLL), they are still susceptible to severe multipath. Moreover, while signal processing techniques could be extended to receivers that exploit cellular signals opportunistically for navigation, antenna techniques that mitigate multipath by filtering out signals with lower elevation angles are not useful, since most received signals from terrestrial 5G base stations (referred to as gNBs) have low elevation angles.

Machine learning algorithms have found their way into the navigation field [26]. A neural network (NN)-based DLL (NNDLL) was proposed in [27] for multipath mitigation in GPS receivers. The type of multipath environment and receiver motion was identified via an NN in [28] in order to adjust the receiver's tracking strategy. The ability of different NNs to mitigate multipath signals for opportunistic navigation with downlink 5G signals was considered in [29]. The paper presented two NN designs, namely feed-forward NNs (FFNNs) and time-delay NNs (TDNNs), to learn multipath-induced errors on a 5G receiver's code phase estimate. Experimental results in a multipath-rich environment were presented demonstrating that the proposed TDNN achieved ranging root-mean squared error (RMSE) reduction of 27.1% compared to a conventional DLL. However, such NNs are limited due to the dependence on DLL for training data; hence, the NN only corrects the DLL estimates. This paper addresses this limitation by proposing a reinforcement learning (RL)-based approach to learn multipath errors that corrupt the TOA estimate in a 5G opportunistic navigation receiver. The proposed RLNN seeks to learn the multipath behavior by making a sequence of decisions, each with a certain reward and penalty.

This paper assesses the ability of RL-based convolutional NN (CNN) to mitigate multipath signals for opportunistic navigation with downlink 5G signals. The NNs use inputs

from the autocorrelation function (ACF) to learn the errors in the code phase estimate of a conventional DLL. A ray tracing algorithm is used to produce high fidelity training data that could model the dynamics between the line of sight (LOS) component and the non-line of sight (NLOS) components. Experimental results on a ground vehicle navigating in an urban environment are presented demonstrating that the proposed RL-CNN achieved a position root-mean squared error (RMSE) of 14.7 m compared to 20.6 m with a conventional DLL.

This paper is organized as follows. Section II introduces the structure of 5G signals and models the synchronization signals being exploited for navigation. Section III presents the proposed RL-based multipath mitigation approach along with the simulator that was used to generate the training and testing data. Section V presents experimental results in an urban environment. Section VI gives concluding remarks.

II. 5G Signal Structure

This section discusses the 5G signal structure and provides a model for 5G reference signals that can be exploited for opportunistic navigation.

A. 5G Frame Structure

5G systems implement orthogonal frequency-division multiplexing (OFDM) with an adaptive subcarrier spacing $\Delta f = 2^{\mu} \times 15$ kHz, where $\mu \in \{0, 1, 2, 3, 4\}$ is defined as the numerology. 5G is designed to support transmission at different frequency ranges (from 450 MHz to 52.6 GHz). In the time-domain, 5G signals are transmitted in frames of duration $T_f = 10$ ms, which are divided into 10 subframes with a duration of 1 ms each. Subframes are then further divided into 2^{μ} time slots which contain 14 OFDM symbols each of duration $T_{\text{symb}} = \frac{1}{\Delta f}$. In the frequency domain, subframes are divided into a number of resource grids consisting of resource blocks with 12 subcarriers each. The number of resource grids in a frame is determined by higher level parameters. Moreover, a resource element defines the smallest unit of the resource grid spanning a duration of one OFDM symbol and a bandwidth of one subcarrier.

5G systems utilize two maximal-length synchronization signals (SS) of length $N_{\text{SS}} = 127$, known as the primary synchronization signal (PSS) and secondary synchronization signal (SSS) to enable cell search and synchronization at the user equipment (UE). There is a total of three possible PSS sequences, each mapped to an integer representing the sector ID of the gNB denoted by $N_{\text{ID}}^{(2)}$. On the other hand, the SSS is one of 336 possible sequences, each mapped to an integer representing the gNB's group identifier denoted by $N_{\text{ID}}^{(1)}$. This results in a total of 1008 cell identifiers denoted by $N_{\text{ID}}^{\text{cell}} = 3N_{\text{ID}}^{(1)} + N_{\text{ID}}^{(2)}$.

The SS are transmitted along with the physical broadcast channel (PBCH) signal and its associated demodulation reference signal (DM-RS) on a block known as the SS/PBCH block, which spans 20 resource blocks (i.e., 240 subcarriers) and four consecutive OFDM symbols. The SS/PBCH is transmitted numerous times, where each set of these transmitted block is called an SS/PBCH burst. However, each SS/PBCH block in the burst is beamformed in a different direction with a periodicity that can be 5 ms, 10 ms, 20 ms, 40 ms, 80 ms or 160 ms.

B. Signal Model

For the purpose of opportunistic navigation with 5G, the signals of interest for a given $N_{\text{ID}}^{\text{cell}}$ could be modeled as

$$s_{\text{SS}}(t) = \begin{cases} \text{IFT}\{S_{\text{PSS}}(f)\}, & \text{for } t \in (0, T_{\text{symb}}) \\ \text{IFT}\{S_{\text{SSS}}(f)\}, & \text{for } t \in (2T_{\text{symb}}, 3T_{\text{symb}}) \\ 0, & \text{otherwise,} \end{cases}$$

where $S_{\text{PSS}}(f)$ and $S_{\text{SSS}}(f)$ are the frequency-domain representations of the PSS and SSS, respectively. A navigation receiver correlates the replicated SS signal with the received signal, forming the autocorrelation function (ACF), denoted by $R(\tau)$ according to

$$\begin{aligned} R(\tau) &\triangleq y(t) \circledast s_{\text{SS}}(t) \\ &= \text{IFFT}\{Y(f) S_{\text{SS}}^{*}(f)\} \quad (1) \\ &= \text{sinc}\,(B\tau) \quad (2) \end{aligned}$$

where the symbols $\circledast$ and * denote the circular correlation and the complex conjugate operators, respectively, IFFT denotes the inverse fast Fourier transform, and $y(t)$ and $Y(f)$ are the time- and frequency-domain representations of the received signal with a bandwidth of $B = N_{\text{subcarriers}} \cdot \Delta f$, where $N_{\text{subcarriers}}$ is the number of subcarriers allocated for the synchronization signal. Since each symbol of the SS is mapped onto one subcarrier, then $N_{\text{subcarriers}} = N_{\text{SS}} = 127$. It is important to note that while the ACF has a triangular shape for GPS signals, the ACF produced by the correlator of an opportunistic receiver exploiting 5G signals has the shape of the sinc function. This follows from the OFDM modulation of the two maximal-length sequences (m-sequences) PSS and SSS. Equation (2) follows from (1) since $S_{\text{SS}}(f)$ is an m-sequence that takes the values $\{-1, +1\}$, and $S_{\text{SS}}(f) S_{\text{SS}}^{*}(f) = |S_{\text{SS}}(f)|^2 = \text{rect}(\frac{f}{B})$, where rect(.) denotes the standard rectangular function with a bandwidth of B.

III. Proposed Approach

RL is a machine learning technique that seeks modeling a certain environment following the cut-and-try approach. The trained model is denoted by an agent that evaluates a current situation (state). The agent takes a sequence of actions, each receives a feedback (reward/penalty) from an environment. The environment represents the training data to which the agent is making actions. Positive feedback represents a reward for making a correct decision, while negative feedback represents a penalty for making the wrong decision. In other words, RL learns the best action via a trail-and-error approach while interacting with an environment to maximize a long-term reward. The long-term reward is a combination of short-term rewards that are observed in every state after taking a set of coherent actions while interacting with the environment. A block diagram depicting RL is hown in Fig. 1

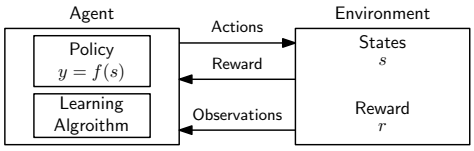

Fig. 1. RL block diagram.

The proposed RL approach consists of the following

- Environment: represents the physical environment on which the agent operates. In particular, it is represented via the ACF $R(\tau)$ that captures all rays impinging on the receiver's antenna including both LOS and NLOS components and the receiver's states.
- State: represents the current situation of the agent. As such, the code phase error is an informative state of the agent while seeking to maintain tracking in presence of multipath.
- Reward: represents the feedback from the environment to evaluate the agent's performance. Here, a potential choice of the reward function r_t is chosen to penalize the code phase error and its first order derivative according to

$$r_t = -|\tilde{\tau}| - \frac{d|\tilde{\tau}|}{dt}, \qquad (3)$$
$$\tilde{\tau} \triangleq \tau_k - \hat{\tau}_k,$$

  where τ, $\hat{\tau}$, $\tilde{\tau}$ are the actual code phase, estimated code phase, and code phase error, respectively. The reward in (3) represents the short-term reward. In addition to that, a milestone reward for surviving five seconds is applied, where surviving inhere denotes $\tilde{\tau} < \frac{B}{4}$, where B is bandwidth of the received 5G signals. Exceeding this bound results in killing the agent and starting another episode. It is worth mentioning that this long-term reward helps with the initial convergence as it helps in filtering out the agents that are immediately killed and gives the agent a push to the right decision.
- Policy: maps the agent's state s to actions $y = f(s)$. To do so, an NN is implemented to decide the actions to be taken. For the proposed approach, a CNN with sixteen 21×3 filters, with a stride of 21×1 were designed. The CNN has 42,757 learnable parameters. Note that "21" represents the number of ACF taps used with 10 delay taps, which are the user's design choices. Fig. 2 shows the proposed RL network design. It worth mentioning that the input is 42×10 instead of 21×10 due to the fact that the real and imaginary parts of each sample point are fed separately to the network.

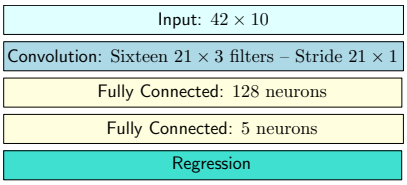

Fig. 2. RL network design.

IV. Training and Data Generation

To simulate a realistic environment, map and terrain data were obtained through OpenStreetMap [30] and Global Multiresolution Terrain Elevation Data (GMTED) [31] for the area around Aldrich Park at the University of California, Irvine (UCI). An opportunistic 5G receiver was then simulated to be moving around the park at a walking speed of 2 m/s. The simulated environment and trajectory are presented in Fig. 3(a). Moreover, the location of the simulated gNB correspond to real gNB positions on top of the Engineering Tower at UCI. The power, delay, and phase of each path were then computed for the entire trajectory using the ray tracing methods available through MATLAB's RadioFrequency (RF) toolbox [32]. The channel impulse response (CIR) was generated in this manner to ensure that the simulator would capture the dynamics between the LOS and NLOS components. Fig. 3(b) shows the simulation environment in MATLAB with the rays traced from the gNB to four sample points within the trajectory along with the received power for each path. It is worth noting that the material used for buildings was concrete with a relative permittivity of 5.31 and a conductivity of 0.0548 Siemens per meter. These values were chosen according to the international telecommunication union (ITU) recommendations, which provide methods, equations, and values used to calculate real relative permittivity, conductivity, and complex relative permittivity for common materials [33].

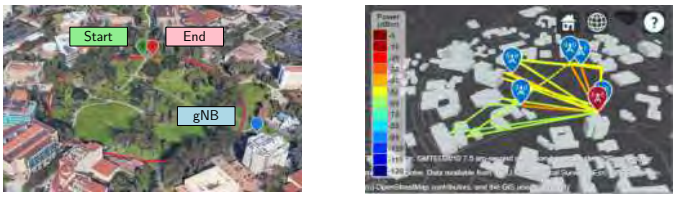

(a) (b)

Fig. 3. (a) Receiver Trajectory around Aldirch Park. (b) Rays traced from transmitter (red) to sample points of trajectory (blue).

Next, the obtained CIRs are used to simulate the tracking results for an opportunistic 5G receiver traversing the aforementioned trajectory shown in Fig. 3(a). The tracking loops of the receiver uses inputs from the output of the correlator $R(\tau)$, which is simulated from the CIR according to

$$R_k(\tau) = \sum_{i=1}^{N_k^{\text{paths}}} \alpha_k^i R(\tau - \tau_k^i),$$

where k is the time index with a duration equivalent to that of the SS (set to 20 ms based on an observation of a real 5G transmission scenario), $R_k(\tau)$ is the correlator output of the opportunistic receiver accounting for the different traversed paths at the k-th time-step, $R(.)$ is the ACF of the synchronization signal defined in (2), N_k^{paths} is the total number of paths traversed by the signal, $\alpha_k^i \in \mathcal{C}$ is a complex number representing the power and phase of the signal component corresponding to the i-th path, and τ_k^i represents its delay (time of flight).

Finally, the simulated data contained samples (x_k, y_k) with an equivalent duration of 438.51 seconds. The input $x_k \in \mathcal{C}^{2N_x+1}$ is formed of $2N_x + 1$ samples of the correlator output at the k-th time-step centered around the DLL's code phase estimate, such that $x_k = [x_k^{-N_x}, \ldots, x_k^{N_x}]^\mathsf{T}$, where $x_k^d = R_k(\tau + \hat{\tau}_k^{\mathrm{DLL}} + d/f_s)$ and f_s is the frequency at which the ACF was sampled. For the remainder of this paper, the sampling frequency is set to $f_s \triangleq 4B = 7.62$, and the number of ACF taps used as inputs is $2N_x+1 = 11$. The sample target points $y_k \in \mathcal{R}$ are the errors incurred by the DLL estimate $e(x_k) = \tau_k^{\mathrm{LOS}} - \hat{\tau}_k^{\mathrm{DLL}}$, where the true LOS delays at the k-th time-step τ_k^{LOS} are obtained from the simulated CIR.

V. Experimental Results

This section validates the proposed framrwork on a ground vehicle in an urban environment.

A. Experimental Setup and Environmental Layout

The experiment was performed on the Fairview road in Costa Mesa, California, USA. A quad-channel National Instrument (NI) universal software radio peripheral (USRP)-2955 was mounted on a vehicle, where two channels were used to sample 5G signals with a sampling ratio of 10 MSps. The receiver was equipped with two consumer-grade cellular omnidirectional Laird antennas. The USRP was tuned to listen to 5G signals from AT&T and T-Mobile U.S. cellular providers (see Table I). The vehicle was equipped with a Septentrio AsteRx-i V integrated GNSS-inertial measurement unit (IMU) to produce the ground truth trajectory.

TABLE I
GNBs's Characteristics

gNB	Carrier frequency [MHz]	N_{ID}^{Cell}	Cellular provider
1	872	608	AT&T
2	632.55	398	T-Mobile

B. Signal Tracking Performance

Two gNBs were present in the environment whose positions were mapped prior to the experiment. In the tracking stage, the 5G signals from both gNBs were tracked for 100 seconds. Fig. 4 shows the tracking results of the two gNBs, while Fig. 5 shows the cumulative distribution function (CDF) of the errors.

C. Navigation Solution

An extended Kalman filter, as discussed in [18], was used to estimate the vehicle-mounted receiver's trajectory. The measurement variances were found to vary between 1.3 and 25.7 m. Fig. 6 shows the environment layout, location of gNBs, navigation solution of DLL-based and RL-based 5G, and receiver's ground truth. The proposed 5G RL approach achieved a position RMSE of 14.7 m compared to 20.6 m with a conventional DLL-based 5G receiver. It is worth noting that the receiver presented in [18] used additional reference signals (not used in this study), namely physical broadcast channel (PBCH) and its associated demodulation reference signal (DM-RS).

VI. Conclusion

This paper presented a proof-of-concept of the power of RL in learning multipath errors that corrupt the TOA estimate in a 5G opportunistic navigation receiver. The proposed approach is the first of its kind to not depend on a DLL, as it learns the errors from observed ACFs directly. The RL-CNN used inputs from the ACF to learn the errors in the code phase estimates. A ray tracing algorithm was used to produce high fidelity training data that could model the dynamics between the LOS component and the NLOS components. Experimental results in a multipath-rich environment were presented demonstrating that the proposed RL-CNN achieved a position RMSE of 14.7 m compared to 20.6 m achieved using the conventional DLL.

Acknowledgment

This work was supported in part by the Office of Naval Research (ONR) under Grant N00014-19-1-2511 and Grant N00014-19-1-2613, in part by the U.S. Department of Transportation (USDOT) under Grant 69A3552047138 for the CARMEN University Transportation Center (UTC), and in part under the financial assistance award 70NANB17H192 from U.S. Department of Commerce, National Institute of Standards and Technology (NIST). Map data copyrighted OpenStreetMap contributors and available from https://www.openstreetmap.org.

References

[1] A. Mannesson, M. Yaqoob, B. Bernhardsson, and F. Tufvesson, "Tightly coupled positioning and multipath radio channel tracking," *IEEE Transactions on Aerospace and Electronic Systems*, vol. 52, no. 4, pp. 1522–1535, August 2016.

[2] J. del Peral-Rosado, R. Estatuet-Castillo, J. Lopez-Salcedo, G. Seco-Granados, Z. Chaloupka, L. Ries, and J. Garcoa-Molina, "Evaluation of hybrid positioning scenarios for autonomous vehicle applications," in *Proceedings of ION International Technical Meeting Conference*, January 2017, pp. 2541–2553.

[3] T. Kang, H. Lee, and J. Seo, "TOA-based ranging method using CRS in LTE signals," *Journal of Advanced Navigation Technology*, vol. 23, no. 5, pp. 437–443, October 2019.

[4] K. Shamaei, J. Morales, and Z. Kassas, "A framework for navigation with LTE time-correlated pseudorange errors in multipath environments," in *Proceedings of IEEE Vehicular Technology Conference*, April 2019, pp. 1–6.

[5] X. Chen, Q. Wei, F. Wang, Z. Jun, S. Wu, and A. Men, "Super-resolution time of arrival estimation for a symbiotic FM radio data system," *IEEE Transactions on Broadcasting*, vol. 66, no. 4, pp. 847–856, December 2020.

[6] L. Xu and J. Rife, "Modeling multipath effects on frequency locked loops," in *Proceedings of ION International Technical Meeting*, 2020, pp. 698–712.

[7] H. Dun, C. Tiberius, and G. Janssen, "Positioning in a multipath channel using OFDM signals with carrier phase tracking," *IEEE Access*, vol. 8, pp. 13 011–13 028, 2020.

[8] P. Wang and Y. Morton, "Performance comparison of time-of-arrival estimation techniques for LTE signals in realistic multipath propagation channels," *NAVIGATION, Journal of the Institute of Navigation*, vol. 67, no. 4, pp. 691–712, December 2020.

[9] T. Kazaz, G. Janssen, J. Romme, and A. Van der Veen, "Delay estimation for ranging and localization using multiband channel state information," *IEEE Transactions on Wireless Communications*, pp. 1–16, September 2021.

[10] C. Jin, I. Bajaj, K. Zhao, W. Tay, and K. Ling, "5G positioning using code-phase timing recovery," in *Proceedings of IEEE Wireless Communications and Networking Conference*, 2021, pp. 1–7.

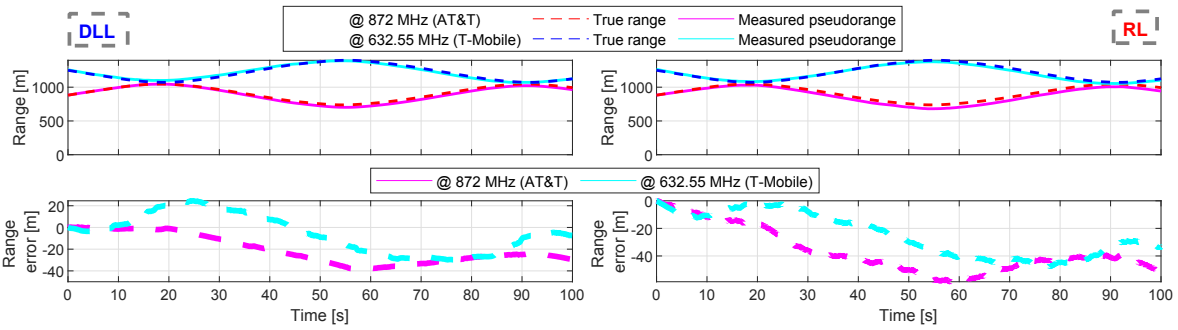

Fig. 4. Cellular 5G signal tracking results of the two gNBs for both DLL and RL approaches showing: (i) pseudorange estimate in solid lines versus true range in dashed lines after removing the initial bias and (ii) range errors.

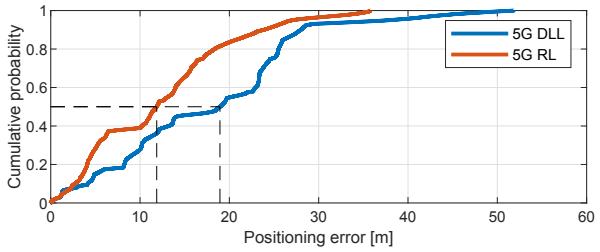

Fig. 5. CDF of positioning errors for DLL-based and RL-based approaches.

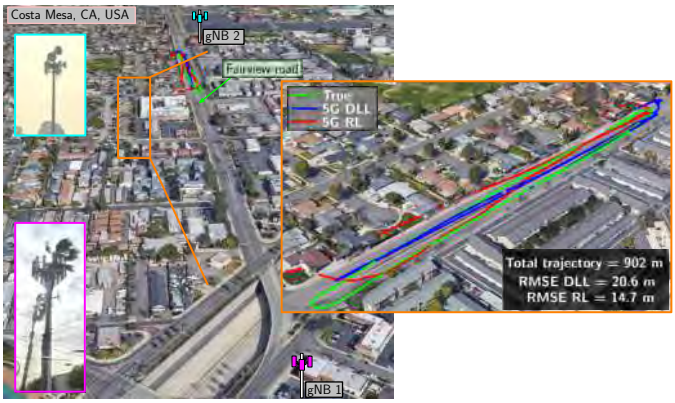

Fig. 6. 5G gNBs' locations and traversed trajectory: true (white), DLL-based estimate (blue), and RL-based estimate (red). Image: Google Earth.

[11] N. Souli, P. Kolios, and G. Ellinas, "Online relative positioning of autonomous vehicles using signals of opportunity," *IEEE Transactions on Intelligent Vehicles*, pp. 1–1, 2021.

[12] K. Shamaei and Z. Kassas, "Receiver design and time of arrival estimation for opportunistic localization with 5G signals," *IEEE Transactions on Wireless Communications*, vol. 20, no. 7, pp. 4716–4731, 2021.

[13] I. Lapin, G. Seco-Granados, O. Renaudin, F. Zanier, and L. Ries, "Joint delay and phase discriminator based on ESPRIT for 5G NR positioning," *IEEE Access*, vol. 9, pp. 126 550–126 563, 2021.

[14] A. Abdallah, J. Khalife, and Z. Kassas, "Experimental characterization of received 5G signals carrier-to-noise ratio in indoor and urban environments," in *Proceedings of IEEE Vehicular Technology Conference*, April 2021, pp. 1–5.

[15] A. Shahmansoori, G. Garcia, G. Destino, G. Seco-Granados, and H. Wymeersch, "Position and orientation estimation through millimeter-wave MIMO in 5G systems," *IEEE Transactions on Wireless Communications*, vol. 17, no. 3, March 2018.

[16] N. Garcia, H. Wymeersch, E. Larsson, A. Haimovich, and M. Coulon, "Direct localization for massive MIMO," *IEEE Transactions on Signal Processing*, vol. 65, no. 10, pp. 2475–2487, May 2017.

[17] K. Han, Y. Liu, Z. Deng, L. Yin, and L. Shi, "Direct positioning method of mixed far-field and near-field based on 5G massive MIMO system," *IEEE Access*, vol. 7, pp. 72 170–72 181, 2019.

[18] A. Abdallah, K. Shamaei, and Z. Kassas, "Assessing real 5G signals for opportunistic navigation," in *Proceedings of ION GNSS Conference*, 2020, pp. 2548–2559.

[19] Z. Kassas, A. Abdallah, and M. Orabi, "Carpe signum: seize the signal – opportunistic navigation with 5G," *Inside GNSS Magazine*, vol. 16, no. 1, pp. 52–57, 2021.

[20] A. Abdallah and Z. Kassas, "UAV navigation with 5G carrier phase measurements," in *Proceedings of ION GNSS Conference*, September 2021, pp. 3294–3306.

[21] D. Aloi and M. Sharawi, "High fidelity antenna model validation results of a GNSS multipath limiting antenna," *IEEE Transactions on Aerospace and Electronic Systems*, vol. 47, no. 1, pp. 3–14, January 2011.

[22] A. van Dierendonck, P. Fenton, and T. Ford, "Theory and performance of narrow correlator spacing in a GPS receiver," *NAVIGATION, Journal of the Institute of Navigation*, vol. 39, no. 3, pp. 265–283, September 1992.

[23] L. Garin, F. van Diggelen, and J. Rousseau, "Strobe and edge correlator multipath mitigation for code," in *Proceedings of ION International Technical Meeting*, January 1996, pp. 657–664.

[24] G. McGraw and M. Braasch, "GNSS multipath mitigation using gated and high resolution correlator concepts," in *Proceedings of ION National Technical Meeting*, January 1999, pp. 333–342.

[25] A. Abdallah and Z. Kassas, "Multipath mitigation via synthetic aperture beamforming for indoor and deep urban navigation," *IEEE Transactions on Vehicular Technology*, vol. 70, no. 9, pp. 8838–8853, September 2021.

[26] J. Gante, L. Sousa, and G. Falcao, "Dethroning GPS: Low-power accurate 5G positioning systems using machine learning," *IEEE Journal on Emerging and Selected Topics in Circuits and Systems*, vol. 10, no. 2, pp. 240–252, June 2020.

[27] M. Orabi, J. Khalife, A. Abdallah, Z. Kassas, and S. Saab, "A machine learning approach for GPS code phase estimation in multipath environments," in *Proceedings of IEEE/ION Position, Location, and Navigation Symposium*, April 2020, pp. 1224–1229.

[28] N. Sokhandan, N. Ziedan, A. Broumandan, and G. Lachapelle, "Context-aware adaptive multipath compensation based on channel pattern recognition for GNSS receivers," *NAVIGATION, Journal of the Institute of Navigation*, vol. 70, no. 5, pp. 944–962, September 2017.

[29] M. Orabi, A. Abdallah, J. Khalife, and Z. Kassas, "A machine learning multipath mitigation approach for opportunistic navigation with 5G signals," in *Proceedings of ION GNSS Conference*, September 2021, pp. 2895–2909.

[30] OpenStreetMap contributors, "Planet dump retrieved from https://planet.osm.org," https://www.openstreetmap.org, 2017.

[31] J. Danielson and D. Gesch, *Global multi-resolution terrain elevation data 2010 (GMTED2010)*. US Department of the Interior, US Geological Survey, 2011.

[32] "Matlab RF toolbox," https://www.mathworks.com/help/rf/index.html, 2021.

[33] P. Series, "Effects of building materials and structures on radiowave propagation above about 100 MHz," *Recommendation ITU-R*, pp. 2040–1, 2015.

Multi-Constellation Blind Beacon Estimation, Doppler Tracking, and Opportunistic Positioning with OneWeb, Starlink, Iridium NEXT, and Orbcomm LEO Satellites

Sharbel Kozhaya, Haitham Kanj, and Zaher M. Kassas
Department of Electrical and Computer Engineering
The Ohio State University, Columbus, OH, USA
kozhaya.1@osu.edu, kanj.7@osu.edu, zkassas@ieee.org

***Abstract*—A novel blind spectral approach is proposed for blind beacon estimation, Doppler tracking, and opportunistic positioning with unknown low Earth orbit (LEO) satellite signals. The framework is agnostic to the modulation and multiple access scheme adopted by LEO satellites. First, an analytical derivation of the received signal frequency spectrum is presented, which accounts for the highly dynamic channel between the LEO satellite and a terrestrial receiver. Second, a frequency domain-based blind Doppler discriminator is proposed. Third, a Kalman filter (KF)-based Doppler tracking algorithm is developed. Fourth, a blind beacon estimation framework for LEO satellites is proposed and its convergence properties are studied. Simulation results are presented showing successful beacon estimation and Doppler tracking of Starlink LEO satellites transmitting 5G orthogonal division multiple access (OFDM) signals. Experimental results are presented demonstrating the efficacy of the proposed framework on multi-constellation LEO satellites, namely OneWeb, Starlink, Orbcomm, and Iridium NEXT. Despite adopting different modulation and multiple access transmission schemes, the proposed framework is capable of successfully estimating the beacon and tracking the Doppler, in a blind fashion, of 8 LEO satellites (2 OneWeb, 4 Starlink, 1 Iridium NEXT, and 1 Orbcomm) over a period of about 560 seconds with Hz-level accuracy. The produced Doppler measurements were fused through a nonlinear least-squares estimator to localize a stationary receiver to an unprecedented level of accuracy. Starting with an initial estimate about 3,600 km away, a final three-dimensional (3–D) position error of 5.8 m and 2–D position error of 5.1 m was achieved. Aside from achieving this unprecedented accuracy, these results represent the first successful opportunistic tracking of unknown OneWeb LEO signals and their exploitation for positioning.**

***Index Terms*—Positioning, navigation, signals of opportunity, blind Doppler tracking, low Earth orbit satellite, OneWeb.**

I. Introduction

Navigation from low Earth orbit (LEO) will usher a new era for positioning, navigation, and timing (PNT). Megaconstellations of LEO satellites are being born (e.g., Starlink, OneWeb, and Kuiper), joining existing LEO constellations (e.g., Orbcomm, Globalstar, Iridium NEXT, among others) [1]. These satellites will shower the Earth with a plethora of signals, diverse in frequency and direction, which could be utilized for PNT in a dedicated fashion [2] or opportunistically [3].

To compensate for the limitations of global navigation satellite systems (GNSS) [4], [5], researchers over the past decade studied the exploitation of terrestrial signals of opportunity (SOPs) for PNT. SOPs include: (i) AM/FM radio [6]; (ii) digital television [7]; (iii) WiFi [8]; and (iv) cellular 3G [9], [10], 4G [11], [12], and 5G [13], [14]; with cellular SOPs showing the most promise, as they achieved lane-level positioning on ground vehicles [15], [16], meter-level positioning on high-altitude aircraft [17], and submeter-level positioning on low-altitude unmanned aerial vehicles [18], [19], and are usable in environments under intentional GPS jamming [20]. Exploiting SOPs did not stay earthly, as LEO satellites have received considerable attention recently as potential SOPs [21]. Many theoretical and experimental studies have been conducted on LEO-based PNT [22]–[27].

LEO satellites possess desirable attributes for PNT [2], [3]: (i) they are around twenty times closer to the Earth compared to GNSS satellites, which reside in medium Earth orbit (MEO), which could yield significantly higher carrier-to-noise ratio; (ii) they are becoming abundant as tens thousands of broadband Internet satellites are expected to be deployed into LEO; and (iii) they transmit in different frequency bands and are placed in varying orbits, making LEO satellite signals diverse in frequency and direction. However, exploiting broadband LEO satellite signals for PNT purposes comes with challenges [28], as they are owned by private operators that typically do not disclose crucial information about the satellites': (i) ephemerides, (ii) clock synchronization and stability, and (iii) signal specifications.

To address the first challenge, several approaches have been recently proposed, including differential navigation utilizing a known base receiver [29], [30], simultaneous tracking and navigation (STAN) [31], and analytical/machine-learning satellite

This work was supported in part by the Office of Naval Research (ONR) under Grants N00014-19-1-2511 and N00014-22-1-2242, in part by the Air Force Office of Scientific Research (AFOSR) under Grant FA9550-22-1-0476, and in part by the U.S. Department of Transportation (USDOT) under Grant 69A3552047138 for the CARMEN University Transportation Center (UTC).

orbit tracking [32], [33]. Approaches to address the second challenge have been offered in [24], [34]. To address the third challenge, the paradigm of cognitive opportunistic navigation, which estimates the minimally known LEO satellite signals in a *blind* fashion has been showing tremendous promise [35]. Most recently, this paradigm allowed for the exploitation of unknown Starlink LEO satellites, from which navigation observables were produced via (i) a carrier phase tracking approach [27] and (ii) a generalized likelihood ratio (GLR) Doppler detection approach [36], with the former localizing a receiver to within a two-dimensional (2D) error of 25.9 m, while the latter achieving a 2D error of 10 m.

This paper addresses the third challenge by developing a blind beacon estimation and Doppler tracking framework that is agnostic to the modulation and multiple access scheme adopted by LEO satellites. The proposed framework generates navigation observables from broadband LEO satellites without the need to know their signal specifications. Previous researchers have proposed frameworks for blind estimation of spreading sequences in direct sequence spread spectrum in communication systems [37] and for GPS signals under non-cooperative conditions [38]. However, these approaches cannot be applied to LEO because they do not account for the high dynamics channel between the LEO satellite and a terrestrial receiver. Previous literature has proposed methods for Doppler tracking with M-ary phase shift keying (M-PSK) and orthogonal frequency division multiplexing (OFDM) signals [39]–[41]. The aforementioned approaches aim to generate a peak in the frequency-domain by either relying on nonlinear operations (for M-PSK signals) or increasing the coherent processing interval (CPI) (for OFDM signals). After generating the peak, the methods track it using a peak tracking algorithm to estimate the Doppler shift. However, using nonlinear operations could degrade the signal-to-noise ratio (SNR), while increasing the CPI is not straightforward with the highly dynamic channels encountered with LEO satellites. Also, peak tracking is prone to generate invalid observables and even divergence whenever the spectrum is contaminated by noisy DC peaks.

This paper proposes a novel spectral-based framework to mitigate the above challenges. The proposed framework relies on the presence of a repetitive sequence (also known as a beacon) in the signal transmitted by the LEO satellite that will induce a prominent feature in the received spectrum. The proposed blind Doppler tracker locks on the satellite's feature in the frequency domain and uses the cross-correlation method to track the Doppler shift.While spectral cross-correlation has been studied in the literature [42] and used for noise reduction in speech [43] and detection of stars and planets [44], to the author's knowledge, this approach is newly applied to track Doppler from LEO satellites.

This paper makes the following contributions: (i) develop an analytical approximation of the received signal frequency spectrum under high dynamics channel, (ii) propose a novel blind Doppler estimator using spectral cross-correlation and a Kalman filter (KF)-based tracking loop, (iii) demonstrate successful acquisition, tracking, and positioning with multi-constellation LEO satellite, namely Orbcomm, Iridium NEXT, Starlink, and OneWeb. To the author's knowledge, this paper is the first to show tracking and navigation solution results with the OneWeb LEO constellation. It is important to note that the main purpose of this blind navigation beacon estimation framework is to estimate the time-domain waveform of the repetitive sequence present in the LEO signals. Decoding the repetitive sequence using its modulation scheme is an extra step presented in this paper for the sake of presentation; however, the refined time-domain waveform alone is sufficient to be used to generate navigation observables from LEO satellites. The highlight of the proposed framework is its ability of estimating the transmitted beacon on-the-fly even if the signal structure employed at the satellite's end changes.

In light of recent partnerships by broadband LEO satellite operators and terrestrial cellular providers, it is expected that broadband LEO satellite constellations will move to adopting the 5G new radio (NR) (and generally, the third generation partnership project (3GPP)) standards for cellular communications. In preparation for this, simulation results are presented showing successful beacon estimation and Doppler tracking of Starlink LEO satellites transmitting 5G-NR OFDM signals. Experimental results are also presented demonstrating the efficacy of the proposed framework on multi-constellation LEO satellites, namely OneWeb, Starlink, Orbcomm, and Iridium NEXT. Despite adopting different modulation and multiple access transmission schemes, the proposed framework is capable of successfully estimating the beacon and tracking the Doppler, in a blind fashion, of 8 LEO satellites (2 OneWeb, 4 Starlink, 1 Iridium NEXT, and 1 Orbcomm) over a period of about 560 seconds with Hz-level accuracy. The produced Doppler measurements were fused through a nonlinear least-squares estimator to localize a stationary receiver to an unprecedented level of accuracy. Starting with an initial estimate about 3,600 km away, a final three-dimensional (3–D) position error of 5.8 m and 2–D position error of 5.1 m was achieved. Aside from achieving this unprecedented accuracy, these results represent the first successful opportunistic tracking of unknown OneWeb LEO signals and their exploitation for positioning.

The paper is organized as follows. Section II derives the signal model. Section III introduces the blind Doppler tracking. Section IV develops the code phase tracking. Section V presents the blind beacon estimation. Section VI presents simulation results. Section VIII presents experimental results. Section VIII presents the positioning framework and solution. Section IX gives concluding remarks.

II. Signal Model

This section presents a model of the received signal which takes into account the high dynamics channel between the LEO satellite and ground-based receiver. Then, it derives an analytical expression of the signal's frequency spectrum.

A. Existence of Repetitive Sequences

The proposed framework relies on the existence of a repetitive sequence in the signal transmitted by the LEO satellite. The existence of repetitive sequences in any communication system is not a strong assumption as they are either inherently defined by the source and channel encoding, modulation, and multiplexing schemes, or abundantly transmitted by the communication source for synchronization purposes at the UE. For example, code division multiple access (CDMA) in cellular 3G [45], GPS [46], and Globalstar LEO [47], employ repetitive sequences in the form of pseudorandom noise (PRN) codes to spread the data before transmission. In OFDM used in 4G long-term evolution (LTE) [48] and 5G [49], the primary synchronization sequence (PSS) and secondary synchronization sequence (SSS) define repetitive sequences in the signal transmitted by cellular towers. Moreover, permanently or temporarily repeated patterns in the transmitted user data can define a repetitive sequence. As an example, Orbcomm LEO satellites transmit their ephemeris packets every 4 seconds [50]. The ephemeris packet contains the current date and time, which is temporarily repetitive (the same) along the symbols corresponding to the day, month, and year.

B. Baseband Received Signal Model

Let $x(t)$ be the unknown signal transmitted by a LEO satellite before carrier modulation. The proposed framework does not assume knowledge of any particular modulation or multiplexing scheme. The only assumption is that the transmitted signal $x(t)$ can be written as $x(t) = s(t) + n_d(t)$, where $s(t)$ is a deterministic repetitive signal, and $n_d(t)$ is a random signal driven by the user data. The proposed framework assumes the following properties of $s(t)$:

1) It is periodic with period T_0.
2) It is uncorrelated with the user data $n_d(t)$.
3) It is zero-mean and has a stationary power spectral density (PSD) $\left|\mathcal{F}\left\{s(t)w_{T_0}(t)\right\}\right|^2 = S_s(f)$, where $w_{T_0}(t)$ is a windowing function that is unity within the interval $[0, T_0)$ and zero elsewhere.

Consider $x(t)$ being transmitted at a carrier frequency f_c. Let $\tau_d(t)$ denote the apparent delay between the transmitted signal $x_c(t) \triangleq x(t)\exp(j2\pi f_c t)$ and the received signal at the receiver's antenna. The apparent delay $\tau_d(t)$ is the composition of multiple effects: (i) the time-of-flight along the line-of-sight (LOS) between the transmitter and receiver (i.e., $d_{LOS}(t)/c$, where $d_{LOS}(t)$ is the LOS distance between the LEO satellite's transmitter and the receiver and c is the speed of light); (ii) combined effect of the transmitter's and receiver's clock biases, denoted $\delta t_{clk}(t)$; (iii) ionospheric and tropospheric delays $\delta t_{iono}(t)$ and $\delta t_{tropo}(t)$, respectively; and (iv) other unmodeled errors. After propagating in an additive white Gaussian channel, the resulting received signal before baseband mixing can be expressed as

$$\begin{aligned} r_c(t) &= x_c\left(t - \tau_d(t)\right) + n_c(t) \\ &= x(t - \tau_d(t)) \exp\left[\, j2\pi f_c \left[t - \tau_d\left(t\right)\right]\right] + n_c(t), \end{aligned}$$

where $n_c(t)$ is complex, zero-mean, white Gaussian noise with two-sided PSD $N_0/2$. Let $r^-(t)$ denote the received signal after baseband mixing and filtering, which can be expressed as

$$\begin{aligned} r^-(t) &\triangleq r_c(t)\exp\left(-j2\pi f_c t\right) \\ &= x(t - \tau_d(t))\exp\left[\, j\theta(t)\right] + n^-(t), \end{aligned}$$

where $n^-(t)$ is the low-pass filtered version of $n_c(t)$, and $\theta(t)$ is the carrier phase of the received signal expressed as

$$\theta(t) \triangleq -2\pi f_c \tau_d(t). \tag{1}$$

Using a Taylor series expansion (TSE), at time instant $t_k = t_0 + kT_0$, where k is the sub-accumulation index and t_0 is some initial time; the carrier phase of the received signal $\theta_k(t) \triangleq \theta(t)w_{T_0}(t - t_k)$ for $t \in [0, T_0)$ can be approximated as

$$\theta_k(t) \approx \theta(t_k) + \dot{\theta}(t_k)(t - t_k) + \frac{1}{2}\ddot{\theta}(t_k)(t - t_k)^2. \tag{2}$$

By definition, $f_D(t) \triangleq \frac{\dot{\theta}(t)}{2\pi}$ is the apparent Doppler shift and $\dot{f}_D(t) \triangleq \frac{\ddot{\theta}(t)}{2\pi}$ is the apparent Doppler rate. It is important to note that the channel between the LEO satellite and the opportunistic receiver is highly dynamic, thus, high Doppler shift and rate will be observed by the receiver. On the other, at the k-th sub-accumulation, $\tau_d(t)$ is approximated by its zero-order TSE term $d_k \approx \tau_d(t_k)$ and the higher-order terms are dropped to simplify the following signal analysis. It worth noting that the higher-order terms in the code phase account for compression and dilation of the code in the time-domain, but this paper ignores this effect. The experimental results presented in Section VIII show that such effect is indeed negligible for the Orbcomm, Iridium NEXT, Starlink, and OneWeb LEO constellations. Finally, the expression of the received signal before carrier wipe-off at the k-th sub-accumulation can be expressed as

$$\begin{aligned} r_k^-(t) &\triangleq r^-(t)w_{T_0}(t - t_k) \\ &= s_k(t)\exp\left[\, j\theta_k(t)\right] + n_k^-(t), \end{aligned} \tag{3}$$

where $s_k(t) \triangleq s(t - d_k)w_{T_0}(t)$ and the term $n_k^-(t) \triangleq \left[n^-(t - d_k) + n_d(t - d_k)\right] w_{T_0}(t)$ represents the lumped user data and channel noise. The received signal $r_k(t)$ after carrier wipe-off using the carrier phase estimate, denoted $\hat{\theta}_k(t)$, generated by the tracking loop discussed in Section III-B, can be expressed as

$$\begin{aligned} r_k(t) &= r_k^-(t)\exp\left[\, -j\hat{\theta}_k(t)\right] \\ &= s_k(t)\exp\left[\, j\tilde{\theta}_k(t)\right] + n_k(t), \end{aligned} \tag{4}$$

where $\tilde{\theta}_k(t) = \theta_k(t) - \hat{\theta}_k(t)$ is the residual carrier phase.

C. Frequency Spectrum of the Received Signal

This section derives an analytical expression of the received signal's frequency spectrum at the k-th sub-accumulation, i.e., $S_{r_k}(f) = \left|\mathcal{F}\left\{r_k(t)\right\}\right|^2$. Using the third property of $s(t)$, the

Wigner distribution function (WDF) of $s_k(t)$ for $t \in [0, T_0)$ can be written as

$$W_s(t,f) \triangleq \int_{-\infty}^{\infty} s_k\left(t+\frac{\tau}{2}\right) s_k^*\left(t-\frac{\tau}{2}\right) \exp(-2\pi f\tau)\, d\tau = \frac{S_s(f)}{T_0},$$

where s^* denotes the complex conjugate of s. It can be shown that the WDF of the residual carrier phase at the k-th sub-accumulation $C_k(t) = \exp(j\tilde{\theta}_k(t))$, for $t \in [0, T_0)$, is

$$W_{C_k}(t,f) = \delta\left(f - \frac{\dot{\tilde{\theta}}_k}{2\pi} - \frac{\ddot{\tilde{\theta}}_k}{2\pi} t\right),$$

where $\delta(\cdot)$ is the Dirac delta function. Using the second property of $s(t)$, WDF of $r_k(t)$ in (4), for $t \in [0, T_0)$, becomes

$$W_{r_k}(t,f) = \frac{S_s(f)}{T_0} \circledast \delta\left(f - \frac{\dot{\tilde{\theta}}_k}{2\pi} - \frac{\ddot{\tilde{\theta}}_k}{2\pi} t\right) + W_{n_k}(t,f),$$

where $(f \circledast g)(t) = \int_{-\infty}^{\infty} f(\tau) g(t-\tau) d\tau$ is the convolution of f and g and $W_{n_k}(t,f)$ is the WDF of the noise and data at the k-th sub-accumulation.

Using the projection property of WDF, the frequency spectrum $S_{r_k}(f) \triangleq \int_0^{T_0} W_{r_k}(t,f)\, dt$ can be further expressed as

$$\begin{aligned} S_{r_k}(f) &= \frac{S_s(f)}{T_0} \circledast \int_0^{T_0} \delta\left(f - \frac{\dot{\tilde{\theta}}_k}{2\pi} - \frac{\ddot{\tilde{\theta}}_k}{2\pi} t\right) dt + S_{n_k}(f) \\ &= S_s(f) \circledast \frac{2\pi}{\left|\ddot{\tilde{\theta}}_k\right| T_0} \int_0^{T_0} \delta\left(t - \frac{2\pi f - \dot{\tilde{\theta}}_k}{\ddot{\tilde{\theta}}_k}\right) dt + S_{n_k}(f) \\ &= S_s(f) \circledast \Pi\left(f; \dot{\tilde{\theta}}_k, \ddot{\tilde{\theta}}_k\right) + S_{n_k}(f), \end{aligned} \tag{5}$$

where $S_{n_k}(f) = \int_0^{T_0} W_{n_k}(t,f)\, dt$ and

$$\Pi\left(f; \dot{\theta}, \ddot{\theta}\right) \triangleq \frac{2\pi}{\left|\ddot{\theta}\right| T_0} \begin{cases} 1, & \left| f - \dfrac{\dot{\theta} + \dfrac{|\ddot{\theta}|}{2} T_0}{2\pi} \right| < \dfrac{|\ddot{\theta}|}{4\pi} T_0 \\ 0, & \text{elsewhere} \end{cases}.$$

Equation (5) implies that the received signal's frequency spectrum consists of a shifted and dilated version of the repetitive sequence's frequency spectrum alongside noise. The shift in the received spectrum is due to the residual Doppler $\dot{\tilde{\theta}}_k$, while the dilation is due to the residual Doppler rate $\ddot{\tilde{\theta}}_k$.

III. Blind Doppler Tracking

This section derives the Doppler discriminator and formulates the KF-based Doppler tracking loop.

A. Frequency Domain-Based Doppler Discriminator

The nonlinear least-squares (NLS) estimator of the residual Doppler $\dot{\tilde{\theta}}_k$ at the k-th sub-accumulation is given by

$$\dot{\tilde{\theta}}_k = \underset{\dot{\theta}}{\operatorname{argmin}} \left\| S_{r_k}(f) - S_s(f) \circledast \Pi\left(f; \dot{\theta}, \ddot{\theta}\right) \right\|^2 \tag{6}$$

$$\begin{aligned} \dot{\tilde{\theta}}_k &= \underset{\dot{\theta}}{\operatorname{argmin}} \|S_{r_k}(f)\|^2 + \left\| S_s(f) \circledast \Pi\left(f; \dot{\theta}, \ddot{\theta}\right) \right\|^2 \\ &\quad -2 \left(S_{r_k} \star S_s\right)(f) \circledast \Pi\left(f; \dot{\theta}, \ddot{\theta}\right) \qquad (7) \\ &= \underset{\dot{\theta}}{\operatorname{argmax}} \left(S_{r_k} \star S_s\right)(f) \circledast \Pi\left(f; \dot{\theta}, \ddot{\theta}\right) \\ &\approx \underset{\dot{\theta}}{\operatorname{argmax}} \left(S_{r_k} \star S_s\right)(f) \circledast \delta\left(f - \frac{\dot{\theta}}{2\pi}\right), \quad \text{for} \quad \ddot{\tilde{\theta}}_k \approx 0 \\ &= 2\pi \underset{f}{\operatorname{argmax}} \left(S_{r_k} \star S_s\right)(f), \qquad (8) \end{aligned}$$

where $(f \star g)(\tau) = \int_{-\infty}^{\infty} f^*(t) g(t+\tau) dt$ is the cross-correlation of f and g. The first two terms in the minimization problem in (7) are a constant function of the optimization parameter $\dot{\theta}$; therefore, they are ignored. Since the blind receiver does not have prior knowledge of $S_s(f)$, it starts with an initial estimate $\hat{S}_s(f) \equiv S_{r_0}(f)$ and refines the repetitive sequence's spectrum with every sub-accumulation. This initialization approach introduces a Doppler ambiguity $\dot{\tilde{\theta}}_0$ invoked by taking $S_{r_0}(f)$ as initial spectral reference for Doppler tracking. Nonetheless, this Doppler ambiguity can be resolved as will be discussed in the Section V-C. Note that the assumption $\ddot{\tilde{\theta}}_k \approx 0$ (i.e., regime of small residual Doppler rate values) invoked in (8) is a reasonable assumption, since the Doppler rate between two consecutive sub-accumulations is nearly constant for LEO satellite channels.

B. KF-Based Tracking Loop

The continuous-time signal in (4) is sampled at a constant sampling interval $T_s = 1/F_s$. The discrete-time received signal before carrier wipe-off at the k-th sub-accumulation can be written as

$$r_k^-[n] = s[n - d_k] \exp\left(j\Theta_k[n]\right) + n_k^-[n], \tag{9}$$

where $n \in [0, L-1]$; $s[n]$ is the discrete-time equivalent of $s(t)$ with period $L = T_0/T_s$; $\Theta_k[n]$ and d_k are the discrete-time carrier phase and code phase, respectively, of the received signal at the k-th sub-accumulation; and $n_k^-[n]$ is the discrete-time equivalent of $n_k^-(t)$.

The continuous-time carrier phase state vector is defined as $\boldsymbol{\theta}(t) \triangleq \left[\theta(t),\ \dot{\theta}(t),\ \ddot{\theta}(t)\right]^{\mathsf{T}}$, with dynamics modeled as

$$\dot{\boldsymbol{\theta}}(t) = \mathbf{A}\boldsymbol{\theta}(t) + \mathbf{B}\boldsymbol{w}(t), \tag{10}$$

$$\mathbf{A} \triangleq \begin{bmatrix} 0 & 1 & 0 \\ 0 & 0 & 1 \\ 0 & 0 & 0 \end{bmatrix}, \quad \mathbf{B} \triangleq \begin{bmatrix} 0 \\ 0 \\ 1 \end{bmatrix},$$

where $\boldsymbol{w}(t)$ is a zero-mean white noise process with PSD q_w. The continuous-time model (10) is discretized at a constant sampling time $T_0 = LT_s$ leading to

$$\boldsymbol{\Theta}_{k+1} = \mathbf{F}\boldsymbol{\Theta}_k + \mathbf{w}_k, \tag{11}$$

where $\boldsymbol{\Theta}_k \triangleq \left[\theta_k,\ \dot{\theta}_k,\ \ddot{\theta}_k\right]^{\mathsf{T}}$ is the carrier phase state at the k-th sub-accumulation, $\mathbf{F} \triangleq e^{\mathbf{A}T_0}$ is the state transition matrix, and $\mathbf{w}_k$ is a discrete-time process noise, which is

a zero-mean white random sequence with covariance $\mathbf{Q} = q_w \int_0^{T_0} e^{\mathbf{A}t}\mathbf{B}\big(e^{\mathbf{A}t}\mathbf{B}\big)^{\mathsf{T}} dt$. The reconstructed sequence of the carrier phase that is used to perform carrier wipe-off can be written as a second-order piecewise polynomial given by $\hat{\Theta}_k[n] = \hat{\theta}_{k-1} + \hat{\dot{\theta}}_k n T_s + \frac{1}{2}\hat{\ddot{\theta}}_k (nT_s)^2$, $n \in [0, L-1]$. After carrier wipe-off, the received signal's sequence becomes

$$\begin{aligned} r_k[n] &= r_k^-[n] \exp\left[-j\hat{\Theta}_k[n]\right] \\ &= s\left[n - d_k\right] \exp\left[j\tilde{\Theta}_k[n]\right] + n_k[n]. \end{aligned} \tag{12}$$

Equation (12) will be used to determine the residual Doppler $\tilde{\dot{\theta}}_k$ at the k-th sub-accumulation, which is fed as innovation to a KF loop that uses the observation model

$$z_k = \mathbf{C}\boldsymbol{\Theta}_k + v_k, \quad \mathbf{C} \triangleq \begin{bmatrix} 0 & 1 & 0 \end{bmatrix}, \tag{13}$$

where v_k is a discrete-time zero-mean white noise sequence with variance $\sigma^2_{\tilde{\theta}}$. The proposed KF innovation ν_k is the fast Fourier transform (FFT)-based discrete version of (8).

$$\nu_{\text{KF}}(k) = \tilde{\dot{\theta}}_k = 2\pi \operatorname*{argmax}_f |R_k[f]|^2 \star \left|\hat{S}_k[f]\right|^2,$$

where $R_k[f]$ and $\hat{S}_k[f]$ are the FFT of $r_k[n]$ and $s[n]$, respectively. The proposed blind Doppler tracking loop can be considered to be in the locked regime whenever the innovation sequence ν_k becomes nearly white and its variance stabilizes. In this regime, $\tilde{\boldsymbol{\Theta}}_k \approx [0,0,0]^{\mathsf{T}}$ and $r_k[n] \approx s\left[n - d_k\right] + n_k[n]$.

Note that the KF is initialized with $\hat{\boldsymbol{\Theta}}_0 \equiv \left[\hat{\theta}_0,\, \hat{\dot{\theta}}_0,\, \hat{\ddot{\theta}}_0\right]^{\mathsf{T}}$ that gives rise to an initial carrier phase state error $\tilde{\boldsymbol{\Theta}}_0 \equiv \left[\tilde{\theta}_0,\, \tilde{\dot{\theta}}_0,\, \tilde{\ddot{\theta}}_0\right]^{\mathsf{T}}$. It can be readily shown that for the observation matrix $\mathbf{C}$ defined in (13), the initial carrier phase error $\tilde{\theta}_0$ is unobservable. This will induce a shift in the phase of the estimated repetitive sequence, causing the initial Doppler error $\tilde{\dot{\theta}}_0$ to persist as an ambiguity in the tracked Doppler $\hat{\dot{\theta}}_k$ (since it is embedded into the first received sub-accumulation which is taken as reference for tracking). Due to the linearity and time-invariance of (11) and (13), it can be readily shown that the residual carrier phase state vector $\tilde{\boldsymbol{\Theta}}_k$ will converge to zero. Fig. 1 summarizes the proposed blind Doppler tracking.

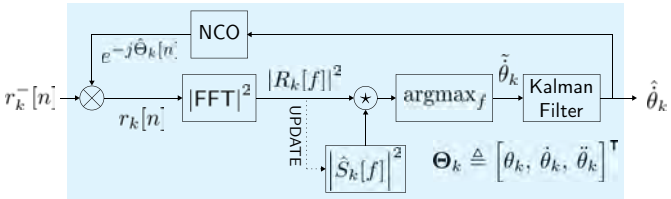

Fig. 1. Block diagram of the proposed blind Doppler tracking loop. NCO: numerically controlled oscillator.

IV. Code Phase Tracking

After the blind Doppler tracking loop achieves lock, the blind receiver starts to correct the carrier phase changes and tracks the code phase of the repetitive sequence. Given (12), the NLS estimate of the code phase at the k-th sub-accumulation is given by

$$\begin{aligned} \hat{d}_k &= \operatorname*{argmin}_d \|r_k[n] - s[n-d]\|^2 \\ &= \operatorname*{argmin}_d \left\{\|r_k[n]\|^2 + \|s[n-d]\|^2 - 2(r_k \star s)[d]\right\} \\ &= \operatorname*{argmax}_d (r_k \star s)[d]. \end{aligned} \tag{14}$$

It is important to note that the NLS code phase estimator given by (14) is only valid while the Doppler tracking loop is locked and the carrier phase changes are tracked and wiped-off at every sub-accumulation. Without the lock condition, the residual carrier phase sequence $\tilde{\Theta}_k[n]$ present in (12) deteriorates the NLS estimator performance drastically. Furthermore, as the blind receiver does not have prior knowledge of $s[n]$, it starts with an initial estimate $\hat{s}[n] \equiv r_0[n]$ and uses it as a reference to track the code phase $\hat{d}_k$. This initialization approach introduces a code phase ambiguity d_0. After tracking the code phase $\hat{d}_k$, the receiver corrects for this code phase shift as follows

$$\begin{aligned} \bar{r}_k[n] &\triangleq r_k[n] \otimes \hat{d}_k \\ &= s\left[n - \tilde{d}_k\right] \exp\left[j\tilde{\Theta}_k[n]\right] + n_k[n], \end{aligned} \tag{15}$$

where $(x[n] \otimes d)$ denotes the circular shift operation that shifts the sequence $x[n]$ by d samples, and $\tilde{d}_k = d_k - \hat{d}_k$ is the code phase error at the k-th sub-accumulation.

V. Blind Navigation Beacon Estimation

This section discusses the blind navigation beacon estimation framework. Given (9), the time-varying parameters modulating the deterministic repetitive beacon sequence $s[n]$ are: (i) the carrier phase state vector $\boldsymbol{\Theta}_k$ and (ii) the code phase d_k. Sections III and IV discussed the mechanism of tracking and wiping-off the effect of these time-varying parameters. In the regime of successful Doppler and code phase tracking $\left\{\tilde{\Theta}_k[n] \approx 0,\ \tilde{d}_k \approx 0\right\}$, (15) simplifies to $\bar{r}_k[n] \approx s[n] + n_k[n]$. At this stage, the receiver is ready to (i) blindly estimate the deterministic repetitive sequence present in (15) and (ii) resolve for the Doppler ambiguity associated with the estimated repetitive sequence.

A. Beacon Estimator Formulation

Let $\boldsymbol{r}_k$, $\boldsymbol{n}_k$, $\boldsymbol{s}$, $\boldsymbol{y}$, $\mathbf{H}$, and $\boldsymbol{w}$ denote the equivalent complex vector form of the terms in (15) such that

$$\begin{aligned} \boldsymbol{r}_k &\triangleq \begin{bmatrix} \bar{r}_k[0], & \ldots, & \bar{r}_k[L-1] \end{bmatrix}^{\mathsf{T}}, \\ \boldsymbol{n}_k &\triangleq \begin{bmatrix} n_k[0], & \ldots, & n_k[L-1] \end{bmatrix}^{\mathsf{T}}, \\ \boldsymbol{s} &\triangleq \begin{bmatrix} s[0], & \ldots, & s[L-1] \end{bmatrix}^{\mathsf{T}}, \\ \boldsymbol{y} &\triangleq \begin{bmatrix} \boldsymbol{r}_1^{\mathsf{T}}, & \ldots, & \boldsymbol{r}_M^{\mathsf{T}} \end{bmatrix}^{\mathsf{T}}, \\ \boldsymbol{w} &\triangleq \begin{bmatrix} \boldsymbol{n}_1^{\mathsf{T}}, & \ldots, & \boldsymbol{n}_M^{\mathsf{T}} \end{bmatrix}^{\mathsf{T}}, \\ \mathbf{H} &\triangleq \begin{bmatrix} \mathbf{I}_L, & \ldots, & \mathbf{I}_L \end{bmatrix}^{\mathsf{T}}, \end{aligned}$$

where $\mathbf{I}_L$ denotes the identity matrix of size $L \times L$; $\boldsymbol{r}_k$ and $\boldsymbol{n}_k$ denote the vectors of observed and noise samples

at the k-th sub-accumulation, respectively; $\boldsymbol{y}$ and $\boldsymbol{w}$ denote the vectors of concatenated observations and noise of M sub-accumulations, respectively; $\boldsymbol{s}$ denotes the vector of the deterministic repetitive sequence present in the received signal that is sought to be estimated; and $\mathbf{H}$ denotes the observation matrix of the M sub-accumulations in the regime of Doppler and code phase tracking lock. One can readily write the vector of observed samples as

$$\boldsymbol{y} = \mathbf{H}\boldsymbol{s} + \boldsymbol{w}, \tag{16}$$

where $\boldsymbol{w}$ is as zero-mean white noise sequence with covariance $\mathbf{R} = \sigma_n^2 \mathbf{I}_{L\times M}$. Given the observation model in (16), the least-squares estimate of the repetitive sequence $\boldsymbol{s}$ is given by

$$\hat{\boldsymbol{s}}_M = \left(\mathbf{H}^{\mathsf{H}}\mathbf{H}\right)^{-1}\mathbf{H}^{\mathsf{H}}\boldsymbol{y} = \frac{1}{M}\sum_{k=1}^{M}\boldsymbol{r}_k, \tag{17}$$

where $(.)^{\mathsf{H}}$ denotes the Hermitian transpose operator.

B. Convergence Property

This section studies the convergence property and stopping criterion for the beacon estimator given in (17). The energy in the estimated sequence, $\hat{\boldsymbol{s}}_M$, after M sub-accumulations can be expressed as

$$\begin{aligned}\mathbb{E}\left\{\|\hat{\boldsymbol{s}}_M\|^2\right\} &= \mathbb{E}\left\{\frac{1}{M^2}\sum_{j=1}^{M}\sum_{k=1}^{M}\boldsymbol{r}_j{}^{\mathsf{H}}\boldsymbol{r}_k\right\}\\ &= \|\boldsymbol{s}\|^2 + \frac{2}{M}\sum_{k=1}^{M}\mathbb{E}\left\{\boldsymbol{s}^{\mathsf{H}}\boldsymbol{n}_k\right\} + \frac{1}{M^2}\sum_{j=1}^{M}\sum_{k=1}^{M}\mathbb{E}\left\{\boldsymbol{n}_j{}^{\mathsf{H}}\boldsymbol{n}_k\right\}\\ &= \|\boldsymbol{s}\|^2 + \frac{L\sigma_n^2}{M}.\end{aligned} \tag{18}$$

The fact that $\mathbb{E}\left\{\boldsymbol{s}^{\mathsf{H}}\boldsymbol{n}_k\right\} = 0$ follows from the second and third properties of $s(t)$, while $\mathbb{E}\left\{\boldsymbol{n}_j{}^{\mathsf{H}}\boldsymbol{n}_k\right\} = L\sigma_n^2\delta_{ij}$, where δ_{ij} is the Kronecker delta function, follows from the assumed whiteness of the noise. According to (18), $\lim_{M\to\infty}\mathbb{E}\left\{\|\hat{\boldsymbol{s}}_M\|^2\right\} = \|\boldsymbol{s}\|^2$; therefore, the energy in the estimated beacon decreases with every additional observed sub-accumulation until reaching a steady-state value equal to the energy of the true beacon $\|\boldsymbol{s}\|^2$. This gives a recipe for a stopping criterion for the beacon estimator given as

$$\frac{\|\hat{\boldsymbol{s}}_M\|^2}{\|\hat{\boldsymbol{s}}_{M-1}\|^2} \geq \eta_{th},$$

where η_{th} is a predetermined constant chosen to be 0.9 for the purposes of this paper.

C. Doppler Ambiguity Resolution

To resolve the Doppler ambiguity $\tilde{\dot{\theta}}_0$ present in the estimated repetitive sequence, the receiver relies on the relationship between the carrier and code phase tracking loops discussed in Section III and Section IV, respectively. Let $\dot{\theta}_k = \hat{\dot{\theta}}_k - \tilde{\dot{\theta}}_0 + \nu_{\dot{\theta},k}$ denotes the true ambiguity-free Doppler shift, where $\nu_{\dot{\theta},k}$ is a discrete-time frequency noise. Therefore, the true carrier phase θ_k can be expressed as

$$\begin{aligned}\theta_k &\triangleq \sum_{j=0}^{k-1}\dot{\theta}_j T_0 + \theta_0 = \sum_{j=0}^{k-1}(\hat{\dot{\theta}}_j - \tilde{\dot{\theta}}_0)T_0 + \nu_{\theta,k}\\ &= \hat{\theta}_k - \tilde{\dot{\theta}}_0 k T_0 + \theta_0 + \nu_{\theta,k},\end{aligned} \tag{19}$$

where θ_0 is the initial carrier phase ambiguity.

Let $d_k = \hat{d}_k + d_0 + \nu_{d,k}$ be the true code phase, where $\nu_{d,k}$ is the discrete-time code phase noise. The discretization of (1) relating the code and carrier phase yields

$$\theta_k = -2\pi f_c d_k = -2\pi f_c(\hat{d}_k + d_0 + \nu_{d,k}). \tag{20}$$

Equating (19) and (20) leads to

$$y_k = \tilde{\dot{\theta}}_0(kT_0) + b_0 + \nu_k, \tag{21}$$

where $y_k = \hat{\theta}_k + 2\pi f_c \hat{d}_k$ denotes the residual carrier phase, which is a function of the ambiguous Doppler term $\tilde{\dot{\theta}}_0$, $b_0 = -(\theta_0 + 2\pi f_c d_0)$ is the lumped ambiguity term, and $\nu_k = (\nu_{\theta,k} - 2\pi f_c \nu_{d,k})$ is the lumped code and carrier phase noise. With enough sub-accumulations M, $\tilde{\dot{\theta}}_0$ can be estimated from (21) by fitting a linear regression model with y_k as the target variable and kT_0 as the regressor.

VI. Simulation Results

This section demonstrates, via numerical simulations, the ability of the proposed framework to blindly estimate the beacon transmitted by a LEO satellite. To this end, following the notation described in (9), the deterministic repetitive sequence $s[n]$ is chosen to be the Synchronization Sequence Block (SSB) of the 5G-NR frame structure with period T_0, bandwidth B, and energy $\|\boldsymbol{s}\|^2$, as described by the 3GPP. The phase $\Theta_k[n]$ was assumed to follow the Doppler profile of a Starlink LEO satellite and the noise component of the signal $n_k^-[n]$ is modeled as a white random process with PSD $L\sigma_n^2$. Table I summarizes all other simulation parameters.

TABLE I
Simulation Parameters of Emulated 5G Signals Transmitted by Starlink LEO Satellites

Parameter	Value	Unit
$\|\boldsymbol{s}\|^2$	0.003	J
B	5	MHz
SNR	0	dB
T_0	20	ms
f_D	[-250 , 250]	kHz
$\dot{f}_D$	[-3 , 0]	kHz

The first step in the process of blindly estimating the beacon is to perform Doppler wipe-off. As described in Section III-A, the proposed framework only relies on the assumption that the PSD of the deterministic repetitive sequence in a received signal is stationary. Therefore, the framework is capable of tracking and wiping off the Doppler with no *a priori* knowledge of the temporal or spectral signal structure. After

successful Doppler wipe-off, the receiver begins the estimation and refinement of the repetitive sequence. Fig. 2 shows the simulation results of the proposed blind framework, which demonstrates its ability to successfully estimate the 5G frame transmitted by a Starlink LEO satellite.

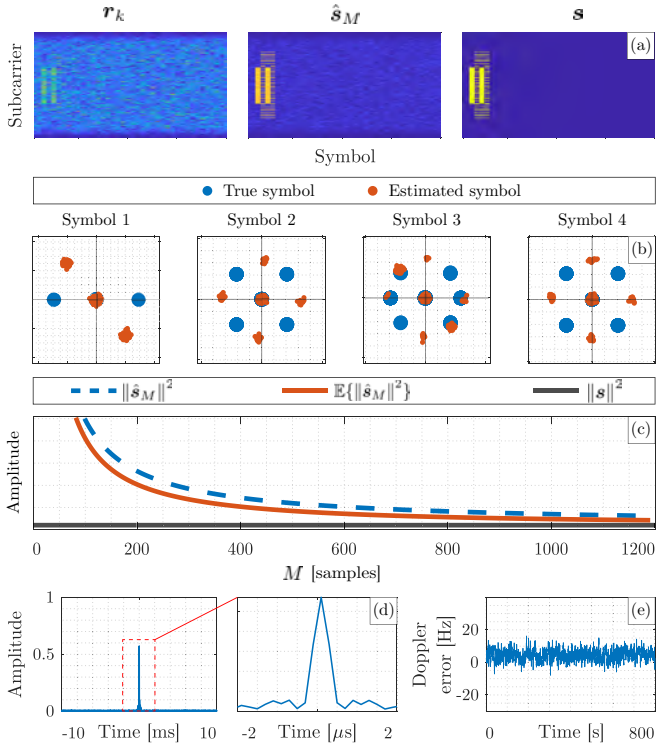

Fig. 2. Simulation results showing successful blind beacon estimation and Doppler tracking of emulated 5G-NR signals transmitted by Starlink LEO satellites: (a) Left: frame of an observed sample sub-accumulation on the left, Middle: refined repetitive sequence after M sub-accumulations, Right: ground truth repetitive sequence's frame. (b) In-phase and quadrature (IQ) components of the estimated sequence and the true sequence. (c) Black: true repetitive sequence's energy. Blue: the energy of the realization shown in (a) and (b). Orange: the expected energy (cf. (18)) of the the estimated sequence $\|\hat{s}_M\|^2$ versus the number of observed sub-accumulations M, respectively. (d) The normalized cross-correlation function between the estimated and true repetitive sequence. (e) The error between the true Doppler shift and the one estimated using the proposed blind Doppler tracker.

In particular, Fig. 2(a) shows the frame of (i) an observed sample sub-accumulation $\boldsymbol{r}_k$ that is composed of the repetitive sequence alongside data and channel noise, (ii) the refined repetitive sequence $\hat{\boldsymbol{s}}_M$ after M sub-accumulations, and (iii) the ground truth repetitive sequence. Fig. 2(b) compares the IQ components of the estimated sequence versus the true sequence. The 5G-NR SSB, which is taken as the repetitive sequence for this simulation, consists of 4 OFDM symbols which are the: (i) PSS at symbol 1, (ii) SSS at symbol 3, and (iii) physical broadcast channel (PBCH) at symbols 2 to 4. Moreover, Fig. 2(b) shows the unobservable constant phase shift $\tilde{\theta}_0$, which is embedded into the estimated sequence relative to the true sequence's constellation. Fig. 2(c) plots in blue the energy of the estimated sequence $\|\hat{\boldsymbol{s}}_M\|^2$ versus the number of observed sub-accumulations M. This curve follows the shape of the theoretical curve $\mathbb{E}\left\{\|\hat{\boldsymbol{s}}_M\|^2\right\}$ discussed in Section V-B, shown in orange. The black curve represent the true repetitive sequence's energy, $\|\boldsymbol{s}\|^2$, which lower-bounds the energy of the estimated sequence. Fig. 2(d) shows the normalized cross-correlation function between the estimated and true repetitive sequence. The prominent cross-correlation peak is an indicator of successful beacon estimation. Finally, Fig. 2(e) shows the error between the true Doppler shift and the one estimated using the proposed blind Doppler tracker during the satellite pass, implying that the proposed framework is capable of tracking the Doppler with Hz-level accuracy– this will also be demonstrated experimentally on the four LEO constellations: Orbcomm, Iridium NEXT, Starlink, and OneWeb in Section VIII-C.

VII. Experimental Results: Beacon Estimation and Blind Doppler Tracking of Orbcomm, Iridium NEXT, Starlink, and OneWeb LEO Constellations

This section presents experimental results demonstrating successful beacon estimation and blind Doppler tracking for four LEO constellations, namely Orbcomm, Iridium NEXT, Starlink, and OneWeb, which transmit their downlink signals according to different modulation schemes. The receiver initializes with and tracks the signal's stationary PSD to generate Doppler observables. Finally, a positioning solution is generated using the estimated observables. Fig. 3 overviews the hardware components used to receive downlink signals from the four LEO constellations. The captured samples were stored and then processed via a software-defined radio implementation (SDR) of the proposed framework.

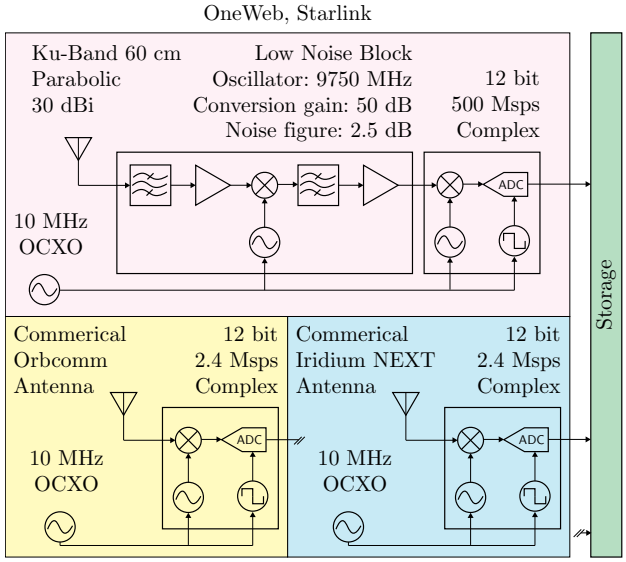

Fig. 3. Block diagram of Orbcomm, Iridium NEXT, Starlink, and OneWeb satellites signal capture setup.

A. Orbcomm LEO Constellation

The proposed blind beacon estimation method was applied to downlink Orbcomm LEO satellite signals. To this end, a stationary National Instrument (NI) universal software radio peripheral (USRP) E312 was equipped with a commercial

Orbcomm antenna to receive signals in the VHF–band. The sampling bandwidth F_s was set to 2.4 MHz and the carrier frequency f_c was set to 137 MHz. The duration of the recorded data was 900 seconds. Orbcomm satellites transmit at a predefined set of frequency pairs in the user downlink spectrum with an effective channel bandwidth $B = 4.8$ kHz. After collection, the Orbcomm signal was fed to the proposed blind beacon estimator and Doppler tracker. On the other hand, for comparative purposes, the true transmitted data of the Orbcomm satellites was decoded using the scheme described in [51]. After decoding, the signal auto-correlation showed repetitive behavior every T_0 intervals equating to 1 second. The decoded data was averaged in a T_0-window over a sufficient number of sub-accumulations to increase the effective energy of the repetitive sequence. Finally, the blindly estimated beacon was compared against the true sequence obtained by the averaging process. Fig. 4(a) shows the true versus estimated sequences in-phase time-domain waveform. Fig. 4(b) shows the IQ plot of the estimated repetitive sequence; this reveals that the modulation scheme of the repetitive sequence for Orbcomm is 4-PSK . Fig. 4(c) shows the cross-correlation function between the true and estimated sequence. The prominent peak indicates successful estimation of the repetitive sequence.

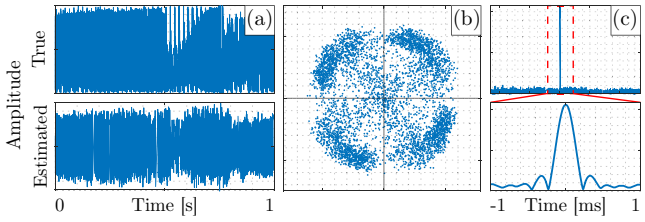

Fig. 4. Blind beacon estimation of Orbcomm LEO satellite signals: (a) In-quadrature waveform of the true versus estimated Orbcomm's repetitive sequence. (b) IQ plot of the estimated repetitive sequence. (c) Cross-correlation function between the true and estimated repetitive sequence. The bottom figure is a zoomed version of the peak in the top figure, which confirms successful beacon estimation.

Furthermore, Fig. 5 shows the result of correlating the estimated repetitive sequence with the collected Orbcomm data. The correlation peaks confirms correct estimation of the repetitive sequence.

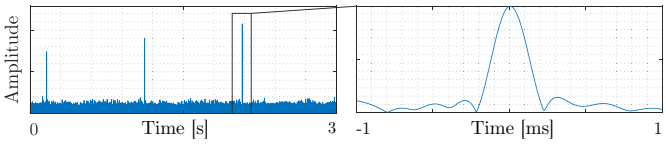

Fig. 5. Correlation of estimated repetitive sequence and Orbcomm data.

B. Iridium NEXT LEO Constellation

An NI-USRP E312 was used to capture raw signal measurements received by a commercial Iridium NEXT antenna. The sampling bandwidth F_s was set to 2.4 MHz, the carrier frequency f_c was set to 1626.2708 MHz in the L–band, which coincide with the ring alert (RA) channel of Iridium satellites, and the total capture duration was 600 seconds. Iridium NEXT satellites employs both time division multiple access (TDMA) and frequency division multiple access (FDMA). The Iridium spectrum consists of multiple channels, namely, the RA, paging channel, voice channel, and duplex user channels. The RA channel bandwidth is $B = 41.667$ kHz and the repetitive sequence period is $T_0 = 90$ ms. Running the blind framework on the collected signal resulted in the repetitive sequence estimate shown in Fig. 6(a). Taking a closer look at the estimated sequence reveals a pure tone sequence (green region) followed by an alternating Binary Phase Shift Keying (BPSK) sequence (red region). This specific estimated repetitive sequence is well-known in the communication literature: it is the typical TDMA synchronization preamble employed in TDMA-based satellite systems [52]. The IQ plot of the estimated repetitive sequence is shown in Fig. 6(b), which indeed matches Figure (1) in [52]. Fig. 6(c) shows the auto-correlation profile of the estimated preamble sequence, which confirms successful sequence estimation. Furthermore, Fig. (7) shows the result of correlating the estimated repetitive sequence with the collected Iridium NEXT data. The correlation peaks separated confirms correct estimation of the repetitive sequence.

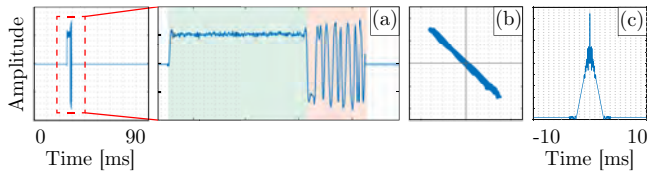

Fig. 6. Blind beacon estimation of Iridium NEXT LEO satellite signals: (a Left: In-phase waveform of the estimated Iridium NEXT's repetitive sequence. Right: zoomed version showing the estimated pure tone sequence (green region) followed by alternating BPSK sequence (red region). (b) IQ plot of the estimated repetitive sequence. (c) Auto-correlation function of the estimated repetitive sequence, which confirms successful beacon estimation.

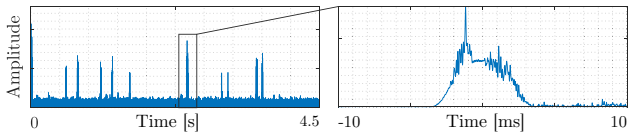

Fig. 7. Correlation of estimated repetitive sequence and Iridium NEXT data.

C. Starlink LEO Constellation

The signal capture setup for Starlink utilized the NI-USRP x410 to collect raw IQ measurements. The sampling bandwidth F_s was set to 500 MHz, the carrier frequency f_c was set to 11.325 GHz, which is roughly at the center of one of Starlink's downlink channels in the Ku–band. According to the Federal Communications Commission (FCC), the Starlink user downlink signal spectrum spans the 10.7 – 12.7 GHz frequency band. This spectrum is dissected into 8 equidistant channels, each with bandwidth $B = 240$ MHz. The period of the repetitive sequence was determined by inspecting the auto-correlation function of a data snapshot that entails many frames. The repetitive sequence present in the frames of the data snapshot induces an impulse train in the auto-correlation function with spacing equal to T_0, which was recorded to

be equal to $4/3$ ms for Starlink downlink signals. A low-noise block (LNB) downconverter was coupled with a 30 dBi conversion gain Ku–band parabolic dish in order to improve the received SNR. The dish was continuously pointed towards the Starlink satellite throughout its passing– propagating the satellite's trajectory from the publicly available TLE files governs the direction in which the dish should be pointed. The NI-USRP x410 was set to record for a duration of 900 seconds. Next, the proposed framework was used to acquire and track the signals present in the collected data. Taking a closer look at the estimated Starlink repetitive sequence reveals an interesting signal structure. Fig. 8(a) shows the auto-correlation profile of the estimated sequence. The different peaks in this figure reveals special values in Starlink's OFDM frame structure, such as the symbol duration, cyclic prefix duration (which is defined as the number of samples taken from the end of a symbol and repeated at its beginning), and the frame duration. Fig. 8(b) shows that the estimated sequence has repetitive components in symbols [1,2,3,5,7]. The parameter estimates from Fig. 8(a) are sufficient to allow for removal of the cyclic prefix from each symbol, which is then followed by applying a short-term Fourier transform (STFT) to the sequence estimate. This allows for spectral analysis of the repetitive sequence which, as shown in Fig. 8(c), reveals 4 silent subcarriers in the middle of the signal bandwidth. In fact, this is the bandwidth location where some tones can be observed sometimes. Fig. 8(d) shows the IQ plot of some of the synchronization sequence bearing symbols. Observing the constellations, it is noted that these synchronization symbols use a 4-quadrature amplitude modulation (QAM) scheme.Note that the first plot (left) is derived from the time domain representation of the symbol whereas the other 2 are derived from the frequency domain representation of the symbols. The estimated repetitive sequences are comparable to the synchronization sequences employed in a 5G-NR (PSS, SSS, and PBCH) frame according to the 3GPP standard.

D. OneWeb LEO Constellation

The signal capture setup for OneWeb downlink signals was the same as that of Starlink with the sampling frequency F_s set to 50 MHz and the carrier frequency f_c set to 11.075 GHz. According to the FCC, OneWeb's user downlink signal spectrum spans the 10.7 – 12.7 GHz frequency band. This spectrum is dissected into 8 equidistant channels, each with bandwidth $B = 250$ MHz. The repetitive sequence period was estimated to be $T_0 = 10$ ms from the data snapshot auto-correlation function. The proposed blind beacon estimation framework was capable of estimating a repetitive sequence which can be used to generate Doppler and code phase observables; these will be shown in the positioning solution presented in Section VIII. To the authors' knowledge, the achieved acquisition and tracking of OneWeb signals is unprecedented in the literature. Fig. (10) shows the result of correlating the estimated repetitive sequence with the collected OneWeb data. The clean correlation peaks separated by T_0 seconds confirms correct estimation of the repetitive sequence. Furthermore, Fig. (9) shows the result of correlating the estimated repetitive sequence with the collected Starlink data. The clean correlation peaks separated by T_0 seconds confirms correct estimation of the repetitive sequence.

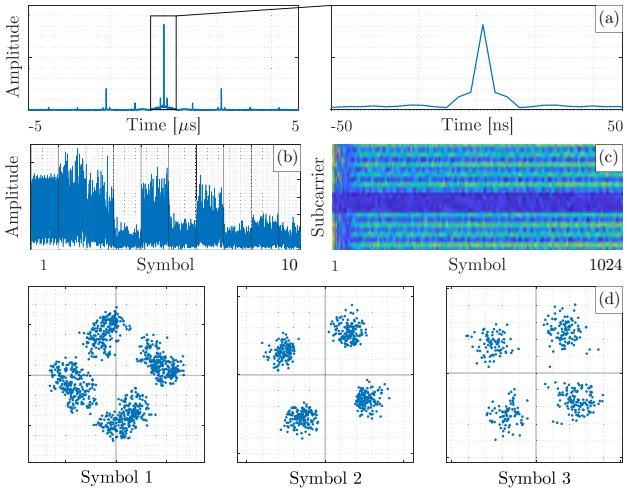

Fig. 8. Blind beacon estimation of Starlink LEO satellite signals: (a) auto-correlation profile of the estimated sequence, (b) frame structure of the estimated time domain repetitive sequence, (c) the OFDM frame structure of the estimated repetitive sequence, and (d) IQ plots of the first three symbols within the sequence.

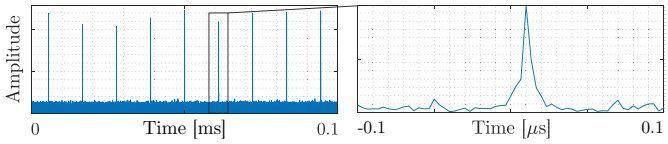

Fig. 9. Correlation of estimated repetitive sequence and Starlink data.

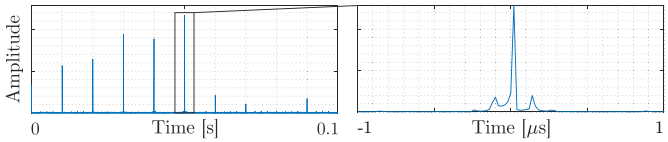

Fig. 10. Correlation of estimated repetitive sequence and OneWeb data.

VIII. Experimental Results: Positioning with Orbcomm, Iridium NEXT, Starlink, and OneWeb LEO Constellations

This section presents the first ever multi-constellation positioning results, exploiting signals from Orbcomm, Iridium NEXT, Starlink, and OneWeb LEO constellations. The carrier phase navigation observables produced by the proposed blind beacon estimation and Doppler tracking framework, for each individual constellation as well as fused from all four constellations, are used to localize a stationary receiver.

A. Carrier Phase Measurement Model

Let $i \in [1, L]$ denote the satellite's index, where L is the total number of satellites. The carrier phase observable $\Phi_i(k) \triangleq \sum_{j=0}^{k-1} c\frac{\hat{\theta}_j}{2\pi f_c} T_0$ obtained by integrating the Doppler

measurement to the i-th satellite at time-step k, which represents the discrete-time instant $t_k = t_0 + kT_0$ for an initial time t_0, expressed in meters, is modeled as

$$\Phi_i(k) = \|\boldsymbol{r}_r - \boldsymbol{r}_{SV_i}(k')\|_2 + c\cdot[\delta t_r(k) - \delta t_{SV_i}(k')] + c\cdot[\delta t_{trop_i}(k) + \delta t_{iono_i}(k)] + \lambda_j N_i + \nu_i(k), \quad (22)$$

where $\boldsymbol{r}_r \triangleq [x_r, y_r, z_r]^\mathsf{T}$ is the stationary receiver's position vector in the East-North-Up (ENU) frame; $\boldsymbol{r}_{SV_i} \triangleq [x_{SV_i}, y_{SV_i}, z_{SV_i}]^\mathsf{T}$ is the i-th satellite's position vector in the ENU frame; δt_r and δt_{SV_i} are the receiver's and i-th satellite's clock biases, respectively; δt_{trop_i} and δt_{iono_i} are the ionospheric and tropospheric delays between the receiver and i-th satellite, respectively; c is the speed-of-light; λ_i is the wavelength of the i-th satellite's signal; N_i is the carrier phase ambiguity between the receiver and i-th satellite; and ν_i is the measurement noise, which is modeled as a discrete-time zero-mean white sequence with variance $\sigma^2_{\Phi,i}$. In (22), the time index k' represents discrete time-step $t_k = t_0 + kT_0 - \delta t_{TOF_i}$, where δt_{TOF_i} is the time-of-flight of the signal from the i-th satellite to the receiver. This paper assumes $k' \approx k$ to simplify the formulation of the NLS positioning framework. This approximation introduces an error in the LEO satellite position and clock bias. The error introduced by this approximation in the LEO satellite position is negligible compared to the position error in TLE files, which can be as high as few kilometers. The error introduced by this approximation in the LEO satellite clock will be lumped into a combined term and estimated as described next.

The receiver and LEO satellite clock error states (bias and drift) are modeled according to the standard double integrator model [3]. The terms $\delta t_r(k)$, $\delta t_{SV_i}(k)$, $\delta t_{iono_i}(k)$, $\delta t_{trop_i}(k)$ will be lumped together and approximated as a first-order TSE. Under these assumptions, (22) can be approximated as

$$\Phi_i(k) \approx \|\boldsymbol{r}_r - \boldsymbol{r}_{SV_i}(k)\|_2 + a_i + b_i k T_0 + \nu_i(k), \quad (23)$$

where $a_i \triangleq c\cdot(\delta t_r - \delta t_{SV_i} + \delta t_{iono_i} + \delta t_{trop_i})$ and $b_i \triangleq c\cdot\left(\dot{\delta} t_r - \dot{\delta} t_{SV_i} + \dot{\delta} t_{iono_i} + \dot{\delta} t_{trop_i}\right)$ are the zero- and first-order TSE terms, respectively, of the lumped clock errors and atmospheric delays.

B. Batch NLS Estimator

Next, define the state vector $\boldsymbol{x} \triangleq \left[\boldsymbol{r}_r{}^\mathsf{T}, a_1, b_1, \ldots, a_L, b_L\right]^\mathsf{T}$. Let $\boldsymbol{z}(k)$ denote the vector of carrier phase observables from all LEO satellites, available at time-step k, stacked together, i.e. $\boldsymbol{z}(k) \triangleq [\Phi_1(k), \ldots, \Phi_L(k)]^\mathsf{T}$. The vector of all available observables is defined as $\boldsymbol{z} \triangleq [\boldsymbol{z}(0), \ldots, \boldsymbol{z}(M)]^\mathsf{T}$, where M is the total number of observations during the satellite's pass. Let $\boldsymbol{v}_z$ denote the vector of all measurement noises stacked together. Then, one can readily write the measurement equation given by $\boldsymbol{z} = \boldsymbol{g}(\boldsymbol{x}) + \boldsymbol{v}_z$, where $\boldsymbol{g}(\boldsymbol{x})$ is the nonlinear mapping from the state space $\boldsymbol{x}$ to the measurement space $\boldsymbol{z}$. The positioning solution is achieved by iterating over the NLS update equation

$$\Delta\hat{\boldsymbol{x}}_p = \left(\mathbf{H}_p^\mathsf{T}\mathbf{H}_p\right)^{-1}\mathbf{H}_p^\mathsf{T}\left(\boldsymbol{z} - \mathbf{g}(\hat{\boldsymbol{x}}_p)\right),$$
$$\hat{\boldsymbol{x}}_{p+1} = \hat{\boldsymbol{x}}_p + \Delta\hat{\boldsymbol{x}}_p, \quad (24)$$

where $p \in \{1, 2, \ldots, p^*\}$ denotes the recursion index; p^* is the index when $\|\Delta\hat{\boldsymbol{x}}_p\|_2$ reaches a predetermined stopping criterion (chosen to be 10^{-6}); $\mathbf{H}_p \triangleq \frac{\partial \boldsymbol{g}(\boldsymbol{x})}{\partial \boldsymbol{x}}|_{\boldsymbol{x}=\hat{\boldsymbol{x}}_p}$ is the measurement Jacobian matrix.

C. Experimental Results

Signals from 1 Orbcomm, 1 Iridium NEXT, 4 Starlink, and 2 OneWeb LEO satellites were collected via the setup described in Fig. 3. Fig. 12(a) shows the skyplot of the LEO satellites, while Fig. 12(b) shows the hardware used for data collection. The hardware included: (i) an LNB with conversion gain of 50 dB and noise figure of 2.5 dB connected to a Ku-band 60 cm parabolic offset dish with gain of 30 dBi to receive Starlink and OneWeb satellite signals, (ii) a commercial Orbcomm antenna, and (iii) a commercial Iridium NEXT antenna. The satellite positions, $\{\boldsymbol{r}_{SV_i}\}_{i=1}^8$, were obtained from TLE files and an SGP4 orbit determination software. The TLE epoch time was adjusted for each satellite to account for ephemeris errors. This was achieved by minimizing the carrier phase residuals for each satellite [27]. The blind Doppler tracking framework discussed in III was used to acquire and track satellite signals with $q_w = (0.1)^2$ rad^2/s^6 and $\sigma_{\dot{\theta}} = \frac{\pi}{6}$ rad/s. Results of 8 different satellites are shown in Fig. 11. Note that cut-offs in Doppler tracking for OneWeb and Starlink are caused by the inability to continuously point the highly directional dish manually towards the satellite position. The top graphs in the figure show the estimated (dashed) versus the TLE+SGP4-predicted (solid) Doppler shift profile for every tracked satellite. The bottom graphs show the KF innovation $\nu_{KF}(k)$ during the tracking period. It is worth noting that even though the studied LEO constellations suffer from high Doppler (up to ∼250 kHz), the blind Doppler tracking framework was able to track the Doppler with an error less than 10 Hz.

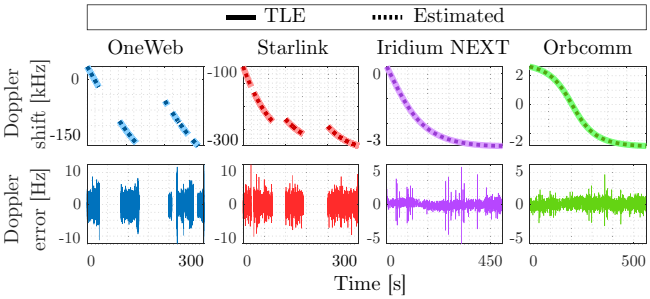

Fig. 11. Top: Doppler shift profiles for 2 OneWeb, 4 Starlink, 1 Iridium NEXT, and 1 Orbcomm LEO satellites: solid curves denote the estimated Doppler from the proposed framework, while dotted curves denote the predicted Doppler from TLE+SGP4. Bottom: KF innovation during the tracking period of each satellite.

Next, the batch NLS estimator described in (24) was employed using measurements from all LEO satellites to obtain the final estimate $\hat{\boldsymbol{x}}_{p^*}$. The receiver's initial position estimate, $\hat{\boldsymbol{r}}_{r,0}$, was set on the roof of the Engineering parking structure at the University of California, Irvine, USA, approximately 3,600 km away from the true position, which was on the roof of The Ohio State University's Electroscience Laboratory (ESL), Columbus, Ohio, USA. Fig. 13 summarizes the positioning

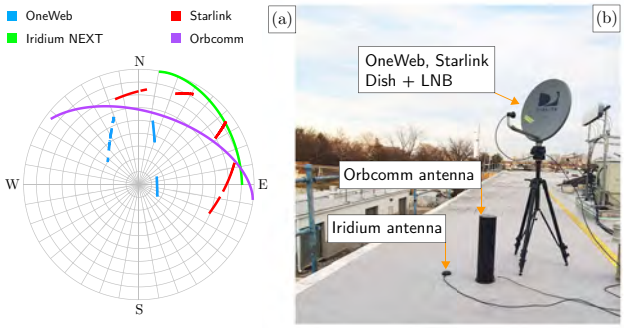

Fig. 12. (a) Skyplot of 2 OneWeb, 4 Starlink, 1 Iridium NEXT, and 1 Orbcomm LEO satellites which were tracked during the experiment. (b) Hardware setup used in data collection.

results. Specifically, Fig. 13(a) shows the trajectories of the 8 satellites from the 4 LEO constellations, Fig. 13(b) shows the initial and final position estimates, and Fig. 13(c) shows the true and estimated receiver's position. The final 3–D position error was found to be 5.8 m, while the 2–D position error was 5.1 m (i.e., upon considering only the east and north coordinates in the ENU frame). For comparative purposes, the batch NLS estimator was employed with the individual LEO constellations. The results are summarized in Table II.

IX. Conclusion

This paper proposed a novel framework for blind beacon estimation and Doppler tracking of LEO satellites. First, it provided a derivation of an analytical expression for the received signal frequency spectrum. Second, a novel frequency-based Doppler discriminator was proposed. Third, a KF-based Doppler tracking algorithm was developed. Fourth, a blind beacon estimation framework was proposed and demonstrated with four LEO constellations, namely, Orbcomm, Iridium NEXT, Starlink, and OneWeb. Finally, the paper showed the first result of stationary receiver localization with multi-constellation LEO satellite including OneWeb, achieving a 2–D position error of 5.1 m.

Acknowledgment

The authors would like to thank the Electroscience Laboratory (ESL) and Mr. Jeffrey Blankenship for his readiness and generous support in the experimental setup.

TABLE II
Comparison of Positioning Results with Different LEO Constellations

Constellation	Visibility [s]	2–D Error [m]
OneWeb	132	30.68
Starlink	215	33.69
Iridium NEXT	490	34.48
Orbcomm	560	31.57
All	560	5.1

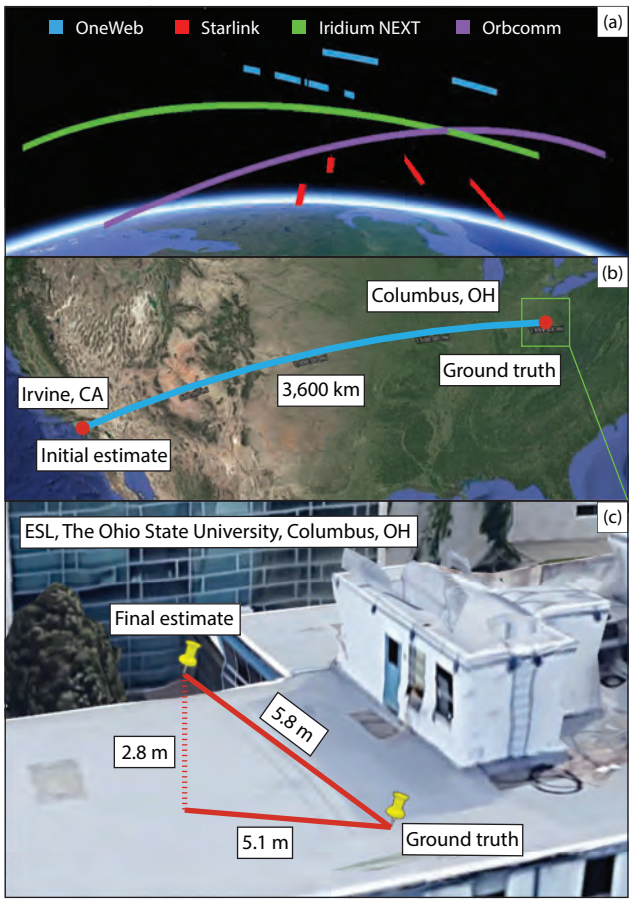

Fig. 13. Positioning results with 2 OneWeb, 4 Starlink, 1 Iridium NEXT, and 1 Orbcomm LEO satellites: (a) LEO satellite trajectories. (b) Initial and final estimated positions. (c) Final errors relative to the receiver's true position.

References

[1] G. Curzi, D. Modenini, and P. Tortora, "Large constellations of small satellites: A survey of near future challenges and missions," *Aerospace*, vol. 7, no. 9, pp. 1–18, September 2020.

[2] T. Reid, T. Walter, P. Enge, D. Lawrence, H. Cobb, G. Gutt, M. O'Conner, and D. Whelan, "Position, navigation, and timing technologies in the 21st century," J. Morton, F. van Diggelen, J. Spilker, Jr., and B. Parkinson, Eds. Wiley-IEEE, 2021, vol. 2, ch. 43: Navigation from low Earth orbit – Part 1: concept, current capability, and future promise, pp. 1359–1379.

[3] Z. Kassas, "Position, navigation, and timing technologies in the 21st century," J. Morton, F. van Diggelen, J. Spilker, Jr., and B. Parkinson, Eds. Wiley-IEEE, 2021, vol. 2, ch. 43: Navigation from low Earth orbit – Part 2: models, implementation, and performance, pp. 1381–1412.

[4] R. Faragher, "Effects of multipath interference on radio positioning systems," Ph.D. dissertation, University of Cambridge, England, 2007.

[5] R. Ioannides, T. Pany, and G. Gibbons, "Known vulnerabilities of global navigation satellite systems, status, and potential mitigation techniques," *Proceedings of the IEEE*, vol. 104, no. 6, pp. 1174–1194, February 2016.

[6] X. Chen, Q. Wei, F. Wang, Z. Jun, S. Wu, and A. Men, "Super-resolution time of arrival estimation for a symbiotic FM radio data system," *IEEE Transactions on Broadcasting*, vol. 66, no. 4, pp. 847–856, December 2020.

[7] L. Chen, P. Thevenon, G. Seco-Granados, O. Julien, and H. Kuusniemi, "Analysis on the TOA tracking with DVB-T signals for positioning," *IEEE Transactions on Broadcasting*, vol. 62, no. 4, pp. 957–961, December 2016.

[8] R. Faragher and R. Harle, "Towards an efficient, intelligent, opportunistic smartphone indoor positioning system," *NAVIGATION, Journal of the Institute of Navigation*, vol. 62, no. 1, pp. 55–72, 2015.

[9] J. Khalife, K. Shamaei, and Z. Kassas, "A software-defined receiver architecture for cellular CDMA-based navigation," in *Proceedings of IEEE/ION Position, Location, and Navigation Symposium*, April 2016, pp. 816–826.

[10] C. Yang, T. Nguyen, and E. Blasch, "Mobile positioning via fusion of mixed signals of opportunity," *IEEE Aerospace and Electronic Systems Magazine*, vol. 29, no. 4, pp. 34–46, April 2014.

[11] J. del Peral-Rosado, J. López-Salcedo, F. Zanier, and G. Seco-Granados, "Position accuracy of joint time-delay and channel estimators in LTE networks," *IEEE Access*, vol. 6, pp. 25 185–25 199, 2018.

[12] K. Shamaei and Z. Kassas, "A joint TOA and DOA acquisition and tracking approach for positioning with LTE signals," *IEEE Transactions on Signal Processing*, pp. 2689–2705, 2021.

[13] A. Xhafa, J. del Peral-Rosado, J. López-Salcedo, and G. Seco-Granados, "Evaluation of 5G positioning performance based on UTDoA, AoA and base-station selective exclusion," *Sensors*, vol. 22, no. 1, pp. 101–118, 2021.

[14] A. Abdallah, J. Khalife, and Z. Kassas, "Exploiting on-demand 5G downlink signals for opportunistic navigation," *IEEE Signal Processing Letters*, 2023, accepted.

[15] J. Peral-Rosado, J. Lopez-Salcedo, S. Kim, and G. Seco-Granados, "Feasibility study of 5G-based localization for assisted driving," in *Proceedings of International Conference on Localization and GNSS*, June 2016, pp. 1–6.

[16] M. Maaref, J. Khalife, and Z. Kassas, "Lane-level localization and mapping in GNSS-challenged environments by fusing lidar data and cellular pseudoranges," *IEEE Transactions on Intelligent Vehicles*, vol. 4, no. 1, pp. 73–89, March 2019.

[17] Z. Kassas, A. Abdallah, C. Lee, J. Jurado, J. Duede, Z. Hoeffner, T. Hulsey, R. Quirarte, S. Wachtel, and R. Tay, "Protecting the skies: GNSS-less aircraft navigation with terrestrial cellular signals of opportunity," in *Proceedings of ION GNSS Conference*, September 2022, pp. 1014–1025.

[18] J. Del Peral-Rosado, P. Nolle, S. Razavi, G. Lindmark, D. Shrestha, F. Gunnarsson, F. Kaltenberger, N. Sirola, O. Särkkä, J. Roström, K. Vaarala, P. Miettinen, G. Pojani, L. Canzian, H. Babaroglu, E. Rastorgueva-Foi, J. Talvitie, and D. Flachs, "Design considerations of dedicated and aerial 5G networks for enhanced positioning services," in *Proceedings of Workshop on Satellite Navigation Technology*, April 2022, pp. 1–12.

[19] J. Khalife and Z. Kassas, "On the achievability of submeter-accurate UAV navigation with cellular signals exploiting loose network synchronization," *IEEE Transactions on Aerospace and Electronic Systems*, vol. 58, no. 5, pp. 4261–4278, October 2022.

[20] Z. Kassas, J. Khalife, A. Abdallah, and C. Lee, "I am not afraid of the GPS jammer: resilient navigation via signals of opportunity in GPS-denied environments," *IEEE Aerospace and Electronic Systems Magazine*, vol. 37, no. 7, pp. 4–19, July 2022.

[21] N. Jardak and Q. Jault, "The potential of LEO satellite-based opportunistic navigation for high dynamic applications," *Sensors*, vol. 22, no. 7, pp. 2541–2565, 2022.

[22] F. Farhangian, H. Benzerrouk, and R. Landry, "Opportunistic in-flight INS alignment using LEO satellites and a rotatory IMU platform," *Aerospace*, vol. 8, no. 10, pp. 280–281, 2021.

[23] M. Psiaki, "Navigation using carrier Doppler shift from a LEO constellation: TRANSIT on steroids," *NAVIGATION, Journal of the Institute of Navigation*, vol. 68, no. 3, pp. 621–641, September 2021.

[24] K. Wang and A. El-Mowafy, "LEO satellite clock analysis and prediction for positioning applications," *Geo-spatial Information Science*, vol. 25, no. 1, pp. 14–33, 2022.

[25] M. Hartnett, "Performance assessment of navigation using carrier Doppler measurements from multiple LEO constellations," Master's thesis, Air Force Institute of Technology, Ohio, USA, 2022.

[26] P. Iannucci and T. Humphreys, "Fused low-Earth-orbit GNSS," *IEEE Transactions on Aerospace and Electronics Systems*, 2022, accepted.

[27] J. Khalife, M. Neinavaie, and Z. Kassas, "The first carrier phase tracking and positioning results with Starlink LEO satellite signals," *IEEE Transactions on Aerospace and Electronic Systems*, vol. 56, no. 2, pp. 1487–1491, April 2022.

[28] Z. Kassas, M. Neinavaie, J. Khalife, N. Khairallah, J. Haidar-Ahmad, S. Kozhaya, and Z. Shadram, "Enter LEO on the GNSS stage: Navigation with Starlink satellites," *Inside GNSS Magazine*, vol. 16, no. 6, pp. 42–51, 2021.

[29] J. Khalife and Z. Kassas, "Performance-driven design of carrier phase differential navigation frameworks with megaconstellation LEO satellites," *IEEE Transactions on Aerospace and Electronic Systems*, pp. 1–20, 2023, accepted.

[30] C. Zhao, H. Qin, N. Wu, and D. Wang, "Analysis of baseline impact on differential doppler positioning and performance improvement method for LEO opportunistic navigation," *IEEE Transactions on Instrumentation and Measurement*, pp. 1–10, 2023.

[31] Z. Kassas, J. Morales, and J. Khalife, "New-age satellite-based navigation – STAN: simultaneous tracking and navigation with LEO satellite signals," *Inside GNSS Magazine*, vol. 14, no. 4, pp. 56–65, 2019.

[32] D. Shen, J. Lu, G. Chen, E. Blasch, C. Sheaff, M. Pugh, and K. Pham, "Methods of machine learning for space object pattern classification," in *Proceedings of IEEE National Aerospace and Electronics Conference*, 2019, pp. 565–572.

[33] J. Haidar-Ahmad, N. Khairallah, and Z. Kassas, "A hybrid analytical-machine learning approach for LEO satellite orbit prediction," in *Proceedings of International Conference on Information Fusion*, 2022, pp. 1–7.

[34] N. Khairallah and Z. Kassas, "An interacting multiple model estimator of LEO satellite clocks for improved positioning," in *Proceedings of IEEE Vehicular Technology Conference*, 2022, pp. 1–5.

[35] S. Kozhaya and Z. Kassas, "Blind receiver for LEO beacon estimation with application to UAV carrier phase differential navigation," in *Proceedings of ION GNSS Conference*, 2022, pp. 2385–2397.

[36] M. Neinavaie, J. Khalife, and Z. Kassas, "Acquisition, Doppler tracking, and positioning with Starlink LEO satellites: First results," *IEEE Transactions on Aerospace and Electronic Systems*, vol. 58, no. 3, pp. 2606–2610, June 2022.

[37] H. Choi and H. Moon, "Blind estimation of spreading sequence and data bits in direct-sequence spread spectrum communication systems," *IEEE Access*, vol. 8, pp. 148 066–148 074, 2020.

[38] Z. Rui, X. Ouyang, F. Zeng, and X. Xu, "Blind estimation of GPS M-Code signals under noncooperative conditions," *Wireless Communications and Mobile Computing*, vol. 2022, 2022.

[39] J. Khalife, M. Neinavaie, and Z. Kassas, "Blind Doppler tracking from OFDM signals transmitted by broadband LEO satellites," in *Proceedings of IEEE Vehicular Technology Conference*, April 2021, pp. 1–5.

[40] C. Zhao, H. Qin, and Z. Li, "Doppler measurements from multiconstellations in opportunistic navigation," *IEEE Transactions on Instrumentation and Measurement*, vol. 71, pp. 1–9, 2022.

[41] C. Huang, H. Qin, C. Zhao, and H. Liang, "Phase - time method: Accurate Doppler measurement for Iridium NEXT signals," *IEEE Transactions on Aerospace and Electronic Systems*, vol. 58, no. 6, pp. 5954–5962, 2022.

[42] T. Frederick, "Time-frequency estimation for cyclostationary signals," Ph.D. dissertation, Florida Atlantic University, USA, 1997.

[43] S. Vaseghi, *Advanced digital signal processing and noise reduction*. John Wiley & Sons, 2008.

[44] S. Zucker, "Cross-correlation and maximum-likelihood analysis: a new approach to combining cross-correlation functions," *Monthly Notices of the Royal Astronomical Society*, vol. 342, no. 4, pp. 1291–1298, 2003.

[45] 3GPP2, "Physical layer standard for cdma2000 spread spectrum systems (C.S0002-E)," 3rd Generation Partnership Project 2 (3GPP2), TS C.S0002-E, June 2011.

[46] A. Flores, "NAVSTAR GPS space segment/navigation user interfaces," https://www.gps.gov/technical/icwg/IS-GPS-200N.pdf, August 2022.

[47] R. Hendrickson, "Globalstar for the military," in *Proceedings of IEEE Military Communications Conference*, vol. 3, November 1997, pp. 1173–1178.

[48] 3GPP, "Evolved universal terrestrial radio access (E-UTRA); multiplexing and channel coding," 3rd Generation Partnership Project (3GPP), TS 36.212, January 2010. [Online]. Available: http://www.3gpp.org/ftp/Specs/html-info/36212.htm

[49] 3GPP, "Physical channels and modulation," https://www.etsi.org/deliver/etsi-ts/138200-138299/138211/15.02.00-60/ts-138211v150200p.pdf, 5G; NR; 3rd Generation Partnership Project (3GPP), TS 38.211, July 2018.

[50] S. Reid, "ORBCOMM system overview," December 2001.

[51] Orbcomm, "Ever wondered what is on the Orbcomm satellite downlink?" http://mdkenny.customer.netspace.net.au/Orbcomm.pdf, 2002.

[52] M. Nezami, "Dsp-based carrier acquisition and tracking for burst TDMA mobile land and satellite receivers," *Applied Microwave & Wireless Magazine*, vol. 13, no. 9, pp. 24–41, 2001.

Navigation with Multi-Constellation LEO Satellite Signals of Opportunity: Starlink, OneWeb, Orbcomm, and Iridium

Zaher M. Kassas, Sharbel Kozhaya, Haitham Kanj, Joe Saroufim, Samer W. Hayek, and Mohammad Neinavaie
Department of Electrical and Computer Engineering
The Ohio State University, Columbus, OH, USA

Nadim Khairallah and Joe Khalife
Department of Mechanical and Aerospace Engineering
University of California, Irvine, CA, USA

***Abstract*—This paper summarizes current state-of-the-art navigation results with multi-constellation low Earth orbit (LEO) satellite signals of opportunity. Experimental results with four LEO satellite constellations are presented: Starlink, OneWeb, Orbcomm, and Iridium. Two receiver designs are presented: (R1) a cognitive opportunistic navigation approach, which utilizes minimal, publicly available prior knowledge about the LEO satellite signal structure and (R2) a blind approach, which assumes no prior knowledge of the signals. Stationary positioning and mobile ground vehicle navigation results are presented. For the ground vehicle, results with two frameworks are presented: (N1) a LEO-aided inertial navigation system (INS) simultaneous tracking and navigation (STAN) and (N2) a LEO-aided differential STAN. The results reveal the tremendous promise of exploiting multi-constellation LEO satellite signals of opportunity for navigation. For positioning: (i) with R1, starting with an initial estimate about 179 km away, by exploiting signals from 6 Starlink, 1 Orbcomm, and 4 Iridium, a final two-dimensional (2–D) position error of 6.5 m was achieved and (ii) with R2, starting with an initial estimate about 3,600 km away, by exploiting signals from 4 Starlink, 2 OneWeb, 1 Orbcomm, and 1 Iridium, a final 2–D position error of 5.1 m was achieved. For navigation, a ground vehicle was equipped with an industrial-grade inertial measurement unit (IMU) and an altimeter. (i) With R1 and N1, the vehicle traversed 4.15 km in 150 seconds (GNSS signals were only available for the first 2.33 km). By exploiting signals from 3 Starlink, 2 Orbcomm, and 1 Iridium, the 3–D position root mean squared error (RMSE) and final 3-D error were 18.4 m and 27.1 m, respectively. The GNSS-aided INS position RMSE and final 3-D error were 118.5 m and 472.7 m, respectively. (ii) With R2 and N2, the vehicle traversed 1.03 km in 110 seconds (GNSS signals were only available for the first 0.11 km). By exploiting signals from 4 Starlink, 1 OneWeb, 2 Orbcomm, and 1 Iridium, the 3–D position RMSE and final 3-D error were 9.5 m and 4.4 m, respectively. The GNSS-aided INS position RMSE and final 3-D error were 205 m and 525 m, respectively.**

***Index Terms*—Positioning, navigation, signals of opportunity, Doppler tracking, low Earth orbit satellite, Starlink, OneWeb.**

This work was supported in part by the Office of Naval Research (ONR) under Grants N00014-19-1-2511 and N00014-22-1-2242, in part by the Air Force Office of Scientific Research (AFOSR) under Grant FA9550-22-1-0476, and in part by the U.S. Department of Transportation (USDOT) under Grant 69A3552047138 for the CARMEN University Transportation Center (UTC).
Corresponding author: Z. Kassas, zkassas@ieee.org.

I. Introduction

We are witnessing a renewed space race. From technology giants, to startups, to governments, everyone is claiming stake in launching their own LEO constellation. These constellations promise to transform our daily lives, offering broadband connectivity anywhere on Earth [1], and will benefit scientific inquiry in fields such as remote sensing [2], [3]. However, not all such constellations are created equal. So-called meg-constellations comprising tens of thousands of satellites are on their way to become a reality, with SpaceX's Starlink being the clear frontrunner with their plan to deploy nearly 12,000 LEO satellites. These constellations will be welcomed by current constellations inhabiting LEO, and collectively they could usher a new era for positioning, navigation, and timing (PNT) [4]–[8].

The promise of utilizing LEO satellites for PNT has been the subject of extensive recent studies [9]–[18]. These studies can be categorized into three groups. The first considers providing a standalone navigation solution by launching PNT-dedicated LEO constellations or transmitting PNT signals from existing LEO constellations [19]–[26]. The second considers augmenting global navigation satellite systems (GNSS) with LEO constellations [27]–[33]. The third exploits LEO signals from *any* constellation in an opportunistic fashion [34]–[41].

LEO satellites possess desirable attributes for PNT [42], [43]: (i) they are around twenty times closer to the Earth compared to GNSS satellites, which reside in medium Earth orbit (MEO), which could yield significantly higher carrier-to-noise ratio; (ii) they are becoming abundant as tens of thousands of broadband Internet satellites are expected to be deployed into LEO; and (iii) they transmit in different frequency bands and are placed in varying orbits, making LEO satellite signals diverse in frequency and direction.

However, exploiting LEO satellite signals for PNT purposes in an opportunistic fashion comes with challenges [44], as these constellations are owned by private operators that typi-

cally do not disclose crucial information about the satellites': (i) ephemerides, (ii) clock synchronization and stability, and (iii) signal specifications.

To address the first challenge, several approaches have been proposed, including differential navigation utilizing known base receiver(s) [45]–[47], simultaneous tracking and navigation (STAN) [48], and analytical/machine-learning satellite orbit tracking [49]–[52]. Approaches to address the second challenge have been offered in [53]–[55]. To address the third challenge, the paradigm of cognitive opportunistic navigation [56], which estimates the minimally known LEO satellite signals in a *blind* fashion has been showing tremendous promise [57].

This paper summarizes recent progress with exploiting multi-constellation LEO satellites for PNT. The focus of the paper is to present the navigation solution achieved with real LEO signals of opportunity on stationary and mobile platforms in a standalone and a differential fashion. To the authors' knowledge, these results represent the most accurate positioning and navigation results reported in the literature with multi-constellation LEO signals of opportunity.

Experimental results with four LEO constellations are presented: Starlink, OneWeb, Orbcomm, and Iridium. Two receiver design approaches are presented:

- **R1:** a cognitive opportunistic navigation approach, which utilizes minimal, publicly available prior knowledge about the LEO satellite signal structure
- **R2:** a blind approach, which assumes no prior knowledge of the signals

Stationary positioning and mobile ground vehicle navigation results are presented. For the ground vehicle, results with two frameworks are presented:

- **N1:** a LEO-aided inertial navigation system (INS) simultaneous tracking and navigation (STAN)
- **N2:** a LEO-aided differential STAN (DSTAN).

For positioning: (i) with R1, starting with an initial estimate about 179 km away, by exploiting signals from 6 Starlink, 1 Orbcomm, and 4 Iridium, a final two-dimensional (2–D) position error of 6.5 m was achieved and (ii) with R2, starting with an initial estimate about 3,600 km away, by exploiting signals from 4 Starlink, 2 OneWeb, 1 Orbcomm, and 1 Iridium, a final 2–D position error of 5.1 m was achieved. For navigation, a ground vehicle was equipped with an industrial-grade inertial measurement unit (IMU) and an altimeter. (i) With R1 and N1, the vehicle traversed 4.15 km in 150 seconds (GNSS signals were only available for the first 2.33 km). By exploiting signals from 3 Starlink, 2 Orbcomm, and 1 Iridium, the 3–D position root mean squared error (RMSE) and final 3-D error were 18.4 m and 27.1 m, respectively. The GNSS-aided INS position RMSE and final 3-D error were 118.5 m and 472.7 m, respectively. (ii) With R2 and N2, the vehicle traversed 1.03 km in 110 seconds (GNSS signals were only available for the first 0.11 km). By exploiting signals from 4 Starlink, 1 OneWeb, 2 Orbcomm, and 1 Iridium, the 3–D position RMSE and final 3-D error were 9.5 m and 4.4 m, respectively. The GNSS-aided INS position RMSE and final 3-D error were 205 m and 525 m, respectively. The results presented in this paper reveal the tremendous promise of exploiting multi-constellation LEO satellite signals of opportunity for navigation

The paper is organized as follows. Section II overviews the LEO constellations considered in this paper. Section III presents experimental results with the cognitive opportunistic navigation receiver with Starlink, Orbcomm, and Iridium NEXT on a stationary receiver and a mobile ground vehicle navigating via the LEO-aided STAN framework. Section IV presents experimental results with the opportunistic navigation receiver with Starlink, OneWeb, Orbcomm, and Iridium NEXT on a stationary receiver and a mobile ground vehicle navigating via the LEO-aided DSTAN framework. Section V gives concluding remarks.

II. Overview of LEO Constellations

Table I compares the four LEO constellations considered in this paper. The number of satellites specified in the table represent the current number, as of the writing of this paper.

TABLE I
COMPARISON OF LEO CONSTELLATIONS

Parameter	**Starlink**	**OneWeb**	**Orbcomm**	**Iridium**
Bandwidth	240 MHz	230 MHz	4.8 kHz	31.5 kHz
Beacon length	4/3 ms	10 ms	1 s	90 ms
Number of satellites	3,660	542	36	66
Modulation	OFDM	OFDM	SD-QPSK	DE-QPSK
Frequency band	Ku, Ka	Ku	VHF	L
Downlink frequency	10.7–12.7 GHz	10.7–12.7 GHz	137 MHz	1.616–1.626 GHz
Number of channels	8	8	2	240
Number of beams	$\approx$ 48	16	N/A	48
Altitude	550 km	1,200 km	750 km	780 km

III. Navigation with Starlink, Orbcomm, and Iridium NEXT LEO Satellites: A Cognitive Opportunistic Navigation Approach

This section presents multi-constellation navigation results exploiting Starlink, Orbcomm, and Iridium NEXT LEO satellites with R1 and N1.

A. Stationary Positioning

Signals from a total of 11 LEO satellites (6 Starlink, 1 Orbcomm, and 4 Iridium NEXT) were recorded on top of a parking structure at the University of California, Irvine, CA, USA. The receiver presented in [58] was used to process Orbcomm and Iridium NEXT signals, from which it produced Doppler navigation observables. The receiver presented in [59] was used to process Starlink signals, from which it produced carrier phase observables. It is worth mentioning that not all satellites were visible simultaneously, and the signals were recorded as satellites passed overhead. The hardware setup is described in [58], [59]. Fig. 1 illustrates the skyplot of the LEO satellites.

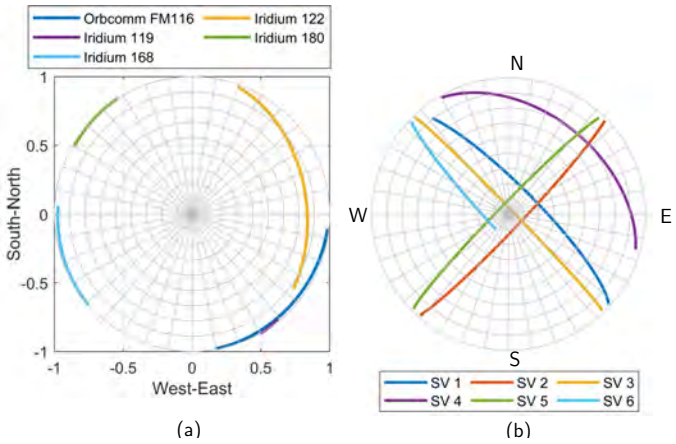

Fig. 1. (a) Skyplot of 6 Starlink, 1 Orbcomm, and 4 Iridium NEXT LEO satellites which were tracked during the experiment.

The navigation observables were processed through an extended Kalman filter, which estimated the receiver's 2–D position (the receiver's height was known). The EKF was initialized 179 km away from the true receiver position. The EKF's final position estimate converged to within 6.5 m. Fig. 2 illustrates the LEO satellite trajectories, initial estimate and ground truth receiver position, and final estimate along with the 99$^{\text{th}}$ percentile estimation error ellipse.

B. Mobile Navigation via LEO-Aided STAN

A ground vehicle was equipped with a Septentrio AsteRx-I V integrated GNSS-INS system with an industrial-grade IMU and an altimeter, from which the ground truth was derived. The hardware setup is described in [48]. The vehicle was driven on the CA-55 freeway next to Irvine, California, USA, for 4.15 km in 150 seconds. During the experiment, signals from 6 LEO satellites (3 Starlink, 2 Orbcomm, and 1 Iridium NEXT) were recorded. The skyplot of satellites' trajectory during the experiment are shown in Fig. 3. The receiver presented in [60] was used to process Orbcomm signals, from which it produced carrier phase navigation observables. The receiver presented in [58] was used to process Iridium NEXT signals, from which it produced Doppler navigation observables. The receiver presented in [61] was used to process Starlink signals, from which it produced Doppler navigation observables. The vehicle navigated via the LEO-aided STAN framework described in [48].

GNSS signals were available for the first 80 seconds of the experiment but were fictitiously cut off for the last 70 seconds, during which the vehicle traveled 1.82 km. The GNSS-INS navigation solution drifted to a final 3-D position error of 472.7 m and a 3-D position RMSE of 118.5 m over the true trajectory. The STAN LEO-aided INS yielded a final 3-D position error of 27.1 m and a 3-D position RMSE of 18.4 m. Fig. 4 summarizes the experimental results. For details about the data processing, EKF formulation, and additional results and analyses, the reader is referred to [48].

Fig. 2. (a) Trajectories of 11 LEO satellites (6 Starlink, 1 Orbcomm, and 4 Iridium NEXT) used to localize the stationary receiver. (b) Initial and final estimated positions. (c) Final errors relative to the receiver's true position.

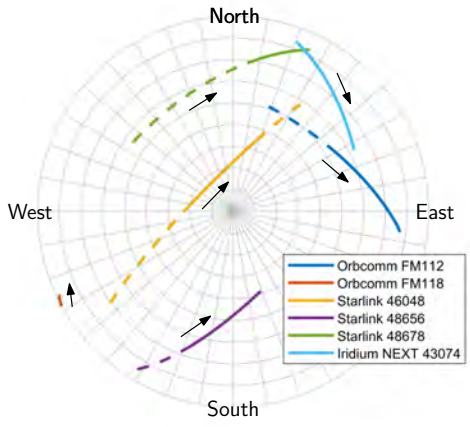

Fig. 3. Skyplot of 3 Starlink, 2 Orbcomm, and 1 Iridium NEXT LEO satellites which were tracked during the experiment.

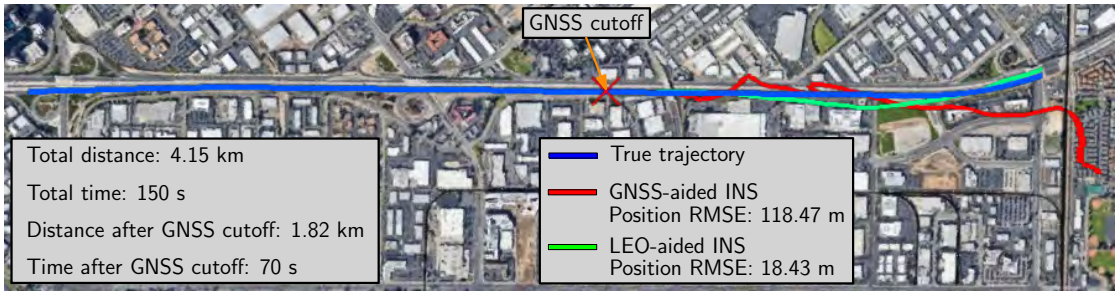

Fig. 4. Experimental results showing the ground vehicle's trajectory and estimated trajectory with GNSS-aided INS and STAN with LEO-aided INS using signals from 3 Starlink, 2 Orbcomm, and 1 Iridium NEXT satellites. Map data: Google Earth.

IV. Navigation with Starlink, OneWeb, Orbcomm, and Iridium NEXT LEO Satellites: A Blind Navigation Approach

This section presents multi-constellation navigation results exploiting Starlink, OneWeb, Orbcomm, and Iridium NEXT LEO satellites with R2 and N2.

A. Stationary Positioning

Signals from a total of 8 LEO satellites (4 Starlink, 2 OneWeb, 1 Orbcomm, and 1 Iridium NEXT) were recorded on top of the ElectroScience Laboratory (ESL) at The Ohio State University, Columbus, OH, USA. The receiver presented in [57] was used to process all LEO signals, from which it produced Doppler navigation observables. It is worth mentioning that not all satellites were visible simultaneously, and the signals were recorded as satellites passed overhead. The hardware setup is described in [57]. Fig. 1 illustrates the skyplot of the LEO satellites.

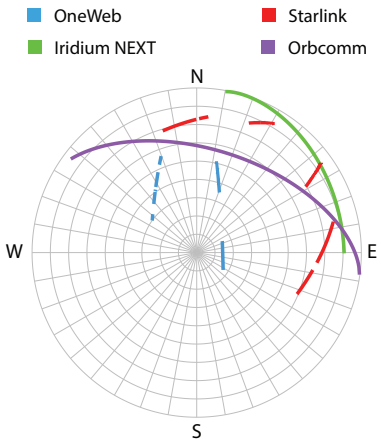

Fig. 5. Skyplot of 4 Starlink, 2 OneWeb, 1 Orbcomm, and 1 Iridium NEXT LEO satellites which were tracked during the experiment.

The Doppler navigation observables were processed through a nonlinear least-squares (NLS) estimator, which estimated the receiver's 3–D position. The NLS was initialized in Irvine, CA, USA, about 3,600 km away from the true receiver position. The NLS's final position estimate converged to within a 2–D error of 5.1 m. Fig. 6 illustrates the LEO satellite trajectories, initial estimate, ground truth receiver position, and final estimate. For additional details about the data processing, NLS formulation, and additional results and analyses, the reader is referred to [57].

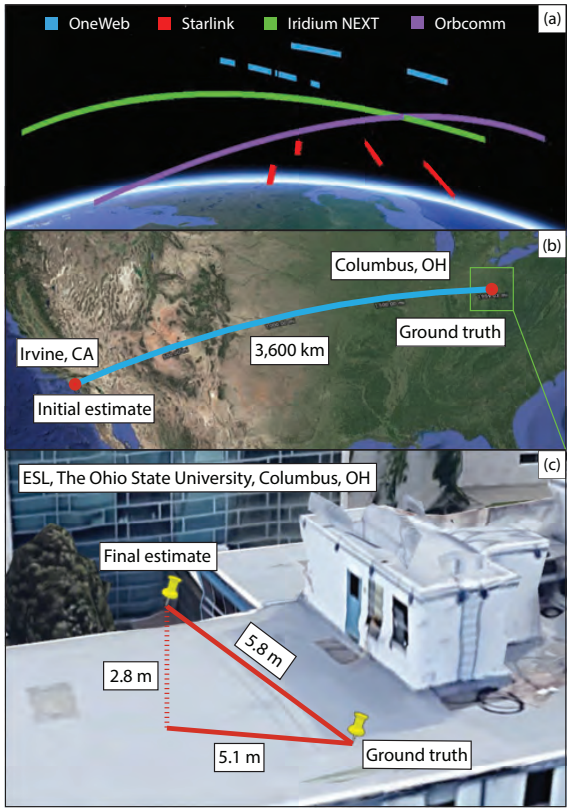

Fig. 6. Positioning results with 4 Starlink, 2 OneWeb, 1 Iridium NEXT, and 1 Orbcomm LEO satellites: (a) LEO satellite trajectories. (b) Initial and final estimated positions. (c) Final errors relative to the receiver's true position.

B. Mobile Navigation via LEO-Aided DSTAN

A ground vehicle was equipped with a Septentrio AsteRx SBi3 Pro+integrated GNSS-INS system with an industrial-grade IMU and an altimeter, from which the ground truth was derived. A differential base station with a known position was set up on top of ESL at The Ohio State University campus, about 2.2 km away from the rover (ground vehicle). The ground vehicle traversed a trajectory of 1.03 km in 110 seconds. During the experiment, signals from 8 LEO satellites (4 Starlink, 1 OneWeb, 2 Orbcomm, and 1 Iridium NEXT)

were recorded. The receiver presented in [57] was used to process signals collected by the base station and the rover, from which it produced Doppler navigation observables. The vehicle navigated via the DSTAN framework described in [47].

GNSS signals were available for the first 7 seconds of the experiment but were fictitiously cut off for the last 103 seconds, during which the vehicle traveled 0.92 km. The GNSS-INS navigation solution drifted to a final 3-D position error of 525 m and a 3-D position RMSE of 205 m over the true trajectory. The DSTAN LEO-aided INS yielded a final 3-D position error of 4.4 m and a 3-D position RMSE of 9.5 m. Fig. 7 summarizes the experimental results.

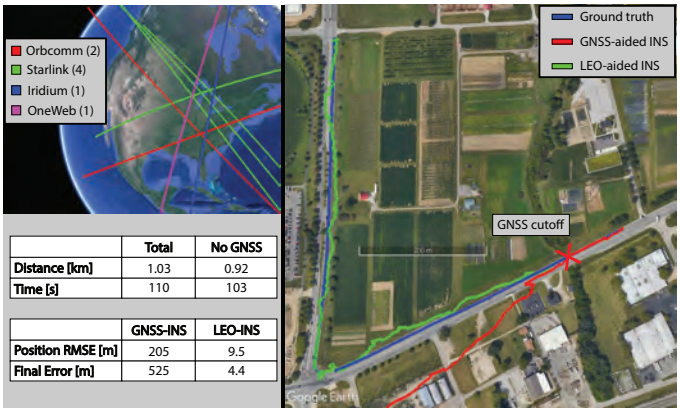

	Total	No GNSS
Distance [km]	1.03	0.92
Time [s]	110	103

	GNSS-INS	LEO-INS
Position RMSE [m]	205	9.5
Final Error [m]	525	4.4

Fig. 7. Navigation results with 1 OneWeb, 4 Starlink, 1 Iridium NEXT, and 2 Orbcomm LEO satellites: ground truth trajectory (blue), GNSS-aided INS (red), and DSTAN LEO-aided INS (green).

V. Conclusion

This paper summarized the current state-of-the-art with exploiting multi-constellation LEO satellite signals of opportunity for positioning and navigation. Exploiting 6 Starlink, 1 Orbcomm, and 4 Iridium via a cognitive opportunistic navigation receiver is shown to yield a stationary 2–D position error of 6.5 m, starting with an initial estimate about 179 km away. With signals from 3 Starlink, 2 Orbcomm, and 1 Iridium NEXT, a ground vehicle equipped with an industrial-grade IMU traveling for 4.15 km in 150 s (the last 1.82 km in 70 s of which without GNSS) could achieve a 3–D position RMSE of 18.4 m via the LEO-aided STAN framework. Exploiting 4 Starlink, 2 OneWeb, 1 Orbcomm, and 1 Iridium via a blind navigation receiver is shown to yield a stationary 2–D position error of 5.1 m, starting with an initial estimate about 3,600 km away. With signals from 4 Starlink, 1 OneWeb, 2 Orbcomm, and 1 Iridium, a ground vehicle equipped with an industrial-grade IMU traveling for 1.03 km in 110 s (the last 0.92 km in 103 s of which without GNSS) could achieve a 3–D position RMSE of 9.5 m via the LEO-aided DSTAN framework

Acknowledgment

The authors would like to thank the Electroscience Laboratory (ESL) and Mr. Jeffrey Blankenship for his readiness and generous support with the experiment. The authors would also like to thank Mu Jia for his help with data collection.

References

[1] A. Yadav, M. Agarwal, S. Agarwal, and S. Verma, "Internet from space anywhere and anytime - Starlink," in *Proceedings of International Conference on Advancement in Electronics & Communication Engineering*, July 2022, pp. 1–8.

[2] Y. Morton, D. Xu, and Y. Jiao, "Ionospheric scintillation effects on signals transmitted from LEO satellites," in *Proceedings of ION GNSS Conference*, September 2022, pp. 2980–2988.

[3] Y. Yi, J. Johnson, and X. Wang, "Diurnal variations in ocean wind speeds measured by CYGNSS and other satellites," *IEEE Geoscience and Remote Sensing Letters*, vol. 19, pp. 1–5, 2022.

[4] T. Reid, B. Chan, A. Goel, K. Gunning, B. Manning, J. Martin, A. Neish, A. Perkins, and P. Tarantino, "Satellite navigation for the age of autonomy," in *Proceedings of IEEE/ION Position, Location and Navigation Symposium*, 2020, pp. 342–352.

[5] D. Egea-Roca, M. Arizabaleta-Diez, T. Pany, F. Antreich, J. Lppez-Salcedo, M. Paonni, and G. Seco-Granados, "GNSS user technology: State-of-the-art and future trends," *IEEE Access*, vol. 10, pp. 39 939–39 968, 2022.

[6] F. Prol, R. Ferre, Z. Saleem, P. Välisuo, C. Pinell, E. Lohan, M. Elsanhoury, M. Elmusrati, S. Islam, K. Celikbilek, K. Selvan, J. Yliaho, K. Rutledge, A. Ojala, L. Ferranti, J. Praks, M. Bhuiyan, S. Kaasalainen, and H. Kuusniemi, "Position, navigation, and timing (PNT) through low earth orbit (LEO) satellites: A survey on current status, challenges, and opportunities," *IEEE Access*, vol. 10, pp. 83 971–84 002, 2022.

[7] N. Jardak and Q. Jault, "The potential of LEO satellite-based opportunistic navigation for high dynamic applications," *Sensors*, vol. 22, no. 7, pp. 2541–2565, 2022.

[8] T. Janssen, A. Koppert, R. Berkvens, and M. Weyn, "A survey on IoT positioning leveraging LPWAN, GNSS and LEO-PNT," *IEEE Internet of Things Journal*, 2023, accepted.

[9] Z. Kassas, J. Morales, and J. Khalife, "New-age satellite-based navigation – STAN: simultaneous tracking and navigation with LEO satellite signals," *Inside GNSS Magazine*, vol. 14, no. 4, pp. 56–65, 2019.

[10] Q. Wei, X. Chen, and Y. Zhan, "Exploring implicit pilots for precise estimation of LEO satellite downlink Doppler frequency," *IEEE Communications Letters*, vol. 24, no. 10, pp. 2270–2274, 2020.

[11] T. Mortlock and Z. Kassas, "Performance analysis of simultaneous tracking and navigation with LEO satellites," in *Proceedings of ION GNSS Conference*, September 2020, pp. 2416–2429.

[12] M. Psiaki, "Navigation using carrier Doppler shift from a LEO constellation: TRANSIT on steroids," *NAVIGATION, Journal of the Institute of Navigation*, vol. 68, no. 3, pp. 621–641, September 2021.

[13] C. Pinell, "Receiver architectures for positioning with low Earth orbit satellite signals," Master's thesis, Lulea University of Technology, School of Electrical Engineering, Sweden, 2021.

[14] W. Van Uytsel, T. Janssen, R. Halili, and M. Weyn, "Exploring positioning through pseudoranges using low earth Orbit satellites," in *Proceedings of International Conference on P2P, Parallel, Grid, Cloud and Internet Computing*, 2022, pp. 278–287.

[15] M. Hartnett, "Performance assessment of navigation using carrier Doppler measurements from multiple LEO constellations," Master's thesis, Air Force Institute of Technology, Ohio, USA, 2022.

[16] H. More, E. Cianca, and M. Sanctis, "Positioning performance of LEO mega constellations in deep urban canyon environments," in *Proceedings of International Symposium on Wireless Personal Multimedia Communications*, 2022, pp. 256–260.

[17] R. Sabbagh and Z. Kassas, "Observability analysis of receiver localization via pseudorange measurements from a single LEO satellite," *IEEE Control Systems Letters*, vol. 7, no. 3, pp. 571–576, 2023.

[18] H. Kanamori, K. Kobayashi, and N. Kubo, "A map-matching based positioning method using Doppler tracking and estimation by a software-defined receiver for multi-constellation LEO satellites," in *Proceedings of ION International Technical Meeting*, January 2023, pp. 649–663.

[19] T. Reid, A. Neish, T. Walter, and P. Enge, "Broadband LEO constellations for navigation," *NAVIGATION, Journal of the Institute of Navigation*, vol. 65, no. 2, pp. 205–220, 2018.

[20] C. Ardito, J. Morales, J. Khalife, A. Abdallah, and Z. Kassas, "Performance evaluation of navigation using LEO satellite signals with periodically transmitted satellite positions," in *Proceedings of ION International Technical Meeting Conference*, 2019, pp. 306–318.

[21] A. Nardin, F. Dovis, and J. Fraire, "Empowering the tracking performance of LEO-based positioning by means of meta-signals," *IEEE Journal of Radio Frequency Identification*, vol. 5, no. 3, pp. 244–253, 2021.

[22] J. Ji, Y. Liu, W. Chen, D. Wu, H. Lu, and J. Zhang, "A novel signal design and performance analysis in NavCom based on LEO constellation," *Sensors*, vol. 21, no. 23, pp. 8235–8262, December 2021.

[23] S. Bilardi, "A GNSS signal simulator and processor for evaluating acquisition and tracking of GPS-like signals from satellites in LEO," Master's thesis, University of Colorado at Boulder, CO, USA, 2021.

[24] D. Egea-Roca, J. Lopez-Salcedo, G. Seco-Granados, and E. Falletti, "Performance analysis of a multi-slope chirp spread spectrum signal for PNT in a LEO constellation," in *Proceedings of Workshop on Satellite Navigation Technology*, September 2022, pp. 1–9.

[25] P. Iannucci and T. Humphreys, "Fused low-Earth-orbit GNSS," *IEEE Transactions on Aerospace and Electronics Systems*, 2022, accepted.

[26] R. Cassel, D. Scherer, D. Wilburne, J. Hirschauer, and J. Burke, "Impact of improved oscillator stability on LEO-based satellite navigation," in *Proceedings of ION International Technical Meeting*, January 2022, pp. 893–905.

[27] D. Racelis, B. Pervan, and M. Joerger, "Fault-free integrity analysis of mega-constellation-augmented GNSS," in *Proceedings of ION GNSS Conference*, January 2019, pp. 465–484.

[28] M. Li, T. Xu, M. Guan, F. Gao, and N. Jiang, "LEO-constellation-augmented multi-GNSS real-time PPP for rapid re-convergence in harsh environments," *GPS Solutions*, vol. 26, no. 1, pp. 1–12, 2022.

[29] K. Wang, A. El-Mowafy, W. Wang, L. Yang, and X. Yang, "Integrity monitoring of PPP-RTK positioning; part II: LEO augmentation," *Remote Sensing*, vol. 14, no. 7, pp. 1599–1620, March 2022.

[30] K. Wang, J. Liu, H. Su, A. El-Mowafy, and X. Yang, "Real-time LEO satellite orbits based on batch least-squares orbit determination with short-term orbit prediction," *Remote Sensing*, vol. 15, no. 1, pp. 133–153, December 2022.

[31] M. Jiang, H. Qin, C. Zhao, and G. Sun, "LEO Doppler-aided GNSS position estimation," *GPS Solutions*, vol. 26, no. 1, pp. 1–18, 2022.

[32] J. Muyuan, Q. Honglei, C. Zhao, and S. Guiyu, "LEO Doppler-aided GNSS position estimation," *GPS Solutions*, vol. 26, no. 1, pp. 1–18, 2022.

[33] M. Jiang, H. Qin, Y. Su, F. Li, and J. Mao, "A design of differential-low Earth orbit opportunistically enhanced GNSS (D-LoeGNSS) navigation framework," *Remote Sensing*, vol. 15, no. 8, pp. 2136–2158, April 2023.

[34] M. Leng, F. Quitin, W. Tay, C. Cheng, S. Razul, and C. See, "Anchor-aided joint localization and synchronization using SOOP: Theory and experiments," *IEEE Transactions on Wireless Communications*, vol. 15, no. 11, pp. 7670–7685, November 2016.

[35] F. Farhangian and R. Landry, "Multi-constellation software-defined receiver for Doppler positioning with LEO satellites," *Sensors*, vol. 20, no. 20, pp. 5866–5883, October 2020.

[36] U. Singh, M. Shankar, and B. Ottersten, "Opportunistic localization using LEO signals," in *Proceedings of Asilomar Conference on Signals, Systems, and Computers*, 2022, pp. 894–899.

[37] C. Huang, H. Qin, C. Zhao, and H. Liang, "Phase - time method: Accurate Doppler measurement for Iridium NEXT signals," *IEEE Transactions on Aerospace and Electronic Systems*, vol. 58, no. 6, pp. 5954–5962, 2022.

[38] C. Zhao, H. Qin, and Z. Li, "Doppler measurements from multiconstellations in opportunistic navigation," *IEEE Transactions on Instrumentation and Measurement*, vol. 71, pp. 1–9, 2022.

[39] N. Jardak and R. Adam, "Practical use of Starlink downlink tones for positioning," *Sensors*, vol. 23, no. 6, pp. 3234–3253, March 2023.

[40] W. Stock, C. Hofmann, and A. Knopp, "LEO-PNT with Starlink: Development of a burst detection algorithm based on signal measurements," in *Proceedings of International ITG Workshop on Smart Antennas and Conference on Systems, Communications, and Coding*, February 2023, pp. 1–6.

[41] M. Neinavaie and Z. Kassas, "Unveiling Starlink LEO satellite OFDM-like signal structure enabling precise positioning," *IEEE Transactions on Aerospace and Electronic Systems*, 2023, accepted.

[42] T. Reid, T. Walter, P. Enge, D. Lawrence, H. Cobb, G. Gutt, M. O'Conner, and D. Whelan, "Position, navigation, and timing technologies in the 21st century," J. Morton, F. van Diggelen, J. Spilker, Jr., and B. Parkinson, Eds. Wiley-IEEE, 2021, vol. 2, ch. 43: Navigation from low Earth orbit – Part 1: concept, current capability, and future promise, pp. 1359–1379.

[43] Z. Kassas, "Position, navigation, and timing technologies in the 21st century," J. Morton, F. van Diggelen, J. Spilker, Jr., and B. Parkinson, Eds. Wiley-IEEE, 2021, vol. 2, ch. 43: Navigation from low Earth orbit – Part 2: models, implementation, and performance, pp. 1381–1412.

[44] Z. Kassas, M. Neinavaie, J. Khalife, N. Khairallah, J. Haidar-Ahmad, S. Kozhaya, and Z. Shadram, "Enter LEO on the GNSS stage: Navigation with Starlink satellites," *Inside GNSS Magazine*, vol. 16, no. 6, pp. 42–51, 2021.

[45] J. Khalife and Z. Kassas, "Performance-driven design of carrier phase differential navigation frameworks with megaconstellation LEO satellites," *IEEE Transactions on Aerospace and Electronic Systems*, pp. 1–20, 2023, accepted.

[46] C. Zhao, H. Qin, N. Wu, and D. Wang, "Analysis of baseline impact on differential doppler positioning and performance improvement method for LEO opportunistic navigation," *IEEE Transactions on Instrumentation and Measurement*, pp. 1–10, 2023.

[47] J. Saroufim, S. Hayek, and Z. Kassas, "Simultaneous LEO satellite tracking and differential LEO-aided IMU navigation," in *Proceedings of IEEE/ION Position Location and Navigation Symposium*, April 2023, accepted.

[48] Z. Kassas, N. Khairallah, and S. Kozhaya, "Ad astra: Simultaneous tracking and navigation with megaconstellation LEO satellites," *IEEE Aerospace and Electronic Systems Magazine*, 2023, accepted.

[49] D. Shen, J. Lu, G. Chen, E. Blasch, C. Sheaff, M. Pugh, and K. Pham, "Methods of machine learning for space object pattern classification," in *Proceedings of IEEE National Aerospace and Electronics Conference*, 2019, pp. 565–572.

[50] N. Khairallah and Z. Kassas, "Ephemeris closed-loop tracking of LEO satellites with pseudorange and Doppler measurements," in *Proceedings of ION GNSS Conference*, September 2021, pp. 2544–2555.

[51] J. Haidar-Ahmad, N. Khairallah, and Z. Kassas, "A hybrid analytical-machine learning approach for LEO satellite orbit prediction," in *Proceedings of International Conference on Information Fusion*, 2022, pp. 1–7.

[52] R. Deng, H. Qin, H. Li, D. Wang, and H. Lv, "Noncooperative LEO satellite orbit determination based on single pass Doppler measurements," *IEEE Transactions on Aerospace and Electronic Systems*, vol. 59, no. 2, pp. 1096–1106, April 2023.

[53] Z. Yang, H. Liu, C. Qian, B. Shu, L. Zhang, X. Xu, Y. Zhang, and Y. Lou, "Real-time estimation of low Earth orbit (LEO) satellite clock based on ground tracking stations," *Remote Sensing*, vol. 12, no. 12, pp. 2050–2067, June 2020.

[54] N. Khairallah and Z. Kassas, "An interacting multiple model estimator of LEO satellite clocks for improved positioning," in *Proceedings of IEEE Vehicular Technology Conference*, 2022, pp. 1–5.

[55] K. Wang and A. El-Mowafy, "LEO satellite clock analysis and prediction for positioning applications," *Geo-spatial Information Science*, vol. 25, no. 1, pp. 14–33, 2022.

[56] M. Neinavaie, J. Khalife, and Z. Kassas, "Cognitive opportunistic navigation in private networks with 5G signals and beyond," *IEEE Journal of Selected Topics in Signal Processing*, vol. 16, no. 1, pp. 129–143, 2022.

[57] S. Kozhaya, H. Kanj, and Z. Kassas, "Multi-constellation blind beacon estimation, Doppler tracking, and opportunistic positioning with OneWeb, Starlink, Iridium NEXT, and Orbcomm LEO satellites," in *Proceedings of IEEE/ION Position, Location, and Navigation Symposium*, April 2023, accepted.

[58] M. Orabi, J. Khalife, and Z. Kassas, "Opportunistic navigation with Doppler measurements from Iridium Next and Orbcomm LEO satellites," in *Proceedings of IEEE Aerospace Conference*, March 2021, pp. 1–9.

[59] J. Khalife, M. Neinavaie, and Z. Kassas, "The first carrier phase tracking and positioning results with Starlink LEO satellite signals," *IEEE Transactions on Aerospace and Electronic Systems*, vol. 56, no. 2, pp. 1487–1491, April 2022.

[60] J. Khalife, M. Neinavaie, and Z. Kassas, "Navigation with differential carrier phase measurements from megaconstellation LEO satellites," in *Proceedings of IEEE/ION Position, Location, and Navigation Symposium*, April 2020, pp. 1393–1404.

[61] M. Neinavaie, J. Khalife, and Z. Kassas, "Acquisition, Doppler tracking, and positioning with Starlink LEO satellites: First results," *IEEE Transactions on Aerospace and Electronic Systems*, vol. 58, no. 3, pp. 2606–2610, June 2022.

Correspondence

No GPS No Problem: Exploiting Cellular OFDM-Based Signals for Accurate Navigation

***Abstract*— This paper presents a receiver that could exploit downlink orthogonal frequency-division multiplexing (OFDM)-based cellular signals to navigate opportunistically to meter-level accuracy in a real-world GPS-denied environment. The proposed receiver exploits signals from multiple logical antenna ports simultaneously, which dramatically improves the receiver's sensitivity. The efficacy of the proposed receiver is demonstrated experimentally in an environment under intentional GPS jamming, in which the ground vehicle-mounted receiver navigated for 5 km in 180 seconds. The receiver was able to acquire and track signals from 7 long-term evolution (LTE) eNodeBs, one of which was more than 25 km away, achieving a two-dimensional position root mean-squared error (RMSE) of 2.6 m.**

***Index Terms*— Signals of opportunity, OFDM, cellular, navigation, GPS jamming.**

I. Introduction

The past decades witnessed extensive research to utilize cellular signals for navigation purposes. Among various cellular generations, 4G and 5G orthogonal frequency-division multiplexing (OFDM)-based systems have shown tremendous promise [1], [2]. Cellular navigation approaches can be categorized into: network-based and user-based. This paper considers the latter approach, in which the user equipment (UE) exploits downlink signals, in an opportunistic fashion, from any cellular provider without being a subscriber in the network.

Previous studies have demonstrated meter-level and submeter-level positioning accuracy on ground vehicles and unmanned aerial vehicles, respectively, with 4G and 5G signals [3]–[10], in which synchronization reference signals (RSs) were exploited to extract navigation observables [11], [12]. A particularly desirable RS for navigation is the cell-specific RS (CRS), due to its high bandwidth. Due to OFDM's spectral nature, the CRS is transmitted on distinct OFDM symbols and subcarriers, also known as logical ports. In [13], a maximum likelihood-based method to estimate the first path was proposed, which utilized one antenna port. Positioning in multipath environments was studied in [14] and [15], both of which

This work was supported in part by the Office of Naval Research under Grant N00014-19-1-2511, in part by the Air Force Office of Scientific Research (AFOSR) under Grant FA9550-22-1-0476, and in part by the U.S. Department of Transportation under Grant 69A3552047138 for the CARMEN University Transportation Center. DISTRIBUTION STATEMENT A. Approved for public release; Distribution is unlimited 412TW-PA-20399. Z. Kassas is with the Department of Electrical and Computer Engineering, The Ohio State University, Columbus, OH 43210, USA. A. Abdallah is with the Department of Electrical Engineering and Computer Science, University of California, Irvine, CA 92697, USA. *Corresponding author: Z. Kassas*, email: zkassas@ieee.org

0018-9251 © 2023 IEEE

considered one antenna port. A recent study developed a tracking algorithm that adaptively mitigated multipath in long-term evolution (LTE) positioning receivers, while utilizing CRS from one antenna port [4]. The effect of antenna ports on time-of-arrival (TOA) estimation using CRS was investigated in [16]. The study showed that different channel responses were recorded for different antenna ports, which can diversify the incoming signals and improve positioning. The signal diversity provided via multiple antenna ports was exploited for cycle slip detection in LTE carrier phase measurements in [3]. Exploiting two antenna ports was considered in [17], where signals from each port was treated as a separate measurements, while [18] tracked signals from each port independently. However, none of the aforementioned studies considered the *simultaneous* exploitation of *all* antenna ports as a *single* navigation source. In general, to extract navigation observables from OFDM signals, existing methods have approached the receiver design from a communication systems perspective [15].

This paper exploits additional LTE available resources in generating the receiver's locally generated code, which offers two advantages: (i) construct a pseudorandom noise (PRN)-like code that possesses a higher bandwidth; thus, improving the precision of TOA estimates and (ii) increase the power by exploiting more available resource elements. The acquisition of LTE signals can be modeled as a detection problem. Increasing the power results in an increase in the carrier-to-noise ratio (CNR), which in turn results in a better probability of detection. Moreover, in terms of estimation of the code and carrier phase, it is known that the phase estimation errors depends on the CNR and the correlation properties [19]. Exploiting the CRS corresponding to all the antenna ports results in less code and carrier phase error (better tracking performance), leading to more precise navigation observables.

This paper presents a novel opportunistic OFDM-based navigation receiver design that exploits all available resources from various antenna ports simultaneously. Unlike previous generation receivers, the proposed receiver exploits the orthogonality property of OFDM signals without the need for reconstructing the received OFDM frame. The proposed approach significantly improves the receiver's sensitivity, amplifying the received power by a factor up to 120, while also improving the carrier phase estimation accuracy. Experimental results in a real-world GPS-denied environment are presented to demonstrate the efficacy of the proposed receiver. A ground vehicle was driven at Edwards Air Force Base (AFB), California, USA, during NAVFEST: a live GPS jamming event with high-powered jammers transmitting a variety of waveforms at a jamming-to-signal ratio (J/S) exceeding 100 dB. A previous state-of-the-art LTE navigation receiver [20] was able to acquire and track only one LTE eNodeB as far as 5 km away, achieving a two-dimensional (2-D) position root mean-squared error (RMSE) of 29.4 m over a trajectory of 5 km [21]. In contrast, the proposed receiver was able to acquire and track 7 LTE eNodeBs with favorable geometry, one of which was more than 25 km away, achieving a 2-D position RMSE of 2.6 m. To the authors' knowledge, the proposed design represents the most sensitive OFDM receiver to-date, achieving unprecedented navigation accuracy in an exclusory GPS-denied environment.

This paper is structured as follows. Section II overviews the LTE OFDM frame structure and discusses the idea behind exploiting the transmitter's multiple antenna ports. Section III presents the proposed time-domain-based receiver design. Section IV shows experimental results in a real-world GPS-jammed environment, demonstrating the superiority of the proposed receiver to previous receiver design. Section V gives concluding remarks.

II. Frame Structure: Exploiting Multiple Antenna Ports

The third generation partnership project (3GPP) standard defines what is known as an antenna port for 4G LTE cellular system. Antenna ports do not necessarily correspond to physical antennas, but rather, they are logical entities distinguished by their reference sequences [22]. A single logical antenna port can include multiple RSs that correspond to the same physical antenna. Correspondingly, a single antenna port can be spread across multiple transmit antennas. The formal definition of an antenna port is: "An antenna port is defined such that the channel over which an OFDM symbol on the antenna port is conveyed can be inferred from the channel over which another symbol on the same antenna port is conveyed [23]." There is one resource grid per antenna port, and the antenna ports used for transmission of a physical channel or signal depends on the number of antenna ports configured for the physical channel or signal.

This paper proposes an opportunistic navigation approach; thus, it only considers the downlink signals, which use OFDM with cyclic prefix (CP) as its modulation. An LTE OFDM frame has a duration of 10 ms. The subcarrier spacing in LTE is fixed and defined as $\Delta f = 15$ kHz. In the time-domain, each subframe breaks down into multiple OFDM symbols. In the frequency-domain, a slot can be decomposed into multiple resource elements (REs). Thus, the subcarrier and symbol are the frequency and time indices of an RE, respectively. Further details about the LTE frame structure can be found in [20].

Fig. 1 shows CRS allocation within the LTE OFDM frame for all antenna ports. The number of subcarriers in an LTE frame, N_c, and the number of used subcarriers, N_r, are not unique and are assigned by the network provider. They can only take the values that are tabulated in Table I [23]. The subcarrier spacing is typically $\Delta f = 15$ kHz. Hence, the occupied bandwidth can be calculated using $W = N_r \Delta f$ (which, here, equals 20 MHz, after adding a 2 MHz guard band). The CRS spans the entire bandwidth of the 4G LTE system and is known to the UE. For CRS, the associated antenna ports p can be $p = 0$, $p \in \{0, 1\}$, or $p \in \{0, 1, 2, 3\}$. Although, by definition, different antenna ports do not have to correspond to different physical antennas for the

various LTE RSs, the CRS is a special RS that has a one-to-one mapping between logical and physical antennas. For LTE, there are 504 possible eNodeB physical Cell IDs, leading to 504 possible URS sequences resulting from the possible CRS sequences. In the proposed receiver, different sectors of the same eNodeB, i.e., Cell IDs with different primary synchronization signal (PSS) but the same secondary synchronization signal (SSS) are combined to form the proposed URS. In other words, the three sectors of a particular eNodeB will have one unique URS, which is generated once as a local code in the receiver. As a result, the correlation of signals coming from different sectors of a particular eNodeB with its corresponding locally generated URS can be considered as the coherent summation of the correlation of signals coming from every sector of a particular eNodeB with the locally generated URS.

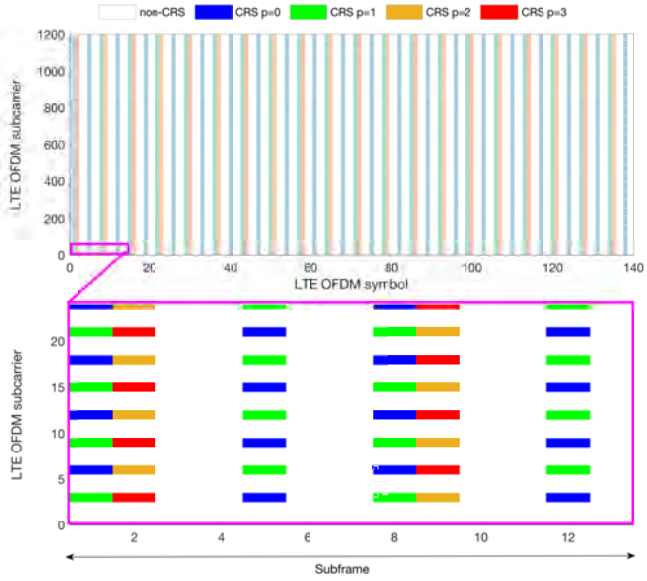

Fig. 1. CRS allocation within the LTE OFDM frame for all antenna ports. The vertical axes show the subcarrier index of each resource element, while the horizontal axes show the symbol index. In the lower figure, one subframe that consists of 14 symbols is zoomed upon to better illustrate the spread of CRS across subcarriers and symbols.

TABLE I
LTE System Bandwidths and Number of Subcarriers

Bandwidth (W) (MHz)	**Total number of subcarriers (N_c)**	**Number of subcarriers used (N_r)**
1.4	128	72
3	256	180
5	512	300
10	1024	600
15	1536	900
20	2048	1200

While previous work in the literature only exploited the CRS from one antenna port ($p = 0$), this paper exploits the CRS from all antenna ports $p \in \{0, 1, 2, 3\}$ simultaneously. This is achieved by adopting a novel representation of an OFDM frame to obtain navigation observables. Detecting active CRS subcarriers is a challenging problem that requires reconstructing the OFDM frame, while tracking the signal for each received frame. In conventional receivers, the timing sequences (PSS and SSS) are used to detect the OFDM frame start time. Then, the CRSs corresponding to one antenna port are detected in the frame and exploited for navigation. In general, conventional OFDM-based receivers in communication and navigation systems use the following steps for timing and synchronization: (i) estimation of the frame start time for each individual OFDM frame, (ii) reconstruction of the OFDM frame, (iii) detection of the CRS subcarriers, and (iv) exploiting the CRS to estimate the channel impulse response (for communication purposes) and provide the navigation observable, e.g., TOA (for navigation purposes). This paper proposes an unorthodox method to exploit the CRSs of different antenna ports for navigation purposes, which allows the receiver to track the code and carrier phase in a way that is similar to a GPS receiver. Recall that the GPS receiver regenerates a replica of the satellites' PRN code. Generating a PRN-like code in OFDM-based systems is more challenging: other CRSs corresponding to different antenna ports are spread among different subcarriers. The idea presented in this paper is to use the time series representation of an OFDM frame as a code (similar to GPS PRN). The time series representation of the OFDM frame should contain all the available resources (including the PSS, SSS, and CRSs corresponding to all antenna ports), and is referred to as the ultimate reference signal (URS). In this paper, in order to generate the URS, the subcarriers corresponding to all antenna ports are used. After reconstruction of the OFDM frame (which is performed only once at the receiver) and considering all the available resource elements, including the CRSs corresponding to all antenna ports, the time representation of the frame (i.e., the URS) is used as a PRN-like code in the GPS-like tracking loops. The phase-locked-loop (PLL) and the delay-locked loop (DLL) track the carrier and code phases of the URS, respectively, eliminating the need to reconstruct the frame and detect the CRS at every time epoch corresponding to the frame start time.

In state-of-the-art opportunistic LTE receiver in [20], only one OFDM symbol of the CRS resources corresponding to $p = 0$ was exploited, as shown in blue in Fig. 1. Two metrics are defined to compare state-of-the-art receiver with the proposed receiver

- $r_{\mathrm{B,RS}}$: bandwidth ratio of the RS versus the entire downlink bandwidth of the LTE signal. Higher $r_{\mathrm{B,RS}}$ means narrower autocorrelation function (ACF), which results in more precise TOA estimation.
- $r_{\mathrm{T,RS}}$: duty factor, i.e., the percentage of time in which the RS is active. Higher $r_{\mathrm{T,RS}}$ results in a more accurate carrier phase and Doppler estimation.

The state-of-the-art receiver has $r_{\mathrm{T,CRS}} = \frac{1}{140} = 0.71\%$ (only one OFDM symbol is active), where 140 is the total number of OFDM symbols in an OFDM

frame. In the proposed approach, the various available ports are utilized. The combined CRSs from different antenna ports define the so-called URS. In other words, the combined OFDM REs depicted in Fig. 1 represent the URS. To study the spectral efficiency $r_{\mathrm{B,URS}}$ and duty factor $r_{\mathrm{T,URS}}$ of the URS, the number of active subcarriers and symbols were obtained from the URS frame structure, as shown in Fig. 2.

Assuming a URS symbol is active if 10 or more subcarriers are active within that OFDM symbol results in having 60 active symbols; hence, $r_{\mathrm{T,URS}} = \frac{60}{140} = 42.86\%$ (in contrast to $r_{\mathrm{T,CRS}} = 0.71\%$). For the bandwidth ratio, Fig. 2 shows that $r_{\mathrm{B,URS}} = r_{\mathrm{B,CRS}} = 100\%$. Therefore, one concludes the following advantages of the proposed URS:

- The proposed URS exploits 24,000 REs compared to 200 REs in past receivers, which means the received *power* is amplified by a factor up to $120 \approx 21$ dB. Fig. 3 shows the relative normalized magnitude of the CRS-based and the proposed URS-based squared ACF, assuming unity equivalent power among all REs. The gain factor results in $r_{\mathrm{gain}} \approx \sqrt{\frac{1}{6.29687\times10^{-5}}} = 126.02$. This gain increase is due to the additional CP REs before converting the frame to serial data by taking the inverse fast Fourier transform (IFFT) of each OFDM symbol.
- The proposed URS improves the duty cycle by a factor of 60, which improves the carrier phase estimation accuracy and initial Doppler shift estimation.

Essentially, exploiting more REs in the time-domain has a direct impact on increasing the accuracy of code phase estimation. In the DLL tracking loop, the correlation between the received signal and the URS updates the prompt correlations whose phase has a direct impact on the performance of the PLL tracking loop from which carrier phase is estimated. As such, higher duty cycle improves the accuracy of the carrier phase estimation, leading to less carrier phase error. Besides, increasing the duty factor, i.e., exploiting more symbols in the URS, results in accumulating more power. Increasing the power results in an increase in the CNR, which in turn results in improving the probability of detection. Moreover, in terms of estimating the code and carrier phase, it is known that phase estimation error depend on the CNR and correlation properties [17]. Exploiting the CRS corresponding to all antenna ports results in higher duty factor, which yields less code and carrier phase errors.

III. Proposed Time-Domain Receiver

This section presents a time-domain-based receiver that operates on the proposed URS to exploit time orthogonality and extract navigation observables from the received LTE signals. State-of-the-art LTE navigation receivers only consider the orthogonality of the synchronization and channel estimation RSs in the frequency-domain, i.e., the transmitted OFDM frame is always

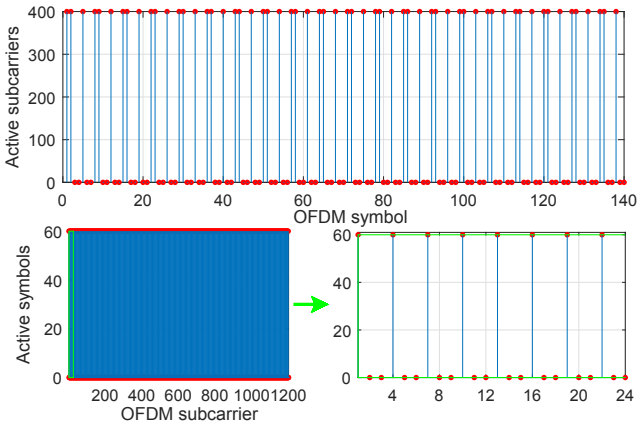

Fig. 2. Top: number of active subcarriers for each URS symbol. Bottom: number of active symbols for each URS subcarrier.

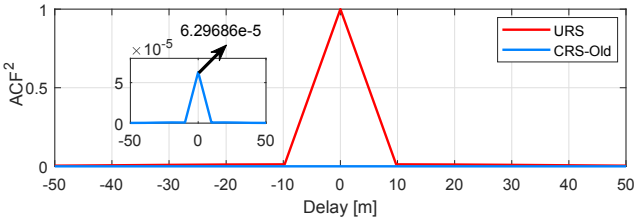

Fig. 3. Comparison of CRS-based and proposed URS-based ACF.

reconstructed from the received time-domain serial data. Then, the navigation observables are estimated by utilizing the RS with the highest bandwidth. This approach was adopted from a communication perspective, in which it is necessary to reconstruct the OFDM frame to extract various system information, which allows two-ways communication between the UE and the eNodeB. However, for opportunistic UE-based navigation, the ultimate goal is to obtain navigation observables by utilizing the most available frequency (bandwidth) and time (duty factor) resources in the received signal. The proposed receiver exploits all available REs, which are combined and used simultaneously in a time-domain-based URS denoted by $\boldsymbol{URS}_i^t$, where i is the eNodeB physical Cell ID. The rest of the section presents: (i) URS generation and (ii) receiver stages: acquisition and tracking.

A. URS Generation

In the frequency-domain, the CRS sequences corresponding to different antenna ports and subframes are generated and mapped to the OFDM frame according to Section 6.10.1 in [24]. After allocating all CRS REs in the OFDM frame and assigning zero to the rest of REs. The resulting frame represents the frequency-domain URS denoted as $\mathbf{URS}_i^f$. The $\mathbf{URS}_i^f$ is converted into a serial time-domain-based sequence $\boldsymbol{URS}_i^t$ by zero-padding $\frac{1}{2}N_{\mathrm{RB}}^{\max,\mathrm{DL}} - N_{\mathrm{RB}}^{\mathrm{DL}}$ REs on both sides of the signals in the frequency-domain. Then, the IFFT is taken, and the CP elements are added, which are nothing but an identical copy of the portion of the OFDM symbol ap-

pended before the OFDM symbol to prevent intersymbol interference (ISI). This procedure is the exact procedure occurring at the eNodeB, except for having zeros instead of having data in the data allocated REs, which is a necessary condition to prevent interference and guarantee orthogonality of the $\boldsymbol{URS}_i^t$.

B. Acquisition and Tracking

After generating the URS, acquisition is performed to determine eNodeBs in the UE's proximity and find their corresponding coarse estimates of code phase and Doppler shift. Next, GPS-like receiver tracking loops (as in [25]) can be employed to refine these estimates and produce navigation observables. This can be done by essentially replacing the GPS code generator by the URS generator.

IV. Experimental Results

This section presents an experimental demonstration of the proposed receiver mounted on a ground vehicle navigating in a real-world GPS-denied environment. A mapping campaign was conducted before the experiment to locate LTE eNodeBs in the environment. The vehicle was driven in the Mojave Desert at Edwards AFB, California, USA, during the intentional GPS jamming exercises, known as NAVFEST. The vehicle's trajectory was composed of three segments: (A) GPS signals were available (0–40 seconds; 1.1 km), (B) GPS signals were intermittent (40–50 seconds; 0.4 km), and (C) GPS signals were not available (50–180 seconds; 3.5 km).

A. Hardware Setup

Six high-power jammers and one portable box jammer were spread over an area of approximately 50 miles north of Edwards AFB. Fig. 4 shows the J/S heatmap; which actually extends outside the depicted rectangle; however, this was the only data provided by Edwards AFB.

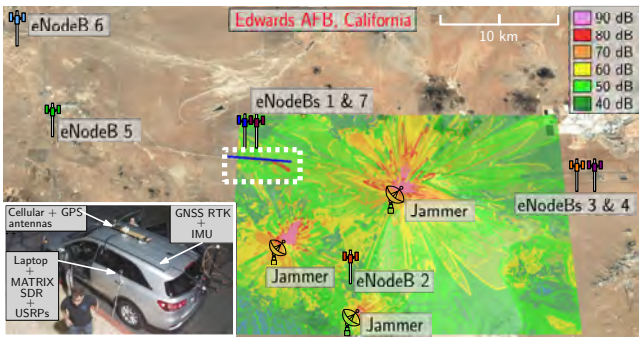

Fig. 4. Environment layout and J/S heatmap. The ground vehicle vehicle's trajectory is within the dashed white rectangle.

The ground vehicle, shown in Fig. 4, was equipped with a National Instrument (NI) universal software radio peripheral (USRP), two consumer-grade Laird cellular antennas, PCIe cable, laptop, and a Septentrio GNSS-inertial measurement unit (IMU) system, comprising a multi-frequency GNSS AsteRx-i V receiver, an industrial-grade Vectornav VN-100 micro-electromechanical system (MEMS) IMU, and a dual-GNSS antenna system. The vehicle-mounted GNSS-IMU was used to obtain the vehicle's ground truth trajectory, utilizing signals from non-jammed GNSS constellations (Galileo and GLONASS). The USRP utilized a GNSS-disciplined oscillator (GNSSDO) and was tuned to listen to two carrier frequencies corresponding to the U.S. cellular providers: Verizon Wireless and T-Mobile, as tabulated in Table II.

TABLE II
eNodeBs' Characteristics

eNodeB	Carrier frequency	Cell ID	Cellular provider
1	751 MHz	417	Verizon
2	751 MHz	399	Verizon
3	751 MHz	393	Verizon
4	751 MHz	402	Verizon
5	2145 MHz	186	T-Mobile
6	2145 MHz	195	T-Mobile
7	2145 MHz	489	T-Mobile

B. Tracking Results

The receiver discussed in Section III was used to acquire and track signals from 7 LTE eNodeBs (see Fig. 4). A second-order PLL with bandwidth of 6 Hz was employed to track the carrier phase, and a carrier-aided DLL whose loop filter is a simple gain $K = 0.2$ was used to track the code phase.

Fig. 5 shows the code phase tracking error. From Table II and Fig. 5, it can be inferred that the receiver was able to track LTE signals at 751 MHz and 2145 MHz, with the tracking loops failing to track as the receiver drove further away from the eNodeBs. It is worth noting that not all seven eNodeBs were continuously tracked along the entire trajectory. In particular, while eNodeB 1, 2, and 7 were continuously tracked along the receiver's trajectory, eNodeBs 5 and 6 were tracked during the earlier part of the trajectory, while eNodeBs 3 and 4 were tracked during the latter part of the trajectory.

Fig. 6 shows the tracking results: (i) CNR, (ii) pseudorange estimates versus expected ranges (the latter calculated from the receiver's ground truth trajectory and eNodeBs' positions), and (iii) range error (i.e., difference between pseudorange and range). The CNR is calculated from CNR $= \frac{P_r - N0}{N_0 T}$, where P_r, N_0, and T denote the received signal power, noise power, and subaccumulation time interval, which is set to the LTE frame duration.

From Fig. 6(a), it can be seen that the CNR for tracked eNodeBs is about 50 dB-Hz, with some of the closer eNodeBs having a CNR exceeding 75 dB-Hz. The intermittency in tracking is due to the receiver tracking loops failing to acquire/track all eNodeBs along the entire trajectory. From Fig. 6(b), it can be seen that eNodeBs 3 and 6 were tracked, while being 25.5 km and 23.6 km, respectively, away from the vehicle. The drift in the range error in Fig. 6(c) is due to the combined receiver–eNodeB's clock error, which is dominated by

the eNodeB's clock error, since the receiver possessed a GNSSDO. These drifts are indicative of the eNodeBs being equipped with high-quality oven-controlled crystal oscillators (OCXOs). The correlatedness observed among some of the eNodeBs could be due to the "loose" network synchronization: eNodeBs need to be synchronized, as per the 3GPP standards, with certain eNodeBs tend to exhibit tighter synchronization, forming so-called "clusters" [6]. It is worth noting in Fig. 6(c) starting segment (C), which is when GPS signals become completely unavailable, there seems to be an "inflection" point impacting the range error. It is speculated that this is due to the jamming impact on eNodeBs' clocks; however, it is difficult to assert such statement.

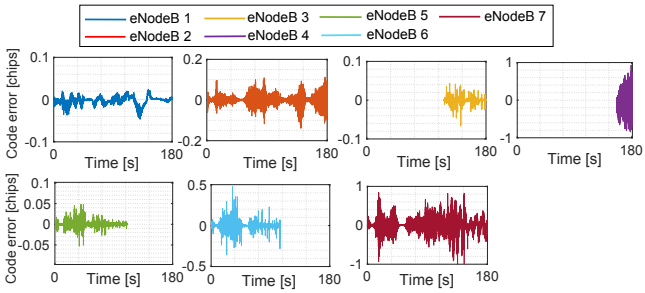

Fig. 5. Cellular LTE code phase tracking error results.

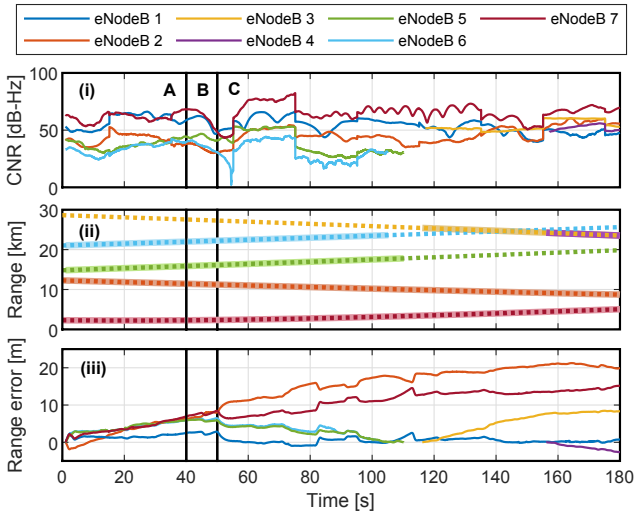

Fig. 6. Cellular LTE tracking results: (i) CNR, (ii) pseudorange estimates in solid lines versus expected ranges in dashed lines (after removing the initial biases), and (iii) range error.

C. Navigation Solution

The navigation filter fused code phase measurements from all eNodeBs via an extended Kalman filter (EKF) to estimate the vehicle-mounted receiver's 3-D position $\boldsymbol{r}_r$ and velocity $\dot{\boldsymbol{r}}_r$ and relative clock bias and drift between the receiver's and eNodeBs' clocks $\{\delta t_r - \delta t_{s,u}\}_{u=1}^{7}$ and $\{\dot{\delta} t_r - \dot{\delta} t_{s,u}\}_{u=1}^{7}$, respectively. As observed in [21], and due to high vertical dilution of precision when using terrestrial eNodeBs alone, the vertical estimation error was much higher than horizontal errors. As such, 2-D navigation errors are reported and compared with those achieved in [21]. The EKF dynamics and measurement models are described in [21]. Using expressions relating CNR to measurement noise variances [20], the variances were found to vary between 0.2 – 22 m^2.

After traversing a trajectory of 5 km in 180 seconds, a 2-D position RMSE of 2.6 m and a 2-D maximum error of 4.5 m were achieved using only LTE signals, without using other sensors (see Fig. 7). This unprecedented accuracy is an order of magnitude lower than previously published results in the same environment and same collected raw LTE in-phase and quadrature samples, in which a 2-D position RMSE of 29.4 m was achieved [21]. While the state-of-the-art receiver in [21] was only able to acquire and track the 5 km-away eNodeB 1, the proposed receiver acquired and tracked weaker signals from eNodeBs 2–6. The GPS-IMU navigation solution exhibited a position RMSE of 237.9 m.

Zaher M. Kassas, Senior Member, IEEE
The Ohio State University, USA

Ali Abdallah
University of California, Irvine, USA

V. Conclusion

A high-sensitivity receiver was presented, which could exploit downlink OFDM-based cellular signals from multiple logical antenna ports simultaneously. The efficacy of the receiver was demonstrated in a real-world GPS-denied environment, in which the receiver produced pseudorange estimates to 7 LTE eNodeBs. The pseudoranges were fused via an EKF to navigate a ground vehicle for 5 km in 180 seconds, achieving a two-dimensional position RMSE of 2.6 m. One of the eNodeBs was more than 25 km away. It is worth highlighting that while cellular frequencies were not directly jammed, it is known that cellular infrastructure timing is disciplined to GPS/GNSS timing. Nevertheless, despite GPS jamming, the cellular signals were profitably exploitable via the proposed receiver, while the timing of each cellular transmitter was estimated via the navigation filter. This enabled the vehicle to navigate to an unprecedented level of accuracy without GNSS signals. This paper justified conclusively "No GPS, No Problem."

Acknowledgment

The authors would like to thank Mr. Chiawei Lee at Edwards AFB for inviting the ASPIN Laboratory to conduct experiments during NAVFEST. The authors would like to thank Shaghayegh Shahcheraghi, Mohammad Neinavaie, and Joe Khalife for insightful discussions and Joshua Morales, Kimia Shamaei, Mahdi Maaref, Kyle Semelka, MyLinh Nguyen, and Trier Mortlock for their help with data collection.

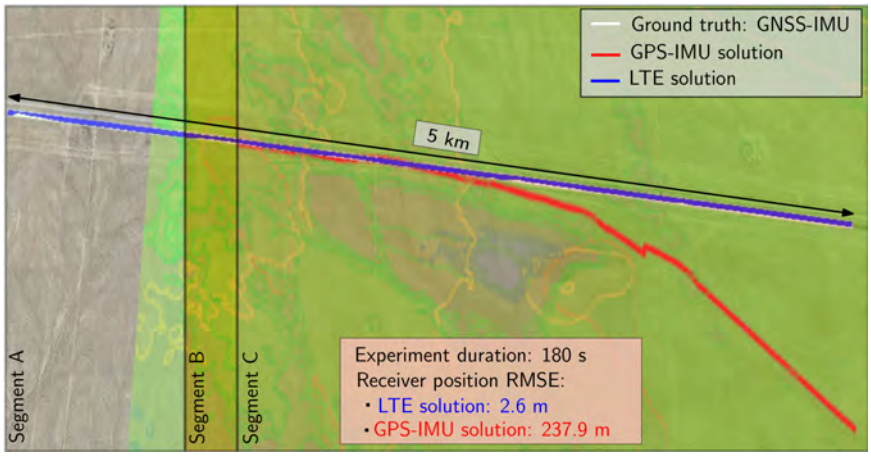

Fig. 7. Navigation solutions of GNSS-IMU, GPS-IMU, and cellular LTE. Map data: Google Earth.

REFERENCES

[1] J. del Peral-Rosado, R. Raulefs, J. Lopez-Salcedo, and G. Seco-Granados, "Survey of cellular mobile radio localization methods: from 1G to 5G," *IEEE Communications Surveys & Tutorials*, vol. 20, no. 2, pp. 1124–1148, 2018.

[2] G. Fokin and D. Volgushev, "Software-defined radio network positioning technology design. problem statement," in *Proceedings of Systems of Signals Generating and Processing in the Field of on Board Communications*, March 2022, pp. 1–6.

[3] K. Shamaei and Z. Kassas, "Sub-meter accurate UAV navigation and cycle slip detection with LTE carrier phase," in *Proceedings of ION GNSS Conference*, September 2019, pp. 2469–2479.

[4] P. Wang, Y. Wang, and J. Morton, "Signal tracking algorithm with adaptive multipath mitigation and experimental results for LTE positioning receivers in urban environments," *IEEE Transactions on Aerospace and Electronic Systems*, vol. 58, no. 4, pp. 2779–2795, August 2022.

[5] R. Whiton, J. Chen, T. Johansson, and F. Tufvesson, "Urban navigation with LTE using a large antenna array and machine learning," in *Proceedings of IEEE Vehicular Technology Conference*, 2022, pp. 1–5.

[6] J. Khalife and Z. Kassas, "On the achievability of submeter-accurate UAV navigation with cellular signals exploiting loose network synchronization," *IEEE Transactions on Aerospace and Electronic Systems*, vol. 58, no. 5, pp. 4261–4278, October 2022.

[7] L. Chen, X. Zhou, F. Chen, L. Yang, and R. Chen, "Carrier phase ranging for indoor positioning with 5G NR signals," *IEEE Internet of Things Journal*, vol. 9, no. 13, pp. 10 908–10 919, July 2022.

[8] J. Khalife and Z. Kassas, "Differential framework for submeter-accurate vehicular navigation with cellular signals," *IEEE Transactions on Intelligent Vehicles*, vol. 8, no. 1, pp. 732–744, January 2023.

[9] A. Abdallah and Z. Kassas, "Opportunistic navigation using sub-6 GHz 5G downlink signals: A case study on a ground vehicle," in *Proceedings of European Conference on Antennas and Propagation*, 2022, pp. 1–5.

[10] J. Tian, L. Fangchi, T. Yafei, and L. Dongmei, "Utilization of non-coherent accumulation for LTE TOA estimation in weak LOS signal environments," *EURASIP Journal on Wireless Communications and Networking*, vol. 2023, no. 1, pp. 1–31, 2023.

[11] A. Soderini, P. Thevenon, C. Macabiau, L. Borgagni, and J. Fischer, "Pseudorange measurements with LTE physical channels," in *Proceedings of ION International Technical Meeting*, January 2020, pp. 817–829.

[12] I. Lapin, G. Seco-Granados, O. Renaudin, F. Zanier, and L. Ries, "Joint delay and phase discriminator based on ESPRIT for 5G NR positioning," *IEEE Access*, vol. 9, pp. 126 550–126 563, 2021.

[13] W. Xu, M. Huang, C. Zhu, and A. Dammann, "Maximum likelihood TOA and OTDOA estimation with first arriving path detection for 3GPP LTE system," *Transactions on Emerging Telecommunications Technologies*, vol. 27, no. 3, pp. 339–356, 2016.

[14] P. Wang and Y. Morton, "Multipath estimating delay lock loop for LTE signal TOA estimation in indoor and urban environments," *IEEE Transactions on Wireless Communications*, vol. 19, no. 8, pp. 5518–5530, 2020.

[15] H. Dun, C. Tiberius, and G. Janssen, "Positioning in a multipath channel using OFDM signals with carrier phase tracking," *IEEE Access*, vol. 8, pp. 13 011–13 028, 2020.

[16] C. Yang, T. Pany, and P. Weitkemper, "Effect of antenna ports on TOA estimation with 4G LTE signals in urban mobile environments," in *Proceedings of ION GNSS+ Conference*, January 2020, pp. 2166–2181.

[17] M. Driusso, C. Marshall, M. Sabathy, F. Knutti, H. Mathis, and F. Babich, "Vehicular position tracking using LTE signals," *IEEE Transactions on Vehicular Technology*, vol. 66, no. 4, pp. 3376–3391, April 2017.

[18] I. Lapin, G. Granados, J. Samson, O. Renaudin, F. Zanier, and L. Ries, "STARE: Real-time software receiver for LTE and 5G NR positioning and signal monitoring," in *Proceedings of Workshop on Satellite Navigation Technology*, April 2022, pp. 1–11.

[19] E. Kaplan and C. Hegarty, *Understanding* GPS/GNSS*: Principles and applications*, 3rd ed. Artech House, 2017.

[20] K. Shamaei and Z. Kassas, "LTE receiver design and multipath analysis for navigation in urban environments," *NAVIGATION, Journal of the Institute of Navigation*, vol. 65, no. 4, pp. 655–675, December 2018.

[21] Z. Kassas, J. Khalife, A. Abdallah, and C. Lee, "I am not afraid of the GPS jammer: resilient navigation via signals of opportunity in GPS-denied environments," *IEEE Aerospace and Electronic Systems Magazine*, vol. 37, no. 7, pp. 4–19, July 2022.

[22] 3GPP, "Evolved universal terrestrial radio access (E-UTRA); user equipment (UE) radio transmission and reception," 3rd Generation Partnership Project (3GPP), TS 136.101, June 2011. [Online]. Available: http://www.3gpp.org/ftp/Specs/html-info/36212.htm

[23] 3GPP, "Evolved universal terrestrial radio access (E-UTRA); physical channels and modulation," 3rd Generation Partnership Project (3GPP), TS 36.211, January 2011. [Online]. Available: http://www.3gpp.org/ftp/Specs/html-info/36211.htm

[24] 3GPP, "LTE; evolved universal terrestrial radio access (E-UTRA); physical channels and modulation," 3rd Generation Partnership Project (3GPP), TS 36.211, May 2019.

[25] M. Braasch and A. Dempster, "Tutorial: GPS receiver architectures, front-end and baseband signal processing," *IEEE Aerospace and Electronic Systems Magazine*, vol. 34, no. 2, pp. 20–37, 2019.

Observability Analysis of Opportunistic Receiver Localization with LEO Satellite Pseudorange Measurements

Ralph Sabbagh, *University of California, Irvine*
Zaher M. Kassas, *The Ohio State University*

BIOGRAPHY

Ralph Sabbagh is a Ph.D. student in the Department of Mechanical and Aerospace Engineering at the University of California, Irvine and a member of the Autonomous Systems Perception, Intelligence, and Navigation (ASPIN) Laboratory. He received a B.E. in Mechanical Engineering with High Distinction from the American University of Beirut. His research interests include satellite-based opportunistic navigation and estimation theory.

Zaher (Zak) M. Kassas is a Professor at The Ohio State University and director of the Autonomous Systems Perception, Intelligence, and Navigation (ASPIN) Laboratory. He is also director of the U.S. Department of Transportation Center: CARMEN (Center for Automated Vehicle Research with Multimodal AssurEd Navigation), focusing on navigation resiliency and security of highly automated transportation systems. He received a B.E. in Electrical Engineering from the Lebanese American University, an M.S. in Electrical and Computer Engineering from The Ohio State University, and an M.S.E. in Aerospace Engineering and a Ph.D. in Electrical and Computer Engineering from The University of Texas at Austin. He is a recipient of the 2018 National Science Foundation (NSF) CAREER award, 2019 Office of Naval Research (ONR) Young Investigator Program (YIP) award, 2022 Air Force Office of Scientific Research (AFOSR) YIP award, 2018 IEEE Walter Fried Award, 2018 Institute of Navigation (ION) Samuel Burka Award, and 2019 ION Col. Thomas Thurlow Award. He is a Senior Editor of the IEEE Transactions on Intelligent Vehicles and an Associate Editor of the IEEE Transactions on Aerospace and Electronic Systems and the IEEE Transactions on Intelligent Transportation Systems. His research interests include cyber-physical systems, navigation systems, autonomous vehicles, and intelligent transportation systems.

ABSTRACT

An observability analysis of terrestrial receiver localization via pseudorange measurements extracted from a single low Earth orbit (LEO) satellite is presented. It is concluded that a stationary receiver with an unknown state (position and time) can localize itself with measurements from a LEO satellite with a known state (position, velocity, and time). In addition, bounds on the determinant of the observability matrix are derived. The relationship between the satellite's relative orbital inclination angle and geometric diversity of the line-of-sight vectors from the receiver to the satellite is analyzed, leading to geometric interpretations indicating directions of poor observability. Experimental results are presented showcasing the conclusions of the observability analysis for a receiver localizing itself with a single Starlink LEO satellite or a single Orbcomm LEO satellite. Finally, an observability-aided LEO satellite selection strategy is discussed.

I. INTRODUCTION

We are witnessing the era of Low Earth orbit (LEO) satellite megaconstellations (Reid et al., 2020; Kulu, 2021). These megaconstellations promise to revolutionize several domains, bringing unprecedented high-resolution images; remote sensing; and global, high-availability, high-bandwidth, and low-latency Internet (Liu et al., 2021; Judice et al., 2022; Okasha et al., 2022). Due to LEO satellites' inherently desirable attributes (Kassas et al., 2019), namely: (i) geometric and spectral diversity, (ii) abundance, (iii) high received signal power, and (iv) high orbital velocity, LEO satellites offer an attractive alternative to global navigation satellite systems (GNSS), which reside in medium Earth orbit (MEO) (Reid et al., 2021; Kassas, 2021; Prol et al., 2022; Jardak and Jault, 2022). The promise of utilizing LEO satellites for navigation has been the subject of numerous recent theoretical (Wei et al., 2020; Thompson et al., 2020; Psiaki, 2021; Nardin et al., 2021; Hartnett, 2022; Cassel et al., 2022; Jiang et al., 2022; Iannucci and Humphreys, 2022; Elgamoudi et al., 2020) and experimental (Tan et al., 2019; Farhangian and Landry, 2020; Farhangian et al., 2021; Wang and El-Mowafy, 2022; Huang et al., 2022; Li et al., 2022; Khalife et al., 2022; Neinavaie et al., 2022; Zhao et al., 2022) studies.

LEO satellites orbit the Earth at much higher rates than GNSS satellites. Contrast, for example, the orbital period of a GPS MEO satellite (11 hr, 58 min) with that of Orbcomm LEO satellites (about 99 min) and Starlink LEO satellites (about 96 min). This yields significant change in their geometry, which can be exploited to localize a terrestrial receiver with fewer satellites. In

particular, while four GNSS satellites are needed to estimate the states of the receiver via a static estimator (e.g., nonlinear least squares), a single LEO satellite can be used to localize the receiver via a dynamic estimator (e.g., an extended Kalman filter (EKF)) by fusing consecutive LEO measurements taken over a relatively short period of time. A few studies demonstrating the impact of receiver localization using a small number of satellites have been conducted in the literature. In (Pike et al., 2022), pseudorange and Doppler measurements were combined for stationary receiver positioning using two and three satellites without the use of a base station or differential positioning techniques.

Observability analysis with LEO satellites has been studied in the context of space situational awareness with relative position measurements (Ou and Zhang, 2018; Yong and Zhang, 2019; Friedman, 2020) and orbit determination with angles-only measurements (Kaufman et al., 2016; Sullivan et al., 2018; Friedman and Frueh, 2021). Moreover, observability of *planar* environments comprising terrestrial transmitters with unknown positions and time have been studied in (Kassas and Humphreys, 2012), where estimability was *numerically* assessed from the EKF's estimation error covariance, and in (Morales and Kassas, 2019), where the Riccati equation was analyzed to conclude that *simultaneously* estimating the receiver's and transmitter's time is stochastically unobservable. However, observability analysis with a small number of LEO satellites in the context of localization has not been thoroughly studied. In (Sabbagh and Kassas, 2023), an observability analysis of *three-dimensional* receiver localization via pseudorange measurements extracted from the signals of a single LEO satellite was conducted. It was shown that a stationary receiver with an unknown state (position and time) can theoretically localize itself with a LEO satellite with a known state (position, velocity, and time). In addition, *analytical* bounds on the determinant of the l-step observability matrix were derived indicating directions of poor observability. It was concluded that the system becomes unobservable if the receiver is in the satellite's orbital plane or along the normal to the satellite's orbital plane.

This paper aims to summarize the results presented in (Sabbagh and Kassas, 2023), with an emphasis on the implications of the analysis on observability-aided LEO satellite selection. Namely, empirical surface plots of the observability matrix can aid in selecting the satellite with desired (i) visibility duration, (ii) elevation profile, and (iii) altitude and relative orbital inclination angle. Finally, experimental results are presented showcasing the conclusions of the observability analysis for a receiver localizing itself with a single Starlink satellite or a single Orbcomm satellite.

The remainder of the paper is organized as follows. Section II describes the dynamics and measurement models. Section III analyzes analytically the observability of receiver localization using pseudorange measurements from a single LEO satellite and gives geometric interpretations of the derived results. Section IV presents experimental results with Orbcomm and Starlink LEO satellites, demonstrating the implications of the observability analysis on the estimation performance. Section V presents a discussion on observability-aided LEO satellite selection for improved receiver localization.

II. PRELIMINARIES AND MODEL DESCRIPTION

1. *Observability of LTV Systems*

Consider the discrete-time (DT) linear time-varying (LTV) dynamical system $\mathbf{\Sigma}$ given by

$$\mathbf{\Sigma}: \begin{cases} \boldsymbol{x}(k+1) & = \mathbf{F}(k)\,\boldsymbol{x}(k) + \mathbf{G}(k)\,\boldsymbol{u}(k), \\ \boldsymbol{y}(k) & = \mathbf{H}(k)\,\boldsymbol{x}(k), \end{cases} \tag{1}$$

where $\boldsymbol{x} \in \mathbb{R}^n$, $\boldsymbol{u} \in \mathbb{R}^p$, and $\boldsymbol{y} \in \mathbb{R}^q$ are the system state, input, and measurement vectors at time-step k, respectively, and $k \in \mathbb{N}$. The state transition matrix corresponding to $\mathbf{\Sigma}$ from time-step j to time-step i is given by

$$\mathbf{\Phi}(i,j) \triangleq \begin{cases} \mathbf{F}(i-1)\,\mathbf{F}(i-2)\cdots\mathbf{F}(j), & \text{if } i > j, \\ \mathbf{I}_{n\times n}, & \text{if } i = j, \end{cases}$$

where $\mathbf{I}_{n\times n}$ denotes an $n \times n$ identity matrix. The following theorem characterizes the observability of DT LTV systems via the l-step observability matrix (Rugh, 1996).

Theorem I: The DT LTV system (1) is l-step observable if and only if its corresponding l-step observability matrix

$$\mathcal{O}(k, k+l-1) \triangleq \begin{bmatrix} \mathbf{H}(k)\,\mathbf{\Phi}(k,k) \\ \mathbf{H}(k+1)\,\mathbf{\Phi}(k+1,k) \\ \vdots \\ \mathbf{H}(k+l-1)\,\mathbf{\Phi}(k+l-1,k) \end{bmatrix}, \tag{2}$$

is full rank. Theorem I can be applied to nonlinear systems by linearizing at each time-step k around $\boldsymbol{x}(k)$. The achieved observability results therein will only be valid locally (Huang et al., 2010).

2. *Receiver Dynamics*

The terrestrial receiver's position $\boldsymbol{r}_r \in \mathbb{R}^3$ is assumed to be fixed in the Earth-centered inertial (ECI) frame and its distance from the center of Earth is denoted by $r = \|\boldsymbol{r}_r\|_2$. The dynamics of the receiver's clock error states (i.e., bias δt_r and drift $\dot{\delta} t_r$) is modeled as a double integrator driven by process noise (Bar-Shalom et al., 2002). The receiver's dynamics is given by

$$\boldsymbol{x}_r(k+1) = \mathbf{F}_r\, \boldsymbol{x}_r(k) + \boldsymbol{w}_r(k),$$

where $\boldsymbol{x}_r \triangleq \left[\boldsymbol{r}_r^{\mathsf{T}},\, c\,\delta t_r,\, c\,\dot{\delta} t_r\right]^{\mathsf{T}}$ is the receiver's state vector, c denotes the speed of light, and $\boldsymbol{w}_r$ is a process noise modeled as a zero-mean white random sequence with covariance $\mathbf{Q}_r = \text{diag}\left[\mathbf{0}_{3\times 3},\, \mathbf{Q}_{cr}\right]$. The receiver state matrix is

$$\mathbf{F}_r = \begin{bmatrix} \mathbf{I}_{3\times 3} & \mathbf{0}_{3\times 2} \\ \mathbf{0}_{2\times 3} & \mathbf{F}_{\text{clk}} \end{bmatrix}, \quad \mathbf{F}_{\text{clk}} = \begin{bmatrix} 1 & T \\ 0 & 1 \end{bmatrix},$$

where T is the sampling period. In this letter, the simplest receiver dynamics was considered to focus on the change in geometry due to the moving satellite. More elaborate receiver dynamics could be considered in future work.

3. *LEO Satellite Dynamics*

The LEO satellite is assumed to follow a circular Keplerian orbit with fixed inclination and a prescribed orbital radius denoted by $a = \|\boldsymbol{r}_s(t)\|_2$ where $0 < r < a$. Under the action of Earth's gravitational field, the satellite's orbital dynamics in continuous-time will be assumed to follow a simplified two-body model given by

$$\ddot{\boldsymbol{r}}_s(t) = -\frac{\mu}{a^3}\, \boldsymbol{r}_s(t) + \boldsymbol{w}_s(t), \tag{3}$$

where $\boldsymbol{r}_s \in \mathbb{R}^3$ is the satellite's position in the ECI frame and $\boldsymbol{w}_s$ is a process noise vector of acceleration perturbations resulting from Earth's non-uniform gravitational potential, atmospheric drag, solar radiation pressure, gravitational pull of other celestial bodies, and general relativity (Montenbruck and Gill, 2000). The following constraints on the satellite dynamics hold $\forall\, t > 0$

$$\begin{aligned} \langle \boldsymbol{r}_s(t)\,, \boldsymbol{r}_s(t) \rangle &= a^2, \\ \langle \dot{\boldsymbol{r}}_{\boldsymbol{s}}(t)\,, \dot{\boldsymbol{r}}_{\boldsymbol{s}}(t) \rangle &= \alpha^2\, a^2, \\ \langle \boldsymbol{r}_s(t)\,, \dot{\boldsymbol{r}}_{\boldsymbol{s}}(t) \rangle &= 0\,, \end{aligned}$$

where $\alpha^2 \triangleq \mu/a^3$. The dynamics of the satellite's clock bias δt_s and drift $\dot{\delta} t_s$ are modeled similarly to the receiver's clock error dynamics (Bar-Shalom et al., 2002). Next, the satellite dynamics in (3) can be discretized at a sampling period T to yield

$$\boldsymbol{x}_s(t_{k+1}) = \mathbf{F}_s\, \boldsymbol{x}_s(t_k) + \boldsymbol{w}_s(t_k),$$

where $\boldsymbol{x}_s = \left[\boldsymbol{r}_s^{\mathsf{T}},\, \dot{\boldsymbol{r}}_s^{\mathsf{T}},\, c\,\delta t_s,\, c\,\dot{\delta} t_s\right]^{\mathsf{T}}$ is the satellite's state vector and $\boldsymbol{w}_s$ is a process noise modeled as a zero-mean white random sequence with covariance $\mathbf{Q}_s$, and $\mathbf{F}_s$ is given by

$$\mathbf{F}_s = \begin{bmatrix} \cos(\alpha T)\, \mathbf{I}_{3\times 3} & (1/\alpha)\, \sin(\alpha T)\, \mathbf{I}_{3\times 3} & \mathbf{0}_{3\times 2} \\ -\alpha\, \sin(\alpha T)\, \mathbf{I}_{3\times 3} & \cos(\alpha T)\, \mathbf{I}_{3\times 3} & \mathbf{0}_{3\times 2} \\ \mathbf{0}_{2\times 3} & \mathbf{0}_{2\times 3} & \mathbf{F}_{\text{clk}} \end{bmatrix}.$$

4. *Measurement Model*

The pseudorange measurement extracted by the receiver (Pinell, 2021) from the satellite signals at time-step k, after compensating for ionospheric and tropospheric delays (Kassas, 2021), is modeled as

$$\rho(k) = \|\boldsymbol{r}_r - \boldsymbol{r}_s(k')\|_2 + c\, \left(\delta t_r(k) - \delta t_s(k')\right) + \boldsymbol{v}(k), \tag{4}$$

where k' represents discrete-time $t_k = k\,T - \delta t_{TOF}$ with δt_{TOF} being the transmission delay of the signal. The term $\boldsymbol{v}$ is the measurement noise, which is modeled as a zero-mean white Gaussian sequence with variance σ^2.

III. OBSERVABILITY ANALYSIS

This section summarizes the analytical observability results derived in (Sabbagh and Kassas, 2023) for receiver localization with a single LEO satellite under two scenarios. The first scenario considers a receiver with *unknown* position states but *known* clock error states. Results from this simple scenario will serve as a stepping stone towards the second scenario, which considers a receiver with *unknown* position states and *unknown* clock error states. In each scenario, the satellite's states are assumed to be known, which is the case whenever (i) a satellite transmits its ephemeris and clock errors (e.g., Orbcomm satellites transmit their states, estimated from onboard GPS receivers (Kassas, 2021)) or (ii) an estimator is employed to estimate the LEO satellite's states (e.g., via a differential navigation framework utilizing a known base receiver (Khalife et al., 2020), via a simultaneous tracking and navigation (STAN) framework (Kassas, 2021)), or via an analytical and/or machine-learning satellite tracking framework (Shen et al., 2019; Khairallah and Kassas, 2021; Haidar-Ahmad et al., 2022)). It is worth noting that instead of estimating the receiver's clock error states, the following analysis readily extends to the case of estimating the *difference* between the receiver's and LEO satellite's clock error states (Khairallah and Kassas, 2022), $\Delta\delta t \triangleq \delta t_r - \delta t_s$ and $\Delta\dot{\delta} t \triangleq \dot{\delta} t_r - \dot{\delta} t_s$, which could be desirable for stochastic observability considerations (Morales and Kassas, 2019).

The nonlinear pseudorange measurement (4) is linearized at time-step k with respect to the unknown receiver states and the corresponding Jacobian matrix is used to build the l-step observability matrix. The scenarios are summarized below

- **Scenario 1:** A stationary receiver with *unknown position states* but *known clock error states* makes pseudorange measurements to a LEO satellite with *known states*. The measurement Jacobian is given by $\mathbf{H}(k) = \boldsymbol{l}_k^\mathsf{T}$.
- **Scenario 2:** A stationary receiver with *unknown position states and clock error states* makes pseudorange measurements to a LEO satellite with *known states*. The measurement Jacobian is given by $\mathbf{H}(k) = \begin{bmatrix}\boldsymbol{l}_k^\mathsf{T} & 1 & 0\end{bmatrix}$.

Above, $\boldsymbol{l}_k \in \mathbb{R}^3$ denotes the unit line-of-sight (LOS) vector between the receiver and satellite at time-step k, given by

$$\boldsymbol{l}_k \triangleq \frac{\boldsymbol{r}_r - \boldsymbol{r}_s(k)}{\|\boldsymbol{r}_r - \boldsymbol{r}_s(k)\|_2}.$$

In what follows, the l-step observability of the aforementioned scenarios is investigated, and bounds on the determinants of observability matrices therein are derived.

1. *Scenario 1: Pseudorange Measurements with Unknown Receiver Position States but Known Clock Error States*

In this scenario, the only unknown states are the receiver's position, and the 3-step observability matrix is given by

$$\mathcal{O}(k, k+2) = \begin{bmatrix}\boldsymbol{l}_k & \boldsymbol{l}_{k+1} & \boldsymbol{l}_{k+2}\end{bmatrix}^\mathsf{T}, \tag{5}$$

where the transition matrix $\boldsymbol{\Phi} = \mathbf{I}_{3\times 3}$ and the measurement Jacobian $\mathbf{H}(k) = l_k^\mathsf{T}$ are used to build $\mathcal{O}(k, k+2)$. Let $\mathcal{O}(k, k+2) \triangleq \mathcal{O}_3$. An expression for $\det(\mathcal{O}_3)$ is derived as a function of the relative geometry between the receiver and the satellite.

Theorem II: Let $c_n \triangleq \cos(\alpha n T)$, $s_n \triangleq \sin(\alpha n T)$, and

$$\beta^k \triangleq \frac{1}{\|\Delta\boldsymbol{r}(k)\|_2 \, \|\Delta\boldsymbol{r}(k+1)\|_2 \, \|\Delta\boldsymbol{r}(k+2)\|_2},$$

where $\Delta\boldsymbol{r}(k) \triangleq \boldsymbol{r}_r - \boldsymbol{r}_s(k)$. The determinant of the 3-step observability matrix in (5) is given by

$$\det(\mathcal{O}_3) = \beta^k \, (2\, s_1 - s_2)\, a^2 \, r \, \sin(\theta), \tag{6}$$

where θ is the angle between the receiver's position vector $\boldsymbol{r}_r$ and the orbital plane of the LEO satellite.

Proof: The determinant of $\mathcal{O}_3$ is equal to the scalar triple product of its rows which are given by the unit LOS vectors $\boldsymbol{l}_k$, $\boldsymbol{l}_{k+1}$, and $\boldsymbol{l}_{k+2}$. Expanding this product in terms of the state variables of the receiver-satellite dynamics will yield the desired result (for details of the proof see (Sabbagh and Kassas, 2023, Theroem II)). ■

Hereafter, θ is referred to as the *relative orbital inclination angle* between the receiver and the LEO satellite. Ideally, θ is assumed constant for a stationary receiver during the time window through which it is seeing a LEO satellite. In what follows, time-independent bounds on $\det(\mathcal{O}_3)$ are derived.

Corollary I: The determinant of the 3-step observability matrix in (5) can be bounded as follows

$$0 \leq L(\theta) \leq \det(\mathcal{O}_3) \leq U(\theta),$$
$$L(\theta) = \frac{(2\,s_1 - s_2)\,a^2\,r\,\sin(\theta)}{(a^2 + r^2 + 2\,a\,r\,\cos(\theta))^{3/2}},$$
$$U(\theta) = \frac{(2\,s_1 - s_2)\,a^2\,r\,\sin(\theta)}{(a^2 + r^2 - 2\,a\,r\,\cos(\theta))^{3/2}},$$

where $0 \leq \theta \leq \pi/12$ and $0 \leq \alpha\,k\,T \leq \pi/6$ for all $k \in \mathbb{N}$.

Proof: Using the law of cosines, it can be deduced that the coefficient β^k satisfies $\left(a^2 + r^2 + 2\,a\,r\,\sin(\theta)\right)^{-3/2} \leq \beta^k \leq \left(a^2 + r^2 - 2\,a\,r\,\sin(\theta)\right)^{-3/2}$ for all $k \in \mathbb{N}$ (for details of the proof see (Sabbagh and Kassas, 2023, Corollary I)). ■

The inequalities on θ and $\alpha\,k\,T$ are placed with the understanding that a LEO satellite should be visible for a long enough time to provide useful measurements. From the observability analysis of Scenario I, the following can be deduced:

Proposition I: If the receiver is in the orbital plane of the LEO satellite, the system is not l-step observable.

Proof: If the receiver is in the orbital plane of the LEO satellite, then $\theta = 0$. This implies that $U(\theta) = 0$. As a result, $\det(\mathcal{O}_3) = 0$ and $\mathcal{O}_3$ is rank deficient. In fact, the rows of $\mathcal{O}_l$, which represent consecutive unit LOS vectors tracing the satellite's orbit, are coplanar lying in the orbital plane of the satellite. As a result, rank$[\mathcal{O}_l] \leq 2$, for all $l \geq 2$. ■.

Remark I: The unobservable subspace in the case above is spanned by the normal to the satellite's orbital plane, otherwise known as the satellite's cross direction. This implies that initial receiver position states along this direction are indistinguishable. The impact of this on localization using a single overhead LEO satellite is demonstrated in Section IV.

Proposition II: If the receiver is not in the orbital plane of the LEO satellite, the system is l-step observable for $l \geq 3$.

Proof: If the receiver is not in the orbital plane of the LEO satellite, then $\theta \neq 0$. As a result, $L(\theta) > L(0) > 0$, and $\det(\mathcal{O}_3) \neq 0$ with rank$[\mathcal{O}_l] = 3$, for all $l \geq 3$. In fact, the rows of $\mathcal{O}_l$, which represent consecutive unit LOS vectors tracing the satellite's orbit, are no longer coplanar. This implies that the corresponding scalar triple product of any three consecutive unit LOS vectors is nonzero within a single orbital period. ■

2. *Relationship Between the relative orbital inclination θ and the Geometric Diversity of the LOS Vectors*

The above analysis and (6) show that the size of θ normalized by the cube of the receiver-satellite range can measure how close the l-step observability matrix is to singularity. In other words,

$$\det(\mathcal{O}_3) \;\propto\; \beta^k\,\sin(\theta).$$

As a result, a relationship between the singularity of $\mathcal{O}_3$ and the geometric diversity of the unit LOS vectors can be established. Namely, the following observations can be made:

- For small θ, the receiver is near the orbital plane of the satellite so that the LOS vectors are almost *coplanar*.
- For large θ, the receiver is far enough from the satellite so that the LOS vectors are almost *collinear*.
- In both extremes, the LOS vectors have poor geometric diversity.

As a visual aid to illustrate the impact of θ on the determinant of the observability matrix, an exaggerated comparison between the geometric diversity of the LOS vectors created between the LEO satellite and three receivers A, B, and C is shown is shown in Figure 1. These receivers result in three drastically different values of θ, which result in LOS vectors with varying geometric diversity. For example, receiver A makes LOS measurements that are relatively closer to each other compared to receiver C (large θ), and receiver B makes LOS measurements that are coplanar in the orbital plane of the LEO satellite (small θ).

A study on the singularity of $\mathcal{O}_3$ is shown in Figure 2(a), where the values of $\det(\mathcal{O}_3)$ were computed from simulated LOS vectors created between a stationary receiver and a satellite traveling along a circular orbit at an altitude of 521 km (computations were repeated for varying values of $\theta \in [0,\ \pi/12]$). It is observed that $\det(\mathcal{O}_3)$ drastically diminishes for θ values which are too small or too large, implying that a "favorable" relative orbital inclination region (shown in Figure 2 in yellow) lying in between

the two extremes exists where $\det(\mathcal{O}_3)$ is ideal over the navigation window of the receiver. In summary, for configurations with θ larger than zero, the geometric diversity of the LOS vectors improves up to a certain point, which is a favorable region that optimizes the geometric diversity of the LOS vectors. Upon further increasing θ, the geometric diversity starts to slowly degrade.

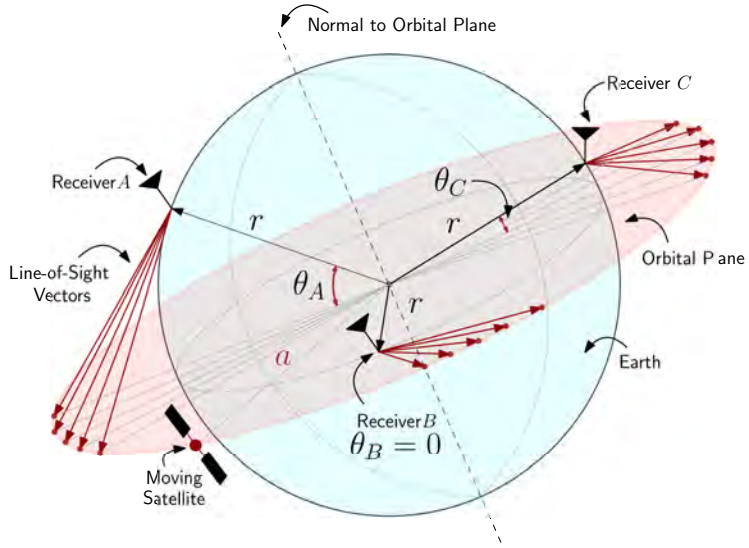

Figure 1: *Comparison between the geometric diversity of the LOS vectors based on the relative orbital inclinations θ_A, θ_B, and θ_C ($\theta_A \gg \theta_C \gg \theta_B$) created between the LEO satellite and receivers A, B, and C, respectively. Receiver A makes LOS measurements that are relatively closer to each other compared to receiver C (large θ), and receiver B makes LOS measurements that are coplanar in the orbital plane of the LEO satellite (small θ).*

3. *Scenario 2: Pseudorange Measurements with Unknown Receiver Position States and Unknown Clock Error States*

In this scenario, the receiver state is unknown, and the 5-step observability matrix is given by

$$\mathcal{O}(k,k+4) = \begin{bmatrix} \boldsymbol{l}_k & \boldsymbol{l}_{k+1} & \boldsymbol{l}_{k+2} & \boldsymbol{l}_{k+3} & \boldsymbol{l}_{k+4} \\ 1 & 1 & 1 & 1 & 1 \\ 0 & T & 2T & 3T & 4T \end{bmatrix}^{\mathsf{T}}, \tag{7}$$

where the transition matrix $\boldsymbol{\Phi} = \mathbf{F}_r \in \mathbb{R}^{5\times 5}$ and the measurement Jacobian $\mathbf{H}(k) = \begin{bmatrix} l_k^{\mathsf{T}} & 1 & 0 \end{bmatrix} \in \mathbb{R}^{1\times 5}$ are used to build $\mathcal{O}(k,k+4)$. Let $\mathcal{O}(k,k+4) \triangleq \mathcal{O}_5$. Next, an expression for $\det(\mathcal{O}_5)$ is derived as a function of the relative geometry between the receiver and the satellite.

Proposition III: Let m, n, and $p \in \mathbb{N}$ with $m < n < p$, then the following equality holds

$$\boldsymbol{l}_m \cdot (\boldsymbol{l}_n \times \boldsymbol{l}_p) = \gamma_{mnp}\, \beta_{mnp}^k\, a^2\, r\, \sin(\theta),$$

where the scalars $\gamma_{mnp} > 0$ and $\beta_{mnp}^k > 0$ are given by

$$\gamma_{mnp} \triangleq s_{n-m} + s_{p-n} - s_{p-m},$$
$$\beta_{mnp}^k \triangleq \frac{1}{\|\Delta\boldsymbol{r}(k+m)\|_2\, \|\Delta\boldsymbol{r}(k+n)\|_2\, \|\Delta\boldsymbol{r}(k+p)\|_2},$$

where $0 \leq \theta \leq \pi/12$ and $0 \leq \alpha\, k\, T \leq \pi/6$ for all $k \in \mathbb{N}$.

Proof: The proof proceeds similarly to that of Theorem II. ■

Theorem III: The determinant of the 5-step observability matrix in (7) is given by

$$\det(\mathcal{O}_5) = T\,(a_1 - a_2 + a_3 - a_4)\, a^2\, r\, \sin(\theta), \tag{8}$$

where a_1, a_2, a_3, and a_4 are scalars given by

$$
\begin{aligned}
a_1 &= \gamma_{012}\,(\beta^k_{012} + \beta^k_{234}) + \gamma_{014}\,(\beta^k_{014} + \beta^k_{034}),\\
a_2 &= 2\,\left(\gamma_{013}\,\beta^k_{013} + \gamma_{024}\,\beta^k_{024} + \gamma_{134}\,\beta^k_{134}\right),\\
a_3 &= 3\,\gamma_{023}\,\left(\beta^k_{023} + \beta^k_{124}\right),\\
a_4 &= 4\,\gamma_{123}\,\beta^k_{123}.
\end{aligned}
$$

Proof: The determinant of $\mathcal{O}_5$ can be expressed in terms of a product of determinants involving block partitions of $\mathcal{O}_5$ via the Schur complement formula. This yields an alternative expression for $\det(\mathcal{O}_5)$, given by

$$
\det(\mathcal{O}_5) = T \begin{vmatrix} \boldsymbol{l}_k^{\mathsf{T}} - 4\,\boldsymbol{l}_{k+3}^{\mathsf{T}} + 3\,\boldsymbol{l}_{k+4}^{\mathsf{T}} \\ \boldsymbol{l}_{k+1}^{\mathsf{T}} - 3\,\boldsymbol{l}_{k+3}^{\mathsf{T}} + 2\,\boldsymbol{l}_{k+4}^{\mathsf{T}} \\ \boldsymbol{l}_{k+2}^{\mathsf{T}} - 2\,\boldsymbol{l}_{k+3}^{\mathsf{T}} + \boldsymbol{l}_{k+4}^{\mathsf{T}} \end{vmatrix}.
$$

By expanding the above determinant, the resulting terms can be grouped using Proposition III, resulting in (8). ■

Time-independent bounds on $\beta^k_{m,n,p}$ can be derived as in the proof of Corollary I, so that $d_{max}^{-3} \leq \beta^k_{mnp} \leq d_{min}^{-3}$ for all k, m, n, and $p \in \mathbb{N}$. Bounds on $\det(\mathcal{O}_5)$ are presented next.

Corollary II: The determinant of the 5-step observability matrix in (8) can be bounded as follows

$$
\begin{aligned}
L(\theta) \leq \det(\mathcal{O}_5) &\leq U(\theta),\\
L(\theta) &= 16\,s_1^3\,(1-c_1)\,a^2\,r\,T\,\left(\frac{1}{d_{max}^3} - \frac{1}{d_{min}^3}\right)\,\sin(\theta),\\
U(\theta) &= 16\,s_1^3\,(1-c_1)\,a^2\,r\,T\,\left(\frac{1}{d_{min}^3} - \frac{1}{d_{max}^3}\right)\,\sin(\theta),
\end{aligned}
$$

where $0 \leq \theta \leq \pi/12$ and $0 \leq \alpha\,k\,T \leq \pi/6$ for all $k \in \mathbb{N}$.

Proof: The proof proceeds similarly to that of Corollary I. ■

Based on Theorem III and Corollary II, the following observability results are deduced.

Proposition IV: If the receiver is in the orbital plane of the satellite or along the normal to the orbital plane of the satellite, the system is not l-step observable.

Proof: By construction, unobservable directions in Scenario I are inherited into Scenario II where additional receiver states are now unknown. Furthermore, if the receiver is along the normal to the orbital plane of the satellite, the minimum and maximum Euclidean distances between the receiver and the LEO satellite become equal which results in $U(\theta) = U(\frac{\pi}{2}) = 0$ and $L(\theta) = L(\frac{\pi}{2}) = 0$, implying that $\det(\mathcal{O}_5) = 0$. In fact, since a constant distance is maintained between the receiver-satellite pair, the stationary receiver can no longer disambiguate between its initial clock bias and the initial range from the satellite, no matter how many pseudorange measurements it makes from that satellite. At best, a one-dimensional unobservable subspace of $\mathbb{R}^5$ is maintained, so that $\text{rank}[\mathcal{O}_l] \leq 4$, for all $l \geq 4$. ■

Proposition V: If the receiver is not in the orbital plane of the satellite, nor along the normal to the satellite's orbital plane, the system is l-step observable for $l \geq 5$.

Proof: It is enough to show by contradiction that the matrix $\mathcal{O}_5$ in this setting is non-singular (for details of the proof see (Sabbagh and Kassas, 2023, Proposition V)). ■

4. *Comparison between Scenario I and Scenario II*

The same study on the singularity of $\mathcal{O}_5$ is done and the corresponding observability surface is generated and compared to the previous Scenario. It can be observed that the observability surface in Figure 2(b) is smaller compared to Figure 2(a). This reflects poorer observability conditions and loss of information due to the addition of unknown receiver states to the system. Additionally, while in both scenarios, the determinant of the observability matrix vanishes when the receiver is in the orbital plane, as θ grows past the favorable region, the determinant in Scenario II approaches singularity much faster.

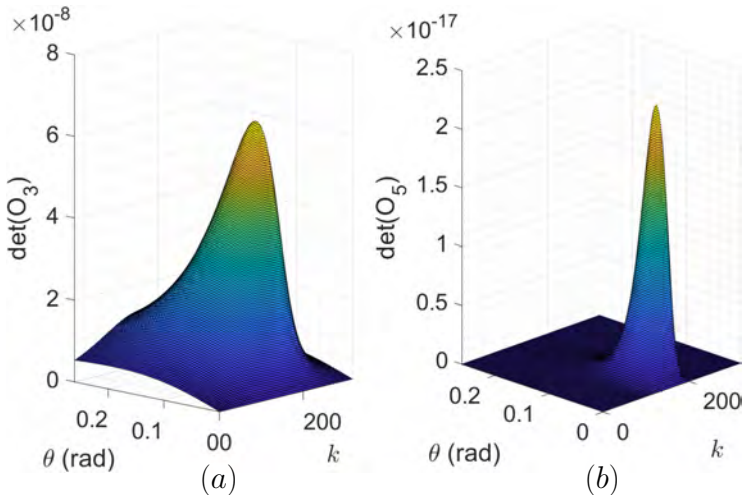

Figure 2: *Values of* $\det(\mathcal{O}_3)$ *(left) and* $\det(\mathcal{O}_5)$ *(right) computed for different values of* θ *in radians at each time-step* k*.*

Finally, it is important to note that while the unobservable subspaces discussed are of zero measure and assume an ideal setting (perfect knowledge of a circular satellite ephemeris, non-rotating spherical Earth, etc), in a real setting, the satellite's orbit will experience random perturbations such that a receiver localizing itself would not lie along the derived unobservable subspaces. This suggests that theoretically, a receiver with an unknown state can indeed localize itself using pseudorange measurements from a single LEO satellite. Section IV will show the effect of the unobservable direction to receiver localization.

IV. EXPERIMENTAL RESULTS

To demonstrate the conclusions of the observability analysis on receiver localization, an experiment was conducted whereby pseudorange measurements, extracted from carrier phase observables (Khalife et al., 2020, 2022), from one Starlink satellite and one Orbcomm satellite were used to localize a stationary receiver using an EKF for LEO satellite visibility durations of 74 and 317 seconds, respectively. The Starlink and Orbcomm satellites possess average relative orbital inclinations of $\theta = 0.01457$ rad and $\theta = 0.00410$ rad, respectively, indicating that the receiver is relatively close to being in their orbital planes during each navigation window. For both satellites, the analysis in Section III shows that the determinant of the corresponding observability

Table 1: Receiver localization error

Satellite	Direction	Initial Error	Final Error
Starlink	Along (m)	-603.94	-67.14
	Cross (m)	-682.25	–768.41
	Radial (m)	-555.90	81.40
	Overall (m)	1,067.35	775.62
Orbcomm	Along (m)	604.47	-51.35
	Cross (m)	-722.25	-689.29
	Radial (m)	-856.47	7.79
	Overall (m)	1,273.30	691.24

matrices is expected to be small enough so that the directions normal to the LEO satellites' orbital planes become nearly unobservable. The objective of the experiment is therefore to demonstrate that receiver localization using near-overhead passing LEO satellites will suffer from poor information in the direction normal to the LEO satellite's orbital plane. This implies that any initial receiver position error in the direction along the normal to the LEO satellite's orbital plane will not reduce in the EKF, due to the observability matrix being nearly singular. For the Starlink satellite, the satellite's states were estimated according to the framework discussed in (Khalife et al., 2022), which estimated the satellite's ephemeris via simplified general perturbation 4 (SGP4) orbit propagator initialized with two-line element (TLE) files. For the Orbcomm satellite, the satellite's states were obtained by decoding the downlink signal, which contains ephemeris and clock errors, estimated via the satellite's onboard GPS receivers (Khalife et al., 2020).

The localization results are shown in Figs. 3 and 4, where the receiver's position estimation errors and the $\pm 3\sigma$-bounds are resolved along the LEO satellite's body frame (along-track, cross-track, and radial directions). Table 1 shows the initial and final receiver position estimation errors in each direction. It can be seen from Figs. 3 and 4 and Table 1 that while the receiver's position error in the along-track and radial directions decreases, there is no improvement in the cross-track direction. This confirms the observability result discussed in Section III, stating that the direction normal to the orbital plane of the satellite is unobservable for a receiver making measurements from incoming overhead satellites.

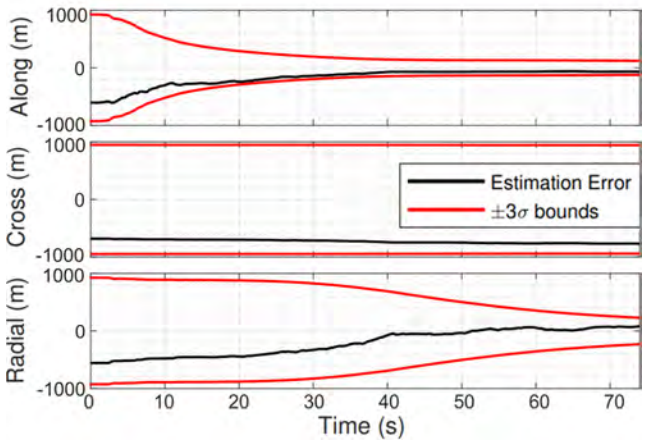

Figure 3: *Receiver position estimation errors resolved along the Starlink satellite body frame (in black) with $\pm 3\sigma$ bounds (in red).*

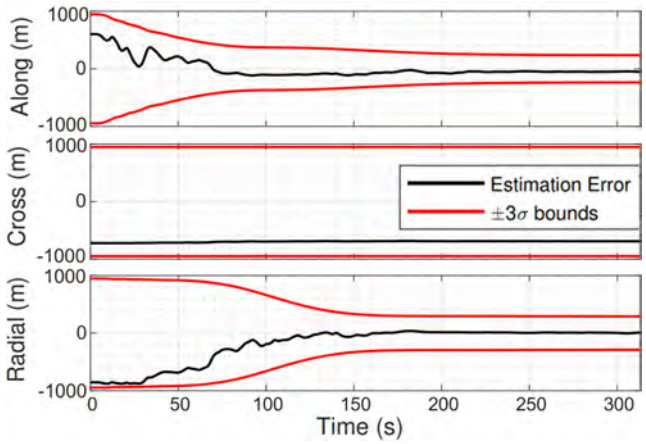

Figure 4: *Receiver position estimation errors resolved along the Orbcomm satellite body frame (in black) with $\pm 3\sigma$ bounds (in red).*

V. OBSERVABILITY-AIDED LEO SATELLITE SELECTION

From a geometric point of view, it may be viable to utilize publicly available TLE files in order to predict LEO satellites that will produce measurements which are most favorable when it comes to the observability of a stationary receiver. Namely, Figure 2 can be utilized for observability-based satellite selection to improve receiver localization based on LEO satellite's SGP4-propagated TLE files. This can be done by mapping the LEO satellite's trajectory with respect to the stationary receiver (which can be guessed *a priori* via information about the satellite's altitudes as well as angles θ of their orbital planes with the receiver) to curves along the observability surfaces (see Figure 5). Then, one may predict and select the satellite which will generate a navigation scenario which is "most" observable by selecting the satellites whose curves are lying in the "favorable" region of the observability surface. Namely, given a set of LEO satellites, one can identify *a priori* the one which will result in the best receiver localization performance, by taking into account the following criteria, which are all features of the observability surfaces shown in Figure 2:

- The visibility duration of the LEO satellite: This can be inferred from the projected length of the satellite's curve on the observability surface, along the time axis.
- The elevation profile of the LEO satellite during this time: This corresponds to the shape of the satellite's curve on the observability surface.
- Satellite altitudes and relative orbital inclinations θ: This corresponds to the position of the satellite's curve on the observability surface, along the θ axis.

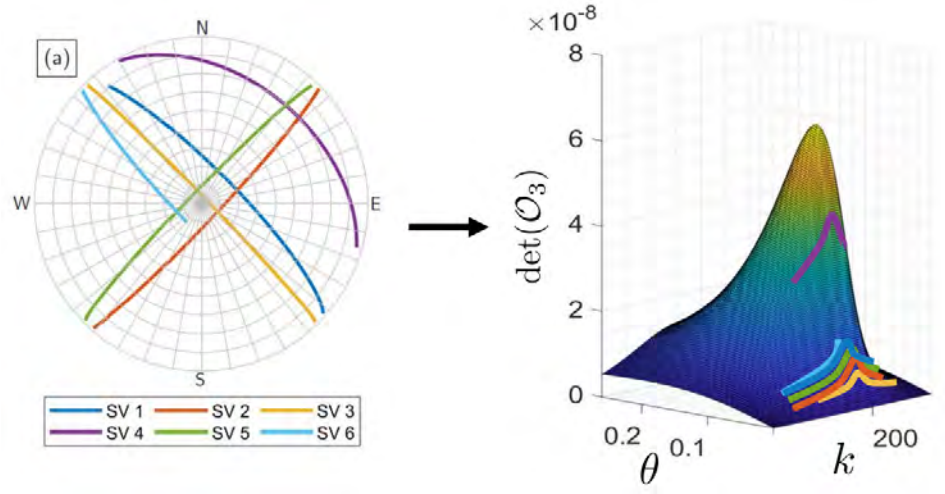

Figure 5: Starlink predicted skyplots

To illustrate the above idea, consider the collection of six Starlink satellites shown in Figure 5. Their propagated TLE files can be used to predict how they will pass above a stationary receiver compared to each other. Knowing *a priori* the average values of their altitudes, θ, and the skyplots shown, it may be possible to map this information directly onto an observability surface, which may then be used to choose the satellite that will provide better measurements. In that case, it is expected that space vehicle (SV) 4 will yield the best localization results, given that it provides measurements for a long enough time and in the "favorable" region from an observability perspective. While the analysis in this paper considered a single LEO satellite, future work could generalize to multiple satellites and develop an observability-aided LEO satellite selection approach that determines the satellites that are expected to provide the best measurements for receiver localization.

ACKNOWLEDGEMENTS

This work was supported in part by the National Science Foundation (NSF) under Grants 1929965 and 1929571 and in part by the U.S. Department of Transportation (USDOT) under Grant 69A3552047138 for the CARMEN University Transportation Center (UTC).

REFERENCES

Bar-Shalom, Y., Li, X., and Kirubarajan, T. (2002). *Estimation with Applications to Tracking and Navigation*. John Wiley & Sons, New York, NY.

Cassel, R., Scherer, D., Wilburne, D., Hirschauer, J., and Burke, J. (2022). Impact of improved oscillator stability on LEO-based satellite navigation. In *Proceedings of ION International Technical Meeting*, pages 893–905.

Elgamoudi, A., Benzerrouk, H., Elango, G., and Landry, R. (2020). Gauss Hermite h∞ filter for UAV tracking using LEO satellites TDOA/FDOA measurement—part I. *IEEE Access*, 8:201428–201440.

Farhangian, F., Benzerrouk, H., and Landry, R. (2021). Opportunistic in-flight INS alignment using LEO satellites and a rotatory IMU platform. *Aerospace*, 8(10):280–281.

Farhangian, F. and Landry, R. (2020). Multi-constellation software-defined receiver for Doppler positioning with LEO satellites. *Sensors*, 20(20):5866–5883.

Friedman, A. (2020). *Observability analysis for space situational awareness*. PhD thesis, Purdue University.

Friedman, A. and Frueh, C. (2021). Observability and estimability analysis of geosynchronous objects with angles-only measurements. *The Journal of the Astronautical Sciences*, 68(2):503–534.

Haidar-Ahmad, J., Khairallah, N., and Kassas, Z. (2022). A hybrid analytical-machine learning approach for LEO satellite orbit prediction. In *Proceedings of International Conference on Information Fusion*, pages 1–7.

Hartnett, M. (2022). Performance assessment of navigation using carrier Doppler measurements from multiple LEO constellations. Master's thesis, Air Force Institute of Technology, Wright-Patterson Air Force Base, Ohio, USA.

Huang, C., Qin, H., Zhao, C., and Liang, H. (2022). Phase - time method: Accurate Doppler measurement for Iridium NEXT signals. *IEEE Transactions on Aerospace and Electronic Systems*, pages 1–9.

Huang, G., Mourikis, A., and Roumeliotis, S. (2010). Observability-based rules for designing consistent EKF SLAM estimators. *International Journal of Robotics Research*, 29(5):502–528.

Iannucci, P. and Humphreys, T. (2022). Fused low-Earth-orbit GNSS. *IEEE Transactions on Aerospace and Electronics Systems*. accepted.

Jardak, N. and Jault, Q. (2022). The potential of LEO satellite-based opportunistic navigation for high dynamic applications. *Sensors*, 22(7):2541–2565.

Jiang, M., Qin, H., Zhao, C., and Sun, G. (2022). LEO Doppler-aided GNSS position estimation. *GPS Solutions*, 26(1):1–18.

Judice, A., Venusamy, K., and Livin, J. (2022). Multilayer LEO satellite constellation coverage analysis and its current research directions. In *Proceedings of IEEE International Conference on Distributed Computing and Electrical Circuits and Electronics*, pages 1–5.

Kassas, Z. (2021). Position, navigation, and timing technologies in the 21st century. volume 2, chapter 43: Navigation from low Earth orbit – Part 2: models, implementation, and performance, pages 1381–1412. Wiley-IEEE.

Kassas, Z. and Humphreys, T. (2012). Observability and estimability of collaborative opportunistic navigation with pseudorange measurements. In *Proceedings of ION GNSS Conference*, pages 621–630.

Kassas, Z., Morales, J., and Khalife, J. (2019). New-age satellite-based navigation – STAN: simultaneous tracking and navigation with LEO satellite signals. *Inside GNSS Magazine*, 14(4):56–65.

Kaufman, E., Lovell, T., and Lee, T. (2016). Nonlinear observability for relative orbit determination with angles-only measurements. *The Journal of the Astronautical Sciences*, 63(1):60–80.

Khairallah, N. and Kassas, Z. (2021). Ephemeris closed-loop tracking of LEO satellites with pseudorange and Doppler measurements. In *Proceedings of ION GNSS Conference*, pages 2544–2555.

Khairallah, N. and Kassas, Z. (2022). An interacting multiple model estimator of LEO satellite clocks for improved positioning. In *Proceedings of IEEE Vehicular Technology Conference*, pages 1–5.

Khalife, J., Neinavaie, M., and Kassas, Z. (2020). Navigation with differential carrier phase measurements from megaconstellation LEO satellites. In *Proceedings of IEEE/ION Position, Location, and Navigation Symposium*, pages 1393–1404.

Khalife, J., Neinavaie, M., and Kassas, Z. (2022). The first carrier phase tracking and positioning results with Starlink LEO satellite signals. *IEEE Transactions on Aerospace and Electronic Systems*, 56(2):1487–1491.

Kulu, E. (2021). Satellite constellations–2021 industry survey and trends. In *Proceedings of Annual Small Satellite Conference*, pages 1–20.

Li, M., Xu, T., Guan, M., Gao, F., and Jiang, N. (2022). LEO-constellation-augmented multi-GNSS real-time PPP for rapid re-convergence in harsh environments. *GPS Solutions*, 26(1):1–12.

Liu, S., Gao, Z., Wu, Y., Kwan Ng, D., Gao, X., Wong, K., Chatzinotas, S., and Ottersten, B. (2021). LEO satellite constellations for 5G and beyond: How will they reshape vertical domains? *IEEE Communications Magazine*, 59(7):30–36.

Montenbruck, O. and Gill, E. (2000). *Satellite orbits: models, methods, and applications*. Springer.

Morales, J. and Kassas, Z. (2019). Stochastic observability and uncertainty characterization in simultaneous receiver and transmitter localization. *IEEE Transactions on Aerospace and Electronic Systems*, 55(2):1021–1031.

Nardin, A., Dovis, F., and Fraire, J. (2021). Empowering the tracking performance of LEO-based positioning by means of meta-signals. *IEEE Journal of Radio Frequency Identification*, 5(3):244–253.

Neinavaie, M., Khalife, J., and Kassas, Z. (2022). Acquisition, Doppler tracking, and positioning with Starlink LEO satellites: First results. *IEEE Transactions on Aerospace and Electronic Systems*, 58(3):2606–2610.

Okasha, N., Zekry, A., and Newagy, F. (2022). Hybrid VLC vehicle to vehicle and LEO satellite communication system for highway road coverage. In *Proceedings of International Conference on Computing, Control and Industrial Engineering*, pages 571–583.

Ou, Y. and Zhang, H. (2018). Observability-based Mars autonomous navigation using formation flying spacecraft. *The Journal of Navigation*, 71(1):21–43.

Pike, E., van Graas, F., and Ugazio, S. (2022). Two and three satellite positioning using Doppler and pseudorange. In *Proceedings of International Technical Meeting of The Institute of Navigation*, pages 671–685.

Pinell, C. (2021). Receiver architectures for positioning with low Earth orbit satellite signals. Master's thesis, Lulea University of Technology, School of Electrical Engineering, Sweden.

Prol, F., Ferre, R., Välisuo, Z. S. P., Pinell, C., Lohan, E., Elsanhoury, M., Elmusrati, M., Islam, S., Celikbilek, K., Selvan, K., Yliaho, J., Rutledge, K., Ojala, A., Ferranti, L., andM. Bhuiyan, J. P., Kaasalainen, S., and Kuusniemi, H. (2022). Position, navigation, and timing (PNT) through low earth orbit (LEO) satellites: A survey on current status, challenges, and opportunities. *IEEE Access*, 10:83971–84002.

Psiaki, M. (2021). Navigation using carrier Doppler shift from a LEO constellation: TRANSIT on steroids. *NAVIGATION, Journal of the Institute of Navigation*, 68(3):621–641.

Reid, T., Chan, B., Goel, A., Gunning, K., Manning, B., Martin, J., Neish, A., Perkins, A., and Tarantino, P. (2020). Satellite navigation for the age of autonomy. In *Proceedings of IEEE/ION Position, Location and Navigation Symposium*, pages 342–352.

Reid, T., Walter, T., Enge, P., Lawrence, D., Cobb, H., Gutt, G., O'Conner, M., and Whelan, D. (2021). Position, navigation, and timing technologies in the 21st century. volume 2, chapter 43: Navigation from low Earth orbit – Part 1: Concept, Current Capability, and Future Promise, pages 1359–1379. Wiley-IEEE.

Rugh, W. (1996). *Linear System Theory*. Prentice Hall, Upper Saddle River, NJ, second edition.

Sabbagh, R. and Kassas, Z. (2023). Observability analysis of receiver localization via pseudorange measurements from a single LEO satellite. *IEEE Control Systems Letters*, 7(3):571–576.

Shen, D., Lu, J., Chen, G., Blasch, E., Sheaff, C., Pugh, M., and Pham, K. (2019). Methods of machine learning for space object pattern classification. In *Proceedings of IEEE National Aerospace and Electronics Conference*, pages 565–572.

Sullivan, J., Lovell, T., and D'Amico, S. (2018). Angles-only navigation for autonomous on-orbit space situational awareness applications. In *Proceedings of AAS/AIAA Astrodynamics Specialist Conference*.

Tan, Z., Qin, H., Cong, L., and Zhao, C. (2019). New method for positioning using IRIDIUM satellite signals of opportunity. *IEEE Access*, 7:83412–83423.

Thompson, S., Martin, S., and Bevly, D. (2020). Single differenced Doppler positioning with low Earth orbit signals of opportunity and angle of arrival estimation. In *Proceedings of ION International Technical Meeting*, pages 497–509.

Wang, K. and El-Mowafy, A. (2022). LEO satellite clock analysis and prediction for positioning applications. *Geo-spatial Information Science*, 25(1):14–33.

Wei, Q., Chen, X., and Zhan, Y. (2020). Exploring implicit pilots for precise estimation of LEO satellite downlink Doppler frequency. *IEEE Communications Letters*, 24(10):2270–2274.

Yong, L. and Zhang, A. (2019). Observability analysis and autonomous navigation for two satellites with relative position measurements. *Acta Astronautica*, 163:77–86.

Zhao, C., Qin, H., and Li, Z. (2022). Doppler measurements from multiconstellations in opportunistic navigation. *IEEE Transactions on Instrumentation and Measurement*, 71:1–9.

Observability Analysis of Receiver Localization via Pseudorange Measurements From a Single LEO Satellite

Ralph Sabbagh, *Student Member, IEEE*, and Zaher M. Kassas, *Senior Member, IEEE*

***Abstract*—This letter presents an observability analysis for terrestrial receiver localization via pseudorange measurements extracted from a single low Earth orbit (LEO) satellite. It is shown that a stationary receiver with an unknown state (position and time) can theoretically localize itself with a LEO satellite with a known state (position, velocity, and time). In addition, bounds on the determinant of the *l*-step observability matrix are derived and geometric interpretations are presented indicating directions of poor observability. The implications of the analysis on observability-aided LEO satellite selection are discussed. Experimental results are presented showcasing the conclusions of the observability analysis for a receiver localizing itself with a single Starlink satellite or a single Orbcomm satellite.**

***Index Terms*—Observability analysis, satellite selection, low Earth orbit, Starlink, Orbcomm.**

I. Introduction

THE ADVENT of low Earth orbit (LEO) satellite mega-constellations promises to revolutionize several domains, bringing unprecedented high-resolution images; remote sensing; and global, high-availability, high-bandwidth, and low-latency Internet [1]. Due to LEO satellites' inherently desirable attributes, namely: (i) geometric and spectral diversity, (ii) abundance, (iii) high received signal power, and (iv) high orbital velocity, LEO satellites offer an attractive alternative to global navigation satellite systems (GNSS), which reside in medium Earth orbit (MEO) [2], [3].

The promise of utilizing LEO satellites for navigation has been the subject of recent theoretical and experimental studies [4], [5]. In [6], a generalized geometric dilution of precision (GDOP) analysis was presented that used Doppler shifts extracted from eight or more LEO satellites to localize a receiver via a static estimator. In [7], an adaptive Kalman filter was developed, achieving the first carrier phase tracking and positioning results using six Starlink LEO satellites.

LEO satellites orbit the Earth at much higher rates than GNSS satellites. Contrast, for example, the orbital period of a GPS MEO satellite (11 hr, 58 min) with that of Orbcomm LEO satellites (about 99 min) and Starlink LEO satellites (about 96 min). This yields significant change in their geometry, which can be exploited to localize a terrestrial receiver with fewer satellites. In particular, while four GNSS satellites are needed to estimate the states of the receiver via a static estimator (e.g., nonlinear least squares), a single LEO satellite can be used to localize the receiver via a dynamic estimator (e.g., an extended Kalman filter (EKF)) by fusing consecutive LEO measurements taken over a relatively short period of time. A few studies demonstrating the impact of receiver localization using a small number of satellites have been conducted in the literature. In [8], pseudorange and Doppler measurements were combined for stationary receiver positioning using two and three satellites without the use of a base station or differential positioning techniques.

Observability analysis with LEO satellites has been studied in the context of space situational awareness with relative position measurements [9] and orbit determination with angles-only measurements [10]. Moreover, observability of *planar* environments comprising terrestrial transmitters with unknown positions and time have been studied in [11], where estimability was *numerically* assessed from the EKF's estimation error covariance, and in [12], where the Riccati equation was analyzed to conclude that *simultaneously* estimating the receiver's and transmitter's time is stochastically unobservable. However, observability analysis with a small number of LEO satellites in the context of localization has not been thoroughly studied. This letter analyzes the observability of *three-dimensional* receiver localization via pseudorange measurements extracted from the signals of a single LEO satellite. It is shown that a stationary receiver with an unknown state (position and time) can theoretically localize itself with a LEO satellite with a known state (position, velocity, and time). In addition, *analytical* bounds on the determinant of the *l*-step observability matrix are derived indicating directions of poor observability. It is concluded that the system becomes unobservable if the receiver is in the satellite's orbital plane or along the normal to the satellite's orbital plane. The implications of the analysis

Manuscript received 21 March 2022; revised 25 May 2022; accepted 17 June 2022. Date of publication 30 June 2022; date of current version 15 September 2022. This work was supported in part by the National Science Foundation (NSF) under Grant 1929965 and Grant 1929571, and in part by the U.S. Department of Transportation (USDOT) for the CARMEN University Transportation Center (UTC) under Grant 69A3552047138. Recommended by Senior Editor V. Ugrinovskii. *(Corresponding author: Zaher M. Kassas.)*

Ralph Sabbagh is with the Department of Mechanical and Aerospace Engineering, University of California, Irvine, CA 92697 USA (e-mail: rsabbag1@uci.edu).

Zaher M. Kassas is with the Department of Electrical and Computer Engineering, The Ohio State University, Columbus, OH 43210 USA (e-mail: zkassas@ieee.org).

Digital Object Identifier 10.1109/LCSYS.2022.3187522

2475-1456 © 2022 IEEE. Personal use is permitted, but republication/redistribution requires IEEE permission.
See https://www.ieee.org/publications/rights/index.html for more information.

Authorized licensed use limited to: The Ohio State University. Downloaded on September 16,2022 at 01:50:48 UTC from IEEE Xplore. Restrictions apply.

on observability-aided LEO satellite selection are discussed, where the presented surface plots of the observability matrix can aid in selecting the satellite with desired (i) visibility duration, (ii) elevation profile, and (iii) altitude and relative orbital inclination angle. Experimental results are presented showcasing the conclusions of the observability analysis for a receiver localizing itself with a single Starlink satellite or a single Orbcomm satellite.

This letter is structured as follows. Section II describes the dynamics and measurement models. Section III analyzes analytically the observability of receiver localization using pseudorange measurements from a single LEO satellite and gives geometric interpretations of the derived results. Section IV presents experimental results with Orbcomm and Starlink LEO satellites, demonstrating the implications of the observability analysis on the estimation performance.

II. Preliminaries and Model Description

A. Observability of LTV Systems

Consider the discrete-time (DT) linear time-varying (LTV) dynamical system Σ given by

$$\Sigma : \begin{cases} \boldsymbol{x}(k+1) = \mathbf{F}(k)\,\boldsymbol{x}(k) + \mathbf{G}(k)\,\boldsymbol{u}(k), \\ \boldsymbol{y}(k) = \mathbf{H}(k)\,\boldsymbol{x}(k), \end{cases} \tag{1}$$

where $\boldsymbol{x} \in \mathbb{R}^n$, $\boldsymbol{u} \in \mathbb{R}^p$, and $\boldsymbol{y} \in \mathbb{R}^q$ are the system state, input, and measurement vectors at time-step k, respectively, and $k \in \mathbb{N}$. The state transition matrix corresponding to Σ from time-step j to time-step i is given by

$$\Phi(i,j) \triangleq \begin{cases} \mathbf{F}(i-1)\,\mathbf{F}(i-2)\cdots\mathbf{F}(j), & \text{if } i > j, \\ \mathbf{I}_{n\times n}, & \text{if } i = j, \end{cases}$$

where $\mathbf{I}_{n\times n}$ denotes an $n \times n$ identity matrix. The following theorem characterizes the observability of DT LTV systems via the l-step observability matrix [13].

Theorem 1: The DT LTV system (1) is l-step observable if and only if its corresponding l-step observability matrix

$$\mathcal{O}(k, k+l-1) \triangleq \begin{bmatrix} \mathbf{H}(k)\,\Phi(k,k) \\ \mathbf{H}(k+1)\,\Phi(k+1,k) \\ \vdots \\ \mathbf{H}(k+l-1)\,\Phi(k+l-1,k) \end{bmatrix}, \tag{2}$$

is full rank. Theorem 1 can be applied to nonlinear systems by linearizing at each time-step k around $\boldsymbol{x}(k)$. The achieved observability results therein will only be valid locally [14].

B. Receiver Dynamics

The terrestrial receiver's position $\boldsymbol{r}_r \in \mathbb{R}^3$ is assumed to be fixed in the Earth-centered inertial (ECI) frame and its distance from the center of Earth is denoted by $r = \|\boldsymbol{r}_r\|_2$. The dynamics of the receiver's clock error states (i.e., bias δt_r and drift $\dot{\delta t}_r$) is modeled as a double integrator driven by process noise [15]. The receiver's dynamics is then given by

$$\boldsymbol{x}_r(k+1) = \mathbf{F}_r\,\boldsymbol{x}_r(k) + \boldsymbol{w}_r(k),$$

where $\boldsymbol{x}_r \triangleq \left[\boldsymbol{r}_r^\mathsf{T},\, c\,\delta t_r,\, c\,\dot{\delta t}_r\right]^\mathsf{T}$ is the receiver's state vector, c denotes the speed of light, and $\boldsymbol{w}_r$ is a process noise modeled as a zero-mean white random sequence with covariance $\mathbf{Q}_r = \mathrm{diag}[\mathbf{0}_{3\times3},\, \mathbf{Q}_{cr}]$. The receiver state matrix is given by

$$\mathbf{F}_r = \begin{bmatrix} \mathbf{I}_{3\times3} & \mathbf{0}_{3\times2} \\ \mathbf{0}_{2\times3} & \mathbf{F}_{\text{clk}} \end{bmatrix}, \quad \mathbf{F}_{\text{clk}} = \begin{bmatrix} 1 & T \\ 0 & 1 \end{bmatrix},$$

where T is the sampling period. In this letter, the simplest receiver dynamics was considered to focus on the change in geometry due to the moving satellite. More elaborate receiver dynamics could be considered in future work.

C. LEO Satellite Dynamics

The LEO satellite is assumed to follow a circular Keplerian orbit with fixed inclination and a prescribed orbital radius denoted by $a = \|\boldsymbol{r}_s(t)\|_2$ where $0 < r < a$. Under the action of Earth's gravitational field, the satellite's orbital dynamics in continuous-time will be assumed to follow a simplified two-body model given by

$$\ddot{\boldsymbol{r}}_s(t) = -\frac{\mu}{a^3}\,\boldsymbol{r}_s(t) + \boldsymbol{w}_s(t), \tag{3}$$

where $\boldsymbol{r}_s \in \mathbb{R}^3$ is the satellite's position in the ECI frame and $\boldsymbol{w}_s$ is a process noise vector of acceleration perturbations resulting from Earth's non-uniform gravitational potential, atmospheric drag, solar radiation pressure, gravitational pull of other celestial bodies, and general relativity [16]. The following constraints on the satellite dynamics hold $\forall\, t > 0$

$$\begin{aligned} \langle \boldsymbol{r}_s(t), \boldsymbol{r}_s(t) \rangle &= a^2, \\ \langle \dot{\boldsymbol{r}}_s(t), \dot{\boldsymbol{r}}_s(t) \rangle &= \alpha^2\, a^2, \\ \langle \boldsymbol{r}_s(t), \dot{\boldsymbol{r}}_s(t) \rangle &= 0, \end{aligned}$$

where $\alpha^2 \triangleq \mu/a^3$. The dynamics of the satellite's clock bias δt_s and drift $\dot{\delta t}_s$ are modeled similarly to the receiver's clock error dynamics [15]. Next, the satellite dynamics in (3) can be discretized at a sampling period T to yield

$$\boldsymbol{x}_s(t_{k+1}) = \mathbf{F}_s\,\boldsymbol{x}_s(t_k) + \boldsymbol{w}_s(t_k),$$

where $\boldsymbol{x}_s = [\boldsymbol{r}_s^\mathsf{T},\, \dot{\boldsymbol{r}}_s^\mathsf{T},\, c\,\delta t_s,\, c\,\dot{\delta t}_s]^\mathsf{T}$ is the satellite's state vector and $\boldsymbol{w}_s$ is a process noise modeled as a zero-mean white random sequence with covariance $\mathbf{Q}_s$, and $\mathbf{F}_s$ is given by

$$\mathbf{F}_s = \begin{bmatrix} \cos(\alpha T)\,\mathbf{I}_{3\times3} & (1/\alpha)\,\sin(\alpha T)\,\mathbf{I}_{3\times3} & \mathbf{0}_{3\times2} \\ -\alpha\,\sin(\alpha T)\,\mathbf{I}_{3\times3} & \cos(\alpha T)\,\mathbf{I}_{3\times3} & \mathbf{0}_{3\times2} \\ \mathbf{0}_{2\times3} & \mathbf{0}_{2\times3} & \mathbf{F}_{\text{clk}} \end{bmatrix}.$$

D. Measurement Model

The pseudorange measurement extracted by the receiver from the satellite signals at time-step k, after compensating for ionospheric and tropospheric delays [3], is modeled as

$$\rho(k) = \|\boldsymbol{r}_r - \boldsymbol{r}_s(k')\|_2 + c\left(\delta t_r(k) - \delta t_s(k')\right) + \nu(k), \tag{4}$$

where k' represents discrete-time $t_k = k\,T - \delta t_{TOF}$ with δt_{TOF} being the transmission delay of the signal. The term ν is the measurement noise, which is modeled as a zero-mean white Gaussian sequence with variance σ^2.

Authorized licensed use limited to: The Ohio State University. Downloaded on September 16,2022 at 01:50:48 UTC from IEEE Xplore. Restrictions apply.

III. Observability Analysis

This section analyzes the observability of receiver localization with a single LEO satellite under two scenarios. The first scenario considers a receiver with *unknown* position states but *known* clock error states. Results from this simple scenario will serve as a stepping stone towards the second scenario, which considers a receiver with *unknown* position states and *unknown* clock error states. In each scenario, the satellite's states are assumed to be known, which is the case whenever (i) a satellite transmits its ephemeris and clock errors (e.g., Orbcomm satellites transmit their states, estimated from onboard GPS receivers [3]) or (ii) an estimator is employed to estimate the LEO satellite's states (e.g., via a differential navigation framework utilizing a known base receiver [17] or via a simultaneous tracking and navigation (STAN) framework [3]). It is worth noting that instead of estimating the receiver's clock error states, the following analysis readily extends to the case of estimating the *difference* between the receiver's and LEO satellite's clock error states, $\Delta\delta t \triangleq \delta t_r - \delta t_s$ and $\Delta\dot{\delta} t \triangleq \dot{\delta} t_r - \dot{\delta} t_s$, which could be desirable for stochastic observability considerations [12]. The nonlinear pseudorange measurement (4) is linearized at time-step k with respect to the unknown receiver states and the corresponding Jacobian matrix is used to build the l-step observability matrix. The scenarios are summarized below

- *Scenario 1:* A stationary receiver with *unknown position states* but *known clock error states* makes pseudorange measurements to a LEO satellite with *known states*. The measurement Jacobian is given by $\mathbf{H}(k) = \boldsymbol{l}_k^{\mathsf{T}}$.
- *Scenario 2:* A stationary receiver with *unknown position states and clock error states* makes pseudorange measurements to a LEO satellite with *known states*. The measurement Jacobian is given by $\mathbf{H}(k) = \begin{bmatrix}\boldsymbol{l}_k^{\mathsf{T}} & 1 & 0\end{bmatrix}$.

Above, $\boldsymbol{l}_k \in \mathbb{R}^3$ denotes the unit line-of-sight (LOS) vector between the receiver and satellite at time-step k, given by

$$\boldsymbol{l}_k \triangleq \frac{\boldsymbol{r}_r - \boldsymbol{r}_s(k)}{\|\boldsymbol{r}_r - \boldsymbol{r}_s(k)\|_2}.$$

In what follows, the l-step observability of the aforementioned scenarios is investigated, and bounds on the determinants of observability matrices therein are derived.

A. Scenario 1: Pseudorange Measurements With Unknown Receiver Position States But Known Clock Error States

In this scenario, the only unknown states are the receiver's position, and the 3-step observability matrix is given by

$$\mathcal{O}(k, k+2) = \begin{bmatrix}\boldsymbol{l}_k & \boldsymbol{l}_{k+1} & \boldsymbol{l}_{k+2}\end{bmatrix}^{\mathsf{T}}, \tag{5}$$

where the transition matrix $\Phi = \mathbf{I}_{3\times 3}$ and the measurement Jacobian $\mathbf{H}(k) = l_k^{\mathsf{T}}$ are used to build $\mathcal{O}(k, k+2)$. Let $\mathcal{O}(k, k+2) \triangleq \mathcal{O}_3$. An expression for $\det(\mathcal{O}_3)$ is derived as a function of the relative geometry between the receiver and the satellite.

Theorem 2: Let $c_n \triangleq \cos(\alpha n T)$, $s_n \triangleq \sin(\alpha n T)$, and

$$\beta^k \triangleq \frac{1}{\|\Delta\boldsymbol{r}(k)\|_2 \, \|\Delta\boldsymbol{r}(k+1)\|_2 \, \|\Delta\boldsymbol{r}(k+2)\|_2},$$

where $\Delta\boldsymbol{r}(k) \triangleq \boldsymbol{r}_r - \boldsymbol{r}_s(k)$. The determinant of the 3-step observability matrix in (5) is given by

$$\det(\mathcal{O}_3) = \beta^k \, (2\, s_1 - s_2)\, a^2 \, r \, \sin(\theta), \tag{6}$$

where θ is the angle between the receiver's position vector $\boldsymbol{r}_r$ and the orbital plane of the LEO satellite.

Proof: Since $\mathcal{O}_3$ is a 3×3 matrix, its determinant is equal to the scalar triple product of its rows which are given by the unit LOS vectors $\boldsymbol{l}_k$, $\boldsymbol{l}_{k+1}$, and $\boldsymbol{l}_{k+2}$ as follows

$$\begin{aligned}\det(\mathcal{O}_3) &= \boldsymbol{l}_k \cdot (\boldsymbol{l}_{k+1} \times \boldsymbol{l}_{k+2}) \\ &= \beta^k \, \Delta\boldsymbol{r}(k) \cdot (\Delta\boldsymbol{r}(k+1) \times \Delta\boldsymbol{r}(k+2)),\end{aligned} \tag{7}$$

where the terms $r_s(k+1)$ in $\Delta r(k+1)$ and $r_s(k+2)$ in $\Delta r(k+2)$ can be written in terms of $r_s(k)$ and $\dot{r}_s(k)$ using the satellite dynamics $\mathbf{F}_s$ defined in Section II-C as follows

$$\Delta\boldsymbol{r}(k+1) = \boldsymbol{r}_r - c_1 \, \boldsymbol{r}_s(k) - \frac{1}{\alpha} s_1 \, \dot{\boldsymbol{r}}_s(k), \tag{8}$$

$$\Delta\boldsymbol{r}(k+2) = \boldsymbol{r}_r - c_2 \, \boldsymbol{r}_s(k) - \frac{1}{\alpha} s_2 \, \dot{\boldsymbol{r}}_s(k). \tag{9}$$

Plugging (8) and (9) in (7) yields

$$\begin{aligned}\det(\mathcal{O}_3) &= \frac{\beta^k \, (2\, s_1 - s_2)}{\alpha} \left(\boldsymbol{r}_r \cdot (\boldsymbol{r}_s(k) \times \dot{\boldsymbol{r}}_s(k))\right) \\ &= \beta^k \, (2\, s_1 - s_2)\, a^2 \, r \, \sin(\theta).\end{aligned}$$

■

Hereafter, θ is referred to as the *relative orbital inclination angle* between the receiver and the LEO satellite. Ideally, θ is assumed constant for a stationary receiver during the time window through which it is seeing a LEO satellite. In what follows, time-independent bounds on $\det(\mathcal{O}_3)$ are derived.

Corollary 1: The determinant of the 3-step observability matrix in (5) can be bounded as follows

$$0 \le L(\theta) \le \det(\mathcal{O}_3) \le U(\theta),$$

$$L(\theta) = \frac{(2\, s_1 - s_2)\, a^2 \, r \, \sin(\theta)}{\left(a^2 + r^2 + 2\, a\, r \, \cos(\theta)\right)^{3/2}},$$

$$U(\theta) = \frac{(2\, s_1 - s_2)\, a^2 \, r \, \sin(\theta)}{\left(a^2 + r^2 - 2\, a\, r \, \cos(\theta)\right)^{3/2}},$$

where $0 \le \theta \le \pi/12$ and $0 \le \alpha \, k \, T \le \pi/6$ for all $k \in \mathbb{N}$.

Proof: Using the law of cosines, the minimum and maximum Euclidean distances between the receiver and the satellite; denoted by d_{min} and d_{max}, respectively, are given by

$$\min_{k\in\mathbb{N}} \|\boldsymbol{r}_r - \boldsymbol{r}_s(k)\|_2 = \left(a^2 + r^2 - 2\, a\, r \, \sin(\theta)\right)^{1/2}, \tag{10}$$

$$\max_{k\in\mathbb{N}} \|\boldsymbol{r}_r - \boldsymbol{r}_s(k)\|_2 = \left(a^2 + r^2 + 2\, a\, r \, \sin(\theta)\right)^{1/2}, \tag{11}$$

such that $d_{max}^{-3} \le \beta^k \le d_{min}^{-3}$ for all $k \in \mathbb{N}$. ■

The inequalities on θ and $\alpha \, k \, T$ are placed with the understanding that a LEO satellite should be visible for a long enough time to provide useful measurements. Next, observability results and geometric interpretations are deduced.

Proposition 1: If the receiver is in the orbital plane of the LEO satellite, the system is not l-step observable.

Proof: If the receiver is in the orbital plane of the LEO satellite, then $\theta = 0$. This implies that $U(\theta) = U(0) = 0$. As a result, $\det(\mathcal{O}_3) = 0$ and $\mathcal{O}_3$ is rank deficient. In fact, the rows of $\mathcal{O}_l$, which represent consecutive unit LOS vectors tracing the satellite's orbit, are coplanar lying in the orbital plane of the satellite. As a result, $\text{rank}[\mathcal{O}_l] \le 2$, for all $l \ge 2$. ■

Authorized licensed use limited to: The Ohio State University. Downloaded on September 16,2022 at 01:50:48 UTC from IEEE Xplore. Restrictions apply.

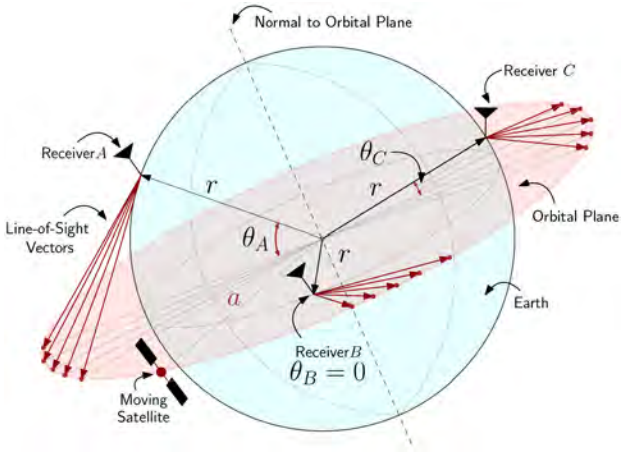

Fig. 1. Comparison between the geometric diversity of the LOS vectors based on the relative orbital inclinations θ_A, θ_B, and θ_C ($\theta_A \gg \theta_C \gg \theta_B$) created between the LEO satellite and receivers A, B, and C, respectively. Receiver A makes LOS measurements that are relatively closer to each other compared to receiver C (large θ), and receiver B makes LOS measurements that are coplanar in the orbital plane of the LEO satellite (small θ).

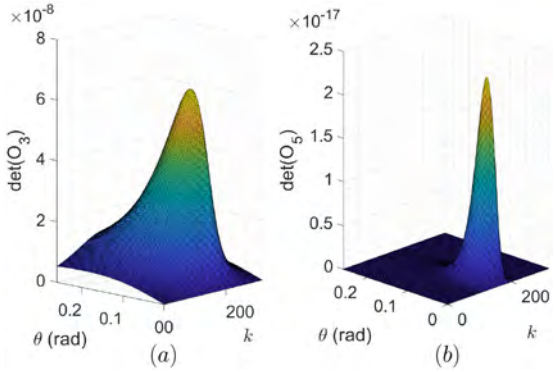

Fig. 2. Values of $\det(\mathcal{O}_3)$ (left) and $\det(\mathcal{O}_5)$ (right) computed for different values of θ in radians at each time-step k.

Remark 1: The unobservable subspace in the case above is spanned by the normal to the satellite's orbital plane, otherwise known as the satellite's cross direction. This implies that initial receiver position states along this direction are indistinguishable. The impact of this on localization using a single overhead LEO satellite is demonstrated in Section IV.

Proposition 2: If the receiver is not in the orbital plane of the LEO satellite, the system is l-step observable for $l \geq 3$.

Proof: If the receiver is not in the orbital plane of the LEO satellite, then $\theta \neq 0$. As a result, $L(\theta) > L(0) > 0$, and $\det(\mathcal{O}_3) \neq 0$ with $\text{rank}[\mathcal{O}_l] = 3$, for all $l \geq 3$. In fact, the rows of $\mathcal{O}_l$, which represent consecutive unit LOS vectors tracing the satellite's orbit, are no longer coplanar. This implies that the corresponding scalar triple product of any three consecutive unit LOS vectors is nonzero within a single orbital period. ■

The above analysis and (6) show that the size of θ normalized by the cube of the receiver-satellite range can measure how close the l-step observability matrix is to singularity ($\det(\mathcal{O}_3) \propto \beta^k \sin(\theta)$). As a result, a relationship between the singularity of $\mathcal{O}_3$ and the geometric diversity of the unit LOS vectors can be established. Namely, for small θ, the receiver is near the orbital plane of the satellite so that the LOS vectors are almost *coplanar*. For large θ, the receiver is far enough from the satellite so that the LOS vectors are almost *collinear*. In both extremes, the LOS vectors have poor geometric diversity. An exaggerated comparison illustrating the impact of θ on the geometric diversity of the LOS vectors is shown in Fig. 1, where three receiver positions resulting in three drastically different values of θ result in LOS vectors with varying geometric diversity. A study on the singularity of $\mathcal{O}_3$ is shown in Fig. 2(a), where the values of $\det(\mathcal{O}_3)$ were computed from simulated LOS vectors created between a stationary receiver and a satellite traveling along a circular orbit at an altitude of 521 km (computations were repeated for varying values of $\theta \in [0,\ \pi/12]$). It is observed that $\det(\mathcal{O}_3)$ drastically diminishes for θ values which are too small or too large, implying that a "favorable" relative orbital inclination region (shown in Fig. 2 in yellow) lying in between the two extremes exists where $\det(\mathcal{O}_3)$ is maximal over the navigation window of the receiver. Implications of this on observability-based satellite selection is discussed in Section IV.

B. Scenario 2: Pseudorange Measurements With Unknown Receiver Position States and Unknown Clock Error States

In this scenario, the receiver state is unknown, and the 5-step observability matrix is given by

$$\mathcal{O}(k, k+4) = \begin{bmatrix} \boldsymbol{l}_k & \boldsymbol{l}_{k+1} & \boldsymbol{l}_{k+2} & \boldsymbol{l}_{k+3} & \boldsymbol{l}_{k+4} \\ 1 & 1 & 1 & 1 & 1 \\ 0 & T & 2T & 3T & 4T \end{bmatrix}^{\mathsf{T}}, \quad (12)$$

where the transition matrix $\Phi = \mathbf{F}_r \in \mathbb{R}^{5\times 5}$ and the measurement Jacobian $\mathbf{H}(k) = [\boldsymbol{l}_k^{\mathsf{T}} \quad 1 \quad 0] \in \mathbb{R}^{1\times 5}$ are used to build $\mathcal{O}(k, k+4)$. Let $\mathcal{O}(k, k+4) \triangleq \mathcal{O}_5$. Next, an expression for $\det(\mathcal{O}_5)$ is derived as a function of the relative geometry between the receiver and the satellite.

Proposition 3: Let m, n, and $p \in \mathbb{N}$ with $m < n < p$, then the following equality holds

$$\boldsymbol{l}_m \cdot (\boldsymbol{l}_n \times \boldsymbol{l}_p) = \gamma_{mnp}\, \beta_{mnp}^k\, a^2\, r\, \sin(\theta),$$

where the scalars $\gamma_{mnp} > 0$ and $\beta_{mnp}^k > 0$ are given by

$$\gamma_{mnp} \triangleq s_{n-m} + s_{p-n} - s_{p-m},$$
$$\beta_{mnp}^k \triangleq \frac{1}{\|\Delta \boldsymbol{r}(k+m)\|_2\, \|\Delta \boldsymbol{r}(k+n)\|_2\, \|\Delta \boldsymbol{r}(k+p)\|_2},$$

where $0 \leq \theta \leq \pi/12$ and $0 \leq \alpha\, k\, T \leq \pi/6$ for all $k \in \mathbb{N}$.

Proof: The proof proceeds similarly to that of Theorem 2. ■

Theorem 3: The determinant of the 5-step observability matrix in (12) is given by

$$\det(\mathcal{O}_5) = T\,(a_1 - a_2 + a_3 - a_4)\, a^2\, r\, \sin(\theta), \quad (13)$$

where a_1, a_2, a_3, and a_4 are scalars given by

$$a_1 = \gamma_{012}\,(\beta_{012}^k + \beta_{234}^k) + \gamma_{014}\,(\beta_{014}^k + \beta_{034}^k),$$
$$a_2 = 2\left(\gamma_{013}\,\beta_{013}^k + \gamma_{024}\,\beta_{024}^k + \gamma_{134}\,\beta_{134}^k\right),$$
$$a_3 = 3\,\gamma_{023}\left(\beta_{023}^k + \beta_{124}^k\right),$$
$$a_4 = 4\,\gamma_{123}\,\beta_{123}^k.$$

Authorized licensed use limited to: The Ohio State University. Downloaded on September 16,2022 at 01:50:48 UTC from IEEE Xplore. Restrictions apply.

Proof: The determinant of $\mathcal{O}_5$ can be expressed in terms of a product of determinants involving block partitions of $\mathcal{O}_5$ via the Schur complement formula as follows

$$\det(\mathcal{O}_5) = \det(\mathbf{D})\,\det(\mathbf{A} - \mathbf{B}\mathbf{D}^{-1}\mathbf{C}), \tag{14}$$

where the matrices $\mathbf{A}$, $\mathbf{B}$, $\mathbf{C}$, and $\mathbf{D}$ are given by

$$\mathbf{A} = \begin{bmatrix} \boldsymbol{l}_k & \boldsymbol{l}_{k+1} & \boldsymbol{l}_{k+2} \end{bmatrix}^{\mathsf{T}},\ \mathbf{B} = \begin{bmatrix} 1 & 1 & 1 \\ 0 & T & 2T \end{bmatrix}^{\mathsf{T}},$$

$$\mathbf{C} = \begin{bmatrix} \boldsymbol{l}_{k+3} & \boldsymbol{l}_{k+4} \end{bmatrix}^{\mathsf{T}},\ \text{and}\ \mathbf{D} = \begin{bmatrix} 1 & 1 \\ 3T & 4T \end{bmatrix}^{\mathsf{T}}.$$

Plugging the above expressions for matrices $\mathbf{A}$, $\mathbf{B}$, $\mathbf{C}$, and $\mathbf{D}$ in equation (14) and expanding yields

$$\det(\mathcal{O}_5) = T \begin{vmatrix} \boldsymbol{l}_k^{\mathsf{T}} - 4\boldsymbol{l}_{k+3}^{\mathsf{T}} + 3\boldsymbol{l}_{k+4}^{\mathsf{T}} \\ \boldsymbol{l}_{k+1}^{\mathsf{T}} - 3\boldsymbol{l}_{k+3}^{\mathsf{T}} + 2\boldsymbol{l}_{k+4}^{\mathsf{T}} \\ \boldsymbol{l}_{k+2}^{\mathsf{T}} - 2\boldsymbol{l}_{k+3}^{\mathsf{T}} + \boldsymbol{l}_{k+4}^{\mathsf{T}} \end{vmatrix}.$$

Hence, $\det(\mathcal{O}_5)$ is now expressed in terms of the determinant of a 3×3 matrix which is equal to the scalar triple product of its rows. By expanding this product, the resulting terms can be grouped using Proposition 3, resulting in (13). ■

Time-independent bounds on $\beta^k_{m,n,p}$ can be derived as in the proof of Corollary 1, so that $d_{max}^{-3} \leq \beta^k_{mnp} \leq d_{min}^{-3}$ for all k, m, n, and $p \in \mathbb{N}$. Bounds on $\det(\mathcal{O}_5)$ are presented next.

Corollary 2: The determinant of the 5-step observability matrix in (13) can be bounded as follows

$$L(\theta) \leq \det(\mathcal{O}_5) \leq U(\theta),$$

$$L(\theta) = 16\, s_1^3\,(1 - c_1)\, a^2\, r\, T \left(\frac{1}{d_{max}^3} - \frac{1}{d_{min}^3} \right) \sin(\theta),$$

$$U(\theta) = 16\, s_1^3\,(1 - c_1)\, a^2\, r\, T \left(\frac{1}{d_{min}^3} - \frac{1}{d_{max}^3} \right) \sin(\theta),$$

where $0 \leq \theta \leq \pi/12$ and $0 \leq \alpha\, k\, T \leq \pi/6$ for all $k \in \mathbb{N}$.

Proof: The proof proceeds similarly to that of Corollary 1. ■

Based on Theorem 3 and Corollary 2, the following observability results and geometric interpretations are deduced.

Proposition 4: If the receiver is in the orbital plane of the satellite or along the normal to the orbital plane of the satellite, the system is not l-step observable.

Proof: By construction, unobservable directions in Scenario I are inherited into Scenario II where additional receiver states are now unknown. Furthermore, if the receiver is along the normal to the orbital plane of the satellite, the minimum and maximum Euclidean distances between the receiver and the LEO satellite become equal which results in $U(\theta) = U(\frac{\pi}{2}) = 0$ and $L(\theta) = L(\frac{\pi}{2}) = 0$, implying that $\det(\mathcal{O}_5) = 0$. In fact, since a constant distance is maintained between the receiver-satellite pair, the stationary receiver can no longer disambiguate between its initial clock bias and the initial range from the satellite, no matter how many pseudorange measurements it makes from that satellite. At best, a one-dimensional unobservable subspace of $\mathbb{R}^5$ is maintained, so that $\text{rank}[\mathcal{O}_l] \leq 4$, for all $l \geq 4$. ■

Proposition 5: If the receiver is not in the orbital plane of the satellite, nor along the normal to the satellite's orbital plane, the system is l-step observable for $l \geq 5$.

Proof: It is enough to show by contradiction that the matrix $\mathcal{O}_5$ in this setting is non-singular. To that end, assume that there exists a nontrivial vector $\boldsymbol{v} \in \mathbb{R}^5$ such that $\mathcal{O}_5 \cdot \boldsymbol{v} = \mathbf{0}_{5\times 1}$. By partitioning $\boldsymbol{v}$ such that $\boldsymbol{v} = [\boldsymbol{u}^{\mathsf{T}}\ \ s\ \ w]^{\mathsf{T}}$ where $\boldsymbol{u} \in \mathbb{R}^3$, $s \in \mathbb{R}$, one obtains the following system of 5 equations:

$$\begin{cases} \langle \boldsymbol{l}_k, \boldsymbol{u} \rangle = -s \\ \langle \boldsymbol{l}_{k+1}, \boldsymbol{u} \rangle = -s - T\,w \\ \langle \boldsymbol{l}_{k+2}, \boldsymbol{u} \rangle = -s - 2\,T\,w \\ \langle \boldsymbol{l}_{k+3}, \boldsymbol{u} \rangle = -s - 3\,T\,w \\ \langle \boldsymbol{l}_{k+4}, \boldsymbol{u} \rangle = -s - 4\,T\,w. \end{cases} \tag{15}$$

From (15), it follows that $\boldsymbol{u}$ must make either constant or linearly increasing angles with 5 consecutive unit LOS vectors tracing the satellite's circular Keplerian orbit. Since the receiver is not in the orbital plane of the satellite, any 3 vectors chosen from 5 consecutive unit LOS vectors within a single orbital period are non-coplanar. If in addition, the receiver is not along the normal to the orbital plane of the satellite, then the corresponding difference vectors between the 5 unit LOS vectors are not coplanar and with same length. This implies that $\boldsymbol{u}$ must be the trivial vector, concluding the proof. ■

The observability surface in Fig. 2(b) is significantly smaller compared to Fig. 2(a). This reflects poorer observability conditions and loss of information due to the addition of unknown receiver states to the system. Finally, while the unobservable subspaces discussed are of zero measure and assume an ideal setting (perfect knowledge of a circular satellite ephemeris, non-rotating spherical Earth, etc), in a real setting, the satellite's orbit will experience random perturbations such that a receiver localizing itself would not lie exactly along the derived unobservable subspaces. Despite this, Section IV will show that a receiver still fails to localize itself due to the unobservable direction derived in the ideal setting.

IV. Experimental Results

To demonstrate the conclusions of the observability analysis on receiver localization, an experiment was conducted whereby pseudorange measurements, extracted from carrier phase observables [7], [17], from one Starlink satellite and one Orbcomm satellite were used to localize a stationary receiver using an EKF for LEO satellite visibility durations of 74 and 317 seconds, respectively. The Starlink and Orbcomm satellites possess average relative orbital inclinations of $\theta = 0.01457$ rad and $\theta = 0.00410$ rad, respectively, indicating that the receiver is relatively close to being in their orbital planes during each navigation window. For both satellites, the analysis in Section III shows that the determinant of the corresponding observability matrices is expected to be small enough so that the directions normal to the LEO satellites' orbital planes become nearly unobservable. The objective of the experiment is therefore to demonstrate that receiver localization using near-overhead passing LEO satellites will suffer from poor information in the direction normal to the LEO satellite's orbital plane. This implies that any initial receiver position error in the direction along the normal to the LEO satellite's orbital plane will not reduce in the EKF, due to the observability matrix being nearly singular. For the Starlink satellite, the satellite's states were estimated according to the framework discussed in [7], which estimated the satellite's ephemeris via simplified general perturbation 4 (SGP4)

Authorized licensed use limited to: The Ohio State University. Downloaded on September 16,2022 at 01:50:48 UTC from IEEE Xplore. Restrictions apply.

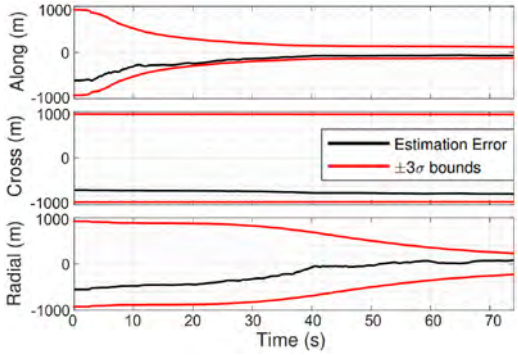

Fig. 3. Receiver position estimation errors resolved along the Starlink satellite body frame (in black) with $\pm 3\sigma$ bounds (in red).

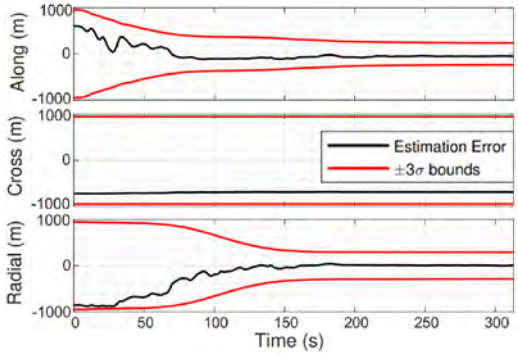

Fig. 4. Receiver position estimation errors resolved along the Orbcomm satellite body frame (in black) with $\pm 3\sigma$ bounds (in red).

TABLE I
RECEIVER LOCALIZATION ERROR

Satellite	Direction	Initial Error	Final Error
Starlink	Along (m)	-603.94	-67.14
	Cross (m)	-682.25	–768.41
	Radial (m)	-555.90	81.40
	Overall (m)	1,067.35	775.62
Orbcomm	Along (m)	604.47	-51.35
	Cross (m)	-722.25	-689.29
	Radial (m)	-856.47	7.79
	Overall (m)	1,273.30	691.24

orbit propagator initialized with two-line element (TLE) files. For the Orbcomm satellite, the satellite's states were obtained by decoding the downlink signal, which contains ephemeris and clock errors, estimated via the satellite's onboard GPS receivers [17]. The localization results are shown in Figs. 3 and 4, where the receiver's position estimation errors and the $\pm 3\sigma$-bounds are resolved along the LEO satellite's body frame (along-track, cross-track, and radial directions). Table I shows the initial and final receiver position estimation errors in each direction. It can be seen from Figs. 3 and 4 and Table I that while the receiver's position error in the along-track and radial directions decreases, there is no improvement in the cross-track direction. This confirms the observability result discussed in Section III, stating that the direction normal to the orbital plane of the satellite is unobservable for a receiver making measurements from incoming overhead satellites. Fig. 2 can be utilized for observability-based satellite selection to improve receiver localization. To this end, based on LEO satellite's SGP4-propagated TLE files, estimates for their respective altitudes as well as angles θ of their orbital planes with the receiver can be used to predict and select the satellite which will generate a navigation scenario which is most observable. Namely, given a set of LEO satellites, one can identify the one which will result in the best receiver localization performance, by taking into account the following criteria, which are all features of the observability surfaces shown in Fig. 2:

- The duration of time for which the satellite will be visible.
- The elevation profile of the satellite during this time.
- Satellite altitudes and relative orbital inclinations θ.

While the analysis in this letter considered a single LEO satellite, future work could generalize to multiple satellites and develop an observability-aided LEO satellite selection approach that determines the satellites that are expected to provide the best measurements for receiver localization.

REFERENCES

[1] S. Liu *et al.*, "LEO satellite constellations for 5G and beyond: How will they reshape vertical domains?" *IEEE Commun. Mag.*, vol. 59, no. 7, pp. 30–36, Jul. 2021.

[2] T. Reid *et al.*, "Navigation from low earth orbit—Part 1: Concept, current capability, and future promise," in *Position, Navigation, and Timing Technologies in the 21st Century*, vol. 2, J. Morton, F. van Diggelen, J. Spilker, Jr., and B. Parkinson, Eds. Hoboken, NJ, USA: Wiley-IEEE, 2021, ch. 43, pp. 1359–1379.

[3] Z. Kassas, "Navigation from low earth orbit—Part 2: Models, implementation, and performance," in *Position, Navigation, and Timing Technologies in the 21st Century*, vol. 2, J. Morton, F. van Diggelen, J. Spilker, Jr., and B. Parkinson, Eds. Hoboken, NJ, USA: Wiley-IEEE, 2021, ch. 43, pp. 1381–1412.

[4] Q. Wei, X. Chen, and Y. F. Zhan, "Exploring implicit pilots for precise estimation of LEO satellite downlink doppler frequency," *IEEE Commun. Lett.*, vol. 24, no. 10, pp. 2270–2274, Oct. 2020.

[5] S. Thompson, S. Martin, and D. Bevly, "Single Differenced doppler positioning with low earth orbit signals of opportunity and angle of arrival estimation," in *Proc. ION Int. Tech. Meeting*, 2020, pp. 497–509.

[6] M. Psiaki, "Navigation using carrier doppler shift from a LEO constellation: TRANSIT on steroids," *J. Inst. Navig.*, vol. 68, no. 3, pp. 621–641, Sep. 2021.

[7] J. Khalife, M. Neinavaie, and Z. Kassas, "The first carrier phase tracking and positioning results with starlink LEO satellite signals," *IEEE Trans. Aerosp. Electron. Syst.*, vol. 56, no. 2, pp. 1487–1491, Apr. 2022.

[8] E. Pike, F. van Graas, and S. Ugazio, "Two and three satellite positioning using doppler and pseudorange," in *Proc. Int. Tech. Meeting Inst. Navig.*, 2022, pp. 671–685.

[9] A. Friedman, "Observability analysis for space situational awareness," Ph.D. dissertation, Dept. Aeronaut. Astronaut., Purdue Univ., West Lafayette, IN, USA, 2020.

[10] E. Kaufman, T. Lovell, and T. Lee, "Nonlinear observability for relative orbit determination with angles-only measurements," *J. Astronaut. Sci.*, vol. 63, no. 1, pp. 60–80, 2016.

[11] Z. Kassas and T. Humphreys, "Observability and estimability of collaborative opportunistic navigation with pseudorange measurements," in *Proc. ION GNSS Conf.*, Sep. 2012, pp. 621–630.

[12] J. Morales and Z. Kassas, "Stochastic observability and uncertainty characterization in simultaneous receiver and transmitter localization," *IEEE Trans. Aerosp. Electron. Syst.*, vol. 55, no. 2, pp. 1021–1031, Apr. 2019.

[13] W. Rugh, *Linear System Theory*, 2nd ed. Upper Saddle River, NJ, USA: Prentice Hall, 1996.

[14] G. Huang, A. Mourikis, and S. Roumeliotis, "Observability-based rules for designing consistent EKF SLAM estimators," *Int. J. Robot. Res.*, vol. 29, no. 5, pp. 502–528, Apr. 2010.

[15] Y. Bar-Shalom, X. Li, and T. Kirubarajan, *Estimation With Applications to Tracking and Navigation*. New York, NY, USA: Wiley, 2002.

[16] O. Montenbruck and E. Gill, *Satellite Orbits: Models, Methods, and Applications*. Heidelberg, Germany: Springer, 2000.

[17] J. Khalife, M. Neinavaie, and Z. Kassas, "Navigation with differential carrier phase measurements from Megaconstellation LEO satellites," in *Proc. IEEE/ION Position Location Navig. Symp.*, Apr. 2020, pp. 1393–1404.

Authorized licensed use limited to: The Ohio State University. Downloaded on September 16,2022 at 01:50:48 UTC from IEEE Xplore. Restrictions apply.

On the Achievability of Submeter-Accurate UAV Navigation With Cellular Signals Exploiting Loose Network Synchronization

JOE KHALIFE, Member, IEEE
ZAHER M. KASSAS, Senior Member, IEEE
University of California, Irvine, CA USA

A framework that could achieve submeter-level unmanned aerial vehicle (UAV) horizontal navigation in multipath-free environments with cellular carrier phase measurements is developed. This framework exploits the "loose" synchronization between cellular base transceiver station (BTS) clocks. It is shown through extensive experimental data that the beat frequency stability of cellular BTSs approaches that of atomic standards and that the clock deviations can be realized as a stable autoregressive moving average model. This BTS clock model is referred to as loose network synchronization. A rule-of-thumb is established for clustering the clock deviations to minimize the position estimation error, while significantly reducing the computational complexity. The presented models allow the UAV to achieve sustained carrier phase-based meter- to submeter-accurate navigation. To demonstrate the efficacy of the developed framework, this article presents three UAV flight experiments in Southern California, USA, utilizing signals from different cellular providers transmitting at different frequencies. The three experiments took place in open, semiurban environments with nearly multipath-free, line-of-sight (LOS) conditions, in which the UAV traveled 1.72, 3.07, and 0.61 km, achieving a horizontal position root mean squared error of 36.61, 88.58, and 89.33 cm, respectively, with respect to the UAV's on-board navigation system.

Manuscript received 19 January 2022; released for publication 11 March 2022. Date of publication 31 March 2022; date of current version 11 October 2022.

DOI. No. 10.1109/TAES.2022.3162770

Refereeing of this contribution was handled by S. Khanafseh.

This work was supported in part by the Office of Naval Research (ONR) under Grant N00014-16-1-2305 and Grant N00014-19-1-2511 and in part by the U.S. Department of Transportation (USDOT) under Grant 69A3552047138 for the CARMEN University Transportation Center (UTC).

Authors' addresses: The authors are with the Department of Mechanical and Aerospace Engineering, University of California, Irvine, CA 92617 USA, E-mail: (jjkhalife@gmail.com; zkassas@ieee.org). *(Corresponding author: Zaher M. Kassas.)*

0018-9251 © 2022 IEEE

I. INTRODUCTION

Unmanned aerial vehicles (UAVs) will demand a resilient, accurate, and tamper-proof navigation system [1]. Current UAV navigation systems will not meet these stringent demands as they are dependent on global navigation satellite system (GNSS) signals, which are jammable, spoofable, and may not be usable in certain environments (e.g., deep urban canyons) [2]–[4]. The potential of signals of opportunity (SOPs) (e.g., AM/FM radio [5]–[7], low Earth orbit (LEO) satellite [8]–[12], Wi-Fi [13]–[16], digital television [17]–[21], and cellular [22]–[32]) as complementary or alternative navigation sources have been the subject of extensive research recently. Navigation with SOPs has been demonstrated on ground vehicles and UAVs, achieving a localization accuracy ranging from meters to tens of meters, with the latter accuracy corresponding to ground vehicles in deep urban canyons with severe multipath conditions [33]–[39]. Cellular signals, particularly 3G code-division multiple access (CDMA), 4G long-term evolution (LTE), and 5G new radio (NR), are among the most attractive SOP candidates for navigation. These signals are abundant, received at a much higher power than GNSS signals, offer a favorable horizontal geometry, and are free to use. Unlike ultra-wide bandwidth positioning [40], [41], cellular SOP-based navigation does not require additional transmitter infrastructure. Several receiver designs have been proposed recently that produce navigation observables from cellular CDMA, LTE, and NR signals [23], [42]–[45]. Moreover, error sources pertaining to code phase-based navigation with cellular CDMA systems have been derived and performance under such errors has been characterized [24], [44]. While cellular signals are jammable and spoofable [46]–[49], they are typically received outdoors at carrier-to-noise ratios that are more than 30 dB higher than GNSS signals [50]. As such, considerably higher power would be needed to jam cellular signals than is needed to jam GNSS signals. Moreover, cellular signals are transmitted in multiple frequency bands. The cellular 3G, 4G, and 5G spectrum spans the 700 MHz to nearly 6 GHz bands. The 5G millimeter wave (mmWave) spectrum is envisioned to span several GHz of spectrum, with some bands reaching up to 400 MHz of bandwidth. Unless most cellular bands are simultaneously attacked, an SOP receiver could detect the attack by leveraging redundancy in the measurements. This makes staging a successful, clandestine attack on cellular SOPs generally challenging, as the attacker would need to target the entire cellular spectrum. Although not impossible, the capability of completely jamming cellular SOPs has not become as accessible yet as in the case of jamming GNSS signals, which can be readily performed through illegal but widely available personal privacy devices. As jamming technology becomes more capable, navigation systems can be made more robust by exploiting more signals, whether dedicated navigation signals or other forms of SOPs.

A challenge that arises in cellular-based navigation is the unknown states of cellular base transceiver stations (BTSs), namely their position and clock errors (bias and drift).

Authorized licensed use limited to: The Ohio State University. Downloaded on October 12,2022 at 17:26:44 UTC from IEEE Xplore. Restrictions apply.

This is in sharp contrast to GNSS-based navigation, where the states of the satellites are transmitted to the receiver in the navigation message. To deal with this challenge, a base/rover framework was proposed in [24], [44], [51], in which the base and rover make pseudorange measurements to the same BTSs in the environment. The base was assumed to have complete knowledge of its states (e.g., by having access to GNSS signals), while estimating the states of BTSs in its environment, and sharing these estimates with a rover that had no knowledge of its states. Another framework was developed in which the rover estimated its states simultaneously with the states of the BTSs in the environment, i.e., performed radio simultaneous localization and mapping (radio SLAM) [52]–[55]. It is worth noting that since cellular BTSs are spatially stationary, their positions may be mapped prior to navigation (e.g., by dedicated mapping receivers [56] or from satellite imagery and cellular databases). However, the BTSs' clocks errors must be continuously estimated, whether in the base/rover framework or radio SLAM framework, since these errors are stochastic and dynamic.

A preliminary study for cellular carrier phase-based nondifferential single UAV navigation was conducted in [25]. The proposed framework relied on the relative stability of 3G CDMA cellular BTS clocks. It was revealed that while these clocks are not perfectly synchronized to GNSS, the clock biases of different neighboring BTSs are dominated by a common term. Another study was conducted for 4G LTE cellular BTSs, also known as eNBs, in the presence of real GPS jamming [57]. The study showed that LTE eNBs maintain tight synchronization for at least 90 min, even in the absence of GPS signals. These key findings suggest that precise carrier phase navigation with cellular signals is achievable with or without a base.

This article presents a comprehensive study in which a UAV navigating using cellular carrier phase measurements could achieve submeter-level accuracy in a multipath-free environment with line-of-sight (LOS) conditions. It is assumed that the UAV has knowledge of its position for a period of time, e.g., from a GNSS receiver or from the cellular-based differential framework proposed in [51], before loss of communication with the base, whether initially or intermittently. It is important to note that the algorithms presented in this article are agnostic to the cellular signal type (3G, 4G, 5G, and beyond) as long as navigation observables can be produced from these signals. This article studies 3G and 4G signals and the carrier phase observables were obtained using the receivers proposed in [23] and [44]. The proposed framework assumes a certain level of synchronization between the towers, which has been observed in 3G and 4G systems [25], [57]. This article shows that while cellular networks are not as tightly synchronized as GPS, since they are not intended for navigation, there are strong correlations between the BTS clock biases. This level of synchronization is referred to as "loose" network synchronization. A clock bias clustering algorithm is developed, motivated by the strong correlations between the clock biases. This results in a tradeoff between 1) lost accuracy due to eliminating some clock biases and 2) improved precision by reducing the dilution of precision (DOP). The proposed clustering method aims at exploiting the correlations between BTS clock biases to resolve this tradeoff by minimizing the resulting position error. In particular, this article extends [25] by making the following three contributions:

1) A comprehensive method to obtain the statistics of the BTS clock deviations is presented. It is shown that the beat frequency stability of cellular BTSs approaches that of atomic standards and that the clock deviations can be realized as a stable autoregressive moving average (ARMA) model. The stationarity of such deviations is validated experimentally.
2) The navigation performance is analyzed extensively as a function of clustering frequency.
3) Extensive experimental results with 3G CDMA and 4G LTE signals from different cellular providers transmitting at different frequencies are presented, demonstrating the efficacy of the proposed framework. The UAV flight experiments took place in Southern California, USA, in three different open semiurban environments with multipath-free LOS conditions. In all experiments, the UAV remained within the same sector of each BTS. The UAV achieved a horizontal position root mean-squared error (RMSE) of: 1) 36.61 cm over a trajectory of 1.72 km, 2) 88.58 cm over a trajectory of 3.07 km, and 3) 89.33 cm over a trajectory of 609 m. The RMSEs were calculated relative to the UAV's on-board navigation solution.

The rest of this article is organized as follows. Section II describes the cellular carrier phase observable model. Section III describes the single-UAV navigation framework that leverages the relative stability of cellular SOPs. Section IV provides experimental results demonstrating the proposed framework, showing submeter-level UAV navigation accuracy in nearly multipath-free environments. Finally, Section V concludes this article.

II. CELLULAR CARRIER PHASE OBSERVABLE MODEL

In cellular systems, several known signals are transmitted for synchronization or channel estimation purposes. In cellular CDMA systems, a pilot signal consisting of a pseudorandom noise sequence, known as the short code, is modulated by a carrier signal and broadcast by each BTS for synchronization purposes [58]. Therefore, by knowing the shortcode, the receiver may measure the code phase of the pilot signal as well as its carrier phase; hence, forming a pseudorange measurement to each BTS transmitting the pilot signal. In LTE, two synchronization signals [primary synchronization signal (PSS) and secondary synchronization signal (SSS)] are broadcast by each BTS, referred to evolved node B (eNodeB) in LTE systems [59]. In addition to the PSS and SSS, a reference signal known as the cell-specific reference signal (CRS), is transmitted by each eNodeB for channel estimation purposes [59]. The PSS,

Authorized licensed use limited to: The Ohio State University. Downloaded on October 12,2022 at 17:26:44 UTC from IEEE Xplore. Restrictions apply.

SSS, and CRS may be exploited to draw carrier phase and pseudorange measurements on neighboring eNodeBs [23], [37]. In the rest of this article, availability of code phase, Doppler frequency, and carrier phase measurements of cellular CDMA and LTE signals is assumed (e.g., from specialized navigation receivers [23], [35], [37], [42]–[44], [60]).

Let $n \in \{1, \ldots, N\}$ denote the cellular SOP index, where N is the total number of SOPs. Moreover, let $k = 0, 1, \ldots,$ denote the time index, which represents time at $t_k = t_0 + kT$, where t_0 is some initial time and T is the subaccumulation period in the receiver. The carrier phase at time-step k, expressed in meters, can be parameterized in terms of the receiver and cellular SOP states as

$$z_n(k) = \sqrt{\left\|\boldsymbol{r}_r(k) - \boldsymbol{r}_{s_n}\right\|_2^2 + \Delta z_{r,s_n}^2(k)} + c \cdot \left[\delta t_r(k) - \delta t_{s_n}(k)\right] + \lambda N_n + v_n(k) \quad (1)$$

where $\boldsymbol{r}_r \triangleq [x_r, y_r]^{\mathsf{T}}$ is the receiver's two-dimensional (2-D) position vector; $\boldsymbol{r}_{s_n} \triangleq [x_{s_n}, y_{s_n}]^{\mathsf{T}}$ is the cellular BTS's known 2-D position vector; $\Delta z_{r,s_n} \triangleq z_r(k) - z_{s_n}$ is the difference between the receiver' and BTS's altitude; c is the speed of light; δt_r and δt_{s_n} are the receiver's and cellular BTS's clock biases, respectively; λ is the signal's wavelength; N_n is the carrier phase ambiguity; and $v_n(k)$ is the measurement noise, which is modeled as a discrete-time zero-mean white Gaussian sequence with variance $\sigma_n^2(k)$. Note that a coherent phase-locked loop (PLL) may be employed in CDMA and LTE navigation receivers, since the cellular synchronization and reference signals do not carry any data. As such, the measurement noise variance can be expressed as [61]

$$\sigma_n^2(k) = \lambda^2 \frac{B_{\text{PLL}}}{C/N_{0,n}(k)} \quad (2)$$

where B_{PLL} is the receiver's PLL noise equivalent bandwidth and $C/N_{0,n}(k)$ is the cellular SOP's measured carrier-to-noise ratio at time-step k. The remainder of this article assumes zero-mean Gaussian measurement noise. The actual measurement noise statistics may differ from the what is assumed in (2). Therefore, instead of using (2), Gaussian overbounds of the true measurement noise distribution could be used, if known. Methods described in [62]–[64] could be used to compute overbounds of the measurement noise statistics in different environments. Note that small UAVs and hearable cellular BTSs are typically at comparable altitudes, which makes the vertical diversity very poor. Therefore, one can only estimate the UAV's horizontal position using cellular SOPs without introducing significant errors. As such, the proposed frameworks assume that the UAV and BTS altitudes, $z_r(k)$ and z_{s_n}, respectively, are known and only the UAV's 2–D position is estimated.

It is important to note that the channels between the UAVs and the cellular BTSs do not suffer from severe multipath, as a strong LOS component is usually observed in the received signal [65]. In the case of severe multipath or non-LOS (NLOS) conditions, it is assumed that either 1) signal processing techniques at the SOP receiver level [37], [66]–[72] or 2) measurement outlier rejection techniques [62] are used to mitigate multipath or exclude measurements with large errors due to multipath. Concepts of receiver autonomous integrity monitoring may also be used to exclude measurements with large errors, which can be considered as faulty measurements [73]–[75]. Alternatively, multipath error models may be used to predict and mitigate large measurement errors, either through multipath prediction maps [63], [76] or statistical models [77]. To this end, it is assumed in the rest of this article that the effect of multipath has either 1) been mitigated or 2) included in the measurement model (1).

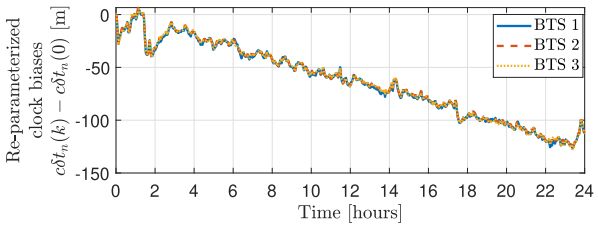

Fig. 1. Experimental data showing $c\delta t_n(k) - c\delta t_n(0)$ obtained from carrier phase measurements over 24 hours for three neighboring BTSs. It can be seen that the clock biases $c\delta t_n(k)$ in the carrier phase measurement are very similar, up to an initial bias $c\delta t_n(0)$ which has been removed. *Remark:* The receiver's clock was derived from a GPS-disciplined oven-controlled crystal oscillator (OCXO), which do not typically have a long-term drift. Therefore, the observed drift is most likely due to the BTS clocks. However, this does not affect the new clock model as it does not disambiguate between the BTS and receiver clock biases and only considers their difference, as per (11).

III. PRECISE NAVIGATION WITH SOP CARRIER PHASE MEASUREMENTS

This section discusses a cellular carrier phase navigation framework that is employable on a single UAV.

A. Combined Clock Errors

The terms $c[\delta t_r(k) - \delta t_{s_n}(k) + \frac{\lambda}{c} N_n]$ are not needed to be estimated individually and are thus combined into one term defined as

$$c\delta t_n(k) \triangleq c\left[\delta t_r(k) - \delta t_{s_n}(k) + \frac{\lambda}{c} N_n\right]. \quad (3)$$

The combined clock errors of three BTSs over a 24-h period are shown in Fig. 1. It was noted in [78] that while large differences between the BTSs' clock biases may be observed (the code phase synchronization requirement as per the cellular protocol is to be within 3 μs), cellular BTSs possess tight carrier frequency synchronization, as seen by the Allan deviations computed for the three BTSs over 24 h and shown in Fig. 2. Therefore, the resulting clock biases in the carrier phase estimates will be very similar, up to an initial bias, as shown in Fig. 1. This level of synchronization is referred to as loose network synchronization. Consequently, one may leverage this relative frequency stability to eliminate parameters that need to be estimated. Moreover, this allows one to use a static estimator (e.g., a WNLS) to estimate the position of the UAV. To achieve this, in what follows,

Authorized licensed use limited to: The Ohio State University. Downloaded on October 12,2022 at 17:26:44 UTC from IEEE Xplore. Restrictions apply.

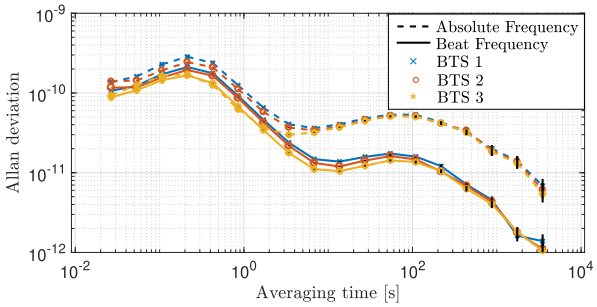

Fig. 2. Allan deviations of absolute and beat frequencies for the 3 BTSs shown in Fig. 1. The beat frequency is calculated from the clock drift between two BTSs, whereas the absolute frequency is the clock drift between the receiver and BTS. The Allan deviations were calculated from data collected over 24 h. The carrier frequency was 883.98 MHz. It is worth noting that while the beat frequency stability approaches that of atomic standards, it is not quite the same as it tends upwards for relatively short averaging periods of 0.1 to 100 s. This could be due to the fact that GPS corrections on the BTSs' clocks happen gradually over several seconds.

the carrier phase measurement is first reparameterized and a WNLS estimation framework is subsequently developed. In what follows, it is assumed that the UAV remains within one sector of a particular BTS. A complete treatment of clock bias mismatches arising due to crossing BTS sectors is discussed in [24] and [44].

B. Carrier Phase Measurement Reparametrization

Motivated by the experimental results in [78], the following reparametrization is proposed

$$c\bar{\delta t}_n(k) \triangleq c\delta t_n(k) - c\delta t_n(0) \equiv c\delta t(k) + \epsilon_n(k) \tag{4}$$

where $c\delta t$ is a time-varying common bias term and ϵ_n is the deviation of $c\bar{\delta t}_n$ from this common bias and is treated as measurement noise. Using (4), the carrier phase measurement (1) can be reparameterized as

$$z_n(k) = \sqrt{\|\boldsymbol{r}_r(k) - \boldsymbol{r}_{s_n}\|_2^2 + \Delta z_{r,s_n}^2(k)} + c\delta t(k) + c\delta t_{0_n} + \eta_n(k) \tag{5}$$

where $c\delta t_{0_n} \triangleq c\delta t_n(0)$ and $\eta_n(k) \triangleq \epsilon_n(k) + v_n(k)$ is the overall measurement noise. The statistics of ϵ_n will be discussed in Section III-E. Note that $c\delta t_{0_n}$ can be obtained knowing the initial position and given the initial measurement $z_n(0)$ according to $c\delta t_{0_n} \approx z_n(0) - \sqrt{\|\boldsymbol{r}_r(0) - \boldsymbol{r}_{s_n}\|_2^2 + \Delta z_{r,s_n}^2(0)}$. This approximation ignores the contribution of the initial measurement noise. If the receiver is initially stationary for a period $k_0 T$ seconds, which is short enough such that $\delta t(k) \approx 0$ for $k = 1, \ldots, k_0$, then the first k_0 samples may be averaged to obtain a more accurate estimate of $c\delta t_{0_n}$.

It is proposed that instead of lumping all N clock biases into one bias $c\delta t$ to be estimated, the clocks get clustered into L clusters, each of size N_l such as

$$\sum_{l=1}^{L} N_l = N. \tag{6}$$

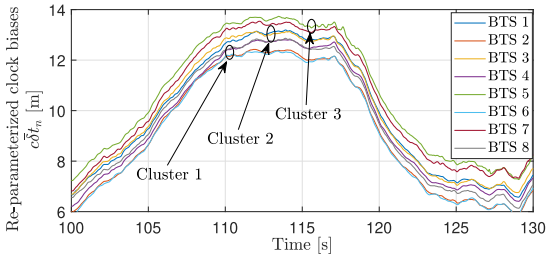

Fig. 3. Experimental data for re-parameterized clock biases $c\bar{\delta t}_n(k)$ over 30 s for 8 BTSs. The clock biases have been visually clustered into three clusters as an illustrative example.

As such, the clocks in a cluster l are lumped into one bias $c\delta t_l$ to be estimated. This gives finer granularity for the parametrization (4), since naturally, certain groups of cellular SOPs will be more synchronized with each other than with other groups (e.g., corresponding to the same network provider, transmission protocol, etc.) or some may lose synchronization altogether in some unlikely event. In the case of complete loss of synchronization, a framework for navigation with asynchronous SOPs could be used instead at the price of lower position accuracy [79]. An illustrative experimental plot is shown in Fig. 3. The figure shows an oscillating, dominant common term that is most likely due to the receiver's clock bias. Note that since the 2-D position vector of the UAV is being estimated along with L clock biases, the number of clusters L cannot exceed $N-2$, otherwise there would be more unknowns than measurements.

Without loss of generality, it assumed that the carrier phase measurements have been ordered such that the first N_1 measurements were grouped into the first cluster, the second N_2 measurements were grouped into the second cluster, et. Next, obtaining the navigation solution with a WNLS is discussed.

C. Navigation Solution

Given $N \geq 3$ pseudoranges modeled according to (5) and $L \leq N-2$ SOP clusters, the receiver may solve for its current position $\boldsymbol{r}_r$ and the current set of common biases $c\boldsymbol{\delta t} \triangleq [c\delta t_1, \ldots, c\delta t_L]^\mathsf{T}$ using a WNLS estimator. The state to be estimated is defined by $\boldsymbol{x} \triangleq [\boldsymbol{r}_r{}^\mathsf{T}, c\boldsymbol{\delta t}^\mathsf{T}]^\mathsf{T}$. An estimate $\hat{\boldsymbol{x}}$ may be obtained using the iterated WNLS equations as

$$\hat{\boldsymbol{x}}^{(j+1)}(k) = \hat{\boldsymbol{x}}^{(j)}(k) + \left(\mathbf{H}^\mathsf{T}\mathbf{R}_\eta^{-1}\mathbf{H}\right)^{-1}\mathbf{H}^\mathsf{T}\mathbf{R}_\eta^{-1}\delta\boldsymbol{z}(k) \tag{7}$$

where $\delta\boldsymbol{z}(k) \triangleq [\delta z_1(k), \ldots, \delta z_N(k)]^\mathsf{T}$ and $\delta z_n(k) \triangleq z_n(k) - \left[\sqrt{\|\hat{\boldsymbol{r}}_r^{(j)}(k) - \boldsymbol{r}_{s_n}\|_2^2 + \Delta z_{r,s_n}^2(k)} + c\hat{\delta t}_{l(n)}^{(j)}(k) + c\delta t_{0_n}\right]$, $\mathbf{R}_\eta = \mathrm{diag}[\sigma_1^2 + \sigma_{\epsilon_1}^2, \ldots, \sigma_N^2 + \sigma_{\epsilon_N}^2]$ is the measurement noise covariance, where $\sigma_{\epsilon_n}^2$ will be discussed in Section III-E, j is the WNLS iteration index, and $\mathbf{H}$ is the measurement Jacobian given by

$$\mathbf{H} \triangleq [\mathbf{G} \quad \boldsymbol{\Gamma}], \qquad \boldsymbol{\Gamma} \triangleq \begin{bmatrix} \mathbf{1}_{N_1} & \ldots & \mathbf{0} \\ \vdots & \ddots & \vdots \\ \mathbf{0} & \ldots & \mathbf{1}_{N_L} \end{bmatrix} \tag{8}$$

Authorized licensed use limited to: The Ohio State University. Downloaded on October 12,2022 at 17:26:44 UTC from IEEE Xplore. Restrictions apply.

$$\mathbf{G} \triangleq \begin{bmatrix} \frac{[\hat{\boldsymbol{r}}_r^{(j)}(k)-\boldsymbol{r}_{s_1}]^{\mathsf{T}}}{\sqrt{\|\hat{\boldsymbol{r}}_r^{(j)}(k)-\boldsymbol{r}_{s_1}\|_2^2+\Delta z_{r,s_1}^2(k)}} \\ \vdots \\ \frac{[\hat{\boldsymbol{r}}_r^{(j)}(k)-\boldsymbol{r}_{s_N}]^{\mathsf{T}}}{\left\|\sqrt{\|\hat{\boldsymbol{r}}_r^{(j)}(k)-\boldsymbol{r}_{s_N}\|_2^2+\Delta z_{r,s_N}^2(k)}\right\|_2} \end{bmatrix} \tag{9}$$

and $\mathbf{1}_{N_l} \triangleq [1, \ldots, 1]^{\mathsf{T}}$. Note that

$$l(n) = \begin{cases} 1, & \text{for } n = 1, \ldots, N_1 \\ 2, & \text{for } n = N_1+1, \ldots, \sum_{l=1}^{2} N_l \\ \vdots & \vdots \\ L, & \text{for } n = \sum_{l=1}^{L-1} N_l + 1, \ldots, N. \end{cases} \tag{10}$$

After convergence [i.e., $\hat{\boldsymbol{x}}^{(j+1)}(k) \approx \hat{\boldsymbol{x}}^{(j)}(k)$] the final estimate is obtained by setting $\hat{\boldsymbol{x}}(k) \equiv \hat{\boldsymbol{x}}^{(j+1)}(k)$. In the rest of this article, it is assumed that $\mathbf{H}$ is always full column rank. Observability conditions and their relation to the rank of $\mathbf{H}$ has been studied in [79] and [80]. It is important to note that this article makes the assumption that $\mathbf{R}_\eta$ is diagonal. In practice, it may not be. In this case, a degradation in the performance is expected. To fully address this issue, the correlation between ϵ_n must be characterized and accounted for in $\mathbf{R}_\eta$. Characterizing these correlations is rather involved and is deferred for future work. The sequel assumes that $\mathbf{R}_\eta$ remains diagonal.

D. Common Clock Bias Parametrization

Note that the clock bias clusters $\{c\delta t_l\}_{l=1}^{L}$ are "virtual clock biases," which are introduced to group SOPs whose carrier frequency is more synchronized than others. This would in turn yield more precise measurement models, reducing the estimation error. This section parameterizes $c\delta t_l$ as a function of $c\delta t_n$. This parametrization is based on the following theorem.

THEOREM III.1: Consider $N \geq 3$ carrier phase measurements. Assume that the contribution of the relative clock deviation ϵ_n is much larger than the carrier phase measurement noise v_n and that ϵ_n are uncorrelated with identical variances σ^2. Then, the position error at any time instant $\delta\boldsymbol{r}_r(k)$ due to relative clock deviations is independent of $c\delta t_l$.

PROOF: See Appendix A.

In plain words, Theorem III.1 is saying that the position error is fully characterized by $\{\epsilon_n\}_{n=1}^{N}$, assuming it dominates the measurement noise, regardless of the actual values of $\{c\delta t_l\}_{l=1}^{L}$. The assumption that the contribution of the relative clock deviation ϵ_n is much larger than the carrier phase measurement noise v_n comes from experimental data, where $\|\boldsymbol{\epsilon}\|_2$ was observed to be within 0.2 and 4 m, whereas σ_n was on the order of a few cm. To illustrate that, Fig. 4(a) shows the time history of ϵ_n for the three BTSs shown in Fig. 1 over 24 h, from which it is clearly seen that $\|\boldsymbol{\epsilon}\|_2$ can be in the order of a few meters. Although ϵ_n is stable, Fig. 4(b) shows that the process appears to be initially

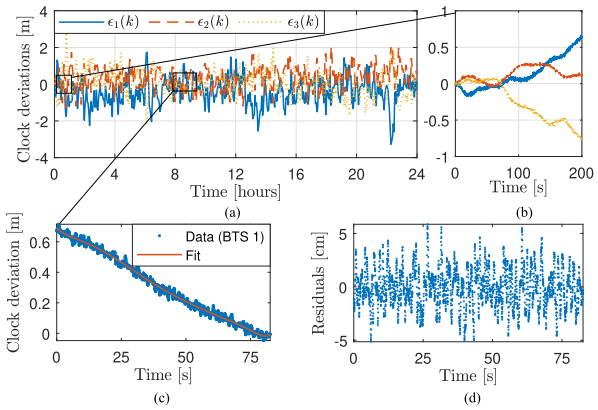

Fig. 4. (a) Time history of ϵ_n for the three BTSs shown in Fig. 1 over 24 h. (b) First 200 s of $\epsilon_n(k)$ showing that the clock deviation process appears to have a diverging short-term behavior. (c) A 75-s portion of ϵ_1 around the eighth hour, as well as a polynomial fit. (d) Residuals between the data and the polynomial fit, whose standard deviation was calculated to be 1.85 cm.

diverging. This apparently diverging short-term behavior is also discussed in Section IV-A. Fig. 4(c) shows a 75-s portion of ϵ_1 around the eighth hour, as well as a polynomial fit. The residuals between the data and the polynomial fit are shown in Fig. 4(d), whose standard deviation was calculated to be 1.85 cm. These residuals contain the effect of $v_1(k)$ as well as $w_{\epsilon_1}(k)$; therefore, σ_n is upper bounded by 1.85 cm, which validates the assumption that the relative clock deviation ϵ_n is much larger than the carrier phase measurement noise v_n.

The reparametrization of $c\bar{\delta t}_n(k)$ in (4) does not assume a specific mapping to $c\delta t(k)$ and $\epsilon_n(k)$ other than being the sum of the two latter terms. Theorem III.1 shows that for a given clustering, the clock bias error term contributing the receiver position error (denoted $\tilde{\epsilon}_n$ in Appendix A) are only a function of 1) $\{c\bar{\delta t}_n\}_{n=1}^{N}$ and 2) the SOP clock bias clustering [see (36)]. Following the result in (36), the following parametrization is adopted

$$c\delta t_l(k) \equiv \frac{1}{N_l}\sum_{i=1}^{N_l} c\bar{\delta t}_{l_i}(k),\ \epsilon_n(k) \equiv c\bar{\delta t}_n(k) - c\delta t_{l(n)}(k) \tag{11}$$

where $l_i \triangleq (\sum_{u=1}^{l-1} N_u) + i$, for $i \in 1, \ldots, N_l$. The term $c\delta t_l(k)$ is equivalent to $c\delta t(k)$ in (4) for the case of multiple clusters. Note that the UAV can perform an exhaustive search over the different clustering possibilities to minimize its position error while it has access to GPS. The number of possible clusters is given by $N_{\text{clus}} = \sum_{L=1}^{N-2} \binom{N}{L} = \sum_{L=1}^{N-2} \frac{N!}{L!(N-L)!}$. It can be seen that this number becomes impractically large as N increases. A rule-of-thumb that significantly reduces N_{clus} is discussed in Section III-G. Note that it is assumed that cycle slips in the receiver are uncommon. As such, they will be treated as almost constant offsets and will not affect the clustering process.

Authorized licensed use limited to: The Ohio State University. Downloaded on October 12,2022 at 17:26:44 UTC from IEEE Xplore. Restrictions apply.

E. Statistics of the Clock Deviations

It was found that ϵ_n is appropriately modeled to evolve according to the ARMA model given by [25]

$$\epsilon_n(k+1) = \sum_{i=1}^{p} \phi_i \epsilon_n(k-i+1) + \sum_{i=1}^{q} \psi_i w_{\epsilon_n}(k-i+1) + w_{\epsilon_n}(k) \tag{12}$$

where p and $\{\phi_i\}_{i=1}^{p}$ are the order and the coefficients of the autoregressive (AR) part, respectively; q and $\{\psi_i\}_{i=1}^{q}$ are the order and the coefficients of the moving average (MA) part, respectively; and w_ϵ is a white sequence. Identifying p and q and their corresponding coefficients can be readily obtained with standard system identification techniques [81], and it was found that $p = q = 6$ was usually enough to whiten w_{ϵ_n} [25]. Therefore, ϵ_n will also be a Gaussian sequence. Without loss of generality, it is assumed that $\epsilon_n(i-p) = 0$ for $i = 1, \ldots, p$. Subsequently, $\mathbb{E}[\epsilon_n(k)] = 0$. The variance of $\epsilon_n(k)$ is discussed next. The ARMA process in (12) may be represented in state-space according to

$$\boldsymbol{\xi}_n(k+1) = \mathbf{F}_{\xi_n} \boldsymbol{\xi}_n(k) + \boldsymbol{\Gamma}_{\xi_n} w_{\epsilon_n}(k) \tag{13}$$

$$\epsilon_n(k) = \boldsymbol{h}_{\epsilon_n}^{\mathsf{T}} \boldsymbol{\xi}_n(k) \tag{14}$$

where $\boldsymbol{\xi}_n$ is the underlying dynamic AR process, $\mathbf{F}_{\xi_n}$ is its state transition matrix, $\boldsymbol{\Gamma}_{\xi_n}$ is the input matrix, and $\boldsymbol{h}_{\epsilon_n}^{\mathsf{T}}$ is the output matrix. The eigenvalues of $\mathbf{F}_{\xi_n}$ were computed to be inside the unit circle, implying stability of $\boldsymbol{\xi}_n$. The covariance of $\boldsymbol{\xi}_n$, denoted $\mathbf{P}_{\xi_n}$, evolves according to

$$\mathbf{P}_{\xi_n}(k+1) = \mathbf{F}_{\xi_n} \mathbf{P}_{\xi_n}(k) \mathbf{F}_{\xi_n}^{\mathsf{T}} + \mathbf{Q}_{\xi_n} \tag{15}$$

where $\mathbf{Q}_{\xi_n} \triangleq \sigma_{w_{\epsilon_n}}^2 \boldsymbol{\Gamma}_{\xi_n} \boldsymbol{\Gamma}_{\xi_n}^{\mathsf{T}}$ and the variance of the clock deviation ϵ_n at any given time-step is given by

$$\sigma_{\epsilon_n}^2(k) = \boldsymbol{h}_{\epsilon_n}^{\mathsf{T}} \mathbf{P}_{\xi_n}(k) \boldsymbol{h}_{\epsilon_n}. \tag{16}$$

Since $\boldsymbol{\xi}_n$ is stable, $\mathbf{P}_{\xi_n}(k)$ will converge to a finite steady-state covariance denoted $\mathbf{P}_{\xi_n,\mathrm{ss}}$ given by the solution to the discrete-time matrix Lyapunov equation

$$\mathbf{P}_{\xi_n,\mathrm{ss}} = \mathbf{F}_{\xi_n} \mathbf{P}_{\xi_n,\mathrm{ss}} \mathbf{F}_{\xi_n}^{\mathsf{T}} + \mathbf{Q}_{\xi_n}. \tag{17}$$

Subsequently, the steady-state variance of the clock deviation is given by

$$\sigma_{\epsilon_n}^2 = \boldsymbol{h}_{\epsilon_n}^{\mathsf{T}} \mathbf{P}_{\xi_n,\mathrm{ss}} \boldsymbol{h}_{\epsilon_n}. \tag{18}$$

F. Statistics of the Residuals

In this section, the resulting residuals w_ϵ are studied. To this end, the autocorrelation function (acf) and the probability density function (pdf) of the residuals are computed for the three realizations of ϵ_n shown in Fig. 4. Note that half of the data was used for system identification and the other half was used to validate the model. The acf and pdf of the residuals obtained with the second half of the data are plotted in Fig. 5(a)–(c). A Gaussian pdf fit (red) was also plotted. It can be seen that $\{w_{\epsilon_n}\}_{n=1}^{3}$ are zero-mean white Gaussian sequences, with variances $\{\sigma_{w_{\epsilon_n}}^2\}_{n=1}^{3}$.

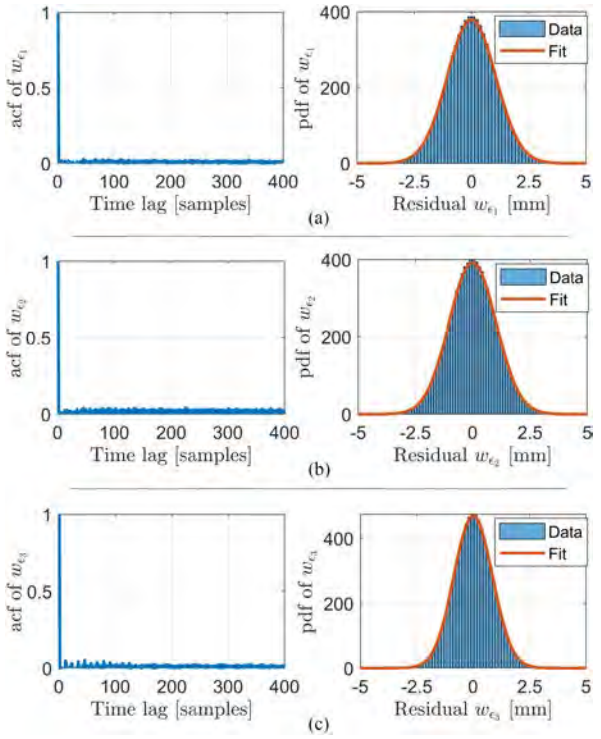

Fig. 5. (a), (b), and (c) show the acfs and pdfs of w_{ϵ_1}, w_{ϵ_2}, and w_{ϵ_3}, respectively. The acfs show that the sequences $\{w_{\epsilon_n}\}_{n=1}^{3}$ are approximately white and the pdfs show that the sequences are Gaussian.

G. Clustering of the Clock Biases

It was mentioned in Section III-D that an exhaustive search may be performed to cluster the clock biases $c\delta t_n$ in order to minimize the position estimation error. This amounts to finding the matrix $\boldsymbol{\Gamma}$ that minimizes

$$J_p(\boldsymbol{\Gamma}) \triangleq \sum_{k=1}^{k_0} \|\delta \boldsymbol{r}_r(k)\|_2^2 = \sum_{k=1}^{k_0} \left\| \left[\mathbf{G}^{\mathsf{T}} \left(\mathbf{I} - \boldsymbol{\Gamma} \left(\boldsymbol{\Gamma}^{\mathsf{T}} \boldsymbol{\Gamma} \right)^{-1} \boldsymbol{\Gamma}^{\mathsf{T}} \right) \mathbf{G} \right]^{-1} \mathbf{G}^{\mathsf{T}} \left(\mathbf{I} - \boldsymbol{\Gamma} \left(\boldsymbol{\Gamma}^{\mathsf{T}} \boldsymbol{\Gamma} \right)^{-1} \boldsymbol{\Gamma}^{\mathsf{T}} \right) \boldsymbol{\epsilon}(k) \right\|_2^2$$

$$= \sum_{k=1}^{k_0} \left\| \left(\mathbf{G}^{\mathsf{T}} \boldsymbol{\Psi} \mathbf{G} \right)^{-1} \mathbf{G}^{\mathsf{T}} \boldsymbol{\Psi} \boldsymbol{\epsilon}(k) \right\|_2^2 \tag{19}$$

where $\boldsymbol{\Gamma}$ and $\boldsymbol{\Psi}$ are defined in (8) and (33), respectively. This optimization problem is nonconvex and intractable. Instead of optimizing $J_p(\boldsymbol{\Gamma})$, a tractable rule-of-thumb is provided next. First, consider the modified cost function

$$J(\boldsymbol{\Gamma}) \triangleq \left\| \left(\mathbf{G}^{\mathsf{T}} \boldsymbol{\Psi} \mathbf{G} \right)^{-1} \mathbf{G}^{\mathsf{T}} \boldsymbol{\Psi} \boldsymbol{\epsilon}(k_0) \right\|_2^2 = \left\| \left(\mathbf{G}^{\mathsf{T}} \boldsymbol{\Psi}\, \boldsymbol{\Psi} \mathbf{G} \right)^{-1} \mathbf{G}^{\mathsf{T}} \boldsymbol{\Psi} \boldsymbol{\Psi} \boldsymbol{\epsilon}(k_0) \right\|_2^2$$

$$\leq \left\| \left(\mathbf{G}_\Gamma^{\mathsf{T}} \mathbf{G}_\Gamma \right)^{-1} \mathbf{G}_\Gamma^{\mathsf{T}} \right\|_2^2 \|\boldsymbol{\Psi} \boldsymbol{\epsilon}(k_0)\|_2^2 \tag{20}$$

where $\mathbf{G}_\Gamma \triangleq \boldsymbol{\Psi} \mathbf{G}$. Using the fact that the square of the two-norm of some real matrix $\mathbf{A}$ is the maximum eigenvalue of $\mathbf{A}\mathbf{A}^{\mathsf{T}}$ [82, p. 266 and 341], denoted by $\lambda_{\max}(\mathbf{A}\mathbf{A}^{\mathsf{T}})$, one can

Authorized licensed use limited to: The Ohio State University. Downloaded on October 12,2022 at 17:26:44 UTC from IEEE Xplore. Restrictions apply.

show that

$$\left\| \left(\mathbf{G}_{\Gamma}^{\mathsf{T}} \mathbf{G}_{\Gamma} \right)^{-1} \mathbf{G}_{\Gamma}^{\mathsf{T}} \right\|_2^2 = \lambda_{\max} \left(\mathbf{P}_{\boldsymbol{r}_r} \right) \tag{21}$$

where $\mathbf{P}_{\boldsymbol{r}_r} \triangleq (\mathbf{G}_{\Gamma}^{\mathsf{T}} \mathbf{G}_{\Gamma})^{-1}$ is the estimation error covariance associated with the receiver's position. Consequently, the cost $J(\mathbf{\Gamma})$ may be bounded by

$$J(\mathbf{\Gamma}) \leq \lambda_{\max} \left(\mathbf{P}_{\boldsymbol{r}_r} \right) \| \mathbf{\Psi} \boldsymbol{\epsilon}(k_0) \|_2^2 . \tag{22}$$

Next, two theorems are presented that will help derive the rule-of-thumb for clustering the clock biases.

THEOREM III.2 Assume a clock bias clustering with $L < N - 2$ clusters and denote $J_L \triangleq \| \mathbf{\Psi} \boldsymbol{\epsilon}(k) \|_2^2$. Then, there exists a clustering with $L + 1$ clusters such that $J_L \geq J_{L+1}$.

PROOF See in Appendix B.

From Theorem III.2, it can be implied that $\| \mathbf{\Psi} \boldsymbol{\epsilon}(k) \|_2^2$ is minimized when $L = N - 2$, i.e., the maximum number of clusters is used. This also implies that using more SOP clusters will decrease $\| \mathbf{\Psi} \boldsymbol{\epsilon}(k_0) \|_2^2$ in the upper bound expression of $J(\mathbf{\Gamma})$ given in (22).

THEOREM III.3 Consider $N \geq 3$ carrier phase measurements for estimating the receiver's position $\boldsymbol{r}_r$ and a clustering of L clock states $c\boldsymbol{\delta t}$. Adding a carrier phase measurement from an additional cellular SOP while augmenting the clock state vector $c\boldsymbol{\delta t}$ by its corresponding additional clock state will neither change the position error nor the position error uncertainty.

PROOF: See in Appendix C.

From Theorem III.3, it can be implied that it is required that $N_l \geq 2$ in order for cluster l to contribute in estimating the position state; hence, reducing $\lambda_{\max}(\mathbf{P}_{\boldsymbol{r}_r})$.

Theorems III.2 and III.1 pose a tradeoff on L. On the one hand, Theorem III.2 states that increasing L decreases $\| \mathbf{\Psi} \boldsymbol{\epsilon}(k) \|_2^2$. On the other hand, Theorem III.1 states that L must be decreased to decrease $\lambda_{\max}(\mathbf{P}_{\boldsymbol{r}_r})$. Consequently, a good rule of thumb is to have at least one cluster with $N_l \geq 3$ (to ensure observability) and $N_l \geq 2$ for the remaining clusters. Combined with (6), this implies that L should satisfy

$$L \leq L_{\max} \triangleq \frac{N - 3}{2} + 1 \tag{23}$$

which significantly reduces the number of possible clusters in the exhaustive search algorithm, which is summarized in Algorithm 1. The algorithm produces the matrix $\mathbf{\Gamma}$, which is then used to solve the WNLS. It is important to note that the tradeoff on L is similar to the tradeoff between accuracy and precision discussed in [82], to which the reader is referred for more mathematical details. While clustering is performed, the UAV navigates using its known position.

Algorithm 1: Clock bias clustering algorithm.

input: $\{\{z_n(k)\}_{k=1}^{k_0}, \boldsymbol{r}_{s_n}\}_{n=1}^{N}, \{\boldsymbol{r}_r(k)\}_{k=0}^{k_0}$.
output: L, $\mathbf{\Gamma}$, $\{c\hat{\delta}t_l\}_{l=1}^{L}$.
procedure Cluster$\{c\delta t_n\}_{n=1}^{N}$
    Compute the maximum number of clusters $L_{\max}$ from (23)
    Perform clustering when GPS is available.
    if GPS available **then**
        for $L = 1$ to $L_{\max}$ **do**
            Find all possible combinations of L clusters.
            Evaluate (19) for each combination of clusters.
            Save the combination of clusters that minimizes (19)
        Select the clustering that minimizes (19) over all values of L.
        Form the $N \times L$ matrix $\mathbf{\Gamma}$ according to the clustering: the nth row of $\mathbf{\Gamma}$ is all zeros with a 1 in the lth column, where l is the index of the cluster in which ϵ_n belongs.

IV. EXPERIMENTAL RESULTS

This section presents results from three experiments conducted in different environments at different times demonstrating submeter-level UAV navigation in multipath-free environments using the framework developed in this article. As mentioned in Section II, only the 2-D position of the UAV is estimated as its altitude may be obtained using other sensors (e.g., altimeter). The UAV's position is estimated in the horizontal plane of an East-North-Up (ENU) frame centered at the average of the BTS positions. In the following experiments, the altitude of the UAV was obtained from its on-board navigation system. Alternatively, the UAV's altitude may be obtained from a barometric altimeter. Moreover, the noise equivalent bandwidths of the receivers' PLLs were set to $B_{\text{PLL}} = 3$ Hz in all experiments. The experiment setups and results are discussed next.

A. Experiment 1

In the first experiment, an Autel Robotics X-Star Premium UAV was equipped with an Ettus E312 universal software radio peripheral (USRP), a consumer-grade 800/1900 MHz cellular antenna, and a small consumer-grade GPS antenna to discipline the on-board oscillator. The receiver was tuned to a 882.75 MHz carrier frequency (i.e., $\lambda = 33.96$ cm), which is a cellular CDMA channel allocated for the U.S. cellular provider Verizon Wireless. Samples of the received signals were stored for offline postprocessing. The cellular carrier phase measurements were given at a rate of 37.5 Hz, i.e., $T = 0.0267$ s. The ground-truth reference for the UAV trajectory was taken from its on-board integrated navigation system, which uses GPS, an inertial measurement unit (IMU), and other sensors. The UAV traversed a trajectory of 1.72 km, which was completed in 3 min with a trajectory radius of 270 m. The trajectory radius is defined as the distance between the center of the trajectory and the furthest point on the trajectory.

Authorized licensed use limited to: The Ohio State University. Downloaded on October 12,2022 at 17:26:44 UTC from IEEE Xplore. Restrictions apply.

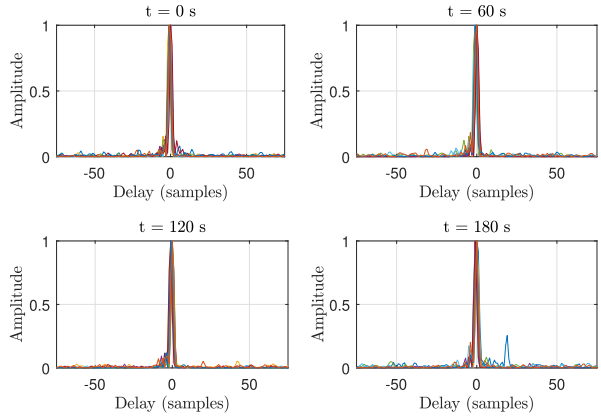

Fig. 6. Channel impulse response measured using the autocorrelation function of the CDMA shortcode for all 9 BTSs over 180 s in the environment near Riverside, California, USA.

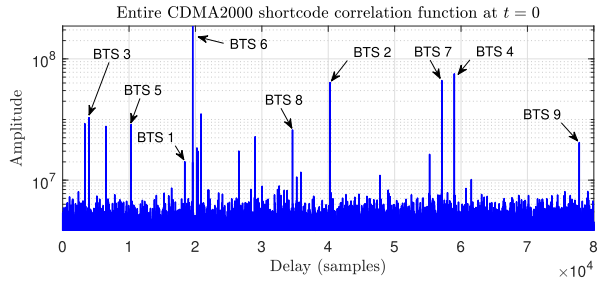

Fig. 7. Entire CDMA shortcode correlation showing multiple peaks pertaining to the different BTSs in the environment.

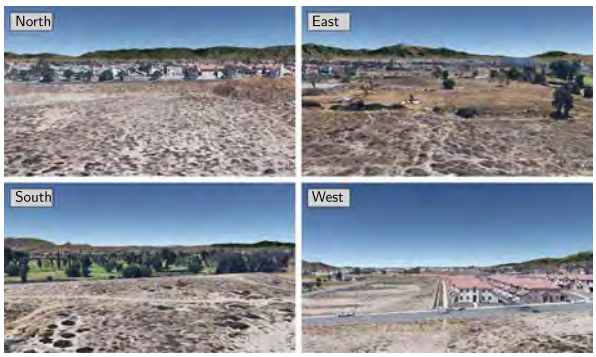

Fig. 8. Panorama of the environment from the UAV's vantage point for the environment near Riverside, California, USA.

Over the course of the experiment, which took place in an open semiurban environment with multipath-free LOS conditions near Riverside, California, USA, the receiver was listening to 9 CDMA BTSs whose 3-D positions were mapped prior to the experiment according to the framework in [56] and refined using Google Earth. A panorama of the environment from the UAV's vantage point is shown in Fig. 8, and the channel impulse response measured using the autocorrelation function of the CDMA shortcode for all 9 BTSs over 180 s is shown in Fig. 6. The curves in Fig. 6 demonstrate a dominant LOS component and nearly multipath-free conditions. Similar channels were observed for the second and third experiments. The entire correlation of the CDMA2000 shortcode is shown in Fig. 7. A plot of

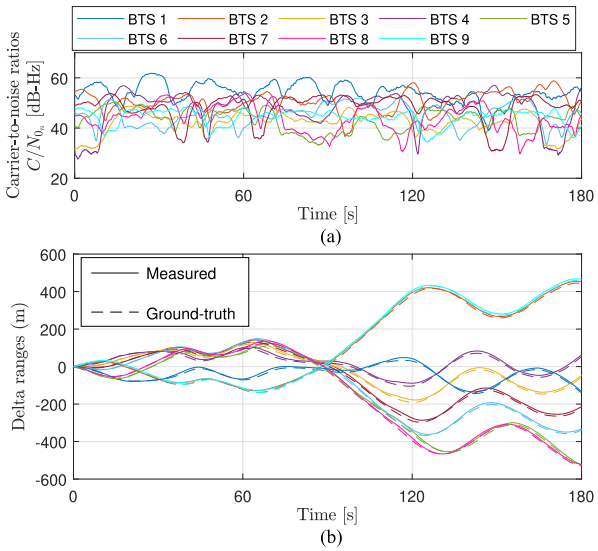

Fig. 9. (a) Carrier-to-noise ratios $\{C/N_{0_n}\}_{n=1}^{9}$ of all the cellular BTSs measured by the UAV in the CD-cellular experiment. (b) Measured and calculated delta ranges to all the cellular BTSs from the UAV in the CD-cellular experiment. Similarly, the base's measured delta ranges closely matched the calculated delta ranges.

the carrier-to-noise ratios of all the BTSs measured by the UAV and the time history of the delta ranges (deviation from the initial range) are given in Fig. 9(a) and (b), respectively.

The UAV had access to GPS for 10 s, then GPS was cut off. During the time where GPS was available, the cellular signals were used to cluster the cellular SOPs, as described in Section III-G. The BTS clock biases obtained from ground-truth are shown in Fig. 10(a) for all nine BTSs. While Fig. 10(a) shows $\{c\delta t_n(k)\}_{n=1}^{9}$ for the entire trajectory, only the first 10 s were used for clustering. The optimal clustering was found to be $\mathcal{C}_1 = \{\text{BTS 1}, \text{BTS 5}, \text{BTS 7}, \text{BTS 8}\}$, $\mathcal{C}_2 = \{\text{BTS 2}, \text{BTS 3}, \text{BTS 6}\}$, and $\mathcal{C}_3 = \{\text{BTS 4}, \text{BTS 9}\}$. The resulting clock deviations $\{\epsilon_n\}_{n=1}^{9}$ and the cluster clock biases $\{c\delta t_l\}_{l=1}^{3}$ are shown in Fig. 10(b) and (c), respectively. Note that $\{\epsilon_n\}_{n=1}^{9}$ appear to be diverging, similarly to the behavior in Fig. 4(b). However, it is found next that these processes are stable.

Then, the state-space models of $\{\epsilon_n\}_{n=1}^{9}$ were identified according to Section III-E for $p = q = 6$ using MATLAB's System Identification Toolbox. Appendix D shows the ARMA coefficients as well as the resulting $\{\sigma_{w_{\epsilon_n}}\}_{n=1}^{9}$. Fig. 11 shows the residuals between $\{\epsilon_n\}_{n=1}^{9}$ and the identified models, which were found to be white sequences. The steady-state values of $\{\sigma_{\epsilon_n}\}_{n=1}^{9}$ were calculated from (18) and used in the WNLS.

Next, the time evolution of $\{\sigma_{\epsilon_n}^2\}_{n=1}^{9}$ and their steady-state values were computed according to Section III-E. Fig. 12 shows the time evolution of $\{\sigma_{\epsilon_n}\}_{n=1}^{9}$. The time axis was extended longer than the experiment duration to show the convergence of $\{\sigma_{\epsilon_n}\}_{n=1}^{9}$, indicating that $\{\epsilon_n\}_{n=1}^{9}$ are stable processes.

Subsequently, the position of the UAV and the clusters's clock biases were estimated according to Section III-C. The

Authorized licensed use limited to: The Ohio State University. Downloaded on October 12,2022 at 17:26:44 UTC from IEEE Xplore. Restrictions apply.

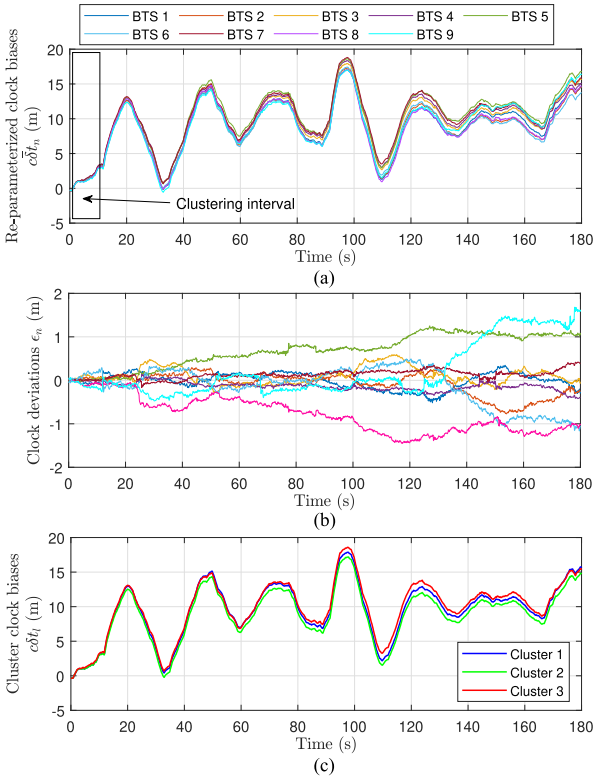

Fig. 10. (a) BTS Clock biases in Experiment 1 obtained from ground-truth. (b) Deviations of the BTS clock biases after clustering. Note that the legend of (b) is the same as (a). (c) BTS clusters' clock biases. Clustering was performed in the first 10 seconds while GPS was available.

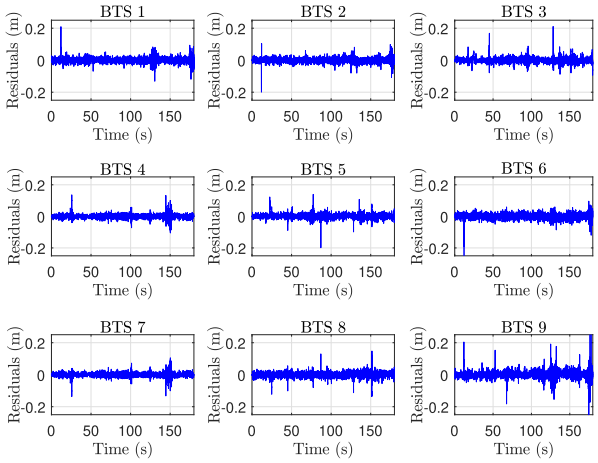

Fig. 11. Residuals of the clock deviation ARMA models for all the nine BTSs in Experiment 1 obtained using MATLAB's System Identification Toolbox for $p = q = 6$. A correlation analysis shows that the residuals are white.

horizontal position RMSE was calculated to be 36.61 cm. The carrier phase measurements were used to estimate the navigating UAV's trajectory via the framework developed in Section III. The experimental setup, the cellular BTS layout, and the true trajectory (from the UAV's on-board integrated navigation system) and estimated trajectory (from the proposed framework) of the navigating UAV are shown in Fig. 13, the x- and y- errors over the entire trajectory are

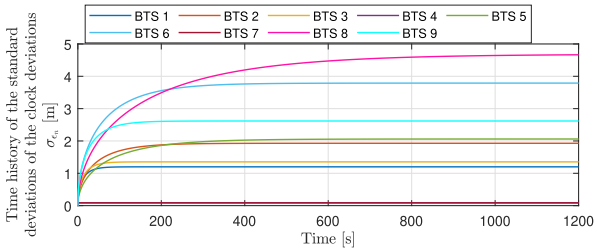

Fig. 12. Time evolution of $\{\sigma_{\epsilon_n}\}_{n=1}^{9}$ calculated according to Section III-E. The time axis was extended longer than the experiment duration to show the convergence of $\{\sigma_{\epsilon_n}\}_{n=1}^{9}$, indicating that $\{\epsilon_n\}_{n=1}^{9}$ are stable processes.

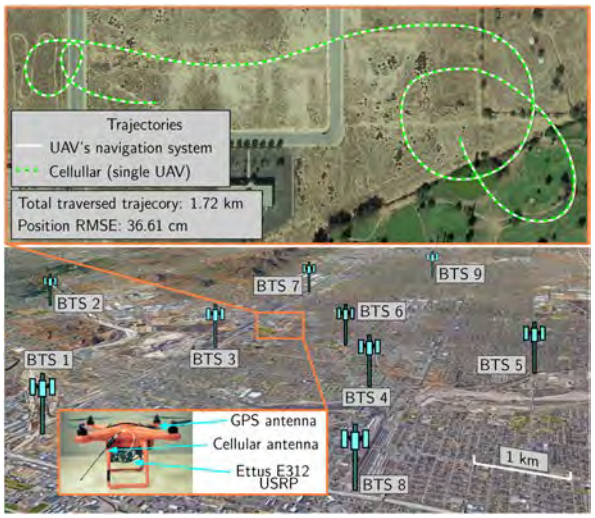

Fig. 13. Experiment 1 setup, BTS layout, and navigation solution demonstrating a single UAV navigating with precise cellular carrier phase measurements. The true and estimated trajectories are shown in solid and dashed lines, respectively. Map data: Google Earth.

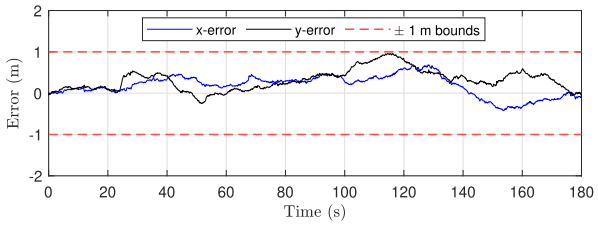

Fig. 14. Experiment 1 x- and y-errors over the entire trajectory as well as the ± 1m bounds showing that the position errors remain below 1 meter throughout the experiment.

shown in Fig. 14, and the estimated cluster clock biases are shown in Fig. 15.

Next, the frequency of clock bias clustering is considered. That is, it is assumed that the UAV regains knowledge of its position for a short period of time throughout the experiment either through the CD-cellular framework (e.g., flying in the vicinity of a base) or via GPS. During these short periods, the UAV updates the clock bias clusters. To this end, the frequency at which the UAV performs clustering was varied from 1 to 2, and then to 4 times during the experiment. The clustering events were uniformly spaced in time. Every time the UAV regains of its position, the

Authorized licensed use limited to: The Ohio State University. Downloaded on October 12,2022 at 17:26:44 UTC from IEEE Xplore. Restrictions apply.

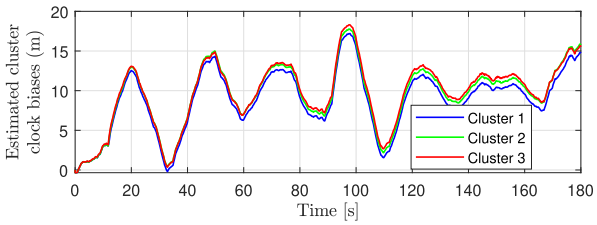

Fig. 15. Estimated cluster clock biases for the first experiment. The estimated biases match closely the cluster biases shown in Fig. 10(c).

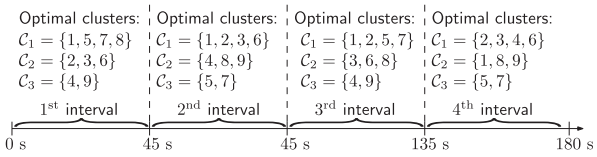

Fig. 16. Optimal BTS clusters for each interval in Experiment 1.

latter is made available for 10 s to perform clustering and is cut off again. The position RMSEs were found to be 36.61, 45.11, and 18.1 cm for clustering frequencies of 1, 2, and 4, respectively. The optimal clusters for each interval of the trajectory are shown in Fig. 16. Note that new initial clock bias estimates are produced every time clustering is performed.

B. Experiment 2

In the second experiment, a DJI Matrice 600 was equipped with the same hardware described in Section IV-A and the on-board USRP was tuned to the same carrier frequency. The cellular carrier phase measurements were also given at a rate of 37.5 Hz, i.e., $T = 0.0267$ s. The ground-truth reference for the UAV trajectory was taken from its on-board navigation system, which also uses GPS, an IMU, and other sensors. The experimental setup and SOP BTS layout for the second experiment are shown in Fig. 17. The ground-truth reference for the UAV trajectory was taken from its on-board integrated navigation system, which also uses GPS, IMU, and other sensors. The UAV traversed a trajectory of 3.07 km completed in 325 s with a trajectory radius of 320 m. The receiver was listening to the seven CDMA BTSs shown in Fig. 17. The UAV remained in the same BTS sectors throughout the experiments. A plot of the carrier-to-noise ratios of all the BTSs and the time history of the delta ranges are given in Fig. 19(a) and (b), respectively. The same steps as in Experiment 1 were taken to cluster the BTS clock biases and characterize the clock deviation statistics. The optimal clustering for a one-time clustering was found to be $\mathcal{C}_1 = \{$BTS 1, BTS 2, BTS 3, BTS 4, BTS 6$\}$ and $\mathcal{C}_2 = \{$BTS 5, BTS 7$\}$. The position RMSE was calculated to be 88.58 cm. The navigation results are shown in Fig. 17 and the x- and y- errors are shown in Fig. 18.

A similar study as in Experiment 1 is perform to characterize the RMSE under varying clustering frequencies. The same approach was taken as in the previous experiment. The position RMSEs were found to be 88.58, 84.17, and 83.07 cm for clustering frequencies of 1, 2, and 4, respectively.

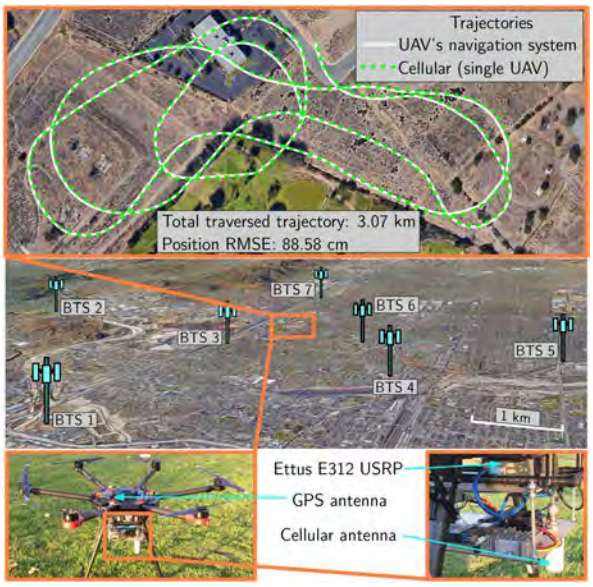

Fig. 17. Experiment 2 setup, BTS layout, and navigation solution demonstrating a single UAV navigating with precise cellular carrier phase measurements. The true and estimated trajectories are shown in solid and dashed lines, respectively. Map data: Google Earth.

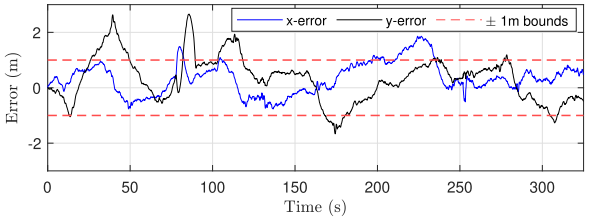

Fig. 18. Experiment 2 x- and y-errors over the entire trajectory as well as the $\pm$1m bounds showing that the position errors remain below 1 meter most of the time.

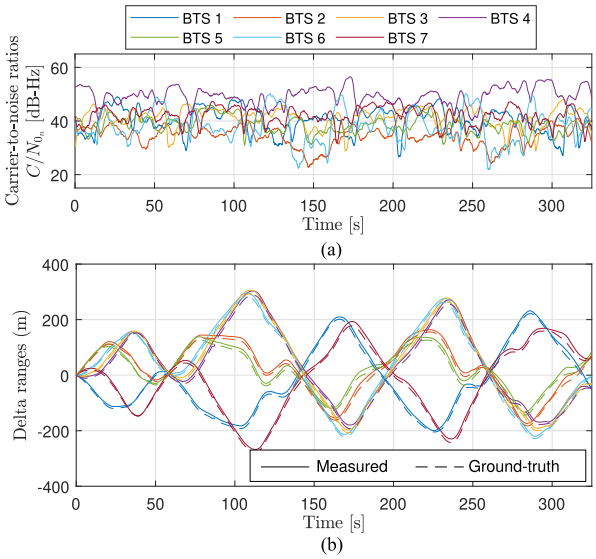

Fig. 19. (a) Carrier-to-noise ratios $\{C/N_{0_n}\}_{n=1}^{7}$ of all the cellular BTSs measured by the single UAV in Experiment 2. (b) Measured and calculated delta ranges to all the cellular BTSs from the single UAV.

Authorized licensed use limited to: The Ohio State University. Downloaded on October 12,2022 at 17:26:44 UTC from IEEE Xplore. Restrictions apply.

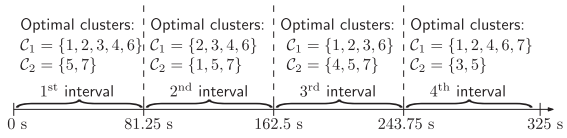

Fig. 20. Optimal BTS clusters for each interval in Experiment 2.

Fig. 21. Panorama of the environment from the UAV's vantage point for the environment in Aliso Viejo, California, USA.

The optimal clusters for each interval of the trajectory are shown in Fig. 20.

C. Experiment 3

In the third experiment, the Matrice UAV was equipped with 1) a four-channel National Instrument (NI) USRP-2955 to sample LTE signals at four different carrier frequencies; 2) four consumer-grade 800/1900 MHz cellular antennas; 3) a small consumer-grade GPS antenna to discipline the on-board oscillator; and 4) a dual antenna, multi-frequency Septentrio AsteRx-i V GNSS-inertial navigation system (INS) with RTK capabilities to provide ground-truth of the UAV's position and attitude. The four receiver channels were tuned to 1955 MHz ($\lambda = 15.33$ cm), 2145 MHz ($\lambda = 13.98$ cm), 2125 MHz ($\lambda = 14.11$ cm), and 739 MHz ($\lambda = 40.57$ cm), which are all LTE frequencies and allocated to the U.S. cellular operators AT&T, T-Mobile, and Verizon. Over the course of the experiment, which took place in an open semiurban environment with multipath-free LOS conditions near Aliso Viejo, California, USA, the receivers were listening to 11 LTE BTSs, also known as eNBs, whose 3-D positions were also mapped prior to the experiment according to the framework in [56] and refined using Google Earth. A panorama of the environment from the UAV's vantage point is shown in Fig. 21 .

In this experiment, the cellular carrier phase measurements were given at a rate of 1 Hz, i.e., $T = 1$ s. The UAV traversed a trajectory of 609 m completed in 175 s with a trajectory radius of 68 m and remained in the same eNB sectors throughout the experiment. A plot of the carrier-to-noise ratios of all the eNBs and the time history of the delta ranges are given in Fig. 24(a) and (b), respectively. The same steps as in Experiment 1 were taken to cluster the eNB clock biases and characterize the clock deviation statistics. The optimal clustering for a one-time clustering was found to be $\mathcal{C}_1 = \{\text{eNB 2, eNB 8, eNB 9, eNB 10, eNB 11}\}$ and

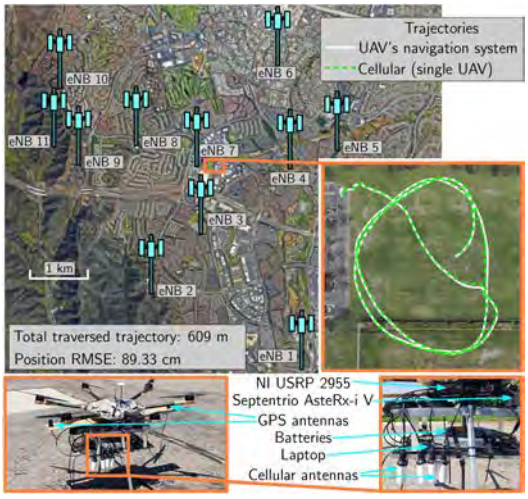

Fig. 22. Experiment 3 setup, eNB layout, and navigation solution demonstrating a single UAV navigating with precise cellular carrier phase measurements. The true and estimated trajectories are shown in solid and dashed lines, respectively. Map data: Google Earth.

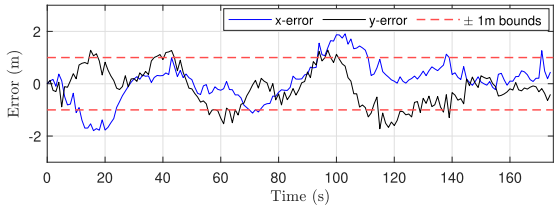

Fig. 23. Experiment 3 x- and y-errors over the entire trajectory as well as the $\pm$1m bounds showing that the position errors remain below 1 meter most of the time.

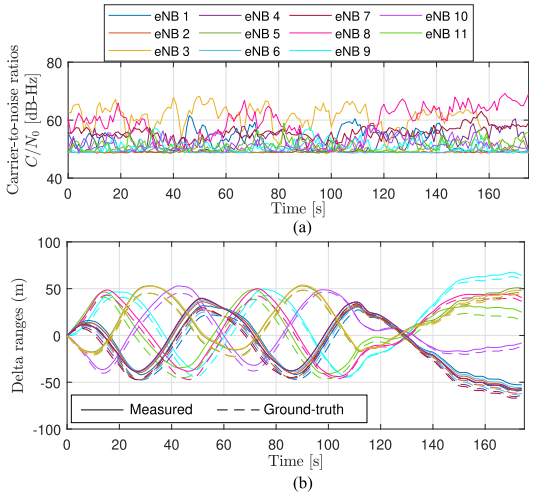

Fig. 24. Measured and calculated delta ranges to all the cellular eNBs from the single UAV in Experiment 3.

$\mathcal{C}_2 = \{\text{eNB 1, eNB 3, eNB 4, eNB 5, eNB 6, eNB 7}\}$. The position RMSE was calculated to be 89.33 cm. The navigation results are shown in Fig. 22 and the x- and y-errors are shown in Fig. 23.

A similar study as in Experiments 1 and 2 is performed to characterize the RMSE under varying clustering frequencies. The same approach was taken as in the previous experiments. The position RMSEs were found to be 89.33,

Authorized licensed use limited to: The Ohio State University. Downloaded on October 12,2022 at 17:26:44 UTC from IEEE Xplore. Restrictions apply.

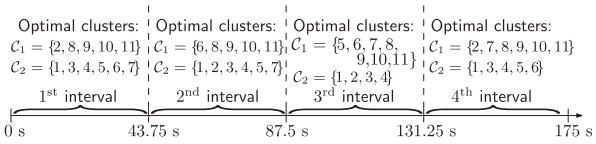

Fig. 25. Optimal eNB clusters for each interval in Experiment 3.

TABLE I
Lowest Position RMSEs for the Three Experiments

	Experiment 1	Experiment 2	Experiment 3
Duration	180 s	325 s	175 s
Distance traveled	1.72 km	3.07 km	0.61 km
Trajectory radius	270 m	320 m	68 m
Position RMSE	18.1 cm	83.07 cm	80.96 cm

TABLE II
Position RMSEs of the Three Experiments for Different Clustering Frequencies

	Clustering frequency		
	1	2	4
Experiment 1	36.61 cm	45.11 cm	18.1 cm
Experiment 2	88.58 cm	84.17 cm	83.07 cm
Experiment 3	89.33 cm	81.07 cm	80.96 cm

TABLE III
Comparison of Position RMSEs for the Exploited Levels of Synchronization

Exploited level of synchronization	Experiment 1	Experiment 2	Experiment 3
Loose	36.6 cm	88.58 cm	89.53 cm
Asynchronous	2.94 m	5.99 m	1.96 m

81.07, and 80.96 cm for clustering frequencies of 1, 2, and 4, respectively. The optimal clusters for each interval of the trajectory are shown in Fig. 25.

The lowest achieved position RMSE for each experiment are tabulated in Table I and the RMSEs for different clustering frequencies are summarized in Table II, which shows that in general, updating the clustering yields better performance than fixing the clusters once at the beginning. The increase in RMSE in Experiment 1 between clustering frequencies of 1 and 2 can be attributed to the diverging short-term behavior of ϵ_n, as discussed above.

REMARK The proposed method assumes a certain level of synchronization between BTSs, referred to as loose synchronization. If this synchronization is completely absent or unexploited using the proposed framework, the method in [79], which addresses asynchronous networks, could be used instead. However, this will come at the cost of larger position errors. For example, the position RMSE of experiment 1 will increase from 36.6 cm to 2.94 m, the position RMSE of experiment 2 will increase from 88.58 cm to 5.99 m [79], and the position RMSE of experiment 3 will increase from 89.53 cm to 1.96 m. These results are summarized in Table III. As such, in the case of the three experiments presented herein, submeter-level position RMSE is achieved by exploiting loose network synchronization using the proposed method in a multipath-free environment with LOS conditions. The RMSEs are calculated relative to a GPS-IMU solution in the case of Experiments 1 and 2, and relative to an GNSS-IMU RTK system in the case of Experiment 3.

D. Discussion

The following are key takeaways and remarks from the experimental results presented above. First, it is important to note that the RMSEs for the first two experiments were calculated with respect to the trajectory returned by the UAVs' on-board navigation system. Although these systems use multiple sensors for navigation, they are not equipped with high precision GPS receivers, e.g., RTK systems. Therefore, some errors are expected in what is considered to be "true" trajectories taken from the on-board sensors. The hovering horizontal precision of the UAVs are reported to be 2 m for the X-Star Premium by Autel Robotics and 1.5 m for the Matrice 600 by DJI. In contrast, the ground-truth system for the third non-differential single-UAV experimental results uses RTK and is rated at 0.6 cm horizontal precision by Septentrio. Moreover, some errors may be due to uncertainties in the BTS positions, which were obtained from Google Earth imagery. While the accuracy of Google Earth is not officially known, studies show that it is below 20 cm in the areas of interest [83].

Second, the reported RMSEs are for optimal clustering. In the 10 s during which GPS was available, a search was performed to optimally cluster the clock biases using the rule-of-thumb discussed in Section III-G. The search took less than 3 s in each case. The RMSEs without clustering (only one bias is estimated) are 48 cm, 97 cm, and 1.78 m for the first, second, and third single-UAV experiments, respectively. As such, optimal clustering following the analysis proposed in Section III resulted in approximately 24%, 9%, 48% reductions in the position RMSEs, respectively, over not clustering at all.

Third, the experiments showed that reliable navigation with cellular signals is possible when the proper models are used in an open semiurban environment. Some of the experiments went over 5 min, indicating that the UAV could rely *exclusively* on cellular carrier phase measurements for sustained meter-level accurate navigation. Note that the proposed frameworks does not account for unmodeled errors such as multipath or signal blockage. Such errors could be partially mitigated at the receiver level [37]. It is expected for the performance to degrade in the presence of such errors.

Fourth, throughout the experiments, the UAV remained within the same BTS or eNB sectors. BTSs and eNBs typically transmit in three different sectors, each of which covering 120°. When crossing between sectors, the receiver would need to perform a "handover," which involves acquiring and tracking the signal from the new sector [44]. If the BTS sectors are not completely synchronized, the handover may introduce meter-level errors to the BTSs' clock bias model. One way to reduce the effect of the errors introduced by crossing BTS sectors is to use the approach proposed in [24].

Authorized licensed use limited to: The Ohio State University. Downloaded on October 12,2022 at 17:26:44 UTC from IEEE Xplore. Restrictions apply.

Fifth, it was assumed that the UAVs had short access to GPS to perform clustering and initialize proposed framework. Alternatively, if a base receiver is continuously or intermittently present throughout the navigation period, the UAV could leverage the cellular-based differential framework proposed in [51] to perform clustering periodically. This would completely eliminate the dependency on GPS. Moreover, it was shown in [57] that under real GPS jamming conditions, cellular BTSs maintain the same level of synchronization for at least 90 min, and that a cellular SOP receiver can navigate for 5 km in the presence of jamming. This implies that the navigation performance of the proposed framework will not suffer under GPS jamming for a significant period of time.

Sixth, Fig. 12 shows that the clock deviations are stable processes with bounded standard deviations. However, Table II shows that, in general, keeping the same clustering performs worse than updating the clustering when GPS is available. This is due the fact that some of the ϵ_n processes, while stable, reach stationarity at a much slower rate than the rate at which positioning is performed. Therefore, optimal clusters may change in the short-term. In the long-term, if clustering is performed only once, the steady-state values of σ_{ϵ_n} will determine the accuracy of the position solution. According to Fig. 12, $\sigma_{\epsilon_n} < 5$ m, which is equivalent to GPS pseudorange precision. It is also worth mentioning that the ubiquity of cellular SOPs offers a low horizontal dilution of precision (HDOP). In fact, the HDOP remained below unity in all experiments. The low HDOP further reduces the effect of a large σ_{ϵ_n}.

Seventh, the UAV-mounted receiver's clock bias is accounted for as part of the common clock bias terms. As such, the magnitude of the receiver's clock bias should not affect the position estimate. It has been proven in [24] [c.f. (30)] that the position error is independent of common errors, which is the receiver's clock bias in this case. This implies that the quality of the receiver's clock should not affect the navigation performance, as long as the receiver can maintain track of the signals. As an example, the USRPs used in Experiments 1 and 2 are equipped with GPS-disciplined TCXOs, whereas the one used in Experiment 3 was equipped with a GPS-disciplined OCXO; yet, the navigation performances were comparable.

Eighth, in order to assess the effect of altimeter errors on the 2-D navigation solution, a zero-mean, Gaussian measurement noise error was simulated in $\Delta z_{r,s_n}$ with a 100 m^2 variance. The 2-D position RMSEs for experiments 1, 2, and 3 in the presence of altimeter errors were 38.3 cm (increase of 1.7 cm), 1.03 m (increase of 14.4 cm), and 94.6 cm (increase of 4.3 cm), respectively. The degradation in the 2-D navigation solution is up to two orders of magnitudes less than the altimeter errors.

Ninth, the reclustering idea is related to intermittent self-calibration of clocks using ground-based SOPs [84]. The main difference, however, lies in the fact the proposed method keeps estimating clock biases after reclustering, albeit a subset of the clock biases. The subset of clock biases is selected via the clustering algorithm. This ensures a robust navigation solution against unexpected time varying behaviors of clock biases while minimizing the number of estimated parameters to reduce the DOP. Moreover, this article assumed periodic reclustering; however, reclustering could be performed whenever the UAV regains access to GPS or following some metric defined by the desired application.

V. CONCLUSION

This article presented a framework for UAV navigation with cellular carrier phase measurements where submeter accuracy is achievable under multipath-free LOS conditions and the UAV not crossing BTS sectors. The proposed framework leverages the relative stability of cellular BTSs clocks, referred to as loose network synchronization. This stability also allows to parameterize the SOP clock biases by a common term plus some small deviations from the common term. The clock deviations were subsequently modeled as a stochastic sequence and the model is validated through extensive experimental data. Analysis of these deviations revealed that they can be clustered to minimize the resulting position error. Next, a rule-of-thumb for clustering the clock deviations was established to significantly reduce the complexity of the clustering step. To demonstrate the efficacy of the developed framework, three UAV flight experiments in Southern California, USA, were presented. The three experiments took place in open, semiurban environments with nearly multipath-free LOS conditions, in which the UAV traveled 1.72, 3.07, and 0.61 km, achieving submeter horizontal position RMSEs of 36.61, 88.58, and 89.33 cm, respectively, relative to the UAV's on-board navigation solution.

APPENDIX A
PROOF OF THEOREM III.1

This appendix provides the proof of Theorem III.1 stating that the position error at any time instant $\delta \boldsymbol{r}_r(k)$ due to relative clock deviations is independent of $c\delta t_l$.

PROOF Denote the measurement noise covariance of $\boldsymbol{\eta} \triangleq [\eta_1 \ldots, \eta_n]^\mathsf{T}$ as $\mathbf{R}_\eta$. It is assumed that the WNLS had converged very closely to the true state in the absence of clock deviations. The clock deviations are then suddenly introduced into the measurements, which will induce an incremental change in the receiver state estimate given by

$$\begin{aligned}\delta \boldsymbol{x}(k) &= -\left(\mathbf{H}^\mathsf{T}\mathbf{R}_\eta^{-1}\mathbf{H}\right)^{-1}\mathbf{H}^\mathsf{T}\mathbf{R}_\eta^{-1}\boldsymbol{\epsilon}(k) \\ &= -\left(\bar{\mathbf{H}}^\mathsf{T}\bar{\mathbf{H}}\right)^{-1}\bar{\mathbf{H}}^\mathsf{T}\bar{\boldsymbol{\epsilon}}(k) \end{aligned} \tag{24}$$

where

$$\bar{\mathbf{H}} \triangleq \mathbf{R}_\eta^{-\frac{1}{2}}\mathbf{H}, \quad \bar{\boldsymbol{\epsilon}}(k) \triangleq \mathbf{R}_\eta^{-\frac{1}{2}}\boldsymbol{\epsilon}(k) \tag{25}$$

and $\boldsymbol{\epsilon} \triangleq [\epsilon_1, \ldots, \epsilon_N]^\mathsf{T}$. The matrix product $\bar{\mathbf{H}}^\mathsf{T}\bar{\boldsymbol{\epsilon}}(k)$ can be further expressed as

$$\bar{\mathbf{H}}^\mathsf{T}\bar{\boldsymbol{\epsilon}}(k) = \begin{bmatrix}\bar{\mathbf{G}}^\mathsf{T} \\ \bar{\boldsymbol{\Gamma}}^\mathsf{T}\end{bmatrix}\bar{\boldsymbol{\epsilon}}(k) = \begin{bmatrix}\bar{\mathbf{G}}^\mathsf{T}\bar{\boldsymbol{\epsilon}}(k) \\ \bar{\boldsymbol{\Gamma}}^\mathsf{T}\bar{\boldsymbol{\epsilon}}(k)\end{bmatrix} \tag{26}$$

where

$$\bar{\mathbf{G}} \triangleq \mathbf{R}_\eta^{-\frac{1}{2}}\mathbf{G}, \quad \bar{\boldsymbol{\Gamma}} \triangleq \mathbf{R}_\eta^{-\frac{1}{2}}\boldsymbol{\Gamma}. \tag{27}$$

Authorized licensed use limited to: The Ohio State University. Downloaded on October 12,2022 at 17:26:44 UTC from IEEE Xplore. Restrictions apply.

Next, $(\bar{\mathbf{H}}^{\mathsf{T}}\bar{\mathbf{H}})^{-1}$ is expressed as

$$\left(\bar{\mathbf{H}}^{\mathsf{T}}\bar{\mathbf{H}}\right)^{-1} = \begin{bmatrix} \bar{\mathbf{G}}^{\mathsf{T}}\bar{\mathbf{G}} & \bar{\mathbf{G}}^{\mathsf{T}}\bar{\mathbf{\Gamma}} \\ \bar{\mathbf{\Gamma}}^{\mathsf{T}}\bar{\mathbf{G}} & \bar{\mathbf{\Gamma}}^{\mathsf{T}}\bar{\mathbf{\Gamma}} \end{bmatrix}^{-1} \triangleq \begin{bmatrix} \mathbf{A} & \mathbf{B} \\ \mathbf{B}^{\mathsf{T}} & \mathbf{D} \end{bmatrix} \tag{28}$$

where $\mathbf{A}$ is a 2×2 symmetric matrix, $\mathbf{B}$ is a $2 \times L$ matrix, and $\mathbf{D}$ is an $L \times L$ symmetric matrix. The estimation error becomes

$$\delta\boldsymbol{x}(k) = \begin{bmatrix} \delta\boldsymbol{r}_r(k) \\ \delta\left(c\delta t(k)\right) \end{bmatrix} = -\begin{bmatrix} \left(\mathbf{A}\bar{\mathbf{G}}^{\mathsf{T}} + \mathbf{B}\bar{\mathbf{\Gamma}}^{\mathsf{T}}\right)\bar{\boldsymbol{\epsilon}}(k) \\ \left(\mathbf{B}^{\mathsf{T}}\bar{\mathbf{G}}^{\mathsf{T}} + \mathbf{D}\bar{\mathbf{\Gamma}}^{\mathsf{T}}\right)\bar{\boldsymbol{\epsilon}}(k) \end{bmatrix}. \tag{29}$$

Using the matrix block inversion lemma, the following may be obtained:

$$\begin{aligned} \mathbf{A} &= \left(\bar{\mathbf{G}}^{\mathsf{T}}\bar{\mathbf{\Psi}}\bar{\mathbf{G}}\right)^{-1} \\ \mathbf{B} &= -\left(\bar{\mathbf{G}}^{\mathsf{T}}\bar{\mathbf{\Psi}}\bar{\mathbf{G}}\right)^{-1}\bar{\mathbf{G}}^{\mathsf{T}}\bar{\mathbf{\Gamma}}\left(\bar{\mathbf{\Gamma}}^{\mathsf{T}}\bar{\mathbf{\Gamma}}\right)^{-1} \\ \mathbf{D} &= \left(\bar{\mathbf{\Gamma}}^{\mathsf{T}}\bar{\mathbf{\Gamma}}\right)^{-1}\left[\mathbf{I} + \bar{\mathbf{\Gamma}}^{\mathsf{T}}\bar{\mathbf{G}}\left(\bar{\mathbf{G}}^{\mathsf{T}}\bar{\mathbf{\Psi}}\bar{\mathbf{G}}\right)^{-1}\bar{\mathbf{G}}^{\mathsf{T}}\bar{\mathbf{\Gamma}}\left(\bar{\mathbf{\Gamma}}^{\mathsf{T}}\bar{\mathbf{\Gamma}}\right)^{-1}\right] \end{aligned} \tag{30}$$

where $\bar{\mathbf{\Psi}} \triangleq \mathbf{I} - \bar{\mathbf{\Gamma}}(\bar{\mathbf{\Gamma}}^{\mathsf{T}}\bar{\mathbf{\Gamma}})^{-1}\bar{\mathbf{\Gamma}}^{\mathsf{T}}$. This yields the position error given by

$$\delta\boldsymbol{r}_r(k) = -\left(\bar{\mathbf{G}}^{\mathsf{T}}\bar{\mathbf{\Psi}}\bar{\mathbf{G}}\right)^{-1}\bar{\mathbf{G}}^{\mathsf{T}}\bar{\mathbf{\Psi}}\bar{\boldsymbol{\epsilon}}(k). \tag{31}$$

When $\mathbf{R}_\eta = \sigma^2\mathbf{I}$, the above simplifies to

$$\delta\boldsymbol{r}_r(k) = -\left(\mathbf{G}^{\mathsf{T}}\mathbf{\Psi}\mathbf{G}\right)^{-1}\mathbf{G}^{\mathsf{T}}\mathbf{\Psi}\boldsymbol{\epsilon}(k) \tag{32}$$

$$\boldsymbol{\epsilon}(k) \triangleq [\epsilon_1(k), \ldots, \epsilon_N(k)]^{\mathsf{T}}, \quad \mathbf{\Psi} \triangleq \mathbf{I} - \mathbf{\Gamma}\left(\mathbf{\Gamma}^{\mathsf{T}}\mathbf{\Gamma}\right)^{-1}\mathbf{\Gamma}^{\mathsf{T}}. \tag{33}$$

Note that $\mathbf{\Psi}$ is the annihilator matrix of $\mathbf{\Gamma}$ and satisfies $\mathbf{\Psi}\mathbf{\Psi} = \mathbf{\Psi}$. It can be readily shown that

$$\mathbf{\Psi} = \operatorname{diag}\left[\mathbf{I}_{N_1} - \frac{1}{N_1}\mathbf{1}_{N_1}\mathbf{1}_{N_1}{}^{\mathsf{T}}, \ldots, \mathbf{I}_{N_L} - \frac{1}{N_L}\mathbf{1}_{N_L}\mathbf{1}_{N_L}{}^{\mathsf{T}}\right]. \tag{34}$$

Consequently, (32) implies that the effect on the position error $\delta\boldsymbol{r}_r$ comes from the vector

$$\tilde{\boldsymbol{\epsilon}}(k) \triangleq \mathbf{\Psi}\boldsymbol{\epsilon}(k) = -\begin{bmatrix} \boldsymbol{\epsilon}_1(k) - \mu_1(k)\mathbf{1}_{N_1} \\ \vdots \\ \boldsymbol{\epsilon}_L(k) - \mu_L(k)\mathbf{1}_{N_L} \end{bmatrix} \tag{35}$$

where $\boldsymbol{\epsilon}(k) = [\boldsymbol{\epsilon}_1^{\mathsf{T}}(k), \ldots, \boldsymbol{\epsilon}_L^{\mathsf{T}}(k)]^{\mathsf{T}}$, $\boldsymbol{\epsilon}_l(k) = [\epsilon_{l_1}, \ldots, \epsilon_{l_{N_l}}]^{\mathsf{T}}$, and $\mu_l(k) \triangleq \frac{1}{N_l}\sum_{i=1}^{N_l}\epsilon_{l_i}(k)$. Noting that $\epsilon_n(k) = c\delta t_{l(n)}(k) - c\delta t_n(k)$, the following holds:

$$\begin{aligned} \tilde{\epsilon}_n(k) &= \frac{1}{N_l}\sum_{i=1}^{N_l}\left[c\delta t_{l(n)}(k) - c\bar{\delta t}_{l_i}(k)\right] - \left[c\delta t_{l(n)}(k) - c\bar{\delta t}_n(k)\right] \\ &= c\bar{\delta t}_n(k) - \frac{1}{N_l}\sum_{i=1}^{N_l}c\bar{\delta t}_{l_i}(k) \end{aligned} \tag{36}$$

which is independent of $c\delta t_l(k)$. □

APPENDIX B
PROOF OF THEOREM III.2

This appendix provides the proof of Theorem III.2, which states that given a clock bias clustering with $L < N - 2$ clusters and $J_L \triangleq \|\mathbf{\Psi}\boldsymbol{\epsilon}(k)\|_2^2$; then, there exists a clustering with $L + 1$ clusters such that $J_L \geq J_{L+1}$.

PROOF: First, note that J_L may be expressed as

$$\begin{aligned} J_L = \|\mathbf{\Psi}\boldsymbol{\epsilon}(k)\|_2^2 &= \left\| \begin{bmatrix} \boldsymbol{\epsilon}_1(k) - \mu_1(k)\mathbf{1}_{N_1} \\ \vdots \\ \boldsymbol{\epsilon}_L(k) - \mu_L(k)\mathbf{1}_{N_L} \end{bmatrix} \right\|_2^2 \\ &= \sum_{l=1}^{L}\left\|\boldsymbol{\epsilon}_l - \mu_l(k)\mathbf{1}_{N_l}\right\|_2^2 = \sum_{l=1}^{L}\sum_{j=1}^{N_l}\left[\epsilon_{l_j}(k) - \mu_l(k)\right]^2 \\ &= \sum_{l=1}^{L-1}\sum_{j=1}^{N_l}\left[\epsilon_{l_j}(k) - \mu_l(k)\right]^2 + \sum_{j=1}^{N_L}\left[\epsilon_{L_j}(k) - \mu_l(k)\right]^2 \\ &= a + \sum_{j=1}^{N_L}(\epsilon_{L_j}(k) - \mu_L(k))^2 \end{aligned} \tag{37}$$

where $a \triangleq \sum_{l=1}^{L-1}\sum_{j=1}^{N_l}[\epsilon_{l_j}(k) - \mu_l(k)]^2$. In what follows, the time argument k will be dropped for simplicity of notation. Now, add an additional cluster by partitioning $\boldsymbol{\epsilon}_L$ according to $\boldsymbol{\epsilon}_L = [\boldsymbol{\epsilon}'^{\mathsf{T}}_L, \epsilon_{L+1}]^{\mathsf{T}}$ and define

$$J_{L+1} = a + \sum_{j=1}^{N_L-1}\left(\epsilon_{L_j} - \mu'_L\right)^2 + \left(\epsilon_{L+1} - \mu_{L+1}\right)^2 \tag{38}$$

where $\mu'_L \triangleq \frac{1}{N_L-1}\sum_{j=1}^{N_L-1}\epsilon_{L_j}$ and $\mu_{L+1} = \epsilon_{L+1}$. Subsequently, J_{L+1} may be expressed as

$$J_{L+1} = a + \sum_{j=1}^{N_L-1}(\epsilon_{L_j} - \mu_L)^2. \tag{39}$$

The second term in J_L may be expressed as

$$\begin{aligned} \sum_{j=1}^{N_L}(\epsilon_{L_j} - \mu_L)^2 &= \sum_{j=1}^{N_L}\epsilon_{L_j}^2 - N_L\mu_L^2 \\ &= \sum_{j=1}^{N_L-1}\epsilon_{L_j}^2 - N_L\mu_L^2 + \epsilon_{L_{N_L}}^2. \end{aligned} \tag{40}$$

The term $N_L\mu_L^2$ may be expressed as

$$\begin{aligned} N_L\mu_L^2 &= N_L\left(\frac{1}{N_L}\sum_{j=1}^{N_L}\epsilon_{L_j}\right)^2 \\ &= \frac{1}{N_L}\left(\sum_{j=1}^{N_L-1}\epsilon_{L_j} + \epsilon_{L_{N_L}}\right)^2 \\ &= \frac{1}{N_L}\left[(N_L - 1)\,\mu'_L + \epsilon_{L_{N_L}}\right]^2 \\ &= \frac{(N_L-1)^2\,\mu'^2_L}{N_L} + \frac{2(N_L-1)\mu'_L\epsilon_{L_{N_L}}}{N_L} + \frac{\epsilon^2_{L_{N_L}}}{N_L} \\ &= (N_L - 1)\,\mu'^2_L - \frac{(N_L-1)\,\mu'^2_L}{N_L} \\ &\quad + \frac{2(N_L-1)\mu'_L\epsilon_{L,N_L}}{N_L} + \frac{\epsilon^2_{L_{N_L}}}{N_L} + \epsilon^2_{L_{N_L}} - \epsilon^2_{L_{N_L}} \\ &= (N_L - 1)\,\mu'^2_L - \frac{(N_L-1)}{N_L}(\epsilon_{L_{N_L}} - \mu'_L)^2 + \epsilon^2_{L_{N_L}}. \end{aligned} \tag{41}$$

Authorized licensed use limited to: The Ohio State University. Downloaded on October 12,2022 at 17:26:44 UTC from IEEE Xplore. Restrictions apply.

Substituting back in the second term of J_L yields

$$\sum_{j=1}^{N_L}(\epsilon_{L_j}-\mu_L)^2 = \sum_{j=1}^{N_L-1}(\epsilon_{L_j}-\mu'_L)^2+\frac{(N_L-1)}{N_L}(\epsilon_{L_{N_L}}-\mu'_L)^2. \quad (42)$$

Substituting back in J_L yields

$$J_L = a+\sum_{j=1}^{N_L-1}(\epsilon_{L_j}-\mu'_L)^2+\frac{(N_L-1)}{N_L}(\epsilon_{L_{N_L}}-\mu'_L)^2 = J_{L+1}+\frac{(N_L-1)}{N_L}(\epsilon_{L_{N_L}}-\mu'_L)^2. \quad (43)$$

Since $\frac{(N_L-1)}{N_L}(\epsilon_{L_{N_L}}-\mu'_L)^2 \geq 0$, then $J_L \geq J_{L+1}$. □

APPENDIX C
PROOF OF THEOREM III.3

This appendix provides the proof of Theorem III.3 stating that adding a carrier phase measurement from an additional cellular SOP while augmenting the clock state vector $c\boldsymbol{\delta t}$ by its corresponding additional clock state will neither change the position error nor the position error uncertainty.

PROOF: The augmented Jacobian matrix is given by

$$\mathbf{H}' = \begin{bmatrix}\mathbf{G} & \boldsymbol{\Gamma} & \mathbf{0}\\ \boldsymbol{g}^{\mathsf{T}} & \mathbf{0}^{\mathsf{T}} & 1\end{bmatrix} \quad (44)$$

where $\boldsymbol{g} \triangleq \frac{\hat{\boldsymbol{r}}_r-\boldsymbol{r}_{s_{N+1}}}{\sqrt{\|\hat{\boldsymbol{r}}_r-\boldsymbol{r}_{s_{N+1}}\|_2^2+\Delta z^2_{r,s_{N+1}}}}$. The new information matrix is subsequently given by

$$\mathbf{H}'^{\mathsf{T}}\mathbf{H}' = \begin{bmatrix}\mathbf{G}^{\mathsf{T}}\mathbf{G}+\boldsymbol{g}\boldsymbol{g}^{\mathsf{T}} & \mathbf{G}^{\mathsf{T}}\boldsymbol{\Gamma} & \boldsymbol{g}\\ \boldsymbol{\Gamma}^{\mathsf{T}}\mathbf{G} & \boldsymbol{\Gamma}^{\mathsf{T}}\boldsymbol{\Gamma} & \mathbf{0}\\ \boldsymbol{g}^{\mathsf{T}} & \mathbf{0}^{\mathsf{T}} & 1\end{bmatrix} = \begin{bmatrix}\mathbf{M}_{11} & \boldsymbol{m}_{12}\\ \boldsymbol{m}_{12}^{\mathsf{T}} & 1\end{bmatrix} \quad (45)$$

where

$$\mathbf{M}_{11} \triangleq \begin{bmatrix}\mathbf{G}^{\mathsf{T}}\mathbf{G}+\boldsymbol{g}\boldsymbol{g}^{\mathsf{T}} & \mathbf{G}^{\mathsf{T}}\boldsymbol{\Gamma}\\ \boldsymbol{\Gamma}^{\mathsf{T}}\mathbf{G} & \boldsymbol{\Gamma}^{\mathsf{T}}\boldsymbol{\Gamma}\end{bmatrix}, \boldsymbol{m}_{12} \triangleq \begin{bmatrix}\boldsymbol{g}\\ \mathbf{0}\end{bmatrix}.$$

The new covariance is given by

$$\mathbf{P}' = \left(\mathbf{H}'^{\mathsf{T}}\mathbf{H}'\right)^{-1} = \begin{bmatrix}\mathbf{A}' & \boldsymbol{b}'\\ \boldsymbol{b}'^{\mathsf{T}} & d'\end{bmatrix} \quad (46)$$

where

$$\mathbf{A}' = \left(\mathbf{M}_{11}-\boldsymbol{m}_{12}\boldsymbol{m}_{12}^{\mathsf{T}}\right)^{-1}$$
$$\boldsymbol{b}' = -\left(\mathbf{M}_{11}-\boldsymbol{m}_{12}\boldsymbol{m}_{12}^{\mathsf{T}}\right)^{-1}\boldsymbol{m}_{12}$$
$$d' = 1+\boldsymbol{m}_{12}^{\mathsf{T}}\left(\mathbf{M}_{11}-\boldsymbol{m}_{12}\boldsymbol{m}_{12}^{\mathsf{T}}\right)^{-1}\boldsymbol{m}_{12}.$$

The matrix $\mathbf{A}'$ may be expressed as

$$\mathbf{A}' = \left(\begin{bmatrix}\mathbf{G}^{\mathsf{T}}\mathbf{G}+\boldsymbol{g}\boldsymbol{g}^{\mathsf{T}} & \mathbf{G}^{\mathsf{T}}\boldsymbol{\Gamma}\\ \boldsymbol{\Gamma}^{\mathsf{T}}\mathbf{G} & \boldsymbol{\Gamma}^{\mathsf{T}}\boldsymbol{\Gamma}\end{bmatrix}-\begin{bmatrix}\boldsymbol{g}\boldsymbol{g}^{\mathsf{T}} & \mathbf{0}\\ \mathbf{0}^{\mathsf{T}} & \mathbf{0}\end{bmatrix}\right)^{-1} = \begin{bmatrix}\mathbf{G}^{\mathsf{T}}\mathbf{G} & \mathbf{G}^{\mathsf{T}}\boldsymbol{\Gamma}\\ \boldsymbol{\Gamma}^{\mathsf{T}}\mathbf{G} & \boldsymbol{\Gamma}^{\mathsf{T}}\boldsymbol{\Gamma}\end{bmatrix}^{-1} = \mathbf{P} \quad (47)$$

which indicates that the new uncertainty in the position state is unchanged. The new covariance can be expressed as

$$\mathbf{P}' = \begin{bmatrix}\mathbf{P} & -\mathbf{P}\boldsymbol{m}_{12}\\ -\boldsymbol{m}_{12}^{\mathsf{T}}\mathbf{P} & 1+\boldsymbol{m}_{12}^{\mathsf{T}}\mathbf{P}\boldsymbol{m}_{12}\end{bmatrix} = \begin{bmatrix}\mathbf{P}'_{11} & \mathbf{P}'_{12} & \mathbf{P}'_{13}\\ \mathbf{P}'^{\mathsf{T}}_{12} & \mathbf{P}'_{22} & \mathbf{P}'_{23}\\ \mathbf{P}'^{\mathsf{T}}_{13} & \mathbf{P}'^{\mathsf{T}}_{23} & \mathbf{P}'_{33}\end{bmatrix} \quad (48)$$

where

$$\mathbf{P}'_{11} = \left(\mathbf{G}^{\mathsf{T}}\boldsymbol{\Psi}\mathbf{G}\right)^{-1}$$
$$\mathbf{P}'_{12} = -\left(\mathbf{G}^{\mathsf{T}}\boldsymbol{\Psi}\mathbf{G}\right)^{-1}\mathbf{G}^{\mathsf{T}}\boldsymbol{\Gamma}\left(\boldsymbol{\Gamma}^{\mathsf{T}}\boldsymbol{\Gamma}\right)^{-1}$$
$$\mathbf{P}'_{13} = -\left(\mathbf{G}^{\mathsf{T}}\boldsymbol{\Psi}\mathbf{G}\right)^{-1}\boldsymbol{g}$$
$$\mathbf{P}'_{22} = \left(\boldsymbol{\Gamma}^{\mathsf{T}}\boldsymbol{\Gamma}\right)^{-1}\boldsymbol{\Gamma}^{\mathsf{T}}\left[\mathbf{I}+\mathbf{G}\left(\mathbf{G}^{\mathsf{T}}\boldsymbol{\Psi}\mathbf{G}\right)^{-1}\mathbf{G}^{\mathsf{T}}\right]\boldsymbol{\Gamma}\left(\boldsymbol{\Gamma}^{\mathsf{T}}\boldsymbol{\Gamma}\right)^{-1}$$
$$\mathbf{P}'_{23} = \left(\boldsymbol{\Gamma}^{\mathsf{T}}\boldsymbol{\Gamma}\right)^{-1}\boldsymbol{\Gamma}^{\mathsf{T}}\mathbf{G}\left(\mathbf{G}^{\mathsf{T}}\boldsymbol{\Psi}\mathbf{G}\right)^{-1}\boldsymbol{g}$$
$$\mathbf{P}'_{33} = 1+\boldsymbol{g}^{\mathsf{T}}\left(\mathbf{G}^{\mathsf{T}}\boldsymbol{\Psi}\mathbf{G}\right)^{-1}\boldsymbol{g}.$$

The new estimation error is given by

$$\delta\boldsymbol{r}'_r(k) = -\mathbf{P}'\mathbf{H}'^{\mathsf{T}}\boldsymbol{\epsilon}'(k) \quad (49)$$

where $\boldsymbol{\epsilon}'(k) \triangleq [\boldsymbol{\epsilon}^{\mathsf{T}}(k), \epsilon_{N+1}(k)]^{\mathsf{T}}$ and $\epsilon_{N+1}(k)$ is the error from the $(N+1)^{\text{st}}$ measurement. Using the expressions of $\mathbf{P}'$, $\mathbf{H}'$, and $\boldsymbol{\epsilon}'$, it can be readily shown that

$$\delta\boldsymbol{r}'_r(k) = -\left(\mathbf{G}^{\mathsf{T}}\boldsymbol{\Psi}\mathbf{G}\right)^{-1}\mathbf{G}^{\mathsf{T}}\boldsymbol{\Psi}\boldsymbol{\epsilon}(k) = \delta\boldsymbol{r}_r(k). \quad (50)$$

Therefore, the addition of a measurement while augmenting the clock state vector by one state will not improve the position estimate nor the position error uncertainty. □

APPENDIX D

Table of ARMA Coefficients for Experiment 1

BTS	AR coefficients	MA coefficients	$\sigma_{w_{\epsilon_n}}$ (mm)
1	[1, -1.167, -0.023, -0.508, 0.743, 0.323, -0.363]	[1 ,-0.349, -0.399, -0.834, 0.0960, 0.406, 0.087]	3.1
2	[1, -1.596, 0.934, 0.132, -0.826, 0.508, -0.035]	[1,-0.692, 0.224, 0.328, -0.485, -0.073, 0.004]	2.5
3	[1, -1.052, -0.407, 0.356, -0.121, 0.588, -0.352]	[1,-0.368, -0.657, -0.240, -0.208, 0.525, -0.011]	3.6
4	[1, -0.208, -0.512, 0.506, -0.564, -0.340, 0.5742]	[1,0.439, -0.203, 0.388, -0.417, -0.626, 0.161]	2.9
5	[1, -1.06, 0.006, -0.484, 0.596, 0.329, -0.331]	[1,-0.250, -0.270, -0.771, -0.009, 0.402, -0.009]	2.9
6	[1, -2.350, 2.450, -1.750, 0.890, -0.243, 0.0419]	[1, -1.417, 1.062, -0.714, 0.212, -0.099, 0.103]	2.9
7	[1, -0.208, -0.512, 0.505, -0.564, -0.340, 0.574]	[1, 0.43, -0.203, 0.388, -0.417, -0.626, 0.161]	2.9
8	[1, 0.835, -0.656, -0.629, -0.028, 0.270, 0.221]	[1, 1.569, 0.484, -0.350, -0.383, -0.005, 0.146]	3.3
9	[1, 0.134, -0.450, 0.518, -0.427, -0.391, 0.468]	[1, 0.995, 0.230, 0.552, 0.0380, -0.608, -0.128]	57.5

ACKNOWLEDGMENT

The authors would like to thank Joshua Morales, Kimia Shamaei, and Mahdi Maaref for their help in data collection.

REFERENCES

[1] R. Loh, Y. Bia, and T. Roe
UAVs in civil airspace: Safety requirement
IEEE Aerosp. Electron. Syst. Mag., vol. 24, no. 1, pp. 5–17, Jan. 2009.

Authorized licensed use limited to: The Ohio State University. Downloaded on October 12,2022 at 17:26:44 UTC from IEEE Xplore. Restrictions apply.

[2] A. Kerns, D. Shepard, J. Bhatti, and T. Humphreys
Unmanned aircraft capture and control via GPS spoofing
J. Field Robot., vol. 31, no. 4, pp. 617–636, 2014.

[3] D. Borio, F. Dovis, H. Kuusniemi, and L. Presti
Impact and detection of GNSS jammers on consumer grade satellite navigation receivers
Proc. IEEE, vol. 104, no. 6, pp. 1233–1245, Jun. 2016.

[4] N. Kbayer and M. Sahmoudi
Performances analysis of GNSS NLOS bias correction in urban environment using a threedimensional city model and GNSS simulator
IEEE Trans. Aerosp. Electron. Syst., vol. 54, no. 4, pp. 1799–1814, Aug. 2018.

[5] J. McEllroy
Navigation using signals of opportunity in the AM transmission band
M.S. thesis, Air Force Inst. of Technol., Wright-Patterson Air Force Base, OH, USA, 2006.

[6] V. Moghtadaiee and A. Dempster
Indoor location fingerprinting using FM radio signals
IEEE Trans. Broadcast., vol. 60, no. 2, pp. 336–346, Jun. 2014.

[7] X. Chen, Q. Wei, F. Wang, Z. Jun, S. Wu, and A. Men
Super-resolution time of arrival estimation for a symbiotic FM radio data system
IEEE Trans. Broadcast., vol. 66, no. 4, pp. 847–856, Dec. 2020.

[8] T. Reid, A. Neish, T. Walter, and P. Enge
Broadband LEO constellations for navigation
NAVIGATION, J. Inst. Navig., vol. 65, no. 2, pp. 205–220, 2018.

[9] J. Khalife, M. Neinavaie, and Z. Kassas
Navigation with differential carrier phase measurements from megaconstellation LEO satellites
In *Proc. IEEE/ION Position, Location, Navig. Symp.*, 2020, pp. 1393–1404.

[10] F. Farhangian and R. Landry
Multi-constellation software-defined receiver for Doppler positioning with LEO satellites
Sensors, vol. 20, no. 20, pp. 5866–5883, Oct. 2020.

[11] F. Farhangian, H. Benzerrouk, and R. Landry
Opportunistic in-flight INS alignment using LEO satellites and a rotatory IMU platform
Aerospace, vol. 8, no. 10, pp. 280–281, 2021.

[12] Z. Kassas *et al.*
Enter LEO on the GNSS stage: Navigation with Starlink satellites
Inside GNSS Mag., vol. 16, no. 6, pp. 42–51, 2021.

[13] N. Chang, R. Rashidzadeh, and M. Ahmadi
Robust indoor positioning using differential Wi-Fi access points
IEEE Trans. Consum. Electron., vol. 56, no. 3, pp. 1860–1867, Aug. 2010.

[14] R. Faragher, C. Sarno, and M. Newman
Opportunistic radio SLAM for indoor navigation using smartphone sensors
In *Proc. IEEE/ION Position Location Navigation Symp.*, 2012, pp. 120–128.

[15] I. Bisio *et al.*
A trainingless WiFi fingerprint positioning approach over mobile devices
IEEE Antennas Wireless Propag. Lett., vol. 13, pp. 832–835, 2014.

[16] Y. Zhuang and N. El-Sheimy
Tightly-coupled integration of WiFi and MEMS sensors on handheld devices for indoor pedestrian navigations
IEEE Sensors J., vol. 16, no. 1, pp. 224–234, Jan. 2016.

[17] M. Rabinowitz and J. Spilker
The rosum television positioning technolog
In *Proc. Annu. Meeting Inst. Navigation CIGTF Guid. Test Symp.*, 2003, pp. 528–541.

[18] P. Thevenon *et al.*
Positioning using mobile TV based on the DVB-SH standard
J. Inst. Navigation, vol. 58, no. 2, pp. 71–90, 2011.

[19] J. Yang, X. Wang, M. Rahman, S. Park, H. Kim, and Y. Wu
A new positioning system using DVB-T2 transmitter signature waveforms in single frequency networks
IEEE Trans. Broadcast., vol. 58, no. 3, pp. 347–359, Sep. 2012.

[20] L. Chen, O. Julien, P. Thevenon, D. Serant, A. Pena, and H. Kuusniemi
TOA estimation for positioning with DVB-T signals in outdoor static tests
IEEE Trans. Broadcast., vol. 61, no. 4, pp. 625–638, Dec. 2015.

[21] C. Yang and A. Soloviev
Mobile positioning with signals of opportunity in urban and urban canyon environments
In *Proc. IEEE/ION Position, Location, Navigation Symp.*, 2020, pp. 1043–1059.

[22] C. Yang and T. Nguyen
Tracking and relative positioning with mixed signals of opportunity
J. Inst. Navig., vol. 62, no. 4, pp. 291–311, Dec. 2015.

[23] K. Shamaei, J. Khalife, and Z. Kassas
Exploiting LTE signals for navigation: Theory to implementation
IEEE Trans. Wireless Commun., vol. 17, no. 4, pp. 2173–2189, Apr. 2018.

[24] J. Khalife and Z. Kassas
Navigation with cellular CDMA signals — Part II: Performance analysis and experimental results
IEEE Trans. Signal Process., vol. 66, no. 8, pp. 2204–2218, Apr. 2018.

[25] J. Khalife and Z. Kassas
Precise UAV navigation with cellular carrier phase measurements
In *Proc. IEEE/ION Position, Location, Navig. Symp.*, 2018, pp. 978–989.

[26] J. del Peral-Rosado, R. Raulefs, J. López-Salcedo, and G. Seco-Granados
Survey of cellular mobile radio localization methods: From 1G to 5G
IEEE Commun. Surv. Tut., vol. 20, no. 2, pp. 1124–1148, Apr.–Jun. 2018.

[27] E. Kim and Y. Shin
Feasibility analysis of LTE-based UAS navigation in deep urban areas and DSRC augmentation
Sensors, vol. 19, no. 9, pp. 4192–4207, Apr. 2019.

[28] T. Kang, H. Lee, and J. Seo
TOA-based ranging method using CRS in LTE signals
J. Adv. Navig. Technol., vol. 23, no. 5, pp. 437–443, Oct. 2019.

[29] C. Yang, T. Pany, and P. Weitkemper
Effect of antenna ports on TOA estimation with 4G LTE signals in urban mobile environments
In *Proc. ION Int. Tech. Meeting Conf.*, 2020, pp. 2166–2181.

[30] J. Mortier, G. Pages, and J. Vila-Valls
Robust TOA-based UAS navigation under model mismatch in GNSS-denied harsh environments
Remote Sens., vol. 12, no. 18, pp. 2928–2947, Sep. 2020.

[31] H. Dun, C. Tiberius, and G. Janssen
Positioning in a multipath channel using OFDM signals with carrier phase tracking
IEEE Access, vol. 8, pp. 13011–13028, 2020.

[32] J. Gante, L. Sousa, and G. Falcao
Dethroning GPS: Low-power accurate 5G positioning systems using machine learning
IEEE Trans. Emerg. Sel. Topics Circuits Syst., vol. 10, no. 2, pp. 240–252, Jun. 2020.

[33] C. Gentner, T. Jost, W. Wang, S. Zhang, A. Dammann, and U. Fiebig
Multipath assisted positioning with simultaneous localization and mapping

Authorized licensed use limited to: The Ohio State University. Downloaded on October 12,2022 at 17:26:44 UTC from IEEE Xplore. Restrictions apply.

IEEE Trans. Wireless Commun., vol. 15, no. 9, pp. 6104–6117, Sep. 2016.

[34] P. Muller, J. del Peral-Rosado, R. Piche, and G. Seco-Granados
Statistical trilateration with skew-t distributed errors in LTE networks
IEEE Trans. Wireless Commun., vol. 15, no. 10, pp. 7114–7127, Oct. 2016.

[35] M. Driusso, C. Marshall, M. Sabathy, F. Knutti, H. Mathis, and F. Babich
Vehicular position tracking using LTE signals
IEEE Trans. Veh. Technol., vol. 66, no. 4, pp. 3376–3391, Apr. 2017.

[36] Z. Kassas, J. Morales, K. Shamaei, and J. Khalife
LTE steers UAV
GPS World Mag., vol. 28, no. 4, pp. 18–25, Apr. 2017.

[37] K. Shamaei and Z. Kassas
LTE receiver design and multipath analysis for navigation in urban environments
J. Inst. Navig., vol. 65, no. 4, pp. 655–675, Dec. 2018.

[38] Z. Kassas, M. Maaref, J. Morales, J. Khalife, and K. Shamaei
Robust vehicular localization and map matching in urban environments through IMU, GNSS, and cellular signals
IEEE Intell. Transp. Syst. Mag., vol. 12, no. 3, pp. 36–52, Jun. 2020.

[39] N. Souli, P. Kolios, and G. Ellinas
Online relative positioning of autonomous vehicles using signals of opportunity
IEEE Trans. Intell. Veh., to be published, doi: 10.1109/TIV.2021.3124727.

[40] G. Retscher, H. Hofer, A. Kealy, V. Gikas, and F. Obex
Cooperative localization in indoor environments using constrained differential Wi-Fi and UWB measurements
In *Proc. 30th Int. Tech. Meeting Satell. Division Inst. Navigation Conf.*, 2017, pp. 2869–2882.

[41] T. Zhao, K. Zhao, C. Yu, D. Dong, Z. Zheng, and Y. Zhang
Application of differential time synchronization in indoor positioning
In *Proc. Int. Conf. Wireless Commun. Signal Process.*, 2019, pp. 1–6.

[42] J. del Peral-Rosado *et al.*
Software-defined radio LTE positioning receiver towards future hybrid localization systems
In *Proc. Int. Commun. Satell. Syst. Conf.*, 2013, pp. 1–11.

[43] C. Yang, T. Nguyen, and E. Blasch
Mobile positioning via fusion of mixed signals of opportunity
IEEE Aerosp. Electron. Syst. Mag., vol. 29, no. 4, pp. 34–46, Apr. 2014.

[44] J. Khalife, K. Shamaei, and Z. Kassas
Navigation with cellular CDMA signals - Part I: Signal modeling and software-defined receiver design
IEEE Trans. Signal Process., vol. 66, no. 8, pp. 2191–2203, Apr. 2018.

[45] K. Shamaei and Z. Kassas
Receiver design and time of arrival estimation for opportunistic localization with 5G signals
IEEE Trans. Wireless Commun., vol. 20, no. 7, pp. 4716–4731, Jul. 2021.

[46] M. Lichtman, R. Jover, M. Labib, R. Rao, V. Marojevic, and J. Reed
LTE/LTE-A jamming, spoofing, and sniffing: Threat assessment and mitigation
IEEE Commun. Mag., vol. 54, no. 4, pp. 54–61, Apr. 2016.

[47] M. Lichtman, R. Rao, V. Marojevic, J. Reed, and R. Jover
5G NR jamming, spoofing, and sniffing: Threat assessment and mitigation
In *Proc. IEEE Int. Conf. Commun. Workshops*, 2018, pp. 1–6.

[48] A. Gupta, R. Jha, P. Gandotra, and S. Jain
Bandwidth spoofing and intrusion detection system for multistage 5G wireless communication network
IEEE Trans. Veh. Technol., vol. 67, no. 1, pp. 618–632, Jan. 2018.

[49] W. Xu, C. Yuan, S. Xu, H. Ngo, and W. Xiang
On pilot spoofing attack in massive MIMO systems: Detection and countermeasure
IEEE Trans. Inf. Forensics Secur., vol. 16, pp. 1396–1409, 2021.

[50] A. Abdallah, J. Khalife, and Z. Kassas
Experimental characterization of received 5G signals carrier-to-noise ratio in indoor and urban environments
In *Proc. IEEE Veh. Technol. Conf.*, 2021, pp. 1–5.

[51] J. Khalife, K. Shamaei, S. Bhattacharya, and Z. Kassas
Centimeter-accurate UAV navigation with cellular signals
In *Proc. 31st Int. Techn. Meeting Satell. Division Inst. Navigation Conf.*, 2018, pp. 2321–2331.

[52] Z. Kassas
Analysis and synthesis of collaborative opportunistic navigation systems
Ph.D. dissertation, University of Texas, Austin, TX, USA, 2014.

[53] C. Yang and A. Soloviev
Simultaneous localization and mapping of emitting radio sources-SLAMERS
In *Proc. 28th Int. Tech. Meeting Satell. Division Inst. Navigation Conf.*, 2015, pp. 2343–2354.

[54] C. Gentner, B. Ma, M. Ulmschneider, T. Jost, and A. Dammann
Simultaneous localization and mapping in multipath environments
In *Proc. IEEE/ION Position Location Navigation Symp.*, 2016, pp. 807–815.

[55] J. Morales and Z. Kassas
Tightly-coupled inertial navigation system with signals of opportunity aiding
IEEE Trans. Aerosp. Electron. Syst., vol. 57, no. 3, pp. 1930–1948, Jun. 2021.

[56] J. Morales and Z. Kassas
Optimal collaborative mapping of terrestrial transmitters: Receiver placement and performance characterization
IEEE Trans. Aerosp. Electron. Syst., vol. 54, no. 2, pp. 992–1007, Apr. 2018.

[57] Z. Kassas, J. Khalife, A. Abdallah, and C. Lee
I am not afraid of the jammer: Navigating with signals of opportunity in GPS-denied environments
In *Proc. 33rd Int. Tech. Meeting Satell. Division Inst. Navigation Conf.*, 2020, pp. 1566–1585.

[58] *Physical Layer Standard for CDMA2000 Spread Spectrum Systems (C.S0002-E)*, 3GPP2, 3rd Generation Partnership Project 2 (3GPP2), TS C.S0002-E, Jun. 2011.

[59] *Evolved Universal Terrestrial Radio Access (E-UTRA); Physical Channels and Modulation*, 3GPP, 3rd Generation Partnership Project (3GPP), TS 36.211, Jan. 2011. [Online]. Available: http://www.3gpp.org/ftp/Specs/html-info/36211.htm

[60] M. Ulmschneider and C. Gentner
Multipath assisted positioning for pedestrians using LTE signals
In *Proc. IEEE/ION Position, Location, Navigation Symp.*, 2016, pp. 386–392.

[61] P. Misra and P. Enge
Global Positioning System: Signals, Measurements, and Performance, 2nd ed. Lincoln, MA, USA: Ganga-Jamuna Press, 2010.

[62] M. Maaref and Z. Kassas
Measurement characterization and autonomous outlier detection and exclusion for ground vehicle navigation with cellular signals
IEEE Trans. Intell. Veh., vol. 5, no. 4, pp. 670–683, Dec. 2020.

[63] S. Ragothaman, M. Maaref, and Z. Kassas
Autonomous ground vehicle path planning in urban environments using GNSS and cellular signals reliability maps: Models and algorithms
IEEE Trans. Aerosp. Electron. Syst., vol. 57, no. 2, pp. 1562–1580, Jun. 2021.

[64] M. Maaref, J. Khalife, and Z. Kassas
Aerial vehicle protection level reduction by fusing GNSS and

Authorized licensed use limited to: The Ohio State University. Downloaded on October 12,2022 at 17:26:44 UTC from IEEE Xplore. Restrictions apply.

terrestrial signals of opportunity
IEEE Trans. Intell. Transp. Syst., vol. 22, no. 9, pp. 5976–5993, Sep. 2021.

[65] Qualcomm Technologies, Inc. LTE unmanned aircraft systems Tech. Rep. 1.0.1, May 2017. [Online]. Available: https://www.qualcomm.com/documents/lte-unmanned-aircraft-systems-trial-report/

[66] X. Chen, F. Dovis, and M. Pini
An innovative multipath mitigation method using coupled amplitude delay lock loops in GNSS receivers
In *Proc. IEEE/ION Position, Location, Navigation Symp.*, 2010, pp. 1118–1126.

[67] O. Bialer, D. Raphaeli, and A. Weiss
Efficient time of arrival estimation algorithm achieving maximum likelihood performance in dense multipath
IEEE Trans. Signal Process., vol. 60, no. 3, pp. 1241–1252, Mar. 2012.

[68] J. del Peral-Rosado, J. López-Salcedo, F. Zanier, and G. Seco-Granados
Position accuracy of joint time-delay and channel estimators in LTE networks
IEEE Access, vol. 6, pp. 25185–25199, 2018.

[69] Y. Quan, L. Lau, G. Roberts, X. Meng, and C. Zhang
Convolutional neural network based multipath detection method for static and kinematic GPS high precision positioning
Remote Sens., vol. 10, no. 12, Dec. 2018, Art. no. 2052.

[70] P. Wang and Y. Morton
Performance comparison of time-of-arrival estimation techniques for LTE signals in realistic multipath propagation channels
NAVIGATION, J. Inst. Navigation, vol. 67, no. 4, pp. 691–712, Dec. 2020.

[71] P. Wang and Y. Morton
Multipath estimating delay lock loop for LTE signal TOA estimation in indoor and urban environments
IEEE Trans. Wireless Commun., vol. 19, no. 8, pp. 5518–5530, Aug. 2020.

[72] A. Abdallah and Z. Kassas
Multipath mitigation via synthetic aperture beamforming for indoor and deep urban navigation
IEEE Trans. Veh. Technol., vol. 70, no. 9, pp. 8838–8853, Sep. 2021.

[73] M. Joerger and B. Pervan
Fault detection and exclusion using solution separation and chi-squared ARAIM
IEEE Trans. Aerosp. Electron. Syst., vol. 52, no. 2, pp. 726–742, Apr. 2016.

[74] N. Zhu, J. Marais, D. Betaille, and M. Berbineau
GNSS position integrity in urban environments: A. review of literature
IEEE Trans. Intell. Transp. Syst., vol. 19, no. 9, pp. 2762–2778, Sep. 2018.

[75] N. Zhu, D. Betaille, J. Marais, and M. Berbineau
GNSS integrity monitoring schemes for terrestrial applications in harsh signal environments
IEEE Intell. Transp. Syst. Mag., vol. 12, no. 3, pp. 81–91, Mar. 2020.

[76] N. Ziedan
Multipath channel estimation and pattern recognition for environment-based adaptive tracking
In *Proc. 25th Int. Tech. Meeting Satell. Division Inst. Navigation Conf.*, 2012, pp. 394–407.

[77] Y. Wang, X. Chen, and P. Liu
Statistical multipath model based on experimental GNSS data in static urban canyon environment
Sensors, vol. 18, no. 4, Apr. 2018, Art. no. 1149.

[78] J. Khalife and Z. Kassas
Evaluation of relative clock stability in cellular networks
In *Proc. 30th Int. Tech. Meeting Satell. Division Inst. Navigation Conf.*, 2017, pp. 2554–2559.

[79] J. Khalife and Z. Kassas
Opportunistic UAV navigation with carrier phase measurements from asynchronous cellular signals
IEEE Trans. Aerosp. Electron. Syst., vol. 56, no. 4, pp. 3285–3301, Aug. 2020.

[80] J. Morales and Z. Kassas
Stochastic observability and uncertainty characterization in simultaneous receiver and transmitter localization
IEEE Trans. Aerosp. Electron. Syst., vol. 55, no. 2, pp. 1021–1031, Apr. 2019.

[81] L. Ljung
System Identification: Theory for the User. 2nd ed. Englewood Cliffs, NJ, USA: Prentice-Hall, 1999.

[82] J. Khalife, C. Sevinc, and Z. Kassas
Performance evaluation of TOA positioning in asynchronous cellular networks using stochastic geometry models
IEEE Wireless Commun. Lett., vol. 9, no. 9, pp. 1422–1426, Sep. 2020.

[83] J. Wirth, E. Bonugli, and M. Freund
Assessment of the accuracy of Google Earth imagery for use as a tool in accident reconstruction
In *Proc. SAE World Congr. Exhib.*, 2015, pp. 1–17.

[84] C. Yang and T. Nguyen
Self-calibrating position location using signals of opportunity
In *Proc. 22nd Int. Tech. Meeting Satell. Division Inst. Navigation Conf.*, 2009, pp. 1055–1063.

Joe Khalife (Member, IEEE) received the B.E. degree in electrical engineering and the M.S. degree in computer engineering from the Lebanese American University (LAU), Beirut, Lebanon, in 2011 and 2014, respectively and the Ph.D. degree in electrical engineering and computer science from the University of California, Irvine, CA, USA, in 2020.

He is a Postdoctoral Fellow with the University of California, Irvine and member of the Autonomous Systems Perception, Intelligence, and Navigation (ASPIN) Laboratory. From 2012 to 2015, he was a Research Assistant with LAU, and has been a member of the ASPIN Laboratory since 2015. His research interests include opportunistic navigation, autonomous vehicles, and software-defined radio.

Dr. Khalife is a recipient of the 2016 IEEE/ION Position, Location, and Navigation Symposium (PLANS) Best Student Paper Award and the 2018 IEEE Walter Fried Award.

Zaher M. Kassas (Senior Member, IEEE) received the B.E. degree in electrical engineering from the Lebanese American University, Beirut, Lebanon, the M.S. degree in electrical and computer engineering from The Ohio State University, Columbus, OH, USA, and the M.S.E. degree in aerospace engineering and the Ph.D. degree in electrical and computer engineering from The University of Texas at Austin, Austin, TX, USA.

He is currently an Associate Professor with the University of California, Irvine, CA, USA, and the Director of the Autonomous Systems Perception, Intelligence, and Navigation (ASPIN) Laboratory. He is also the Director of the U.S. Department of Transportation Center: CARMEN (Center for Automated Vehicle Research with Multimodal AssurEd Navigation), focusing on navigation resiliency and security of highly automated transportation systems. His research interests include cyber-physical systems, estimation theory, navigation systems, autonomous vehicles, and intelligent transportation systems.

Prof. Kassas is a recipient of the 2018 National Science Foundation (NSF) Faculty Early Career Development Program (CAREER) award, 2019 Office of Naval Research (ONR) Young Investigator Program (YIP) award, 2022 Air Force Office of Scientific Research (AFOSR) YIP award, 2018 IEEE Walter Fried Award, 2018 Institute of Navigation (ION) Samuel Burka Award, and 2019 ION Col. Thomas Thurlow Award. He is a Senior Editor of the IEEE TRANSACTIONS ON INTELLIGENT VEHICLES and an Associate Editor of the IEEE TRANSACTIONS ON AEROSPACE AND ELECTRONIC SYSTEMS and the IEEE TRANSACTIONS ON INTELLIGENT TRANSPORTATION SYSTEMS.

Authorized licensed use limited to: The Ohio State University. Downloaded on October 12,2022 at 17:26:44 UTC from IEEE Xplore. Restrictions apply.

Feature Article:

DOI. No. 10.1109/MAES.2022.3178664

Opportunistic Autonomous Integrity Monitoring for Enhanced UAV Safety

Joe Khalife, Mahdi Maaref, and Zaher M. Kassas, **University of California, Irvine, CA 92697 USA**

INTRODUCTION

Autonomous unmanned aerial vehicles (UAVs) are predicted to revolutionize a wide range of sectors, such as surveying, farming, filming, construction, transportation, emergency response, infrastructure inspection, and package delivery. As these vehicles approach full-autonomy, the accuracy and integrity of their navigation system become ever more stringent [1]–[4]. While the notion of accuracy is self-explanatory, the notion of integrity is less obvious, but it is of utmost importance in the safety critical application of aviation. Integrity is a criterion to evaluate the reliability and to measure the level of trust in the information produced by a navigation system. A high-integrity navigation system must be able to detect and reject faulty measurements and provide an integrity measure of the confidence in the system performance at any time. Integrity monitoring can be provided through the global navigation satellite system (GNSS) navigation messages to indicate satellite anomalies, such as clock errors. However, this type of integrity information is not useful for real-time applications, as it may take on average, about an hour (or less based on recent data), to identify and broadcast the satellite service failure. Thus, alternative frameworks for integrity monitoring have been developed, which can be categorized into internal and external [5]. External methods [e.g., ground-based augmentation system (GBAS) and satellite-based augmentation system (SBAS)] leverage a network of ground monitoring stations to monitor the transmitted signals [6], while internal methods [e.g., receiver autonomous integrity monitoring (RAIM)] typically use the redundant information within the transmitted navigation signals. RAIM inherently possesses desirable characteristics due to its design flexibility and adaptability [5]. RAIM is a technique primarily based on checking the consistency of redundant measurements. RAIM assesses the availability performance by calculating the protection level (PL) on-the-fly, which is the radius of a circular area centered around the position solution and is guaranteed to contain the true position within the specifications of RAIM, i.e., with a probability less than or equal to an acceptable integrity risk [7]. By comparing the PL with a predefined alert limit (AL), the availability of the navigation system could be determined; specifically, if the PL is less than the AL, the navigation solution is deemed reliable for the predefined integrity risk, and unreliable otherwise.

RAIM was initially proposed for GPS-based navigation. Recently, advanced RAIM (ARAIM) algorithms have been developed for multiconstellation navigation systems, which use measurements from different GNSS [8]. Nevertheless, relying on GNSS signals alone poses an alarming vulnerability for UAV navigation due to unintentional interference [9], intentional jamming [10], and spoofing [11]. Besides, due to the geometric configuration of GNSS satellites, the vertical error of the GNSS navigation solution is too large for safe UAV navigation in urban environments [12]. To account for GNSS limitations, alternative sensors have been integrated into the UAV's navigation system, and the integrity of these sensors has been the subject of recent studies. Recently, different RAIM schemes incorporating other sensing modalities have been proposed, such as i) multi-GNSS constellation RAIM (e.g., Galileo-GPS, [13] GLONASS-GPS, [8] Beidou-GPS [14], and ii) GNSS-sensor RAIM (e.g., GPS, inertial measurement units (IMUs), wheel speed encoders, and cameras [15]; GNSS-aided inertial navigation system (INS) [16]; GPS and vision [17]; GNSS and IMU [18]; GNSS, lidar, and IMU [19]; and GPS and lidar [20]).

In addition to sensors, ambient radio signals in the environment, which are not intended for navigation, have been recently considered as a supplement or an alternative to GNSS signals [21]. These signals, termed signals of opportunity (SOPs), can be terrestrial (e.g., cellular signals, digital television signals, AM/FM signals) or space-based (e.g, low Earth orbit (LEO) satellites). SOPs possess

Authors' current address: The authors are with the University of California, Irvine, CA 92697 USA (e-mail: zkassas@ieee.org).

Manuscript received 12 September 2021, revised 11 February 2022; accepted 13 May 2022, and ready for publication 9 June 2022.

Review handled by Giancarmine Fasano.

0885-8985/22/$26.00 © 2022 IEEE

Authorized licensed use limited to: The Ohio State University. Downloaded on May 15,2023 at 19:40:44 UTC from IEEE Xplore. Restrictions apply.

Image licensed by Ingram Publishig

desirable characteristics for navigation purposes: i) ubiquity, ii) high received power, iii) large transmission bandwidth, iv) wide range of transmission frequencies, and v) geometric diversity. Recent research has demonstrated that cellular SOPs could yield submeter-level-accurate navigation on UAVs [22] and meter-level-accurate navigation on high altitude aircraft [23]. Moreover, it has been demonstrated that fusing GNSS and cellular SOPs results in significant reduction in the UAV's position uncertainty and PLs [12].

As the number of systems that rely on SOPs for navigation grows, the need for modeling measurement errors and monitoring the integrity of SOP-based navigation systems increases. Over the past few years, research has been conducted to model different error sources that deteriorate SOP measurements [24], [25]. In [25], it was shown that while adding more measurements from other satellites decreases the PLs, measurements from SOPs are more effective in minimizing the PL than GNSS satellites. This is due to the fact that terrestrial SOP measurements are received from negative elevation angles, as the UAV can fly above terrestrial SOPs. As a consequence, a combined GNSS-SOP system will benefit from a doubled elevation angle range. However, the integrity of SOP-based navigation systems has been barely studied in the existing literature. This article presents a new paradigm, termed opportunistic ARAIM (OARAIM), which reduces the PLs of UAVs by fusing GNSS and terrestrial SOP pseudorange measurements. It is shown that by incorporating SOPs, the PLs can be made smaller than the ones from any combination of current GNSS constellations, as shown in Figure 1. This reduction is essential in order to meet stringent integrity standard needed for safe UAV operations, especially in i) GNSS-challenged environments and ii) environments with poor satellite-to-user geometry.

Preliminary studies to assess the PL reduction due to using SOPs have been considered in [12], [24], [26]. These studies investigated a classical RAIM-based approach, where a maximum of only one measurement outlier at each time-step was considered. However, in the complicated wireless environments (e.g., deep urban canyons, nearby buildings, SOP blind spots, etc.) where the signals are heavily affected by multipath and line-of-sight-(LOS)-blockage, the assumption of experiencing only one measurement outlier may not be valid anymore. Moreover, at high altitudes [e.g., UAVs flying at an altitude of 250 m above ground level (AGL)], signal interference could be experienced [27]. To thoroughly tackle these problems, this article extends previous work through three contributions. First, in contrast to previous work, this article aims to detect more than one outlier induced into measurements due to LOS signal blockage or multipath. To this end, this article establishes a GNSS-SOP OARAIM framework and calculates the corresponding vertical PL (VPL) and horizontal PL (HPL). Second, a fault-tree and the associated fault probabilities for a combined GNSS-SOP system is developed. Then, the corresponding integrity support message (ISM) parameters for SOPs are discussed (e.g., user range error (URE), user range accuracy (URA), maximum nominal bias, etc.). Third, experimental results with cellular SOPs are presented evaluating the efficacy of the proposed OARAIM framework on a UAV for different fault conditions. A stress test shows that in faulty conditions, the OARAIM algorithm detects the faults in GPS satellites while GPS-only ARAIM fails to detect such faults. Moreover, the OARAIM algorithm reduces the gaps between the VPL and HPL and vertical and horizontal position errors (PEs) by more than 55% and 70%, respectively, compared to only using GNSS measurements.

The rest of this article is organized as follows. The section "OARAIM Framework" presents the proposed OARAIM framework. "Performance Evaluation" evaluates the performance of the OARAIM framework numerically and experimentally. Last, we present the "Conclusion."

OARAIM FRAMEWORK

This section develops the OARAIM framework to perform integrity monitoring for GNSS-SOP-based navigation. A well-designed integrity monitoring framework provides the UAV with the PLs, i.e., horizontal and vertical regions

Authorized licensed use limited to: The Ohio State University. Downloaded on May 15,2023 at 19:40:44 UTC from IEEE Xplore. Restrictions apply.

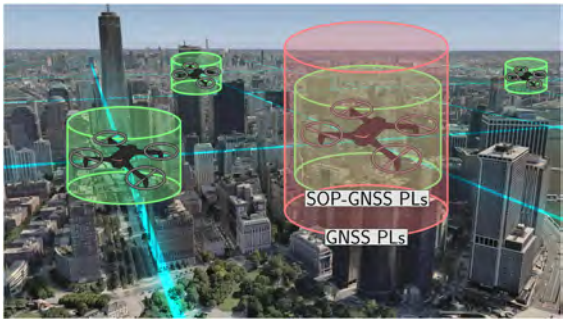

Figure 1.
UAV PLs with ARAIM (GNSS only) and OARAIM (SOP-GNSS).

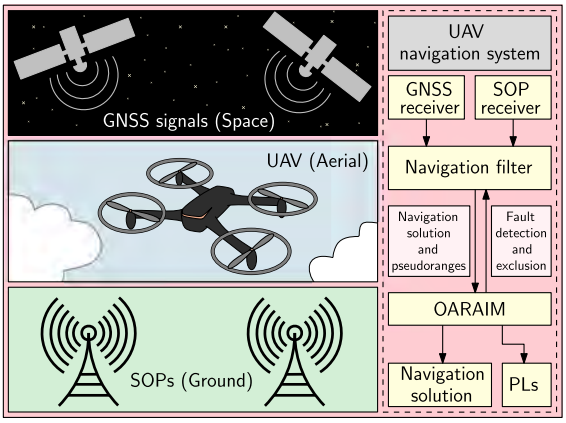

Figure 2.
Opportunistic navigation framework with OARAIM.

centered at the UAV's true position, which are guaranteed to contain the UAV's estimated position with a certain level of confidence. In this article, a baseline multiple hypothesis solution separation (MHSS) ARAIM, which was introduced in [28] is used to calculate the PLs. In the sequel, ARAIM will refer to MHSS ARAIM, for simplicity. ARAIM is a robust framework for combining navigation signals from different navigation sources with different signal properties, e.g., different URA values and different probabilities of single or multiple simultaneous faults. As such, ARAIM is well-suited for combining SOP signals with GNSS signals to form OARAIM. In addition to providing PLs, OARAIM performs fault detection and exclusion to mitigate the effect of SOP and/or GNSS system faults on the navigation solution. Figure 2 summarizes the OARAIM GNSS-SOP framework for UAV navigation.

FAULT TREE AND FAULT MODES

OARAIM operates on a fault tree. By definition, a fault tree refers to a set of assumptions about the environment in which a RAIM algorithm is applied. The measurements are supposed to be in one out of a set of different branches of the fault tree, to each of which an *a priori* probability of occurrence is assigned. Therefore, the fault tree can be employed to identify different sources of faults. OARAIM performs multiple statistical tests to detect faults, and then it attempts to exclude the detected faults. The HPL and VPL are subsequently calculated.

OARAIM considers a list of faults that need to be monitored and determines the corresponding prior probabilities that must be assigned to each mode. For simplicity, a GPS-SOP fault tree will be discussed. Extension to other GNSS constellations is expected to be straightforward. In [28], a method was presented to determine the faults that need to be monitored and the associated probabilities of faults. Using the same methodology, in this article, a maximum of three simultaneous faults are considered. Also, the probability of a constellation fault (i.e., a fault that affects all transmitters) for both GPS and SOP transmitters are assumed to be sufficiently improbable. This assumption relies on historical record of these signals. GPS records show that there is no evidence of a constellation fault since the first GPS satellites were launched [29]. Moreover, no SOP "constellation" faults were experienced in any of the tests performed in [25]; however, since there is not enough SOP data to compute this probability yet, this may be an optimistic assumption. The resulting GPS-SOP fault tree is depicted in Figure 3. It is assumed that the true SOP "constellation" fault will not change the number of faults to be monitored in the current fault tree. In the case that the number of faults change, the fault tree should be updated accordingly

To calculate the mode probabilities, the probability of GPS satellite and SOP transmitter failures must be known, namely $\{P_{\text{GPS},i}\}_{i=1}^{N_{\text{GPS}}}$ and $\{P_{\text{SOP},i}\}_{i=1}^{N_{\text{SOP}}}$, respectively; where N_{GPS} and N_{GPS} are the numbers of visible GPS satellites and SOP transmitters, respectively. In this article, all SOP transmitter failure probabilities were set to $\{P_{\text{SOPi},i}\}_{i=1}^{N_{\text{SOP}}} = P_{\text{SOP}} = 10^{-4}$ and all GPS satellite failure probabilities were set to $\{P_{\text{GPS},i}\}_{i=1}^{N_{\text{GPS}}} = P_{\text{GPS}} = 10^{-5}$, according to the historical records detailed in [30]. The choice of P_{SOP} is discussed in the Experimental Results section. Subsequently, the GPS-SOP fault probability for Mode n can be expressed as

$$P_{\text{Mode},n} = \binom{N_{\text{GPS}}}{k_{\text{GPS},n}} P_{\text{GPS}}^{k_{\text{GPS},n}} (1-P_{\text{GPS}})^{(N_{\text{GPS}}-k_{\text{GPS},n})} \cdot \binom{N_{\text{SOP}}}{k_{\text{SOP},n}} P_{\text{SOP}}^{k_{\text{SOP},n}} (1-P_{\text{SOP}})^{(N_{\text{SOP}}-k_{\text{SOP},n})} \quad (1)$$

where $n = 0, \ldots, 10$, is the mode index and $k_{\text{GPS},n}$ and $k_{\text{SOP},n}$ are the number of faulty GPS satellites and SOP transmitters in Mode n, respectively. Modes 1 to 9 correspond to the faulty operations, including one, two, and three simultaneous faults, while Mode 10 is assumed to never occur.

Authorized licensed use limited to: The Ohio State University. Downloaded on May 15,2023 at 19:40:44 UTC from IEEE Xplore. Restrictions apply.

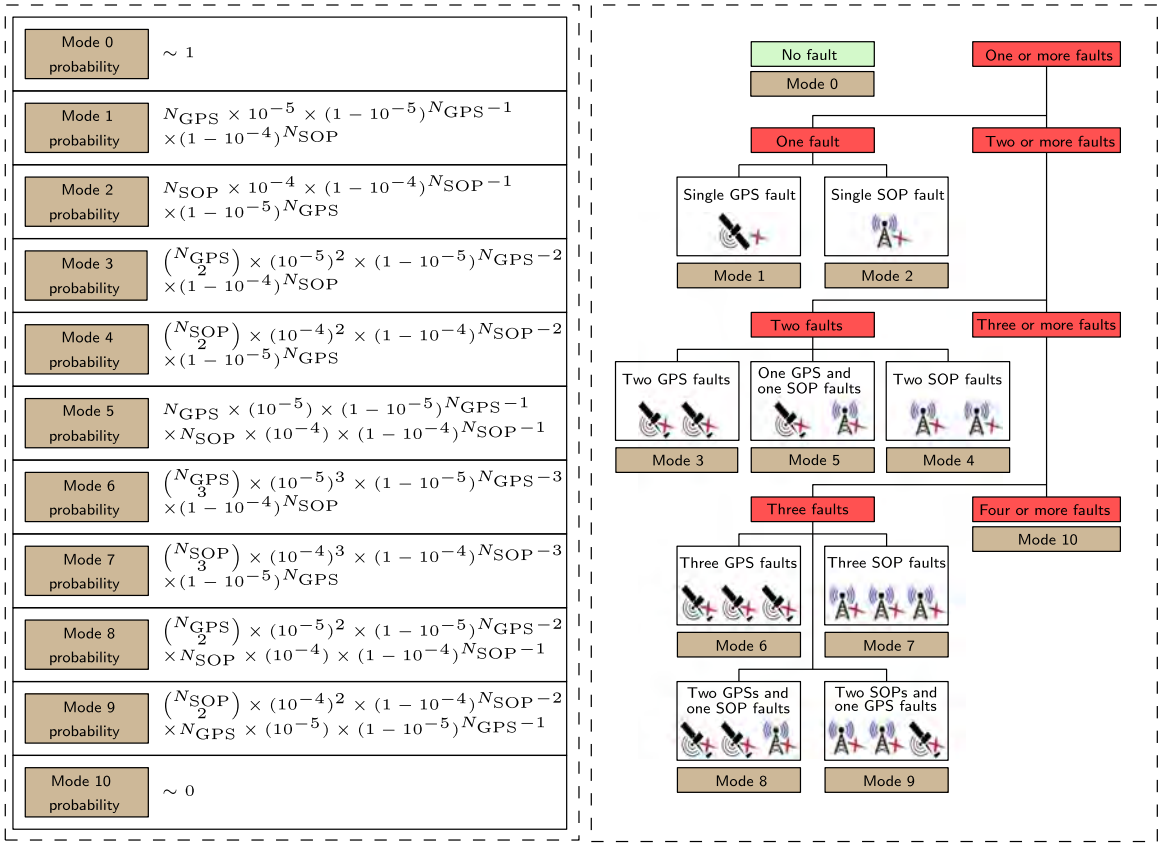

Figure 3.
GPS-SOP fault tree and the associated probabilities calculated according to (1).

OARAIM ALGORITHM

OARAIM shares some common inputs and constant parameters used by ARAIM [28]. While some values are independent of the signal type (e.g., total integrity budget, probability of false alarm, etc.), other values are SOP-specific. The ORAIM inputs are tabulated in Table 1. In contrast to traditional RAIM frameworks, where pseudorange measurement errors are assumed to have zero-mean, ARAIM accounts for unknown but bounded pseudorange biases denoted by $\{b_{\mathrm{nom,GPS},i}\}_{i=1}^{N_{\mathrm{GPS}}}$. For GPS measurements, these biases bound nominal errors, mainly due to the code correlation peak deformation [31]. The values of the biases are extracted from the ISM and can be limited to 0.75 m [5]. A similar value can be conservatively used for biases in SOP measurements, denoted by $\{b_{\mathrm{nom,SOP},i}\}_{i=1}^{N_{\mathrm{SOP}}}$, as SOP signals are unaffected by atmospheric errors.

A summary of the OARAIM algorithm is given below. The steps below highlight the differences between the ARAIM and OARAIM algorithm. The details of the ARAIM algorithm can be found in [28].

Step 1: Compute the pseudorange error covariance matrices denoted $\mathbf{C}_{\mathrm{int}}$ and $\mathbf{C}_{\mathrm{acc}}$, where the former is computed using the URA standard deviations $\{\sigma_{\mathrm{URA,GPS},i}\}_{i=1}^{N_{\mathrm{GPS}}}$ and $\{\sigma_{\mathrm{URA,SOP},i}\}_{i=1}^{N_{\mathrm{SOP}}}$, and the latter using the URE standard deviations $\{\sigma_{\mathrm{URE,GPS},i}\}_{i=1}^{N_{\mathrm{GPS}}}$ and $\{\sigma_{\mathrm{URE,SOP},i}\}_{i=1}^{N_{\mathrm{SOP}}}$. Without loss of generality, it is assumed that the combined GPS-SOP measurements are ordered as GPS measurements first then SOP. The diagonal elements of $\mathbf{C}_{\mathrm{int}}$ and $\mathbf{C}_{\mathrm{acc}}$ pertaining to GPS satellites are calculated according to, [28] and the ones pertaining to SOPs are given by

$$\mathbf{C}_{\mathrm{int}}(N_{\mathrm{GPS}}+i, N_{\mathrm{GPS}}+i) = \sigma^2_{\mathrm{URA,SOP},i} \tag{2}$$

$$\mathbf{C}_{\mathrm{acc}}(N_{\mathrm{GPS}}+i, N_{\mathrm{GPS}}+i) = \sigma^2_{\mathrm{URE,SOP},i}, \tag{3}$$

for $i = 1, \ldots, N_{\mathrm{SOP}}$.

Step 2: Compute the all-in-view position solution using weighted least-squares estimation with weight matrix $\mathbf{C}_{\mathrm{int}}^{-1}$. All available GNSS and SOP measurements are used in this step.

Step 3: Determine the fault modes, which are the faults that need to be monitored and their associated probabilities. These modes for the OARAIM algorithm are summarized in the fault tree shown in Figure 3.

Step 4: Evaluate the fault-tolerant positions and associated standard deviations and biases for each fault mode. A fault-tolerant position for a certain mode is computed using all measurements except the measurements of the assumed faulty GNSS satellites or SOPs in that given

Authorized licensed use limited to: The Ohio State University. Downloaded on May 15,2023 at 19:40:44 UTC from IEEE Xplore. Restrictions apply.

Table 1.

Inputs to the GPS-SOP DARAIM Algorithm		
Input	Description	Obtained from
$\{z_{\text{GPS,i}}\}_{i=1}^{N_{\text{GPS}}}$	GPS pseudorange measurements	GPS front-end and tracking loop
$\{z_{\text{SOP,i}}\}_{i=1}^{N_{\text{SOP}}}$	SOP pseudorange measurements	SOP front-end and tracking loop
$\{\sigma_{\text{URA,GPS,i}}\}_{i=1}^{N_{\text{GPS}}}$	Standard deviation of GPS user range accuracy	ISM
$\{\sigma_{\text{URA,SOP,i}}\}_{i=1}^{N_{\text{SOP}}}$	Standard deviation of SOP user range accuracy	The value of URE multiplied by 1.5
$\{\sigma_{\text{URE,GPS,i}}\}_{i=1}^{N_{\text{GPS}}}$	Standard deviation of the GPS user range error	ISM
$\{\sigma_{\text{URE,SOP,i}}\}_{i=1}^{N_{\text{SOP}}}$	Standard deviation of the SOP user range error	[25]
$\{b_{\text{nom,GPS,i}}\}_{i=1}^{N_{\text{GPS}}}$	Maximum bias for a GPS measurement	ISM
$\{b_{\text{nom,SOP,i}}\}_{i=1}^{N_{\text{SOP}}}$	Maximum bias for a SOP measurement	Similar to the GPS maximum bias
$\{P_{\text{GPS,i}}\}_{i=1}^{N_{\text{GPS}}}$	Probability of a single GPS fault	Historical records. Currently used value is 10^{-5}
$\{P_{\text{SOP,i}}\}_{i=1}^{N_{\text{SOP}}}$	Probability of a single SOP fault	Experimental campaign. Proposed value is 10^{-4}
$P_{\text{Const,GPS}}$	Probability of GPS constellation fault	Historical records. Currently used value is 0
$P_{\text{Const,SOP}}$	Probability of SOP constellation fault	Experimental campaign. Proposed value is 0

mode. In particular, this step derives the following parameters for each fault mode:

The variances of the fault-tolerant position components (East, North, Up) for each fault mode.

The difference between the fault-tolerant position and the all-in-view position and the variance of this difference.

The worst-case impact of the nominal biases $\{b_{\text{nom,GPS},i}\}_{i=1}^{N_{\text{GPS}}}$ and $\{b_{\text{nom,SOP},i}\}_{i=1}^{N_{\text{SOP}}}$ on the position estimate.

Step 5: Perform two sets of tests:

Solution separation tests:

- Compute the solution separation test thresholds from the probability of false alarm.
- Perform the test on all the components of the difference between the fault-tolerant and all-in-view solutions for each fault mode. If any test fails, exclusion must be attempted.

A chi-squared test:

- A chi-squared test is performed on the measurement residuals for the all-in-view solution with weight matrix $\mathbf{C}_{\text{acc}}$ calculated in **Step 1**.
- The threshold is computed using the inverse chi-squared cumulative density function (cdf) and a pre-defined probability of false alarm.
- If the chi-squared test fails, the PLs cannot be considered valid and exclusion cannot be attempted. If this test fails while none of the solution separation tests fail, then the fault is most likely outside the threat model. The chi-square test is a sanity check for that purpose.

Step 6: Calculate the PLs if all of the solution separation tests and the chi-squared test pass and formulate the vertical positioning performance criteria:

1) Criterion 1: 95% accuracy parameter, which is the achievable positioning accuracy in the vertical domain 95% of the time. According to the Localizer Performance with Vertical guidance (LPV)- 200 standard, the 95% accuracy must be limited to 4 m.
2) Criterion 2: 10^{-7} fault-free position error bound, which is the achievable positioning accuracy in the vertical domain 99.99999% of the fault-free time. According to the LPV-200 standard, the 10^{-7} fault-free position error bound must be limited to 10 m.
3) Criterion 3: Effective monitor threshold (EMT), which is a parameter that takes into account the faults with a prior greater than or equal to 10^{-5}. According to the LPV-200 standard, EMT must be limited to 15 m.

If the chi-squared test passes but any of the solution separation tests fail, the following steps are performed instead.

Step 7: Exclude the faults by first determining the candidate subset to exclude. This is achieved by performing a search over all possible subsets to find the subset that yields the highest discrepancy between the fault-tolerant and all-in-view solution. Once the best candidate subset is determined, an exclusion test is performed to account for the wrong exclusion probability.

Step 8: Compute the PLs after exclusion. This step is similar to **Step 6** except that it accounts for the wrong exclusion probability.

Authorized licensed use limited to: The Ohio State University. Downloaded on May 15,2023 at 19:40:44 UTC from IEEE Xplore. Restrictions apply.

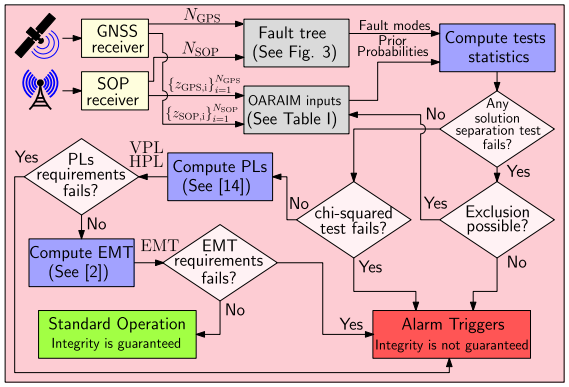

Figure 4.
OARAIM algorithm.

Step 9: Compute the 95% accuracy criterion after exclusion to account for fault modes.

Remark: Note that the above used LPV-200 requirements, which were developed for aircraft operation, since no formal integrity requirements established for small UAVs as of yet. As stakeholders develop such requirements for UAVs, the parameters in the OARAIM algorithm can be adjusted accordingly.

Figure 4 summarizes the proposed OARAIM algorithm.

PERFORMANCE EVALUATION

This section evaluates the performance of the OARAIM framework numerically and experimentally. The OARAIM algorithm was implemented using the MATLAB Algorithm Availability Simulation Tool (MAAST) [29], [32].

SIMULATION RESULTS

In order to study the performance of the OARAIM algorithm under fault-free and faulty conditions, a simulation was performed with two SOPs. For this test, GPS signals were obtained from a stationary receiver at the Madrid Deep Space Communications Complex (MDSCC). The elevation and azimuth angles of the GPS satellite constellation above the receiver over a 24-h period was computed using GPS ephemeris files collected at the MDSCC. The GPS observations were extracted from the recorded Receiver Independent Exchange Format (RINEX) file. Then, the SOP signals were simulated using a high-fidelity SOP simulator that has been used in previous research [24]. The SOP and receiver's clock qualities were modeled as typical oven-controlled crystal oscillator (OCXO) and temperature-compensated crystal oscillator (TCXO), respectively. To overcome the unknown nature of the SOP transmitter's clock bias and its drift, which in GNSS-based navigation are known through the navigation message, a reference receiver, referred to as the base, is assumed to be present in the UAV's environment to provide differential corrections. Moreover, it is assumed that the base has direct line-of-sight (LOS) to all of the cellular towers to eliminate the possibility of common errors. The impact of using a base receiver on an SOP-based integrity monitoring framework has been fully investigated in [24], where a base receiver was employed to estimate the SOP clock biases through a Kalman filter. Considering that the base receiver could be deployed on top of a building, it can be assumed that it has access to unobstructed GNSS signals from which it can estimate its own clock bias. Hence, for the purpose of this study, it is assumed that the base has complete knowledge of its position and its clock bias and that it does not introduce a nonzero mean common mode error in the UAV's differential measurements. Once the measurements are corrected, a common clock bias term remains to be estimated, and is added to the set of constellation clock biases to be estimated.

In the first scenario, both SOPs were fault-free. In the second scenario, a fault of a magnitude of 30 m was injected into the second SOP measurement. To illustrate the accuracy and integrity performances simultaneously, a so-called Stanford diagram was plotted in Figure 5, where PE, PL, and AL are shown for four scenarios: GPS-only (black dots), GPS-SOP in fault-free operation (blue dots), GPS-SOP without OARAIM fault exclusion (red dots), and GPS-SOP with OARAIM fault exclusion (blue dots). The AL was set to 30 m.

Note that except for the red points, the PLs in Figure 5 are calculated only after tests have passed, or after exclusion in the case where faults are detected. However, similar to [7], the PLs before exclusion (red) are shown in the Stanford plot for a comparative analysis. The following may be

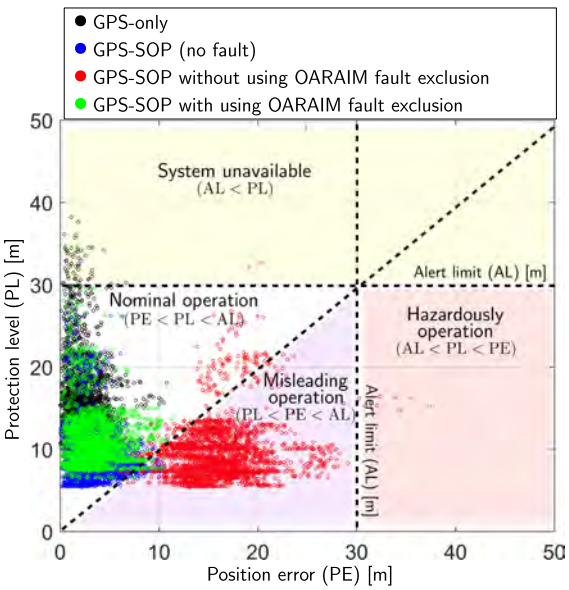

Figure 5.
The Stanford diagram demonstrating the horizontal accuracy and integrity performances simultaneously.

Authorized licensed use limited to: The Ohio State University. Downloaded on May 15,2023 at 19:40:44 UTC from IEEE Xplore. Restrictions apply.

concluded from Figure 5. First, by comparing the blue and black dots, it can be seen that adding SOPs eliminates system unavailability. Second, injecting the fault into an SOP measurement caused a misleading operation (red dots); however, the OARAIM algorithm rejected the faulty measurement to achieve nominal operation (green dots). Third, by comparing the red and green dots, it can be seen that as expected, fault exclusion results in reducing the PE. However, one can spot green and blue dots in the misleading operation region. With only two SOPs, the integrity system will heavily couple the GPS and SOP "constellations" since there are not enough SOPs to compute an SOP-only position solution. This could explain the occasional green or blue point in the misleading operation region. However, one can see that the PL is reduced on average when SOPs are used with GPS for integrity, as shown by the lowered green and blue cloud points compared to the GPS's black point cloud.

EXPERIMENTAL RESULTS

In order to evaluate the performance of the proposed OARAIM framework in a real-world scenario, a DJI Matrice 600 UAV was equipped with a dual-channel National Instrument (NI) universal software radio peripheral (USRP)-2955 to sample cellular long-term evolution (LTE) SOPs at four LTE carrier frequencies: 739, 1955, 2125, and 2145 MHz. These frequencies are allocated for the U.S. cellular providers AT&T, T-Mobile, and Verizon. The ground-truth reference for the UAV's trajectory was taken from a Septentrio AsteRx-i V integrated GNSS-IMU system, which is capable of producing a submeter-level accurate real-time kinematic (RTK) navigation solution. Figure 6 shows the experimental hardware and software setup and Figure 7 shows the experimental environment.

The UAV flew for 4 min, while collecting LTE signals from 11 LTE SOP transmitters in the environment. The stored LTE signals were then processed by the LTE module of the Multichannel Adaptive Transceiver Information eXtractor (MATRIX) SDR to produce LTE SOP pseudoranges, which were then fused with GPS pseudorange measurements obtained from the Septentrio receiver to produce the navigation solution along with the corresponding OARAIM integrity measures, as shown in Figure 7.

Two scenarios were considered to evaluate the impact of SOP measurements on navigation and safety: (i) fault-free conditions and (ii) faulty conditions with faults in two GPS satellites. The faults were injected artificially as a stress test for the OARAIM and ARAIM frameworks in postprocessing in the form of 10 m biases in the pseudorange measurements from GPS PRN 5 and PRN 25 over a period of 1 min. For each scenario, two sets of results are computed: (a) a navigation solution and ARAIM integrity measures using GPS measurements only and (b) a navigation solution and OARAIM integrity measures using GPS and cellular

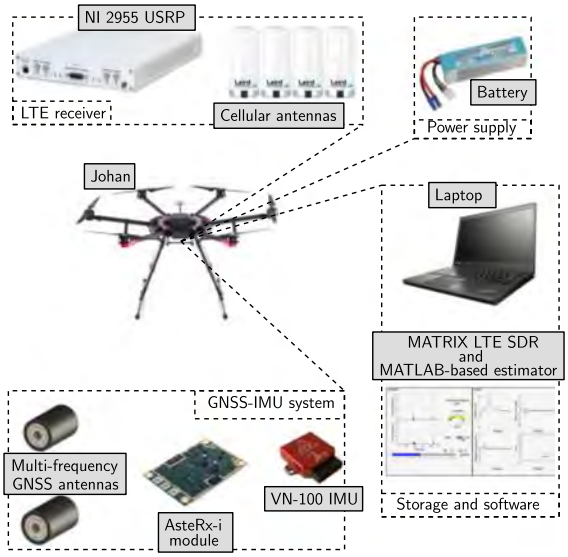

Figure 6.
Experimental hardware and software setup.

LTE SOP measurements. A very preliminary study characterizing the measurement statistics of cellular SOPs shows that $\sigma_{\mathrm{URE,SOP},i}$ is around 0.75 m at high altitudes in a semiurban environment [12]. While the UAV is flown in a similar environment in this article, this value of $\sigma_{\mathrm{URE,SOP},i}$ was inflated by 25% to be more conservative. As such, the ARAIM and OARAIM algorithms were implemented with $\sigma_{\mathrm{URA,GPS},i} = 1.1$ m, $\sigma_{\mathrm{URE,GPS},i} = 0.75$ m, $\sigma_{\mathrm{URA,SOP},i} = 1.4$ m, $\sigma_{\mathrm{URE,SOP},i} = 0.9375$ m, $\{b_{\mathrm{nom,GPS},i}\}_{i=1}^{N_{\mathrm{GPS}}} = 0.5$ m, and $\{b_{\mathrm{nom,SOP},i}\}_{i=1}^{N_{\mathrm{SOP}}} = 0.75$ m, for all i. Moreover, it was found in[12] that the measurement error for UAV flights is less than 5.42 m. Using this standard deviation as a definition of a fault at high altitude in a semiurban environment yields an SOP fault probability of about 10^{-4} (corresponding to $3.89\sigma_{\mathrm{URA,SOP},i}$). Therefore, the prior satellite fault probabilities were set to 10^{-5} and the prior SOP fault probabilities were set to 10^{-4}, with zero probability for constellation faults. The $\sigma_{\mathrm{URE,SOP},i}$ and $\sigma_{\mathrm{URA,SOP},i}$ values are relatively low since cellular signals received by UAVs do not suffer from severe multipath by virtue of the favorable channel between base stations and UAVs. In fact, a recent study of UAV connectivity to the cellular network demonstrated that the received cellular signal power on low-altitude UAVs (30 m to 120 m) are stronger than the receiver power on ground-based receivers, despite the downward-tilted cellular antennas[33]. The study attributes these findings to the fact that "free space propagation conditions at altitude more than make up for antenna gain reductions." It is important to note that the reliability of cellular SOP has not been fully characterized yet. As such, a 10^{-4} fault probability could be either conservative or optimistic. However, in the case of the latter, it has been shown in [34] that OARAIM would still yield improvement over

Authorized licensed use limited to: The Ohio State University. Downloaded on May 15,2023 at 19:40:44 UTC from IEEE Xplore. Restrictions apply.

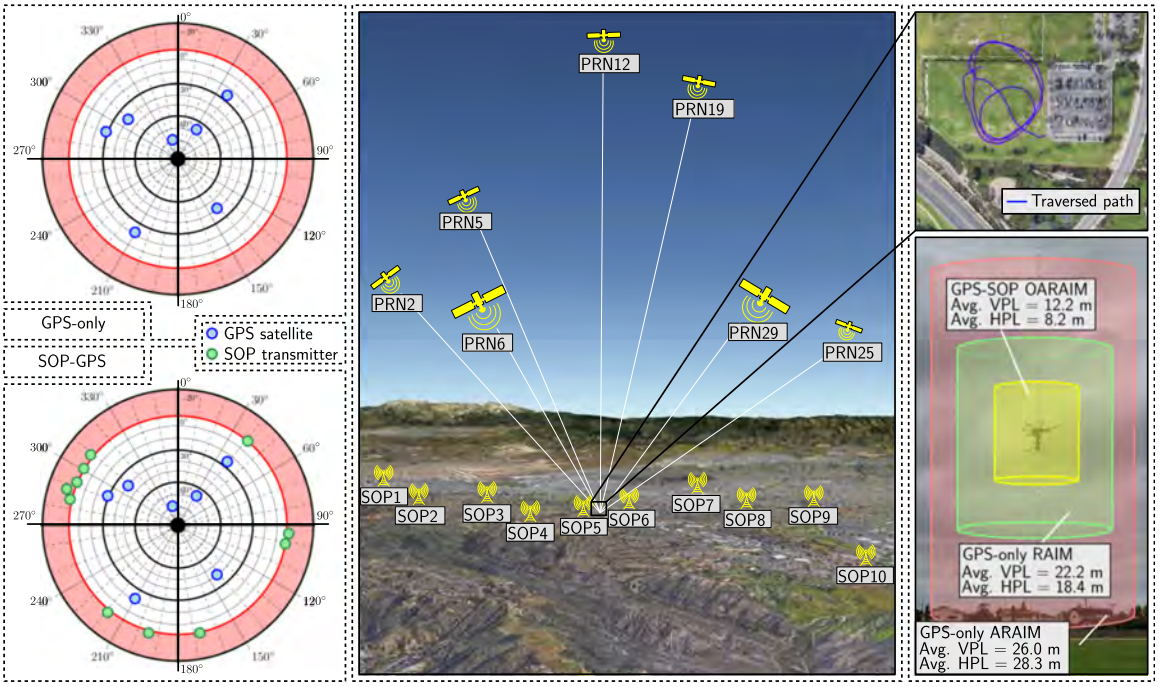

Figure 7.
Experimental environment, experimental setup, and experimental results showing the traversed trajectory, the GPS-only and SOP-GPS sky-plots showing satellite-to-user and SOP transmitter-to-user geometry. The average fault-free PLs across the entire trajectory using GPS-only RAIM, GPS-only ARAIM, and GPS-SOP OARAIM are plotted for comparison.

ARAIM for high and unlikely SOP fault probabilities of 10^{-2}.

One important integrity functionality studied in these experiments is fault detection. Figure 8 shows the chi-squared test results for the GPS-only and GPS-SOP systems in fault-free and faulty conditions. The main takeaway from Figure 8 is that although the test threshold increases by adding SOP measurements (a straightforward property of chi-squared-distributed random variables), the test statistic itself becomes more sensitive to faults. This also

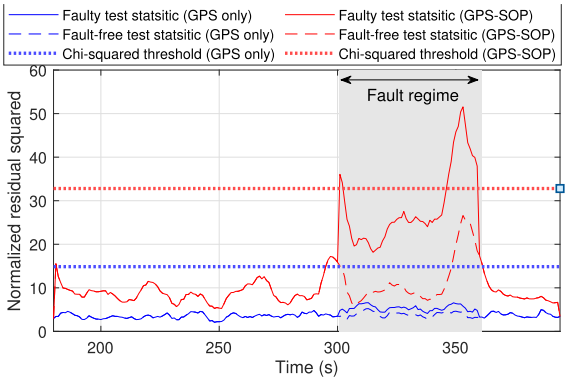

Figure 8.
Time history of the chi-squared test statistic for GPS-only and GPS-SOP with their respective test thresholds. The test-statistic for each system are shown in fault-free and faulty conditions. The shaded area represents faulty conditions.

applies to the solution separation tests, which are not shown here for brevity. No faults were detected by the GPS-only ARAIM system in the fault regime, whereas the GPS-SOP OARAIM system detected such faults. It is worth pointing out that while Figure 8 studied the chi-squared test results, studying the solution separation test results would yield a large number of cases, which is deferred to future work.

Next, the gap between the HPL and the horizontal position error (HPE), and the gap between the VPL and vertical position error (VPE) were studied. The gap between PLs and PEs is an indicator of the tightness of the PLs. The gaps are calculated according to $\Delta V \triangleq VPL - VPE$ and $\Delta H \triangleq HPL - HPE$. The root mean-squared error (RMSE) of ΔV and ΔH were computed for both GPS-only and GPS-SOP and in fault-free and faulty conditions. The results are tabulated in Table 2 and Figure 9.

The following can be concluded from Table 2 and Figure 9. First, ΔH and ΔV are reduced significantly when SOP measurements are added, with more than 70% reduction in the ΔH RMSE and more than 55% in the ΔV RMSE. Figure 9 shows that while the PLs were significantly reduced, the PEs slightly reduce as well. This implies that adding SOP measurements significantly tighten the PLs toward the PEs without the PEs exceeding the PL. This is a desirable behavior as it moves the system more to the left of the "Nominal operation" region shown in Figure 5. Second, the change in the ΔH RMSE between fault-free and faulty conditions for

Authorized licensed use limited to: The Ohio State University. Downloaded on May 15,2023 at 19:40:44 UTC from IEEE Xplore. Restrictions apply.

Table 2.

RMSE Values of ΔH and ΔV for GPS-Only ARAIM and GPS-SOP ARAIM in Fault-Free and Faulty Conditions

Approach	Condition	ΔH RMSE	ΔV RMSE
GPS-only ARAIM	Fault-free	26.9 m	24.7 m
GPS-SOP OARAIM	Fault-free	7.5 m	11.0 m
GPS-only ARAIM	Faulty	25.3 m	24.8 m
GPS-SOP OARAIM	Faulty	7.6 m	11.4 m

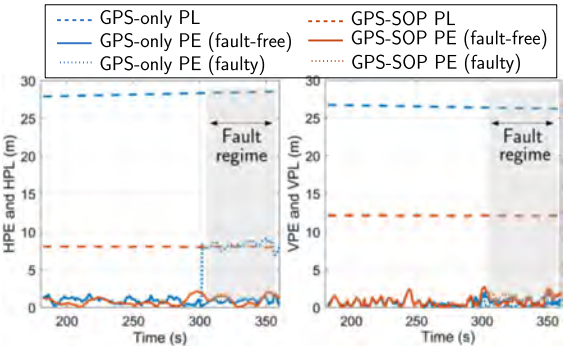

Figure 9.
The PE versus PL values for GPS-only ARAIM and GPS-SOP OARAIM in fault-free and faulty conditions.

GPS-only is much greater than the change for the GPS-SOP, i.e., around 6% compared to 1.3%, respectively. The reduction in the GPS-only ΔH RMSE is due to the HPEs getting larger because of the undetected faults while the HPL remained unchanged. This undesirable behavior brings the system closer to the "Misleading operation" region of Figure 5. In the case of GPS-SOP, the faults are detected and excluded properly, maintaining low ΔH and ΔV RMSEs in the presence of faults. It is important to note that in this particular experiment, the VPL is lower than the HPL in the case of GPS-only, as shown in Figure 9. This may be due to the fact the probability of hazardous misleading information (PHMI) for the VPL is about 100 times the PHMI for the HPL when using standard ARAIM parameters from the GPS ISM, as shown in Table 1. However, the ARAIM system does not necessarily need to detect the faults with high probability. In this study, both the GPS-SOP OARAM and the GPS-only ARAIM algorithms were set up with standard ISM values shown in Table 1 for a comparative analysis. Tuning and designing the OARAIM and ARAIM parameters for optimal performance is left for future work.

Remark: While the presented simulation and experiment results look promising, they are not enough to generalize the conclusions. They provide an insight into the potential of SOPs in improving integrity monitoring. Extensive simulations and experiments are needed to generalize the results obtained in this article and are left as future work.

CONCLUSION

To improve the availability of the integrity monitoring system, the capability to detect faults must be improved and PLs must remain small. This article showed that by incorporating SOPs, the fault detection probability is increased and PLs can be made smaller than the ones from current GNSS constellations. To this end, the article presented an OARAIM framework for enhanced UAV safety. OARAIM enables safe UAV navigation by fusing GNSS signals with ambient SOPs, producing tight PLs, while identifying and excluding faults, if present. A fault tree was constructed for GPS-SOP-based navigation and the OARAIM algorithm was presented. Simulation results were presented demonstrating that adding SOPs eliminates system unavailability of the integrity system. Experimental results were presented showing that in faulty conditions, the OARAIM algorithm detects the faults in GPS satellites while GPS-only ARAIM failed to detect such faults. Moreover, the OARAIM algorithm reduces the gaps between vertical and horizontal PLs and PEs by more than 55% and 70%, respectively, compared to only using GNSS measurements. The PL reduction in OARAIM translates to higher availability of the integrity monitoring system, allowing the UAV navigation system to meet more stringent integrity standards than ARAIM with GNSS only.

ACKNOWLEDGMENTS

The authors would like to thank Kimia Shamaei for her help in data collection. This work was supported in part by the National Science Foundation (NSF) under Grant 1929965, in part by the Office of Naval Research (ONR) under Grant N00014-19-1-2613, and in part by the U.S. Department of Transportation (USDOT) under Grant 69A3552047138 for the CARMEN University Transportation Center (UTC).

REFERENCES

[1] R. Loh, Y. Bia, and T. Roe, "UAVs in civil airspace: Safety requirement," *IEEE Aerosp. Electron. Syst. Mag.*, vol. 24, no. 1, pp. 5–17, Jan. 2009.

[2] Z. Kassas, P. Closas, and J. Gross, "Navigation systems for autonomous and semi-autonomous vehicles: Current trends and future challenges," *IEEE Aerosp. Electron. Syst. Mag.*, vol. 34, no. 5, pp. 82–84, May 2019.

[3] R. Sabatini *et al.*, "Avionics systems panel research and innovation perspectives," *IEEE Aerosp. Electron. Syst. Mag.*, vol. 35, no. 12, pp. 58–72, Dec. 2020.

Authorized licensed use limited to: The Ohio State University. Downloaded on May 15,2023 at 19:40:44 UTC from IEEE Xplore. Restrictions apply.

[4] "NextGen annual report: A report on the history, current status, and future of national airspace system modernization," U.S. Dept. Transp., Federal Aviation Administration, 2020, pp. 1–154.

[5] V. Kropp, "Advanced receiver autonomous integrity monitoring for aircraft guidance using GNSS," Ph.D. dissertation, Univ. of Munich, Munich, Germany, 2018.

[6] R. Sabatini, T. Moore, and C. Hill, "Avionics-based GNSS integrity augmentation synergies with SBAS and GBAS for safety-critical aviation applications," in *Proc. IEEE/AIAA Digit. Avionics Syst. Conf.*, 2016, pp. 1–10.

[7] S. Bhattacharyya and D. Gebre-Egziabher, "Kalman filter-based RAIM for GNSS receivers," *IEEE Trans. Aerosp. Electron. Syst.*, vol. 51, no. 3, pp. 2444–2459, Jul. 2015.

[8] T. Walter, J. Blanch, M. J. Choi, T. Reid, and P. Enge, "Incorporating GLONASS into aviation RAIM receivers," in *Proc. Int. Tech. Meeting Inst. Navigation*, 2013, pp. 239–249.

[9] C. Hegarty, D. Bobyn, J. Grabowski, and A. Van Dierendonck, "An overview of the effects of out-of-band interference on GNSS receivers," *J. Inst. Navigation*, vol. 67, no. 1, pp. 143–161, Mar. 2020.

[10] D. Borio, F. Dovis, H. Kuusniemi, and L. Presti, "Impact and detection of GNSS jammers on consumer grade satellite navigation receivers," *Proc. IEEE*, vol. 104, no. 6, Jun. 2016, pp. 1233–1245.

[11] C. Günther, "A survey of spoofing and counter-measures," *J. Inst. Navigation*, vol. 61, no. 3, pp. 159–177, 2014.

[12] M. Maaref, J. Khalife, and Z. Kassas, "Aerial vehicle protection level reduction by fusing GNSS and terrestrial signals of opportunity," *IEEE Trans. Intell. Transp. Syst.*, vol. 22, no. 9, pp. 5976–5993, Sep. 2021.

[13] A. Ene, J. Blanch, and T. Walter, "Galileo-GPS RAIM for vertical guidance," in *Proc. Nat. Tech. Meeting Inst. Navigation*, 2006, pp. 18–20.

[14] Y. Liu and Y. Zhu, "Design and performance evaluation of airspace-ground cooperative GPS/BeiDou dual-constellation RAIM algorithm," in *Proc. ION Int. Tech. Meeting*, 2014, pp. 127–136.

[15] R. Toledo-Moreo, D. Betaille, and F. Peyret, "Lane-level integrity provision for navigation and map matching with GNSS, dead reckoning, and enhanced maps," *IEEE Trans. Intell. Transp. Syst.*, vol. 11, no. 1, pp. 100–112, Mar. 2010.

[16] O. Garcia Crespillo, A. Grosch, B. Belabbas, and M. Rippl, "GNSS-aided INS integrity concept," in *Proc. 27th Int. Techn. Meeting Satell. Division Inst. Navigation*, 2014, pp. 2069–2077.

[17] L. Fu, J. Zhang, R. Li, X. Cao, and J. Wang, "Vision-aided RAIM: A new method for GPS integrity monitoring in approach and landing phase," *Sensors*, vol. 15, no. 9, pp. 22854–22873, 2015.

[18] T. Needham and M. Braasch, "Gravity model error considerations for high-integrity GNSS-aided INS operations," in *Proc. IEEE/ION Position, Location, Navigation Symp.*, 2018, pp. 822–832.

[19] A. Hassani, N. Morris, M. Spenko, and M. Joerger, "Experimental integrity evaluation of tightly-integrated IMU/LiDAR including return-light intensity data," in *Proc. 32nd Int. Techn. Meeting Satell. Division Inst. Navigation*, 2019, pp. 2637–2658.

[20] T. Li *et al.*, "P3-LOAM: PPP/LiDAR loosely coupled SLAM with accurate covariance estimation and robust RAIM in urban canyon environment," *IEEE Sensors J.*, vol. 21, no. 5, pp. 6660–6671, Mar. 2021.

[21] J. Raquet *et al.*, "Position, navigation, and timing technologies in the 21st century," *Part D: Position, Navigation, and Timing Using Radio Signals-of-Opportunity*, vol. 2. J. Morton, F. van Diggelen, J. Spilker, Jr., and B. Parkinson, Eds. Hoboken, NJ, USA: Wiley-IEEE, 2021, ch. 35–43, pp. 1115–1412.

[22] J. Khalife and Z. Kassas, "On the achievability of submeter-accurate UAV navigation with cellular signals exploiting loose network synchronization," *IEEE Trans. Aerosp. Electron. Syst.*, early access, Mar. 31, 2022, doi: 10.1109/TAES.2022.3162770.

[23] Z. Kassas *et al.*, "Assessment of cellular signals of opportunity for high altitude aircraft navigation," *IEEE Aerosp. Electron. Syst. Mag.*, early access, Jun. 29, 2022, doi: 10.1109/MAES.2022.3187142.

[24] M. Maaref and Z. Kassas, "Measurement characterization and autonomous outlier detection and exclusion for ground vehicle navigation with cellular signals," *IEEE Trans. Intell. Veh.*, vol. 5, no. 4, pp. 670–683, Dec. 2020.

[25] M. Maaref and Z. Kassas, "Autonomous integrity monitoring for vehicular navigation with cellular signals of opportunity and an IMU," *IEEE Trans. Intell. Transp. Syst.*, vol. 23, no. 6, pp. 5586–5601, Jun. 2022.

[26] M. Maaref, J. Khalife, and Z. Kassas, "Enhanced safety of autonomous driving by incorporating terrestrial signals of opportunity," in *Proc. IEEE Int. Conf. Acoust., Speech, Signal Process.*, 2020, pp. 9185–9189.

[27] A. Colpaert, E. Vinogradov, and S. Pollin, "Aerial coverage analysis of cellular systems at LTE and mmWave frequencies using 3D city models," *Sensors*, vol. 18, no. 12, Dec. 2018, Art. no. 4311.

[28] J. Blanch *et al.*, "Advanced RAIM user algorithm description: Integrity support message processing, fault detection, exclusion, and protection level calculation," in *Proc. 25th Int. Tech. Meeting Satell. Division Inst. Navigation*, 2012, pp. 2828–2849.

[29] "Advanced RAIM technical subgroup reference airborne algorithm description document," 3rd Generation Partnership Project (3GPP), Working Group-C, Tech. Rep., Jun. 2019. [Online]. Available: http://web.stanford.edu/group/scpnt/gpslab/website_files/maast/ARAIM_TSG_Reference_ADD_v3.1.pdf

Authorized licensed use limited to: The Ohio State University. Downloaded on May 15,2023 at 19:40:44 UTC from IEEE Xplore. Restrictions apply.

[30] T. Walter and J. Blanch, "Characterization of GNSS clock and ephemeris errors to support ARAIM," in *Proc. ION Pacific PNT Meeting, Conf.*, 2015, pp. 920–931.

[31] D. Imparato, "GNSS-based receiver autonomous integrity monitoring for aircraft navigation," Ph.D. dissertation, Delft Univ. of Technol., CD Delft, Netherlands, 2016.

[32] J. Shau, W. Chan, and T. Walter, "MATLAB algorithm availability simulation tool," *GPS Solutions*, vol. 13, pp. 327–332, 2009.

[33] "LTE unmanned aircraft systems," QualcommTechnologies Inc., Tech. Rep. 1.0.1, May 2017. [Online]. Available: https://www.qualcomm.com/documents/lte-unmanned-aircraft-systems-trial-report/

[34] M. Jia, J. Khalife, and Z. Kassas, "Evaluation of ground vehicle protection level reduction due to fusing GPS with faulty terrestrial signals of opportunity," in *Proc. ION Int. Tech. Meeting*, 2021, pp. 354–365.

Authorized licensed use limited to: The Ohio State University. Downloaded on May 15,2023 at 19:40:44 UTC from IEEE Xplore. Restrictions apply.

Opportunistic Navigation Using Sub-6 GHz 5G Downlink Signals: A Case Study on A Ground Vehicle

Ali A. Abdallah * and Zaher M. Kassas *†
*Department of Electrical Engineering & Computer Science, University of California, Irvine, USA, abdalla2@uci.edu
†Department of Mechanical & Aerospace Engineering, University of California, Irvine, USA, zkassas@ieee.org

***Abstract*—A user equipment (UE)-based navigation framework that opportunistically exploits 5G signals is developed. The proposed framework exploits the "always on" 5G downlink signals in a time-domain-based receiver. To this end, a so-called ultimate synchronization signal (USS) is proposed to utilize the time-domain orthogonality of the orthogonal frequency division multiplexing (OFDM)-based 5G signals. This approach simplifies the receiver's complexity and enhances the performance of the 5G opportunistic navigation framework. Experimental results are presented to evaluate the efficacy of the proposed framework on a ground vehicle navigating in a suburban environment, while utilizing sub-6 GHz 5G signals from two gNBs. It is shown that while a state-of-the-art frequency-domain-based 5G opportunistic navigation receiver can only reliably track the gNBs' signals over a trajectory of 1.02 km traversed in 100 seconds, producing a position root mean-squared error (RMSE) of 14.93 m; the proposed time-domain-based receiver was able to track over a trajectory of 2.17 km traversed in 230 seconds, achieving a position RMSE of 9.71 m.**

***Index Terms*—5G, signals of opportunity, positioning navigation, ground vehicles, software-defined radio.**

I. Introduction

In January 2021, the U.S. Department of Transportation (USDOT)'s National Highway Traffic Safety Administration (NHTSA) announced the expansion of the Automated Vehicle Transparency and Engagement for Safe Testing (AV TEST) Initiative from a pilot to a full program [1], in which dozens of companies and governments agencies are now participating. Globally, hundreds of companies are involved in bringing automated vehicles to our roads. As automated vehicles approach full autonomy (referred to as Level 5 [2]), strict guarantees emerge on their navigation system accuracy, robustness, and integrity [3].

Among the different sensors (e.g., lidars, inertial measurement unit (IMUs), global navigation satellite system (GNSS) receivers, radars, cameras) with which automated vehicles are equipped, GNSS receivers are the only ones that provide a navigation solution in a global frame, do not require aiding from an external source, and are unaffected by weather conditions. Cellular signals possess similar attributes, making them an attractive replacement to GNSS signals in situations where GNSS signals are unusable. Cellular signals, particularly 3G code-division multiple access (CDMA) and 4G long-term evolution (LTE), have shown high ranging and localization accuracy via specialized software-defined receivers (SDR) [4]–[9].

The cellular system is currently in its fifth generation (5G). The navigation capabilities of 5G has been studied extensively in the past few years [10], [11]. Different approaches have been proposed, in which direction-of-arrival (DOA) [12], direction-of-departure (DOD) [13], time-of-arrival (TOA) [14], or a combination thereof [15] was used to achieve accurate positioning from 5G signals. All the aforementioned studies were either limited to simulations and laboratory emulated 5G signals or were based on restrictive assumptions. In particular, the proposed approaches required the user to be in the network to enable network-based localization approaches (i.e., utilizing downlink and uplink signals from the 5G gNB to the user and back). This compromises the user's privacy by revealing their accurate location and limits the user to only gNBs of the network to which they are subscribed.

In contrast to aforementioned approaches, downlink 5G signals can be exploited opportunistically for navigation (i.e., without communicating back with the 5G gNB nor subscribing to the network). In [16], a comprehensive approach for opportunistic navigation with 5G exploiting the downlink signal was developed. The proposed approach extracted navigation observables from the "always-on" transmitted synchronization signals and was validated experimentally, where the ranging error standard deviation was shown to be 1.19 m. In [17], the proposed SDR in [16] was modified to extract navigation observables from different synchronization signals. Experimental results were presented of a ground vehicle navigating with the frequency-domain-based 5G SDR in a suburban environment while receiving signals from two 5G gNBs. It was shown that over a trajectory of 1.02 km traversed in 100 seconds, the position root mean-squared error (RMSE) was 14.93 m. In [18], a more challenging urban environment compared to [17] was considered. The ground vehicle navigated while receiving signals from five gNBs intermittently over the entire trajectory. It was shown that over a trajectory of 773 m traversed in 110 seconds, the position RMSE was 4.1 m. In [19], a more precise navigation approach based on 5G carrier phase measurements was developed and demonstrated on an unmanned aerial vehicle (UAV).

This paper extends the approach in [19] by developing a time-domain-based SDR produce 5G carrier phase measurements. The developed SDR is evaluated experimentally on a ground vehicle with sub-6 GHz 5G cellular signals.

It is shown that while the frequency-domain-based 5G opportunistic navigation receiver [16] can only reliably track the gNBs' signals over a trajectory of 1.02 km traversed in 100 seconds, producing a position RMSE of 14.93 m; the proposed time-domain-based receiver was able to track over a trajectory of 2.17 km traversed in 230 seconds, achieving a position RMSE of 9.71 m.

The remainder of the paper is organized as follows. Section II discusses 5G opportunistic navigation, in which the 5G signal structure is presented, the so-called ultimate synchronization signal (USS) is presented to extract 5G carrier phase measurements via a time-domain-based navigation SDR, and an extended Kalman filter is implemented to estimate the ground vehicle's position using only 5G measurements. Section III evaluates the proposed approach experimentally on a ground vehicle in a semi-urban environment, Section IV gives concluding remarks.

II. 5G Opportunistic Navigation

This section overviews 5G opportunistic navigation. First, the 5G signal structure is studied to exploit potential "always-on" 5G reference signals for navigation purposes. Next, a specialized time-domain-based SDR is presented to extract carrier phase measurements from received 5G signals. Finally, the extracted measurements are fed to an EKF to produce the 5G navigation solution.

A. 5G Signal Structure

This paper proposes an opportunistic navigation approach; thus, it only considers 5G downlink signal, which use orthogonal frequency division multiplexing (OFDM) with cyclic prefix (CP) as a modulation technique. A 5G frame has a duration of 10 ms and consists of 10 subframes with durations of 1 ms. A frame can also be decomposed into two half-frames, where subframes 0 to 4 form half-frame 0 and subframes 5 to 9 form half-frame 1.

In the time-domain, each subframe breaks down into numerous slots, each of which contains 14 OFDM symbols for a normal CP length. The number of slots per subframe depends on the subcarrier spacing. The subcarrier spacing in 5G is flexible and is defined as $\Delta f = 2^{\mu} \cdot 15$ [kHz], where μ is a pre-defined numerology such that $\mu \in \{0, \cdots, 4\}$. This paper considers frequency range 1 (FR1) (i.e., sub-6 GHz) in the experimental evaluation due to the limited FR2 (i.e., mmWave) infrastructure. In FR1, subcarrier spacings of 15 and 30 kHz are used, i.e., $\mu = 0$ and $\mu = 1$.

In the frequency-domain, each subframe is divided into numerous resource grids, each of which has multiple resource blocks with 12 subcarriers. The number of resource grids in the frame is provided to the user equipment (UE) from higher level signallings. A resource element is the smallest element of a resource grid that is defined by its symbol and subcarrier number. Fig. 1 summarizes the 5G frame structure.

The 5G frame contains two synchronization signals that can be exploited that can be exploited for navigation:

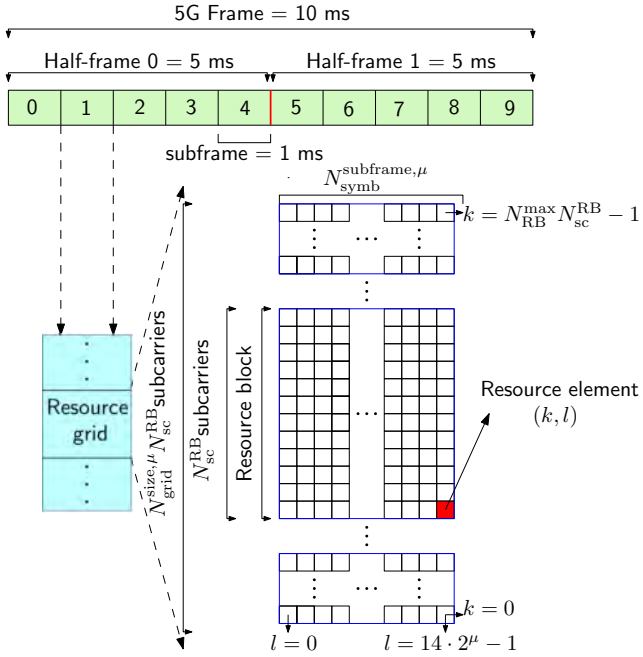

Fig. 1. 5G frame structure.

primary synchronization signal (PSS) and secondary synchronization signal (SSS). Which are two orthogonal maximal length sequences of length 127. PSS has 3 possible sequences and specifies the sector ID of the gNB, and SSS has 336 possible sequences, which specifies the group identifier of the gNB. Together, they provide the frame start time and the gNB physical cell ID N_{ID}^{Cell}. The physical broadcast channel (PBCH) demodulation reference signal (DM-RS) is also transmitted in the same symbols as the synchronization signals. All together, they forms what is called as SS/PBCH block. The length of the block is 240 subcarriers, which gives its a range of bandwidth between 3.6 to 57.6 MHz depending on μ

B. 5G Software-Defined Navigation Receiver

In previous 5G-based opportunistic navigation approaches, the proposed navigation receivers considered the orthogonality of the synchronization and channel estimation signals in the frequency-domain, i.e., the transmitted OFDM frame is always re-constructed from the received time-domain data, then navigation observables are extracted by utilizing the reference signal with the highest bandwidth. This conventional approach is necessary for communication applications, in which the UE has to extract various system information to initiate two-ways communication with the gNB. However, for UE-based navigation applications, the goal is to produce navigation observables by utilizing the entire frequency and time-domain resources in the signal. For this purpose, the proposed receiver exploits the orthogonality property of OFDM signals in both frequency and time-domains, where all available synchronization signals are combined into one signal referred to by the ultimate synchronization signal (USS). The USS consists of the PSS, SSS, and PBCH DM-RS corresponding to each gNB physical cell ID. Then the

time-domain-based sequence is obtained by zero-padding both sides of the signals in the frequency domain. Then, the inverse fast Fourier transform (IFFT) is taken, and the L_{CP} elements are added. This procedure is exactly the procedure happening at the gNB, except for having zeros instead of having data outside the SS/PBCH block. Fig. 2 shows an example of a locally-generated frame showing the USS frequency components for gNB with $N_{ID}^{Cell} = 0$, $\mu = 0$, and 20 MHz bandwidth.

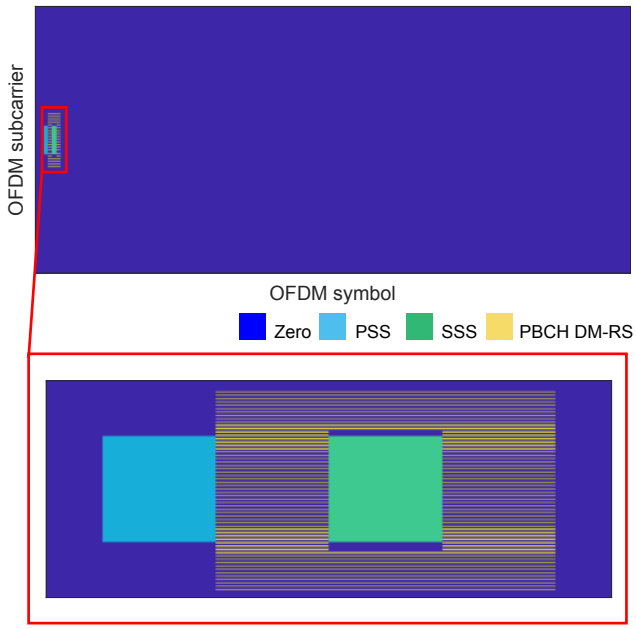

Fig. 2. The 5G OFDM locally-generated frame (i.e., the so-called ultimate synchronization signal (USS).

The developed time-domain-based navigation receiver operates on the USS sequences corresponding to all possible cell IDs. The receiver has two stages: (i) acquisition and (ii) tracking. In the acquisition stage, coarse estimates of the code start times and Doppler frequencies of detected gNBs are obtained. It is worth mentioning that the PSS sequence is not unique for every USS and is common for $N_{ID}^{Cell} \pmod 3$; thus, only SSS and PBCH DM-RS are utilized for acquisition.

In the tracking stage, the receiver refines and maintains the coarse estimates produced in the acquisition stage via tracking loops. The developed receiver deploys a phase-locked loop (PLL) and a delay-locked loop (DLL) to track the carrier and codes phases, respectively.

C. Navigation Filter

The receiver's carrier phase output is multiplied by the received signal wavelength λ resulting in the pseudorange estimate, which is modeled as

$$\rho^{(u)}(n) = \|\boldsymbol{r}_r(n) - \boldsymbol{r}_{s,u}\|_2 + c\cdot[\delta t_r(n) - \delta t_{s,u}(n)] + \nu_u(n), \quad (1)$$

where n is a discrete-time index, $\boldsymbol{r}_r = [x_r, y_r, z_r]^{\mathsf{T}}$ is the receiver's three-dimensional (3–D) position vector, $\boldsymbol{r}_{s,u} = [x_{s,u}, y_{s,u}, z_{s,u}]^{\mathsf{T}}$ is the u-th gNB's 3-D position vector, δt_r is the receiver's clock bias, $\delta t_{s,u}$ is the gNB's clock bias, and ν_u is the measurement noise, which is modeled as a zero-mean, white Gaussian random sequence with variance σ_2^u. In (1), the initial carrier phase is lumped into the relative clock bias term. The gNBs positions $\{\boldsymbol{r}_{s,u}\}_{u=1}^{U}$ are assumed to be known, e.g., from radio mapping or cloud-hosted database. The 5G measurements are fed to an EFK to estimate the state vector $\boldsymbol{x}$ defined as

$$\boldsymbol{x} \triangleq \left[\boldsymbol{x}_r^{\mathsf{T}}, \boldsymbol{x}_{\mathrm{clk}}^{\mathsf{T}}\right]^{\mathsf{T}}, \quad \boldsymbol{x}_r \triangleq \left[\boldsymbol{r}_r^{\mathsf{T}}, \dot{\boldsymbol{r}}_r^{\mathsf{T}}\right]^{\mathsf{T}}$$

where and $\boldsymbol{x}_{\mathrm{clk}}$ is the clock error state vector defined as $\boldsymbol{x}_{\mathrm{clk}} \triangleq \left[c\Delta\delta t_1, c\Delta\dot{\delta} t_1, \cdots, c\Delta\delta t_U, c\Delta\dot{\delta} t_U\right]^{\mathsf{T}}$, where $\{\Delta\delta t_u \triangleq \delta t_r - \delta t_{s,u}\}_{u=1}^{U}$ and $\{\Delta\dot{\delta} t_u \triangleq \dot{\delta} t_r - \dot{\delta} t_{s,u}\}_{u=1}^{U}$ are the relative clock bias and drift between the receiver and the u-th gNB. The temporal evolution of $\boldsymbol{x}_r$ used in the EKF is assumed to follow a nearly constant velocity dynamics and the clock error dynamics is assumed to follow a double integrator driven by process noise, as discussed in [17].

III. Experimental Results

This section validates the proposed cellular 5G opportunistic navigation receiver and the navigation framework experimentally on a ground vehicle in a suburban environment using ambient 5G signals.

A. Experimental Setup and Environmental Layout

The experiment was performed on the Fairview Road in Costa Mesa, California, USA. In this experiment, a quad-channel National Instrument (NI) universal software radio peripheral (USRP)-2955 was mounted on a vehicle, where only two channels were used to sample 5G signals with a sampling ratio of 10 MSps. The receiver was equipped with two consumer-grade cellular omnidirectional Laird antennas. The USRP was tuned to listen to 5G signals from AT&T and T-Mobile U.S. cellular providers as summarized in Table I. The vehicle was equipped with a Septentrio AsteRx-i V integrated GNSS-IMU to be used as a ground truth in this experiment. Fig. 3 shows the experimental hardware and software setup.

TABLE I
GNBs'S CHARACTERISTICS

gNB	Carrier frequency [MHz]	N_{ID}^{Cell}	Cellular provider
1	872	608	AT&T
2	632.55	398	T-Mobile

B. Signal Acquisition and Tracking Performance

The signal acquisition was performed to detect the hearable gNBs. Two gNBs were detected as shown in Fig. 4. The gNBs' positions were mapped prior to the experiment. In the tracking stage, the 5G signals from both gNBs were tracked for 230 seconds. Fig. 5 shows the tracking results of the two gNBs including: (i) carrier-to-noise ratio (CNR), (ii) Doppler frequency estimate versus expected Doppler obtained using the ground vehicle's ground truth reference, (iii) pseudorange estimate versus expected range after removing the initial bias, and (iv) range errors.

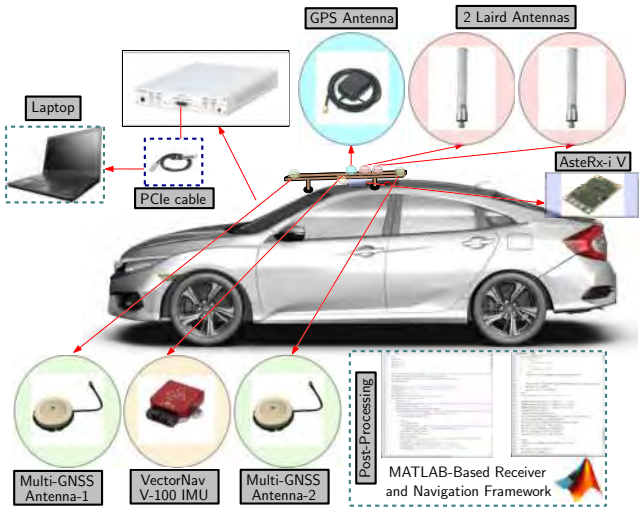

Fig. 3. Experimental hardware and software setup.

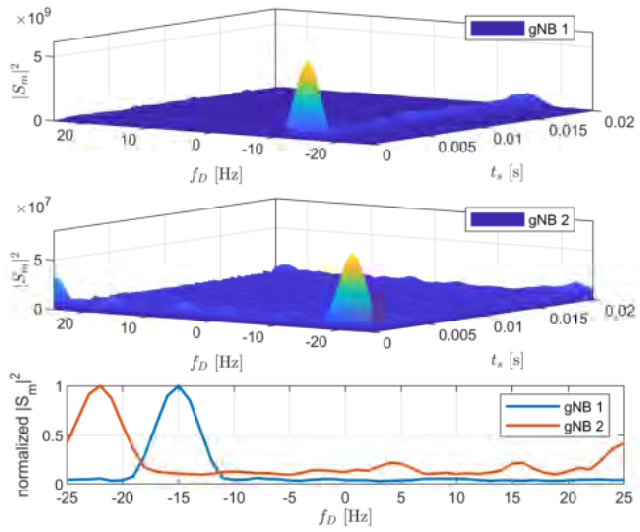

Fig. 4. Cellular 5G signal acquisition results showing squared correlation magnitude $|S_m|^2$ versus initial estimates of the code start time $\hat{t}_{s_0}$ and Doppler frequency $\hat{f}_{D_0}$ for the two detected gNBs.

C. Navigation Solution

The vehicle traversed a trajectory of 2.17 km in 230 seconds. The receiver's position and velocity state vectors and their corresponding covariances were initialized from the GNSS-IMU system. Using the expressions of measurement noise variances as a function of the CNR and receiver parameters in [9], the variances were found to vary between 0.67 to 12.78 m^2. Fig. 6 shows the environmental layout, 5G gNBs location, and the navigation solution of the proposed 5G framework versus ground truth. The proposed 5G opportunistic navigation framework tracked the 5G signals, achieving a position RMSE of 9.71 m. In contrast, the previous generation 5G SDR [16], [17] was only able to track over a shorter segment of 1.02 km, achieving a position RMSE of 14.93 m. It is worth noting that due to bad gNB geometric diversity, the majority of errors are in the east direction. Fig. 7 shows the EKF errors

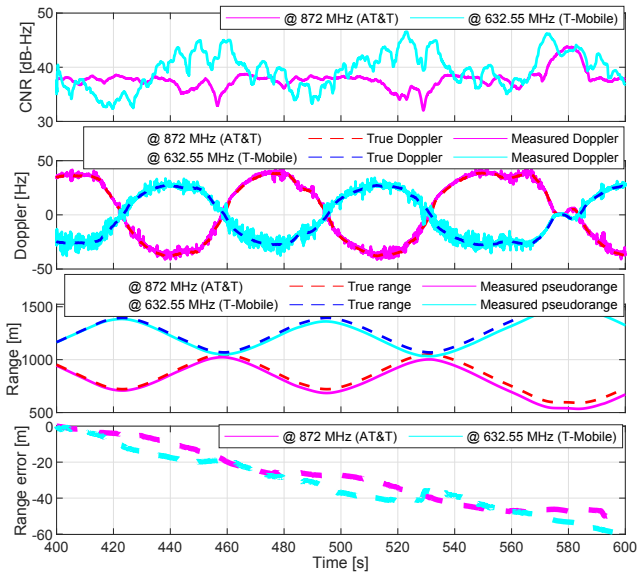

Fig. 5. Cellular 5G signal tracking results of the two gNBs showing: (i) CNR, (ii) Doppler frequency estimate in solid lines versus expected Doppler obtained using the vehicle's ground-truth reference in dashed lines, (iii) pseudorange estimate in solid lines versus expected range in dashed lines after removing the initial bias, and (iv) range errors.

of the ground vehicle's (a) east-position, (b) north-position, along with the associated $\pm 1\sigma$ bounds, and (c) position errors along the east and the north directions.

IV. Conclusion

This paper presented a UE-based navigation framework in which downlink 5G signals are opportunistically exploited for navigation purposes. The framework includes: (i) a time-domain-based receiver to extract carrier phase measurements exploiting a so-called USS that combines all "always on" 5G signals and (ii) an EKF to estimate the ground vehicle's position, velocity, and relative clock biases and drifts between the receiver and each gNB. Experimental results were presented to assess the performance on a ground vehicle navigating a suburban environment. It is shown that over a trajectory of 2.17 km traversed in 230 seconds, the position RMSE with the proposed time-domain-based receiver was 9.71 m.

Acknowledgment

The authors would like to thank Joe Khalife for his help in data collection. This work was supported in part by the Office of Naval Research (ONR) under Grant N00014-19-1-2511, in part under the financial assistance award 70NANB17H192 from U.S. Department of Commerce, National Institute of Standards and Technology (NIST), and in part by the U.S. Department of Transportation (USDOT) under Grant 69A3552047138 for the CARMEN University Transportation Center (UTC).

References

[1] National Highway Traffic Safety Administration (NHTSA), "U.S. Department of Transportation announces expansion of AV TEST initiative," https://www.nhtsa.gov/press-releases/us-department-transportation-announces-expansion-av-test-initiative, January 2021.

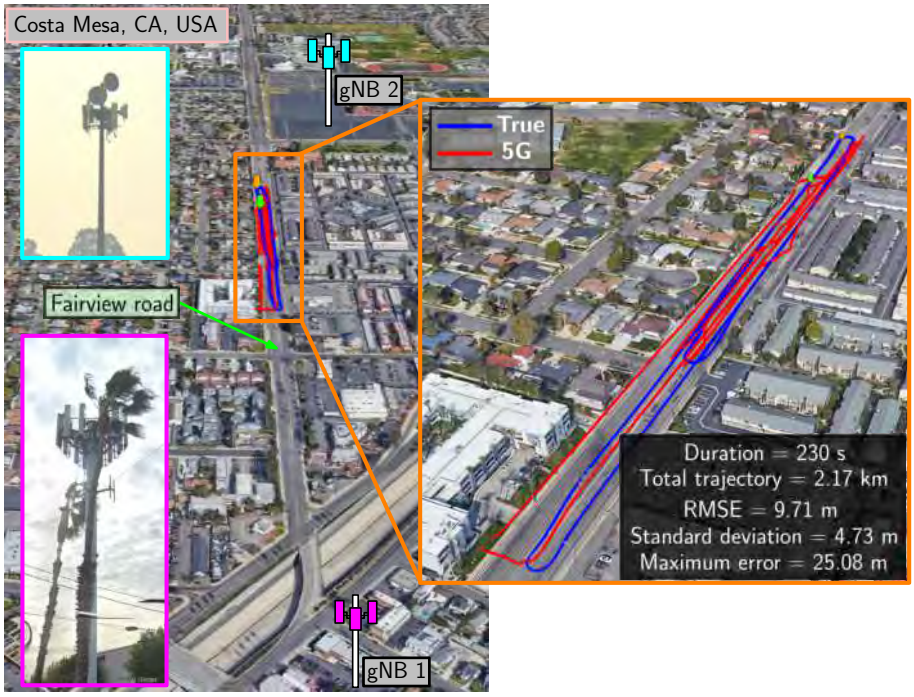

Fig. 6. Environmental layout with 5G gNBs and the traversed trajectory (ground truth versus estimated with 5G signals). Image: Google Earth.

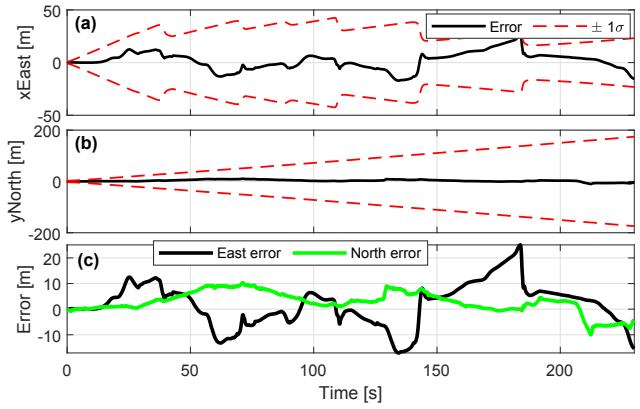

Fig. 7. The EKF estimation of the ground vehicle's (a) east-position and (b) north-position along with the associated $\pm 3\sigma$ bounds. (c) A comparison of the position errors along the east and the north directions.

[2] SAE International, "Taxonomy and definitions for terms related to driving automation systems for on-road motor vehicles," Tech. Rep., June 2018.

[3] A. Eskandarian, C. Wu, and C. Sun, "Research advances and challenges of autonomous and connected ground vehicles," *IEEE Transactions on Intelligent Transportation Systems*, vol. 22, no. 2, pp. 683–711, February 2021.

[4] J. del Peral-Rosado, R. Estatuet-Castillo, J. Lopez-Salcedo, G. Seco-Granados, Z. Chaloupka, L. Ries, and J. Garcoa-Molina, "Evaluation of hybrid positioning scenarios for autonomous vehicle applications," in *Proceedings of ION International Technical Meeting Conference*, January 2017, pp. 2541–2553.

[5] T. Kazaz, G. Janssen, J. Romme, and A. Van der Veen, "Delay estimation for ranging and localization using multiband channel state information," *IEEE Transactions on Wireless Communications*, pp. 1–16, September 2021.

[6] K. Avval, "Cellular-based localization for mobile devices with structured motion," Master's thesis, University of Toronto, Canada, 2020.

[7] H. Dun, C. Tiberius, and G. Janssen, "Positioning in a multipath channel using OFDM signals with carrier phase tracking," *IEEE Access*, vol. 8, pp. 13 011–13 028, 2020.

[8] P. Wang and Y. Morton, "Multipath estimating delay lock loop for LTE signal TOA estimation in indoor and urban environments," *IEEE Transactions on Wireless Communications*, vol. 19, no. 8, pp. 5518–5530, 2020.

[9] Z. Kassas, "Position, navigation, and timing technologies in the 21st century," J. Morton, F. van Diggelen, J. Spilker, Jr., and B. Parkinson, Eds. Wiley-IEEE, 2021, vol. 2, ch. 38: Navigation with Cellular Signals of Opportunity, pp. 1171–1223.

[10] J. Gante, L. Sousa, and G. Falcao, "Dethroning GPS: Low-power accurate 5G positioning systems using machine learning," *IEEE Journal on Emerging and Selected Topics in Circuits and Systems*, vol. 10, no. 2, pp. 240–252, June 2020.

[11] I. Lapin, G. Seco-Granados, O. Renaudin, F. Zanier, and L. Ries, "Joint delay and phase discriminator based on ESPRIT for 5G NR positioning," *IEEE Access*, vol. 9, pp. 126 550–126 563, 2021.

[12] N. Garcia, H. Wymeersch, E. Larsson, A. Haimovich, and M. Coulon, "Direct localization for massive MIMO," *IEEE Transactions on Signal Processing*, vol. 65, no. 10, pp. 2475–2487, May 2017.

[13] C. Guo, J. Yu, W. Guo, Y. Deng, and J. Liu, "Intelligent and ubiquitous positioning framework in 5G edge computing scenarios," *IEEE Access*, vol. 8, pp. 83 276–83 289, 2020.

[14] X. Cui, T. Gulliver, J. Li, and H. Zhang, "Vehicle positioning using 5G millimeter-wave systems," *IEEE Access*, vol. 4, pp. 6964–6973, 2016.

[15] M. Koivisto, M. Costa, J. Werner, K. Heiska, J. Talvitie, K. Leppanen, V. Koivunen, and M. Valkama, "Joint device positioning and clock synchronization in 5G ultra-dense networks," *IEEE Transactions on Wireless Communications*, vol. 16, no. 5, pp. 2866–2881, May 2017.

[16] K. Shamaei and Z. Kassas, "Receiver design and time of arrival estimation for opportunistic localization with 5G signals," *IEEE Transactions on Wireless Communications*, vol. 20, no. 7, pp. 4716–4731, 2021.

[17] A. Abdallah, K. Shamaei, and Z. Kassas, "Assessing real 5G signals for opportunistic navigation," in *Proceedings of ION GNSS Conference*, 2020, pp. 2548–2559.

[18] Z. Kassas, A. Abdallah, and M. Orabi, "Carpe signum: seize the signal – opportunistic navigation with 5G," *Inside GNSS Magazine*, vol. 16, no. 1, pp. 52–57, 2021.

[19] A. Abdallah and Z. Kassas, "UAV navigation with 5G carrier phase measurements," in *Proceedings of ION GNSS Conference*, September 2021, pp. 3294–3306.

Opportunistic Navigation with Doppler Measurements from Iridium Next and Orbcomm LEO Satellites

Mohamad Orabi
Department of Electrical Engineering and Computer Science
University of California, Irvine
Irvine, CA 92697
orabim@uci.edu

Joe Khalife
Department of Mechanical and Aerospace Engineering
University of California, Irvine
Irvine, CA 92697
khalifej@uci.edu

Zaher M. Kassas
Department of Mechanical and Aerospace Engineering
Department of Electrical Engineering and Computer Science
University of California, Irvine
Irvine, CA 92697
zkassas@ieee.org

***Abstract*—A framework for opportunistic navigation with multi-constellation low Earth orbit (LEO) satellite signals is proposed. A receiver architecture suitable for processing both time division (TDMA) and frequency division multiple access (FMDA) signals from Orbcomm and Iridium NEXT satellites is presented to produce Doppler frequency measurements from multi-constellation LEO satellites. An extended Kalman filter (EKF)-based estimator is formulated to solve for a stationary receiver's position using the resulting Doppler measurements. Experimental results are presented showing receiver positioning with one Orbcomm satellite and four Iridium NEXT satellite with an unprecedented final position error 22.7 m.**

TABLE OF CONTENTS

1. INTRODUCTION

As cyber-physical systems move towards full autonomy, the need for accurate and resilient positioning, navigation, and timing (PNT) is now more critical than ever. This need is also nourished by emerging technologies such as autonomous vehicles [1]. Furthermore, PNT has become entangled with critical infrastructure that could affect the national and economic security of the entire Nation [2]. On a similarly important front, PNT is envisioned to enable high-rate, low-latency communication systems, particularly by enabling beam-forming for fifth-generation (5G) cellular networks [3, 4]. Global navigation satellite systems (GNSS) have been the leading providers of PNT solutions. However, they are vulnerable to unintentional interference, intentional jamming, and malicious spoofing [5, 6]. These vulnerabilities could results in large-scale disruptions and millions of dollars worth of losses [7], especially that jamming and spoofing capabilities are becoming alarmingly accessible to the masses [8]. While some signal processing techniques have been developed to detect and mitigate such attacks [9–11], they do not provide full protection against jamming or spoofing. Instead of relying mainly on GNSS, which makes them a single point of failure, a more robust way to address their vulnerabilities is by exploiting other sources for navigation, such as signals of opportunity (SOPs).

SOPs are abundant and span wide frequency bands, which makes them far more robust than GNSS signals against jamming and spoofing attacks. Previous work has demonstrated navigation solutions for both (i) terrestrial SOPs, such as AM/FM radio [12–15], cellular [16–26], and digital television signals [27–31], as well as (ii) non-terrestrial signals from low Earth orbit (LEO) satellites [32–36]. Although SOPs were not designed with PNT in mind, they are still capable of providing submeter-level accuracy on aerial vehicles as was shown in [37–39]. What is more, the exploitation of cellular SOPs for resilient navigation in GPS-denied environments under GPS jamming conditions has been shown to be effective in [40].

In addition to cellular SOPs, LEO broadband communication satellite signals have been considered as possible reliable sources for navigation by various theoretical and experimental studies [41–47]. Tens of thousand of LEO satellites will be launched for broadband communication in the next five years. These signals have desirable attributes for opportunistic navigation, namely: (i) their location in LEO provides higher received signal power than that of GNSS satellites which reside in medium Earth orbit (MEO); (ii) LEO satellites are more abundant due to the larger number of satellites required to provide full earth coverage; and (iii) LEO satellites are deployed into unique constellations and are transmitting in different frequency bands, providing both spatial and spectral diversity.

The potential of these future LEO megaconstellations has triggered a renaissance of research in LEO-based PNT. The approaches in the literature can be grouped into three categories: (i) LEO GNSS, (ii) GNSS augmentation with LEO satellite signals, or (iii) opportunistic navigation exclusively with LEO satellite signals. In the first approach, LEO satellites are assumed to be equipped with navigation payloads to provide PNT services similar to traditional GNSS

978-1-7281-7436-5/21/$31.00 ©2021 IEEE

[41, 43]. While GNSS-like performance can be achieved in such approaches, the additional cost of navigation payloads is imposed on the LEO broadband companies and the users. In the second approach, LEO satellite signals are fused with GNSS signals, such as in [48], where simulated pseudorange measurements from Iridium NEXT satellites were used to augment the pseudoranges from GPS satellites with the goal of reducing the dilution of precision. The third approach is fully opportunistic, either in a simultaneous tracking and navigation (STAN) framework that estimates both the receiver's and satellites' states using Doppler and/or pseudorange measurements from real LEO satellite signals [35], or in a differential framework using LEO carrier phase differential (CD-LEO) measurements [49]. These opportunistic frameworks were experimentally demonstrated on ground vehicles and unmanned aerial vehicles (UAVs) using exclusively signals from two Orbcomm LEO satellites (without GNSS), achieving position root mean-squared errors (RMSEs) of (i) 416 m for a ground vehicle using the STAN framework after traversing a 7.5 km trajectory in 258 seconds, the last 228 seconds of which without GNSS signals [35], (ii) 5.3 m for a UAV using the STAN framework after traversing a 1.53 km trajectory in 155 seconds, the last 30 of which without GNSS signals [47]; (iii) 14.8 m for a UAV using the CD-LEO framework and traversing a 1.14 km trajectory in 2 minutes [36], all of which without GNSS signals []; and (iv) 21.2 m for a UAV using a *blind* Doppler tracking approach within the CD-LEO framework after traversing a 782 m trajectory in 90 seconds, all of which without GNSS signals [50]. Experimental results with Iridium NEXT satellite signals using an opportunistic approach were presented in [51], where a 22 m RMSE was achieved for a stationary receiver over a 30-minute period. One challenge in using LEO satellite signals opportunistically is the unknown nature of the LEO satellite positions and velocities. While two-line element (TLE) files and orbit determination software (e.g., simplified general perturbation 4 (SGP4)) could be used to predict LEO satellite positions and velocities, the resulting estimates could be off by a few kilometers and a few meters per second, respectively [35, 52].

Despite these errors in the predicted LEO satellite orbits, the aforementioned experimental results have shown remarkable potential for opportunistic navigation with LEO satellites. However, the experiments therein only utilized signals from a single LEO constellation, which does not exploit the spatial and spectral diversity of LEO constellations. Moreover, LEO satellites are designed to cover as much of the Earth's surface with as few satellites as possible, making it improbable to listen to a large number of satellites (6 or more) from the same constellation simultaneously. This is illustrated in Figure 1, which shows the percentage of time L *or more* satellites are simultaneously visible over a period of 2 days. The LEO satellite trajectories were generated using TLE files and SGP4 software [53]. Figure 1 shows the importance of being able to exploit multi-constellation LEO satellites for PNT. Currently, the literature presenting experimental results with multi-constellation LEO-based PNT is rather sparse. As opposed to [51], which investigated opportunistic navigation using only Iridium NEXT satellites, this paper uses both Iridium Next and Orbcomm satellite signals to investigate multi-constellation LEO satellite-based opportunistic navigation. This paper makes three contributions. First, an extended Kalman filter (EKF)-based full opportunistic framework for navigating with Doppler measurements from multi-constellation LEO satellite signals is developed. Second, a receiver architecture capable of producing such Doppler measurements from multi-constellation LEO satellite signals is provided. Third, experimental results are presented, showing stationary receiver positioning using Doppler measurements from the Iridium NEXT and Orbcomm constellations simultaneously, with a final two-dimensional (2–D) position error of 23 m. Next to [54] [1], this paper presents the first experimental results for multi-constellation LEO satellite-based opportunistic navigation.

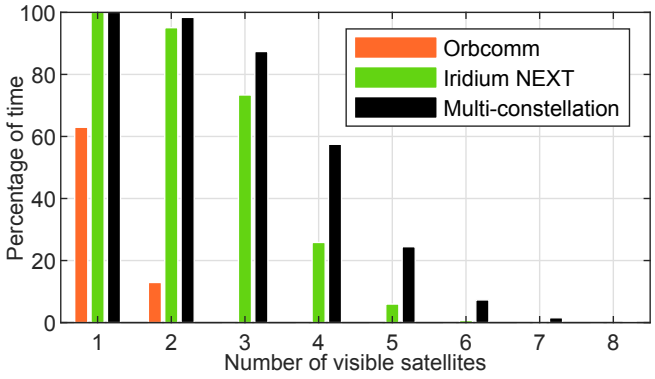

Figure 1. Percentage of time when L *or more* satellites are visible simultaneously for Orbcomm and Iridium NEXT satellite constellations for a simulated duration of 2 days.

The rest of the paper is organized as follows. Section 2 describes the received signal model and LEO receiver architecture. Section 3 presents an EKF-based framework to navigate with the Doppler measurements estimated by the multi-constellation LEO receiver. Section 4 gives an overview of the Iridium NEXT and Orbcomm LEO satellite constellations. Section 5 presents experimental results. Section 6 gives concluding remarks.

2. Received Signal Model and LEO Receiver Architecture

This section presents the received multi-constellation LEO signal model and the proposed receiver architecture.

Received LEO Satellite Signal Model

This paper considers a stationary receiver that listens to both continuous signals and burst signals from multi-constellation LEO satellites on various channels. Let L denote the total number of visible LEO satellites and U the total number of constellations to which these satellites belong. Furthermore, let L_u denote the number of visible satellites in the u-th constellation, where $u = 1, 2, \ldots, U$. It follows that $\sum_{u=1}^{U} L_u = L$. The baseband received signal for the u-th constellation at the input of an opportunistic LEO receiver can be modeled as

$$r_u(i) = \sum_{l_u=1}^{L_u} s_{l_u}(i) + n_u(i), \quad i = 0, 1, \ldots, u = 1, 2, \ldots, U, \tag{1}$$

where $n_u(i) \triangleq n_{I_u}(i) + j n_{Q_u}(i)$, with n_{I_u} and n_{Q_u} are modeled as zero-mean white Gaussian noise with variance $\frac{N_0}{2T_s}$; T_s is the sampling time; i represents time $t_i \triangleq t_0 + iT_s$

[1] The results in this work were achieved independently from [54], which was published shortly after the first submission of this manuscript, which achieved a 2–D position error of 132 m.

for some initial time t_0; $s_{l_u}(i)$ is given by

$$s_{l_u}(i) \triangleq \sqrt{C_{l_u}} a_{l_u}(i) \exp\{j2\pi[f_{D,l_u}(i) + f_{\mathrm{IF},l_u}]iT_s + j\theta_{l_u}(i)\},$$

where C_{l_u} is the received signal power of the l_u-th satellite; a_{l_u} is the transmitted symbol at time i; $f_{D,l_u}(i)$ and $\theta_{l_u}(i)$ are the time-varying Doppler frequency and carrier phase of the l_u-th satellite, respectively; and $f_{\mathrm{IF,l_u}}$ is the intermediate frequency of the l_u-th satellite. It is assumed that the symbols a_{l_u} are drawn from an M-ary phase shift keying (M-PSK) constellation, i.e., $a_{l_u} \triangleq \exp\left[j\left(\frac{q2\pi}{M}\right)\right]$ for $q \in \{0, 1, \ldots, M-1\}$.

It is important to note that (1) holds for both continuously transmitted and burst signals. The difference between these signals is the domain of the time index i. For continuous signals, i goes from zero to infinity. For burst signals, i is defined only over burst intervals, which requires knowledge of the burst start-time, period, and duration. The burst period and duration are known for the signals of interest (Iridium NEXT), and the start-time can be acquired through an energy detector.

Multi-Constellation LEO Receiver Architecture

The navigation receiver architecture in Figure 3, which operates on the samples of $r_u(i)$ from (1), was designed to account for both time-division multiple access (TDMA) schemes (used by Iridium NEXT) and frequency-division multiple access (FDMA) schemes (used by both Iridium NEXT and Orbcomm). The receiver performs recursively the steps discussed next to obtain an estimate of the Doppler frequency for the l_u-th satellite, denoted $\hat{f}_{D,l_u}$. An extra step is required for TDMA signals at initialization to acquire the burst start time, which can be done using an energy detector. To this end, it is assumed that an initial Doppler frequency estimate $\hat{f}_{D,l_u}(0)$ and the burst start time $t_{\mathrm{burst}_{l_u}}(0)$ and associated index $i_{0_{l_u}}$ are given.

1. The receiver first wipes-off the intermediate frequency f_{IF,l_u} to obtain

$$d_{l_u}(i) \triangleq r_u(i) \exp[-j2\pi f_{\mathrm{IF},l_u} iT_s]. \quad (2)$$

2. Next, the receiver groups samples of $d_{l_u}(i)$ into data blocks of size N_u, denoted by

$$\mathrm{d}_{l_u}^k = [d_{l_u}(kN_u + i_{0_{l_u}}), d_{l_u}(kN_u + 1 + i_{0_{l_u}}), \ldots, d_{l_u}((k+1)N_u - 1 + i_{0_{l_u}})],$$

where $k = 0, 1, \ldots,$ is the data block index. These data blocks have a duration $T_{\mathrm{block}_u} = N_u T_s$, which is equal to that of the burst for satellites that employ TDMA, or that is an integer multiple of the symbol period T_{symb_u} for continuously transmitting satellites. For TDMA schemes, only samples of the burst signal are chosen to form the data blocks. For a burst duration T_{burst_u} and period $P_{\mathrm{burst}_u} \geq T_{\mathrm{burst}_u}$, the samples between two bursts are dumped by the receiver. The duration of the dumped samples is given by $T_{\mathrm{dump}_u} = P_{\mathrm{burst}_u} - T_{\mathrm{burst}_u}$, as shown in Figure 2.
It is clear that $P_{\mathrm{burst}_u} > T_{\mathrm{burst}_u}$ for TDMA signals, which makes T_{dump_u} strictly positive, and $P_{\mathrm{burst}_u} = T_{\mathrm{burst}_u}$ for continuous signal transmission, which implies $T_{\mathrm{dump}_u} = 0$. It is assumed the Doppler frequencies are approximately constant during a data block duration, i.e.,

$$f_{D,l_u}(i) = f_{D,l_u}[k], \quad kN_u \leq i < (k+1)N_u, k = 0, 1, \ldots. \quad (3)$$

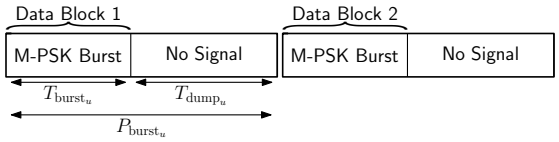

Figure 2. TDMA data block.

3. The data blocks $\mathrm{d}_{l_u}^k$ are then raised to the M-th power to wipe off the M-PSK symbols, resulting in a pure tone at a frequency of $M \cdot f_{D,l_u}(i)$.
4. A Fast Fourier Transform (FFT) of the signal is then taken, which results in an impulse-like peak at the next Doppler frequency $M\hat{f}_{D,l_u}(k)$, which will be around $M\hat{f}_{D,l_u}(k-1)$. Therefore, the search for the FFT peak is limited to $[\hat{f}_{D,l_u}(k-1) - \Delta f, \hat{f}_{D,l_u}(k-1) + \Delta f]$, where Δf is chosen to be greater than the maximum expected frequency deviation in a period of T_{block_u}. The Doppler estimates are then normalized by M.
5. In order to successfully track a burst signal, it is important to update the burst start time acquired at the initialization of the receiver. This is due to the change in the distance and hence delay between the satellite and the receiver. The delay can be predicted from the estimated Doppler frequency according to

$$t_{\mathrm{burst}_{l_u}}(k) = t_{\mathrm{burst}_{l_u}}(k-1) - \frac{\hat{f}_{D,l_u}(k)}{f_{c,u} + f_{\mathrm{IF},l_u}} P_{burst}, \quad (4)$$

where $f_{c,u}$ is the carrier frequency of the u-th constellation. The burst start time index is then updated accordingly. Compensating for the change delay using (4) results in slight variations in the value of $T_{\mathrm{dump}_{l_u}}$.

The receiver architecture is summarized in Figure 3.

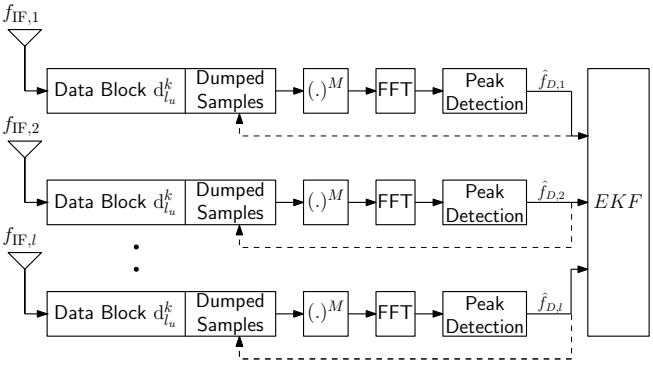

Figure 3. Block diagram for the mutli-constellation receiver architecture presented in this paper. The dashed lines represent optional feedback of the estimated Doppler to update T_{dump_u}.

3. MULTI-CONSTELLATION LEO SATELLITE-BASED NAVIGATION FRAMEWORK

This section develops an EKF-based framework to navigate with the Doppler measurements estimated by the multi-constellation LEO receiver discussed in Section 2. The goal is to estimate the receiver's three dimensional (3–D) position vector $\boldsymbol{r}_r \triangleq [x_r, y_r, z_r]^{\mathsf{T}}$ using the Doppler measurements

obtained from the receiver developed in the paper. In what follows, the pseudorange rate model is first described and the EKF model is then provided.

Pseudorange Rate Measurement Model

Given a Doppler measurement $\hat{f}_{D,l_u}(k)$, a pseudorange rate measurement can be formed according to

$$z_{\text{leo},l_u}(k) \triangleq c\frac{\hat{f}_{D,l_u}(k)}{f_{c,u}+f_{\text{IF},l_u}}, \quad k=0,1,\ldots, \tag{5}$$

where $l_u = 1,\ldots,L_u$, $u = 1,\ldots,U$, and c is the speed of light. Let the pseudorange rate measurements $\left\{\{z_{\text{leo},l_u}(k)\}_{l_u=1}^{L_u}\right\}_{u=1}^{U}$ for $k=0,1,\ldots$, be re-indexed according $\{z_{\text{leo},l}(k)\}_{l=1}^{L}$ for compactness of notation. Hence, the pseudorange rate measurement of the l-th satellite produced by the receiver could be expressed as

$$\begin{aligned} z_{\text{leo},l}(k) =& \frac{\dot{\boldsymbol{r}}_{\text{leo},l}^{\mathsf{T}}(k)\left[\boldsymbol{r}_r-\boldsymbol{r}_{\text{leo},l}(k)\right]}{\|\boldsymbol{r}_r-\boldsymbol{r}_{\text{leo},l}(k)\|}+c[\dot{\delta}t_r(k)-\dot{\delta}t_{\text{leo},l}] \\ &+c\left[\dot{\delta}t_{\text{iono},l}(k)+\dot{\delta}t_{\text{trop},l}(k)\right]+v_{\text{leo},l}(k), \end{aligned} \tag{6}$$

where $\boldsymbol{r}_{\text{leo},l}$ and $\dot{\boldsymbol{r}}_{\text{leo},l}$ are the l-th LEO satellite's 3–D position and velocity vectors, respectively; $\dot{\delta}t_r$ and $\dot{\delta}t_{\text{leo},l}$ are the receiver's and l-th LEO satellite's clock drifts, respectively; $\dot{\delta}t_{\text{iono},l}$ and $\dot{\delta}t_{\text{trop},l}$ are the l-th satellite's ionospheric and tropospheric delay rates, respectively; and $v_{\text{leo},l}$ is the measurement noise, which is modeled as a zero-mean white Gaussian random sequence with variance $\sigma^2_{\text{leo},l}$. It is assumed that the receiver's clock drift $\dot{\delta}t_r$ and the satellites' clock drifts $\left\{\dot{\delta}t_{\text{leo},l}\right\}_{l=1}^{L}$ are constant within the 10-minute satellite visibility window. Moreover, since it not necessary to estimate the receiver and satellite's clock drifts individually, they will be lumped into one term $\Delta\dot{\delta}t_l \triangleq \dot{\delta}t_r - \dot{\delta}t_{\text{leo},l}$. In case of multiple passes, $\left\{\Delta\dot{\delta}t_l\right\}_{l=1}^{L}$ are re-initialized at the beginning of each pass. Note that at any time-step k, the l-th satellite's position and velocity vectors can be obtained from the TLE files and SGP4 software. For the brief duration of LEO satellite visibility, the ionospheric and tropospheric delay rates are negligible; hence, $\dot{\delta}t_{\text{iono}_l}$ and $\dot{\delta}t_{\text{trop}_l}$ are ignored in the measurement, yielding the measurement model given by

$$z_{\text{leo},l}(k) \approx \frac{\dot{\boldsymbol{r}}_{\text{leo},l}^{\mathsf{T}}(k)\left[\boldsymbol{r}_r-\boldsymbol{r}_{\text{leo},l}(k)\right]}{\|\boldsymbol{r}_r-\boldsymbol{r}_{\text{leo},l}(k)\|}+c\Delta\dot{\delta}t_l+v_{\text{leo},l}(k). \tag{7}$$

EKF Model

From (7), it can be seen that the state vector to be estimated is $\boldsymbol{x} \triangleq \left[\boldsymbol{r}_r^{\mathsf{T}}, c\Delta\dot{\delta}t_1,\ldots,c\Delta\dot{\delta}t_L\right]^{\mathsf{T}}$. Subsequently, an EKF is designed to produce an estimate $\hat{\boldsymbol{x}}(k|m)$ of $\boldsymbol{x}(k)$ using all pseudorange rate measurements from time-step 1 to $m \le k$. The estimation error is denoted $\tilde{\boldsymbol{x}}(k|m) \triangleq \boldsymbol{x}(k) - \hat{\boldsymbol{x}}(k|m)$. The EKF also calculates the estimation error covariance $\mathbf{P}(k|m) \triangleq \mathbb{E}\left[\tilde{\boldsymbol{x}}(k|m)\tilde{\boldsymbol{x}}^{\mathsf{T}}(k|m)\right]$. Given a prior $\hat{\boldsymbol{x}}(0|0)$ and $\mathbf{P}(0|0)$, the standard EKF equations are iterated. Since the state vector $\boldsymbol{x}$ is constant, the EKF state and estimation error covariance time-update equations are given by

$$\hat{\boldsymbol{x}}(k+1|k)=\hat{\boldsymbol{x}}(k|k), \quad \mathbf{P}(k+1|k)=\mathbf{P}(k|k)+\mathbf{Q},$$

where $\mathbf{Q}$ is the process noise covariance. Note that $\mathbf{Q}$ should theoretically be a zero matrix; however, in order to prevent the estimation error covariance from converging to zero, $\mathbf{Q}$ is chosen to be $\mathbf{Q} \equiv \epsilon\mathbf{I}_{(3+L)\times(3+L)}$, where ϵ is a very small positive number. Given an innovation vector $\boldsymbol{\nu}(k+1)$, the state and covariance measurement update equations are given by

$$\begin{aligned} \hat{\boldsymbol{x}}(k+1|k+1) &= \hat{\boldsymbol{x}}(k+1|k)+\mathbf{K}(k+1)\boldsymbol{\nu}(k+1), \\ \mathbf{P}(k+1|k+1) &= \left[\mathbf{I}-\mathbf{K}(k+1)\mathbf{H}(k+1)\right]\mathbf{P}(k+1|k), \end{aligned}$$

where $\mathbf{K}(k+1)$ is the standard Kalman gain, $\mathbf{H}(k+1)$ is the measurement Jacobian given by

$$\begin{aligned} \mathbf{H}(k+1) &= \left[\boldsymbol{h}_{\text{leo},1}(k+1) \quad \ldots \quad \boldsymbol{h}_{\text{leo},L}(k+1)\right]^{\mathsf{T}}, \\ \boldsymbol{h}_{\text{leo},l}(k+1) &\triangleq \left[\boldsymbol{h}_{r,l}^{\mathsf{T}}(k+1), \boldsymbol{e}_l^{\mathsf{T}}\right]^{\mathsf{T}} \end{aligned}$$

where $\boldsymbol{e}_l$ is the standard $L\times 1$ basis vector whose l-th element is 1 and the remaining elements are 0,

$$\begin{aligned} \boldsymbol{h}_{r,l}(k) \triangleq& \frac{\dot{\boldsymbol{r}}_{\text{leo},l}(k+1)}{\|\hat{\boldsymbol{r}}_r(k+1|k)-\boldsymbol{r}_{\text{leo},l}(k+1)\|} \\ &-\left[\hat{\boldsymbol{r}}_r(k+1|k)-\boldsymbol{r}_{\text{leo},l}(k+1)\right] \\ &\times\frac{\dot{\boldsymbol{r}}_{\text{leo},l}^{\mathsf{T}}(k+1)\left[\hat{\boldsymbol{r}}_r(k+1|k)-\boldsymbol{r}_{\text{leo},l}(k+1)\right]}{\|\hat{\boldsymbol{r}}_r(k+1|k)-\boldsymbol{r}_{\text{leo},l}(k+1)\|^3}, \end{aligned}$$

and $\hat{\boldsymbol{r}}_r(k+1|k)$ is the receiver's position prediction at time-step $k+1$. The innovation vector $\boldsymbol{\nu}(k+1)$ is formed according to

$$\boldsymbol{\nu}(k+1)=\left[\nu_{\text{leo},1}(k+1),\ldots,\nu_{\text{leo},L}(k+1)\right]^{\mathsf{T}},$$

where $\nu_{\text{leo},l}(k+1) = z_{\text{leo},l}(k+1) - \hat{z}_{\text{leo},l}(k+1)$, such that

$$\begin{aligned} \hat{z}_{\text{leo},l}(k+1) =& \frac{\dot{\boldsymbol{r}}_{\text{leo},l}^{\mathsf{T}}(k+1)\left[\hat{\boldsymbol{r}}_r(k+1|k)-\boldsymbol{r}_{\text{leo},l}(k+1)\right]}{\|\hat{\boldsymbol{r}}_r(k+1|k)-\boldsymbol{r}_{\text{leo},l}(k+1)\|} \\ &+c\hat{\dot{\delta}}t_l(k+1|k). \end{aligned}$$

It is important to note that the altitude of the receiver is assumed to be known. Therefore, the initial estimate of z_r is set to the known altitude and its corresponding initial uncertainty is set to be very small.

4. Overview of the Iridium NEXT and Orbcomm LEO Constellations

This section provides an overview of the two LEO constellations used in the experimental results: Iridium NEXT and Orbcomm.

Iridium NEXT System Overview

The Iridium NEXT constellation is the next-generation Iridium constellation which provides voice and data information coverage to satellite phones, pagers, and integrated transceivers over the entire Earth surface on the L-band [55].

Iridium NEXT LEO Satellite Constellation— The Iridium Next constellation consists of 75 active satellites that orbit the Earth in 6 different orbital planes spaced 30° apart [55], as shown in Figure 4. The planes are near-polar orbits with 86.4° inclination angle and 780 km orbital altitude. Originally, the Iridium constellation was designed to incorporate 66 satellites (gathered in 6 groups of 11) in order to provide coverage for the entire Earth surface. Later, Iridium decided to enlarge the initial constellation (referred to as the NEXT campaign) by launching 12 extra satellites in order to provide 24/7 real-time coverage, which would add two extra satellites on each of the original orbital planes. Unfortunately, 3 of them are not active since they experienced technical difficulties once they were launched and thus the current constellation remains at 75 satellites.

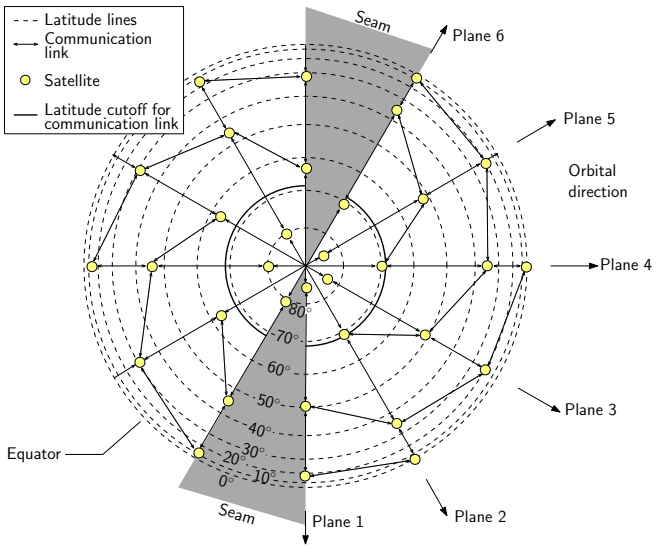

Figure 4. Polar view of the Iridium NEXT Constellation.

Iridium NEXT Downlink Signals—Iridium NEXT signals are transmitted over the 1616–1626.5 MHz band, which is part of the L-band. There are 252 carriers in both the uplink and downlink channels, with carrier spacings of 41.6667 kHz with a required bandwidth of 35 kHz [55]. These carrier frequencies are grouped into sub-bands of 8 carriers, with the 32nd group containing 4 carriers. A small portion of the Iridium NEXT spectrum, namely 1626–1626.5 MHz is assigned for paging and acquisition [55]. On this part of the spectrum are 5 simplex downlink channel with the same frequency spacing as the standard channels and with 35 kHz of bandwidth. Doppler measurements are extracted from the simplex downlink channels.

Iridium NEXT uses a TDMA scheme for downlink channel multiplexing. The signal structure over the uplink and downlink channels consists of signal bursts that are sent periodically over the TDMA frame. Each burst is composed of an unmodulated tone, succeeded by a unique word and the information data. On the simplex channel, Iridium NEXT satellites transmit the ring alert as well as paging/acquisition messages, which have the same burst structure as the standard carriers. As such, the pure tone transmitted at the beginning of each burst can be used to extract Doppler measurements. However, the burst duration is 2.56 ms and the burst period is about 1700 times longer at 4.32 seconds. This large scaling will yield poor Doppler frequency measurements if not accounted for, as discussed in Section 2.

Orbcomm System Overview

The Orbcomm system is a wide area two-way communication system that uses a constellation of LEO satellites to provide worldwide geographic coverage for sending and receiving alphanumeric packets [56].

Orbcomm LEO Satellite Constellation—The Orbcomm constellation, at maximum capacity, has up to 47 satellites in 7 orbital planes A–G, illustrated in Figure 5. Planes A, B, and C are inclined at 45° to the equator and each contains 8 satellites in a circular orbit at an altitude of approximately 815 km. Plane D, also inclined at 45°, contains 7 satellites in a circular orbit at an altitude of 815 km. Plane E is inclined at 0° and contains 7 satellites in a circular orbit at an altitude of 975 km. Plane F is inclined at 70° and contains 2 satellites in a near-polar circular orbit at an altitude of 740 km. Plane G is inclined at 108° and contains 2 satellites in a near-polar elliptical orbit at an altitude varying between 785 km and 875 km.

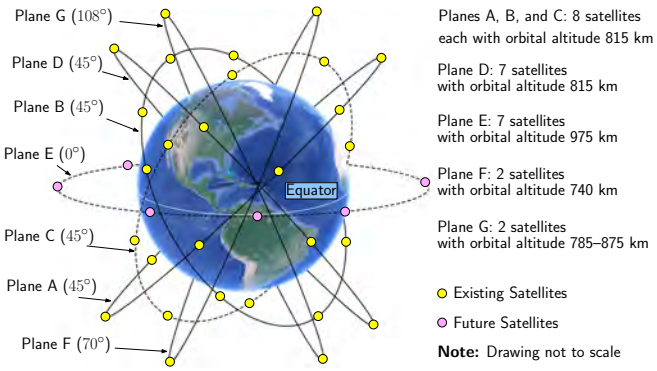

Figure 5. Orbcomm LEO satellite constellation. Map data: Google Earth.

Orbcomm Downlink Signals— Orbcomm uses an FDMA scheme for downlink channel multiplexing. Satellite radio frequency (RF) downlinks are within the 137–138 MHz VHF band. Downlink channels include 12 channels for transmitting to users and one gateway channel, which is reserved for transmitting to the ground stations. Each satellite transmits to users on one of the 12 subscriber downlink channels through a frequency-sharing scheme that provides four-fold channel reuse. The Orbcomm satellites have a subscriber transmitter that provides a continuous 4800 bits-per-second (bps) stream of packet data using symmetric differential-quadrature phase shift keying (SD-QPSK). Each satellite also has multiple subscriber receivers that receive short bursts from the users at 2400 bps.

Note that Orbcomm satellites are also equipped with a specially constructed 1-Watt ultra high frequency (UHF) transmitter that is designed to emit a highly stable signal at 400.1 MHz. The transmitter is coupled to a UHF antenna designed to have a peak gain of approximately 2 dB. The UHF signal is used by the Orbcomm system for user positioning. However, experimental data shows that the UHF beacon is absent. Moreover, even if the UHF beacon was present, one would need to be a paying subscriber to benefit from positioning services. Consequently, only downlink channel VHF signals are exploited for navigation.

5. Experimental Results

An experiment was conducted to demonstrate the proposed receiver architecture and navigation framework. To this end, two universal software radio peripherals (USRPs) Ettus E312 were used to collect multi-constellation LEO satellite signals. One USRP was equipped with a VHF quadrifilar helix antenna to sample Orbcomm signals at a carrier frequency of 137.5 MHz, which is the central frequency of the Orbcomm band [56], and the other was equipped with an AT 1621-12 Iridium antenna to sample Iridium NEXT signals at a carrier frequency of 1626.2708 MHz, which is the central frequency of the Iridium ring alert burst signal according to [51]. Both USRPs were set to sample data at 2.4 Msps over a 410-second period. The samples were stored for offline processing, and a software-defined radio (SDR) implementation of the aforementioned receiver architecture was used to post-process the collected data. The experimental setup is illustrated in Figure 6. Moreover, the M-PSK constellation size was set to 2 for the Orbcomm signals and 1 for the Iridium signals, respectively. Note that Orbcomm satellites transmits quadrature PSK (QPSK) signals ($M = 4$); however, raising the signal to the second power yielded better results than $M = 4$. The M-PSK constellation size was chosen to be 1 for Iridium NEXT since their satellites transmit a pure tone as part of the burst. Moreover, T_{block} and T_{dump}, where set to 100 ms and zero, respectively, for the Orbcomm constellation. For the Iridium constellation, they were set to $T_{\text{block}} = 2.56$ ms and $T_{\text{dump}} = 4.3174$ s, enabling burst processing for a signal with a period of $P_{\text{block}} = 4.32$ s, equivalent to that of the ring alert burst signal. The SDR produced Doppler measurements for five satellites, consisting of (i) one continuously transmitting Orbcomm satellite and (ii) four burst transmitting Iridium NEXT satellites. The Doppler measurements were provided at a rate of 100 ms for the Orbcomm satellite and 4.32 s for the Iridium NEXT satellites. The satellites' positions and velocities were determined using a MATLAB-based SGP4 propagation software and publicly available TLE files. The positions of the satellites along with the skyplot with respect to the receiver are shown in Figure 8.

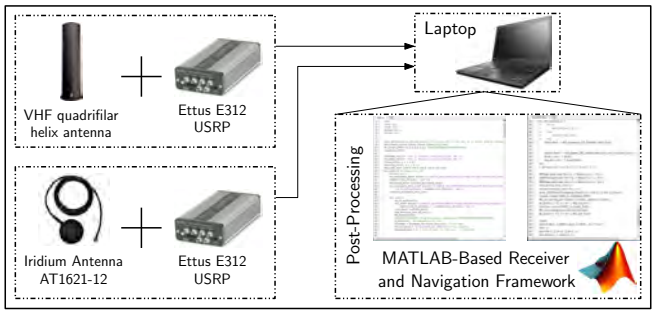

Figure 6. Experimental setup.

Figure 7 shows the true and estimated pseudorange rates obtained from the TLE files and the receiver, respectively, for each of the five satellites. The satellites were not all tracked for the entire duration of their availability due to bad signal reception at low elevation angles. Figure 7 also illustrates the availability of the satellites within the 410 s window when the data was recorded. The Orbcomm satellite was available throughout the entire window and was providing measurements every 100 ms. However, for the Iridium constellation, three satellites are tracked initially and are then lost at 78, 118, and 217 s, respectively. The EKF continues to estimate the receiver's position using one Orbcomm satellite

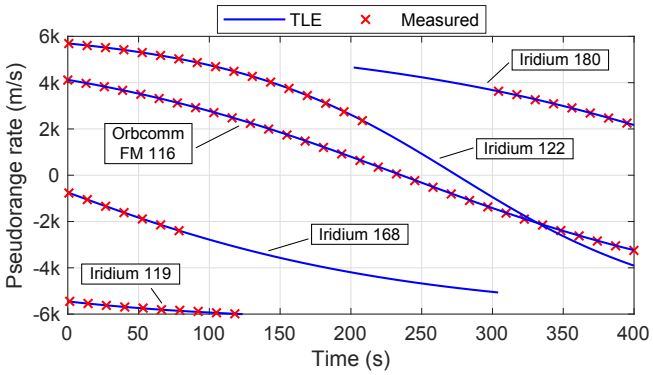

Figure 7. Pseudorange rates time history predicted using TLE files for the satellites tracked by the proposed receiver along with the actual measurements produced by the receiver.

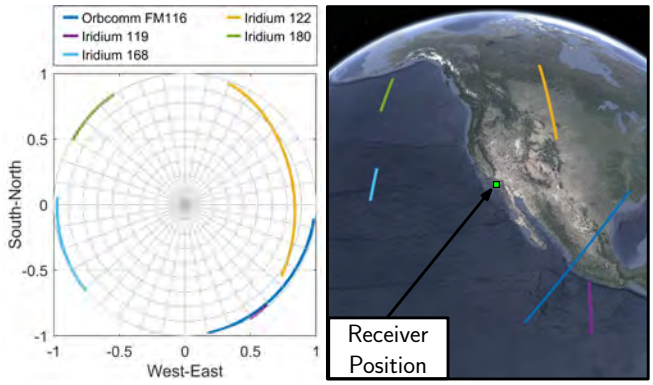

Figure 8. Skyplot and satellite positions of the tracked Orbcomm and Iridium NEXT satellites.

until the receiver starts extracting measurements from another Iridium NEXT satellite at 304 seconds. Figure 7 illustrate the availability of Orbcomm and Iridium NEXT satellites during the experiment window as well as the actual number of LEO satellites that were tracked by the receiver. It is worth mentioning that tracking an Iridium NEXT satellite for 100 seconds only produces around 23 pseudorange rate measurements.

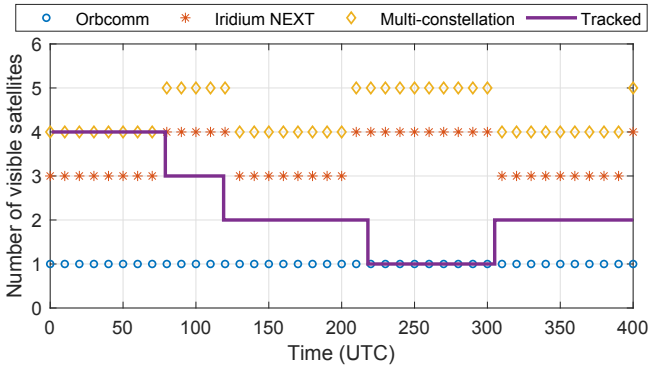

Figure 9. Number of tracked and available satellites as a function of time.

The horizontal position estimate was initialized around 200 km away from the receiver's true position, and the initial horizontal uncertainty was set to 10^{10} m^2. The receiver's

altitude was initialized according to Section 3, with a 0.1 m^2 initial uncertainty. Figure 10 shows the time evolution of the EKF position errors in the east and north coordinates along with the $\pm 3\sigma$ bounds, reaching a final position error of 22.7 m. The small jumps seen in the EKF errors happen at a period of 4.32 s, which is the rate at which pseudorange rate measurements were produced from the Iridium NEXT satellite signals. The receiver's true and estimated positions are shown in Figure 11. It is also worth noting that some of the position error could be attributed to errors in the LEO satellites' positions and velocities predicted by the TLEs and SGP4 orbit determination software.

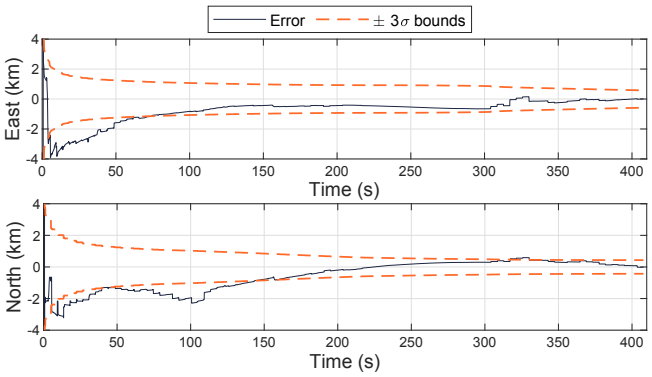

Figure 10. The time evolution of the EKF east and north position estimation errors as a function of time.

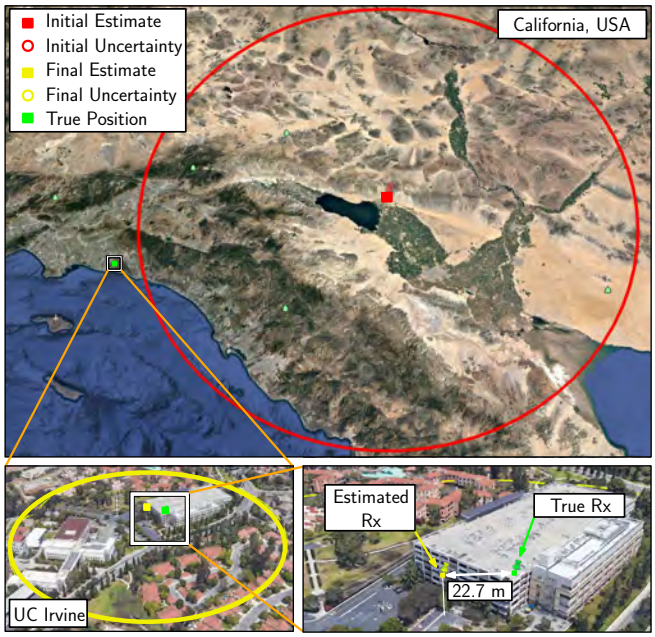

Figure 11. True position of the receiver along with the estimate produced by the EKF using pseudorange rate measurements for one Orbcomm and four Iridium NEXT satellites.

6. Conclusion

This paper proposed a framework for opportunistic navigation with multi-constellation LEO satellite signals. A receiver architecture suitable for processing both TDMA and FDMA signals from Orbcomm and Iridium NEXT satellites to produced Doppler frequency measurements to LEO satellites was proposed. An EKF-based estimator was formulated to solve for a stationary receiver's position using Doppler measurements from multi-constellation LEO satellites. Unprecedented experimental were presented showing receiver positioning with one Orbcomm satellite and four Iridium NEXT satellite with a final position error less than 23 m.

Acknowledgements

This work was supported in part by the Office of Naval Research (ONR) under Grant N00014-19-1-2511 and in part by the U.S. Department of Transportation (USDOT) under University Transportation Center (UTC) Program Grant 69A3552047138. The authors would also like to thank Carlos Acebes for his contributions to the paper and Nadim Khairallah for his help with data collection.

References

[1] Z. Kassas, P. Closas, and J. Gross, "Navigation systems for autonomous and semi-autonomous vehicles: Current trends and future challenges," *IEEE Aerospace and Electronic Systems Magazine*, vol. 34, no. 5, pp. 82–84, May 2019.

[2] United States, Executive Office of the President, "Executive order on strengthening national resilience through responsible use of positioning, navigation, and timing services," Febraury 2020.

[3] F. Boccardi, R. Heath, A. Lozano, T. Marzetta, and P. Popovski, "Five disruptive technology directions for 5G," *IEEE Communications Magazine*, vol. 52, no. 2, pp. 74–80, February 2014.

[4] M. Agiwal, A. Roy, and N. Saxena, "Next generation 5G wireless networks: A comprehensive survey," *IEEE Communications Surveys Tutorials*, vol. 18, no. 3, pp. 1617–1655, February 2016.

[5] R. Ioannides, T. Pany, and G. Gibbons, "Known vulnerabilities of global navigation satellite systems, status, and potential mitigation techniques," *Proceedings of the IEEE*, vol. 104, no. 6, pp. 1174–1194, February 2016.

[6] D. Borio, F. Dovis, H. Kuusniemi, and L. Presti, "Impact and detection of GNSS jammers on consumer grade satellite navigation receivers," *Proceedings of the IEEE*, vol. 104, no. 6, pp. 1233–1245, February 2016.

[7] M. Thomas, "Global navigation space systems: reliance and vulnerabilities," *The Royal Academy of Engineering*. http://www.raeng.org.uk/news/publications/list/reports/RAoE_Global_Navigation_Systems_Report.pdf, March 2011.

[8] S. Pullen and G. Gao, "GNSS jamming in the name of privacy: Potential threat to GPS aviation," *Inside GNSS*, pp. 34–43, March/April 2012.

[9] D. Akos, "Who's afraid of the spoofer? GPS/GNSS spoofing detection via automatic gain control (AGC)," *NAVIGATION, Journal of the Institute of Navigation*, vol. 59, no. 4, pp. 281–290, 2012.

[10] C. Günther, "A survey of spoofing and countermeasures," *NAVIGATION, Journal of the Institute of Navigation*, vol. 61, no. 3, pp. 159–177, 2014.

[11] M. Psiaki and T. Humphreys, "GNSS spoofing and detection," *Proceedings of the IEEE*, vol. 104, no. 6, pp. 1258–1270, June 2016.

[12] T. Hall, C. Counselman III, and P. Misra, "Radiolocation using AM broadcast signals: Positioning performance," in *Proceedings of ION GPS Conference*, September 2002, pp. 921–932.

[13] A. Popleteev, "Indoor positioning using FM radio signals," Ph.D. dissertation, University of Trento, Italy, 2011.

[14] G. Park, D. Kim, H. Kim, and H. Kim, "Maximum-likelihood angle estimator for multi-channel FM-radio-based passive coherent location," *IET Radar, Sonar Navigation*, vol. 12, no. 6, pp. 617–625, 2018.

[15] M. Psiaki and B. Slosman, "Tracking of digital FM OFDM signals for the determination of navigation observables," in *Proceedings of ION GNSS Conference*, September 2019, pp. 2325–2348.

[16] C. Yang and T. Nguyen, "Tracking and relative positioning with mixed signals of opportunity," *NAVIGATION, Journal of the Institute of Navigation*, vol. 62, no. 4, pp. 291–311, December 2015.

[17] M. Ulmschneider and C. Gentner, "Multipath assisted positioning for pedestrians using LTE signals," in *Proceedings of IEEE/ION Position, Location, and Navigation Symposium*, April 2016, pp. 386–392.

[18] J. Khalife and Z. Kassas, "Navigation with cellular CDMA signals – part II: Performance analysis and experimental results," *IEEE Transactions on Signal Processing*, vol. 66, no. 8, pp. 2204–2218, April 2018.

[19] Z. Kassas, J. Khalife, K. Shamaei, and J. Morales, "I hear, therefore I know where I am: Compensating for GNSS limitations with cellular signals," *IEEE Signal Processing Magazine*, pp. 111–124, September 2017.

[20] K. Shamaei, J. Khalife, and Z. Kassas, "Exploiting LTE signals for navigation: Theory to implementation," *IEEE Transactions on Wireless Communications*, vol. 17, no. 4, pp. 2173–2189, April 2018.

[21] K. Shamaei and Z. Kassas, "LTE receiver design and multipath analysis for navigation in urban environments," *NAVIGATION, Journal of the Institute of Navigation*, vol. 65, no. 4, pp. 655–675, December 2018.

[22] J. Khalife and Z. Kassas, "Opportunistic UAV navigation with carrier phase measurements from asynchronous cellular signals," *IEEE Transactions on Aerospace and Electronic Systems*, vol. 56, no. 4, pp. 3285–3301, August 2020.

[23] J. del Peral-Rosado, R. Raulefs, J. Lopez-Salcedo, and G. Seco-Granados, "Survey of cellular mobile radio localization methods: from 1G to 5G," *IEEE Communications Surveys & Tutorials*, vol. 20, no. 2, pp. 1124–1148, 2018.

[24] T. Kang, H. Lee, and J. Seo, "TOA-based ranging method using CRS in LTE signals," *Journal of Advanced Navigation Technology*, vol. 23, no. 5, pp. 437–443, October 2019.

[25] A. Abdallah, K. Shamaei, and Z. Kassas, "Performance characterization of an indoor localization system with LTE code and carrier phase measurements and an IMU," in *Proceedings of International Conference on Indoor Positioning and Indoor Navigation*, September 2019, pp. 1–8.

[26] P. Wang and Y. Morton, "Multipath estimating delay lock loop for LTE signal TOA estimation in indoor and urban environments," *IEEE Transactions on Wireless Communications*, vol. 19, no. 8, pp. 5518–5530, 2020.

[27] M. Rabinowitz and J. Spilker, Jr., "A new positioning system using television synchronization signals," *IEEE Transactions on Broadcasting*, vol. 51, no. 1, pp. 51–61, March 2005.

[28] P. Thevenon, S. Damien, O. Julien, C. Macabiau, M. Bousquet, L. Ries, and S. Corazza, "Positioning using mobile TV based on the DVB-SH standard," *NAVIGATION, Journal of the Institute of Navigation*, vol. 58, no. 2, pp. 71–90, 2011.

[29] J. Yang, X. Wang, M. Rahman, S. Park, H. Kim, and Y. Wu, "A new positioning system using DVB-T2 transmitter signature waveforms in single frequency networks," *IEEE Transactions on Broadcasting*, vol. 58, no. 3, pp. 347–359, September 2012.

[30] C. Yang, T. Nguyen, and E. Blasch, "Mobile positioning via fusion of mixed signals of opportunity," *IEEE Aerospace and Electronic Systems Magazine*, vol. 29, no. 4, pp. 34–46, April 2014.

[31] L. Chen, O. Julien, P. Thevenon, D. Serant, A. Pena, and H. Kuusniemi, "TOA estimation for positioning with DVB-T signals in outdoor static tests," *IEEE Transactions on Broadcasting*, vol. 61, no. 4, pp. 625–638, 2015.

[32] L. Gill, D. Grenier, and J. Chouinard, "Use of XM radio satellite signal as a source of opportunity for passive coherent location," *IET Radar, Sonar Navigation*, vol. 5, no. 5, pp. 536–544, June 2011.

[33] D. Lawrence, H. Cobb, G. Gutt, M. OConnor, T. Reid, T. Walter, and D. Whelan, "Navigation from LEO: Current capability and future promise," *GPS World Magazine*, vol. 28, no. 7, pp. 42–48, July 2017.

[34] R. Landry, A. Nguyen, H. Rasaee, A. Amrhar, X. Fang, and H. Benzerrouk, "Iridium Next LEO satellites as an alternative PNT in GNSS denied environments–part 1," *Inside GNSS Magazine*, pp. 56–64., May 2019.

[35] Z. Kassas, J. Morales, and J. Khalife, "New-age satellite-based navigation – STAN: simultaneous tracking and navigation with LEO satellite signals," *Inside GNSS Magazine*, vol. 14, no. 4, pp. 56–65, 2019.

[36] Z. Kassas, J. Khalife, M. Neinavaie, and T. Mortlock, "Opportunity comes knocking: overcoming GPS vulnerabilities with other satellites' signals," *Inside Unmanned Systems Magazine*, pp. 30–35, June/July 2020.

[37] J. Khalife and Z. Kassas, "Precise UAV navigation with cellular carrier phase measurements," in *Proceedings of IEEE/ION Position, Location, and Navigation Symposium*, April 2018, pp. 978–989.

[38] J. Khalife, K. Shamaei, S. Bhattacharya, and Z. Kassas, "Centimeter-accurate UAV navigation with cellular signals," in *Proceedings of ION GNSS Conference*, September 2018, pp. 2321–2331.

[39] K. Shamaei and Z. Kassas, "Sub-meter accurate UAV navigation and cycle slip detection with LTE carrier phase," in *Proceedings of ION GNSS Conference*, September 2019, pp. 2469–2479.

[40] Z. Kassas, J. Khalife, A. Abdallah, and C. Lee, "I am not afraid of the jammer: navigating with signals of opportunity in GPS-denied environments," in *Proceedings of ION GNSS Conference*, 2020, pp. 1566–1585.

[41] M. Joerger, L. Gratton, B. Pervan, and C. Cohen, "Analysis of Iridium-augmented GPS for floating carrier phase positioning," *NAVIGATION, Journal of the Institute of Navigation*, vol. 57, no. 2, pp. 137–160, 2010.

[42] K. Pesyna, Z. Kassas, and T. Humphreys, "Constructing a continuous phase time history from TDMA signals for opportunistic navigation," in *Proceedings of IEEE/ION Position Location and Navigation Symposium*, April 2012, pp. 1209–1220.

[43] T. Reid, A. Neish, T. Walter, and P. Enge, "Broadband LEO constellations for navigation," *NAVIGATION, Journal of the Institute of Navigation*, vol. 65, no. 2, pp. 205–220, 2018.

[44] D. Racelis, B. Pervan, and M. Joerger, "Fault-free integrity analysis of mega-constellation-augmented GNSS," in *Proceedings of ION GNSS Conference*, January 2019, pp. 465–484.

[45] T. Reid, K. Gunning, A. Perkins, S. Lo, and T. Walter, "Going back for the future: Large/mega LEO constellations for navigation," in *Proceedings of ION GNSS Conference*, September 2019, pp. 2452–2468.

[46] T. Reid, T. Walter, P. Enge, D. Lawrence, H. Cobb, G. Gutt, M. O'Conner, and D. Whelan, "Position, navigation, and timing technologies in the 21st century," J. Morton, F. van Diggelen, J. Spilker, Jr., and B. Parkinson, Eds. Wiley-IEEE, 2021, vol. 2, ch. 43: Navigation from low Earth orbit – Part 1: Concept, Current Capability, and Future Promise, pp. 1359–1379.

[47] Z. Kassas, "Position, navigation, and timing technologies in the 21st century," J. Morton, F. van Diggelen, J. Spilker, Jr., and B. Parkinson, Eds. Wiley-IEEE, 2021, vol. 2, ch. 43: Navigation from low Earth orbit – Part 2: models, implementation, and performance, pp. 1381–1412.

[48] L. Xiao and Z. Lei, "Analysis of Iridium-augmented GPS positioning performance," *The Journal of Engineering*, vol. 2019, no. 20, pp. 7139–7143, 2019.

[49] J. Khalife, M. Neinavaie, and Z. Kassas, "Navigation with differential carrier phase measurements from megaconstellation LEO satellites," in *Proceedings of IEEE/ION Position, Location, and Navigation Symposium*, April 2020, pp. 1393–1404.

[50] M. Neinavaie, J. Khalife, and Z. Kassas, "Blind Doppler tracking and beacon detection for opportunistic navigation with LEO satellite signals," in *Proceedings of IEEE Aerospace Conference*, March 2021, accepted.

[51] Z. Tan, H. Qin, L. Cong, and C. Zhao, "New method for positioning using IRIDIUM satellite signals of opportunity," *IEEE Access*, vol. 7, pp. 83 412–83 423, 2019.

[52] T. Mortlock and Z. Kassas, "Assessing machine learning for LEO satellite orbit determination in simultaneous tracking and navigation," in *Proceedings of IEEE Aerospace Conference*, March 2021, accepted.

[53] J. Vetter, "Fifty years of orbit determination: Development of modern astrodynamics methods," *Johns Hopkins APL Technical Digest*, vol. 27, no. 3, pp. 239–252, November 2007.

[54] F. Farhangian and R. Landry, "Multi-constellation software-defined receiver for Doppler positioning with LEO satellites," *Sensors*, vol. 20, no. 20, pp. 5866–5883, October 2020.

[55] Iridium Constellation LLC, "Iridium NEXT engineering statement," http://licensing.fcc.gov/myibfs/download.do?attachment_key=1031348.

[56] Orbcomm, https://www.orbcomm.com/en/networks/satellite.

Mohamad Orabi *is a graduate student at the Department of Electrical Engineering and Computer Science at University of California, Irvine and member of the Autonomous Systems Perception, Intelligence, and Navigation (ASPIN) Laboratory. He received a B.E. in Electrical Engineering from the Lebanese American University (LAU). His research interest include opportunistic navigation, software-defined radio, machine learning, and iterative learning control.*

Joe Khalife *is a postdoctoral fellow at the University of California, Irvine and member of the Autonomous Systems Perception, Intelligence, and Navigation (ASPIN) Laboratory. He received a B.E. in Electrical Engineering, an M.S. in Computer Engineering from the Lebanese American University (LAU) and a Ph.D. in Electrical Engineering and Computer Science from the University of California, Irvine. From 2012 to 2015, he was a research assistant at LAU, and has been a member of the ASPIN Laboratory since 2015. He is a recipient of the 2016 IEEE/ION Position, Location, and Navigation Symposium (PLANS) Best Student Paper Award and the 2018 IEEE Walter Fried Award. His research interests include opportunistic navigation, autonomous vehicles, and software-defined radio.*

Zaher (Zak) M. Kassas *is an associate professor at the University of California, Irvine and director of the Autonomous Systems Perception, Intelligence, and Navigation (ASPIN) Laboratory. He is also director of the U.S. Department of Transportation Center: CARMEN (Center for Automated Vehicle Research with Multimodal AssurEd Navigation), focusing on navigation resiliency and security of highly automated transportation systems. He received a B.E. in Electrical Engineering from the Lebanese American University, an M.S. in Electrical and Computer Engineering from The Ohio State University, and an M.S.E. in Aerospace Engineering and a Ph.D. in Electrical and Computer Engineering from The University of Texas at Austin. He received the 2018 National Science Foundation (NSF) Faculty Early Career Development Program (CAREER) award, and 2019 Office of Naval Research (ONR) Young Investigator Program (YIP) award. He is a recipient of the 2018 IEEE Walter Fried Award, 2018 Institute of Navigation (ION) Samuel Burka Award, and 2019 ION Col. Thomas Thurlow Award. He is an Associate Editor for the IEEE Transactions on Aerospace and Electronic Systems and the IEEE Transactions on Intelligent Transportation Systems. His research interests include cyber-physical systems, estimation theory, navigation systems, autonomous vehicles, and intelligent transportation systems.*

Performance Analysis of Opportunistic ARAIM for Navigation With GNSS Signals Fused With Terrestrial Signals of Opportunity

Mu Jia, *Graduate Student Member, IEEE*, Joe Khalife, *Student Member, IEEE*, and Zaher M. Kassas, *Senior Member, IEEE*

***Abstract*— Integrity monitoring of a vehicular navigation system that utilizes multi-constellation global navigation satellite systems (GNSS) signals fused with terrestrial signals of opportunity (SOPs) is considered. An opportunistic advanced receiver autonomous integrity monitoring (OARAIM) framework is developed to detect faults and calculate protection levels (PLs). The influence of fusing SOPs on the integrity performance is analyzed. It is shown that fusing a single SOP with GNSS signals essentially increases both the horizontal PL (HPL) and vertical PL (VPL), while fusing two or more SOPs could reduce the PLs and improves fault detection. Performance sensitivity analysis for the probability of SOP fault and user range error is conducted to characterize the fault-free HPL under different regimes. Experimental results on an unmanned aerial vehicle (UAV) navigating with GPS signals fused with cellular SOPs are presented to validate the effectiveness of the OARAIM framework and demonstrate the analysis of the integrity performance in the horizontal direction.**

***Index Terms*— Navigation, integrity, RAIM, protection level, GNSS, signals of opportunity.**

NOMENCLATURE

z_m^{G}	m-th GNSS pseudorange measurement.
$\boldsymbol{r}_{\mathrm{r}}$	Receiver's position vector.
$\boldsymbol{r}_m^{\mathrm{G}}$	m-th GNSS satellite postion vector.
$\delta t_{\mathrm{r},j}^{\mathrm{G}}$	Receiver's clock bias with respect to the i-th GNSS constellation's reference time.
v_m^{G}	Measurement noise for the m-th GNSS satellite.
$z_m^{\mathrm{G}'}$	GNSS pseudorange measurement before compensation.
$\hat{\delta}t^{\mathrm{G}}$	GNSS satellite's clock bias estimate.
$\hat{\delta}t_{\mathrm{iono}}$	Estimated ionospheric dalay.
$\delta t_{\mathrm{tropo}}$	Estimated troposheric delay.
$\boldsymbol{r}_n^{\mathrm{S}}$	Position of n-th SOP transmitter.
$\bar{\delta}t_{\mathrm{r}}$	SOP receiver's clock bias.
δt_n^{S}	Clock bias of the n-th SOP transmitter.
$\bar{v}_n^{\mathrm{S}}$	SOP pseudorange measurement noise.
$\delta t_{\mathrm{r},j}^{\mathrm{S}}$	SOP receiver's clock bias with respect to the j-th SOP subgroup (constellation).
$\delta t_{n,0}^{\mathrm{S}}$	Initial SOP clock bias.
N_{const}	Number of SOP constellations.
M_{const}	Number of GNSS constellations.
M_{s}	Number of GNSS satellites.
N_{s}	Number of SOP transmitters.
v_n^{S}	SOP pseudorange measurement noise in the re-parameterized measurement model.
$\boldsymbol{x}$	UAV state vector.
$\boldsymbol{z}$	Measurement vector.
$\mathbf{H}$	Measurement Jacobian matrix.
$\hat{\boldsymbol{x}}$	Estimated state vector.
$\mathbf{W}$	Wighting matrix in estimators.
$\hat{\boldsymbol{z}}^{(\infty)}$	Converged measurement prediction.
$\boldsymbol{y}$	Estimation residual vector.
$\mathbf{G}$	Geometry matrix.
$\mathbf{B}$	Measurement Jacobian associated with clock states.
el_l	Elevation angle.
az_l	Azimuth angle.
$d_{\mathrm{min}}^{\mathrm{S}}$	Minimum SOP horizontal distance.
$d_{\mathrm{max}}^{\mathrm{S}}$	Maximum SOP horizontal distance.
σ_{URA}	User Range Accuracy.
b_{nom}	Maximum nominal error.
P_{s}	Probability of single ranging source fault.
P_{const}	Probability of constellation-wide fault.
P_{thresh}	Integrity risk budget for unmonitored fault modes.
N_{f}	Number of fault modes to be monitored.
$P_{\mathrm{f}}^{(i)}$	Probability of fault mode i.
$\hat{\boldsymbol{x}}^{(i)}$	Fault-tolerant solution.
$\hat{\boldsymbol{x}}^{(0)}$	All-in-view solution.
$\Delta\hat{\boldsymbol{x}}^{(i)}$	Solution separation for the i-th fault mode.
$\mathbf{W}^{(i)}$	Integrity wighting matrix for fault mode i.
$\sigma_q^{(i)}$	Standard deviation of the i-th fault-tolerant navigation solution in the q-th directin.
$b_q^{(i)}$	Worst-case bias.
$\sigma_{ss,q}^{(i)}$	Standard deviation of solution separation.
$T_{i,q}$	Test threshold.

Manuscript received 8 April 2022; revised 4 November 2022 and 25 March 2023; accepted 3 May 2023. Date of publication 21 August 2023; date of current version 4 October 2023. This work was supported in part by the U.S. Department of Transportation (USDOT) through the Center for Automated Vehicle Research with Multimodal AssurEd Navigation (CARMEN) University Transportation Center (UTC) under Grant 69A3552047138 and in part by the National Science Foundation (NSF) under Grant 1929965. The Associate Editor for this article was S.-H. Kong. *(Corresponding author: Zaher M. Kassas.)*

Mu Jia and Zaher M. Kassas are with the Department of Electrical and Computer Engineering, The Ohio State University, Columbus, OH 43210 USA (e-mail: jia.641@osu.edu; zkassas@ieee.org).

Joe Khalife was with the Department of Mechanical and Aerospace Engineering, University of California, Irvine, CA 92697 USA. He is now with Apple, Cupertino, CA 95014 USA (e-mail: khalifej@uci.edu).

Digital Object Identifier 10.1109/TITS.2023.3277393

1558-0016 © 2023 IEEE. Personal use is permitted, but republication/redistribution requires IEEE permission.
See https://www.ieee.org/publications/rights/index.html for more information.

Authorized licensed use limited to: The Ohio State University. Downloaded on October 13,2023 at 15:38:43 UTC from IEEE Xplore. Restrictions apply.

$\hat{x}_q^{(i)}$	Fault-tolerant solution in the q-th direction.
$\hat{x}_q^{(0)}$	All-in-view solution in the q-th direction.
P_{NM}	Probability of faults not monitored.
PL_q	Protection level in q-th direction.
$P_{\mathrm{FA\_H}}$	Coninuity budget in the horizontal direction.
$P_{\mathrm{FA\_V}}$	Coninuity budget in the vertical direction.
$PHMI_{\mathrm{H}}$	Integrity budget in the horizontal direction.
$PHMI_{\mathrm{V}}$	Integrity budget in the vertical direction.

I. Introduction

In safety-of-life navigation applications, e.g. aviation, the passenger and mission safety highly depends on the accuracy and reliability of the navigation system. This is particularly the case for civil aircraft autopilot systems, and unmanned aerial vehicles (UAVs), which are quickly becoming popular in a wide range of civilian and military applications [1]. Semi- and fully-automated autopilot systems, whether on ground or aerial vehicles, rely on global navigation satellite systems (GNSS) receivers and a suite of onboard sensors, e.g., radar, inertial navigation system (INS), etc. [2]. GNSS are relied upon to provide a navigation solution in a global frame and to correct for accumulating errors due to sensor dead reckoning.

While achieving higher levels of navigation accuracy has been a classic requirement, the trustworthiness in the navigation solutions, commonly assessed by navigation integrity, is evermore vital in safety critical applications. To ensure safe navigation, autopilot systems need to detect changes or anomalies in navigation signal characteristics that could affect the accuracy of the position calculated by the user equipment. Navigation systems need to tightly bound the position errors and ensure that the probability of position errors being not properly bounded is below a certain limit. However, current GNSS technologies are insufficient to support the full flight procedure, e.g., vertical guidance down to altitudes of 200 ft (LPV-200) [3]. To provide high-integrity navigation for UAVs and urban air mobility can be even more challenging, as these aerial vehicles may fly in urban environments, where GNSS signals are challenged and could be compromised via interference, jamming, or spoofing [4], [5].

Recently, terrestrial radio signals [6] have been shown to be an attractive alternative or supplement to GNSS signals [7], [8], either in an opportunistic manner, e.g., cellular signals [9], [10], digital television signals [11], [12], and FM radio signals [13], [14], or as radio beacons dedicated to navigation, e.g., Locata and NextNav [15]. While cellular base stations are already abundant in most locales, the number of base stations for future cellular generations keeps increasing dramatically, with the base station density of 5G projected to grow to 40-50 per km^2 [16]. Terrestrial signals of opportunity (SOPs) are particularly attractive for aerial integrity monitoring, as they can provide additional geometric diversity from below aerial vehicles [17].

Integrity monitoring relies on a priori knowledge of the nominal performance and fault rates of the ranging constellations. For GPS, the ground stations provide periodic updates regarding the safety-critical parameters contained in the Integrity Support Message (ISM). The safety-critical parameters include user range accuracy (URA) and user range error (URE), which are the standard deviations of the nominal errors used for integrity and continuity, respectively, and a priori probability of satellite failure. For SOPs and dedicated beacons, those parameters are either not fully characterized by enough data, or completely unknown. Hence, the impact of adding terrestrial signals with variable safety-critical parameters on integrity monitoring is still to be studied.

This paper conducts a thorough study on the impact of adding terrestrial measurements, whether from SOPs or dedicated beacons, with variable safety-critical parameters on GNSS-SOP integrity monitoring. It is shown that adding one SOP actually increases both the horizontal protection level (HPL) and vertical protection level (VPL). This happens when there is only one SOP available in the environment or the clocks of the SOPs are not synchronized (herein referred to as coming from different SOP constellations). In such cases, adding any SOP to the system would augment the state vector with an additional clock term, and the information from the additional SOP gets consumed in estimating the additional clock term. While the additional SOP is desirable from the perspective of improving the geometric diversity, it does not add redundancy in the measurements, and in fact, adds a vulnerability exhibited by an increase in the PLs. While new-generation cellular networks are evolving to support precise positioning, the current time synchronization requirement for both LTE and 5G is 3 μs [18], which corresponds to ranging errors of about 900 m. A recent study modeled, based on experimental data, the level of synchronization across cellular base stations [19]. This paper adopts such models and shows that adding two or more SOPs with synchronized clocks potentially reduces the HPL within a fairly large regime of safety-critical parameters.

This paper presents an opportunistic advanced receiver autonomous integrity monitoring (OARAIM) framework that utilizes multi-constellation GNSS signals fused with terrestrial SOPs, while detecting faults and calculating the PLs. The paper makes three contributions:

- It analytically shows that there needs to be at least two SOPs in an SOP constellation to possibly reduce PLs.
- It characterizes the horizontal integrity performance via extensive Monte Carlo simulations for adding a different number of SOPs with variable safety-critical parameters.
- It presents UAV experimental results demonstrating the efficacy of the proposed OARAIM to bound the integrity risk and comparing against the theoretical conclusions on the influence of adding terrestrial SOP measurements on HPL.

The remainder of this paper is organized as follows. Section II surveys related work about integrity monitoring and opportunistic navigation. Section III presents the navigation models, which include GNSS and SOP measurement models, weighted nonlinear least square (WLNS) estimator, and terrestrial SOP geometry model. Section IV presents the critical elements for OARAIM, namely definitions, safety-critical parameters and algorithm framework, which are foundational for the analysis in this paper. Section V analytically

Authorized licensed use limited to: The Ohio State University. Downloaded on October 13,2023 at 15:38:43 UTC from IEEE Xplore. Restrictions apply.

proves that adding only one SOP in an additional constellation increases the PLs, indicating that to possibly improve navigation integrity, at least two or more SOPs are needed. Section VI presents the sensitivity analysis of integrity performance over variable SOP safety-critical parameters. Section VII discusses the experiment setup and results demonstrating the OARAIM framework. Section VIII concludes this paper by summarizing the analytical, simulation, and experimental results.

II. Related Work

The concept of navigation integrity, which measures the confidence of the information correctness provided by the navigation system. was introduced in the early 1990s to deal with safety threats caused by GPS faults in safety-critical missions [20]. The integrity information is provided by (i) external aiding systems, e.g. Ground Based Augmentation System (GBAS) [21] and Satellite Based Augmentation System (SBAS) [22]; (ii) onboard sensors, e.g. through the Airborne Based Augmentation System (ABAS). ABAS is usually referred as receiver autonomous integrity monitoring (RAIM), which is exceptionally attractive, as it is cost-effective and does not require building additional infrastructure [23]. RAIM for GPS constellation has been used since the mid-1990s. With the deployment of new GNSS constellations and the development of sensor technology, Advanced RAIM (ARAIM) has been proposed to account for multi-constellation GNSS measurements [24] (e.g. Galileo [25], GLONASS [26], and Beidou [27]), aiding sensors (e.g., INS-GPS [28], lidar-GNSS [29], and vision-GPS [30]). Since the introduction of ARAIM concept in the GPS Evolutionary Architecture Study (GEAS) phase II report [31], the cooperation between U.S. and E.U. on GPS/Galileo, through Working Group C Advanced Receiver Autonomous Integrity Monitoring Technical Subgroup (ARAIM SG), keeps improving the availability of safety-critical service, which is supposed to maintain integrity and continuity simultaneously [32]. As an extension to the original framework which only covers single-fault cases, [33] explicitly proposed the methods to compute the PLs for hypotheses with simultaneous faults. The estimator and detector design is optimized in [34] and [35] to minimize integrity risk in RAIM.

With the remarkable developments of BeiDou System (BDS) and GLONASS in the past decade, researcher has started to investigate utilizing multi-constellation ARAIM to meet more stringent integrity requirements. Foundational definitions, assertions, and assumptions for multi-constellation ARAIM are delicately checked and clarified for current RAIM-based operations [36]. The impact of incorporating more constellations to ARAIM on navigation performance is characterized, and a method of grouping multiple fault hypotheses to reduce high computational load caused by increasing number of measurements is proposed in [37]. The sensitivity of availability in response to changes in error model parameters is analyzed for multi-constellation ARAIM [38].

While GNSS has monopolized global navigation for decades, researchers have been working on developing new radionavigation systems and exploiting ambient signals for positioning. Opportunistic navigation has been widely studied over the last two decades [39], [40], [41], [42]. SOPs are exploited to provide a navigation solution in a global frame in a standalone fashion [43], [44] or could be used as aiding sources to dead reckoning sensors (e.g., lidar [45] and INS [46]). Among the different types of terrestrial SOPs, cellular signals are particularly attractive due to their inherent attributes: abundance, desirable geometric and spectral diversity, high received power, and large bandwidth. Cellular signals have shown high ranging and localization accuracy even in multipath environments [47], [48], [49], [50], [51] and on high-altitude aircraft [52], [53]. Recently, 5G signals have been studied for navigation purposes [54], [55], [56], and have been demonstrated on UAVs and ground vehicles [57], [58]. [59] develops a framework to exploit the entire bandwidth for navigation by using both "always-on" and "on-demand" reference signals. Recent studies have exploited terrestrial SOPs to enhance integrity monitoring performance by fusing GPS signals with SOPs. which has been shown to achieve improvement of integrity, in terms of PLs, over GPS-only for both aerial and ground vehicles [17], [60], [61]. However, the analyses are based on preliminary signal characterization and/or assumptions on safety-critical parameters of SOPs [62], [63]. On one hand, the SOP URE value in [17] is adopted based on signal characterization from a few hours worth of collected data, which is insufficient in the strict context of integrity. On the other hand, [61] assumed the SOP probability of fault to be 10 times that of GPS.

While multi-constellation GNSS ARAIM and opportunistic navigation has been extensively studied, the analyses do not directly apply to GNSS-SOP integrity monitoring. This is because: (i) terrestrial SOP transmitters have different geometry than GNSS satellites. Instead of orbiting above aerial vehicles, terrestrial SOPs usually are located below aerial vehicles; (ii) the safety-critical parameters of SOPs could have different order of magnitudes than those of GNSS.

III. Navigation Model Description

This section describes the pseudorange measurement models of the GNSS satellites and terrestrial SOPs and the WNLS estimator used to estimate the receiver's position. Furthermore, the terrestrial SOP geometry model used for the OARAIM performance analysis is presented.

A. GNSS Pseudorange Measurement Model

The aerial vehicle-mounted receiver makes pseudorange measurements to M_{s} GNSS satellites from M_{const} GNSS constellations. Let $i \in \{1, \ldots, M_{\mathrm{const}}\}$ denote the index of the constellation to which the m-th GNSS satellite belongs. The m-th GNSS pseudorange measurement from the i-th GNSS constellation at time-step k, after compensating for ionospheric delays, tropospheric delays, and the satellite's clock bias, is modeled as [64]

$$z_m^{\mathrm{G}}(k) = \|\boldsymbol{r}_{\mathrm{r}}(k) - \boldsymbol{r}_m^{\mathrm{G}}(k)\|_2 + c \cdot \delta t_{\mathrm{r},i}^{\mathrm{G}}(k) + v_m^{\mathrm{G}}(k), \quad (1)$$

where $z_m^{\mathrm{G}}(k) = z_m^{\mathrm{G}'}(k) + c\hat{\delta}t_m^{\mathrm{G}}(k) - c \cdot \hat{\delta}t_{\mathrm{iono}}(k) - c \cdot \hat{\delta}t_{\mathrm{tropo}}(k)$; $z_m^{\mathrm{G}'}(k)$ is the pseudorange from the m-th GNSS satellite before

Authorized licensed use limited to: The Ohio State University. Downloaded on October 13,2023 at 15:38:43 UTC from IEEE Xplore. Restrictions apply.

compensation; c is the speed of light; $\hat{\delta}t_m^{\mathrm{G}}(k)$ is the m-th GNSS satellite's clock bias estimate; $\hat{\delta}t_{\mathrm{iono}}(k)$ and $\hat{\delta}t_{\mathrm{tropo}}(k)$ are the estimated ionospheric and tropospheric delays, respectively; $\boldsymbol{r}_{\mathrm{r}}(k)$ and $\boldsymbol{r}_m^{\mathrm{G}}(k)$ are the receiver and m-th satellite's three-dimension (3D) position vectors, respectively; $\delta t_{\mathrm{r},i}^{\mathrm{G}}(k)$ is the receiver's clock bias with respect to the i-th GNSS constellation's reference time; and v_m^{G} is the lumped noise term including residual ionospheric errors, which is modeled as a zero-mean, white Gaussian sequence with standard deviation σ_m^{G}.

B. Terrestrial SOP Pseudorange Measurement Model

The aerial vehicle-mounted receiver also makes pseudorange measurements from N_{s} terrestrial SOP transmitters, which are assumed to be stationary with known positions. Unlike GNSS satellites that transmit their clock parameters from which their clock error states can be deduced, terrestrial SOPs may not transmit any information about their clock error states. The n-th SOP measurement at time-step k can be modeled as

$$\bar{z}_n^{\mathrm{S}}(k) = \|\boldsymbol{r}_r(k) - \boldsymbol{r}_n^{\mathrm{S}}(k)\|_2 + c \cdot [\bar{\delta}t_{\mathrm{r}}(k) - \delta t_n^{\mathrm{S}}(k)] + \bar{v}_n^{\mathrm{S}}(k), \tag{2}$$

where $\boldsymbol{r}_n^{\mathrm{S}}(k)$ and $\delta t_n^{\mathrm{S}}(k)$ are the 3D position and clock bias of the n-th SOP transmitter, respectively; $\bar{\delta}t_{\mathrm{r}}(k)$ is the SOP receiver's clock bias with respect to the true time; and $\bar{v}_n^{\mathrm{S}}$ is the measurement noise, which is modeled as a zero-mean white Gaussian sequence with standard deviation $\bar{\sigma}_n^{\mathrm{S}}$.

The recent study [19] concluded that there exists a certain level of clock synchronization between cellular transmitters, i.e., the clock biases of different neighboring transmitters are dominated by one common term, due to the synchronization of the cellular network, leading to the model

$$c \cdot [\bar{\delta}t_{\mathrm{r}}(k) - \delta t \ldots\ldots \mathrm{S}_n(k)] = c\delta t_{\mathrm{r}}^{\mathrm{S}}(k) + c\delta t_{0,n}^{\mathrm{S}} + \epsilon_n(k), \tag{3}$$

where $c\delta t_{\mathrm{r}}^{\mathrm{S}}(k)$ is a common term driving the difference between the receiver and a subgroup of SOP clock biases, and $\epsilon_n(k)$ is an error term modeled as a zero-mean Gaussian random variable with variance $\sigma_{\epsilon_n}^2$. The initial biases $\left\{c\delta t_{0,n}^{\mathrm{S}}\right\}_{n=1}^{N_{\mathrm{s}}}$ can be obtained knowing the initial receiver position and given the initial measurement $\bar{z}_n^{\mathrm{S}}(0)$ according to $c\delta t_{0,n}^{\mathrm{S}} \approx \bar{z}_n^{\mathrm{S}}(0) - \|\boldsymbol{r}_r(0) - \boldsymbol{r}_n^{\mathrm{S}}(0)\|_2$. The initial receiver position can be estimated from GNSS measurements during a pre-calibration stage or before GNSS is cut off. The details of this calibration method can be found in [65].

A subgroup of SOPs whose clock biases are driven by a common term can be considered as an SOP constellation. This could happen when the transmitters have the same transmission protocol and are from the same network provider. Suppose that the SOPs can be grouped into N_{const} subgroups. i.e., SOP constellations. Let $j \in \{1, \ldots, N_{\mathrm{const}}\}$ denote the index of the constellation to which the n-th SOP belongs. After initial bias calibration, the n-th SOP pseudorange measurement $z_n^{\mathrm{S}}(k)$ can be remodeled as

$$z_n^{\mathrm{S}}(k) = \|\boldsymbol{r}_r(k) - \boldsymbol{r}_n^{\mathrm{S}}(k)\|_2 + c\delta t_{\mathrm{r},j}^{\mathrm{S}}(k) + v_n^{\mathrm{S}}(k), \tag{4}$$

where $c\delta t_{\mathrm{r},j}^{\mathrm{S}}(k)$ is the receiver's clock bias with respect to the j-th SOP subgroup's common reference time and the lumped measurement noise for the re-parameterized pseudorange measurement $v_n^{\mathrm{S}}(k) \triangleq \epsilon_n(k) + \bar{v}_n^{\mathrm{S}}(k)$ is modeled as a white Gaussian sequence with variance $\sigma_{\epsilon_n}^2 + \sigma_n^{\mathrm{S}^2}$.

Equations (2) and (4) represent two different ways of modeling SOP pseudorange measurements. The grouping of SOPs in equation (4) enables the receiver to use a static estimator (e.g., WNLS) to estimate the position of the aerial vehicle. It is worth noting that the measurement error terms in the two models are modeled differently, hence, the noise variances should be characterized differently according to the two models. For cellular SOPs, a preliminary characterization of measurement errors was carried out in [17] by overbounding the error distribution of the experimentally recorded data over a period of 24 hours using DeCleene's single cdf-overbounding approach [66].

C. Navigation Solution

The receiver estimates its position vector using GNSS and SOP pseudorange measurements along with the GNSS and SOP receivers' biases vectors via a WNLS. The vector to be estimated is given by

$$\boldsymbol{x}(k) \triangleq \left[\boldsymbol{r}_r(k), c\boldsymbol{\delta t}^{\mathrm{G}^{\mathsf{T}}}(k), c\boldsymbol{\delta t}^{\mathrm{S}^{\mathsf{T}}}(k)\right]^{\mathsf{T}},$$

where

$$c\boldsymbol{\delta t}^{\mathrm{G}}(k) = \left[c\delta t_1^{\mathrm{G}}(k), \ldots, c\delta t_{M_{\mathrm{const}}}^{\mathrm{G}}(k)\right]^{\mathsf{T}},$$
$$c\boldsymbol{\delta t}^{\mathrm{S}}(k) = \left[c\delta t_1^{\mathrm{S}}(k), \ldots, c\delta t_{N_{\mathrm{const}}}^{\mathrm{S}}(k)\right]^{\mathsf{T}}$$

The time argument is omitted in the following for compactness of notation. The all-in-view combined GNSS-SOP measurement vector can be formed according to

$$\boldsymbol{z} \triangleq \left[z_1^{\mathrm{G}}, \ldots, z_{M_{\mathrm{s}}}^{\mathrm{G}}, z_1^{\mathrm{S}}, \ldots, z_{N_{\mathrm{s}}}^{\mathrm{S}}\right]^{\mathsf{T}}.$$

A WNLS is then iterated to obtain an estimate of $\boldsymbol{x}$, denoted by $\hat{\boldsymbol{x}}$, using $\boldsymbol{z}$. Let h denote the iteration number, $\hat{\boldsymbol{x}}_h$ the estimate at iteration h, and $\hat{\boldsymbol{z}}_h$ the measurement prediction calculated using $\hat{\boldsymbol{x}}_h$. The all-in-view navigation solution update is obtained from the normal equations according to

$$\Delta\boldsymbol{x}_h = \left(\mathbf{H}_h^{\mathsf{T}}\mathbf{W}\mathbf{H}_h\right)^{-1}\mathbf{H}_h^{\mathsf{T}}\mathbf{W}\left(\boldsymbol{z} - \hat{\boldsymbol{z}}_h\right), \tag{5}$$

where $\mathbf{H}_h$ is the measurement Jacobian evaluated at $\hat{\boldsymbol{x}}_h$ and $\mathbf{W}$ is the weighting matrix. The weighting matrix is given by $\mathbf{W} = \mathbf{C}_{\mathrm{acc}}^{-1}$, where $\mathbf{C}_{\mathrm{acc}}$ is a diagonal matrix whose diagonal elements $\{\mathbf{C}_{\mathrm{acc}}(l,l)\}_{l=1}^{N_{\mathrm{s}}+M_{\mathrm{s}}}$ are the measurement noise variances used for continuity and accuracy. Details about $\mathbf{C}_{acc}$ can be found in Appendix A. The WNLS estimate at the $(h+1)$-th iteration is updated according to

$$\hat{\boldsymbol{x}}_{h+1} = \hat{\boldsymbol{x}}_h + \Delta\boldsymbol{x}_h,$$

and the iteration number is subsequently increased, i.e., $h \leftarrow h+1$. After convergence, the all-in-view navigation solution is denoted $\hat{\boldsymbol{x}}^{(\infty)}$, the measurement prediction after convergence

Authorized licensed use limited to: The Ohio State University. Downloaded on October 13,2023 at 15:38:43 UTC from IEEE Xplore. Restrictions apply.

is denoted $\hat{\boldsymbol{z}}^{(\infty)}$, and the residual at convergence is denoted $\boldsymbol{y}$, which is defined as

$$\boldsymbol{y} \triangleq \boldsymbol{z} - \hat{\boldsymbol{z}}^{(\infty)}.$$

Let $\mathbf{H}$ denote the measurement Jacobian after convergence, which is an $(N_s + M_s) \times (3 + M_{\text{const}} + N_{\text{const}})$ matrix, that can be parameterized by the GNSS satellites and SOP transmitters' azimuth and elevation angles according to

$$\mathbf{H} \triangleq [\mathbf{G}, \mathbf{B}], \tag{6}$$

where $\mathbf{G}$ is the geometry matrix, and $\mathbf{B}$ is the time matrix. The l-th row of $\mathbf{G}$ matrix can be defined as

$$\mathbf{G}_l \triangleq [-c(el_l)s(az_l) \ -c(el_l)c(az_l) \ -s(el_l)],$$

where $c(\cdot)$ and $s(\cdot)$ denote the cos$(\cdot)$ and sin$(\cdot)$ functions, respectively; el_l and az_l are elevation angle and azimuth angle, respectively, of the l-th GNSS satellite or terrestrial SOP transmitter. The clock bias Jacobian can be expressed as

$$\mathbf{B} \triangleq \begin{bmatrix} \mathbf{B}^{\text{G}} & \mathbf{0}_{M_s \times N_{\text{const}}} \\ \mathbf{0}_{N_s \times M_{\text{const}}} & \mathbf{B}^{\text{S}} \end{bmatrix}, \tag{7}$$

where $\mathbf{B}^{\text{G}}$ is an $M_s \times M_{\text{const}}$ matrix denoting the GNSS clock bias Jacobian, whose m, i-th entry, denoted by $B_{m,i}$, is given by

$$B_{m,i} = \begin{cases} 1 & \text{if } m\text{-th satellite belongs to } i\text{-th constellation,} \\ 0 & \text{otherwise.} \end{cases}$$

$\mathbf{B}^{\text{S}}$ is measurement Jacobian associated with the SOP clock bias, which is defined similarly to $\mathbf{B}^{\text{G}}$.

D. Terrestrial SOP Geometry Model

To capture the randomness in the SOP transmitter locations, the terrestrial SOP network is modeled as a binomial point process (BPP) [67], [68], where the horizontal positions of N SOPs are independently and uniformly distributed over an annular region centered at the receiver, i.e., $\mathbb{B}_r(d^{\text{S}}_{\min}, d^{\text{S}}_{\max}) = \pi({d^{\text{S}}_{\max}}^2 - {d^{\text{S}}_{\min}}^2)$ [69], where $d^{\text{S}}_{\min}$ is the minimum horizontal distance required for the far-field assumption to hold and $d^{\text{S}}_{\max}$ is the maximum horizontal distance for which ranging signals can be detected by the receiver (Figure 1 (a) shows an example of an SOP realization for $N = 15$). The altitudes of the SOPs relative to the receiver are assumed to be uniformly distributed between $h^{\text{S}}_{\min}$ and $h^{\text{S}}_{\max}$. As shown in Figure 1(b), the location of the n-th SOP is represented by $(d^{\text{S}}_n, h^{\text{S}}_n, az^{\text{S}}_n)$, where d^{S}_n and h^{S}_n are the horizontal and vertical distances between the n-th SOP and the receiver, respectively, and az^{S}_n is the azimuth angle of the n-th SOP. As a result, the elevation angle of the n-th SOP el^{S}_n and the range to the n-th SOP r_{S_n} can be calculated as

$$el^{\text{S}}_n = \tan^{-1}\left(\frac{h^{\text{S}}_n}{d^{\text{S}}_n}\right),$$
$$r^{\text{S}}_n = \sqrt{{d^{\text{S}}_n}^2 + {h^{\text{S}}_n}^2}.$$

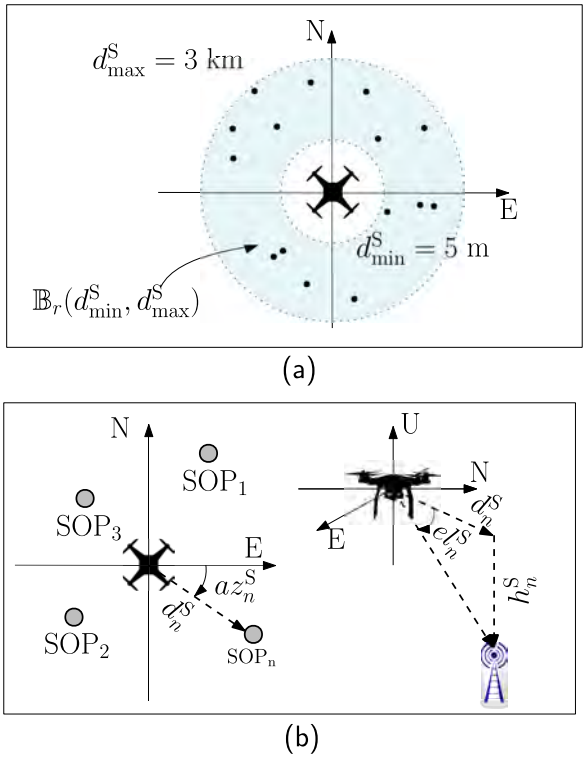

Fig. 1. (a) BPP realization with $N = 15$, in the angular region constrained by $d^{\text{S}}_{\min}$ and $d^{\text{S}}_{\max}$. The aerial vehicle is depicted in the center of the North-East frame. (b) Geometry of aerial vehicle-to-SOP. The aerial vehicle is the center of the North-East-Up frame.

IV. Critical Elements for OARAIM

This section presents the definitions, parameters, and algorithm framework for OARAIM, which are foundational for requirement and performance analysis. OARAIM is developed based on the baseline ARAIM [70], which is designed for GNSS navigation. Although ARAIM has the flexibility of incorporating multi-source measurements, it must be adapted when incorporating SOPs as discussed next.

A. Definitions for OARAIM

The definitions of key concepts, e.g., fault and nominal states, have been discussed and evolved based the of-the-time perspective of RAIM since the introduction of RAIM. However, integrity definitions for SOPs have not been explicitly made in the literature. In this subsection, the definitions for GNSS ARAIM are reviewed and the definitions for OARAIM are proposed thereafter. The definitions are discussed to provide foundations for the design and evaluation of the OARAIM algorithm. The discussion reveals that the conventions of defining transmitter performance allow for different definitions of integrity parameters. Therefore, the integrity parameters could take different values according to different ways of defining the transmitter performance. Most of the definitions are based on [71].

In terms of integrity, the characteristics of interest for navigation signals are mainly the nominal behavior and the probability that the signals might be in a faulty state. In OARAIM, there are four safety-critical parameters, inher-

Authorized licensed use limited to: The Ohio State University. Downloaded on October 13,2023 at 15:38:43 UTC from IEEE Xplore. Restrictions apply.

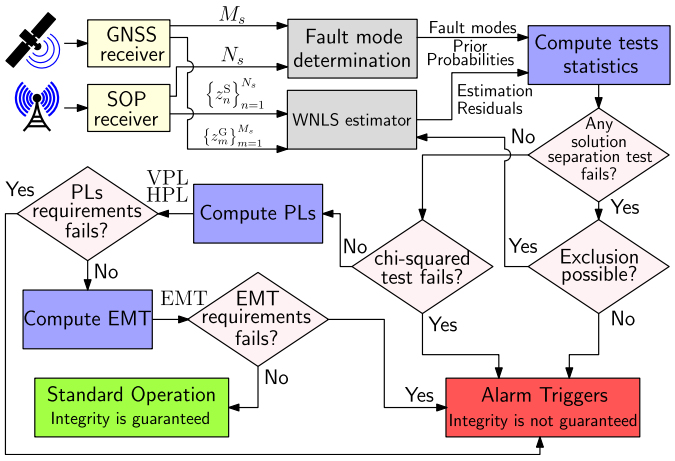

Fig. 2. OARAIM Flowchart. Note that M_S and N_S are the number of GNSS and SOP pseudoranges, respectively, and EMT denotes effective monitor threshold.

ited from the baseline ARAIM, that must be provided a priori to the user [24]:

- $\{\sigma_{\mathrm{URA},m}\}_{m=1}^{M_s}$: URA, the standard deviation of a Gaussian distribution that overbounds the nominal clock and ephemeris error at the worst-case location on Earth, to be used for the determination of integrity. The parameter σ_{URA} is a conservative representation of the unfaulted error distribution.
- $\{b_{\mathrm{nom},m}\}_{m=1}^{M_s}$: bound on the maximal bias affecting the nominal error of ranging source m to be used for the determination of integrity.
- $\{P_{\mathrm{s},m}\}_{m=1}^{M_s}$: the probability that a ranging source m is faulty at a given time.
- $\{P_{\mathrm{const},i}\}_{i=1}^{M_{\mathrm{const}}}$: the probability of a constellation-wide fault.

The safety-critical parameters for GPS have been thoroughly characterized over the last several decades. The ARAIM SG provides values for URA, $b_{\mathrm{nom},m}$, and probability of satellite and constellation fault for GNNS agreed by the groups. However, the values for the safety-critical parameters of SOPs have not been characterized due to limited adoption of these signals in safety-critical applications and the fact that one needs sufficient historical data to characterize these parameters, which has not materialized yet. Therefore, this paper will conduct a sensitivity analysis of performance on the safety-critical parameters for SOPs.

B. OARAIM Framework

This section presents the OARAIM framework introduced in [60] and [72] to incorporate GNSS pseudorange measurements and SOP pseudorange measurements. The solution separation tests and PL calculation are introduced to provide foundations for the analysis in later sections. OARAIM performs fault detection and exclusion (FDE) and PL calculation based on the multiple hypothesis solution separation (MHSS) algorithm [23]. Figure 2 shows the OARAIM algorithm flowchart.

OARAIM first determines the fault modes to monitor, based on the GNSS and SOP ranging sources visible to the receiver, so that the probability of fault modes other than the monitored ones is smaller than a predefined threshold P_{thresh}, i.e.,

$$1-\sum_{i=0}^{N_{\mathrm{f}}} P_{\mathrm{f}}^{(i)} \le P_{\mathrm{thresh}}, \tag{8}$$

where N_{f} is the number of fault modes to be monitored and $P_{\mathrm{f}}^{(i)}$ is the probability of fault mode i ($i \in \{1,\ldots,N_{\mathrm{f}}\}$). For each fault mode, a fault-tolerant solution $\hat{\boldsymbol{x}}^{(i)}$ is defined as the navigation solution obtained from measurements excluding the hypothesized faulty measurements in the corresponding fault mode. The difference between the fault-tolerant solutions $\hat{\boldsymbol{x}}^{(i)}$ and the all-in-view solution $\hat{\boldsymbol{x}}^{(0)}$ serves as the test statistics for each alternative hypothesis. The difference vector for the i-th fault mode is computed as [70]

$$\Delta\hat{\boldsymbol{x}}^{(i)} = \hat{\boldsymbol{x}}^{(i)} - \hat{\boldsymbol{x}}^{(0)} = (\mathbf{S}^{(i)} - \mathbf{S}^{(0)})\boldsymbol{y}$$
$$\mathbf{S}^{(i)} = (\mathbf{H}^{\mathsf{T}}\mathbf{W}^{(i)}\mathbf{H})^{-1}\mathbf{H}^{\mathsf{T}}\mathbf{W}^{(i)}$$

where $\mathbf{W}^{(i)}$ is a diagonal weighting matrix, defined as

$$\mathbf{W}^{(i)}(l,l) = \begin{cases} \mathbf{C}_{\mathrm{int}}^{-1}(l,l), & \text{if measurement } l \text{ is hypothesized faulty,} \\ 0, & \text{otherwise,} \end{cases}$$

where $\mathbf{C}_{\mathrm{int}}$ is the diagonal covariance matrix characterizing the nominal error model used for integrity. Details about nominal error models used in OARAIM can be found in Appendix A.

Let the index $q \in \{1,2,3\}$ denotes the east, north, and up components, respectively. The variances of the q-th coordinate of i-th fault-tolerant navigation solution $\hat{x}_q^{(i)}$ are calculated as

$$\sigma_q^{(i)2} = (\mathbf{H}^{\mathsf{T}}\mathbf{W}^{(i)}\mathbf{H})_{q,q}^{-1}. \tag{9}$$

To bound the impact of the nominal bias for each measurement, $b_{\mathrm{nom},j}$, on the position solutions, OARAIM calculates the worst-case bias for the every fault mode i. The worst-case bias can be given by

$$b_q^{(i)} = \sum_{l=1}^{M_{\mathrm{s}}+N} \left|\mathbf{S}_{q,l}^{(i)}\right| b_{\mathrm{nom},l}. \tag{10}$$

The variance of the difference $\Delta\hat{\boldsymbol{x}}^{(i)}$ between the all-in-view and the fault-tolerant position solutions is given by

$$\sigma_{\mathrm{ss},q}^{(i)2} = \boldsymbol{e}_q^{\mathsf{T}}\left(\mathbf{S}^{(i)} - \mathbf{S}^{(0)}\right)\mathbf{C}_{\mathrm{acc}}\left(\mathbf{S}^{(i)} - \mathbf{S}^{(0)}\right)^{\mathsf{T}}\boldsymbol{e}_q, \tag{11}$$

where $\boldsymbol{e}_q$ denotes the vector whose q-th entry is 1 and all other entries are 0, $\mathbf{C}_{\mathrm{acc}}$ is the diagonal covariance matrix characterizing the nominal error model used for accuracy and continuity, whose details can be found in Appendix A.

The test threshold for the q-th coordinate of fault mode i is denoted by

$$T_{i,q} = K_{\mathrm{fa},q}\sigma_{\mathrm{ss},q}^{(i)}, \tag{12}$$

where

$$K_{\mathrm{fa},1} = K_{\mathrm{fa},2} = Q^{-1}\left(\frac{P_{\mathrm{FA\_H}}}{4N_{\mathrm{f}}}\right),$$
$$K_{\mathrm{fa},3} = Q^{-1}\left(\frac{P_{\mathrm{FA\_V}}}{2N_{\mathrm{f}}}\right),$$

Authorized licensed use limited to: The Ohio State University. Downloaded on October 13,2023 at 15:38:43 UTC from IEEE Xplore. Restrictions apply.

where $Q^{-1}(\cdot)$ is the inverse Q-function, and $P_{\text{FA\_H}}$ and $P_{\text{FA\_V}}$ are continuity budget allocated for false alarm in the horizontal and vertical direction, respectively. For each i and q, the solution separation test coefficient is defined by

$$\tau_{i,q} = \frac{|\hat{x}_q^{(i)} - \hat{x}_q^{(0)}|}{T_{i,q}}. \tag{13}$$

The solution separation test is conducted by testing $\tau_{i,q} \leq 1$ over all fault modes, i.e., $i \in \{1, \ldots, N_{\text{f}}\}$ and all directions, i.e., $q \in \{1, 2, 3\}$.

If any of the tests fails, the algorithm will try to perform fault exclusion. After the fault detection and exclusion is performed, the PL for each direction can be calculated. For HPL, the algorithm first computes PLs for the two horizontal directions, i.e., $q \in \{1, 2\}$, by solving the following equation [23]

$$2Q\left(\frac{PL_q - b_q^{(0)}}{\sigma_q^{(0)}}\right) + \sum_{i=1}^{N_{\text{f}}} P_{\text{f}}^{(i)} Q\left(\frac{PL_q - T_{i,q} - b_q^{(i)}}{\sigma_q^{(i)}}\right) = \frac{1}{2} PHMI_{\text{H}} \left(1 - \frac{P_{\text{NM}}}{PHMI_{\text{V}} + PHMI_{\text{H}}}\right), \tag{14}$$

where $Q(\cdot)$ is the Q-function; P_{NM} is the probability of the faults that are not included in the fault modes; and $PHMI_{\text{V}}$ and $PHMI_{\text{H}}$ are the integrity budget for the vertical and horizontal components, respectively. The HPL is calculated from

$$HPL = \sqrt{PL_1^2 + PL_2^2}. \tag{15}$$

The VPL can be calculated similarly by solving

$$2Q\left(\frac{PL_3 - b_3^{(0)}}{\sigma_3^{(0)}}\right) + \sum_{i=1}^{N_{\text{f}}} P_{\text{f}}^{(i)} Q\left(\frac{PL_3 - T_{i,3} - b_3^{(i)}}{\sigma_3^{(i)}}\right) = PHMI_{\text{V}} \left(1 - \frac{P_{\text{NM}}}{PHMI_{\text{V}} + PHMI_{\text{H}}}\right), \tag{16}$$

and $VPL = PL_3$.

Equations (8)-(14) for OARAIM are inherited from multi-constellation GNSS ARAIM. However, it is worth noting that a significant difference between multi-constellation GNSS ARAIM and OARAIM is that the definition of constellation in multi-constellation GNSS ARAIM is clear, while the grouping of SOPs and augmentation of system state space, i.e., adding a SOP 'constellation', depends on the relative synchronization of SOP clocks, as mentioned in Section III-B.

V. Analysis of Protection Level Reduction Due to Fusing SOPs With GNSS

This section analyzes the effect of fusing SOP pseudoranges with GNSS pseudoranges on the PL. It is shown that adding only one pseudorange measurement from an additional SOP constellation (i) reduces the fault detection sensitivity and (ii) increases the computed PLs over GNSS only. Therefore, to possibly improve integrity, there need to be at least two SOPs in the same constellation. The ARAIM is valid as long as the total number of pseudorange measurements is larger than the number of estimation states, so that the algorithm has measurement redundancy to perform solution separation [70]. However, the numerical study in [60] shows that adding only one SOP increases PLs. This paper extends the previous study by seeking analytical explanations of the performance degradation after adding only one SOP. Extending the analytical expressions derived in this section to two or more SOPs is analytically intractable. As such, Section VI resorts to Monte Carlo numerical simulations to show that the PL can be reduced under certain integrity parameters.

The case where only one pseudorange measurement from one SOP constellation arises if (i) there is only one SOP in the environment or (ii) the SOP does not share relative clock stability with other SOPs in the environment, as discussed in Section III-B. Recall that upon adding a single SOP, the state vector $\boldsymbol{x}$ is augmented with the SOP's corresponding additional clock state $c\delta_n^{\text{S}}$. It has been proved in [19] that adding one pseudorange measurement from an additional constellation does not improve the position estimate. Specifically, adding one pseudorange measurement from an additional constellation will change neither the position error nor the position error uncertainty. However, whether adding one SOP improves the integrity performance has not been studied. The following theorems show the influence of adding one SOP on the integrity performance, in terms of fault detection sensitivity and computed PLs, respectively.

Theorem 1: Consider M_{s} pseudorange measurements from M_{const} constellations in the ARAIM algorithm, where $M_{\text{s}} \geq 3 + M_{\text{const}}$. Assume that there exists another constellation to be used for ranging. Suppose that the probability of single and constellation-wide faults for the ranging sources is such that the maximum number of simultaneous faults to be monitored is 1. Adding one pseudorange measurement from an additional constellation will make the algorithm less sensitive to the faults of the original M_{s} measurements. Furthermore, the algorithm cannot detect faults from the additional measurement.

Proof. See Appendix C.

From Theorem 1, it can be implied that the number of SOP measurements in a constellation to benefit detection of GNSS fault is no less than 2. Furthermore, the number of SOP measurements in a constellation for faults in those SOPs being possibly detectable by OARAIM is no less than 2. The influence of adding one measurement from an additional constellation on the computed PLs is shown by the following theorem.

Theorem 2: Consider M_{s} pseudorange measurements from M_{const} constellations , where $M_{\text{s}} \geq 3 + M_{\text{const}}$ for the ARAIM algorithm to perform fault detection and compute PLs under baseline specifications. Assume that there exists another constellation to be used for ranging. Suppose that the probability of single and constellation-wide faults is such that the maximum number of simultaneous faults to be monitored is 1. Adding one pseudorange measurement from the additional constellation increases the vertical and horizontal protection levels.

Proof. See Appendix D.

As a demonstration of Theorem 2, Figure 3 shows the average PL reduction by adding one SOP with different probability of SOP fault over 5000 realizations of Monte Carlo simulation, whose setup is present in detail in the following

Authorized licensed use limited to: The Ohio State University. Downloaded on October 13,2023 at 15:38:43 UTC from IEEE Xplore. Restrictions apply.

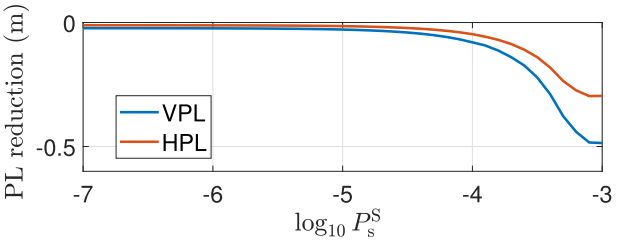

Fig. 3. Simulation result showing PL increases after adding one SOP with different P_s^S. Note that PL reduction denotes the PL after adding one SOP subtracted by the PL before adding the SOP.

section. From Figure 3, adding one SOP with different P_s^S always increases the PLs, which matches Theorem 2. It is worth noting that with larger P_s^S, the PL increase becomes larger, which is also declared by (32).

Note that Theorem 1 and Theorem 2 do not address the influence of adding $N_s \geq 2$ SOPs, while, however, is studied in Section VI via simulations.

VI. Fault-Free Integrity Performance Sensitivity Analysis

The impact of adding SOP measurements on the integrity performance is not completely obvious. On one hand, adding SOP measurements increases redundancy; hence, it presumably reduces the integrity risk. On the other hand, it is possible that adding more measurements increases the probability of hazardous misleading information (HMI), especially when the additional measurements have large probability of fault. Moreover, the safety-critical parameters are not fully characterized, which makes the impact of adding SOP measurements more difficult to track. As such, this section conducts simulation studies to characterize the integrity performance, specifically, HPL, upon incorporating SOPs with different assumptions of safety-critical characteristics, namely, σ_{URA}^S and P_s^S.

In order to quantify the integrity risk of the position solution and its error bound, a trusted model of the signals' safety-critical features is needed. However, these models for SOPs are not fully developed yet. From the integrity perspective, the navigation signal can be characterized by a nominal model and a model of potential threats. The nominal model describes the expected measurement error when no faults are present. The faults are by definition, instances where the nominal model is not valid. Based on the analyses in Section IV-A, the distinction between nominal and faulted conditions can be arbitrary. For example, one could choose to model common (but bounded) faults by inflating the nominal error model.

Besides that the fault condition can be "arbitrarily" defined, SOP signals have not been fully characterized by large-scale experimental campaigns (i.e., spanning very long duration and different environments). While an attempt to characterize the pseudorange error distribution has been made in [17], [62], this paper does not assume the availability of such characterization. Instead, the OARAIM performance is studied via Monte Carlo simulation for adding SOP, with varying safety-critical parameters, namely, σ_{URA}^S and P_s^S.

TABLE I
Simulation Setup

Parameter	Description	Value
I_{REQ}	Total integrity budget	10^{-7}
$PHMI_{\text{H}}$	Integrity budget allocated to vertical direction	9.9×10^{-8}
$PHMI_{\text{V}}$	Integrity budget allocated to horizontal direction	10^{-9}
$C_{\text{REQ,FA}}$	Continuity budget allocated to false alarm	10^{-7}
$P_{\text{FA\_H}}$	False alarm budget allocated to horizontal direction	9.9×10^{-8}
$P_{\text{FA\_V}}$	False alarm budget allocated to vertical direction	10^{-9}
P_{thresh}	Upper bound for the integrity risk from unmonitored faults	6×10^{-8}
$\{\sigma_{\text{URA},m}^{\text{GPS}}\}_{m=1}^{M_s}$	User range accuracy for GPS satellites	1 m
$\{b_{\text{nom},m}^{\text{GPS}}\}_{m=1}^{M_s}$	Nominal bias for GPS satellites	0.75 m
$\{P_{s,m}^{\text{GPS}}\}_{m=1}^{M_s}$	Narrow fault probability for GPS satellites	10^{-5}
$\{P_{s,n}^{S}\}_{n=1}^{N_s}$	Narrow fault probability for SOP transmitters	$[10^{-7}, 10^{-1}]$
$P_{\text{const}}^{\text{GPS}}$	GPS constellation fault probability	10^{-8}
P_{const}^{S}	SOP constellation fault probability	10^{-4}

In the simulation, terrestrial SOP pseudoranges are fused with GPS pseudoranges. This paper assumes a stationary receiver located in Orange County, California, USA. The receiver position is fixed at $\boldsymbol{r}_r = 10^6 \times [-2.482345, -4.700049, 3.513616]$, expressed in the Earth-Centered-Earth-Fixed (ECEF) frame. It is shown that the difference of integrity performance along the longitude direction is negligible [24]. The influence of the receiver's latitude is not the focus of this study. As such, this paper chooses to fix the receiver's position, while the geometric distribution of GPS satellites is varied by randomizing the time. As the nominal orbital period of a GPS satellite is 11 hours and 58 minutes, which is almost half of a sidereal day, one can randomly choose time in an approximately 24-hour interval to get GPS satellite positions, without having to randomize the date. Cellular SOP base stations are placed randomly based on the BPP model mentioned in the Section III-D.

Table I shows the OARAIM constants and inputs used in the simulation [70]. Note that this study employs LPV-200 requirements. P_s^S is varied from 10^{-7} to 10^{-1}, and σ_{URA}^S is varied from 0.5 to 25. For each combination of P_s^S and σ_S^S, there are 5000 Monte Carlo realizations. The 5000 Monte Carlo realizations uniformly span time of a day to obtain GPS

Authorized licensed use limited to: The Ohio State University. Downloaded on October 13,2023 at 15:38:43 UTC from IEEE Xplore. Restrictions apply.

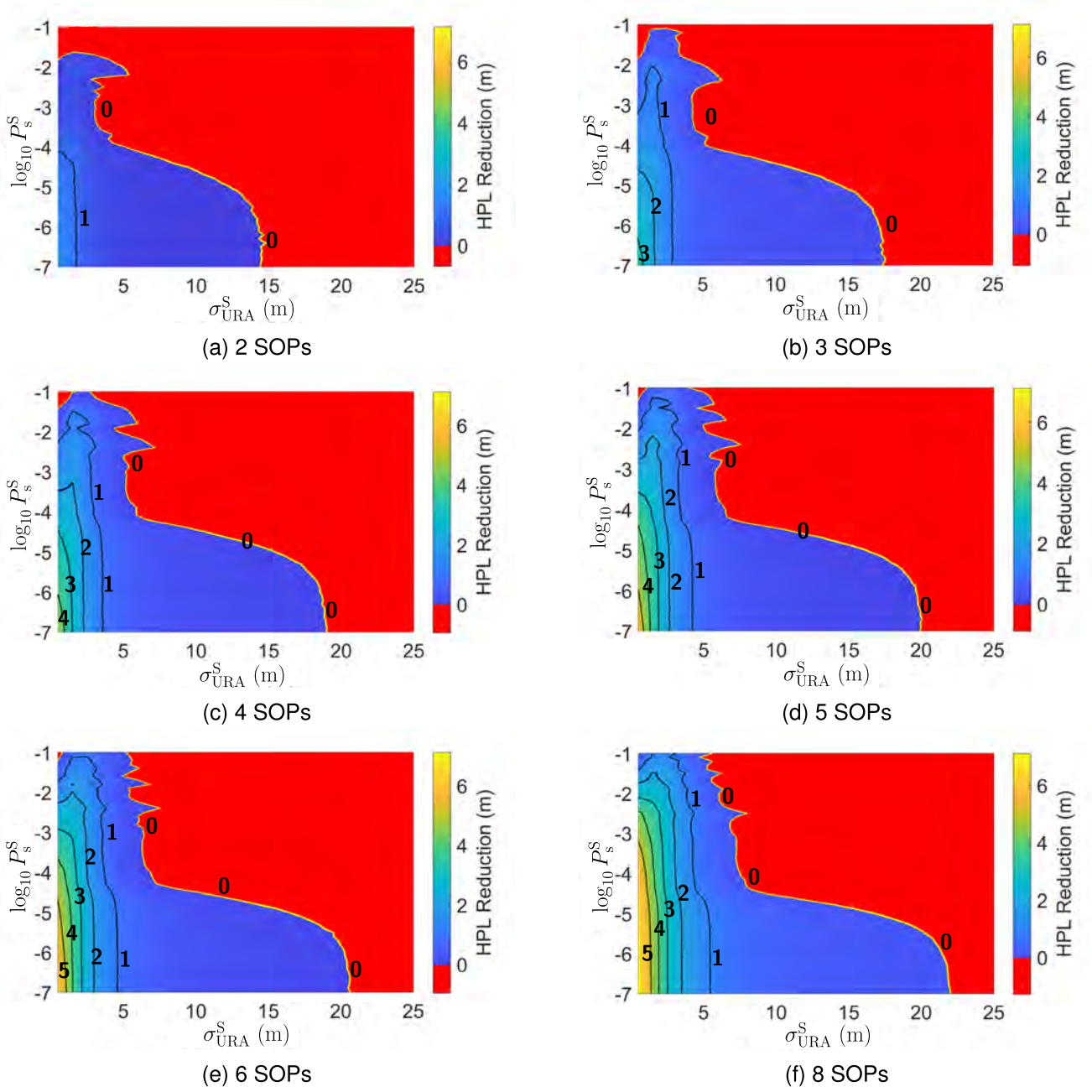

Fig. 4. Color map of HPL reduction for different $\sigma_{\mathrm{URA,SOP}}$ and P_{S}: (a) 2 SOPs; (b) 3 SOPs; (c) 4 SOPs; (d) 5 SOPs; (e) 6 SOPs; (f) 8 SOPs. The red region is where HPL reduction is below zero, indicating that HPL increases after adding SOPs, while other regions are where the HPL reduces after adding SOPs.

satellite position. Cellular transmitters are placed randomly based on the BPP model for each realization. The HPL reduction is calculated by averaging over the 5000 realizations. The sensitivity analysis results are shown in Figure 4. The following conclusions can be drawn from the simulation results: (i) adding no less than 2 "regular" SOPs (i.e., SOPs with reasonably small $\sigma_{\mathrm{URA}}^{\mathrm{S}}$ and $P_{\mathrm{s}}^{\mathrm{S}}$) will reduce the HPL; (ii) for two and more SOPs, with $P_{\mathrm{s}}^{\mathrm{S}}$ and $\sigma_{\mathrm{URA}}^{\mathrm{S}}$ increasing, the PL reduction decreases; (iii) with the number of SOPs increasing, the $\sigma_{\mathrm{URA}}^{\mathrm{S}}$ required for HPL reduction increases, which can be seen from that the boundary between positive and negative region of PL reduction moves to the right-hand side with more SOPs; and (iv) for the scenario of adding 2 SOPs with extremely large probability of fault, e.g., $P_{\mathrm{s}}^{\mathrm{S}} = 0.1$, the PL always increases, no matter how small $\sigma_{\mathrm{URA}}^{\mathrm{S}}$ is.

From Figure 4, it can be concluded that as number of SOPs increase, there will be less scenarios where adding SOPs degrades the performance. With enough SOPs, even signals with less favorable safety-critical characteristics (e.g., $\sigma_{\mathrm{URA}}^{\mathrm{S}}$ is 20 times larger than $\sigma_{\mathrm{URA}}^{\mathrm{GPS}}$ and $P_{\mathrm{s}}^{\mathrm{S}}$ is 100 times larger than $P_{\mathrm{s}}^{\mathrm{GPS}}$) would still reduce the HPL.

It is worth noting that the conclusions made in this section only apply to HPL. Terrestrial SOPs have relatively less geometric diversity in the vertical direction– they usually possess similar altitudes. The vertical integrity performance is sensitive to the SOPs' vertical geometric distribution and

Authorized licensed use limited to: The Ohio State University. Downloaded on October 13,2023 at 15:38:43 UTC from IEEE Xplore. Restrictions apply.

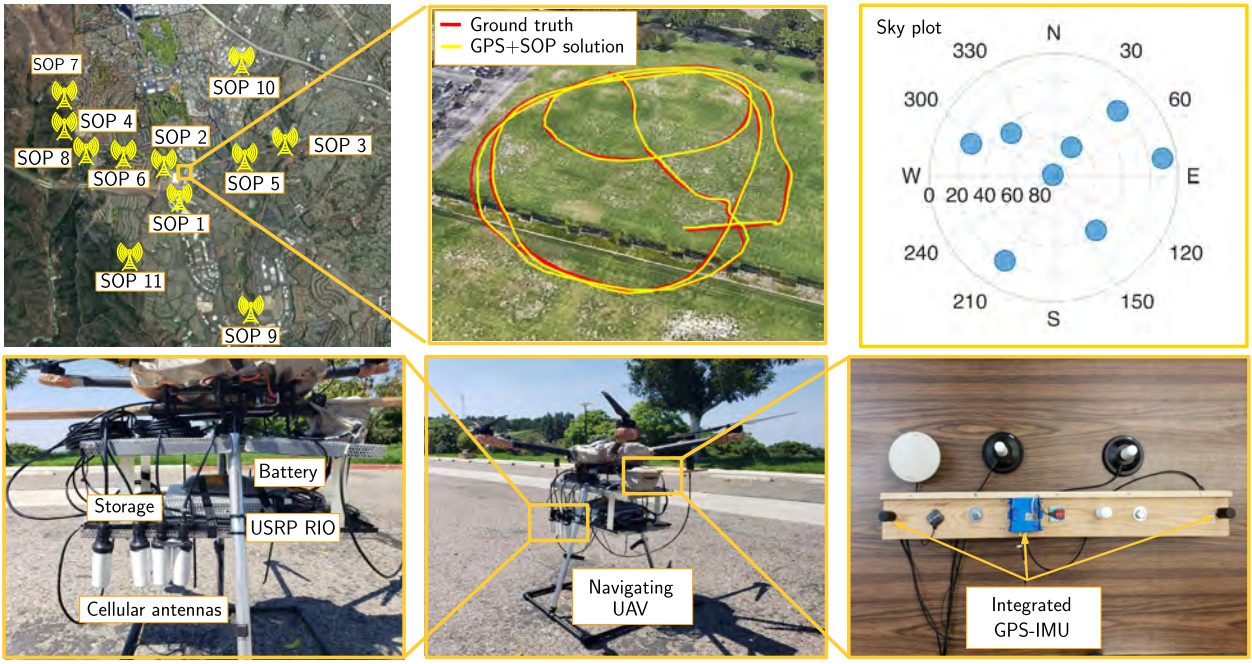

Fig. 5. Experimental hardware setup, navigation solution, and the traversed trajectory along with the position of cellular LTE SOP towers and the sky plot of GPS satellite positions.

their relative positions with respect to the receiver (e.g., a receiver may be located at the same altitude, higher, or lower than terrestrial SOPs, which is radically different than the relative geometry with respect to GNSS satellites). The influence of SOP geometry on the vertical integrity performance is not studied in this paper and is deferred to future work.

VII. Experimental Results

This section presents the experimental results on a UAV to demonstrate the proposed OARAIM framework and validate the sensitivity analysis of the integrity performance. First, Theorem 1 is demonstrated by showing detection sensitivity before and after adding one SOP pseudorange measurement over an experiment trajectory. Second, the experiment shows that the HPL bounds the horizontal position error (HPE) along the experiment trajectory, indicating OARAIM's ability to protect against integrity risk.

A. Experiment Setup

Figure 5 shows the environment and hardware setup for the experiment. A DJI Matrice 600 UAV was equipped with a dual-channel National Instrument (NI) universal software radio peripheral (USRP)-2955, driven by a GPS disciplined oscillator (GPSDO), to sample LTE SOPs. Four LTE carrier frequencies, 739, 1955, 2125, and 2145 MHz, were collected during the experiments. These frequencies are channels allocated for the U.S. cellular providers AT&T, T-Mobile, and Verizon. The sampling rate was set to 10 MSps and the sampled LTE signals were recorded on a laptop for post-processing. An LTE software-defined receiver (SDR) developed in [73] was used to process the sampled LTE signals to get the LTE pseudorange measurements.

The UAV was also equipped with a Septentrio AsteRx-i V, which has dual antenna multi-frequency GNSS receiver with RTK and a Vectornav VN-100 micro electromechanical systems (MEMS) inertial measurement unit (IMU). The integrated GNSS-IMU system provides both the raw GNSS measurements and ground-truth navigation solution. The raw GNSS measurements, after ionospheric and tropospheric corrections using Klobuchar Ionospheric Model and the Hopfield Tropospheric Model [74], and the LTE pseudorange measurements are fed into the WNLS estimator to calculate the GNSS-SOP coupled navigation solution. The integrity parameters are set the same as the simulation setup in Table I, except $\{P^{\mathrm{S}}_{\mathrm{s},n}\}_{n=1}^{N_s}$ is set to be 10^{-4}. As mentioned earlier, the probability of SOP fault has not been fully characterized nor agreed upon by standards bodies. The choice of $\{P^{\mathrm{S}}_{\mathrm{s},n}\}_{n=1}^{N_s}$ is only intended for the demonstration of the analytical and simulation results in this work.

The GPS and SOP pseudorange measurements were fed into the navigation framework discussed in Section III to produce the navigation solution and calculate the HPE. Over the course of the experiment, the UAV traversed a trajectory of 815 m in 220 s, while listening to 11 LTE towers. The locations of the towers in the environment were mapped prior to the experiment.

B. HPL Bounding

In this subsection, the ability of the OARAIM to bound the integrity risk, i.e., to bound the HPE with real-time HPLs, is validated. Over the course of the experiment, all GPS satellites above an elevation angle of 15° and all available SOPs were used to produce the navigation solution and compute HPLs. Figure 6 shows that HPE can always be bounded by real-time HPLs for the GPS+SOP framework.

Authorized licensed use limited to: The Ohio State University. Downloaded on October 13,2023 at 15:38:43 UTC from IEEE Xplore. Restrictions apply.

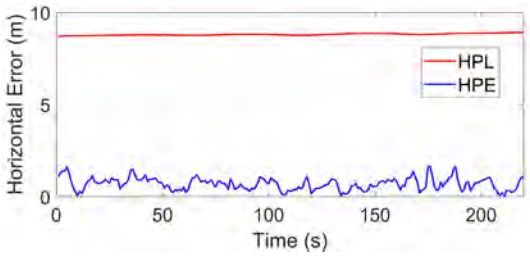

Fig. 6. HPE and corresponding HPL.

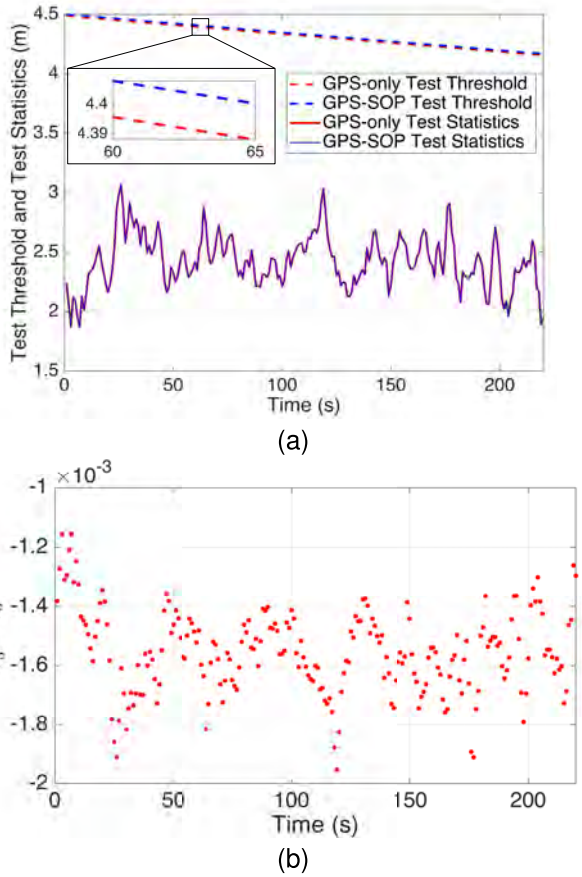

Fig. 7. Experiment results for fault detection corresponding to the GPS fault mode where GPS satellite with PRN number of 8 is faulty: (a) test threshold and statistics for GPS-only and GPS with one SOP, showing that adding one SOP does not change the test statistics while increases the test threshold; (b) the difference of test coefficients for the GPS fault mode between GPS-only and GPS with one SOP.

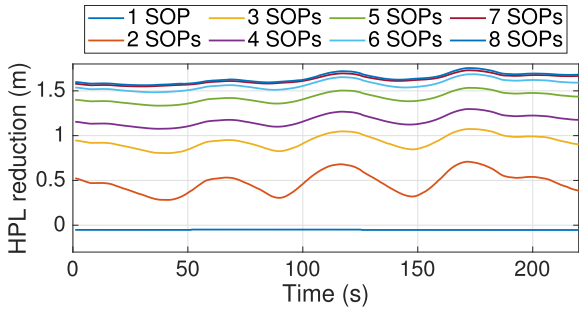

Fig. 8. HPL reduction for different numbers of SOPs over the experiment trajectory.

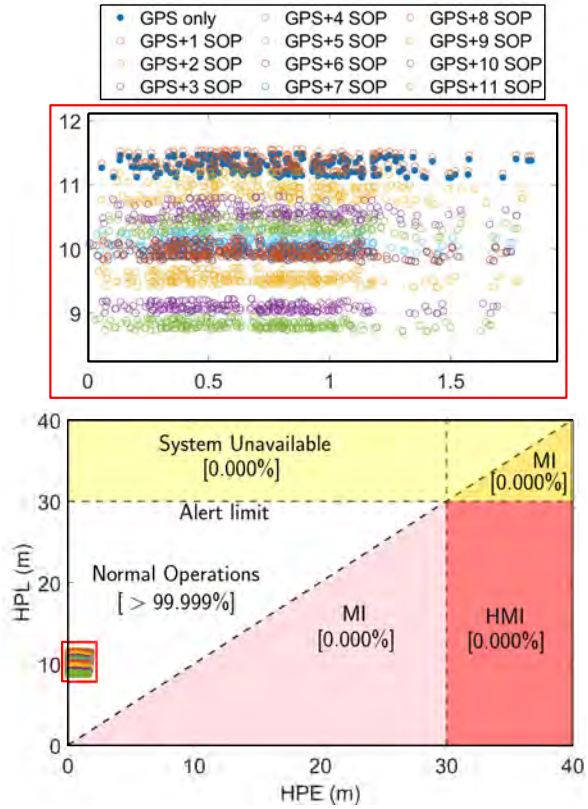

Fig. 9. The Stanford Diagram showing HPE and HPL for GPS only and GPS with different numbers of SOPs. On top is the zoom-in view of the data points. Note that MI denotes misleading information.

C. Detection Sensitivity

This subsection presents experimental results evaluating Theorem 1. This theorem was demonstrated by comparing the test statistics, thresholds, and coefficients for using GPS only pseudorange measurements and GPS pseudorange measurements with an additional SOP pseudorange measurement, i.e. SOP 1 shown in Figure 5. Figure 7(a) shows the test thresholds and statistics for the fault mode where the GPS satellite with PRN number of 8 is faulty. It is shown that adding one SOP from an additional constellation does not change the test statistics, whereas increases the test threshold. Figure 7(b) shows the test coefficient will be reduced by adding one additional SOP pseudorange measurement. This indicates that the detection sensitivity for GPS fault modes is reduced.

D. HPL Reduction for Adding SOPs

Next, the PL reduction after adding SOPs is demonstrated. Based on the common definition of narrow fault mentioned in Subsection IV-A, $P_s^S = 10^{-4}$ is chosen as a sample value in the experiment to compute HPLs for adding SOPs. As the experiment was conducted in a semi-urban area, σ_{URA}^S was chosen to be 3, which is the characterized value of semi-urban model from [17].

To calculate the HPL reduction, GPS-only HPL was first calculated and subtracted from the corresponding HPL for the GPS-SOP solution with different number of SOPs. The order of adding SOPs followed the numbering in Figure 5. Figure 8

Authorized licensed use limited to: The Ohio State University. Downloaded on October 13,2023 at 15:38:43 UTC from IEEE Xplore. Restrictions apply.

shows the HPL reduction over the experiment course. One can see that adding one SOP slightly increases the HPL, which affirms Theorem 2. For two or more SOPs, the results show HPL reduction over the experiment trajectory. Note that results for only up tp 8 SOPs are plotted in Figure 5 to avoid the plot being discernible.

The Stanford Diagram, which expresses the working regime of the algorithm by the visualization of each epoch's HPL and HPE with respect to the alert limit, is plotted in Figure 9 for GPS only and GPS with different number of SOPs. There are a total of 2880 epochs, among which 100% are in the normal operations, which shows that OARAIM indeed meets the integrity requirement. One can also notice from the zoom-in view in Figure 9 that adding one SOP does not change the HPE, but it increases the HPL. Adding two or more SOPs reduces both the HPL and HPE.

VIII. Conclusion

This paper analyzed the integrity performance of OARAIM after incorporating terrestrial SOP measurements with variable safety-critical parameters. These analyses were conducted to support RAIM algorithm design for SOPs whose safety-critical parameters are not fully characterized with adequate historical data. First, the GNSS and SOP pseudorange measurement models were presented. In particular, two SOP pseudorange measurement model were proposed, one of which enables grouping of SOPs to support static estimators. Moreover, the OARAIM framework was proposed to incorporate SOPs with multi-constellation GNSS. The critical elements for OARAIM was also explicitly discussed. The least number of SOP pseudorange measurements to possibly improve integrity performance was proved to be no less than 2. This theoretical derivation also showed that to get integrity improvement with NLS-based ARAIM, the SOP pseudorange measurements need to be grouped into an SOP constellation. Then, the HPL reduction after adding different number of terrestrial SOPs with variable safety-critical parameters was analyzed through simulation. Finally, an experimental study was conducted to validate the OARAIM framework, theoretical study, and performance characterization.

Appendix A
Nominal Error Models

$$\mathbf{C}_{\text{int}}(l,l) = \sigma^2_{\text{URA},l} + \sigma^2_{\text{iono},l} + \sigma^2_{\text{tropo},l} + \sigma_{\text{user},l},$$
$$\mathbf{C}_{\text{acc}}(l,l) = \sigma^2_{\text{URE},l} + \sigma^2_{\text{iono},l} + \sigma^2_{\text{tropo},l} + \sigma_{\text{user},l},$$

where $\sigma_{\text{URE},l}$ is the standard deviation of the clock and ephemeris error of GNSS satellite l used for accuracy and continuity; $\sigma_{\text{URE},l}$ is different from $\sigma_{\text{URA},l}$ in the sense that $\sigma_{\text{URE},l}$ is the average, other than overbounding standard deviation of the nominal errors; $\sigma_{\text{iono},l}$ and $\sigma_{\text{tropo},l}$ denote the standard deviation of the residual ionospheric and tropospheric errors, respectively; and $\sigma_{\text{user},l}$ denotes the standard deviation of the code noise and multipath errors. Terrestrial SOPs are not influenced by ionospheric and tropospheric delays. Therefore, the nominal error models for terrestrial SOPs do not contain $\sigma_{\text{iono},l}$ and $\sigma_{\text{tropo},l}$. For dual-frequency GNSS receivers, the ionospheric delay in the pseudorange measurements can be completely eliminated by dual-frequency. Therefore, the error models do not contain the residual ionospheric delay.

Appendix B
Calculation of Fault Mode Probability

The calculation of fault mode probability $P_{\text{f}}^{(i)}, i \in \{1,\ldots,N_{\text{f}}\}$ is performed using the probabilities of single-ranging-source fault and the probabilities of constellation-wide fault as described in [32]. Suppose there are a total of N_s GNSS satellites and/or SOP towers available in the environment, belonging to N_{const} constellations. The probability of single-ranging-source fault is denoted by $P_{s,m}, m \in \{1,\ldots,N_{\text{s}}\}$. The probability of constellation-wide fault is denoted by $P_{\text{const},n}, n \in \{1,\ldots,N_{\text{const}}\}$. To generalize the notations, the single-ranging-source faults and constellation-wide faults are unified into events, i.e.,

$$P_{\text{event},m} = P_{\text{s},m}, \quad m \in \{i,\ldots,N_{\text{s}}\}$$
$$P_{\text{event},N_{\text{s}}+n} = P_{\text{const},n} \quad n \in \{i,\ldots,N_{\text{const}}\}.$$

The probability of fault mode i is given by

$$P_{\text{f}}^{(i)} = \prod_{l}^{N_{\text{s}}+N_{\text{const}}} P_{\text{event},l}^{B_{l,i}} \left(1 - P_{\text{event},l}\right)^{B_{l,i}}, \tag{17}$$

where

$$B_{l,i} = \begin{cases} 1, & \text{if event } l \text{ is in fault mode } i \\ 0, & \text{otherwise.} \end{cases}$$

Appendix C
Proof of Theorem 1

Proof: Assume that M_{s} pseudorange measurements and WNLS be formulated as discussed in Section III. After adding one pseudorange measurement, the number of fault modes to be monitored will increase by 1, i.e.,

$$N'_{\text{f}} = N_{\text{f}} + 1.$$

Without loss of generality, assume that the N_{f} fault modes correspond to these where one of the original single measurements or constellations is faulty, i.e., for $i = 1,\ldots,N_{\text{f}}$, the measurement vector

$$z^{(i)\prime} = \left[z^{(i)\mathsf{T}}, z_{\text{S}}\right]^{\mathsf{T}},$$

where $z^{(i)\prime}$ and $z^{(i)}$ are the measurement vectors for the new and old systems, respectively, and z_{S} is the additional SOP pseudorange measurement.

One can notice that the measurement vector of the $(N_{\text{f}}+1)$-th fault mode from the new system is identical to the all-in-view measurement vector from the old system, i.e.,

$$z^{(N_{\text{f}}+1)\prime} = z^{(0)}.$$

Based on Theorem III.3 in [19], the addition of a measurement while augmenting the clock state vector by one state

Authorized licensed use limited to: The Ohio State University. Downloaded on October 13,2023 at 15:38:43 UTC from IEEE Xplore. Restrictions apply.

will not improve the position estimate nor the position error uncertainty, i.e., for $i = 0, \ldots, N_{\mathrm{f}}$,

$$\hat{\boldsymbol{x}}^{(i)\prime} = \hat{\boldsymbol{x}}^{(i)}, \tag{18}$$

$$\sigma_q^{(i)\prime} = \sigma_q^{(i)}. \tag{19}$$

It can be readily shown that for $i = 0, \ldots, N_{\mathrm{f}}$

$$\hat{x}_q^{(i)\prime} - \hat{x}_q^{(0)\prime} = \hat{x}_q^{(i)} - \hat{x}_q^{(0)}, \tag{20}$$

$$\sigma_{\mathrm{ss},q}^{(i)\prime} = \sigma_{\mathrm{ss},q}^{(i)}. \tag{21}$$

The test threshold coefficients from (12) for the new system become

$$\begin{aligned} K'_{\mathrm{fa},1} = K'_{\mathrm{fa},2} &= Q^{-1}\left[\frac{P_{\mathrm{FA\_H}}}{2\,(N_{\mathrm{f}}+1)}\right] \\ &> K_{\mathrm{fa},1} = K_{\mathrm{fa},2}, \\ K'_{\mathrm{fa},3} &= Q^{-1}\left[\frac{P_{\mathrm{FA\_V}}}{2\,(N_{\mathrm{f}}+1)}\right] > K_{\mathrm{fa},3}. \end{aligned}$$

The above inequality uses the fact that the inverse Q function is monotonically decreasing. Therefore,

$$T'_{i,q} > T_{i,q}, \quad \text{for } i = 1, \ldots, N_{\mathrm{f}}. \tag{22}$$

Combining the above with (20) yields

$$\frac{\left|\hat{x}_q^{(i)\prime} - \hat{x}_q^{(0)\prime}\right|}{T'_{i,q}} < \frac{\left|\hat{x}_q^{(i)} - \hat{x}_q^{(0)}\right|}{T_{i,q}}, \quad \text{for } i = 1, \ldots, N_{\mathrm{f}}.$$

This means that the new system is less sensitive to faults from the original constellations. Recall from (13) that $\tau_{i,q} = \frac{|\hat{x}_q^{(i)} - \hat{x}_q^{(0)}|}{T_{i,q}}$ is compared to 1 as the fault detection test.

For the fault mode corresponding to the new measurement,

$$\hat{\boldsymbol{x}}^{(N_{\mathrm{f}}+1)\prime} = \hat{\boldsymbol{x}}^{(0)\prime}$$

Therefore, for $q = 1, 2, 3$,

$$|\hat{x}_q^{(N_{\mathrm{f}}+1)\prime} - \hat{x}_q^{(0)\prime}| = 0 < T'_{N_{\mathrm{f}}+1,q}$$

will always hold. This means the new system cannot detect faults from the additional constellation.

□

Appendix D
Proof of Theorem 2

Proof: The proof of this theorem will first consider PL_3 (VPL). From Theorem III.3 in [19], it can be readily shown that

$$\mathbf{S}^{(i)\prime} = \begin{cases} \left[\mathbf{S}^{(i)}, \mathbf{0}\right] & i = 0, \ldots, N_{\mathrm{f}} \\ \mathbf{S}^{(0)} & i = N_{\mathrm{f}}+1. \end{cases}$$

Assume unimodal overbounding of the nominal error for the additional pseudorange, i.e., $b_{\mathrm{nom},j} = 0$ for $j = M_{\mathrm{s}}+1$. It can readily shown that the worst-case bias of the new system for the fault modes corresponding to the original measurements ($i = 1, \ldots, N_{\mathrm{f}}$)

$$b_q^{(i)\prime} = \sum_{j=1}^{M_{\mathrm{s}}+1} \left|\mathbf{S}_{q,j}^{(i)\prime}\right| b_{\mathrm{nom},j} = \sum_{j=1}^{M_{\mathrm{s}}} \left|\mathbf{S}_{q,j}^{(i)}\right| b_{\mathrm{nom},j} = b_q^{(i)}. \tag{23}$$

For the fault mode corresponding to the new measurement

$$b_q^{(N_{\mathrm{f}}+1)\prime} = \sum_{j=1}^{M_{\mathrm{s}}+1} \left|\mathbf{S}_{q,j}^{(N_{\mathrm{f}}+1)\prime}\right| b_{\mathrm{nom},j} = \sum_{j=1}^{M_{\mathrm{s}}} \left|\mathbf{S}_{q,j}^{(i)}\right| b_{\mathrm{nom},j} = b_q^{(0)}. \tag{24}$$

First, assume the probability of single fault for the additional measurement $P_{\mathrm{s,new}} = 0$. For $i = 1, \ldots, N_{\mathrm{f}}$,

$$P_{\mathrm{f}}^{(i)\prime} = P_{\mathrm{f}}^{(i)}. \tag{25}$$

For $i = N_{\mathrm{f}} + 1$, one also has

$$P_{\mathrm{f}}^{(N_{\mathrm{f}}+1)\prime} = 0. \tag{26}$$

The probability of fault modes not monitored

$$P'_{\mathrm{NM}} = P_{\mathrm{NM}}. \tag{27}$$

Substituting (19) and (23)-(27) into (16), the equation to compute VPL for the new system with P_{new} becomes

$$\begin{aligned} &2Q\left(\frac{PL'_{3,0} - b_3^{(0)}}{\sigma_3^{(0)}}\right) + \sum_{i=1}^{N_{\mathrm{f}}} P_{\mathrm{f}}^{(i)} Q\left(\frac{PL'_{3,0} - T'_{i,3} - b_3^{(i)}}{\sigma_3^{(i)}}\right) \\ &\quad = PHMI_V\left(1 - \frac{P_{\mathrm{NM}}}{PHMI_V + PHMI_H}\right). \end{aligned} \tag{28}$$

Considering inequality (22) and the monotonicity of the Q function yields that the computed VPL for $P_{\mathrm{s,new}} = 0$,

$$PL'_{3,0} > PL_3. \tag{29}$$

This means that adding one measurement with the probability of fault $P_{\mathrm{s,new}} = 0$ from an additional constellation will increase the computed VPL.

Second, the case when $P_{\mathrm{s,new}} > 0$ is considered. Without loss of generality, assume the same probability of narrow fault $P_{\mathrm{s,old}}$ for all the previous ranging sources and the probability of wide fault to be 0 for all the previous ranging constellations. The probability of fault modes not monitored for the new system can be given by

$$\begin{aligned} P'_{\mathrm{NM}} &= 1 - \sum_{i=0}^{N_{\mathrm{f}}+1} P_{\mathrm{f}}^{(i)\prime} \\ &= 1 - (1 - P_{\mathrm{s,old}})^{M_{\mathrm{s}}} - M_{\mathrm{s}}(1 - P_{\mathrm{s,old}})^{M_{\mathrm{s}}-1} P_{\mathrm{s,old}} \\ &\quad + P_{\mathrm{new}} M_{\mathrm{s}}(1 - P_{\mathrm{s,old}})^{M_{\mathrm{s}}-1} P_{\mathrm{s,old}} \end{aligned}$$

Let $x = PL'_3$, $y = P_{\mathrm{s,new}}$, and

$$\begin{aligned} f(x, y) &= 2Q\left(\frac{PL'_3 - b_3^{(0)\prime}}{\sigma_3^{(0)\prime}}\right) \\ &\quad + \sum_{i=1}^{N_{\mathrm{f}}+1} P_{\mathrm{f}}^{(i)\prime} Q\left(\frac{PL'_3 - T'_{i,3} - b_3^{(i)\prime}}{\sigma_3^{(i)\prime}}\right) \\ &\quad - PHMI_{\mathrm{V}}\left(1 - \frac{P'_{\mathrm{NM}}}{PHMI_{\mathrm{V}} + PHMI_{\mathrm{H}}}\right) \end{aligned}$$

$$f(x, y) = 2Q\left(\frac{x - b_3^{(0)}}{\sigma_3^{(0)}}\right) + y\left(1 - P_{\mathrm{s,old}}\right)^M Q\left(\frac{x - b_3^{(0)}}{\sigma_3^{(0)}}\right)$$

Authorized licensed use limited to: The Ohio State University. Downloaded on October 13,2023 at 15:38:43 UTC from IEEE Xplore. Restrictions apply.

$$+ (1-y)\sum_{i=1}^{N_{\mathrm{f}}} P_{\mathrm{f}}^{(i)} Q\left(\frac{x - T'_{i,3} - b_3^{(i)}}{\sigma_3^{(i)}}\right) + y \cdot a \cdot M_{\mathrm{s}}(1-P_{\mathrm{s,old}})^{M_{\mathrm{s}}-1} P_{\mathrm{s,old}} - PHMI'_{\mathrm{V}}, \tag{30}$$

where

$$a = \frac{PHMI_{\mathrm{V}}}{PHMI_{\mathrm{V}} + PHMI_{\mathrm{H}}},$$
$$PHMI'_{\mathrm{V}} = PHMI_V\left[1 - \frac{d}{PHMI_{\mathrm{V}} + PHMI_{\mathrm{H}}}\right],$$
$$d = 1 - \left(1 - P_{\mathrm{s,old}}\right)^M - M\left(1 - P_{\mathrm{s,old}}\right)^{M-1} P_{\mathrm{s,old}}.$$

Considering that the Q function is monotonically decreasing, it can be readily shown that $f_x < 0$, where f_x denotes the derivative of $f(x, y)$ with respect to x. Taking derivative of $f(x, y)$ with respect to y yields

$$f_y = a \cdot M_{\mathrm{s}}(1-P_{\mathrm{s,old}})^{M_{\mathrm{s}}-1} P_{\mathrm{s,old}} + (1-P_{\mathrm{s,old}})^{M_{\mathrm{s}}} Q\left(\frac{x - b_3^{(0)}}{\sigma_3^{(0)}}\right) - (1-P_{\mathrm{s,old}})^{M_{\mathrm{s}}-1} P_{\mathrm{s,old}} \sum_{i=1}^{M_{\mathrm{s}}} Q\left(\frac{x - T'_{i,3} - b_3^{(i)}}{\sigma_3^{(i)}}\right) \tag{31}$$

Under baseline specifications, the first term dominates the above equation. Therefore

$$f_y > 0.$$

Letting $f(x, y) = 0$ and taking the total derivative yields

$$\frac{dx}{dy} = -\frac{f_y}{f_x} > 0$$

This indicates that PL'_3 increases with P_{new} increasing. Therefore,

$$PL'_3 > PL'_{3,0} > PL_3 \tag{32}$$

Using similar steps, the same conclusion can be achieved for the two horizontal directions. □

REFERENCES

[1] R. Sabatini et al., "Avionics systems panel research and innovation perspectives," *IEEE Aerosp. Electron. Syst. Mag.*, vol. 35, no. 12, pp. 58–72, Dec. 2020.

[2] A. Schütz, D. E. Sánchez-Morales, and T. Pany, "Precise positioning through a loosely-coupled sensor fusion of GNSS-RTK, INS and LiDAR for autonomous driving," in *Proc. IEEE/ION Position, Location Navigat. Symp. (PLANS)*, Apr. 2020, pp. 219–225.

[3] D. Imparato, A. El-Mowafy, and C. Rizos, "Integrity monitoring: From airborne to land applications," in *Multifunctional Operation and Application of GPS*. London, U.K.: IntechOpen, 2018, pp. 23–43.

[4] X. Wang, C. Toth, and D. Grejner-Brzezinska, "A survey on integrity monitoring of GNSS navigation for ground vehicles," in *Proc. 34th Int. Tech. Meeting Satell. Division Inst. Navigat. (ION GNSS)*, Oct. 2021, pp. 2591–2601.

[5] F. A. C. de Oliveira, F. S. Torres, and A. García-Ortiz, "Recent advances in sensor integrity monitoring methods—A review," *IEEE Sensors J.*, vol. 22, no. 11, pp. 10256–10279, Jun. 2022.

[6] J. Raquet et al., "Part D: Position, navigation, and timing using radio signals-of-opportunity," in *Position, Navigation, and Timing Technologies in the 21st Century*, vol. 2, J. Morton, F. van Diggelen, J. Spilker Jr., and B. Parkinson, Eds. Hoboken, NJ, USA: Wiley, 2021, chs. 35–43, pp. 1115–1412.

[7] N. Souli, R. Makrigiorgis, P. Kolios, and G. Ellinas, "Real-time relative positioning system implementation employing signals of opportunity, inertial, and optical flow modalities," in *Proc. Int. Conf. Unmanned Aircr. Syst. (ICUAS)*, Jun. 2021, pp. 229–236.

[8] K. Strandjord, Y. J. Morton, and P. Wang, "Evaluating the urban signal environment for GNSS and LTE signals," in *Proc. 34th Int. Tech. Meeting Satell. Division Inst. Navigat. (ION GNSS)*, Oct. 2021, pp. 2166–2182.

[9] M. Maaref and Z. Kassas, "Ground vehicle navigation in GNSS-challenged environments using signals of opportunity and a closed-loop map-matching approach," *IEEE Trans. Intell. Transp. Syst.*, vol. 21, no. 7, pp. 2723–2738, Jul. 2020.

[10] C. Yang, M. Arizabaleta-Diez, P. Weitkemper, and T. Pany, "An experimental analysis of cyclic and reference signals of 4G LTE for TOA estimation and positioning in mobile fading environments," *IEEE Aerosp. Electron. Syst. Mag.*, vol. 37, no. 9, pp. 16–41, Sep. 2022.

[11] N. Souli, P. Kolios, and G. Ellinas, "Online relative positioning of autonomous vehicles using signals of opportunity," *IEEE Trans. Intell. Vehicles*, vol. 7, no. 4, pp. 873–885, Dec. 2022.

[12] Z. Jiao et al., "Carrier phase ranging with DTMB signals for urban pedestrian localization and GNSS aiding," *Remote Sens.*, vol. 15, no. 2, pp. 423–446, 2023.

[13] X. Chen, Q. Wei, F. Wang, Z. Jun, S. Wu, and A. Men, "Super-resolution time of arrival estimation for a symbiotic FM radio data system," *IEEE Trans. Broadcast.*, vol. 66, no. 4, pp. 847–856, Dec. 2020.

[14] M. L. Psiaki and B. D. Slosman, "Tracking digital FM OFDM signals for the determination of navigation observables," *Navigat., J. Inst. Navigat.*, vol. 69, no. 2, 2022, Art. no. navi.521.

[15] R. X. T. Kor, P. A. Iannucci, and T. E. Humphreys, "Autonomous signal-situational-awareness in a terrestrial radionavigation system," in *Proc. IEEE Int. Intell. Transp. Syst. Conf. (ITSC)*, Sep. 2021, pp. 3965–3971.

[16] Y. Hao, M. Chen, L. Hu, J. Song, M. Volk, and I. Humar, "Wireless fractal ultra-dense cellular networks," *Sensors*, vol. 17, no. 4, pp. 847–853, 2017.

[17] M. Maaref, J. Khalife, and Z. Kassas, "Aerial vehicle protection level reduction by fusing GNSS and terrestrial signals of opportunity," *IEEE Trans. Intell. Transp. Syst.*, vol. 22, no. 9, pp. 5976–5993, Sep. 2021.

[18] *Evolved Universal Terrestrial Radio Access (E-UTRA); Requirements for Support of Radio Resource Management*, document TS 36.133, 3GPP, Apr. 2010. [Online]. Available: https://www.3gpp.org/dynareport/36133.htm

[19] J. Khalife and Z. Kassas, "On the achievability of submeter-accurate UAV navigation with cellular signals exploiting loose network synchronization," *IEEE Trans. Aerosp. Electron. Syst.*, vol. 58, no. 5, pp. 4261–4278, Oct. 2022.

[20] N. Zhu, J. Marais, D. Bétaille, and M. Berbineau, "GNSS position integrity in urban environments: A review of literature," *IEEE Trans. Intell. Transp. Syst.*, vol. 19, no. 9, pp. 2762–2778, Sep. 2018.

[21] B. Belabbas, P. Remi, and M. Meurer, "Performance assessment of GBAS CAT III using GPS and Galileo," in *Proc. ION GNSS Conf.*, Sep. 2008, pp. 2945–2952.

[22] R. Sabatini, T. Moore, and C. Hill, "Avionics-based GNSS integrity augmentation synergies with SBAS and GBAS for safety-critical aviation applications," in *Proc. IEEE/AIAA 35th Digit. Avionics Syst. Conf. (DASC)*, Sep. 2016, pp. 1–10.

[23] J. Blanch, T. Walter, Y. Lee, B. Pervan, M. Rippl, and A. Spletter, "Advanced RAIM user algorithm description: Integrity support message processing, fault detection, exclusion, and protection level calculation," in *Proc. ION GNSS Conf.*, Sep. 2012, pp. 2828–2849.

[24] J. Blanch et al., "Critical elements for a multi-constellation advanced RAIM," *Navigat., J. Inst. Navigat.*, vol. 60, no. 1, pp. 53–69, 2013.

[25] A. Ene, J. Blanch, and T. Walter, "Galileo-GPS RAIM for vertical guidance," in *Proc. Nat. Tech. Meeting Inst. Navigat.*, Jan. 2006, pp. 18–20.

[26] T. Walter, J. Blanch, M. J. Choi, T. Reid, and P. Enge, "Incorporating GLONASS into aviation RAIM receivers," in *Proc. Int. Tech. Meeting Inst. Navigat.*, Jan. 2013, pp. 239–249.

[27] Y. Liu, J. Zhang, R. Xue, and Z. Wang, "Performance analysis of advanced RAIM with the inclusion of BeiDou," in *Proc. ION Int. Tech. Meeting*, 2014, pp. 3629–3636.

[28] P. F. Roysdon and J. A. Farrell, "GPS-INS outlier detection & elimination using a sliding window filter," in *Proc. Amer. Control Conf. (ACC)*, May 2017, pp. 1244–1249.

Authorized licensed use limited to: The Ohio State University. Downloaded on October 13,2023 at 15:38:43 UTC from IEEE Xplore. Restrictions apply.

[29] T. Li et al., "P3-LOAM: PPP/LiDAR loosely coupled SLAM with accurate covariance estimation and robust RAIM in urban canyon environment," *IEEE Sensors J.*, vol. 21, no. 5, pp. 6660–6671, Mar. 2021.

[30] L. Fu, J. Zhang, R. Li, X. Cao, and J. Wang, "Vision-aided RAIM: A new method for GPS integrity monitoring in approach and landing phase," *Sensors*, vol. 15, no. 9, pp. 22854–22873, Sep. 2015.

[31] FAA GEAS Panel. *Phase II of the GNSS Evolutionary Architecture Study*. Accessed: Feb. 2010. [Online]. Available: http://www.faa.gov/about/officeorg/headquartersoffices/ato?/serviceunits/techops/navservices/gnss/library/documents/media/GEASPhaseIIFinal.pdf

[32] *Advanced RAIM Technical Subgroup Reference Airborne Algorithm Description Document*, document, 3GPP, Working Group-C (WG-C), Jun. 2019. [Online]. Available: http://web.stanford.edu/group/scpnt/gpslab/websitefiles/maast/ARAIM TSG Reference ADD v3.1.pdf

[33] J. Blanch, T. Walter, and P. Enge, "RAIM with optimal integrity and continuity allocations under multiple failures," *IEEE Trans. Aerosp. Electron. Syst.*, vol. 46, no. 3, pp. 1235–1247, Jul. 2010.

[34] M. Joerger, S. Stevanovic, S. Langel, and B. Pervan, "Integrity risk minimisation in RAIM Part 1: Optimal detector design," *Navig. J. Inst. Navig.*, vol. 69, no. 3, pp. 449–467, May 2016.

[35] M. Joerger, S. Stevanovic, S. Langel, and B. Pervan, "Integrity risk minimisation in RAIM Part 2: Optimal detector design," *Navig. J. Inst. Navig.*, vol. 69, no. 4, pp. 709–728, 2016.

[36] M. Joerger, Y. Zhai, I. Martini, J. Blanch, and B. Pervan, "ARAIM continuity and availability assertions, assumptions, and evaluation methods," in *Proc. Int. Tech. Meeting Inst. Navigat.*, Feb. 2020, pp. 404–420.

[37] Y. Zhai, X. Zhan, J. Chang, and B. Pervan, "ARAIM with more than two constellations," in *Proc. ION Pacific PNT Meeting*, May 2019, pp. 925–941.

[38] X. Zheng, Y. Liu, G. Guan, J. Zhao, and C. Xu, "Analyses of the sensitivity of multi-constellation advanced receiver autonomous integrity monitoring vertical protection level availability to error parameters and a failure model over China," *Adv. Mech. Eng.*, vol. 10, no. 6, pp. 1–11, 2018.

[39] Z. Madadi, F. Quitin, and W. P. Tay, "Receiver tracking using signals of opportunity from asynchronous RF beacons in GNSS-denied environments," in *Proc. IEEE 84th Veh. Technol. Conf. (VTC-Fall)*, Sep. 2016, pp. 1–5.

[40] N. Ikhtiari, "Navigation in GNSS denied environments using software defined radios and LTE signals of opportunities," M.S. thesis, Air Force Inst. Technol., Wright-Patterson Air Force Base, OH, USA, 2019.

[41] N. Souli, P. Kolios, and G. Ellinas, "Relative positioning of autonomous systems using signals of opportunity," in *Proc. IEEE 91st Veh. Technol. Conf. (VTC-Spring)*, May 2020, pp. 1–6.

[42] N. Jardak and Q. Jault, "The potential of LEO satellite-based opportunistic navigation for high dynamic applications," *Sensors*, vol. 22, no. 7, pp. 2541–2565, 2022.

[43] Z. Kassas, M. Maaref, J. Morales, J. Khalife, and K. Shamei, "Robust vehicular localization and map matching in urban environments through IMU, GNSS, and cellular signals," *IEEE Intell. Transp. Syst. Mag.*, vol. 12, no. 3, pp. 36–52, Fall. 2020.

[44] Z. Kassas, J. Khalife, A. Abdallah, and C. Lee, "I am not afraid of the GPS jammer: Resilient navigation via signals of opportunity in GPS-denied environments," *IEEE Aerosp. Electron. Syst. Mag.*, vol. 37, no. 7, pp. 4–19, Jul. 2022.

[45] M. Maaref, J. Khalife, and Z. Kassas, "Lane-level localization and mapping in GNSS-challenged environments by fusing LiDAR data and cellular pseudoranges," *IEEE Trans. Intell. Vehicles*, vol. 4, no. 1, pp. 73–89, Mar. 2019.

[46] J. Morales and Z. Kassas, "Tightly coupled inertial navigation system with signals of opportunity aiding," *IEEE Trans. Aerosp. Electron. Syst.*, vol. 57, no. 3, pp. 1930–1948, Jun. 2021.

[47] H. Dun, C. C. J. M. Tiberius, and G. J. M. Janssen, "Positioning in a multipath channel using OFDM signals with carrier phase tracking," *IEEE Access*, vol. 8, pp. 13011–13028, 2020.

[48] P. Wang and Y. J. Morton, "Performance comparison of time-of-arrival estimation techniques for LTE signals in realistic multipath propagation channels," *Navigat., J. Inst. Navigat.*, vol. 67, no. 4, pp. 691–712, Dec. 2020.

[49] P. Wang and Y. J. Morton, "Multipath estimating delay lock loop for LTE signal TOA estimation in indoor and urban environments," *IEEE Trans. Wireless Commun.*, vol. 19, no. 8, pp. 5518–5530, Aug. 2020.

[50] T. Kazaz, G. Janssen, J. Romme, and A. Van der Veen, "Delay estimation for ranging and localization using multiband channel state information," *IEEE Trans. Wireless Commun.*, vol. 21, no. 4, pp. 2591–2607, Apr. 2022.

[51] A. Abdallah and Z. Kassas, "Multipath mitigation via synthetic aperture beamforming for indoor and deep urban navigation," *IEEE Trans. Veh. Technol.*, vol. 70, no. 9, pp. 8838–8853, Sep. 2021.

[52] Z. Kassas et al., "Assessment of cellular signals of opportunity for high-altitude aircraft navigation," *IEEE Aerosp. Electron. Syst. Mag.*, vol. 37, no. 10, pp. 4–19, Oct. 2022.

[53] Z. Kassas et al., "Flight demonstration of high altitude aircraft navigation with cellular signals," *IEEE Intell. Transp. Syst. Mag.*, vol. 15, no. 4, pp. 150–165, Oct. 2023.

[54] J. Gante, L. Sousa, and G. Falcao, "Dethroning GPS: Low-power accurate 5G positioning systems using machine learning," *IEEE J. Emerg. Sel. Topics Circuits Syst.*, vol. 10, no. 2, pp. 240–252, Jun. 2020.

[55] K. Shamaei and Z. Kassas, "Receiver design and time of arrival estimation for opportunistic localization with 5G signals," *IEEE Trans. Wireless Commun.*, vol. 20, no. 7, pp. 4716–4731, Jul. 2021.

[56] L. Chen, X. Zhou, F. Chen, L. Yang, and R. Chen, "Tracking digital FM OFDM signals for the determination of navigation observables," *IEEE Internet Things J.*, vol. 9, no. 13, pp. 10908–10919, 2022.

[57] A. Abdallah and Z. Kassas, "UAV navigation with 5G carrier phase measurements," in *Proc. 34th Int. Tech. Meeting Satell. Division Inst. Navigat. (ION GNSS)*, Oct. 2021, pp. 3294–3306.

[58] A. Abdallah and Z. Kassas, "Opportunistic navigation using sub-6 GHz 5G downlink signals: A case study on a ground vehicle," in *Proc. 16th Eur. Conf. Antennas Propag. (EuCAP)*, Mar. 2022, pp. 1–5.

[59] A. Abdallah, J. Khalife, and Z. Kassas, "Exploiting on-demand 5G downlink signals for opportunistic navigation," *IEEE Signal Process. Lett.*, vol. 30, pp. 389–393, 2023.

[60] M. Jia, J. Khalife, and Z. Kassas, "Evaluation of ground vehicle protection level reduction due to fusing GPS with faulty terrestrial signals of opportunity," in *Proc. Int. Tech. Meeting Inst. Navigat.*, Feb. 2021, pp. 354–365.

[61] M. Jia, H. Lee, J. Khalife, Z. Kassas, and J. Seo, "Ground vehicle navigation integrity monitoring for multi-constellation GNSS fused with cellular signals of opportunity," in *Proc. IEEE Int. Intell. Transp. Syst. Conf. (ITSC)*, Sep. 2021, pp. 3978–3983.

[62] M. Maaref and Z. Kassas, "Measurement characterization and autonomous outlier detection and exclusion for ground vehicle navigation with cellular signals," *IEEE Trans. Intell. Vehicles*, vol. 5, no. 4, pp. 670–683, Dec. 2020.

[63] M. Maaref and Z. Kassas, "Autonomous integrity monitoring for vehicular navigation with cellular signals of opportunity and an IMU," *IEEE Trans. Intell. Transp. Syst.*, vol. 23, no. 6, pp. 5586–5601, Jun. 2022.

[64] E. Kaplan and C. Hegarty, *Understanding GPS: Principles and Applications*, 2nd ed. Norwood, MA, USA: Artech House, 2005.

[65] J. Khalife and Z. Kassas, "Evaluation of relative clock stability in cellular networks," in *Proc. 30th Int. Tech. Meeting Satell. Division Inst. Navigat. (ION GNSS)*, Nov. 2017, pp. 2554–2559.

[66] B. DeCleene, "Defining pseudorange integrity-overbounding," in *Proc. Int. Tech. Meeting Satell. Division Inst. Navigat.*, Sep. 2000, pp. 1916–1924.

[67] M. Haenggi, J. G. Andrews, F. Baccelli, O. Dousse, and M. Franceschetti, "Stochastic geometry and random graphs for the analysis and design of wireless networks," *IEEE J. Sel. Areas Commun.*, vol. 27, no. 7, pp. 1029–1046, Sep. 2009.

[68] J. Khalife, C. Sevinc, and Z. Kassas, "Performance evaluation of TOA positioning in asynchronous cellular networks using stochastic geometry models," *IEEE Wireless Commun. Lett.*, vol. 9, no. 9, pp. 1422–1426, Sep. 2020.

[69] S. Aditya, H. S. Dhillon, A. F. Molisch, R. M. Buehrer, and H. M. Behairy, "Characterizing the impact of SNR heterogeneity on time-of-arrival-based localization outage probability," *IEEE Trans. Wireless Commun.*, vol. 18, no. 1, pp. 637–649, Jan. 2019.

[70] J. Blanch et al., "Baseline advanced RAIM user algorithm and possible improvements," *IEEE Trans. Aerosp. Electron. Syst.*, vol. 51, no. 1, pp. 713–732, Jan. 2015.

[71] T. Walter, J. Blanch, K. Gunning, M. Joerger, and B. Pervan, "Determination of fault probabilities for ARAIM," *IEEE Trans. Aerosp. Electron. Syst.*, vol. 55, no. 6, pp. 3505–3516, Dec. 2019.

[72] J. Khalife, M. Maaref, and Z. Kassas, "Opportunistic autonomous integrity monitoring for enhanced UAV safety," *IEEE Aerosp. Electron. Syst. Mag.*, vol. 38, no. 5, pp. 34–44, May 2023.

Authorized licensed use limited to: The Ohio State University. Downloaded on October 13,2023 at 15:38:43 UTC from IEEE Xplore. Restrictions apply.

[73] K. Shamaei and Z. Kassas, "LTE receiver design and multipath analysis for navigation in urban environments," *Navigat., J. Inst. Navigat.*, vol. 65, no. 4, pp. 655–675, Dec. 2018.

[74] J. Spilker Jr., "Overview of GPS operation and design," in *Global Positioning System: Theory and Applications*. Washington, DC, USA: American Institute of Aeronautics and Astronautics, 1996, ch. 2, pp. 57–119.

Mu Jia (Graduate Student Member, IEEE) received the B.E. degree in vehicle engineering from Shandong University, the M.E. degree in mechanical engineering from the University of Defense Technology, and the M.S. degree in mechanical engineering from Duke University. He is currently pursuing the Ph.D. degree with The Ohio State University. He is a member of the Autonomous Systems Perception, Intelligence, and Navigation (ASPIN) Laboratory. His current research interests include autonomous vehicles, integrity monitoring, and opportunistic navigation.

Joe Khalife (Student Member, IEEE) received the B.E. degree in electrical engineering and the M.S. degree in computer engineering from Lebanese American University and the Ph.D. degree in electrical engineering and computer science from the University of California at Irvine. He was a Post-Doctoral Fellow with the University of California at Irvine and a member of the ASPIN Laboratory. He was a recipient of the 2016 IEEE/ION Position, Location and Navigation Symposium (PLANS) Best Student Paper Award and the 2018 IEEE Walter Fried Award.

Zaher (Zak) M. Kassas (Senior Member, IEEE) received the B.E. degree in electrical engineering from Lebanese American University, the M.S. degree in electrical and computer engineering from The Ohio State University, and the M.S.E. degree in aerospace engineering and the Ph.D. degree in electrical and computer engineering from The University of Texas at Austin. He is currently a Professor with The Ohio State University, the Director of the ASPIN Laboratory, and the Director of the U.S. Department of Transportation, Center for Automated Vehicle Research with Multimodal Assured Navigation (CARMEN), where he is focusing on navigation resiliency and security of highly automated transportation systems. His research interests include cyber-physical systems, navigation systems, autonomous vehicles, and intelligent transportation systems. He is a fellow of the ION and a Distinguished Lecturer of the IEEE Aerospace and Electronic Systems Society. He was a recipient of the 2018 National Science Foundation (NSF) CAREER Award, the 2018 IEEE Walter Fried Award, the 2018 Institute of Navigation (ION) Samuel Burka Award, the 2019 ION Colonel Thomas Thurlow Award, the 2019 Office of Naval Research (ONR) Young Investigator Program (YIP) Award, and the 2022 Air Force Office of Scientific Research (AFOSR) YIP Award. He is an Associate Editor of the IEEE TRANSACTIONS ON AEROSPACE AND ELECTRONIC SYSTEMS and the IEEE TRANSACTIONS ON INTELLIGENT TRANSPORTATION SYSTEMS.

Authorized licensed use limited to: The Ohio State University. Downloaded on October 13,2023 at 15:38:43 UTC from IEEE Xplore. Restrictions apply.

Performance-Driven Design of Carrier Phase Differential Navigation Frameworks With Megaconstellation LEO Satellites

JOE KHALIFE, Member, IEEE
University of California, Irvine, CA USA

ZAHER (ZAK) M. KASSAS, Senior Member, IEEE
The Ohio State University, Columbus, OH USA

A navigation framework with carrier phase differential measurements from megaconstellation low Earth orbit (LEO) satellite signals is developed. The measurement errors due to ephemeris errors and ionospheric and tropospheric delays are derived and the statistics of the dilution of precision is characterized. Moreover, the joint probability density function of the megaconstellation LEO satellites' azimuth and elevation angles is derived to 1) enable performance characterization of navigation frameworks with LEO satellites in a computationally efficient way and 2) facilitate parameter design, namely, the differential baseline, to meet desired performance requirements. The Starlink constellation is used as a specific LEO megaconstellation example to demonstrate the developed carrier phase differential LEO (CD-LEO) navigation framework. Simulation results are presented demonstrating the efficacy of the proposed CD-LEO framework for an unmanned aerial vehicle (UAV) navigating for 15.1 km in 300 s, while using signals from 44 Starlink satellites, achieving a 3-D position root mean squared error (RMSE) of 2.2 m and a 2-D RMSE of 32.4 cm. Experimental results are presented showing UAV navigating for 2.28 km in 2 min over Aliso Viejo, CA, USA, using exclusively signals from only two Orbcomm LEO satellites, achieving an unprecedented position RMSE of 14.8 m.

Manuscript received 9 July 2021; revised 17 February 2022 and 23 July 2022; accepted 1 November 2022. Date of publication 6 January 2023; date of current version 9 June 2023.

DOI. No. 10.1109/TAES.2023.3234521

Refereeing of this contribution was handled by J. Blanch.

This work was supported in part by the Office of Naval Research (ONR) under Grant N00014-19-1-2511, in part by the Air Force Office of Scientific Research (AFOSR) under Grant FA9550-22-1-0476, in part by the National Science Foundation (NSF) under Grant 1929965, and in part by the U.S. Department of Transportation (USDOT) under Grant 69A3552047138 for the CARMEN University Transportation Center (UTC)

Authors' addresses: Joe Khalife was with the Department of Mechanical and Aerospace Engineering, University of California, Irvine, CA 92697, USA, E-mail: (jjkhalife@gmail.com); Zaher (Zak) M. Kassas is with the Department of Electrical and Computer Engineering, The Ohio State University, Columbus, OH 43210, USA, E-mail: (zkassas@ieee.org). *(Corresponding author: Zaher (Zak) M. Kassas.)*

0018-9251 © 2023 IEEE

I. INTRODUCTION

The coming decade is slated to witness a space revolution with the launch of tens of thousands of low Earth orbit (LEO) satellites for broadband communication [1], [2]. The promise of utilizing LEO satellites for positioning, navigation, and timing (PNT) has been the subject of recent studies [3], [4], [5], [6], [7], [8], [9], [10], [11], [12], [13], [14], [15], [16], [17], [18]. While some of these studies call for tailoring the broadband protocol to support navigation capabilities [19], [20], other studies propose to exploit existing broadband LEO constellations for navigation in an opportunistic fashion [21], [22], [23], [24], [25], [26], [27]. The former studies allow for simpler receiver architectures and navigation algorithms. However, they require changes to existing infrastructure [28], the cost of which private companies, such as OneWeb, SpaceX, Boeing, and others, which are planning to aggregately launch tens of thousands of broadband Internet satellites into LEO, may not be willing to pay. Moreover, if the aforementioned companies agree to that additional cost, there will be no guarantees that they would not charge extra for "navigation services." In this case, exploiting broadband LEO satellite signals opportunistically for navigation becomes the more viable approach. An opportunistic approach also offers two additional advantages: 1) it maintains the privacy of the user, as only downlink LEO signals are utilized without communicating back with the LEO satellites and 2) it allows utilization of multiple constellations without being limited to only the subscription constellation. This article assesses opportunistic navigation with carrier phase differential measurements, also known as real-time kinematic (RTK), from broadband LEO satellite signals.

To address the limitations and vulnerabilities of global navigation satellite system (GNSS), opportunistic navigation has received significant attention over the past decade or so [29]. Opportunistic navigation is a paradigm that relies on exploiting ambient radio signal of opportunity (SOPs) for PNT. Besides LEO satellite signals, other SOPs include AM/FM radio [30], [31], [32], digital television [33], [34], and cellular [35], [36], [37], [38], [39], [40], [41], [42], [43], [44], with the latter showing the promise of a submeter-accurate navigation solution for unmanned aerial vehicles (UAVs) when carrier phase measurements from cellular signals are used [45], [46].

LEO satellites possess desirable attributes for positioning in GNSS-challenged environments [1], [2]: 1) they are around 20 times closer to Earth compared to GNSS satellites, which reside in medium Earth orbit (MEO), making their received signal power between 24 to 34-dBs higher than GNSS signals; 2) they will become abundant as tens of thousands of broadband Internet satellites are expected to be deployed into LEO; and 3) each broadband provider will

Authorized licensed use limited to: The Ohio State University. Downloaded on October 13,2023 at 15:28:54 UTC from IEEE Xplore. Restrictions apply.

deploy broadband Internet satellites into unique constellations, transmitting at different frequency bands, making LEO satellite signals diverse in frequency and direction. While the ephemerides of LEO satellites are not as precisely known as those of GNSS satellites, estimates of the Keplerian elements parameterizing the orbits of these LEO satellites are made publicly available by the North American Aerospace Defense Command (NORAD) and are updated daily in the two-line element (TLE) files. Using TLEs and orbit determination algorithms (e.g., SGP4), the positions and velocities of these satellites can be estimated, albeit not precisely [47], [48], [49]. In addition, some of these broadband LEO satellites, such as Orbcomm satellites, are equipped with GPS receivers and broadcast their GPS solution to terrestrial receivers.

This article considers the problem of navigating exclusively with LEO satellite signals in environments where GNSS signals are unavailable or untrustworthy (e.g., in the presence of jamming or spoofing). To this end, there are several challenges that must be addressed. First, there are no publicly available receivers that can produce navigation observables from LEO satellite signals. Recent papers on navigation with LEO satellites have addressed this challenge for some of the existing constellations [21], [50], [51], [52], [53]. Second, existing navigation frameworks do not apply in a straight forward fashion to megaconstellation LEO satellites due to the unique error sources associated with megaconstellation LEO satellites. The literature on navigation with LEO satellites either 1) assumes that the orbit and clock errors of LEO satellites are precisely determined [54], [55], [56], [57], [58], 2) relies on TLEs [21], [50], [51], [52], 3) or simultaneously track LEO satellites and navigate [59], [60]. Obtaining precise LEO orbits and clocks requires additional infrastructure, the cost of which LEO broadband providers may not be willing to bare. Moreover, the error in the orbits obtained from the publicly available TLEs may be on the order of a few kilometers as the orbit is propagated way beyond the epoch at which the TLE file was generated. Blindly using the satellite positions obtained from the TLE files introduces significant errors in the measurement residuals [61]. Tracking the satellite orbits while navigating may reduce the error in satellite orbits; however, the augmented system becomes poorly estimable, especially for long period of navigation, i.e., 4 min or more [61]. An LEO carrier phase differential navigation framework was introduced in [62] to tackle the problem of large measurement errors due to LEO satellite orbit and clock errors. However, the framework was geared toward the Orbcomm constellation only. A third challenge is the unknown achievable navigation performance with megaconstellation LEO satellites. The navigation performance has been partially characterized in [62] and [63]. In [62], only the Orbcomm constellation was characterized, while none of the sources of errors were studied. In [63], stochastic models of the LEO satellite elevation and azimuth angles were developed to characterize the performance of LEO megaconstellations. However, the effect of satellite position errors on the measurement error were partially analyzed for a specific location, and ionospheric and tropospheric delays were not considered in the analysis.

The high level of precision of carrier phase measurements enables a submeter level navigation solution as has been demonstrated in GNSS [64] and cellular SOPs [45], [46]. This precision comes at the cost of added ambiguities that need to be resolved, for which the least-squares ambiguity decorrelation adjustment (LAMBDA) method can be employed [65]. Carrier phase differential measurements from LEO satellites have been used previously to accelerate integer ambiguity resolution in the case of GNSS [3], [4], [5], [66]. On one hand, the authors in [3] and [66] propose a method for resolving GNSS ambiguities by augmenting GNSS carrier phase measurements with ones taken from LEO satellites. On the other hand, Joerger et al. [4] and [5] discussed navigation and integrity monitoring with GNSS augmented with carrier phase measurements from Iridium satellites. Contrary to the aforementioned papers, this article does not assume that the rover can augment GNSS measurements with LEO measurements; thus, the rover is navigating exclusively with carrier phase differential measurements from LEO satellites. Moreover, the analysis in this article is not limited to one LEO constellation, but is generalized to multiple LEO megaconstellations.

Once the ambiguities are resolved, the rover can perform real-time positioning. As mentioned above, two major sources of error that have to be considered in the so-called carrier phase differential (CD)-LEO framework are 1) the error in the satellite positions obtained from the TLE files and 2) residual ionospheric and tropospheric delays as LEO satellites reside above the ionosphere and troposphere. Although the double-difference carrier phase measurements will cancel out most of satellite position errors and ionospheric and tropospheric delays, there will still be significant errors if the base and rover are "too far apart." These errors are too large to ignore if an accurate navigation solution is desired. This article characterizes this error and its statistics as a function of the differential baseline, from which the baseline can be designed to guarantee a desirable performance.

This article presents a study for carrier phase differential navigation with megaconstelation LEO satellites and considers the following scenario. A receiver onboard a "rover" with *unknown* states makes carrier phase measurements to LEO satellites, and a "base" station with known position in the vicinity of the rover makes carrier phase measurements to the same LEO satellites. One can form differential carrier phase measurements from base and rover measurements and solve for the rover's position as well as for the resulting ambiguities. Without any position priors, the rover cannot perform real-time positioning and must wait until there is enough change in satellite geometry to use a batch least-squares estimator to estimate its position and the integer ambiguities or use a dynamic estimator, such as an extended Kalman filter (EKF). The goal of the article is to develop a methodology for designing CD-LEO frameworks and analyzing their performance. Stochastic geometry models

Authorized licensed use limited to: The Ohio State University. Downloaded on October 13,2023 at 15:28:54 UTC from IEEE Xplore. Restrictions apply.

have been used to characterize relevant metrics in terrestrial wireless communication systems [67]. Recent studies extended such models to LEO-based wireless communication systems [68], [69], [70], [71] to characterize coverage probabilities, interference, as well as Doppler spreads. This article aims to develop stochastic models for LEO satellite azimuth and elevation angles to characterize navigation performance metrics and error sources, namely, the dilution of precision (DOP), ephemeris errors, and atmospheric effects. Stochastic geometry models are an efficient alternative to full orbit simulations. Furthermore, they can still be used even when not enough information is known to simulate a given constellation. Stochastic geometry models can be used to calculate exact statistics of some performance metrics, either using numerical integration, or, although rarely simple, by deriving closed-form expressions in some instances. This article makes four contributions as follows.

1) First, a carrier phase differential (CD)-LEO navigation framework is developed for LEO satellite signals and the measurement residuals due to ephemeris, and ionospheric and tropospheric delays are derived.
2) Second, the probability density functions (pdfs) of megaconstellation LEO satellites' azimuth and elevation angles are used to characterize the cumulative density functions (cdfs) of the DOPs, namely, position DOP (PDOP), horizontal DOP (HDOP), and vertical DOP (VDOP).
3) Third, the statistics and cdfs of measurement residuals due to ephemeris errors and ionospheric and tropospheric delays are characterized as a function of the baseline. This study allows to design the system parameters to guarantee a desired performance, namely, the differential baseline.
4) Fourth, simulation and experimental results are presented showing a UAV localizing itself with LEO satellite signals using carrier phase differential measurements to an unprecedented level of accuracy. The simulation results show a UAV navigating for 15.1 km in 300 s, while using signals from 44 Starlink LEO satellites, achieving a 3-D position root mean squared error (RMSE) of 2.2 m and a 2-D RMSE of 32.4 cm. The experimental results show a UAV navigating for 2.28 km in 2 min over Aliso Viejo, CA, USA, using exclusively signals from only two Orbcomm LEO satellites, achieving a position RMSE of 14.8 m.

The rest of this article is organized as follows. Section II describes the measurement models used and the CD-LEO framework. Section III models the errors in the CD-LEO measurements due to ephemeris errors and ionospheric and tropospheric delays. Section IV derives the joint pdf of the megaconstellation LEO satellites' azimuth and elevation angles. Section V uses these models to characterize the performance of the CD-LEO framework and proposes a methodology to design system parameters to meet a desired performance. Section VI presents simulation results showing the potential of centimeter-accurate UAV navigation with fully deployed LEO magaconstellations. Section VII presents experimental results demonstrating a UAV navigating with CD-LEO measurements. Finally, Section VIII concludes this article.

II. MEASUREMENT MODELS AND CD-LEO FRAMEWORK DESCRIPTION

This section describes the measurement models and the CD-LEO framework used in the article. From here on out, a satellite will be referred to as a space vehicle (SV).

A. LEO Satellite Position Error

Let $\boldsymbol{r}_{\text{leo},l} \triangleq [x_{\text{leo},l}, y_{\text{leo},l}, z_{\text{leo},l}]^{\mathrm{T}}$ denote the lth LEO SV true position vector in the East–North–Up (ENU) frame. If the true LEO SV positions are not known, they may be estimated utilizing TLE files and orbit determination algorithms (e.g., SGP4), resulting with an estimate $\hat{\boldsymbol{r}}_{\text{leo},l}$. Denote the estimation error as $\tilde{\boldsymbol{r}}_{\text{leo},l} \triangleq \boldsymbol{r}_{\text{leo},l} - \hat{\boldsymbol{r}}_{\text{leo},l}$. Due to the large ephemeris errors in TLE files, $\|\tilde{\boldsymbol{r}}_{\text{leo},l}\|_2$ can be on the order of a few kilometers.

B. LEO Carrier Phase Observation Model

In this article, availability of carrier phase measurements from LEO SV signals is assumed. For example, the receiver proposed in [21] may be used to obtain carrier phase measurements from Orbcomm LEO SV signals and the one in [72] can be used for Starlink LEO SV signals. Note that Orbcomm LEO SVs transmit their SV ID. As such, data association for Orbcomm LEO SVs can be readily performed. However, little is known about Starlink LEO SV signals and data association must be performed. The problem of data association has been extensively studied in literature [73], [74] and its adaptation to the CD-LEO framework is left as future work. In the rest of the article, it is assumed that data association is performed perfectly. Note that since LEO satellite orbits are above the ionosphere, their signals will suffer from ionospheric and tropospheric delays. Let $\delta t^{(i)}_{\text{iono},l}(k)$ and $\delta t^{(i)}_{\text{trop},l}(k)$ denote the ionospheric and tropospheric delays from the lth LEO SV to the ith receiver at time-step k, respectively, where i denotes either the base B or the rover R. An estimate of the ionospheric and tropospheric delays, denoted $\hat{\delta} t^{(i)}_{\text{iono},l}(k)$ and $\hat{\delta} t^{(i)}_{\text{trop},l}(k)$, respectively, may be obtained using standard models [75]. After ionospheric and tropospheric delay correction, the carrier phase measurement $z^{(i)}_l(k)$ expressed in meters can be parameterized in terms of the receiver and LEO SV states as

$$z^{(i)}_l(k) = \left\|\boldsymbol{r}_{r,i} - \boldsymbol{r}_{\text{leo},l}(k)\right\|_2 + c\left[\delta t_{r,i}(k) - \delta t_{\text{leo},l}(k)\right] + \lambda_l N^{(i)}_l + c\tilde{\delta} t^{(i)}_{\text{trop},l}(k) + c\tilde{\delta} t^{(i)}_{\text{iono},l}(k) + v^{(i)}_l(k) \quad (1)$$

where $\boldsymbol{r}_{r,i} \triangleq [x_{r,i}, y_{r,i}, z_{r,i}]^{\mathrm{T}}$ is the ith receiver's position vector in ENU; c is the speed of light; $\delta t_{r,i}$ and $\delta t_{\text{leo},l}$ are the ith receiver's and lth LEO SV clock biases, respectively; $\tilde{\delta} t^{(i)}_{\text{iono},l} \triangleq \delta t^{(i)}_{\text{iono},l} - \hat{\delta} t^{(i)}_{\text{iono},l}$ and $\tilde{\delta} t^{(i)}_{\text{trop},l} \triangleq \delta t^{(i)}_{\text{trop},l} - \hat{\delta} t^{(i)}_{\text{trop},l}$ are the ionospheric and tropospheric delay errors, respectively; λ_l is the lth LEO SV signal's wavelength; $N^{(i)}_l$ is the carrier

Authorized licensed use limited to: The Ohio State University. Downloaded on October 13,2023 at 15:28:54 UTC from IEEE Xplore. Restrictions apply.

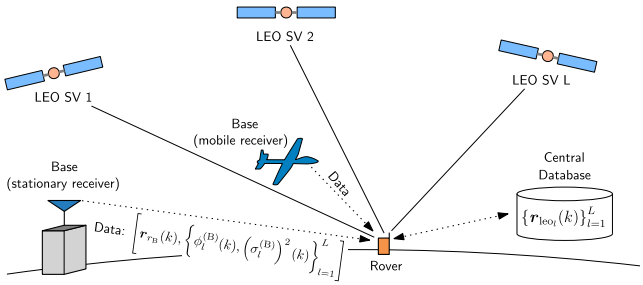

Fig. 1. Base/rover CD-LEO framework. The base receiver can be either (a) stationary or (ii) mobile (e.g., high-flying aerial vehicle).

phase ambiguity; and $v_l^{(i)}$ is the measurement noise, which is modeled as a discrete-time zero-mean white Gaussian sequence with variance $\left[\sigma_l^{(i)}(k)\right]^2$. It is assumed that $\left\{v_l^{(i)}\right\}_{l=1}^{L}$ are independent and identically distributed, but with different values of $\left[\sigma_l^{(i)}(k)\right]^2$.

C. CD-LEO Framework

The framework consists of a rover and a base receiver in an environment comprising L visible LEO SVs. The base receiver (B), is assumed to have knowledge of its own position state, e.g., 1) a stationary receiver deployed at a surveyed location or 2) a high-flying aerial vehicle with access to GNSS. The rover (R) does not have knowledge of its position. The base communicates its own position and carrier phase observables with the rover. The LEO SVs' positions are known through the TLE files and orbit determination software, or by decoding the transmitted ephemerides, if any. As such, one of two differential measurements may be used by the rover for navigating: 1) single difference or 2) double difference carrier phase measurements. Both of these measurements are discussed next. Fig. 1 illustrates the base/rover CD-LEO framework.

D. LEO Single Difference Carrier Phase Framework

In what follows, the objective is to estimate the rover's position using single difference carrier phase measurements. While these measurements eliminate the time-varying component of SV clock biases, the relative clock bias between the base and rover receivers as well as the carrier phase ambiguities cannot be resolved in the single difference measurements. As such, either 1) a precise prior is needed to estimate the initial ambiguities or 2) a dynamic estimator must be employed to estimate the ambiguities over time. The latter approach is adopted and an EKF is formulated to estimate the rover's position from single difference carrier phase measurements.

1) *LEO Single Difference Carrier Phase Observation Model:* First, define the single difference across receivers adjusted for the base-LEO SV range as

$$\begin{aligned} z_l^{(\mathrm{R,B})}(k) &\triangleq z_l^{(\mathrm{R})}(k) - z_l^{(\mathrm{B})}(k) + \left\|\boldsymbol{r}_{r,\mathrm{B}} - \hat{\boldsymbol{r}}_{\mathrm{leo},l}(k)\right\|_2 \\ &= \left\|\boldsymbol{r}_{r_\mathrm{R}} - \boldsymbol{r}_{\mathrm{leo},l}(k)\right\|_2 + c\delta t_r^{(\mathrm{R,B})}(k) + \lambda_l N_l^{(\mathrm{R,B})} \\ &\quad + c\tilde{\delta} t_{\mathrm{iono},l}^{(\mathrm{R,B})}(k) + c\tilde{\delta} t_{\mathrm{trop},l}^{(\mathrm{R,B})}(k) \\ &\quad - \tilde{r}_{\mathrm{leo},L}^{(\mathrm{B})}(k) + v_l^{(\mathrm{R,B})}(k) \end{aligned} \tag{2}$$

where

$$\begin{aligned} \delta t_r^{(\mathrm{R,B})}(k) &\triangleq \delta t_{r_\mathrm{R}}(k) - \delta t_{r_\mathrm{B}}(k) \\ \lambda_l N_l^{(\mathrm{R,B})} &\triangleq \lambda_l N_l^{(\mathrm{R})} - \lambda_l N_l^{(\mathrm{B})} \\ \tilde{\delta} t_{\mathrm{iono},l}^{(\mathrm{R,B})}(k) &\triangleq \tilde{\delta} t_{\mathrm{iono},l}^{(\mathrm{R})}(k) - \tilde{\delta} t_{\mathrm{iono},l}^{(\mathrm{B})}(k) \\ \tilde{\delta} t_{\mathrm{trop},l}^{(\mathrm{R,B})}(k) &\triangleq \tilde{\delta} t_{\mathrm{trop},l}^{(\mathrm{R})}(k) - \tilde{\delta} t_{\mathrm{trop},l}^{(\mathrm{B})}(k) \\ \tilde{r}_{\mathrm{leo},L}^{(\mathrm{B})}(k) &\triangleq \left\|\boldsymbol{r}_{r,\mathrm{B}} - \boldsymbol{r}_{\mathrm{leo},l}(k)\right\|_2 - \left\|\boldsymbol{r}_{r,\mathrm{B}} - \hat{\boldsymbol{r}}_{\mathrm{leo},l}(k)\right\|_2 \\ v_l^{(\mathrm{R,B})}(k) &\triangleq v_l^{(\mathrm{R})}(k) - v_l^{(\mathrm{B})}(k). \end{aligned}$$

Define $\tilde{\delta} t_{\mathrm{atmo},l}^{(\mathrm{R,B})}(k) \triangleq \tilde{\delta} t_{\mathrm{iono},l}^{(\mathrm{R,B})}(k) + \tilde{\delta} t_{\mathrm{trop},l}^{(\mathrm{R,B})}(k)$ as the overall delay in the lth single difference measurement due to atmospheric effects. Subsequently, $z_l^{(\mathrm{R,B})}(k)$ can be expressed as

$$\begin{aligned} z_l^{(\mathrm{R,B})}(k) &= h_l^{(\mathrm{R})}(k) + c\delta t_r^{(\mathrm{R,B})}(k) + \lambda_l N_l^{(\mathrm{R,B})} \\ &\quad + \tilde{r}_{\mathrm{leo},L}^{(\mathrm{R,B})}(k) + c\tilde{\delta} t_{\mathrm{atmo},l}^{(\mathrm{R,B})}(k) + v_l^{(\mathrm{R,B})}(k) \end{aligned} \tag{3}$$

where $h_l^{(\mathrm{R})}(k) \triangleq \|\boldsymbol{r}_{r_\mathrm{R}} - \hat{\boldsymbol{r}}_{\mathrm{leo},l}(k)\|_2$, $\tilde{r}_{\mathrm{leo},L}^{(\mathrm{R,B})}(k) \triangleq \tilde{r}_{\mathrm{leo},L}^{(\mathrm{R})}(k) - \tilde{r}_{\mathrm{leo},L}^{(\mathrm{B})}(k)$, and $\tilde{r}_{\mathrm{leo},L}^{(\mathrm{R})}(k) \triangleq \|\boldsymbol{r}_{r,\mathrm{R}} - \boldsymbol{r}_{\mathrm{leo},l}(k)\|_2 - \|\boldsymbol{r}_{r,\mathrm{R}} - \hat{\boldsymbol{r}}_{\mathrm{leo},l}(k)\|_2$. In vector form, the measurement equation becomes

$$\begin{aligned} \boldsymbol{z}(k) &= \boldsymbol{h}^{(\mathrm{R})}(k) + c\delta t_r^{(\mathrm{R,B})}(k)\mathbf{1}_L + \boldsymbol{A} \\ &\quad + \tilde{\boldsymbol{r}}_{\mathrm{leo}}^{(\mathrm{R,B})}(k) + c\tilde{\boldsymbol{\delta}} t_{\mathrm{atmo}}^{(\mathrm{R,B})}(k) + \boldsymbol{v}(k) \end{aligned} \tag{4}$$

where $\mathbf{1}_L$ is an $L \times 1$ vector of ones and

$$\begin{aligned} \boldsymbol{z}(k) &\triangleq \left[z_1^{(\mathrm{R,B})}(k), \ldots, z_L^{(\mathrm{R,B})}(k)\right]^{\mathrm{T}} \\ \boldsymbol{h}^{(\mathrm{R})}(k) &\triangleq \left[h_1^{(\mathrm{R})}(k), \ldots, h_L^{(\mathrm{R})}(k)\right]^{\mathrm{T}} \\ \boldsymbol{A} &\triangleq \left[\lambda_1 N_1^{(\mathrm{R,B})}, \ldots, \lambda_L N_L^{(\mathrm{R,B})}\right]^{\mathrm{T}} \\ \tilde{\boldsymbol{r}}_{\mathrm{leo}}^{(\mathrm{R,B})}(k) &\triangleq \left[\tilde{r}_{\mathrm{leo}_1}^{(\mathrm{R,B})}(k), \ldots, \tilde{r}_{\mathrm{leo},L}^{(\mathrm{R,B})}(k)\right]^{\mathrm{T}} \\ \tilde{\boldsymbol{\delta}} t_{\mathrm{atmo}}^{(\mathrm{R,B})}(k) &\triangleq \left[\tilde{\delta} t_{\mathrm{atmo},1}^{(\mathrm{R,B})}(k), \ldots, \tilde{\delta} t_{\mathrm{atmo},L}^{(\mathrm{R,B})}(k)\right]^{\mathrm{T}} \\ \boldsymbol{v}(k) &\triangleq \left[v_1^{(\mathrm{R,B})}(k), \ldots, v_L^{(\mathrm{R,B})}(k)\right]^{\mathrm{T}}. \end{aligned}$$

The covariance matrix of $\boldsymbol{v}(k)$ is given by $\mathbf{R}(k) \triangleq \mathrm{diag}\left[\left[\sigma_1^{(\mathrm{R,B})}(k)\right]^2, \ldots, \left[\sigma_L^{(\mathrm{R,B})}(k)\right]^2\right]$, where $\left[\sigma_l^{(\mathrm{R,B})}(k)\right]^2 \triangleq \left[\sigma_l^{(\mathrm{R})}(k)\right]^2 + \left[\sigma_l^{(\mathrm{B})}(k)\right]^2$.

2) *EKF Model:* In this framework, the rover may be stationary or mobile. Here, the position and velocity of the rover are estimated, along with the vector of ambiguities, yielding the state vector

$$\boldsymbol{x}_{\mathrm{EKF}}(k) = \left[\boldsymbol{r}_{r_\mathrm{R}}^{\mathrm{T}}(k), \quad \dot{\boldsymbol{r}}_{r_\mathrm{R}}^{\mathrm{T}}(k), \quad \boldsymbol{x}_{\mathrm{clk},r}^{(\mathrm{R,B})^{\mathrm{T}}}(k), \quad \boldsymbol{A}^{\mathrm{T}}\right]^{\mathrm{T}} \tag{5}$$

where $\boldsymbol{x}_{\mathrm{clk},r}^{(\mathrm{R,B})}(k) \triangleq \left[c\delta t_r^{(\mathrm{R,B})}(k), \quad c\dot{\delta} t_r^{(\mathrm{R,B})}(k)\right]^{\mathrm{T}}$ and $c\dot{\delta} t_r^{(\mathrm{R,B})}(k)$ is the relative drift between the rover and base clocks. Since the dynamics of the rover are not necessarily known, a simple, yet reasonable dynamical model is assumed for the rover's position and velocity,

Authorized licensed use limited to: The Ohio State University. Downloaded on October 13,2023 at 15:28:54 UTC from IEEE Xplore. Restrictions apply.

namely, a velocity random walk model, which can be expressed as [76]

$$\boldsymbol{x}_{\text{pv}}(k+1) = \mathbf{F}_{\text{pv}}\boldsymbol{x}_{\text{pv}}(k) + \boldsymbol{w}_{\text{pv}}(k) \tag{6}$$

where $\boldsymbol{x}_{\text{pv}(k)} \triangleq \left[\boldsymbol{r}_{r_{\text{R}}}^{\text{T}}(k),\ \dot{\boldsymbol{r}}_{r_{\text{R}}}^{\text{T}}(k)\right]^{\text{T}}$, $\mathbf{F}_{\text{pv}} \triangleq \begin{bmatrix} \mathbf{I}_{3\times3} & T\mathbf{I}_{3\times3} \\ \mathbf{0}_{3\times3} & \mathbf{I}_{3\times3} \end{bmatrix}$ is the state matrix, $\mathbf{I}_{n\times n}$ is the $n \times n$ identity matrix, $\mathbf{0}_{n\times n}$ is the $n \times n$ zero matrix, T is the sampling interval, and $\boldsymbol{w}_{\text{pv}}(k)$ is the process noise, which is modeled as a zero-mean, white random vector with covariance $\mathbf{Q}_{\text{pv}}$. In general, a clock error state $\boldsymbol{x}_{\text{clk}} \triangleq [c\delta t, c\dot{\delta}t]^{\text{T}}$ is modeled to evolve according to a standard double integrator driven by process noise [76], according to the dynamics model

$$\boldsymbol{x}_{\text{clk}}(k+1) = \mathbf{F}_{\text{clk}}\boldsymbol{x}_{\text{clk}}(k) + \boldsymbol{w}_{\text{clk}}(k) \tag{7}$$

where $\mathbf{F}_{\text{clk}} \triangleq \begin{bmatrix} \mathbf{I}_{2\times2} & T\mathbf{I}_{2\times2} \\ \mathbf{0}_{2\times2} & \mathbf{I}_{2\times2} \end{bmatrix}$ and $\boldsymbol{w}_{\text{clk}}(k)$ is the process noise, which is modeled as a zero-mean, white random vector with covariance $\mathbf{Q}_{\text{clk}}$. Since $\boldsymbol{x}_{\text{clk},r}^{(\text{R,B})}$ is the difference between the rover and base clock error states, then its dynamics will be similar to (7) except that its process noise covariance, denoted by $\mathbf{Q}_{\text{clk},r}^{(\text{R,B})}$, will be the sum of the two process noise covariances, i.e.,

$$\mathbf{Q}_{\text{clk},r}^{(\text{R,B})} = \mathbf{Q}_{\text{clk},r}^{(\text{R})} + \mathbf{Q}_{\text{clk},r}^{(\text{B})} \tag{8}$$

where $\mathbf{Q}_{\text{clk},r}^{(\text{R})}$ and $\mathbf{Q}_{\text{clk},r}^{(\text{B})}$ are the rover and base's clock error process noise covariances, respectively. Consequently, the overall dynamics of $\boldsymbol{x}_{\text{EKF}}$ will be given by

$$\boldsymbol{x}_{\text{EKF}}(k+1) = \mathbf{F}_{\text{EKF}}\boldsymbol{x}_{\text{EKF}}(k) + \boldsymbol{w}_{\text{EKF}}(k) \tag{9}$$

where $\mathbf{F}_{\text{EKF}} = \text{diag}[\mathbf{F}_{\text{pv}}, \mathbf{F}_{\text{clk}}, \mathbf{I}_{L\times L}]$ and $\boldsymbol{w}_{\text{EKF}}(k)$ is the overall process noise which is modeled as a zero-mean, white random vector with covariance $\mathbf{Q}_{\text{EKF}} = \text{diag}\left[\mathbf{Q}_{\text{pv}}, \mathbf{Q}_{\text{clk},r}^{(\text{R,B})}, \mathbf{0}_{L\times L}\right]$. Note that the block pertaining to the ambiguity vector is not exactly zero in the process noise covariance but is set to a small value $\epsilon\mathbf{I}$ to avoid numerical instabilities in the EKF [77]. The EKF can be readily implemented, with the measurement Jacobian given by

$$\mathbf{H}(k) = [\mathbf{G}(k) \quad \mathbf{1}_L \quad \mathbf{0}_L \quad \mathbf{I}] \tag{10}$$

where $\mathbf{G}(k)$ is the geometry matrix at time-step k, which can be parameterized by the SVs' azimuth and elevation angles $\{\phi_l\}_{l=1}^{L}$ and $\{\theta_l\}_{l=1}^{L}$, respectively, according to (11) equation shown at the bottom of this page.

E. LEO Double Difference Carrier Phase Framework

In what follows, the objective is to estimate the rover's position using double difference carrier phase measurements. While these measurements completely remove the dependency on clock biases, they have inherent ambiguities that must be resolved. Recall that $(L-1)$ measurements are obtained from L visible satellites [75], with one unknown ambiguity associated with each double difference measurement. Using only one set of carrier phase measurements with no *a priori* knowledge on the rover position results in an underdetermined system: $(L+2)$ unknowns (3 position states and $(L-1)$ ambiguities) with only $(L-1)$ measurements. Therefore, when no *a priori* information on the position of the rover is known, a batch weighted nonlinear least-squares (B-WNLS) over a window of K time-steps is employed to solve for the rover's position and ambiguities. The rover could either remain stationary or move during the batch window. Subsequently, the rover uses measurements collected at different times in a batch estimator, resulting in an overdetermined system [75]. The total number of measurements will be $K \times (L-1)$ in the batch window. If the rover remains stationary, the total number of unknowns will remain $(L+2)$. Otherwise, the number of unknowns becomes $(3\tilde{K} + L - 1)$: 3 position states at each time-step and $(L-1)$ ambiguities. The dimensions of the unknown parameters and the measurement vector set a necessary condition on K and L in order to obtain a solution. Once an estimate of the ambiguities is obtained, the rover position can be estimated in real-time using a point-solution weighted nonlinear least-squares (PS-WNLS) estimator. Both the B-WNLS and PS-WNLS estimate the rover's position from LEO double difference carrier phase measurements, which is described next.

1) *LEO Double Difference Carrier Phase Observation Model:* Without loss of generality, the first LEO SV is taken as the reference, yielding the double difference measurements

$$\begin{aligned}\bar{\boldsymbol{z}}(k) &\triangleq \mathbf{T}\boldsymbol{z}(k) \\ &= \bar{\boldsymbol{h}}^{(\text{R})}(k) + \bar{\boldsymbol{A}} + \bar{\tilde{\boldsymbol{r}}}_{\text{leo}}^{(\text{R,B})}(k) + c\bar{\tilde{\boldsymbol{\delta}}}t_{\text{atmo}}^{(\text{R,B})}(k) + \bar{\boldsymbol{v}}(k)\end{aligned} \tag{12}$$

where $\bar{\boldsymbol{h}}^{(\text{R})}(k) \triangleq \mathbf{T}\boldsymbol{h}^{(\text{R})}(k)$, $\bar{\boldsymbol{A}} \triangleq \mathbf{T}\boldsymbol{A}$, $\bar{\tilde{\boldsymbol{r}}}_{\text{leo}}^{(\text{R,B})}(k) \triangleq \mathbf{T}\tilde{\boldsymbol{r}}_{\text{leo}}^{(\text{R,B})}(k)$, $\bar{\boldsymbol{v}}(k) \triangleq \mathbf{T}\boldsymbol{v}(k)$, $\bar{\tilde{\boldsymbol{\delta}}}t_{\text{atmo}}^{(\text{R,B})}(k) \triangleq \mathbf{T}\tilde{\boldsymbol{\delta}}t_{\text{atmo}}^{(\text{R,B})}(k)$, and $\mathbf{T} \triangleq [-\mathbf{1}_{L-1} \ \ \mathbf{I}_{(L-1)\times(L-1)}]$ is the differencing matrix. Note that the covariance matrix of $\bar{\boldsymbol{v}}(k)$ is given by $\bar{\mathbf{R}}(k) = \mathbf{T}\mathbf{R}(k)\mathbf{T}^{\text{T}}$. If $\lambda_l \neq \lambda_1$, then $\bar{\boldsymbol{A}}$ cannot be expressed as $\lambda\boldsymbol{N}$, where $\boldsymbol{N}$ is a vector of integers. If $\lambda_l = \lambda\ \forall\ l$, then $\bar{\boldsymbol{A}} = \lambda\boldsymbol{N}$ and the LAMBDA method is used to resolve the integer ambiguities.

2) *B-WNLS Solution:* If the rover remains stationary during the batch window, then the parameter to be estimated is given by

$$\boldsymbol{x}_{\text{stationary}} \triangleq \left[\boldsymbol{r}_{r,\text{R}}^{\text{T}}(0), \bar{\boldsymbol{A}}^{\text{T}}\right]^{\text{T}}$$

$$\mathbf{G}(k) \triangleq -\begin{bmatrix} \cos[\theta_1(k)]\sin\left[\phi_1(k)\right] & \cos[\theta_1(k)]\cos\left[\phi_1(k)\right] & \sin[\theta_1(k)] \\ \vdots & \vdots & \vdots \\ \cos[\theta_L(k)]\sin\left[\phi_L(k)\right] & \cos[\theta_L(k)]\cos\left[\phi_L(k)\right] & \sin[\theta_L(k)] \end{bmatrix}. \tag{11}$$

Authorized licensed use limited to: The Ohio State University. Downloaded on October 13,2023 at 15:28:54 UTC from IEEE Xplore. Restrictions apply.

otherwise, it is given by

$$\boldsymbol{x}_{\text{mobile}} \triangleq \left[\boldsymbol{r}_{r,\text{R}}^{\text{T}}(0), \ldots, \boldsymbol{r}_{r,\text{R}}^{\text{T}}(K-1), \overline{\boldsymbol{A}}^{\text{T}}\right]^{\text{T}}.$$

The parameter $\boldsymbol{x}_{\text{stationary}}$ or $\boldsymbol{x}_{\text{mobile}}$ are estimated from the collection of measurements from 0 to $(K-1)$ given by

$$\overline{\boldsymbol{z}}^{K} \triangleq \left[\overline{\boldsymbol{z}}^{\text{T}}(0), \ldots, \overline{\boldsymbol{z}}^{\text{T}}(K-1)\right]^{\text{T}}$$

to yield an estimate $\hat{\boldsymbol{x}}_{\text{stationary}}$ or $\hat{\boldsymbol{x}}_{\text{mobile}}$, respectively. Let $\widetilde{\boldsymbol{A}}$ denote the estimate of $\overline{\boldsymbol{A}}$. For a mobile receiver, the estimation error covariance $\mathbf{Q}_A$ associated with $\widetilde{\boldsymbol{A}}$ is given by

$$\mathbf{Q}_A = \left(\sum_{k=0}^{K-1} \mathbf{Y}_k^{\frac{1}{2}} \boldsymbol{\Omega}_k \mathbf{Y}_k^{\frac{1}{2}}\right)^{-1}$$

where $\mathbf{Y}_k^{\frac{1}{2}}$ is a square-root of $\mathbf{Y}_k \triangleq \overline{\mathbf{R}}^{-1}(k)$, and

$$\boldsymbol{\Omega}_k \triangleq \mathbf{I}_{(L-1)\times(L-1)} - \boldsymbol{\Psi}_k$$
$$\boldsymbol{\Psi}_k \triangleq \mathbf{Y}_k^{\frac{1}{2}} \mathbf{T}\mathbf{G}(k) \left[\mathbf{G}^{\text{T}}(k)\mathbf{T}^{\text{T}}\mathbf{Y}_k\mathbf{T}\mathbf{G}(k)\right]^{-1} \mathbf{G}^{\text{T}}(k)\mathbf{T}^{\text{T}}\mathbf{Y}_k^{\frac{1}{2}}$$

where $\mathbf{G}(k)$ is given in (11).

REMARK 1 In this article, the well-known LAMBDA method is adopted to resolve integer ambiguities. However, the CD-LEO framework may be implemented with a different integer ambiguity resolution method. Regardless of the resolution method used, the integers may not be resolved properly, especially that many of the LEO megaconstellations of interest will be transmitting in the Ka band and above. Since the wavelength is very small (3 cm or less), the difference between the float and integer solution will also be very small. In this case, errors due to uncertainty in the ephemeris would dominate. This source of error is one of the main sources characterized in this article. Nevertheless, the methodology developed in this article can be readily extended to study the effect of the integer resolution algorithm and the batch window size on the navigation performance of the CD-LEO framework and is left as future work.

3) *PS-WNLS Solution:* After resolving the ambiguities, a point solution for the rover position can be computed at each time-step. Let $\check{\boldsymbol{N}}$ denote the integer estimates of $\boldsymbol{N}$. Hence, the double difference measurement vector adjusted for the integer ambiguities expressed as

$$\overline{\boldsymbol{z}}_f(k) \triangleq \overline{\boldsymbol{z}}(k) - \lambda\check{\boldsymbol{N}} = \overline{\boldsymbol{h}}, \text{R}(k) + \lambda\tilde{\boldsymbol{N}} + \overline{\tilde{\boldsymbol{r}}}_{\text{leo}}^{(\text{R,B})}(k) + \overline{\boldsymbol{v}}(k) \tag{13}$$

where $\tilde{\boldsymbol{N}} \triangleq \boldsymbol{N} - \check{\boldsymbol{N}}$ is the integer ambiguity error. The rover uses $\overline{\boldsymbol{z}}_f(k)$ to solve for $\boldsymbol{r}_{r_\text{R}}(k)$ in a PS-WNLS. For small measurement noise variances, which is typically the case for high-frequency carriers, the positioning performance heavily depends on $\overline{\tilde{\boldsymbol{r}}}_{\text{leo}}^{(\text{R,B})}(k)$, which is characterized in Section V.

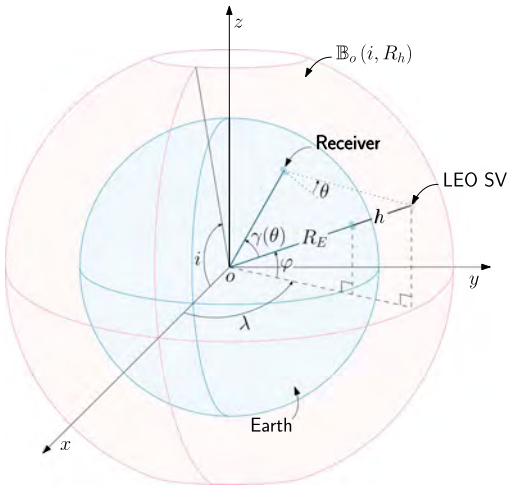

Fig. 2. LEO SV-to-receiver geometry. The subscripts j and l are omitted for simplicity.

III. LEO MEGACONSTELLATION AND ERROR MODELS

This section describes the LEO megaconstellation orbit model as well as models of ephemeris and ambiguity resolution errors.

A. LEO Megaconstellation Orbit Model

Consider a LEO megaconstellation composed of J LEO constellations of L_j SVs each, where $j = 1, \ldots, J$. The total number of SVs in the megaconstellation is given by

$$L = \sum_{j=1}^{J} L_j. \tag{14}$$

The orbit of a LEO SV belonging to constellation j is defined by its inclination angle i_j and orbital altitude h_j. Define the normalized orbital radius

$$\alpha_j \triangleq 1 + \frac{h_j}{R_E} \tag{15}$$

where R_E is the average radius of the Earth, which is assumed to be spherical. The surface over which the LEO SV can exist is defined as $\mathbb{B}_o(i_j, R_{h_j})$, which is a capless sphere of radius $R_{h_j} \triangleq \alpha_j R_E$, as shown in Fig. 2. The subsequent analysis can be done independently for different LEO constellation; hence, the subscript j will be dropped for simplicity of notation. Let ϕ_l and θ_l denote the azimuth and elevation angles, respectively, of the lth LEO SV. These angles are specific to a receiver location given by longitude λ_0 and latitude φ_0. Moreover, let $\gamma(\theta_l)$ denote the angle between the LEO SV and receiver position vectors. Using the law of sines, $\gamma(\theta_l)$ can be expressed as

$$\gamma(\theta_l) = \cos^{-1}\left[\frac{1}{\alpha}\cos\theta_l\right] - \theta_l. \tag{16}$$

The constellation parameters are obtained from the proposed Starlink constellation in [78] and are summarized in Table I.

Authorized licensed use limited to: The Ohio State University. Downloaded on October 13,2023 at 15:28:54 UTC from IEEE Xplore. Restrictions apply.

TABLE I
Starlink Orbital Configuration

Parameter	LEO constellation				
Satellites per altitude	1600	1600	400	375	450
Altitude (km)	1150	1110	1130	1275	1325
Inclination (°)	53	53.8	74	81	70

B. Measurement Errors Due to Ephemeris Errors

Recall that the SV positions are obtained by nonprecise ephemerides. The effect of the estimated SV position error onto the CD-LEO measurement is first characterized as a function of the SV elevation angle. Next, the pdf of the elevation angle derived in Section IV is used to obtain the cdf of the measurement error due to ephemeris errors. A first-order Taylor series expansion around $\hat{\boldsymbol{r}}_{\text{leo},l}$ yields

$$\left\|\boldsymbol{r}_{r,i}-\boldsymbol{r}_{\text{leo},l}\right\|_2 \approx \left\|\boldsymbol{r}_{r,i}-\hat{\boldsymbol{r}}_{\text{leo},l}\right\|_2 + \boldsymbol{h}_{i,l}^{\mathrm{T}}\tilde{\boldsymbol{r}}_{\text{leo},l}^{(i)} \tag{17}$$

where $\boldsymbol{h}_{i,l}$ is the unit line-of-sight vector between the lth LEO SV and the ith receiver and $\tilde{\boldsymbol{r}}_{\text{leo},l}^{(i)}$ is the lth LEO SV's position error vector expressed in the ith receiver's ENU frame. A first-order Taylor series expansion around $\boldsymbol{h}_{\text{B},l}$ yields

$$\boldsymbol{h}_{\text{R},l} \approx \boldsymbol{h}_{\text{B},l} + \frac{1}{\left\|\boldsymbol{r}_{r,\text{B}}-\hat{\boldsymbol{r}}_{\text{leo},l}\right\|_2}\left(\mathbf{I}-\boldsymbol{h}_{\text{B},l}\boldsymbol{h}_{\text{B},l}^{\mathrm{T}}\right)\Delta\boldsymbol{r}_b \tag{18}$$

where $\Delta\boldsymbol{r}_b$ is the baseline vector between the base and the rover. Subsequently, the residual due to SV position errors can be expressed as

$$\begin{aligned}\tilde{r}_{\text{leo},l}^{(\text{R,B})} &= \left\|\boldsymbol{r}_{r,\text{R}}-\boldsymbol{r}_{\text{leo},l}\right\|_2 - \left\|\boldsymbol{r}_{r,\text{B}}-\boldsymbol{r}_{\text{leo},l}\right\|_2 \\ &\quad - \left\|\boldsymbol{r}_{r,\text{R}}-\hat{\boldsymbol{r}}_{\text{leo},l}\right\|_2 + \left\|\boldsymbol{r}_{r,\text{B}}-\hat{\boldsymbol{r}}_{\text{leo},l}\right\|_2 \\ \Rightarrow \tilde{r}_{\text{leo},l}^{(\text{R,B})} &\approx \frac{\left(\boldsymbol{\Xi}_l\tilde{\boldsymbol{r}}_{\text{leo},l}^{(B)}\right)^{\mathrm{T}}\left(\boldsymbol{\Xi}_l\Delta\boldsymbol{r}_b\right)}{d_l^{(\text{B})}}\end{aligned} \tag{19}$$

where $\boldsymbol{\Xi}_l \triangleq (\mathbf{I}-\boldsymbol{h}_{\text{B},l}\boldsymbol{h}_{\text{B},l}^{\mathrm{T}})$ and $d_l^{(\text{B})} \triangleq \|\boldsymbol{r}_{r,\text{B}}-\hat{\boldsymbol{r}}_{\text{leo},l}\|_2$. Using the law of sines and (16), $d_l^{(i)}$ can be expressed as

$$d_l^{(i)} = R_E\left(\sqrt{\alpha^2-\cos^2\theta_l^{(i)}}-\sin\theta_l^{(i)}\right) \tag{20}$$

where $\theta_l^{(i)}$ denotes the lth LEO SV's elevation angle in the ith receiver's coordinate frame. The residual in (19) can be interpreted as the dot product between the baseline projected onto the range-space of $\boldsymbol{\Xi}_l$, denoted $\mathcal{R}(\boldsymbol{\Xi}_l)$, and the SV position error vector also projected onto $\mathcal{R}(\boldsymbol{\Xi}_l)$, as shown in Fig. 3(a). Practically, the rover can be assumed to be on the base's local plane East–North (EN) plane, i.e., its elevation angle with respect to the base is zero. Moreover, let $\omega_{\text{R}}^{(\text{B})}$ denote the rover's azimuth angle with respect to the base, as shown in Fig. 3(b). As such, the baseline can be parameterized as

$$\Delta\boldsymbol{r}_b = \Delta r_b\boldsymbol{u}_{\text{R}}^{(\text{B})} \tag{21}$$

where $\boldsymbol{u}_{\text{R}}^{(\text{B})} \triangleq [\sin\omega_{\text{R}}^{(\text{B})}, \cos\omega_{\text{R}}^{(\text{B})}, 0]^{\mathrm{T}}$ is a unit vector representing the baseline direction and Δr_b is the baseline magnitude.

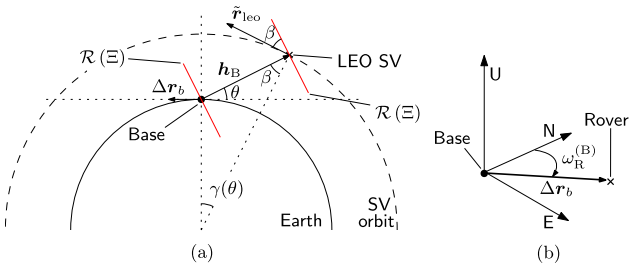

Fig. 3. Baseline-to-SV geometry. The subscript l was omitted for simplicity. The red lines show the range-space of $\boldsymbol{\Xi}$, denoted by $\mathcal{R}(\boldsymbol{\Xi})$, which is orthogonal to the unit line-of-sight vector $\boldsymbol{h}_{\text{B}}$.

Moreover, let $\psi_l^{(\text{B})}$ denote the orientation of the LEO SV's ground track in the base's ENU frame. As such, the LEO SV's position error vector may be expressed in the base's ENU frame as

$$\tilde{\boldsymbol{r}}_{\text{leo},L}^{(\text{B})} = e_{\text{leo},L}\boldsymbol{u}_{\text{leo},L}^{(\text{B})} \tag{22}$$

where $e_{\text{leo},L}$ is the magnitude of the SV position error and $\boldsymbol{u}_{\text{leo},L}^{(\text{B})}$ is the unit direction vector of the SV error in the base's ENU frame. Using (16) and the geometry in Fig. 3, one can show that $\boldsymbol{u}_{\text{leo},L}^{(\text{B})}$ can be expressed as

$$\begin{aligned}\boldsymbol{u}_{\text{leo},L}^{(\text{B})} \triangleq \frac{1}{\alpha}\Big[&\sin\psi_l^{(\text{B})}\cos\theta_l^{(\text{B})}, \cos\psi_l^{(\text{B})}\cos\theta_l^{(\text{B})}, \\ &\sqrt{\alpha^2-\cos^2\theta_l^{(\text{B})}}\Big]^{\mathrm{T}}.\end{aligned} \tag{23}$$

Using (19)–(23), the measurement residual due to SV position error can be expressed as

$$\tilde{r}_{\text{leo},l}^{(\text{R,B})} = f\left(\theta_l^{(\text{B})}, \phi_l^{(\text{B})}, \omega^{(\text{B})}, \text{R}, \psi_l^{(\text{B})}, \alpha\right)\frac{\Delta r_b\cdot e_{\text{leo},L}}{R_E} \tag{24}$$

where

$$\begin{aligned}f(\theta,\phi,\omega,\psi,\alpha) \triangleq \frac{\cos\theta}{\alpha\left(\sqrt{\alpha^2-\cos^2\theta}-\sin\theta\right)} \\ \cdot\Big[\cos(\psi-\omega)-\cos(\psi-\phi)\cos\theta \\ -\alpha\cos(\omega-\phi)-\frac{\sin\theta\sqrt{\alpha^2-\cos^2\theta}}{\cos\theta}\Big].\end{aligned} \tag{25}$$

While (24) shows the mapping between SV position error and measurement residual, it is worth looking at an upper bound of the residual magnitude for worst case scenario analysis. It can be seen from Fig. 3(a) that the magnitude of $\tilde{r}_{\text{leo},l}^{(\text{R,B})}$ is maximized when the SV's ground track is collinear with the baseline. In such cases, using (20), the magnitude of $\tilde{r}_{\text{leo},l}^{(\text{R,B})}$ may be bounded according to

$$\left|\tilde{r}_{\text{leo},l}^{(\text{R,B})}\right| \le \left|g\left(\theta_l^{(\text{B})}, \alpha_l\right)\right|\frac{\Delta r_b\cdot e_{\text{leo},L}}{R_E} \tag{26}$$

where

$$g(\theta,\alpha) = \frac{\frac{1}{\alpha}}{\frac{1}{\sin\theta}-\frac{1}{\sqrt{\alpha^2-\cos^2\theta}}}. \tag{27}$$

Authorized licensed use limited to: The Ohio State University. Downloaded on October 13,2023 at 15:28:54 UTC from IEEE Xplore. Restrictions apply.

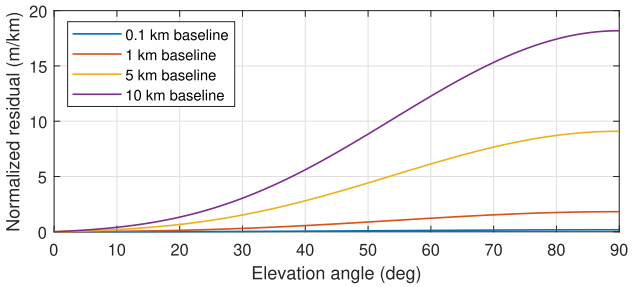

Fig. 4. Normalized residual as a function of the elevation angle for different baseline values.

Fig. 4 shows $|g(\theta_l^{(\mathrm{B})}, \alpha_l)|\frac{\Delta r_b}{R_E}$ as a function of $\theta_l^{(\mathrm{B})}$ for different values of Δr_b. This quantity, called normalized residual, represents the maximum residual error per unit of SV position error.

C. Measurement Errors Due to Atmospheric Effects

In case the LEO receiver is not making corrections for ionospheric and tropospheric delays, a residual error in the CD-LEO measurements will be introduced. In GPS, differential measurements at a "short" baseline of 20 km or less may almost completely cancel out the measurement errors due to atmospheric effects. However, such baselines may still yield significant errors in the CD-LEO measurements. In general, ionospheric and tropospheric delays can be modeled as the product of the delay at zenith and a mapping function of the elevation angle [75], known as the obliquity factor. As the elevation angle of the SV decreases, the obliquity factor increases due to the fact that signals at low elevation angles propagate longer in the ionosphere and troposphere. Differential GNSS exploits the fact that MEO SVs have almost the same elevation angles for a baseline of tens of kilometers, which means that the ionospheric and tropospheric delays cancel out almost completely when forming the differential GNSS measurements. However, LEO SVs are much closer to Earth than MEO SVs, more than 36 times closer in the case of Starlink, which means that the equal elevation angle approximation for typical GNSS baselines does not hold anymore. The residual errors due to atmospheric effects are subsequently studied as a function of the elevation angle and the baseline for LEO SVs.

The ionospheric and tropospheric delays in the carrier phase measurement from the lth LEO SV in the ith receiver can be estimated as

$$\hat{\delta}t_{\mathrm{iono},l}^{(i)} = {}^{\mathrm{z}}\hat{\delta}t_{\mathrm{iono}}^{(i)} f_{\mathrm{iono}}\left(\theta_l^{(i)}\right) \tag{28}$$

$$\hat{\delta}t_{\mathrm{trop},l}^{(i)} = {}^{\mathrm{z,w}}\hat{\delta}t_{\mathrm{trop}}^{(i)} f_{\mathrm{trop,w}}\left(\theta_l^{(i)}\right) + {}^{\mathrm{z,d}}\hat{\delta}t_{\mathrm{trop}}^{(i)} f_{\mathrm{trop,d}}\left(\theta_l^{(i)}\right) \tag{29}$$

where ${}^{\mathrm{z}}\hat{\delta}t_{\mathrm{iono}}^{(i)}$, ${}^{\mathrm{z,w}}\hat{\delta}t_{\mathrm{trop}}^{(i)}$, and ${}^{\mathrm{z,d}}\hat{\delta}t_{\mathrm{trop}}^{(i)}$ are the ionospheric, tropospheric wet, and tropospheric dry delays for the ith receiver at zenith, respectively, and $f_{\mathrm{iono}}(\theta_l^{(i)})$, $f_{\mathrm{trop,w}}(\theta_l^{(i)})$, and $f_{\mathrm{trop,d}}(\theta_l^{(i)})$ are the ionospheric, tropospheric wet, and tropospheric dry obliquity factors, respectively.

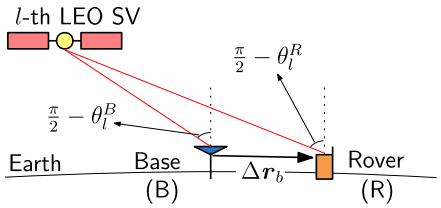

Fig. 5. Base-rover-LEO SV geometry when $\Delta\theta_l$ is maximized, i.e., the 2–D position of the LEO SV is collinear with the base and rover positions.

Assuming that ${}^{\mathrm{z}}\hat{\delta}t_{\mathrm{iono}}^{(\mathrm{R})} = {}^{\mathrm{z}}\hat{\delta}t_{\mathrm{iono}}^{(\mathrm{B})}$ and using a first-order Taylor series expansion of $f_{\mathrm{iono}}(\theta_l^{(\mathrm{R})})$ around $\theta_l^{(\mathrm{B})}$, the residual in the single difference CD-LEO measurement due to ionospheric delays can be approximated as

$$\begin{aligned}\hat{\delta}t_{\mathrm{iono},l}^{(\mathrm{R,B})} &\triangleq \hat{\delta}t_{\mathrm{iono},l}^{(\mathrm{R})} - \hat{\delta}t_{\mathrm{iono},l}^{(\mathrm{B})} \\ &\approx {}^{\mathrm{z}}\hat{\delta}t_{\mathrm{iono}}^{(\mathrm{B})} \cdot \frac{d}{d\theta} f_{\mathrm{iono}}(\theta)\Big|_{\theta_l^{(\mathrm{B})}} \Delta\theta_l \end{aligned} \tag{30}$$

where $\Delta\theta_l \triangleq \theta_l^{(\mathrm{R})} - \theta_l^{(\mathrm{B})}$. Fig. 5 illustrates the geometry between the LEO SV and the base and rover receivers when the 2-D position of the LEO SV is collinear with the base and rover positions. It can be shown that $|\Delta\theta_l|$ is maximized in such configurations. Using the law of sines and assuming that $d_l^{(\mathrm{R})} = d_l^{(\mathrm{B})}$, one can show that

$$|\Delta\theta_l| \le |\Delta\theta_l|_{\max} \tag{31}$$

where $|\Delta\theta_l|_{\max}$ is a function of the baseline and elevation angle at the base receiver given by

$$|\Delta\theta_l|_{\max} \triangleq \left|\sin^{-1}\left[\frac{\sin\theta_l^{(\mathrm{B})}\Delta r_b}{R_E\left(\sqrt{\alpha^2 - \cos^2\theta_l^{(\mathrm{B})}} - \sin\theta_l^{(\mathrm{B})}\right)}\right]\right|. \tag{32}$$

Combining (30) and (31) yields the following bound:

$$\left|\hat{\delta}t_{\mathrm{iono},l}^{(\mathrm{R,B})}\right| \le \left|{}^{\mathrm{z}}\hat{\delta}t_{\mathrm{iono}}^{(\mathrm{B})} \cdot \frac{d}{d\theta} f_{\mathrm{iono}}(\theta)\Big|_{\theta_l^{(\mathrm{B})}}\right| \cdot |\Delta\theta_l|_{\max}. \tag{33}$$

A similar bound is obtained for residuals due to tropospheric delays as

$$\begin{aligned}\left|\hat{\delta}t_{\mathrm{trop},l}^{(\mathrm{R,B})}\right| \le \Bigg|&{}^{\mathrm{z,w}}\hat{\delta}t_{\mathrm{trop}}^{(\mathrm{B})} \cdot \frac{d}{d\theta} f_{\mathrm{trop,w}}(\theta)\Big|_{\theta_l^{(\mathrm{B})}} \\ &+ {}^{\mathrm{z,d}}\hat{\delta}t_{\mathrm{trop}}^{(\mathrm{B})} \cdot \frac{d}{d\theta} f_{\mathrm{trop,d}}(\theta)\Big|_{\theta_l^{(\mathrm{B})}}\Bigg| \cdot |\Delta\theta_l|_{\max}. \end{aligned} \tag{34}$$

Equations (33) and (34) indicate that the magnitude of ionospheric and tropospheric delay residuals will be upper bounded by terms proportional to $|\Delta\theta_l|_{\max}$, which is the maximum difference between the elevation angles of the lth SV with respect to the base and rover, respectively. Fig. 6 shows $|\Delta\theta_l|_{\max}$ as a function of $\theta_l^{(\mathrm{B})}$ for different baseline values. As expected from (32), $|\Delta\theta_l|_{\max}$ is maximized when the SV is at zenith. Moreover, Fig. 6 suggests that the small angle approximation holds with respect to the baseline

Authorized licensed use limited to: The Ohio State University. Downloaded on October 13,2023 at 15:28:54 UTC from IEEE Xplore. Restrictions apply.

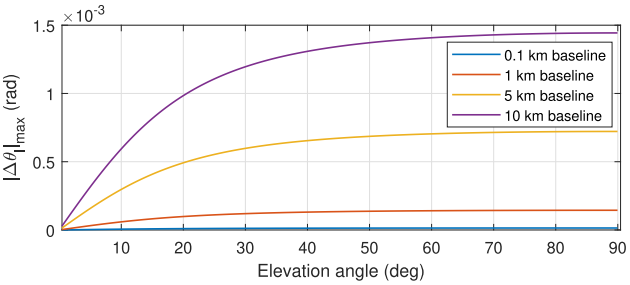

Fig. 6. Plot of $|\Delta\theta_l|_{\max}$ as a function of $\theta_l^{(\mathrm{B})}$ for different baseline values.

Δr_b. As such, one can approximate the upper bound on the magnitude of the ionospheric and tropospheric delay residuals to be proportional to the baseline.

IV. JOINT DISTRIBUTION OF MEGACONSTELLATION LEO SVS' AZIMUTH AND ELEVATION ANGLES

The joint pdf of megaconstellation LEO SVs' azimuth and elevation angles offers an efficient way to characterize the performance of the CD-LEO framework as well as to enable performance-driven design of the CD-LEO framework, such as the differential baseline selection. To this end, the LEO SV orbits are defined, such as in Section III-A. Moreover, it as assumed that the probability p_j of the lth LEO SV belonging to constellation j is given by

$$p_j \triangleq \Pr\left[\mathrm{SV}_l \in \mathrm{const}_j\right] = \frac{L_j}{L}, \quad j = 1, \ldots, J, l = 1, \ldots, L. \tag{35}$$

The following analysis holds for both receivers; hence, the superscripts j, B, and R will be dropped for simplicity of notation.

A. Satellite Elevation and Azimuth Distribution Model

Let λ_l and φ_l denote the lth LEO SV's longitude and latitude, respectively. Recall that the Earth is assumed to be spherical and the SV orbits are assumed to be circular. Moreover, it is assumed that the right ascension of the ascending node (RAAN) is uniformly distributed over 2π. As such, it can be shown that the pdfs of λ_l and φ_l are given by [63]

$$f_\Lambda(\lambda_l) = \begin{cases} \frac{1}{2\pi}, & 0 \le \lambda_l < 2\pi \\ 0, & \text{elsewhere} \end{cases} \tag{36}$$

$$f_\Psi(\varphi_l) = \begin{cases} \frac{\cos\varphi_l}{\pi\sqrt{\sin^2 i - \sin^2\varphi_l}}, & |\varphi_l| < i \\ 0, & \text{elsewhere} \end{cases} \tag{37}$$

with the joint pdf given by

$$f_{\Lambda,\Psi}(\lambda_l, \varphi_l) = f_\Lambda(\lambda_l) f_\Psi(\varphi_l). \tag{38}$$

The histogram obtained from the Starlink constellation and the analytical pdfs for $i = 53^\circ$ are shown in Fig. 7.

The joint pdf of ϕ_l and θ_l for an SV in constellation j, parameterized by the receiver's longitude λ_0 and latitude φ_0, the normalized orbital radius α_j, inclination angle i_j, and elevation mask $\theta_{\min}$, was derived in [63] and is denoted by

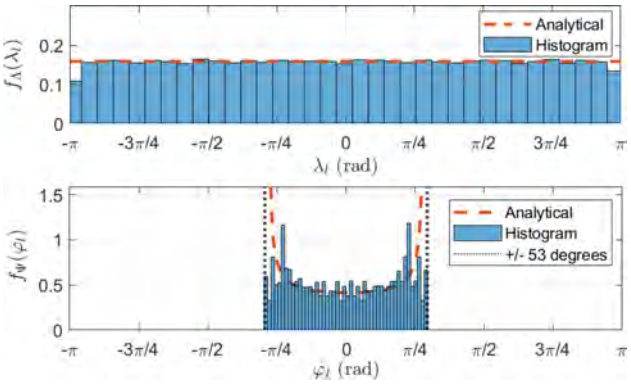

Fig. 7. Histogram and analytical pdfs of λ_l and φ_l for $i = 53^\circ$.

${}^l f_{\Phi,\Theta}^{\theta_{\min}}(\phi_l, \theta_l; \alpha_j, i_j, \lambda_0, \varphi_0)$. This pdf can be obtained from $f_{\Lambda,\Psi}(\lambda_l, \varphi_l)$ through coordinate transformation. To this end, the mapping from the pair (ϕ_l, θ_l) to (λ_l, φ_l) must be established. The result is captured in the following lemma. Note that the subscript j will be omitted for simplicity of notation.

LEMMA IV.1 Given a spherical Earth, an SV orbit characterized by i_l and α_l, and a receiver's longitude λ_0 and latitude φ_0, the inverse mapping from (ϕ_l, θ_l) to (λ_l, φ_l) is given by

$$\boldsymbol{y}(\phi_l, \theta_l) \triangleq \begin{bmatrix} \lambda_l \\ \varphi_l \end{bmatrix} = \begin{bmatrix} \tan^{-1}\left[\frac{a_{02}(\phi_l,\theta_l)}{a_{01}(\phi_l,\theta_l)}\right] \\ \sin^{-1}\left[a_{03}(\phi_l, \theta_l)\right] \end{bmatrix} \tag{39}$$

where

$$\begin{aligned}
a_{01}(\phi_l, \theta_l) &\triangleq \sin\left[\gamma(\theta_l)\right] f_{01}(\phi_l, \theta_l) + \frac{1}{\alpha}\cos\varphi_0\cos\lambda_0 \\
a_{02}(\phi_l, \theta_l) &\triangleq \sin\left[\gamma(\theta_l)\right] f_{02}(\phi_l, \theta_l) + \frac{1}{\alpha}\cos\varphi_0\sin\lambda_0 \\
a_{03}(\phi_l, \theta_l) &\triangleq \sin\left[\gamma(\theta_l)\right] f_{03}(\phi_l, \theta_l) + \frac{1}{\alpha}\sin\varphi_0, \\
f_{01}(\phi, \theta) &\triangleq \cos\varphi_0\cos\lambda_0\tan\theta - \sin\lambda_0\sin\phi \\
&\quad - \sin\varphi_0\cos\lambda_0\cos\phi \\
f_{02}(\phi, \theta) &\triangleq \cos\varphi_0\sin\lambda_0\tan\theta + \cos\lambda_0\sin\phi \\
&\quad - \sin\varphi_0\sin\lambda_0\cos\phi \\
f_{03}(\phi, \theta) &\triangleq \sin\varphi_0\tan\theta + \cos\varphi_0\cos\phi.
\end{aligned}$$

PROOF See Appendix A. ■

Finally, $f_{\Phi,\Theta}(\phi_l, \theta_l)$ is given by

$$f_{\Phi,\Theta}(\phi_l, \theta_l) = \begin{cases} \frac{|\det[\mathbf{J}_y(\phi_l,\theta_l)]|\sqrt{1-a_{03}^2(\phi_l,\theta_l)}}{2\pi^2\sqrt{\sin^2 i - a_{03}^2(\phi_l,\theta_l)}}, & |a_{03}(\phi_l, \theta_l)| < \sin i \\ 0, & \text{elsewhere} \end{cases} \tag{40}$$

where $\mathbf{J}_y(\phi_l, \theta_l) \triangleq \begin{bmatrix} \frac{\partial\lambda_l}{\partial\phi_l} & \frac{\partial\lambda_l}{\partial\theta_l} \\ \frac{\partial\varphi_l}{\partial\phi_l} & \frac{\partial\varphi_l}{\partial\theta_l} \end{bmatrix}$. The expression of $\mathbf{J}_y(\phi_l, \theta_l)$ and its determinant are given in Appendix B.

B. Azimuth and Elevation Joint Distribution for a Set Elevation Mask

Since the visible SVs have nonnegative elevation angles, one is interested to know the pdf for $\theta_l \ge 0$. In practice, a

Authorized licensed use limited to: The Ohio State University. Downloaded on October 13,2023 at 15:28:54 UTC from IEEE Xplore. Restrictions apply.

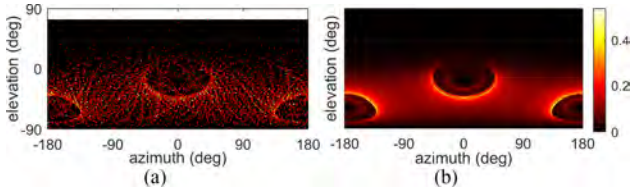

Fig. 8. Joint (ϕ_l, θ_l) pdfs calculated from (a) a histogram of azimuth and elevation angles of the SVs from the proposed Starlink LEO constellation and (b) from the analytical solution in (43). Note that the different orbital shells can be seen in the pdfs, especially in the analytical one in (b). The receiver is located at $\varphi_0 = 33.642673^\circ$, $\lambda_0 = -117.838747^\circ$, and zero altitude. .

positive elevation mask $\theta_{\min}$ is set. The pdf for $\theta_l \geq \theta_{\min}$ is hence given by

$$f_{\Phi,\Theta}^{\theta_{\min}}(\phi_l, \theta_l) = \begin{cases} \frac{|\det[\mathbf{J}_y(\phi_l,\theta_l)]|\sqrt{1-a_{03}^2(\phi_l,\theta_l)}}{C_{l,\theta_{\min}}\sqrt{\sin^2 i - a_{03}^2(\phi_l,\theta_l)}}, & (\phi_l, \theta_l) \in \mathcal{D}_{l,\theta_{\min}} \\ 0, & \text{elsewhere} \end{cases} \quad (41)$$

where the domain $\mathcal{D}_{l,\theta_{\min}}$ is defined as

$$\mathcal{D}_{l,\theta_{\min}} = \left[(\phi_l, \theta_l)\,|(|a_{03}(\phi_l, \theta_l)| < \sin i) \cap (\theta_l \geq \theta_{\min})\right]$$

and the normalization constant $C_{l,\theta_{\min}}$ is given by

$$C_{l,\theta_{\min}} = 2\pi^2 \int\int_{\mathcal{D}_{l,\theta_{\min}}} f_{\Phi,\Theta}(\phi_l, \theta_l) d\phi_l d\theta_l.$$

Note that one can find the average number of visible satellites $\bar{L}$ according to

$$\bar{L} = L \times \Pr[\theta_l \geq \theta_{\min}] = L\frac{C_{l,\theta_{\min}}}{2\pi^2} \quad (42)$$

where L is the total number of SVs in the constellation.

C. Multiconstellation Azimuth and Elevation Joint Distribution

Recall that the pdf in (41) is constellation-specific, i.e., it is parameterized by one inclination angle $i = i_j$ and one normalized orbital radius $\alpha = \alpha_j$. For the case of multiconstellations, as is the case for LEO megaconstellation, the joint pdf for all constellations, each of which defined by is given by

$${}^{\text{all}}f_{\Phi,\Theta}^{\theta_{\min}}(\phi_l, \theta_l) = \sum_{j=1}^{J} p_j\, {}^{j}f_{\Phi,\Theta}^{\theta_{\min}}(\phi_l, \theta_l) \quad (43)$$

where ${}^{j}f_{\Phi,\Theta}^{\theta_{\min}}(\phi_l, \theta_l)$ is the pdf of the jth constellation obtained according to (41). Fig. 8 shows the joint pdf of (ϕ_l, θ_l) estimated from a histogram of azimuth and elevation angles of the proposed Starlink constellation as well as the analytical pdf calculated in (43). The receiver location was set in Irvine, CA, USA, with $\varphi_0 = 33.642673^\circ$, $\lambda_0 = -117.838747^\circ$, zero altitude. It can be seen that the two pdfs match closely.

V. PERFORMANCE CHARACTERIZATION AND PERFORMANCE-DRIVEN CD-LEO FRAMEWORK DESIGN

This section studies leverages the models developed in Section III and Section IV to develop a performance characterization methodology that can inform the design of CD-LEO frameworks, namely, in baseline selection. First, the cdf and statistics of the PDOP are evaluated, followed by the statistics and cdfs of the CD-LEO measurement residual errors due to ephemeris errors and atmospheric effects. Note that the following analysis is concerned with the single-epoch position estimation performance after the integer ambiguities have been resolved, i.e., for the PS-WNLS. The performance characterization is conducted using a Monte Carlo approach: several realizations of the elevation and azimuth angles are obtained from the joint pdf derived in Section IV and the cdf or statistics of the performance metric are computed numerically. To do so, the average number of visible satellites $\bar{L}$ is determined according to (42) and the elevation mask. Then, $\bar{L}$ realizations of joint azimuth and elevation angles are determined by sampling the joint PDF given in (43). The PDF is sampled using a standard rejection sampling method [79]. Then, the variable of interest is calculated as a function of the azimuth and elevation angle in realization. Finally, the cdf of the variable of interest is computed from all the Monte Carlo realizations. It is important to note that the same methodology can be used to characterize performance in different environments, such as multipath errors or SV visibility in deep urban canyons.

A. PDOP Statistics Characterization

One important measure of the estimability (i.e., degree of observability) of the receiver's position is the PDOP. Assuming equal measurement noise variances, the PDOP in the CD-LEO framework is given by $\text{PDOP} = \sqrt{\text{trace}[\mathbf{P}]}$, where $\mathbf{P}$ is the PDOP matrix given by

$$\mathbf{P} = 2\left[\mathbf{G}^{\mathrm{T}}\mathbf{T}^{\mathrm{T}}\left(\mathbf{T}\mathbf{T}^{\mathrm{T}}\right)^{-1}\mathbf{T}\mathbf{G}\right]^{-1}. \quad (44)$$

Another metric of interest is the horizontal dilution of precision (HDOP), which gives a measure of the estimability of the horizontal components of the position vector. This metric is appropriate to study in the case where the rover is equipped with an altimeter and is using LEO signals mainly to estimate its horizontal position. Otherwise, the vertical dilution of precision (VDOP) becomes an important metric to study as well. The HDOP is calculated according to $\text{HDOP} = \sqrt{\text{trace}[\mathbf{P}_{2\times2}]}$, where $\mathbf{P}_{2\times2}$ indicates the 2×2 block of the PDOP matrix corresponding to the horizontal position coordinates, and the VDOP is given by $\text{VDOP} = \sqrt{\mathbf{P}_{3\times3}}$, where $\mathbf{P}_{3\times3}$ is the third diagonal element of $\mathbf{P}$, corresponding to the vertical position coordinate. The PDOP, HDOP, and VDOP cdfs are characterized numerically using the pdfs of the SV azimuth and elevation angles derived in Section IV for the Starlink constellation with the parameters in Table I. The cdfs, shown in Fig. 9 are computed for a receiver in Irvine, CA, USA, with

Authorized licensed use limited to: The Ohio State University. Downloaded on October 13,2023 at 15:28:54 UTC from IEEE Xplore. Restrictions apply.

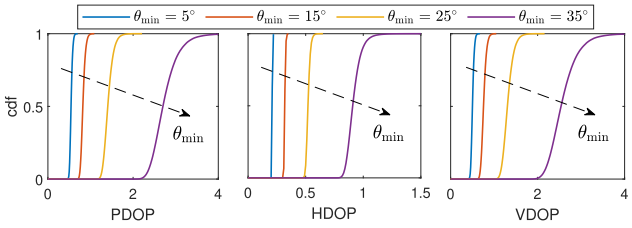

Fig. 9. Cdf of the PDOP, HDOP, and VDOP in the CD-LEO framework for the Starlink constellation for a receiver located at $\varphi_0 = 33.642673°$, $\lambda_0 = -117.838747°$, and zero altitude. The dashed arrows indicate the direction of the curves when $\theta_{\min}$ increases. The cdfs were computed from 10^5 PDOP, HDOP, and VDOP realizations.

$\varphi_0 = 33.642673°$, $\lambda_0 = -117.838747°$, zero altitude, and for four elevation angle masks: 5°, 15°, 25°, and 35°. While 5° might be unrealistically low for LEO SVs, it is included in the analysis to study a wider range of the DOP values. Fig. 9 shows that the PDOP is mostly less than 2 for elevation angle masks of 25° or below, and above 2 almost all the time for elevation angle masks of 35°. This is mainly due to the fact that the vertical component becomes poorly observable for such elevation angle masks. This is validated in the HDOP cdf, which shows that the HDOP is almost always below unity for elevation masks of 35° or below. In fact, the HDOP is mostly below 0.6 for elevation angles of 25°, showing that highly accurate horizontal positioning may be achieved.

Moreover, heat maps showing the average PDOP, HDOP, and VDOP were computed in Fig. 10. The figure shows that the average DOP is less than 1.5 for all latitudes between $-60°$ and 60°. Note that only the aforementioned range of latitudes is considered as 1) this is the region of interest and 2) the elevation angles become very low and the SVs are obstructed at the poles as the orbits have a 55 ° inclination yielding very large DOP values.

B. Measurement Error Statistics Characterization

1) *Ephemeris Errors:* The cdf of $|\tilde{r}_{\text{leo}_l}{}^{(\text{R,B})}|$ can be characterized from (26) and the joint distribution of the LEO SVs' azimuth and elevation angles derived in Section IV. To this end, the cdf of $g(\theta, \alpha)$ is calculated for the Starlink LEO constellation using the parameters in Table I. The receiver was assumed to be on the University of California, Irvine (UCI) campus. The cdf was computed for three elevation masks: $\theta_{\min} = 5°$, $\theta_{\min} = 25°$, and $\theta_{\min} = 35°$. The cdf of $g(\theta, \alpha)$ is shown in Fig. 11(a), and the expected value of $g(\theta, \alpha)$, denoted by $\mathbb{E}[g(\theta, \alpha)]$, is shown in Fig. 11(b) as a function of $\theta_{\min}$.

Next, to characterize the effect of ephemeris errors on CD-LEO measurements, the measurement errors are computed for a given distribution of the SV position error. The distribution of the SV position error was obtained from published root mean-squared error (RMSE) data by Celestrack for current Starlink SVs, which represent the SV position RMSE at the TLE epoch. A histogram of the SV position RMSE as well as a pdf fit are shown in Fig. 12. It was found that the Burr distribution best fit the RMSE data. It is assumed that the SV position error is independent

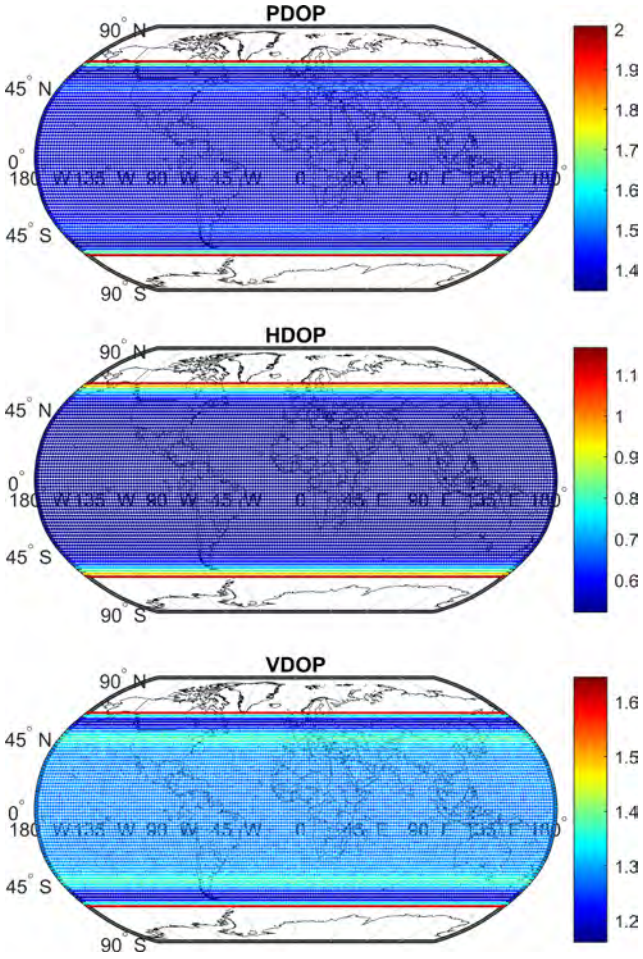

Fig. 10. Heat maps of the average PDOP, HDOP, and VDOP for the CD-LEO navigation framework. The heat maps were computed from 10^3 PDOP, HDOP, and VDOP realizations for an elevation mask of 25°.

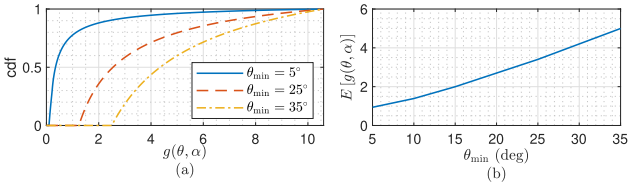

Fig. 11. (a) Cdf of $g(\theta, \alpha)$ for $\theta_{\min} = 5°$, $\theta_{\min} = 25°$, and $\theta_{\min} = 35°$. (b) Expected value of $g(\theta, \alpha)$ as a function of $\theta_{\min}$.

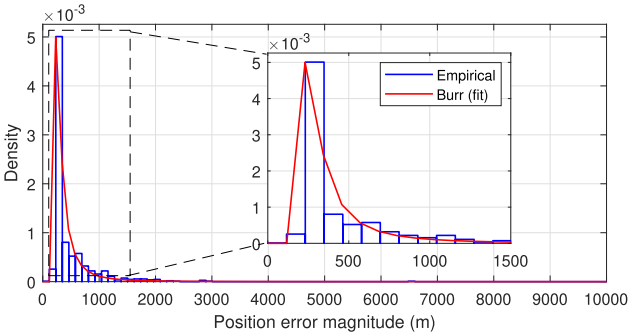

Fig. 12. Histogram of Starlink LEO SV position RMSE as obtained from Celestrack along with a pdf fit. It was found that the Burr distribution best fit the empirical data.

Authorized licensed use limited to: The Ohio State University. Downloaded on October 13,2023 at 15:28:54 UTC from IEEE Xplore. Restrictions apply.

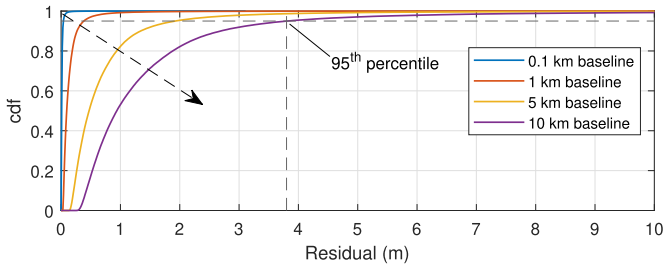

Fig. 13. Cdf of the CD-LEO measurement error due to SV position errors. The dashed arrows indicate the direction of the curves when the baseline increases. The cdf was computed from 10^5 residual realizations.

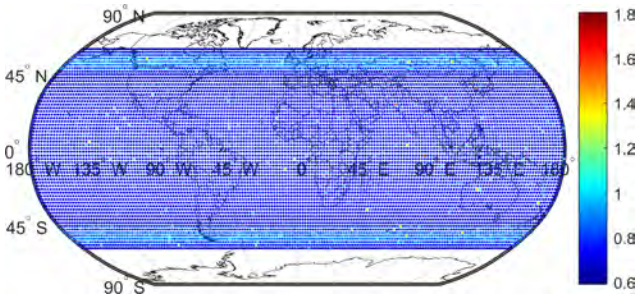

Fig. 14. Heat map of the average measurement error magnitude in CD-LEO measurements due to SV position error for a 5-km baseline. The heat map was computed from 10^4 residual realizations.

of the SV azimuth and elevation angles; hence, it is sampled independently from the Burr distribution fit.

Fig. 13 shows the cdf of the measurement errors for $\theta_{\min} = 25^\circ$ and for different values of the baseline. The SV position errors were drawn from the Burr distribution described above. The receiver was assumed to be on the UCI campus. The black arrow indicates the direction in which the baseline increases. It can be seen from Fig. 13 that the 95th percentile for a 10-km baseline is 3.8 m, which indicates that the measurement error 95th percentile is lower than 3.8 m for all baselines less than 10 km.

A heat map of the average measurement error magnitude is then computed for a baseline of 5 km and shown in Fig. 14. The heat map shows that the average measurement error in the CD-LEO measurements due to SV position error is less than 2 m almost anywhere between -60° and 60° latitudes.

2) *Atmospheric Effects:* Since the ${}^{\mathrm{z}}\hat{\delta}t^{(i)}_{\mathrm{iono},l}$, ${}^{\mathrm{z,w}}\hat{\delta}t^{(i)}_{\mathrm{iono},l}$, and ${}^{\mathrm{z,d}}\hat{\delta}t^{(i)}_{\mathrm{trop},l}$ are also functions of several unknown parameters, such as carrier frequency, TECV, atmospheric pressure, temperature, etc., the effect of ionospheric and tropospheric delays on CD-LEO measurements will be characterized through the mapping functions derived from (33) and (34) as

$$\bar{f}_{\mathrm{iono}}(\theta) \triangleq \left| \frac{d}{d\theta} f_{\mathrm{iono}}(\theta) \Delta\theta_{\max} \right| \tag{45}$$

$$\bar{f}_{\mathrm{trop,w}}(\theta) \triangleq \left| \frac{d}{d\theta} f_{\mathrm{trop,w}}(\theta) \Delta\theta_{\max} \right| \tag{46}$$

$$\bar{f}_{\mathrm{trop,d}}(\theta) \triangleq \left| \frac{d}{d\theta} f_{\mathrm{trop,d}}(\theta) \Delta\theta_{\max} \right|. \tag{47}$$

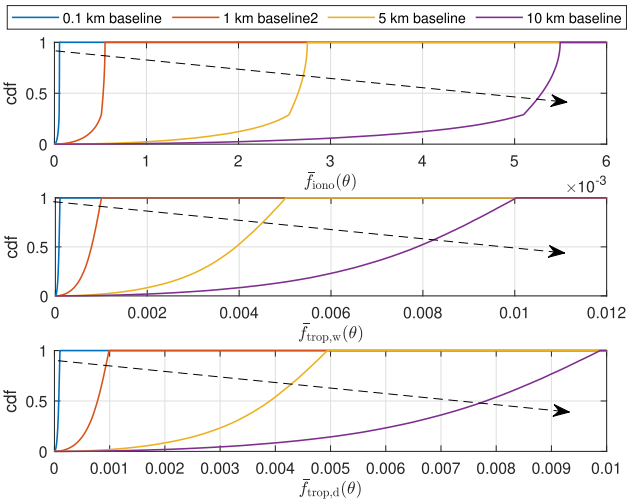

Fig. 15. Cdf of the ionospheric and tropospheric delay mapping functions in (45)–(47) for $\theta_{\min} = 25^\circ$. The dashed arrows indicate the direction of the curves when the baseline increases. The cdf was computed from 10^5 realizations.

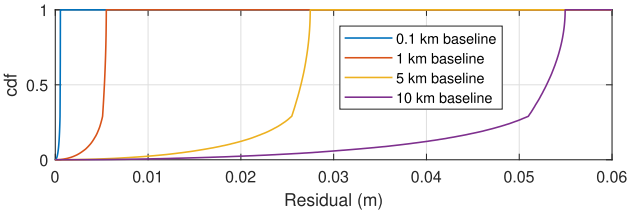

Fig. 16. Cdf of the error in the CD-LEO measurements due to the ionospheric delays for $\theta_{\min} = 25^\circ$ and ionospheric delay of 10 m at zenith. The cdf was computed from 10^5 residual realizations.

The cdf of $\bar{f}_{\mathrm{iono}}(\theta)$, $\bar{f}_{\mathrm{trop,w}}(\theta)$, and $\bar{f}_{\mathrm{trop,d}}(\theta)$ are shown in Fig. 15. The cdf of the measurement errors can be computed knowing the ionospheric and wet and dry tropospheric delays by simply multiplying them by the corresponding mapping functions in (45)–(47). For example, Fig. 16 shows the cdf of the CD-LEO measurement error due to ionospheric delays for an ionospheric delay of 10 m at zenith.

Heat maps of the average ionospheric and tropospheric delay mapping functions are then computed for a baseline of 5 km and shown in Fig. 17. The heat maps show that the average error magnitude in the CD-LEO measurements due to ionospheric delays is less than 4 mm per meters of zenith ionospheric delay almost anywhere between -60° and 60° latitudes.

REMARK 2 It is important to note that the goal of the article is to develop a methodology for characterizing the performance of a CD-LEO system and designing key system parameters. The Starlink constellation is taken as an example and several values for the baselines were considered for illustrative purposes. Other values of the baseline can be evaluated as well. Designing the CD-LEO baseline is a function of available resources and desired performance. Such a study is beyond the scope of this article and is left as future work.

Authorized licensed use limited to: The Ohio State University. Downloaded on October 13,2023 at 15:28:54 UTC from IEEE Xplore. Restrictions apply.

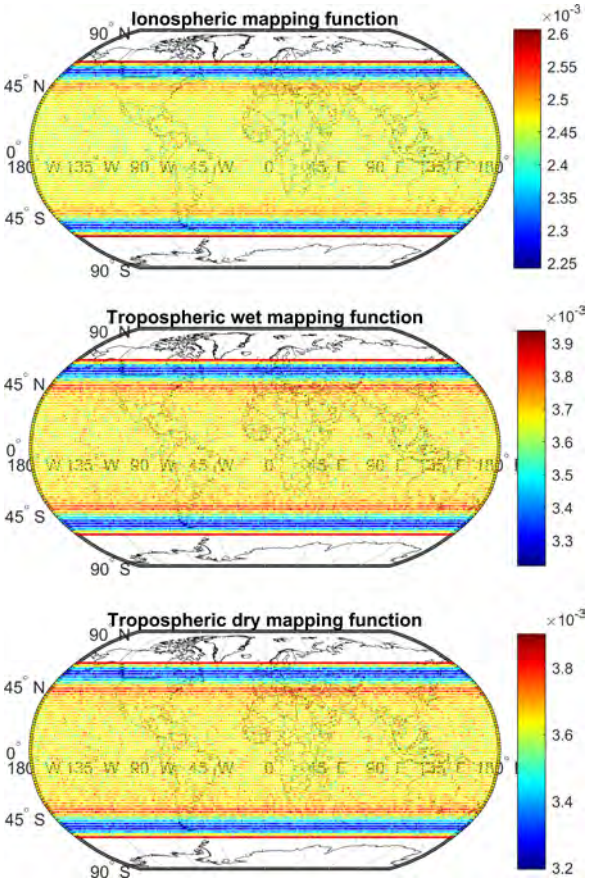

Fig. 17. Heat map of the average ionospheric and tropospheric delay mapping functions for a 5 km baseline. The heat map was computed from 10^4 residual realizations.

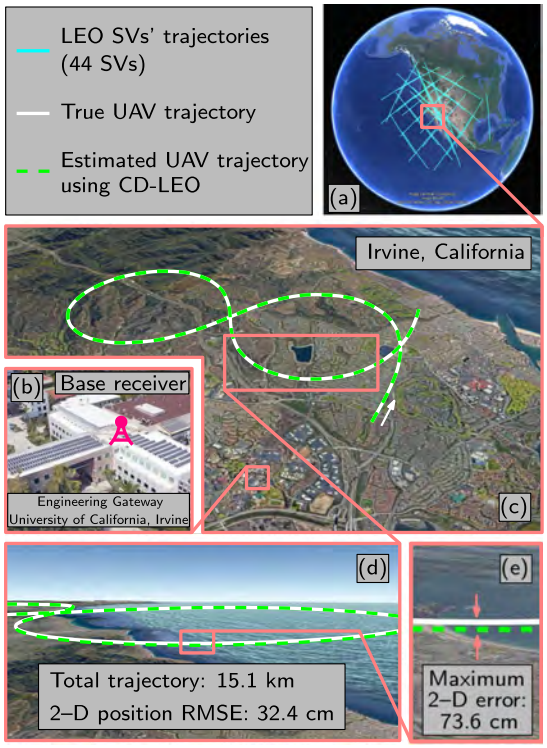

Fig. 18. Simulation results showing a fixed-wing UAV navigating using the proposed CD-LEO framework. (a) Starlink LEO SVs' trajectories (elevation mask set at 15°). (b) Base receiver location. (c) True and estimated UAV trajectories. (d)–(e) Close-up of the UAV trajectory showing precise navigation with the CD-LEO framework and a maximum 2–D position error of 73.6 cm.

VI. SIMULATION RESULTS

This section details simulation results of a fixed-wing UAV navigating with signals from the proposed Starlink LEO SV megaconstellation under the double difference CD-LEO framework discussed in Section II. The UAV, representing the rover, flew a total trajectory of 15.1 km in 300 s over Irvine, CA. The simulated UAV compares in performance to a small private plane with a cruise speed of roughly 50 m/s. The trajectory of the UAV, shown in white in Fig. 18(c) consisted of a straight segment, followed by a figure-eight pattern over Irvine, CA, USA, and then a final straight segment. The UAV flew at a constant altitude of 2.5 km, while executing the rolling and yawing maneuvers. A stationary base, shown in Fig. 18(b), was located on top of the Engineering Gateway at the UCI campus. The distance between the base and the UAV throughout the UAV's trajectory ranged between a maximum of 3.826 km to a minimum of 2.489 km. The elevation angle mask was set to 15° in both receivers. The UAV and base station both received signals from 44 simulated LEO SVs, whose trajectories are depicted in blue in Fig. 18(a). To simulate ephemeris errors, the true anomaly of each satellite was randomly shifted such that the satellite position errors were distributed between 75 m and 3.5 km. It was assumed that the UAV had access to GNSS for the first 50 s, during which the B-WNLS is solved. After 50 s, the UAV solves for its 3-D position using CD-LEO measurements and the integer ambiguities estimates obtained by solving the B-WNLS. The total 3-D and 2-D position RMSE were 2.2 m and 32.4 cm, respectively, while the maximum 2-D position error was 73.6 cm. Given that the baseline ranges from 2.5 to 3.8 km, the cdf of the measurement errors will be between the red and yellow curves in Fig. 9. As such, measurement errors on the order of 1 m are expected due to ephemeris errors. Note that the signal wavelength was assumed to be 3 cm (10 GHz). Therefore, the ephemeris errors will dominate the measurement errors. Moreover, similar to GNSS, the vertical uncertainty in the CD-LEO framework is larger than the horizontal uncertainty due to less geometric diversity in the vertical direction since the VDOP will be high relative to the HDOP, as seen in Figs. 9 and 10. The simulation layout and the true and estimated UAV trajectories are shown in Fig. 18.

VII. EXPERIMENTAL RESULTS

This section presents experimental results of a UAV navigating with signals from Orbcomm LEO SVs via the CD-LEO framework discussed in Section II. First, the experimental setup is discussed. Then, the navigation frameworks implemented in the experiments and their associated results are presented.

Authorized licensed use limited to: The Ohio State University. Downloaded on October 13,2023 at 15:28:54 UTC from IEEE Xplore. Restrictions apply.

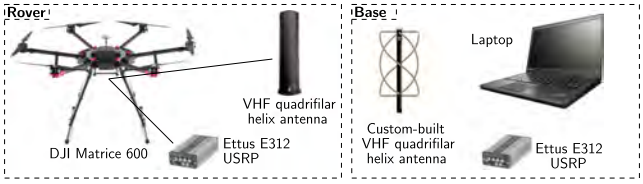

Fig. 19. Base/rover experimental setup of the CD-LEO framework.

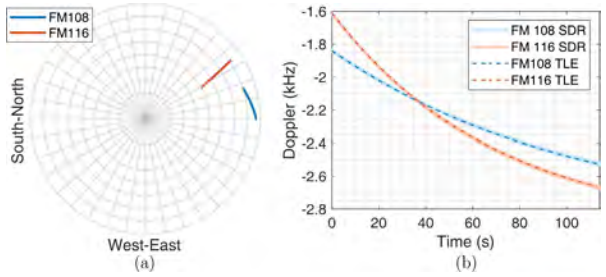

Fig. 20. (a) Sky plot of the geometry of the 2 Orbcomm SVs during the experiment. (b) The measured Doppler frequencies using the proprietary SDR and the expected Doppler calculated from the TLE for both Orbcomm SVs.

A. Experimental Setup

To demonstrate the CD-LEO framework discussed in Section II, the rover was a DJI Matrice 600 UAV equipped with an Ettus E312 USRP, a high-end VHF antenna, and a small consumer-grade GPS antenna to discipline the on-board oscillator. The base was a stationary receiver equipped with an Ettus E312 USRP, a custom-made VHF antenna, and a small consumer-grade GPS antenna to discipline the on-board oscillator. The receivers were tuned to a 137-MHz carrier frequency with 2.4-MHz sampling bandwidth, which covers the 137–138-MHz band allocated to Orbcomm SVs. Samples of the received signals were stored for off-line postprocessing using the software-defined radio (SDR) developed in [21]. The LEO carrier phase measurements were produced at a rate of 4.8 kHz and were downsampled to 10 Hz. The the base's position was surveyed on Google Earth, and the UAV trajectory was taken from its on-board navigation system, which uses GNSS (GPS and GLONASS), an inertial measurement unit (IMU), and other sensors. The hovering horizontal precision of the UAV is reported to be 1.5 m by DJI. The experimental setup is shown in Fig. 19. The UAV traversed a total trajectory of 2.28 km in 120 s.

Over the course of the experiment, the receivers onboard the base and the UAV were listening to two Orbcomm SVs, namely, FM 108 and FM 116. The SVs transmit a telemetry message which includes system time, SV position, and SV velocity as estimated by their on-board GPS receivers. These positions were decoded and used as ground-truth. A position estimate of FM 108 and FM 116 was also obtained from TLE files and SGP4 software [80]. The satellites were simultaneously visible for 2 min. A sky plot of the 2 Orbcomm SVs is shown in Fig. 20(a). The Doppler frequency measured by the rover using the SDR in [21] for the 2 Orbcomm SVs is shown along

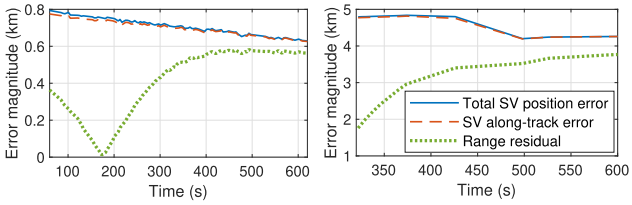

Fig. 21. Total SV position error magnitude and along-track SV position error magnitude for 2 Orbcomm LEO SVs, as well as the range residual due to ephemeris errors as observed by a terrestrial LEO receiver. .

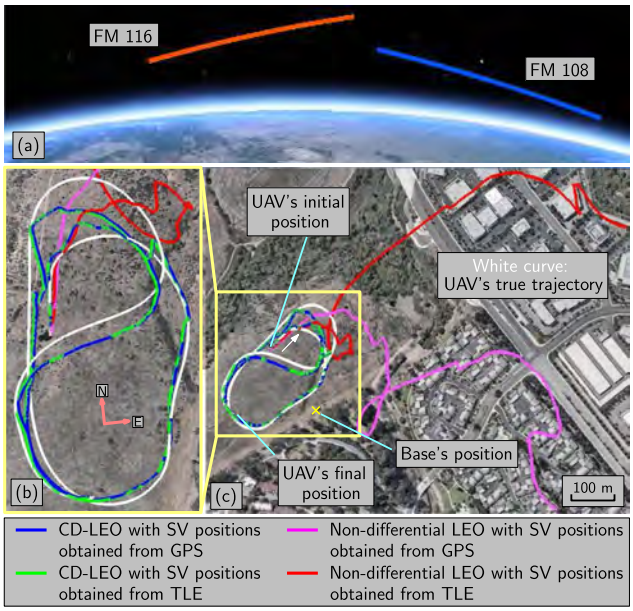

Fig. 22. (a) Trajectories of the 2 Orbcomm LEO SVs. (b)–(c) True and estimated trajectories of the UAV. Map data: Google Earth.

the expected Doppler calculated from the TLE files in Fig. 20(b). The SV position error and the range residuals are shown in Fig. 21 for each SV. Fig. 22(a) shows the SV trajectories. Note that the base and rover were closer than 1 km over the experiment; hence, ionospheric and tropospheric delay residuals were negligible. Since only two satellites were visible at a time, which is typically the case the Orbcomm constellation [53], the single difference CD-LEO framework discussed in Section II is used to estimate the 3–D position and velocity of the UAV from single difference CD-LEO measurements along with altitude measurements, taken from the UAV's on-board navigation solution. To demonstrate the potential of the CD-LEO navigation framework, two frameworks were implemented for comparison: 1) the CD-LEO framework discussed in Section II-D and 2) a nondifferential framework that employs carrier phase LEO measurements from the UAV's receiver only. The second framework is exactly equivalent to the one proposed [81] except that carrier phase measurements from LEO satellites are used instead of cellular transmitters. The results of each framework are presented next.

Authorized licensed use limited to: The Ohio State University. Downloaded on October 13,2023 at 15:28:54 UTC from IEEE Xplore. Restrictions apply.

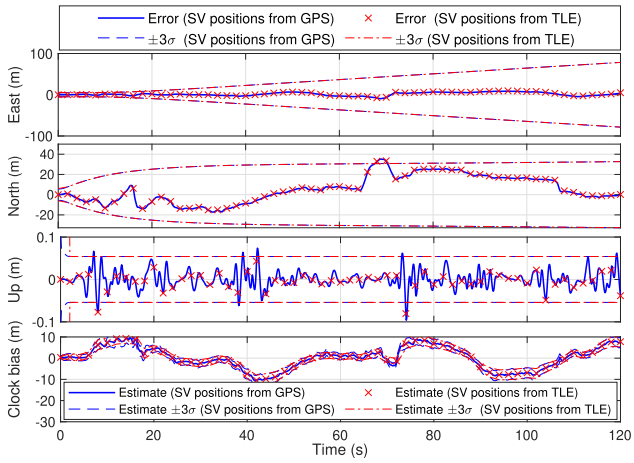

Fig. 23. EKF position estimation error and $\pm 3\sigma$ bounds for the CD-LEO framework. The estimates and sigma bounds for the case where SV positions are obtained from GPS and the ones for the case where the SV positions are obtained from TLE files are almost identical. The top legend corresponds to the position errors and the bottom legend corresponds to the clock bias estimate.

B. CD-LEO Framework Experimental Results

Single difference measurements provide more information on the SV-to-receiver geometry than double difference measurements since the differencing matrix $\mathbf{T}$ is not applied [82]. This comes at the cost of an additional state to be estimated: the common clock bias $\delta t_r^{(\mathrm{R,B})}(k)$. To this end, the UAV's position and velocity states were estimated along with the common clock bias $\delta t_r^{(\mathrm{R,B})}(k)$ and the constant ambiguity $N_2^{(\mathrm{R,B})}$. Note that $N_1^{(\mathrm{R,B})}$ was lumped into $\delta t_r^{(\mathrm{R,B})}(k)$. The UAV's continuous-time acceleration process noise spectra were set to $\tilde{q}_x = \tilde{q}_y = 1$ m$^2/s^5$ and $\tilde{q}_z = 0.01$ m$^2/s^5$ for the East, North, and up components, respectively. The choice of these spectra follows from the fact that the UAV is maneuvering in the horizontal direction only. The position and velocity process noise covariance can be readily obtained from these power spectra [76]. The UAV's and base's oscillator quality is assumed to be that of a typical temperature-compensated crystal oscillator (TCXO), from which the process noise covariance can also be readily obtained according to [76]. A prior for the UAV position and velocity was obtained from the UAV's on-board system. The prior was used to initialize the EKF. After initialization, the EKF was using single-difference Orbcomm LEO SV measurements to estimate the states of the UAV. To study the effect of ephemeris errors on the navigation solution, two EKFs were implemented: 1) one that uses the Orbcomm LEO SV positions estimated by the SVs' on-board GPS receiver and 2) one that uses the Orbcomm LEO SV positions estimated from TLE files. The estimated trajectories are shown in Fig. 22(b) and (c). The EKF position estimation errors are shown in Fig. 23 along with the 3σ bounds. Note that since the UAV mainly travels in the North direction, the East direction becomes poorly estimable; hence, the 3σ bounds in the East direction increase at a higher rate than the 3σ bound in the North direction, as shown in Fig. 23. The common clock bias estimate and the corresponding $\pm 3\sigma$ bounds are also shown in Fig 23. The 3-D position RMSEs and final errors for both EKFs are shown in Table II.

TABLE II
Experimental Results: 3-D RMSEs and 3-D Final Errors

Framework	SV position source	RMSE	Final error
CD-LEO	GPS	14.8 m	3.9 m
CD-LEO	TLE	15.0 m	4.8 m
Nondifferential	GPS	338.6 m	590.4 m
Nondifferential	TLE	405.4 m	759.5 m

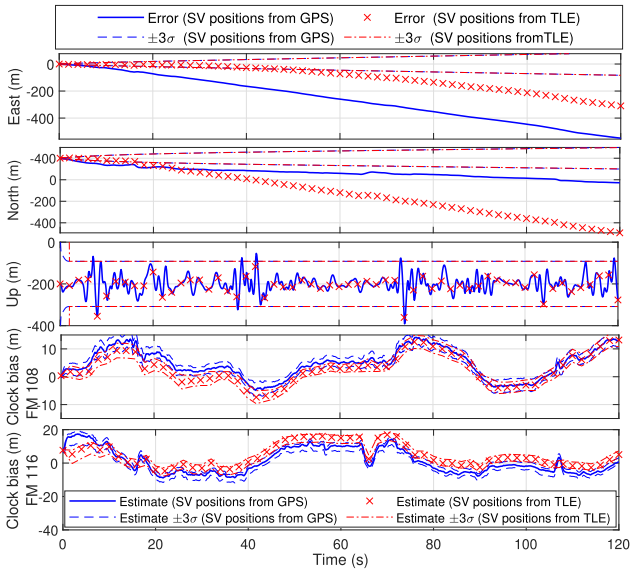

Fig. 24. EKF position estimation error and $\pm 3\sigma$ bounds for nondifferential LEO framework. The sigma bounds for the case where SV positions are obtained from GPS and the ones for the case where the SV positions are obtained from TLE files are almost identical. The top legend corresponds to the position errors and the bottom legend corresponds to the clock bias estimate. Also note that in the nondifferential framework, two clock biases are estimated: one for each SV.

C. Nondifferential LEO Framework Experimental Results

To demonstrate the importance of the CD-LEO framework, a nondifferential LEO framework is implemented. To this end, the UAV's position and velocity are estimated in an EKF using the nondifferential measurements in (1). In this case, two clock biases must be estimated capturing the difference between the receiver's clock bias and each of the Orbcomm LEO SVs' bias. The same dynamics models and initialization method employed in Section VII-B were used in the nondifferential framework, except that the SV's oscillators was assumed to be that of typical oven-controlled crystal oscillators (OCXO) [76]. Similarly to Section VII-B, two EKFs were implemented: 1) one that uses the Orbcomm LEO SV positions estimated by the SVs' on-board GPS receiver and 2) one that uses the Orbcomm LEO SV positions estimated from TLE files. The estimated trajectories are shown in Fig. 22(b) and (c). The EKF position estimation errors are shown in Fig. 24 along with the associated 3σ bounds. The clock bias estimates associated with FM 108

Authorized licensed use limited to: The Ohio State University. Downloaded on October 13,2023 at 15:28:54 UTC from IEEE Xplore. Restrictions apply.

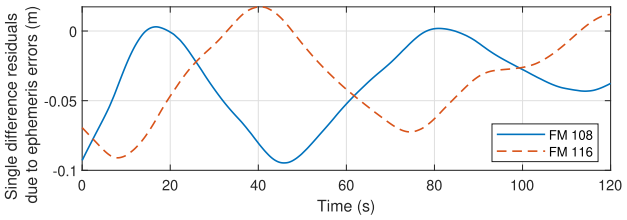

Fig. 25. Single difference residuals due to ephemeris errors for Orbcomm LEO SVs FM 108 and FM 116.

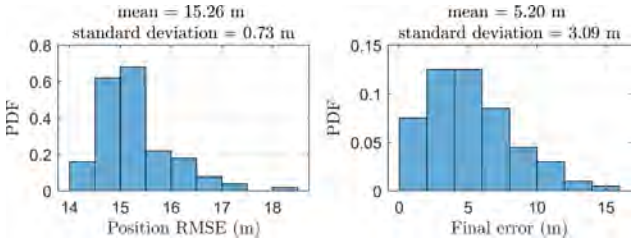

Fig. 26. Histogram of the position RMSE and final error obtained from 100 Monte Carlo realizations, where the initial position estimate of the UAV is drawn from a Gaussian distribution centered at the true UAV position with covariance $9 \times \mathbf{I}_{3\times 3}\text{m}^2$.

and FM 116 and the corresponding $\pm 3\sigma$ bounds are also shown in Fig 24. The 3-D position RMSEs and final errors for both EKFs are shown in Table II.

D. Discussion

Table II summarizes the experimental results for the CD-LEO and nondifferential LEO frameworks. It can be seen from Fig. 21 that the residuals in the nondifferential carrier phase measurements are on the order of kilometers, which explains the unacceptably large RMSEs of the nondifferential framework. While using the SV positions transmitted by the Orbcomm SVs reduces the RMSEs, the errors remain unacceptably large in the nondifferential framework due to other unmodeled errors. Such errors cancel out in the CD-LEO framework, yielding acceptable performance whether SV positions from GPS or TLE are used. The accuracy of these results is *unprecedented*, considering that 1) only 2 LEO SVs were used, 2) no other sensors were fused into the navigation, and 3) these LEO SVs are not intended for navigation and are exploited opportunistically. The predicted single difference residual due to ephemeris errors, $\{\tilde{r}^{\text{R,B}}_{\text{leo},l}\}_{l=1}^{2}$ were calculated according to (19), and are shown in Fig. 25. During the experiment, the baseline varied between 20 and 200 m. According to Section II-A, the function $g(\theta, \alpha)$ averages to 1.346 for the Orbcomm constellation, which has an inclination angle of 45° and orbital altitude of 800 km and $\theta_{\min} = 5°$. From the SV position errors in Fig. 21, the expected range of the residuals is from 0.3 to 16 cm. It can be seen from Fig. 25 that the magnitude of the single difference residual is on the order of *centimeters* and matches the expected values, showing 1) the robustness of the CD-LEO framework against ephemeris errors and 2) the accuracy of the performance analysis framework discussed in Section V. These small residuals explain the small change in performance between using TLE-derived SV positions and GPS-derived SV positions in the differential framework.

REMARK 3 To see the effect of small initialization errors on the CD-LEO framework performance, the EKF for the CD-LEO framework with SV position obtained from TLE was randomized over 100 Monte Carlo realizations. The initial estimate was drawn from a Gaussian distribution centered at the true UAV position with covariance $9 \times \mathbf{I}_{3\times 3}$ m^2. The histograms of the position RMSE and final error are shown in Fig. 26 along with their means and standard deviations. The results show that the EKF is robust against small initial errors.

REMARK 4 The CD-LEO frameworks were also implemented without altimeter measurements. The 3-D position RMSE and final position error when using SV position estimates from GPS were calculated to be 15.1 and 15.0 m, respectively. The 3-D position RMSE and final position error when using SV position estimates from TLE were calculated to be 14.3 and 8.4 m, respectively. Note that the RMSE in the latter case improved slightly; however, the final error degraded significantly. Nevertheless, the performance obtained with only CD-LEO measurements is comparable with that of CD-LEO and altimeter.

REMARK 5 In order to test the double difference framework, the CD-LEO framework was also implemented with the UAV acting as the base and the stationary receiver acting as a stationary rover. The 2-D position error of the stationary rover after the B-WNLS was calculated to be 10.9 m when using SV position estimates from TLE, and 8.2 m when using SV position estimates from GPS. The HDOP was found to be 29.2. Assuming a precision of $\lambda/2$ in the CD-LEO measurements, it is found that the position errors obtained in this experiment are well below the 1σ bound.

VIII. CONCLUSION

This article proposes a differential framework for opportunistic navigation with carrier phase measurements from megaconstellation LEO satellites. Models of the measurement errors due to ephemeris errors and ionospheric and tropospheric delays were derived as a function of the SV elevation angle. Moreover, the joint pdf of the megaconstellation LEO satellites' azimuth and elevation angle was characterized. A performance characterization of the proposed CD-LEO framework was conducted using derived joint azimuth and elevation angle pdf, showing the potential of LEO satellite signals for precise navigation. The performance characterization conducted in this article also facilitates system parameter design to meet desired performance requirements. Simulation and experimental results are presented showing a UAV localizing itself with LEO satellite signals using carrier phase differential measurements to an unprecedented level of accuracy. The simulation results show a UAV navigating for 15.1 km in 300 s, while using

Authorized licensed use limited to: The Ohio State University. Downloaded on October 13,2023 at 15:28:54 UTC from IEEE Xplore. Restrictions apply.

signals from 44 Starlink LEO satellites, achieving a 3-D position RMSE of 2.2 m and a 2-D RMSE of 32.4 cm. The experimental results show a UAV navigating for 2.28 km in 2 min over Aliso Viejo, CA, USA, using exclusively signals from only two Orbcomm LEO satellites, achieving a position RMSE of 14.8 m. Additional experiments could be conducted to characterize the CD-LEO performance with varying baselines in future work.

ACKNOWLEDGMENT

The authors would like to thank Dr. Chris Bartone for the insightful discussions and Joshua Morales, MyLinh Nguyen, Ali Abdallah, Mohammad Orabi, Kimia Shamaei, Mahdi Maaref, and Naji Tarabay for their help in data collection.

APPENDIX A
PROOF OF LEMMA IV.1

This appendix proves the inverse mapping from (ϕ_l, θ_l) to (λ_l, φ_l) is given in Lemma IV.1.

PROOF For a spherical Earth, the lth satellite position in Earth-centered Earth-fixed (ECEF) may be expressed as

$$\bar{\boldsymbol{r}}_{\text{leo},L} = \alpha_l R_E \left[\cos\varphi_l \cos\lambda_l, \quad \cos\varphi_l \sin\lambda_l, \quad \sin\varphi_l\right]^{\mathrm{T}}.$$

Subsequently, given $\bar{\boldsymbol{r}}_{\text{leo},L}$, the longitude and latitude λ_l and φ_l, respectively, may be obtained according to

$$\lambda_l = \tan^{-1}\left[\frac{\boldsymbol{e}_2^{\mathrm{T}}\bar{\boldsymbol{r}}_{\text{leo},L}}{\boldsymbol{e}_1^{\mathrm{T}}\bar{\boldsymbol{r}}_{\text{leo},L}}\right], \quad \varphi_l = \sin^{-1}\left[\frac{\boldsymbol{e}_3^{\mathrm{T}}\bar{\boldsymbol{r}}_{\text{leo},L}}{\left\|\bar{\boldsymbol{r}}_{\text{leo},L}\right\|_2}\right]. \quad (48)$$

The SV position in ENU can also be expressed as

$$\boldsymbol{r}_{\text{leo},l} \triangleq d_l \left[\cos\theta_l \sin\phi_l, \quad \cos\theta_l \cos\phi_l, \quad \sin\theta_l\right]^{\mathrm{T}}. \quad (49)$$

Using coordinate frame transformation, the SV position in ECEF can be obtained from $\boldsymbol{r}_{\text{leo}}$ through

$$\bar{\boldsymbol{r}}_{\text{leo}_l} = \mathbf{R}^{\mathrm{T}}(\varphi_0, \lambda_0)\boldsymbol{r}_{\text{leo},l} + \bar{\boldsymbol{r}}_r \quad (50)$$

where $\bar{\boldsymbol{r}}_r = R_E[\cos\varphi_0 \cos\lambda_0, \cos\varphi_0 \sin\lambda_0, \sin\varphi_0]^{\mathrm{T}}$ is the receiver's position in ECEF and $\mathbf{R}(\varphi_0, \lambda_0)$ is the ECEF to ENU rotation matrix with

$$\mathbf{R}(\varphi_0, \lambda_0) \triangleq \begin{bmatrix} -\sin\lambda_0 & \cos\lambda_0 & 0 \\ -\sin\varphi_0\cos\lambda_0 & -\sin\varphi_0\sin\lambda_0 & \cos\varphi_0 \\ \cos\varphi_0\cos\lambda_0 & \cos\varphi_0\sin\lambda_0 & \sin\varphi_0 \end{bmatrix}.$$

Equation (39) is readily obtained by combining (48)–(50). □

APPENDIX B
DERIVATION OF THE JACOBIAN IN (40)

In the following, the subscripts j and l are omitted for compactness of notation.

$$\text{Define } g_\gamma(\theta) \triangleq \frac{\partial \sin\left[\gamma(\theta)\right]}{\partial\theta} = \left[\frac{\sin\theta}{\alpha\sqrt{1-\frac{\cos^2\theta}{\alpha^2}}} - 1\right]\cos\left[\gamma(\theta)\right]$$

$$g_{01}^{\phi}(\phi,\theta) \triangleq \frac{\partial f_{01}(\phi,\theta)}{\partial\phi} = \sin\lambda_0\sin\phi - \sin\varphi_0\cos\lambda_0\cos\phi$$

$$g_{01}^{\theta}(\phi,\theta) \triangleq \frac{\partial f_{01}(\phi,\theta)}{\partial\theta} = \frac{\cos\varphi_0\cos\lambda_0}{\cos^2\theta}$$

$$g_{02}^{\phi}(\phi,\theta) \triangleq \frac{\partial f_{02}(\phi,\theta)}{\partial\phi} = -\cos\lambda_0\sin\phi - \sin\varphi_0\sin\lambda_0\cos\phi$$

$$g_{02}^{\theta}(\phi,\theta) \triangleq \frac{\partial f_{02}(\phi,\theta)}{\partial\theta} = \frac{\cos\varphi_0\sin\lambda_0}{\cos^2\theta}$$

$$g_{03}^{\phi}(\phi,\theta) \triangleq \frac{\partial f_{03}(\phi,\theta)}{\partial\phi} = \cos\varphi_0\cos\phi$$

$$g_{03}^{\theta}(\phi,\theta) \triangleq \frac{\partial f_{03}(\phi,\theta)}{\partial\theta} = \frac{\sin\varphi_0}{\cos^2\theta}$$

$$b_{01}^{\phi}(\phi,\theta) \triangleq \frac{\partial a_{01}(\phi,\theta)}{\partial\phi} = \sin\left[\gamma(\theta)\right] g_{01}^{\phi}(\phi,\theta)$$

$$b_{01}^{\theta}(\phi,\theta) \triangleq \frac{\partial a_{01}(\phi,\theta)}{\partial\theta} = g_\gamma(\theta) f_{01}(\phi,\theta) + \sin\left[\gamma(\theta)\right] g_{01}^{\theta}(\phi,\theta)$$

$$b_{02}^{\phi}(\phi,\theta) \triangleq \frac{\partial a_{02}(\phi,\theta)}{\partial\phi} = \sin\left[\gamma(\theta)\right] g_{02}^{\phi}(\phi,\theta)$$

$$b_{02}^{\theta}(\phi,\theta) \triangleq \frac{\partial a_{02}(\phi,\theta)}{\partial\theta} = g_\gamma(\theta) f_{02}(\phi,\theta) + \sin\left[\gamma(\theta)\right] g_{02}^{\theta}(\phi,\theta)$$

$$b_{03}^{\phi}(\phi,\theta) \triangleq \frac{\partial a_{03}(\phi,\theta)}{\partial\phi} = \sin\left[\gamma(\theta)\right] g_{03}^{\phi}(\phi,\theta)$$

$$b_{03}^{\theta}(\phi,\theta) \triangleq \frac{\partial a_{03}(\phi,\theta)}{\partial\theta} = g_\gamma(\theta) f_{03}(\phi,\theta) + \sin\left[\gamma(\theta)\right] g_{03}^{\theta}(\phi,\theta).$$

Since by definition $\|\boldsymbol{r}_{\text{leo},l}\|_2 = \alpha R_E$, then the following holds:

$$a_{01}^2(\phi,\theta) + a_{02}^2(\phi,\theta) + a_{03}^2(\phi,\theta) = 1. \quad (51)$$

Subsequently, the elements of the Jacobian matrix $\mathbf{J}_y(\phi,\theta)$ are given by

$$\frac{\partial\lambda}{\partial\phi} \triangleq \frac{b_{02}^{\phi}(\phi,\theta)a_{01}(\phi,\theta) - b_{01}^{\phi}(\phi,\theta)a_{02}(\phi,\theta)}{a_{01}^2(\phi,\theta) + a_{02}^2(\phi,\theta)}$$

$$\frac{\partial\lambda}{\partial\theta} \triangleq \frac{b_{02}^{\theta}(\phi,\theta)a_{01}(\phi,\theta) - b_{01}^{\theta}(\phi,\theta)a_{02}(\phi,\theta)}{a_{01}^2(\phi,\theta) + a_{02}^2(\phi,\theta)}$$

$$\frac{\partial\varphi}{\partial\phi} \triangleq \frac{b_{03}^{\phi}(\phi,\theta)}{\sqrt{a_{01}^2(\phi,\theta) + a_{02}^2(\phi,\theta)}}$$

$$\frac{\partial\varphi}{\partial\theta} \triangleq \frac{b_{03}^{\theta}(\phi,\theta)}{\sqrt{a_{01}^2(\phi,\theta) + a_{02}^2(\phi,\theta)}}$$

and the determinant of $\mathbf{J}_y(\phi,\theta)$ is given by

$$\left|\mathbf{J}_y(\phi,\theta)\right| = \frac{a_{01}\left(b_{02}^{\phi}b_{03}^{\theta} - b_{02}^{\theta}b_{03}^{\phi}\right) - a_{02}\left(b_{01}^{\phi}b_{03}^{\theta} - b_{01}^{\theta}b_{03}^{\phi}\right)}{\left(a_{01}^2 + a_{02}^2\right)^{\frac{3}{2}}}. \quad (52)$$

REFERENCES

[1] T. Reidet al., "Navigation from low Earth orbit–Part 1 Concept, current, capability, and future promise," in *Position, Navigation, and Timing Technologies in the 21st Century*, J. Morton, F. van Diggelen, J. Spilker Jr, and B. Parkinson, Eds., Hoboken, NJ, USA: Wiley, vol. 2, ch. 43, 2021, pp. 1359–1379.

Authorized licensed use limited to: The Ohio State University. Downloaded on October 13,2023 at 15:28:54 UTC from IEEE Xplore. Restrictions apply.

[2] Z. Kassas, "Navigation from low Earth orbit–Part 2: Models, implementation, and performance," in *Position, Navigation, and Timing Technologies in the 21st Century*, J. Morton, F. van Diggelen, J. Spilker Jr, and B. Parkinson, Eds., Hoboken, NJ, USA: Wiley, vol. 2, ch. 43, 2021, pp. 1381–1412.
[3] M. Rabinowitz, "A differential carrier-phase navigation system combining GPS with low earth orbit satellites for rapid resolution of integer cycle ambiguities," Ph.D. dissertation, Stanford Univ., Stanford, CA, USA, 2000.
[4] M. Joerger, L. Gratton, B. Pervan, and C. Cohen, "Analysis of iridium-augmented GPS for floating carrier phase positioning," *J. Inst. Navigation*, vol. 57, no. 2, pp. 137–160, 2010.
[5] M. Joerger, J. Neale, S. Datta-Barua, and B. Pervan, "Ionospheric error modeling for carrier phase-based multiconstellation navigation systems," *IEEE Trans. Aerosp. Electron. Syst.*, vol. 49, no. 1, pp. 451–467, Jan. 2013.
[6] T. Reid, A. Neish, T. Walter, and P. Enge, "Broadband LEO constellations for navigation," *J. Inst. Navigation*, vol. 65, no. 2, pp. 205–220, 2018.
[7] Z. Kassas, J. Morales, and J. Khalife, "New-age satellite-based navigation–STAN: Simultaneous tracking and navigation with LEO satellite signals," *Inside GNSS Mag.*, vol. 14, no. 4, pp. 56–65, 2019.
[8] J. Fischer, "Resilient timekeeping for critical infrastructure," in *Proc. ION Precise Time Interval Syst. Appl. Meeting*, 2020, pp. 234–240.
[9] R. Morales-Ferre, E. Lohan, G. Falco, and E. Falletti, "GDOP-based analysis of suitability of LEO constellations for future satellite-based positioning," in *Proc. IEEE Int. Conf. Wireless Space Extreme Environments*, 2020, pp. 147–152.
[10] Q. Wei, X. Chen, and Y. Zhan, "Exploring implicit pilots for precise estimation of LEO satellite downlink Doppler frequency," *IEEE Commun. Lett.*, vol. 24, no. 10, pp. 2270–2274, Oct. 2020.
[11] D. Racelis and M. Joerger, "Impact of cascading faults on mega-constellation-augmented GNSS PPP integrity," in *Proc. ION GNSS Conf.*, 2020, pp. 3055–3070.
[12] S. Thompson, S. Martin, and D. Bevly, "Single differenced doppler positioning with low earth orbit signals of opportunity and angle of arrival estimation," in *Proc. ION Int. Tech. Meeting Conf.*, 2021, pp. 497–509.
[13] J. Khalife, M. Neinavaie, and Z. Kassas, "Blind doppler tracking from OFDM signals transmitted by broadband LEO satellites," in *Proc. IEEE Veh. Technol. Conf.*, 2021, pp. 1–6.
[14] Z. Kassaset al., "Enter LEO on the GNSS stage: Navigation with starlink satellites," *Inside GNSS Mag.*, vol. 16, no. 6, pp. 42–51, 2021.
[15] R. Sabbagh and Z. Kassas, "Observability analysis of receiver localization via pseudorange measurements from a single LEO satellite," *IEEE Contr. Syst. Lett.*, vol. 7, no. 3, pp. 571–576, 2023.
[16] M. Hartnett, "Performance assessment of navigation using carrier doppler measurements from multiple LEO constellations," Master's thesis, Air Force Inst. Technol., Wright-Patterson AFB, OH, USA, 2022.
[17] M. Jiang, H. Qin, C. Zhao, and G. Sun, "LEO doppler-aided GNSS position estimation," *GPS Solutions*, vol. 26, no. 1, 2022, Art. no. 31.
[18] N. Jardak and Q. Jault, "The potential of LEO satellite-based opportunistic navigation for high dynamic applications," *Sensors*, vol. 22, no. 7, pp. 2541–2565, 2022.
[19] T. Reidet al., "Satellite navigation for the age of autonomy," in *Proc. IEEE/ION Position Location Navigation Symp.*, 2020, pp. 342–352.
[20] A. Nardin, F. Dovis, and J. Fraire, "Empowering the tracking performance of LEO-based positioning by means of meta-signals," *IEEE J. Radio Freq. Identif.*, vol. 5, no. 3, pp. 244–253, Sep. 2021.
[21] J. Khalife and Z. Kassas, "Receiver design for Doppler positioning with LEO satellites," in *Proc. IEEE Int. Conf. Acoust. Speech Signal Process.*, 2019, pp. 5506–5510.
[22] R. Landry, A. Nguyen, H. Rasaee, A. Amrhar, X. Fang, and H. Benzerrouk, "Iridium next LEO satellites as an alternative PNT in GNSS denied environments—Part I," *Inside GNSS Mag.*, vol. 14, no. 3, pp. 56–64, May 2019.
[23] F. Farhangian, H. Benzerrouk, and R. Landry, "Opportunistic in-flight INS alignment using LEO satellites and a rotatory IMU platform," *Aerospace*, vol. 8, no. 10, pp. 280–281, 2021.
[24] A. Elgamoudi, H. Benzerrouk, G. Elango, and R. Landry, "Gauss Hermite H∞ filter for UAV tracking using LEO satellites TDOA/FDOA measurement—Part I," *IEEE Access*, vol. 8, pp. 201428–201 440, 2020.
[25] M. Neinavaie, J. Khalife, and Z. Kassas, "Blind doppler tracking and beacon detection for opportunistic navigation with LEO satellite signals," in *Proc. IEEE Aerosp. Conf.*, 2021, pp. 1–8.
[26] C. Pinell, "Receiver architectures for positioning with low earth orbit satellite signals," Master's thesis, School Electr. Eng., Lulea Univ. Technol., Lulea, Sweden, 2021.
[27] C. Huang, H. Qin, C. Zhao, and H. Liang, "Phase - time method: Accurate Doppler measurement for iridium NEXT signals," *IEEE Trans. Aerosp. Electron. Syst.*, vol. 58, no. 6, pp. 5954–5962, Dec. 2022.
[28] P. Iannucci and T. Humphreys, "Economical fused LEO GNSS," in *Proc. IEEE/ION Position Location Navigation Symp.*, 2020, pp. 426–443.
[29] J. Raquet et al., "Part D: Position, navigation, and timing using radio signals-of-opportunity," in *Position, Navigation, and Timing Technologies in the 21st Century*, J. Morton, F. van Diggelen, J. Spilker Jr, and B. Parkinson, Eds. Hoboken, NJ, USA: Wiley, 2021, vol. 2, ch. 35–43, pp. 1115–1412.
[30] J. McEllroy, J. Raquet, and M. Temple, "Use of a software radio to evaluate signals of opportunity for navigation," in *Proc. ION GNSS Conf.*, 2006, pp. 126–133.
[31] X. Chen, Q. Wei, F. Wang, Z. Jun, S. Wu, and A. Men, "Super-resolution time of arrival estimation for a symbiotic FM radio data system," *IEEE Trans. Broadcast.*, vol. 66, no. 4, pp. 847–856, Dec. 2020.
[32] M. Psiaki and B. Slosman, "Tracking digital FM OFDM signals for the determination of navigation observables," *J. Inst. Navigation*, vol. 69, no. 2, 2022, Art. no. navi.521.
[33] C. Yang and A. Soloviev, "Mobile positioning with signals of opportunity in urban and urban canyon environments," in *Proc. IEEE/ION Position, Location, Navigation Symp.*, 2020, pp. 1043–1059.
[34] N. Souli, P. Kolios, and G. Ellinas, "Online relative positioning of autonomous vehicles using signals of opportunity," *IEEE Trans. Intell. Veh.*, vol. 7, no. 4, pp. 873–885, Dec. 2022, doi: 10.1109/TIV.2021.3124727.
[35] J. Khalife and Z. Kassas, "Navigation with cellular CDMA signals—Part II: Performance analysis and experimental results," *IEEE Trans. Signal Process.*, vol. 66, no. 8, pp. 2204–2218, Apr. 2018.
[36] T. Kang, H. Lee, and J. Seo, "TOA-based ranging method using CRS in LTE signals," *J. Adv. Navigation Technol.*, vol. 23, no. 5, pp. 437–443, Oct. 2019.
[37] P. Wang and Y. Morton, "Multipath estimating delay lock loop for LTE signal TOA estimation in indoor and urban environments," *IEEE Trans. Wireless Commun.*, vol. 19, no. 8, pp. 5518–5530, Aug. 2020.
[38] J. Gante, L. Sousa, and G. Falcao, "Dethroning GPS: Low-power accurate 5 G positioning systems using machine learning," *IEEE Trans. Emerg. Sel. Topics Circuits Syst.*, vol. 10, no. 2, pp. 240–252, Jun. 2020.
[39] H. Dun, C. Tiberius, and G. Janssen, "Positioning in a multipath channel using OFDM signals with carrier phase tracking," *IEEE Access*, vol. 8, pp. 13011–13028, 2020.
[40] K. Shamaei and Z. Kassas, "Receiver design and time of arrival estimation for opportunistic localization with 5G signals," *IEEE Trans. Wireless Commun.*, vol. 20, no. 7, pp. 4716–4731, Jul. 2021.
[41] A. Abdallah and Z. Kassas, "Opportunistic navigation using sub-6 GHz 5G downlink signals: A case study on a ground vehicle," in *Proc. Eur. Conf. Antennas Propag.*, 2022, pp. 1–5.
[42] T. Kazaz, G. Janssen, J. Romme, and A. Van der Veen, "Delay estimation for ranging and localization using multiband channel state information," *IEEE Trans. Wireless Commun.*, vol. 21, no. 4, pp. 2591–2607, Apr. 2022.

Authorized licensed use limited to: The Ohio State University. Downloaded on October 13,2023 at 15:28:54 UTC from IEEE Xplore. Restrictions apply.

[43] I. Lapin, G. Seco-Granados, O. Renaudin, F. Zanier, and L. Ries, "Joint delay and phase discriminator based on ESPRIT for 5G NR positioning," *IEEE Access*, vol. 9, pp. 126550–126563, 2021.
[44] G. Fokin and D. Volgushev, "Software-defined radio network positioning technology design. Problem statement," in *Proc. Syst. Signals Generating Process. Field Board Commun.*, 2022, pp. 1–6.
[45] J. Khalife and Z. Kassas, "On the achievability of submeter-accurate UAV navigation with cellular signals exploiting loose network synchronization," *IEEE Trans. Aerosp. Electron. Syst.*, vol. 58, no. 5, pp. 4261–4278, Oct. 2022.
[46] J. Khalife and Z. Kassas, "Differential framework for submeter-accurate vehicular navigation with cellular signals," *IEEE Trans. Intell. Veh.*, vol. 8, no. 1, pp. 732–744, 2023, doi: 10.1109/TIV.2022.3187957.
[47] D. Vallado and P. Crawford, "SGP4 orbit determination," in *Proc. AIAA/AAS Astrodynamics Specialist Conf. Exhibit*, 2008, pp. 6770–6799.
[48] X. Tian, G. Chen, E. Blasch, K. Pham, and Y. Bar-Shalom, "Comparison of three approximate kinematic models for space object tracking," in *Proc. Int. Conf. Inf. Fusion*, 2013, pp. 1005–1012.
[49] B. Li, J. Huang, Y. Feng, F. Wang, and J. Sang, "A machine learning-based approach for improved orbit predictions of LEO space debris with sparse tracking data from a single station," *IEEE Trans. Aerosp. Electron. Syst.*, vol. 56, no. 6, pp. 4253–4268, Dec. 2020.
[50] H. Benzerrouk, Q. Nguyen, F. Xiaoxing, A. Amrhar, A. Nebylov, and R. Landry, "Alternative PNT based on iridium next LEO satellites Doppler/INS integrated navigation system," in *Proc. Saint Petersburg Int. Conf. Integr. Navigation Syst.*, 2019, pp. 1–10.
[51] Z. Tan, H. Qin, L. Cong, and C. Zhao, "New method for positioning using IRIDIUM satellite signals of opportunity," *IEEE Access*, vol. 7, pp. 83412–83423, 2019.
[52] F. Farhangian and R. Landry, "Multi-constellation software-defined receiver for Doppler positioning with LEO satellites," *Sensors*, vol. 20, no. 20, pp. 5866–5883, Oct. 2020.
[53] M. Orabi, J. Khalife, and Z. Kassas, "Opportunistic navigation with doppler measurements from iridium next and orbcomm LEO satellites," in *Proc. IEEE Aerosp. Conf.*, 2021, pp. 1–9.
[54] H. Geet al., "Initial assessment of precise point positioning with LEO enhanced global navigation satellite systems (LeGNSS)," *Remote Sens.*, vol. 10, no. 7, pp. 984–999, 2018.
[55] B. Li, H. Ge, M. Ge, L. Nie, Y. Shen, and H. Schuh, "LEO enhanced global navigation satellite system (LeGNSS) for real-time precise positioning services," *Adv. Space Res.*, vol. 63, no. 1, pp. 73–93, 2019.
[56] M. Su, X. Su, Q. Zhao, and J. Liu, "BeiDou augmented navigation from low earth orbit satellites," *Sensors*, vol. 19, no. 1, pp. 198–214, 2019.
[57] D. Racelis, B. Pervan, and M. Joerger, "Fault-free integrity analysis of mega-constellation-augmented GNSS," in *Proc. ION GNSS Conf.*, 2019, pp. 465–484.
[58] L. Ye, Y. Yang, X. Jing, L. Deng, and H. Li, "Single-satellite integrated navigation algorithm based on broadband LEO constellation communication links," *Remote Sens.*, vol. 13, no. 4, pp. 703–729, Feb. 2021.
[59] T. Mortlock and Z. Kassas, "Performance analysis of simultaneous tracking and navigation with LEO satellites," in *Proc. ION GNSS Conf.*, 2020, pp. 2416–2429.
[60] S. Kozhaya, J. Haidar-Ahmad, A. Abdallah, Z. Kassas, and S. Saab, "Comparison of neural network architectures for simultaneous tracking and navigation with LEO satellites," in *Proc. ION GNSS Conf.*, 2021, pp. 2507–2520.
[61] N. Khairallah and Z. Kassas, "Ephemeris closed-loop tracking of LEO satellites with pseudorange and Doppler measurements," in *Proc. ION GNSS Conf.*, 2021, pp. 2544–2555.
[62] J. Khalife and Z. Kassas, "Assessment of differential carrier phase measurements from orbcomm LEO satellite signals for opportunistic navigation," in *Proc. ION GNSS Conf.*, 2019, pp. 4053–4063.
[63] J. Khalife, M. Neinavaie, and Z. Kassas, "Navigation with differential carrier phase measurements from megaconstellation LEO satellites," in *Proc. IEEE/ION Position, Location, Navigation Symp.*, 2020, pp. 1393–1404.
[64] K. Pesyna, T. Humphreys, R. Heath, T. Novlan, and J. Zhang, "Exploiting antenna motion for faster initialization of centimeter-accurate GNSS positioning with low-cost antennas," *IEEE Trans. Aerosp. Electron. Syst.*, vol. 53, no. 4, pp. 1597–1613, Aug. 2017.
[65] P. Teunissen, "The least-squares ambiguity decorrelation adjustment: A method for fast GPS integer ambiguity estimation," *J. Geodesy*, vol. 70, no. 1, pp. 65–82, Nov. 1995.
[66] M. Rabinowitz, B. Parkinson, C. Cohen, M. O'Connor, and D. Lawrence, "A system using LEO telecommunication satellites for rapid acquisition of integer cycle ambiguities," in *Proc. IEEE/ION Position Location Navigation Symp.*, 1998, pp. 137–145.
[67] M. Haenggi, J. Andrews, F. Baccelli, O. Dousse, and M. Franceschetti, "Stochastic geometry and random graphs for the analysis and design of wireless networks," *IEEE J. Sel. Areas Commun.*, vol. 27, no. 7, pp. 1029–1046, Sep. 2009.
[68] T. Khan and M. Afshang, "A stochastic geometry approach to Doppler characterization in a LEO satellite network," in *Proc. IEEE Int. Conf. Commun.*, 2020, pp. 1–6.
[69] N. Okati, T. Riihonen, D. Korpi, I. Angervuori, and R. Wichman, "Downlink coverage and rate analysis of low earth orbit satellite constellations using stochastic geometry," *IEEE Trans. Commun.*, vol. 68, no. 8, pp. 5120–5134, Aug. 2020.
[70] A. Talgat, M. Kishk, and M. Alouini, "Stochastic geometry-based analysis of LEO satellite communication systems," *IEEE Commun. Lett.*, vol. 25, no. 8, pp. 2458–2462, Aug. 2021.
[71] D. Jung, J. Ryu. Byun, and J. Choi, "Performance analysis of satellite communication system under the shadowed-Rician fading: A stochastic geometry approach," *IEEE Trans. Commun.*, vol. 70, no. 4, pp. 2707–2721, Apr. 2022.
[72] J. Khalife, M. Neinavaie, and Z. Kassas, "The first carrier phase tracking and positioning results with starlink LEO satellite signals," *IEEE Trans. Aerosp. Electron. Syst.*, vol. 56, no. 2, pp. 1487–1491, Apr. 2022.
[73] Y. Bar-Shalom, T. Kirubarajan, and X. Lin, "Probabilistic data association techniques for target tracking with applications to sonar, radar and EO sensors," *IEEE Aerosp. Electron. Syst. Mag.*, vol. 20, no. 8, pp. 37–56, Aug. 2005.
[74] A. Wrabel, R. Graef, and T. Brosch, "A survey of artificial intelligence approaches for target surveillance with radar sensors," *IEEE Aerosp. Electron. Syst. Mag.*, vol. 36, no. 7, pp. 26–43, Jul. 2021.
[75] P. Misra and P. Enge, *Global Positioning System: Signals, Measurements, and Performance*, 2nd ed. Lincoln, MA, USA: Ganga-Jamuna Press, 2010.
[76] Z. Kassas and T. Humphreys, "Observability analysis of collaborative opportunistic navigation with pseudorange measurements," *IEEE Trans. Intell. Transp. Syst.*, vol. 15, no. 1, pp. 260–273, Feb. 2014.
[77] Y. Bar-Shalom, X. Li, and T. Kirubarajan, *Estimation With Applications to Tracking and Navigation*. Hoboken, NJ, USA: Wiley, 2002.
[78] SpaceX, "FCC file number: SATMOD2018110800083," *IB FCC Rep.*, Nov. 2018. [Online]. Available: https://licensing.fcc.gov/cgi-bin/ws.exe/prod/ib/forms/attachment_menu.hts?id_app_num=128513&acct=599269&id_form_num=15&filing_key=-425955
[79] G. Casella, C. Robert, and M. Wells, "Generalized accept-reject sampling schemes," *Lecture Notes-Monograph Ser.*, vol. 45, pp. 342–347, 2004.
[80] J. Vetter, "Fifty years of orbit determination: Development of modern astrodynamics methods," *Johns Hopkins APL Tech. Dig.*, vol. 27, no. 3, pp. 239–252, Nov. 2007.
[81] J. Khalife and Z. Kassas, "Opportunistic UAV navigation with carrier phase measurements from asynchronous cellular signals," *IEEE Trans. Aerosp. Electron. Syst.*, vol. 56, no. 4, pp. 3285–3301, Aug. 2020.

Authorized licensed use limited to: The Ohio State University. Downloaded on October 13,2023 at 15:28:54 UTC from IEEE Xplore. Restrictions apply.

[82] J. Morales, J. Khalife, and Z. Kassas, "Information fusion strategies for collaborative inertial radio SLAM," *IEEE Trans. Intell. Transp. Syst.*, vol. 23, no. 8, pp. 12935–12952, Aug. 2022.

Joe Khalife (Member, IEEE) received the B.E. degree in electrical engineering and the M.S. degree in computer engineering from the Lebanese American University (LAU), Beirut, Lebanon, in 2011 and 2014, and the Ph.D. degree in electrical engineering and computer science from the University of California, Irvine, CA, USA, in 2020.

He was a Postdoctoral Fellow with the University of California and member of the Autonomous Systems Perception, Intelligence, and Navigation (ASPIN) Laboratory. From 2012 to 2015, he was a Research Assistant with LAU, and has been a member of the ASPIN Laboratory, since 2015. His research interests include opportunistic navigation, autonomous vehicles, and software-defined radio.

Dr. Khalife was the recipient of the 2016 IEEE/ION Position, Location, and Navigation Symposium (PLANS) Best Student Paper Award, 2018 IEEE Walter Fried Award, and 2021 IEEE AESS Robert T. Hill Best Dissertation Award.

Zaher (Zak) M. Kassas (Senior Member, IEEE) received the B.E. degree in electrical engineering from the Lebanese American University, Beirut, Lebanon, the M.S. degree in electrical and computer engineering from The Ohio State University, Columbus, OH, USA, the M.S.E. degree in aerospace engineering and the Ph.D. in electrical and computer engineering from the University of Texas at Austin, Austin, TX, USA.

He is currently a Professor of Electrical and Computer Engineering with The Ohio State University and Director of the Autonomous Systems Perception, Intelligence, and Navigation (ASPIN) Laboratory. He is also the Director of the U.S. Department of Transportation Center: CARMEN (Center for Automated Vehicle Research with Multimodal AssurEd Navigation), Ohio State University, focusing on navigation resiliency and security of highly automated transportation systems. His research interests include cyber-physical systems, estimation theory, navigation systems, autonomous vehicles, and intelligent transportation systems.

Dr. Kassas was the recipient of the 2018 National Science Foundation CAREER Award, 2019 Office of Naval Research Young Investigator Program Award, 2022 Air Force Office of Scientific Research YIP Award, 2018 IEEE Walter Fried Award, 2018 Institute of Navigation (ION) Samuel Burka Award, and 2019 ION Col. Thomas Thurlow Award. He is an Associate Editor for IEEE TRANSACTIONS ON AEROSPACE AND ELECTRONIC SYSTEMS and IEEE TRANSACTIONS ON INTELLIGENT TRANSPORTATION SYSTEMS. He is a Distinguished Lecturer of the IEEE Aerospace and Electronic Systems Society.

Authorized licensed use limited to: The Ohio State University. Downloaded on October 13,2023 at 15:28:54 UTC from IEEE Xplore. Restrictions apply.

Positioning with Starlink LEO Satellites: A Blind Doppler Spectral Approach

Sharbel E. Kozhaya and Zaher M. Kassas
Department of Electrical and Computer Engineering, The Ohio State University, Columbus, OH, USA
Emails: kozhaya.1@osu.edu and zkassas@ieee.org

***Abstract*—A blind Doppler spectral approach is proposed for exploiting *unknown* Starlink low Earth orbit (LEO) satellite signals for positioning. First, an analytical derivation of the received signal frequency spectrum is presented, which accounts for the highly dynamic channel between the LEO satellite and a ground-based receiver. Second, a frequency domain-based blind Doppler discriminator is proposed. Third, a Kalman filter (KF)-based Doppler tracking algorithm is developed. Finally, experimental results are presented of a stationary receiver tracking the Doppler, in a blind fashion, of six Starlink LEO satellites over a period of about 800 seconds with Hz-level accuracy. The Doppler measurements were fused through a nonlinear least-squares estimator to localize the receiver to an unprecedented level of accuracy. Starting with an initial estimate 200 km away, the proposed approach achieved a final horizontal two-dimensional (2D) position error of 4.3 m.**

***Index Terms*—Positioning, navigation, signals of opportunity, blind Doppler tracking, low Earth orbit satellite.**

I. Introduction

Global navigation satellite systems (GNSS) are at the core of modern navigation systems. GNSS receivers are routinely used to navigate today's ground and aerial vehicles and are embedded into mass marketed consumer devices (smart phones, watches, notepads, etc.) [1]. However, GNSS signals are prone to multipath and interference [2]. There has been a considerable effort recently to exploit ambient radio frequency (RF) signals of opportunity as complement or alternative to GNSS signals. These signals range from terrestrial sources (e.g., cellular [3], [4] and digital television [5], [6]) to extraterrestrial sources (e.g., low Earth orbit (LEO) [7], [8] and geostationary Earth orbit (GEO) [9] satellites).

The past few years ushered the new era of LEO megaconstellations, where thousands of LEO space vehicles (SVs) have been launched and tens of thousands scheduled for launch [10]. Using broadband LEO SV signals for navigation offers several desirable attributes [11], [12]: (i) higher received signal power compared to GNSS SVs that reside in medium Earth orbit (MEO), (ii) high availability and favorable geometry, and (iii) spectral diversity in the RF spectrum. However, using broadband LEO SV signals for navigation purposes comes with challenges [13], [14], as they are owned by private operators that typically do not disclose crucial information about the SVs': (i) ephemerides, (ii) clock synchronization and stability, and (iii) signal specifications.

To address the first challenge, several approaches have been recently proposed, including differential navigation utilizing a known base receiver [15], [16], simultaneous tracking and navigation (STAN) [17], and analytical/machine-learning SV orbit tracking [18], [19]. Approaches to address the second challenge have been offered in [20], [21]. To address the third challenge, the paradigm of cognitive opportunistic navigation, which estimates the minimally known LEO SV signals in a blind fashion has been showing tremendous promise [22], [23]. Most recently, this paradigm allowed for the exploitation of unknown Starlink LEO SVs, from which navigation observables were produced via (i) a carrier phase tracking approach [24] and (ii) a generalized likelihood ratio (GLR) Doppler detection approach [25], with the former localizing a receiver to within a two-dimensional (2D) error of 25.9 m, while the latter achieving a 2D error of 10 m.

This paper proposes a novel blind Doppler spectral approach to address the first challenge without the need to know the LEO SVs' donwlink signal specification. While the method is generalizable to any LEO constellation, Starlink SVs are chosen to demonstrate the proposed method's efficacy. Previous literature has proposed methods for Doppler tracking with M-ary phase shift keying (M-PSK) and orthogonal frequency division multiplexing (OFDM) signals [26]–[30]. The aforementioned approaches aim to generate a peak in the frequency-domain by either relying on nonlinear operations (for M-PSK signals) or increasing the coherent processing interval (CPI) (for OFDM signals). After generating the peak, the methods track it using a peak tracking algorithm to estimate the Doppler shift. However, using nonlinear operations could degrade the signal-to-noise ratio (SNR), while increasing the CPI is not straightforward with the highly dynamic channels encountered with LEO SVs. Also, peak tracking is prone to generate invalid observables and even divergence whenever the spectrum is contaminated by noisy DC peaks.

This paper proposes a novel approach to mitigate the above challenges and offers the following contributions: (i) derive an analytical approximation of the received signal frequency spectrum for highly dynamic channels and (ii) develop a blind Doppler spectral estimator via frequency-domain cross-correlation and a Kalman filter (KF)-based tracking loop. The proposed approach relies on the presence of a repetitive sequence in the LEO SV's downlink, to which the blind spectral Doppler tracker locks and cross-correlation is used to track the Doppler shift. While spectral cross-correlation has been studied in the literature [31] and used for noise reduction in speech [32] and detection of stars and planets [33], to the author's knowledge, this approach is newly applied

to tracking the Doppler of LEO SVs. Experimental results with six Starlink SVs are presented showing the superiority of the proposed approach over state-of-the-art blind positioning methods. The proposed approach yielded an unprecedented Hz-level Doppler tracking accuracy and 2D positioning error of 4.3 m, which is 57% lower than the most accurate results with Starlink reported in the literature to-date.

This paper is organized as follows. Section II derives the signal model. Section III introduces the blind Doppler discriminator and tracking approach. Section IV presents experimental results. Section V gives concluding remarks.

II. Signal Model

This section presents a model of the received signal, which takes into account the high dynamics channel between the LEO SV and ground-based receiver. Then, it derives an analytical expression of the signal's frequency spectrum.

A. Received Baseband Signal Model

Let $x(t)$ be the unknown LEO SV signal, expressed at baseband. The proposed framework does not assume any particular modulation or multiplexing scheme. The only assumption is that $x(t)$ can be written as $x(t) = s(t) + n_d(t)$, where $s(t)$ is a deterministic repetitive signal and $n_d(t)$ is a random signal driven by the user data. Examples of repetitive sequences are the pseudorandom noise (PRN) used in GPS [34], Globalstar LEO SVs [35], and CDMA2000 [36] and the primary and secondary synchronization sequences (PSS and SSS) used in 4G long-term evolution (LTE) [37] and 5G [38]. The proposed framework assumes the following properties of $s(t)$:

1) It is periodic with period T_0.
2) It is uncorrelated with the data $n_d(t)$.
3) It is zero-mean, has a stationary power spectral density (PSD) with $\left|\mathcal{F}\left\{s(t)w_{T_0}(t)\right\}\right|^2 = S_s(f)$, where $w_{T_0}(t)$ is a windowing function that is unity within the interval $[0, T_0]$ and zero elsewhere.

Consider $x(t)$ being transmitted at a carrier frequency f_c. Let $\tau_d(t)$ denote the apparent delay between the transmitted signal $x_c(t) \triangleq x(t)\exp(j2\pi f_c t)$ and the received signal at the receiver's antenna. The apparent delay $\tau_d(t)$ is composed of (i) the time-of-flight along the line-of-sight (LOS) between the transmitter and receiver (i.e., $d_{LOS}(t)/c$, where $d_{LOS}(t)$ is the LOS distance between the LEO SV's transmitter and the receiver and c is the speed of light); (ii) combined effect of the transmitter's and receiver's clock biases, denoted $\delta t_{clk}(t)$; (iii) ionospheric and tropospheric delays $\delta t_{iono}(t)$ and $\delta t_{tropo}(t)$, respectively; and (iv) other unmodeled errors. After propagating in an additive white Gaussian channel, the resulting received signal before baseband mixing can be expressed as

$$\begin{aligned}\bar{r}(t) &= x_c\left(t - \tau_d(t)\right) + \bar{n}(t) \\ &= x(t - \tau_d(t))\exp\left(j2\pi f_c\left[t - \tau_d\left(t\right)\right]\right) + \bar{n}(t),\end{aligned}$$

where $\bar{n}(t)$ is a complex white Gaussian noise with PSD $N_0/2$.

Let $r(t) \triangleq \bar{r}(t)\exp\left(-j2\pi f_c t\right)$ denote the received signal after baseband mixing and filtering. Then, $r(t)$ can be expressed as $r(t) = x(t - \tau_d(t))\exp\left(j\theta(t)\right) + n(t)$, where $n(t)$ is the low-pass filter output of $\bar{n}(t)$, and $\theta(t) = -2\pi f_c \tau_d(t)$ is the carrier phase of the received signal. Using a Taylor series expansion, at time instant $t_k = t_0 + kT_0$, where k is the sub-accumulation index and t_0 is some initial time, the carrier phase of the signal can be expressed as

$$\theta(t) = \theta(t_k) + \dot{\theta}(t_k)t + \frac{1}{2}\ddot{\theta}(t_k)t^2 + H.O.T. \tag{1}$$

Denote $\theta_k(t)$ as $\theta(t)$ in (1), after dropping the higher-order terms ($H.O.T.$). By definition, $f_D(t) \triangleq \frac{\dot{\theta}(t)}{2\pi}$ is the apparent Doppler shift and $\dot{f}_D(t)$ is the apparent Doppler rate.

It is important to note that the channel between the LEO SV and the ground-based receiver is highly dynamic, thus, high Doppler shift and rate will be observed by the receiver. On the other hand, at the k-th sub-accumulation, $\tau_d(t)$ is approximated by its zero-order term $d_k = \tau_d(t_k)$, while the higher order terms are dropped to simplify the following signal analysis. Due to the first property, one can arbitrarily choose $\tau_d(t)$ to denote the code start time. It is important to note that the higher order terms in $\tau_d(t)$ stretch or contract the code in the time-domain, but this paper ignores this effect, which seems to be of little impact on Starlink LEO SV codes.

Finally, the expression of the received signal at the k-th sub-accumulation can be written as $r_k^-(t) = r(t)w_{T_0}(t - t_k) = s_k(t)\exp\left(j\theta_k(t)\right) + n_k^-(t)$, where $s_k(t) = s(t - d_k)w_{T_0}(t)$ and $n_k^-(t) = n(t - d_k)w_{T_0}(t)$. The received signal $r_k(t)$ after carrier wipe-off using the carrier phase estimate, denoted $\hat{\theta}_k(t)$, generated by the tracking loop discussed in Section III-B, can be expressed as

$$\begin{aligned}r_k(t) &= r_k^-(t)\exp(-j\hat{\theta}_k(t)) \\ &= s_k(t)\exp(j\tilde{\theta}_k(t)) + n_k(t),\end{aligned} \tag{2}$$

where $\tilde{\theta}_k(t) = \theta_k(t) - \hat{\theta}_k(t)$ is the residual carrier phase.

B. Frequency Spectrum of the Received Signal

The received signal's frequency spectrum at the k-th sub-accumulation is $S_{r_k}(f) = \left|\mathcal{F}\left\{r_k(t)\right\}\right|^2$. Using the third property of $s(t)$, the Wigner distribution function (WDF) of $s_k(t)$ for $t \in [0, T_0]$ can be written as

$$\begin{aligned}W_s(t, f) &\triangleq \int_{-\infty}^{\infty} s_k\left(t + \frac{\tau}{2}\right) s_k^*\left(t - \frac{\tau}{2}\right)\exp(-2\pi f\tau)\, d\tau \\ &= \frac{S_s(f)}{T_0}.\end{aligned}$$

It can be shown that the WDF of the residual carrier phase at the k-th sub-accumulation $C_k(t) = \exp(j\tilde{\theta}_k(t))$, for $t \in [0, T_0]$, is $W_{C_k}(t, f) = \delta\left(f - \frac{\dot{\tilde{\theta}}_k}{2\pi} - \frac{\ddot{\tilde{\theta}}_k}{2\pi}t\right)$, where $\delta(\cdot)$ denotes the Dirac delta function. Using the second property of $s(t)$, the WDF of $r_k(t)$ in (2), for $t \in [0, T_0]$, can be written as

$$W_{r_k}(t, f) = \frac{S_s(f)}{T_0} \circledast \delta\left(f - \frac{\dot{\tilde{\theta}}_k}{2\pi} - \frac{\ddot{\tilde{\theta}}_k}{2\pi}t\right) + W_{n_k}(t, f),$$

where $(f \circledast g)(t) = \int_{-\infty}^{\infty} f(\tau)g(t - \tau)d\tau$ is the convolution, $W_{n_k}(t, f)$ is the WDF of the noise and data at the k-th sub-accumulation. Noting that $S_{r_k}(f) = \int_0^{T_0} W_{r_k}(t, f)\, dt$ and using the projection property of WDF, the following follows

$$
\begin{aligned}
S_{r_k}(f) &= \frac{S_s(f)}{T_0} \circledast \int_0^{T_0} \delta\left(f - \frac{\tilde{\dot{\theta}}_k}{2\pi} - \frac{\tilde{\ddot{\theta}}_k}{2\pi} t\right) dt + S_{n_k}(f) \\
&= S_s(f) \circledast \frac{2\pi}{\left|\tilde{\ddot{\theta}}_k\right| T_0} \int_0^{T_0} \delta\left(t - \frac{2\pi f - \tilde{\dot{\theta}}_k}{\tilde{\ddot{\theta}}_k}\right) dt + S_{n_k}(f) \\
&= S_s(f) \circledast \Pi\left(f; \tilde{\dot{\theta}}_k, \tilde{\ddot{\theta}}_k\right) + S_{n_k}(f), \qquad (3)
\end{aligned}
$$

where $S_{n_k}(f) = \int_0^{T_0} W_{n_k}(t, f)\, dt$ and

$$
\Pi\left(f; \dot{\theta}, \ddot{\theta}\right) = \frac{2\pi}{\left|\ddot{\theta}\right| T_0} \begin{cases} 1, & \left| f - \dfrac{\dot{\theta} + \dfrac{|\ddot{\theta}|}{2} T_0}{2\pi} \right| < \dfrac{|\ddot{\theta}|}{4\pi} T_0, \\ 0, & \text{elsewhere.} \end{cases}
$$

Equation (3) states that the received signal's frequency spectrum consists of a shifted and dilated version of the repetitive sequence's frequency spectrum alongside a noise floor. The shifting in the received spectrum is mainly due to residual Doppler $\tilde{\dot{\theta}}_k$ and the dilation is due to residual Doppler rate $\tilde{\ddot{\theta}}_k$.

III. Blind Doppler Tracking

This section derives the Doppler discriminator and formulates the KF-based Doppler tracking loop.

A. Frequency-Domain Based Doppler Discriminator

The nonlinear least-squares (NLS) estimator of the residual Doppler $\tilde{\dot{\theta}}_k$ at the k-th sub-accumulation is given by

$$
\begin{aligned}
\tilde{\dot{\theta}}_k &= \underset{\dot{\theta}}{\operatorname{argmin}} \left\| S_{r_k}(f) - S_s(f) \circledast \Pi\left(f; \dot{\theta}, \ddot{\theta}\right) \right\|^2 \\
&= \underset{\dot{\theta}}{\operatorname{argmin}} \left\| S_{r_k}(f) \right\|^2 + \left\| S_s(f) \circledast \Pi\left(f; \dot{\theta}, \ddot{\theta}\right) \right\|^2 \\
&\quad - 2\left(S_{r_k} \star S_s\right)(f) \circledast \Pi\left(f; \dot{\theta}, \ddot{\theta}\right) \qquad (4) \\
&= \underset{\dot{\theta}}{\operatorname{argmax}} \left(S_{r_k} \star S_s\right)(f) \circledast \Pi\left(f; \dot{\theta}, \ddot{\theta}\right) \\
&\approxeq \underset{\dot{\theta}}{\operatorname{argmax}} \left(S_{r_k} \star S_s\right)(f) \circledast \delta\left(f - \frac{\dot{\theta}}{2\pi}\right), \quad \text{for} \quad \tilde{\ddot{\theta}}_k \approx 0 \\
&= 2\pi \underset{f}{\operatorname{argmax}} \left(S_{r_k} \star S_s\right)(f), \qquad (5)
\end{aligned}
$$

where $(f \star g)(\tau) = \int_{-\infty}^{\infty} f^*(t) g(t+\tau) dt$ is the cross-correlation. The first two terms in the minimization problem (4) are a constant function of the search parameter $\dot{\theta}$; therefore, they are ignored. As the blind receiver does not have prior knowledge of $S_s(f)$, it starts with an initial estimate $\hat{S}_s(f) \triangleq S_{r_0}(f)$ and refines the repetitive sequence's spectrum with every sub-accumulation. It is worth pointing that the regime of small residual Doppler rate values assumed in (5) is a reasonable assumption, since the Doppler rate between two consecutive sub-accumulations is nearly constant.

B. Kalman Filter-Based Tracking Loop

The continuous-time signal in (2) is sampled at a sampling interval $T_s = 1/F_s$, the discrete-time received signal before carrier wipe-off at the k-th sub-accumulation can be written as

$$
r_k^-[n] = s[n - d_k] \exp\left(j\tilde{\Theta}_k[n]\right) + n_k^-[n],
$$

where $n \in [0, L-1]$, $s[n]$ is the discrete-time sequence of $s(t)$ with period $L = T_0/T_s$ and $\Theta_k[n]$ and d_k are the discrete-time carrier phase and code start time, respectively, of the received signal at the k-th sub-accumulation.

The carrier phase state vector is defined as $\boldsymbol{\theta}(t) \triangleq \left[\theta(t),\ \dot{\theta}(t),\ \ddot{\theta}(t)\right]^{\mathsf{T}}$, whose dynamics is modeled as

$$
\dot{\boldsymbol{\theta}}(t) = \mathbf{A}\boldsymbol{\theta}(t) + \mathbf{B}\boldsymbol{w}(t), \qquad (6)
$$

$$
\mathbf{A} \triangleq \begin{bmatrix} 0 & 1 & 0 \\ 0 & 0 & 1 \\ 0 & 0 & 0 \end{bmatrix}, \quad \mathbf{B} \triangleq \begin{bmatrix} 0 \\ 0 \\ 1 \end{bmatrix},
$$

where $\boldsymbol{w}(t)$ is a zero-mean white noise process with power spectral density q_w. The continuous-time dynamics in (6) is discretized at a sampling time $T_0 = LT_s$, leading to $\boldsymbol{\Theta}_{k+1} = \mathbf{F}\boldsymbol{\Theta}_k + \mathbf{w}_k$, where $\boldsymbol{\Theta}_k \triangleq \left[\theta_k,\ \dot{\theta}_k,\ \ddot{\theta}_k\right]^{\mathsf{T}}$, $\mathbf{F} \triangleq e^{\mathbf{A}T_0}$ is the state transition matrix, $\mathbf{w}_k$ is a discrete-time process noise vector, which is a zero-mean white sequence with covariance $\mathbf{Q} = q_{\tilde{w}} \int_0^{T_0} e^{\mathbf{A}t}\mathbf{B}\left(e^{\mathbf{A}t}\mathbf{B}\right)^{\mathsf{T}} dt$. The reconstructed sequence of the carrier phase used to perform carrier wipe-off can be written as a second order piecewise polynomial given by $\hat{\Theta}_k[n] = \hat{\theta}_{k-1} + \hat{\dot{\theta}}_k n T_s + \frac{1}{2}\hat{\ddot{\theta}}_k (nT_s)^2$, $n \in [0, L-1]$. After carrier wipe-off, the received signal's sequence can be expressed as

$$
r_k[n] = s[n - d_k] \exp\left(j\tilde{\Theta}_k[n]\right) + n_k[n]. \qquad (7)
$$

Equation (7) will be used to determine the residual Doppler $\tilde{\dot{\theta}}_k$ at the k-th sub-accumulation, which is fed as innovation to a KF loop that uses the observation model $z_k = \mathbf{H}\boldsymbol{\Theta}_k + v_k$, where $\mathbf{H} \triangleq [0\ \ 1\ \ 0]$ and v_k is a discrete-time zero-mean white noise sequence with variance $\sigma_{\dot{\theta}}^2$. The KF innovation ν_k is the fast Fourier transform (FFT)-based discrete-time version of (5). It is worth noting that the Doppler tracked using the proposed approach has a real-valued ambiguity part $\dot{\theta}_N$ that needs to be resolved to retrieve back the actual Doppler shift.

IV. Experimental Results

This section demonstrates the proposed blind Doppler estimator and tracking loop with Starlink LEO SV signals. To this end, a stationary National Instrument (NI) universal software radio peripheral (USRP) 2945R was equipped with a consumer-grade Ku antenna and low-noise block (LNB) downconverter to receive Starlink signals in the Ku-band. The sampling bandwidth was set to 2.5 MHz and the carrier frequency f_c was set to 11.325 GHz. Samples of the Ku signal were stored for off-line processing via a software-defined radio (SDR). The experimental hardware is shown in Fig. 1.

Fig. 1. Experimental hardware.

A. Blind Doppler Tracking Results

The USRP was set to record Ku signals over a period of 800 seconds. During this period, a total of six Starlink SVs passed over the receiver, one at a time. The framework discussed in Section III was used to acquire and track the signals from these SVs with $q_w = (0.1)^2$ rad^2/s^6 and $\sigma_{\dot{\theta}} = \frac{\pi}{6}$ rad/s. The SVs' skyplot, time history of the KF innovation ν_k, and tracked Doppler shift $\hat{f}_{D_k} = \hat{\dot{\theta}}_k/2\pi$ for each SV is shown in Fig. 2.

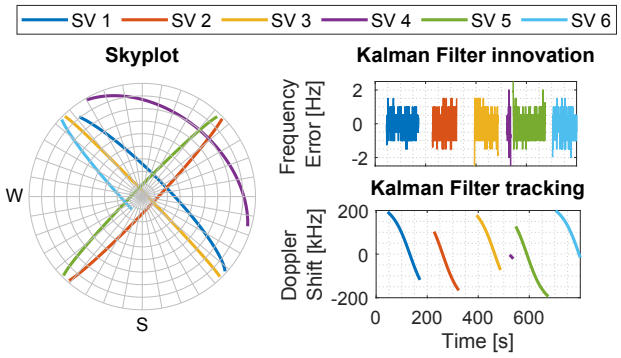

Fig. 2. Left: Skyplot of the six Starlink LEO SVs. Right: time history of the KF innovation ν_k and tracked Doppler shift $\hat{f}_{D_k}$ for each SV.

B. Position Solution

Let $i \in [1, 6]$ denote the SV index. The pseudorange rate observable $z^i(k) \triangleq c\frac{\hat{f}_{D_k}}{f_c}$ of the i-th SV at time-step k, expressed in meters, is modeled as

$$z^i(k) = \frac{\dot{\boldsymbol{r}}_{\mathrm{SV}_i}^{\mathsf{T}}(k)\left[\boldsymbol{r}_r - \boldsymbol{r}_{\mathrm{SV}_i}(k')\right]}{\|\boldsymbol{r}_r - \boldsymbol{r}_{\mathrm{SV}_i}(k')\|_2} + a_i + v_{z_i}(k), \qquad (8)$$

where $\boldsymbol{r}_r$ and $\boldsymbol{r}_{\mathrm{SV}_i}$ are the receiver's and i-th Starlink SV's 3D position vectors; $\dot{\boldsymbol{r}}_{\mathrm{SV}_i}$ is the i-th SV's 3D velocity vector; k' is the time at the i-th SV; a_i is a bias that models the (i) unknown Doppler ambiguity $\dot{\theta}_N$, (ii) lumped receiver–SV clock drift, and (iii) ionospheric and tropospheric delay rate; $v_{z_i}(k)$ is the measurement noise, which is modeled as a zero-mean, white Gaussian random sequence with variance σ_i^2.

Next, define the parameter vector $\boldsymbol{x} \triangleq \left[\boldsymbol{r}_r{}^{\mathsf{T}}, a_1, \ldots, a_6\right]^{\mathsf{T}}$. Let $\boldsymbol{z}$ denote the vector of all the pseudorange observables stacked together, and let $\boldsymbol{v}_z$ denote the vector of all measurement noises stacked together. Then, one can readily write the measurement equation given by $\boldsymbol{z} = \boldsymbol{g}(\boldsymbol{x}) + \boldsymbol{v}_z$, where $\boldsymbol{g}(\boldsymbol{x})$ is a vector-valued function that maps the parameter $\boldsymbol{x}$ to the pseudorange rate observables according to (8). Next, an NLS estimator is used to obtain an estimate of $\boldsymbol{x}$. The SV positions were obtained from TLE files and SGP4 orbit propagator. It is important to note that the TLE epoch time was adjusted for each SV to account for ephemeris errors. This was achieved by minimizing the pseudorange rate residuals for each SV. Subsequently, the receiver position was estimated using the aforementioned NLS. The receiver position was initialized 200 km away from the true position. The final 3D position error was found to be 19.4 m, while the horizontal 2D position error was 4.3 m. The results are summarized in Fig. 3.

Table I compares the results achieved with the proposed approach against the only positioning results with Starlink LEO SV signals reported in the literature. Using the same recorded samples from Starlink SVs in [24], [25], the proposed approach reduced the 3D and 2D positioning error by 15.3% and 57%, respectively, over the most accurate positioning results with Starlink reported in the literature to-date.

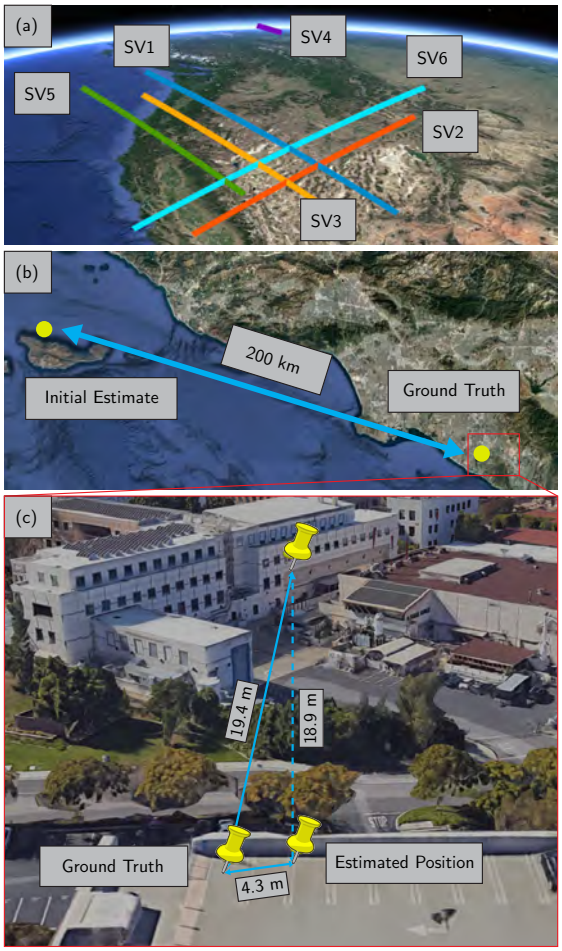

Fig. 3. Environment layout summarizing the positioning results

TABLE I
COMPARISON OF STARLINK POSITIONING RESULTS.

	Carrier phase [24]	GLR Doppler [25]	Proposed approach
3D error (m)	33.5	22.9	19.4
2D error (m)	25.9	10.0	4.3

V. CONCLUSION

This paper proposed a novel approach for blind Doppler tracking of LEO SVs. First, an analytical expression for the received signal frequency spectrum was derived, which accounts for high LEO SVs' dynamic channels. Second, a novel frequency-domain-based Doppler discriminator was proposed. Third, a KF-based Doppler tracking algorithm was developed. Finally, experimental results were presented showing Hz-level Doppler tracking of six Starlink LEO SV signals. Starting with an initial estimate 200 km away, the proposed approach achieved a 2D error of 4.3 m.

ACKNOWLEDGMENTS

The authors thank Dr. Joe Khalife for his help with data collection. This work was supported in part by the Office of Naval Research (ONR) under Grants N00014-19-1-2511 and N00014-22-1-2242 and in part by the U.S. Department of Transportation (USDOT) under Grant 69A3552047138 for the CARMEN University Transportation Center (UTC).

REFERENCES

[1] N. Gogoi, A. Minetto, and F. Dovis, "On the cooperative ranging between Android smartphones sharing raw GNSS measurements," in *Proceedings of IEEE Vehicular Technology Conference*, 2019, pp. 1–5.

[2] S. Sand, P. Unterhuber, D. B. Ahmed, F. Muller, A. Lehner, I. Rashdan, M. Schmidhammer, R. Karasek, B. Siebler, O. Heirich, C. Gentner, M. Walter, S. Kaiser, M. Ulmschneider, M. Schaab, L. Wientgens, and T. Strang, "Radio interference measurements for urban cooperative intelligent transportation systems," in *Proceedings of IEEE Vehicular Technology Conference*, 2021, pp. 1–6.

[3] R. Whiton, J. Chen, T. Johansson, and F. Tufvesson, "Urban navigation with LTE using a large antenna array and machine learning," in *Proceedings of IEEE Vehicular Technology Conference*, 2022, pp. 1–5.

[4] I. Lapin, G. Granados, J. Samson, O. Renaudin, F. Zanier, and L. Ries, "STARE: Real-time software receiver for LTE and 5G NR positioning and signal monitoring," in *Proceedings of Workshop on Satellite Navigation Technology*, April 2022, pp. 1–11.

[5] N. Souli, R. Makrigiorgis, P. Kolios, and G. Ellinas, "Cooperative relative positioning using signals of opportunity and inertial and visual modalities," in *Proceedings IEEE Vehicular Technology Conference*, 2021, pp. 1–7.

[6] Z. Jiao, L. Chen, X. Lu, Z. Liu, X. Zhou, Y. Zhuang, and G. Guo, "Carrier phase ranging with DTMB signals for urban pedestrian localization and GNSS aiding," *Remote Sensing*, vol. 15, no. 2, pp. 423–446, 2023.

[7] N. Jardak and Q. Jault, "The potential of LEO satellite-based opportunistic navigation for high dynamic applications," *Sensors*, vol. 22, no. 7, pp. 2541–2565, 2022.

[8] M. Hartnett, "Performance assessment of navigation using carrier Doppler measurements from multiple LEO constellations," Master's thesis, Air Force Institute of Technology, Ohio, USA, 2022.

[9] Y. Gao, X. Zhao, S. Wang, Y. Xiang, C. Huang, and Y. Hua, "Positioning via GEO communication satellites' signals of opportunity," *IET Radar, Sonar Navigation*, vol. 15, no. 11, pp. 1472–1482, July 2021.

[10] S. Liu, Z. Gao, Y. Wu, D. Kwan Ng, X. Gao, K. Wong, S. Chatzinotas, and B. Ottersten, "LEO satellite constellations for 5G and beyond: How will they reshape vertical domains?" *IEEE Communications Magazine*, vol. 59, no. 7, pp. 30–36, July 2021.

[11] T. Reid, T. Walter, P. Enge, D. Lawrence, H. Cobb, G. Gutt, M. O'Conner, and D. Whelan, "Position, navigation, and timing technologies in the 21st century," J. Morton, F. van Diggelen, J. Spilker, Jr., and B. Parkinson, Eds. Wiley-IEEE, 2021, vol. 2, ch. 43: Navigation from low Earth orbit – Part 1: concept, current capability, and future promise, pp. 1359–1379.

[12] Z. Kassas, "Position, navigation, and timing technologies in the 21st century," J. Morton, F. van Diggelen, J. Spilker, Jr., and B. Parkinson, Eds. Wiley-IEEE, 2021, vol. 2, ch. 43: Navigation from low Earth orbit – Part 2: models, implementation, and performance, pp. 1381–1412.

[13] Z. Kassas, M. Neinavaie, J. Khalife, N. Khairallah, J. Haidar-Ahmad, S. Kozhaya, and Z. Shadram, "Enter LEO on the GNSS stage: Navigation with Starlink satellites," *Inside GNSS Magazine*, vol. 16, no. 6, pp. 42–51, 2021.

[14] F. Prol, R. Ferre, Z. Saleem, P. Välisuo, C. Pinell, E. Lohan, M. Elsanhoury, M. Elmusrati, S. Islam, K. Celikbilek, K. Selvan, J. Yliaho, K. Rutledge, A. Ojala, L. Ferranti, J. Praks, M. Bhuiyan, S. Kaasalainen, and H. Kuusniemi, "Position, navigation, and timing (PNT) through low earth orbit (LEO) satellites: A survey on current status, challenges, and opportunities," *IEEE Access*, vol. 10, pp. 83 971–84 002, 2022.

[15] J. Khalife and Z. Kassas, "Performance-driven design of carrier phase differential navigation frameworks with megaconstellation LEO satellites," *IEEE Transactions on Aerospace and Electronic Systems*, pp. 1–20, 2023, accepted.

[16] C. Zhao, H. Qin, N. Wu, and D. Wang, "Analysis of baseline impact on differential doppler positioning and performance improvement method for LEO opportunistic navigation," *IEEE Transactions on Instrumentation and Measurement*, pp. 1–10, 2023.

[17] Z. Kassas, N. Khairallah, and S. Kozhaya, "Ad astra: Simultaneous tracking and navigation with megaconstellation LEO satellites," *IEEE Aerospace and Electronic Systems Magazine*, 2023, accepted.

[18] D. Shen, J. Lu, G. Chen, E. Blasch, C. Sheaff, M. Pugh, and K. Pham, "Methods of machine learning for space object pattern classification," in *Proceedings of IEEE National Aerospace and Electronics Conference*, 2019, pp. 565–572.

[19] J. Haidar-Ahmad, N. Khairallah, and Z. Kassas, "A hybrid analytical-machine learning approach for LEO satellite orbit prediction," in *Proceedings of International Conference on Information Fusion*, 2022, pp. 1–7.

[20] N. Khairallah and Z. Kassas, "An interacting multiple model estimator of LEO satellite clocks for improved positioning," in *Proceedings of IEEE Vehicular Technology Conference*, 2022, pp. 1–5.

[21] K. Wang and A. El-Mowafy, "LEO satellite clock analysis and prediction for positioning applications," *Geo-spatial Information Science*, vol. 25, no. 1, pp. 14–33, 2022.

[22] M. Neinavaie, J. Khalife, and Z. Kassas, "Blind Doppler tracking and beacon detection for opportunistic navigation with LEO satellite signals," in *Proceedings of IEEE Aerospace Conference*, 2021, pp. 1–8.

[23] S. Kozhaya and Z. Kassas, "Blind receiver for LEO beacon estimation with application to UAV carrier phase differential navigation," in *Proceedings of ION GNSS Conference*, 2022, pp. 2385–2397.

[24] J. Khalife, M. Neinavaie, and Z. Kassas, "The first carrier phase tracking and positioning results with Starlink LEO satellite signals," *IEEE Transactions on Aerospace and Electronic Systems*, vol. 56, no. 2, pp. 1487–1491, April 2022.

[25] M. Neinavaie, J. Khalife, and Z. Kassas, "Acquisition, Doppler tracking, and positioning with Starlink LEO satellites: First results," *IEEE Transactions on Aerospace and Electronic Systems*, vol. 58, no. 3, pp. 2606–2610, June 2022.

[26] Z. Tan, H. Qin, L. Cong, and C. Zhao, "New method for positioning using IRIDIUM satellite signals of opportunity," *IEEE Access*, vol. 7, pp. 83 412–83 423, 2019.

[27] F. Farhangian and R. Landry, "Multi-constellation software-defined receiver for Doppler positioning with LEO satellites," *Sensors*, vol. 20, no. 20, pp. 5866–5883, October 2020.

[28] C. Zhao, H. Qin, and Z. Li, "Doppler measurements from multiconstellations in opportunistic navigation," *IEEE Transactions on Instrumentation and Measurement*, vol. 71, pp. 1–9, 2022.

[29] C. Huang, H. Qin, C. Zhao, and H. Liang, "Phase - time method: Accurate Doppler measurement for Iridium NEXT signals," *IEEE Transactions on Aerospace and Electronic Systems*, vol. 58, no. 6, pp. 5954–5962, 2022.

[30] J. Khalife, M. Neinavaie, and Z. Kassas, "Blind Doppler tracking from OFDM signals transmitted by broadband LEO satellites," in *Proceedings of IEEE Vehicular Technology Conference*, April 2021, pp. 1–6.

[31] T. Frederick, "Time-frequency estimation for cyclostationary signals," Ph.D. dissertation, Florida Atlantic University, USA, 1997.

[32] S. Vaseghi, *Advanced digital signal processing and noise reduction*. John Wiley & Sons, 2008.

[33] S. Zucker, "Cross-correlation and maximum-likelihood analysis: a new approach to combining cross-correlation functions," *Monthly Notices of the Royal Astronomical Society*, vol. 342, no. 4, pp. 1291–1298, 2003.

[34] A. Flores, "NAVSTAR GPS space segment/navigation user interfaces," https://www.gps.gov/technical/icwg/IS-GPS-200N.pdf, August 2022.

[35] R. Hendrickson, "Globalstar for the military," in *Proceedings of IEEE Military Communications Conference*, vol. 3, November 1997, pp. 1173–1178.

[36] 3GPP2, "Physical layer standard for cdma2000 spread spectrum systems (C.S0002-E)," 3rd Generation Partnership Project 2 (3GPP2), TS C.S0002-E, June 2011.

[37] 3GPP, "Evolved universal terrestrial radio access (E-UTRA); multiplexing and channel coding," 3rd Generation Partnership Project (3GPP), TS 36.212, January 2010. [Online]. Available: http://www.3gpp.org/ftp/Specs/html-info/36212.htm

[38] 3GPP, "Physical channels and modulation," https://www.etsi.org/deliver/etsi-ts/138200-138299/138211/15.02.00-60/ts-138211v150200p.pdf, 5G; NR; 3rd Generation Partnership Project (3GPP), TS 38.211, July 2018.

Protecting the Skies: GNSS-less Aircraft Navigation with Terrestrial Cellular Signals of Opportunity

Zaher M. Kassas
The Ohio State University
Ali Abdallah
University of California, Irvine
Chiawei Lee, Juan Jurado, Steven Wachtel, Jacob Duede, Zachary Hoeffner, Thomas Hulsey, and Rachel Quirarte
United States Air Force
RunXuan Tay
Republic of Singapore Air Force

BIOGRAPHY

Zaher (Zak) M. Kassas is a Professor at The Ohio State University and director of the Autonomous Systems Perception, Intelligence, and Navigation (ASPIN) Laboratory. He is also director of the U.S. Department of Transportation Center: CARMEN (Center for Automated Vehicle Research with Multimodal AssurEd Navigation), focusing on navigation resiliency and security of highly automated transportation systems. He received a B.E. in Electrical Engineering from the Lebanese American University, an M.S. in Electrical and Computer Engineering from The Ohio State University, and an M.S.E. in Aerospace Engineering and a Ph.D. in Electrical and Computer Engineering from The University of Texas at Austin. He is a recipient of the 2018 National Science Foundation (NSF) CAREER award, 2019 Office of Naval Research (ONR) Young Investigator Program (YIP) award, 2022 Air Force Office of Scientific Research (AFOSR) YIP award, 2018 IEEE Walter Fried Award, 2018 Institute of Navigation (ION) Samuel Burka Award, and 2019 ION Col. Thomas Thurlow Award. He is a Senior Editor of the IEEE Transactions on Intelligent Vehicles and an Associate Editor of the IEEE Transactions on Aerospace and Electronic Systems and the IEEE Transactions on Intelligent Transportation Systems. His research interests include cyber-physical systems, navigation systems, autonomous vehicles, and intelligent transportation systems.

Ali Abdallah received his M.S. degree in Electrical Engineering and Computer Science (EECS) from University of California at Irvine and was a member of the Autonomous Systems Perception, Intelligence, and Navigation (ASPIN) Laboratory. He is currently a research intern at Google. He is a recipient of the 2020 IEEE/ION Position, Location, and Navigation Symposium (PLANS) Best Student Paper Award and the 2020 IEEE Signal Processing Society video contest for beamforming research (5-MICC) Grand Prize.

Chiawei Lee is an Assistant Professor and Instructor Flight Test Engineer at the U.S. Air Force Test Pilot School. He serves as the Test Management Program Director where he oversees about a dozen student and staff led flight test projects each year. In addition, he is the Chief Test Safety Officer responsible for the safe execution of curriculum and flight test project safety packages. He received a B.S. in Aerospace Engineering from University of California, Los Angeles and a M.S. in Aero/Astro Engineering from Stanford University.

Juan Jurado is a U.S. Air Force Lieutenant Colonel and the Director of Education at the U.S. Air Force Test Pilot School. He holds a B.S. from Texas A&M University, an M.S. from the Air Force Test Pilot School, and M.S. and Ph.D. from the Air Force Institute of Technology. Previously, he served as Director of Engineering for the 413th Flight Test Squadron and oversaw various C-130, V-22, and H-1 flight test programs. His research interests include aircraft performance modeling, online sensor calibration, image processing, visual-inertial navigation, and statistical sensor management for multi-sensor navigation problems.

Steven Wachtel is a U.S. Air Force Captian and a Flight Test Engineer, assigned to the 780th Test Squadron, Eglin Air Force Base, FL. He received a B.S. in Mechanical Engineering from The Ohio State University, an M.S. in Flight Test Engineering from the U.S. Air Force Test Pilot School, and an M.S. in Systems Engineering from the Air Force Institute of Technology.

Jacob Duede is a Major in the U.S. Air Force. He was trained as a Communication/Navigation/Mission Systems apprentice on C-17 Globmaster II aircraft and stationed at McChord Air Force Base, WA. He graduated from the U.S. Air Force Academy as a commissioned officer with a B.S. in Mechanical Engineering. He attended the Undergraduate Pilot Training at Columbus

Air Force Base, MS. In 2020, he graduated from the U.S. Air Force Test Pilot School at Edwards Air Force Base, CA. He is a Senior Pilot with over 2,000 hours and holds an M.S. in Engineering from the University of Arkansas and an M.S. in Flight Test Engineering from Air University.

Zachary Hoeffner is a flight test engineer at the U.S. Air Force. He received a a B.S. in Nuclear Engineering from the U.S. Air Force Academy, an M.S. in Flight Test Engineering from the U.S. Air Force Test Pilot School, an M.S. in Engineering Physics and Applied Physics from the Air Force Institute of Technology, and an M.S. in Nuclear Engineering from the Air Force Institute of Technology.

Thomas Hulsey is a U.S. Air Force Flight Commander of Operations Engineering. He received a B.S. in Aerospace Engineering from Missouri University of Science and Technology, an M.S. in Aeronautical Engineering from the Air Force Institute of Technology, and an M.S. in Experimental Flight Test Engineering from the United States Air Force Test Pilot School.

Rachel Quirarte is a KC-46 and KC-135 programmatic flight commander and test pilot in the 418th Flight Test Squadron in the U.S. Air Force. She received a a B.S. in Aeronautical Engineering from the U.S. Air Force Academy, an M.S. in Flight Test Engineering from the U.S. Air Force Test Pilot School, and an M.S. in Mechanical Engineering from Rice University.

RunXuan Tay received a B.S. degree in Electrical Engineering from the University California, San Diego and an M.S. degree in Flight Test Engineering from the U.S. Air Force Test Pilot School. He is currently a test pilot at Air Warfare Center, Republic of Singapore Air Force, where he works on fixed wing test programs.

ABSTRACT

This paper shows how to protect our skies from harmful radio frequency interference (RFI) to global navigation satellite system (GNSS) signals, by offering terrestrial cellular signals of opportunity (SOPs) as a viable aircraft navigation system backup. An extensive flight campaign was conducted by the Autonomous Systems Perception, Intelligence, and Navigation (ASPIN) Laboratory in collaboration with the United States Air Force (USAF) to study the potential of cellular SOPs for high-altitude aircraft navigation. A multitude of flight trajectories and altitudes were exercised in the flight campaign in two different regions in Southern California, USA: (i) rural and (ii) semi-urban. Samples of the ambient downlink cellular SOPs were recorded, which were fed to ASPIN Laboratory's MATRIX (Multichannel Adaptive TRansceiver Information eXtractor) software-defined receiver (SDR), which produced carrier phase measurements from these samples. These measurements were fused with altimeter data via an extended Kalman filter (EKF) to estimate the aircraft's trajectory. This paper shows for the first time that at altitudes as high as about 11,000 ft above ground level (AGL), more than 100 cellular long-term evolution (LTE) eNodeBs can be reliable tracked, many of which were more than 100 km away, with carrier-to-noise ratio (C/N_0) exceeding 40 dB-Hz. The paper shows pseudorange and Doppler tracking results from cellular eNodeBs along with the C/N_0 and number of tracked eNodeBs over the two regions, while performing ascending, descending, and grid maneuvers. In addition, the paper shows navigation results in the semi-urban and rural regions, showing a position root mean-squared error of 9.86 m and 10.37, respectively, over trajectories of 42.23 km and 56.56 km, respectively, while exploiting an average of about 19 and 10 eNodeBs, respectively.

I. INTRODUCTION

A quick search of the phrase "global positioning system (GPS)" on the aviation safety reporting system (ASRS) returns 579 navigation-related incidents since January 2000. Out of these incidents, 508 were reported to be due to a malfunction or failure in GPS and other satellite navigation components. Among these, 100 are suspected to due to GPS jamming and interference leading to the loss of the main and auxiliary GPS units in some cases.

Over the past few years, global navigation satellite system (GNSS) radio frequency interference (RFI) incidents skyrocketed, jeopardizing safe and efficient aviation operations. RFI sources include repeaters and pseudolites, GNSS jammers, and systems transmitting outside the GNSS frequency bands (Blasch et al., 2019). According to EUROCONTROL, a pan-European, civil-military organization dedicated to supporting European aviation, there were 4,364 GNSS outages reported by pilots in 2018, which represents more than a 2,000% increase over the previous year (EUROCONTROL, Aviation Intelligence Unit, 2021). What is alarming is that while the majority of RFI hotspots appear to be due to conflict zones, they affected civil aviation at distances of up to 300 km from these zones. The majority of RFI (about 81%) affected en-route flights, even though this is where RFI should be at its lowest, as the aircraft is faraway from a ground-based interferer. In 2019, the International Civil Aviation Organization (ICAO) issued a Working Paper titled "An Urgent Need to Address Harmful Interferences to GNSS," where it concluded that harmful RFI to GNSS would prevent the full continuation of safety and efficiency benefits of GNSS-based services (International Civil Aviation Organization (ICAO), 2019). ICAO followed this by an "Action Required" letter for "Strengthening of Communications, Navigation, and Surveillance (CNS) Systems Resilience and Mitigation of Interference to Global Navigation Satellite System (GNSS)" (International Civil Aviation Organization (ICAO), 2020).

In 2021, the National Institute of Standards and Technology (NIST) issued a report on "Foundational PNT Profile: Applying

the Cybersecurity Framework for the Responsible Use of PNT Services," where it identified signals of opportunity (SOPs) and terrestrial RF sources (e.g., cellular) as a mitigation category that apply to the PNT profile (Bartock et al., 2021). Indeed, SOPs (Leng et al., 2016; Casado et al., 2018; Mortier et al., 2020; Kassas et al., 2020; Zhu et al., 2021; Psiaki and Slosman, 2022), particularly from cellular infrastructure, have shown tremendous promise over the past decade as an alternative PNT source (del Peral-Rosado et al., 2017; Ikhtiari, 2019; Souli et al., 2020; Gante et al., 2020; Kassas, 2021; Souli et al., 2021a; Xhafa et al., 2021; Ivanov et al., 2023).

Among various cellular generations, the forth-generation (4G) long-term evolution (LTE), which adopts orthogonal frequency division multiplexing (OFDM) as a modulation technique, possesses desirable attributes for navigation purposes:

- **Abundance:** LTE transmitters (also known as evolved Node Bs or eNodeBs) are abundant in many locales of interest.
- **Geometric diversity:** eNodeBs possess favorable geometric configurations by construction of the cellular infrastructure.
- **Frequency diversity:** eNodeBs transmit in a wide range of frequencies.
- **High received power:** LTE's received carrier-to-noise (C/N_0) ratio is tens of dBs higher than that of GNSS signals, even indoors (Abdallah et al., 2021).
- **High bandwidth:** LTE's bandwidth can be up to 20 MHz, which allows for more accurate time-of-arrival estimation (Shamaei et al., 2017).
- **Free to use:** The LTE infrastructure is already operational; thus, with specialized receivers, navigation observables can be extracted from LTE's "always on" transmitted signals.

Cellular LTE signals have shown high ranging and localization accuracy (del Peral-Rosado et al., 2018; Kang et al., 2019; Gadka et al., 2019; Han et al., 2019; Shamaei and Kassas, 2021; Souli et al., 2021b; Kazaz et al., 2022; Yang et al., 2022; Wang and Morton, 2022), even in urban and indoor environments experiencing severe multipath (Wang and Morton, 2020; Dun et al., 2020; Wang and Morton, 2020; Abdallah and Kassas, 2021; Strandjord et al., 2021; Wang et al., 2022; Whiton et al., 2022; Jao et al., 2022; Pan et al., 2022) and environments under intentional GPS jamming (Kassas et al., 2022b). Experimental navigation results with LTE signals demonstrated meter-level positioning accuracy on ground vehicles (Shamaei et al., 2019; del Peral-Rosado et al., 2019; Yang et al., 2020; Soderini et al., 2020; Hong et al., 2021; Maaref and Kassas, 2022; Lapin et al., 2022) and sub-meter-level positioning accuracy on unmanned aerial (UAVs) (Khalife and Kassas, 2022b,a).

However, the potential of cellular LTE signals for high-altitude aircraft navigation has been largely unstudied (Kim and Shin, 2019; Stevens and Younis, 2021). To the authors' knowledge, the first such studies appeared in (Kassas et al., 2022a,c). The results therein where achieved from a collaboration between the United States Air Force (USAF) at Edwards Air Force Base (AFB), California and the Autonomous Systems Perception, Intelligence, and Navigation (ASPIN) Laboratory through a week-long flight campaign called "SNIFFER: Signals of opportunity for Navigation In Frequency-Forbidden EnviRonments." In SINFFER, ASPIN Laboratory's Multichannel Adaptive TRansceiver Information eXtractor (MATRIX) specialized software-defined receiver (SDR) was flown on a Beechcraft C-12 Huron, a fixed-wing USAF aircraft, to collect ambient cellular LTE signals. The collected data consisted of combinations of flight runs performed over three regions: (A) Edwards: rural; (B) Palmdale: semi-urban; (C) Riverside: urban. The flights spanned different altitudes (up to 23,000 ft above ground level (AGL)) and a multitude of trajectories including straight segments, banking turns, benign and aggressive maneuvers, and ascending and descending teardrops with a descent rate ranging between 0 to 1500 ft/min. The flights were performed by members of the USAF Test Pilot School (TPS). Terabytes of LTE data was collected over the three regions under various conditions.

The main conclusions from the studies in (Kassas et al., 2022a,c) were:

- Cellular LTE signals are surprisingly powerful at both (i) high altitudes, exhibiting C/N_0 of 25–55 dB-Hz at altitudes of 2,000–23,000 ft AGL and (ii) faraway horizontal distances, exhibiting C/N_0 of about 30 dB-Hz for towers as far as 50 km, while flying at about 16,000 ft AGL.
- The two-ray model fits the measured C/N_0 sufficiently well for towers more than 10 km away, while flying at an altitude of 16,000 ft AGL. For towers closer than 10 km, the antenna radiation pattern should be incorporated into the two-ray model to improve model fitting.
- With carrier phase navigation observables produced by the MATRIX SDR from 5 4G LTE eNodeBs and 6 3G code-division multiple-access (CDMA) base transceiver stations (BTSs), fused with altimeter measurements via an extended Kalman filter (EKF), a three-dimensional (3–D) position root mean-squared error (RMSE) of 10.5 m was achieved over a 51-km trajectory traversed in 9 minutes.

Upon improving the MATRIX SDR design to exploit an eNodB's multiple antenna ports and the time-orthogonality of OFDM signals, the number of acquirable and trackable LTE eNodeBs grew monumentally, from less than a dozen as reported in (Kassas et al., 2022a,c) to more than 100. This paper presents these findings. In particular, for three different maneuvers (climbing

teardrop, descending teardrop, and grid) in Regions A and B[1], the results were consistent: the number of tracked eNodeBs at altitudes as high as 11,000 ft AGL can be higher than 100, with C/N_0 over 40 dB-Hz. In addition, upon fusing the carrier phase observables with altimeter data via an EKF, a sustained accurate and robust navigation solution was achieved. In particular, over trajectories of 42.23 km and 56.56 km in regions B and A, respectively, traversed in 450 s and 600 s, respectively, a 3–D position RMSE of 9.86 m and 10.37, respectively, was achieved by exploiting an average of about 19 and 10 eNodeBs[2], respectively.

The rest of the paper is organized as follows: Section II overviews the hardware and software setup with which the aircraft was equipped and overviews the environments in which the flight campaigns took place. Section III presents experimental characterization of tracked cellular LTE signals as a function of their C/N_0 and total number over different aircraft maneuvers. Section IV summarizes the cellular LTE navigation results. Section V gives concluding remarks.

II. EXPERIMENTAL SETUP AND FLIGHT REGIONS

This section overviews the hardware and software setup used for data collection and processing. It also describes the flight regions and aircraft maneuvers.

1. Hardware and Software Setup

For this study, the C-12 aircraft, called Ms. Mabel, was equipped with

- A quad-channel universal software radio peripheral (USRP)-2955.
- Three consumer-grade 800/1900 MHz Laird cellular antennas.
- A peripheral component interconnect express (PCIe) cable.
- A desktop computer equipped with a solid-state drive for data storage.
- A laptop computer running ASPIN Laboratory's MATRIX SDR for real-time monitoring of the signals, which was operated during the flight by a flight engineer to determine when, where, and what cellular signals were available to tune the USRP accordingly.
- A GPS antenna to (i) feed GPS measurements for the aircraft navigation system and (ii) discipline the USRP's onboard GPS-disciplined oscillator (GPSDO).

Figure 1 shows the C-12 aircraft and the USAF pilots and ASPIN researchers. The equipment was assembled at the ASPIN Laboratory on a special rack provided by the USAF and was shipped to be mounted on the C-12 aircraft. The three Laird antennas were connected to the USRP to capture impinging 4G LTE signals, and the USRP was tuned to listen to three carrier frequencies corresponding to two 4G U.S. cellular providers and one 3G[3] U.S. cellular provider as shown in Figure 2. Terabytes of in-phase and quadrature samples were collected throughout the experiment with a sampling rate of 10 MSps per channel. The 4G cellular module of the MATRIX SDR (Kassas et al., 2020) was then used to post-process the stored samples to produce navigation observables: Doppler frequency, carrier phase, and pseudorange, along with corresponding C/N_0's. The hardware and software setup are shown in Figures 2–3, respectively.

2. Flight Regions and Aircraft Maneuvers

The campaign took place in three regions: (i) Region A: a rural region in Edwards AFB, California, (ii) Region B: a semi-urban region in Palmdale, California, and (iii) Region C: an urban region in Riverside, California. Different maneuvers were planned over the three regions to test several aspects of aircraft navigation with cellular SOPs.

Figure 4 shows the regions in which the experiments were performed. More than 70 3G BTSs and 4G eNodeBs were mapped throughout the experiment via the method described in (Morales and Kassas, 2018). The mapped towers were cross-checked via Google Earth and online databases and are shown in Figure 4. This paper investigates the potential of cellular SOPs for navigation; therefore, mapping the SOPs will not be discussed.

Two main types of maneuvers were performed in each region (see Figure 4). The first was a teardrop-like pattern while climbing/descending. The patterns have a focal point that is aligned with a geographic points of interest (see the green "$\times$" in Figure 4). The measurements used to characterize the C/N_0 were taken exactly above the geographic point of interest to maintain the horizontal distance between the aircraft and the cellular base stations. The second was a grid-like pattern with many turns and straight segments. Such patterns were used as stress-test for the navigation receivers to assess their ability to track cellular synchronization signals in a robust and accurate fashion as well as to evaluate the navigation solution.

[1] At the time of writing of this paper, the data collected in Region C has not been processed with the improved MATRIX SDR yet.

[2] At the time of writing of this paper, not all 100+ eNodeBs in the environment were mapped yet. Only eNodeBs whose positions were mapped were used in the EKF.

[3] This paper focuses on the 4G LTE signals only. Results for 3G signals were published in (Kassas et al., 2022c).

Figure 1: USAF Pilots and ASPIN researchers with the C-12 aircraft.

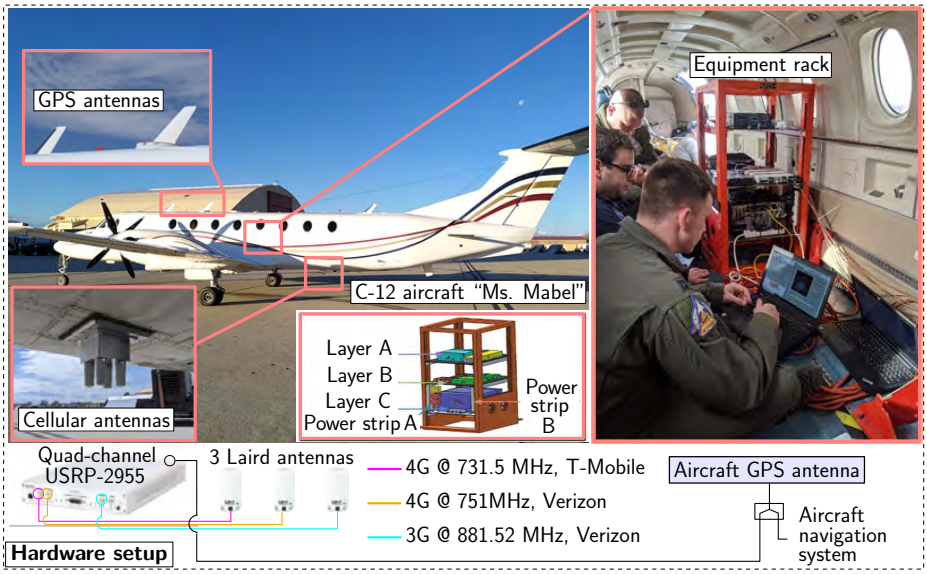

Figure 2: Hardware setup with which the C-12 aircraft was equipped.

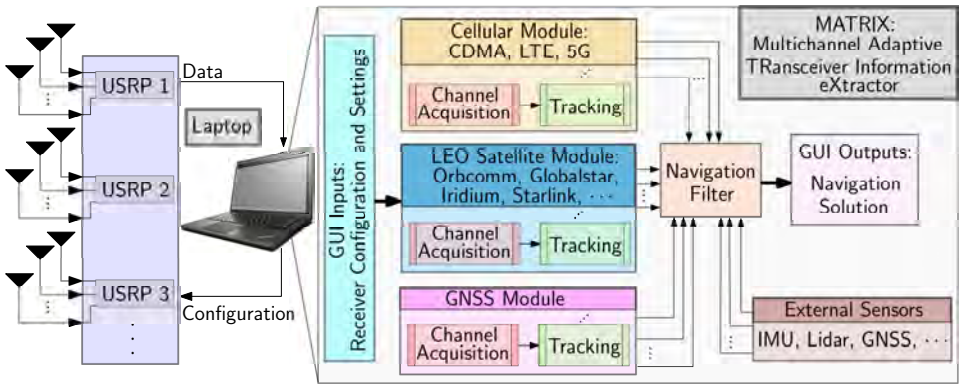

Figure 3: Software setup used for cellular SOP signal collection.

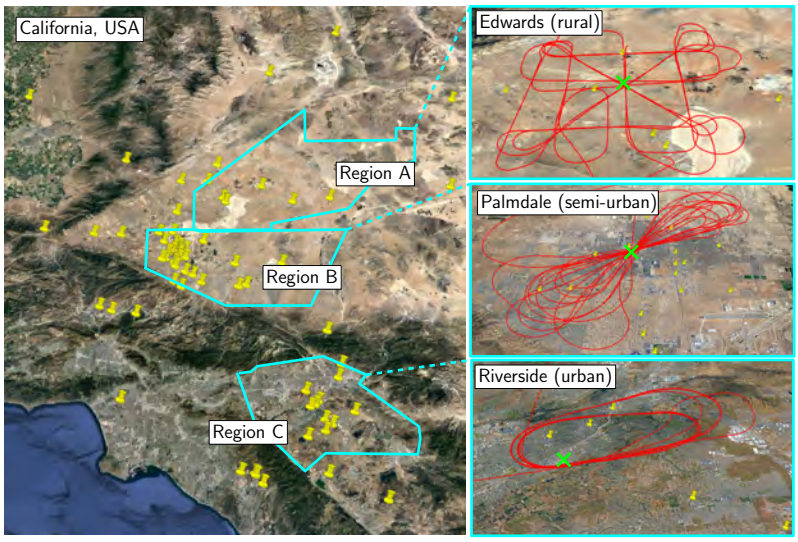

Figure 4: Regions A, B, and C in which the flight campaigns took place. The yellow pins represent 3G and 4G cellular towers that were mapped and analyzed in this study. The right figures show the aircraft trajectory in all regions (shown in red).

III. CELLULAR LTE AVAILABILITY AND C/N_0 CHARACTERIZATION

This section presents experimental results evaluating cellular LTE availability in Regions A and B with the improved MATIX SDR. To this end, Figures 5 – 10 show the outputs of the navigation observables produced by the receiver (pseudorange and Doppler) along with the C/N_0 and number of tracked LTE eNodeBs during various flight trajectories.

The following conclusions can be made from these results. First, while the results presented in (Kassas et al., 2022c,a) revealed tremendous potential for tracking cellular LTE signals at high-altitude aircraft, there is more room for improvement from a receiver design perspective. In particular, the improved receiver design increased the sensitivity of the receiver, enabling it to track much weaker signals from further away eNodeBs. Second, in rural and semi-urban regions, the aircraft could track more than 100 eNodeBs simultaneously, some of which were more than 100 km away. No matter the aircraft maneuvers, tens of eNodeBs were trackable. A significant factor behind the change in the number of tracked eNodeBs is attributed to the aircraft's body and wings causing signal blockage and severe attenuation during banking.

IV. CELLULAR LTE NAVIGATION RESULTS

The navigation carrier phase observables produced by the improved MATRIX SDR were fused with altimeter data through the EKF navigation filter as described in (Kassas et al., 2022c). Note that the EKF employed herein employed a continuous Wiener process acceleration model for the aircraft's dynamics, in place of the nearly constant velocity dynamical model adopted in (Kassas et al., 2022c). The navigation performance in all three Regions is summarized in Table 1. It is worth emphasizing that the reported performance is expected to improve significantly if an inertial navigation system (INS) is coupled with the LTE navigation observables (e.g., via a tightly-coupled SOP-aided INS (Morales and Kassas, 2021)) and/or all the tracked eNodeBs (see Figures 5 – 10) are exploited in the EKF.

Table 1: Navigation Performance with Cellular LTE Signals

Metric	Region B	Region A
Number of cellular towers used	11 – 28	5 – 16
Cellular frequencies (MHz)	731.5	731.5
	751	751
	739	
Flight duration (sec)	450	600
Flight length (km)	42.23	56.56
Altitude AGL (m)	2,295 – 2,316	1,079 – 1,394
Position RMSE (m)	9.86	10.37
Standard deviation (m)	5.92	4.39
Maximum position error (m)	35.26	24.42

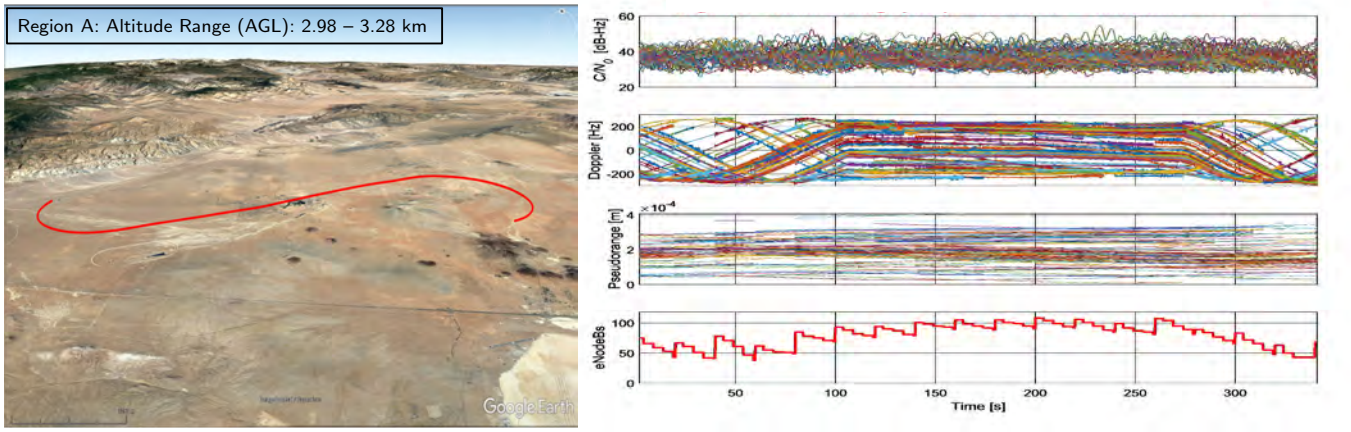

Figure 5: Left: climbing teardrop aircraft trajectory in Region A. Right: receiver's pseudorange and Doppler tracking results from cellular LTE eNodeBs during this trajectory along with the C/N_0 and number of tracked eNodeBs.

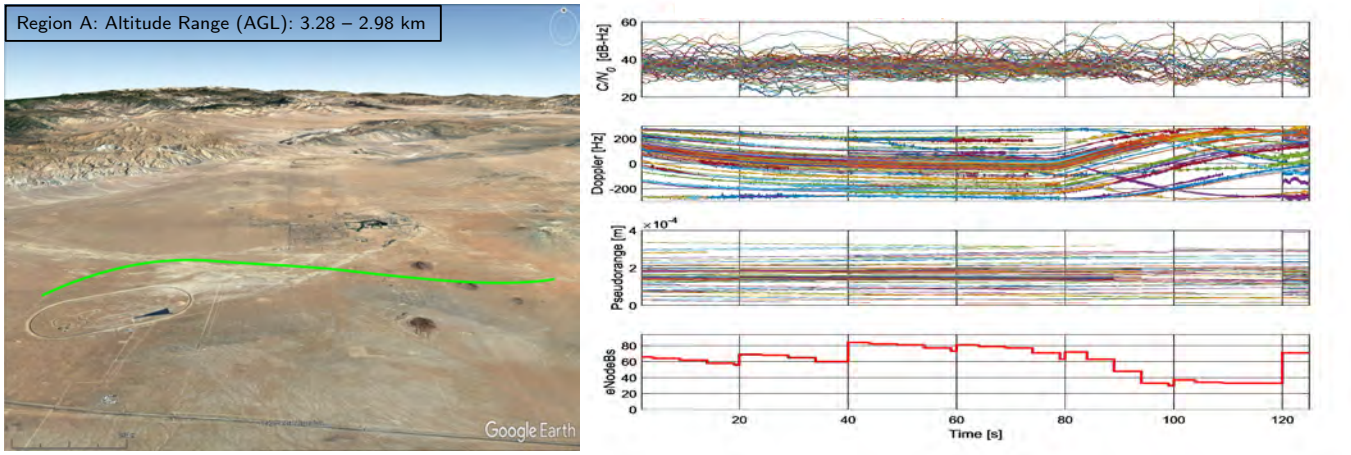

Figure 6: Left: descending teardrop aircraft trajectory in Region A. Right: receiver's pseudorange and Doppler tracking results from cellular LTE eNodeBs during this trajectory along with the C/N_0 and number of tracked eNodeBs.

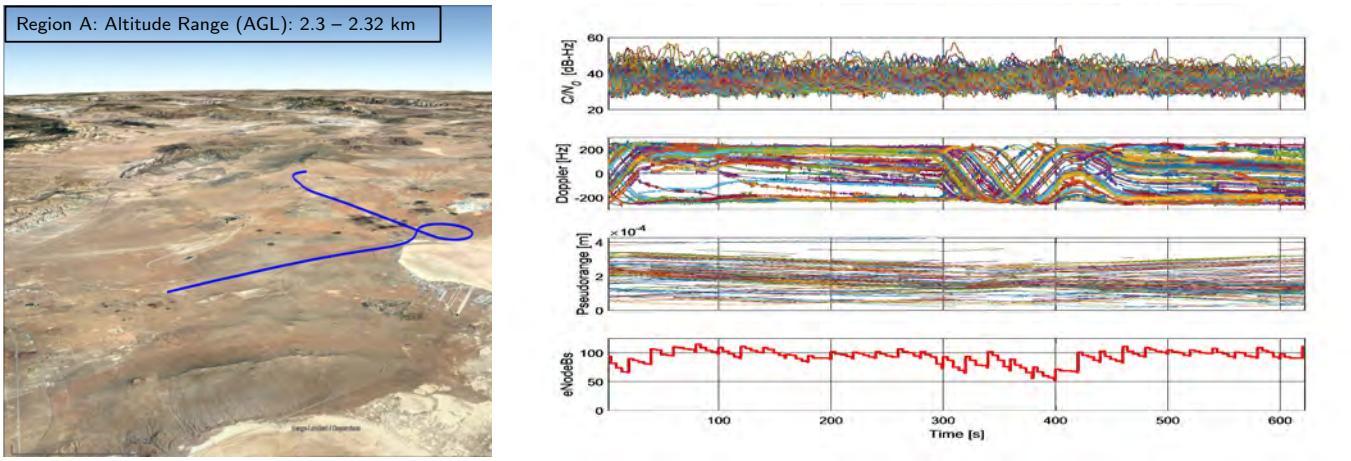

Figure 7: Left: grid aircraft trajectory in Region A. Right: receiver's pseudorange and Doppler tracking results from cellular LTE eNodeBs during this trajectory along with the C/N_0 and number of tracked eNodeBs.

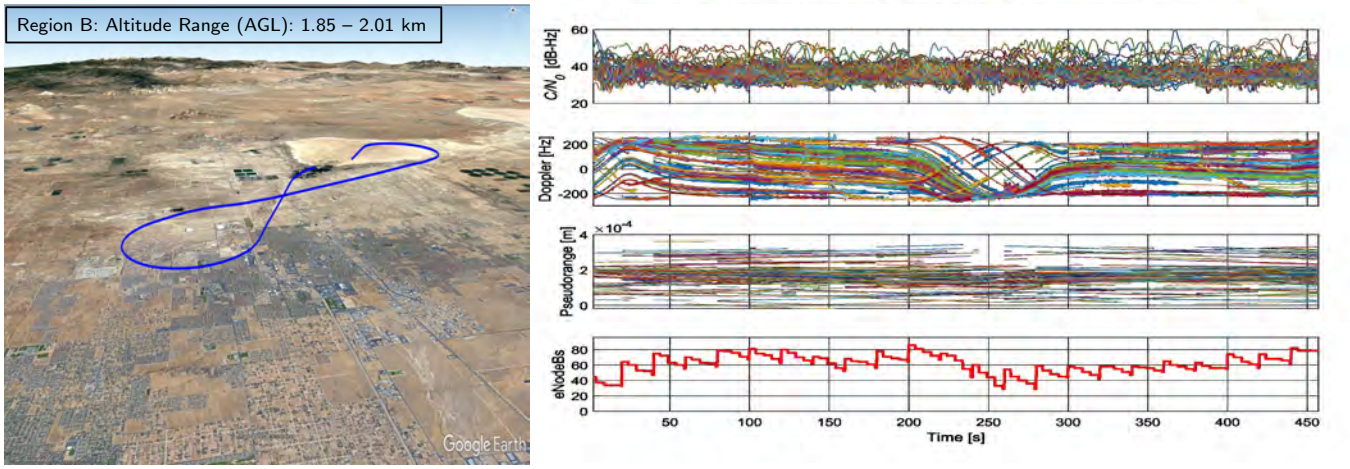

Figure 8: Left: climbing teardrop aircraft trajectory in Region B. Right: receiver's pseudorange and Doppler tracking results from cellular LTE eNodeBs during this trajectory along with the C/N_0 and number of tracked eNodeBs.

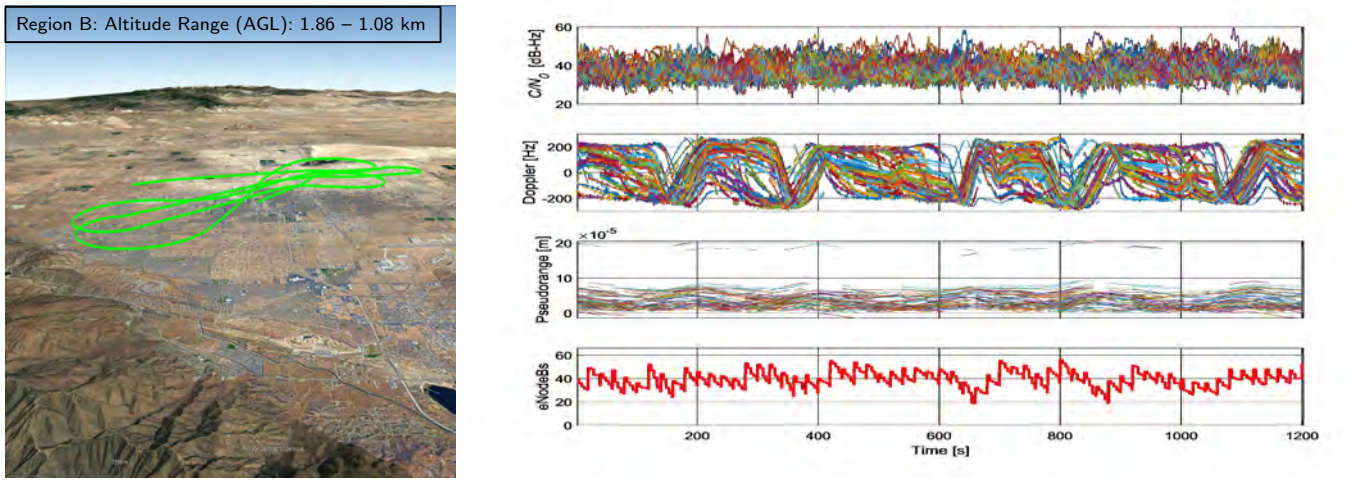

Figure 9: Left: descending teardrop aircraft trajectory in Region B. Right: receiver's pseudorange and Doppler tracking results from cellular LTE eNodeBs during this trajectory along with the C/N_0 and number of tracked eNodeBs.

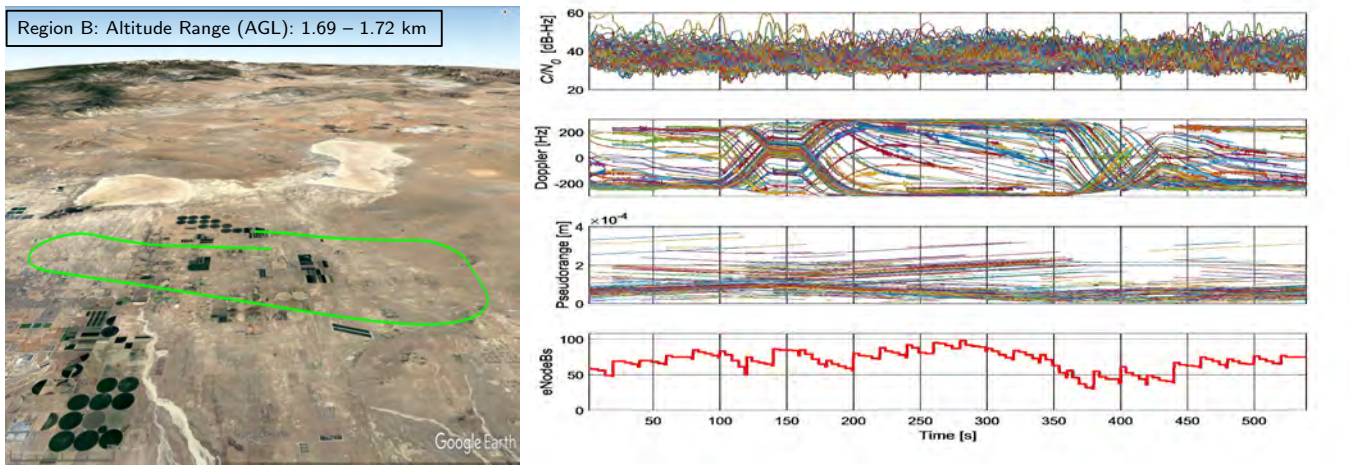

Figure 10: Left: grid aircraft trajectory in Region B. Right: receiver's pseudorange and Doppler tracking results from cellular LTE eNodeBs during this trajectory along with the C/N_0 and number of tracked eNodeBs.

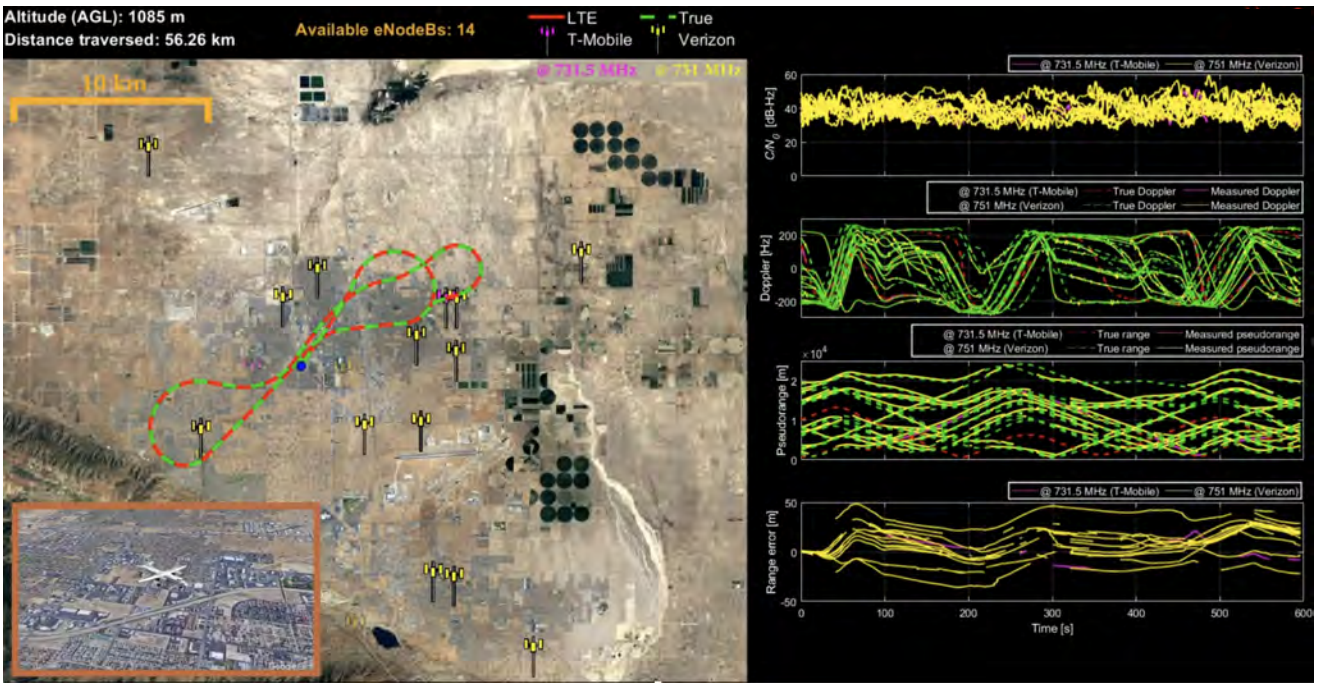

Figure 11: Left: Region A environment layout showing the cellular eNodeBs' locations and aircraft's true and estimated trajectories (from LTE signals). Right: LTE pseudorange and Doppler tracking during this trajectory along with C/N_0 and number of tracked LTE eNodeBs.

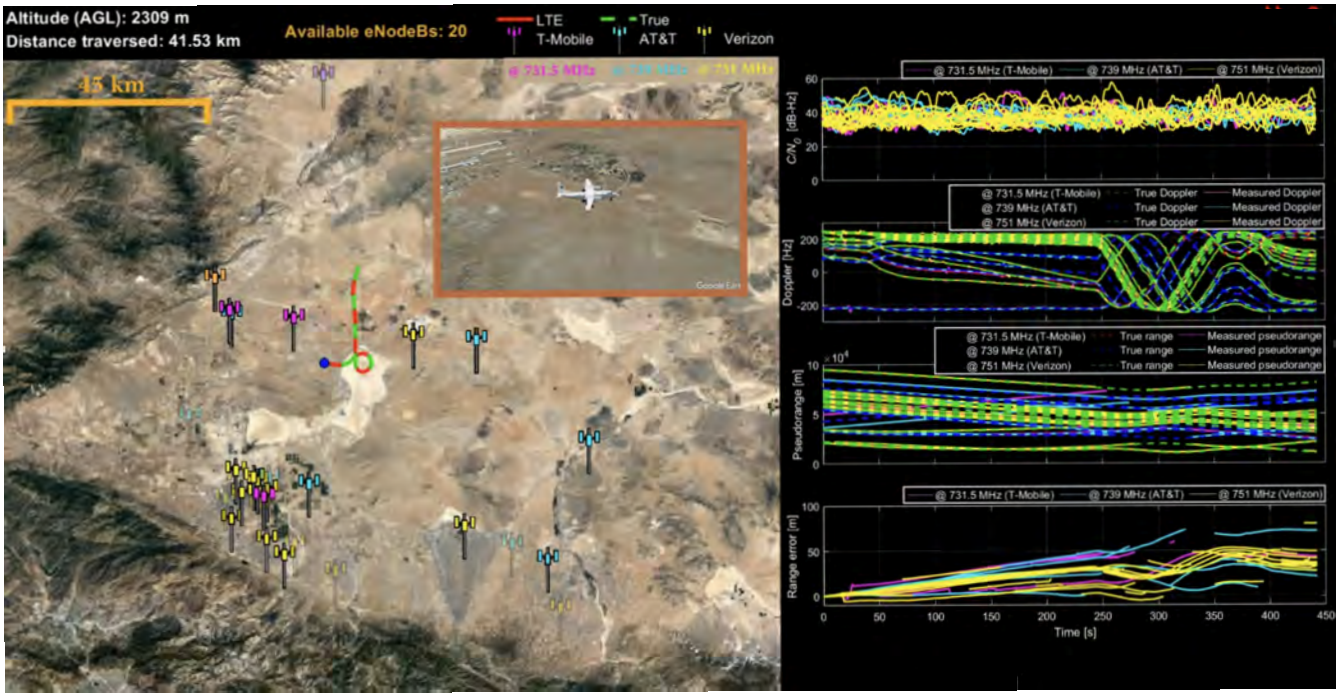

Figure 12: Left: Region B environment layout showing the cellular eNodeBs' locations and aircraft's true and estimated trajectories (from LTE signals). Right: LTE pseudorange and Doppler tracking during this trajectory along with C/N_0 and number of tracked LTE eNodeBs.

V. CONCLUSION

This paper unveiled the tremendous potential of cellular SOPs as a viable aircraft navigation system backup. SNIFFER flight campaign data were re-processed with an improved LTE receiver design, enabling the tracking of more than 100 eNodeBs simultaneously, many of which were more than 100 km away, with C/N_0 exceeding 40 dB-Hz. In addition, the paper showed navigation results in rural and semi-urban regions, showing a position root mean-squared error of 9.86 m and 10.37, respectively,

over trajectories of 42.23 km and 56.56 km, respectively, while exploiting an average of about 19 and 10 eNodeBs, respectively.

ACKNOWLEDGEMENTS

The authors would like to thank Edwards AFB and Holloman AFB for inviting the ASPIN Laboratory to conduct experiments on Air Force aircraft in the "SNIFFER: Signals of opportunity for Navigation In Frequency-Forbidden EnviRonments" flight campaign. The authors would like to thank Joshua Morales, Kimia Shamaei, Mahdi Maaref, Kyle Semelka, MyLinh Nguyen, and Trier Mortlock for their help with preparing for data collection. DISTRIBUTION STATEMENT A. Approved for public release; Distribution is unlimited. 412TW-PA-20146.

This work was supported in part by the Office of Naval Research (ONR) under Grant N00014-19-1-2511 and Grant N00014-19-1-2613, in part by the National Science Foundation (NSF) under Grant 2240512, in part by the U.S. Department of Transportation (USDOT) under Grant 69A3552047138 for the CARMEN University Transportation Center (UTC), and in part by the Air Force Office of Scientific Research (AFOSR) under Grant FA9550-22-1-0476. This work was also supported in part by the Laboratory Directed Research and Development program at Sandia National Laboratories, a multimission laboratory managed and operated by National Technology and Engineering Solutions of Sandia LLC, a wholly owned subsidiary of Honeywell International Inc. for the U.S. Department of Energy's National Nuclear Security Administration under contract DE-NA0003525. This paper describes objective technical results and analysis. Any subjective views or opinions that might be expressed in the paper do not necessarily represent the views of the U.S. Department of Energy or the United States Government. SAND2022-13901 C

REFERENCES

Abdallah, A. and Kassas, Z. (2021). Multipath mitigation via synthetic aperture beamforming for indoor and deep urban navigation. *IEEE Transactions on Vehicular Technology*, 70(9):8838–8853.

Abdallah, A., Khalife, J., and Kassas, Z. (2021). Experimental characterization of received 5G signals carrier-to-noise ratio in indoor and urban environments. In *Proceedings of IEEE Vehicular Technology Conference*, pages 1–5.

Bartock, M., Brule, J., Li-Baboud, Y., Lightman, S., McCarthy, J., Reczek, K., Northrip, D., Scholz, A., and Suloway, T. (2021). Foundational PNT profile: Applying the cybersecurity framework for the responsible use of positioning, navigation, and timing (PNT) services. *National Institute of Standards and Technology (NIST)*, (NISTIR 8323).

Blasch, E., Sabatini, R., Roy, A., Kramer, K., Andrew, G., Schmidt, G., Insaurralde, C., and Fasano, G. (2019). Cyber awareness trends in avionics. In *Proceedings of IEEE/AIAA Digital Avionics Systems Conference*, pages 1–8.

Casado, A., Krauthammer, A., Olsen, S., and Valles, E. (2018). Environment-RF-based positioning using machine learning. In *Proceedings of ION GNSS+ Conference*, pages 3327–3334.

del Peral-Rosado, J., Estatuet-Castillo, R., Lopez-Salcedo, J., Seco-Granados, G., Chaloupka, Z., Ries, L., and Garcoa-Molina, J. (2017). Evaluation of hybrid positioning scenarios for autonomous vehicle applications. In *Proceedings of ION International Technical Meeting Conference*, pages 2541–2553.

del Peral-Rosado, J., López-Salcedo, J., Zanier, F., and Seco-Granados, G. (2018). Position accuracy of joint time-delay and channel estimators in LTE networks. *IEEE Access*, 6:25185–25199.

del Peral-Rosado, J., Renaudin, O., Gentner, C., Raulefs, R., Dominguez-Tijero, E., Fernandez-Cabezas, A., Blazquez-Luengo, F., Cueto-Felgueroso, G., Chassaigne, A., Bartlett, D., Grec, F., Ries, L., Prieto-Cerdeira, R., Lopez-Salcedo, J., and Seco-Granados, G. (2019). Physical-layer abstraction for hybrid GNSS and 5G positioning evaluations. In *Proceedings of IEEE Vehicular Technology Conference*, pages 1–6.

Dun, H., Tiberius, C., and Janssen, G. (2020). Positioning in a multipath channel using OFDM signals with carrier phase tracking. *IEEE Access*, 8:13011–13028.

EUROCONTROL, Aviation Intelligence Unit (2021). Does radio frequency interference to satellite navigation pose an increasing threat to network efficiency, cost-effectiveness and ultimately safety? Technical report.

Gadka, P., Sadowski, J., and Stefanski, J. (2019). Detection of the first component of the received LTE signal in the OTDoA method. *Wireless Communications and Mobile Computing*, pages 1–12.

Gante, J., Sousa, L., and Falcao, G. (2020). Dethroning GPS: Low-power accurate 5G positioning systems using machine learning. *IEEE Journal on Emerging and Selected Topics in Circuits and Systems*, 10(2):240–252.

Han, S., Kang, T., and Seo, J. (2019). Smartphone application to estimate distances from LTE base stations based on received signal strength measurements. In *International Technical Conference on Circuits/Systems, Computers and Communications*, pages 1–3.

Hong, T., Sun, J., Jin, T., Yi, Y., and Qu, J. (2021). Hybrid positioning with DTMB and LTE signals. In *Proceedings of International Wireless Communications and Mobile Computing*, pages 303–307.

Ikhtiari, N. (2019). Navigation in GNSS denied environments using software defined radios and LTE signals of opportunities. Master's thesis, University of Canterbury, Christchurch, New Zealand.

International Civil Aviation Organization (ICAO) (2019). An urgent need to address harmful interferences to GNSS. Technical report.

International Civil Aviation Organization (ICAO) (2020). Strengthening of communications, navigation, and surveillance (CNS) systems resilience and mitigation of interference to global navigation satellite system (GNSS). Technical report.

Ivanov, A., Koshnicharova, D., Tonchev, K., and Poulkov, V. (2023). Localization in cellular and heterogeneous networks for 5G and beyond: A review. *Journal of Mobile Multimedia*, pages 47–72.

Jao, C., Abdallah, A., Chen, C., Seo, M., Kia, S., Kassas, Z., and Shkel, A. (2022). Sub-meter accurate pedestrian indoor navigation system with dual ZUPT-aided INS, machine learning-aided LTE, and UWB signals. In *Proceedings of ION GNSS+ Conference*. accepted.

Kang, T., Lee, H., and Seo, J. (2019). Analysis of the maximum correlation peak value and RSRQ in LTE signals according to frequency bands and sampling frequencies. In *International Conference on Control, Automation and Systems*, pages 1182–1186.

Kassas, Z. (2021). Position, navigation, and timing technologies in the 21st century. volume 2, chapter 38: Navigation with Cellular Signals of Opportunity, pages 1171–1223. Wiley-IEEE.

Kassas, Z., Abdallah, A., Khalife, J., Lee, C., Jurado, J., Duede, J., Hoeffner, Z., Hulsey, T., Quirarte, R., Wachtel, S., and Tay, R. (2022a). Received power characterization of terrestrial cellular signals on high altitude aircraft. In *Proceedings of IEEE Aerospace Conference*, pages 1–8.

Kassas, Z., Khalife, J., Abdallah, A., and Lee, C. (2020). I am not afraid of the jammer: navigating with signals of opportunity in GPS-denied environments. In *Proceedings of ION GNSS Conference*, pages 1566–1585.

Kassas, Z., Khalife, J., Abdallah, A., and Lee, C. (2022b). I am not afraid of the GPS jammer: resilient navigation via signals of opportunity in GPS-denied environments. *IEEE Aerospace and Electronic Systems Magazine*, 37(7):4–19.

Kassas, Z., Khalife, J., Abdallah, A., Lee, C., Jurado, J., Wachtel, S., Duede, J., Hoeffner, Z., Hulsey, T., Quirarte, R., and Tay, R. (2022c). Assessment of cellular signals of opportunity for high altitude aircraft navigation. *IEEE Aerospace and Electronic Systems Magazine*, 37(10):4–19.

Kazaz, T., Janssen, G., Romme, J., and Van der Veen, A. (2022). Delay estimation for ranging and localization using multiband channel state information. *IEEE Transactions on Wireless Communications*, 21(4):2591–2607.

Khalife, J. and Kassas, Z. (2022a). Differential framework for submeter-accurate vehicular navigation with cellular signals. *IEEE Transactions on Intelligent Vehicles*. accepted.

Khalife, J. and Kassas, Z. (2022b). On the achievability of submeter-accurate UAV navigation with cellular signals exploiting loose network synchronization. *IEEE Transactions on Aerospace and Electronic Systems*. accepted.

Kim, E. and Shin, Y. (2019). Feasibility analysis of LTE-based UAS navigation in deep urban areas and DSRC augmentation. *Sensors*, 19(9):4192–4207.

Lapin, I., Granados, G., Samson, J., Renaudin, O., Zanier, F., and Ries, L. (2022). STARE: Real-time software receiver for LTE and 5G NR positioning and signal monitoring. In *Proceedings of Workshop on Satellite Navigation Technology*, pages 1–11.

Leng, M., Quitin, F., Tay, W., Cheng, C., Razul, S., and See, C. (2016). Anchor-aided joint localization and synchronization using SOOP: Theory and experiments. *IEEE Transactions on Wireless Communications*, 15(11):7670–7685.

Maaref, M. and Kassas, Z. (2022). Autonomous integrity monitoring for vehicular navigation with cellular signals of opportunity and an IMU. *IEEE Transactions on Intelligent Transportation Systems*, 23(6):5586–5601.

Morales, J. and Kassas, Z. (2018). Optimal collaborative mapping of terrestrial transmitters: receiver placement and performance characterization. *IEEE Transactions on Aerospace and Electronic Systems*, 54(2):992–1007.

Morales, J. and Kassas, Z. (2021). Tightly-coupled inertial navigation system with signals of opportunity aiding. *IEEE Transactions on Aerospace and Electronic Systems*, 57(3):1930–1948.

Mortier, J., Pages, G., and Vila-Valls, J. (2020). Robust TOA-based UAS navigation under model mismatch in GNSS-denied harsh environments. *Remote Sensing*, 12(18):2928–2947.

Pan, M., Liu, P., Liu, S., Qi, W., Huang, Y., You, X., Jia, X., and Li, X. (2022). Efficient joint DOA and TOA estimation for indoor positioning with 5G picocell base stations. *IEEE Transactions on Instrumentation and Measurement*, 71:1–19.

Psiaki, M. and Slosman, B. (2022). Tracking digital FM OFDM signals for the determination of navigation observables. *NAVIGATION, Journal of the Institute of Navigation*, 69(2).

Shamaei, K. and Kassas, Z. (2021). A joint TOA and DOA acquisition and tracking approach for positioning with LTE signals. *IEEE Transactions on Signal Processing*, pages 2689–2705.

Shamaei, K., Khalife, J., and Kassas, Z. (2017). Comparative results for positioning with secondary synchronization signal versus cell specific reference signal in LTE systems. In *Proceedings of ION International Technical Meeting Conference*, pages 1256–1268.

Shamaei, K., Morales, J., and Kassas, Z. (2019). A framework for navigation with LTE time-correlated pseudorange errors in multipath environments. In *Proceedings of IEEE Vehicular Technology Conference*, pages 1–6.

Soderini, A., Thevenon, P., Macabiau, C., Borgagni, L., and Fischer, J. (2020). Pseudorange measurements with LTE physical channels. In *Proceedings of ION International Technical Meeting*, pages 817–829.

Souli, N., Kolios, P., and Ellinas, G. (2020). Relative positioning of autonomous systems using signals of opportunity. In *Proceedings of IEEE Vehicular Technology Conference*, pages 1–6.

Souli, N., Kolios, P., and Ellinas, G. (2021a). Online relative positioning of autonomous vehicles using signals of opportunity. *IEEE Transactions on Intelligent Vehicles*, pages 1–1.

Souli, N., Makrigiorgis, R., Kolios, P., and Ellinas, G. (2021b). Real-time relative positioning system implementation employing signals of opportunity, inertial, and optical flow modalities. In *Proceedings of International Conference on Unmanned Aircraft Systems*, pages 229–236.

Stevens, B. and Younis, M. (2021). Detection algorithm for cellular synchronization signals in airborne applications. *IEEE Access*, 9:55555–55566.

Strandjord, K., Morton, Y., and Wang, P. (2021). Evaluating the urban signal environment for GNSS and LTE signals. In *Proceedings of ION GNSS+ Conference*, pages 2166–2182.

Wang, P. and Morton, Y. (2020). Multipath estimating delay lock loop for LTE signal TOA estimation in indoor and urban environments. *IEEE Transactions on Wireless Communications*, 19(8):5518–5530.

Wang, P. and Morton, Y. (2020). Performance comparison of time-of-arrival estimation techniques for LTE signals in realistic multipath propagation channels. *NAVIGATION, Journal of the Institute of Navigation*, 67(4):691–712.

Wang, P. and Morton, Y. (2022). Impact analysis of inter-cell interference in cellular networks for navigation applications. *IEEE Transactions on Aerospace and Electronic Systems*. accepted.

Wang, P., Wang, Y., and Morton, J. (2022). Signal tracking algorithm with adaptive multipath mitigation and experimental results for LTE positioning receivers in urban environments. *IEEE Transactions on Aerospace and Electronic Systems*, 58(4):2779–2795.

Whiton, R., Chen, J., Johansson, T., and Tufvesson, F. (2022). Urban navigation with LTE using a large antenna array and machine learning. In *Proceedings of IEEE Vehicular Technology Conference*, pages 1–5.

Xhafa, A., del Peral-Rosado, J., López-Salcedo, J., and Seco-Granados, G. (2021). Evaluation of 5G positioning performance based on UTDoA, AoA and base-station selective exclusion. *Sensors*, 22(1):101–118.

Yang, C., Arizabaleta-Diez, M., Weitkemper, P., and Pany, T. (2022). An experimental analysis of cyclic and reference signals of 4g LTE for TOA estimation and positioning in mobile fading environments. *IEEE Aerospace and Electronic Systems Magazine*, 37(9):16–41.

Yang, C., Pany, T., and Weitkemper, P. (2020). Effect of antenna ports on TOA estimation with 4G LTE signals in urban mobile environments. In *Proceedings of ION International Technical Meeting*, pages 2166–2181.

Zhu, H., Xu, W., Sang, Y., Yao, Z., Liu, L., and Okonkw, M. (2021). Mobile communication signal selection algorithm for signal of opportunity navigation. In *Proceedings of International Conference on Advanced Communication Technology*, pages 166–171.

Received Power Characterization of Terrestrial Cellular Signals on High Altitude Aircraft

Zaher M. Kassas
Department of Mechanical and Aerospace Engineering
University of California, Irvine
Irvine, CA 92697
zkassas@ieee.org

Ali A. Abdallah
Department of Electrical Engineering and Computer Science
University of California, Irvine
Irvine, CA 92697
abdalla2@uci.edu

Joe Khalife
Department of Mechanical and Aerospace Engineering
University of California, Irvine
Irvine, CA 92697
khalifej@uci.edu

Chiawei Lee, Juan Jurado, Steven Wachtel, Jacob duede, Zachary Hoeffner, Thomas Hulsey, Rachel Quirarte, and RunXuan Tay
U.S. Air Force
Edwards, CA 93524

***Abstract*— The received power of terrestrial cellular 3G code division multiple access (CDMA) and 4G long-term evolution (LTE) signals on a high altitude aircraft is experimentally characterized. The conducted experiments were performed on a Beechcraft C-12 Huron, a fixed-wing U.S. Air Force aircraft. Two types of flight patterns were performed: (i) teardrop-like patterns to characterize the carrier-to-noise ratio (C/N_0) versus altitude and (ii) grid-like patterns to characterize C/N_0 versus the horizontal distance between the aircraft and cellular towers. Flight campaigns in two regions were conducted: (i) a rural region in Edwards, California, USA, and (ii) an urban region in Riverside, California, USA. It was observed that cellular signals are surprisingly powerful at both (i) high altitudes, exhibiting C/N_0 of 25–55 dB-Hz at altitudes of 2,000–23,000 ft above ground level (AGL) and (ii) faraway horizontal distances, exhibiting C/N_0 of about 30 dB-Hz for towers as far as 50 km, while flying at about 16,000 ft AGL. In addition, two propagation models were evaluated to describe the behavior of the measured C/N_0: (i) free-space path loss model and (ii) two-ray model. It was observed that the two-ray model fits the measured C/N_0 sufficiently well, for towers more than 10 km away, while flying at an altitude of 16,000 ft AGL. For towers closer than 10 km, the antenna radiation pattern should be incorporated into the two-ray model to improve model fitting.**

TABLE OF CONTENTS

1. INTRODUCTION

Global navigation satellite systems (GNSS) are heavily relied upon in today's aviation communications, navigation, and surveillance (CNS) systems as well as air traffic management [1]. The upsurge in GNSS radio frequency interference (RFI) is jeopardizing safe and efficient aviation operations [2, 3]. RFI sources include repeaters and pseudolites [4, 5], GNSS jammers [6, 7], and systems transmitting outside the GNSS frequency bands [8, 9]. There were 4,364 GNSS outages reported by pilots in 2018, which represents more than a 2,000% increase over the previous year [10]. What is alarming is that RFI is affecting civil aviation at distances of up to 300 km from conflict zones (where GNSS jammers tend to be prevent) and that the majority of RFI (about 81%) affects en-route flights. In 2019, the International Civil Aviation Organization (ICAO) issued a Working Paper titled "An Urgent Need to Address Harmful Interferences to GNSS," where it concluded that harmful RFI to GNSS would prevent the full continuation of safety and efficiency benefits of GNSS-based services. Moreover, there was a call for supporting multi-disciplinary development of alternative positioning, navigation, and timing (PNT) strategy and solutions to complement the use of GNSS in aviation [11].

Cellular signals have shown tremendous promise as an alternative PNT source [12–23]. This is due to their inherently desirable attributes [24]: (i) they are ubiquitous, (ii) they are transmitted in a wide range of frequencies and in many directions which makes them spectrally and geometrically diverse, (iii) they possess a high received carrier-to-noise (C/N_0) ratio (tens of dBs higher than GNSS), and (iv) they are readily available for free as their infrastructure is well established and the signals are broadcasted to billions of users worldwide. Recent results have shown the ability of cellular signals to yield meter-level-accurate navigation on ground vehicles [25–29] in urban environments and submeter-level-accurate navigation on UAVs [30, 31]. Moreover, the robustness and availability of cellular signals have been demonstrated in a GPS-jammed environment [32].

Assessing cellular signals for aerial vehicles has been the subject of several studies recently [33–37]. It was concluded that commercial cellular networks are capable of providing connectivity to aerial vehicles at low altitudes [38, 39]. However, the majority of existing studies considered low altitude aerial vehicles traveling at low speeds and focused on evaluating cellular signals for communication purposes with little attention to evaluating them for PNT [40].

A joint effort between the Autonomous Systems Perception, Intelligence, and Navigation (ASPIN) Laboratory and Edwards Air Force Base, California, USA led to a weeklong flights in March 2020 in a mission called "SNIFFER: Signals of opportunity for Navigation In Frequency-Forbidden EnviRonments." The flights took place on a Beechcraft C-12 Huron, a fixed-wing U.S. Air Force aircraft, to study the efficacy of terrestrial cellular signals for aircraft navigation. This paper presents findings from these flights to characterize

978-1-6654-3760-8/22/$31.00 ©2022 IEEE

C/N_0 of terrestrial cellular 3G code division multiple access (CDMA) and 4G long-term evolution (LTE) signals. The C/N_0 provides a measure of the precision of the navigation observables (pseudorange and carrier phase) [41], which are used to calculate the PNT solution [42, 43]. Two types of flight patterns were performed: (i) teardrop-like patterns to characterize the carrier-to-noise ratio (C/N_0) versus altitude and (ii) grid-like patterns to characterize C/N_0 versus the horizontal distance between the aircraft and cellular towers. Flight campaigns in two regions were conducted: (i) a rural region in Edwards, California, USA, and (ii) an urban region in Riverside, California, USA. It was observed that cellular signals are surprisingly powerful at both (i) high altitudes, exhibiting C/N_0 of 25–55 dB-Hz at altitudes of 2,000–23,000 ft above ground level (AGL) and (ii) faraway horizontal distances, exhibiting C/N_0 of about 30 dB-Hz for towers as far as 50 km, while flying at about 16,000 ft AGL. In addition, two propagation models were evaluated to describe the behavior of the measured C/N_0: (i) free-space path loss model and (ii) two-ray model. It was observed that the two-ray model fits the measured C/N_0 sufficiently well, for towers more than 10 km away, while flying at an altitude of 16,000 ft AGL. For towers closer than 10 km, the antenna radiation pattern should be incorporated into the two-ray model to improve model fitting to the measured C/N_0.

The remainder of the paper is organized as follows. Section 2 overviews (i) hardware and software setup, (ii) flight maneuvers, and (iii) flight regions. Section 3 characterizes the measured C/N_0 of 3G and 4G cellular signals as a function of altitude and horizontal distance to the towers in the both regions. It also evaluates the free-space path loss model and the two-ray model. Section 4 gives concluding remarks.

2. High-Altitude Aircraft Navigation with Terrestrial Cellular Signals

This section presents the hardware and software setup with which the aircraft was equipped and flight maneuvers and regions.

Hardware and Software Setup

The C-12 aircraft was equipped with a universal software radio peripheral (USRP) with consumer-grade cellular antennas to sample three cellular bands and store the samples on a desktop computer for off-line processing. The stored samples were post-processed with the 3G and 4G cellular modules of ASPIN Laboratory's SDR, called MATRIX: Multichannel Adaptive TRansceiver Information eXtractor [32]. The SDR produces navigation observables: Doppler frequency, carrier phase, and pseudorange, along with the corresponding C/N_0. The hardware setup is shown in Figure 1.

Flight Maneuvers

Two types of maneuvers were performed in each region. The first is a teardrop-like pattern while climbing/descending. The pattern has a focal point that is aligned with a geographic point of interest. The measurements used to characterize C/N_0 and multipath were taken exactly above the geographic point of interest to maintain the horizontal distance between the aircraft and the cellular base stations. The second type of maneuver is a grid-like pattern with many turns and straight segments. Such patterns were used as a stress test on ASPIN Laboratory's SDRs to assess the performance of signal acquisition, tracking loops, and navigation solution. The two types of maneuvers are shown in Figure 2.

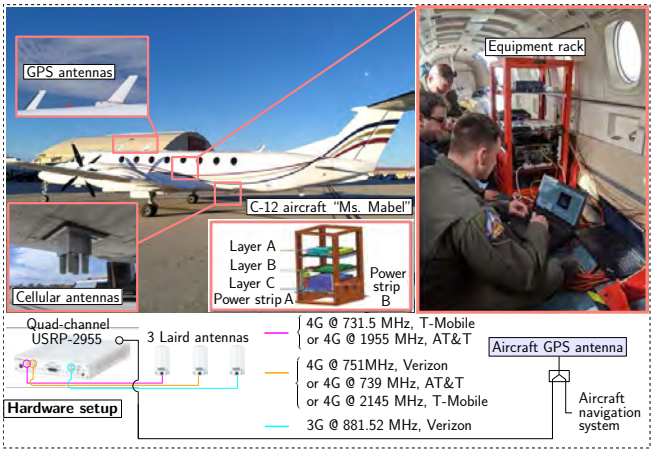

Figure 1. Hardware setup with which the C-12 aircraft was equipped.

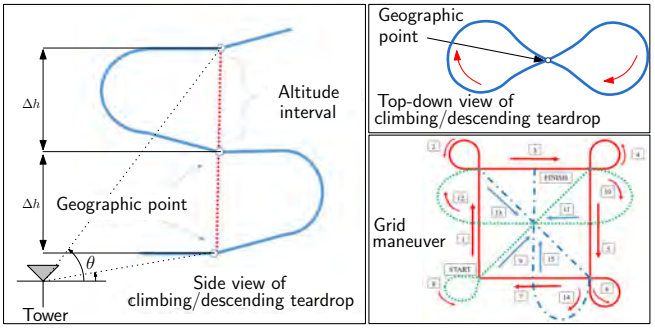

Figure 2. Maneuvers performed by the C-12 aircraft. The altitude step and elevation angle are denoted by Δh and θ, respectively.

Flight Regions

Figure 3 shows the regions in which the experiments were performed: (i) Region A, a rural region in Edwards, California, USA and (ii) Region C, an urban region in Riverside, California, USA.

3. Received C/N_0 Characterization

This section characterizes the C/N_0 of received cellular signals in regions A and C. Different channel models are evaluated to find the best model that represents the C/N_0 behavior. The precision of navigation observables (pseudorange and carrier phase) is a function of C/N_0, which ultimately determines the precision of the navigation solution. As its name suggests, the pseudorange is not quite the range between the transmitter and the receiver, but the sum of the range and the bias due to the difference between the transmitter and receiver's clocks. Essentially, the pseudorange measurement is constructed by measuring the time-of-arrival (TOA) of the signal. The TOA is obtained by correlating the received cellular signals with known synchronization sequences [24]. The C/N_0 can be calculated according to [41]

$$C/N_0 = \frac{C}{N_0} = \frac{C}{\sigma^2_{\text{noise}} T},$$

where C is the carrier power in Watts (W), N_0 is the noise power spectral density in W/Hz, which can b expressed as $N_0 = \sigma^2_{\text{noise}} T$, where $\sigma^2{}_{\text{noise}}$ is the discretized noise variance

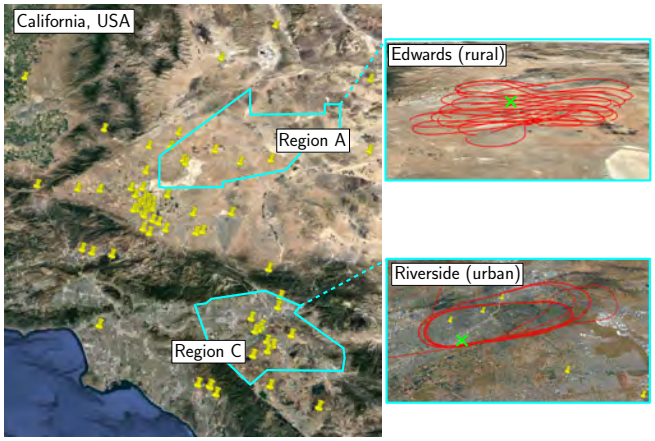

Figure 3. Regions A and C in which the flight campaigns took place. The yellow pins in the left figure represent 3G and 4G cellular towers that were mapped and analyzed in this study. The right figures show the aircraft trajectory in both regions (shown in red). Geographic points of interest in each region, shown in green crosses, were chosen according to the designed trajectories.

and T is the accumulation period, or the period over which correlation is performed. Typically, the C/N_0 should be above 35 dB-Hz for reliable acquisition, and above 25 dB-Hz to maintain track [41]. High sensitivity receivers can acquire and track at lower values of C/N_0 [44–46].

Free-Space Path Loss Model

The free-space path loss (FSPL) model is a simple, yet informative for aerial vehicles' wireless channels. The FSPL accounts only for the propagation loss between two isotropic radiators in free space and can be expressed as [47]

$$\frac{C}{N_0}(h) = \frac{C}{N_0}(R_0) - 10\alpha \log_{10} \sqrt{D} + w, \qquad (1)$$

where R_0 is the initial range; D is the line-of-sight given by $D = d^2 + h^2$, where d and h are the horizontal and vertical distances to the tower, respectively; α is the pathloss exponent; and w is a zero-mean random variable. Figure 4 depicts the variables involved in the FSPL model.

The measured C/N_0 as a function of altitudes for Region A and both signal types (3G CDMA and 4G LTE) are shown in Figures 5 and 6. Also shown are the FSPL model fit, where the pathloss exponent was assumed to be $\alpha = 2$ (free space). The aircraft-mounted SDR was able to maintain tracking of all acquired cellular signals up to the maximum altitude it reached, namely 23,000 ft AGL.

The C/N_0 for six 3G and 4G base stations in Region C are plotted as a function of the horizontal distance in Figure 7. It is worth noting that the aircraft was flying at an altitude of a little above 16,000 ft AGL. At such an altitude, the elevation angles are very high. Since cellular base station antennas are tilted downwards and are directional in the elevation direction, the loss due to the directive radiation pattern of cellular base station antennas dominate the pathloss. This explains why some of the C/N_0s in Figure 7 have an increasing trend, especially at shorter horizontal distances where the change in elevation angle is more significant. The big hole between 22 to 38 km in Figure 7 is purely due to the fact that some cellular towers happened to be located either too close or too far with respect to the trajectory traversed by the aircraft. In other words, none of the lines get disconnected in this gap; instead, the C/N_0 of the two base stations in the region below the 22 km horizontal distance are different from the four base stations in the region right to the 38 km horizontal distance. The aircraft-mounted SDR was able to maintain tracking of cellular towers as far as 50 km away.

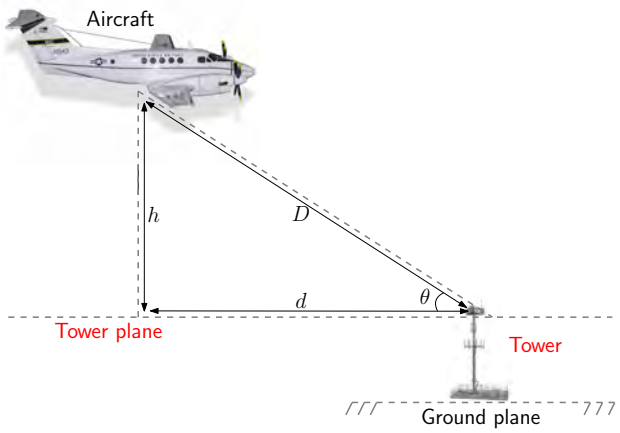

Figure 4. The free path loss model diagram.

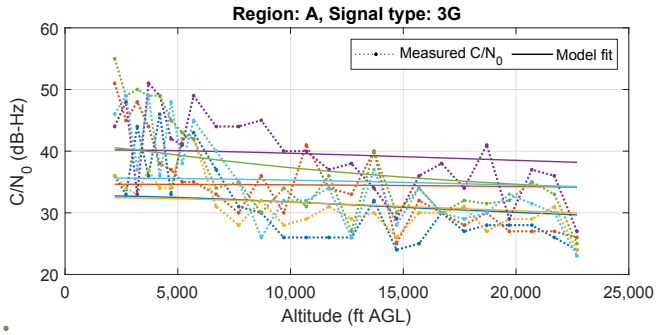

Figure 5. The C/N_0 of 7 3G towers as a function of altitude in Region A. The model fit is obtained by fitting the measured data to (1) for $\alpha = 2$.

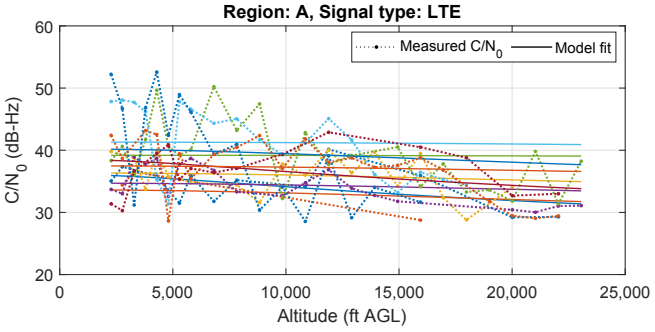

Figure 6. The C/N_0 of 14 4G towers as a function of altitude in Region A. The model fit is obtained by fitting the measured data to (1) for α=2.

Two-Ray Model

Next, a more sophisticated model is evaluated, namely the two-ray model. The two-ray model can be expressed as [47]

$$\frac{C}{N_0}(D) = \frac{C}{N_0}(D_0) - 20 \log_{10} \left[r_p \left| \frac{1}{D} + \Gamma(\psi) \frac{e^{-j\Delta\phi}}{D + \Delta D} \right| \right],$$

where

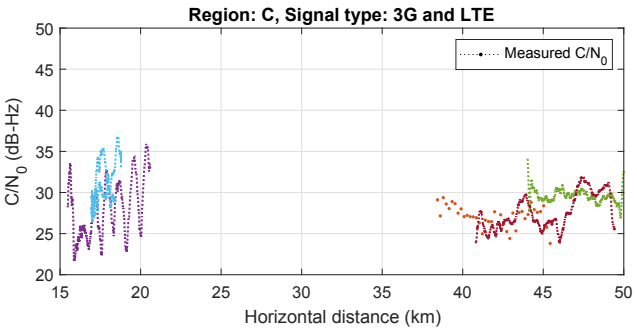

Figure 7. The C/N_0 as a function of the horizontal distance for four 3G towers (blue, red, yellow, and purple) and two LTE towers (green and light blue). The aircraft was flying at an altitude a little above 16,000 ft AGL.

$$\Delta D \triangleq \sqrt{(h_{\rm A}+h_{\rm S})^2+d^2} - \sqrt{(h_{\rm A}-h_{\rm S})^2+d^2},$$
$$\Delta\phi \triangleq \frac{2\pi\Delta D}{\lambda},$$
$$\Gamma(\psi) \triangleq \frac{\epsilon_g \sin\psi - \sqrt{\epsilon_g - \cos^2\psi}}{\epsilon_g \sin\psi + \sqrt{\epsilon_g - \cos^2\psi}},$$

where ϵ_g is the relative permittivity of the ground; $h_{\rm A}$ and $h_{\rm S}$ are the aircraft's and cellular tower's altitude, respectively; d is the horizontal distance; D is the line-of-sight distance; r_p is the antenna radiation pattern defined as $r_p = \cos(\theta)^\beta$, with θ and $\beta = 100$ being the elevation angle and the radiation pattern exponent, respectively; and ψ is the angle between the ground and the reflected ray. The C/N_0 of one 4G towers and one 3G tower as a function of horizontal distance in Region A is shown in Figure 9. For the 4G tower, the far-field two-ray model (green curve) appears to capture the measured C/N_0 (red dots) sufficiently accurately. It is worth noting that the far-field model does not account for the antenna's radiation pattern. However, this did not affect the model fitting, since the tower was already far enough (it was tracked from about 16 km through about 36 km). For the 3G tower, the far-field model (orange curve) did not fit the measured C/N_0 (blue dots) well for small horizontal distances. This discrepancy is due to not accounting for the tower's antenna directivity, which plays a significant role at lower horizontal distances. By accounting to the radiation pattern into the far-field model, a closer fit to the measured C/N_0 was achieved (magenta curve). Nevertheless, a slight mismatch can be seen at horizontal distances less than 10 km, even after accounting for the elevation angle between the aircraft and the cellular tower antenna, which could be due to the fact that the tilting angle of the tower's antenna is not exactly known.

Discussion

The obtained C/N_0 results demonstrate the promise of utilizing cellular signals for aircraft navigation. It was observed that both 3G CDMA and 4G LTE signals exhibited measured C/N_0 between 25 and 55 dB-Hz at altitudes of 2,000–23,000 ft AGL. The aircraft-mounted SDRs were able to maintain reliable tracking of acquired cellular signals throughout as the aircraft ascended/descended along the teardrop flight trajectory. In addition, cellular signals were tracked up to a horizontal distance of 50 km, while flying at about 16,000 ft AGL. These unprecedented results are the first of their kind, showing the tremendous potential of cellular signals for aircraft navigation.

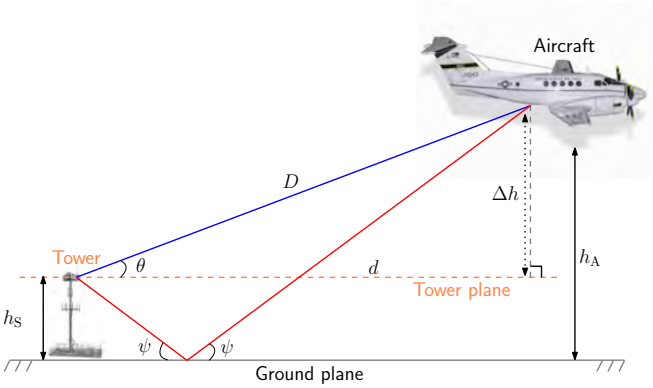

Figure 8. The two-ray model diagram.

The two-ray propagation model appears to fit the measured C/N_0 when flying at an altitude of 16,000 ft AGL, when the cellular transmitter's horizontal distances ranged between 10 km and about 33 km. For distances lower than 10 km, the mismatch between the measured C/N_0 and the two-ray model fit grew. Incorporating the transmitter's antenna radiation pattern reduced this mismatch, albeit did not remove completely. This could be due to the fact that the exact radiation pattern of the transmitter is not precisely known.

4. Conclusion

This paper characterized the received C/N_0 of terrestrial cellular 3G and 4G signals on a Beechcraft C-12 Huron, a fixed-wing U.S. Air Force aircraft. Two types of flight patterns were performed in two different regions. It was observed that cellular signals are surprisingly powerful at both (i) high altitudes, exhibiting C/N_0 of 25–55 dB-Hz at altitudes of 2,000–23,000 ft above ground level (AGL) and (ii) faraway horizontal distances, exhibiting C/N_0 of about 30 dB-Hz for towers as far as 50 km, while flying at about 16,000 ft AGL. In addition, two propagation models were evaluated to describe the behavior of the measured C/N_0: (i) free-space path loss model and (ii) two-ray model. It was observed that the two-ray model fits the measured C/N_0 sufficiently well, for towers more than 10 km away, while flying at an altitude of 16,000 ft AGL. For towers closer than 10 km, the antenna radiation pattern should be incorporated into the two-ray model to improve model fitting.

Acknowledgements

his work was supported in part by the Office of Naval Research (ONR) under Grant N00014-19-1-2511 and Grant N00014-19-1-2613, in part by Sandia National Laboratories under Award 1655264, and in part by the U.S. Department of Transportation (USDOT) under Grant 69A3552047138 for the CARMEN University Transportation Center (UTC). The authors would like to thank Edwards AFB and Holloman AFB for inviting the ASPIN Laboratory to conduct experiments on Air Force aircraft in the "SNIFFER: Signals of opportunity for Navigation In Frequency-Forbidden EnviRonments" flight campaign. The authors would like to thank Joshua Morales, Kimia Shamaei, Mahdi Maaref, Kyle Semelka, MyLinh Nguyen, and Trier Mortlock for their help with preparing for data collection. DISTRIBUTION STATEMENT A. Approved for public release; Distribution is unlimited. 412TW-PA-20146.

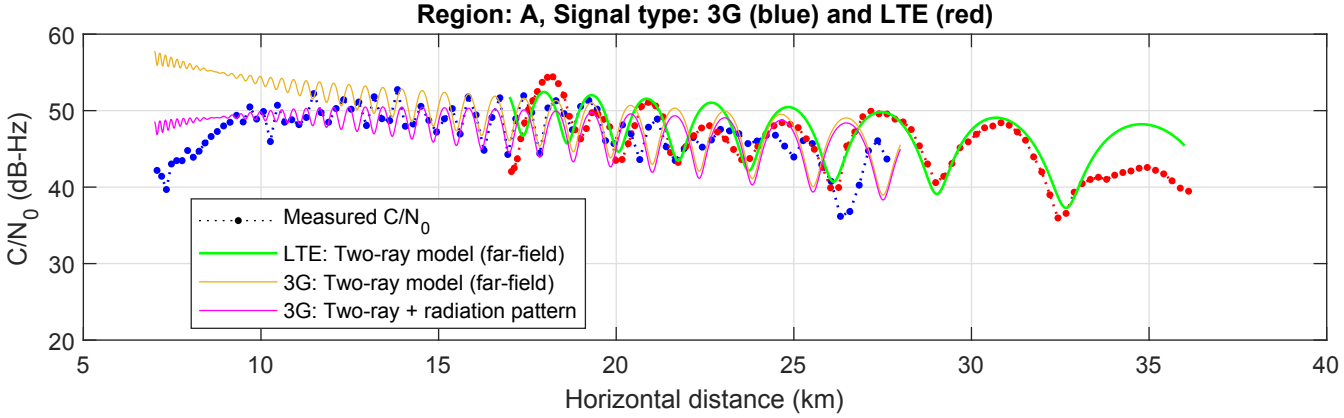

Figure 9. The measured C/N_0 of a 4G tower (red dots) and a 3G tower (blue dots) as a function of horizontal distance in Region A. The model fit is obtained by fitting the measured C/N_0 using the two-ray model and two-ray + cellular tower antenna radiation pattern.

REFERENCES

[1] R. Sabatini, A. Roy, E. Blasch, K. Kramer, , G. Fasano, I. Majid, O. Crespillo, D. Brown, and R. Ogan, "Avionics systems panel research and innovation perspectives," *IEEE Aerospace and Electronic Systems Magazine*, vol. 35, no. 12, pp. 58–72, December 2020.

[2] R. Ioannides, T. Pany, and G. Gibbons, "Known vulnerabilities of global navigation satellite systems, status, and potential mitigation techniques," *Proceedings of the IEEE*, vol. 104, no. 6, pp. 1174–1194, February 2016.

[3] E. Blasch, R. Sabatini, A. Roy, K. Kramer, G. Andrew, G. Schmidt, C. Insaurralde, and G. Fasano, "Cyber awareness trends in avionics," in *Proceedings of IEEE/AIAA Digital Avionics Systems Conference*, 2019, pp. 1–8.

[4] K. Kwon, Y. Jang, C. Yang, and D. Shim, "Impacts of GPS pseudolite signals on GPS software receivers," *Journal of Advanced Navigation Technology*, vol. 16, no. 4, pp. 627–634, August 2012.

[5] T. Marathe, S. Daneshmand, and G. Lachapelle, "Pseudolite interference mitigation and signal enhancements using an antenna array," in *Proceedings of International Conference on Indoor Positioning and Indoor Navigation*, October 2015, pp. 1–9.

[6] J. Grabowski, "Personal privacy jammers: locating Jersey PPDs jamming GBAS safety-of-life signals," *GPS World Magazine*, pp. 28–37, April 2012.

[7] D. Borio, F. Dovis, H. Kuusniemi, and L. Presti, "Impact and detection of GNSS jammers on consumer grade satellite navigation receivers," *Proceedings of the IEEE*, vol. 104, no. 6, pp. 1233–1245, February 2016.

[8] R. La Valle, J. Garcia, and P. Roncagliolo, "Antenna coupling and out of band interference effects on a high precision GNSS receiver," in *Proceedings of Argentine Conference on Electronics*, 2019, pp. 47–51.

[9] C. Hegarty, D. Bobyn, J. Grabowski, and A. Van Dierendonck, "An overview of the effects of out-of-band interference on GNSS receivers," *NAVIGATION, Journal of the Institute of Navigation*, vol. 67, no. 1, pp. 143–161, March 2020.

[10] EUROCONTROL, Aviation Intelligence Unit, "Does radio frequency interference to satellite navigation pose an increasing threat to network efficiency, cost-effectiveness and ultimately safety?" Tech. Rep.

[11] International Civil Aviation Organization (ICAO), "An urgent need to address harmful interferences to GNSS," https://www.iata.org/contentassets/e45e5219cc8c4277a0e80562590793da/address-harmful-interferences-gnss.pdf, Tech. Rep., May 2019.

[12] J. del Peral-Rosado, R. Estatuet-Castillo, J. Lopez-Salcedo, G. Seco-Granados, Z. Chaloupka, L. Ries, and J. Garcoa-Molina, "Evaluation of hybrid positioning scenarios for autonomous vehicle applications," in *Proceedings of ION International Technical Meeting Conference*, January 2017, pp. 2541–2553.

[13] J. del Peral-Rosado, R. Raulefs, J. López-Salcedo, and G. Seco-Granados, "Survey of cellular mobile radio localization methods: From 1G to 5G," *IEEE Communications Surveys Tutorials*, vol. 20, no. 2, pp. 1124–1148, 2018.

[14] T. Kang, H. Lee, and J. Seo, "TOA-based ranging method using CRS in LTE signals," *Journal of Advanced Navigation Technology*, vol. 23, no. 5, pp. 437–443, October 2019.

[15] J. Khalife and Z. Kassas, "Opportunistic UAV navigation with carrier phase measurements from asynchronous cellular signals," *IEEE Transactions on Aerospace and Electronic Systems*, vol. 56, no. 4, pp. 3285–3301, August 2020.

[16] N. Ikhtiari, "Navigation in GNSS denied environments using software defined radios and LTE signals of opportunities," Master's thesis, University of Canterbury, Christchurch, New Zealand, 2019.

[17] P. Wang and Y. Morton, "Multipath estimating delay lock loop for LTE signal TOA estimation in indoor and urban environments," *IEEE Transactions on Wireless Communications*, vol. 19, no. 8, pp. 5518–5530, 2020.

[18] J. Gante, L. Sousa, and G. Falcao, "Dethroning GPS: Low-power accurate 5G positioning systems using machine learning," *IEEE Journal on Emerging and Selected Topics in Circuits and Systems*, vol. 10, no. 2, pp. 240–252, June 2020.

[19] H. Dun, C. Tiberius, and G. Janssen, "Positioning in a multipath channel using OFDM signals with car-

rier phase tracking," *IEEE Access*, vol. 8, pp. 13 011–13 028, 2020.

[20] P. Wang and Y. Morton, "Performance comparison of time-of-arrival estimation techniques for LTE signals in realistic multipath propagation channels," *NAVIGATION, Journal of the Institute of Navigation*, vol. 67, no. 4, pp. 691–712, December 2020.

[21] J. Mortier, G. Pages, and J. Vila-Valls, "Robust TOA-based UAS navigation under model mismatch in GNSS-denied harsh environments," *Remote Sensing*, vol. 12, no. 18, pp. 2928–2947, September 2020.

[22] T. Kazaz, G. Janssen, J. Romme, and A. Van der Veen, "Delay estimation for ranging and localization using multiband channel state information," *IEEE Transactions on Wireless Communications*, pp. 1–16, September 2021.

[23] A. Abdallah and Z. Kassas, "UAV navigation with 5G carrier phase measurements," in *Proceedings of ION GNSS Conference*, September 2021, pp. 3294–3306.

[24] Z. Kassas, "Position, navigation, and timing technologies in the 21st century," J. Morton, F. van Diggelen, J. Spilker, Jr., and B. Parkinson, Eds. Wiley-IEEE, 2021, vol. 2, ch. 38: Navigation with Cellular Signals of Opportunity, pp. 1171–1223.

[25] Z. Kassas, M. Maaref, J. Morales, J. Khalife, and K. Shamaei, "Robust vehicular localization and map matching in urban environments through IMU, GNSS, and cellular signals," *IEEE Intelligent Transportation Systems Magazine*, vol. 12, no. 3, pp. 36–52, June 2020.

[26] M. Driusso, C. Marshall, M. Sabathy, F. Knutti, H. Mathis, and F. Babich, "Vehicular position tracking using LTE signals," *IEEE Transactions on Vehicular Technology*, vol. 66, no. 4, pp. 3376–3391, April 2017.

[27] J. del Peral-Rosado, O. Renaudin, C. Gentner, R. Raulefs, E. Dominguez-Tijero, A. Fernandez-Cabezas, F. Blazquez-Luengo, G. Cueto-Felgueroso, A. Chassaigne, D. Bartlett, F. Grec, L. Ries, R. Prieto-Cerdeira, J. Lopez-Salcedo, and G. Seco-Granados, "Physical-layer abstraction for hybrid GNSS and 5G positioning evaluations," in *Proceedings of IEEE Vehicular Technology Conference*, September 2019, pp. 1–6.

[28] C. Yang and A. Soloviev, "Mobile positioning with signals of opportunity in urban and urban canyon environments," in *Proceedings of IEEE/ION Position, Location, and Navigation Symposium*, April 2020, pp. 1043–1059.

[29] M. Maaref and Z. Kassas, "Autonomous integrity monitoring for vehicular navigation with cellular signals of opportunity and an IMU," *IEEE Transactions on Intelligent Transportation Systems*, 2021, accepted.

[30] J. Khalife and Z. Kassas, "Precise UAV navigation with cellular carrier phase measurements," in *Proceedings of IEEE/ION Position, Location, and Navigation Symposium*, April 2018, pp. 978–989.

[31] K. Shamaei and Z. Kassas, "Sub-meter accurate UAV navigation and cycle slip detection with LTE carrier phase," in *Proceedings of ION GNSS Conference*, September 2019, pp. 2469–2479.

[32] Z. Kassas, J. Khalife, A. Abdallah, and C. Lee, "I am not afraid of the jammer: navigating with signals of opportunity in GPS-denied environments," in *Proceedings of ION GNSS Conference*, 2020, pp. 1566–1585.

[33] G. Athanasiadou, M. Batistatos, D. Zarbouti, and G. Tsoulos, "LTE ground-to-air field measurements in the context of flying relays," *IEEE Wireless Communications*, vol. 26, no. 1, pp. 12–17, February 2019.

[34] X. Cai, N. Wang, J. Rodriguez-Pineiro, X. Yin, A. Yuste, W. Fan, G. Zhang, G. Pedersen, and L. Tian, "Low altitude air-to-ground channel characterization in LTE network," in *Proceedings of European Conference on Antennas and Propagation*, April 2019, pp. 1–5.

[35] W. Khawaja, I. Guvenc, D. Matolak, U. Fiebig, and N. Schneckenburger, "A survey of air-to-ground propagation channel modeling for unmanned aerial vehicles," *IEEE Communications Surveys & Tutorials*, vol. 21, no. 3, pp. 2361–2391, 2019.

[36] A. Abdalla and V. Marojevic, "Communications standards for unmanned aircraft systems: The 3GPP perspective and research drivers," *IEEE Communications Standards Magazine*, vol. 5, no. 1, pp. 70–77, March 2021.

[37] R. Amorim, J. Wigard, I. Kovacs, and T. Sorensen, "UAV communications for 5G and beyond," Y. Zeng, I. Guvenc, R. Zhang, G. Geraci, and D. Matolak, Eds. Wiley-IEEE, 2021, ch. 5: Performance Enhancements for LTE-Connected UAVs: Experiments and Simulations, pp. 139–161.

[38] Qualcomm Technologies, Inc., "LTE unmanned aircraft systems," Tech. Rep. 1.0.1, May 2017. [Online]. Available: https://www.qualcomm.com/documents/lte-unmanned-aircraft-systems-trial-report/

[39] Y. Zeng, Q. Wu, and R. Zhang, "Accessing from the sky: A tutorial on UAV communications for 5G and beyond," *Proceedings of the IEEE*, vol. 107, no. 12, pp. 2327–2375, December 2019.

[40] E. Kim and Y. Shin, "Feasibility analysis of LTE-based UAS navigation in deep urban areas and DSRC augmentation," *Sensors*, vol. 19, no. 9, pp. 4192–4207, April 2019.

[41] P. Misra and P. Enge, *Global Positioning System: Signals, Measurements, and Performance*, 2nd ed. Ganga-Jamuna Press, 2010.

[42] J. Khalife and Z. Kassas, "Navigation with cellular CDMA signals – part II: Performance analysis and experimental results," *IEEE Transactions on Signal Processing*, vol. 66, no. 8, pp. 2204–2218, April 2018.

[43] K. Shamaei and Z. Kassas, "LTE receiver design and multipath analysis for navigation in urban environments," *NAVIGATION, Journal of the Institute of Navigation*, vol. 65, no. 4, pp. 655–675, December 2018.

[44] A. Razavi, D. Gebre-Egziabher, and D. Akos, "Carrier loop architectures for tracking weak GPS signals," *IEEE Transactions on Aerospace and Electronic Systems*, vol. 44, no. 2, pp. 697–710, 2008.

[45] M. Lashley, D. Bevly, and J. Hung, "Performance analysis of vector tracking algorithms for weak GPS signals in high dynamics," *IEEE Journal of Selected Topics in Signal Processing*, vol. 3, no. 4, pp. 661–673, August 2009.

[46] C. Zhu and X. Fan, "A novel method to extend coherent integration for weak GPS signal acquisition," *IEEE Communications Letters*, vol. 19, no. 8, pp. 1343–1346, 2015.

[47] T. Rappaport, *Wireless communications: principles and practice*. Prentice hall PTR New Jersey, 1996, vol. 2.

BIOGRAPHY

Zaher (Zak) M. Kassas *is an associate professor at the University of California, Irvine and director of the Autonomous Systems Perception, Intelligence, and Navigation (ASPIN) Laboratory. He received a B.E. in Electrical Engineering from the Lebanese American University, an M.S. in Electrical and Computer Engineering from The Ohio State University, and an M.S.E. in Aerospace Engineering and a Ph.D. in Electrical and Computer Engineering from The University of Texas at Austin. In 2018, he received the National Science Foundation (NSF) Faculty Early Career Development Program (CAREER) award, and in 2019, he received the Office of Naval Research (ONR) Young Investigator Program (YIP) award. He is a recipient of 2018 IEEE Walter Fried Award, 2018 Institute of Navigation (ION) Samuel Burka Award, and 2019 ION Col. Thomas Thurlow Award. He is an Associate Editor for the IEEE Transactions on Aerospace and Electronic Systems and the IEEE Transactions on Intelligent Transportation Systems. His research interests include cyber-physical systems, estimation theory, navigation systems, autonomous vehicles, and intelligent transportation systems.*

Ali Abdallah *is a Ph.D. student in the Department of Electrical Engineering and Computer Science (EECS) at the University of California, Irvine (UCI) and a member of the Autonomous Systems Perception, Intelligence, and Navigation (ASPIN) Laboratory. He is a recipient of the Best Student Paper Award at the 2020 IEEE/ION Position, Location, and Navigation Symposium (PLANS) and the Grand Prize of the 2020 IEEE Signal Processing Society video contest for beamforming research (5-MICC).*

Joe Khalife *is a postdoctoral fellow at the University of California, Irvine and member of the Autonomous Systems Perception, Intelligence, and Navigation (ASPIN) Laboratory. He received a B.E. in Electrical Engineering, an M.S. in Computer Engineering from the Lebanese American University (LAU) and a Ph.D. in Electrical Engineering and Computer Science from the University of California, Irvine. From 2012 to 2015, he was a research assistant at LAU, and has been a member of the ASPIN Laboratory since 2015. He is a recipient of the 2016 IEEE/ION Position, Location, and Navigation Symposium (PLANS) Best Student Paper Award and the 2018 IEEE Walter Fried Award. His research interests include opportunistic navigation, autonomous vehicles, and software-defined radio.*

Chiawei Lee *is an Assistant Professor and Instructor Flight Test Engineer at the U.S. Air Force Test Pilot School. He serves as the Test Management Program Director where he oversees about a dozen student and staff led flight test projects each year. In addition, he is the Chief Test Safety Officer responsible for the safe execution of curriculum and flight test project safety packages. He received a B.S. in Aerospace Engineering from University of California, Los Angeles and a M.S. in Aero/Astro Engineering from Stanford University.*

Juan Jurado *is a U.S. Air Force Lieutenant Colonel and the Director of Education at the U.S. Air Force Test Pilot School. He holds a B.S. from Texas A&M University, a M.S. from the Air Force Test Pilot School, and M.S. and Ph.D. from the Air Force Institute of Technology. Previously, he served as Director of Engineering for the 413th Flight Test Squadron and oversaw various C-130, V-22, and H-1 flight test programs. His research interests include aircraft performance modeling, online sensor calibration, image processing, visual-inertial navigation, and statistical sensor management for multi-sensor navigation problems.*

Steven Wachtel *is a U.S. Air Force Captian and a Flight Test Engineer, assigned to the 780th Test Squadron, Eglin AFB, FL. He received a B.S. in Mechanical Engineering from The Ohio State University, an M.S. in Flight Test Engineering from the U.S. Air Force Test Pilot School, and an M.S. in Systems Engineering from the Air Force Institute of Technology.*

Thomas Hulsey *is a U.S. Air Force Flight Commander of Operations Engineering. He received a B.S. in Aerospace Engineering from Missouri University of Science and Technology, an M.S. in Aeronautical Engineering from the Air Force Institute of Technology, and an M.S. in Experimental Flight Test Engineering from the United States Air Force Test Pilot School.*

Zachary Hoeffner *is a flight test engineer at the U.S. Air Force. He received a a B.S in Nuclear Engineering from the U.S. Air Force Academy, an M.S. in Flight Test Engineering from the U.S. Air Force Test Pilot School, an M.S. in Engineering Physics and Applied Physics from the Air Force Institute of Technology, and an M.S. in Nuclear Engineering from the Air Force Institute of Technology.*

Jacob Duede *is a Major in the U.S. Air Force. He was trained as a Communication/Navigation/Mission Systems apprentice on C-17 Globmaster II aircraft and stationed at McChord Air Force Base, WA. He graduated from the U.S. Air Force Academy as a commissioned officer with a B.S. in Mechanical Engineering. He attended the Undergraduate Pilot Training at Columbus Air Force Base, MS. In 2020, he graduated from the U.S. Air Force Test Pilot School at Edwards Air Force Base, CA. He is a Senior Pilot with over 2,000 hours and holds an M.S. in Engineering from the University of Arkansas and an M.S. in Flight Test Engineering from Air University.*

Rachel Quirarte *is a KC-46 and KC-135 programmatic flight commander and test pilot in the 418th Flight Test Squadron in the U.S. Air Force. She received a a B.S. in Aeronautical Engineering from the U.S. Air Force Academy, an M.S. in Flight Test Engineering from the U.S. Air Force Test Pilot School, and an M.S. in Mechanical Engineering from Rice University.*

RunXuan Tay *received a B.S. degree in Electrical Engineering from the University California, San Diego and M.S. degree in Flight Test Engineering from the U.S. Air Force Test Pilot School. He is currently a test pilot at Air Warfare Center, Republic of Singapore Air Force, where he works on fixed wing test programs.*

Robust Receiver Design for High Altitude Aircraft Navigation with Terrestrial Cellular Signals

Zaher M. Kassas
The Ohio State University
Columbus, OH, USA
zkassas@ieee.org

Shaghayegh Shahcheraghi
The Ohio State University
Columbus, OH, USA
shahcheraghi.1@osu.edu

Ali Kaiss
The Ohio State University
Columbus, OH, USA
kaiss.1@osu.edu

Chiawei Lee
United States Air Force
Edwards Air Force Base, CA, USA

Juan Jurado
United States Air Force
Edwards Air Force Base, CA, USA

Steven Wachtel
United States Air Force
Edwards Air Force Base, CA, USA

Jacob Duede
United States Air Force
Edwards Air Force Base, CA, USA

Zachary Hoeffner
United States Air Force
Edwards Air Force Base, CA, USA

Thomas Hulsey
United States Air Force
Edwards Air Force Base, CA, USA

Rachel Quirarte
United States Air Force
Edwards Air Force Base, CA, USA

RunXuan Tay
Republic of Singapore Air Force
Singapore, Republic of Singapore

***Abstract*—A robust receiver design to exploit long-term evolution (LTE) terrestrial cellular signals of opportunity (SOPs) for high altitude aircraft navigation is presented. Conventional receivers employ phase-locked loops (PLLs) to track the carrier phase of received signals. In this paper, a Kalman filter (KF) is developed to replace the receiver's PLLs. To evaluate the performance of the proposed receiver, a flight campaign was conducted over two regions in California, USA: (i) Region A: Edwards Air Force Base (rural) and (ii) Region B: Palmdale (semi-urban). It is shown that the proposed receiver provides robust tracking of received LTE signals compared to a conventional PLL-based receiver, in which the latter could only track intermittently, especially during sharp turns. The produced carrier phase observables to 5 LTE eNodeBs in each region were fused with altimeter data via an extended Kalman filter (EKF) to estimate the aircraft's trajectory. Over trajectories of 51 km and 57 km in regions A and B, traversed in 9 min and 11 min, at flying altitudes of 5,000 and 7,000 ft above ground level, respectively, the proposed KF-based receiver reduced the position root-mean squared error (RMSE) by 74.8% and 30.7%, respectively, over the PLL-based receiver.**

***Index Terms*—Aircraft navigation, signals of opportunity, LTE**

I. Introduction

Radio frequency interference (RFI) incidents in global navigation satellite system (GNSS) bands have skyrocketed in the past few years, jeopardizing safe and efficient aviation operations [1]. National agencies, from the U.S. Department of Transportation (USDOT) [2] to the National Institute of Standards and Technology (NIST) [3], and international agencies, from the International Civil Aviation Organization (ICAO) [4], [5] to the International Telecommunication Union (ITU) [6], have called for both protecting against harmful RFI in GNSS bands and to finding complementary navigation technologies. In its highly regarded 2021 report, NIST identified signals of opportunity (SOPs) and terrestrial RF sources (e.g., cellular) as a mitigation category.

SOPs have demonstrated promising potential for navigation when GNSS signals become unreliable or unavailable [7]. Even though these signals were not intended for navigation purposes, researchers have shown that they can be exploited for such purpose. SOPs can be terrestrial (e.g., AM/FM radio [8]–[10], cellular [11]–[13], and digital television [14]–[16]), or space-based (e.g., low Earth orbit (LEO) satellites [17]–[19] and geostationary Earth orbit (GEO) satellites [20]).

Cellular SOPs have been shown to be particularly effective as a navigation source in challenging GNSS environments, such as indoors [21], [22], deep urban canyons [23], [24], and intentionally GPS-jammed environments [25]. This is attributed to their inherent features, which are desirable for navigation: abundance, geometrical and spectral diversity, and reception with a high carrier-to-noise ratio (CNR). When it comes to aerial vehicle navigation, cellular signals have yielded submeter-level accuracy on low altitude unmanned aerial vehicles (UAVs) [26], [27] and meter-level accuracy on high altitude aircraft [28]–[30].

Assessing cellular signals for aerial vehicles have been the subject of several studies recently [31], [32]. These studies span radio channel modeling [33], [34]; evaluation of signal quality in terms of received signal power [35], [36], interference from cellular transmitters [37], [38], and coverage and connectivity [39], [40]; and standards recommendations

[41], [42]. However, the majority of these studies focused on evaluating cellular signals for communication purposes with little attention to evaluating them for navigation purposes [43], [44]. Moreover, they considered UAVs flying at low altitudes (up to 500 ft) and slow speeds (up to 50 km/h).

To the authors knowledge, the first studies to evaluate the potential of cellular signals for high altitude aircraft navigation appeared in [28]–[30]. These studies were the result of an unprecedented aerial campaign conducted by the Autonomous Systems Perception, Intelligence, and Navigation (ASPIN) Laboratory in collaboration with the United States Air Force (USAF) at the Edwards Air Force Base (AFB), California, USA. The cellular software-defined radios (SDRs) of the ASPIN Laboratory were flown on a USAF Beechcraft C-12 Huron, a fixed-wing aircraft, to collect ambient cellular signals. This unique dataset consists of combinations of flights run over rural and semi-urban environments with altitudes ranging up to 23,000 ft and a multitude of trajectories and maneuvers including straight segments, banking turns, holding patterns, and ascending and descending teardrops, performed by members of the USAF Test Pilot School.

Conventional receivers [45], including the one used in [28]–[30], employ phase-locked loops (PLLs) to track the carrier phase of received signals. Kalman filter (KF)-based tracking loops are known to improve tracking robustness [46], [47], which are adopted in this paper. The proposed KF-based receiver was evaluated on recorded long-term evolution (LTE) samples over two regions in California, USA: (i) Region A: Edwards Air Force Base (rural) and (ii) Region B: Palmdale (semi-urban). This paper shows that the KF-based receiver provides robust tracking compared to a conventional PLL-based receiver, in which the latter could only track intermittently, especially during sharp turns. The produced carrier phase observables to 5 LTE eNodeBs in each region were fused with altimeter data via an extended Kalman filter (EKF) to estimate the aircraft's trajectory. Over trajectories of 51 km and 57 km in regions A and B, traversed in 9 min and 11 min, at flying altitudes of 5,000 and 7,000 ft above ground level (AGL), respectively, the proposed KF-based receiver reduced the position root-mean squared error (RMSE) by 74.8% and 30.7%, respectively, over the PLL-based receiver.

The rest of this article is organized as follows. Section II describes the proposed KF-based tracking loops. Section III evaluates the tracking performance of the proposed receiver. Section IV describes the EKF settings and compares the aircraft navigation results obtained using the PLL-based receiver versus the proposed KF-based receiver. Section V gives concluding remarks.

II. Proposed KF-Based Tracking Loops

This section outlines the proposed KF-based tracking loops, which are later shown to improve carrier phase tracking robustness over PLL-based tracking. Aside from the tracking loops, the remainder of the receiver components remain identical to the receiver used in [28]–[30].

A. KF-based Tracking Design

In [28], it was shown that during aircraft banking, tracking was lost, which resulted in large navigation error. One reason for the tracking loss was that the PLL could not cope with such high dynamics. To address this issue, the PLL is replaced with a KF to track the carrier phase, Doppler, and Doppler rate.

1) Received Signal Dynamical Model: Using a Taylor series expansion, the carrier phase of the received signal can be represented as

$$\theta = \theta_0 + \dot{\theta}(t)t + \frac{1}{2}\ddot{\theta}(t)t^2 + \cdots. \tag{1}$$

In this paper, the carrier phase is approximated up to its second-order term to provide robust tracking by estimating both the Doppler frequency and Doppler rate. The state vector is defined as $\boldsymbol{x}(t) = [\theta(t), \dot{\theta}(t), \ddot{\theta}(t)]$, whose dynamics is modeled as

$$\begin{aligned} \dot{\boldsymbol{x}}(t) &= \mathbf{A}\boldsymbol{x}(t) + \mathbf{B}\tilde{\boldsymbol{w}}(t) \\ \mathbf{A} = \begin{bmatrix} 0 & 1 & 0 \\ 0 & 0 & 1 \\ 0 & 0 & 0 \end{bmatrix}, &\quad \mathbf{B} = \begin{bmatrix} 0 \\ 0 \\ 1 \end{bmatrix}, \end{aligned} \tag{2}$$

where $\tilde{\boldsymbol{w}}(t)$ is a zero-mean white noise process with power spectral density $q_{\tilde{w}}$. The continuous-time model in (2) is discretized at a time interval, known as subaccumulation interval, T_{sub}, yielding

$$\boldsymbol{x}_{k+1} = \mathbf{F}\boldsymbol{x}_k + \boldsymbol{w}_k, \tag{3}$$

where $\mathbf{F} = e^{\mathbf{A}T_{sub}}$; $T_{sub} = LT_s$, where T_s is the baseband sampling time, and L is the number of samples in each T_{sub}; $\boldsymbol{w}_k$ is a discrete-time process noise vector, which is a zero-mean white sequence with covariance $\mathbf{Q} = q_{\tilde{w}} \int_0^{T_{sub}} e^{\mathbf{A}T_{sub}} (e^{\mathbf{A}T_{sub}})^{\mathsf{T}} dt$.

B. Kalman Filter-Based Tracking Loop

In the proposed receiver, a third-order KF-based algorithm is designed to track the carrier phase, Doppler frequency, and Doppler rate. Denote $\hat{\boldsymbol{\theta}}_{k|k}$ as the estimate of the state vector at time-step k, given all the measurements up to time-step k. The estimate of the state vector is $\hat{\boldsymbol{\theta}} = [\hat{\theta}_0, 2\pi\hat{f}_D, 2\pi\hat{\dot{f}}_D]$. The initial state vector estimate is $\hat{\boldsymbol{\theta}}_{0|0} = [0, 2\pi f_{D_0}, 0]$, where f_{D_0} is estimated from the acquisition step. The estimated carrier phase $\hat{\theta} = \hat{\theta}_0 + 2\pi\hat{f}_D n T_s + 2\pi\frac{\hat{\dot{f}}_D}{2} n^2 T_s^2$ is used for both Doppler and Doppler rate wipe-off according to $\tilde{\boldsymbol{r}}[n] = \boldsymbol{r}[n]\exp(-j\hat{\theta})$, where $\boldsymbol{r}[n]$ is the received baseband signal, which can be expressed as

$$\begin{aligned} r[n] = \alpha c[\tau_n - t_s[n]]\exp(j\theta[\tau_n]) \\ + d[\tau_n - t_s[n]]\exp(j\theta[\tau_n]) + w[n], \end{aligned} \tag{4}$$

where α is the complex channel gain between the receiver and the eNodeB, τ_n is the sample time expressed in the receiver time, $c[n]$ is the periodic reference signal (namely, the secondary synchronization signal (SSS) and cell-specific reference signal (CRS), in this paper), $t_s[n]$ is the code phase

related to the distance between the receiver and the eNodeB at the nth time instant, $\theta[\tau_n]$ is the carrier phase in radians, $d[\tau_n]$ represents the data samples transmitted from the eNodeB, and $w[n]$ the measurement noise, modeled as an independent and identically distributed white noise.

Equivalently, the received signal can be represented as

$$r[n] = s[n] + w_{equ}[n], \tag{5}$$

where the desired received signal can be represented as

$$s[n] = \alpha c[\tau_n - t_s[n]] \exp(j\theta[\tau_n]) \tag{6}$$

and the equivalent noise is

$$w_{equ}[n] = d[\tau_n - t_s[n]] \exp(j\theta[\tau_n]) + w[n]. \tag{7}$$

After compensating for the carrier phase, the received signal can be written as

$$r[n] = \alpha c[\tau_n - t_s[n]] \exp(j\tilde{\theta}[\tau_n]) + n_k[n], \tag{8}$$

where $\tilde{\theta}_k[n] = \theta_k[n] - \hat{\theta}_k[n]$ is the carrier phase estimation error. The wiped-off sequence is correlated with the locally generated code. The angle of this correlation is considered as the residual error and is fed as an innovation to the KF loop using the observation model

$$\boldsymbol{z}_k = \mathbf{H}\boldsymbol{x}_k + \boldsymbol{v}_k, \quad \mathbf{H} = \begin{bmatrix} 1 & 0 & 0 \end{bmatrix}, \tag{9}$$

where $\boldsymbol{v}_k$ is the observation noise, which is modeled as discrete-time zero-mean white sequence with variance σ_θ^2. After calculating the innovation and performing a measurement-update step, the posterior carrier phase state $\hat{\boldsymbol{\theta}}_{k|k}$ is estimated and used in the refinement of the tracking.

C. Carrier-Aided Delay-Locked Loop

The carrier-aided delay-locked loop (DLL) uses a dot-product discriminator [48] to calculate the code phase error using the prompt, early, and late correlations, represented by S_p, S_e, and S_l. The early and late correlations are computed by correlating the received signal with an early and delayed version of the prompt code sequence, respectively to yield

$$e_k = C \cdot \left[(I_{e,k} - I_{l,k}) I_{p,k} + (Q_{e,k} - Q_{l,k}) Q_{p,k} \right], \tag{10}$$

where $S_{p,k} = I_{p,k} + jQ_{p,k}$, $S_{e,k} = I_{e,k} + jQ_{e,k}$, and $S_{l,k} = I_{l,k} + jQ_{l,k}$ and the constant C relates to the CNR and chip interval. The DLL loop filter is a simple gain K, which relates to the noise-equivalent bandwidth, $B_{n,DLL} = \frac{K}{4} = 0.05$. The output of the DLL filter, $\nu_{DLL,k}$, is the rate of change of the code phase, expressed in $\frac{\text{s}}{\text{s}}$. Assuming low-side mixing, the code start time is updated at time intervals of T_{sub} according to

$$\hat{t}_{s_{k+1}} = \hat{t}_{s_k} - (\nu_{DLL,k} + \frac{\hat{f}_{Dk}}{f_c}) T_{sub}, \tag{11}$$

where f_c is the carrier frequency, $\hat{f}_{Dk}$ is the Doppler frequency estimated by the KF, and T_{sub} is the subaccumulation interval.

III. Tracking Results

To evaluate the performance of the proposed receiver, the same LTE samples used in [28]–[30] was re-processed. The tracking results from proposed receiver versus [30] are compared in this section.

A. Region A

The first test trajectory is shown in Fig. 1. During this flight, data was sampled from two LTE channels with carrier frequencies at (i) 731.5 MHz, a 4G LTE channel allocated for the US cellular provider T-Mobile, and (ii) 751 MHz, a 4G LTE channel allocated for the US cellular provider AT&T. The robustness of the proposed receiver is evaluated by comparing its performance for the five eNodeBs that were acquired and tracked in [30]. Fig. 2a illustrates the time history of the pseudoranges obtained from carrier phase measurements that were estimated using the proposed KF-based receiver versus the ground truth ranges for the five LTE eNodeBs. Fig. 2b shows the time history of the measured pseudoranges estimated in [30] versus the ground truth ranges for those five LTE eNodeBs. The results demonstrate that pseudorange tracking is lost only for one eNodeB (around 350 s), while in [30], tracking was lost for three eNodeBs, starting around 300 s, the time at which the aircraft performed a banking turn.

Fig. 1: Experimental environment in region A showing the aircraft trajectory and the locations of the 5 LTE eNodeBs.

B. Region B

The second test trajectory is shown in Fig. 3. During this flight, two LTE channels were sampled at (i) 731.5 MHz, a 4G LTE channel allocated for T-Mobile, and (ii) 739 MHz, a 4G LTE channel allocated for Verizon. In [30], five LTE eNodeBs were acquired and tracked during this flight. Fig. 4a illustrates the time history of the pseudoranges estimated using the proposed KF-based receiver versus the ground truth ranges for the five LTE eNodeBs. Fig. 4b shows the time history of the measured pseudoranges estimated in [30] versus the ground truth ranges for those five LTE eNodeBs. It can be seen that the KF-based receiver tracks more eNodeBs for longer time compared with [30].

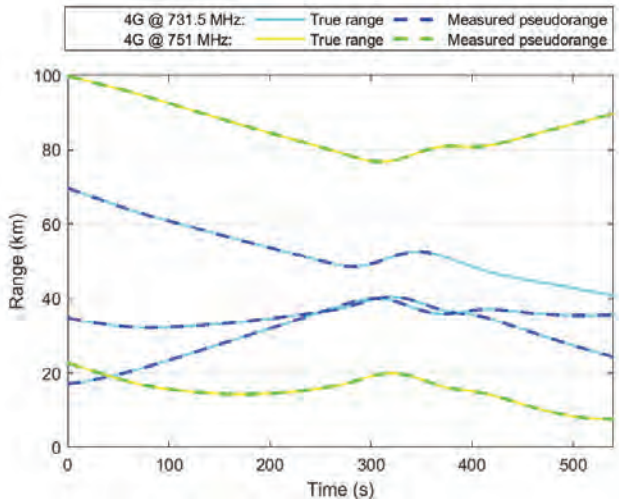

(a)

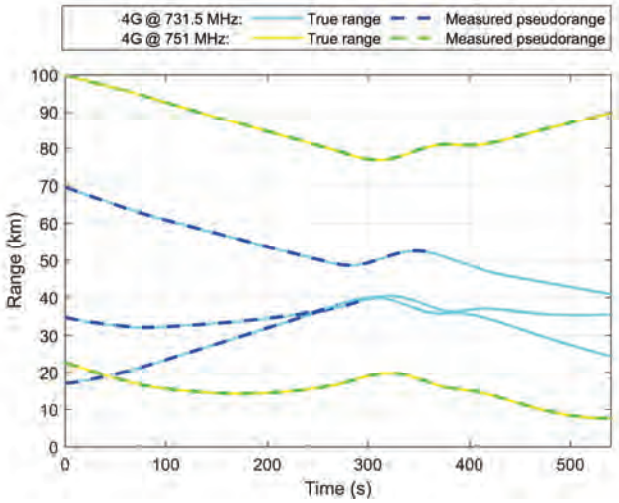

(b)

Fig. 2: Time history of the pseudoranges and the corresponding true range in Region A using (a) the proposed KF-based receiver and (b) the PLL-based received used in [30]. The initial values of the pseudoranges were subtracted out for ease of comparison.

C. Discussion

The results presented in Subsections III-A and III-B highlight the robustness of the proposed KF-based tracking loop compared to PLL-based tracking. Using a third-order KF enabled tracking more eNodeBs for a longer period of time. This improved performance is due to the fact that using a third-order KF, the Doppler rate is also tracked. In addition, in each iteration, the carrier phase error is used to update the measurement variance, which affects Doppler estimation, and improves the tracking. It is worth noting that the loss of tracking in the proposed KF-based receiver could be attributed to the blockage caused by the wings or the body of the aircraft,

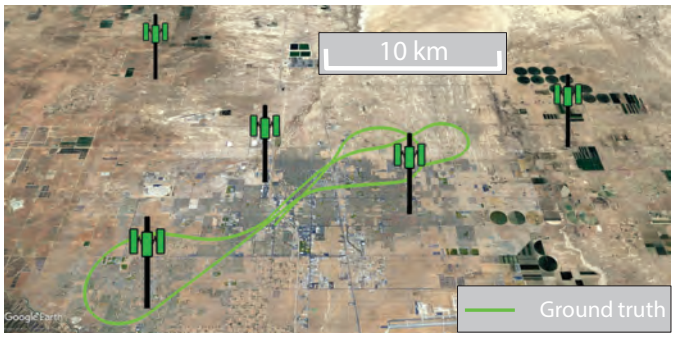

Fig. 3: Experimental environment in region A showing the aircraft trajectory and the locations of the 5 LTE eNodeBs.

which attenuate the signal. It could be also attributed to the KF failing to keep up with highly dynamic aircraft maneuvers. Investigation of this phenomenon is deferred to future research.

IV. Navigation Results

The produced carrier phase observables to five LTE eNodeBs in each region were fused with altimeter data via an EKF to estimate the aircraft's trajectory. The EKF used in this paper is similar to the one adopted in [30]. The EKF settings are summarized next.

The receiver and nth LTE eNodeB clock process noise covariance matrices were set to

$$c^2\mathbf{Q}_{clk_r} = \begin{bmatrix} 4.22 \times 10^{-5} & 3.37 \times 10^{-7} \\ 3.37 \times 10^{-7} & 6.74 \times 10^{-5} \end{bmatrix}$$

$$c^2\mathbf{Q}_{clk_{sn}} = \begin{bmatrix} 3.59 \times 10^{-5} & 3.54 \times 10^{-9} \\ 3.54 \times 10^{-9} & 7.09 \times 10^{-7} \end{bmatrix},$$

where c is the speed of light and $n = 1, 2, \ldots, 5$. The measurement sampling time was $T = 0.01$ s. The jerk process noise spectra were chosen to $\tilde{q}_N = \tilde{q}_E = 15\,\mathrm{m}^2/\mathrm{s}^5$ and $\tilde{q}_D = 5\,\mathrm{m}^2/\mathrm{s}^5$. The altimeter measurement noise variance $\sigma^2_{alt}(k)$ was set to $5\,\mathrm{m}^2$. The measurement noise variance was calculated from the CNR.

The navigation performance of the proposed receiver is compared with PLL-based receiver in Table II and Table III for both regions. Over trajectories of 51 km and 57 km in regions A and B, traversed in 9 min and 11 min, at flying altitudes of 5,000 and 7,000 ft AGL, respectively, the proposed KF-based receiver reduced the position RMSE by 74.8% and 30.7%, respectively, over the PLL-based receiver. The PLL-based receiver in [30] lost track of several eNodeBs during the banking turns. It is worth noting that the results presented in [30] included signals received from cellular 3G code-division multiple access (CDMA), which yielded a meter-level accurate navigation solution. These CDMA signals are omitted in this papers to focus on assessing the performance of only LTE signals. It is expected that adding the omitted CDMA pseudoranges into the EKF would yield meter-level accurate navigation which would be more accurate than the results reported in [30].

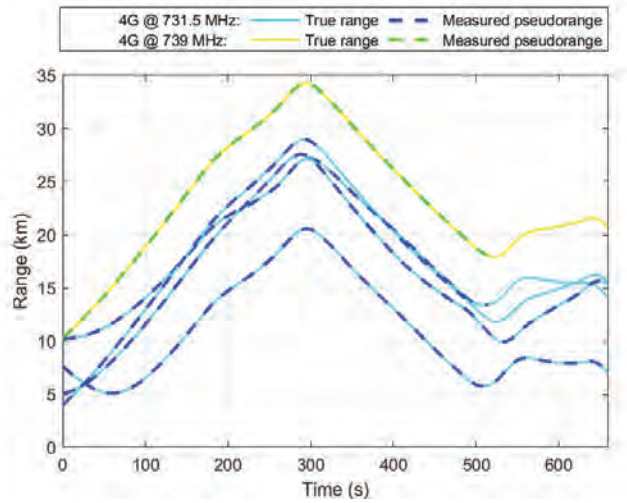

(a)

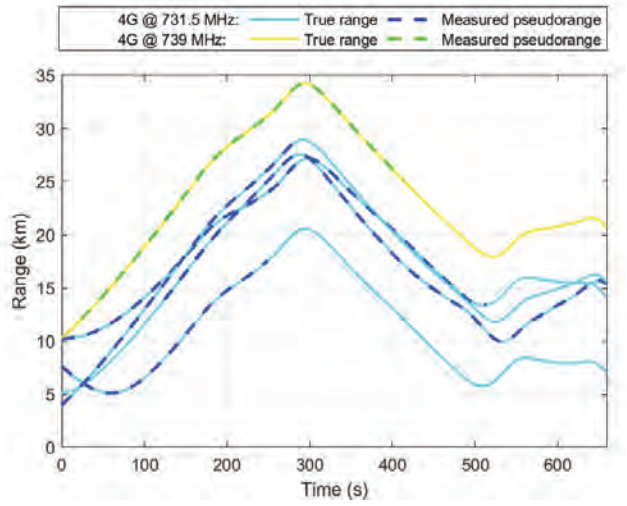

(b)

Fig. 4: Time history of the pseudoranges and the corresponding true range in Region B using (a) the proposed KF-based receiver and (b) the PLL-based received used in [30]. The initial values of the pseudoranges were subtracted out for ease of comparison.

V. Conclusion

This paper presented a KF-based receiver design to track the carrier phase of terrestrial cellular LTE signals on high altitude aircraft. Re-processing the dataset recorded in the SNIFFER flight campaign with the proposed KF-based receiver was shown to produce robust tracking compared with a PLL-based receiver. In addition, the produced carrier phase observables were fused with altimeter data via an EKF to estimate the aircraft's trajectory. Over trajectories of 51 km and 57 km in regions A and B, traversed in 9 min and 11 min, at altitude of 5,000 ft and 7,000 ft AGL, respectively, the proposed KF-based receiver reduced the position RMSE by 74.8% and 30.7%, respectively, over the PLL-based receiver.

TABLE I: Navigation Performance in Region A

Metric	PLL	Proposed KF
Number of eNodeBs used	5	5
Cellular Frequency [MHz]	731.5	731.5
	751	751
Flight duration [min]	9	9
Flight length [km]	44	44
Altitude AGL [ft]	5,000	5,000
Position RMSE [m]	119.25	30.03
Position error standard deviation [m]	88.51	20.79

TABLE II: Navigation Performance in Region B

Metric	PLL	Proposed KF
Number of eNodeBs used	5	5
Cellular Frequency [MHz]	731.5	731.5
	739	739
Flight duration [min]	11	11
Flight length [km]	57	57
Altitude AGL [ft]	7,000	7,000
Position RMSE [m]	211.33	146.44
Position error standard deviation [m]	183.11	113.25

Acknowledgment

This work was supported in part by the Air Force Office of Scientific Research (AFOSR) under Grant FA9550-22-1-0476 and in part by the U.S. Department of Transportation (USDOT) under Grant 69A3552047138 for the CARMEN University Transportation Center (UTC). The authors would like to thank Edwards AFB and Holloman AFB for inviting the ASPIN Laboratory to conduct experiments on USAF aircraft in the "SNIFFER: Signals of opportunity for Navigation In Frequency-Forbidden EnviRonments" flight campaign. The authors would like to thank Joshua Morales, Kimia Shamaei, Mahdi Maaref, Kyle Semelka, MyLinh Nguyen, and Trier Mortlock for their help with preparing for data collection and Joe Khalife and Ali Abdallah for their help with data processing. DISTRIBUTION STATEMENT A. Approved for public release; Distribution is unlimited. 412TW-PA-20146.

References

[1] EUROCONTROL, Aviation Intelligence Unit, "Does radio frequency interference to satellite navigation pose an increasing threat to network efficiency, cost-effectiveness and ultimately safety?," tech. rep., March 2021.

[2] A. Hansen, S. Mackey, H. Wassaf, E. Wallischeck, C. Scarpone, M. Barzach, and E. Baskerville, "Complementary PNT and GPS backup technologies demonstration report: Sections 1 through 10," *John A. Volpe National Transportation Systems Center (US)*, no. DOT-VNTSC-20-07, 2021.

[3] M. Bartock, J. Brule, Y. Li-Baboud, S. Lightman, J. McCarthy, K. Reczek, D. Northrip, A. Scholz, and T. Suloway, "Foundational PNT profile: Applying the cybersecurity framework for the responsible use of positioning, navigation, and timing (PNT) services," *National Institute of Standards and Technology (NIST)*, February 2021.

[4] International Civil Aviation Organization (ICAO), "An urgent need to address harmful interferences to GNSS," tech. rep., May 2019.

[5] International Civil Aviation Organization (ICAO), "Strengthening of communications, navigation, and surveillance (CNS) systems resilience and mitigation of interference to global navigation satellite system (GNSS)," tech. rep., 2020.

[6] International Telecommunication Union , "Prevention of harmful interference to radio navigation satellite service receivers in the 1559 – 1610 mhz frequency band," tech. rep., July 2022.

[7] J. Raquet *et al.*, "Position, navigation, and timing technologies in the 21st century," vol. 2, Part D: Position, Navigation, and Timing Using Radio Signals-of-Opportunity, ch. 35–43, pp. 1115–1412, Wiley-IEEE, 2021.

[8] J. McEllroy, J. Raquet, and M. Temple, "Use of a software radio to evaluate signals of opportunity for navigation," in *Proceedings of ION GNSS Conference*, pp. 126–133, September 2006.

[9] X. Chen, Q. Wei, F. Wang, Z. Jun, S. Wu, and A. Men, "Super-resolution time of arrival estimation for a symbiotic FM radio data system," *IEEE Transactions on Broadcasting*, vol. 66, pp. 847–856, December 2020.

[10] M. Psiaki and B. Slosman, "Tracking digital FM OFDM signals for the determination of navigation observables," *NAVIGATION, Journal of the Institute of Navigation*, vol. 69, no. 2, 2022.

[11] A. Abdallah, J. Khalife, and Z. Kassas, "Exploiting on-demand 5G downlink signals for opportunistic navigation," *IEEE Signal Processing Letters*, vol. 30, pp. 389–393, 2023.

[12] J. Tian, L. Fangchi, T. Yafei, and L. Dongmei, "Utilization of non-coherent accumulation for LTE TOA estimation in weak los signal environments," *EURASIP Journal on Wireless Communications and Networking*, vol. 2023, no. 1, pp. 1–31, 2023.

[13] S. Morgan and S. Martin, "Performance analysis of a cellular LTE and GPS L1 C/A vector tracking receiver, a simulation study," in *Proceedings of ION International Technical Meeting*, pp. 692–707, January 2023.

[14] N. Souli, P. Kolios, and G. Ellinas, "Relative positioning of autonomous systems using signals of opportunity," in *Proceedings of IEEE Vehicular Technology Conference*, pp. 1–6, 2020.

[15] T. Hong, J. Sun, T. Jin, Y. Yi, and J. Qu, "Hybrid positioning with DTMB and LTE signals," in *Proceedings of International Wireless Communications and Mobile Computing*, pp. 303–307, July 2021.

[16] Z. Jiao, L. Chen, X. Lu, Z. Liu, X. Zhou, Y. Zhuang, and G. Guo, "Carrier phase ranging with DTMB signals for urban pedestrian localization and GNSS aiding," *Remote Sensing*, vol. 15, no. 2, pp. 423–446, 2023.

[17] C. Pinell, "Receiver architectures for positioning with low Earth orbit satellite signals," Master's thesis, Lulea University of Technology, School of Electrical Engineering, Sweden, 2021.

[18] C. Zhao, H. Qin, N. Wu, and D. Wang, "Analysis of baseline impact on differential doppler positioning and performance improvement method for LEO opportunistic navigation," *IEEE Transactions on Instrumentation and Measurement*, pp. 1–10, 2023.

[19] Z. Kassas, N. Khairallah, and S. Kozhaya, "Ad astra: Simultaneous tracking and navigation with megaconstellation LEO satellites," *IEEE Aerospace and Electronic Systems Magazine*, 2023. accepted.

[20] Y. Gao, X. Zhao, S. Wang, Y. Xiang, C. Huang, and Y. Hua, "Positioning via GEO communication satellites' signals of opportunity," *IET Radar, Sonar Navigation*, vol. 15, pp. 1472–1482, July 2021.

[21] A. Abdallah and Z. Kassas, "Multipath mitigation via synthetic aperture beamforming for indoor and deep urban navigation," *IEEE Transactions on Vehicular Technology*, vol. 70, pp. 8838–8853, September 2021.

[22] C. Jao, A. Abdallah, C. Chen, M. Seo, S. Kia, Z. Kassas, and A. Shkel, "PINDOC: Pedestrian indoor navigation system integrating deterministic, opportunistic, and cooperative functionalities," *IEEE Sensors Journal*, vol. 22, pp. 14424–14435, July 2022.

[23] Z. Kassas, M. Maaref, J. Morales, J. Khalife, and K. Shamaei, "Robust vehicular localization and map matching in urban environments through IMU, GNSS, and cellular signals," *IEEE Intelligent Transportation Systems Magazine*, vol. 12, pp. 36–52, June 2020.

[24] R. Whiton, J. Chen, T. Johansson, and F. Tufvesson, "Urban navigation with LTE using a large antenna array and machine learning," in *Proceedings of IEEE Vehicular Technology Conference*, pp. 1–5, 2022.

[25] Z. Kassas, J. Khalife, A. Abdallah, and C. Lee, "I am not afraid of the GPS jammer: resilient navigation via signals of opportunity in GPS-denied environments," *IEEE Aerospace and Electronic Systems Magazine*, vol. 37, pp. 4–19, July 2022.

[26] J. Khalife and Z. Kassas, "On the achievability of submeter-accurate UAV navigation with cellular signals exploiting loose network synchronization," *IEEE Transactions on Aerospace and Electronic Systems*, vol. 58, pp. 4261–4278, October 2022.

[27] J. Khalife and Z. Kassas, "Differential framework for submeter-accurate vehicular navigation with cellular signals," *IEEE Transactions on Intelligent Vehicles*, vol. 8, pp. 732–744, January 2023.

[28] Z. Kassas, J. Khalife, A. Abdallah, C. Lee, J. Jurado, S. Wachtel, J. Duede, Z. Hoeffner, T. Hulsey, R. Quirarte, and R. Tay, "Assessment of cellular signals of opportunity for high-altitude aircraft navigation," *IEEE Aerospace and Electronic Systems Magazine*, vol. 37, pp. 4–19, October 2022.

[29] Z. Kassas, A. Abdallah, J. Khalife, C. Lee, J. Jurado, J. Duede, Z. Hoeffner, T. Hulsey, R. Quirarte, S. Wachtel, and R. Tay, "Received power characterization of terrestrial cellular signals on high altitude aircraft," in *Proceedings of IEEE Aerospace Conference*, pp. 1–8, March 2022.

[30] Z. Kassas, J. Khalife, A. Abdallah, C. Lee, J. Jurado, J. Duede, Z. Hoeffner, T. Hulsey, R. Quirarte, S. Wachtel, and R. Tay, "Flight demonstration of high altitude aircraft navigation with cellular signals," *IEEE Intelligent Transportation Systems Magazine*. accepted.

[31] Qualcomm Technologies, Inc., "LTE unmanned aircraft systems," Tech. Rep. 1.0.1, May 2017.

[32] Y. Zeng, Q. Wu, and R. Zhang, "Accessing from the sky: A tutorial on UAV communications for 5G and beyond," *Proceedings of the IEEE*, vol. 107, pp. 2327–2375, December 2019.

[33] X. Cai, J. Rodriguez-Pineiro, X. Yin, N. Wang, B. Ai, G. Pedersen, and A. Yuste, "An empirical air-to-ground channel model based on passive measurements in LTE," *IEEE Transactions on Vehicular Technology*, vol. 68, pp. 1140–1154, February 2019.

[34] W. Khawaja, I. Guvenc, D. Matolak, U. Fiebig, and N. Schneckenburger, "A survey of air-to-ground propagation channel modeling for unmanned aerial vehicles," *IEEE Communications Surveys & Tutorials*, vol. 21, no. 3, pp. 2361–2391, 2019.

[35] K. Matheou, R. Apaza, A. Downey, R. Kerczewski, J. Jung, C. Ippolito, and H. Modi, "Analysis of at-altitude LTE power spectra for small unmanned aircraft system C2 communications," in *Proceedings of Integrated Communications, Navigation and Surveillance Conference*, pp. 1–12, April 2019.

[36] X. Cai, N. Wang, J. Rodriguez-Pineiro, X. Yin, A. Yuste, W. Fan, G. Zhang, G. Pedersen, and L. Tian, "Low altitude air-to-ground channel characterization in LTE network," in *Proceedings of European Conference on Antennas and Propagation*, pp. 1–5, April 2019.

[37] I. Kovacs, R. Amorim, H. Nguyen, J. Wigard, and P. Mogensen, "Interference analysis for UAV connectivity over LTE using aerial radio measurements," in *Proceedings of IEEE Vehicular Technology Conference*, pp. 1–6, September 2017.

[38] R. Amorim, J. Wigard, I. Kovacs, and T. Sorensen, "UAV communications for 5G and beyond," ch. 5: Performance Enhancements for LTE-Connected UAVs: Experiments and Simulations, pp. 139–161, Wiley-IEEE, 2021.

[39] E. Teng, J. Diogo Falcao, and B. Iannucci, "Holes-in-the-sky: A field study on cellular-connected UAS," in *Proceedings of International Conference on Unmanned Aircraft Systems*, pp. 1165–1174, June 2017.

[40] B. Stevens and M. Younis, "Detection algorithm for cellular synchronization signals in airborne applications," *IEEE Access*, vol. 9, pp. 55555–55566, April 2021.

[41] A. Abdalla and V. Marojevic, "Communications standards for unmanned aircraft systems: The 3GPP perspective and research drivers," *IEEE Communications Standards Magazine*, vol. 5, pp. 70–77, March 2021.

[42] H. Maattanen, "UAV communications for 5G and beyond," ch. 6: 3GPP Standardization for Cellular-Supported UAVs, pp. 163–180, Wiley-IEEE, 2021.

[43] E. Kim and Y. Shin, "Feasibility analysis of LTE-based UAS navigation in deep urban areas and DSRC augmentation," *Sensors*, vol. 19, pp. 4192–4207, April 2019.

[44] J. Mortier, G. Pages, and J. Vila-Valls, "Robust TOA-based UAS navigation under model mismatch in GNSS-denied harsh environments," *Remote Sensing*, vol. 12, pp. 2928–2947, September 2020.

[45] M. Braasch and A. Dempster, "Tutorial: GPS receiver architectures, front-end and baseband signal processing," *IEEE Aerospace and Electronic Systems Magazine*, vol. 34, no. 2, pp. 20–37, 2019.

[46] J. Won, T. Pany, and B. Eissfeller, "Characteristics of Kalman filters for GNSS signal tracking loop," *IEEE Transactions on Aerospace and Electronic Systems*, vol. 48, pp. 3671–3681, October 2012.

[47] J. Vila-Valls, P. Closas, M. Navarro, and C. Fernandez-Prades, "Are PLLs dead? a tutorial on Kalman filter-based techniques for digital carrier synchronization," *IEEE Aerospace and Electronic Systems Magazine*, vol. 32, no. 7, pp. 28–45, 2017.

[48] A. van Dierendonck, P. Fenton, and T. Ford, "Theory and performance of narrow correlator spacing in a GPS receiver," *NAVIGATION, Journal of the Institute of Navigation*, vol. 39, pp. 265–283, September 1992.

Signal Mode Transition Detection in Starlink LEO Satellite Downlink Signals

Mohammad Neinavaie and Zaher M. Kassas
Department of Electrical and Computer Engineering
The Ohio State University, Columbus, OH, USA
neinavaie.1@osu.edu, zkassas@ieee.org

***Abstract*—A receiver architecture for detection and tracking of Starlink orthogonal frequency division multiplexing (OFDM)-based signals is proposed. The proposed receiver enables exploiting all the transmitted periodic beacons of Starlink low Earth orbit (LEO) signals to draw carrier phase, code phase, and Doppler observables. The reference signals (RSs) of modern OFDM-based systems contain both always-on and on-demand components. These components can be unknown and *subject to dynamic transmission modes*. Thanks to a matched subspace-based detection algorithm, the proposed receiver is shown to be capable of *cognitive detection* of both always-on and on-demand components in the Starlink OFDM-based RSs. It is shown that despite the dynamic nature of Starlink RSs, the proposed matched subspace detector senses the *transition between the transmission modes* of Starlink RSs, and detects all the accessible RSs with a predetermined probability of false alarm. Experimental results are provided to validate the performance of the proposed receiver in transmission mode detection in Starlink downlink signals.**

***Index Terms*—Positioning, navigation, signals of opportunity, low Earth orbit satellite, Starlink, OFDM, 5G, on-demand.**

I. Introduction

Abundant man-made terrestrial and extraterrestrial signals of opportunity (SOPs) have been shown to possess promising features for positioning, navigation, and timing [1]–[4]. *High bandwidth and diverse* synchronization signals of orthogonal frequency division multiplexing (OFDM) signals in cellular fourth-generation (4G) long-term evolution (LTE) and 5G new radio (NR) systems enabled meter-level and decimeter-level navigation on ground vehicles [5], [6] and unmanned aerial vehicles (UAVs) [7], [8], respectively. Similarly to 4G LTE and 5G NR, Starlink low Earth orbit (LEO) space vehicles (SVs) also adopt OFDM [9] signals with considerably high bandwidth [10]. While a single LTE channel has a bandwidth of up to 20 MHz, the bandwidth of a single 5G NR channel goes up to 100 MHz and 400 MHz for FR1 and FR2, respectively [11]. On the other hand, Starlink downlink signals occupy 250 MHz bandwidth of the Ku band to provide high rate broadband connectivity [12]. The OFDM reference signals (RSs) are spread across the whole bandwidth, which promises *good correlation properties*, leading to high ranging and localization accuracy.

This work was supported in part by the Office of Naval Research (ONR) under Grant N00014-22-1-2242, in part by the Air Force Office of Scientific Research (AFOSR) under Grant FA9550-22-1-0476, and in part by the U.S. Department of Transportation (USDOT) under Grant 69A3552047138 for the CARMEN University Transportation Center (UTC).

SOP-based navigation receivers typically rely on known synchronization sequences or beacons transmitted by SOP sources to draw time-of-arrival (TOA), direction-of-arrival (DOA), and frequency-of-arrival (FOA) measurements [13]. Due to the unknown and dynamic nature of modern communication signals in private networks, such as Starlink, a navigation receiver that is based on reverse engineering the downlink signals either (i) fails to exploit the whole available bandwidth unless *all* RSs get determined or (ii) fails to operate if the operator changes their signal. As such, designing receivers that can cognitively acquire *partially known*, *unknown*, or *dynamic* beacon signals is an emerging need for the future of cognitive opportunistic navigation [14]–[17].

Cognitive opportunistic navigation [17] has recently been introduced to address the following challenges of navigation with SOPs in modern and private networks. First, opportunistic navigation frameworks usually exploit the broadcast RSs for navigation [13]. In public networks, these signals are known by the user equipment (UE) and are universal across network operators. Hence, they can be exploited for positioning without the need for the UE to be a network subscriber. However, in *private networks*, the signal specifications may not be available to the public or are subject to change, which makes acquiring and tracking these signals impossible for conventional opportunistic navigation receivers [17]. Second, conventional cellular networks broadcast RSs at regular and known time intervals, regardless of the number of UEs in the environments (e.g., the cell-specific reference signal (CRS) in LTE). Modern communication systems, such as 5G NR, minimize the transmission of *always-on* signals, by adopting an *ultra-lean* design which entails transmitting some of the RSs only when necessary or *on-demand* [18].

Matched subspace detectors have been widely adopted to solve the detection problem of sources with unknown parameters in the presence of other interfering sources [19], [20]. In the signal processing literature, matched subspace detectors were used to detect the unknown signal activities in multiple-input multiple-output (MIMO) radars, passive bistatic radars, and blind array signal processing [21]–[23]. Recently, machine learning approaches have also been proposed for unknown transmitter detection, identification, and classification [24], [25]. In the navigation literature, the detection of unknown signals has been studied to design frameworks that are capable of navigating with unknown or partially known signals. The problem of detecting Galileo and Compass satellites signals

was studied in [26], which revealed the spread spectrum codes for these satellites. Preliminary experiments on navigation with partially known signals from low and medium Earth orbit satellites were conducted in [14]–[16], [27]. In particular, a chirp parameter estimator was used in [14] to blindly estimate the GPS pseudorandom noise (PRN) codes. In [16], a blind channel estimator was proposed to exploit Orbcomm satellite signals for navigation purposes. In [15], OFDM signals were emulated from Orbcomm LEO SVs, and a fast Fourier transform (FFT)-based Doppler estimator was proposed to exploit these signals for navigation purposes.

The first positioning results with always-on Starlink SV signals were presented in [28]–[30]. Following these studies, [9] was the first to exploit Starlink's OFDM signals for navigation. The contribution of this paper is (i) the detection of transmission mode change between on-demand and always-on and (ii) tracking the carrier phase when the on-demand signal is not beamed towards the receiver.

The rest of this paper is organized as follows. Section II presents the received baseband signal model. Section III summarizes the receiver architecture. Section IV presents experimental results. Section V gives concluding remarks.

II. Signal Model

The frame structure in OFDM-based transmission is either fixed or identified based on the physical requirements [31]. Each OFDM frame contains always-on and on-demand RSs which are transmitted for synchronization and channel estimation purposes. The period of the RSs is usually equal to the frame length of the OFDM signal. Acquisition and tracking OFDM RSs require knowledge of the frame length. While the frame length is known in public networks, such as 5G NR, it is usually unknown (and subject to change) in private networks, e.g., Starlink LEO broadband system. For private networks, the frame length should be estimated and updated cognitively. Estimation of the frame length of Starlink LEO downlink is discussed in [9].

A. Baseband Signal Model

The common feature of always-on and on-demand RSs is periodicity. If a subcarrier is being periodically transmitted, it will get detected, estimated, and used to derive carrier phase, code phase, and Doppler observables. The channel between the ith satellite and the UE is considered to have a single tap with a complex channel gain α_i. Denoting a continuous-time beacon at time t by $c(t)$, and the discrete-time beacon at time instant n by $c[n]$, the received baseband signal samples can be modeled as

$$r[n] = \sum_{i=1}^{N} \alpha_i[n] \left(c_i^{\mathrm{I}}\left(\tau_r[n]\right) + c_i^{\mathrm{II}}\left(\tau_r[n]\right) + d_i\left(\tau_r[n]\right)\right) \exp\left(j\theta_i[n]\right) + w[n], \quad (1)$$

where $r[n]$ is the received signal at the nth time instant; $\alpha_i[n]$ is the complex channel gain between the UE and the ith satellite at time instant n; and $\tau_r[n] \triangleq \tau_n - t_{s_i}[n]$, where $t_{s_i}[n]$ is the code-delay corresponding to the UE and the ith satellite at the nth time instant, and τ_n is the sample time expressed in the receiver time. Moreover, N is the number of unknown satellite RSs; $c_i^{\mathrm{I}}[n]$ and $c_i^{\mathrm{II}}[n]$ represent the samples of the always-on waveform $c_i^{\mathrm{I}}(t)$ and on-demand waveform $c_i^{\mathrm{II}}(t)$ periodic RSs corresponding to the ith satellite with a period of L samples, respectively; $\theta_i[n] = 2\pi f_{D_i}[n] T_s n$ is the carrier phase in radians, where $f_{D_i}[n]$ is the Doppler frequency at the nth time instant and T_s is the sampling time; $d_i[n]$ represents the samples of some data transmitted from the ith satellite; and $w[n]$ is a zero-mean independent and identically distributed noise with $\mathbb{E}\left\{w[m]w^*[n]\right\} = \sigma_w^2 \delta[m-n]$, where $\delta[n]$ is the Kronecker delta function, and $w^*[n]$ denotes the complex conjugate of random variable $w[n]$. By defining $c_i[n] \triangleq c_i^{\mathrm{I}}[n] + c_i^{\mathrm{II}}[n]$, the received signals can be expressed in terms of the equivalent RS from the ith satellite, denoted by $s_i[n]$, and the equivalent noise, denoted by w_{eq_i}, which are defined as

$$s_i[n] \triangleq \alpha_i[n] c_i(\tau_n - t_{s_i}[n]) \exp\left(j\theta_i[n]\right), \quad (2)$$

$$w_{\mathrm{eq}_i}[n] = \alpha_i[n] d_i(\tau_n - t_{s_i}[n]) \exp\left(j\theta_i[n]\right) + w[n]. \quad (3)$$

Using (2) and (3), the baseband samples can be rewritten as

$$r[n] = \sum_{i=1}^{N} \left(s_i[n] + w_{\mathrm{eq}_i}[n] \right). \quad (4)$$

Remark 1: In this paper, the Doppler frequency is modeled as a linear chirp, i.e., $f_{D_i}[n] = f_{D_{i_0}} + \beta_i T_s n$, where $f_{D_{i_0}}[n]$ is the initial Doppler frequency and $\beta_i[n]$ is the Doppler rate.

Definition 1: The CPI is defined as the number of periods of an RS in a time interval during which the Doppler $f_{D_{i_0}}$, Doppler rate β_i, delay t_{s_i}, and channel gain α_i, are considered to be constant.

III. Receiver Architecture

This section summarizes the receiver architecture.

A. Acquisition

The received signal at the nth time instant when the Doppler rate is wiped-off is denoted by $r'[n] \triangleq \exp(-j2\pi\beta_i T_s^2 n^2) r[n]$. Due to the periodicity of $c(\tau_n)$, $s_i[n]$ has the following property

$$s_i[n + mL] = s_i[n] \exp\left(j\omega_i mL\right) \quad 0 \le n \le L-1, \quad (5)$$

where $\omega_i = 2\pi f_{D_{i_0}} T_s$ is the normalized Doppler, corresponding to the ith transmitting satellite, and $-\pi \le \omega_i \le \pi$. A vector of L observation samples corresponding to the mth period of the signal is formed as $\mathbf{z}_m \triangleq [r'[mL], r'[mL+1], \ldots, r'[(m+1)L-1]]^{\mathsf{T}}$. The CPI vector is constructed by concatenating K number of $\mathbf{z}_m$ vectors to form the $KL \times 1$ vector

$$\mathbf{y} = \sum_{i=1}^{N} \mathbf{H}_i \mathbf{s}_i + \mathbf{w}, \quad (6)$$

where $\mathbf{s}_i = [s_i[1], s_i[2], \ldots, s_i[L]]^{\mathsf{T}}$, and the $KL \times L$ Doppler matrix is defined as $\mathbf{H}_i \triangleq [\mathbf{I}_L, \exp\left(j\omega_i L\right)\mathbf{I}_L, \ldots, \exp\left(j\omega_i (M-1)L\right)\mathbf{I}_L]^{\mathsf{T}}$, where $\mathbf{I}_L$ is an $L \times L$ identity matrix, and $\mathbf{w}$ is the noise vector.

Similar to [9], the concept of *sequential matched subspace detection* is used to provide an initial estimate for the unknown parameters which are: (i) the number of unknown satellites, (ii) corresponding RSs, and (iii) the chirp parameters. A hypothesis testing problem is solved sequentially in multiple stages to detect the active satellites in the environment. Unlike [17], where a constant Doppler subspace was used to distinguish between different satellites, in this paper, the matched subspace is defined based on the chirp parameters of each satellite. At each stage, a test is performed to detect the most powerful satellite, while the *chirp subspace* of the previously detected satellite RSs are nulled. The so-called *general linear detectors* [32] is used at each stage of the sequential detection algorithm. In the first stage of the sequential algorithm, the presence of a single satellite is tested and if the null hypothesis is accepted, then $\hat{N} \equiv 0$, which means that no satellite is detected to be present in the environment under the test. If the test rejects the null hypothesis, the algorithm asserts the presence of at least one satellite and performs the test to detect the presence of other satellites in the presence of the previously detected satellite. The unknown chirp parameters and the RSs of each satellite are estimated at each stage. In general, if the null hypothesis at the ith level of the sequential algorithm is accepted, the algorithm is terminated and the estimated number of satellites will be $\hat{N} = i - 1$. It should be pointed out that while [17] only considered the Doppler space to distinguish between different unknown satellite RSs, in this paper, the Doppler rate space is also used to define the satellite subspace.

The detection problem of the ith RS is defined as a binary hypothesis test

$$\begin{cases} \mathcal{H}_0^i: & i\text{th satellite is absent} \\ \mathcal{H}_1^i: & i\text{th satellite is present.} \end{cases} \tag{7}$$

Under $\mathcal{H}_1^i$, the signal model can be expressed as

$$\mathbf{y} = \mathbf{H}_i \mathbf{s}_i + \mathbf{B}_{i-1}\boldsymbol{\theta}_{i-1} + \mathbf{w}_{\mathrm{eq}_i}, \tag{8}$$

where, $\mathbf{B}_{i-1} \triangleq [\mathbf{H}_1, \mathbf{H}_2, \ldots, \mathbf{H}_{i-1}]$ and $\boldsymbol{\theta}_{i-1} \triangleq [\mathbf{s}_1^{\mathsf{T}}, \mathbf{s}_2^{\mathsf{T}}, \ldots, \mathbf{s}_{i-1}^{\mathsf{T}}]^{\mathsf{T}}$ stores the chirp parameters and estimated RS in the previous steps. The decision criterion for the satellite detection is developed based on the Generalize Likelihood Ratio (GLR) (see [32, Section 9.4.3]). The likelihood of the GLR detector is derived as

$$\mathcal{L}_i(\mathbf{y}|\omega_i, \beta_i) = \frac{\mathbf{y}^{\mathsf{H}}\mathbf{P}_{\mathbf{S_i}}\mathbf{y}}{\mathbf{y}^{\mathsf{H}}\mathbf{P}^{\perp}_{\mathbf{B_{i-1}}}\mathbf{P}^{\perp}_{\mathbf{S_i}}\mathbf{P}^{\perp}_{\mathbf{B_{i-1}}}\mathbf{y}}, \tag{9}$$

for a given normalized Doppler frequency, Doppler rate, and CPI, denoted by ω_i, and β_i. Vector $\mathbf{y}^{\mathsf{H}}$ is the Hermitian transpose of $\mathbf{y}$, $\mathbf{P}_{\mathbf{X}} \triangleq \mathbf{X}(\mathbf{X}^{\mathsf{H}}\mathbf{X})^{-1}\mathbf{X}^{\mathsf{H}}$, denotes the projection matrix to the column space of $\mathbf{X}$, and $\mathbf{P}^{\perp}_{\mathbf{X}} \triangleq \mathbf{I} - \mathbf{P}_{\mathbf{X}}$ denotes the projection matrix onto the space orthogonal to the column space of $\mathbf{X}$. Also, $\mathbf{S}_i = \mathbf{P}^{\perp}_{\mathbf{B}_{i-1}}\mathbf{H}_i$. It should be pointed out that $\mathbf{H}_i^{\mathsf{H}}\mathbf{P}^{\perp}_{\mathbf{B}_{i-1}}\mathbf{H}_i = \lambda_i \mathbf{I}$, where the scalar λ_i is the Schur complement of block $\mathbf{C}_{i-1}$, i.e., the upper $(i-1)\times(i-1)$ block of the matrix $\mathbf{C}_i$, whose ijth element is [17]

$$c_{ij} \triangleq \sum_{k=0}^{K-1} \exp\left(j(\omega_j - \omega_i)Lk\right). \tag{10}$$

It can be seen from (10) that the elements of the matrix $\mathbf{C}_i$, and consequently the scalar λ_i, are scalar functions of the Doppler frequency difference between the ith satellite and the previously detected satellites.

The simplified likelihood can be written as [17]

$$\mathcal{L}_i^*(\mathbf{y}) = \arg\max_{\omega_i, \beta_i} \frac{\|\lambda_i^{-1}\hat{\mathbf{H}}_i^{\mathsf{H}}\hat{\mathbf{P}}^{\perp}_{\mathbf{B}_{i-1}}\mathbf{y}\|^2}{\|\hat{\mathbf{P}}^{\perp}_{\mathbf{B}_{i-1}}\mathbf{y}\|^2 - \|\lambda_i^{-1}\hat{\mathbf{H}}_i^{\mathsf{H}}\hat{\mathbf{P}}^{\perp}_{\hat{\mathbf{B}}_{i-1}}\mathbf{y}\|^2}. \tag{11}$$

The likelihood should be compared with a predetermined threshold η_i which is designed based on a particular probability of false alarm.

The ML estimates of the chirp parameters, i.e., $\hat{f}_{D_i}$, $\hat{\beta}_i$, can be obtained by maximizing $\mathcal{L}_i(\mathbf{y})$. Accordingly, the least squares (LS) estimate of the ith satellite $\mathbf{s}_i$, is given by

$$\hat{\mathbf{s}}_{\mathrm{acq}_i} = \lambda_i^{-1}\mathbf{H}_i^{\mathsf{H}}\mathbf{P}^{\perp}_{\mathbf{B}_{i-1}}\mathbf{y}. \tag{12}$$

B. Tracking

The initial estimate of the Doppler frequencies corresponding to each Starlink LEO SV and the associated likelihood functions are fed to the tracking stage along with the estimated RSs. By employing a phase-locked loop (PLL) and a delay-locked loop (DLL), the Doppler and delay are tracked over time. The tracking loops are based on the design discussed in [17], with compensation for compression and stretching due to high LEO dynamics.

IV. Experimental Results

This section presents experimental results with the receiver discussed in Section III showing successful detection of Starlink mode transition between on-demand and always-on. It also shows that while the DLL fails to track the code phase when the on-demand signal is turned off, the PLL continues to track the carrier phase of the always-on signal.

A. Starlink RS Transmission Modes and Correlation Properties

Starlink LEO SVs transmit nine pure tones located in a roughly, 1 MHz gap at the center of the transmission bandwidth of the Ku band. The pure tones were exploited for Doppler positioning in [28]–[30]. In this subsection, more details about the RSs of Starlink LEO SVs and their corresponding properties are assessed. In particular, it will be shown that two types of RSs with two different correlation properties are being transmitted.

In this experiment, a stationary National Instrument (NI) universal software radio peripheral (USRP) 2945R consumer-grade Ku antenna and low-noise block (LNB) downconverter to receive Starlink signals in the Ku-band in the parking structure of the University of California, Irvine. The sampling rate was set to 2.5 MHz and the carrier frequency was set to 11.325 GHz to record Ku signals over a period of 800 s. The origin points of time instants shown in the figures are considered to be the recording start time in each experiment. Six SVs were detected during the period of 800 s.

1) Always-on and On-demand RSs: The trajectories of the tracked satellites are plotted in Fig. 1. To avoid redundancy, this subsection analyzes the transmission modes and the correlation properties of the RSs corresponding to one of the six detected satellites in the experiment, namely SV 6 (Starlink-45694). The signals from other Starlink LEO SVs in this experiment follow the same pattern.

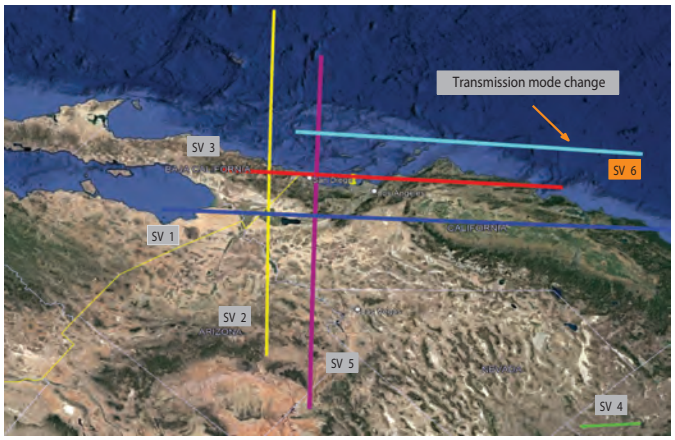

Fig. 1. Skyplot of the six satellites tracked in the experiment. The position on the trajectory of SV 6 in which the transmission mode occurred is indicated with an orange arrow.

Fig. 2 concentrates on the time epochs in which a transmission mode change has occurred. The autocorrelation and the likelihood functions at time epochs of $t = 606$ s and $t = 607$ s are plotted in Fig. 2. The RS structure and correlation properties change in the transition between these two time epochs for Starlink-45694. Fig. 2(a) and (b) demonstrate the autocorrelation function at $t = 606$ s and $t = 607$ s. The amplitude of the impulses follows the sinc-function behavior, which is due to the Doppler rate effect. These impulses are approximately 1.33 ms apart. However, at $t = 607$ s, the ambiguity function impulses disappeared. While the autocorrelation function is suggesting that the periodic RSs are not being transmitted at $t = 607$ s, the likelihood function shows a surprising behavior. At $t = 606$ s, the likelihood includes two different components which are shown in a black and a red box in Fig. 2(c).

Recall that when the likelihood passes the threshold, the existence of an RS with a period of approximately 1.33 ms is guaranteed by the detector with a certain probability of detection. The likelihood at $t = 607$ s shows that the component in the black box is not being transmitted anymore, while the component in the red box is *still on*. The signal in the red box is periodic with a period of 1.33 ms, which is associated with the OFDM RSs. However, as it can be seen in Fig. 2(b), the signal in the red box does not have good *time correlation* properties. The signal in the red box is continuously transmitted when the boradband OFDM signal is active and is referred to as always-on RS in this paper. The behavior of the signal in the black box is similar to 5G NR on-demand RSs which are not always active and, therefore, are referred to as on-demand RSs in this paper.

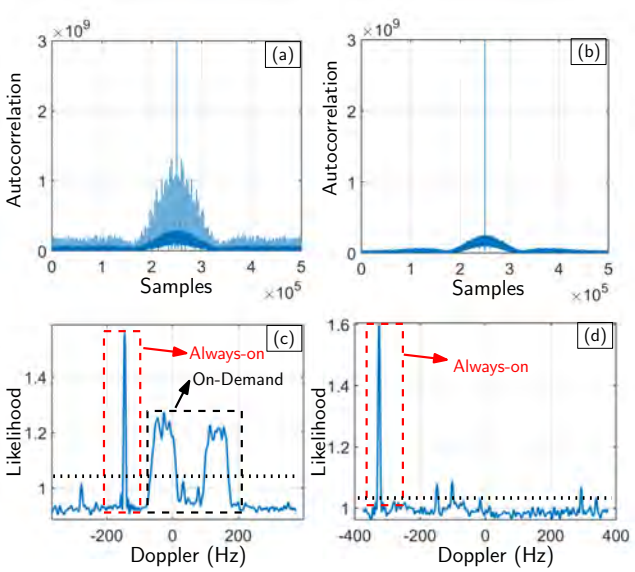

Fig. 2. (a) and (b) demonstrate the autocorrelation at $t = 606$ s and $t = 607$ s, respectively. It can be seen that at $t = 606$ s, the RS is showing a time autocorrelation and at $t = 607$ s the time autocorrelation is lost. (c) and (d) demonstrate the likelihood function at $t = 606$ s and $t = 607$ s, respectively. Two components can be seen in the likelihood functions (the red box and the black box) at $t = 606$ s. The component in the black box is not being transmitted at $t = 607$ s.

Fig. 3 shows the code phase and carrier phase tracking results for Starlink-45694 during this time interval. The tracking results give a better understanding of the correlation properties of the two detected RSs in the feedback tracking loops. The bandwidth of the PLL was set to 65 Hz and the bandwidth of the DLL was set to be 0.02 Hz.

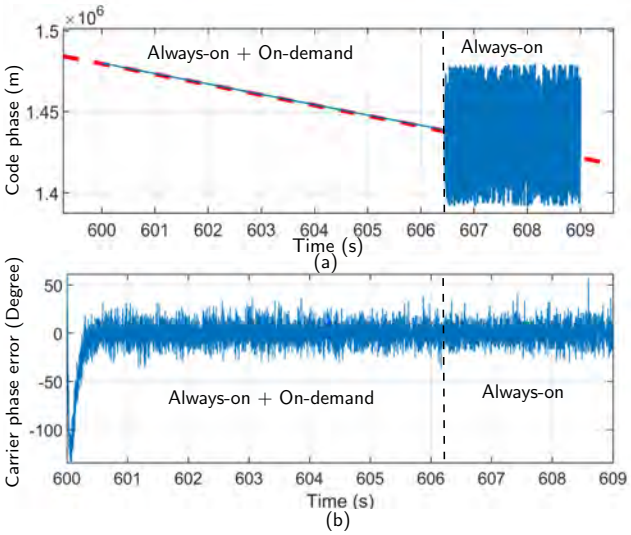

Fig. 3. (a) Code phase tracking, and (b) carrier phase tracking of Starlink-45694. As it was expected, at a time epoch between $t = 606$ s and $t = 607$ s the code phase tracking is lost. This is due to the fact that the on-demand signal which has suitable time autocorrelation properties is not active anymore at this time epoch. However, Fig. 3(b) shows that the carrier phase tracking loop is still locked.

As expected, at a time epoch between $t = 606$ s and $t = 607$ s, code phase tracking is lost. This is due to the fact that the on-demand signal, which has suitable time autocorrelation properties, is not active anymore at this time

epoch. However, Fig. 3(b) shows that the carrier phase tracking loop is still locked. This is due to the fact that the always-on signal (the signal in the red box in Fig. 2(c)) is showing good frequency correlation properties. The frequency-domain correlation property of the always-on signal guarantees carrier phase tracking even if the on-demand signal is not active.

Remark 2: Starlink RSs may dynamically change during one satellite pass. A method that only relies on a static design based on an RS with good time correlation properties may not provide continuous navigation observables. The proposed method cognitively detects all available RSs and yields continuous carrier and code phase tracking (when applicable).

V. Conclusion

Signal mode transition between on-demand and always-on in Starlink satellite downlink signals was studied. Via a matched subspace-based detection algorithm, all the transmitted periodic beacons of Starlink LEO signals were detected to draw navigation observables. It was shown that similar to the RSs of modern OFDM-based systems, the RSs of Starlink downlink signals contain both always-on and on-demand components. The proposed method was able to detect the transmission mode change in Starlink downlink signals and maintain carrier phase tracking when the on-demand component was not beamed towards the receiver.

References

[1] J. Raquet *et al.*, "Position, navigation, and timing technologies in the 21st century," J. Morton, F. van Diggelen, J. Spilker, Jr., and B. Parkinson, Eds. Wiley-IEEE, 2021, vol. 2, Part D: Position, Navigation, and Timing Using Radio Signals-of-Opportunity, ch. 35–43, pp. 1115–1412, doi: 10.1002/9781119458555.ch35.

[2] N. Jardak and Q. Jault, "The potential of LEO satellite-based opportunistic navigation for high dynamic applications," *Sensors*, vol. 22, no. 7, pp. 2541–2565, 2022.

[3] M. Hartnett, "Performance assessment of navigation using carrier Doppler measurements from multiple LEO constellations," Master's thesis, Air Force Institute of Technology, Ohio, USA, 2022.

[4] F. Prol, R. Ferre, Z. Saleem, P. Välisuo, C. Pinell, E. Lohan, M. Elsanhoury, M. Elmusrati, S. Islam, K. Celikbilek, K. Selvan, J. Yliaho, K. Rutledge, A. Ojala, L. Ferranti, J. Praks, M. Bhuiyan, S. Kaasalainen, and H. Kuusniemi, "Position, navigation, and timing (PNT) through low earth orbit (LEO) satellites: A survey on current status, challenges, and opportunities," *IEEE Access*, vol. 10, pp. 83 971–84 002, 2022.

[5] J. Peral-Rosado, J. Lopez-Salcedo, S. Kim, and G. Seco-Granados, "Feasibility study of 5G-based localization for assisted driving," in *Proceedings of International Conference on Localization and GNSS*, June 2016, pp. 1–6.

[6] C. Yang, M. Arizabaleta-Diez, P. Weitkemper, and T. Pany, "An experimental analysis of cyclic and reference signals of 4G LTE for TOA estimation and positioning in mobile fading environments," *IEEE Aerospace and Electronic Systems Magazine*, vol. 37, no. 9, pp. 16–41, 2022.

[7] J. Del Peral-Rosado, P. Nolle, S. Razavi, G. Lindmark, D. Shrestha, F. Gunnarsson, F. Kaltenberger, N. Sirola, O. Särkkä, J. Roström, K. Vaarala, P. Miettinen, G. Pojani, L. Canzian, H. Babaroglu, E. Rastorgueva-Foi, J. Talvitie, and D. Flachs, "Design considerations of dedicated and aerial 5G networks for enhanced positioning services," in *Proceedings of Workshop on Satellite Navigation Technology*, April 2022, pp. 1–12.

[8] J. Khalife and Z. Kassas, "On the achievability of submeter-accurate UAV navigation with cellular signals exploiting loose network synchronization," *IEEE Transactions on Aerospace and Electronic Systems*, vol. 58, no. 5, pp. 4261–4278, October 2022.

[9] M. Neinavaie and Z. Kassas, "Unveiling Starlink LEO satellite OFDM-like signal structure enabling precise positioning," *IEEE Transactions on Aerospace and Electronic Systems*, 2023, accepted.

[10] S. Liu, Z. Gao, Y. Wu, D. Kwan Ng, X. Gao, K. Wong, S. Chatzinotas, and B. Ottersten, "LEO satellite constellations for 5G and beyond: How will they reshape vertical domains?" *IEEE Communications Magazine*, vol. 59, no. 7, pp. 30–36, July 2021.

[11] J. del Peral-Rosado, R. Raulefs, J. López-Salcedo, and G. Seco-Granados, "Survey of cellular mobile radio localization methods: From 1G to 5G," *IEEE Communications Surveys Tutorials*, vol. 20, no. 2, pp. 1124–1148, 2018.

[12] I. Del Portillo, B. Cameron, and E. Crawley, "A technical comparison of three low earth orbit satellite constellation systems to provide global broadband," *Acta Astronautica*, vol. 159, pp. 123–135, 2019.

[13] K. Shamaei and Z. Kassas, "A joint TOA and DOA acquisition and tracking approach for positioning with LTE signals," *IEEE Transactions on Signal Processing*, pp. 2689–2705, 2021.

[14] M. Neinavaie, J. Khalife, and Z. Kassas, "Blind opportunistic navigation: Cognitive deciphering of partially known signals of opportunity," in *Proceedings of ION GNSS Conference*, September 2020, pp. 2748–2757.

[15] J. Khalife, M. Neinavaie, and Z. Kassas, "Blind Doppler tracking from OFDM signals transmitted by broadband LEO satellites," in *Proceedings of IEEE Vehicular Technology Conference*, April 2021, pp. 1–5.

[16] M. Neinavaie, J. Khalife, and Z. Kassas, "Blind Doppler tracking and beacon detection for opportunistic navigation with LEO satellite signals," in *Proceedings of IEEE Aerospace Conference*, 2021, pp. 1–8.

[17] M. Neinavaie, J. Khalife, and Z. Kassas, "Cognitive opportunistic navigation in private networks with 5G signals and beyond," *IEEE Journal of Selected Topics in Signal Processing*, vol. 16, no. 1, pp. 129–143, 2022.

[18] S. Parkvall, Y. Blankenship, R. Blasco, E. Dahlman, G. Fodor, S. Grant, E. Stare, and M. Stattin, "5G NR release 16: Start of the 5G evolution," *IEEE Communications Standards Magazine*, vol. 4, no. 4, pp. 56–63, 2020.

[19] L. Scharf and B. Friedlander, "Matched subspace detectors," *IEEE Transactions on signal processing*, vol. 42, no. 8, pp. 2146–2157, 1994.

[20] S. Kraut, L. Scharf, and L. McWhorter, "Adaptive subspace detectors," *IEEE Transactions on Signal Processing*, vol. 49, no. 1, pp. 1–16, 2001.

[21] M. Korso, R. Boyer, A. Renaux, and S. Marcos, "Statistical resolution limit for source localization with clutter interference in a MIMO radar context," *IEEE Transactions on Signal Processing*, vol. 60, no. 2, pp. 987–992, 2012.

[22] A. Zaimbashi, M. Derakhtian, and A. Sheikhi, "GLRT-based CFAR detection in passive bistatic radar," *IEEE Transactions on Aerospace and Electronic Systems*, vol. 49, no. 1, pp. 134–159, 2013.

[23] F. Izedi, M. Karimi, and M. Derakhtian, "Joint DOA estimation and source number detection for arrays with arbitrary geometry," *Signal Processing*, vol. 140, pp. 149–160, 2017.

[24] D. Roy, T. Mukherjee, M. Chatterjee, E. Blasch, and E. Pasiliao, "RFAL: adversarial learning for RF transmitter identification and classification," *IEEE Transactions on Cognitive Communications and Networking*, vol. 6, no. 2, pp. 783–801, 2019.

[25] M. Baek, S. Kwak, J. Jung, H. Kim, and D. Choi, "Implementation methodologies of deep learning-based signal detection for conventional MIMO transmitters," *IEEE Transactions on Broadcasting*, vol. 65, no. 3, pp. 636–642, 2019.

[26] G. Gao, "Towards navigation based on 120 satellites: Analyzing the new signals," Ph.D. dissertation, Stanford University, 2008.

[27] J. Merwe, S. Bartl, C. O'Driscoll, A. Rügamer, F. Förster, P. Berglez, A. Popugaev, and W. Felber, "GNSS sequence extraction and reuse for navigation," in *Proceedings of ION GNSS+ Conference*, 2020, pp. 2731–2747.

[28] J. Khalife, M. Neinavaie, and Z. Kassas, "The first carrier phase tracking and positioning results with Starlink LEO satellite signals," *IEEE Transactions on Aerospace and Electronic Systems*, vol. 56, no. 2, pp. 1487–1491, April 2022.

[29] M. Neinavaie, J. Khalife, and Z. Kassas, "Acquisition, Doppler tracking, and positioning with Starlink LEO satellites: First results," *IEEE Transactions on Aerospace and Electronic Systems*, vol. 58, no. 3, pp. 2606–2610, June 2022.

[30] M. Neinavaie, Z. Shadram, S. Kozhaya, and Z. M. Kassas, "First results of differential Doppler positioning with unknown Starlink satellite signals," in *Proceedings of IEEE Aerospace Conference*, March 2022, pp. 1–14.

[31] K. Takeda, H. Xu, T. Kim, K. Schober, and X. Lin, "Understanding the heart of the 5G air interface: An overview of physical downlink control channel for 5G new radio," *IEEE Communications Standards Magazine*, vol. 4, no. 3, pp. 22–29, 2020.

[32] S. Kay, *Fundamentals of statistical signal processing: Detection Theory*. Prentice-Hall, Upper Saddle River, NJ, 1993, vol. II.

The First Carrier Phase Tracking and Positioning Results With Starlink LEO Satellite Signals

Letter

This letter shows the first carrier phase tracking and positioning results with Starlink's low earth orbit (LEO) satellite signals. An adaptive Kalman filter based algorithm for tracking the beat carrier phase from the unknown Starlink signals is proposed. Experimental results show carrier phase tracking of six Starlink satellites and a horizontal positioning error of 7.7 m with known receiver altitude.

I. INTRODUCTION

Low earth orbit (LEO) broadband communication satellite signals have been considered as possible reliable sources for navigation by various theoretical and experimental studies [1]–[4]. With SpaceX having launched more than a thousand space vehicles (SVs) into LEO, a renaissance in LEO-based navigation has started. Signals from LEO SVs are received with higher power compared to medium earth orbit where GNSS SVs reside. Moreover, LEO SVs are more abundant than GNSS SVs to make up for the reduced footprint, and their signals are spatially and spectrally diverse.

Opportunistic navigation frameworks with LEO SV signals have drawn attention recently as they do not require additional, costly services or infrastructure from the broadband provider [5]. One major requirement in such frameworks is the ability to draw navigation observables from these LEO SV signals of opportunity. However, broadband providers do not usually disclose the transmitted signal structure to protect their intellectual property. As such, one would have to dissect LEO SV signals to draw navigation observables. A cognitive approach to tracking the Doppler frequency of unknown LEO SV signals was proposed in [6]. However, the aforementioned method cannot estimate the carrier phase, nor it can be adopted here since it requires knowledge of the period of the beacon within the transmitted signal, which is unknown in the case of Starlink LEO SVs.

Manuscript received June 25, 2021; released for publication September 7, 2021. Date of publication September 20, 2021; date of current version April 12, 2022.

DOI. No. 10.1109/TAES.2021.3113880

This work was supported in part by the Office of Naval Research (ONR) under Grant N00014-19-1-2511, in part by the National Science Foundation (NSF) under Grant 1929965, and in part by the U.S. Department of Transportation (USDOT) under Grant 69A3552047138 for the CARMEN University Transportation Center (UTC).

Authors' addresses: Joe Khalife and Mohammad Neinavaie are with the Department of Mechanical and Aerospace Engineering, University of California, Irvine, CA 92697 USA, E-mail: (khalifej@uci.edu; mneinava@uci.edu); Zaher M. Kassas is with Department of Mechanical and Aerospace Engineering, University of California, Irvine, CA 92697 USA, and also with the Ohio State University, Columbus, OH 43210 USA, E-mail: (zkassas@ieee.org). *(Corresponding author: Zaher M. Kassas.)*

0018-9251 © 2021 IEEE

Authorized licensed use limited to: The Ohio State University. Downloaded on October 12,2022 at 17:32:55 UTC from IEEE Xplore. Restrictions apply.

This letter develops a carrier phase tracking algorithm for Starlink signals without prior knowledge of their structure.

Recent efforts in carrier synchronization showed the benefit of using Kalman filter (KF) based tracking loops over traditional Costas-based phase-locked loops (PLLs) [7]–[10]. These adaptive methods either 1) update the process noise covariance using the residuals or 2) update the measurement noise covariance using the carrier-to-noise ratio. However, high fluctuations in the process noise covariance may cause the filter to diverge [10]. Moreover, the carrier-to-noise ratio cannot be reliably estimated when the signal structure is unknown, as is the case with Starlink signals.

This letter makes the following contributions. First, the Starlink signals are analyzed and a model suitable for carrier phase tracking is developed. Second, an adaptive KF-based tracking loop is developed where the measurement noise is updated based on a heuristic of the residuals. Third, a demonstration of the first carrier phase tracking and positioning results with real Starlink signals is presented, showing a horizontal position error of 7.7 m with six Starlink SVs.

II. RECEIVED SIGNAL MODEL

In this letter, all signals are represented as complex signals (both in-phase and quadrature baseband components).

A. Starlink Downlink Signals

Little is known about Starlink downlink signals or their air interface in general, except for the channel frequencies and bandwidths. One cannot readily design a receiver to track Starlink signals with the aforementioned information only as a deeper understanding of the signals is needed. Software-defined radios (SDRs) come in handy in such situations, since they allow one to sample bands of the radio frequency spectrum. However, there are the following two main challenges for sampling Starlink signals: 1) the signals are transmitted in *Ku*/*Ka*-bands, which is beyond the carrier frequencies that most commercial SDRs can support, and 2) the downlink channel bandwidths can be up to 240 MHz, which also surpasses the capabilities of current commercial SDRs. The first challenge can be resolved by using a mixer/downconverter between the antenna and the SDR. However, the sampling bandwidth can only be as high as the SDR allows. In general, opportunistic navigation frameworks do not require much information from the communication/navigation source (e.g., decoding telemetry or ephemeris data or synchronizing to a certain preamble). Therefore, the aim of the receiver is to exploit enough of the downlink signal to be able produce raw navigation observables (e.g., Doppler and carrier phase). Fortunately, a look at the FFT of the downlink signal at 11.325 GHz carrier frequency and sampling bandwidth of 2.5 MHz shows nine "carrier peaks," as shown in Fig. 1(a). Furthermore, the waterfall plot in Fig. 1(b) shows that these carrier peaks vary as the Doppler frequency over an 80-s interval. The Doppler frequency was predicted using two-line element (TLE) files.

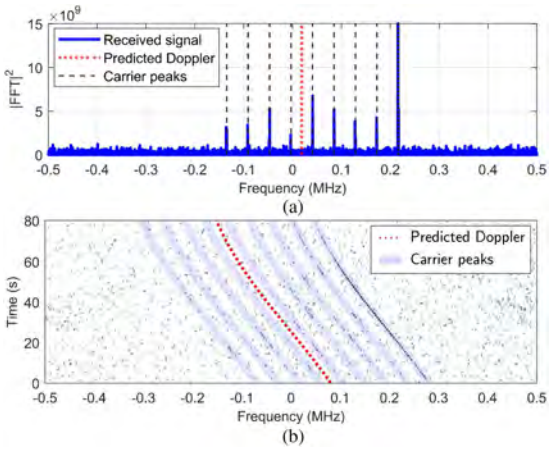

Fig. 1. (a) Snapshot of the square of the FFT of the received signal along with the Doppler frequency predicted using TLEs and the nine observed carrier peaks. (b) Waterfall plot of the FFT of the received signal over an 80-s interval showing the nine peaks varying as the predicted Doppler. The peaks seem to be uniformly separated by approximately 44 kHz.

It was observed that the relative amplitudes of these nine peaks vary from one SV to the other. Therefore, only the strongest peak will be tracked. Moreover, this letter makes no assumptions on the position of the peaks relative to the center frequency of the signal. This results in a Doppler ambiguity that is addressed in the rest of this letter. The following section discusses the assumed transmitted signal model.

B. Continuous-Time Transmitted Baseband Signal Model

Let $x(t)$ denote the continuous-time transmitted signal. As mentioned previously, only one of the nine peaks will be tracked. Motivated by the results in Fig. 1, the transmitted signal $x(t)$ can be modeled as

$$x(t) = \alpha \exp\left[j(2\pi f_p(t - t_0) + \bar{\theta}(t_0)\right] + y(t) \qquad (1)$$

where f_p is the frequency shift of the peak of interest from the center frequency; $\alpha > 0$ is a real, positive amplitude; t_0 is some initial time; $\theta(t_0)$ is some initial phase; and $y(t)$ models the remaining components of the transmitted signals. Also, motivated by Fig. 1, the following assumption is made:

$$\frac{1}{\alpha T}\left|\int_t^{t+T} y(\tau)\exp\left[j2\pi(f_p+f)\tau\right]d\tau\right| \ll 1, -\frac{\Delta f}{2} \le f \le \frac{\Delta f}{2} \qquad (2)$$

where Δf is the separation between the peaks and T is the integration period. The assumption in (2) formally states that $y(t)$ is considered as low interference around the peak of interest, which explains the existence of the peaks in Fig. 1(a). The signal $x(t)$ is then mixed to *Ku*-band for transmission.

C. Discrete-Time Received Baseband Signal Model

The Starlink LEO SV's transmitted signal will suffer from very high Doppler shifts, as shown in Fig. 1(b). Note

Authorized licensed use limited to: The Ohio State University. Downloaded on October 12,2022 at 17:32:55 UTC from IEEE Xplore. Restrictions apply.

that ionospheric delays are negligible for the Starlink SV signals in the *Ku*-band. Tropospheric delays are discussed in Section IV-B. After downmixing, low-pass filtering, and bandpass sampling, the nth sample of the discrete-time received signal $r(n)$ can be expressed as

$$r(n) = \alpha \exp\left[j(2\pi f_p n T_s + \bar{\theta}(n))\right] + \beta(n) \tag{3}$$

where T_s is the sampling interval, $\bar{\theta}(n)$ is the true beat carrier phase at time-step n, and β captures the effect of the channel noise and interference and is modeled as a complex, zero-mean white sequence with variance σ_β^2. The Starlink receiver described next will operate on the samples $r(n)$.

III. CARRIER PHASE TRACKING ALGORITHM

It is important to note that the receiver does not have knowledge of f_p. As such, the modified beat carrier phase is defined as $\theta(n) \triangleq \bar{\theta}(n) + 2\pi f_p n T_s$, which will be the quantity tracked by the receiver. Instead of a conventional PLL, an adaptive KF-based tracking loop is developed. The KF formulation allows for arbitrary model order selection, which is crucial in the LEO SVs' high-dynamics. The adaptive KF-based carrier tracking algorithm is described as follows.

A. Beat Carrier Phase Dynamics Model

The time-varying component of the continuous-time true beat carrier phase is a function of 1) the true range between the LEO SV and the receiver, denoted by $d(t)$, and 2) the time-varying difference between the receiver's and LEO SV's clock bias, denoted by $b(t)$ and expressed in meters. Specifically, the modified beat carrier phase can be expressed as

$$\theta(t) = 2\pi\left[-\frac{d(t)}{\lambda} + \frac{b(t)}{\lambda} + f_p(t - t_0)\right] + \bar{\theta}(t_0) \tag{4}$$

where λ is the carrier wavelength. The clock bias is assumed to have a constant drift a, i.e., $b(t) = a \cdot (t - t_0) + b_0$, where b_0 is the initial bias. Moreover, simulations with Starlink LEO SVs show that the following dynamics model for $d(t)$ holds for short periods of time (between carrier phase updates)

$$\dddot{d}(t) = \tilde{w}(t) \tag{5}$$

where $\tilde{w}$ is a zero-mean white noise process with power spectral density $q_{\tilde{w}}$. Subsequently, the kinematic model of the modified beat carrier phase state vector $\boldsymbol{\theta}(t) \triangleq [\theta(t), \dot{\theta}(t), \ddot{\theta}(t)]^\mathsf{T}$ is given by

$$\dot{\boldsymbol{\theta}}(t) = \mathbf{A}\boldsymbol{\theta}(t) + \boldsymbol{b}\tilde{w}(t) \tag{6}$$

$$\mathbf{A} \triangleq \begin{bmatrix} 0 & 1 & 0 \\ 0 & 0 & 1 \\ 0 & 0 & 0 \end{bmatrix}, \quad \boldsymbol{b} \triangleq \begin{bmatrix} 0 \\ 0 \\ \frac{2\pi}{\lambda} \end{bmatrix}$$

and the initial state is given by $\boldsymbol{\theta}(t_0) = [\bar{\theta}(t_0) + \frac{2\pi}{\lambda}(b_0 - d(t_0)), 2\pi f_p + \frac{2\pi}{\lambda}(a - \dot{d}(t_0)), -\frac{2\pi}{\lambda}\ddot{d}(t_0)]^\mathsf{T}$. The abovementioned system is discretized at a sampling interval of $T = N \cdot T_s$, also known as the subaccumulation period, where N is the number of subaccumulated samples. Let k denote the time index corresponding to $t_k = kT + t_0$. The discrete-time model of (6) can be expressed as

$$\boldsymbol{\theta}(k+1) = \mathbf{F}\boldsymbol{\theta}(k) + \boldsymbol{w}(k) \tag{7}$$

where $\mathbf{F} \triangleq e^{\mathbf{A}T}$ is the discrete-time state transition matrix and $\boldsymbol{w}$ is the discrete-time process noise vector, which is a zero-mean white sequence with covariance $\mathbf{Q} = q_{\tilde{w}} \int_0^T e^{\mathbf{A}t}\boldsymbol{b}(e^{\mathbf{A}t}\boldsymbol{b})^\mathsf{T} dt$.

B. Adaptive KF-Based Carrier Tracking

The adaptive KF-based tracking algorithm operates in a similar fashion to Costas loops, except that the loop filter is replaced with a KF, where the measurement noise variance is varied adaptively. Let $\hat{\boldsymbol{\theta}}(k|l)$ denote the KF estimate of $\boldsymbol{\theta}(k)$ given all the measurements up to time-step $l \leq k$, and $\mathbf{P}(k|l)$ denote the corresponding estimation error covariance. The initial estimate and its corresponding covariance are denoted by $\hat{\boldsymbol{\theta}}(0|0)$ and $\mathbf{P}(0|0)$, respectively, and are calculated as discussed in Section III-B4. The KF-based tracking algorithm steps are discussed as follows:

1) *KF Time Update:* The standard KF time update equations are preformed to yield $\hat{\boldsymbol{\theta}}(k+1|k)$ and $\mathbf{P}(k+1|k)$.

2) *KF Measurement Update:* The KF measurement update step is similar to a Costas loop: a carrier wipe-off is first performed, followed by an accumulation and discrimination step. The wipe-off and accumulation are performed as

$$s(k+1) = \frac{1}{N}\sum_{n=0}^{N-1} r(n+kN)\exp\left[-j\hat{\theta}(k+n|k)\right] \tag{8}$$

where $\hat{\theta}(k+n|k) = \hat{\theta}(k|k) + \hat{\dot{\theta}}(k|k)nT_s + \frac{1}{2}\hat{\ddot{\theta}}(k|k)(nT_s)^2$, which is obtained by propagating the initial condition $\hat{\boldsymbol{\theta}}(k|k)$ by nT_s using the dynamics in (6). Since the tracked signal in (3) is dataless, an atan2 discriminator can be used to obtain an estimate of the carrier phase error according to

$$\begin{aligned} \nu(k+1) &\triangleq \text{atan2}\left(\Im\{s(k+1)\}, \Re\{s(k+1)\}\right) \\ &= \theta(k+1) - \hat{\theta}(k+1|k) + v(k+1) \end{aligned} \tag{9}$$

where $\Re\{\cdot\}$ and $\Im\{\cdot\}$ denote the real and imaginary parts, respectively, and $v(k+1)$ is the measurement noise, which is modeled as a zero-mean, white Gaussian sequence with variance $\sigma_v^2(k+1)$. Since the measurement noise variance is not known, an estimate $\hat{\sigma}_v^2(k+1)$ is used instead in the KF. This estimate is updated adaptively according to the following section. It is important to note that $\nu(k+1)$ is the KF innovation and gives a direct measure of the modified beat carrier phase error. Hence, the standard KF measurement update equations are performed using $\nu(k+1)$, $\hat{\sigma}_v^2(k+1)$, and the measurement matrix $\mathbf{H} \triangleq [1\ 0\ 0]$.

3) *Measurement Noise Variance Estimate Update:* As the signal quality fluctuates, it is important to match the measurement noise variance to the actual noise statistics. This cannot be done readily as the channel between the LEO SV and the receiver is highly dynamic and unknown. Instead, a heuristic model is used to update $\hat{\sigma}_v^2(k)$ over time, and is given by

$$\hat{\sigma}_v^2(k+1) = \gamma\hat{\sigma}_v^2(k) + (1-\gamma)u(k) \tag{10}$$

Authorized licensed use limited to: The Ohio State University. Downloaded on October 12,2022 at 17:32:55 UTC from IEEE Xplore. Restrictions apply.

where $0 < \gamma < 1$ is a "forgetting" factor (close to one) [11] and $u(k) \triangleq \frac{1}{K_v} \sum_{m=k-K_v+1}^{k} \nu^2(m)$, where K_v is the number of samples used to estimate the measurement noise variance. The heuristic model in (10) adapts to the quality of the measurements while filtering out abrupt changes in the phase error variance.

4) *KF Initialization:* The steps abovementioned assumed that an initial estimate and corresponding covariance are available. The initial estimate can be readily obtained from the data. Since a PLL cannot resolve the true initial carrier phase, the initial estimate $\hat{\theta}(0|0)$ is set to zero with zero uncertainty. This initial ambiguity is accounted for in the navigation filter. Initial estimates of the first and second derivatives of θ can be obtained by performing a search over the Doppler and the Doppler rate to maximize the FFT of the received signal. The search yields the Doppler and Doppler rate estimates denoted by $\hat{f}_D(0)$ and $\hat{\dot{f}}_D(0)$, respectively. In the following, let Δf_D and $\Delta \dot{f}_D$ denote the sizes of the Doppler and Doppler rate search bins, respectively. It is assumed that the initial Doppler and Doppler rate errors are uniformly distributed within one bin, and their initial probability density functions (pdfs) are bounded by Gaussian pdfs with zero-mean and standard deviations $\frac{\Delta f_D}{6}$ and $\frac{\Delta \dot{f}_D}{6}$, respectively. As such, Δf_D and $\Delta \dot{f}_D$ represent the $\pm 3\sigma$ intervals of the Gaussian pdfs. The KF is initialized as

$$\hat{\boldsymbol{\theta}}(0|0) = \left[0, 2\pi \hat{f}_D(0), 2\pi \hat{\dot{f}}_D(0)\right]^{\mathsf{T}} \tag{11}$$

$$\mathbf{P}(0|0) = \operatorname{diag}\left[0, \frac{4\pi^2}{36}\Delta f_D^2, \frac{4\pi^2}{36}\Delta \dot{f}_D^2\right]. \tag{12}$$

IV. EXPERIMENTAL RESULTS

This section provides the first results for carrier phase tracking and positioning with Starlink signals. To this end, a stationary National Instrument universal software radio peripheral (USRP) 2945R was equipped with a consumer-grade *Ku* antenna and low-noise block downconverter to receive Starlink signals in the *Ku*-band. The sampling bandwidth was set to 2.5 MHz and the carrier frequency was set to 11.325 GHz, which is one of the Starlink downlink frequencies. The samples of the *Ku* signal were stored for offline processing. The tracking results are presented in the following.

A. Carrier Phase Tracking Results

The USRP was set to record *Ku* signals over a period of 800 s. During this period, a total of six Starlink SVs transmitting at 11.325 GHz passed over the receiver, one at a time. The framework discussed in Section III was used to acquire and track the signals from these satellites with $\gamma = 0.99, K_v = 200, \Delta f_D = 250$ Hz, $\Delta \dot{f}_D = 50$ Hz/s, $q_{\tilde{w}} = (0.577)^2$ m^2/s^5, and $\hat{\sigma}_v^2(0) = \frac{1}{9}(\frac{\pi}{2})^2$ rad^2. The time history of $\nu(k)$ for each SV is shown in Fig. 2.

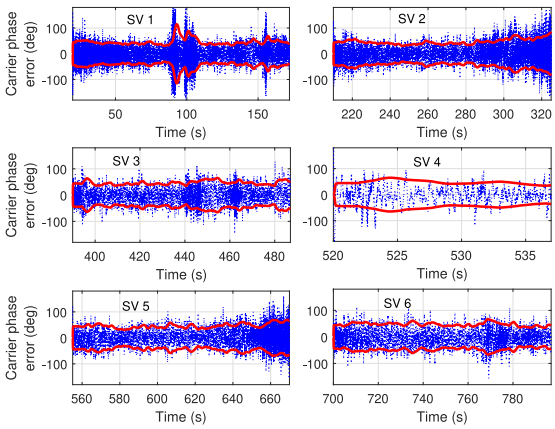

Fig. 2. Time history of $\nu(k)$ for each SV (dotted blue curves) and their corresponding $\pm 3\sigma$ bounds (solid red curves).

B. Position Solution

In the following, carrier phase observables are formed from the tracked modified beat carrier phases by (i) downsampling by a factor $D = 10$ to avoid large time-correlations in the carrier phase observables and (ii) multiplying by the wavelength to express the carrier observable in meters. Let $i \in \{1, 2, 3, 4, 5, 6\}$ denote the SV index. The carrier phase observable to the ith SV at time-step $\kappa = k \cdot D$, expressed in meters, is modeled as

$$z_i(\kappa) = \left\| \boldsymbol{r}_r - \boldsymbol{r}_{\mathrm{SV}_i}(\kappa) \right\|_2 + a_i\, \kappa DT + b_i + c\, T_{\mathrm{tropo},i}(\kappa) + v_{z_i}(\kappa) \tag{13}$$

where $\boldsymbol{r}_r$ and $\boldsymbol{r}_{\mathrm{SV}_i}(\kappa)$ are the receiver's and ith Starlink SV 3-D position vectors expressed in an east-north-up frame centered at the receiver's true position; a_i and b_i are the coefficients of the first-order polynomial modeling the errors due to the initial carrier phase, clock bias, and unknown frequency shift f_p; c is the speed of light, $T_{\mathrm{tropo},i}(\kappa)$ is the tropospheric delay for the ith SV; and $v_{z_i}(\kappa)$ is the measurement noise, which is modeled as a zero-mean, white Gaussian random variable with variance $\sigma_i^2(\kappa)$. The value of $\sigma_i^2(\kappa)$ is nothing but the first diagonal element of $\mathbf{P}(\kappa|\kappa)$, expressed in m^2. Tropospheric delay estimates $\hat{T}_{\mathrm{tropo},i}(\kappa)$ are obtained using the Hopfield model [12] and subtracted from $z_i(\kappa)$ yielding the corrected measurement $\hat{z}_i(\kappa) \triangleq z_i(\kappa) - \hat{T}_{\mathrm{tropo},i}(\kappa)$. In the following, define the parameter vector

$$\boldsymbol{x} \triangleq \left[\boldsymbol{r}_r^{\mathsf{T}}, a_1, b_1, \ldots, a_6, b_6\right]^{\mathsf{T}}. \tag{14}$$

Let $\hat{\boldsymbol{z}} \triangleq [z_1(0), \hat{z}_1(1), \ldots, \hat{z}_1(K_1), \ldots, \hat{z}_6(0), \hat{z}_6(1), \ldots, \hat{z}_6(K_6)]^{\mathsf{T}}$, where K_i denoted the total number of measurements from the ith SV, and let $\boldsymbol{v}_z \triangleq [v_{z_1}(0), v_{z_1}(1), \ldots, v_{z_1}(K_1), \ldots, v_{z_6}(0), v_{z_6}(1), \ldots, v_{z_6}(K_6)]^{\mathsf{T}}$, which is a zero-mean Gaussian random vector with a diagonal covariance $\mathbf{R}$ whose diagonal elements are given by $\sigma_i^2(\kappa)$. Then, one can readily write the measurement equation

$$\boldsymbol{z} = \boldsymbol{g}(\boldsymbol{x}) + \boldsymbol{v}_z \tag{15}$$

Authorized licensed use limited to: The Ohio State University. Downloaded on October 12,2022 at 17:32:55 UTC from IEEE Xplore. Restrictions apply.

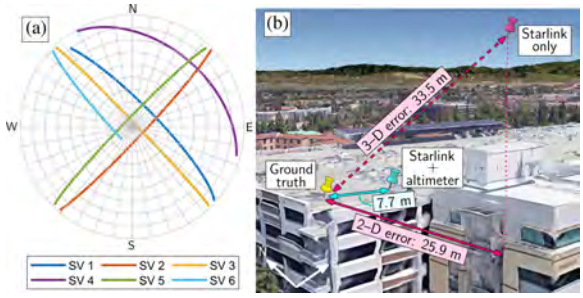

Fig. 3. (a) Skyplot showing the Starlink SVs' trajectories during the experiment. (b) Environment layout and positioning results.

where $\boldsymbol{g}(\boldsymbol{x})$ is a vector-valued function that maps the parameter $\boldsymbol{x}$ to the carrier phase observables according to (13). In the following, a weighted nonlinear least-squares (WNLS) estimator with weight matrix $\mathbf{R}^{-1}$ is solved to obtain an estimate of $\boldsymbol{x}$. The SV positions were obtained from TLE files and simplified general perturbation 4 software. It is important to note that the TLE epoch time was adjusted for each SV to account for ephemeris errors. This was achieved by minimizing the range residuals for each SV.

Subsequently, the receiver position was estimated using the aforementioned WNLS. The receiver position was initialized as the centroid of all SV positions, projected onto the surface of the earth, yielding an initial position error of 179 km. The clock biases and drifts were initialized to zero. The final 3-D position error was found to be 33.5 m, while the 2-D position error was 25.9 m. Upon equipping the receiver with an altimeter (to know its altitude), the 2-D position error goes down to 7.7 m. A skyplot of the Starlink SVs, the environment layout, and the positioning results are shown in Fig. 3.

V. CONCLUSION

This letter showed the first carrier phase tracking and positioning results with real Starlink LEO SV signals. A model of a Starlink SV's transmitted signal was formulated, and an adaptive KF-based carrier phase tracking algorithm was developed to track the Starlink signal. Experimental results showed carrier phase tracking of six Starlink LEO SVs over a period of approximately 800 s. The resulting positioning performance was: 7.7 m 2-D error when the receiver's altitude is known, and 25.9 m 2-D error and 33.5 m 3-D error when the receiver's altitude is unknown.

JOE KHALIFE, Member, IEEE
MOHAMMAD NEINAVAIE, Student Member, IEEE
ZAHER M. KASSAS, Senior Member, IEEE
University of California, Irvine, CA USA
The Ohio State University, Columbus, OH USA

REFERENCES

[1] D. Racelis, B. Pervan, and M. Joerger
Fault-free integrity analysis of mega-constellation-augmented GNSS
In *Proc. 32nd Int. Tech. Meeting Satellite Division Inst. Navigat.*, 2019, pp. 465–484.

[2] T. Reid *et al.*
Navigation from low earth orbit — Part 1: Concept, current capability, and future promise
In *Position, Navigation, and Timing Technologies in the 21st Century*, vol. 2, J. Morton, F. van Diggelen, J. Spilker Jr., and B. Parkinson, Eds. Hoboken, NJ, USA: Wiley, 2021, ch. 43, pp. 1359–1379.

[3] Z. Kassas
Navigation from low earth orbit — Part 2: Models, implementation, and performance
in Position, Navigation, and Timing Technologies in the 21st Century, J. Morton, F. van Diggelen, J. Spilker Jr., and B. Parkinson, Eds. Hoboken, NJ, USA: Wiley, 2021, vol. 2, ch. 43, pp. 1381–1412.

[4] M. Orabi, J. Khalife, and Z. Kassas
Opportunistic navigation with Doppler measurements from Iridium Next and Orbcomm LEO satellites
In *Proc. IEEE Aerosp. Conf.*, 2021, pp. 1–9.

[5] Z. Kassas, J. Khalife, M. Neinavaie, and T. Mortlock
Opportunity comes knocking: Overcoming GPS vulnerabilities with other satellites' signals
Inside Unmanned Syst. Mag., pp. 30–35, 2020.

[6] M. Neinavaie, J. Khalife, and Z. Kassas
Blind Doppler tracking and beacon detection for opportunistic navigation with LEO satellite signals
In *Proc. IEEE Aerosp. Conf.*, 2021, pp. 1–8.

[7] K. Kim, G. Jee, and J. Song
Carrier tracking loop using the adaptive two-stage Kalman filter for high dynamic situations
Int. J. Control, Autom. Syst., vol. 6, no. 6, pp. 948–953, 2008.

[8] L. Zhang, Y. Morton, and M. Miller
A variable gain adaptive Kalman filter-based GPS carrier tracking algorithms for ionosphere scintillation signals
In *Proc. ION Int. Tech. Meeting*, 2010, pp. 3107–3114.

[9] J. Won and B. Eisfeller
A tuning method based on signal-to-noise power ratio for adaptive PLL and its relationship with equivalent noise bandwidth
IEEE Commun. Lett., vol. 17, no. 2, pp. 393–396, Feb. 2013.

[10] J. Vila-Valls, P. Closas, M. Navarro, and C. Fernandez-Prades
Are PLLs dead? a tutorial on Kalman filter-based techniques for digital carrier synchronization
IEEE Aerosp. Electron. Syst. Mag., vol. 32, no. 7, pp. 28–45, Jul. 2017.

[11] Q. Xiang, Y. Yang, Q. Zhang, J. Cao, and Y. Yao
Adaptive and joint frequency offset and carrier phase estimation based on Kalman filter for 16 QAM signals
Opt. Commun., vol. 430, pp. 336–341, 2019.

[12] P. Misra and P. Enge
Global Positioning System: Signals, Measurements, and Performance, *2nd ed*. Kathmandu, Nepal: Ganga-Jamuna Press, 2010.

Authorized licensed use limited to: The Ohio State University. Downloaded on October 12,2022 at 17:32:55 UTC from IEEE Xplore. Restrictions apply.

UAV Navigation With 5G Carrier Phase Measurements

Ali A. Abdallah and Zaher M. Kassas
University of California, Irvine

BIOGRAPHIES

Ali A. Abdallah is a Ph.D student in the Department of Electrical Engineering and Computer Science at the University of California, Irvine and a member of the Autonomous Systems Perception, Intelligence, and Navigation (ASPIN) Laboratory. He received a B.E. in Electrical Engineering from the Lebanese American University (LAU). His current research interests include opportunistic navigation, software-defined radio, long-term evolution (LTE), 5G, and indoor localization.

Zaher (Zak) M. Kassas is an associate professor at the University of California, Irvine and director of the Autonomous Systems Perception, Intelligence, and Navigation (ASPIN) Laboratory. He is also director of the U.S. Department of Transportation Center: CARMEN (Center for Automated Vehicle Research with Multimodal AssurEd Navigation), focusing on navigation resiliency and security of highly automated transportation systems. He received a B.E. in Electrical Engineering from the Lebanese American University, an M.S. in Electrical and Computer Engineering from The Ohio State University, and an M.S.E. in Aerospace Engineering and a Ph.D. in Electrical and Computer Engineering from The University of Texas at Austin. He is a recipient of the 2018 National Science Foundation (NSF) Faculty Early Career Development Program (CAREER) award, 2019 Office of Naval Research (ONR) Young Investigator Program (YIP) award, 2018 IEEE Walter Fried Award, 2018 Institute of Navigation (ION) Samuel Burka Award, and 2019 ION Col. Thomas Thurlow Award. His research interests include cyber-physical systems, estimation theory, navigation systems, autonomous vehicles, and intelligent transportation systems.

ABSTRACT

A framework for unmanned aerial vehicle (UAV) navigation using downlink cellular fifth-generation (5G) signals is presented. In the proposed framework, a software-defined receiver (SDR) is developed to extract carrier phase measurements from received 5G signals. The SDR utilizes the time-domain orthogonality of the orthogonal frequency division multiplexing (OFDM)-based 5G signals. A so-called ultimate synchronization signal (USS) to combine all available resources is proposed. The proposed 5G SDR includes two stages: (i) acquisition stage, in which only unique USS resources are utilized to detect the hearable gNBs and (ii) tracking stage, in which the entire USS is utilized to produce 5G carrier phase measurements. These measurements are processed in an extended Kalman filter (EKF) to assess the navigation performance of the proposed 5G opportunistic SDR. Experimental results are presented of an UAV navigating with the proposed 5G SDR, while receiving signals from four 5G base stations (known as gNBs). It is shown that over a trajectory of 500 m traversed in 145 seconds, the position root mean-squared error (RMSE) was 3.35 m.

I. INTRODUCTION

The dramatic growth in the unmanned aerial vehicle (UAV) industry and their public adoption is propelling researchers and designers to develop integrated navigation systems that ensure continuous, trusted operation. Towards this end, one could diversify the navigation sources, either by introducing (a) complementary sensors (e.g., inertial measurement units (IMUs) [1, 2], cameras [3, 4], lidar [5, 6], etc.) and/or (b) complementary signal-based navigation signals (e.g., WiFi [7, 8], UWB [9, 10], cellular [11–15], low Earth orbit (LEO) satellites [16, 17], etc.). The focus of this paper is to develop a navigation system that exploit 5G cellular signals.

Recent research has considered the use of cellular signals as complementary and alternative navigation system GNSS signals. Code-division multiple access (CDMA) and long-term evolution (LTE), have shown high ranging and localization accuracy using specialized software-defined receivers (SDR) [18–20]. The performance of these SDRs

Copyright © 2021 by A. Abdallah and Z. Kassas

Preprint of the 2021 ION GNSS+ Conference St. Louis, Missouri, September 20–24, 2021

have been evaluated in different navigation frameworks (standalone, differential, and integrated with other sensors), both indoors and outdoors, where experimental results demonstrated meter-level accuracy positioning accuracy on ground-based receivers [21–24] and sub-meter-level positioning accuracy on aerial vehicle-based receivers [25, 26].

Unconventionally, 5G will be the first cellular system to coexist with the previous system (namely, LTE). Similar to LTE, 5G deploys a structure that uses orthogonal frequency division multiplexing (OFDM) for downlink transmission. The 5G system is very attractive by design for navigation purposes due to:

- High carrier frequencies: High carrier frequencies yield precise carrier phase navigation observables and reduce multipath effects due to high path signal loss.
- Abundance: 5G tackles the problem of high signal path loss of millimeter waves (mmWaves) by using beamforming techniques and small cells, which makes the 5G base stations (also known as gNodeBs (gNB)) ubiquitous.
- Geometric diversity: Cellular towers have favorable geometry by construction of the cells to provide better coverage.
- Large bandwidth: While a single LTE signal has a bandwidth up to 20 MHz, a single 5G signal has a bandwidth up to 400 MHz for mmWave band, which makes it less susceptible to multipath errors, i.e., it can differentiate multipath components with shorter delays from the line-of-sight (LOS) signal.
- High received power: The received carrier-to-noise-ratio C/N_0 of cellular signals from nearby cellular towers is more than 20 dB-Hz higher than GPS signals [27].

The positioning capabilities of 5G has been studied over the past few years. Different approaches have been proposed, in which direction-of-arrival (DOA), direction-of-departure (DOD), time-of-arrival (TOA), or combination of them is used to achieve accurate positioning from 5G signals. In [28], the authors investigated the positioning performance of six different 5G impulse radio waveforms, where 5G had no generally accepted waveform at the time. The performance analysis showed the capability of mmWaves in achieving sub-meter level accuracy, where the best performance was achieved when using Gaussian raised-cosine, Gaussian pulse, and Sinc-RCP impulse radio waveforms. The capability of massive multiple-input-multiple-output (mMIMO) systems in providing very accurate localization when relying on DOA was studied in [29]. The paper addressed the limitation of DOA in mMIMO systems in the presence of multipath by proposing a compressed sensing navigation framework which relied on the channel properties to distinguish LOS from multipath components. The proposed algorithm showed sub-meter accuracy in simulation. Another approach to reduce 5G small cell interference and multipath effect in angular localization methods by combining near-field and far-field effects was proposed in [30]. Simulation results showed that the proposed approach improved the angular resolution by orders of magnitude. In [31], a GNSS/5G integrated positioning framework was developed, in which device-to-device (D2D) range and angle measurements are assumed between mobile terminals (MTs). An experiment was performed with real GNSS data and emulated 5G D2D data, in which the integrated system reduced the GNSS position root mean-squared error (RMSE) from around 5 m to 3 m assuming 10 MTs. A similar study was conducted in [32], where the performance of different hybrid navigation filters exploiting GPS, Galileo and 5G TOA measurements in multipath environment was assessed. The hybrid GNSS/5G was studied for different type of filters with a specific design of the assumed Gaussian errors. Simulation results showed an accuracy of less than 2 m for the hybrid GNSS/5G assuming an urban environment. In [33], a network-based positioning framework using joint TOA and DOA was proposed using cascaded extended Kalman filters (EKFs). The proposed framework considered the clock biases between the user equipment (UE) and the gNBs, and among the gNBs themselves. The framework was evaluated by simulating a real 5G scenario using three-dimensional (3-D) ray tracing, where sub-meter-level positioning accuracy was demonstrated. In [34], the positioning capabilities of 5G on edge devices was studied. A preliminary simulation study was conducted, in which an integrated 5G/IMU navigation solution exhibited a positioning horizontal absolute error ranging around 2.5 m.

On one hand, all the aforementioned studies are limited to simulations and laboratory emulated 5G signals as well as outdated or restrictive assumptions. In particular the proposed approaches require the user to be in the network so that network-based localization approaches (i.e., utilizing downlink and uplink channels from the gNB to the user and back). This compromises the user privacy by revealing their accuracte location and limits the user to only the gNBs of the network they are subscribed to.

In contrast to existing literature, the authors studied real downlink 5G signals for opportunistic exploitation (i.e., without communicating back with the 5G gNB nor subscribing to the network). In [35], a comprehensive approach for opportunistic navigation with 5G that exploits the downlink channel was developed. The proposed approach extracted navigation observables from the "always-on" transmitted synchronization signals. The proposed SDR was

validated experimentally, where the ranging performance with real 5G signals was evaluated. After removing the effect of the clock bias and drift from the estimated pseudorange, the ranging error standard deviation was shown to be 1.19 m. In [36], the proposed SDR in [35] was modified to extract navigation observables from different synchronization signals. These observables were analyzed and fused in an EKF to estimate the 2-D position and velocity of the receiver, along with the relative clock bias and drift between the receiver and each gNB. Experimental results were presented of a ground vehicle navigating with the 5G SDR in a suburban environment: Costa Mesa, California, USA, while receiving signals from two gNBs. It was shown that over a trajectory of 1.02 km traversed in 100 seconds, the position RMSE and standard deviation were 14.93 m and 8.28 m, respectively. In [37], a more challenging environment compared to [36] was considered for experimental demonstration, where the ground vehicle navigated in an urban environment: Santa Ana, California, USA, while receiving signals from five gNBs intermittently over the entire trajectory. It was shown that over a trajectory of 773 m traversed in 110 seconds, the position RMSE and standard deviation were 4.1 m and 2 m, respectively.

This paper considers UAVs as the navigation platform and develops a more precis navigation approach than the previous work. This paper makes the following contributions:

- First, it develops a carrier phase-based 5G SDR to opportunistically extract 5G carrier phase measurements. The proposed receiver exploits the orthogonality property of OFDM signals in both frequency and time-domains, where all available synchronization signals are combined into one ultimate signal.
- Second, it implements a navigation framework to obtain an accurate navigation on a UAV platform.
- Third, it assesses the proposed system experimentally on a UAV using exiting sub-6 GHz 5G cellular signals.

The remainder of the paper is organized as follows. Section II discusses 5G signal model, frame structure, and potential reference signals for opportunistic navigation. Also, it proposes a 5G ultimate synchronization signal (USS). Section III proposes a USS-based carrier-aided code-based 5G opportunistic navigation receiver. Section IV presents a navigation framework, in which an EKF is used to estimate the UAV's position using 5G carrier phase measurements. Section V demonstrates the experimental results. Section VI gives concluding remarks.

II. 5G SIGNAL STRUCTURE

A. Frame Structure and System Information

OFDM with cyclic prefix (CP) is used as a modulation technique for 5G downlink signals, which is the same waveform LTE has adopted for its downlink signal. This paper discusses an opportunistic UE-based navigation approach; thus, only 5G downlink signal structure is discussed. In OFDM, a multi-carrier transmission scheme is used, where transmitted data symbols are mapped into multiple narrowband subcarriers in the frequency-domain, which reduces frequency selective fading effect caused by multipath. The serial data symbols $\{S_1, \cdots, S_{N_r}\}$ are parallelized in group symbols, each of length N_r, where N_r is the number of subcarriers carrying the data. Then, a guard band in the frequency-domain is applied by zero-padding both sides of the signal and extending the N_r subcarriers into N_c subcarriers. At this step, an inverse fast Fourier transform (IFFT) is taken, and the last L_{CP} elements are repeated in the beginning, which serves as a guard band in the time-domain to protect the OFDM signals from inter-symbol interference (ISI).

At the receiver, the transmitted symbols are demodulated by executing the aforementioned steps in reverse order. The obtained OFDM signals are arranged in a 2-D frame. The structure of this frame depends on the transmission type of the 5G signal, which can be either time division duplexing (TDD) or frequency division duplexing (FDD). This paper will use 5G signals from FR1, where most cellular providers are using FDD due to its superior performance in providing better coverage and less latency.

Compared to LTE numerology (i.e., subcarrier spacing (SCS) and symbol length), which supports only one type of subcarrier spacing, $\Delta f = 15$ kHz, 5G supports different types of subcarrier spacing.

The duration of the FDD 5G frame is

$$T_f = \frac{\Delta f_{\max} N_f}{100} \cdot T_c = 10\,\text{ms},$$

where, $\Delta f_{\max} = 480\,\text{kHz}$, $N_f = 4096$, and $T_c = \frac{1}{\Delta f_{\max} N_f} = 0.509$ ns is the basic time unit for 5G. Each 5G frame consists of ten subframes, with duration 1 ms each. The number of OFDM symbols per subframe is $N_{\text{symb}}^{\text{subframe},\mu} = N_{\text{symb}}^{\text{slot}} N_{\text{slot}}^{\text{subframe},\mu}$. The frame is divided into two equally-sized half-frames consisting of five subframes each and denoted by: (i) half-frame 0 consisting of subframes 0-4 and (ii) half-frame 1 consisting of subframes 5-9.

For a predefined μ, the number of slots is denoted by $n_s^\mu \in \{0, 1, \cdots, N_{\text{slot}}^{\text{subframe},\mu}\}$ or $n_s^\mu \in \{0, 1, \cdots, N_{\text{slot}}^{\text{frame},\mu}\}$ in an increasing order within a subframe or a frame, respectively. The number of symbols per slot $N_{\text{symb}}^{\text{slot}}$ depends on the type of cyclic prefix and the specified numerology. For different numerologies: the subcarrier spacing, CP type, number of OFDM symbols per slot, number of slots per frame, number of slots per subframe, symbol duration, and CP duration.

A resource block (RB) is defined as $N_{\text{sc}}^{\text{RB}} = 12$ subcarriers in the frequency-domain and has the time length of a resource grid $N_{\text{symb}}^{\text{subframe},\mu}$. A resource block consists of resource elements. The minimum and maximum number of resource blocks along with the corresponding bandwidth for different numerologies are summarized in Table I. Each element in the 5G frame is uniquely identified for a specific antenna port p and subcarrier configuration μ by $(k, l)_{p,\mu}$, where k is the index in frequency domain l is the symbol position in the time domain relative to some reference point. In the 5G protocol, "Point A" serves as a common reference point and can be obtained as reported in [38].

TABLE I

The minimum and maximum number of resource blocks and the corresponding bandwidths for different numerologies.

μ	$N_{\text{RB}}^{\min}$	$N_{\text{RB}}^{\max}$	**Minimum bandwidth [MHz]**	**Maximum bandwidth [MHz]**
0	24	275	4.32	49.5
1	24	275	8.64	99
2	24	275	17.28	198
3	24	275	34.56	396
4	24	138	69.12	397.44

At the receiver side, the received 5G signal must be converted to frame structure before extracting signals of interest. To do so, the frame start time should be known. For the purpose of providing the frame start time, the gNB broadcasts synchronization signals (SS) with a pre-specified symbol mapping in the 5G frame. The SS includes two reference signals: primary synchronization signal (PSS) and secondary synchronization signal (SSS), which provide symbol and frame timing, respectively. Once the frame start time is known, the CPs can be removed and a fast Fourier transform (FFT) is taken to construct the OFDM symbols in the frame. The SS, the physical broadcast channel (PBCH), and its associated demodulation reference signal (DM-RS) are transmitted in the same 4 symbols block called the SS/PBCH block. The SS/PBCH block consists of 240 contiguous subcarrier (20 RBs) and four consecutive OFDM symbols. Within the SS/PBCH, the subcarriers are numbered in an ascending order from 0 to 239. Note that the position of PBCH-DM-RS varies with v, and the value v changes depending on the physical cell ID N_{ID}^{Cell}. The SS/PBCH block is transmitted every two frames and is transmitted numerous times, where each set of these transmitted block is called an SS/PBCH burst. The SS/PBCH burst has to be confined within a half-frame window (5 ms). Each block in the SS/PBCH burst is beamformed in a different direction and has an identifier denoted as $\bar{i}_{\text{ssb}}$. The $\bar{i}_{\text{ssb}}$ is a time-dependent part of the DM-RS scrambling initialization specified as an integer from 0 to 7, which is derived in the SS burst configuration from the least significant bits (LSBs) of the SS/PBCH block index and the half-frame number. The frequency location of the SS/PBCH within the 5G frame depends on the 5G high-level signaling. The time location of the SS/PBCH block and the size of the SS/PBCH burst in the frame depends on the transmission frequency f_c and the numerology μ as shown in Table II, where index 0 corresponds to the first OFDM symbol of the first slot in a half-frame.

The PSS and SS are two orthogonal maximum-length sequences (m-sequences) of length 127 and are transmitted on contiguous subcarriers. The PSS has three possible sequences $N_{ID}^{(2)} \in \{0, 1, 2\}$, each of which maps to an integer representing the sector ID of the gNB. The SSS has 336 possible sequences $N_{ID}^{(1)} \in \{0, \cdots, 335\}$, each of which maps to an integer representing the group identifier of the gNB. See Section 7.4.2 of [38]. Both $N_{ID}^{(1)}$ and $N_{ID}^{(2)}$ define the physical cell identity of the gNB according to

$$N_{ID}^{Cell} = 3N_{ID}^{(1)} + N_{ID}^{(2)}.$$

TABLE II

SYMBOL NUMBERS CONTAINING SS/PBCH BLOCK FOR DIFFERENT NUMEROLOGIES AND FREQUENCY BANDS

subcarrier spacing (kHz)	**Carrier frequency**	**Symbol number**	**Slot number n**
Case A: 15	$f_c \leq 3$ GHz $3 < f_c \leq 6$ GHz	$\{2, 8\} + 14n$	$\{0, 1\}$ $\{0, \cdots, 3\}$
Case B: 30	$f_c \leq 3$ GHz $3 < f_c \leq 6$ GHz	$\{4, 8, 16, 20\} + 28n$	$\{0\}$ $\{0, 1\}$
Case C: 30	$f_c \leq 3$ GHz $3 < f_c \leq 6$ GHz	$\{2, 8\} + 14n$	$\{0, 1\}$ $\{0, \cdots, 3\}$
Case D: 120	$f_c > 6$ GHz	$\{4, 8, 16, 20\} + 28n$	$\{0, \cdots, 3,$ $5, \cdots, 8,$ $10, \cdots, 13,$ $15, \cdots, 18\}$
Case E: 240	$f_c > 6$ GHz	$\{8, 12, 16, 20, 32,$ $36, 40, 44\} + 56n$	$\{0, \cdots, 8\}$

PBCH is a physical channel that is used to transmit the system information required to establish the connection between the gNB and the UE. The decoding of the PBCH parameters is explained in details in [35]. The DM-RS signal associated with the PBCH is used for decoding purposes and estimate the channel frequency response. The PBCH DM-RS sequence is generated as explained in Section 7.4.1.4 of [38].

B. 5G Ultimate Synchronization Signal

In previous 5G-based opportunistic navigation approaches, the proposed navigation receivers considered the orthogonality of the synchronization and channel-estimation signals in frequency-domain, i.e., the transmitted OFDM frame is always re-constructed from the received time-domain data by executing the transmission steps discussed in Subsection II-A in a reverse order, then navigation are estimated by utilization the reference signal with the highest bandwidth. This conventional approach is necessary for communication applications, in which the UE has to extract various system information to initiate two-ways communication with the gNB; however, for UE-based navigation applications, the goal is to produce navigation observables by utilizing the entire frequency and time-domain resources in the signal. For this purpose, this paper presents a navigation receiver that exploits the orthogonality property of OFDM signals in both frequency and time-domains. In this receiver, all available synchronization signals are combined into one signal denoted by the USS. The USS consists of the PSS, SSS, and PBCH DM-RS as shown Fig. 1. Then the time-domain-based sequence is obtained by zero-padding both sides of the signals in the frequency domain. Then, the IFFT is taken, and the L_{CP} elements are added. This procedure is exactly the procedure happening at the gNB, except for having zeros instead of having data outside the SS/PBCH block.

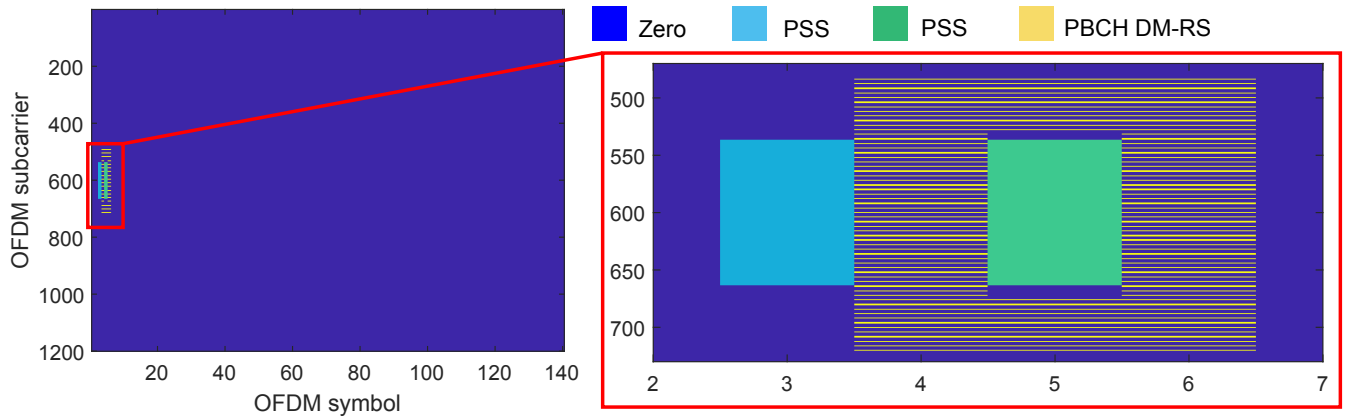

Fig. 1. The 5G OFDM locally-generated frame (i.e., the so-called ultimate synchronization signal (USS).

III. 5G SDR STRUCTURE

In this section, a carrier-aided code phase-based SDR to opportunistically extract TOA measurements from 5G signals is developed. The proposed receiver exploits the USS as a one ultimate sequence. The receiver has three main stages: (i) 5G carrier frequency extraction, (ii) acquisition, and (iii) tracking. The first stage was discussed in the authors' previous work and does not change in the proposed SDR [35, 36]. The rest of this section discusses the other stages.

A. Acquisition

The objective of this stage is to determine which gNBs are in the receiver's proximity and to obtain a coarse estimate of their corresponding code start times and Doppler frequencies. For this purpose, and after extracting the carrier frequency of the surrounding gNBs, the UE starts sampling the 5G signals with at least a sufficient sampling rate to capture the entire SS/PBCH (i.e., USS) bandwidth and convert the signals to the baseband domain by wiping out the carrier frequency. The received discrete-time signal is denoted by $x[n]$, where n is a discrete-time instance. Then, a search over the code start time and Doppler frequency is performed to detect the presence of a signal in $x[n]$ at $n = 0$. For 5G, there are 1008 possible USS sequences resulting from the possible sequences of PSS and SSS and denoted by

$$\mathrm{USS}_{N_{ID}^{Cell}}, \quad \text{for} \quad N_{ID}^{Cell} \in \{0, 1, \cdots, 1007\}. \tag{1}$$

It is worth mentioning that the USS is not transmitted every frame and has a periodicity of 5 ms, 10 ms, 20 ms, 40 ms, 80 ms, or 160 ms. However, a UE can assume a default periodicity of 20 ms during initial cell search or idle mode mobility. In this case, while the USS has a frame duration of 10 ms, it is zero-padded in the time-domain to obtain a 20 ms sequence.

The PSS sequence is not unique for every USS and is common for N_{ID}^{Cell} (mod 3). If the proposed USS is used, as is, to detect the existing N_{ID}^{Cell} in the received 5G signals, signals with same PSS will be also detected as long as the PSS received power is enough to pass the detection threshold. This will cause faulty detection of 5G gNBs. To circumvent this, a USS$^{'}$ is used in the acquisition stage, in which only SSS and PBCH DM-RS are utilized. After detecting the available gNBs, another acquisition is performed using the USS in which PSS is also utilized to obtain more accurate initial estimates of the Doppler frequency $\hat{f}_{D_0}$ and the code start time $\hat{t}_{s_0}$, which are then fed to the tracking loops.

B. Tracking

After obtaining an initial coarse estimate of the code start time and Doppler frequency, the receiver refines and maintains these estimates via tracking loops. In the proposed design, a phase-locked loop (PLL) is employed to track the carrier phase and a carrier-aided delay-locked loop (DLL) is used to track the code phase.

The PLL consists of a phase discriminator, a loop filter, and a numerically-controlled oscillator (NCO). Since USS is a data-less pilot channel, an atan2 discriminator, which remains linear over the full input error range of $\pm\pi$, could be used without the risk of having phase ambiguities. Given the limited dynamics of small UAVs, it was found that a second-order PLL is sufficient to maintain track of the carrier phase. The loop filter transfer function is given by

$$F_{\mathrm{PLL}}(s) = \frac{2\zeta w_n s + w_n^2}{s}, \tag{2}$$

where $\zeta \equiv \frac{1}{\sqrt{2}}$ is the damping ratio and w_n is the undamped natural frequency, which can be related to the PLL's noise-equivalent bandwidth $B_{n,\mathrm{PLL}}$ by $B_{n,\mathrm{PLL}} = \frac{w_n}{8\zeta}\left(4\zeta^2 + 1\right)$ [39]. The output of the loop filter at the m-th subaccumulation $v_{\mathrm{PLL,m}}$ is the rate of change of the carrier phase error, expressed in rad/s. Then, the Doppler frequency estimate is obtained as $\hat{f}_{D_m} = \frac{v_{\mathrm{PLL,m}}}{2\pi}$. The carrier phase estimate is modeled as

$$\hat{\theta}(t_n) = 2\pi \hat{f}_{D_m} t_n + \theta_0, \tag{3}$$

where $t_n = nT_s$ is the sample time expressed in receiver time, T_s is the sampling time, and θ_0 is the initial beat carrier phase of the received signal.

The carrier-aided DLL employs the non-coherent dot product discriminator, in which the prompt, early, and late correlations, denoted by S_{p_m}, S_{e_m}, and S_{l_m}, respectively. The DLL loop filter is a simple gain K, with a noise-equivalent bandwidth $B_{n,\mathrm{DLL}} = \frac{K}{4} \equiv 0.05$ Hz. The output of the DLL loop filter $v_{\mathrm{DLL,m}}$ is the rate of change of the code phase, expresses in s/s. Assuming low-side mixing, the code start time is updated according to

$$\hat{t}_{s_{m+1}} = \hat{t}_{s_m} - (v_{\mathrm{DLL,m}} + \hat{f}_{D_m}/f_c) \cdot N_s T_s, \tag{4}$$

where f_c is the carrier frequency of the received signal and N_s is the number of samples per subaccumulation.

IV. NAVIGATION FRAMEWORK

This section presents a navigation framework, in which an EKF is deployed to estimate the UAV's position using 5G carrier phase measurements.

A. 5G Carrier Phase Measurements

As discussed in Subsection III-B, the carrier phase estimate is obtained as shown in (3). Then the pseudorange estimate corresponding to the u-th gNB $\rho^{(u)}$ can therefore be deduced by multiplying the carrier phase estimate by the wavelength $\lambda^{(u)} = \frac{c}{f_c^{(u)}}$, where c is the speed of light. The pseudorange between the receiver and the u-th gNB at the n-th time-step can be modeled as

$$\rho^{(u)}(n) = \|\boldsymbol{r}_r(n) - \boldsymbol{r}_{s,u}\|_2 + c \cdot [\delta t_r(n) - \delta t_{s,u}(n)] + \nu_u(n), \quad n = 1, 2, \cdots, \tag{5}$$

where in the model above,the term $\lambda^{(u)}\theta_0$ is lumped in the initial relative clock bias, $\boldsymbol{r}_r = [x_r, y_r, z_r]^{\mathsf{T}}$ is the receiver's 3-D position vector, $\boldsymbol{r}_{s,u} = [x_{s,u}, y_{s,u}, z_{s,u}]^{\mathsf{T}}$ is the u-th gNB's 3-D position vector, δt_r is the receiver's clock bias, $\delta t_{s,u}$ is the gNB's clock bias, and ν_u is the measurement noise, which is modeled as a zero-mean, white Gaussian random sequence with variance σ_2^u. The gNBs positions $\{\boldsymbol{r}_{s,u}\}_{u=1}^{U}$ are assumed to be known, e.g., from radio mapping or cloud-hosted databases.

B. EKF Implementation

The EKF state vector consists of the receiver's position and velocity, and the relative clock bias and drift between the receiver and each gNB, given by

$$\boldsymbol{x} \triangleq \left[\boldsymbol{x}_r^{\mathsf{T}}, \boldsymbol{x}_{\mathrm{clk}}^{\mathsf{T}}\right]^{\mathsf{T}},$$

where $\boldsymbol{x}_r = \left[\boldsymbol{r}_r^{\mathsf{T}}, \dot{\boldsymbol{r}}_r^{\mathsf{T}}\right]$ and $\boldsymbol{x}_{\mathrm{clk}}$ is the clock state vector $\boldsymbol{x}_{\mathrm{clk}}$ defined as $\boldsymbol{x}_{\mathrm{clk}} \triangleq \left[c\Delta\delta t_1, c\Delta\dot{\delta} t_1, \cdots, c\Delta\delta t_U, c\Delta\dot{\delta} t_U\right]^{\mathsf{T}}$, where $\{\Delta\delta t_u \triangleq \delta t_r - \delta t_{s,u}\}_{u=1}^{U}$ and $\{\Delta\dot{\delta} t_u \triangleq \dot{\delta} t_r - \dot{\delta} t_{s,u}\}_{u=1}^{U}$ are the relative clock bias and drift between the receiver and the u-th gNB. The clock error dynamics are assumed to evolve according to the following discrete-time dynamics

$$\boldsymbol{x}_{\mathrm{clk}_j}(n+1) = \mathbf{F}_{\mathrm{clk}} \boldsymbol{x}_{\mathrm{clk}_j}(n) + \boldsymbol{w}_{\mathrm{clk}_j}(n),$$

where

$$\boldsymbol{x}_{\mathrm{clk}_j} \triangleq \begin{bmatrix} c\delta t_j \\ c\dot{\delta} t_j \end{bmatrix}, \quad \mathbf{F}_{\mathrm{clk}} = \begin{bmatrix} 1 & T \\ 0 & 1 \end{bmatrix}, \quad \boldsymbol{w}_{\mathrm{clk}_j} = \begin{bmatrix} w_{\delta t_j} \\ w_{\dot{\delta} t_j} \end{bmatrix}, \quad \text{for } j \in \{r, s_u\},$$

where $T \equiv T_f$ is the measurement's sampling time and $\boldsymbol{w}_{\mathrm{clk}_j}$ is the process noise, which is modeled as a discrete-time zero-mean white sequence with covariance $\mathbf{Q}_{\mathrm{clk}_j}$ with

$$\mathbf{Q}_{\mathrm{clk}_j} \triangleq c^2 \cdot \begin{bmatrix} S_{\tilde{w}_{\delta t_j}} T + S_{\tilde{w}_{\dot{\delta} t_j}} \frac{T^3}{3} & S_{\tilde{w}_{\delta t_j}} \frac{T^2}{2} \\ S_{\tilde{w}_{\dot{\delta} t_j}} \frac{T^2}{2} & S_{\tilde{w}_{\dot{\delta} t_j}} T \end{bmatrix},$$

where $S_{\tilde{w}_{\delta t,j}}$ and $S_{\tilde{w}_{\dot{\delta} t,j}}$ are the clock bias and drift process noise power spectra, respectively. The values of $S_{\tilde{w}_{\delta t,j}}$ and $S_{\tilde{w}_{\dot{\delta} t,j}}$ depend on the clock's quality [20].

The receiver is assumed to move in a 2-D plane with a constant known height $z_r \equiv z_0$. The receiver's motion is assumed to evolve according to a nearly constant velocity dynamics, i.e.,

$$\ddot{\boldsymbol{r}}(t) = \tilde{\boldsymbol{w}},$$

where $\tilde{\boldsymbol{w}}$ is a process noise vector, which is modeled as zero-mean white random process with power spectral density $\tilde{\mathbf{Q}}_{\text{ped}} = \text{diag}[\tilde{q}_x, \tilde{q}_y]$, where $\tilde{q}_x$ and $\tilde{q}_y$ are the power spectral densities of the acceleration in the $x-$ and $y-$ directions, respectively [40]. The receiver's discrete-time dynamics are hence given by

$$\boldsymbol{x}_r(i+1) = \mathbf{F}_r \boldsymbol{x}_r(i) + \boldsymbol{w}_r(i),$$

where

$$\boldsymbol{x} \triangleq \begin{bmatrix} x_r \\ y_r \\ \dot{x}_r \\ \dot{y}_r \end{bmatrix}, \quad \mathbf{F}_r = \begin{bmatrix} 1 & 0 & T & 0 \\ 0 & 1 & 0 & T \\ 0 & 0 & 1 & 0 \\ 0 & 0 & 0 & 1 \end{bmatrix},$$

and $\boldsymbol{w}_r$, the process noise, which is modeled as a discrete-time zero-mean white sequence with covariance $\mathbf{Q}_r$, where

$$\mathbf{Q}_r = \begin{bmatrix} \tilde{q}_x \frac{T^3}{3} & 0 & \tilde{q}_x \frac{T^2}{2} & 0 \\ 0 & \tilde{q}_y \frac{T^3}{3} & 0 & \tilde{q}_y \frac{T^2}{2} \\ \tilde{q}_x \frac{T^2}{2} & 0 & \tilde{q}_x T & 0 \\ 0 & \tilde{q}_y \frac{T^2}{2} & 0 & \tilde{q}_y T \end{bmatrix}.$$

V. EXPERIMENTAL RESULTS

This section validates the proposed cellular 5G opportunistic navigation receiver and the navigation framework experimentally on a UAV in an urban environment using ambient 5G signals.

A. Experimental Setup and Environmental Layout

An experiment was conducted in Santa Ana, California, USA. In the experiment, the navigator was an Autel Robotics X-Star Premium UAV equipped with a single-channel Ettus 312 USRP connected to a consumer-grade 800/1900 MHz cellular antenna and a small consumer-grade GPS antenna to discipline the on-board oscillator. The cellular receivers were tuned to the cellular carrier frequency 632.55 MHz, which is a 5G frequency allocated to the U.S. cellular provider T-Mobile. The Samples of the received signals were stored for off-line postprocessing with a sampling ratio of 10 MSps. The ground-truth reference trajectory was taken from the on-board Ettus 312 universal software radio peripheral (USRP) GPS solution. The UAV traversed a trajectory of 500 m in 145 seconds. Figures 2 and 3 show the experimental setup and the environment layout, respectively.

Fig. 2. Experimental setup.

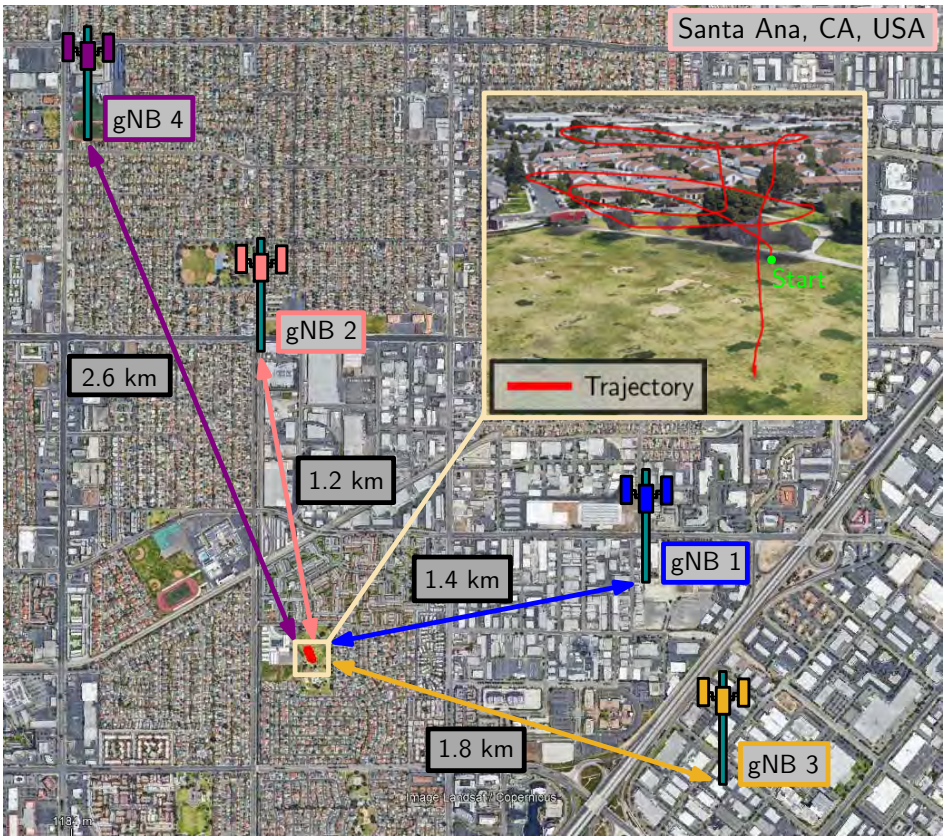

Fig. 3. Environment layout and UAV trajectory.

B. Receiver Output

Next, the signal acquisition stage was applied to detect the ambient 5G signals. Based on experimental data, the Doppler frequency search window was chosen to be between -25 and 25 Hz. The code start time search window was chosen to be one code interval with a delay spacing of one sample. Four gNBs were detected, three of which were hearable starting at $t_n = 0$ seconds, and a fourth gNB was hearable at $t_n = 25$ seconds. The gNBs' positions were mapped prior to the experiment.

In the tracking stage, the noise-equivalent bandwidths $B_{n,\text{PLL}}$ and $B_{n,\text{DLL}}$ were chosen to be 6 Hz and 0.05 Hz, respectively. Fig. 4 shows cellular 5G signal tracking results of the four gNBs including: (i) carrier-to-noise ratio (CNR), (ii) Doppler frequency estimate in solid lines versus expected Doppler obtained using the UAV's ground-truth reference in dashed lines, (iii) Pseudorange estimate in solid lines versus expected range in dashed lines after removing the initial bias, and (iv) range error estimate in solid lines versus measured error in dashed lines.

C. Navigation Solution

The UAV traversed a distance of 500 m in 145 seconds. The receiver's position and velocity state vectors and their corresponding covariances were initialized using the output of the Ettus 312 USRP GPS solution. The initial relative clock biases were eliminated, i.e., the EKF's relative clock biases were initialized to zero. The first two 5G measurements were dropped, where the first two position from the Ettus 312 GPS solution were used to initialize the relative clock drifts. Table III presents the EKF settings.

Fig. 5 shows the navigation solution of the USS-based 5G receiver versus the Ettus 312 GPS solution. The proposed receiver yielded a UAV position RMSE of 3.35 m.

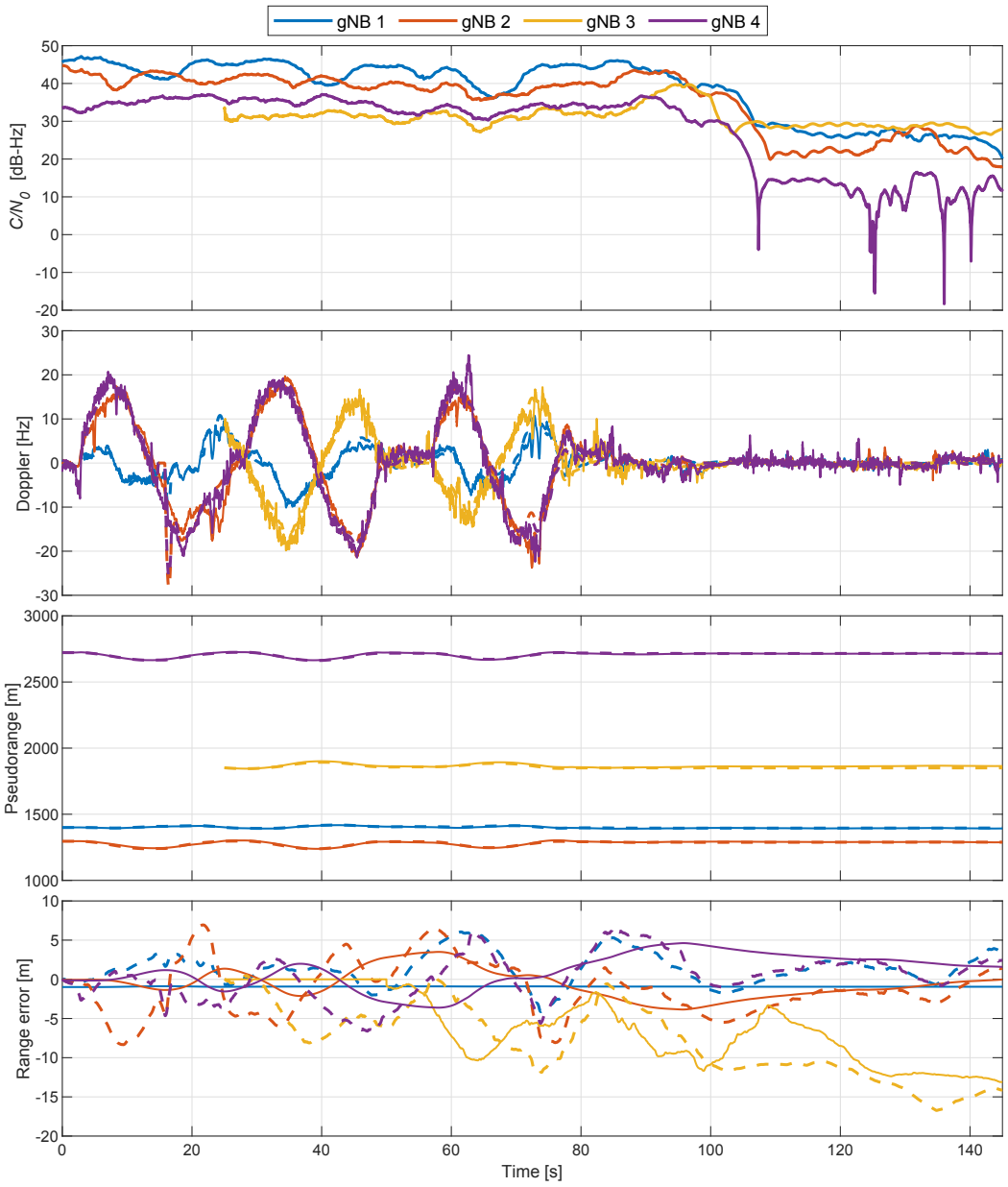

Fig. 4. Cellular 5G signal tracking results of the four gNBs showing: (i) carrier-to-noise ratio (CNR), (ii) Doppler frequency estimate in solid lines versus expected Doppler obtained using the UAV's ground-truth reference in dashed lines, (iii) Pseudorange estimate in solid lines versus expected range in dashed lines after removing the initial bias, and (iv) range error estimate in solid lines versus measured error in dashed lines.

VI. CONCLUSION

This paper presented a 5G opportunistic navigation framework using 5G carrier phase. A 5G SDR was presented, in which the 5G time-domain orthogonality is utilized to combine all available resources in the received 5G signal into one ultimate signal, denoted by USS. The proposed 5G SDR includes two stages: (i) the acquisition stage in which only unique 5G resources (i.e., SSS and PBCH DM-RS) are utilized to detect the hearable gNBs and (ii) the tracking stage in which the entire USS is utilized to produce 5G navigation observable. An EKF was implemented to process the observables and estimate the UE's position and velocity, along with the relative clock bias and drift between the receiver and each gNB. An experiment was conducted on a UAV to assess the navigation performance of the proposed framework. In the experiment, the UAV-mounted receiver navigated using 5G signals from four gNBs

TABLE III
EKF Settings.

Component	Parameter(s)
UAV's motion	$\{\tilde{q}_x, \tilde{q}_y\} \equiv \{1, 1\}\,(\mathrm{m}^2/\mathrm{s}^3)$
UAV's clock	$\left\{S_{\tilde{w}_{\delta t_j}}, S_{\tilde{w}_{\dot{\delta} t_j}}\right\} \equiv \left\{1.3 \times 10^{-22}, 7.9 \times 10^{-25}\right\}$
gNB 1	$\left\{S_{\tilde{w}_{\delta t_j}}, S_{\tilde{w}_{\dot{\delta} t_j}}\right\} \equiv \left\{1.3 \times 10^{-22}, 7.9 \times 10^{-25}\right\}$
gNBs 2,3, and 4	$\left\{S_{\tilde{w}_{\delta t_j}}, S_{\tilde{w}_{\dot{\delta} t_j}}\right\} \equiv \left\{4 \times 10^{-20}, 7.9 \times 10^{-22}\right\}$

Fig. 5. The 5G navigation solution exhibited a position RMSE of 3.35 m versus the ground-truth reference navigation solution. Image: Google Earth.

for 500 m in 145 seconds. The proposed framework exhibited a position RMSE of 3.35 m, while listening to signals from one cellular provider.

ACKNOWLEDGMENT

The authors would like to thank Moahamad Orabi for his help in data collection. This work was supported in part by the Office of Naval Research (ONR) under Grant N00014-19-1-2511 and Grant N00014-19-1-2613, in part by the U.S. Department of Transportation (USDOT) under Grant 69A3552047138 for the CARMEN University Transportation Center (UTC), and in part under the financial assistance award 70NANB17H192 from U.S. Department of Commerce, National Institute of Standards and Technology (NIST).

References

[1] L. Carrillo, A. López, R. Lozano, and C. Pégard, "Combining stereo vision and inertial navigation system for a quad-rotor UAV," *Journal of Intelligent & Robotic Systems*, vol. 65, no. 1, pp. 373–387, 2012.

[2] J. Gross, Y. Gu, and M. Rhudy, "Robust uav relative navigation with DGPS, INS, and peer-to-peer radio ranging," *IEEE Transactions on Aerospace and Electronic Systems*, vol. 12, no. 3, pp. 935–944, July 2015.

[3] B. Schnaufer, P. Hwang, J. Nadke, G. McGraw, and D. Venable, "Collaborative image navigation simulation and analysis for UAVs in GPS challenged conditions," in *Proceedings of IEEE/ION Position Location and Navigation Symposium*, April 2012, pp. 719–729.

[4] N. Mandel, F. Alvarez, M. Milford, and F. Gonzalez, "Towards simulating semantic onboard UAV navigation," in *Proceedings of the IEEE Aerospace Conference*, 2020, pp. 1–15.

[5] J. Kim, I. Bae, C. Quan, S. Lee, W. Son, J. Rhee, S. Kim, and J. Seo, "Collaborative navigation of UAV and UGV using vision and LIDAR sensors," in *Proceedings of ION Pacific PNT Meeting*, April 2013, pp. 762–768.

[6] T. Gee, J. James, W. V. D. Mark, P. Delmas, and G. Gimel'farb, "Lidar guided stereo simultaneous localization and mapping (SLAM) for UAV outdoor 3-D scene reconstruction," in *International Conference on Image and Vision Computing*, November 2016, pp. 1–6.

[7] Y. Zhuang, Y. Li, H. Lan, Z. Syed, and N. El-Sheimy, "Wireless access point localization using nonlinear least squares and multi-level quality control," *IEEE Wireless Communications Letters*, vol. 4, no. 6, pp. 693–696, 2015.

[8] T. Kazaz, G. Janssen, J. Romme, and A. Van der Veen, "Delay estimation for ranging and localization using multiband channel state information," *IEEE Transactions on Wireless Communications*, pp. 1–16, September 2021.

[9] Y. Xu, Y. Shmaliy, Y. Li, and X. Chen, "UWB-based indoor human localization with time-delayed data using EFIR filtering," *IEEE Access*, vol. 5, pp. 16 676–16 683, 2017.

[10] Z. Koppanyi, C. Toth, and D. Grejner Brzezinska, "Scalable ad-hoc UWB network adjustment," in *Proceedings of IEEE/ION Position, Location, and Navigation Symposium*, April 2018, pp. 1502–1508.

[11] M. Driusso, F. Babich, F. Knutti, M. Sabathy, and C. Marshall, "Estimation and tracking of LTE signals time of arrival in a mobile multipath environment," in *Proceedings of International Symposium on Image and Signal Processing and Analysis*, September 2015, pp. 276–281.

[12] C. Yang and T. Nguyen, "Tracking and relative positioning with mixed signals of opportunity," *NAVIGATION, Journal of the Institute of Navigation*, vol. 62, no. 4, pp. 291–311, December 2015.

[13] M. Ulmschneider and C. Gentner, "Multipath assisted positioning for pedestrians using LTE signals," in *Proceedings of IEEE/ION Position, Location, and Navigation Symposium*, April 2016, pp. 386–392.

[14] Z. Kassas, M. Maaref, J. Morales, J. Khalife, and K. Shamaei, "Robust vehicular localization and map matching in urban environments through IMU, GNSS, and cellular signals," *IEEE Intelligent Transportation Systems Magazine*, vol. 12, no. 3, pp. 36–52, June 2020.

[15] J. del Peral-Rosado, O. Renaudin, C. Gentner, R. Raulefs, E. Dominguez-Tijero, A. Fernandez-Cabezas, F. Blazquez-Luengo, G. Cueto-Felgueroso, A. Chassaigne, D. Bartlett, F. Grec, L. Ries, R. Prieto-Cerdeira, J. Lopez-Salcedo, and G. Seco-Granados, "Physical-layer abstraction for hybrid GNSS and 5G positioning evaluations," in *Proceedings of IEEE Vehicular Technology Conference*, September 2019, pp. 1–6.

[16] H. Benzerrouk, Q. Nguyen, F. Xiaoxing, A. Amrhar, A. Nebylov, and R. Landry, "Alternative PNT based on Iridium Next LEO satellites Doppler/INS integrated navigation system," in *Proceedings of Saint Petersburg International Conference on Integrated Navigation Systems*, May 2019, pp. 1–10.

[17] Z. Kassas, J. Morales, and J. Khalife, "New-age satellite-based navigation – STAN: simultaneous tracking and navigation with LEO satellite signals," *Inside GNSS Magazine*, vol. 14, no. 4, pp. 56–65, 2019.

[18] C. Yang, T. Nguyen, and E. Blasch, "Mobile positioning via fusion of mixed signals of opportunity," *IEEE Aerospace and Electronic Systems Magazine*, vol. 29, no. 4, pp. 34–46, April 2014.

[19] M. Driusso, C. Marshall, M. Sabathy, F. Knutti, H. Mathis, and F. Babich, "Indoor positioning using LTE signals," in *Proceedings of International Conference on Indoor Positioning and Indoor Navigation*, October 2016, pp. 1–8.

[20] Z. Kassas, "Position, navigation, and timing technologies in the 21st century," J. Morton, F. van Diggelen, J. Spilker, Jr., and B. Parkinson, Eds. Wiley-IEEE, 2021, vol. 2, ch. 37: Navigation with Cellular Signals of Opportunity, pp. 1171–1223.

[21] C. Gentner, E. Munoz, M. Khider, E. Staudinger, S. Sand, and A. Dammann, "Particle filter based positioning with 3GPP-LTE in indoor environments," in *Proceedings of IEEE/ION Position, Location and Navigation Symposium*, April 2012, pp. 301–308.

[22] M. Maaref and Z. Kassas, "Ground vehicle navigation in GNSS-challenged environments using signals of opportunity and a closed-loop map-matching approach," *IEEE Transactions on Intelligent Transportation Systems*, vol. 21, no. 7, pp. 2723–2723, July 2020.

[23] A. Abdallah and Z. Kassas, "Deep learning-aided spatial discrimination for multipath mitigation," in *Proceedings of IEEE/ION Position, Location, and Navigation Symposium*, April 2020, pp. 1324–1335.

[24] C. Yang and A. Soloviev, "Mobile positioning with signals of opportunity in urban and urban canyon environments," in *IEEE/ION Position, Location, and Navigation Symposium*, April 2020, pp. 1043–1059.

[25] J. Khalife, K. Shamaei, S. Bhattacharya, and Z. Kassas, "Centimeter-accurate UAV navigation with cellular signals," in *Proceedings of ION GNSS Conference*, September 2018, pp. 2321–2331.

[26] K. Shamaei and Z. Kassas, "Sub-meter accurate UAV navigation and cycle slip detection with LTE carrier phase," in *Proceedings of ION GNSS Conference*, September 2019, pp. 2469–2479.

[27] A. Abdallah, J. Khalife, and Z. Kassas, "Experimental characterization of received 5G signals carrier-to-noise ratio in indoor and urban environments," in *Proceedings of IEEE Vehicular Technology Conference*, April 2021, pp. 1–5.

[28] X. Cui, T. Gulliver, J. Li, and H. Zhang, "Vehicle positioning using 5G millimeter-wave systems," *IEEE Access*, vol. 4, pp. 6964–6973, 2016.

[29] N. Garcia, H. Wymeersch, E. Larsson, A. Haimovich, and M. Coulon, "Direct localization for massive MIMO," *IEEE Transactions on Signal Processing*, vol. 65, no. 10, pp. 2475–2487, May 2017.

[30] K. Han, Y. Liu, Z. Deng, L. Yin, and L. Shi, "Direct positioning method of mixed far-field and near-field based on 5G massive MIMO system," *IEEE Access*, vol. 7, pp. 72 170–72 181, 2019.

[31] L. Yin, Q. Ni, and Z. Deng, "A GNSS/5G integrated positioning methodology in D2D communication networks," *IEEE Transactions on Signal Processing*, vol. 36, no. 2, pp. 351–362, February 2018.

[32] A. Tobie, A. Garcia-Pena, P. Thevenon, J. Vezinet, and M. Aubault, "Hybrid navigation filters performances between GPS, Galileo and 5G TOA measurements in multipath environment," in *Proceedings of ION GNSS Conference*, 2020, pp. 2107–2140.

[33] M. Koivisto, M. Costa, J. Werner, K. Heiska, J. Talvitie, K. Leppanen, V. Koivunen, and M. Valkama, "Joint device positioning and clock synchronization in 5G ultra-dense networks," *IEEE Transactions on Wireless Communications*, vol. 16, no. 5, pp. 2866–2881, May 2017.
[34] C. Guo, J. Yu, W. Guo, Y. Deng, and J. Liu, "Intelligent and ubiquitous positioning framework in 5G edge computing scenarios," *IEEE Access*, vol. 8, pp. 83 276–83 289, 2020.
[35] K. Shamaei and Z. Kassas, "Receiver design and time of arrival estimation for opportunistic localization with 5G signals," *IEEE Transactions on Wireless Communications*, vol. 20, no. 7, pp. 4716–4731, 2021.
[36] A. Abdallah, K. Shamaei, and Z. Kassas, "Assessing real 5G signals for opportunistic navigation," in *Proceedings of ION GNSS Conference*, 2020, pp. 2548–2559.
[37] Z. Kassas, A. Abdallah, and M. Orabi, "Carpe signum: seize the signal – opportunistic navigation with 5G," *Inside GNSS Magazine*, vol. 16, no. 1, pp. 52–57, 2021.
[38] 3GPP, "Physical channels and modulation," https://www.etsi.org/deliver/etsi-ts/138200-138299/138211/15.02.00-60/ts-138211v150200p.pdf, 5G; NR; 3rd Generation Partnership Project (3GPP), TS 38.211, July 2018.
[39] P. Misra and P. Enge, *Global Positioning System: Signals, Measurements, and Performance*, 2nd ed. Ganga-Jamuna Press, 2010.
[40] X. Li and V. Jilkov, "Survey of maneuvering target tracking. Part I: Dynamic models," *IEEE Transactions on Aerospace and Electronic Systems*, vol. 39, no. 4, pp. 1333–1364, 2003.

Universal Receiver Architecture for Blind Navigation with Partially Known Terrestrial and Extraterrestrial Signals of Opportunity

Joe Khalife, M. Neinavaie, and Zaher M. Kassas
University of California, Irvine

BIOGRAPHIES

Joe Khalife is a postdoctoral fellow at the University of California, Irvine and member of the Autonomous Systems Perception, Intelligence, and Navigation (ASPIN) Laboratory. He received a B.E. in Electrical Engineering, an M.S. in Computer Engineering from the Lebanese American University and a Ph.D. in Electrical Engineering and Computer Science from the University of California, Irvine. From 2012 to 2015, he was a research assistant at LAU, and has been a member of the ASPIN Laboratory since 2015. He is a recipient of the 2016 IEEE/ION Position, Location, and Navigation Symposium (PLANS) Best Student Paper Award and the 2018 IEEE Walter Fried Award. His research interests include opportunistic navigation, autonomous vehicles, and software-defined radio.

Mohammad Neinavaie is a Ph.D. student at the University of California, Irvine and member of the Autonomous Systems Perception, Intelligence, and Navigation (ASPIN) Laboratory. He received a B.E. in electrical engineering and an M.S. in digital communication systems from Shiraz University. His research interests include opportunistic navigation, blind opportunistic navigation, cognitive radio, wireless communication systems and software-defined radio.

Zaher (Zak) M. Kassas is an associate professor at the University of California, Irvine and director of the Autonomous Systems Perception, Intelligence, and Navigation (ASPIN) Laboratory. He is also director of the U.S. Department of Transportation Center: CARMEN (Center for Automated Vehicle Research with Multimodal AssurEd Navigation), focusing on navigation resiliency and security of highly automated transportation systems. He received a B.E. in Electrical Engineering from the Lebanese American University, an M.S. in Electrical and Computer Engineering from The Ohio State University, and an M.S.E. in Aerospace Engineering and a Ph.D. in Electrical and Computer Engineering from The University of Texas at Austin. He is a recipient of the 2018 National Science Foundation (NSF) Faculty Early Career Development Program (CAREER) award, 2019 Office of Naval Research (ONR) Young Investigator Program (YIP) award, 2018 IEEE Walter Fried Award, 2018 Institute of Navigation (ION) Samuel Burka Award, and 2019 ION Col. Thomas Thurlow Award. His research interests include cyber-physical systems, estimation theory, navigation systems, autonomous vehicles, and intelligent transportation systems.

ABSTRACT

A universal receiver architecture that is capable of exploiting partially known signals of opportunity (SOPs) for navigation is presented. A partially known signal refers to a signal to which only the center frequency and bandwidth are known to the receiver. Assuming that the SOP follows a standard modulation scheme, e.g., phase shift keying (PSK) or quadrature amplitude modulation (QAM), and a standard multiplexing scheme, e.g., code-division multiple access (CDMA) or orthogonal frequency-division multiplexing (OFDM), the proposed receiver architecture can blindly acquire and track the SOP to provide a navigation solution. Experimental results are presented showing the proposed receiver successfully producing meter-level-accurate navigation solutions from different types of terrestrial and space signals: GPS, cellular 4G long-term evolution (LTE) and 5G, and Starlink LEO satellites, under the aforementioned partially known assumption.

I. INTRODUCTION

Meter-level accurate ground and aerial vehicular navigation with terrestrial signals of opportunity (SOPs) have been demonstrated in the recent years [1–9]. In addition to the demonstrated remarkable potential of SOPs as complement or alternative to global navigation satellite systems (GNSS), especially in challenging environments, plans of private

Copyright © 2021 by Z. M. Kassas

Preprint of the 2021 ION GNSS+ Conference
St. Louis, Missouri, September 20–24, 2021

companies such as OneWeb, SpaceX, and Boeing to launch thousands of broadband Internet satellites into low Earth orbit (LEO) will trigger a renaissance in navigation with SOPs [10, 11]. Several theoretical and experimental studies characterized broadband LEO satellite signals as potential reliable sources for navigation [12–18]. Much like cellular signals, the most attractive attributes of LEO satellite signals are mainly their abundance and diversity in geometry and frequency [19–21]. This diversity increases the availability of a navigation system and provides immunity against interference, jamming, and spoofing. However, one must emphasize that the major underlying assumption in existing SOP navigation frameworks is that the structure of these SOPs is known at the receiver side [22]. Many of the LEO broadband communication systems are using proprietary protocols and have made barely any information about their signal structure available. Similarly, there are several reference signals in 4G long-term evolution (LTE) and 5G new radio (NR) systems that are not exploited by current opportunistic receivers, as these typically high-bandwidth references signals are either unknown to these opportunistic receivers or are only transmitted on demand [23, 24]. A natural question arises from the unknown nature of the upcoming LEO broadband and some of the cellular reference signals: is it possible to still exploit these unknown signals for navigation purposes? This paper aims at answering this question by proposing a computationally-efficient universal receiver architecture that can extract navigation observables from any partially known signal with a periodic beacon.

A partially known signal here refers to a signal to which only the center frequency and bandwidth are known to the receiver, and a periodic beacon refers to a sequence of any kind that is periodically transmitted for synchronization, channel estimation, or positioning purposes [25]. Assuming that the SOP follows a standard modulation scheme, e.g., phase shift keying (PSK) or quadrature amplitude modulation (QAM), and a standard multiplexing scheme, e.g., code-division multiple access (CDMA) or orthogonal frequency-division multiplexing (OFDM), the proposed receiver architecture can blindly acquire and track the signal to provide a navigation solution. Most communication systems employ a synchronization beacon for receiver timing and carrier recovery. For example, in cellular CDMA, pseudorandom noise (PN) sequences are used on the forward-link pilot channel for synchronization proposes [26]. Other examples of such beacons are the primary synchronization signal (PSS) and secondary synchronization signal (SSS) in 4G LTE and 5G NR systems. Even though different broadband providers may use known modulation schemes, their underlying configuration and parameters can be different. For instance, the Globalstar satellite system uses similar protocol to the IS-95 cellular CDMA system but with different PN sequences [26, 27]. Without knowing these PN sequences, a standard opportunistic receiver cannot draw navigation observables from these signals. As such, a crucial stage in the architecture of the proposed universal receiver is to blindly estimate the unknown beacon sequence of the SOP on-the-fly.

The problem of discovering the unknown signal characteristics has been considered in both communications and navigation literature for CDMA and OFDM signals, e.g., see [28–37]. The algorithms for blindly detecting synchronization sequences proposed in the communications literature rely on coherently integrating samples of the transmitted signals [28, 29, 31–34]. However, such approaches do not account for the time-varying Doppler shifts and delays, especially for LEO-based signals, which make it impossible to accumulate enough signal power to detect the beacon signal. Alternative approaches make use of high-gain antennas to accumulate enough signal power for PN sequence detection [31]. In contrast with these approaches, the proposed receiver has the flexibility of *cognitively* detecting the unknown beacon of any broadband signal using a particular communication standard, e.g. CDMA or OFDM. Therefore, unlike [31], which concentrates on deciphering one particular system, the proposed receiver is universal and capable of cognitively deciphering beacons of partially known SOPs in a computationally-efficient way and in turn produce Doppler and pseudorange measurements.

The two main factors defining the proposed receiver architecture are (i) the periodicity and (ii) the correlation properties of the beacon sequence. Exploiting the "desirable" correlation properties of the beacon sequence allows the proposed receiver to track the beacon's Doppler and phase as it is repeated over time. While this may seem intuitive for CDMA signals, it applies to a larger family of signals as well, including OFDM signals. OFDM is widely adopted in different communication generations such as 4G LTE and 5G NR communication systems and attracted a lot of attention in opportunistic navigation systems. It is also anticipated that OFDM will be used in future LEO megaconstellations such as SpaceX's Starlink constellation [20]. In OFDM systems, data symbols are mapped onto multiple carrier frequencies called subcarriers. The serial data symbols are first parallelized in groups. Then, each group is zero-padded to make the data vector length an even power of two, and an inverse fast Fourier transform (IFFT) is taken. The zero-padding provides a guard band in the frequency-domain. Finally, to protect the data from multipath effects, the last few symbols are repeated at the beginning of the data, which are called the cyclic

prefix (CP). The transmitted symbols can be obtained at the receiver by executing these steps in reverse order. A traditional LTE or NR opportunistic receiver would use a local replica of the known PSS and SSS to correlate with the received signals and recover timing and the frame structure. In the case where these sequences are unknown, as in the case of future broadband LEO satellite systems or some of the on-demand reference signals in 5G NR signals, acquiring and tracking of these SOPs becomes impossible unless the receiver blindly and adaptively estimates these sequences. As such, the often forgotten time-domain orthogonality of OFDM signals is exploited to jointly estimate all the reference signals contained within the received OFDM signal, without the need to reconstruct the frame. This shortcut alleviates a significant computational burden. A similar approach is used for other types of signals, e.g., CDMA. Another important part of the proposed receiver are traditional phase-locked loops (PLLs) and delay-locked loops (DLLs) to track the carrier and code phases of the estimated beacon sequence. However, it will be shown that the estimated Doppler will have an ambiguity that is an integer multiple of some fundamental frequency inherent to the signal. This ambiguity needs to be resolved to perform proper carrier tracking and aiding.

This paper extends the work in [38] and [39] through the following contributions. First, a universal signal model for blind Doppler and code phase tracking is derived from standard signal models, namely CDMA and OFDM. Second, a receiver architecture capable of estimating the unknown beacon sequences and produce Doppler and pseudorange measurements from the universal signal model is proposed. Third, extensive experimental results are presented showing successful tracking and navigation solution production from multiple sources using the proposed receiver for different types of signals: GPS, cellular 4G LTE and 5G, and Starlink LEO satellites, under the aforementioned partially known assumption.

The remainder of the paper is organized as follows. Section II presents the signal model. Section III overviews the proposed blind universal receiver architecture. Section IV characterizes and demonstrates the proposed receiver in producing a navigation solution with GPS, cellular 4G LTE and 5G signals, and Starlink LEO satellite signals. Section V gives concluding remarks.

II. SIGNAL MODEL

Let $x(t)$ be the unknown signal transmitted by a navigation source. The proposed framework does not assume any particular modulation or multiplexing scheme. The only assumptions are the following:

1. The transmitted signal $x(t)$ comprises M periodic synchronization signals $\{s_m(t)\}_{m=1}^{M}$, with the m-th signal having a period T_m. The total number of periodic signals M may be unknown. Furthermore, these periodic signals may be multiplexed in time, frequency, and/or code.
2. The periodic signals $\{s_m(t)\}_{m=1}^{M}$ have "nice" autocorrelation and cross-correlation properties, i.e.,

$$\begin{aligned} R_{s_m s_m}(\tau) &\triangleq \int_{-\frac{T_m}{2}}^{\frac{T_m}{2}} s_m(t+\tau) s_m^*(t) dt \\ &= \begin{cases} g_{\text{bell}_\text{m}}(\tau), & |\tau| \leq \gamma_m T_m, \\ g_{\text{tail}_\text{m}}(\tau), & \text{otherwise}, \end{cases} \end{aligned} \tag{1}$$

   where g_{bell_m} is a bell-shaped function, γ is a positive real number close to one, and $g_{\text{tail}_\text{m}}(\tau)$ is the tail of the autocorrelation function such as $|g_{\text{tail}_\text{m}}(\tau)| < \epsilon$ for all $|\tau| > \gamma_m T_m$, where ϵ is a small, positive real number; and

$$R_{s_m s_{m'}}(\tau) \triangleq \int_{-\frac{T_m+T_{m'}}{2}}^{\frac{T_m+T_{m'}}{2}} s_m(t+\tau) s_{m'}^*(t) dt, \quad m' \neq m, \tag{2}$$

   where $\left|R_{s_m s_{m'}}(\tau)\right| < \epsilon$, $\forall\, \tau$.

As such, $x(t)$ is modeled as,

$$x(t) = \sum_{n=-\infty}^{\infty} \sum_{m=1}^{M} s_m(t - nT_m) + y(t), \tag{3}$$

where $y(t)$ denotes the remaining, non-periodic signals in the original transmitted signal $x(t)$. Let T_0 denotes the least common multiplier of $\{T_m\}_{m=1}^{M}$. Subsequently, one can define a periodic signal $s(t)$ with period T_0 as

$$s(t) = \sum_{m=1}^{M} s_m(t). \tag{4}$$

The transmitted signal can now be expressed as

$$x(t) = \sum_{n=-\infty}^{\infty} s(t - nT_0) + y(t), \tag{5}$$

where $s(t)$ encompasses *all* periodic signals contained in $x(t)$.

Fig. 1 shows examples of synchronization sequences with correlation properties that satisfy (1) and (1): (a) the primary and secondary synchronization sequences (PSS and SSS, respectively) in 5G signals as well as the demodulation reference signal (DM-RS) and (b) a GPS L1 C/A pseudorandom noise (PRN) sequence as well as the downlink pseudo-noise (PN) sequence in cdma2000.

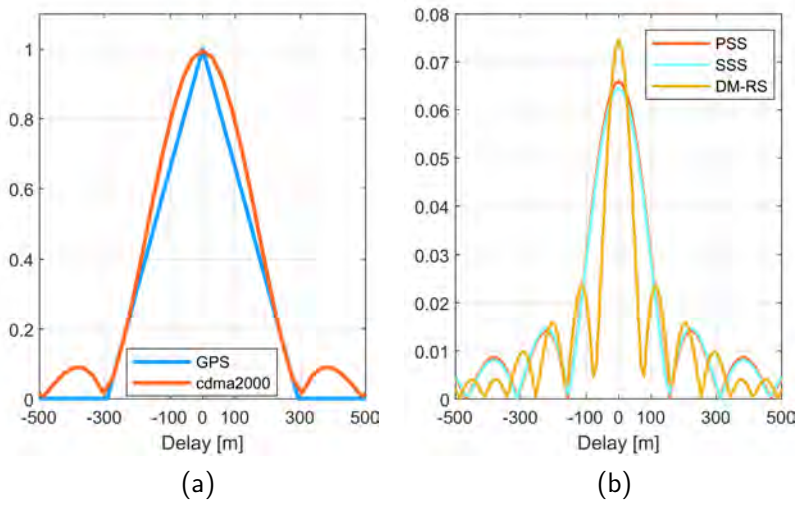

Fig. 1. Correlation function of (a) GPS C/A PRN and cellular cdma2000 PN and (b) cellular LTE/5G PSS and SSS and cellular 5G DM-RS.

III. Blind Universal Receiver Architecture

Fig. 2 shows a block diagram of the proposed universal receiver architecture. Similar to correlation-based receivers, the universal receiver consists of a phase-locked loop (PLL) and a delay-locked loop (DLL) to track the carrier and code phase of the synchronization sequence present in the received signal. The proposed receiver has two additional blocks: (i) a block that refines the estimate of the unknown synchronization sequence [38] and (ii) a block that resolves ambiguities in the estimated Doppler before switching to carrier aiding.

The receiver is initialized with a Doppler estimate that can be obtained in one of two ways: (i) using the maximum likelihood approach described in [24] or (ii) from the phase of the inner product of two consecutive received frames. Either way, the initial Doppler will have an ambiguity of $\frac{N}{T_0}$, where N is an integer. The initial Doppler estimate $\hat{f}_{D_0}$ can be expressed as follows:

$$\hat{f}_{D_0} = f_{D_0} + \frac{N}{T_0} + \epsilon_0,$$

where f_{D_0} is the true initial Doppler and ϵ_0 is the initial error due to noise. The Doppler estimate produced by the tracking loops will have the aforementioned ambiguity. To use the Doppler estimate for carrier aiding, the ambiguity

must be resolved. This can be performed by comparing the Doppler constructed by the delay estimate to the Doppler produced by the tracking loops. Once the Doppler ambiguity is resolved, the receiver can switch to carrier aiding to produce smooth code phase estimates.

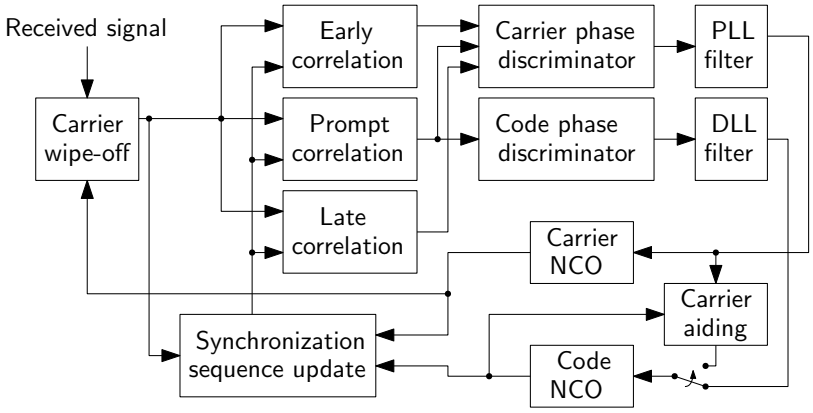

Fig. 2. Blind universal receiver architecture.

The above receiver is first tested to track a simulated Globalstar-like signal. The inner-product approach was used to initialize the Doppler. Fig. 3 summarizes the simulation results, which show that the Doppler and delay estimates converge to the true ones at varying carrier-to-noise ratios (CNRs). Fig 3 also shows the norm squared of the estimated sequence, $|S|^2$ which converges to its maximum at steady-state. Fig. 4 shows a scatterplot of the estimate sequence at varying CNRs.

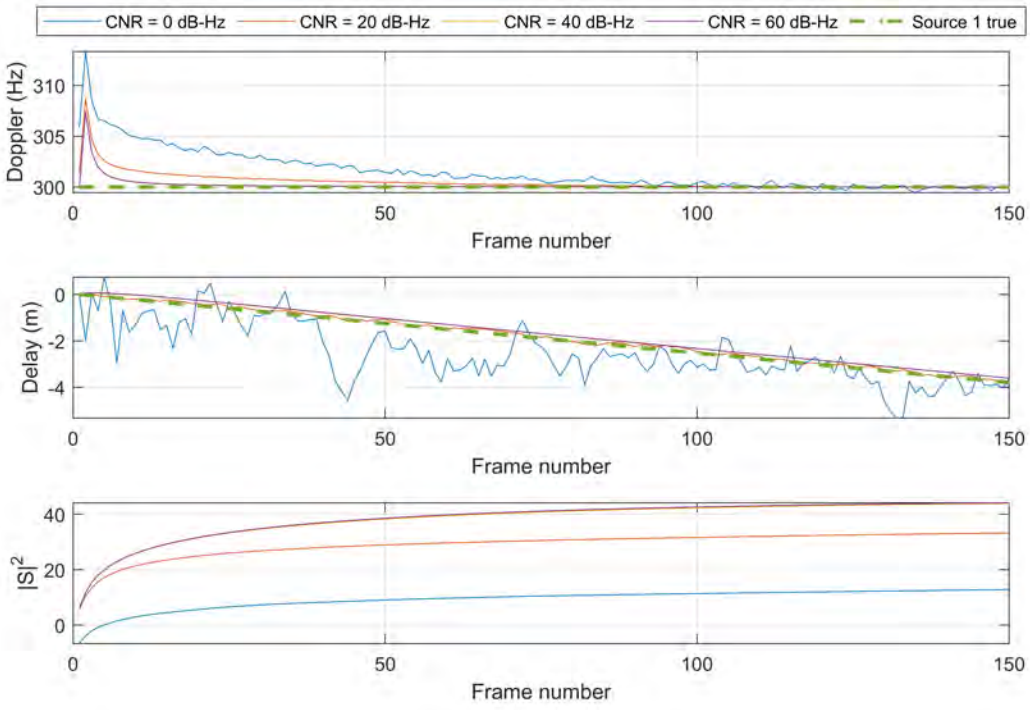

Fig. 3. Simulation results showing the Doppler and delay estimates converging to the true ones at varying CNRs. The figure also shows the norm squared of the estimated sequence, $|S|^2$ which converges to its maximum at steady-state.

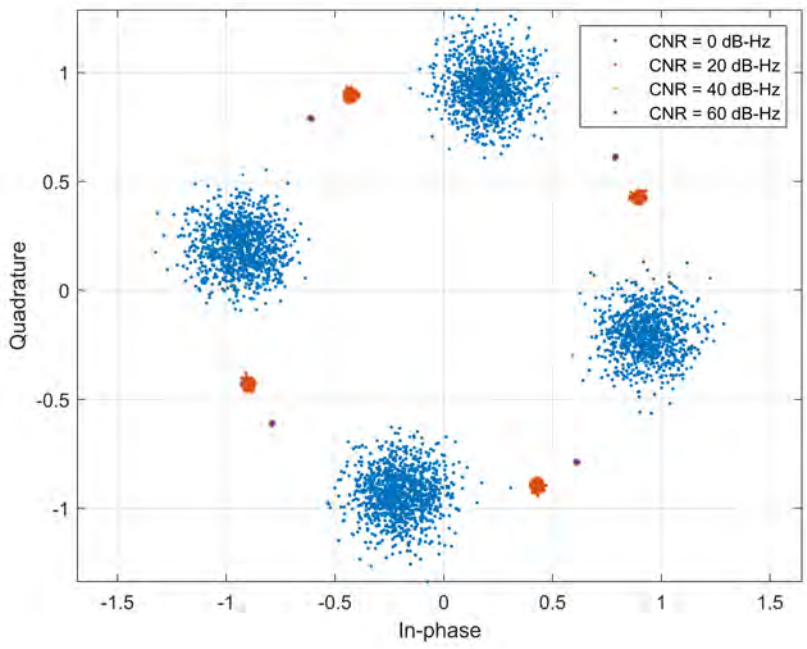

Fig. 4. Simulation results showing the estimated synchronization sequence at varying CNRs.

IV. EXPERIMENTAL RESULTS

This section shows experimental application of the blind universal cognitive receiver in producing a navigation solution with GPS L1 C/A signals, cellular 4G LTE and 5G signals, and Starlink LEO satellite signals.

A. GPS Signals

In order to test the proposed receiver with GPS L1 C/A signals, a GPS antenna which was mounted on the roof of the Winston Chung Hall at the University of California, Riverside, USA. The GPS signals were down-mixed and sampled via a National Instruments universal software radio peripheral (USRP), driven by a GPS-disciplined oscillator (GPSDO). The samples of the received signals were stored for off-line post-processing. The GPS L1 C/A signals contain PRN codes at 1.023 Mega chips per second (Mcps), modulated by binary PSK (BPSK) ($M = 2$) navigation bits at 50 bits per second (bps). Multiple GPS satellites transmit simultaneously in the same channel using CDMA. As such, the maximum likelihood approach in [24] was used to initialize the Doppler of four GPS satellites. The correlation function between the estimated and true PRNs of the 4 GPS satellites are shown in Fig. 5. The decoded PRNs are then used in an SDR to produce pseudorange measurements on GPS satellites and in turn solve for a stationary receiver's position. The acquisition and tracking results of PRN 21 are shown in Fig. 6. Note that the GPS signals were used opportunistically; hence, no clock corrections were performed and the satellites' positions were obtained by propagating the two-line element (TLE) files available for the visible satellites [38]. The final position error was found to be 54.5 m. The experimental layout and the true and estimated receiver positions are shown in Fig. 7.

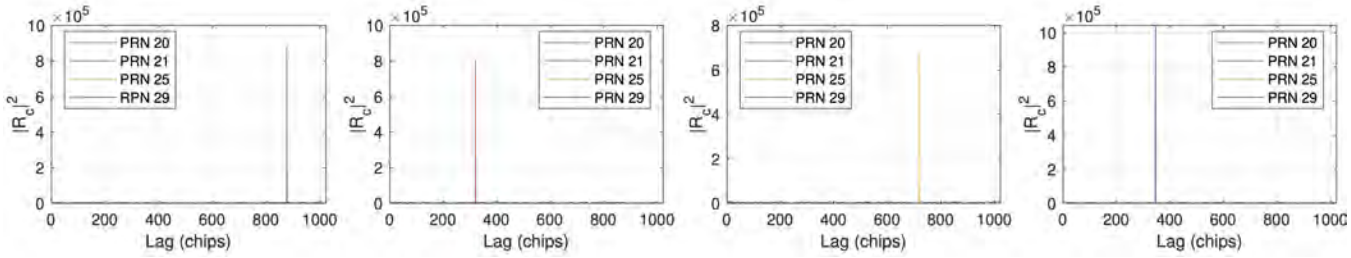

Fig. 5. Correlations between the decoded PRN of each GPS satellite and the true PRNs

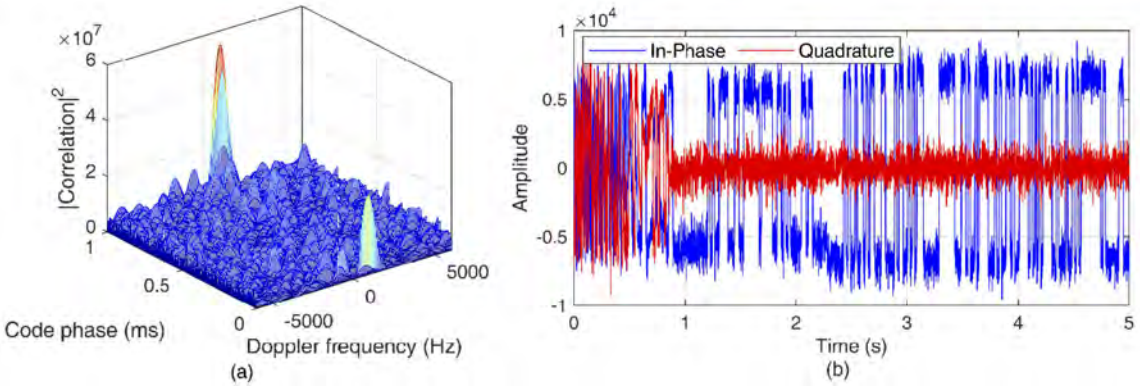

Fig. 6. GPS signal acquisition for PRN 21 using the decoded beacon. (b) Signal tracking of PRN 21 over a period of 5 seconds.

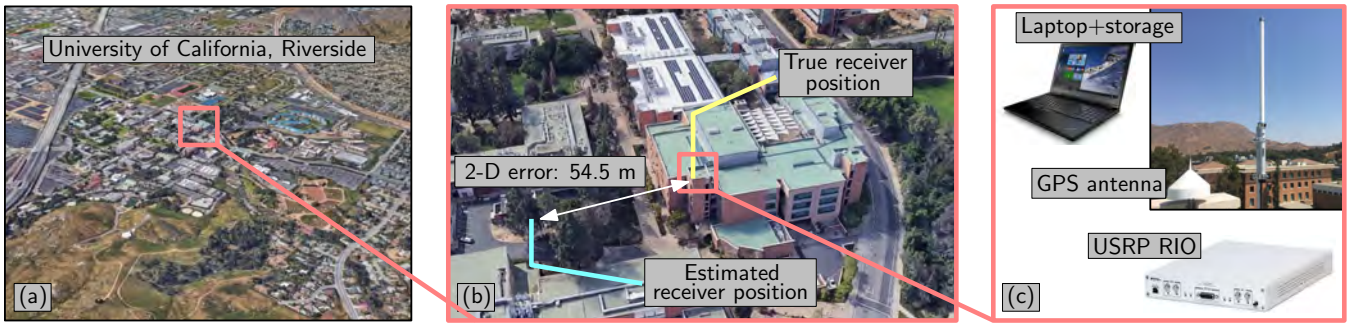

Fig. 7. (a) Experimental environment for GPS L1 C/A signals. (b) True and estimated receiver positions. (c) Experimental hardware setup.

B. Cellular 4G LTE Signals

In this experiment with LTE signals, a DJI Matrice 600 UAV was equipped with an NI USRP-2955 and four consumer grade 800/1900 MHz cellular antennas to sample LTE signals near Aliso Viejo, California, USA. The channels of the USRP were tuned to 1955, 2145, 2125, and 739 MHz carrier frequencies, respectively, which are 4G LTE frequencies allocated to the U.S. cellular providers AT&T, T-Mobile, and Verizon. The sampling rate for each channel was set to 10 MSps and the sampled LTE signals were stored on a laptop for post-processing. The UAV was equipped with a Septentrio GNSS-aided INS for ground-truth. The UAV traversed a trajectory of 609 m. Fig. 8 shows the environment layout and the UAV trajectory. The blind receiver was used to produce pseudorange and carrier phase measurements and estimate the UAV trajectory [24]. The position RMSE from both the blind receiver and a conventional receiver was found to be 2.07 m. Fig. 9 shows the true and estimated UAV trajectories.

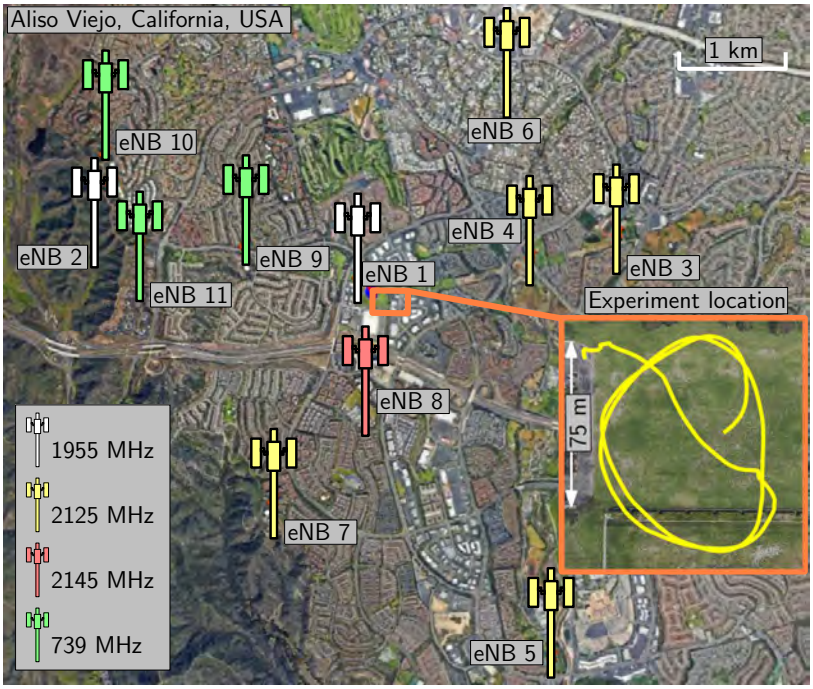

Fig. 8. LTE eNodeB layout.

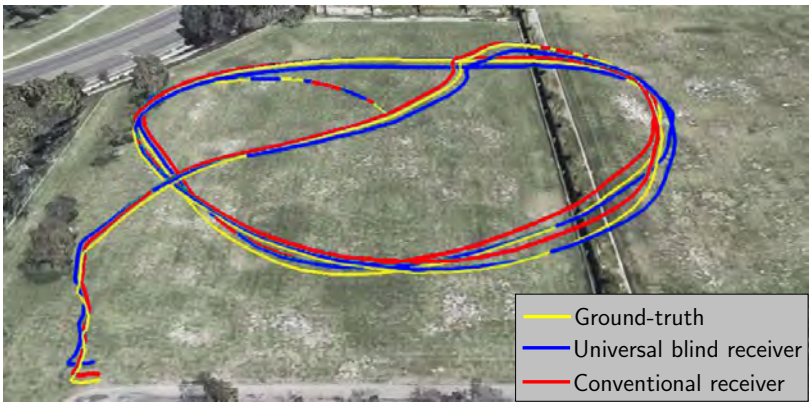

Fig. 9. Navigation results. Total traversed trajectory was 609 m and Position RMSE: 2.07 m (Universal blind and conventiona receiverss

C. Cellular 5G Signals

In this experiment with 5G signals, an Autel Robotics X-Star Premium UAV equipped with a single-channel Ettus 312 USRP connected to a consumer-grade 800/1900 MHz cellular antenna and a small consumer-grade GPS antenna to discipline the on-board oscillator. The cellular receivers were tuned to the cellular carrier frequency 632.55 MHz, which is a 5G NR frequency allocated to the U.S. cellular provider T-Mobile. Samples of the received signals were stored for off-line post-processing. The ground-truth reference trajectory was taken from the on-board Ettus 312 USRP GPS solution. The UAV traversed a trajectory of 416 m. Fig. 10 shows the environment layout and the vehicle trajectory. The blind receiver was used to produce pseudorange and carrier phase measurements and estimate the UAV trajectory [24]. The position RMSE was found to be 4.35 m. Fig. 11 shows the true and estimated UAV trajectories.

Fig. 10. 5G gNB layout.

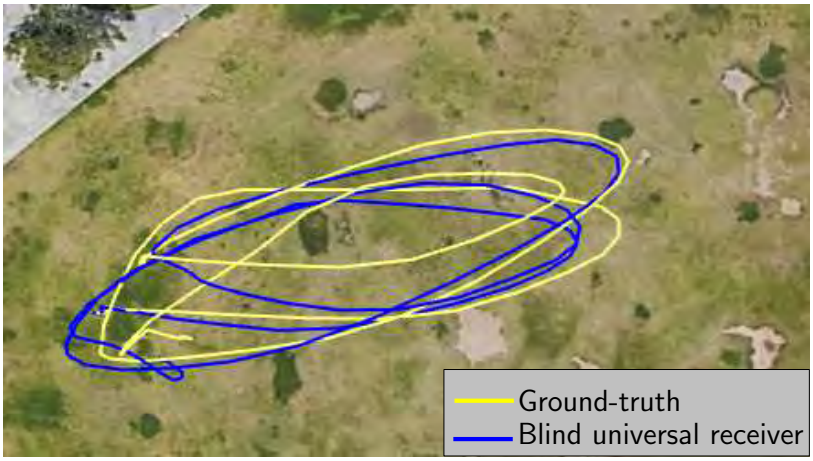

Fig. 11. 5G Navigation results. Total traversed trajectory was 416 m and position RMSE was 4.35 m.

D. Starlink LEO Signals

In this experiment with Starlink signals, a stationary NI USRP-2945R was equipped with a consumer-grade Ku antenna and low-noise block downconverter (LNB) to receive Starlink signals in the Ku-band. The sampling bandwidth was set to 2.5 MHz and the carrier frequency was set to 11.325 GHz, which is one of the Starlink downlink frequencies. The samples of the Ku signal were stored for off-line processing. The USRP was set to record Ku signals over a period of 800 seconds. During this period, a total of six Starlink space vehicles (SVs) transmitting at 11.325 GHz passed over the receiver, one at a time. The universal receiver was adapted to acquire and track the signals from these satellites using the Starlink signal model discussed in [40]. The final 3–D position error was found to be 33.5 m, while the 2–D position error was 25.9 m. Upon equipping the receiver with an altimeter (to know its altitude), the 2–D position error goes down to 7.7 m. A skyplot of the Starlink SVs, the environment layout, and the positioning results are shown in Fig. 12.

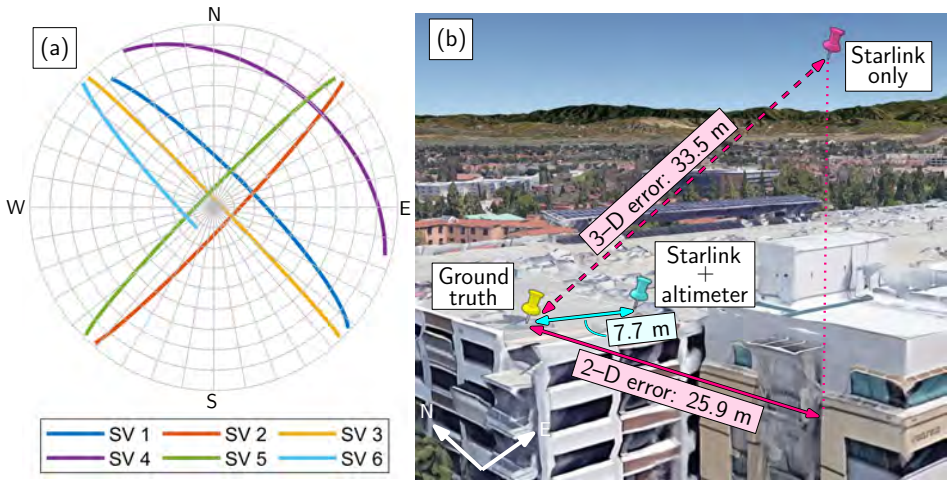

Fig. 12. Positioning results with Starlink LEO satellites.

V. CONCLUSION

This paper presented a universal receiver architecture for blindly exploiting terrestrial and space SOPs for navigation. The only assumption the receiver makes is knowledge of the center frequency and bandwidth of the SOP. Experimental results were presented showing the proposed receiver successfully producing meter-level-accurate navigation solutions from different types of terrestrial and space signals: GPS, cellular 4G LTE and 5G, and Starlink LEO satellites, under the aforementioned partially known assumption.

ACKNOWLEDGMENT

This work was supported in part by the Office of Naval Research (ONR) under Grant N00014-19-1-2511 and Grant N00014-19-1-2613, and in part by the U.S. Department of Transportation (USDOT) under Grant 69A3552047138 for the CARMEN University Transportation Center (UTC).

References

[1] C. Yang and T. Nguyen, "Tracking and relative positioning with mixed signals of opportunity," *NAVIGATION, Journal of the Institute of Navigation*, vol. 62, no. 4, pp. 291–311, December 2015.

[2] M. Driusso, C. Marshall, M. Sabathy, F. Knutti, H. Mathis, and F. Babich, "Vehicular position tracking using LTE signals," *IEEE Transactions on Vehicular Technology*, vol. 66, no. 4, pp. 3376–3391, April 2017.

[3] J. del Peral-Rosado, R. Raulefs, J. López-Salcedo, and G. Seco-Granados, "Survey of cellular mobile radio localization methods: From 1G to 5G," *IEEE Communications Surveys Tutorials*, vol. 20, no. 2, pp. 1124–1148, 2018.

[4] J. Khalife and Z. Kassas, "Opportunistic UAV navigation with carrier phase measurements from asynchronous cellular signals," *IEEE Transactions on Aerospace and Electronic Systems*, vol. 56, no. 4, pp. 3285–3301, August 2020.

[5] M. Maaref and Z. Kassas, "Ground vehicle navigation in GNSS-challenged environments using signals of opportunity and a closed-loop map-matching approach," *IEEE Transactions on Intelligent Transportation Systems*, vol. 21, no. 7, pp. 2723–2723, July 2020.

[6] C. Yang and A. Soloviev, "Mobile positioning with signals of opportunity in urban and urban canyon environments," in *IEEE/ION Position, Location, and Navigation Symposium*, April 2020, pp. 1043–1059.

[7] Z. Kassas, J. Khalife, A. Abdallah, and C. Lee, "I am not afraid of the jammer: navigating with signals of opportunity in GPS-denied environments," in *Proceedings of ION GNSS Conference*, 2020, pp. 1566–1585.

[8] W. Pelgrum and C. Schue, "Position, navigation, and timing technologies in the 21st century," J. Morton, F. van Diggelen, J. Spilker, Jr., and B. Parkinson, Eds. Wiley-IEEE, 2021, vol. 2, ch. 41: Navigation with Low-Frequency Radio Signals, pp. 1281–1333.

[9] A. Abdallah and Z. Kassas, "UAV navigation with 5G carrier phase measurements," in *Proceedings of ION GNSS Conference*, September 2021, accepted.

[10] T. Reid, K. Gunning, A. Perkins, S. Lo, and T. Walter, "Going back for the future: Large/mega LEO constellations for navigation," in *Proceedings of ION GNSS Conference*, September 2019, pp. 2452–2468.

[11] Z. Kassas, J. Morales, and J. Khalife, "New-age satellite-based navigation – STAN: simultaneous tracking and navigation with LEO satellite signals," *Inside GNSS Magazine*, vol. 14, no. 4, pp. 56–65, 2019.

[12] M. Joerger, L. Gratton, B. Pervan, and C. Cohen, "Analysis of Iridium-augmented GPS for floating carrier phase positioning," *NAVIGATION, Journal of the Institute of Navigation*, vol. 57, no. 2, pp. 137–160, 2010.

[13] T. Reid, A. Neish, T. Walter, and P. Enge, "Broadband LEO constellations for navigation," *NAVIGATION, Journal of the Institute of Navigation*, vol. 65, no. 2, pp. 205–220, 2018.

[14] D. Racelis, B. Pervan, and M. Joerger, "Fault-free integrity analysis of mega-constellation-augmented GNSS," in *Proceedings of ION GNSS Conference*, January 2019, pp. 465–484.

[15] T. Mortlock and Z. Kassas, "Performance analysis of simultaneous tracking and navigation with LEO satellites," in *Proceedings of ION GNSS Conference*, September 2020, pp. 2416–2429.

[16] S. Thompson, S. Martin, and D. Bevly, "Single differenced doppler positioning with low Earth orbit signals of opportunity and angle of arrival estimation," in *Proceedings of ION International Technical Meeting*, 2020, pp. 497–509.

[17] M. Psiaki, "Navigation using carrier doppler shift from a LEO constellation: TRANSIT on steroids," *NAVIGATION, Journal of the Institute of Navigation*, vol. 68, no. 3, pp. 621–641, September 2021.

[18] N. Khairallah and Z. Kassas, "Ephemeris closed-loop tracking of LEO satellites with pseudorange and Doppler measurements," in *Proceedings of ION GNSS Conference*, September 2021, accepted.

[19] D. Lawrence, H. Cobb, G. Gutt, M. OConnor, T. Reid, T. Walter, and D. Whelan, "Navigation from LEO: Current capability and future promise," *GPS World Magazine*, vol. 28, no. 7, pp. 42–48, July 2017.

[20] P. Iannucci and T. Humphreys, "Economical fused LEO GNSS," in *Proceedings of IEEE/ION Position, Location and Navigation Symposium*, 2020, pp. 426–443.

[21] J. Khalife, M. Neinavaie, and Z. Kassas, "Navigation with differential carrier phase measurements from megaconstellation LEO satellites," in *Proceedings of IEEE/ION Position, Location, and Navigation Symposium*, April 2020, pp. 1393–1404.

[22] "Position, navigation, and timing technologies in the 21st century," J. Morton, F. van Diggelen, J. Spilker, Jr., and B. Parkinson, Eds. Wiley-IEEE, 2021, vol. 2, Part D: Position, Navigation, and Timing Using Radio Signals-of-Opportunity, ch. 35–43, pp. 1115–1412.

[23] K. Shamaei and Z. Kassas, "Receiver design and time of arrival estimation for opportunistic localization with 5G signals," *IEEE Transactions on Wireless Communications*, vol. 20, no. 7, pp. 4716–4731, 2021.

[24] M. Neinavaie, J. Khalife, and Z. Kassas, "Cognitive opportunistic navigation in private networks with 5G signals and beyond," *IEEE Journal of Selected Topics in Signal Processing*, 2021, accepted.

[25] D. Tse and P. Viswanath, *Fundamentals of wireless communication*. Cambridge university press, 2005.

[26] L. Schiff and A. Chockalingam, "Signal design and system operation of Globalstar TM versus IS-95 CDMA – Similarities and differences," *Wireless Networks*, vol. 6, no. 1, pp. 47–57, February 2000.

[27] R. Hendrickson, "Globalstar for the military," in *Proceedings of IEEE Military Communications Conference*, vol. 3, November 1997, pp. 1173–1178.

[28] M. Tsatsanis and G. Giannakis, "Blind estimation of direct sequence spread spectrum signals in multipath," *IEEE Transactions on Signal Processing*, vol. 45, no. 5, pp. 1241–1252, May 1997.

[29] M. Tanda, "Blind symbol-timing and frequency-offset estimation in OFDM systems with real data symbols," *IEEE Transactions on Communications*, vol. 52, no. 10, pp. 1609–1612, October 2004.

[30] A. Al-Dweik, "A novel non-data-aided symbol timing recovery technique for OFDM systems," *IEEE Transactions on Communications*, vol. 54, no. 1, pp. 37–40, January 2006.

[31] G. Gao, "Towards navigation based on 120 satellites: Analyzing the new signals," Ph.D. dissertation, Stanford University, 2008.

[32] W. Liu, J. Wang, and S. Li, "Blind detection and estimation of OFDM signals in cognitive radio contexts," in *International Conference on Signal Processing Systems*, vol. 2, July 2010, pp. 347–351.

[33] T. Zhang, S. Dai, W. Zhang, G. Ma, and X. Gao, "Blind estimation of the PN sequence in lower SNR DS-SS signals with residual carrier," *Digital Signal Processing*, vol. 22, no. 1, pp. 106–113, 2012.

[34] Y. Wei, L. Liu, and J. Zhang, "Blind estimation of PN sequence of DS-CDMA signal in multipath," in *Proceedings of International Conference on Consumer Electronics, Communications and Networks*, 2012, pp. 1695–1699.

[35] D. Roy, T. Mukherjee, M. Chatterjee, E. Blasch, and E. Pasiliao, "RFAL: adversarial learning for RF transmitter identification and classification," *IEEE Transactions on Cognitive Communications and Networking*, vol. 6, no. 2, pp. 783–801, 2019.

[36] A. Al-Habob, E. Makled, O. Dobre, and O. Üreten, "Blind signal detection in cellular bands," *IEEE Transactions on Instrumentation and Measurement*, vol. 69, no. 3, pp. 657–659, 2020.

[37] Y. Liu and F. Wang, "Blind data detection with unknown channel coding," *IEEE Communications Letters*, vol. 24, no. 4, pp. 758–761, 2020.

[38] M. Neinavaie, J. Khalife, and Z. Kassas, "Blind opportunistic navigation: Cognitive deciphering of partially known signals of opportunity," in *Proceedings of ION GNSS Conference*, September 2020, pp. 2748–2757.

[39] J. Khalife, M. Neinavaie, and Z. Kassas, "Blind Doppler estimation from LEO satellite signals: A case study with real 5G signals," in *Proceedings of ION GNSS Conference*, September 2020, pp. 3046–3054.

[40] J. Khalife, M. Neinavaie, and Z. Kassas, "The first carrier phase tracking and positioning results with Starlink LEO satellite signals," *IEEE Transactions on Aerospace and Electronic Systems*, 2021, accepted.

Letter

Unveiling Starlink LEO Satellite OFDM-Like Signal Structure Enabling Precise Positioning

***Abstract*— This letter unveils the unknown structure of Starlink low Earth orbit (LEO) satellites' orthogonal frequency division multiplexing (OFDM)-like reference signals (RSs). The spectrum of Starlink's dowlink signals is presented, and the frame length is estimated. A blind receiver is proposed, which acquires via a sequential generalized likelihood ratio test multiple satellites, estimates their RSs and respective Doppler, and tracks their carrier and code phases. Experimental results are presented showing six tracked Starlink LEO satellites, three of which transmitted pure tones, while the other transmitted OFDM-like signals. The achieved horizontal positioning error with the six satellites was 6.5 m.**

***Index Terms*— signals of opportunity, matched subspace detector, Doppler positioning, low Earth orbit, Starlink.**

I. Introduction

Navigation with low Earth orbit (LEO) space vehicles (SVs) is receiving significant attention [1]–[3]. Research has shown that one could exploit LEO SVs' broadband communication signals opportunistically for navigation purposes [4].

The first positioning results with Starlink LEO SV signals were presented in [5], [6]. These papers, exploited a train of pure tones in the downlink of Starlink signals to obtain carrier phase and Doppler measurements. Starlink downlink signals occupy 250 MHz bandwidth of the Ku-band to provide high-rate broadband connectivity [7]. However, to the authors' knowledge, in the current literature, nothing beyond the pure tones transmitted in the downlink of Starlink SVs have been detected, tracked, and exploited for navigation purposes.

This letter unveils for the first time Starlink's orthogonal frequency division multiplexing (OFDM) reference signal (RS) structure, from which the frame length is estimated. Next, a blind receiver is proposed, which acquires multiple SVs, estimates their RSs and Doppler, and tracks their carrier and code phases. Upon processing the data collected in [6] from six Starlink LEO SVs via the proposed receiver, it turns out that while three of the SVs were transmitting pure tones, three were also transmitting OFDM-like signals. When the OFDM-like signals were fused into the positioning framework, the horizontal positioning error reduced from 10 m to 6.5 m.

This work was supported in part by the Office of Naval Research under Grants N00014-19-1-2511 and N00014-22-1-2242, in part by the Air Force Office of Scientific Research (AFOSR) under Grant FA9550-22-1-0476, and in part by the U.S. Department of Transportation under Grant 69A3552047138 for the CARMEN University Transportation Center.
M. Neinavaie and Z. Kassas are with the Department of Electrical & Computer Engineering, The Ohio State University, USA. *Corresponding author: Z. Kassas*, email: zkassas@ieee.org

0018-9251 © 2023 IEEE

II. Received Signal Model

A. OFDM-Like Signal Frame Length

Starlink uses a 250 MHz signal bandwidth in the Ku-band for the satellite-to-user downlink [7]. Starlink SVs broadcast nine pure tones which are approximately 43.9 KHz apart. In this letter, these tones are referred to as *central tones*, since they are located at the center of the 250 MHz bandwidth. At a first glance, a white signal containing the central tones is visible in the spectrum [5]. It should be pointed out that due to the high dynamics of Starlink SVs, the downlink signals suffer from Doppler rates which can be on the order of thousands of Hz/s. The Doppler rate distorts the frequency components and imposes a whitening effect on the transmitted signals. Fig. 1 demonstrates the spectrum of Starlink downlink signals after the Doppler rate wipe-off. The details of the Doppler rate wipe-off process are provided in the following subsection. It can be seen that along with the central tones, OFDM-like subcarriers are also visible in the spectrum of Starlink downlink signals.

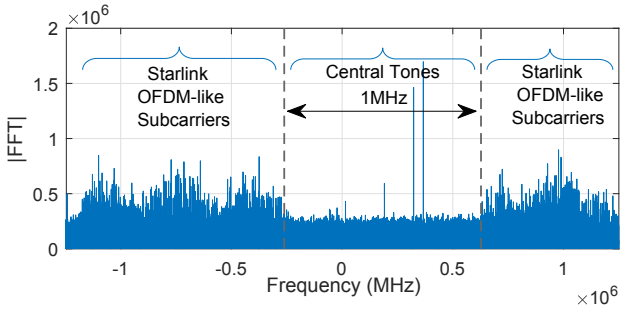

Fig. 1. The spectrum of Starlink downlink signals after Doppler rate wipe-off: OFDM-like subcarriers appeared along with central tones.

OFDM signals contain frames in which some periodic RSs reside, and are sent for synchronization purposes. The frame length, i.e., the period of the synchronization signals, can be obtained according to the autocorrelation function of a time segment of the received signal. The autocorrelation of a large enough time segment of the received signal will result in an impulse train, and the distances between two consecutive impulses are equal the OFDM frame length. Fig. 2(a) demonstrates the autocorrelation of a 100 ms time segment of the Starlink downlink signal after Doppler rate wipe-off. It can be seen that the distance between the impulses of the resulting train is about 1.32 ms. Also, as a comparison, Fig. 2(b) shows the same processing on a 40 ms time segment of a 5G new radio (NR) signal, resulting in a frame length estimate of 10 ms, which matches the standard frame length of 5G NR downlink signals.

B. Baseband Signal Model

Based on the signal analysis in the previous subsection, the downlink signals from multiple Starlink SVs are modeled as unknown RSs of OFDM-like signals in the presence of noise [8]. Therefore, the received baseband

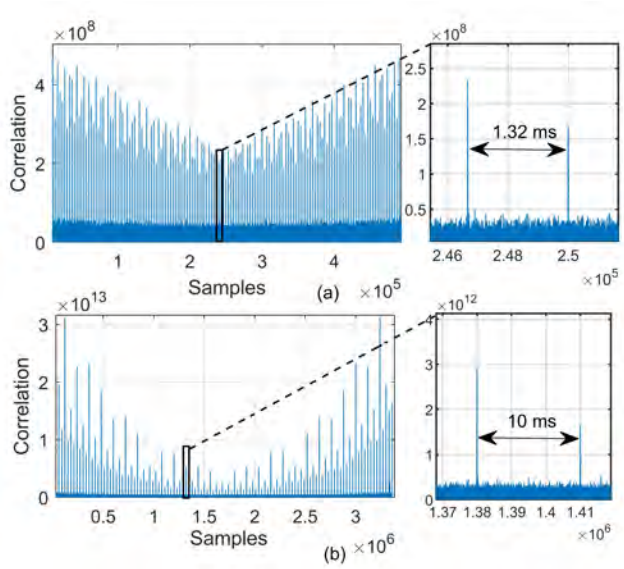

Fig. 2. Autocorrelation of the recorded signal after Doppler wipe-off: (a) Autocorrelation of 100 ms of Starlink downlink signal shows a frame length of about 1.32 ms. (b) Autocorrelation of 40 ms of 5G NR downlink signal which shows the frame length of 10 ms (5G NR standard frame length).

signal samples can be written as

$$r[n] = \sum_{i=1}^{N} \alpha_i(\tau_n) c_i[\tau_n - t_{s_i}[n]] \exp\left(j\theta_i[\tau_n]\right) + w[n], \quad (1)$$

where $r[n]$ is the received signal at the nth time instant; N is the total number of Starlink SVs; $\alpha_i(\tau_n)$ is the complex channel gain between the receiver and ith Starlink SV; τ_n is the sample time expressed in receiver time; $c_i[n]$ represents samples of the complex periodic RS with a period of L samples; $t_{s_i}[n]$ is the instantaneous code-delay of the ith SV at the nth time instant; $\theta_i[\tau_n] = 2\pi f_{D_i}[n] T_s n$ is the carrier phase in radians, where $f_{D_i}[n]$ is the instantaneous Doppler frequency at the nth time instant and T_s is the sampling time; and $w[n]$ captures the effect of noise and transmitted data and is modeled as a complex zero-mean independent and identically-distributed Gaussian sequence with variance σ_w^2.

It is observed that during the processing interval, the instantaneous Doppler frequency $f_{D_i}[n]$ and the instantaneous code-delay $t_{s_i}[n]$ are almost linear functions of time; i.e., $f_{D_i}[n] = f_{D_i} + \beta_i n$ and $t_{s_i}[n] = t_{s_i} + \gamma_i n$; where f_{D_i} is referred to as Doppler, t_{s_i} is referred to as code-delay, β_i is the Doppler rate, and γ_i is referred to as the Doppler stretch corresponding to the ith Starlink SV. The coherent processing interval (CPI) is defined as the time interval in which the channel gain $\alpha_i(\tau_n)$, Doppler f_{D_i}, code-delay t_{s_i}, Doppler rate β_i, and Doppler stretch γ_i are all constant. The received signal at the nth time instant when the Doppler rate is wiped off is denoted by $r'[n] \triangleq \exp(-j2\pi\beta_i n^2) r[n]$. Assuming a constant Doppler rate, one can define $c_i'(\tau_n) \triangleq c_i[(1-\gamma_i)\tau_n - t_{s_i}]$. Due to the priodicity of the RS, $c'(\tau_n)$ is also periodic with period $L' \triangleq \frac{L}{1-\gamma_i}$. Moreover, one can define $s_i[n] \triangleq \alpha_i c'[\tau_n] \exp\left(j2\pi f_{D_i} T_s n\right)$ to obtain

$r'[n] = \sum_{i=1}^{N} s_i[n] + w[n]$. Due to the periodicity of $c'(\tau_n)$, $s_i[n]$ has the following property

$$s_i[n+mL'] = s_i[n] \exp(j\omega_i mL'), \quad 0 \le n \le L'-1, \quad (2)$$

where $\omega_i = 2\pi f_{D_i} T_s$ is the normalized Doppler and $-\pi \le \omega_i \le \pi$. A vector of L' observation samples corresponding to the mth period of the signal is formed as $\mathbf{z}_m \triangleq [r'[mL'], r'[mL'+1], \ldots, r'[(m+1)L'-1]]^{\mathsf{T}}$. The CPI vector is constructed by concatenating K vectors of $\mathbf{z}_m$ to form the $KL' \times 1$ vector

$$\mathbf{y} = \sum_{i=1}^{N} \mathbf{H}_i \mathbf{s}_i + \mathbf{w}, \quad (3)$$

where $\mathbf{s}_i = [s_i[1], s_i[2], \ldots, s_i[L']]^{\mathsf{T}}$; $\mathbf{H}_i \triangleq [\mathbf{I}_{L'}, \exp(j\omega_i L')\mathbf{I}_{L'}, \ldots, \exp(j\omega_i (M-1)L')\mathbf{I}_{L'}]^{\mathsf{T}}$ is a $KL' \times L'$ Doppler matrix with $\mathbf{I}_{L'}$ being an $L' \times L'$ identity matrix; and $\mathbf{w}$ is the noise vector.

III. Receiver Structure

This section presents the structure of the proposed receiver, consisting of two stages: acquisition and tracking.

A. Acquisition: Sequential Matched Subspace Detection

In this paper, the acquisition stage is formulated as a *sequential matched subspace detection* problem [9], [10]. The reader is referred to [8], [11] for further interpretations of matched subspace detectors. In the first step of the proposed sequential algorithm, the presence of a single Starlink SV is tested, and if the null hypothesis is accepted, then $\hat{N} = 0$, which means that no Starlink SV is detected to be present in the environment under the test. If the test rejects the null hypothesis, the algorithm asserts the presence of at least one source and performs the test to detect the presence of other SVs in the presence of the previously detected SVs, sequentially. The Doppler and RS of each SV are estimated at each step as follows.

In order to test the presence of $\mathbf{s}_i$ at the ith stage of the acquisition algorithm, the observation vector (3) can be written as $\mathbf{y} = \mathbf{H}_i \mathbf{s}_i + \mathbf{B}_{i-1}\boldsymbol{\theta}_{i-1} + \mathbf{w}$, where, $\mathbf{B}_{i-1} \triangleq [\mathbf{H}_1, \mathbf{H}_2, \ldots, \mathbf{H}_{i-1}]$ and $\boldsymbol{\theta}_{i-1} \triangleq [\mathbf{s}_1^{\mathsf{T}}, \mathbf{s}_2^{\mathsf{T}}, \ldots, \mathbf{s}_{i-1}^{\mathsf{T}}]^{\mathsf{T}}$. The generalized likelihood ratio (GLR) test for detecting $\mathbf{s}_i$ at each stage can be written as [8]

$$\mathcal{L}(\mathbf{y}) = \frac{\|\mathbf{H}_i^{\mathsf{H}} \mathbf{P}^{\perp}_{\mathbf{B}_{i-1}} \mathbf{y}\|^2}{\|\mathbf{P}^{\perp}_{\mathbf{B}_{i-1}} \mathbf{y}\|^2} \underset{\mathcal{H}_0^i}{\overset{\mathcal{H}_1^i}{\gtrless}} \eta_i, \quad (4)$$

where $\mathcal{H}_1^i$ is the hypothesis that $\mathbf{s}_i$ is present at the ith stage of the acquisition, $\mathcal{H}_0^i$ is the hypothesis that $\mathbf{s}_i$ is absent, $\mathbf{y}^{\mathsf{H}}$ is the Hermitian transpose of $\mathbf{y}$, $\mathbf{P}_{\mathbf{X}} \triangleq \mathbf{X}(\mathbf{X}^{\mathsf{H}}\mathbf{X})^{-1}\mathbf{X}^{\mathsf{H}}$ denotes projection matrix to the column space of $\mathbf{X}$, and $\mathbf{P}^{\perp}_{\mathbf{X}} \triangleq \mathbf{I} - \mathbf{P}_{\mathbf{X}}$. The threshold η_i is a predetermined threshold at the ith stage. The maximum likelihood (ML) estimate of ω_i is obtained by maximizing the likelihood function under $\mathcal{H}_1^i$, which yields

$$\hat{\omega}_i = \arg\max_{\omega_i} \|\mathbf{H}_i^{\mathsf{H}} \mathbf{P}^{\perp}_{\mathbf{B}_{i-1}} \mathbf{y}\|^2, \quad (5)$$

and is used to construct $\mathbf{P}_{\mathbf{B}_{i-1}}$ and $\mathbf{H}_i$ used in the next stage (with $\mathbf{P}_{\mathbf{B}_0} \equiv \mathbf{I}$). The ML estimate of the ith Starlink RS $\mathbf{s}_i$, is given by $\hat{\mathbf{s}}_i = \frac{1}{\lambda_i} \mathbf{H}_i^{\mathsf{H}} \mathbf{P}^{\perp}_{\mathbf{B}_{i-1}} \mathbf{y}$, where $\lambda_i \mathbf{I} = \mathbf{H}_i^{\mathsf{H}} \mathbf{P}^{\perp}_{\mathbf{B}_{i-1}} \mathbf{H}_i$. If the null hypothesis at the ith stage of the sequential algorithm is accepted, the algorithm is terminated and the estimated number of Starlink SVs will be $\hat{N} = i - 1$.

B. Tracking

After obtaining coarse estimates of the Doppler frequencies and estimates of the RSs in the acquisition stage, the receiver refines and maintains these estimates via tracking loops. Specifically, phase-locked loops (PLLs) are employed to track the carrier phases of the detected RSs and carrier-aided delay-locked loops (DLLs) [12] are used to track the RSs' code phases as in [8]. Each detected source has its own dedicated tracking loop.

IV. Experimental Results

This section presents experimental results showing the first precise positioning results that exploit Starlinks' OFDM-like signals. A stationary National Instrument (NI) universal software radio peripheral (USRP) 2945R was equipped with a consumer-grade Ku antenna and a low-noise block (LNB) downconverter to receive Starlink signals in the Ku-band. The sampling rate was set to 2.5 MHz and the carrier frequency was set to 11.325 GHz to record Ku signals over a period of 800 s. Six Starlink SVs were broadcasting nine pure tones during this period, and the algorithm detected OFDM-like signals in the downlink of three of these SVs. To avoid redundancy, the acquisition and tracking results of only one of the OFDM transmitting SVs are presented next.

A. Acquisition

The detection threshold was set $\eta_i = 1.02$ and K was set to 220. Doppler estimation was performed by searching for the maximizer of the likelihood function (5) with a step-size of 1 Hz. The acquisition stages in the proposed receiver are illustrated in Fig. 3, where in the first stage, one source is detected at frequency -249.288 Hz; in the second stage, another source is detected at 207.212 Hz; and finally, in the third stage, the Doppler subspace of the first two sources are nulled and the resulting likelihood is less than the threshold, leading to $\hat{N} = 2$. It should be pointed out that the detected sources can be either an SV or a false alarm (multipath or other unwanted sources). It will be demonstrated in the next subsection that if at the acquisition stage, a false alarm occurs (i.e., a source is mistakenly detected), the carrier phase error will not converge in the tracking loops. In this case, the proposed receiver should neglect such a source. Fig. 4 demonstrates the correlation properties of the estimated RSs. The shape of the autocorrelation function reveals that all the available bandwidth ($\frac{1}{0.4\times10^{-6}} = 2.5$ MHz, in this experiment) is exploited.

B. Tracking

Fig. 5 demonstrates the carrier phase error for the two detected sources. It can be seen that the carrier phase error for the source located at 207.212 Hz is not converging.

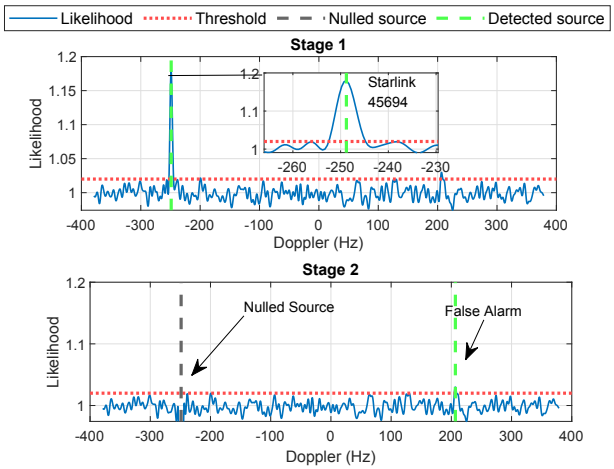

Fig. 3. Acquisition – Stage 1: source at −249.288 Hz is detected. Stage 2: The first source is nulled and a source at 207.212 is detected.

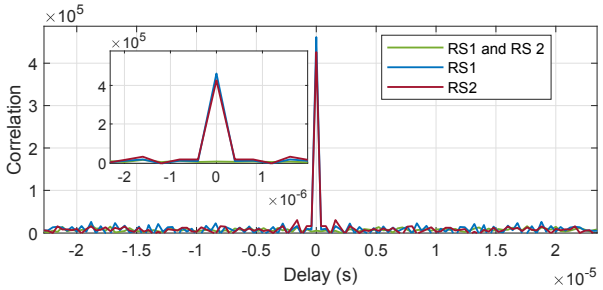

Fig. 4. Autocorrelation function of estimated RS of Starlink 45694 (RS 1), Starlink 45693 (RS 2), and their crosscorrelation function.

Hence, the proposed receiver rejects this source as false alarm and excludes it. Six Starlink SVs were tracked using the proposed receiver. While all six SVs broadcasted pure tones, three of them also transmitted OFDM-like signals.

The receiver's position is estimated via a weighted nonlinear least-squares (WNLS) from Doppler measurements extracted from the three SVs with pure tones and the three SVs with OFDM-like signals. The WNLS formulation is similar to [6]. The receiver's position estimate was initialized as the centroid of all SV positions, projected onto the surface of the earth, yielding an initial position error of 179 km. Recall that the final horizontal position with the pure tones was shown in [6] to be 10 m. When the OFDM-based Doppler measurements are incorporated, the error was reduced to 6.5 m. The positioning results are summarized in Fig. 6.

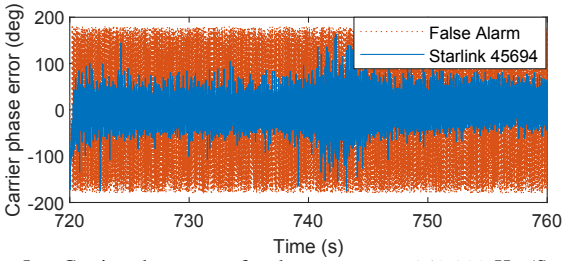

Fig. 5. Carrier phase error for the source at −249.288 Hz (Starlink 45694) and the source at 207.212 Hz (false alarm).

Mohammad Neinavaie, Member, IEEE
The Ohio State University, USA

Zaher M. Kassas, Senior Member, IEEE
The Ohio State University, USA

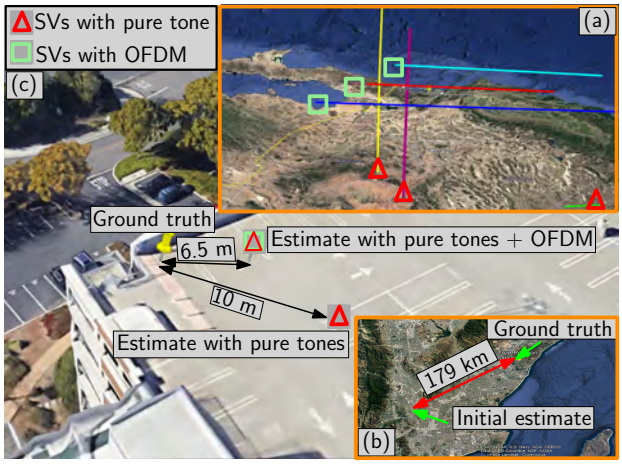

Fig. 6. (a) Starlink SVs trajectories, (b) initial estimate relative to true position, (c) positioning results with six Starlink SVs.

REFERENCES

[1] M. Hartnett, "Performance assessment of navigation using carrier Doppler measurements from multiple LEO constellations," Master's thesis, Air Force Institute of Technology, Ohio, USA, 2022.

[2] N. Jardak and Q. Jault, "The potential of LEO satellite-based opportunistic navigation for high dynamic applications," *Sensors*, vol. 22, no. 7, pp. 2541–2565, 2022.

[3] F. Prol, R. Ferre, Z. Saleem, P. Välisuo, C. Pinell, E. Lohan, M. Elsanhoury, M. Elmusrati, S. Islam, K. Celikbilek, K. Selvan, J. Yliaho, K. Rutledge, A. Ojala, L. Ferranti, J. Praks, M. Bhuiyan, S. Kaasalainen, and H. Kuusniemi, "Position, navigation, and timing (PNT) through low earth orbit (LEO) satellites: A survey on current status, challenges, and opportunities," *IEEE Access*, vol. 10, pp. 83 971–84 002, 2022.

[4] Z. Kassas, "Position, navigation, and timing technologies in the 21st century," J. Morton, F. van Diggelen, J. Spilker, Jr., and B. Parkinson, Eds. Wiley-IEEE, 2021, vol. 2, ch. 43: Navigation from low Earth orbit – Part 2: models, implementation, and performance, pp. 1381–1412.

[5] J. Khalife, M. Neinavaie, and Z. Kassas, "The first carrier phase tracking and positioning results with Starlink LEO satellite signals," *IEEE Transactions on Aerospace and Electronic Systems*, vol. 56, no. 2, pp. 1487–1491, April 2022.

[6] M. Neinavaie, J. Khalife, and Z. Kassas, "Acquisition, Doppler tracking, and positioning with Starlink LEO satellites: First results," *IEEE Transactions on Aerospace and Electronic Systems*, vol. 58, no. 3, pp. 2606–2610, June 2022.

[7] I. Del Portillo, B. Cameron, and E. Crawley, "A technical comparison of three low earth orbit satellite constellation systems to provide global broadband," *Acta Astronautica*, vol. 159, pp. 123–135, 2019.

[8] M. Neinavaie, J. Khalife, and Z. Kassas, "Cognitive opportunistic navigation in private networks with 5G signals and beyond," *IEEE Journal of Selected Topics in Signal Processing*, vol. 16, no. 1, pp. 129–143, 2022.

[9] L. Scharf and B. Friedlander, "Matched subspace detectors," *IEEE Transactions on signal processing*, vol. 42, no. 8, pp. 2146–2157, 1994.

[10] F. Gini and A. Farina, "Vector subspace detection in compound-Gaussian clutter. part I: survey and new results," *IEEE Transactions on Aerospace and Electronic Systems*, vol. 38, no. 4, pp. 1295–1311, 2002.

[11] H. Bolvardi, M. Derakhtian, and A. Sheikhi, "Dynamic clutter suppression and multitarget detection in a DVB-T-based passive radar," *IEEE Transactions on Aerospace and Electronic Systems*, vol. 53, no. 4, pp. 1812–1825, 2017.

[12] M. Braasch and A. Dempster, "Tutorial: GPS receiver architectures, front-end and baseband signal processing," *IEEE Aerospace and Electronic Systems Magazine*, vol. 34, no. 2, pp. 20–37, 2019.

Urban Road Safety Prediction: A Satellite Navigation Perspective

IMAGE LICENSED BY INGRAM PUBLISHING

Halim Lee and Jiwon Seo*
Are with Yonsei University, Incheon, 21983, Korea.
E-mail: halim.lee@yonsei.ac.kr; jiwon.seo@yonsei.ac.kr

Zaher M. Kassas*
Is with The Ohio State University, Columbus, Ohio, 43210, USA.
E-mail: zkassas@ieee.org

Digital Object Identifier 10.1109/MITS.2022.3181557
Date of current version: 18 August 2022

*Corresponding authors

1939-1390/22©2022IEEE
Authorized licensed use limited to: The Ohio State University. Downloaded on April 13,2023 at 05:02:10 UTC from IEEE Xplore. Restrictions apply.

***Abstract*—**Predicting the safety of urban roads for navigation via global navigation satellite systems (GNSS) signals is considered. To ensure the safe driving of automated vehicles, a vehicle must plan its trajectory to avoid navigating on unsafe roads (e.g., icy conditions, construction zones, narrow streets, and so on). Such information can be derived from roads' physical properties, the vehicle's capabilities, and weather conditions. From a GNSS-based navigation perspective, the reliability of GNSS signals in different locales, which is heavily dependent on the road layout within the surrounding environment, is crucial to ensure safe automated driving. An urban road environment surrounded by tall objects can significantly degrade the accuracy and availability of GNSS signals. This article proposes an approach to predict the reliability of GNSS-based navigation to ensure safe urban navigation. Satellite navigation reliability at a given location and time on a road is determined based on the probabilistic position error bound of the vehicle-mounted GNSS receiver. A metric for GNSS reliability for ground vehicles is suggested, and a method to predict the conservative probabilistic error bound of the GNSS navigation solution is proposed. A satellite navigation reliability map is generated for various navigation applications. As a case study, the reliability map is used in a proposed optimization problem formulation for automated ground vehicle safety-constrained path planning.

For the safe and reliable control of automated ground vehicles, various road information needs to be estimated. Road information typically include road surface conditions, such as dryness, wetness, and iciness, as well as shapes, including curvature, bank angles, and slope angles. Satellite-based navigation reliability should also be considered important road information because automated vehicles use various navigation sensors that are dependent on positioning, navigation, and timing from global navigation satellite systems (GNSS). In particular, reliable and accurate GNSS-derived positions are crucial for short-range driving control and long-range navigation and path planning, while timing is crucial for onboard sensor fusion, cooperative planning and control, and information exchanges with other vehicles and the infrastructure. The reliability and accuracy of received GNSS signals is heavily dependent on the road layout within the surrounding environment.

An automated vehicle usually relies on GNSS, such as GPS in the United States, GLONASS in Russia, Galileo in Europe, and Beidou in China, to obtain its absolute position on Earth. Although other sensors, including vision [1], [2], radar [3], [4], lidar [5], [6], and ultrasonic [7] sensors and sensor networks [8], [9], can measure relative distances to nearby objects, GNSS receivers are the primary sensing modality for determining a vehicle's absolute position. This absolute position information is crucial, especially for initializing urban navigation processes using other sensors. For example, given a GNSS position solution, one can narrow the search space in digital maps, which are used with 3D point clouds from a scanning lidar, to estimate in real time a vehicle's position and heading to lane-level accuracy to avoid collisions [10]. In addition, when integrated with vision simultaneous localization and mapping [2], GNSS can mitigate the accumulative positioning error. Furthermore, GNSS measurements can be used to fix the drift of inertial measurement units (IMUs) for determining a vehicle's linear and angular motion [11], [12].

GNSS and differential correction stations alone can provide centimeter-level positioning accuracy if the signal reception environment and solar activity are favorable [17]. Urban canyons impose harsh signal reception conditions [18]. Tall buildings, trees, and nearby vehicles frequently block GNSS signals. Non-line-of-sight (NLOS) reception of GNSS signals without the reception of LOS signals, i.e., the NLOS-only condition, which occasionally occurs on urban roads, can cause arbitrarily large position errors. In addition, the accuracy of pseudoranges (i.e., measured distances between a user's receiver and GNSS satellites, without compensating for the receiver's clock bias and atmospheric delays) is degraded in an urban environment where LOS and NLOS signals are simultaneously received, i.e., the LOS + NLOS condition. Therefore, it is important to predict the reliability of GNSS signals on urban roads to ensure the safe operation of automated ground vehicles.

Various studies have utilized 3D building models with and without ray tracing to overcome the unfavorable GNSS signal reception conditions in urban environments [13], [14], [19]–[21]. Power matching [22], shadow matching [20], specular matching [21], and urban trench modeling [19] were developed to decrease positioning error by predicting the NLOS conditions of GNSS satellites by using a 3D building map. In [13] and [14], 3D building models along with ray-tracing techniques were utilized to predict pseudoranges at a given location in an urban multipath environment. The future state uncertainty [13] and predicted positioning error [14] were then calculated based on the predicted pseudoranges. However, while GNSS signal blockage due to buildings was considered, blockage due to other objects

Authorized licensed use limited to: The Ohio State University. Downloaded on April 13,2023 at 05:02:10 UTC from IEEE Xplore. Restrictions apply.

(e.g., trees and nearby vehicles) was not considered, nor did the predicted positioning error consider the detection and exclusion of possible faulty satellite signals and the probabilistic error bound of the predicted position solution.

The probabilistic error bound of the GNSS position solution, which is referred to as the *protection level* (*PL*), as well as the concept of navigation integrity have been actively studied for safety-critical applications, such as aviation [23], [24]. In [15], a receiver autonomous integrity monitoring (RAIM) algorithm was developed to predict the horizontal position error bound [i.e., the horizontal PL (HPL)] as a measure of satellite navigation reliability for ground vehicles. However, this algorithm did not perform fault detection and exclusion (FDE), and it did not consider multiple signal faults, which are expected in urban environments. Furthermore, urban NLOS-only and LOS + NLOS conditions were not considered, and it was assumed that all GPS signals were received by direct LOS.

To overcome these limitations, a multiple hypothesis solution separation (MHSS) RAIM method was applied in [16], which considered multiple signal faults to predict the HPL. However, FDE was still not performed, and the performance of the proposed method was not validated experimentally. Upon attempting to validate this method experimentally, it was discovered that the method did not accurately predict the HPL. This was due to the complexity of predicting the multipath environment sufficiently accurately and due to signal blockage owing to tall objects other than buildings. As presented in Table 1, the method proposed in the current study addresses the aforementioned issues.

The contributions of this study are summarized as follows:

- A conservatively predicted multiconstellation GNSS HPL, after detecting and excluding multiple signal faults, is suggested as a metric for GNSS reliability for ground vehicles. This metric considers more realistic urban GNSS signal environments than those in Table 1.
- A method to conservatively predict GNSS HPLs for ground vehicles is proposed. While performing ray-tracing simulations with 3D urban digital maps, possible driving lanes and surrounding vehicles are considered, and the most conservative value is selected at each longitudinal location along the test roads.
- It is experimentally shown that the proposed metric (i.e., the conservatively predicted HPL) successfully overbounds the HPL calculated using real pseudorange measurements during field tests in two cities.
- An optimization problem formulation for safety-constrained path planning is proposed. Unlike previous studies, the unavailability of GNSS signals and continuous GNSS signal outages are considered in the problem formulation. A specific implementation to solve this problem is also presented and experimentally demonstrated. The proposed method enables automated ground vehicles to select the path that ensures navigation safety.

Prediction of Satellite Navigation Reliability on Urban Roads

A GNSS receiver estimates its 3D position and clock bias by using pseudorange measurements from at least four GNSS satellites. Because a pseudorange is directly related to the signal travel time from a satellite to a user's receiver, which is measured by a receiver clock, various errors, such as satellite clock bias and ionospheric and tropospheric delay errors, contaminate the pseudorange measurement. These errors should be corrected for to bring the pseudorange closer to the true range. The receiver clock bias is treated as an additional unknown variable, which is obtained alongside the receiver position through a solution estimation process. This section presents various error sources for satellite navigation systems and introduces the proposed method to predict pseudoranges and conservative position error

Table 1. The comparison of GNSS reliability prediction methods.

Method	Metric for GNSS Reliability	Considered Obstacles	Verification Method
Shetty and Gao [13]	State uncertainty bound (3σ) that encloses the uncertain future state distributions	Buildings in virtual urban environments	Simulations only
Zhang and Hsu [14]	GPS positioning error	Real-world buildings, without consideration of driving lanes	Experiments (mean of the measured and predicted positioning errors differed by a maximum of 17.7 m)
Maaref and Kassas [15]	GPS HPL without consideration of measurement faults	Not considered (all GPS signals assumed to be direct LOS)	Experiments (no performance comparison between the predicted and measured HPLs reported)
Lee et al. [16]	GPS HPL with consideration of multiple measurement faults (FDE not performed)	Real-world buildings, without consideration of driving lanes	Simulations only
Proposed	Conservative multiconstellation GNSS HPL with consideration of multiple measurement faults (FDE performed)	Real-world buildings and surrounding vehicles, with consideration of driving lanes	Experiments (conservatively predicted HPL bounded the measured HPL 100% of the time)

Authorized licensed use limited to: The Ohio State University. Downloaded on April 13,2023 at 05:02:10 UTC from IEEE Xplore. Restrictions apply.

bounds as measures of satellite navigation reliability on urban roads.

Error Sources for Satellite Navigation

The performance of GNSS-based navigation can be degraded by anomalous ionospheric behavior [25]–[27], radio frequency interference [28], [29], signal reflection and blockage [30], [31], and poor geometric diversity of satellites in view [32], [33]. In particular, signal reflection and blockage due to buildings and other tall objects is a significant error source for ground vehicle navigation in urban canyons. When N GNSS satellites are in view, the nth pseudorange measurement in an urban environment at time step t, after satellite clock bias corrections, can be modeled as follows:

$$\begin{aligned}\rho^n(t) &= R^n_{\mathrm{LOS}}(t) + \rho^n_{\mathrm{bias}}(t) + \varepsilon^n(t) \\ &= \| \boldsymbol{r}_u(t) - \boldsymbol{r}^n(t) \|_2 + c \cdot \delta t_u(t) \\ &\quad + I^n(t) + T^n(t) + \rho^n_{\mathrm{bias}}(t) + \varepsilon^n(t), \end{aligned} \tag{1}$$

where the descriptions of the symbols are given in Table 2.

Considerable common-mode errors can exist between a user and a nearby reference station, such as atmospheric delays and satellite ephemeris errors. These errors can be largely mitigated using differential GNSS (DGNSS). A DGNSS reference station broadcasts correction messages to nearby users, enabling the users to eliminate common-mode errors. However, site-specific errors caused by NLOS-only and LOS + NLOS signal reception cannot be mitigated using DGNSS.

Four GNSS signal reception conditions can occur in urban canyons: 1) the LOS-only condition, in which only the LOS signal is received; 2) the NLOS-only condition, in which only NLOS signals are received; 3) the LOS + NLOS condition, in which both LOS and NLOS signals are received; and 4) the no-signal condition, in which a signal is completely blocked by an object. Figure 1 illustrates the difference between the NLOS-only and LOS + NLOS conditions. In the field of satellite navigation, the NLOS-only and LOS + NLOS conditions are treated differently, as they cause different types of pseudorange errors. Moreover, simulation methods to predict these errors are different, as discussed in the following.

Under the NLOS-only condition, the NLOS-only bias term, which is ρ^n_{NLOS} in Figure 1(a), reflects the extra travel distance (i.e., $\rho^n_1 - R^n_{\mathrm{NLOS}}$ where ρ^n_1 is the travel distance along the reflected path) due to signal reflection, which

Table 2. The mathematical notations related to pseudorange measurement modeling in urban environments.

Symbol	Description
ρ^n	The nth pseudorange measurement in an urban environment after satellite clock bias corrections
R^n_{LOS}	Length of the LOS path between a user's receiver and the nth satellite, including delays due to receiver's clock bias, ionosphere, and troposphere
ρ^n_{bias}	Either 1) the bias due to an NLOS-only condition (i.e., ρ^n_{NLOS}) which represents the extra travel distance of the NLOS signal compared with R^n_{LOS} [see Figure 1(a)], or 2) the bias due to an LOS + NLOS condition (i.e., $\rho^n_{\mathrm{L+N}}$) where both LOS and NLOS signals are received [see Figure 1(b)]
ρ^n_{NLOS}	Bias due to an NLOS-only condition
$\rho^n_{\mathrm{L+N}}$	Bias due to an LOS + NLOS condition
$\boldsymbol{r}_u$	Position vector of a user's receiver
$\boldsymbol{r}^n$	Position vector of the nth satellite
c	Speed of light
δt_u	User's receiver clock bias
I^n	Ionospheric delay in the nth pseudorange measurement
T^n	Tropospheric delay in the nth pseudorange measurement
ε^n	Remaining errors (e.g., noise, unmodeled effects, and so on) in the nth pseudorange measurement

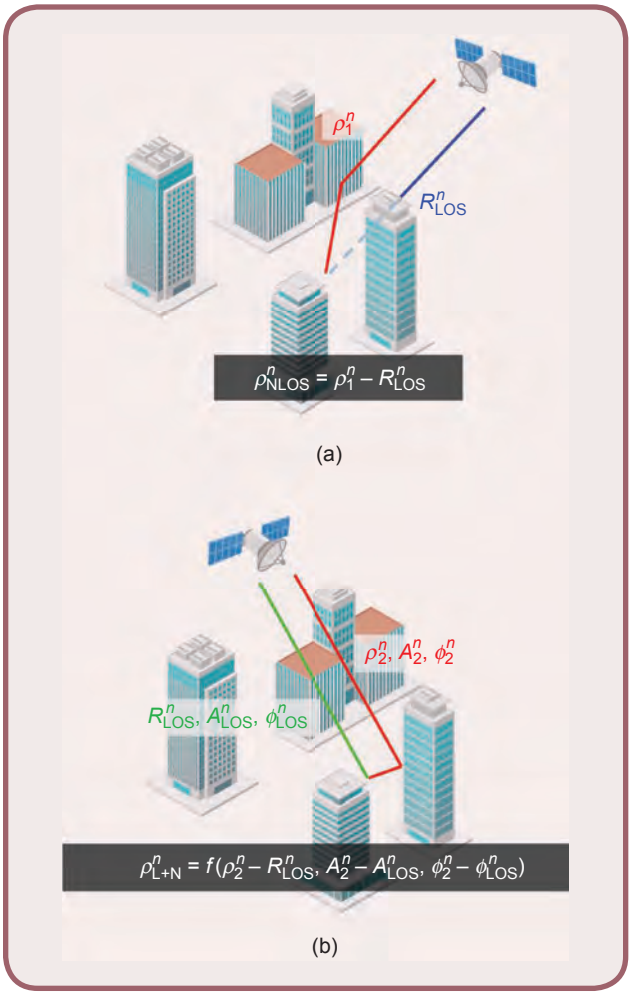

FIG 1 The GNSS (a) NLOS-only and (b) LOS + NLOS conditions in an urban environment and corresponding pseudorange biases.

Authorized licensed use limited to: The Ohio State University. Downloaded on April 13,2023 at 05:02:10 UTC from IEEE Xplore. Restrictions apply.

can be arbitrarily large. If this bias remains in the pseudorange measurement, it can cause a large unbounded positioning error. A typical way to predict ρ^n_{NLOS} at a given location is to calculate the difference between the lengths of the direct and reflected paths (i.e., the LOS and NLOS paths) from a satellite to a receiver, which represents the extra travel distance. Ray-tracing simulation using 3D urban digital maps can be performed to estimate the length of the reflected path. The positions of the satellites at a given time for ray-tracing simulation are calculated based on the satellite broadcast almanac information. The complete blockage of a signal (i.e., the no-signal condition) can also be predicted by ray-tracing simulation.

In an urban environment, the LOS + NLOS condition is more frequently observed than the NLOS-only condition. Unlike the NLOS-only bias term, the LOS + NLOS bias term, which is $\rho^n_{\mathrm{L+N}}$ in Figure 1, is bounded. Reflected signals with a large delay when compared with the 1.5-chip width of the GNSS signal (e.g., a 300-m width for a GPS L1 C/A-code chip) do not cause any bias in the pseudorange measurements if the direct signal is also received and tracked [34]. For short-delay reflected signals (i.e., the delay is less than 1.5 chips), $\rho^n_{\mathrm{L+N}}$ depends on the receiver's correlator design, and it is a function of the difference of the travel distances (i.e., $\rho^n_2 - R^n_{\mathrm{LOS}}$), received signal amplitudes (i.e., $A^n_2 - A^n_{\mathrm{LOS}}$), and phases (i.e., $\phi^n_2 - \phi^n_{\mathrm{LOS}}$) of the reflected and direct signals, where $(\cdot)^n_2$ and $(\cdot)^n_{\mathrm{LOS}}$ represent the reflected and direct signals from the nth satellite, respectively [see Figure 1(b)].

The receiver used in the field experiments of this study, which will be explained in the "Experimental Field Test Results" section, utilizes the a posteriori multipath estimation (APME) method [35]; therefore, the multipath error envelop of the APME method was used to predict $\rho^n_{\mathrm{L+N}}$ in this study. The amplitudes and phases of the received reflected and direct signals were obtained through ray-tracing simulations.

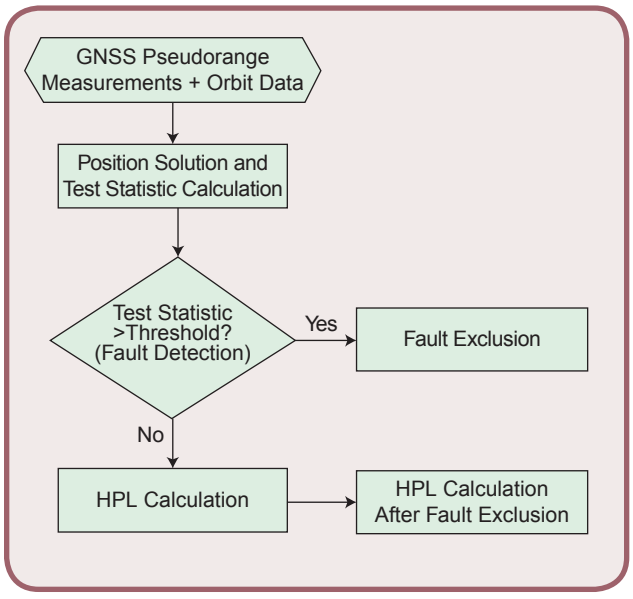

FIG 2 The FDE and HPL calculation of the RAIM algorithm.

Probabilistic Error Bound and Advanced RAIM

Accuracy in the field of navigation usually refers to the 95th-percentile value of the positioning error distribution [36]. However, when navigation safety is of concern, a considerably higher probability (e.g., 99.99999% for the vertical guidance of aircraft) should be considered to obtain an error bound [23]. This error bound (i.e., the PL) includes the true position of a user with a required high probability. If the PL is larger than the alert limit (AL) of a certain safety-critical operation (e.g., 35 m for the vertical guidance of an aircraft down to 200 ft above the runway), the position output from the navigation system is deemed unreliable because it is not guaranteed that the true position is within the AL with the required probability. In this case, the navigation system is declared unavailable and must not be used to ensure navigation safety (i.e., navigation integrity is guaranteed by a timely alert).

Among various methods and augmentation systems—e.g., ground-based augmentation systems [37]–[39] and satellite-based augmentation systems [40], [41]—to guarantee the integrity of satellite navigation systems, RAIM is often preferred because it requires no or minimal support from infrastructure. The basic idea of RAIM is to check the consistency among position solutions obtained by subsets of pseudorange measurements. If all the subset solutions are almost identical, all the signals can be confirmed to be fault free, and the position output of a receiver is deemed reliable.

Many RAIM algorithms have the functionality of FDE and PL calculations. FDE rejects faulty signals that cause erroneous position solutions through a consistency check using redundant measurements. A minimum of six pseudorange measurements is necessary to detect and exclude a single fault. PL is a probabilistic error bound of a position solution, and HPL is particularly relevant to ground vehicles. For aerial vehicles, the vertical PL should also be considered [42], [43]. After performing FDE, the HPL can be calculated, as shown in Figure 2.

It should be noted that RAIM is suitable for the real-time integrity monitoring of received GNSS signals; however, the focus of this study is not on guaranteeing real-time navigation integrity. Instead, a method is proposed to predict satellite navigation reliability at every location on urban roads before an automated vehicle arrives at a location. The probabilistic position error bound (i.e., the HPL) is used as a safety metric to represent satellite navigation reliability. After the reliability is predicted and provided to a vehicle as part of the road information, the vehicle can detour around the low-reliability region (i.e., the high-HPL region) or prepare

Authorized licensed use limited to: The Ohio State University. Downloaded on April 13,2023 at 05:02:10 UTC from IEEE Xplore. Restrictions apply.

its other navigation sensors to not utilize GNSS measurements when passing through the low-reliability region.

For this purpose, advanced RAIM (ARAIM) with an MHSS algorithm [36], [44] that can handle multiple faults and constellations is adopted in this study. It is expected that a ground vehicle will experience multiple GNSS signal faults on urban roads. Currently, most GNSS receivers used by automated vehicles are capable of tracking multiple GNSS constellations (e.g., GPS and GLONASS were used in this study). By introducing multiple hypotheses of signal failures, ARAIM can detect and exclude multiple faults in multiple constellations and consider the possibility of further fault modes when calculating the HPL. Therefore, ARAIM, among various RAIM algorithms [45], is appropriate for FDE based on predicted pseudoranges and HPL prediction for automated ground vehicles in urban environments.

The MHSS-based FDE algorithm detects faulty signals by using a solution separation threshold test. Solution separation is the difference between fault-free and fault-tolerant position solutions. The receiver's state $\boldsymbol{x}$, which is $\hat{\boldsymbol{x}} + \Delta\hat{\boldsymbol{x}}$, can be estimated by the weighted least-squares estimator, whose update equation is given by [34], [44]

$$\Delta\hat{\boldsymbol{x}} = (\mathbf{G}^{\top}\mathbf{W}\mathbf{G})^{-1}\mathbf{G}^{\top}\mathbf{W}\Delta\boldsymbol{\rho}, \tag{2}$$

where the descriptions of the symbols are given in Table 3. The fault-free position solution is estimated from the all-in-view satellites, whereas the fault-tolerant position solution assumes one or more possible faulty signals; thus, it is estimated from a subset of satellites. Then, the solution separation threshold test is expressed as [44]

$$|\hat{x}_q^{(0)} - \hat{x}_q^{(k)}| \leq T_{k,q}, \tag{3}$$

where the descriptions of the symbols are given in Table 3. If the solution separation for any axis exceeds a certain threshold, signal faults are likely to exist, and exclusion of these faults should be attempted.

If the solution separation threshold test passes without excluding any satellite signals, the HPL is computed as follows. In the MHSS-based HPL calculation method, the HPL is obtained as a bound that includes all the HPLs corresponding to the fault-free and fault-tolerant position solutions. The HPL for the q-axis (i.e., HPL_q) is calculated as [44]

Table 3. The mathematical notations related to HPL calculation.

Symbol	Description
$\boldsymbol{x}$	State vector of a user's receiver, which is defined as $[\boldsymbol{r}_u^{\mathrm{T}}, c\delta t_u]^{\mathrm{T}}$
$\boldsymbol{\rho}$	Pseudorange measurement vector, which is defined as $[\rho^1, \ldots, \rho^N]^{\mathrm{T}}$
$\Delta\hat{\boldsymbol{x}}$	Difference between a receiver's state vector $\boldsymbol{x}$ and its estimate from the previous iteration $\hat{\boldsymbol{x}}$
$\Delta\boldsymbol{\rho}$	Difference between the pseudorange measurement vector $\boldsymbol{\rho}$ and the expected pseudorange vector $\hat{\boldsymbol{\rho}}$ based on the satellite positions and $\hat{\boldsymbol{x}}$
$\mathbf{G}$	Geometry matrix
$\mathbf{W}$	Weighting matrix, which is the inverse of a diagonal matrix whose diagonal elements are the measurement noise variances
q	Either $q = 1$ or $q = 2$ for the east or north axis of the horizontal plane, respectively
$\hat{x}_q^{(0)}$	Fault-free position solution for the q-axis estimated from the all-in-view satellites
$\hat{x}_q^{(k)}$	Fault-tolerant position solution for the q-axis and kth fault mode
$T_{k,q}$	Solution separation threshold for the q-axis and kth fault mode ($k = 0$ represents the fault-free condition)
HPL_q	HPL for the q-axis
$\mathbf{Q}(\cdot)$	Tail probability function of the standard Gaussian distribution
$b_q^{(k)}$	Nominal bias of the position solution for the q-axis and kth fault mode
$\sigma_q^{(k)}$	Standard deviation of the position solution for the q-axis and kth fault mode
$N_{\text{fault modes}}$	Total number of fault modes
$p_{\text{fault},k}$	Probability that the kth fault mode occurs
$PHMI_{\text{HOR}}$	Probability of hazardously misleading information for the horizontal component
$PHMI_{\text{VERT}}$	Probability of hazardously misleading information for the vertical component
$P_{\text{sat,not monitored}}$	Probability that independent simultaneous satellite faults are not monitored
$P_{\text{const,not monitored}}$	Probability that simultaneous constellation faults are not monitored

Authorized licensed use limited to: The Ohio State University. Downloaded on April 13,2023 at 05:02:10 UTC from IEEE Xplore. Restrictions apply.

$$2\mathbf{Q}\left(\frac{HPL_q - b_q^{(0)}}{\sigma_q^{(0)}}\right) + \sum_{k=1}^{N_{\text{fault modes}}} p_{\text{fault},k}\,\mathbf{Q}\left(\frac{HPL_q - T_{k,q} - b_q^{(k)}}{\sigma_q^{(k)}}\right) = \frac{1}{2}PHMI_{\text{HOR}}\left(1 - \frac{P_{\text{sat,not monitored}} + P_{\text{const,not monitored}}}{PHMI_{\text{VERT}} + PHMI_{\text{HOR}}}\right), \quad (4)$$

where the descriptions of the symbols are given in Table 3. Detailed information and mathematical formulations of the ARAIM user algorithm are provided in [44]. If the solution separation threshold test does not pass (i.e., a fault is detected), fault exclusion should be attempted. After the exclusion of faulty signals, the HPL should be calculated considering the probability of wrong exclusion. The HPL equation in this case has an additional factor to (4). Detailed discussions are available in [44].

Prediction of Conservative HPL in Urban Environments

Predicting the exact HPL of a vehicle at a certain location and time is virtually impossible due to imperfections in 3D urban digital maps as well as the presence of nearby dynamic objects, which cannot be predicted. For example, nearby vehicles can block satellite signals, as illustrated in Figure 3(a). Therefore, the HPL will be predicted conservatively by assuming that the vehicle of interest is always surrounded by taller vehicles. Considering the height of the vehicle used for the field test (1.7 m), the height and width of a typical dump truck (3.3 and 2.5 m, respectively), and the typical width of a lane (3.7 m), an elevation mask of 33° was set, including a slight margin. In other words, to be conservative, satellite signals with less than a 33° elevation are assumed to be blocked by nearby vehicles.

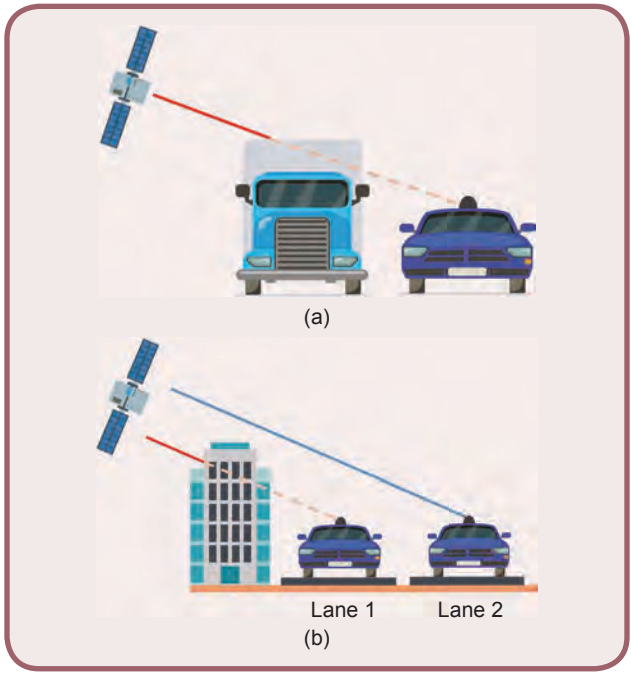

FIG 3 (a) The GNSS signal blockage due to a nearby vehicle. (b) The different signal reception conditions in two lanes.

FIG 4 The ray tracing at a single node within a 3D urban digital map.

Signal reflection and blockage due to static objects, such as buildings, can be predicted by ray-tracing simulation if exact 3D urban digital maps are available [46], [47]. However, it should be noted that the signal reception conditions in each lane can vary significantly [48]. For example, a vehicle can have an LOS reception of a certain satellite signal in one lane but may not receive the signal from the same satellite in another lane because of building blockage [see Figure 3(b)].

To perform ray-tracing simulations to predict signal blockage due to buildings and NLOS-only or LOS + NLOS bias (i.e., ρ^n_{NLOS} or $\rho^n_{\text{L+N}}$ in Figure 1), commercial 3D urban digital maps from 3dbuildings and Wireless InSite commercial ray-tracing software were used. Figure 4 shows an example of a ray-tracing simulation. It was assumed that the exterior walls of all buildings were made of concrete. The time of arrival (TOA) of GNSS signals was calculated using the shooting and bouncing ray (SBR) method described in [49], which is used to find geometrical propagation paths between a transmitter and a receiver using a 3D map. In the SBR method, among the rays transmitted from the source, the rays that hit the building are specularly reflected and traced until the maximum number of reflections is reached. Then, ρ^n_{NLOS} or $\rho^n_{\text{L+N}}$ is predicted using the simulated TOAs, amplitudes, and phases of GNSS signals from ray tracing according to the signal reception condition. The GPS and GLONASS constellations were considered based on their almanac information.

To reduce the computational complexity of the ray-tracing simulation, it was assumed that the receiver received only direct and single reflected signals. If a signal was reflected by buildings more than once, it was assumed that the signal was not received by the vehicle. This assumption does not significantly affect the accuracy of conservative HPL prediction because the received signal strength of multiple reflected signals is low, and a receiver may not track such signals.

With the predicted pseudoranges from the ray-tracing simulation, the HPL can be predicted following the procedure in Figure 2. An example map of the conservatively predicted HPL is given in Figure 5. If the number of visible satellites at a certain location is insufficient for FDE, the location is marked as unavailable because the HPL prediction is not performed in this case. It should be noted that the HPL

Authorized licensed use limited to: The Ohio State University. Downloaded on April 13,2023 at 05:02:10 UTC from IEEE Xplore. Restrictions apply.

at a given location varies with time because GNSS satellites move. Fortunately, future satellite positions are reliably predictable based on ephemerides [34]. Thus, the conservative HPLs over a certain time horizon at each location can be calculated in advance in a cloud server. Automated vehicles can use this information without concern about their onboard computational power. Since the conservative HPL prediction at each location and time can be performed independently, a cloud server with enough parallel processors can quickly generate HPL prediction maps of regions of interest.

Experimental Field Test Results

To verify the proposed methodology for conservatively predicting HPL in urban environments, field tests were performed to calculate the HPL based on actual pseudorange measurements. Then, the HPL based on measured pseudoranges (i.e., the measured HPL) was compared with the conservative HPL based on predicted pseudoranges (i.e., the conservatively predicted HPL). The HPL varies over time, as satellite geometry changes. Further, the HPL is impacted by the surrounding environment. To check if the proposed methodology is applicable to various times and environments, field tests were performed in two different cities: Irvine, California, and Riverside, California.

During the experiments, GPS and GLONASS measurements were collected using a Septentrio AsteRx-i V receiver. The GNSS antenna was placed on top of the ground vehicle (Figure 6). GNSS constellations during the experiments in Irvine and Riverside are included in Figure 7. Figure 8 presents a small portion of the urban test environment in Irvine as an example, which included several tall buildings that significantly changed the measured HPL values. In Riverside, complex-shaped buildings were distributed along the test trajectory. The experiments were conducted along approximately 4.5- and 1.6-km roads in Irvine and Riverside, respectively.

As shown in Figure 3(b), the signal reception condition can dramatically change according to the lateral location of a vehicle on the road. It is theoretically possible to predict the HPL at every location, as in Figure 5; however, the prediction accuracy depends on the accuracy of the 3D building and road maps. For example, a slight height error of a building model or a lateral position error of a road model in a digital map can cause a visible satellite to be predicted as invisible during ray-tracing simulation. Unfortunately, commercially available 3D digital maps have limited accuracy. As a conservative approach, multiple ray-tracing simulations were performed by changing the vehicle's lateral location across the road. If a certain satellite was invisible at one location, the satellite was treated as an invisible satellite when predicting the HPL at the given longitudinal location of the road. Furthermore, ρ^n_{NLOS} and $\rho^n_{\mathrm{L+N}}$ were also predicted at every lateral location across the road, and the largest value was chosen for the pseudorange prediction, to be conservative.

Figure 9 describes the conservatively predicted HPL along two 1.5-km roads with tall buildings. The ground vehicle freely changed its driving lane during the field tests. However, its measured HPL was always less than the conservatively predicted HPL that assumed the most challenging lateral location, having the largest number of signal blockages and largest NLOS-only and LOS + NLOS biases. When the vehicle drove along a lane with better satellite visibility (i.e., a lane distant from a tall building), the measured HPL was significantly lower than the conservatively predicted HPL that assumed the most challenging lane with poor satellite visibility, as in the case of a 1.3-km distance location in Figure 9(b). Nevertheless, the most challenging lane needs to be assumed when the HPL is predicted because it is not practical to restrict the driving lane of a vehicle.

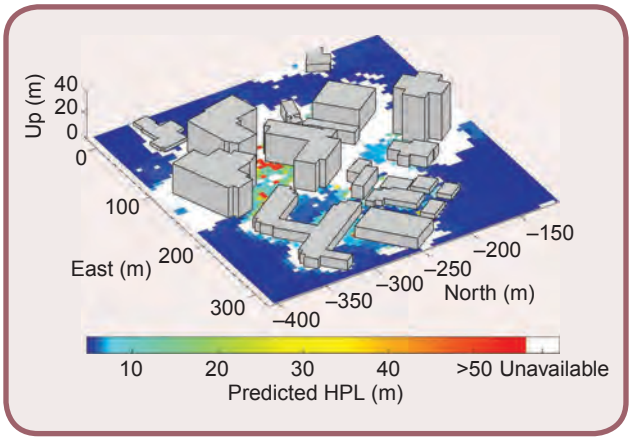

FIG 5 The conservatively predicted HPL with a 33° elevation mask at a certain time epoch. This map varies with time because of GNSS satellite motion.

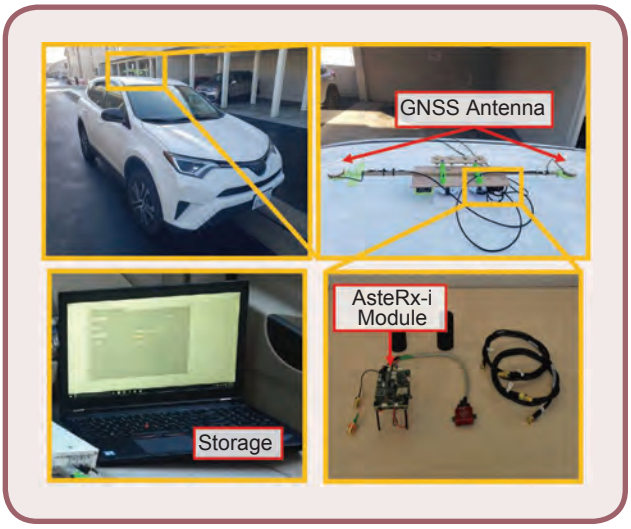

FIG 6 The experimental settings. A GNSS antenna is attached to the top of a ground vehicle. The GNSS signals are processed using a Septentrio AsteRx-i receiver module. GNSS measurements and navigation data are stored on a laptop placed inside the vehicle.

Authorized licensed use limited to: The Ohio State University. Downloaded on April 13,2023 at 05:02:10 UTC from IEEE Xplore. Restrictions apply.

Application Case Study: Safety-Constrained Path Planning

The predicted satellite navigation reliability map (i.e., the HPL prediction map) can be utilized by an automated vehicle for various purposes to ensure safe driving. Because the reliability of satellite navigation signals is already known through the HPL prediction map, an automated vehicle can plan a safe trajectory ahead of time. If the navigation sensors of the vehicle rely heavily on GNSS, it would be better to detour around high-HPL regions. Most automated vehicles utilize IMUs, which are calibrated using GNSS. Therefore, IMU outputs in a high-HPL region should not be relied on.

As an application case study, the path planning of an automated vehicle based on the HPL prediction map is considered. Unlike traditional strategies for path planning to minimize travel distances and times, the primary focus here is the navigation safety of an automated vehicle. Therefore, the optimization problem is formulated with safety considerations as

$$\begin{aligned} \underset{\pi\in\mathcal{P}}{\text{minimize}} \quad & \sum_{p_k\in\pi} dist(p_{k-1},p_k)\cdot HPL(p_k,t) \\ \text{subject to} \quad & \frac{N(HPL(p_k,t)<T_{\text{HPL}})}{N_{\text{nodes}}} > T_{\text{safe}} \\ & D_{\text{HPL unacceptable}} < D_{\text{safe}}, \end{aligned} \tag{5}$$

where the descriptions of the symbols are given in Table 4.

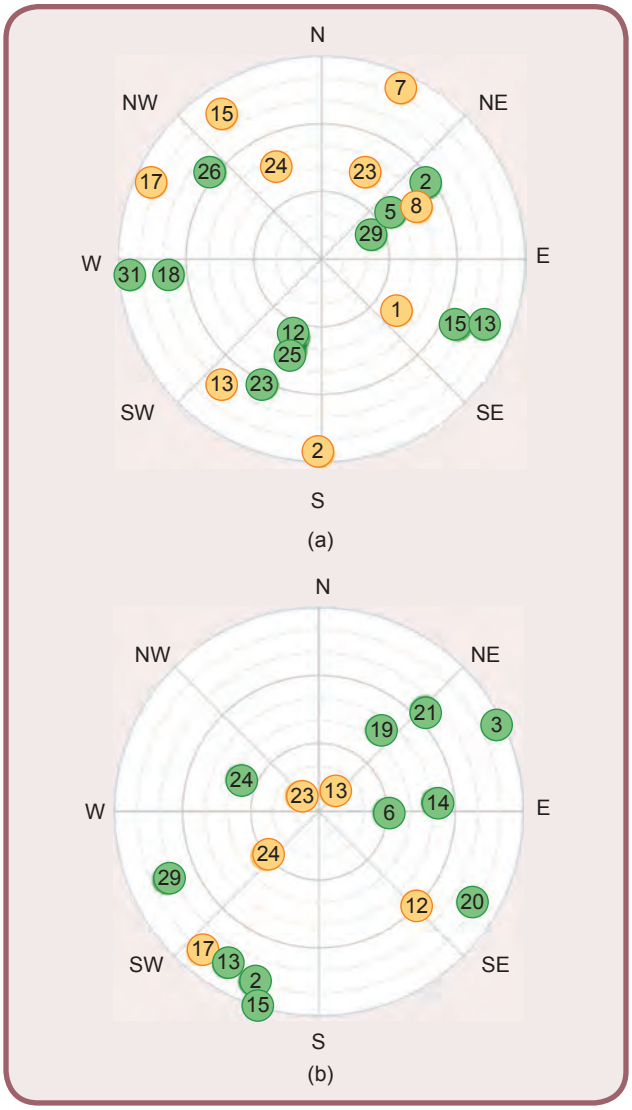

FIG 7 The GPS (green) and GLONASS (yellow) constellations during the field tests in (a) Irvine and (b) Riverside.

FIG 8 The urban test environment in Irvine.

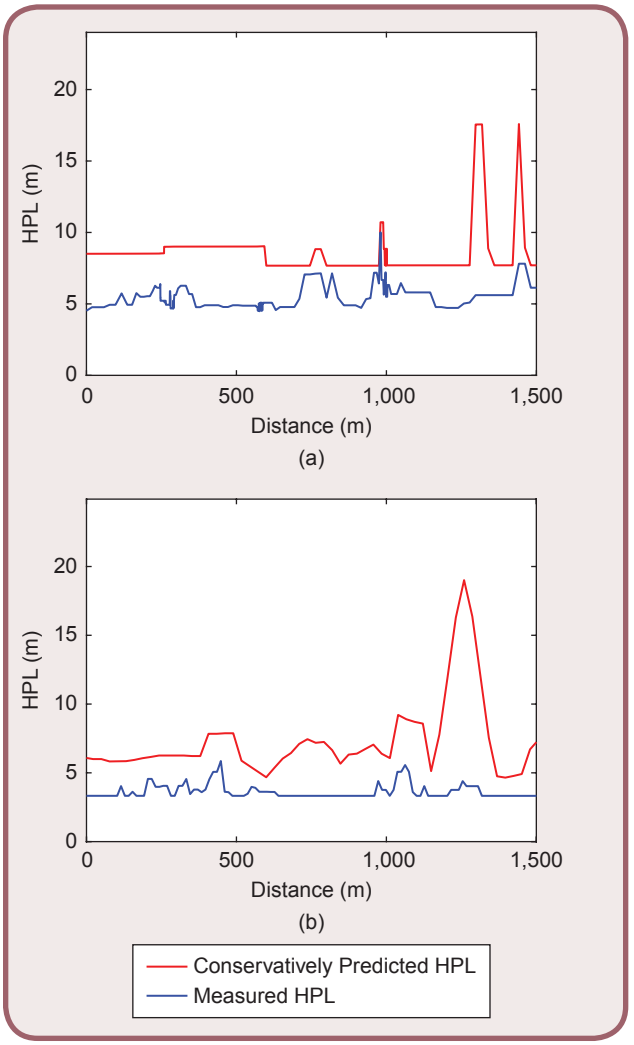

FIG 9 The experimental results in (a) Irvine and (b) Riverside. Conservatively predicted HPLs overbound measured HPLs along sample paths.

Authorized licensed use limited to: The Ohio State University. Downloaded on April 13,2023 at 05:02:10 UTC from IEEE Xplore. Restrictions apply.

The cost function in (5) aims to find an optimal path that minimizes both the travel distance and HPL along the path (recall that a smaller HPL indicates a higher satellite navigation reliability). The first constraint in (5) considers the ratio of the number of safe nodes to that of the total nodes. For example, if T_{HPL} is set to 10 m and T_{safe} is set to 95%, a candidate path with more than 5% of nodes having an HPL of more than 10 m will not be selected as an optimal path. The second constraint in (5) ensures the avoidance of a candidate path with continuous signal outages. The outputs from automotive-grade IMUs quickly diverge if GNSS signals are unavailable or unreliable for a certain period. Therefore, continuous signal outages are more problematic than intermittent signal outages for similar total outage durations. For example, if D_{safe} is set to 150 m, a candidate path with continuous signal outages for more than a 150-m distance will not be selected as an optimal path.

Table 5 compares the optimization problem formulations of previous studies [14], [15] and the current study. Unlike the previous studies, where only travel distance and navigation reliability (i.e., the positioning error [14] and the HPL without considering measurement faults [15]) were considered, the proposed optimization problem considers GNSS unavailability and continuous signal outages, as well, to obtain a more realistic solution.

To solve the optimization problem in (5), the A* algorithm [50] was applied, which is a widely used search algorithm that can find an optimal path to a given target node. The A* algorithm was implemented as shown in Algorithm 1 to find an optimal solution to the safety-constrained path planning problem. The overall road structure of a given map, which is expressed by a graph composed of nodes and edges, is denoted by $\mathcal{P}$. Given start and target nodes, the A* algorithm finds the cheapest path [i.e., a sequence of nodes that minimizes the cost function in (5)] based on the sum of the backward cost (the cumulative cost) and forward cost (the heuristic cost). The open set, which is implemented as a priority queue that stores nodes that have been visited but whose successors have not been explored, is denoted by O. p_{current} denotes the currently visited node, and p_{neighbor} denotes a neighbor node of p_{current}.

For each iteration, all neighbor nodes of p_{current} are stored in O and the overall cost f of each neighbor node is calculated. The overall cost f is defined as the sum of cumulative cost g and heuristic cost h. The Euclidean distance (i.e., the straight line distance) to the target node was used as the heuristic cost. After calculating the cost of each neighbor node, the node in O with the smallest f is selected as p_{current} and is moved to the close set C. The iteration ends when the target node is reached or when the open set O becomes empty. If the target node is reached, the final optimal path π can be found by reconstructing the nodes in C.

Considering the four candidate paths in Figure 10, which are between Costa Mesa, California, and Irvine, the key metrics related to the optimization problem in (5) along each candidate path are summarized in Table 6. The GPS and GLONASS pseudoranges were measured along the paths during the field tests to obtain the measured HPL. The results of this experiment are summarized as follows:

- The costs, which are the output of the cost function in (5), of paths 1, 2, 3, and 4 were 56,428, 52,137, 110,398, and 92,805, respectively. Therefore, path 2 has the minimum cost. Because path 2 satisfies all the constraints in (5), it was selected as the optimal path.
- Although the average HPLs of the four paths were similar, the ratios of safe nodes and the maximum continuous distances with unacceptable HPLs (i.e., the predicted HPL is unavailable or above T_{HPL}) were significantly different. In particular, in path 2, the ratio of safe nodes was 100%, and there was no section where the predicted HPL was unacceptable. This implies that an autonomous vehicle can know path 2 has better

Table 4. The mathematical notations related to the proposed safety-constrained path planning algorithm.

Symbol	Description
π	Sequence of nodes between start node p_{start} and target node p_{target}, i.e., $\pi = \{p_{\text{start}}, p_2, p_3, \ldots, p_{\text{target}}\}$
N_{nodes}	Total number of nodes along a path
$dist(p_{k-1}, p_k)$	Euclidean distance between nodes p_{k-1} and p_k ($p_1 = p_{\text{start}}$ and $p_{N_{\text{nodes}}} = p_{\text{target}}$)
$HPL(p_k, t)$	Conservatively predicted HPL at node p_k and time t, which is given by the HPL prediction map
T_{HPL}	Maximum allowable HPL value (i.e., the HPL threshold)
$N(\cdot)$	Number of nodes satisfying the given condition
T_{safe}	Threshold for the ratio of nodes satisfying HPL threshold T_{HPL}
$D_{\text{HPL unacceptable}}$	Continuous distance where the predicted HPL is unavailable or above T_{HPL}
D_{safe}	Threshold for $D_{\text{HPL unacceptable}}$

Table 5. The comparison of optimization problem formulations for safety-constrained path planning.

Method	Travel Distance	Navigation Reliability	GNSS Unavailability	Continuous GNSS Outage
Zhang and Hsu [14]	✓	✓	✗	✗
Maaref and Kassas [15]	✓	✓	✗	✗
Proposed	✓	✓	✓	✓

Authorized licensed use limited to: The Ohio State University. Downloaded on April 13,2023 at 05:02:10 UTC from IEEE Xplore. Restrictions apply.

Algorithm 1. The A* algorithm implementation for safety-constrained path planning.

Data: $\mathcal{P}$, p_{start}, p_{target}, HPL, D_{safe}, T_{HPL}
Result: π
$f(p_{start}) \leftarrow dist(p_{start}, p_{target})$
$D_{HPL\ unacceptable}(p_{start}) \leftarrow 0$
$safenode(p_{start}) \leftarrow 1$
$O \leftarrow p_{start}$
while O is not empty **do**
  $p_{current} \leftarrow$ node in O having smallest f
  $O \leftarrow O - p_{current}$
  if $D_{HPL\ unacceptable}(p_{current}) \geq D_{safe}$ **then**
    continue
  end
  if $p_{current}$ is p_{target} **then**
    $\pi \leftarrow$ reconstructed path from C
    $N_{nodes} \leftarrow$ total number of nodes in π
    $N_{safe\ nodes} \leftarrow$ sum of *safenode* of all nodes in π
    if $N_{safe\ nodes}/N_{nodes} > T_{safe}$ **then**
      return π
    end
    continue
  end
  $C \leftarrow C + p_{current}$
  for every neighbor of $p_{current}$ **do**
    $g(p_{neighbor}) \leftarrow dist(p_{neighbor}, p_{current}) \cdot HPL(p_{neighbor}) + g(p_{current})$
    $h(p_{neighbor}) \leftarrow dist(p_{neighbor}, p_{target})$
    $f(p_{neighbor}) \leftarrow g(p_{neighbor}) + h(p_{neighbor})$
    if $HPL(p_{neighbor})$ is unacceptable **then**
      $safenode(p_{neighbor}) \leftarrow 0$
      $D_{HPL\ unacceptable}(p_{neighbor}) \leftarrow$
      $D_{HPL\ unacceptable}(p_{current}) + dist(p_{neighbor}, p_{current})$
    else
      $safenode(p_{neighbor}) \leftarrow 1$
      $D_{HPL\ unacceptable}(p_{neighbor}) \leftarrow 0$
    end
    $O \leftarrow O + p_{neighbor}$
  end
end
return failure

GNSS signal quality than the other paths before driving by solving the optimization problem in (5) using the HPL prediction map and Algorithm 1.

- Paths 1 and 4 are also feasible solutions because they satisfied all the constraints of (5). However, neither path 1 nor path 4 is an optimal solution according to the proposed cost function that considers both travel distances and predicted HPLs.
- Path 3 is not a feasible solution because it violated the second constraint that requires $D_{\text{HPL unacceptable}}$ to be less than D_{safe}, which was set to 150 m. The proposed optimization problem successfully screened a path with continuous GNSS signal outages that could potentially threaten the vehicle's driving safety.
- In all cases, the conservatively predicted HPL bounded the measured HPL 100% of the time.

Conclusion

The reliability of GNSS signals is crucial to ensure driving safety because various navigation sensors of automated vehicles rely on GNSS signals. This article considered the HPL obtained by the ARAIM algorithm as a metric to measure navigation reliability at a given location and time on urban roads. Due to the uncertainty of nearby dynamic objects and the limited accuracy of 3D urban digital maps, a method to conservatively predict the HPL was proposed and validated experimentally. The pseudorange biases and presence of signal reflections and blockages, which are necessary to predict the HPL in urban environments, were simulated by ray-tracing with 3D maps. The generated HPL prediction map can serve as useful road information for various navigation applications. As a case study, the HPL prediction map was applied for the safety-constrained path planning of an automated ground vehicle. Unlike previous studies, the proposed optimization problem considered the unavailability of GNSS signals and continuous GNSS signal

FIG 10 The four candidate paths between Costa Mesa and Irvine. GNSS signals along the paths were collected during four consecutive days.

Authorized licensed use limited to: The Ohio State University. Downloaded on April 13,2023 at 05:02:10 UTC from IEEE Xplore. Restrictions apply.

Table 6. The comparison of key optimization metrics along four candidate paths.

Path	Travel Distance (m)	Average Predicted HPL (m)	Average Measured HPL (m)	Ratio of Safe Nodes (%)	Maximum Continuous Distance With Unacceptable HPL (m)
Path 1	9,746	6.49	5.57	98.5	131.90
Path 2	9,631	7.91	5.60	100	0
Path 3	14,244	7.67	5.52	97.2	208.72
Path 4	10,629	8.50	5.64	97.1	103.95

outages that occur in urban environments. A specific implementation of the A* algorithm to find an optimal path was also suggested and demonstrated.

Acknowledgments

The authors would like to thank Mahdi Maaref for data collection and insightful discussions. This work was supported in part by the Ministry of Science and Information and Communications Technology (MSIT), Korea, under the High-Potential Individuals Global Training Program (grant 2020-0-01531), supervised by the Institute of Information and Communications Technology Planning and Evaluation; in part by the Unmanned Vehicles Core Technology Research and Development Program through the National Research Foundation of Korea (NRF) and the Unmanned Vehicle Advanced Research Center, funded by the MSIT (grant 2020M3C1C1A01086407); in part by the Basic Science Research Program, through the NRF, funded by the Ministry of Education (grant 2021R1A6A3A13046688); in part by the National Science Foundation, under grant 1929965; and in part by the U.S. Department of Transportation, under grant 69A3552047138, for the Center for Automated Vehicle Research With Multimodal AssurEd Navigation (CARMEN) University Transportation Center.

About the Authors

Halim Lee (halim.lee@yonsei.ac.kr) earned her B.S. degree in integrated technology from Yonsei University, Incheon, 21983, Korea, where she is a Ph.D. student in the School of Integrated Technology. Her research interests include motion planning, integrity monitoring, and opportunistic navigation.

Jiwon Seo (jiwon.seo@yonsei.ac.kr) earned his Ph.D. degree in aeronautics and astronautics in 2010 from Stanford University. He is an associate professor in the School of Integrated Technology, Yonsei University, Incheon, 21983, Korea. His research interests include global navigation satellite systems and complementary positioning, navigation, and timing systems. He is a member of the International Advisory Council of the Resilient Navigation and Timing Foundation and a member of several advisory committees of the Ministry of Oceans and Fisheries and the Ministry of Land, Infrastructure, and Transport, Korea. He is a Member of IEEE.

Zaher (Zak) M. Kassas (zkassas@ieee.org) earned his Ph.D. degree in electrical and computer engineering from the University of Texas at Austin. He is a professor of electrical and computer engineering at The Ohio State University, Columbus, Ohio, 43210, USA, and the director of the Autonomous Systems Perception, Intelligence, and Navigation Laboratory. He is also the director of the U.S. Department of Transportation Center for Automated Vehicle Research With Multimodal AssurEd Navigation (CARMEN). His research interests include cyberphysical systems, estimation theory, navigation systems, autonomous vehicles, and intelligent transportation systems. He is a senior editor of *IEEE Transactions on Intelligent Vehicles* and an associate editor of the *Transactions on Aerospace and Electronic Systems* and *IEEE Transactions on Intelligent Transportation Systems*. He is a Senior Member of IEEE.

References

[1] J. Kim, J.-W. Kwon, and J. Seo, "Multi-UAV-based stereo vision system without GPS for ground obstacle mapping to assist path planning of UGV," *Electron. Lett.*, vol. 50, no. 20, pp. 1431–1432, 2014, doi: 10.1049/el.2014.2227.

[2] Y. Li, Z. Hu, Y. Cai, H. Wu, Z. Li, and M. Sotelo, "Visual map-based localization for intelligent vehicles from multi-view site matching," *IEEE Trans. Intell. Transp. Syst.*, vol. 22, no. 2, pp. 1068–1079, 2021, doi: 10.1109/TITS.2019.2962183.

[3] Y. Shin, S. Lee, and J. Seo, "Autonomous safe landing-area determination for rotorcraft UAVs using multiple IR-UWB radars," *Aerosp. Sci. Technol.*, vol. 69, pp. 617–624, Oct. 2017, doi: 10.1016/j.ast.2017.07.018.

[4] Z. Feng, M. Li, M. Stolz, M. Kunert, and W. Wiesbeck, "Lane detection with a high-resolution automotive radar by introducing a new type of road marking," *IEEE Trans. Intell. Transp. Syst.*, vol. 20, no. 7, pp. 2430–2447, 2019, doi: 10.1109/TITS.2018.2866079.

[5] A. Joshi and M. James, "Generation of accurate lane-level maps from coarse prior maps and lidar," *IEEE Intell. Transp. Syst. Mag.*, vol. 7, no. 1, pp. 19–29, 2015, doi: 10.1109/MITS.2014.2364081.

[6] C. Peng and Y. Zhenglin, "Modeling analysis for positioning error of mobile lidar based on multi-body system kinematics," *Intell.*

Authorized licensed use limited to: The Ohio State University. Downloaded on April 13,2023 at 05:02:10 UTC from IEEE Xplore. Restrictions apply.

Autom. Soft Comput., vol. 25, no. 4, pp. 827–834, 2019, doi: 10.31209/2019.100000086.
[7] J. Rhee and J. Seo, "Low-cost curb detection and localization system using multiple ultrasonic sensors," *Sensors*, vol. 19, no. 6, pp. 1389–1410, 2019, doi: 10.3390/s19061389.
[8] J. Wang, X. Qiu, and Y. Tu, "An improved MDS-MAP localization algorithm based on weighted clustering and heuristic merging for anisotropic wireless networks with energy holes," *Comput., Mater. Continua*, vol. 60, no. 1, pp. 227–244, 2019, doi: 10.32604/cmc.2019.05281.
[9] J. Wang, L. Cheng, Y. Tu, and S. Gu, "A novel localization approach for irregular wireless sensor networks based on anchor segmentation," *IEEE Sensors J.*, vol. 22, no. 7, pp. 7267–7276, 2022, doi: 10.1109/JSEN.2022.3143826.
[10] M. Montemerlo *et al.*, "Junior: The Stanford entry in the urban challenge," *J. Filed Robot.*, vol. 25, no. 9, pp. 569–597, 2008, doi: 10.1002/rob.20258.
[11] M. Atia *et al.*, "A low-cost lane-determination system using GNSS/IMU fusion and HMM-based multistage map matching," *IEEE Trans. Intell. Transp. Syst.*, vol. 18, no. 11, pp. 3027–3037, Nov. 2017, doi: 10.1109/TITS.2017.2672541.
[12] Z. Kassas, M. Maaref, J. Morales, J. Khalife, and K. Shamaei, "Robust vehicular localization and map matching in urban environments through IMU, GNSS, and cellular signals," *IEEE Intell. Transp. Syst. Mag.*, vol. 12, no. 3, pp. 36–52, Jun. 2020, doi: 10.1109/MITS.2020.2994110.
[13] A. Shetty and G. Gao, "Predicting state uncertainty bounds using nonlinear stochastic reachability analysis for urban GNSS-based UAS navigation," *IEEE Trans. Intell. Transp. Syst.*, vol. 22, no. 9, pp. 5952–5961, 2021, doi: 10.1109/TITS.2020.3040517.
[14] G. Zhang and L. Hsu, "A new path planning algorithm using a GNSS localization error map for UAVs in an urban area," *J. Intell. Robot. Syst.*, vol. 94, no. 1, pp. 219–235, 2019, doi: 10.1007/s10846-018-0894-5.
[15] M. Maaref and Z. Kassas, "Optimal GPS integrity-constrained path planning for ground vehicles," in *Proc. IEEE/ION Position, Location, Navig. Symp.*, 2020, pp. 655–660, doi: 10.1109/PLANS46316.2020.9109898.
[16] H. Lee, J. Seo, and Z. Kassas, "Integrity-based path planning strategy for urban autonomous vehicular navigation using GPS and cellular signals," in *Proc. ION GNSS Conf.*, 2020, pp. 2347–2357, doi: 10.33012/2020.17589.
[17] J. Jackson, B. Davis, and D. Gebre-Egziabher, "A performance assessment of low-cost RTK GNSS receivers," in *Proc. IEEE/ION Position, Location, Navig. Symp.*, 2018, pp. 642–649, doi: 10.1109/PLANS.2018.8373438.
[18] E. Costa, "Simulation of the effects of different urban environments on GPS performance using digital elevation models and building databases," *IEEE Trans. Intell. Transp. Syst.*, vol. 12, no. 3, pp. 819–829, Sep. 2011, doi: 10.1109/TITS.2011.2122258.
[19] D. Betaille, F. Peyret, M. Ortiz, S. Miquel, and L. Fontenay, "A new modeling based on urban trenches to improve GNSS positioning quality of service in cities," *IEEE Intell. Transp. Syst. Mag.*, vol. 5, no. 3, pp. 59–70, 2013, doi: 10.1109/MITS.2013.2263460.
[20] L. Wang, P. Groves, and M. Ziebart, "GNSS shadow matching: Improving urban positioning accuracy using a 3D city model with optimized visibility scoring scheme," *Navig. J. Inst. Navig.*, vol. 60, no. 3, pp. 195–207, 2013, doi: 10.1002/navi.38.
[21] K. Strandjord, P. Axelrad, and S. Mohiuddin, "Improved urban navigation with shadow matching and specular matching," *Navig., J. Inst. Navig.*, vol. 67, no. 3, pp. 547–565, 2020, doi: 10.1002/navi.378.
[22] S. Saab and Z. Kassas, "Power matching approach for GPS coverage extension," *IEEE Trans. Intell. Transp. Syst.*, vol. 7, no. 2, pp. 156–166, 2006, doi: 10.1109/TITS.2006.874720.
[23] T. Walter, P. Enge, J. Blanch, and B. Pervan, "Worldwide vertical guidance of aircraft based on modernized GPS and new integrity augmentations," *Proc. IEEE*, vol. 96, no. 12, pp. 1918–1935, Dec. 2008, doi: 10.1109/JPROC.2008.2006099.
[24] J. Lee, Y. Morton, J. Lee, H. Moon, and J. Seo, "Monitoring and mitigation of ionospheric anomalies for GNSS-based safety critical systems," *IEEE Signal Process. Mag.*, vol. 34, no. 5, pp. 96–110, 2017, doi: 10.1109/MSP.2017.2716406.
[25] J. Seo and T. Walter, "Future dual-frequency GPS navigation system for intelligent air transportation under strong ionospheric scintillation," *IEEE Trans. Intell. Transp. Syst.*, vol. 15, no. 5, pp. 2224–2236, 2014, doi: 10.1109/TITS.2014.2311590.
[26] A. Sun *et al.*, "Markov chain-based stochastic modeling of deep signal fading: Availability assessment of dual-frequency GNSS-based aviation under ionospheric scintillation," *Space Weather*, vol. 19, no. 9, pp. 1–19, Sep. 2021, doi: 10.1029/2020SW002655.
[27] H. Lee, S. Pullen, J. Lee, B. Park, M. Yoon, and J. Seo, "Optimal parameter inflation to enhance the availability of single-frequency GBAS for intelligent air transportation," *IEEE Trans. Intell. Transp. Syst.*, early access, 2022, doi: 10.1109/TITS.2022.3157138.
[28] K. Park and J. Seo, "Single-antenna-based GPS antijamming method exploiting polarization diversity," *IEEE Trans. Aerosp. Electron. Syst.*, vol. 57, no. 2, pp. 919–934, 2021, doi: 10.1109/TAES.2020.3034025.
[29] W. Kim, P.-W. Son, S. Park, S. Park, and J. Seo, "First demonstration of the Korean eLoran accuracy in a narrow waterway using improved ASF maps," *IEEE Trans. Aerosp. Electron. Syst.*, vol. 58, no. 2, pp. 1492–1496, Apr. 2022, doi: 10.1109/TAES.2021.3114272.
[30] J. Lesouple, T. Robert, M. Sahmoudi, J. Tourneret, and W. Vigneau, "Multipath mitigation for GNSS positioning in an urban environment using sparse estimation," *IEEE Trans. Intell. Transp. Syst.*, vol. 20, no. 4, pp. 1316–1328, 2019, doi: 10.1109/TITS.2018.2848461.
[31] G. Zhang and L. Hsu, "Performance assessment of GNSS diffraction models in urban areas," *Navig., J. Inst. Navig.*, vol. 68, no. 2, pp. 369–389, 2021, doi: 10.1002/navi.417.
[32] S. Saab and Z. Kassas, "Map-based land vehicle navigation system with DGPS," in *Proc. IEEE Intell. Veh. Symp.*, vol. 1, pp. 209–214, Jun. 2002, doi: 10.1109/IVS.2002.1187953.
[33] J. Bresler, P. Reisdorf, M. Obst, and G. Wanielik, "GNSS positioning in non-line-of-sight context: A survey," in *Proc. 19th IEEE Int. Conf. Intell. Transp. Syst.*, 2016, pp. 1147–1154, doi: 10.1109/ITSC.2016.7795701.
[34] P. Misra and P. Enge, *Global Positioning System: Signals, Measurements, and Performance*, 2nd ed. Lincoln, MA, USA: Ganga-Jamuna Press, 2010.
[35] J. Sleewaegen and F. Boon, "Mitigating short delay multipath: A promising new technique," in *Proc. ION Int. Tech. Meeting Conf.*, 2010, pp. 204–213.
[36] J. Blanch, A. Ene, T. Walter, and P. Enge, "An optimized multiple hypothesis RAIM algorithm for vertical guidance," in *Proc. ION GNSS Conf.*, 2007, pp. 2924–2933.
[37] J. Lee, J. Seo, Y. Park, S. Pullen, and P. Enge, "Ionospheric threat mitigation by geometry screening in ground-based augmentation systems," *J. Aircr.*, vol. 48, no. 4, pp. 1422–1433, 2011, doi: 10.2514/1.C031309.
[38] J. Seo, J. Lee, S. Pullen, P. Enge, and S. Close, "Targeted parameter inflation within ground-based augmentation systems to minimize anomalous ionospheric impact," *J. Aircr.*, vol. 49, no. 2, pp. 587–599, 2012, doi: 10.2514/1.C031601.
[39] J. Lee, S. Pullen, S. Datta-Barua, and J. Lee, "Real-time ionospheric threat adaptation using a space weather prediction for GNSS-based aircraft landing systems," *IEEE Trans. Intell. Transp. Syst.*, vol. 18, no. 7, pp. 1752–1761, 2017, doi: 10.1109/TITS.2016.2627600.
[40] R. Toledo-Moreo, M. Zamora-Izquierdo, B. Ubeda-Miarro, and A. Gomez-skarmeta, "High-integrity IMM-EKF-based road vehicle navigation with low-cost GPS/SBAS/INS," *IEEE Trans. Intell. Transp. Syst.*, vol. 8, no. 3, pp. 491–511, 2007, doi: 10.1109/TITS.2007.902642.
[41] T. Walter and J. Blanch, "Improved user position monitor for WAAS," *Navig., J. Inst. Navig.*, vol. 64, no. 1, pp. 165–175, 2017, doi: 10.1002/navi.180.
[42] J. Morales, J. Khalife, and Z. Kassas, "Opportunity for accuracy," *GPS World Mag.*, vol. 27, no. 3, pp. 22–29, Mar. 2016.
[43] M. Maaref, J. Khalife, and Z. Kassas, "Aerial vehicle protection level reduction by fusing GNSS and terrestrial signals of opportunity," *IEEE Trans. Intell. Transp. Syst.*, vol. 22, no. 9, pp. 5976–5993, Sep. 2021, doi: 10.1109/TITS.2021.3095184.
[44] J. Blanch *et al.*, "Baseline advanced RAIM user algorithm and possible improvements," *IEEE Trans. Aerosp. Electron. Syst.*, vol. 51, no. 1, pp. 713–732, 2015, doi: 10.1109/TAES.2014.130739.
[45] N. Zhu, J. Marais, D. Betaille, and M. Berbineau, "GNSS position integrity in urban environments: A review of literature," *IEEE Trans. Intell. Transp. Syst.*, vol. 19, no. 9, pp. 2762–2778, 2018, doi: 10.1109/TITS.2017.2766768.
[46] N. Ziedan, "Urban positioning accuracy enhancement utilizing 3-D buildings model and accelerated ray tracing algorithm," in *Proc. ION GNSS Conf.*, Sep. 2017, pp. 3253–3268, doi: 10.33012/2017.15366.
[47] S. Zhang, S. Lo, Y. Chen, T. Walter, and P. Enge, "GNSS multipath detection in urban environment using 3D building model," in *Proc. IEEE/ION Position, Location Navig. Symp.*, 2018, pp. 1053–1058, doi: 10.1109/PLANS.2018.8373486.
[48] S. Miura, L. Hsu, F. Chen, and S. Kamijo, "GPS error correction with pseudorange evaluation using three-dimensional maps," *IEEE Trans. Intell. Transp. Syst.*, vol. 16, no. 6, pp. 3104–3115, 2015, doi: 10.1109/TITS.2015.2432122.
[49] J. Schuster and R. Luebbers, "Comparison of site-specific radio propagation path loss predictions to measurements in an urban area," in *Proc. IEEE Antennas Propag. Soc. Int. Symp.*, 1996, pp. 1210–1213, doi: 10.1109/APS.1996.549814.
[50] S. Russell and P. Norvig, *Artificial Intelligence: A Modern Approach*, 3rd ed. Hoboken, NJ, USA: Prentice Hall, 2010.

ITS

Authorized licensed use limited to: The Ohio State University. Downloaded on April 13,2023 at 05:02:10 UTC from IEEE Xplore. Restrictions apply.